8ACEE

8th Asia Conference on Earthquake Engineering

9~11 November, 2022
Taipei, Taiwan

Proceedings

Host

NCREE

NARLabs National Applied Research Laboratories
National Center for Research on Earthquake Engineering

Co-hosts

NCDR

Proceedings of
the 8th Asia Conference on Earthquake Engineering

November 9-11, 2022, Taipei, Taiwan

Edited by

Chung-Che Chou
Jui-Liang Lin
Ming-Chieh Chuang
Chiu-Ping Fan

National Center for Research on Earthquake Engineering

Editors: Chung-Che Chou, Jui-Liang Lin, Ming-Chieh Chuang, Chiu-Ping Fan
Publisher: National Center for Research on Earthquake Engineering,
National Applied Research Laboratories
Distribution: National Center for Research on Earthquake Engineering,
National Applied Research Laboratories
Address: 200, Sec. 3, Xinhai Rd., Taipei 106219, Taiwan, R.O.C.
Tel: +886-2-6630-0888
Fax: +886-2-6630-0858
Email: 8acee@narlabs.org.tw
Website: www.ncree.narl.org.tw
Publish Date: February 2023, First edition
ISBN: 978-986-89629-5-8

Preface

The 8th Asia Conference on Earthquake Engineering (8ACEE) was successfully held in Taipei, Taiwan, ROC, during the period November 9-11, 2022, with the theme "Earthquake-Resilient and Sustainable Communities". 8ACEE was jointly organized by the National Center for Research on Earthquake Engineering (NCREE), the Chinese Society of Structural Engineering (CSSE), the Chinese Taiwan Society for Earthquake Engineering (CTSEE), the Chinese Institute of Civil and Hydraulic Engineering (CICHE), and the National Science and Technology Center for Disaster Reduction (NCDR).

8ACEE was approved and sponsored by the National Science and Technology Council, Taiwan, ROC. Due to the COVID-19 pandemic, 8ACEE was organized as a hybrid conference comprising on-site and online events. The venue for the on-site meetings was the office building of the NCREE. The program of 8ACEE included five plenary sessions and six concurrent sessions. Twelve keynote speeches and ten invited speeches were delivered by 22 distinguished scholars for the plenary and concurrent sessions, respectively, and the banquet also featured a special talk, all speeches being of real benefit to the attendees. During 8ACEE, a total of 155 papers were delivered by scientists and engineers from nearly 19 countries and there were nearly 220 conferees. For more details about this wonderful event, please visit the conference website (http://8ACEE.ncree.org.tw).

8ACEE provided an excellent forum to bring together researchers, professionals, engineers, and academics to promote and exchange new ideas and experiences in the fields of earthquake engineering, disaster management, seismic risk reduction, and many other fields. Despite the challenges of the COVID-19 pandemic, all participants had a fruitful experience.

As the conference chairperson of 8ACEE, I thank the members of Advisory Committee, International Scientific Committee, and Local Organizing Committee for their valuable suggestions on organizing the conference. I would also like to thank all sponsors for their generous supports. All participants who participated in the 8ACEE are deeply appreciated. Finally, I would like to express my special thanks to my colleagues of the 8ACEE Secretariat for doing their best to conduct this conference. In addition, I gratefully acknowledge the full-hearted support of my colleague Ms. Chiu-Ping Fan. Without her talent and diligence, the completion of the proceedings would not have been made possible.

Chung-Che Chou

Director General and Conference Chair
National Center for Research on Earthquake Engineering (NCREE), Taiwan, ROC

Table of Contents

Host

National Center for Research on Earthquake Engineering (NCREE)

Co-hosts

Chinese Institute of Civil and Hydraulic Engineering (CICHE)
Chinese Society of Structural Engineering (CSSE)
Chinese Taiwan Society for Earthquake Engineering (CTSEE)
National Science and Technology Center for Disaster Reduction (NCDR)

Collaborative Partnership

Institute of Earth Sciences, Academia Sinica
China Corporation Register of Shipping
CECI Engineering Consultants Inc. Taiwan
Department of Civil Engineering, Chung Yuan Christian University
Department of Civil Engineering, Feng Chia University
Bureau of Energy, Ministry of Economic Affairs
Architectire and Building Research Institute, Ministry of the Interior
Department of Civil Engineering, National Central University
Department of Civil Engineering, National Cheng Kung University
Department of Civil Engineering, National Chi Nan University
Department of Civil and Water Resources Engineering, National Chiayi University
Department of Civil Engineering, National Chung Hsing University
Department of Civil Engineering, National Kaohsiung University of Science and Technology
Department of Construction Engineering, National Kaohsiung University of Science and Technology
Department of Civil Engineering, National Taipei University of Technology
Department of Civil Engineering, National Taiwan University
Department of Civil and Construction Engineering, National Taiwan University of Science and Technology
Department of Civil and Disaster Prevention Engineering, National United University
Department of Civil Engineering, National University of Kaohsiung
Department of Civil Engineering, National Yang Ming Chiao Tung University
Department of Civil and Construction Engineering, National Yunlin University of Science and Technology
Sinotech Engineering Consultants Inc.
Sinotech Engineering Consultants LTD.
Taiwan Offshore Winf Turbine Foundation and Marine Engineering Association
Taiwan Power Company
Taiwan Wind Energy Association
T. Y. Lin International Taiwan
Department of Civil Engineering, Tamkang University

Chair and Co-chairs

Chair

Prof. Chung-Che Chou

Director General of National Center for Research on Earthquake Engineering

President of Chinese Taiwan Society for Earthquake Engineering

Co-chairs

Prof. Hongey Chen

Director of National Science and Technology Center for Disaster Reduction

Prof. Chien-Kuo Chiu

President of Chinese Society of Structural Engineering

Prof. Yu-Chi Sung

President of Chinese Institute of Civil and Hydraulic Engineering

Advisory Committee

Dr. Juin-Fu Chai
National Center for Research on Earthquake Engineering

Prof. Kuo-Chun Chang
National Taiwan University

Prof. Shih-Huang Chen
National Central University

Prof. Chien-Kuo Chiu
National Taiwan University of Science and Technology

Dr. Lap-Loi Chung
National Center for Research on Earthquake Engineering

Engr. Juanito Cunanan (ASEP President)
Association of Structural Engineers of the Philippines, Inc. (ASEP)

Prof. Shang-Hsien Hsieh
National Taiwan University

Prof. Hsuan-Teh Hu
National United University

Prof. Chiung-Shiann Huang
National Yang Ming Chiao Tung University

Prof. Jenn-Shin Hwang
National Taiwan University of Science and Technology

Prof. Shyh-Jiann Hwang
National Taiwan University

Engr. Ronaldo Ison (ACEE Founding Chair)
Association of Structural Engineers of the Philippines, Inc. (ASEP)

Prof. Shen-Haw Ju
National Cheng Kung University

Prof. Wen-I Liao
National Taipei University of Technology

Prof. Chi-Chang Lin
National Chung Hsing University

Prof. Chin-Hsiung Loh
National Taiwan University

Prof. Yu-Chi Sung
National Taipei University of Technology

Prof. Keh-Chyuan Tsai
National Taiwan University

Prof. Wei-Chih Wang
National Yang Ming Chiao Tung University

Dr. Chiun-Lin Wu
National Center for Research on Earthquake Engineering

Prof. Jian-Hong Wu
National Cheng Kung University

Prof. George C. Yao
National Cheng Kung University

International Scientific Committee

Engr. Adam Abinales
Association of Structural Engineers of the Philippines, Inc., Philippines

Prof. Norman Abrahamson
University of California, Berkeley, USA

Prof. Naveed Anwar
Asian Institute of Technology, Thailand

Prof. Yousef Bozorgnia
University of California, Los Angeles, USA

Prof. Tak-Ming Chan
The Hong Kong Polytechnic University, Hong Kong

Prof. Jiun-Shyan Chen
University of California, San Diego, USA

Prof. Jian-Guo Dai
The Hong Kong Polytechnic University, Hong Kong

Prof. Shirley J. Dyke
Purdue University, USA

Prof. Ken Elwood
The University of Auckland, New Zealand

Prof. Larry A. Fahnestock
University of Illinois, Urbana-Champaign, USA

Prof. Peter Fajfar
University of Ljubljana, Slovenia

Prof. Michael Fardis
University of Patras, Greece

Prof. Hanbin Ge
Meijo University, Japan

Prof. Muhammet Gül
Munzur University, Turkey

Prof. Jerome F. Hajjar
Northeastern University, USA

Prof. Huanjun Jiang
Tongji University, China

Prof. Kazuhiko Kasai
Tokyo Institute of Technology, Japan

Prof. Cheol-Ho Lee
Seoul National University, Korea

Prof. Guoqiang Li
Tongji University, China

Prof. Gregory MacRae
University of Canterbury, New Zealand

Prof. Jason P. McCormick
University of Michigan, Ann Arbor, USA

Prof. Rodolfo Mendoza, Jr.
De La Salle University, Philippines

Prof. Eduardo Miranda
Stanford University, USA

Prof. Masakatsu Miyajima
Kanazawa University, Japan

Prof. Yi-Lung Mo
University of Houston, USA

Prof. Khalid M. Mosalam
University of California, Berkeley, USA

Prof. Gilberto Mosqueda
University of California, San Diego, USA

Prof. Norhazilan Bin Md. Noor
Universiti Teknologi Malaysia, Malaysia

Prof. Andres W. C. Oreta
De La Salle University, Philippines

Dr. Farhang Ostadan
Bechtel Corporation, USA

Prof. Peng Pan
Tsinghua University, China

Prof. Tso-Chien Pan
Nanyang Technological University, Singapore

Prof. Hong-Gun Park
Seoul National University, Korea

Prof. James M. Ricles
Lehigh University, USA

Prof. Taiki Saito
Toyohashi University of Technology, Japan

Prof. I Wayan Sengara
Asosiasi Ahli Rekayasa Gempa Indonesia (AARGI), Indonesia

Prof. B. F. Spencer, Jr
University of Illinois, Urbana-Champaign, USA

Prof. Kenneth Stokoe
The University of Texas at Austin, USA

Prof. Kunitomo Sugiura
Kyoto Univeristy, Japan

Prof. Toru Takeuchi
Tokyo Institute of Technology, Japan

Prof. Chia-Ming Uang
University of California San Diego, USA

Prof. Pennung Warnitchai
Asian Institute of Technology, Thailand

Prof. Andrew S. Whittaker
University at Buffalo, USA

Prof. Tony T. Y. Yang
The University of British Columbia, Canada

Prof. Xueqing Zhang
The Hong Kong University of Science and Technology, Hong Kong

Local Organizing Committee

Prof. Chuin-Shan Chen
National Taiwan University

Prof. Rong-Song Chen
National Chung Hsing University

Prof. Shi-Shuenn Chen
National Taiwan University of Science and Technology

Prof. Tung-Yang Chen
National Cheng Kung University

Prof. Chin-Tung Cheng
National Kaohsiung University of Science and Technology

Prof. Jiunn-Shyang Chiou
National Taiwan University

Prof. Louis Ge
National Taiwan University

Prof. Hsieh-Lung Hsu
National Central University

Prof. Yin-Nan Huang
National Taiwan University

Prof. Chung-Chan Hung
National Cheng Kung University

Prof. Jin-Hung Hwang
National Central University

Prof. Liang-Jenq Leu
National Taiwan University

Prof. Wen-Cheng Liao
National Taiwan University

Prof. Tzu-Kang Lin
National Yang Ming Chiao Tung University

Prof. Lyan-Ywan Lu
National Cheng Kung University

Prof. Kuo-Fong Ma
Academia Sinica

Prof. Yu-Chen Ou
National Taiwan University

Prof. Ruey-Juin Rau
Taiwan Earthquake Research Center

Prof. Chung-Yue Wang
National Central University

Prof. Shiang-Jung Wang
National Taiwan University of Science and Technology

Prof. Yuan-Sen Yang
National Taipei University of Technology

Secretariat

Secretary General：Dr. Jui-Liang Lin

Executive Secretary：Dr. Ming-Chieh Chuang

Dr. Che-Yu Chang

Dr. Wei-Tze Chang

Dr. Chih-Shian Chen

Dr. Kuan-Yu Chen

Dr. Kai-Ning Chi

Ms. Chia-Hui Chiang

Mr. Bo-Yuan Hou

Mr. Hung-Hao Hsieh

Dr. Shang-Yi Hsu

Dr. Wei-Hung Hsu

Ms. Ching-Hsien Huang

Mr. Han-Wei Huang

Ms. Tsu-Hui Huang

Ms. Ling-Yu Kung

Dr. Bo-Han Lee

Mr. Chun-Yi Lin

Mr. Hsien-Chung Lin

Dr. Wang-Chuen Lin

Dr. Yu-Fang Liu

Ms. Su-Yueh Lu

Mr. Wen-Cheng Shen

Ms. Ya-Chuan Tsou

Mr. Yung-Kang Wang

Mr. Chi-Hung Wu

Dr. Cheng-Tao Yang

Sponsors

National Science and Technology Council (NSTC)

ITT Enidine, Inc.

P-WAVER Inc.

Sinodynamics Enterprise Co., Ltd.

Well-Link Industry Co., Ltd.

CECI Engineering Consultants, Inc., Taiwan

Conn-Tek Vibration Control Inc.

Sanlien Technology Corp.

Sinotech Engineering Consultants, Inc.

Sinotech Engineering Consultants, Ltd.

Keynote Speakers

Prof. Norman Abrahamson

University of California, Berkeley, USA

Topic： Key Issues for Fault Rupture Models for Probabilistic Rupture Hazard Analysis

(The material of the speaker's presentation has not been authorized for publication in the proceedings.)

Prof. Kuo-Chun Chang

National Taiwan University, Taiwan

Topic： Damage-Based Seismic Design and Evaluation for Reinforced Concrete Bridges

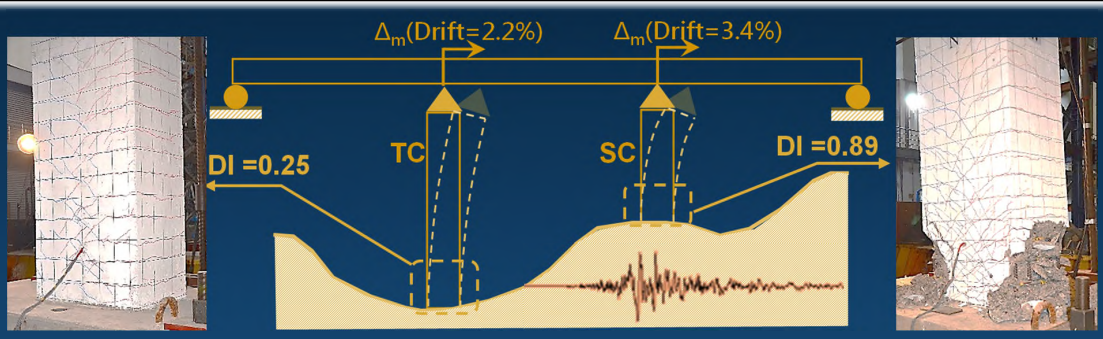

Damage-Based Seismic Design and Evaluation for Reinforced Concrete Bridges

Kuo-Chun Chang
- Professor
Department of Civil Engineering,
National Taiwan University

Ping-Hsiung Wang
- Assistant Professor
Department of Civil Engineering,
National Taipei University of Technology

Outline

1) Capacity-Based Inelastic Disp. Spectra

2) Application to Seismic Evaluation and Seismic Design

3) Domestic Dual Spectra

4) Conclusions

Road Map for Seismic Bridge Codes

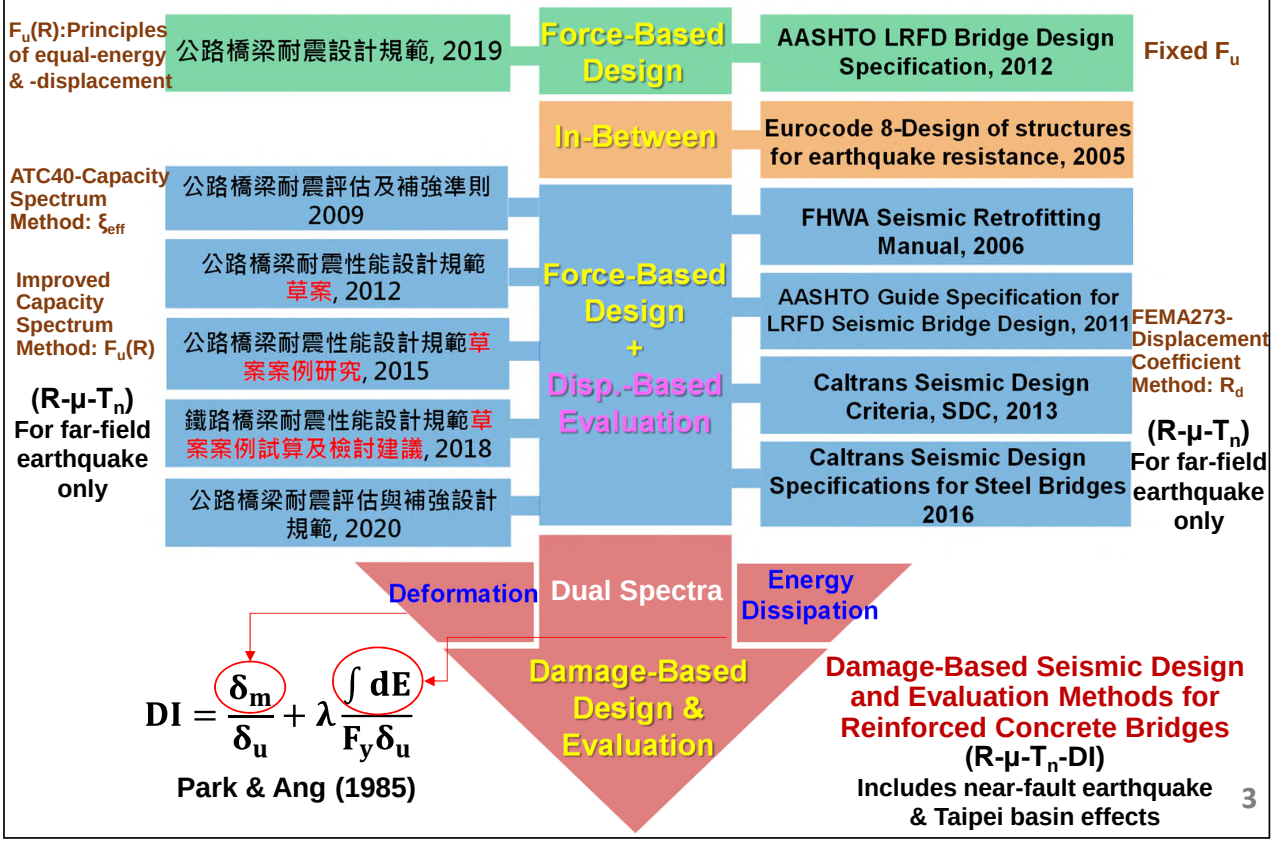

Capacity-Based Inelastic Disp. Spectra

- **Dual Spectra** were constructed using **smooth hysteresis model** and a series of SDOF nonlinear time history analysis, which can evaluate the **maximum inelastic displacement** and the corresponding **damage index**, with the effects of various **column design parameters**.

$$C_R = \frac{\Delta_{inelastic}}{\Delta_{elastic}} \qquad DI = \frac{\Delta_m}{\Delta_u} + \lambda \frac{\int dE}{F_y \Delta_u} \qquad R(or\ F_u) = \frac{F_e}{F_y} = \frac{mS_{ae}}{mS_{ay}}$$

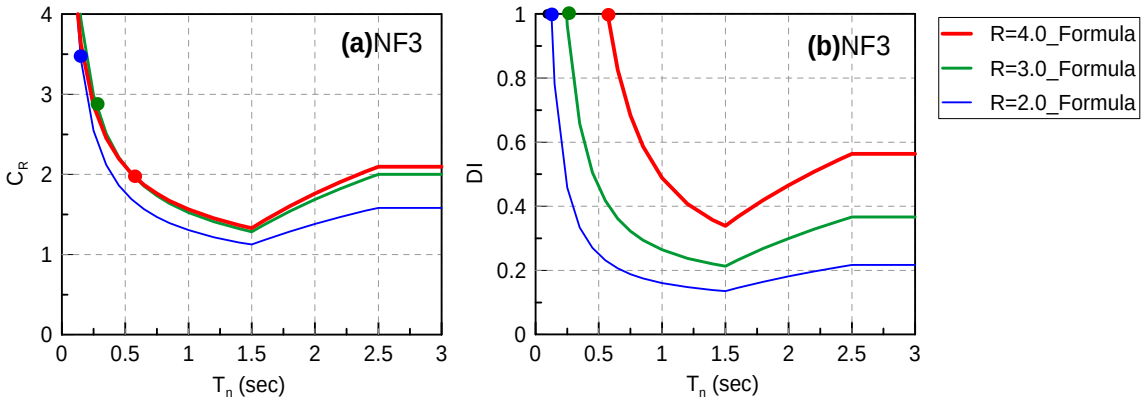

Period limit, before which the failure probability is larger than 20%

Smooth Hysteresis Model

$$z(t) = h(z)\frac{\{A\dot{u} - \nu[\beta|\dot{u}||z|^{n-1}z + \gamma\dot{u}|z|^n]\}}{\eta}$$

$$h(z) = 1 - \xi_1 \exp\left\{-\frac{[z\,sgn(\dot{u}) - q\,z_u]^2}{\xi_2^2}\right\}\left|\frac{sgn(\dot{u}) + sgn(z)}{2}\right|$$

Bouc-Wen family model

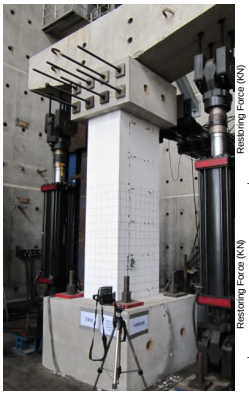

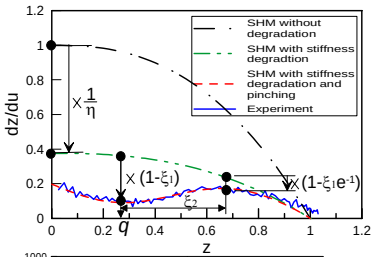

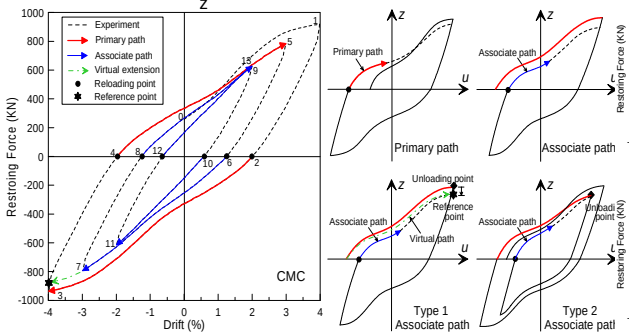

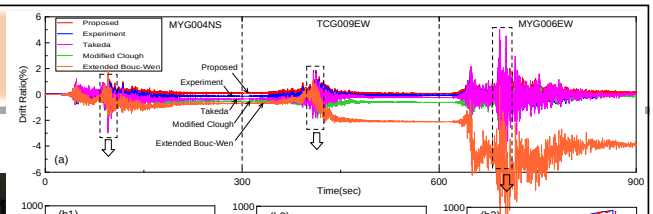

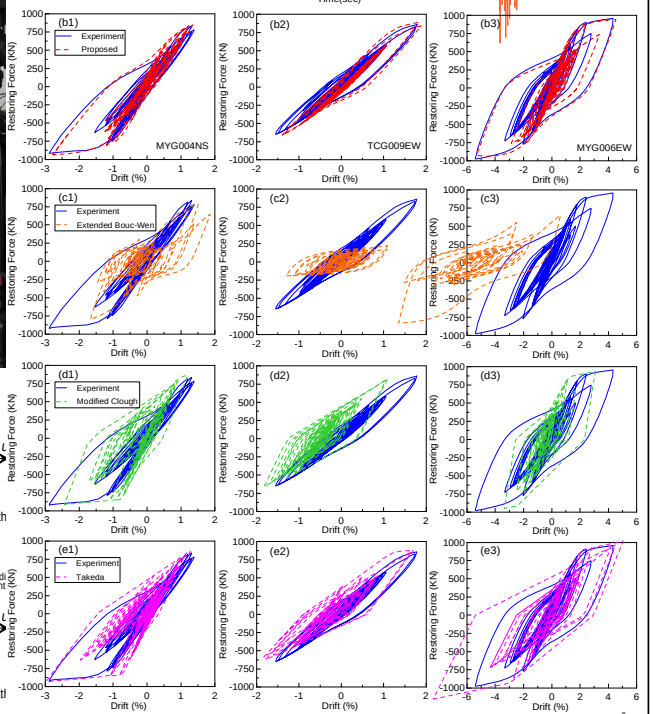

■ Ping-Hsiung Wang, Yu-Chen Ou, Kuo-Chun Chang (2017). A New Smooth Hysteretic Model for Ductile Flexural-dominated Reinforced Concrete Bridge Columns. Earthquake Engineering and Structural Dynamics, 46: 2237-2259.

Damage Index vs. Strength Deterioration

■ The **Damage Index** proposed by **Park and Ang (1985)** was used in the proposed **Smooth Hysteretic Model** to predict the onset of **strength deterioration.**

$$DI = \frac{\Delta_m}{\Delta_u} + \lambda\frac{\int dE}{F_y\Delta_u}$$

Damage caused by **maximum displacement**

Damage caused by **hysteretic energy dissipation**

Damage parameters, Δ_u in association with λ, can be obtained from analytical and experimental results.

D=1.0 corresponds to 20% strength deterioration

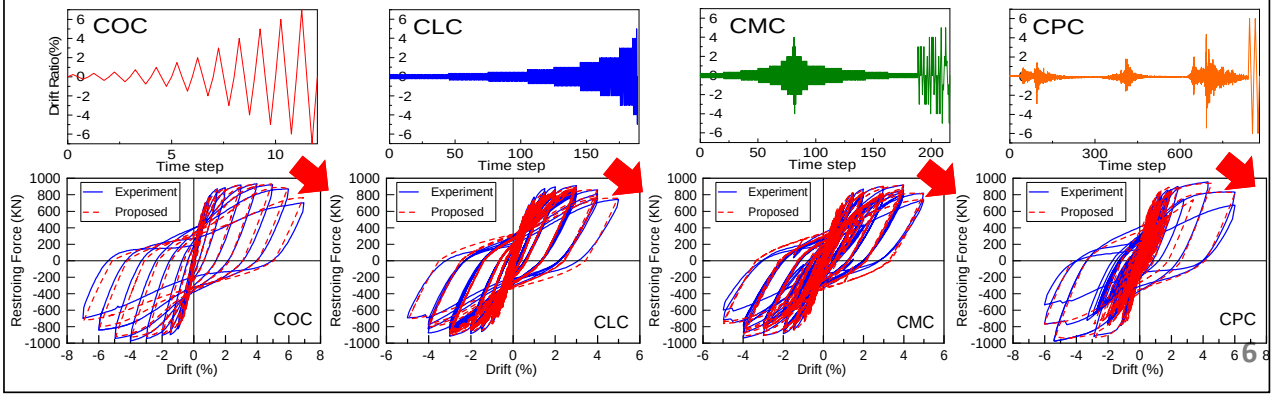

Damage Index vs. Actual Damage State

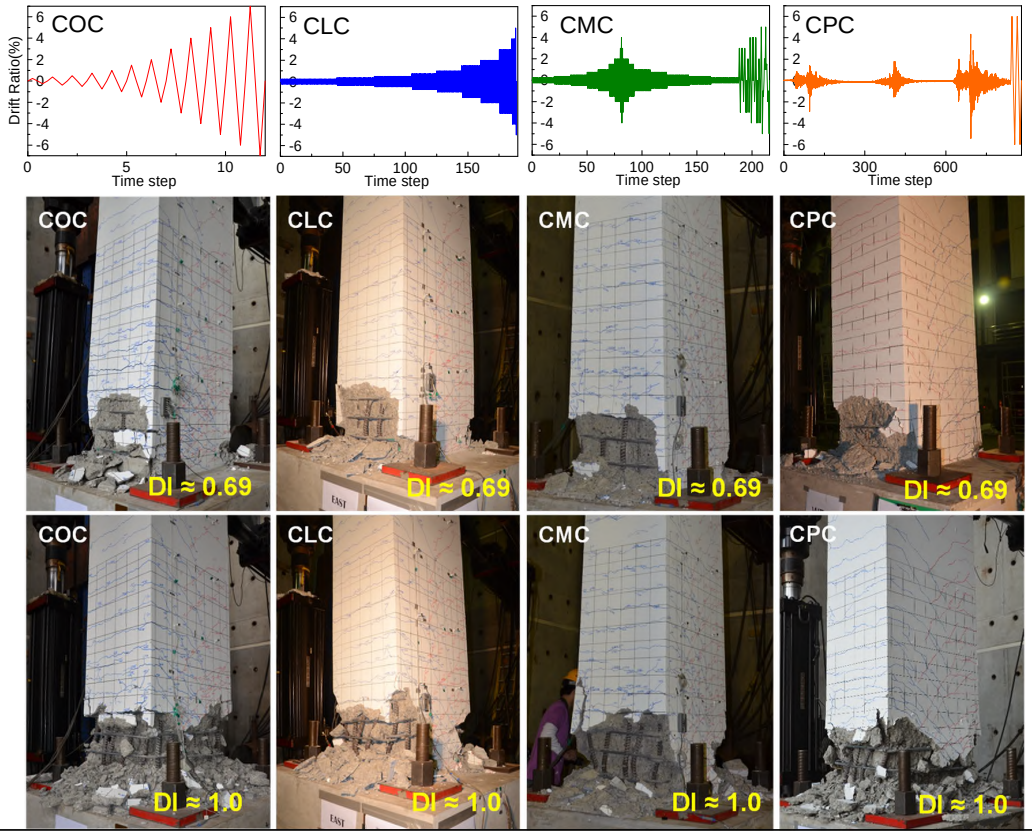

7

Damage Index vs. Actual Damage State

Column COC

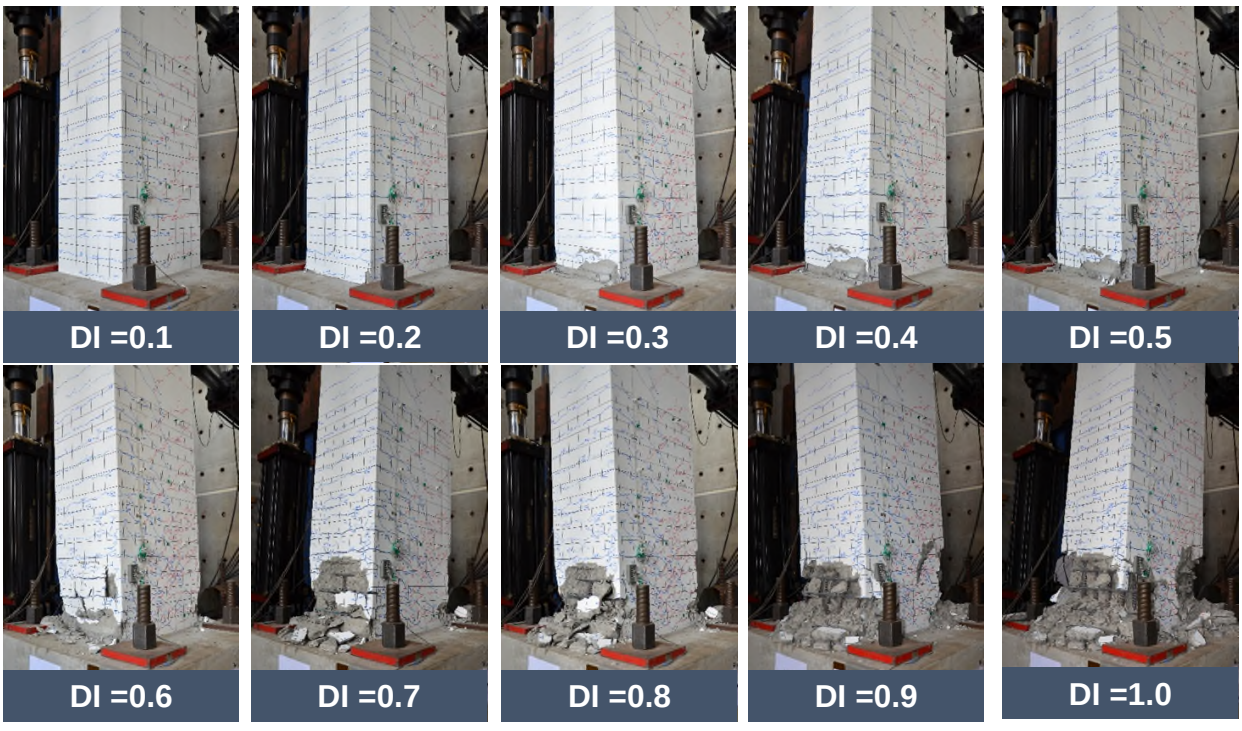

8

Damage Database for RC Bridge Columns

National Center for Research on Earthquake Engineering NCREE

PEER SPD Structural Performance Database

Main Design Parameters :

1. Circular and rectangular sections, spiral and ties
2. Longitudinal steel ratio, ρ_l
3. Aspect ratio, L/D

Major Outputs :

1. Hysteresis loop for hysteresis model calibration
2. Damage parameters identification, Δu and λ
3. Correlation between damage index and failure photos

Applications:

1. Dual spectra construction
2. Seismic evaluation
3. Seismic design
4. Post-earthquake examination

Circular Spiral Column Test

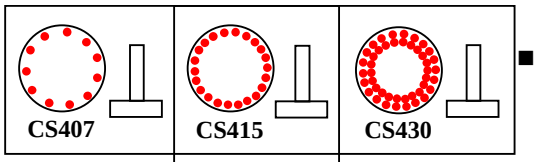

Leman and Moehle (2000)

- Lehman, D. E., and Moehle, J. P., "Seismic Performance of Well-Confined Concrete Bridge Columns," Report No. PEER 1998/01, University of California, Berkeley, 2000, 295 pp.

Column	Δ_u (mm)	λ
CS407	272	0.153
CS415	234	0.045
CS430	215	0.028
CS815	778	0.130
CS1015	1108	0.103

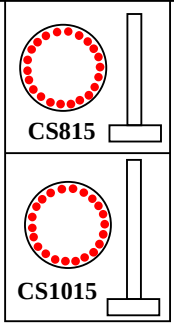

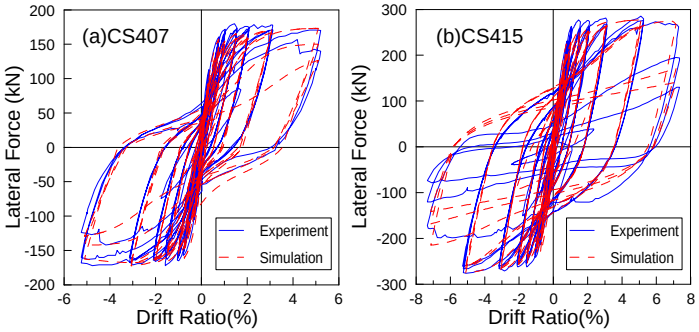

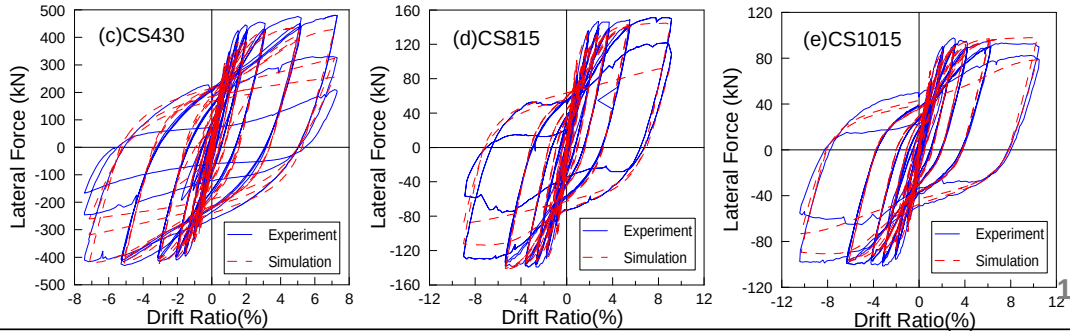

Rectangular Tied Column Test

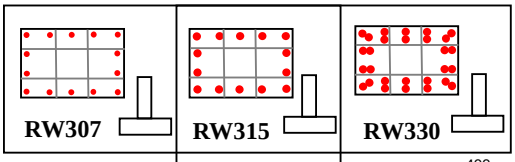

Wang et al. (2020)

- Ping-Hsiung Wang, Kuo-Chun Chang, Wei-Chung Cheng (2022). Deteriorated Hysteresis Behaviors of Reinforced Concrete Bridge Columns. *ACI Structural Journal*. (SCI) (in press)

Column	Δ_u (mm)	λ
RW307	161	0.140
RW315	136	0.057
RW330	107	0.025
RW615	356	0.066
RW1015	822	0.140

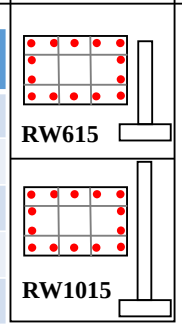

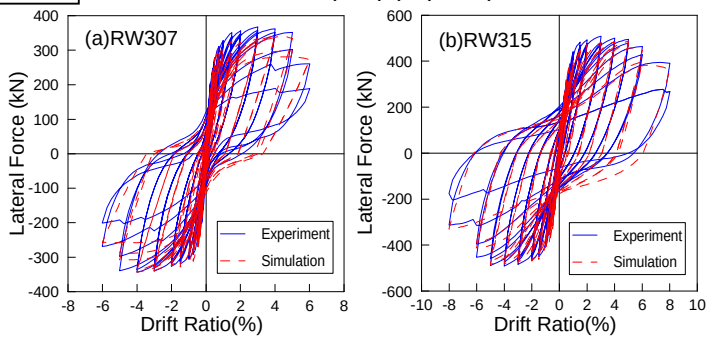

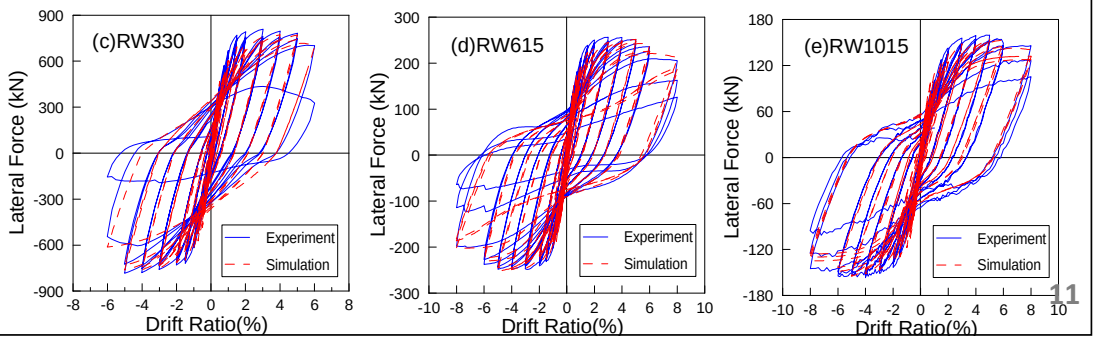

11

Spectral Parameters

1) Fundamental period, T_n

T_n = 0.05, 0.15, 0.25, 0.35, 0.45, 0.55, 0.65, 0.75, 0.85, 1.0, 1.2, 1.4, 1.6, 1.8, 2.0, 2.2, 2.4, 2.6, 2.8, 3.0

20

2) Strength coefficient, R

R = 1.5, 2.0, 3.0, 4.0, 5.0

5

3) Hysteresis model, M

9

M1 :	EPP	
M2, M3 :	a/D= 10, 4	(ρ_l= 1.5%, ρ_t = 0.72%, P=0.07f'$_c$A$_g$)
M4, M5 :	ρ_l= 0.75,3.0%	(ρ_t= 0.72%, P=0.07f'$_c$A$_g$, a/d=4)
M6, M7 :	ρ_t = 1.26, 1.79%	(ρ_l= 2.1%, P=0.1f'$_c$A$_g$, a/d ≈ 3.3)
M8, M9 :	P=0.09, 0.23f'$_c$A$_g$	(ρ_l= 2.2%, ρ_t =0.94%, a/d = 3.8)

Leman (2000)
Wang et al.(2017)
Ou et al.(2015)
Wehbe et al.(2001)

4) Ground excitation, FF & NF

NEHRP 2000	
Site Class	V_{s30} (m/sec)
B	760-1525
C	360-760
D	180-360
E	180-

Far-Field : FFC (Site Class C)
FFD (Site Class D)
Near-Fault : NF1 (T_p=0.5~2.5 s)
NF2 (T_p=2.5~5.5 s)
NF3 (T_p=5.5~10.5 s)

75

67500 runs

12

Comparison Between FF & NF Ground Motions

M3 Hysteresis Model

Far-Field — **FFC** (Site Class C)

Near-Fault — **NF3** (T_p = 5.5-10.5 s)

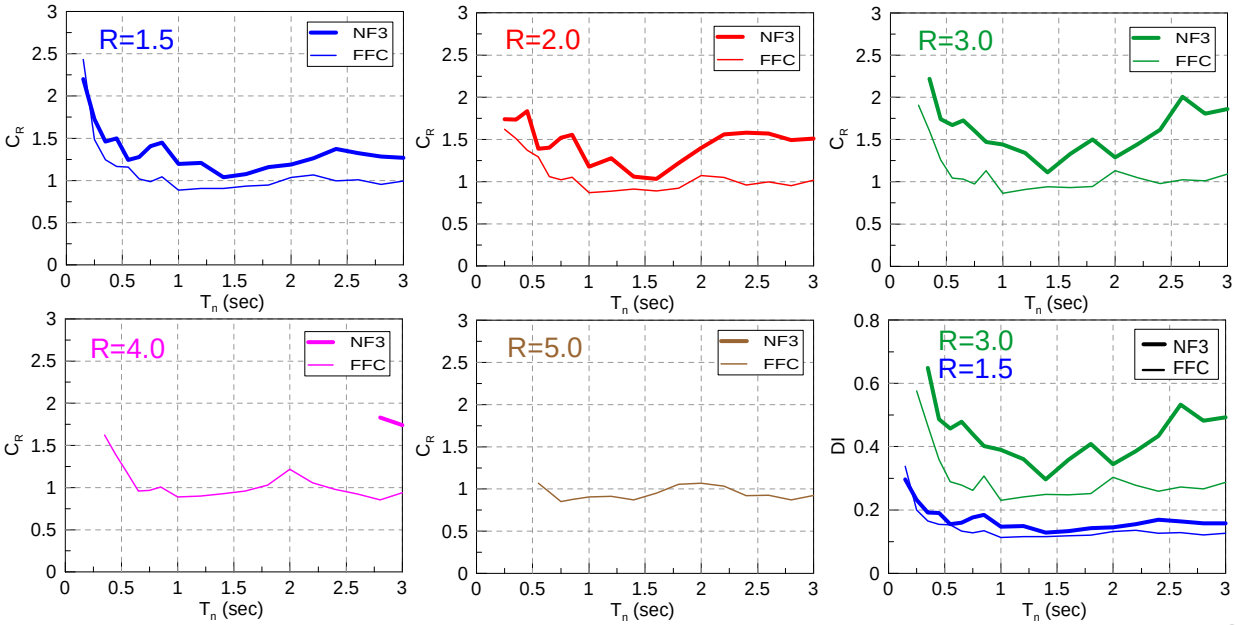

■ Ping-Hsiung Wang, Kuo-Chun Chang, Yu-Chen Ou (2019). Capacity-Based Inelastic Displacement Spectra for Reinforced Concrete Bridge Columns. Earthquake Engineering and Structural Dynamics, 48(14): 1536-1555.

Proposed Spectral Formula for FF Ground Motions

Far-field ground motions

$$R_d = \left(1-\frac{1}{\mu_D}\right)\frac{T^*}{T}+\frac{1}{\mu_D} \quad for\ T < T^*$$
$$= 1.0 \quad for\ T \geq T^*$$

AASHTO
T* = 1.25T_s
μ_D = 6 for SDC D

$$C_R = \begin{cases} \left(1-\frac{1}{R}\right)\frac{T_1^*}{T_n}+\frac{1}{R} \geq C_{R\_min}, & T_n \leq T_1^* \\ C_{R\_min}, & T_1^* < T_n \leq 3.0s \end{cases}$$

$$T_1^* = \begin{cases} 1.25T_s & (Site\ Class\ C) \\ 1.45T_s & (Site\ Class\ D) \end{cases} \quad C_{R\_min} = \begin{cases} 1.0 & (Site\ Class\ C) \\ 1.1 & (Site\ Class\ D) \end{cases}$$

$$DI = \begin{cases} \left(C_{DI}-\frac{C_{DI}}{R}\right)\left(\frac{T_2^*}{T_n}\right)^n+\frac{C_{DI}}{R}, & T_n \leq T_2^* \\ C_{DI}, & T_2^* < T_n \leq 3.0s \end{cases}$$

$$T_2^* = \{0.37\,ln(R)+1.3\}T_s$$

$$n = 0.1R + 1.1$$

$$C_{DI} = \begin{cases} \{0.065-0.010\,ln(AD)+0.017LR-0.013\,ln(TR)\}R & (Site\ Class\ C) \\ \{0.077-0.006\,ln(AD)+0.015LR-0.017\,ln(TR)\}R & (Site\ Class\ D) \end{cases}$$

Aspect ratio — Longitudinal steel ratio — Transverse steel ratio

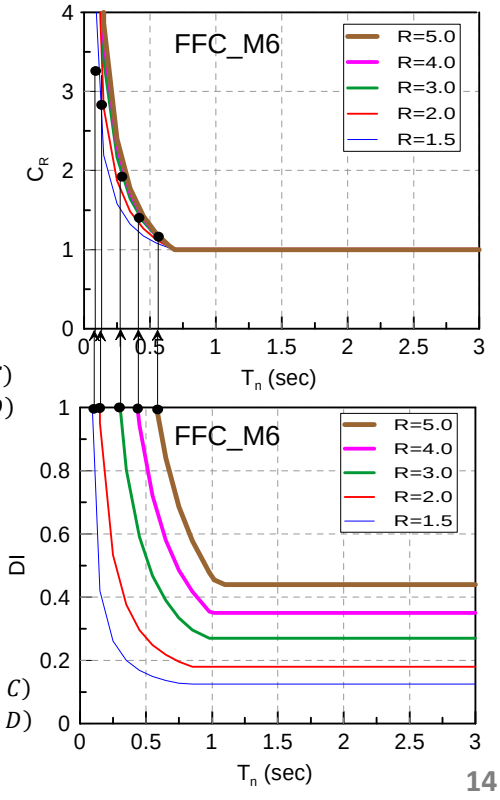

Proposed Spectral Formula for NF Ground Motions

Near-fault ground motions

$$C_R = \begin{cases} \left(C_{BR} - \frac{C_{BR}}{R}\right)\left(\frac{T_1^*}{T_n}\right)^{n_1} + \frac{C_{BR}}{R} + \frac{\Delta_1}{3}T_n, & T_n \le 3.0s\ (T_p = 0.5 \sim 5.5s) \\ \left(C_{BR} - \frac{C_{BR}}{R}\right)\left(\frac{T_1^*}{T_n}\right)^{n_1} + \frac{C_{BR}}{R}, & T_n \le 1.5s\ (T_p = 5.5 \sim 10.5s) \\ \left(C_{BR} - \frac{C_{BR}}{R}\right)\left(\frac{T_1^*}{1.5}\right)^{n_1} + \frac{C_{BR}}{R} + k_1 \times ln\left(\frac{T_n}{1.5}\right), & 1.5s < T_n \le 2.5s\ (T_p = 5.5 \sim 10.5s) \\ \left(C_{BR} - \frac{C_{BR}}{R}\right)\left(\frac{T_1^*}{1.5}\right)^{n_1} + \frac{C_{BR}}{R} + k_1 \times ln\left(\frac{2.5}{1.5}\right), & 2.5s < T_n \le 3.0s\ (T_p = 5.5 \sim 10.5s) \end{cases}$$

$$C_{BR} = \begin{cases} 1 & (T_p = 0.5 \sim 2.5s) \\ -0.069R^2 + 0.473R + 0.546 & (T_p = 2.5 \sim 10.5s) \end{cases}$$

$$DI = \begin{cases} \left(C_{DI} - \frac{C_{DI}}{R}\right)\left(\frac{T_2^*}{T_n}\right)^{n_2} + \frac{C_{DI}}{R} + \frac{\Delta_2}{3}T_n, & T_n \le 3.0s\ (T_p = 0.5 \sim 2.5s) \\ \left(C_{DI} - \frac{C_{DI}}{1.5}\right)\left(\frac{T_2^*}{T_n}\right)^{n_2} + \frac{C_{DI}}{1.5} + \frac{\Delta_2}{3}T_n, & T_n \le 3.0s\ (T_p = 2.5 \sim 5.5s) \\ \left(C_{DI} - \frac{C_{DI}}{1.5}\right)\left(\frac{T_2^*}{T_n}\right)^{n_2} + \frac{C_{DI}}{1.5}, & T_n \le 1.5s\ (T_p = 5.5 \sim 10.5s) \\ \left(C_{DI} - \frac{C_{DI}}{1.5}\right)\left(\frac{T_2^*}{1.5}\right)^{n_2} + \frac{C_{DI}}{1.5} + k_2 \times ln\left(\frac{T_n}{1.5}\right), & 1.5s < T_n \le 2.5s\ (T_p = 5.5 \sim 10.5s) \\ \left(C_{DI} - \frac{C_{DI}}{1.5}\right)\left(\frac{T_2^*}{1.5}\right)^{n_2} + \frac{C_{DI}}{1.5} + k_2 \times ln\left(\frac{2.5}{1.5}\right), & 2.5s < T_n \le 3.0s\ (T_p = 5.5 \sim 10.5s) \end{cases}$$

$$C_{DI} = \begin{cases} \{0.056 - 0.010\,ln(AD) + 0.028LR - 0.029\,ln(TR)\}R & (T_p = 0.5 \sim 2.5s) \\ \{0.075 - 0.009\,ln(AD) + 0.021LR - 0.027\,ln(TR)\}R & (T_p = 2.5 \sim 10.5s) \end{cases}$$

Aspect ratio | Longitudinal steel ratio | Transverse steel ratio

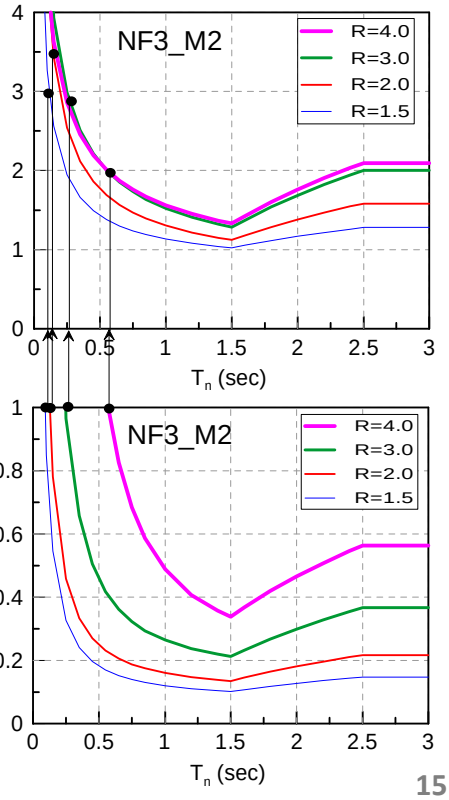

Seismic Evaluation Procedure

1. Pushover Analysis of Bridge

- Perform pushover analysis
- Conversion of equivalent SDOF
- Obtain strength reduction factor $R=S_{ae}/S_{ay}$

2. Capacity-Based Dual Spectra

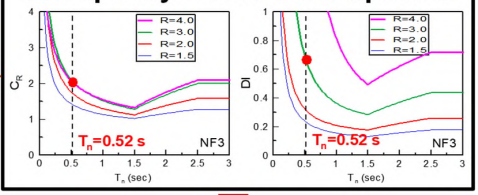

3. Maximum Responses of Bridge

- Compute maximum inelastic spectral displacement from C_R
- Obtain maximum inelastic responses of bridge

4. Damage Evaluation of Bridge

- Compute total dissipated energy E_{total} from DI
- Distribute E_{total} to each column
- Compute DI of each column

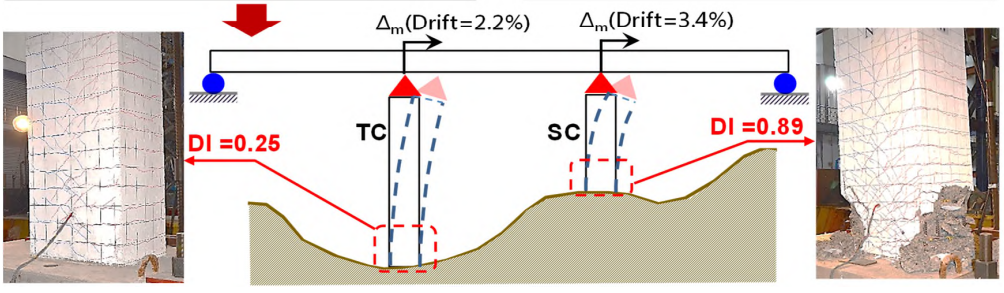

■ Ping-Hsiung Wang, Kuo-Chun Chang, Dzong-Chwang Dzeng, Tzu-Kang Lin, Hsiao-Hui Hung, Wei-Chung Cheng (2021). Seismic Evaluation of Reinforced Concrete Bridges Using Capacity-Based Inelastic Displacement Spectra. Earthquake Engineering and Structural Dynamics, 50: 1845-1863.

Validation of Proposed Method to NTHA

Far-field, FFC **Long. direction** Near-fault, NF3

No	Maximum Displacement (mm)			Damage Index (*DI*)				
	NTHA	Proposed	Error (%)	NTHA		Proposed		
				TC	SC	TC	SC	EQ
FFC01	146.1	142.7	-2.34	0.19	0.67	0.19	0.66	0.48
FFC02	**265.8**	**272.4**	**2.46**	**0.49**	**1.74**	**0.52**	**1.82**	**1.26**
FFC03	176.6	170.6	-3.43	0.23	0.76	0.22	0.75	0.55
FFC04	87.6	88.3	0.85	0.10	0.40	0.12	0.39	0.29
FFC05	251.3	250.3	-0.43	0.30	0.97	0.30	0.98	0.73
FFC06	146.0	139.6	-4.34	0.19	0.64	0.18	0.62	0.45
FFC07	126.7	123.3	-2.70	0.18	0.72	0.20	0.69	0.49
FFC08	**273.0**	**284.8**	**4.34**	**0.35**	**1.16**	**0.36**	**1.21**	**0.89**
FFC09	133.9	140.0	4.56	0.17	0.68	0.20	0.70	0.50
FFC10	105.7	106.7	0.93	0.12	0.44	0.13	0.44	0.32
FFC11	189.9	193.4	1.86	0.23	0.79	0.24	0.81	0.60
FFC12	**NA**	**NA**	**NA**	**NA**	**NA**	**NA**	**NA**	**NA**
FFC13	169.1	149.0	-11.93	0.23	0.81	0.21	0.73	0.53
FFC14	**NA**	**NA**	**NA**	**NA**	**NA**	**NA**	**NA**	**NA**
FFC15	183.8	184.0	0.13	0.25	0.89	0.26	0.89	0.64
Average	156.1	153.4	-1.53	0.20	0.71	0.21	0.70	0.51

No	Maximum Displacement (mm)			Damage Index (*DI*)				
	NTHA	Proposed	Error (%)	NTHA		Proposed		
				TC	SC	TC	SC	EQ
NF301	68.5	64.2	-6.22	0.07	0.25	0.07	0.23	0.18
NF302	213.9	189.8	-11.30	0.26	0.84	0.23	0.76	0.56
NF303	221.3	211.0	-4.63	0.26	0.84	0.24	0.81	0.61
NF304	203.1	201.4	-0.83	0.24	0.79	0.24	0.79	0.59
NF305	247.2	268.8	8.74	0.30	0.94	0.31	1.03	0.77
NF306	80.8	89.4	10.62	0.09	0.28	0.09	0.31	0.24
NF307	86.6	84.4	-2.55	0.11	0.47	0.13	0.44	0.31
NF308	134.2	128.3	-4.40	0.18	0.68	0.19	0.63	0.46
NF309	127.2	117.6	-7.56	0.15	0.55	0.15	0.49	0.36
NF310	**311.5**	**302.7**	**-2.84**	**0.56**	**1.75**	**0.50**	**1.75**	**1.23**
NF311	85.7	83.4	-2.77	0.10	0.33	0.10	0.32	0.24
NF312	51.3	53.0	3.35	0.05	0.20	0.06	0.20	0.15
NF313	134.8	117.5	-12.86	0.15	0.51	0.13	0.45	0.33
NF314	143.6	129.6	-9.70	0.18	0.63	0.17	0.56	0.41
NF315	97.2	99.2	2.11	0.11	0.38	0.11	0.38	0.28
Average	135.4	131.3	-2.71	0.16	0.55	0.16	0.53	0.39

TC: Tall Column; SC: Short Column; EQ: Equivalent SDOF System
NTHA: Nonlinear Time History Analysis

Performance Objectives

Performance Objectives

1. Level I Earthquake

Remains elastic

ex: R < 1.0

2. Level II Earthquake

DI, II,L <= 0.6

$$\delta_{II} \le 0.20 \frac{M_{ult}}{P_D}$$

DI =0.6

3. Level III Earthquake

DI, III,L <= 0.9

$$\delta_{III} \le 0.25 \frac{M_{ult}}{P_D}$$

DI =0.9

Proposed Seismic Design Procedure

1. Preliminary bridge design
- Determine preliminarily the main design parameters of bridge (AD, LR, TR, T_n)

2. Performance objective
- Determine the anticipated equivalent damage index $DI,eq,_{II}$ under level II earthquake and $DI,eq,_{III}$ under level III earthquake

3. Strength reduction factor
- Obtain the strength reduction factor R_{II} (R_{III})from the DI spectrum Based on the $DI,eq,_{II}$ ($DI,eq,_{III}$), T_n and AD, LR, TR of the critical column.
- Calculate the design seismic forces V_D

4. Seismic design
- Determine the distribution of lateral seismic forces according to seismic design code and then apply these forces to the corresponding nodes.
- Perform the detailed bridge design based on the obtain member forces and obtain the revised design parameters (AD, LR, TR, T_n)

Phase 1 Design

Phase 2 Evaluation

5. Pushover Analysis of Bridge
- Perform pushover analysis
- Conversion of equivalent SDOF to get Say
- Obtain strength reduction factor R=Sae/Say

6. Capacity-Based Dual Spectra
- Form Capacity-Based Dual Spectra based on the revised design parameters
- Obtain the equivalent DI,eq, and C_R,eq of the equivalent SDF system for level II and III earthquake

7. Maximum Responses of Bridge
- Compute maximum inelastic spectral displacement S_{dm} for the equivalent SDF system from C_R,eq
- Obtain maximum inelastic responses for each column

8. Damage Evaluation of Bridge
- Compute total dissipated energy E_{total} from DI,eq
- Distribute E_{total} to each column
- Compute $DI_{,i}$ of each column

9. Check
Check If $DI,_{LII} < 0.6$
$DI,_{LIII} < 0.9$
Check P-Δ effects

No
Increase LR or adjust column size

Yes
Capacity design

Design Demonstration

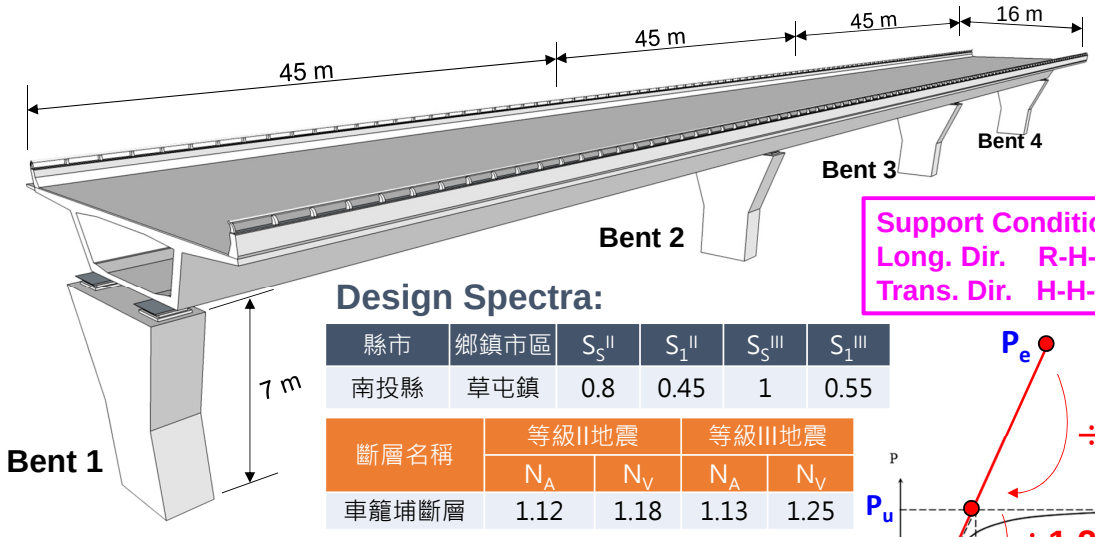

Support Conditions:
Long. Dir. R-H-H-R
Trans. Dir. H-H-H-H

Design Spectra:

縣市	鄉鎮市區	S_S^{II}	S_1^{II}	S_S^{III}	S_1^{III}
南投縣	草屯鎮	0.8	0.45	1	0.55

斷層名稱	等級II地震		等級III地震	
	N_A	N_V	N_A	N_V
車籠埔斷層	1.12	1.18	1.13	1.25

$$V_{III} = \frac{I}{1.2\alpha_y}\left(\frac{S_{a,III}}{F_{u,III}}\right)_{\mu} W$$

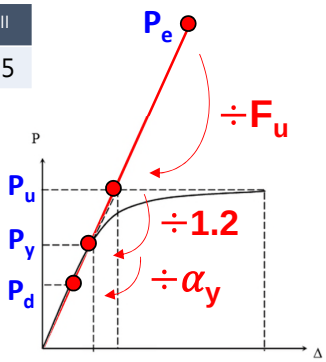

PREMISE:
1. **Design EQ force modification, initial yielding amplification factor (load /resistance factors), and EQ direction combination are not considered.**
2. **In current method M_u shall not be greater than M_n.**
3. **In new method M_u shall not be greater than M_P due to the lack of 1.2 in V_{III}.**

Comparison of Design Results

Regular Bridge

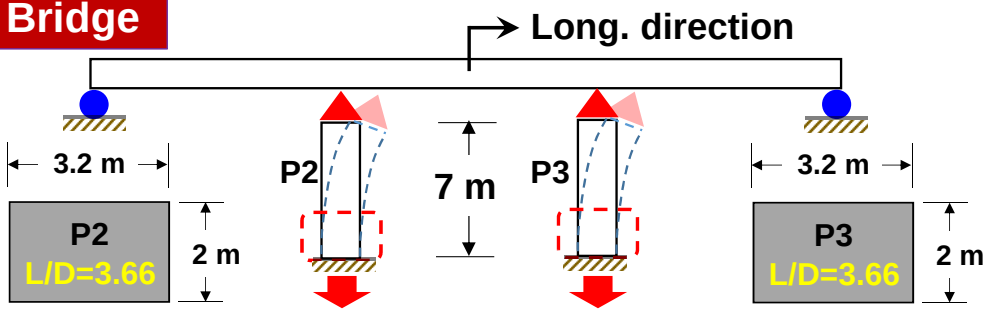

Method	ρ_l(%) P2-P3	DI_2 (III)	DI_3 (III)	Earthquake
Taiwan Code	1.7%-1.7%	1.14 (NG)	1.16 (NG)	
AASHTO	1.5%-1.5%	1.39 (NG)	1.42 (NG)	Near-Fault (NF3)
Proposed	2.3%-2.3%	0.82	0.84	
Taiwan Code	1.7%-1.7%	0.49	0.51	
AASHTO	1.5%-1.5%	0.54	0.56	Far-Filed(FFD)
Proposed	1.3%-1.3%	0.58	0.60	

Comparison of Design Results

Irregular Bridge

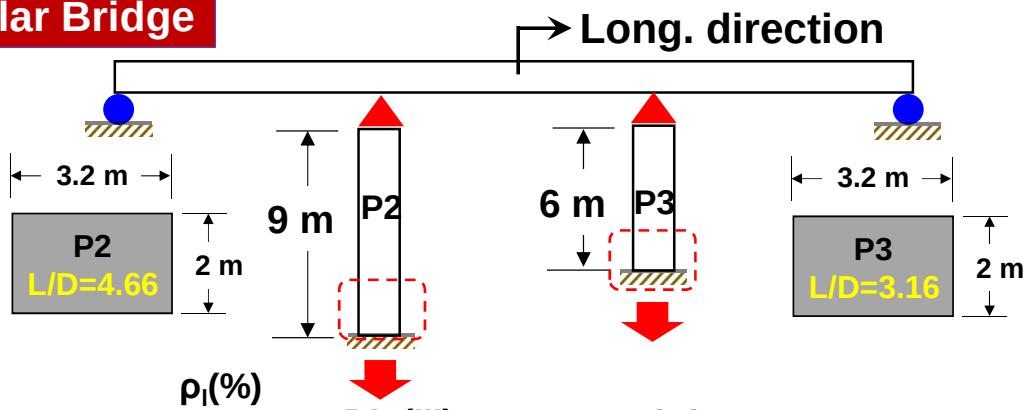

Method	ρ_l(%) P2-P3	DI_2 (III)	DI_3 (III)	Earthquake
Taiwan Code	1.2%-2.3%	0.76	2.65 (NG)	
AASHTO	1.5%-2.4%	0.46	1.32 (NG)	Near-Fault (NF3)
Proposed	2.0%-2.3%	0.35	0.83	

The cross-sectional size of P2 was 1.2 times scaled up.

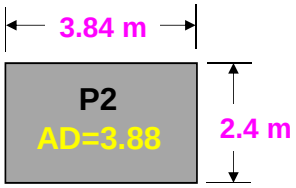

Proposed Domestic Dual Spectra

Earthquake Characteristics:

1) **Site Class 1** (V_{s30} > 270 m/s)
2) **Site Class 2** (180 m/s < V_{s30} <270 m/s)
3) **Site Class 3** (V_{s30} < 180 m/s)
4) **Taipei Basin Zone 1**
5) **Taipei Basin Zone 2**
6) **Taipei Basin Zone 3**
7) **Near Active Faults**

(Fling Step, Forward Directivity, Non Plus-Like, Magnitude, Distance, etc.)

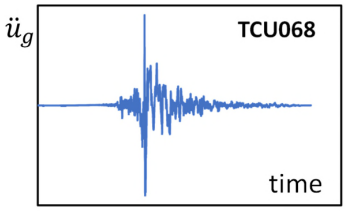

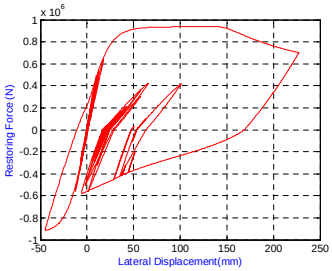

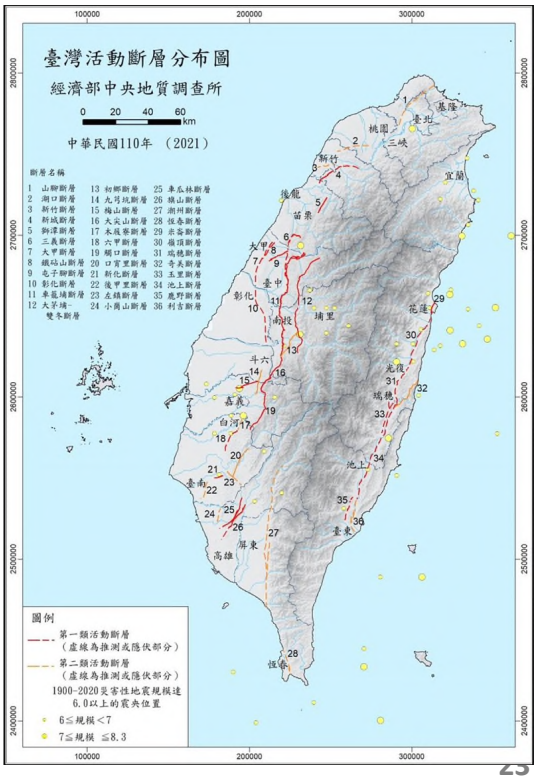

23

Taipei Basin Response Spectra

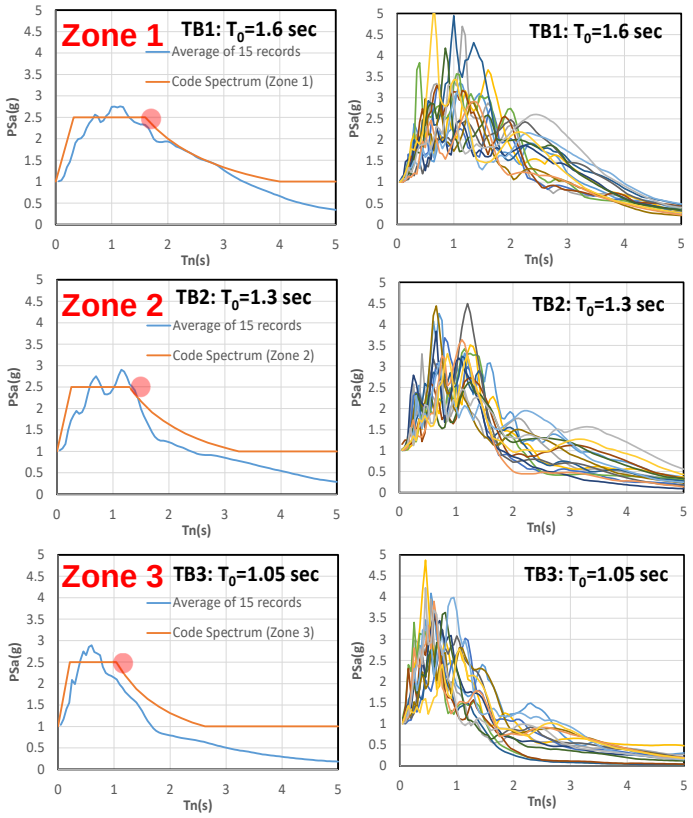

Earthquakes dominating the seismic hazard of Taipei Basin are those being major, shallow, and far-field earthquakes (Magnitude > 6.5)

1. 1999 Chi-Chi (921)Earthquake
2. 2002 Hualien (331) Earthquake
3. 2004 Yilan (1015) Earthquake

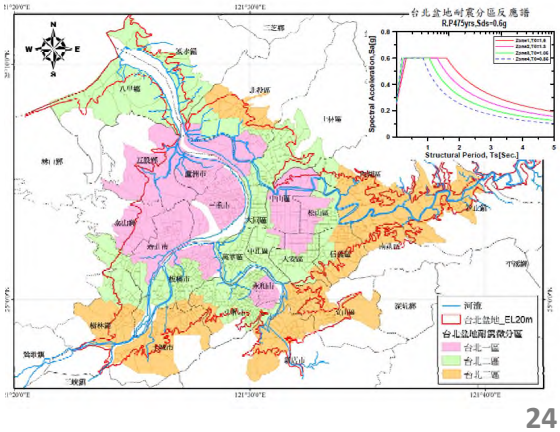

24

Dual Spectra vs. Taiwan R-μ-T Formula

(Taipei Basin Zone 1)

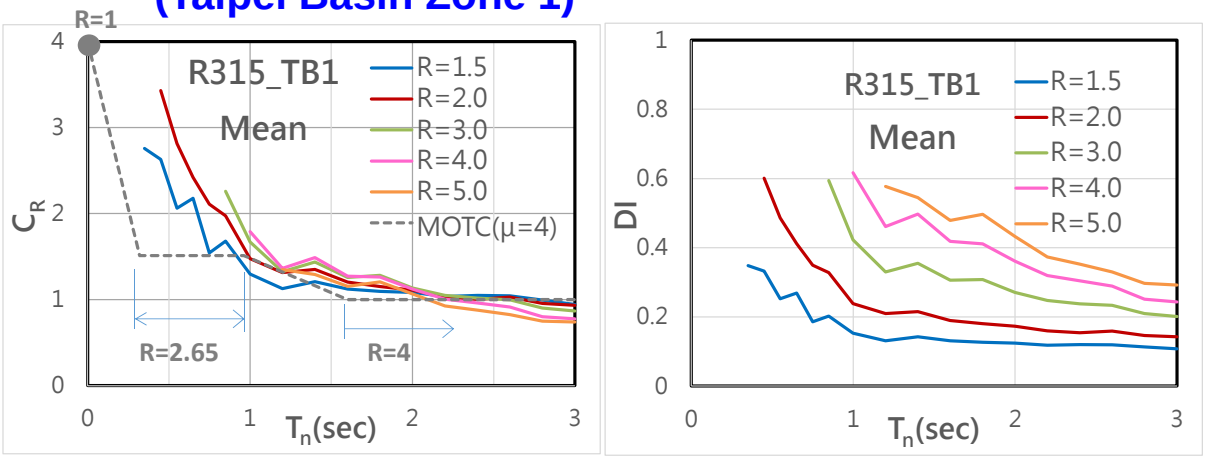

TB1: T_0=1.6 sec

$$C_R = \frac{\Delta_i}{\Delta_e} = \frac{\Delta_i/\Delta_y}{\Delta_e/\Delta_y} = \frac{\mu}{R}$$

$$R = \frac{mS_a}{F_y}$$

$$R = (F_u) \begin{cases} \mu & ;T \geq T_0 \\ \sqrt{2\mu-1} + (\mu - \sqrt{2\mu-1}) \times \dfrac{T - 0.6T_0}{0.4T_0} & ;\ 0.6T_0 \leq T \leq T_0 \\ \sqrt{2\mu-1} & ;\ 0.2T_0 \leq T \leq 0.6T_0 \\ \sqrt{2\mu-1} + (\sqrt{2\mu-1} - 1) \times \dfrac{T - 0.2T_0}{0.2T_0} & ;T \leq 0.2T_0 \end{cases}$$

25

Taipei Basin vs. Near-Fault Effects

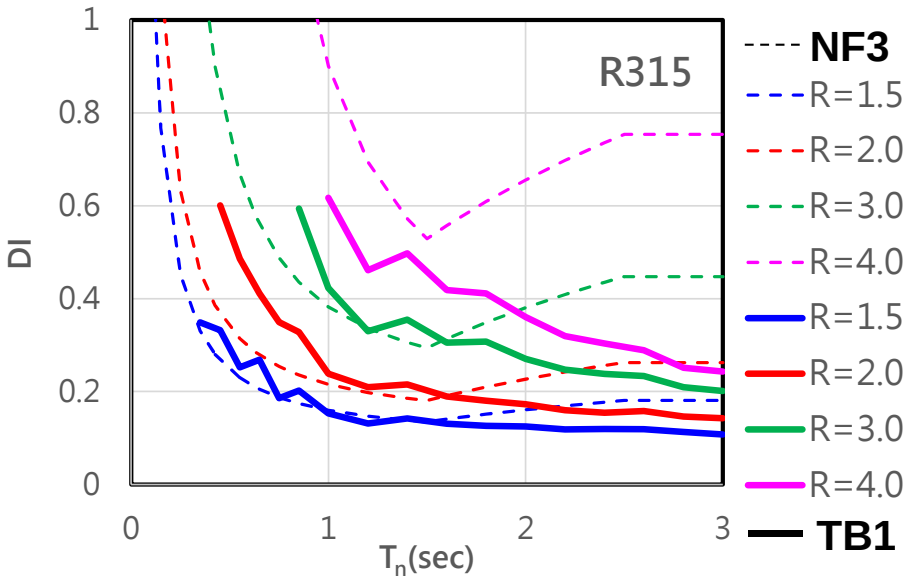

- Preliminary study shows that when T_n< 1.0 s & R< 3.0, the DI of Taipei basin zone 1 could be greater than that of near-fault ground motion.

26

Conclusions

1. **Dual spectra are proposed to consider the seismic damage of RC bridges caused by various earthquake characteristics.**
2. **Damage-based seismic design and evaluation methods using dual spectra are developed to better realize the seismic performance of RC bridges.**
3. **Correlation between damage index and actual failure photo can be achieved by AI technology for visualized seismic design and evaluation and post-earthquake examination.**

The End

Thank You for Your Attention

Prof. Shih-Ho (Simon) Chao

The University of Texas at Arlington, USA

Topic：An Innovative Horizontal Seismic Force-Resisting System for Improved Seismic Resilience of Steel Buildings

AN INNOVATIVE HORIZONTAL SEISMIC FORCE-RESISTING SYSTEM FOR IMPROVED SEISMIC RESILIENCE OF STEEL BUILDINGS

Kyoung Sub Park,[1] Shih-Ho Chao, [2] and Chia-Ming Uang[3]

[1] Postdoctoral Research Fellow, University of Texas at Arlington, Arlington, TX, USA
[2] Professor, Department of Civil Engineering, University of Texas at Arlington, Arlington, TX, USA
[3] Professor, Department of Structural Engineering, University of California San Diego, La Jolla, CA, USA
Email: kyoungsub.park@uta.edu, shchao@uta.edu, cmu@ucsd.edu

ABSTRACT

This study explores a new concept, which transforms a seismic-resistant steel building's energy-dissipation system from the traditional vertical seismic force-resisting system (V-SFRS) into a horizontal seismic force-resisting system (H-SFRS). Energy-dissipation devices like buckling-restrained braces (BRBs) are placed between the diaphragm and the V-SFRS to separate the diaphragm from the V-SFRS and the gravity load resisting system (GLRS). A diaphragm is connected to the V-SFRS only by the BRBs placed in both directions of the structure, while the low-friction PTFE (Teflon)-bearing pads placed between the steel beams and the diaphragm allow the diaphragm to slide in horizontal directions. The seismically induced horizontal inertial force transferred to the V-SFRS is limited by the capacity of the reusable and replaceable BRBs. Consequently, the force transferred to the V-SFRS can be controlled to minimize damage to both the V-SFRS and nonstructural components. V-SFRS then can be designed economically to remain essentially elastic with a re-centering capability. The proposed low-damage, high-performance system has the potential to achieve a resilient structure with lower repair costs and less repair time due to limited damage. Its functionality is minimally affected or can be recovered quickly and economically after a seismic event. Results from the preliminary nonlinear time-history analyses of the proposed system with moment frame V-SFRS and braced frame V-SFRS are discussed.

Keywords: vertical seismic force-resisting system, horizontal seismic force-resisting system, buckling-restrained braces, nonstructural components, re-centering, resilient, diaphragm

INTRODUCTION

Vertical seismic force-resisting systems (V-SFRS) are commonly used in seismic-resistant steel buildings as the energy-dissipation system. The horizontal earthquake inertial force is transferred through a diaphragm to its collectors and chords and then resisted by the V-SFRS. A diaphragm also transfers the gravity loads to the gravity load resisting system (GLRS). Structural fuses of a V-SFRS are designed to behave in a ductile manner and dissipate the earthquake energy inelastically. The consequence of this design approach leads to large lateral story drifts under a major earthquake, which can cause significant P-Delta forces and the possibility of collapse. The large story drifts can also cause severe damage to nonstructural elements such as façade and partition walls. According to FEMA P-58 (2018a, 2018b), the economic loss due to damage in the exterior cladding (façade) system due to story drifts of V-SFRS can be as high as 50% of the total loss in an M6.5 earthquake. In addition, inelastic deformations of structural members lead to residual displacements, which can considerably affect the post-earthquake repair work and delay the functional recovery of the structure. Furthermore, peak floor accelerations in the diaphragm can be much larger than the peak ground accelerations (Ray-Chaudhuri and Hutchinson, 2011). The high floor accelerations can cause damage in acceleration-sensitive nonstructural elements such as suspended ceiling systems and equipment. The high ductility demands in the structural fuses call for costly detailing and fabrication. Post-earthquake repair or replacement of these fuses such as moment connections and column bases can be very challenging and time-consuming. Notably, it is estimated that the functional recovery time for code-compliant buildings could be on the order of days, weeks, or even months (EERI, 2019).

Considering these issues with conventional V-SFRS, an alternative design approach limiting the inertial force being transferred from diaphragms to V-SFRS has been suggested (Tsampras et al., 2016) and experimentally verified. Extending from this inertial force-limiting concept, this study explores a low-damage high-performance system which transforms a seismic resistant steel building's energy-dissipation system from the traditional V-SFRS into a horizontal seismic force-resisting system (H-SFRS). Energy-dissipation components like buckling-restrained braces (BRBs) are placed between the diaphragm and the V-SFRS to separate the diaphragm (a major source of seismic masses) from the V-SFRS and GLRS as shown in Figure 1. A diaphragm is connected to the V-SFRS only by the BRBs placed in both directions of the structure, while low-friction polytetrafluoroethylene (PTFE) pads, also known as Teflon-bearing pads, are placed between the steel beams and the diaphragm, allowing the diaphragm to slide in a controlled manner in the horizontal directions. The seismically induced horizontal inertial force transferred to the V-SFRS is limited by the capacity of the reusable and replaceable energy-dissipating components. Consequently, the force transferred to the V-SFRS can be controlled to minimize damage to both the V-SFRS and nonstructural components. V-SFRS then can be designed economically to remain essentially elastic with a re-centering capability.

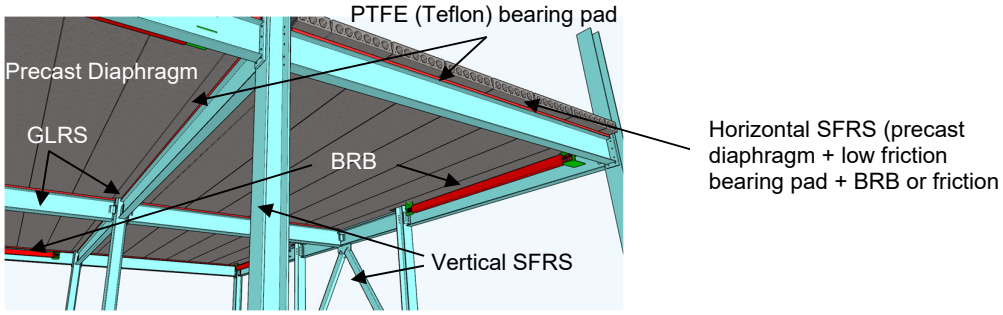

Figure 1. Proposed steel building system with horizontal seismic force-resisting system (H-SFRS).

PRELIMINARY ANALYTICAL RESULTS

The effectiveness and advantages of the proposed concept is demonstrated by preliminary nonlinear time-history analyses carried out on a four-story steel building. Its floor plan view is shown in Figure 2. This building has three-bay special moment frames (SMFs) in one direction and one-bay special concentrically braced frames (SCBFs) in the orthogonal direction. The former is a flexible steel system while the latter is a stiff steel system. The baseline SMF and SCBF are designed according to AISC 341 (AISC, 2016) and presented in the AISC Seismic Design Manual (AISC, 2018).

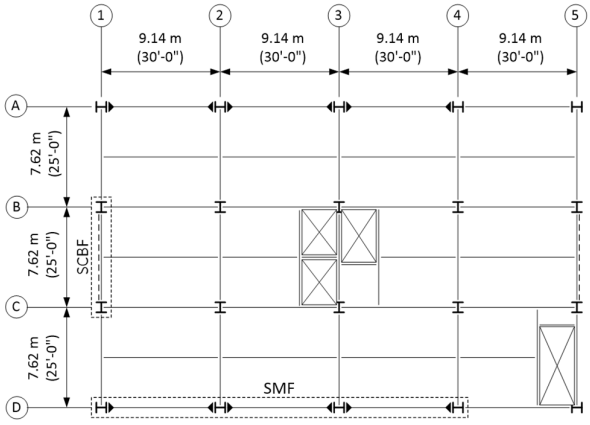

Figure 2. Floor plan and associated special moment frame and special concentrically braced frame.

The two redesigned frames based on the proposed concept used BRBs as the energy-dissipation components in the H-SFRS. In this pilot study, the strength of each floor's BRBs were determined by

trial-and-error since the diaphragm design forces specified in ASCE 7 (ASCE, 2022) are not applicable for the proposed system. Each level uses two BRBs in each direction, and the required BRB strength is about 110 to 180 kN (25 to 40 kips). Figure 3a shows Model 1, which represents the original AISC SMF from the AISC Seismic Design Manual (AISC, 2018), where reduced beam sections (RBS) are used at each beam end. Leaning (gravity) columns are used to consider the P-Delta effect. These leaning columns are connected to the SMF by truss elements. Figure 3b shows Model 2, which is a modified SMF using the proposed concept. BRBs are placed parallel to the steel beams and in-between the floor masses and the SMF; that is, the V-SFRS and the diaphragm are separated by the BRBs, and inertial force is transferred from the diaphragm to the V-SFRS only through the BRBs. The sizes of beams and columns are the same as those in the original SMF (Figure 3a) except that no RBS are used at the beam ends. Model 3 is the same as Model 2 with two exceptions: (1) fixed column bases are replaced by hinged column bases (commonly used in steel braced frames), since the expected drifts in the proposed system are reduced, and (2) stiffer columns (of nearly the same weight) are used to compensate for the reduced lateral stiffness by using hinged column bases (Figure 3c). Further, plastic hinging at a fixed column base is generally inevitable in a major earthquake; hence, minimizing inelastic deformation at the column bases can increase the post-earthquake repairability. All analyses were carried out by using the Perform-3D program with the BRB model calibrated from actual testing (Sahoo and Chao, 2015) (Figure 3d).

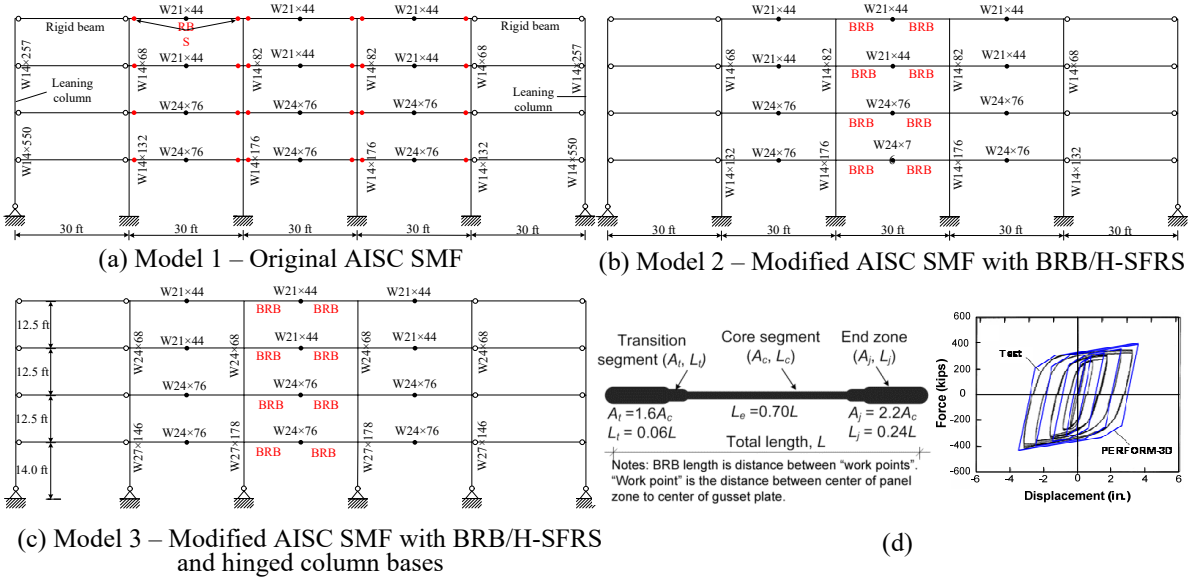

(a) Model 1 – Original AISC SMF

(b) Model 2 – Modified AISC SMF with BRB/H-SFRS

(c) Model 3 – Modified AISC SMF with BRB/H-SFRS and hinged column bases

(d)

Figure 3. Steel SMFs for the proof-of-concept analyses: (a) original AISC frame, (b) modified frame with H-SFRS and fixed column bases, (c) modified frame with H-SFRS and hinged column bases, and (d) the BRB model (1 kip = 4.448 kN, 1 in. = 25.4 mm, and 1 ft = 0.3 m).

Figure 4a presents the roof drift ratio responses of the three models under two design basis earthquakes (El Centro and Northridge). The moment frame system with the proposed H-SRFS shows two major features: (1) peak roof drift ratios are less than 50% of the peak roof drift ratios in the conventional SMF system; (2) residual drift ratio is negligible while significant residual drifts are noticed in the conventional SMF system. Notably, prior studies have indicated that buildings are no longer practically usable if residual drift ratios are greater than 0.05 radian (McCormick et al., 2008). Figure 4b indicates that the proposed system can effectively eliminate or minimize the development of plastic hinges in the beams and columns of a moment frame. This enhances the post-earthquake structural repairability and occupiability, as well as allowing a more economical design with relaxed seismic detailing in all the connections in the V-SFRS. Figure 4c reveals another feature of the proposed system where the absolute peak floor accelerations are about 30% to 50% of the absolute peak floor accelerations in the conventional SMF system.

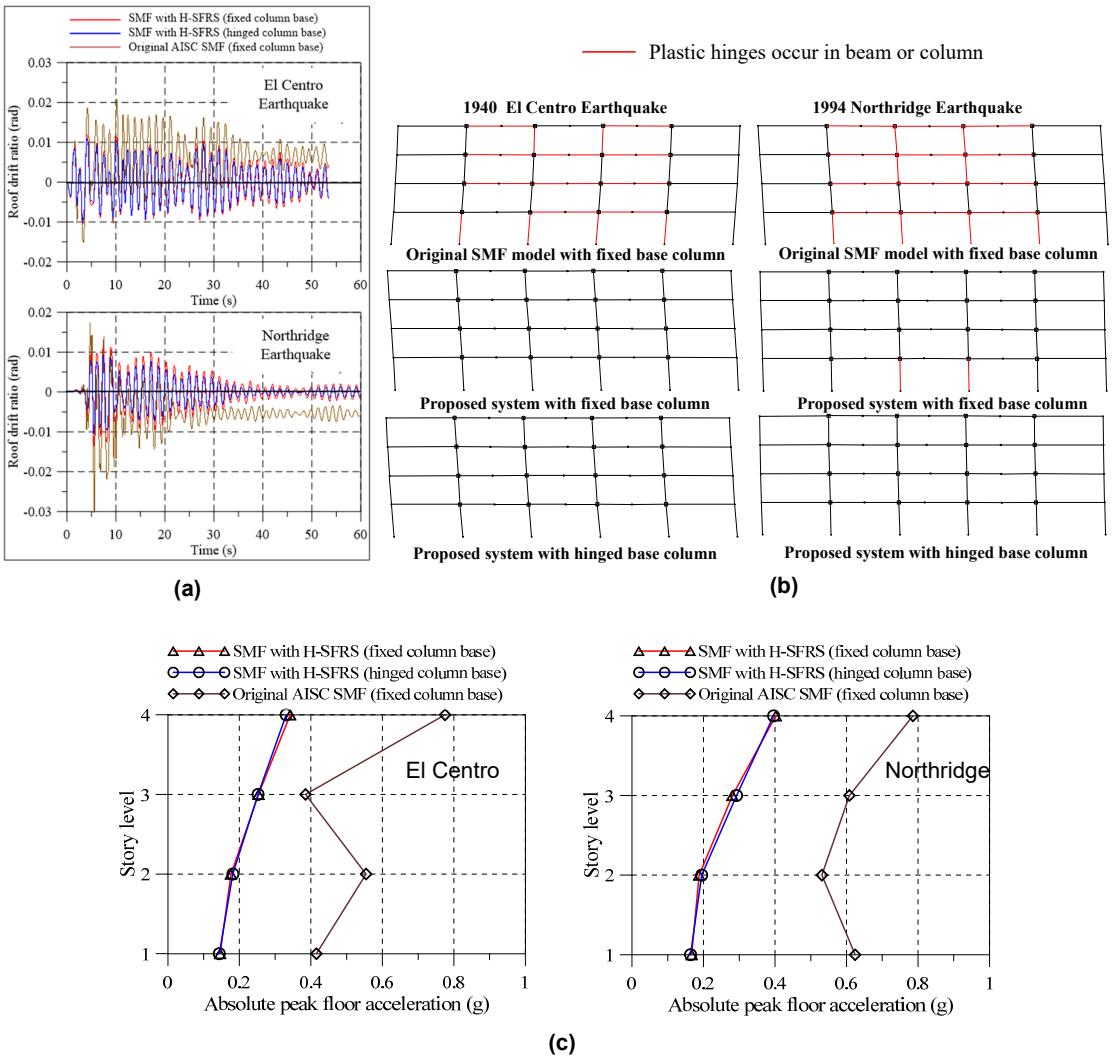

Figure 4. Seismic response comparison between conventional SMF design and proposed moment frame systems with H-SFRS.

Figure 5 shows an SCBF with conventional V-SFRS (AISC, 2018) and the proposed H-SFRS where 3-m (120-in.) long BRBs are used to separate the masses and the V-SFRS. Figure 6a compares time-history responses of the two frames subjected to the two design basis ground motions. The results indicate the proposed system has a maximum roof ratio of approximately 35% and a residual drift ratio that is approximately 10% of the conventional SCBF. Figure 6b shows that, without severe buckling, diagonal braces in the proposed system remained essentially elastic under the El Cento Earthquake while experiencing smaller inelastic deformations. Figure 7 shows the deformation histories of BRBs in the H-SFRS. The largest deformation is approximately 75 to 110 mm (3 to 4.5 in.) or a 3% to 5% core strain. The BRBs used in the preliminary analyses experienced a small cumulative inelastic strain compared to their expected low-cycle fatigue life (Li et al., 2022). Note that the deformation in the BRBs is also the same as the relative displacement between the diaphragm and the V-SFRS; hence, nonstructural components, as well as the firestopping attached to the diaphragm need to be designed to accommodate this expected displacement. In addition, a re-centering mechanism in the diaphragm, such as the self-centering BRBs (Chou et al., 2016) or post-tensioning device [30] can be used to re-center the diaphragm. An optimized design should be investigated to adjust the strength of BRBs (hence the required lateral strength of V-SFRS) to have a smaller BRB strain and diaphragm displacement thereby avoiding use of overly strong BRBs and V-SFRS.

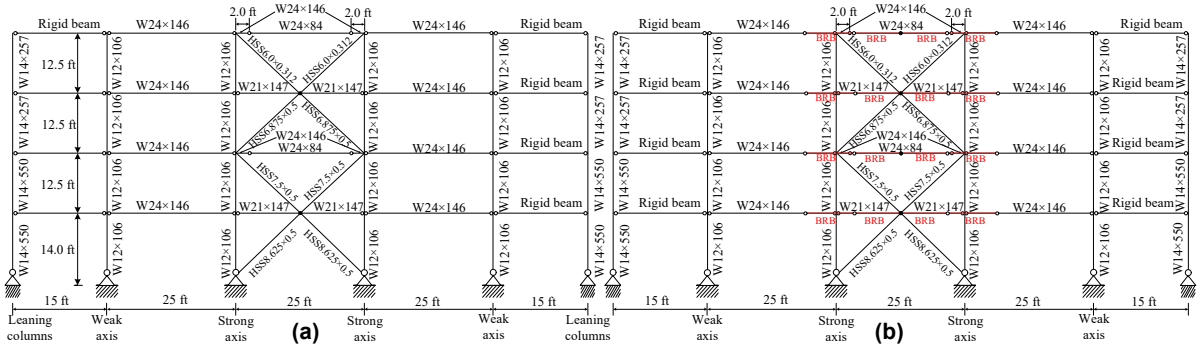

Figure 5. SCBFs for proof-of-concept analyses: (a) original AISC SCBF (AISC, 2018) and (b) modified SCBF with H-SFRS (1 ft = 0.3 m).

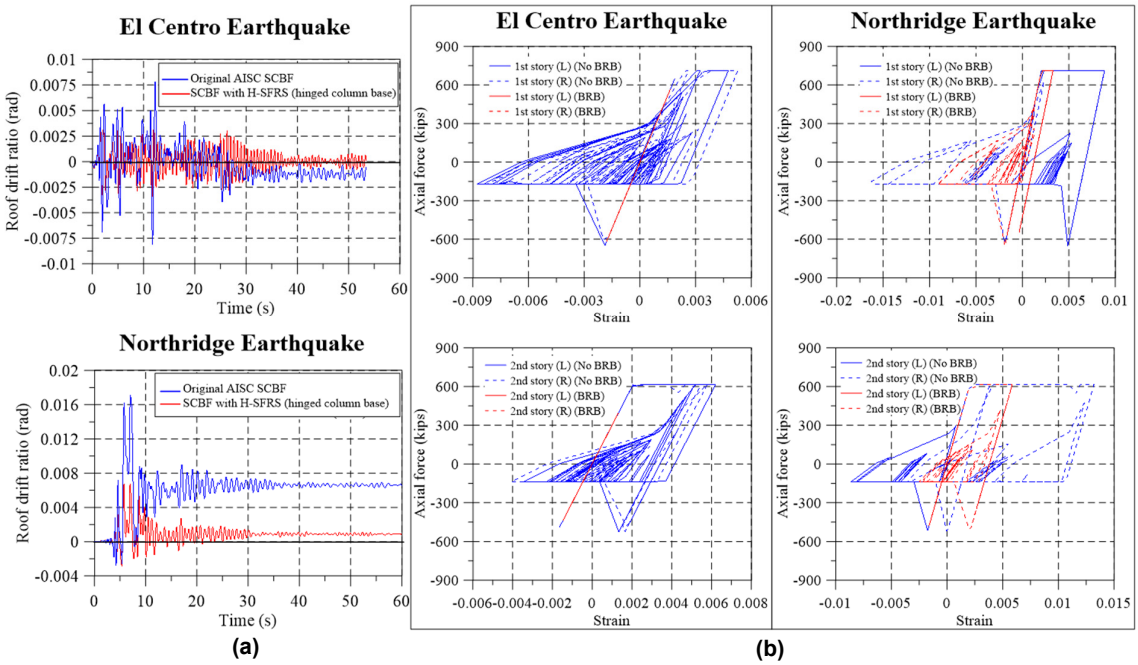

Figure 6. Seismic responses between original AISC SCBF frame and modified SCBF with H-SFRS (1 kips = 4.448 kN).

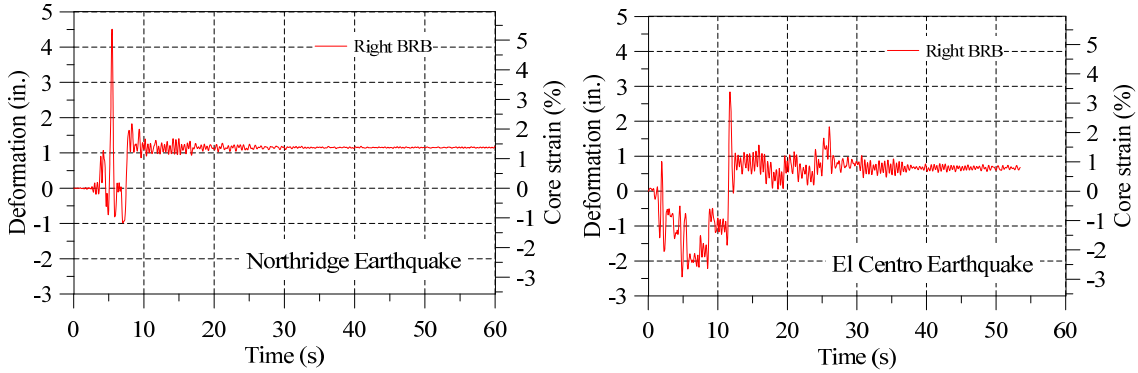

Figure 7. First-story BRB deformation time-history in the modified SCBF with H-SFRS (1 in. = 25.4 mm).

SUMMARY AND CONCLUSIONS

As reflected in modern seismic steel design codes, conventional seismic-resistant steel buildings rely on designated vertical seismic force-resisting systems (V-SFRS) that are interconnected through stiff floor diaphragms for seismic resistance. Since selected "ductile" elements in the V-SFRS are designed to be sacrificial, strength and stiffness degradation in the V-SFRS, compounded by the P-Delta effect at large lateral drifts, is responsible for collapse. The lateral story drifts and large floor accelerations are the primary causes of damage to the nonstructural element and the accompanying economical losses, based on the time needed for functional recovery when a building is subjected to a major earthquake event. To improve the seismic resilience and functional recovery, self-centering and rocking have been proposed, yet the improvements are still focused on V-SFRS. Despite the proven effectiveness of base isolation, in the U.S., this "advanced" design alternative is still limited in practical use.

This study explores a drastically different but practical concept that decouples the floor and roof diaphragms from the vertical systems (both V-SFRS and gravity load-resisting systems). The new approach minimizes the drawbacks of the traditional V-SFRS by using a horizontal seismic force-resisting system (H-SFRS) to limit the force transferred from the diaphragm to the V-SFRS. The energy-dissipation and yielding elements are devices like BRBs, which connect the V-SFRS and diaphragms. The V-SFRS is capacity-designed to remain essentially elastic such that expensive ductility detailing required in current codes can be relaxed; an elastic V-SFRS also serves as a re-centering mechanism.

A pilot study with preliminary nonlinear time-history analyses on prototype four-story steel buildings with SMF V-SFRS or SCBF V-SFRS indicates that buildings using the proposed H-SFRS show much smaller drift ratios (35% to 50%) and absolute peak floor accelerations (30% to 50%), as well as negligible residual drift ratios when compared to buildings with conventional V-SFRS. The V-SFRS in buildings with the proposed H-SFRS remained essentially elastic or had limited ductility demands. These reduced drift demands, ductility demands, and floor accelerations consequently eliminated the P-Delta-induced collapse potential, allowing a re-centering of the building, and minimized nonstructural element damage. All of these advantages can enhance the resilience and functional recovery of buildings in high seismic regions. Further research is needed to investigate the re-centering mechanism to minimize the residual displacements of the H-SFRS. System level testing and further analytical studies are needed in the future to verify the proposed concept.

REFERENCES

American Institute of Steel Construction (AISC). (2016). Seismic Provisions for Structural Steel Buildings, ANSI/AISC 341-16, Chicago, IL.

American Institute of Steel Construction (AISC). (2018). Seismic Design manual, 3rd Edition, Chicago, IL.

American Society of Civil Engineers (ASCE). (2022). Minimum Design Loads and Associated Criteria for Buildings and Other Structures. Reston, VA: American Society of Civil Engineers.

Chou, C.-C. Chung, P.-T. and Cheng, Y.-T. (2016). "Experimental Evaluation of Large-Scale Dual-Core Self-Centering Braces and Sandwiched Buckling-Restrained Braces," Engineering Structures, Vol. 116, pp. 12-25.

Earthquake Engineering Research Institute (EERI) (2019). "Functional Recovery: A Conceptual Framework with Policy Options – *white paper of the Earthquake Engineering Research Institute*," 21 pages, December 2019.

Federal Emergency Management Agency (FEMA) (2018a). Seismic Performance Assessment of Buildings – Volume 1: Methodology & Volume 2: Implementation Guide. 2nd edition, FEMA P-58-1 & FEMA P-58-2, December 2018.

Federal Emergency Management Agency (FEMA) (2018b). Building the Performance You Need – A Guide to State-of-the-Art Tools for Seismic Design and Assessment, FEMA P-58-7, December 2018.

Li, C.-H. Vidmar, Z. Saxey, B. Reynolds, M. and Uang, C.-M. (2022). "Procedure for Assessing Low-Cycle Fatigue Life of Buckling-Restrained Braces," *ASCE Journal of Structural Engineering*, Vol. 148, No. 2, 2022, pp. 04021259-1 to 04021259-15.

McCormick, J. Aburano, H., Ikenaga, M., and Nakashima, M. (2008). "Permissible residual deformation levels for building structures considering both safety and human elements." *Proceedings of the 14th World Conference of Earthquake Engineering* (14WCEE), Seismological Press, Beijing.

Ray-Chaudhuri, S. and Hutchinson, T. C. (2011). "Effect of Nonlinearity of Frame Buildings on Peak Horizontal Floor Acceleration," *Journal of Earthquake Engineering*, Vol. 15, No. 1, pp. 124–142, Jan. 2011.

Sahoo, D. R. and Chao, S.-H. (2015). "Stiffness-based Design for Mitigation of Residual Displacements of Buckling-restrained Braced Frames" *ASCE Journal of Structural Engineering*, Vol. 141, No. 9, pp. 04014229-1 to 04014229-13.

Tsampras, G., Sause, R. Zhang, D., Fleischman, R. B., Restrepo, J. I., Mar, D., and Maffei, J. (2016). "Development of Deformable Connection for Earthquake-Resistant Buildings to Reduce Floor Accelerations and Force Responses," *Earthquake Engineering & Structural Dynamics*, Vol. 45, No. 9, pp. 1473–1494, Jul. 2016,

Prof. Tung-Yang Chen

National Cheng Kung University, Taiwan

Topic： Seismic Composite Metamaterials: An Overview

(The material of the speaker's presentation has not been authorized for publication in the proceedings.)

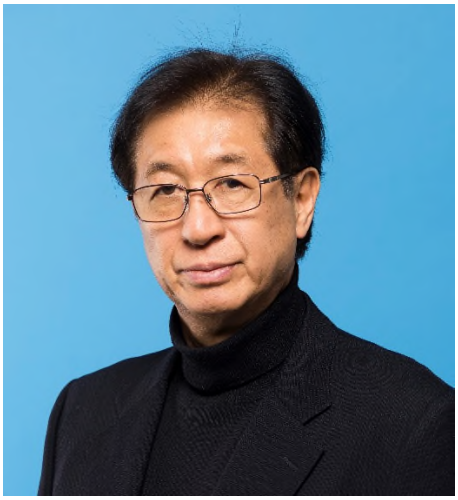

Prof. Kazuhiko Kasai

Tokyo Institute of Technology, Japan

Topic：Method to Greatly Reduce DOF for Fast Dynamic Analysis of Super-Tall Building with/without Dampers

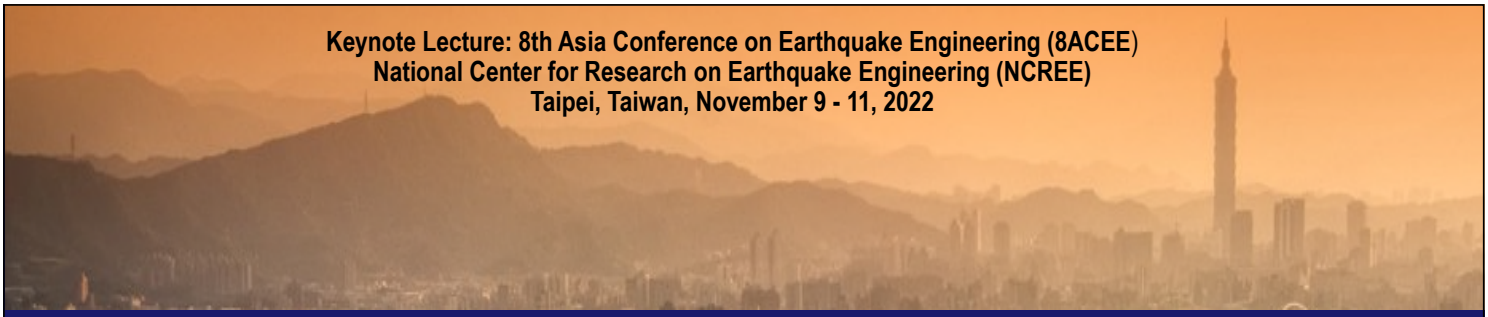

Keynote Lecture: 8th Asia Conference on Earthquake Engineering (8ACEE)
National Center for Research on Earthquake Engineering (NCREE)
Taipei, Taiwan, November 9 - 11, 2022

Method to Greatly Reduce DOF for Fast Dynamic Analysis of Super-Tall Building with/without Dampers

Kazuhiko KASAI
Professor Emeritus, Tokyo Institute of Technology

Yu MU
Post-Doctoral Researcher, Tokyo Institute of Technology

Acknowledgement:

This study was conducted jointly by Tokyo Institute of Technology and Takenaka Corporation who was the designer & contractor of Japan's tallest building "Abeno Harukas".

The financial support from Takenaka Corporation is greatly appreciated. The members are Dr. Watai, Mr. Maeda, Mr. Oka, Mr. Suzuki, Mr. Iino, and Dr. Nakai of Takenaka Corporation, and Prof. Kasai, Prof. Sato, and Dr. Mu from Tokyo Institute of Technology.

Method to Greatly Reduce DOF for Fast Dynamic Analysis of Super-Tall Building with/without Dampers

- Super-tall buildings are increasingly constructed. For bidding the project, good design (performance/economy) must be proposed (i.e., promised) within limited time.
- Thus, efficient and accurate dynamic analysis scheme is needed for preliminary design iterations against earthquake/wind.
- Analysis using member-to-member (M) model is time-consuming, and not suitable for such design iterations.
- Reduced models like shear (S) model / bending-shear (B) model calculate story shear, overturning-moment, drifts, accelerations, and ductilities much faster.

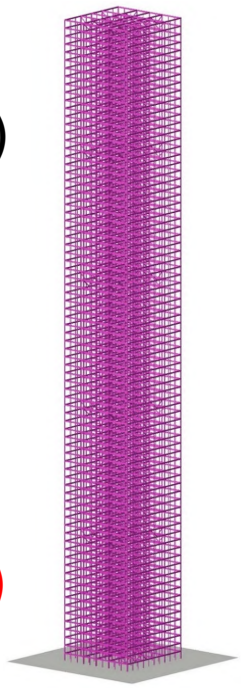

Member-to-member (M-) Model (400m : 14,377DOF)

8 hrs. by mainframe computer

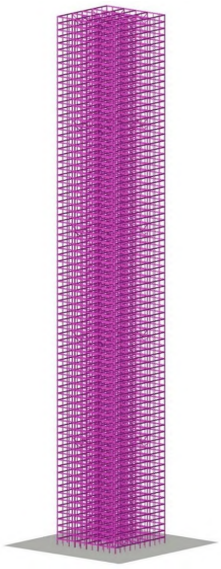

Member-to-member (M) model
400m (80-story) : 14,377 DOF

40 sec. by PC

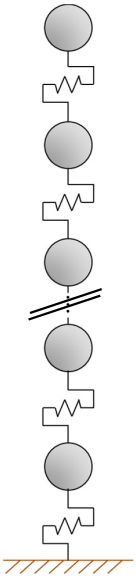

Shear (S) model
N = 80 DOF, only 0.6%

1 min. by PC

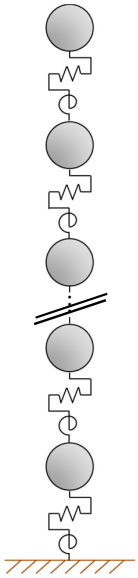

Bending-shear (B) model
2N = 160 DOF, only 1.1%

5

Method to Greatly Reduce DOF for Fast Dynamic Analysis of Super-Tall Building with/without Dampers

6

Damped 43-Story Bldg.（Viscous Wall）

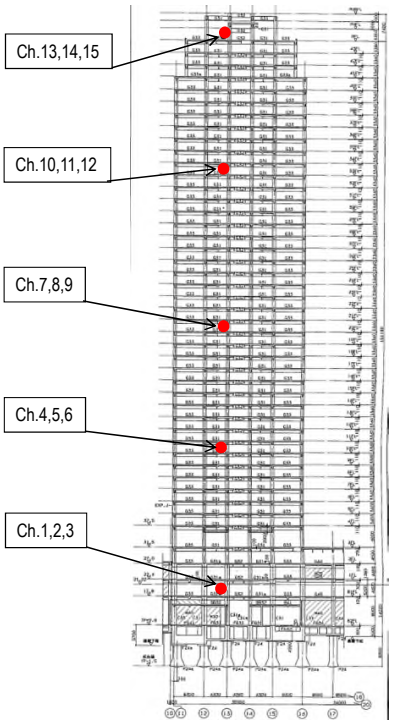

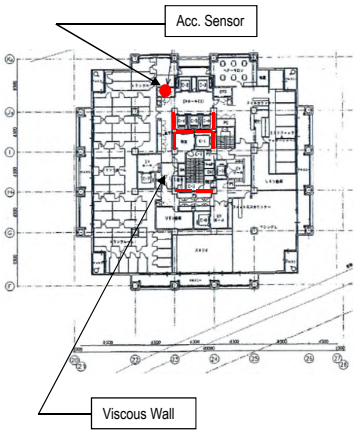

- 43-Story(+ 2-story basement and 2-story tower)
- Total building area: 7,337m^2
  Total floor area: 49,567m^2
- Column : CFT
- Beam : SRC & S
- Viscous wall No.: 344
- Viscous walls are installed between 1st floor and 43th floor in both X- and Y- Directions.

Damped 43-Story Bldg.

Viscous Wall

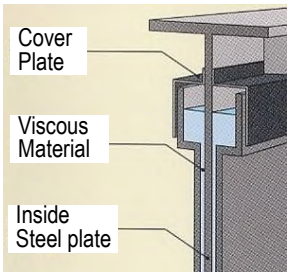

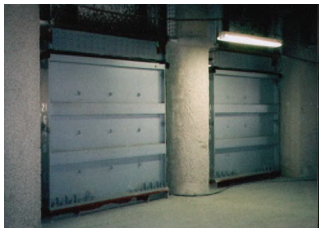

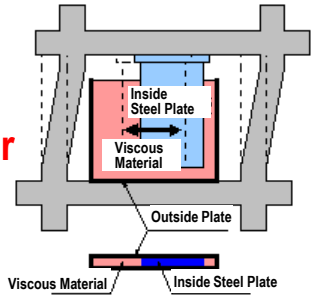

Shear drift causes damper deformation.

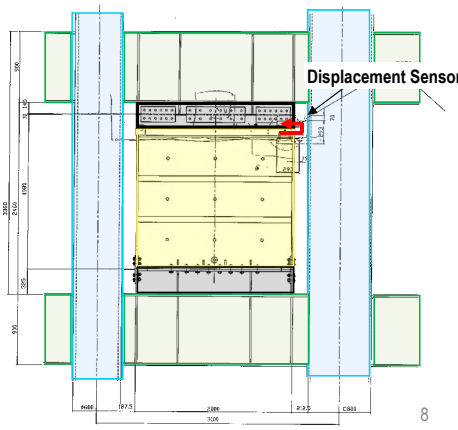

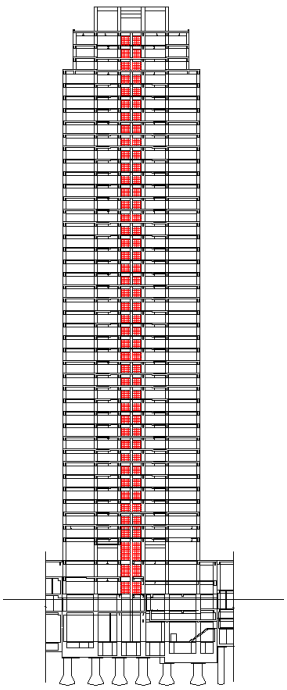

8

Both local and global responses were recorded in April 11, 2011 (One month after the 2011 Tohoku Earthquake)

Record (—) vs. Analysis (—) using $S^{(1)}$ model with dampers

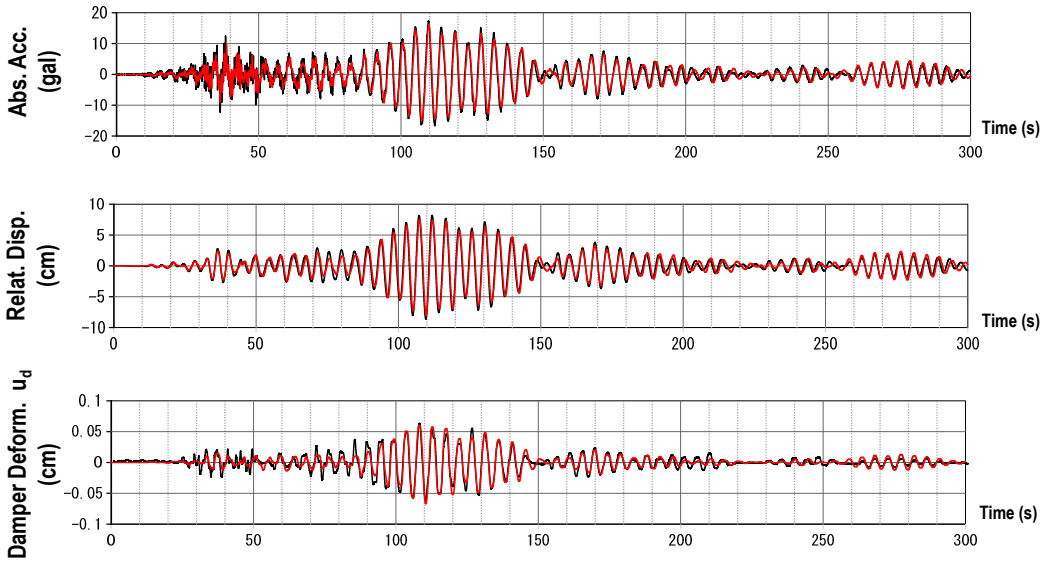

Damper deformation ≈ only 0.2 times the story drift at the upper story !

Simple shear (S) model is found to work well for local (damper u_d) and global simulations !

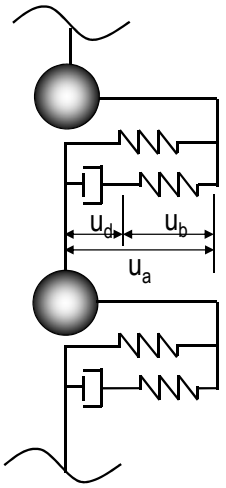

Method to Greatly Reduce DOF for Fast Dynamic Analysis of Super-Tall Building with/without Dampers

1. Introduction
   - 1.1 Member-to-member (M) model and reduced (S & B) models
   - 1.2 Example performance of S model with dampers
2. Reduced Models without Dampers
   - 2.1 Shear (S) model vs. Mode-matched Shear ($S^{(1)}$) model
   - 2.2 Bending-shear (B) model vs. Mode-matched Bending-shear ($B^{(1)}$) model
3. NR-$B^{(1)}$ model with Dampers
   - 3.1 No-damper / Rigid-damper (N/R) states
   - 3.2 NR-$B^{(1)}$ model for continuous / discrete distributions of dampers
4. Conclusions

Example Buildings

- Super tall building with height 80 to 400m, aspect ratio 1.6 to 8.0.
- Variations by removing/adding core frame and outrigger.

Model		80m	150m	300m	400m
Height	(m)	82.0	146.1	300.0	400.0
Plan	(m)	51.2 × 35.2	64.8 × 28.8	50.0 × 50.0	50.0 × 50.0
Aspect ratio	-	1.6	2.3	6.0	8.0
Story	-	20	37	60	80
1st mode natural period	(s)	3.648	4.852	5.288	6.938
Natural period / Height	(s/m)	0.044	0.033	0.018	0.017

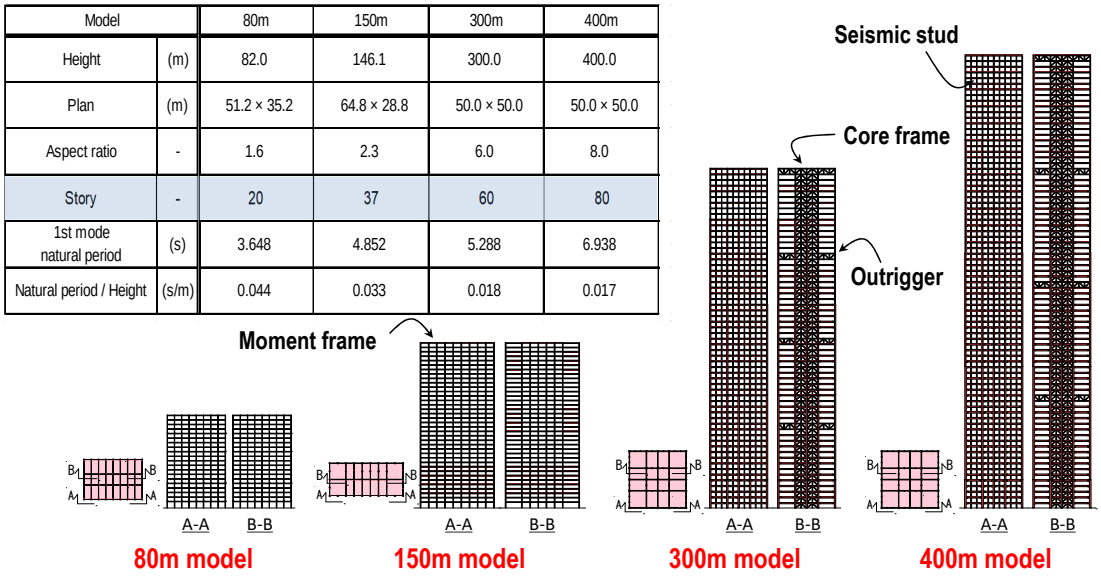

In the super-tall building having high aspect ratio, bending disp. Is large at upper story levels (rigid body disp. due to rotation θ_i of lower story levels).

Up to 30 to 40 story building, however, the most simple shear (S) model (shear beam) can simulate well the total of shear and bending drifts.

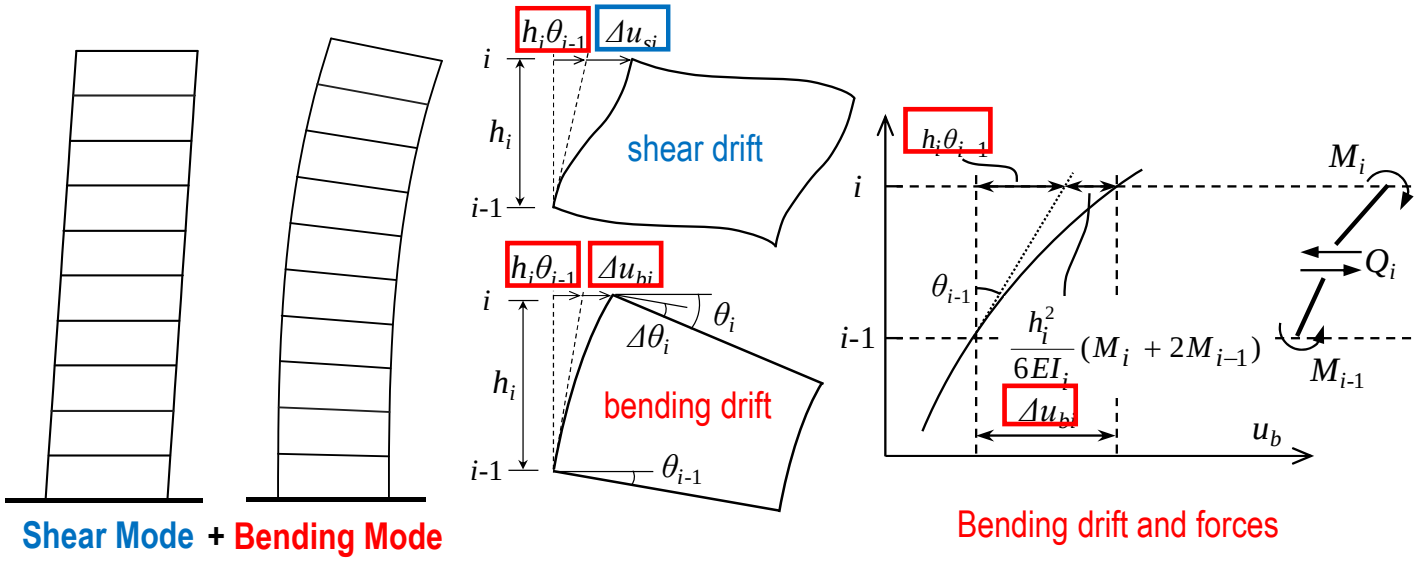

Shear Mode + Bending Mode

Bending drift and forces

S model

Apply design shear Q_i to M model. Get drift Δu_i and shear stiffness K_{siUse}

$$K_{si} = Q_i / \Delta u_i \quad , \quad \Delta u_i = u_i - u_{i-1}$$

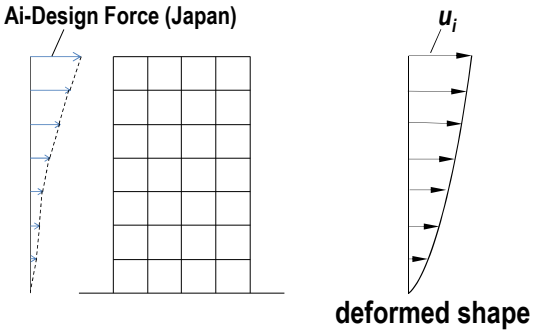

S(1) model

Use 1st mode shear $Q_i^{(1)}$ of M model. Get shear stiffness K_{si} using 1st mode drift $\Delta\phi_{i1}$ ($K\varphi_1 = \omega_1^2 M\varphi_1$)

$$Q_i^{(1)} = \sum_{k=i}^{N} F_k^{(1)} = \omega_1^2 \sum_{k=i}^{N} (m_k \varphi_{k1})$$

$$K_{si} = Q_i^{(1)} / \Delta\phi_{i1} \quad , \quad \Delta\phi_{i1} = \varphi_{i1} - \varphi_{i-1,1}$$

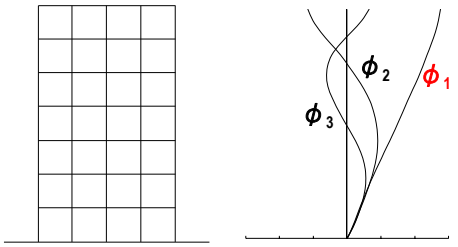

Vibration Periods of M-, S-, S(1)-, B-, and B(1)-models

Height	80m			150m			300m			400m		
Period	T_1 (s)	T_2 (s)	T_3 (s)	T_1 (s)	T_2 (s)	T_3 (s)	T_1 (s)	T_2 (s)	T_3 (s)	T_1 (s)	T_2 (s)	T_3 (s)
M-model	3.648	1.357	0.811	4.852	1.684	0.999	5.288	1.611	0.838	6.938	2.152	1.133
S-model	3.650 (1.00)	1.391 (1.03)	0.850 (1.05)	4.855 (1.00)	1.747 (1.04)	1.073 (1.07)	5.192 (0.98)	2.032 (1.26)	1.288 (1.54)	6.606 (0.95)	2.825 (1.31)	1.750 (1.54)
S(1)-model	3.648 (1.00)	1.397 (1.03)	0.856 (1.06)	4.852 (1.00)	1.761 (1.05)	1.089 (1.09)	5.288 (1.00)	2.231 (1.38)	1.421 (1.70)	6.938 (1.00)	3.093 (1.44)	1.969 (1.74)
B-model	3.649 (1.00)	1.365 (1.01)	0.825 (1.02)	4.852 (1.00)	1.694 (1.01)	1.019 (1.02)	5.089 (0.96)	1.565 (0.97)	0.823 (0.98)	6.491 (0.94)	2.068 (0.96)	1.091 (0.96)
B(1)-model	3.648 (1.00)	1.356 (1.00)	0.816 (1.01)	4.852 (1.00)	1.680 (1.00)	1.002 (1.00)	5.288 (1.00)	1.627 (1.01)	0.892 (1.06)	6.938 (1.00)	2.145 (1.00)	1.149 (1.01)

Note: ( ) = Each period / M-model period , = ±3% or more error

S model vs. $S^{(1)}$ model

Participation vectors $\beta_i \Phi_i (i = 1 \text{ to } 3)$ — M model — S model — $S^{(1)}$ model

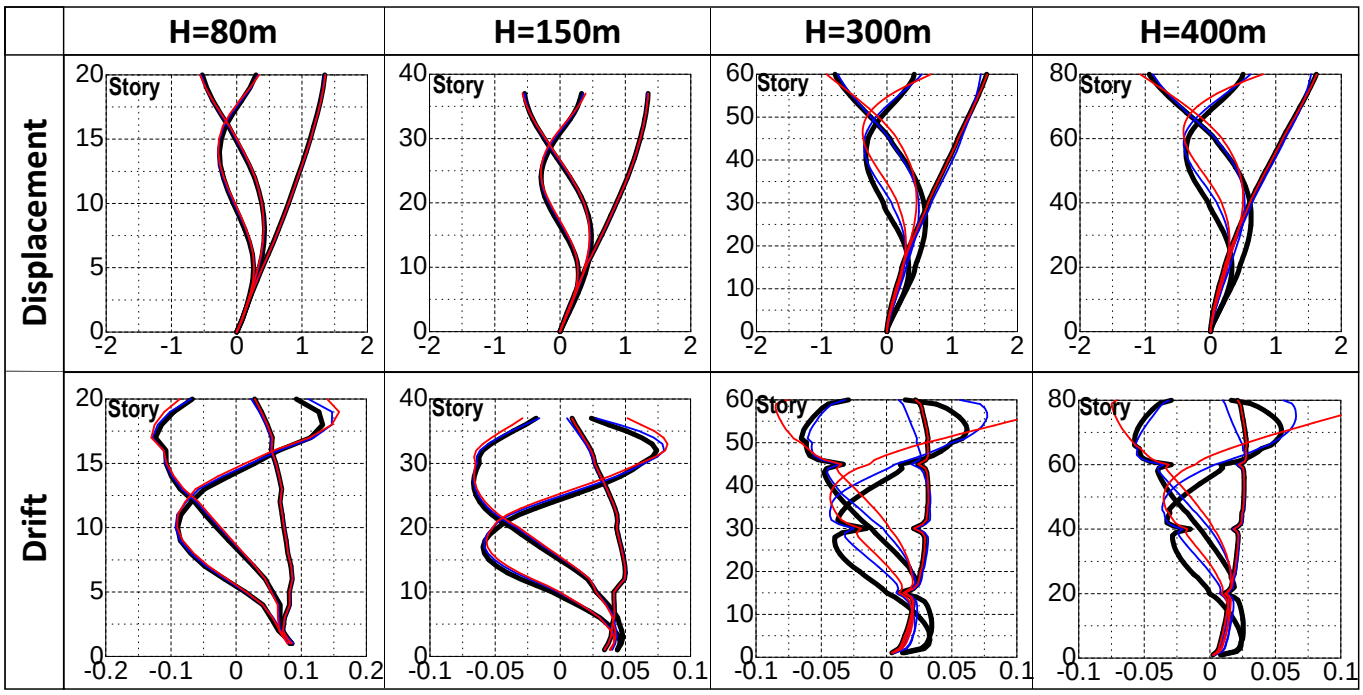

S model vs. $S^{(1)}$ model

Participation vectors $\beta_i \Phi_i (i = 1 \text{ to } 3)$ — M model — S model — $S^{(1)}$ model

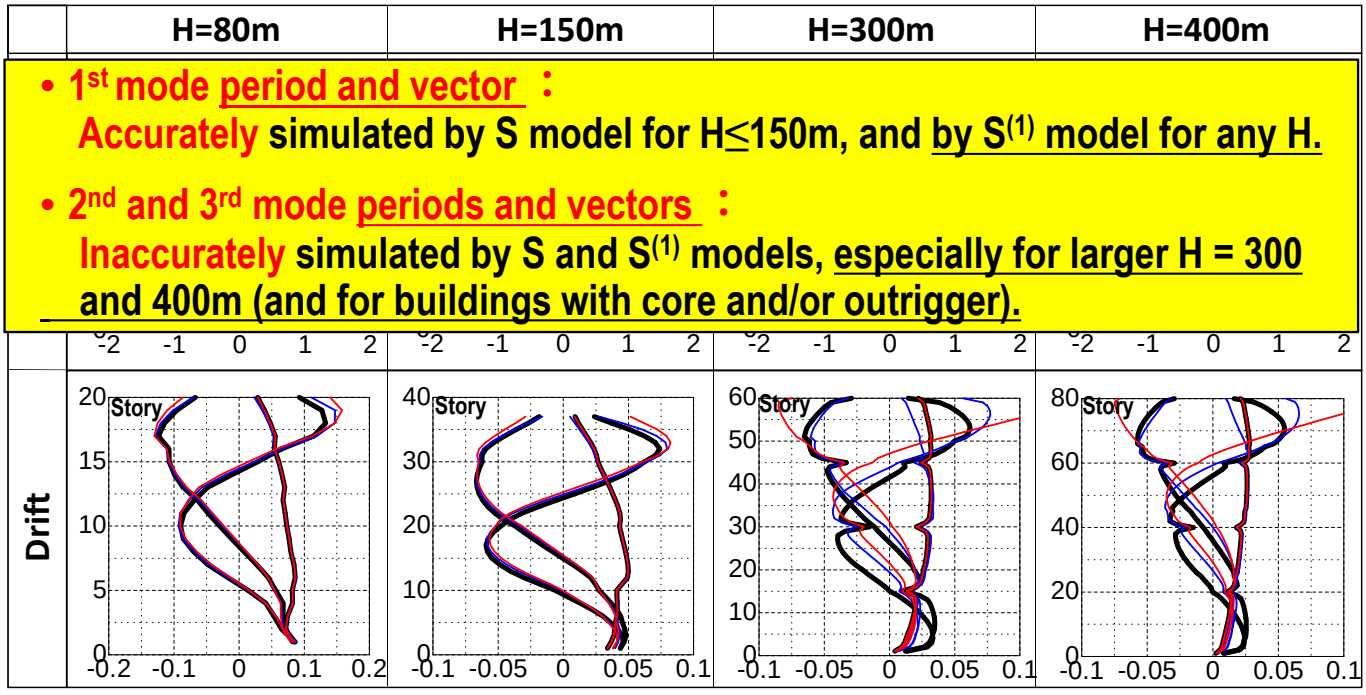

- 1st mode period and vector ：
  Accurately simulated by S model for H≤150m, and by $S^{(1)}$ model for any H.
- 2nd and 3rd mode periods and vectors ：
  Inaccurately simulated by S and $S^{(1)}$ models, especially for larger H = 300 and 400m (and for buildings with core and/or outrigger).

S model vs. S(1) model Building H=150m

Time histories (BCJ-L2)

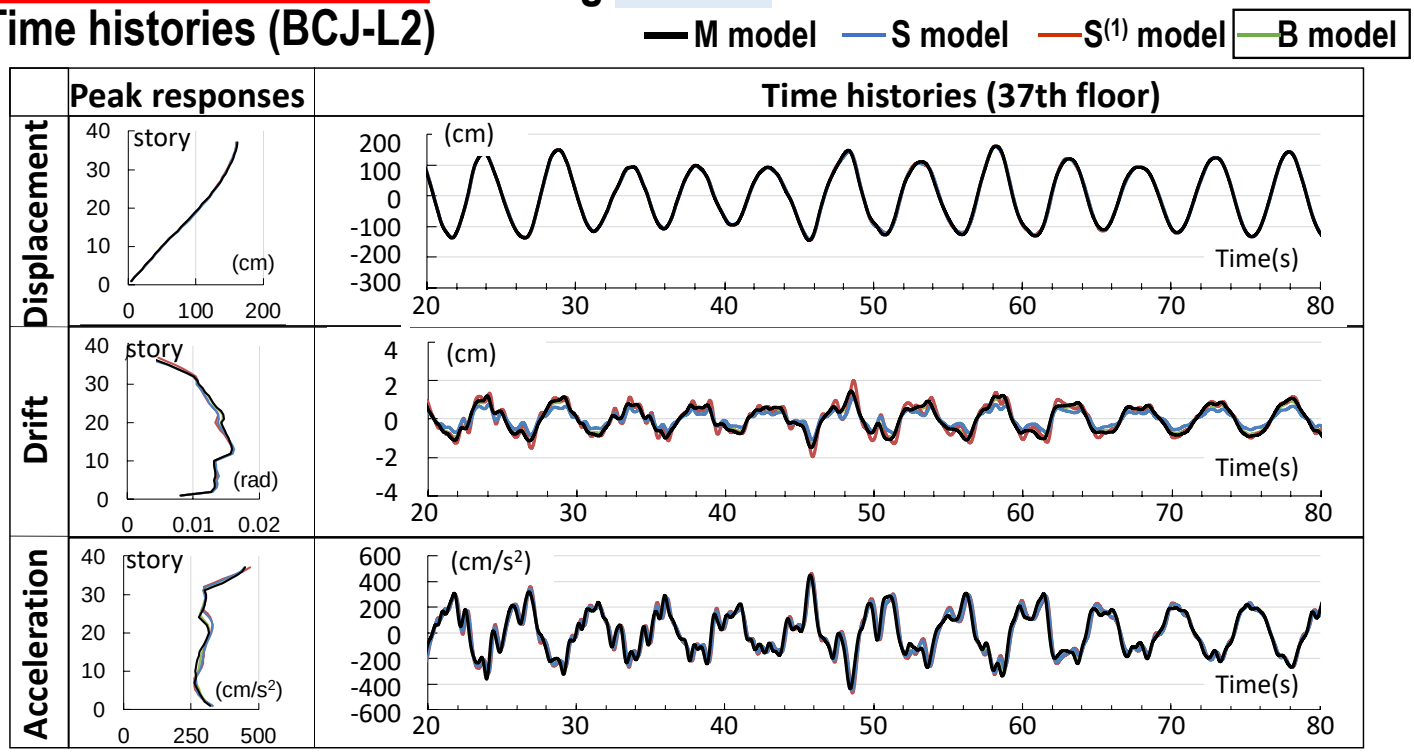

S model vs. S(1) model Building H=400m

Time histories (BCJ-L2)

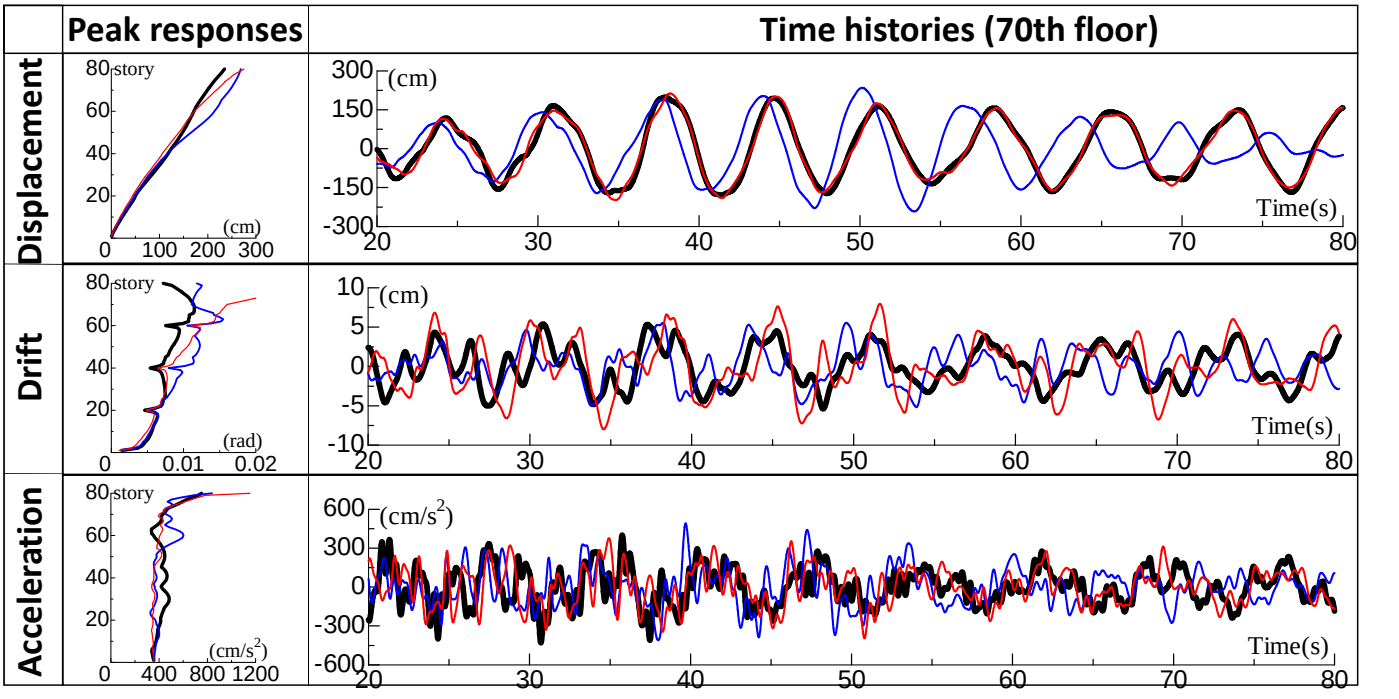

S model vs. $S^{(1)}$ model Building H=400m

Time histories (BCJ-L2)

— M model — S model — $S^{(1)}$ model

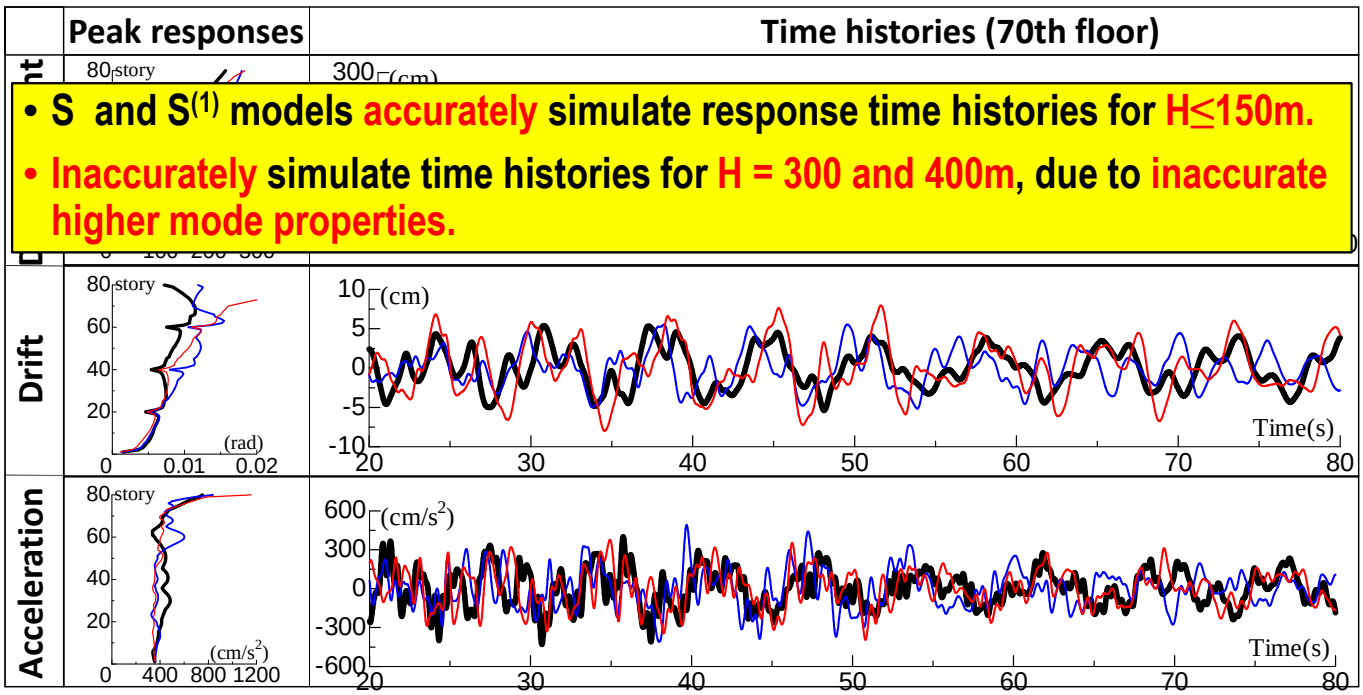

Method to Greatly Reduce DOF for Fast Dynamic Analysis of Super-Tall Building with/without Dampers

1. Introduction
   - 1.1 Member-to-member (M) model and reduced (S & B) models
   - 1.2 Example performance of S model with dampers
2. Reduced Models without Dampers
   - 2.1 Shear (S) model vs. Mode-matched Shear ($S^{(1)}$) model
   - 2.2 Bending-shear (B) model vs. Mode-matched Bending-shear ($B^{(1)}$) model
3. NR-$B^{(1)}$ model with Dampers
   - 3.1 No-damper / Rigid-damper (N/R) states
   - 3.2 NR-$B^{(1)}$ model for continuous / discrete distributions of dampers
4. Conclusions

In the super-tall building having high aspect ratio, bending mode tends to govern at upper story levels.

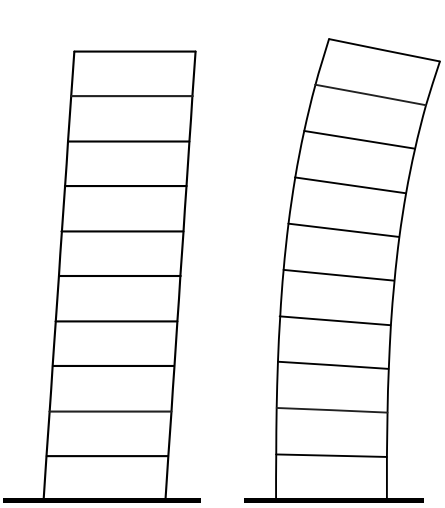

Shear Mode + Bending Mode

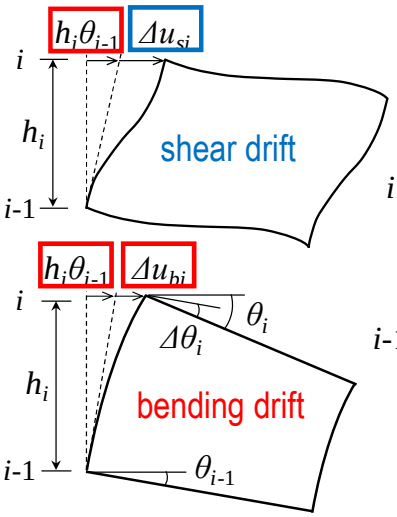

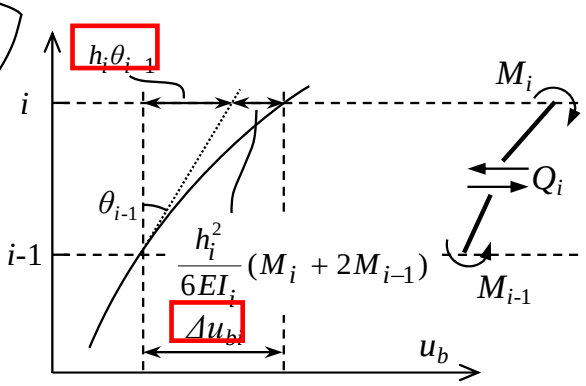

Bending drift and forces

B Model (Muto et al. 1979)

1. Analysis of M Model

- Apply design shear Q_i and get total drift Δu_i
- Get equiv. story rotation matching total strain energies of all vertical members.
- Get energy-equivalent beam EI_{ei}

$$\Delta\theta_{ei} = \sum_{j=1}^{s_i}\left(N_{ij}\Delta v_{ij}\right)\Big/\sum_{j=1}^{s_i}\left(N_{ij}l_{ij}\right)$$

$$EI_{ei} = h_i\left(M_{i+1}+M_i\right)/2\Delta\theta_{ei}$$

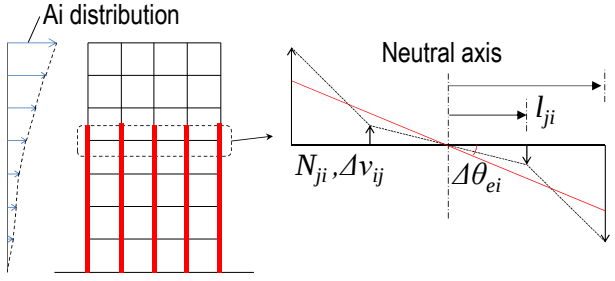

B(1) Model (Kasai et al. 2021)

1. Analysis of M Model

- Apply pure moment M at top of M model.
- Get curvature from story displacement.
- Get beam EI_i

$$p_i = 2\left(\Delta u_{bi} - h_i\theta_{i-1}\right)/h_i^2 \qquad \theta_i = \theta_{i-1} + h_i p_i$$

$$EI_i = M_0/p_i$$

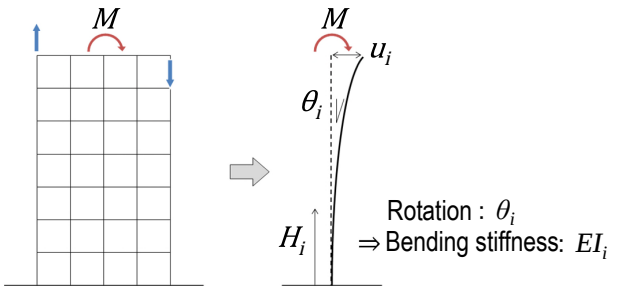

B model (Muto et al. 1979)

2. Making B Model

- Get bending drift Δu_{bi} by beam formula & EI_{ei}
- Get shear drift $\Delta u_{si} = \Delta u_i - \Delta u_{bi}$
- Get shear stiffness $K_{si} = Q_i / \Delta u_{si}$

$$\Delta u_{bi} = \frac{h_i^2}{6EI_{ei}}\left(M_{i+1} + 2M_i\right) + h_i \sum_{k=1}^{i-1} \Delta\theta_k$$

$$K_{si} = Q_i \Big/ \left(\Delta u_i - \Delta u_{bi}\right)$$

$B^{(1)}$ model (Kasai et al. 2021)

2. Making $B^{(1)}$ Model

- Get bending drift $\Delta\phi_{bi}$ by beam formula & EI_i
- Get shear drift $\Delta\phi_{si} = \Delta\phi_i - \Delta\phi_{bi}$
- Get shear stiffness $K_{si} = Q_i^{(1)} / \Delta\phi_{si}$

$$\Delta\theta_{i1} = \frac{h_i}{2EI_i}\left(M_{i+1}^{(1)} + M_i^{(1)}\right)$$

$$\Delta\varphi_{bi} = \frac{h_i^2}{6EI_i}\left(M_{i+1}^{(1)} + 2M_i^{(1)}\right) + h_i \sum_{k=1}^{i-1} \Delta\theta_k$$

$$K_{si} = Q_i^{(1)} \Big/ \left(\Delta\varphi_i - \Delta\varphi_{bi}\right)$$

1st mode period and vector will exactly match with those of M model.

Do eigenvalue analysis of the $B^{(1)}$ model, and compare the 2nd mode period with M model.

Reduce EI_i and repeat above calculation till 2nd mode period matches, while maintaining exactness of 1st mode. Typical scaling factor for $EI_i \approx 0.8$ to 1.

For N-story bldg:

- $S^{(1)}$ model used N shear springs to match 1st mode shape and period.
- $B^{(1)}$ model uses N shear springs and N bending springs to match 1st mode shape and period, and additionally 2nd mode period.

$B^{(1)}$ model (Kasai et al. 2021)

2. Making $B^{(1)}$ Model

- Get bending drift $\Delta\phi_{bi}$ by beam formula & EI_i
- Get shear drift $\Delta\phi_{si} = \Delta\phi_i - \Delta\phi_{bi}$
- Get shear stiffness $K_{si} = Q_i^{(1)} / \Delta\phi_{si}$

$$\Delta\theta_{i1} = \frac{h_i}{2EI_i}\left(M_{i+1}^{(1)} + M_i^{(1)}\right)$$

$$\Delta\varphi_{bi} = \frac{h_i^2}{6EI_i}\left(M_{i+1}^{(1)} + 2M_i^{(1)}\right) + h_i \sum_{k=1}^{i-1} \Delta\theta_k$$

$$K_{si} = Q_i^{(1)} \Big/ \left(\Delta\varphi_i - \Delta\varphi_{bi}\right)$$

1st mode period and vector will exactly match with those of M model.

Do eigenvalue analysis of the $B^{(1)}$ model, and compare the 2nd mode period with M model.

Reduce EI_i and repeat above calculation till 2nd mode period matches, while maintaining exactness of 1st mode. Typical scaling factor for $EI_i \approx 0.8$ to 1.

Vibration Periods of M-, S-, $S^{(1)}$-, B-, and $B^{(1)}$-models

Height	80m			150m			300m			400m		
Period	T_1 (s)	T_2 (s)	T_3 (s)	T_1 (s)	T_2 (s)	T_3 (s)	T_1 (s)	T_2 (s)	T_3 (s)	T_1 (s)	T_2 (s)	T_3 (s)
M-model	3.648	1.357	0.811	4.852	1.684	0.999	5.288	1.611	0.838	6.938	2.152	1.133
S-model	3.650 (1.00)	1.391 (1.03)	0.850 (1.05)	4.855 (1.00)	1.747 (1.04)	1.073 (1.07)	5.192 (0.98)	2.032 (1.26)	1.288 (1.54)	6.606 (0.95)	2.825 (1.31)	1.750 (1.54)
$S^{(1)}$-model	3.648 (1.00)	1.397 (1.03)	0.856 (1.06)	4.852 (1.00)	1.761 (1.05)	1.089 (1.09)	5.288 (1.00)	2.231 (1.38)	1.421 (1.70)	6.938 (1.00)	3.093 (1.44)	1.969 (1.74)
B-model	3.649 (1.00)	1.365 (1.01)	0.825 (1.02)	4.852 (1.00)	1.694 (1.01)	1.019 (1.02)	5.089 (0.96)	1.565 (0.97)	0.823 (0.98)	6.491 (0.94)	2.068 (0.96)	1.091 (0.96)
$B^{(1)}$-model	3.648 (1.00)	1.356 (1.00)	0.816 (1.01)	4.852 (1.00)	1.680 (1.00)	1.002 (1.00)	5.288 (1.00)	1.627 (1.01)	0.892 (1.06)	6.938 (1.00)	2.145 (1.00)	1.149 (1.01)

Note: ( ) = Each period / M-model period , = ±3% or more error

B model vs. $B^{(1)}$ model

Participation vectors $\beta_i \Phi_i (i = 1 \text{ to } 3)$ — M model — B model — $B^{(1)}$ model

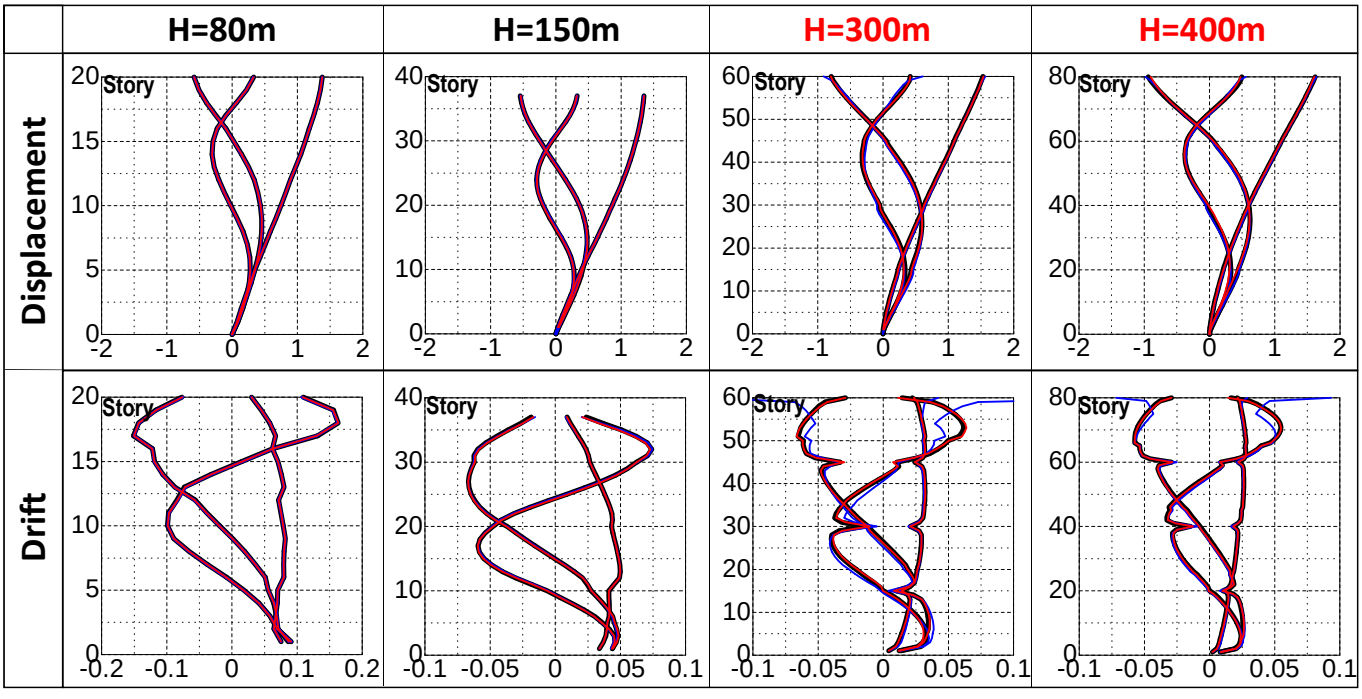

B model vs. $B^{(1)}$ model

Participation vectors $\beta_i \Phi_i (i = 1 \text{ to } 3)$ — M model — B model — $B^{(1)}$ model

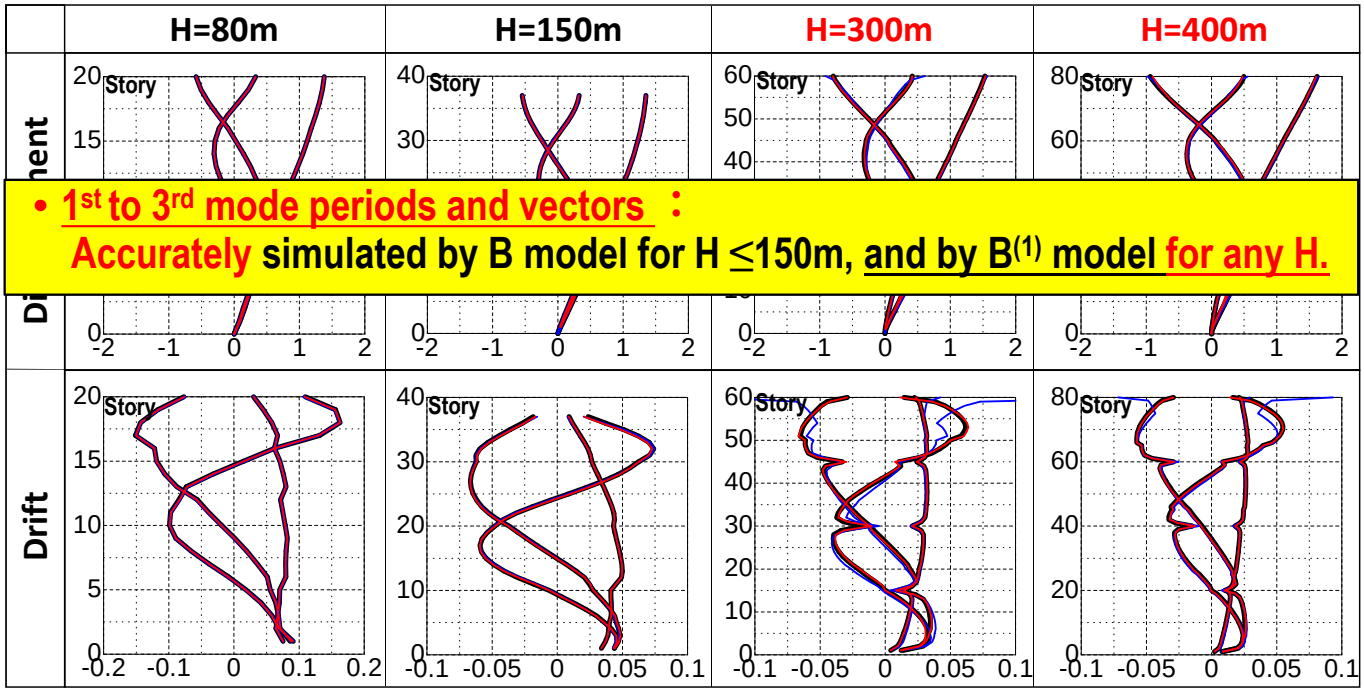

- 1st to 3rd mode periods and vectors : Accurately simulated by B model for H ≤150m, and by $B^{(1)}$ model for any H.

B model vs. $B^{(1)}$ model Building H=400m

Time histories (BCJ-L2) — M model — B model — $B^{(1)}$ model

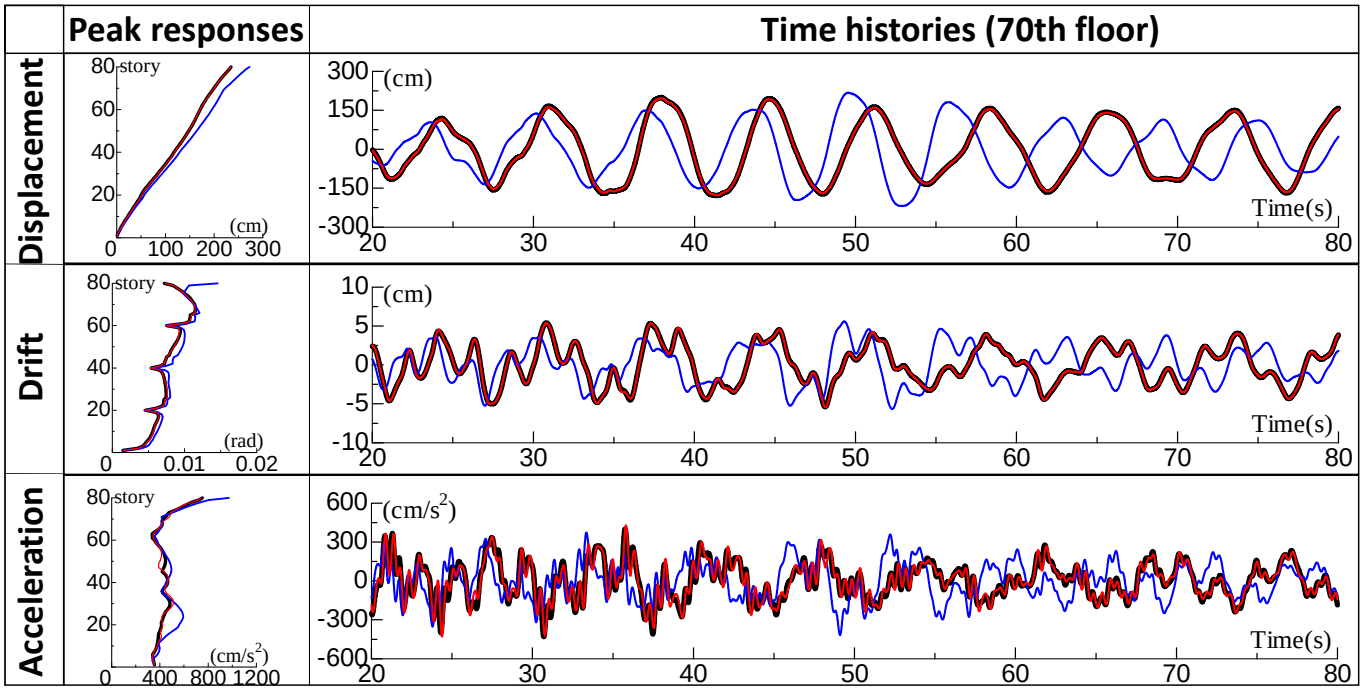

B model vs. $B^{(1)}$ model Building H=400m

Time histories (BCJ L2)

—M model —B model —$B^{(1)}$ model

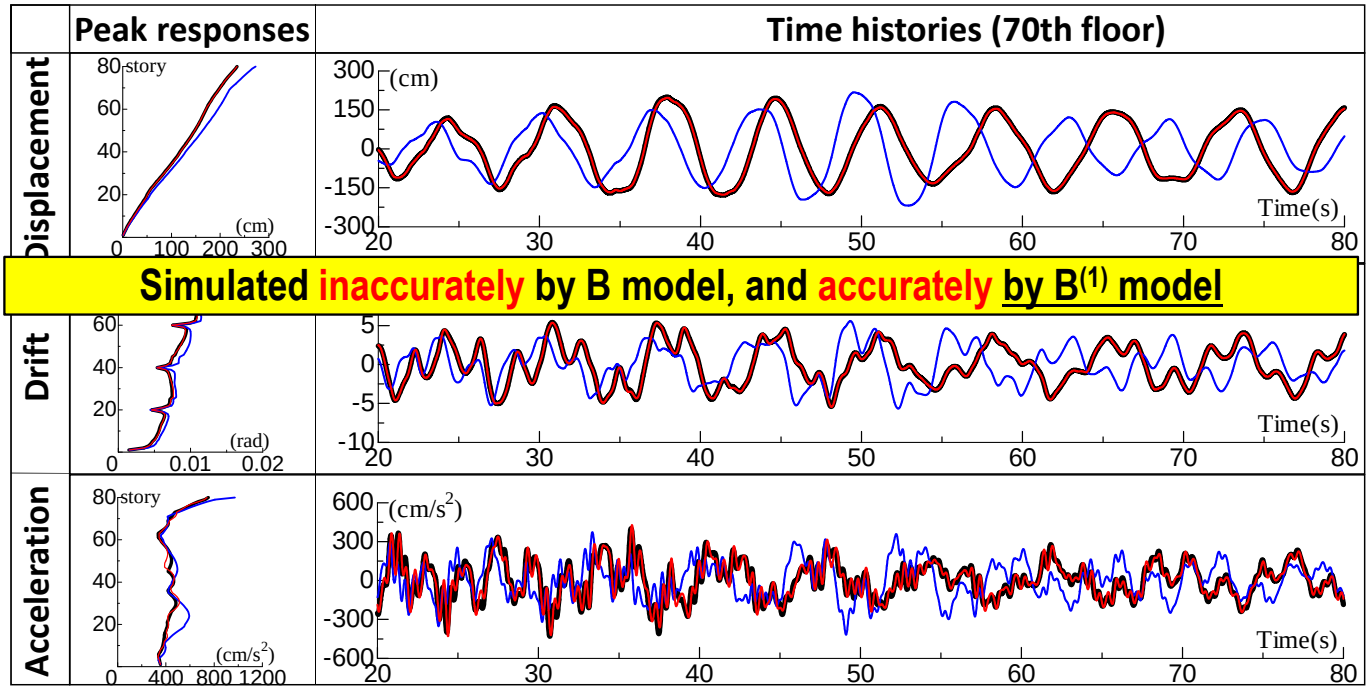

Response spectrurm(BCJ-L2 vs. JMA-Kobe, h=0.02)

BCJ-L2 (Building Center of Japan, Artificial Record for Level 2 Earthq.)

1995 JMA-Kobe Record

※ Periods specified: H= 400m, outrigger & core frame

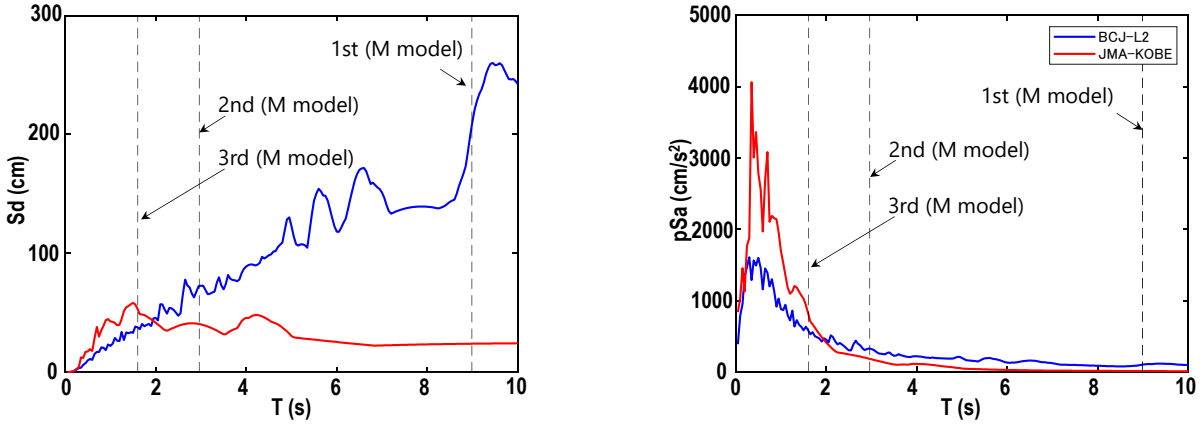

a) Displacement b) Pseudo Acceleration

Response spectrum（h=0.02）

Model accuracies for different earthquakes: 1995 JMA-Kobe record (Higher modes excited)

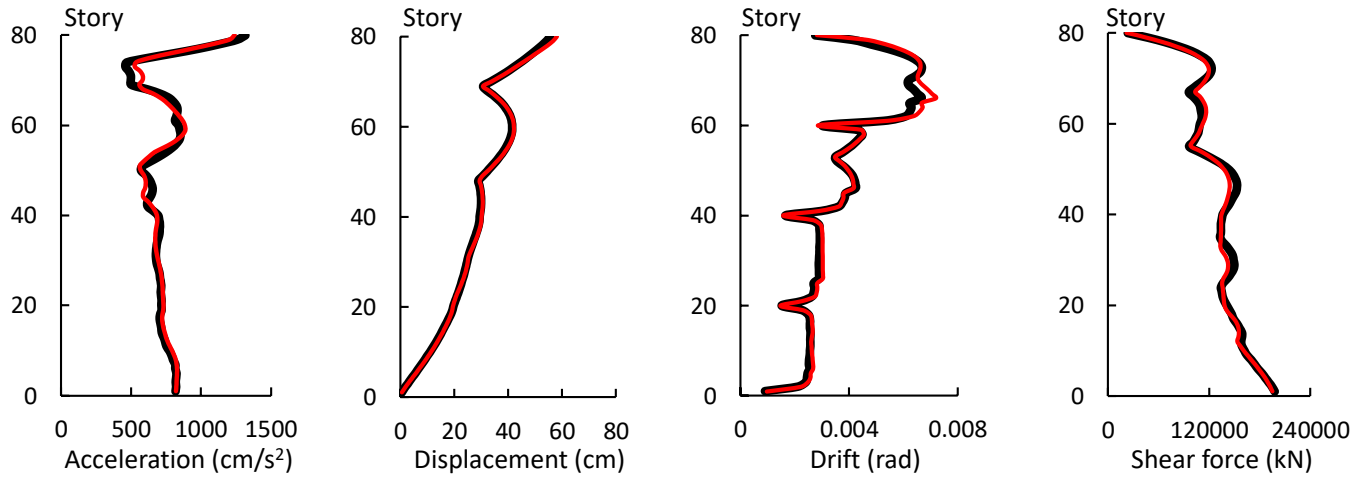

Earthquake responses of 400m Outrigger & Core frame

Response time histories of H=400m building (70th floor)

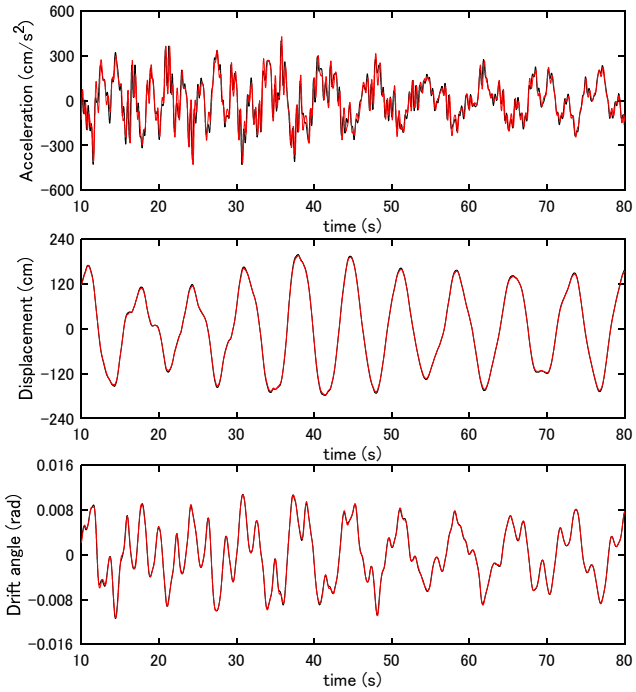

a) BCJ-L2 Artificial Earthq.

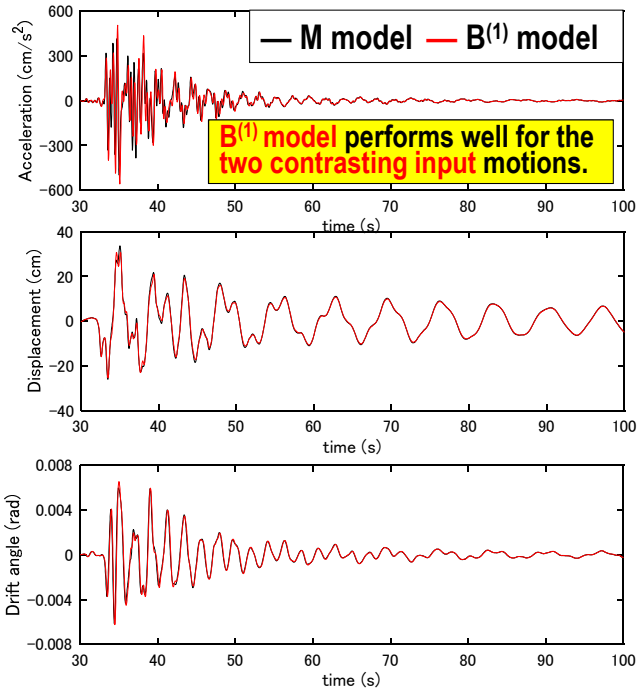

b) 1995 JMA-Kobe Record

Method to Greatly Reduce DOF for Fast Dynamic Analysis of Super-Tall Building with/without Dampers

Shear (S) Model + Dampers (Kasai & Iwasaki, 2006, Ishii & Kasai 2010)
Unique Static Condensation + Conversion to Spring Model

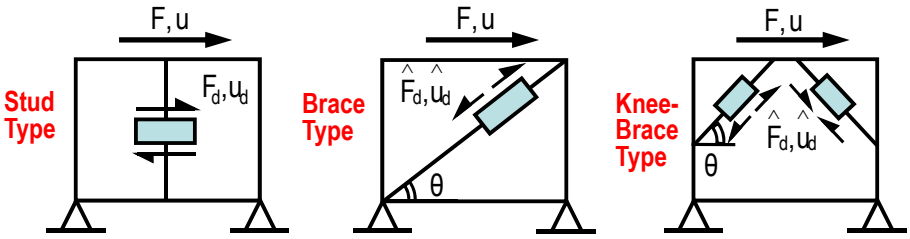

MDOF Frame

$$\begin{bmatrix} F \\ 0 \end{bmatrix} = \begin{bmatrix} K_{11} & K_{12} \\ K_{21} & K_d + K_{22} \end{bmatrix} \begin{bmatrix} u \\ u_d \end{bmatrix}$$

Spring Model

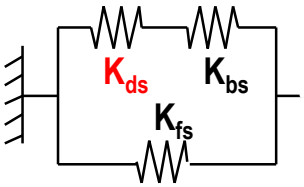

$$\begin{bmatrix} F_s \\ 0 \end{bmatrix} = \begin{bmatrix} K_{bs} + K_{fs} & -K_{bs} \\ -K_{bs} & K_{ds} + K_{bs} \end{bmatrix} \begin{bmatrix} u_s \\ u_{ds} \end{bmatrix}$$

States N/R analyses to convert M model to Shear (S) model.

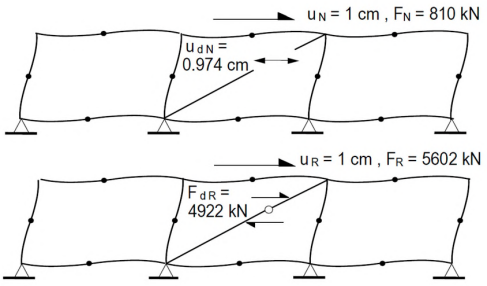

K_N = 810 kN/cm
α_N = 0.974

(a) 状態 N：ダンパー解除

K_R = 5602 kN/cm
α_R = 0.879

(b) 状態 R：ダンパー固定

States N & R analyses for brace-type dampers

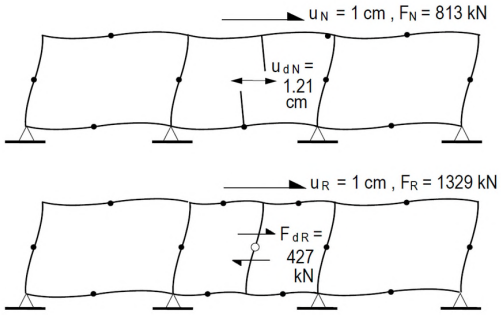

K_N = 813 kN/cm
α_N = 1.21

(a) 状態 N：ダンパー解除

K_R = 1329 kN/cm
α_R = 0.321

(b) 状態 R：ダンパー固定

States N & R analyses for stud- or panel-type dampers

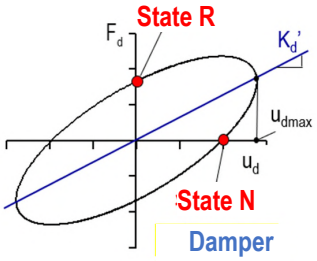

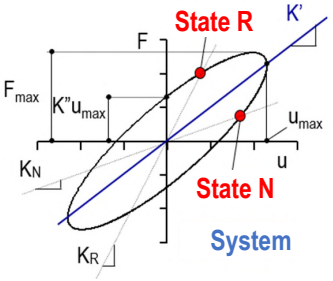

Phase difference between VE-damper and System

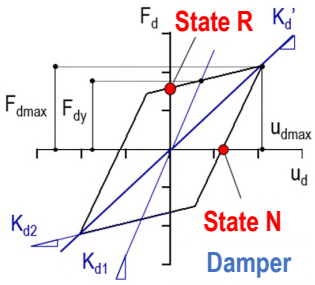

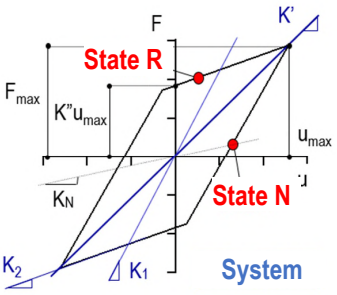

Phase difference between EP-damper and System

Tuning Mode-matched Bending-Shear ($B^{(1)}$) Model to Reflect Damper Effect

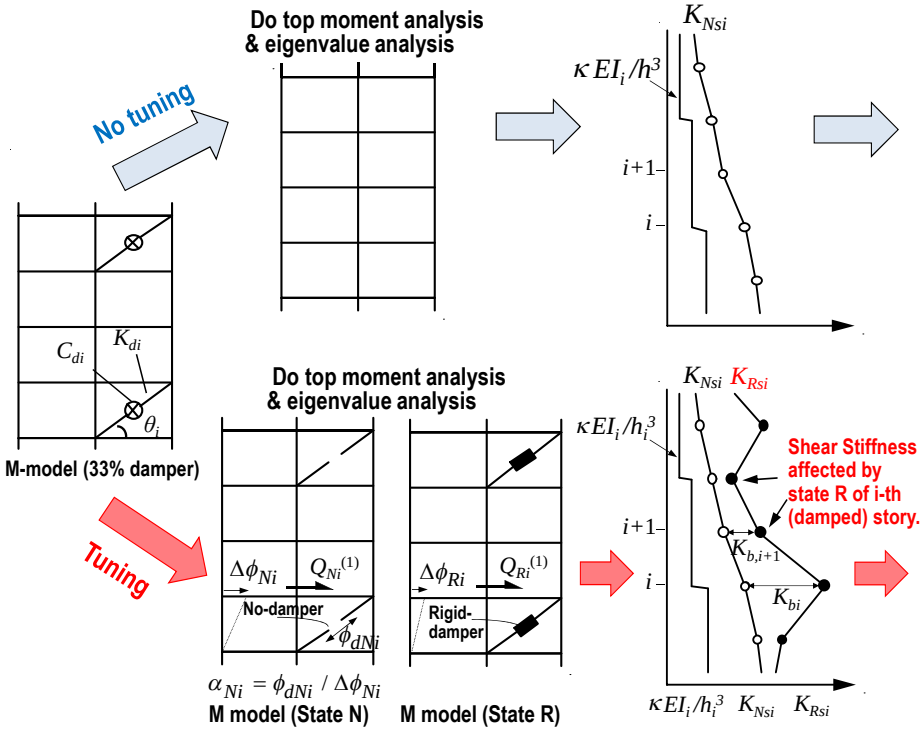

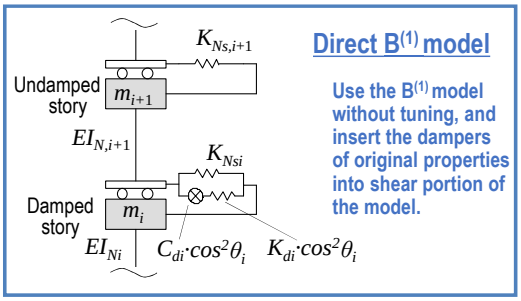

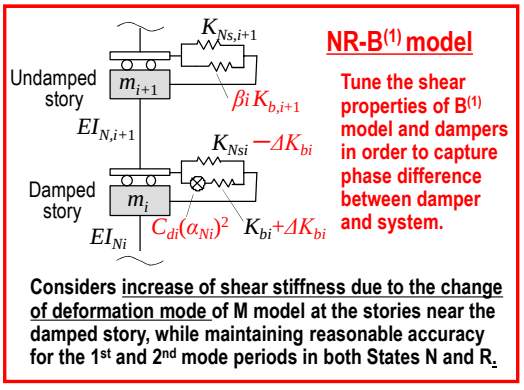

Considers increase of shear stiffness due to the change of deformation mode of M model at the stories near the damped story, while maintaining reasonable accuracy for the 1st and 2nd mode periods in both States N and R.

Details of Shear Stiffness Tuning

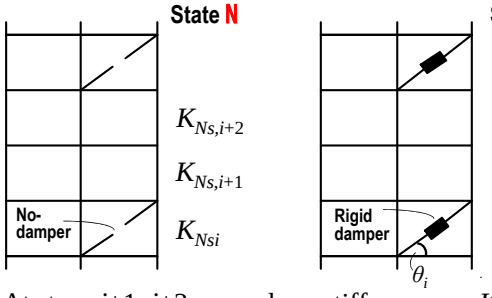

$K_{Rs,i+2}=K_{Ns,i+2}+K_{b,i+2}$

$K_{Rs,i+1}=K_{Ns,i+1}+K_{b,i+1}$

$K_{Rsi}=K_{Nsi}+K_{bi}$ ⇒ get equivalent brace deformation ratio $\lambda_i=\dfrac{C_{di}\alpha_{Ni}^2\omega}{K_{bi}}$

At damped story i, determine βi that will tune the shear stiffness of story i, i+1, i+2 …

$\beta_i=0.9\lambda_i$ (≤ 1)

∴ At story i+1, i+2, …, shear stiffness = $K_{Ns,i+1}+\beta_i K_{b,i+1}$, $K_{Ns,i+2}+\beta_i K_{b,i+2}$, …

At story i, shear stiffness = $K_{Nsi}-\beta_i(K_{b,i+1}+K_{b,i+2}+\cdots)$

brace stiffness = $K_{bi}+\beta_i(K_{b,i+1}+K_{b,i+2}+\cdots)$

Added component at story i

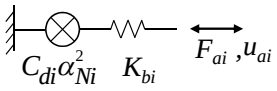

Storage stiffness $K'_{ai}=\dfrac{K_{bi}}{1+(1/\lambda_i)^2}$

Loss stiffness $K''_{ai}=\dfrac{C_{di}\alpha_{Ni}^2\omega}{1+\lambda_i^2}$

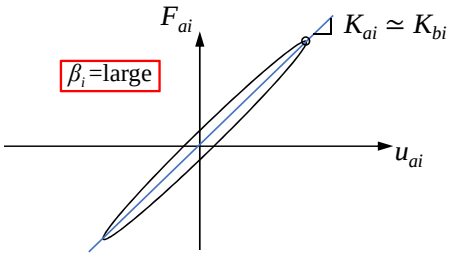

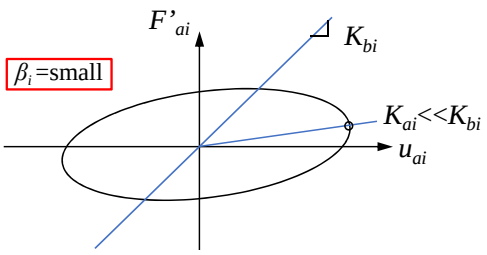

Method to Greatly Reduce DOF for Fast Dynamic Analysis of Super-Tall Building with/without Dampers

1. Introduction
   - 1.1 Member-to-member (M) model and reduced (S & B) models
   - 1.2 Example performance of S model with dampers
2. Reduced Models without Dampers
   - 2.1 Shear (S) model vs. Mode-matched Shear ($S^{(1)}$) model
   - 2.2 Bending-shear (B) model vs. Mode-matched Bending-shear ($B^{(1)}$) model
3. NR-$B^{(1)}$ model with Dampers
   - 3.1 No-damper / Rigid-damper (N/R) states
   - 3.2 NR-$B^{(1)}$ model for continuous / discrete distributions of dampers
4. Conclusions

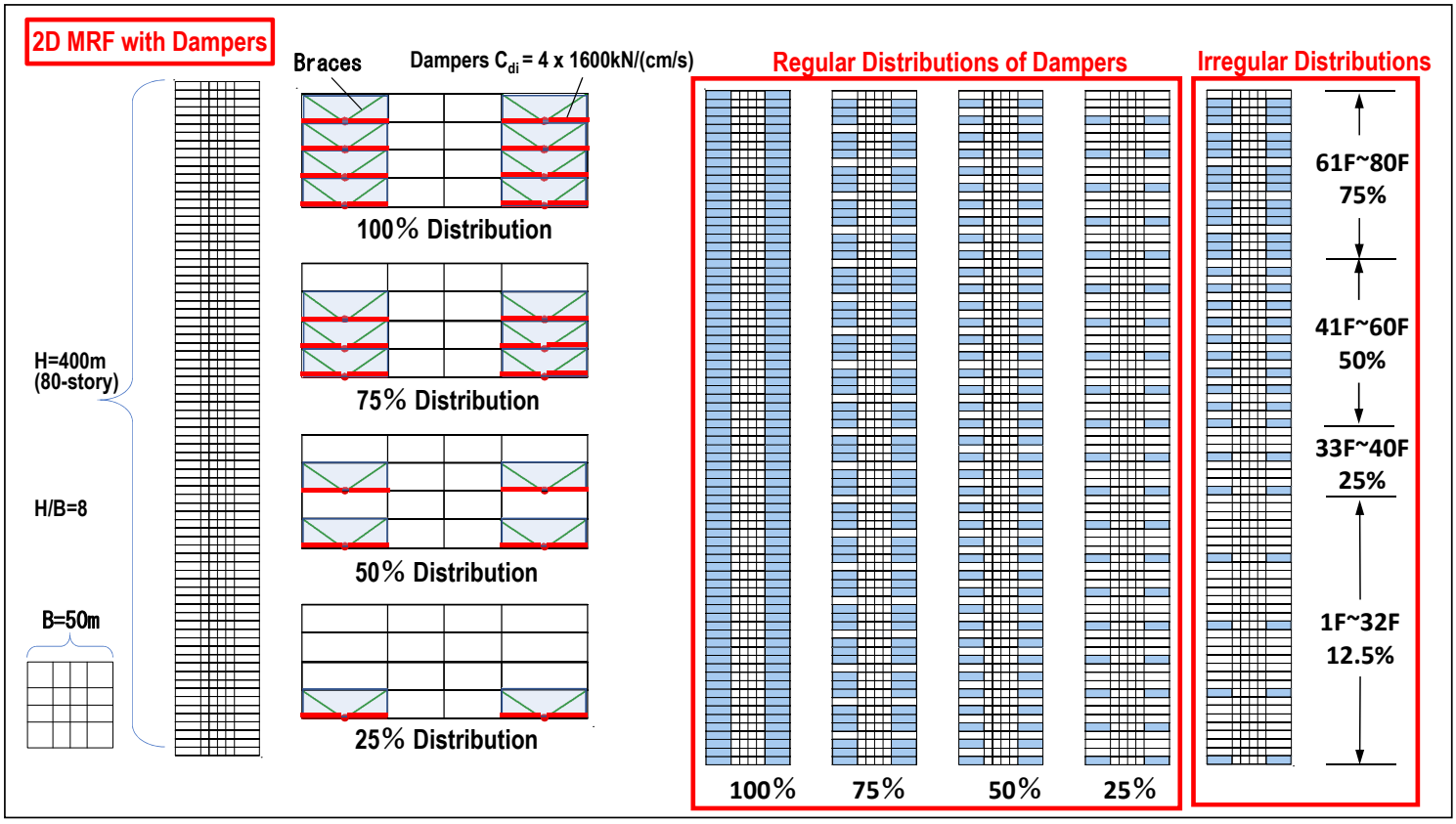
2D MRF with Dampers
Braces
Dampers C_{di} = 4 x 1600kN/(cm/s)
100% Distribution
75% Distribution
50% Distribution
25% Distribution
H=400m
(80-story)
H/B=8
B=50m
Regular Distributions of Dampers
100%
75%
50%
25%
Irregular Distributions
61F~80F
75%
41F~60F
50%
33F~40F
25%
1F~32F
12.5%

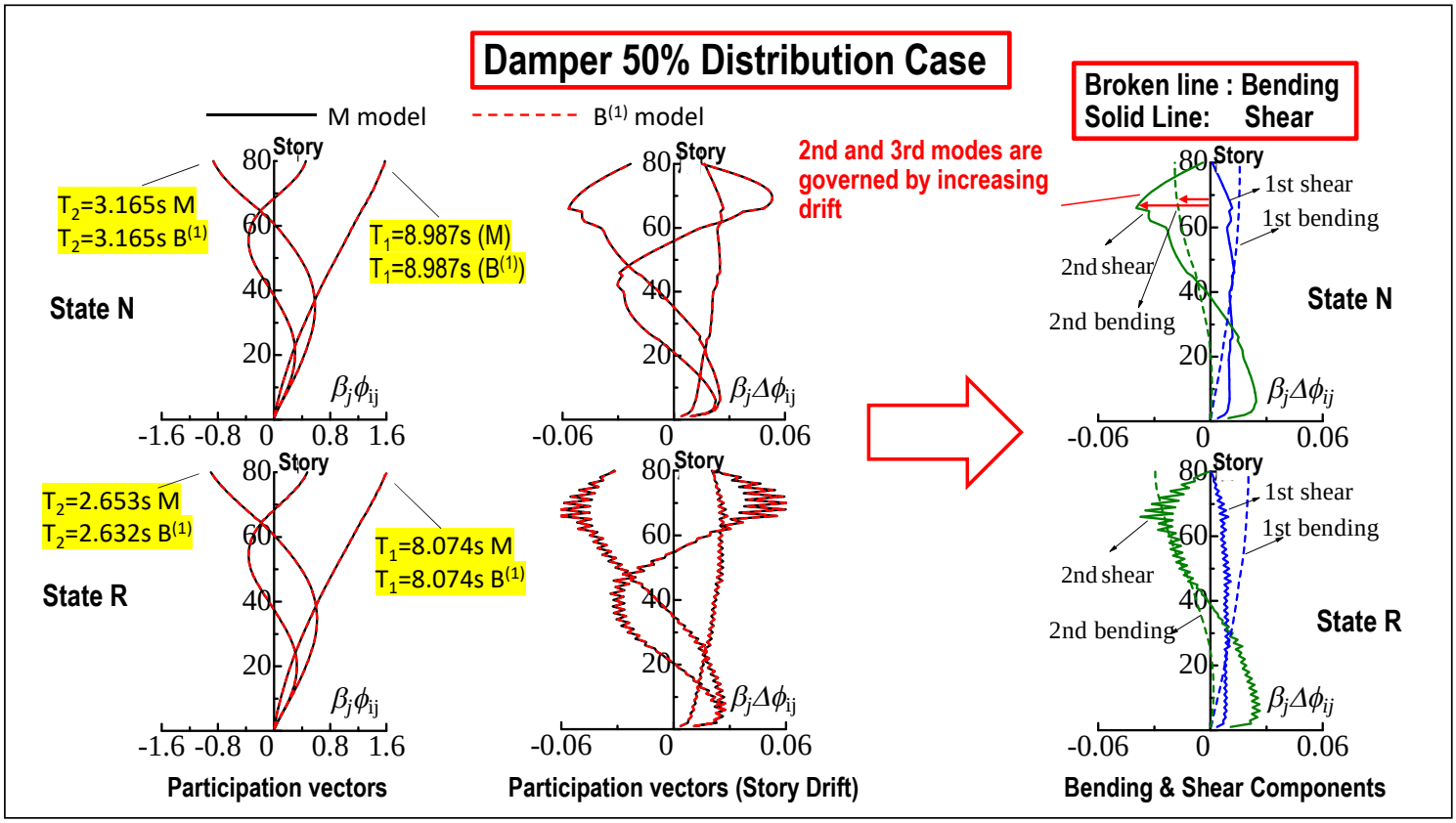
Damper 50% Distribution Case
M model
$B^{(1)}$ model
T_2=3.165s M
T_2=3.165s $B^{(1)}$
State N
T_1=8.987s (M)
T_1=8.987s ($B^{(1)}$)
T_2=2.653s M
T_2=2.632s $B^{(1)}$
State R
T_1=8.074s M
T_1=8.074s $B^{(1)}$
Story
$\beta_j\phi_{ij}$
$\beta_j\Delta\phi_{ij}$
Participation vectors
Participation vectors (Story Drift)
2nd and 3rd modes are governed by increasing drift
Broken line : Bending
Solid Line: Shear
1st shear
1st bending
2nd shear
2nd bending
Bending & Shear Components

Response reduction of different damper distributions H=400m

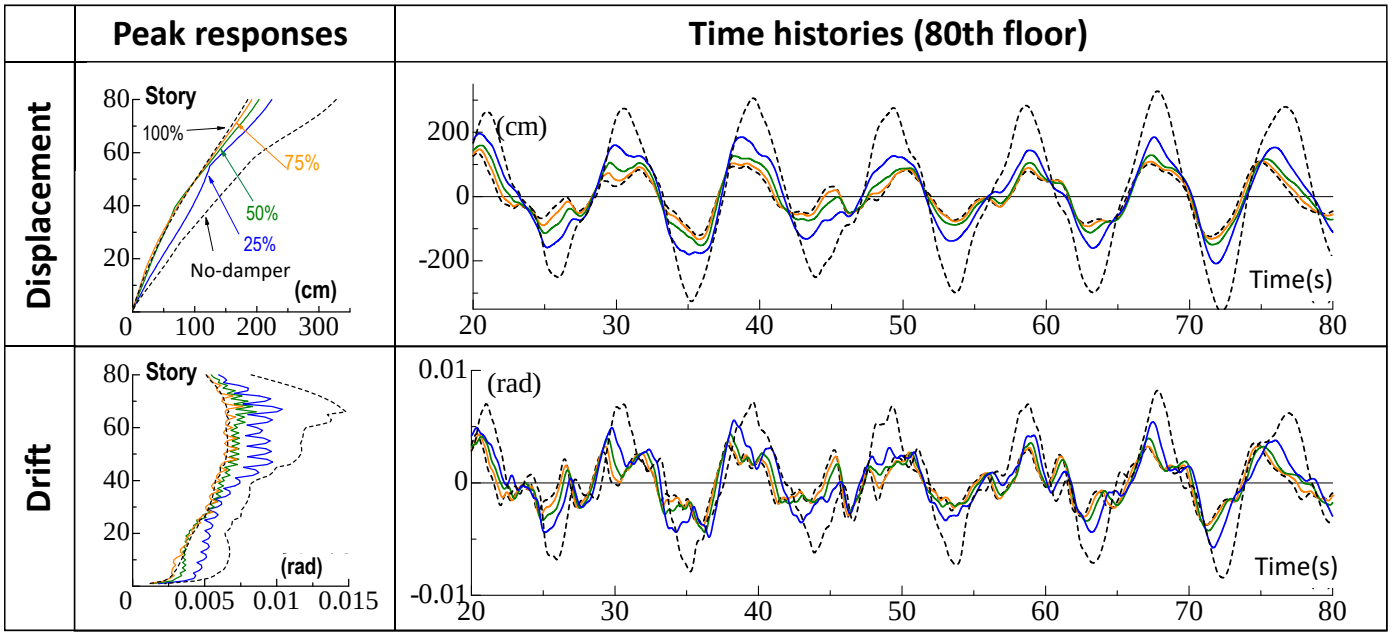

Response reduction by different damper distributions H=400m

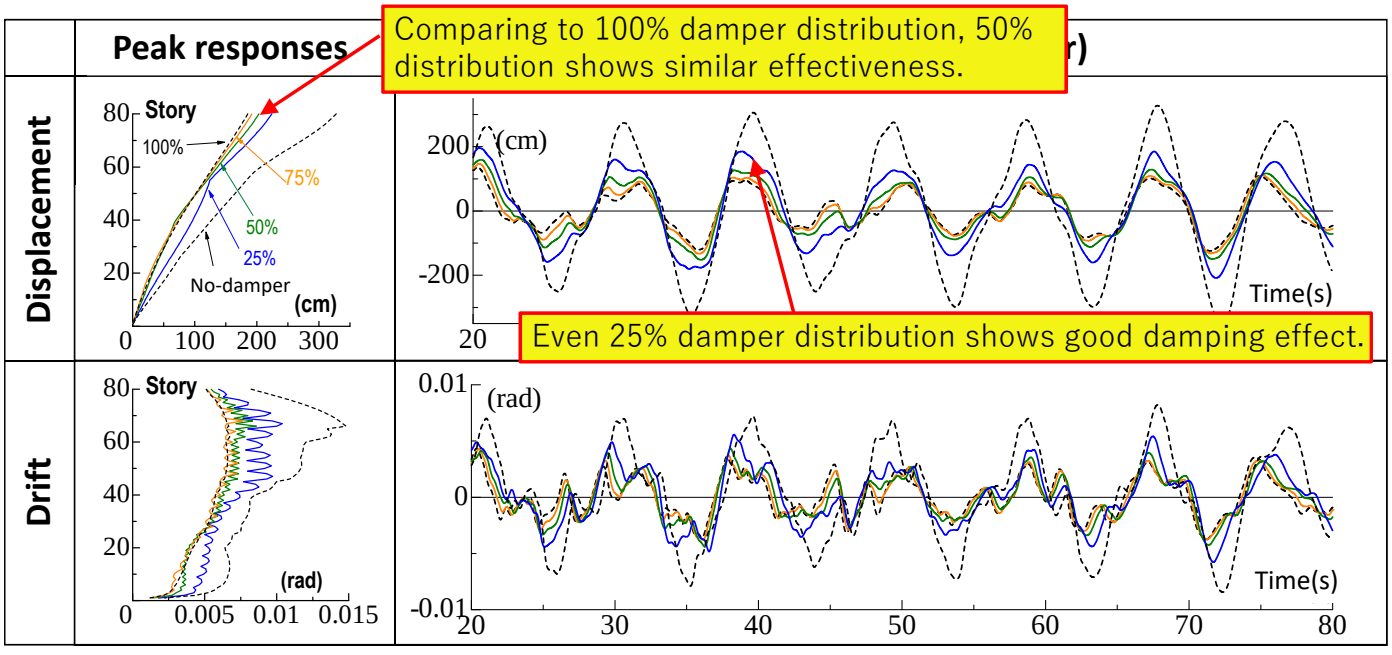

Response reduction by different damper distributions H=400m

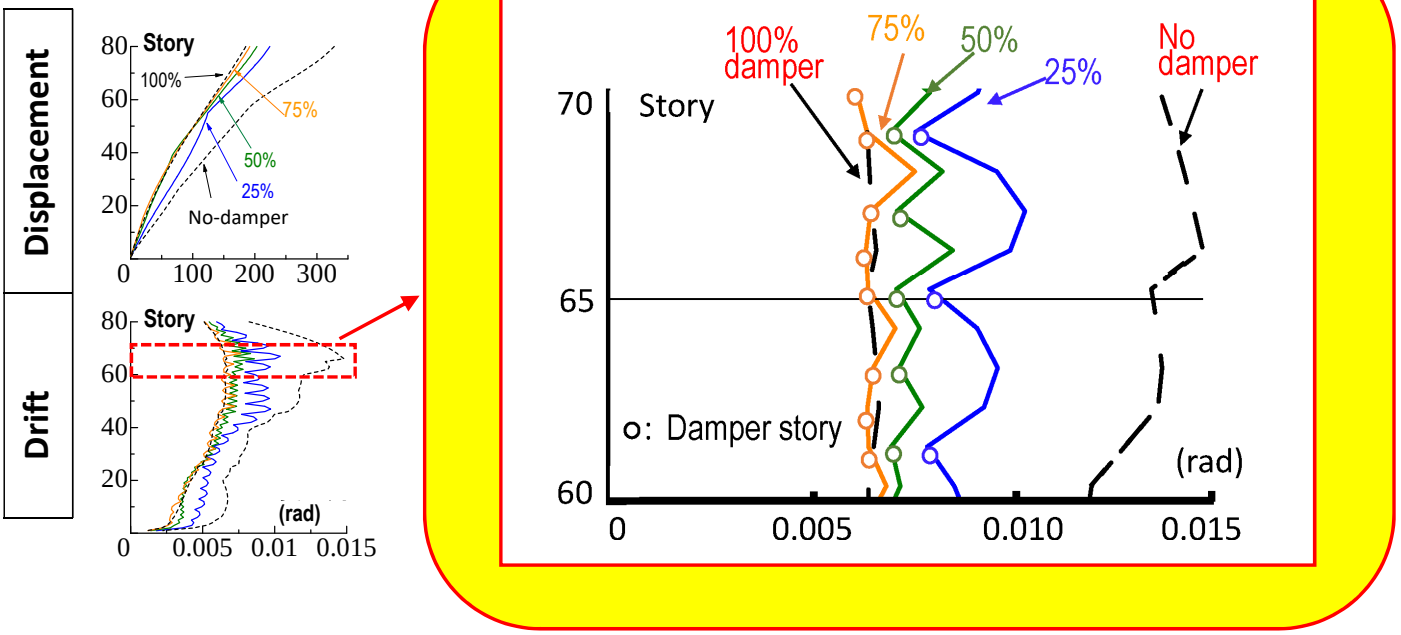

Direct-B(1) model vs. NR-B(1) Time histories (BCJ-L2) H=400m

— M model —Direct B(1) model —NR-B(1) model

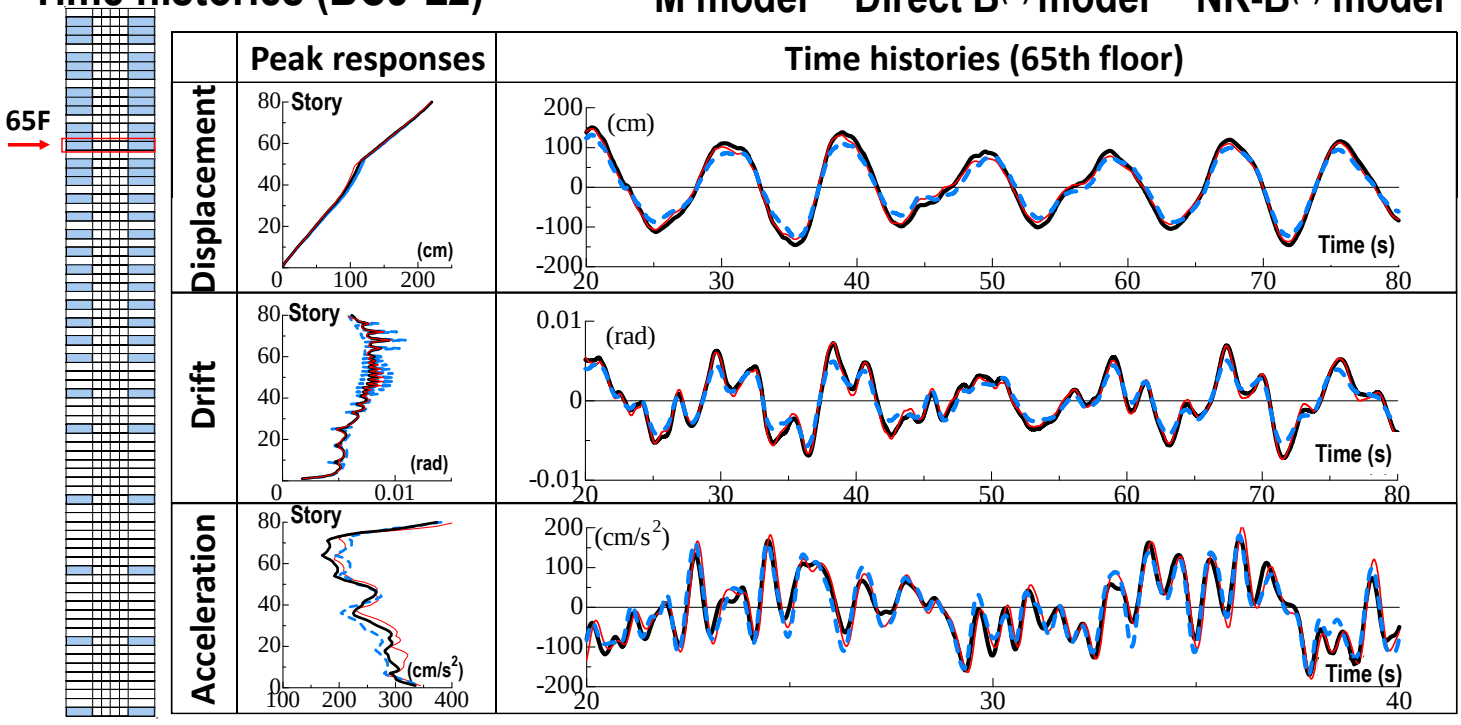

Direct B(1) model vs. NR-B(1) model H=400m

Time histories (BCJ-L2)

— M model — Direct B(1) model — NR-B(1) model

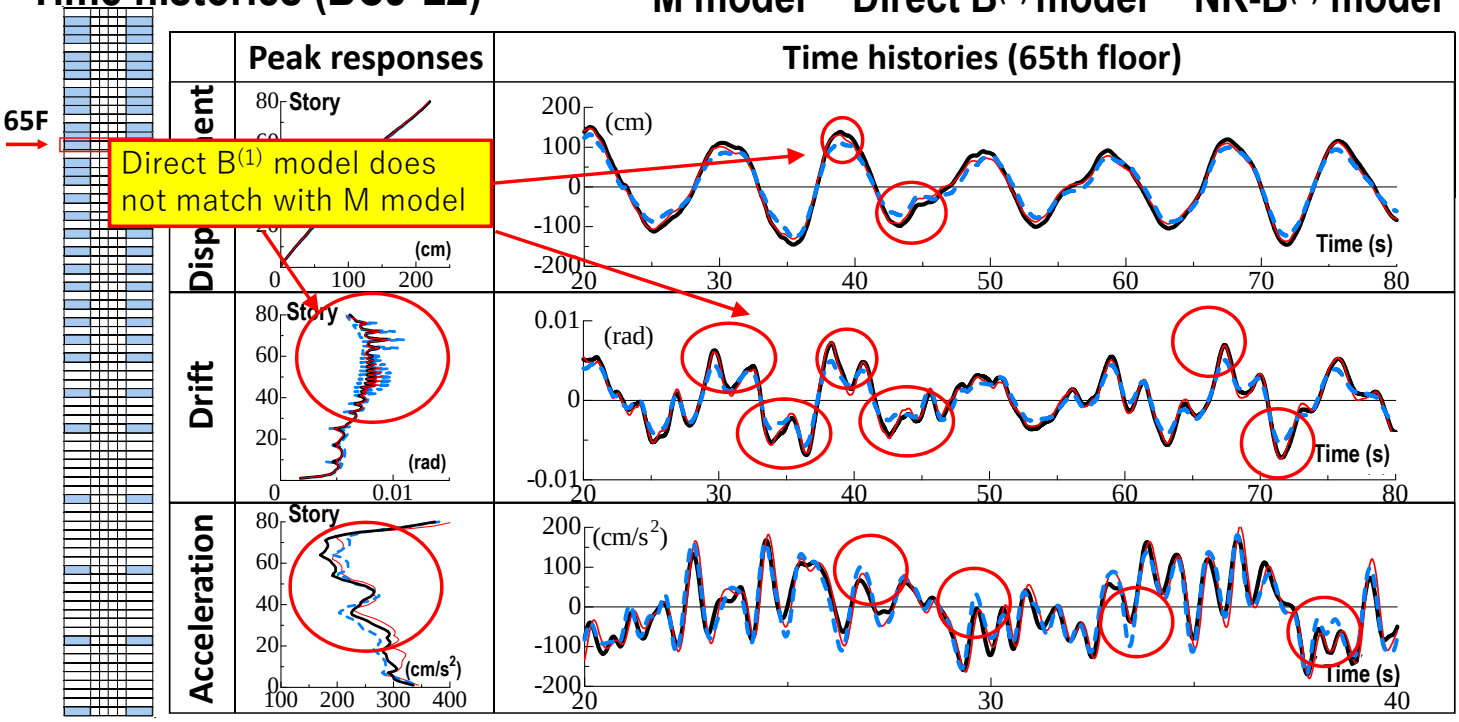

Convert damper responses from NR-B(1) model to M model：

After obtaining damper force F_{dsi} and deformation u_{dsi} of NR-B(1) model, convert to total damper force F_{di} and average deformation u_{di} of the four dampers in the M model.

$$F_{di} = F_{dsi} / \alpha_{Ni}\,,\quad u_{di} = u_{dsi}\alpha_{Ni}$$ (Damper deformation ratio $\alpha_{Ni} = \phi_{dNi} / \Delta\phi_{Ni}$)

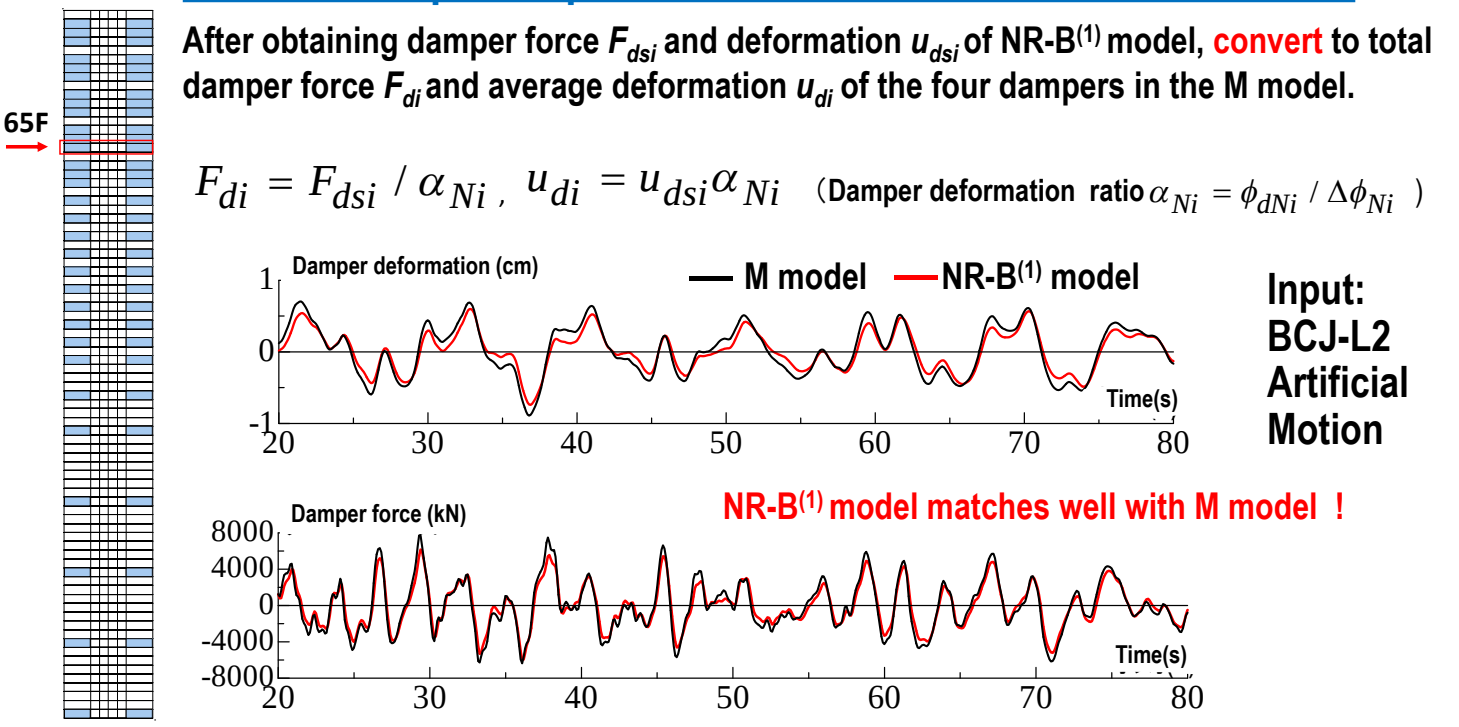

Input: BCJ-L2 Artificial Motion

NR-B(1) model matches well with M model ！

Energy Dissipation by Higher Modes:

One advantage of the NR-B(1) method is ability to find mode by mode the shear drift component causing damper deformation. Extension to multi-mode spectra-based damper design would be possible.

※ result below is obtained by approximate approach, and will be reproduced by more rigorous approach being explored now.

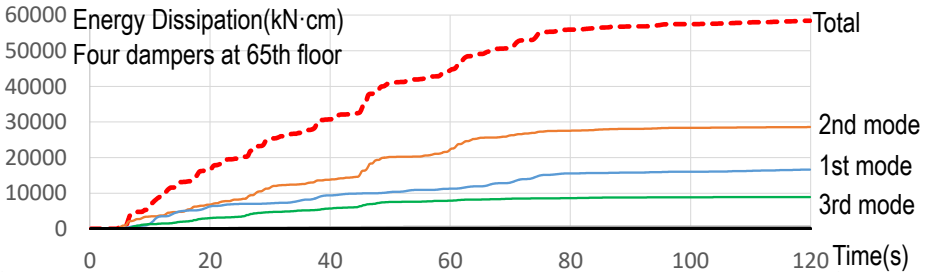

2nd and 3rd modes are governed by increasing drift

Broken line : Bending
Solid Line: Shear

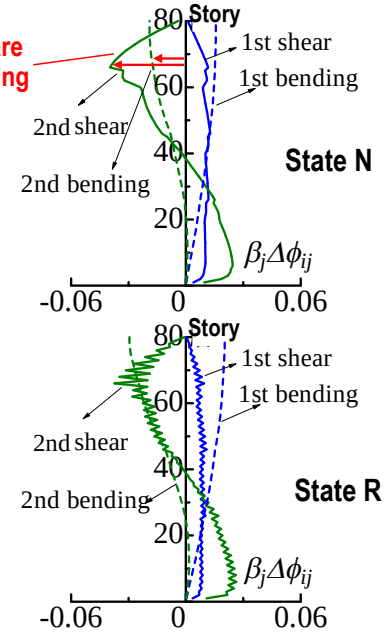

Example of Other Models: Miranda & Taghavi (without damper) :

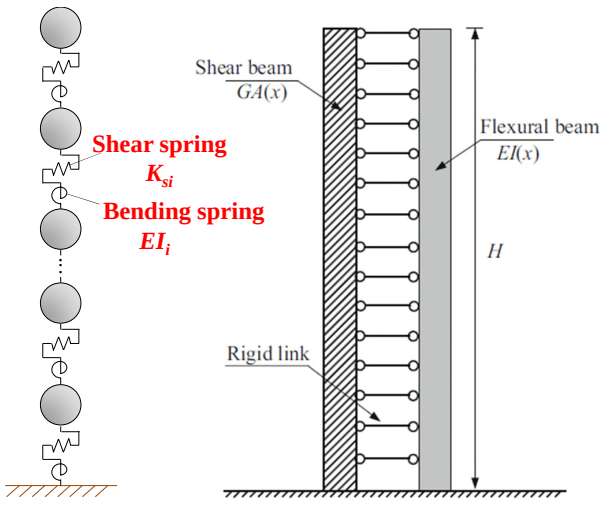

Mode-matched Bending-shear model ($B^{(1)}$ model)

Miranda and Taghavi *1 Flexural-shear model

Flexure and Shear Beams Connected in Parallel

$EI(x)$ and $GA(x)$ are commonly expressed by $S(x)$:

$$EI_{(x)} = EI_0 S_{(x)} \qquad GA_{(x)} = GA_0 S_{(x)}$$

$$S_{(x)} = 1-(1-\delta)x^{\lambda}$$

EI_0 and GA_0 = values at 1st story
x = normalized height
$\delta = EI(1)/EI_0$ or $GA(1)/GA_0$
λ=1 to 2

*1 Eduardo Miranda and Shahram Taghavi; Approximate Floor Acceleration Demands in Multistory Buildings. I: Formulation, Journal of Structural Engineering, Volume 131, Issue 2, pp.203-211, 2005.2

Method to Greatly Reduce DOF for Fast Dynamic Analysis of Super-Tall Building with/without Dampers

1. Introduction
   - 1.1 Member-to-member (M) model and reduced (S & B) models
   - 1.2 Example performance of S model with dampers
2. Reduced Models without Dampers
   - 2.1 Shear (S) model vs. Mode-matched Shear ($S^{(1)}$) model
   - 2.2 Bending-shear (B) model vs. Mode-matched Bending-shear ($B^{(1)}$) model
3. NR-$B^{(1)}$ model with Dampers
   - 3.1 No-damper / Rigid-damper (N/R) states
   - 3.2 NR-$B^{(1)}$ model for continuous / discrete distributions of dampers
4. Conclusions

49

Fast and Accurate Time-History Analysis:

- **Building without dampers:** Shear (S), mode-matched shear ($S^{(1)}$), bending-shear (B), and mode-matched bending-shear ($B^{(1)}$) models were discussed. **$B^{(1)}$ model** is outstandingly accurate for taller buildings.
- **Building with dampers:** $B^{(1)}$ model tuned by N/R method, **"NR-$B^{(1)}$ model"** works well for various frame types and vertical (continuous/discrete) distributions of dampers.

Other Important Points (NR-$B^{(1)}$ model):

- Ideal for the preliminary design of **macroscopic balancing** between the frame and dampers.
- Can indicate damper effectiveness for **discrete (vertical) distribution saving damper cost.**
- Enables higher-mode-based damper design by **estimating shear and bending drifts mode-by-mode.**

50

Prof. Junji Kiyono

Kyoto University, Japan

Topic：Strain Imposed on a Water Pipeline by Stationary Loads for Seismic Design

STRAIN IMPOSED ON A WATER PIPELINE BY STATIONARY LOADS FOR SEISMIC DESIGN

Junji Kiyono[1], Joji Kubota[2], Aiko Furukawa[3], Hiromoto Onuma[4] and Hideki Omuro[5]
1. Professor, Graduate School of Engineering, Kyoto University, Kyoto, Japan
2. Master Course Student, Graduate School of Engineering, Kyoto University, Kyoto, Japan
3. Associate Professor, Graduate School of Engineering, Kyoto University, Kyoto, Japa
4. Director, Onuma Waterworks Technical Institute, Niigata, Japan
5. Polyethylene Piping System Integrated Technology and Engineering Center (POLITEC), Tokyo, Japan
Email: kiyono.junji.5x@kyoto-u.ac.jp

ABSTRACT

In the seismic design of pipelines, as set out in the guidelines for earthquake-resistant construction of water-works facilities, the seismic capacity is evaluated by adding together the strain due to stationary loads (internal pressure, vehicle load, temperature change, differential settlement) and the strain due to earthquake ground motion. When comparing the experiments' results done by Polyethylene Piping System Integrated Technology and Engineering Center (POLITEC) to the result obtained using the calculation model of the Japan Water Works Association, we found a marked difference in the strains due to the above stationary loads. A possible cause is that the calculations for a buried pipeline do not take into account the effect of constraints exerted by the ground on the deformation of the pipeline. We found that the Japan Water Works Association's calculation model yields excessively high strain figures. In this study, new formulations for the internal pressure and temperature change are proposed. The calculation results are in good agreement with experiments' results.

Keywords: HPPE distribution pipe, axial strain, stationary loads, soil–pipe interaction

INTRODUCTION

In the seismic design of pipelines in the Waterworks Facility Earthquake-Resistant Construction Method Guideline & Explanation by Japan Water Works Association (1997), seismic capacity is evaluated by adding together the strains due to stationary loads (internal pressure, vehicle load, temperature change, differential settlement) and the strain due to earthquake ground motion. However, the strain due to those stationary loads, obtained as a result of the experiments using buried higher performance polyethylene (HPPE) pipes (herein-after referred to as blue PE pipes), differs markedly from the result obtained by using the Japan Water Works Association's strain calculation model. A possible cause is that the calculations for a buried pipeline do not take into account the effect of constraints exerted by the ground on the deformation of the pipeline. As such, for the internal pressure and temperature change, which are stationary loads that have a particularly significant effect on axial strain, this research introduced soil springs in the axial direction of a pipe to take into account the effect of the surrounding ground when formulating the calculations. For stationary loads, we review here the equations for calculating the strain that occurs in the axial direction of a steel pipe that is an integral part of a pipeline.

FORMULATING PIPE STRAIN

Axial Strain due to Internal Pressure

In the calculation example of the seismic capacity of a buried pipeline by JWWA (1997), the strain in the axial direction of a buried steel pipe due to the internal pressure of the pipeline where the axial displacement is constrained is given by the equation below. In this equation, the circumferential stress and the strain are found from an equilibrium of forces with the internal pressure, using the mean diameter. The axial strain is then obtained using Poisson's ratio.

$$\varepsilon_{li} = \frac{P_i(D-t)}{2E}\nu \tag{1}$$

where ε_{li} is the pipe axial strain due to internal pressure, ν is Poisson's ratio, P_i is the internal pressure, D is the outside diameter, t is the pipe thickness, and E is the modulus of elasticity.

In this research we considered an experimentally simulated pipeline of length L, as shown in Fig. 1. We formulated the calculations using a model provided with soil springs in the axial direction, to take into account the effect of the surrounding ground.

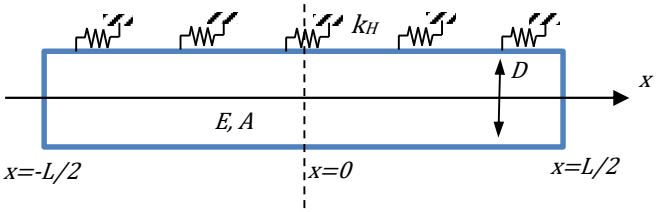

Figure 1. Pipeline model that takes soil springs into account

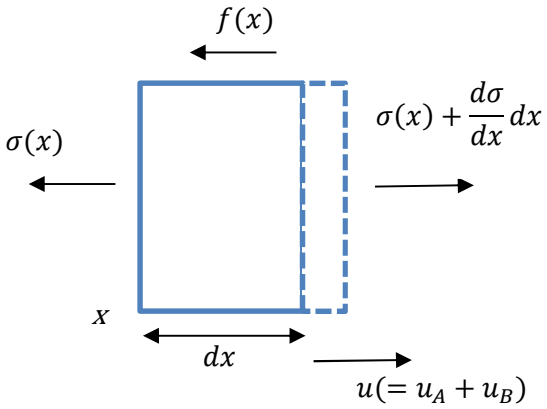

Figure 2. Equilibrium of forces of minute elements near point x

The stress application in a minute section dx is as shown in Fig. 2, where the dotted line represents the elongation of the pipe. Let u_A be the elongation due to axial stress and u_B the elongation due to Poisson's ratio resulting from internal pressure. u_B can then be expressed by:

$$u_B = \frac{\sigma_\theta}{E}\nu x \tag{2}$$

where σ_θ is the circumferential stress due to the internal pressure. The overall displacement u is expressed by the following equation:

$$\boldsymbol{u = u_A + u_B} \tag{3}$$

We can set up an equation for the equilibrium of forces in a minute section dx as follows:

$$\boldsymbol{EA\frac{d^2u_A}{dx^2} - \pi D f(x) = 0} \tag{4}$$

We have here

$$f(x) = k_H\left(u_A + \frac{\sigma_\theta}{E}\nu x\right) \tag{5}$$

Hence, Eq. (4) can be expressed as:

$$\frac{d^2u_A}{dx^2} - \frac{\pi D k_H}{EA}\left(u_A + \frac{\sigma_\theta}{E}\nu x\right) = 0 \tag{6}$$

We let

$$k^2 = \frac{\pi D k_H}{EA} \tag{7}$$

Eq. (6) now becomes:

$$\frac{d^2u_A}{dx^2} - k^2 u_A = k^2 \frac{\sigma_\theta}{E}\nu x \tag{8}$$

We further let

$$\alpha = k^2 \frac{\sigma_\theta}{E}\nu \tag{9}$$

We now have the inhomogeneous differential equation:

$$\frac{d^2u_A}{dx^2} - k^2 u_A = \alpha x \tag{10}$$

where we consider the boundary conditions: when $x=0$, $u=0$; when $x=L/2$, $\sigma=\sigma(L/2)$; and $\sigma=E\varepsilon=E\,du_A/dx$. Finally we have the general solution:

$$u_A = \frac{\sigma(\frac{L}{2})+\sigma_\theta\nu}{kE}\cdot\frac{sinhkx}{cosh\frac{kL}{2}} - \frac{\sigma_\theta}{E}\nu x \tag{11}$$

Therefore, the displacement u at the point x and the axial strain ε are expressed by the following equations:

$$u = u_A + \frac{\sigma_\theta}{E}\nu x = \frac{\sigma(\frac{L}{2})+\sigma_\theta\nu}{kE}\cdot\frac{sinhkx}{cosh\frac{kL}{2}} \tag{12}$$

$$\varepsilon = \frac{du}{dx} = \frac{\sigma(\frac{L}{2})+\sigma_\theta\nu}{E}\cdot\frac{coshkx}{cosh\frac{kL}{2}} \tag{13}$$

Note that $k = \sqrt{\frac{\pi D k_H}{EA}}$ from Eq. (7).

Axial Strain due to Temperature Change

In the calculation example by JWWA (1997) of the seismic capacity of a buried pipeline, the pipe axial strain due to temperature change of the steel pipe is given by:

$$\varepsilon_{lt} = \alpha\Delta T \tag{14}$$

where ε_{lt} is the strain in the pipe's axial direction due to temperature change, α is the coefficient of linear expansion, and ΔT is the temperature change.

In this research we considered an experimentally simulated pipeline of length L (as shown in Fig. 1), as with a pipeline subjected to internal pressure. We formulated the calculations using a model provided with soil springs in the pipe's axial direction, to take into account the effect of the surrounding ground.

As with internal pressure, the overall elongation u of the pipe was defined as the sum of the elongation u_A, due to stress acting in the axial direction, and the elongation $\alpha\Delta Tx$, due to expansion by temperature change. Water is circulating and thus freely flows through the pipe ends, the boundary condition being that when $x=L/2$, $\sigma(L/2)=0$.

The overall elongation u is expressed by:

$$u = u_A + \alpha\Delta Tx \tag{15}$$

The differential equation of the pipe elongation due to temperature change is as follows:

$$\frac{d^2u_A}{dx^2} - \frac{\pi D k_H}{EA}\{u_A + \alpha\Delta Tx\} = 0 \tag{16}$$

Setting the conditions that when $x=0$, $u=0$; when $x=L/2$, $\sigma=0$; and $k^2=(\pi Dk_H)/EA$, solving this differential equation, as in the case of internal pressure, yields the following equation:

$$u_A = \alpha\Delta T\left(\frac{1}{k}\cdot\frac{sinhkx}{cosh\frac{kL}{2}} - x\right) \tag{17}$$

Substituting this into Eq. (15) gives:

$$u = \frac{\alpha\Delta T}{k}\cdot\frac{sinhk}{cosh\frac{kL}{2}} \tag{18}$$

Hence, the axial strain ε due to temperature change is expressed by the following equation:

$$\varepsilon = \frac{du}{dx} = \alpha\Delta T\cdot\frac{coshk}{cosh\frac{kL}{2}} \tag{19}$$

COMPARISON WITH THE EXPERIMENTAL RESULTS

In order to grasp the stretching behaviour of a blue PE pipe buried underground when its internal pressure or temperature changes, we verify here the suitability of the formulation in the previous section, using the results by JWWA (1998) of measurement of strain due to internal pressure change or temperature change of a buried blue PE pipe. The experiment measured the strain due to temperature change (from 15.1°C to 40.5°C) of a blue PE pipe buried outside, and the strain due to internal pressure change (from zero to 1.0 MPa) under the same burial conditions. The burial conditions were as follows: an overburden of 1.2 m; decomposed granite as the backfilling soil; a compaction method of six rounds, with a compaction rammer for each 30 cm backfilling. The measured items were the pipe temperature (five points) and the pipe strain (20 points in the pipe's axial direction x 4 directions (up and down, left and right)). The experiment was made with a 20 m pipeline, comprising four straight pipes of length 5 m and bore 75 mm connected by electrofusion (EF) or butt fusion. Here we make a comparison with the result of EF connection.

Experiment to Measure Strain due to Internal Pressure Change

Experiment report to measure strain due to internal pressure change was published by POLITEC (2020). Blue PE pipes of length 20 m and bore 75 mm, connected by EF or butt fusion, are buried side by side. The water pressure fixtures at both ends are set to be fixed in the pipe's elongation direction and to be free in the compression direction. Running water is then circulated. When the pipe temperature is constant, the pipe strain is measured by applying water pressures of 0.5 MPa, 0.75 MPa, and 1.0 MPa. Fig. 3 is a diagrammatic sketch of the experiment to measure strain due to water pressure change, and Fig. 4 provides the obtained results.

As seen in Fig. 4, the axial strain in the buried area was a maximum of approximately -0.015% (compression) in the case of an EF connection.

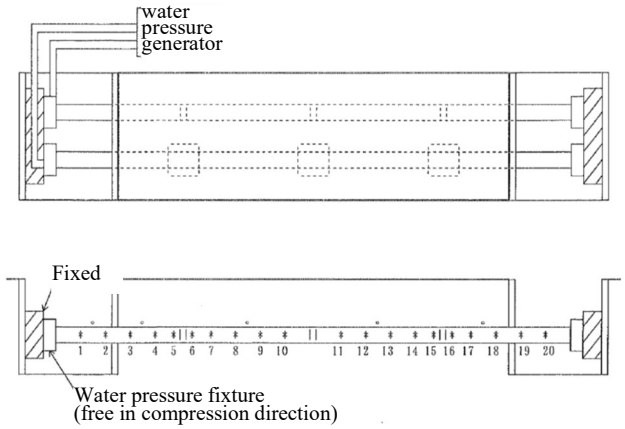

Figure 3. Diagrammatic sketch of the experiment to measure strain due to internal pressure change (POLITEC 2021)

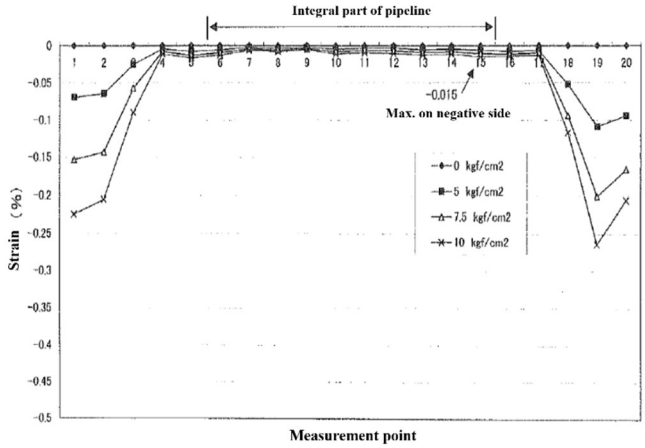

Figure 4. Pipe axial strain due to internal pressure change (POLITEC 2021)

Experiment to Measure Strain due to Temperature Change

Cold or hot water was circulated inside the pipe, and a temperature change of approximately 25°C (from about 15°C to 40°C) was generated. The strain that occurred in the pipe was measured. Fig. 5 shows the outline of the experiment to measure strain due to temperature change, and Fig. 6 provides the obtained results.

The axial strain of the buried area of the EF-connected pipe was a maximum of approximately 0.001%.

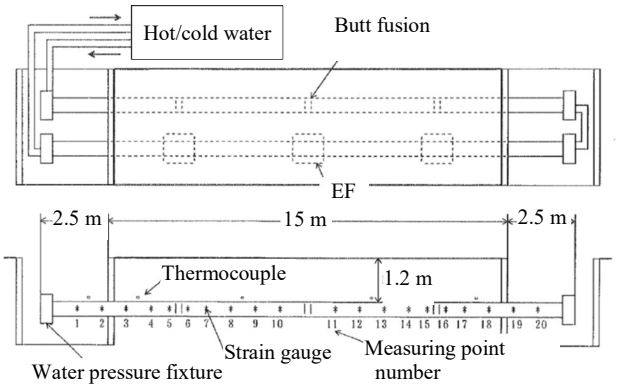

Figure 5. Diagrammatic sketch of the experiment to measure strain due to temperature pressure change (POLITEC 2021)

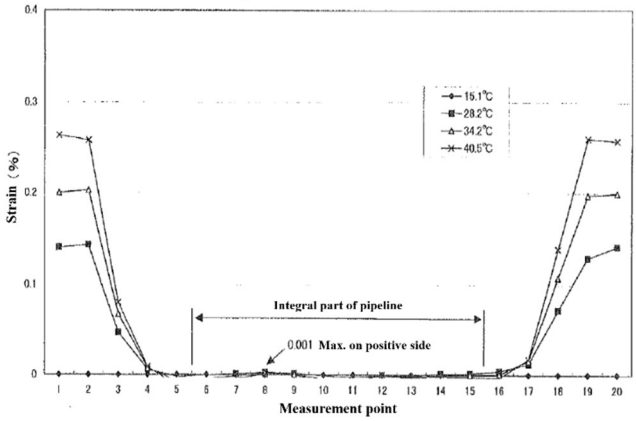

Figure 6. Pipe axial strain due to temperature change (POLITEC 2021)

Axial Strain upon Internal Pressure Change Obtained from the Proposed Equation

The values below are used as data of the blue PE pipe and are substituted into Eq. (13). The axial strains at intervals of 1 m within the range of -7.5≤ x≤7.5 are shown in Fig. 7. The average strain in the range of -5 m to 5 m (where the value varies little) is -0.00046% and the maximum strain at $\pm\mathbf{5}\boldsymbol{m}$ is -0.00380%, which is one fourth value of the experiment (0.015%: Fig.4). The boundary condition at $x=L/2$, $\sigma(L/2)$, is given by

$$\boldsymbol{\sigma}\left(\frac{\boldsymbol{L}}{\mathbf{2}}\right)=\mathbf{0} \tag{20}$$

By contrast, calculating the strain value on the basis of Eq. (1), from the equation to find the axial strain due to internal pressure when not taking into account the resistance by soil, yields ε = (-)0.229 [%]. This is about 15 times larger than the experimental value and is excessively high. The parameters given to the proposed equation are as follows:

P: internal pressure (1.0×10^3 [kN/m^2])

ν: Poisson's ratio (0.46)

D: outside diameter (0.09 [m])

t: pipe thickness (0.0082 [m])

E: modulus of elasticity (1.0×10^6 [kN/m^2])

L: pipe length (15 [m])

k_H: coefficient of horizontal subgrade reaction (2.0×10^4 [kN/m^3])

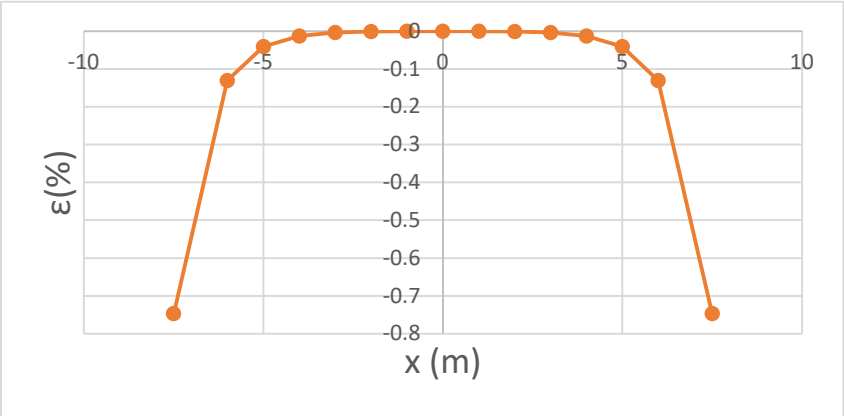

Figure 7. Pipe axial strain due to internal pressure change obtained from the proposed equation

Axial Strain upon Temperature Change Obtained from the Proposed Equation

The values below are used as data of the blue PE pipe and are substituted into Eq. (19). The axial strains at intervals of 1 m within the range of -7.5≤x≤7.5 are shown in Fig. 8. The average strain in the range of -5 m to 5 m (where the value varies little) is 0.0006% and the maximum strain at $\pm 5m$ is -0.0050%, which is a half of the experimental value (0.001%: Fig.6).

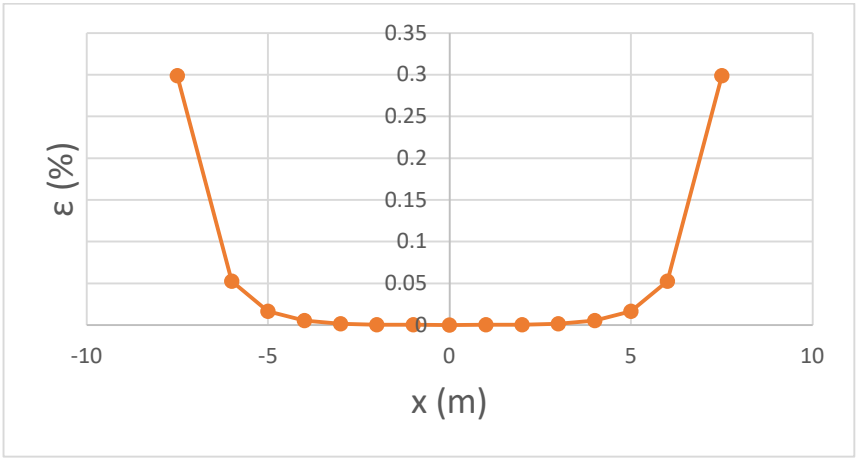

Figure 8. Pipe axial strain due to temperature change obtained from the proposed equation

By contrast, calculating the strain value on the basis of Eq. (14), from the equation to find the axial strain due to temperature change when not taking into account the resistance by soil, yields ε=0.300 [%]. This is 300 times more than the experimental value and is excessively high. The parameters given to the proposed equation are as follows:

α: coefficient of linear expansion (1.2×10^{-4} [/°C])

ΔT: temperature change (25 [°C])

D: outside diameter (0.09 [m])

t: pipe thickness (0.0082 [m])

E: modulus of elasticity (1.0×10^{6} [kN/m^2])

L: pipe length (15 [m])

k_H: coefficient of horizontal subgrade reaction (2.0×10^{4} [kN/m^3]).

Comparison and Discussion

The summary of comparison is shown in Table 1. JWWA's calculation example is subject to the steel pipe of which elastic modulus is about 200 times larger than blue PE pipe. This means that excessively large strain is expected for the relatively low stiffness pipe as a stationary load.

Table 1. Comparison of the strain values for JWWA equation, experiment and proposed equation

	JWWA Equation (%)	Experiment (%)	Proposed Equation (%)
Internal Pressure	(-)0.229	-0.015 (maximum)	-0.0038 (maximum)
Temperature	0.300	0.001 (maximum)	0.0050 (maximum)

CONCLUSIONS

In this research we considered internal pressure and temperature change, which are stationary loads that cause significant deformation in a pipe's axial direction, and formulated calculations by taking into account the effect of the surrounding ground. We then compared the results with experimental results to verify their suitability and usefulness. We found that the Japan Water Works Association's calculation model, which does not take into account the constraints imposed by the surrounding ground, yields excessively high strain especially for the relatively low rigidity pipe such as HPPE pipe.

REFERENCES

Japan Water Works Association (1997). Suidou Shisetsu Taishin Kouhou Shishin Kaisetsu [Waterworks Facility Earthquake-Resistant Construction Method Guideline & Explanation], pp. 291–301. (in Japanese)

Japan Water Works Association (1998). Suidou Haisuiyou Poriechilen Kan Tsugite ni Kansuru Tyousa Houkokusyo [Research Report on Polyethylene Pipes and Fittings for Water Supply] pp. 32–33. (in Japanese)

POLITEC Seismic Resistance Evaluation Committee material (November 12, 2021) of the Polyethylene Piping System Integrated Technology and Engineering Center. (in Japanese)

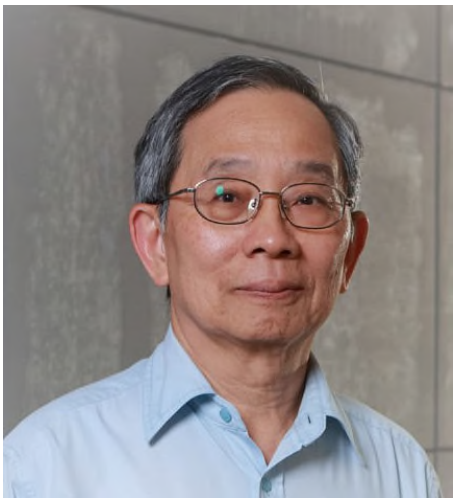

Prof. Chin-Hsiung Loh

National Taiwan University, Taiwan

Topic：A Review of Seismic Monitoring and Vibration-Based Damage Assessment in Civil Structures

A Review of Seismic Monitoring and Vibration-based Damage Detection in Civil Structures

Chin-Hsiung Loh

Adjunct Prof. of CE Dept., NTU
Adjunct Prof. of SME, UCSD
Advisor, NCREE

Acknowledgements

Contributions from co-authors

Ms. Yu-Tzu Huang

Graduate student
NTU

Prof. Chung-Che Chou

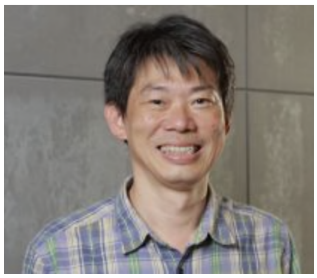

Professor of CE Dept, NTU
Director, NCREE

Ms. Wen-Hui Chen

Senior Engineer
P-Waver, Inc.

Contents

1. Introduction

Core of SHM

A. Monitoring strategy

Selection of monitored parameters, Selection of monitoring systems, Design of sensor network

B. Installation of SHM system

Installation of sensors and software

C. Data management

Collecting data, Storage of data (local or remote), Providing for access to data, Visualization, Interpretation and data analysis, The use of data

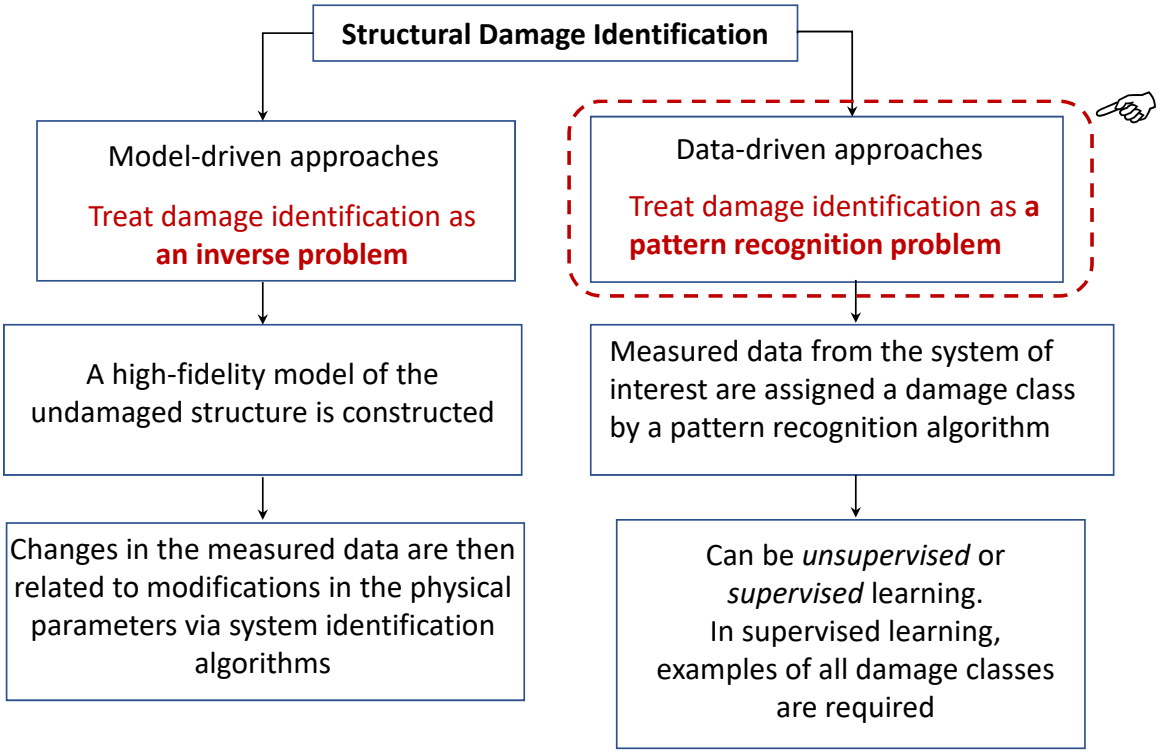
Structural Damage Identification
Model-driven approaches
Treat damage identification as an inverse problem
Data-driven approaches
Treat damage identification as a pattern recognition problem
A high-fidelity model of the undamaged structure is constructed
Measured data from the system of interest are assigned a damage class by a pattern recognition algorithm
Changes in the measured data are then related to modifications in the physical parameters via system identification algorithms
Can be unsupervised or supervised learning. In supervised learning, examples of all damage classes are required

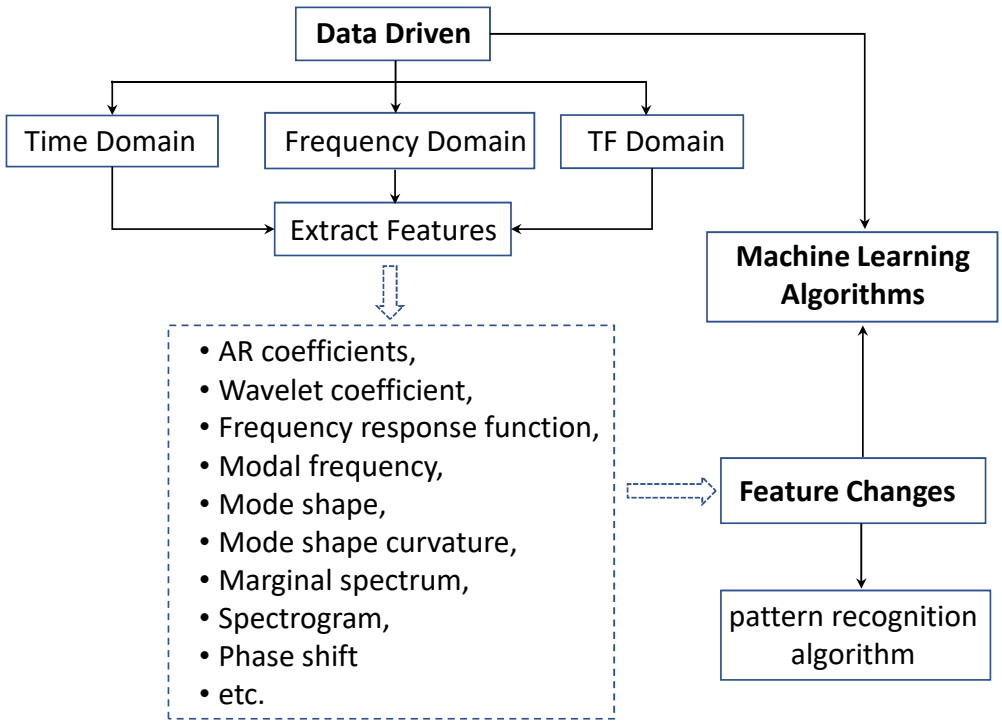
Data Driven
Time Domain
Frequency Domain
TF Domain
Extract Features
Machine Learning Algorithms
• AR coefficients,
• Wavelet coefficient,
• Frequency response function,
• Modal frequency,
• Mode shape,
• Mode shape curvature,
• Marginal spectrum,
• Spectrogram,
• Phase shift
• etc.
Feature Changes
pattern recognition algorithm

Analysis on structural response data

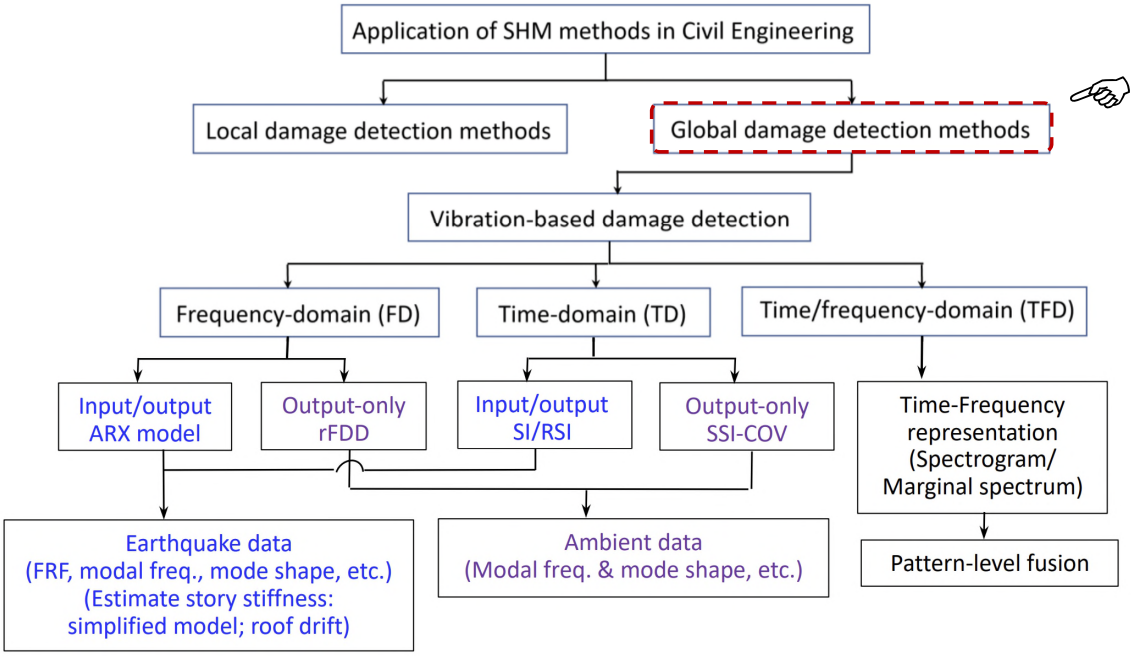

NCREE building

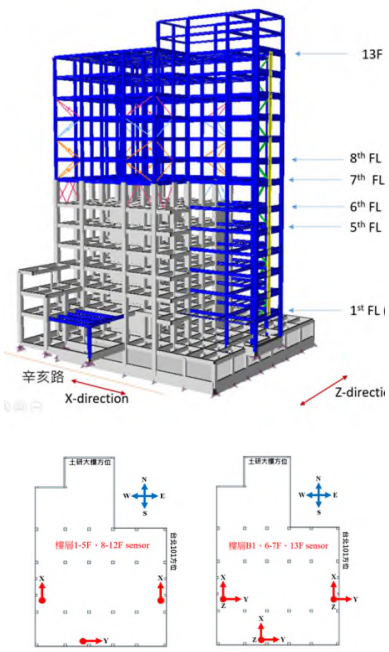

No.	Event No.	Time	Magnitude	Depth (km)	Epicenter distance (km)	Peak Accel. of Roof (gal)
1	110014	2021-02-09 00:58:02	5.6	24.7	86.3	43
2	110025	2021-04-18 22:11:39	5.8	16.3	127.3	18
3	110026	2021-04-18 22:14:37	6.2	14.4	128.4	67
4	110047	2021-06-23 13:40:24	4.8	23.6	105.1	5
5	110049	2021-06-29 13:30:56	4.9	71.1	83.6	4
6	110055	2021-07-08 06:11:55	5.5	8.2	125.0	24
7	110077	2021-08-05 05:50:45	6.0	7.0	81.8	50
8	110079	2021-08-06 16:11:04	5.6	13.3	69.8	23
9	**110103**	**2021-10-24 13:11:34**	**6.5**	**66.8**	**59.4**	**245**
10	110104	2021-10-24 13:12:42	5.5	64.1	54.8	48
11	**111001**	**2022-01-03 17:46:37**	**6.0**	**19.4**	**128.1**	**223**
12	111007	2022-01-25 22:35:53	5.1	64.7	59.1	9
13	111011	2022-02-07 18:58:25	5.5	33.2	81.5	39
14	111012	2022-02-12 00:43:13	5.6	26.4	131.6	53
15	111019	2022-03-23 01:41:38	6.7	25.7	179.2	54
16	111020	2022-03-23 01:43:25	6.2	22.6	177.3	28
17	111050	2022-04-24 01:53:48	5.1	69.3	51.0	8
18	111054	2022-05-09 14:23:03	6.2	16.8	152.9	47
19	111059	2022-06-20 09:05:07	6.0	6.8	148.3	45
20	111086	2022/09/17 21:41:19	6.4	7.3	219.0	63
21	**111111**	**2022/09/18 14:44:15**	**6.8**	**7.0**	**211.7**	**181**

Acceleration Response Spectrum

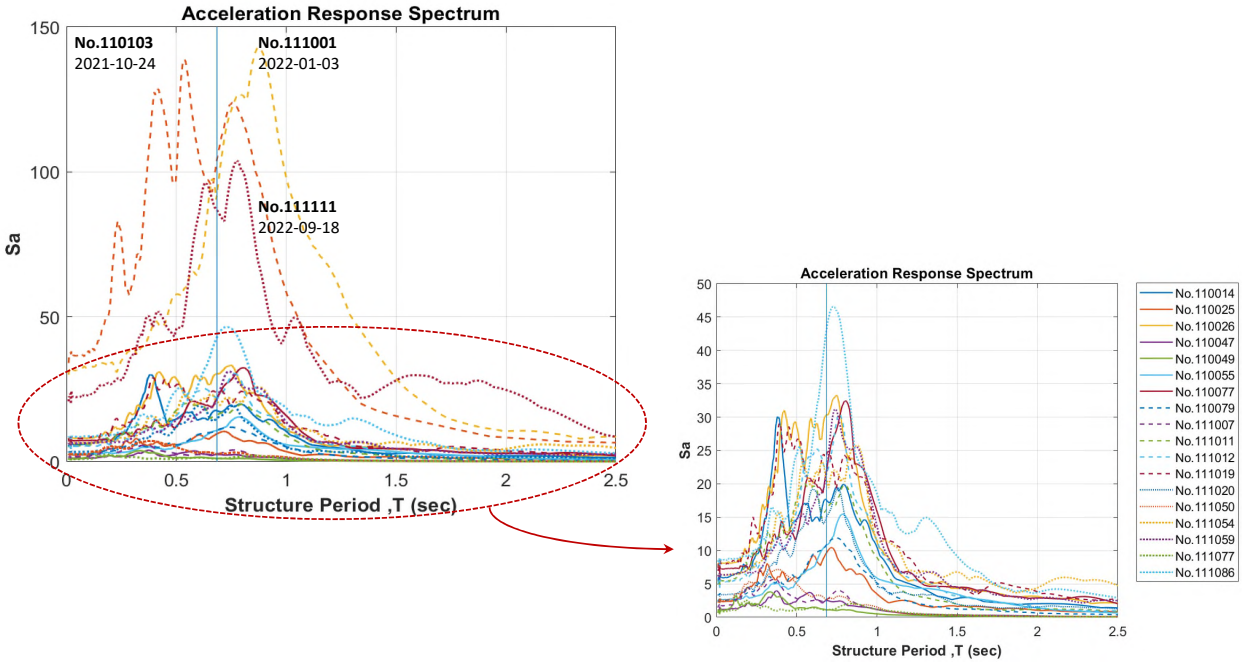

2. Analysis on building seismic response data

(a) Subspace ID (SI) and Recursive Subspace ID (RSI)

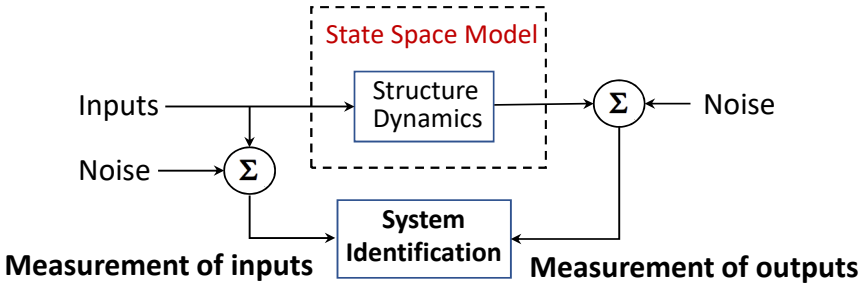

(b) Identification of system transfer function

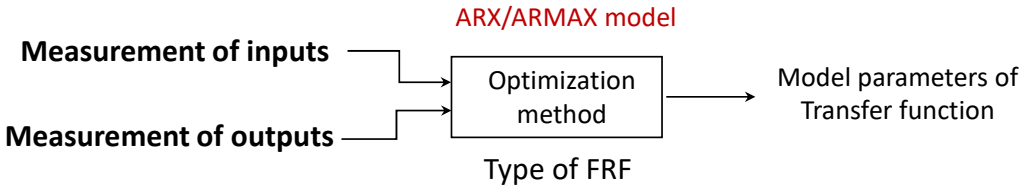

2a. Identify modal parameters using Subspace Identification

$$M\ddot{x}_{(t)} + C\dot{x}_{(t)} + Kx_{(t)} = F_{(t)} = \mathrm{L}\,u_{(t)}$$

$$A_c = \begin{bmatrix} 0 & I_n \\ -M^{-1}K & -M^{-1}C \end{bmatrix} \qquad B_c = \begin{bmatrix} 0 \\ M^{-1}\mathrm{L} \end{bmatrix}$$

$$X_{(k+1)} = A_d \cdot X_{(k)} + B_d \cdot u_{(k)} + w_{(k)}$$

$$y_{(k+1)} = C_c \cdot X_{(k)} + D_c \cdot u_{(k)} + v_{(k)}$$

$\begin{bmatrix} Y_p \\ Y_f \end{bmatrix}$ and $\begin{bmatrix} U_p \\ U_f \end{bmatrix}$

Hankel Matrix

$$\Xi_p = \begin{bmatrix} U_p \\ Y_p \end{bmatrix}$$

Construct an instrumental variable (IV) matrix

Step-1: Projection matrix

$$O^{Oblique}_{(k)} = (Y_{f(k)} / U_{f(k)} \Xi_{p(k)}) / U^{\perp}_{f(k)}$$

$$= \Gamma_i \cdot X_f / U^{\perp}_{f(k)}$$

$$= USV^{\mathrm{T}} = \begin{bmatrix} U_1 & U_2 \end{bmatrix} \begin{bmatrix} S_1 & 0 \\ 0 & S_2 \approx 0 \end{bmatrix} \begin{bmatrix} V_1^{\mathrm{T}} \\ V_2^{\mathrm{T}} \end{bmatrix} \approx U_1 S_1 V_1^{\mathrm{T}}$$

Step-2: Numerical Decomposition

$\Gamma_i^{Oblique}$ U_1

Step-3: Identification

A & C : system matrices
(Modal characteristic)

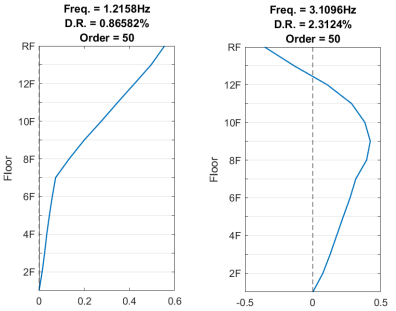

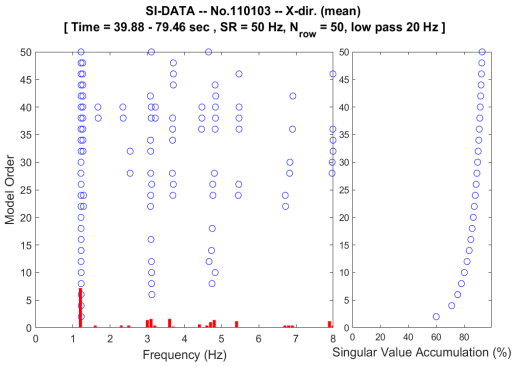

Matrix Input-Output Equations

$$Y_f = \Gamma_i X_f + H_i \cdot U_f + G_i \cdot W_f + V_f$$

$$\Gamma_i \equiv \begin{bmatrix} C_c \\ C_c A_d \\ C_c A_d^2 \\ \vdots \\ C_c A_d^{i-1} \end{bmatrix} \in \mathbb{R}^{li \times 2n}$$

Matrix I/O Eq.

Alternative approach
LQ-decomposition

$$\begin{bmatrix} U_{f(k)} \\ \Xi_{p(k)} \\ Y_{f(k)} \end{bmatrix}_{2i(m+l)\times j} = \begin{bmatrix} L_{11(k)} & 0 & 0 \\ L_{21(k)} & L_{22(k)} & 0 \\ L_{31(k)} & L_{32(k)} & L_{33(k)} \end{bmatrix}_{2i(m+l)\times 2i(m+l)} \cdot \begin{bmatrix} Q^T_{1(k)} \\ Q^T_{2(k)} \\ Q^T_{3(k)} \end{bmatrix}_{2i(m+l)}$$

$$O^{Oblique}_{(k)} = Y_{f(k)} / U_{f(k)} \Xi_{p(k)} / U^{\perp}_{f(k)} = L_{32(k)} Q^T_{2(k)}$$

Subspace Identification using building seismic response data

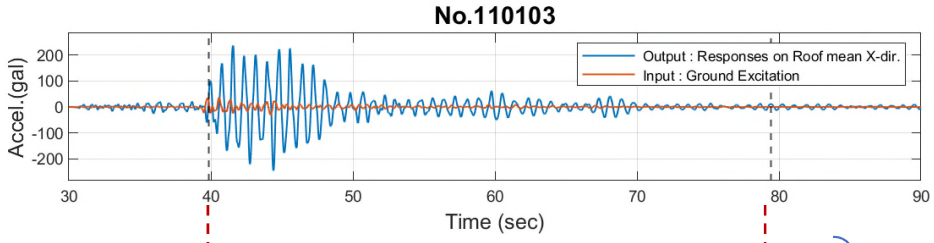

Subspace Identification (SI)

Duration: Arias Intensity 1% ~ 99%

Identify modal frequency & mode shape

Table for Identified Frequency (SI) and RF peak Accel.

	No.110014	No.110025	No.110026	No.110055	No.110077	No.110079
Frequency (Hz)	1.33	1.35	1.30	1.34	1.29	1.32
RF Peak Accel. (gal)	43	18	67	24	50	23

	No.110103	No.111001	No.111012	No.111019	No.111086	No.111111
Frequency (Hz)	1.22	1.20	1.23	1.22	1.22	1.20
RF Peak Accel. (gal)	245	223	53	54	63	181

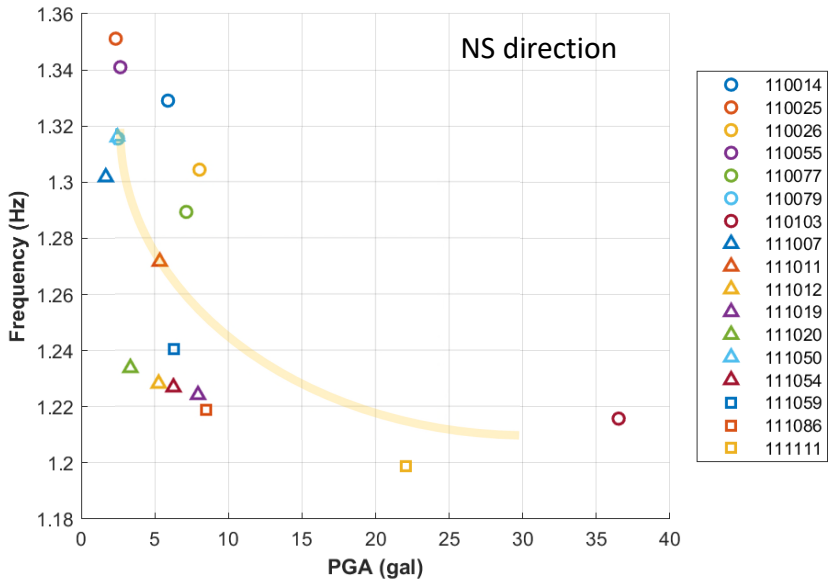

Identified modal frequencies & damping ratio (seismic event along NS-direction)

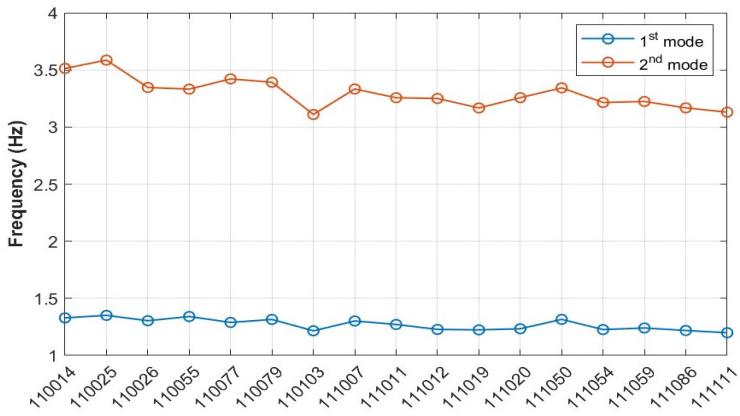

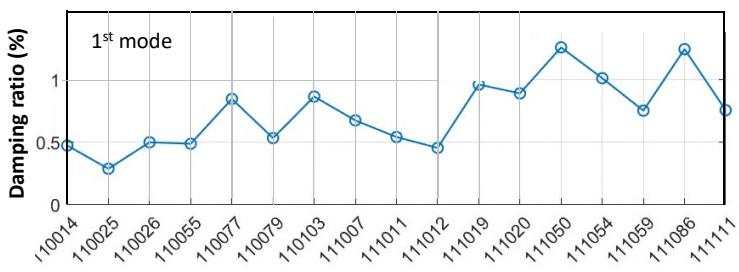

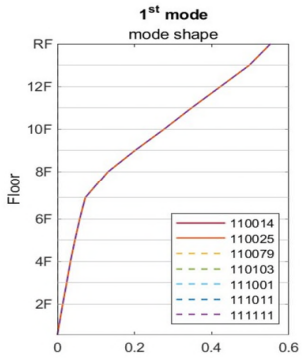

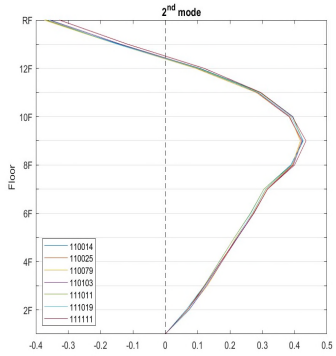

2b. Identify inter-story stiffness (simplified model)

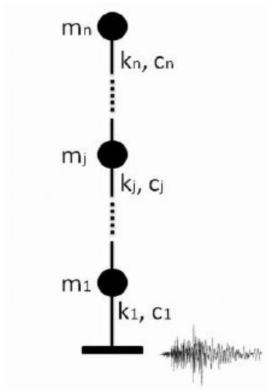

n -DOF Lumped mass model of a shear building.

Eigen-equation of the n-DOF system

$$\mathbf{K}_{\text{System}}\boldsymbol{\Phi}_r = \omega_r^2 \mathbf{M}_{\text{System}}\boldsymbol{\Phi}_r$$

ω_r and $\boldsymbol{\Phi}_r$ From subspace ID

$$\mathbf{M}=\begin{bmatrix} m_1 & 0 & \cdots & 0 & 0 \\ 0 & m_2 & \cdots & 0 & 0 \\ \vdots & \vdots & \ddots & \vdots & \vdots \\ 0 & 0 & \cdots & m_{n-1} & 0 \\ 0 & 0 & \cdots & 0 & m_n \end{bmatrix}$$

system mass matrix is known

$$\mathbf{K}=\begin{bmatrix} k_1+k_2 & -k_2 & & & 0 \\ -k_2 & k_2+k_3 & \ddots & & \\ & \ddots & \ddots & & \\ & & k_{n-1}+k_n & -k_n & \\ 0 & & -k_n & k_n & \end{bmatrix}$$

unknown variables of inter-story stiffness of each floor

2b. Identify inter-story stiffness (simplified model)

Least Squares Stiffness Method (LSSM)

- Use identified modal frequencies and mode shapes by subspace ID, together with the information of mass

Eigen-equation of the n-DOF system

$$\mathbf{K}_{\text{System}}\boldsymbol{\Phi}_r = \omega_r^2 \mathbf{M}_{\text{System}}\boldsymbol{\Phi}_r$$

$$\begin{bmatrix} \boldsymbol{\Delta}_1 \\ \boldsymbol{\Delta}_2 \\ \vdots \\ \boldsymbol{\Delta}_s \end{bmatrix}_{(s\times n)\times n} \times \begin{bmatrix} k_1 \\ k_2 \\ k_3 \\ \vdots \\ k_n \end{bmatrix}_{(n\times 1)} = \begin{bmatrix} \boldsymbol{\Lambda}_1 \\ \boldsymbol{\Lambda}_2 \\ \vdots \\ \boldsymbol{\Lambda}_s \end{bmatrix}_{(s\times n)\times 1}$$

$$k = \Delta^{-1}\Lambda$$

Least-squares (member stiffness)

$$\boldsymbol{\Delta}_r = \begin{bmatrix} \phi_{1,r} & \phi_{1,r}-\phi_{2,r} & 0 & \cdots & 0 \\ 0 & \phi_{2,r}-\phi_{1,r} & \phi_{2,r}-\phi_{3,r} & \cdots & 0 \\ \vdots & \vdots & \vdots & \ddots & \vdots \\ 0 & 0 & \cdots & \phi_{n-1,r}-\phi_{n-2,r} & \phi_{n-1,r}-\phi_{n,r} \\ 0 & 0 & \cdots & 0 & \phi_{n,r}-\phi_{n-1,r} \end{bmatrix}$$

$$\boldsymbol{\Lambda}_r = \omega^2_{(t=k),r} \times \begin{bmatrix} m_1\phi_{1,r} \\ m_2\phi_{2,r} \\ m_3\phi_{3,r} \\ \vdots \\ m_n\phi_{n,r} \end{bmatrix}$$

Modal parameter matrices

Ref: J. M. Caicedo, S.J. Dyke and E. A. Johnson. (2004), Natural excitation technique and eigensystem realization algorithm for phase I of the IASC-ASCE benchmark problem: simulated data, Journal of Engineering Mechanics, Vol.130, No.1, p49-60.

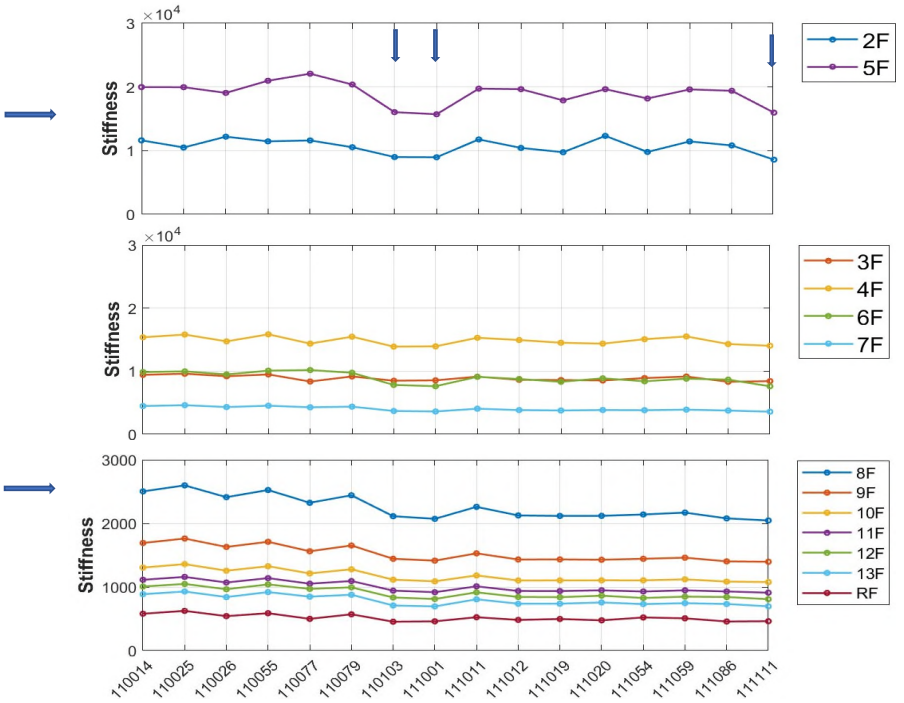
×10^4
Stiffness
2F
5F
3F
4F
6F
7F
8F
9F
10F
11F
12F
13F
RF
110014
110025
110026
110055
110077
110079
110103
111001
111011
111012
111019
111020
111054
111059
111086
111111

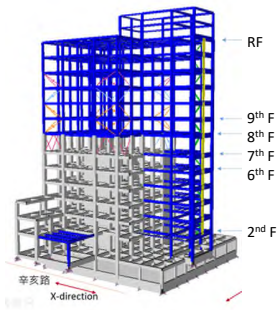
RF
9th F
8th F
7th F
6th F
2nd F
辛亥路
X-direction

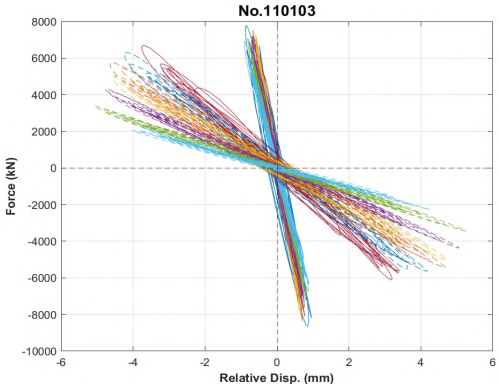
No.110103
Force (kN)
Relative Disp. (mm)

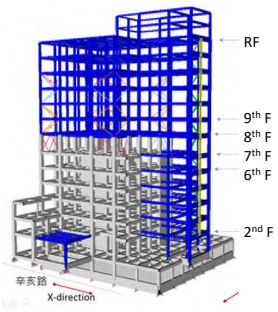
RF
9th F
8th F
7th F
6th F
2nd F
辛亥路
X-direction

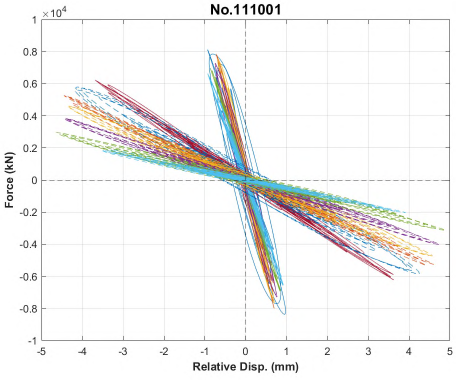
No.111001
×10^4
Force (kN)
Relative Disp. (mm)

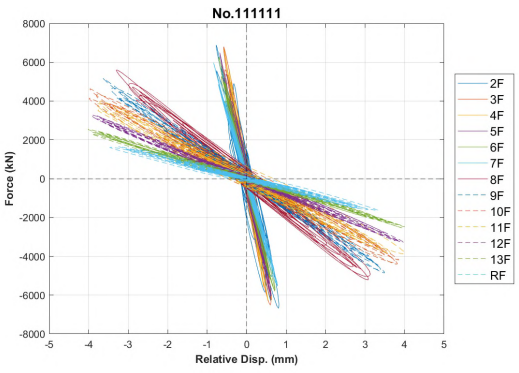
No.111111
Force (kN)
Relative Disp. (mm)
2F
3F
4F
5F
6F
7F
8F
9F
10F
11F
12F
13F
RF

2c. PCA-based measures for damage assessment in structures (using FRF)

Establish the reference model

Select the reference cases

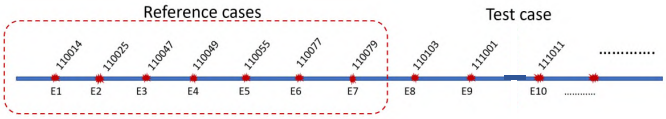

Identify FRF of each floor (ARX model)

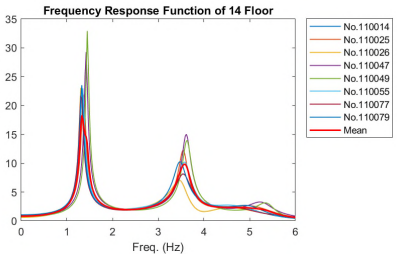

Extract the major principal component

$$[X]_i = \begin{bmatrix} FRF_{E1} \\ FRF_{E2} \\ \vdots \\ FRF_{Em} \end{bmatrix}_{m \times N} \quad ; m = Ref.cases;\ i = Floor\ No.$$

$$[C]_{N\times N} = cov(X) = \frac{X^T X}{N-1}$$

Eigen decomposition of [C] to obtain the 1st Principal Component {Φ}

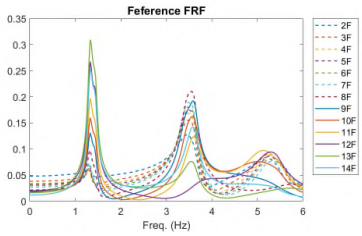

2c. PCA-based measures for damage assessment in structures (using FRF)

Step-1: Create X matrix (consider data from m sensingnode and each with N-data point)

***Sensor i*: FRF of i-th floor**
***m*: total floor number**

$$[X] = \begin{bmatrix} FRF\ R-1 \\ FRF\ R-2 \\ \vdots \\ FRF\ A-FR \\ FRFn\ B-1 \\ FRFn\ B-2 \\ \vdots \\ FRFn\ B-FR \end{bmatrix}_{2FR\times N}$$

Reference case "A"

Test case "B"

Step-2: Develop Covariance matrix

$$[C]_{m\times m} = cov(X) = \frac{XX^T}{M-1}$$

Step-3: Solve the eigenvalue & eigenvector of $[C]_{m\times m}$

The eigenvalue is $[\Lambda] = diag(\lambda_1, \lambda_2, \cdots, \lambda_m)$ and the corresponding eigenvectors

Step-4: Project the high dimension space $[X]$ matrix into a 2-dimension space

(by selecting the two major principal components, PC. Normalization on each PC is needed)

$$[X]_{2D-PCA} = \begin{bmatrix} x_{11} & x_{12} \\ x_{21} & x_{22} \\ \vdots & \vdots \\ x_{m1} & x_{m2} \end{bmatrix}$$

Step-5: Plot the $[X]_{2D-PCA}$ on a complex plain as defined

$$P_{ref} = \begin{Bmatrix} \vec{p}_1 \\ \vec{p}_2 \\ \vec{p}_3 \\ \vdots \\ \vec{p}_m \end{Bmatrix} = \begin{Bmatrix} \vec{p}_1 = x_{11} - ix_{12} \\ \vec{p}_2 = x_{21} - ix_{22} \\ \vec{p}_3 \\ \cdots\cdots\cdots \\ \vec{p}_m = x_{m1} - ix_{m2} \end{Bmatrix}$$

Test the similarities between test case and reference case through 2D-PCA mapping

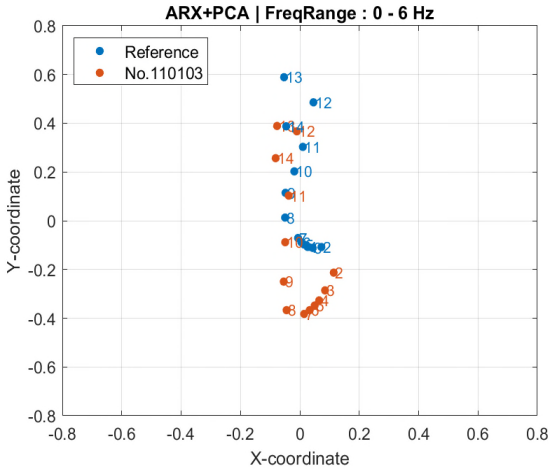

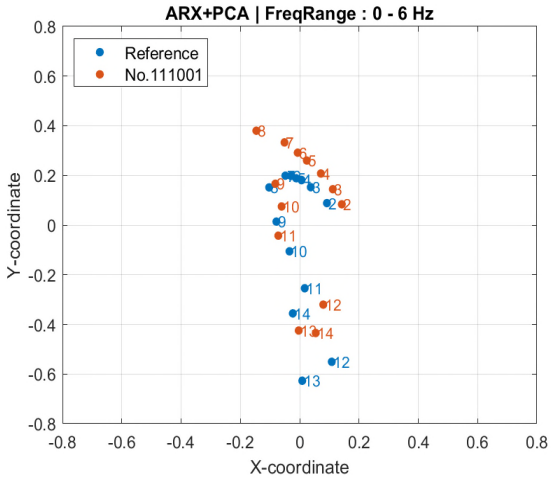

Test the similarities among all reference test cases

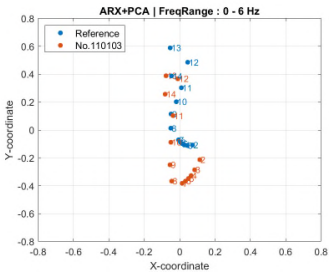

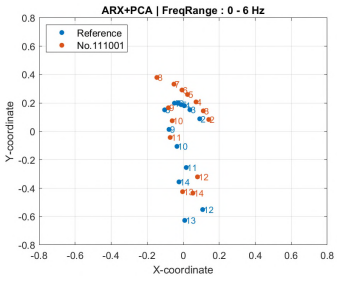

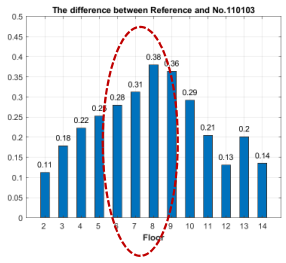

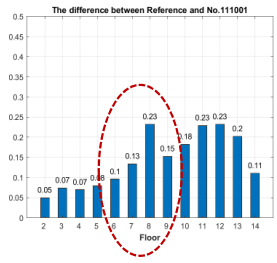

PA ~ 200 gal
Duration ~ 40 sec

PA ~ 200 gal
Duration ~ 25 sec

No.110103/Ref.

No.111001/Ref.

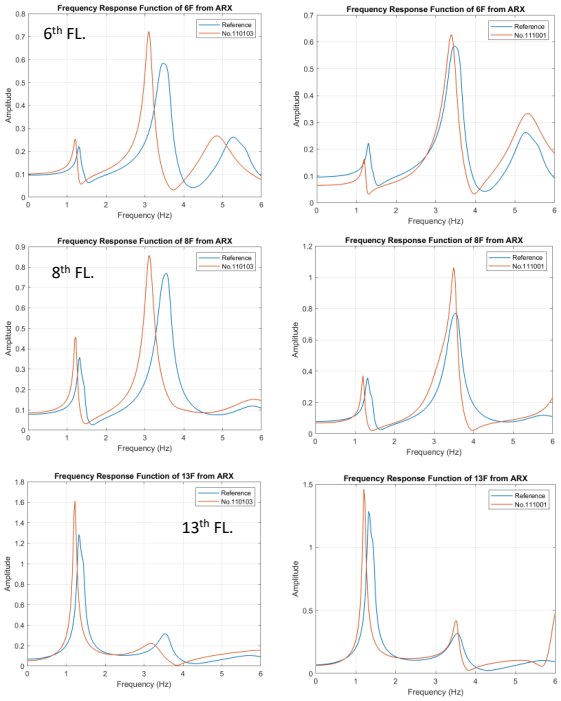

2c. Use BonaFide RSI (Fixed-length window) to detect time-varying 3-D mode shape

(using all measurement from each seismic event)

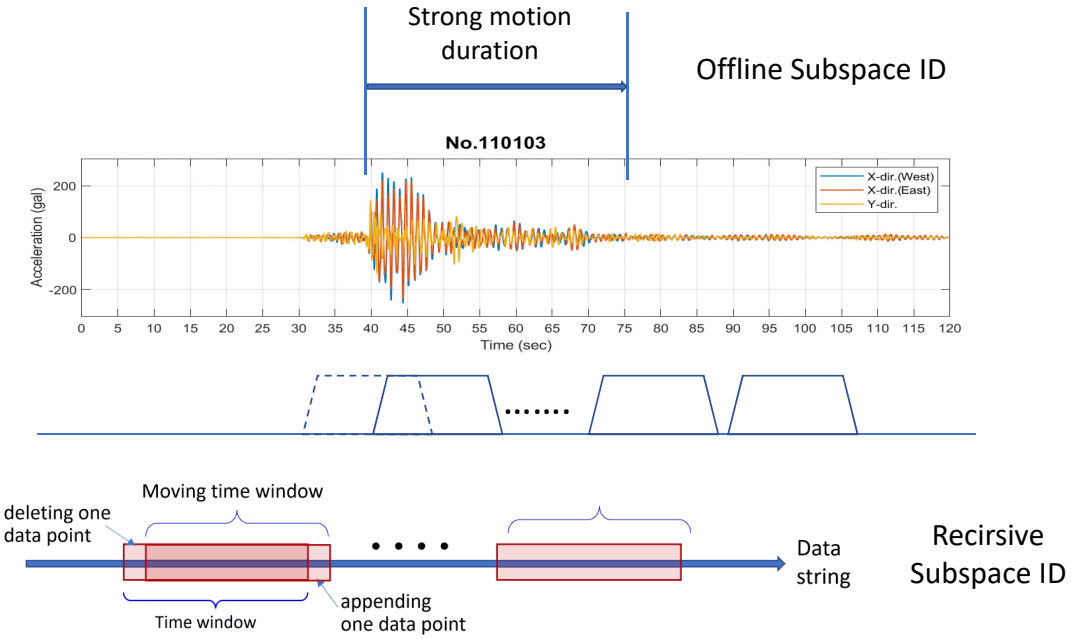

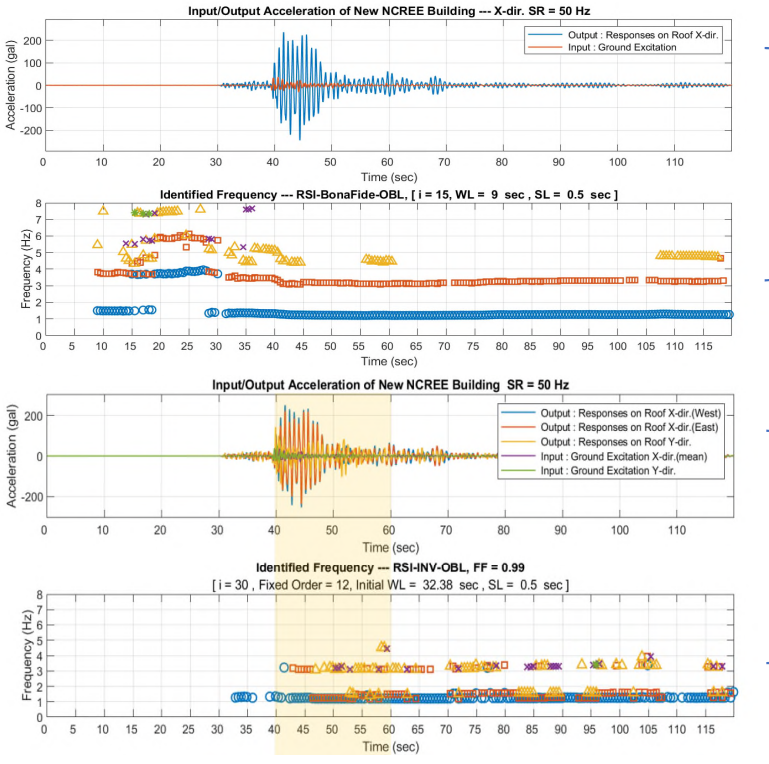

Using the average data of X-east & X-west

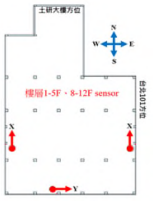

Using data from X-east, X-west & Y-direction

Seismic event No.110103

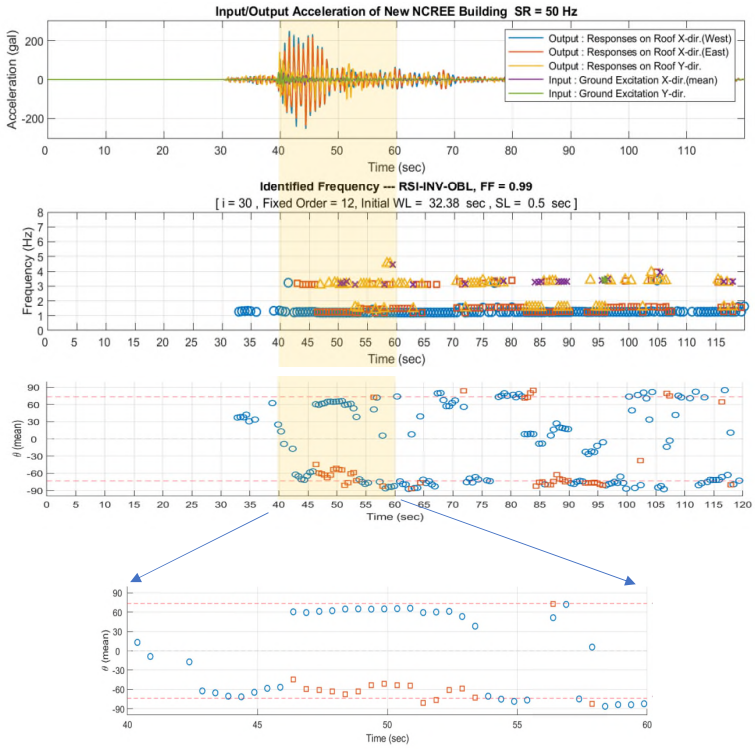

3D mode shape

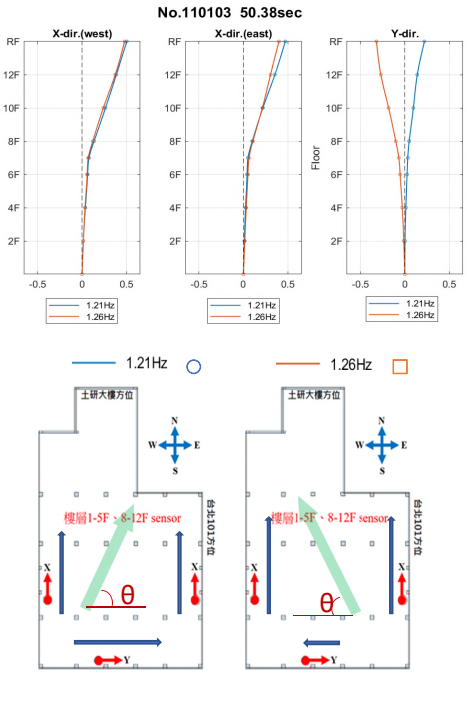

3. Time domain Analysis (on data under operating condition): using SSI-COV algorithm

- Subspace Identification for Operational Modal Analysis (FD, SSI, etc)

Extract the modal parameters from the dynamic response to operational forces. (*Features*: A vector of system natural frequencies, mode shapes, etc.)

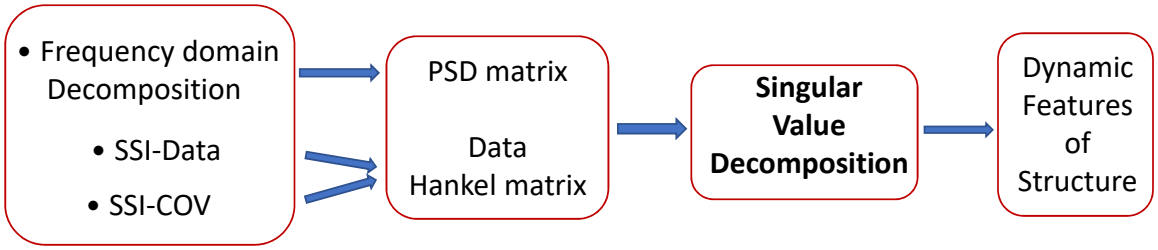

(Event by event)

SSI-COV: Conduct SVD of Toeplitz matrix
SSI-Data: Using projection (row space of future output into the row space of past output)

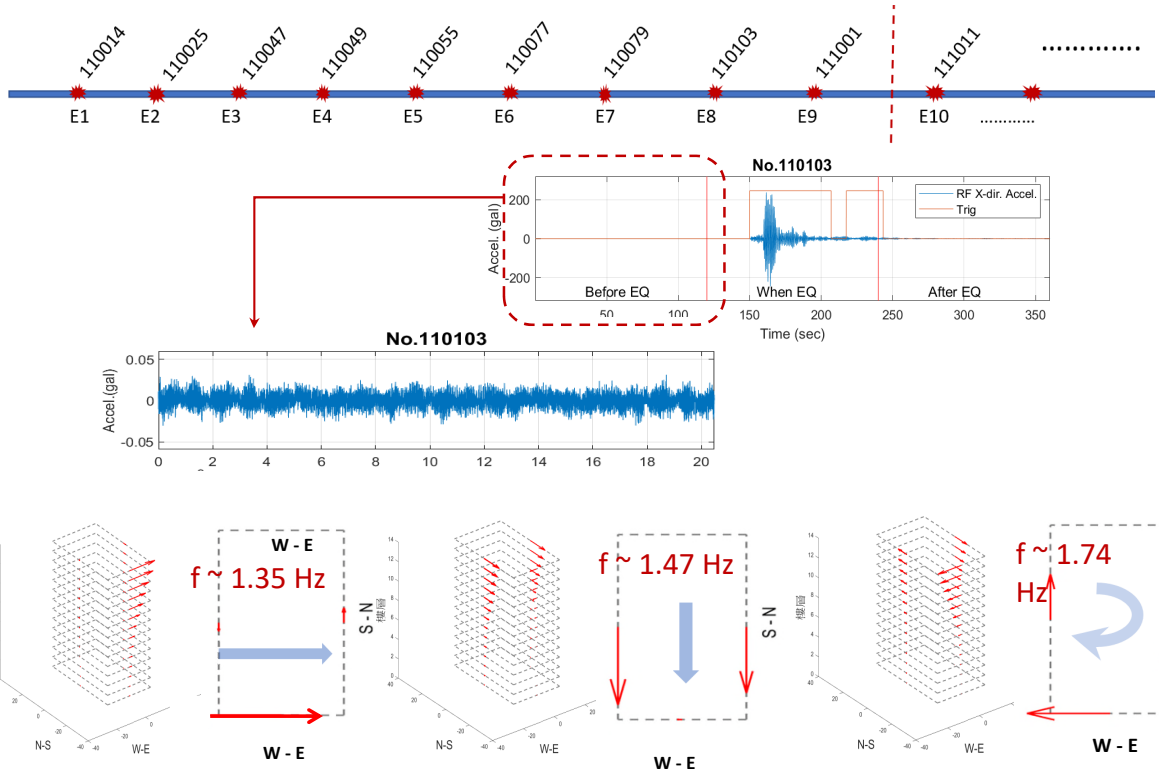

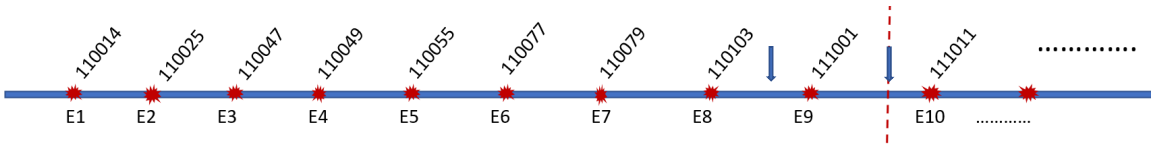

Use MAC to check mode correlation

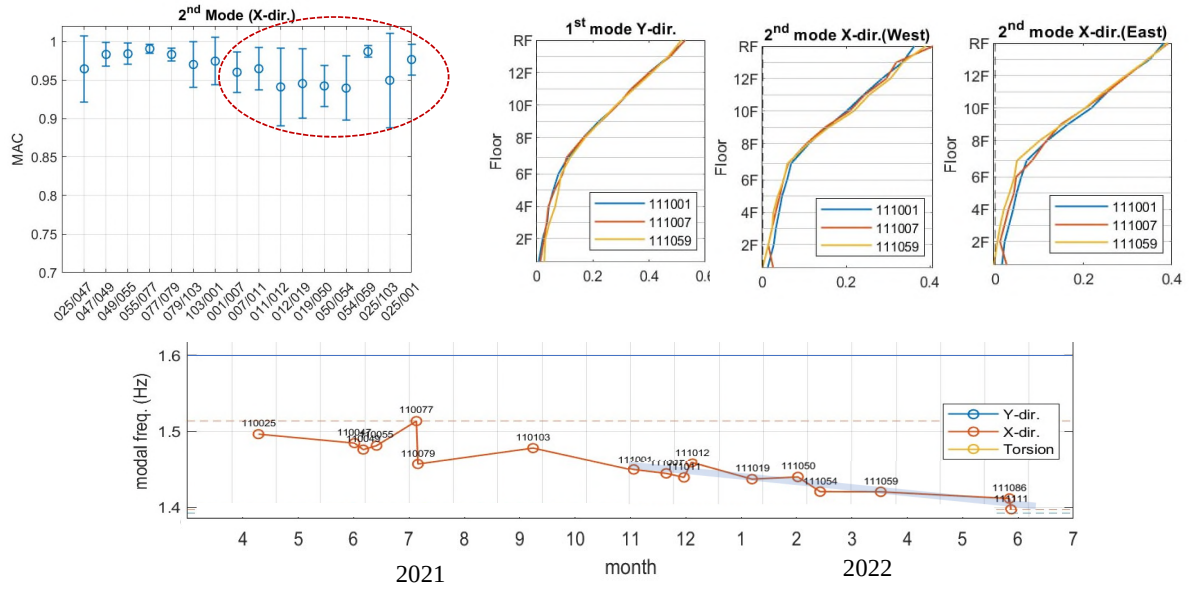

Summary: In relating to damage measure, the goal of this study is to develop damage prognosis solution with a SHM system for civil infrastructures.

1. Detect changes in resonance frequencies of structure under operating condition and during earthquake excitation,
2. Identify the changes in mode shape (or curvature) and FRF
3. Change in stiffness matrix

$$\left.\begin{aligned}[K] &\approx \sum_{i=1}^{n} \omega_i^{\,2} \phi_i \phi_i^{\,T} \\ [K]^{*} &\approx \sum_{i=1}^{n} \omega_i^{\,*2} \phi_i^{\,*} \phi_i^{\,*T}\end{aligned}\right\} \quad [\Delta K_d] = [K] - [K]^{*} \qquad ;\{D_i\} = [\Delta K_d]\{\phi_i\}^{*}$$

Summary:

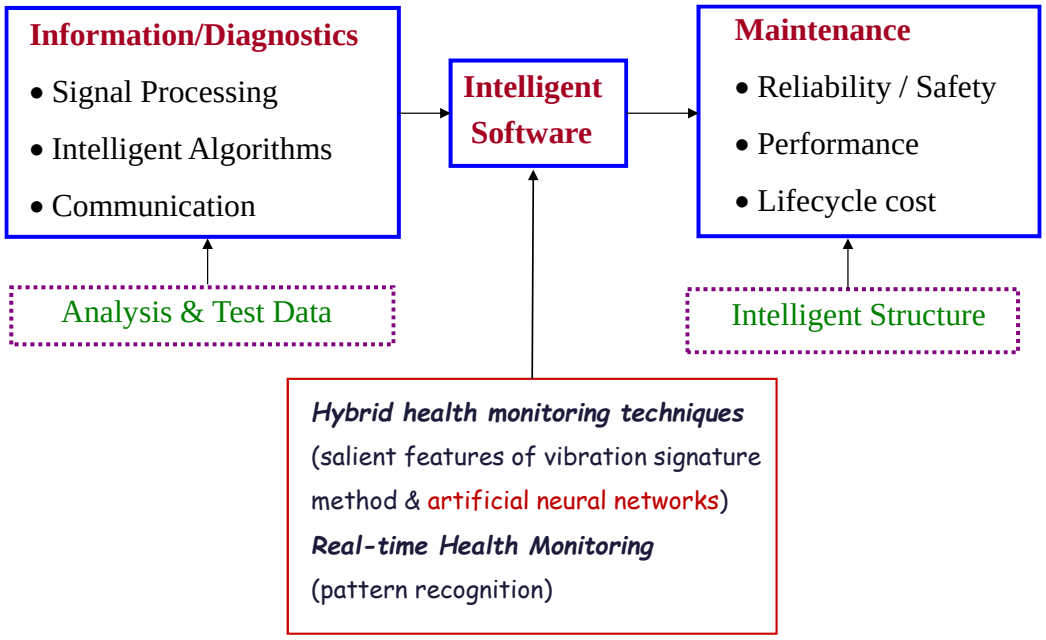

Thank you for your attention !

Questions ?

Prof. Kuo-Fong Ma

Institute of Earth Sciences, Academia Sinica, Taiwan

Topic：Observation and Modeling of Strong-Velocity Pulses of Earthquakes

Observation and Modeling of Strong-Velocity Pulses of Earthquakes

Kuo-Fong Ma

馬國鳳

Institute of Earth Sciences, Academia Sinica

Department of Earth Sciences, National Central University, Taiwan

Large velocity pulse observed in the 1999 Mw7.6 earthquake

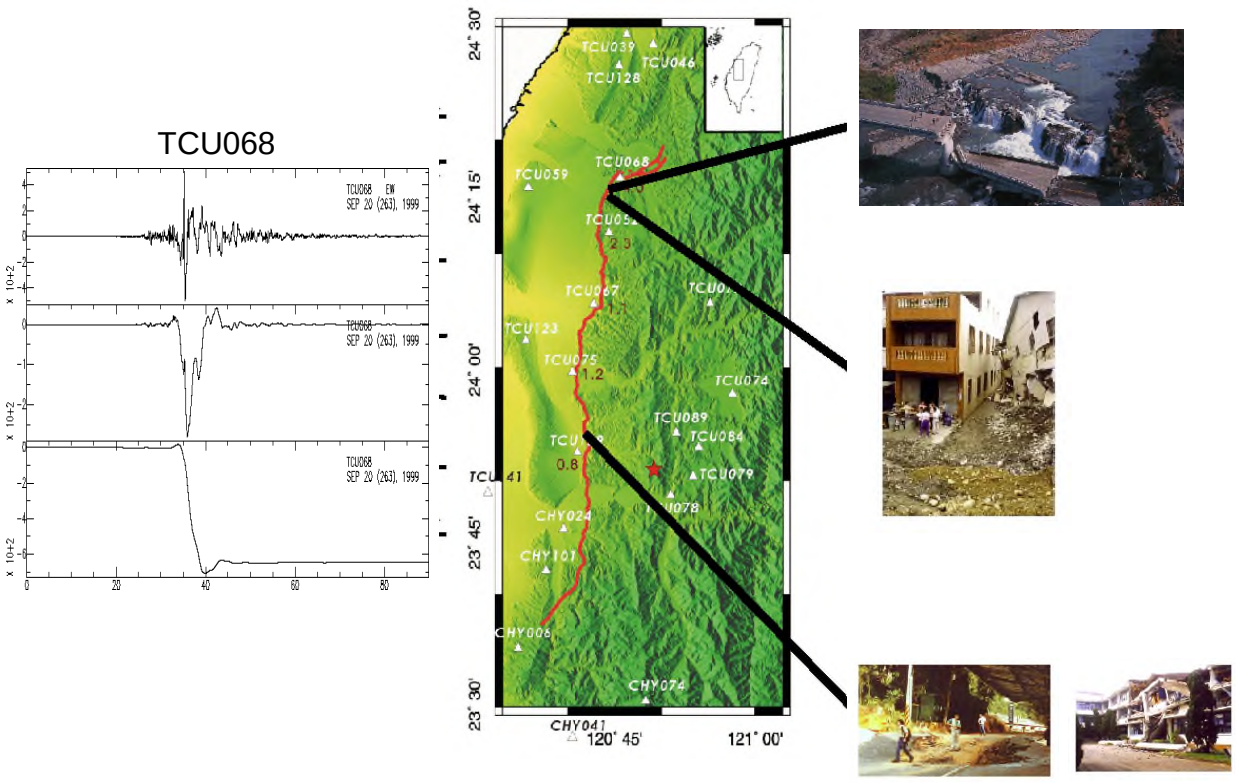

1999 Chi-Chi (Mw7.6) Earthquake

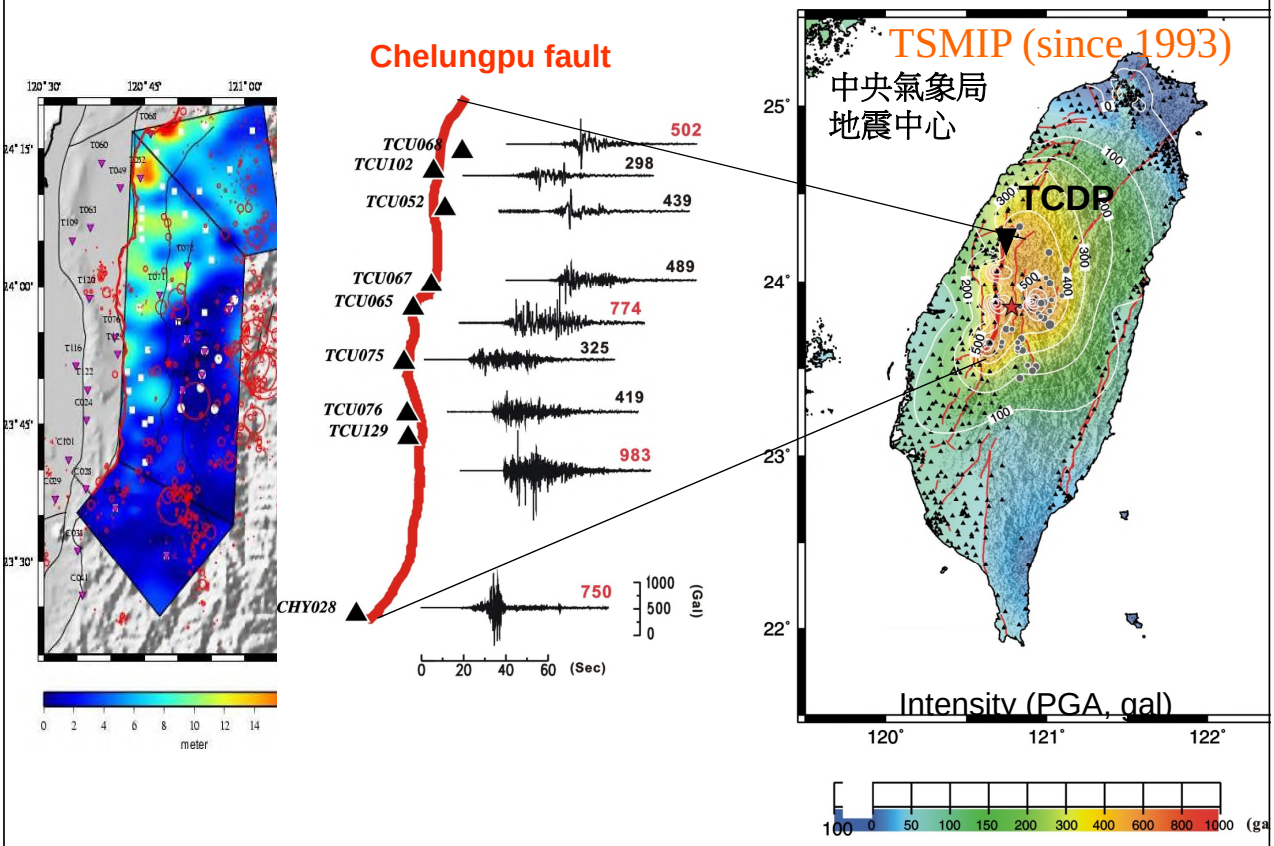

Evidence for fault lubrication Ma et al. (2003)

- **Start at T1**
- **Impulsive acc. waveform between T2 (max.) and T3 (small)**
- **T3: max. velocity**
- **Continue slip until T4**

=>Widening of the fault gap and reduction of asperity collision (displacement increase yields large lubrication pressure)

*** Change of frequency contains after T3**

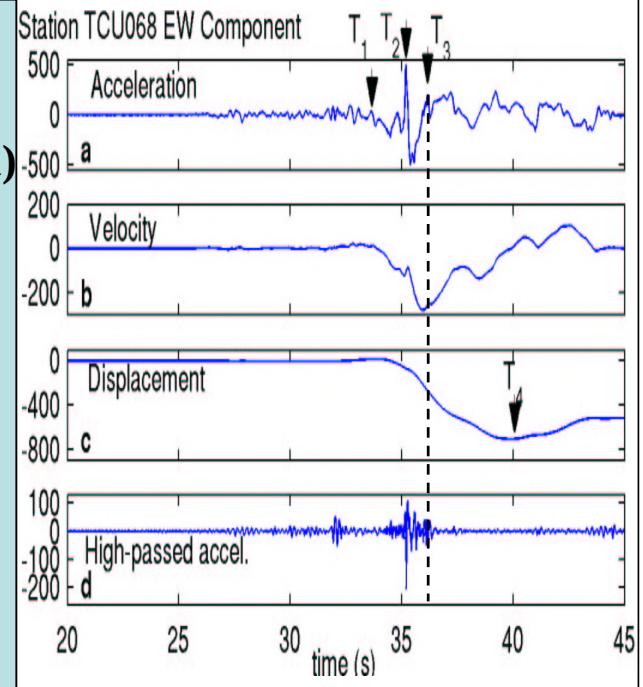

Large velocity pulses are now commonly observed with and without static offset

Mw6.4 Meinong earthquake

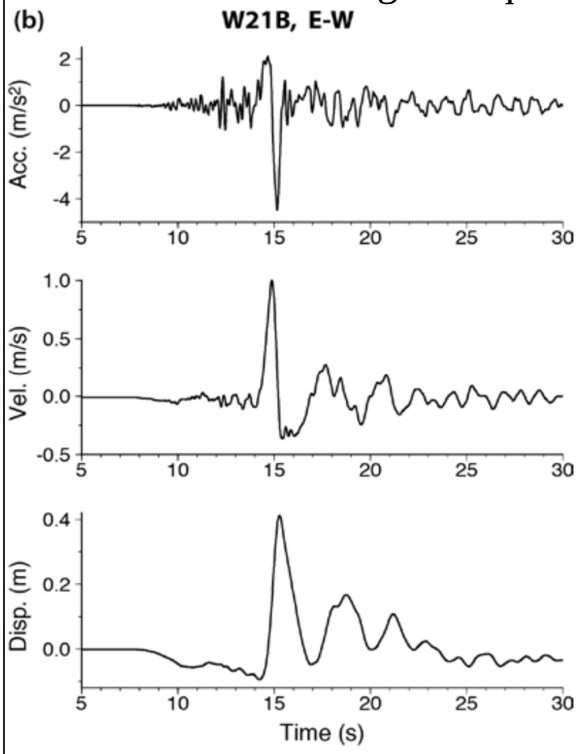

Mw7.6 Chi-Chi earthquake

Station TCU068

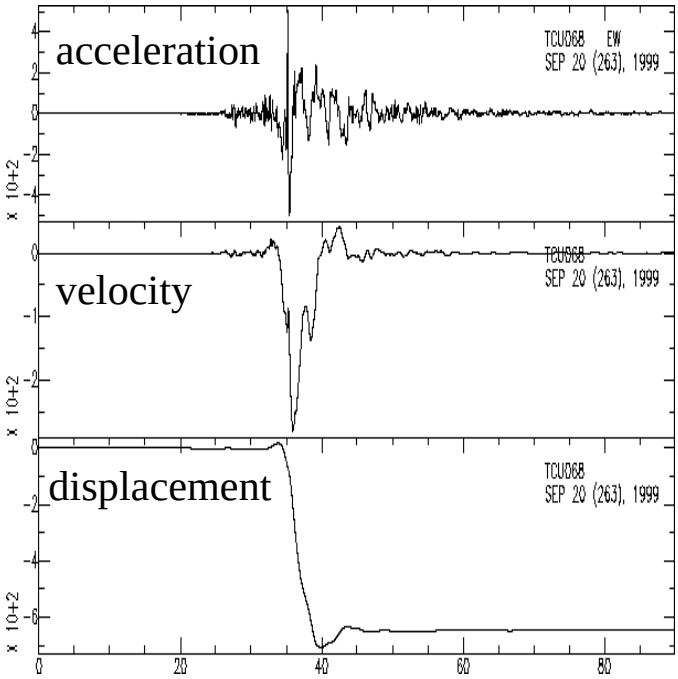

Any PGV scaling relationship to Asperity Distance, and Period to Magnitudes ?

Ground-Motion Velocity from Large Earthquakes

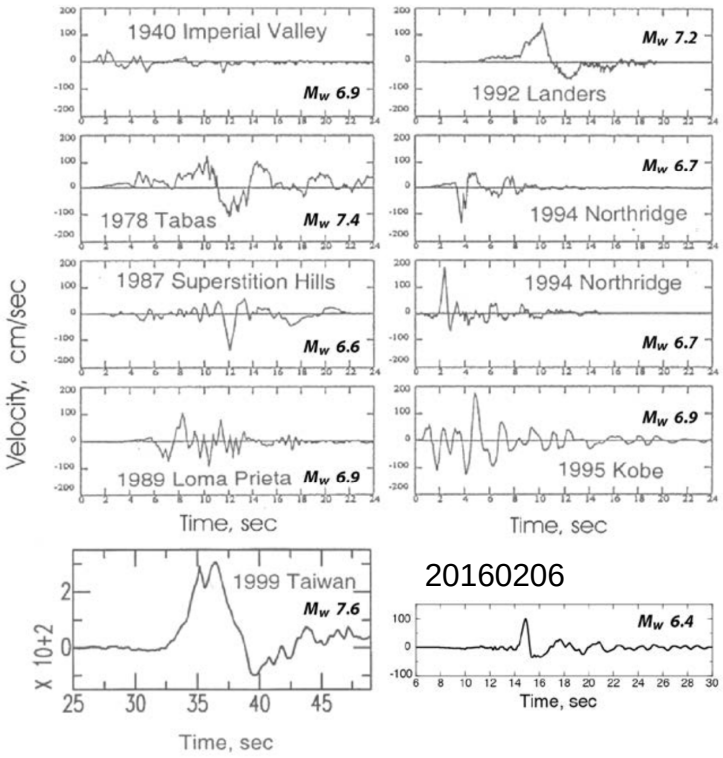

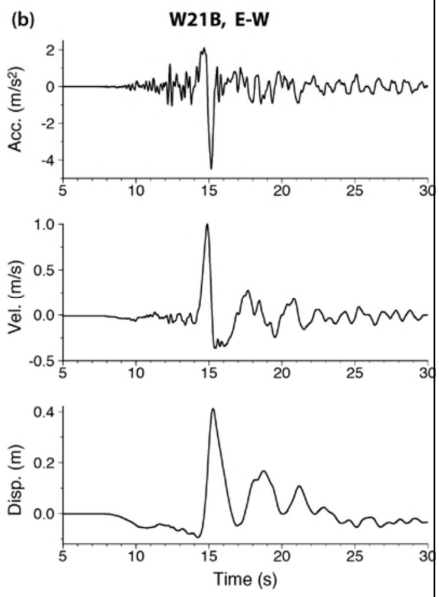

*20180206 Hualiean earthquake, W028 ;
* 20220918 Mw7.0 Chihshan earthquake

20160206 Meinong Earthquake

Dense Seismic Array: (Understanding the source from unfiltered Data) Palert, CWB RTD, Real-time strong motion, BATS

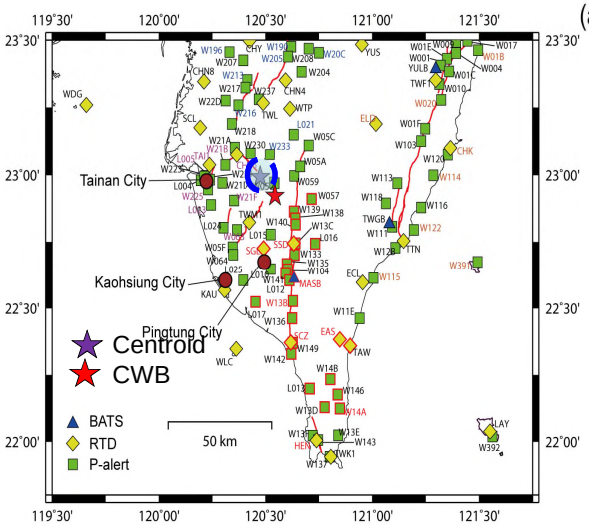

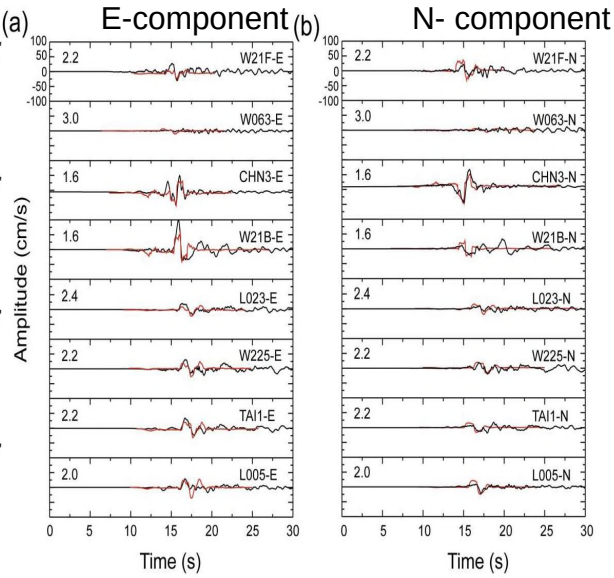

Asperity (Patch) Model Simulation

- Large Pulsive velocity motion was directly from the asperity.

- Asperity was formed in rupture direction, but, the large PGV from asperity directly, not directivity.

****Important message for ground motion prediction!**

Lin et al. (BSSA, 2018)

20160206 Meinong Earthquake PGV/PGA with GMPE

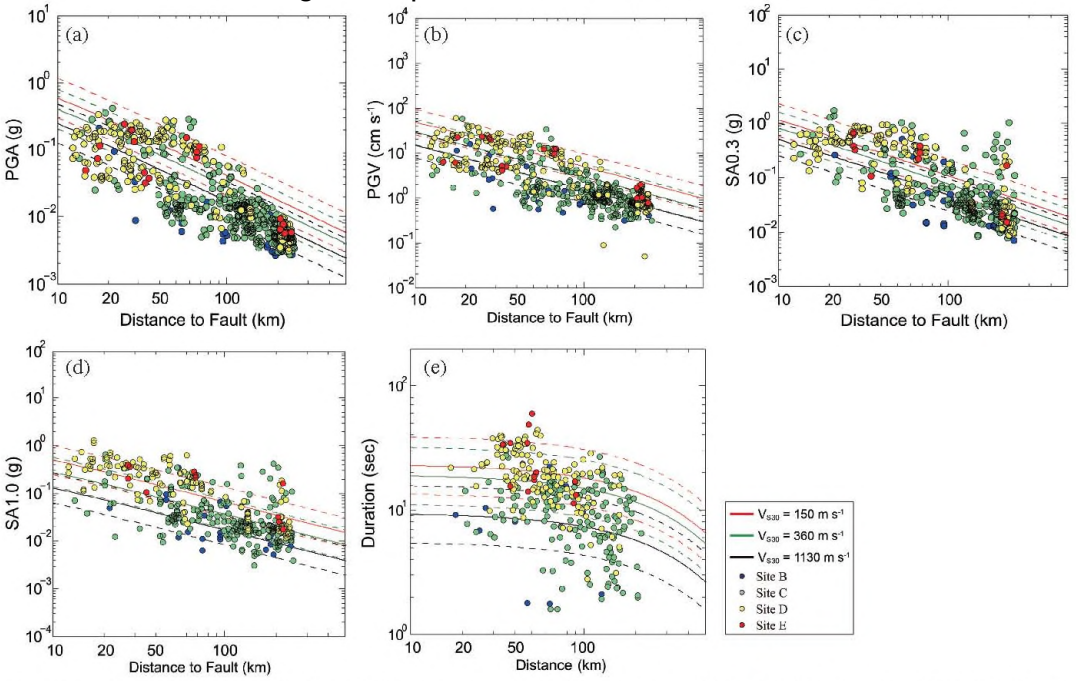

Fig. 3. Comparison between observations from the Meinong earthquake and the attenuation model developed by Lin et al. (2012) for (a) PGA, (b) PGV, SA for the following periods (c) 0.3 s; (d) 1.0 s; and (d) shaking duration by Lee et al. (2015). The solid lines are the median of the attenuation models and the dashed lines are curves for the median plus one standard deviation. The lines in red, green and black denote the attenuation model for the sites with Vs30 of 150, 360, and 1130 m s^{-1}, respectively.

=> Any PGV scaling relationship to Asperity Distance?

Lee et al., (2017)

1994 Northridge (California)
5 slip models

[e.g. Dreger, 1994]

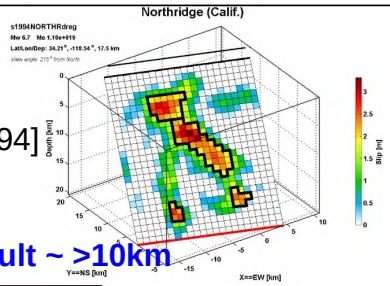

Asperity D>1.5Dav

Extreme PGA/PGV to the fault ~ >10km **to the asperity < 10km**

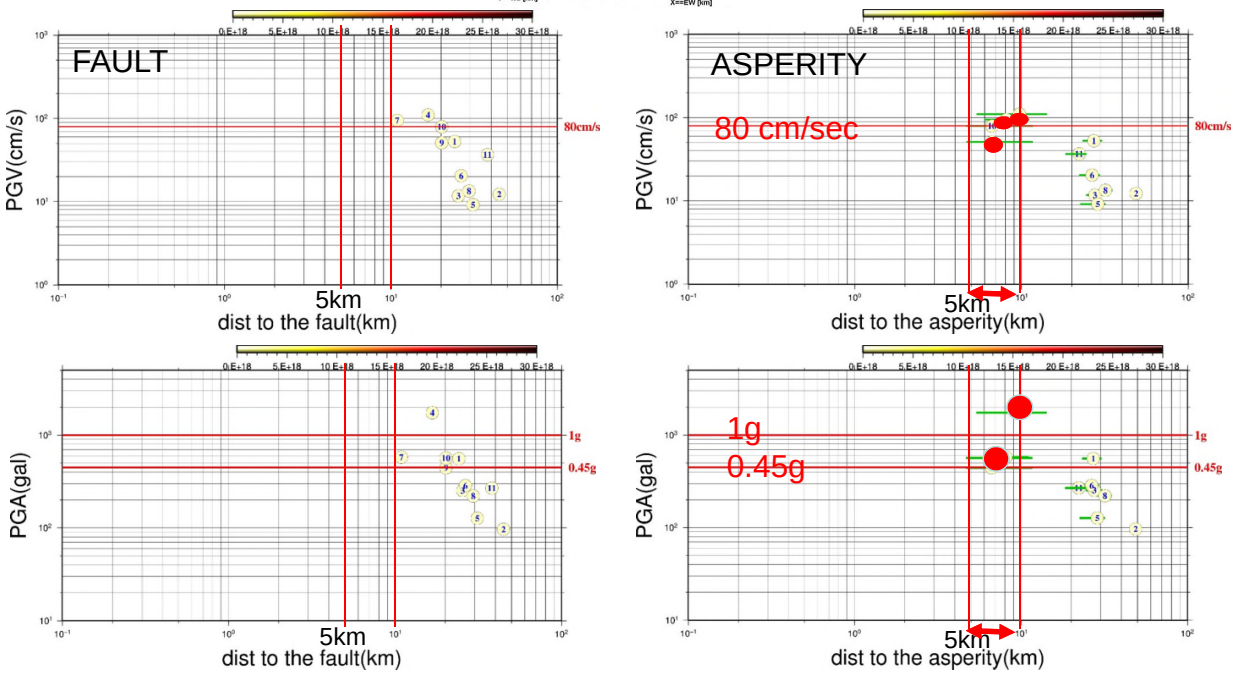

ChiChi (Taiwan)

1999 ChiChi (Taiwan)
20 slip models

[e.g. Ma et al., 2001]

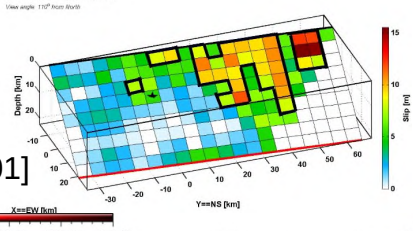

Asperity: D>1.5Dav

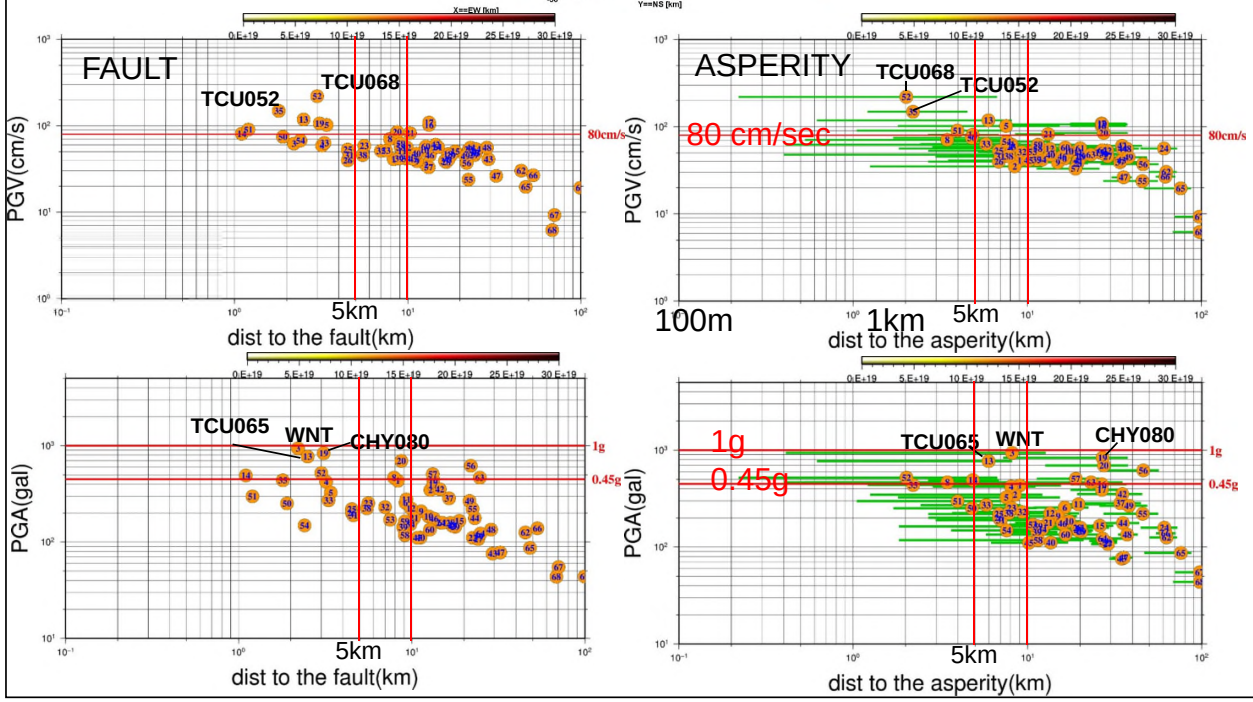

Moderate earthquakes occurred more frequently, and, thus, require further attention!

Within- and Between-Event Variabilities of Strong-Velocity Pulses of Moderate Earthquakes within Dense Seismic Arrays

Yen, M.-H., S. von Specht, Y.-Y. Lin, F. Cotton, and K.-F. Ma (2021). Bull. Seismol. Soc. Am. 112, 361–380, doi: 10.1785/0120200376

TABLE 1
Summary of the Parameters of the Earthquakes Considered in This Work

Event	UTC Time (yyyy/mm/dd hh:mm:ss)	Epicenter	Focal Depth (km)	Strike and Dip	Rake	M_w	Faulting Type
Kumamoto foreshock	2016/04/14 12:26:36	32.7417° N, 130.8087° E	11.39	205° and 74°	180°	6.1	Strike slip
Kumamoto mainshock	2016/04/15 16:25:06	32.7545° N, 130.7630° E	12.45	205° and 72°	−142°	7.04	Strike slip
				235° and 65°	−142°		Strike slip
Meinong	2016/02/05 19:57:27	22.92° N, 120.54° E	14.6	295° and 22°	20°	6.4	Strike-slip like
Hualien	2018/02/06 15:50:43	24.132° N, 121.659° E	10.6	216° and 56°	26°	6.4	Oblique slip
Darfield	2010/09/03 16:35:46	−43.6148° N, 172.0386° E	10.84	85° and 82°	154°	7.02	Strike slip

Values of the pulse period, ❄🔲, as a function of earthquake moment magnitudes.
Adoptive Tp using Shahi and Baker (2014)
The extracted pulse period with static-offset removal for this study.

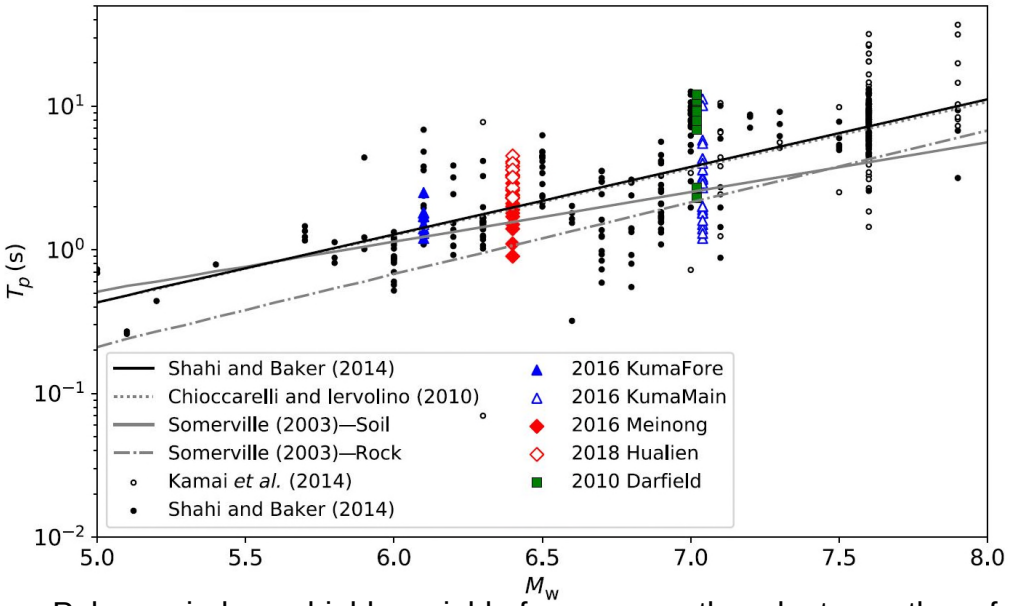

Pulse periods are highly variable from one earthquake to another of similar magnitude (between-event variability) or even for various records of a single earthquake (within-event variability).

Pulse retrieval with and without static-offset (2016 Kumamoto mainshock)

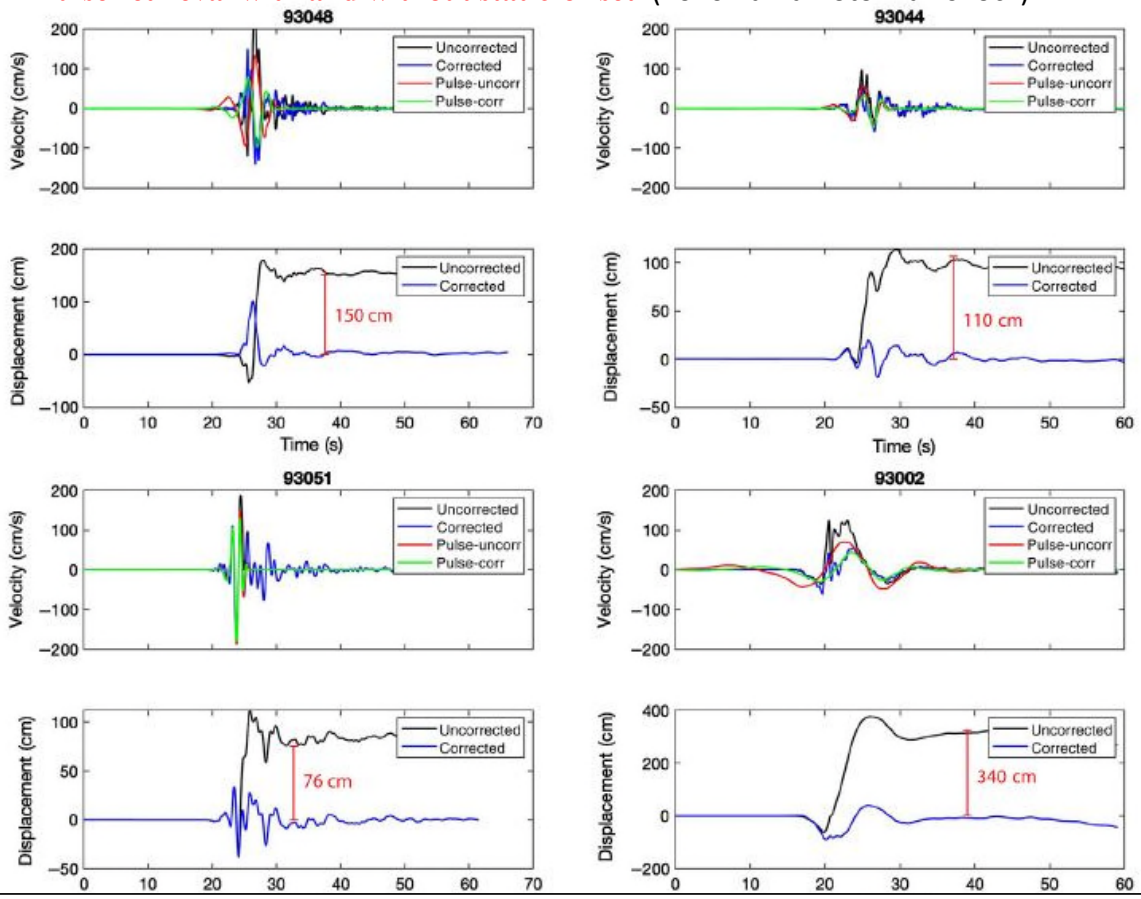

Pulse velocity and period before and after the static-offset removal for the cases of the pulses of the 2016 Kumamoto mainshock (dark outline) and the 2010 Darfield earthquake (light outline).

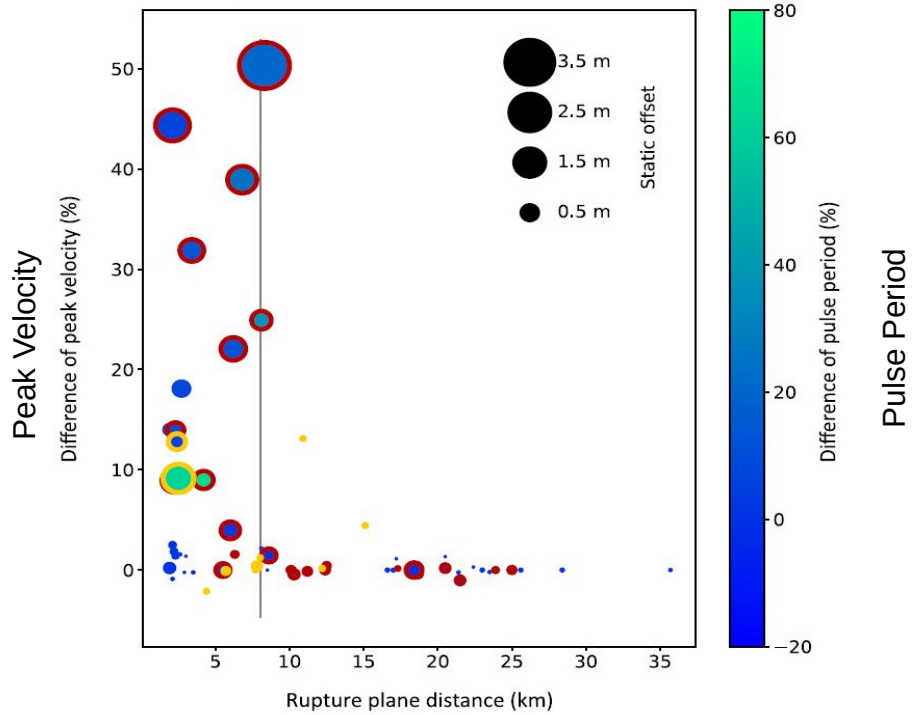

Strong-velocity pulses without the static-offset effect and finite-fault slip distributions of the five moderate earthquakes. The color in circles represent the pules period, ❄🔲.

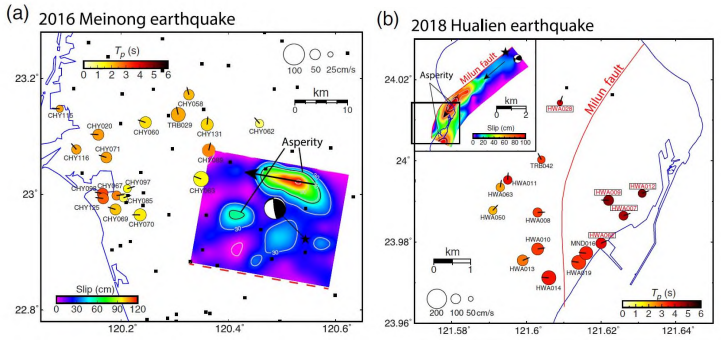

The identified asperity and the rupture direction of slip distribution.

Squares represent the station without pulses. The stations names with frame of which represent the pulses that are impacted upon the static offset.

Finite-fault models, Lee et al. (2016; 2019)

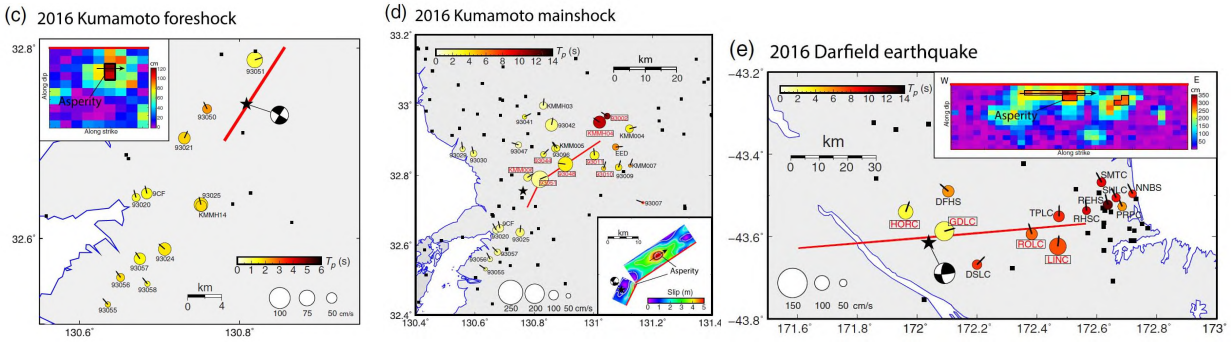

Kobayashi *et al.* (2017), Asano and Iwata (2016), Hayes (NEIC, Darfield 2010

Rotated ground motions along pulse orientations (thick curve) and extracted pulses (dashed curve)

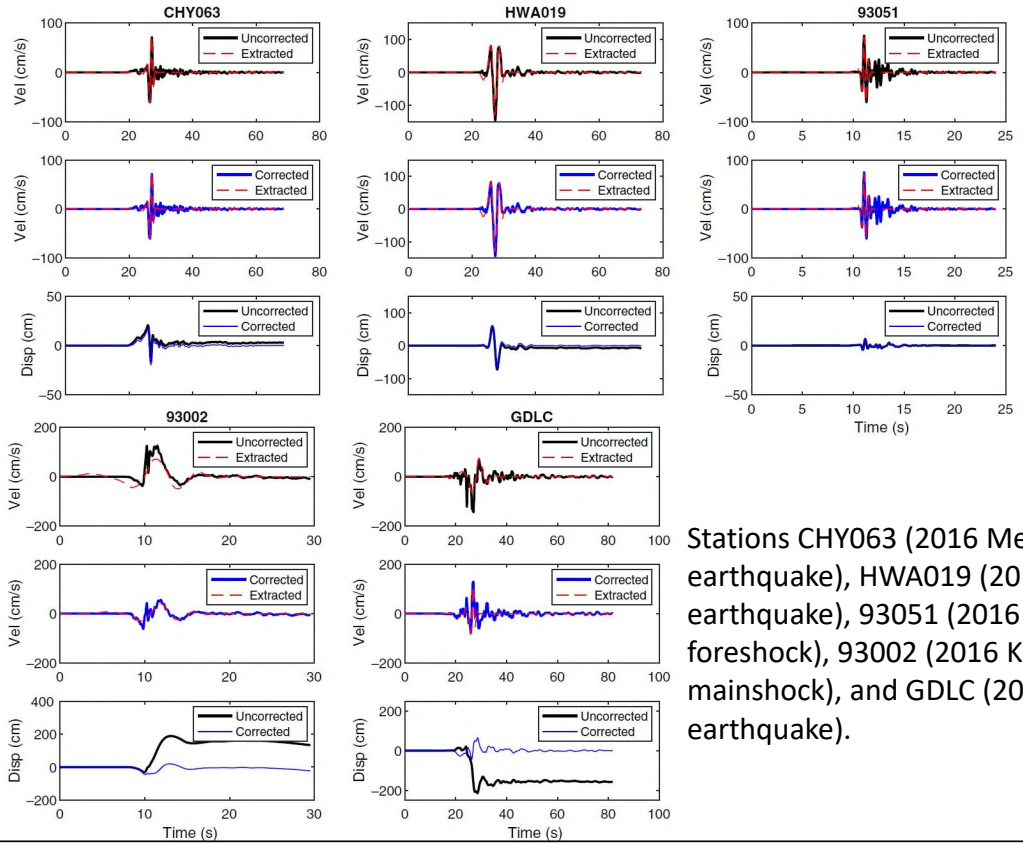

Stations CHY063 (2016 Meinong earthquake), HWA019 (2018 Hualien earthquake), 93051 (2016 Kumamoto foreshock), 93002 (2016 Kumamoto mainshock), and GDLC (2010 Darfield earthquake).

Values of the pulse period, ❄□, as a function of earthquake moment magnitudes.

Adoptive Tp using Shahi and Baker (2014)

The extracted pulse period with static-offset removal for this study.

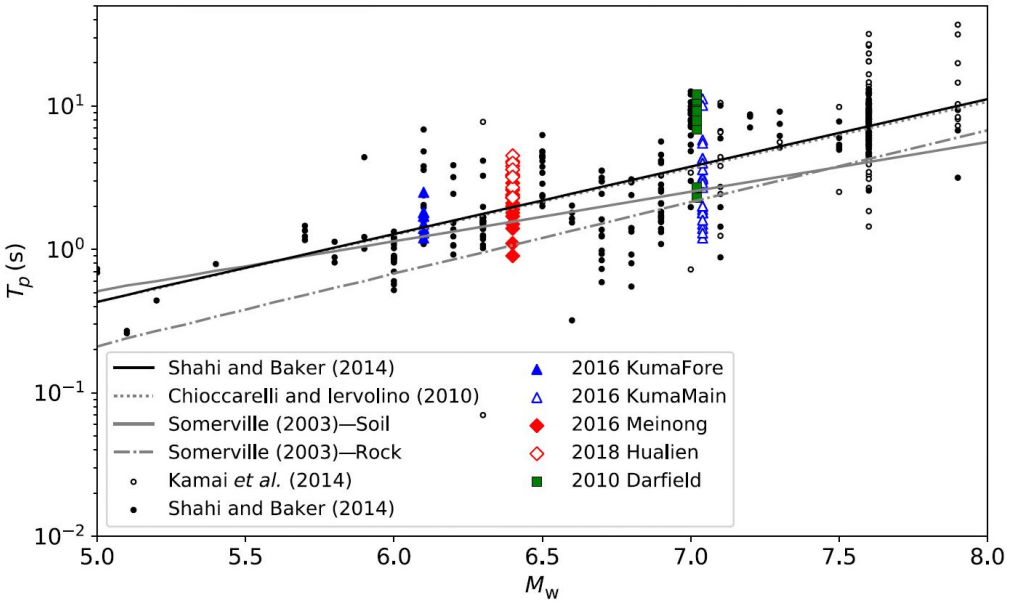

Pulse periods are highly variable from one earthquake to another of similar magnitude (between-event variability) or even for various records of a single earthquake (within-event variability).

Modeling the within and between events variables for the 2018 Hualien earthquake

(a)

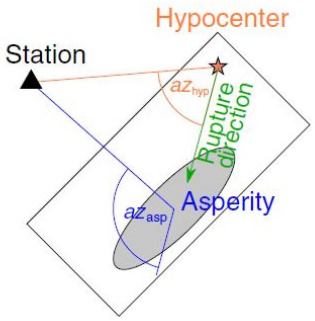

Geometrical setting for the definitions of the azimuth from the hypocenter (♋⌘〰▱□□) and the azimuth from the asperity (♋⌘♋⬧□). Azimuth indicates the angle between the station's azimuth to the rupture direction within the asperity.

Peak ground velocity (PGV) as a function of 'stations' azimuth

(b)

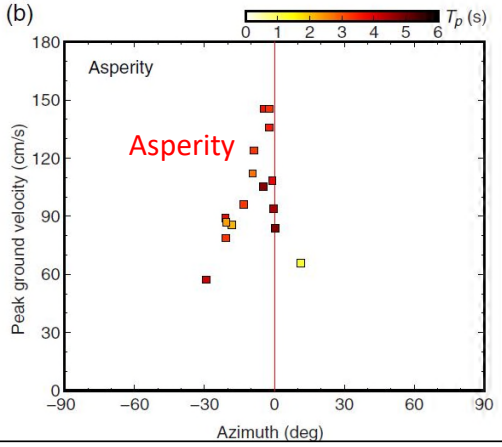

(c)

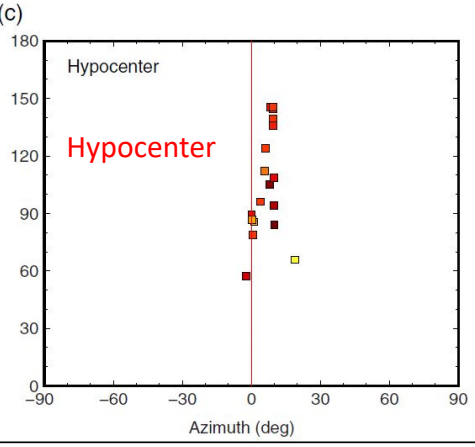

Scaling of (a) PGV and (b) pulse period, ❄□, according to the rupture plane distance. The static offset of the events has been removed.

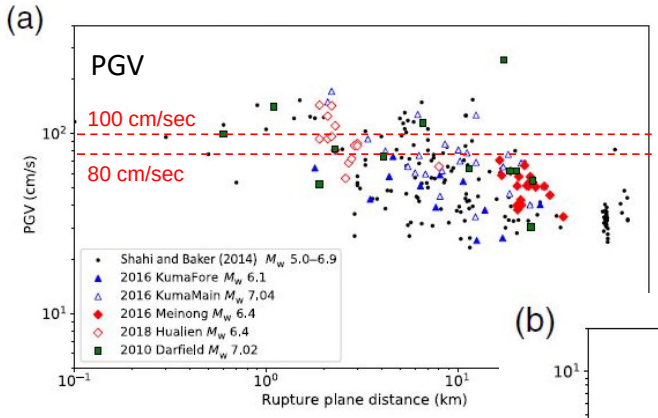

PGV decreased with rupture plane distance, while Tp shows large variance between and within events

PGV > 100 cm/sec, R< 3km
PGV > 80cm/sec, R<10km

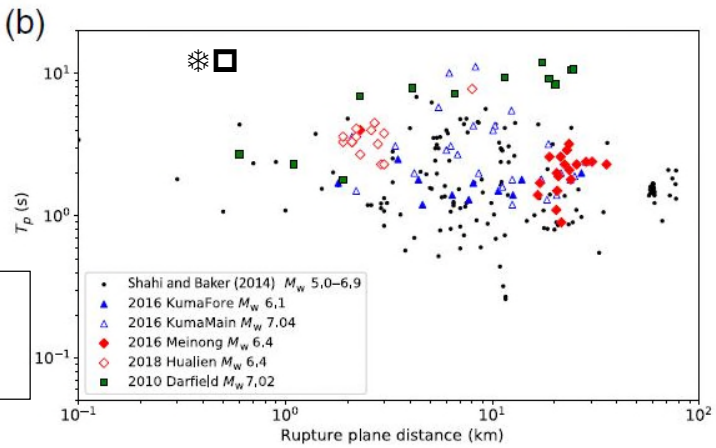

The data of Shahi and Baker (2014) are shown for earthquakes magnitudes between 5.0 and 6.9.

Modeling the strong-velocity pulses
Simulation setting

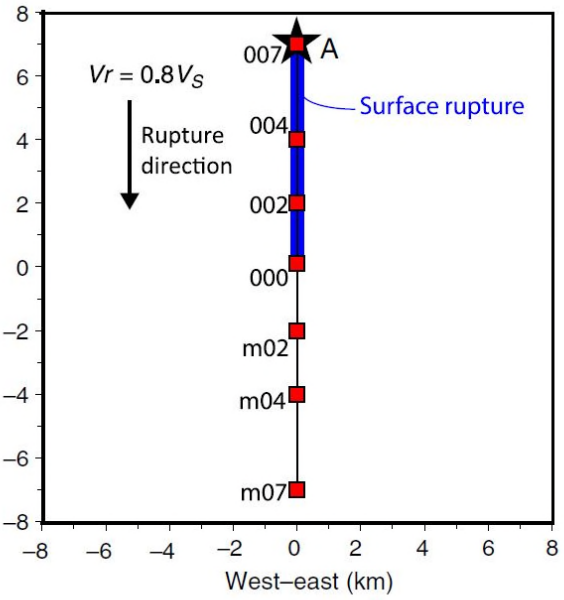

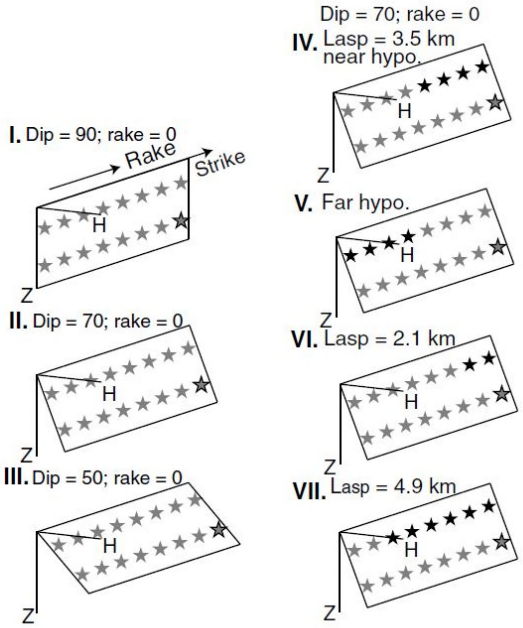

Fault geometry models.
Black stars are asperities (💣◆🗄🖱). Gray stars are the subevents with background slips.

Simulated ground motions (black) and extracted pulses (red)

Pulse indicator (PI): reliability level

PI>10 as a threshold

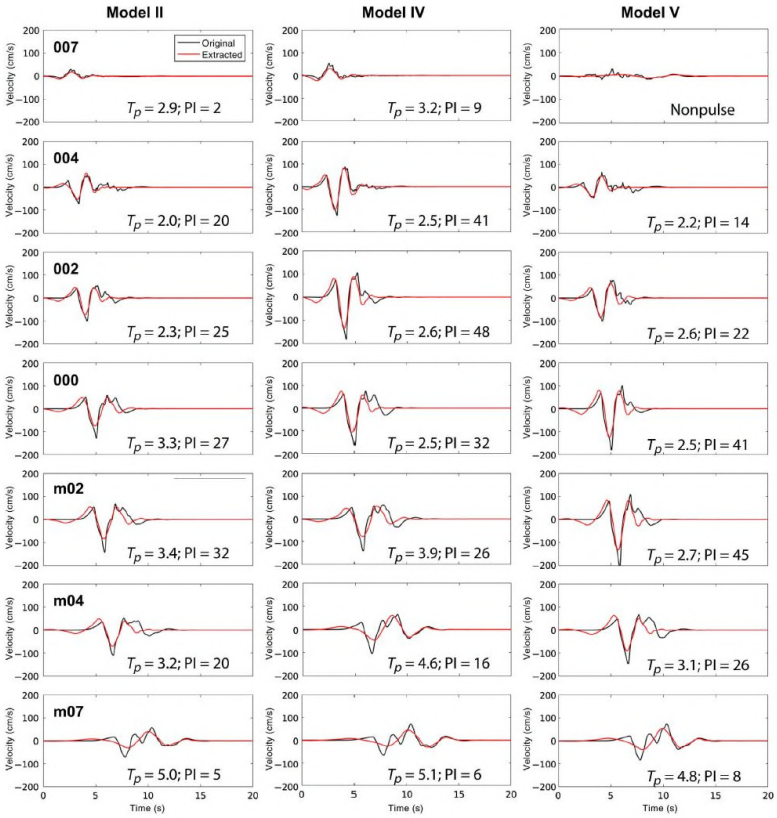

PI distribution of simulations

homogenous slip

asperity near the hypocenter

asperity far from the hypocenter

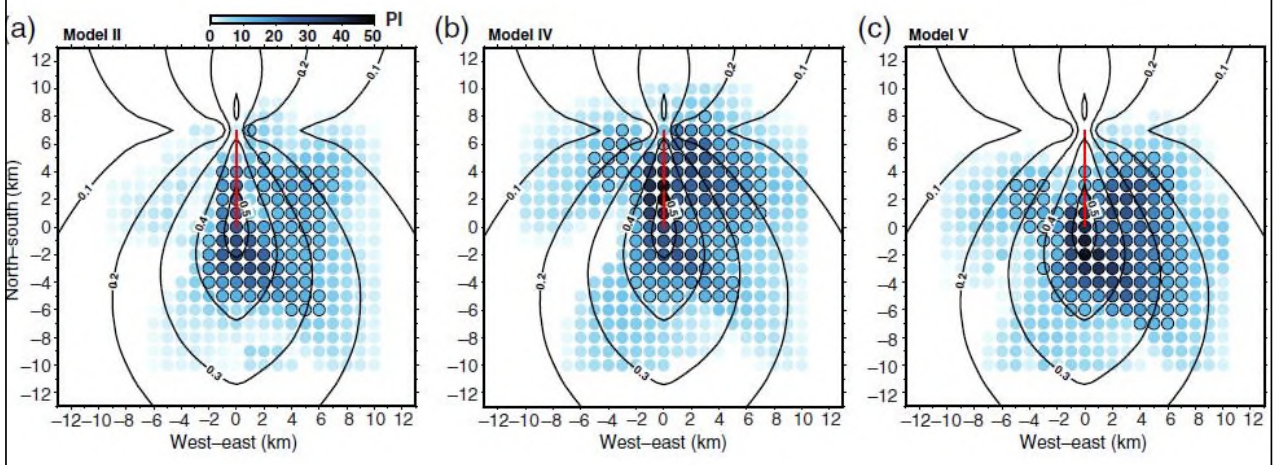

The contours indicate the probability of pulses (Shahi and Baker, 2014, equation 23). Circles indicate the pulses from the simulations. The color shows the PI values. The circles with outlines represent the pulses with PI > 10.

Probability of pulses (Shahi and Baker, 2014, equation 23) overestimated spatially, but, underestimated in near-fault distance.

Distribution of the pulses for various asperity locations and sizes

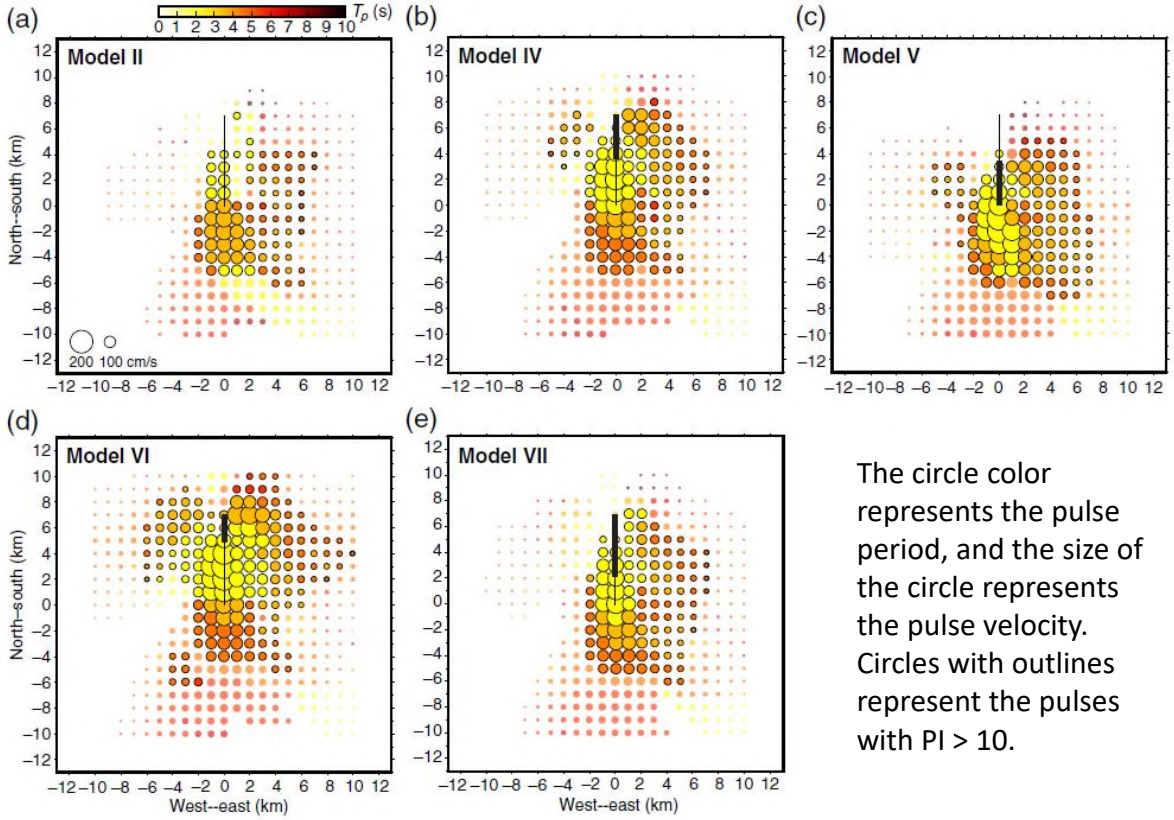

The circle color represents the pulse period, and the size of the circle represents the pulse velocity. Circles with outlines represent the pulses with PI > 10.

Pulse velocities as a function of azimuth for various dipping angle cases and five moderate earthquakes in this study.

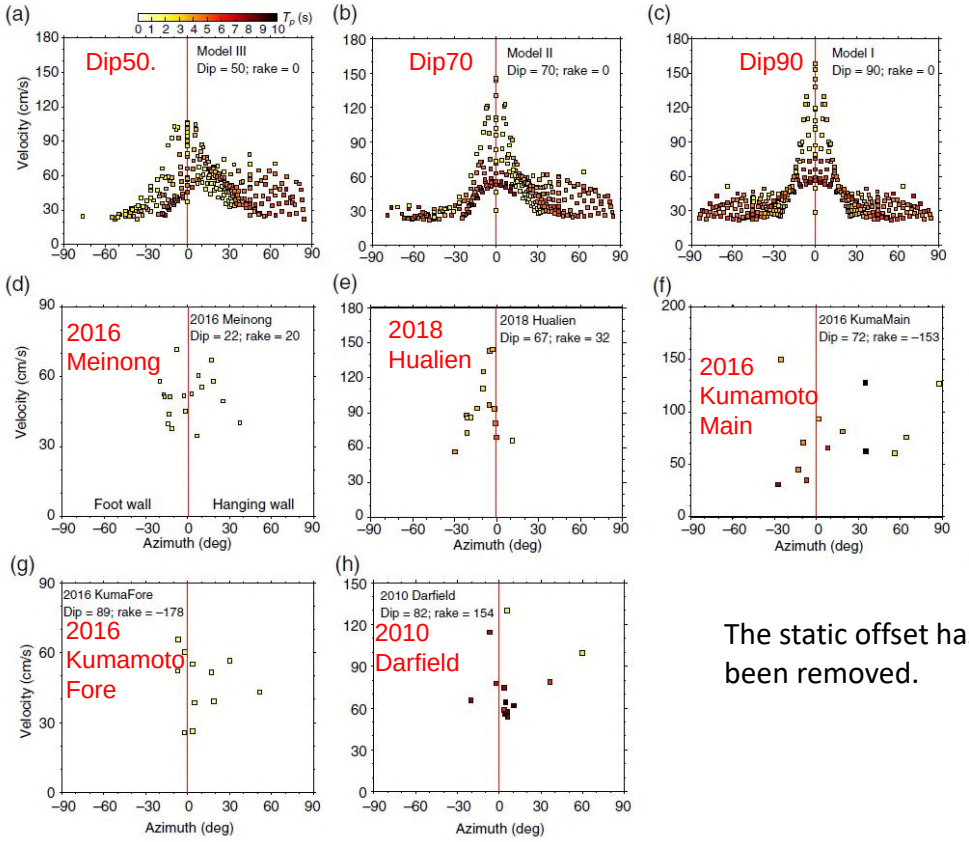

synthetics

observations

The static offset has been removed.

Comparison of the observed (obs.) mean pulse periods from all pulses in the events and the mean ❄🔲

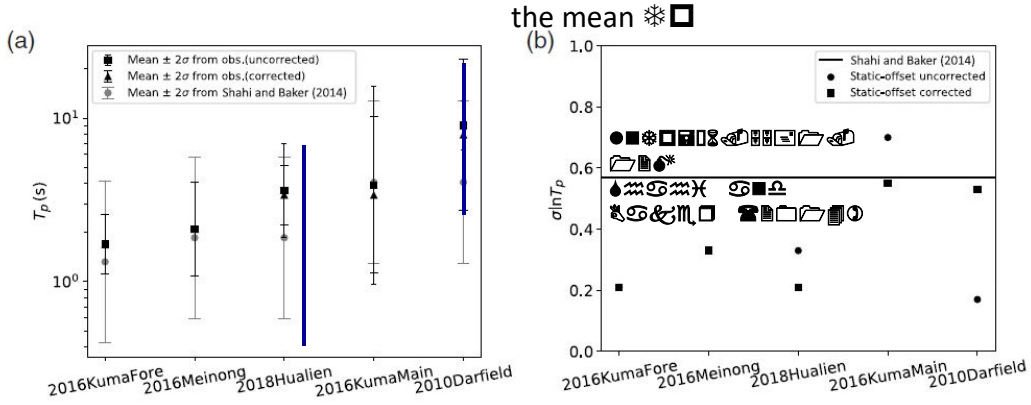

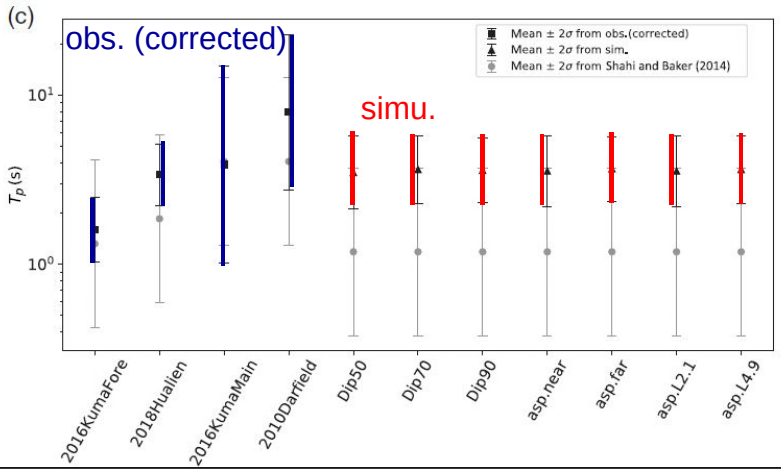

Comparison of the observed (obs.) and simulated (sim.) mean pulses periods within a rupture distance of 15 km and the ❄🔲 periods.

20220918 MW7.0 Chinshan earthquake

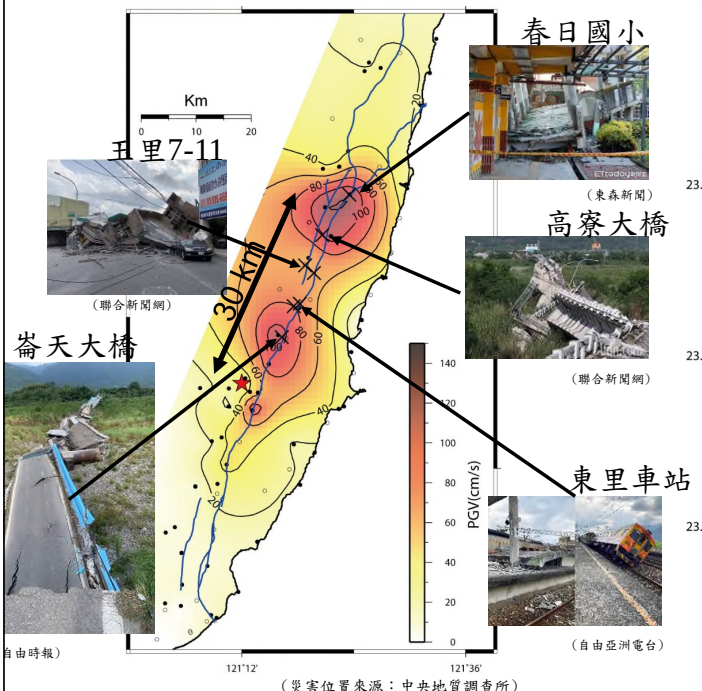

PGV distribution

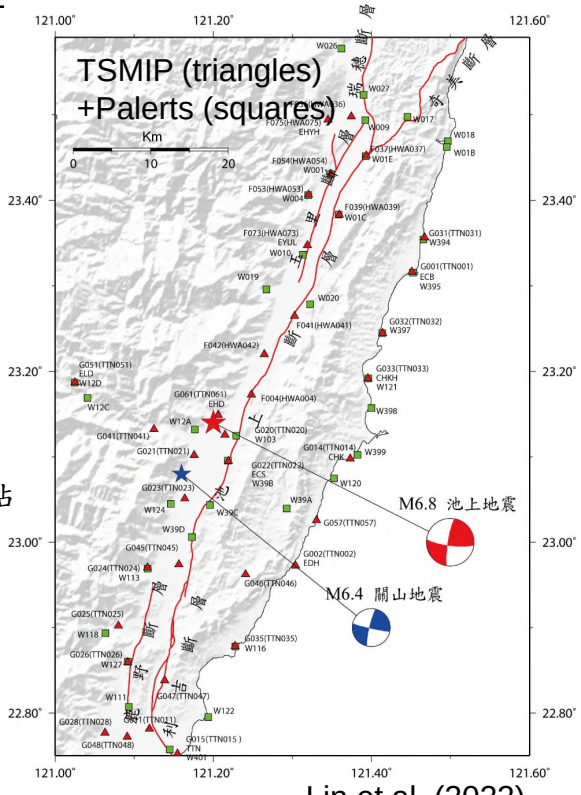

Lin et al. (2022)

(pulse-like velocity motion along the Chihshan fault)

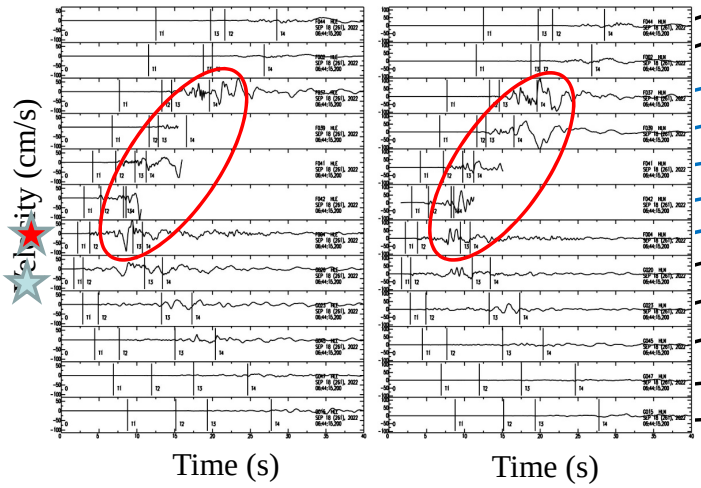

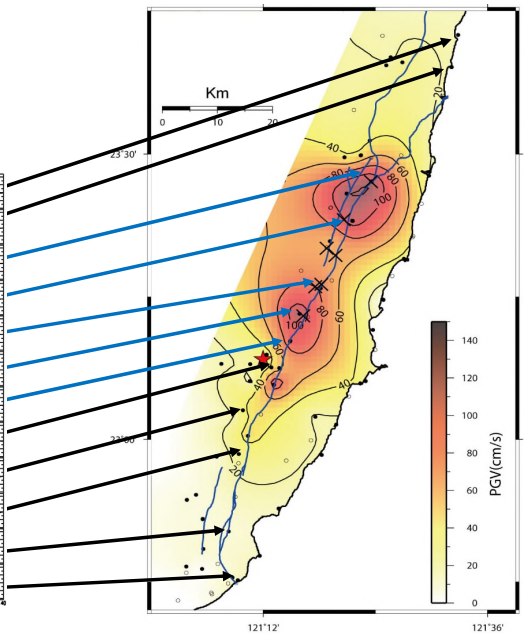

（災害位置來源：中央地質調查所）

F039 Gaoliao Bridge
高寮大橋 PGV=108.0 cm/s (at least)

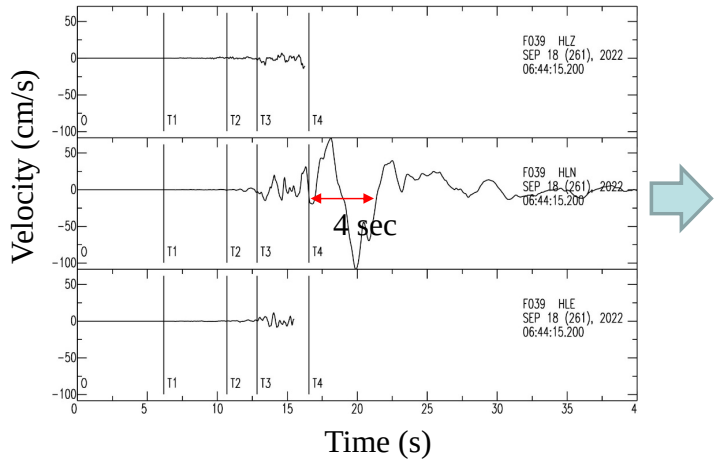

（聯合新聞網）

Conclusions

- Near-fault strong-velocity pulses, causing significant damage to buildings and structures, had been commonly observed from the dense seismic strong motion array for moderate to large earthquakes.
- Similar features were observed in the recent 18th September, 2022 M6.8 earthquake.
- Physical factors from static offset, and source asperity relating the scaling of pulse periods with magnitude are characterized using the method of Shahi and Baker (2014) .
- The scaling from five moderate earthquakes shows large within-event variability of the pulses.
- The simulations using the frequency–wavenumber algorithm suggest that the asperity properties have a high impact on the pulse periods and amplitudes at nearby stations.

Prof. Gregory MacRae

University of Canterbury, New Zealand

Topic：Recovery after the Canterbury Earthquakes

8th Asia Conference on Earthquake Engineering
Taipei, Taiwan
9~11 November, 2022

UNIVERSITY OF CANTERBURY
Te Whare Wānanga o Waitaha
CHRISTCHURCH NEW ZEALAND

RECOVERY AFTER THE CANTERBURY EARTHQUAKES

by

Gregory MacRae
University of Canterbury, New Zealand

PREAMBLE

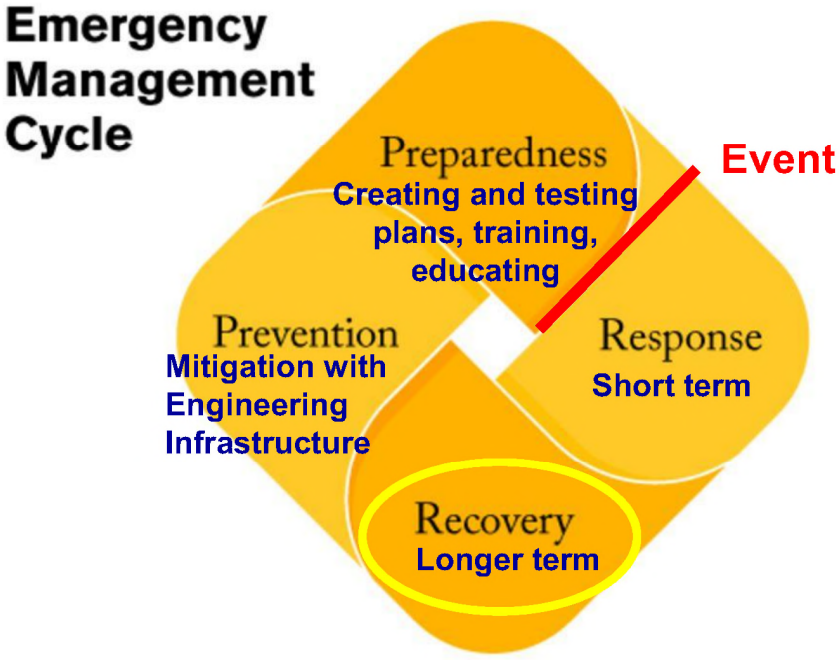

https://resilience.acoss.org.au/the-six-steps/leading-resilience/emergency-management-prevention-preparedness-response-recovery

PREAMBLE

Recovery Goal:

to build "a city that will be stronger, smarter and more resilient to the physical, social, and economic challenges"

(Christchurch City Council, 2016a; 2016b)

OUTLINE

- Pre-Quake Considerations
- The Event
- The Rebuild
- Societal Considerations
- Conclusions

OUTLINE

- **Pre-Quake Considerations**
- The Event
- The Rebuild
- Societal Considerations
- Conclusions

PRE-QUAKE

2011/2/06

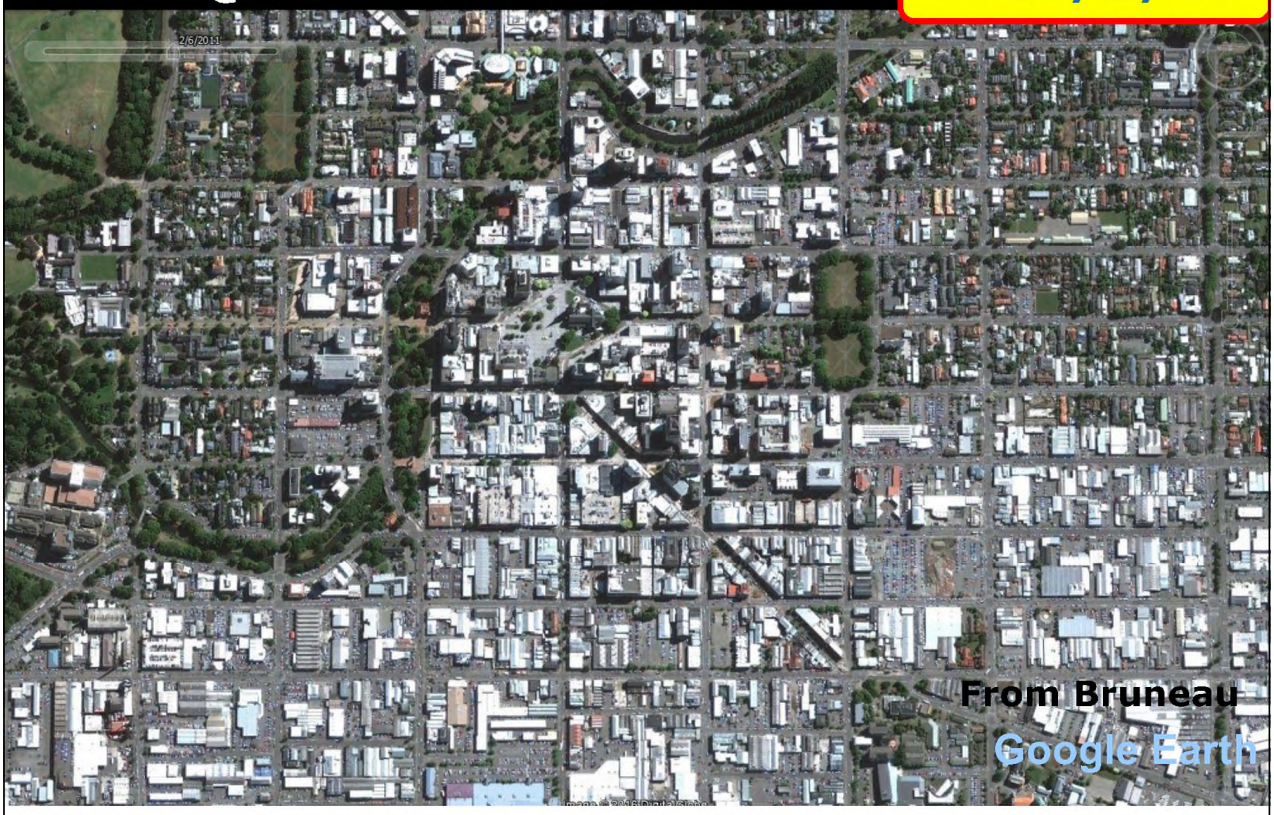

- **Dominant concrete construction** (following Park and Paulay)

PRE-QUAKE

INSURANCE

For most personal, and private infrastructure

PRE-QUAKE

- Building Legislative Framework:

Performance Based Approach

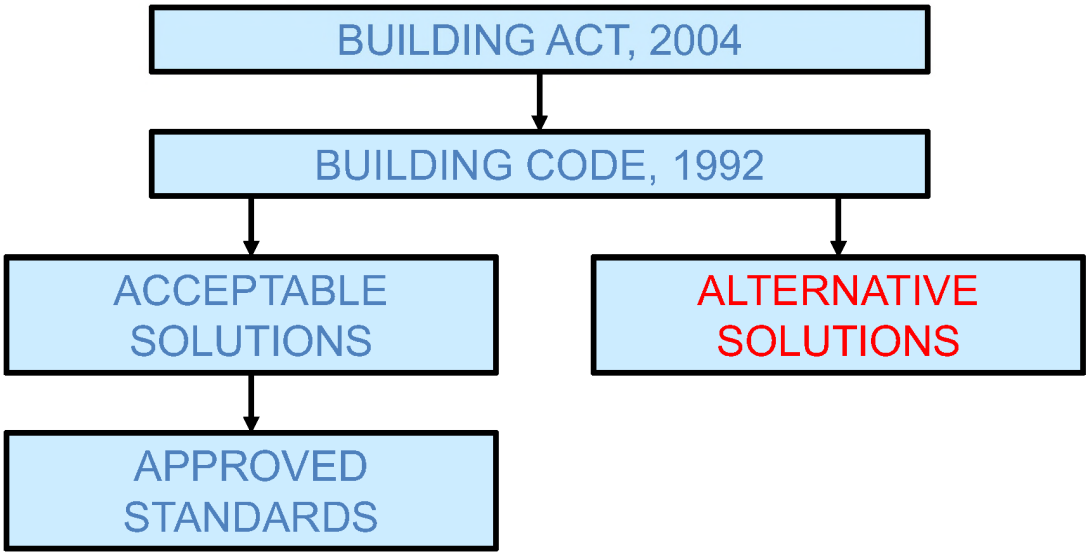

https://www.building.govt.nz/building-code-compliance/

PRE-QUAKE

- **The Price of Steel had Reduced**

PRE-QUAKE

- **Information about many new structural systems**

Bull, D., "Understanding the Complexities of Designing Diaphragms in Buildings for Earthquakes", *Paulay and Park Symposium, Christchurch, 2003*

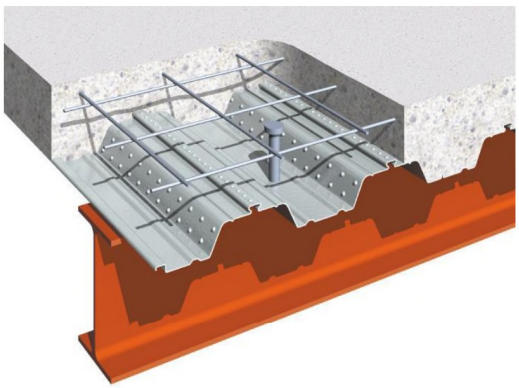

E.g. Comflor decking
https://www.miproducts.co.nz/imagesdb/album/64571 8aa-f85c-45f0-a368-4c96bfd84e29.jpg

PRE-QUAKE

- **Information about many new structural systems**

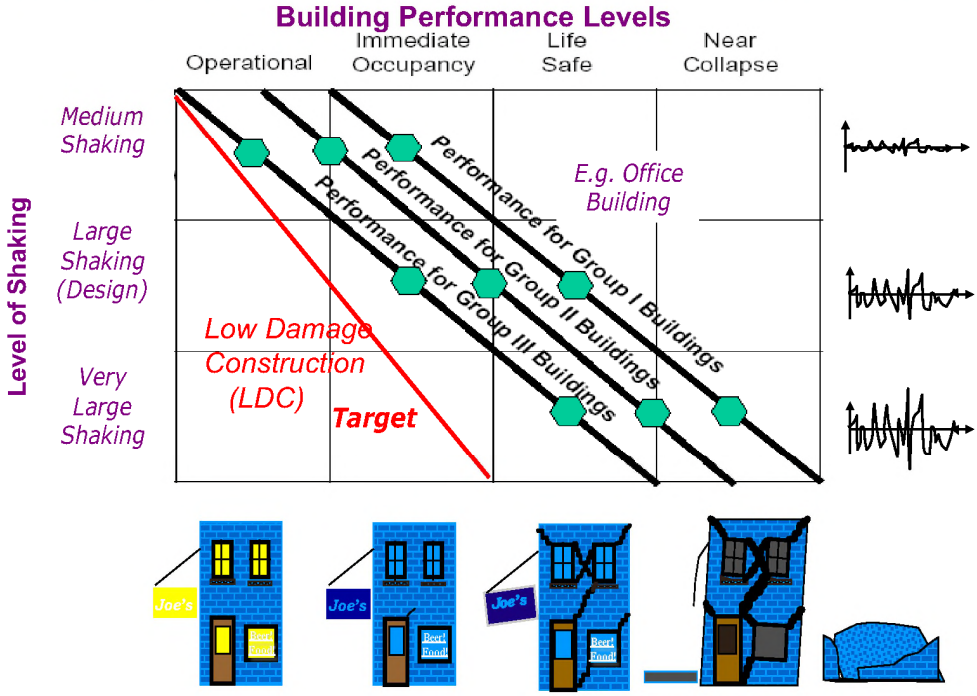

MacRae G. A., 2010. "University of Canterbury Research", in Proce. of the Steel Structures Workshop 2010, University of Canterbury, 13-14 April., Hamburger

OUTLINE

- Pre-Quake Considerations
- **The Event**
- The Rebuild
- Societal Considerations
- Conclusions

THE EVENT

Canterbury Quakes

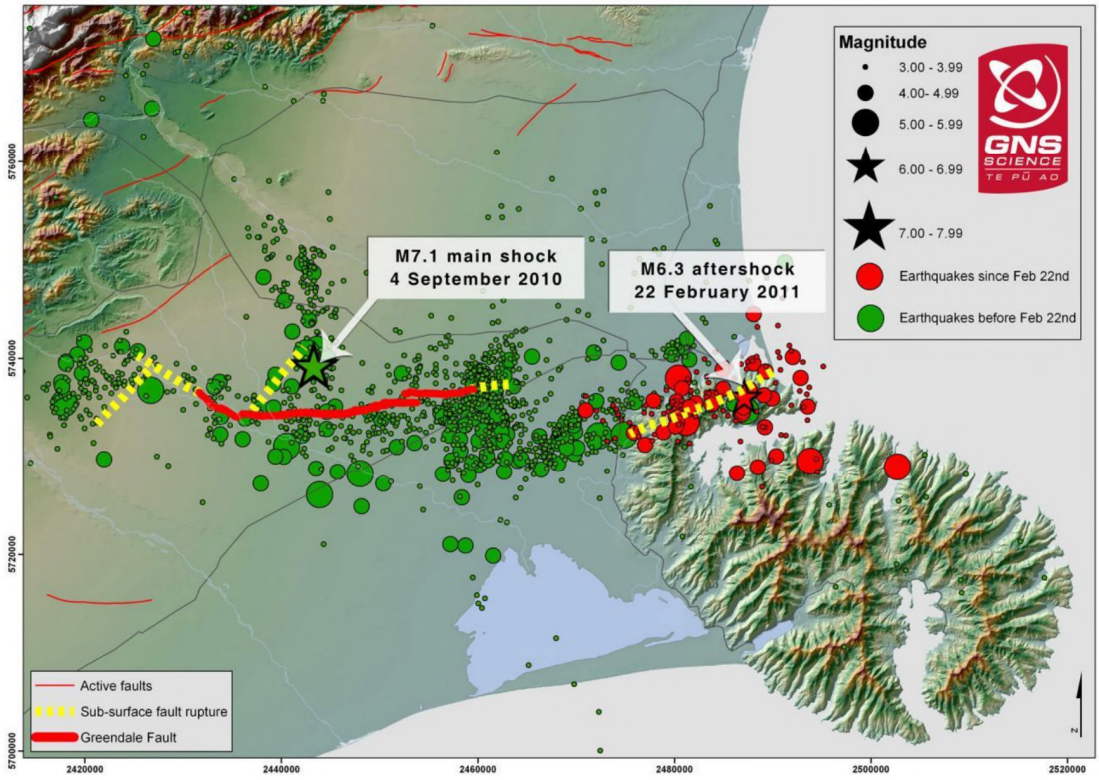

THE EVENT

The Canterbury Earthquakes

THE EVENT

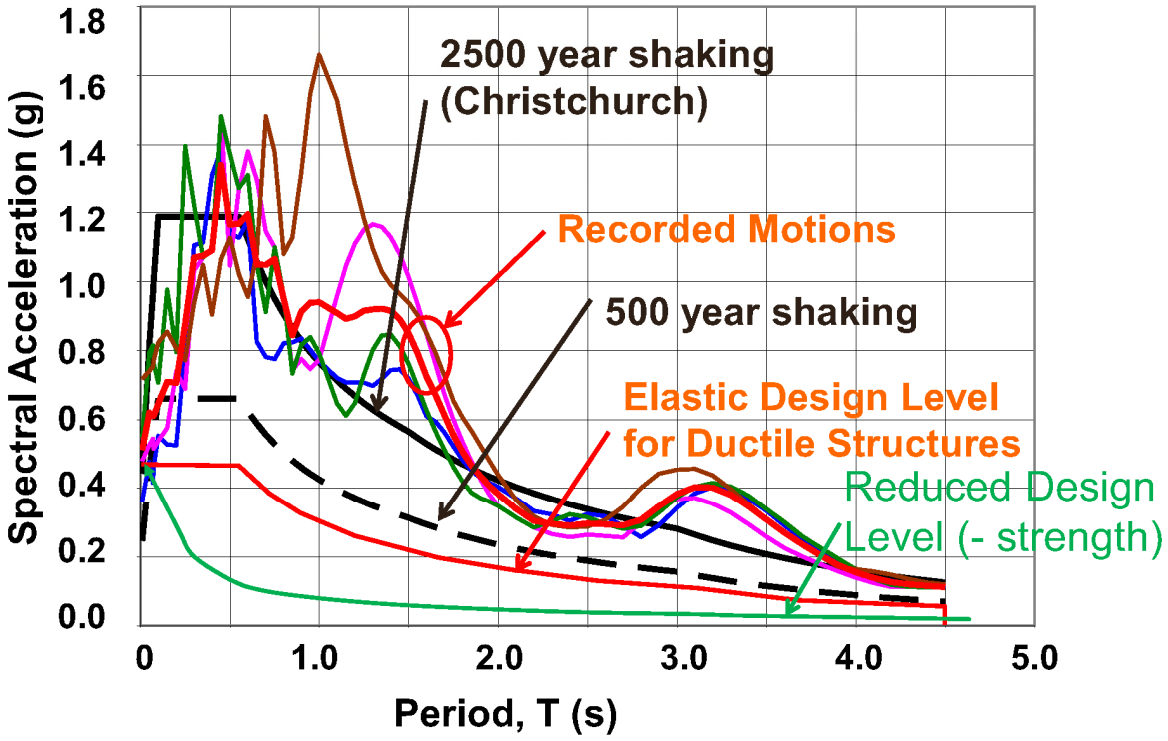

22 February 2011 M6.3 Response Spectra (Geonet)

THE EVENT

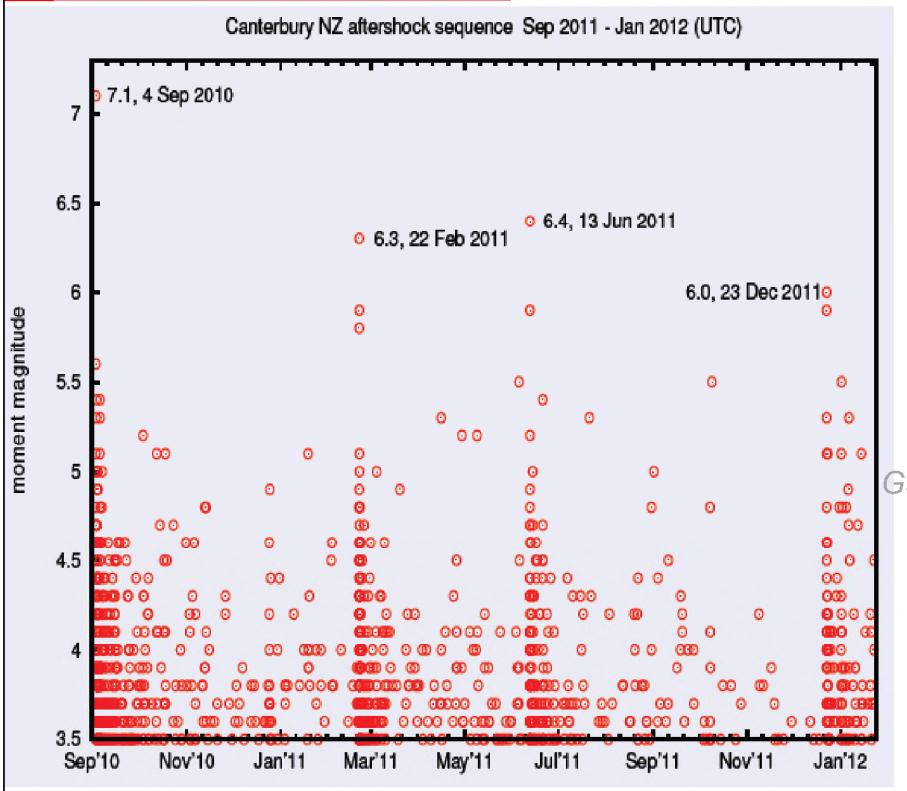

Gavin, Nigbor et al. (2012)

In one building the internal partitions were replaced 4 times!

THE EVENT

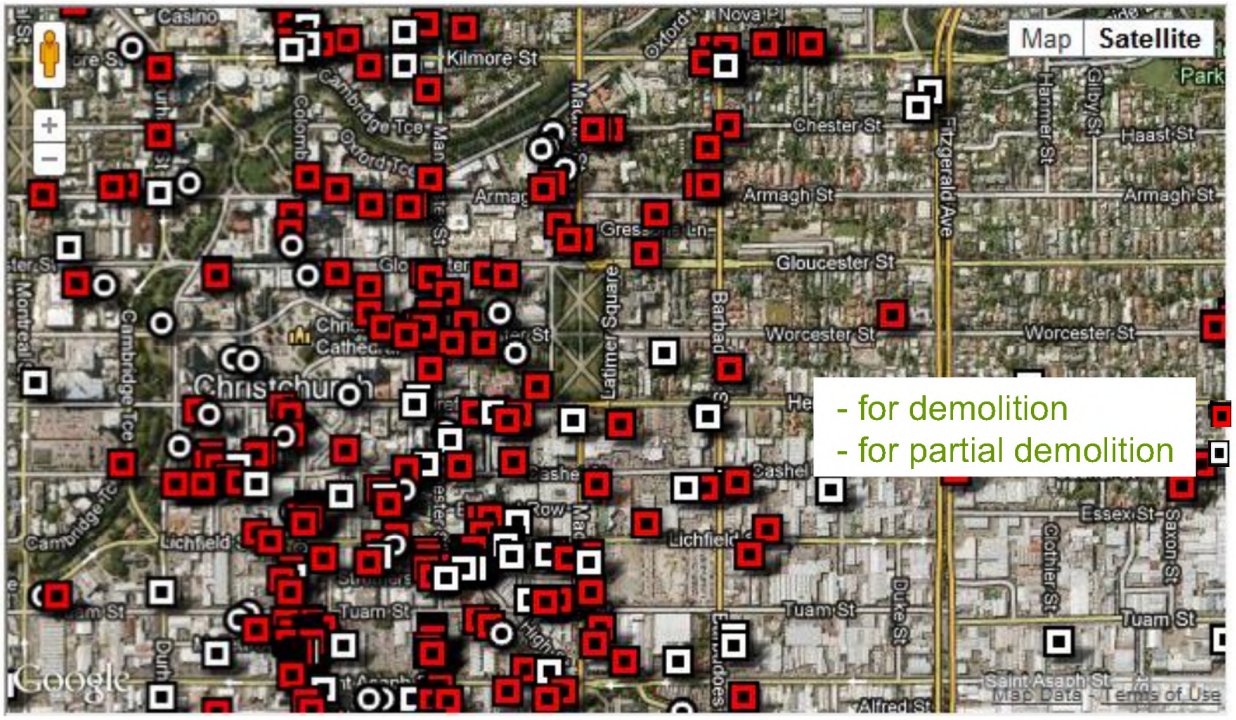
Map
Satellite
- for demolition
- for partial demolition
Many remained standing!
We can prevent life loss with current good design/construction
http://www.stuff.co.nz/the-press/news/christchurch-earthquake-2011/5282824/Quake-damaged-buildings-map

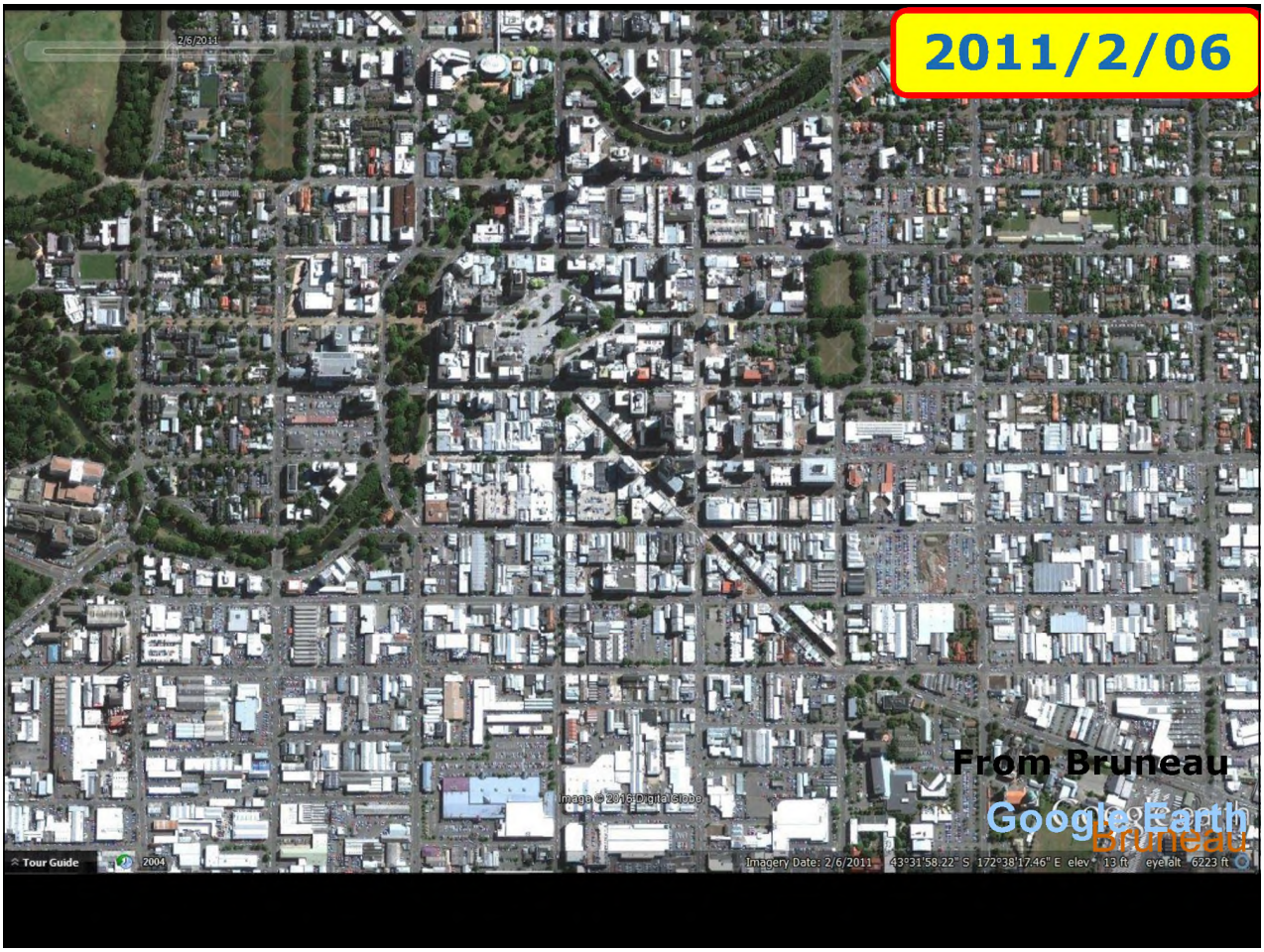
2011/2/06
From Bruneau
Google Earth
Bruneau

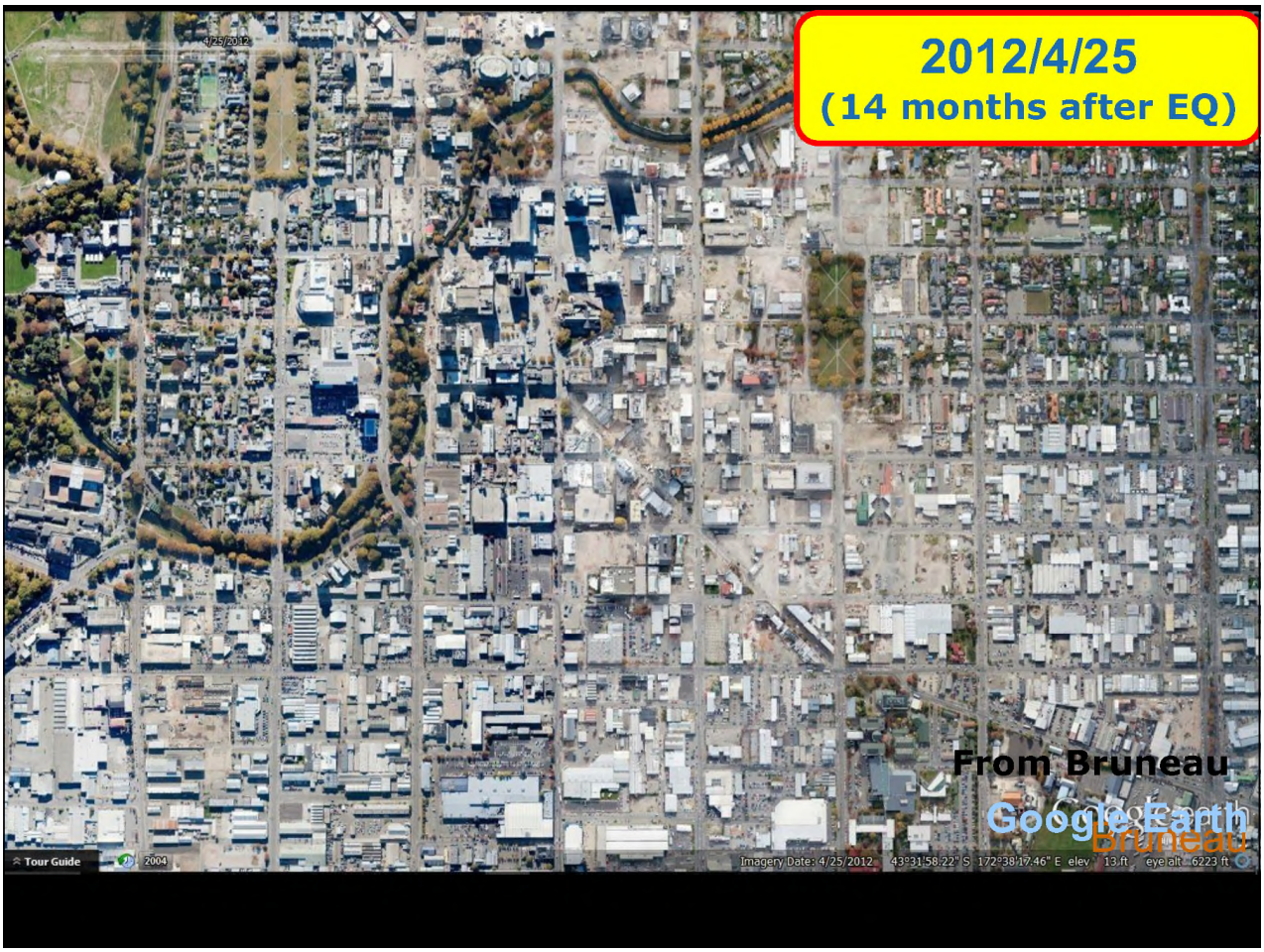
2012/4/25
(14 months after EQ)
From Bruneau
Google Earth
Bruneau
Tour Guide
2004
Imagery Date: 4/25/2012


Bruneau

THE EVENT

Ground effects

Photos courtesy Cubrinovski

THE EVENT

Some structural forms are more reparable than others

SESOC Guide for Concrete Structures (2012)

THE EVENT

Some structural forms are more reparable than others

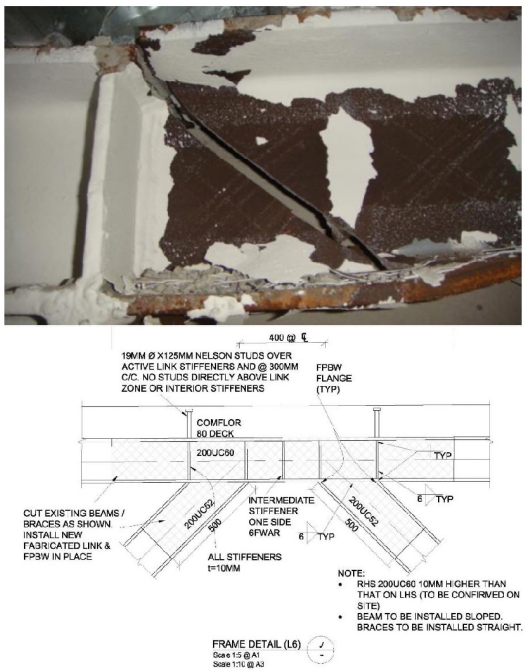

Photos courtesy Ingham/SESOC

Photos courtesy Sean Gardiner

THE EVENT

26 April 2016

http://www.stuff.co.nz/the-pr

OUTLINE

- Pre-Quake Considerations
- The Event
- **The Rebuild**
- Societal Considerations
- Conclusions

THE REBUILD

AFTER 2010-2011 Canterbury Earthquakes

Royal Commission made 189 recommendations, some related to structural design.

Some many were made with respect to concrete structures (E.g. wall performance), and to concrete floor diaphragm performance. Some, related to loading, are described in the following slides.

Changes were initially listed in B1/VM1 which cites the NZS1170.5 (2011), and then changes were made to the standard, NZS1170.5, Amendment 1, 2016.

https://www.mbie.govt.nz/assets/27c53c4193/responses-cerc-recommendations.pdf

THE REBUILD

1. Seismic Hazard

Changes for Christchurch:

An increase in Zone Hazard Factor, Z, from 0.22 to 0.30.

Before 2010 -2011 Earthquakes

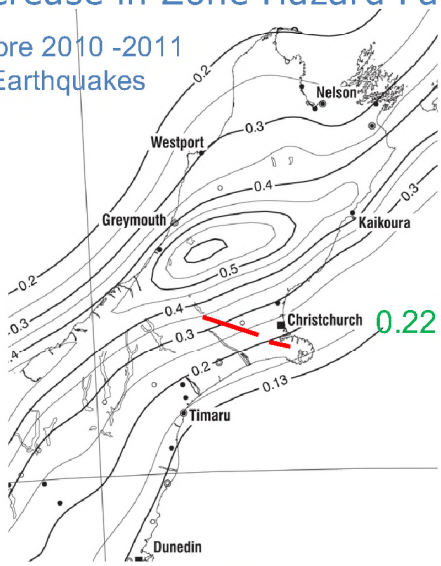

0.22

After 2010 -2011 Earthquakes

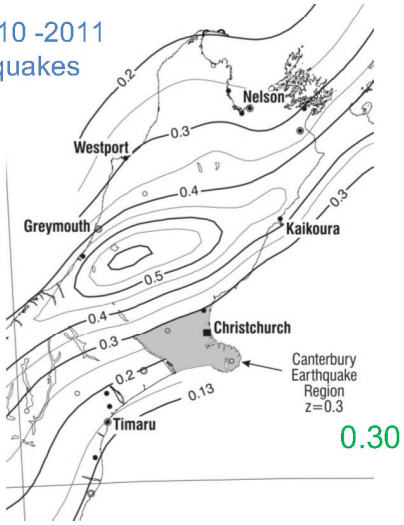

0.30

Temporary increase in serviceability factor, R_s, from 0.25 to 0.33.

=> 1.8 times increase in lateral design force

THE REBUILD

2. Elements Supported on Ledges

https://en.wikipedia.org/wiki/Forsyth_Barr_Building

Stairs unseating / collapse

Increase in stair overlap

($2/S_p$ = 2.86 times!)

THE REBUILD

3. Ratcheting

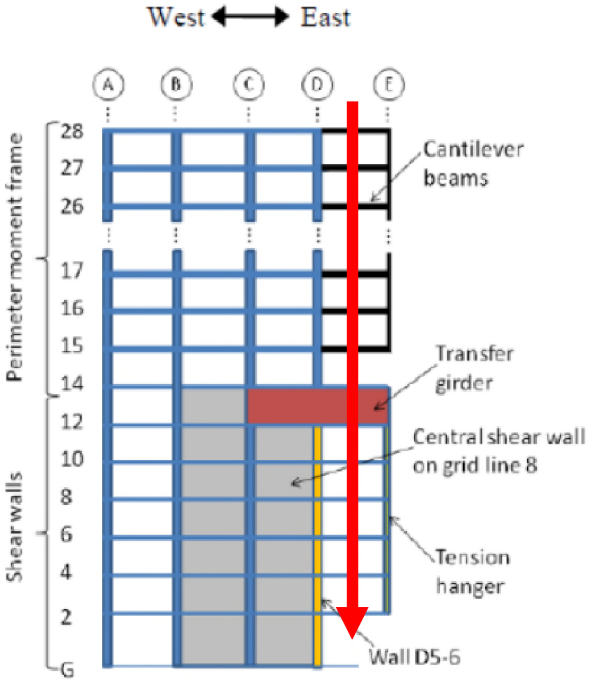

Hotel Grand Chancellor
(Canterbury Earthquakes Royal Commission, 2012

RECENT CHANGES TO DESIGN

3. Ratcheting:

https://canterbury.royalcommission.govt.nz/documents-by-key/20120229.3475\

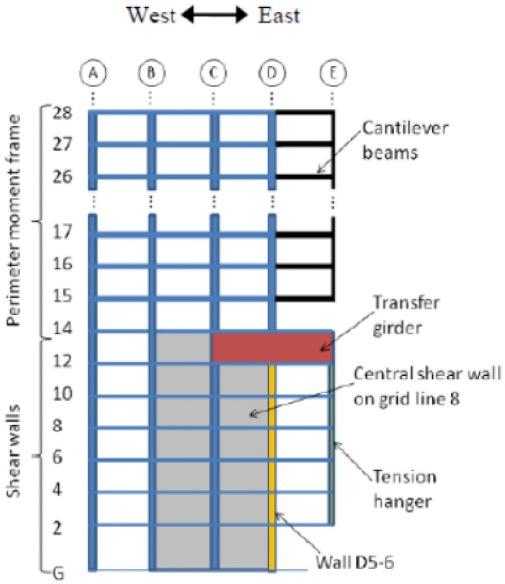

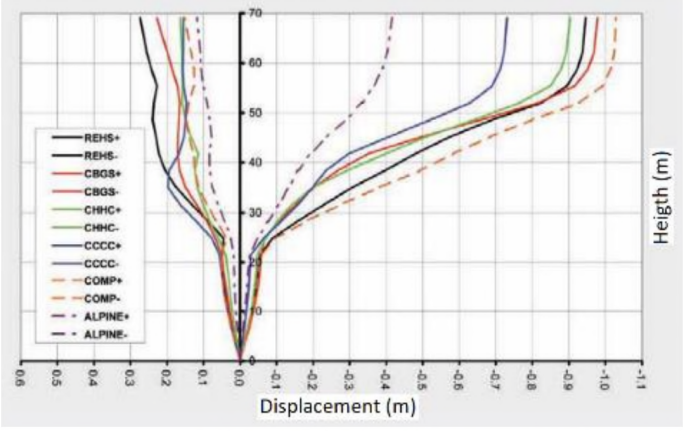

(a) Schematic Elevation **(b) Peak Displacements**

Hotel Grand Chancellor
(Canterbury Earthquakes Royal Commission, 2012)

RECENT CHANGES TO DESIGN

4. Inelastic Torsion:

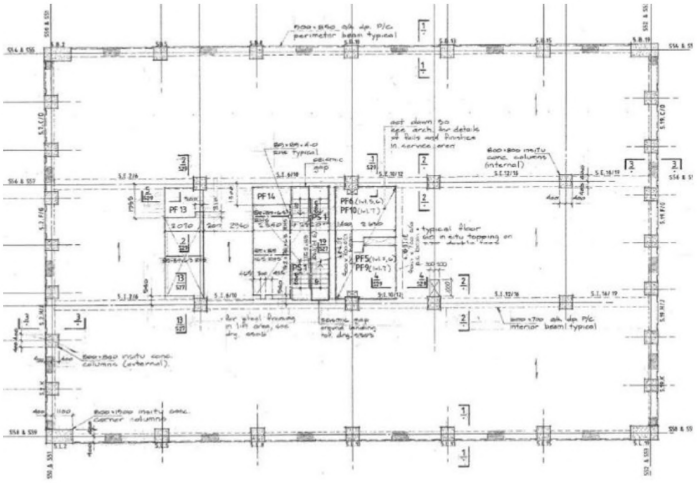

https://en.wikipedia.org/wiki/Clarendon_Tower

https://canterbury.royalcommission.govt.nz/documents-by-key/20120229.3475

THE REBUILD

4. Inelastic Torsion:

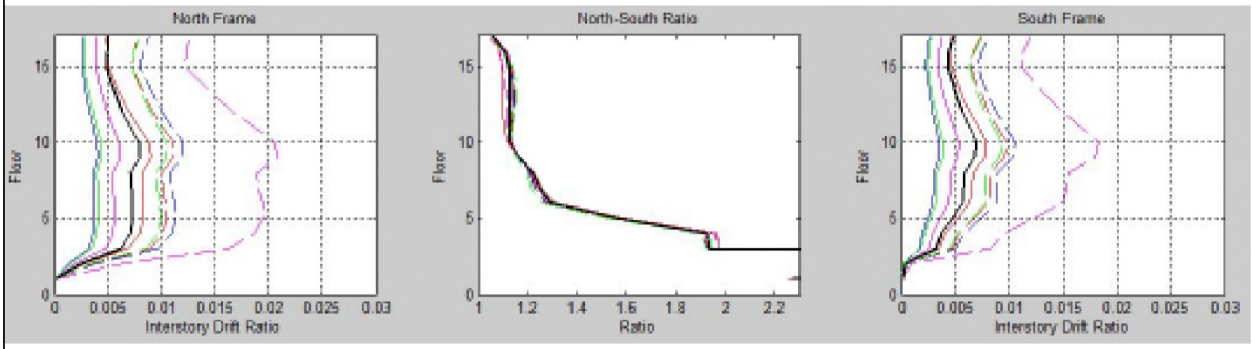

Clarendon Towers

(Canterbury Earthquakes Royal Commission, 2012)

https://canterbury.royalcommission.govt.nz/documents-by-key/20120229.3475

CONSTRUCTION FORMS

a) Existing Construction
b) Strong (Elastically Responding) Systems
c) BRB Systems
d) Rocking structures
e) Base Isolation
f) Friction types
g) Lead dissipaters
h) Supplemental dampers

MacRae G. A and Clifton G. C, "Low Damage Steel Construction", Steel Innovations Conference, Steel Construction New Zealand, Wigram, Christchurch, 21-22 February 2013, Paper 1.

THE REBUILD

EXISTING SYSTEMS

THE REBUILD

a) Existing Construction (?)

Courtesy Mac Rae

J. Kirk (Kirk Roberts)

THE REBUILD

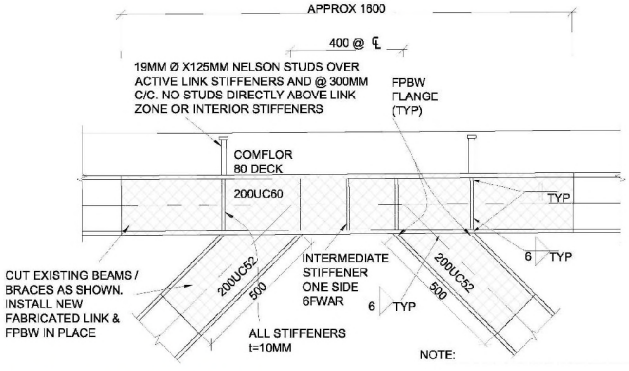

Gardiner S. et al. (2013)

NOMINALLY ELASTIC SYSTEMS

THE REBUILD

Lichfield Street Bus Exchange

THE REBUILD

Lichfield Street Bus Exchange
Photo MacRae
15 February 2016

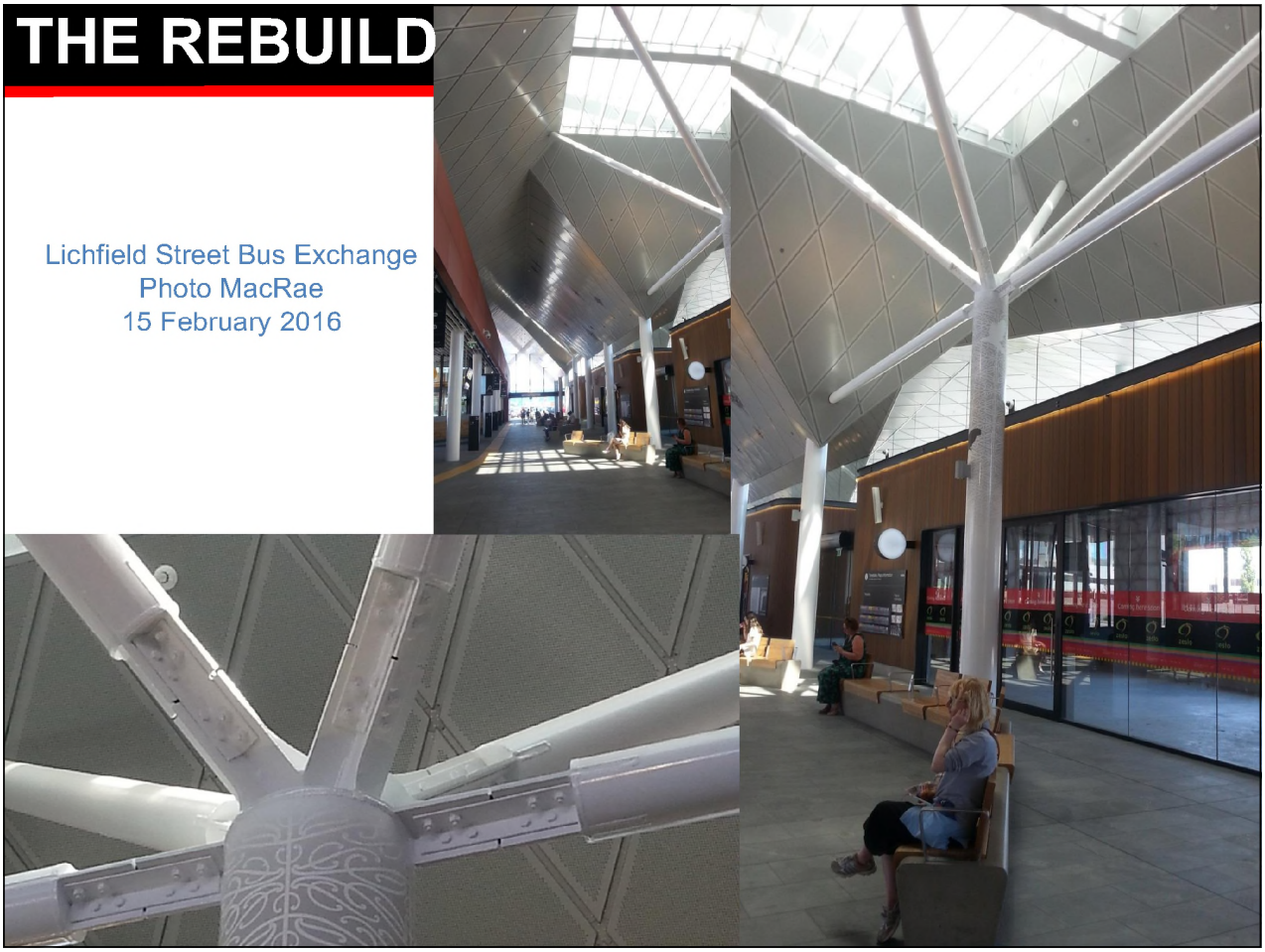

THE REBUILD

BUCKLING RESTRAINED BRACE (BRB) SYSTEMS

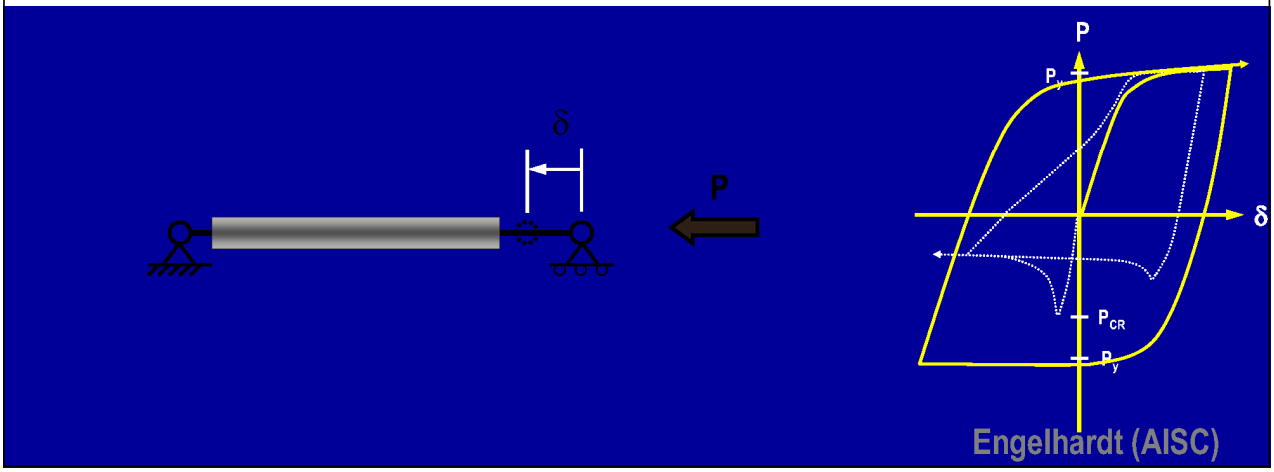


14 Hazeldean Rd, Addington, Christchurch 8024
East Side, MacRae, March 2015

THE REBUILD


254 Montreal Street, Photo: MacRae

THE REBUILD

THE REBUILD

THE REBUILD

NE Corner of Lichfield and Colombo St
15 February 2016

THE REBUILD

NEW STRUCTURAL SYSTEMS

Could William Tell do it again?
Was he just lucky?
What if the boy were moving?

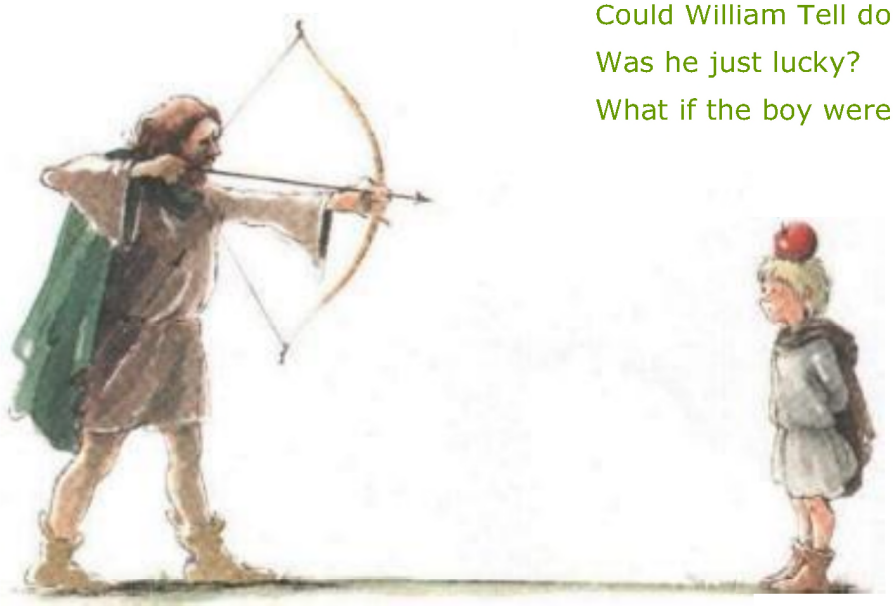

http://www.potatofeed.com/the-10-most-famous-characters-that-never-existed/

BRBs and their gusset plates

BRB and gusset plate failure

(Tsai and Hsaio 2008)

US design recommendation k_g equal to 0.65-0.70

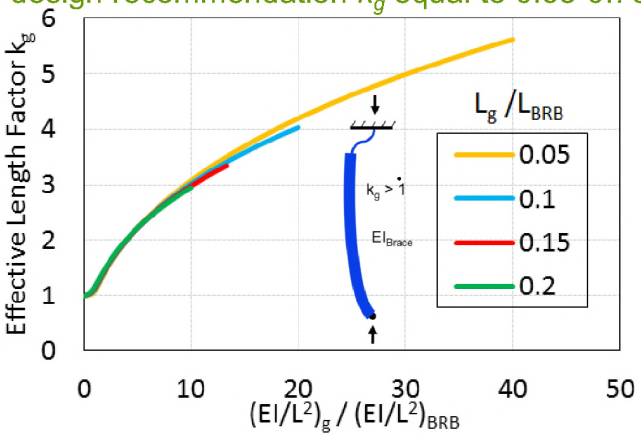

Gusset Plate Effective Length Factor
(Westeneng and Crake, 2014)

Realistic k_g may exceed 3

Westeneng, Lee et al. (2014, 2015), MacRae (SRP Tokyo, 2015), Jones, Lee et al. (2015)

THE REBUILD

BRBs and their gusset plates

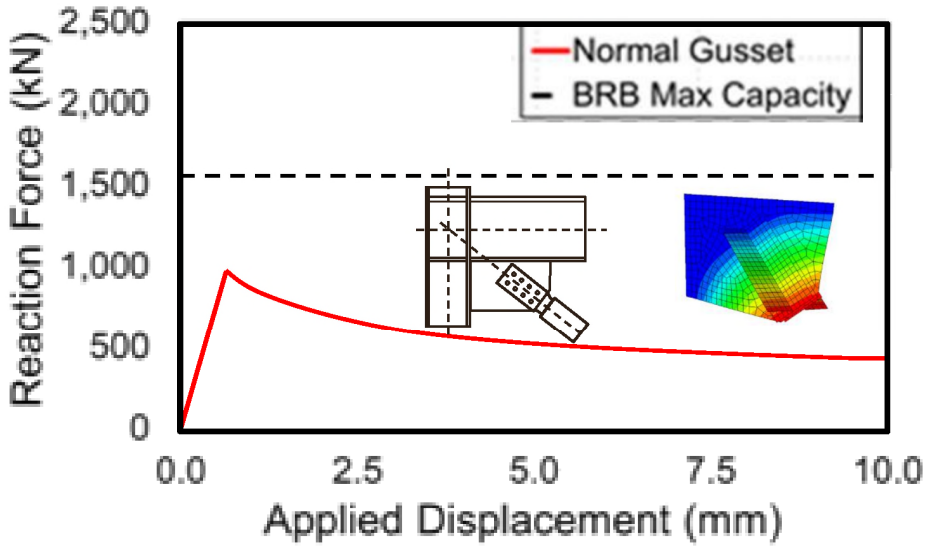

Strength Assessment
(Westeneng and Crake, 2014,
following Tsai and Hsaio, 2008)

BRBs and their gusset plates

Other factors affecting gusset plates with BRBs:

- in-plane bending from
  - brace (if brace not pin-ended)

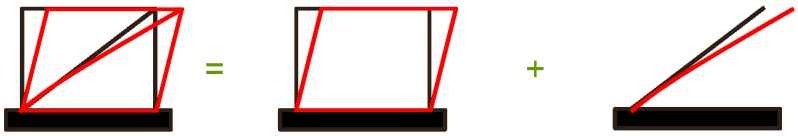

- frame action
  (e.g. Chou 2011, Tsai 2012)

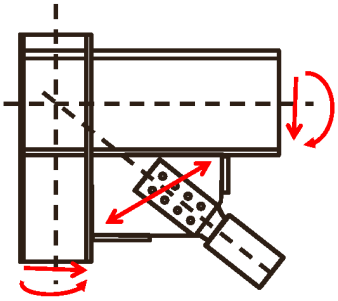

THE REBUILD

BRBs and their gusset plates

Factors affecting gusset plates with BRBs (contd):

- out-of-plane
  - stiffness of frame at gusset connection
  - brace inertia effects
  - frame deformation effects (- from Wada)

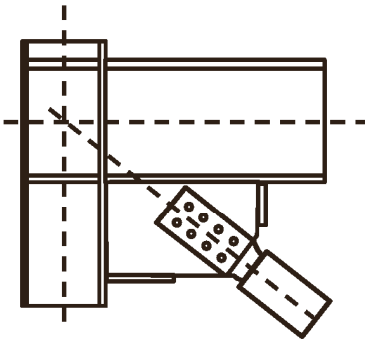

- strength of adjoining elements (e.g. beams, and beam webs)
- welding approach (butt, or fillet with distribution factor of 1.25, 1.4?)

Hewitt C. M. and Thornton W. A. Rationale Behind and Proper Application of the Ductility Factor for Bracing Connections Subjected to Shear and Transverse Loading, ENGINEERING JOURNAL / FIRST QUARTER / 2004, pp1-6.

BRBs and their gusset plates

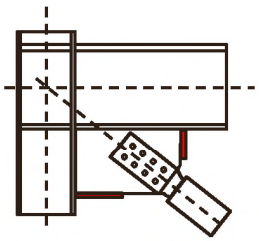

Ways to deal with gusset plate issues:

1) Place stiffeners on gusset plates (e.g. Tsai, Taiwan)
2) Require out-of-plane force (e.g. 2.5%*P* in NZ)
3) Consider failure mechanism (e.g. Takeuchi, Japan)
4) Used increased design length (e.g. Bruneau's book, Corebrace), and others?

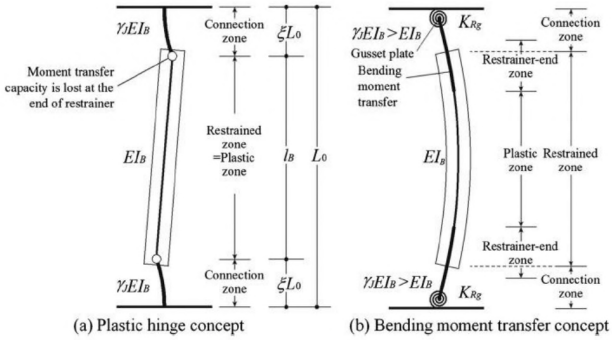

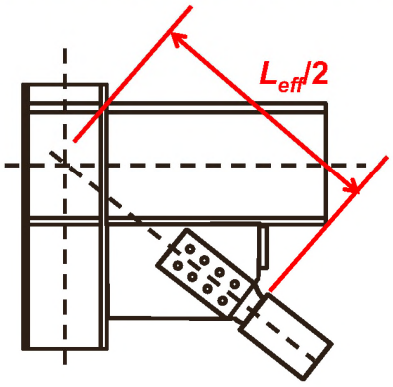

Takeuchi

Nakamura Method (Bruneau's book)

THE REBUILD

BRBs and their gusset plates

STESSA Conference, Shanghai, 2015

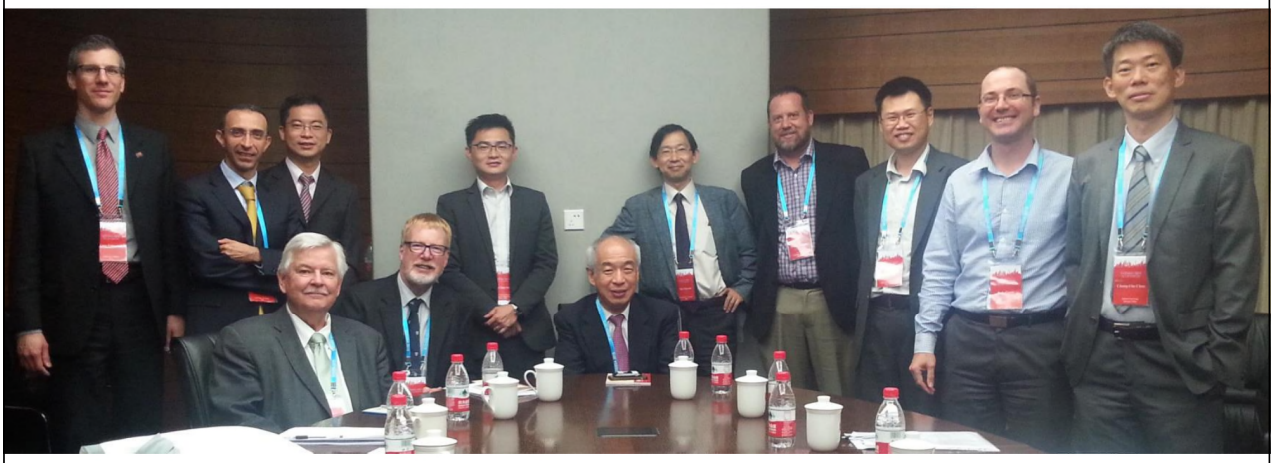

THE REBUILD

BRBs and their gusset plates

NZSEE Conference, Christchurch, 4/2016

THE REBUILD

BRBs and their gusset plates

HERA House, Auckland, 6/2016

THE REBUILD

BRBs and their gusset plates

WCEE (2017, Santiago, Chile) - 3 sessions

THE REBUILD

BRBs and their gusset plates

STESSA (2018, Christchurch, NZ)

THE REBUILD

BRBs and their gusset plates

Ngai Tahu Property Site, 48 Hereford Street, 15 February 2016

THE REBUILD

BRBs and their gusset plates

Externally Mounted Tension-Compression Yielding Devices (EMTCYD), Mini-BRBs

Trimble building
Christchurch
Photos: MacRae
April 2016

BRBs and their gusset plates

Externally Mounted Tension-Compression Yielding Devices (EMTCYD), Mini-BRBs

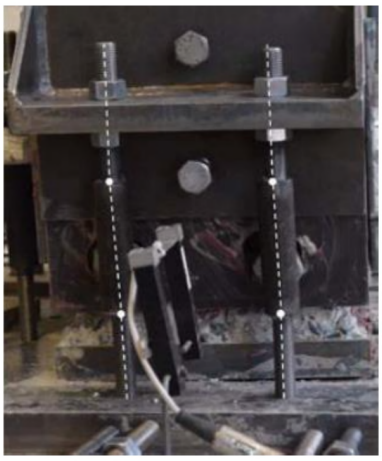

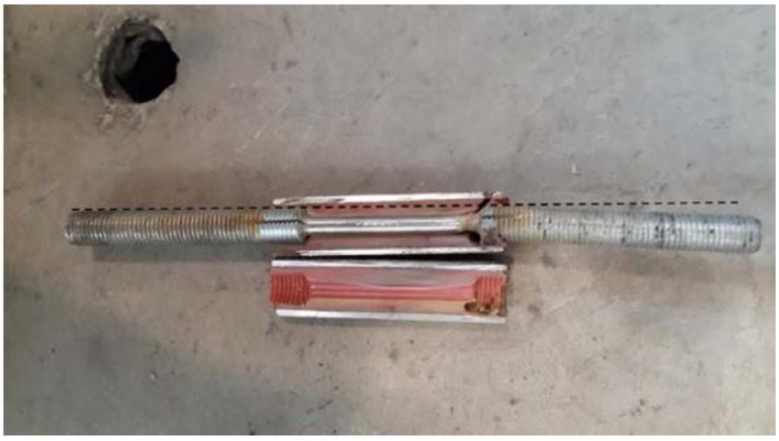

From: NZSEE Conference 2015 Gultom, R., & Ma, Q. T.

THE REBUILD

ROCKING FRAME SYSTEMS

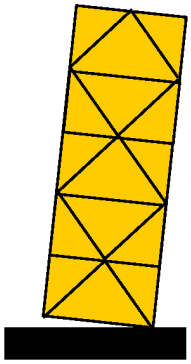

THE REBUILD

Rocking Frames

Recent frames all are separated from gravity system to prevent damage to floor slab and restraint from gravity columns

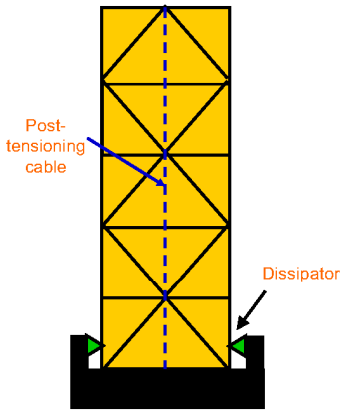

Pros:
No expensive springs at base required

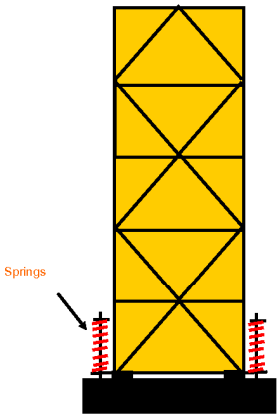

Do not need to size frame members to carry post-tension force over whole height.
Can be used for frames all heights

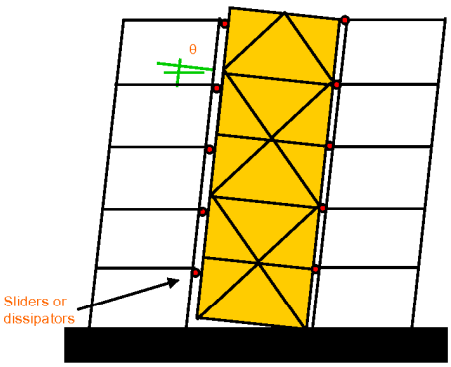

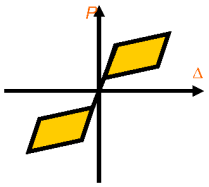

THE REBUILD

Rocking Frames

Forte Health – Hospital (132 Peterborough Street and Kilmore Street, Christchurch)
Google Maps, 26/4/2016

THE REBUILD

Rocking Frames

THE REBUILD

Rocking Frames in NS Direction

141 Cambridge Terrace

MacRae Photo, March 2016

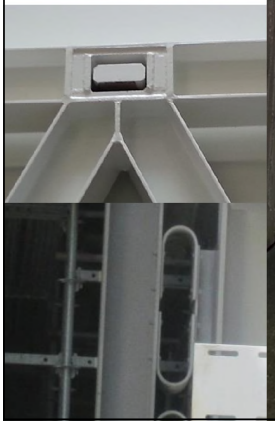

Rocking Frames

Rocking occurred in Wellington Te Puni rocking frame during 2014 Seddon earthquakes. 4mm of movement was seen on the friction slider (Courtesy of Gledhill, Aurecon)

THE REBUILD

ECCENTRICALLY BRACED FRAME (EBF) SYSTEMS

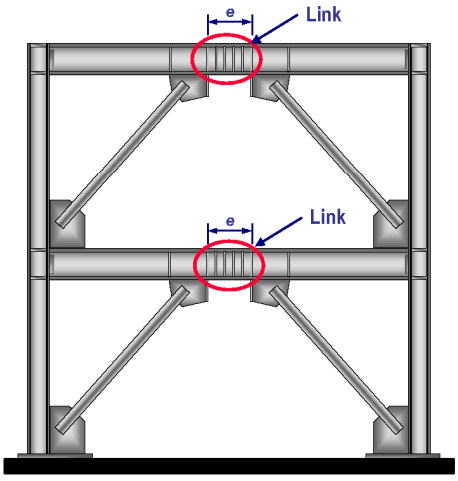

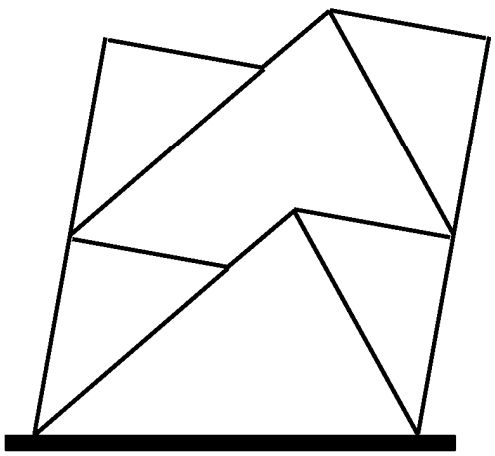

THE REBUILD

EBF

Traditional Links vs Replaceable links

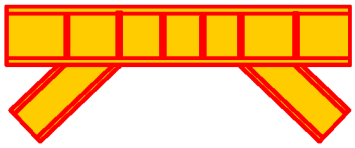

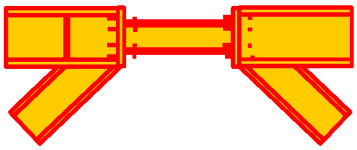

THE REBUILD

THE REBUILD

208 Barbadoes St

THE REBUILD

Lichfield Street on NW corner of Lichfield and Barbadoes Streets, traditional EBF

THE REBUILD

BASE ISOLATION

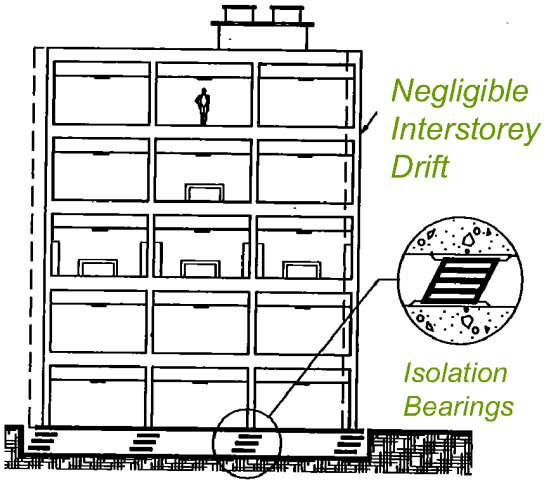

From Mayes R. in Naeim F. The Seismic Design Handbook, 2001

THE REBUILD

151

151 Cambridge Terrace
Base Isolated

THE REBUILD

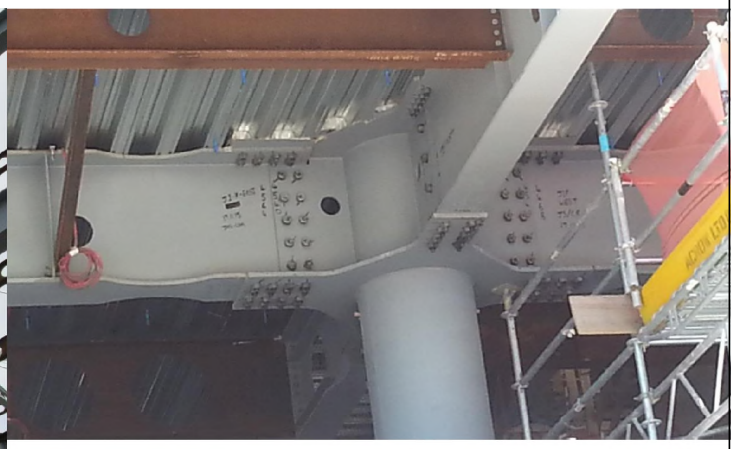

Justice Precinct,
121 Tuam Street, Christchurch
Photo MacRae, March 2015
Base Isolated

THE REBUILD

Justice Precinct
15 February 2016, Photo: MacRae

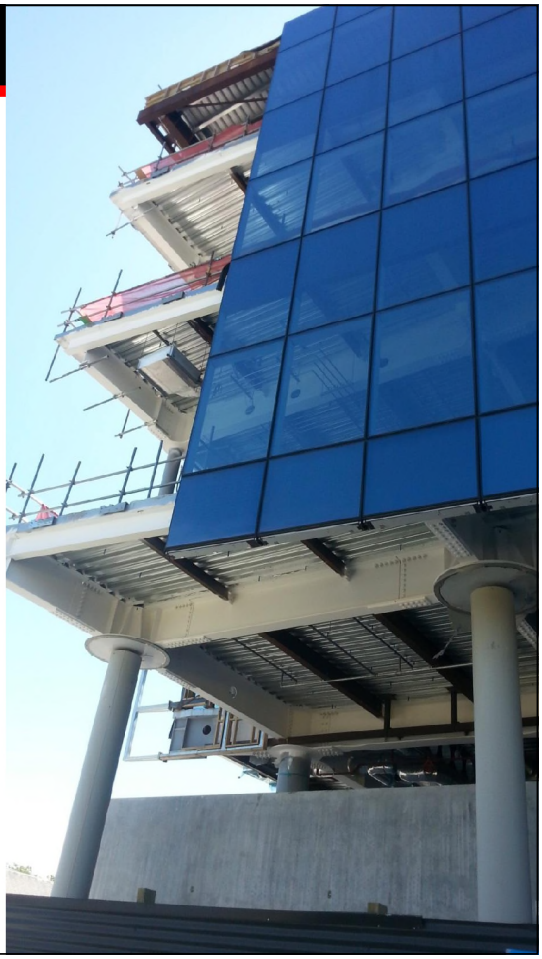

THE REBUILD

FRICTION MOMENT CONNECTIONS

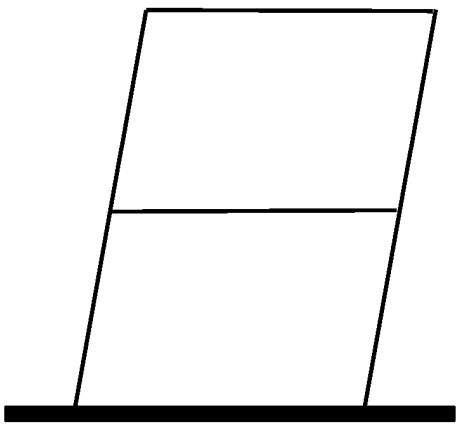

THE REBUILD

Friction Connections

sliding hinge joint (shj)

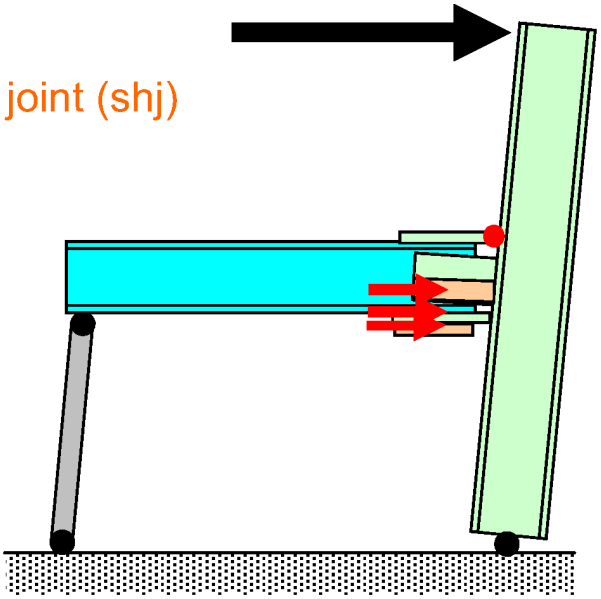

Clifton 2005, MacRae et al. 2010 + Khoo, Chanchi, Xie, Borzouie, Shahab + others

THE REBUILD

Friction Connections

DETAILS:

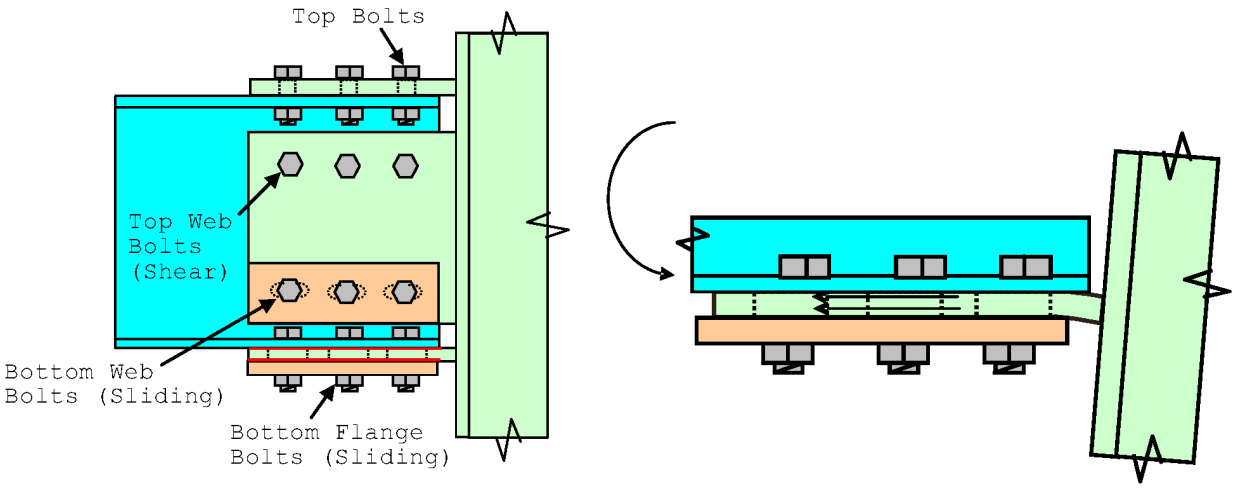

THE REBUILD

Friction Connections

Deformations:

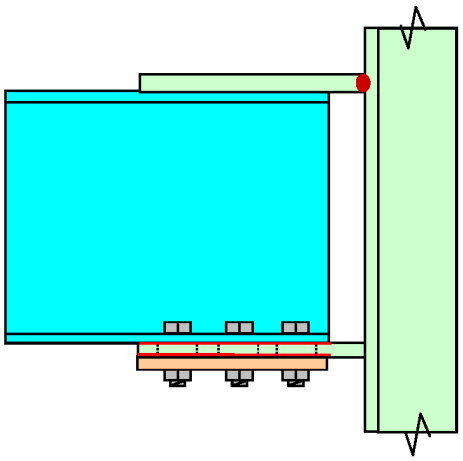

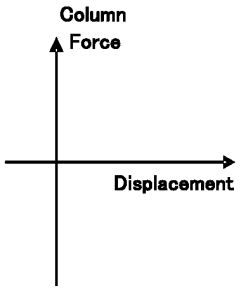

1

THE REBUILD

Friction Connections

Deformations:

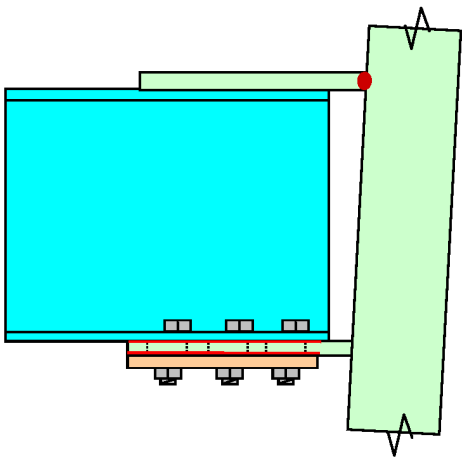

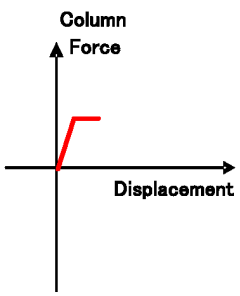

2

THE REBUILD

Friction Connections

Deformations:

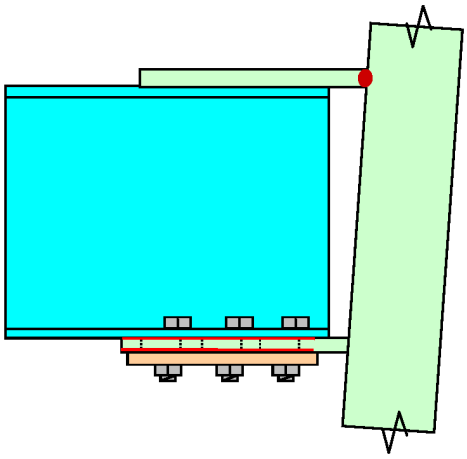

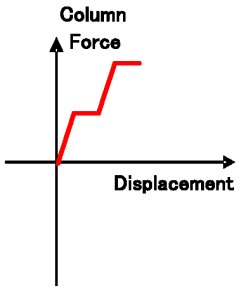

3

THE REBUILD

Friction Connections

Deformations:

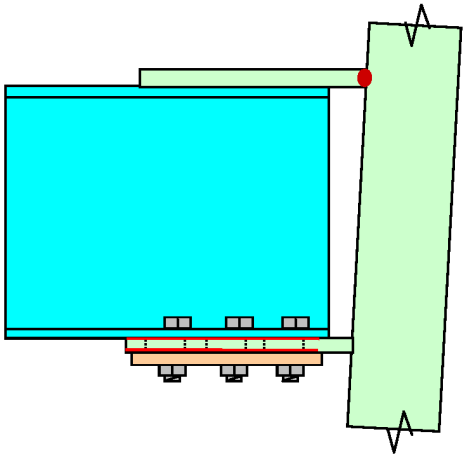

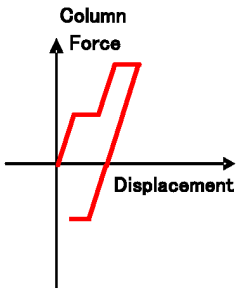

4

THE REBUILD

Friction Connections

Deformations:

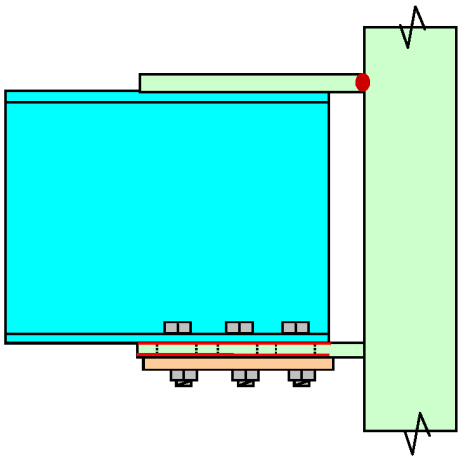

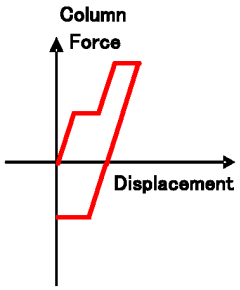

5

THE REBUILD

Friction Connections

Deformations:

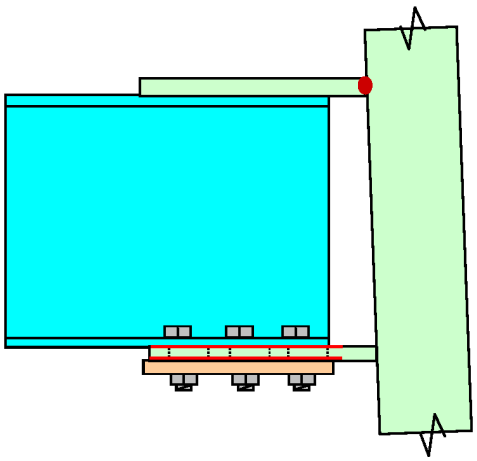

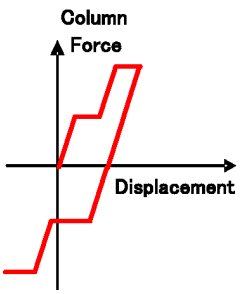

6

Friction Connections, Te Puni Apartments, Wellington

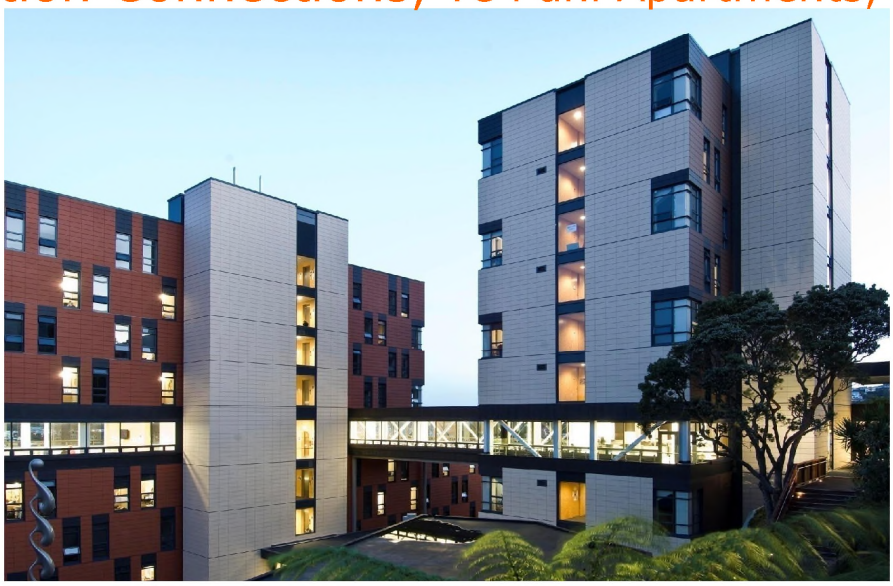

Courtesy: Geoff Sidwell, Aurecon

Related Projects: Robin Xie / Jamaledin Borzouie / Shahab Ramhormozian / Jose Chanchi

Friction Connections, Te Puni Apartments, Wellington

Courtesy: Darrin Bell of Connell-Wagner, 2007

THE REBUILD

THE REBUILD

The Resilient Slip Friction Connection (RSFJ)

Tectonus – University of Auckland – Pierre Quenneville

RSFJ Connections

Nelson Airport Terminal

https://www.tectonus.com/

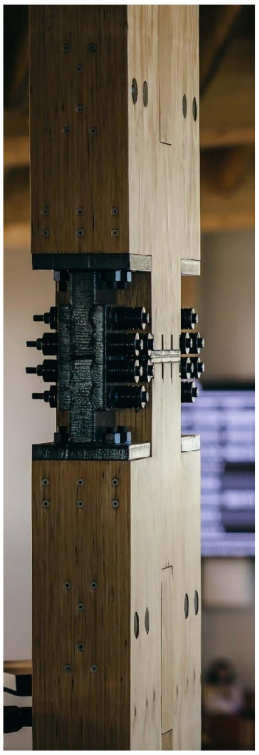

QUAKETEK, Saint-Laurent QC

Lincoln Hub

https://www.quaketek.com/

lincolnhub.co.nz

THE REBUILD

SUPPLEMENTAL VISCOUS DAMPERS

THE REBUILD

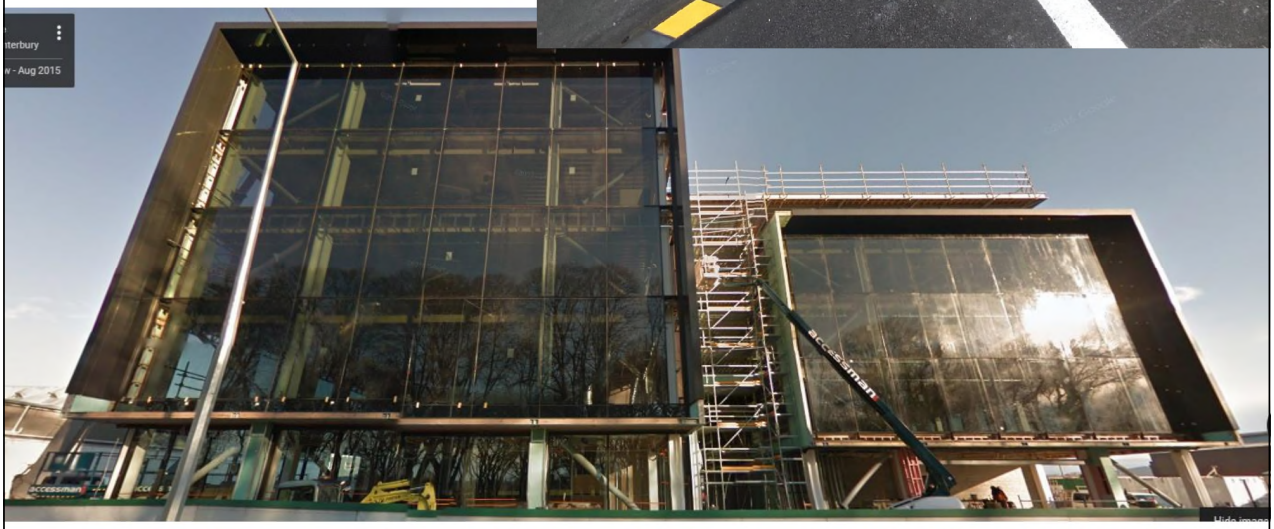

12c Moorhouse+Ave, Addington, Christchurch 8011 (Google Maps)

THE REBUILD

CONCENTRICALLY BRACED FRAME (CBF) SYSTEMS

THE REBUILD

124 Kilmore Street
Consortium Construction/Peebles Group
15 February 2016, Photo MacRae

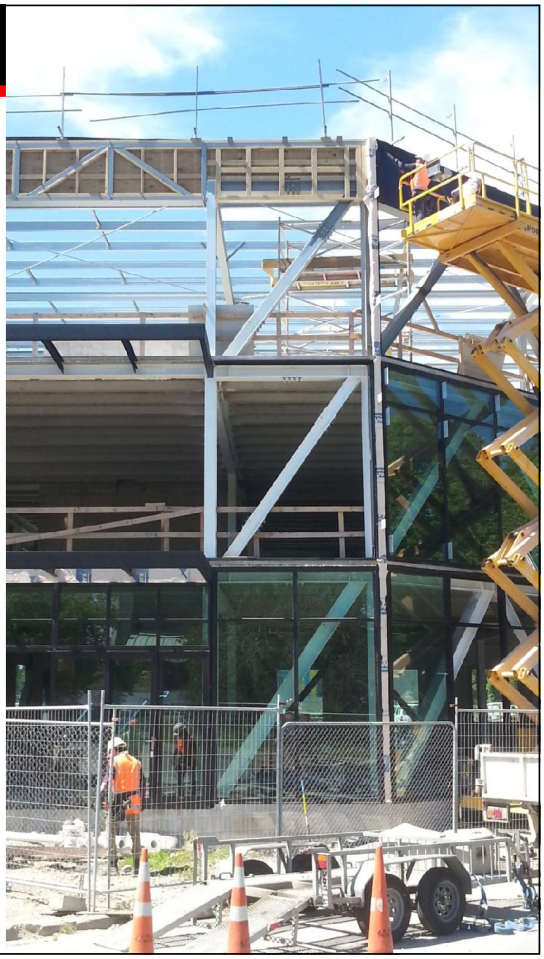

THE REBUILD

THE REBUILD

THE REBUILD

THE REBUILD

Some Interesting Examples

#1. CBF System

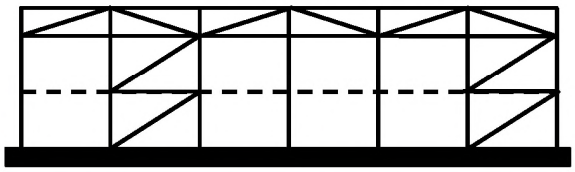

Univ. of Canterbury Engineering Hub
Photo MacRae, March 2016

THE REBUILD

#2. EBF building (136 Moorehouse Avenue)

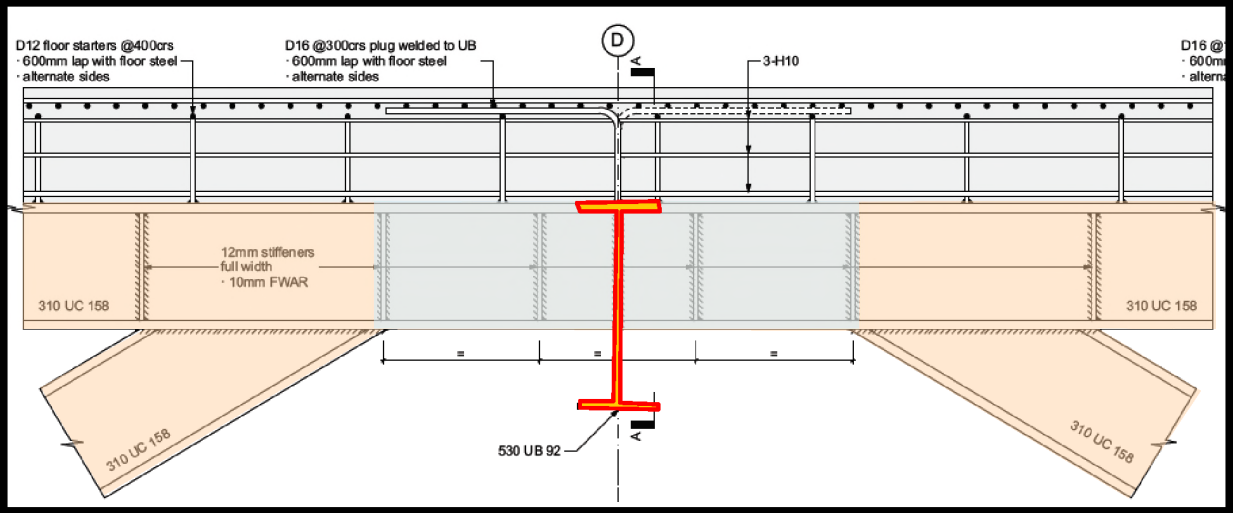

2) EBF building (136 Moorehouse Avenue)

THE REBUILD

3) BRB building

32 Oxford Terrace, Christchurch, Photo from Tuam Street, MacRae, March 2015

THE REBUILD

INTERESTING SYSTEMS

4) CBF System

SW Corner of Cambridge Terrace and Armagh Street, MacRae Photo, March 2016

THE REBUILD

INTERESTING SYSTEMS

5) Friction Connections

Building with Sliding Hinge Joint Beams and Columns

Boulcott St, between St Mary of the Angels Church/O'Reily Ave and Willis Street.

Photos courtesy of Scarry 2 August 2015

THE REBUILD

INTERESTING SYSTEMS

6) CBF Structure, Auckland

Westgate Pac'n'Save, Courtesy J. Scarry 2015

THE REBUILD

7) Nelson Structure (Courtesy Ashby/Bull) Received 9 May 2016

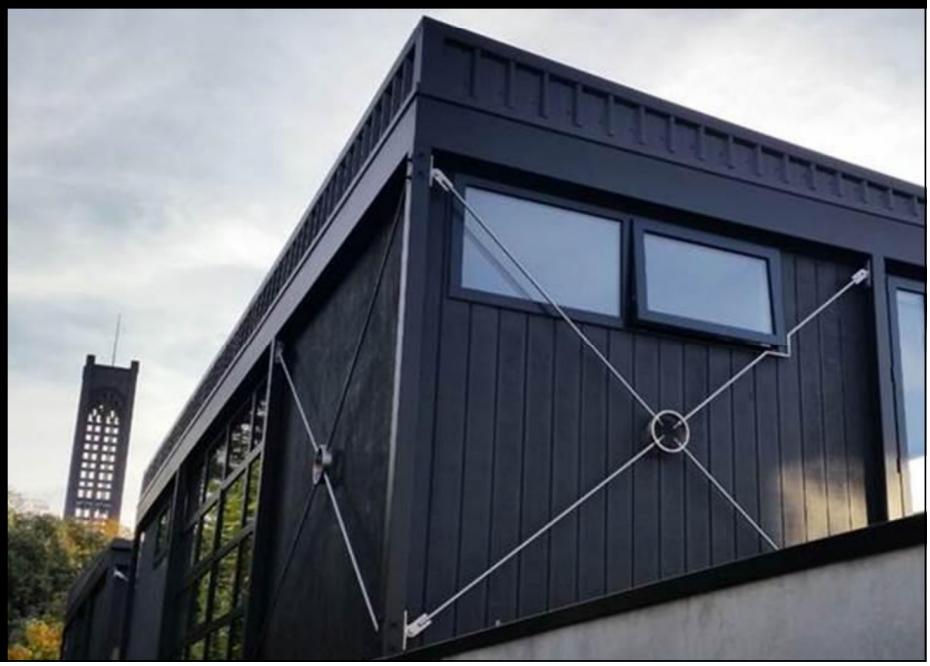

THE REBUILD

8) Other newly built structures shown found to be deficient

(a) Masterton, 2016

Falling through the cracks: experts warn of a wave of new buildings failing earthquake standards

Piers Fuller • 15:47, Oct 08 2016

A *Stuff* investigation has found 13 near-new buildings have structural weaknesses in Masterton, raising fears of systemic failings in the engineering industry.

https://www.stuff.co.nz/business/84488823/falling-through-the-cracks-experts-warn-of-a-wave-of-new-buildings-failing-earthquake-standards

THE REBUILD

8) Other newly built structures shown found to be deficient

(b) Christchurch – High Street
7 storey building

New Christchurch building has serious flaws - engineers

Wednesday, 22 May 2019, 10:31 am
Article: RNZ

"The leaked report - from engineering firm Beca to the Ministry of Business, Innovation and Employment - said the narrow, glass-fronted block at 230 High Street has:

* piles about 10 times too weak

* a support column overloaded by five times

* steel frame fixings not strong enough

* inadequate foundations"

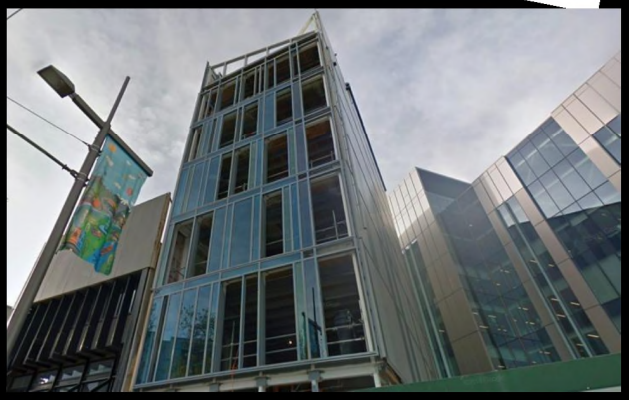

http://www.scoop.co.nz/stories/HL1905/S00114/new-christchurch-building-has-serious-flaws-engineers.htm

THE REBUILD

Systems that were NOT popular

1) POST-TENSIONED BEAMS (with steel)

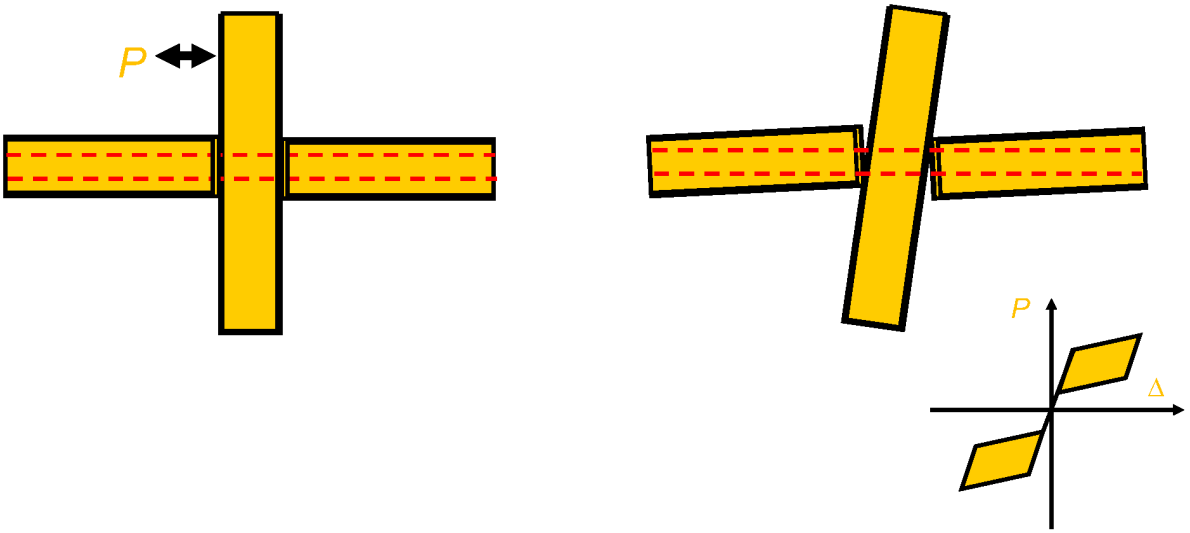

THE REBUILD

Systems that were NOT popular

1) Post-Tensioned Beams (with steel)

System Issues:

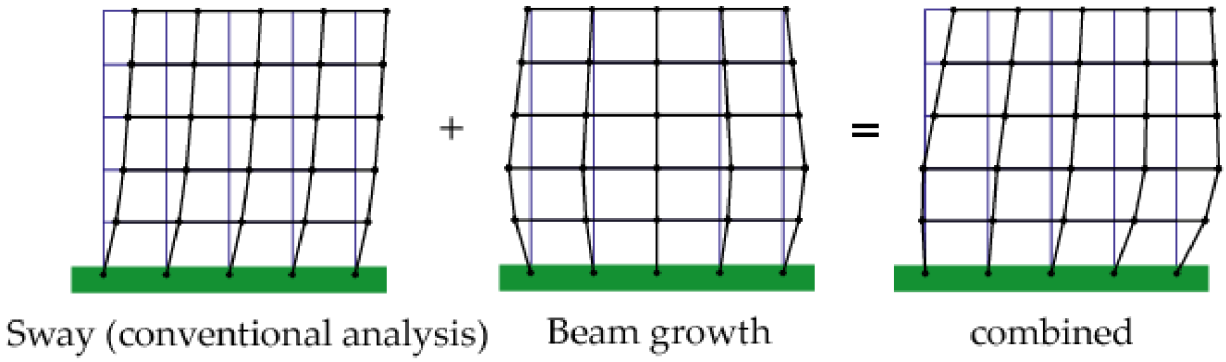

Kim J., Stanton J., and MacRae G. A., "Effect of Beam Growth on Reinforced Concrete Frames", Journal of Structural Engineering, ASCE, 130(9), pp. 1333-1342, September 2004.

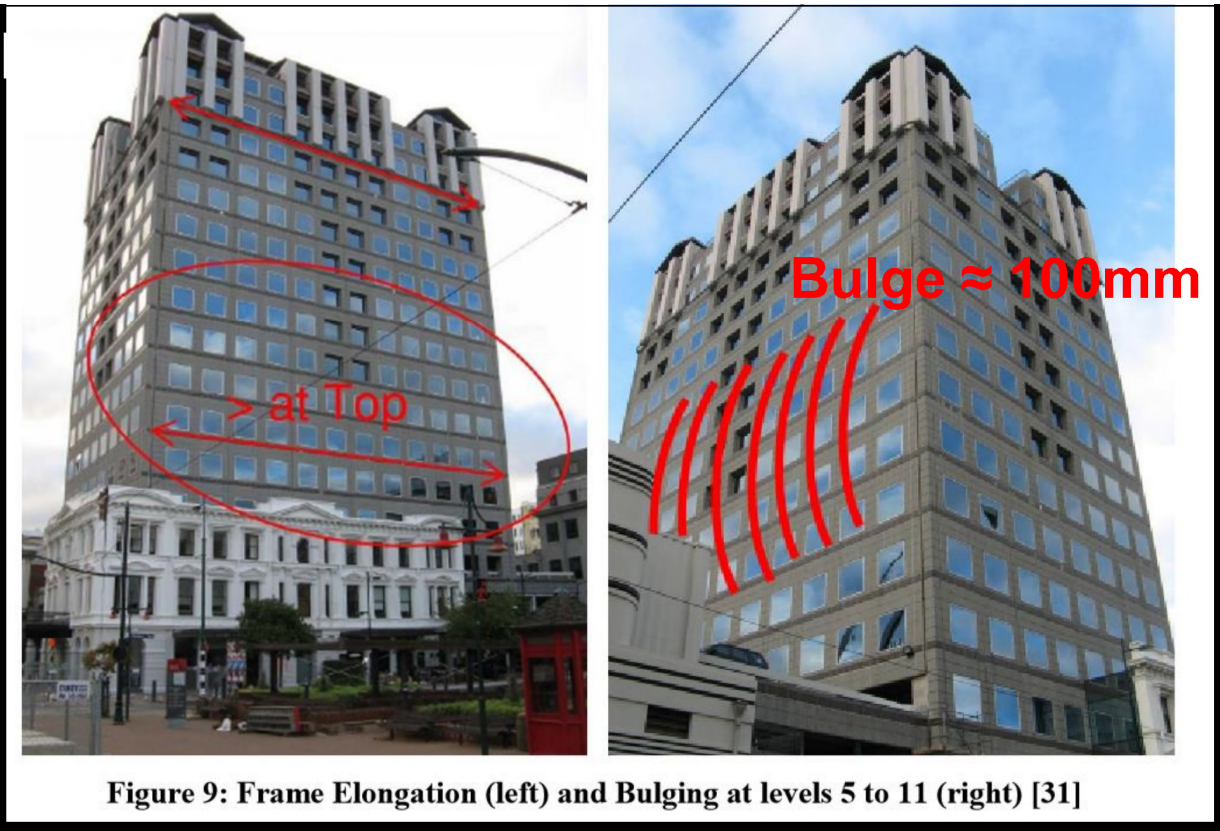

Figure 9: Frame Elongation (left) and Bulging at levels 5 to 11 (right) [31]

https://canterbury.royalcommission.govt.nz/documents-by-key/20120229.3475

Systems that were NOT popular

1) Post-Tensioned Beams (with steel)

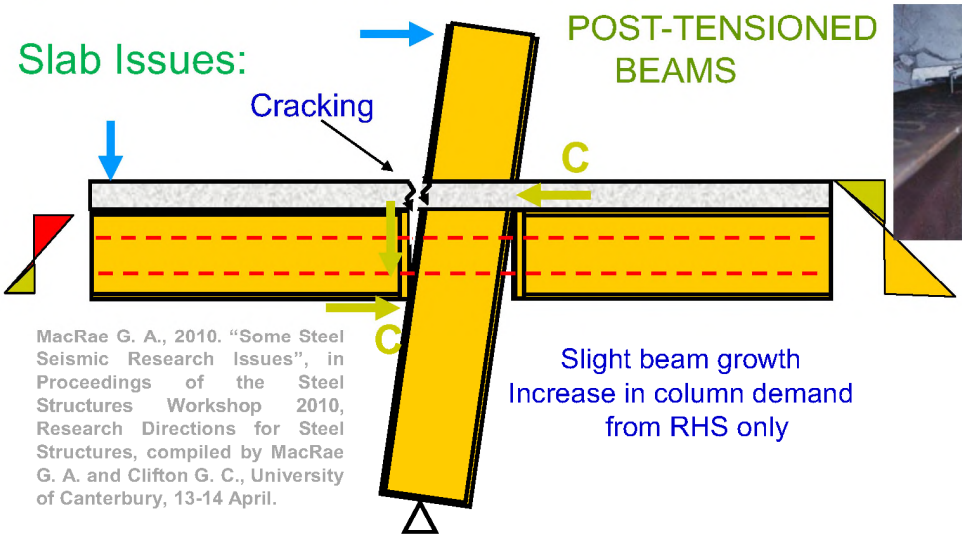

Slab damage

(Clifton G. C. 2005. Semi-Rigid Joints for Moment Resisting Steel Framed Seismic Resisting Systems. PhD Thesis, Department of Civil and Environmental Engineering, University of Auckland)

MacRae G. A., 2010. "Some Steel Seismic Research Issues", in Proceedings of the Steel Structures Workshop 2010, Research Directions for Steel Structures, compiled by MacRae G. A. and Clifton G. C., University of Canterbury, 13-14 April.

Slight beam growth
Increase in column demand from RHS only

It is possible to mitigate some of these slab issues for some structures.
SESOC does not recommend the use of post-tensioned beam systems

Design of Conventional Structural Systems Following the Canterbury Earthquakes: Structural Engineering Society of New Zealand, ENG.SESOC.0016.1, Version No. 4– 21 December 2011, http://canterbury.royalcommission.govt.nz/documents-by-key/20110930.14

THE REBUILD

Systems that were NOT popular

2) RC Moment Frame Structures

It may be because they were perceived to be:

- difficult to repair

- often too flexible causing damage to
  - non-skeletal elements (NSEs), and
  - slab

- susceptible to
  - beam elongation
  - large permanent drifts

THE REBUILD

Drivers for Structural

Form Decisions

Bruneau and MacRae

http://resources.quakecentre.co.nz/reconstructing-christchurch/

8015 downloads
30 June 2022

November 2017

THE REBUILD

UC

Why does there seem to be a lot of steel construction?

Opinions galore !

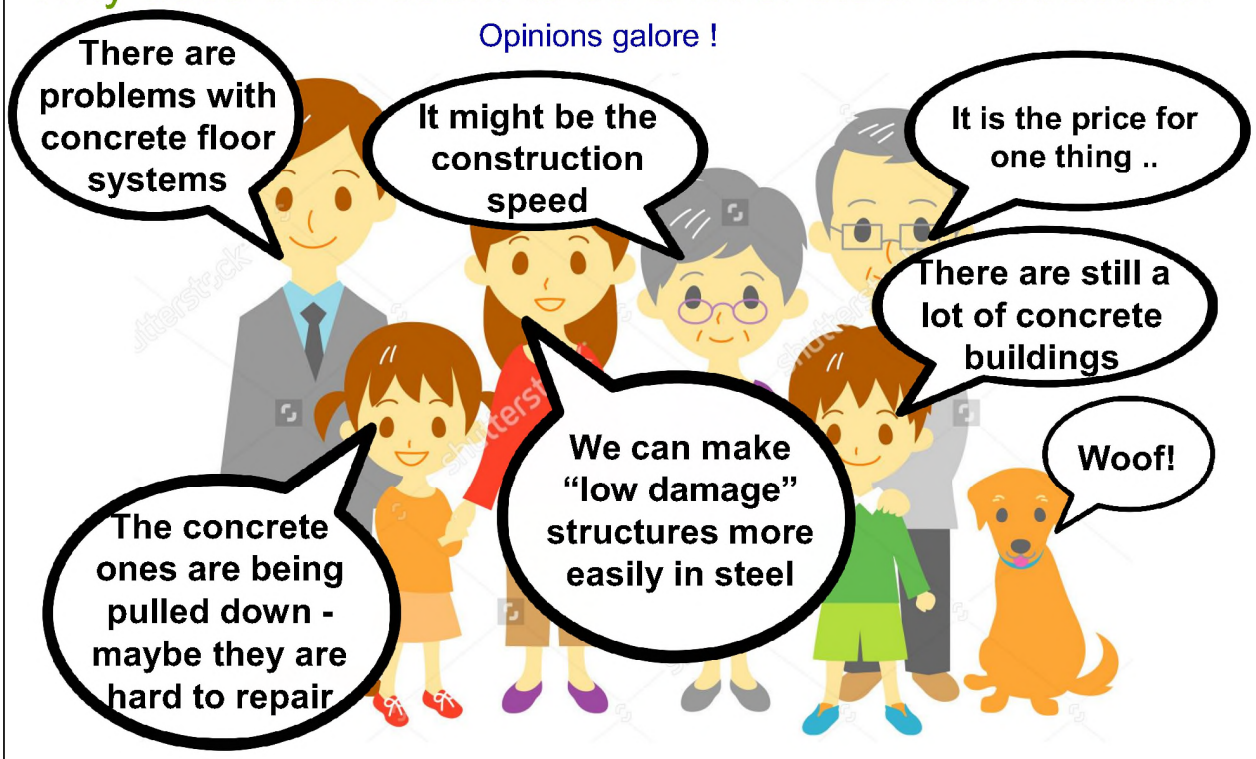

http://laoblogger.com/image-post/79710-family-cat-dog-clipart-1.jpg.html

THE REBUILD

This study was undertaken to determine:

1) What structures were actually being built …

2) What were the drivers for the choice of structural system…

THE REBUILD

Methodology:

Bruneau and MacRae

Databases – Christchurch City Council

- Steel Construction NZ

Street Survey

+ information from consultants






THE REBUILD

Number of Buildings (Steel / RC / Timber)

Cumulative **number of new buildings** having lateral-load resisting systems of each **material** type

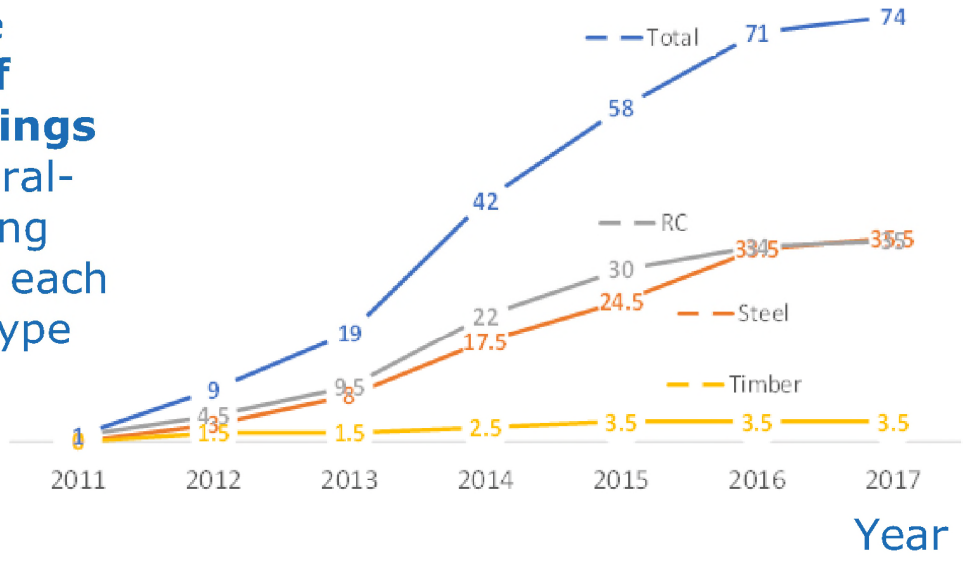

Bruneau and MacRae

THE REBUILD

Floor Area of New Buildings (m²)

Floor area of new buildings having lateral-load resisting systems (LFRSs) of each material type:

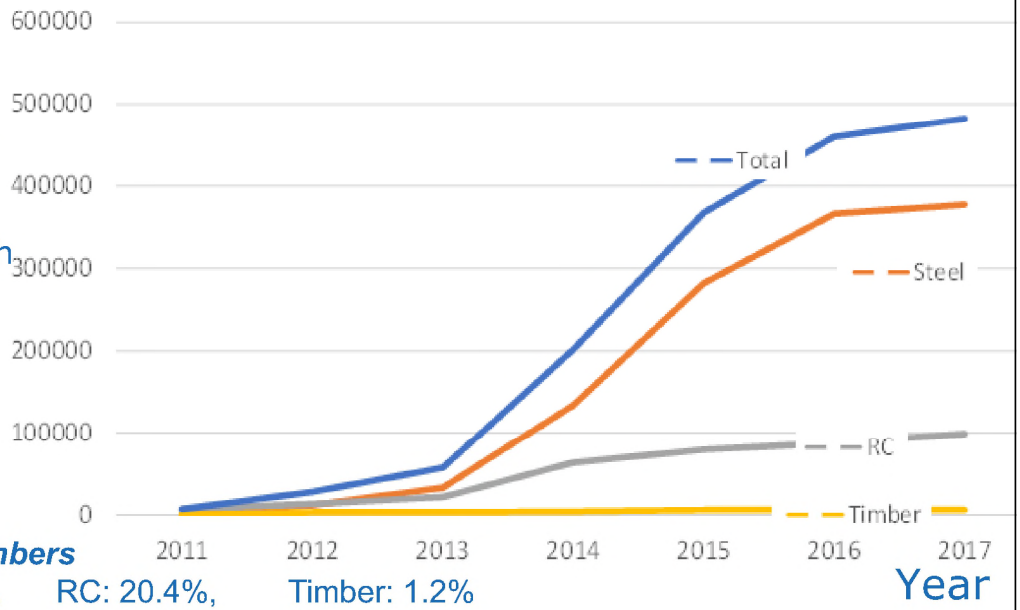

Cumulative numbers
Steel: 78.4%, RC: 20.4%, Timber: 1.2%

Buildings with structural steel systems: 95% area (approx.)

Bruneau and MacRae

THE REBUILD

THE DRIVERS

Methodology: Chatting with people

http://www.huffingtonpost.com/amanda-schneider/brainstorming_b_3832389.html

Engineers in Christchurch, Wellington and Auckland (many companies)

- An Architect
- A Developer
- A Project Manager

Meetings:

2016 – March

2017 – March / April

To find out more:

Bruneau M. and MacRae G. A., (2019) Building Structural Systems in Christchurch's Post-Earthquake Reconstruction. Earthquake Spectra: November 2019, Vol. 35, No. 4, pp. 1953-1978. https://doi.org/10.1193/052818EQS126O

OUTLINE

- Pre-Quake Considerations
- The Event
- The Rebuild
- **Societal Considerations**
- Conclusions

ORGANISATIONS

The strength of a society resides in its institutions

https://www.youtube.com/watch?v=TMbZqDh2V-g

Bas van Bavel

https://www.socialevraagstukken.nl/author/bas-van-bavel/

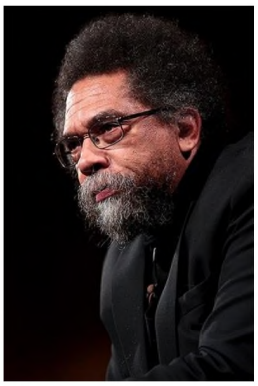

"There is no fundamental social change by being simply of individual and interpersonal actions. You have to have organizations and institutions that make a fundamental difference"

https://www.pbs.org/wgbh/pages/frontline/shows/race/interviews/west.html

Cornel West

https://en.wikipedia.org/wiki/Cornel_West

Christchurch has good institutions and they worked well in general, but we can learn from the debates …

ORGANISATIONS

Key resources:

1) Canterbury Earthquake Symposium

Venue:	University of Canterbury
Location:	29-30 November 2018 highlighting the social aspects of the recovery
Purpose:	"To give thanks we are here"
Who:	Key political and social figures in the rebuild
Website:	http://www.eqrecoverylearning.org/connect/symposium/

2) Internet (links provided in paper)

3) Anecdotes and experiences
(with links when possible)

ORGANISATIONS

Organizations Existing PreEarthquake

ORGANISATIONS

Ministry of Business Innovation and Employment (MBIE)

https://www.mbie.govt.nz/ Brunsden and Stannard (CES, 2018) stated that:

Shaking led to public loss of confidence in building safety

No post-disaster legislative framework address aspects

Little technical leadership

Constant scrutiny

ORGANISATIONS

Christchurch City Council (CCC)

- https://www.ccc.govt.nz/

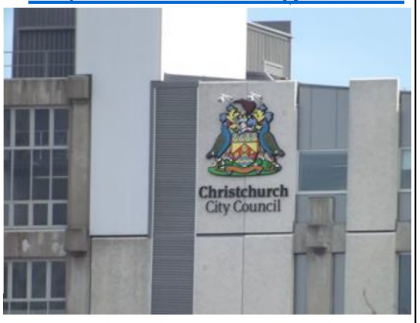

Overloaded before earthquakes

Now made busier!

Constant criticism from government

Lack of harmony in management

ORGANISATIONS

Christchurch City Council (CCC)

Overloaded before earthquakes

Now made busier!

Constant criticism from government

Lack of harmony in management

Controversial Marryatt to leave Christchurch council

Glenn Conway • 12:28, Sep 13 2013

Brownlee slams council housing failure

LOIS CAIRNS • 17:21, Nov 21 2013

POLITICS / CANTERBURY

Brownlee bows out of Christchurch rebuild

9:36 pm on 24 April 2017

Share this

ORGANISATIONS

Earthquake Commission (EQC)

- https://www.eqc.govt.nz/

- Provides residential insurance of $100,000.
- Created ***Culture of insurance*** (Marquis et al. 2015).
- > 500,000 claims for > 13 shaking events (EQC 2018).
- Employed many staff
- Purchased poor land (red zoned), $1.5b
- Responsible for repairs (with Fletchers)

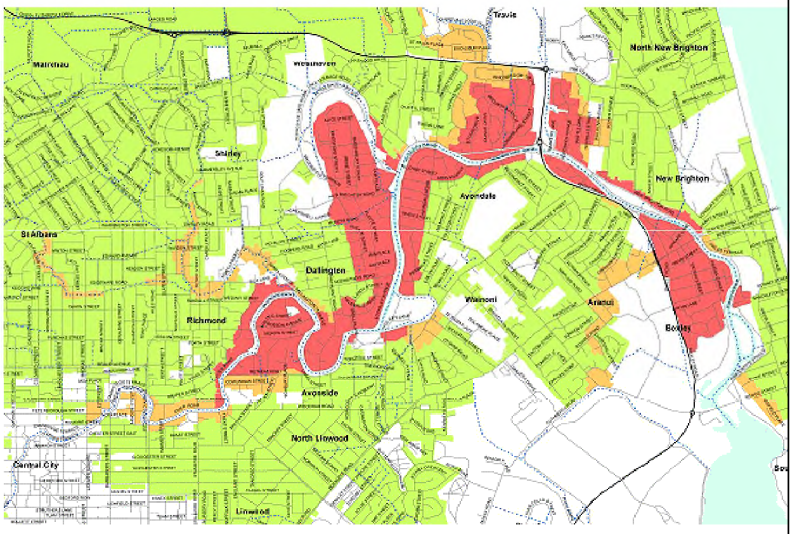

https://www.building.govt.nz/assets/Uploads/building-code-compliance/canterbury-rebuild/repairing-and-rebuilding-houses/canterbury-guidance-introduction.pdf
https://www.interest.co.nz/sites/default/files/embedded_images/image/chc-red-zone.gif

ORGANISATIONS

Earthquake Commission (EQC)

- https://www.eqc.govt.nz/

Just after 2010 earthquakes

Google maps (20 March 2019)

Banks, insurers, homeowners sifting through quaqmire of information over red-zone pay-outs and insurance claims

Posted in Insurance July 01, 2011 - 01:06pm, Hannah Lynch Tweet

EQC boss says Fletcher Building is liable for bad repairs

LAW / HOUSING

Don't buy a house repaired by EQC, Christchurch homeowner warns

Liz McDonald · 20:34

From Checkpoint, 5:43 pm on 15 March 2018

ORGANISATIONS

UC

Insurance Companies

Government announces $500m bailout for insurer AMI

ROELAND VAN DE' ... MARTIN KAY · 11:25, Apr 07 2011

No more cheap home insurance

by Rebecca Macfie / 30 July, 2011

Since the Christchurch earthquakes, homeowners face massive cost increases an some may fail to get insurance at any price.

Insurers put embargo on transferring home insurance from vendors to buyers from Rakaia to Masterton; Wellington deals frozen as mortgages impossible without insurance, say agents; Boom stopped dead in its tracks

Posted in News UPDATED November 17, 2016 - 10:23am, Bernard Hickey Tweet

ORGANISATIONS

New Organizations

CERA Plan

https://ceraarchive.dpmc.govt.nz/sites/default/files/Documents/christchurch-central-recovery-plan-summary.pdf

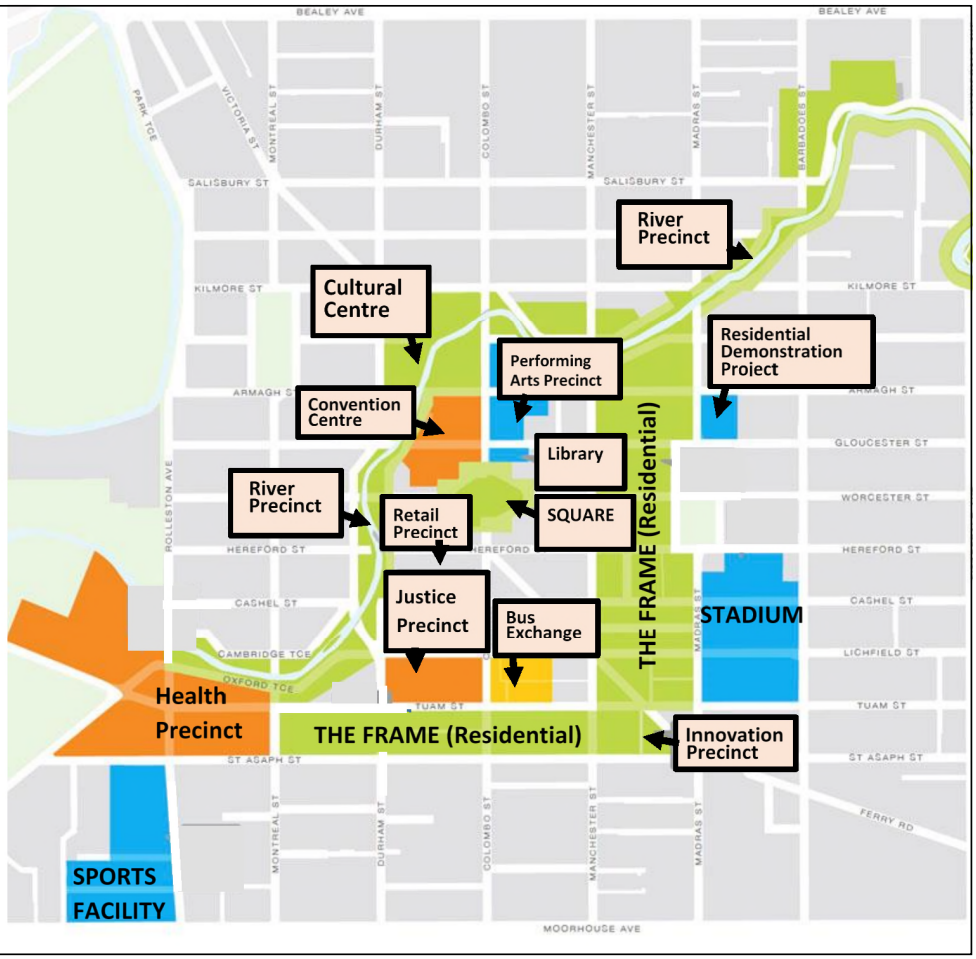

ORGANISATIONS

Canterbury Earthquake Recovery Agency (CERA)

(June 2011- April 2016) - https://ceraarchive.dpmc.govt.nz/

ORGANISATIONS

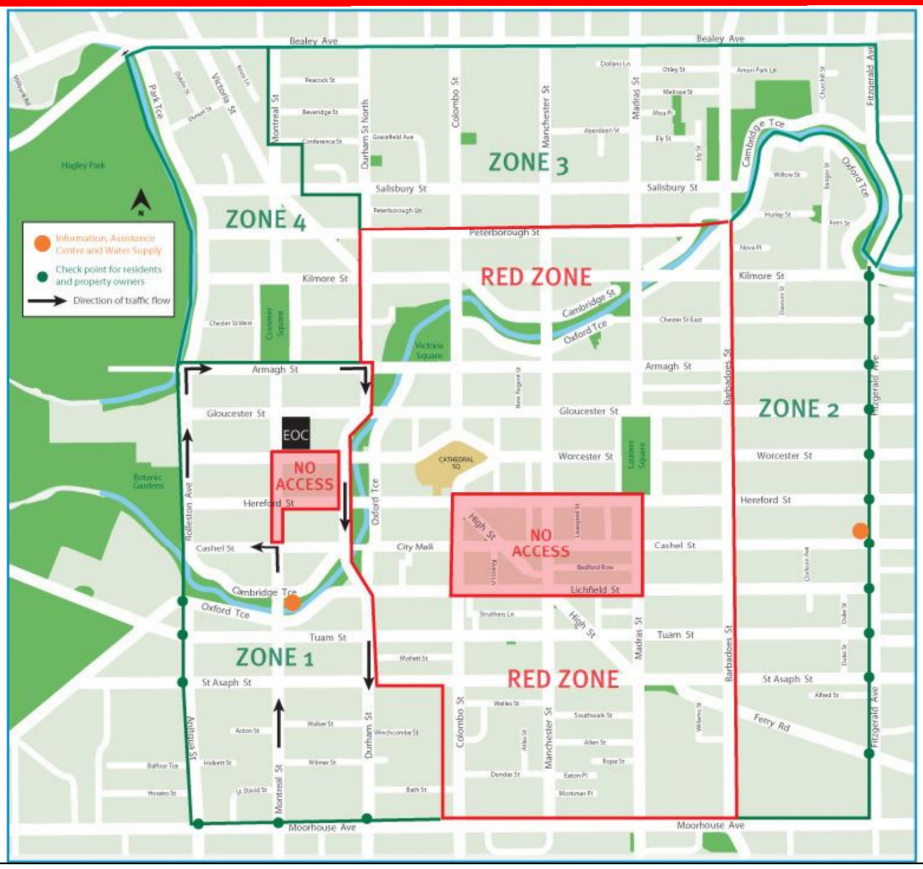

ORGANISATIONS

Recover Canterbury
(2011- 2014)

http://www.recovercanterbury.co.nz/rebuilding-after-the-christchurch-earthquake/

Formed by Business Groups

- assisted >3000 businesses access premises
- supported 400 businesses with $6.1m
- saved > 617 jobs,
- kept $39 million in the economy.

ORGANISATIONS

Stronger Christchurch Infrastructure Rebuild Team (SCIRT) 2011 – 2017

- Rebuilding **horizontal infrastructure**
  (pipes, pump stations, roads, bridges, retaining walls)
- 700 individual projects
- ***Competitive Collaboration***
- Very successful : https://scirtlearninglegacy.org.nz/

ORGANISATIONS

Canterbury Earthquakes Royal Commission (CERC)

2011 – 2013 https://canterbury.royalcommission.govt.nz/About-the-Terms-of-Reference

https://ssl.c.photoshelter.com/img-get2/I0000cmfg3gdHiSo/fit=1000x750/SNPA050912002.jpg

Determining:

(i) causes of building failure / injury

(ii) adequacy of current requirements

(design, construction and maintenance)

not liability

Many parties were called to testify about their act immediately after the major shaking.

ORGANISATIONS

Indigenous Involvement

Ngai Tahu Maori Tribe (South Island)

- involved with recovery **at all levels**
- participation was regarded highly

https://ngaitahu.iwi.nz/our_stories/big-ups-canterbury-marae/

ORGANISATIONS

Churches

Many buildings damaged

https://rubbletoresurrection.org.nz/

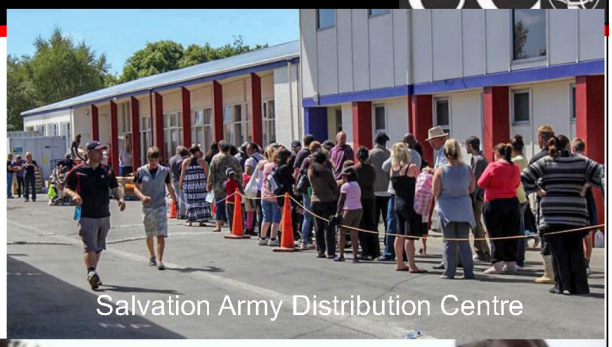

Salvation Army Distribution Centre

http://ketechristchurch.peoplesnetworknz.info/places_and_streets/images/show/40060-oxford-terrace-baptist-church-288-oxford-terrace#.XEKPIFUzaM8

https://epsombaptist.wordpress.com/tag/oxford-terrace-baptist-church/

ORGANISATIONS

Residential Advisory Service (RAS)

https://advisory.org.nz/about

Greedy insurers and insurees!

Adversarial with a low level of trust and sector failure.

Provided free impartial advice relating to home repair/rebuild insurance

> 12,000 calls received

ORGANISATIONS

Project Lyttelton https://lyttelton.net.nz/about-project-lyttelton/earthquake

Time-banking system

https://www.theguardian.com/sustainable-business/2015/dec/16/new-zealand-time-banking-currency-community-earthquake#img-2

ORGANISATIONS

Transitional City Programme http://volumeproject.org/the-transitional-city/

Gapfiller

ORGANISATIONS

Transitional City Programme http://volumeproject.org/the-transitional-city/

Gapfiller

ORGANISATIONS

Transitional City Programme http://volumeproject.org/the-transitional-city/

Gapfiller

ORGANISATIONS

Transitional City Programme http://volumeproject.org/the-transitional-city/

Gapfiller

ORGANISATIONS

Canterbury Earthquake Digital Archive (CEISMIC)

http://www.ceismic.org.nz/ University of Canterbury Linguistic department, NZ Institute of Language Brain and Behaviour

- narratives of individuals and groups regarding the earthquakes
- "contains 722 stories in 13 languages – 120 hours of video.

UC Student Volunteer Army https://sva.org.nz/

This group was very active in and assisted with many activities.

Sam Johnson
(from Dalziel)

ORGANISATIONS

Ministry of Business Innovation and Employment (MBIE)

BUILDING PERFORM.

EAG Support for MBIE & Canterbury Rebuild

Residential guidance

Liquefaction/Slope stability

Multi units

Optimising use of scarce resources

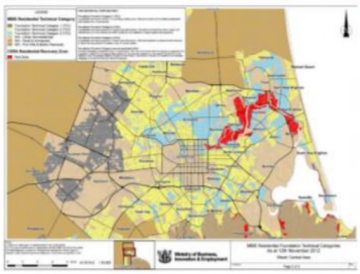

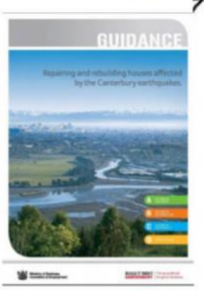

Industrial guidance

Keeping businesses operating

Foundation design

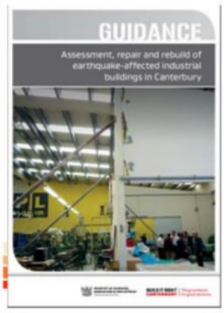

Detailed Damage Evaluation, DDE

Formerly DEE

Seismicity review

Time varying hazard

MINISTRY OF INNOVATION & EMPLOYMENT HĪKINA WHAKATUTUKI

New Zealand Government

Brunsdon and Stannard, https://www.eqrecoverylearning.org/assets/Uploads/CES-Construction-Housing-Panel-1200-Brunsden.pdf

ORGANISATIONS

Ministry of Business Innovation and Employment (MBIE)

BUILDING PERFORM.

Geotechnical Improvements - examples

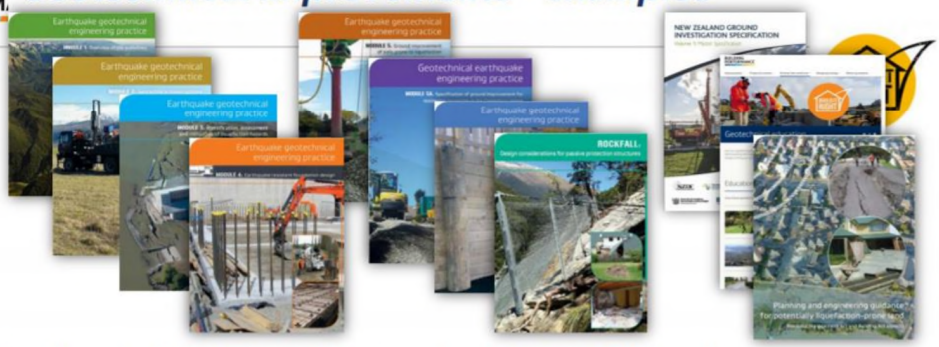

Earthquake Geotechnical Engineering Guidance & Practice

New Zealand Geotechnical Database

MINISTRY OF BUSINESS, INNOVATION & EMPLOYMENT HĪKINA WHAKATUTUKI

New Zealand Geotechnical Soc

Government

Brunsdon and Stannard, https://www.eqrecoverylearning.org/assets/Uploads/CES-Construction-Housing-Panel-1200-Brunsden.pdf

ORGANISATIONS

Ministry of Business Innovation and Employment (MBIE)

https://www.mbie.govt.nz/

Building inspection placards:

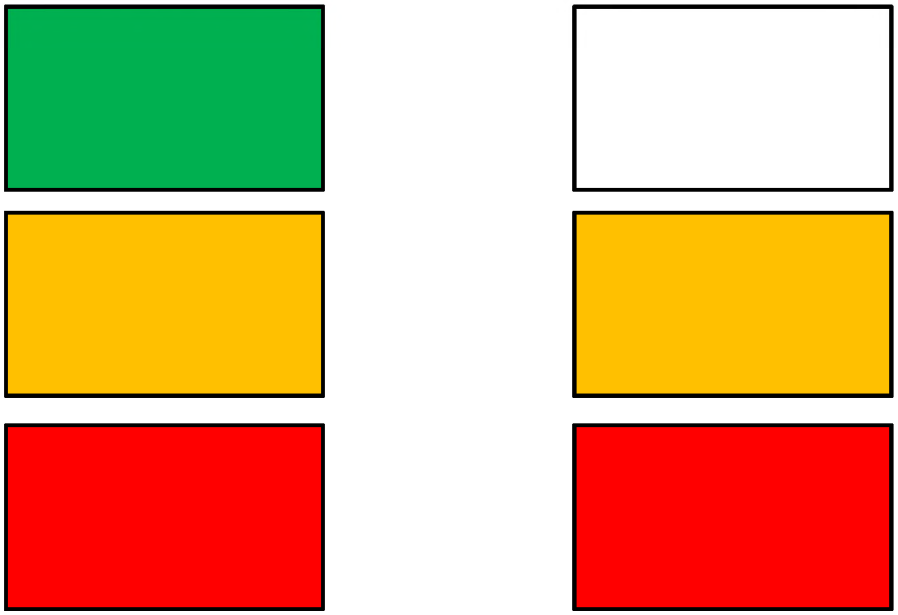

OTHER ISSUES

Population

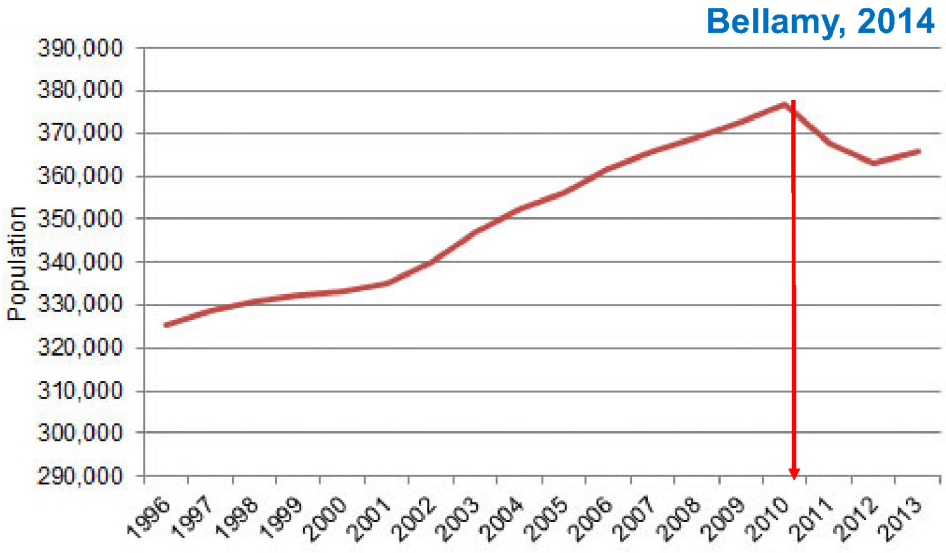

https://www.parliament.nz/en/pb/research-papers/document/00PlibC51211/social-effects-of-the-canterbury-earthquakes

OTHER ISSUES

Population

https://www.parliament.nz/en/pb/research-papers/document/00PlibC51211/social-effects-of-the-canterbury-earthquakes

OTHER ISSUES

Mental Health

How the Christchurch earthquakes devastated mental-health services by Sally Blundell / 03 May, 2018

HEALTH / CANTERBURY

Christchurch sitting on mental health 'time bomb'

Share this

From **Checkpoint**, 5:12 pm on 1 June 2017

OTHER ISSUES

Mental Health

Symptoms include anger, volatility, bed wetting, …… there were children who were even self-harming and feeling suicidal.
.... the level of post-quake PTSD was on par with children in homes where there was domestic violence, or where a parent has died unexpectedly.

Where to get help:

Lifeline: 0800 543 354
Suicide Crisis Helpline: 0508 828 865 / 0508 TAUTOKO (24/7). This is a service for people who may be thinking about suicide, or those who are concerned about family or friends.
Depression Helpline: 0800 111 757 (24/7)
Samaritans: 0800 726 666 (24/7)
Youthline: 0800 376 633 (24/7) or free text 234 (8am-12am), or email talk@youthline.co.nz
What's Up: online chat (7pm-10pm) or 0800 WHATSUP / 0800 9428 787 children's helpline (1pm-10pm weekdays, 3pm-10pm weekends)
Kidsline (ages 5-18): 0800 543 754 (24/7)
Rural Support Trust Helpline: 0800 787 254
Healthline: 0800 611 116

OTHER ISSUES

What could have been better?

Barnaby Bennett, activist stated :

http://festa.org.nz/wp-content/uploads/2014/08/barnaby-bennett-400x400.jpg

Good things included
- Ngai Tahu involvement,
- the transitional movement
- some funding agencies.

But, **it was wrong to**

(i) demolish 80% of heritage structures,
(ii) have a group like CERA that 80% of people distrusted,
(iii) have poor planning with stadium/convention centre.
(iv) not sort out the failure of public transport, and
(v) not properly fund mental health.

OTHER ISSUES

Criticism of the Convention Centre

There was no case for the centre discussed in the media. It was meant to be an early win. Eight years later was still not started.

Original price tag was $284m (2012)

Updated budget is $475 million (2018)

Government pays full cost

Some elements of the budget remain confidential ..

https://www.stuff.co.nz/the-press/news/96090557/convention-centre-cost-updated-to-475m?rm=m

OTHER ISSUES

What could have been better?

Barnaby Bennett considered that we would have been better with

- a minister with a collegial leadership style
- more public discussion than political control of the message
- more focus on process than efficiency
- some other public service people
- placement of authority in people with knowledge/experience
- follow up of the “share an idea campaign” (with 10,000 ideas)
- funding for Cathedral Square
- a stronger media

“Democracy is messy, and we need to celebrate inefficiency.”

OTHER ISSUES

What could have been better?

https://www.bing.com/th?id=OIP.P6b3TGhN3OMqn85BMGYTfwHaFj&pid=Api&rs=1&p=0

http://anglicantaonga.org.nz/var/taonga/storage/images/news/tikanga-pakeha/cathedral-to-come/christchurch-cathedral-a-very-dangerous-building-says-the-bishop.-photo-john-kirk-anderson-fairfax-nz/106571-1-eng-AU/ChristChurch-Cathedral-a-very-dangerous-building-says-the-bishop.-Photo-John-Kirk-Anderson-Fairfax-NZ_photoDisplay.jpg

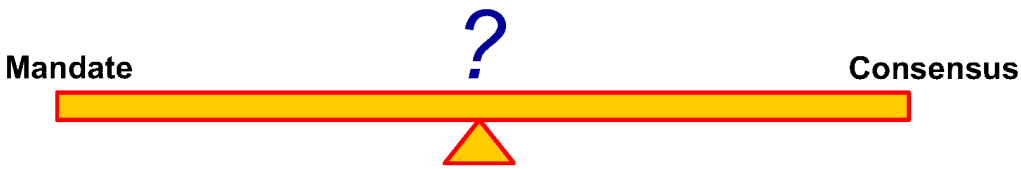

OUTLINE

- Pre-Quake Considerations
- The Event
- The Rebuild
- Societal Considerations
- **Conclusions**

CONCLUSIONS

Some aspects of the recovery from the Canterbury earthquake are described. It was shown that:

1) The recovery does not occur in a vacuum, but depends on the previous preparation, planning, response, as well as the magnitude of the event(s).
2) Some examples of buildings in the rebuild were described. Christchurch now has a new city. Some structures may be better than others. Some possible drivers for decisions in the rebuild were briefly mentioned.
3) A number of different organizations were instrumental in the recovery. The role of the organization, as well as the characteristics of the personnel involved, affected their contribution to the recovery.
4) As well as infrastructure, people were affected.
5) There were concerns about the decisions made. Such frank dialogue is useful in planning for future events.
6) A number of quotations/thoughts indicate that recovery from a disaster can be a long and messy process. However, as a result of the recovery, Christchurch is a more pleasant city.

FINAL THOUGHT

Maori saying

"He aha te mea nui o te ao.
He tāngata, he tāngata, he tāngata".

"What is the most important thing in the world?
It is people, it is people, it is people".

Questions?

https://www.bing.com/th?id=OIP.362urcEuCVnmdgsRvQVjAQHaC2&pid=Api&rs=1&p=0

Prof. Andres Oreta

De La Salle University, Philippines

Topic：Heritage Conservation Asset Value Rating of Buildings in a School Campus for Disaster Risk Assessment

HERITAGE CONSERVATION ASSET VALUE RATING OF BUILDINGS IN A SCHOOL CAMPUS FOR DISASTER RISK ASSESSMENT

Corinne Wesnee D. Yu[1], Carlyse Nicole L. Kah[1], Aldrei Charles C. Navera[1], Charles Janzen C. Sy[1], Rodolfo P. Mendoza, Jr. [2] and Andres Winston C. Oreta[3]
1) BSCE, De La Salle University, Manila, Philippines
2) Associate Professor, De La Salle University, Manila, Philippines
3) Professor, De La Salle University, Manila, Philippines
Email: andres.oreta@dlsu.edu.ph, rodolfo.mendoza@dlsu.edu.ph, corinne_wesnee_yu@dlsu.edu.ph

ABSTRACT

A campus is an area occupied by the buildings of an educational facility, usually a university or college. A school campus, especially those located in hazard-prone regions, must be safe and resilient to various disasters like earthquake, wind or flood to protect the community of learners and teachers and to assure the continuous operation of the school. Hence, the existing buildings in a campus must be assessed to determine if immediate repair or retrofitting is necessary. Structural assessment and retrofitting is costly and time consuming, though, especially if there is a large population of school buildings in a campus. Hence, a rapid assessment that is not expensive and easy to implement must be conducted first before any detailed inspection and retrofitting be implemented. To prioritize which buildings need immediate detailed inspection, risk assessment using a disaster risk reduction and management (DRRM) framework may be used. The disaster risk assessment framework involves the interaction of hazard, vulnerability, and asset. At the center of disaster risk assessment is the "Asset" which has an associated value that depends on the importance and function of the building. In this study, the value of a school building is viewed with a heritage conservation perspective. A simple and qualitative asset value rating of existing buildings in a campus considering educational function and the building's architecture and history is presented. The asset value rating can then be integrated to the DRRM framework for the overall risk assessment of existing buildings in a campus. A case study of the qualitative asset value rating and seismic risk assessment of De La Salle University campus in Manila, Philippines is presented. In the case study, two important buildings with significant heritage value to the university were identified.

Keywords: disaster risk assessment, asset value, campus, heritage conservation, De La Salle University

INTRODUCTION

The Philippines is one of the most hazard-prone countries in the world. It is regularly subjected to various hazards because of its geologic and geographic conditions. The Philippines is an earthquake country where at least five earthquakes occur per day. The country has experienced disastrous earthquakes such as the 1990 Luzon earthquake which affected many buildings in Baguio and Dagupan and recent Mindanao earthquakes (Davao del Sur in Dec 2019 and Davao Oriental in Aug 2021). Aside for earthquakes, the country has also been regularly devastated by typhoons and floods. On the average, 20 typhoons occur in the Philippines within the period from July to November. Moreover, other natural and man-made hazards like fire endanger the built environment. With this disaster-prone condition of the Philippines, there should be an intensive effort to assure the safety of the community and the built environment. And as a start, assessment of existing buildings at a site like a campus to various hazards must be extensively conducted.

A campus is an area occupied by the buildings of an educational facility, usually a university or college. In a school campus, there are many buildings, some old and some new that may be vulnerable to hazards like strong earthquakes or wind. School administrators must assure that the campus and its buildings are safe and resilient to various disasters to protect the community of learners and teachers from harm and to assure the continuous operation of the school even after a hazardous event. Hence, the existing buildings in a campus must be assessed to determine if immediate repair or retrofitting is necessary. Structural assessment and retrofitting is costly and time consuming, though, especially if there is a large

population of school buildings in a campus. Thus, this paper aims to address the need to develop rapid and simple assessment framework that can be used for disaster risk reduction and management (DRRM) purposes with a special focus on heritage conservation.

RISK ASSESSMENT FRAMEWORK

Risk assessment aims to rank and prioritize structures from a pool of existing buildings at a site that must be given immediate attention for detailed structural assessment and retrofitting. A common framework in the disaster risk reduction and management (DRRM) community is a multi-hazard risk assessment methodology which considers the relationship of the following parameters: hazard, vulnerability, asset, and risk as shown in Figure 1.

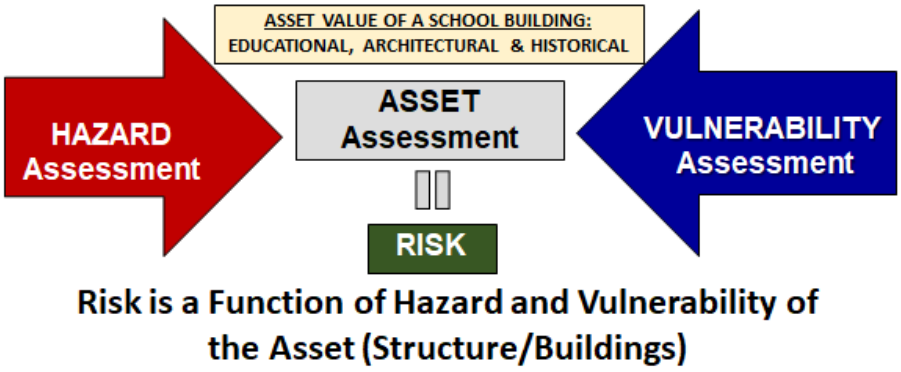

Figure 1. Risk Assessment Framework considering heritage preservation

The first component in the framework is "Hazard" which is defined as a "potentially damaging physical event, phenomenon or human activity that may cause losses in life or injury, property damage, social and economic disruption or environmental degradation" (UNISDR 2015). Natural Hazards include earthquake, typhoon, flood, tsunami, landslide, storm surge, drought, volcanic eruption, while human-induced hazards include terrorism, fire, war, and industrial catastrophe. Hazard assessment aims to determine the impact of a hazard to an asset like buildings by considering quantitative parameters that contribute to the degree of severance of the hazard. Among the parameters that are important in a hazard assessment are (a) size of the hazard (e.g., earthquake magnitude, peak ground acceleration, wind speed, precipitation, flood depth) and (b) amplifying factors of the hazard (e.g., nearness to the fault, rivers or slopes, soil type). The second component in the framework is "Vulnerability" which is referred to as the "conditions determined by physical, social, economic and environmental factors or processes, which increase the susceptibility of a community to the impact of hazards" (UNISDR 2015). With respect to structures or buildings, vulnerability is the degree of susceptibility of the structural and non-structural elements of the building to specific hazards. A qualitative and semi-quantitative vulnerability assessment aims to assess if a building has vulnerable elements to a specific hazard. A building that possesses many vulnerable elements has a greater "risk" to perform poorly to the specific hazard. Finally, at the center of the Risk Assessment Framework is the "Asset" or the building which has an associated quantitative value based on investment and construction cost (monetary) and qualitative value based on its importance related to the institution which can educational function for schools, architecture and history for heritage conservation, commercial use and tourism for business. Combining the three components of the framework results to risk (R) which is determined using the general relationship: $R=(H\times V)\times A$, where R, H, V, and A are indices corresponding to the risk, hazard, vulnerability, and asset value, respectively; the latter three indices are referred to as sub-indices.

ASSET VALUE ASSESSMENT

Assigning a value to structures is a challenge because different values can be ascribed to these structures or buildings especially if viewed from a heritage conservation perspective. Of course, the quantitative value of a building can be easily assigned based on its cost of construction which can be given in monetary units. However, the value of the structure is multivalent and can be viewed by various

perspectives not only based on investment. A building asset may be considered important and valuable due to the following reasons: (a) Functional – because the asset serves basic operational functions of the organization, (b) Historical - because the asset is associated to past events or because it is old, (c) Aesthetic – because the asset is beautiful and a fine work of architecture, (d) Economic – because it is a real estate property and provides income to the community, (e) Political – because it may represent a social order or class, (f) Tourism – because it is a recognized landmark and attracts tourists or (g) Spiritual – because it is a place of worship (churches).

A campus or a land area consisting of educational facilities houses many buildings of various importance and uses. Spaces in school buildings may be used as a classroom, library, administrative office, laboratory, or study area. The importance of the function to the school's mission may be a criterion for the assigning of the value of a building as low or high. Oreta and Brizuela (2013) assigned values to a school building based on three parameters: (a) population (a building with more occupants has high value), (b) consequence to the function or operation of the school (a building that will affect the school's basic educational function when damage has a high value) and (c) type of equipment/data stored in the building (a building that houses expensive laboratory equipment or priceless data like student records are rated high). Illumin and Oreta (2018) assigned values to a school building from a perspective of schools being used as evacuation centers and the floor area was the main parameter used since it is correlated to the number of people that can be accommodated during evacuation. An educational institution, although its primary mission is to promote development and advanced knowledge to the new generation of learners must also preserve its history and heritage. Usually, a campus consists of buildings that have attached memories and historical significance to its founders, administrators, faculty, and students that needs to be preserved. Some school buildings also have unique architecture designs that highlight the identity of the school. A building's value can also be attached to history and architecture. Studies on risk assessment of heritage structures for adaptive reuse assigned values to buildings based on heritage, architectural, commercial, tourism and adaptive reuse values (Yu and Oreta 2015, De Jesus et al. 2021). In the asset value assessment in these studies, an asset value index was obtained by taking the weighted sum of the asset value indicators where the weights for the indicators are either assumed or determined through a survey using analytical hierarchical process (AHP) or a focus group discussion.

HERITAGE CONSERVATION ASSET VALUE ASSESSMENT

This paper presents a framework (Figure 1) on asset value assessment of buildings in a campus based on a heritage conservation perspective. A qualitative asset value rating integrating the studies on safe schools (Oreta and Brizuela 2013, Illumin and Oreta 2018) and heritage structures (De Jesus et al. 2021) was adapted to the present context. The asset value of a school building is associated to its function as an educational institution and to heritage which is represented by the architecture and history of the building. Thus, each building in a campus is rated based on the three criteria: a) Architectural (AV_1), Historical (AV_2) and (c) Educational (AV_3) values.

Architectural Value

In terms of architectural value, this refers to the sensual qualities of a site, making it a strong contributor to its cultural affiliation (De la Torre, 2002). Cultural heritage preservation is all about maintaining the people's shared links with the past and the architecture of the building is one symbol that connects a university to its past. The architectural value of a building is rated as Low (1), Moderate (2), and High (3) through the following three indicators: (a*) The building captures the architecture, design, and culture of the past generation*, (b) *The building's architecture is retained since the year it was built*, and (c) *The building's architecture is eye-catching and stands out among other buildings*. Through these three architectural value indicators, a building is rated on its design, authenticity, and visual appeal.

Historical Value

Heritage value is associated with history or age. Republic Act No. 10066 or the National Cultural Heritage Act of 2009 states that "structures dating at least fifty (50) years old are included in the list of important cultural property that will be protected against exportation, modification, or demolition." A

school or university needs to preserve its rich history. A building in a campus may be a link to significant events or important people. The historical and heritage value of a building is rated by answering the following indicators: (a) *Is the building recognized locally, nationally, or internationally as a heritage structure?* (b) *How old is the building?* (Age is assumed to be directly related to heritage and history as conveyed in RA No. 10066), (c) *Does the building have a history that is worth telling and preserving to the new generation?* (d) *Does the building reflects the cultural heritage and identity of the school?* and (e) *Does the building have historically significant places or monuments?* To answer these indicators, there is a need to do research about a building's construction and history. There may be a need also to conduct focus group discussions where the participants are former administrators, faculty, and students to capture the significant historical value of the building. From the five indicators, the historical value of a building is assessed on its heritage, age, history, identity, and significant monuments.

Educational Value

The educational asset value (*AV*3) of a building is based on the various functions of a school. The prioritization of the functionality of the school buildings were based on the study of Ilumin and Oreta (2018). The educational or functional value of a building is rated based on the total area of the type of occupancy such as: (a) classroom, (b) laboratory, (c) office and (d) other functionalities such as conference room, library, or canteen. The rating scale based on floor area for (a), (b) and (d) as follows: (1) 25% or less of the total floor area, (2) 26% to 50% of the total floor area, or (3) 51% or more of the total floor area. On the other hand, offices were rated based on floor area using a different scale: (1) 15% or less of the total floor area, (2) 16% to 25% of the total floor area, or (3) 26% or more of the total floor area.

For each indicator in the asset value criterion, a qualitative rating as Low (1), Moderate (2), and High (3) is assigned and then combined through a weighted sum. Finally, the three asset values (architectural, historical and educational values) of a building are combined to obtain the asset value, $AV = w_1 \, x \, AV_1 + w_2 \, x \, AV_2 + w_3 \, x \, AV_3$. Figure presents a sample application of the qualitative asset value rating checklist with assigned scores (1, 2, or 3) and weights. For this example, equal weight of 1/3 was assigned to each *AV* value resulting to $AV = 2.35$ which is categorized as high with respect to asset value for this building assuming a scale for *AV*: a) Low (0-1), b) Med (1-2) and c) High (2-3).

	L	*M*	*H*	Weight	Value
A. ARCHITECTURAL VALUE (AV1)	1	2	3	W1	AV1 x W1
A1. The building captures the architecture, design and culture of the past generation.		3		0.33	0.99
A2. The building's architecture is retained since the year it was built.		3		0.33	0.99
A3. The building's architecture is eye-catching and stands out among other buildings.		3		0.33	0.99
AV1 (AVERAGE)		3		0.99	2.97
B. HISTORICAL VALUE (AV2)	1	2	3	W2	AV1 x W2
B1. The building has historical value: (1) locally, (2) nationally or (3) internationally.		3		0.2	0.6
B2. The age of the building is (1) 15 to 25 years, (2) 26 to 50 years, or (3) 51 years +		3		0.2	0.6
B3. The building has a history that is worth telling and preserving to the new generation.		3		0.2	0.6
B4. The building's history reflects the cultural heritage of De La Salle University.		3		0.2	0.6
B5. The building has historically significant places, such as chapels, occupying (1) 15% or less of the total floor area, (2) 16% to 25% of the total floor area, or (3) 26% or more of the total floor area		1		0.2	0.2
AV2 (AVERAGE)		2.6		1	2.6
C. EDUCATIONAL VALUE (AV3)	*1*	*2*	*3*	W3	AV3 x W3
C1. This building has classrooms occupying (1) 25% or less of the total floor area, (2) 26% to 50% of the total floor area, or (3) 51% or more of the total floor area.		*1*		0.2782	0.2782
C2. This building has laboratories occupying (1) 25% or less of the total floor area, (2) 26% to 50% of the total floor area, or (3) 51% or more of the total floor area		*1*		0.2423	0.2423
C3. This building has offices occupying (1) 15% or less of the total floor area, (2) 16% to 25% of the total floor area, or (3) 26% or more of the total floor area		*1*		0.2382	0.2382
C4. The building has other functionailities (conference rooms, library, canteen) occupying (1) 25% or less of the total floor area, (2) 26% to 50% of the total floor area, or (3) 51% or more of the total floor area.		*3*		0.2414	0.7242
AV3 (AVERAGE)		1.5		1.000	1.4829
ASSET VALUE (AV) = Σ (AVi x Wi)				2.35	

Figure 2. Qualitative Asset Value Rating for St. La Salle Hall at DLSU Campus

CASE STUDY: DE LA SALLE UNIVERSITY, MANILA

De La Salle University (DLSU), a private university founded in 1910 is located in Manila, Philippines. The DLSU campus has a rich history and one of its oldest buildings. St. La Salle Hall, completed in 1924, was used to house displaced civilians and wounded soldiers during World War II. The constant bombings during the war had brought several damages to the structure which brought to its reconstruction in 1948 (Celestino et al., 2013). Now a four-story neoclassical architecture, St. La Salle Hall is known to be the most historic building in DLSU (Virgula, 2010) with the Most Blessed Sacrament Chapel being the site of the World War II massacre in 1945. St. La Salle Hall has undergone several changes but remains its appearance and architecture due to its identification as "DLSU's most historic building." Additionally, this historical building is the only building in the Philippines that appeared in the '1001 Buildings You Must See Before You Die: The World's Architectural Masterpieces' (Irving, 2007). by Mark Irving which was published by Quintessence Editions Ltd. in 2007.

At present, the DLSU-Manila campus (Figures 3 and 4) includes twenty-three buildings along the stretch of Taft Avenue in Malate, Manila. Sixteen of which hosts most of the population including students, faculty, and administrative authorities.

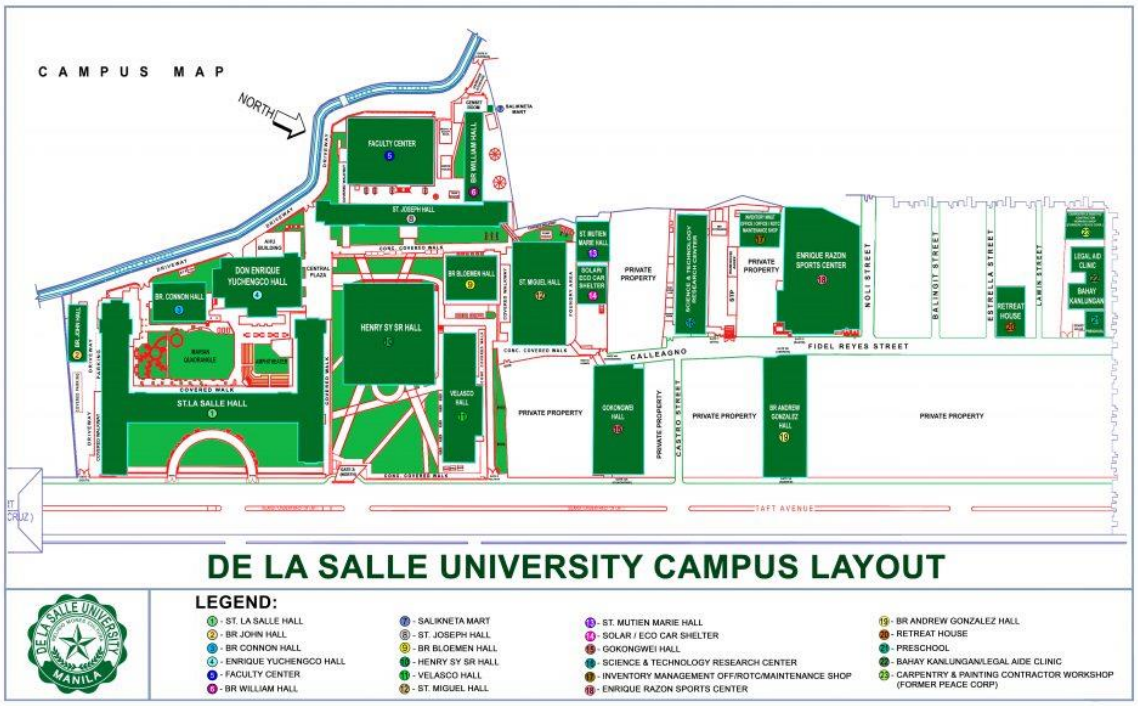

Figure 3. DLSU, Manila Campus Map (https://www.dlsu.edu.ph/inside/campus-map/)

Figure 4. DLSU, Manila campus with St. La Salle Hall at the left.
(https://www.dlsu.edu.ph/about-dlsu/).

The qualitative asset value rating checklist (Figure 2) can be applied to the other buildings in the campus. Table 1 presents the summary of the asset value ratings and seismic risk assessment of the 16 buildings at DLSU. The buildings were ranked based on asset value in this table to highlight the asset value assessment.

Table 1. Asset Value and Seismic Risk Assessment of the DLSU – Manila Campus

ASSET VALUE ASSESSMENT						SEISMIC RISK ASSESSMENT			
	Asset Value Ratings					Hazard	Vulnerability		Risk Index
Building ID	AV1	AV2	AV3	AV	Remark	HR	SVR	HR x SVR	R=HR x SVR x AV
LS	2.97	2.60	1.48	2.35	H	2.33	1.89	4.42	10.39
SJ	2.31	2.20	1.48	2.00	H	2.33	2.34	5.46	10.91
YUCH	2.64	1.60	1.48	1.91	M	2.33	2.16	5.05	9.64
FACULTY CENTER	1.98	1.20	1.72	1.63	M	2.33	1.98	4.61	7.53
RAZON	1.98	1.40	1.48	1.62	M	2.33	2.34	5.45	8.84
AGH	1.98	1.40	1.48	1.62	M	2.33	1.91	4.46	7.22
HENRY	1.98	1.60	1.24	1.61	M	2.33	2.18	5.08	8.16
JOHN	1.65	1.20	1.96	1.60	M	2.33	2.04	4.76	7.63
WILLIAM	0.99	1.80	1.96	1.58	M	2.33	1.98	4.61	7.30
BLOEMEN	1.65	1.60	1.48	1.58	M	2.33	1.86	4.35	6.86
MM	1.65	1.20	1.80	1.55	M	2.33	1.92	4.48	6.94
GOKS	1.65	1.20	1.76	1.54	M	2.33	2.66	6.21	9.53
STRC	1.65	1.20	1.73	1.53	M	2.33	1.89	4.42	6.74
SM	1.65	1.40	1.48	1.51	M	2.33	1.99	4.65	7.02
VELASCO	1.65	1.20	1.48	1.44	M	2.33	2.35	5.49	7.93
CONNON	0.99	1.20	1.96	1.38	M	2.33	1.89	4.41	6.10

The various ratings can be used to group the buildings based on the specific value or parameter and color coded scale. For example, Figure 5 shows the buildings classified in terms of architectural value (AV_1) using the scale: Low (0-1), Med (1-2) and High (2-3). St. John Hall, St. La Salle Hall, and Yuchengco Hall rated high because of the neo-classical architectural style which is common in the buildings in France, where the founder St. La Salle was born. The two buildings are also more than 50 years old, rating high with respect to heritage, age, and history.

Figure 6, on the other hand, shows the buildings grouped based on the asset value (AV) which is the sum of the weighted asset values on architecture, history, and educational function. Figure 6 shows two buildings – the St. La Salle Hall (LS) and the St. Joseph Building (SJ) that have the highest asset values among the buildings in the campus. The LS Hall was rated high for architectural and historical value indicators for highly capturing the architectural neo-classical look, capturing the past culture and has been retained since the year it was built, as shown in the sample qualitative asset value rating in Figure

2. The building exists for more than 50 years and is internationally known. With this, it can be noted that LS Hall is worth preserving for the next generation as its history reflects the culture of the school. The SJ Hall, on the other hand, captures a semi-modern and neoclassical take, due to its façade scheme that has been retained since it was built. The building is known locally and exists for 67 years, reflecting the culture of the university and housed the classrooms, chemistry, and physics laboratories of many undergraduate students who are now successful and prominent alumni.

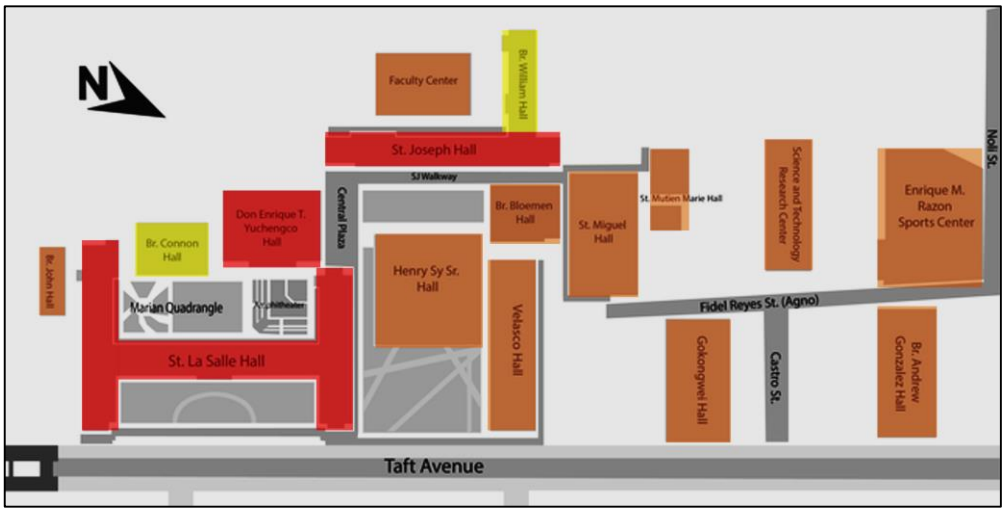

Figure 5. Architectural Value (AV_1) Categorical Map (Color Legend: **High, Med, Low**)

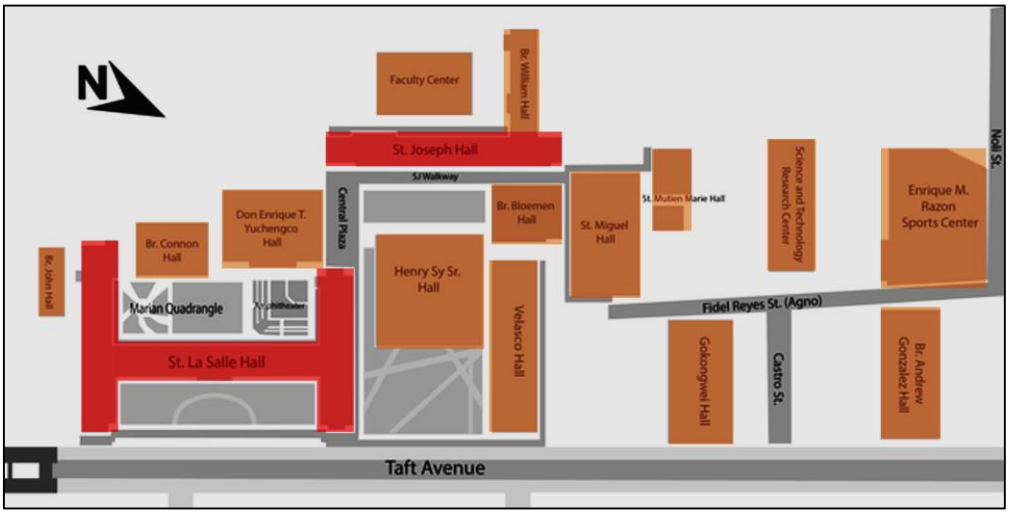

Figure 6. Asset Value (*AV*) Categorical Map (Color Legend: **High, Med, Low**)

The seismic hazard and vulnerability assessment from De Jesus et al. (2021) was adopted in the final seismic risk assessment. The buildings, since they are located in the same site with slight variations in soil conditions will usually have the same hazard (*HR*) ratings as shown in Table 1. The seismic vulnerability ratings (*SVR*), on the other hand, will depend on the building condition and applicable vulnerabilities like plan and vertical irregularities, design code used, structural system and type of material.

The seismic risk index is obtained as $R = HR \times SVR \times AV$. Table 1 shows that asset value is a major factor in risk assessment, where the two buildings with the highest asset value rated also highest with respect to risk. However, asset value is not only the deciding factor in the prioritization and ranking as observed in Table 1. There are buildings with a high-risk index like building ID: GOKS, WILLIAM and RAZON but medium asset value. Figure 7 shows the mapping of the buildings based on the seismic risk index. Through this seismic risk index map, decision makers will be guided on the prioritization on

which buildings need immediate attention for a more detailed structural inspection and possible seismic retrofitting based on a heritage conservation perspective.

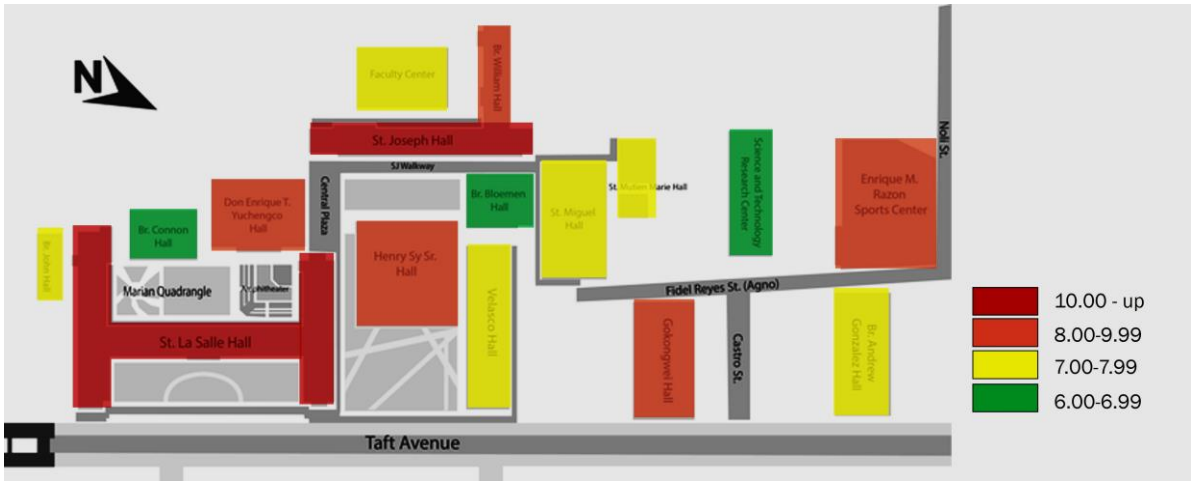

Figure 7. Seismic Risk Assessment Graduated Map

CONCLUSIONS

The paper presented a simple qualitative asset value rating of existing buildings in a campus with respect to heritage conservation. Buildings are assessed based on architectural, historical, and educational values and an asset value index (*AV*) is obtained through the weighted sum of the asset value indicators. The index (*AV*) can be integrated to hazard and vulnerability assessment to complete the risk assessment of the school buildings in a campus with respect to a specific hazard. The case study for DLSU campus presented the qualitative asset value rating and seismic risk assessment.

REFERENCES

Celestino, C., Montinola, J. F., & Mendoza, A. (2013, August 7). A La Salle story. *The Lasallian*. https://thelasallian.com/2013/08/07/a-la-salle-storey/

De la Torre, M. (2002). *Assessing the Values of Cultural Heritage*. Getty Conservation Institute.

De Jesus, R., Oreta, A., Grio M., Mendoza, R., Ibabao, R., Sevieri, G. and Galasso, C. (2021). "Seismic Screening and Structural Investigation of Heritage Buildings for Adaptive Reuse: A Survey Study at Iloilo City, Philippines," *9th AUN/SEED-Net Regional Conference on Natural Disaster*, Dec 15-16, 2021

Illumin, R. and Oreta, A. (2018). "A Post-Disaster Functional Asset Value Index for School Buildings," *Procedia Engineering*, 212 (2018) 230–237, 7th International Conference on Building Resilience (7ICBR), Nov. 26-29, 2017, Bangkok, Thailand

Irving, Mark (2007). *1001 Buildings You Must See Before You Die: The World's Architectural Masterpieces*, Quintessence Editions Ltd.

Oreta, A.W.C. and Brizuela, K. (2013). "A Computer-Aided Seismic Hazard Risk Management Tool to Promote Safe School Communities," *Proceeding the 6th Civil Engineering Conference in Asia Region: Embracing the Future through Sustainability*, Aug. 20-22, 2013, Jakarta, Indonesia, ISBN 978-602-8605-08-3

Philippines 2009 Republic Act No. 10066: National Cultural Heritage Act of 2009, https://www.officialgazette.gov.ph/2010/03/26/republic-act-no-10066/

Thomas, V. et al. (2013). *Climate-Related Disasters in Asia and the Pacific*. Working Paper, Asian Development Bank. UNECE. "Climate Change and Sustainable Transport, http://www.unece.org/trans/theme_global_warm.html\

Yu, Kirk and Oreta, A.W.C. (2015). "Multi-hazard Risk and Asset Value Assessment of Heritage Buildings (Case study in Iloilo City, Philippines)," *International Association for Bridge & Structural Engineering (IABSE) Conference*, Nara, Japan, May 13-15, ISBN 978-3-85748-138-3, Published by IABSE, Printed in Japan

Prof. I Wayan Sengara

Asosiasi Ahli Rekayasa Gempa Indonesia (AARGI), Indonesia

Topic：Development of Risk-Targeted Ground-Motions Criteria in Indonesian Seismic Building Code

Development of Risk-Targeted Ground-Motions Criteria in Indonesian Seismic Building Code

Presented by:

I Wayan Sengara

- Professor, Civil and Environmental Engineering Faculty, Institut Teknologi Bandung, Bandung – Indonesia
- Indonesian Earthquake Engineering Association

8th Asia Conference on Earthquake Engineering (8ACEE), Taipei-Taiwan, 9-11 November, 2022

Acknowledgement

Masyhur Irsyam, Indra Djati Sidi, Andri Mulia, Muhammad Asrurifak, Daniel Hutabarat, Windu Partono

- **PUSGEN - Indonesian Department of Public Work**
- **Indonesian Earthquake Engineering Association**

8th Asia Conference on Earthquake Engineering (8ACEE), Taipei-Taiwan, 9-11 November, 2022

Presentation Outline

1. Hazard and Risk-Targeted Spectra Criteria
2. Revision on Maximum Considered Earthquake (MCE) Hazard Maps for Indonesia
   (a) 2010 Hazard Maps
   (b) New 2017 Hazard Maps
3. Risk-Targeted Ground-Motions Mapping
   (a) Notes on Ground-Motion Direction of Maximum Response
   (b) Revision on β -value
   (c) RTGM Calculation and Results of RTGM Maps
4. Revision on Spectral Amplification Factors

1. Hazard and Risk-Targeted Spectra Criteria

➡ **Previous Approach**:

- Seismic safety was *implied* by past design approaches through **HAZARD-Based** Spectra Criteria
- Spectra design criteria was purely based on earthquake Hazard through PSHA or DHSA
- Seismic Risk for the resulting structures (annual probability of *seismically-induced failure)* associated with hazard-based criteria was not explicitly quantified in the design process, or in the development of the design process by regulators (Luco, 2016)

➡ **New Approach :**

RISK-Targeted Spectra Criteria

Seismic Risk Quantification

Meanwhile, for decades now (e.g., ATC 3-06, 1978) …

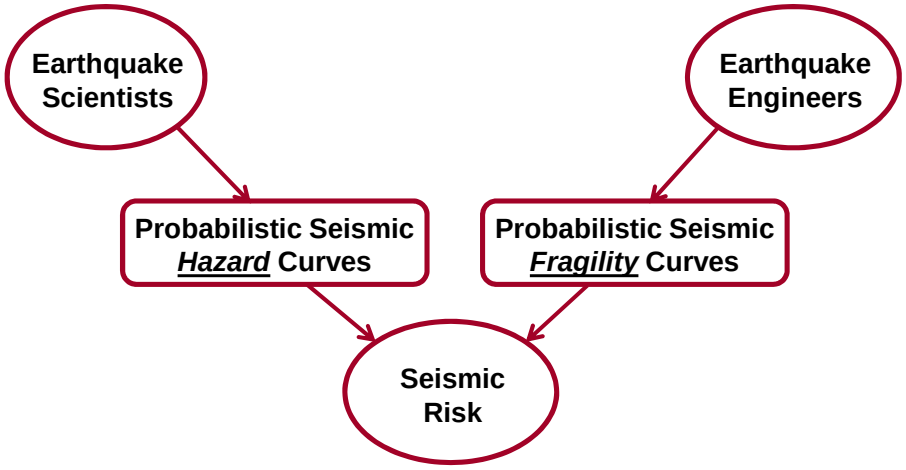

(Source: Luco, 2016)

Probabilistic Seismic *Hazard* Curves

Results of Probabilistic Seismic Hazard Analysis (PSHA), pioneered by the late Prof. C. Allin Cornell in 1968.

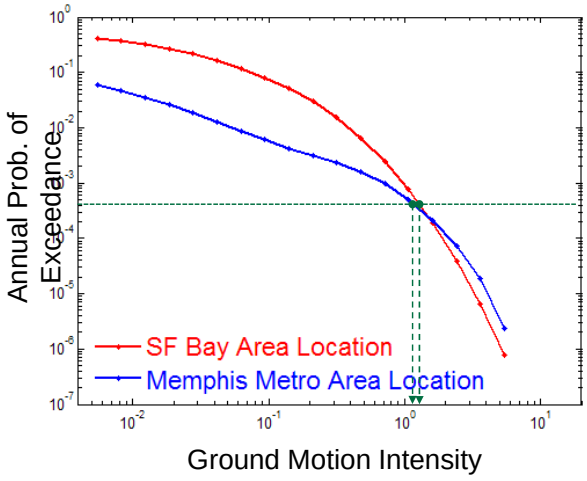

Notes:

Hazard curves are interpolated to derive aforementioned "hazard maps".

Shapes of hazard curves can vary significantly with location.

(Source: Luco, 2016)

Probabilistic Seismic *Fragility* Curves

Based on the performance of similar structures in past earthquakes, and/or numerical simulations.

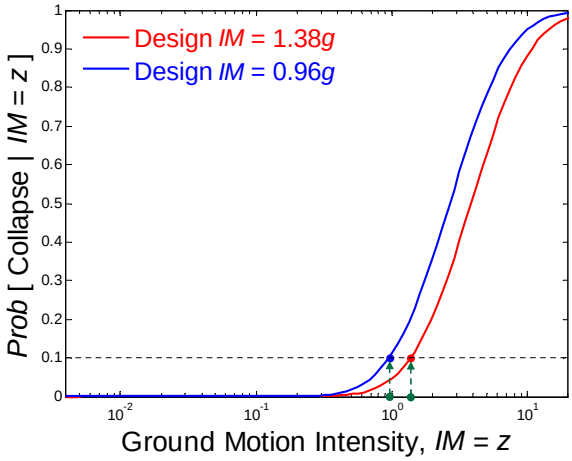

Notes:

Fragility curve depends on the ground motion intensity for which the structure was designed ("Design *IM*").

It also depends on the prescriptive requirements that are used to design the structure (e.g., those for buildings vs. nuclear power plants).

(Source: Luco, 2016)

Risk Integral

Combination of such hazard and fragility curves is an application of the total probability theorem …

$$P[Collapse] = \int_0^\infty \frac{dP[Collapse|IM = z]}{dz} P[IM > z]\, dz$$

Risk

Fragility

Hazard

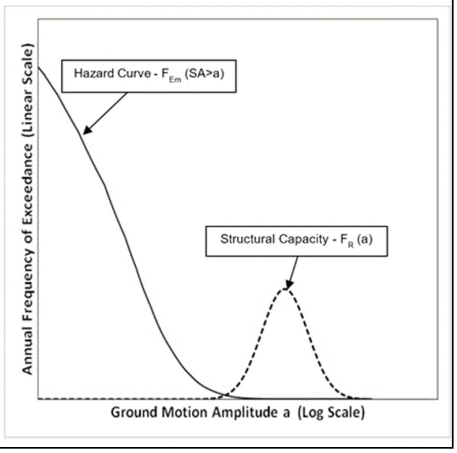

Hazard and Risk-Targeted Spectra Criteria

USGS NSHM	NEHRP Provisions	ASCE-7 Standard	IBC
1996	1997, 2000	1998, 2002	2000, 2003
2002	2003	2005	2006
2008	2009	2010	2012, 2015
2014	2015	2016	2018

For USA

Since 2009/2010, RTGM was introduced for Earthquake Ground-Motions Map

Development of Indonesian Seismic Building Codes

Transition from :

SNI-1726-2002 → SNI-1726-2012 → SNI-1726-2019

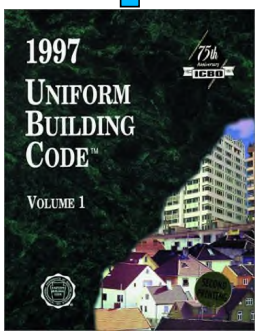

HAZARD-Based Spectra

RISK-Targeted Based Spectra

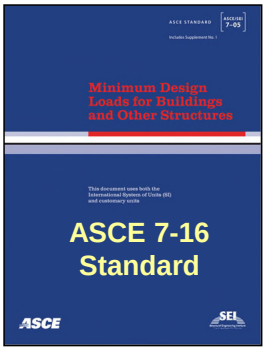

RISK-Targeted Based Spectra

Update of Indonesian Seismic RTGM Maps

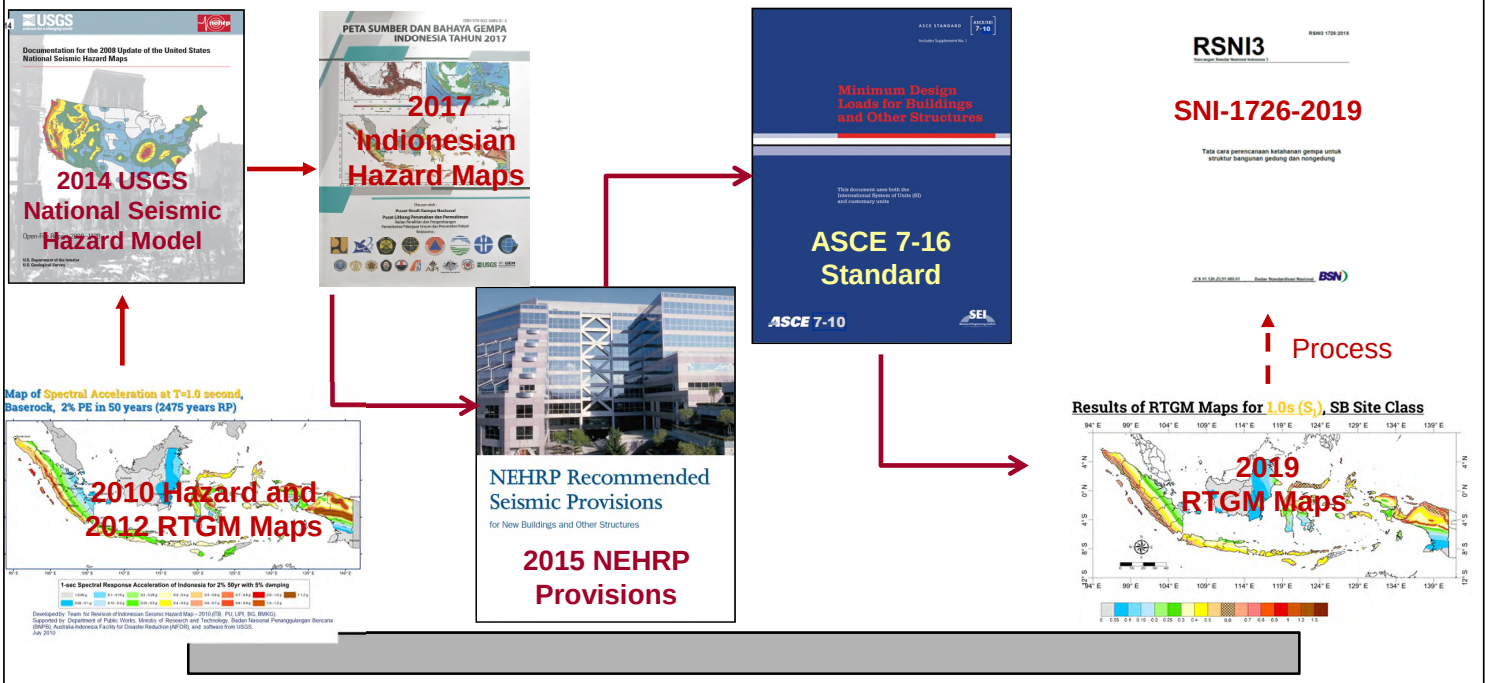

2

Revision on Maximum Considered Earthquake Hazard Maps for Indonesia

(a) 2010 Hazard Maps

(b) 2017 Hazard Maps

Seismo-Tectonic Map of Indonesia

Indonesia is one of the most seismically active countries in the world

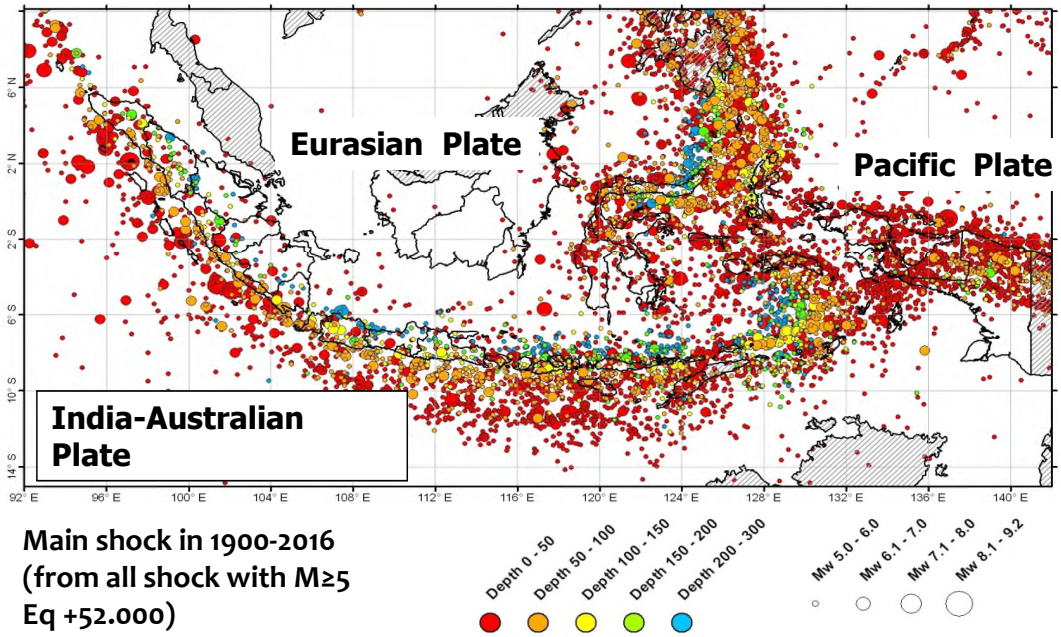

Main shock in 1900-2016
(from all shock with M≥5
Eq +52.000)

SEISMIC HAZARD ANALYSIS

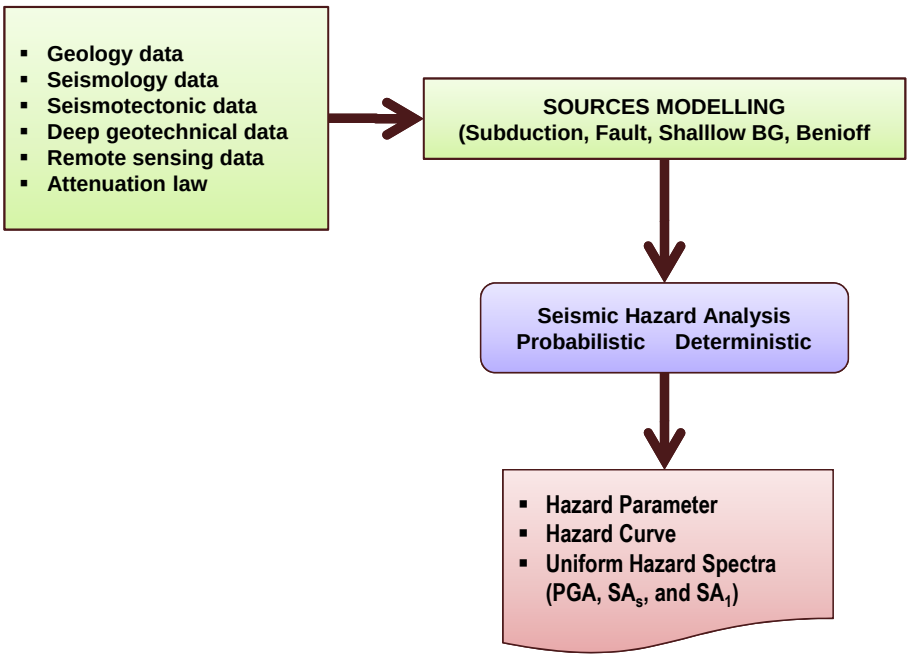

PROBABILISTIC SEISMIC HAZARD ANALYSIS

- Use of Total Probability Theorem: The earthquake Peak Acceleration depends on Magnitude (M) and hypocenter (r) as continuous independent random variables, expressed as :

$$H(a) = \sum v_i \iint P[A > a | m, r] \, f_{Mi}(m) \, f_{Ri|Mi}(r,m) dr dm$$

where :

- **H(a) is annual frequency of earthquakes that produce ground motion Amplitute A > a.**
- **v_i is annual rate of earthquakes (with magnitude higher than some threshold value of M_{oi}) in source I,**
- **f_{Mi} (m) and $f_{Ri|Mi}$(r,m) are PDF on magnitude and distance, respectively.**
- **P[A > a| m, r is the probability that an earthquake of magnitude m at distance r produces a peak acceleration A at the site that is > a.**

PSHA PROCESS

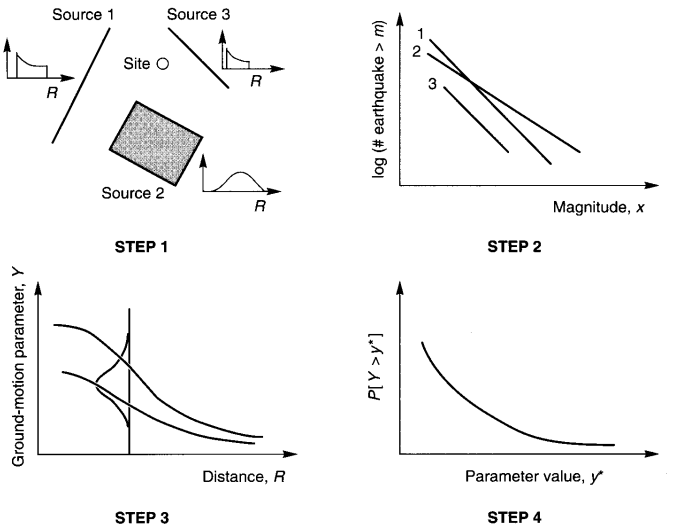

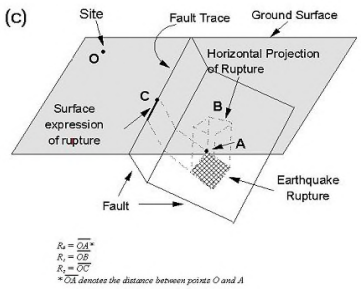

a. Earthquake Data/Catalog Collection

b. Earthquake Source Zoning

c. Use of appropriate GMMs

d. Recurrence Models

e. Ground Motion Characteristics

- USGS Software
- EZ-Frisk Computer Program (Risk Engineering, 2017)

SEISMIC SOURCE MODEL

Well identified Seismotectonic → Subduction Fault

Region Lack of Seismotectonic data → Background

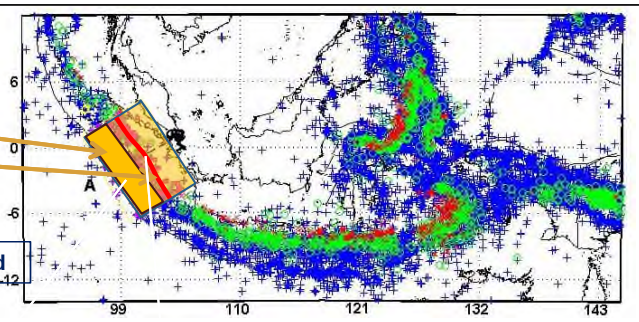

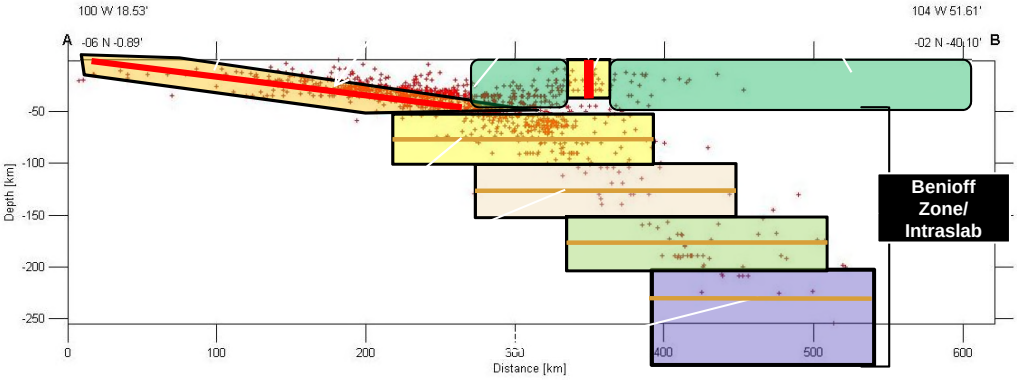

Seismic Hazard Map -2010

Sa, 1 second, 2475 yr RP

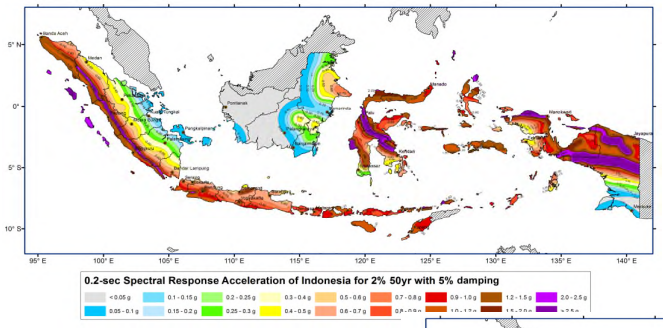

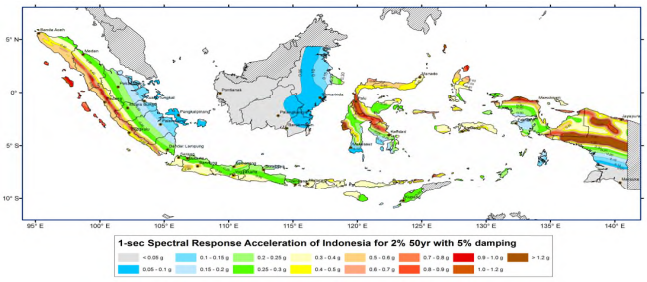

Sa, 0.2 second, 2475 yr RP

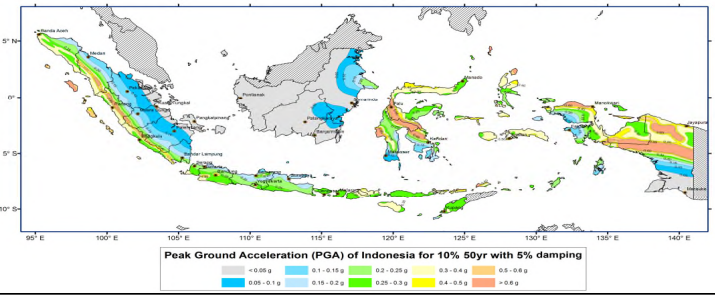

PGA, 475 yr RP

(Team 9, 2010)

New 2017 Indonesian Seismic Hazard Map & Risk-Targeted Ground Motions Analysis

2017 seismic hazard maps are updated by considering as follows:

1. **Quality improvement with updating new seismic sources of geological, geodetic, seismology & instrumentation, and updated GMMs.**
2. **New information regarding the identification of active faults with a significant number (from 81 to 251 faults; from previously 11 to 13 subduction zones.**
3. **Availability of more topographic data with better resolution, namely SRTM-30, IFSAR, and LIDAR topographic data.**
4. **The use of a more complete and more accurate earthquake catalogue by updating the earthquake catalogue until 2016.**

2010 Source Zones and Parameters

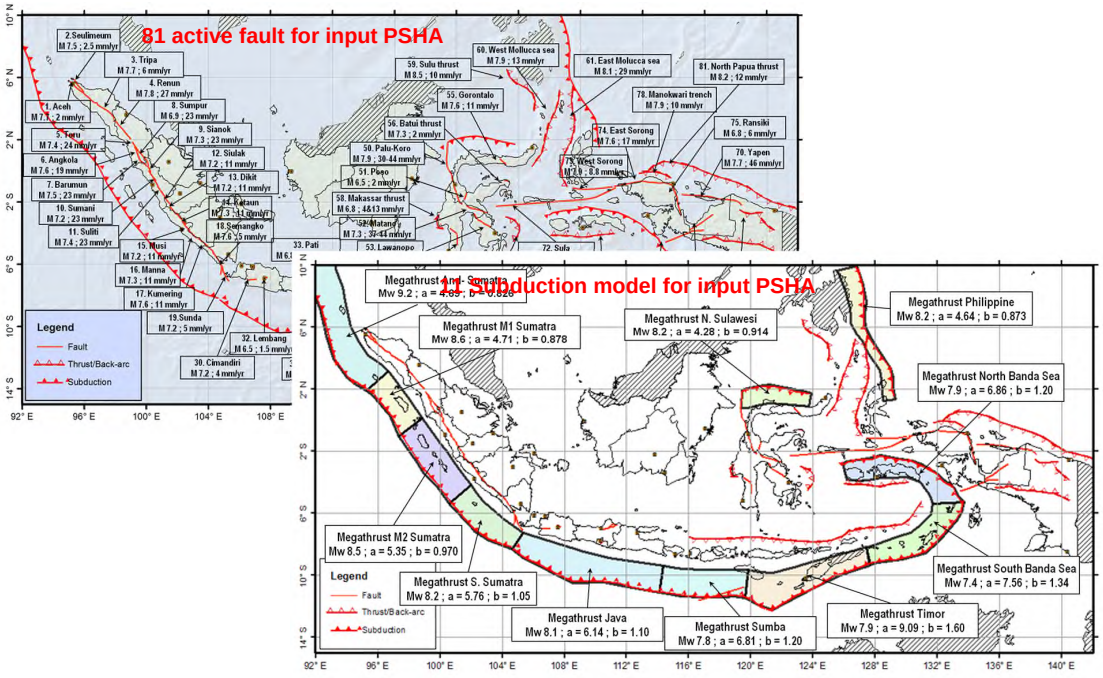

Input Parameters Indonesian Hazard Map, 2010

NEW 2017 PARAMETER FOR SEISMIC SOURCES
(251 ACTIVE FAULT FOR INPUT PSHA)

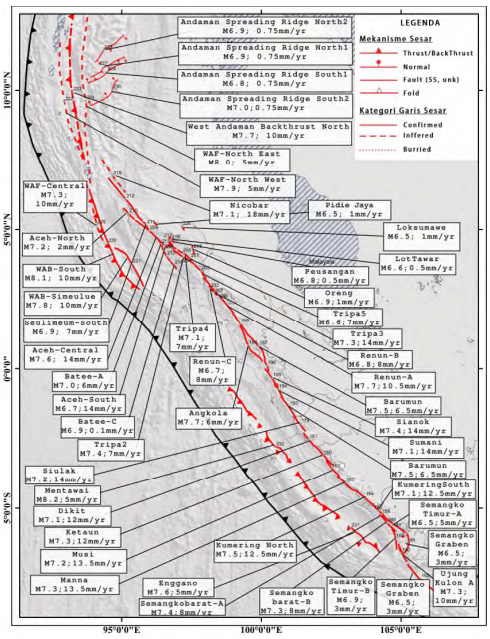

SUMATRA ACTIVE FAULT AND SURROUNDING

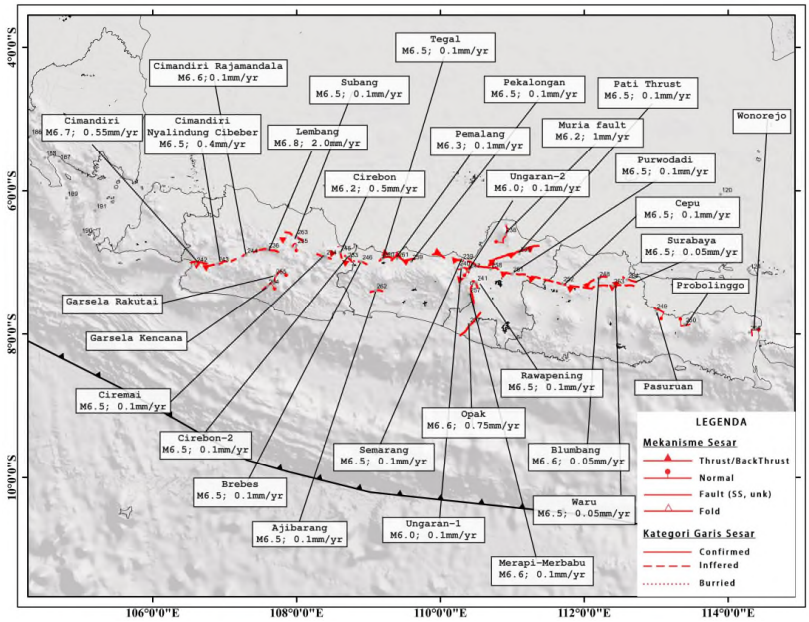

JAVA ACTIVE FAULT AND SURROUNDING

(Developed by: Tim Pemutakhiran Sumber dan Hazard Gempa Indonesia 2016)

NEW 2017 SUBDUCTION SOURCE ZONES AND PARAMETERS

From previously
11 to 13
Zones

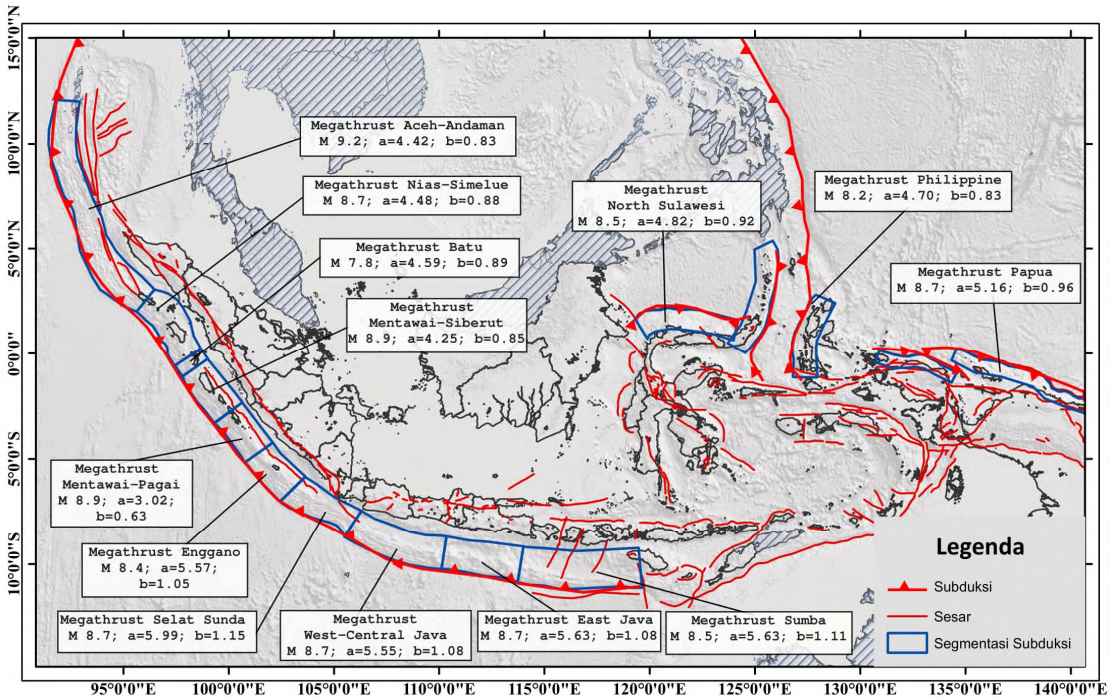

SUBDUCTION SOURCE MODEL

(Developed by: Tim Pemutakhiran Sumber dan Hazard Gempa Indonesia 2016)

UPDATE ON INPUT DATA PARAMETERS AND SUITE OF GMMs FOR 2010 AND 2017 MAPS

PARAMETERS	MAP 2010	MAP 2017
Eq. Catalog	• For BG sources non relocation	• For BG sources relocation
Seismic sources	• Input PSHA = 81 active fault	• Input PSHA = 251 active fault
Software	• USGS Software • EZ-Frisk Software (as control)	• USGS Software • OpenQuake Sofware • EZ-Frisk Soft ware (sebagai kontrol)
GMMs Shallow-Crustal	1. Boore-Atkinson NGA, 2008) 2. Campbell-Bozorgnia NGA, 2008 3. Chiou-Youngs NGA, 2008	1. Boore-Atkinson (NGA, 2008) 2. Campbell-Bozorgnia (NGA, 2008) 3. Chiou-Youngs (NGA, 2008) + Update NGA West-2 (2015)
Subduction Interface (Megathrust)	1. Youngs et al, SRL, 1997 2. Atkinson & Boore, 2003 3. Zhao et al, 2006)	1. Youngs et al, SRL, 1997 2. Atkinson & Boore, 2003 3. Zhao et al, 2006) + BC Hydro (Abrahamson et al 2015)
Deep Intraplate (Benioff)	1. Atkinson -Boore, 1995) 2. Youngs et al, 1997) 3. AB 2003 intraslab seismicity world data , BC-rock cond. (Atkinson - Boore, 2003)	1. Atkinson -Boore, 1995) 2. Youngs et al, 1997) 3. AB 2003 intraslab seismicity world data , BC-rock cond. (Atkinson - Boore, 2003) + BC Hydro (Abrahamson et al 2015)

FEATURES OF NEW GMMs IN 2017 MAPS

NGA-West2 Crustals:

- More strong-motions database
- Additional epistemic uncertainties
- Decay much faster with distance
- Applicability to further distance 300 km

BC-Hydro Subduction:

- More strong-motions database of large M (including M8.8 Chili and M9 Tohuku)
- Attenuation to larger distance up to 1000km
- Decay faster with distance for Interface

Seismic Hazard Map -2017

Sa, 1 second, 2475 yr RP

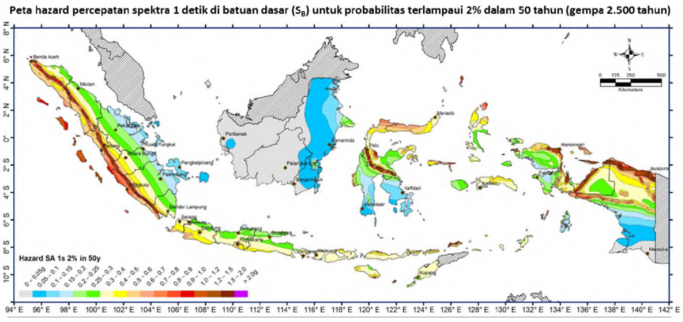

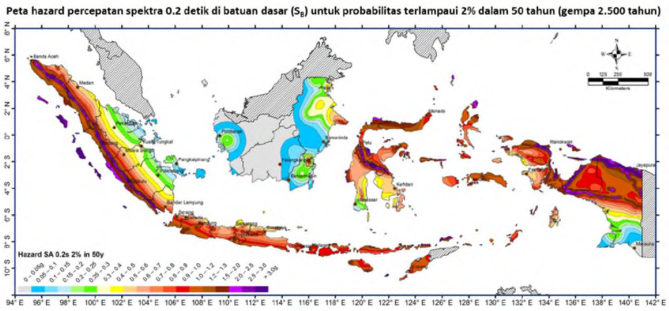

Sa, 0.2 second, 2475 yr RP

PGA and SAs:
Average values of two horizontal components (RotD50)

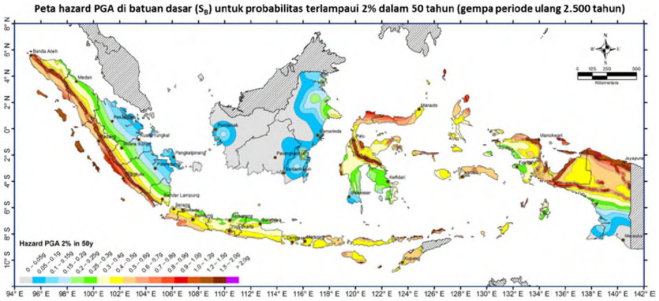

PGA, 2475 yr RP

Kerja sama:

(Developed by: Indonesian Team for Revision of Seismic Hazard Map, 2017)

3 Risk-Targeted Ground-Motions Mapping

(a) Notes on Ground-Motion Direction of Maximum Response

(b) Revision on β -value

(c) RTGM Calculation

(d) Results of RTGM Maps for SNI-1726-2019

Probabilistic Ground-Motions

From the site-specific procedures (Ch. 21) of *ASCE 7-10 & 2009 NEHRP Provisions* …

21.2.1, Probabilistic Ground Motion: *The probabilistic spectral response accelerations shall be taken as the spectral response accelerations in the direction of maximum horizontal response represented by a 5 percent damped acceleration response spectrum that is expected to achieve a 1 percent probability of collapse within a 50-yr. period.*

21.2.1.2, Method 2: *At each spectral response period for which the acceleration is computed, ordinates of the probabilistic ground motion response spectrum shall be determined from iterative integration of a site-specific hazard curve with a lognormal probability density function representing the collapse fragility (i.e., probability of collapse as a function of spectral response acceleration). The ordinate of the probabilistic ground-motion response spectrum at each period shall achieve a 1 percent probability of collapse within a 50-yr. period for a collapse fragility having (i) a 10 percent probability of collapse at said ordinate of the probabilistic ground-motion response spectrum and (ii) a logarithmic standard deviation values of 0.6.*

(Source: Luco, 2016)

Risk-Targeted Ground Motion

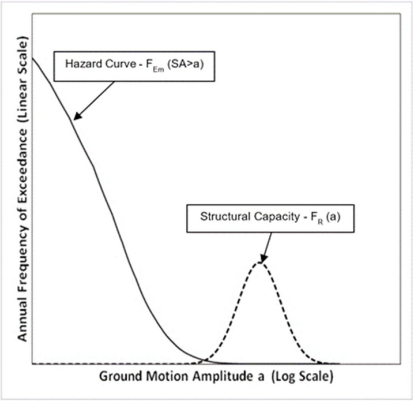

- **Several studies show that earthquake resistance structures, which were designed using a similar hazard, give different response or risk (e.g., Liel et al, 2015).**
- **The behavior of structure resistance is random following log-normal distribution (Luco et al., 2007).**
- **In general, the following equation shows the probability of failure from the structure (or risk) caused by the earthquake (Luco et al., 2007):**

$$\text{Risk, Pf} = \int_0^\infty f_R\,(a)\, f_{E_m}(\text{SA}>a)\, da$$

$$f_R(a) = \frac{1}{a\beta\sqrt{2\pi}} \exp\left[-\frac{(\ln a - (\ln(\text{RTGM}) + 1.28\beta))^2}{2\beta^2}\right]$$

Where:
f_{E_m}(a) = hazard curve
f_R(a) = structural capacity against the earthquake load

Building Fragility Curves

Relate ground motion spectral acceleration to building collapse probability; depend on RTGM

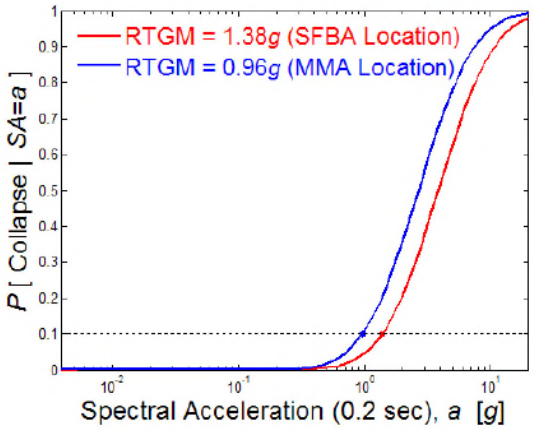

Generic fragility curve equation:

$$P[Collapse|SA = a] = \left[\frac{\ln a - (\ln RTGM + 1.28 \times 0.8)}{0.8}\right]$$

where

$\Phi[\cdot] \equiv$ Normal/Gaussian CDF

Source: Luco, 2006, Towards Risk Targeted Earthquake Ground Motion)

a) Notes on Ground Motion Direction of Maximum Response

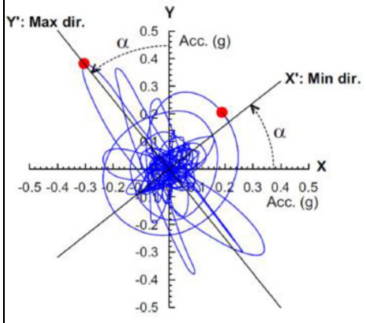

(Huang et al., 2008)

NGA-West2 Model

Ground motion intensity is not uniform in all orientations.

$Sa_{RotD100}$ is a more meaningful IM than Sa_{RotD50} for structural design

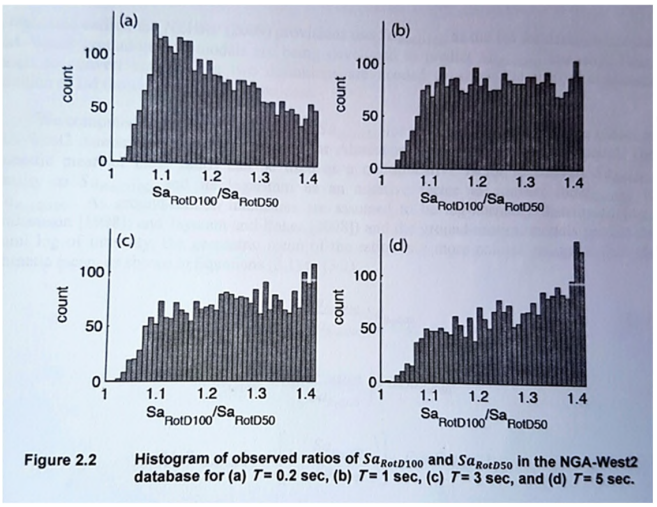

Figure 2.2 Histogram of observed ratios of $Sa_{RotD100}$ and Sa_{RotD50} in the NGA-West2 database for (a) T= 0.2 sec, (b) T= 1 sec, (c) T= 3 sec, and (d) T= 5 sec.

Sa_{RotD50}
(Median ground-motion Sa)

$Sa_{RotD100}$
(Maximum Sa over all orientations)

(After Shahi and Baker, 2013)
PEER - Center

Notes on Ground Motion
Direction of Maximum Response

NGA-West2 Model

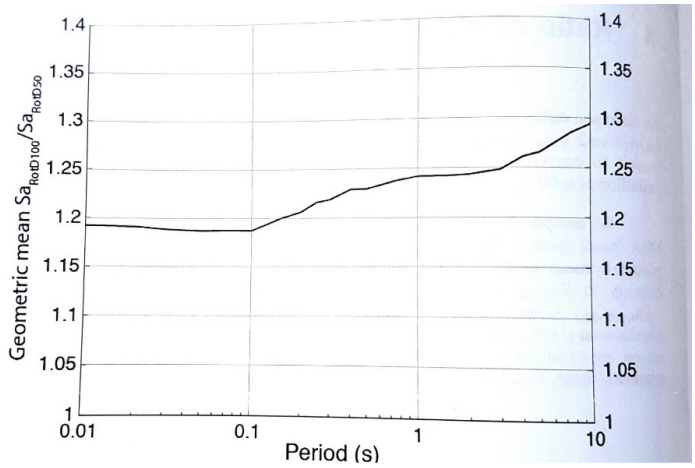

Geometric Mean
$Sa_{RotD100}/Sa_{RotD50}$

(After Shahi and Baker, 2013)
PEER - Center

- **The collapse of structure occurred due to the effect of two direction horizontal movement (Kicher, 2009). This issue has been accomodated with applying directionality coefficient for each period of interest.**
- **The SNI-1726-2012 adopts directionality coefficient of 1.05 for short (T=0.2 sec) periods and 1.15 for long (T=1.0 sec) periods.**
- **FEMA/NEHRP and Whittaker (2009) suggest the directionality coefficient for maximum response of 1.1 at short periods and 1.3 at a period of 1.0 second. These factors are adopted in this study.**

(b) Revision of β -value

- **Analysis and recommendation on representative β values for Indonesian buildings has been conducted through hazard analysis and probability-based factor of safety by Sidi I.D. (2011).**
- **The analysis suggests that β values for Indonesia is between 0.65 – 0.7 (within the range of ATC-63 Project and Luco,et.al.,2007).**
- **For the development of SNI-1726-2012, a relatively high value of $\beta = 0.7$ was adopted.**
- **While for the new proposed code, the representative value was drawn in an experts consensus held in January 2018, agreeing to adopt the value of $\beta = 0.65$, as proposed by Sidi I.D. (2018).**

(b) Revision of β -value

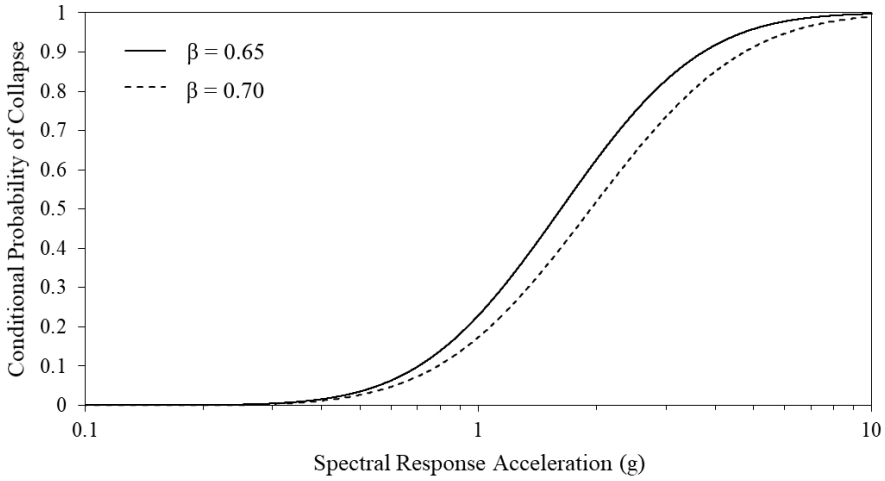

Typical of change in collapse fragility curve (considering a mapped **0.2-s spectral response acceleration** of **0.788g** for Jakarta), change from **β of 0.70 to 0.65**

RTGM Calculation

- **Considering a site-specific hazard curve corrected by the directivity factor, the probability of failure can be derived as follows:**

$$P_F = \int_0^{\sim} \gamma(a) \frac{1}{a\beta\sqrt{2\pi}} \exp\left[-\frac{(\ln a - (\ln(\mathrm{RTGM}) + 1.28\beta))^2}{2\beta^2}\right] da$$

- **The RTGM can be directly computed through numerical integration and iterative process**
- **A Risk Coefficient is a ratio of RTGM with MCE being corrected by the directivity factor**

$$C_{RT} = \frac{RTGM_T}{MCE_T * DF_T}$$

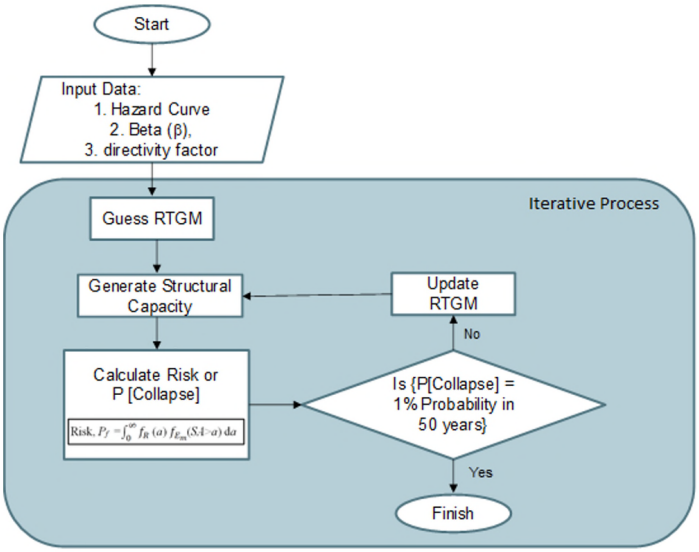

RTGM Calculation (A Case for City of Jakarta)

- Risk Integral for T = 0.2 second.
- RTGM = 0.680 g

C_R = (RTGM / $MCE_{\_DC}$)
= 0.98

Where *DC* is directionality coefficient

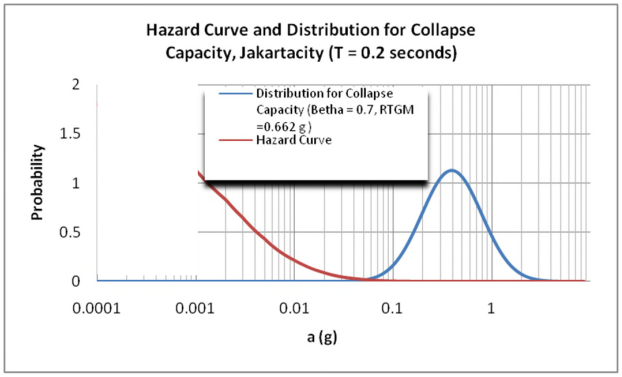

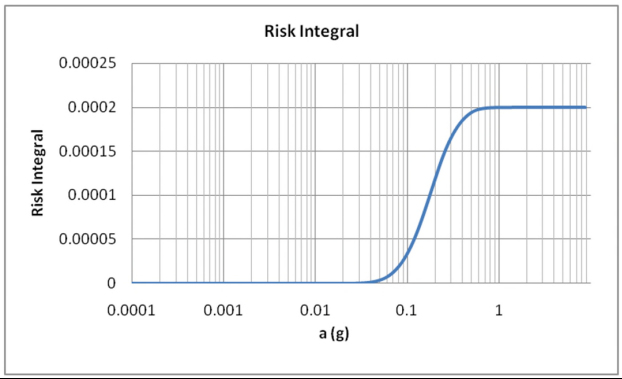

RTGM Calculation for all Indonesia

- Calculation of RTGM for the whole Indonesian region consisting of approximately **96,000 cells** for two spectral values at T=0.2 second and T=1.0 second.
- Results of the RTGM is presented in risk coefficient (C_R) defined as MCE_R/MCE.
- RTGM Distribution Map of :
  - C_{RS} (C_R value correspond to spectral values at 0.2 second period) and
  - C_{R1} (C_R value correspond to spectral values at 1.0 second period)

Results of C_{rs} Maps

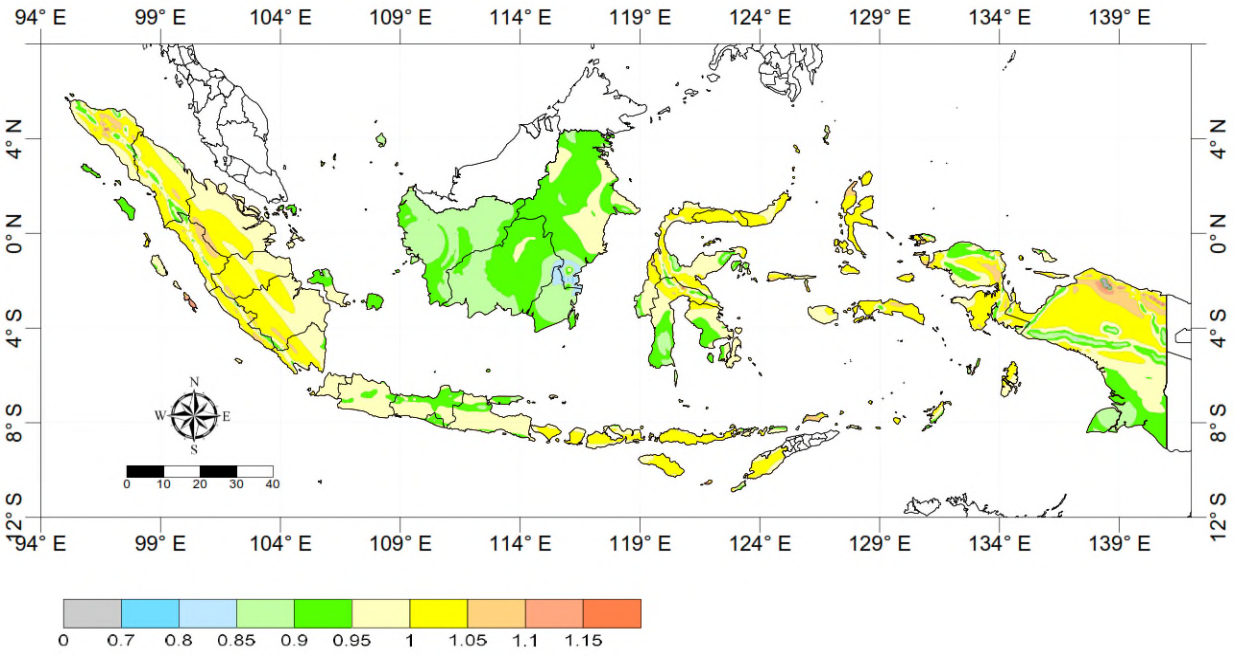

(Developed by: Team for MCE_R and C_R Revision Maps of Indonesia 2019)

Results of C_{r1} Maps

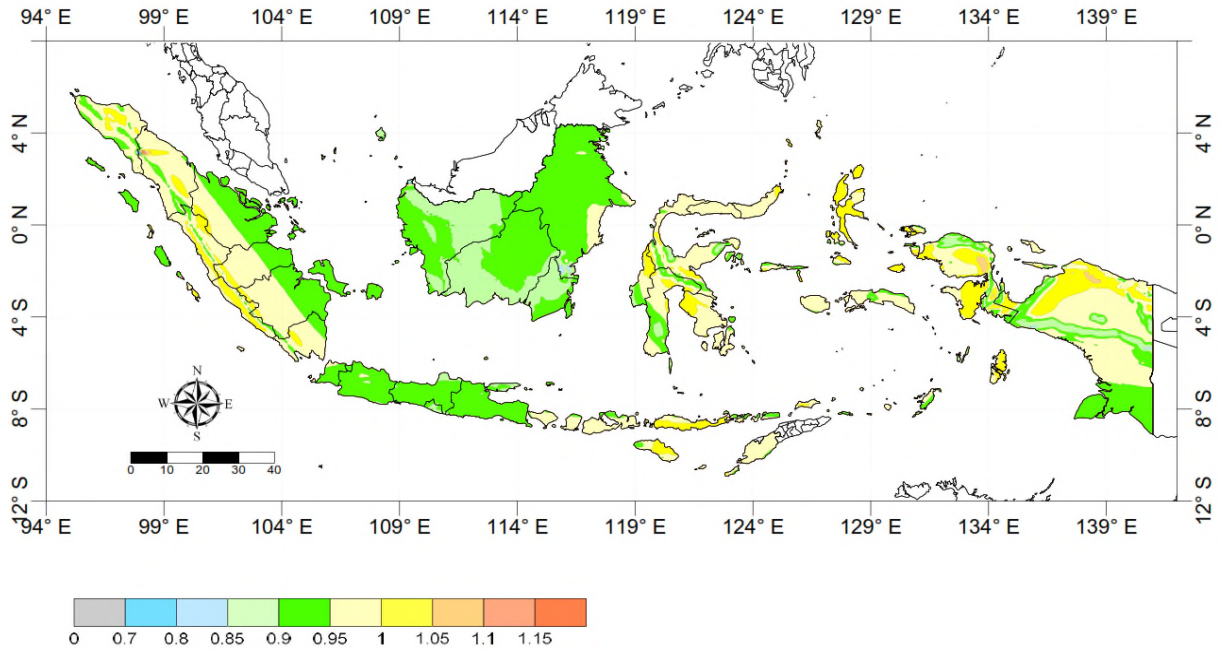

(Developed by: Team for MCE_R and C_R Revision Maps of Indonesia 2019)

Distribution of C_R values in percentage
Total District: 6326

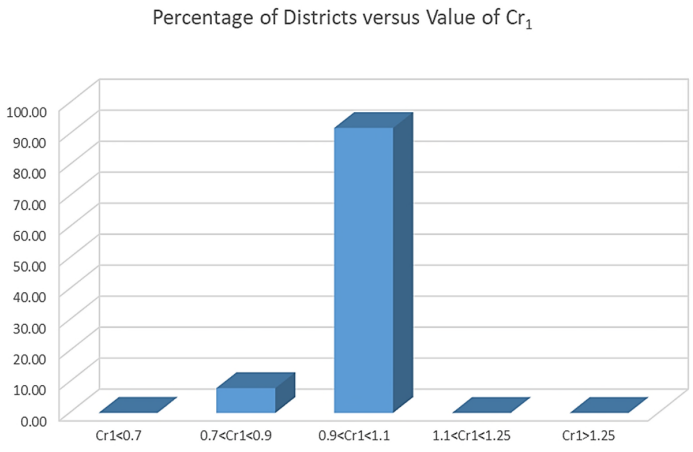

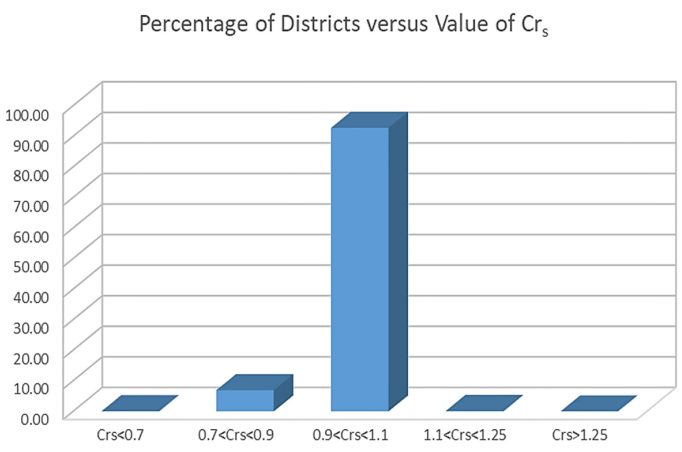

Results of RTGM Maps for 0.2s (S_s), SB Site Class

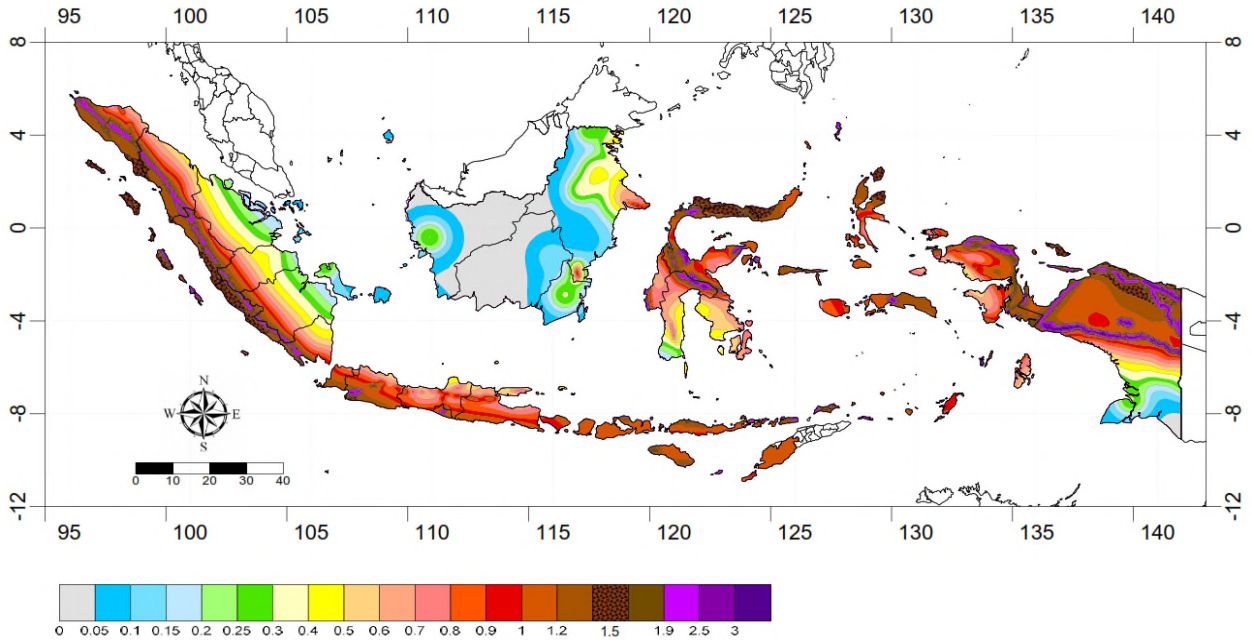

(Developed by: Team for MCE_R and C_R Revision Maps of Indonesia 2019)

Results of RTGM Maps for 1.0s (S_1), SB Site Class

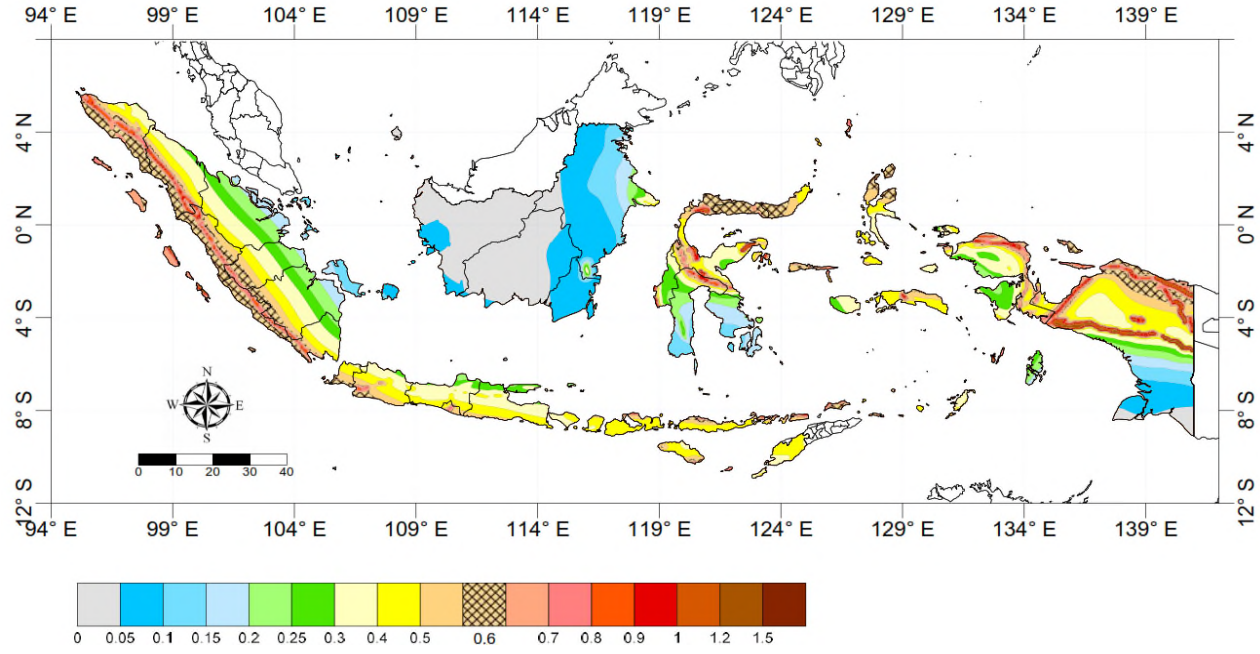

(Developed by: Team for MCE_R and C_R Revision Maps of Indonesia 2019)

Risk-Targeted Maximum Considered Earthquake (MCE_R) in SNI-1726-2012 and SNI-1726-2019

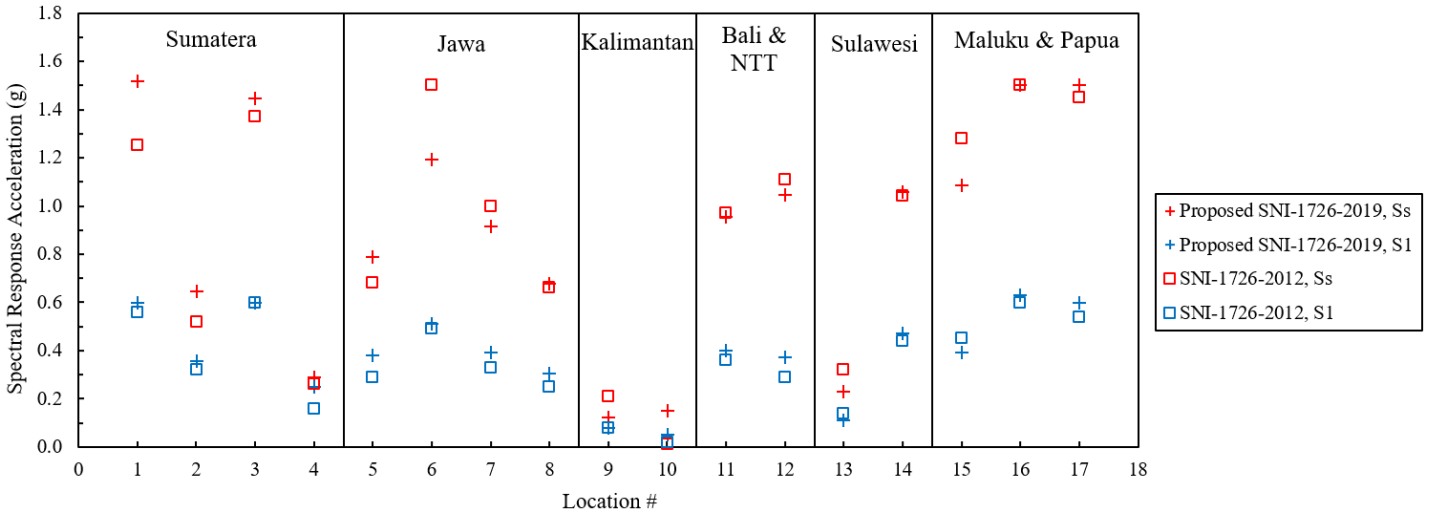

Risk Coefficient values in SNI-1726-2012 and SNI-1726-2019

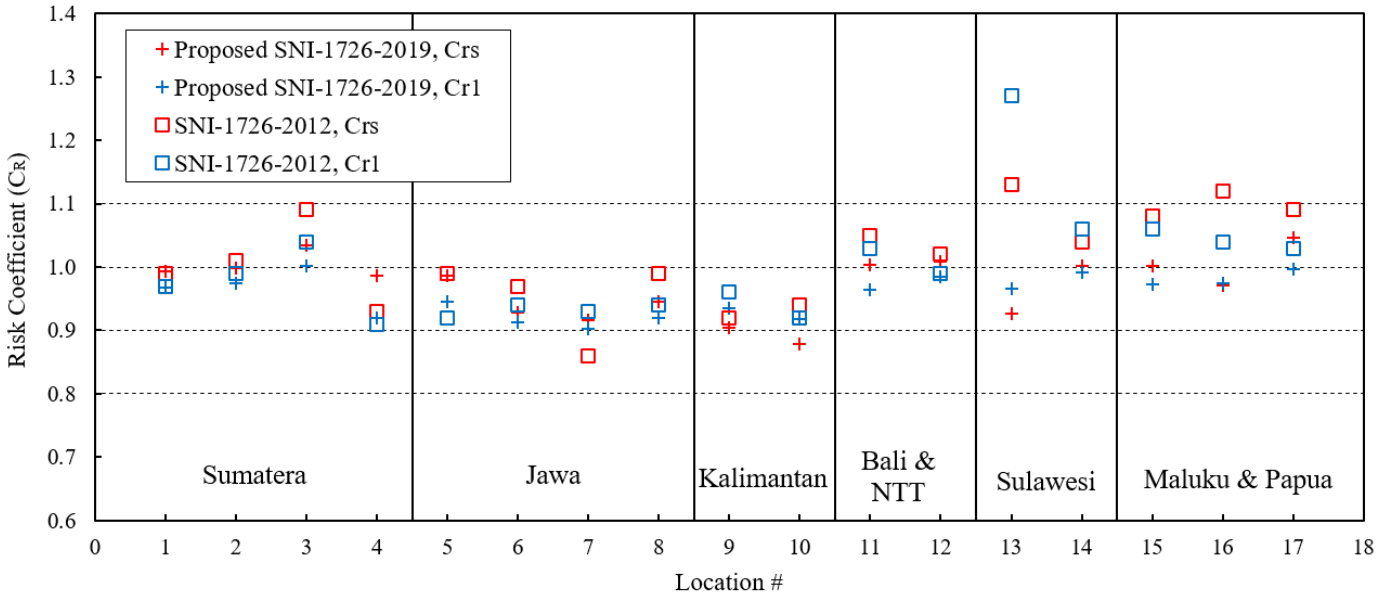

4

Revision on Spectral Amplification Factors

Design Response Spectra
For Design of Structures

3

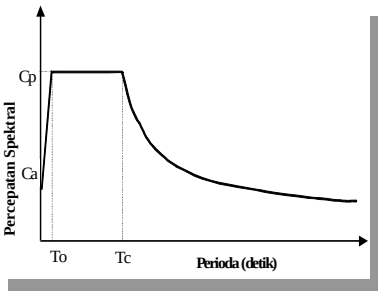

Ground Surface

SSRA → 2b

R

2a

Site

BaseRock

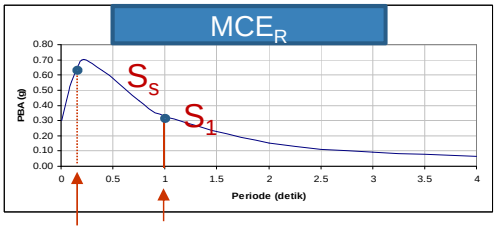

Faults

Magnitude M

1

PSHA

$T_{short\ period}$ T_1 second period

Revision on Spectral Amplification Factors

- **Separately from the updates to the RTGM maps, the site coefficients used to adjust the mapped values for soil properties have also been updated for the SNI-1726-2019.**

- **This modification is due to Site-Class SB of GM map is not consistent with the Vs30=760m/s which is actually correspond to border of Site-Class SB-SC . Previously the ASCE-7-10 (or SNI-1726-2012) assumed Vs30=760m/s as SB.**

Short-Period Site Coefficient, Fa (Proposed SNI-1726-2019)

Site Class	Mapped Risk-Targeted Maximum Considered Earthquake (MCE_R) Spectral Response Acceleration Parameter at Short Period					
	$S_S \leq 0,25$	$S_S = 0,5$	$S_S = 0,75$	$S_S = 1,0$	$S_S = 1,25$	$S_S \geq 1,5$
SA	0,8	0,8	0,8	0,8	0,8	0,8
SB	0,9	0,9	0,9	0,9	0,9	0,9
SC	1,3	1,3	1,2	1,2	1,2	1,2
SD	1,6	1,4	1,2	1,1	1,0	1,0
SE	2,4	1,7	1,3	1,1 (1,2)*	0,9 (1,2)*	0,8 (1,2)*

Note: *Coefficient in the parentheses ( ) is short-period site coefficient (Fa) of ASCE-7-16

1-Second Period Site Coefficient, Fv (Proposed SNI-1726-2019)

Site Class	Mapped Risk-Targeted Maximum Considered Earthquake (MCE_R) Spectral Response Acceleration Parameter at 1-s Period					
	$S_1 \leq 0,1$	$S_1 = 0,2$	$S_1 = 0,3$	$S_1 = 0,4$	$S_1 = 0,5$	$S_1 \geq 0,6$
SA	0,8	0,8	0,8	0,8	0,8	0,8
SB	0,8	0,8	0,8	0,8	0,8	0,8
SC	1,5	1,5	1,5	1,5	1,5	1,4
SD	2,4	2,2	2,0	1,9	1,8	1,7
SE	4,2	3,3	2,8	2,4	2,2	2,0

Site Coefficient F_{PGA} (Proposed SNI-1726-2019)

Site Class	PGA ≤ 0,1	PGA = 0,2	PGA = 0,3	PGA = 0,4	PGA = 0,5	PGA ≥ 0,6
SA	0,8	0,8	0,8	0,8	0,8	0,8
SB	0,9	0,9	0,9	0,9	0,9	0,9
SC	1,3	1,2	1,2	1,2	1,2	1,2
SD	1,6	1,4	1,3	1,2	1,1	1,1
SE	2,4	1,9	1,6	1,4	1,2	1,1

Ratios of the updated Site Coefficient in SNI-1726-2019 divided by those in SNI-1726-2012

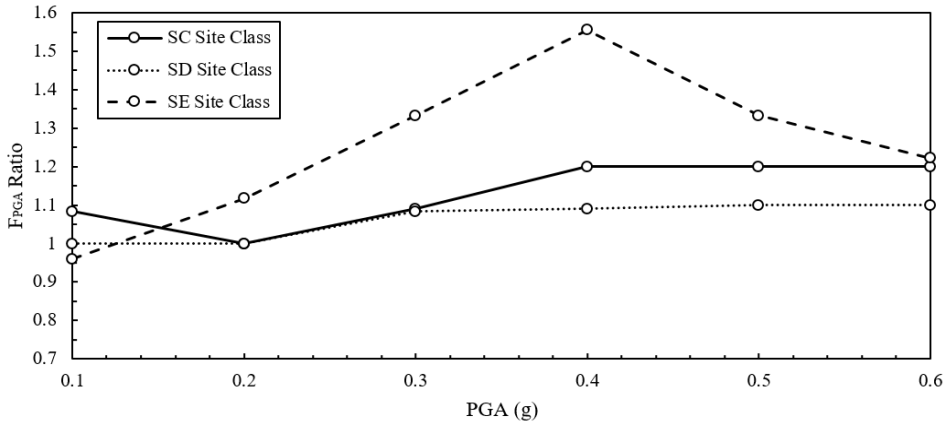

F_{PGA} Ratio

Ratios of the updated Site Coefficient in SNI-1726-2019 compared to those in SNI-1726-2012

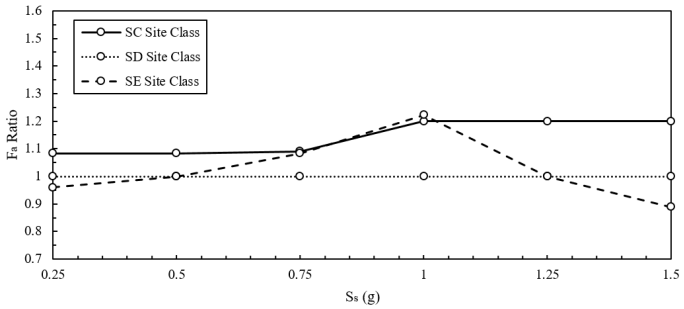

F_A Ratio

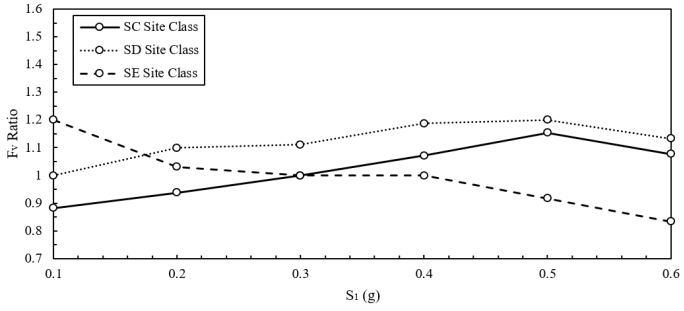

F_V Ratio

Concluding Remarks

- RTGM (MCE_R) maps for Indonesia has been developed based on New 2017 hazard maps that has been revised with new faults database from **81 to 251** total faults with updated seismic parameters with an improved estimates of maximum magnitudes and slip rates. Most recent global **GMMs** have been adopted.
- The significant changes in the New 2019 Indonesian MCE_R Maps is due:
  - *New-2017 MCE hazard maps*
  - *Revision on directivity coeff. for maximum response* ***(1.1 and 1.3 for Ss and S1)***
  - *Log-normal-standard-deviation (β) or Slope of fragility curve* ***(from β=0.7 to β=0.65)***
- Evaluating the $RTGM_{0.2s}$ values, it is identified that most changes vary in the range of **-25% to +20%, and** $RTGM_{1s}$ changes vary in the range of **-15% to +25%.**
- Results of calculation show that Risk Coefficients **(C_R)** for both spectral periods are more than **90%** are within the range of **0.9 to 1.1**, which is mostly not significantly different from the previous MCE_R maps.

Concluding Remarks

- Site coefficient for **Fa, Fv, and PGA** in the proposed SNI-1726-2019 have been updated with partial reference to ASCE 7-16. Most of the values tend to increase. Reason: The Site coefficient in the previous code is actually for Vs30=760m/s (**border of Site-Class SB-SC)**, whereas the GM Map is **Site-Class SB.**
- The newly developed RTGM maps and site coefficient have been adopted in the Proposed 2019 Indonesian Seismic Building Codes SNI-1726-2019.

Prof. Keh-Chyuan Tsai

National Taiwan University, Taiwan

Topic：Long Span Buckling Restrained Braces for Mega Braced Frames

LONG-SPAN BUCKLING RESTRAINED BRACES FOR MEGA BRACED FRAMES

Keh-Chyuan Tsai[1], An-Chien Wu[2]
Chun Chen[3], Yu-Chen Lin[3], Lu-An Chen[3], I-Chen Chang Chien[3], Ming-Chieh Chuang[2]

1. Professor, Department of Civil Engineering, National Taiwan University, Taipei, Taiwan, R.O.C.
2. Associate Researcher, National Center for Research on Earthquake ENG, Taipei, Taiwan, R.O.C.
3. Graduate Research Assistant, Department of Civil ENG, National Taiwan University, Taipei, Taiwan, R.O.C.

Email: kctsai@ntu.edu.tw, acwu@narlabs.org.tw, mcchuang@narlabs.org.tw

ABSTRACT

This study investigates the seismic deformational demands on the long-span truss-confined buckling-restrained braces (TC-BRBs) in a 24-story prototype mega braced frame to be constructed in Taipei. Results of nonlinear response history analysis of the prototype building, using a suite of maximum considered earthquakes, indicate that the zig-zag-spanned BRBs can promote a rather uniform distribution of peak lateral drifts (less than 0.015 radian) computed for every 4-story. The proposed long-span BRB can be constructed from using three truss frames each with a cosine-shape varying depth to restrain the BRB's center casing and core. Cyclic loading tests of two 1/3-scale specimens confirm that the proposed TC-BRB can meet the severe seismic service requirements, as it can sustain a peak lateral drift demand greater than 3% and with a cumulative plastic deformation index greater than 236.

Keywords: buckling-restrained brace, mega braced frame, nonlinear response history analysis, cyclic loading test

INTRODUCTION

Various types of buckling-restrained braces (BRBs) have been developed over the past few decades. Numerous experiments conducted have confirmed that BRBs are capable of sustaining multiple seismic events without failure (Black *et al*., 2004; Uang *et al*., 2004; Tremblay *et al*., 2006; Fahnestock *et al*., 2007; Lin *et al*., 2012 and 2016; Tsai *et al*., 2014; Li *et al*., 2022). As a result, buckling-restrained braced frame (BRBF) have become a popular lateral load-resisting system in seismic buildings (Chuang *et al*., 2015; Takeuchi and Wada, 2017). With regard to the buckling restraining mechanism, the overall flexural buckling and local high-mode buckling of the steel core have been inhibited by a mortar- or concrete-filled steel casing (Black *et al*., 2004; Tsai *et al*., 2014; Li *et al*., 2022) or an all-metal built-up construction (Usami *et al*., 2012; Wu *et al*., 2014). Although all-metal BRBs feature with low self-weight and without secondary construction from the grouting and curing of concrete or mortar, most of the BRBs used worldwide are equipped with infilled casings. This is because a composite restrainer is relatively more reliable at providing sufficient buckling resistance than a metal built-up restrainer. Recently, a rigid truss-confined BRB (TC-BRB), which was composed of rigid truss frames attached to the outside of a double-tube BRB, was investigated (Guo *et al*., 2017a and 2017b). In this paper, an evolutionary TC-BRB is proposed to achieve a more robust buckling restraining mechanism and a more attractive architectural appearance for long-span spatial structures. As shown in Fig. 1, the truss confining system can be applied to a mortar- or concrete-filled casing to efficiently prevent possible local buckling failure. The truss confining system is assigned to have a fusiform shape with varying cross sections along the restrainer. The novel restraining system reduces the truss material usage and improves its physical attractiveness. In order to investigate the seismic performance of the proposed TC-BRB, cyclic loading tests on two constant-section and four varying-section specimens with different force capacities, depths, and member sectional dimensions of the corresponding truss confining systems have been conducted in NCREE (Chen *et al*., 2021; Chen, 2021).

PROTOTYPE MEGA BRACED FRAMES

In order to represent the proposed TC-BRB as a component of a mega braced frame for the prototype 24-story building (Fig. 2), a diagonal brace inclined at approximately 45 degrees across four stories, each with a story height of 3.7m, was designed and extensively analyzed (Chang Chien, 2021). The foot print of the building is 42.5×42.5m to be constructed in Taipei Zone 2 (DBE spectrum is shown in Fig. 3). The symmetrical lateral force resisting system consists of perimeter moment resisting frame and BRBFs dual system in the two principal axes. The four columns adjacent to the service core are gravity columns. All BRB core steel is SN490B. All the frame beams are SN490B grade wide-flange sections, whilst all columns are SN490B built-up box sections with 56MPa in-fill concrete. The fundamental period is about 2.22s in each of two principal directions. A suite of 21 historical ground accelerations are scaled considering the geometric means of the spectra for the two horizontal components and according to the procedures prescribed in the model building codes. From the PISA3D nonlinear response history analysis (NLRHA) results in Fig. 3, it can be found that the peak and standard deviation of the inter-story drift ratios (IDRs) are 1.49% and 0.53%, whilst the distributions of the peak averaged lateral drifts computed for every four-story are rather uniform with a peak value of about 1% under the DBEs applied simultaneously in three directions. It appears that the long-span BRBs zig-zag-spanned every four-story have transformed the 24-story dual-frame into a mega 6-story structure.

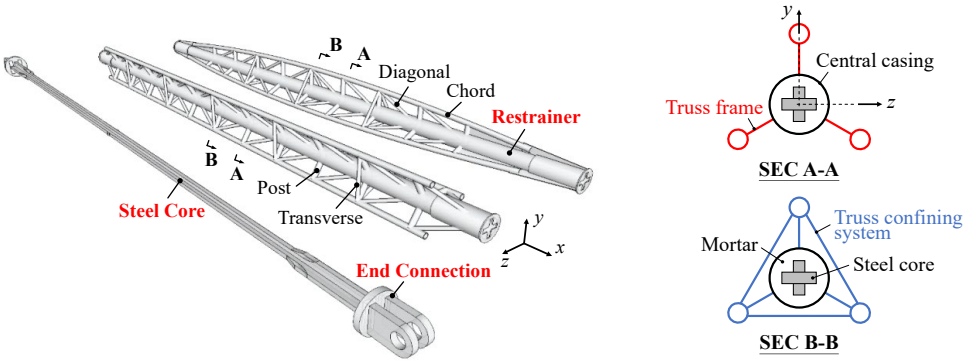

Figure 1. Schematic of the proposed TC-BRB.

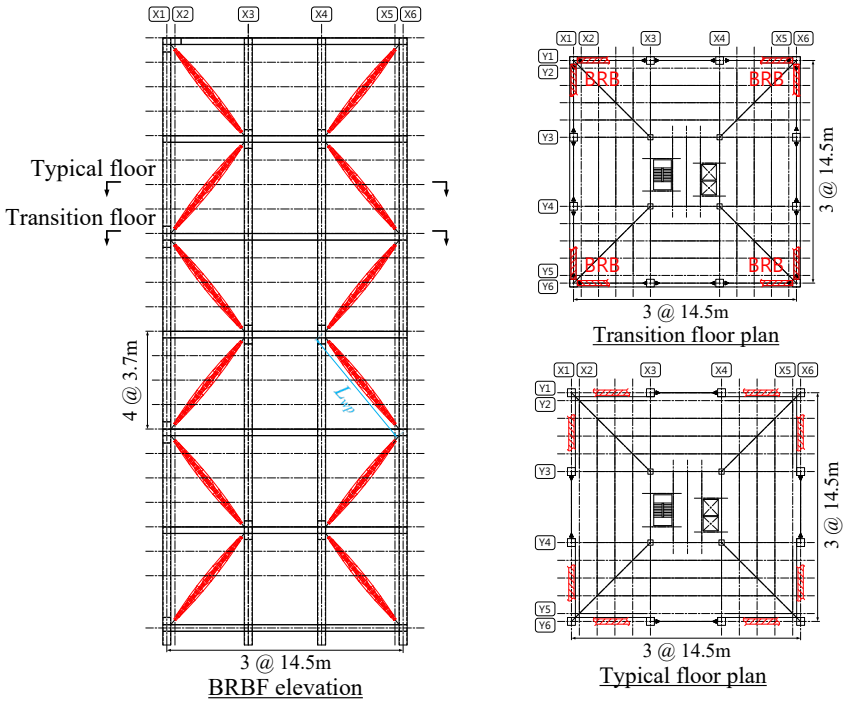

Figure 2. Application of TC-BRBs in a mega-frame structure.

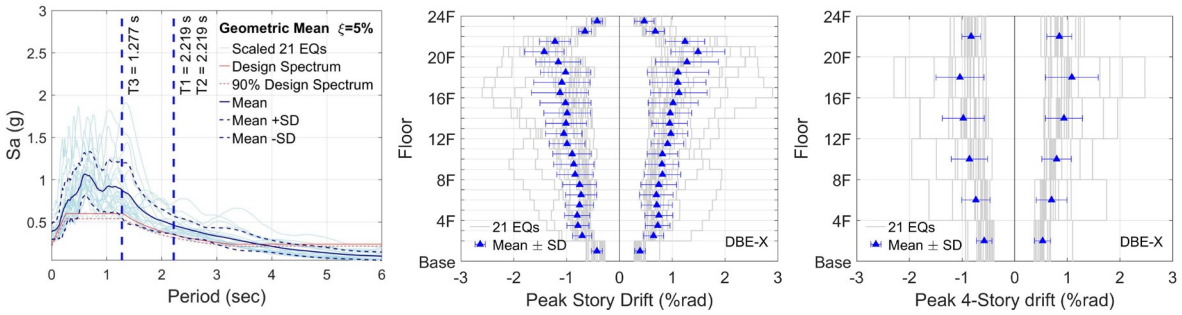

Figure 3. Design vs scaled response spectra (left),
peak averaged lateral drifts (middle), peak 4-story lateral drifts for the DBEs (right).

EXPERIMENTAL PERFORMANCE OF THE PROPOSED TC-BRBS

Design of Specimens

Due to the limitations of the test facility, the prototype TC-BRB in the mega braced frame was scaled down by approximately 1/3 to have a total height of 4.9m in the four-story braced reference frame, with a brace work point-to-work point length L_{wp} of 6.9m. A total of six TC-BRB specimens, namely CT, 2CT, VT, 2VT, 3VT, and 4VT (Chen *et al*., 2021; Chen, 2021), were then designed with a total length L_B of about 6.3m as shown in Fig. 4. Specimens CT and VT have a nominal yield capacity P_{yn} of 1016kN and the others have a P_{yn} of 853kN, all having a cruciform core cross-section made from 25-mm-thick SN490B steel plate. Each end of the steel core was connected to an end plate welded to a pair of lug plates with a pin connection details. The steel casings were made from the 139.6×4mm STK490 steel tubes and infilled with 56MPa mortar. The chord of the truss confining system was shaped to have the center-to-center distance between the steel casing and the chord varied along the BRB. The shape agrees with a function of $h(x) = h_0\cos(a\pi x/L_{sc})$, where L_{sc} is the casing length; a controls the curvature of the chord; h_0 is the central height of the truss frame; $x = 0$ and $x = L_{sc}/2$ are locations at the casing midspan and end, respectively. When $a = 0$, the TC-BRB would have a constant cross-sectional depth truss system. This type of TC-BRB was investigated by other researchers (Guo *et al*., 2017a and 2017b). In this paper, the details and test results of specimens 2VT and 4VT only are presented. While h_0 was 290 and 330mm, the values of a were 0.85 and 0.89 chosen for specimens 2VT and 4VT, respectively. The nominal cross-sectional dimensions of the chord and the post in specimen 2VT were 48.4×3.2mm, while they were 48.4×3mm in specimen 4VT. The sizes of the diagonal and transverse tubes are 33.8×2.8mm for both specimens. Both specimens' truss frames were divided into twelve truss segments with equal spacing L_s between two adjacent posts.

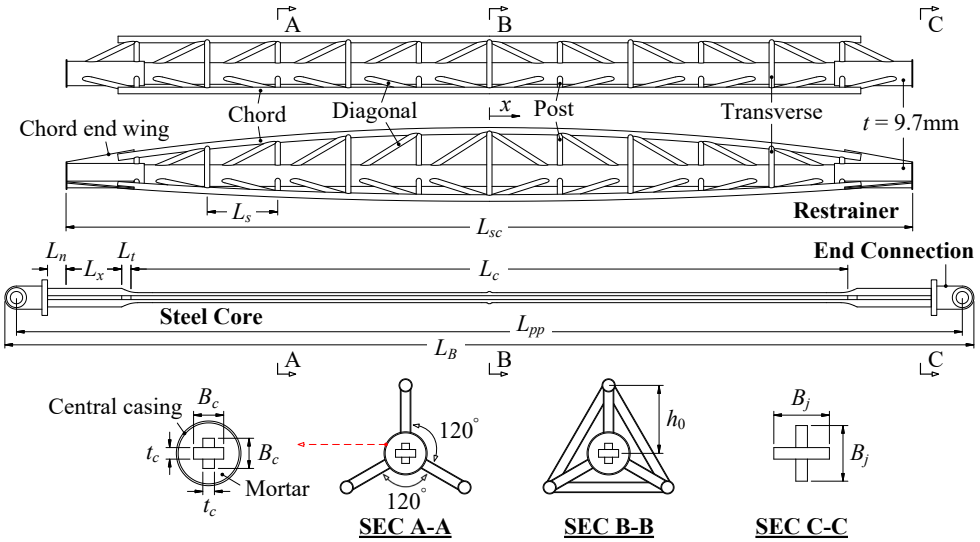

Figure 4. Cross-sectional details of the proposed TC-BRB.

Test Setup and Procedure

The specimens were tested using the multi-axial testing system (MATS) at Taiwan National Center for Research on Earthquake Engineering (Lin *et al*., 2017) by applying cyclically increasing displacements prescribed in the AISC specifications (AISC 2016). Two steel connectors were made to anchor the specimen's pin ends to the reaction wall or MATS platen, and to provide end boundary conditions for the gussets. A pair of displacement transducers were mounted at each brace end to measure the axial deformations. A motion capture system was adopted in order to record the in-plane and out-of-plane deformations along the specimens. The standard loading proceeded with increasing axial deformations considering lateral drift ratios (LDRs) ranging from 0.5% to 2% for two cycles at each deformation level. The extended loading was continued with five cycles of 2% LDR to achieve an index of 200 cumulative plastic deformation (CPD) prescribed in the model specification. In order to trigger possible instability of the specimens, the axial deformations correspond to 3% to 5% LDRs were applied following the last cycle of 2% LDR until failure occurred.

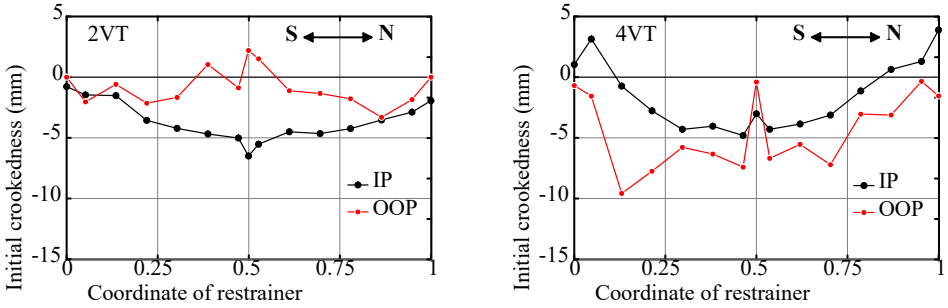

Figure 5. Initial crookedness of specimens.

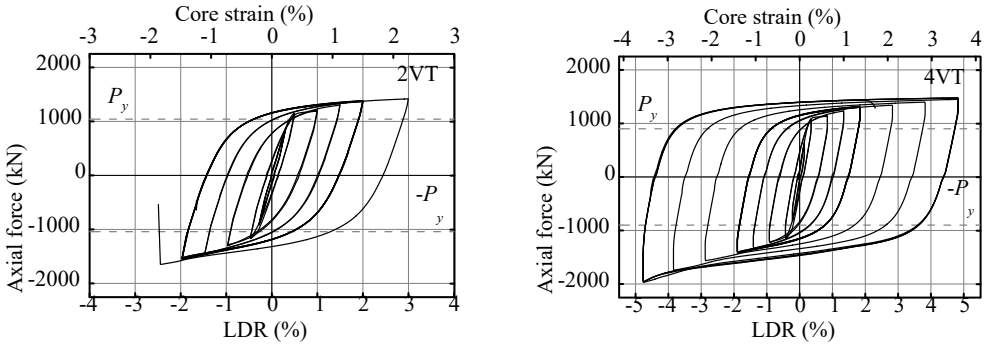

Figure 6. Hysteresis behavior of specimens 2VT and 4VT.

Test Results

The BRB's initial imperfection can result from the fabrication error and self-weight. Figure 5 shows the initial crookedness of the specimens, where the negative in-plane values are toward the gravity direction and the positive out-of-plane ones are toward the east. The measured results reveal that the initial in-plane crookedness of the specimens was slightly larger than that in the out-of-plane direction, which could result from the effect of self-weight. However, the averaged in-plane crookedness (including the deflections due to the self-weight) was less than 1/1000 with a maximum value lower than 1/500, which is within most construction tolerances in practice. As shown in Fig. 6, both specimens exhibited stable and repeatable hysteresis behavior with a maximum core strain larger than 1.4% throughout the standard loading and the first five cycles of the extended loading without any observable instability or damage. During the abovementioned loadings, the over-strength ratios due to the strain hardening effect (ω) were 1.28 and 1.48, while the peak compression-to-tension ratios (β) were 1.14 and 1.10 for specimens 2VT and 4VT, respectively, when the 2% LDR cycle was completed. Specimen 2VT buckled with the obvious in-plane flexural deformation developed along the restraining system (Fig. 7) at the first cycle of 3% LDR loading, and the axial compressive strength dropped drastically after reaching 1647kN with

a CPD value of 236. Specimen 4VT sustained the subsequent 3% to 5% LDR loadings and its steel core eventually fatigue fractured at the 5th cycle in the 5% drift loadings. During the entire test, the developed maximum tension and compression of 1480 and 1971kN in specimen 4VT was recorded. The maximum ratios of ω and β calculated were 1.66 and 1.36, and the gained CPD value was 625. In addition, from the axial force versus deformation relationships given in Fig. 4, it can be seen that the axial stiffness and compressive strength rose slightly when specimen 4VT was compressed to axial deformations larger than 100mm or 3% LDR. This kind of phenomenon should be caused by the effects of severe high-mode buckling developed along the core, or when the compressible spacing at any one end of the inelastic core is exhausted.

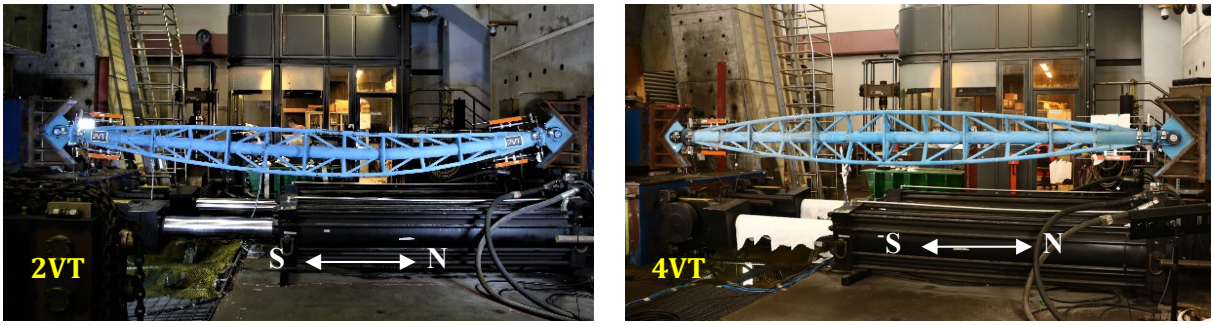

Figure 7. Damage conditions of specimens at the end of test.

CONCLUSIONS

From the NLRHA results, the proposed mega-braced dual framing system using long-span BRBs seems effective in smoothing the peak lateral drift distribution over the full height of tall buildings. The proposed TC-BRB with a varying cross-sectional depth truss confining system appears feasible and practical for long-span BRBs. Its novel restraining system may have remarkable advantages on the efficient flexural rigidity, less self-weight and the associated architectural appearance when it is adopted as a large load-carrying and long-span brace in mega braced frame structures. The two 1/3-scale TC-BRBs, with different mid-span heights of the truss frame of their restraining systems, represent a brace length of about 20m and a nominal yield capacity of 7650kN in the prototype mega braced frame, were investigated. Their experimental performance demonstrates satisfactory hysteretic behavior complying with the requirements prescribed in the model specifications. Test results indicate that properly fabricated TC-BRB specimen designed with a stiffer truss confining system is able to sustain a larger CPD without flexural buckling. It is confirmed that the proposed TC-BRB can be designed and fabricated to achieve an excellent seismic performance. A simplified method in estimating the elastic buckling strength of the TC-BRB has been developed. Its accuracy was verified through the finite element model analysis.

ACKNOWLEDGMENTS

The authors very much appreciate the financial support provided by the Taiwan Ministry of Science and Technology (MOST110-2221-E-002-107-MY3), and the technical support provided by the Taiwan National Center for Research on Earthquake Engineering.

REFERENCES

American Institute of Steel Construction (2016). *Seismic Provisions for Structural Steel Buildings (AISC 341-16)*, AISC, Chicago, Illinois.

Black, C.J., Makris, N. and Aiken, I.D. (2004). "Component testing, seismic evaluation and characterization of buckling-restrained braces," *Journal of Structural Engineering*, **130**(6), 880-894.

Chen, C., Lin, Y.C., Wu, A.C., Chen, L.A. and Tsai, K.C. (2021). "Long-span buckling-restrained braces using truss-confined restrainers," *Structural Engineering*, **36**(2), 5-50. (in Chinese)

Chen, L.A. (2021). A Study of BRBs using Varying Section Steel Truss Restrainers, *Master Thesis*, National Taiwan University, Taipei, Taiwan. (in Chinese)

Chang Chien, I.C. (2021). Seismic Design and Analysis of Steel Frames with Long-Span BRBs, *Master Thesis*, National Taiwan University, Taipei, Taiwan. (in Chinese)

Chuang, M.C., Tsai, K.C., Lin, P.C. and Wu, A.C. (2015). "Critical limit states in seismic buckling-restrained brace and connection designs," *Earthquake Engineering & Structural Dynamics*, **44**(10), 1559-1579.

Fahnestock, L.A., Ricles, J.M. and Sause, R. (2007). "Experimental evaluation of a large-scale buckling-restrained braced frame," *Journal of Structural Engineering*, **133**(9), 1205-1214.

Guo, Y.L., Zhou, P., Wang, M.Z., Pi, Y.L. and Bradford, M.A. (2017a). "Numerical studies of cyclic behavior and design suggestions on triple-truss-confined buckling-restrained braces," *Engineering Structures*, **146**, 1-17.

Guo, Y.L., Zhou, P., Wang, M.Z., Pi, Y.L., Bradford, M.A. and Tong, J.Z. (2017b). "Experimental and numerical studies of hysteretic response of triple-truss-confined buckling-restrained braces," *Engineering Structures*, **148**, 157-174.

Li, C.H., Vidmar, Z., Saxey, B., Reynolds, M. and Uang, C.M. (2022). "A procedure for assessing low-cycle fatigue life of buckling-restrained braces," *Journal of Structural Engineering*, **148**(2), 04021259.

Lin, P.C., Tsai, K.C., Wang, K.J., Yu, Y.J., Wei, C.Y., Wu, A.C., Tsai, C.Y., Lin, C.H., Chen, J.C., Schellenberg, A.H., Mahin, S.A. and Roeder, C.W. (2012). "Seismic design and hybrid tests of a full-scale three-story buckling-restrained braced frame using welded end connections and thin profile," *Earthquake Engineering & Structural Dynamics*, **41**(5), 1001-1020.

Lin, P.C., Tsai, K.C., Chang, C.A., Hsiao, Y.Y. and Wu, A.C. (2016). "Seismic design and testing of buckling-restrained braces with a thin profile," *Earthquake Engineering & Structural Dynamics*, **45**(3), 339-358.

Lin, T.H., Chen, P.C. and Lin, K.C. (2017). "The multi-axial testing system for earthquake engineering researches," *Earthquakes and Structures*, **13**(2), 165-176.

Takeuchi, T. and Wada, A. (2017). *Buckling-Restrained Braces and Applications*, The Japan Society of Seismic Isolation, Tokyo, Japan.

Tremblay, R., Bolduc, P., Neville, R. and DeVall, R. (2006). "Seismic testing and performance of buckling-restrained bracing systems," *Canadian Journal of Civil Engineering*, **33**(2), 183-198.

Tsai, K.C., Wu, A.C., Wei, C.Y., Lin, P.C., Chuang, M.C. and Yu, Y.J. (2014). "Welded end-slot connection and debonding layers for buckling-restrained braces," *Earthquake Engineering & Structural Dynamics*, **43**(12), 1785-1807.

Uang, C.M., Nakashima, M. and Tsai, K.C. (2004). "Research and application of buckling-restrained braced frames," *International Journal of Steel Structures*, **4**(4), 301-313.

Usami, T., Wang, C.L. and Funayama, J. (2012). "Developing high-performance aluminum alloy buckling-restrained braces based on series of low-cycle fatigue tests," *Earthquake Engineering & Structural Dynamics*, **41**(4), 643-661.

Wu, A.C., Lin, P.C. and Tsai, K.C. (2014). "High-mode buckling responses of buckling-restrained brace core plates," *Earthquake Engineering & Structural Dynamics*, **43**(3), 375-393.

Special Talk

Prof. Shyh-Jiann Hwang

National Taiwan University, Taiwan

Topic： Seismic Retrofitting Program of School Buildings in Taiwan

NARLabs

Nov. 10, 2022

Seismic Retrofitting Program of School Buildings in Taiwan

Shyh-Jiann Hwang

Professor
National Taiwan University

Former Director General
National Center for Research on Earthquake Engineering

Outlines

- Introduction
- Technical Preparation
- School Retrofitting Program
- International Collaboration
- Conclusions

Introduction

Seismicity in Taiwan

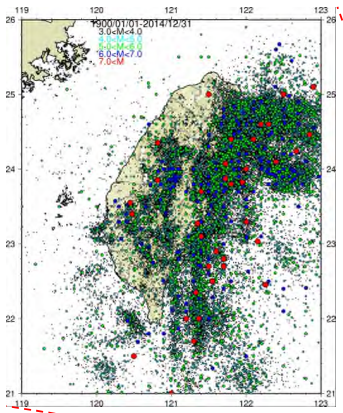

Taiwan

Earthquake Distribution of Taiwan (A.D.1900-2014)

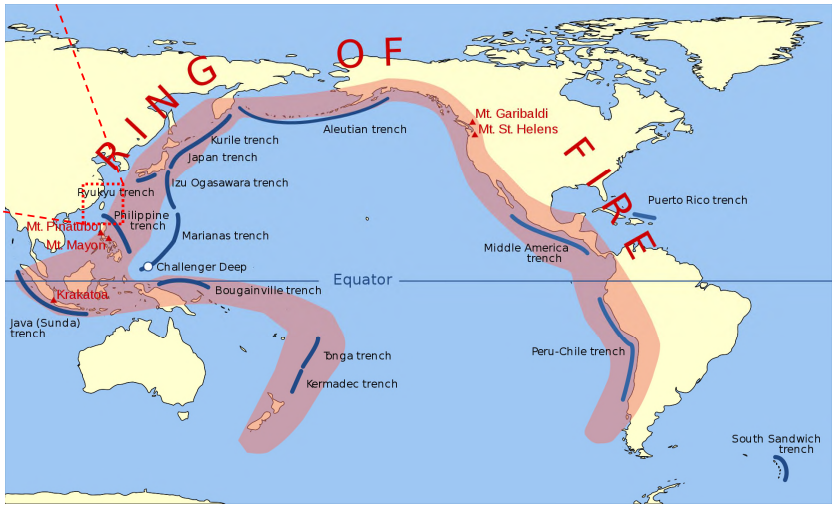

School Buildings Attacked by Chi-Chi EQ

M_L = 7.3; 01:47 am, Sep. 21, 1999

NARLabs 國家實驗研究院 National Applied Research Laboratories

School Retrofitting Project in Taiwan

1999 → **2009** → **2022**

Preparation – 10 yrs

Execution – 14 yrs

- **Strategy**
- **Technology Development**

- **Administration measures**
- **Budgets US$ 4 billions**

$$\frac{\text{Retrofitted}}{\text{Total}} = \frac{10,163}{27,227} = 37\%$$

NARLabs 國家實驗研究院 National Applied Research Laboratories

Technical Preparation

Strategy for School Upgrading in Taiwan

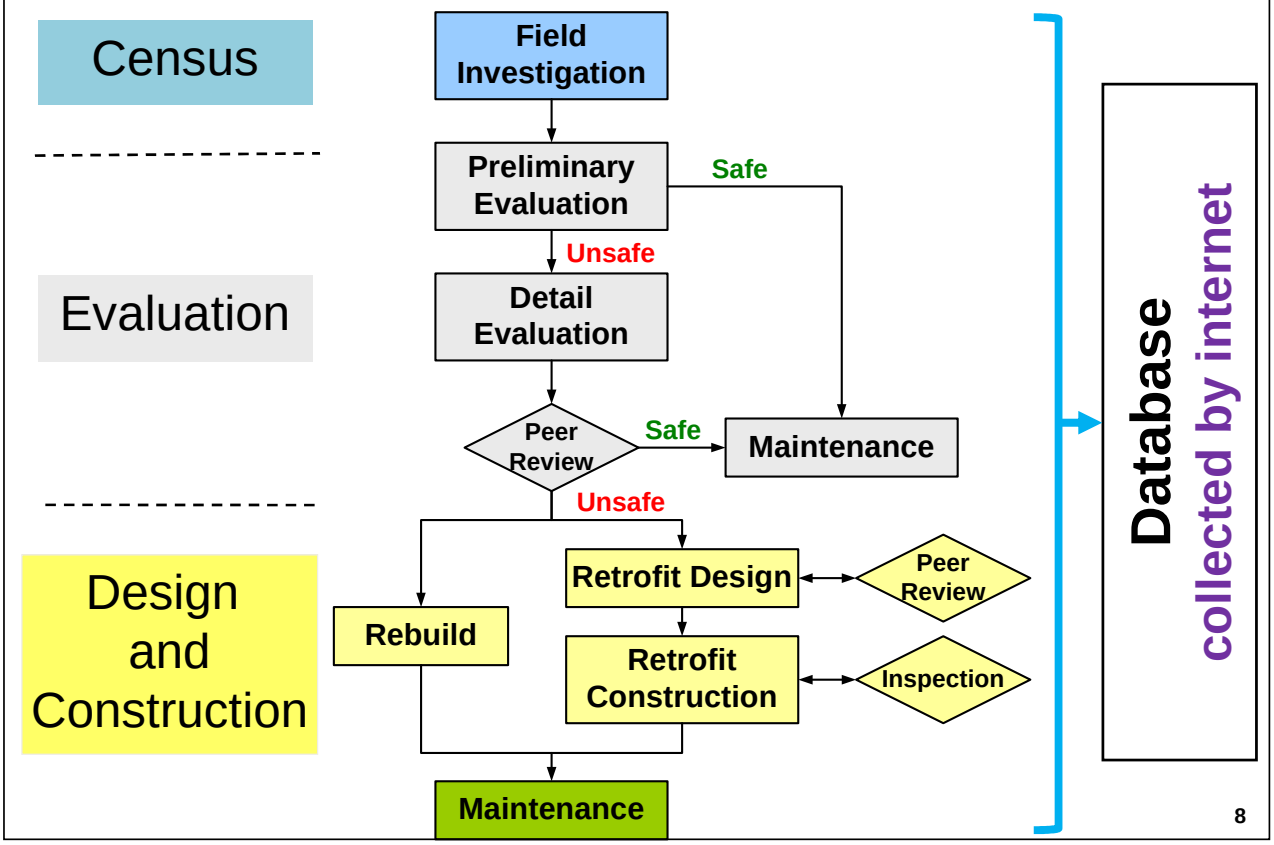

Screening Process

Field Investigation

Preliminary Evaluation

Detailed Evaluation

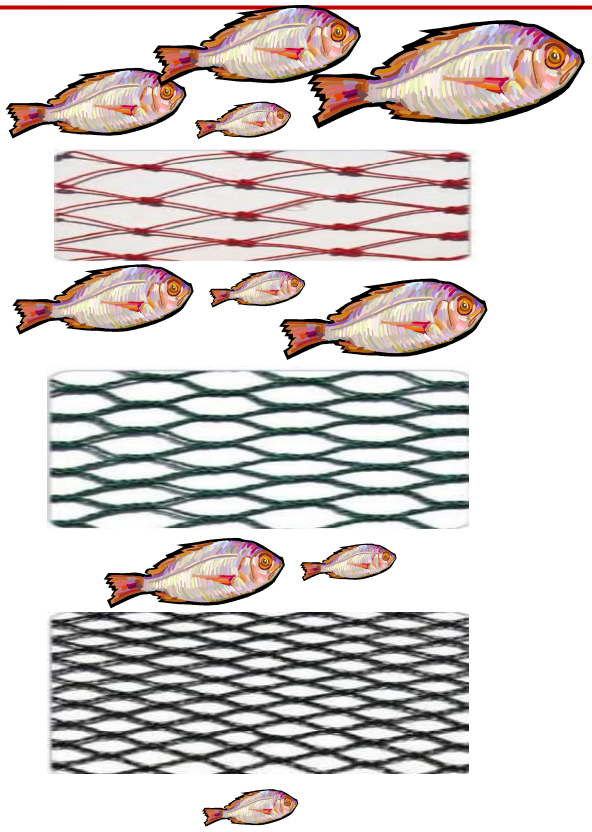

Screening

NARLabs 國家實驗研究院 National Applied Research Laboratories

9

Field Investigation (2009-2011)

Simple Survey:

- 3,721 public schools
  25,843 buildings
- 228 college students
  4,426 days per person

School building included:

- Buildings constructed before 1999
- Buildings occupied by students or teachers

NARLabs 國家實驗研究院 National Applied Research Laboratories

Preliminary Evaluation

Seismic Index: $\dfrac{Capacity}{Demand} = \dfrac{\tau_C A_C + \tau_W A_W}{a_g \times w \times \Sigma A_f}$

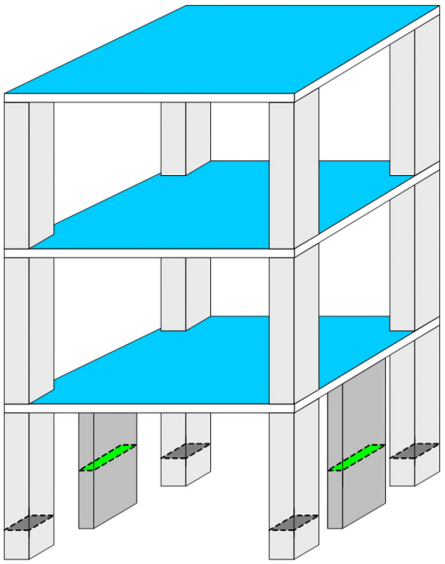

ΣA_f 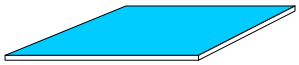

Total Floor Area above 1st Floor

A_C

A_W 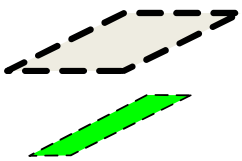

1st Floor Capacity

Detailed Evaluation

Performance Based Engineering

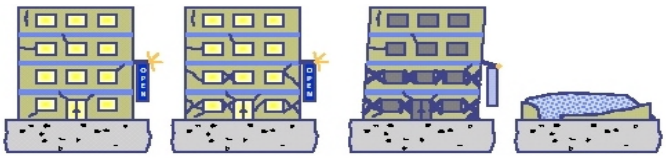

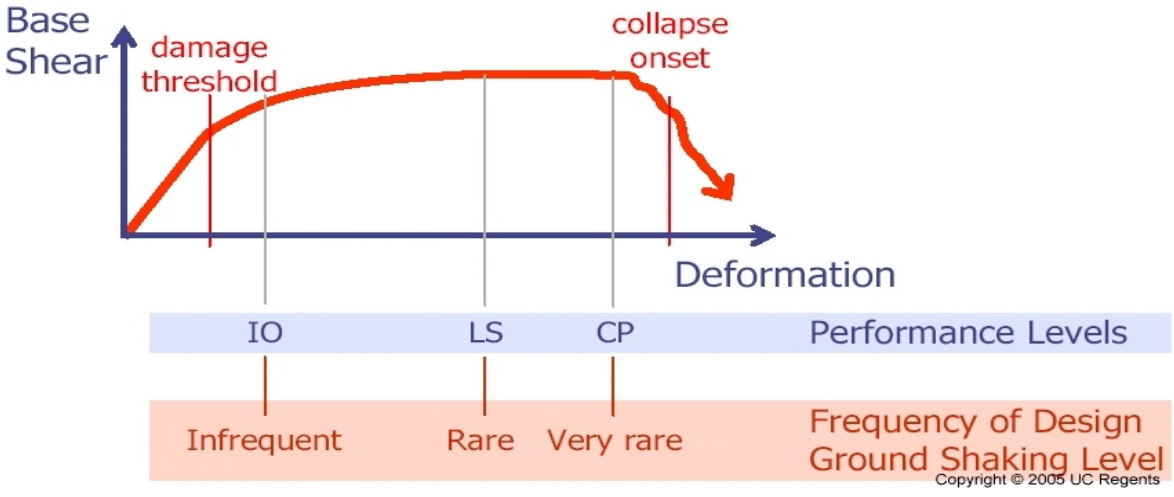

Nonlinear Static Analysis

Pushover Analysis ⇒ **Capacity Spectrum Analysis**

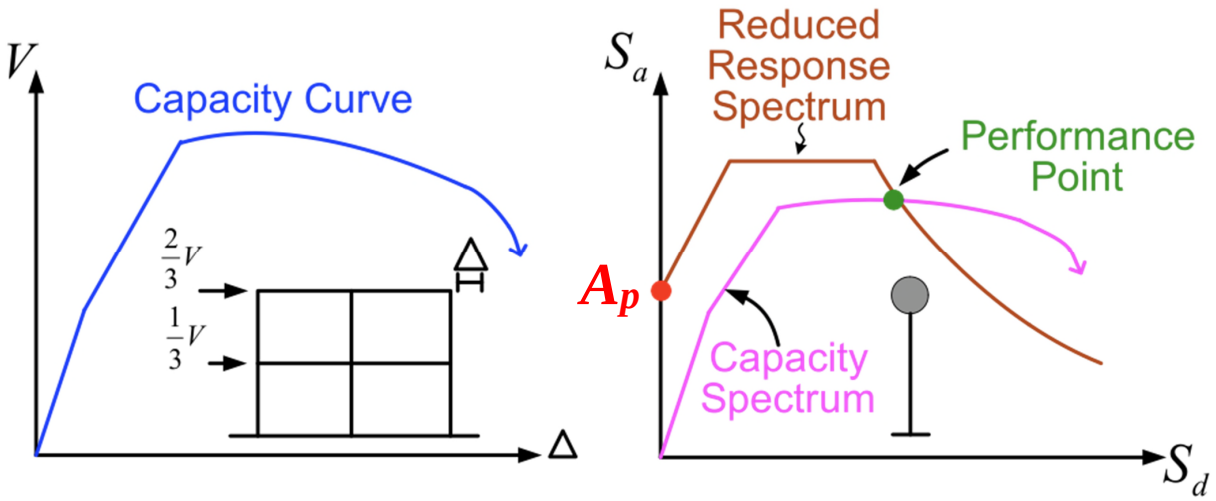

⇒ Performance-Target Ground Acceleration A_p

Backbone Curves for Shear Critical Members

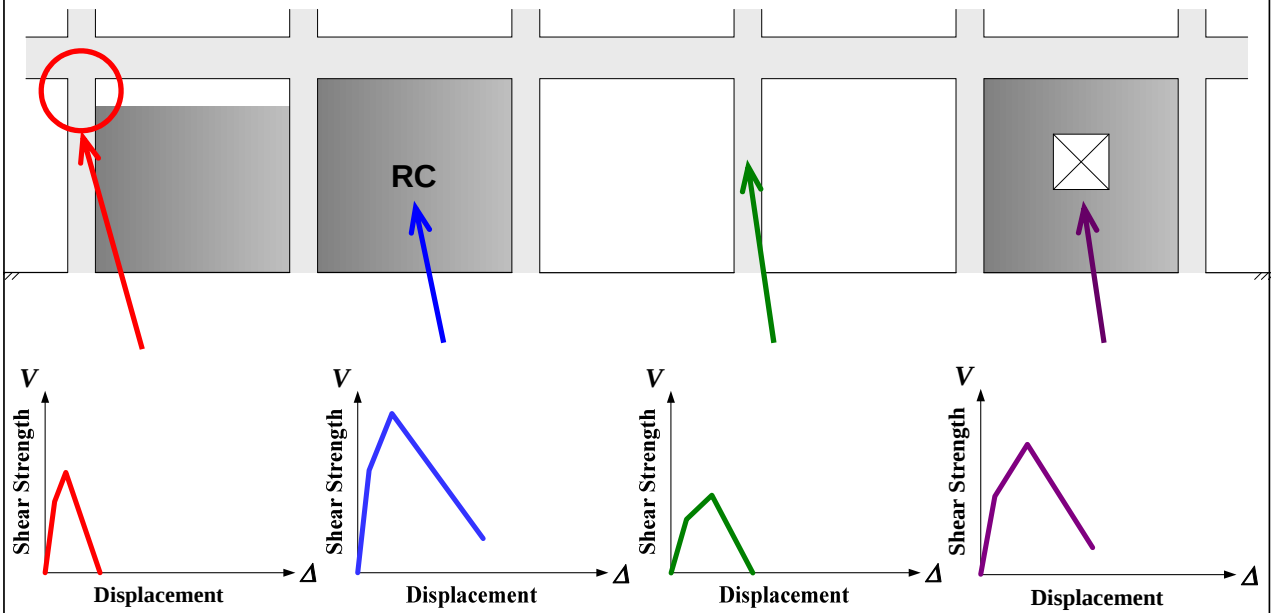

Softened Strut-and-Tie Model

Research on Seismic Capacity of Members

Static Test

Column

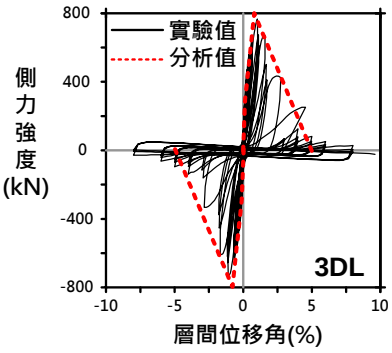

Shaking Table Test

Columns

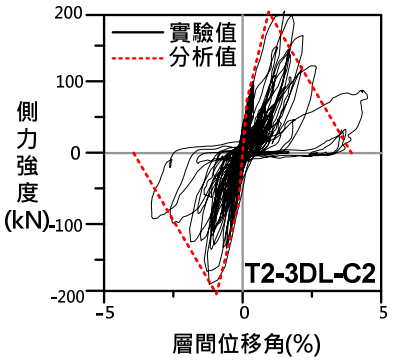

Static Test

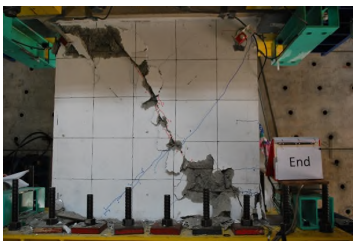

Wall

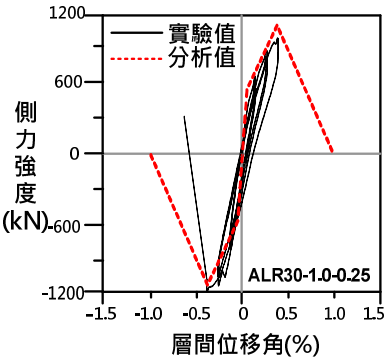

Shaking Table Tests for Column Collapse Behavior

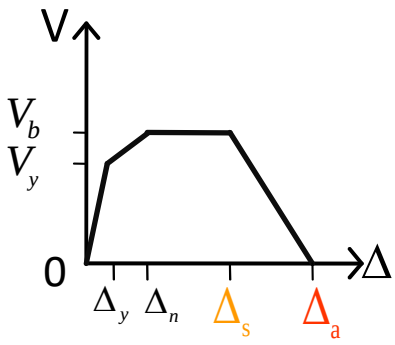

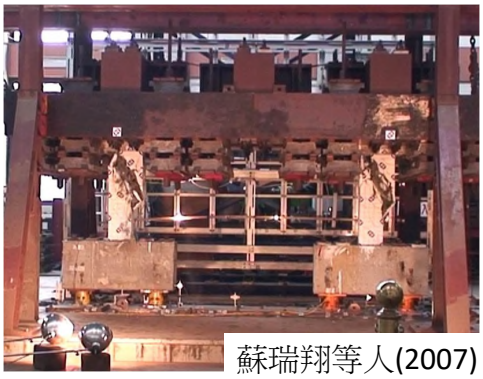

蘇瑞翔等人(2007)

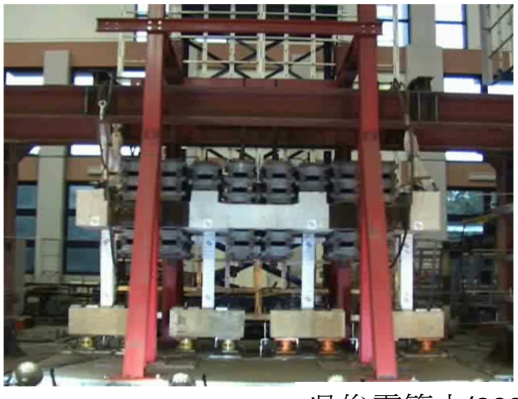

吳俊霖等人(2009)

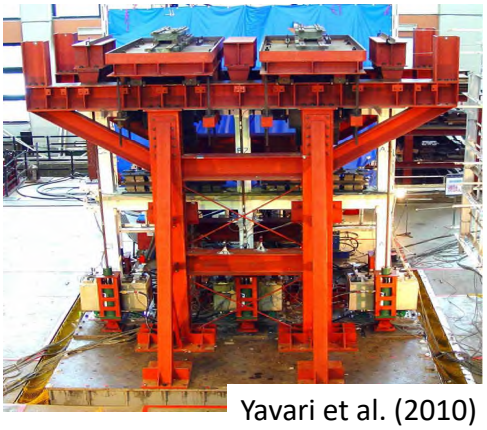

Yavari et al. (2010)

Test Setup of Monotonic Loading

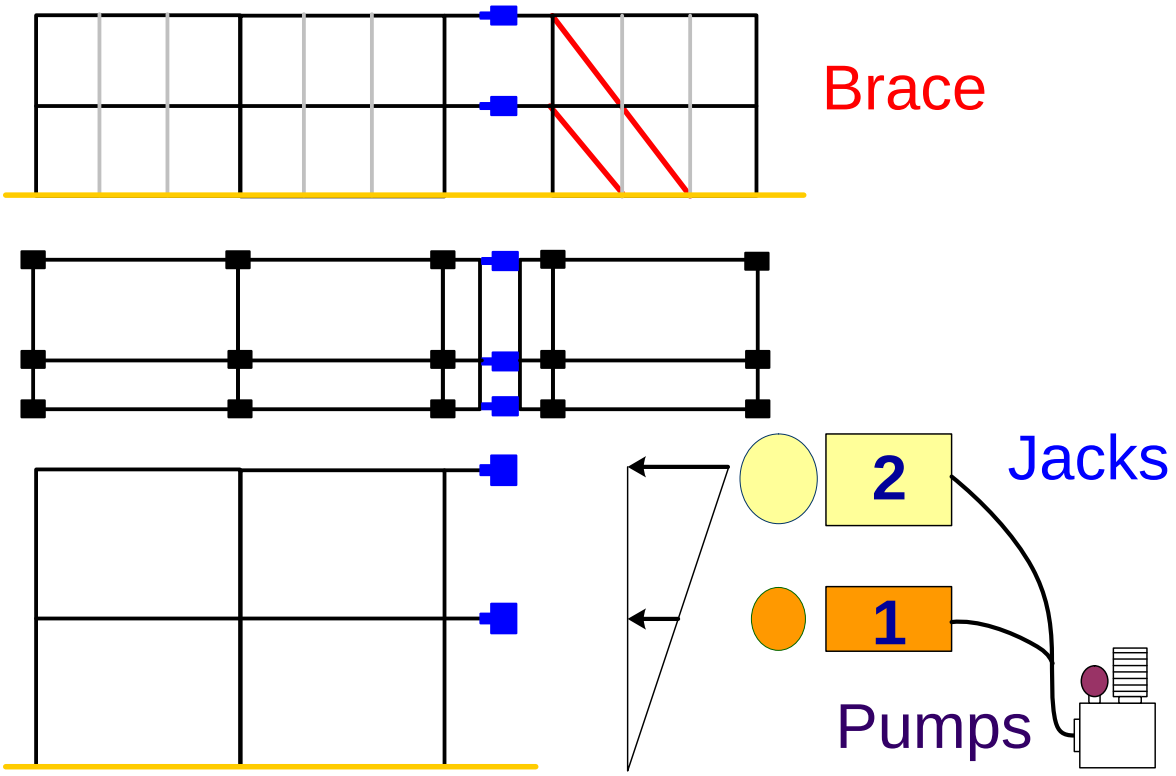

Test Video of Monotonic Loading

Pseudo-Dynamic and Cyclic Tests Setup

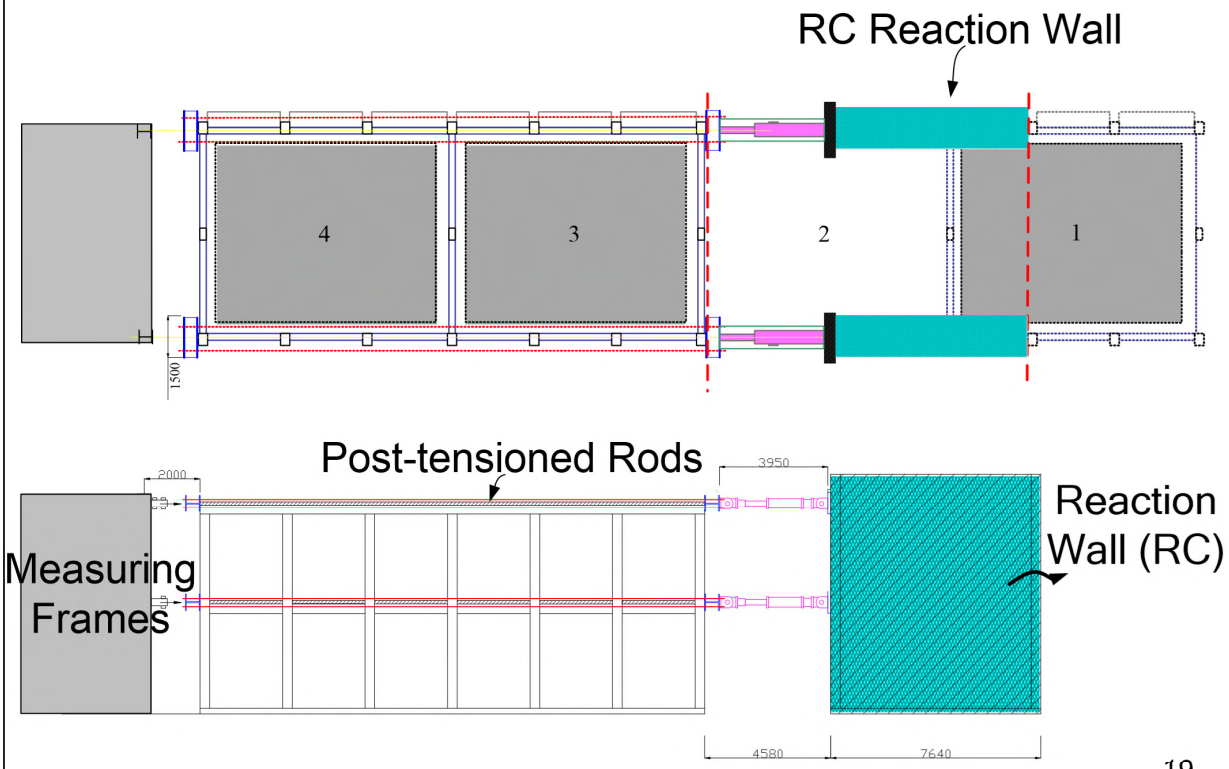

19

Pseudo Dynamic Test (# 3), Courtesy of Dr. Min-Lang Lin

In-Situ Tests of School Buildings – Verification of Pushover Analysis

Hua-Lien (2005)

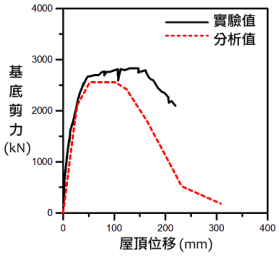

Yun-Lin (2005)

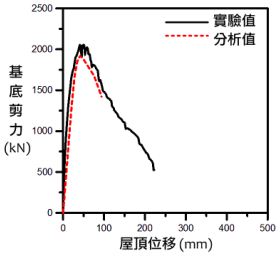

Tao-Yuan (2006)

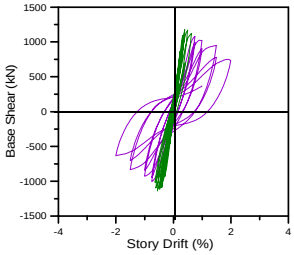

Tainan (2007)

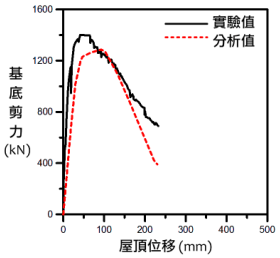

Common Retrofitting Techniques

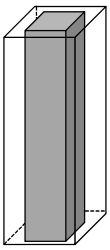

Jacketed column

Shear wall

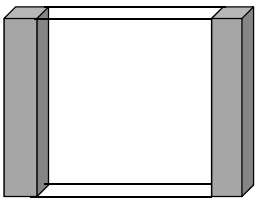

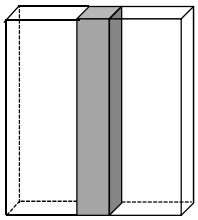

Wing wall

In-Situ Tests of School Buildings – Verification of Retrofitting Methods

RC Wing Wall (2005)

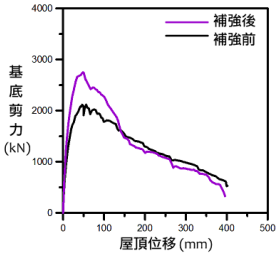

Composite Column (2006)

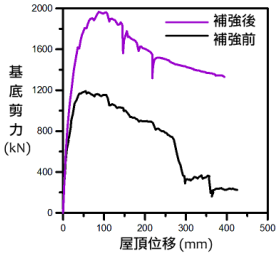

RC Jacketing (2007)

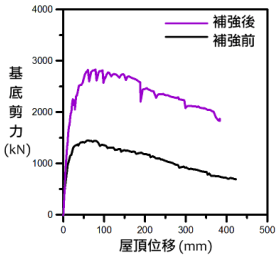

Steel Jacketing (2007)

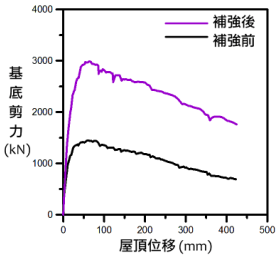

Chi-Chi Earthquake Damage Database of School Buildings in Taiwan

- **Basic Methodology from ATC-13**

Structural Properties

Plan, Dimensions,
Section details,
~~Material strength,~~
~~Soil condition~~

Damaged Conditions

Damage records,
Definition of "damage"

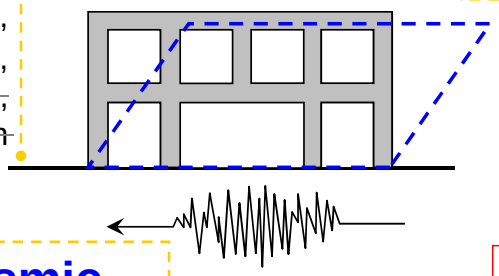

Seismic Magnitude

Site PGA,
Longitudinal PGA for individual building

NCREE-07-023 Tu et al.

Verification of Acceptance Criteria (35 Buildings)

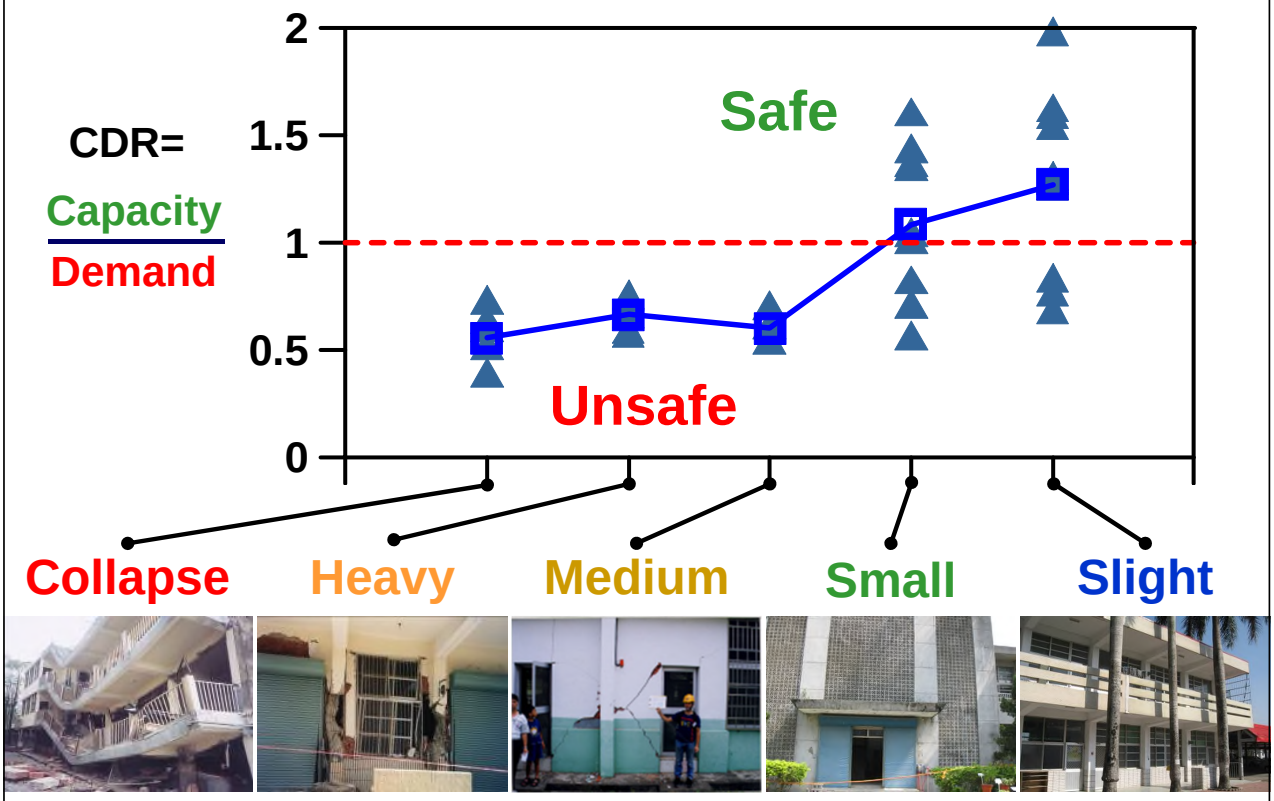

25

School Retrofitting Program
2009-2022

NARLabs 國家實驗研究院 National Applied Research Laboratories

26

Unification of Process

- Complex Parties: governmental official, school teacher, engineer, constructor, student, parent
- Tight Schedule: annual budget, short construction period
- Unification Document: operation specification, contract document, design manual

Budget Control - Service Payment

New Construction

Seismic Retrofitting

Design Payment = Rate × Construction Fee

Design Payment = Rate × Floor Area

Payment per Quantity

Innovation for Quality

Budget Control - Economic Methods

Traditional Retrofitting Method ⇨ Encouraged

RC Column Jacketing

RC Wing Wall

RC Shear Wall

Seismic Devices with Patents ⇨ Prohibited

Isolated Device

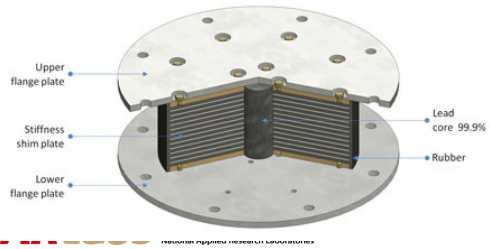

Damper

Quality Control - Review and Inspection

- **Peer Review for Design**

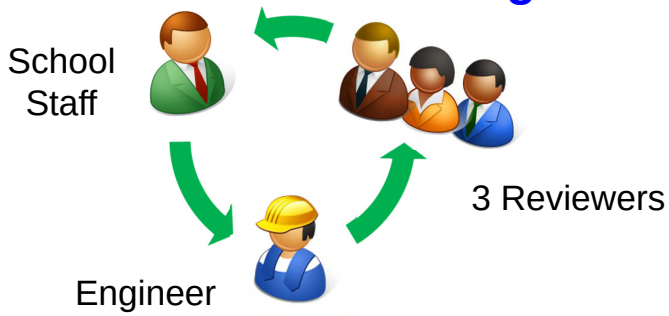

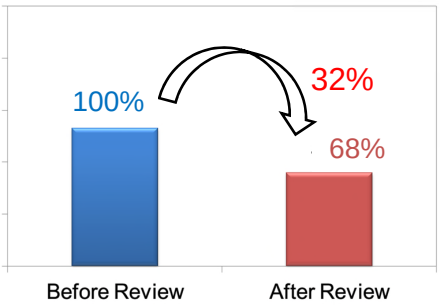

- **Inspection for Construction**

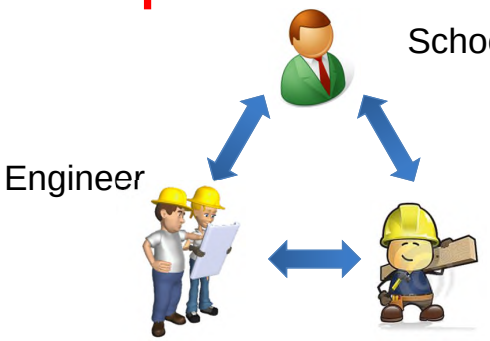

Quality Control - Workshops

- Workshops for Engineers, School Administrators, Educational Officials




- Case Study





Website and Database

https://school.ncree.org.tw

Database

- Data Collecting
- News Announcement
- Download Service
- Exchange of Information

- Process monitoring
- Decision making

Retrofitting Effectiveness

Kaohsiung Jia-Xian EQ
M_L = 6.4, March 4, 2010

Cost of School Retrofitting in Taiwan

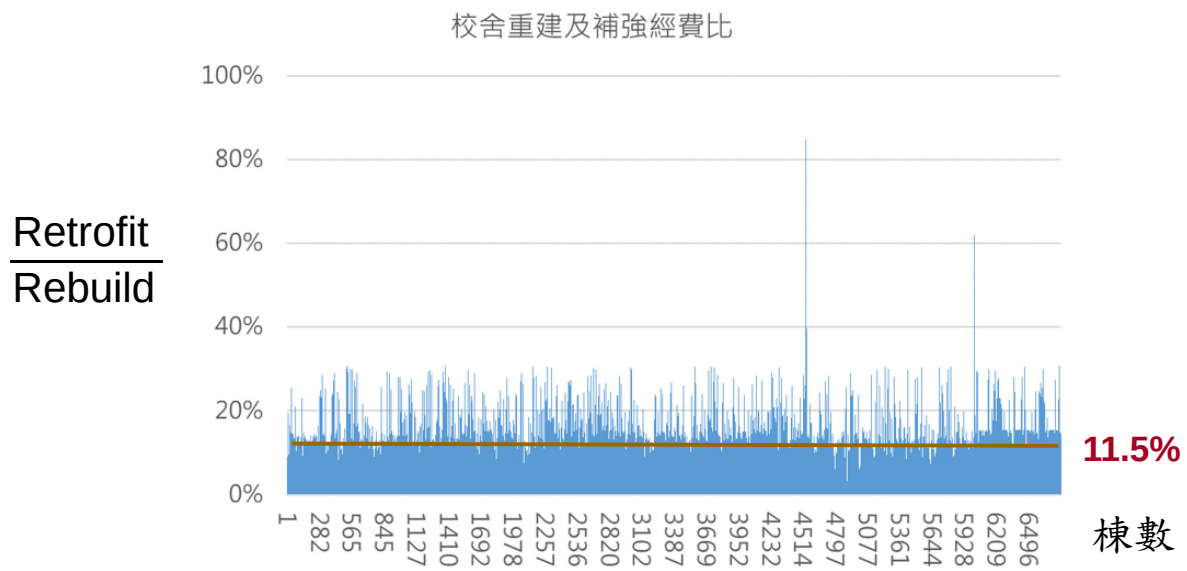

Actual Cost: $\frac{\text{Retrofitting fee}}{\text{Rebuilt fee}} = \frac{\text{NT\$ 2,995 /m}^2}{\text{NT\$ 26,000 /m}^2} = 11.5\%$

NARLabs 國家實驗研究院 National Applied Research Laboratories

School Buildings Upgrading Projects

- Project span from 2009 to 2022
- Upgrading rate by construction up to 37%

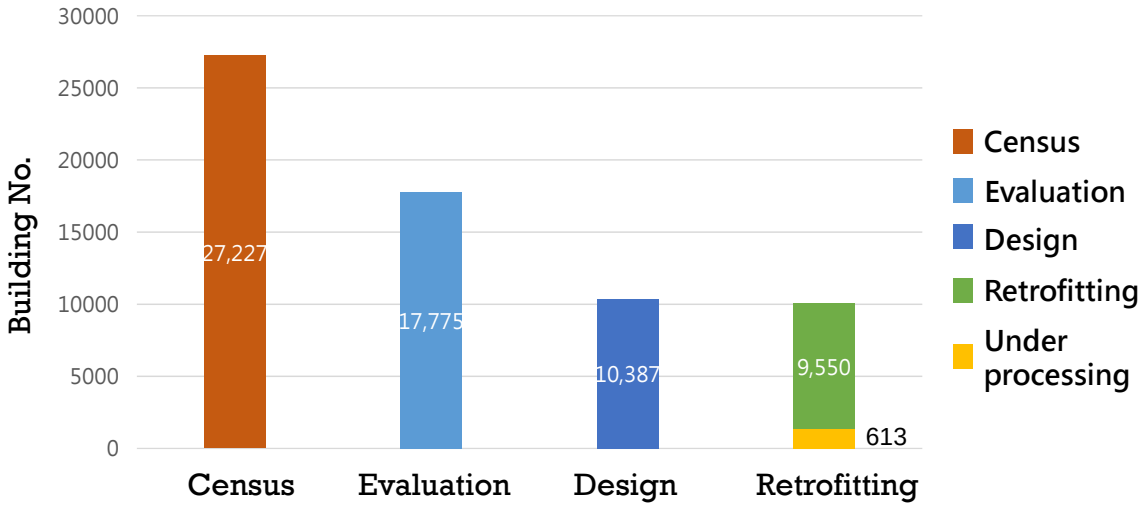

Data deadline： 2021.12.31

International Collaboration

International Collaboration - Thailand

- AIT-KMUTT

AIT Asian Institute of Technology

Prof. Pennung Warnitchai

King Mongkut's University of Technology Thonburi

Prof. Sutat Leelataviwat

- Soft First Story – Column Jacketing

Thailand 2014 ,
Ching Lai EQ , M_w 6.2

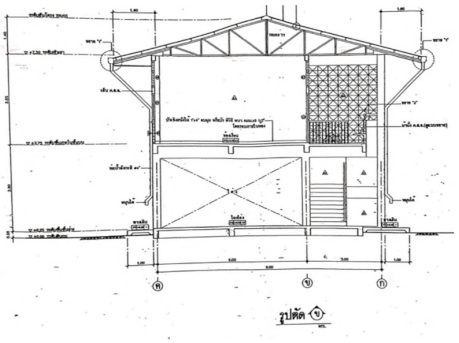

Laboratory Study - NCREE

- Column Tests of RC Jacketing

Specimen without rebar planting

Specimen with rebar planting

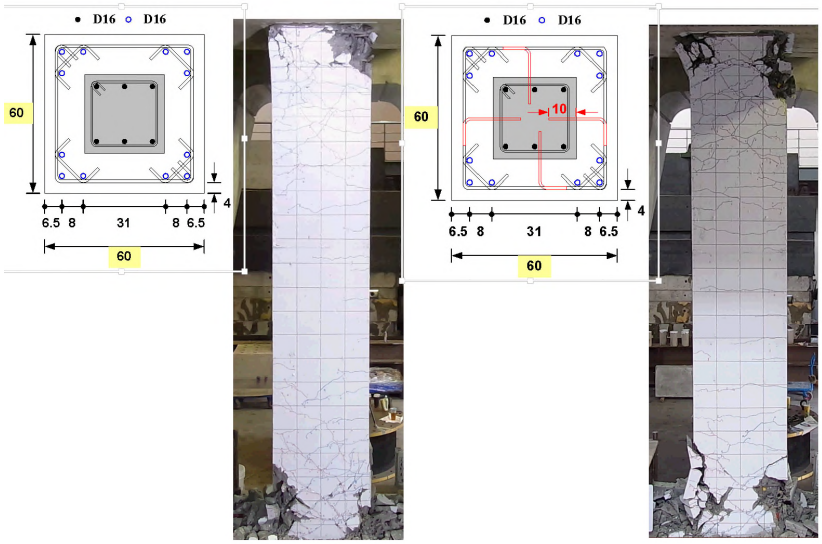

Rebar planting – 10% higher strength

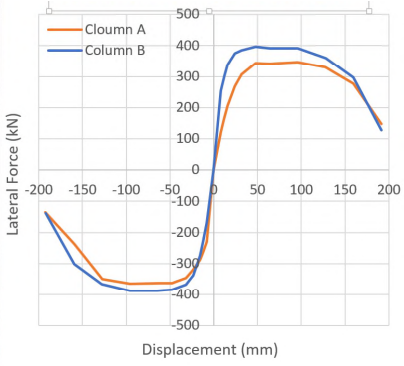

Schools Retrofitted in Thailand June, 2021

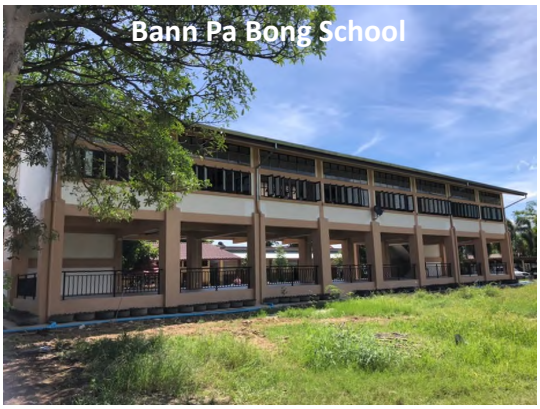

Sri Toi Sun Thorn Rat wittaya School

International Collaboration - Indonesia

- ITB

AARGI ASOSIASI AHLI REKAYASA GEMPA INDONESIA

INSTITUT TEKNOLOGI BANDUNG

Dr. Erwin Lim

- Confined Masonry

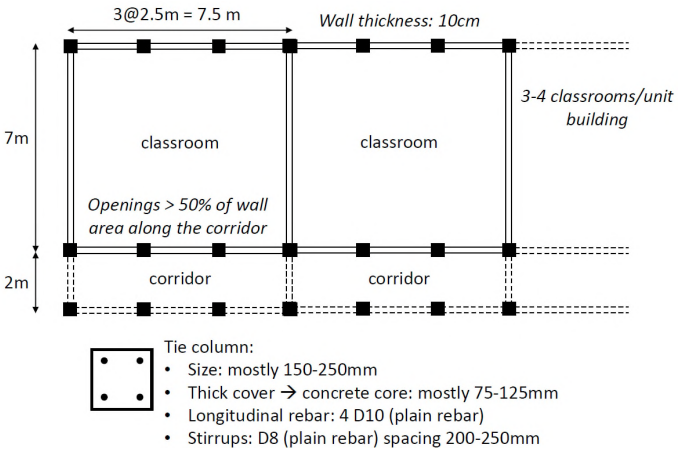

Tie column:
- Size: mostly 150-250mm
- Thick cover → concrete core: mostly 75-125mm
- Longitudinal rebar: 4 D10 (plain rebar)
- Stirrups: D8 (plain rebar) spacing 200-250mm

Laboratory Study – ITB on going

Retrofitted specimens

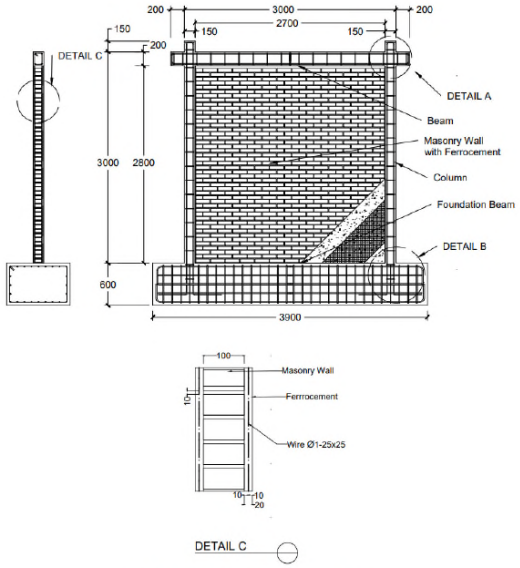

Ferrocement retrofitting

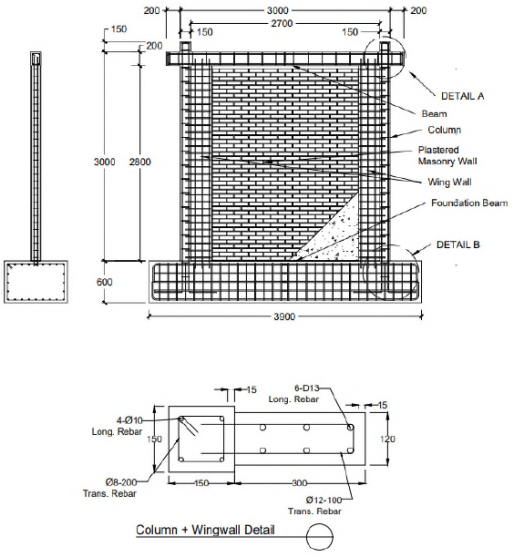

Wing wall retrofitting

Conclusions

Features of Project

Compulsory	• Field investigation
Technology	• Advanced evaluation method
	• Screen and prioritization
Administration	• Unified procedure
	• Budget and quality control
Monitoring	• Website and database
Collaboration	• International collaboration

NCREE

NARLabs 國家實驗研究院 National Applied Research Laboratories

Acknowledgement

- Ministry of Education (MOE)
- Ministry of Science and Technology (MOST)
- National Applied Research Laboratories (*NARLabs*)
- Schools of Cheng Junior High, Kou-Hu Elementary, Ruei-Pu Elementary and Guan-Miao Elementary
- County Governments of Hualien, Yunlin, Taoyuan and Tainan
- Universities of NTU, NTUST, NYUST, NCKU, NKFUST, NCTU, etc.

Thank you for your attention

Residential Building Program

Earthquake Damages of Buildings with Soft and Weak First Story



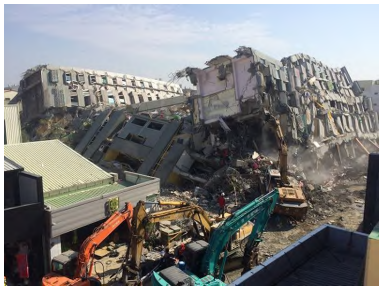

14-story Condominium
2016 Meinong EQ

12-story Condominium
2018 Hualien EQ

11-story Hotel
2018 Hualien EQ

NARLabs 國家實驗研究院 National Applied Research Laboratories

Characteristics of Damaged Buildings

- Older RC building
- Soft and weak first story

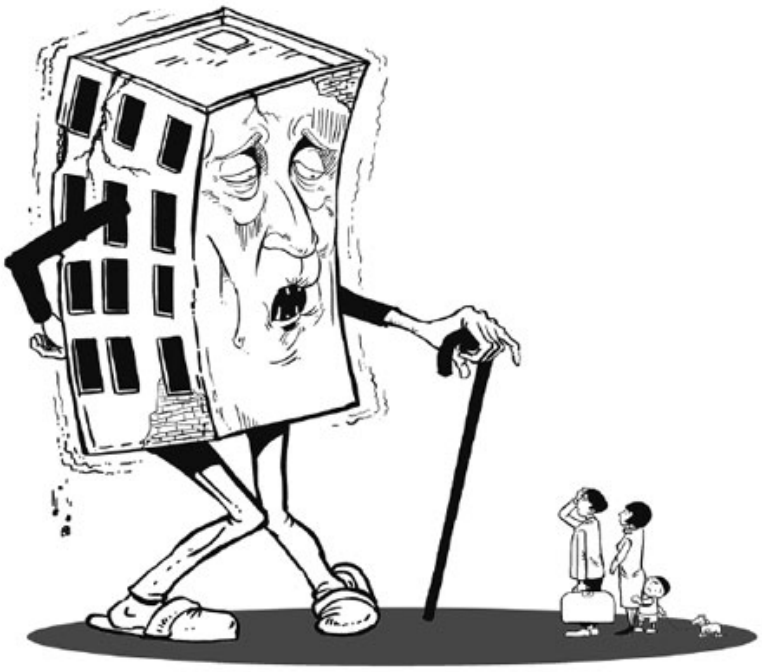

Source : DEGENKOLB RECONNAISANCE TEAM
2016 MEINONG TAIWAN EARTHQUAKE DEBRIEF

Seismic Retrofitting of Soft First Story

Building with soft first story

Removal of seismic deficiency

Prevent Building Collapse Immediately during Earthquake

Seismic Retrofitting Case – Shear Walls

- Story： 6F/B1
- Floor area：4900 m^2
- Construction Floor：1F (690 m^2)
- Addition of Shear Walls
- Budget: US$ 85,000/690
- = US$ 125 dollars/m^2

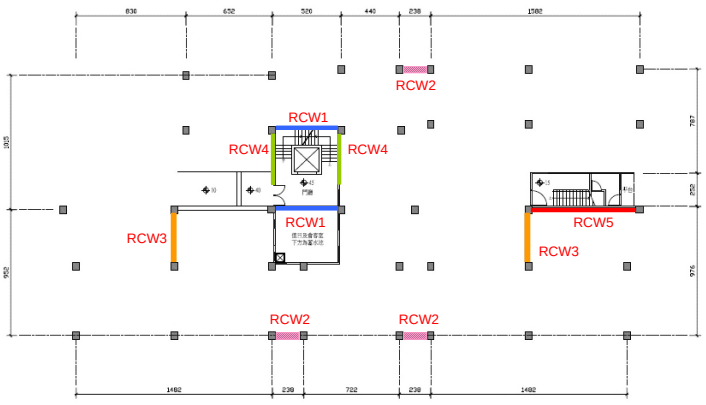

1F Parking Space

Seismic Retrofitting Case – External Frames

City	Building type	Process	Method
Tainan	7-story Condominium + 1F market	Open bidding	Addition of external frames

UBE TAIWAN CO., LTD.
Design U Frame, 2020

Invited Speakers

Dr. Ramesh Guragain

National Society for Earthquake Technology, Nepal

Topic：Lessons on Building Code Implementation and Seismic Retrofitting in Nepal: Build Better Now

(The material of the speaker's presentation has not been authorized for publication in the proceedings.)

Prof. Chung-Chan Hung

National Cheng Kung University, Taiwan

Topic：Use of UHPC Shotcrete for Retrofitting Masonry Infilled RC Frames

Use of UHPC Shotcrete for Retrofitting Masonry Infilled RC Frames

MS student **Yu-Chi Wang**
PhD student **Tuong-Dat-Dinh Do**
Professor and Director **Chung-Chan Hung**

Dept. of Civil Engineering, National Cheng Kung University
NCKU Research Center for Earthquake Engineering and Vibration Control

Acknowledgements

- NSTC 國家科學及技術委員會 National Science and Technology Council
- NARLabs 國家實驗研究院 國家地震工程研究中心 National Center for Research on Earthquake Engineering
- 國立成功大學 National Cheng Kung University 1931

C.-C. Hung
Dept of Civil Engineering, NCKU

Masonry-Infilled RC Frames (MIFs)

Source: "街屋台灣：100間街屋，100種看見台灣的方式！(2019)"

C.-C. Hung
Dept of Civil Engineering, NCKU

Background: Brittle Failure of Masonry Walls

- Damage and collapse of thousands of MIFs under earthquakes

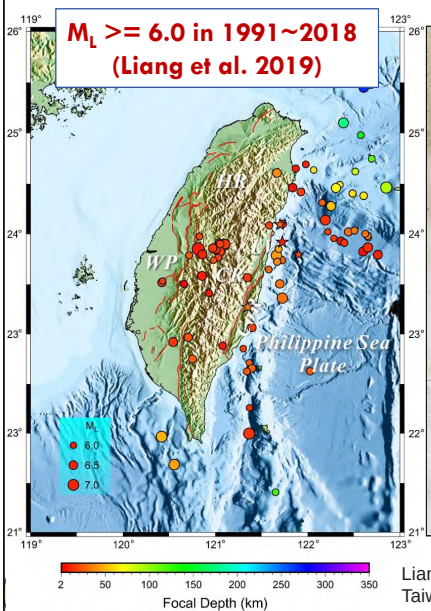

2022 Taitung Earthquake

2016 Tainan Earthquake

Liang et al. (2019). Crowdsourcing platform toward seismic disaster reduction: The Taiwan scientific earthquake reporting (TSER) system. *Frontiers in Earth Science*, *7*, 79.

C.-C. Hung
Dept of Civil Engineering, NCKU

New Retrofitting Materials

■ Ultrahigh Performance Concrete (UHPC)

Short fibers

SP

Good workability

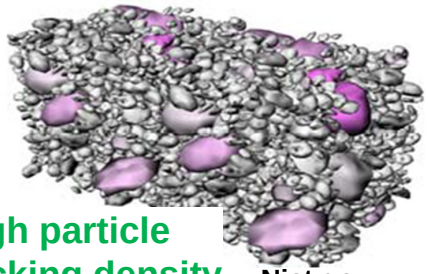

High particle packing density

Nist.gov

Pozzolanic materials

American Coal Ash Association

C.-C. Hung
Dept of Civil Engineering, NCKU

Ultrahigh Performance Concrete (UHPC)

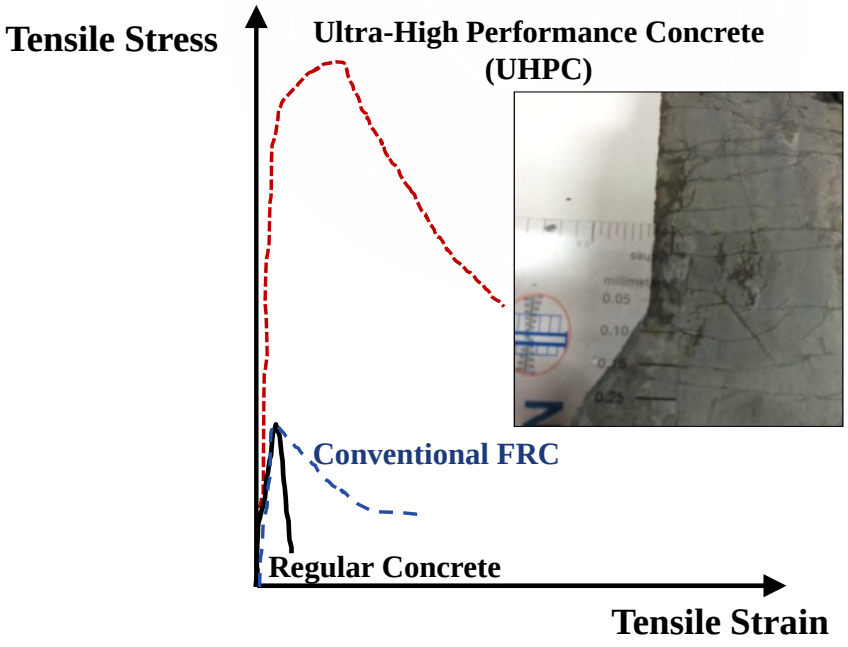

C.-C. Hung
Dept of Civil Engineering, NCKU

UHPC - COMPRESSION

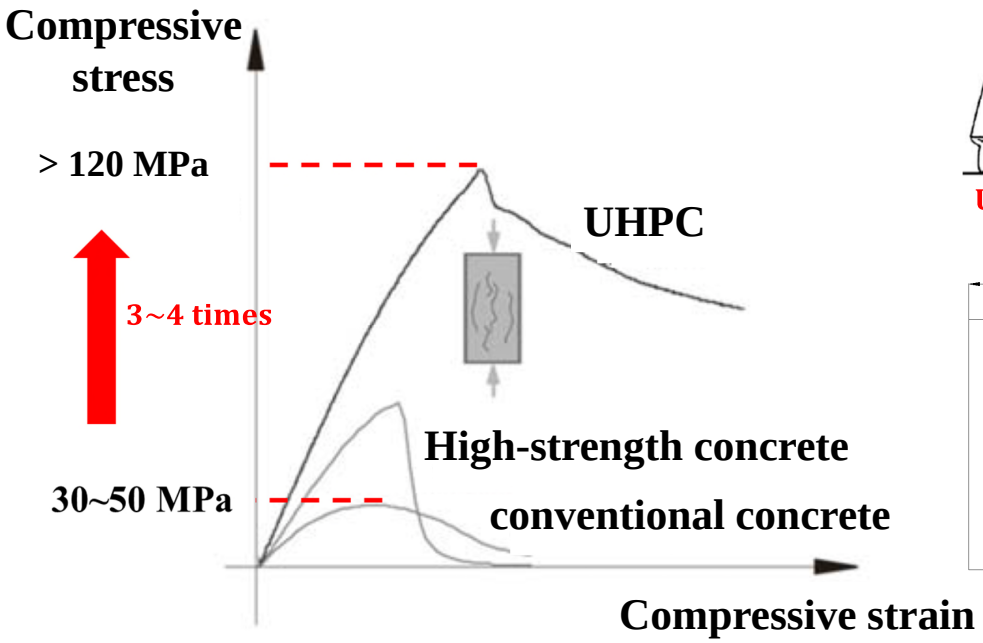

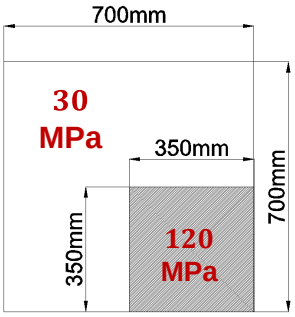

C.-C. Hung
Dept of Civil Engineering, NCKU

UHPC - High Shear Strength

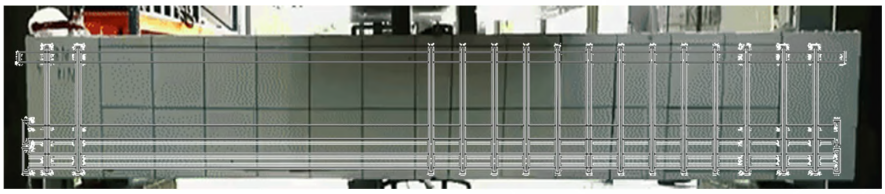

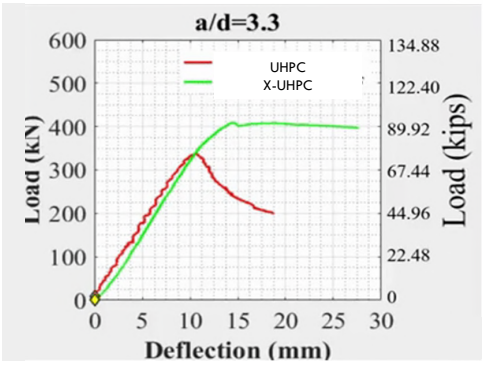

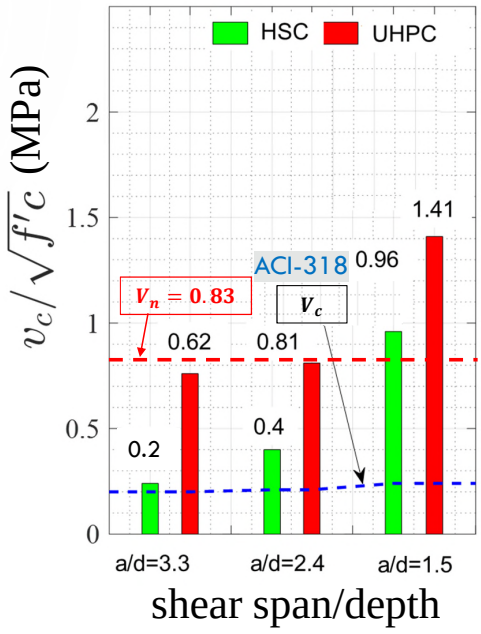

C.-C. Hung
Dept of Civil Engineering, NCKU

Research Objectives

- To investigate the effectiveness of **sprayed UHPC** to retrofit MIFs.
  - ➢ To prevent structural collapse under earthquakes
  - ➢ To reduce post-earthquake damage repairs
- Development of **computational models** for MIFs retrofitted with sprayed UHPC.

Full collapse of MIFs at school

Collapse of school buildings under ChiChi Earthquake
(credit of photo:柯金源:數位島嶼)

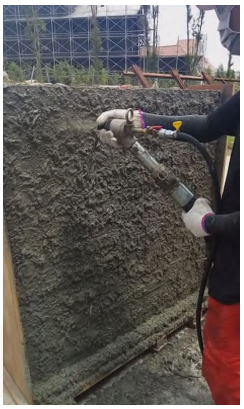

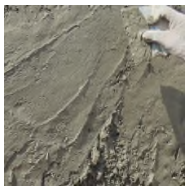

C.-C. Hung
Dept of Civil Engineering, NCKU

EXPERIMENTAL PROGRAM – 1/2
Masonry Assemblages Retrofitted With Sprayed UHPC

ASTM E519/E519M-21:
Standard Test Method for Diagonal Tension (Shear) in Masonry Assemblages

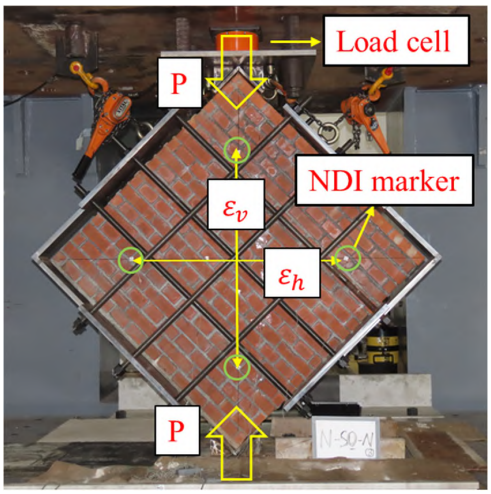

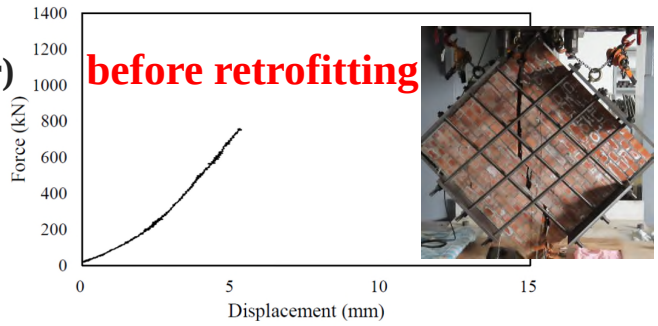

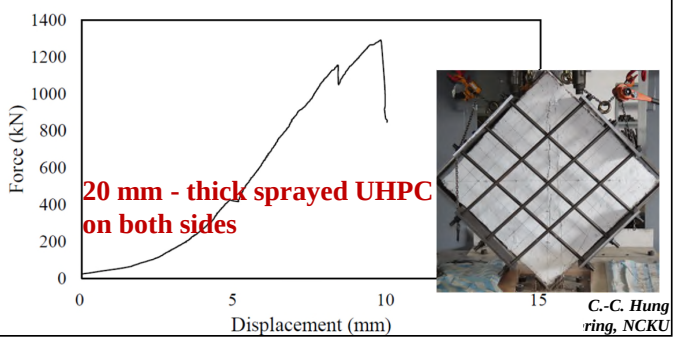

C.-C. Hung
ring, NCKU

Experimental Program – 2/2

- Two full-scale as-built specimens

Frame

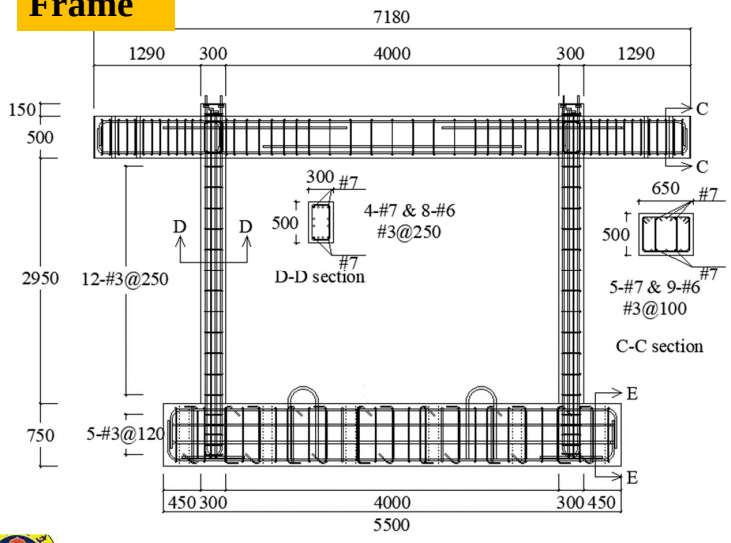

MIF

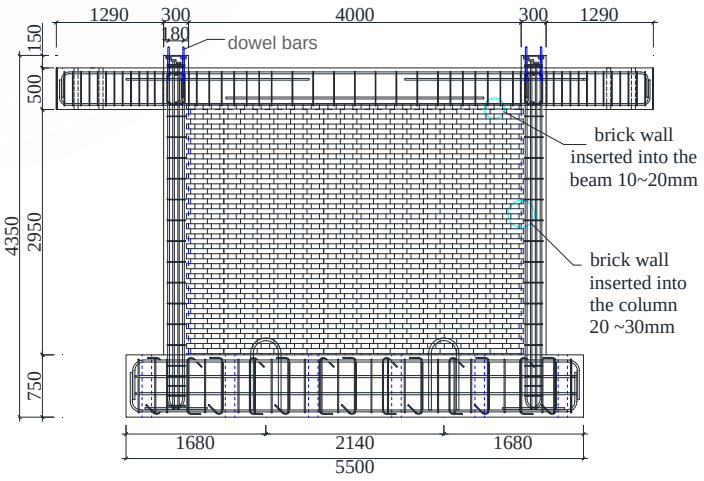

- Unit: mm (25.4 mm = 1 in.)

C.-C. Hung
Dept of Civil Engineering, NCKU

Experimental Program – 2/2

Retrofitted specimen: 2-side 40 mm-thick sprayed UHPC
UHPC layer and foundation/beam: dowel bars
UHPC layer and masonry: screw anchors

U-MIF

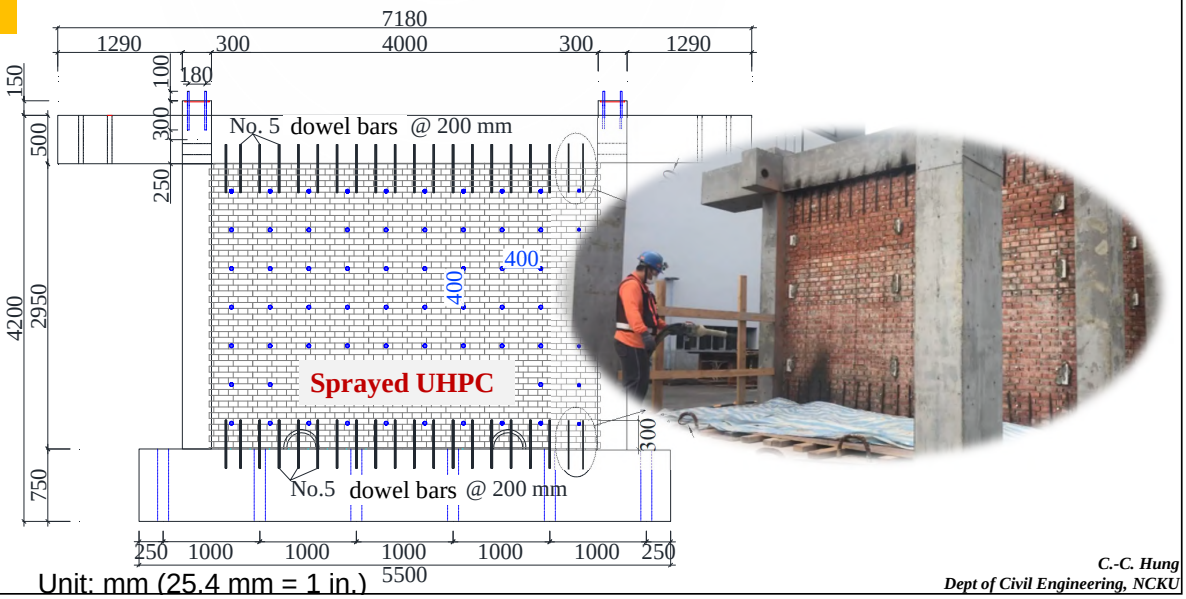

Unit: mm (25.4 mm = 1 in.)

C.-C. Hung
Dept of Civil Engineering, NCKU

Test Setup and Loading Protocol

- Tainan Laboratory of the National Center for Research on Earthquake Engineering
- Double-curvature structural deformation
- Constant 10% axial load ratio

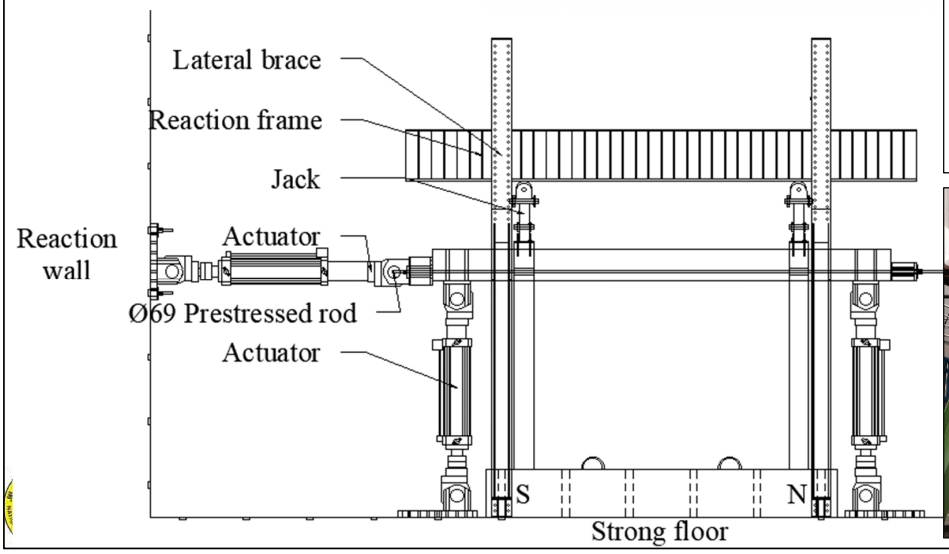

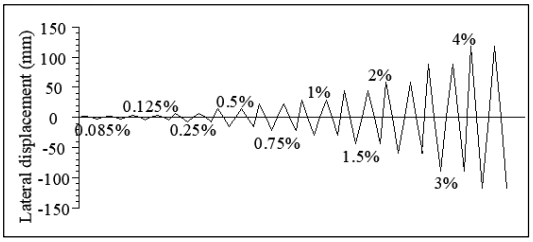

C.-C. Hung
Dept of Civil Engineering, NCKU

Test results - Cyclic behavior and failure mode

Frame

- **flexural-shear failure**

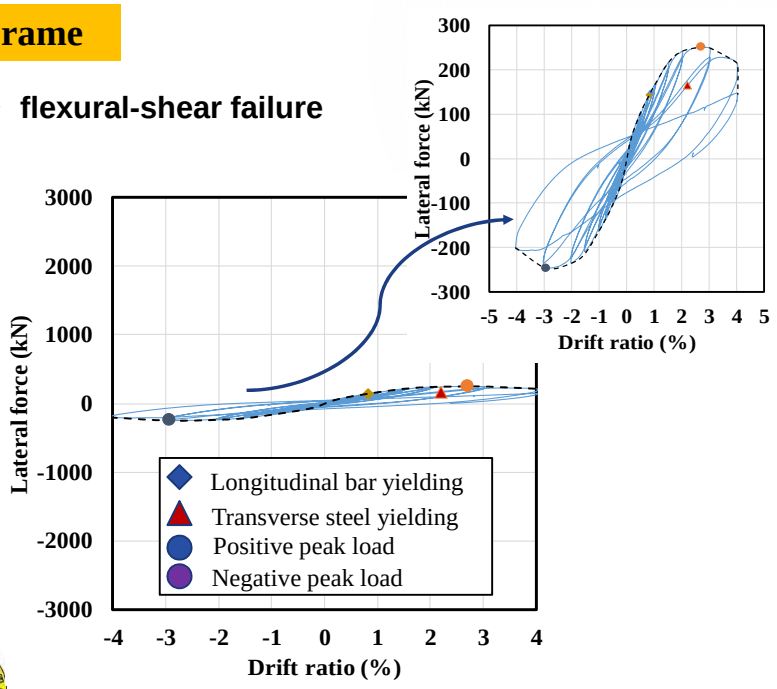

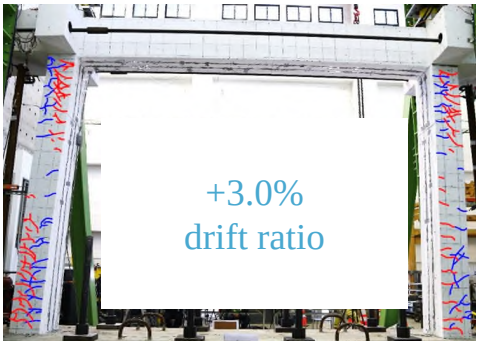

C.-C. Hung
Dept of Civil Engineering, NCKU

Test results - Cyclic behavior and failure mode

MIF

- Diagonal tension failure in the masonry wall
- Significant shear cracking at column ends

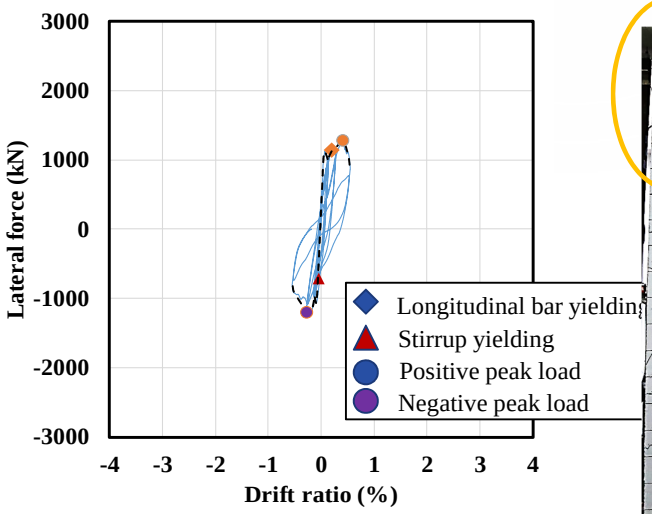

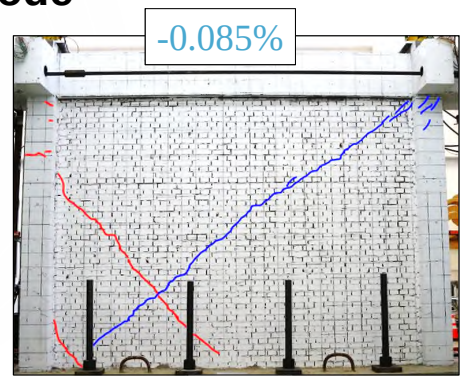

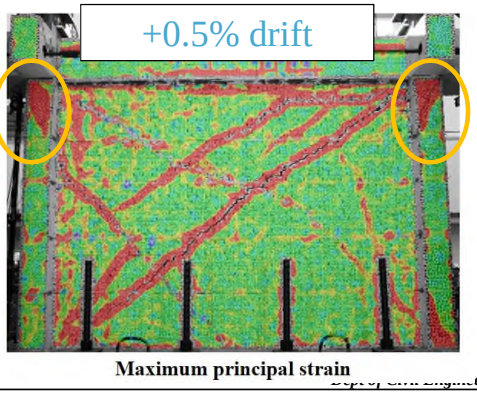

Test results - Cyclic behavior and failure mode

U-MIF

- Wall-beam interface damage
- Localized shear cracks at column ends
- No visible damage in the UHPC layer

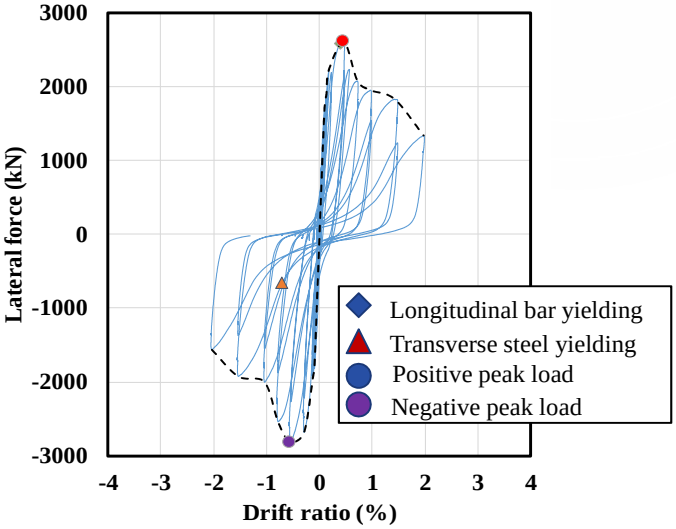

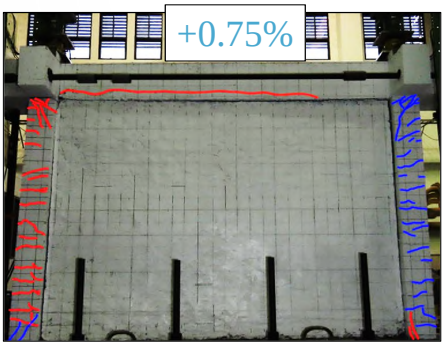

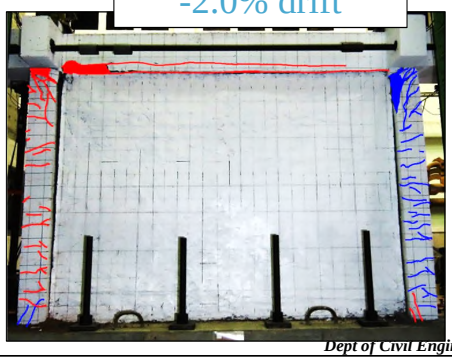

C.-C. Hung
Dept of Civil Engineering, NCKU

Strength Envelopes

- The inclusion of masonry increased the structural strength by 400%.
- Sprayed UHPC increased the strength (by 120%) and ultimate drift capacity.

RC frame

Masonry-infilled frame

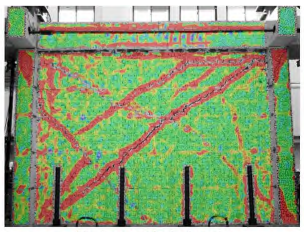

Maximum principal strain

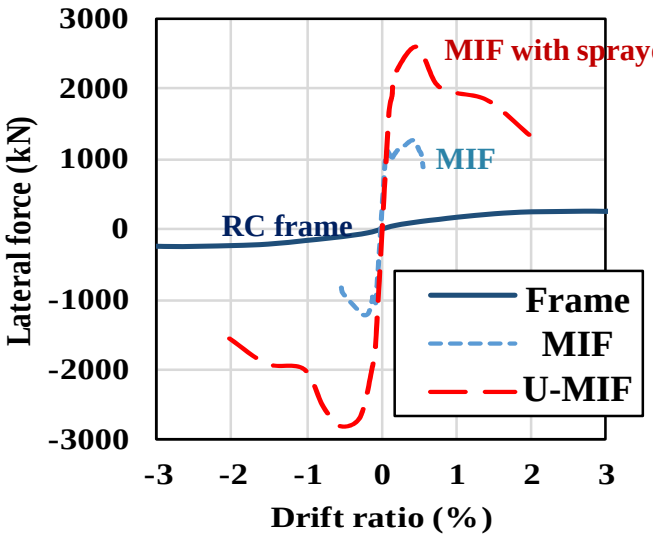

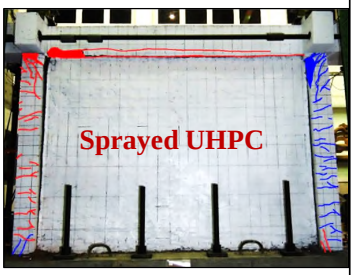

C.-C. Hung
Dept of Civil Engineering, NCKU

Stiffness degradation

- Inclusion of masonry wall greatly increased the initial stiffness of the RC frame by about 43 times. However, the stiffness degraded rapidly and diminished at 0.5% drift ratio.
- The UHPC shotcrete only increased the initial stiffness of MIF by 17%.

$$K = (P^+ + P^-)/(\delta^+ + \delta^-)$$

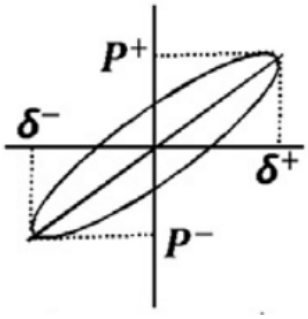

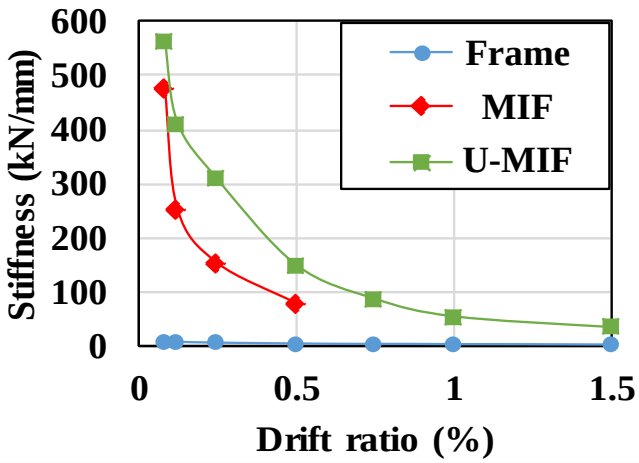

Hung
NCKU

Development of Computational Models for MIFs with Sprayed UHPC

- OpenSees: The Open System for Earthquake Engineering Simulation

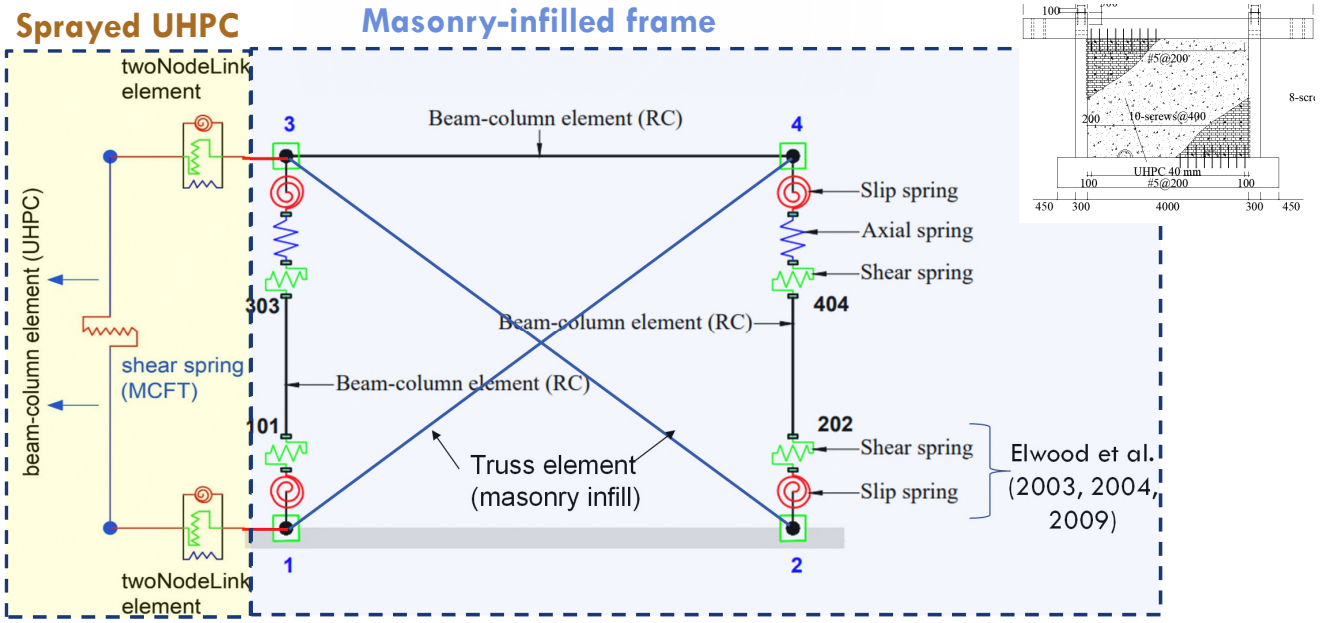

- Elwood, K.; Moehle, J., Shake table tests and analytical studies on the gravity load collapse of reinforced concrete frames, PEER Report 2003/01. *University of California, Berkeley* 2003.
- Elwood, K. J., Modelling failures in existing reinforced concrete columns. *Canadian Journal of Civil Engineering* 2004, *31* (5), 846-859.
- Elwood, K. J.; Eberhard, M. O., Effective stiffness of reinforced concrete columns. *ACI Structural Journal* 2009, *106* (4), 476.

C.-C. Hung
Dept of Civil Engineering, NCKU

Analytical Models: OpenSees

- Strut in Masonry Wall: Decanini and Fantin (1986)

$$b_m = \left(\frac{K_1}{\lambda_h} + K_2\right) d \qquad \lambda_h = \sqrt{\frac{E_m t_m \sin(2\theta)}{4 E_c I h_m}}\, h$$

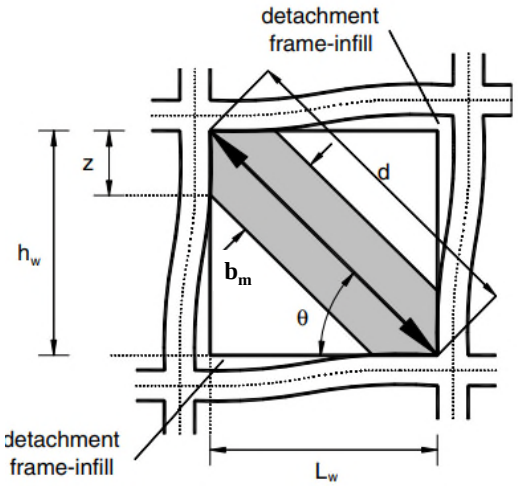

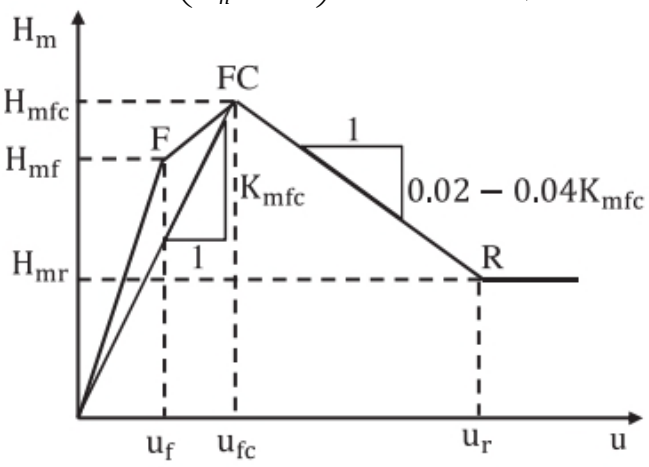

Decanini, L.; Fantin, G. (1986), "Modelos simplificados de la mampostería incluida en porticos". *Caracteristicas de stiffnessy resistencia lateral en estado limite. Jornadas Argentinas de Ingeniería Estructural*, Vol 2, 817-836. (in Spanish)

C.-C. Hung
Dept of Civil Engineering, NCKU

Analytical Models: OpenSees

➢ UHPC layer: flexural, shear, and axial responses

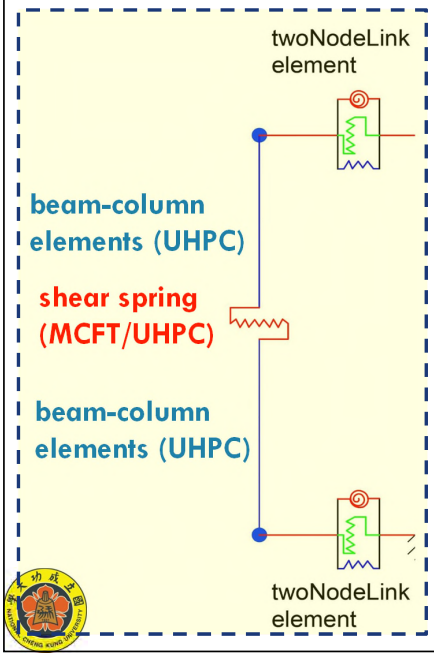

➢ **Uniaxial constitutive laws for UHPC**

Hung & El-Tawil (2009)

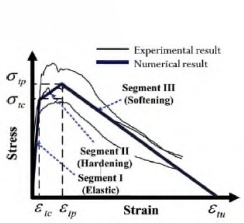

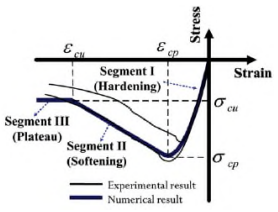

➢ **Compression-softening effect for UHPC**

Fukuyama et al. (2003)

$$f_{c2} = f_{c2max}\left[2\left(\frac{\varepsilon_2}{\varepsilon_c'}\right) - \left(\frac{\varepsilon_2}{\varepsilon_c'}\right)^2\right]$$

$$= \beta_f \cdot f_c'\left[2\left(\frac{\varepsilon_2}{\varepsilon_{c'}}\right) - \left(\frac{\varepsilon_2}{\varepsilon_{c'}}\right)^2\right]$$

$$\beta_f = \frac{1.0}{0.68 + 0.45 \cdot \left(\frac{\varepsilon_1}{\varepsilon_c'} + 0.13\right)^{0.36}}$$

➢ **Shear resistance on the crack surface for UHPC**

Cho and Kim (2009)

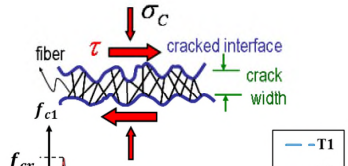

➢ **Tension stiffening of UHPC**

Hung et al. (2019)

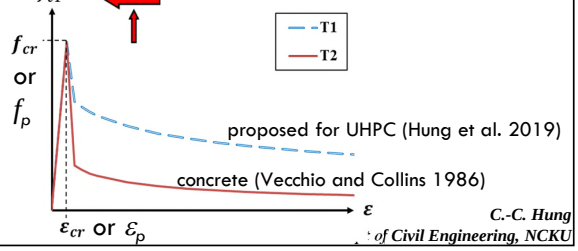

C.-C. Hung
Dept of Civil Engineering, NCKU

Comparisons of Experimental and Modeling Results

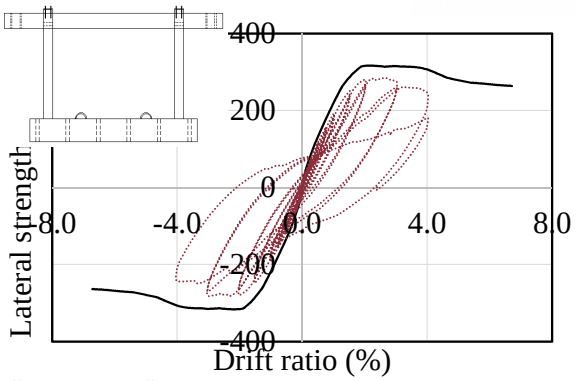

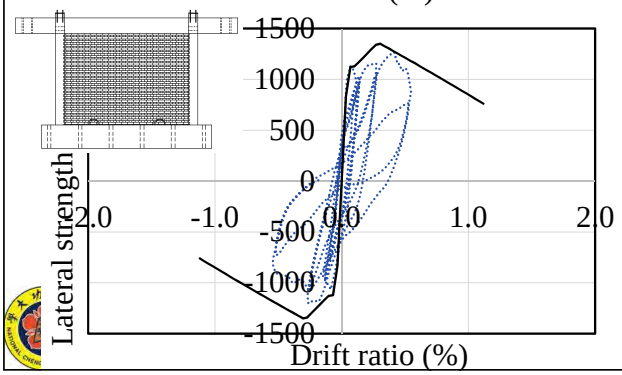

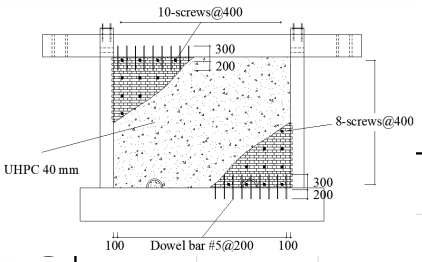

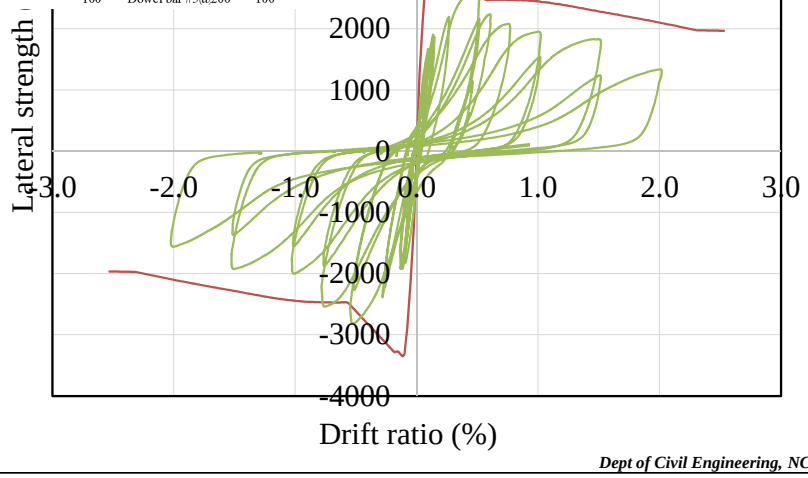

ng
Dept of Civil Engineering, NCKU

Conclusions

- The presence of masonry wall significantly increased the RC frame's strength by 5 times and stiffness by 40 times.
- While the sprayed UHPC considerably enhanced the masonry-infilled frame's strength and drift capacity, it only slightly increased the stiffness by 17%.
- Application of sprayed UHPC prevented diagonal cracks in the masonry wall and structural collapse.
- The strength degradation of U-MIF was controlled by the shear failure of RC columns and detachment of the UHPC layer and the original frame.
- While the developed OpenSees model reasonably captured the strength envelopes of the test specimens, it overestimated the initial stiffness of RF.

C.-C. Hung
Dept of Civil Engineering, NCKU

APPLICATION OF SPRAYED UHPC FOR MIFS IN TAIWAN

- Sprayed UHPC

- Trowel finish UHPC surface

C.-C. Hung
Dept of Civil Engineering, NCKU

THANK YOU

Chung-Chan Hung

cchung@ncku.edu.tw

Prof. Jin-Hung Hwang

National Central University, Taiwan

Topic： Soil Liquefaction: A Natural Fuse for Earthquake-resistant System- Observations and Interpretations of the Failure Mechanism of Bridge Piers during the 2022/09/18 Chihshang Earthquake

8th Asia Conference on Earthquake Engineering
Taipei, Taiwan ■ November 9-11, 2022

SOIL LIQUEFACTION-A NATURAL FUSE FOR BRIDGE SEISMIC SYSTEM :

OBSERVATIONS ON THE FAILURE MODES OF BRIDGE PIERS DURING THE 2022/09/18 CHIHSHANG ML6.8 EARTHQUAKE

Jin-Hung Hwang[1] , Yu-Wei Hwang[2], and Chih-Chieh Lu[3]

Prof., Dept. of Civil Engineering, National Central University, Taoyuan, Taiwan, R.O.C.

Assistant Prof., Dept. of Civil Engineering, National Yaming Chiaotung University, Taoyuan, Taiwan, R.O.C.

Researcher, National Center for Research on Earthquake Engineering, Taipei, Taiwan, R.O.C.

Outline

- Background of Earthquake Event
- Failure Modes of the Gaoliao Bridge
- Seismic Response of the New Xiuguluanxi Railway Bridge
- Conclusions and Suggestion

Background of Earthquake Event

- 2022/09/18 M_L6.8 Chihshang Earthquake
- Relevant Fault System
- Ground Ruptures
- Strong Ground Motions
- Building Damages
- Bridge Damages

2022/09/18 M_L6.8 Chihshang Earthquake

- Focal depth=7km
- The relevant fault system

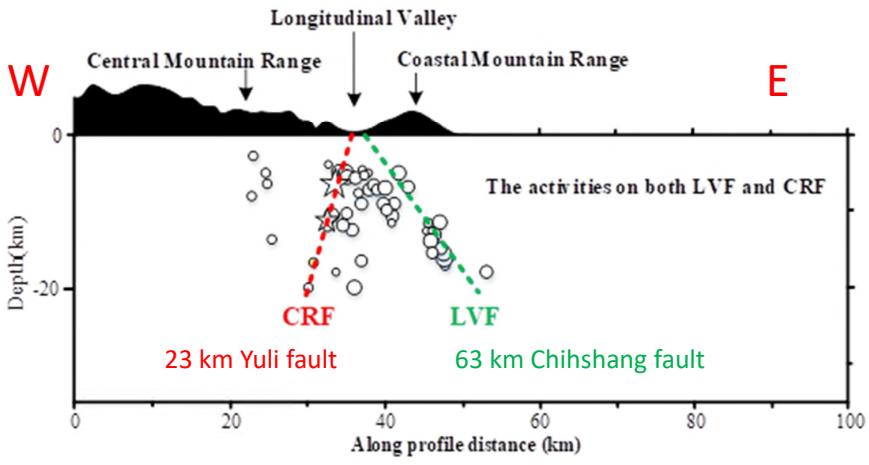

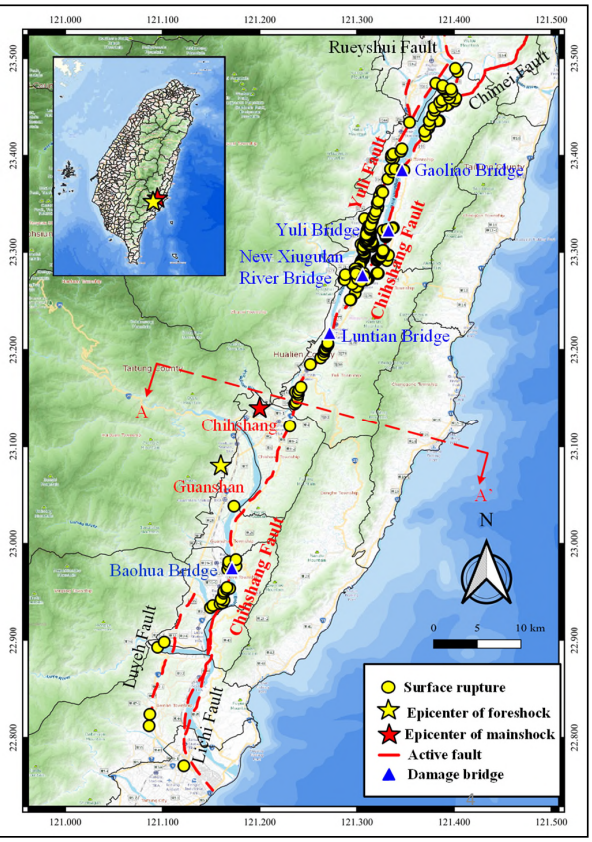

Ground Ruptures

- Central Range Fault
  - Yuli Fault (Segment)
  - Thrust left-lateral strike-slip fault
  - Dipping to the west
  - Dip angle about 56 °～69°
- Longitudinal Valley Fault
  - Chichshang Fault (Segament)
  - Left-lateral strike-slip thrust fault
  - dipping to the east
  - Dip angle about 50 °～63°

(a) Horizontal offset in watermelon field

(b) Vertical offset in watermelon field

(a) vertical offset at courtyard of farmhouse

(b) vertical offset at Dongli Middle School

Strong Ground Motions

- peak horizontal accelerations of the longitudinal valley from Chishang town to the northern end of Yuli are about 0.3-0.5g
- peak vertical accelerations are about 0.25-0.45g
- peak velocities near the epicenter and the northern end of Yuli can reach 103 cm/sec (HWA004) and 89 cm/sec (HWA054)

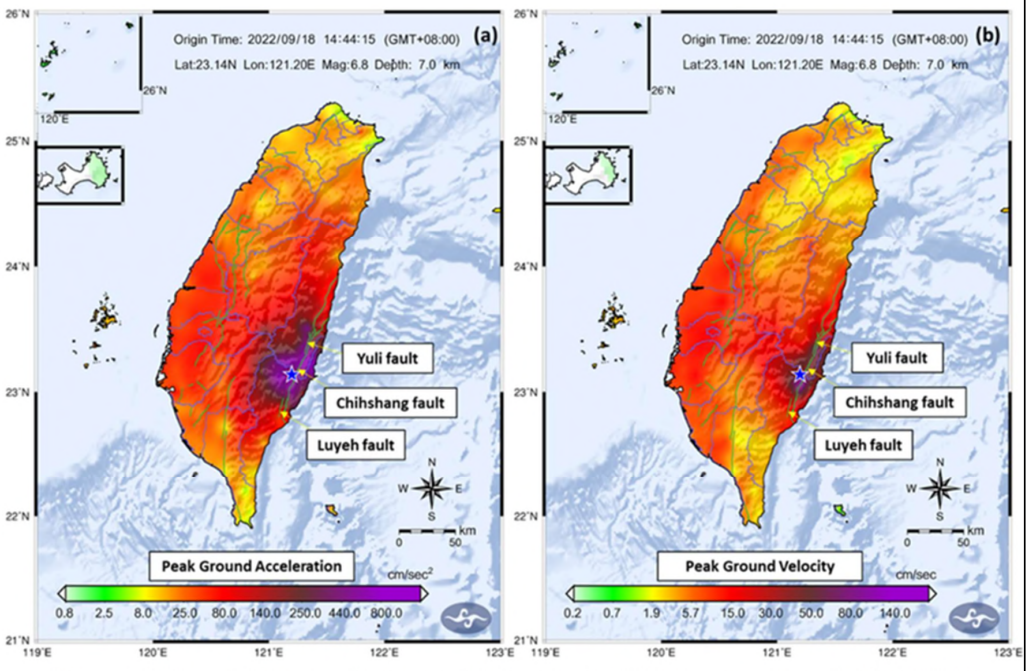

Figure 2 PGA and PGV intensity maps of Taiwan in the Chihshang earthquake(CWB,2022)

Building Damages

■Only two 3-story modern RC buildings completely collapsed

Collapse of a 7-11 superstore

(a) before earthquake

(b) collapsed after earthquake

7

Building Damages

Collapse of a religious building

(a) Panorama of the collapsed building

(b) The floor was penetrated by columns

8

Bridge Damages

- Gaoliao Bridge (completely collapsed)
- Luntian Bridge (almost completely collapsed)
- New Xiuguluanxi Railway Bridge (severe displacement of girders)
- Baohua Bridge (moderate damaged)

Basic Data of the Gaoliao Bridge

- Basic data
  - completed in June, 1991
  - a two-lane road bridge
  - width of bridge deck is 7.6m
  - a total length of 879.1 m
  - 22 spans, span length≒40m
  - 21 piers and 2 abutments
  - Three pre-stressed I-Girders
  - Rubber bearing pad
  - T-type bridge pier
  - Foundation type is unknown

Fig. 3 Superstructure system of the Gaoliao bridge

Failure conditions of the Gaoliao Bridge

- 20 of the 21 piers were knocked down by strong motions to the north direction (downstream side)
- Among the 20 piers, only the EP2 and EP4 (pier numbers are counted from the east) seriously tilted and settled without any visible damage and crack on the surfaces of the piers

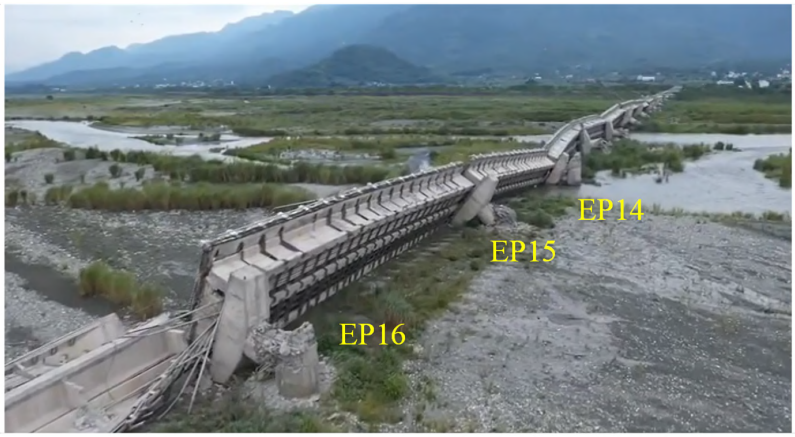

Failure Modes of the Gaoliao Bridge

- Flexural failure mode
  - EP12, EP13, EP15, EP16, EP17, EP18, EP19, EP20
- Flexural Shear failure mode
  - EP3, EP5, EP6, EP7, EP8, EP9, EP10
- Shear failure mode
  - EP14
- Foundation failure mode
  - EP2, EP4
- No failure
  - EP1

Flexural failure mode

- The pier failure is due to the main rebars were pulled off owing to insufficient rebar size and spacing of stirrup, and improper position of rebar lap splices in the middle or the bottom parts of the pier.

13

Flexural Shear failure mode

- The pier failure is due to the combined action of bending moment, axial and shear forces owing to insufficient rebar size and spacing of stirrup, and improper position of rebar lap splices in the middle part of the pier.

14

Shear failure mode

- The pier failure is owing to the combined action of large axial and shear forces without enough stirrup confinement

Foundation failure mode

- The piers seriously tilted and settled owing to insufficient bearing capacity of bridge foundation. It is speculated that this mode is caused by liquefaction of foundation soil.

Inclination
of
EP2 and EP4

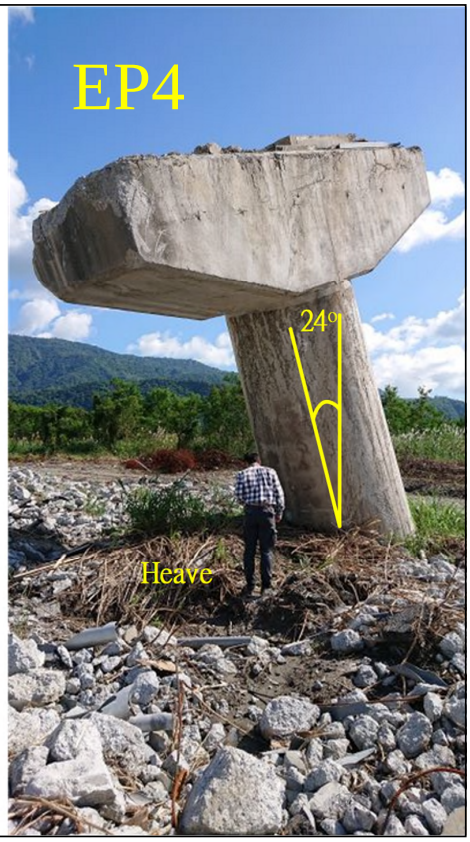

Soil liquefaction around EP2

(a) Gap with erupted sediment (b) Mud with underlying sand (c) Ejecta sand

Fig. 6 Traces of soil liquefaction around the EP2 pier

18

Soil liquefaction around EP4

(a) Gap between pier and ground (b) A sand volcano

Fig. 8 Traces of soil liquefaction around the EP4 pier

Grain Size Distribution Curves of the Liquefied Soils around EP2 and EP4

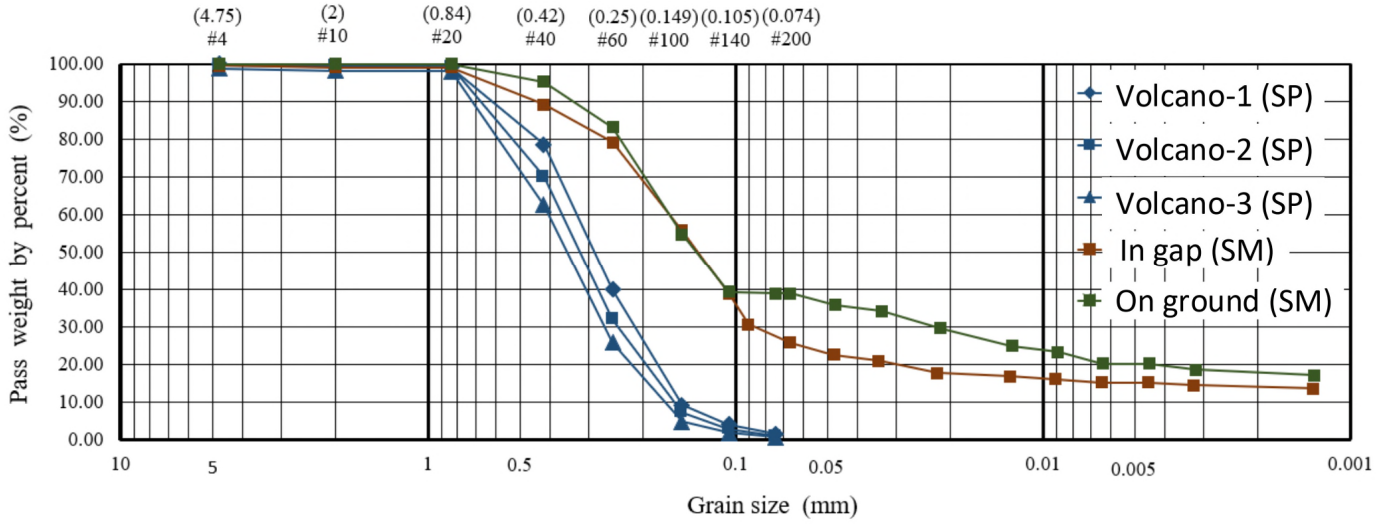

Basic Data of the New Xiuguluanxi Railway Bridge

- An electrified double track railway bridge
- A total length of 640 m (16 spans, span length=40m)
- The width of bridge deck is about 10.9m
- 15 piers and 2 abutments
- Four pre-stressed I-girders
- Rubber bearing pad
- T-type bridge pier
- 4×4 piled group foundation
- All casing pile with D=1.2m and L=15m

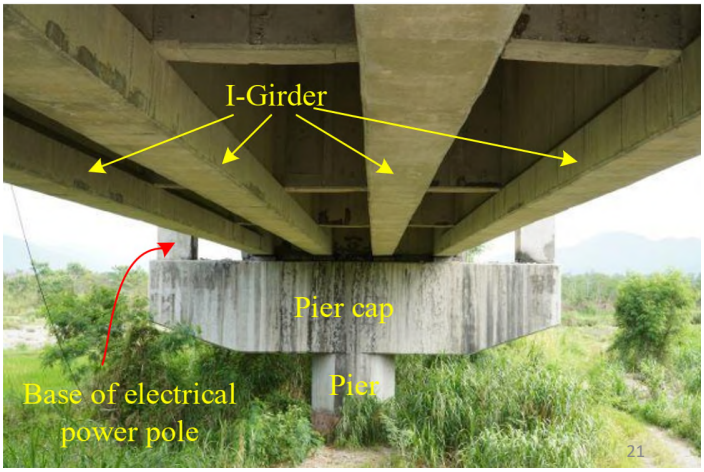

Seismic response of the southern section of the New Xiuguluanxi Railway Bridge

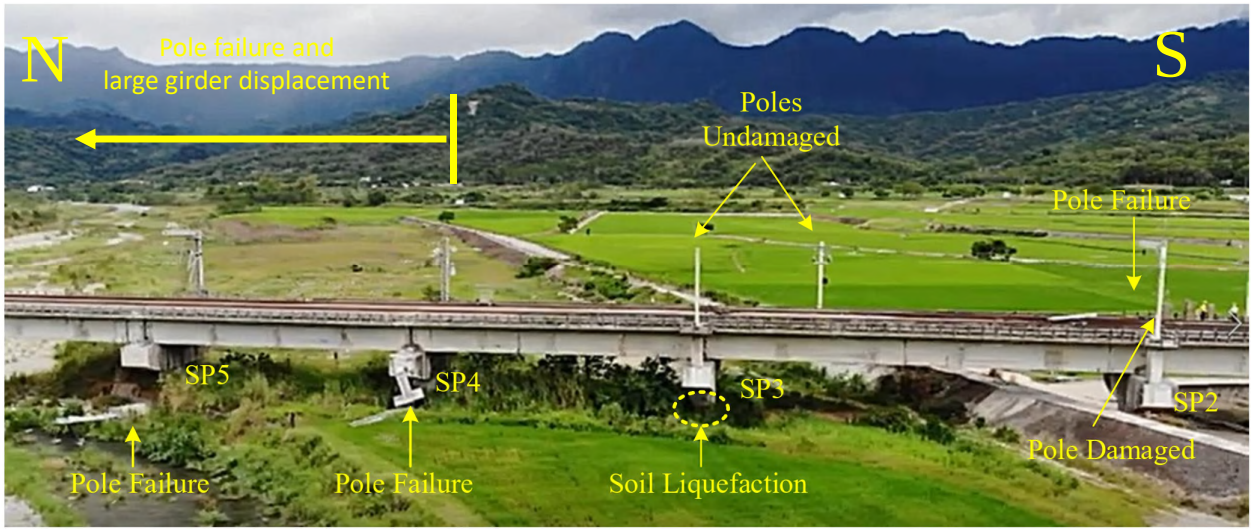

22

Seismic response of the southern section of the New Xiuguluanxi Railway Bridge

- Some girders displaced 20～100 cm
- Many electricity poles were damaged and some of them fell down to the river bed
- Only the electricity poles on the SP3 pier are undamaged
- In the same time, significant soil liquefaction was found around SP3 pier only

Damages of the New Xiuguluanxi Railway Bridge

Fig. 12 No permanent girder displacement at SP3

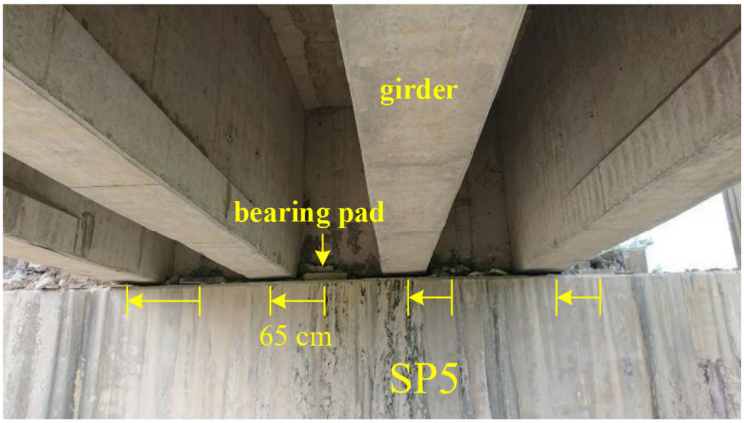

Fig. 13 Large permanent girder displacement at SP5

Soil Liquefaction around SP3

(a) east side of SP3 (b) west side of SP3 (c) plastic soils at gap bottom

Fig. 14 Traces of soil liquefaction at SP3

25

Grain Size Distribution Curves of the Liquefied Soils around SP3

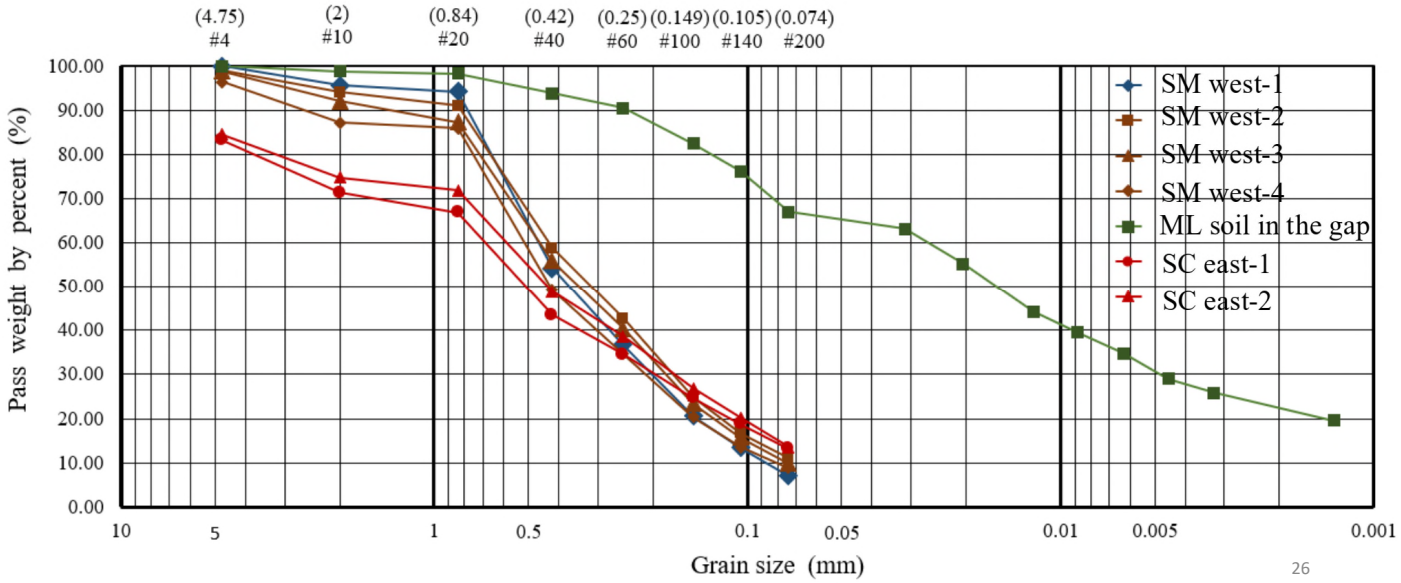

26

Conclusions and suggestion

- During the 2022/09/18 Chihshang earthquake, 20 of the 21 piers of the Gaoliao Bridge were knocked down by strong ground motions. Among the 20 piers, only 2 piers seriously tilted and settled without suffering any visible damage. In particular, soil liquefaction was observed around these 2 piers.
- A similar phenomenon seems to be found in the New Xiuguluanxi Railway Bridge.
- The preliminary interpretation is that the liquefaction of the foundation soil has a seismic isolation effect on the superstructure, thus causing such a different failure mode of the bridge piers.

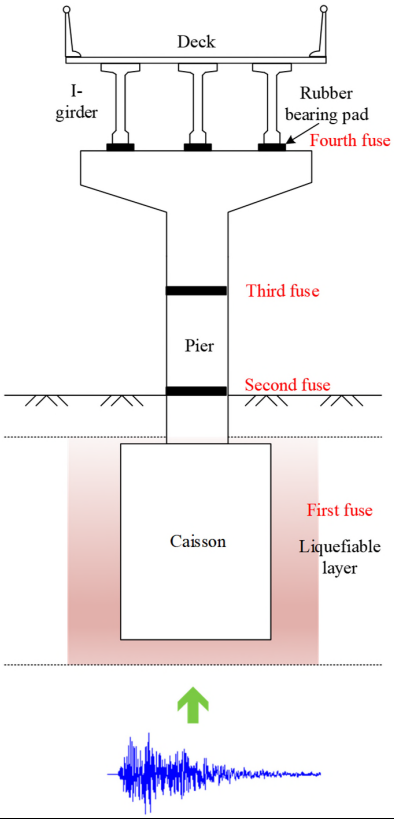

Soil Liquefaction-A Natural Fuse

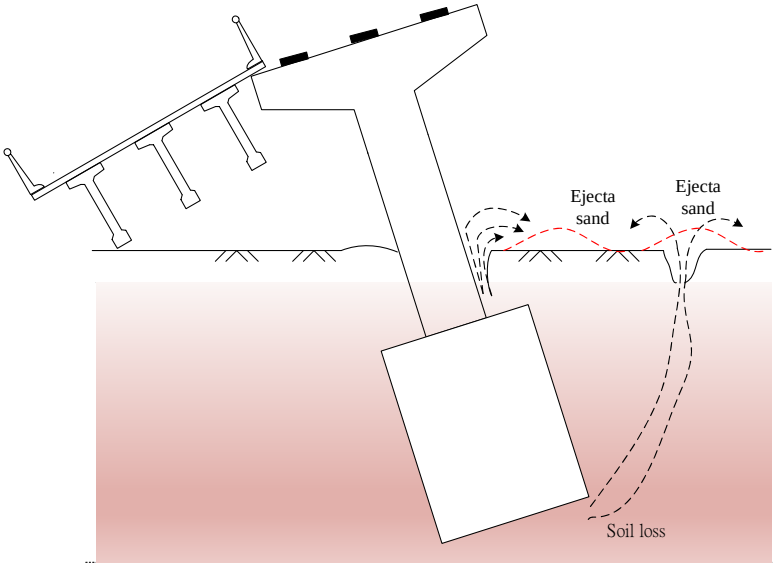

Conclusions and suggestion

- These field observations suggest that soil liquefaction could be a natural fuse for the bridge seismic system. If foundation soil liquefies first, the substructure can avoid severe structural damage and can be re-used in the restoration work after earthquake.
- This observation and interpretation need further investigation and research to verify. It is strongly suggested that drilling and pit excavation are required to clarify the foundation type and size, and the depth and extent of soil liquefaction, and the possible failure mechanisms.

Prof. Wen-Cheng Liao

National Taiwan University, Taiwan

Topic：Shear Behavior of High Strength Steel Fiber Reinforced Columns under Different Axial Loading Levels

SHEAR BEHAVIOR OF HIGH STRENGTH STEEL FIBER REINFORCED COLUMNS UNDER DIFFERENT AXIAL LOADING LEVELS

Wen-Cheng Liao[1] and Wisena Perceka[2]
1. Professor, Department of Civil Engineering, National Taiwan University, Taipei, Taiwan, R.O.C.
2. Assistant Professor, Department of Civil Engineering, Parahyangan Catholic University, Bandung, Indonesia
Email: wcliao@ntu.edu.tw, wperceka@unpar.ac.id

ABSTRACT

High strength concrete exhibits brittle failure after reaching the ultimate strength. Traditionally, the seismic behavior of reinforced concrete columns is improved by increasing transverse reinforcement; however, excessively dense stirrup always leads to construction difficulty. This study evaluates the replacement of shear reinforcement with steel fibers. The shear behavior of high strength steel fiber reinforced columns under different axial levels is studied. In addition, the shear strength and the shear design formula of high-strength steel fiber reinforced concrete columns are also proposed.

Keywords: axial loading, fiber reinforced concrete, high strength concrete, high strength steel, shear strength

INTRODUCTION

By knowing that concrete is brittle material, the transverse reinforcement in accordance with every requirement of ACI 318-14 or newer (ACI, 2014; 2019) is needed to prevent the brittleness of an RC column; therefore, the column can dissipate seismic energy through flexural mechanism. According to studies conducted by Elwood et al. (2009), more transverse reinforcement is required as axial loading level increases. However, for column with small cross-section size, the high amount of transverse reinforcement may lead to construction difficulties. One of methods that can be used to keep not using large cross-section size of the RC column without losing the strength is by using high strength concrete and steel reinforcing bars. Therefore, the demand for high strength steel reinforcing bars increases, since by reducing the amount of reinforcing bars can reduce the reinforcing bars congestion, particularly the amount of shear reinforcing bars in plastic hinge region (Ou and Kurniawan, 2015a; Liao et al, 2017a)
It is worth mentioning that the mechanical behavior of high strength concrete and steel reinforcing bars is different from that of normal strength materials. The experimental and analytical studies of high strength concrete and steel reinforcing bars, therefore, are still being performed. One of countries that started research works on the use of high strength concrete and steel reinforcement was Japan in 1995, where the project was named as New RC project. In 2008, Taiwan New RC project was begun. In Taiwan New RC project, the minimum concrete compressive strength, yield stress of deformed reinforcement for longitudinal reinforcement, and yield stress of deformed reinforcement for transverse reinforcement, respectively, were 70 MPa, 685 MPa (SD685), and 785 MPa (SD785) (Lee and Chen, 2014). Currently, with advancements in material production technology in Taiwan, the high strength concrete can be supplied by many ready mix companies in Taiwan and the high strength steel reinforcing bars are commercially available.
On the other hand, it well known that concrete turns more brittle as its strength increases. Moreover, the presence of high axial compression load increases the brittleness of high strength concrete (Ou and Kurniawan, 2015b). Theoretically, the high strength transverse reinforcement can be provided such that the brittle behavior can be avoided. However, there is condition where column with larger cross-section size is still required, like in the 20-storey building or higher. In the high-rise building, without increasing size of column, there is possibility of occurrence of reinforcement congestion. Furthermore, ACI 318 code attempts to defender against extreme widths of crack by limiting the maximum shear strength provided by transverse reinforcement. In order to get strength and ductility, an alternative material can

be proposed; therefore, the RC column with moderate or even minimum transverse reinforcement can still achieve targeted strength and ductility.
Several research studies showed that adding short and discontinuous steel fibers to concrete material could improve its post-peak behavior and toughness (Naim and Naaman, 1991; Hsu and Hsu, 1994; Mansur et al., 1999; Liao et al., 2015; Perceka et al., 2019). Steel fibers provide bridging action across microcracks in the matrix and improve resistance to crack opening owing to the existence of the bond strength between steel fibers and matrix (Parra, 2005; Liao et al., 2006; Thomas and Ramaswamy, 2007). Additionally, the use of steel fibers in concrete improved shear and bending resistance of reinforced concrete members, and led to improvement in the bond of reinforcing bars under monotonic and cyclic loading. Thus, these advantages enticed researchers to apply steel fiber in earthquake resistant reinforced concrete members. Therefore, a comprehensive experimental study of shear behavior of high strength SFRC column with high strength reinforcement under lateral cyclic and different axial compression ratios shall be performed. Through the shear tests, the shear strength and behavior of SFRC columns with high strength material and different axial compression ratios can be clearly observed.

EXPERIMENTAL PROGRAM

In order to provide a comprehensive understanding of the overall shear behavior of SFRC columns with high strength concrete and steel reinforcement, an experimental study of shear behavior of high strength SFRC columns with high strength reinforcement subjected to lateral cyclic and different axial compression ratios was performed. Large scale SFRC columns made of high-strength concrete with a compressive strength of 70 MPa, and high-strength steel reinforcement with yield stresses of 685 MPa and 785 MPa, respectively, for longitudinal and transverse reinforcement were tested. Data presented here are considered unique in the sense that they provide main information on the effect of fiber volume fraction and axial compression load on the shear behavior of large scale SFRC columns.

Materials

The cementitious materials used in this study were ASTM Type I Portland Cement, ground granulated blast furnace slag, and silica fume. The coarse aggregate had a maximum size of 9.50 mm and consisted of solid crushed limestone from a local source, with a density of approximately 2.70 g/cm^3. Superplasticizer was also used in the mixture. Hooked-end steel fiber with a circular cross-section, tensile strength of 2300 MPa, and aspect ratio of 79 was used. At least three cylinders corresponding to each specimen were tested in the day with the corresponding column specimen. In addition, three samples of steel reinforcing bar from each used diameter were tested before the specimens constructed in order to obtain the actual mechanical properties.

Detail of column specimens

Eight large scale double curvatures high-strength SFRC columns were prepared. Every column had a square cross-section of 600 mm x 600 mm and clear height of 1800 mm. A rigid concrete block at each column end was constructed as well. The top rigid concrete block had length, depth, width of 1900 mm, 900 mm, and 850 mm, respectively, while the bottom rigid concrete block had length, depth, and width of 2000 mm, 1000 mm, and 850 mm, respectively. These rigid concrete blocks simulated rigid floor system or rigid foundation at the bottom of column in ground floor in a high-rise building. The specimen geometries referred to specimens designed and tested by Ou and Kurniawan (2015a, 2015b). The main parts (columns) were made of high strength SFRC with concrete compressive stress of 70 MPa, while both rigid concrete blocks were constructed using normal concrete with compressive stress of 40 MPa.
High strength deformed longitudinal reinforcing bar with diameter of 32 mm (D32) with specified yield strength of 685 MPa (SD685) were selected and placed uniformly around the perimeter of the column cross section. Every longitudinal reinforcing bar were continuous without lap slices. In addition, high strength deformed reinforcing bar with diameter of 13 mm (D13) with specified yield strength of 785 MPa (SD785) were used for the transverse reinforcement.
The column design details are shown in Table 1 and Figure 1. The configuration of longitudinal and transverse reinforcement was selected and exercised such that the failure mode of column was shear

prior to flexural. The shear strength prediction equations for an SFRC beam proposed by Perceka et al. (2019) was adopted to design column specimens. Two values of fiber volume fraction of 0.75% and 1.50% were used. As seen in Table 1, the notations of the column are as follows: "S" denotes specimens; the numbers following the capital "S", namely number 1 to 8 denote the specimen number; two numbers "500" and "540" denote the ties spacing; "0.75" and "1.50" denote fiber volume fraction of 0.75% and 1.5%, respectively, and the numbers "0.1", "0.2", "0.3", and "0.4" denote axial load ratio ($P/A_g f_c'$).

Table 1. Specimen design

ID	$b_c = h_c$ (mm)	Concrete strength	Longitudinal reinforcement bar		Transverse reinforcement bar		Steel fibers		Axial load ratio (%)
		f'_c (MPa)	$f_{yl,spec}$ (MPa)	ρ_l (%)	$f_{yt,spec}$ (MPa)	ρ_w (%)	$\alpha_f = L_f/D_f$	V_f (%)	
S1-500-0.75-0.10	600	70	685	4.52 (20D 32)	785	0.10 (D13-500)	79	0.75	10
S2-500-0.75-0.20									20
S3-500-0.75-0.30									30
S4-500-0.75-0.40									40
S5-540-1.50-0.10						0.09 (D13-540)		1.50	10
S6-540-1.50-0.20									20
S7-540-1.50-0.30									30
S8-540-1.50-0.40									40

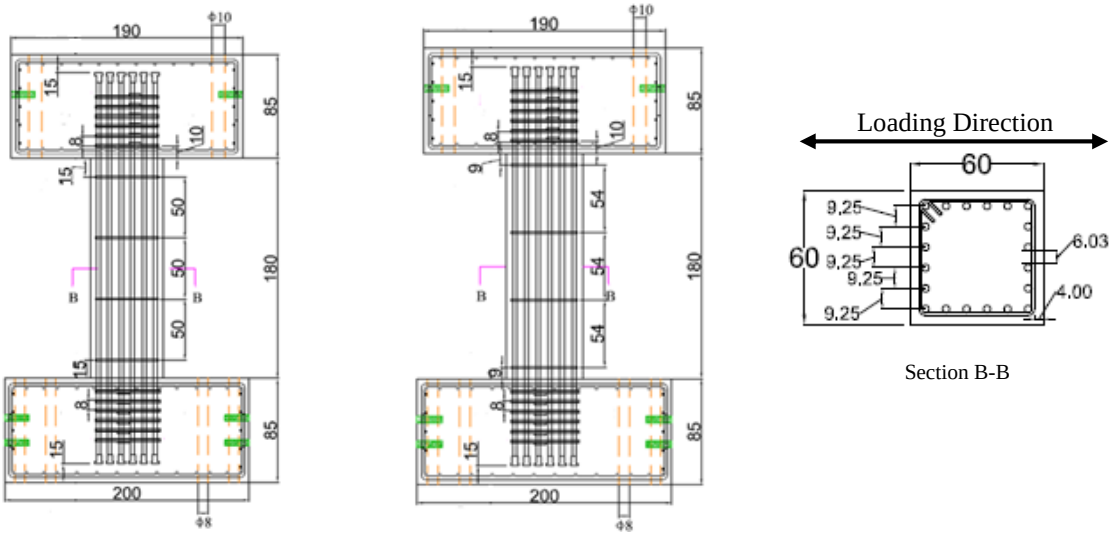

(a) (b) (c)

Unit: cm

Figure 1. Specimen elevation: (a) Specimens S1-500-0.75-0.1, S2-500-0.75-0.2, S3-500-0.75-0.3, S4-500-0.75-0.4; (b) Specimens S5-540-1.50-0.1, S6-540-1.50-0.2, S7-540-1.50-0.3, S8-540-1.50-0.4; (c) Specimen cross-section

EXPERIMENTAL RESULTS

Force-displacement relationships

The P-Δ effect due to lateral movements of applied axial load is expected significant. The correction is required accordingly. Correction methodology is done by Liao et al. (2017b). Once the P-delta effect has been corrected, a complete cyclic force-drift relationship for each column specimen could be plotted correctly. The lateral force-drift and axial compression force-drift relationships of specimens with fiber volume fraction of 0.75% and those of specimens with fiber volume fraction of 1.50%, respectively, are shown in Figures 2 and 3. Important events during the test are also noted in those figures.

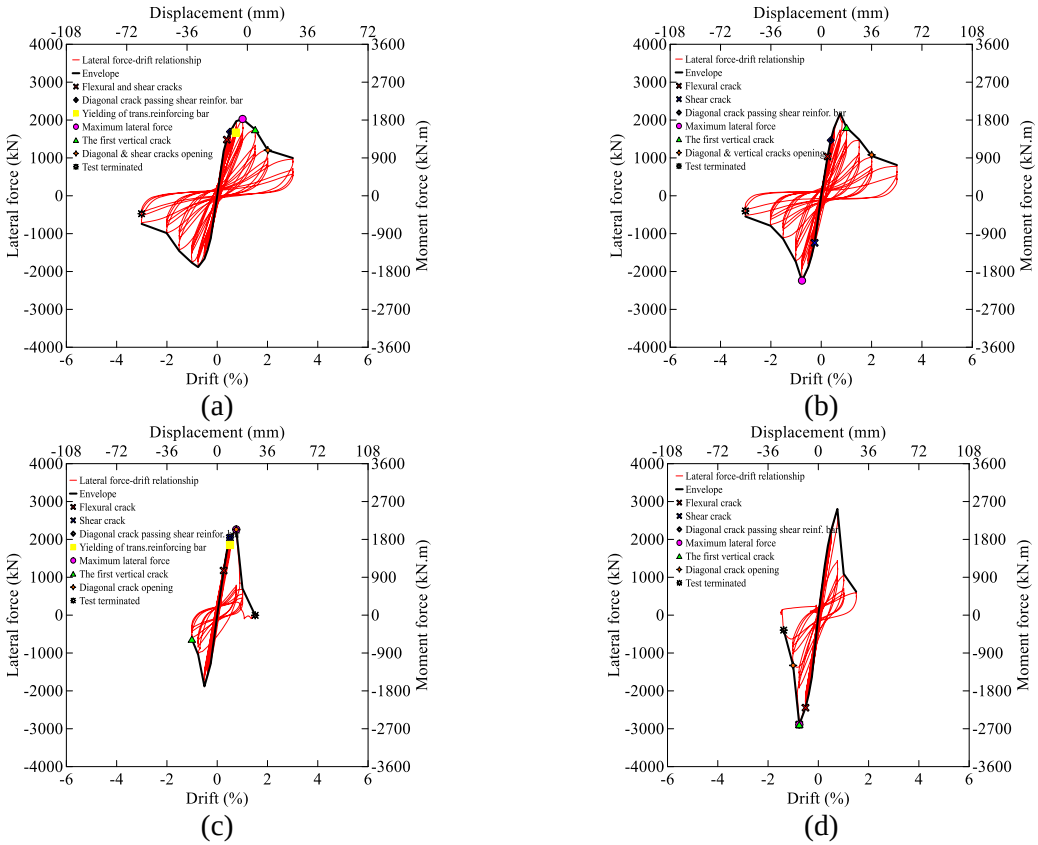

Figure 2. The lateral force-drift relationships of specimens with fiber volume fraction of 0.75%: (a) S1-500-0.75-0.1; (b) S2-500-0.75-0.2; (c) S3-500-0.75-0.3; (d) S4-500-0.75-0.4

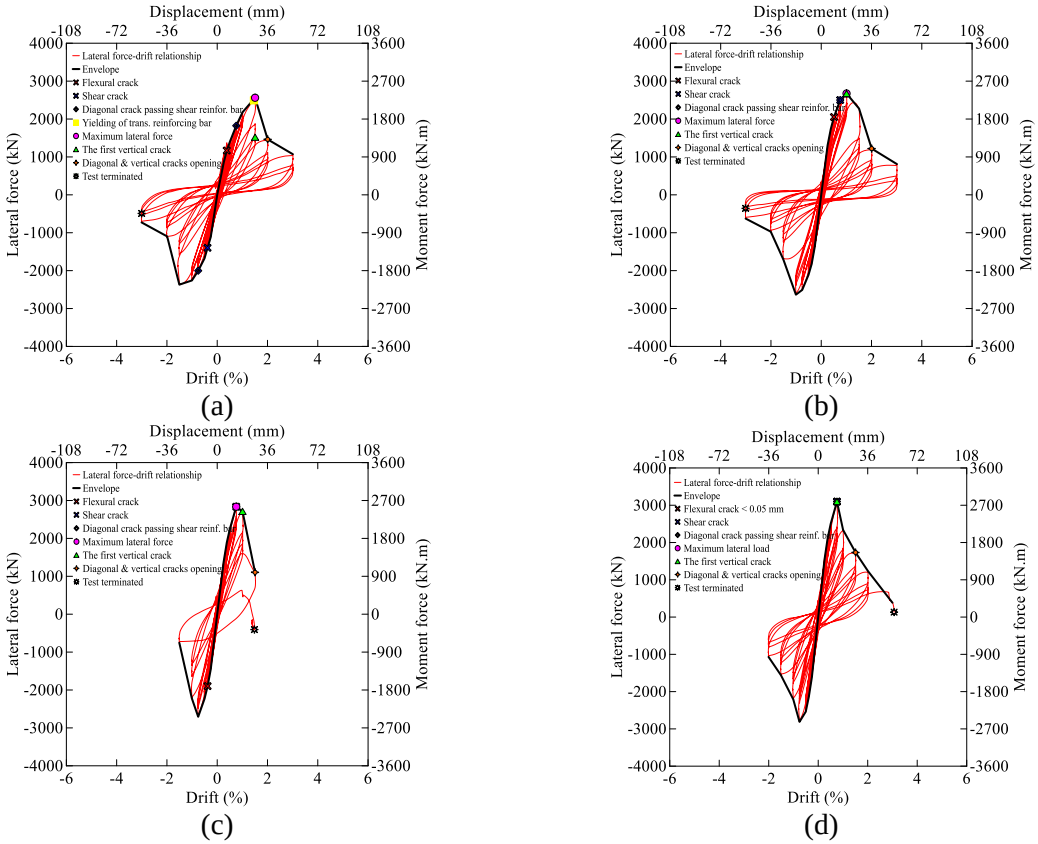

Figure 3. The lateral force-drift relationships of specimens with fiber volume fraction of 1.50%: (a) S5-540-1.50-0.1; (b) S6-540-1.50-0.2; (c) S7-540-1.50-0.3; (d) S8-540-1.50-0.4

For specimens with fiber volume fraction of 0.75%, the greatest lateral force was found in specimen S4-500-0.75-0.4 that was subjected to axial load ratio of 0.4. Both specimens S3-500-0.75-0.3 and S4-500-0.75-0.4 failed in shear followed by axial failure. The nominal drift ratio corresponding to peak applied lateral force of specimens S3-500-0.75-0.3 and S4-500-0.75-0.4 was similar to that of specimen S2-500-0.75-0.2, but smaller than that of specimen S1-500-0.75-0.1. Specimens S1-500-0.75-0.1 and S2-500-0.75-0.2 with axial load ratios of 0.1 and 0.2, respectively, failed in shear only, since their axial capacities remained unchanged up to the third cycle of -3% drift (negative direction), as shown in Figures 2a and 2b. According to Figures 2c and 2d, the axial capacity of S3-500-0.75-0.3 and S4-500-0.75-0.4 dropped significantly. The tests on S1-500-0.75-0.1 and S2-500-0.75-0.2 were terminated at the third cycle of drift of -3%. By contrast, S3-500-0.75-0.3 and S4-500-0.75-0.4 failed at drift of 1.5%. In addition, the buckling of longitudinal reinforcement and rupture of transverse reinforcement in specimens S3-500-0.75-0.3 and S4-500-0.75-0.4 were seen. Increasing axial load ratio from 0.1 to 0.2, 0.2 to 0.3, and 0.3 to 0.4 increased the peak lateral strength by 10.46%, 1.01%, and 27.73%, respectively. As observed from the results of specimens S3-500-0.75-0.3 and S4-500-0.75-0.4, high axial compression ratio turned the post-peak behavior to be more brittle. Unlike specimens under high axial compression ratio, the post-peak lateral strengths in specimens S1 and S2 were found to decrease gradually.

According to the test results of specimens with fiber volume fraction of 1.5%, the greatest lateral force was found specimen S8-540-1.5-0.4. Specimens S7-540-1.5.0.3 and S8-540-1.5-0.4 that were subjected to axial ratio of 0.3 and 0.4, respectively, failed in shear-axial failure, while specimens under low axial compression ratio (S5-540-1.5-0.1 and S6-540-1.5-0.2) failed in shear only. As axial load increased, the drift corresponding to peak applied lateral force decreased. This can be observed from the comparison between drift corresponding to peak applied lateral force of S5-540-1.5-0.1 and S6-540-1.5-0.2. Furthermore, the drift corresponding to applied peak lateral force of S7-540-1.5.0.3 and S8-540-1.5-0.4 were less than that of S5-540-1.5-0.1 and S6-540-1.5-0.2. According to the axial compression force-drift relationship shown in Figures 3a and 3b, the axial capacity of specimens S5 and S6 was constant up to the end of test that was terminated at the third cycle of drift of -3%. Specimen S7-540-1.5.0.3 lost the axial capacity suddenly at 1.5% drift. For specimen S8-540-1.5-0.4, it had sudden loss of axial capacity before finishing the first cycle of drift of 3%. Although the specimen S8-540-1.5-0.4 failed at drift of almost 3%, the measured post-peak applied lateral strengths dropped significantly as drift increased. By contrast, the post-peak lateral force of S5-540-1.5-0.1 and S6-540-1.5-0.2 decreased gradually as drift increased. Compared to specimens S5-540-1.5-0.1 and S6-540-1.5-0.2, the post peak behavior of S7-540-1.5.0.3 and S8-540-1.5-0.4 was more brittle once drift increased larger than drift corresponding to peak applied lateral strength. Increasing axial load ratio from 0.1 to 0.2, 0.2 to 0.3, and 0.3 to 0.4 for specimen with V_f of 1.5% increased the lateral capacity by 4.34%, 6.10%, and 9.26%, respectively.

By comparing lateral force-displacement relationships for the specimens with constant fiber volume fraction under different axial loading level, it can be known that in general, increasing axial compression force turns the post-peak behavior of SFRC column to be more brittle. With increasing axial compression force, the lateral force increased, but the displacement corresponding to the peak lateral force decreased. Therefore, based on observations on specimens under constant axial compression force with different fiber volume fractions, it can be known that the maximum lateral capacity increase with increasing fiber volume fraction. However, increasing fiber volume fraction had little or no effect on drift corresponding to maximum lateral force, particularly for the specimen with axial compression force ratio of 0.2 or greater. Increasing fiber volume fraction by 100% (from fiber volume fraction of 0.75% to 1.5%) increased the maximum lateral force by 26.36%, 20.83%, 24.67%, and 9.10% for specimen with axial load ratio of 0.1, 0.2, 0.3, and 0.4, respectively.

Shear strength component

The contribution of shear strength provided by concrete and transverse reinforcement was measured as well. This section presents the shear strength components at crack and peak conditions. The strength components at post-peak behavior tends to be difficult to observe, since measured strain was unreliable due to the occurring damages might disturb the strain gauges. The experimental shear strength provided

by concrete can be calculated by subtracting the experimental shear strength provided by transverse reinforcing bars from experimental ultimate shear strength, as expressed in Eq. 1.

$$V_{c,test} = V_{test} - V_{s,test} \quad (1)$$

where V_{test} is the experimental ultimate shear strength, $V_{c,test}$ is the experimental concrete strength, and $V_{s,test}$ is the experimental shear strength provided by transverse reinforcement bars.

Effect of axial load on concrete strength in SFRC columns

For specimens under low axial load, the peak strengths were greater than the cracking strengths. This was because of the occurrence of the strength redistribution from concrete to transverse reinforcement. There was no reduction concrete strength when cracking condition turned into peak condition. This proves that the steel fiber bridging action across the micro-cracks avoided strain localization and prevented crack opening that could lead concrete to achieve premature failure. For specimens under high axial loading level (except S3-500-0.75-0.3), the crack condition showed the same strength as the peak condition. This is due to the first strength redistribution occurred simultaneously with reaching maximum shear capacity. As previously mentioned, with increasing drift larger than drift at peak strength, the concrete might not be able to distribute more force to transverse reinforcement, since concrete has experienced damages.
At cracking condition, for specimens with V_f of 0.75%, increasing axial compression load from 0.1 to 0.2, 0.2 to 0.3, and 0.3 to 0.4 increased the concrete shear strength by -0.36%, 33.51%, and 46.06%, respectively. At peak condition, the concrete shear strength increased by 15.99%, 5.36%, and 39.74% with increasing axial compression load from 0.1 to 0.2, 0.2 to 0.3, and 0.3 to 0.4, respectively. For specimens with V_f of 1.5%, at cracking condition, the concrete shear strength increased by 51.10%, 33.11%, and 10.59% as axial compression load increased from 0.1 to 0.2, 0.2 to 0.3, and 0.3 to 0.4, respectively. At peak condition, with increasing axial compression load from 0.1 to 0.2, 0.2 to 0.3, and 0.3 to 0.4, the concrete shear strength increased by 5.64%, 18.79%, and 10.49%, respectively. In general, it can be concluded that the concrete shear strength increases with axial compression; however higher axial compression load tended to reduce the rate of increase of concrete shear strength.

Effect of fiber volume fraction on concrete strength in SFRC columns

The effect of fiber volume fraction on concrete shear strength can be observed. S1-500-0.75-0.1 is compared with S5-540-1.50-0.1, S2-500-0.75-0.2 is compared with S6-540-1.50-0.2, S3-500-0.75-0.3 is compared with S7-540-1.50-0.3, and S4-500-0.75-0.4 is compared with S8-540-1.50-0.4. At first cracking stage, the increase of fiber volume fraction resulted the improvement of concrete shear strength by -4.51%, 44.80%, 44.37%, and 9.31% for specimens with axial load ratios of 0.1, 0.2, 0.3, and 0.4, respectively. In addition, increasing fiber volume fraction improved concrete shear strength 34.68%, 22.63%, 38.28%, and 9.31% at the peak strength stage, respectively for specimen with axial load ratios of 0.1, 0.2, 0.3, and 0.4, respectively. It can be observed that the improvement of fiber volume fractions up to 100% was not proportional to the improvement of SFRC column shear strength, particularly for a column subjected to high axial loading level.

CONCLUSIONS

From the experimental results conducted in this study, the following conclusions can be drawn:

1. For specimens with constant fiber volume fraction, with increasing axial compression load, the maximum shear strength increased, but the post-peak behavior turned more brittle. Meanwhile, for specimens under the same low axial loading level, increasing fiber volume fraction increased the column shear strength and improved post-peak behavior.
2. For specimen under high axial loading level, the increase of shear strength was not as greater as increase of the shear strength of specimens under low axial loading level. Also, for specimens

under high axial loading level, increasing fiber volume fraction from 0.75% to 1.5% gave no effect on drift ratio corresponding to peak lateral force.

3. Higher axial load reduced the difference between diagonal cracking strength and peak strength. This indicates that the redistribution of internal forces from concrete to transverse reinforcement occurred in specimens under low axial loading level, but not in specimens under moderate or high axial loading level. Furthermore, the deformation capacity decreased as axial load ratio increased.
4. The failure mode of specimens under low axial loading level was shear failure only, while the specimens under high axial loading level achieved shear-buckling failures.
5. Based on strain gauges attached on longitudinal reinforcement, no strain exceeded yield strain. Meanwhile, according to strain reading from strain gauges attached on transverse reinforcement, the yield strain was found in specimens with axial load ratio of 0.1 only.
6. As axial loading level increased, the contribution of transverse reinforcement in an SFRC column decreased. This can be found in specimens under high axial loading level, where the peak experimental lateral force was almost similar to the experimental shear strength provided by concrete.
7. The effect of increase of axial loading level on concrete shear strength in SFRC columns with constant fiber volume fraction was the decrease of the rate of increase of concrete shear strength. Also, for specimens under the same axial loading level, the improvement of fiber volume fraction up to 100% was not proportional to the improvement of SFRC column shear strength, particularly for columns subjected to high axial loading level.

REFERENCES

ACI Committee 318 (2014), "Building Code Requirements for Structural Concrete (ACI 318-14) and Commentary (318R-14)," American Concrete Institute, Farmington Hills, MI, 520 pp.

ACI Committee 318 (2019), "Building Code Requirements for Structural Concrete (ACI 318-19) and Commentary (318R-19)," American Concrete Institute, Farmington Hills, MI, 520 pp.

Elwood, K. J., Maffei, J., Riederer, K. A., and Telleen, K. (2009), "Improving Column Confinement Part I: Assessment of Design Provisions," Concrete International, pp. 32 – 39.

Hsu, L.S., and Thomas Hsu, C.T., (1994), "Stress-Strain Behavior of Steel-Fiber High-Strength Concrete under Compression," ACI Structural Journal, V. 91, No. 4, pp. 448-457.

Liao, W. C., Perceka, W., Liu, E. J. (2015), "Compressive Stress-Strain Relationship of High Strength Steel Fiber Reinforced Concrete," Journal of Advanced Concrete Technology, V. 13, No. 8, pp. 378-392.

Liao, W. C., Perceka, W., Yu, L. C. (2017a), "Systematic Mix Procedures for Highly Flowable-Strain Hardening Fiber Reinforced Concrete (HF-SHFRC) by using Tensile Strain Hardening Responses as Performance Criteria," Science of Advanced Materials, V. 9, No. 7, pp. 1157-1168.

Liao, W.-C., Perceka, W., Wang, M. (2017b), "Experimental Study of Cyclic Behavior of High- Strength Reinforced Concrete Columns with Different Transverse Reinforcement Detailing Configurations," Engineering Structures, V. 153, pp. 290-301

Mansur, M.A., Chin, M.S., Wee, T.H., (1999), "Stress-Strain Relationship of High Strength Fiber Concrete in Compression," Journal of Materials in Civil Engineering, V. 11, No. 1, pp. 21-29.

Najm, H., and Naaman, A.E., (1991), "Bond-Slip Mechanism of Steel Fiber in Concrete," ACI Material Journal, Technical Paper, V. 88, No. 2, pp. 135-145.

Ou, Y-. C., and Kurniawan, D. P. (2015a), "Shear Behavior of Reinforced Concrete Columns with High-Strength Steel and Concrete," ACI Structural Journal, V. 112, No. 1, pp. 35 – 46.

Ou, Y-. C., and Kurniawan, D. P. (2015b), "Effect of Axial Compression on Shear Behavior of High-Strength Reinforced Concrete Columns," ACI Structural Journal, V. 112, No. 2, pp. 209 – 220.

Parra-Montesinos, G.J. (2005), "High-Performance Fiber-Reinforced Cement Composites: An Alternative for Seismic Design of Structures," ACI Structural Journal, V.102, No. 5, 668 – 675.

Perceka, W., Liao, W. C., and Wang, Y. D. (2016), "High Strength Concrete Columns under Axial Compression Load: Hybrid Confinement Efficiency of High Strength Transverse Reinforcement and Steel Fibers," Materials, V. 9, No. 4.

Perceka, W., Liao, W.-C., Wu, Y.-F. (2019), "Shear Strength Prediction Equations and Experimental Study of High Strength Steel Fiber-Reinforced Concrete Beams with Different Shear Span-to-Depth Ratios," Applied Sciences, 9(22), 4790.

Thomas, J., and Ramaswamy, A., (2007), "Mechanical Properties of Steel Fiber-Reinforced Concrete," Journal of Materials in Civil Engineering, V. 19, No. 5, pp. 385-392.

Prof. Tzu-Kang Lin

National Yang Ming Chiao Tung University, Taiwan

Topic： An Intelligent Isolation System Based on Long Short-term Memory Module Model of Ground Motion Characteristics Prediction

(The material of the speaker's presentation has not been authorized for publication in the proceedings.)

Prof. Lyan-Ywan Lu

National Cheng Kung University, Taiwan

Topic：Seismic Risk Assessment Considering Multi-Performance Levels for Base-Isolated Building

SEISMIC RISK ASSESSMENT CONSIDERING MULTI-PERFORMANCE LEVELS FOR BASE-ISOLATED BUILDINGS

Lyan-Ywan Lu[1*] Fu-Pei Hsiao[2] Natalia Nur Ramadhanti[3] Natalia Lioe[3]
Yu-Shi Tang[4] Yin-Nan Huang[5]

1. Corresponding author, Professor, Department of Civil Engineering, National Cheng Kung University, Tainan, Taiwan
2. Research fellow, National Center for Research on Earthquake Engineering, Taipei, Taiwan
3. Master student, Department of Civil Engineering, National Cheng Kung University, Tainan, Taiwan
4. Master of Science, Department of Civil Engineering, National Cheng Kung University, Tainan, Taiwan
5. Associate Professor, Department of Civil Engineering, National Taiwan University, Taipei, Taiwan

E-mail: lylu@ncku.edu.tw, fphsiao@narlabs.org.tw, natalianurramadhanti@gmail.com, nataliaalioe@gmail.com, sincos0311@gmail.com, ynhuang@ntu.edu.tw

ABSTRACT

Presently, the majority of existing seismic assessment methods aim to evaluate the collapse-resistance capacity of building structures. This type of assessment methods may not be appropriate for buildings with higher seismic performance demand, such as base-isolated buildings, which are usually required to maintain functionality after a major earthquake. In order to accommodate the above needs, this study proposes a practical procedure, consisting of 7 operational steps, for seismic risk assessment of isolated structures considering multiple performance levels (PLs). To demonstrate the operation of the proposed assessment method, a 5-story old apartment building retrofitted by sliding isolators and supplementary dampers was considered in this study. The seismic performance of the building with and without the isolators was evaluated in various PLs. The assessment outcomes show that installing the isolators significantly reduces the exceedance failure probability of Collapse Prevention PL of the building to about 1/7 of the original level under the Maximum Considered Earthquake (MCE), and reduced the failure probability of Immediate Occupancy PL to 1/10 of the original value under the Service Level Earthquake. Installation of dampers in the isolation system (IS) is able to reduce the IS failure probability to about 1/4 of the original value under the MCE.

Keywords: Isolated building, seismic performance assessment, probabilistic assessment, multiple performance levels, incremental dynamic analysis, fragility analysis.

INTRODUCTION

Advanced seismic-resistant technologies, such as seismic isolation (SI), are able to not only protect a building structure from fatal damage (e.g. collapse) but also maintain its functionality under the attack of a strong earthquake. Through seismic performance assessment, some studies showed that seismic isolation offers a lower failure probability than that of non-isolated buildings, in terms of the damage to both structural (Karimi and Genes, 2019) and non-structural components (Ryu et al., 2018; Kitayama and Constantinou, 2019). Nonetheless, because most of conventional seismic assessment methods aim to evaluate the collapse risk of building structures (Ibarra and Krawinkler, 2005; Haelton and Deierlein, 2008; Hsieh et al. 2018; Lu et al., 2021), their damage criteria are solely connected to the structural collapse mechanism. Therefore, these assessment methods may not be suitable for evaluating seismic isolated structures or structures required higher seismic performance, such as the vital infrastructures that need to maintain functionality following a major earthquake.

The seismic performance assessment of isolated building has been conducted by Fanaie et al. (2017) and Bhandari et al. (2019) by defining the performance levels (PLs) based on different structural damage

levels, such as slight, moderate, extensive, and complete. Nevertheless, the definitions of these performance levels exclusively depend on the superstructural response; therefore, they are not applicable to the isolation system. Even though the seismic probabilistic assessment for isolated buildings have been studied by some researchers (Ryu et al., 2018; Kitayama and Constantinou, 2019; Cardone et al., 2018), a comprehensive assessment method that considers the multiple performance levels either for general buildings or isolated buildings has not been clearly defined. To this end, this study proposes a general procedure for the seismic risk assessment of seismically isolated or non-isolated structures by taking into account multiple performance levels. Moreover, in this study, a 5-story RC building will be employed to demonstrate how the proposed assessment procedure with the multiple PLs is applied. The following three structural types will be considered for the RC building: (1) the original structure (non-isolated), (2) the isolated structure, and (3) the isolated structure with SI dampers.

GENERAL PROCEDURE OF ASSESSMENT

The probabilistic seismic assessment procedure for buildings used in this paper is mainly developed base on FEMA P-58 by Hsieh et al. (2018) and further extended by Tang (2018), so that it can be applied to evaluate multiple performance levels of buildings. The procedure is mainly divided into the following seven steps:

(1) Establish 3D nonlinear numerical model
The built-in model must be able to simulate and reflect to the nonlinear behavior of each component of the structure, such as the plastic hinge of the component after it enters the yielding stage. For structural systems with seismic isolation and energy dissipation elements (or dampers), the hysteretic energy dissipation behavior should be represented.

(2) Select a target response spectrum and ground motions
A target response spectrum is required to be prescribed as it is used to select ground motions. The bidirectional ground motion pairs should match the target response spectrum. This paper suggests using 11 pairs of ground motion whose geo-mean response spectra have to match with the shape of the pre-determined target response spectrum, which may be selected according to FEMA P-58 and ASCE 7-16 recommendations, or local seismic design code.

(3) Select performance levels and damage criteria
The performance levels are chosen according to the seismic performance demands, such as the functionality, life safety, or collapse prevention. Moreover, quantified by certain engineering demand parameter (EDP), the damage criterion corresponding to each performance level has to be defined in order to determine the occurrence of the damage for each PL.

(4) Perform incremental dynamic analysis (IDA)
With the ground motion intensity gradually increased from low to high for each of the 11 ground motions, the IDA is performed on the numerical model, and record the intensity when the building reaches any damage criterion for a specific PL. In the IDA, the spectral acceleration at the structural fundamental period is used as the seismic intensity measure.

(5) Construct the fragility curve for each PL
A fragility curve for a specific PL represents the exceedance occurrence probability of the PL at a given ground motion intensity. The fragility curve for each performance level can be produced using the data obtained from the IDA, which generates two statistic parameters, namely, regression median and logarithmic standard deviation by the maximum likelihood method.

(6) Calculate the performance index of each performance level
Performance index is an index to judge the seismic performance of the evaluated structure. In this study, the performance index for a certain PL is defined as the exceedance probability of the PL under a specified ground motion intensity, such as the maximum considered earthquake (MCE).

(7) Check acceptability of the seismic performance
The seismic performance of the evaluated structure represented by the performance indices is checked to see whether they conform to the acceptable level specified by a standard, guidelines or demand of building stackholders.

DEMONSTRATION OF PROPOSED ASSESSMENT PROCEDURE

In this section, the implementation of the proposed seismic assessment procedure with multiple-PLs, which consists of 7 operational steps, will be demonstrated step-by-step, by using a RC structure.

Step 1 – Establish Three-dimensional Nonlinear Numerical Model

Structure properties

A 5-story RC building located in Wufeng District of Taichung, which is near active fault area, is selected as the target structure in this study. The building was designed according to early Taiwanese seismic code and contains 3 spans 6.475 meters in north-south direction, 2 spans 8.875 meters in east-west direction, 4.3 meters first floor height, and the total height is 17.1 meters. The section of all columns is 50×50cm with 10#6 main rebar and #3 shear rebar. The detail building information is described by Tang (2018). For comparison purpose, the following three structural types are modeled in this study: (1) the original structure (non-isolated), (2) the structure retrofitted with an SI system, and (3) the structure retrofitted with an SI system and SI dampers. In types (2) and (3), friction pendulum isolators (FPIs) are used for the SI. Following Taiwanese design code (2011) and a performance-based design method (Lu et al., 2016), the friction coefficient of μ=0.031 and the radius of curvature R=6.03m for the FPIs are used. A damping ratio of 10% is chosen for the SI dampers.

Numerical model

To accurately simulate the seismic responses of the 5-story RC structure, a 3D numerical model that is able to reflect nonlinear characteristics of the structure is established by the ETABS software as shown in Figure 1. The built numerical model does not consider the stiffness of the wall, but the weight of the wall is treated as the static load. The stiffness reduction factor 0.7 is adopted so that effective stiffness of the structure is not lower than that of the real structure. Furthermore, nonlinear plastic hinges are added to structural components in the numerical model in order to simulate the nonlinear yielding behavior of the structural members. The parameters of the plastic-hinge backbone curve will use the recommended values of ASCE 41-13, and the hysteresis behavior of the plastic hinge will be simulated using the Takeda hysteresis model built in the ETABS.

.

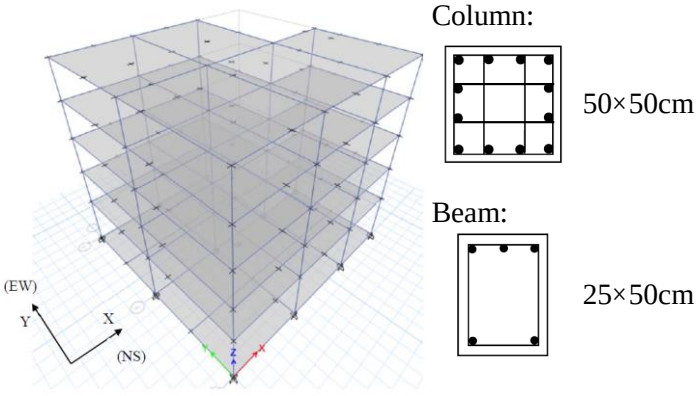

Figure 1. 3D-view of the structural model

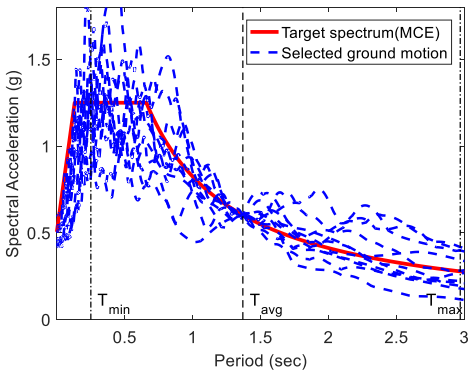

Figure 2. Response spectra of 11 selected ground motions

Step 2 – Select Target Response Spectrum and Ground Motions

FEMA P-58 (2018) recommends that as least 11 pairs of bi-directional horizontal ground motions have to be chosen for the response history analysis of the assessed building. The ground motions have to be selected based on a target response spectrum. For practical concern, this study suggests

that the MCE-level response spectrum specified in the local seismic code be used as the target spectrum. The average of geometric-mean response spectra of the 11 selected ground motions has to be consistent with the pre-determined target spectrum within the period range (T_{min}, T_{max}), as shown in Figure 2. Notably, the average spectrum is consistent within the both period ranges of the isolated and non-isolated cases.

Step 3 – Define Performance Levels and Damage Criteria

Seismic Performance Levels

For common buildings, seismic performance regarding life safety is of the major concern, so preventing building collapse may be the only performance objective in the seismic assessment (Ibarra and Krawinkler, 2005). However, for important buildings with SI, which are usually expected to maintain their functionality after an earthquake, performance objectives regarding functionality must also be considered. For this reason, this paper adopts the following four seismic performance levels in the assessment of isolated structures: Immediate Occupancy (IO), Life Safety (LS), Collapse Prevention (CP), and Isolation Limit (IL). The performance levels IO, LS and CP, adopted from ASCE 41-13 (2014), are designated for the assessment of the superstructure, while the IL performance level is designated for the assessment of the SI system. Note that the IO is related to functionality performance.

Damage Criteria for Each Performance Level

For each of the four PLs mentioned above, the corresponding damage criteria are assigned. The damage criteria for IO, LS and CP are further divided into global and local criterion. The superstructure is under the damage state of a certain PL if either the global or local damage criterion corresponding to that PL is met. For global damage criteria, this paper adopts the definition of FEMA 356 (2000), in which the damage states of the IO, LS, CP are defined as when the maximum drift of any story reaches 1%, 2%, and 4%, respectively. For the local damage criteria, this paper refers to Lu et al. (2021) and ASCE 41-13 (2014), which defines the damage states of various structural components for each of the IO, LS, and CP performance levels. For example, the IO local damage state is said to occur when any vertical element reaches the IO damage criteria defined by ASCE 41. Moreover, the damage criterion for the IL performance level is defined as when the displacement of any isolator exceeds the maximum design value (D_{TM} = 0.78m) obtained from the design code.

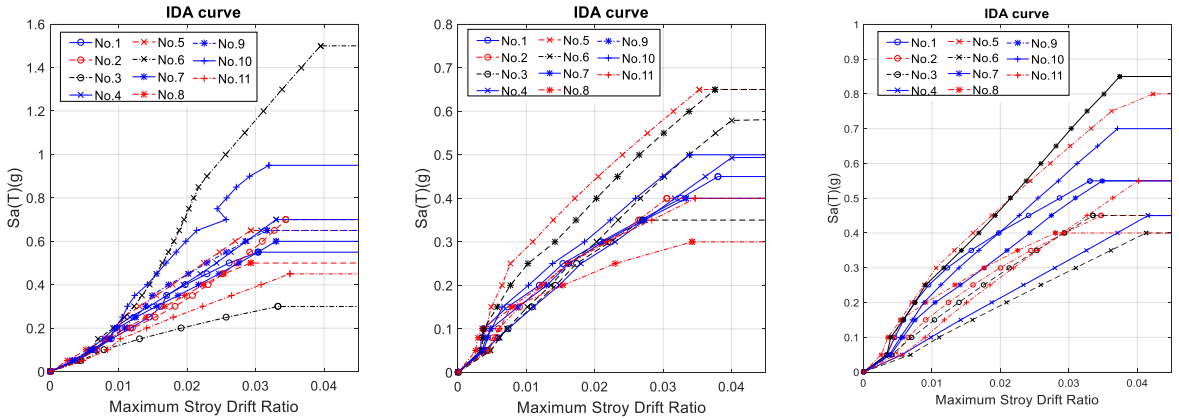

(a) Original building (b) Isolated building (c) Isolated building with dampers

Figure 3. Incremental dynamic analysis

Step 4 – Perform Incremental Dynamic Analysis (IDA)

The purpose of the IDA is to find out at which seismic intensity level the damage criterion of a certain performance level is achieved by gradually increased the intensity of the ground motions. The IDAs of the considered three cases in this study are shown in Figure 3. In the IDA, the geo-mean spectral

acceleration $S_{gm}(\bar{T})$ (where $\bar{T}$ is the structural fundamental period) is used as the intensity measure (IM) and the nonlinear response histories of the evaluated building, maximum story drift ratio, is chosen to be the engineering demand parameter (EDP). Notably, the fundamental period $\bar{T}$ for each of the structural types in Fig. 3 is different. For a ground motion with certain intensity, if the simulated response meets or exceeds any damage criterion defined for a certain PL (see Step 3), the structure is said to reach that PL. For a given intensity, the number of the ground motions for which a certain PL is reached will determine the total probability of the damages exceeding that PL under the given intensity.

Step 5 – Construct Fragility Curves

The fragility curve for each of the four PLs can be obtained by using the IDA data and following the data regression process suggested by FEMA P-58 and Baker (2015). Notably, in the fragility curves, instead of using the dispersion from regression, the dispersions, which are able to reflect construction quality and modeling uncertainties, suggested by FEMA P58 are used. Figure 4 shows the fragility curves of all PLs (IO, LS, CP, IL) for the three structural types mentioned previously. A fragility curve in Fig. 4, which can be described mathematically as $P(PL|\, S_a(\bar{T})= x)$, represents the exceedance damage probability of a certain PL as a function of seismic intensity $S_a(\bar{T})= S_{gm}(\bar{T})= x$. In certain intensities, the IL curve crosses the other PL curves in Fig. 4, which means beyond those intensities, IL has higher damage probability than the other PLs'. Notably, the fundamental period $\bar{T}$ for each of the structural types is different as shown in Fig. 4.

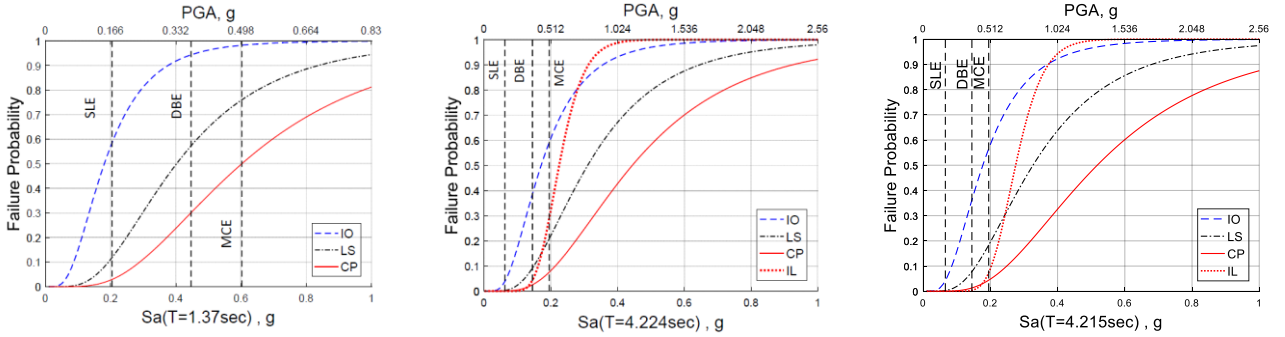

(a) Original structure (b) Isolated structure (c) Isolated structure with dampers

Figure 4. Fragility curves of all performance levels for different structural types

Step 6 – Determine Seismic Performance Index

In this study, the seismic performance index is defined as the exceedance damage probability of a certain PL under the seismic intensities of concern. The following three levels of seismic intensities are considered in the assessment: service level earthquake (SLE), design basis earthquake (DBE), and maximum considered earthquake (MCE). The return periods for the SLE, BDE and MCE are 75, 475 and 2475 years, respectively. The three vertical lines in Figs. 4(a)-(c) represent the seismic intensities of these three level earthquakes. The intersections of these lines with the fragility curve of a particular PL represent the damage probabilities of that PL when the building is subjected to the three level earthquakes. For the three structural types, the damage probabilities for the four PLs under SLE, DBE, and MCE are summarized in the 3rd to 5th columns of Table 1.

Step 7 – Check Acceptability of Seismic Performance

To check the acceptability of seismic performance for a building, the acceptance criteria for the seismic performance index has to be determined first. The acceptance criteria used in this study is shown in the last column of Table 1. The acceptance criterion for the CP performance level recommended by the FEMA P-695 (2009) and ASCE 7-16 (2016) is that the exceedance collapse probability under the MCE

must be less than 10% for Risk Category I and II structures. Due to lack of references, this paper recommends the acceptance criterion for the IL is as that of the CP (i.e., exceedance damage probability <10%), since the IL damage for an isolated structure may cause the instability of the whole structure and is as critical as the CP damage. Also, due to lack of reference for acceptance criteria of the IO and LS damages, they may be determined according to the need of stakeholders.

Table 1. Comparison of seismic performance indexes for different types of structures.

Structural type	**Performance level**	**Performance index**			**Recommended acceptance criterion**
		Damage probability under			
		SLE	DBE	MCE	
Original structure (fixed-base)	IO	**57.15%**	94.04%	98.21%	-
	LS	11.13%	**56.29%**	75.81%	-
	CP	2.71%	29.18%	**49.76%**	< 10% (under MCE)
Isolated structure	IO	**4.80%**	38.66%	59.08%	-
	LS	0.34%	**9.17%**	20.83%	-
	CP	0%	2.52%	**7.51%**	< 10% (under MCE)
	IL	0%	4.38%	**28.91%**	< 10% (under MCE)
Isolated structure with dampers	IO	**4.28%**	36.17%	56.50%	-
	LS	0.27%	**7.80%**	18.35%	-
	CP	0%	1.32%	**4.40%**	< 10% (under MCE)
	IL	0%	0.37%	**7.42%**	< 10% (under MCE)

DISCUSSION ON ASSESSMENT RESULTS

Table 1 indicates that the fixed-base original structure has a CP damage probability of 49.76% under MCE, which is much higher than the acceptable value of 10%. As a result, the original structure required to be retrofitted since it does not have sufficient seismic capacity. The damage probabilities for the superstructure performance levels (IO, LS, CP) are significantly decreased after the structure is isolated with FPIs. The damage probability for CP under the MCE is reduced from 49.76% to 7.51% (< 10%), while the damage probability of the IO under the SLE is reduced from 57.15% to 4.80%. Low damage probability of IO in SLE verified that retrofitting with the FPIs is suitable for the structure that required more stringent performance design in smaller earthquake level which occurs frequently. Table 1 further reveals that the damage probability of the IL under the MCE for the isolated structure is higher than the allowable value of 10% at 28.91%. Nevertheless, after the supplemental dampers are introduced to the SI system, the damage probability of the IL is substantially decreased from 28.91% to 7.42% (<10%) in the MCE, while the damage probabilities of the other PLs relating the superstructure essentially remain the same.

CONCLUSIONS

Based on the framework of FEMA P-58, this study proposes a practical procedure for probabilistic seismic assessment of general building considering multiple performance levels, including immediate occupancy (IO), life safety (LS), collapse prevention (CP), and additionally isolation limit (IL) for the isolated building. The proposed procedure that consists of 7 operational steps can be easily implemented by engineers. For demonstration, the proposed method was employed to evaluate the seismic performance of a 5-story old apartment RC building before and after retrofitted with sliding-type isolators and further installed with isolation dampers. The assessment result indicates that the installation of the isolators under the building significantly reduces the damage probabilities of the superstructure associated with IO, LS, CP performance levels, while adding the dampers in the isolation system further lowers the IL damage probability of the isolation system to the acceptable level. The demonstration illustrates that the proposed method is applicable to assess the different seismic performance levels of both isolated and non-isolated structures under various earthquake levels.

REFERENCES

ASCE 41-13 (2014). *Seismic rehabilitation of existing building*, American Society of Civil Engineers.

ASCE 7-16 (2016). *Minimum Design Loads and Associated Criteria for Buildings and Other Structures*, American Society of Civil Engineers.

Baker, J.W. (2015). "Efficient analytical fragility function fitting using dynamic structural analysis," *Earthquake Spectra*, **31**(1): 579-599.

Bhandari, M., S.D. Bharti, M.K. Shrimali, and T.K. Datta (2019). "Seismic fragility analysis of base-isolated building frames excited by near- and far-field earthquakes," *Journal of Performance of Constructed Facilities*, **33**(3):04019029.

Cardone, D., G. Perrone and V. Piesco (2018). "Developing collapse fragility curves for base-isolated buildings," *Earthquake Engineering and Structural Dynamic*, **48**(1): 78-102.

CPA (2011). *Seismic Design Code and Commentary for Buildings*, Construction and Planning Agency, Ministry of Interior Affair, Taipei, Taiwan. (in Chinese)

Fanaie, N., M.S. Kolbadi and E.A. Dizaj (2017). "Probabilistic seismic demand assessment of steel moment resisting frames isolated by LRB." *Numerical Methods in Civil Engineering*, **2**(2):52-62.

FEMA 356 (2000). *Prestandard and commentary for the seismic rehabilitation of buildings*, Federal Emergency Management Agency.

FEMA P-58 (2018). *Seismic Performance Assessment of Buildings*, Federal Emergency Management Agency.

FEMA P-695 (2009). *Quantification of building seismic performance factors*, Federal Emergency Management Agency.

Haselton, C.B. and G.G. Deierlein (2008). "Assessing collapse safety of modern reinforced concrete moment frame buildings," *PEER Report No. 2007/08*, Pacific Earthquake Engineering Research Center, University of California at Berkeley, Berkeley, CA.

Hsieh, W.H., L.Y. Lu, F.P. Hsiao, Y.S. Tang and Y.N. Huang (2018). "Probabilistic assessment of seismic performance and collapse risk for mid-rise buildings," *Structural Engineering*, **33**(2):89-120. (in Chinese)

Ibarra, L.F. and H. Krawinkler (2005). "Global collapse of frame structures under seismic excitations," *Report No. 152*, The John A. Blume Earthquake Engineering Research Center, Stanford University, Stanford, CA.

Kitayama, S. and M.C. Constantinou (2019). "Probabilistic seismic performance assessment of seismically isolated buildings designed by the procedures of ASCE/SEI 7 and other enhanced criteria," *Engineering Structures*, **179**:566-582.

Karimi, M.R.B. and M.C. Genes (2019). "Probabilistic behavior assessment of base-isolated buildings and base isolation systems subjected to various earthquakes with different components," *Arabian Journal for Science and Engineering*, **44**:8265-8288.

Lu, L.Y., F.P. Hsiao, Y.N. Huang and W.H. Hsieh (2021). "Collapse seismic risk assessment for irregular mid-rise buildings," *The 11th International Structural Engineering and Construction Conference*, Cairo, Egypt, July 26-31, 2011, paper no. STR-37.

Lu, L.Y., L.W. Wang, C.H. Chen, K.F. Lee, T.Y. Lee and C.C. Tsai (2016). "Performance-oriented two-stage design method for base-isolated structures," *Structural Engineering*, **31**(3):33-61. (in Chinese)

Ryu, Y, S. Kwag , B. Ju (2018). "Fragility assessment of multi-story piping systems within a seismically isolated low-rise building," *Sustainability*, **10**:3775.

Tang, Y.S. (2018). Seismic isolation design and its probabilistic performance assessment considering near-fault pulse effect, *Master Thesis*, National Cheng Kung University. (in Chinese)

Prof. Yu-Chen Ou

National Taiwan University, Taiwan

Topic：Use of Lap Spliced Inner Hoops in the Plastic Hinge Regions of Beams of Reinforced Concrete Special Moment Frames

Use of Lap-spliced Inner Hoops in the Plastic Hinge Regions of Beams of Reinforced Concrete Special Moment Frames

Yu-Chen Ou, Ph.D.

Distinguished Professor
Department of Civil Engineering
National Taiwan University

November 9th, 2022

8th Asia Conference on Earthquake Engineering
Taipei, Taiwan ■ November 9-11, 2022

Outline

Background
- ACI 318-19 Code Requirements
- Common Practice in Taiwan

Increasing Constructability
- Previous Research About Lap-spliced Hoops and the Code Requirements
- Introduction of the Lap-spliced Hoops
- Method of Construction of the Lap-spliced Hoops

Experiment
- Experimental Set Up
- Test Results

Conclusions

The Code

Hoops Requirements

ACI 318-19

- **18.6.4.1** Hoops shall be provided in a beam over a length equal to twice the beam depth measured from the face of the supporting column toward midspan, at both ends of the beam.
- 18.4.6.2
- 18.4.6.3
- 25.7.2.3

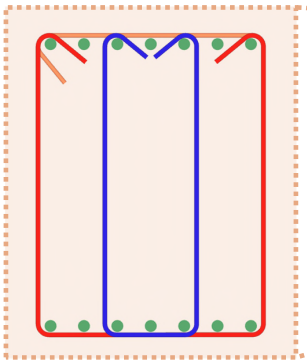

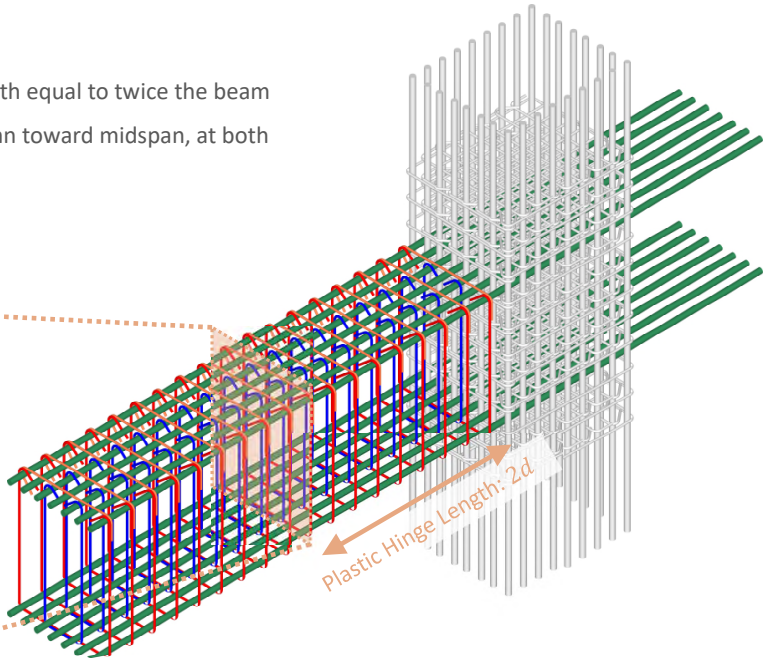

The Code

Hoops Requirements

ACI 318-19

- 18.4.6.1
- **18.4.6.2** Where hoops are required, primary longitudinal reinforcing bars closest to the tension and compression faces shall have lateral support in accordance with **25.7.2.3.**
- **25.7.2.3**
  a) Every corner and alternate longitudinal bar shall have lateral support provided by the corner of a tie with an included angle of not more than 135 degrees;
  b) No unsupported bar shall be farther than 150 mm clear on each side along the tie from a laterally supported bar.

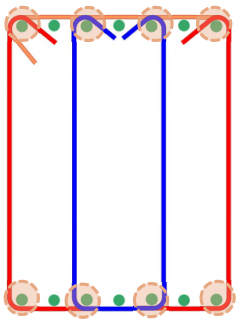

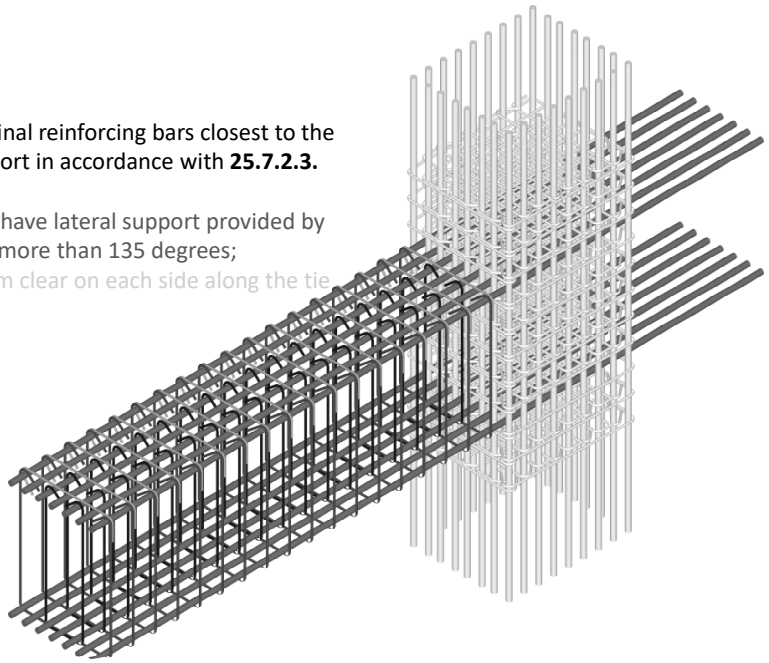

The Code

Hoops Requirements

ACI 318-19

- 18.4.6.1
- **18.4.6.2** Where hoops are required, primary longitudinal reinforcing bars closest to the tension and compression faces shall have lateral support in accordance with **25.7.2.3.**
- **25.7.2.3**
  a) Every corner and alternate longitudinal bar shall have lateral support provided by the corner of a tie with an included angle of not more than 135 degrees;
  b) No unsupported bar shall be farther than 150 mm clear on each side along the tie from a laterally supported bar.

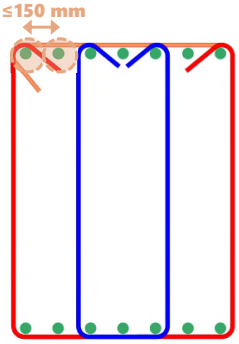

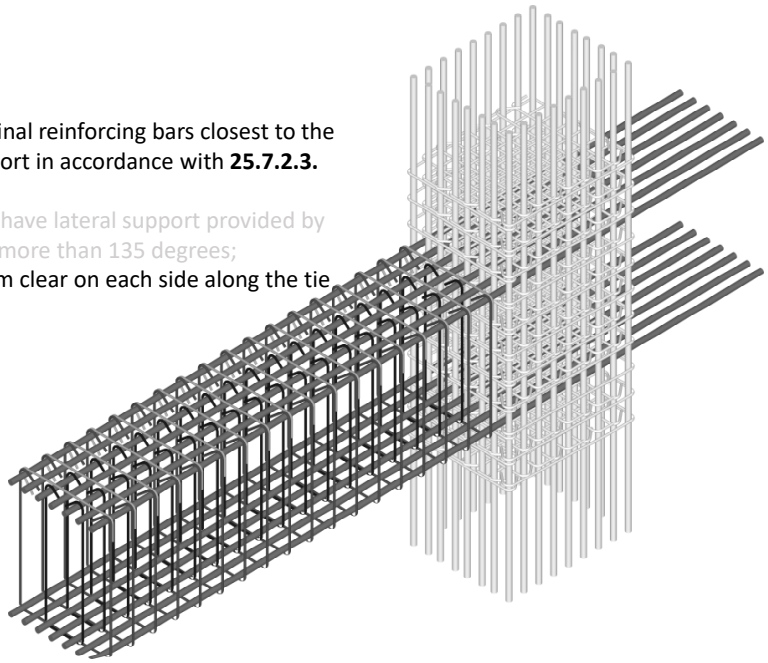

The Code

Hoops Requirements

ACI 318-19

- 18.6.4.1
- 18.4.6.2
- **18.4.6.3** Hoops in beams shall be permitted to be made up of two pieces of reinforcement: a stirrup having seismic hooks at both ends and closed by a crosstie.
- 25.7.2.3

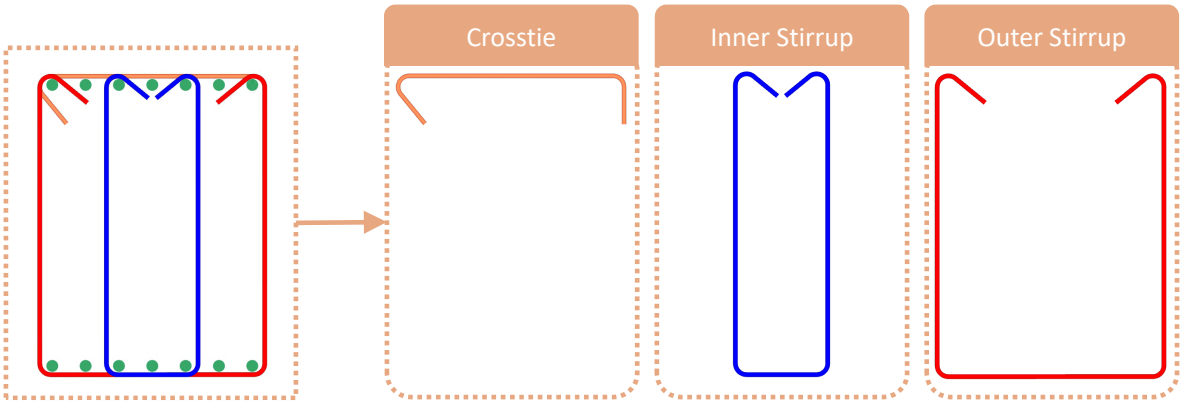

Current Practice in Taiwan

國立臺灣大學 National Taiwan University

Hoops Configurations

- Double-overlapping perimeter hoops without inner hoops are commonly used in Taiwan
- Higher constructability
- The **ACI 318-19 (27.5.2.3)** requirements for lateral support of longitudinal reinforcement are not satisfied

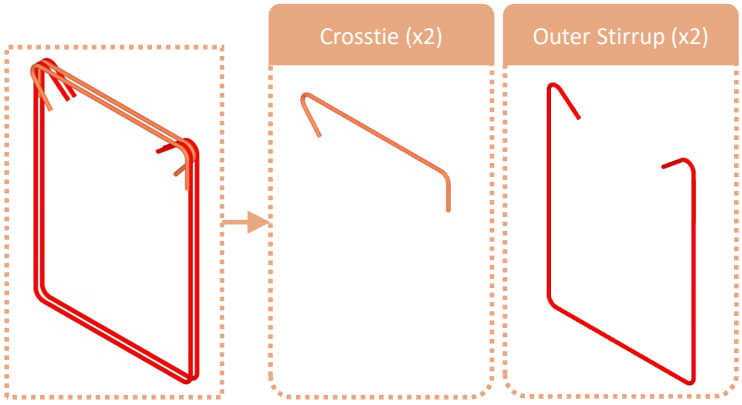

Increasing Constructability

國立臺灣大學 National Taiwan University

Previous Research

❖ Tanaka et al. (1985)

- Four-column specimens (400 mm x 400 mm) with different types of perimeter and inner hoops were built.
- The test used combined axial compressive load held constant at $P_e = 0.2 f_c' A_g$ and a reversible horizontal load H, consisting of two cycles to nominal displacement ductility factors ($\mu_N = \Delta/\Delta_y$) of $\pm 2, \pm 4, \pm 6, \pm 8, \pm 10$ and ± 12.

Specimen	Types of Crossties	Types of Perimeter Hoops
UNIT 1	$180^o/180^o$ Hooks	135^o Hooks
UNIT 2	$180^o/90^o$ Hooks	135^o Hooks
UNIT 3	180^o Hooks, Lap-spliced J-Crossties (Lap-splice length: $24d_b = 288\ mm$)	Lap-spliced U-stirrups (Lap-splice length: $17d_b = 204\ mm$)
UNIT 4	180^o Hooks, Lap-spliced J-Crossties (Lap-splice length: $24d_b = 288\ mm$)	135^o Hooks

Lap-spliced Bars

Note: The ACI 318-19 lap-splice length: $1.3l_d = 299\ mm$

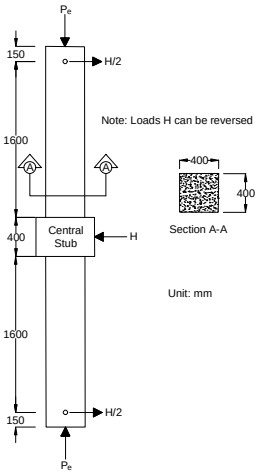

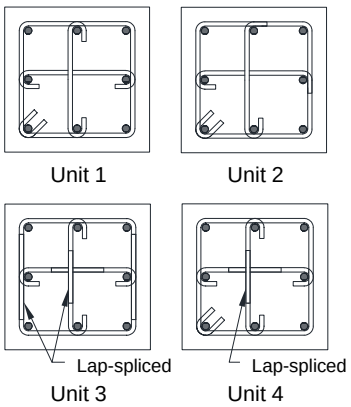

Increasing Constructability

Previous Research

❖ Tanaka et al. (1985)

Unit 1	Unit 2	Unit 3	Unit 4
The transverse reinforcement was still effective at $\mu_N = 12$	The 90^o hooks at one end of the interior crossties had opened at $\mu_N = 12$	The lap-spliced U-Stirrups perimeter hoops had become ineffective at $\mu_N = 8$	The lap-spliced J-Crossties were still effective at $\mu_N = 12$

- Crossties with 90^o end hooks (Unit 2) and lap-spliced perimeter hoops (Unit 3) were less effective for controlling the buckling of longitudinal bars.

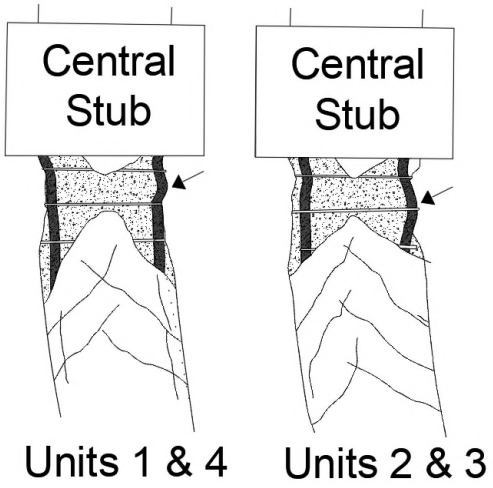

Increasing Constructability

Previous Research

❖ Li et al. (2018)

- Four-column specimens with different types of crossties and inner hoops;
- Tested under cyclic loading up to a 5% drift ratio with 3 cycles for each drift ratio.

Specimen	Types of Crossties and Inner Hoops
C-90/135	$90^o/135^o$ Hooks
C-180/180	$180^o/180^o$ Hooks
C-LS/180	180^o Hooks, Lap-spliced J-Crossties (Lap-splice length: 520 mm)
C-LS/cn	Lap-spliced U-stirrups (Lap-splice length: 520 mm)

Lap-spliced Bars

Note: The ACI 318-19 lap-splice length: $1.3l_d = 483\ mm$

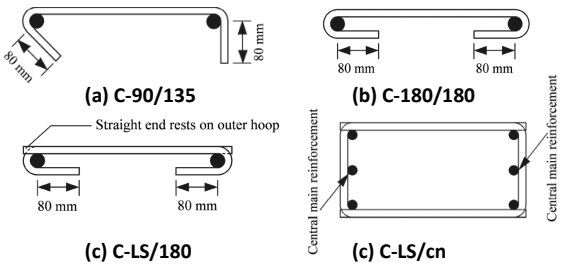

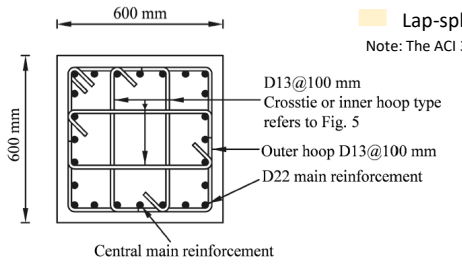

Column cross section of Specimen C-90/135

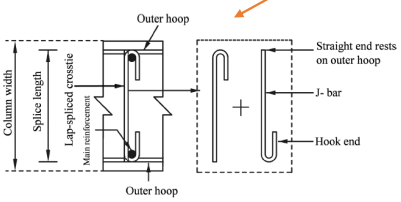

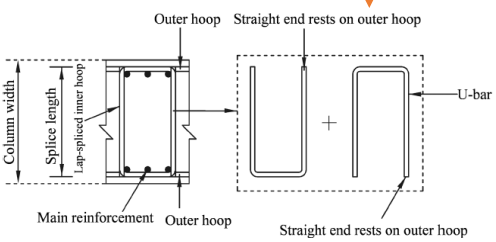

Increasing Constructability

國立臺灣大學 National Taiwan University

Previous Research

❖ Li et al. (2018)

- Plastic hinge rotation capacity

C-LS/180 (Lap-spliced J-Crossties) **23%** > C-90/135 (Conventional Crossties)

C-LS/180 (Lap-spliced J-Crossties) ≈ C-180/180 (Crossties with 180^o Hooks at both ends)

C-LS/cn (Lap-spliced U-Stirrups) **29%** > C-90/135 (Conventional Crossties)

C-LS/cn (Lap-spliced U-Stirrups) **14%** > C-180/180 (Crossties with 180^o Hooks at both ends)

- Constructability

C-LS/cn (Lap-spliced U-Stirrups) ≈ C-LS/180 (Lap-spliced J-Crossties) > C-90/135 (Conventional Crossties) > C-180/180 (Crossties with 180^o Hooks at both ends)

- Conclusions

❖ The plastic hinge rotation capacity of lap-spliced J-crossties with 180^o hooks is similar to the continuous crossties with 180^o hooks at both ends and higher than the conventional crossties;

❖ The plastic hinge rotation capacity of lap-spliced U-Stirrups is higher than the conventional crossties and the continuous crossties with 180^o hooks at both ends;

❖ Lap-spliced J-Crossties and lap-spliced U-Stirrups had higher plastic hinge rotation and constructability.

Increasing Constructability

國立臺灣大學 National Taiwan University

ACI 318-19 Code

❖ Lap-spliced Closed Stirrups (Perimeter Hoops)

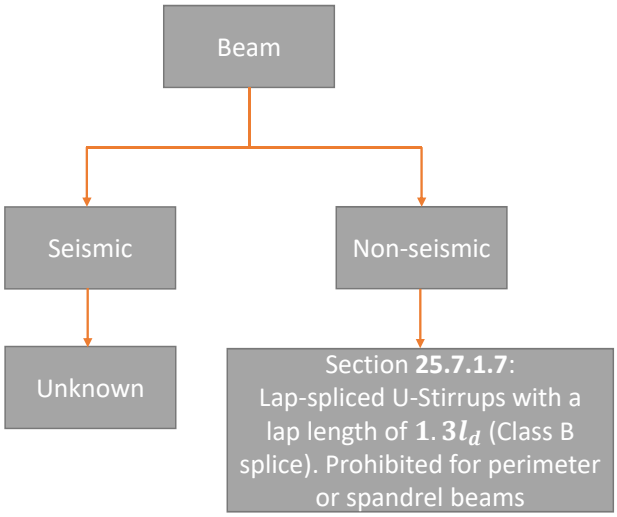

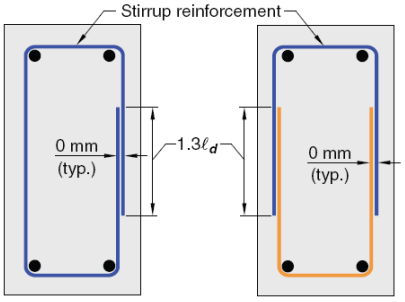

Closed stirrup configuration for beams

There is no previous research about lap-spliced closed stirrup as an inner hoop for beam of special moment frame

Increasing Constructability

The Current Research

❖ **So what is new?**

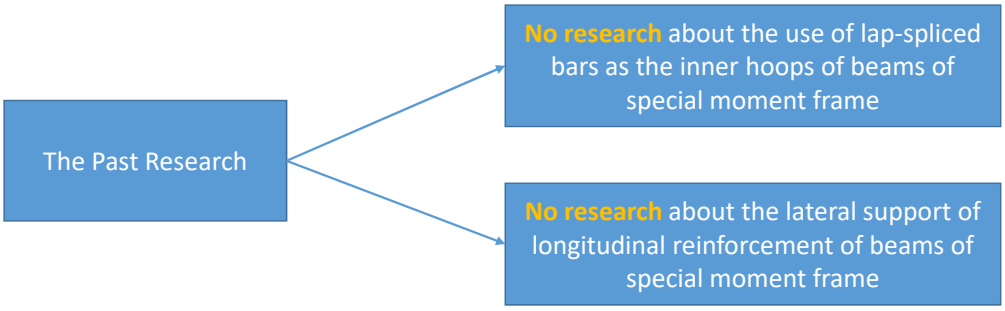

15

Increasing Constructability

Types of Hoops

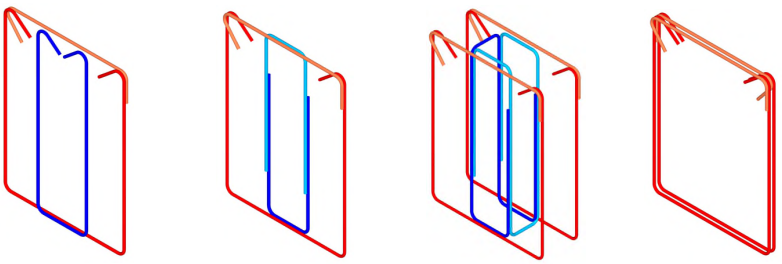

Specimens	S1	SL1	SL2	S3
Types of Hoops	Conventional Hoops	Lap-spliced Hoops		Common in Taiwan
Design Codes	ACI 318-19	?		Not meeting code requirements
Testing Variables		Lap-spliced Inner Hoops		Lateral support of longitudinal bars

17

Increasing Constructability

國立臺灣大學 National Taiwan University

Method of Construction

Specimen SL1

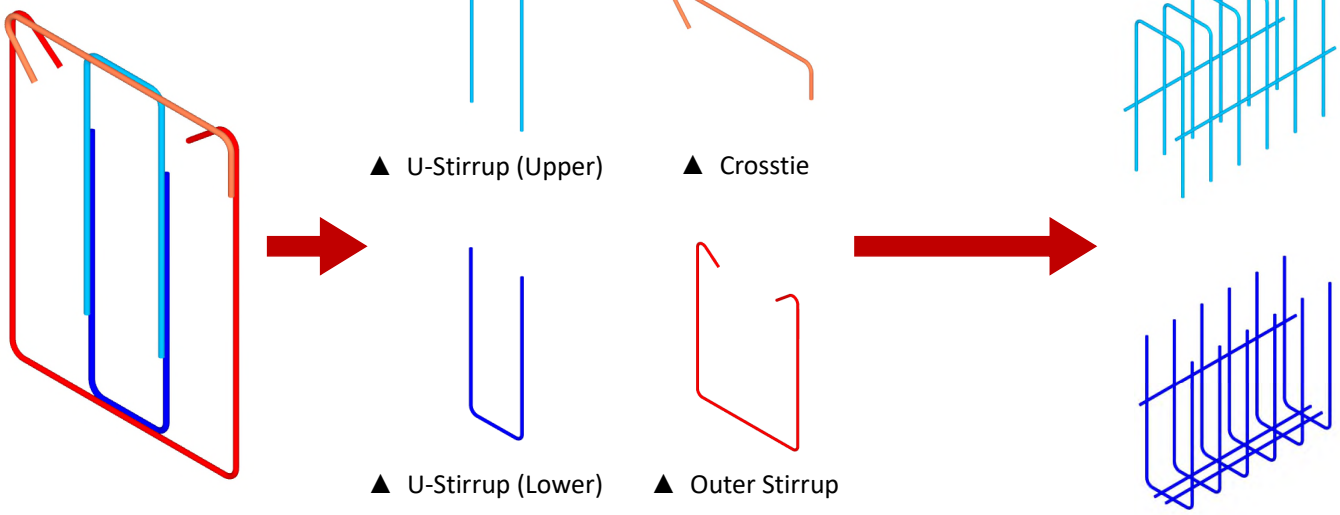

▲ U-Stirrup (Upper)　▲ Crosstie

▲ U-Stirrup (Lower)　▲ Outer Stirrup

Increasing Constructability

國立臺灣大學 National Taiwan University

Method of Construction

Specimen SL2

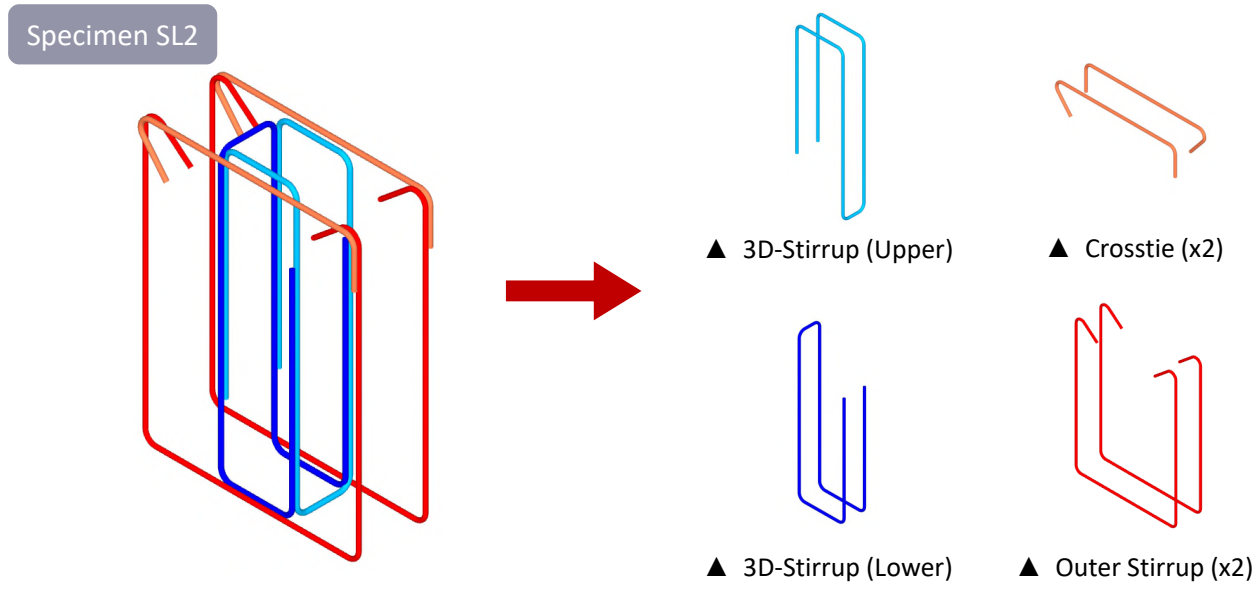

▲ 3D-Stirrup (Upper)　▲ Crosstie (x2)

▲ 3D-Stirrup (Lower)　▲ Outer Stirrup (x2)

Experimental Set Up

國立臺灣大學 National Taiwan University

Single Curvature Cyclic Loading Test

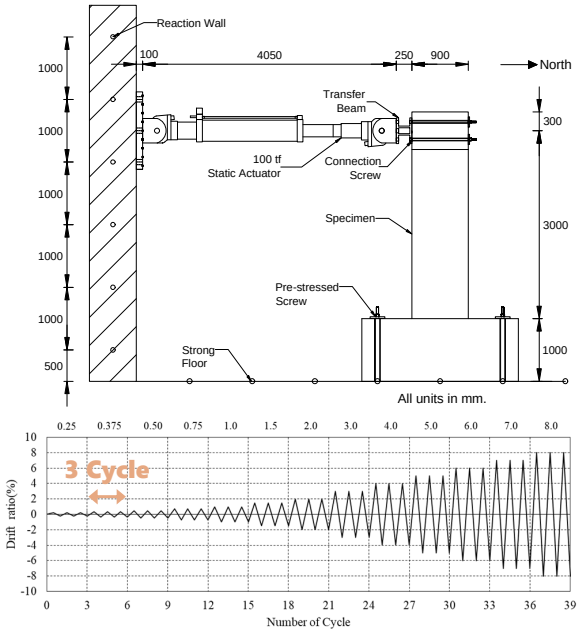

Test Results

國立臺灣大學 National Taiwan University

5% Drift Ratio

Specimens	S1	SL1	SL2	S3
Damage (East Side)	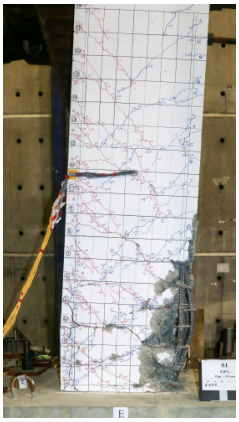	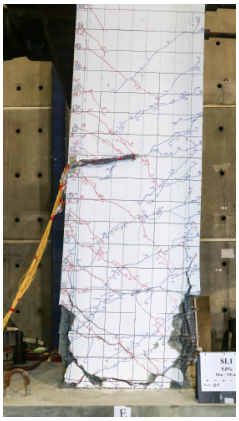	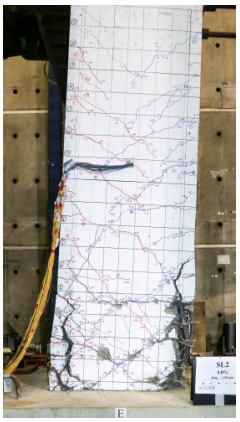	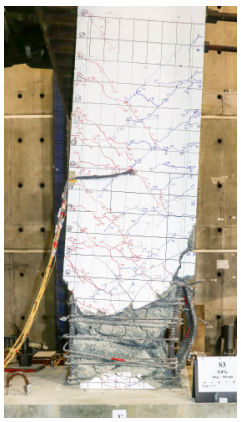

Test Results

國立臺灣大學 National Taiwan University

5% Drift Ratio

Specimens	S1	SL1	SL2	S3
Damage (Top/North Side)		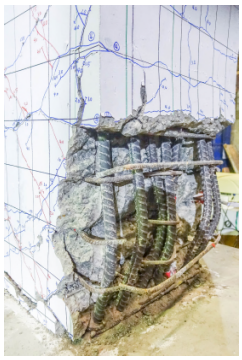	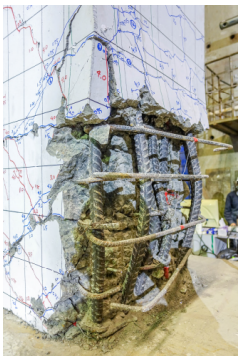	
	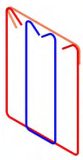	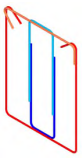	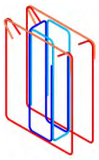	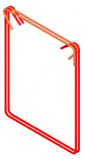

Test Results

國立臺灣大學 National Taiwan University

Hysteresis Curves

Specimens	S1	SL1	SL2	S3
	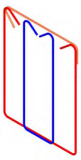	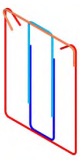	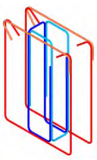	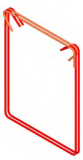
Hysteresis Curves	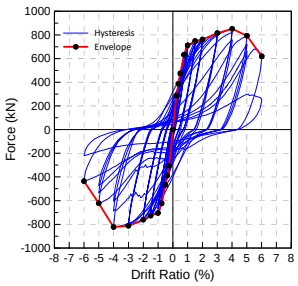	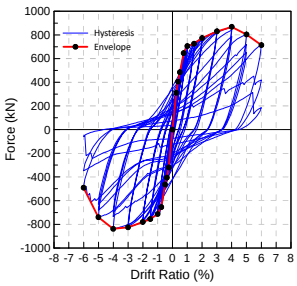	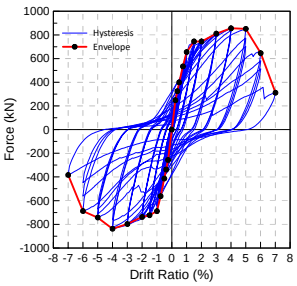	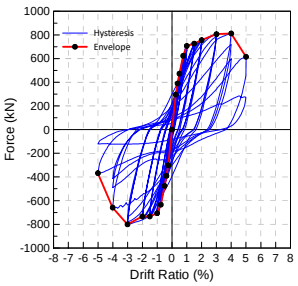

Conclusions

國立臺灣大學 National Taiwan University

Several conclusions can be drawn from this discussion:

- ❖ The beams with proposed lap-spliced inner hoops showed a flexural strength and ductility higher than that with the conventional hoops specified in the ACI 318-19 code;
- ❖ The beam with only the outer hoops as commonly seen in Taiwanese practice showed a flexural strength and ductility lower than that with the conventional hoops conforming to the ACI 318-19 code. This shows the importance of lateral support to longitudinal reinforcement in compression. However, enforcing Section 25.7.2.3 of ACI 318-19 in Taiwan is not easy as it increases the cost of reinforcing work by 30%-50%.

References

國立臺灣大學 National Taiwan University

- ACI Committee. (2019). ACI 318-19: Building Code Requirements for Structural Concrete and Commentary. *American Concrete Institute: Farmington Hills, MI, USA*.
- Lee, T. K., Chen, C. C., & Zhan, K. S. (2018). The cyclic performance of reinforced concrete columns using the lap-spliced crosstie and lap-spliced inner hoop. Structural Concrete, 19(4), 1146-1156.
- Tanaka, H., Park, R., & McNamee, B. (1985). Anchorage of transverse reinforcement in rectangular reinforced concrete columns in seismic design. *Bulletin of the New Zealand Society for Earthquake Engineering*, *18*(2), 165-190.

Thank You for Your Attention

Any Questions?

Dr. Chih-Hsuan Sung

University of California, Berkeley, USA

Topic：Fully Non-Ergodic Ground Motion Models for Taiwan

FULLY NON-ERGODIC GROUND-MOTION MODELS FOR TAIWAN

Chih-Hsuan Sung[1] and Norman Abrahamson[2] and Jyun-Yan Huang[3] and Shu-Hsien Chao[4]
1. Post-Doc Researcher, Dept. of Civil & Environmental Engineering, UC Berkeley, CA, U.S.A
2. Adjunct Professor, Dep. of Civil & Environmental Engineering, UC Berkeley, CA, U.S.A
3. Associate Research Fellow, NCREE, National Applied Research Laboratories, Taipei, Taiwan
4. Research Fellow, NCREE, National Applied Research Laboratories, Taipei, Taiwan
Email: karensung@berkeley.edu, abrahamson@berkeley.edu, jyhuang@narlabs.org.tw,1206015@narlabs.org.tw

ABSTRACT

This study shows the fully non-ergodic model for the Taiwan region, which applies the Bayless and Abrahamson (2019) GMM as the base ergodic model and further incorporates the non-ergodic source, site, and path terms. The recent approaches for non-ergodic GMMs include the site and source-specific path effects through an isotropic source-specific geometrical spreading term or through cell-specific linear-distance scaling that mimics the effects of a 2-D Q structure. In this study, we capture the additional path effect related to the 3-D velocity structure using the resulting within-site residual to estimate the spatial distribution of the non-ergodic path terms through the varying coefficient model for each site separately. Furthermore, the mean and epistemic uncertainty of the non-ergodic terms can vary by geographical locations. We adopt the Fourier amplitude spectrum GMM rather than the spectral acceleration to build the model because the Fourier transform is a linear operator, so linear effects from small magnitudes can be applied to larger magnitudes. The results show that the fully non-ergodic model leads to an aleatory standard deviation of residual values for the GMM that is reduced by 40-75%, which can have large implications for seismic hazard calculations for the Taiwan region.

Keywords: nonergodic, ground-motion, sigma, aleatory variability, FAS

INTRODUCTION

Probabilistic seismic hazard analysis (PSHA) results are sensitive to the standard deviation for empirical ground-motion models (GMMs), and even small reductions in sigma may significantly impact the hazard level, especially with long return periods. In the past decade, GMMs have been regionalized, but within a region, they are based on the ergodic assumption, which assumes that ground motion follows the same scaling with magnitude, distance, and site conditions within the broad tectonic category. The median and aleatory variability of the ergodic GMM is assumed to be applicable everywhere. In contrast, the non-ergodic GMM captures the systematic source, path, and site effects that change the median (either increase or decrease) and reduce the aleatory variability compared to the ergodic model. As the ground-motion data sets have grown, there has been a trend of moving from ergodic to non-ergodic GMMs.

Lin et al. (2011) estimated the reduction in the aleatory variability between ergodic and non-ergodic GMMs using the Taiwan data sub with multiple recording at a site from sources located at similar locations. The base GMM is ergodic, but they apply the Close index (CI) value to capture the path term from the empirical data. Their results show that by including the systematic source, site, and path effects, there is about a 40% reduction in the total aleatory standard deviation compared to the ergodic GMM. Many studies have shown that the apparent reduction for the specific site with different datasets, we call the partially non-ergodic variance, which is about 10-20% of the ergodic standard deviation (e.g., Atkinson, 2006; Lin et al., 2011; Sung & Lee, 2019).

For the Taiwan partially non-ergodic model, Sung and Lee (2019) built more than 700 single-station GMMs for the Taiwan region. In this approach, site-specific GMMs are developed independently using the ground motions recorded at a single station each station. Each site has its own GMM so there is no site term. This corresponds to fine regionalization of the GMM. The standard deviation is less than the traditional single-station sigma because regional path and source terms are included in the GMM. ; Compared to the ergodic version, there is about a 10-20% reduction in the single-station aleatory

standard deviation. The coefficients and aleatory variability of the single-station GMM can be interpolated to the new site location via the Kriging approach, implying the spatial distribution. This is the simple way to develop a partially non-ergodic GMM; however, this approach cannot provide estimates of the epistemic uncertainty at the new locations as current non-ergodic models do.

The fully non-ergodic GMMs have been developed with different data sets for the pseudo-spectral acceleration (PSA) or Fourier amplitude spectrum (FAS), such as California, France, Cascadia, and southern CA (Abrahamson et al., 2019; Lavrentiadis et al., 2022; Sung et al., 2022a, b). Lavrentiadis et al. (2022) provide an overview of non-ergodic GMMs and introduce the s different methods used in developing non-ergodic terms with an emphasis on Gaussian Process (GP) regression. The varying coefficient model (VCM) is the primary approach used to estimate the non-ergodic terms via the GP regression (Landwehr et al., 2016). The VCM allows the GMM coefficient be random variables following assumed prior distributions that constrain the behavior (posterior distribution) for each non-ergodic term. Furthermore, the VCM GP approach uses hyperparameters (correlation length and variance) that allow for continuously varying non-ergodic terms over the region. .

Most GMMs for engineering applications are developed for 5%-damped pseudo-spectral acceleration (PSA); however, PSA scaling depends on the spectral shape, so the linear source, path, and site effects will not have the same scaling on the PSA values for small and large magnitudes. In contrast, the Fourier transform is a linear operator, so linear effects from small magnitudes can be applied to larger magnitudes. Therefore, the non-ergodic model is developed for the Fourier amplitude spectra (FAS) values rather than for the PSA values in this study.

Here, we apply the Bayless and Abrahamson (2019) empirical FAS GMM for shallow crustal earthquakes in California (BA19) as our base model with a modification to the geometrical spreading term at short distance (< 20 km) from the small-magnitude earthquakes. The combination of a VCM and the cell-specific anelastic attenuation is used to build the Taiwan fully non-ergodic FAS model based on the Taiwan subset data for 0.1Hz to 20Hz. The results of the model are the median value and epistemic uncertainty for the non-ergodic terms for each frequency which can be visualized in a map.

DATA

Fig. 1 shows a map with the event and station locations for the data set that was selected. The National Center for Research on Earthquake Engineering Taiwan SSHAC Level 3 PSHA Project (NCREE, 2018) developed a ground-motion database that includes the records from the Taiwan Strong-Motion Instrumentation Program with available data on all three components. We selected a subset with magnitude greater than 3.5 and the shortest distance from the site to the rupture plane (R_{rup}) less than 300 km and less than the maximum usable distance Rmax. In addition, data from crustal earthquakes are selected using the following criteria: (1) the source type given in the ground motion database is shallow crustal, (2) there are 10 or more recordings for each earthquake, (3) there are 3 or more recordings for each station, (4) the earthquake is not far from the coast, and (5) there are no errors in the location of the station. The resulting subset has 12140 recordings from 184 crustal events that occurred between 1992 and 2018.

The intensity measured used in the ground-motion model is the “Effective Amplitude Spectrum” (EAS) defined by Goulet et al. (2018). The EAS is an orientation-independent measure of the average horizontal-component FAS of the ground acceleration:

$$EAS(f) = \sqrt{\frac{1}{2}[FAS_{H1}(f)^2 + FAS_{H2}(f)^2]}. \quad (1)$$

The EAS is smoothed over a frequency band using the $\log_{10}$-scale Konno and Ohmachi (1998) smoothing window with weights defined as follows:

$$W(f) = \left(\frac{\sin\left(b \log\left(f/f_1\right)\right)}{b \log\left(f/f_1\right)} \right)^4 \quad (2)$$

in which f_1 is the center frequency of the window, b is the window parameter ($=2\pi/b_w$) and b_w is a smoothing parameter. The Konno and Ohmachi smoothing window was selected for use in PEER projects because it led to minimal bias on the amplitudes of the smoothed EAS compared with the unsmoothed EAS. The PEER procedure uses b_w=0.0333 for the smoothing parameter because it leads to a minimal effect on the statistical moments of the EAS that are used in RVT to convert the EAS model to a response spectrum model

ERGODIC MODEL

In this paper, the Taiwan ergodic EAS model is based on a form of the BA19 GMM. We use thee same independent parameters: magnitude, rupture distance, Vs30, $Z_{1.0}$ and Z_{tor} scaling in the ergodic GMM:

$$\ln(EAS_{es}) = c_1 + c_2(\mathbf{M} - 6) + c_3 \ln\left(1 + e^{c_n(c_M - \mathbf{M})}\right) + c_4 \ln\left(R_{rup} + c_5 \cosh(c_6 \max(\mathbf{M} - c_{hm}, 0))\right) + (-0.5 - c_4) \ln\left(\sqrt{R_{rup}^2 + c_{RB}^2}\right) + c_7 R_{rup} + c_8 \ln\left(\frac{\min(V_{S30}, V_{Ref})}{V_{Ref}}\right) + f_{LN} + c_9 \min(Z_{tor}, 20) + c_{10} \ln\left(\frac{\min(Z_{1.0}, 2) + 0.01}{Z_{1.0,Ref} + 0.01}\right) + f_{adj}(M, R_{rup}) + f_{radiation}(M) + \delta B_e + \delta S2S_s + \delta WS_{es} \quad (3)$$

in which M is the moment magnitude; R_{rup} is the shortest distance from the site to the rupture plane in km; c_{RB} is the midpoint of the transition in distance scaling, and was set as 50 km from analyses of next-generation attenuation (NGA) data sets; V_{S30} is in m/s; the reference value of V_{S30}, $V_{Ref,}$ is 1130 m/s; Z_{tor} is the depth to the top of the rupture plane in km; δB_e, $\delta S2S_s$ and δWS_{es} are between-event, between-site, and within-site residuals in nature logarithm unit. The nonlinear site amplification, f_{LN}, is based on an analytical model rather than obtaining it from the empirical dataset, so we consider the same nonlinear-site coefficient from BA19. We did not include the style-of-faulting term here due to the strong trade-off with the Z_{tor} term.

We apply the V_{S30}-$Z_{1.0}$ relationship are based on the Taiwan conditions from NCREE (2018) to define the reference $Z_{1.0}$ value:

$$Z_{1.0,Ref} = \frac{1}{1000} \exp\left(\frac{-4.06}{2} \ln\left(\frac{V_{S30}^2 + 352.7^2}{1750^2 + 352.7^2}\right)\right) \quad (4)$$

The BA19 model does not capture the steeper distance slope at short distances (< 20 km) for small magnitudes seen in recent ground-motion data sets from induced and natural earthquakes (Abrahamson et al. 2020). This is a limitation of the current NGA-West2 GMMs as well. We applied an adjustment function for short distances from small-magnitude earthquakes developed by Abrahamson et al. (2020): $f_{adj}(M, R_{RUP}) = (c_1 + f_R(R_{RUP}, M))T_m(M)$. Here, the $f_R(R_{RUP}, M)$ and $T_m(M)$ are the distance adjustment function and magnitude taper function in equation (8) and equation (9) of Abrahamson et al. (2020), respectively. $f_{radiation}(M)$ is the radiation pattern term for Taiwan (Huang et al., 2022).

NON-ERGODIC MODEL

The non-ergodic model extends the ergodic GMM to account for systematic/repeatable source, site, and path effects. That is, there are source-, site-, and path-specific adjustment terms that are added to the ergodic median prediction, which make the median ground motion dependent on the coordinates of sources and sites:

$$\mu_{nonerg}(M, R, S, t_e, t_s) = \mu_{erg}(M, R, S, \dots) + \delta L2L(t_e) + \delta S2S(t_s) + \delta P2P_Q(t_e, t_s) + \delta P2P_V(t_e, t_s) \quad (5)$$

in which t_e and t_s are the coordinates of the earthquake and the site, respectively, $\delta L2L(t_e)$ is the adjustment to the source term, $\delta S2S(t_s)$ is the site term, and $\delta P2P(t_e, t_s)$ is the path term. The path term can be separated into a term related to the effects of the 2-D Q structure, $\delta P2P_Q(t_e, t_s)$, and a term related to the effects of the 3-D velocity structure, $\delta P2P_V(t_e, t_s)$.

The adjustment map of $\delta L2L(t_e)$ and $\delta S2S(t_s)$ for 5 Hz are captured via the VCM and are shown in **Fig. 2** and **Fig. 3**. These adjustment terms go to zero in regions with sparse data (or without data) and have strong positive or negative values for cells close to observed data. The standard deviations of the epistemic uncertainty of the adjustments for the source and site terms are also shown in the same plots. The lower epistemic uncertainty values are constrained to locations where data are available, whereas the uncertainty is larger for the region with sparse or no data. These epistemic uncertainty values are used in the logic tree for the non-ergodic terms in the hazard calculation.

The recent non-ergodic GMMs include the $\delta P2P_Q(t_e, t_s)$ term by replacing the linear R term by cells. The calculation of the non-ergodic anelastic attenuation term is based on the methodology proposed by Dawood and Rodriguez-Marek (2013) or modified to use the Bayesian formulation described by Kuehn et al. (2019). That is, the linear R scaling is removed from the reference ergodic GMM, the region is broken into a grid of cells, and attenuation through each cell is estimated:

$$\delta P2P_Q(t_e, t_s) = \sum_i^{Nc} \theta_{Attn,i} \, \Delta R_{Rup,i} \tag{6}$$

in which the $\Delta R_{Rup,i}$ is the length of the ray (between the source and the site) in the ith cell (see Fig.5 in Sung et al., 2022b). **Fig. 4ab** show the number of rays that pass through each cell (10km * 10km) at 5 Hz. For Taiwan, there are data to provide good constraints on the path effect per cell. We apply the non-ergodic cell-specific anelastic attenuation terms to modify the ergodic term in the GMM using the cell-specific approach from Kuehn et al. (2019). **Fig. 4cd** show the mean values and epistemic uncertainty of the posterior distribution of the θ_{Attn} per cell at 5.0 Hz. Greater anelastic attenuation coefficients (lower Q) occur in western whereas the smaller values (higher Q) in southern Taiwan. These results are similar to the Taiwan Qs from Wang et al. (2009). However, if the cell did not include any path ray or the final cell-specific anelastic attenuation coefficient (ergodic + non-ergodic adjustment) is positive, the non-ergodic cell-specific anelastic attenuation coefficient (adjustment) goes to zero. That is, the final cell-specific anelastic attenuation coefficient gets back the ergodic liner R term.

The cell-specific anelastic attenuation terms can capture significant path effects on the short-period median ground motion at large distances. For long periods (T > 1sec), the anelastic attenuation coefficient is small and there is little or no effect on the ground motion (Kuehn et al., 2019; Sung et al., 2022b). The limitation of the cells approach is that it does not capture the 3-D path effects at short distances and at long periods that are seen in 3-D simulations. Therefore, a second term, $\delta P2P_V(t_e, t_s)$, is needed to capture the additional path effects due to the 3-D velocity structure. **Fig. 5** is an example of $\delta P2P_V(t_e, t_s)$ for the given site for 1Hz and 5Hz. The correlation length of the path effect is seen by the dimensions of the contours of $\delta P2P_V(t_e, t_s)$.

Fig. 6 shows the aleatory standard-deviations terms for the ergodic, VCM non-ergodic (including source and site terms), non-ergodic (including source, site and $\delta P2P_Q$ terms) and fully non-ergodic (including source, site, $\delta P2P_Q$ and $\delta P2P_V$ terms) GMMs for each frequency. There is a significant reduction of the aleatory variability for the non-ergodic model. For example, at 5 Hz, the ergodic aleatory standard deviation is 0.70, the VCM non-ergodic aleatory standard deviation is 0.52, the non-ergodic aleatory standard deviation without $\delta P2P_V(t_e, t_s)$ is 0.44, and the fully non-ergodic aleatory standard deviation with $\delta P2P_V(t_e, t_s)$ is 0.36. This corresponds to a 49% reduction in standard deviation from the ergodic to the fully non-ergodic GMM. At long periods, there is a reduction in the standard deviation by including the $\delta P2P_Q(t_e, t_s)$ term without the $\delta P2P_V(t_e, t_s)$. This is due to some of the effects of the 3-D velocity structure being mapped into the $\delta P2P_Q(t_e, t_s)$ for this data.

CONCLUSIONS

The recent approaches for non-ergodic GMMs only include the site/source-specific path effects through an isotropic source-specific geometrical spreading term or through cell-specific linear-distance scaling that mimics the effects of a 2-D Q structure. Neither of the recent approaches used in non-ergodic GMMs capture the path effects due to the 3-D velocity structure seen in the 3-D simulations. Although the new path term ($\delta P2P_V$) is still considered in the 2-D, the results show that it captures the path effects in addition to the effects of the 2-D Q structure and significantly reduces the aleatory variability.

The non-ergodic GMM was developed for EAS rather than PSA to avoid the scaling issue being affected by differences in the response spectral shape which allows the use of non-ergodic terms estimated from small-magnitude earthquakes to be applied to large-magnitude earthquakes; however, the response spectrum is still necessary for engineering applications. So, in the next step, the non-ergodic and ergodic GMMs for EAS developed in this study can be converted to GMMs for response spectral values using RVT.

The fully non-ergodic GMM considering the source, site and path terms has about 40-55% smaller total aleatory standard deviation than the ergodic model. That is, the non-ergodic hazard curves can lead to a steeper slope than the ergodic version. In regions with no data, the non-ergodic GMMs can still be used: the mean hazard will approximate the ergodic mean hazard, but the uncertainty range will be broader and provide a better estimate of the uncertainty and the value of collecting/simulating ground-motion data.

REFERENCES

Abrahamson NA, Kuehn NM, Walling M, Landwehr N (2019) Probabilistic seismic hazard analysis in California using non-ergodic ground-motion models. Bull Seism Soc Am 109 (4): 1235–1249.

Abrahamson, NA, Chiou B, Kuehn NM. Modification of the NGA West2 GMMs for Application to Induced Earthquakes. Report to BCHydro, 2020.

Atkinson GM (2006). Single-station sigma, Bull. Seism. Soc. Am., 96, 446–455.

Bayless J, Abrahamson NA (2019) Summary of the BA18 Ground-Motion Model for Fourier Amplitude Spectra for Crustal Earthquakes in California. Bull Seismol Soc Am. 109(5): 2088–2105.

Dawood HM, Rodriguez-Marek A (2013) A method for including path effects in ground-motion prediction equations: An example using the Mw 9.0 Tohoku earthquake aftershocks. Bull Seismol Soc Am. 103 (2B): 1360–1372.

Goulet, C. A., A. Kottke, D. M. Boore, Y. Bozorgnia, J. Hollenback, T. Kishida, A. Der Kiureghian, O. J. Ktenidou, N. M. Kuehn, E. M. Rathje, et al. (2018). Effective amplitude spectrum (EAS) as a metric for ground motion modeling using Fourier amplitudes, 2018 Seismology of the Americas Meeting, Miami, Florida, 14–17 May 2018.

Huang, J.-Y, C.-H Sung, S.-H Chao, and N. Abrahamson (2022) Including Radiation Pattern Effects in Ground-Motion Models for Taiwan, Bull. Seismol. Soc. Am. (submitted)

Landwehr, N., N. M. Kuehn, T. Scheffer, and N. Abrahamson (2016). A non-ergodic ground-motion model for California with spatially varying coefficients, Bull. Seismol. Soc. Am. 106, no. 6, 2574–2583.

Lavrentiadis. G, N. Abrahamson, K. Nicolas, Y. Bozorgnia, and more (2022) Overview and Introduction to Development of Non-Ergodic Earthquake Ground-Motion Models, Bulletin of Earthquake Engineering. doi.org/10.48550/arXiv.2111.07921.

Lin, PS, Chiou B, Abrahamson NA, Walling M, Lee CT, Cheng CT (2011) Repeatable source, site, and path effects on the standard deviation for empirical ground-motion prediction models. Bull Seismol Soc Am. 101: 2281–2295.

Kuehn NM, Abrahamson NA, Walling MA. Incorporating non-ergodic path effects into the NGA-West2 ground-motion prediction equations. Bulletin of the Seismological Society of America 2019; 109 (2): 575–585.

Konno, K., and T. Ohmachi (1998). Ground-motion characteristics estimated from spectral ratio between horizontal and vertical components of microtremor, Bull. Seismol. Soc. Am. 88, 228–241.

National Center for Research on Earthquake Engineering (NCREE) (2018), Web page for reevaluation of probabilistic seismic hazard of nuclear facilities in Taiwan using SSHAC level 3 methodology project, available at http://sshac.ncree.org.tw.

Sung, C.-H. and N. Abrahamson (2022a). A Partially Non-Ergodic Ground-Motion Model for Cascadia Interface Earthquakes, Bulletin of the Seismological Society of America. doi: 10.1785/0120210330.

Sung, C.-H., N. Abrahamson, N. Kuehn, P. Traversa, and I. Zentner (2022b). A non-ergodic ground-motion model of Fourier amplitude spectra for France, Bulletin of Earthquake Engineering. DOI: 10.1007/s10518-022-01403-1.

Sung, C.-H. and C.-T. Lee (2019). Improvement of the Quantification of Epistemic Uncertainty 480 Using Single-Station Ground-Motion Prediction Equations, Bulletin of the Seismological Society 481 of America 109(4), 1358–1377

Yu-Ju Wang, Kuo-Fong Ma, Frederic Mouthereau and Donna Eberhart-Phillips (2010) Three-dimensional Qp- and Qs-tomography beneath Taiwan orogenic belt: implications for tectonic and thermal structure, Geophysical Journal International, 180(2), 891–910.

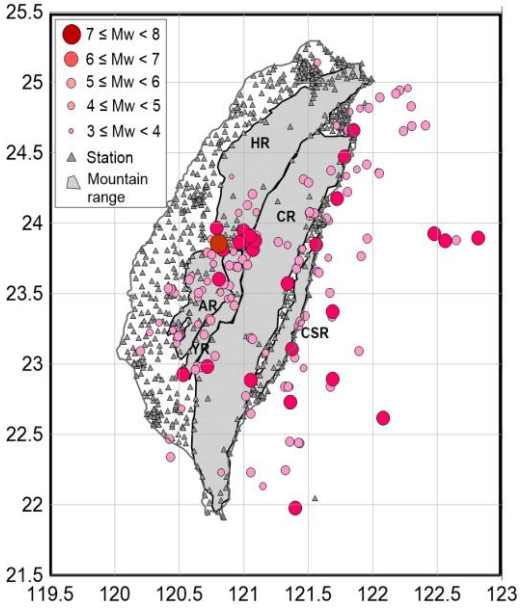

Figure 1. Map showing locations of the strong-motion stations and crustal earthquakes of Taiwan used in this study.

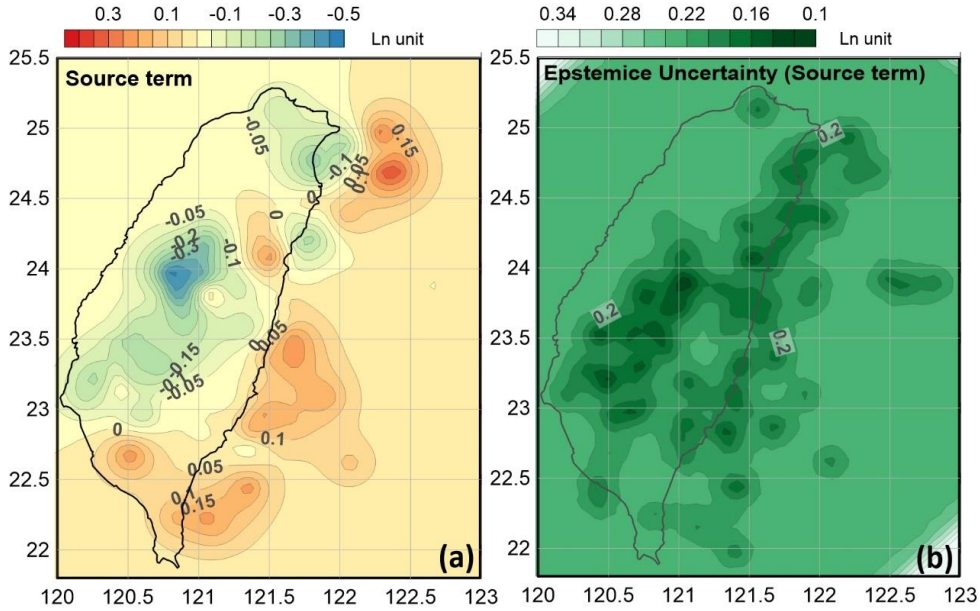

Figure 2. Spatially varying adjustment of (a) constant event terms and (b) epistemic uncertainty.

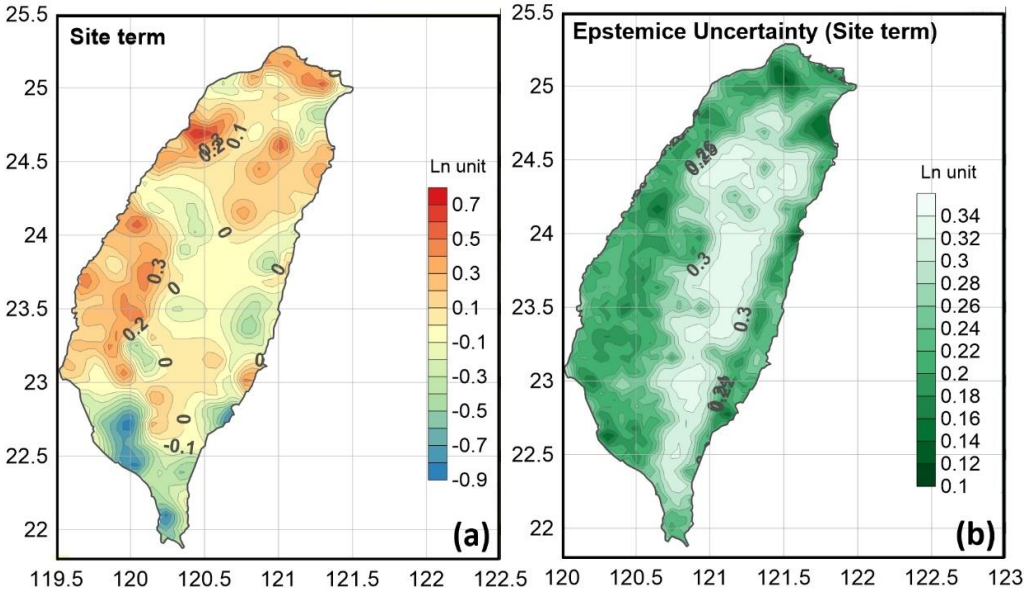

Figure 3. Spatially varying adjustment of (a) constant site terms and (b) epistemic uncertainty.

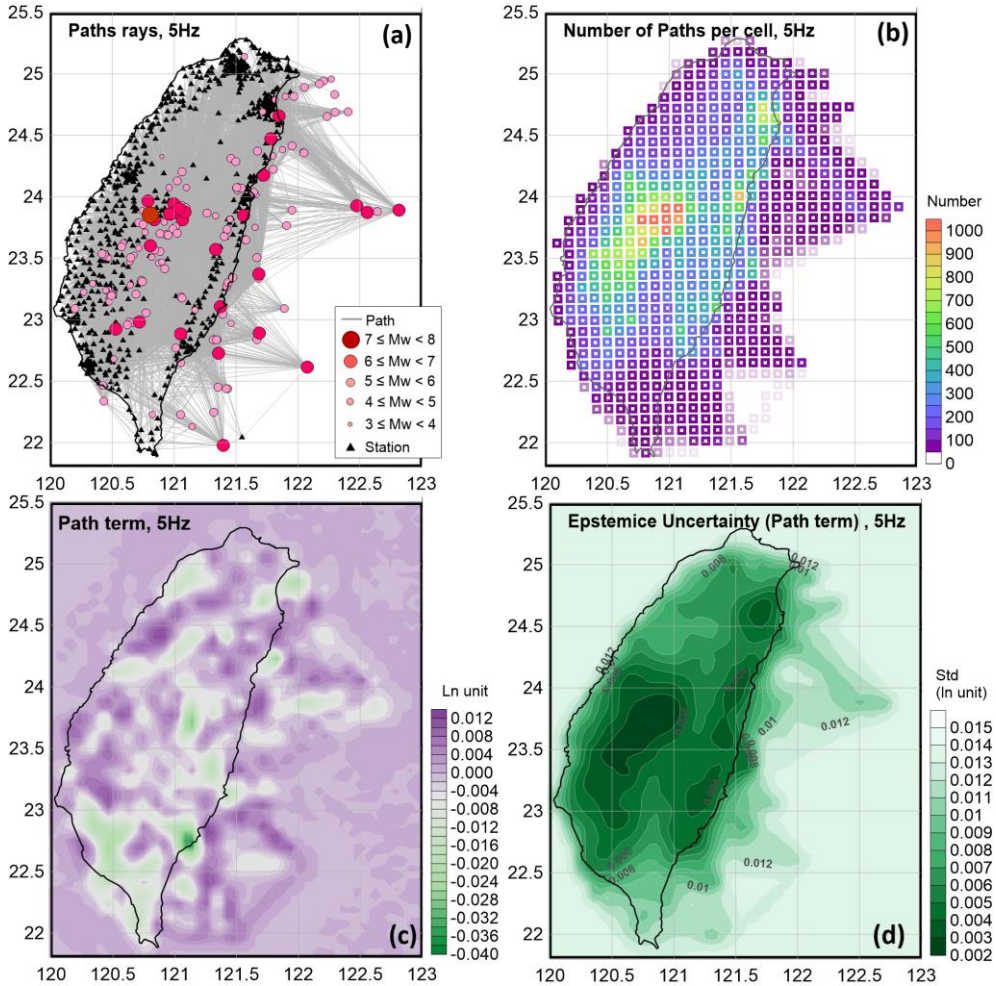

Figure 4. (a) Map of path rays with stations and earthquakes at 5.0 Hz, each gray line shows the path from the earthquake to the recording station. (b) Number of paths per cell, the cell size is 10km times 10km. (c) Mean values of the posterior distribution of the θ_{Attn} per cell. (d) Standard deviation of the posterior distribution of the θ_{Attn} per cell.

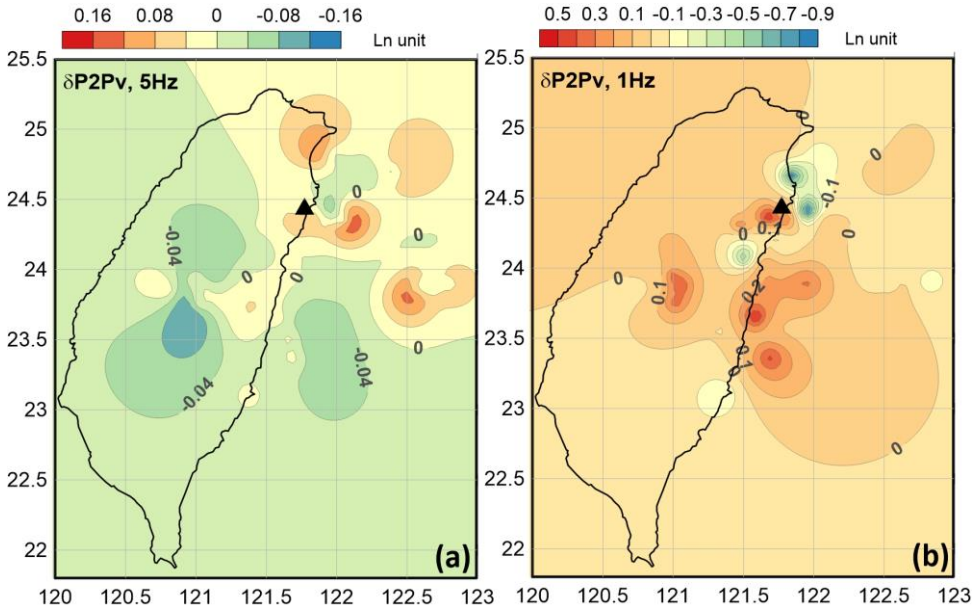

Figure 5. Mean values of the posterior distribution of the $\delta P2P_V$ per cell for the given site (ILA066). (a) 5Hz and (b) 1Hz.

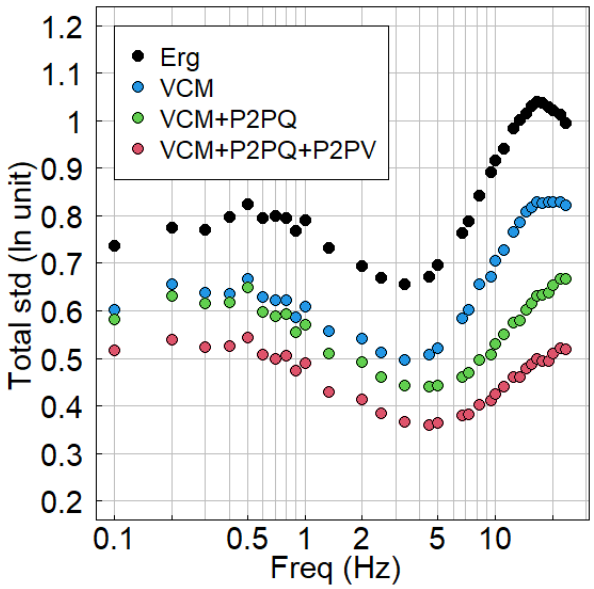

Figure 6. The aleatory standard deviation (ln unit) of ergodic, VCM non-ergodic, non-ergodic, and fully non-ergodic GMMs.

Prof. Georgios Tsampras

University of California San Diego, USA

Topic：Reusable Force-Limiting Connection with Variable Friction Force for High-Performance Buildings

REUSABLE FORCE-LIMITING CONNECTION WITH VARIABLE FRICTION FORCE FOR HIGH-PERFORMANCE BUILDINGS

Kaixin Chen[1], Georgios Tsampras[2], Kyoungyeon Lee[1], and C. Franco Mayorga[1]
1. Graduate Student Researcher, University of California San Diego, La Jolla, USA
2. Assistant Professor, University of California San Diego, La Jolla, USA
Email: kac011@ucsd.edu, gtsampras@ucsd.edu, kyl008@ucsd.edu, cfmayorg@ucsd.edu

ABSTRACT

This paper presents a reusable force-limiting deformable connection with a discrete variable friction force for high-performance reinforced concrete core wall buildings. The connection is designed to limit the seismic-induced horizontal forces transferred from the floors to the core wall piers, control the relative displacement between the floors and the core wall piers, and accommodate the three-dimensional kinematics expected between the floors and the core wall piers. The connection is simple to manufacture and assemble. It is designed to withstand multiple earthquake events without damage. The components and the assembly of the friction-based force-limiting deformable connection are presented. The expected kinematics and the expected force-displacement response are discussed. Preliminary numerical simulation results are used to validate the expected cyclic force-displacement response of the connection. Limited results from preliminary earthquake numerical simulations of an eighteen-story reinforced concrete core wall building model are discussed. The numerical simulation results show that it is possible to design a reusable force-limiting connection with friction force that increases at target design displacement levels to limit the magnitude of the seismic responses in the eighteen-story reinforced concrete core wall building model and accommodate the three-dimensional kinematics expected between the floors and the core wall piers.

Keywords: friction-based force-limiting connection; structural component reusability; high-performance buildings; reinforced concrete core wall structure

INTRODUCTION

Practical force-limiting deformable connections between the floors and the vertical elements of seismic force-resisting systems (e.g., reinforced concrete planar structural walls and self-centering concentrically-braced steel frames) have been developed (Zhang et al. 2014; Tsampras 2016; Tsampras et al. 2016, 2017, 2018; Zhang et al. 2018; Tsampras and Sause 2022). Figure 1(a) shows a schematic example of a building with reinforced concrete planar structural walls and force-limiting connections. The force-limiting connections consist of buckling-restrained braces or friction devices and low-damping rubber bearings. The force-limiting connections allow relative displacement between the floors and the seismic force-resisting system and transfer the seismic-induced horizontal forces from the floors to the seismic force-resisting system. The compressive stiffness of the rubber bearings ensures the out-of-plane stability of the structural walls. The shear stiffness of the rubber bearings provides post-elastic stiffness to the force-limiting connections required to limit the inelastic deformation demands between the floors and the planar structural walls. Figure 1(b) shows a sketch of the friction device developed and tested by Tsampras et al. (2018). Results from earthquake numerical simulations showed that buildings with planar reinforced concrete structural walls and force-limiting connections have reduced magnitude and dispersion in the force and acceleration responses compared to conventional buildings (Tsampras et al. 2016, 2017, 2018).

Tall buildings commonly use a core wall or multiple core walls instead of planar structural walls to resist the seismic-induced horizontal forces. Lee et al. (2022) conducted a preliminary study to assess the seismic response of an eighteen-story building with a reinforced concrete core wall and friction-based force-limiting connections between the floors and the core wall piers. Lee et al. (2022) showed that it is not possible to use low-damping rubber bearings to add post-elastic stiffness in force-limiting

connections between floors and core wall piers since the compressive stiffness of the rubber bearings practically restrains the horizontal displacement of the floors relative to the core wall piers. To eliminate restraining the horizontal displacement of the floors relative to the core wall piers, Lee et al. (2022) assumed a modified force-limiting connection that consists of a friction device without low-damping rubber bearings. The force of the assumed modified friction-based force-limiting connection was designed to increase at predetermined displacement values resulting to a discrete variable friction force. The discrete variable friction force in the assumed modified friction-based force-limiting connection resulted in a non-zero effective post-elastic stiffness. Results from the preliminary earthquake numerical simulations of the eighteen-story core wall building model showed that it is possible to use the assumed modified friction-based force-limiting connection with discrete variable friction force to limit the magnitude of the force and acceleration responses while maintaining reasonable force-limiting connection deformation demand.

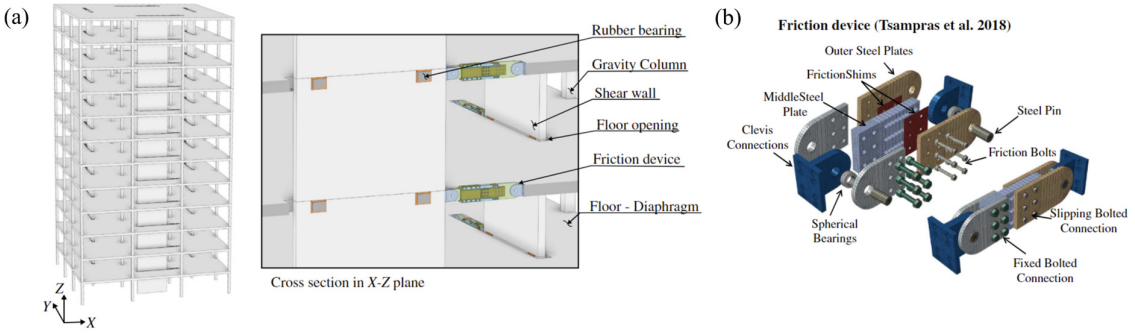

Figure 1 (a) Schematic example of a building with reinforced concrete planar structural walls and force-limiting connections. (b) Sketch of the friction device developed by Tsampras et al. (2018).

In this paper, the preliminary physical embodiment of a reusable force-limiting connection with discrete variable friction force is presented. The connection is termed Modified Friction Device (Modified FD) in this paper. The term Modified is used to indicate that a non-zero effective post-elastic stiffness is achieved through the discrete variable friction force. The components and the assembly of the Modified FD are discussed. Results from preliminary numerical simulations are used to validate the expected kinematics and the expected force-displacement response of the Modified FD. Limited preliminary earthquake numerical simulation results are used to compare the seismic response of an eighteen-story reinforced concrete core wall building model with Modified FDs with the seismic response of the building model with assumed monolithic connections between the floors and the core wall piers.

REUSABLE FRICTION-BASED FORCE-LIMITING CONNECTION

Components

Figure 2 shows a sketch of the components, the exploded view, the assembly, and the front view of the Modified FD. The Modified FD consists of an internal plate, two external plates, four curved edge plates, four rectangular friction shims, four curved edge friction shims, ten structural bolts with flat washers and nuts, and a spherical bearing. The end clevises used to attach a Modified FD on a floor and a core wall pier are not shown in Figure 2. Pretension load is applied to the bolts to clamp the external plates, the curved edge plates, the friction shims, and the internal plate. The bolted components create the assembly of the Modified FD. Friction interfaces are established in the contact surfaces between the internal plate and the friction shims. The rectangular friction shims are not expected to move relative to the external plates. The curved edge friction shims are not expected to move relative to the curved edge plates. The slots in the internal plate allow the longitudinal motion of the friction shims, the external plates, and the curved edge plates relative to the internal plate. The curved edge plates and the curved edge friction shims are positioned within slots in the external plates, and they are not expected to move relative to the internal plate until the curved edges of the friction shims and the plates are in contact with

the external plates. The gap between the curved edge plates and the short slots in the external plates is termed D_1, and the gap between the curved edge plates and the long slots in the external plates is termed D_2, as shown in Figure 2(d). The spherical bearings at the ends of the Modified FD allow the rotational motions and restrain the translational motions within the plane of the plates. As a result, the Modified FD is expected to develop axial load along its longitudinal direction and zero moments at the ends.

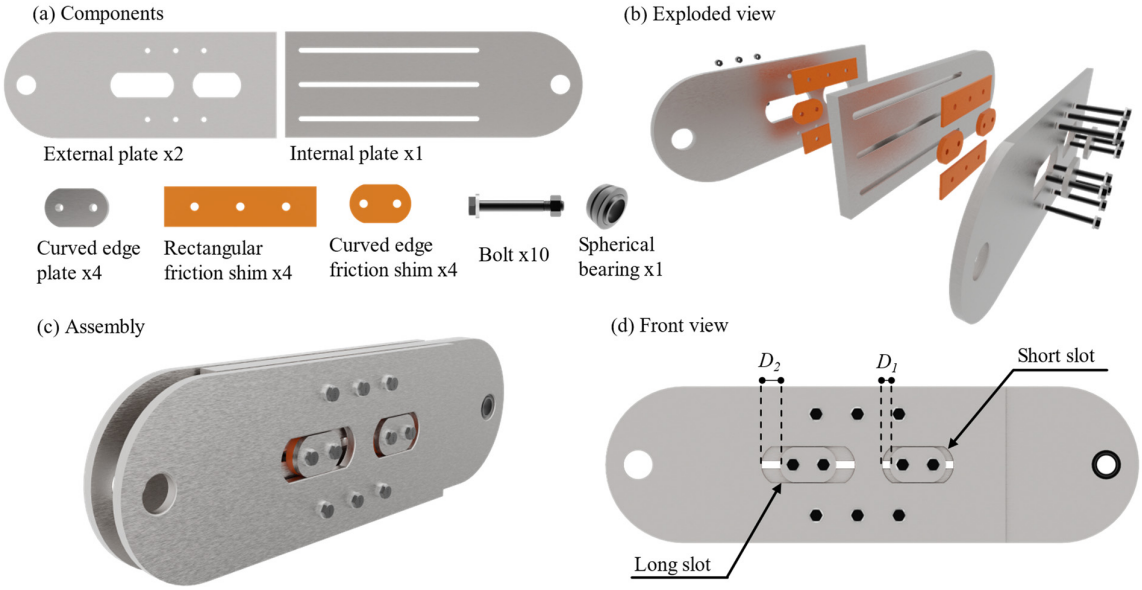

Figure 2 Modified FD (a) components, (b) exploded view, (c) assembly, and (d) front view with initial gap dimensions D1 and D2 between the curved edge plates and the slots in the external plates.

Expected kinematics and expected force-displacement response

Figure 3 shows the expected kinematics and the expected force-displacement response of the Modified FD. The term "expected" is used in this paper because the kinematics and force-displacement response have not been validated through experimental testing yet. The following parameters define the expected kinematics and the expected force-displacement response: the initial gap between the curved edge plates and the short slot in each external plate, D_1; the initial gap between the curved edge plates and the long slot in each external plate, D_2; the friction force generated by the frictional interface between the internal plate and the rectangular friction shims, F_1; the friction force generated by the frictional interface between the internal plate and the curved edge friction shims in the short slot of the external plates, F_2; the friction force generated by the frictional interface between the internal plate and the curved edge friction shims in the long slot of the external plates, F_3; and the values of the elastic stiffnesses K_1, K_2, and K_3. Six phases define the expected kinematics of the Modified FD that result to the expected force-displacement response. The expected kinematics and the expected force-displacement response described below assume that the translational motion of the internal plate is restrained (i.e., pinned condition at the end of the internal plate) and that a displacement along the longitudinal direction of the Modified FD is applied at the ends of the external plates. Positive displacement results in axial compression in the Modified FD and negative displacement results in axial tension in the Modified FD. The following section presents the six phases. In this paper, the discussion of the kinematics in the six phases ignores the elastic deformations F_1/K_1, F_2/K_2, and F_3/K_3 assuming $K_1=K_2=K_3 \cong \infty$. Thus, the rigid body kinematics of the Modified FD components are considered.

Phase 1 – Sliding along the positive direction of motion with friction force F_1: The increase of the imposed displacement in the Modified FD results in increasing force with stiffness K_1. When the force in the Modified FD becomes equal to F_1 the rectangular friction shims and the external plates start moving relative to the internal plate. The sliding at the frictional interface between the internal plate and the rectangular friction shims results to F_1. F_1 can be estimated using Coulomb theory, $F_1 = n_{s1}N_1\mu_{s1}$,

where $n_{s1} = 2$ is the number of friction interfaces; N_1 is the total load from the six bolts acting normal to the friction interfaces between the rectangular friction shims and the internal plate; μ_{s1} is the coefficient of friction in the friction interfaces between the rectangular friction shims and the internal plate.

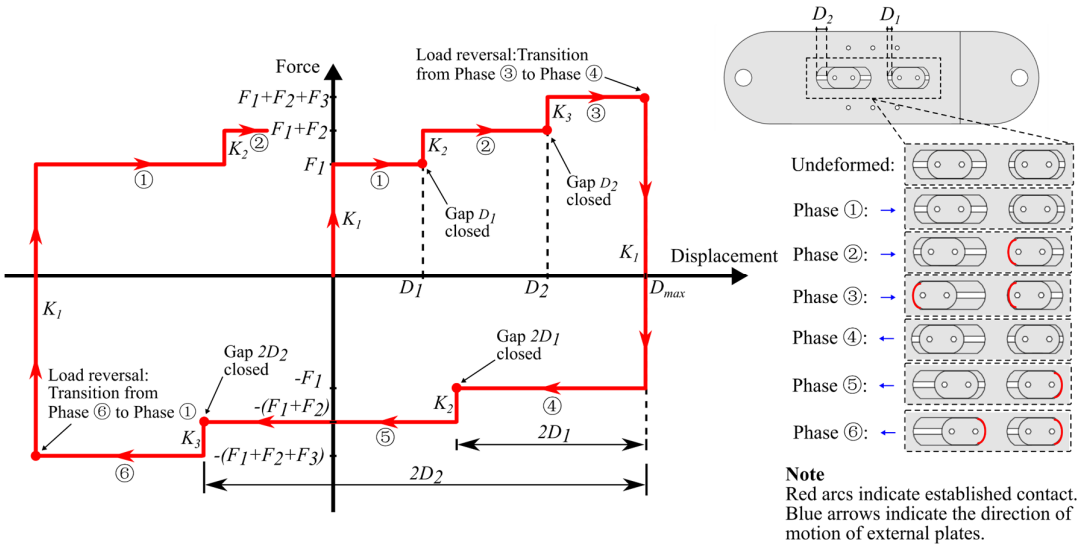

Figure 3 Expected kinematics and expected force-displacement response of Modified FD.

Phase 2 – Sliding along the positive direction of motion with friction force F_1+F_2: Assuming that the elastic deformations are negligible, once the value of displacement reaches D_1, the external plates contact the curved edge plates located in the short slots. As the displacement in the Modified FD increases, the force in the Modified FD increases with stiffness K_2. When the force in the Modified FD becomes equal to F_1+F_2, the curved edge plates and the curved edge friction shims in the short slots start moving relative to the internal plate. The sliding at the frictional interface between the internal plate and the curved edge friction shims in the short slots results to F_2. F_2 can be estimated using Coulomb theory, $F_2 = n_{s2}N_2\mu_{s2}$, where $n_{s2} = 2$ is the number of friction interfaces; N_2 is the total load from the two bolts acting normal to the friction interfaces between the curved edge friction shims in the short slots and the internal plate; μ_{s2} is the coefficient of friction in the friction interfaces between the curved edge friction shims in the short slot and the internal plate. The total force in the Modified FD during this phase is F_1+F_2.

Phase 3 – Sliding along the positive direction of motion with friction force $F_1+F_2+F_3$: Assuming that the elastic deformations are negligible, once the value of the displacement reaches D_2, the external plates contact the curved edge plates located in the long slots. As the displacement in the Modified FD increases, the force in the Modified FD increases with stiffness K_3. When the force in the Modified FD becomes equal to $F_1+F_2+F_3$, the curved edge plates and the curved edge friction shims in the long slots start moving relative to the internal plate. The sliding at the frictional interface between the internal plate and the curved edge friction shims in the long slots results to F_3. F_3 can be estimated using Coulomb theory, $F_3 = n_{s3}N_3\mu_{s3}$, where $n_{s3} = 2$ is the number of friction interfaces; N_3 is the total load from the two bolts acting normal to the friction interfaces between the curved edge friction shims in the long slot and the internal plate; μ_{s3} is the coefficient of friction in the friction interfaces between the curved edge friction shims in the long slots and the internal plate. The total force in the Modified FD during this phase is $F_1+F_2+F_3$. The motion continues until the Modified FD reaches the maximum imposed displacement D_{max}.

Phase 4 – Sliding along the negative direction of motion with friction force $-F_1$: The reversal of the imposed displacement reduces the force in the Modified FD with elastic stiffness K_1. When the force in the Modified FD becomes equal to $-F_1$ the external plates start moving relative to the internal plate along the negative direction. The curved edge friction shims are not expected to move relative to the internal

plate during this phase. The rectangular friction shims and the external plates move relative to the internal plate resulting to a force with magnitude equal to F_1.

Phase 5 – Sliding along the negative direction of motion with friction force $-(F_1+F_2)$: Assuming that the elastic deformations are negligible, once the value of displacement reaches D_{max} - $2D_1$, the external plates contact the curved edge plates located in the short slots. As the displacement in the Modified FD decreases, the force in the Modified FD decreases with stiffness K_2. When the force in the Modified FD becomes equal to $-(F_1+F_2)$, the curved edge plates and the curved edge friction shims in the short slots start moving relative to the internal plate. The sliding at the frictional interface between the internal plate and the curved edge friction shims in the short slots results to a force with magnitude equal to F_2. The total force in the Modified FD during this phase is $-(F_1+F_2)$.

Phase 6 – Sliding along the negative direction of motion with friction force $-(F_1+F_2+F_3)$: Assuming that the elastic deformations are negligible, once the value of displacement reaches D_{max} - $2D_2$, the external plates contact the curved edge plates located in the long slots. As the displacement in the Modified FD decreases, the force in the Modified FD decreases with stiffness K_3. When the force in the Modified FD becomes equal to $-(F_1+F_2+F_3)$, the curved edge plates and the curved edge friction shims in the long slots start moving relative to the internal plate. The sliding at the frictional interface between the internal plate and the curved edge friction shims in the long slots results to a force with magnitude equal to F_3. The total force in the Modified FD during this phase is $-(F_1+F_2+F_3)$.

Preliminary numerical force-displacement response

The development of the Modified FD requires experimental characterization of its kinematics and its force-displacement response. However, finite element analysis can be used for the preliminary assessment and the rapid digital prototyping of the Modified FD.

Preliminary numerical simulations with two types of finite element models are conducted to validate numerically the expected force-displacement response of the Modified FD. The first model uses solid finite elements, and it is termed *Solid Model* in this paper. The Solid Model simulates explicitly the internal plate, the external plates, the curved edge plates, and the friction shims. The Solid Model simulates explicitly the contact interfaces between the modeled components of the Modified FD. The second model simulates the expected force-displacement response of the Modified FD at a macroscopic level using a truss finite element model. The second model is termed *Truss Model* in this paper. The Truss Model is used to simulate the force-displacement response of the Modified FD in earthquake numerical simulations of buildings. The Solid Model and the Truss model assume D_1 = 2 cm (i.e., 0.8 in.); D_2 = 5 cm (i.e., 2 in.); F_1 = 596 kN (i.e., 134 kips). $F_2 = F_3$ = 222.4 kN (i.e., 50 kips). A pseudo-static sinusoidal axial displacement loading history is applied to the Modified FD models. The maximum applied displacement is equal to 6.35 cm (i.e., 2.5 in). Figure 4 shows the force-displacement response computed from the numerical simulations. The Solid Model confirmed the expected kinematics and the expected force-displacement response in the Modified FD. The Truss Model approximated reasonably well the force-displacement response computed using the Solid Model.

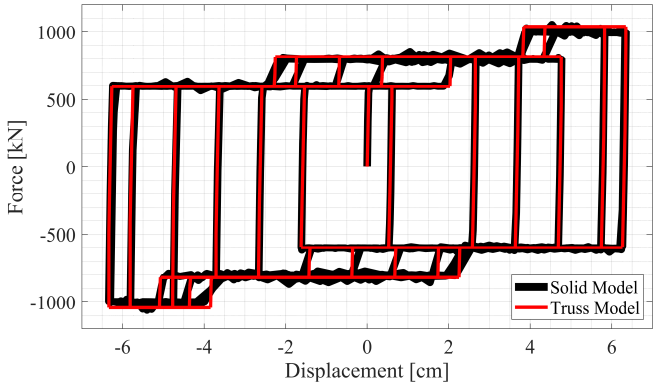

Figure 4 Preliminary numerical simulation results.

PRELIMINARY EARTHQUAKE NUMERICAL SIMULATIONS

Preliminary earthquake numerical simulations of an eighteen-story reinforced concrete core wall building are conducted to compare the seismic response of a building model with Modified FDs to the seismic response of a building model with monolithic connections between the floors and the core wall piers. This study uses a building model developed by Lee et al. (2022).

The building model was subjected to a ground motion recorded at Shin-Osaka station during the 1995 earthquake in Kobe, Japan. Figure 5(a) and Figure 5(b) show the scaled ground acceleration time histories of the two horizontal components SHI000 (H1) and SHI090 (H2), respectively. Figure 5(c) shows the response spectra of the scaled ground motion and the design spectrum. H1 and H2 are applied at the base of the model along the global X and Y direction, respectively.

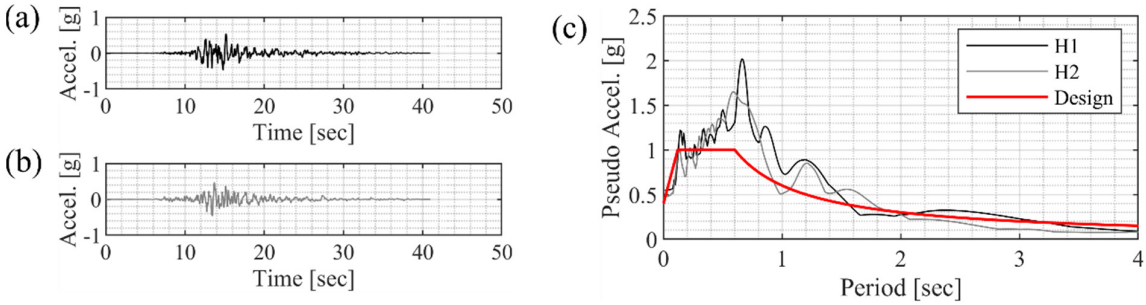

Figure 5 Scaled ground acceleration of the two horizontal components (a) SHI000 (H1) and (b) SHI090 (H2), and (c) pseudo acceleration response spectra of scaled ground motions and design spectrum with a 5% damping ratio.

Figure 6 shows the time history response of the roof total acceleration of the building model with the monolithic connections and with the Modified FD. The use of the Modified FD reduces the roof total acceleration. There is a 38% and 27% reduction in the peak total acceleration in global X-direction and in global Y-direction, respectively.

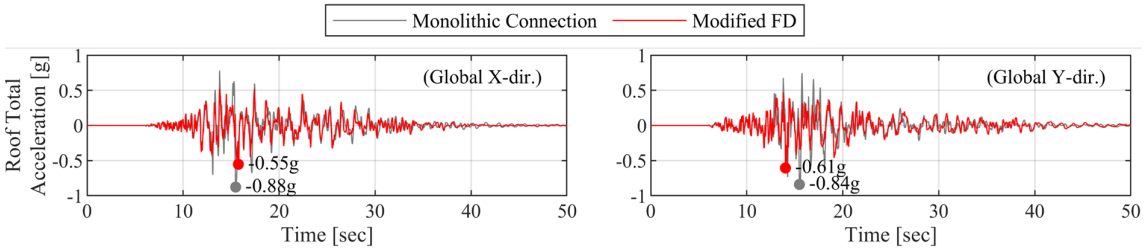

Figure 6 Time history response of the roof total acceleration.

Figure 7 shows the distribution of the strain demand at the base section of the core wall piers at the time when the moment reaction is equal to the absolute maximum value of the moment reactions from the four core wall piers. The use of the Modified FD reduced the absolute values of the maximum and minimum strain in the core wall base section by approximately 49% and 54%, respectively, compared to the use of monolithic connections. The reduction in the magnitude of the strain demands indicates a potential reduction in the expected structural damage in the core wall piers.

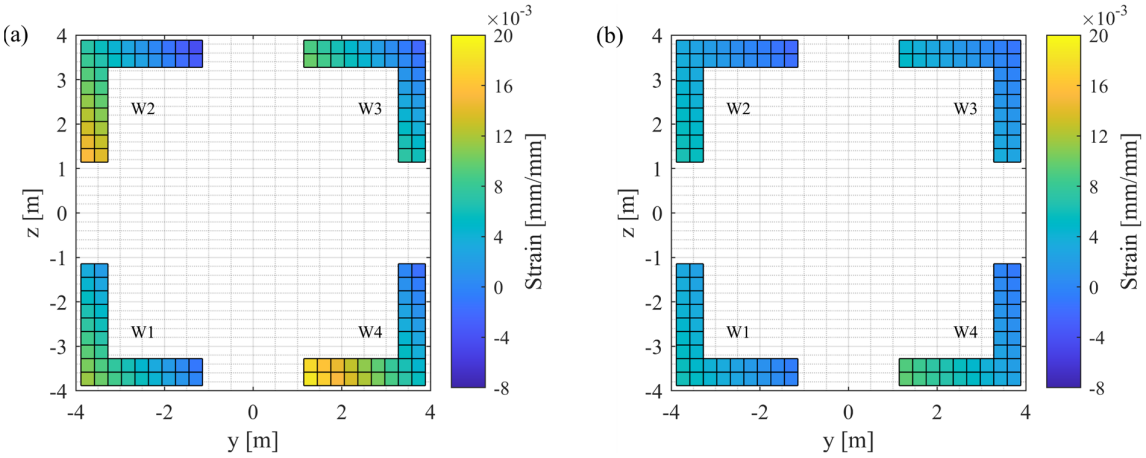

Figure 7 Strain distribution at the base of the core wall piers for the case with (a) monolithic connections and (b) Modified FDs.

CONCLUSIONS

This paper presented a reusable force-limiting deformable connection with a discrete variable friction force for high-performance reinforced concrete core wall buildings. The force-limiting connection was termed Modified FD. The Modified FD aims to limit the seismic-induced horizontal forces transferred from the floors to the core wall piers of reinforced concrete core wall buildings, control the relative displacement between the floors and the core wall piers, and accommodate the three-dimensional kinematics expected between the floors and the core wall piers. The expected kinematics and the expected force-displacement response of the Modified FD were discussed. Preliminary finite element analyses conducted for the preliminary assessment of the kinematics and the force-displacement response of the Modified FD. Limited earthquake numerical simulation results show that the use of Modified FDs between the floors and the core wall piers in an eighteen-story reinforced concrete core wall building model reduces the magnitude of the roof total acceleration and the strain at the core wall base compared to a model of a conventional core wall building. The results indicated that the use of the Modified FD could potentially limit the residual damage in core wall structures.

Parametric earthquake numerical simulations are required to determine the values of the design parameters of the Modified FD that result to acceptable seismic performance of core wall buildings. Experimental characterization of the kinematics and the force-displacement response of the Modified FD is required.

ACKNOWLEDGMENTS

The authors are grateful for financial support provided by Structural Engineering Distinguished Fellowship and additional support from the Department of Structural Engineering at UC San Diego. Any opinions, findings, and conclusions expressed in this paper are those of the authors and do not necessarily reflect the views of the parties acknowledged here.

REFERENCES

Lee, Kyoungyeon, Kaixin Chen, and Georgios Tsampras. 2022. “Seismic Response of Core Wall Building with Friction-Based Force- Limiting Connections.” in *3rd European Conference on Earthquake Engineering & Seismology (3ECEES)*.

Tsampras, Georgios. 2016. “Force-Limiting Deformable Floor Diaphragm Connection for Earthquake-Resistant Buildings.” Doctoral dissertation, Lehigh University.

Tsampras, Georgios, and Richard Sause. 2022. "Force-Based Design Method for Force-Limiting Deformable Connections in Earthquake-Resistant Buildings." *Journal of Structural Engineering* 148(10):04022150. doi: 10.1061/(ASCE)ST.1943-541X.0003456.

Tsampras, Georgios, Richard Sause, Robert B. Fleischman, and Jose I. Restrepo. 2017. "Experimental Study of Deformable Connection Consisting of Buckling-Restrained Brace and Rubber Bearings to Connect Floor System to Lateral Force Resisting System: Experimental Validation of BRB+RB Deformable Connection." *Earthquake Engineering & Structural Dynamics* 46(8):1287–1305. doi: 10.1002/eqe.2856.

Tsampras, Georgios, Richard Sause, Robert B. Fleischman, and José I. Restrepo. 2018. "Experimental Study of Deformable Connection Consisting of Friction Device and Rubber Bearings to Connect Floor System to Lateral Force Resisting System." *Earthquake Engineering & Structural Dynamics* 47(4):1032–53. doi: 10.1002/eqe.3004.

Tsampras, Georgios, Richard Sause, Dichuan Zhang, Robert B. Fleischman, Jose I. Restrepo, David Mar, and Joseph Maffei. 2016. "Development of Deformable Connection for Earthquake-resistant Buildings to Reduce Floor Accelerations and Force Responses." *Earthquake Engineering & Structural Dynamics* 45(9):1473–94. doi: 10.1002/eqe.2718.

Zhang, D., R. Fleischman, J. Restrepo, R. Sause, J. Maffei, D. Mar, and G. Monti. 2014. "Development of a Floor Inertial Force Limiting Anchorage System Building Seismic Response." in *10th U.S. National Conference on Earthquake Engineering*.

Zhang, Zhi, Robert B. Fleischman, Jose I. Restrepo, Gabriele Guerrini, Arpit Nema, Dichuan Zhang, Ulina Shakya, Georgios Tsampras, and Richard Sause. 2018. "Shake-Table Test Performance of an Inertial Force-Limiting Floor Anchorage System." *Earthquake Engineering & Structural Dynamics* 47(10):1987–2011. doi: 10.1002/eqe.3047.

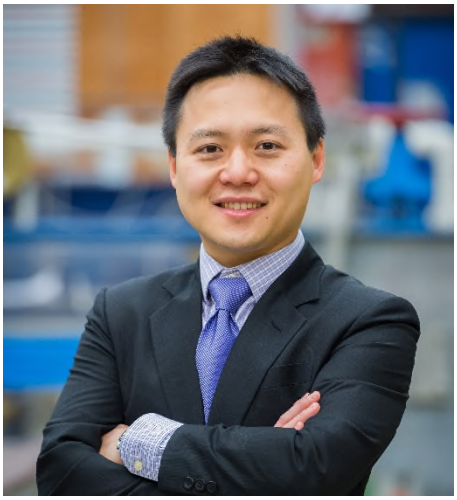

Prof. Tony Yang

The University of British Columbia, Canada

Topic： Development of high-performance carbon neutral resilient infrastructures

(The material of the speaker's presentation has not been authorized for publication in the proceedings.)

(1b) Ground motion prediction equations and engineering applications of ground motion simulation

A METHODOLOGY FOR DEVELOPING EMPIRICAL GROUND-MOTION MODELS COMPATIBLE WITH SHEAR-WAVE VELOCITY PROFILES AND KAPPA

Van-Bang Phung[1] and Norman Abrahamson[2]

1. Post-doc, Dept. of Civil Engineering, University of California, Berkeley, CA 94720, USA.
2. Adjunct Professor Dept. of Civil Engineering, University of California, Berkeley, CA 94720.

Email: phungvb@earth.sinica.edu.tw, abrahamson@berkeley.edu

ABSTRACT

A method is presented for developing empirical effective amplitude spectrum (EAS) ground-motion models (GMMs) that include the 1-D shear-wave (V_S) velocity profiles and the high-frequency attenuation parameter (κ) which are consistent with the site scaling in the GMM. Rather than simply providing the site scaling in terms of the time-averaged shear-wave velocity over the top 30 m (V_{S30}), the method also provides the corresponding depth-dependent $V_S(z)$ profiles and the κ value for the selected V_{S30} value as a result of the inverse quarter-wave-length method (IQWL). Holding the V_{S30} scaling due to the inverted 1-D profiles fixed, the regression for the GMM coefficients is repeated to allow the path and source terms to adjust to the fixed V_{S30} scaling for the 1-D V_S profiles. Not all of the empirical amplification can be explained by the 1-D V_S profiles and κ values. For soft sites ($V_{S30} < 500$ m/s), and intermediate periods (0.5-2 sec), there is additional amplification in the empirical data which is attributed to 3-D path and site effects. Using the proposed method, the resulting GMM provides a V_S profile, κ, and 3-D effect for each V_{S30} value, which provides a more informative handoff of ground-motion information for use in site-specific site response studies.

Keywords: Ground Motion Models, Effective Amplitude Spectrum, Inverse Quarter Wave Length, Shear-Wave Profiles, Site Amplification, and kappa

INTRODUCTION

Site effects in GMMs are typically characterized by the V_{S30}; however, the V_{S30} is not a fundamental parameter for site amplification. The V_{S30} scaling in the GMM is only applicable to sites for which the site-specific $V_S(z)$ profile is consistent with the average $V_S(z)$ profile represented by GMM for the given V_{S30} value. Therefore, the full $V_S(z)$ profile and kappa are required to estimate the site factors implied by the V_{S30} scaling in GMMs. This concept is used as part of the $V_S - \kappa$ correction approach to adjusting GMMs from one region to another (Williams & Abrahamson, 2021). Given the two Vs profiles (one for GMM and one for a site), the ratio of the site amplification is used to adjust ground motion from the GMM to the site-specific ground motion according to the following equation:

$$SA_{site}(T) = \left(\frac{AMP_{site-Vs}(T)}{AMP_{GMM-Vs}(T)}\right) SA_{GMM}(T) \quad (1)$$

Most empirical GMMs do not provide the $V_S(z)$ profile and the κ, so they are estimated by the user of the GMM which can have large uncertainties and may be inconsistent with the scaling in the GMM. Rather than have the users of GMMs estimate these parameters, a better approach is for GMMs to include the $V_S(z)$ profile and the kappa that is consistent with the V_{S30} scaling in the GMM. In this paper, we propose a procedure for developing the V_{S30} −dependent 1-D velocity profiles and kappa values as part of the GMM development, rather than estimating the V_S profile and kappa independent of the development of the GMM. A subset of the NGA-W2 data from earthquakes in California is used for this application. The selected dataset includes 12039

ground motions from 227 earthquakes in the magnitude range of M3.0 - M7.3 recorded at 1452 sites in the distances range of 0 - 350 km. The ground-motion measure selected for the analysis is the effective amplitude spectrum (EAS), which is the square root of average power on the FAS from two horizontal components.

APPROACH FOR DEVELOPING GMMS WITH COMPATIBLE VS-PROFILES

The traditional approach for developing GMMs is to conduct the regression one frequency at a time for all V_{S30} values, but the 1-D velocity profile for a given V_{S30} value affects the site amplification at all frequencies. We use an iterative method that alternate between frequency-by-frequency FAS model development for all V_{S30} values and V_{S30}-by-V_{S30} 1-D V_S profile development for all frequencies. The steps in this approach are listed below:

Step 1.

Develop an initial GMM for the Fourier Amplitude Spectrum with the site factor relative to a hard-rock site condition (V_S=3500 m/s) including random effects for the site and event terms. To demonstrate the methodology, a simple functional form is used:

$$\begin{aligned} ln(EAS) = {} & a_1 + a_2(M-6) + a_3(M-8.5)^2 + \left(a_4 + a_5(M-6)\right) \\ & \cdot ln\left(R_{rup} + 5 \cdot e^{0.4\cdot(M-6)}\right) + a_6 R_{rup} + f_{site}(V_{S30}) + f_{basin}(z_{2.5}) \\ & + f_{NL-site}(V_{S30}, EAS_{1000}) + \delta B + \delta S2S + \delta W \end{aligned} \quad (2)$$

where M is moment magnitude; R_{rup} is the rupture distance; V_{S30} is the average shear-wave velocity over the top 30 m; $z_{2.5}$is the basin depth parameter; $\hat{z}_{2.5}$is average basin depth inferred from CB14 given V_{S30}; δB, $\delta S2S$ and δW are the between event residual, between site residual, and single site residual, respectively. The linear site term, $f_{site}(V_{S30})$, is usually modeled by a linear function of $\ln(V_{S30})$, but we used a tri-linear form to better capture the V_{S30} scaling in the data. The resulting linear site amplification relative to VS=3500 m/s is shown in Fig 1.

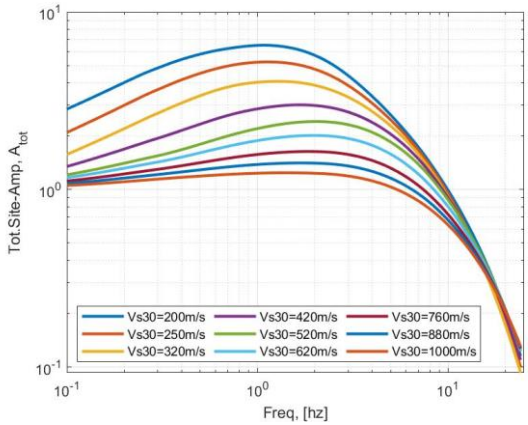

Figure 1. Site amplification relative to a hard-rock site condition with V_S=3500 m/s

Step 2

The site amplification from step 1 has the combined effect of the amplification due to the V_S profile and the attenuation due to κ_0. For a set of V_{S30} values, the effect of κ_0 is removed. The kappa-corrected amplification is used to invert for the 1-D Vs profile for each V_{S30} using the inverse quarter-wavelength (QWL) method described by Al Atik & Abrahamson (2021). An example of this process is shown in Fig. 2 for V_{S30}=250 m/s. Starting with the site amplification shown by the black curve in Fig. 2a, an initial estimate of the site

amplification due to the V_S profile, based on adjusted Kamai et al. (2016) V_S profiles for California (shown by the red curve) is removed. The kappa is estimated from the slope of the high-frequency FAS (pink curve). The kappa-corrected amplification is then computed, as shown by the blue curve. The inverted Vs profile is shown in Fig 2b. These same steps are applied to each V_{S30}. As can be seen from Figure 2b, the V_{S30} of inverted V_S profiles for soil sites is much less than the specified value. This inconsistency is addressed in Step 3.

Step 3

Apply constraints to the V_S profile in the top 30 m so that V_{S30} value from the inverted V_S profile is consistent with the specified V_{S30} and to the profile at depth so that it matches the median $z_{2.5}$ values from California. The resulting V_S profiles for a set of V_{S30} are shown in Fig 3.

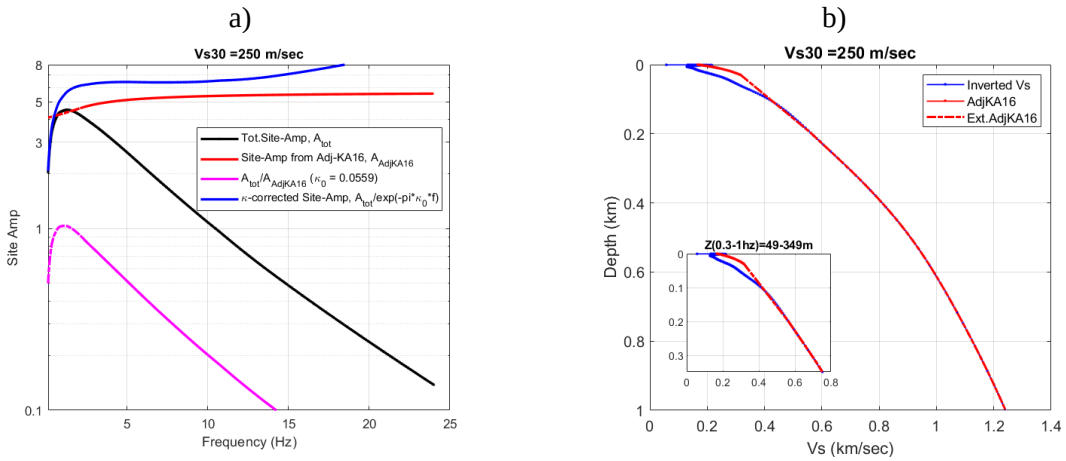

Figure 2. Steps for the derivation of the kappa and kappa-corrected site amplification as input for the IQWL method: a) total site amplification with and without kappa, b) the inverted Vs-profile and its corrected version.

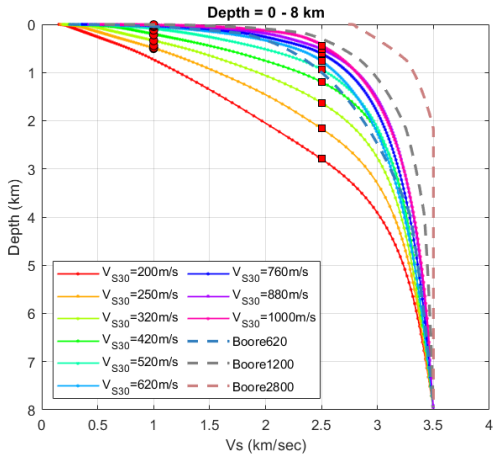

Figure 3. The V_{S30}-consistent Vs-profiles for a suite of V_{S30} values.

Step4

Compute the frequency-dependent site amplification for the 1-D Vs profiles from step 3 (Fig 3). The resulting site amplification is shown as a function of frequency in Fig 4a. The site amplification from the

inverted profiles is shown as function of V_{S30} in Fig 4b. The site amplification is computed using the QWL amplification with a scale factor to account for the differences between the amplification computed using the QWL method and the amplification computed using a traditional site response from a 1-D profile. GMMs typically model the V_{S30} scaling as a simple linear function of the ln(V_{S30}) at a given frequency. The inverted profiles are approximately linear with for the central V_{S30} range, but there is curvature that we include in the model as a non-parametric model in the GMM.

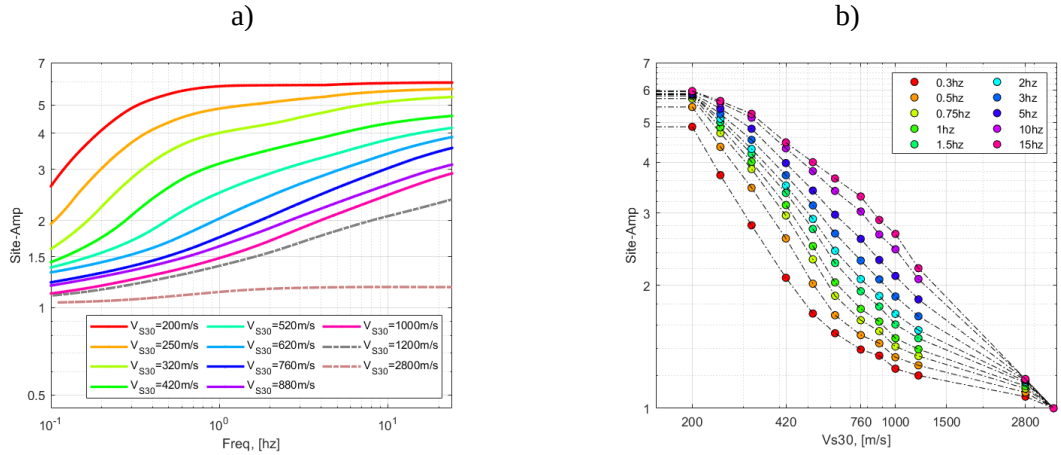

Figure 4. The linear 1-D site amplification from the 1-D profiles. (a) shown as a function of frequency for a given V_{S30} value. (b) shown as a function of V_{S30} for a given frequency.

Step 5

Holding the site amplification from step 4 and the smoothed kappa model from step 2 as fixed, repeat the regression for the EAS GMM to estimate the source and path coefficients in the GMM. This step allows the GMM coefficients to adjust to the fixed site terms consistent with the 1-D Vs profiles and κ values. Any residuals trend in the high-frequency between-site residuals is used to compute an additional kappa term. The net kappa is the sum of the additional kappa term and the kappa from step 2. The initial and net kappa values are shown in Fig 5.

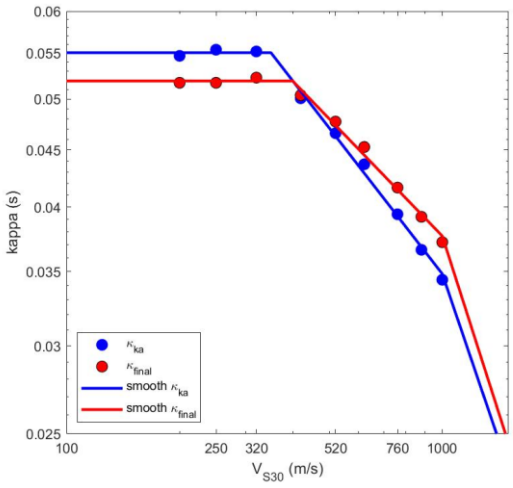

Figure 5. Initial kappa (blue curve) and net kappa (red curve).

The between-site residuals of the updated regression show trends in the period range of 0.5 to 2sec for soil sites. For example, the between-site residuals for 1 Hz are shown in Fig 6a. This trend in the residuals is modelled by an additional $f_{3D}(V_{S30})$ term which we interpret as 3-D effects that are not captured by the 1-D wave propagation.

$$f_{3D} = a_8 min\left(ln\left(\frac{V_{S30}}{500}\right), 0\right) \tag{2}$$

The size of f_{3D} relative to the total site amplification is shown in Fig 6b.

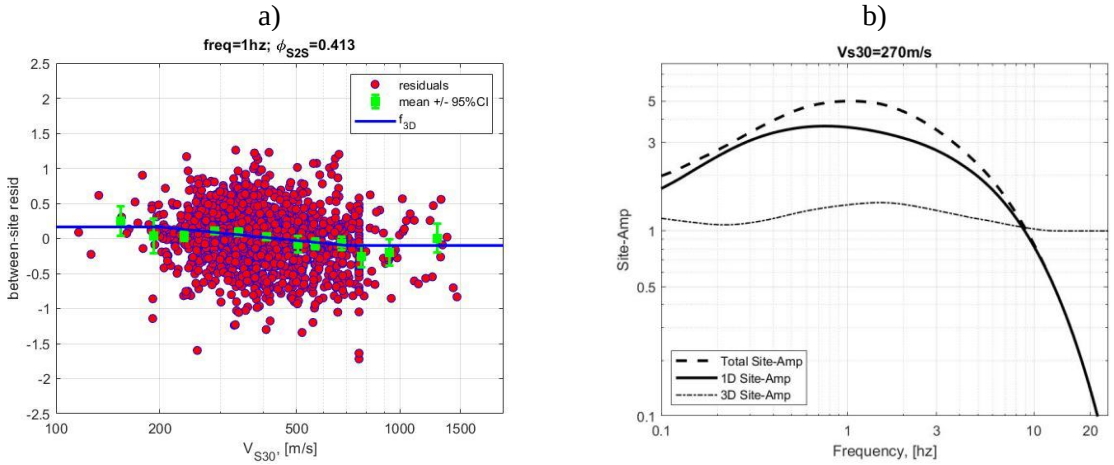

Figure 6. a) Between site residuals of the 1-D site response model showing bias with V_{S30}. b) Comparison of the 3-D site amplification with the 1-D site amplification for V_{S30} = 270 m/s.

CONCLUSIONS

The methodology given in this paper provides a method for GMM developers to include the estimation of the $V_S(z)$ profile and κ as a part of the GMM development. In addition to providing the information needed for the $V_S - \kappa$ correction approach, providing $V_S(z)$ profiles as part of the GMM will help to clarify that the V_{S30} value is just an index for a $V_S(z)$ profile and not a fundamental parameter of site amplification. A key result of the example application of the approach is that the empirical site amplification at long periods for soft sites cannot be fully explained by 1-D site response. The 1-D Vs profiles can explain by about 75% of the total site amplification relative to hard-rock. We attributed this underestimation of the long-period amplification to 3-D effects. The total amplification (1-D plus 3-D effects) can be up to a factor of 1.5 larger than the amplification due only to 1-D effects.

There are potential implications of the underprediction of the site amplification using the inverted 1-D profiles that need further study. A common approach in seismic hazard is to use rock motion as the input to 1 1D soil profile. There are only small 3-D effects for soft-rock sites, so the input motion will not have 3-D effects. Using a site-specific 1-D profile to compute the site amplification relative to the input rock motion will not capture the 3-D effects. This leads to the question: are there missing 3-D effects in the input motion at depth for soil sites? The alternative, is that there is a bias in our approach. Further work is needed to resolve the physical cause of the unexplained amplification for soil sites.

ACKNOWLEDGMENTS

Partial financial support for this work was provided by the PG&E Geosciences Department of Long-Term Seismic Program.

REFERENCES

1. Williams, T., & Abrahamson, N. (2021). Site-Response Analysis Using the Shear-Wave Velocity Profile Correction Approach. Bulletin of the Seismological Society of America, 111(4), 1989–2004. https://doi.org/10.1785/0120200345
2. Boore, D. (2016). Determining generic velocity and density models for crustal amplification calculations, with an update of the Boore and Joyner (1997) Generic Site Amplification for Graphic Site Amplification. In Bulletin of the Seismological Society of America (Vol. 106, Issue 1, p. 316320). https://doi.org/10.1785/0120150229
3. Al Atik, L., & Abrahamson, N. (2021). A Methodology for the Development of 1D Reference VS Profiles Compatible with Ground-Motion Prediction Equations: Application to NGA-West2 GMPEs. Bulletin of the Seismological Society of America, 111(4), 1765–1783. https://doi.org/10.1785/0120200312.
4. Kamai, R., Abrahamson, N. A., & Silva, W. J. (2016). VS30 in the NGA GMPEs: Regional Differences and Suggested Practice. Earthquake Spectra, 32(4), 2083–2108. https://doi.org/10.1193/072615EQS121M.

A SIMPLE SCHEME TO PREPARE SITE-SPECIFIC DESIGN GROUND MOTIONS BASED ON LOCAL MICROTREMOR MEASUREMENT AND GLOBALLY-AVAILABLE STRONG MOTION DATABASES

Atsushi Nozu[1]
1. Director of Earthquake Disaster Prevention Engineering Department, Port and Airport Research Institute, Japan
Email: nozu@p.mpat.go.jp

ABSTRACT

Earthquake ground motions are quite site-specific; it is preferable to use site-specific design ground motions in the design of structures. Now site-specific design ground motions are routinely evaluated and used in the design of port and airport structures in Japan. This process is largely benefitted from the existence of strong motion networks in Japan; it is not easy to implement exactly the same procedure in countries and regions where a similar network is not available. On the other hand, microtremor measurement is a truly universal tool that can be applied to countries and regions without sufficient strong motion data. Based on this understanding, in this article, a new simple scheme is proposed to prepare site-specific design ground motions based on local microtremor measurement and globally-available strong motion databases such as those in Japan. The idea is to select a record from a database which is consistent with the earthquake scenario at the construction site not only in terms of magnitude and fault distance but also in terms of the site effects. Microtremor H/V spectrum is used as a signature of the site characteristics to find a strong motion station that exhibits similar site characteristics with the construction site.

Keywords: site effect, design ground motion, strong motion database, microtremor

INTRODUCTION

Earthquake ground motions are significantly affected by the site effects. Even for a similar magnitude and distance, earthquake ground motions can vary significantly due to the difference of the site effects. In a previous article (Nozu, 2020), the author discussed how introducing site-specific design ground motions can contribute to the safety of society. The importance of site-specific design ground motions is also briefly discussed in this article in the next section.

Now site-specific design ground motions are routinely evaluated and used in the design of port and airport structures in Japan. The details can be found in OCDI (2020). As will be explained later in this article, the process of preparing site-specific design ground motions is largely benefitted from the existence of strong motion networks (Aoi et al., 2020; Nagasaka and Nozu, 2021) and the resultant database of empirical site amplification factors in Japan (https://www.pari.go.jp/bsh/jbn-kzo/jbn-bsi/taisin/siteamplification_jpn.html). Therefore, it is not necessarily easy to implement exactly the same procedure in countries and regions where a similar network or database is not available.

On the other hand, microtremor measurement is a truly universal tool that can be applied to countries and regions without sufficient strong motion data. Based on this understanding, in this article, a new simple scheme is proposed to prepare site-specific design ground motions based on local microtremor measurement and globally-available strong motion databases such as those in Japan. The idea is to select a record from a database which is consistent with the earthquake scenario at the construction site not only in terms of magnitude and fault distance but also in terms of the site effects. Microtremor H/V spectrum (Nakamura, 2008) is used as a signature of the site characteristics to find a strong motion station that exhibits similar site characteristics with the construction site.

IMPORTANCE OF SITE-SPECIFIC DESIGN GROUND MOTIONS

In general, earthquake ground motions are affected by three factors, namely, the source, path and site effects (Fig. 1). The source effects can be defined as the characteristics of seismic waves generated at the earthquake source as a result of a rupture process on the fault. The path effects can be defined as the attenuation and deformation of seismic waves during their propagation from the source to the upper boundary of the seismological bedrock below the site. The site effects can be defined as the influence of sediments above the seismological bedrock on the seismic waves. The seismological bedrock can be defined as the layers having a shear wave velocity greater than or equal to 3 km/s and it is often composed of granite in Japan. Among those effects, the influence of sediments above the seismological bedrock is so significant that it is important to accurately evaluate the site effects to estimate ground motions during future earthquakes at a construction site. Regarding the site effects, it has been increasingly recognized that, in addition to the influence of shallower sediments above the engineering bedrock, the influence of deeper sediments below the engineering bedrock is also significant (Japan Society of Civil Engineers, 2000). In-situ earthquake observations and microtremor measurements can be a useful tool to evaluate the site effects.

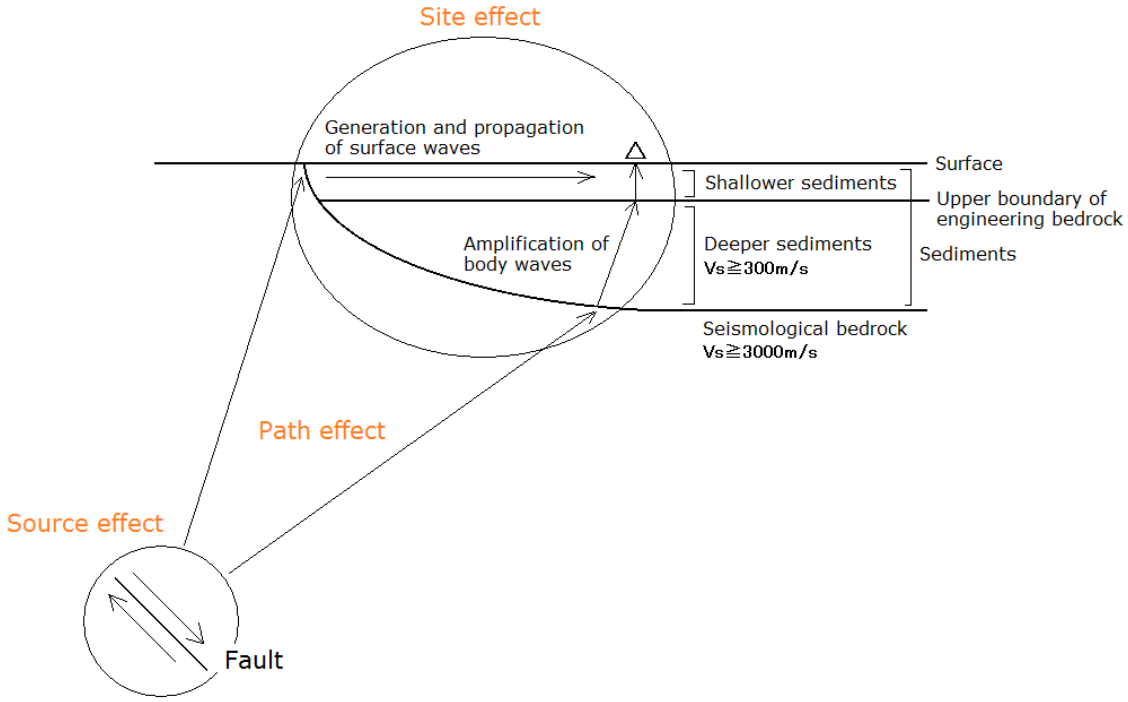

Figure 1. Source, path and site effects.

There have been a lot of case histories in which earthquake ground motions were significantly affected by the existence of sediments. For example, Fig. 2 shows the Fourier spectra observed at 17 K-NET and KiK-net stations (Aoi et al., 2020) in Iwate Prefecture, Japan, during the 2011 Tohoku earthquake (M_w9.0) and the site amplification factors at the same stations evaluated prior to the Tohoku earthquake using small earthquakes. It is obvious that the frequency content of strong ground motions during the Tohoku earthquake was quite site-dependent. The spectral peaks appearing in the site amplification factors also appeared in the Fourier spectra during the Tohoku event, with a slight shift to lower frequencies because of nonlinear soil behavior.

A similar figure was plotted for the K-NET station ‘MYG010’ and the station ‘Sendai-G’ (Fig. 3). The latter station belongs to Strong-Motion Earthquake Observation in Japanese Ports (Nagasaka and Nozu, 2021) (https://www.eq.pari.go.jp/kyosin/en). There is a significant difference between the observed Fourier spectra at MYG010 and Sendai-G during the 2011 Tohoku earthquake, although the difference of the fault distance is not so significant. MYG010 is located at (141.282E, 38.429N). Sendai-G is

located at (141.012E, 38.286N). Around 0.7 Hz, the spectrum at MYG010 is greater than the spectrum at Sendai-G by a factor of 10. The difference can be attributed to the difference of the site amplification factors. It should be noted that such a big difference cannot be attributed merely to the difference of the ground conditions above the engineering bedrock (Fig. 1). The difference should be attributed to the difference of the entire sediments down to the seismological bedrock (Fig. 1).

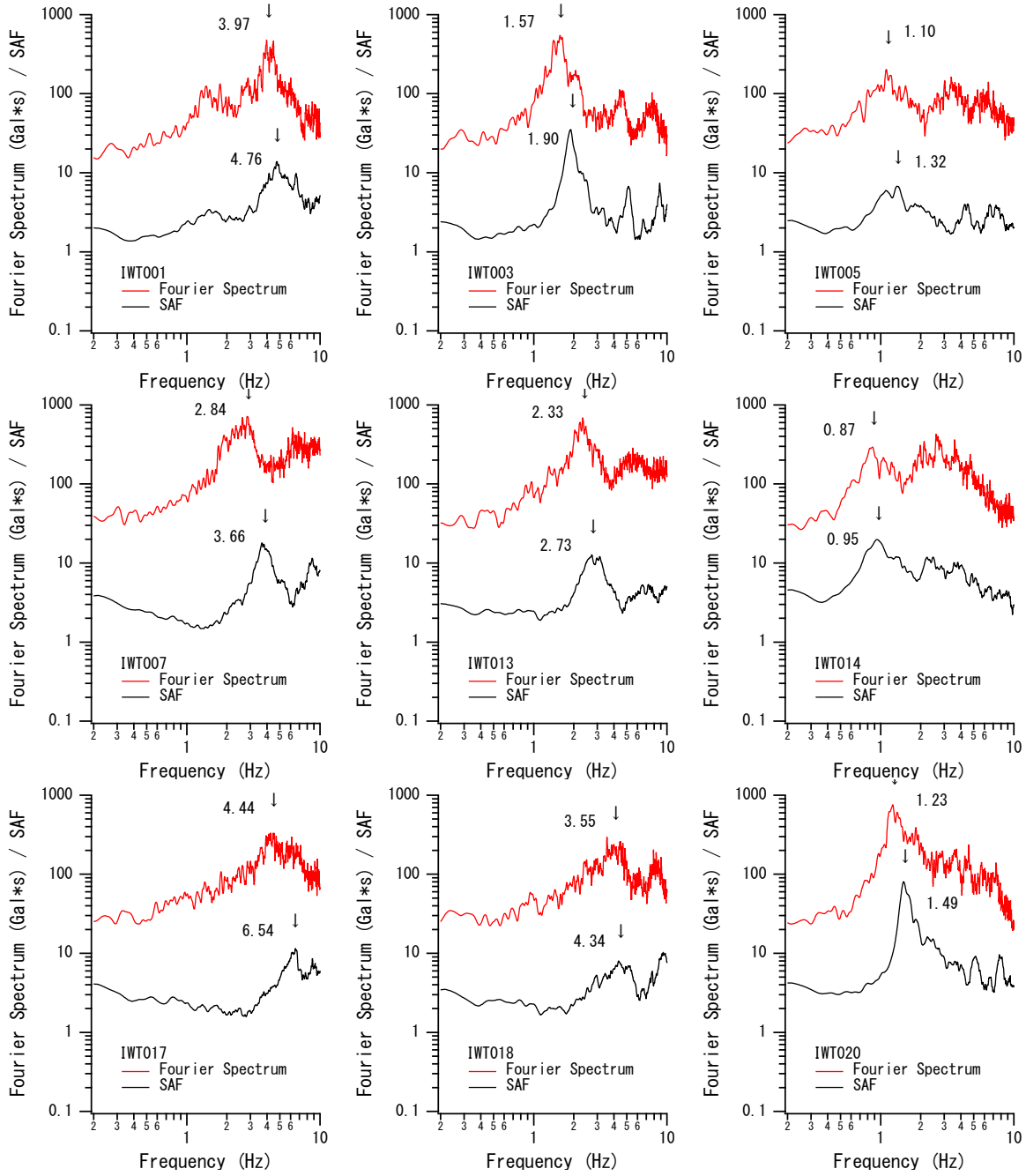

Figure 2. Fourier spectra observed at 17 K-NET and KiK-net stations in Iwate Prefecture, Japan, during the 2011 Tohoku earthquake (M_w9.0) (red) and the site amplification factors at the same stations evaluated prior to the Tohoku earthquake using small earthquakes (https://www.pari.go.jp/bsh/jbn-kzo/jbn-bsi/taisin/siteamplification_jpn.html) (black). The Fourier spectra are the root of the squared sum of two horizontal components, smoothed with a Parzen window with a band width of 0.05 Hz.

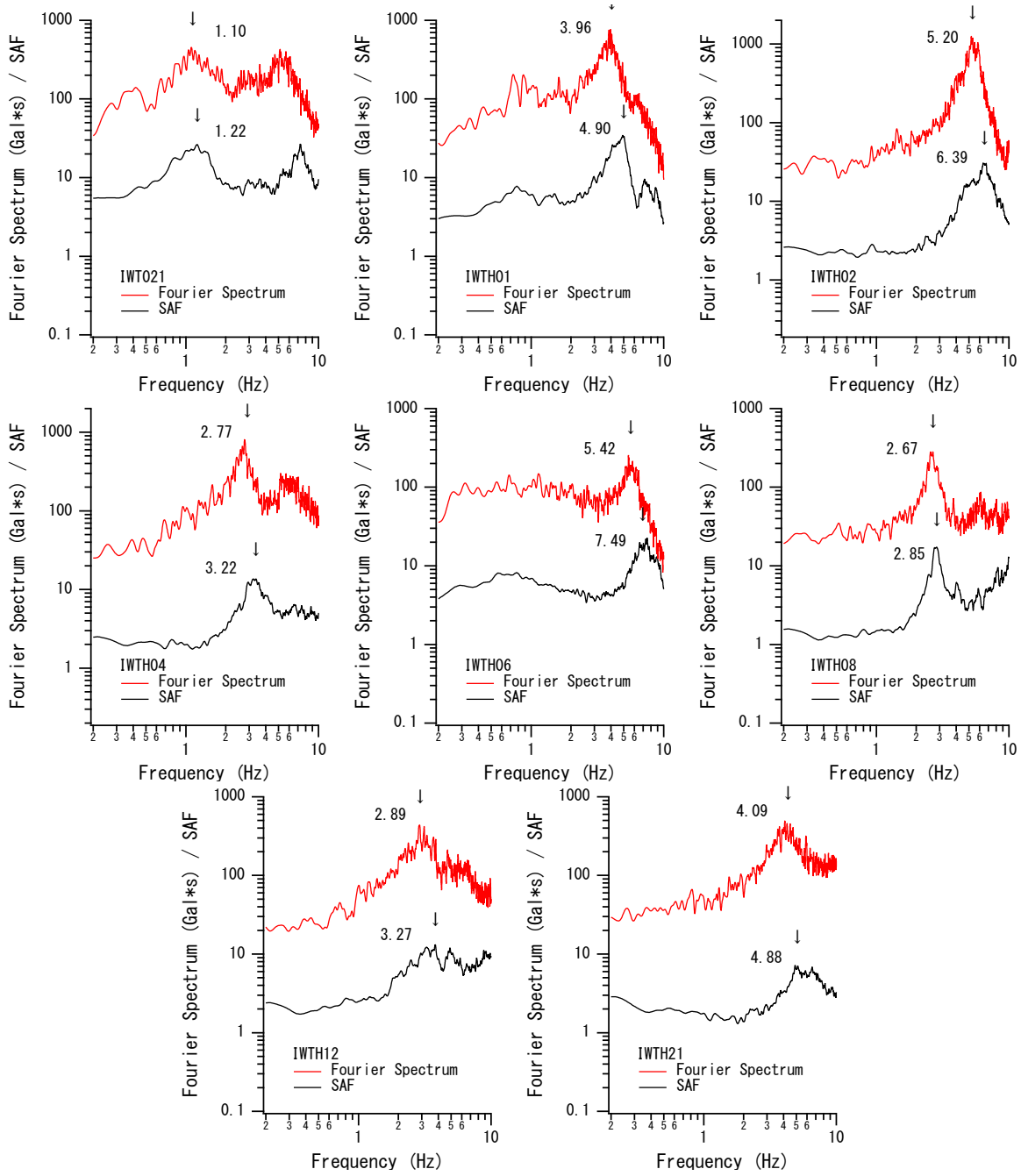

Figure 2. (continued)

Such a big difference should be considered in the design of structures by introducing site-specific design ground motions. Further discussion on the advantage of introducing site-specific design ground motions can be found in Nozu (2020).

PRACTICE IN JAPAN

Now site-specific design ground motions are routinely evaluated and used in the design of port and airport structures in Japan. The details can be found in OCDI (2020). This document is a translated version of the "Technical Standards and Commentaries for Port and Harbour Facilities in Japan" and can be freely accessed by registered users (https://ocdi.or.jp/wordpress/technical-st).

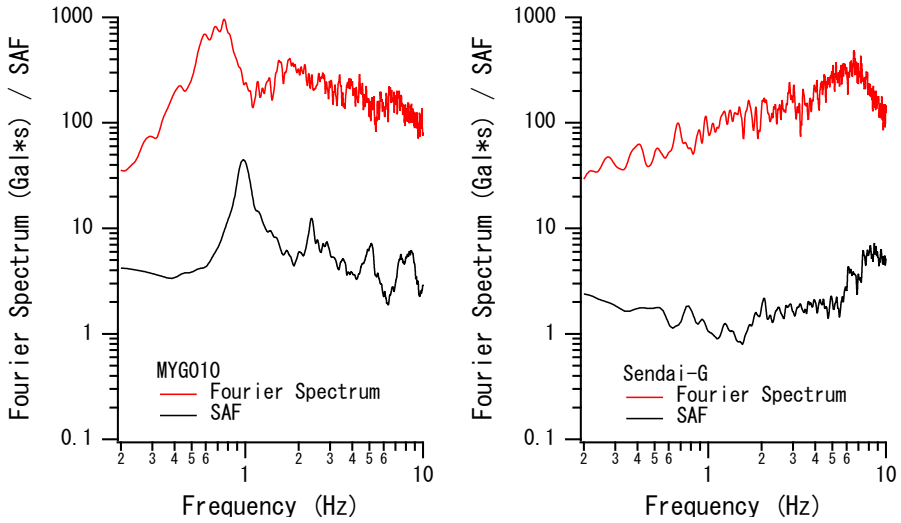

Figure 3. Fourier spectra observed at MYG010 and Sendai-G in Miyagi Prefecture, Japan, during the 2011 Tohoku earthquake (M_w9.0) (red) and the site amplification factors at the same stations evaluated prior to the Tohoku earthquake using small earthquakes (https://www.pari.go.jp/bsh/jbn-kzo/jbn-bsi/taisin/siteamplification_jpn.html) (black). The Fourier spectra are the root of the squared sum of two horizontal components, smoothed with a Parzen window with a band width of 0.05 Hz.

There are two categories of design ground motions: level-1 and level-2 design ground motions. Level-1 ground motions are defined as those having a probability of exceedance of 1/75 a year. In general, level-1 ground motions are determined by means of a probabilistic seismic hazard analysis considering the source and path effects and the site amplification factor at the construction site. Time history data of level-1 ground motions at major ports, etc. that were determined taking account of regional source and path effects are available at the website of the National Institute for Land and Infrastructure Management at http://www.ysk.nilim.go.jp/kakubu/kouwan/sisetu/sisetu.html. Detailed procedures for the determination can be found in Takenobu et al. (2014).

Level-2 ground motions can be defined as those having greatest intensity among anticipated ground motions at a construction site. In general, Level-2 ground motions are determined based on strong motion simulations, taking into account the source and path effects and the site amplification factor at the construction site. The corrected empirical Green's function method (Kowada et al., 1998; Nozu and Sugano, 2008) is often used for the simulation. A FORTRAN program based on this method is available at https://www.pari.go.jp/bsh/jbn-kzo/jbn-bsi/taisin/sourcemodel/somodel_program.html.

Both for the level-1 and level-2 ground motions, the evaluation of the site amplification factor is necessary. The most reliable method to reveal the site amplification factor at a construction site is to conduct earthquake observations. Therefore, we first consider the availability of strong motion stations of existing networks such as K-NET, KiK-net (Aoi et al., 2020) and Strong-Motion Earthquake Observation in Japanese Ports (Nagasaka and Nozu, 2021). The database of the empirical site amplification factors at existing strong motion stations can be found at https://www.pari.go.jp/bsh/jbn-kzo/jbn-bsi/taisin/siteamplification_jpn.html.

We conduct microtremor measurements at the construction site and a nearby strong motion station. If the characteristics of microtremors are similar between the two locations, it is reasonable to assume that the site characteristics are similar between the two locations. In that case the site amplification factor at the nearby strong motion station will be used for the design. However, if the results of the microtremor measurements indicate that the site characteristics are different between the construction site and the nearby strong motion station, it is desirable to evaluate the site amplification factor at the construction site by means of in-situ temporary earthquake observations, depending on the importance

of the project. In that case, spectral ratios between the temporary station and a nearby strong motion station are used to evaluate the site amplification factor at the construction site. Fig. 4 shows an example of in-situ temporary earthquake observation, which was conducted by the Chugoku regional development bureau at the Port of Iwakuni. In this case the spectral ratios were calculated between the temporary station and a nearby strong motion station YMG016, which was 5 km away. Although it is preferable to correct the site amplification factor based on earthquake observations as shown in Fig. 4, we sometimes correct the site amplification factor by merely relying upon the results of microtremor measurements (OCDI, 2020).

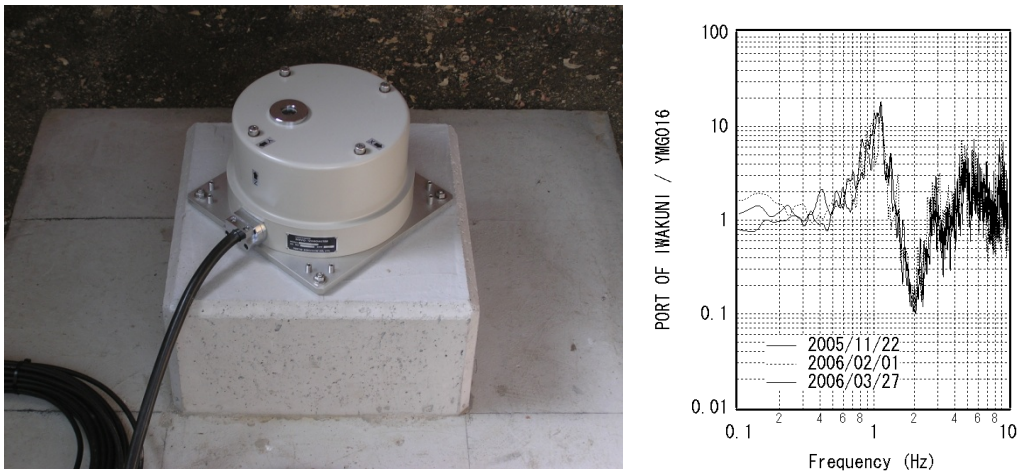

Figure 4. In-situ temporary earthquake observation conducted by the Chugoku regional development bureau at the Port of Iwakuni.

PROPOSED SCHEME

As shown in the previous section, the process of preparing site-specific design ground motions in Japan is largely benefitted from the existence of strong motion networks (Aoi et al., 2020; Nagasaka and Nozu, 2021) and the resultant database of empirical site amplification factors in Japan (https://www.pari.go.jp/bsh/jbn-kzo/jbn-bsi/taisin/siteamplification_jpn.html). Therefore, it is not necessarily easy to implement exactly the same procedure in countries and regions where a similar network or database is not available. On the other hand, microtremor measurement is a truly universal tool that can be applied to countries and regions without sufficient strong motion data. Based on this understanding, in the following, a new simple scheme is proposed to prepare site-specific design ground motions based on in-situ microtremor measurement and globally-available strong motion databases such as those in Japan.

The idea is to select a record from a database which is consistent with the earthquake scenario at the construction site not only in terms of magnitude and fault distance but also in terms of the site effects. Microtremor H/V spectrum is used as a signature of the site characteristics to find a strong motion station that exhibits similar site characteristics with the construction site. The procedure will be as follows:

1) Choose a strong motion database which is located in a similar tectonic setting as the project. For example, for a project in Tonga, a Japanese database could be useful because the tectonic setting in Tonga is similar to that of Japan in a sense that it is near a subduction zone.
2) Observe microtremors at the construction site. It is recommended to observe at multiple locations.
3) Calculate microtremor H/V spectra and compare them with those at strong motion stations to find a station that exhibits similar site characteristics with the construction site.
4) Select a strong motion record which is consistent with the earthquake scenario at the construction site not only in terms of magnitude and fault distance but also in terms of the site effects.

Microtremor measurement is one of the most economical methods of geophysical survey. In addition, Japanese strong motion data is freely available. Therefore, the proposed scheme could be the most economical way of preparing site-specific design ground motions.

There are two most accessible sources of Japanese strong motion data. One is the K-NET and KiK-net website operated by the National Institute for Earth Science and Disaster Resilience (NIED) (https://www.kyoshin.bosai.go.jp/). K-NET is observing surface ground motions, while KIK-net is observing both surface and borehole ground motions. The other source of Japanese strong motion data is the website of the Strong-Motion Earthquake Observation in Japanese Ports, operated by our research institute (https://www.eq.pari.go.jp/kyosin/en). This network covers Japanese major ports. It involves several vertical arrays.

Even in Japan, records of earthquakes exceeding M8.0 are rare. If we are to use earthquakes exceeding M8.0, we have only three choices (except for very distant earthquakes).

The M8.2 Hokkaido Toho-oki earthquake of October 4, 1994
The M8.0 Tokachi-oki earthquake of September 26, 2003
The M9.0 Tohoku earthquake of March 11, 2011

The records were obtained over a wide range of distance. Ground motions are affected not only by the distance but also by the site effects. Therefore, it is important to select a record with appropriate distance and appropriate site effects. The 1994 event was an intraslab event, so, we should avoid this event if we are to consider a plate-boundary earthquake.

In terms of distance, it is recommended to use the distance from the fault plane rather than the hypocentral distance or the epicentral distance, because the latter two can only consider the distance from the rupture initiation. For a project near a subduction zone, it is reasonable to consider the shortest distance from the project to the upper surface of the subducting plate. To measure the distance from the fault planes of the 2003 Tokachi-oki and the 2011 Tohoku earthquakes, one could use the Earthquake Source Model Database (http://equake-rc.info/srcmod/). It should be noted that the websites of strong motion databases usually provide the information of epicentral distance only.

In this scheme, microtremor H/V spectrum is used as a signature of the site characteristics to find a strong motion station that exhibits similar site characteristics with the construction site. Microtremor measurement is obviously more cost-effective compared to borehole survey, but it can still provide useful information in term of site amplifications. In Fig. 5, microtremor H/V spectra, i.e., horizontal to vertical spectral ratios of microtremors at MYG010 and Sendai-G are plotted and compared with the site amplification factors obtained from small earthquakes. It can be seen that the microtremor H/V spectra captures the fundamental characteristics of the site amplification factors.

CONCLUSIONS

In this article, a new simple scheme was proposed to prepare site-specific design ground motions based on local microtremor measurement and globally-available strong motion databases such as those in Japan. The idea is to select a record from a database which is consistent with the earthquake scenario at the construction site not only in terms of magnitude and fault distance but also in terms of the site effects. Microtremor H/V spectrum is used as a signature of the site characteristics to find a strong motion station that exhibits similar site characteristics with the construction site. Microtremor measurement is one of the most economical methods of geophysical survey. In addition, Japanese strong motion data is freely available. Therefore, the proposed scheme could be the most economical way of preparing site-specific design ground motions.

Another advantage of using observed ground motions could be the fact that everybody feels they are realistic. In Japanese design we often use simulated ground motions and the author does think that simulated ground motions are realistic enough when the simulation method is good. However, sometimes engineers can more easily agree to use observed ground motions.

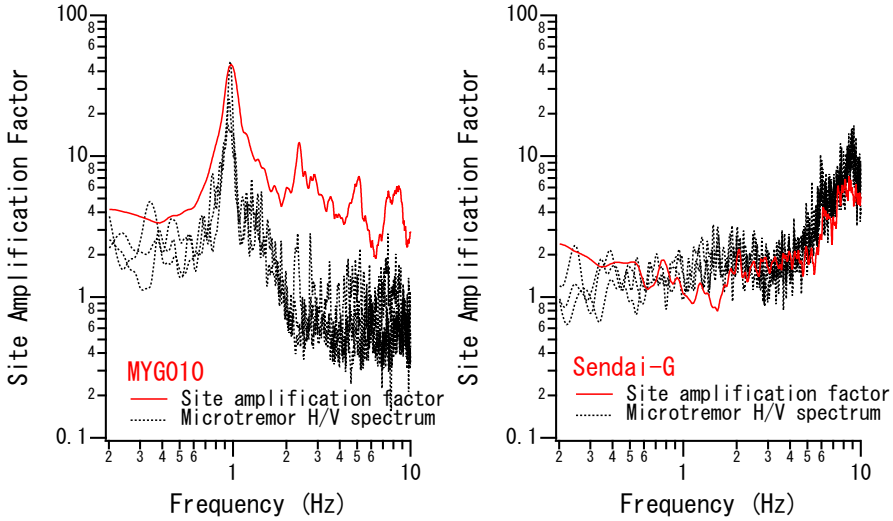

Figure 5. Microtremor H/V spectra, i.e., horizontal to vertical spectral ratios of microtremors at MYG010 and Sendai-G (black), compared with the site amplification factors obtained from small earthquakes (https://www.pari.go.jp/bsh/jbn-kzo/jbn-bsi/taisin/siteamplification_jpn.html) (red).

ACKNOWLEDGMENTS

The author would like to thank the National Institute for Earth Science and Disaster Resilience for the K-NET and KiK-net data.

REFERENCES

Aoi, S., Y. Asano, T. Kunugi, T. Kimura, K. Uehira, N. Takahashi, H. Ueda, K. Shiomi, T. Matsumoto and H. Fujiwara (2020). "MOWLAS: NIED observation network for earthquake, tsunami and volcano," *Earth, Planets and Space*, 72:126.

Japan Society of Civil Engineers (2000). "Proposal and commentary on seismic design standards for infrastructures: the third proposal," (in Japanese).

Kowada, A., M. Tai, Y. Iwasaki and K. Irikura (1998). "Evaluation of horizontal and vertical strong ground motions using empirical site-specific amplification and phase characteristics," *Journal of Structural and Construction Engineering*, AIJ, No.514, pp.97-104 (in Japanese with English abstract).

Nakamura, Y. (2008). "On the H/V spectrum," *Proceedings of the 14th World Conference on Earthquake Engineering*, Beijing, China, October 12th to 17th, 2008.

Nagasaka, Y. and A. Nozu (2021). "Annual report on strong-motion earthquake records in Japanese ports (2019)," *Technical Note of the Port and Airport Research Institute*, No.1394, https://www.pari.go.jp/search-pdf/TECHNICAL%20NOTE1394.pdf (in Japanese with English abstract).

Nozu, A. (2020). "Can ground motion studies contribute to anti-catastrophe design?" *Proceedings of the 17th World Conference on Earthquake Engineering*, Sendai, Japan, September 13th to 18th, 2020.

Nozu, A. and T. Sugano (2008). "Simulation of strong ground motions based on site-specific amplification and phase characteristics – Accounting for causality and multiple nonlinear effects –," *Technical Note of the Port and Airport Research Institute*, No.1173, https://www.pari.go.jp/search-pdf/no1173.pdf (in Japanese with English abstract).

OCDI (2020), "Technical standards and commentaries for port and harbour facilities in Japan," https://ocdi.or.jp/wordpress/technical-st.

Takenobu, M., A. Nozu, M. Miyata, Y. Sato and S. Asai (2014). "Comprehensive report for setting up level-1 earthquake ground motion with a probabilistic time history waveform for seismic design of port facilities," *Technical Note of National Institute for Land and Infrastructure Management*, No.812, http://www.nilim.go.jp/lab/bcg/siryou/tnn/tnn0812pdf/ks0812.pdf (in Japanese with English abstract).

DEVELOPMENT OF PREDICTION EQUATION ON LONG PERIOD GROUND MOTION IN BANGKOK

Xi-Han Li[1], Subedi Bidhya[2], Junji Kiyono[3]
1. Graduate Student, Dept. of Urban Management, Graduate School of Engineering, Kyoto University.
2. PhD Student, Dept. of Urban Management, Graduate School of Engineering, Kyoto University
3. Professor, Dept. of Urban Management, Kyoto University
Email: li.xihan.36a@st.kyoto-u.ac.jp, subedi.bidhya.24s@st.kyoto-u.ac.jp, kiyono.junju.5x@kyoto-u.ac.jp,

ABSTRACT

Long-period ground motions can take place at long distances from hypocenter and might cause huge damages to high-rise structures in distant basins. Among numerous ground motion intensity measures, absolute velocity response correlates well with the indoor conditions of high-rise buildings during long- period ground motions. However, it has rarely been studied in previous studies. As the earthquake records may not be enough for developing an attenuation equation for the parameter in Bangkok. Therefore, firstly we developed attenuation equations for absolute velocity response, relative velocity response and peak ground velocity using earthquake records from Japan. Then we used the attenuation equations to calculate two correlation coefficients $\alpha_1$and α_2. They can be used to estimate absolute velocity responses for a site in real-time earthquake event, by using suitable attenuation equations of other ground motion parameters for the site. Results show that the regression model in this study might underestimate situation in Bangkok. Besides that, estimation equations proposed in this study might be applicable, however, future evaluation is indispensable for existence of suitable attenuation model in Bangkok.

Keywords: long period ground motion, ground motion prediction equation, absolute velocity response spectra, Bangkok, estimation equation.

INTRODUCTION

Long-Period Ground Motions (LPGM) are usually generated from large earthquakes with period larger than around one second. Resonance may occur when natural period of buildings coincides with period of ground motion. Recently, LPGM has been taken increasingly consideration as increase in the number of large-scale structures such as high-rise buildings, oil storage tanks and suspension bridges which commonly have larger natural period (Koketsu et al., 2008). In addition, LPGM attenuate slowly with distance, and site effect might amplify motions in distant basins so that they can propagate over longer distance compared with short period ground motions (Kawase et al, 2003). Therefore, during large earthquakes, damage caused by vibration of large-scale structures that are far away from epicenter can be observed when long-period ground motions happen. Bangkok is the capital city of Thailand and locates far from the seismic sources, previous studies show that Bangkok is at risk from damaging ground motion induced by distant and large earthquakes. For instance, during 2016 M_w 6.8 earthquake in Myammar, moderate tremors shook high-rise buildings as far away as in Bangkok (about 1000 km from epicenter). Since the earthquake occurred during working hours, residents had to be evacuated from buildings causing wide panic (Fig. 1).

Targeting on situation in high-rise buildings, Japan Meteorological Agency (JMA) has recently proposed a new intensity scale for LPGM based on effect on people and indoor condition for buildings with height larger than 45 m. According to the JMA investigation, maximum floor velocity response can best differentiate the level of moving for people and degree of damage of furniture inside the buildings which can be calculated as absolute velocity response spectra (AVRS) using recorded data from ground seismometers. Fig. 2 shows the difference in applying AVRS and relative velocity response spectra (RVRS) for long- and short-period ground motions. When natural period of a single-degree of freedom (SDOF) system (T_S) is larger than period of an input ground motion (T_G), the

oscillator moves in opposite direction than ground motion and becomes nearly static with respect to immobile space. Therefore, relative velocity response (RVR) has some value whereas absolute velocity response (AVR) becomes very small or almost zero. When T_S is smaller than T_G, the oscillator moves together with ground, so RVR is small whereas AVR is relatively large or nearly equal to the ground velocity. Therefore, AVRS is more suitable than RVRS for LPGM. The new intensity scale is classified into four levels based on maximum AVRS computed from observation data on the ground with natural period band 1.6 to 7.8 s with 5% damping ratio (Nakamura, 2013).

Figure 1. People in high-rise buildings in Bangkok scurried out (private information from O. Teraphan).

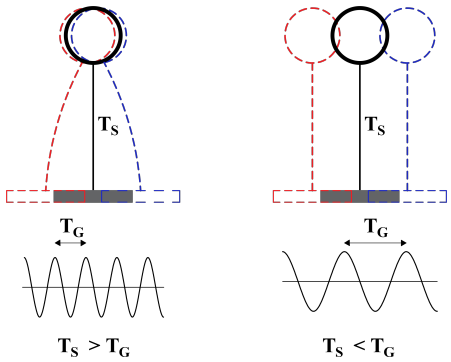

Figure 2. Difference by applying AVRS and RVRS during short (left) and long (right) period ground motions.

As long-period ground motions prevail at long distance from hypocenter and can cause severe damage to high-rise buildings, earthquake early warning (EEW) for LPGM is indispensable by providing caution and dissemination to people in most affected area. Ground motion prediction equations (GMPEs), also known as attenuation equations, has been one of the well-studied aspect of seismology and earthquake engineering. GMPEs usually take earthquake magnitude parameter, source to site distance parameter and may have some other variables to characterize earthquake source, propagation path, and/or local site conditions. Lifelines Program of the Pacific Earthquake Engineering Research Center (PEER) developed "Next Generation of Ground-Motion Attenuation Models" in NGA project using vast database. They developed GMPEs for various intensity measures such as peak ground acceleration (PGA), peak ground velocity (PGV), and acceleration response spectra, etc. In Japan, numerous attenuation models for peaks and spectral response are available. JMA employs attenuation equation by Si and Midorikawa (1999) to estimate the maximum velocity amplitude on engineering bedrock to estimate the seismic intensity for EEW.

The objective of this paper is to obtain prediction model with minimum-demand information for EEW of long-period ground motion in Bangkok. Attenuation equation for AVRS in this paper is based on Dhakal et al. (2015) with parameters as hypocemtral distance and magnitude. There are not many attenuation equations for AVRS as of other parameters. Dhakal et al. (2015) developed a GMPE of AVRS using records from Japan for early warning of LPGM. They concluded that their results reproduced the observed intensities for 98% of the records within a difference of one intensity without any site corrections. As Bangkok locates far away from active faults in Thailand and lack of observation data, it is difficult to do regression for AVRS by using data in Bangkok directly. Therefore, in this study regression analysis is done based on data recorded from JMA observation sites in Japan. In calculation of AVRS for Bangkok in absence of observation data, we propose two estimation equations; one with RVRS and PGV, and the other one using absolute acceleration response spectra (AARS). According to this procedure, AVRS for Bangkok can be calculated if suitable attenuation equations on RVRS, PGV or AARS exist. Applicability of the regression model as well as estimation equations in Bangkok are also examined.

DATA COLLECTION AND PROCESSING

Acceleration time histories in NS, EW and UD direction are collected from six earthquakes with M_w 5.1 or greater from November 22, 2016 to March 13, 2020 at 950 JMA observation sites in total. These earthquakes are selected to cover wide magnitude and distance range in the JMA long-period range in the JMA long-period earthquake catalog. Earthquake information are listed in Table 1. Distribution of recordings with respect to magnitude and hypocentral distances is shown in Fig. 3. Intensity level of each event is determined by maximum of intensity levels from various observation stations.

Table 1. List of events used in this study.

SN	Hypocenter Information Provided by JMA						Mw	JMA long-period class
	Origin Time (UT)	Latitude (°)	Longitude (°)	Region	Depth (km)	Number of sites		
1	2020/03/12 17:18:46.77	37.2797	136.8245	Noto Peninsula Region	12.33	69	5.4	2
2	2019/06/18 13:22:19.98	38.608	139.4793	W Off Yamagata Pref	13.99	202	6.8	3
3	2018/09/05 18:07:59.33	42.6908	142.0067	Ishikari Depression	37.04	156	6.7	4
4	2018/05/12 01:29:30.08	36.6325	137.901	Northern Nagano Pref	10.86	57	5.1	1
5	2016/12/28 12:38:49.04	36.7202	140.5742	Northern Ibaraki Pref	10.84	179	6.3	1
6	2016/11/21 20:59:46.89	37.3547	141.6042	E Off Fukushima Pref	24.5	287	7.3	2

Velocity time histories are calculated by integration of acceleration time histories in frequency domain and PGV is obtained by taking a peak of absolute value. Integration of acceleration records may have drifts due to presence of long-period noise. High-pass filter employed in this study utilize a cut-off frequency of 0.067 Hz (T=15 s) and following a cosine function for frequency range of 0.067–0.1 Hz. In calculation of absolute velocity response time histories, relative velocity response with damping ratio of 5% is calculated by linear acceleration method, then velocity time histories are added in time domain for corresponding natural period. AVRS is obtained by taking a maximum of absolute value.

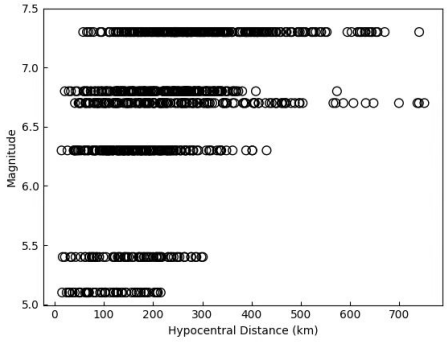

Figure 3. Distribution of data with respect to magnitude and hypocentral distance.

Soil condition for all observation sites is evaluated by calculation of S-wave velocity up to 30 m depth (V_{s30}). In Japan, mapping of V_{s30} in Japan is provided and data is available at K-NET and KiK-net observation sites (Mastuoka et al., 2005). Since observation data applied in this study is recorded from JMA observation sites, V_{s30} data of the nearest K-NET and KiK-net observation stations are referred for evaluation. Among all 950 observation sites, there are 421 sites left after removal of duplicates. Distribution of V_{s30} obtained is shown in Fig. 4 with distance to nearest K-NET and KiK-net observation stations up to1 km, 5 km, and 15 km from JMA sites respectively. Site classification is based on National Earthquake Hazard Reduction Program (NEHRP) and the result shows that in most

sites range of V_{s30} lies between corresponding site class C and D that the soil is in favorable condition considered as stiff and dense soil (BSSC, 2004).

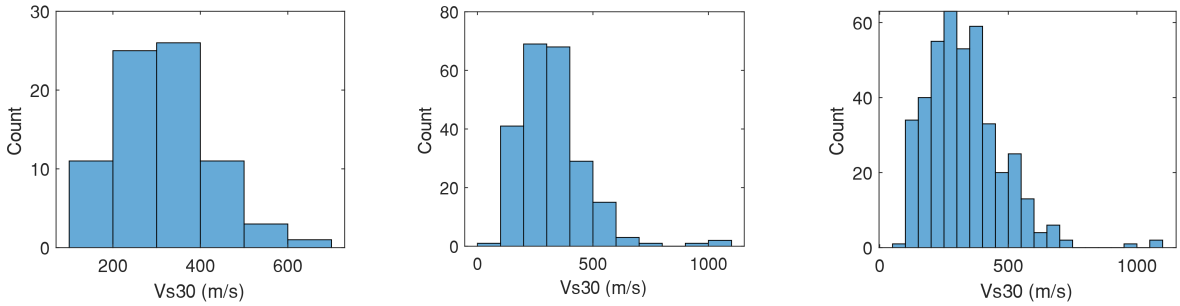

Figure 4. Distribution of V_{s30} around JMA sites to nearest K-NET and Kik-net stations with distance up to1 km (left side), 5 km (middle) and 15 km (right side).

REGRESSION MODEL

We used the regression model with moment magnitude and hypocentral distance parameters based on the LPGM study by Dhakal et al. (2015) as of Eq. 1:

$$log_{10}Y_{ij} = c + aM_i - \mathrm{b}R_{ij} - log_{10}R_{ij} + \varepsilon_{ij} + \eta_i \quad (1)$$

where, Y_{ij} is ground velocity parameter in cm/s from event i at observation station j, M is magnitude, R is hypocentral distance in km, ε_{ij} is intra-event error, η_i is inter-event error. Coefficients *a, b*, and *c* are regression coefficients for magnitude, anelastic attenuation and constant respectively.
We used the two-stage regression analysis of Joyner and Boore (1993) to eliminate the systematic errors in one-stage due to the correlation between magnitude and distance. We have not considered the effects of tectonic environment due to the complexity of tectonic regimes in Japan. GMPEs adopting additional parameters like fault distance, fault type etc. may further improve the accuracy of estimation, however such information is unavailable for real-time EEW.

Comparison of regression coefficients calculated in this paper based on Eq. (1) and from Dhakal et al. (2015) model are shown in Fig. 5. Maximum value of AVRS in NS and EW direction are taken in regression analysis and regression coefficients are calculated with natural period 0.1 to 10 s. Constant *c* decreases as natural period increases and coefficient *a* increases with the increment of natural period. In general, anelastic attenuation coefficient *b* in this paper decreases as natural period increases. Both studies show similar values and trends for coefficients of regression *a* and *c*, but for anelastic attenuation *b* the results show difference to some extent. Main reason is the difference of data set. Dhakal et al. (2015) included earthquakes with magnitude 6 to 8.5 and included subduction zone earthquakes as well. We collected earthquakes data with magnitude 5.1 to 7.3 without subduction zone earthquakes considering type of earthquakes happened which can be felt in Bangkok during recent years.

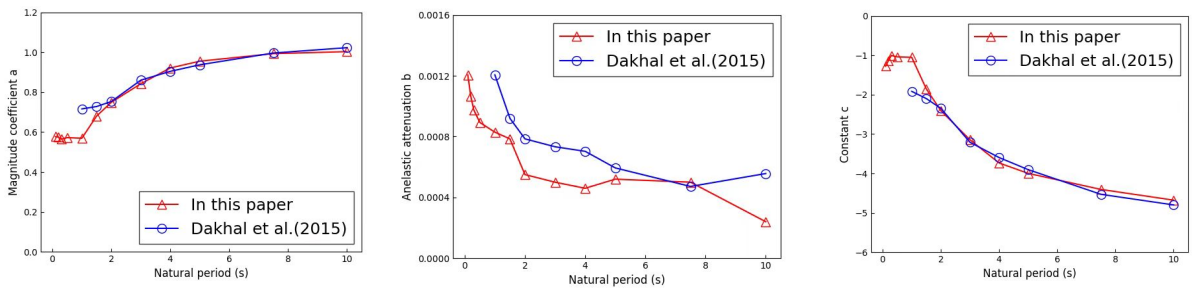

Figure 5. Comparison of regression coefficients.

CALCULATION OF AVRS FOR BANGKOK

Bangkok located at relatively remote distance from seismic sources, and the major active faults are far away from Bangkok city around 400 to 1000 km. As the number of earthquake observation data are limited, it is difficult to establish regression model using AVRS directly. On the other hand, Japan is situated along subduction zone and existence of remarkable number of active faults. Several earthquakes with various fault types occur every year, and existence of large amount of strong-motion data recorded by sites from K-NET, KiK-net and JMA. Therefore, various strong-motion parameters can be calculated from observation data involving PGA, PGV, AARS, and RVRS etc (Si et al., 1999). In this paper, two estimation equations are proposed with coefficients, α, by using same sets of earthquake data in Japan to calculate AVRS for Bangkok in absence of recorded data. These coefficients can be applied to estimate AVRS values for any sites for EEW.

METHOD 1: ESTIMATION WITH PGV AND RVRS

Conventionally, AVR is calculated by taking the sum of ground velocity and the relative velocity response time histories for given natural period. We propose the first estimation equation to calculate *AVRS(T)* in absence of observation data using *PGV* and *RVRS(T)* as:

$$AVRS(T) = RVRS(T) + \alpha_1(T)PGV \tag{2}$$

where $\alpha_1(T)$ is coefficient at corresponding natural period, T. In calculation of regression coefficient, α, in the first step, regression analysis is done on $AVRS(T)$, $RVRS(T)$, and PGV based on Eq. (1). Fig. 6 shows example plot of regression curves on AVRS and RVRS with magnitude of 7.3 and 5.4 which corresponding to EQ 1 and EQ 6.at natural period 2 s, as well as regression results on PGV. After that, 10,000 random values are generated from probability density function of hypocentral distance data (Fig. 7) based on the JMA data set used in this study. Range of random values for hypocentral distance are generated between 10 km to 800 km, and between 4.9 to 8.5 for magnitude. For given natural period, $\alpha_1(T)$ is calculated based on Eq. (4) by taking mean value (Fig. 8). Therefore, we will use the $\alpha_1(T)$ to estimate AVRS(T) from RVRS(T) and PGV for Bangkok. RVRS(T) and PGV will be estimated by the existing GMPEs that were found suitable for Thailand by previous studies.

METHOD 2: ESTIMATION WITH AARS

We propose another estimation equation using AARS shown in Eq. (3).

$$AVRS(T) = \alpha_2(T)\, AARS(T)\frac{T}{2\pi} \tag{3}$$

where $\alpha_2(T)$ is coefficient at corresponding natural period, T. Calculation of coefficient, α_2, follows same procedure as previously done to obtain α_1 in which regression analysis on *AARS(T)* is done based on Eq. (1). Fig. 9 shows plot of mean value of $\alpha_2(T)$ and standard deviation for each natural period.

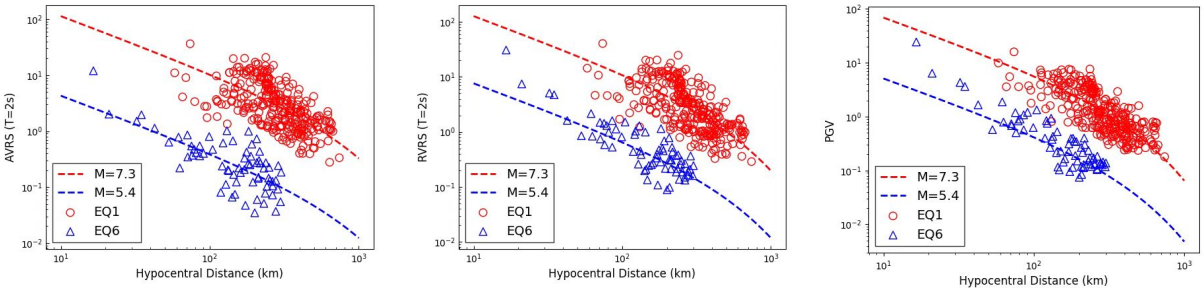

Figure 6. Regression model with AVRS(T), RVRS(T) at T= 2 s and PGV.

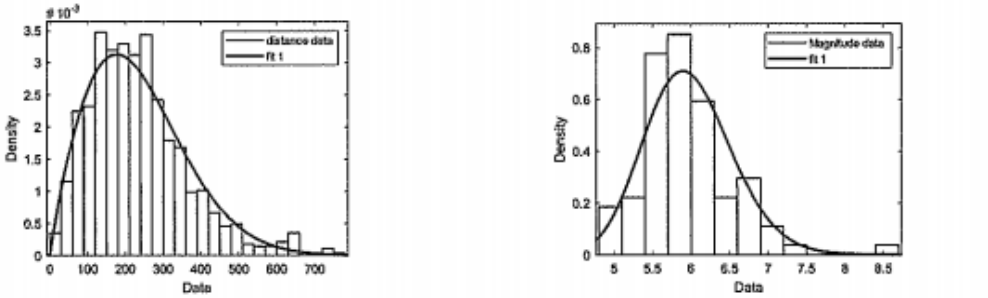

Figure 7. Distribution of hypocentral distance (left) and magnitude data (right).

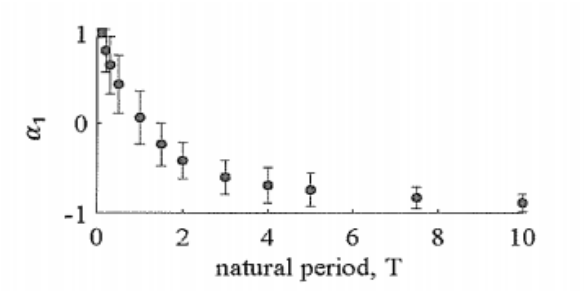

Figure 8. $\alpha_1(T)$ with standard deviation.

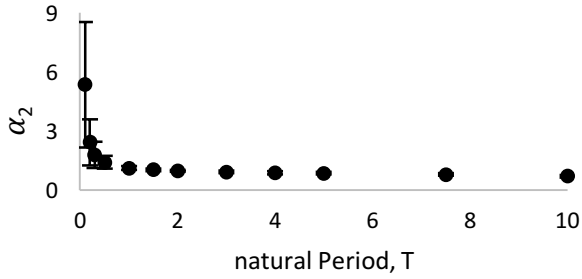

Figure 9. $\alpha_2(T)$ with standard deviation.

DISCUSSION

In this study, we obtained acceleration time histories of three components for only two earthquake records at one Thai Meteorological Department (TMD) observation site. One is the 2011 M_w 6.8 Tarlay earthquake in Myanmar, and the other one is the 2014 M_w 6.1 Mae Lao earthquake in Thailand with hypocentral distance 786 km and 674 km respectively. AVRS with natural period at 1.5 s, 2 s, 3 s, 4 s, 5 s, 7.5 s are calculated in NS, EW and UD directions corresponding to the range of natural period for intensity scale provided by JMA. For sake of comparison, maximum values (larger peak value of NS and EW directions) as well as geometric mean of AVRS in NS and EW direction is obtained, where geometric mean is calculated as square root of multiplications of AVRS in two directions. Applicability of regression curves with magnitude of 6.8 and 6.1 for AVRS directly using Eq. (1) is examined for Bangkok.

The results show that the observed absolute velocity response spectra at all the periods in Bangkok observation site are larger than the estimated value based on the proposed attenuation model as shown in Fig. 10. One possible reason for underestimation shown in the results might due to site amplification effect from soft clay. Soil condition of JMA sites obtained in our study is classified as stiff and dense soil. Bangkok is located on the central part of a large lower Plain known as Chao Phraya basin. The plain consists of deposits generated from the sedimentation at the delta of rivers. Soil underlying this area is alternating layers of clay and sand. The soft clay layer under metropolitan area of Bangkok has thickness of 15-20 m. Microtremor survey conducted by Subedi et al. (2021) at 5 sites in Bangkok basin shows the existence of soft clay layer which has low Vs values: 82–120 m/s at depths of 11–14.3 m. Therefore, it appears that sediment-induced amplification is a potential concern in Bangkok. In addition, the term of anelastic attenuation shown in Eq. (1) is supposed to be affected by the inhomogeneity of the crust. Therefore, the use of distance attenuation equation with Japan data might be another possible reason for underestimation.

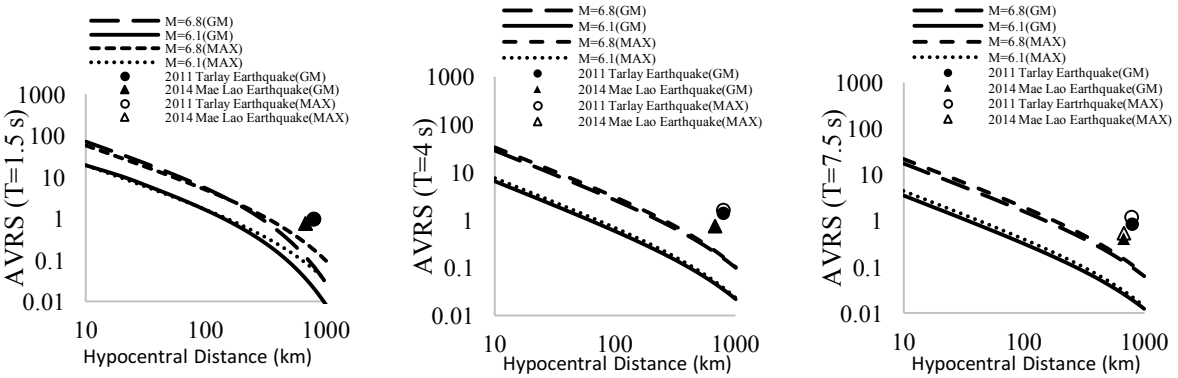

Figure 10. Regression curve using maximum (MAX) and geometric mean (GM).

We also examined the applicability of two proposed estimation equations. According to previous studies on suitable attenuation equations for Thailand (Tanapalungkorn et al., 2020; Chintanapakdee et al., 2008), attenuation model on RVRS is not examined. In addition, Boore et al. model (2008) is most appropriate models to predict AARS and PGA (Tanapalungkorn et al., 2020). Both models can estimate PGV, however, the limited distance range (< 200 km) might affect the results for case in Bangkok as distances from observation sites to epicenter are all larger than 600 km in this study. Therefore, we could not apply an appropriate attenuation model to evaluate PGV and RVRS for Bangkok to further evaluate the applicability of the estimation equation. We evaluate the applicability by using the observation data from the two earthquakes mentioned above instead. Fig. 11 shows the relevance between estimated and observed absolute velocity response spectra in which along the line denotes same value. $\alpha_1(T)$ is applicable to estimate AVRS despite of slight underestimation of estimated AVRS than observed one. For applicability of proposed estimation equation Eq. (3), estimated and observed absolute velocity response spectra is shown in Fig. 13 by using same earthquake data in Bangkok. Result from $\alpha_2(T)$ shows same tendency with $\alpha_1(T)$. The extremely limited size of observation data from Bangkok may also have influence on the results to some extent. In this study, the data was provided by TMD and if more observation recordings are available in the future in Thailand, further assessment could be implemented.

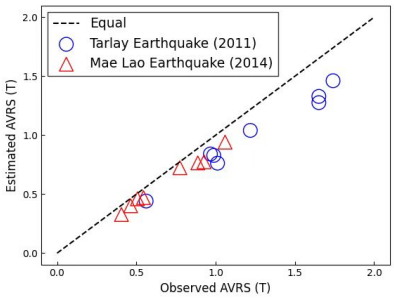

Fig. 11 Estimated and observed AVRS use α_1.

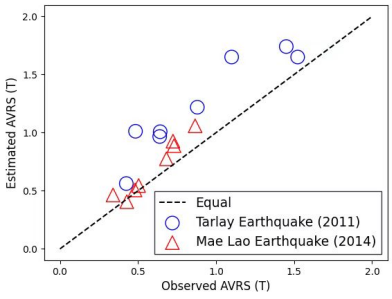

Fig. 12 Estimated and observed AVRS use α_2.

CONCLUSIONS

We developed GMPE of AVRS in the period range of 0.1 to 10 s with aim of EEW in Bangkok based on the JMA intensity for long-period ground motions. Because of lack in observation data from Bangkok, regression analysis is done by collecting data from JMA stations in Japan. We performed two stage regression analysis of AVRS with magnitude and hypocentral distance as independent parameters. In addition to that, we also proposed two prediction equations to estimate AVRS in Bangkok in absence of observation data under the existence of proper attenuation on RVRS and PGV or AARS for Thailand.

Regression curves and AVRS calculated from observation data in Bangkok suggests that our model underestimates the value for several natural periods due to the limited size of data available and lack in

site evaluation in the model as soft clay underlying Bangkok city could cause amplification during earthquakes. On account of lack in suitable attenuation equation to calculate PGV and RVRS for Bangkok, we evaluate the estimation equations by using real observation data from two earthquakes. The results show somehow positive feedback, but it is suggested that a further evaluation if appropriate attenuation equations are developed in the future.

ACKNOWLEDGMENTS

The authors would like to express their gratitude to Prof. Ono (Tottori Univ), Dr. Furukawa (Kyoto Univ), Dr. Kitaoka (Kansai Univ), Dr. Latcharote (Mahidol Univ), Dr. Charatpangoon for their useful discussions. They especially thank Prof. Matsuoka (Tokyo Inst. of Technology) for providing V_{s30} data of K-NET and KiK-net sites. The strong ground motion records used in this paper were offered by the Japan Meteorological Agency. This research was done under the support of the Supporting Program for Interaction-based Initiative Team Studies (SPIRITS) funded by Kyoto University.

REFERENCES

Building Seismic Safety Council (BSSC) (2004). "NEHRP Recommended Provisions for Seismic Regulations for New Buildings and Other Structures, Part 1 and Part 2 (Commentary)", Report prepared for the Federal Emergency Management Agency, Washington, D.C.

Boore, D. M., and J. J. Bommer (2005). "Processing of strong-motion accelerograms: needs, options and consequences", *Soil Dyn. Earthq. Eng.*, **25**, 93-115.

Chintanapakdee, C., Naguit, M.E. and Charoenyuth, M. (2008). "Suitable Attenuation Model for Thailand", *Proc. 14th World Conf. Eqk. Eng.*, October, Beijing, China.

Dhakal, Y. P., Suzuki, W., Kunugi, T. and Aoi, S. (2015). "Ground Motion Prediction Equations for Absolute Velocity Response Spectra (1-10 s) in Japan for Earthquake Early Warning", *Journal of Japan Association for Earthquake Engineering*, **15**(6), pp. 91-111.

Joyner, W. B. and Boore, D. M. (1993). "Methods for Regression Analysis of Strong-Motion Data, *Bulletin of Seismological Society America*", **83**, 469-487.

Kawase (2003), "Site effects on strong ground motions in International Handbook of Earthquake and Engineering Seismology", (edited by W. H. K. Lee, Kanamori, H., Jennings, P. C. and Kisslinger, C.), Chapter 61, *Academic Press*, 1013–1030.

Koketsu, K. and Miyake, H. (2008). "A seismological overview of long-period ground motion", *J. Seismol*. **12**(2), 133-143.

Nakamura, M. (2013). "Information on Long-Period Ground Motion of the Japan Meteorological Agency", Proceedings *10th International Workshop on Seismic Microzoning and Risk Reduction*, Paper ID 12.

Likitlersuang, S., Plengsiri, P., Zalbuin Mase, L. and Tanapalungkorn, W. (2020). "Influence of spatial variability of ground on seismic response analysis : a case study of Bangkok subsoils". *Bull. Eng. Geol. Environ*. **79**, 39–51.

Sadigh, K., Chang, C., Egan, J., Makdisi, F. and Youngs, R. (1997). "Attenuation Relationships for Shallow Crustal Earthquakes Based on California Strong Motion Data". *Seismological Research Letters*, **68**(1), 180-189.

Subedi, B., Kiyono, J., Furukawa, A., Ono, Y., Ornthammarath, T., Kitaoka, T., Charatpangoon, B. and Latcharote, P. (2021). "Estimation of Ground Profiles Based on Microtremor Survey in the Bangkok Basin", *Frontiers in Built Environment*, **7**.

Tanapalungkorn W, Mase LZ, Latcharote P and Likitlersuang S, (2020). "Verification of attenuation models based on strong ground motion data in Northern Thailand". *Soil Dyn Earthq Eng*, **133**(106145):1–9.

8th Asia Conference on Earthquake Engineering
Taipei, Taiwan ■ November 9-11, 2022

Toward the seismic hazard assessment of the stable continental region from the strong-motion data recorded of a significant earthquake: Example for Northern Vietnam

Bang V. Phung[1], Bor S. Huang[1], Minh L. Nguyen[2], Duong V. Nguyen[2] ,

Cong Nghia Nguyen[1, 2, 3] , and Ha Vinh Long[1, 2, 3]

[1] Institute of Earth Sciences, Academia Sinica, Academia, 115201, Taiwan.

[2] Institute of Geophysics, Vietnam Academy of Science and Technology, Hanoi, 122480, Vietnam.

[3] Taiwan International Graduate Program Earth System Sciences, Academia Sinica, 115201, Taiwan.

Email: phungvb@earth.sinica.edu.tw, hwbs@earth.sinica.edu.tw, nlminh79@gmail.com,

nghianc@hus.edu.vn, duongnv@g.ncu.edu.tw, havinhlong1988@g.ncu.edu.tw

ABSTRACT

It is challenging to develop ground motion prediction equations (GMMs) for seismic hazard assessments purpose at a region with light to moderate seismicity due to the scant recorded data. In this study, we present a methodology for developing the ground motion model using the data from a significant earthquake (2020 Moc Chau, Vietnam), which characterizes the seismic condition in Northern Vietnam. The collected data were first used to evaluate ground shaking in northern Vietnam (NVN). Then, the earthquake model of Abrahamson et al. 2014 (ASK14) modified their prediction efficiencies by fitting the observed data. The modified ASK14 was used to simulate seismic risk scenarios of large earthquakes in NVN and compared with the structures' design spectra of Hanoi city. Our analyses revealed the possibility of damage resulting from shaking in the Hanoi metropolitan area caused by recognized earthquake sources in NVN. Our results give an indication to the engineer's community that considering seismic design for buildings, bridges and infrastructures should have been taken in future construction projects.

Keywords**:** *Moc Chau earthquake, Vietnam, ground motion prediction, site effect, and GMM*

INTRODUCTION

An earthquake with a magnitude (Mw) of 5.0 occurred near the Moc Chau district in the northwest region of Vietnam on July 27, 2020 (referred to herein as the 2020 Moc Chau earthquake; Figure 1). This event has caused considerable damage to the infrastructure in the vicinity of the epicenter. Although the magnitude was moderate, people reported feeling strong shaking in the high-rise buildings of Hanoi and other provinces on the Red River delta, which is approximately 100 to 170 km away from the epicenter. This low-frequency shaking had not been previously reported and

underscores the importance of the seismic hazard assessment of the potential damage of future large earthquakes in Vietnam.

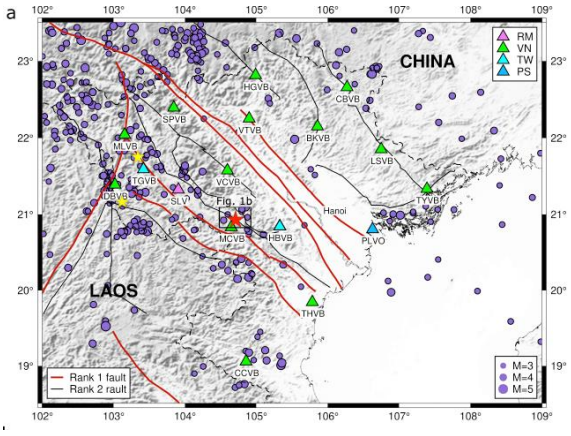

Figure 1. Map of seismicity in northern Vietnam from 1990 to 2021. The red star symbol represents the epicenter of the 2020 Moc Chau earthquake, and the yellow star symbols represent the locations of the events discussed in this study (Figure from C.N Nguyen 2021).

Northern Vietnam (NVN), which is known to be the result of complex motions triggered by relative motions between several microcontinents such as 1) the South China Block masses extrusion motion that was promoted by the indentation of the India Block (IB) into the Eurasian Continent since the Tertiary period (Tapponnier et al., 1982). Over the past decade, many studies primarily investigated tectonic dynamism have assessed the seismic risk of the region (Huang et al., 2009). Earthquakes in NVN are characterized as shallow (Nguyen and Le, 2005; Nguyen et al., 2019). Destructive earthquakes with maximum magnitudes of M6 or greater have occurred in NVN (Das, 2015), two of which occurred in the last century (Figure 1): the 1935 Dien Bien earthquake, which had a surface wave magnitude (Ms) of 6.8, and the 1983 Tuan Giao earthquake, which had a Ms of 6.7. Both earthquakes caused significant infrastructural damage and economic loss (Duong et al., 2013).

In response to the urbanization and construction of large public facilities in Hanoi, Vietnam, various seismic hazard reduction measures, including the modification of the global earthquake prediction model by Abrahamson et al. (2014, ASK14) GMMs, have been proposed in this study. Then, a new evaluation technique is developed using 148 high-quality earthquake data records from all 15 broadband seismic stations in NVN.

DATA GATHERING NETWORK AND STRONG MOTION RECORD

a. Seismological gathering network

The national seismological network, Vietnam (VNNET) land-based broadband stations were started setup in early 2010 with three first stations in Dien Bien Phu (DBVB), Bac Giang (BGVB), Lang Chanh (LAVB), and Con Cuong (CCVB). Then, from 2012 to 2018 total of 30+ stations

were deployed (Triangle - Figure 1). The stations equipped the high-gain broadband seismometer co-located with strong motion Kinemetric/Episensor FBA-EST sensor, both connected with Quanterra/Kinemetric Q330HR/Q330HRS digital datalogger, real-time transmission of the data to the datacenter by optical fiber cable internet (FTTH), with approximately 3500 megabytes per day. The station's locations are not only along the main fault section, which is mostly located in the mountainous area, but also situated in the delta and east coastal line region; the distribution of the VNNET provided good coverage of seismicity observation for internal Northern Vietnam. Although primarily intended for real-time monitoring, the seismic activity region on the NorthWest side, the VNNET stations were set up with the distance station-to-station with a grid of nearly 50km in the West and 80 to 100km in the East and far Eastern, respectively.

b. Strong-motion data

The Moc Chau earthquake occurred at 05:15 (UTC; local time: 12:15) on July 27, 2020. The hypocenter was located at 20.929°N, 104.708°E, approximately 12 km away from the town of Moc Chau (Figure 1). Infrastructure in the region of the epicenter was severely damaged by the earthquake (Nguyen et al., 2021). Also, People in the nearby cities and in the region near the earthquake felt strong shaking during the quake. Some descriptions of shaking, mostly from high-rise buildings in Hanoi, were classified as grade III according to the MSK-64 intensity scale (Medvedev and Sponheuer, 1969). Numerous aftershocks followed the mainshock, all of which were concentrated in a small region (Nguyen et al., 2021). Table 1 displays the details of the main shock and two aftershocks regarding the epicenter and source-related parameters.

Table 1. List of 3 largest events used in this study.

Event id	M_L	M_w	Location	Depth (km)	N. of records
202007270514 (Main shock)	5	5	20.929°N 104.708°E	7.1	12
202008170113	4.4	4.4	20.907°N 104.749°E	6.9	13
202007280125	4.1	4.1	20.910°N 104.716°E	5.3	13

The mainshock (M = 5.0) and its aftershocks with magnitudes > 3 (11 events, as indicated in Figure 1 – black box) were considered in our analysis. Figure 2a presents the time histories of the one-component accelerations caused by the main shock at station MCVB. The peak ground motion accelerations (PGAs) observed at this station were 35.9, 29.3, and 26.7 cm/s^2 in the vertical, east-west (E–W), and north-south (N–S) components, respectively. The maximum peak ground velocity (PGV) derived from the integration of the acceleration time histories in the E–W component was weak (0.72 cm/s; Figure 2b).

In a modern broadband station, signals from both the accelerometer and the broadband velocity sensor are continuously recorded at the same site and share the same data logger. The combined broadband velocity and acceleration exhibit a large dynamic range concerning the recorded ground motion. This implies that the broadband network may record extra data, such as recordings for distant large events or smaller local events untriggered by the independent strong ground accelerations, for use in earthquake engineering.

a)

b)

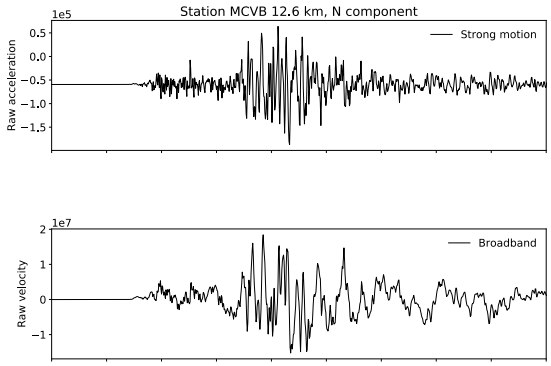

Figure 2. The recordings of corrected acceleration (a) and velocity integrated from acceleration (b) of the 2020 Moc Chau earthquake, as recorded by station MCVB – 12.6 km away from the epicenter. The unit of raw acceleration and raw velocity are nm/s^2 and nm/s, respectively.

DEVELOPMENT OF EARTHQUAKE PREDICTION MODEL

For a purpose of evaluating seismic hazards due to the Moc-Chau earthquakes, we modified ASK14, which was recognized as the model that can have a better comparison with the observed data than the other candidate models. We examined the residual analysis and generally observed that the total residual (the difference between observed data and the GMM in the natural logarithm unit) shows both significant mean offset and significant trend with respect to magnitude. Based on the peculiarities of the ground motion characteristics from the residuals, we identify two coefficients that control the ground motion in the considering earthquakes; constant a_1 measuring mean offset and coefficient a_6 representing small magnitude scaling. Our method to modify ASK14 is to replace a_1 and a_6 in ASK14 with new terms. Hence, the median prediction of ASK14 without a_1 and small magnitude scaling is:

$$f_{ASK14-VN} = f_{ASK14} - \left(a_1 + a_6(M-5)\right) \quad (1)$$

The natural logarithm of spectral acceleration can be expressed as follows:

$$ln(y_{es}) = f_{ASK14-VN} + \left(a_{1vn} + a_{6vn}(M-5)\right) + \delta B_e + \delta W_{es} \quad (2)$$

whereas e refers to an eth earthquake and $\boldsymbol{s}$ refers to *sth* station. The quantity y_{es} is an observed spectral acceleration. δB_e, δW_{es} are between event residual and within event residual, which are assumed to be normally distributed with standard deviation τ and ϕ, respectively. The method to modify ASK14 to account for the Moc Chau earthquakes is based on the mixed effect regression described in Abrahamson et al., (1992).

Figure 3a shows the residual analysis concerning the magnitude and distance; it indicates that residual trends of both δB_e in magnitude range and δW_{es} in the distance of 200 km are improved for the after-regression model (i.e., modified ASK14) as compared with that for the before-regression model. Figure 3b displays the comparison of the distance attenuation of the modified ASK14 and ASK14 for M = 3, 4, and 5 with observed data. The results indicate an improvement of the modified ASK14 relative to the original ASK14. With this improvement, the modified ASK14 can be used further for the hazard assessment.

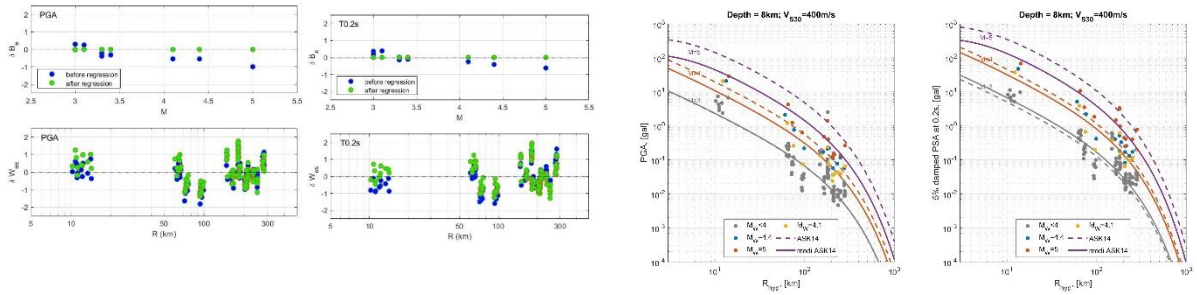

Figure 3. (a) Residual of modified ASK14 and ASK14 plotted as a function of magnitude and distance for PGA and T0.2 sec PSA. (b) Comparison of distance attenuation of the modified ASK14 and AKS14 with the observed data.

SEISMIC RISK EVALUATIONS FOR HANOI

The elastic seismic demand spectra for performance-based design are usually represented by the design acceleration response spectra S_e proposed in a seismic design code. The seismic design code for buildings in Vietnam is the TCVN 9386:2012 (IBST, 2012). This seismic design code of Vietnam (TCVN 9386:2012) was developed based on Eurocode 8 (EC-8; 2005) and with consideration of the Vietnamese seismic zone map (Nguyen, 2005), which provides information about the ground acceleration (a_g) for different zones of Vietnam. In this study, the ground acceleration range for each zone in the study region was selected from two seismic zone maps (Nguyen et al., 2020), as illustrated in Fig. 4. The later seismic zone map of Nguyen et al. published in 2020 provides a more detail zonation of the Hanoi metropolitan area than the map of Nguyen (2005).

To evaluate seismic hazards in Vietnam, given a ground acceleration level for each zone, the design spectra can be computed according to the seismic design code TCVN 9386:2012. The horizontal elastic response spectrum $S_e(T)$ is determined by the following equations:

$$T \le T_B:\ S_e(T) = a_g \cdot S \cdot \left[1 + \frac{T}{T_B} \cdot (\eta \cdot 2.5 - 1)\right] \quad (3)$$

$$T_B \le T \le T_C:\ S_e(T) = a_g \cdot S \cdot \eta \cdot 2.5 \quad (4)$$

$$T_C \le T \le T_D:\ S_e(T) = a_g \cdot S \cdot \eta \cdot 2.5 \cdot \left[\frac{T_C}{T}\right] \quad (5)$$

$$T_D \le T:\ S_e(T) = a_g \cdot S \cdot \eta \cdot 2.5 \cdot \left[\frac{T_C \cdot T_D}{T^2}\right] \quad (6)$$

in which $S_e(T)$ is the elastic response spectrum; T is the vibration period of a linear SDOF system; ag is the design ground acceleration on type A ground ($a_g = \gamma_I \cdot a_{gR}$); T_B and T_C are the lower and upper limits of the period of the constant spectral acceleration branch, respectively; T_D is the value defining the beginning of the constant displacement response range of the spectrum; S is the soil factor; and η is the damping correction factor, with a reference value of $\eta = 1$ for viscous damping $\xi = 0.05$.

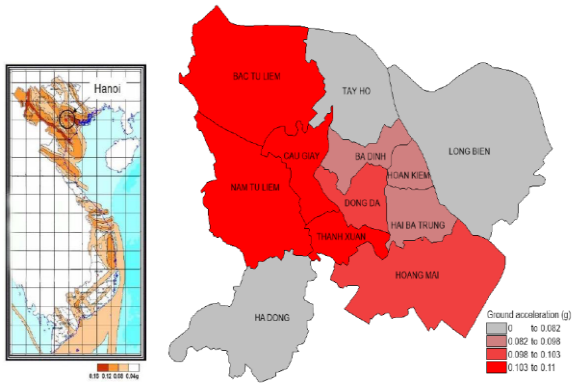

Figure 4. Estimated ground acceleration zone maps for (a) Vietnam (Nguyen, 2005) and (b) Hanoi (Nguyen et al., 2020).

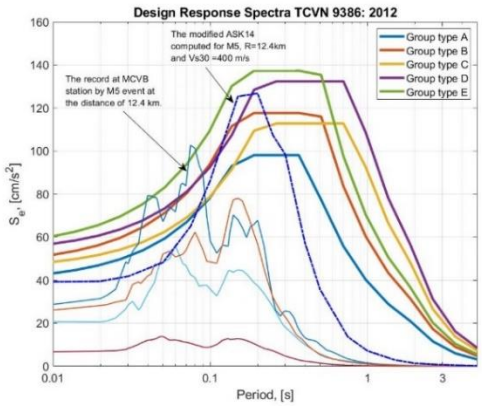

Figure 5. Superposition of the acceleration spectra from station MCVB modified ASK14 and the design spectra. The design ground acceleration (a_g) was 0.04g used to generate this plot.

To construct the design spectra in Hanoi, the design acceleration was referred to as the mean value of the lowest ground acceleration zone of Hanoi (zone of gray color in Fig. 4), and ag = 0.04g was selected. Figure 5 presents the design spectra for ground types A, B, C, D, and E in Hanoi with ag = 0.04g. In Figure 6, the computed spectral accelerations of the seismograms recorded at station MCVB (12.4 km away from the epicenter) during the 2020 Moc Chau

earthquake sequence were superimposed with the design spectra of TCVN 9386:2012 for comparison. The acceleration spectra of the main shock (M = 5) exceeded the TCVN 9386:2012 design spectra at periods of approximately 0.03 to 0.1s; the maximum site amplifications (i.e., group D and E in Figure 5) were included for a conservative comparison. This implies that a similar earthquake (M= 5) occurred approximately 10 to 15 km away from Hanoi, which may have damaged buildings and infrastructure. However, the distance from the earthquake source to Hanoi is more than 120 km; at this distance, the observed acceleration response spectra from other stations at similar distances did not exceed the design spectra, which implies that the earthquakes could not have damaged buildings in the Hanoi area. However, previous seismic hazard evaluations have suggested that a giant super shear rupture destructive earthquake may occur along the Red River fault (Das, 2015). A larger earthquake occurring along the fault will likely greatly damage buildings in Hanoi, and engineers and decision-makers must not ignore this possibility.

TOWARD PROBABILISTIC SEISMIC HAZARD ANALYSIS

When PSHA is applied to seismic hazard assessment, the aim is to quantify and integrate ground motion uncertainties to produce an explicit description of the distribution of future shaking that may occur at a site (Baker, 2013). PSHA depends on ground motion computations using GMMs; the standard PSHA procedure involves the selection of a set of appropriate GMMs, which predict the means and standard deviations of ground motion. Therefore, the GMM candidates for PSHA must be carefully selected to ensure the applicability of the PSHA results. The total residuals (the natural logarithmic difference between a GMM and the observed data) can be used to evaluate the suitability of a GMM. Figure 6 presents the total residuals plotted against distance (R_{hyp}) and magnitude (**M**) for modified ASK14 and "raw" ASK14 for periods of 0.01 and 0.2 s. The means and standard deviations were also computed and are presented in each subplot. The mean offset (mean residual) can be used to generally indicate the overall model fit (all magnitudes and distance ranges). For example, the residual at T = 0.2 s of the modified model shows a mean near 0 indicating a better fit than the residual at T = 0.01 s. However, the residuals as shown in ASK14 are strongly associated with magnitude when T = 1 or 3s, indicating that the ASK14 model exhibits low predictive accuracy even though the residual mean is near 0. In addition, the magnitude scaling of the ASK14 is unsuitable for long-period motion (1 and 3 s), for which it exhibits overprediction for M5 (by a factor of 3) and underprediction for M3 (by a factor of 2). The poor fit of the ASK14 model leads to high standard deviations for the long-period motion; the average acceptable standard deviation value for PSHA is approximately 0.8 (GeoPentech, 2015). In this study, the estimated sigma (σ) values of the ASK14 predictions tested by the 2020 Moc Chau earthquake recordings were 10% to 50% greater than the standard values for PSHA studies. Therefore, none of the GMMs considered in this study can be recommended for use in PSHA for NVN without further refinement. We suggest developing new GMMs using the ASK14 as an initial model and updating it according to new observed local data.

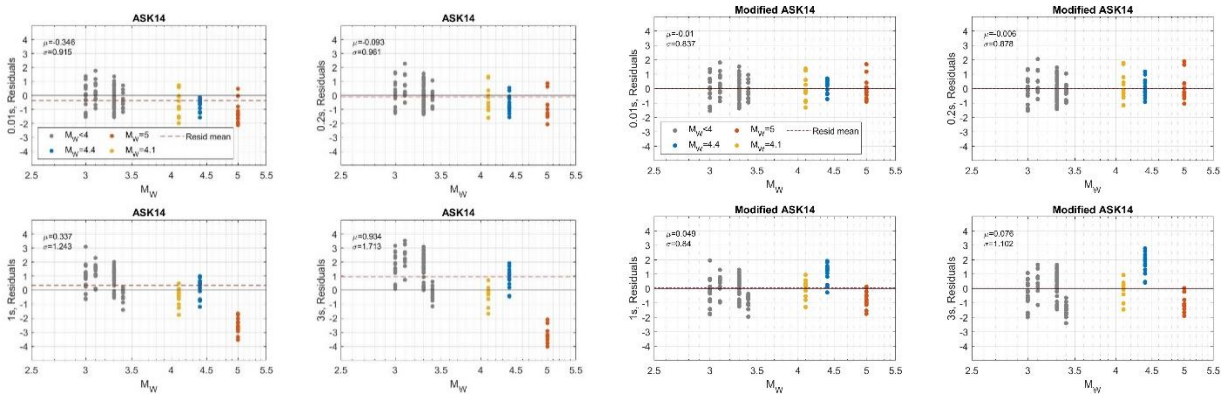

Figure 6. The residual of ASK14 (left) and modified ASK14 (right) GMM is plotted as a function of magnitude and distance, which shows a bias with magnitude. The prediction values are done in the same of site and model conditions.

CONCLUSIONS

The 2020 Moc Chau earthquake (M = 5) and its aftershocks elucidated several aspects of ground motion characteristics and their effects on structural damage. Based on the comparison of the computed response spectra of the records and the design spectra, our examination of the seismic risk scenarios of large earthquakes in NVN indicated the possibility of damage resulting from shaking in the Hanoi metropolitan area caused by earthquake sources in NVN. Furthermore, the vertical ground motion observed at the MCVB station being greater than the GM of its horizontal components should be carefully considered in the seismic design of structures because the effects of vertical motion are often neglected by engineers. The comparison between the recorded ground motion and the predictions of the selected foreign GMMs revealed that ASK14 fit the data more closely than any of the other GMMs. However, as indicated by the total residual analysis, none of the existing GMMs perform well enough for PSHA in NVN. Therefore, we develop a local GMM based on the ASK14 using the Moc Chau data. However, this data is limited to a small subset. We suggest developing a new GMM soon based on additional input data collected from existing broadband seismic records and the new Vietnam broadband seismic network. Careful integration of the old and new seismic data will improve the accuracy of seismic hazard assessment in Vietnam,

REFERENCES

Abrahamson, N. A., and R. R. Youngs (1992), A stable algorithm for regression analyses using the random effects model, Bulletin of the Seismological Society of America, 82(1), 505-510, doi:10.1785/bssa0820010505.

Akkar, S., Sandıkkaya, M. A., and Bommer, J. J. (2014). “Empirical ground-motion models for point- and extended-source crustal earthquake scenarios in Europe and the Middle East.” Bulletin of Earthquake Engineering, 12(1), 359–387.

Baker, J. W. (2013), An Introduction to Probabilistic Seismic Hazard Analysis (PSHA), edited.

Das, S. (2015), Supershear Earthquake Ruptures – Theory, Methods, Laboratory Experiments and Fault Superhighways: An Update, in Perspectives on European Earthquake Engineering and Seismology, edited, pp. 1-20, doi:10.1007/978-3-319-16964-4_1.

Duong, N. A., T. Sagiya, F. Kimata, T. D. To, V. Q. Hai, D. C. Cong, N. X. Binh, and N. D. Xuyen (2013), Contemporary horizontal crustal movement estimation for northwestern Vietnam inferred from repeated GPS measurements, Earth, Planets and Space, 65(12), 1399-1410, doi:10.5047/eps.2013.09.010.

GeoPentech (2015), Southwestern United States Ground Motion Characterization SSHAC Level 3– Technical Report Rev.2Rep.

Huang, B.-S., T. S. Le, C.-C. Liu, D. V. Toan, W.-G. Huang, Y.-M. Wu, Y.-G. Chen, and W.-Y. Chang (2009), Portable broadband seismic network in Vietnam for investigating tectonic deformation, the Earth's interior, and early-warning systems for earthquakes and tsunamis, Journal of Asian Earth Sciences, 36(1), 110-118, doi:10.1016/j.jseaes.2009.02.012.

Medvedev, S. V. a. S., W. (1969), Scale of seismic intensity. , paper presented at The 5th World Conference Earthquake Engineering, Santiago.

Nghia Nguyen, C., et al. (2022), Characteristics of earthquake source and ground motions in Northern Vietnam investigated through the 2020 Moc Chau M5.0 earthquake sequence, Journal of Asian Earth Sciences, 229, doi:10.1016/j.jseaes.2022.105144.

Nguyen, D. X., and Le, T. S. (2005), Research and Forecasting Earthquakes and Ground Movements in Vietnam (In Vietnamese).Rep., Vietnam Institute of Geophysics, Hanoi, Vietnam

Nguyen, D. X., and Le, T. S. (2005), Seismic hazard assessment for Vietnam Territory." In: Proceeding of the 4th Conference of Vietnamese Association of Geophysics, paper presented at The 4th Conference of Vietnamese Association of Geophysics, Publishing House of Science and Technology, Hanoi, Vietnam, Ha Noi, Viet Nam.

Nguyen, H. P., T. T. Pham, and T. N. Nguyen (2019), Investigation of long-term and short-term seismicity in Vietnam, Journal of Seismology, 23(5), 951-966, doi:https://doi.org/10.1007/s10950-019-09846-x.

Nguyen, V.-Q., M. Aaqib, D.-D. Nguyen, N.-V. Luat, and D. Park (2020), A Site-Specific Response Analysis: A Case Study in Hanoi, Vietnam, Applied Sciences, 10(11), doi:10.3390/app10113972.

Tapponnier, P., G. Peltzer, A. Y. Le Dain, R. Armijo, and P. Cobbold (1982), Propagating extrusion tectonics in Asia: New insights from simple experiments with plasticine, *Geology, 10(12),* doi:10.1130/0091-7613(1982)10<611:Petian>2.0.Co;2.

NON-ERGODIC GROUND-MOTION MODEL FOR TAIWAN SUBDUCTION EARTHQUAKES USING 3-D SIMULATIONS

Chih-Hsuan Sung[1] and Ming-Che Hsieh[2] and Norman Abrahamson[3]
1. Post-Doc Researcher, Dept. of Civil & Environmental Engineering, UC Berkeley, CA, U.S.A
2. Associate Research Fellow, Earthquake Disaster & Risk Evaluation and Management Center (E-DREaM), National Central University,Taoyuan ,Taiwan
3. Adjunct Professor, Dep. of Civil & Environmental Engineering, UC Berkeley, CA, U.S.A
Email: karensung@berkeley.edu, mchsieh@g.ncu.edu.tw, abrahamson@berkeley.edu

ABSTRACT

As sets of 3D simulations become more widely available, it is good opportunity to incorporate the information from the 3D simulations into ground motion model (GMM) used in seismic hazard calculations. Non-ergodic effects on the ground motions have been seen in the suite of numerical simulations of ground motions from megathrust earthquakes, such as the western US region, Seattle and Wasatch Front, Utah. In this study, we generated the suite of numerical simulations of ground motions from megathrust earthquakes on the Ryukyu subduction zone through a 3-D structure and chose a small site region in the middle Hualien that nears this subduction zone. Chao et al. (2020) (CCHL20) subduction zone GMM is ergodic, so we follow the process of Sung and Abrahamson (2022) to build the non-ergodic GMM based on the 3-D simulation results. First, the basin term of the CCHL20 GMM is modified to be consistent with the basin scaling from the 3-D simulations. Then, the spatial distribution of the non-ergodic terms is estimated using the varying coefficient model for the region covered by the simulations. In this case, we can see the strong radiation/directivity effects from 3-D simulation are captured through non-ergodic terms.

Keywords: nonergodic, ground-motion, 3D simulation, sigma, aleatory variability

INTRODUCTION

With the large increase in the number of recorded ground motions, there are large systematic differences in ground-motion scaling can be seen in some regions, such as the western US region and Taiwan. The ergodic GMMs assume that ground motion follows the same scaling with magnitude, distance, and site conditions within the broad tectonic category. That is, ergodic GMMs are poor predictors of the ground motion at a specific site from a specific source and overestimate the aleatory variability. In contrast, the non-ergodic GMM can capture the systematic source, path, and site effects and also reduce the aleatory variability (Abrahamson et al., 2019; Lavrentiadis et al., 2022; Sung et al., 2022; Sung and Abrahamson, 2022).

In the Cascadia region, the 3-D simulations from the M9 project (Frankel et al., 2018) showed that there are large systematic differences in the site and path effects due to the 3-D velocity structure in the Cascadia region. Sung and Abrahamson (2022) future incorporate the 3-D simulation results into AG20 GMM to replace with the basin scaling based on the M9 simulation and include the non-ergodic site/path terms. Their results show that the non-ergodic aleatory variability was reduced by 15-25% compared to the ergodic sigma for Cascadia. The application of non-ergodic GMMs requires an estimate of the epistemic uncertainty in the non-ergodic terms. For the Cascadia case, there are no multiple simulation results for 3-D velocity models, so the epistemic uncertainty of the non-ergodic term is less than 0.1. Therefore, Sung and Abrahamson (2022) assumed that the epistemic uncertainty due to uncertainty in the 3-D velocity model is one-half of the between-site standard deviation from the simulations.

For the Taiwan region, the empirical ground-motion data from subduction zone earthquakes are not available to constrain the non-ergodic terms. As an alternative to empirical ground-motion data from

subduction zone events, 3-D simulations can be used to constrain the repeatable source, path, and site effects within the region. Therefore, we generated the 3-D simulations from the M8 subduction zone events close to east Taiwan and chose a relatively small and nearest region, the middle Hualien, as the target site in this study.

We adopted the CCHL20 model as our ergodic ground-motion model for subduction events. Before moving to the non-ergodic version, the scaling of the basin effects as a function of the depth to a shear-wave velocity of 1.0 km/s (Z1.0) in the CCHL20 model should be replaced with the Z1.0 scaling from the 3-D simulations. Then, the CCHL20 model with the new basin scaling is modified to be a non-ergodic GMM based on the combined non-ergodic effects determined from the M8 simulation results. Our goal is to incorporate these features into a non-ergodic GMM in a manner that is consistent with the development of GMMs for use in Taiwan seismic hazard calculations in the future step.

SYNTHETIC GROUND-MOTION DATA

According to the comprehensive earthquake catalog from Central Weather Bureau in Taiwan and previous studies (Kao, 1998; Theunissen et al., 2010; Hsu et al., 2012), an M8 historical earthquake took place offshore east Taiwan in 1920. To estimate the possible ground motions in eastern Taiwan if earthquakes with similar magnitudes happen again, we assume an M8 scenario earthquake in the Ryukyu subduction zone. We focus only on the R1 segment of the Ryukyu trench because the 1920 event probably occurred near the R1 segment. From the empirical relationship of Yen and Ma (2012), the R1 segment has a possible moment magnitude of about 8. To preliminarily compare the synthetic ground motions with ground motion models, we prescribe kinematic fault-rupture models with nine different rupture initiation points for the M8-scenario ground motion simulations (Figure 1). Macro and micro source parameters are referred to as the working flow of the Recipe (Irikura and Miyake, 2012). A single asperity is placed on the fault plane, and the asperity represents 22% of the total fault-plane area. Amounts of slips are 5.2 m and 3 m in the asperity and the background areas, respectively. An average rupture speed of 3 km/s is set for rupture propagation. The fault plane has a length and a width of 161 and 51 km, and it is discretized to 161 x 56 subfaults. A 2-s gaussian wavelet yielding a resolvable frequency up to 0.8 Hz is applied for each subfault. The above settings produce nine rupture cases, and we treated these simulation cases as nine realizations. Detailed fault-rupture parameters are shown in Table 1.

We conduct a 3-D traction-image finite-difference method (FDM, Zhang and Chen, 2006; Zhang et al., 2012) to perform full-waveform ground motion simulations. The tomographic P- and S-wave velocity models used in the simulation are from Kuo-Chen et al. (2012). The ETOPO1 topographic model (Amante and Eakins, 2009) is also implemented when building the numerical mesh of FDM calculation. Thus, wave propagation in the 3-D model with considering scatterings from topographic relief and bathymetry is mannered in our modeling. The simulation cost about 14 hours with using 96 CPU cores to simulate 150-s wave propagation in the target region. A total of 24,755 fictitious stations with an inter-station spacing of 500 m are deployed to output 3-component synthetic waveforms. We adopt the RotD50 approach to calculate spectral acceleration and pick 3- and 5-second PSAs for ground motion model analysis.

GROUND-NOTION MODEL

One example of the 3-sec PSA map of the middle Hualien area for the one simulation scenario (Figure 2a) is shown in Figure 2b and the CCHL20 model in Figure 2c. The result shows that the traditional ergodic GMM cannot present the 3-D crustal structure due to the ground motion following the same scaling with magnitude, distance, and site conditions within the broad tectonic category. So, in this session, we show the process of moving the ergodic model to the non-ergodic model.

Ergodic Model

The basin scaling of the CCHL20 model is replaced with the basin scaling in the M8 simulations. To evaluate the basin scaling from the simulations, the total residuals, $\delta\varepsilon$, from the 3-D simulations are computed relative to the CCHL20 model without the basin term:

$$\delta\epsilon = \ln(PSA_{SIM}) - CCHL20(M, R, \dots) - f_{basin}(Z_{1.0}) \quad (1)$$

$f_{basin}(Z_{1.0})$ is the basin term of the CCHL20 model. $Z_{1.0}$ refers to the Engineering Geological Database maintained by NCREE (NCREE, 2018).

The total residuals ($\delta\varepsilon$) at T = 3 s are shown as a function of $Z_{1.0}$ in Figure 3, and the pink points are the mean residual for different $Z_{1.0}$ bins. The total residuals were fit to the following basin-depth model:

$$f_{3D-basin} = C_{SIM} + b_2 \ln\left(\frac{\max(Z_{1.0},\ 100)}{Z_{1.0,ref}}\right) \quad (2)$$

The new basin-depth scaling ($f_{3D-basin}$) and the basin term of the CCHL20 model (f_{basin}), for T = 3 sec, are shown in the same plot, using the solid blue line and pink dashed line, respectively. Comparing the slope of the new basin term (b_2= 0.152) with the original CCHL20 basin term (0.164), the M8 simulations have a $Z_{1.0}$ slope similar to the CCHL20 basin scaling. However, the basin term for the simulation cannot show the site amplification for the $Z_{1.0}$ over 100 meters due to the rough resolution for the 3D crustal velocity model at the shallow soil depth. Therefore, we fix the scaling for the new basin term after the $Z_{1.0}$ > 100 meters. C_{SIM} (= 0.66) is the difference between the fit to the residuals and the new basin term at $Z_{1.0}$ = 100 m as the constant shift to center the simulations on the CCHL20 model.

The CCHL20 model with the modified basin-depth scaling is given by:

$$CCHL20_{Erg}(M, R, \dots) = CCHL20(M, R, \dots) - f_{basin}(Z_{1.0}) + f_{3D-basin} - C_{SIM} \quad (3)$$

$CCHL20_{Erg}$ (M, R, …) is the final ergodic model. If the user wants centered the ergodic model on the average amplitude from the M8 simulations, the C_{SIM} term can be added to ergodic median model. Then, using the $CCHL20_{Erg}$ model, we recomputed the residuals for the M8 simulations:

$$\delta\epsilon_{SIM} = \ln(PSA_{SIM}) - (CCHL20_{Erg}(M, R, \dots) + C_{SIM}) \quad (4)$$

in which $\delta\epsilon_{SIM}$ is the total residual between simulation data and new ergodic model.

Non-Ergodic Model

Similar to the Cascadia case, the sources are all M8 earthquakes for in this study, so we cannot separate the path effects from the site/source effects. That is, we build a non-ergodic GMM that combines the path and site/source terms into a single site term and uses the CCHL20 model with the modified basin-depth scaling as the ergodic mode:

$$\mu_{Nonerg\_SIM}(M, R, \dots, t_s) = CCHL20_{Erg}(M, R, \dots) + C_{SIM} + \Delta(t_s) \quad (5)$$

$\Delta(t_s)$ is the non-ergodic term that is varied by the site location.

Hyperparameter

An estimation of the hyperparameters which include variance (θ) and spatial correlation length (ρ) of the non-ergodic term relative to the separation distance between two sites, which is estimated using the

R-ILAN based on the Matern covariance function. The covariance function between a pair of sites for cov(x_{sta}, x'_{sta}) is defined as

$$cov(x_{sta}, x'_{sta}) = \theta^2 \frac{2^{1-\upsilon}}{\Gamma(\upsilon)} \left(\frac{\sqrt{8\upsilon}||x_{sta} - x'_{sta}||}{\rho} \right)^{\upsilon} \mathrm{K}_{\upsilon}(\frac{\sqrt{8\upsilon}||x_{sta} - x'_{sta}||}{\rho})$$

in which Γ is the Gamma function; ρ is the correlation lenght, θ is the marginal standard deviation of the spatial field; υ is the smoothness parameter; x_{sta} and x'_{sta} are the coordinates of the two sites depending on the coefficient; K_{υ} is the modified Bessel function of second kind and order $\upsilon > 0$.

Mean and epistemic uncertainty

For the new location, the mean and epistemic uncertainty for non-ergodic terms are estimated from samples of the posterior distribution of the model at the mesh nodes used by Integrated Nested Laplace Approximation (INLA) based on the VCM. For the R-ILAN package, there are tools that can sample from the posterior distribution of the model at the mesh nodes and interpolate the distribution to new locations. It provides estimates of the mean (μ) and variance (σ) of the marginal distribution for the individual latent effect $\Delta(t_s)$ (non-ergodic term). The epistemic uncertainty depends on the density of the data near the specified location.

A map of the non-ergodic term for T=3 sec is shown in Figure 4a. These terms show the larger positive values for sites close to the eastern and southern portions of the middle Hualien. The results show that the contribution for the non-ergodic term is based on the radiation pattern/directivity, not the 3D velocity model, so the non-ergodic term here should be the source terms. Non-ergodic terms can be extrapolated to the outside region without data due to the correlation length of the covariance function. Moreover, the epistemic uncertainty would be higher in the region without the simulation than in including the data. Figure 4b shows the non-ergodic PSA from the non-ergodic model, which is almost identical to the simulation result (Fig 2b). That is, the non-ergodic term can capture the 3D structure from the simulation result well.

CONCLUSIONS

The 3D simulations can be incorporated into the median and aleatory standard deviation of GMMs to capture the non-ergodic effect. Integrating the current set of simulations for Taiwan into a non-ergodic version of the CCHL20 GMM provides one GMM that can be used in PSHA calculations. The non-ergodic model does not change the average level of the ground motion from the original CCHL20 GMM; it only changes the spatial distribution of the non-ergodic terms and the aleatory variability.

The critical limitations of the current model are that: (1) the basin term for the simulation cannot show the apparent site amplification for the Z1.0 due to the rough resolution for the 3D crustal velocity model at the shallow soil depth, and (2) the epistemic uncertainty in the non-ergodic terms due to uncertainty in the 3-D velocity model is based on assumed values without the benefit of simulation results for a suite of alternative 3-D velocity models to constrain the estimates. Therefore, our next step is the development of the non-ergodic model for the 3-D simulation based on the multiple 3-D velocity models with finer resolution in the shallow depth.

A concern with 3D simulations is that they are only for limited regions, but the seismic hazard needs to be computed for larger regions not covered by the 3D simulations. For the non-ergodic approach, the reduced aleatory variability is used with a zero median adjustment but with large epistemic uncertainty in the non-ergodic terms when sites are outside the simulation region. To help with the application of the non-ergodic GMM to a broader region, that will be good to apply this approach to the larger region covered by the simulations.

REFERENCES

Abrahamson NA, Kuehn NM, Walling M, Landwehr N (2019) Probabilistic seismic hazard analysis in California using non-ergodic ground-motion models. Bull Seism Soc Am 109 (4): 1235–1249.

Amante, C. and B. W. Eakins, (2009) ETOPO1 1 Arc-Minute Global Relief Model: Procedures, Data Sources and Analysis, NOAA Technical Memorandum, NESDIS NGDC-24, 19 pp.

Frankel, A., E. Wirth, N. Marafi, J. Vidale, and W. Stephenson (2018). Broadband synthetic seismograms for magnitude 9 earthquakes on the Cascadia megathrust based on 3D simulations and stochastic synthetics, Part 1: Methodology and overall results, Bulletin of the Seismological Society of America 108(5A), 2347–2369.

Chao, S.-H., B. Chiou, C.-C. Hsu, and P.-S. Lin (2020) A horizontal ground-motion model for crustal and subduction earthquakes in Taiwan, 36(2): 463, https://doi.org/10.1177/8755293019891711.

Hsu, Y.-J., M. Ando, S.-B. Yu, and M. Simons (2012) The potential for a great earthquake along the southernmost Ryukyu subduction zone, Geophys. Res. Lett., 39, L14302, doi:10.1029/2012GL052764.

Irikura, K. and H. Miyake, (2011) Recipe for predicting strong ground motion from crustal earthquake scenarios. Pure and Appl. Geophs., 168, 85–104.

Kao, H. (1998) Can great earthquakes occur in the southernmost Ryukyu arc-Taiwan region?, Terr. Amos. Oceanic Sci., 9, 487–508.

Kuo-Chen, H., F. Wu, D. M. Jenkins, J. Mechie, S. Roecker, C.-Y. Wang, and B.-S. Huang (2012) Seismic evidence for the α-β quartz transition beneath Taiwan from Vp/Vs tomography, Geophys. Res. Lett., doi:10.1029/2012GL053649

Lavrentiadis. G, N. Abrahamson, K. Nicolas, Y. Bozorgnia, and more (2022) Overview and Introduction to Development of Non-Ergodic Earthquake Ground-Motion Models, Bulletin of Earthquake Engineering. doi.org/10.48550/arXiv.2111.07921.

National Center for Research on Earthquake Engineering (NCREE) (2018), Web page for reevaluation of probabilistic seismic hazard of nuclear facilities in Taiwan using SSHAC level 3 methodology project, available at http://sshac.ncree.org.tw.

Sung, C.-H. and N. Abrahamson (2022a). A Partially Non-Ergodic Ground-Motion Model for Cascadia Interface Earthquakes, Bulletin of the Seismological Society of America. doi: 10.1785/0120210330.

Sung, C.-H., N. Abrahamson, N. Kuehn, P. Traversa, and I. Zentner (2022b). A non-ergodic ground-motion model of Fourier amplitude spectra for France, Bulletin of Earthquake Engineering. DOI: 10.1007/s10518-022-01403-1.

Theunissen, T., Y. Font, S. Lallemand, and W.-T. Liang (2010) The largest instrumentally recorded earthquake in Taiwan: Revised location and magnitude, and tectonic significance of the 1920 event, Geophys. J. Int., 183, 1119–1133, doi:10.1111/j.1365-246X.2010.04813.x.

Yen, Y.-T. and K.-F. Ma, (2011) Source-Scaling relationship for M 4.6–8.9 earthquakes, specifically for earthquakes in the collision zone of Taiwan. Bull. Seismo. Soc. Am., 101(2), 464–481, doi: 10.1785/0120100046.

Zhang, W. and X. Chen (2006) Traction image method for irregular free surface boundaries in finite difference seismic wave simulation, Geophys. J. Int., 167, 337–353.

Zhang, W., Z. Zhang, and X. Chen, (2012) Three-dimensional elastic wave numerical modeling in the presence of surface topography by a collocated-grid finite-difference method on curvilinear grids, Geophys. J. Int., 190, 358–378.

Table 1. Source Parameters of the M8 Earthquake Scenarios

Hypocenters					
9 hypocenters on the presumed fault plane					
Macro Source Parameters					
M_W	Fault Length	Fault Width	Strike	Dip	Rake
8.0	161 km	56 km	294°	30°	90°
Micro Source Parameters					
Slip in the asperity area	Slip in the background area	Source Time Function			
5.2 m	3.0 m	2.0-s Gaussian wavelet			

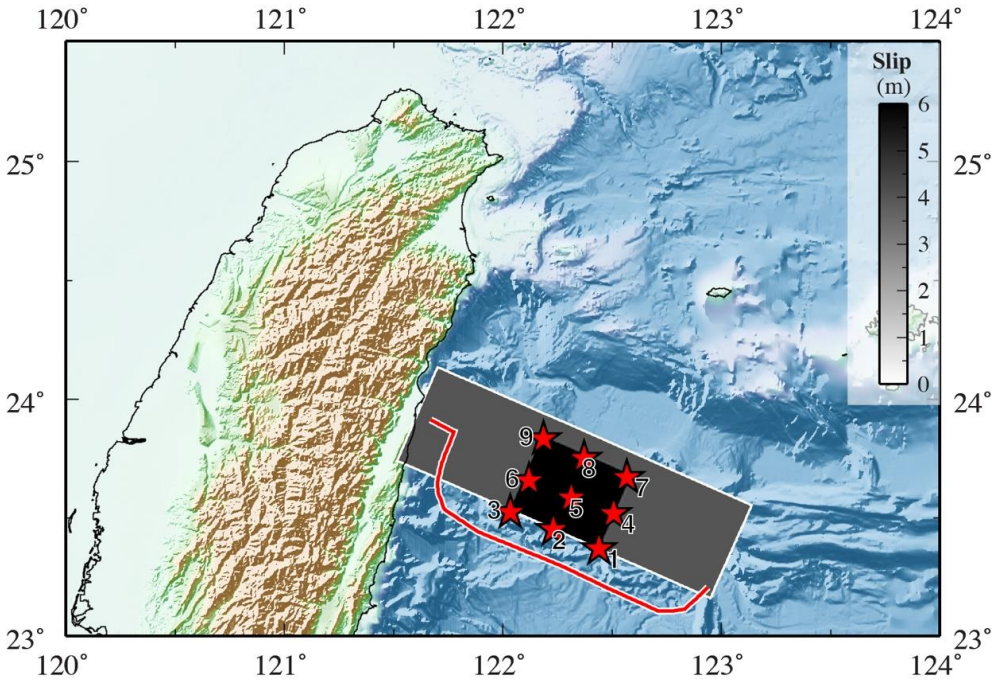

Figure 1. The settings of fault geometry, asperity location, and hypocenters in this study. The Red line indicates the R1 segment of the Ryukyu Trench. On the fault plane, the gray-shaded color scale represents amounts of slip. The red stars with IDs labeled the 9 hypocenters equivalent to the rupture initiation points of these scenarios.

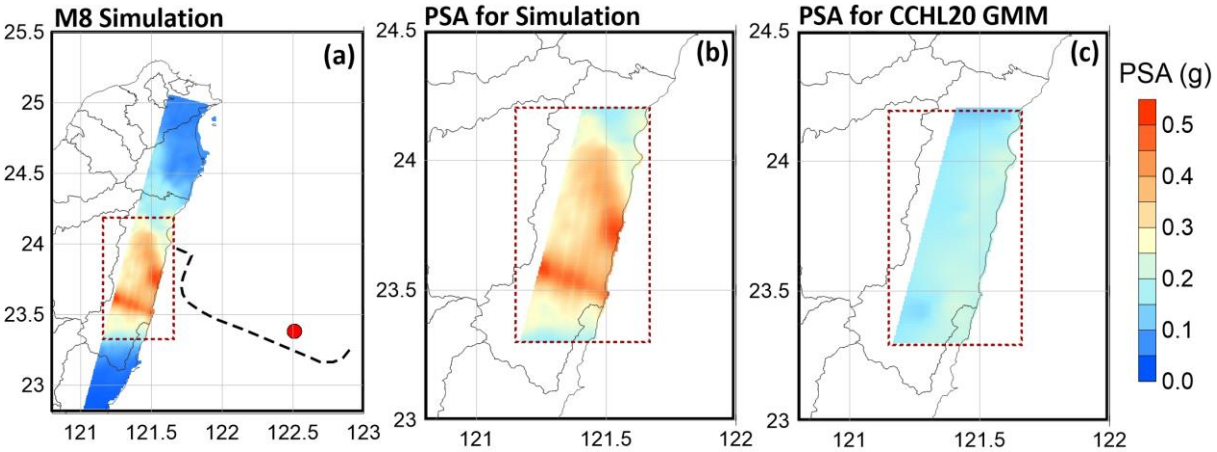

Figure 2. Map of the spectral acceleration at T=3 sec for (a) one M8 simulation in the whole region, (b) the M8 simulation within the target site, and (c) the CCHL20 GMM.

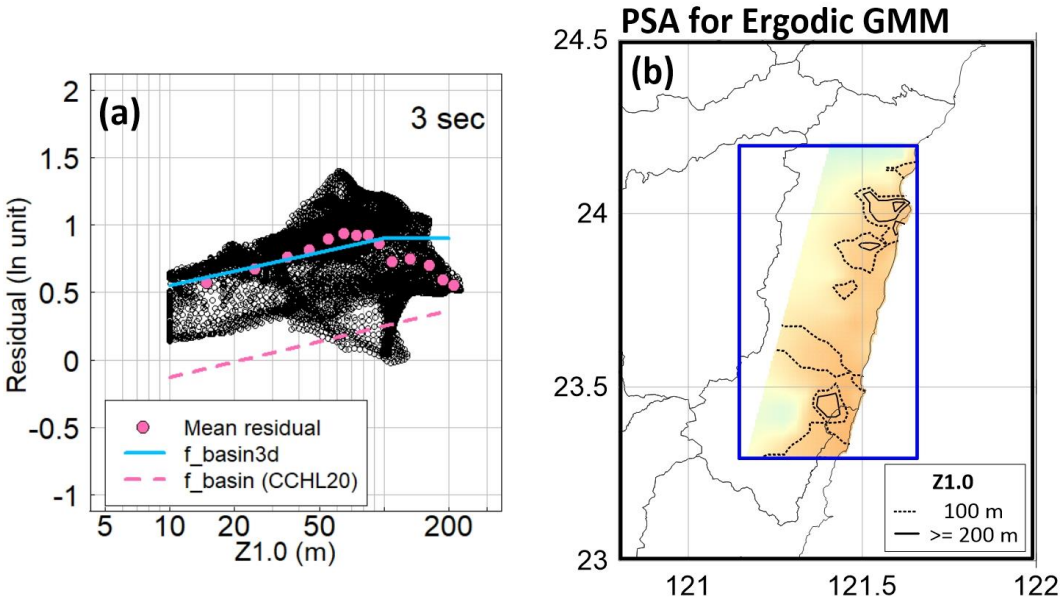

Figure 3. (a) An example for new basin-depth term at T = 3 sec. (b) Map of the spectral acceleration at T=3 sec for the ergodic model.

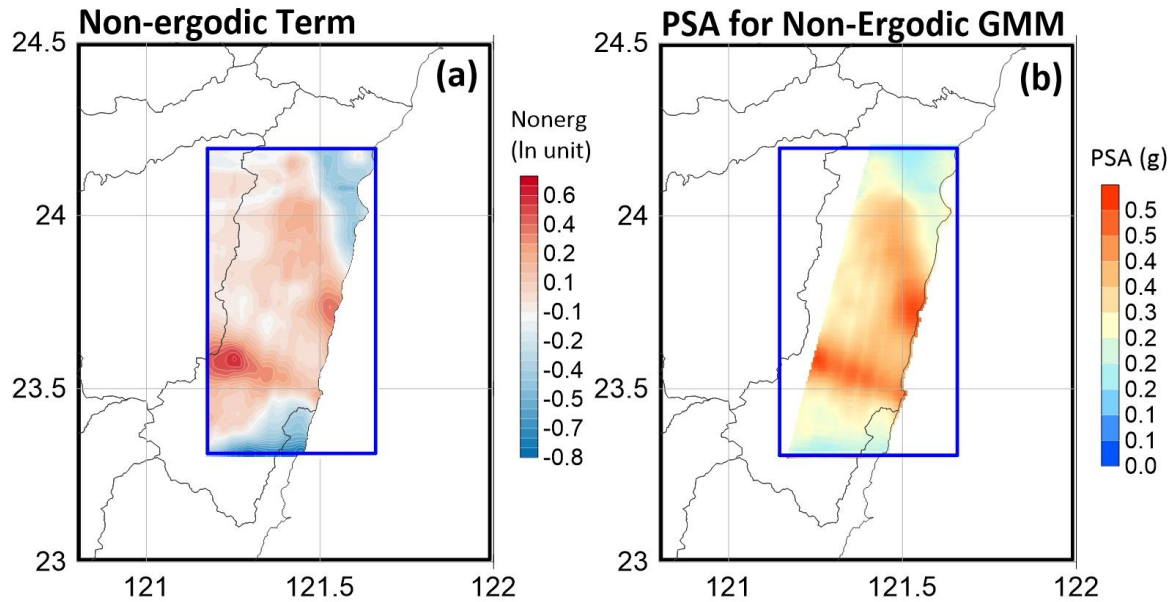

Figure 4. (a) Spatial distribution of non-ergodic terms at the target site. (b) Map of the spectral acceleration at T=3 sec for the non-ergodic model.

OCCURRENCE RATE AND PERIOD OF PULSE-LIKED GROUND MOTION BASED ON GROUND MOTION SIMULATION TECHNIQUE: SHANCHIAO FAULT IN NORTHERN TAIWAN

Jyun-Yan Huang[1], Shu-Hsien Chao[2], Che-Min Lin[2], Shang-Yi Hsu[1], Chung-Che Chou*[3,4], Chin-Hsiung Loh[5] and Chiun-Lin Wu[6]

1. Associate Research Fellow, National Center for Research on Earthquake Engineering, Taipei, Taiwan
2. Research Fellow, National Center for Research on Earthquake Engineering, Taipei, Taiwan
3. Professor, Department of Civil Engineering, National Taiwan University, Taipei, Taiwan
4. Director General, National Center for Research on Earthquake Engineering, Taipei, Taiwan
5. Distinguished Professor, Department of Civil Engineering, National Taiwan University, Taipei, Taiwan
6. Deputy Director General, National Center for Research on Earthquake Engineering, Taipei, Taiwan

Email: jyhuang@narlabs.org.tw, shchao@narlabs.org.tw, cmlin@narlabs.org.tw, syhsu@narlabs.org.tw, cechou@ntu.edu.tw, lohc0220@ntu.edu.tw, clwu@narlabs.org.tw

ABSTRACT

A site-specific, near-fault effect for an on-fault site was investigated by a combined methodology of ground motion model and ground motion simulation methods in Huang et al. (2022). Twenty-one pseudo stations parallel to the Sanchiao fault as a followed-up study were used to evaluate the influence of related site location to the fault. The near-fault pulse effects could be separately discussed by assigning the same linear site response from an empirical transfer function to the stochastic finite-fault simulation technique for the whole pseudo stations, after considering moving random asperity models. Simulation results indicated that the pulse occurrence rate has a significant difference on hanging wall and footwall sites in a similar rupture distance. In addition, the on-fault and hanging wall sites generate a long period of velocity pulse compared to footwall sites for the particular fault geometry (i.e., the Sanchiao fault in northern Taiwan). Moreover, the mode period of velocity pulse (Tp) varied from approximately 3 to 7 s, which was not obtained by the previous Tp model by only considering the magnitude in ergodic assumption (Shahi and Baker, 2014).

Keywords: Velocity pulse, Near-fault effect simulation, the Sanchiao fault, Northern Taiwan

INTRODUCTION

Understanding the mechanism of generating velocity pulse by a fault is very important in seismic hazard and building damage evaluation. Shahi and Baker (2011, 2014) provided an effective method to determine velocity pulse from strong motion records and developed an empirical model to predict the pulse period from earthquake magnitude and the impact on response spectrum induced by velocity pulse. The empirical dataset they used provides an ergodic consideration to model near-fault pulse effect in ground motion model and seismic hazard. Owing to the relative lack of near-fault strong motion records in worldwide research, site-specific (nonergodic) consideration for near-fault effect was still very difficult that need to be supported from evidence of ground motion simulation technique. Huang *et al.* (2022) validated the ability of near-fault pulse motions that could be reconstructed by using stochastic finite-fault simulation with proper seismic parameters of source and path effect and suitable empirical transfer function (ETF, Huang *et al.*, 2017) to represent site effects. And indicated that variability of period of velocity pulse (Tp) was mainly controlled by location and its size of asperity on fault and could be simulated from the finite-fault procedure, in which random phase setting of each point source may not significantly bias simulated velocity time history. Since it is difficult to decide proper asperity location before a future earthquake, a moving random asperity model method was applied to identify possible occurrence rate of velocity pulse and mode Tp that could be used in pulse model in ground motion models (Chao *et al.*, 2019; Shahi and Baker, 2014) Their result has pointed out that for a specific

location near a seismic fault the pulse period Tp was mostly approximately 6 s, different from a prediction of 2.5 s in aforementioned pulse models with ergodic assumption based on the occurrence rate of velocity pulse for weighted pulse model considering different Tp in site-specific near-fault motions. In this study, a series of pseudo sites were conducted using a sensitivity evaluation, which was constructed by three lines located on a foot wall, fault and hanging wall individually that were parallel to each other to comprehend the influence of relative site location to the fault with a near-fault effect.

METHODOLOGY

The simulation technique in this study uses the stochastic Green's function with finite fault procedure method (Boore, 2009), the ETF method (Huang *et al.*, 2017), and a moving random asperity model (Huang *et al.*, 2022). The seismic source and path effects and ETF of a site class C for the Taipei Basin are grabbed from Huang *et al.* (2017), in which a site-specific κ (kappa) was transformed by the Vs30-κ equation built in Chang *et al.* (2019). Table 1 lists all parameters used in the stochastic simulation. Noted that class C site ETF was applied because Vs30 for rock motion beneath a specific site was estimated to be 450 m/s, derived from previous site effect studies in the Taipei Basin (Wen and Peng, 1998). Meanwhile, a site-specific site transfer function from ETF was needed for the near-fault evaluation because the Tp estimation is influenced by local site effect (Rodriguez-Marek and Bray, 2006).

Table 1. Seismic parameters used in stochastic finite-fault simulation

Shear-wave velocity (VS)	3.6 km/s	**Crustal amplification**	ENA-A (general transfer function of site class A in East North America, Atkinson and Boore, 2006)
Density (ρ)	$2.8 gm/cm^3$	**Site ETF**	TAP_general_C (general ETF of site class C in Taipei basin)
Geometric spreading R^b: b	-1.0 (1-50 km); 0 (50-170km) -0.5(>170 km)	**Stress drop (bar)**	90
Quality factor	$80f^{0.9}$	**Rupture velocity**	0.8 VS (2.88 km/s)
κ (kappa)	0.0578 sec. (from Vs30-κ relation, Chang *et al.*, 2019, Vs30=450m/s)		

Fig. 1 shows twenty-one pseudo stations near the Sanchiao fault. Station intervals are 3 km in fault perpendicular direction and 6 km in fault parallel direction. The finite-fault parameters used for the Sanchiao fault are listed in Table 2. Those pseudo stations are parallelly located to the fault with similar distance to the fault surface rupture for hanging wall (southeast direction) and foot wall (northwest direction) stations. As seen in Fig. 1, a sampled asperity model that would be moved from one edge of surface layer toward another edge of the bottom of the fault in moving random asperity model with red color subfaults. The asperity carried approximately 5 times slip compared to surrounding background subfaults and depended on fault size followed Japan's recipe (Irikura *et al.*, 2004; NIED, 2009; Irikura and Miyake, 2011).

Table 2. Fault dimension used in finite-fault simulation for stations near the Sanchiao fault

Mw	6.7	**Fault length and width**	30 km × 16 km
Fault Type	Normal	**Sub-Fault size**	1 km × 1km
Strike, dip, depth of fault	212.19, 52.5, 0		

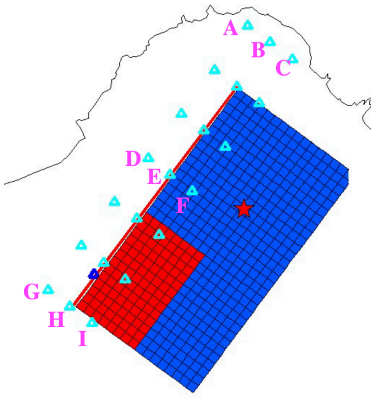

Figure 1. Distribution map of twenty-one pseudo stations near the Sanchiao fault in Taipei, Taiwan. A sample asperity model showed high slip region located at southwest edge, top layer on fault is represented in red color.

Finally, the moving random asperity model generated 144 sets of asperity models with the same size of high slip asperity region that corresponded to the fault dimension of the Sanchiao fault, as mentioned in Huang *et al.* (2022). Each asperity provided a synthetic velocity waveform for all pseudo stations and a group of sample results as shown in Fig. 2. The simulated velocity waveform (black waveforms) was recognized as a velocity pulse if it passed the criteria of Shahi and Baker's (2014) extraction method (red waveforms).

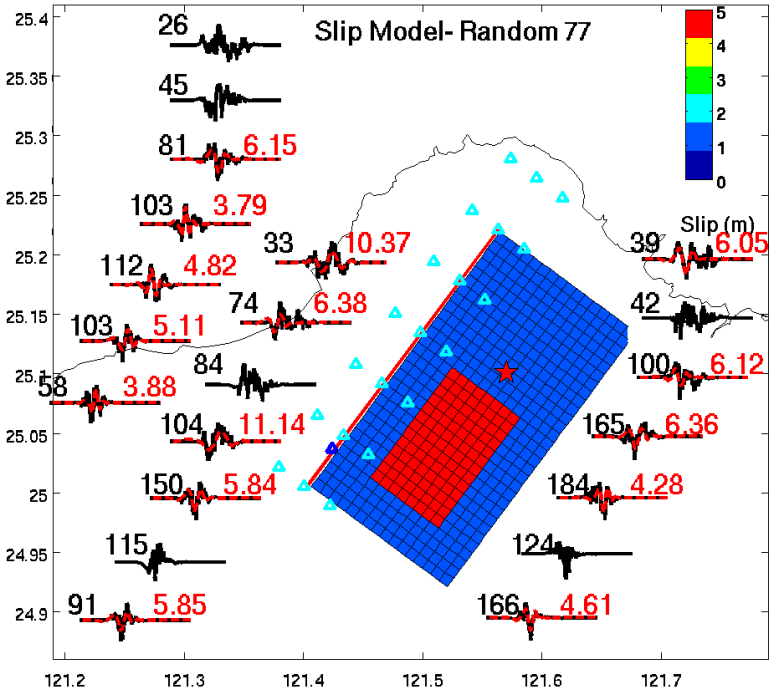

Figure 2. Synthetic waveforms of 21 pseudo stations near the Sanchiao fault for a sampled moving random asperity model. Black waveforms, red waveforms, black number and red number are synthetic velocity waveform by finite-fault simulation, extracted velocity pulse by Shahi and Baker's (2014) method, peak ground velocity (cm/s) and extracted Tp if there's a velocity pulse existed, respectively.

RESULTS AND DISCUSSIONS

Fig. 2 shows a clear characteristic that the stations closed to the high slip region (asperity) produce high peak ground velocity (PGV) with an occurrence of velocity pulse. In general, foot wall stations (northwest side) have lower PGV than hanging wall (southeast side) sites, which may relate to close rupture distances for hanging wall sites corresponding to a 52.5 dipping geometry to southeast direction for the assumed Sanchiao fault. Meanwhile, the closest station on fault (the middle part of the pseudo

stations) may sometimes not generate the largest PGV compared to stations on both sides of the fault. This may induce by a comprehensive finite-fault effect consisted of a superposition process in time history for whole subfaults, and an influence of relative distance to the asperity region, in which it is needed to be further considered in site-specific near-fault effect for ground motion models (GMMs). Fig. 3 showed extracted Tp and occurrence rate of velocity pulse for a group of sampled pseudo stations. For those cases that did not extract velocity pulse, No VP on the left side category was marked in the figure, in which the total number subtract cases number of No VP represents the occurrence rate of velocity pulse of each pseudo station. Moreover, several features can be identified such as: 1) On-fault stations (site e and h) have higher occurrence rates of velocity pulse than the stations of both sides that may be due to shorter fault rupture distance and may be easier induced higher PGV for whole asperity models, 2) Hanging wall sites have extracted longer period Tp compared to on fault and footwall sites, and footwall sites have shorter period Tp, based on fault geometry of a specific fault. The pulse period Tp of hanging wall sites (site c, f, i), on fault sites (site b, e, h) and footwall sites (site a, d, g) are approximately 5-8 s, 5-7 s and 3 s, respectively. This Tp difference between pseudo stations highlighted large variance in Tp generated for an event with the same magnitude and may need site-specific consideration for the near-fault effect. 3) Stations, located at both edge of the fault which has similar hypocenter distance, indicated a different feature that southwestern sites (sites g, h, i) generated more velocity pulse (higher occurrence rate of velocity pulse) due to the shorter distance to the asperity locations compared to northeastern sites (sites a, b, c), which suggested that the distance to the high slip region on fault may control the occurrence of velocity pulse rather than the rupture distance used in most GMMs.

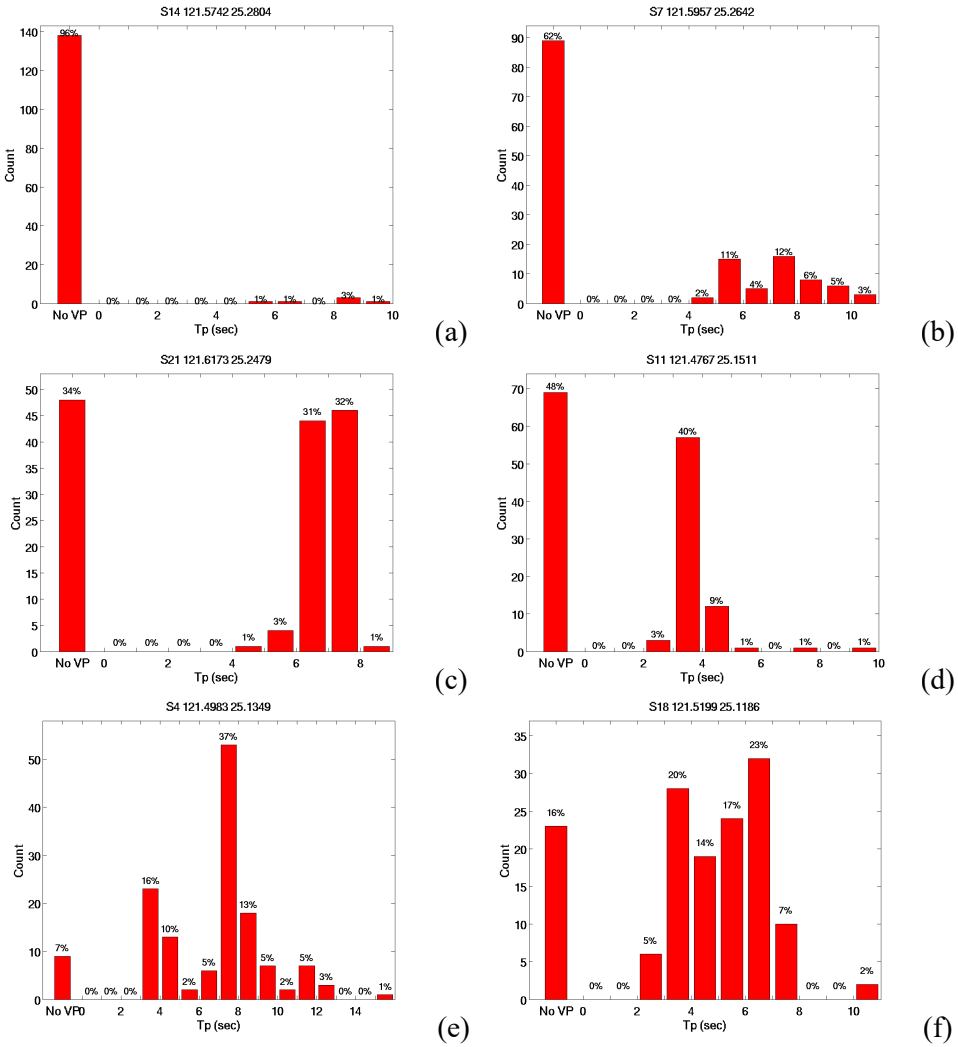

Figure 3. Occurrence rate of velocity pulse and their corresponding Tp of a group of sampled pseudo stations in finite-fault simulation. (a), (b), (c)……to (i) is correlated to site location showed in Fig. 1.

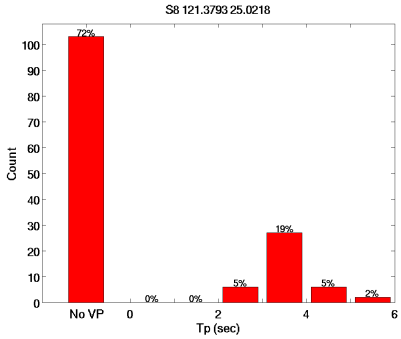

(g)

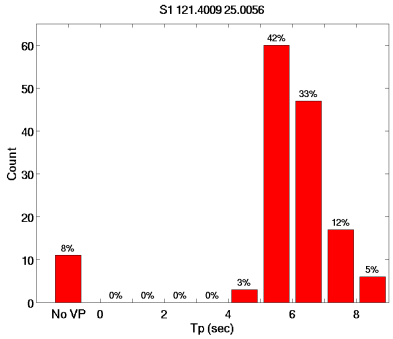

(h)

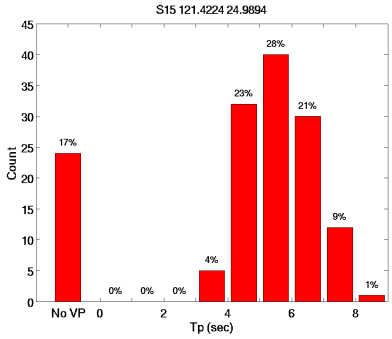

(i)

Figure 3. (Continued)

CONCLUSIONS

Near-fault effects produced by a specific fault in northern Taiwan were investigated, indicating the importance of site-specific consideration for near-fault velocity pulse. The occurrence rate and Tp varied from 4-93% and 3-8 s, respectively for an Mw 6.7 earthquake induced by the Sanchiao fault in different locations. In contrast, an ergodic consideration of pulse model provides a 2.5 s Tp from previous studies (Chao *et al.*, 2019; Shahi and Baker, 2014). This study is a part of work of Chao *et al.* (2022) which verifies that the site-specific consideration, including more detailed simulation for different relative sites and fault geometry to model the main behavior of the velocity pulse for near-fault effect, is needed in engineering applications, such as design spectrum, structural performance evaluation, and retrofit.

REFERENCES

Atkinson, G.M. and D.M. Boore (2006). "Earthquake Ground-Motion Prediction Equations for Eastern North America," *Bull. Seismol. Soc. Am.*, **96**(6), 2181-2205.

Boore, D.M. (2009). "Comparing Stochastic Point-Source and Finite-Source Ground-Motion Simulations: SMSIM and EXSIM," *Bull. Seismol. Soc. Am.*, **99**(6), 3202-3216.

Chang, S.C., K.L. Wen, M.W. Huang, C.H. Kuo, C.M. Lin, C.T. Chen and J.Y. Huang (2019). "The High Frequency Decay Parameter (Kappa) in Taiwan," *Pure Appl. Geophys.*, **176**(11), 4861-4879.

Chao, S.H., C.H. Kuo, H.H. Huang, C.C. Hsu and J.C. Jan (2019). "Observed Pulse-Liked Ground Motion and Rupture Directivity Effect In Taiwan Ground Motion Dataset. In proc. of international conference in commemoration of 20th anniversary of the 1999 Chi-Chi earthquake, 15-19 Sep., Taipei, Taiwan.

Chao, S.H., J.Y. Huang, C.M. Lin, S.Y. Hsu, Y.W. Chang, C.W. Chang, C.C. Hsu, L.H. Huang, W.K. Chang, C.P. Fan, C.H. Loh, C.L. Wu and C.C. Chou (2022). "Response Spectrum and Time History of Ground Motion for a Near-Fault Site in Taiwan – A Case Study of Sanchiao Fault", NCREE report, report number: NCREE-22-008. (In Chinese)

Huang, J.Y., K.L. Wen, C.M. Lin, C.H. Kuo, C.T. Chen and S.C. Chang (2017). "Site Correction of A High-Frequency Strong-Ground-Motion Simulation Based on An Empirical Transfer Function," *J. Asian Earth Sci.*, **138**, 399-415.

Huang, J.Y., S.H. Chao, C.M. Lin, S.Y. Hsu, C.C. Chou, C.L. Wu, and C.H. Loh (2022). "Site-Specific Response Spectra Developed by Considering Near-Fault Motions in Taiwan," *Engineering Geology*. (Preprint under review, http://dx.doi.org/10.2139/ssrn.4156511)

Irikura, K., H. Miyake, T. Iwata, K. Kamae, H. Kawabe and L.A. Dalguer (2004). Recipe for Predicting Strong Ground Motions from Future Large Earthquakes. In Proc. of 13th World Conference on Earthquake Engineering (13WCEE), Vancouver, Canada, Paper No. 1371.

Irikura, K. and H. Miyake (2011). "Recipe for Predicting Strong Ground Motion from Crustal Earthquake Scenarios," *Pure Appl. Geophys.*, **168**, 85-104.

National research Institute for Earth science and Disaster prevention (NIED) (2009). Strong Ground Motion Prediction Method ("Recipe") for Earthquakes with Specified Source Faults. Technical note of NIED 336, Appendix 1-50.

Rodriguez-Marek, A. and J. D. Bray (2006). "Seismic Site Response for Near-Fault Forward Directivity Ground Motions," *Journal of Geotechnical and Geoenvironmental Engineering*, **132**(12), 1611-1620.

Shahi, S.K. and J.W. Baker (2011). "An Empirically Calibrated Framework for Including the Effects of Near-Fault Directivity in Probabilistic Seismic Hazard Analysis," *Bull. Seismol. Soc. Am.*, **101**(2), 742-755.

Shahi, S.K. and J.W. Baker (2014). "An Efficient Algorithm to Identify Strong Velocity Pulses in Multi-Component Ground Motions," *Bull. Seismol. Soc. Am.*, **104**(5), 2456-2466.

Wen, K.L. and H.Y. Peng (1998). "Site Effect Analysis in The Taipei Basin: Results from TSMIP Network Data," *Terr. Atmos. Ocean. Sci.*, **9**(4), 691-704.

RE-EVALUATING GROUND MOTION INTENSITY CONVERSION EQUATIONS (GMICE) FOR CALIFORNIA, U.S.A.

Molly Gallahue[1] and Norman Abrahamson[2]
1. Department of Earth and Planetary Sciences, Northwestern University, Evanston, Illinois, U.S.A.
2. Department of Civil and Environmental Engineering, University of California, Berkeley, California, U.S.A
Email: mollygallahue2023@u.northwestern.edu, abrahamson@berkeley.edu

ABSTRACT

Ground-motion intensity conversion equations (GMICE) are used globally to describe the relationship between ground-motion amplitude and shaking intensity. These relationships are crucial for comparisons of results of probabilistic seismic hazard analysis (PSHA) to observations of historical shaking characterized by intensity. Current GMICE use simple regression equations that allow direct conversion between intensity and peak ground motion (PGM). We will show that GMICE using the common approach overestimate the variability of predicted intensity because residuals of the intensity from an intensity prediction equation (IPE) and the residuals of the PGM from a ground-motion model (GMM) are only partially correlated. We explore these effects and their causes using data and GMICE from California. For this study, we primarily consider the Worden et al. (2012) relation, PGA as the ground motion parameter, and MMI as the intensity unit. These conclusions can be generalized to other GMICE and regions.

Keywords: Ground motion intensity conversion equations, PGA, MMI, California

INTRODUCTION

Ground-motion intensity conversion equations (GMICE) are used globally to describe the relationship between ground-motion amplitude and shaking intensity. GMICE have been developed for the global average (Caprio *et al*., 2015) and for specific regions such as California (Worden *et al*., 2012) Iran (Ahmadzadeh *et al*., 2020), New Zealand (Moratalla *et al*., 2021), China (Tian *et al*., 2021), and Italy (Zanini *et al*., 2019). Intensity data for these models are measured on several scales, including modified Mercalli intensity (MMI), Mercalli-Cancani-Sieberg (MCS), and European Macroseismic Scale (EMS-98), while ground-motion amplitudes are typically expressed as peak ground acceleration (PGA) or peak ground velocity (PGV).

GMICE are particularly useful when they can be used to convert directly from ground motion to intensity, without the inclusion of the contributing earthquake magnitude or distance between the event and the recording. As such, current GMICE use simple regression equations that allow these conversions to occur (Worden *et al*., 2012; Caprio *et al*., 2015; Zanini *et al*., 2019; Ahmadzadeh *et al*., 2020; Moratalla *et al*., 2021; Tian *et al*., 2021). The common approach to developing such GMICE is to conduct an initial regression for the intensity as a function of the peak ground motion (PGM) parameters (Worden *et al*., 2012; Caprio *et al*., 2015; Zanini *et al*., 2019; Ahmadzadeh *et al*., 2020; Moratalla *et al*., 2021; Tian *et al*., 2021). Using the residuals from the initial regression, subsequent regressions incorporate the magnitude and/or distance scaling, but these terms are only added into the initial equation that predicts intensity as a function of PGM. In the application of a GMICE developed using a two-step approach for the regression, there is an implicit assumption that the magnitude and distance scaling of the intensity and the PGM parameter are the same. As discussed later, this can lead to biased estimates of the intensity for above-average PGM values that control seismic hazard.

While useful, we show that GMICE using the common two-step approach overestimate the variability of predicted intensity for two reasons: (1) the differences in the M and R scaling are mapped into the slope on the ln(PGA) and (2) the residuals of the intensity from an intensity prediction equation (IPE)

and the residuals of the PGM from a ground-motion model (GMM) are only partially correlated. We explore these effects, and the causes of, using data and GMICE from California. We consider the Worden et al. (2012) relation (hereafter: WGRW12), PGA as the ground motion parameter, and MMI as the intensity unit, but we note that the challenges presented herein are applicable to other GMICE.

SLOPE OF THE GMICE

Modern GMICEs have the form:

$$MMI = c_1 + c_2 \ln(PGA) \quad (1)$$

where MMI is the intensity unit and PGA is the ground-motion parameter. The c_2 parameter represents the slope of the relation between PGA and MMI and is computed via regression on these variables.

For many years, c_2 has been relatively stable as new GMICE are developed. Using the PGA/MMI relation, Gutenberg and Richter (1942) identified c_2 as 3.03, which is consistent with Trifunac and Brady's (1975) value of 3.33 and WGRW12's value of 3.70 (the latter two are for higher intensities, roughly MMI> 4).

We will show that these steep slopes are appropriate for median ground motions, but perform poorly for individual observations, which could fall above or below the median. While peak ground motions and intensity are correlated, they are also both dependent on magnitude and distance in different ways (Fig. 1). Regressions that do not take magnitude and distance into consideration in the initial step cause some of the magnitude/distance dependence to be mapped into the c_2 parameter, thus inflating the apparent correlation between peak ground motions and intensity. We demonstrate this in the following sections.

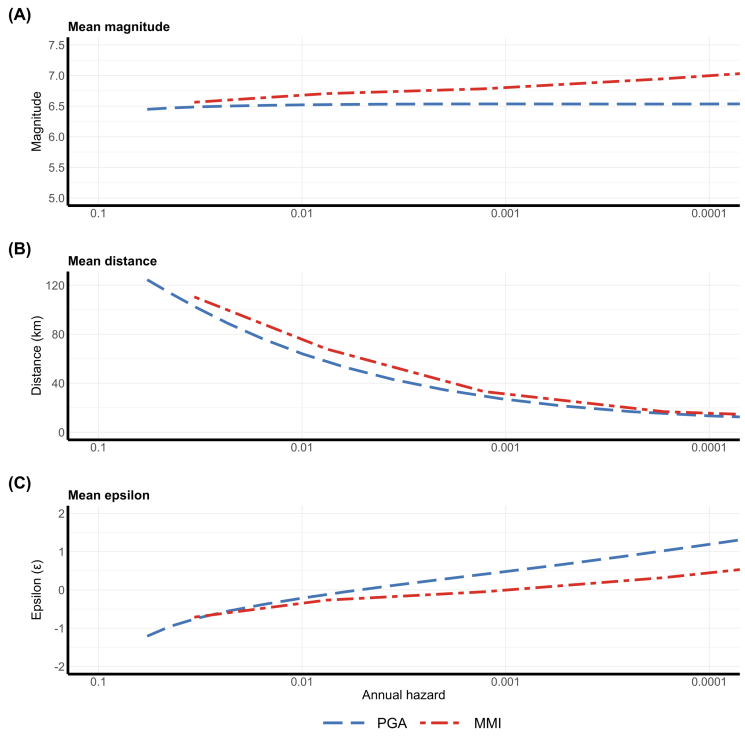

Figure 1. a) Mean magnitude (a), distance (b), and ϵ (c), deaggregations for simulated MMI hazard and PGA hazard. a and b), MMI scales more strongly with magnitude and distance than PGA. GMICE derived from regressions that do not include magnitude and distance as primary predictors of PGA thus steepen the slope of the line in Fig. 3 causing predicted MMI to often be too high. c) ϵ_{PGA} and ϵ_{MMI} also scale differently and are only partially

correlated ($\rho < 1$). Thus, a high ϵ_{PGA} corresponds to a lower ϵ_{MMI} at any hazard level.

GMICE PERFORM WELL ONLY FOR MEDIAN GROUND MOTIONS

We simulate PGA values from magnitude and distance combinations via the Boore et al. (2014) GMM (hereafter BSSA14) and the MMI values from the same scenarios via the Atkinson et al. (2014) IPE (hereafter AWW14). We convert the simulated PGA values to MMI using WGRW12. Fig. 2 shows the results.

When an observed PGA is a median value for a scenario and is converted to MMI, the GMICE performs well (Fig. 2). However, when the same value of PGA is rarer for a scenario (i.e., falling 1-2 standard deviations (ϵ_{PGA}) above the median) and is converted to MMI, the GMICE overpredicts the expected MMI by 1-2 units (Fig. 2)

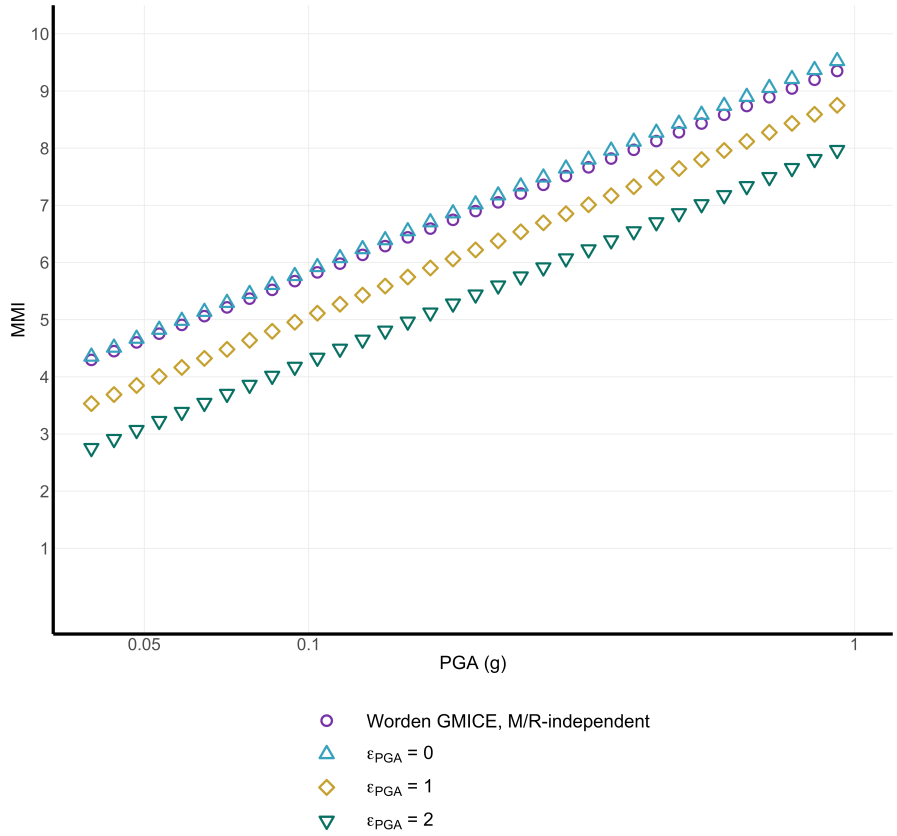

Figure 2. PGA at ϵ_{PGA} = 0, 1, and 2, and the corresponding MMI, derived from calculating ϵ_{MMI} assuming ρ = 0.5 (partially correlated). WGRW12's GMICE estimates MMI well when ϵ_{PGA} = 0 (median), but when ϵ_{PGA}= 1 or 2, WGRW12's GMICE estimates MMI too high by 1-2 intensity units.

This can be further demonstrated by considering expected ground motions and intensities from specific scenarios and comparing these to the estimated value by a GMICE. Fig. 3a plots simulated MMI against simulated PGA for varying magnitude and distance combinations. The estimated MMI from WGRW12 based on the simulated PGA is shown as a solid line. From Fig. 3, a PGA at ϵ_{PGA} = 1 from a **M** 6 event would be the same as a PGA at ϵ_{PGA} = 0.5 from a **M** 7 event at the same distance. AWW14 would expect these two scenarios to have differing MMIs, ~6.5 and ~7.5, respectively, but WGRW12 would overestimate both, estimating an MMI of ~8.

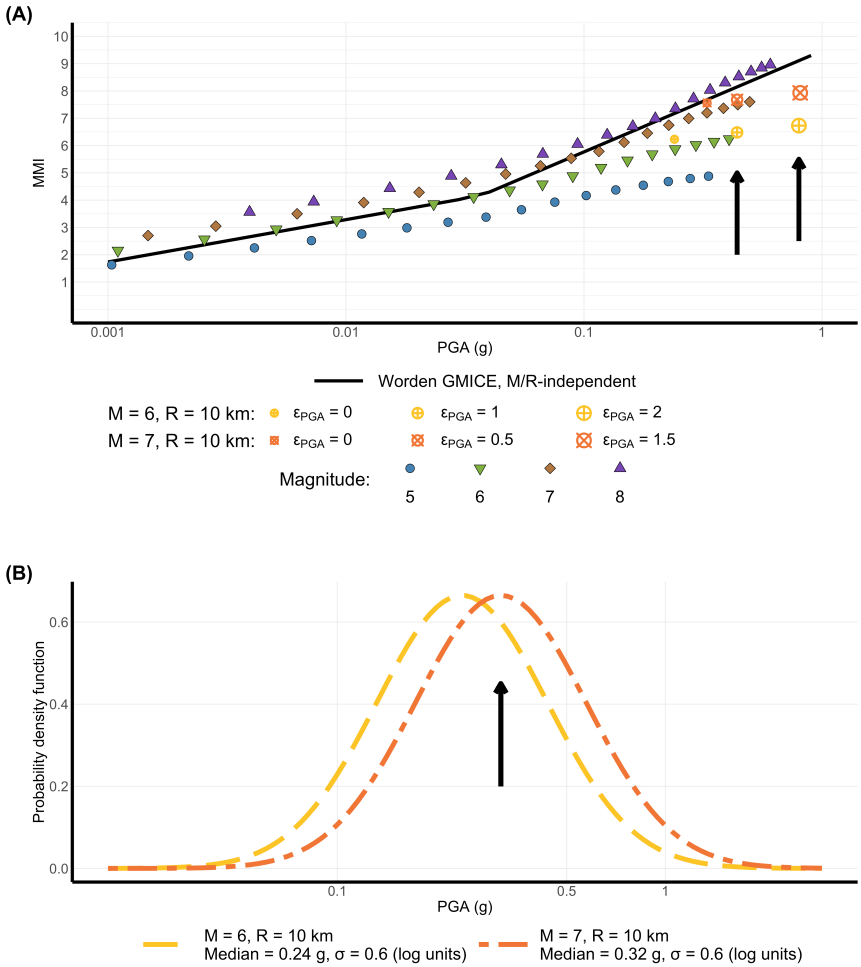

Figure 3. a) Simulated PGA (g) plotted against simulated MMI for varying magnitude and distance scenarios. WGRW12 M/R-independent GMICE is plotted over the data. Notice the slope between measurements from the same scenario but with different ϵ_{PGA} is shallower than the slope of the GMICE. Slope on the black line is c_2 from Eq. 1. b) Probability density functions for a **M** 6 earthquake at 10km and **M** 7 earthquake at 10 km. The median PGA for the **M** 7 event corresponds to a higher ϵ_{PGA} of the **M** 6 event, but via WGRW12 would correspond to the same MMI.

We calculated ϵ_{PGA} and ϵ_{MMI} using WGRW12's data and the corresponding expected values from BSSA14 and AWW14. Fig. 4 shows these values and the correlations between them. Modern GMICE assume ϵ_{PGA} and ϵ_{MMI} are fully correlated ($\rho = 1$), but the line of best fit indicates a correlation of only $\rho = 0.388$. Thus, ϵ_{PGA} and ϵ_{MMI} are only partially correlated.

This observation is the fundamental problem with current GMICE methodology. Current GMICE methodology assumes that PGA can directly inform MMI (requiring ρ to be closer to 1 than observed in data), but this is not the case because they are only partially correlated and the relation between ln(PGA) and MMI is not casual. Instead, median PGA and MMI are both well correlated with the contributing magnitude and distance scenario. Thus, GMICE essentially map a PGA to a scenario and predict MMI from that scenario. This works well for median observations, which are well correlated with the contributing scenario, but does not work for non-median observations because those are poorly correlated with any particular contributing scenario.

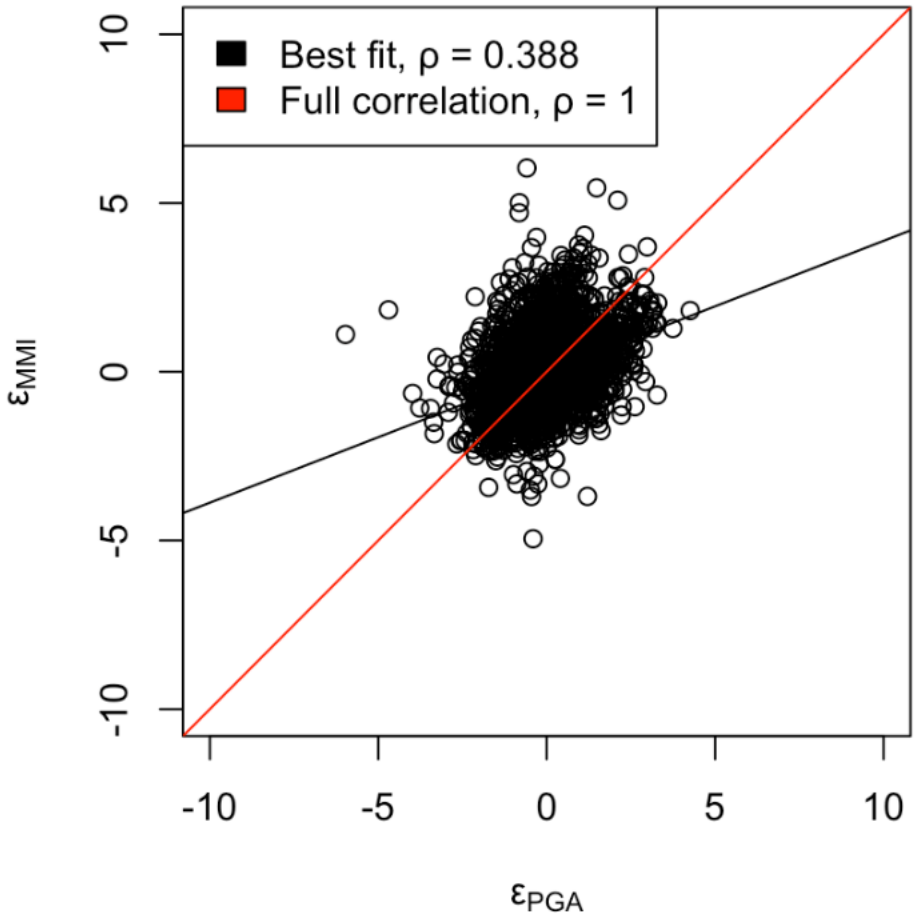

Figure 4. ϵ_{MMI} plotted against ϵ_{PGA}. The line of best fit is shown ($\rho = 0.388$) as well as a line assuming full correlation ($\rho = 1$). Because the ϵ's are only partially correlated, GMICE perform poorly when the input values are not at the median.

CONCLUSION

Current GMICE only perform well for relating the median PGA to the median MMI. This poses a challenge for using GMICE to evaluate seismic hazard results because the seismic hazard is typically controlled by "rarer" ground motions that fall above the median. Specifically, current GMICE overestimate variability which overestimates the hazard estimates. Current GMICE derivation practices should be reconsidered to better model the relation between ground motion and intensity for evaluating seismic hazard maps.

REFERENCES

Ahmadzadeh, S., G.J. Doloei and H. Zafarani (2020). "Ground motion to intensity conversion equations for Iran," *Pure and Applied Geophysics*, **177**(11), 5435-5449.

Atktinson, G.M., C.B. Worden and D.J. Wald (2014). "Intensity prediction equations for North America," *Bulletin of the Seismological Society of America*, **104**(6), 3084-3093.

Boore, D.M., J.P. Stewart, E. Seyhan and G.M. Atkinson (2014). "NGA-West2 equations for predicting PGA, PGV, and 5\% damped PSA for shallow crustal earthquakes," *Earthquake Spectra*, **30**(3), 1057-1085.

Caprio, M., B. Tarigan, C.B. Worden, S. Wiemer, D.J. Wald (2015). "Ground motion to intensity conversion equations (GMICEs): A global relationship and evaluation of regional dependency," *Bulletin of the Seismological Society of America*, **105**(3), 1476-1490.

Gutenberg, B. and C.F. Richter (1942). "Earthquake magnitude, intensity, energy, and acceleration," *Bulletin of the Seismological Society of America*, **32**, 163-191.

Moratalla, J.M., T. Goded, D.A. Rhoades, S. Canessa and M.C. Gerstenberger (2021). "New ground motion to intensity conversion equations (GMICEs) for New Zealand," *Seismological Society of America*, **92**(1), 448-459.

Tian, X., Z. Wen, W. Zhang and J. Yuan (2021). "New Ground Motion to Intensity Conversion Equations for China," *Shock and Vibration*.

Trifunac, M.D. and A.G. Brady (1975). "On the correlation of seismic intensity scales with the peaks of recorded strong ground motion," *Bulletin of the Seismological Society of America*, **65**(1), 139-162.

Worden, C.B., M.C. Gerstenberger, D.A. Rhoades and D.J. Wald (2012). "Probabilistic relationships between ground-motion parameters and modified Mercalli intensity in California," *Bulletin of the Seismological Society of America*, **102**(1), 204-221.

Zanini, M.A., L. Hofer and F. Faleschini (2019). "Reversible ground motion-to-intensity conversion equations based on the EMS-98 scale," *Engineering Structures*, **180**, 310-320.

(1c) Velocity structures and site effect

SHALLOW CRUSTAL VELOCITY STRUCTURES OF THE HENGCHUN PENINSULA REVEALED BY AMBIENT SEISMIC NOISE

Yu-Chih Huang[1], Che-Min Lin[2], Hung-Hao Hsieh[3], Chih-Wei Chang[4], Kuo-En Ching[5], Strong Wen[6]

1. Associate Researcher, National Center for Research on Earthquake Engineering, Taipei, Taiwan, R.O.C.
2. Research Fellow, National Center for Research on Earthquake Engineering, Taipei, Taiwan, R.O.C.
3. Assistant Researcher, National Center for Research on Earthquake Engineering, Taipei, Taiwan, R.O.C.
4. Assistant Technologist, National Center for Research on Earthquake Engineering, Taipei, Taiwan, R.O.C.
5. Associate Professor, Department of Geomatics, National Cheng Kung University, Tainan, Taiwan, R.O.C.
6. Associate Professor, Department of Earth and Environmental Sciences, National Chung Cheng University, Chayi, Taiwan, R.O.C.

Email: huangyc@narlabs.org.tw, cmlin@narlabs.org.tw, hhhsieh@narlabs.org.tw, chihwei@narlabs.org.tw, jingkuen@mail.ncku.edu.tw, strong@eq.ccu.edu.tw

ABSTRACT

The Hengchun Peninsula is an accretionary prism formed by plate collision and it is dominated by fold-and-thrust belts. The Hengchun Fault is an eastward-dipping thrust fault that is located near the intersection of the foothills and the plains, with both ends suspected to extend into the sea. Recently, a temporary seismic network was operated by the National Center for Research on Earthquake Engineering with twelve broadband seismometers along the Hengchun Fault with an interstation spacing of approximately 5 km. Some nearby broadband stations were also included to study shallow crustal velocity structures underneath the Hengchun Peninsula. In this research, time domain empirical Green's functions are obtained with long-term stacking from the cross-correlation of daily vertical-component data between 2018 and 2020. The 0.5–15 s Rayleigh-wave phase-velocity dispersion curves are found and then 1–5 s Rayleigh-wave phase-velocity maps are constructed. The lateral resolution is determined through a checkerboard resolution test and shallow crustal S-wave velocity structures within 3 km depths of the surface are derived. High velocities may imply the presence of Miocene strata or mud diapirs. More detailed velocity distributions are compared with the information for geological structures, groundwater distribution, and other associated phenomena.

Keywords: Hengchun Peninsula, ambient seismic noise, tomography, velocity structures

TECTONIC SETTING AND GEOLOGICAL STRUCTURE

Taiwan is located at a convergent plate boundary where the Eurasian Plate interacts with the Philippine Sea Plate and is characterized by complex tectonics and intense seismicity (Tsai *et al.*, 1977; Tsai, 1986). Due to the complexity of tectonic conditions, the origins and mechanisms of geologic settings are still under frequently debate (e.g., Suppe, 1981; Suppe, 1984; Angelier, 1986; Hsu and Sibuet, 1995; Wu *et al.*, 1997; Lin, 2000; Simoes *et al.*, 2007; Seno and Kawanishi, 2009; Huang *et al.*, 2015). The Hengchun Peninsula is located on the southernmost tip of Taiwan and connects to the Hengchun Ridge to the south. It is an accretionary prism formed by plate tectonics and is dominated by fold-and-thrust belts. The strata are generally older in the middle of the accretionary prism and gradually young on both sides, and the accretionary prism thickens and widens toward the north. (Chen *et al.*, 2005).

Furthermore, the deformation front, out-of-sequence thrust, and Hengchun Fault are major tectonic structures from west to east, among the fold-and-thrust belts. The deformation front connects to the Manila Trench in the south and may extend to the geological boundaries between the Western Foothills and the Western Coastal Plains on the Taiwan Island in the north. The out-of-sequence thrust may connect with the Shoushan and Chishan Faults on land, and the Hengchun Fault may connect with the Chaochou Fault (Fig. 1; Lin *et al.*, 2009).

The Hengchun Fault is categorized as a late Pleistocene active fault according to the announcements from the Central Geological Survey (CGS) in 2021. The Hengchun Fault is an eastward-dipping thrust fault, located along the intersection of the foothills and the plains, with both ends suspected to extend into the sea (Giletycz *et al.*, 2017; Chan *et al.*, 2020). Hence, the Hengchun Peninsula is considered to have high seismic risk. However, the seismic events were most located in the offshore regions of the Hengchun Peninsula (Fig. 1). These events were caused by plate tectonic interaction, rather than activity along the Hengchun Fault. Moreover, many mud volcanoes and mud diapirs have been discovered in the southwest offshore regions of Taiwan after detailed surveys over many years (Chen *et al.*, 2014). They could be connected to similar onshore structures and be correlated with geological structures, such as anticlines, faults, and tablelands (Chen *et al.*, 2016; Ching *et al.*, 2016). The mud diapirs are still active and are characterized by high gravity anomalies, which may be related to high pore pressures caused by plate tectonic processes (Doo *et al.*, 2015).

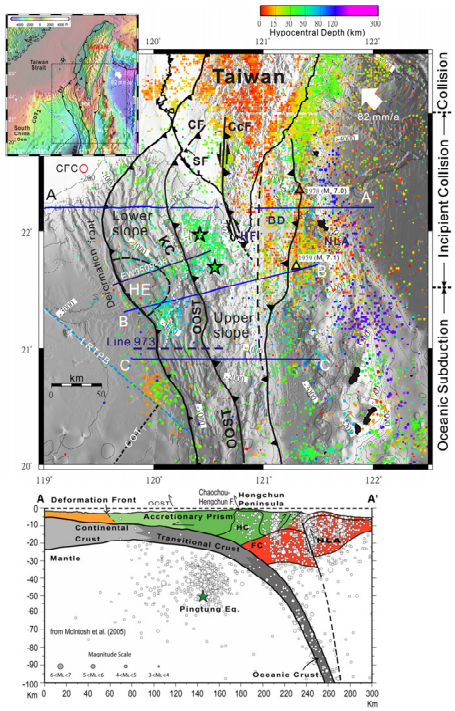

Figure 1. The tectonic setting and seismic activity of the Hengchun Peninsula and its surroundings (Lin *et al.*, 2009).

SEISMIC NETWORK AND DATA PROCESSING

Recently, a temporary seismic network was operated by the National Center for Research on Earthquake Engineering (NCREE) to monitor the seismic activity in the Hengchun Peninsula. The network used twelve Güralp CMG-6TD broadband seismometers along the Hengchun Fault with an interstation spacing of approximately 5 km (Fig. 2). Some nearby broadband stations operated by the NCREE were also included to study shallow crustal velocity structures underneath the Hengchun Peninsula.

Since the basic theorem of ambient seismic noise analysis has been generally verified, investigations of subsurface velocity structures have provided important insights for various parts of the world. Ambient seismic noise contains diffuse wavefields with passive structural signals and is caused by a variety of factors, such as human activities, atmospheric pressure changes, and the interaction of ocean waves with the coast and seafloor (Webb, 2007). The propagation is similar to that of surface waves, hence exhibiting dispersion properties related to underground velocity structures. The time domain empirical Green's functions (TDEGFs) can be obtained from the cross-correlation of station pairs with

simultaneous and continuous ambient seismic noise signals (Weaver, 2005). Relatively stable and representative TDEGFs could be enhanced after long-term stacking.

After data preparation, the daily CCFs were calculated using one-bit cross-correlation and spectral whitening for enhancing the spectral energy of the ambient seismic noise. The basic concepts of these two methods have been verified and regularly utilized for research on ambient seismic noise (Cupillard and Capdeville, 2010). Phase image analysis and far-field approximation methods employed to measure the Rayleigh-wave phase-velocity dispersion curves for each station pair (Yao *et al.*, 2006; Yao, 2009). Then, the tomographic method was applied to construct phase-velocity maps and a checkerboard resolution test (CRT) was used to assess the lateral resolution of the obtained phase velocities. The S-wave velocity (Vs) structures were constructed, and it was shown that the depth range is positively related to the aperture of the seismic network and its lateral resolution is positively related to the density of seismic stations. Figure 3 shows the data analysis procedures for processing ambient seismic noise in this study; they are similar to those of Huang *et al.* (2017) and Huang *et al.* (2018).

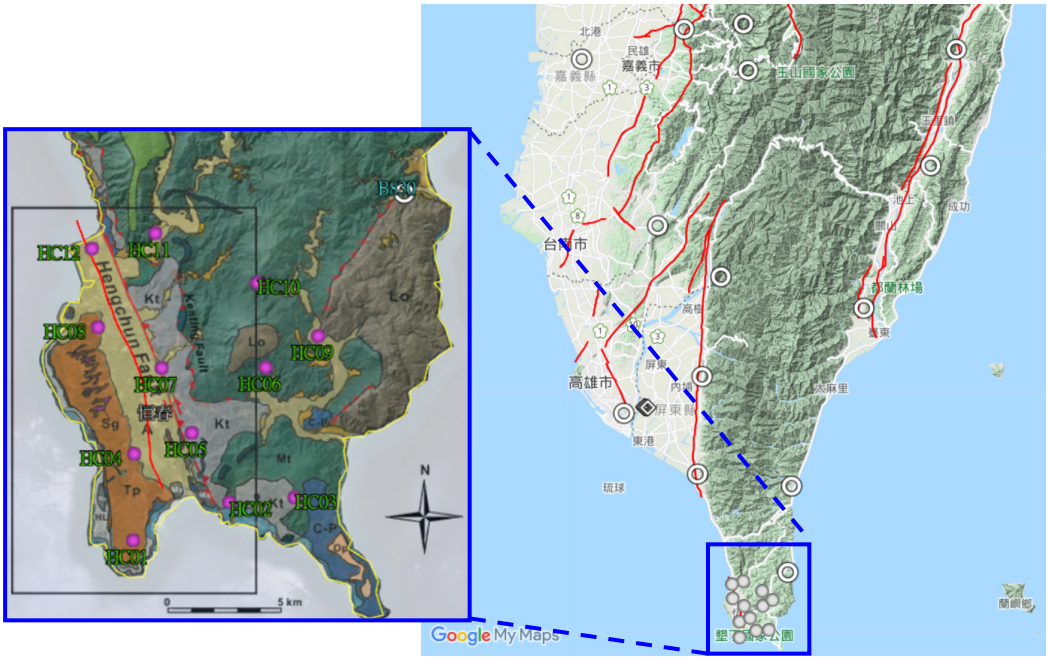

Figure 2. The geological structure (Giletycz *et al.*, 2017) and broadband seismic stations operated by the NCREE along the Hengchun Fault (purple solid circles) and other networks (white circles and diamonds).

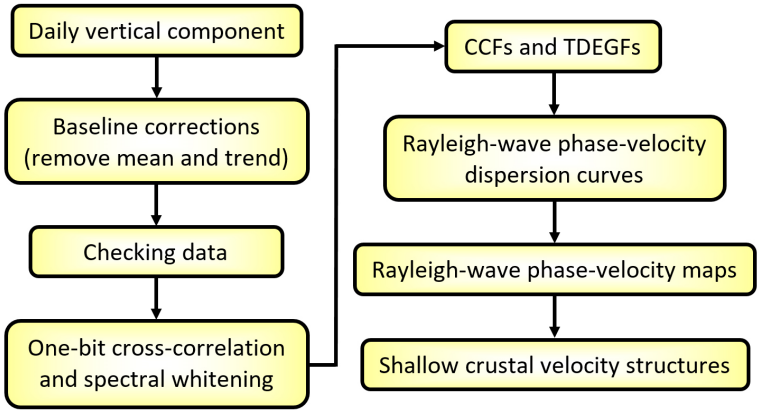

Figure 3. Data processing of ambient seismic noise in this study.

RESULTS

The daily vertical-component data from 2018 to 2020 were first assessed for quality and then downsampled from 100 Hz to 20 Hz. Daily cross-correlation functions (CCFs) were calculated using a 100-s lag time in the 0.5–15 s period band. Figure 4 shows the measured Rayleigh-wave phase-velocity dispersion curves, including the averages and standard deviations. The CRT models were examined at 0.025°, 0.05° and 0.25° anomalies with 0.01°, 0.02°, and 0.1° grid spacing, respectively. The recovery results indicate that the regions with high station densities near the Hengchun Fault were recovered with 0.025° and 0.05° anomalies. In contrast, for other regions with low station densities on the Hengchun Peninsula, the CRT could only be recovered with a 0.25° anomaly.

Based on CRT recovery results, a 0.02° grid spacing was applied for the construction of 1–5 s Rayleigh-wave phase-velocity maps around the Hengchun Fault (Fig. 5). At every grid point, the Rayleigh-wave phase-velocity dispersion curves were extracted from the phase-velocity maps. An initial velocity model with related physical parameters was provided, and the SURF program (Herrmann, 2013) was then employed to derive 1-D Vs structures. Figure 6 presents three 2-D Vs profiles within 3 km depths near the Hengchun Fault. Small-scale, near-surface high velocities anomalies were found to be distributed near the surface expression of the Hengchun Fault, and large-scale high velocity anomalies occur below the hills on the north and east sides of the Hengchun Fault. Hence, it is speculated that the high velocities may indicate the locations of Miocene strata or mud diapirs (which produce high gravity anomalies).

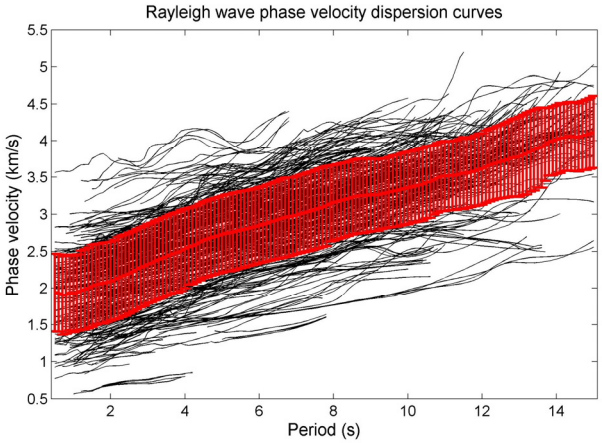

Figure 4. Measured 0.5–15 s Rayleigh-wave phase-velocity dispersion curves. Black lines indicate individual dispersion curves and the red band represents the average with standard deviation.

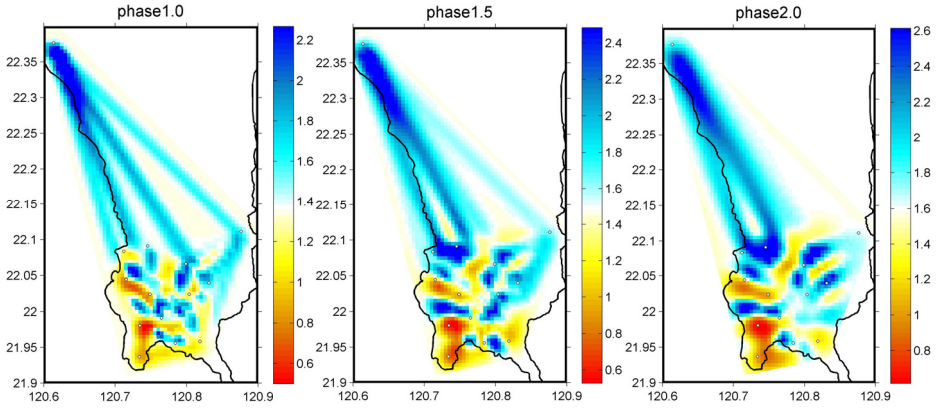

Figure 5. Rayleigh-wave phase-velocity maps near the Hengchun Fault at periods of 1.0s, 1.5 s and 2.0 s.

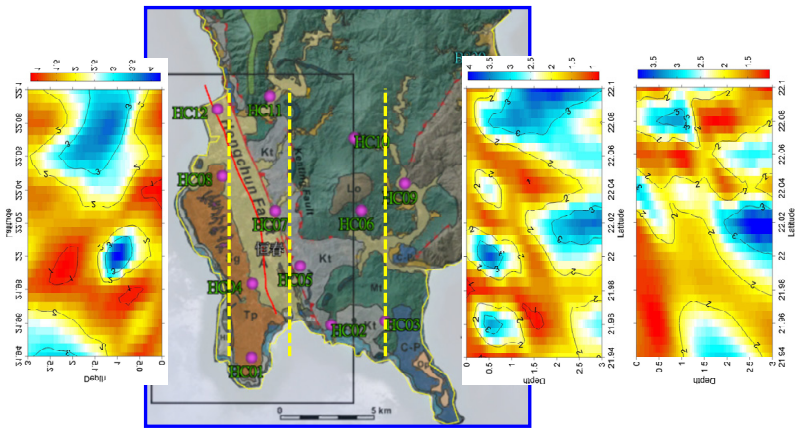

Figure 6. Three 2-D Vs profiles to depths of 3 km near the Hengchun Fault.

CONCLUSIONS AND FUTURE STUDIES

In this research, the TDEGFs were obtained from the cross-correlation of daily vertical-component data between 2018 and 2020, with a temporary broadband seismic network along the Hengchun Fault was operated by the NCREE. Shallow crustal S-wave velocity structures within 3 km depths of the surface are derived underneath the Hengchun Peninsula. High velocities may imply the presence of Miocene strata or mud diapirs which produce high gravity anomalies.

In the near future, more detailed shallow crustal Vs structures beneath the Hengchun Peninsula will be obtained to provide comparisons with the information derived from geological structures, groundwater distribution, and associated phenomena. Based on these observations, the earthquake probabilities of seismogenic structures such as the Hengchun Fault can be evaluated with more confidence. The parameters are important for constructing strong ground motion, assessing seismic hazards, and numerically simulating potential seismic risks.

ACKNOWLEDGMENTS

This study is partially supported by the Ministry of Science and Technology, Taiwan under Grant no. MOST 109-2116-M-492-003, MOST 110-2116-M-492-006, and MOST 111-2116-M-492-005.

APPENDIX

Some of the results in this article were published in research papers, academic conferences or the project reports of the Ministry of Science and Technology.

REFERENCES

Angelier, J. (1986). "Geodynamics of the Eurasia-Philippine Sea Plate boundary: Preface," *Tectonophys.*, **125**, IX-X.

Chan, C. H., K. F. Ma, J. B. H. Shyu, Y. T. Lee, Y. J. Wang, J. C. Gao, Y. T. Yen and R. J. Rau (2020). "Probabilistic seismic hazard assessment for Taiwan: TEM PSHA2020," *Earthq. Spectra.*, **36(1_Suppl)**, 137-159.

Chen, S. C., S. K. Hsu, C. H. Tsai, Y. Wang, C. S. Horng and F. W. Kuo (2016). "The Influence of mud diapirism on the tectonic evolution in nearshore and onshore areas of the West Hengchun Hill," *Min. Metal.*, **60**, 7-22. (in Chinese with English abstract)

Chen, S.-C., S.-K. Hsu, Y. Wang, S.-H. Chung, P.-C. Chen, C.-H. Tsai, C.-S. Liu, H.-S. Lin and Y.-W. Lee (2014). "Distribution and characters of the mud diapirs and mud volcanoes off southwest Taiwan," *J. Asian Earth Sci.*, **92**, 201-214.

Chen, W. S., W. C. Lee, N. W. Huang, I. C. Yen, C. C. Yang, H. C. Yang, Y. C. Chen and S. H. Sung (2005). "Characteristics of accretionary prism of Hengchun Peninsula, southern Taiwan: Holocene activity of the Hengchun Fault," *Western Pacific Earth. Sci.*, **5**, 129-154. (in Chinese with English abstract)

Ching, K. E., J. R. Gourley, Y. H. Lee, S. C. Hsu, K. H. Chen and C. L. Chen (2016). "Rapid deformation rates due to development of diapiric anticline in southwestern Taiwan from geodetic observations," *Tectonophys.*, **292**, 241-251.

Cupillard, P. and Y. Capdeville (2010). "On the amplitude of surface waves obtained by noise correlation and the capability to recover the attenuation: a numerical approach," *Geophys. J. Int.*, **181**, 1687-1700.

Doo, W. B., S. K. Hsu, C. L. Lo, S. C. Chen, C. H. Tsai, J. Y. Lin, Y. P. Huang, Y. S. Huang, S. D. Chiu and Y. F. Ma (2015). "Gravity anomalies of the active mud diapirs off southwest Taiwan," *Geophys. J. Int.*, **203**, 2089–2098.

Giletycz, S. J., C. P. Chang, A. T. S. Lin, K. E. Ching and J. B. H. Shyu (2017). "Improved alignment of the Hengchun Fault (southern Taiwan) based on fieldwork, structure-from-motion, shallow drilling, and levelling data," *Tectonophys.*, **721**, 435-447.

Herrmann, R. B. (2013). "Computer Programs in Seismology: An Evolving Tool for Instruction and Research," *Seismol. Res. Lett.*, **84**, 1081-1088.

Hsu, S. K. and J. C. Sibuet (1995). "Is Taiwan the result of arc-continent or arc-arc collision?," *Earth Planet. Sci. Lett.*, **136**, 315-324.

Huang, T. Y., Y. Gung, B. Y. Kuo, L. Y. Chiao and Y. N. Chen (2015). "Layered deformation in the Taiwan orogen," *Science*, **349**, 720-723.

Huang, Y. C., C. H. Lin and T. Kagiyama (2017). "Shallow crustal velocities and volcanism suggested from ambient noise studies using a dense broadband seismic network in the Tatun Volcano Group of Taiwan," *J. Volcanol. Geotherm. Res.*, **341**, 6-20.

Huang, Y. C., T. Ohkura, T. Kagiyama, S. Yoshikawa and H. Inoue (2018). "Shallow volcanic reservoirs and pathways beneath the Aso caldera revealed using ambient seismic noise tomography," *Earth Planets Space*, **70**, 169.

Lin, A. T., B. Yao, S. K. Hsu, C. S. Liu and C. Y. Huang (2009). "Tectonic features of the incipient arc-continent collision zone of Taiwan: Implications for seismicity," *Tectonophys.*, **479**, 28-42.

Lin, C. H. (2000). "Thermal modeling of continental subduction and exhumation constrained by heat flow and seismicity in Taiwan," *Tectonophys.*, **324**, 189-201.

Seno, T. and Y. Kawanishi (2009). "Reappraisal of the arc-arc collision in Taiwan," *Terr. Atmos. Ocean. Sci.*, **20**, 573-585.

Simoes, M., J. P. Avouac, O. Beyssac, B. Goffé, K. A. Farley and Y. G. Chen (2007). "Mountain building in Taiwan: A thermokinematic model," *J. Geophys. Res.*, **112**, B11405.

Suppe, J. (1981). "Mechanics of mountain building and metamorphism in Taiwan," *Mem. Geol. Soc. China*, **4**, 67-89.

Suppe, J. (1984). "Kinematics of arc-continent collision, flipping of subduction, and back-arc spreading near Taiwan," *Mem. Geol. Soc. China*, **6**, 21-33.

Tsai, Y. B. (1986), "Seismotectonics of Taiwan," *Tectonophys.*, **125**, 17-37.

Tsai, Y. B., T. L. Teng, J. M. Chiu and H. L. Liu (1977). "Tectonic implications of the seismicity in the Taiwan region," *Mem. Geol. Soc. China*, **2**, 13-41.

Weaver, R. L. (2005). "Information from seismic noise," *Science*, **307**, 1568-1569.

Webb, S. C. (2007). "The Earth's 'hum' is driven by ocean waves over the continental shelves," *Nature*, **445**, 754-756.

Wu, F. T., R. J. Rau and D. Salzberg (1997). "Taiwan orogeny: thin-skinned or lithospheric collision?," *Tectonophys.*, **274**, 191-220.

Yao, H. (2009). Ambient noise interferometry and surface-wave array tomography in southeastern Tibet, *Ph.D. Thesis*, Massachusetts Institute of Technology, Cambridge.

Yao, H., R. D. van der Hilst and M. V. de Hoop (2006). "Surface-wave array tomography in SE Tibet from ambient seismic noise and two-station analysis - I. Phase velocity maps," *Geophys. J. Int.*, **166**, 732-744.

NUMERICAL ANALYSIS OF MULTICHANNEL ANALYSIS OF SURFACE WAVES (MASW)

Maria Desti Natalin[1] and Jiunn-Shyang Chiou[2]
1. Ph.D. Student, Department of Civil Engineering, National Taiwan University, Taipei, Taiwan, R.O.C.
2. Associate Professor, Department of Civil Engineering, National Taiwan University, Taipei, Taiwan, R.O.C.
Email: mariadesti25@gmail.com, jschiou@ntu.edu.tw

ABSTRACT

Multichannel analysis of surface waves (MASW) is a well-known non-invasive wave test used to construct shear wave velocity, which is important for geotechnical earthquake engineering. The finite element program ABAQUS is used in the present study to simulate the MASW tests and then compared with field measurements. The effects of element mesh, damping ratio, and near-field are investigated. Model validation is firstly carried out using two different soil profiles, homogeneous and multiple soil layer. Then, the numerical findings are validated by an experimental study which was conducted at the NTU Sports Field. The results show that element mesh influences the identified maximum frequency, whereas the damping ratio influences the phase velocity at a higher frequency. Underestimation of phase velocity due to the near-field effect can be observed at a lower frequency which leads to underestimation of shear wave velocity (v_s) at a deeper soil depth. However, errors of shear wave velocity (v_s) due to the near-field effect can only be seen in the multiple soil layer case. Furthermore, this study confirms two important issues, specifically the near-field and soil nonlinearity effects. Therefore, 3D numerical analysis with a detailed damping ratio profile is recommended for further study to overcome these issues.

Keywords: MASW, numerical analysis, element mesh, damping ratio, near-field effect

INTRODUCTION

Shear wave velocity (v_s) is the most important parameter for geotechnical earthquake engineering, representing the stiffness of the soil layer. Multichannel analysis of surface waves (MASW) is a non-invasive wave propagation test usually utilized to construct the shear wave velocity (v_s) profile. Three main steps of MASW (Park *et al.*; 1999) are field measurements using a set of geophones, construction of a dispersion curve, and inversion analysis or back-calculation of the shear wave velocity profile from the calculated dispersion curve. MASW focuses on the dispersion of surface wave propagation in detail, which means that different frequencies with different wavelengths travel at different velocities. Besides the construction of shear wave velocity profile, the MASW has been used in many engineering practices, e.g., an assessment of soil liquefaction potential (Lin *et al.*, 2004), evaluation of an unknown bridge foundation (Nguyen *et al.*, 2016), detection of a shallow buried rock obstruction (Liu *et al.*, 2021) and other applications.

Researchers have extensively studied the MASW test experimentally and numerically after its introduction by Park *et al.* (1999). However, research on the detailed numerical analysis for simulating the surface wave propagation test is relatively limited. In numerical analysis, the spatial-temporal discretization within the mesh is the main important factor affecting the accuracy of wave propagation simulation. In addition, the treatment of damping also influences the numerical accuracy of finite element simulation. Previously, Zerwer *et al.* (2002) proposed a new simplified method considering the effect of mesh dispersion effect and damping ratio for a half-space finite element model and reported that an appropriate element mesh combined with stiffness damping could eliminate or reduce the effect of spatial aliasing, parasitic mode, and unwanted reflection. Besides the element mesh and damping ratio, the near-field effect must be taken into account when modeling an active MASW test. Near-field effects are an erroneous measurement of Rayleigh wave dispersion due to a very close

distance between the seismic source and the first geophone. In that case, the assumption of a purely plane Rayleigh wave may be incorrect. The wave field actually consists of both cylindrically propagating Rayleigh waves and body waves (Zywicki, 1999; Rix *et al.*, 2001). Near-field effects cause the underestimation of Rayleigh-wave phase velocity at low frequencies (Bodet *et al.*, 2009; Yoon and Rix, 2009) and affect the inverted shear wave velocity (v_s) profile. Roy and Jakka (2017) used a detailed finite element method to study the near-field effects of MASW tests considering different shear wave velocity (v_s) profiles and impedance scenarios. Their study reported an underestimation of phase velocity occurred due to the impedance contrasts between the overlying soil layer and half-space layer, shear wave velocity model, and far and near offset distances. However, limited previous studies have fully discussed the effects of elemental mesh, damping ratio, and near-field in the numerical analysis of MASW tests. Therefore, the combined effects of element mesh, damping ratio, and near-field are completely investigated in the present study.

In the present study, the wave propagation tests are numerically investigated using the finite element method (FEM) and then compared with field measurements. The objective of the present study is to well simulate full-wave propagation with considering the influence of element mesh and damping ratio. As mentioned before, proper element mesh and damping ratio are required for developing a reliable and accurate finite element model to simulate wave propagation. In addition, the near-field effect is also discussed in the present study. Different shear wave velocity profiles studied by Roy and Jakka (2017) are used for model validation of the finite element model. Then, a site-specific field study is conducted to demonstrate the numerical findings.

METHODOLOGY

In this study, numerical analysis is performed to assess the feasibility of the Multichannel Analysis of Surface Waves (MASW) tests in various soil profiles. The finite element program ABAQUS is used to simulate the full-wave propagation due to impulsive loading caused by a sledgehammer. From numerical analysis, the velocity records are assembled. Then, the frequency-wavenumber analysis is used to generate the dispersion curve. The generated dispersion curves are compared with the theoretical solution based on the stiffness matrix method by Kausel and Roësset (1981). The matrix methods originate in the work of Thomson (1950) and Haskell (1953), assuming a horizontal soil layering model. In addition, the nonlinearity of the soil is not considered in the stiffness matrix method, which means the damping ratio is neglected in the analysis.

It needs to be emphasized that the element mesh and damping are important for the simulation of wave propagation in numerical analysis. According to Zerwer *et al.* (2002), the element mesh is chosen concerning the highest frequency (f_{max}) for the lowest velocity wave (v_R) for wave propagation problems. Higher frequencies could be filtered by coarser mesh, whereas finer mesh can cause numerical instability. An approximate element mesh (g) for square mesh can be calculated by using the following equations:

$$g \leq \chi \, \lambda_{min} \tag{1}$$

where

$$\lambda_{min} = \frac{V_R}{f_{max}} \tag{2}$$

in which λ_{min} is the minimum wavelength. The constant χ must be less than 0.5 because of the Nyquist limit. Rayleigh wave velocity (v_R) can be assumed as described by Park et a. (1999), where the shear wave velocity at depth (v_s) is estimated as 1.09 times the experimental Rayleigh wave phase velocity at the frequency.

In addition to the element mesh, the time increment also must be carefully chosen to maintain numerical accuracy and stability. Larger time increment may cause the divergence of the solution,

whereas shorter time increment may cause spurious oscillations (Gibb's phenomenon). The calculation of time increment depends on the element mesh dimension computed in the following equation:

$$\frac{1}{10}\frac{g}{V_P} \leq \tau \leq \frac{g}{V_P} \tag{3}$$

where τ = characteristic time and V_P = compression wave velocity.

In dynamic finite element analysis, the governing equation of motion is expressed as:

$$[M]\{\ddot{u}\} + [C]\{\dot{u}\} + [K]\{u\} = \{F\} \tag{4}$$

where M, C, and K are the mass matrix, viscous damping matrix, and stiffness matrix, respectively. Meanwhile, ü, u̇, and u are the acceleration, velocity, and displacement vectors, respectively. Caughey (1960) showed that the damping matrix could be expressed as a linear combination of the mass and stiffness matrices or called Rayleigh damping. The relationship between damping ratio and Rayleigh damping is given by the following equation:

$$D = \frac{\eta_1}{2\omega} + \frac{\eta_2 \omega}{2} \tag{4}$$

where D is the damping ratio, ω is the natural frequency of the first vibration modes, and η_1 and η_1 are constants for the mass and stiffness damping, respectively. The more detailed information for determining the damping ratio can be seen in Zerwer *et al.* (2002).

MODEL VALIDATION

In this study, model validation is firstly carried out using two different soil profiles, hereinafter referred to as Case I and Case II. Case I is a homogenous half-space soil layer with a constant velocity of 200 m/s, and Case II is multiple soil layer (three soil layers above the half-space soil layer). The detailed information regarding soil profiles can be seen in Table 1. In addition, the density of soil and Poisson's ratio are kept constants for all cases due to their insignificant effects on Rayleigh wave dispersion, as mentioned in previous studies (Roy and Jakka, 2017). The numerical model of both cases is shown in Fig. 1. The finer mesh is used to simulate the wave propagation more accurately, and then the coarser mesh is used from a certain distance to prevent excessive calculation times without hindering the accuracy of the computation.

Table 1. Details of soil profiles for validation

Thickness (m)	Velocity (m/s)		Poisson's Ratio	Density (kg/m^3)
	Case I	Case II		
5	200	180	0.3	1800
7		240		
12		300		
Half-space		360		

Infinite elements are used for the lateral boundaries and a fixed boundary is simulated at the bottom of the soil profiles. Impulsive loading is simulated using a half-sine pulse acting for a short duration. The peak of loading is 12 kN which appears for a short duration of 0.012 s at the middle of the soil surface. Total time duration of the simulation is kept at 2 s with a time step of 0.0001 s. Velocity records from 192 modeled geophones with 1 m spacing are obtained from the numerical analysis and the dispersion analysis was carried out by using those records. Then, the shear wave velocity profile (v_s) is generated by inversion analysis. In addition, dispersion curves are generated in a frequency range from 4 Hz to 60 Hz, which is mainly associated with the frequency range of engineering interests. In order to gain an understanding of full-wave propagation simulation in numerical analysis, the element mesh (M) and damping ratio (D) are varied in this study. Fine and coarse meshes are represented by element

mesh of 0.5 m and 1 m, respectively. The assumption of a zero or very small damping ratio is usually used in previous studies. For example, Yoon (2005) reported that the damping ratio could be set as zero as the effect of the damping ratio on the near-field effect is negligible. However, the effect of the damping ratio is significant in the far-field. Therefore, the zero (0%) and small damping ratio (0.5%, 1%, 2%, 3%) are used in this study.

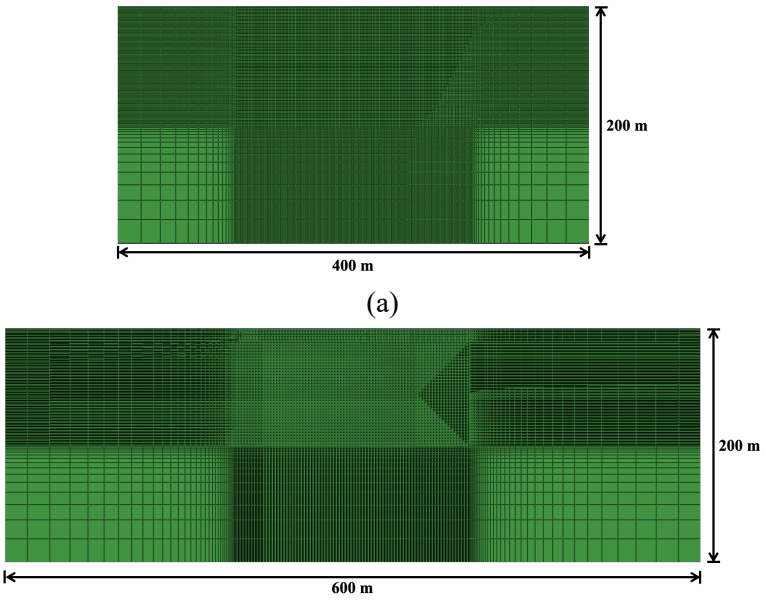

Figure 1. Numerical model for (a) Case I and (b) Case II

Results and Discussions

Case I: Homogenous soil layer

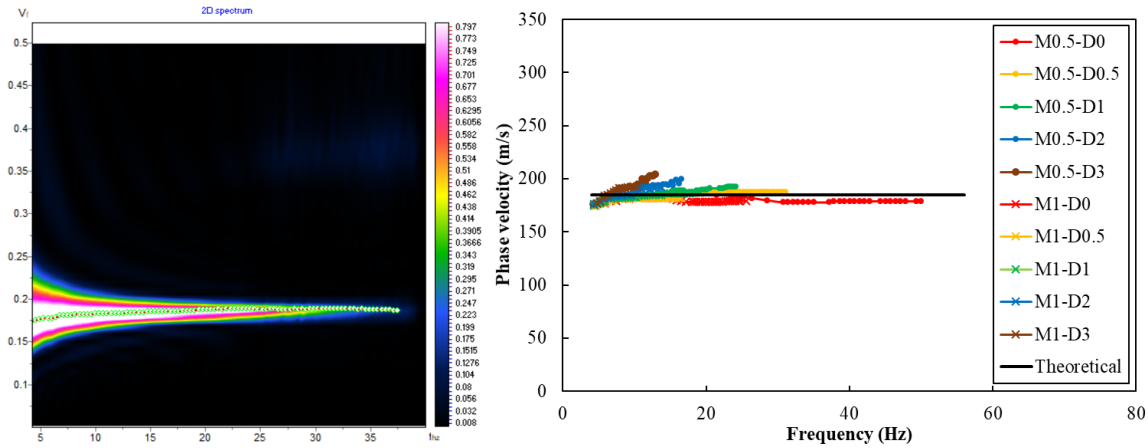

(a) (b)

Figure 2. (a) Dispersion curve after frequency-wavenumber analysis, and (b) dispersion curves for different mesh and damping ratio for Case I (homogeneous soil layer)

Generated phase velocity from the dispersion curve for the homogeneous soil layer is shown in Fig. 2. Considering the element mesh, the fine mesh (0.5 m) results in a longer frequency than the coarse mesh (1 m), which may lead to poor resolution of shear wave velocity (v_s) at the ground surface. In addition, the increased damping ratio increases the phase velocity and decreases the observed maximum frequency. No damping cases (M0.5-D0 and M1-D0) show a different phase velocity pattern than those with a damping ratio, particularly underestimation at a higher frequency. Roy and Jakka (2017) reported that the underestimation of phase velocity due to the near-field effect could be

observed in lower frequencies. In this study, the near-field effect also can be observed where a slightly downward trend is seen at the lower frequencies. From all the cases, it can be concluded that the fine mesh (0.5 m) with a very small damping ratio (0.5% and 1%) shows a good agreement with the theoretical solution and can be used for further simulations. Fig. 3(a) shows the calculated shear wave velocity profile obtained from the inversion analysis by using the stiffness matrix method. The same velocity as the input profile shear wave velocity (v_s) profile can be obtained in this homogeneous soil layer. In addition, it is seen that the underestimation of phase velocity due to the near-field effect does not affect the calculated shear wave velocity in the homogeneous soil layer.

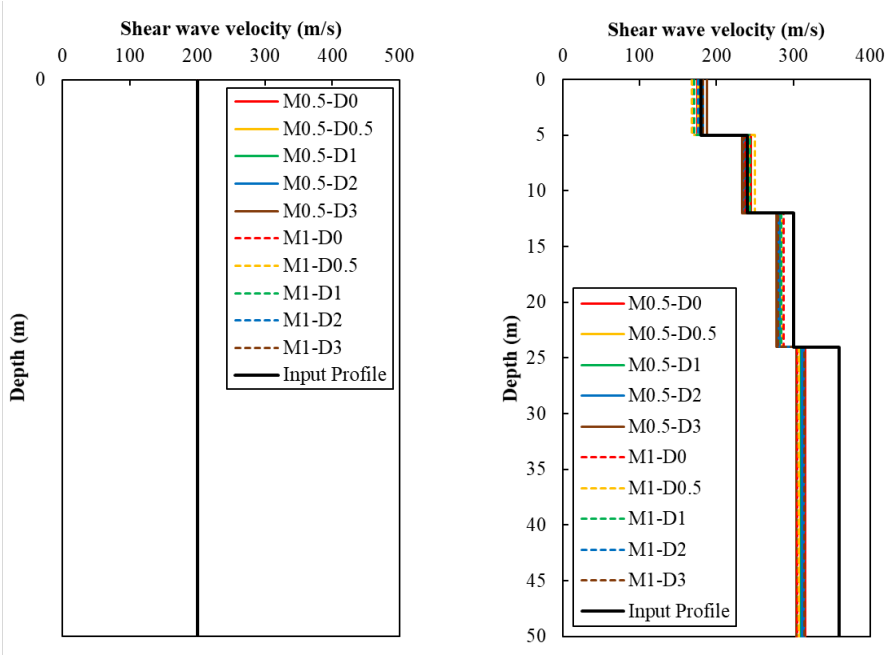

(a) (b)

Figure 3. Shear wave velocity (v_s) profile for (a) Case I and (b) Case II

Case II: Multiple soil layer

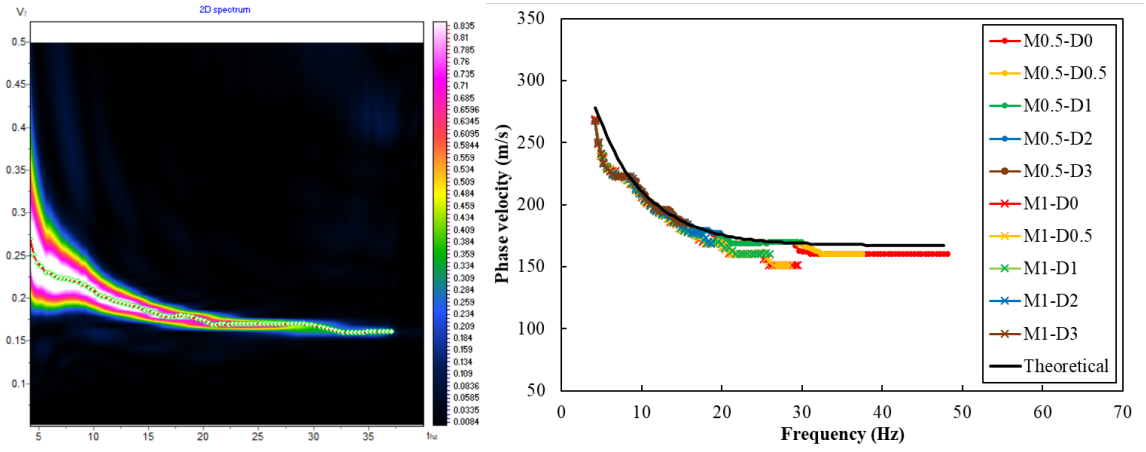

(a) (b)

Figure 4. (a) Dispersion curve after frequency-wavenumber analysis, and (b) dispersion curves for different mesh and damping ratio for Case II (multiple soil layer)

Fig. 4 shows the generated phase velocity from the dispersion curve for the multiple soil layer. Same as Case I, the fine mesh (0.5 m) results in a longer frequency than the coarse mesh (1 m), and the increased damping ratio increases the phase velocity. However, the influence of the element mesh is more pronounced than the damping ratio in this case, particularly in higher frequency.

Underestimation of phase velocity due to the near-field effect can clearly be observed in lower frequency; this underestimation is not affected by either element mesh or damping ratio. It can be seen that the generated phase velocity by the fine mesh shows a good agreement with the theoretical solution; however, it should be emphasized that the near-field effect must be overcome in order to obtain an accurate shear wave velocity (v_s) profile. Those phenomena influence the shear wave velocity (v_s) profile obtained from the inversion analysis by using the stiffness matrix method, as shown in Fig. 3(b). Contrary to the calculated shear wave velocity in the homogeneous soil layer, errors due to the near-field effect can clearly be seen in the deep soil layers (layer III and half-space soil layer). This is because the phase velocity at lower frequencies affects deeper soil layers. Underestimation of the shear wave velocity at deeper soil layers is due to the use of the stiffness matrix method to analyze data containing near-field effects. In addition to the assumption of the horizontal soil layering model, the stiffness matrix method is also not suitable for solving 3D soil problems. Therefore, enhancement of the inversion method needs to be done in further study. Despite the underestimation of shear wave velocity (v_s) at deeper soil layers, the calculated shear wave velocity with the fine mesh (0.5 m) with various damping ratios accurately predicts the shear wave velocity at the soil surface. From Cases I and II, it is concluded that the fine mesh (0.5 m) with a very small damping ratio (0.5% and 1%) can be used to simulate the experimental study.

EXPERIMENTAL STUDY

The numerical findings are validated by an experimental study in this section. An active MASW test was conducted at the National Taiwan University (NTU) Sports Field with geophones configuration as shown in Fig. 5. 24-channel geophones were used lined up in a straight line on the surface of the test site. The spacing between geophones was 2 m and the total length of the spread was 46 m. The natural frequency of each geophone is 4.5 Hz. The shot points were at the middle of the spread using 10 kg sledgehammer as a source. The recording time was 2000 ms and the sampling rate was 1 ms.

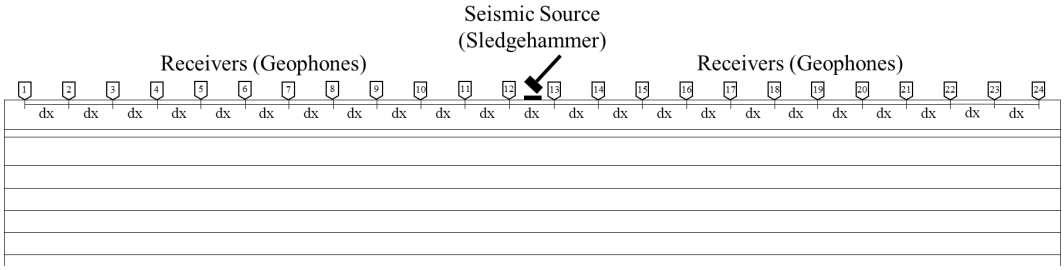

Figure 5. Configuration of MASW test

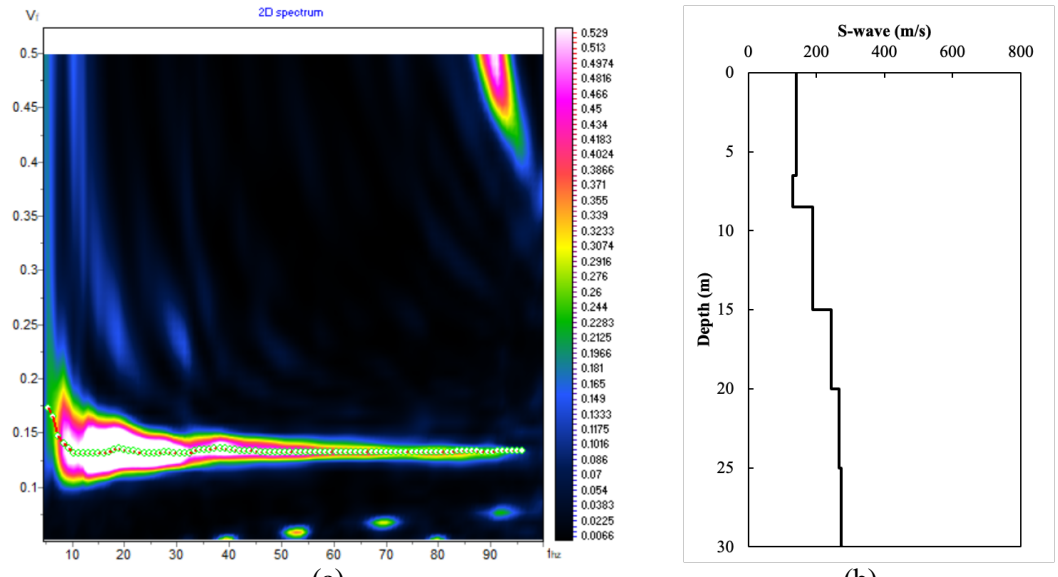

(a) (b)

Figure 6. (a) Dispersion curve and (b) shear wave velocity (vs) profile from the experimental study

Fig. 6 shows the generated dispersion curve and shear wave velocity (vs) profile from the experimental study. Due to the ambient noise in the field, the phase velocity can be generated from 6 Hz to 96 Hz as shown in Fig. 6(a). From the shear wave velocity (vs) profile, the numerical model is simulated into six soil layers above the half-space soil layer with the same numerical model as Case II (Fig.1b). From the validation results, it is determined that the fine mesh (0.5 m) with a very small damping ratio (0.5% and 1%) are used to simulate the experimental study.

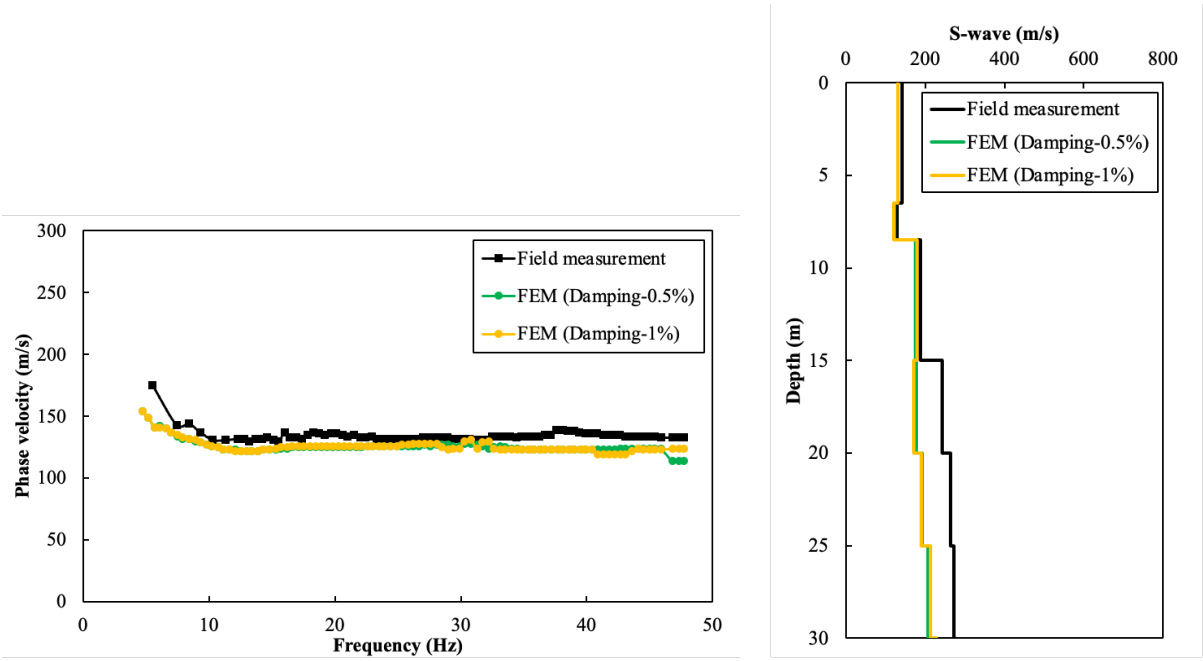

(a) (b)

Figure 7. Comparison of (a) dispersion curve and (b) shear wave velocity (vs) profile of experimental study and numerical analysis

As shown in Fig. 7(a), the finite element model with the damping ratio of 1% case shows a good agreement with the field measurement. Due to the element mesh, the phase velocity can only be generated from 6 Hz to 48 Hz. Therefore, a finer mesh than 0.5 m is recommended for further study to obtain a longer observed frequency. Meanwhile, the effect of the damping ratio can be observed at a higher frequency. For example, the phase velocity tends to decrease for the damping ratio of 0.5% case which will affect the calculated shear wave velocity (v_s) at the soil surface. The effect of the damping ratio shows the nonlinearity of soil at shallow soil depths. In addition, the relative error between phase velocity from the field measurement and numerical analysis for damping 0.5% and 1% is 7.9% and 7.7%, respectively. According to the validation results, the underestimation of phase velocity in lower frequency due to the near-field effect can also be observed in this model. Due to the near-field effect, the underestimation of shear wave velocity (v_s) at deeper depth can be seen in Fig. 7(b). To overcome the near-field effect, 3D numerical analysis can be used in further study. In conclusion, this study confirms two important issues, specifically the near-field and soil nonlinearity effects in the simulation of MASW tests, which will be discussed in our future study.

CONCLUSIONS

The finite element program ABAQUS is used in the present study to simulate the Multichannel Analysis of Surface Waves (MASW) tests and then compared with field measurements. In numerical analysis, proper element mesh and damping ratio are required for developing a reliable and accurate finite element model. Therefore, the effects of element mesh and damping ratio are investigated. In addition, the near-field effect is also discussed in the present study. From the numerical analysis, the phase-velocity and shear wave velocity are generated by using the frequency-wavenumber analysis

and the stiffness matrix method, respectively. Model validation is firstly carried out using two different soil profiles, namely Case I (homogeneous soil layer) and Case II (multiple soil layer). Then, the numerical findings are validated by an experimental study which was conducted at NTU Sports Field. Based on the numerical analysis results, the conclusions of this study are as follows:

1. Fine mesh results in longer frequency than coarse mesh and the increased damping ratio increases the phase velocity for both cases (homogeneous and multiple soil layers). In addition, underestimation of phase velocity due to the near-field effect at lower frequencies can clearly be observed for both cases (homogeneous and multiple soil layers).
2. The same velocity as the input profile shear wave velocity (v_s) profile can be obtained in the homogeneous soil layer case. However, errors of shear wave velocity (v_s) profile due to the near-field effect can clearly be seen in the deep soil layers in the multiple soil layer case.
3. From the comparison between field testing and numerical analysis, the relative error between phase velocity from field measurement and numerical analysis is relatively small. This study confirms two important issues, specifically the near-field and soil nonlinearity effects. 3D numerical analysis is recommended to overcome the near-field effect in further study; meanwhile, the detailed damping ratio profile must be carefully determined to overcome the soil nonlinearity effect at the ground surface.

REFERENCES

Haskell, N.A. (1953). "The dispersion of surface waves on multilayered media." *Bulletin of the Seismological Society of America*, **43**(1): 17–34.

Bodet, L., Abraham, O., and Clorennec, D. (2009). "Near-offset effects on Rayleigh-wave dispersion measurements: physical modelling." *Journal of Applied Geophysics*, **68**:95–103.

Kausel, E., and Roësset, J.M. (1981). "Stiffness matrices for layered soils." *Bulletin of the Seismological Society of America*, **71**(6): 1743–1761.

Lin, C.H., Chang, C.C., and Chang, T.S. (2004). "The use of MASW method in the assessment of soil liquefaction potential." *Soil Dynamics and Earthquake Engineering*, **24**, 689–698.

Liu, Y.H., Zhang, Y.H., Nilot, E., Ng Yannick, C.H., Yang, P., and Ku, T.S. (2021). "Detection of a shallow-buried rock obstruction using 2D full waveform inversion." *Soil Dynamics and Earthquake Engineering*, **143**, 106644.

Nguyen, T.D., Tran, K.M., and McVay, M. (2016). "Evaluation of Unknown Foundations Using Surface-Based Full Waveform Tomography." *Journal of Bridge Engineering*, **21**(5): 04016013.

Park, C.B., Miller, R.D., and Xia, J.H. (1999). "Multichannel analysis of surface waves." *Geophysics*, **64**(3), 800-808.

Rix, G.J., Lai, C.G., and Foti, S. (2001). "Simultaneous measurement of surface wave dispersion and attenuation curves." *Geotechnical Testing Journal*, **24**(4): 350–8.

Roy, N. and Jakka, R.S. (2017). "Near-field effects on site characterization using MASW technique." *Soil Dynamics and Earthquake Engineering*, **97**, 289-303.

Thomson, W.T. (1950). "Transmission of elastic waves through a stratified solid medium." *Journal of Applied Physics*, **21**(2): 89–93.

Yoon, S. (2005). Array-based measurement of surface wave dispersion and attenuation using frequency-wave number analysis, *Ph.D. thesis*, Georgia Institute of Technology, Atlanta.

Yoon, S., Rix, G.J. (2009). "Near-field effects on array-based surface wave methods with active sources." *Journal of Geotechnical and Geoenvironmental Engineering*,**135**:399–406.

Zerwer, A., Cascante, G., and Hutchinson, J. (2002). "Parameter estimation in finite element simulations of Rayleigh waves." *Journal of Geotechnical and Geoenvironmental Engineering*, **128**(3):250–261.

Zywicki, D.J. (1999). Advanced signal processing methods applied to engineering analysis of seismic surface waves, *Ph.D. thesis*, Georgia Institute of Technology, Atlanta.

THREE-DIMENSIONAL FINITE DIFFERENCE GROUND MOTION SIMULATION OF THE BANGKOK BASIN, THAILAND

Bidhya Subedi[1], Junji Kiyono[2] and Aiko Furukawa[3]

1. Research Assistant, Department of Urban Management, Kyoto University, Kyoto, Japan
2. Professor, Department of Urban Management, Kyoto University, Kyoto, Japan
3. Associate Professor, Department of Urban Management, Kyoto University, Kyoto, Japan

Email: subedi.bidhya.8x@kyoto-u.ac.jp, kiyono.junji.5x@kyoto-u.ac.jp, furukawa.aiko.3w@kyoto-u.ac.jp

ABSTRACT

Multiple earthquakes occurring far away were felt in high-rise buildings of the Bangkok basin. The ground motions recorded in the basin show long period amplifications. Long-period ground motions were simulated using three-dimensional (3D) finite difference method in the open-source GMS program. A four-layered 3D velocity structure of Bangkok was modelled using a real earthquake event as the point source. The simulated waveforms show sedimentary basin generated long-period ground motions with a predominant period of 2 s.

Keywords: 3-D finite difference simulations, Bangkok basin, long-period ground motions

INTRODUCTION

Numerous distant earthquakes have been felt in high-rise buildings of Bangkok. Bangkok lies in the Chao Phraya Plain, Thailand, which is a wide depositional flat plain with an irregular basement at 500–2000 m below the ground surface. The basement is filled with a sequence of fluvial, alluvial, and deltaic sediments (Sinsakul, 2000). The top clay layer is soft and highly compressible (Phien-wej et al., 2006). Low-velocity sedimentary soil layers in a deep basin amplify seismic waves in the long period range. Some examples of such basin amplifications include the Mexico City in the 1985 Michoacan earthquake, the Taipei basin in the 1999 Chi-Chi earthquake and the Kathmandu basin during the 2015 Gorkha-Nepal earthquake. Bangkok is densely populated and has a growing number of high-rise buildings and long-period structures.

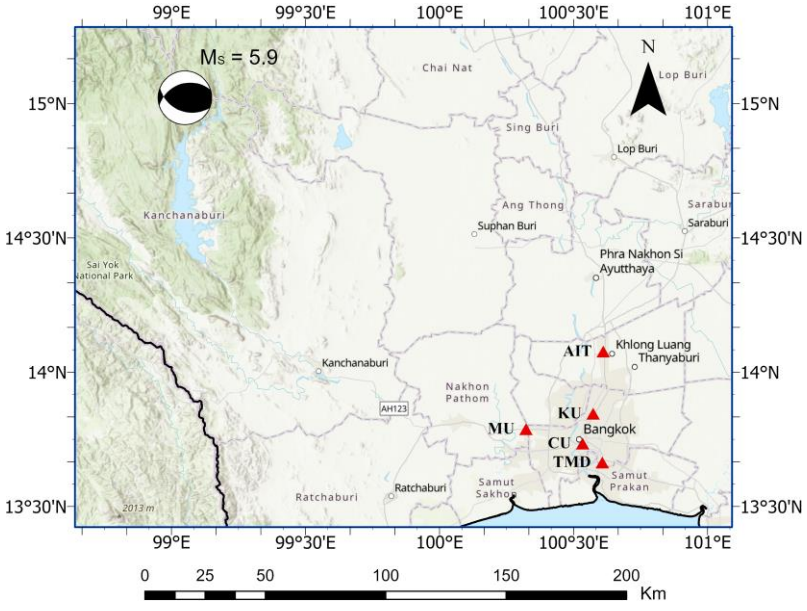

Figure 1. Observation stations (red triangles) and the point source used in 3D FDM simulations.

3D VELOCITY STRUCTURE MODEL

A three-dimensional (3D) site response analysis using numerical methods such as the finite difference method (FDM) and finite element method is important for studying the sediment-induced amplification in basin structures. Such 3D analysis requires a 3D ground velocity structure. Subedi et al. (2021b) discusses the 3D ground surfaces estimated by interpolation of borehole data from hydrogeological survey. Subedi et al. (2021a) performed a microtremor survey at five sites (red triangles in the Fig. 1) in the Bangkok region to study the long period amplifications. Inversion profiles from the study were used to estimate a 3D velocity structure of the region in Subedi et al. (2021c). The 3D structure consisted of four layers above the bedrock with V_s of 2000 m/s. First to fourth layers from the top correspond to V_s of 82–120 m/s, 330–337 m/s, 605–650 m/s, and 900 m/s, respectively. The Bangkok basin has an irregular basement, and the 3D V_s structure was created from just five inversion profiles. Therefore, we further estimated a 3D V_s structure model of the basin combining the experimental dispersion curves from Subedi et al. (2021a) and hydrogeological data from Subedi et al. (2021b). The model better represents the geological layers of the site due to the use of borehole information and is further used in simulating long-period ground motions using 3D FDM.

Including low V_s layers in simulation increases the computational requirements due to necessity of modelling with finer grids; therefore, we started from the layer with V_s of 400 m/s. A four layered model was used for the simulations with first–fourth layer from the top having the V_s of 400, 700, 1200 and 2000 m/s, respectively. We used V_s of 3200m/s for the bedrock. The maximum depth of the Layers 1–4 is 155, 524, 612 and 2084 m, respectively. Fig 2. shows the bottom geometry of the layers.

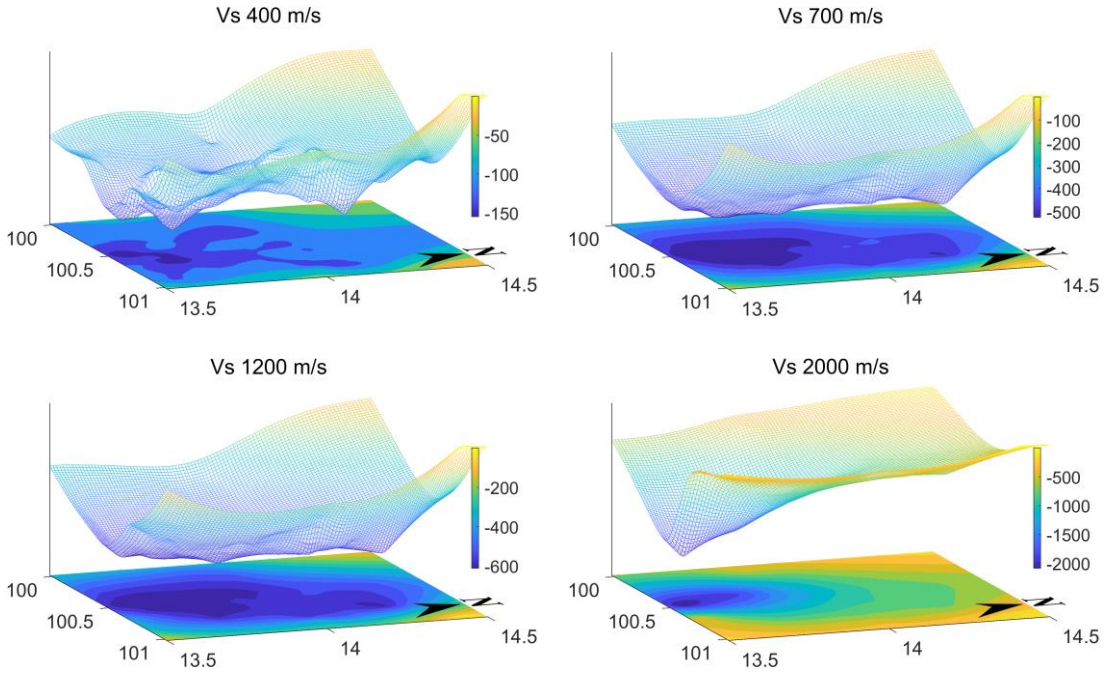

Figure 2. Bottom geometry of the velocity layers used for ground motion simulations.

Accurate estimation of earthquake ground motions requires incorporating anelastic attenuation because of its high effect in the ground-motion amplitudes. Olsen et al. (2000) shows that simulations with attenuation may reduce the predicted peak velocity by a factor up to 2.5 relative to lossless simulations. The regional variations of the seismic Q exist and there are no prior studies on the Q value for the study region. Various studies suggest estimating frequency independent value of Q from V_s for long period (> 0.5 sec) strong motion simulations (Olsen et al., 2000; Satoh, 2004). ERC Japan (2017) estimated Q using the empirical relation: $Q = V_s/5$ (V_s is in meters per second), for the subsurface velocity structure of Japan. We fixed Q of top four layers based on this equation. Table 1 shows the physical properties of the layers and underlying bedrock.

Table 1. Properties of the layer model used in 3D FDM

V_p (m/s)	V_s (m/s)	Density (kg/m^3)	Q
1665	400	1800	80
2100	700	2000	140
2685	1200	2100	240
3593	2000	2300	400
5500	3200	2650	400

GROUND MOTIONS SIMULATIONS USING GMS

We used GMS (Ground Motion Simulator) developed by NIED Japan for the long-period ground motion simulations. GMS is a freely available open-source 3D Finite Difference Simulation tool consisting of a parameter generation tool, 3D FD solver and result visualization tools. GMS requires parameters such as 3D velocity structure of the simulation area, station locations, source models and calculation configurations for 3D FDM simulations, which can be entered using Graphical User Interface (Aoi et al., 2004). GMS adopts a discontinuous grid, which largely reduces the computation load (Aoi and Fujiwara, 1999). GMS allows the use of three times coarser grid spacing in the deep region than the shallow region. Aoi et al. (2004) provides the discrete forms of the equations for velocity and stress-strain relations for the 3D FD calculation of wave field in the GMS program.

The point source used in the simulation is the main shock (m_b= 5.8, M_s= 5.9) among a series of reservoir induced earthquake, occurring on April 22, 1983. The focal mechanism strikes 255°, dips 48° and slips 63.5°. The epicenter is near the Srinagarind reservoir [14.92°N 99.05°E] which is about 190 km northwest of Bangkok. The focal depth used in the simulation was 8 km and seismic moment of the earthquake was 3.86 x 10^{24} dyne-cm, as estimated by Chung and Liu (1992).

Table 2. Structural model used in GMS program for ground motion simulations

Lattice size (m)

Region I			Region II		
dx1	dy1	dz1	dx2	dy2	dz2
70	70	70	210	210	210

Number of grids

Region I			Region II		
nx1	ny1	nz1	nx2	ny2	nz2
2204	2673	32	734	891	32

Table 3. Parameters used in GMS program for ground motion simulations

Calculation time interval (seconds)	0.0056 s
Thickness of absorption boundary	60 grids
Absorption power	0.005
Frequency limit	1 Hz
Grid points per wavelength	5

Five microtremor survey sites from Subedi et al. (2021a) were used as the observation sites in the simulations (Fig. 1). Observation stations were placed at multiple depths for each site and velocity waveforms were recorded. Table 2 shows the details of the structural model and Table 3 lists the parameters used for the simulations. Velocity-stress formulation of fourth order approximation was used for wavefield calculation. We took five grid points per wavelength for a frequency limit of 1 Hz. Isotropic grids of 70 m size were used for the shallow part of the model and the grid size was updated to 210 m for the deeper region. Smoothed ramp source time function was used for simulations. The time increment from the stability condition was 0.0056 s. The thickness of the absorbing boundary was 60 grids, and the damping coefficient was 0.005 (Cerjan et al., 1985).

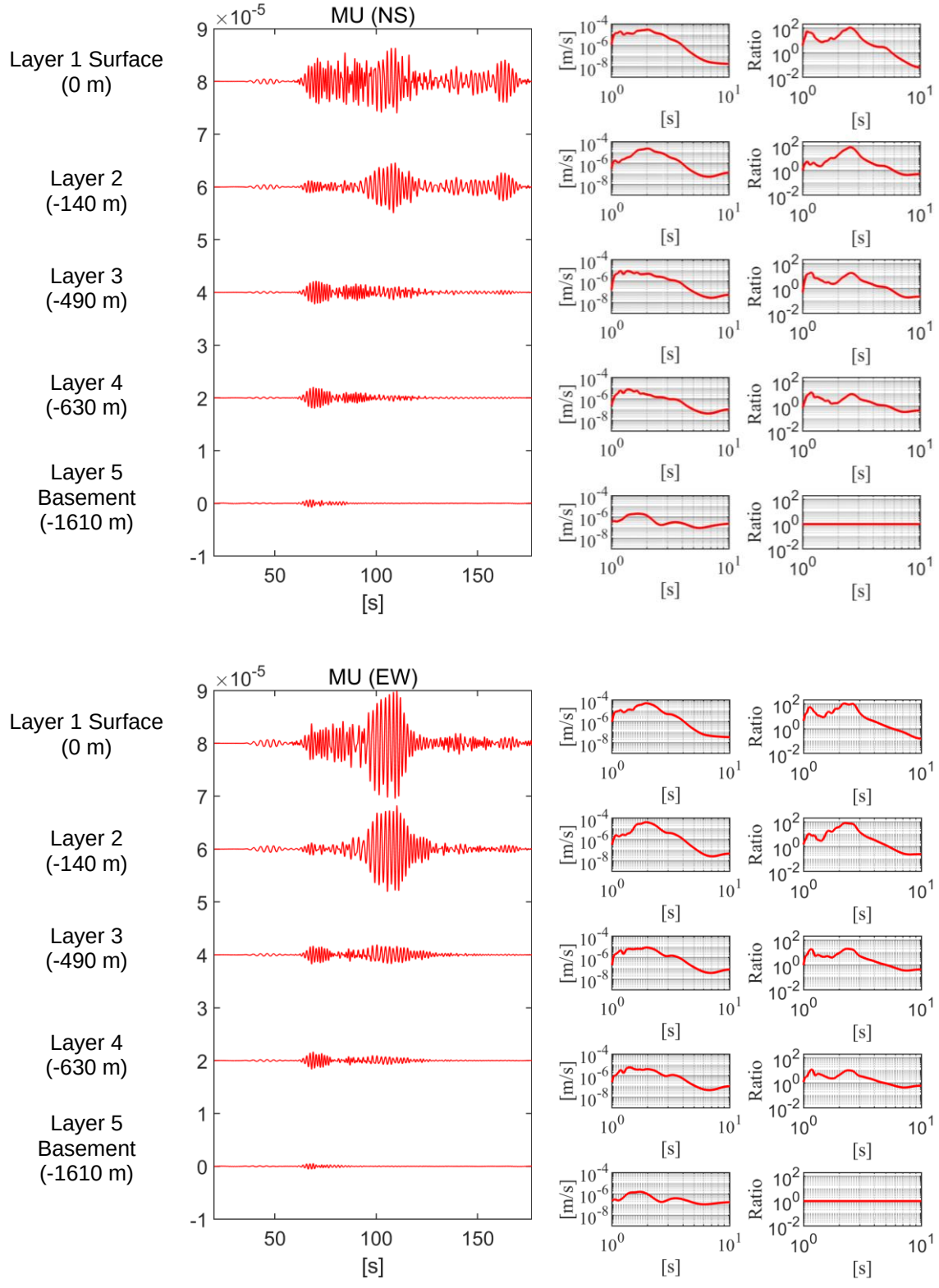

Figure 3. Simulated velocity waveforms and their Fourier spectra for NS and EW directions at the site MU.

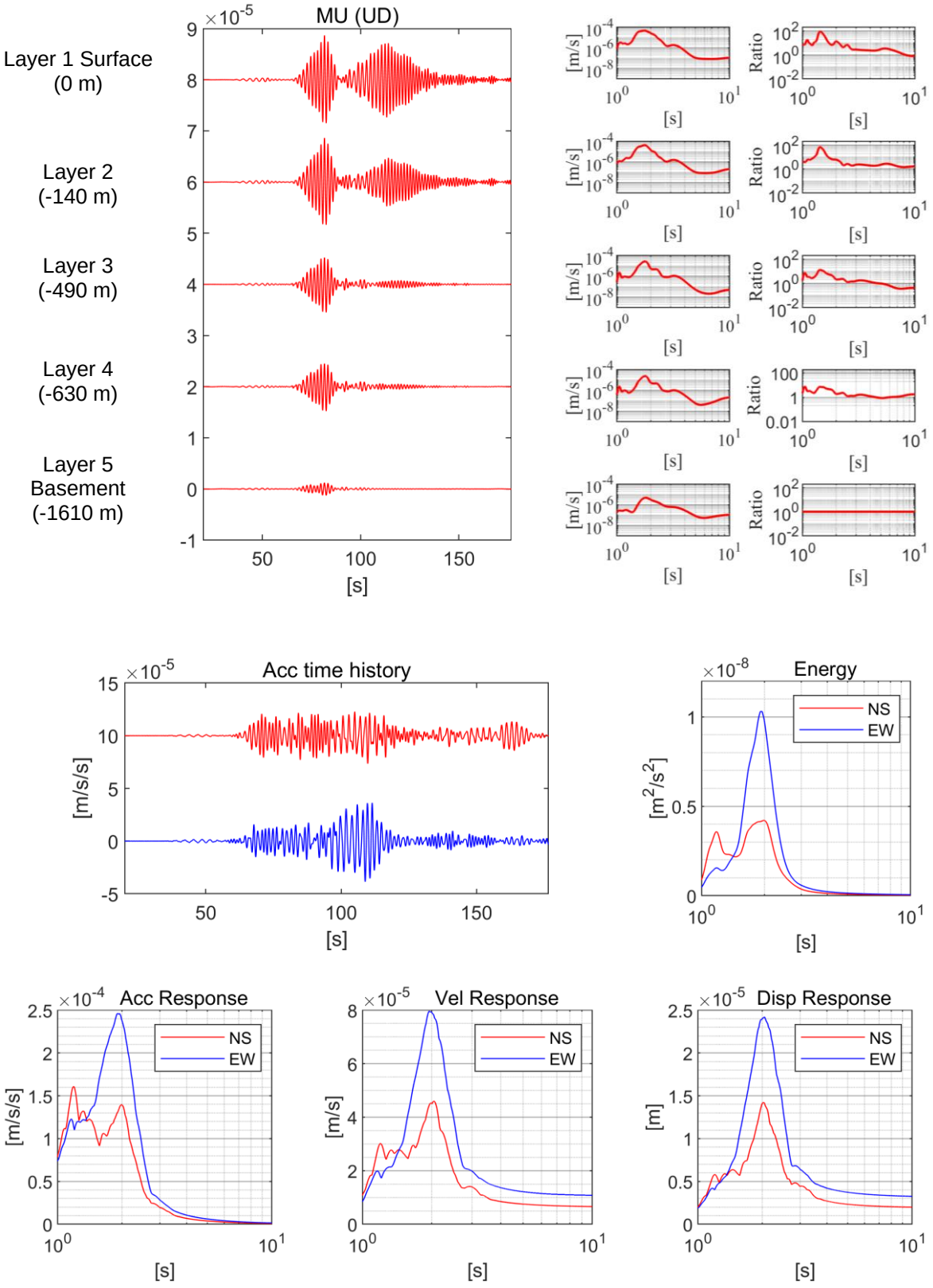

Figure 4. Simulated velocity waveforms and their Fourier spectra at the site MU (top); acceleration time history, energy spectra, and acceleration, velocity and displacement responses at the surface station (bottom).

DISCUSSIONS

Figs. 3 and 4 shows the simulation results in three directions at the site MU. There are five observation stations placed on the surface, in bedrock and near the upper boundary of Layer 2–4 for each site. The velocity time history was bandpass filtered from 0.1–1 Hz. The waveforms show sedimentary basin generated long-period ground motions. The Fourier spectra shows a peak at around 2 s. The ratio of Fourier spectra at upper four observation stations to the spectra at the basement shows high amplification for periods 2–3 s. The comparison of this ratio of the top four layers shows gradual amplification of long-period ground motions from the bottom to the top layers. For the station at the surface, shorter period ground motions at around 1 s amplifies as well. Fig. 4 shows the acceleration time histories in NS and EW directions at the surface station of the site MU. The energy spectra and acceleration, velocity and displacement response spectra estimated for the surface station show a clear peak at 2 s. The results in remaining sites also show the same trend as the site MU.

Long-period structures in Bangkok

When the predominant period of ground matches the natural period of a building, the building shows larger responses due to the resonance. Warnitchai (2004) performed an ambient vibration survey and used frequency-domain identification method to identify the dynamic properties of around 50 buildings in Bangkok with heights from 20 to 210 m. They obtained the relation between building height, and first and second mode natural periods. The buildings with 100 m height have the first mode of vibration at around 2 s (Fig. 4). There are more than 108 buildings taller than 150 m in Bangkok (Skyscrapercenter, 2021). Currently there are five Skytrain lines, and five more Skytrain lines will be completed in a few years (Mrta, 2021).

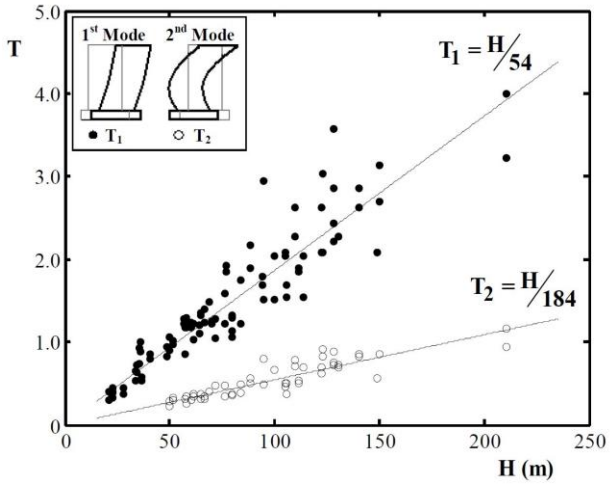

Figure 4. Relation between natural periods and height of buildings in Bangkok (Warnitchai, 2004).

CONCLUSIONS

Open-source GMS program was used for 3D finite difference simulations of long-period ground motions using a four-layered velocity structure model. A real earthquake event was used as the point source. The simulated velocity waveforms show sedimentary basin generated long-period ground motions. The Fourier spectra of waveforms shows a clear peak at around 2 s. The results show high amplification ratio between the surface and basement for periods 2–3 s.

ACKNOWLEDGMENTS

This study was supported by the project of “International Collaborative Research on Long-period Earthquake Early Warning for the Bangkok Metropolitan Area”, which is part of the Supporting Program for Interaction-Based Initiative Team Studies (SPIRITS) funded by Kyoto University.

REFERENCES

Aoi, S. and Fujiwara, H. (1999). "3-D finite difference method using discontinuous grids," *Bulletin of the Seismological Society of America*, Vol. 89, pp. 918-930.

Aoi, S., Hayakawa, T., and Fujiwara, H., "Ground Motion Simulator (2004). GMS," *Butsuri-Tansa (Geophysical Exploration)*, 57, 651-666. (In Japanese with English abstract)

Cerjan, C., Kosloff, D., and Reshef, M. (1985). "A nonreflecting boundary condition for discrete acoustic and elastic wave equations," *Geophysics* 500: pp. 705-708.

Chung, W.-Y. and Liu, C. (1992). "The reservoir-associated earthquakes of April 1983 in western Thailand: Source modeling and implications for induced seismicity," *Pure Appl. Geophys*, Vol. 138, pp. 17–41, https://doi.org/10.1007/BF00876712.

ERC Japan (2017). *Explanatory material on Kanto region shallow/deep integrated ground structure model*, Earthquake Research Committee, Japan. (In Japanese)

Mrta (2021). https://www.mrta.co.th/en/projectelectrictrain/construction_progress_ report/ (Accessed on 2021/06/22)

Olsen, K. B., Nigbor, R. and Konno, T. (2000). "3D viscoelastic wave propagation in the Upper Borrego Valley, California, constrained by borehole and surface data," *Bulletin of Seismological Society of America* 90, pp. 134-150.

Phien-wej N, Giao PH and Nutalaya P (2006). "Land Subsidence in Bangkok, Thailand," *Engineering Geology*, 82: 187–201.

Satoh, T. (2004). "Inversion of incident angle and Q value of sediments from deep borehole seismograms using adaptive simulated annealing method," *Proceedings of the 13th World Conference on Earthquake Engineering, Vancouver, Canada*.

Sinsakul S (2000). "Late Quaternary geology of the Lower Central Plain, Thailand," *Journal of Asian Earth Sciences*, 18(4), 415-426.

Skyscrapercenter (2021). https://www.skyscrapercenter.com/country/thailand/ buildings (Accessed on 2021/06/22)

Subedi B, Kitaoka T and Kiyono J (2021b). "3D stratigraphic modelling of the Bangkok basin using Kriging on borehole data," *IOP Conference Series: Earth and Environmental Science*. 851. 012014. 10.1088/1755-1315/851/1/012014.

Subedi B, Kiyono J, Furukawa A, Ono Y, Ornthammarath T, Kitaoka T, Charatpangoon B and Latcharote P (2021a). "Estimation of Ground Profiles Based on Microtremor Survey in the Bangkok Basin," *Front. Built Environ*. 7:651902. doi: 10.3389/fbuil.2021.651902

Subedi B, Kiyono J, Furukawa A, Ono Y, Ornthammarath T, Kitaoka T, Charatpangoon B and Latcharote P (2021c). "Deep Subsurface Structure of Bangkok Basin Using Microtremor Observations," *Proceedings of the 17th World Conference on Earthquake Engineering, Sendai, Japan*.

Warnitchai, P. (2004, August). "Development of seismic design requirements for buildings in Bangkok against the effects of distant large earthquakes," *In Proceedings of the 13th world conference on earthquake engineering, Vancouver*.

SITE CHARACTERISTICS OF CHIANG MAI, THAILAND FROM ARRAY MICROTREMOR OBSERVATIONS

Nakhorn Poovarodom[1] Amorntep Jirasakjamroonsri[2] and Pennung Warnitchai[3]
1. Professor, Faculty of Engineering, Thammasat University, Thailand.
2. Lecturer, Faculty of Science and Technology, Thammasat University, Thailand.
3. Professor, School of Engineering & Technology, Asian Institute of Technology, Thailand.
Email: pnakhorn@engr.tu.ac.th, amorntep@tu.ac.th, pennung.ait@gmail.com

ABSTRACT

This paper presents results of microtremor surveys for site characterization in Chiang Mai, the second largest city in Thailand. The Horizontal to Vertical spectral ratio (H/V) method was used to estimate the site predominant period and the Centerless Circular Array (CCA) method was employed to derive the velocity structure of thick sediments. Altogether 50 sites distributed almost uniformly in the basin were surveyed. The results of the predominant period, average shear wave velocity from the surface to 30-m depth (VS30) and estimated depth of basement or thickness of Quaternary sediments are presented. The results show that in most sites, which are situated on Alluvium deposits, the predominant period ranges within 0.1 to 0.3 second, VS30 is from 200 to 400 m/s and the estimated depth of basement rock varies mainly from 200 m to 500 m.

Keywords: Site Effects, Array Microtremor, Shear Wave Velocity, Chiang Mai, Thailand

INTRODUCTION

Shear wave velocity structures and predominant period can substantially influence the characteristics of ground shaking, such as amplitude, frequency content, duration, and earthquake damages. Several examples from catastrophic earthquakes have revealed that ground motion intensity was amplified, frequency contents became narrow band, and duration of shaking was lengthened due to a seismic interaction of soft shallow soil layers with deep basin structure below at the site. To examine these effects, soil characterization and ground response analysis of the area are required. Understanding of the effects could enable engineers to establish appropriate measures for earthquake resistant design of structures. In particular, site effects are important in densely populated areas founded on recent and soft deposits.

Chiang Mai is the largest city in northern Thailand and the second largest city in the nation after metropolitan Bangkok. It is situated in a mountainous region, about 700 km north of Bangkok. Economic expansion has been progressed in this area steadily due to commercial and tourism activities causing increase in construction of infrastructures and buildings in recent decades. The city has been threaten by occasional tremors from near faults in Thailand and the neighboring countries. The recent examples are Mw 6.8 Talay (Myanmar) earthquake on March 24, 2011 located 230 km away and Mw 6.0 Mae Lao earthquake on May 5, 2014 located 140 km away. Both events caused strong shaking in buildings and raised public awareness of seismic risks. The city is situated on the flood plain with the top surface is unconsolidated sediments. Ground motion amplifications have been observed, however, seismic mitigation of the area have been comprehended based on limited supporting research studies especially on site effects.

In this study, the main objective is to explore site characteristics of the sediments underneath Chiang Mai municipality using microtremor observations in order to acquire sufficient data for comprehensive site characterizations and further improvement of the design standard. The Horizontal to Vertical spectral ratio (H/V) method (Nakamura 1989) and the Centerless Circular Array (CCA) method (Cho et. al., 2006) were employed to estimate the predominant period and the dispersive characteristics of

phase velocity, respectively. An inversion analysis was subsequently used to inverse the dispersion curve to the shear wave velocity profile down to a depth of rocklike material layers. The results of 50 microtremor observation sites, in approximately 54 km (north-south) by 38 km (east-west) area are presented.

AREA OF STUDY

Thailand has been perceived to be a low to moderate seismic hazard zone. A number of small- and medium-sized earthquakes from active faults in the northern and western regions of the country and the neighboring countries have been frequently recorded. From PSHA study (Ornthammarath et al. 2010, Pailoplee and Charusiri 2016), Thailand's highest seismic hazard areas are located near faults in northern and western Thailand. Chiang Mai city is situated on Chiang Mai Basin, with a maximum width of about 35 km and a north-south length of 140 km surrounded by eastern and western mountain range. The approximate elevation varies from 335 m in the north to 280 m in the south (Wattananikorn et al. 1995). From an interpretation of gravity survey (Wattananikorn et al. 1995), the most prominent features on Chiang Mai basin are a thick section of lower density rocks, which are Quaternary alluvium, terrace deposits and Tertiary sequence. The unconsolidated Quaternary alluvium deposits cover most of the basin. These Quaternary sediments are characterized as high terrace, low terrace and floodplain deposits (Chuamthaisong 1971). High terrace deposits of Lower Pleistocene-Pliocene age are located along both sides of the basin. The deposits contain thick sand and gravel beds. The low terrace deposits of Middle-Upper Pleistocene are located next to the high terrace and on lower elevations. These deposits contain thick clay with intercalation of sand and gravel lenses. The floodplain deposits of Holocene age are located in the central part of the basin. The deposits consist of clays, silts, sands and gravel with thickness from 10 to 60 m (Intrasuta, 1983; Asanachinda, 1992). NEHRP site classification based on the average of shear wave velocity from the surface to 30-m depth (Vs30) obtained from MASW study indicates that Chiang Mai subsoils in mostly site class D (Thitimakorn 2013). However, there is no information of deeper velocity structures.

The investigated area is located within latitudes 18° 28' N to 18° 57' N and longitudes 98° 47' E to 99° 10' E, covering Chiang Mai and Lamphun provinces. The area lies on a large flood plain of Ping River, which runs southward. The subsoils of most sites are classified as Alluvium deposits (Qa) and some sites near the study boundary are located on Terrace deposits (Qt). Figure 1 shows the investigated area and the distributions of 50 observation sites are presented by markers.

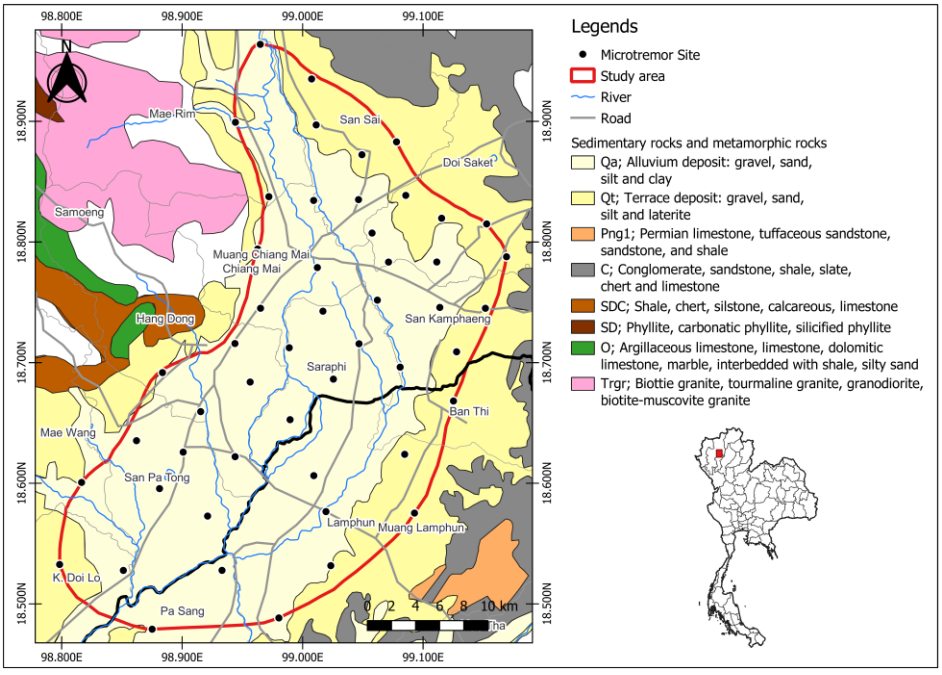

Figure 1. Area of study and microtremor observation points

MICROTREMOR OBSERVATION AND ANALYSIS

The techniques of microtremor observations employed in this study are the Horizontal-to-Vertical spectral ratio (H/V) method to estimate the predominant period of amplification and the Centerless Circular Array (CCA) method to determine shear wave velocity profiles.

Horizontal to Vertical (H/V) Spectral Ratio Method

Nakamura (1989) proposed this technique to interpret records of microtremor for the dominant period of subsoil sediments and also the estimated amplification level. In this method, the ratios of horizontal to vertical Fourier Spectra of microtremor are used to eliminate the source effect. This technique requires the horizontal and vertical component of microtremor measured at a single station only. The H/V spectrum plots are obtained by taking the ratio of the Fourier Spectra of the horizontal to the Fourier Spectra of the vertical component. It is assumed that the horizontal to vertical spectral ratio is similar to the transfer function for horizontal motion of surface layer. The H/V spectrum plots are obtained by taking the ratio of the Fourier Spectra of the horizontal to the Fourier Spectra of the vertical component, as shown in Eq. 1.

$$\text{H/V spectrum} = \sqrt{\frac{(F_{NS})^2 + (F_{EW})^2}{2F_{UD}}} \tag{1}$$

where F_{NS}, F_{EW} and F_{UD} are the Fourier amplitude spectra in the north-south, east-west and up-down directions, respectively. The period and amplitude at a peak of the H/V spectrum plot are interpreted as predominant period and amplification ratio, respectively.

Centerless Circular Array method (CCA)

This technique was proposed and developed by Cho et. al. (2006) based on spectral ratio representations. The spectral ratio which contains information of phase velocities is an integration of all information on the field of vertical component of microtremors. Field works require to deploy a circular array of radius r and record the vertical component of microtremor $z(t,r,\theta)$. Define the average value $Z_0(t,r)$ along the circumference and its weighted average $Z_1(t,r)$ as;

$$Z_0(t,r) = \int_{-\pi}^{\pi} z(t,r,\theta)d\theta \tag{2}$$

$$Z_1(t,r) = \int_{-\pi}^{\pi} z(t,r,\theta)\exp(i\theta)d\theta \tag{3}$$

Assume that the fundamental Rayleigh wave mode dominates the vertical component of the microtremor field, the ratio of their power spectra densities, $G_0(r,r;\omega)$ and $G_1(r,r;\omega)$, can be written as;

$$\frac{G_0(r,r;\omega)}{G_1(r,r;\omega)} = \frac{J_0^{\,2}(rk(\omega))}{J_1^{\,2}(rk(\omega))} \tag{4}$$

Where J_1 is the Bessel function of the first kind with the first order. The wavenumber, and phase velocity, are then estimated by fitting the observed spectral ratio with a theoretical ratio of $J_0^2(rk(\omega))/J_1^2(rk(\omega))$.

Inversion Analysis of Shear Wave Velocity Profile

The shear wave velocity profile from surface to basement rock level can be derived by an inversion analysis. The dispersion relation of phase velocity and frequency from field observations are compared with those derived theoretically from a horizontally layered earth model by iteration procedure to provide the best-fit shear wave velocity–depth profile. However, there are always be several possible solutions from the inversion analysis indicating the problem of non-uniqueness solutions. This study carefully selects the solutions with minimum level of misfits and employs two algorithms for inversion analysis as; the combination of Down Hill Simplex Method with Very Fast Simulated Annealing (Yokoi, 2005) and the neighbourhood algorithm (Wathelet, 2008).

Field Measurement

The equipment used for field observation consists of four units of highly sensitive, servo velocity sensors having frequency range of 0.1 to 70 Hz, and data acquisition instruments with 32 bits A/D converter. Time synchronization between each unit was enabled by GPS clock with a resolution of 1/100 seconds. The arrangement of sensors for array observation was an equilateral triangular array where one unit is placed at the center of circular and the other three are on the perimeter. The duration for recording microtremor data was about 40 minutes for each array. Four different sized array arrangements were set at each site with radius ranging from 5 to 150 m depending on the area of the site. Figure 2 show the equipment and array configuration.

Figure 2. Microtremor equipment and arrangement of array observation

RESULTS AND DISCUSSION

From field observation, site characterization based on the predominant period (Tp), the average shear wave velocity from the surface to 30-m depth (VS30) and the depth of basement are presented. The variations of the identified results are depicted as a contour plot in Figure 3 to 5 for Tp, VS30 and the depth of basement, respectively. The spatial interpolation from the data at discrete locations was done by the inverse distance weighting method. Figure 6 shows relations among the values of these results.

From Figure 3 and 6, the predominant period ranges mainly within 0.1 to 0.3 second. The area with longer period lies along Ping River which runs from north to south of the study area. It should be noted that in many sites, there is no clear peak of H/V spectral plot and the result is excluded.

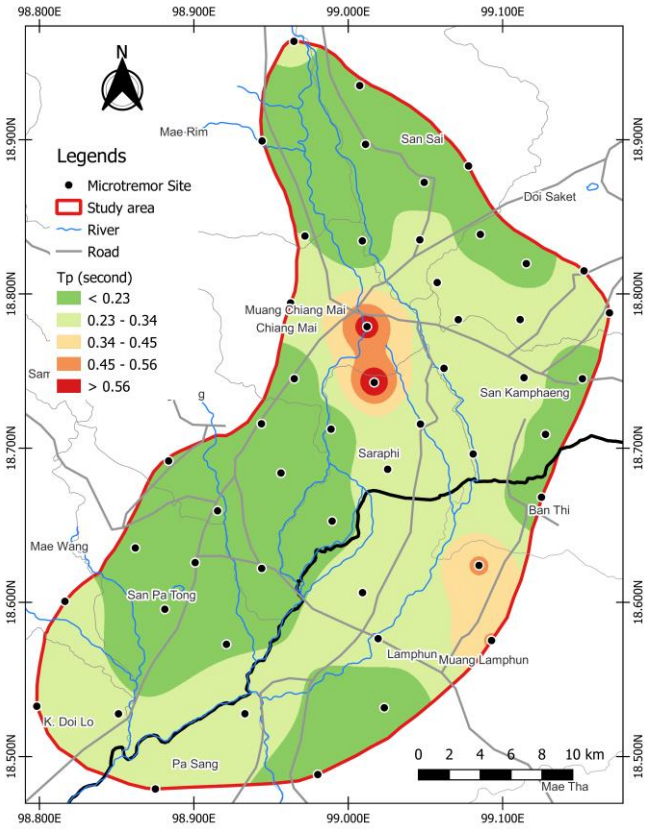

Figure 3. Map of the predominant period

The shallow shear wave velocity structure is presented as the average of shear wave velocity from the surface to 30-m depth (VS30). The results reveal that most sites exhibit VS30 from 200 to 400 m/s. The map of the distribution of VS30 in the study area is presented in Figure 4. Variability of Vs30 is found in some area as the VS30 increases to 500 - 800 m/s. It can be observed that the areas near Ping River show lower VS30 while some sites near the western boundary of the study area show relatively higher VS30. The results are similar to those obtained by MASW (Thitimakorn 2013) in which VS30 in most areas varies from 250 to 500 m/s.

From shear wave velocity profile along depth at a site, the estimated depth of basement rock could be inferred from the level having clear contrasts of shear wave velocity. The velocity at this level changes abruptly to be about 2000 m/s or more. The estimated depth of basement rock found in this study varies mainly from 200 m to 500 m. This finding is in agreement with the depth of the Quaternary sediments interpreted from results of gravity survey (Wattananikorn et al. 1995). Sites with estimate deep basement of about 500 to 800 m are found along Ping River. The shallow basement sites, about 100 m, are located near the mountain hills in the west and the north of the study area. Figure 5 shows the map of the estimated basement depth.

Figure 6 (a) to (c) present relations among Tp and VS30, Tp and depth of basement, VS30 and depth of basement, respectively. In Figure 6 (a), a general tendency of an inverse variation between Tp and VS30 could be observed indicating correlation between the identified predominant period and the shallow velocity structure. However, the plots in Figure 6 (b) and (c) show that the depth of basement does not exhibit clear relation with Tp or VS30. In other words, Tp and VS30 are not sufficiently accurate to represent deep structure, and therefore they are inadequate for site effects assessment of a deep basin.

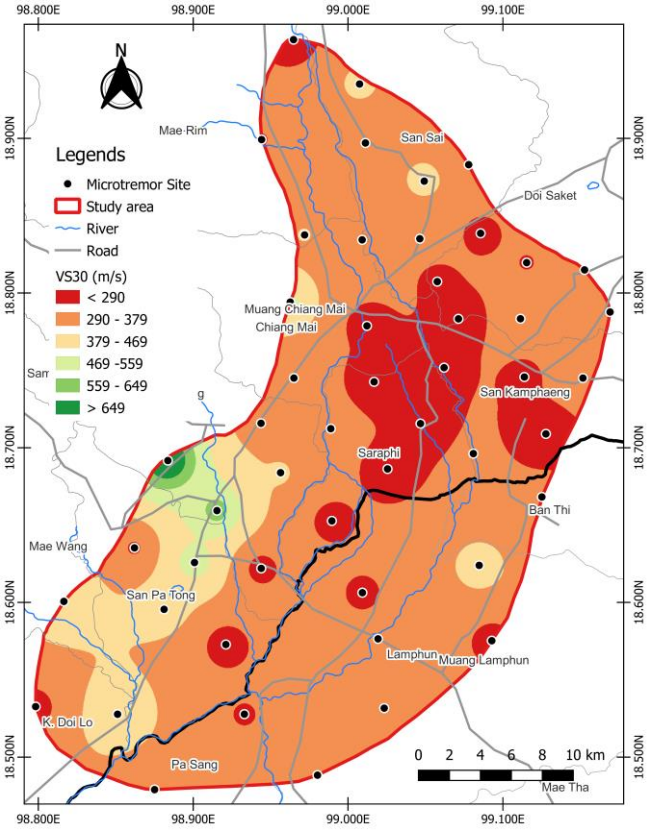

Figure 4. Map of the average of shear wave velocity from the surface to 30-m depth (VS30)

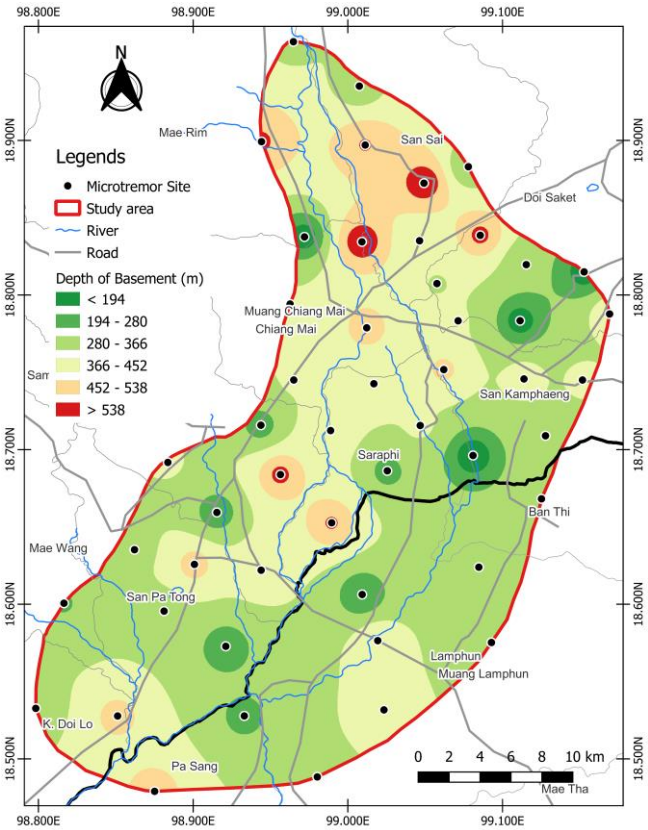

Figure 5. Map of depth of basement

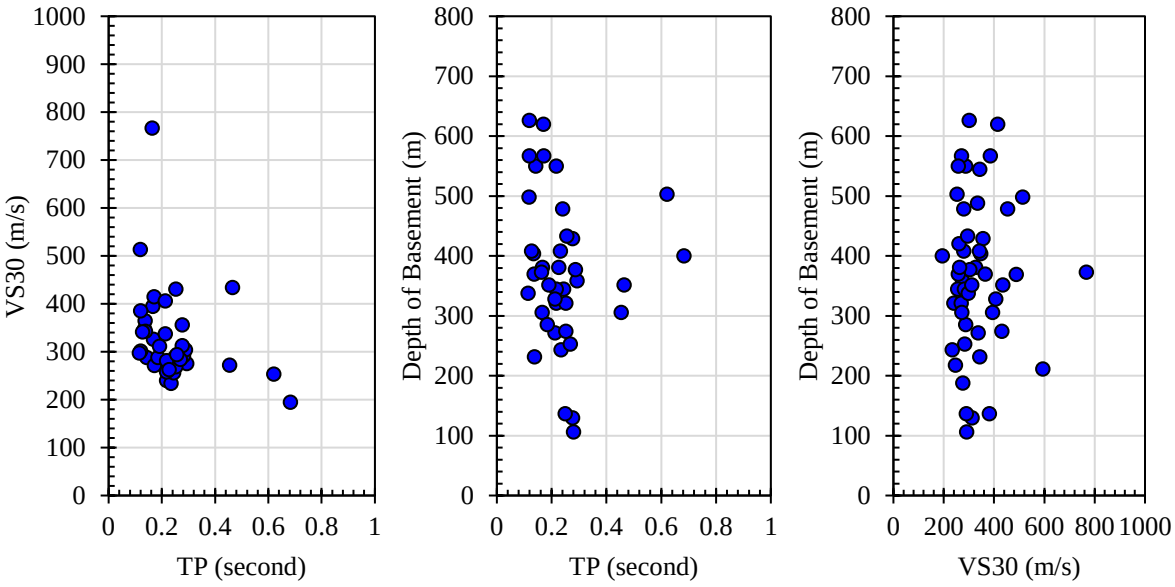

(a) (b) (c)

Figure 6. Relations among the predominant period, VS30 and depth of basement

CONCLUSIONS

This study investigates site characteristics of the sediments underneath Chiang Mai City by microtremor techniques. Results of 50 observation sites situated on Alluvium deposits, the predominant period, average shear wave velocity from the surface to 30-m depth (VS30) and estimated depth of basement, are presented. The results show some degree of variations such that the predominant period ranges within 0.1 to 0.3 second, VS30 is from 200 to 400 m/s and the estimated depth of basement rock varies mainly from 200 m to 500 m. The central area of the city, which lies along a main river, exhibit relatively low VS and deep sediment compared with the area along the western boundary. The velocity structures from surface to basement change considerably from site to site. This important finding could result in spatial variation of amplification characteristics in the area. Further study on ground amplification of the basin modelled by the velocity structures obtained from this pioneer and extensive results are under investigation.

ACKNOWLEDGMENTS

This study is supported by Thailand Science Research and Innovation, research number RDG6230009 and National Research of Council Thailand, research number SS65000874. The sources of support are gratefully acknowledged.

REFERENCES

Asanachinda, P. (1992). "Hydrochemistry of groundwaters in the Chiang Mai Basin, Northern Thailand. *Ph.D. Thesis*, University of London.

Cho, I., Tada, T. and Shinozaki, Y (2006). "Centerless circular array method: Inferring phase velocities of Rayleigh wave in broad wavelength range using microtremor records," *Journal of Geophysical Research*, **111**, B09315.

Chuamthaisong C. (1971). "Geology and grourd water resources of the Chiang Mai Basin, Thailand," *Unpub. M.Sc. thesis*, University of Alabama.

Intrasuta, T (1983). "Ground water potential in unconsolidated sediments in Chiang Mai Basin," *Proc. of the First Symp. on Geomorphology and Quaternary Geology of Thailand*, Bangkok, 179-195.

Nakamura, Y (1989). "A Method for Dynamic Characteristics Estimation of Subsurface Using Microtermor on the Ground Surface," *Quarterly Report of RTRI*, **30**(1), 25-30 .

Ornthammarath, T., Warnitchai, P., Worakanchana, K., Zaman, S., Sigbjörnsson R and Lai, C.G. (2010). "Probabilistic seismic hazard assessment for Thailand," *Bull Earthquake Eng*, DOI 10.1007/s10518-010-9197-3

Pailoplee, S. and Charusiri, P (2016). "Seismic hazards in Thailand: a compilation and updated probabilistic analysis," *Planets and Space*, **68**(98), DOI 10.1186/s40623-016-0465-6

Thitimakorn, T (2013). "Development of a NEHRP site classification map of Chiang Mai city, Thailand, based on shear-wave velocity using the MASW technique," *Journal of Geophysics and Engineering*, **10**(4), 045007, DOI 10.1088/1742-2132/10/4/045007

Wattananikorn, K., Beshir, J.A., and Nochaiwong, A (1995). "Gravity interpretation of Chiang Mai basin, northern Thailand: concentrating on Ban Thung Sieo area," *Journal of Southeast Asian Earth Sciences*, **12**(1/2), 53-64.

Wathelet, M) 2008 .("An improved neighborhood algorithm :parameter conditions and dynamic scaling," *Geophysical Research Letters*, **35**, L09301, DOI 10.1029/2008GL033256.

Yokoi, T (2005), "Combination of down hill simplex algorithm with very fast simulated annealing method-an effective cooling schedule for inversion of surface wave's dispersion curve," *Proc. of the Fall Meeting of Seismological Society of Japan*, B049.

(2a) Soil dynamic and ground response

CENTRIFUGAL MODEL TEST ON SEISMIC RETROFIT OF SLOPE WITH BENCH AGAINST SHALLOW SLIDING

Shanzhi Tao[1] and Thirapong Pipatpongsa[2]
1. PhD Student, Department of Urban Management, Kyoto University.
2. Associate Professor, Department of Urban Management, Kyoto University.
Email: tao.shanzhi.43e@st.kyoto-u.ac.jp, pipatpongsa.thirapong.4s@kyoto-u.ac.jp

ABSTRACT

Shallow sliding is one of the failure patterns of a slope under the earthquake. Bench reinforcement is a feasible way to prohibit this failure from happening. Although this method has been used long time ago, its mechanism is still not fully clear. Thus, two dynamic centrifugal tests were conducted with two soil slopes in each case, reinforced by different types of benches. The slopes were applied with five sequent horizontal seismic waves by the in-flight shaking table on the centrifuge under 50g to examine the maximum resistance of slopes against the earthquake with or without the retrofit bench. The heights of benches were selected based on Culmann's method and pseudo-static analysis. Results indicated that appropriate reinforcement could make the slope bear more intense seismic waves and transfer the potential toe sliding into a slighter one.

Keywords: slope stability, pseudo-static, Culmann's method, bench, dynamic centrifuge

INTRODUCTION

The geometry design is vital for seismic slope stability. With a certain shape, the safety of a slope during an earthquake can be evaluated by using a circular or log-spiral failure surface based on the pseudo-static method traditionally (Farshidfar and Mirhosseini, 2007). But due to its complexity, it is difficult to weigh the importance of each parameter.

Culmann (1866) proposed a wedge stability analysis at a prescribed plane failure surface and it was extended to seismic conditions (Ling et al., 1999). Benched slopes prevail in open-pit mining to increase the stability of the mining pit and prevent rockfall (Alejano et al., 2007). As a practical reinforcement method, the empirical technique is always adopted to devise the bench, lacking theory foundation and experimental verification. In this paper, Culmann's method in seismic conditions was used for bench design and two dynamic centrifugal tests were conducted to prove the theory.

MATERIAL PROPERTIES

The material used in this study, namely Hiroshima sand, is the mountain sand taken from Kure Shi, Hiroshima prefecture. It was preprocessed by the sieve with a diameter of 1mm. The bulk density ρ_t of it is 1.7 g/cm^3 with water content w of 8% under degree of compaction D_c of 90%. The grain size distribution of this sand is drawn in Figure 1. The constant-load direct shear test was conducted to measure the strength parameters of this sand, for which six different normal pressures were chosen. The Rowe's stress ratio – dilatancy relation is used here to obtain both the peak strength and the critical-state strength of Hiroshima sand, as shown in Figure 2.

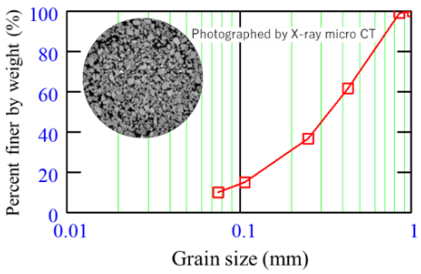

Figure 1. Grain size distribution curve of Hiroshima sand

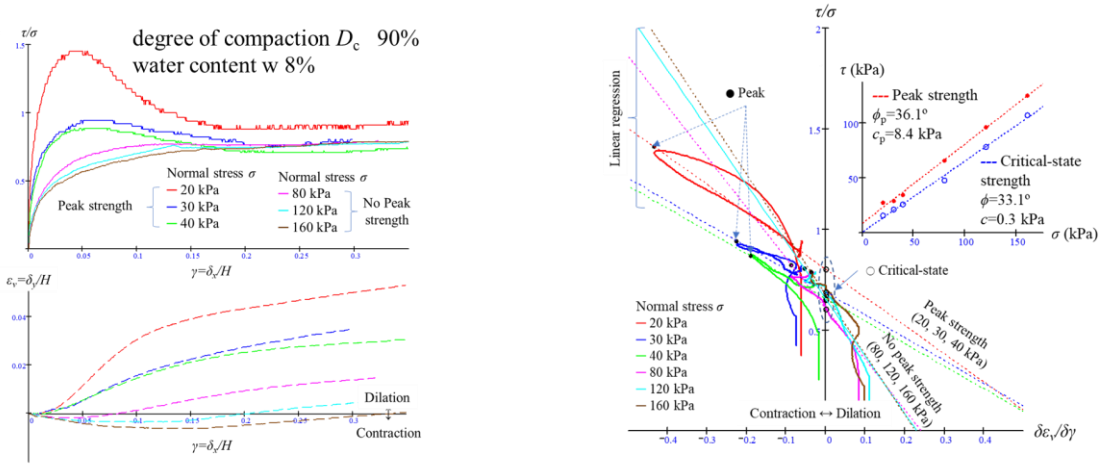

(a) (b)

Figure 2. Shear strength parameters of Hiroshima sand
(a) Direct shear test (b) Rowe's dilatancy method

The method is illustrated in Figure 2 (b). Firstly. The six pairs of curves gotten in the traditional way are transferred in terms of $\delta\varepsilon_v/\delta\gamma$ vs τ/σ. Secondly, by linear regression, six dash lines can be drawn and then the peak points at the minimum $\delta\varepsilon_v/\delta\gamma$ and the critical point at $\delta\varepsilon_v/\delta\gamma$ =0 can be located by the intersection and extrapolation using the dash lines. Once having these points, two fitting lines of σ~τ can be achieved. The result shows that both c and ϕ of the critical-state strength of sand was smaller than the peak strength and the c of the former was nearly 0.

The summary of shear strength parameters is listed as: peak strength: c=8.4 kPa, ϕ=36.1°; critical-state strength: c=0.3 kPa, ϕ=33.1°. So, the soil suction plays an insignificant role in the critical property of soil, since the cohesion shows in peak strength is actually caused by the dilatancy. Anyway, the peak strength was adopted in this work.

BENCH DESIGNED BY CULMANN'S METHOD

Culmann's method in dynamic condition

A straight failure surface is assumed by Culmman to determine the most possible sliding surface in a slope. The force diagram of a potential wedge-shaped sliding block is shown in Figure 3 with a cross section of the slope.

Where;

Table 1. Parameters used in Culmann's method

W	the weight of the soil block	k_h	the horizontal pseudo-static seismic coefficient
H	the height of the slope in prototype	α	the angle of the failure plane
β	the angle of the slope	B	the inner breadth perpendicular to the section
A_H	the area of the wedge section	ϕ	the internal friction angle of soil
c	the cohesion of soil	ρ_t	the bulk density of the soil

Along the slope direction, the driving force F_D consists of components of W and $k_h \cdot W$, and the resisting force S_α is provided by the friction force and the cohesive force on the failure surface based on the Mohr-Coulomb failure criterion.

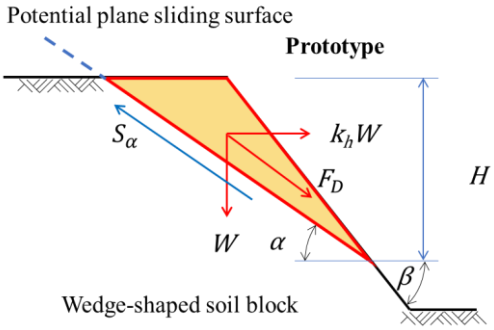

Figure 3. Force diagram of potential sliding soil block in Culmann's method

$$A_H = \frac{H^2(cot\alpha - cot\beta)}{2} \tag{1}$$

$$W = \rho_t \cdot g \cdot A_H \cdot B \tag{2}$$

$$F_D = W \cdot sin\alpha + k_h \cdot W \cdot cos\alpha \tag{3}$$

$$S_\alpha = W \cdot (cos\alpha - k_h \cdot sin\alpha) \cdot tan\phi + c \cdot B \cdot H \cdot csc\alpha \tag{4}$$

The factor of safety can be defined as follows.

$$FS = \frac{S_\alpha}{F_D} = \frac{W \cdot (cos\alpha - k_h \cdot sin\alpha) \cdot tan\phi + c \cdot B \cdot Hcsc\alpha}{W \cdot sin\alpha + k_h \cdot W \cdot cos\alpha} \tag{5}$$

In order to determine the angle of failure plane, the partial derivative of FS with respect to α is taken and the result is set to zero for minimization. By calculation, the resultant α is a simple combination of β, ϕ and k_h as follows.

$$\frac{\partial FS}{\partial \alpha} = 0 \tag{6}$$

$$\alpha = \frac{\beta + \phi - tan^{-1}k_h}{2} \tag{7}$$

Substitute Eq. 7 into Eq. 5, the FS can be achieved. If $FS > 1$, the slope stays safe theoretically.

Bench design

Then, substitute Eqs. 1 and 2 into Eq. 5,

$$FS = \frac{(cos\alpha - k_h \cdot sin\alpha) \cdot tan\phi + \dfrac{2 \cdot c \cdot csc\alpha}{\rho_t \cdot g \cdot H \cdot (cot\alpha - cot\beta)}}{sin\alpha + k_h \cdot cos\alpha} \tag{8}$$

The FS increases with decreasing H. The target of bench design is to reduce the height of the part exposed on a slope by applying the bench to protect the toe part.

As shown in Figure 4, there is a bench with a parallelogram-shaped section marked 3 leaning on the toe of the slope. The height of the bench is h and the thickness of it is b. The slope is divided into two parts, one of which marked 2 is the toe of the slope and another one marked 1, acting as thrust force on the toe from above.

O_1A_1 is the initial critical plane without the bench. If the additional resistance force for the toe part provided by the bench is enough to protect it from sliding along O_1A_1, then the potential sliding surface will change to O_2A_2 in the exposed part of the slope above the bench. In a certain k_h, O_2A_2 is parallel to O_1A_1.

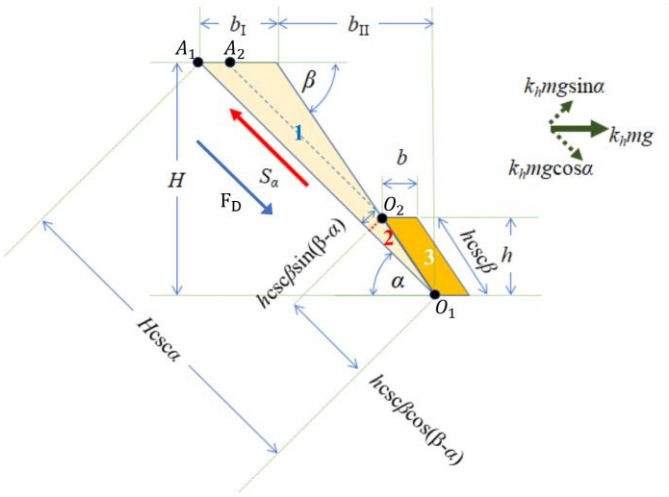

Figure 4. Seismic stability analysis with the bench

CENTRIFUGAL MODEL TESTS FOR VERIFYING THE USABILITY OF THE BENCH

Experimental setup

Two cases were conducted for the centrifugal model test. The container of both models is a soil chamber made of aluminum alloy fabricated with transparent reinforced glass for visual observation in the front, having a dimension of 63 × 20 × 20 cm (length × width × height). It is shown in Figure 5.

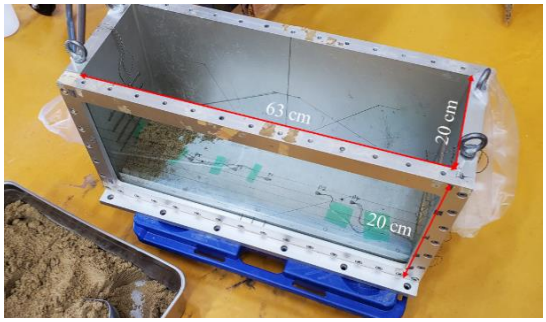

Figure 5. Soil chamber

The soil model with two slopes was built in this chamber with the soil whose properties being tested in the direct shear test above. It was constructed by compacting the soil of 3 cm for each layer, until the total height (18 cm) of the model, then, the center of this compacted soil foundation was dug transversely and cut carefully to form two slopes. The general schematic diagrams of the two models in the top and front view are displayed in Figure 6 in a model scale, including the basic sensor arrangement.

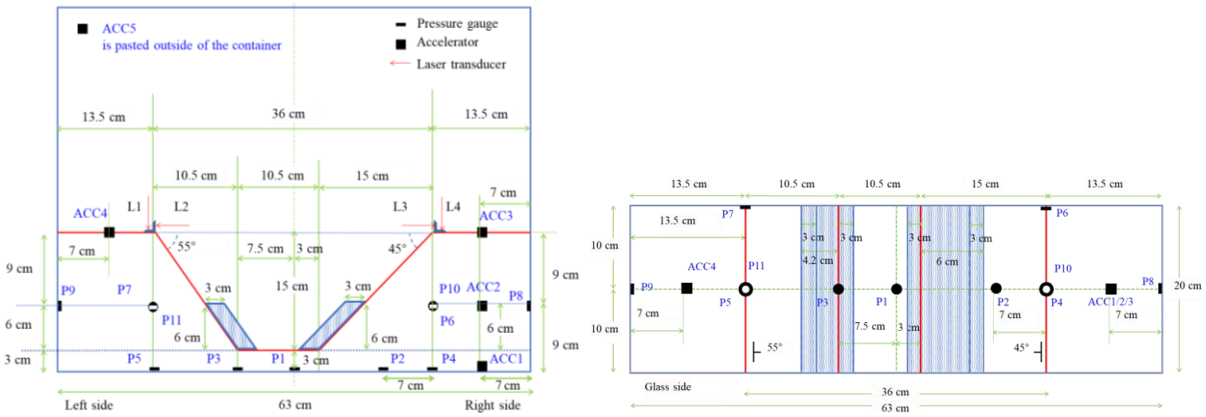

(a) (b)

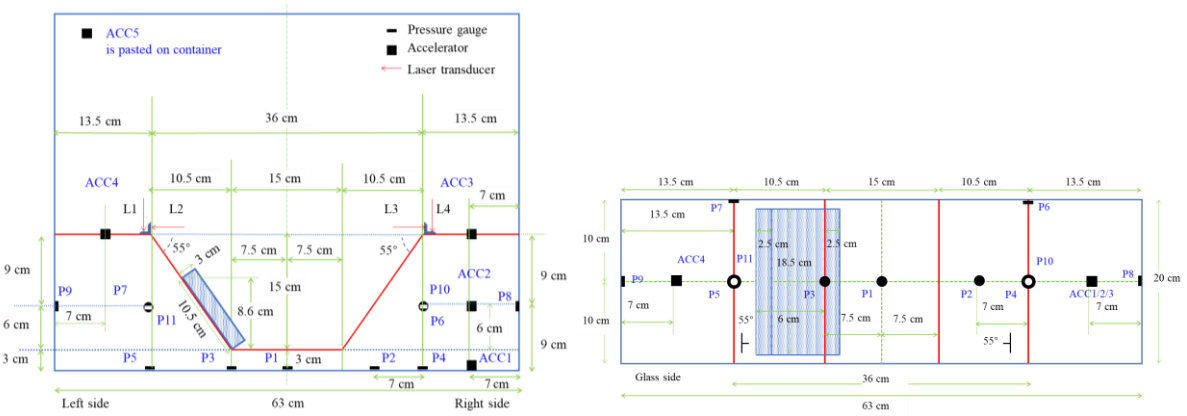

(c) (d)

Figure 6. The schematic diagram of the two cases (model scale) (a) The front view of the case 1 (b) The top view of the case 1 (c) The front view of the case 2 (d) The top view of the case 2

In case 1, the shaded part represents the bench part formed by carving, but in case 2, the bench was made by placing a block of plasticine on the slope surface. Detailed configuration is as Table 2.

Table 2. Sensor arrangement in the model

Case		Instrument No	Instrument Date	Earth pressure gauge											Accelerometer					Laser sensor				a	b	c	d	e	f
With bench	soil	1	220 414	P1	P2	P3	P4	P5	P6	P7	P8	P9	P 10	P 11	AC C1	AC C2	AC C3	AC C4	AC C5	LD 1	LD 2	LD 3	LD 4	55°	45°	2	6	3	20
	plast icine	2	220 426																					55°	55°	1	8.6	3	18.5

a=the angle of left slope, b=the angle of right slope, c=the number of benches, d=the height of benches (cm), e=the thickness of benches (cm), f=the width of benches (cm).

Both cases were conducted in the geotechnical centrifuge facilities at DPRI. The centrifuge has an effective radius of 2.5 m, the maximum centrifugal acceleration is 200 g.

Experimental procedure

After preparing the slope model, it was accelerated to 50 G gradually, and kept in that state for a certain time in the geotechnical centrifuge. Then, the seismic excitation using a shaking table was started. A series of ramped sine waves were used in sequence based on the datum wave (Figure 7), whose amplifications were gradually magnified and converted to k_h (prototype scale) can as shown in Table 3.

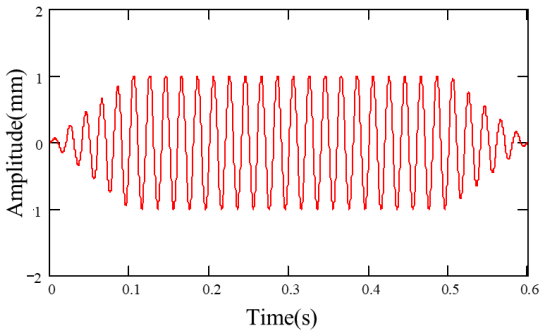

Figure 7. Datum sine wave (model scale)

Table 3. Five different seismic waves

Waves	Magification	Shaking (case 1)	k_h (case 1)	Shaking (case 2)	k_h (case 2)
Wave A	1.9	323	0.33	372	0.38
Wave B	2.5	441	0.45	519	0.53
Wave C	2.7	500	0.51	558	0.57
Wave D	2.7	500	0.51	558	0.57
Wave E	3.0	578	0.59	627	0.64

Experiment results

Pictures below show the states of slope model before and after every time of shaking in case 1. The seismic waves recorded by ACC1 are also attached in the Figure 8. ACC1 is the accelerometer inserted on the bottom of the soil, and the value of it is used to represent the state of the soil model during shaking.

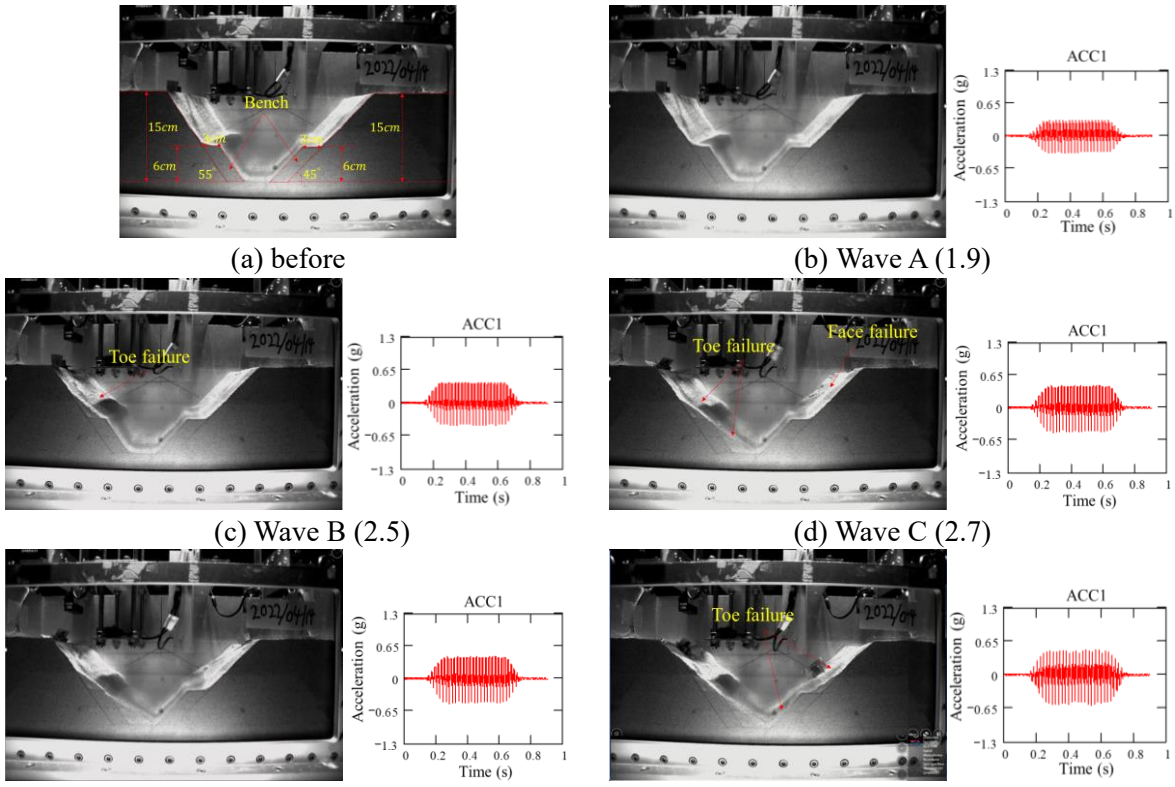

(a) before (b) Wave A (1.9)

(c) Wave B (2.5) (d) Wave C (2.7)

(e) Wave D (2.7) (f) Wave E (3.0)

Figure 8. the resultant state of each seismic wave

From the pictures above, it is obvious that both slopes resisted the first wave A ($k_h = 0.33$). Then a toe failure happened on the left-hand side in wave B ($k_h = 0.45$), and this failure was located above the bench part. When applying wave C ($k_h = 0.51$), the failure of the left slope deteriorated, the bench also failed at this time, in the meantime, the right slope had a face failure at the center of the slope above the bench. Next, the seismic wave C was repeated once as wave D ($k_h = 0.51$), the state of two slopes didn't change much before and after this wave. Finally, wave E ($k_h = 0.59$) was applied, the failure on the left slope developed a step further and the face failure on the right slope expanded to a toe one, the bench on the right-hand side also failed.

With regard to failure part, Figure 8 shows that bench could change the position where sliding tended to happen. If the toe of a slope was protected well by an appropriate bench, only the part above the bench would have had shallow sliding during earthquake.

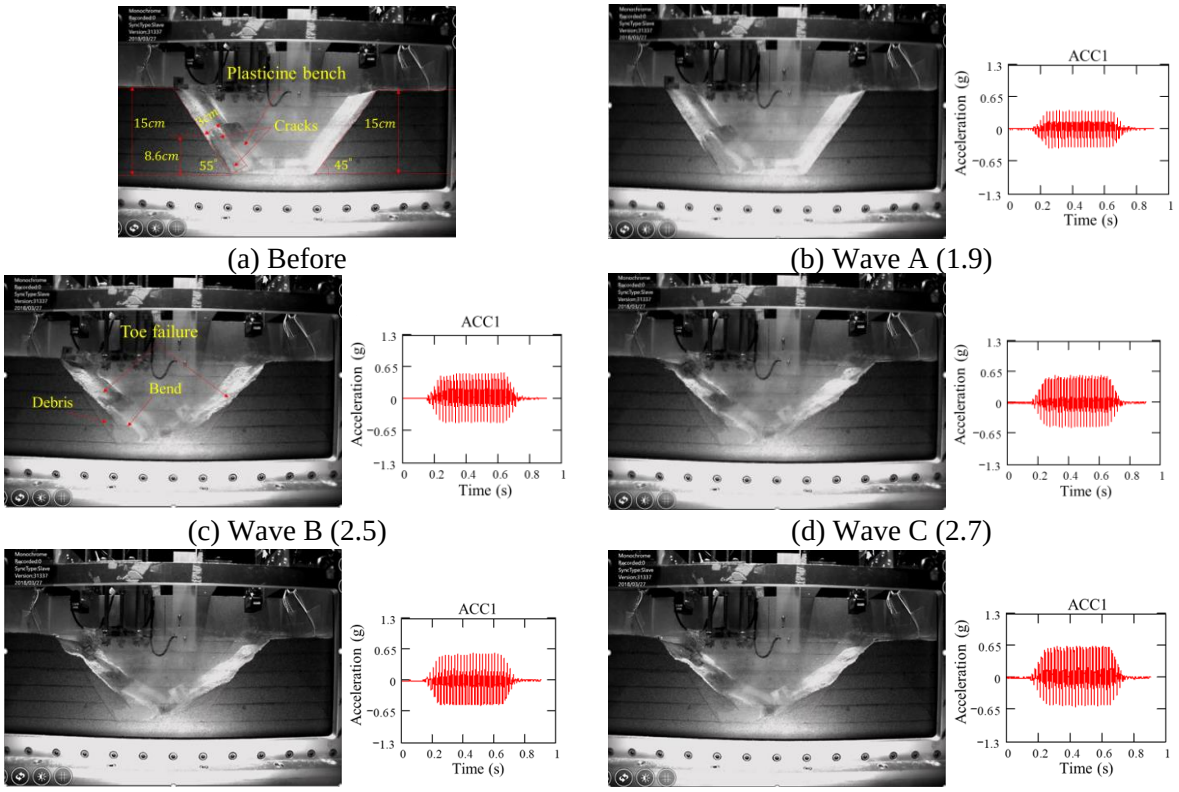

(a) Before (b) Wave A (1.9)

(c) Wave B (2.5) (d) Wave C (2.7)

(e) Wave D (2.7) (f) Wave E (3.0)

Figure 9. the resultant state of each seismic wave

In order to find a suitable material for bench, not only soil, a block of plasticine was chosen to replace the soil bench in case 2. It leant on the slope as Figure 9 (a). There were two cracks initiating in the plasticine because of the deformation caused by acceleration of 50g before shaking. Then, both slops kept stable during the wave A ($k_h = 0.38$) although the plasticine further deformed. However, in the wave B ($k_h = 0.53$), they failed together. The plasticine on the left slope bended seriously by the thrust force of soil debris falling behind it, so it seemed to malfunction this time. The following several waves aggravated the failure on both sides.

COMPARISON BETWEEN EXPERIMENTAL RESULTS AND PREDICTION

According to Eq. 8, the predicted k_h (prototype scale) when the toe failure would happen in a slope can be calculated. The value of predicted k_h with and without bench are shown in Figure 10, also the value when the shallow sliding really happened in experiments with the form of face or toe.

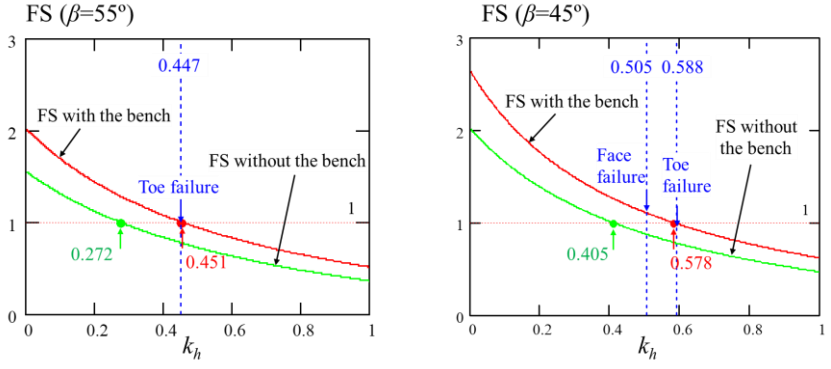

(a) (b)

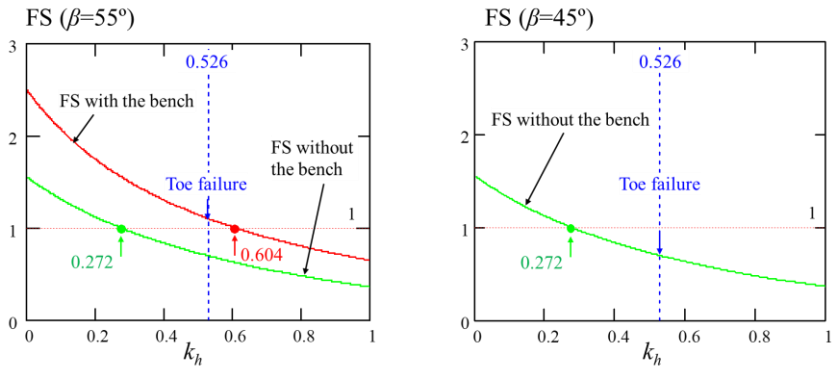

(c) (d)

Figure 10. Comparison between prediction and experimental results (a) left slope of case 1 (b) right slope of case 1 (c) left slope of case 2 (d) right slope of case 2

In Fig. 10, the lower curve in each figure represents the safety factor of the whole slope with respect to the increase of k_h without bench while the upper curve represents that of the slope part whose toe is located above the stable bench. There is only one curve in Fig. 10 (d) because there is no bench in the right slope. The vertical dash lines remark the observed values at failure. For case 1, if there is no bench, the toe failure for the left slope would appear when k_h = 0.272. Due to the existence of bench, the slope failed at $k_h = 0.447$ in experiment which is consistent with $k_h = 0.451$ in prediction. For the right slope, the predicted k_h without and with bench are 0.405 and 0.578, respectively, despite a face failure happened before the toe one. Therefore, the slope reinforced by a bench at the toe can enhance the slope's seismic stability. The theory over-predicted k_h in case 2 because the plasticine bench excessively deformed with cracks by the second wave owing to its relatively low stiffness. However, the right slope without bench failed at a k_h higher than its prediction in the first wave; hence, the theory stands on the safe side and the reproduced test is necessary to make additional comparison.

CONCLUSIONS

Resorting to dynamic Culmann's method, bench can be designed to protect the soil slope from shallow sliding in earthquake. Dynamic centrifugal tests were conducted with a variety of benches to study the reliability of this retrofit method. This paper presents how the bench functions and records the reaction of slope against earthquake with and without the bench. The conclusions are 1) Culmann's method can predict the toe failure of a slope well and always be the lower boundary, so it is a safe way and can be beneficial for preliminary slope design, but it isn't suitable for predicting the face failure, 2) A robust bench can protect the toe of a slope, shrinking the potential failure height and making a slope stronger and 3) Due to the thrust force behind the bench, enough strength of it is needed, otherwise, it will slide or bend, losing effectiveness. Thus, the shape of the bench needs to be studied in the future.

AKNOWLEDGEMENT

This work was supported by W-NEXCO and JSPS KAKENHI Grant Number 20H02242. Sincere thanks are also given to A Siga for his valuable assistance with the laboratory testing.

REFERENCES

Culmann, K. (1866). "Die graphische Statik", Zürich : Meyer & Zeller.

Alejano, L. R., Pons, B., Bastante, F. G., Alonso, E., & Stockhausen, H. W. (2007). Slope geometry design as a means for controlling rockfalls in quarries. International Journal of Rock Mechanics and Mining Sciences, 44(6), 903-921.

Farshidfar, N., Keshavarz, A., & Mirhosseini, S. M. (2020). Yield acceleration of reinforced soil slopes using the modified pseudo-dynamic method. SN Applied Sciences, 2(5), 1-14.

Ling, H. I., Y. Mohri, and T. Kawabata. "Seismic analysis of sliding wedge: extended Francais–Culmann's analysis." Soil Dynamics and Earthquake Engineering 18.5 (1999): 387-393.

RESPONSE OF MACHINE FOUNDATIONS ON REINFORCED SOIL

Neeraj Kumar Das[1] and Prishati Raychowdhury[2]

1. Research Scholar, Dept of Civil Engg, Indian Institute of Technology, Kanpur (IITK)
2. Associate Professor, Dept of Civil Engg, Indian Institute of Technology, Kanpur (IITK)

Email: nrjkmr@iitk.ac.in, nrjkmr.das@gmail.com,prishati@iitk.ac.in

ABSTRACT

Foundations subjected to vibrations or periodic loadings in the case of turbines, heavy machinery may cause crack and excessive vibration in the nearby structures. Using geosynthetics in the subsoil is well established as it may increase the soil's strength and reduce the foundations vibration. The present study focuses on using reinforced soil to mitigate the vibration caused by the dynamic loading on the foundation. A series of block vibration tests are conducted on the full-scale footing on a reinforced soil bed using the mechanical oscillator in vertical and horizontal directions. The geogrid reinforced bed is of the size 2.2 m x 2.2 m x 1 m, and the footing is of size 1 m x 1 m x 0.3 m. The tests are conducted on the unreinforced bed and a single layer of geogrid at 0.2 m depth. The responses are recorded with the help of accelerometer sensors placed on the footing. The Butterworth filter is applied to the raw data. The foundation soil system's resonant frequency, amplitude, and damping are evaluated. The effect of geogrid reinforcement in mitigating the vibration, a significant reduction of up to 84% in the vibration-based amplitude, is observed.
Keywords: Machine foundation, Mechanical oscillator, Dynamic properties, Resonant frequency, Reinforced soil

INTRODUCTION

In case of foundation under heavy machinery like turbines,compressors etc. may be subjected to the harmonic or periodic loading. It may cause excessive vibration and crack in the nearby structures. Therefore, the design of foundation is such that it can withstand vibration and damage if it exceeded the limiting state. It is also noted that the soil foundation interaction is govern by the dynamic properties of the soil bed as it interacts and dissipiates energy due to the wave propagation in the underlying soil bed. To understand the soil foundation interaction, the large scale field studies are best suitable compared to the laboratory experiments as there is boundary effects due to the presence of the rigid or flexible boundary interfaces.

Reissner, 1936 calculated the theoretical expression for the periodic displacement solution at the center of circular loaded area. Lysmer, 1965 has presented the stiffness and damping constanats which is frequency independent refered to as Lysmer's analog. Gazetas, 1991 presented dimension formulaes and charts for the value of dynamic stiffness and damping for any arbitrary shaped foundations subjected to harmonic loading considering both surface and embeded foundations. The block vibration test is a routine test for the performance evaluation of machine footing and calculation of its dynamic charcateristics. The block vibration tests considering different modes on the model concrete footing subjected to harmonic loading, Bhoumik, 1989. To understand the effect of presence of rigid layer and layering on the sand on the dynamic properties of the footing, Baidya *et al*., 2004.

Kumar and Reddy, 2006 has conducted a series of block vibration tests on the foundation with the spring-mounted base resulting in the reduction of amplitude and resonant frequency of the foundation. Baidya and Rathi, 2004 has studied the effect of layering of soil underlain by a rigid layer through block vibration test in the vertical direction. Swain and Ghosh, 2016 has conducted a large number of experiments on a pair of footing (active footing that is being excited and its consequences on passive footing) at IIT Kanpur campus soil to understand the dynamic interference of footing. The study helps

in the design of the machine foundation in case of a foundation in groups. The transmission ratio is plotted with frequency to predict the effect of active footing on the passive footing. Das and Raychowdhury, 2018 has conducted the block vibration test on the IIT Kanpur campus soil for the determination of displacement amplitude, resonant frequency, and damping and compared with the values earlier determined by (Bhoumik, 1989; Swain and Ghosh, 2016). The proper understanding of the dynamic parameters primarily at resonance condition and nature of the foundation bed is indeed helpful. There is a gradual increase in the amplitude with frequency and at resonance, there is sudden shoot in the amplitude values because of matching between the frequency given to the mechanical oscillator with the natural frequency of the soil-foundation system.

Geosynthetics products are widely used in erosion, ground improvement, retaining wall, slope stability and many other large construction projects. There is plenty of literature available on the use of biaxial geogrid (Geosynthetics product) in the case of static loading (Binquet and Lee, 1975;Yoo, 2001). Binquet and Lee, 1967 has conducted tests on the performance of geogrid in the slope stability case. Yoo, 2001 has performed tests on small scale model footing and validated with the finite element analysis for finding the optimum depth for the full utilization of reinforcement strength. Abd and Utili, 2017 studied the use of geosynthetics in case of slope stability problems in cohesive backfills. However, there are limited studies on the performance of geogrid under the application of dynamic loading for the case of the machine foundation bed. Boominathan, 1991 has conducted block vibration test on reinforced soil bed with geotextile and geogrid under vertical vibration. There is a reduction in the value of displacement amplitude, an increase in shear modulus and a slight increase in the frequency at resonance condition. Clement, 2015 has conducted laboratory test namely free vibration and forced vibration on geogrid reinforced dense sand bed. Hegde and Sitharam, 2016 studied the geocell combined with geogrid reinforced soil by conducting a series of cyclic plate load tests. Significant increase in bearing capacity, reduction in settlement and increase in stiffness of the soil bed. Venkateswarlu *et al.*, 2018 studied the use of geocell and geogrid reinforced soil bed under machine foundation and reported improvement in reducing the amplitude.

In the present study, an attempt is made to understand the performance evaluation of geogrid reinforced soil bed under the machine foundation. A series of block vibration tests are conducted where the bi-axial geogrid is laid at a different depth to find the optimum location for the significant reduction of the peak displacement amplitude.

EXPERIMENTAL PROGRAM

The block vibration test setup was based on IS:456, 2000 code provision guidelines and the experimental program used by (Richart *et al*., 1970; Lopes and Reibeiro, 1975; Bhoumik, 1989; Rao, 1998; Baidya and Rathi, 2004; Kumar and Reddy, 2006; Swain and Ghosh, 2016; Das *et al.*, 2018; Das *et al.*, 2020; Das and Raychowdhury, 2020). The block vibration test setup is consisting of an eccentric mass shaker equipment (MX 100A), Micron Industries Limited. The eccentric mass shaker is the mechanical oscillator that is capable of producing 10000 kgf. The principle mechanism of the eccentric mass shaker to produce a sinusoidal harmonic variation is due to the counter-clockwise rotating shafts which can able to produce periodic vertical force. The horizontal mode is given by changing the orientation of the oscillator. The eccentricity angle inside the mechanical oscillator can be set up to from zero to 180 degrees. The shaft of the oscillator is driven by the help of 5HP DC motor and it can run up to 3000 rpm.

The base plate (MS plate) is connected to the foundation through the help of guide bars. Then the square-shaped bottom plate is connected to the four guide bars. After the calibration, the mechanical oscillator is placed on the bottom plate of the oscillator so that the whole system vibrates as a single entity. The layout of experimental test setup in layout (front view) and the plan is shown in Fig. 1a) and b).

Preparation of reinforced foundation bed

The site is first cleaned and then excavation is done to remove the topsoil up to a depth of 1m so that the pit size being 2.2m x 2.2m x 1.0m as shown in Fig.2a). The soil specimen from various depth is checked for the in-situ density through the core cutter sample. The optimum amount of water content and density were determined from the standard Procter test. Therefore, pit length is taken as 2.2B where

B is the width of the foundation. The soil was air-dried for 48 hours. The water is added as per the optimum moisture content. The pit was prepared with 95 % of the in-situ density as shown in Fig. 2b).

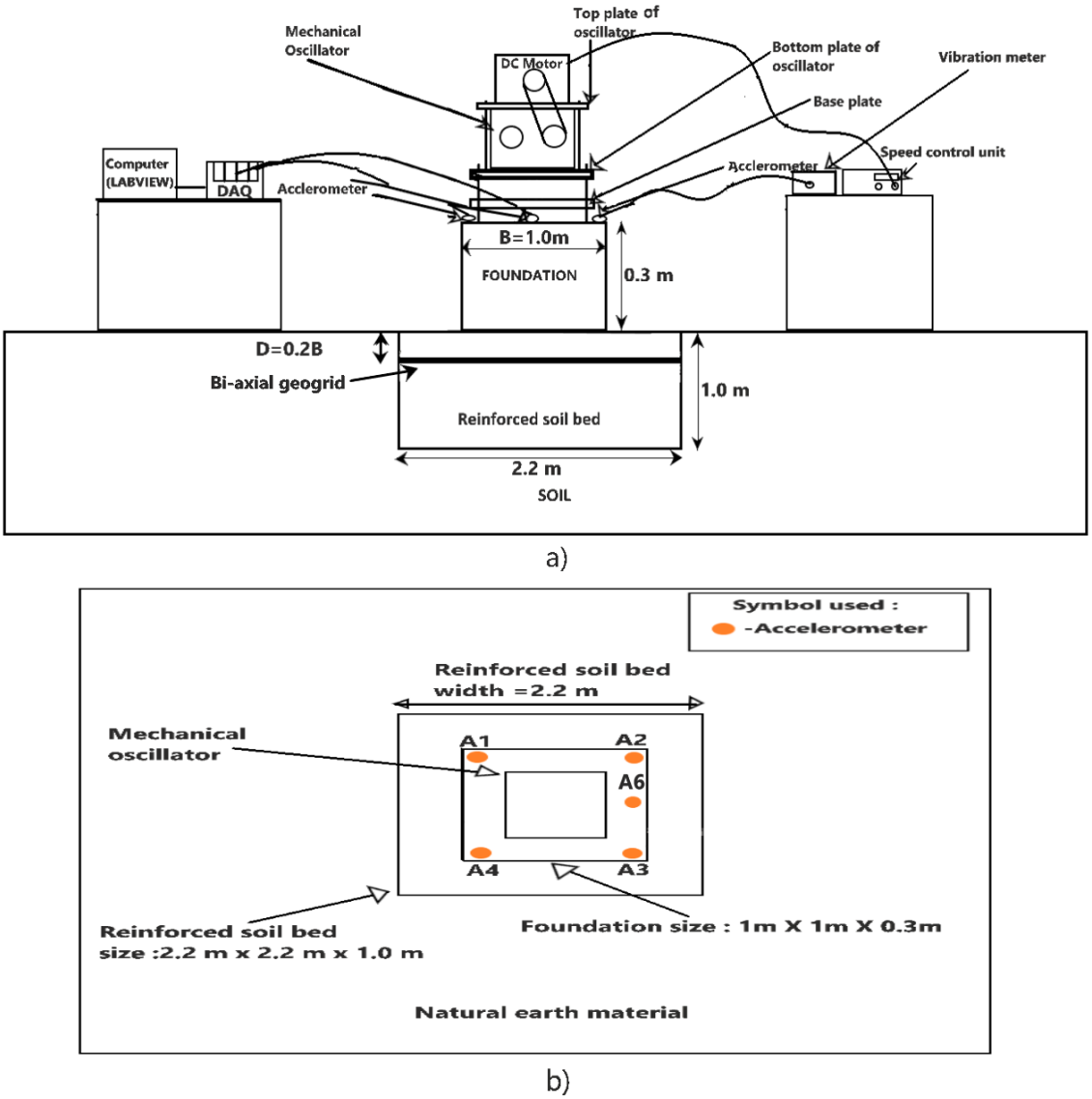

Figure 1. Layout of block vibration test setup a) front view (elevation); b) plan of the experimental program.

The manual mode of compaction was considered with compaction effort equal to the standard Procter test. A steel rammer of weight 12.17 kg is utilized for that purpose. The pit was prepared in ten layers each of 10 cm depth. Then, bi-axial geogrid as a reinforcement being introduced to the well-compacted soil strata at the required depth as shown in the Fig. 2c). The bi-axial geogrid used is made from fine grades of polypropylene with carbon black content. The bi-axial geogrid has high tensile strength and stiffness. The properties of the biaxial geogrid are given in Table 1. The depth of the single layer (D) of the bi-axial geogrid reinforcement chosen as 0.2B where B is the width of the footing. Finally, the foundation bed is prepared for the experimentation as shown in the Fig. 2d).

After preparing the cast-in-situ foundation and proper setup of the mechanical oscillator the placement of sensors like accelerometer was done. Overall five accelerometers were connected to the foundation. The four accelerometer is placed on the outer four edges (numbered A1, A2, A3, and A4 as shown in Fig. 1b) in the clockwise direction from Southside direction).

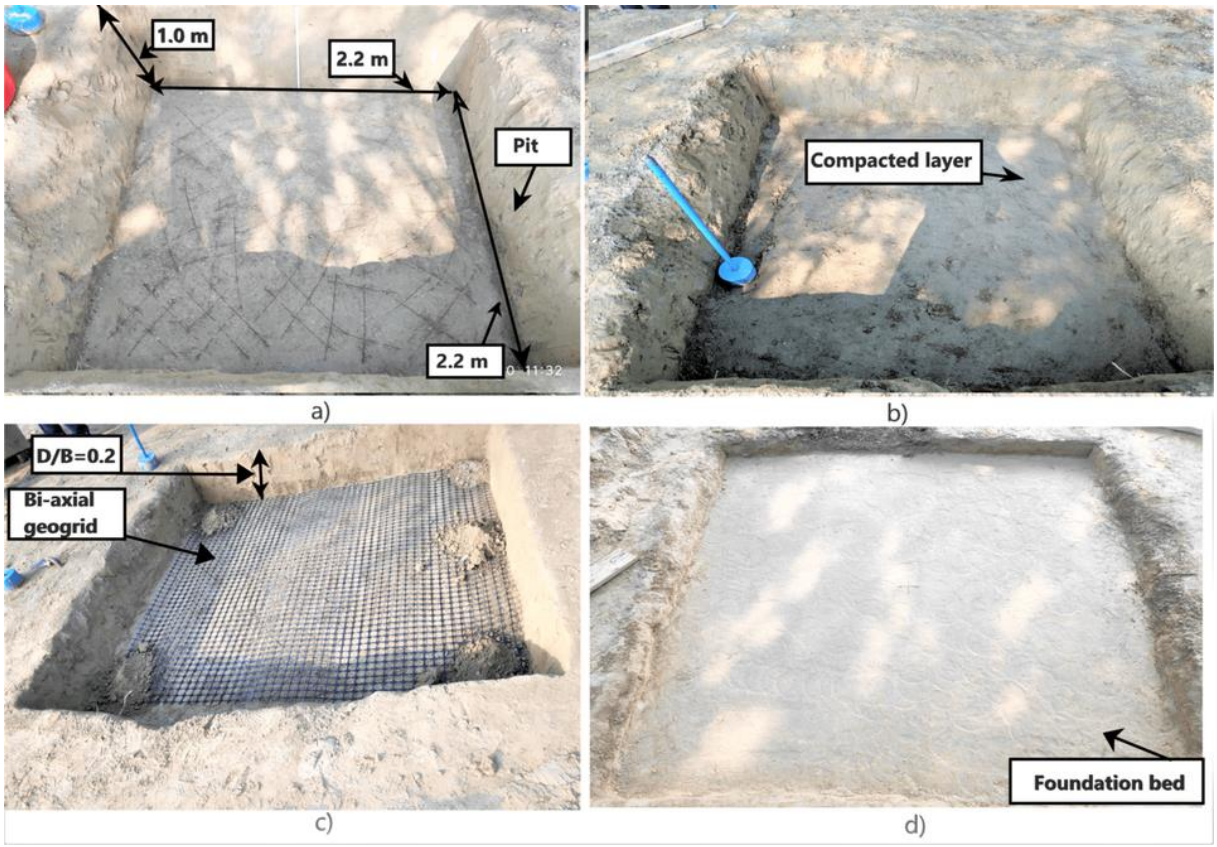

Figure 2. The preparation of the foundation beds a) excavating a pit of size 2.2m x 2.2m x 1.0m b) preparing the compacted layers to Procter density c) Bi-axial geogrid reinforcement at D/B=0.2 d) pit is ready for experimentation.

Table 1 – Properties of the reinforcement material

Property	**Quantity**
Bi-axial Geogrid	
Pitch size (MD x XMD) (mm)	30 x 30
Shape of the aperature	Square
Material	Polyproplene

The accelerometer sensor is connected to the 32-bit data acquisition system (DAQ). The DAQ is further connected to a computer having LABVIEW installed in it for recording the raw data. The MEMS accelerometer (numbered A6 as shown in Fig. 1b) is placed on the centerline of the foundation. This MEMS based sensor is further connected to the vibration meter which gives a direct reading of acceleration, velocity, and displacement. The placement of accelerometer sensors along with the block vibration test setup is as shown in Fig. 1b).

The soil strata at the field site are clayey silt. The water table is 6.5 m below the ground table so that it is well below the zone of influence ie. B depth below the base of the footing where B is the width of the foundation. The specific gravity of the soil is 2.67. The dry density of the soil is 16.42 kN/m^3. The liquid limit is found to be 26.70 %. The plasticity is found in the range of low to medium.

Experimental procedure

The block vibration test for the vertical vibration case is conducted on an isolated square foundation of size 1m x 1m x 0.3m for different values of eccentric force and with a range of forcing frequencies. The power is fed into AC to DC converter to run the 5HP DC motor which causes the two shafts of the eccentric mass shaker to run in counter-clockwise direction thereby canceling the horizontal forces and addition of forces in the vertical direction. For the horizontal loading, the orientation of the oscillator is changed. The desired forcing frequency is set by setting the revolution per minute (rpm) by the speed control unit. The eccentricity angle range is from 0 to 180 degrees. The speed control unit range is from 300 rpm to 3000 rpm thereby the forcing frequency range is from 5Hz to 50 Hz. The capacity of the mechanical oscillator is 10000 kgf. The eccentric force depends upon the angle of eccentricity between the unbalanced mass inside the mechanical oscillator and the speed of rotation. The eccentric force generated is given by following Eq. 1 as follows

$$F = m_e \times e \times \omega^2 = 0.85624 \times \sin(\theta/2) \times \omega^2 \quad (1)$$

where F is the force generated in Newton, m_e is the unbalanced mass rotating with the radius of e inside the mechanical oscillator in meters, and θ is the angle between the eccentric masses.

First the calibration of the accelerometer sensor was performed so to record the response (g values) with accelerometer sensors with the help of LABVIEW software using a data acquisition system connected with the accelerometer sensor. The micron MEMS accelerometer sensor (A6) connected to the vibration meter which gives the direct value of acceleration, velocity and displacement values. After recording the data in LABVIEW software from different accelerometers (A1, A2, A3, and A4), the recorded data are multiplied with 9.81 so to convert it in m/s^2. Then the raw data is processed with MATLAB. The samples are recorded at 2000 samples per second so that the Nyquist frequency of the system is 1000 Hz. The baseline correction is made to the acceleration values. The Butterworth filter of the 4^{th} order is applied in the selected frequency bandwidth to capture the fundamental mode of the present system. The velocity is calculated by integrating the acceleration values and displacement is calculated by integrating the velocity values. The peak displacement value is calculated by taking the average of the peak displacement as obtained from the sensor placed on the edges.

The peak displacement response is plotted with frequency as shown in Fig. 3a) and b) for each of the two eccentric angles of 13 and 19 degrees for the case of vertical loading. A total of 6 tests are conducted for the unreinforced, reinforcement foundation bed at D/B=0.2 particularly at two eccentricity angle settings including two trial tests.

Similarly for the horizontal loading, the peak displacement response is shown in Fig. 4a) and b) for each of the two eccentric angles of 5 and 9 degrees. A total of 6 tests are conducted for the unreinforced, reinforcement foundation bed at D/B=0.2 particularly at two eccentricity angle settings including two trial tests.

RESULT AND DISCUSSION

The block vibration test is conducted on the model foundation of size 1 m x 1 m x 0.3 m resting on field site near field laboratory, IIT Kanpur. After attaining the steady-state, the reading from the accelerometer sensors is recorded. The displacement values are calculated from numerically double integration of the acceleration values for each forcing frequency. Finally, the response curve is plotted with the function of frequency from each of the peak displacement amplitude at different frequencies.

First discussing the unreinforced foundation bed case as per Fig. 3a), as the eccentricity angle is 13 degrees, the peak displacement amplitude at resonance condition is ie. 174.08 μm (ie. 0.174mm) as shown in Table 2 where μ refers to the usual mathematical power of 10^{-6}. As the eccentric angle is

increased to 19 degrees thus resulting in larger dynamic loading, the peak displacement increased to 190.01 µm thus creating larger ground amplitude as shown in Fig. 3a) and in Table 2.

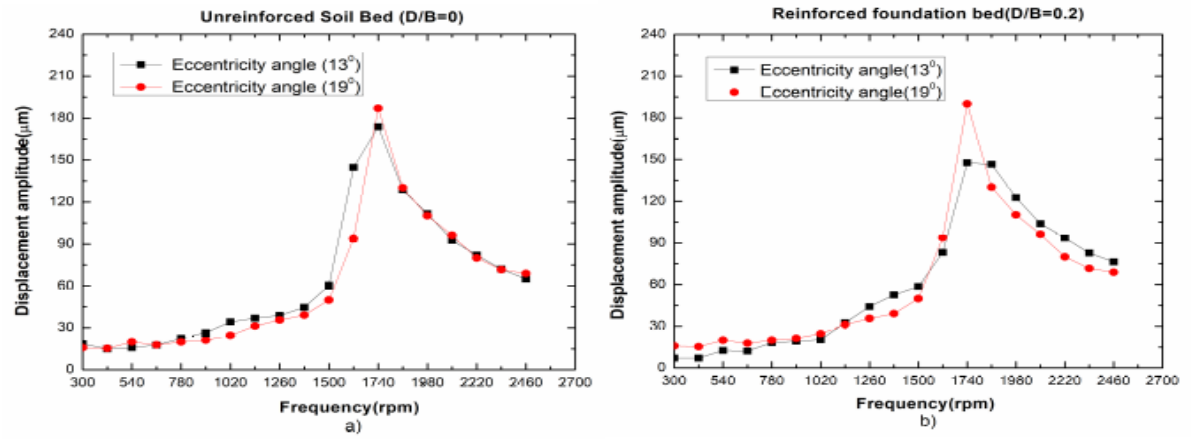

Figure 3. Displacement amplitude variation with frequency at different eccentric force settings for vertical vibration- a) Unreinforced foundation bed; b) Reinforced foundation bed at D/B=0.2

The inclusion of bi-axial geogrid to the foundation bed at D/B=0.2, there is a decrease in the displacement amplitude as shown in Fig. 3b) and Table 2 in case of an eccentricity angle of 13 degrees. The peak displacement amplitude at resonance condition under vertical loading is reduced to 143.94µm (ie. 0.143 mm). The reason behind it is the improvement in the resistance of soil of the soil as offered by the tensile strength of biaxial geogrid by providing the frictional mobilisation inside the soil mass. However, the natural frequency is kept almost the same with 0.2m geogrid inclusion. The inclusion of a single layer of bi-axial geogrid did reduce the vibration induced displacement amplitude. However there is not much reduction in amplitude value is seen at 19 degrees which may be due to insufficient shear mobilisation.

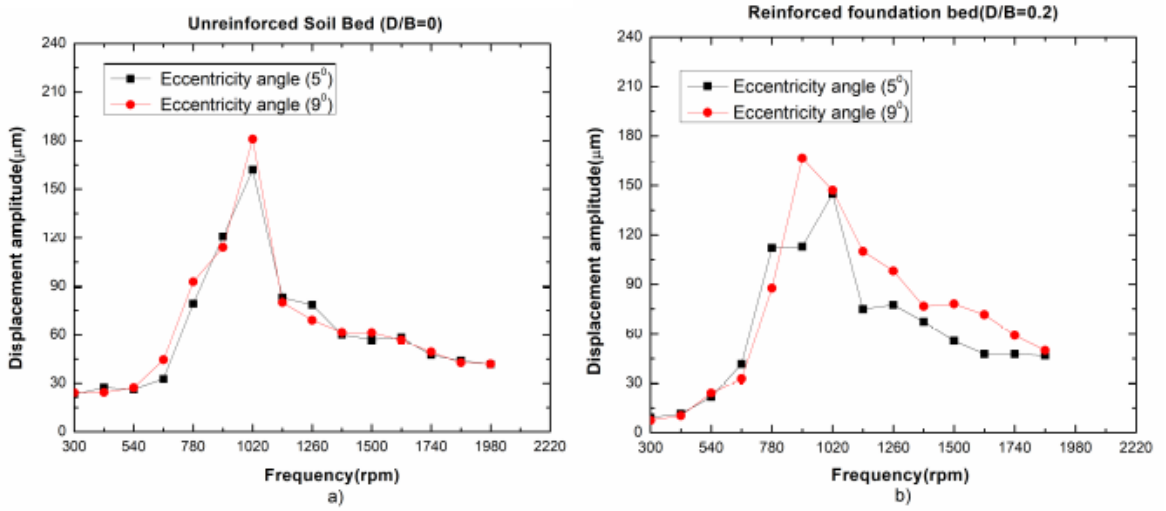

Figure 4. Displacement amplitude variation with frequency at different eccentric force for horizontal vibration a) Unreinforced foundation bed; b) Reinforced foundation bed at D/B=0.2

It is clear from the results as seen from Fig. 4a) and b) and Table 3, that the inclusion of the single layer of bi-axial geogrid at different depth can reduce the ground vibration to a significant amount thereby altering the soil foundation interaction in the horizontal direction. As evident at eccentricity angle of 5 degrees, the amplitude is 162.97 µm in unreinforced soil bed which is reduced to 143.94 µm under the effect of reinforced soil in mitigating vibration. However, at 0.2 m depth not much reduction is noticed at eccentricity angle of 9 degrees as the shear mobilisation may occur at greater depth than the 0.2 m depth inside the reinforced soil bed.

A factor δ is defined to depict the effectiveness of the biaxial geogrid reinforcement in reducing the vibration induced amplitude thereby changing the interaction of the soil foundation system. The improvement factor δ is defined in Eq. 1 as the ratio between the peak displacement amplitude at resonance condition in case of reinforced foundation bed to the unreinforced foundation bed case.

$$\delta=(Disp)_{Rf}/(Disp)_{Unrf} \quad (2)$$

Table 2. Test results for the present study for vertical vibration case on model machine foundation under unreinforced and reinforced foundation bed with a single layer of bi-axial geogrid inclusion

Eccentric settings	Unreinforced foundation bed		Reinforced foundation bed (D/B=0.2)	
Angle	Resonance displacement amplitude	δ	Resonance displacement amplitude	δ
(Degree)	(μm)	-	(μm)	-
13	174.68	1	147.54	0.84
19	190.01	1	187.39	0.98

Table 3. Test results for the present study for horizontal vibration case on model machine foundation under unreinforced and reinforced foundation bed with a single layer of bi-axial geogrid inclusion

Eccentric settings	Unreinforced foundation bed		Reinforced foundation bed (D/B=0.2)	
Angle	Resonance displacement amplitude	δ	Resonance displacement amplitude	δ
(Degree)	(μm)	-	(μm)	-
5	162.97	1	143.94	0.88
9	180.92	1	163.54	0.90

The bi-axial geogrid has greater tensile strength and stiffness and causing greater friction resistance between geogrid and soil thereby improving the lateral resistance of the reinforced foundation bed. The present study confirming the utility of bi-axial geogrid in improving and controlling the vibration-based deformation.

CONCLUSIONS

Due to an increase in the construction activity, near to residential buildings,due to changing landscape the use of multi-story buildings and installation of heavy machines which may create strong vibration during its operation at high frequency. This experimental study is an attempt to understand the vibration problem of machine foundation considering vertical and horizontal vibration and that should be duly acknowledged in the design for machine foundation. Large scale field model test was conducted on a machine foundation over reinforced soil bed with the inclusion of the biaxial geogrid at different depth. The problem of soil-foundation interaction is visible from the test results as the value of displacement amplitude of the soil gets significantly reduced with geogrid reinforced foundation bed under the variation of dynamic loading. The use of bi-axial geogrid in controlling the vibration-induced vertical displacement of the reinforced foundation bed is clearly evident from the present study. Further research, is needed in this direction, to fully understand the soil foundation interaction under a reinforced foundation bed.

REFERENCES

Abd, A.H., Utili, S., (2017). "Design of geosynthetic-reinforced slopes in cohesive backfills", *Geotextile and Geomembranes*, **45** (6), 627–641.

Baidya, D.K., Rathi, A. (2004). "Dynamic response of footings resting on a sand layer of finite thicknes", *Journal of Geotechnical and Geoenvironmental Engineering*, ASCE, **130**(6): 651–655.

Binquet, J., Lee, K.L., (1975). "Bearing capacity tests on reinforced earth slabs". *Journal of Geotechnical and Geoenvironmental Engineering*, **101**, ASCE 11792 Proceeding.

Bhoumik, K. (1989). "Coupled vibration of footings on elastic half-space". M.Tech. thesis, IIT-Kanpur.

Boominathan, S., Senathipathi, K., Jayaprakasam, V., (1991). "Field studies on dynamic properties of reinforced earth". *Soil Dynamics and Earthquake. Engineering*. **10** (8), 402–406.

Clement, S., (2015), "Experimental Studies on Dynamic Response of a Block Foundation on Sand Reinforced with Geogrid", *Geosynthetics 2015*, Portland, Oregon, 479–488.

Das, N.K., Raychowdhury, P. and Chaudhuri, S.R. (2018). "A study on dynamic characteristics of shallow foundation from block vibration test",*16th Symposium on Earthquake Engineering*, IIT Roorkee, 316,1- 9.

Das, N.K., Raychowdhury, P. and Chaudhuri, S.R. (2020), "Experimental and Numerical Study of Shallow Foundation Subjected to Vertical Dynamic Load", *7th International Conference on Recent Advances in Geotechnical Earthquake Engineering and Soil Dynamics*, Soil Dynamics, Springer . DOI:10.1007/978-981-33-4001-5_32

Das N.K., Raychowdhury P. (2020), "Behavior of machine foundation on reinforced soil. *17th World conference on Earthquake Engineering* , Sept. 27-Oct.2, 2021, Sendai, Japan,4c-0042,1-10.

Gazetas, G. (1991). "Formulas and charts for impedance of surface and embedded foundations", *Journal of Geotechnical Engineering*. ASCE, **117**(9), 1363-1381.

Hegde, A., Sitharam, T.G., (2016), " Behaviour of geocell reinforced soft clay bed subjected to incremental cyclic loading", *Geomechanics and Engineering*,**10** (4), 405–422.

IS (1992). "Method of test for determination of in-situ dynamic properties of soils", IS:5249, *Indian standard Institution*, Manak Bhavan, New Delhi, India.

IS (2000). "Plain and Reinforced Concrete-Code of Practice", IS :456, *Indian Standards Institution*, Manak Bhavan, New Delhi.

Rao, K.N.S.V. 1998. "*Vibration analysis and foundation dynamics*". Wheeler, New Delhi.

Kumar, J., Reddy, C.O. (2006). "Dynamic response of footing and machine with spring mounting base", *Geotechnical and Geological Engineering*, **24**: 15–27.

Lopes, F.R., Ribeiro, A.T.F., (1985). "Vibration tests for the analysis of machine foundations", *11th International Conference on Soil Mechanics and Foundation Engineering*, San Francisco, **34**(2), 1-4.

Lysmer, J. (1965). "Vertical Motion of Rigid Footings", *Report to WES Contract Report No.3-115*, 340, Dept. of Civil Engineering, University of Michigan.

Mandal, A., Baidya, D.K., and Roy, D. (2012). "Dynamic response of the foundations resting on a two-layered soil underlain by a rigid layer", *Geotechnical and Geological Engineering*, **30**: 775–786.

Reissner E. (1936). "Stationäre, axialsymmetrische Schwingungen eines homogenenelastischen Halbraumes", angeregt durch eine schwingende Masse, *Ingenieur Archiv*, Gesellschaft f¨ur Angewandte Mathematik und Mechanik, **7**(6), 381-396.

Richart, F.E., Hall, J.R., and Woods, R.D. 1970. "*Vibrations of soils and foundations*". Prentice-Hall, Englewood Cliffs, N.J

Yoo, C. (2001). "Laboratory investigation of bearing capacity behavior of strip footing on geogrid-reinforced sand slope". *Geotextile and Geomembranes*, **19**, 279–298.

Venkateswarlu, H., Ujjawal, K.N., Hegde, A. (2018). "Laboratory and numerical investigation of machine foundations reinforced with geogrids and geocells", *Geotextile and Geomembranes*, **46** (6), 882-896.

BEHAVIOR OF EMBANKMENT AFFECTED BY WATER CONTENT FOR COMPACTION STUDIED BY DYNAMIC CENTRIFUGE MODEL TESTS

Siga A[1] and Thirapong Pipatpongsa[2]
1. Ph.D. student, Graduate School of Engineering, Kyoto University, Kyoto, Japan
2. Assoc. Professor, Graduate School of Engineering, Kyoto University, Kyoto, Japan
Email: a.siga.62y@st.kyoto-u.ac.jp, pipatpongsa.thirapong.4s@kyoto-u.ac.jp

ABSTRACT

In order to study the behaviors of embankment affected by the water content, dynamic centrifuge model tests were conducted with a water supply system. Urethane ground is used to simulate the soft ground consolidation settlement under 50G centrifugal acceleration, and then the saturated region is reproduced by supplying fluid inside the model, and the vibration is applied when the steady state is reached and dynamic behavior was observed. The test results showed that:(1) The stress ratio in the cases with high water content (10%-12%) was low, and the cases with low water content were high. (2) The embankment deformation before the dynamic loading was not influenced by water content, and after dynamic loading, the low water content case showed a larger deformation. (3) During the fluid supply process, the max water level has no relationship with water content, but the steady state water content increased with water content increasing. (4) The cases with high water content showed a less shear strain.

Keywords: centrifuge model test, embankment, water content, dynamic loading

INTRODUCTION

The dynamic behavior of the embankment centrifuge will affect by many factors like embankment height or compaction degree. Many researchers have tried to study the dynamic behavior of embankments by centrifuge tests. (e.g. Higo et al., 2014, Enomoto et al., 2014, Okamura et al., 2012). In addition, seismic behavior affected by construction water content and those mechanisms have not been systematically studied.

The shear stress condition is the basis for evaluating the deformation and strength of the embankment. The dynamic shear stress is the important basis for evaluating the behavior of embankment in a centrifuge test. Many researchers have studied the shear stress and shear strain in the embankment centrifuge test. (e.g. Koga et al., 1990, Kazama et al., 1996)

In this study, dynamic centrifugal model tests of embankments under different water contents with a fluid supply system are conducted to verify the dynamic behavior of the embankment in different water content. Embankment models are constructed in the same compaction degree with a water content from 4% to 14%. The metolose will supply into the embankment model after the centrifugal acceleration reaches 50G, and the dynamic wave has been applied to the model. Through the shear stress, deformation, water level, and shear strain of embankment model provided by the earth pressure sensor, pore water pressure sensor, accelerometer and image analysis, the behavior of embankment in different water content was studied.

MODEL PREPARATION AND TEST CONDITION

Materials

The embankment was built by sieved Hiroshima sand and the impermeable soft ground was modeled by Urethane. The Hiroshima sand was collected from Kure City, Hiroshima Prefecture (manufactured

by Yamamoto Kenzai Co., Ltd.) and sieved with the 1mm-particle-diameter maximum size. The non-drainage boundary is reproduced by covering the urethane with vinyl. The properties of the materials were shown in Table 1. The compaction test was conducted and the result is shown in Fig. 1. The compaction degree in all centrifuge cases were 90%, and the water content changed from 4% to 14% in 2% increments, so the water content-dry density points of centrifuge cases can be marked in Fig. 1. The condition of sand is defined as humid with water content of 4% and 6%, as damp in 8%, 10%,12%, and as moist in 14%.

Table 1 Physical properties of materials

Hiroshima sand	
Soil particle density ρ_s	2.633 g/cm^3
D10	0.08 mm
D30	0.20 mm
D50	0.34 mm
D60	0.40 mm
Fine fraction content FC	9.2%
Maximum void ratio e_{max}	1.003
Minimum void ratio e_{min}	0.441
Dry maximum density ρ_{dmax}	1.75g/cm^3
Optimum water content w_{opt}	11.2%
Degree of compaction D_c	90%
Coefficient of permeability k	2.4×$10^{-5}m/s$
Urethane	
Young's modulus	126~129kPa
Poisson's ratio	0.282±0.044
Tensile strength	0.39MPa
Elongation at break	150%
Density	0.18±0.03g/cm^3
25% compression load	29.4~58.8kPa

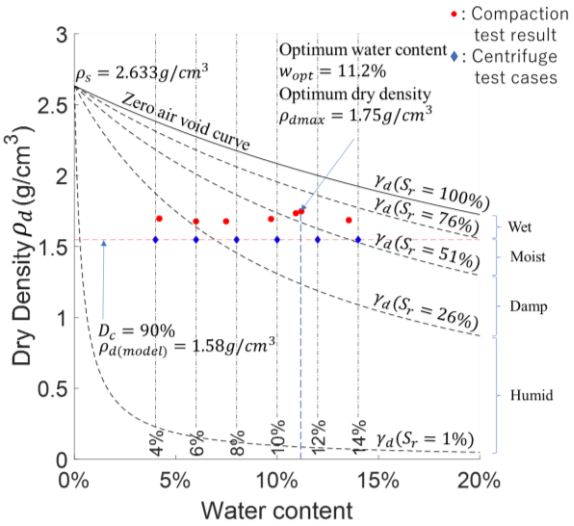

Figure 1. The compaction curve of Hiroshima sand

To suit the permeability coefficient of sand under 50G centrifugal acceleration, Metolose (Shin-Etsu Chemical Co., Ltd.) was used, and the kinematic viscosity was adjusted to 50cSt (50 times that of water) by mixing with water and hydroxypropyl methylcellulose.

Sample preparation

To investigate the impact of water content on the dynamic behavior of the embankment, 8 cases was conducted in different construction water contents. Firstly, the above-mentioned urethane material was placed at the bottom of soil chamber to simulate the soft ground. Secondly, the undrain condition was realized by covering the urethane with vinyl sheet. Then, the embankment model was constructed by the procedure below:

(1) The water content of sand was adjusted. (4%, 6%, 8%, 10%, 12%, 14%)
(2) The wooden plates with a thickness of 1 mm were stacked to provide the temporary boundary for each layers of compaction.
(3) The degree of compaction was kept constant at 90% regardless of water contents. Also, sensors were installed inside the model during compaction.
(4) The wooden mold was removed and the embankment model was trimmed to the desired shape.

The arrangement of measuring instruments in the embankment is the same for the whole series of experimental cases. The model configuration and the location of measuring instruments were demonstrated in Fig. 2 in prototype scale. The experimental data is processed on the assumption of plane strain condition so that there is no difference in the longitudinal direction. Three pressure gauges were installed at the same location at each point for measuring soil pressure in three directions. The three-directional earth pressure sensor is described below.

The test cases and measurement instruments condition are listed in Table 2, the construction water content was changed from 4% to 14% in 2% increments. Where TEP represents the three-directional earth pressure sensor, ACC represents accelerometer, LD represents laser sensor and PP is pore water pressure sensor. For some reason, such as instrument damage, in some cases the measurement values of certain instruments could not be obtained, such situation is marked with a cross in Table 2.

Table 2. Test cases

Case No.	TEP		ACC			LD		PP		Water content
	a	b	a	b	c	vertical	horizonal	a	b	
1	○	○	○	○	○	○	○	×	○	4%
2	○	×	○	○	○	○	○	○	○	4%
3	○	○	○	○	○	○	×	○	○	6%
4	○	○	○	○	○	○	○	○	○	6%
5	○	○	○	○	○	○	○	○	○	8%
6	○	○	○	○	○	○	○	○	○	10%
7	○	○	○	○	○	○	○	○	○	12%
8	×	×	○	○	○	○	○	○	○	14%

Two types of input waves were used in this experiment: white noise and ramped sine wave. The white noise will be introduced first to alleviate the unevenness of density and stress caused by compaction, then the fluid was supplied into the model, and four ramped sine waves with different amplitudes were applied separately. The sine wave is a 1Hz sine wave whose amplitude increases for 5 seconds from the start of vibration, then maintains a constant amplitude for 20 seconds, and then decays in 5 seconds on prototype scale. The single amplitude of each input wave is 70 gal, 110 gal, 185 gal, and 335 gal as measured by the accelerometer placed at bottom of the soil chamber. In this study, all dynamic behavior analysis were based on the final input wave whose amplitude is 335 gal.

DYNAMIC SHEAR STRESS

Shear stress obtained by accelerometers

The shear stress could be obtained by the above-mentioned three-directional earth pressure sensor, but another method was commonly used in centrifuge tests, the shear stress inside the embankment can be obtained by acceleration. Fig. 3 shows a schematic diagram showing how to obtain the shear stress using the wet density (ρ_t), the installation distance (h) between the accelerometer, and the measured value (a) by the accelerometer. The shear stress was computed by:

$$\tau_1 = \sum ma = \rho_t \cdot \left(\frac{h_2}{2} \cdot a_3 + \frac{h_1 + h_2}{2} \cdot a_2 + \frac{h_1}{2} \cdot a_1\right) \quad (1)$$

$$\tau_2 = \sum ma = \rho_t \cdot \frac{h_2}{2} \cdot (a_3 + a_2) \quad (2)$$

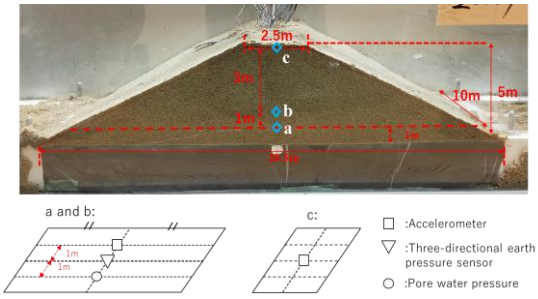

Figure 2. Model configuration

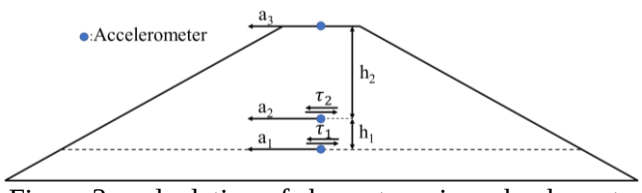

Figure 3. calculation of shear stress in embankment based on acceleration

Three-directional earth pressure sensor

In this research, a test device named three-directional earth pressure sensor was used, and the shear stress, vertical earth pressure, and horizontal earth pressure were calculated by decomposing the measured values. The device was made by processing a high-strength acrylic cube into a triangular prism shape, and three earth pressure sensors were installed on three faces of it. A photograph of the acrylic triangular prism is shown in Fig. 4. The two-dimensional stress tensor formulation for stress decomposition is as follows. The components of σ_1, σ_2, and σ_3 are shown in Fig. 5.

$$M = \frac{1}{2}\begin{bmatrix} 1+cos(2\theta_1) & 1-cos(2\theta_1) & 2\,sin(2\theta_1) \\ 1+cos(2\theta_2) & 1-cos(2\theta_2) & 2\,sin(2\theta_2) \\ 1+cos(2\theta_3) & 1-cos(2\theta_3) & 2\,sin(2\theta_3) \end{bmatrix} \tag{3}$$

$$\begin{Bmatrix} \sigma_y \\ \sigma_x \\ \tau_{xy} \end{Bmatrix} = M^{-1} \cdot \begin{Bmatrix} \sigma_1 \\ \sigma_2 \\ \sigma_3 \end{Bmatrix} \tag{4}$$

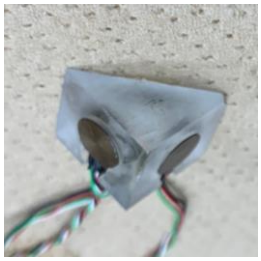

Figure 4. Acrylic triangular prism

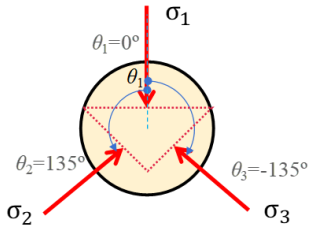

Figure 5. Stress component

Reliability of three-directional earth pressure sensor

As mentioned above, the shear stress could be obtained by the three-directional earth pressure sensor, but the reliability of the calculated result should be checked first. Fig. 6 shows a comparison of the shear stress at point a of case 1. The shear stress was obtained by the three-directional earth pressure sensor was smaller than the result obtained by accelerometers, and the baseline drift was also observed. It may cause the rotation of sensors during the dynamic loading. The results of two methods showed a correlation so the shear stress was obtained by the three-directional earth pressure sensor will be used in analyzing.

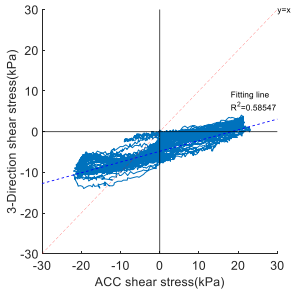

Figure 6. Comparison between ACC and three-directional shear stress at point a

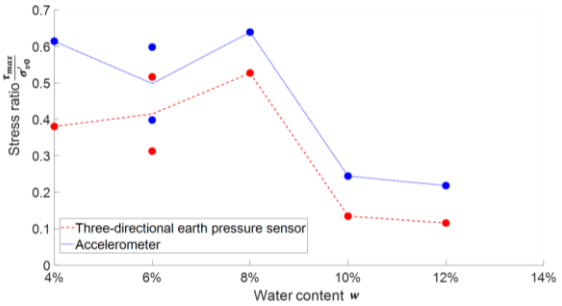

Figure 7. Relationship between Stress ratio and water content at point a

Stress Ratio in different water content

Figure 7 represents the relationship between the shear stress ratio and water content at point a. The maximum shear stress τ_{max} was obtained during the dynamic loading and the initial consolidation stress σ'_{v0} in Fig. 7 was computed by:

$$\sigma'_{v0} = \sigma_{v0} - u_0 \tag{5}$$

Where $\boldsymbol{\sigma_{v0}}$ is the initial vertical stress and u_0 is the initial pore water pressure.

The shear stress was obtained from two methods: The three-directional earth pressure sensor and Accelerometers as mentioned above. The results of two methods showed the same tendency that the stress ratio would be influenced by the construction water content of the material. The largest stress ratio appeared in water content at 8% (0.64 for accelerometer result and 0.53 for three-directional earth pressure sensor result) and the smallest one was observed at 12% (0.22 for accelerometer result and 0.12 for three-directional earth pressure sensor result). The cases with the water content of 10%-12% showed a less shear stress ratio, which means a smaller tendency of liquification.

DEFORMATION OF EMBANKMENT

Reliability of image analysis

The shape of the embankment will be changed due to the loading, and the top and base settlement can be measured by the images of the embankment model as shown in Fig. 8. The central thickness H of embankment can be obtained by the equation below:

$$H = H_0 + S_B - S_T \tag{6}$$

The images of each experimental process can be obtained by capturing the view screen of a high-speed camera. The laser sensor is also used to detect top settlement by the reflection target set at the top of the embankment. The reliability of the calculated result should be checked first by comparing the image analysis results with the laser sensor results. Fig. 9 shows a comparison of top settlement between image analysis and laser sensor.

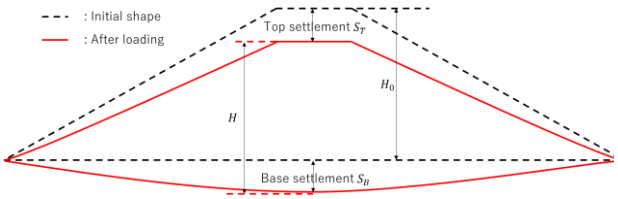

Figure 8. Deformation of embankment model

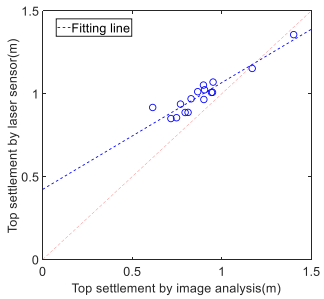

Figure 9. Comparison of top settlement between image measurement and laser sensor

The top settlement was measured by the laser sensor, is larger than the top settlement by image analysis. The possible reason is the image analysis using the initial height measures by image as a reference, and it may change during the compaction. But except that the image analysis shows reliability.

Central thickness and top settlement in different water content

Figures 10 and 11 show the normalized central thickness and top settlement before and after the dynamic loading. The central thickness was obtained by image analysis and the top settlement was obtained by laser sensor.

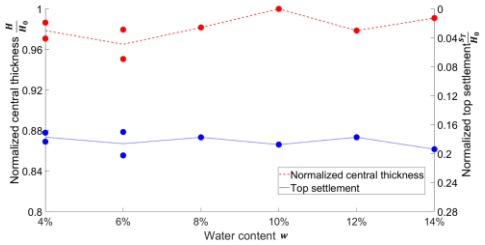

Figure 10. Normalized central thickness and top settlement before dynamic loading

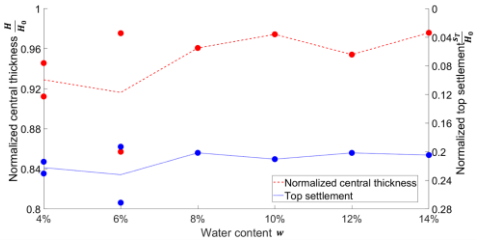

Figure 11. Normalized central thickness and top settlement after dynamic loading

The settlement before dynamic load should cause by the urethane settlement and depends on the weight of the embankment. Since the weight of the embankment increases with the increasing of the construction water content, it is considered that the higher the construction water content ratio, the larger the settlement amount. However, from the experimental results, there is no obvious correlation between the settlement and the construction water content.

The settlement before dynamic load showed the same tendency for both image analysis results and laser sensor results. In the low water content case, the embankment showed a large central thickness change, the largest deformation occurred on the water content of 6% both for two methods. A lower water content showed a large liquefication tendency.

PERMEATION BEHAVIOR IN THE FLUID SUPPLY PROCESS

Figure 12 shows the images from the high-speed camera during fluid supply, summarized for the three stages of initial supply, peak water level, and steady state. The volume of fluid supply was controlled by a water pressure sensor installed at the bottom of the supply fluid tank. After the centrifugal loading reached 50G and white noise was applied, the supply valve of the tank installed outside of the soil chamber was opened, and the metolose was supplied by the fluid supply pipe inside the embankment model. The fluid supply was performed until the value of the pore water pressure gauge placed in the tank decreased by about 5 kPa.

For case 8 (water content 14%), a sudden increase in pore water pressure occurred during the fluid supply process, and a crack occurred in the central part of the embankment before the target fluid supply amount was reached, so the supply was stopped. Therefore, in this section, Cases 1 to 7 are discussed excluding Case 8. There is no big difference in the total volume of fluid supply in whole cases.

Figure 13 shows the schematic diagram of water level measurement by image analysis. The max water level and the steady state water level were measured as well as the water level calculated by the pore water pressure sensor. The result was showed in Fig. 14 and Fig. 15.

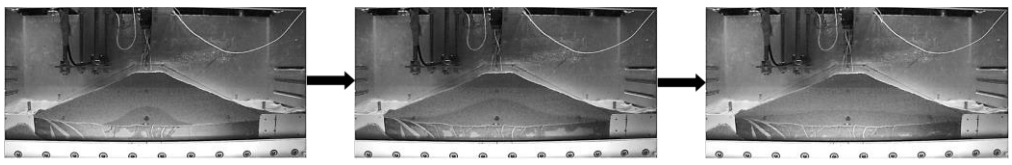

Figure 12. Process of fluid supply

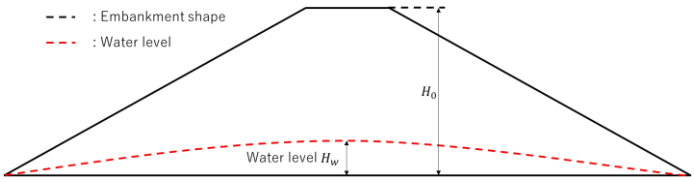

Figure 13. Water level measurement

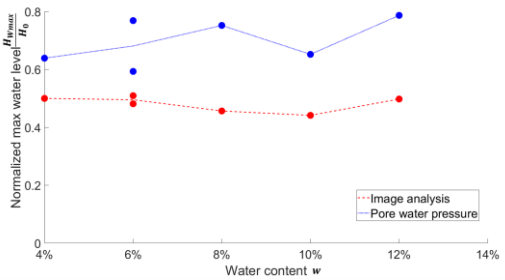

Figure 14. Max water level

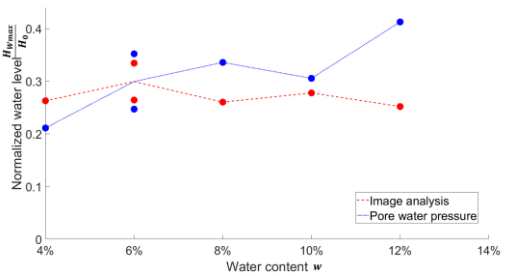

Figure 15. Water level in steady state

The normalized max water did not show a significant tendency in different water content. When the total volume of fluid supply reaches the target volume and the water level reaches the peak during the supply process, the max water level was same as whatever the construction water content is, the max water level will not be influenced by the construction water content.

For the steady state water level, the image analysis result was not influenced by the construction water content either. But the water level calculated by the pore water pressure sensor showed a tendency that increased with the increase of the construction water content. That may cause by the behavior of the soil. The permeability of the soil decreases with the increase in the water content, which leads to pore water pressure increase in fluid supply.

DYNAMIC SHEAR STRAIN

Shear stress obtained by accelerometers

Three accelerometers shown in Fig. 2 and Fig. 3 are used to calculate the horizontal displacement by double integration of acceleration expressed below:

$$\iint (a_n(t)\ dt)dt = d_n \tag{7}$$

The sampling frequency of the measurement is 200Hz, so the interval of time integral dt is 0.005 seconds. However, the integrated displacement usually tends to contain unexpected drift due to errors involved in the record and in numerical computation, Fast Fourier Transfer (FFT) was used to analyze the original acceleration records. After the high-pass filter, the integration is performed in the frequency domain, to exclude the drifting part of the displacement. The shear strain can be calculated from differential displacement between two accelerometers. This is given by Eq. 8, where Δd is equal to differential displacement between two accelerometers, and Δh is equal to distance between two accelerometers.

$$\gamma_n = \Delta d_n / \Delta h_n \tag{8}$$

The reliability of the shear strain calculated by the accelerometer

As mentioned above, the displacement can be obtained by the data of accelerometers, but the reliability of the calculated result should be checked first. Fig. 16 shows a comparison of the displacement measured by the laser sensor and the accelerometer installed at top of the embankment.

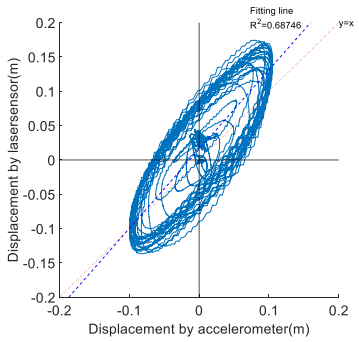

Figure 16. Comparison between the horizontal displacement measured by laser displacement sensor and accelerometer

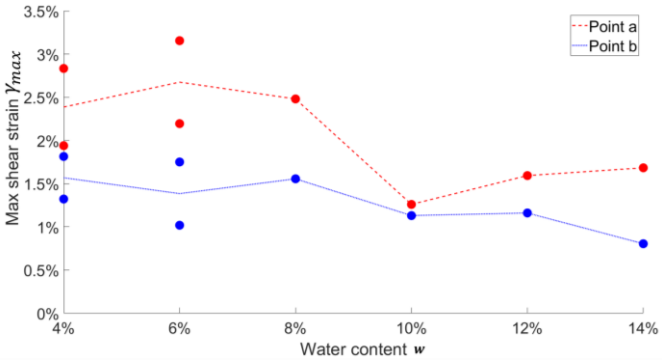

Figure 17. Max shear strain in different water content

The horizontal displacement measured by the laser displacement sensor is about 1.5 times of the displacement obtained by the accelerometers. Though the shaking of the target on the embankment may affect the measurement and the support frame of the laser displacement sensor may not be firmly

installed, the values measured by the accelerometer were employed to calculate the shear strain in the embankment. The results of the laser sensor and accelerometer showed a high correlation, so the acceleration value was used to evaluate the shear strain of the embankment.

Max shear strain during dynamic load

The max shear strain by the double amplitude of different water content is shown in Fig. 17. The differences can be observed when comparing the shear strain at the bottom (point a) and middle (point b), the experiments revealed that the horizontal deformation of the embankment was not like a rigid solid. The bottom strain is larger than the middle strain in all cases. The maximum shear strain shows a tendency of changing with the water content, i.e., the shear strain at low water content is higher than that at high water content, when compared with the test under high water content, cases in low water content showed a greater tendency of liquefaction. The cases with high water content showed a less shear strain.

CONCLUSION

Dynamic centrifuge tests were conducted under different construction water content with a fluid supply system. The behavior of the embankment was obtained by the sensor installed inside the embankment model and image analysis, to verify the influence of the initial construction water content.

The results of the analysis show the following: (1) The stress ratio showed a high liquefication tendency in low water content, and it is lower in cases with high water content. (2) The embankment deformation before the dynamic loading was not influenced by water content, and after dynamic loading, the low water content cases showed a larger deformation. (3) During the fluid supply process, the max water level has no relationship with water content, but the steady state water content increased with water content increasing. (4) The embankment model was not shaking as a rigid solid under dynamic loading in the centrifuge test, and the shear strain in the lower part was larger than the upper part. The max shear strain would be influenced by the water content.

AKNOWLEDGEMENT

This work was supported by JSPS KAKENHI Grant Number 20H02242. Sincere thanks are also given to Shanzhi Tao and Shozo Tsuchida for their valuable assistance with the laboratory testing.

REFERENCES

Enomoto, T. and Sasaki, T. (2015). Several factors affecting seismic behaviour of embankments in dynamic centrifuge model tests. *Soils and Foundations*, **55**(4), 813-828.

Higo, Y., Lee, C. W., Doi, T., Kinugawa, T., Kimura, M., Kimoto, S. and Oka, F. (2015). Study of dynamic stability of unsaturated embankments with different water contents by centrifugal model tests. *Soils and Foundations*, **55**(1), 112-126.

Kazama, M., Toyota, H., Towhata, I. and Yanagisawa, E. (1996). Stress strain relationship of sandy soils obtained from centrifuge shaking table tests. *Doboku Gakkai Ronbunshu*, **1996**(535), 73-82.

Koga, Y., & Matsuo, O. (1990). Shaking table tests of embankments resting on liquefiable sandy ground. *Soils and Foundations*, **30**(4), 162-174.

Okamura, M., Tamamura, S. and Yamamoto, R. (2013). Seismic stability of embankments subjected to pre-deformation due to foundation consolidation. *Soils and Foundations*, **53**(1), 11-22.

Shozo, T. (2022). Effect of different water content on liquefaction resistance of embankments, *Master's Thesis*, Kyoto University.

STABILITY OF LOOSE FILL EMBANKMENT UNDER SEISMIC LOADS STUDIED BY PHYSICAL MODEL AND DISCRETE ELEMENT METHOD

Zi-Rui Lu[1] and Thirapong Piptpongsa[2]
1. PhD Student, Department of Urban Management, Kyoto University, Kyoto, Japan
2. Associate Professor, Department of Urban Management, Kyoto University, Kyoto, Japan
Email: lu.zirui.55e@st.kyoto-u.ac.jp, pipatpongsa.thirapong.4s@kyoto-u.ac.jp

ABSTRACT

As a classical research topic, the stability and pressure distribution of deposited sand heap have been studied for a long time. Hummel and Finnan firstly studied the relationship between pressure distribution and the cross-section of sand heap 100 years ago. They found that the profile of pressure distribution coincides exactly with the surface of the sand heap after horizontal vibration. If the pressure on the base at all points is equal to the vertical height of the column of material above it, it can reach a form of great stability. In this research, both experimental and numerical methods were utilized to verify the stability evolution of the deposited sand heap against horizontal vibration. DEM simulation results agree with the great stability theorem well.

Keywords: horizontal vibration, sand heap, seismic stability, discrete element method

INTRODUCTION

Slumping is regarded as one of important kinds of failure of embankments that cause residual deformations after strong earthquake motion. Large deformation due to lateral spreading can destroy the body of earth structure such as river dikes, earth fills, road and railway fills as well as their embedded lifelines. Performance-based design principle requires the evaluation of seismic displacement which remains after earthquake; however, it is not simple due to difficulties in numerical simulations, parameter determinations and initial conditions at the site. Both solid-like and liquid-like behaviors can be observed in granular materials undergoing plastic deformation. Plastic flow observed in a vibrated granular system depends on the range of strain and loading condition. Under the application of vibrations, a granular medium can behave as a perfect fluid. Many studies have been investigated the dynamics of dry granular media with a free surface and subject to vertical or horizontal vibrations (Evesque and Rajchenbach, 1989; Chen et al., 1997). Therefore, this work aims to study the seismic stability of deposited sand heap against the series of horizontal vibrations in terms of the progressive reorientation of stress distribution above its base.

BACKGROUND

The earthquake sometimes induces a massive amount of destruction to the major infrastructures such as embankments and levees, which may hinder rescue and cause secondary damage. To design these structures with higher stability and reduces their deformation when subjected to seismic waves is an issue worth extensive discussion. Hummel and Finnan (1921) studied the relationships between pressure distribution and the cross section of sand heap. They found that when the shape of sand heap coincides to its vertical pressure profile, the sand heap tends to be stable during horizontal vibration, which is called the “great stability”. Gerner and Henk (2007) simulated the formation process of Faraday heap with CD-CFD method, and discussed the correlation between the stable shape of the heap and vertical vibration. Matsuo et al. (2014) investigated the shape change of sand heap caused by repeating impact perturbation. The discrete element method (DEM) get more and more popular in recent decades in simulating the seismic response of granular materials (Lin et al., 2018; Zhou et al., 2019), and also the formation process of sand heap (Zhao and Shan, 2013). To provide a preliminary design of apparatuses and experimental procedures of the consequent physical models, rather than mechanisms under

earthquake of compacted materials, this work focuses on the phenomenon of a dry and loose sand heap inclined at angle of repose under vibration. A series of experiments were conducted to discuss the relationship between the shape of sand heap and vertical pressure distribution before and after horizontal vibration. Particle flow code (PFC2D) is adopted to simulate the seismic response of sand heap.

EXPERIMENTS

Experiment setups

The prism sand heap was constructed with silica sand No. 6 inside a soil chamber, as shown in Fig. 1. There were 5 laser sensors installed over the sand heap, 5 pressure gauges used to monitor the vertical pressure variation and 4 density pans for the average density of sand. The sand heap was built by dry deposition method without compaction, as all the sand dropped in a height of 100 mm to reach a relatively low void ratio. The repose angle of sand heap is 35°, the same as the friction angle of silica sand No. 6, and the prism sand heap has a width of 400 mm and a height of 140 mm in the beginning. Then, a sine wave (10 Hz, 1 mm) is exerted by the shaking table on the soil chamber. The height of sand heap in Fig. 4 decreased to 92 mm after shaking, and the shape of it became curve. The repose angle of sand heap also decreased from 35° to 20°. The relative density of sand heap increased from 53.78% to 56.17%. The shape of sand heap was depicted on graph paper for further discussion.

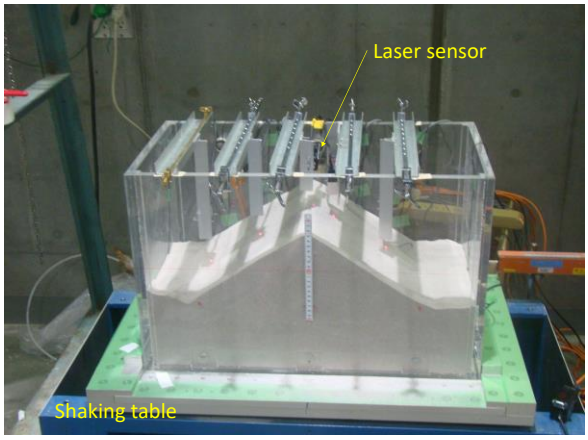

Figure. 1. Experiment setup

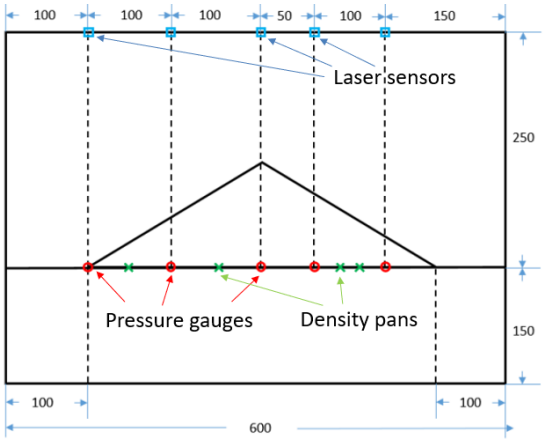

Figure. 2. Location of sensors

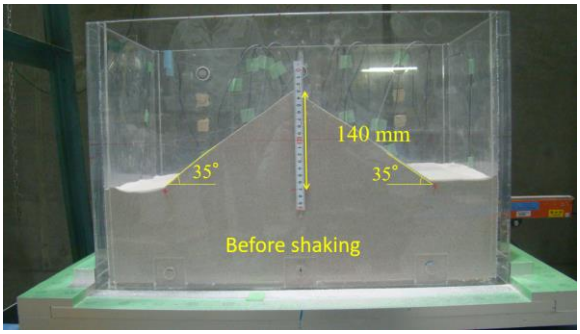

Figure. 3. Profile before shaking

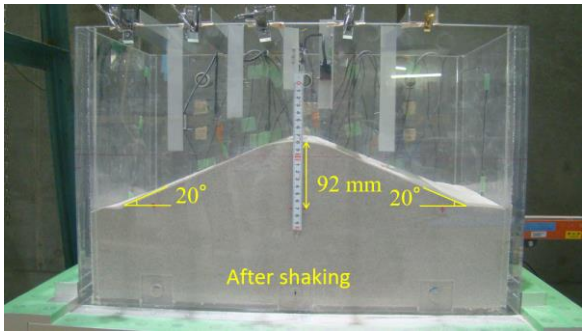

Figure. 4. Profile after shaking

Experiment results

Figure 5 shows the normalized shape and vertical pressure distribution before and after shaking in Test 1. The prism sand heap slumped because of the horizontal vibration, and transformed into a flat curved shape. The vertical pressure changed with the slumping and became somehow close to the shape of sand heap. In Test 2, another prism sand heap was built, and it was shaken twice. The shape of sand heap changed due to the first shaking, and the pressure distribution also changed. After the sand heap got stabilized in a while, the second shaking was exerted on the soil chamber. As shown in Fig. 7, both the

shape and vertical pressure distribution hardly changed. The sand heap transformed into a more stable shape by the first vibration, the shape and the pressure distribution coincided to some extent. Therefore, the impact of the second shaking was mitigated. In Test 3 shown in Fig. 8, the sand heap was built into a stable shape that the pressure distribution coincided with the shape of the sand heap. However, the sand heap slumped after shaking, though the vertical pressure distribution kept unchanged.

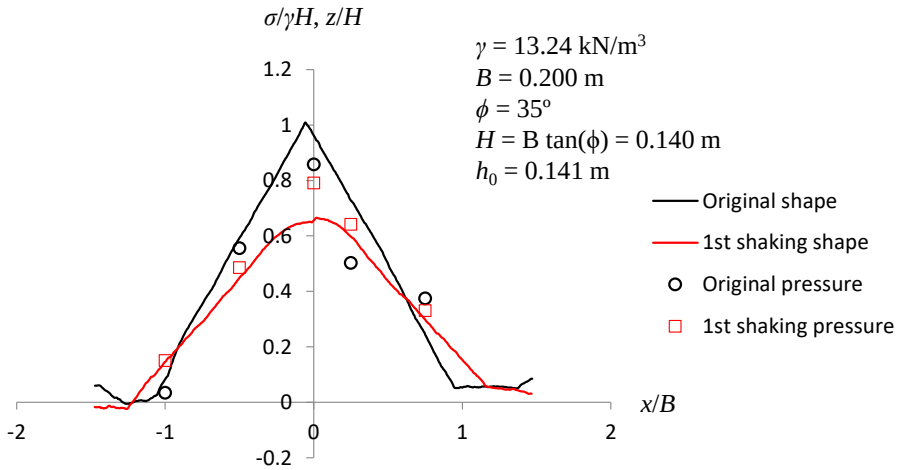

Figure. 5. Profile of z/H ~ $\sigma/\gamma H$ vs x/B in comparison between the original & 1st shaking (Test 1)

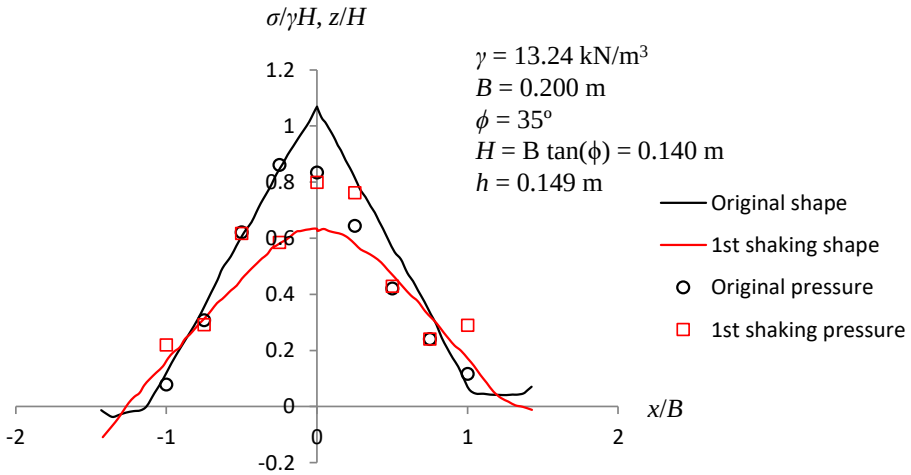

Figure. 6. Profile of z/H ~ $\sigma/\gamma H$ vs x/B in comparison between the original & 1st shaking (Test 2)

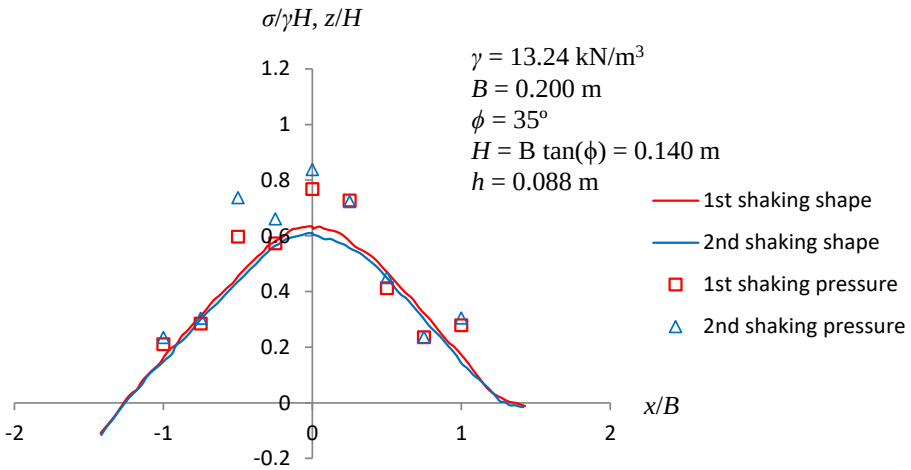

Figure. 7. Profile of z/H ~ $\sigma/\gamma H$ vs x/B in comparison between the 1st & 2nd shaking (Test 2)

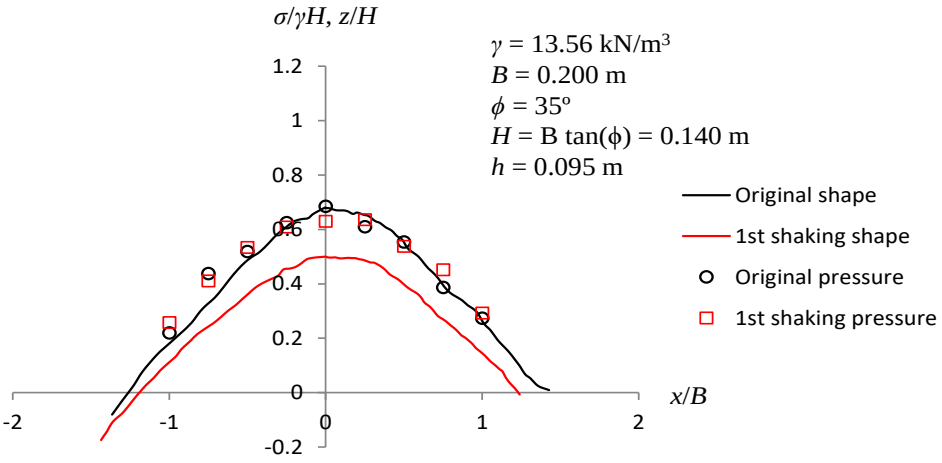

Figure. 8. Profile of z/H ~ $\sigma/\gamma H$ vs x/B in comparison between the original & 1st shaking (Test 3)

DEM SIMULATION

Model setups

DEM simulation was performed by PFC2D to study the seismic response of dry deposited sand heap. The rolling-resistance linear model was adopted, which considers the effect of rolling resistance at contacts between particles and associated energy dissipation. A similar method as the experiment was used to build the model. Firstly, a plate of 400 mm, the same width as the sand heap built in the experiments, was generated horizontally. The particles that fall out of the range of the plate will be deleted. Then, particles were created continuously in the sky and deposited due to gravity, until a triangular heap with a reposed angle of 35° was constructed. Lastly, the plate was removed and a box was created instead. The parameters adopted in simulation are listed in Table 1.

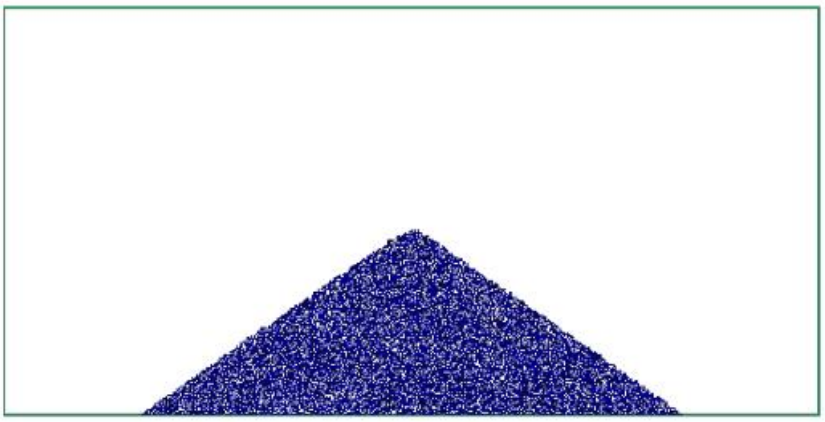

Figure. 9. DEM model for sand heap before shaking

Table 1. Parameters of contact model

Particle size (d/mm)	Effective Modulus (E*/Pa)	Normal-to-shear stiffness ratio (κ*)	Normal damping ratio (β_n)	Shear damping ratio (β_s)	Friction coefficient (μ)	Rollig friction coefficient (μ_r)
1.2~3	5×10^6	1.2	0.6	0.5	0.4	0.35

To simulate the shaking behavior, a sine wave (10 Hz, 1 mm) was applied horizontally to the box as shown in Fig. 10 & 11. The ramped sine wave has a duration of 10 seconds, and its wave form will change at the beginning and ending of the shaking. The amplitude of the sine wave will reduce to 0 after

every shaking until the sand heap gets stabilized, the interval time is at least 3 seconds, and then raise to 1mm to exert another shaking on the box. The contact force of the particles on the bottom of the box will be monitored during the simulation. The bottom plate was partitioned into 9 segments, which in the particle diameter to sensing diameter ratio of 1:22 to alleviate the influence of uneven local stress (Talesnick, 2013). The normal force and shear force between particles and bottom plate in the same segment will be summed up and then divided by the width of the segment as vertical pressure and shear stress, respectively.

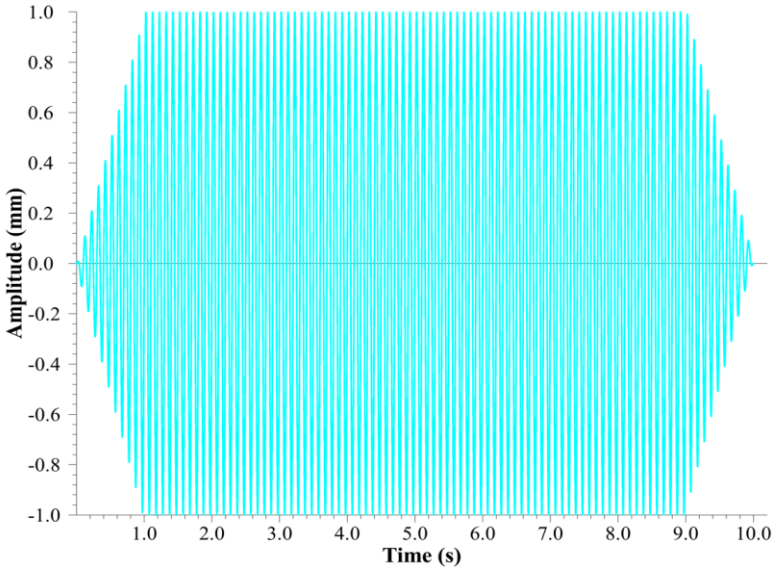

Figure. 10. Input ramped sine wave

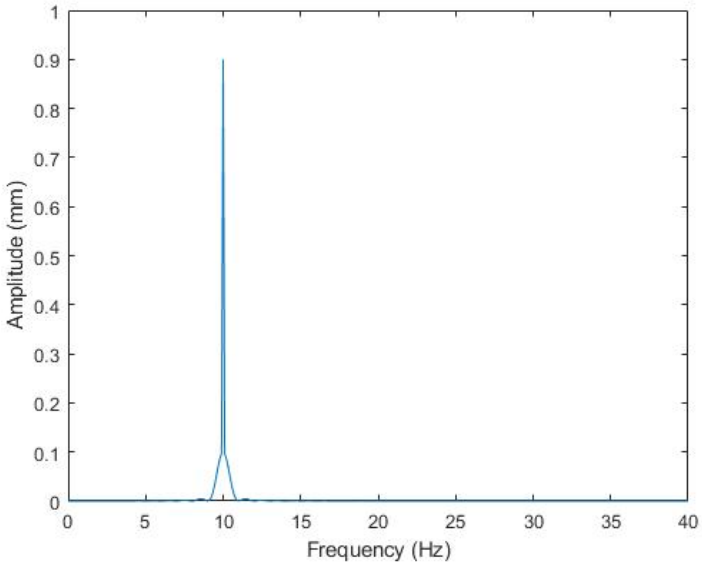

Figure. 11. Frequency domain

Simulation results

Figure 12 presents the shape of sand heap after the 1st shaking, it slumped like experiment results. The normalized profile of vertical pressure distribution and the shape of sand heap was plotted in the Fig.14, 15 and 16. The original shape of both symmetric and asymmetric triangular sand heaps differ from their vertical pressure distribution as proposed by Pipatpongsa et al. (2010) as well as Nguyen and Pipatpongsa (2020) due to the shear stress. After getting stabilized from the first shaking, the shape of sand heap became flat and coincided with the pressure distribution. A circular measuring area was set near the center bottom of the sand heap with a diameter of 6 cm, the total area of voids divided by the

whole area is regarded as the porosity. The porosity of sand heap is 21.2% in the original state, and then decreased to 18.3% after the first shaking as shown in Fig. 13. Because the measuring area is fixed, the curve of porosity fluctuates due to the horizontal translation of the sand heap. After 10 times of shaking, the porosity reached 17.8% while the lowest porosity ever is 17.5%. Shear dilatancy can be observed at the last of simulation, which means the sand heap becomes very dense. The area of the original shape is slightly bigger than the shape after the first shaking, and so does the integral of normalized vertical pressure because the initial specific weight of particles is used for normalization. However, the absolute value of the integral of vertical pressure is the same throughout the simulation.

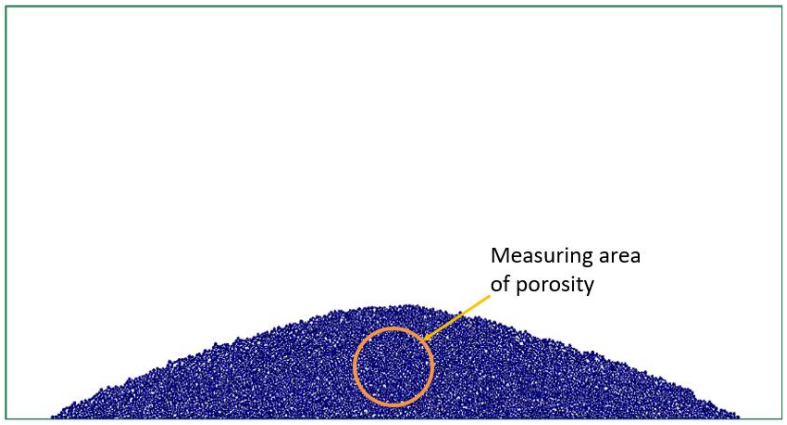

Figure. 12. DEM model after the 1st shaking

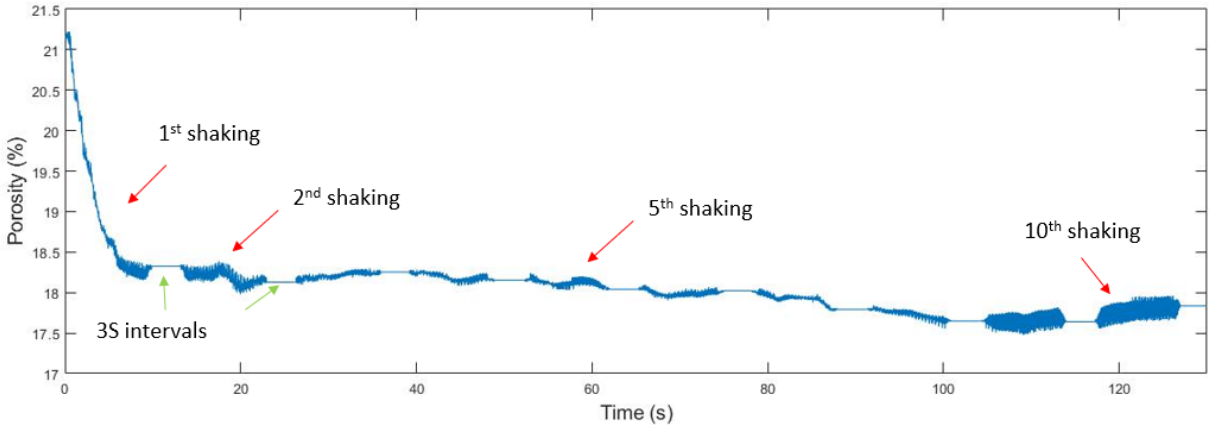

Figure. 13. Porosity of measuring area

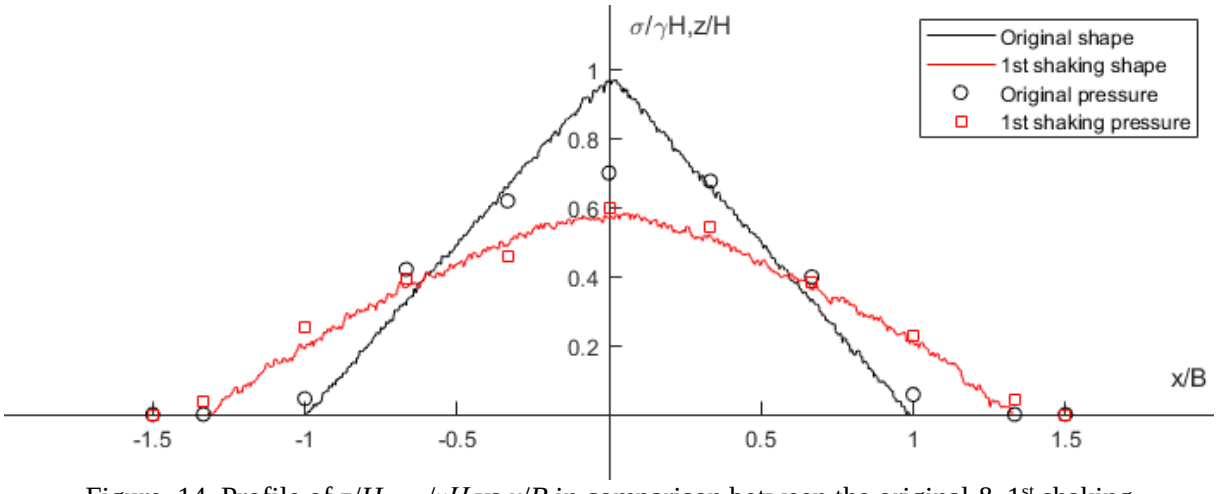

Figure. 14. Profile of z/H ~ $\sigma/\gamma H$ vs x/B in comparison between the original & 1st shaking

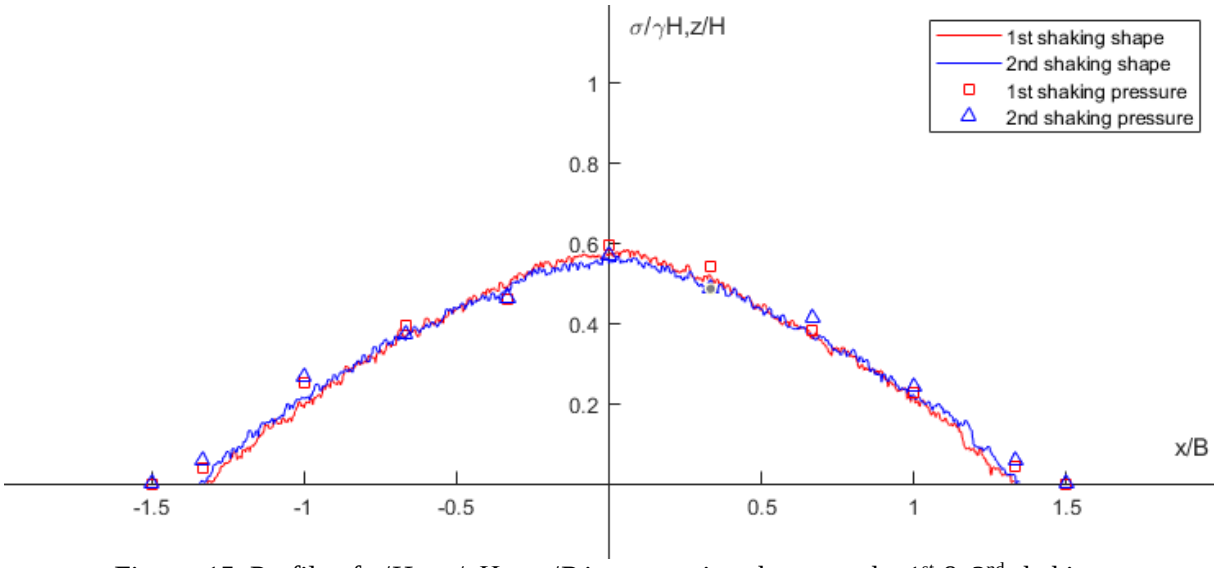

Figure. 15. Profile of z/H ~ $\sigma/\gamma H$ vs x/B in comparison between the 1st & 2nd shaking

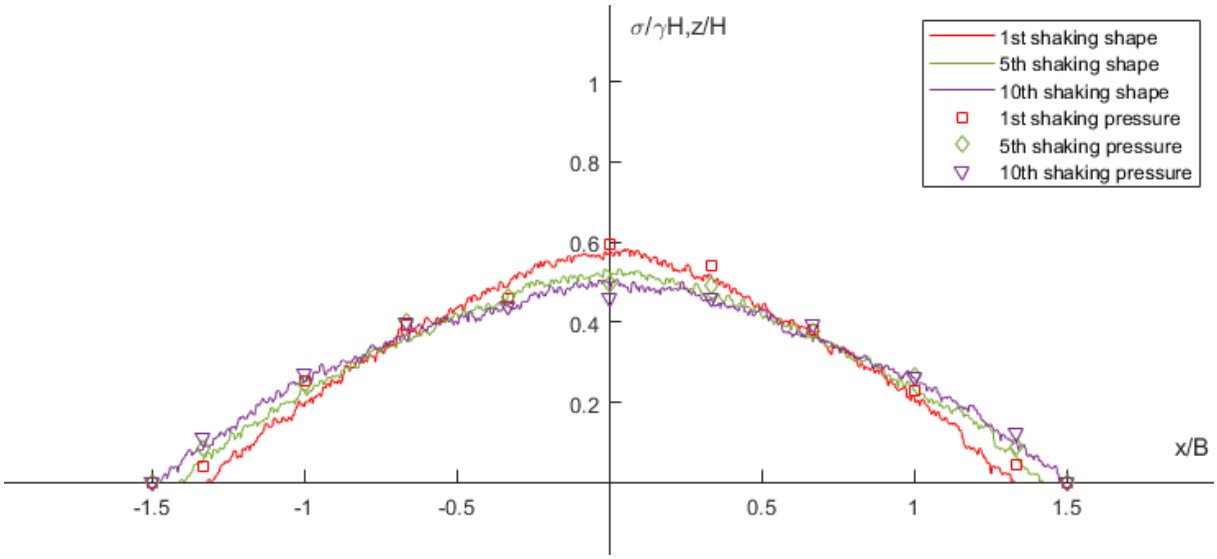

Figure. 16. Profile of z/H ~ $\sigma/\gamma H$ vs x/B in comparison between the 1st & 5th & 10th shaking

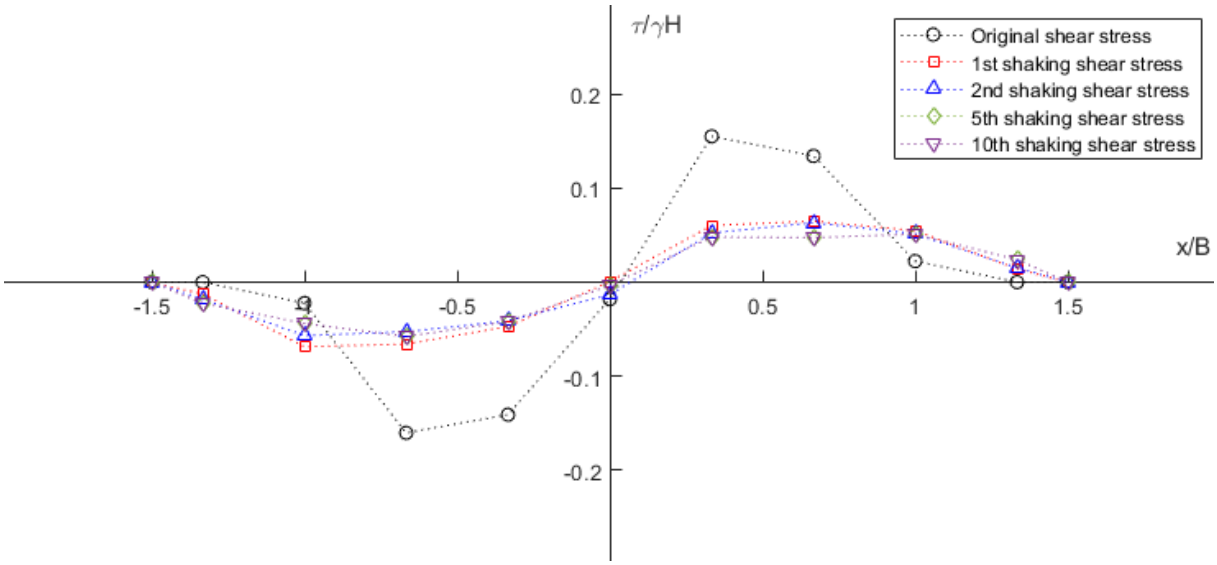

Fig. 17. Profile of $\tau/\gamma H$ vs x/B in comparison between the original & 1st & 2nd & 5th & 10th shaking

After the first shaking, the sand heap deformed and reached the great stability state, that the profile of shape coincides the vertical pressure distribution. The sand heap obtained better stability against the shaking. Therefore, the sand heap hardly changed after the second shaking as shown in Fig. 15. However, great stability does not mean strictly unchangeable. Even if the sand heap has already got seismic resistance, it will still deform slowly if shaking is continuously applied to it though the deformation of it becomes very tiny. The shape of the sand heap will keep consistent with the vertical pressure distribution after the first shaking even new shaking is applied. The shear stress along the bottom plane is plotted in Fig. 17. As a prove of stability enhancement, the basal shear stress will decrease after the first shaking and hardly change due to the later shaking.

CONCLUSIONS

The great stability of sand heap was realized in prismatic shape using shaking table. However, the great stability cannot sustain severe vibration due to excessive change of void ratio in the experiments. Further tests with different shapes of sand heap are necessary (e.g. trapezoidal or irregular) on stiff and fixed-width base. Nevertheless, the simulation results agree with the great stability theorem well, and then proved that the relationship between the shape of sand heap and the vertical pressure distribution can affect the stability of the sand heap.

AKNOWLEDGEMENT

This work was supported by JSPS KAKENHI Grant Number 20H02242. Sincere thanks are also given to Ruoqi Sui, Dr Tan Nguyen and Dr Kun Fang for their valuable assistance with the laboratory testing.

REFERENCES

Chen, W., Wei, R., & Wang, B. (1997). Formation mechanism of the soliton-shape heap and convection in granular materials under vibration. Physics Letters A, 228(4-5), 321-328.

Evesque, P., & Rajchenbach, J. (1989). Instability in a sand heap. Physical review letters, 62(1), 44.

Hummel, F. H., & Finnan, E. J. (1921). The distribution of pressure on surfaces supporting a mass of granular material. In Minutes of the Proceedings of the Institution of Civil Engineers (Vol. 212, No. 1921, pp. 369-392). Thomas Telford-ICE Virtual Library.

Lin, C. H., Li, H. H., & Weng, M. C. (2018). Discrete element simulation of the dynamic response of a dip slope under shaking table tests. Engineering Geology, 243, 168-180.

Matsuo, M. Y., Nishiura, D., & Sakaguchi, H. (2014). Geometric effect of angle of repose revisited. Granular Matter, 16(4), 441-447.

Nguyen, T. and Pipatpongsa, T. (2020), Plastic behaviors of asymmetric prismatic sand heaps on the verge of failure. Mechanics of Materials, Vol. 151, 103624.

Pipatpongsa, T., Heng, S., Iizuka, A., & Ohta, H. (2010). Statics of loose triangular embankment under Nadai's sand hill analogy. Journal of the Mechanics and Physics of Solids, 58(10), 1506-1523.

Talesnick, M. (2013). Measuring soil pressure within a soil mass. Canadian Geotechnical Journal, 50(7), 716-722.

van Gerner, Henk Jan, et al. "Interplay of air and sand: Faraday heaping unravelled." Physical Review E 76.5 (2007): 051305.

Wanjala S. (2017). The dynamic stability of loose fill embankments under seismic loads, Bachelor's Thesis, Department of Urban Management, Kyoto University.

Zhou, Y., Shi, Z., Zhang, Q., Liu, W., Peng, M., & Wu, C. (2019). 3D DEM investigation on the morphology and structure of landslide dams formed by dry granular flows. Engineering Geology, 258, 105151.

Zhao, J., & Shan, T. (2013). Coupled CFD–DEM simulation of fluid–particle interaction in geomechanics. Powder technology, 239, 248-258.

DEVELOPMENT OF FREQUENCY DEPENDENT EQUIVALENT LINEAR PROGRAM FOR DECONVOLUTION ANALYSIS

Ssu-Chieh Chen[1], Chi-Chin Tsai[1] and Duhee Park[2]
1. National Chung Hsing University, Taichung, Taiwan, R.O.C.
2. Hanyang University, Seoul, Korea.
Email: dzxcvbnmanny@gmail.com, tsaicc@nchu.edu.tw, dpark@hanyang.ac.kr

ABSTRACT

This study proposes a frequency dependent equivalent linear (FD-EQL) method for deconvolution analysis to obtain bedrock motion or within soil motion from the surface motion. The developed FD-EQL code is first verified using an idealized 1000 m soil profile, after which it is applied to perform deconvolutions using recordings obtained at three downhole arrays. The results show that the FD-EQL deconvolution procedure reliably predicts the downhole response without a divergence issue and does not require a cutoff frequency, in contrast to the conventional EQL deconvolution analysis. The amplification of high-frequency noise typically accompanied in the deconvolution is automatically suppressed due to the simulated FD soil behavior.

Keywords: Frequency dependent equivalent linear method, deconvolution, convolution, site response analysis.

INTRODUCTION

Site amplification effects on seismic ground motions are typically quantified via site response analysis that involves propagation of earthquake motions from the base rock through the overlying soil layers to the ground surface. It is called a convolution analysis or forward analysis (Figure 1). Several methods including liner (LN), equivalent linear (EQL), and nonlinear (NL) methods have been developed to evaluate the seismic ground response by analyzing one-dimensional propagation of shear waves in horizontally layered media (Tsai & Chen, 2016). For a realistic time-history soil structural response evaluation and seismic assessment of underground structures, the seismic motion needs to be applied at the base of the finite domain of the soil profile. However, seismic ground motions at a depth are rarely available. Therefore, appropriate bedrock or within soil motion is calculated by a deconvolution analysis, where the surface ground motion is inversely propagated to a location at depth (Figure 1).

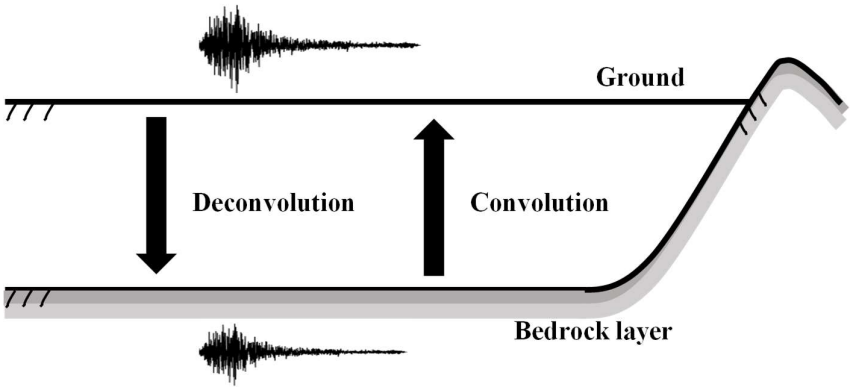

Figure 1. Convolution and deconvolution analysis.

Conventionally, the frequency-domain solution (e.g. SHAKE program (Idriss & Sun, 1992; Schnabel et al., 1972)) is used to deconvolute the surface ground motions for dynamic soil-structure interaction analyses. However, unreliable results may occur in a deconvolution analysis. For instance, the SHAKE program may lead to excessive high frequency responses and even fail to converge in a deconvolution analysis (Chen et al., 1995). This phenomenon aggravates with increases in the deconvolution depth and the damping ratio. Such a divergent problem can be avoided by using a cutoff frequency. However, selection of a suitable cutoff frequency requires an empirical engineering judgement. Silva (1988) recommended to use 15 Hz for the cut off frequency. However, it was not reported whether this cut off frequency is applicable for all depths and damping ratios.

In this study, frequency dependent equivalent linear (FD-EQL) method is proposed to overcome these evident problems accompanied in a deconvolution analysis. The advantage of FD-EQL is that it does not require an artificial filtering or ad-hoc interaction process. The error induced in the high frequency can be automatically suppressed by the modeled FD soil behavior. The developed Matlab code for FD-EQL is validated through the generic case.

FD-EQL METHOD

To better account for the variation of shear strain amplitudes when ground motions are simulated using frequency domain solutions, a series of FD-EQL methods were developed by modifying the EQL algorithm with FD soil parameters (Kausel & Assimaki, 2002; Sugito, 1995; Yoshida et al., 2002), as depicted in Figure 2. The frequency-dependence of the EQL solution arises from the fact that ground motions or responses (e.g. shear strain time histories in Figure 2a) exhibit frequency content that can be represented as a combination of multiple harmonics associated with variable amplitudes in terms of their Fourier spectrum (Figure 2b). Hysteretic nonlinear soil behavior (Figure 2c) is then dependent on amplitudes of cycles corresponding to different frequencies. In other words, higher strain amplitudes within the soil profile are associated with intermediate frequencies of vibration, whereas higher frequency components produce lower amplitudes of shear strain. Therefore, the EQL procedure was modified by using FD soil parameters for both shear modulus and soil damping as illustrated in Figure 2d.

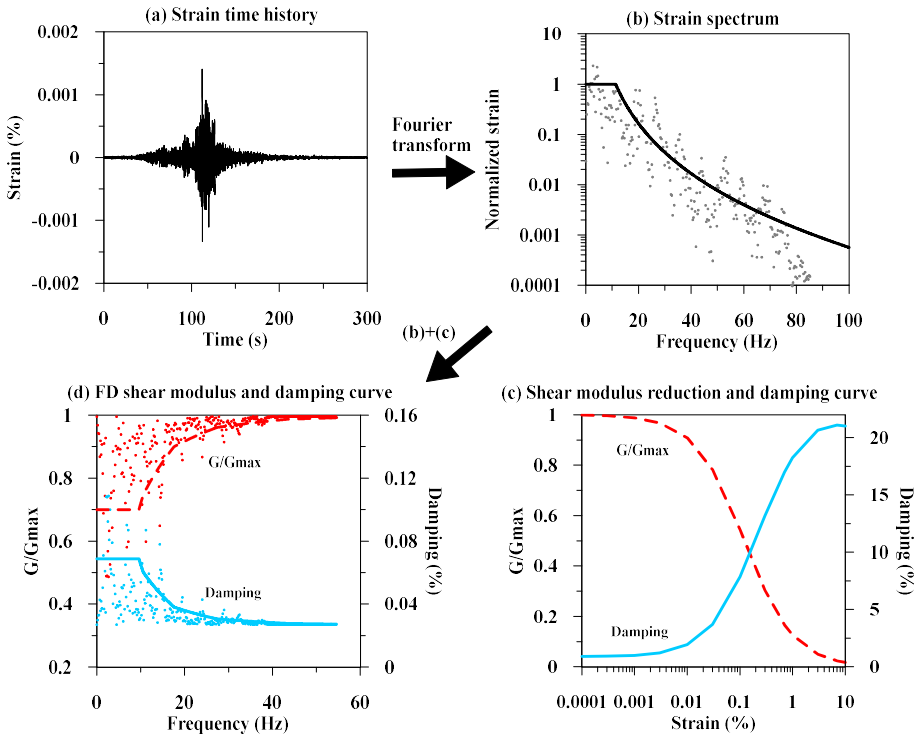

Figure 2. Illustration of FD-EQL method.

Huang et al. (2018) proposed a combination factor used to interpolate the strain spectrum $\gamma(\omega)$ between the EQL and FD-EQL methods using the following weighting factor f

$$\gamma_{M-FD-EQL}(\omega) = \gamma_{EQL}^{1-f}(\omega) * \gamma_{FD-EQL}^{f}(\omega) \quad (1)$$

where $\gamma_{EQL}(\omega)$ and γ_{FD} (ω) are amplitudes of shear strain Fourier spectra calculated by the EQL and FD-EQL methods at frequency ω, whereas $\gamma_{M-FD-EQL}(\omega)$ represents the adjusted value to be used in the modified FD-EQL procedure. An optimal range of f was reported as 0.2–0.3. It was demonstrated that the modified FD-EQL provides improved site response estimates at high frequencies compared with both the EQL and FD-EQL methods.

CODE DEVELOPMENT AND VERIFICATION

The in-house code written by Matlab was developed following the FD-EQL procedure described in the previous section. The code can perform both EQL and FD-EQL analyses by adjusting the factor f. It is essential an EQL model for f=0, whereas for $0 < f < 1$, it becomes a FD-EQL analysis method, as defined in Eq. (1). Most importantly, the code is able to perform convolution and deconvolution using both EQL and FD-EQL methods. It should be noted an alternative code which can perform a FD-EQL deconvolution analysis is not yet available. The developed code was verified by comparing with the other EQL [DEEPSOIL (Hashash et al., 2020)] and FD-EQL [Strata (Kottke & Rathje, 2008) and Huang et al.(2018)] programs using a generic case. Figure 3 shows the 1000 m Vs profile of the generic case. The pressure dependent nonlinear curve (Darendeli, 2001) is used in the analysis.

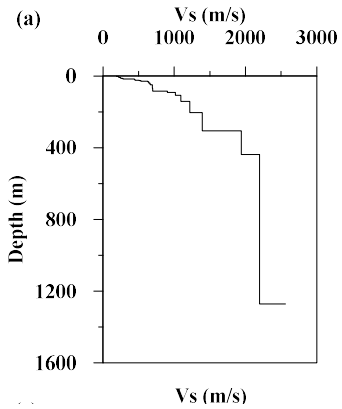

Figure 3. Vs profiles used to test the proposed procedure: Generic case for model validation

Figure 4a shows the surface response spectrum computed by the EQL convolution analysis as well as the input bedrock motion. The predicted response by the program developed in this study matches that calculated from DEEPSOIL and Strata favorably, thus verifying the EQL procedure of this code. Figure 4 b shows the surface response spectrum calculated by the FD-EQL convolution analysis. Two cases are analyzed using the developed code in this study, one using the calculated strain Fourier spectrum obtained from the strain time history and the other using the smoothed strain spectrum proposed in Kausel & Assimaki (2002). Generally, the calculated surface response by the developed program agrees well with those computed by Strata and Huang et al. (Huang et al., 2018) procedure regardless of the used strain spectrum (either smoothed or unsmoothed). The predicted response using the smooth spectrum best matches that calculated by Huang et al. (Huang et al., 2018) procedure, which also uses a smoothed spectrum. The consistent prediction results validates the accuracy of the proposed FD-EQL convolution analysis model. Moreover, it's also observed that using smoothed spectrum produces a higher response compared with that using a real spectrum. The validated code is further adopted to perform the FD-EQL and EQL deconvolution analyses to obtain the bedrock motion from the surface response calculated in the FD-EQL convolution analysis. The EQL deconvolution analysis failed to converge, and thus only the FD-EQL result is shown in Figure 4c. The FD-EQL analysis using both the real and smoothed spectrum successfully predicts the bedrock motion without encountering a convergence issue.

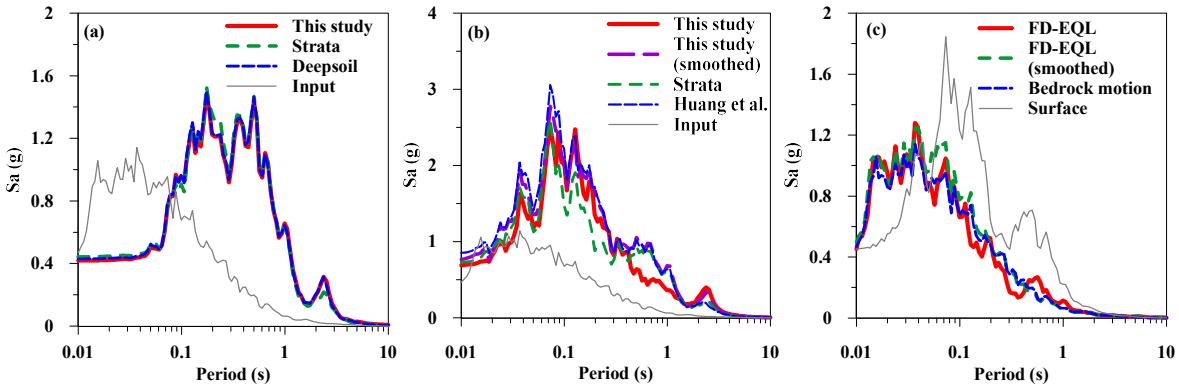

Figure 4. Verification of developed FD-EQL code: (a) EQL convolution analysis, (b) FD-EQL convolution analysis, (c) FD-EQL deconvolution analysis.

CONCLUSIONS

In this study, the FD-EQL method is proposed to overcome the problems encountered with the EQL procedure in the deconvolution analysis. The FD-EQL deconvolution code is developed and verified step by step through comparisons with available EQL convolution and FD-EQL convolution analysis codes for a 1000 m thick soil column. The FD-EQL deconvolution (not functional in the other code) performed by the developed code is proven to be capable of calculating the downhole response consistent with the bedrock motion, whereas the EQL deconvolution fails to converge. However, the FD-EQL deconvolution still needs to be verified by using more actual downhole array records.

ACKNOWLEDGMENTS

This work was supported by the Ministry of Science and Technology in Taiwan, under Award No. MOST 108-2628-E-005 -001 -MY3. The authors gratefully acknowledge such support.

REFERENCES

Chen, L. Y., Chen, J. T., Hong, H.-K., & Chen, C. H. (1995). Application of Cesaro mean and the L-curve for the deconvolution problem. *Soil Dynamics and Earthquake Engineering*, *14*, 361-373.

Darendeli, M. B. (2001). *Development of a new family of normalized modulus reduction and material damping curves* [Ph. D., University of Texas at Austin].

Hashash, Y. M. A., Musgrove, M., Harmon, J. A., Ilhan, O., Xing, G., Groholski, D. R., Phillips, C. A., & Park, D. (2020). *DEEPSOIL 7.0, User Manual and Tutorial*.

Huang, D., Wang, G., Wang, C., & Jin, F. (2018). A Modified Frequency-Dependent Equivalent Linear Method for Seismic Site Response Analyses and Model Validation using KiK-Net Borehole Arrays. *Journal of Earthquake Engineering,*. https://doi.org/https://doi.org/10.1080/13632469.2018.1453418

Idriss, I. M., & Sun, J. I. (1992). *SHAKE91: A computer program for conducting equivalent linear seismic response analyses of horizontally layered soil deposits*. In Department of Civil and Environmental Engineering, University of California Davis.

Kausel, E., & Assimaki, D. (2002). Seismic simulation of inelastic soils via frequency-dependent moduli and damping. *J Eng Mech 128*(1), 34-47.

Kottke, A., & Rathje, E. M. (2008). *Technical manual for Strata* (2008/10). https://nees.org/resources/692

Schnabel, P. B., Lysmer, J., & Seed, H. B. (1972). *SHAKE, A computer program for earthquake response analysis of horizontally layered sites* (Report EERC 72-12).

Silva, W. J. (1988). *Soil Response to Earthquake Motion*.

Sugito, M. (1995). Frequency-dependent equivalent strain for earthquake response analysis of soft ground. In: Proc. IS-Tokyo,'95, the first international conference on earthquake geotechnical engineering,, Tokyo.

Tsai, C. C., & Chen, C. W. (2016). Comparison study of 1D site response analysis method. *Earthquake Spectra*, *32*(2), 1075-1095.

Yoshida, N., Kobayashi, S., Suetomi, I., & Miura, K. (2002). Equivalent linear method considering frequency dependent characteristics of stiffness and damping. *Soil Dynamics and Earthquake Engineering*, *22*(3), 205-222.

INFLUENCE OF WEIGHT OF SHEAR BOX ON DYNAMIC SOIL RESPONSE IN CENTRIFUGE MODEL TEST

Hiroto Nakagawa[1], Hisatoshi Kashiwa[2], Moeko Matoba[3], and Shoichi Nakai[4]
1. Senior Research Engineer, Building Research Institute, Tsukuba, Japan
2. Associate Professor, Osaka University, Suita, Japan
3. Research Engineer, Building Research Institute, Tsukuba, Japan
4. Professor Emeritus, Chiba University, Chiba, Japan
Email: hiroto-n@kenken.go.jp, kashiwa@arch.eng.osaka-u.ac.jp, matoba@kenken.go.jp, nakai@faculty.chiba-u.jp

ABSTRACT

This study aims to investigate the influence of the weight of a shear box on dynamic soil response in centrifuge model test. We compared the experimental test in centrifugal-field and its simulation analysis performed by a three-dimensional finite element (FE) modeling considering the shear box. Comparing the spectral ratios obtained from the experiment and the analysis results has revealed that the weight of the shear box may influence the experimental results. The peak frequencies obtained in the analysis without the shear box were similar to those obtained in the analysis considering the weight of the shear box having approximately 13% of the mass ratio to the model ground.

Keywords: centrifuge model test, shear box, three-dimensional FE analysis, soil nonlinearity

INTRODUCTION

The centrifuge model test is one of the most effective methods to reproduce the seismic behavior of the ground, and numerous experiments have been conducted extensively so far. In order to reduce the influence of boundary conditions of a soil box on a model ground and a specimen, a shear box is often used to investigate the seismic behavior using a shaking table installed on a geotechnical centrifuge. However, only a few studies have examined the influence of the weight of the shear box on the seismic behavior of the model ground. In this study, the influence of the weight of a shear box on the dynamic soil response is investigated based on a centrifuge test and its simulation analysis performed by a three-dimensional finite element (FE) analysis.

CENTRIFUGE MODEL TEST

An experiment was conducted in May 2021, using a geotechnical centrifuge system installed at the building foundation and geotechnical laboratory in the Building Research Institute, Japan in 2020. Figure 1 shows an overview of the experimental apparatus (a shear box + Toyoura sand) used in the experiment. The internal size of the shear box placed on a shaking table is 0.6 m (L) x 0.3 m (W) x 0.5 m (D). The shear box is made of aluminum and consists of 20 layers of frames with a height of 25 mm per layer. The model ground was made using dry Toyoura sand by the air pluviation method, and the relative density of the soil before the experiment was D_r = 51%. (At the end of the experiment, the relative density was about 84%.) In the experiment, horizontal acceleration time histories were measured at four depths. Table 1 shows a list of the excitations in the experiment. Twelve cases of excitations were performed in the experiment. Although the geotechnical centrifuge system is capable of two-directional excitation in the horizontal and vertical directions, excitation in the horizontal direction was only used in the experiment. The amplitude characteristics of the input motions were specified according to the design response spectrum stipulated in the Building Standard Law in Japan, and the peak amplitudes were changed between 25% and 150% (4 amplitude levels) of the design response spectrum. Three types of phase characteristics were considered: Hachinohe, Kobe, and Random, respectively. The experiment was conducted in a 40-g field.

Figure 2 shows the experimental results during the four Kobe type excitations. Hereafter, the values used in this study are converted to full-scale by considering the centrifugal acceleration of 40-g. Figure 2a) shows the peak acceleration distribution measured in the experiment. As can be seen in Fig. 2a), the peak acceleration measured at the ground surface is larger than that obtained at the bottom of the shear box, regardless of the amplitude of excitation. The ratios of the peak acceleration obtained between the two depths are 2.0, 1.6, 1.5, and 1.6 for the input amplitude of 25%, 50%, 100%, and 150%, respectively. Figure 2b) shows the Fourier spectral ratio calculated from accelerations measured at the ground surface and bottom of the shear box. In calculating the spectral ratio, smoothing was performed using the Parzen window with a bandwidth of 0.4 Hz. As can be seen from Fig. 2b), the height of the peak around 2 Hz decreases as the input amplitude increases. Also, as the input amplitude increases, the peak frequency tends to become slightly lower.

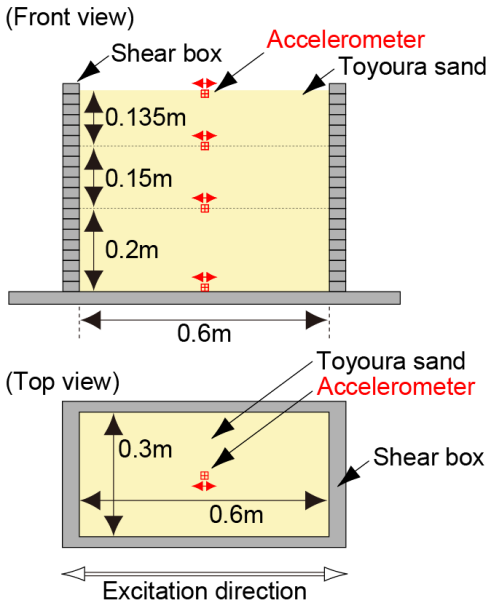

Figure 1. Experimental apparatus.

Table 1. A list of excitations in the experiment

No.	Case name	Phase characteristics	Amplitude level
1	Hachinohe-025	Hachinohe EW	
2	Kobe-025	Kobe EW	25%
3	Random-025	Random	
4	Hachinohe-050	Hachinohe EW	
5	Kobe-050	Kobe EW	50%
6	Random-050	Random	
7	Hachinohe-100	Hachinohe EW	
8	Kobe-100	Kobe EW	100%
9	Random-100	Random	
10	Hachinohe-150	Hachinohe EW	
11	Kobe-150	Kobe EW	150%
12	Random-150	Random	

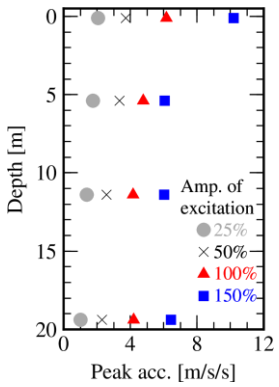

a) Peak accelerations

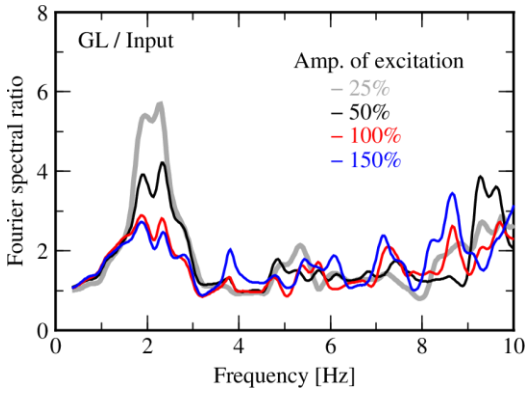

b) Fourier spectral ratios between ground surface (GL) and bottom of the shear box (Input)

Figure 2. Experimental results due to the four Kobe type excitations.

FINITE ELEMENT MODELING

In order to investigate the influence of the weight of the shear box on the dynamic soil response in the aforementioned experimental results, simulation analysis was performed by a three-dimensional FE analysis. The analysis method and model used in this study are briefly explained below.

Soil Constitutive Model

A soil constitutive model considered in this study is based on an elastic perfectly-plastic model (JGS, 2003). In the model, Mohr-Coulomb (MC) failure criterion is considered as a yield function. Drucker-Prager (DP) model is adopted for a plastic potential in order to avoid singular points during the calculation of flow rule. In this MCDP model, the yield function, *f*, and the plastic potential, *g*, are expressed as follows

$$f = -I_1 \cdot \sin\phi + \frac{\sqrt{J_2}}{2}\left\{3(1-\sin\phi)\sin\Theta + \sqrt{3}(3+\sin\phi)\cos\Theta\right\} - 3c\cdot\sin\phi = 0 \tag{1}$$

$$g = -\frac{\tan\psi}{\sqrt{9+12\cdot\tan^2\psi}}\cdot I_1 + \sqrt{J_2} \tag{2}$$

where c, ϕ, ψ, I_1, J_2, and Θ denote cohesion, internal frictional angle, dilatancy angle, the first invariant of the stress tensor, the second invariant of the deviatoric stress tensor, and the Lode angle, respectively. In this study, c is set to 0 because the Toyoura sand is used in the experiment. Also, ψ is set to 0° in order to avoid computational difficulties. In an elasto-plastic analysis by considering elastic-perfectly plastic material, the relationship between increments of stresses and strains can be expressed as

$$\{\Delta\sigma\} = \left[[D_e] - (1-\gamma)\cdot\frac{[D_e]\left\{\frac{\partial g}{\partial\sigma}\right\}\left\{\frac{\partial f}{\partial\sigma}\right\}^T[D_e]}{\left\{\frac{\partial f}{\partial\sigma}\right\}^T[D_e]\left\{\frac{\partial g}{\partial\sigma}\right\}}\right]\{\Delta\varepsilon\} \tag{3}$$

where $[D_e]$ is the elastic stress-strain matrix. The coefficient γ is a value calculated by Eq. (4). As can be seen from Eq. (3), when γ = 1, the material is elastic, and when γ = 0, it is in a plastic state. Therefore, by using Eq. (3), the incremental stress can be calculated from the incremental strain in a unified manner for any stress state (JGS, 2003).

$$\gamma = \frac{-f(\{\sigma\})}{f(\{\sigma\}+[D_e]\{\Delta\varepsilon\}) - f(\{\sigma\})} \tag{4}$$

Based on the MCDP model mentioned above, we carried out FE analyses using a Nested Surface (NS) model to represent the work-hardening effect by considering a number of similar yield surfaces in a stress space, as shown in Fig. 3. The concept of the NS model is introduced by Mróz (1967) and Iwan (1967).

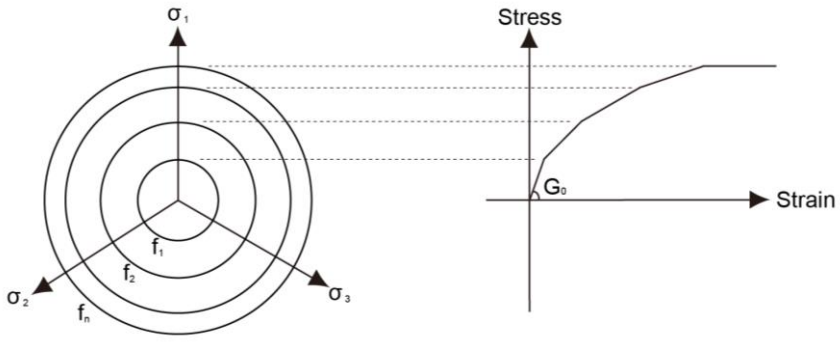

Figure 3. Schematic illustration on nested surface layers in the principal stress space and representation in the shear stress-strain curve.

Non-Iterative Time Integration Scheme

As in the previous studies by the authors (Nakagawa *et al*., 2020; Nakagawa *et al*., 2022), the non-iterative time integration scheme (Sakai *et al*., 1995; Honda *et al*., 2004) is applied for the dynamic elasto-plastic FE analysis in this study. The feature of this scheme is combining an implicit time integration scheme and an explicit scheme by taking their advantages. The scheme enables stable computation without an iteration process for convergence in the non-linear analysis. According to the literature, we can write the equation of motion, using the Newmark method (β = 1/4) as an implicit scheme, as

$$\{\Delta u\}=\left(\frac{4}{\Delta t^2}[M]+\frac{2}{\Delta t}[C]+[K]\right)^{-1}\left(\{\Delta f_{\text{ext}}\}+\{\Delta q\}+[M]\left(\frac{4}{\Delta t}\{\dot{u}\}+2\{\ddot{u}\}\right)+[C]\left(2\{\dot{u}\}\right)\right) \tag{5}$$

where $[M]$, $[C]$, and $[K]$ denote the mass, damping and stiffness matrices; $\{\Delta u\}$, $\{\Delta f_{\text{ext}}\}$, and $\{\Delta q\}$ are the displacement, external force, and the adjusting force vectors in incremental form, respectively; Δt indicates time step; a dot over the variable indicates differentiation with respect to time. $\{\Delta u\}$ is obtained by solving Eq. (5), then velocities and accelerations at the next time step can be obtained by Eqs. (6) and (7), respectively.

$$\{\dot{u}_{t+\Delta t}\}=\frac{\Delta t}{2}\left([M]+\frac{\Delta t}{2}[C]\right)^{-1}\{\Delta q\}+\frac{\Delta t}{2}\{\Delta u\}-\{\dot{u}\} \tag{6}$$

$$\{\ddot{u}_{t+\Delta t}\}=\left([M]+\frac{\Delta t}{2}[C]\right)^{-1}\{\Delta q\}+\frac{4}{\Delta t^2}\{\Delta u\}-\frac{4}{\Delta t}\{\dot{u}\}-\{\ddot{u}\} \tag{7}$$

$\{\Delta q\}$ in the above equations is given by

$$\{\Delta q\}_{\text{elem}}=\int[B]^T\left([D_e]\{\varepsilon\}-\{\sigma\}\right)dV \tag{8}$$

where V indicates the volume of the element. $[B]$ denotes the strain-displacement matrix. It is noted that $\{\Delta q\}_{\text{elem}}$ in Eq. (8) is element-wise while $\{\Delta q\}$ in Eqs. (5) - (7) is a global description.

Analysis Model

Figure 4 shows a FE mesh diagram used in the analysis. The analysis model is a half symmetry model consisting of solid elements to represent the shear box and sandy soil. The number of nodes is 5194, and the number of elements is 3080. In the analysis, acceleration motion measured at the bottom of the shear box during the experiment was the input at the bottom of the analysis model. As shown on the right-hand side of Fig. 4, the elements representing the shear box are rigid, and their nodes are set on x-directional roller conditions. Therefore, each layer of the elements for the shear box does not directory exchange forces with each other, but the forces are applied through elements of sandy soil. There is no gap between the elements because the double nodes are defined with the same coordinates. The density of the element was set to ρ = 2400 kg/m^3, based on a nominal value provided by a manufacturer. In this case, the mass ratio (MR) of the frame of the shear box to the model ground is approximately 50%. Figure 5 shows the settings of the soil properties used in the analysis. Figure 5a) depicts the distribution of initial S-wave velocities in the ground. The figure shows the S-wave velocity distribution for Toyoura sand at D_r = 70% derived from three regression equations proposed by some researchers (Kokusho, 1980; Kishida *et al*., 1997; Lo Presti *et al*., 1997). The S-wave velocity increases with depth using any equations since sand becomes stiffer as the confining pressure increases. The S-wave velocity evaluated by Kokusho's equation is found to be between the S-wave velocities by the other two equations. Based on this comparison, the initial S-wave velocity indicated

by the red line in Fig. 5a) was set according to Kokusho's equation. Figure 5b) shows the shear modulus reduction curve considered in the FE analysis. In this study, 50 yield surfaces were set in the NS model described earlier (see Fig. 3). Thus, the 50 internal frictional angles ϕ_i were set to express the shear modulus reduction curve investigated by Kokusho (1980), as shown in Fig. 5b). The Rayleigh damping was also used in the analysis. The Rayleigh damping of the soil and the shear box was set at 2% and 1%, respectively, at 2 Hz and 8 Hz. In the FE analysis, the time increment and the duration were set to $\Delta t = 0.002$ s and 25 s, respectively.

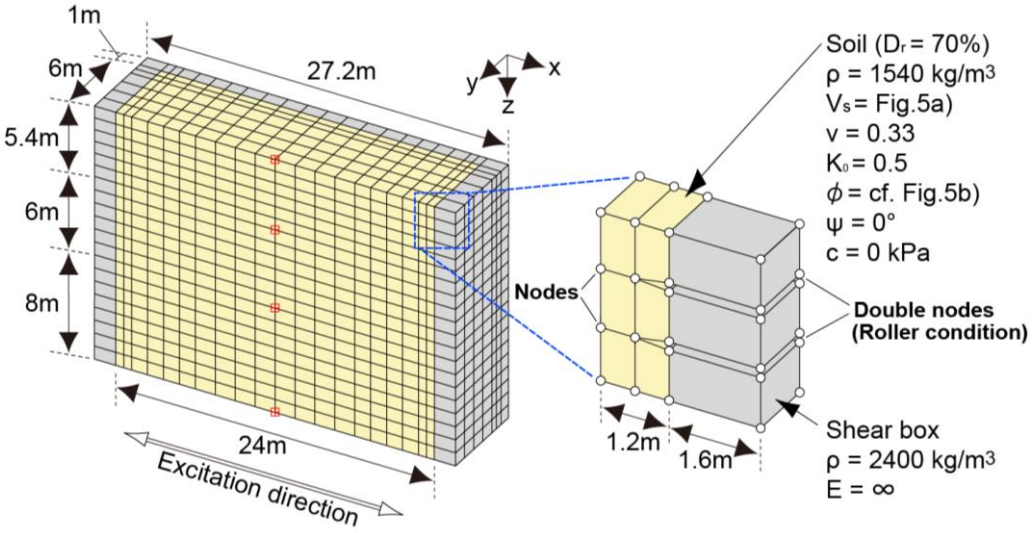

Figure 4. FE mesh diagram (The half symmetry model was used).

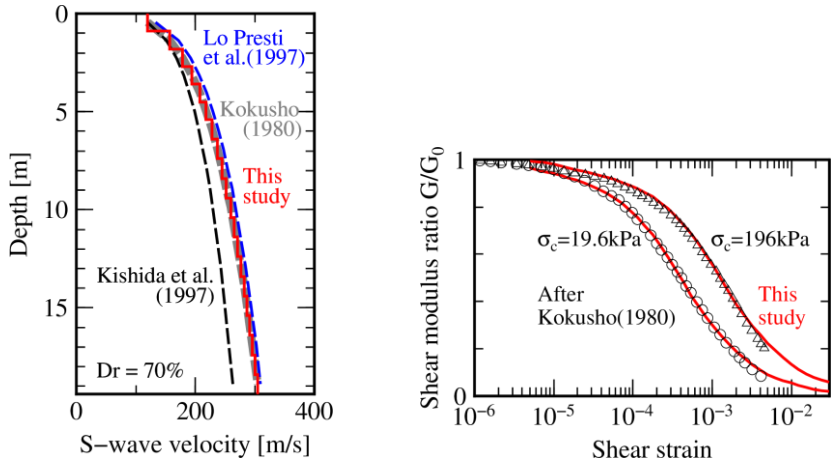

a) Initial S-wave velocity b) Shear modulus reduction curve

Figure 5. Soil properties considered in the FE analysis.

RESULTS AND DISCUSSION

Figure 6 compares acceleration waveforms at the ground surface. The figure shows the case of the input amplitudes of 25%, 50%, 100%, and 150%, from left to right. In the figure, the black line indicates the experimental result, and the blue and red lines denote analysis results. The red line indicates the analysis results for the FE model considering the weight of the shear box shown in Fig. 4. The blue line represents analysis results for only the sandy soil model without the shear box. The analysis without the shear box was performed using a one-dimensional soil column extracted from the

soil elements of the FE model shown in Fig. 4. As seen in Fig. 6, the waveforms computed from the two analyses, with and without the shear box, seem to correspond roughly to the experimental results regardless of the input amplitude. In detail, for the input amplitudes of 25%, 50%, and 100%, the analysis results with the shear box seem to correspond better to the experimental results than those without the shear box. At the 150% input amplitude, the amplitudes of accelerations of the two analyses results are smaller than those of the experimental results. In contrast, the phases of the analysis results roughly correspond to the experimental result. Besides, the maximum shear strains for the analysis with the one-dimensional soil column were 0.059%, 0.13%, 0.40%, and 0.75% at the input amplitudes of 25%, 50%, 100%, and 150%, respectively.

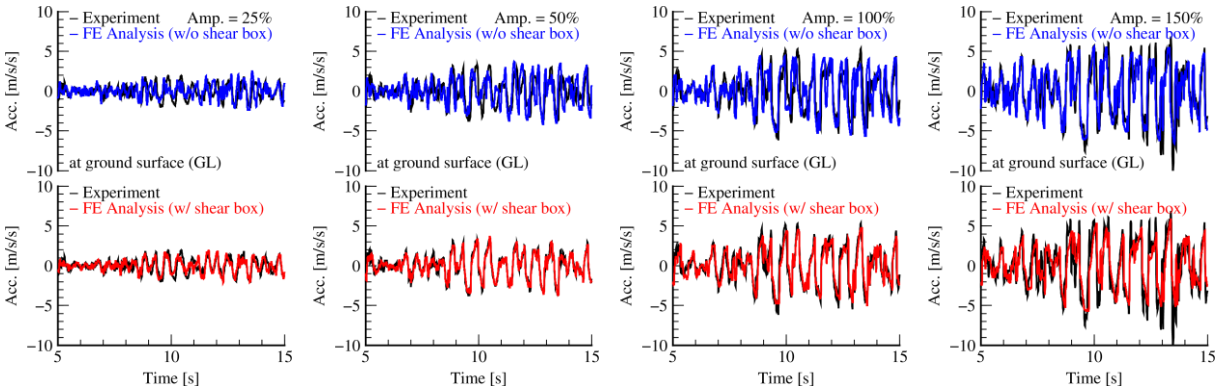

Figure 6. Comparison of acceleration time history at the ground surface.

Figure 7 compares the Fourier spectral ratios calculated from the acceleration waveforms at the ground surface or in the ground and the acceleration waveform at the bottom of the shear box. As in Figure 6, the black line indicates the experimental results, the blue line denotes the analysis results without the shear box, and the red line represents the analysis results with the shear box. As in Figure 6, from left to right, the input amplitudes are 25%, 50%, 100%, and 150%, respectively. In calculating the spectral ratios, both the experimental and analytical results were smoothed by the Parzen window with a bandwidth of 0.4 Hz. As can be seen from Fig. 7a), when the shear box is not considered in the analysis, the peak frequencies that appeared in spectral ratios of the analysis tend to be higher than those of the experiment. It can also be seen that the peak height of the analysis is lower with increasing input amplitude as in the experiment. At the input amplitude of 150%, the peak frequency and height roughly correspond to each other in the analysis and experiment. Next, Fig. 7b) compares the experimental results for the case where the shear box is considered in the analysis. It appears that both the peak frequency and height correspond better with the experimental results for all cases when compared to the results shown in Fig. 7a). However, at the 150% input amplitude, the peak height of the analysis seems to be slightly lower than that of the experiment.

Figure 8 compares the peak frequencies and heights of the spectral ratios calculated from waveforms at the ground surface and the bottom of the shear box. In addition to the previous three results (i.e., the experiment (black line), the case without the shear box (blue line), and the case considering the shear box (red dashed line)), the figure shows the case with shear box weight reduced by 1/2 (MR is about 25%, gray dashed line) and 1/4 (MR is about 13%, black dotted line). The open circles in the figure indicate the experimental results, and the triangles indicate the analysis results. As seen from Fig. 8, as the input amplitude increases, the peak frequency tends to decrease, and the peak height decreases in both the experimental and analysis results. The analysis results considering the shear box reproduce well the peak frequencies and heights of the experimental results. There appears to be a difference from the experimental results when the shear box is not considered in the analysis. When the weight of the shear box is varied in the analysis, the results approach those of the analysis without the shear box as the weight becomes lighter, suggesting that the weight of the shear box affected the experimental results. When the weight of the shear box is set to 1/4, the peak frequencies are generally similar to the peak frequencies obtained from the analysis without the shear box.

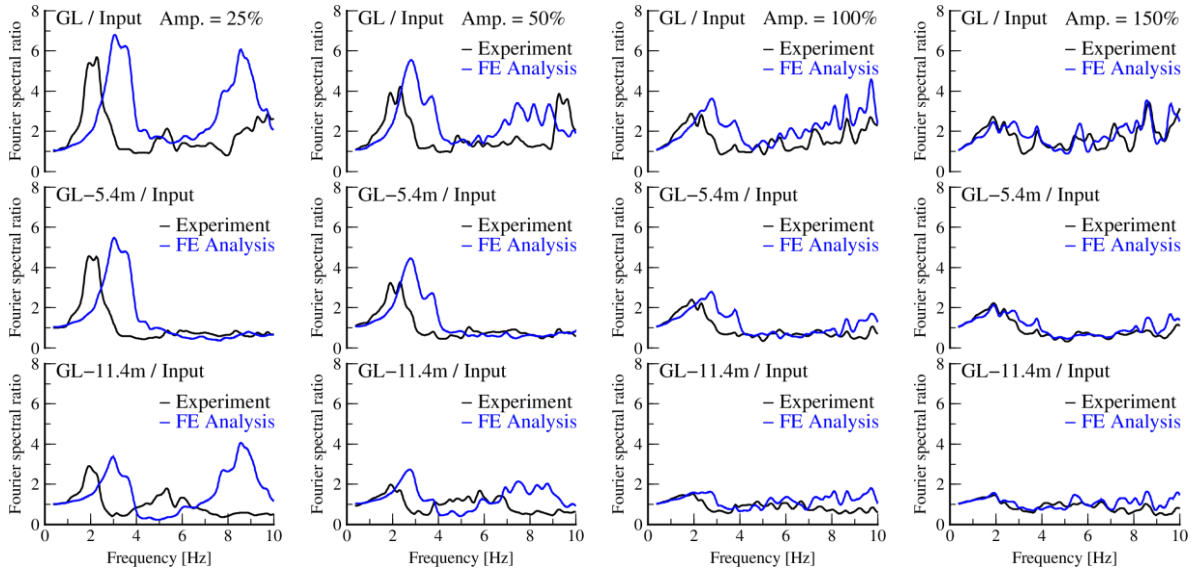

a) without shear box

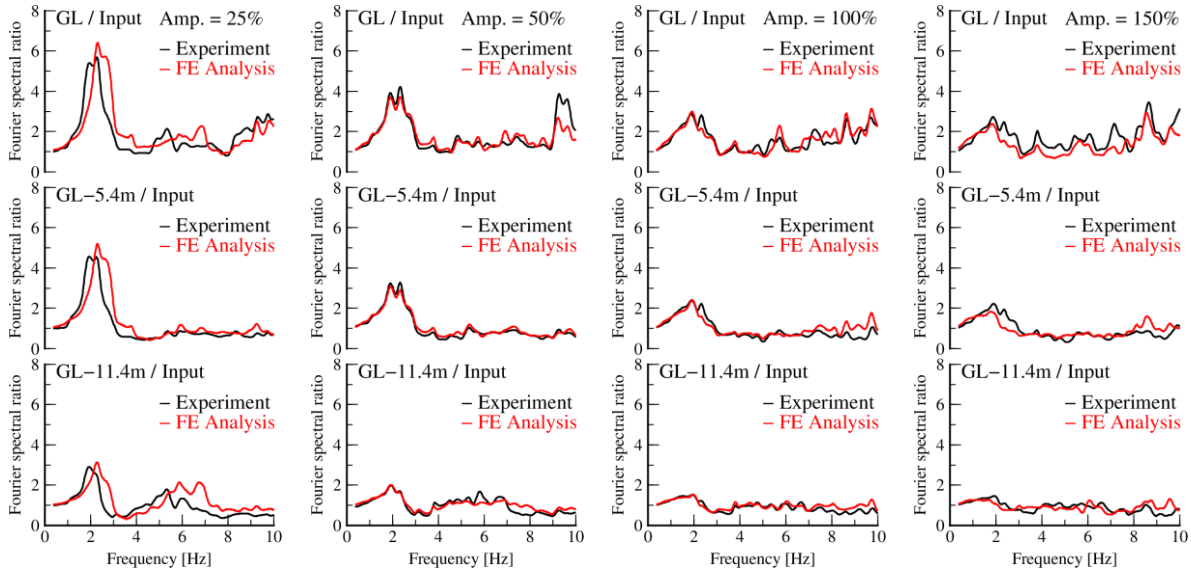

b) with shear box

Figure 7. Comparison of Fourier spectral ratios.

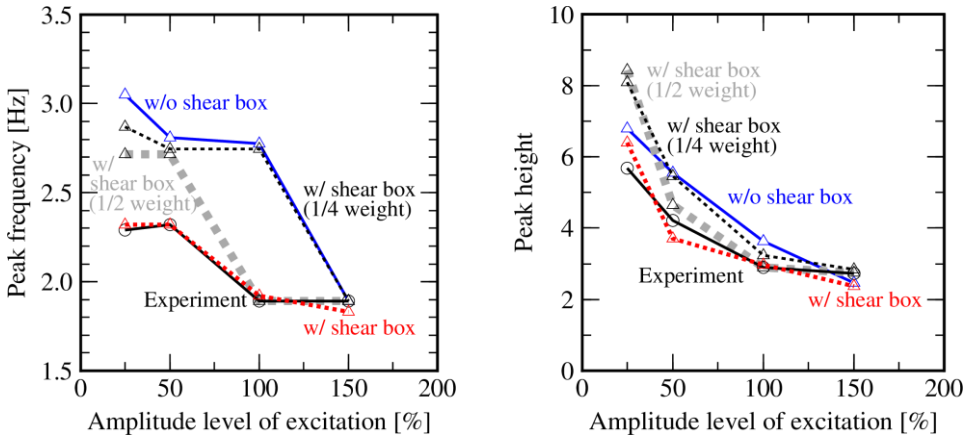

Figure 8. Comparison of peak frequencies and peak amplitudes.

CONCLUSIONS

In this study, the influence of the weight of the shear box on the seismic behavior of the model ground was studied through the centrifuge experiment and its simulation analysis performed by the three-dimensional FE analysis. From the study, the following conclusions can be attained:

- The three-dimensional FE analysis considering the weight of the shear box can approximately represent the characteristics of the spectral ratio between the ground surface (or in the ground) and the bottom of the shear box obtained in the experiments.
- The peak frequency of the spectral ratio between the ground surface and the bottom of the shear box obtained by the analysis without considering the shear box may shifts to a higher frequency than that obtained by the analysis considering the weight of the shear box.
- The weight of the shear box may influence the experimental results since the analysis results become closer to those without the shear box as the weight of the shear box is reduced. Within the scope of this study, the peak frequencies obtained in the analysis without the shear box were similar to those obtained in the analysis considering the weight of the shear box having approximately 13% of the mass ratio to the model ground.

However, the analysis considering the weight of the shear box underestimates the peak height of the spectral ratio at the input amplitude of 150%. It is one of the subjects of future study.

ACKNOWLEDGMENTS

This study was partially supported by JSPS KAKENHI Grant Number 20H02306. The authors utilized Generic Mapping Tool (Wessel & Smith, 1998) to draw some figures herein.

REFERENCES

Honda R, H. Sakai and S. Sawada (2004). "Non-iterative time integration scheme for non-linear dynamic FEM analysis," *Earthquake Engineering and Structural Dynamics*, **33**, 111-132.

Iwan W.D. (1967). "On a class of models for the yielding behavior of continuous and composite systems," *Journal of Applied Mechanics (Transactions of the ASME)*, **34**(3), 612-617.

JGS (2003). *Understanding Elasto-Plastic Finite Element Methods*, Japan Geotechnical Society (JGS). (in Japanese)

Kishida S., Y. Katsura and S. Nishio (1997). "Centrifuge model tests of shear wave and Young's moduli on sand," *Technical Research Report of Shimizu Construction Co., Ltd.*, (65), 9-14. (in Japanese)

Kokusho T. (1980). "Cyclic triaxial test of dynamic soil properties for wide strain range," *Soils and Foundations*, **20** (2), 45-60.

Lo Presti D.C.F., M. Jamiolkowski, O. Pallara, A. Cavallaro and S. Pedroni (1997). "Shear modulus and damping of soils," *Geotechnique*, **47** (3), 603-617.

Mróz Z. (1967). "On the description of anisotropic workhardening," *Journal of the Mechanics and Physics of Solids*, **15**(3), 163-175.

Nakagawa H., H. Kashiwa and S. Nakai (2020). "Three-dimensional finite element analysis of a building with insulated pile foundation," *Proceedings of the 17th World Conference on Earthquake Engineering, Sendai, Japan*, 4c-0050, 12 p.

Nakagawa H., H. Kashiwa and S. Nakai (2022). "Applicability of a simple constitutive model for Three-dimensional finite element analysis on Dynamic Soil-Structure Interaction Problem," *Proceedings of the 3rd European Conference on Earthquake Engineering & Seismology, Bucharest, Romania*, 192-201.

Sakai H., S. Sawada and K. Toki (1995). "Non-iterative computation scheme for nonlinear dynamic finite element method," *J. Japan Soc. Civil Eng.*, **507/I-30**, 137-147. (in Japanese)

Wessel P. and W.H.F. Smith (1998), "New, improved versions of generic mapping tools released," EOS, AGU.

ANTI-PLANE RESPONSES IN FREQUENCY DOMAIN AND TIME DOMAIN INDUCED BY AN OBLIQUE-TRUNCATED SEMICIRCULAR CANYON

Wen-Shinn Shyu[1], Chi-Wei Lu[2] and Po-Kai Wu[3]

1. Professor, Department of Civil Engineering, National Pingtung University of Science and Technology, Pingtung, Taiwan, R.O.C.
2. Professor, Department of Civil and Construction Engineering, National Taiwan University of Science and Technology, Taipei, Taiwan, R.O.C.
3. Associate Professor, Department of Civil and Construction Engineering, National Yunlin University of Science and Technology, Yunlin, Taiwan, R. O. C.

Email: wsshyu@mail.npust.edu.tw, cwlu@mail.ntust.edu.tw, wupokai@yuntech.edu.tw

ABSTRACT

This paper proposes a method for the investigation of displacement amplitude ($|\overline{u}_y|$) in the frequency domain near and along an oblique-truncated semicircular canyon subjected to shear horizontal (*SH*) waves. A mapping function, transfinite interpolation (TFI), was used to mesh the irregular canyon. The hybrid method combined finite element method and Lamb series was applied to investigate the effects of canyon geometry, the incident angle of *SH* waves (θ), and dimensionless frequency (η) on $|\overline{u}_y|$. The site effect including canyon-decay-effect and oblique-effect were observed in the oblique-truncated semicircular canyon. By introducing the inverse fast Fourier transform (IFFT), we also obtained the amplification of u_y in the time domain.

Keywords: *SH* Wave, Scattered Wave, Oblique-truncated Semicircular Canyon, Hybrid Method, Transfinite Interpolation.

INTRODUCTION

Ground motions generated by earthquake increase due to the site of surface irregularities, such as canyons, are measured from the records (Trifunac, 1973). This phenomenon could be attributed to the scattering waves and diffraction waves from the numerical models, such as domain methods, boundary methods, and hybrid methods (Shyu and Teng, 2014). Several theoretical and numerical methods have been developed to analyze the phenomenon. A simple model of shear horizontal waves (*SH* waves) were introduced by different shapes of canyon due to the mode conversion could be ignored. The discussed shapes of canyon included semi-cylindrical canyon (Trifunac, 1973), semi-elliptical canyon (Wong and Trifunac, 1974) circular cylindrical canyon with various depth-to-width ratios (Cao and Lee, 1989), semi-elliptical canyon (Wong and Trifunac, 1974), symmetrical V-shaped (Tsaur *et al*., 2008; Tsaur *et al*., 2010; Zhang *et al*., 2012;), U-shaped canyon (Gao *et al*., 2012), non-symmetrical V-shaped canyon (Zhang *et al*., 2012), a circular-arc cross-section canyon (Yuan *et al*., 1994) and truncated semicircular canyon (Tsaur *et al*., 2009) as well as oblique truncated semicircular canyon (Shyu *et al*., 2015). However, the previous studies almost focused on the frequency domain. Only few study focused on the wave propagation in time domain (Takemiya and Fujuwara, 1994; Tsaur *et al*., 2008). In this study, the scattering of SH waves induced by an oblique-truncated semicircular canyon were solved in frequency domain by using hybrid method with transfinite interpolation (TFI, Knupp and Steinberg, 1994). The incident time signal is set as a Ricker wavelet, and the transient responses are obtained through the inverse fast Fourier transform (FFT).

PROBLEM DESCRIPTION

In Fig.1(a), a 2D model consists of an oblique-truncated semicircular canyon embedded in the half-space and excited by a unit-amplitude plane *SH* wave with circular frequency ω, incident angle θ, and displacement in the *y*-direction. The symbols $2a$, d_1 and d_2 represent the width, left-hand side depth, and the right-hand side depth of the oblique-truncated semicircular canyon, respectively. The elastic half-plane is divided into Ω and Ω^0 by a semi-circular interface *C*. Ω^0 is a finite domain that encloses the oblique-truncated semicircular canyon.

NUMERICAL MODEL

Hybrid Method

The hybrid method was developed based on a boundary value problem (Shyu, *et al.*, 2015). A following matrix equation is obtained as Eq. (1):

$$\begin{bmatrix} \mathbf{K}^{aa} - \omega^2 \mathbf{M}^{aa} & -\mathbf{K}^{ac} \\ -\mathbf{K}^{ca} & \mathbf{K}^{cc} \end{bmatrix} \begin{Bmatrix} \bar{\mathbf{u}}_y^0 \\ \mathbf{c} \end{Bmatrix} = \begin{Bmatrix} \mathbf{P}^a \\ -\mathbf{P}^c \end{Bmatrix} \tag{1}$$

where $\left[\mathbf{K}^{aa}\right]$ and $\left[\mathbf{M}^{aa}\right]$ are the stiffness matrix and mass matrix obtained using the formulation of finite element method. $\left\{\mathbf{P}^a\right\}$ and $\left\{\mathbf{P}^c\right\}$ are the force vectors on boundary *C*. $\left[\mathbf{K}^{ac}\right]$ and $\left[\mathbf{K}^{ca}\right]$ are the coupling matrices, which are formed by combining the displacement in Ω^0 and the traction of the scattered field on the boundary *C*. $\left[\mathbf{K}^{cc}\right]$ is the matrix formed by combining the traction and displacement of the scattered field on the boundary *C*. Vector $\left\{\bar{\mathbf{u}}_y^0\right\}$ is the frequency displacement responses under ω of nodal points in the region . Vector $\{\mathbf{c}\}$ represents the unknown coefficients (C_n) in the scattered field. The scattered waves can be formulated as a series representation with determined coefficients $\{\mathbf{c}\}$. The frequency displacement responses ($\bar{u}_y$) in Ω is shown as:

$$\bar{u}_y = \bar{u}_y^f + \sum_{n=0}^{N} C_n \left(\bar{u}_y^s\right)_n \tag{2}$$

where $\left(\bar{u}_y^s\right)_n$ is a Lamb series which satisfies the traction-free boundary conditions and radiation conditions. $\bar{u}_y^f$ is the frequency displacement responses of half-space under impinging *SH* waves. It is noticed $\left|\bar{u}_y^f\right| = 2.0$ with various incident angles and frequency of *SH* waves.

Transfinite Interpolation

The finite domain Ω^0 including an oblique truncated semicircular canyon shown in Fig. 1(a) could be mapped into a rectangular domain and its finite element meshes are discretized in the rectangular domain (Shyu, *et al.*, 2015). The coordinates in rectangular domain $\mathbf{X} = (X, Z) = (X_{\bar{n}}, Z_{\bar{n}}) = (\bar{X}_n, \bar{Z}_m)$ and $0 \le X, Z \le 1$ are easily chosen, where $\bar{n} = n + (m-1) \times (\bar{N} + 1)$ with $n, m = 1, 2, \cdots \bar{N} + 1$, as well as $\bar{N}$ is the number of nodes on one length of the rectangular domain. The real boundaries of Ω^0 are $\mathbf{x}_b$, $\mathbf{x}_t$, $\mathbf{x}_\ell$ and $\mathbf{x}_r$ as the bottom, top, left, and right boundaries of the finite domain. By using the TFI formula as Eq. (3):

$$\begin{aligned}\left(x_{\bar{n}}, z_{\bar{n}}\right) = &\left(1-\bar{Z}_m\right)\mathbf{x}_b(n) + \bar{Z}_m\mathbf{x}_t(n) + \left(1-\bar{X}_n\right)\mathbf{x}_\ell(m) + \bar{X}_n\mathbf{x}_r(m) \\ &-\left\{\bar{X}_n\bar{Z}_m\mathbf{x}_t^1 + \bar{X}_n\left(1-\bar{Z}_m\right)\mathbf{x}_b^1 + \bar{Z}_m\left(1-\bar{X}_n\right)\mathbf{x}_t^0 + \left(1-\bar{X}_n\right)\left(1-\bar{Z}_m\right)\mathbf{x}_b^0\right\}\end{aligned} \tag{3}$$

where superscript 0 and 1 represent the starting point and end point for the boundaries. Therefore, we can obtain the coordinates of the mesh grids in the region Ω^0 .

Numerical Examples

In this study, two cases are discussed as Case 1 ($d_1/a = 0.5$ and $d_2/a = 0.25$) and Case 2 ($d_1/a = 0.75$ and $d_2/a = 0.5$). An example of FEM mesh of Ω^0 in Case 1 is shown in Fig. 1(b), with 1600 Q8 elements and 4961 nodes. A dimensionless frequency $\eta = 2a/\lambda = \omega a/\pi C_s$ is introduced. η is the ratio of the width of the oblique-truncated semicircular canyon to the incident wave length (λ) of *SH* wave. Figure 2 presents the results of the amplitude of displacement ($|\bar{u}_y|$) on the free surface. The 3D plots show the amplitudes versus x/a (from −5 to 5) and η (from 0.02 to 3.00). In Case1, the results of θ with 0 and $\pi/2$ are shown in Fig. 2(a) and (b). In Case 2, the results of θ with 0 and $\pi/2$ are shown in Fig. 2(c) and (d). To fix a special position, the variation function with frequency could be regarded as a transfer function. According to the transfer functions of frequency domain, we can introduce the inverse fast Fourier transform (IFFT) to obtain the displace responses in time domain.

Time Domain Responses

The transient response is obtained from the frequency domain results through the IFFR algorithm. The incident time signal is a Ricker wavelet:

$$u_{Ric}(t) = \left[2\pi^2 f_c^2 (t-t_s)^2 - 1\right]\exp\left[-\pi^2 f_c^2 (t-t_s)^2\right] \tag{4}$$

where f_c is the characteristic frequency of the wavelet and t_s is the peak amplitude of the wavelet in time domain. In this study, the Ricker parameters are selected at $f_c = 0.5Hz$ and $t_s = 6.0sec$. The Ricker wavelet in time domain and its corresponding Fourier amplitude spectrum are shown in Fig. 3(a) and 3(b), respectively. The absolute value of maximum displacement amplitude in time domain is 1, that means the maximum amplitude is 2 on the surface without canyon. The calculated frequencies are 96 in total, the range from 0.0 to 1.52 with 0.016 intervals. The time window is chosen as 16 *sec*. The half-width of the canyon is set to be 1 *km*. The shear wave propagates vertically with the velocity $C_s = 1km/sec$ and the reference point is set to be $(x,z) = (0, 6/\cos\theta)$ for $t = 0sec$, that means the Ricker wavelet arrives at the position $(x,z) = (0,0)$ without canyon is 6 *sec*. For a particular frequency, $\bar{u}(f)$ should be multiplied by $\bar{u}_{Ric}(f)$ in Fig. 3(b) and the transfer function in Fig. 2. Then the time domain results can be obtained by using the IFFT. The time domain signals of 4 special positions in Case 1 and Case 2 are shown in Fig. 4 and Fig. 6, respectively. Figures 5 and 7 show the

synthetic seismogram which contains 341 time-series received from positions located along the surface of the oblique-truncated semicircular canyon and the half-space between $x = -4$ and 4 *km* in Case 1 and Case 2, respectively. In Figs. 5 and 7, D means the arrival waves, SM1 and SM2 indicate the waves generated by the left and right corners. SR and SL indicate the scattered waves propagated to the right and left directions.

RESULTS AND DISCUSSIONS

This study investigated asymptotic variations $|\overline{u}_y|$ due to an oblique-truncated semicircular canyons in Case 1 and Case 2. In frequency domain, an oblique-effect is suppressed under special frequency, resulting in a decrease $|\overline{u}_y|$ at the surface of oblique-truncated semicircular canyons. A canyon-decay-effect also generates a maximum $|\overline{u}_y|$ at the canyon corner near the wave source, and $|\overline{u}_y|$ decays quickly along the canyon surface. In time domain, it is easily to observe the wave propagations. The incident waves, reflective waves and the scattered waves are clearly shown with various positions and time. It is helpful to figure the phenomenon of the waves around the surface irregularities.

CONCLUSIONS

This study introduced a hybrid method combining a Lamb series and finite element method to solve the scattering of *SH* waves by an oblique-truncated semicircular canyon. A mapping function TFI was used to mesh the irregularities. Under the impinging *SH* waves, the oscillations associated with surface motion on the left-part horizontal increase with an increase in η and θ. The maximum value of $|\overline{u}_y|$ was shown in the top-left corner of the canyon. Between the top corners, the $|\overline{u}_y|$ of the canyon surface are decreased due to the canyon-decay-effect. In the truncated semicircular canyons, a discontinuous slope appears in the bottom corners, leading to a rapid change in $|\overline{u}_y|$, called the oblique-effect.

With the responses in frequency domain (i.e., transfer function), we combined the frequency responses of the impact incident wave (such as the Ricker wavelet) and using the IFFT to calculate the surface responses in time domain. The responses in time domain are helpful to obtain the spectrum. It could be useful for engineers to design the buildings near the canyon surface.

ACKNOWLEDGMENTS

The authors would like to thank the Ministry of Science and Technology, Taiwan R. O. C. for financially supporting this research under Contract No. MOST 111-2221-E-020-015-

REFERENCES

Cao, H., and V. W. Lee (1989). "Scattering of plane *SH* waves by circular cylindrical canyons with variable depth-to-width ratio," *European Earthquake Engineering* **3**, 29-37.

Guo, Y. F., Zhang, N., Li D. Y., Liu H. L., Cai Y. Q. and Wu, Y. X., (2012). "Effects of topographic amplification induced by a U-shaped canyon on seismic waves," *Bulletin of the Seismological Society of America*, **102**, 1748-1763.

Knupp, P., and Steinberg, S., (1994). *Fundamentals of Grid Generation*, CRC Press, Inc.

Shyu, W. S., and Teng T. J., (2014). "Hybrid method combines transfinite interpolation with series expansion to simulate the anti-plane response of a surface irregularity," *Journal of Mechanics*, **30**, 349-360.

Shyu,W. S., Teng, T. J., and Chou, C. S., (2015). "Determining anti-plane responses induced by oblique-truncated semicircular canyon using systematic hybrid method with mapping function," *Soil Dynamics and Earthquake Engineering*, **77**, 24-34.

Takemiya, H., and Fujiwara, A., (1994). "*SH*-wave scattering and propagation analyses at irregular sites by time domain BEM," *Bulletin Seismological Society of America*, **84**, 1443-1455.

Trifunac, M. D., (1973). "Scattering of plane *SH* waves by a semi-cylindrical canyon," *Engineering and Structural Dynamics*, **1**(3), 267-281.

Tsaur, D. H. and Chang, K. H., (2008). "An analytical approach for the scattering of *SH* waves by a symmetrical V-shaped canyon: shallow case," *Geophysical Journal International,* **174**, 255-264.

Tsaur, D. H. and Chang, K. H., (2009). "Scattering of *SH* waves by truncated semicircular canyon," *Journal of Engineering Mechanics*, **135**, 862-870.

Tsaur, D. H., Chang, K. H., and Hsu, M. S., (2010)., "An analytical approach for the scattering of *SH* waves by a symmetrical V-shaped canyon: deep case," *Geophysical Journal International,* **183**, 1501-1511.

Wong, H. L. and Trifunac, M. D., (1974). "Scattering of plane *SH* waves by a semi-elliptical canyon," *Earthquake Engineering and Structural Dynamics*, **3**(2), 157-169.

Yuan, X. M., Liao, Z. P., and Trifunac, M. D., (1994). "Scattering of plane *SH* waves by a cylindrical canyon of circular-arc cross-section," *Soil Dynamics and Earthquake Engineering*, **13**, 407-412.

Zhang, N., Gao Y. F., Li D. Y., Wu, Y. X. and Zhang, F., (2012). "Scattering of *SH* waved by a symmetrical V-shaped canyon : a unified analytical solution," *Earthquake Engineering and Engineering Vibration*, **11**, 445-460.

Zhang, N., Gao, Y. F., Cai Y. Q., Li D. Y. and Wu Y. X., (2012). "Scattering of *SH* waves induced by a non-symmetrical V-shaped canyon," *Geophysical Journal International*, **191**, 243-256.

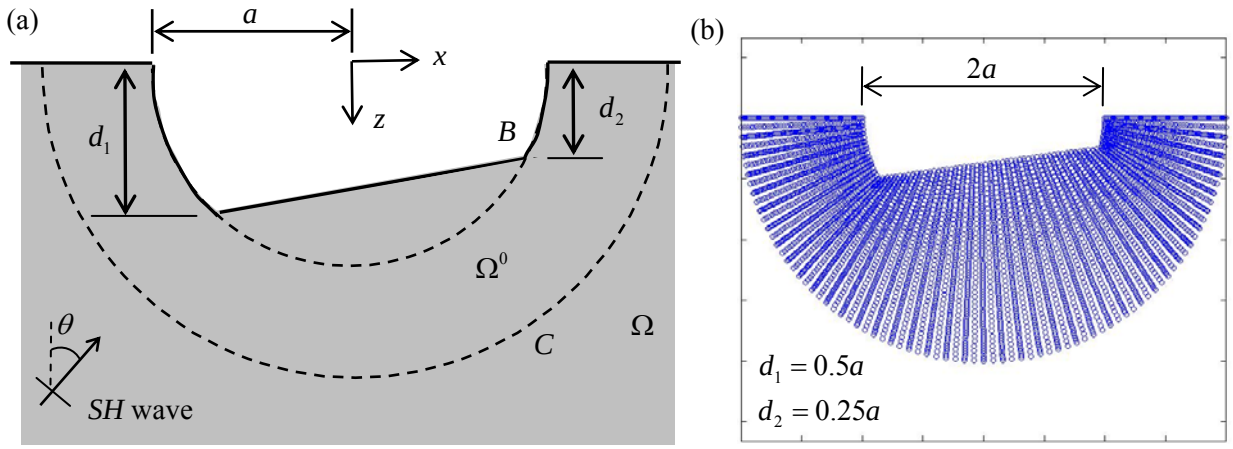

Figure 1. (a) Schematic diagram showing oblique-truncated semicircular canyon (b) FEM mesh of Ω^0 including oblique-truncated semicircular canyon in Case 1

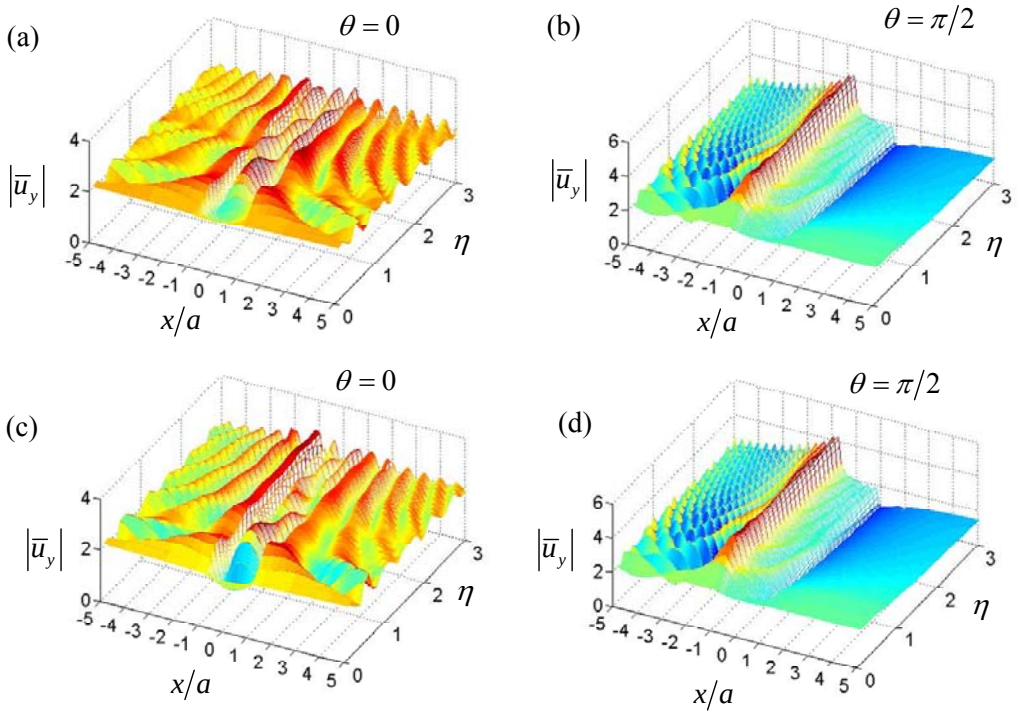

Figure 2. 3D plots showing amplitudes of surface displacement in Case 1 with (a) $\theta = 0$, and (b) $\theta = \pi/2$; in Case 2 with (c) $\theta = 0$, and (d) $\theta = \pi/2$

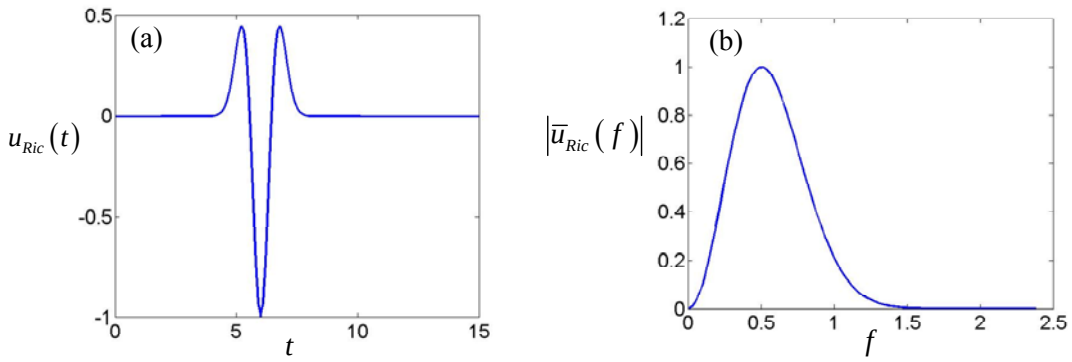

Figure 3 (a) The incident Ricker wavelet in time domain and (b) in frequency domain.

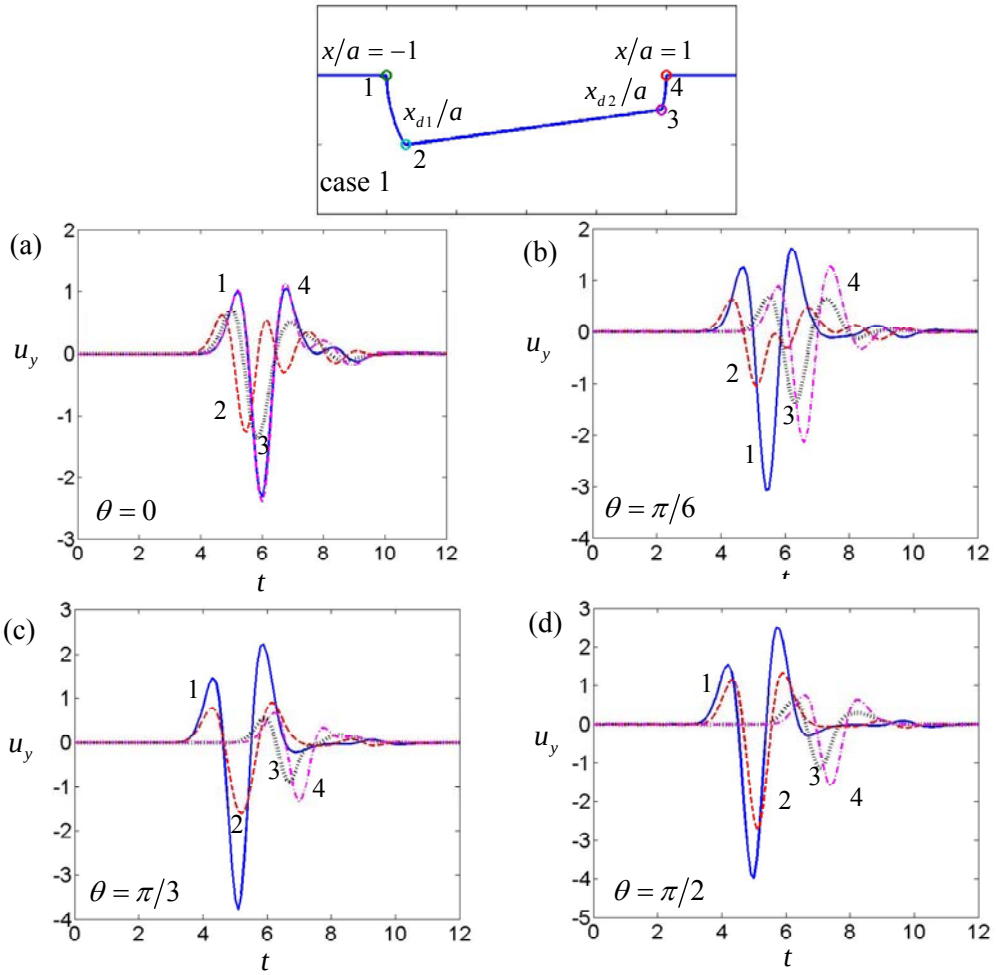

Figure 4. Displacement amplitudes in time domain at four positions and various incident angles for Case 1.

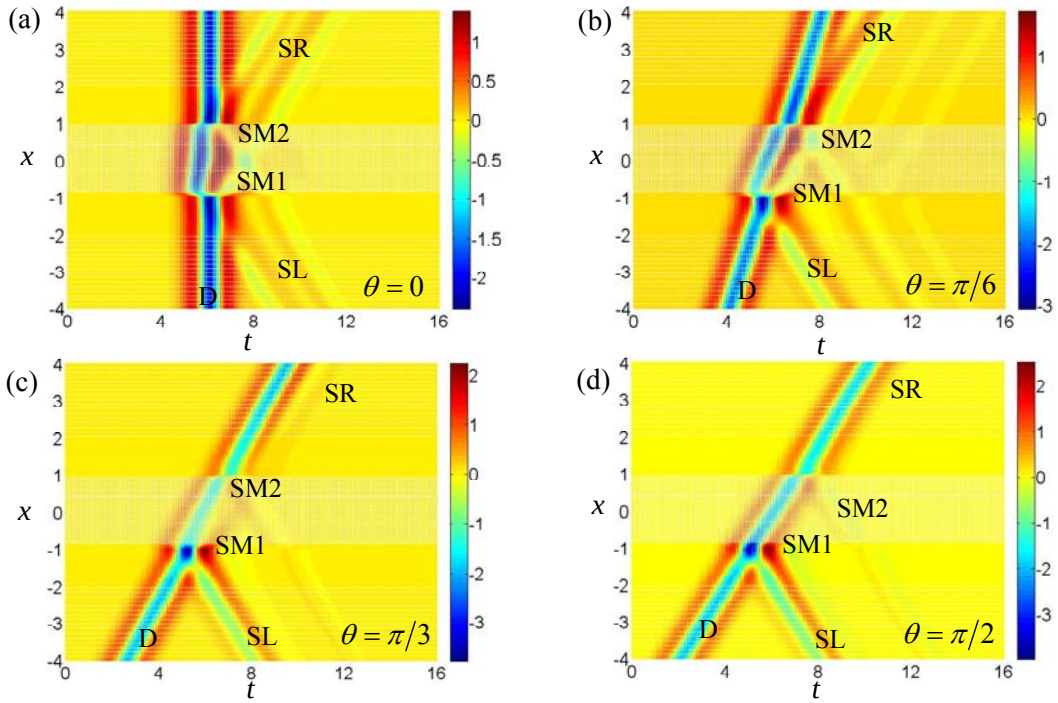

Figure 5. Synthetic seismogram at various incident angles for Case 1

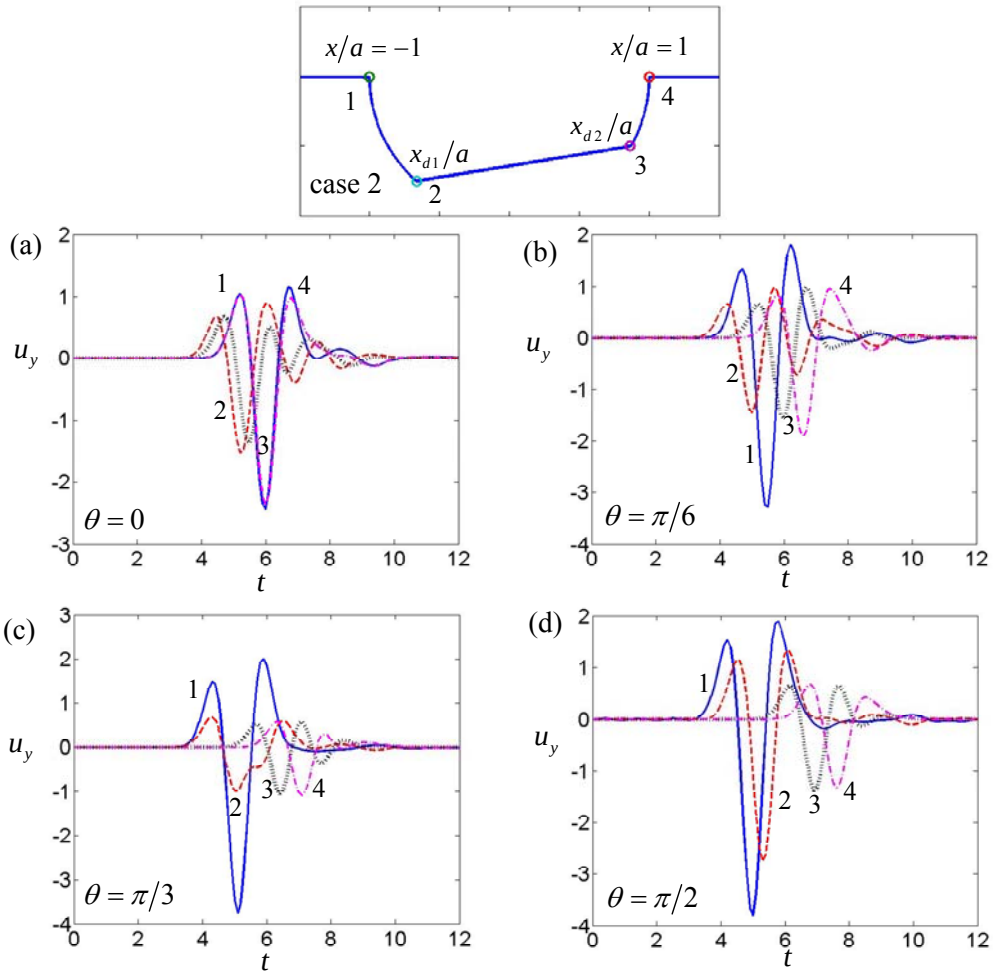

Figure 6. Displacement amplitudes in time domain at four positions and various incident angles for Case 2.

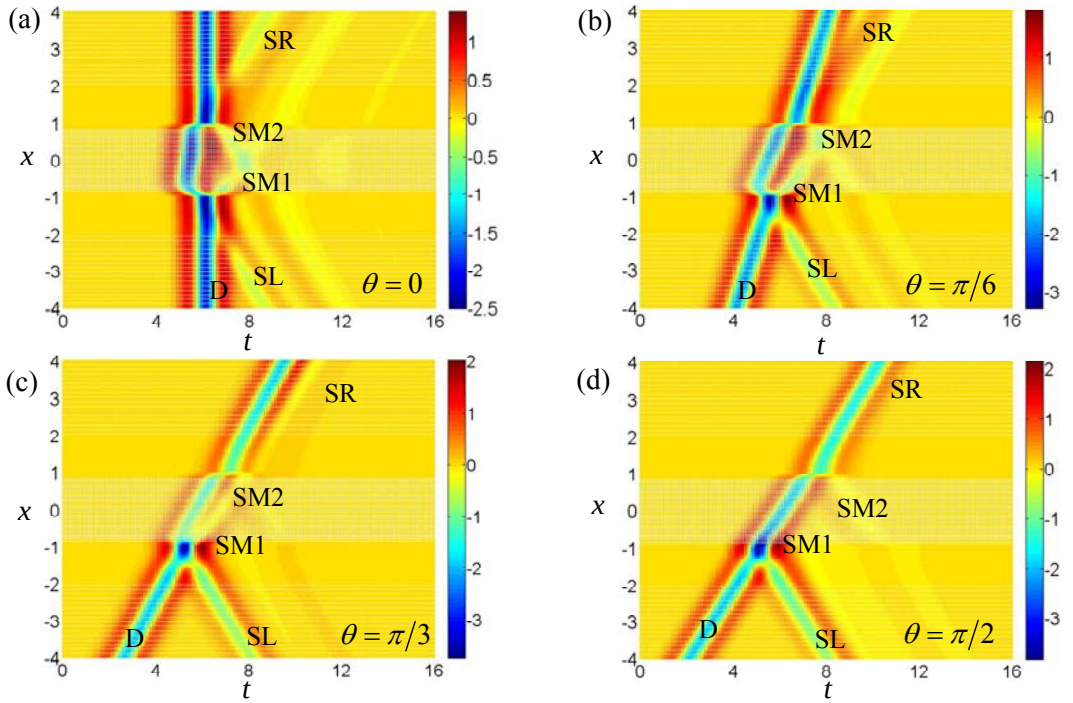

Figure 7. Synthetic seismogram at various incident angles for Case 2

(2b) Soil liquefaction and ground failure

EVALUATION OF LIQUEFACTION RESISTANCE IN UNDRAINED CYCLIC TRIAXIAL TESTS BY USING ENERGY-BASED METHOD

Thirapong Pipatpongsa[1]
1. Associate Professor, Department of Urban Management, Kyoto University, Kyoto, Japan
Email: pipatpongsa.thirapong.4s@kyoto-u.ac.jp

ABSTRACT

The actual earthquake wave is not a harmonic motion of a specific amplitude; therefore, evaluation of liquefaction resistance for design is required to improve the stress-based method. This work confirmed that the relationships between the number of cycles for the initial liquefaction based on the energy approach is independent on relative density; therefore, evaluation of liquefaction resistance is more general and useful than the stress-based method. The number of cycles for the initial liquefaction based on the stress method and the energy method revealed a good agreement through various physical quantities obtained from a series of undrained cyclic triaxial tests.

Keywords: soil liquefaction, cyclic triaxial test, energy-based method, stress-based method

INTRODUCTION

Though the cyclic resistance ratio (CRR) determined from the laboratory using a sine wave motion is widely used in engineering practice, the actual earthquake wave is not a harmonic motion of a specific amplitude. Therefore, evaluation of liquefaction resistance for design still need more researches to improve the stress-based method (SBM). Unlike SBM, the concept of energy-based method (EBM) rooted in the assumption of the dissipation of seismic energy per unit volume of soil has been recently developed (Kokusho 2017; Kokusho 2018; Kokusho 2021) for liquefaction potential evaluations and the associated large liquefaction-induced soil settlement. According to Kokusho (2018), despite the shortcoming of cyclic triaxial test for which the axial strain on the extension is larger than that on the compression side, the cumulative dissipated energy ($\Sigma\Delta W$) based on shear work can determine the liquefaction behaviors. As $\Sigma\Delta W$ is not limited to a harmonic motion, it can be generally applied to irregular seismic motion. The unique relations between the $\Sigma\Delta W$ obtained by EBM and CRR obtained by SBM under a given cyclic stress ratio (CSR) and the number of cycles for liquefaction (N_L) in triaxial tests were found irrespectively of relative density and fine contents of sands. Though the cyclic resistance ratio (CRR) determined from the laboratory using a sine wave motion is widely used in engineering practice, the actual earthquake wave is not a harmonic motion of a specific amplitude. Therefore, evaluation of liquefaction resistance for design still need more researches to improve SBM by developing EBM in the on-going development of a new design concept.

This study aims to investigate various criteria by which the liquefaction resistance is evaluated by the energy dissipation per unit volume using a set of undrained cyclic triaxial tests on reconstituted sand. The characteristics in pore water pressure buildup, the double amplitude of axial strain and the stress ratio of deviatoric stress to the effective mean stress observed in the experiment of different densities to reach the state of soil liquefaction under seismic lading were demonstrated in terms of both cyclic number and dissipated energy.

MATERIALS AND METHODS

Mountain sand taken at Kure City, Hiroshima prefecture was used as the specimen material, and is referred to as Hiroshima sand in this study. Table 1 shows the physical and mechanical properties of Hiroshima sand. The abbreviations of physical quantities are summarized in Table 2. The total number of 9 tests were carried out to investigate the liquefaction resistance for specimens prepared with three different relative densities (D_r) of 45%, 55% and 65% and a certain range of cyclic stress ratios (CSR).

Test conditions are shown in Table 3 where groups A, B and C represent D_r of 45%, 55% and 65%, respectively. As labeled by 1, 2 and 3, three different cyclic stress ratios (CSR) varied between 0.13-0.20 were applied to each group; therefore, tests A1~A3, B1~B3 and C1~C3 are labeled.

Tthe specimen was prepared under the specific degree of compaction in a summit mold (diameter 5 cm and height 10 cm). Constant density is controlled by compacting every 1 cm thick layers. The top of a sample is covered by the filter paper and porous stone and sealed by vinyl tape with some holes for ventilation (see Fig. 1(A). Next, the sample is placed in a desiccator (see Fig. 1(B)), and filled with the distilled water. The processes of deaeration by air suction and exposure to atmospheric pressure around 5 minutes are repeated until the mass of the summit mold by which the specimen is contained becomes constant. By preparing the specimen by this method, the void can be filled with distilled water in advance, and consequently the degree of saturation can be effectively reach 95% or more every time. Then, the specimen is frozen in a freezer for one day so that the specimen can keep its shape after the removal of the summit mold in the undrained cyclic triaxial test (see Fig. 1(C)). Cyclic stress with a constant amplitude is applied until liquefaction occurs and the number of cycles is counted.

Table 1. Material properties of dry Hiroshima sand

Soil particles density ρ_s	g/cm^3	2.633	Maximum dry densiy ρ_{dmax}	g/cm^3	1.75
Fines content F_c	%	9.2	Optimum water content w	%	11
Maximum void ratio e_{max}	-	1.007	Permeability coefficient k	m/s	2.4×10^{-5}
Minimum void ratio e_{min}	-	0.444	Effective friction angle ϕ'	o	31.3

Table 2. List of abbreviations

Abbreviation	Definition	Abbreviation	Definition
D_r	Relative density	M	Stress ratio at critical state
N_c	Number of cyclic loads	N_l	N_c for initial liquefaction
σ_a	Axial stress	σ_r	Radial stress
$\sigma_d=\sigma_a-\sigma_r$	Stress deviator	$\tau_d=\sigma_d/2$	Maximum shear stress
u	Pore water pressure	u_i	Initial u after consolidation
$\Delta u=u-u_i$	Excess pore water pressure	$p=(\sigma_a+2\sigma_r)/3$	Mean total stress
$p'=p-u$	Mean effective stress	p_i	Initial p after consolidation
$\sigma'_c=p_i-u_i$	Pre-consolidation pressure	$\eta=\sigma_d/p'$	Stress ratio
$\Delta u/\sigma'_c$	Excess pore water pressure ratio	u/p	Pore water pressure ratio
ε_a	Axial strain	$\varepsilon_r=-\varepsilon_a/2$	Radial strain
$CSR=\tau_d/\sigma'_c$	Cyclic stress ratio	$DA=2\lvert\varepsilon_a\rvert$	Double amplitude of strain
$\Sigma W/\sigma'_c$	Normalized accumulated elastic strain energy	$\Sigma\Delta W/\sigma'_c$	Normalized accumulated dissipation energy

Table 3. Summary of cyclic stress ratio (CSR) specified to each test with pre-consolidation pressure (σ'_c) shown in brackets

Condition		Cyclic stress ratio (CSR)		
Relative density (D_r)	Test	1	2	3
45%	A	0.13 (83)	0.15 (72)	0.18 (80)
55%	B	0.15 (87)	0.18 (96)	0.20 (81)
65%	C	0.15 (94)	0.18 (97)	0.20 (89)

RESULTS

If power regression is used to relate the cyclic stress ratio (τ_d/σ'_c or $\sigma_d/2\sigma'_c$) and the number of cyclic loads for initial liquefaction (N_l), the simple and its logarithmic form could be considered below.

$$\frac{\sigma_d}{2\sigma'_c}=10^{\alpha}N_c^{\beta} \quad (1)$$

$$\log\left(\frac{\sigma_d}{2\sigma_c'}\right) = \alpha + \beta \log(N_c) \quad (2)$$

where α and β are assumed to be approximated by Eq. (3) and Eq. (4), respectively,

$$\alpha = a_1 + a_2 D_r + a_3 DA + a_4 D_r DA \quad (3)$$

$$\beta = b_1 + b_2 D_r + b_3 DA + b_4 D_r DA \quad (4)$$

For a set of D_r = 45%, 55% and 65% and DA = 2.5%, 5% and 10%, the coefficients a_1, a_2, a_3 and a_4 as well as b_1, b_2, b_3 and b_4 are determined by linear regression using data of Table 5 in Appendix. The liquefaction strength curve is shown in Fig. 1(D) for which the number of cycles to reach double amplitude axial strain of 2.5%, 5%, 10% were considered. As a result, cyclic resistance ratio (CRR) can be determined from Eq. (1) using N_c = 20 for a given D_r and DA as listed in Table 4.

Table 4. Summary of cyclic resistance ratio (CRR) at N_c = 20 for different relative densities (D_r) and double amplitude of strains (DA)

Condition		Double amplitude of strain (DA)		
Relative density (D_r)	Test	2.5%	5%	10%
45%	A	0.118	0.119	0.122
55%	B	0.151	0.153	0.157
65%	C	0.194	0.197	0.201

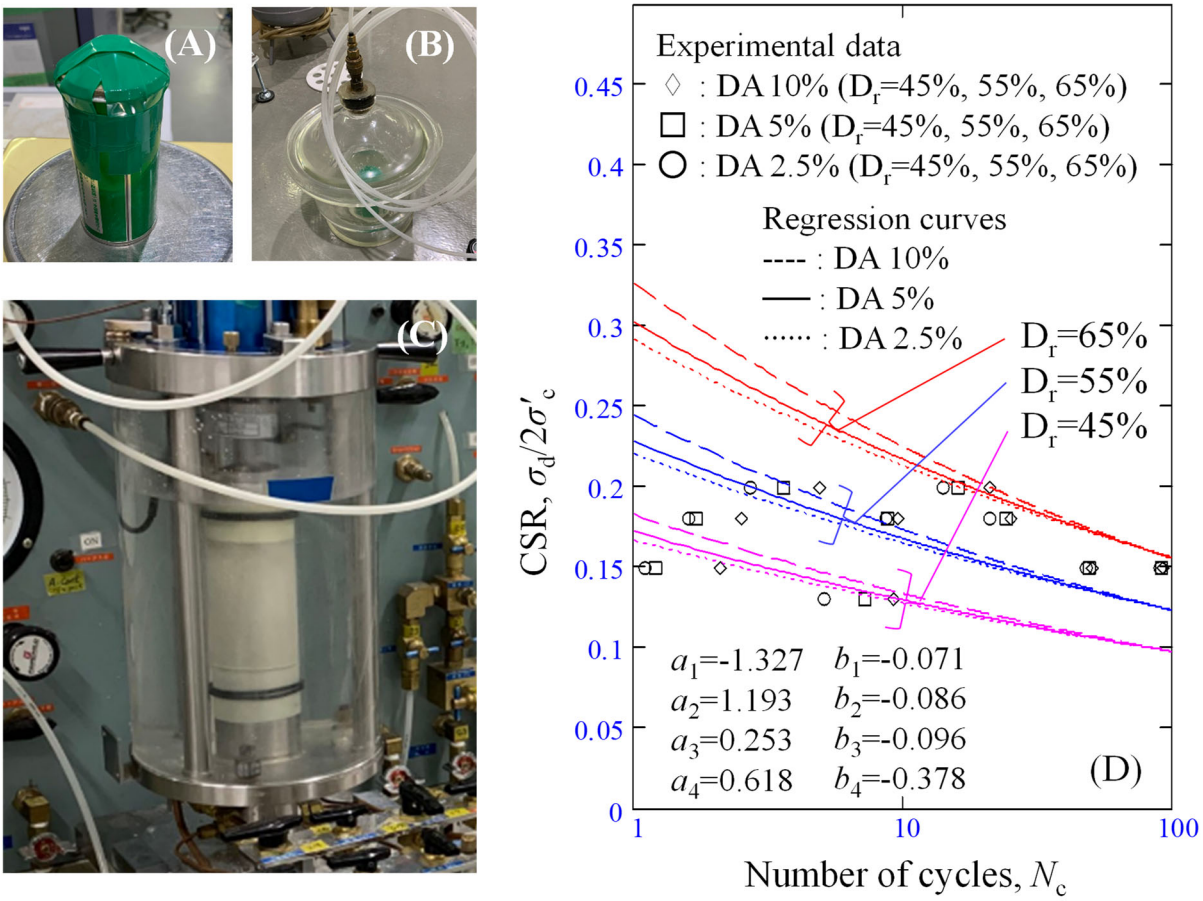

Figure 1. Undrained cyclic triaxial tests (A) Desiccator, (B) Frozen sample, (C) Triaxial apparatus, (D) Liquefaction strength curve

The results of EBM are shown in Figs. 3, 4 and 5 in Appendix. The characteristics of results are discussed in Fig. 2 through unique relationships regardless of relative densities. The relations between DA & $\Delta u/\sigma'_c$ as well as $\Delta u/\sigma'_c$ & $\Sigma\Delta W/\sigma'_c$ can be fitted by parabolic forms shown in Eq. (5), Eq. (6) and Fig. 2(A) as well as Eq. (7), Eq. (8) and Fig. 2(B), respectively.

$$\frac{\Delta u}{\sigma'_c}=\frac{c_2 DA}{c_1+DA},\quad DA=\frac{c_1\dfrac{\Delta u}{\sigma'_c}}{c_2-\dfrac{\Delta u}{\sigma'_c}} \qquad (5),\ (6)$$

$$\frac{\Delta u}{\sigma'_c}=\frac{d_2\dfrac{\Sigma\Delta W}{\sigma'_c}}{d_1+\dfrac{\Sigma\Delta W}{\sigma'_c}},\quad \frac{\Sigma\Delta W}{\sigma'_c}=\frac{d_1\dfrac{\Delta u}{\sigma'_c}}{d_2-\dfrac{\Delta u}{\sigma'_c}} \qquad (7),\ (8)$$

The unique relation between $\Sigma\Delta W/\sigma'_c$ & $\Sigma W/\sigma'_c$ can be fitted by power regression shown in Eq. (9), Eq. (10) and Fig. 2(C). In order to compare with SMB, the number of cycles at the initial liquefaction can be regressed from Eq. (11) using linear relationships with D_r and CSR through Eqs. (12) and (13) and Fig. 2(D).

$$\frac{\Sigma W}{\sigma'_c}=k_1\cdot\left(\frac{\Sigma\Delta W}{\sigma'_c}\right)^{k_2},\quad \frac{\Sigma\Delta W}{\sigma'_c}=\frac{1}{k_1}\cdot\left(\frac{\Sigma W}{\sigma'_c}\right)^{\frac{1}{k_2}} \qquad (9),\ (10)$$

$$N_l=\left(\frac{1}{10^{\lambda}}\frac{\Sigma W}{\sigma'_c}\right)^{\frac{1}{\mu}} \qquad (11)$$

$$\lambda=l_1+l_2D_r+l_3CSR+l_4D_r\cdot CSR,\quad \mu=m_1+m_2D_r+m_3CSR+m_4D_r\cdot CSR \qquad (12),\ (13)$$

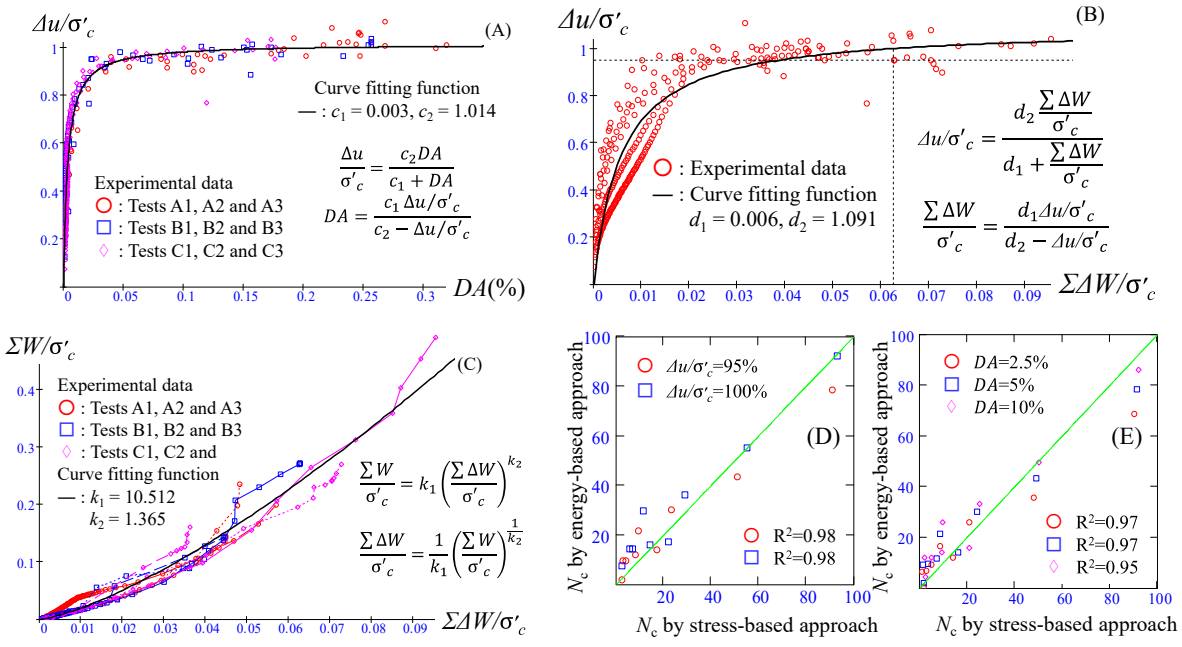

Figure 2. Unique relationships obtained by curve fitting functions: (A) DA & $\Delta u/\sigma'_c$, (B) $\Delta u/\sigma'_c$ & $\Sigma\Delta W/\sigma'_c$, (C) $\Sigma\Delta W/\sigma'_c$ & $\Sigma W/\sigma'_c$, (D) N_c corresponding to $\Delta u/\sigma'_c$ and (E) N_c corresponding to DA

CONCLUSIONS

This work confirmed that the number of cycles for the initial liquefaction based on energy method were agreed well with those based on stress method through unique relationships between various physical quantities obtained from a series of undrained cyclic triaxial tests.

APPENDIX

Experimental datasets of undrained cyclic triaxial tests are summarized by Figs. 1-11 and Table xx-xxx.

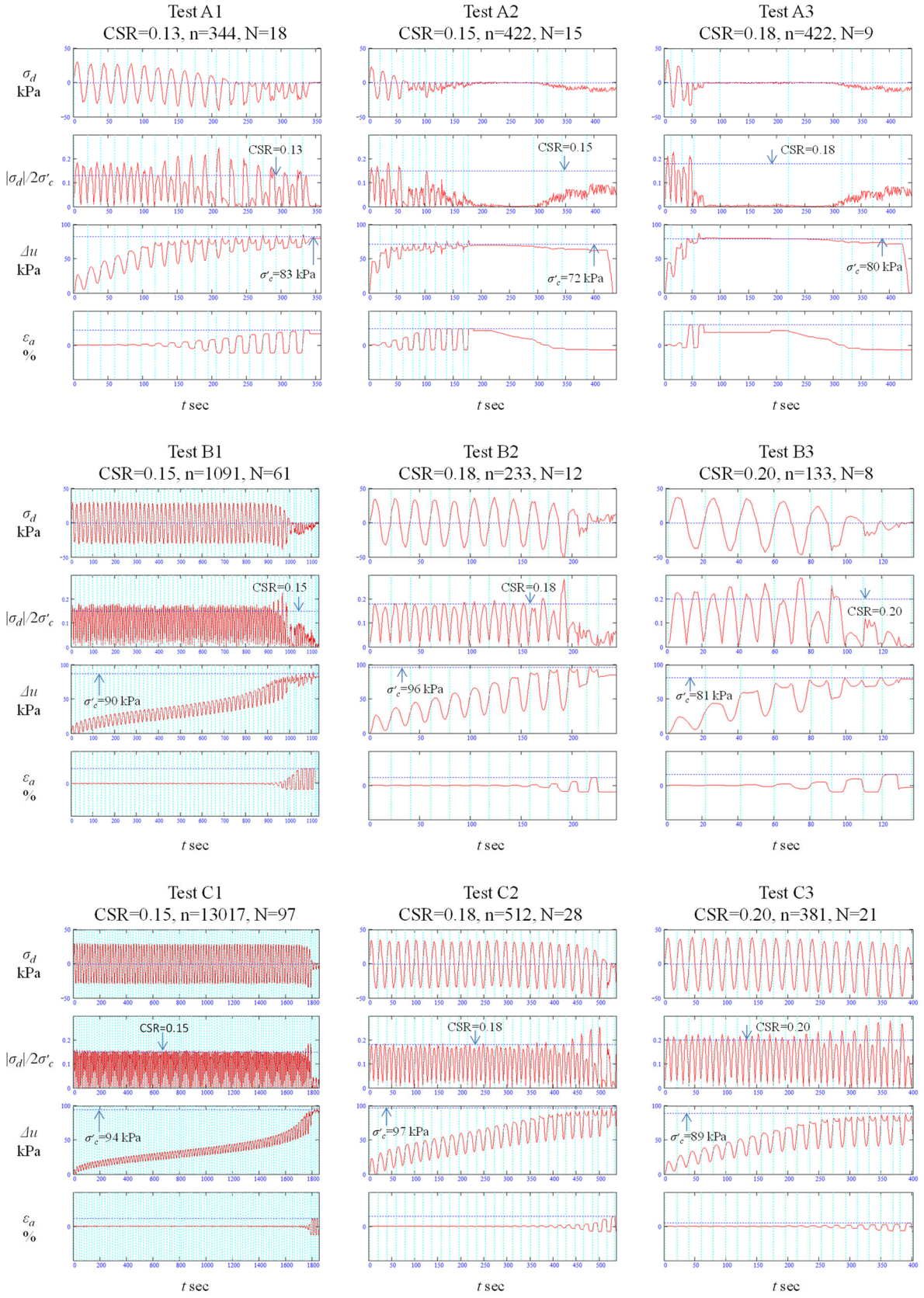

Figure 3. Experimental data for undrained cyclic triaxial tests

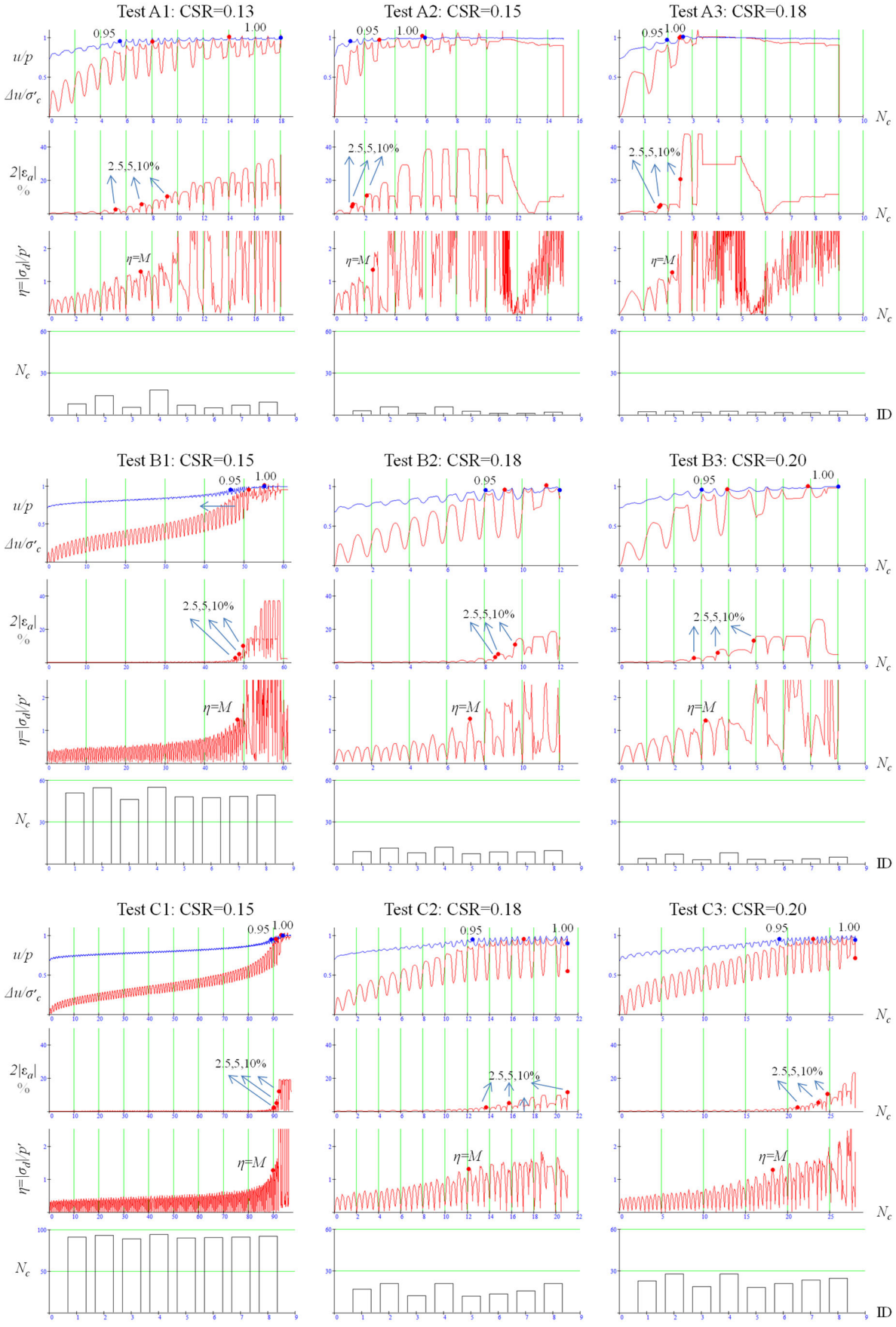

Figure 4. Number of cycles based on liquefaction judgements

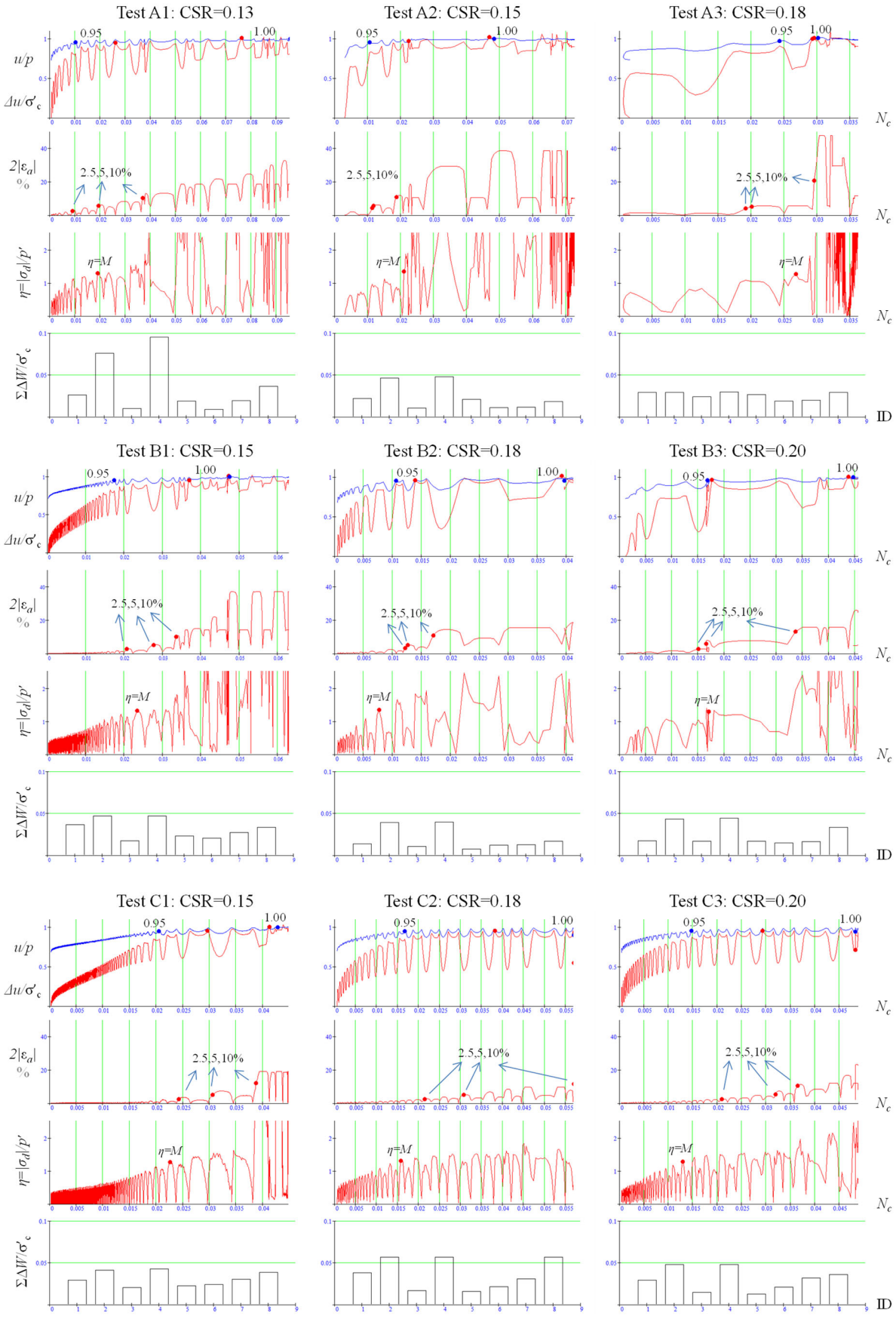

Figure 5. Energy loss based on liquefaction judgements

Table 5. Number of cycles (N_c) by each liquefaction judgement for all tests

Criterion	$\Delta u/\sigma'_c$		u/p		η	DA		
Limit	0.95	1.00	0.95	1.00	M=1.26	2.5%	5%	10%
ID	1	2	3	4	5	6	7	8
N_c (A1)	8	14	5.4	18	7.1	5.1	7.2	9.2
N_c (A2)	2.9	5.76	1	5.9	2.5	1.1	1.2	2.1
N_c (A3)	2.5	2.53	1.9	2.6	2.2	1.6	1.7	2.5
N_c (B1)	51	55	46	55	48	48	49	50
N_c (B2)	9.1	11.3	8	13	7.2	8.6	8.7	9.6
N_c (B3)	3.9	6.97	3	9	3.1	2.7	3.6	4.9
N_c (C1)	91	93	89	94	90	90	91	92
N_c (C2)	23	29	19	29	18	21	24	25
N_c (C3)	17	22	12	22	12	14	16	21

Table 6. Energy loss ($\Sigma\Delta W/\sigma'_c$) by each liquefaction judgement for all tests

Criterion	$\Delta u/\sigma'_c$		u/p		η	DA		
Limit	0.95	1.00	0.95	1.00	M=1.26	2.5%	5%	10%
ID	1	2	3	4	5	6	7	8
$\Sigma\Delta W/\sigma'_c$ (A1)	0.0261	0.0762	0.0103	0.0955	0.019	0.0091	0.0193	0.0370
$\Sigma\Delta W/\sigma'_c$ (A2)	0.0224	0.0468	0.0105	0.0483	0.021	0.0114	0.0118	0.0187
$\Sigma\Delta W/\sigma'_c$ (A3)	0.0293	0.0296	0.0243	0.0301	0.0268	0.0192	0.0201	0.0296
$\Sigma\Delta W/\sigma'_c$ (B1)	0.0369	0.0472	0.0174	0.0474	0.0233	0.0206	0.0276	0.0335
$\Sigma\Delta W/\sigma'_c$ (B2)	0.0138	0.0375	0.0106	0.0674	0.0077	0.0122	0.0127	0.0168
$\Sigma\Delta W/\sigma'_c$ (B3)	0.0176	0.0437	0.0168	0.0291	0.0171	0.0150	0.0166	0.0336
$\Sigma\Delta W/\sigma'_c$ (C1)	0.0296	0.0412	0.0205	0.0427	0.0226	0.0243	0.0306	0.0387
$\Sigma\Delta W/\sigma'_c$ (C2)	0.0293	0.0482	0.0147	0.0482	0.013	0.0209	0.0319	0.0364
$\Sigma\Delta W/\sigma'_c$ (C3)	0.0382	0.0569	0.0167	0.0569	0.0157	0.0215	0.0308	0.0569

ACKNOWLEDGMENTS

This research was supported by JSPS KAKENHI Grant Number 20H02242. Thanks are offered to Mr. Shoya Hirakawa and Mr. Takahiro Uemoto for their assistance with the experiments.

REFERENCES

Kokusho, T. (2017). *Innovative Earthquake Soil Dynamics*, CRC Press.

Kokusho, T. and Y. Kaneko (2018). "Energy evaluation for liquefaction-induced strain of loose sands by harmonic and irregular loading tests," *Soil Dynamics and Earthquake Engineering*, **114**, 362-377.

Kokusho, T. and S. Tanimoto (2021). "Energy capacity versus liquefaction strength investigated by cyclic triaxial tests on intact soils," *Journal of Geotechnical and Geoenvironmental Engineering*, **147**(4), Pages 04021006

Tsuchida, S., Y. Murai, T. Pipatpongsa, Y. Miyazaki (2020). "Centrifugal model tests on the influence of arch action on the liquefaction inside embankment resting on non-liquefiable ground," *Kansai Geo-symposium*, **8**, 106-111 (in Japanese).

Uemoto, T., S. Hirakawa, T. Pipatpongsa and Y. Miyazaki (2021). "Liquefaction resistance of local sandy soil evaluated by cyclic triaxial tests using the energy method," *JSCE Annual Meeting*, III-301 (in Japanese).

A COMPARISON STUDY OF CPT-BASED METHODS FOR ASSESSING LIQUEFACTION POTENTIAL OF SOILS: A HBF SIMPLIFIED METHOD

Jin-Hung Hwang[1], Jiun-Shiang Wang[2], and Chih-Chieh Lu[3]
1. Professor, Dept. of Civil Engineering, National Central University, Taoyuan, Taiwan, R.O.C.
2. Assistant Research Fellow, Earth Sciences and Geotechnical Engineering Division, National Center for Research on Earthquake Engineering, Taipei, Taiwan, R.O.C.
3. Researcher, Earth Sciences and Geotechnical Engineering Division, National Center for Research on Earthquake Engineering, Taipei, Taiwan, R.O.C.
Email: jinhunghwang@gmail.com, jswang@narlabs.org.tw, chchlu@narlabs.org.tw

ABSTRACT

This paper performs a comparative study of cone penetration test-based (CPT-based) methods for assessing soil liquefaction potential using case histories of liquefaction. Since CPT is the major approach for site investigation in offshore wind farm (OWF), the CPT-based methods should be adopted for liquefaction evaluation. Due to the lack of liquefied and non-liquefied cases in marine sites, the available CPT-based methods are established using cases from onshore sites, such that picking one method up to assess soil liquefaction potential is the state-of-art. In order to provide a reference as choosing acceptable methods for the future design code for OWF in Taiwan, a comparison of the success rates of predicting liquefaction of current methods with the HBF method, which is trained by case histories in Taiwan, has been carried out using liquefaction and non-liquefaction cases from Chi-Chi earthquake and from Boulanger and Idriss (2016). The results show that the success rates of most methods are within 91-95% for Chi-Chi earthquake data and within 80-85% for data from Boulanger and Idriss. The success rates for non-liquefied cases are higher than those for liquefied cases for Chi-Chi data. Finally, the relative conservativeness between different methods is presented by statistical indices.

Keywords: Soil liquefaction, cone penetration test, hyperbolic function, 1999 Chi-Chi earthquake

INTRODUCTION

Soil liquefaction is a critical earthquake hazard in Taiwan. Therefore, how to evaluate the impact of soil liquefaction on OWT design is a key issue. Since CPT is the main site investigation mean in OWF practice, the CPT-based methods should be adopted for liquefaction evaluation. However, the available CPT-based methods are established using cases from onshore sites, so that picking one method up to assess soil liquefaction potential is the state-of-art for engineers. In order to suggest acceptable methods in the future Taiwan design code for OWF design, it is necessary to compare the prediction accuracy and conservativeness of different methods.

In this paper, the methods developed by Olsen (1997), NCEER (2001), Hwang et al. (2005), Moss et al. (2006), Robertson (2009), Ku and Juang (2012), Boulanger and Idriss (2016) are selected to do comparison study. Among them, Hwang et al. (2005) developed a Taiwan local CPT-based simplified method based on the liquefaction and non-liquefaction cases in 1999 Chi-Chi earthquake and used hyperbolic function (**H**yper**B**olic **F**unction, HBF) to fit the boundary curve of CRR. It is called the HBF method. This paper will briefly present the HBF simplified procedure at the first because the geotechnical profession is not familiar with this method. Then compare the success rates of prediction by various methods and their relative conservativeness by statistical indices using the data bases from Boulanger and Idriss (2016), and from Chi-Chi earthquake.

INTRODUCTION OF HBF METHOD

Figure1 shows a flowchart that illustrates the procedure of soil liquefaction evaluation using the HBF CPT-based method for soils with a soil behavior index (I_c) less than 2.6 (i.e., sand-like soils). The main

feature of this method is to use the following hyperbolic function to fit the cyclic strength curve for judging whether soil liquefaction occurs or not.

$$\mathrm{CRR}_{7.5} = 0.09 + \frac{0.00028\left(\mathrm{q_{c1N}}\right)_{\mathrm{cs}}}{1-\left(\mathrm{q_{c1N}}\right)_{\mathrm{cs}}/180} \tag{1}$$

where 0.09 corresponds to a CRR_{lim}, the minimum intrinsic value of liquefaction resistance; 0.00028 corresponds to the rate of increase in *CRR* with respect to $(q_{c1N})_{cs}$; and 180 corresponds to $(q_{c1N})_{cs}^{upp}$, an upper bound, beyond which soil will be too dilative to liquefy. The function form is very simple and its three coefficients have physical meanings. The above three coefficients are calibrated to a boundary *CRR* curve with a probability of liquefaction P_L=50%. Thus this *CRR* curve is an unbiased model. The other feature of HBF method is the correction of fines content on *CRR* is a little conservative, especially for non-plastic silty soils. This is due to a lot of liquefied cases of non-plastic silty soils in central Taiwan were observed during Chi-Chi earthquake. The development of the SPT-N version of HBF method can be referred to Hwang et al. (2021). The evaluation procedures and details of other CPT-based methods can be referred to the original papers listed in the reference.

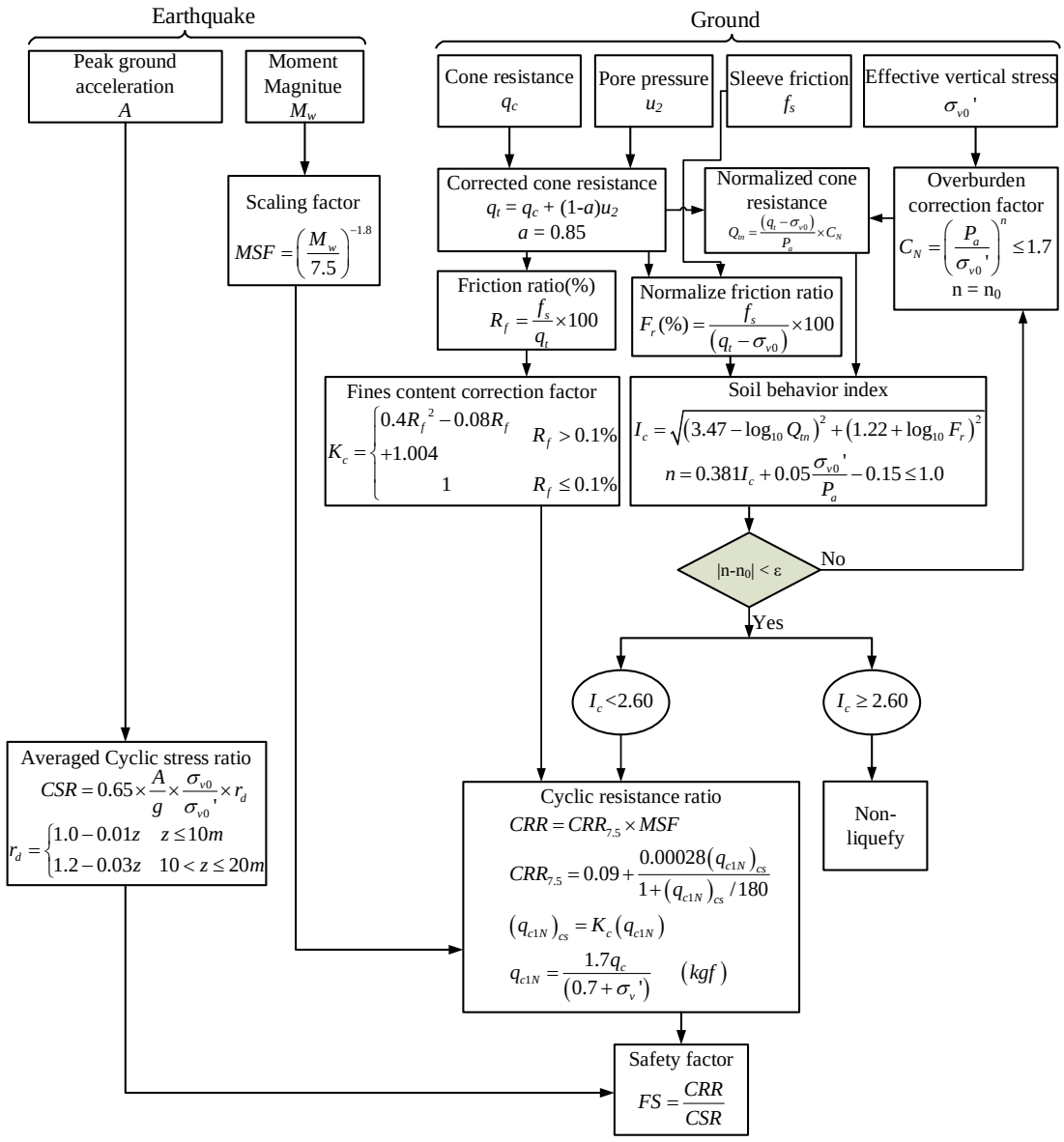

Figure 1. The flowchart of HBF CPT- based method.

DATABASES

This study used two data bases. One is the data base from Chi-Chi earthquake (Chin-Wen Yang, 2003) and the other one is the data base from Boulanger and Idriss (2016). The former is a data base of single earthquake event and includes 182 liquefied cases and 71 non-liquefied cases. The latter is a data base collected from multiple earthquake events worldwide and includes 76 liquefied cases and 53 non-liquefied cases. The soil types of all the cases are plotted in the CPT soil classification chart shown in Figure 2. It can be observed that the majority of the cases (98%) are soil type 5 and 6 which are silty sand to sandy silt, and clean sand to silty sand, respectively.

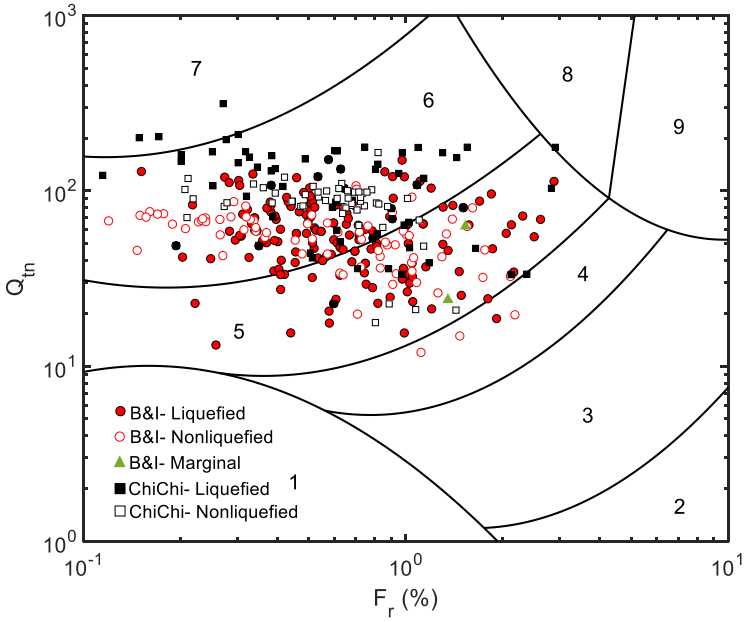

Figure 2. The scatter plot in CPT soil classification chart of all data used in this study.

COMPARISON OF SUCCESS RATES PREDICTED BY VARIOUS METHODS

Table 1 shows the success rates predicted by various methods for liquefied and non-liquefied cases from the data bases of Chin-Wen Yang (2003), Boulanger and Idriss (2016), and all cases. Since Moss et al. (2006) and Boulanger and Idriss (2016) are probabilistic CPT-based methods. They suggested their deterministic CRR curves are the ones corresponding to the probability of liquefaction P_L=15% in their original papers. Therefore, their deterministic CRR curves are biased models. For comparison purpose, these two methods are further divided into the methods that use liquefaction probability P_L=15% and 50% CRR curves as the deterministic CRR curves. They can be denoted as Moss et al. (2006), Moss et al. (2006) (P_L=0.5), B&I (2006), B&I (2006) (P_L=0.5). It can be observed from the table that the success prediction rates of most methods are within 91-95% for the data base of Chi-Chi earthquake and within 72-85% for the data base of Boulanger and Idriss (2016). The success rates for non-liquefied cases are higher than those for liquefied cases for Chi-Chi data, however, the former are lower than the latter for data from Boulanger and Idriss. It also shows the single event data base yields higher success rate than that of the multiple event data base for all the methods due to the data quality and uncertainty. Most methods display the overall prediction success rates within 85-87% with higher success rates for non-liquefaction cases than those for liquefied cases.

Table 1. Success rates predicted for liquefied/non-liquefied cases by various CPT- based methods

Chi-Chi Database	**NCEER**	**Robertson**	**B&I**	**B&I(P_L=0.5)**	**HBF**	**Olsen**	**K&J**	**Moss**	**Moss(P_L=0.5)**
success rates for liq./ non-liq./ all cases(%)	92/ 98/ 95	92/ 98/ 95	91/ 98 94	86/ 98/ 91	92/ 98 /95	87/ 96 /91	93/ 91/ 92	92/ 94/ 95	91/ 98/ 94
B&I(2016) Database	**NCEER**	**Robertson**	**B&I**	**B&I(P_L=0.5)**	**HBF**	**Olsen**	**K&J**	**Moss**	**Moss(P_L=0.5)**
success rates for liq./ non-liq./ all cases(%)	82/ 76/ 80	81/ 75/ 79	96/ 55/ 85	85/ 72/ 81	83/ 75/ 81	73/ 69/ 72	86/ 68/ 81	88/ 65/ 81	79/ 79/ 79
All Database	**NCEER**	**Robertson**	**B&I**	**B&I(P_L=0.5)**	**HBF**	**Olsen**	**K&J**	**Moss**	**Moss(P_L=0.5)**
success rates for liq./ non-liq./ all cases(%)	85/ 85/ 85	85/ 85/ 85	95/ 73/ 88	85/ 83/ 85	86/ 85/ 85	77/ 81/ 78	88/ 77/ 85	90/ 77/ 86	83/ 87/ 84

RELATIVE CONSERVATIVENESS AMONG VARIOUS METHODS

If the factor of safety predicted by HBF is used as a comparative base, the ratio of factor of safety (RFS) can be defined as the factor of safety predicted by the other methods divided by that predicted by HBF method. According to the definition, the smaller the ratio is, the more conservative the method is. The statistical result of RFSs calculated by various methods using all the data bases is shown in Table 2. The statistical average and the coefficient of variation of RFS are denoted by μ and δ, respectively, and shown in the figure. It can be observed that the relative conservativeness among the various methods is in the following descending order: Moss et al. (2006) (P_L=0.5) (the least conservative), Robertson (2009), Hwang et al. (2005), NCEER (2001), Moss et al. (2006), B&I (2006), Ku and Juang (2012) (the most conservative). Since the RFS averages of NCEER (2001), Robertson (2009) methods are close to 1 and the coefficients of variation of RFS are less than 0.13 (the smallest), they can be regarded as the same intermediate conservative level as the HBF method. Ku and Juang (2012) as well as B&I (2006) methods belong to conservative methods. However, Moss et al. (2006) (P_L=0.5), Olsen (1997), and B&I (2006) (P_L=0.5) methods belong to less conservative methods.

Table 2. The statistical result of RFSs calculated by various CPT- based methods

All Database	**NCEER**	**Robertson**	**B&I**	**B&I(P_L=0.5)**	**Olsen**	**K&J**	**Moss**	**Moss(P_L=0.5)**
(μ, δ)	(0.99, 0.13)	(1.03, 0.12)	(0.91, 0.19)	(1.12, 0.19)	(1.19, 0.26)	(0.90, 0.37)	(0.97, 0.28)	(1.23, 0.28)

CONCLUSIONS AND DISCUSSIONS

Based on the above comparison, the following conclusions can be tentatively drawn.

1. All CPT-based methods in the study have acceptable success rates of prediction (85-87%) for liquefied and non-liquefied cases.
2. The relative conservativeness among the various methods has been quantitatively calibrated by the statistical indices of the ratio of safety factor (RFS) with respective to the HBF method.
3. The predicted factor of safety by the HBF method is close to those by NCEER (2001) and Robertson (2009) methods. They belong to the intermediate conservative methods.

The choice of the CPT-based method should consider the conservativeness of the entire design system, including the conservativeness of factors such as earthquake, foundation design method, and soil parameters. The most conservative method may not be the best one because over-conservative design of pile foundation may cause piling difficulties or unpredictable risks during offshore wind turbine construction. Thus, engineers can refer the relative conservativeness of the various methods calibrated in the study to select a method that can balance safety and construction feasibility at the same time.

REFERENCES

Boulanger R.W., Idriss I.M. CPT-based liquefaction triggering procedure. Journal of Geotechnical and Geoenvironmental Engineering, 2016, **142** (2): 04015065-1-11.

Olsen R. Cyclic liquefaction based on the cone penetrometer test. NCEER Workshop on Evaluation of Liquefaction Resistance of Soils 1997: 225–276.

Youd T.L., Idriss I.M., Andrus R.D., Arango I., Castro G., Christian J.T., Dobry R., Liam Finn W.D., Harder Jr., L.F., Hynes M.E., Ishihara K., Koester J.P., Liao S.S.C., Marcuson III W.F., Martin G.R., Mitchell J.K., Moriwaki Y., Power, M.S., Robertson P.K., Seed R.B., Stokoe II K.H. Liquefaction resistance of soils: summary report from the 1996 NCEER and 1998 NCEER/NSF workshops on evaluation of liquefaction resistance of soils. Journal of Geotechnical and Geoenvironmental Engineering, ASCE, 2001, **127** (1): 297–313.

Hwang J.H., Yang C.W., Chen C.H. Simplified methods for assessing liquefaction potential of soils by using hyperbolic cyclic resistance curves. SINO-GEOTECHNICS 2005, **103**: 53-64. (in Chinese).

Moss R.E.S., Seed R.B., Kayen R.E., Stewart J.P., Kiureghian A.D., Cetin K. O., CPT-based probabilistic and deterministic assessment of in situ seismic soil liquefaction potential. Journal of Geotechnical and Geoenvironmental Engineering 2006, **132** (8): 1032-1051.

Robertson P.K. Interpretation of cone penetration tests — a unified approach. Canadian Geotechnical Journal 2009, **46** (11): 1337-1355.

Ku C.S., Juang C.H. Liquefaction and cyclic softening potential of soils – a unified piezocone penetration testing-based approach. Géotechnique 2012, **62** (5): 457–461.

Youd T.L., Idriss I.M., Andrus R.D., Arango I., Castro G., Christian J.T., Dobry R., Liam Finn W.D., Harder Jr., L.F., Hynes M.E., Ishihara K., Koester J.P., Liao S.S.C., Marcuson III W.F., Martin G.R., Mitchell J.K., Moriwaki Y., Power, M.S., Robertson P.K., Seed R.B., Stokoe II K.H. Liquefaction resistance of soils: summary report from the 1996 NCEER and 1998 NCEER/NSF workshops on evaluation of liquefaction resistance of soils. Journal of Geotechnical and Geoenvironmental Engineering, ASCE, 2001, **127** (1): 297–313.

Hwang J.H., Khoshnevisan S., Juang C.H., Lu C.C. Soil liquefaction potential evaluation – An update of the HBF method focusing on research and practice in Taiwan. Engineering Geology 2021, **280**: 105926.

Yang C.W. A Study of full probabilistic method of evaluating soil liquefaction. PhD. Thesis. National Central University. Taoyuan, Taiwan, 2003. (in Chinese).

GEOTECHNICAL INVESTIGATION FOR LIQUEFACTION ASSESSMENT IN CHIANG RAI AND PHAYAO PROVINCES OF NORTHERN THAILAND

Pakawadee Anussornrajkit[1], Weeradetch Tanapalungkorn[2] and Suched Likitlersuang[3]
1. Master student, Department of Civil Engineering, Faculty of Engineering, Chulalongkorn University, Bangkok, Thailand
2. Post-doctoral researcher, Centre of Excellence in Geotechnical and Geoenvironmental Engineering, Department of Civil Engineering, Faculty of Engineering, Chulalongkorn University, Bangkok, Thailand
3. Professor, Centre of Excellence in Geotechnical and Geoenvironmental Engineering, Department of Civil Engineering, Faculty of Engineering, Chulalongkorn University, Bangkok, Thailand 10330
Email: 6372087021@student.chula.ac.th, weeradetch.t@chula.ac.th, fceslk@eng.chula.ac.th

ABSTRACT

This study aims to raise awareness of liquefaction risks in densely populated areas (e.g., Muang Chiang Rai and Muang Phayao) after the liquefaction phenomenon was observed in remote areas in northern Thailand back in 2011. Much of these capital areas are underlain by sandy soil layers, which are susceptible to liquefaction. This research completed the Standard Penetration Test (SPT) on five new boreholes located across downtown Chiang Rai and Phayao. The liquefaction triggering thresholds are estimated using the Simplified Procedure analysis. The study considers two earthquake ground motion scenarios: 10% probability of exceedance in 50 years and 2% probability of exceedance. The results of the analyses show that peak ground acceleration (PGA) value for the 10% in 50 years probability is insufficient to trigger liquefaction in Phayao sites, whereas PGA value for the 2% exceedance can cause relatively high liquefaction potential. Additionally, the liquefaction hazard is controlled by the variation of type and sequence of soil deposits. Since this liquefaction study is primarily based on additional geotechnical data from new boreholes, it has significantly improved the accuracy of estimated liquefaction potential values for these capital areas.

Keywords: Liquefaction potential, Site investigation, Simplified method, Peak ground acceleration, Northern Thailand

INTRODUCTION

The work presents a detailed study to assess liquefaction potential in Chiang Rai and Phayao Provinces in the northern Thailand. Modern records and seismic studies (Ketsap *et* al., 2019; Thitimakorn *et* al., 2018) indicate that this region is subjected to ground shaking sufficient for liquefaction to occur. Liquefaction potential assessment and hazard mapping of Chiang Rai and Phayao was presented in previous research (Soralump *et al*., 2013; Mase *et al*., 2021). However, those studies mainly focused on the areas where liquefaction was observed. Current liquefaction-related work in Chiang Rai and Phayao included the seismic PGA maps (Ketsap *et al*., 2019), the comparison between different methods to predict liquefaction (Mase *et al*., 2020, 2021), and the building codes against liquefaction in 2009. In fact, comprehensive quantitative evaluation of liquefaction in high risk areas has not been performed. Accordingly, a liquefaction analysis for Chiang Rai and Phayao can be improved by incorporating boring logs from populated places (e.g., downtown and university) for the best interests of the public.

Our primary focus is to investigate the impact of local seismicity on liquefaction hazard assessment. Locations we perform liquefaction analysis are Chiang Rai Rajabhat University (CRRU), Muang Chiang Rai and Muang Phayao (see Fig. 1). The liquefaction analysis is carried out based on the standard penetration test (SPT) method (Boulanger *et al*., 2014). This method utilizes a seismic hazard curve in term of PGA, which is obtained from the probability seismic hazard analysis (PSHA) and moment magnitude (M) of an earthquake scenario.

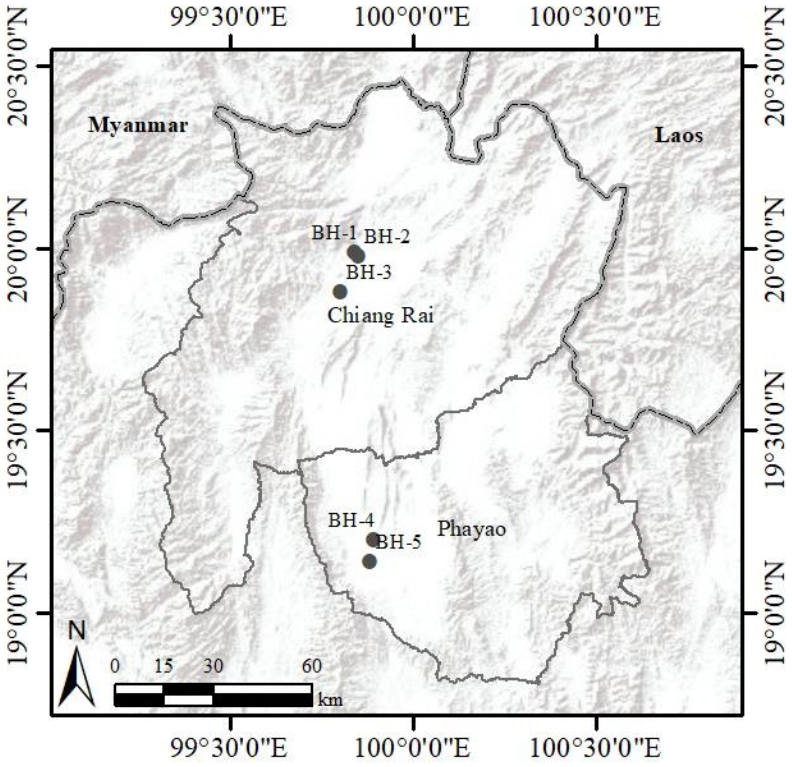

Figure 1. Site locations

We note that similar investigations were carried out by Mase *et al*. (2020) for Mae Sai and Sukkarak *et al*. (2021) for Mae Lao, Chiang Rai. Their studies suggested that Chiang Rai, especially near the Thailand-Myanmar border, was highly prone to liquefaction. This study aims to provide liquefaction potential assessments of populated areas in Muang Chiang Rai and Muang Phayao based on actual dynamic soil characteristics to estimate the liquefaction risk and to determine further mitigation measures.

Liquefaction case history in Chiang Rai and Phayao

Because northern Thailand is subjected to ground shaking sufficient for liquefaction to occur, the areas with a shallow cohesive-less soil are vulnerable to liquefaction. Liquefaction phenomenon in Thailand was first observed in Mae Sai, Chiang Rai caused by 6.8M earthquake occurring on March, 2011 (Soralump *et al*., 2013). The epicenter was close to Tarley City located approximately 30 km from the border of Myanmar. The largest horizontal peak ground acceleration (PGA) recorded at Mae Sai seismic station was 0.2g corresponding to the 475-year return period (Ornthammarath *et al*., 2012) based on the study of probabilistic seismic hazard assessment (PSHA).

Another major earthquake event occurred on May, 2014. The 6.1M earthquake was caused by a movement of Mae Lao Fault in Chiang Rai (Mase *et al*., 2018). The highest PGA recorded by a seismic station at Mae

Suai Dam was 0.33g. The earthquakes damaged more than 10,000 buildings and affected more than 500,000 residents (Sukkarak *et al*., 2021).

Damaged infrastructures, local lateral spreading and liquefaction could be observed across Mae Lao and Mae Sai following the earthquake events. Because of large destruction in these areas, earthquakes have become a great concern to locals.

Liquefaction potential evaluation

In this study, the simplified procedures developed by Seed *et al*., 1971 are used to estimate the factor of safety against soil liquefaction, which is simply defined by Eq. 1:

$$FS = \frac{CSR_{M,\sigma_v'}}{CRR_{M,\sigma_v'}} \tag{1}$$

Liquefaction is predicted to occur when FS ≤ 1, but the acceptable FS value will depend on uncertainty of geotechnical data and safety risk tolerance. The parameters used for the calculation consist of the cyclic stress ratio (CSR), which is a function of ground acceleration and overburden stress of soil; and the cyclic resistance ratio (CRR), which is a resistance of soil to liquefaction.

The CSR of soil at each depth is calculated using the simplified method proposed by Boulanger *et al*. (2014) as follows:

$$CSR_{M,\sigma_v'} = 0.65 \cdot \left(\frac{a_{max}}{g}\right) \cdot \left(\frac{\sigma_v}{\sigma_v'}\right) \cdot r_d \tag{2}$$

where a_{max} is horizontal peak ground acceleration on the surface; g is specific gravity; σ_v is the total vertical stress; $\sigma_v{}'$ is the effective vertical stress at the point of interest; and r_d is the stress reduction coefficient. The depth reduction factor r_d is a correction for soil rigidity, which can be estimated using equations proposed by Boulanger *et al*. (2014), as follows:

$$r_d = \exp[\alpha(z) + \beta(z) \cdot M] \tag{3}$$

in which $$\alpha(z) = -1.012 - 1.126 \cdot \sin\left(\frac{z}{11.73} + 5.133\right) \tag{4}$$

$$\beta(z) = 0.106 + 0.118 \cdot \sin\left(\frac{z}{11.28} + 5.142\right) \text{ for } z < 10 \tag{5}$$

where z is the depth from ground surface to the point of interest.

The CRR is a boundary of CSR separating liquefaction and non-liquefaction occurrences based on in-situ properties of soil. The standard penetration test (SPT) is carried out within a borehole to obtain SPT blow counts in order to determine soil strength. Regarding the variation of hammer energy, variation of fines content and normalized overburden stresses, blow counts measured in the field are corrected using the following equations (Eqs. 6 and 7):

$$(N_1)_{60,cs} = N_1 C_N C_{ER} C_R C_B C_S + \Delta(N_1)_{60} \tag{6}$$

in which $$\Delta(N_1)_{60} = \exp\left(1.63 + \frac{9.7}{FC+0.01} - \left(\frac{15.7}{FC+0.01}\right)^2\right) \tag{7}$$

where FC is fines content; N is SPT blow counts measured in the field; C_{ER} is a correction factor for the variation of hammer's energy; C_N is a correction factor for the overburden stress; C_R is a correction factor for the length of rod; C_B is a correction factor for the diameter of borehole; and C_S is a correction factor for samplers with or without liners.

The correlation of CRR at 7.5 earthquake magnitude and 1 atm vertical effective stress can be calculated from $(N_1)_{60,cs}$ using Eq. 8. For any overburden stress and shaking duration, CRR is corrected using Eq. 9.

$$CRR_{M=7.5,\sigma'_v=1atm} = \exp\left(\frac{(N_1)_{60,cs}}{14.1} + \left(\frac{(N_1)_{60,cs}}{126}\right)^2 - \left(\frac{(N_1)_{60,cs}}{23.6}\right)^3 + \left(\frac{(N_1)_{60,cs}}{25.4}\right)^4 - 2.8\right) \quad (8)$$

$$CRR_{M=7.5,\sigma'_v=1atm} = CRR_{M=7.5,\sigma'_v=1atm} \cdot MSF \cdot K_\sigma \quad (9)$$

where MSF is magnitude scaling factor (Boulanger *et al.*, 2015) and K_σ is overburden correction factor.

Field investigation

Although there are many factors influencing soil liquefaction (e.g., density of soil, depth to groundwater and predicted magnitude of earthquake), this study focuses on factors that are conveniently obtained and measured in the field. The factors comprise the vertical effective stress, the shear wave velocity, the fine content, the historical earthquake magnitude and the recorded peak ground acceleration.

This study utilizes the database collected during site investigation. The field study includes five SPT boreholes installed at five different sites: Planetarium of CRRU, the center of CRRU, downtown Chiang Rai, National Stadium Phayao, and a fertilizer factory in Phayao. Soil stratigraphic columns are shown in Fig 2. We interpret aerial photographs for a preliminary site assessment. The site locations are selected based on their accessibility and significance.

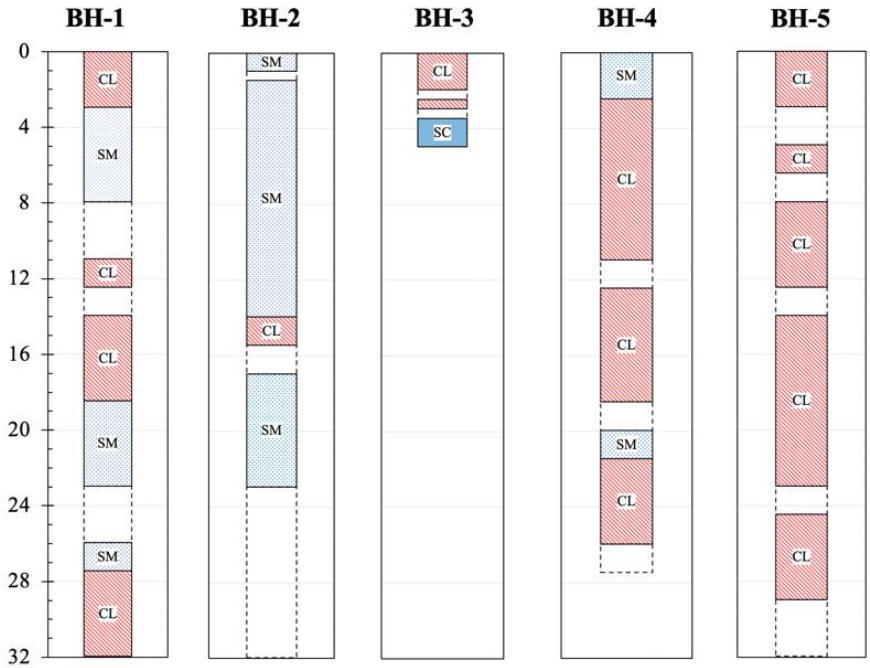

Figure 2. Representative soil profiles

DISCUSSION

This study analyzed 108 data from 5 new boreholes that are installed in capital locations across Chiang Rai and Phayao (e.g., Chiang Rai Rajabhat University, Muang Chiang Rai and Muang Phayao). The factors of safety of each sample with SPT blow count data are calculated separately using the Simplified Procedure (Idriss *et al*., 2014). The relationship between cyclic stress ratio (CSR) and SPT $(N_1)_{60,cs}$ value with liquefaction threshold curve is plotted in Figure 3. For the assessment, 0.18g and 0.36g as maximum ground accelerations corresponding to the 10% and 2% probability of exceedance in 50 years are used in this study, respectively (Ornthammarath *et al*., 2020). Additionally, a magnitude 6.5 earthquake as a seismic scenario value (Sukkarak *et al*., 2021) is employed to analyze the liquefaction potential based on conservative conditions (i.e., a fully saturated soil column assumption).

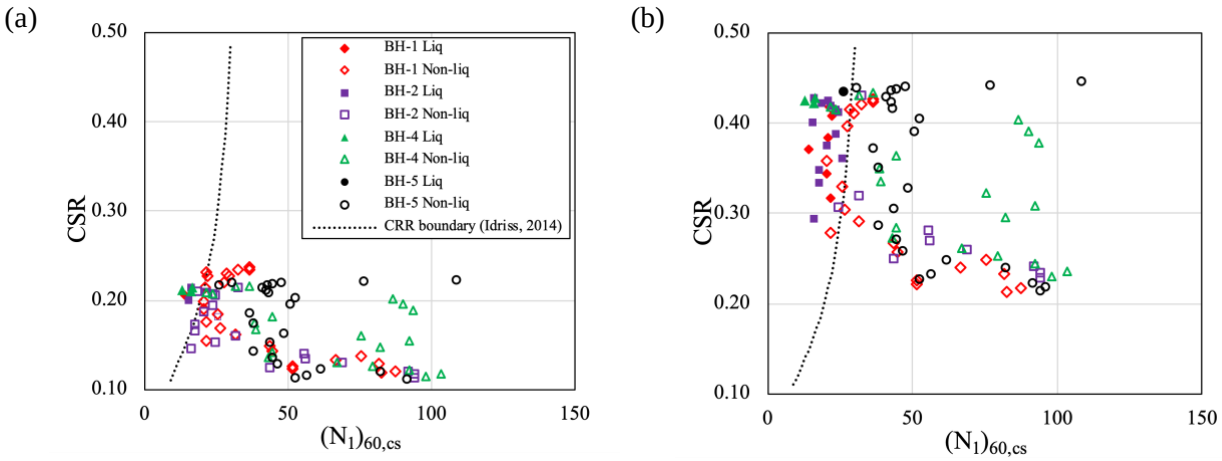

Figure 3. SPT-based liquefaction triggering curve: (a) 10% probability of exceedance PGA and (b) 2% probability of exceedance PGA

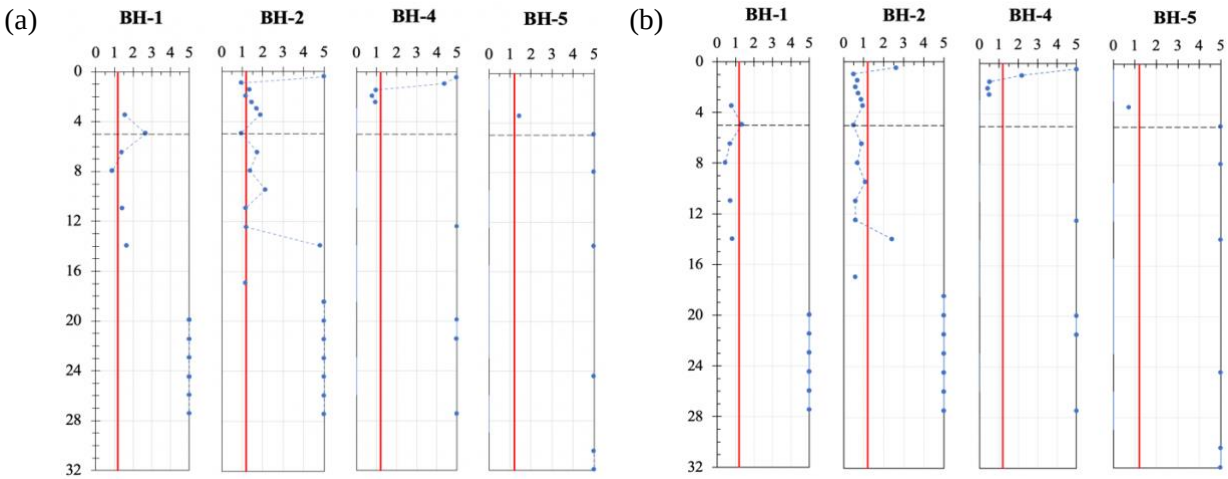

Figure 4. Factors of safety corresponding to PGA: (a) 10% probability of exceedance and (b) 2% probability of exceedance

The impact of earthquakes on liquefaction in downtown areas from the 4 representative site profiles are determined in any depth. It is noted that BH-3, which is located in downtown Chiang Rai, is not susceptible to liquefaction since it has a plasticity index greater than 7% (Boulanger *et al*., 2006). The analysis suggests that all sites except BH-3 contain at least one sand layer susceptible to liquefaction.

Because there is some considerable uncertainty in soil characteristics, a threshold for a factor of safety of 1.2 is assigned. The factors of safety along the depth at a given site are illustrated in Fig 4. Based on the analysis, the 10% probability of exceedance in 50 years ground motion is insufficient to trigger liquefaction in sandy soil found in BH-5 (see Fig 4-a), whereas the liquefaction potential for the 2% probability of exceedance PGA is relatively high across the study area (see Fig 4-b). In conclusion, the liquefaction potential increases with increasing PGA.

To estimate the impact of liquefaction, soil samples are classified as shallow soil (with less than 5 m depth) and deep soil (with more than 5 m depth). The criteria proposed here provides initial steps to evaluate scientific outputs. Generally, liquefaction near ground surface will cause significant damages to pipelines and shallow foundation, which is usually founded within 3 m deep (Ketsap *et al.*, 2019), while liquefaction at deeper locations has a greater effect on deep foundation. A number of classified soil specimens prone to liquefaction (i.e., a factor of safety less than 1.2) at 0.18g and 0.36g ground motion are summarized in Table 1. Accordingly, the sites in Chiang Rai Rajabhat University, the national stadium Phayao and the fertilizer factory Phayao are considered to be susceptible to liquefaction. It is noted that the sites in Chiang Rai are vulnerable to a change in PGA while the sites in Phayao undergo more subtle changes and are appeared to be relatively stable.

Table 1. Liquefaction potential evaluation of soil specimens

Site ID	Location	Specimen retrieved	Liquefied at 0.18g PGA			Liquefied at 0.36g PGA			Increase in liquefaction potential
			Liquefied soil sample	Shallow soil	Deep soil	Liquefied soil sample	Shallow soil	Deep soil	
BH-1	Chiang Rai	26	1	0	1	5	1	4	15.4%
BH-2	Chiang Rai	23	6	3	3	13	7	8	47.8%
BH-4	Phayao	23	3	3	0	3	3	0	0%
BH-5	Phayao	26	0	0	0	1	1	0	3.8%

The analysis shows substantial variation in soil characteristics regardless of the distance (e.g., BH-1 and BH-3), so it is crucial to perform site-specific tests. The type and sequence of soil deposits are laterally variable and inconsistent from one site to another as a result of historical construction of buildings and structures. The complexity of artificial fill deposits limits our ability to accurately predict site response and soil structure across the entire study area.

This study updates the previous estimated liquefaction potential in Muang Chiang Rai and Phayao primarily based on additional geotechnical data from new boreholes. Our estimated factors of safety against liquefaction have not substantially change in magnitude, but our analysis of additional data has significantly reduced the presumption of liquefaction potential values in downtowns Chiang Rai and Phayao.

CONCLUSIONS

Based on the results of this study that incorporates quantitative geotechnical data with seismic hazard criteria, we conclude the following:

(1) This study shows that Muang Chiang Rai and Muang Phayao areas have a potential to liquefy during earthquake. The results are consistent with documented liquefaction studies located within the basin of Chiang Rai and Phayao.

(2) The 10% probability of exceedance PGA is insufficient to trigger the liquefaction in Muang Phayao (e.g., BH-4 and BH-5), whereas the liquefaction in Muang Chiang Rai (e.g., BH-1 and BH-2) can occur.

(3) This distribution of liquefaction potential suggests that further liquefaction studies in densely populated areas, especially in Muang Chiang Rai, are necessary to account for the anticipated increase in liquefaction potential with increasing PGA.

(4) It is recommended to consider the spatial variation of type and sequence of soil deposits. For example, the presence of fine-grained soils in BH-3 causes local ground conditions to deviate from our basic stratigraphic model, which sand layers are expected.

REFERENCES

Boulanger, R. W., & Idriss, I. M. (2006). Liquefaction susceptibility criteria for silts and clays. *Journal of Geotechnical and Geoenvironmental Engineering*, *132*(11), 1413–1426. https://doi.org/10.1061/(asce)1090-0241(2006)132:11(1413)

Boulanger, R.; Idriss, I. CPT and SPT Based Liquefaction Triggering Procedures; Report No. UCD/CGM-14/01; Center for Geotechnical Modeling, Department of Civil and Environmental Engineering, University of California: Davis, CA, USA, 2014.

Boulanger, R. W., & Idriss, I. M. (2015). Magnitude scaling factors in liquefaction triggering procedures. *Soil Dynamics and Earthquake Engineering*, *79*, 296–303. https://doi.org/10.1016/j.soildyn.2015.01.004

Ketsap, A., Hansapinyo, C., Kronprasert, N., & Limkatanyu, S. (2019). Uncertainty and fuzzy decisions in earthquake risk evaluation of buildings. *Engineering Journal*, *23*(5), 89–105. https://doi.org/10.4186/ej.2019.23.5.89

Mase, L. Z., Likitlersuang, S., & Tobita, T. (2018). Analysis of seismic ground response caused during strong earthquake in northern Thailand. *Soil Dynamics and Earthquake Engineering*, *114*, 113–126. https://doi.org/10.1016/j.soildyn.2018.07.006

Mase, L. Z., Likitlersuang, S., & Tobita, T. (2020). Verification of liquefaction potential during the strong earthquake at the border of Thailand-myanmar. *Journal of Earthquake Engineering*, *26*(4), 2023–2050. https://doi.org/10.1080/13632469.2020.1751346

Ornthammarath, T. (2012). A note on the strong ground motion recorded during the MW 6.8 earthquake in Myanmar on 24 March 2011. *Bulletin of Earthquake Engineering*, *11*(1), 241–254. https://doi.org/10.1007/s10518-012-9385-4

Ornthammarath, T., Warnitchai, P., Chan, C.-H., Wang, Y., Shi, X., Nguyen, P. H., Nguyen, L. M., Kosuwan, S., & Thant, M. (2020). Probabilistic seismic hazard assessments for Northern Southeast Asia (Indochina): Smooth seismicity approach. *Earthquake Spectra*, *36*(1_suppl), 69–90. https://doi.org/10.1177/8755293020942528

Seed, H. B., & Idriss, I. M. (1971). Simplified procedure for evaluating soil liquefaction potential. *Journal of the Soil Mechanics and Foundations Division*, *97*(9), 1249–1273. https://doi.org/10.1061/jsfeaq.0001662

Soralump, S., and J. Feungaugsorn. (2013). Probabilistic analysis of liquefaction potential: The first eyewitness case in Thailand. Proceedings of the 18th National Convention of Civil Engineering (NCCE), Chiang Mai, Thailand, May 8–10.

Sukkarak, R., Tanapalungkorn, W., Likitlersuang, S., & Ueda, K. (2021). Liquefaction analysis of sandy soil during strong earthquake in northern Thailand. *Soils and Foundations*, *61*(5), 1302–1318. https://doi.org/10.1016/j.sandf.2021.07.003

Thitimakorn, T., & Raenak, T. (2016). NEHRP site classification and preliminary soil amplification maps of Lamphun City, Northern Thailand. *Open Geosciences*, *8*(1). https://doi.org/10.1515/geo-2016-0046

A STUDY OF DRAINED VOLUMETRIC BEHAVIOUR OF WEAKLY CEMENTED SANDS USING ENZYME-INDUCED CALCITE PRECIPITATION (EICP)

Amali Gitanjali Rayappan Kennedy[1], Yu-Syuan Jhuo[2] and Louis Ge[3]
1. PhD Candidate, Department of Civil Engineering, National Taiwan University, Taipei, Taiwan, R.O.C.
2. Post-Doctoral Researcher, Department of Civil Engineering, National Taiwan University, Taipei, Taiwan, R.O.C.
3. Professor, Department of Civil Engineering, National Taiwan University, Taipei, Taiwan, R.O.C
Email: d07521017@ntu.edu.tw, ymca0777@gmail.com, louisge@ntu.edu.tw

ABSTRACT

Enzyme-Induced Calcite Precipitation (EICP) is a novel ground improvement technique recently gaining attention. This technique utilizes free urease enzymes with urea and calcium chloride for the calcium carbonate precipitation. In this paper, triaxial consolidated drained tests were carried out in poorly graded silica sand, which is susceptible to liquefaction. The sand is mixed with the preferred recipe of EICP solution and subjected to drained monotonic loading at three different confining pressures (50 kPa (low), 100 kPa (medium), and 200 kPa (high). A drained triaxial was chosen here, which neglects the influence of pore pressure. The stress-strain and volumetric strain curves are plotted for one cycle of biocementation treatment and presented in this paper. The biocementation using EICP increases the liquefaction resistance by the clogging of voids in the soil particles by the calcium carbonate precipitation and improves the package of the soil structure. The volumetric strain response of the EICP treated specimen moves to higher dilatancy compared to the untreated pure sand. Higher calcium carbonate content (CCC) is essential for higher strength. Applying high number of treatment cycles may increase the stiffness and stability of the specimen compared to the untreated pure sand.

Keywords: Bio cementation, Enzyme induced calcite Precipitation (EICP), Calcite/Calcium carbonate ($CaCO_3$), Consolidated Drained triaxial test, Confinement, Cementation.

INTRODUCTION

Bio-cementation has been an innovative soil improvement technique in recent days. This method leads to the production of calcium carbonate in the soil and binds the soil particles together. This increases the shear resistance and fills in the pores to reduce the permeability of the soil. Biocementation ameliorates the ground improvement (Gao et al., 2018; Meng, Shu, Gao, Yan, et al., 2021; Putra et al., 2020), liquefaction resistance (Huang & Wang, 2017; Xiao et al., 2018), slope protection (He et al., 2022; Liu et al., 2020; Yuan et al., 2020), seepage control and erosion mitigation (Meng, Shu, Gao, He, et al., 2021). There are two essential techniques in bio cementation of soils, which include Microbial Induced Calcite Precipitation (MICP) (Konstantinou et al., 2021; Wu et al., 2021) and Enzyme-Induced Calcite Precipitation (EICP) (Almajed et al., 2021; Cui et al., 2020; Gao et al., 2018). MICP uses sustainable technology by using ureolytic bacteria like Sporosarcina Pasteurii for the process of hydrolysis of urea. Similarly, EICP uses free urease enzymes derived from plants, filamentous fungi/bacteria, and organic products and lacks nucleation sites, unlike MICP (Yuan et al., 2020). Both methods lead to calcium carbonate precipitation. The precipitated calcium carbonate gets settled among the pore spaces of the soil and helps a lot in inter-particle binding. The cementation of particles and their increased roughness will improve the shear soil's shear strength, stiffness, and dilatancy characteristics biocemented soil behavior of urease (Almajed et al., 2018), relative density (P. Xiao et al., 2019), particle shape (Y. Xiao et al., 2019), and particle size

distribution (Nafisi et al., 2020). There are several strategies for the increase of biocementation. One of the common strategies for biocementation involves multiple cycles of biocementation, as suggested by (Whiffin et al., 2007). This influences the void spaces, pore filling by calcite particles, and distribution of contact points by calcite particles by several cycles of biocementation for higher calcium carbonate precipitation. The primary challenge in adopting the EICP technique is the massive cost of the urease enzyme. Hence it is essential to reduce the cost of urease enzyme for field applications. The high purity and activity of urease enzymes available commercially are expensive at market rates. At the same time, lower activity and purity of urease enzymes lead to less and slower calcite precipitation. The final product of the EICP reaction leads to the settling of ammonium chloride, an undesirable salt in the field. The accumulation of ammonium chloride causes acidification, leading to a reversal of carbonate precipitation. The higher concentration of ammonium chloride leads to less discharge of OH^- and CO_3^{2-} ions. This leads to the degradation of carbonate precipitation and ultimately disrupts the precipitation ratio in the treatment (Hu et al., 2021). Therefore, it is vital to address the environmental degradation caused by the EICP technique is robust stabilization using Enzyme Induced Calcite Precipitation.

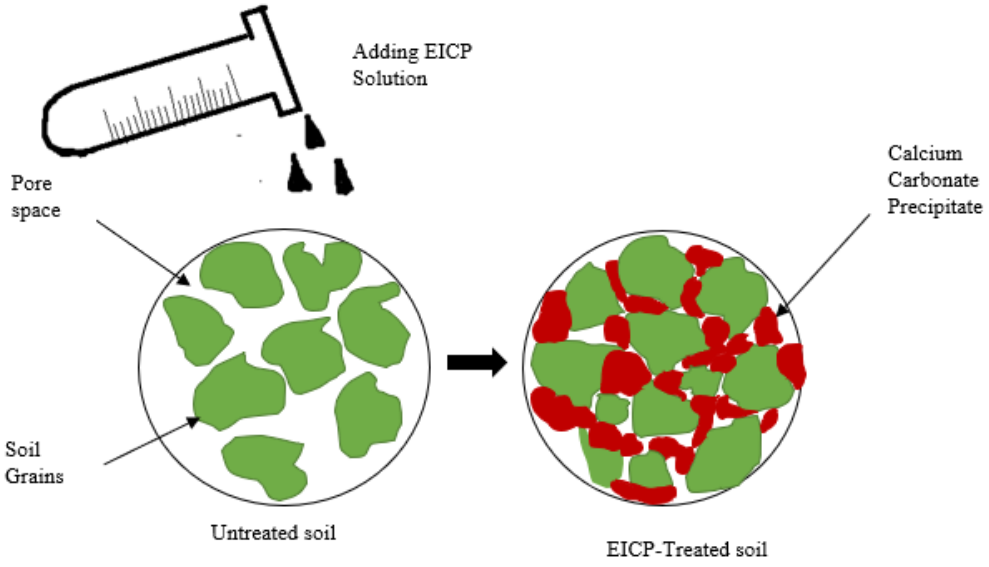

Figure 1. A schematic diagram of $CaCO_3$ precipitation in the pore space of the soil matrix using EICP

The ureolysis process is mentioned below in chemical reactions.

$$CO(NH_2)_{2(s)} + H_2O_{(l)} \xrightarrow{\text{Urease}} CO_{2(g)} + 2NH_3^+{}_{(aq)} + 2OH^-{}_{(aq)} \quad (1)$$

$$CO_{2(g)} + 2NH_3^+{}_{(aq)} + H_2O_{(l)} \rightarrow 2NH_4^+{}_{(aq)} + CO_3^{2-}{}_{(aq)} \quad (2)$$

in the presence of a suitable divalent cation such as calcium, carbonate mineral precipitation can occur

$$CaCl_{2(s)} \rightarrow Ca^{2+}{}_{(aq)} + 2Cl^-{}_{(aq)} \quad (3)$$

The carbonate (CO_3^{2-}) ions react with calcium ions (Ca^{2+}), leading to the formation of calcium carbonate ($CaCO_3$)

$$Ca^{2+}{}_{(aq)} + CO_3^{2-}{}_{(aq)} \leftrightarrow CaCO_{3(s)} \quad (4)$$

The chloride ions ($2Cl^-_{(aq)}$) react with ammonium ions ($2NH_4^+{}_{(aq)}$) which leads to the formation of ammonium chloride. At this time, a reduction in the alkalinity of the solution is reported by Mortenson et al.,2011

$$2NH_4^+{}_{(aq)} + 2Cl^-{}_{(aq)} \rightarrow 2NH_4Cl_{(aq)} \quad (5)$$

Previous studies in EICP have a plethora of research on the compressive strength of the sand. Higher confinements are required to conduct research into the EICP treatment. The confining pressure and cementation significantly affect EICP-treated sand's mechanical behavior (Feng & Montoya, 2016; Simatupang et al., 2019). EICP is an environmentally friendly, sustainable, low carbon emission technique for field application.

MATERIALS USED

Sand

The silica sand used for this study was purchased from Singapore. The particle size distribution curve is shown in fig. 2. The coefficient of uniformity C_u is 1.403, coefficient of curvature C_c is 0.977, and the specific gravity is 2.66. Some of the other geotechnical parameters are D_{60} = 0.205mm, D_{30} =0.171 mm, D_{10} = 0.146mm, e_{max} = 0.911, e_{min} =0.574 and At 50% Relative Density, ρ is 1.527 g/cm^3 adopted in this study.

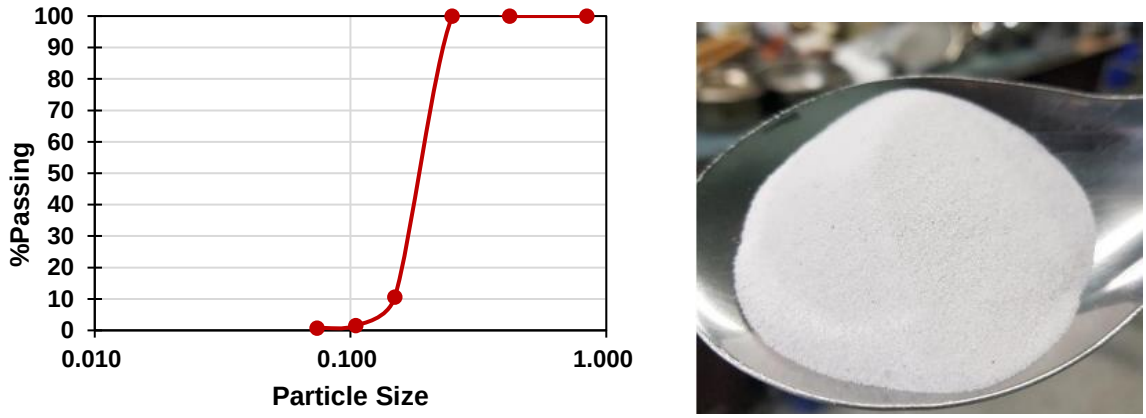

Figure 2. Grain size distribution curve

Characteristics of Urease Enzyme and Reagents

The cementation solution consisting of Calcium chloride dihydrate ($CaCl_2.2H_2O$) and Urea ($CO(NH_2)_2$) with 99% purity were purchased from Bioman Scientific Co.Ltd. The urease enzyme used in this study was extracted from an agricultural source (jack beans). It was purchased from CDH chemicals Pvt Ltd, India. The activity rate of this enzyme used in the research is 3500 Units/gram. After the use of enzyme, it is stored in the refrigerator at 4ºC for future use.

Sample Preparation for Triaxial specimens

The paper mold for triaxial specimen with a diameter of 73mm and height of 150mm for the preparation of EICP treated soil specimens. The percolation method of EICP treatment is adopted in this research. Four holes are drilled on the bottom of the paper mold for drainage purpose. From the knowledge of several

research papers, it is found that the percolation method helps inter-particle soil binding and the ease of removing the specimen from the paper mold. EICP solution is prepared with 1M Urea, 0.67M $CaCl_2$, and 3g/l urease enzyme. Initially, Urea and calcium chloride solution is prepared, and the urease enzyme is added. The urease solution with DI water is made to run in a magnetic stirrer for 10mins, and the cementation solution is added to the urease solution. Then the final solutions are made to run on the magnetic stirrer again for a few minutes. The amount of dry sand is calculated from the dry density of the sand with a relative density of 50%. One pore solution is calculated from the relative density of the soil. The soil is compacted into 5 layers by tamping each layer, and a scratch is made between the layers to increase the binding of the two layers. Thereby, the pure sand triaxial specimen is made. The next stage is EICP treatment; here EICP solution is poured from top to bottom, and the solution gets drained through gravity. In closed end columns the EICP solution retains in the sample, which helps in the uniform calcite precipitation and is akin a saturated condition in the paper mold. After the curing period, the sealant at the bottom of the paper mold is removed. After the curing time, the triaxial specimens are cut by a cutter and transferred to the triaxial apparatus for consolidated drained triaxial testing.

Experimental Procedure

The following tests adopted a strain-controlled GDS triaxial shear apparatus equipped with a data acquisition and control system to carry out consolidation and drained shearing tests. Consolidated Drained (CD) triaxial tests were conducted to evaluate the influence of biocementation on the sand by the stress-strain behavior. The EICP-treated specimen was placed on the triaxial base lined with filter paper and porous stone at the bottom. Then the sample was encased in a latex membrane and placed in a triaxial chamber. Initially, a vacuum pressure of -6Hg was applied to the specimen before a cell pressure of 20 kPa to support the sample. Manual saturation with 9 to 12 ml per minute is performed for one night before proceeding to back pressure saturation. The back pressure was raised to 700 kPa to get a B value higher than 0.95, which indicates the sample is fully saturated. The samples are subjected to three different confining pressure – 50 kPa (low), 100 kPa (medium), and 200 kPa (high). The samples were monotonically sheared with a shear rate of 0.185mm/min. When the axial strain reached 20%, the test was made to stop, and the data were extracted.

RESULTS & DISCUSSIONS

Stress-Strain Response

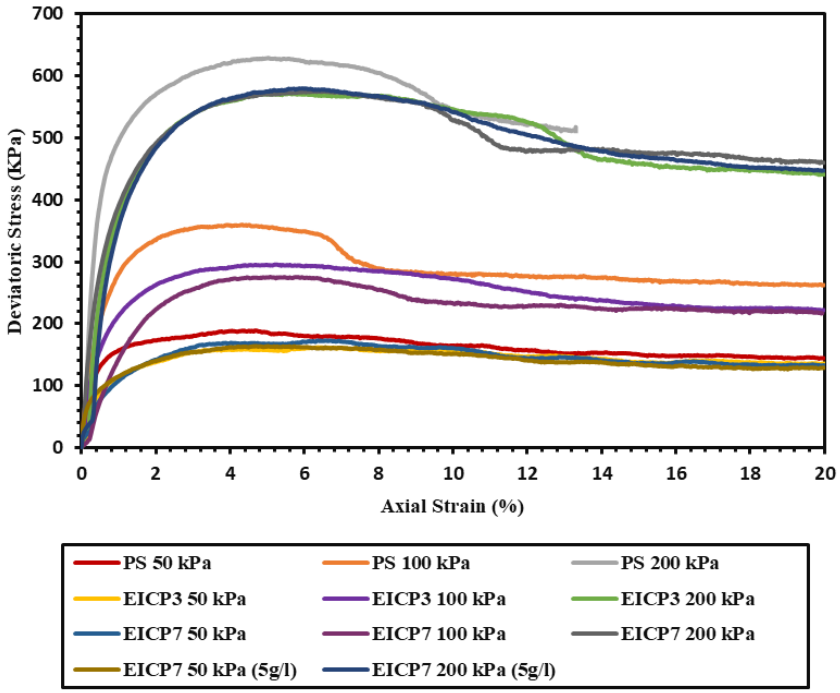

Figure 3. Shear Response curve at different curing times day 3 and day 7 in 50 kPa, 100 kPa, and 200 kPa effective confining pressure.

The shear response curve of consolidated drained triaxial on EICP treated and untreated pure sand is presented in fig. 3 at 50 kPa, 100 kPa, and 200 kPa effective confining pressures and two different curing times on day 3 and day 7. Treated EICP sand generally has a higher peak deviatoric stress than untreated sand. The higher deviatoric priority is due to the high calcium carbonate content. But in this study, it is seen that the peak deviatoric stress at higher effective confining pressures of 100 kPa and 200 kPa showed less strength than the untreated. The strength can be due to a lower amount of CCC. The weak calcite bonds in the soil particles increase the initial stiffness but are destroyed by shear stress, reducing the peak deviatoric stress. The deviatoric stress rises to the peak due to stiffness, with an effective confining pressure increase. The deviatoric stress gradually decreases from peak to post-peak. The weakly cemented EICP specimens have often show strain-softening behaviour and fail with brittle failure pattern at 20% axial strain. The peak deviatoric strain on curing days 3 and 7 was less than pure sand. Repeated tests in the study obtained the same result. The lesser strength in the EICP-treated sand may be due to the breakage of weakly cemented sand among the particle contacts (Wang et al., 2019). The shear strain destroys the weak EICP bonds in the sand, resulting in a lower peak strength. The EICP particle-particle contact highly influences the peak deviatoric strength. The peak deviatoric stress at different curing times increases with an increase in effective confining pressure. The peak deviatoric stress on day three and day seven didn't increase at 200 kPa, which may be due to the lower amount of calcite precipitation in the one cycle of biocementation. The peak deviatoric stress on day 3 and day 7 at 100 kPa effective confining pressure shows a considerable decrease in the untreated sand. Deviatoric stress may have changed between day 3 and day 7 due to the disruption of the triaxial sample during molding. The peak deviatoric stress at 50 kPa for pure sand showed almost the same peak deviatoric stress on day 3 and day 7 curing time for treated specimens. It is possible that the weakly cemented sands are being constrained by low confining pressure. Even after adding 5g/l urease enzyme with the same urea and calcium chloride concentrations, the peak deviatoric stress remains constant at all effective confining pressures. Increased urease enzyme activity resulted in a pronounced dilative behavior of the sand but no increase in peak deviatoric stress. One cycle of biocementation has less calcite precipitation and unstable, weak bonds in the interlocking of soil grains. Therefore, multiple

processes of biocementation may increase the calcite precipitation in the treated specimens. The higher amount of CCC increases initial stiffness and dilative behavior compared to the untreated sample (Wu et al., 2021).

Volumetric Strain Response

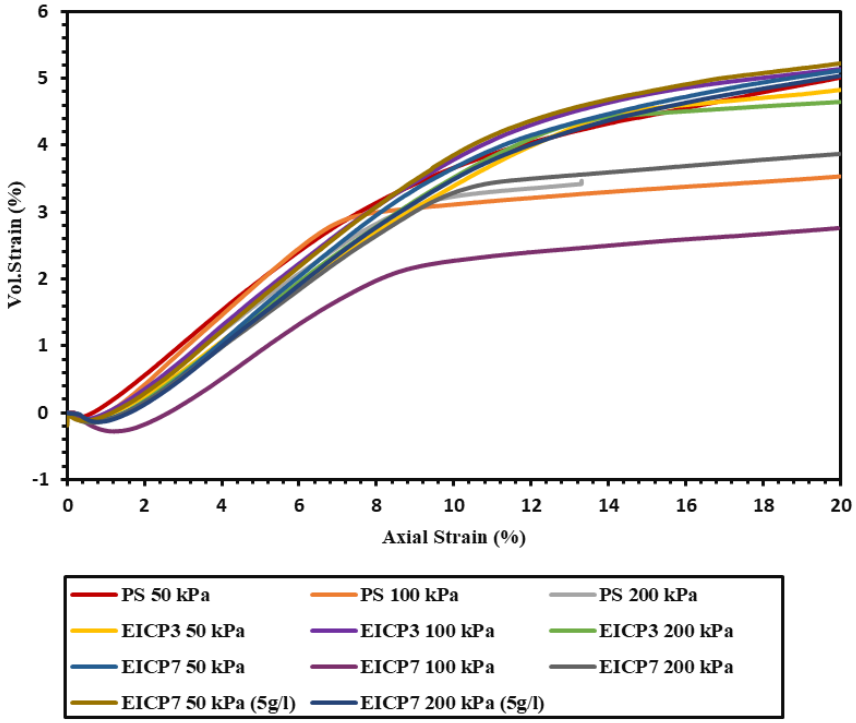

Figure 4. Volumetric strain response curve at different curing times day 3 and day 7 in 50 kPa, 100 kPa, and 200 kPa effective confining pressure.

The volumetric strain is slightly higher than the untreated pure sand. Fig. 4 shows a decrease in volumetric strain with a higher effective confining pressure. The rate of dilation decreases with an increase in effective confining pressure (Safdar et al., 2021). The volumetric strain response graph shows the resistance of calcite bonds in the EICP-treated specimens. Other research papers support this volumetric strain curve (Baxter et al., 2011; Ravi Sharma et al., 2011; Sharma et al., 2011). The volumetric strain response showed an initial contraction followed by significant dilation. The amount of initial contraction has increased in the EICP biocemented sand, which can be seen in the repeatability of consolidated triaxial tests at varying confining pressures and curing times. The increase in cementation in the EICP-treated specimens leads to high compressibility in the initial shearing stage. This increase in compressibility may be due to the breakage of weak calcium carbonate cemented particle contacts in the treated specimens. All the EICP-treated samples illustrated a transition from contractive behavior to dilative behavior after a particular stage of initial shearing. The increase of CCC in EICP-treated specimens induces dilative behavior compared to the untreated samples. The EICP biocementation enhances the particle interlocking capacity between the soil grains by gelling calcite precipitation between the soil particles. In an undrained consolidated drained triaxial test, the excess pore pressure generation is used to assess the liquefaction occurrence (Tarantino et al., 2019). The untreated sand shows a ru value of 1.0, which indicates the highest pore water pressure. This pore water pressure is gradually reduced by the biocementation in the sand, making it resistant to liquefaction. Similarly, consolidated drained triaxial tests were used in the study to investigate the volumetric behavior in one cycle of biocemented treated sand. The peak deviatoric stress remained

unchanged on days 3 and 7, but it showed a slight improvement in dilative behavior in all confining pressures compared to untreated pure sand. The increase in the liquefaction resistance depends strongly on the volumetric strain. The increase in volumetric strain in the treated specimen is noticeably high compared to untreated pure sand with the addition of 3 g/l urease enzyme. This dilative behavior in one cycle of biocementation can help in liquefaction mitigation.

CONCLUSIONS

EICP treatment in the soil is highly influenced by the type of urease enzyme, urease activity, the relative density of soil, specimen preparation, and calcite bonding in the soil particles. The one-phase EICP method gives uniform calcite precipitation along the height of the soil column. Calcium carbonate precipitation has three different types of crystals. The most stable crystal calcite increases the binding capacity of the soil, which increases the stiffness of the soil under high effective confining pressure. Higher peak deviatoric stress and higher stiffness of the treated specimen can be achieved by multiple cycles of treatment. The number of treatment cycles directly influences the precipitation rate in the soil particles. This treatment cycle helps transition poor sand to dense sand with inter-particle binding with calcite by filling the pore voids in the specimens. Biocemented sand improves the dilation compared to the untreated samples. The dilative behavior in the treated model gets destroyed when there is a large amount of shearing or weak cementation. In such cases, the volumetric strain of the treated specimen falls behind the untreated pure sand. The weak cemented bonds can be transformed into more potent calcium carbonated bonds in the treated specimen with the addition of treatment cycles. One cycle of biocementation showed a small but promising effect of dilative behavior in the treated specimen. EICP can be applied for liquefaction resistance as all the EICP-treated specimens fall under contraction at the initial stages of shearing and move towards the dilation side at a higher rate than the untreated pure sand. This trend is seen in the volumetric strain response curve for all EICP-treated specimens. This can be interpreted as minor effects of reduced excess pore pressure generation in the treated specimen in undrained behavior. It can be taken that EICP can be adopted for liquefaction resistance.

REFERENCES

Almajed, A., Khodadadi Tirkolaei, H., & Kavazanjian, E. (2018). Baseline Investigation on Enzyme-Induced Calcium Carbonate Precipitation. *Journal of Geotechnical and Geoenvironmental Engineering*, *144*(11). https://doi.org/10.1061/(asce)gt.1943-5606.0001973

Almajed, A., Lateef, M. A., Moghal, A. A. B., & Lemboye, K. (2021). State-of-the-Art Review of the Applicability and Challenges of Microbial-Induced Calcite Precipitation (MICP) and Enzyme-Induced Calcite Precipitation (EICP) Techniques for Geotechnical and Geoenvironmental Applications. *Crystals*, *11*(4). https://doi.org/10.3390/cryst11040370

Baxter, C. D. P., Sharma, M. S. R., Moran, K., Vaziri, H., & Narayanasamy, R. (2011). Use of A^{-}=0 as a Failure Criterion for Weakly Cemented Soils. *Journal of Geotechnical and Geoenvironmental Engineering*, *137*(2), 161-170. https://doi.org/10.1061/ASCEGT.1943-5606.0000414

Cui, M.-J., Lai, H.-J., Hoang, T., & Chu, J. (2020). One-phase-low-pH enzyme induced carbonate precipitation (EICP) method for soil improvement. *Acta Geotechnica*, *16*(2), 481-489. https://doi.org/10.1007/s11440-020-01043-2

Feng, K., & Montoya, B. M. (2016). Influence of Confinement and Cementation Level on the Behavior of Microbial-Induced Calcite Precipitated Sands under Monotonic Drained Loading. *Journal of Geotechnical and Geoenvironmental Engineering*, *142*(1). https://doi.org/10.1061/(asce)gt.1943-5606.0001379

Gao, Y., Hang, L., He, J., & Chu, J. (2018). Mechanical behaviour of biocemented sands at various treatment levels and relative densities. *Acta Geotechnica*, *14*(3), 697-707. https://doi.org/10.1007/s11440-018-0729-3

He, J., Fang, C., Mao, X., Qi, Y., Zhou, Y., Kou, H., & Xiao, L. (2022). Enzyme-Induced Carbonate Precipitation for the Protection of Earthen Dikes and Embankments Under Surface Runoff: Laboratory Investigations. *Journal of Ocean University of China*, *21*(2), 306-314. https://doi.org/10.1007/s11802-022-4821-9

Hu, W., Cheng, W. C., Wen, S., & Yuan, K. (2021). Revealing the Enhancement and Degradation Mechanisms Affecting the Performance of Carbonate Precipitation in EICP Process. *Front Bioeng Biotechnol*, *9*, 750258. https://doi.org/10.3389/fbioe.2021.750258

Huang, Y., & Wang, L. (2017). Reply to the discussion by Ochoa-Cornejo et al. on "Laboratory investigation of liquefaction mitigation in silty sand using nanoparticles" [Eng.Geol.204:23–32]. *Engineering Geology*, *221*. https://doi.org/10.1016/j.enggeo.2017.02.024

Konstantinou, C., Biscontin, G., Jiang, N.-J., & Soga, K. (2021). Application of microbially induced carbonate precipitation to form bio-cemented artificial sandstone. *Journal of Rock Mechanics and Geotechnical Engineering*, *13*(3), 579-592. https://doi.org/10.1016/j.jrmge.2021.01.010

Liu, B., Zhu, C., Tang, C.-S., Xie, Y.-H., Yin, L.-Y., Cheng, Q., & Shi, B. (2020). Bio-remediation of desiccation cracking in clayey soils through microbially induced calcite precipitation (MICP). *Engineering Geology*, *264*. https://doi.org/10.1016/j.enggeo.2019.105389

Meng, H., Shu, S., Gao, Y., He, J., & Wan, Y. (2021). Kitchen waste for Sporosarcina pasteurii cultivation and its application in wind erosion control of desert soil via microbially induced carbonate precipitation. *Acta Geotechnica*, *16*(12), 4045-4059. https://doi.org/10.1007/s11440-021-01334-2

Meng, H., Shu, S., Gao, Y., Yan, B., & He, J. (2021). Multiple-phase enzyme-induced carbonate precipitation (EICP) method for soil improvement. *Engineering Geology*, *294*. https://doi.org/10.1016/j.enggeo.2021.106374

Nafisi, A., Montoya, B. M., & Evans, T. M. (2020). Shear Strength Envelopes of Biocemented Sands with Varying Particle Size and Cementation Level. *Journal of Geotechnical and Geoenvironmental Engineering*, *146*(3), 04020002. https://doi.org/doi:10.1061/(ASCE)GT.1943-5606.0002201

Putra, H., Yasuhara, H., Erizal, Sutoyo, & Fauzan, M. (2020). Review of Enzyme-Induced Calcite Precipitation as a Ground-Improvement Technique. *Infrastructures*, *5*(8). https://doi.org/10.3390/infrastructures5080066

Ravi Sharma, M. S., Baxter, C. D. P., Moran, K., Vaziri, H., & Narayanasamy, R. (2011). Strength of Weakly Cemented Sands from Drained Multistage Triaxial Tests. *Journal of Geotechnical and Geoenvironmental Engineering*, *137*(12), 1202-1210. https://doi.org/10.1061/(asce)gt.1943-5606.0000537

Safdar, M., Newson, T., & Shah, F. (2021). Consolidated drained (CID) behavior of fibre reinforced cemented Toyoura sand in triaxial loading conditions. *International Journal of Geo-Engineering*, *12*(1). https://doi.org/10.1186/s40703-021-00165-0

Sharma, R., Baxter, C., & Jander, M. (2011). Relationship between shear wave velocity for weakly cemented sands during Drained Triaxial Compression. *Soils and Foundations*, *51*(4), 761-771.

Simatupang, M., Sukri, A. S., Nasrul, Sulha, & Putri, T. S. (2019). Effect of confining pressures on the shear modulus of sand treated with enzymatically induced calcite precipitation. 7th International Conference on Euro Asia Civil Engineering Forum,

Tarantino, A., Zhang, X., Russell, A. R., & Ibraim, E. (2019). Drained volumetric behaviour and static liquefaction of very loose sand reinforced with synthetic fibres. *E3S Web of Conferences*, *92*. https://doi.org/10.1051/e3sconf/20199212001

Wang, Y., Liu, H., Zhang, Z., Xiao, P., He, X., & Xiao, Y. (2019). Study on Low-Strength Biocemented Sands Using a Temperature-Controlled MICP (Microbially Induced Calcite Precipitation) Method. In *New Prospects in Geotechnical Engineering Aspects of Civil Infrastructures* (pp. 15-26). https://doi.org/10.1007/978-3-319-95771-5_2

Whiffin, V. S., van Paassen, L. A., & Harkes, M. P. (2007). Microbial Carbonate Precipitation as a Soil Improvement Technique. *Geomicrobiology Journal*, *24*(5), 417-423. https://doi.org/10.1080/01490450701436505

Wu, S., Li, B., & Chu, J. (2021). Stress-Dilatancy Behavior of MICP-Treated Sand. *International Journal of Geomechanics*, *21*(3). https://doi.org/10.1061/(asce)gm.1943-5622.0001923

Xiao, P., Liu, H., Stuedlein, A. W., Evans, T. M., & Xiao, Y. (2019). Effect of relative density and biocementation on cyclic response of calcareous sand. *Canadian Geotechnical Journal*, *56*(12), 1849-1862. https://doi.org/10.1139/cgj-2018-0573

Xiao, P., Liu, H., Xiao, Y., Stuedlein, A. W., & Evans, T. M. (2018). Liquefaction resistance of bio-cemented calcareous sand. *Soil Dynamics and Earthquake Engineering*, *107*, 9-19. https://doi.org/10.1016/j.soildyn.2018.01.008

Xiao, Y., Stuedlein, A. W., Ran, J., Evans, T. M., Cheng, L., Liu, H., van Paassen, L. A., & Chu, J. (2019). Effect of Particle Shape on Strength and Stiffness of Biocemented Glass Beads. *Journal of Geotechnical and Geoenvironmental Engineering*, *145*(11). https://doi.org/10.1061/(asce)gt.1943-5606.0002165

Yuan, H., Ren, G., Liu, K., Zheng, W., & Zhao, Z. (2020). Experimental Study of EICP Combined with Organic Materials for Silt Improvement in the Yellow River Flood Area. *Applied Sciences*, *10*(21). https://doi.org/10.3390/app10217678

RELATIONSHIP BETWEEN SLOPE FAILURE DISPLACEMENT AND FREQUENCY OF INPUT GROUND MOTION — NUMERICAL STUDY USING THE SPH METHOD

Moe Sasaki[1] and Yusuke Ono[2]
1. Graduate Student, Graduate School of Sustainable Science, Tottori University, Tottori, Japan
2. Professor, Department of Management of Social Systems and Civil Engineering, Tottori University, Tottori, Japan
Email: m22j6010b@edu.tottori-u.ac.jp, ysk@tottori-u.ac.jp

ABSTRACT

Recently, the application of the SPH method has attracted attention as a new seismic response analysis method. In this paper, we investigate the effect of the frequency of input seismic motion on slope failure using seismic response analysis based on the SPH method. The slope model used in this analysis slid down while the soil mass kept its original shape in response to the input seismic motion. Regardless of the frequency response characteristics of the slope model, the amount of soil mass sliding increased with decreasing frequency of the input seismic motion.

Keywords: Numerical analysis, SPH method, slope failure, seismic ground motion

INTRODUCTION

The finite element method, which has been widely used for seismic response analysis, is a mesh-dependent analysis method and is not easily applied to problems with large deformation. The SPH method is a type of particle method that considers a continuum as a set of many particles and performs approximate calculations. The SPH method can easily handle large deformation problems because it does not require the creation of a mesh.

The SPH method has been applied to large deformation problems of soil structures (Ono *et al.*, 2006; Bui *et al.*, 2008; Ono, 2013). In this study, the effect of the frequency of input earthquake motion on slope failure was examined using seismic response analysis based on the SPH method.

ANALYSIS METHOD

The SPH method

Kernel Approximation

The SPH method evaluates a physical quantity $f(x)$ at position x in a continuum using an approximation method called the kernel approximation. The kernel approximation is expressed as

$$f(x) = \int f(x')W(x - x', h)dx' \tag{1}$$

where $W(x\text{-}x',h)$ is the weight function, x' is the coordinate value of the surrounding particles, and h is the radius of influence. In the SPH method, the physical quantities possessed by particles within the radius of influence from the particle at the center of evaluation are weighted according to their distance and added together to obtain an approximation of the physical quantity at the location of the particle at the center of evaluation.

Kernel Approximation and Discretization of Differential Forms

The differential form of Eq. 1 is necessary for the analysis of the continuum body. The kernel approximation of the differential form is expressed as,

$$\nabla \cdot f(x) = -\int f(x') \cdot \nabla W(x - x',\ h) dx' \tag{2}$$

Since the SPH method performs calculations on a particle-by-particle basis, Eqs. 1 and 2 are discretized as follows, respectively.

$$\nabla \cdot f(x^i) = -\sum_{j=1}^{N} \frac{m^j}{\rho^j} f(x^j) \cdot \nabla W(x - x',\ h) \tag{3}$$

where x^j, ρ^j, and m^j are the coordinate values, density, and mass of particles within the radius of influence of particle i.

Discretization of the equations of motion

The equation of motion of the continuum is expressed as,

$$a_a = \frac{1}{\rho} \frac{\partial \sigma_{\alpha\beta}}{\partial x_\beta} + b_\alpha \tag{4}$$

where a_α is the acceleration in the α direction, $\sigma_{\alpha\beta}$ is the stress tensor, b_α is the body force in the α direction. Discretizing Eq. 4 by the SPH method, the following equation is derived.

$$a_\alpha^i = \sum_{j=1}^{N} m \left\{ \frac{\sigma_{\alpha\beta}^i}{(\rho^i)^2} + \frac{\sigma_{\alpha\beta}^i}{(\rho^j)^2} \right\} \frac{\partial W^{ij}}{\partial x_\beta} + b_\alpha \tag{5}$$

On the other hand, the strain rate tensor is calculated by the following equation.

$$\dot{\varepsilon}^{ij} = \frac{1}{2} \left(\frac{\partial v^i}{\partial x^j} + \frac{\partial v^j}{\partial x^i} \right) \tag{6}$$

In the SPH method, $\partial v^i / \partial x^j$ is obtained by the kernel approximation and substituted into Eq. 6 to calculate the strain rate for each particle. Then, from the obtained strain rate, the stress for each particle is calculated according to the constitutive equation, and the acceleration a_α^i at each particle position can be calculated by substituting it into Eq. 5.

Elasto-plastic Analysis

In the elasto-plastic analysis using the SPH method, various constitutive laws for stress-strain relationships can be applied as in the finite element method. In this study, the Drucker-Prager equation was used as the failure criterion and plastic potential of the soil.

Rayleigh damping

Rayleigh damping is commonly used in seismic response analysis using the finite element method. In the present analysis, Rayleigh damping was introduced. To introduce Rayleigh damping into the SPH

method, the following equation is added to the right-hand side of the equation of motion in Eq. 5 (Ono et al., 2013).

$$\alpha_R v_\alpha^i + \beta_R \frac{\Delta g_\alpha^i}{\Delta t} \tag{13}$$

where α_R and β_R are the coefficient of Rayleigh damping; v_α^i is the velocity of the particle i; Δg_α^i is the increment of inner force of the particle i; Δt is the time interval used in the time integral scheme.

Jaumann stress rate

In analyses of large deformations, such as slope failure, rigid body rotation occurs in the object under analysis. The Jaumann stress rate was introduced to remove the effect of rigid body rotation in the stress calculation (Gray *et al.*,2001).

Slope Model

The slope model used in the analysis is shown in Fig. 1. Table 1 shows the material parameters of the slope model. Initially, particles were evenly spaced at 1.0 m intervals. The total number of particles on the slope was 2423. The radius of influence was set to 2.6 m.

Table 1. Material parameters of the slope model.

Density	$\rho_t = 19.4\text{kN/m}^3$
Peak strength	$c_p = 5.9\text{kN/m}^3, \phi_p = 5.9°$
Residual strength	$c_r = 17.5\text{kN/m}^2, \phi_r = 35.0°$
Elastic modulus	$E_0 = 170000 + 825 \cdot P\ \text{kN/m}^2$
Poisson's ratio	$\upsilon = 0.364$

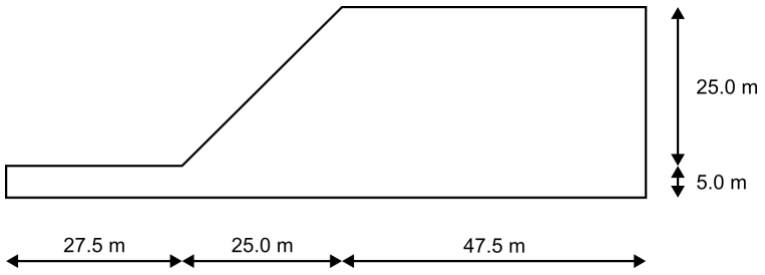

Figure 1. Geometry of the slope model.

Input ground motions

Five input earthquake motions with different frequencies of 0.6, 1.2, 2.4, 3.6, and 4.8 Hz were used in this analysis. The maximum amplitude was the same for all five waveforms and was set to 5.0 m/s2. The seismic motion was applied only in the horizontal direction of the slope model, and the duration was adjusted so that a sinusoidal wave with 15 cycles was input. The waveforms of the input seismic motion used are shown in Fig. 2. The horizontal axis is the dimensionless time obtained as the product of time and frequency of the input seismic motion. When dimensionless time is used, the waveforms are identical in all cases. Before inputting the seismic motion, the slope model was analyzed with only gravity acting on it for 10 seconds to obtain the initial stress state.

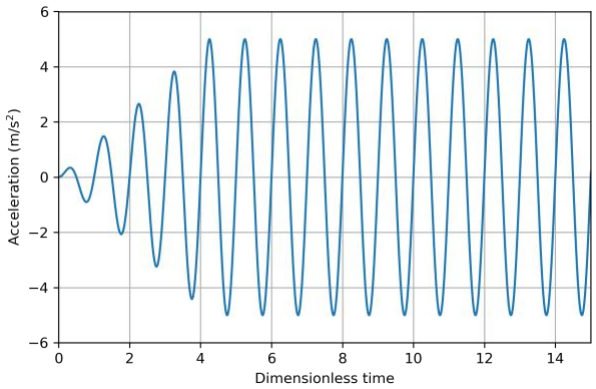

Figure 2. Acceleration time history of the input ground motion. The horizontal axis is dimension time, which is given by multiplying time and the frequency of input ground motion.

RESULTS AND DISCUSSION

Figure 3 shows the initial state SPH particle configurations and the final deformation of the slope in each case. In these figures, the particles are color-coded by normalizing the displacement by the maximum final displacement for each case. In all cases, the soil mass slid while maintaining its original shape.

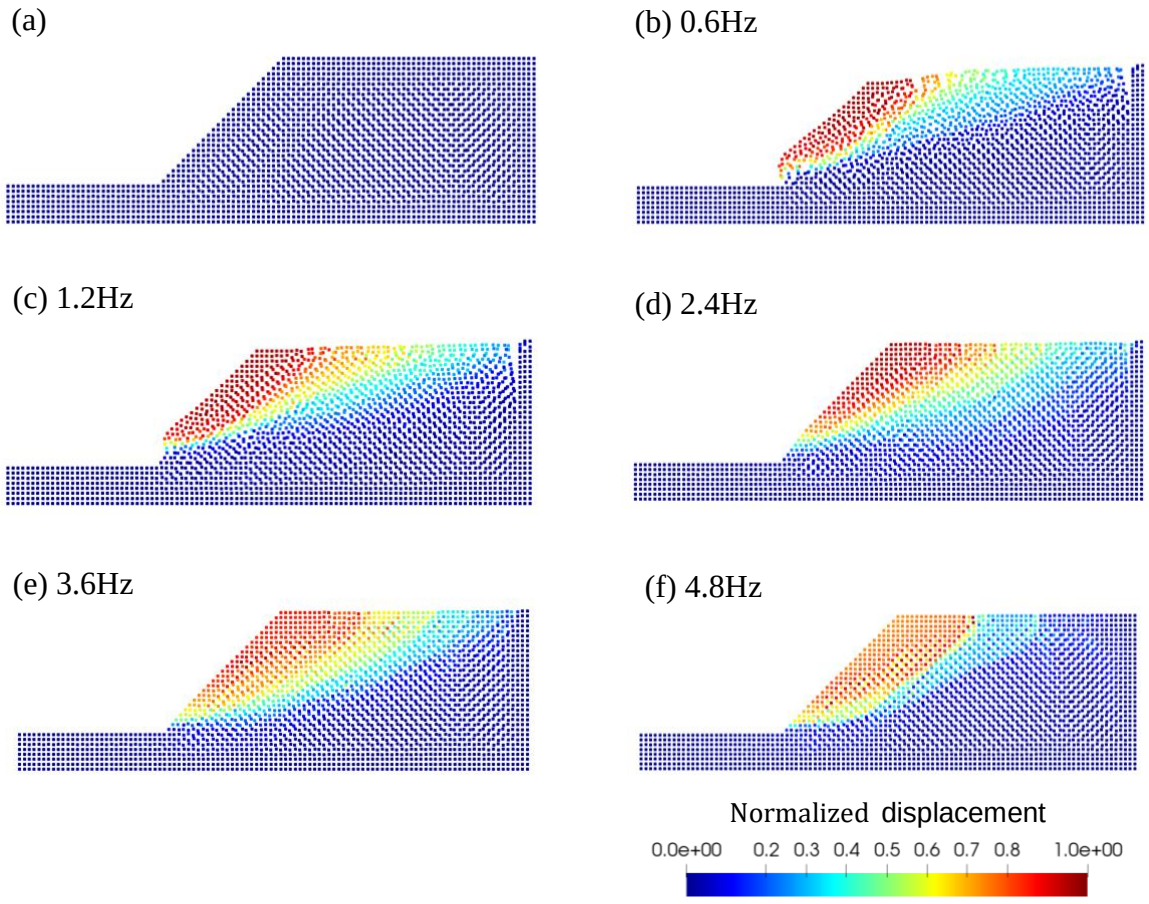

Figure 3. Comparison of the slope geometry before and after excitation: (a) before excitation; (b) - (f) after excitation. The particles are colored by the normalized displacement by the maximum one for each frequency case.

In order to examine the movement of the sliding soil mass, we focused on the particle at the shoulder of the slope. Figure 4 shows the difference in the time history of the horizontal displacement of the slope shoulder depending on the input frequency. The horizontal axis is the number of cycles of the input wave. The vertical axis is the horizontal displacement of the slope shoulder, with the leftward (open) direction of the slope model being negative. For any input frequency, the displacement of the horizontal component of the slope shoulder increases in a staircase-like manner with a constant magnitude. In other words, the displacement of the sliding soil mass for a given duration is obtained as the product of the number of repetitions of the input sine wave and the displacement per cycle.

The average displacement of the sliding soil mass for one cycle of input is calculated and displayed for each frequency in Fig. 5. As the frequency of the input ground motion decreases, the displacement per cycle of the input wave increases.

To investigate the relationship between the frequency response characteristics of the slope model and the displacement of the sliding soil mass, the acceleration amplification factor of the slope shoulder was determined by elastic analysis (Fig. 6). Comparing Figs. 5 and 6, there is no relationship between the acceleration amplification factor at each frequency and the displacement of the soil mass per cycle of the input wave. In other words, the displacement of the soil mass per cycle of the input ground motion is not affected by the frequency response characteristics of the slope model.

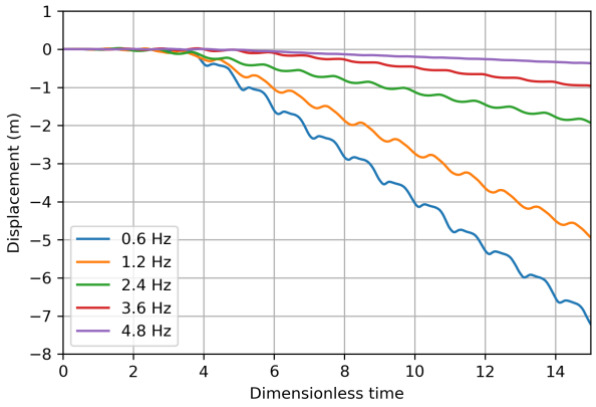

Figure 4. Comparison of horizontal displacement of the slope shoulders.

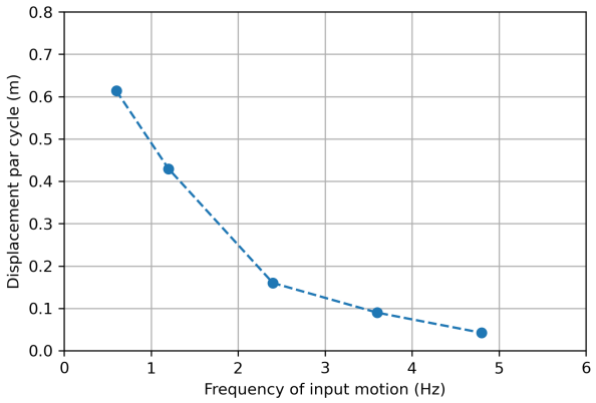

Figure 5. Averaged horizontal displacement of sliding soil mass per one cycle of the input ground motion.

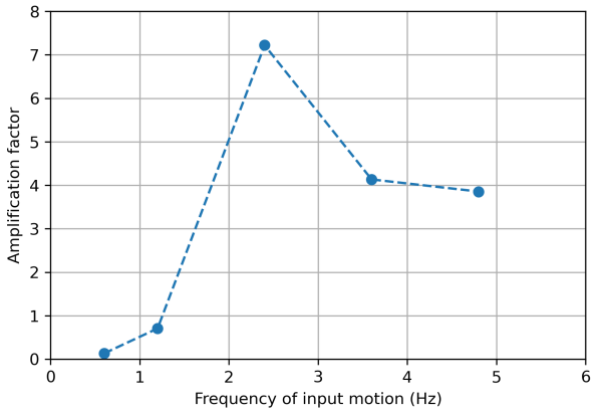

Figure 6. Acceleration amplification factor of the slope shoulder obtained by the elastic analysis.

CONCLUSIONS

This study examined the effect of the frequency of the input seismic motion on the slope failure using the SPH method of seismic response analysis. As a result, the following findings were obtained.

1. The slope model used in the present analysis slipped down while the soil mass kept its shape in response to the seismic input.
2. The sliding displacement of the soil mass was not related to the frequency response characteristics of the slope model.
3. The horizontal displacement of the sliding soil mass per input wave period is related to the frequency of the input wave. The lower the input wave frequency, the greater the horizontal displacement of the sliding soil mass.
4. The final slip displacement of the soil mass was expressed by the product of the displacement per a cycle and the number of cycles of the input ground motion.

In the future, we plan to conduct analyses using actual observation records and varying ground conditions to investigate the effects of input earthquake ground motion on slope failure in more detail.

REFERENCES

Bui, H., Fukagawa, R., Sako, K. and Ohno, S. (2008). "Lagrangian meshfree particles method (SPH) for. large deformation and failure flows of geomaterial using elastic-plastic soil constitutive model", *International Journal for Numerical and Analytical Methods in Geomechanics*, **32**, 1537-1570.

Gray, J. P., Monaghan, J. J. and Swift, R. P. (2001). "SPH elastic dynamics", *Computer Methods in Applied Mechanics and Engineering*, **190**(49-50), 6641-6662.

Ono, Y., Nishida, S. and Kiyono, J. (2006). "Elasto-plastic analysis of earth structure using SPH method", *Journal of Applied Mechanics*, **9**, 717-723 (in Japanese).

Ono, Y. (2013). "SPH simulation of slope failure induced by earthquake ground motion", *Journal of Japan Society of Civil Engineers, Ser. A1 (Structural Engineering & Earthquake Engineering (SE/EE))*, **32**, I_650-I_660 (in Japanese).

INFLUENCE OF LOWERING GROUNDWATER LEVEL ON SOIL LIQUEFACTION POTENTIAL OF TAIPEI BASIN

Yuan-Chang Deng[1] Chih-Chieh Lu[2] Chun-Hung Chen[3] Yi-Tsen Ou[4] Jin-Hung Hwang[5]

1. Assistant Researcher, Earth Sciences and Geotechnical Engineering Division, National Center for Research on Earthquake Engineering, Taipei, Taiwan, R.O.C.
2. Research Fellow, Earth Sciences and Geotechnical Engineering Division, National Center for Research on Earthquake Engineering, Taipei, Taiwan, R.O.C.
3. Director, Water Resources Planning Institute, WRA, MOEA, Taiwan
4. Assistant Researcher, Groundwater Research Center, Water Resources Planning Institute, WRA, MOEA, Taiwan
5. Professor, Department of Civil Engineering, National Central University/ Chairperson, Earth Sciences and Geotechnical Engineering Division, National Center for Research on Earthquake Engineering, Taiwan

Email: ycdeng@narlabs.org.tw

ABSTRACT

The purpose of this study is to discuss influence of practical lowering the groundwater level on soil liquefaction potential of the Taipei Basin. The simplified soil liquefaction evaluations and map production in post-lowering groundwater level considers the increase thickness of surface non-liquefied soil layer. The pre-lowering groundwater level is set as the average water level during the flood season during the implementation of "Home Security Plan, the post-lowering one is set as GL. -3m. The pre-lowering groundwater level results show that the proportion of high potential area is 25.3%, and the post-lowering ones show that the proportion of high potential area is only 6.4%. Lowering groundwater strategies could significantly reduce soil liquefaction potential. The corresponding thickness of surface non-liquefied layer could prevent surface liquefaction damages. The post-lowering water level could be used as a preliminary reference for the management strategies of soil liquefaction disaster prevention in the Taipei Basin.

Keywords: soil liquefaction, lowering the groundwater table, liquefaction potential map, Taipei Basin

INTRODUCTION

In 1999, the 921 Chi-Chi earthquake struck central Taiwan and caused extensive soil liquefaction. This attracted the attention of researchers and engineers, and the study of soil liquefaction subsequently became mainstream, benefitting from the fact that cases of soil liquefaction, earthquake records, and relevant geological information were well documented. Some Taiwanese researchers developed a local simplified procedure based on standard penetration test blow counts (SPT-N) in light of the framework proposed by Seed et al. (1985), namely the hyperbolic function (HBF) procedure (Hwang et al., 2012).

In 2016, approximately 17 years after the 921 Chi-Chi earthquake, the Meinong earthquake, with a local magnitude (M_L) of 6.6, struck southern Taiwan, causing serious building damage due to soil liquefaction in the Tainan area. Because of the great public concern about the risk of soil liquefaction in urban areas after this event, about one month after the Meinong earthquake, the Central Geological Survey disclosed the first version of a soil liquefaction potential map based on data from a limited number of boreholes. This map provided a ranking of liquefaction risk in terms of the liquefaction potential index (P_L). In order to provide the public with a better understanding of soil liquefaction risk, the Construction and Planning Agency Ministry of the Interior (CPA/MOI) then promoted the "Home Security Plan" to produce a refined soil liquefaction potential map for local administrative divisions that contain liquefiable areas. To facilitate the execution of this plan, the National Center for Research on Earthquake Engineering (NCREE) served as general counselors for Taipei City and New Taipei City to establish a standard operating procedure and supervise the contractor (CECI Engineering Consultants) in executing the plan according to the setting requirements. The working group has been

engaged in this project for approximately two years and has accumulated a wealth of experience in its execution.

The refined soil liquefaction potential maps released by the Taipei City Government and the New Taipei City Government show that areas with high liquefaction potential in the Taipei Basin are densely populated, suggesting that the issue of soil liquefaction caused by earthquakes is important with regard to disaster prevention, mitigation strategies, and urban planning in the Taipei Basin Metropolitan Area.

Engineering lower water tables is one of the effective anti-liquefaction strategies being used, but there is little research related to the management of this process for the regional water levels used in the Taipei Basin. Yasuda and Hashimoto (2016) pointed out that the damage to Japanese wooden structures caused by earthquake-induced soil liquefaction could be avoided when groundwater levels were kept to 3 m below the surface.

In order to realize the applications of the work conducted by Yasuda and Hashimoto (2016), this study used their recommendations to examine the differences in the distribution of regional soil liquefaction potential between a benchmark ground water level (set as the average water level during flood season) and a post-lowering ground water level of GL. -3 m. The results can be used as a reference for the formulation of relevant disaster prevention and mitigation strategies in the Taipei Basin.

REFINED BOREHOLE DATABASE OF THE TAIPEI BASIN

The Taipei Basin is a highly developed region in Taiwan. Many large projects including large-scale land development, public rapid transit systems, freeways, and highways have been completed and have operated over recent decades. This public infrastructure has resulted in the generation of a large geological drilling database distributed throughout the Taipei Basin, which is an essential input for soil liquefaction assessment. The total number of boreholes in the Taipei Basin is currently as many as 12962, which means that there are approximately 53 boreholes per square kilometer assuming a uniform spatial distribution. However, since the quality control of the early geological drilling was not well established, much of the submitted borehole data is not reliable enough for use in liquefaction assessment. Therefore, it is necessary to conduct further inspection and screening processes before borehole data can be included. In the screening process, the quality of the drilling data is first classified. The classification principle is based on the complete set of the data including the unified soil classification system (USCS) information, SPT-N value, physical properties of the soil and the judgement of the authors. The first class included data that requires almost no correction nor supplementary data; the second class requires some correction and/or supplementary data; the third class included data that considered unreliable and lacked some essential information; and the fourth class represented data that considered extremely unreliable and lacked essential information.

In this study, the boreholes belonging to the third and fourth classes are discarded and only borehole data of the first and second classes are used for analyses. For these boreholes, where soil sample data are missing they are supplemented using information from neighboring soil samples with similar USCS characteristics. If there are no suitable nearby references, the missing data are constructed from a statistical analysis of reliable soil sample data. After the above processing, the number of remaining boreholes is 5182. Their distribution in the Taipei Basin is shown in Fig. 1. The solid blue circles are boreholes drilled during the “Home Security Plan” project from 2017 to 2018. The purpose of the drilling is mainly for the evaluation of soil liquefaction in the Taipei Basin. In order to reduce operation variability, the automatic drop hammer system is adopted, resulting in improved drilling quality. Based on the energy measurements of selected boreholes, the energy ratio of the automatic drop hammer system in this case is approximately 65~70%. According to the statistical results of the boreholes from the “Home Security Plan”, liquefiable sandy soils, including USCS categories SM, ML, CL-ML, and other gravel soils, account for 58.3% of all soils. Among the liquefiable sandy soils, the SM soils are in the majority and account for 53.5% of the liquefiable soils. The SM soils have an average N value of approximately 12 and an average fines content of 25%, the CL soils have an average N value of 5 and an average fines content of 94%, and the ML soils have an average N value of 9 and an average fines content of 75%.

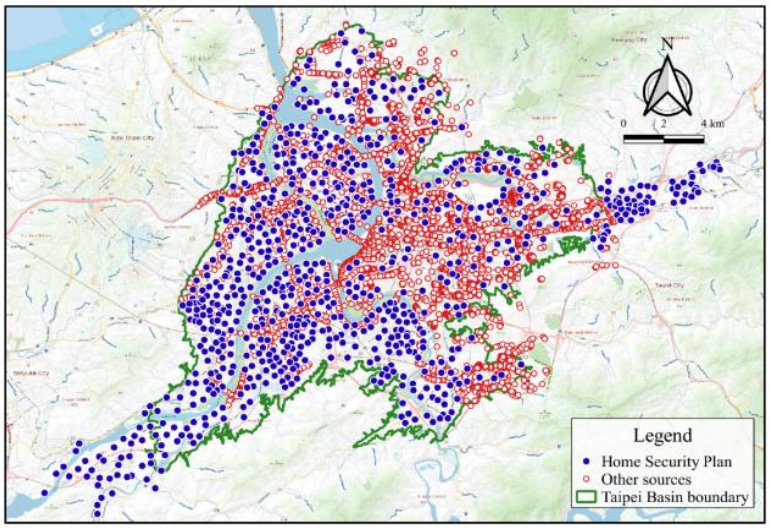

Figure 1. Distribution of boreholes in the Taipei Basin after the screening process are conducted.

SOIL LIQUEFACTION POTENTIAL EVALUATION

Design earthquake parameters and ground water table

The moment magnitude (M_w) and the horizontal peak ground acceleration (PGA) are the earthquake parameters used for the evaluation of soil liquefaction. According to the recommendations of the latest "Seismic design specifications and commentary of buildings", the design earthquake with a return period of 475 years (10% probability of exceedance in 50 years) is required when considering soil liquefaction. In this study, the same concept is used. For a return period of 475 years, the corresponding M_w is 7.3 and its horizontal PGA is 0.24 g. All the boreholes in this study are within or near the Taipei Basin, and both M_w and PGA are consistent throughout.

The ground water table (GWT) is also a critical parameter for soil liquefaction evaluation. However, since the existing GWT data are insufficient, the ground water table of the boreholes drilled by the "Home Security Plan" was measured during the execution of the plan. Based on the GWT measurements, it can be easily shown that the GWT changes throughout the year, and it can be conservatively stated that the contour of the average ground water table in the Taipei Basin during flood season can be reproduced for use in the soil liquefaction evaluation of all boreholes in this study. In order to examine the influence of lowering the groundwater level on the soil liquefaction potential of the Taipei Basin, a lowered ground water level is used, set as GL. -3 m suggested by Yashuda and Hashimoto (2016).

Methods to evaluate soil liquefaction potential

To determine the effect of soil liquefaction in areas that experienced severe liquefaction during the design earthquake, the liquefaction potential index (P_L) proposed by Iwasaki et al. (1978) is commonly used. According to this index, sites with $P_L > 15$ are regarded as having high liquefaction potential, sites with $5 < P_L \leq 15$ are regarded as having middle liquefaction potential, and sites with $P_L \leq 5$ are regarded as having low liquefaction potential. P_L is evaluated from the obtained factors of safety (FS) in light of the Taiwan local HBF method (Hwang et al, 2012, 2021) to predict the potential of liquefaction to cause damage at the surface.

According to Ishihara (1985), the surface non-liquefied layer can restrain the liquefaction-induced ground damage, and the corresponding evaluation can be made by the comparison between the thicknesses of the liquefied and non-liquefied soil layers. The increase thickness of surface non-liquefied soil layers by lowering the groundwater level can restrain the liquefaction-induced ground damage is considered in the analysis case of GWT of GL. -3m. The profile of FS analyzed by HBF method is used to calculate the thickness of surface non-liquefied soil layers H_1 ($FS \geqq 1$) and thickness of liquefied soil layers H_2 ($FS<1$) based on applicable extension of Ishihara (1985). In order to make the P_L contour can better consider the contribution of surface non-liquefied soil layers to restrain the

effect of soil liquefaction on surface structures, this study proposes a P_L modification criterion with adopting the concept of Ishihara (1985) to adjust the calculated P_L values of the boreholes based on Iwasaki et al. (1978). The criterion of liquefaction-induced ground damage of PGA=0.24g can be interpolated from Ishihara (1985). The boreholes with non-liquefied damage are on the right side of the curve of PGA=0.24g, and the corresponding P_L are adjusted as zero. The boreholes with liquefied damage are on the left side of the curve of PGA=0.24g, and the corresponding P_L are kept in the origin values.

P_L and the spatial coordinates of every borehole are used in spatial ordinary Kriging interpolation to produce regional liquefaction potential maps consisting of all discrete cells in the Taipei Basin.

EFFECT OF LOWERING GROUNDWATER LEVEL ON SOIL LIQUEFACTION POTENTIAL

This study compares soil liquefaction between a benchmark groundwater level, which is set as the average ground water table of the Taipei Basin during flood season, and a lowered ground water level, which is set at GL. -3m. The distribution of benchmark groundwater level of boreholes in the Taipei Basin is shown in Fig. 2. In the case of lowered groundwater level, the groundwater level higher than GL. -3m are lowered as GL. -3m, and others are kept in the origin value. The distribution of post-lowering groundwater level of boreholes in the Taipei Basin is shown in Fig. 3. The number of boreholes whose groundwater level are lowered is 2460.

Table 1 shows the percentage distribution of each liquefaction potential level (high, medium, and low PL) among the analyzed boreholes for both ground water levels. The benchmark soil liquefaction evaluation shows that the percentage of boreholes with high, medium, and low liquefaction potential is each approximately one third of the total. The liquefaction potential results for the lowered water table show that the percentage of boreholes with high liquefaction potential reduced to 17.2%, those with middle liquefaction potential reduced to 7.9%, and those with low liquefaction potential increases to 74.9%. This indicates that lowered groundwater level can substantially reduce the risk of liquefaction.

Fig. 3 shows the soil liquefaction potential P_L map using the benchmark groundwater level, and Fig. 4 shows the P_L map using the lowered groundwater level. Table 2 shows the percentage distribution of areas affected by each liquefaction potential levels for both ground water levels. The results of the evaluation using the benchmark groundwater level reveal that the area occupied by each liquefaction potential level is also approximately one third of the total. The area with high liquefaction potential is widely distributed over the middle- and down- stream areas of the Danshui and Keelung Rivers. In general, the areas far from the rivers have little soil liquefaction potential. The results of the soil liquefaction evaluation using the comparative (lowered) groundwater level reveal that the area with high liquefaction potential accounts for a very small fraction of the total, while that with low liquefaction potential increases to two-thirds of the total. This indicates that lowered groundwater level decreases the proportion of high liquefaction potential and increases the proportion of low liquefaction potential area. These values can be used as a preliminary reference for soil liquefaction prevention and disaster mitigation strategies in the Taipei Basin.

Table 1. The percentage distribution of each liquefaction potential level among boreholes for both GWTs

Analysis GWT setting	Borehole proportion (%)		
	Low	Middle	High
Mean GWT during flood season (Benchmark)	38.4	31.7	29.9
GL. -3m (Lowered)	74.9	7.9	17.2

Table 2. The percentage distribution of areas affected by different liquefaction potential levels for both GWTs

Analysis GWT setting	Area proportion (%)		
	Low	Middle	High
Mean GWT during flood season (benchmark)	37.4	37.3	25.3
GL. -3m (Lowered)	69.7	23.9	6.4

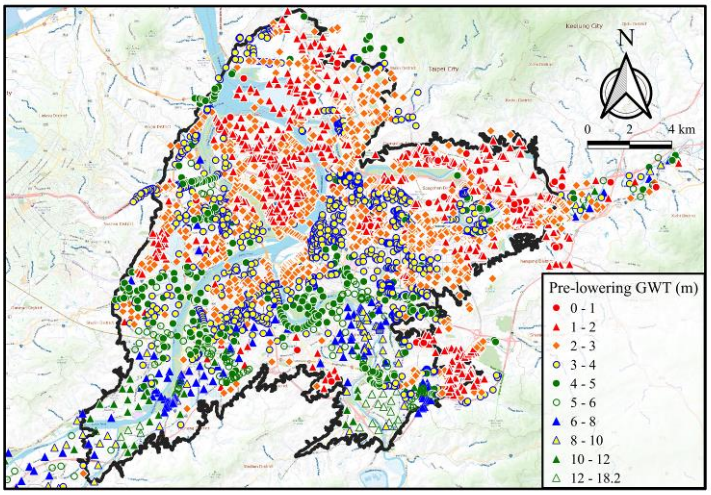

Figure 2. The distribution of pre-lowering groundwater level of boreholes (benchmark level)

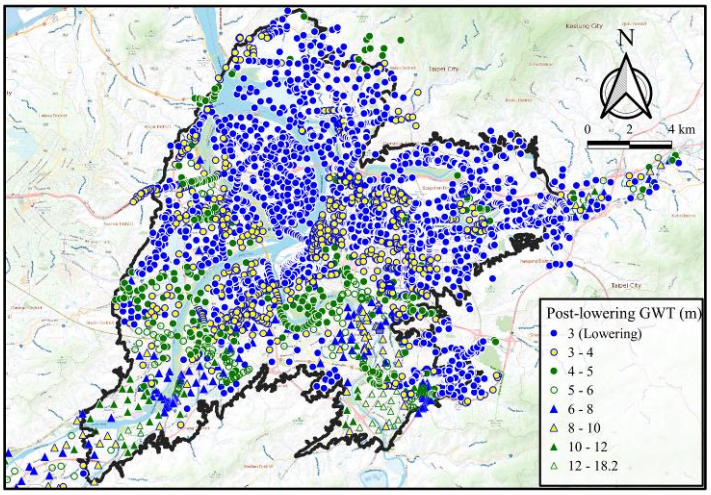

Figure 3. The distribution of post-lowering groundwater level of boreholes (lowered level)

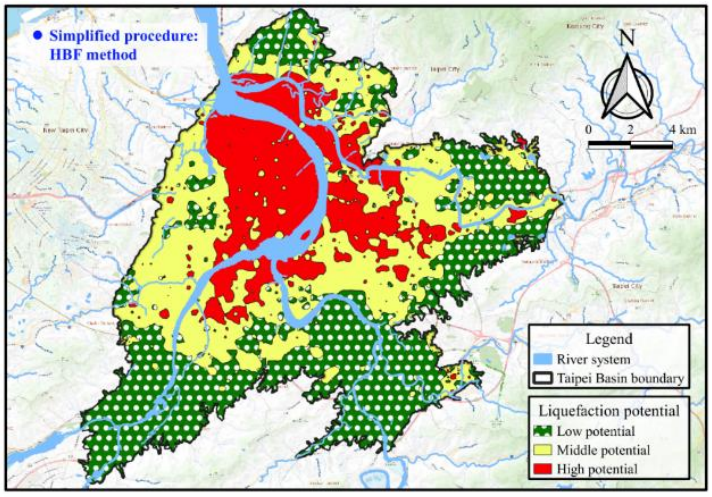

Figure 4. Soil liquefaction potential map of the Taipei Basin (benchmark groundwater level)

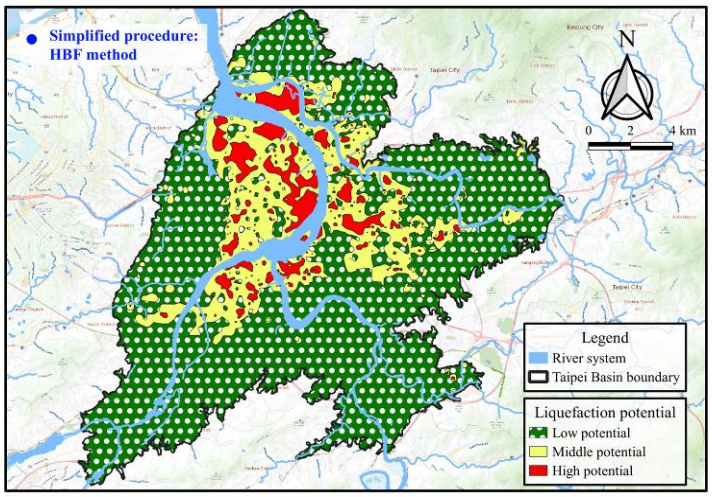

Figure 5. Soil liquefaction potential map of the Taipei Basin (lowered water level of GL. -3m)

CONCLUSION

The effect of lowering the groundwater level on the soil liquefaction potential of the Taipei Basin has examined. The results has suggested that lowering the groundwater level at GL. -3m can significantly decrease the proportion of high potential soil liquefaction area and boreholes. The corresponding surface non-liquefied soil layers can prevent the ground loss and restrain the liquefaction-induced damage on low-story buildings. The results can be used as a preliminary reference for soil liquefaction prevention and disaster mitigation strategies in the Taipei Basin.

The lowering water strategies on anti-liquefaction should be noticed the settlement of neighbor structures induced by pumping system. The barriers of sheet piles are recommended to build around the construction site to make the anti-liquefaction strategies more efficient and safe.

The liquefaction risk of critical infrastructure beneath GL. -3m should be noticed because the analysis results of lowered groundwater level show the soil layers beneath GL. -3m still have high liquefaction potential.

The evaluation of thickness of non-liquefied soil and liquefied soils in this research might not be conservative because of the extended application based on Ishihara (1985). The original configuration of Ishihara is recommended to apply in the engineering practices.

ACKNOWLEDGMENTS

The authors wish to acknowledge the financial support of the Water Resources Planning Institute, Water Resources Agency, Ministry of Economic Affairs, and the data provided by the Construction and Planning Agency Ministry of the Interior, Taipei City, and New Taipei City. The results and the opinions presented in this paper, written or implied, are those of the writers and do not necessarily represent the opinions and policies of Taipei City.

REFERENCES

Seed, H.B., K. Tokimatsu, L.F. Harder, and R.M. Chung (1985). "Influence of SPT Procedures in Soil Liquefaction Resistance Evaluation," J. of Geot.Engr., ASCE, 111(12), 1425-1445.

Hwang, J.H., C.H. Chen, and C.H. Juang (2012). "Calibrating the model uncertainty of the HBF simplified method for assessing liquefaction potential of soils," Sino-geotechnics, 133, 77-86. (in Chinese)

Yasuda, S., and Hashimoto, T. (2016), "New project to prevent liquefaction-induced damage in a wide existing residential area by lowering the ground water table," Soil Dyn. Earthq. Eng., 91, 246–259, 2016.

Construction and Planning Agency, MOI, 2011, Seismic design specifications and commentary of buildings. (in Chinese)

Iwasaki, T., F. Tatsuoka, K. Tokida, and S. Yasuda (1978). "A practical method for assessing soil liquefaction potential based on case studies at various sites in Japan," Proceedings of the 2nd international conference on microzonation for safer construction—research and application, San Francisco, CA, 885-896.

Hwang, J.H., Khoshnevisan, S., Juang, C.H, Lu, C.C. (2021), "Soil liquefaction potential evaluation – An update of the HBF method focusing on research and practice in Taiwan," Engineering Geology, 280, Article 105926.

Ishihara, K. (1985), "Stability of natural deposits during earthquakes," Proceedings of the 11th International Conference on Soil Mechanics and Foundation Engineering, 1, A.A. Balkema,Rotterdam, Netherlands, 321-376.

(2c) Soil structure interaction

ANALYTICAL SEISMIC RESPONSES CONSIDERING SOIL-STRUCTURE INTERACTION WITH STRUCTURAL NONLINEAR PROPERTY

Kuo-Hung Chao[1] Yu-Chi Sung[2] and Xiao-Qin Liu[3]

1. Ph.D. Student, Department of Civil Engineering, National Taipei Univ. of Technology, Taiwan, R.O.C.
2. Professor, Department of Civil Engineering, National Taipei Univ. of Technology, Taiwan, R.O.C.
3. Post-doctoral fellow, Offshore Wind Power Project Office, National Taipei Univ. of Technology, Taiwan, R.O.C.

Email: t108429003@ntut.edu.tw, sungyc@ntut.edu.tw, lisaliu@ntut.edu.tw

ABSTRACT

This study considered soil-structure interaction (SSI) and structural nonlinearity, simultaneously. To achieve this goal, the study first adopted a discrete-time recursive filter approach and frequency-dependent foundation-soil impedance functions to realize the time-frequency domain transfer and solve external forces exerted onto the foundation. Then, the motion equations of the assumed soil-foundation-superstructure (SFS) system subjected to the unidirectional ground motion were derived. Meanwhile, structural nonlinearity was adopted to compare the experimental and analytical results, proving the integral method's accuracy in this study. Last, different properties of soil were used to consider the SSI effect. The results of this study verified the feasibility of the integral method and provided a good understanding of the factors (soil condition and structural nonlinearity) that affect the response of the 3DOF SFS system.

Keywords: discrete-time infinite impulse response filter (IIRF), foundation-soil impedance (FSI) function, soil-structure interaction (SSI)

INTRODUCTION

The soil-structure interaction (SSI) is an important factor in evaluating structural responses. When sitting on a flexible soil bed, a system considering the SSI effect exhibits a larger structural period than the system without SSI consideration. Soil is a type of nonhomogeneous material, and its stiffness and dynamic characteristics are highly sensitive to properties of soil contents and superstructure characteristics. To address such characteristics, Gazetas (1983) suggested a complex frequency-dependent foundation-soil impedance (FSI) function, composed of the real and imaginary components. The real component indicates the stiffness and inertia of the supporting soil, whereas the imaginary component reflects the radiation and material damping of the foundation-soil impedance system. After Gazetas, there have been numerous studies conducted for resolving various soil modeling issues, e.g. considering embedded, non-circular, non-rigid, or piled foundations (Luco, 1974; Gazetas,1983; Veletsos,1971; Apsel, 1987; Kause,1974; Tassoulas, 1981).

Due to the frequency-dependent characteristics of soil, frequency domain analyses are often involved in formation of the equation of motion of the SFS system. However, such practice sacrifices the realistic nonlinear behavior of structure, but it is achievable with integral method.

To incorporate SSI in standard time-history analysis, Safak (2015) proposed a simple method using a discrete-time digital filter to approximate the frequency-dependent FSI function in the time domain. Consequently, the relationship between the foundation forces and displacements can be defined by resultant time-domain finite-difference equations. This method was later adopted by Gash (2017) to solve a multiple-degree-of-freedom (MDOF) motion equation of a shear building, which was supported by a rigid disk foundation and underlying uniform-soil half-space. Sung and Chen (2019) used a z-transferred discrete-time infinite impulse response filter serving as a foundation–soil impedance function to get a transfer function between the ground displacement and foundation shear, and thus derived the base force propagating function to analyze structural responses.

The present study employed a Z-transform discrete-time infinite impulse response filter (IIRF) approach to incorporate the FSI relationship into a three-degrees-of-freedom (3DOF) soil-foundation-superstructure (SFS) model. Meanwhile, structural nonlinearity was adopted to compare the experiment and analytical result proving the accuracy of integral method in this study. Last, two different shear wave velocity V_S = 180 and 365 m/s were used to consider SSI effect, and surveyed the discrepancy from various stiffness and property of soil.

3DOF SFS SYSTEM

Figure 1(a) shows a SDOF system on a fixed base. The SSI effect is not considered by assuming the SDOF system subject to the free-field ground motion. On the other hand, Figure 1(b) displays a 3DOF SFS system consisting of the underlying soil, foundation, and superstructure. The set of 3DOF includes the horizontal displacement u_s of the superstructure mass, and the horizontal displacement u_{FIM} and rotational angle θ_f at the foundation level, which are involved in the SFS system to consider the SSI effect. In Figure 1(b), m_s, c_s, and k_s denote the mass, damping, and stiffness of the superstructure, respectively; h is the height of the superstructure mass. And u_s and u_f are the system's relative horizontal displacements w.r.t. the ground at the superstructure mass level and the foundation level, respectively. As defined in the research by previous scholars, the soil-foundation combination's dynamic stiffness and damping properties are approximated as the transitional and rotational forces— f_h and f_r— at the foundation level.

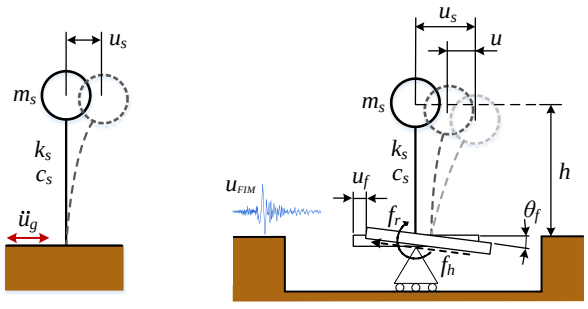

(a) (b)

Figure 1. Structural models: (a) the SDOF system without SSI and (b) the 3DOF system with SSI

Motion Equations

3DOF SFS system concerning the SSI effect is defined as the equation of motion in Eq. (1).

$$\begin{bmatrix} m_s & 0 & 0 \\ 0 & m_f & 0 \\ 0 & 0 & I_f \end{bmatrix} \begin{Bmatrix} \ddot{u}_{s,n} \\ \ddot{u}_{f,n} \\ \ddot{\theta}_{f,n} \end{Bmatrix} + \begin{bmatrix} c_s & -c_s & -c_s h \\ -c_s & c_s & c_s h \\ -c_s h & c_s h & c_s h^2 \end{bmatrix} \begin{Bmatrix} \dot{u}_{s,n} \\ \dot{u}_{f,n} \\ \dot{\theta}_{f,n} \end{Bmatrix} + \begin{bmatrix} k_s & -k_s & -k_s h \\ -k_s & k_s & k_s h \\ -k_s h & k_s h & k_s h^2 \end{bmatrix} \begin{Bmatrix} u_{s,n} \\ u_{f,n} \\ \theta_{f,n} \end{Bmatrix} + \begin{Bmatrix} 0 \\ f_{h,n} \\ f_{r,n} \end{Bmatrix} = -\begin{Bmatrix} m_s \\ m_f \\ 0 \end{Bmatrix} \ddot{u}_{g,n} \quad (1)$$

where m_s and m_f are the masses of the superstructure and foundation, respectively; I_f is the moment inertia of the foundation. c_s and k_s are the damping and stiffness of the superstructure, respectively. The terms u_s, u_f, θ_f and $\dot{u}_s, \dot{u}_f, \dot{\theta}_f$ and $\ddot{u}_s, \ddot{u}_f, \ddot{\theta}_f$ denote the displacement or rotational angle and their first- and second-order derivatives, and $\ddot{u}_g$ is the ground acceleration. The subscripts s and f represent structure- and foundation-related, respectively. n indicates that they occur at time n.

As mentioned by Safak (2015), consequently, the soil impedance is approximated as the transitional and rotational forces at the foundation level, denoted as f_h and f_r in Eqs. (2) and (3):

$$f_{h,n} = b_{h,0} u_{f,n} + \sum_{j=1}^{p} b_{h,j} u_{f,n-j} - \sum_{i=1}^{k} a_{h,i} f_{h,n-i} \quad (2)$$

$$f_{r,n} = b_{r,0}\theta_{f,n} + \sum_{j=1}^{p} b_{r,j}\theta_{f,n-j} - \sum_{i=1}^{k} a_{r,i} f_{r,n-i} \tag{3}$$

Then, Eq. (1) is rearranged into the form of Eq. (4) to deliberately place the terms $\bar{f}_{h,n}$ and $\bar{f}_{r,n}$ to the right side of the equal sign. The terms $\bar{f}_{h,n}$ and $\bar{f}_{r,n}$, as the partial contents of the horizontal force $f_{h,n}$ and moment $f_{r,n}$, respectively, can be derived from the known quantities $u_{f,n-1}$, $\theta_{f,n-1}$, $f_{h,n-1}$ and $f_{r,n-1}$ of the previous time step.

$$\begin{bmatrix} m_s & 0 & 0 \\ 0 & m_f & 0 \\ 0 & 0 & I_f \end{bmatrix} \begin{Bmatrix} \ddot{u}_{s,n} \\ \ddot{u}_{f,n} \\ \ddot{\theta}_{f,n} \end{Bmatrix} + \begin{bmatrix} c_s & -c_s & -c_s h \\ -c_s & c_s & c_s h \\ -c_s h & c_s h & c_s h^2 \end{bmatrix} \begin{Bmatrix} \dot{u}_{s,n} \\ \dot{u}_{f,n} \\ \dot{\theta}_{f,n} \end{Bmatrix} + \begin{bmatrix} k_s & -k_s & -k_s h \\ -k_s & k_s + b_{h,0} & k_s h \\ -k_s h & k_s h & k_s h^2 + b_{r,0} \end{bmatrix} \begin{Bmatrix} u_{s,n} \\ u_{f,n} \\ \theta_{f,n} \end{Bmatrix} = -\begin{Bmatrix} m_s \\ m_f \\ 0 \end{Bmatrix} \ddot{u}_{g,n} + \begin{Bmatrix} 0 \\ \bar{f}_{h,n} \\ \bar{f}_{r,n} \end{Bmatrix} \tag{4}$$

$$\bar{f}_{h,n} = -\sum_{j=1}^{p} b_{h,j} u_{f,n-j} + \sum_{i=1}^{k} a_{h,i} f_{h,n-i} \tag{5}$$

$$\bar{f}_{r,n} = -\sum_{j=1}^{p} b_{r,j} \theta_{f,n-j} + \sum_{i=1}^{k} a_{r,i} f_{r,n-i} \tag{6}$$

Coefficient Estimation

The dynamic FSI function (Gazetas 1983; Veletsos and Verbic 1973; Veletsos and Wei 1971) depends on various foundation geometrics and soil conditions. The dynamic stiffness of the FSI function can be determined using vibration tests and expressed as the ratio of harmonic forces acting on the foundation–soil interface to the corresponding harmonic displacement or rotation angle (Srinivasan et al. 1991).
The following $K(a_0)$ is the general form of the FSI function (Veletsos and Wei 1971; Sieffert and Cevaer 1991):

$$K(a_0) = K_j[k(a_0) + i a_0 c(a_0)] \tag{7}$$

where K_j is the static component of soil impedance, and j represents either the horizontal displacement h, vertical displacement v, or rotational angle r. $k(a_0)$ and $c(a_0)$, as functions of the dimensionless frequency a_0, are the frequency-dependent stiffness and damping components, respectively.
The present study used a Z-transform discrete-time infinite impulse response filter (IIRF) approach to incorporate the FSI relationship into a 3DOF SFS model. The finite-difference equation of a linear and causal discrete-time filter is expressed as follows (Carlson 1998):

$$y[nT] + \sum_{i=1}^{k} a_i y[(n-i)T] = \sum_{j=0}^{p} b_j x[(n-j)T] \tag{8}$$

where T is the sampling time, n is the number of time instant in T; k and p represent the order of the filter, and a_i and b_j are constant coefficients. The terms $y[nT]$ and $x[nT]$ are the output and input signals, respectively, of this discrete-time filter. To prevent the discrete-time filter having an intricate convolution procedure in the time domain, the Z-transform discrete-time infinite impulse response filter (IIRF) was used.
On the basis of the time-delay theorem of Z-transform and the zero-state response condition, the discrete-time single-side Z-transform is defined as follows:

$$Y(z) + \sum_{i=1}^{k} a_i z^{-i} Y(z) = \sum_{j=0}^{p} b_j z^{-j} X(z) \tag{9}$$

where z = exp($i\Omega$).
Let $H(z)$ be the ratio of $Y(z)$ over $X(z)$, Eq. (9) becomes:

$$H(z) = \frac{Y(z)}{X(z)} = \frac{\sum_{j=0}^{p} b_j z^{-j}}{1 + \sum_{i=1}^{k} a_i z^{-i}} \tag{10}$$

Eq. (7) indicates that $K(a_0)$ is expressed using two complex polynomials (Safak 2006), similar to the expression of the transfer function $H(z)$ of the IIRF in Eq. (10). Therefore, the discrete-time force sequence $f(t)$ exerted onto the foundation is used to directly determine the standard form of the Z-transform function $H(z)$ in Eq. (10) and the finite-difference equations in Eq. (8). Through minor modifications, Eq. (8) becomes

$$f[nT] = \sum_{j=0}^{p} b_j u[(n-j)T] - \sum_{i=1}^{k} a_i f[(n-i)T] \tag{11}$$

where the filter coefficients a_i and b_j can be determined through a system identification technique. To express the transfer function $H(z)$ of the IIRF in terms of a known objective function, that is, the foundation–soil impedance function $K(a_0)$, the error between the transfer function $H(z)$ and objective function $K(a_0)$ is expressed as a function, and iterative reweighted least-square approximations (Wolke and Schwetlick 1988) are subsequently used to minimize this error function. The obtained $H(z)$ should be equivalent to the foundation–soil impedance function $K(a_0)$.

SPECIMENS INTRODUCTION WITH CORRESPONDING TEST

Three identical reinforced concrete bridge columns (specimen A, B and C), designed according to the 1995 version of the Taiwan Bridge Design Code (TBDC), shown in figure 2 were cast with a scale of 2/5. Among those, specimen A was proceeded by a cyclic loading test and specimens B and C were subjected to two different strong near-fault ground motions by pseudo dynamic test. Details about the test setup can be found in the reference of Chang et al. (2004).

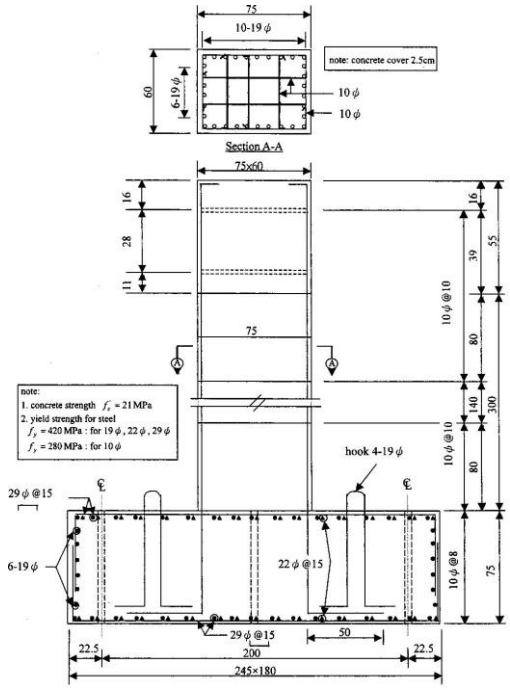

Figure 2. Design diagram for the specimen

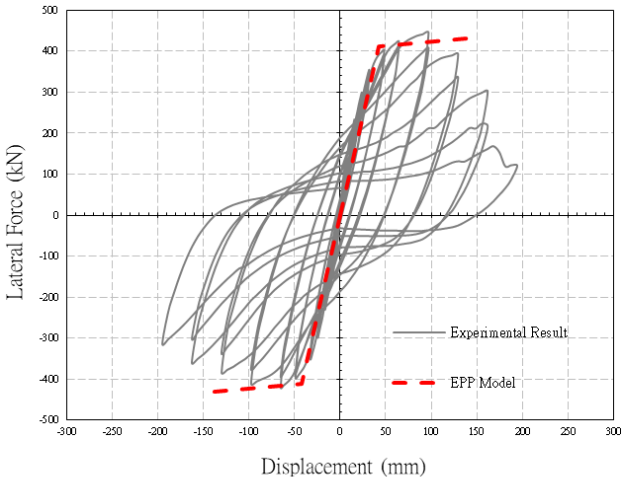

Figure 3. Result of cyclic loading test for specimen A and analytical bilinear model setting

Associated with the experimental results of the cyclic loading test of the specimen A, this paper adopted a bilinear model to present the nonlinear behavior of the specimen, shown in Figure 3. The yielding and ultimate displacements of specimen are found to be $\Delta y = 42.229mm$ and $\Delta u = 150mm$, respectively. The yielding lateral force is 411.681 *kN*, and the ultimate lateral force is 432.694 *kN*. The initial stiffness is 9748.779 MPa, and the unloading stiffness is the same as initial stiffness.

COMPARING FIXED-BASE TIME HISTORY ANALYSIS SOLUTIONS TO PSEUDODYNAMIC TEST RESULTS

This study used ground accelerations record from stations TCU075 and TCU102 as the seismic input, which were caused by the Chelungpu fault. Figure 4 shows the ground acceleration for TCU075. The lumped mass for Specimen B is assumed to be 27,500 kg, which is subjected to the ground acceleration record of TCU075 with a peak ground acceleration of 0.8g. Figure 5 shows the ground acceleration for TCU102. The lumped mass for Specimen C is specified to be 68,000 kg, which is subjected to TCU102 with a peak ground acceleration of 0.7g.

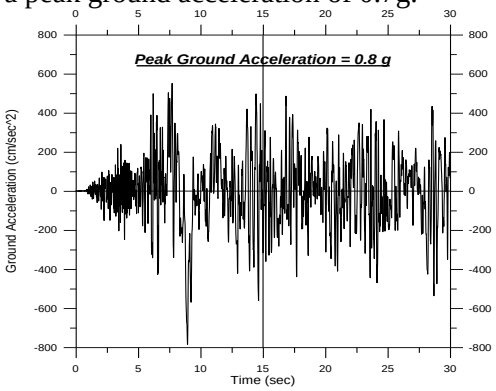

Figure 4. Ground acceleration for TCU075

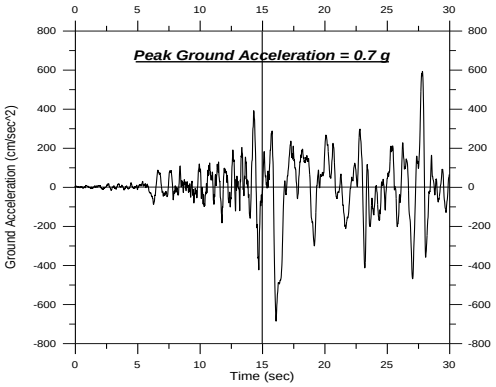

Figure 5. Ground acceleration for TCU102

Figures 6 and 7 expressed the comparison between analytical and experiment result under TCU075 and TCU102, respectively. For specimen B, the maximum displacement and maximum lateral force displayed in the pseudo dynamic responses at t=14.52 s and were 68.32 mm and 467.0 kN, respectively, while the analyzed responses at the same time were 53.71 mm and 413.92 kN.

For specimen C, the maximum displacement and maximum lateral force displayed in the pseudo dynamic responses at t=14.79 s and were 60.98 mm and 477.0 kN, respectively, while the analyzed responses at the same time were 55.60 mm and 413.91 kN. It is apparent that the analytical displacement is larger than the experiment result and the lateral force is lower than experiment result, conversely. Because the concrete cover was severely spalled and steel bar buckled at the bottom of the specimen, the pseudo-dynamic experiment was stopped at t=16.27 s in Figure 7.

The initial stiffness and energy dissipation mechanism of analytical model are representative to the experimental result by observing the area of the hysteretic loops from Figure 6(a) and Figure 7(a).

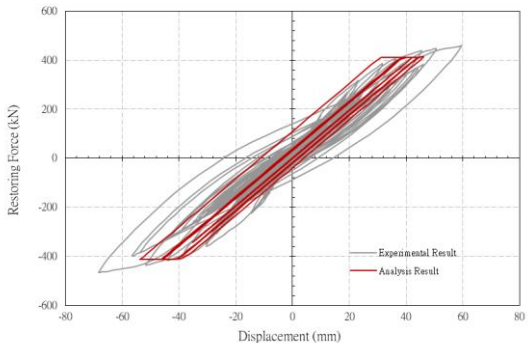

(a) Hysteretic loops

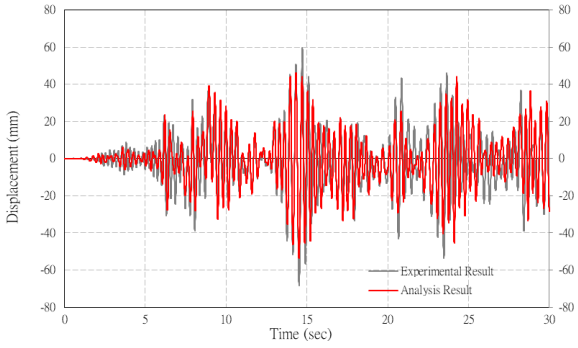

(b) Displacement time history

Figure 6. Comparison between analytical and experimental result subjected to TCU075

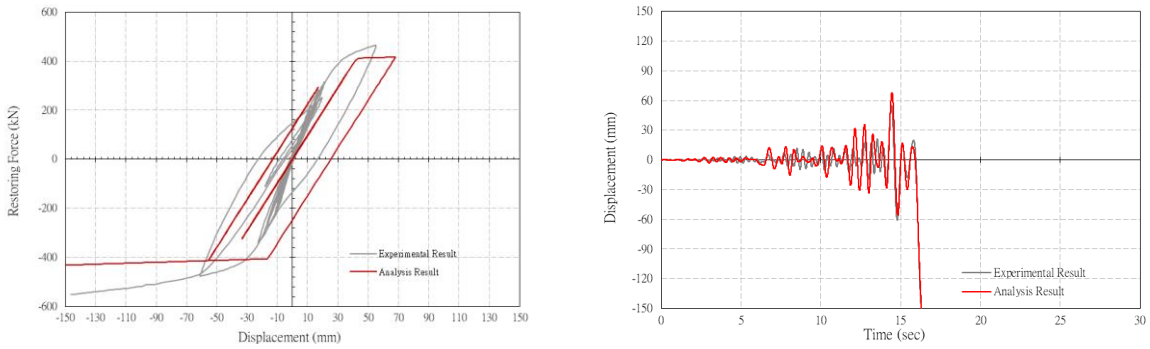

(a) Hysteretic loops (b) Displacement time history

Figure 7. Comparison between analytical and experimental result subjected to TCU102

TIME HISTORY ANALYSIS SOLUTIONS CONSIDERING SSI EFFECT

This study employed two soil conditions with shear wave velocity V_S = 180 and 365 m/s to consider SSI. The structure is assumed to be supported by a rigid disk foundation and underlying uniform-soil half-space. The rigid disk foundation is 0.9 m height with 6 m of diameter, and 160,000 kg of mass. Table 1 presents the modeling parameters pertaining to the soil and foundation.

Table 1. Modeling Parameters of the Soil, Foundation, and Superstructure

Soil			**Foundation**	
Parameters	Loose soil	Dense soil	Height h_f (m)	0.9
Shear modulus G (kN/m^2)	7,287	29,964	Mass W_f (kg)	160,000
Shear wave velocity *Vs* (m/s)	180	365	Diameter d_f (m)	6
Poisson's ratio *v*	1/3			

For the analytical result under TCU075 with V_S = 365 m/s in Figure 8, the displacement and lateral force displayed at t=14.51 s and were 51.36 mm and 413.46 kN, respectively. The displacement is smaller than that of the fixed base at the same time. The analyzed maximum responses occurred at t=14.34 s and were 56.65 mm and 414.50 kN. During the seismic duration, the positive displacement has generated the alternative displacement, which cause the negative displacement smaller at t=14.51 s. It also explains the restrict of the bilinear model and the unload stiffness setting which is always the same as initial stiffness.

For the analytical result under TCU075 with V_S = 180 m/s in Figure 9, the displacement and lateral force displayed at t=14.51 s and were 73.78 mm and 417.93 kN, respectively. The displacement is larger than that of the fixed base at the same time, because the period prolonged considering SSI and changed the structure response. The analyzed maximum responses occurred at t=20.72 s and were 77.06 mm and 418.47 kN. The results showed that the structure response of SFS system is larger than that of fixed base.

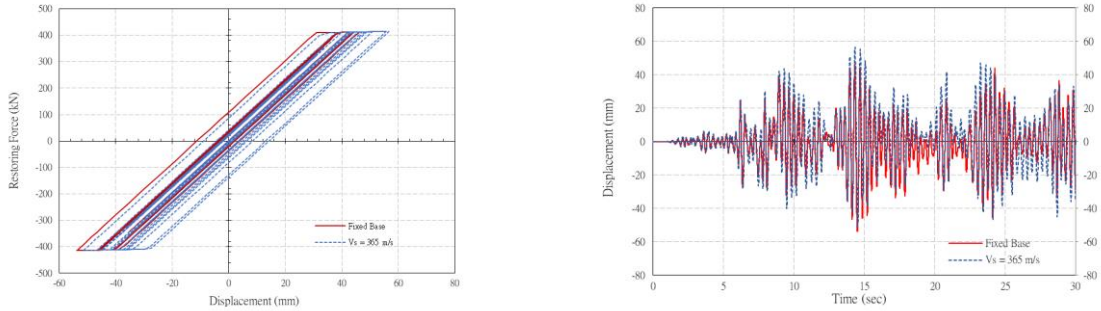

(a) Hysteretic loops (b) Displacement time history

Figure 8. Analytical result comparison between fixed base and V_S = 365 m/s subjected to TCU075

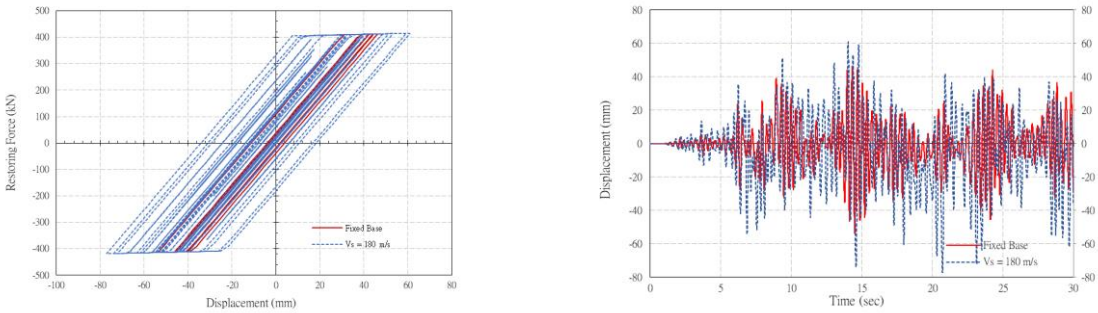

(a) Hysteretic loops (b) Displacement time history

Figure 9. Analytical result comparison between fixed base and V_S = 180 m/s subjected to TCU075

For the analytical result under TCU102 with V_S = 365 m/s in Figure 10, the displacement and lateral force displayed at t=14.79 s and were 51.53 mm and 413.11 kN, respectively. The displacement is smaller than that of the fixed base at that time point. The analyzed maximum responses occurred at t=14.48 s and were 88.47 mm and 420.31 kN.

For the analytical result under TCU102 with V_S = 180 m/s in Figure 11, the displacement and lateral force displayed at t=14.79 s and were 40.49 mm and 410.96 kN, respectively. The analyzed maximum responses occurred at t=14.55 s and were 123.33 mm and 427.10 kN.

The response of SFS system larger than that of fixed base system because of the altered structure and nonlinear properties. The time occurred maximum response of the SFS system is different from that of fixed base, and the SFS system's response considering various conditions of soil is more uncertain.

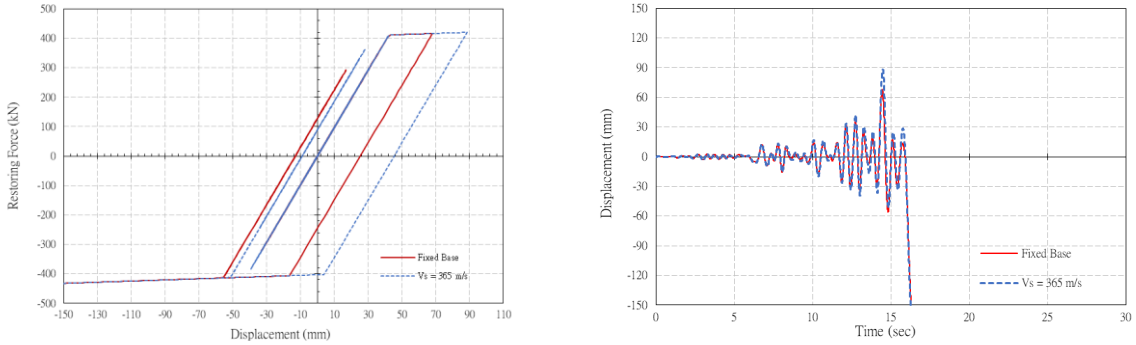

(a) Hysteretic loops (b) Displacement time history

Figure 10. Analytical result comparison between fixed base and V_S = 365 m/s subjected to TCU102

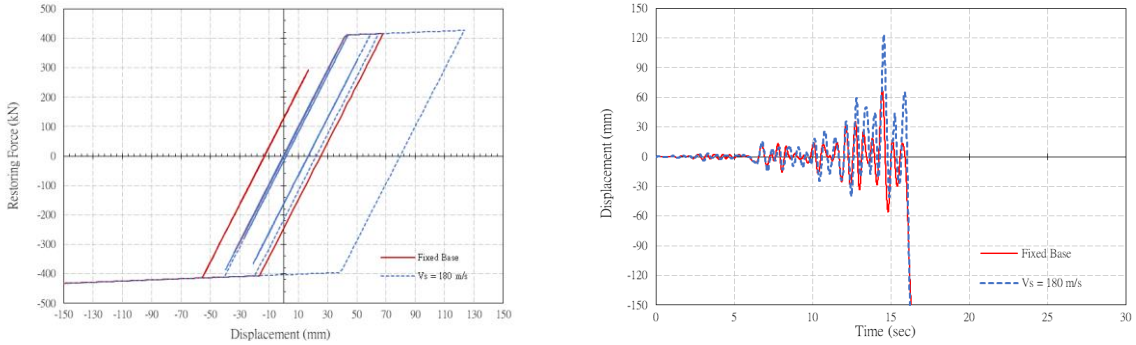

(a) Hysteretic loops (b) Displacement time history

Figure 11. Analytical result comparison between fixed base and V_S = 180 m/s subjected to TCU102

CONCLUSIONS

This study implemented the discrete-time filter techniques and structural nonlinearity into the dynamic structural analysis of a 3DOF SFS system considering SSI. Through the IIRF method, the frequency-

dependent FSI function was transferred into the time domain. The highlights of the study are concluded as follows:

1. The soil impedance function, featuring property of frequency dependence, was applied to consider the characteristics of soil damping. This study used the IIRF system to realize the frequency-dependent soil characteristics in the time domain, and obtained the SFS system responses by the integral method.
2. The accuracy of the integral method and structural nonlinearity is proved by comparing between experimental and analytical result. The initial stiffness and energy dissipation mechanism of analytical model are representative to the experimental result by observing the area of the hysteretic loops and the displacement time history of analysis result.
3. This study employed two different shear wave velocity V_S = 180 and 365 m/s to consider SSI effect. The displacement time history indicated the response of SFS system is larger than that of fixed base system due to the extended structural period considering SSI. However, the structural nonlinearity generated the permanent displacement, therefore, maximum response of both systems occurred in different time point.
4. By cooperated with IIRF method and compact nonlinearity setting, this study provided a simple way to simulate complicated nonlinear behavior of structure considering SSI, precisely.

ACKNOWLEDGMENTS

The research was supported by the Ministry of Science and Technology in Taiwan. (Project No.: 109-2221-E-027 -003 -MY3)

REFERENCES

Apsel, R.J. and J.E. Luco (1987). "Impedance functions for foundations embedded in a layered medium: an integral equation approach," *Earthquake Engineering and Structural Dynamics*, **15**, 213-231.

Carlson, G.E. (1998). *Signal and linear system analysis*, Hoboken, NJ: John Wiley.

Chang, S.Y., Li, Y.F. and C.H. Loh (2004). "Experimental study of seismic behaviors of as-built and carbon fiber reinforced plastics repaired reinforced concrete bridge columns," *Journal of Bridge Engineering*, **9**(4), 391-402.

Gash, R., Seylabi, E.E. and E. Taciroglu (2017). "Implementation and stability analysis of discrete-time filters for approximating frequency-dependent impedance functions in the time domain," *Soil Dynamics and Earthquake Engineering*, **94**, 223-233.

Gazetas, G. (1983). "Analysis of machine foundation vibrations: state of the art," *Soil Dynamics and Earthquake Engineering*, **2**, 2-42.

Luco, J.E. (1974). "Impedance functions for a rigid foundation on a layered medium," *Nuclear engineering and design*, **31**, 204-217.

Şafak, E. (2006). "Time-domain representation of frequency-dependent foundation impedance functions," *Soil Dynamics and Earthquake Engineering*, **26**, 65-70.

Sieffert, J.G. and F. Cevaer (1991). *Handbook of Impedance Function: Surface Foundations*, Ouest Ed., Presses Academiques, Nantes, France.

Su, C.K., Sung, Y.C., Chang, S.Y. and C.H. Huang (2007). "Analytical investigations of seismic responses for reinforced concrete bridge columns subjected to strong near-fault ground motion,"*Earthquake Engineering and Engineering Vibration*, **6**(3), 237-244.

Sung, Y.C. and C.C. Chen (2019). "Z-Transferred discrete-time infinite impulse response filter as foundation–soil impedance function for SDOF dynamic structural response considering soil–structure interaction," *Earthquake Spectra*, **35**, 1003-1022.

Veletsos, A.S. and B. Verbic (1973). "Vibration of viscoelastic foundations," *Earthquake Engineering and Structural Dynamics*, **2**, 87-102.

Veletsos, A.S., and Y. Wei (1971). "Lateral and rocking vibration of footings," *Journal of the Soil Mechanics and Foundations Division*, **97**, 1227-1248.

SITE-SPECIFIC RESPONSE ANALYSIS INVOLVING DYNAMIC SOIL-STRUCTURE INTERACTION

I Wayan Sengara[1], Ahmad Sulaiman[2], Det Komerdevi[3]
1. Professor, Civil and Environmental Engineering Faculty, Institut Teknologi Bandung, Bandung – Indonesia
2. Researcher, Geotechnical Engineering Research Group, Civil and Environmental Engineering Faculty, Institut Teknologi Bandung, Bandung – Indonesia
3. Senior Engineer, WSP Engineering Consultant, Bandung – Indonesia
Email: wayansengara@yahoo.com, 1995.ahmadsulaiman@gmail.com, detkomerdevi@gmail.com

ABSTRACT

There would be an interaction phenomenon between sub-soil layers, foundations, and building structures during earthquake event to yield a unique seismic response. It is important to understand soil-structure-interaction (SSI) effects so that structural and geotechnical engineers could make better decisions on the design and construction of the structures. This study presents results of Site-Specific Response Analysis (SSRA) involving soil-structure interaction (SSI) of basement structures in particular, to better recommend design response spectra at ground surface for dynamic structural analysis of the proposed buildings. Three different SSRA cases were studied, i.e., 1D ground response analysis, 2D ground response analysis without considering structure (free-field) and 2D ground response analysis considering structure interaction. The 1D and 2D nonlinear time-history dynamic analysis is carried out using computer program NERA and FLAC 2D, respectively. There are 11 (eleven) input bedrock motions considered for each 1D and 2D SSRA. In general, it is indicated that the spectral acceleration responses involving SSI tend to be lower compared to those of the 1-D and 2-D free-field motions. Results of the analysis are evaluated with reference to the ASCE-7-2016 and 2022 for the potential reduction of recommended response spectra for building structures.

Keywords: Soil-structure interaction, site-specific response analysis, earthquake, dynamic analysis, time-history, ground-motions

INTRODUCTION

Site-specific response analyses (SSRA) could be conducted for a site to better recommend ground-surface response spectra as seismic design criteria for building structures. Geological and geotechnical soil layers for many major cities in Indonesia particularly city of Jakarta that lies on soft alluvial deposits consisting soft clay layers, stiff to very stiff silty-clay with some sand lenses contributed by many ancient volcanic activities. These conditions have contributed to site-classification variations and therefore, response-spectra varies to great extends. ASCE-SEI-7-16 and 7-22 and Indonesian seismic building codes (SNI-1726-2019) allow SSRA to be conducted to provide more accurate design response spectra for the buildings that could often yields benefits to the project. Traditionally, one-dimensional (1-D) soil column analysis is performed. Even though when the subsurface profile cannot be simplified as horizontal layers, validation of the 1-D analysis is recommendable through more detailed means that capture these site-specific features. Recently, this 1-D SSRA has been employed for many SSRA sites for recommendation of seismic design spectra in Jakarta (Sengara et al., 2012-2020).

Several features such as interaction between structure and buildings during earthquake cannot be captured on the 1-D SSRA. Soil-structure-interaction (SSI) would occur during the seismic event and the effect of both inertial and kinematic interaction would provide more representative response to the system as previously presented in Sengara and Wijayanto, 2008. Therefore, modeling the soil-structural system in the SSRA through two-dimensional (2-D) wave propagation analysis is considered to better represent the soil-structural system compared to more common 1-D SSRA. This is with assumption that the 2-D SSRA need to be conducted with the same of similar soil constitutive modeling of 1-D currently available, where non-linearity in the soil layer moduli and damping ratios are represented in the modeling.

Many software packages are available to conduct 1-D and 2-D SSRA. In this study, a finite-difference program is utilized with the purpose of assessing the importance of several aspects incorporating soil properties, geometry, and structural effects. Formulation of seismic design criteria of a proposed high-rise building in city of Jakarta is used as case study to examine SSRA using both 1-D and 2-D involving both inertial and kinematic effects. The first step is comparing between 1-D and 2-D analysis results in free-field conditions to calibrate several parameters, such as dynamic soil properties and influence of boundary conditions. Next, basement structure is assigned to the 2-D model and inspect the effect of basement and structural mass and stiffness into the spectral response at the ground surfaces. The analysis considers two level earthquake intensity, that is service-level earthquake (SLE) and risk-targeted maximum considered earthquake (MCE_R) ground-motions.

NUMERICAL MODELING PROCEDURE

In this study, site specific response analyses (SSRA) were carried out using 1-D and 2-D modeling approach involving soil-structure systems. The 1-D SSRA was conducted by using NERA (Non-linear Earthquake Response Analysis) computer program developed by Bardet dan Tobita, 2001. The 2-D SSRA with inertial and kinematic basement structure effects were conducted using finite-difference computer FLAC2D computer program, developed by Itasca Consulting Ltd. (Itasca, 2011). The FLAC2D allows the domain of interest to be modeled by elements or zones in which each element or zone behaves according to a prescribed stress-strain constitutive law in response to the applied forces and/or boundary conditions. The program solves dynamic stress-strain problem using an explicit time-stepping procedure. The soil non-linearity can be modelled according to user-defined non-linear models or to the hysteretic damping formulation. This non-linear model is employed in this study that the backbone curve is built by adjusting the tangent shear modulus for each zone in the model as a function of the strain amplitude. In addition to the hysteretic damping, FLAC2D allows us to specify Rayleigh damping according to the full formulation with one control frequency.
It is important to note that whereas most of the constitutive model parameters can be directly evaluated from data obtained from laboratory tests and in-situ investigations, there are always some parameters that are determined through a calibration process as element test simulations. The analyses were conducted with definition of the numerical model, determination of the constitutive model parameters, determination of boundary condition and input-motions, and interpretation of results. The analyses then were verified for each step, including the result interpretation and the post-processing stages.

PROBABILISTIC SEISMIC HAZARD ANALYSIS AND BASE-ROCK MOTIONS

Probabilistic Seismic Hazard Analysis

Probabilistic seismic hazard analysis (PSHA) has been conducted for the site of interest in this study. The PSHA provide uniform hazard spectra at reference base-rock (Site Class B). The PSHA in this study is based on total probability theorem of PSHA implicitly implemented in EZ-FRISK computer program [Risk Engineering, Version 7.62, 2011]. The essential components of the PSHA consist of seismic source zoning, earthquake recurrence, attenuation functions, and logic tree formulation.In this PSHA, mean annual rate of exceedance at the site is computed based on the aggregate risk from potential earthquakes of various magnitudes occurring at different source-to-site distances.
Two intensity levels were considered in this study to represent service level earthquake (SLE) that correspond to 50% probability of exceedance (PE) in 30 years (43-years earthquake return period), and risk-targeted maximum considered earthquake (MCE_R) that correspond to 1% probability of building collapse in 50 years (equivalent to 2,475-years earthquake return period in combination with specified building fragility, as presented in Sengara et al., 2015). These two ground-motion intensity levels are specified at reference base-rock (S_B) of the case site. Uniform Hazard Spectra (UHS) and de-aggregation for each hazard level were also resulted. Summary of PSHA results is presented in Figure 1 as the mean Uniform Hazard Spectra (UHS) for the two return periods. Typical hazard curves representing each seismic source contribution to total hazard at case periods of T=PBA and T=10 second is presented in Figure 2.

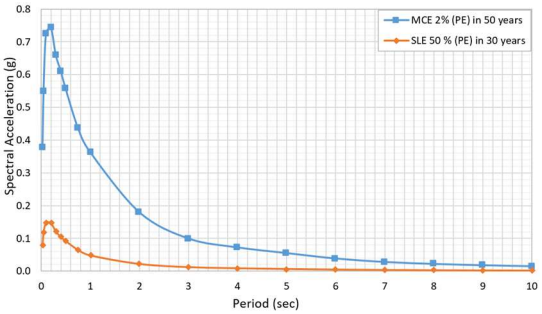

Figure 1. Uniform Hazard Spectra for 2% PE in 50 years and 50% PE in 30 years

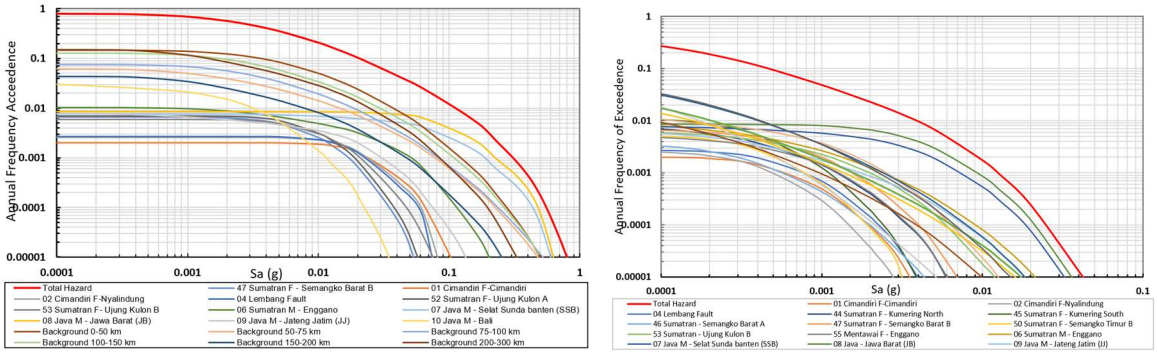

Figure 2. Total Hazard curve for Period T=PBA (left) and T=10.0 sec (right)

Base-Rock Motions

De-aggregation analysis within the PSHA provide controlling magnitude and distance to select Megathrust (6 sources), Benioff (3 sources), and Shallow Crustal/Background (2 sources). Ground-motion selection procedure adopt Quake Manager (V2.1) computer program. To select an appropriate ground-motion, each response spectra is resulted from several different source mechanism and various magnitudes and distances. For spectral matching of ground-motions, each ground-motion component have been scaled such that the average of the spectra from all ground motion components, in each horizontal direction for which ground motions are applied, not be less than the defined target response spectrum, over the period range. Based on structural analyses, the natural period of building of interest is 9.5 sec, therefore range of period to be considered based on ASCE-7-2016 is 0.2 T - 2.0 T (1.9 sec – 14.2 sec). Figure 3 shows spectral matched to the target spectrum for (a) SLE level and (b) MCE_R intensity level. In this case study, eleven (11) input motions have been considered to represent Megathrust and Benioff suductions, Shallow Crustals, and Background source mechanisms. The ground-motions were generated for both SLE and MCE_R intensity levels using tight spectral matching procedures and considering maximum direction (RotD100). The ground-motions selection and scaling to the target spectrum are based on the de-aggregation analysis resulted from the PSHA of the site of interest.

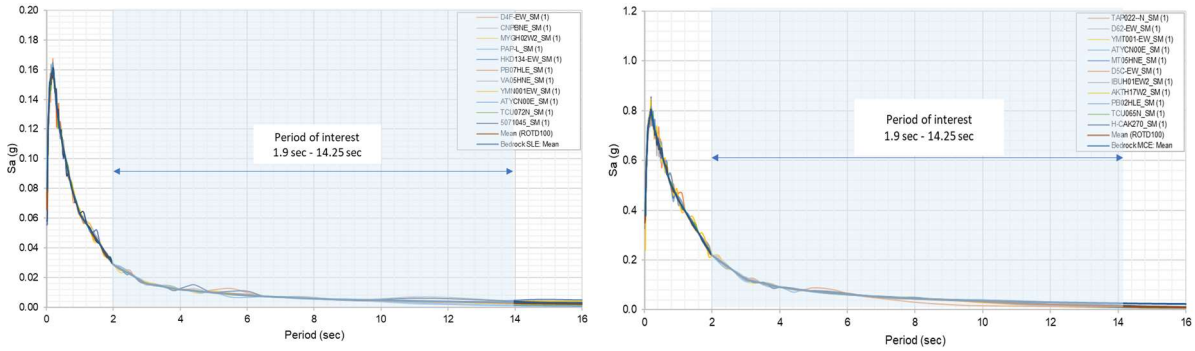

(a) (b)

Figure 3. Matched to the target spectra (a) SLE intensity level and (b) MCE_R intensity level

2-D SSRA AND SOIL-STRUCTURE INTERACTION ANALYSIS

Local Site Conditions

Local site condition is considered from results of Seismic downhole tests (SDT) providing shear wave velocity for the site for the top 30 meters. The site classification based on the SDT is classified as medium soil (S_D) with average shear wave velocity over the top 30 meters of about 206 m/s to 242 m/s. Shear wave velocity (Vs) profile at the site adopted in the analysis is determined based on combination of the SDT and also correlation from N-SPT (Ohta & Goto 1978, and Seed & Idriss 1981), as shown in Figure 4(a). Vs profile below 40 m to 80 m are based on average N-SPT data, and 80 m - 280 m are approached by secondary data of microtremor. Bedrock reference (S_{BC} with Vs=760 m/s) is assumed at depth of ±650 m (Ridwan et al., 2016) and Vs profile is gradually increase from 280 – 650 m, as shown in Figure 4. This Vs profile is used as input in the 1-D and 2-D wave propagation analysis from bedrock to the ground-surface using NERA and FLAC2D, respectively.

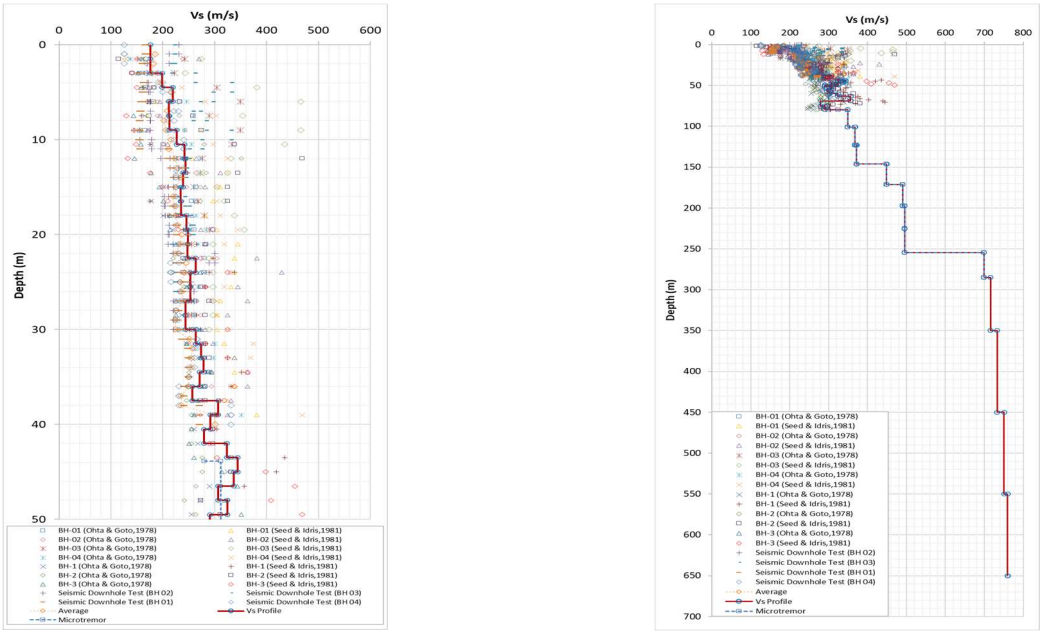

(a) (b)

Figure 4. (a) Shear wave velocity data based on SDT at top 50 meter and (b) shear wave velocity values at the 1D and 2D SSRA along 650 meter-depth

2-D Soil Modelling Analysis

For the 2-D wave propagation analysis, Mohr-Coulomb constitutive model built in the FLAC2D computer program is used adopted. The Mohr-Coulomb criterion models only dilate at failure and not compute the densification effect during cyclic loading below the failure condition. Therefore, this model was modified to simulate the changes of permanent volumetric strains in drained cyclic loading or pore pressures in undrained cyclic loading. In addition, in order to reproduce shear modulus degradation and damping increase over the shear strain increment that may occur during seismic loading, additional hysteretic damping were applied to these model, as shown in Figure 5 (a) and (b). The soil parameters used in the 1-D Free-Field analysis are relatively similar with those in the 2D analysis.

For minimizing the time consumption in the analysis, the soil layers were partitioned into thirty two (32) layers with thickness of about 1.5 to 50 meters until 650 meter-depth. This layers are divided based on similarly consistencies, shear wave velocity values, and shear modulus. It should be noted that the hysteretic damping examined in the analyses were calibrated with publication of Ishibashi and Zhang (1993) for cohesive material. The shear modulus degradation and damping ratio curve adopted in the analyses in respect of its calibration are shown in Figure 5 (a) and (b), respectively. The blue line represents the published data from Ishibashi and Zhang (1993), while the red line shows the calibrated hysteretic damping.

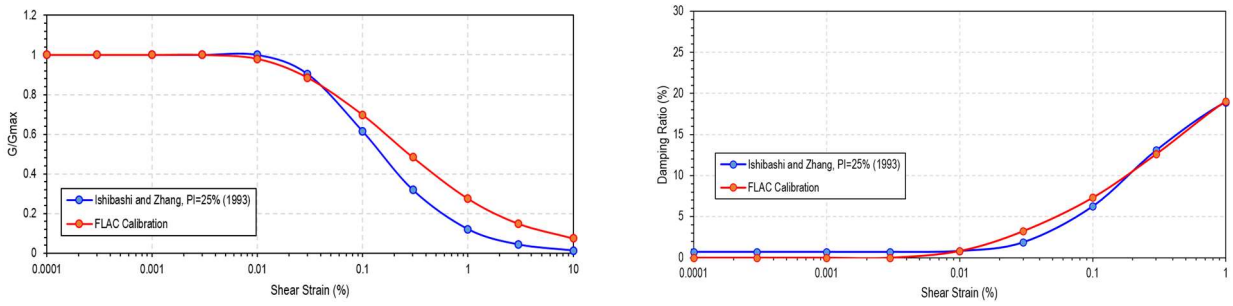

(a) (b)

Figure 5. Clay Fitting between Ishibashi and Zhang (1993) and FLAC Calibration for (a) Degradation Shear Modulus and (b) Damping Ratio

Free-Field Analysis

Before conducting full-scale analysis involving inertial and kinematic basement effect, it is necessary to verify the spectral acceleration on the surface after earthquake excitation load from the bedrock. This analysis referred to as free-field analysis, where the structure has not been installed and there is only the soil layer model. Free-field analysis is carried out to verify the vertical boundaries (quiet boundaries) and horizontal boundaries (free field boundaries). Additionally, the objective of this analysis is to calibrate between wave propagation results of the non-linear 1-D and the nonlinear 2-D analysis. In the free-field analysis, a horizontal soil column was modeled in 2-D plane-strain represented by a stack of rectangular soil element in vertical direction that has one unit length in horizontal direction. On the other hand, 1-D wave propagation analysis had previously been conducted using NERA computer program, as previously explained.

For calibration purposes, spectral accelerations at ground-surface resulted from FLAC2D and NERA are compared. The results show that the FLAC2D analysis provides quite similar pattern and very close agreement with that of non-linear 1-D NERA wave propagation results, as shown in Figure 6 (a) and (b) for SLE and MCE_R earthquake, respectively. The calibration was conducted adopting scaled SLE Coastal Chile ground-motion and scaled MCE_R Takachi Oki ground-motion.

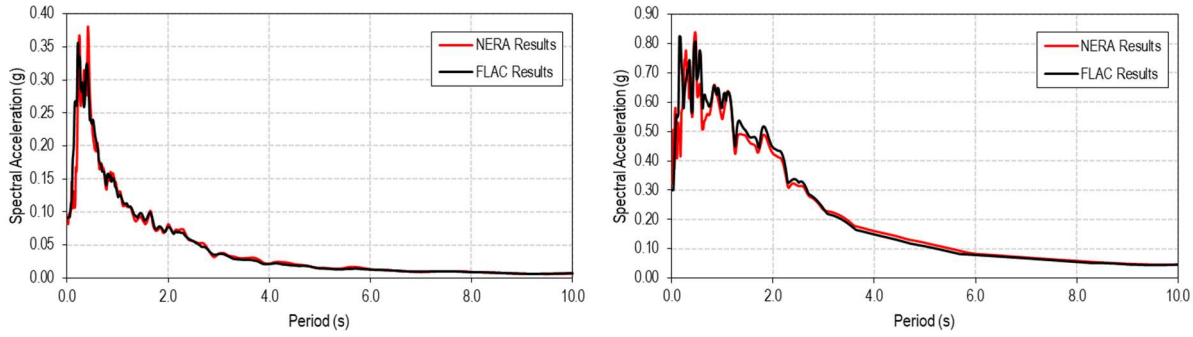

(a) (b)

Figure 6. An Example Comparison of Spectral Acceleration in Ground Surface between NERA and FLAC Results (a) for Scaled SLE and (b) for Scaled MCE_R

Numerical Modeling for Soil-Structure Interaction (SSI) Analysis

2-D modeling involving SSI of basement and upper structures consists of soil and structural modeling parameters, as well as determination and calibration of horizontal and vertical boundaries. Both structural and soil dynamic responses were directly calculated from fully non-linear analyses with FLAC2D (Version 8.1 (Itasca, 2019) computer program. In these analyses, the calculation of seismic soil response is coupled with the calculation of dynamic response of structure.

To establish the state of stress prior to the seismic ground motions loading, a staged construction analysis and a static stress analysis were performed. Firstly, a static analysis considering the effect of gravity with the Mohr-Coulomb elastic perfectly plastic constitutive model is performed to establish the in-situ stresses before seismic loading. The water within the soil is modeled directly.

After the initial stresses were generated, the computation was converted to dynamic mode. In dynamic mode, a minor amount of Rayleigh damping of 0.2% was used at dominant frequency in accordance with the ground-motion that will be used to facilitate convergence and stability in seismic condition. Additionally, the hysteretic behavior, that is shear modulus degradation and damping-ratio curves for the soil layers were applied. For dynamic analysis, the earthquake motions are input as a shear-stress time history which is applied to the nodes along the bottom of the numerical grid.

The four-story basement in this study case were activated after the initial stresses were generated. Upper structures such as the tower, typical slabs, typical raft, shear walls, and DWalls are modeled after the free-field analysis has been completed. The calculations were carried out in plane-strain conditions. The parameters are converted to equivalent plane-strain model from the 3D structural model according to the stiffness, spacing and dimension for each materials. In this study case, there are two tower structures, First tower is modeled as beam element with fc' = 65 MPa, E = 40 GPa, I=45m4, Tower mass = 2300MN (or equivalent with 45kN/m over 326 m height). Second tower is modeled as beam element with fc' = 65 MPa, E = 40 GPa, I=53m^4, Tower mass = 2200MN (equivalent with 50kN/m over 276 m height). Shear wall is modelled using soil cluster element full basement depth and width – 100 mm thick/meter of strip. Podium and tower raft is modelled as continuous beam element with thickness of 1.5 and 4 meter, respectively. DWall is modelled as continuous beam element with thickness of 0.8 meter. The location of point of interests were determined at the bottom and the top right of basement to examine the response of spectral acceleration. The detail model mesh of FLAC2D involving basement and simplified structural element, considering both inertial and kinematic effects, are illustrated in Figure 7.

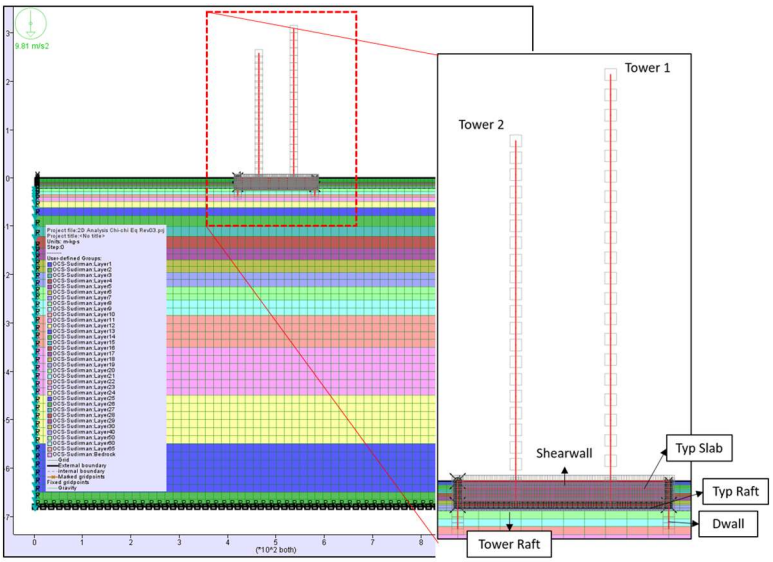

Figure 7. Detail Mesh Distribution and Model for 2-D SSRA

Results and Discussions

Summary graphs has been developed to show the response spectra resulted from this analysis compared to that of the code-based spectra. The average spectral acceleration for 1-D and 2-D site specific response analysis involving the soil-structure interaction effect for SLE and MCE_R intensity level, are depicted in Figure 8 and 9, respectively.

It is indicated from 2-D SSRA involving SSI of basement and its simplified upper structures model that, for both SLE and MCE_R intensity levels, the spectral acceleration responses at ground-surface tend to be lower compared to those of the 1-D and 2-D free-field motions. Significant reduction is identified to be limited to periods of 0-2.5 second. For SLE level, the SSI effect has no effect for period > 2.5 sec, and slight effect for MCE_R level for period 2.5-5 second. For all SLE and MCE_R levels, SSI effect almost has no effect for period > 5 second. These results are relatively similar with the study conducted by Ellison et al. (2015), concluding the presence of the SSI to have a smaller effect on the spectral acceleration responses especially on the higher period, that is higher than 5 seconds. Findings conducted in this study highlight the importance and benefit of considering soil-structure interaction effects particularly on the low natural period structures. For practical purposes, SNI-1726:2019 or ASCE-7-16

allow spectral reduction to be minimum of 80% of the free-field SSRA if SSI with basement is incorporated in the analysis.

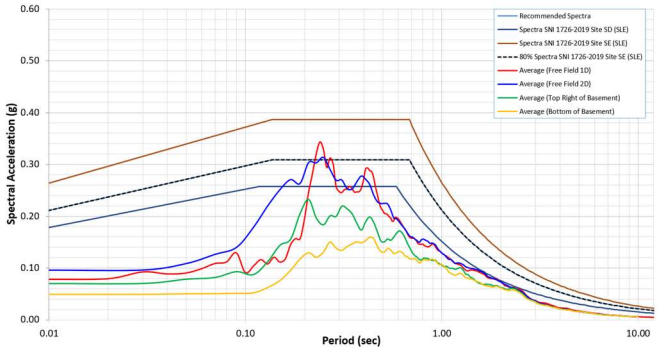

Figure 8. SLE Average Spectral Acceleration involving Soil-Structure Interaction Effect

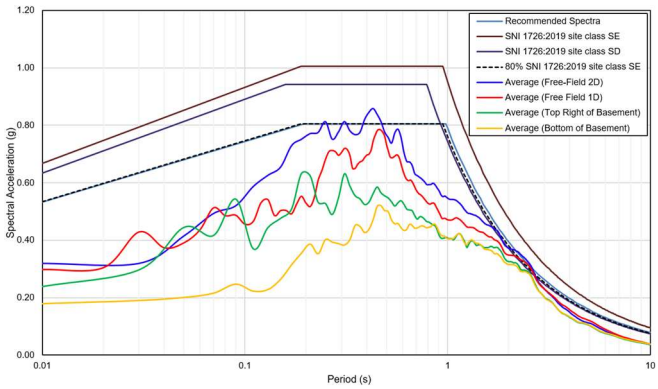

Figure 9. MCE_R Average Spectral Acceleration involving Soil-Structure Interaction Effect

CONCLUDING REMARKS

Site-specific response analysis (SSRA) considering site-specific soil layers condition and various base-rock motion characteristics has been performed to obtain response spectra at ground surface. This analysis consists of performing seismic-hazard analysis to acquire spectral response and ground-motions at reference bed-rock, and later performing wave propagation analysis of the bedrock motions to ground surface to acquire spectral response at ground-surface for recommendation of response spectra the specified building structures. There have been 11 (eleven) input bedrock motions adopted in both 1-D and 2-D SSRA for both SLE and MCE_R for both 1-D and 2-D SSI involving basement structure model. It is indicated from 2D SSRA involving SSI model that, for both SLE and MCE_R intensity levels, the spectral acceleration responses at ground-surface tend to be lower compared to those of the 1-D and 2-D free-field motions. Significant reduction is identified to be limited to periods of 0-2.5 second. For SLE level, the SSI effect has no effect for period > 2.5 sec, and slight effect for MCE_R level for period 2.5 -5 second. For all SLE and MCE_R levels, SSI effect almost has no effect for period > 5 second.
For practical purposes, SNI-1726:2019 or ASCE-7-16 allow spectral reduction to be minimum of 80% of the free-field SSRA if SSI with basement is incorporated in the analysis. The 2D SSRA considering SSI with basement model performed in this study however, only resulted in spectral reduction limited to period range of 0 - 5 second only. Further detail study needs to be conducted for other sites and basement depths.

ACKNOWLEDGMENTS

The authors appreciate support by Dr. Yuamar Basarah who has reviewed the 2D analysis. We also acknowledge Arup's structural engineers, i.e., Marc Tatarsky and David Farnsworth for their input on

the 2D SSRA involving the basement and structural effects, as well as the experience of adopting ASCE-7-16 and ASCE-7-22 in the USA. The soil investigation data and structural data is provided by Mitsubishi Oasis and WSP Engineering Consultant.

REFERENCES

American Society of Civil Engineers Standards, ASCE 7-16. (2016). "Minimum Design Loads for Buildings and Other Structures," *Structural Engineering Institute ASCE*, Virginia, USA.

Bardet J.P., Tobita T. (2001). *NERA, A Computer Program for Nonlinear Earthquake Site Response Analyses pf layered Soil Deposits*, University of Southern California.

Ellison, Kirk C. et al. (2015). "Structure-Soil-Structure Interaction Analysis in a Highly Seismic, Dense Urban Regeneration Zone," *6th International Conference on Earthquake Geotechnical Engineering*, Christchurch, New Zealand.

Hashash, Y.M. A., dan Park, D. (2002). "Viscous damping formulation and high frequency motion propagation in nonlinier site respon analysis," *Soil Dynamics and Earthquake Engineering*, **22**(7), 611-624.

Ishihara, K. (1996). *Soil Behaviour in Earthquake Geotechnics. Oxford Engineering Science Series*, Oxford University Press.

Ishibashi, I and Zhang, X. (1993). *Unified dynamic shear moduli and damping ratios of sand and clay, Soils and Foundations*, Vol. 33. No. I, pp - 182-191.

ITASCA. (2011). *Manual FLAC Version 7.0*, ITASCA Company.

Kuhlemeyer, R. L., and J. Lysmer. (1973). "Finite Element Method Accuracy for Wave Propagation Problems," *J. Soil Mech. & Foundations*, Div. ASCE, 99(SM5), 421-427.

Ohta, Y. and Goto, N. (1978). "Emprical Shear Wave Velocity Equations in terms of Characteristics Soil Indexes," *Earthquake Engineering and Structural Dynamics*, 6:167-187

Ridwan, M., Widiyantoro, S., Irsyam, M. (2016). "Development of an engineering bedrock map beneath Jakarta based on microtremor array measurements," *Geological Society, London, Special Publications*, Vol. 441, pp. 153-165.

Risk Engineering, (2014). *EZ-FRISK (Software for in-depth Seismic Hazard Analysis) User's Manual*, Risk Engineering Inc., Golden, Colorado, USA.

Seed, H.B. and Idris, I. M. (1981). *Evaluation of Liquefaction Potential Sand Deposits based on Observation of Performance in Previous Earthquakes., In situ testing to evaluate liquefaction susceptibility*, ASCE National Convention, Missouri, Preprint, 81–544.

Sengara, IW., Wijayanto, N. (2008). "Soil-Basement Structure Interaction Analysis On Dynamic Lateral Earth Pressure on Basement Wall," *Proceeding International Conference on Earthquake Engineering and Disaster Mitigation-Bali*.

Sengara IW., and Komerdevi, D. (2019). "Site-Specific Response Analysis (SSRA) and pairs of ground motions time-history generation of a site in Jakarta," *4th International Conference Earthquake Engineering Disaster Mitigation (ICEEDM)*, Padang, Indonesia.

Sengara, IW., Yulman, M.A., and Mulia, A. (2016). "Seismic Time-History Ground-Motions for a specific site in Jakarta," *Journal Teknologi Malaysia*, Malaysia

Sengara, IW., Irsyam, M., Sidi, I.D, Mulia, A., Asrurifak, M., Hutabarat, D. (2015). "Development of Earthquake Risk-Targeted Ground-Motions for Indonesian Earthquake Resistance Building Code SNI-1726-2012," *12th International Conference on Applications of Statistics and Probability in Civil Engineering (ICASP)*, July 12-15, Vancouver, Canada

Sengara, IW. (2012). "Investigation on Risk-Targeted Seismic Design for a High-Rise Building in Jakarta-Indonesia," *World Conference on Earthquake Engineering Proceeding*, Lisboa, September 24-28, 2012.

SNI-1726-2019. (2019). *Indonesian Seismic Building Codes, Tata Cara Perencanaan Ketahanan Gempa untuk Struktur Bangunan Gedung dan Non-gedung*, Badan Standarisasi Nasional Indonesia.

(2d) Seismic design of foundations and geotechnical structures

PERFORMANCE OF THE SHALLOW BURIED WATER PIPELINE WITH PROTECTION FEATURE

Che-Yu Chang[1], Hsuan-Chih Yang[2], Gee-Yu Liu[3], and Pao-Ching Chou[4]

1. Assistant Research Fellow, Earth Sciences and Geotechnical Engineering Division, National Center for Research on Earthquake Engineering, Taipei, Taiwan, R.O.C.
2. Associate Research Fellow, Earth Sciences and Geotechnical Engineering Division, National Center for Research on Earthquake Engineering, Taipei, Taiwan, R.O.C.
3. Research Fellow, Earthquake Disaster Simulation Division, National Center for Research on Earthquake Engineering, Taipei, Taiwan, R.O.C.
4. Assistant Research Fellow, Earthquake Disaster Simulation Division, National Center for Research on Earthquake Engineering, Taipei, Taiwan, R.O.C.

Email: cheyu@narlabs.org.tw, hcyang@narlabs.org.tw, karl@narlabs.org.tw, pcchou@narlabs.org.tw

ABSTRACT

Seismic damage to the pipeline systems could result in noticeable impact no less than such to the infrastructures. Interruption of water, oil, and gas pipeline systems not only leads to service instability but also catastrophic events. Protection methods such as trench enlargement, concrete culverts utilization, and the trench backfill material selection are candidate damage mitigation measures. This study focuses on the buried water pipe and analyzes the effectiveness of the controlled low strength material as the trench backfill. As a pioneer step, pipe performance of multiple pipe diameters and various depths of cover are discussed under vehicle load with and without the water internal pressure. The results will serve as reference for using the selected trench backfill material as pipe protection measure.

Keywords: pipeline protection, controlled low strength material, ductile iron pipe, depth of cover, finite element

INTRODUCTION

Historical seismic events have shown that damage to the utility systems could cause scenarios as devastating as such to the infrastructures. The water pipeline damage may result to the system service interruption and possibly local flooding. The damage to the oil and/or gas pipeline system may cause its service interruption and even sever fire events. According to a research report conducted by the Joint Research Centre (JRC) of European Commission (Girgin and Krausmann, 2014), most of the pipeline system damage is caused by geological hazard. In terms of damage resulting from seismic events, fault displacement to directly rupture the pipeline, and support missing due to soil liquefaction or ground movement might be the immediate issues in needs of attention. Protection measures such as trench enlargement, concrete culverts utilization, and the trench backfill material selection are discussed by Gantes and Melissianos (2016) for seismic damage mitigation. In this study, the water pipeline performance with controlled low strength material (CLSM) as protection feature is analyzed. As a pioneer step, a variety of pipe diameters with such protection method under vehicle load is discussed for the effectiveness analysis.

In recent years, CLSM has been widely used as the backfill material because of its high flowability, self-leveling, and self-compacting characteristics. This type of backfill material also solves the problem of subsidence and uneven road due to the imperfection of the backfill rolling task. Furthermore, the pipe type used by the Taiwan Water Company has been switched to a higher strength type of pipe, called the ductile iron pipes (DIP). In addition, given that most of the fundamental civil facilities of the pipeline system have been established in Taiwan, the prior task became the facility maintenance and the replacement of aged pipelines. The task of the replacement of aged pipelines is,

however, complex with difficulties to perform in a city in terms of the construction method, range, and cost. In light of such difficulties and in order to reduce public construction cost, Japan has already evaluated the possibilities for a smaller depth of cover (DOC) required for buried pipelines and issued corresponding new guidelines in 2000 (MLIT, 2000).

This study aims to analyze the behavior of the buried DIP with CLSM as backfill under vehicle load. Multiple DIP diameters with and without internal water pressure are analyzed using finite element models. Results of various DOC are compared to discuss the performance of shallow buried DIP with CLSM as backfill under vehicle load. The results could be the reference for the effectiveness of the selected backfill material to be utilized as a candidate protection measure under potential seismic damage.

NUMERICAL ANALYSIS MODEL

There are seven DIP nominal diameters and four DOCs are carried out in this study. These seven diameters are 100 mm, 300 mm, 500 mm, 1000 mm, 1350 mm, 2000 mm, and 2600 mm. The four DOCs are 30 cm, 60 cm, 90 cm, and 120 cm. These numerical analyses are conducted using the finite element commercial program called ABAQUS. A schematic finite element model is illustrated in Figure 1, where the CLSM is color coded in gray, the surrounding soil media in green, and the DIP in red. As the trench laying the DIP is backfilled by the CLSM, the position of the DIP is inside the CLSM as indicated by the arrow. Shell elements are used for the DIP; while solid elements are used for the CLSM and the soil media in the finite element model. The boundary condition at the bottom of the model is restricted in the three translation directions; while the two sides lateral to the pipe are free to move vertically. The two faces at the ends of the pipe are restricted in the longitudinal direction of the pipe.

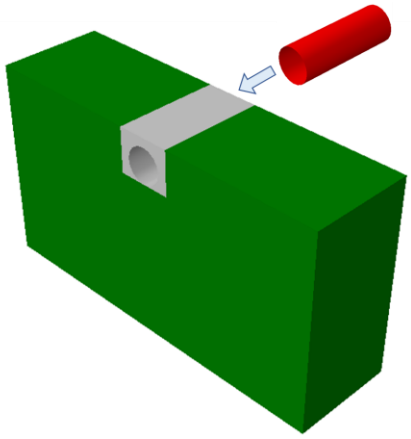

Figure 1. Analysis model scheme.

As for the model dimensions, the length in the longitudinal direction of the DIP is determined by the widely used DIP length as 6 m. The width in the DIP lateral direction from the DIP edge to the trench edge is denoted as B and defined in the Water Pipeline Installation Guidelines (Taiwan Water Corporation, 2020). The total width of the trench could then be determined by adding the DIP nominal diameter, denoted as D, by B on each side of the pipe, which leads to the trench width of D+2B as shown in Table 1. The surrounding soil media extends to three times the trench width on each side of the trench as well as the depth below the trench based on the concept of the pile foundation design and the foundation bearing capacity.

The material properties of the DIP, the backfill material CLSM, and the soil media are listed in Table 2. For the loading condition, the AASHTO HS-20 truck of 16 kips wheel load with a 1.5 impact factor (DIPRA, 2016) to be approximately 10 ton of loading is considered as vehicle load in this study. Such loading is applied uniformly on a 20 cm by 30 cm area representing the wheel contact area. The

internal water pressure is taken as 1.27 MPa based on the suggestion from the Japan Ductile Iron Pipe Association (JDIPA, 2000).

Table 1. Model dimensions.

DIP nominal diameter, D (mm)	Width of DIP edge to trench edge, B (mm)	D+2B (mm)
100	200	500
300	200	700
500	250	1000
1000	350	1700
1350	350	2050
2000	500	3000
2600	500	3600

Table 2. Material properties.

Material	Density (ton/mm^3)	Young's modulus (N/mm^2)	Poisson ratio
CLSM	1.80e-9	8.7e2	0.25
DIP	7.15e-9	1.6e5	0.28
Soil	1.80e-9	20	0.30

ANALYSIS RESULTS AND DISCUSSIONS

The analysis results of the DIP with CLSM backfill protection under vehicle load are discussed in this section. Figure 2 shows the relationship of the DIP maximum von Mises stress of four different DOCs versus the DIP diameter. Part (a) provides the results without internal water pressure; while part (b) offers those with the pipe internal water pressure's presence.

With and without the DIP internal water pressure, the DIPs of diameters larger than 1000 mm do not show noticeable difference in the max. von. Mises stress at the same DOC. Comparing between different DOCs, the max. von Mises stress is similar as well for the DIPs of diameters larger than 1000 mm, except the DOC of 30 cm.

For the DIP diameters smaller than 1000 mm, the DIP max. von Mises stress decreases with the increasing DOC. When there is no internal water pressure, such stress reduces with the increase of the DIP diameter. However, when the internal water pressure presents, such stress rises with the increase of the DIP diameter.

When the DOC being 30 cm, the max. von Mises stress of those with the diameter smaller than 1000 mm is reduced with increasing pipe diameter. Such trend applies on the circumstances with and without the water pressure. For those diameters larger than 1000 mm,

Figure 3 shows the relationship of the DIP max. von Mises stress of seven different diameters versus the DOC. Part (a) shows the results when there is no internal water pressure; while part (b) presents the results with the pipe internal water pressure's presence.

With no internal water pressure, the DIP max. von Mises stress occurs with the DOC of 30 cm for all the DIP diameters. For the circumstances of the DOC being from 60 cm to 120 cm, the DIP max. von Mises stress is not sensitive to the DOC for the DIPs of diameter equal and above 1000 mm. For those less than 1000 mm in diameter, the DIP max. von Mises stress is reduced with the increasing DOC.

When the internal water pressure presents, the DIP max. von Mises stress occurs at the DOC of 30 cm for the DIPs of 100 mm, 300 mm, and 500 mm in diameter. Such stress decreases while the DOC increases, and the stress shows less sensitivity to the DOC when the DIP diameter gets larger. As for the DIPs of diameter larger than 1000 mm, the max. von Mises stress is not sensitive to the DOC.

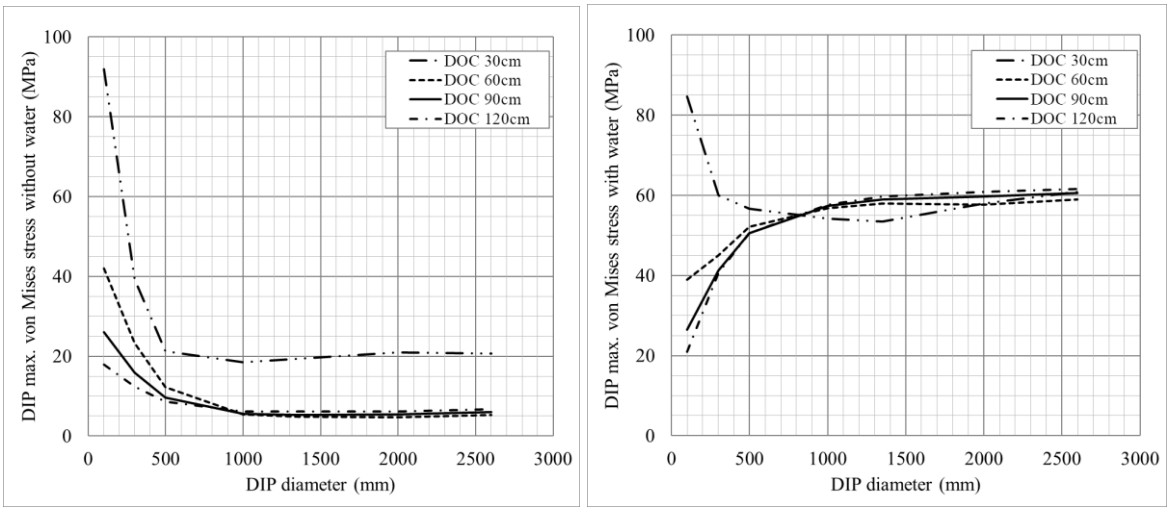

(a) (b)

Figure 2. Relationship of the DIP max. von Mises stress versus the pipe diameter.

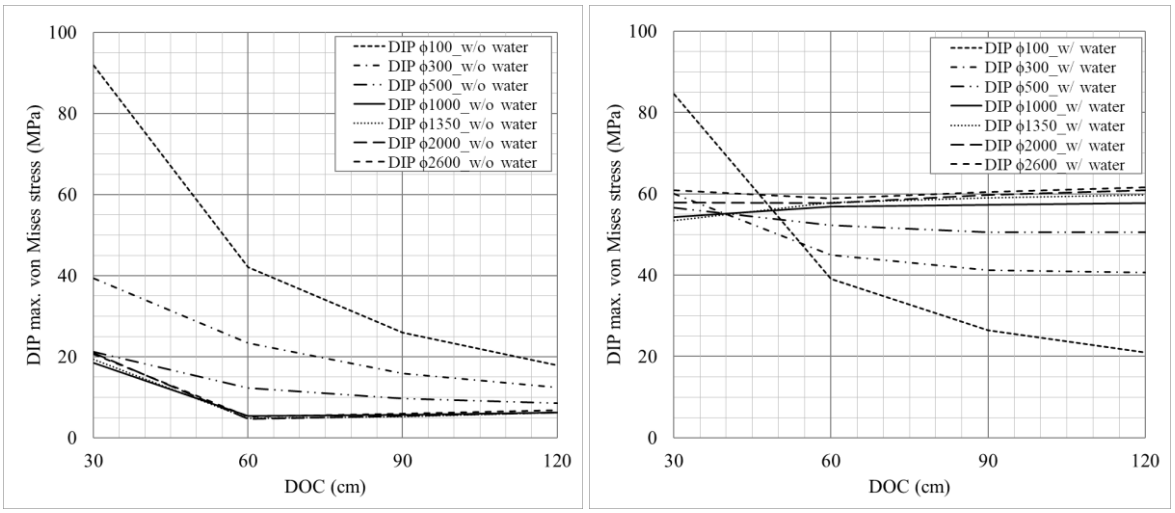

(a) (b)

Figure 3. Relationship of the DIP max. von Mises stress versus the DOC.

CONCLUSIONS

As the seismic impact leading to catastrophic damage to the pipeline systems no less than that to the infrastructures, protection methods are under discussion aiming to mitigate such undesirable outcome. Geological hazard seems to cause most of the pipeline rupture events. Such hazard might be the fault displacement, soil liquefaction, or other ground movement. This study aims to research the effectiveness of the backfill material CLSM which has been widely used in recent years. In addition, shallow bury for the utility systems is becoming a trend for its benefit of construction methods, cost, and activity effecting area. Therefore, this paper presents the results of the performance for currently used water pipe, the ductile iron pipe (DIP), buried with CLSM as trench backfill. Multiple DIP diameters and a variety of the DOCs are discussed with and without the pipe internal water pressure under vehicle load by using finite element modeling.

There are seven DIP diameters, 100 mm, 300 mm, 500 mm, 1000 mm, 1350 mm, 2000 mm, and 2600 mm, and four DOC, 30 cm, 60 cm, 90 cm, and 120 cm, are studied. Without the internal water pressure, the DIP max. von Mises stress occurs at the DOC of 30 cm for all DIP diameters. The DIPs of diameters larger than 1000 mm are not sensitive to the DOC in terms of their max. von Mises stress. With the presence of the internal water pressure, the DIP max. von Mises stress occurs at the DOC of 30 cm for the DIPs of the diameters smaller than 1000 mm. For those diameters larger than 1000 mm, their max. von Mises stress are not sensitive to the DOC.

In summary, the results show that the DIP diameter of 1000 mm and the DOC of 60 cm seem to be dividing points. For the pipe diameters larger than 1000 mm and the DOC larger than 60 cm, the internal water pressure is the control factor of the pipe performance. The max. von Mises stress between DIPs of different diameters is similar. For those diameters smaller than 1000 mm, except 100 mm, the max. von Mises stress decreases with increasing DOC. The DIP with the diameter of 100 mm is a special case. The internal water pressure impact is very insignificant. The DOC is its control factor for the max. von Mises stress.

The analysis results and comparison provided in this study could serve as a reference for using CLSM as a protection measure for the buried DIPs to mitigate the potential geological damage caused by seismic events.

ACKNOWLEDGMENTS

This study is part of the research supported by the Taiwan Water Corporation. The authors are responsible for any flaws in this article.

REFERENCES

Girgin, S. and E. Krausmann (2014). “Analysis of Pipeline Accidents Induced by Natural Hazards: Final Report,” *JRC Technical Report*, European Commission.

Gantes, C. and V. Melissianos (2016). “Evaluation of Seismic Protection Methods for Buried Fuel Pipelines Subjected to Fault Rupture,” *Frontiers in Built Environment*, 2, Article 34.

MLIT (2000). “電線、水管、ガス管又は下水道管を道路の地下に設ける場合における埋設の深さ等について,” 日本建設省 (Ministry of Land, Infrastructure and Transport) (in Japanese). (https://www.mlit.go.jp/notice/noticedata/sgml/071/79000158/79000158.html)

Taiwan Water Corporation (2020). “自來水管埋設施工說明書 (Water Pipeline Installation Guideline),” Taiwan Water Corporation (in Chinese).

DIPRA (2016). “Design of Ductile Iron Pipe,” Ductile Iron Pipe Research Association.

JDIPA (2000). “ダクタイル管の浅層埋設について,” 日本延性鐵管協會[Japan Ductile Iron Pipe Association] (in Japanese).

DEVELOPMENT OF THE DESIGN EARTHQUAKE IN TAIPEI BASIN CONSIDERING THE SHANCHIAO FAULT

Yu-Wen Chang [1], Kuan-Yu Chen [2], Chih-Wei Chang [3] and Chiu-Ping Fan [4]

1. Research Fellow, Earth Sciences and Geotechnical Engineering Division, National Center for Research on Earthquake Engineering, Taipei, Taiwan, R.O.C.
2. Assistant Researcher, Earth Sciences and Geotechnical Engineering Division, National Center for Research on Earthquake Engineering, Taipei, Taiwan, R.O.C.
3. Assistant Technologist, Earth Sciences and Geotechnical Engineering Division, National Center for Research on Earthquake Engineering, Taipei, Taiwan, R.O.C.
4. Research Assistant, Earth Sciences and Geotechnical Engineering Division, National Center for Research on Earthquake Engineering, Taipei, Taiwan, R.O.C.

Email: ywchang@narlabs.org.tw, kuanyu@narlabs.org.tw, chihwei@narlabs.org.tw, cpfan@narlabs.org.tw

ABSTRACT

Apparently, during the 1999 Chi-Chi earthquake (ML7.3; epicenter 150km to the south) and the 2002 Hualien earthquake (ML6.8; epicenter 100km to the southeast), although the epicenter is sufficiently distant from the Taipei Basin, which is usually referred to the "far-field earthquake," it was observed that many buildings still collapsed severely within the Taipei Basin. It is evident that the site effect plays an essential role in the seismic damage potential, especially for the basin topography. On the other hand, the Shanchiao fault located in the Taipei Basin is also a potential threat besides the far-field earthquake. Consequently, the corresponding proper seismic demands at different site conditions within the Taipei Basin in the up-to-date seismic design code are necessary to be further studied to efficiently mitigate the probable earthquake hazard. To understand the hazard contribution of the Shanchiao fault closed to the Taipei Basin for seismic design, the current seismic source and ground motion models are used in probabilistic hazard analysis. This study discusses the seismic requirement's effect considering the Shanchiao fault in the Taipei Basin.

Keywords: Taipei Basin, seismic design, Shanchiao fault, site condition

INTRODUCTION

Taiwan is located at the convergent plate boundary where the Eurasian plate has been eastward underthrusting and colliding with the Philippine Sea plate. This tectonic environment results in high seismicity in and around Taiwan Island. Undoubtedly, earthquake hazard mitigation is an essential issue in Taiwan. It is worthy of noting that Taipei City, the capital of Taiwan and located on a sediment-filled basin, has experienced several damaging earthquakes in which the most recent event occurred on March 31, 2002. Obviously, even though the earthquake was located more than 80-100 km away; it still caused severe damage in the Taipei Basin due to the site or basin effect. The essential way to mitigate the earthquake hazard is to refine the current seismic design code with a more proper definition of seismic demands for different site conditions so that the undesired damage to structures due to earthquake excitations can be efficiently prevented. Due to the fact that the seismic microzonation within the Taipei Basin in the current seismic design code was determined based on the earthquake data recorded. Three subzones of seismic microzonation describe the extent of the long-period effect in the Taipei Basin, including the basin effect and site effect. Even though the intact earthquake records including sufficient damaging earthquakes can more deeply investigate the site amplification effect on the Taipei Basin in response to different levels of excitation, performing the probabilistic seismic hazard analysis for the existed Shanchiao fault will establish exhaustive seismic demand within the Taipei Basin. This paper aims to understand the hazard contribution of the Shanchiao fault located in the Taipei Basin for seismic design not merely the far-field earthquake. The current seismic source and ground motion models are

used in probabilistic hazard analysis. The uniform hazard response spectra (UHRS) with different site conditions in the Taipei basin are developed and discuss the seismic requirement's effect due to the Shanchiao fault in the Taipei Basin.

GEOGRAPHY AND GEOLOGY OF THE TAIPEI BASIN

Taipei Basin, located in Northern Taiwan, contains the metropolitan areas with the highest population densities. The tectonic expansion could have been induced by pure tension, which caused the basin to assume its triangular shape with an area of about 20 km × 20 km. The basin is surrounded by a varied topography, including mountains, tablelands, and a group of volcanoes. This one-sided subsidence made the basin's Tertiary basement into a half-graben shape (see Fig. 1). Four deposited unconsolidated strata were overlaid in the basement of the Taipei Basin. The deepest part of the Tertiary Basement is about 700 m to 1000 m along the western border of the Taipei Basin.

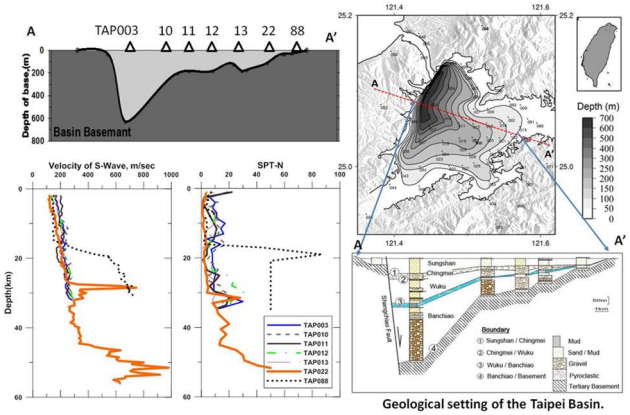

Geological setting of the Taipei Basin.

Figure 1. Topography and geology of the Taipei Basin and the locations of TSMIP network stations. The depth contours denote the Tertiary basement in the basin (Wang et al., 2004). The distribution of SPT-N and shear wave velocity from borehole data of these stations located on the A-A' profile is also shown.

CURRENT SEISMIC DESIGN CODE FOR TAIPEI BASIN

For the current seismic design code for buildings in Taiwan, the elastic seismic demand is represented by the design spectral response acceleration S_{aD} corresponding to a uniform seismic hazard level of 10% probability of exceedance within 50 years. Due to the basin effects, the corner periods noted in the response spectra associated with the earthquake data observed in the Taipei Basin are generally larger than 1.0 seconds (Chiou et al., 2008). It implies that the parameters S_{DS} and S_{D1} prescribed in the design response spectrum for general sites can not be applied directly for locations in the Taipei Basin. The representative values of corner period T_0 between short and moderate period ranges of the design response spectrum are prescribed, as shown in Table 1. In addition, utilizing the uniform hazard analysis, the design spectral response acceleration S_{aD} for a given site can be developed directly from the design spectral response acceleration at short periods S_{DS} (S_{DS}=0.6g) as well as the corner period T_0 for each seismic micro-zone in the Taipei Basin. It can be expressed as:

$$S_{aD} = \begin{cases} S_{DS}\left(0.4 + 3T/T_0\right) & ; \quad T \le 0.2T_0 \\ S_{DS} & ; \quad 0.2T_0 < T \le T_0 \\ S_{DS}T_0/T & ; \quad T_0 < T \le 2.5T_0 \\ 0.4S_{DS} & ; \quad T > 2.5T_0 \end{cases} \tag{1}$$

The distribution of the three micro-zones and the shapes of the corresponding design response spectra in Taipei Basin is shown in Fig. 2. It is found that the microzonation map of the corner period is in

accordance with the basin shape and reflects the thickness of the sedimentary soil layers in the Taipei Basin.

Table 1. Representative values of corner period for each micro-zone in Taipei Basin at 475 years return period.

Micro-zone	Seismic Zone 1	Seismic Zone 2	Seismic Zone 3
Ss	0.6		
T_0 (sec.)	1.60	1.30	1.05

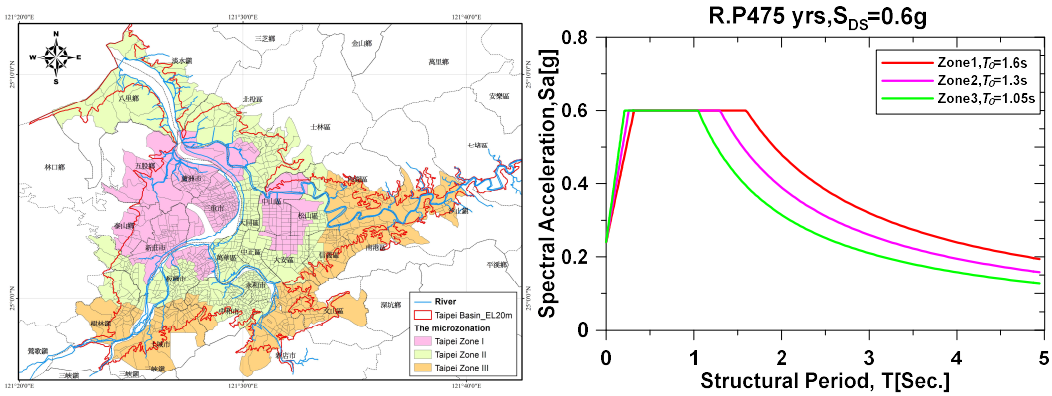

Figure 2. Distribution and the design response spectrum for each microzonation in the Taipei Basin.

THE HAZARD CALCULATION

The Source Model of ShanChiao Fault

The northern offshore region of Taiwan contains a series of normal faults with northeast-southwest strikes, rift basins, and basement highs (Sun, 1982). Fig. 3 shows the seismic source model near the Taipei Basin, particularly the Shanchiao fault. As indicated by the seismicity distribution (Fig. 2), the seismic activity in the Taipei area is significantly lower than in other areas in northern Taiwan, and most of the seismicity is concentrated in the offshore areas. The active faults database published by the Central Geological Survey (Sinotech and CGS, 2021) and the seismicity and subduction zone models refer to Taiwan SSHAC Project (NCREE, 2019). The basic parameters of the Shanchiao fault closed to the Taipei Basin in the hazard calculation, such as the length, geometry, slip rate, and magnitude, are summarized from the Sinotech and CGS report.

The Ground Motion Prediction Equations

The Taiwan ground motion prediction equations (GMPE) were developed using the comprehensive ground-motion database (NCREE, 2019). In hazard calculation, the GMPE models involve six crustal GMPEs, four GMPEs of subduction interface, and intraslab sources. The current GMPE for crustal earthquake, the average shear-wave velocity in the top 30 m (V_{S30}) and the depth to VS=1.0 km/sec (Z1.0) are used to estimate the site amplification correlated with the shear-wave velocity structure of the region. The analytical modeling of Z1 scaling is to constrain the soil depth scaling due to the sparse soil. In Taipei Basin, the stations located the three subzones have the same V_{S30} value but different depths of the Z1.0 values. Fig. 4 shows the dependence of the spectra on Z1.0 for the soil sites with the same V_{S30} = 210 m/s. All soil sites taper together at short periods, since the Z1 scaling only affects periods longer than 0.2 s.

The Design Spectra

The hazard curves at 1.0 sec structure period of six sites located in the Taipei Basin of three subzones (shown in Fig. 4) are shown in Fig. 5. In hazard calculation, considering the single station sigma models and epsilon = 2 for the uncertainty of the ground motion prediction. Based on the mean total hazard

curves of each period, the 5% damping ratio of UHRSs for six sites located in the Taipei Basin at the return periods of 475 years are shown in Fig. 5. The comparison of the design response spectrum and the UHRSs is also shown in Fig. 5. The result indicates that the soil depth affects the response spectra of long periods. On other hand, the hazard contribution from the Shanchiao fault affects the design spectrum at short periods.

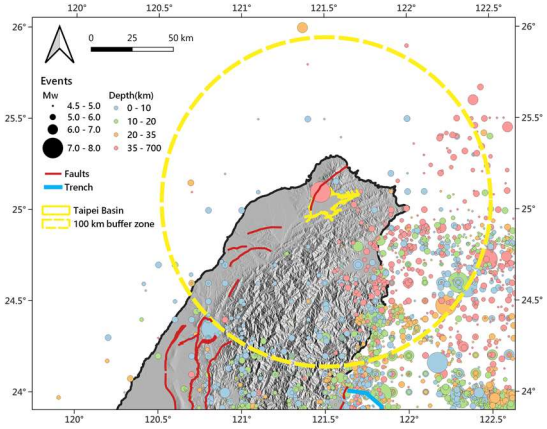

Figure 3. Seismic source characteristics distribution near the Taipei Basin.

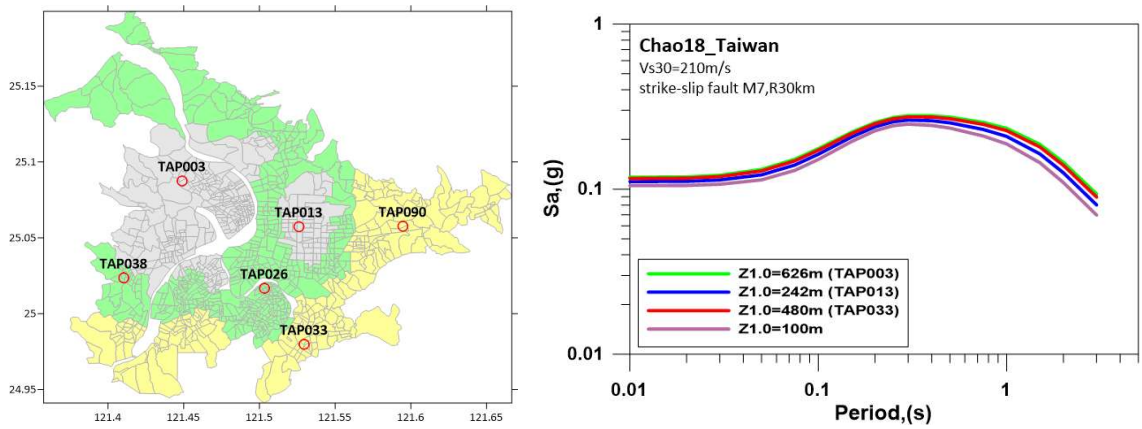

Figure 4. Scaling with soil depth for a M7.0 strike-slip event at a rupture distance of 30 km and VS30 = 210 m/s. (GMPE: Chao et al., 2019)

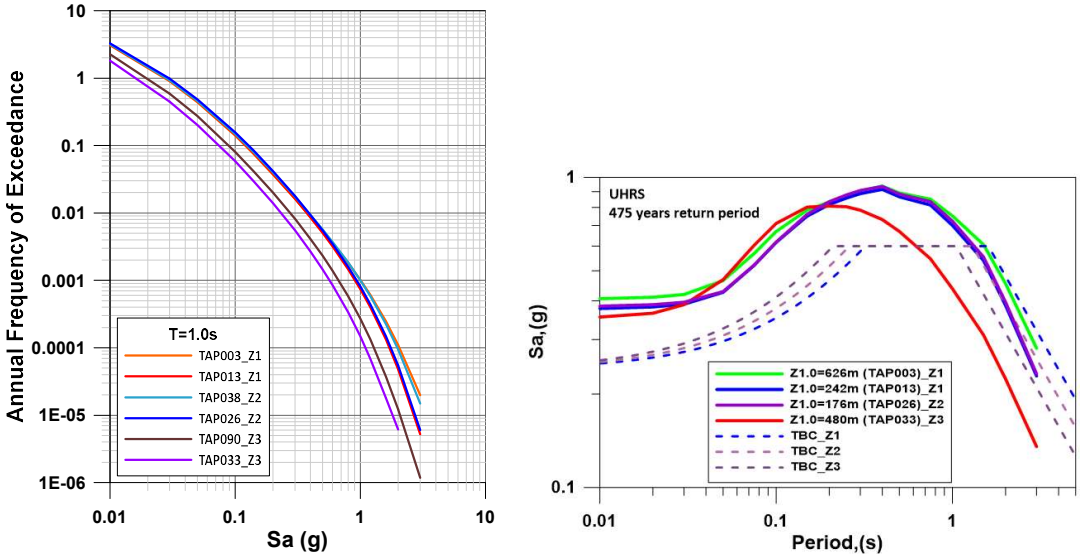

(1) The hazard curves at 1.0s structure period (2) UHRS at 475-year return period

Figure 5. The hazard curves and UHRS of six station located in Taipei Basin.

DISCUSSION AND CONCLUSIONS

The basin effect is not negligible, particularly when the controlling earthquake is a major, shallow, and far-field earthquake such as the 1999 Chi-Chi earthquake or the 2002 Hualien earthquake. In addition, since the seismic microzonation within the Taipei Basin in the current seismic design code (2022) was determined using the earthquake data recorded, including sufficient damaging earthquakes. Based on the recorded data corresponding to the controlling earthquakes such as the 1999 Chi-Chi earthquake and the 2002 Hualien earthquake, the associated acceleration response spectra were determined for each observation station in Taipei Basin. Having calculated the normalized response spectra for each station, all the response spectra of each event were compared with the existing seismic code to facilitate examination of the corner period of the response spectrum for that seismic zone. Fig. 6 shows the comparison of the design response spectrum and observed response spectra of six stations depending on the depth of the Z1.0 values. Although the two similar soil depths at VS=1000 m/s of the two stations in Taipei Basin, the properties of observed response spectra show the long period effect of depth vary depth. The PSHA analytical results show that the seismic design in the Taipei Basin affected by the Shanchiao fault is more significant, such as in accordance with the basin shape and the thickness of the sedimentary soil layers much different compared with the current seismic microzonation.

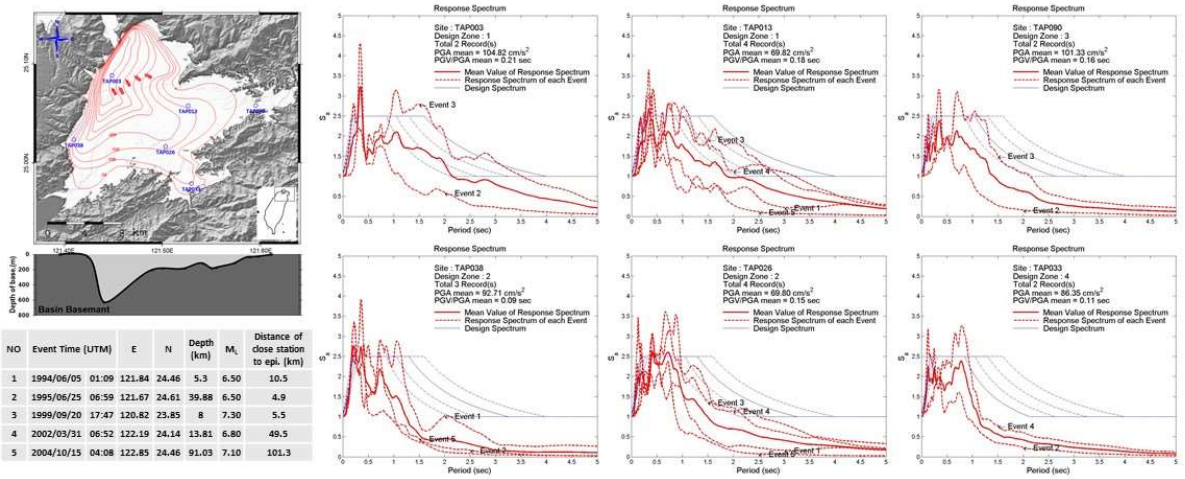

NO	Event Time (UTM)	E	N	Depth (km)	M_L	Distance of close station to epi. (km)
1	1994/06/05 01:09	121.84	24.46	5.3	6.50	10.5
2	1995/06/25 06:59	121.67	24.61	39.88	6.50	4.9
3	1999/09/20 17:47	120.82	23.85	8	7.30	5.5
4	2002/03/31 06:52	122.19	24.14	13.81	6.80	49.5
5	2004/10/15 04:08	122.85	24.46	91.03	7.10	101.3

Figure 5. The hazard curves at 1.0s structure period in the Taipei Basin.

REFERENCES

Chao, S.H., Chiou, B., Hsu, C.C., and Lin, P.S. (2019b). Development of horizontal and vertical ground motion model for crustal earthquakes and subduction earthquakes in Taiwan, NCREE Report, No. NCREE-19-003, National Center for Research on Earthquake Engineering, Taipei, Taiwan.

Chiou S.B, Chang Y.W., Jean W.Y., and Chai J.F. (2008). "A Study on the Microzonation for Design Earthquake in Taipei Basin" (Chinese Version). Research Report, National Center for Research on Earthquake Engineering, NCREE-08-043, Taiwan.

National Center for Research on Earthquake Engineering (2019). "SSC and GMC technique reports of Taiwan SSHAC Level 3 Project".

Sun, S. C. (1981) The Tertiary basins of offshore Taiwan. In Proc. of the Second ASCOPE Conference and Exhibition,125-135.

Wang, C. Y., Y. H. Lee, M. L. Ger, and Y. L. Chen (2004). "Investigating subsurface structures and P- and S-wave velocities in the Taipei Basin", *Terr. Atmos. Ocean. Sci.*, **15**, 609-627.

Sinotech and CGS (2020). "Improvement of Earthquake Probability Assessment for the Active Faults and the Analysis of the parameters for the Seismogenic Structures in Taiwan".

Construction and Planning Agency (2022). Seismic Design Specifications and Commentary of Buildings. (In Chinese)

(2e) Geotechnical engineering innovations

PSEUDO-STATIC STABILITY ANALYSIS OF LATERALLY CONFINED CATACLINAL SLOPE MODEL

Wongchana Pongsakorn[1] and Pipatpongsa Thirapong [2]
1. Ph.D. Student, Department of Urban Management, Kyoto University, Kyoto, Japan
2. Associate Professor, Department of Urban Management, Kyoto University, Kyoto, Japan
Email: wongchana.pongsakorn.62y@st.kyoto-u.ac.jp, pipatpongsa.thirapong.4s@kyoto-u.ac.jp

ABSTRACT

Pseudo-static is a simple approach that statically applies a force to a designated facility and simulates horizontal acceleration in model. When structure has an acceleration, effect of shaking to structure is equivalent to force of seismic coefficient (k_h). This paper aims to demonstrate equivalent approach to performing seismic coefficient by using tilting angle and surcharge loading. The silica sand No.6 is widely used in physical model, thus slope models were installed. In addition, experiments were conducted under two different conditions of slope model, one with and one without lateral supports. Slope models at failure point were recorded with angle and surcharge weight, after then experimental results were plotted as loading path which depends on test procedures. Seismic coefficient can be calculated from surcharge weight and angle at failure. Moreover, the factor of safety can be computed and compared with slope model. The result shows a good agreement with experiment; thus, equivalent slope model can be generated seismic coefficient.

Keywords: Pseudo-static, Seismic coefficient, Loading path, Lateral confinement

INTRODUCTION

The pseudo-static slope stability technique is a simple approach for dynamic load modeling of an earthquake, that was applied to a slope by assuming additional static loads (Towhata, 2008). The pseudo-static load has components in both horizontal and vertical directions; However, the vertical component has a negligible impact on slope stability and is typically neglected in stability analysis. The horizontal seismic coefficient (k_h) can be determined from the tilted angle of the model using a tilting table, a well-known experimental apparatus for generating a pseudo-static horizontal body force on the model.

Testing the slope model carrying out the loading operation and initiating a slope failure using a tilting table is common practice. When assessing the slope of rocks and soil, a tilting table may be used in a variety of ways. Evaluating the slope of soil, the stability of the slope is examined using a pseudo-static analysis, with the tilting table acting as a pseudo-static seismic force. In addition, sliding tests are used to measure the interface parameters between the slope models and the bedding plane (Khosravi *et al*., 2011). The side friction in a compacted slope model can be purposefully raised or lowered for 1g small-scale and centrifugal physical model testing. To observe slope failure, slope is induced by using shaking table, tilting angle, surcharge loading.

In this work, tilting table and surcharge loading were used to assess the stability of slopes. Silica sand No.6 was used as the modeling material. We observed the slope behavior and compared the two techniques (tilting table and surcharge loading). For applying pseudo-static method to slope model, concept can be explained with equivalent static slope model.

BACKGROUND

In engineering practice, pseudo-static slope stability techniques are frequently used to assess the seismic performance of earth structures and natural slopes. Although these methods have the advantage of being comparatively simple to utilize, it should be related to nature geology conditions. Thus, pseudo-static needs to apply for the cataclinal slope model. The pseudo-static theory can be presented as Fig. 1.

Generally, horizontal acceleration is directly applied using shanking table. Using a shaking table can be compensated by adding a surcharge load or tilting angle. Fig. 1(2) Tilting table incline slope model until slope lost stability, this method is equivalent to shaking table. However, surcharge loading is more convenient than using tilting table, the slope model does not depend on weight, it can be added surcharge load until slope collapse. The diagram force is shown in Fig. 1(2). Seismic coefficients effect to reduce normal force and increases driving in slope model. The diagram force of tilting table and surcharge loading follow as shanking table concept. Normal force and driving force for three methods can be illustrated in Fig. 1(4). Loading path for surcharge loading is ABD, slope model firstly incline angle to B point, then surcharge weight is added to rise driving force to D point. Moreover, slope model can add surcharge load until it reaches to failure envelope (ABG), can draw a loading path as AD and AG as followed Eq. 2 and Eq. 3. At the same endpoint, slope models with tilting table are plotted as CD and CFG line, normal force step to C and E point, is subject to weight of slope model and the angle is increased from α to $\alpha + \beta$

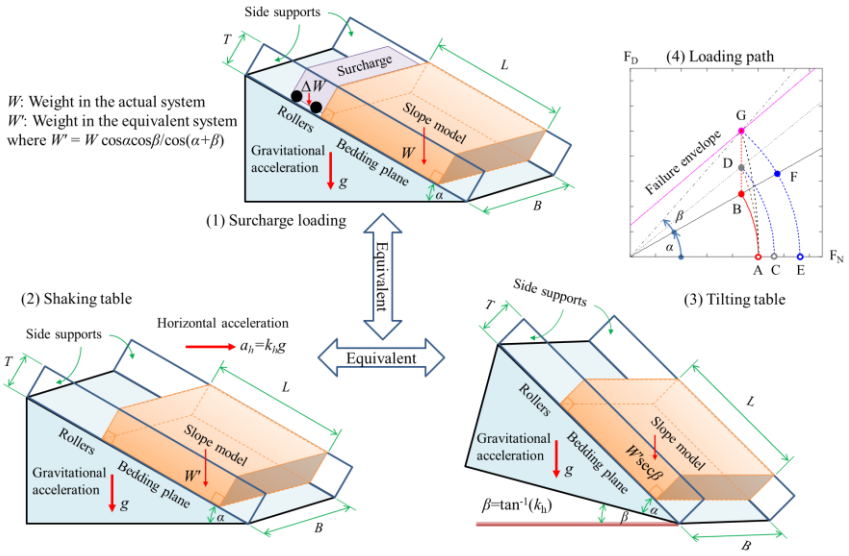

Figure 1. Slope models with surcharge loading, slanted along the bedding plane, and increased slope angles. (1) slope model with shaking table, (2) slope model with tilting table, (3) slope model with surcharge loading and (4) loading path

According to the diagram force and loading path in Fig. 1, slope model for the slope without lateral confinement, the interface friction angle, and the adhesion between the sand block and the bedding plane control the stability of the block through the following equation:

$$R_B = F_N \tan(\phi_i) + C_i BL \tag{1}$$

From force diagram show in Fig. 1, the static method is using surcharge loading, which can be described by following equation:

Static

$$F_{1D} = W_1 sin(\alpha) + \Delta W sin(\alpha) - \Delta W cos(\alpha) \tan(\phi_r) \tag{2}$$

$$F_{1N} = W_1 cos\alpha \tag{3}$$

where

α : initial angle of slope
W_1 : slope model weight
ΔW : Surcharge weight
ϕ_r : Friction angle of roller cart

Pseudo-static

$$F_{2D} = W_2(\sin(\alpha) + k_h\cos(\alpha)) \quad (4)$$
$$F_{2N} = W_2(\cos(\alpha) - k_h\sin(\alpha)) \quad (5)$$
$$k_h = tan(\beta) \quad (6)$$

where
β : incline angle
W_2 : slope model weight
k_h : Seismic coefficient

Substitute Eq. 6 into Eq. 4 and Eq. 5,

$$F_{2D} = \frac{W_2}{cos\beta}\sin(\alpha+\beta) \quad (7)$$
$$F_{2N} = \frac{W_2}{cos\beta}\cos(\alpha+\beta) \quad (8)$$

At the same endpoint, normal force and driving of static method are equal to pseudo-static method.

$$F_{1N} = F_{2N}$$
$$W_2 = W_1\left(\frac{\cos(\alpha)\cos(\beta)}{\cos(\alpha+\beta)}\right) \quad (9)$$
$$F_{1D} = F_{2D} \quad (10)$$
$$r_m = \frac{\Delta W}{W_1}\left(1 - \frac{\tan(\phi_r)}{\tan(\alpha)}\right) \quad (11)$$

Seismic coefficient rearranged to equation below:

$$\beta = -\alpha + tan^{-1}((1+r_m)\tan(\alpha)) \quad (12)$$
$$k_h = \tan\left[-\alpha + tan^{-1}\left((1+r_m)\tan(\alpha)\right)\right] \quad (13)$$

According to Pipatpongsa *et al.* (2022) the slope with lateral confinement, the side friction should be included in seismic coefficient calculation, side friction depends on geometry of slope. The interface friction angle and the adhesion between the sand block and the bedding plane, lateral support control the stability of the block through the following equations:

$$F_R = M \times F_N + C \quad (14)$$
$$M(B,T) = (K_p \cdot \tan(\phi_s) \cdot \frac{T}{B}) + \tan(\phi_i) \quad (15)$$
$$C(B,T) = \frac{2(2r_d \cdot c\sqrt{K_p}\cdot\tan(\phi_s)+c_s)}{\gamma \cdot B} + \frac{c_i}{\gamma \cdot T} \quad (16)$$
$$K_p = tan^2\left(\frac{\pi}{4} + \frac{\phi_d}{2}\right) \quad (17)$$

where
M : attributed function
C : attributed function
K_p : Coefficient passive earth pressure
ϕ_s : Friction angle of side support

Shear strength reduction ratio(r_d) with regard to the shear strength (Dawson *et al.*, 1999; Matsui and San, 1992), is defined as the ratio of τ_d to τ_f, as shown in Eq. 20.

$$\tau_f = \sigma_n' \tan(\phi) + c \quad (18)$$
$$\tau_d = \sigma_n' \tan(\phi_d) + c_d \quad (19)$$

$$r_d = \frac{\tau_d}{\tau_f} = \frac{\tan(\phi_d)}{\tan(\phi)} = \frac{c_d}{c} \quad (20)$$

where

τ_f : Shear strength of soil mass
τ_d : The development of shear stress
ϕ_d : Coefficient passive earth pressure
c_d : Friction angle of side support

$$F_r = F_{2d}\,, F_N = F_{2N}$$
$$F_r = F_{2d}$$
$$\beta = -\alpha + tan^{-1}((M \cdot W) + C) \quad (21)$$
$$k_h(\alpha, B, T) = \frac{\mathrm{M+C-tan\,(\alpha)}}{1+(M+C)\tan(\alpha)} \quad (22)$$

SLOPE STABILITY EXPERIMENT

The slope model was created with silica sand No.6 and was set on an acrylic plate, as shown in Fig. 2. Slope models were conducted with two different models, one without lateral support and one with lateral support. Fig. 2(A) depicts a slope model with no lateral supports sitting on friction interface plane which was made by acrylic plate, whereas Fig. 2(B) depicts a slope model with lateral supports. The lateral supports located at 2 sides of slope model, which were made by the acrylic plate same as bedding plate. After the slope model was set on the plate, it would be installed on the initial condition. Based on the failure mechanism, slope model without side support can collapse more effortless than slope model with side support due to lateral friction. In addition, there are many ways to reduce slope stability, for example, increasing the angle of slope, adding surcharge weight, and adding dynamic loading. These tests were performed by using Tilting angle and Surcharge weight, the method follow as test procedures.

Test procedures

① Tilting procedures
The slope model was rotated continuously until it became unsteady, the slope angle at failure was measured by a digital angle meter.
② Tilting-surcharge-tilting procedures
The slope model was rotated to initial angle. Then, the weight of the surcharge was added to the slope model. After that, tilting table gradually increased until slope model lost stability.
③ Tilting-surcharge procedures
The tilting table was inclined to the desired angle. After then, surcharge weight was applied until the slope collapsed.

Slope models without lateral support were performed by ①tilting angle and ③tilting angle with surcharge weight. The experiments were produced by Techawongsakorn *et al.* (2013), and Kanou *et al.* (2017). On the other hand, Slope models with lateral support were carried out in 6 series that cover 3 test procedures (①,②,③). The experiments were conducted by Kanou *et al*. (2017).

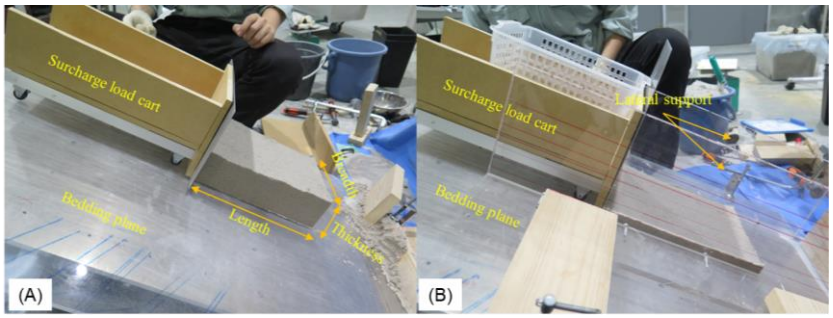

Figure 2. Slope models with surcharge loading, slanted along the bedding plane, and increased slope angles. (A)Without lateral supports, (B) with lateral supports,

According to the set of sliding tests without surcharge weights and with surcharge weights, conducted previously by Techawongsakorn *et al.* (2013), and Kanou *et al.* (2017), respectively. Fig. 3(A) and Fig. 3(B) showed the experimental results, the interface friction angle ϕ_i and adhesion c_i between silica sand No. 6 and the acrylic plate were 29.4°, 0.21 kPa, and 0.26 kPa, respectively. Lateral support is the same material as beading plate which means the friction and adhesion can be the same parameters. Moreover, Kanou's experiments applied surcharge load by using cart deadweight, the friction angle of roller cart (ϕ_s) affects to resist surcharge weight, which was later used in calculation part. On the experiments, the water content remained at 10 percent to contain bulk unit weight (13.68 kN/m^3). Basic properties of silica sand No. 6 and interface strength parameters are shown in Table 1

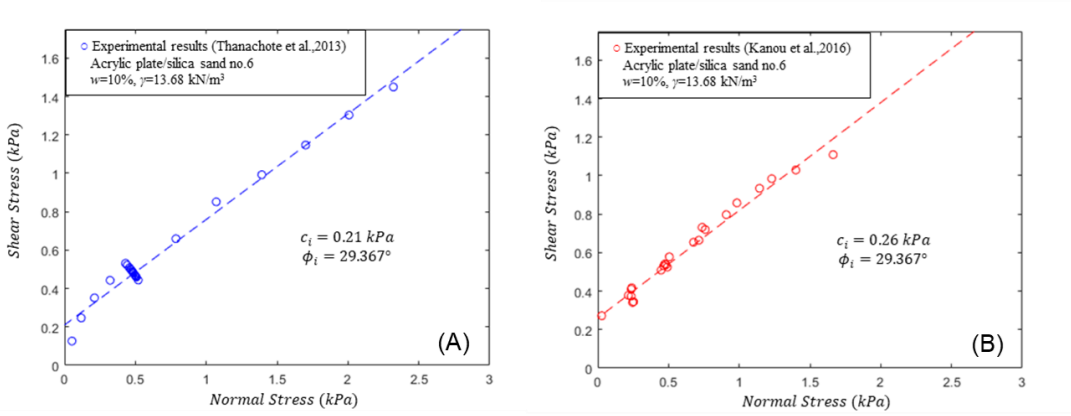

Figure 3. Interface parameters between silica sand No. 6 and acrylic plate (A) siding tests without surcharge weight (B) Sliding tests with surcharge weight

Table 1. Basic properties of silica sand No. 6 and interface strength parameters

Basic properties	silica sand No. 6
Water content (w)	10.0%
Average particle diameter (D_{50})	0.32 mm
Bulk unit weight (γ)	13.68 kN/m^3
Interface Friction angle (ϕ_i)	29.367°
Friction angle of roller cart (ϕ_r)	6.1°
Apparent cohesion (c)	0.57 kPa
Friction angle (ϕ)	33.2°

Experimental results

Figure 4 illustrate loading paths of slope model without lateral support. The loading path are plotted the relation between normal force and driving force by using Eq. 2, Eq. 3, and failure point. Based on test, procedure① were plotted in weight with cosine and sine function due to no applied surcharge weight. Moreover, overlaps loading path ① are shown because experiments were carried out with same dimensions of slope model, but different failure angle. Loading path ③ included surcharge weight function, the curve reaches to endpoint with angle and surcharge weight at failure slope. The experimental results can be normalized in terms of stress ($\frac{F_D}{A}$), or force divided by weight ($\frac{F_D}{W}$). After that, Interface cohesion can be obtained by using y-axis intersection in term of stress. Loading path after normalized to force divided by weight, loading path start at the same original point (x=1) and then it is broken at individual failure envelope. However, deleting adhesion with thickness term led to the diverse of origin point.

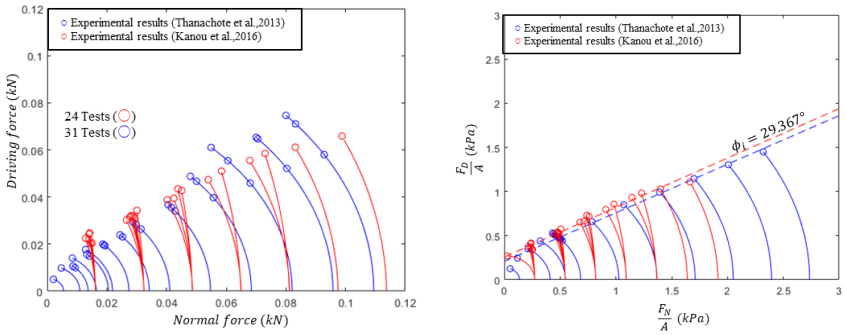

Figure 4(A). Loading paths of slope model without lateral support.

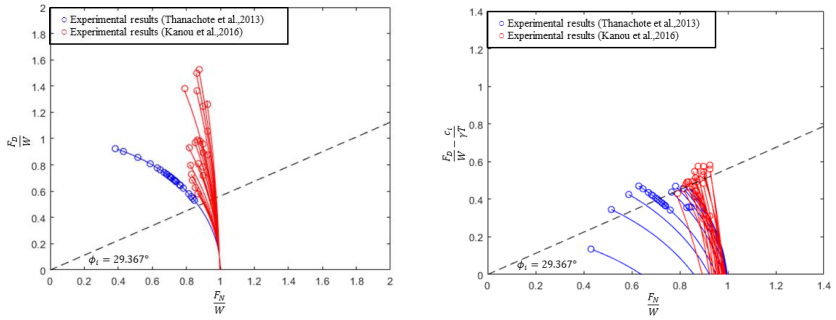

Figure 4(B). Loading paths of slope model without lateral support.

Loading paths of laterally confined slope model were illustrated as Fig. 5. Experiments were operated on 3 test procedures. Test procedures ① was applied to test series 6, ③ is applied to test series 3 and 4, ② is applied to test series 1, 2 and 5. Loading path depends on test procedures and based on Fig. 1(4). However, the endpoint is on failure envelope based on geometry condition which depends on Breadth (B), Length (L) and Thickness (T). For example, series 1 were conducted with 6 different thickness (0.02, 0.04, 0.06, 0.08,0.1 and 0.12 meters). The graph in terms of force and stress shows lowest thickness would produce minimum force and stress the reason why geometry is necessary to include in the seismic coefficient equation. In terms of force divided by weight, loading path start at the same point (x=1) and then it stops at different failure envelope. Therefore, loading path would be helpful to understand soil slope model behavior when the equivalent pseudo-static theory is applied.

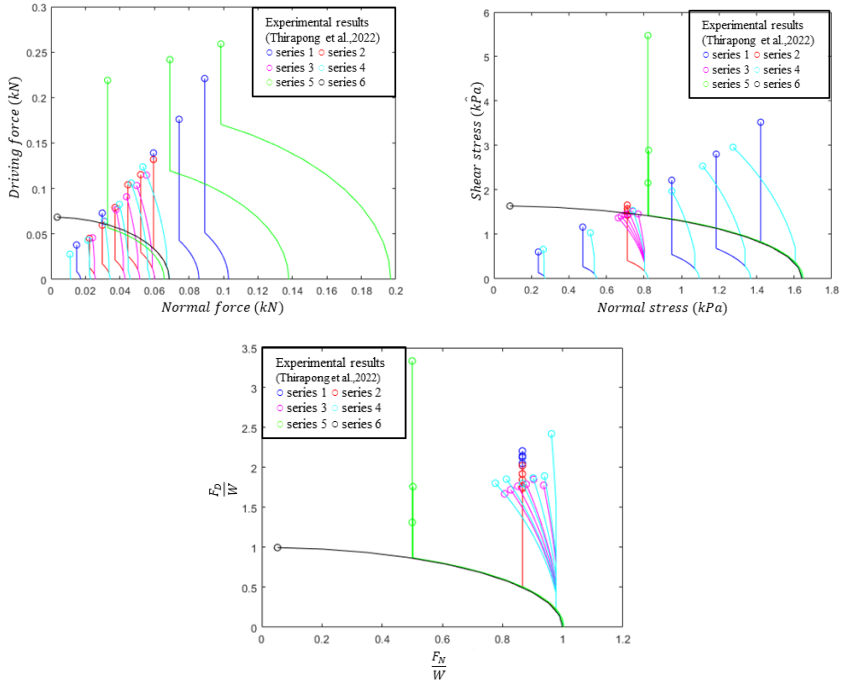

Figure 5. Loading paths of slope model with lateral support

Pseudo-static analysis

The pseudo-static method is a conceptual applying seismic force to a slope model by using static force. Based on experiments, slope models were applied surcharge load and tilted angle of slope as same as pseudo-static technique. These experiments are presented in terms of force, which can convert to seismic coefficient(k_h). from Eq. 14, we can estimate k_h by using effective ratio of surcharge weight (r_m) and angle (α) at failure point. Fig. 6 is shown the relation between k_h and rm, k_h is subject to r_m and α. Tests without lateral support is shown range of r_m between 0.164 to 2.273, is equivalent to k_h between 0.068 to 0.601. In addition, Tests with lateral support using r_m between 0.518 to 7.956 is equivalent to k_h between 0.162 to 1.310. Moreover, Fig. 6 illustrates theoretical analysis curve which matches with experimental results.

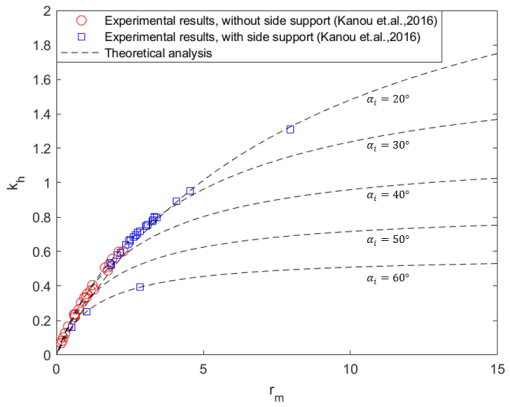

Figure 6. Seismic Coefficient(k_h) and the ratio of surcharge loading(r_m)

However, seismic coefficient based on loading from equivalent slope model of without side support equation is still cannot be used in practice way because nature slope is dependent on geology and geometry condition. the tests based on resistance with lateral supports should be used to analyze for k_h using Eq. 22 and compare with seismic coefficient based on loading. Calculation results show as Fig. 7(A), k_h (seismic coefficient prediction based on geometry and resistance), k_h values with two different methods closely match together. This statement is to prove equivalent equation from 2 methods, can be used to predict k_h from surcharge loading and tilting angle.

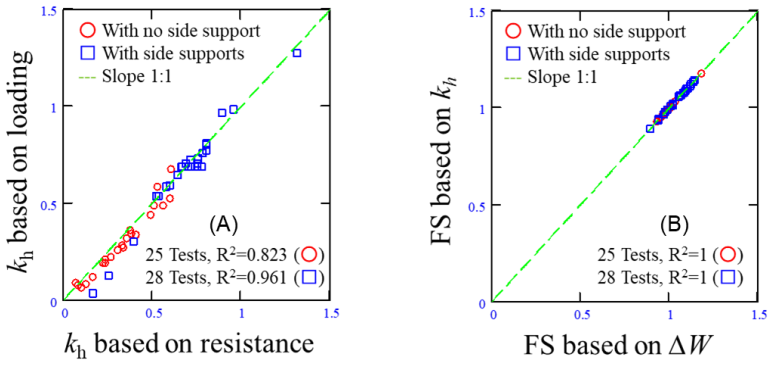

Figure 7. (A)Seismic Coefficient based on resistance (K_h) and Seismic Coefficient based on loading (k_h)
(B) Factor of safety based on k_h and Factor of safety based on ΔW

The method of seismic coefficient is simple and the calculation of the safety factor can be achieved in the same manner as the calculation of static stress, no in-depth analysis is necessary. It greatly facilitated the improvement of seismic safety. Generally, Factor of safety (FS) of slope model can be calculated by resistance force (F_R) divided by driving force (F_D). Eq. 23 shows FS based on equivalent slope model by using surcharge loading and Eq. 24 is FS is based on a slope model that uses the direct seismic coefficient. Fig. 7(B) illustrates FS to compare between two methods. the graph can be explained FS

exactly matched, that mean FS from surcharge loading on slope model and FS based on seismic coefficient can be utilized in the same manner.

$$\mathrm{FS} = \frac{tan\phi_i + tan^2\left(\frac{\pi}{4}+\frac{\phi_d}{2}\right)tan\phi_s\frac{T}{B} + \left(\frac{c_i}{\gamma T} + 2\frac{2r_d ctan\left(\frac{\pi}{4}+\frac{\phi_d}{2}\right)tan\phi_s + c_s}{\gamma B}\right)sec\alpha}{\left(1+\frac{\Delta W}{\gamma TLB}\left(1-\frac{tan\phi_r}{tan\alpha}\right)\right)tan\alpha} \tag{23}$$

$$\mathrm{FS} = \frac{tan\phi_i + tan^2\left(\frac{\pi}{4}+\frac{\phi_d}{2}\right)tan\phi_s\frac{T}{B} + \left(\frac{c_i}{\gamma T} + 2\frac{2r_d ctan\left(\frac{\pi}{4}+\frac{\phi_d}{2}\right)tan\phi_s + c_s}{\gamma B}\right)sec\alpha}{tan\left(\alpha + tan^{-1}(k_h)\right)} \tag{24}$$

CONCLUSIONS

Pseudo-static method is a simple approach to applying seismic acceleration on the static model by using surcharge weight and tilting table. Slope model experiments were conducted with using surcharge weight and tilting table, matched with pseudo-static conception. In general, the slope model can apply seismic by using shaking table. Pseudo-static method can be compensated. However, surcharge weight is more convenient than using tilting angle because tilting angle must add the mass of slope in every step. This paper demonstrates pseudo-static method application with surcharge loading and tilting angle. Seismic coefficient calculation based on loading was corrected and confirmed by calculation based on resistance which is considered with geometry condition. Furthermore, factor of safety was proved by equation and graph between FS based on surcharge loading and FS based on k_h which exactly matched, that mean FS from surcharge loading on slope model and FS based on seismic coefficient can be utilized in the same manner.

ACKNOWLEDGEMENT

This work was supported by EGAT and JSPS KAKENHI Grant Number 20H02242.

REFERENCES

Dawson, E.M., W. Roth and A. Drescher (1999). "Slope stability analysis by strength reduction," *Geotechnique*, **49**(6), 835–840.

Kanou, T., K. Fang, and T. Pipatpongsa (2017). "Physical models on base failure of slope subjected to surcharge loading," *In Proceedings of the 52nd Japan National Conference on Geotechnical Engineering*, 829-830.

Khosravi, M.H., T. Pipatpongsa, A. Takahashi, and J. Takemura (2011). "Arch action over an excavated pit on a stable scarp investigated by physical model tests," *Soils and Foundations*, **51**(4), 723-735.

Matsui, T. and K.C. San (1992). "Finite element slope stability analysis by shear strength reduction technique," *Soils and foundations*, **32**(1), 59-70.

Pipatpongsa, T., K. Fang, C. Leelasukseree and A. Chaiwan (2022). "Stability analysis of laterally confined slope lying on inclined bedding plane," *Landslides*, **19**(8), 1861-1879.

Techawongsakorn, T., H. Hirai, M.H. Khosravi and T. Pipatpongsa (2013). "Slip mechanisms and interface shear strength between moist silica sand and acrylic plate," *In Proceedings of the 48th Japan National Conference on Geotechnical Engineering*, 895-896.

Towhata, I. (2008). "Pseudo-static Limit Equilibrium Analysis," *Geotechnical Earthquake Engineering*, 120-128.

(3a) Practice case studies in seismic retrofits

SEISMIC PERFORMANCE OF RC FRAMES RETROFITTED WITH POST-INSTALLED SHEAR WALLS

Wen-I Liao[1], Yu-Ming Zheng[2], Fu-Pei Hsiao[3] and Zi-En Gu[2]
1. Professor, National Taipei University of Technology, Taipei, Taiwan., R.O.C.
2. Graduate student, National Taipei University of Technology., Taipei, Taiwan, R.O.C.
3. Division Header, National Center for Research on Earthquake Engineering, Tainan, Taiwan, R.O.C.
Email: wiliao@ntut.edu.tw

ABSTRACT

For the existing old reinforced concrete (RC) building structures with low strength concrete and lacking seismic details, installing RC shear walls is one of the effective methods of system retrofitting. For the structure with low strength concrete, the commonly adopted connected construction method on the interface may be not able to provide effective force transfers between the existed and post-installed concretes and may cause unexpected brittle failure in the existing structure. In addition, this unexpected brittle failure often reduces the seismic capacity of the retrofit structure. Therefore, in this study, an improved technique of the post installing RC wall with/without opening is proposed, the key points are to add a new interior column between the RC wall and the existing column, and to install high strength concrete blocks between the wall and existing beam to improve the force transform mechanism on the interface of the existing and post-installed concrete. In addition, a pure frame without retrofit was constructed and tested for comparison.

Keywords: retrofit、RC frame、low strength concrete、seismic performance

INTRODUCTION

Due to the high lateral strength and the stiffness capacity of RC wall panels, the post-installed RC infill wall for the non-ductile RC structures is a widely used technique in seismic retrofit, especially for those low-rise buildings structures. In the past, extensive experimental studies was performed on RC infilled frames. Many types of RC walls, reinforcement layouts, and details were studied [1-3]. Results showed that the RC shear walls increased the lateral capacity of the structures and reduced their lateral deformation. Altin et al. [4] carried out an experimental investigation to study the behavior of RC non-ductile frames with RC infills under lateral loads. Many types of improper lap-splices have been studied. Liao et al. [5] also conducted a test on the seismic performance of non-ductile RC frame retrofitted by infill RC wall and found that the sliding failure may occur on the interface between the post-installed wall and existing components using traditional connection techniques. However, for existing RC structures with low-strength concrete, the commonly used construction method on the interface between existing and post-installed concrete may be not able to provide effective force transfer and may cause unexpected brittle failure in the existing structure due to its low capacity [6].

Therefore, in this experimental study, two improved methods for well connection construction while using a post-installed RC wall are proposed to improve the load transfer mechanism on the interface. The first is the wall with additional interior columns that combine with the existing columns for ensuring stress transfer mechanism and increase the flexural strength of the specimen. Except for the chemical rebar-planting anchorage for connection [7], the additional high-strength concrete blocks were used to paste on the surface of existing beams to increase the shear friction strength and avoid the sliding failure generated on the interface. A typical non-ductile traditional RC frame specimen was built and tested for comparison. Two frame specimens retrofitted using post-installed RC shear walls without/with openings, respectively, were tested for verifying the proposed improved connection construction methods. Reversed cyclic loading is used to test the seismic capacity of these specimens. The test results indicate that the specimen retrofitted by post-installed RC wall with proposed techniques shows good performance in both the strengthening of strength and stiffness.

SPECIFICATIONS OF TEST SPECIMENS

Three RC specimens were tested under lateral cyclic loadings as shown in Figure 1. The first specimen S1:PF is the RC pure frame specimen, it is designed to simulate the behavior of existing non-ductile RC frame structures. The second specimen S2:PF+ISW is the RC frame retrofitted with a post-installed RC shear wall, and the specimen S3:PF+IOSW is the RC frame retrofitted with a post-installed RC shear wall with openings [8]. The existing RC pure frame specimen is a single-span and single-story structure. The height and span of those frame specimens are 190 cm and 340 cm, respectively. The column is 35 x 30 cm in cross-section, whereas the top beam is 50 cm deep and 63 cm wide. The size of the strip foundation is 140 cm in width, 480 cm in length, and 52 cm in height.

For the retrofitted specimen PF+ISW, in order to prevent the damage occurring in the unexpected places of the existing frame, two post-installed columns were added beside the existing column to transfer the stress to the wall. The cross section of the interior column is 20x30 cm. Four #4 (D13) longitudinal SD420 deformed bars were used as longitudinal reinforcements, while the stirrups were made of U-shaped #3 steel bars with spacing 15 cm. The length, thickness, and height of the post-installed RC shear wall are 230, 15, and 190 cm, respectively. Single layer #3 SD280 steel bar mesh at spacing 15 cm was used as vertical and horizontal reinforcement of the RC wall.

The surrounding interfaces of the existing RC frame and the post-installed RC wall and columns were bonded by chemical rebar-planting anchorage. The planting steel bars are # 4 steel bars in a single row with a spacing of 10 cm in the vertical direction and 15 cm spacing in the horizontal direction. In addition to rebar-planting anchorage for connection, the interface at the bottom of the top RC beam of the existing frame is roughened to a roughness of 6 mm, and a total of 23 high strength 5x5x5 cm mortar blocks were pasted using epoxy in the middle of two planting bars.

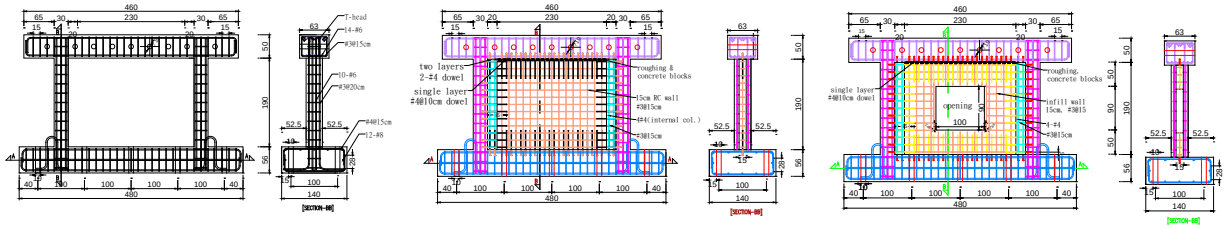

(a) (b) (c)

Figure 1. Configuration of test specimens (a) S1:PF, (b) S2:PF+ISW, (c) S3:PF+IOSW

EXPERIMENTAL SETUP

The test setup of specimens is shown in Figure 2(a). The tests are performed by applying a reversed cyclic lateral loading using hydraulic actuators to the specimen. The applied lateral displacement history is shown in Figure 2(b), where drift is defined as the ratio of horizontal displacement to the specimen height, hw, measured from the center of the displacement application to the base of the wall. Loading is continued to obtain the force-drift relationship until a decrease of 20% in the maximum strength of the specimen is reached. Deformations of specimens were recorded using linear variable differential transformers (LVDTs) and an optical system (NDI) that tracked the motions of “markers” on the surface of specimens.

TEST RESULTS

For the specimen S1-PF, the serious expansion of shear cracks and spalling of concrete was observed at drift 3.0%, and the lateral strength has dropped to about 50% of the maximum strength. The failure mode can be characterized as the flexural failure of the columns with rebar buckling and concrete crushing then causing the bond separation of steel bars and concrete occurred. Figure 3(a) and (b)

shows the photos of the failure status of specimen SPF at drift ratios 3% and 5%, respectively. And the hysteretic loop of this specimen is shown in Figure 3(c).

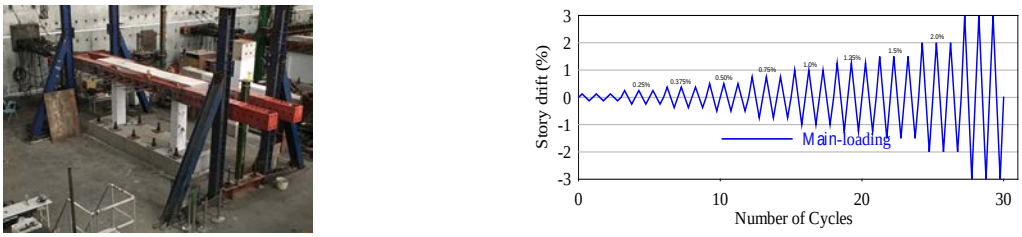

(a) (b)

Figure 2. (a) Photo of test setup for reversed cycling loading. (b) Loading history of the test.

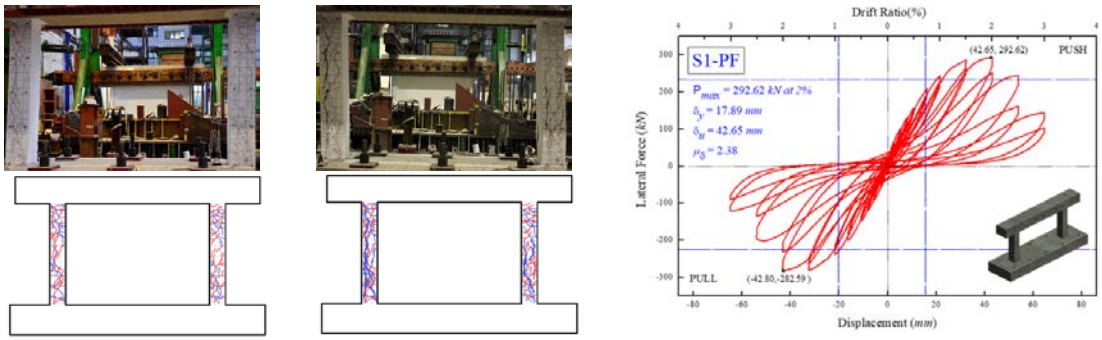

(a) (b) (c)

Figure 3. Cracking patterns and failure status of specimen S1-PF at (a) drift ratio 2% and (b) drift ratio 3%. (c) Hysteretic loop of specimen PF

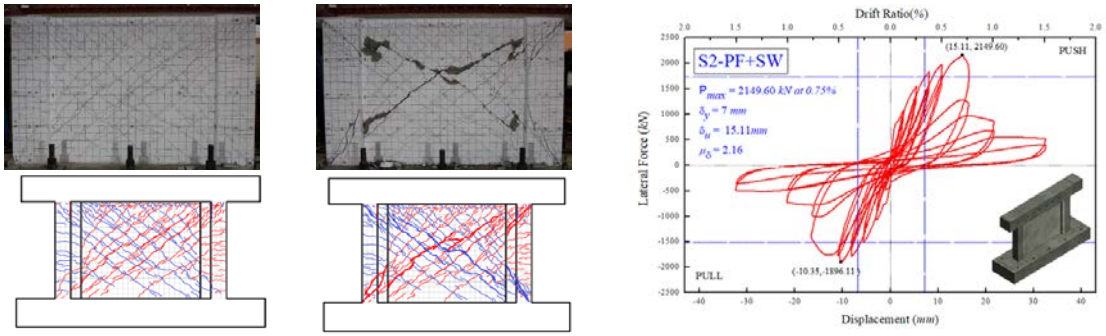

(a) (b) (c)

Figure 4. Cracking patterns and failure status of specimen S2 at (a) drift ratio 0.5% and (b) drift ratio 1.0%. (c) Hysteretic loop of specimen S2.

For specimen S2, during the 1.0% target drift cycles, spalling of concrete progressed diagonally to the upper and lower corners of the wall. Concrete deterioration of the wall worsened, which resulted in the lateral strength dropping to about 50% of the maximum strength. The specimen failure can be characterized as the in-plane shear failure at the retrofit wall web, and the failure mode is as expected of the retrofit design. Figure 4(a), (b) shows the photos of the failure status of specimen S2 at drift ratios 0.5% and 1.0%, respectively. And the hysteretic loop of this specimen is shown in Figure 4(c). Figure 5(a), (b) shows the photos of the failure status of specimen S3 at drift ratios 0.5% and 1.0%, respectively. And the corresponding hysteretic loop of this specimen is shown in Figure 5(c).

CONCLUSIONS

This study is to investigate the retrofit effect of a non-ductile RC frame using improved shear walls without/with an opening. The failure mode of the test results is as expected the shear failure of the

wall panel, which shows that the retrofit method and construction details proposed in this study can effectively improve the old RC structures to achieve their designed strength and deformation capacity. The high-strength mortar blocks on the interface between the post-installed wall and the existing beam can avoid the occurrence of unexpected shear friction failure mode. The internal end columns and RC shear wall with a lower amount of reinforcement not only ensure the stress transfer mechanism between the infill wall and the existing boundary column but also reduce the seismic demand of the existing foundation. The test results also show that the appropriate openings in the shear wall not only meet the requirements of lighting and ventilation but also provide enough strength capacity.

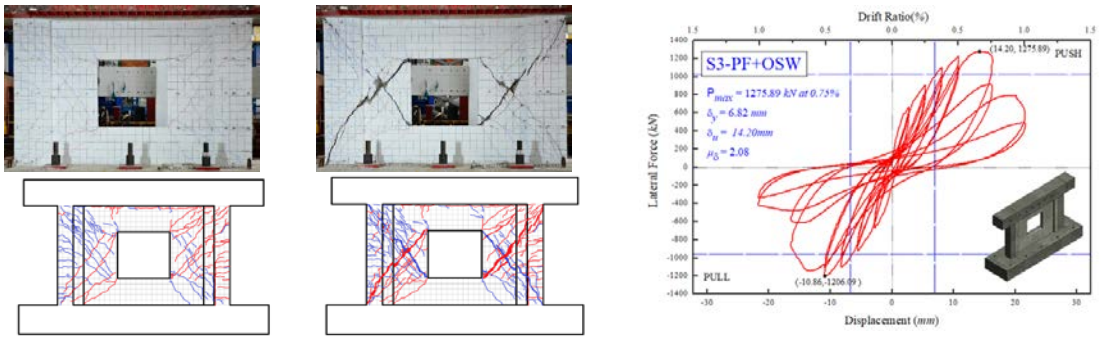

(a) (b) (c)

Figure 5. Cracking patterns and failure status of specimen S3 at (a) drift ratio 0.5% and (b) drift ratio 1.0%. (c) Hysteretic loop of specimen S3

ACKNOWLEDGMENTS

The authors would like to thank the Ministry of Science and Technology of the Republic of China, Taiwan, for financially supporting this research under contract MOST 107-2221-E-027-010. The facilities for research provided by National Center for Research on Earthquake Engineering are also highly appreciated.

REFERENCES

[1] Galal, K., and El-Sokkary, H. (2008) Recent Advancements in Retrofit of RC Shear Walls. The 14th World Conference on Earthquake Engineering, Beijing, China, October 12-17.

[2] Jirsa, JO., Kreger ME. (1989), “Recent research on repair and strengthening of reinforced concrete structures”, In: Kircher CA, Chopra AK, editors. Seismic Engineering, ASCE, 1989, p. 679–688.

[3] Altın S, Ersoy U, Tankut T. (1992), “Hysteretic response of reinforced concrete infilled frames”, ASCE J Struct Eng., vol. 118, no. 8, pp. 2133–2150.

[4] Altin, S., Anil, Ö. and Kara, M.E. (2008), “Strengthening of RC nonductile frames with RC infills: An experimental studies”, Cement and Concrete Composites, vol. 30, no. 7, pp. 612–621.

[5] Liao, W.I., Hsiao, FP., Chiu CK., Ho, CE. (2019), “Structural health monitoring and interface damage detection for infill reinforced concrete walls in seismic retrofit of RC frames using piezoceramic-based transducers under the cyclic loading”, Applied Sciences 9(2):312, DOI: 10.3390/app9020312

[6] Chiu CK., Fu-Pei Hsiao, Wen-I Liao, Samuel Jonathan Quacoo, Chin-En Ho, Zi-En Gu (2019), “Retrofitting non-ductile RC frames for seismic resistance using post-installed shear walls”, ASME 2019 Pressure Vessels & Piping Conference, July 14–19, San Antonio, Texas, USA. DOI: 10.1115/PVP2019-93399

[7] Japan Building Disaster Prevention Association (JBDPA, 2017), Guideline for Seismic Retrofit Design of Existing Reinforced Concrete Buildings. (in Japanese)

[8] Okumura H., Niino E., Takada S., Nakano Y., and Tsutomu Ohta T., (2000), “Seismic Retrofit of RC School Building using Post-installed Walls with Openings”, The 12th World Conference on Earthquake Engineering, Auckland, New Zealand, January 30- February 4.

TAIWAN-THAILAND COLLABORATIVE PROJECT ON SEISMIC STRENGTHENING OF SOFT-STORY SCHOOL BUILDINGS IN NORTHERN THAILAND

Sutat Leelataviwat[1], Pennung Warnitchai[2], Fu-Pei Hsiao[3], Pu-Wen Weng[3]
Shyh-Jiann Hwang[3], and Nattakarn Naiyana[1]

[1]King Mongkut's University of Technology Thonburi, Thailand
[2]Asian Institute of Technology, Thailand
[3]National Center for Research on Earthquake Engineering, Taiwan

Email: sutat.lee@kmutt.ac.th

ABSTRACT

This paper summarizes the collaborative project between Taiwan and Thailand on seismic strengthening of soft-story school buildings in northern Thailand. Following the 2014 Mae Lao Earthquake in northern Thailand, several soft-story school buildings were damaged due to the earthquake demonstrating the inherent weaknesses of these buildings. As a result, a collaborative project between Taiwan and Thailand was carried out to assess the techniques for strengthening of these buildings. Three school buildings located in northern Thailand having the same structural framing and details were strengthened using the concrete jacking method. Background works that formed the basis of the project are briefly discussed. Details and studies regarding the effectiveness of the selected strengthening method are also provided.

Keywords: Seismic Strengthening, Thailand, Taiwan, RC Jacketing

INTRODUCTION

In the past, Thailand is generally thought to be located in an area with low seismic risk. However, since 1975, there have been reports of low- to moderate-sized earthquake activities causing slight damage to buildings. These seismic activities have raised the awareness among the public. Seismic design requirements were finally imposed in 2009. Since then, there has been a change in the design and construction practice to enhance building safety. Despite the new regulations, when a magnitude 6.3 earthquake occurred in Mae Lao, Chiang Rai Province, on May 5th 2014, several school and other buildings were damaged [1]. The earthquake strongly demonstrated the vulnerability of school buildings in seismically active areas in Thailand. Seismic strengthening of these buildings has become a crucial safety issue. As a result, a collaborative project between the National Center for Research on Earthquake Engineering, Taiwan, Asian Institute of Technology, and King Mongkut's University of Technology, Thailand, was carried out to assess the techniques for strengthening of these buildings. Three school buildings were selected for retrofitting in a pilot project to evaluate suitable technology for Thailand and to serve as demonstration sites (Figure 1). A number of retrofitting schemes for RC frames developed in the past were evaluated. This paper focuses on summarizing the Taiwan-Thailand collaborative project. Background works that formed the basis for this Taiwan-Thailand project are presented. Relevant technical details are also presented.

THE 2014 MAE LAO EARTHQUAKE

The earthquake occurred on 5 May 2014 at 11:08:42 UTC. The magnitude was estimated by the Thailand Metrological Department to be 6.3 M_L with a 7 km hypocentral depth near Mae Lao, a small town in Chiang Rai in northern Thailand near the borders between Thailand, Myanmar, and Laos (Figure 1). The earthquake was believed to have occurred along the northeast–southwest left-lateral strike slip Mae Lao fault [1]. This fault is part of the Phayao

active fault zone in the northern part of Thailand. A number of aftershocks followed the main shock, typical for an earthquake of such magnitude. The highest PGA of the main shock as recorded by the instruments nearby was 0.33g at Mae Suai Dam (MSAC) station located at approximately 14 km away from the epicenter. Even though this station was located at the top of the dam and the recorded data was likely to be influence by the dynamic response of the dam, the ground shaking was considered to be one of the highest in Thailand modern time [1]. The ground shaking intensity near the epicenter was estimated to be in the range of Modified Mercalli Intensity (MMI) VII to VIII causing damage to building structures in the 50 km radius.

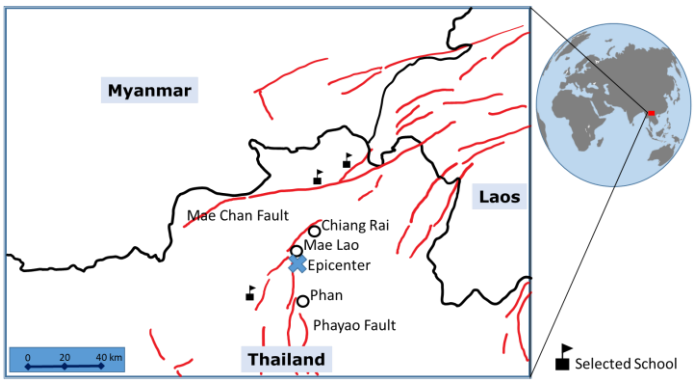

Figure 1. Map of the 2014 Mae Lao Earthquake.

Immediately after the earthquake, the authors conducted a reconnaissance damage survey of several school buildings in the area. Although the buildings inspected were only a small fraction of the buildings damaged by the earthquake, the inspection did provide valuable information as to the strengths and weaknesses of existing school building structures in Thailand. The construction of a typical Thai school is generally based on standard drawings issued by the government with minor modifications to suit local requirements. The design and drawings are normally prepared by engineers appointed by the relevant agency. Because of this, these buildings share similar architectural and structural features. They are usually 2-4 stories in height and are constructed using reinforced concrete. Masonry infill walls are used as partitions. The infill walls are normally made from concrete masonry units, 7-cm thick, with plaster, 2-3 cm think, on both sides. The plan is rectangular in shape. There are normally 6-8 bays in the longitudinal direction and only 1-2 bays in the transverse direction. Although these schools can be considered engineered buildings and many can be considered well-built, most of them were constructed prior to the enforcement of seismic design regulations and were designed only for the gravity loads. Hence, some of these schools lack the lateral strength and ductility required to sustain the ground shaking.

Several other factors also contributed to the vulnerability of these school buildings. The school buildings are generally designed in such a way that they have wide open spaces in the first story for assembly and school activities with minimal amount of infill walls. Compared to the upper stories where classrooms are located and infill walls are used to separate the rooms, the first story is generally much weaker. Under an earthquake the deformation tends to concentrate in the first story where the story shear is generally largest. In addition, because of the wide span length between columns, the beams tend to be generally stronger than the columns exacerbating the soft story problem. The result is that the columns will be damaged while the beams remain almost intact. Figure 2 shows one particular school and its damage pattern. This school building is a 3-story frame structure located in Phan around 20 kilometers south of the epicenter. On one side of the building, masonry infill walls were provided around the staircase. The rest of the ground floor was fully open. The columns were severely damaged as seen from

the figure. The damage pattern indicated that the building moved in a twisting manner in addition to the characteristic soft-story deformation. There was no observable damage to the beams indicating the building responded as “strong beam-weak column” frame. This pattern was undesirable as it could lead to excessive sideways, potentially leading to collapse.

Figure 2. School building damaged by soft story and torsional irregularity.

Although some of these non-ductile structures were severely damaged due to the Mae Lao earthquake, a large number of these buildings survived with only minor damage. This may be attributed to material and structural overstrength as well as the presence of very strong infill walls which contributed significantly to the reserved strength. Hence, lack of ductile detailing may not be the lead cause of the damage but only an important contributing factor. It was observed that the building structures that suffered severe damage were those that also possessed irregularities such as soft-story or torsional irregularities. One of the main strategies to strengthen these non-ductile structures is to increase the lateral strength of the frame such that it is sufficient to inhibit the inelastic deformation especially in the first story. Hence, the technique such as column jacketing is well suited for this type of frame.

DETAILS OF PROTOTYPE FRAMES

Three school buildings were selected for retrofitting in a pilot project to evaluate suitable retrofitting technology for Thai school buildings. Based on the observed weakness described in the previous section, it was decided that soft-story was the most important aspects to eliminate. The overview of one of the buildings and the key plans are shown in Figure 3.

Figure 3. The overview of the study building before retrofitting.

RETROFITTING DESIGN

Strengthening with Concrete Jacketing

As mentioned, increasing the lateral strength is desirable for the soft-story frame. In Concrete Jacketing method, concrete columns are enlarged by casting new concrete around existing columns. A number of retrofitting schemes for RC frames developed in the past were evaluated. It was found that concrete jacketing provided one of the best solutions in terms of performance, cost, and constructability. In this project, selective columns were jacketed. The final design consisted of jacketing alternate columns as shown in Figure 4. The rest of the columns were covered with brick wall to have the same size as the jacketed column for appearance reason. Figures 4 and 5 show the details of the retrofitting plan.

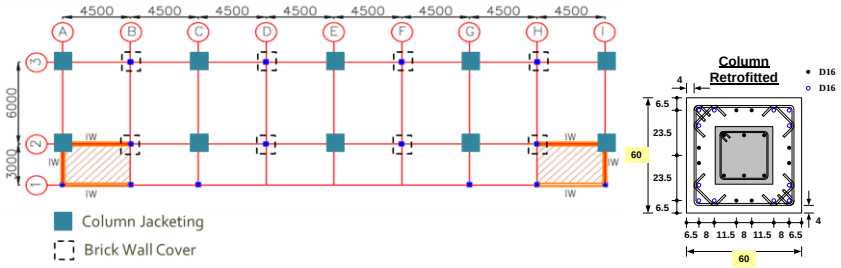

Figure 4. Building Plan and Location of Column Jacketing.

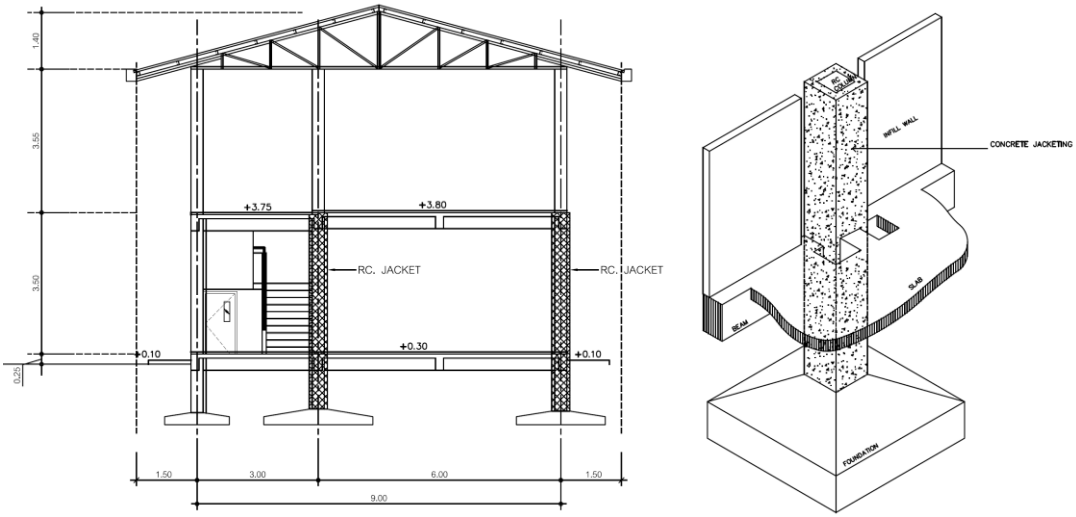

Figure 5. RC Jacketing Detail

It is well known that the bond interface between new and existing concrete are crucial in creating a compatible response between new and existing concrete [2]. In addition, the design is governed by minimum practical requirements for the thickness of the jacket as well as the minimum amount of longitudinal reinforcement in the new concrete. For this project, to save the construction cost and reduce the construction time, dowel bars were not used. An experiment was conducted to evaluate the effect of the dowel bars on the overall strength and stiffness of the jacketed column. Three columns were tested including the existing as-built column and the retrofitted columns with and without dowel bars. The columns were tested by the Multi-Axial Testing System (MATS) at the National Center for Research on Earthquake Engineering (NCREE) in Taipei, Taiwan. Selected test results are shown in Figure 6. As expected, the specimen with dowel bars showed larger strength. However, the strength increase was

approximately 10 percent only. More importantly, there was no significant change in the ductility between the two specimens. For this reason, the design without the dowel bars was eventually adopted.

Analytical models of the structures were also created using a computer software PERFORM 3D [3]. The performance assessment was carried out using inelastic static (pushover) and nonlinear dynamic analysis. The nonlinear dynamic analysis was used to examine the behavior of the structure at the selected level ground motion intensity. The results showed that, because of the increase in the stiffness, the foundation below the jacketed columns were overstressed. Therefore, those foundation were also enlarged. Construction began in 2021. Figure 7 shows the jacketed columns during construction. As can be seen, the jacketing was also done for the columns below the ground level with the new rebars fully embedded into the foundation. The three buildings after the retrofitting are shown in Figure 8.

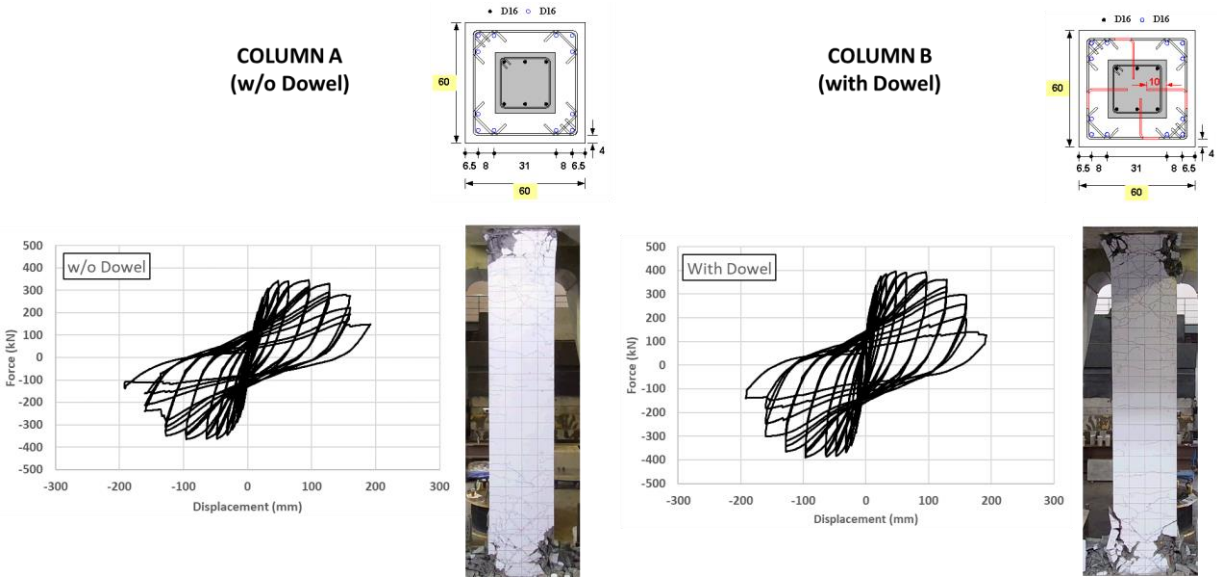

Figure 6. Sample test results of jacketed columns with and without dowel bars.

Figure 7. Column Jacketing during construction.

Figure 8. Three selected schools after retrofitting.

CONCLUSIONS

This paper summarizes the collaborative project between Taiwan and Thailand on seismic strengthening of soft-story school buildings in northern Thailand. A collaborative research effort between Taiwan and Thailand was carried out to assess the techniques for strengthening of these buildings. RC column jacketing was selected as the most versatile and effective way to strengthen this type of structure as it could significantly increase the strength and stiffness of the structure. Three school buildings located in northern Thailand having the same structural framing and details were strengthened using this technique. The project was completed in 2021.

ACKNOWLEDGMENTS

The retrofitting project was supported by the funding from Ministry of Science and Technology (MOST) and the National Center for Research on Earthquake Engineering, Taiwan. The authors gratefully acknowledge the supports from the above agencies. However, the findings and conclusions in this paper are those of the authors and may not necessarily reflect the views of the sponsors.

REFERENCES

1. Ornthammarath, T, and Warnitchai, P. (2016) “5 May 2014 MW 6.1 Mae Lao (Northern Thailand) Earthquake: Interpretations of Recorded Ground Motion and Structural Damage” Earthquake Spectra, 32 (2): 1209–1238.
2. Vandoros, K.G. and Dritsos, S.E. (2008) “Concrete jacket construction detail effectiveness when strengthening RC columns” Construction and Building Materials, 22, 264–276.
3. CSI. 2007. PERFORM 3D user’s manual version 4.0. Computer and Structures Inc., Berkeley, CA, USA.

SEISMIC RETROFITTING OF 100-YEARS OLD 7-STOREYS RC BUILDING USING VISCOELASTIC DAMPERS

Ruel B. Ramirez[1], Nirmala Suwal[2], and Jonathan M. Zabala[3]
1. Principal Structural Engineer, RBRA Consulting Engineers, Manila, Philippines.
2. Structural Engineer, RBRA Consulting Engineers, Manila, Philippines.
3. Structural Engineer, RBRA Consulting Engineers, Manila, Philippines.
Email: rbra_engrs@yahoo.com

ABSTRACT

The energy dissipating property of viscoelastic dampers (VED) has been widely used by many Structural Engineers to improve the performance of existing and new buildings to seismic excitation. The mechanism of VED is to dissipate the mechanical energy of the structure by converting it to heat hence, significantly improving the damping characteristic of the structure. In this study, the bilinear property of VED was used to improve the overall seismic performance of the existing 7-storey 100-year-old reinforced concrete building in Manila, Philippines. To validate the improved performance of the structure to an earthquake with VED, three types of analysis were made, 1) No retrofitting, 2) With Steel Bracing, and 3) With Viscoelastic Dampers. The comparative study of retrofitting the structure with steel bracing and viscoelastic damper shows that viscoelastic damper significantly reduces the seismic demands (floor acceleration and lateral story drift) as compared to using steel bracing. On the other hand, steel bracing increases the base shear and base moment which has a higher chance of damaging the foundation system. This study shows that the VED significantly improves the performance of the building to earthquake compared to traditional steel bracings.

Keywords: Retrofitting, Earthquake, Steel Bracing, Viscoelastic Damper

INTRODUCTION

The Valley Fault System (VFS) that traverse Metro Manila and is expected to generate magnitude 7.2 is a threat to populace not because of the power of the seismic, but because buildings are vulnerable to it! Historically, the cause of deaths and injuries during an earthquake is attributed to the damage of man-made structures. Currently, thousands of earthquake records are available in many sources such as USGS or PEER that Structural Engineers can use in their design. However, implicit in most building codes (ASCE 41-17, ACI-318-14M), the concept of design remains the same, that structural components absorb the earthquake shock through nonlinear behavior of the material which eventually, the culprit of damage in buildings.

In modern days, the structural engineering community is inclined to a resilient-based approach incorporating new engineering innovations to mitigate the damages to buildings during an earthquake. This study aims to present the performance of the 100-year-old reinforced concrete building in Manila retrofitted using the viscoelastic damper (VED). This existing RC structure is composed of moment frames and based on the concrete test following ASTM C42, the average compressive strength is 17MPa. Also, reinforcing bars were made of twisted square bars with a tensile strength of 538MPa.

The existing floor plan layout and isometric 3d view of the un-retrofitted structure are shown in Figure 1(a) and Figure 1(b).

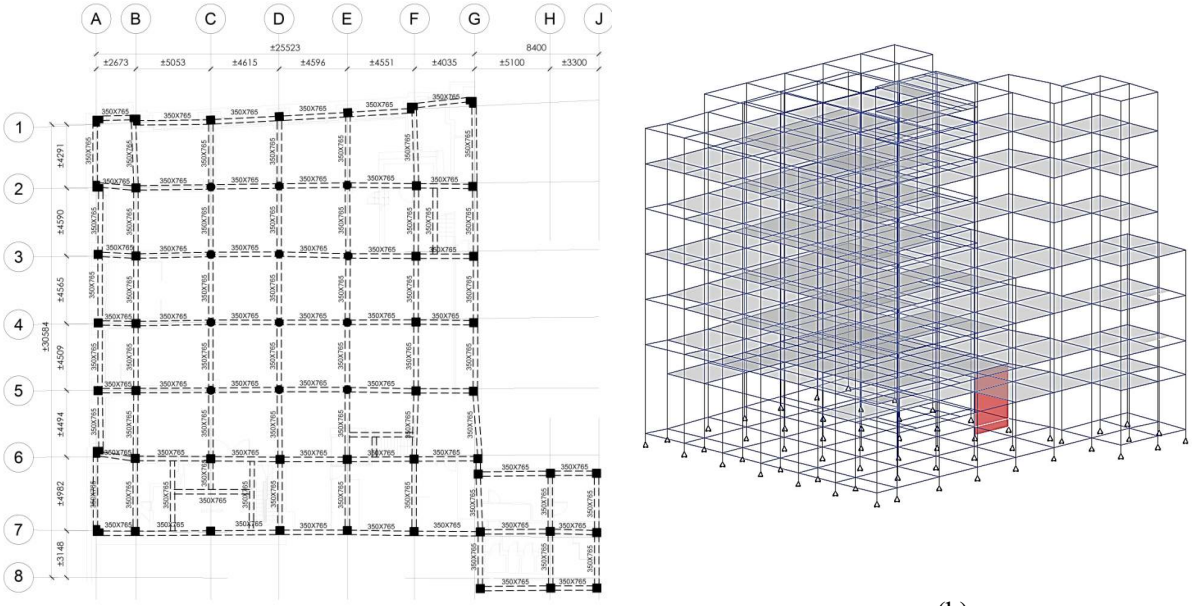

(a) (b)

Figure 1. (a) Existing structural layout plan and (b) 3D isometric view of the case study building.

METHODOLOGY

In this study, retrofitting schemes are investigated by analyzing the existing structure with conventional steel bracing and by using VED. Steel bracing reduces the lateral structural drift of structure during earthquake. On the other hand, VED dissipates seismic energy by transforming mechanical energy to heat energy. To compare the performance of the existing structure with conventional steel bracing and VED, a non-linear time history analysis (NLTHA) was performed for each case. First, as the baseline, the existing structure was analyzed based on the details of the as-built plan taken from the building site (see Figure 1). Second, the building was analyzed with steel braces as shown in Figures 2(a) and 2(b). Finally, the third case, VED was installed in the steel braces to allow flexibility in the steel braces.

Structure with Conventional Steel Bracing

Steel bracing is traditionally used as a retrofitting technique to strengthen the existing buildings against lateral load due to earthquakes. It provides lateral stiffness to the structure and reduces the story drift during strong earthquakes. The proposed locations of the steel bracing in the existing structure are shown in Figures 2(a) and 2(b).

Structure with Viscoelastic Damper (VED)

Viscoelastic dampers (VEDs) dissipate seismic energy by converting mechanical energy into heat energy during a severe earthquake. It also effectively dissipates the wind load in high-rise structures (Aung et al., 2018). In this study, the performance of the 100 years old structure is investigated using the VEDs. The layout of VEDs is shown in Figure 2(a) and elevation is shown in 2(c). Figure 3(a) gives an idea of the picture of VED and 3(b) shows the bilinear property of VED. Table 1 is the list of the properties of VEDs.

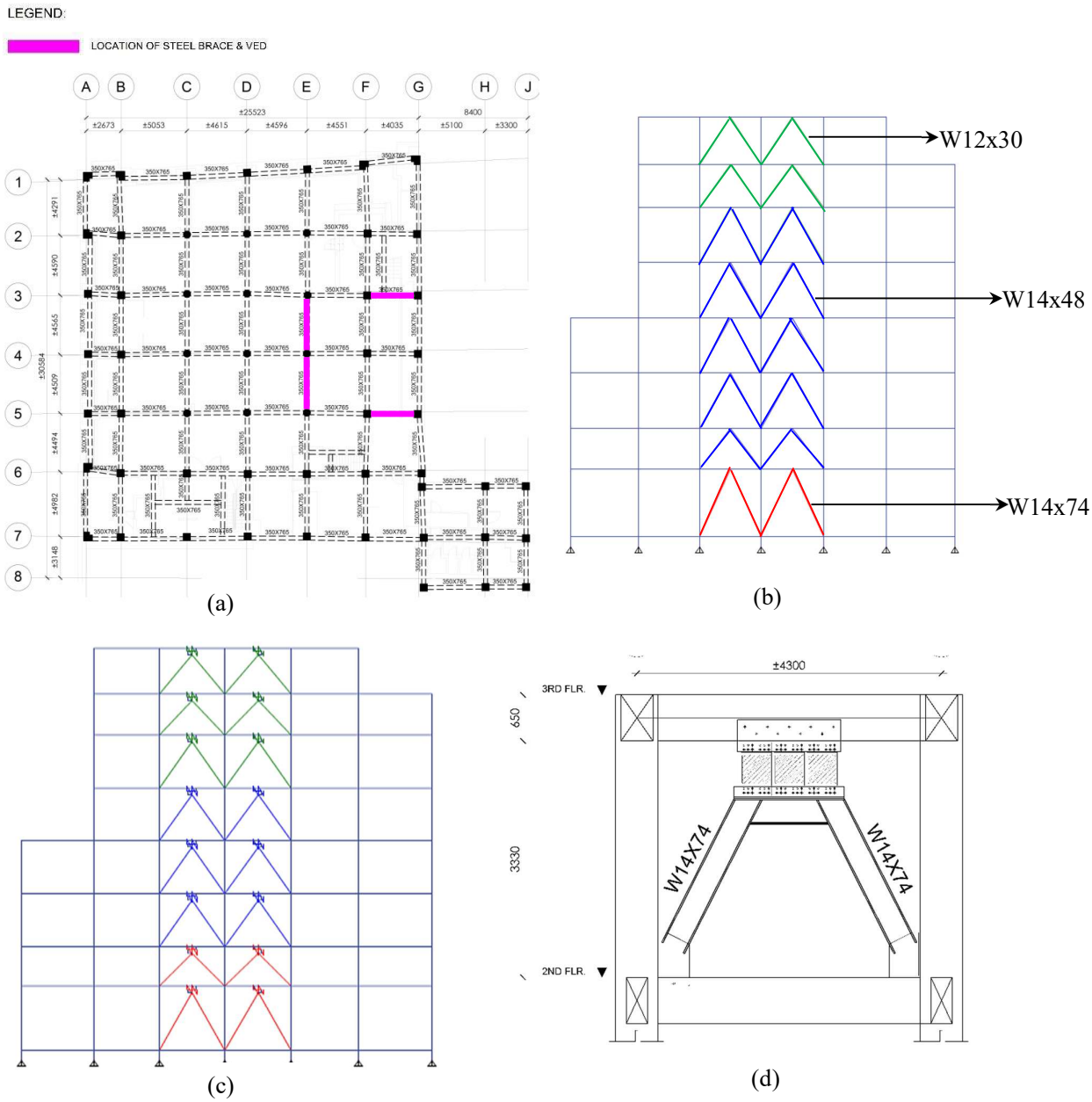

Figure 2. (a) Proposed location of steel bracing and VED in the layout plan, (b) Elevation of steel bracing retrofitting, (c) Elevation of structure with VED, and (d) detailing of VED.

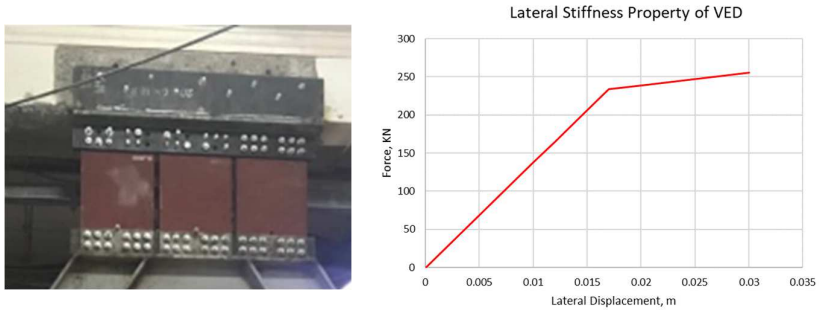

Figure 3. VED and the lateral stiffness property

Table 1. Property of VED

	Ground Floor to 2nd Floor	3rd Floor to 5th Floor	6th floor to Roof
Lateral stiffness	41310 KN/m	27540 KN/m	13770 KN/m
Yielding Force	660KN	440 KN	220KN
Damping Coefficient	59220 KN-s/m	39480 KN-s/m	19740 KN-s/m

Nonlinear Time History Analysis

A set of seven real ground motion records are used including near field and far-field ground motions. The response spectrum and characteristics of each ground motion are shown in figure 4 and Table 2, respectively.

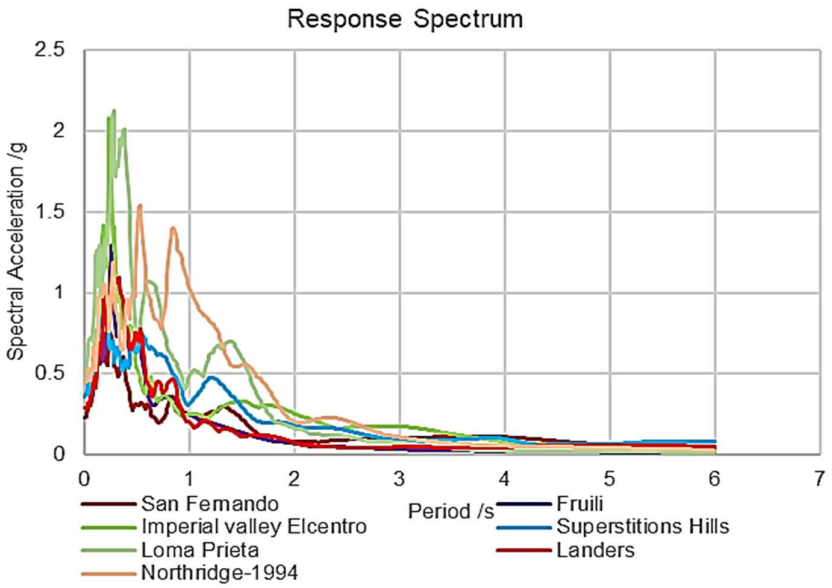

Figure 4. Response spectrum of seven ground motions

Table 2. Characteristics of selected ground motions

Ground Motions	**Station**	**Magnitude**	**PGA**
Imperial Valley	El Centro	6.59	0.31g
Northridge	Beverley Hills	6.9	0.44g
Loma Prieta	Poe Road	6.93	0.52g
Loma Prieta	LGPC	6.93	0.78g
Landers	Lucerne	7.28	0.54g
Chi-Chi	CHY-028	7.62	0.5g
Chi-Chi	TCU-049	7.62	0.21g

Results

Modal properties of structural analysis

The modal time period and mass participation ratio for three different cases are presented in Table 3 below. The result shows that steel bracing reduces the fundamental period of structure compared to that of VED. This implies that steel bracing will make the structure more rigid that will attract more seismic energy.

Table 3. Modal properties of structural analysis

Mode	No Retrofitting			With Steel Bracing			With Viscoelastic Damper		
	Period, sec.	Mass Participation Factor		Period, sec.	Mass Participation Factor		Period, sec.	Mass Participation Factor	
		X-Direction	Y-Direction		X-Direction	Y-Direction		X-Direction	Y-Direction
1	1.353	0.05	0.77	0.99	0.00	0.67	1.29	0.15	0.56
2	1.352	0.01	0.78	0.87	0.69	0.67	1.27	0.73	0.72
3	0.481	0.68	0.78	0.34	0.70	0.82	0.46	0.78	0.78
4	0.47	0.68	0.87	0.33	0.83	0.82	0.45	0.83	0.83
5	0.32	0.69	0.89	0.23	0.83	0.88	0.30	0.85	0.84
6	0.32	0.82	0.89	0.21	0.88	0.88	0.29	0.82	0.89
7	0.25	0.86	0.90	0.16	0.89	0.91	0.23	0.90	0.90
8	0.24	0.89	0.90	0.15	0.91	0.91	0.22	0.91	0.92

Lateral Response Comparison of Nonlinear Time History Analysis

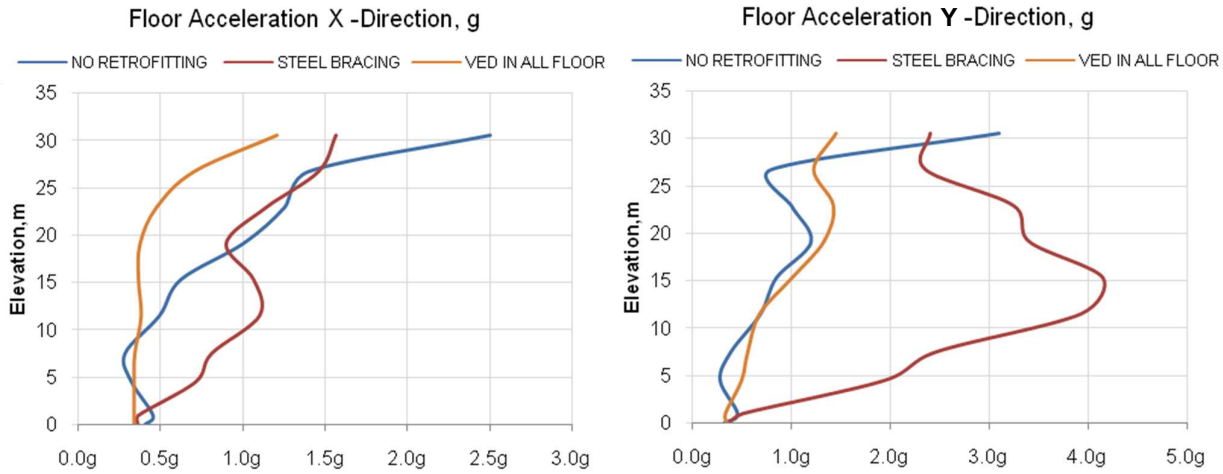

Figure 5. Comparison graph for floor acceleration

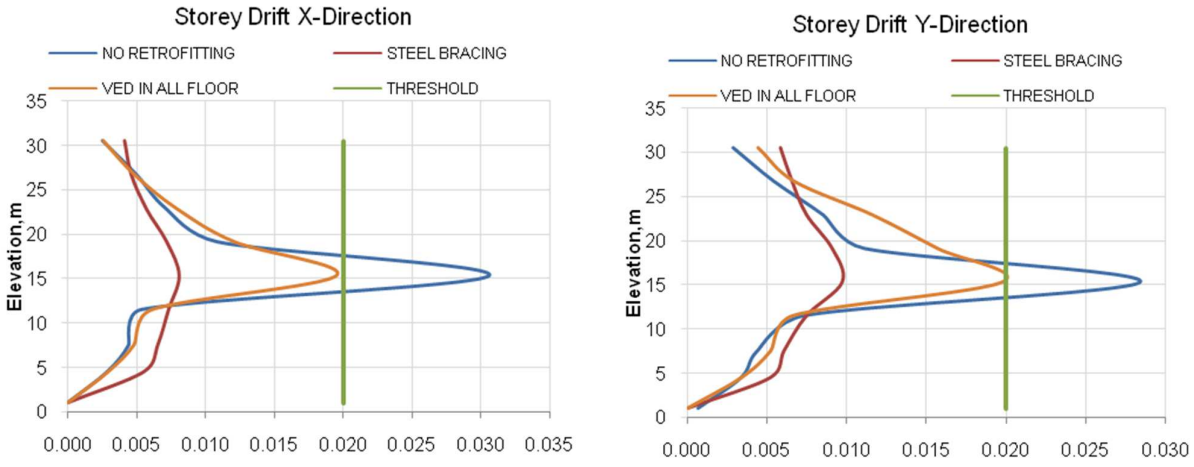

Figure 6. Story drift in X and Y directions

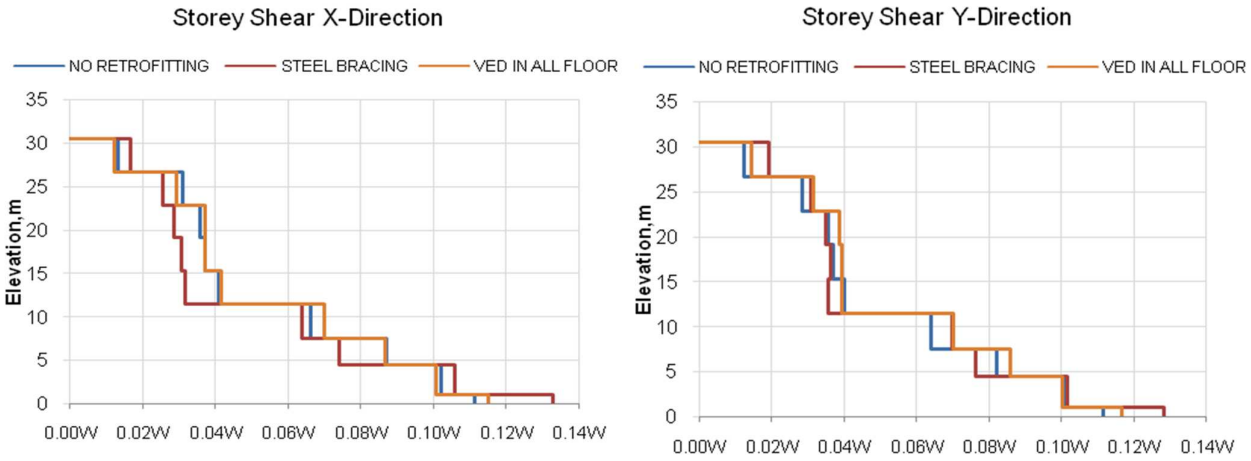

Figure 7. Story shear in X and Y directions

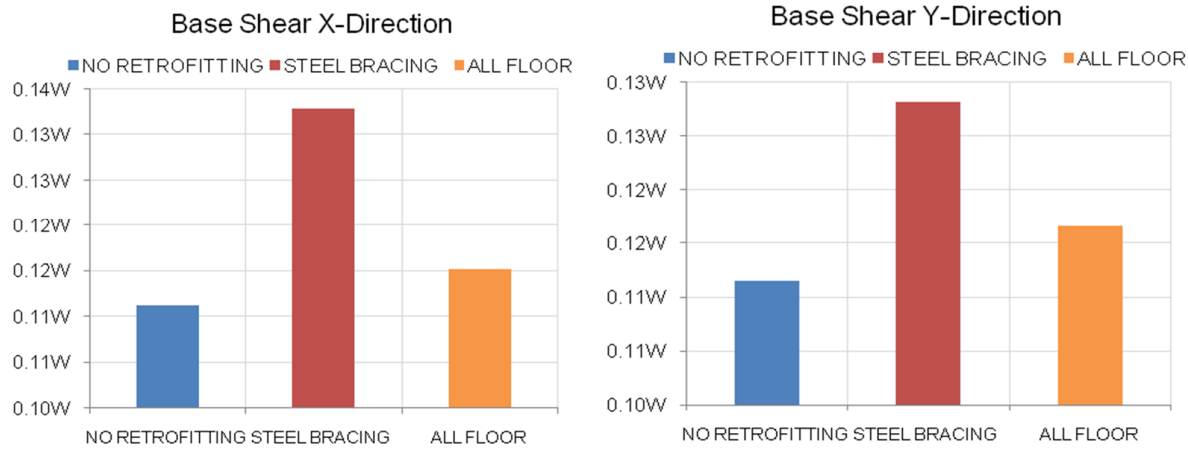

Figure 8. Base shear in X and Y directions

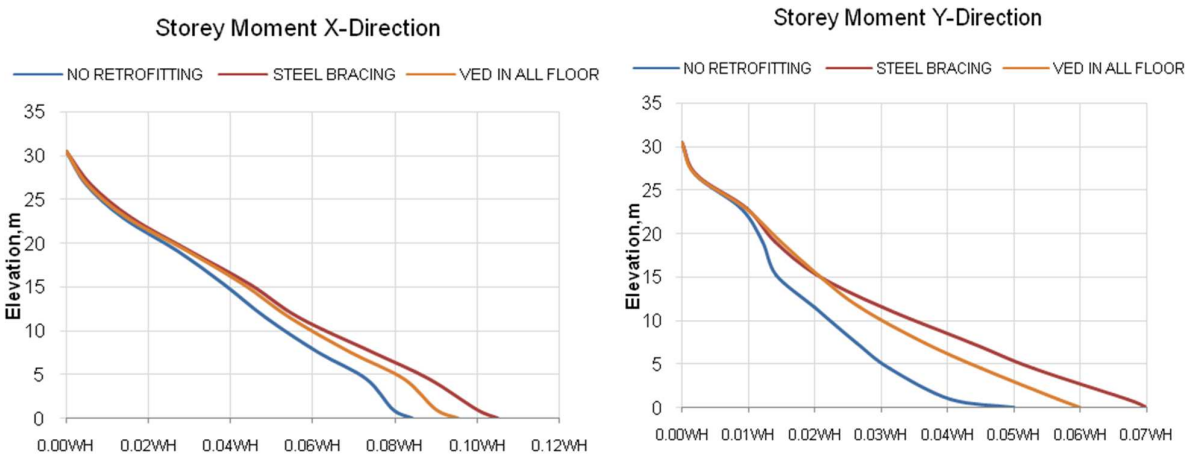

Figure 9. Story moment in X and Y directions

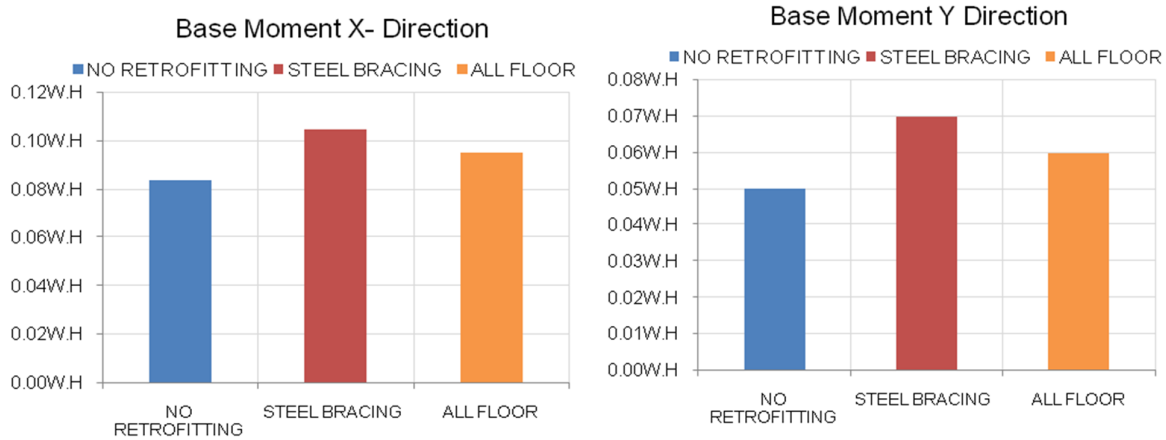

Figure 10. Base moment in X and Y directions

The lateral responses are shown in Figure 5 to Figure 10. In Figure 5, when the structure is steel braced, top floor acceleration reduces by 37.3% and 22.4% in X and Y directions respectively, whereas VED reduces the top floor acceleration by 51.8% and 53.2% in X and Y directions respectively with reference to un-retrofitted case. However, on the 4th floor, steel braced increases floor acceleration by 4.8 times of an un-retrofitted case and 4 times of a VED case. Secondly, in figure 6, steel braced reduces the maximum story drift by 73.7% and 65.8% in the X and Y directions, whereas VED reduces by 36.2% and 30.5% in Y-direction respectively with respect to the un-retrofitted case. In figure 7, story shear is shown for three cases. Steel braced case increases the base shear by 19.5% and 14.9% in the X and Y direction respectively, whereas VED increases base shear by 3.5% and 4.5% in the X and Y directions respectively as shown in figure 8. Similarly, the story moment is shown in figure 9. Steel braced increases base moment by 24.7% and 40% in X and Y directions respectively, whereas VED increases base moment by 13.3% and 20% in X and Y directions respectively as shown in figure 10.

CONCLUSIONS

Conventional retrofitting with Steel bracings stiffens and strengthens the structure and reduces the inter-story drift. However, it attracts more seismic energy which increases the base shear, the overturning moment that could damage the existing foundation system. Also, the increased floor acceleration could damage the content of the building. Using VED, the structural responses such as the story drift and floor acceleration are reduced significantly. Compared to steel bracing, VED is more effective to dissipate seismic energy as compared to the conventional retrofitting using steel bracing which may damage the foundation of the structure.

REFERENCES

ACI Committee 318, (2014). "An ACI standard: Building Code Requirements for Structural Concrete (ACI 318M-14) and Commentary (ACI 318RM-14)," American Concrete Institute, Farmington Hills, MI 48331, 1–524 pp.

ASCE 41-17, (2017). "ASCE 41-17: Seismic Evaluation and Retrofit of Existing Buildings," American Society of Civil Engineers (ASCE), 623 pp.

T.H. Aung, M. Shabir, W. Karlken & N. Answer, (2018). "Case Study: Performance-based Seismic Design of Bearing Wall System Building with Viscoelastic Coupling Dampers in Outrigger System," *The 7th Asia Conference on Earthquake Engineering*, Bangkok, Thailand.

(3b) Design for control of seismic damage

EXPERIMENTAL INVESTIGATION ON ISOLATED STRUT BEHAVIOR OF HIGH STRENGTH STEEL FIBER REINFORCED CONCRETE PANELS

Chia-Chun Kuo, Chung-Wen Hung, Wen-Cheng Liao, and Suyash K. Wagh
Department of Civil Engineering, College of Engineering, National Taiwan University, No.1, Sec.4, Roosevelt Road, Taipei 10617, Taiwan, R.O.C.
Email: R06521229@ntu.edu.tw, R07521220@ntu.edu.tw, wcliao@ntu.edu.tw, D08521030@ntu.edu.tw

ABSTRACT

Fifty-one concrete panels with two different aspect ratios were tested under compression loading condition to evaluate the isolated strut behavior of high strength steel fiber reinforced concrete and addition of steel fiber as alternative to transverse reinforcement. The test results indicated that adequate addition of steel fibers not only exhibit better tensile strength and crack control characteristics but also change the mode of failure of the panel from splitting of the strut to crushing and can replace certain amount of transverse reinforcement for better construction workability. Fiber volume content, location and amount of the transverse reinforcement are found to influence the cracking and ultimate strength of the panel. The panel test results facilitate further development of bottle shaped strut-and-tie model.

Keywords: steel fiber, high strength concrete, panel, isolated strut, strut-and-tie model

INTRODUCTION

High strength reinforced concrete has been widely used in high-rise buildings for several years; however, concrete becomes more brittle with increase in compressive strength. Taiwan New RC Project using high strength concrete along with high strength rebars to reduce the member section sizes and to save material consumption have been conducted since 2009. However, the brittle failure modes owing to the nature of high strength concrete could be a major concern. To mitigate brittle behavior in high shear demanding area, such as beam-column joints, the demand of shear reinforcement is more as per the design codes. This fact results in steel congestion and construction difficulties. Steel fiber reinforced concrete (SFRC) is a structural material characterized by significant ductility, residual tensile strength, and post-cracking toughness. These advantages are due to the bridging effect of steel fibers over the cracks which also reduces crack width and spacing (Susetyo *et al.*, 2011; Kuo, 2019; Hung, 2020). Moreover, SFRC is expected to enhance shear strength and replace certain amount of transverse reinforcement for better construction workability.

Modeling and detailing of the shear critical concrete members can be done reliably with the strut-and-tie method with presumption that, the network of struts and ties transfer the applied load at the interconnected nodes (Sahoo *et al.*, 2008; 2009). Struts basically regulates the flow of compression within a concrete member. Bottle-shaped struts are the most common formation of struts in shear critical regions where the load is applied to a relatively small area of the member. This leads compression to spread out from the support causing tension in the transverse direction of the applied loads as shown in figure 1. Increase in tension beyond tensile strength of concrete can form the tensile cracks in the direction of applied force. To avoid this situation, transverse reinforcement is provided.

According to many experimental results, adding steel fibers in concrete can notably enhance ductility, tensile strength, shear strength and avoids early cover spalling in case of high strength concrete (Liao *et al.*, 2017; Liao and Su, 2018). Fibers can be an alternative to transverse reinforcement to solve the congestion problem. The objective of this study is to investigate the isolated strut behavior of high strength steel fiber reinforced concrete panels for further development of bottle-shaped strut-and-tie model. Series of panel experiments were conducted by varying the parameters such as panel aspect ratio, volume fraction of steel fibers, location and ratio of transverse reinforcement. The test result shows that when adding steel fiber in concrete, specimens with brittle splitting failure could change its failure mode

to concrete crushing. Both cracking strength and ultimate strength increase with the presence of steel fiber. It indicates that apart from reinforcement ratio, location of reinforcement is one of the important design factors.

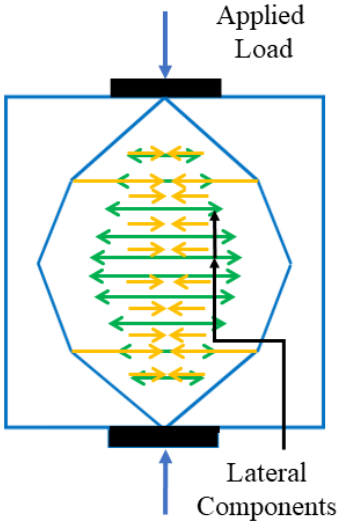

Figure 1. Strut in the panel element with lateral components

EXPERIMENTAL PROGRAM

Specimen Design and Material Properties

A total of 24 square panels of size $90 \times 90 \times 10cm$ (Aspect ratio 1) and 27 rectangular panel specimens of size $120cm \times 60cm \times 15cm$ (Aspect ratio 2) were constructed and tested under uniaxial compression test. To study the effect of parameters on the performance of FRC panels such as fiber volume content, concentration ratio (b/a) (where, b is half-length of symmetrically placed bearing plate and a is half-length of loaded face), aspect ratio of panel specimen, and the ratio and arrangement of transverse reinforcement are taken into consideration. Out of these parameters, fiber volume content, ratio and arrangement of transverse reinforcement were considered as main design parameters. Concentration ratio of 0.33 was obtained from the literature for effective development of transverse tensile forces. With aspect ratio 2, full width of the panel can be engaged with the bottle-strut while, aspect ratio with unity only engages the half the width of the panel. Influence of two different fiber volume content 0.75% and 1.5% were studied in this investigation. The yield strength (f_y), ratio and arrangement of transverse reinforcement was varied and compared with the other specimens to understand the resistance provided by the steel fibers in the transverse direction. Based on the design parameters, table 1 depicts four series of reinforcement layouts for specimens with aspect ratio 1 and 2. Specimens with different series and fiber percentage can be identified with the help of figure 2. All specimens were constructed in high strength steel fiber reinforced concrete with compressive strength 70 MPa. Thickness to height ratio as 0.111 and 0.125 is maintained respectively in the panels with aspect ratio 1 and 2. In literature this ratio is kept between 0.1 and 0.15.
Dramix RC80/30-BP hooked end steel fibers were used in the concrete mix. Before casting the specimens, strain gauges were sticked to the reinforcing bars for the purpose of understanding the stress distribution. Welding method was adopted for anchoring the reinforcement.

Test Setup and Loading Protocol

All the specimens were tested at the National Center for Research on Earthquake Engineering (NCREE) by using the compression testing machine with capacity of 500 tones. A symmetrically placed rectangular stiff steel plate were used at its loaded and supported ends. Figure 3 shows the arrangement of the specimen in the compression testing machine. NDI markers and strain gauges were sticked on the

surface of the concrete panel before testing to elucidate the stress and strain conditions while loading. To stabilize the specimen in the testing machine, 20 to 30 kN seating load was applied and later the specimen was loaded by considering the strain-controlled approach. The loading rate of 0.2mm/min and 0.3mm/min was adopted for the square and rectangular panels respectively. In square panels, before cracking, the lading was suspended after every 120 kN and the specimen was observed for any cracks and photographed. After cracking the loading was suspended after 60 kN. Similarly, for rectangular panels, loading was suspended after every 300 kN before cracking, and every 0.3 mm displacement after cracking.

Table 1. Reinforcement layout of specimens

Aspect Ratio: 1	**Bearing Plate: $30 \times 10 \times 5cm$**			
Panel Specimen [Square]	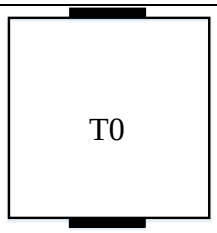	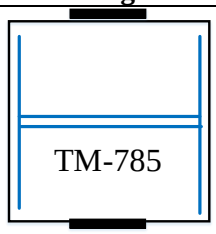	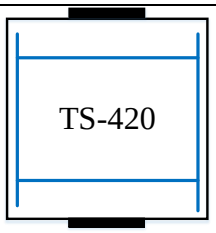	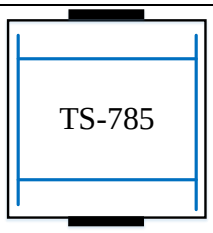
Spacing of Transverse Reinforcement (cm)	NA	4	60	60
Transverse Reinforcement Bar	NA	D13	D13	D13
Yield strength (f_y) MPa	NA	790	790	420
Aspect Ratio: 2	**Bearing Plate: $20 \times 15 \times 5cm$**			
Panel Specimen [Rectangle]	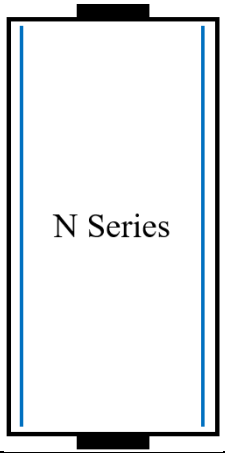	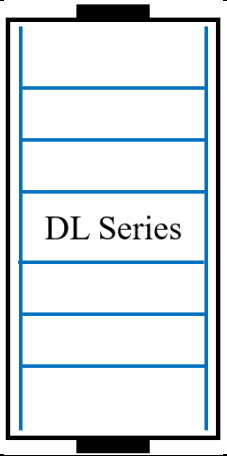	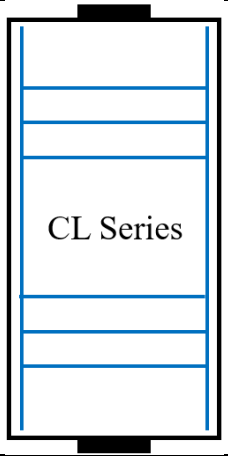	
Spacing of Transverse Reinforcement (cm)	NA	15	10	15
Transverse Reinforcement Bar	NA	D10	D10	D16
Yield strength (f_y) MPa	NA	841	841	848

[F075-TM7851] = Specimen - Aspect Ratio 1
Fiber Percentage 0.75 (0%, 0.75%, 1.5%) –
Series of Panel Specimen TM785 (T0, TM785, TS785, TS420)
Specimen Number 1 (1, 2)

[S075-DL1] = Specimen - Aspect Ratio 2
Fiber Percentage 0.75 (0%, 0.75%, 1.5%) –
Series of Panel Specimen DL (N, DL, CL, DH)
Specimen Number 1 (1, 2, 3)

Figure 2. Specimen Identification

Figure 3. Specimen Arrangement in Compression Testing Machine

TEST RESULTS

Overall Behavior

In the rectangular panels with series S075-N and S150-N (N is series and specimen identification number), despite of the presence of transverse steel, ultimate strength is higher than the cracking strength because of the presence of the steel fibers. Contrarily, in the panels from S0-N series, the cracking and ultimate strength recorded the same. Similar observations are made in the square panels from F075, F150, and F000 series. From figure 4(a) and 4(b) it is worth to note that the CL series exhibited the highest ultimate strength followed by the DH series. Even at lower reinforcement ratio in CL series, with effective reinforcement layout, the strength development is better than the specimens with high reinforcement ratio. Despite of the similar reinforcement layout in the DL and DH series, the strength observed in DH series is higher than DL series because of the higher reinforcement ratio. Higher reinforcement ratio results in the higher lateral tension resistance. In case of rectangular panels, Cracking, and ultimate strength of the SFRC panels after addition of 0.75% (S075) fibers was increased by 20% and 15% respectively. For 1.5% (S150) steel fibers addition, increase in cracking, and ultimate strengths are 40% and 30% respectively.

Cracking, and ultimate strength of the square SFRC panels after addition of 0.75% (F075) fibers was increased by 26% and 47% respectively. Similarly, these values were 35% and 41% in specimens with 1.5% (F150) steel fibers. For square panels without fibers, largest crack development rate, and crack width was observed in the T0 specimen without reinforcement before reaching the ultimate strength, while it was insignificant in the panels from TM785 series. Specimens from TS785 and TS420 series also indicated the increase in crack width with increased loading. Because of the large vertical crack width, brittle failure was occurred in the specimens from T0 series without fibers, and the specimen was split into two pieces instantly, accompanied by a loud noise as shown in figure 5.

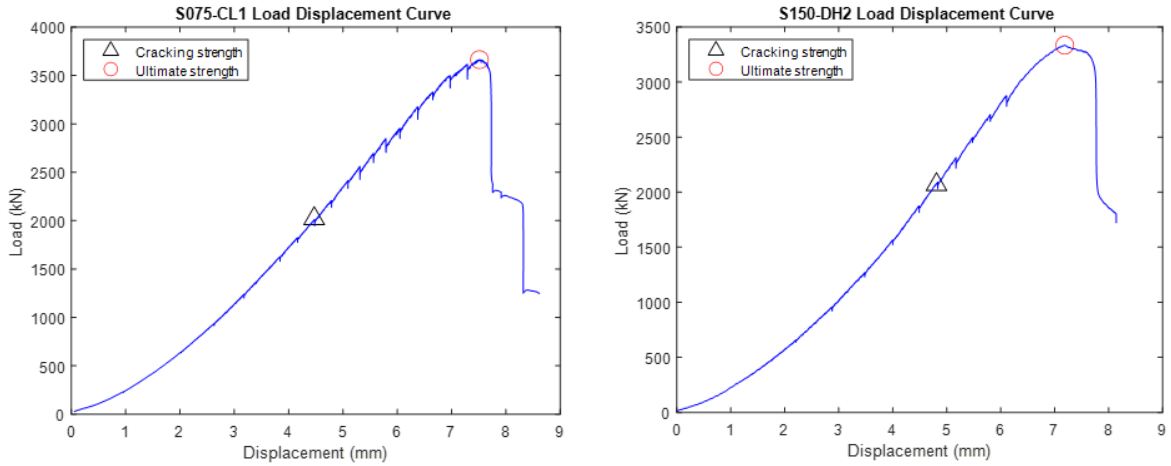

(a) Panel S075-CL1 (b) Panel S150-DH2

Figure 4. Load-Displacement Curve

In addition, because steel fibers can contribute part of the tensile strength, among all the specimens from different series and aspect ratio, the cracking strength observed in the SFRC panels was higher than the plain concrete panels. Increase in fiber content also indicated increased cracking strength in both, square and rectangular specimens. Increase in loading force increased width of crack in the square panel specimens after addition of 0.75% fibers. Figure 6 demonstrates the example of square panel after addition of 0.75% fibers at the ultimate load stage. The maximum crack width of 0.55mm was observed in the panels from the T0 series after 0.75 % fiber addition, which is reduced to 0.4 mm in the panels with 1.5% fiber addition. TM series indicated smallest crack width at the ultimate strength as compared to other specimens with same fiber addition. Compared to plain concrete panels from N series, with 1.5% addition of steel fibers, superior crack controlling, and ultimate strength was observed in the SFRC specimens. This fact avoids the sudden failure by increasing the energy dissipation and illustrates the advantage of adding steel fibers in the concrete. Also, the ultimate strength was improved by 80% and 30% respectively in the panels constructed with and without transverse reinforcement. Similarly, with 0.75% addition of fibers, the ultimate strength was improved by 15% and 70% respectively compared with plain concrete panels with and without transverse reinforcement. Bridging effect of the fibers over the cracked surface resulted into significant improvement in the post cracking strength in the panels from S075 and S150 series.

The specimens from DH series indicated the large resistance to the crack width while N series indicated smaller. The crack propagation pattern in DL, CL, and DH series was also different from the plain concrete specimens; rather than single large crack, multiple small cracks were observed. A single crack with a large crack width and depth, caused brittle failure in the plain concrete panels from S0 series. SFRC panels from S075 and S150 series indicated ductile failure because of small crack width with multiple cracking. The average width of crack in the panels from S0 series with transverse reinforcement was observed to be more than 1 mm. The width of crack in the SFRC panels S075 and S150 was observed respectively as 0.2 and 0.5 mm. It is worth to note that the cracking strength of the specimens from S150 series was observed at the 50% of the ultimate strength.

Strain in the concrete was measured with the strain gauge attached on the surface of the concrete. Strain observed in the vertical direction was greater than the horizontal. strain gauge measurements indicate

the strain at a single point hence, the data obtained is a limited and more strain gauge are required to obtain more data.

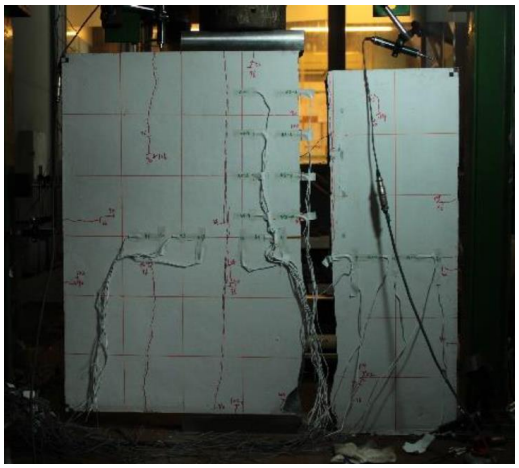

Figure 5. Specimen F000-T02
Vertical Cracking

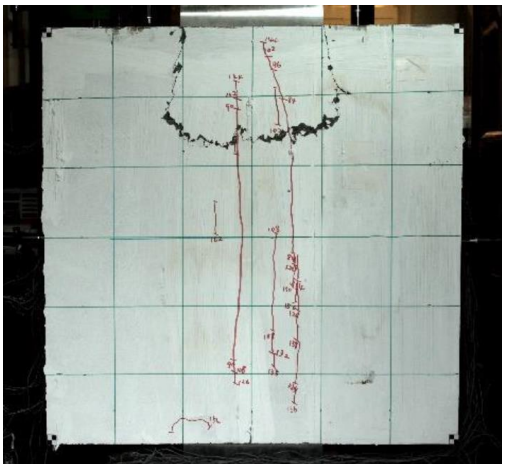

Figure 6. Specimen F075-TM7852
Fan-shaped Cracks Near Bearing Plate

Bar Strain

Steel fibers provides the resistance against tension in the transverse direction together with the reinforcement. Panels with different aspect ratio indicated large strain in each reinforcing bar at the center as indicated in figure 7, and gradually decreased away from the central vertical axis of symmetry, indicating substantial tension closer to the vertical axis of symmetry. This phenomenon was observed both in plain and SFRC panels. Moreover, increase in fiber content also indicated increased resistance to yielding of the reinforcing bars. Unlike other series in rectangular panels specimens, because of the high reinforcement ratio, specimens from DH series indicated relatively small strain without yielding. It can be observed that the strain value of the steel bar changed abruptly before and after cracking of the specimen. Because after concrete cracking all the tensile forces are carried by the reinforcement alone.

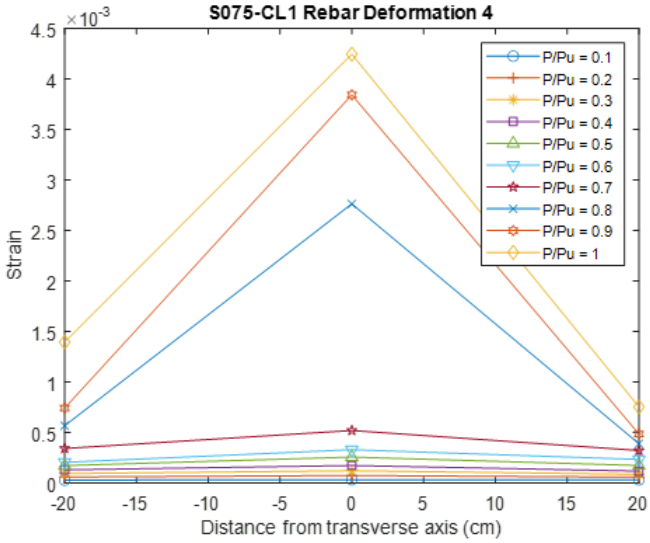

Figure 7. Bar Strain Profile

Failure Pattern

Failure of the specimen can be divided into two types, splitting of the strut, and crushing of the strut. As illustrated in figure 5 and figure 8(a), specimens without steel fibers from T0 and N series, failed due to splitting of the strut. Large crack width was observed in the specimens from T0 and N series but, the presence of the reinforcement in other series reduced the size of the cracks and resulted in single main

crack running parallel to the longitudinal edge, and number of small or secondary cracks in the inclined direction moving towards the edge of the specimen as shown in figure 8(b). Since concrete cannot provide lateral resistance to the tension after cracking hence the resistance is mainly from the fibers bridging effect. This fact also helped in maintaining the integrity of the SFRC panels as shown in figure 8(c) at the ultimate load stage.

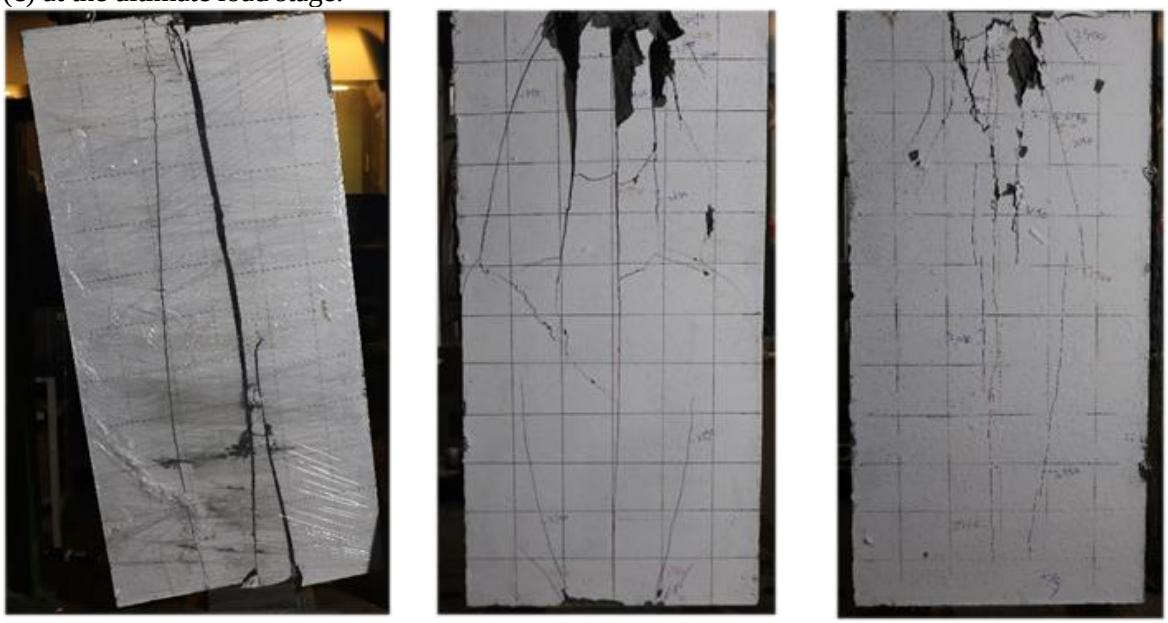

(a) Specimen S0-N2 (b) Specimen S0-CL2 (c) Specimen S075-CL1

Figure 8. Failure Pattern at the Ultimate Load Stage

Failure of Square Specimens

As indicated in figure 5, all the SFRC square specimens indicated fan-shaped cracks near the bearing plate. Failure of all the SFRC specimens from T0, TM785, TS785 and TS420 series was due to crushing of the strut after fan-shaped cracks occurred near the bearing surface causing large vertical cracks in the panel.

Failure of Rectangular Specimens

Panels specimens from N series with and without fibers failed due to splitting of the strut. The failure of the specimens from the DL and CL and DH series can be classified as crushing of the strut. Inclined cracks observed in the DH series were less severe than DL and CL series. DH series also indicated main vertical crack at the center of the specimen. The cracking pattern after addition of 0.75% fibers and 1.5% fibers was similar. Some fine cracks start to develop from the center, and gradually propagated with the increase of loading and no central main crack was observed. In addition, concrete near the bearing plates was crushed during the failure and hence, the specimens were failed due to crushing of the strut. After comprehensive consideration of strength development, crack width, and crack propagation, it was found that the test performance of specimens after addition of 0.75% and 1.5% fibers was similar.

CONCLUSION

Specimens without transverse reinforcement indicated major improvement in the cracking and ultimate strength after addition of fibers. With same reinforcement configuration and different fiber substitution rate indicate increase in fiber content increases cracking and ultimate strength. Bridging effect over the cracks change the failure pattern of the panel specimen from splitting of the strut to crushing of the strut and maintains the integrity of the panel at the ultimate load stage. Panels from F075, F150, S075 and S150 failed due to crushing of the strut. Comparing the crack widths of the specimens with the same

steel fiber volume substitution rate and different rebar arrangement, TM785 series with the reinforcement arranged in the center of the specimen and DH series with high reinforcement ratio indicated effective inhabitation of the crack formation.

ACKNOWLEDGMENTS

The National Center for Research on Earthquake Engineering (NCREE) of Taiwan is gratefully acknowledged.

REFERENCES

Hung, C-W. (2020). The Effect of Steel Fiber on Bottle-Shaped Strut-and-Tie Behavior of High Strength Concrete, *Master Thesis*, National Taiwan University, Taipei.

Kuo, C-C. (2019). Experimental Investigation on Isolated Strut Behavior of High Strength Steel Fiber Reinforced Concrete Panels, *Master Thesis*, National Taiwan University, Taipei.

Liao, W-C., W. Perceka, and L-C. Yu (2017). "Systematic Mix Procedures for Highly Flowable-Strain Hardening Fiber Reinforced Concrete (HF-SHFRC) by Using Tensile Strain Hardening Responses as Performance Criteria," *Science of Advanced Materials.*, **9**, 1157-1168.

Liao, W-C., and W-R. Su (2018). "Implementation of Highly-Flowable Strain Hardening Fiber Reinforced Concrete in New RC Beam-Column Joints," *MATEC Web of Conferences 147*.

Sahoo, D.K., R.K. Gautam, B. Singh, and P. Bhargava (2008). "Strength and Deformation Characteristics of Bottle-Shaped Struts," *Magazine of Concrete Research.*, **60**(2), 137-144.

Sahoo, D.K., B. Singh, and P. Bhargava (2009). "Investigation of Dispersion of Compression in Bottle-Shaped Struts," *ACI Structural Journal.*, **106**(2), 178-186.

Susetyo, J., P. Gauvreau, and F. Vecchio (2011). "Effectiveness of Steel Fiber as Minimum Shear Reinforcement," *ACI Structural Journal.*, **108**(4), 488-496.

RESTORING FORCE CHARACTERISTICS AND EARTHQUAKE RESPONSE OF DOUBLY REINFORCED TALL RM GARDEN WALLS WITH L-SHAPED FOUNDATION

Haruta-Kai[1], Eiichi-Inai[2], Tomofusa-Akita[3], Yorimasa-Hattori[4] and Katsuyuki-Ishii[5]

1. Graduate Student, Graduate School of Sciences and Technology for Innovation, Yamaguchi Univ.
2. Prof., Graduate School of Sciences and Technology for Innovation, Yamaguchi Univ., Dr. Eng.
3. Lecturer, Graduate School of Sciences and Technology for Innovation, Yamaguchi Univ., Dr. Eng.
4. Leader of Technical Support Office, Taiyo Ecobloxx
5. President, Taiyo Ecobloxx Dr. Eng.

Email: c062vew@yamaguchi-u.ac.jp, inai@yamaguchi-u.ac.jp, akita@yamaguchi-u.ac.jp, y-hattori@taiyo-ecobloxx.com, k-ishii@taiyo-ecobloxx.com

ABSTRACT

Horizontal loading tests of doubly reinforced tall RM garden walls with L-shaped foundation were conducted. The restoring force characteristics of the garden walls were modeled based on the results of the lateral loading tests. The earthquake response analyses of the garden wall were also conducted by using the constructed model to investigate the seismic performance. The analyses results indicate that the seismic performance of the garden walls is excellent.

Keywords: RM garden walls, Wall bottom yielding type, Void RM walls, Doubly reinforcement, Earthquake response analysis, Equivalent linearizing method

INTRODUCTION

Japanese traditional garden walls are made of hollow concrete blocks of 120-150 mm thickness, with a height of about 1.0-1.5 m, and are singly reinforced in the direction of out-of-plane of the walls. The newly developed garden walls by authors have a height of about 2.0-3.0 m, are composed of over 210 mm thickness RM units which are formwork blocks for Reinforced Masonry buildings (RM buildings), and are doubly reinforced in the direction of out-of-plane. The RM walls in the buildings are fully filled with concrete or grout materials, but the RM walls in this garden walls are partially filled using styrofoams to reduce the weight. In addition, they have large L-shaped foundation to prevent from turning over and have a failure mechanism that the wall vertical reinforcing bars yield at the wall bottom, namely, at the top of the foundation beam. In this paper, the restoring force characteristics model for the doubly reinforced RM garden walls with L-shaped foundation is constructed based on the results of the lateral loading tests. The earthquake response analyses using the model are performed to investigate the seismic performance of the doubly reinforced RM garden walls.

THE SPECIMENS AND EXPERIMENTAL METHODS

Three types of the garden wall specimens NO. 5, NO. 6, and NO. 7 were investigated, all of specimens are doubly reinforced RM garden walls with a L-shaped foundation. In addition, these are composed of RM units with styrofoams inserted to reduce the weight. These walls are called void RM walls. The specimens NO. 5 and NO.6 have 2-D10@400 as vertical bars of the wall, the assumed height H of them is 2400mm, and the loading height h is 2/3*H from the top of a foundation beam. NO. 6 is a specimen with a foundation slab thickness of 350 mm compared to NO. 5 with a foundation slab thickness of 220 mm. The specimen NO. 7 has 2-D6@400, and H is 1500mm. The upper part from the loading point in all specimens was not made. The lateral loading tests of the RM garden wall specimens were conducted.

The shapes and reinforcement of specimens NO. 5, NO. 6, and NO. 7 are shown in Fig. 1. The shape of RM unit with styrofoam inserted is shown in Photograph 1. The results of material test are shown in Table 1. The method of lateral loading test is shown in Fig. 2.

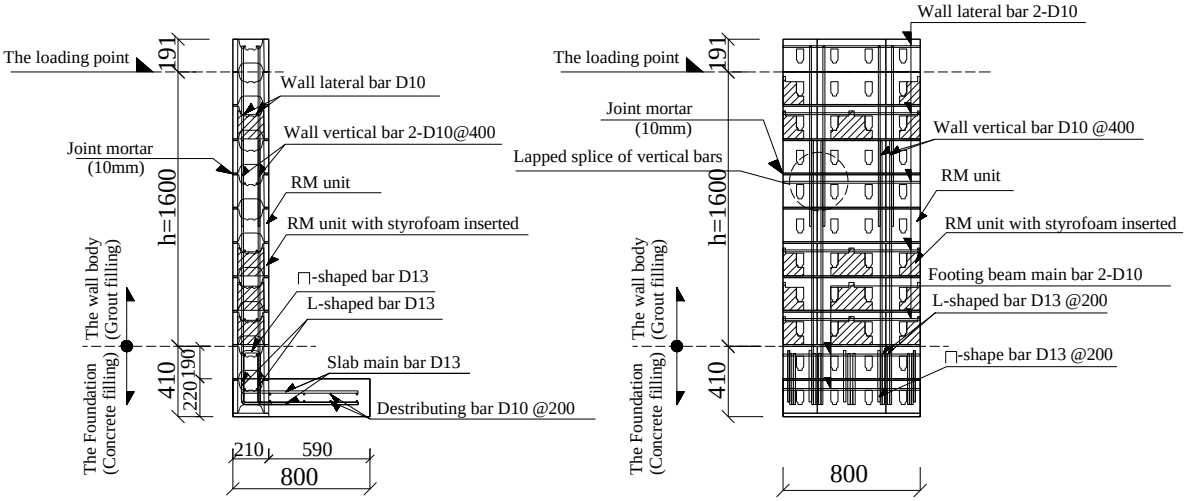

(a) Specimen NO.5

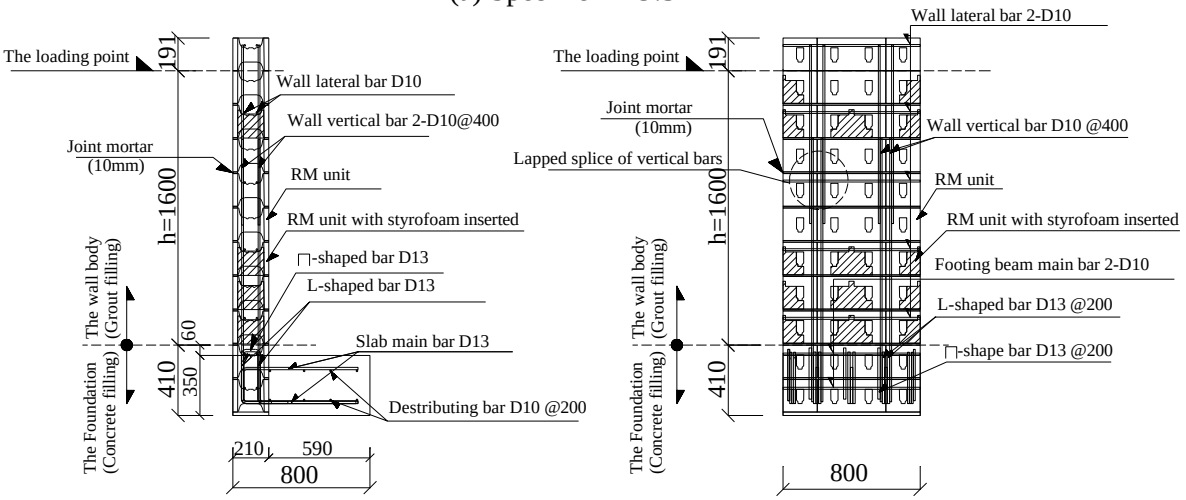

(b) Specimen NO.6

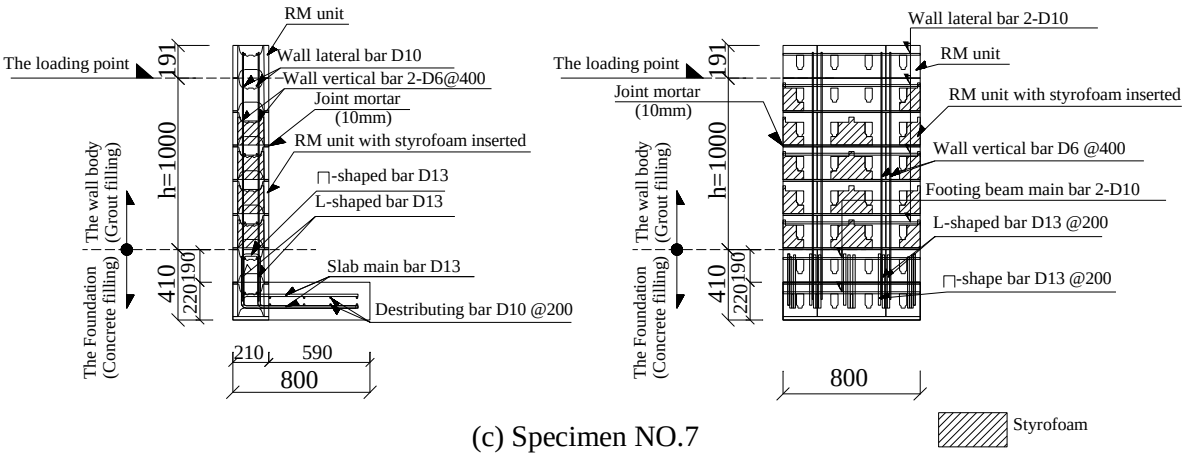

(c) Specimen NO.7

Figure 1. The shapes and reinforcement of specimens NO. 5, NO. 6, and NO. 7

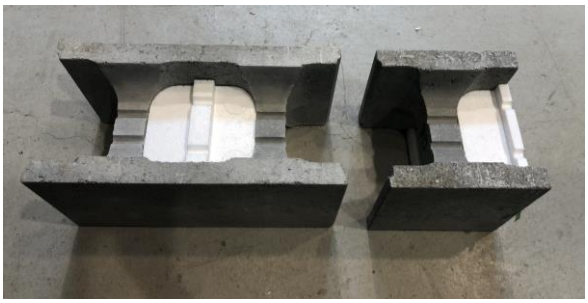

Photograph 1. The shape of RM unit with styrofoam inserted

Table 1. The results of material test

(a) The results of material test of concrete, grout and mortar

Material	Part	Compressive Strength (N/mm²)
RM unit	wall body,foundation beam	53.5
Ordinary concrete	foundation	30.2
pre-mixed grout material	wall body(filling)	71.4
mortar material	wall body(joint)	28.0

(b) The results of material test of reinforcing bars

Material	Specification (N/mm²)	Yield Strength (N/mm²)	Tensile Strength (N/mm²)	Young's modulus (kN/mm²)
D6	SD295	467	558	178
D10	SD295	364	471	186
D13	SD295	345	492	202

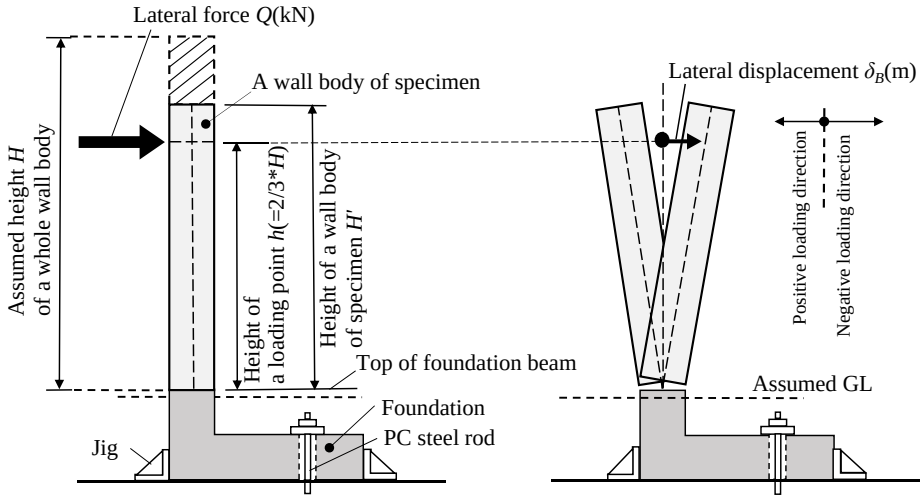

Figure 2. The method of the lateral loading test

THE RESULTS OF LATERAL LOADING TESTS AND THE RESTORING FORCE CHARACTERISTICS MODEL

The lateral force Q - lateral displacement of the garden wall δ_B at the loading point relationships of specimens NO.5 and NO.7 are shown by solid lines in Fig. 3. As a note, the experimental results of specimen NO. 6 are not described in this paper because they are almost identical to those of NO. 5.

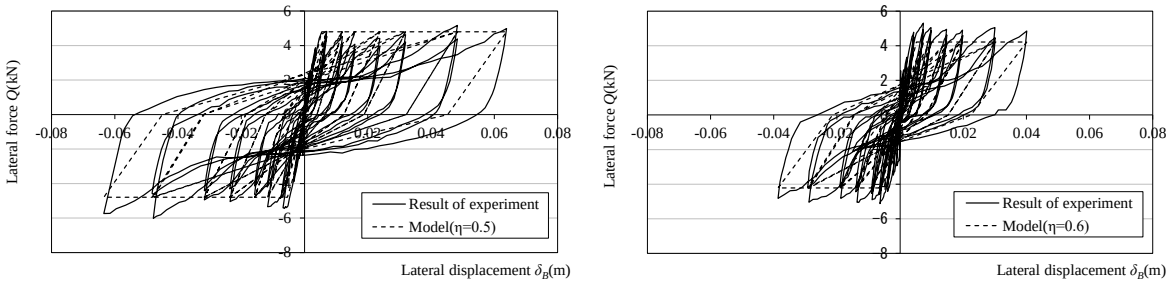

(a) Specimen NO.5 (b) Specimen NO.7

Figure 3. The lateral force Q - lateral displacement δ_B at the loading point relationships

In all specimens, after the bending crack occurred at the top of the foundation beam, the vertical bars of the wall yielded there, and the lateral strength became constant. The crack width expanded as the lateral displacement of the wall increased. As shown in Fig. 3, the observed hysteresis behavior of specimens is similar to that of ordinary RC members because the specimens are doubly reinforced.

The restoring force characteristics models for the specimens are shown by the dashed lines in Fig. 3. The model is a tri-linear type, and the initial stiffness and the yield displacement were derived from the experimental results. The lateral yield strength Q_y was calculated from Eq. (1), and the cracking strength on the skeleton curve was set to 1/3 of the yield strength. The post-yield stiffness was set to zero.

$$Q_y = \frac{M_y}{h} = \frac{a_t \cdot \sigma_y \cdot j + \frac{1}{2} \cdot N \cdot t}{h} \tag{1}$$

where, M_y is the yield moment of wall cross section in the direction of out-of-plane, a_t is the cross-sectional area of the tensile rebar, σ_y is the yield strength of the vertical bar of the wall, j is the stress center distance (=7/8*d), and d is the effective length. N is the axial load and is calculated from Eq. (2).

$$N = \begin{cases} H \cdot L \cdot t \cdot \gamma & \text{(in the earthquake response analysis)} \\ H' \cdot L \cdot t \cdot \gamma & \text{(in the modeling for experimental result)} \end{cases} \tag{2}$$

where, L is the length of the wall, t is thickness of the wall, γ *is* unit weight (=20[kN/m^3]), H is the assumed height of a whole wall body in the analysis, and H' is the height of wall body of the specimen.

The experimental Q -δ_B relationships in Fig. 3 show a difference between the first and the second peak strength in the loading cycle of the same displacement. As shown in Fig. 3, the restoring force characteristics models generally match the second peak strength in each loading cycle.

In the modeling, the hysteresis rules of the origin-oriented model before yielding and the stiffness degrading bi-linear model after yielding were used. However, in the case of the small amplitude after the large amplitude loop, the hysteresis rule of TAKEDA model was used. Equation (3) shows the formula for the damping factor h_{eq} in the experimental results.

$$h_{eq} = \frac{1}{4\pi} \cdot \frac{\Delta W}{W} \tag{3}$$

where, ΔW is the area of one cycle, and W is the elastic potential energy.

The h_{eq}-δ_B relationships of specimens NO.5 and NO.7 are shown by the solid lines in Fig. 4. The dashed lines in Fig. 4 are the calculated damping factors by Eq. (4), which represents the damping factor of the stiffness degrading bi-linear model.

$$h_{eq} = \frac{1}{\pi}(1 - \mu^{\eta-1}) \tag{4}$$

where, μ is the plasticity ratio, and η is the unloading stiffness degrading index.

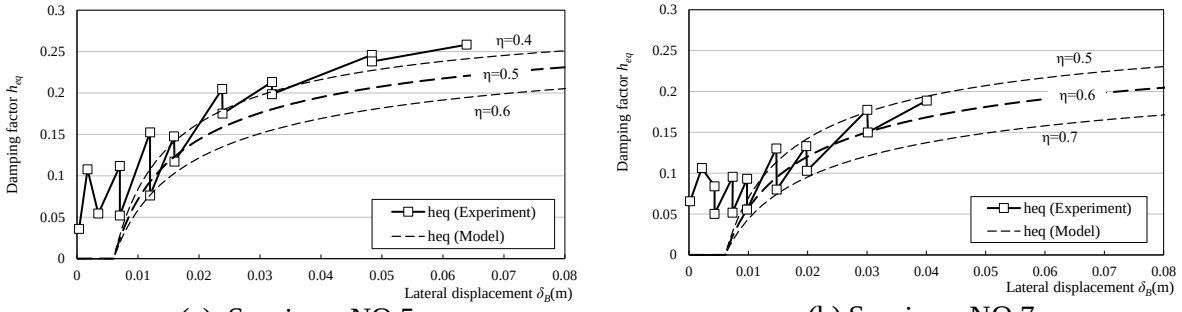

(a) Specimen NO.5 (b) Specimen NO.7

Figure 4. The damping factor h_{eq} - lateral displacement δ_B relationship

As shown in Fig. 4, when the unloading stiffness degrading index η is about 0.5 for specimen NO. 5 and 0.6 for specimen NO. 7, the calculated damping factors by the Eq. (4) match the experimental results.

THE ANALYTICAL MODEL FOR EARTHQUAKE RESPONSE ANALYSIS

In this section, earthquake response analyses using a single degree of freedom system are performed for specimen NO. 5, which has the assumed height H of 2400mm. The analytical model is shown in Fig. 5.

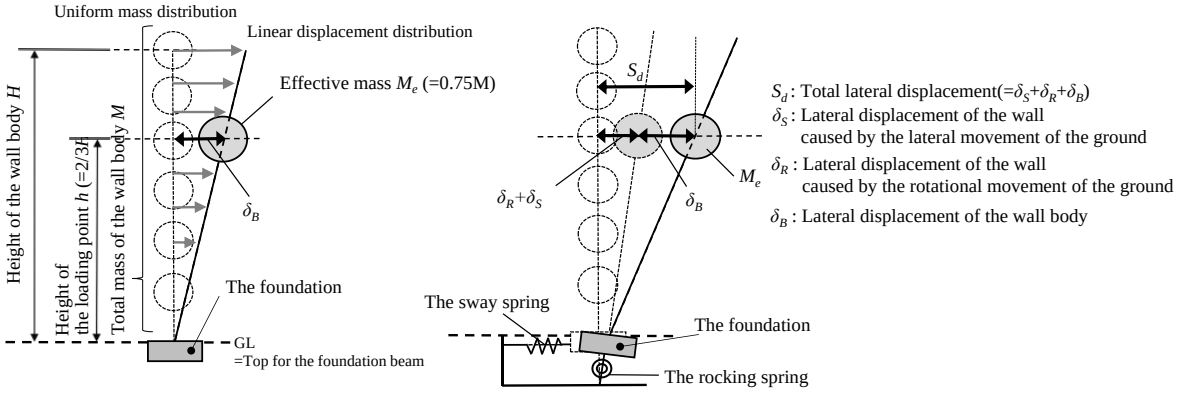

(a)In case of the fixed foundation (b) In case of considering the ground deformation

Figure 5. The analytical models

The garden wall model used in the analysis is a single degree of freedom system obtained from the assumption of a uniform mass distribution in the direction of height and a linear displacement distribution in the first-order mode. The effective mass ratio is 0.75. The effective height of the system is 2/3*H.

In addition to the case of the fixed foundation, earthquake response analyses considering the displacement caused by the ground deformation under the foundation were also performed. In the analysis, two types of ground conditions were used, one was the condition with the poisson ratio v of 0.45 and the shear elastic modulus G of 20,000 (kN/m^2), and the other was the condition with v of 0.45 and G of 10,000 (kN/m^2). The rectangular foundation of 1.5 m in the short direction and 6 m in the long direction was assumed. The viscous damping factor was 5% to the equivalent stiffness of the entire system, and the radiation damping of the ground was not considered. The stiffness of the ground for the

lateral motion K_S and the stiffness of the ground for the rotational motion K_R were determined by Eq. (5) and Eq. (6), respectively. In all cases, the foundation was assumed to be rigid.

$$K_s = \frac{6.77}{1.79 - \nu} Gr \tag{5}$$

$$K_R = \frac{2.52}{1.00 - \nu} Gr^3 \tag{6}$$

where, r is the equivalent radius at the foundation.

In the analyses, the restoring force characteristics model shown in Fig. 3 (a) was used, where the experimental values of the yield displacement and the initial stiffness were used. As an analytical parameter, the value of C_B which is the ratio of the yield strength Q_y to M_e*g, where M_e is the effective mass and g is the gravity acceleration, was varied from 0.2 to 1.2 in increments of 0.1. Newmark's β method where β is 0.25 was used in the calculations, and the integration time increment was 0.001 sec.

The simulated earthquake ground motions used in the analyses were one wave with the random phase and three waves with the phase of the observed waves: Taft EW phase, El Centro NS phase, and JMA Kobe NS phase. The target of the acceleration response spectrum S_{a0} is expressed by Eq. (7) which is the acceleration response spectrum of the sever earthquake in the seismic zone factor Z of 1 and the second soil condition in Japan.

$$S_{a0} = \begin{cases} \dfrac{12 - 4.8}{0.16} T + 4.8 (T < 0.16) \\ 12 (0.16 \le T < 0.864) \\ \dfrac{12 \cdot 0.864}{T} (T \ge 0.864) \end{cases} \tag{7}$$

where, T is the period, and is the equivalent period of the entire system depending on the Q-δ_B relationship of the garden wall in the equivalent linearizing method.

The time history of the acceleration of a simulated earthquake motion with the random phase is shown in Fig. 6, and the acceleration response spectra of four simulated earthquake ground motions are shown in Fig. 7.

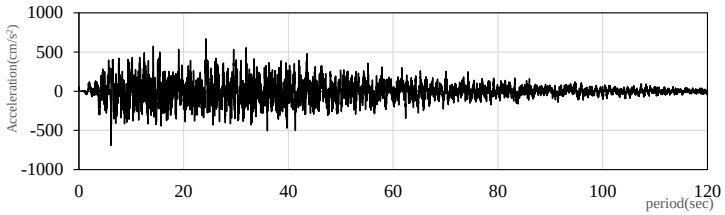

Figure 6. The time history of the simulated earthquake ground motion with random phase

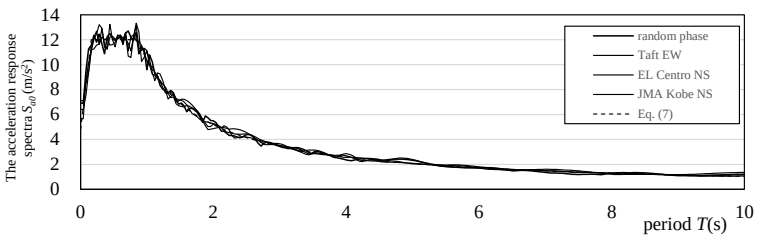

Figure 7. The acceleration response spectra of simulated earthquake ground motions

THE EQUIVALENT LINEARIZING METHODS

The earthquake response of the garden walls was estimated from the equivalent linearizing methods, aside from the earthquake response analyses. The equivalent damping factor h_e of the entire system in the equivalent linearizing method is given by Eq. (8). The response reduction factor F_h due to the damping is given by Eq. (9), and the acceleration response spectrum of the garden wall S_a is given by Eq. (10). The lateral displacement of the entire system S_d is given by Eq. (11). The S_a-S_d relationships are derived from Eqs. (7)-(11), then the C_B (=S_a/g) - δ_B relationships are obtained.

$$h_e = 0.05 + {}_Bh_e \tag{8}$$

$$F_h = {}^{1.5}/_{(1+10h_e)} \tag{9}$$

$$S_a = S_{a0} \cdot F_h \tag{10}$$

$$S_d = S_a \cdot (T/2\pi)^2 \tag{11}$$

where, ${}_Bh_e$ is the equivalent damping factor based on Eq. (4), S_d is the sum of δ_B, δ_S, and δ_R, and there are shown in Fig. 5 (b).

EARTHQUAKE RESPONSE

The marks of ○, ×, □ and △ in Fig. 8 show the C_B-δ_B relationships of the garden wall obtained from the time history response analyses. The two dotted lines in Fig. 8 show the C_B (=S_a/g) - δ_B relationships obtained from the equivalent linearizing methods. One is the relationship in case of ${}_Bh_e$ of zero. The other is the relationship in case of ${}_Bh_e$ given by Eq. (4).

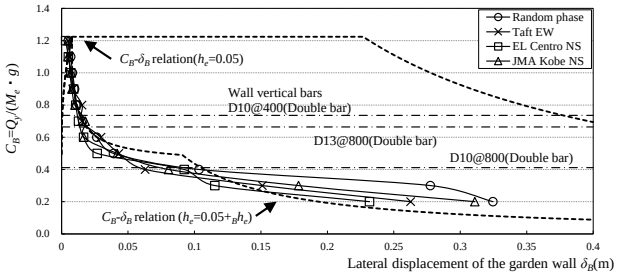

(a) In case of the fixed foundation

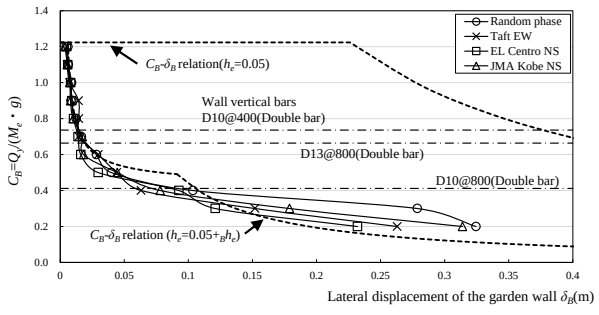

(b) In case of considering ground condition of G=20000(kN/m^2)

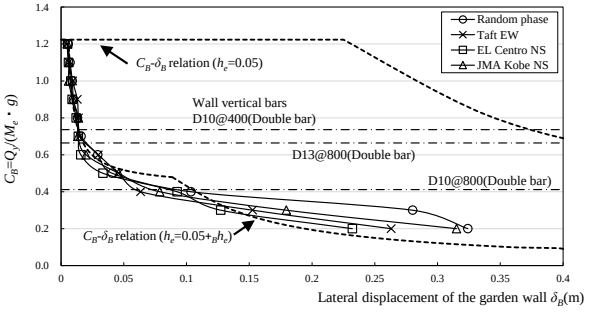

(c) In case of considering ground condition of G=10000(kN/m^2)

Figure 8. C_B -δ_B relationships obtained from the earthquake response analyses and the equivalent linearizing methods

The response displacement considering the damping of Eq. (4) is much smaller than the displacement with no damping. The C_B-δ_B relationship of the garden wall with C_B of more than 0.4 based on the equivalent linearizing method show good correspondence with the results of the time history response

analyses, except for a few cases. The values of C_B in Fig. 8 are determined by the amount of vertical bars of the garden wall. The horizontal dashed lines in Fig. 8 show the values of C_B for the typical amount of vertical bars of the doubly reinforced garden walls. The response displacements of the garden walls are about 0.02 m when the vertical bars of the wall are 2-D10@400 as well as that of specimen NO.5. Figure 8 (a), (b) and (c) shows that there is no significant difference in C_B-δ_B relationships between the case of the fixed foundation and the case of considering ground deformations. Therefore, the doubly reinforced RM garden walls with the proper vertical bar have the excellent seismic performance.

The normalized lateral force $Q/(M_e*g)$ - the lateral displacement of the wall δ_B relationships under various ground conditions obtained from the time history response analyses in the case of the random phase waves and C_B= 0.6 are shown in Fig. 9. There are no significant differences in δ_B between the case of the fixed foundation and the case that ground deformation is considered in Fig. 9.

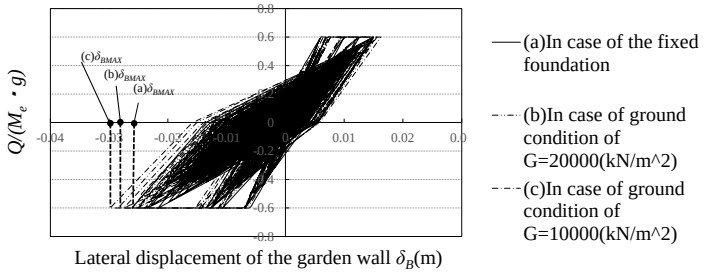

Figure 9. $Q/(M_e*g)$ -δ_B relationships under various ground conditions in case of the random phase wave and C_B of 0.6

CONCLUSIONS

The following conclusions can be drawn from the experimental and analytical investigation reported in this paper.

1. In the lateral loading tests, the RM garden wall specimens showed the hysteresis behavior similar to that of ordinary RC members because the specimens were doubly reinforced.
2. The restoring force characteristics model for the garden walls was constructed based on the results of lateral loading tests, and the model matchs the second peak strength in the loading cycle of the same displacement.
3. The C_B-δ_B relationships of the garden wall with C_B of more than 0.4 obtained from the earthquake response analyses showed good correspondence with the C_B-δ_B relationship of the garden wall obtained from the equivalent linearizing methods.
4. The response displacements of the garden wall were about 2 cm when the vertical bars of the wall were 2-D10@400 as well as that of specimen NO.5.
5. The results of the analyses showed that there was no significant difference in the C_B-δ_B relationships between the case of the fixed foundation and the case of considering ground deformations.
6. The doubly reinforced RM garden walls with the proper vertical bar have the excellent seismic performance.

REFERENCES

Inai, E., Kitamura, K., and Marubashi, N. (2011). *Study on Variation of the Maximum Response of RC Buildings to Design Input Ground Motions and Evaluating Method for the Maximum Response Considering the Variation*, *Journal of Structural and Construction Engineering., AIJ.*, 76(661), 629-637.

Shibata, A. (2014). *Latest Seismic Structure Analysis, 3rd Edition*, *Morikita publishing co., ltd.*, 73-76.

Shibata, A. (2014). *Latest Seismic Structure Analysis, 3rd Edition*, *Morikita publishing co., ltd.*, 97-108.

Shibata, A. (2014). *Latest Seismic Structure Analysis, 3rd Edition*, *Morikita publishing co., ltd.*, 243.

A STUDY ON THE EFFECT OF SEISMIC DAMAGE MITIGATION OF RC SCHOOL BUILDING WITH DIFFERENT IMPORTANCE FACTOR

Taichi Ichioka[1], Tomofusa Akita[2] and Eiichi Inai[3]

1. Graduate Student, Graduate School of Sciences and Technology for Innovation, Yamaguchi Univ.
2. Lecturer, Graduate School of Sciences and Technology for Innovation, Yamaguchi Univ, Dr. Eng.
3. Prof, Graduate School of Sciences and Technology for Innovation, Yamaguchi Univ, Dr. Eng.

Email: c060vew@yamaguchi-u.ac.jp,akita@yamaguchi-u.ac.jp,inai@yamaguchi-u.ac.jp

ABSTRACT

Public buildings need to minimize damage during an earthquake and be ready for use immediately after the earthquake. Therefore, in japan, high seismic resistance is ensured by multiplying the importance factor by the required horizontal load carrying capacity of the building. In this study, we create a building model for study when the importance factors are 1.0, 1.25, and 1.5, input seismic waves in two directions, and conduct the time history response analysis. From the analysis results, the damage index to the columns, beams and shear walls were determined by the deformation angle of members. Then the repair cost was calculated, and the relationship between the importance factor and the repair costs were examined. As a result, the importance factor of 1.5 markedly reduced the repair costs.

Keywords: importance factor, RC school building, repair cost, the required horizontal load carrying capacity, time history response analysis

INTRODUCTION

Public buildings need to minimize damage during an earthquake and be ready for use immediately after the earthquake. Therefore, in japan, high seismic resistance is ensured by multiplying the importance factor by the required horizontal load carrying capacity of the building. Existing research (Matsumura, D., 2019) examined the relationship between the seismic area factor and repair costs. In this study, we create a building model for study when the importance factors are 1.0, 1.25, and 1.5, input seismic waves in two directions, and conduct the time history response analysis. From the analysis results, the damage index to the columns, beams and shear walls were determined by the deformation angle of members. Then the repair cost was calculated, and the relationship between the importance factor and the repair costs were examined. As a result, the importance factor of 1.5 markedly reduced the repair costs.

ANALYSIS METHOD

Analysis Model

In this study, we created three analysis models with different importance factors. The three models created I100, I125 and I150 corresponding to importance factors (I) 1.00, 1,25 and 1.50. I125 was created based on the existing RC school building. The seismic zoning factors (Z) represents the relative ratio of the expectation of the earthquake ground motion obtained by past earthquake records etc. The existing RC school building was built in Japan, which was designed with I=1.25 and Z=0.8. I100 and I150 were created based on I125. I100 reduced the number of reinforcement bar. I150 increased the number of reinforcement bar. In addition, the column width was increased by 100 mm, and the beam width was increased by 50 mm. The cross sections of the foundation beams and shear walls of each model are the same. The 2nd floor framing plan of analysis model is shown in Figure 1. Table 1 and 2 show the beam and column cross section of I100, I125 and I150.

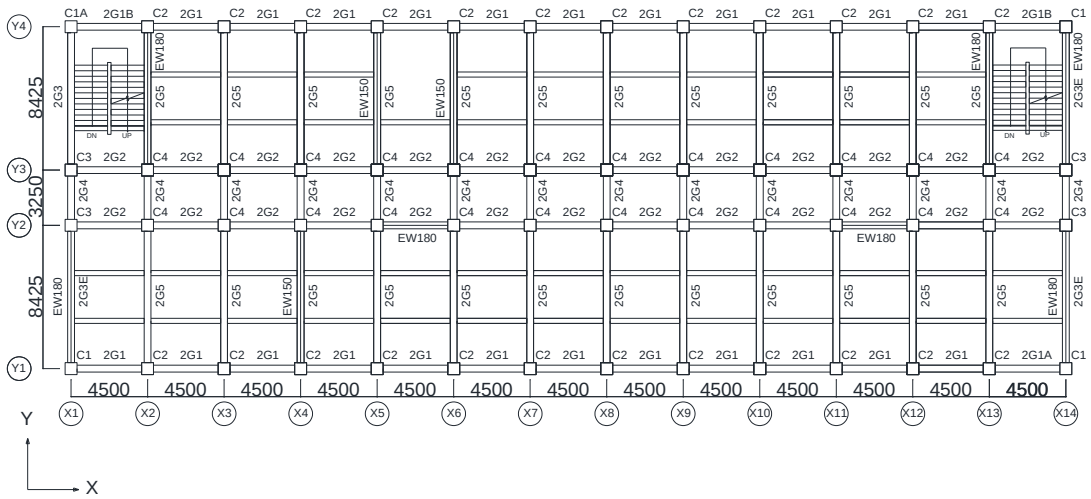

Figure 1. 2nd floor framing plan

Table 1. Beam cross section

(a) I100

				G1	G1A	G2	G3	G3E	G4	G5	
PH	B×D			400×600	—	—	400×650	—	—	400×650	
	Longitudinal bar	Upper	outside	5–D22	—	—	5–D22	—	—	4–D22	
			inside	—	—	—	2–D22	—	—	—	
		Lower	outside	5–D22	—	—	5–D22	—	—	4–D22	
			inside	—	—	—	—	—	—	—	
	Stirrup			3–D13@200	—	—	4–D13@200	—	—	2–D13@200	
RF	B×D			400×600	—	400×600	550×900	400×650	400×650	400×850	
	Longitudinal bar	Upper	outside	3–D22	—	3–D22	4–D22	3–D22	3–D22	3–D22	
			inside	—	—	—	2–D22	—	—	—	
		Lower	outside	3–D22	—	3–D22	4–D22	3–D22	3–D22	3–D22	
			inside	—	—	—	2–D22	—	—	—	
	Stirrup			2–D13@200	—	2–D13@200	3–D13@100	2–D13@200	2–D13@200	2–D13@200	
3F	B×D			400×600	—	400×600	550×900	400×650	400×650	400×850	
	Longitudinal bar	Upper	outside	3–D25	—	3–D25	4–D22	3–D25	3–D25	3–D25	
			inside	—	—	—	2–D22	—	—	—	
		Lower	outside	3–D25	—	3–D25	4–D22	3–D25	3–D25	3–D25	
			inside	—	—	—	2–D22	—	—	—	
	Stirrup			2–D13@200	—	2–D13@200	3–D13@100	2–D13@200	2–D13@200	2–D13@200	
2F	B×D			400×650	400×650	400×650	550×900	400×650	400×650	400×850	
	Longitudinal bar	Upper	outside	3–D25	3–D25	3–D25	4–D25	3–D25	3–D25	3–D25	3–D25
			inside	—	2–D25	1–D25	2–D25	—	—	2–D25	—
		Lower	outside	3–D25	3–D25	3–D25	4–D25	3–D25	3–D25	3–D25	3–D25
			inside	—	2–D25	1–D25	2–D25	—	—	—	2–D25
	Stirrup			3–D13@200	3–D13@200	3–D13@200	3–D13@100	2–D13@200	2–D13@200	2–D13@200	

(b) I125

				G1	G1A	G2	G3	G3E	G4	G5	
PH	B×D			400×600	—	—	400×650	—	—	400×650	
	Longitudinal bar	Upper	outside	5–D22	—	—	5–D22	—	—	4–D22	
			inside	—	—	—	2–D22	—	—	—	
		Lower	outside	5–D22	—	—	5–D22	—	—	4–D22	
			inside	—	—	—	—	—	—	—	
	Stirrup			3–D13@200	—	—	4–D13@200	—	—	2–D13@200	
RF	B×D			400×600	—	400×600	550×900	400×650	400×650	400×850	
	Longitudinal bar	Upper	outside	4–D22	—	4–D22	5–D22	4–D22	4–D22	4–D22	
			inside	—	—	—	2–D22	—	—	—	
		Lower	outside	4–D22	—	4–D22	5–D22	4–D22	4–D22	4–D22	
			inside	—	—	—	2–D22	—	—	—	
	Stirrup			2–D13@200	—	2–D13@200	3–D13@100	2–D13@200	2–D13@200	2–D13@200	
3F	B×D			400×600	—	400×600	550×900	400×650	400×650	400×850	
	Longitudinal bar	Upper	outside	4–D25	—	4–D25	5–D22	4–D25	4–D25	4–D25	
			inside	—	—	—	2–D22	—	—	—	
		Lower	outside	4–D25	—	4–D25	5–D22	4–D25	4–D25	4–D25	
			inside	—	—	—	2–D22	—	—	—	
	Stirrup			2–D13@200	—	2–D13@200	3–D13@100	2–D13@200	2–D13@200	2–D13@200	
2F	B×D			400×650	400×650	400×650	550×900	400×650	400×650	400×850	
	Longitudinal bar	Upper	outside	4–D25	4–D25	4–D25	5–D25	4–D25	4–D25	4–D25	4–D25
			inside	—	2–D25	1–D25	2–D25	—	—	2–D25	—
		Lower	outside	4–D25	4–D25	4–D25	5–D25	4–D25	4–D25	4–D25	4–D25
			inside	—	2–D25	1–D25	2–D25	—	—	—	2–D25
	Stirrup			3–D13@200	3–D13@200	3–D13@200	3–D13@100	2–D13@200	2–D13@200	2–D13@200	

(c) I150

				G1	G1A	G2	G3	G3E	G4	G5	
PH	B×D			450×600	—	—	450×650	—	—	450×650	
	Longitudinal bar	Upper	outside	6-D22	—	—	6-D22	—	—	5-D22	
			inside	—	—	—	2-D22	—	—	—	
		Lower	outside	6-D22	—	—	6-D22	—	—	5-D22	
			inside	—	—	—	—	—	—	—	
	Stirrup			3-D13@200	—	—	4-D13@200	—	—	2-D13@200	
RF	B×D			450×600	—	450×600	550×900	450×650	450×650	450×850	
	Longitudinal bar	Upper	outside	5-D22	—	5-D22	6-D22	5-D22	5-D22	5-D22	
			inside	—	—	—	2-D22	—	—	—	
		Lower	outside	5-D22	—	5-D22	6-D22	5-D22	5-D22	5-D22	
			inside	—	—	—	2-D22	—	—	—	
	Stirrup			2-D13@200	—	2-D13@200	3-D13@100	2-D13@200	2-D13@200	2-D13@200	
3F	B×D			450×600	—	450×600	550×900	450×650	450×650	450×850	
	Longitudinal bar	Upper	outside	5-D25	—	5-D25	6-D22	5-D25	5-D25	5-D25	
			inside	—	—	—	2-D22	—	—	—	
		Lower	outside	5-D25	—	5-D25	6-D22	5-D25	5-D25	5-D25	
			inside	—	—	—	2-D22	—	—	—	
	Stirrup			2-D13@200	—	2-D13@200	3-D13@100	2-D13@200	2-D13@200	2-D13@200	
2F	B×D			450×650	450×650	450×650	550×900	450×650	450×650	450×850	
	Longitudinal bar	Upper	outside	5-D25	5-D25	5-D25	6-D25	4-D25	5-D25	5-D25	5-D25
			inside	—	2-D25	1-D25	2-D25	—	—	2-D25	—
		Lower	outside	5-D25	5-D25	5-D25	6-D25	5-D25	5-D25	5-D25	5-D25
			inside	—	2-D25	1-D25	2-D25	—	—	—	2-D25
	Stirrup			3-D13@200	3-D13@200	3-D13@200	3-D13@100	2-D13@200	2-D13@200	2-D13@200	

Table 2. Column cross section

(a) I100

			C1	C1A	C2	C3	C4
PH	Dx×Dy		700×700	—	700×700	700×700	—
	Longitudinal bar		16-D25	—	12-D25	16-D22	—
	Hoop	X	2-D13@100	—	2-D13@100	2-D13@100	—
		Y	2-D13@100	—	2-D13@100	2-D13@100	—
3F	Dx×Dy		700×700	700×700	700×700	700×700	700×700
	Longitudinal bar		8-D22	16-D25	8-D25	12-D19	8-D25
	Hoop	X	2-D13@100	2-D13@100	2-D13@100	2-D13@100	2-D13@100
		Y	2-D13@100	2-D13@100	2-D13@100	2-D13@100	2-D13@100
2F	Dx×Dy		700×700	700×700	700×700	700×700	700×700
	Longitudinal bar		8-D25	16-D25	10-D25	12-D25	10-D25
	Hoop	X	2-D13@100	2-D13@100	2-D13@100	2-D13@100	2-D13@100
		Y	2-D13@100	2-D13@100	2-D13@100	2-D13@100	2-D13@100
1F	Dx×Dy		700×700	700×700	700×700	700×700	700×700
	Longitudinal bar		12-D25	16-D25	12-D25	12-D25	12-D25
	Hoop	X	2-D13@100	6-D13@100	4-D13@100	2-D13@100	3-D13@100
		Y	2-D13@100	2-D13@100	3-D13@100	2-D13@100	2-D13@100

(b) I125

			C1	C1A	C2	C3	C4
PH	Dx×Dy		700×700	—	700×700	700×700	—
	Longitudinal bar		16-D25	—	12-D25	16-D22	—
	Hoop	X	2-D13@100	—	2-D13@100	2-D13@100	—
		Y	2-D13@100	—	2-D13@100	2-D13@100	—
3F	Dx×Dy		700×700	700×700	700×700	700×700	700×700
	Longitudinal bar		12-D22	20-D25	12-D25	16-D19	12-D25
	Hoop	X	2-D13@100	2-D13@100	2-D13@100	2-D13@100	2-D13@100
		Y	2-D13@100	2-D13@100	2-D13@100	2-D13@100	2-D13@100
2F	Dx×Dy		700×700	700×700	700×700	700×700	700×700
	Longitudinal bar		12-D25	20-D25	14-D25	16-D25	14-D25
	Hoop	X	2-D13@100	2-D13@100	2-D13@100	2-D13@100	2-D13@100
		Y	2-D13@100	2-D13@100	2-D13@100	2-D13@100	2-D13@100
1F	Dx×Dy		700×700	700×700	700×700	700×700	700×700
	Longitudinal bar		16-D25	20-D25	16-D25	16-D25	16-D25
	Hoop	X	2-D13@100	6-D13@100	4-D13@100	2-D13@100	3-D13@100
		Y	2-D13@100	2-D13@100	3-D13@100	2-D13@100	2-D13@100

(c) I150

			C1	C1A	C2	C3	C4
PH	Dx×Dy		750×750	—	750×750	750×750	—
	Longitudinal bar		20-D25	—	16-D25	20-D22	—
	Hoop	X	2-D13@100	—	2-D13@100	2-D13@100	—
		Y	2-D13@100	—	2-D13@100	2-D13@100	—
3F	Dx×Dy		750×750	750×750	750×750	750×750	750×750
	Longitudinal bar		16-D22	24-D25	16-D25	20-D19	16-D25
	Hoop	X	2-D13@100	2-D13@100	2-D13@100	2-D13@100	2-D13@100
		Y	2-D13@100	2-D13@100	2-D13@100	2-D13@100	2-D13@100
2F	Dx×Dy		750×750	750×750	750×750	750×750	750×750
	Longitudinal bar		16-D25	24-D25	18-D25	20-D25	18-D25
	Hoop	X	2-D13@100	2-D13@100	2-D13@100	2-D13@100	2-D13@100
		Y	2-D13@100	2-D13@100	2-D13@100	2-D13@100	2-D13@100
1F	Dx×Dy		750×750	750×750	750×750	750×750	750×750
	Longitudinal bar		20-D25	24-D25	20-D25	20-D25	20-D25
	Hoop	X	2-D13@100	6-D13@100	4-D13@100	2-D13@100	3-D13@100
		Y	2-D13@100	2-D13@100	3-D13@100	2-D13@100	2-D13@100

Pushover analysis

Pushover analysis is carried out to confirm that Qu/Qun of the modified cross section model is equivalent to Qu/Qun of the original design model. Qu/Qun means the horizontal load-carrying capacity margin that divides horizontal load-carrying capacity Qu by required horizontal load-carrying capacity Qun. The pushover analysis finishes when the maximum story drift angle reaches 1/100 rad. External force distribution used for pushover analysis is set based on Ai distribution (The Building Center of Japan, 2016).

Time History Response Analysis

The time history response analysis was carried out about I100 model (I=1.00), I125 model (I=1.25) and I150 model (I=1.50). The seismic waves used in this analysis are three seismic waves of EL Centro NS (1940), EL Centro EW (1940) and EL Centro H2 (1940). Table 3 shows the maximum acceleration and the duration of the three seismic waves used in this analysis. The velocity of the seismic waves were set to 50cm/s. There are a total of 6 types of analysis. Table 4 shows type of the time history response analysis.

Table 3. Maximum acceleration and duration of the three seismic waves

Seismic Wave	Direction	Sort	Maximum Acceleration (cm/s²)	Duration (sec)
EL Centro H2	X,Y	Artificial	571.51	53.74
EL Centro NS	X	Recorded	341.7	53.74
EL Centro EW	Y	Recorded	210.1	53.74

Table 4. Type of the time history response analysis

	Direction		Sort
	X	Y	
Ⅰ	EL Centro H2		Artificial(X)
Ⅱ		EL Centro H2	Artificial(Y)
Ⅲ	EL Centro H2	EL Centro H2	Artificial(XY)
Ⅳ	EL Centro NS		Recorded(X)
Ⅴ		EL Centro EW	Recorded(Y)
Ⅵ	EL Centro NS	EL Centro EW	Recorded(XY)

Modeling Method

3D frame model is used in the pushover analysis and the time history response analysis. Beams are modeled by the uniaxial spring model. Columns and shear walls are modeled by the MN model. In the time history response analysis, Takeda-model is used for hysteresis loops of beams and columns. The damping factor was set to be instantaneous stiffness proportional type, and was 5% with respect to the first eigen period.

THE CALCULATION METHOD OF REPAIR COST

The repair cost is determined based on the angle of the beam and column member obtained by the time history response analysis, and calculated according to the damage index of the member. The damage index to the shear wall shall be considered equivalent to the damage index to the nearby column. The relationship between the damage index, the deformation angle of the member, and the repair cost is shown in Table 5. The relationship between the crack width and the damage index is based on References (Architectural Institute of Japan, 2004). The relationship between the member angle of the column and the crack width is based on existing researches (Minamiguchi, S. and Kishimoto, I., 2012; Nagayama, K. et al., 2001). The relationship between the member angle of the beam and the crack width is based on existing researches (Takahashi, S. et al., 2017). The relationship between repair cost of shear wall and the damage index is based on existing researches (Nakashima, K. et al., 2003). The repair cost was calculated using the minimum and maximum values in Table 5, and the total repair cost for each component was calculated to obtain the total repair cost. If the damage index of the member is different at both member ends, the one with the larger the damage index is adopted. The damage index of the column is the larger of X and Y.

Table 5. Correspondence among damage level member angle and repair cost

Damage degree	Crack width (mm)	Column member angle	Beam member angle	Repair costs for columns and beams (yen)	Repair costs for shear walls (yen)
Ⅰ	0~0.2	Flexural crack	Flexural crack	10,000～50,000	30,000～150,000
Ⅱ	0.2~1.0	Flexural crack	Flexural crack	50,000～100,000	150,000～300,000
Ⅲ	1.0~2.0	1/200 rad	1/150 rad	200,000～400,000	600,000～1,200,000
Ⅳ	2.0~	1/67 rad	1/75 rad	800,000～1,000,000	2,400,000～3,000,000

THE RESULT OF TIME HISTORY RESPONSE ANALYSIS

The maximum story drift angle obtained by the time history response analysis is shown in Figure 2. The maximum story drift angle of the third floor of each case were almost the same, but the maximum story drift angle of the first floor of each case were considerably different. The maximum story drift angle of I100 model was smallest in most every case. The maximum story drift angle of I150 was largest in most every case. The maximum story drift angle is larger in (XY) than in (X) and (Y).

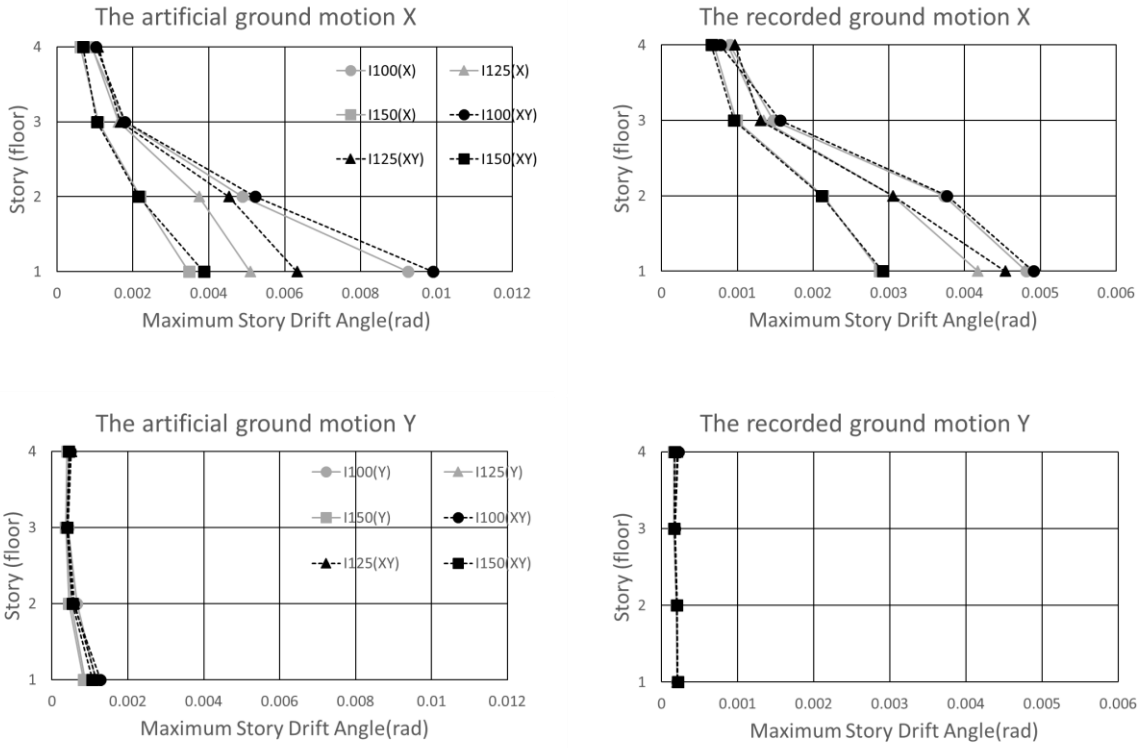

Figure 2. Maximum story drift angle

THE CALCULATION RESULT OF THE DAMAGE INDEX OF MEMBERS

Figure 3 shows Collapse mechanism and damage index of Y4 axis when the artificial ground motion (XY) inputted. I100 has columns and beams with flexural yield on 1st and 2nd floors. The damage index of the members is III on the 1st floor, II on 2nd floor, and I on 3rd and PH floor. I125 has columns with flexural yield on the 1st and 2nd floors. The damage index of the members are III on 1st floor, II on 2nd floor, and I on 3rd and PH floor. I100 has columns with flexural yield on 1st. The damage index of the members are III on 1st floor and I on the other floors.

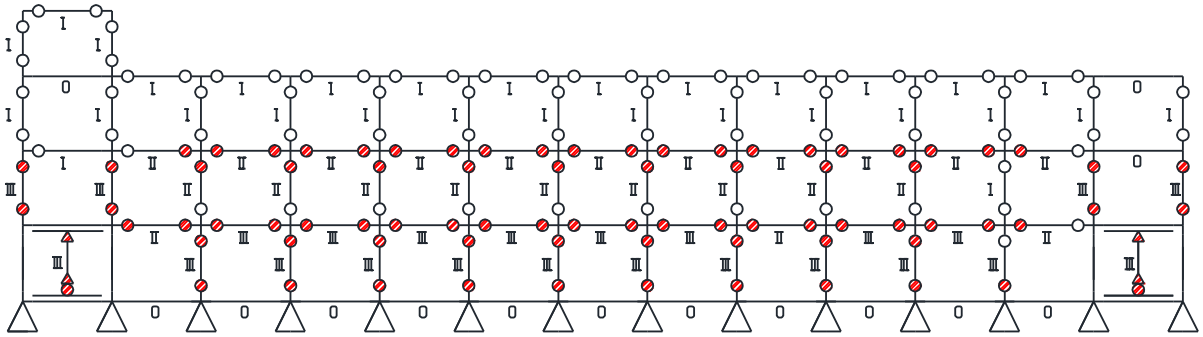

(a) I100

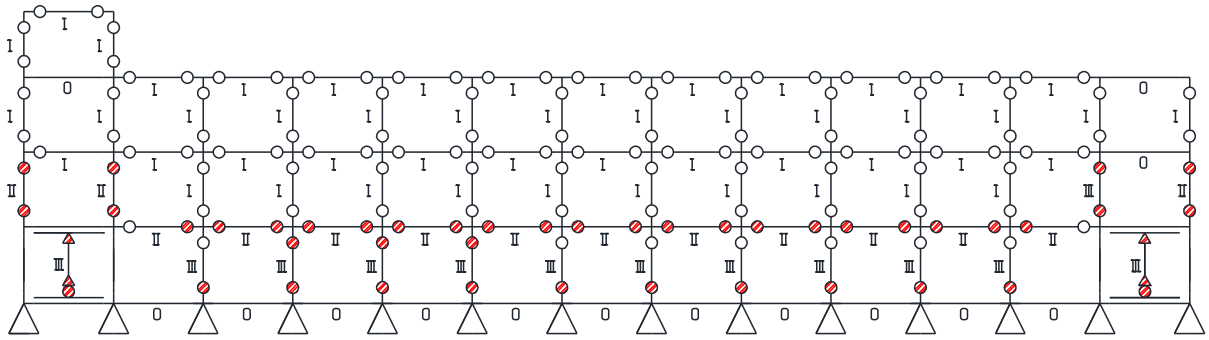

(b) I125

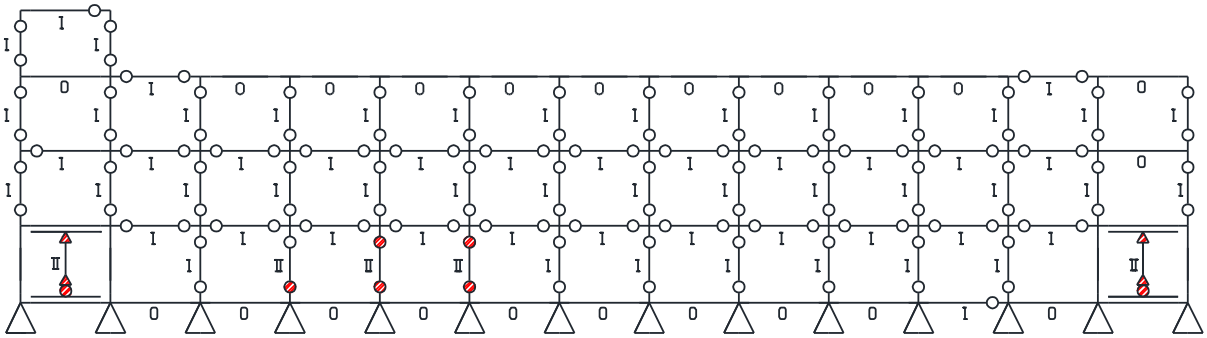

(c) I150

○ : Flexural crack
● : Flexural yield
△ : Shear crack
▲ : Shear yield

Figure 3. Collapse mechanism and damage index of Y4 axis （the artificial ground motion XY）

THE CALCULATION RESULT OF REPAIR COST

Figure 3 shows the result of comparison of repair costs. When compared at the maximum value of the artificial ground motion, the repair cost of I125 is 20% less than that of I100 and I150 is 60% less than I125. When compared with the maximum value of the recorded ground motion, I125 is 40%~50% less than I100 and I150 is 60% less than I125. When compared with the minimum value of the artificial ground motion, I125 is 30% less than I100 and I150 is 80% less than I125. When compared with the minimum value of the previous wave, I125 is 50%~70% less than I100 and I150 is 80% less than I125. On average, I125 is 25% less than I100 and I150 is 70% less than I125 in the artificial ground motion. On average, I125 is 50% less than I100 and I150 is 70% less than I125 on the recorded ground motion.

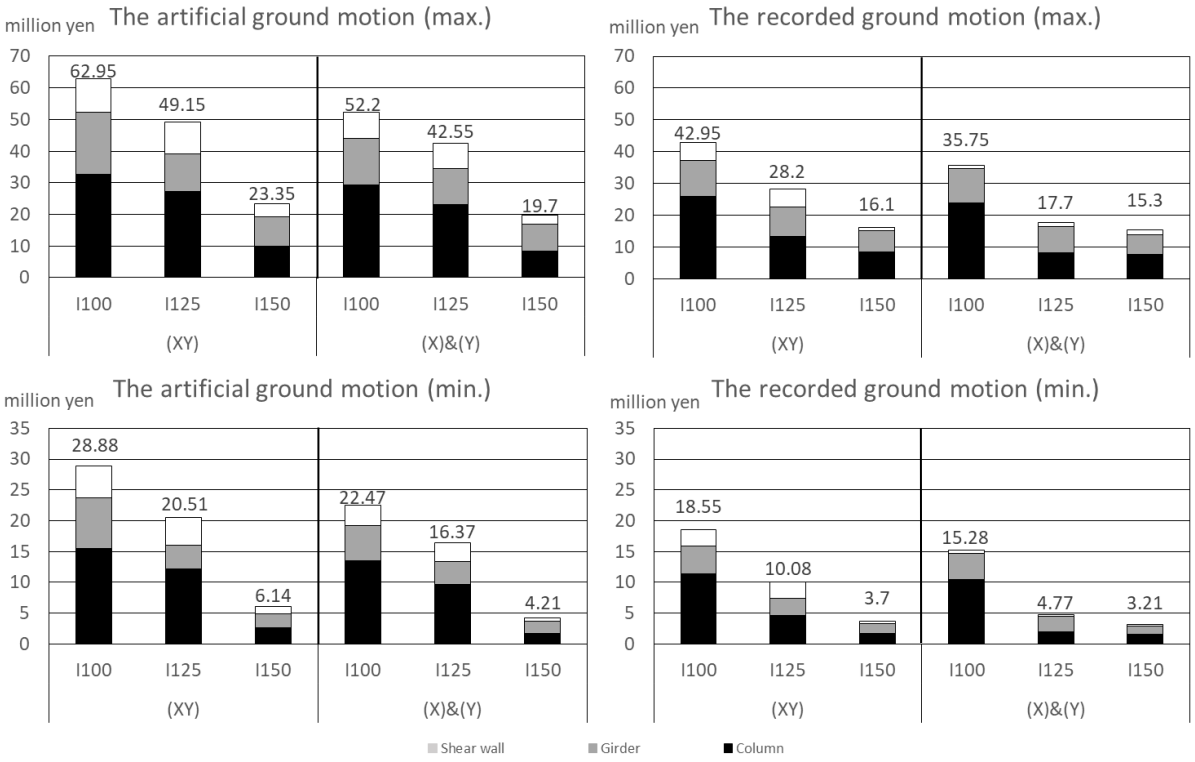

Figure 3. The result of comparison of repair costs

CONCLUSION

The time history response analysis of RC school building models with different importance factor was performed, the damage index to the members was determined, and the repair cost was calculated. I100, I125 and I150 are analysis models of importance factor 1.0, 1.25 and 1.5. The findings are summarized as follows.

1) The repair costs input in two directions of I100 and I125 are higher than the repair costs input in each direction of I100 and I125. For the I150 the repair costs of (XY) and (X)&(Y) are almost the same

2) The repair costs are reduced as the importance factor increases. In the artificial ground motion (XY), the repair cost of I100 is 28.88~62.95 million yen, the repair cost of I125 is 20.51~49.15 million yen, the repair cost of I150 is 6.14~23.35 million yen.

3) The importance factor of 1.5 markedly reduced the repair cost. The repair cost of importance factor of 1.5 is 60%~80% less than the repair cost of importance factor of 1.0.

REFERENCES

Architectural Institute of Japan (2004). "Guidelines for Performance Evaluation of Earthquake Resistant Reinforced Concrete Buildings (Draft)," pp.61-69. (In Japanese)

Matsumura, D., et al. (2019). "A Study on the Influence of Seismic Zoning Factors on the Structure Cost and the Repair Cost of the RC School Building" International Conference in Commemoration of 20th Anniversary of the 1999 Chi-Chi Earthquake Taipei, Taiwan, September 15-19, 2019

Minamiguchi, S., Kishimoto, I. (2012) "Calculation Formula of Crack width on RC Columns under Bending and Shear Force" Transactions of AIJ. Journal of structural and construction engineering 77th-681, pp.1709-1716

Nakashima, K., et al. (2003) **"**Evaluation Method of Earthquake-Resistant Performance in Consideration of Durability and Restoration Performance Pt.2 Proposal of Restoration Expense calculation formula" Architectural Institute of Japan Summaries of technical papers of annual meeting (Tokai). (In Japanese)

Nagayama, K., et al. (2001). "An Evaluation of residual Seismic Capacity of Reinforced Concrete Buildings Based on the Damage of Columns Part 2. The Relation between the Residual Crack Width and the Deformation of the Member" Architectural Institute of Japan Summaries of technical papers of annual meeting (Kanto) pp.453-454. (In Japanese)

Takahashi, S., et al. (2017). "Space and Width of Cracks on Reinforced Concrete Beams under Shear and Flexural Loads" Architectural Institute of Japan Tokai Chapter Architectural Research Meeting, 55th, pp.117-180. (In Japanese)

The Building Center of Japan, (2016). "The Building Standard Law of Japan on CD-ROM May 2016"

8th Asia Conference on Earthquake Engineering
Taipei, Taiwan ■ November 9-11, 2022

UNSTRESSED STEEL STRANDS AS LONGITUDINAL REINFORCEMENT IN REINFORCED CONCRETE ELEMENTS

Jones Joju[1], Yu-Chen Ou[2], Yi-Ching Liu[3], Wen-Chi Hsu[4], and Meng-Yi Hsieh[4]
1. Doctoral Candidate, National Taiwan University, Taipei, Taiwan, R.O.C.
2. Distinguished Professor, National Taiwan University, Taipei, Taiwan, R.O.C.
3. Former Graduate Student, National Taiwan University of Science and Technology, Taipei, Taiwan, R.O.C.
4. Former Graduate Student, National Taiwan University, Taipei, Taiwan, R.O.C.
Email: mjonesjoju@gmail.com, yuchenou@ntu.edu.tw

ABSTRACT

Summarized herein are the motivation, special design details developed, and key findings from an extensive experimental study conducted at National Taiwan University to investigate the effectiveness of using unstressed steel strands as longitudinal reinforcement in reinforced concrete elements. As a part of the study, multiple flexurally dominant columns, shear-critical columns, and beam-column joints were tested under cyclic loading to evaluate seismic behaviour. Special anchorage design details were developed to anchor the unstressed steel strands at the column ends and joint region. Flexurally dominant columns with strands as longitudinal reinforcement exhibited enhanced re-centering capabilities and adequate drift capacities to be qualified for seismic applications, albeit with reduced energy dissipation characteristics. Shear-critical columns tested performed satisfactorily and the available design procedures were able to conservatively estimate the shear strength. Finally, the beam-column joint specimens failed by beam plastic hinge formation as intended in the design. Test results indicated the relative ineffectiveness of strands in compression, where the strand bulged and unwound once the concrete cover deteriorated. Despite this, strands straightened up and continued to sustain tensile stresses under load reversal. Based on the experimental observations, constitutive models were developed for steel strands embedded in concrete for reliable strength prediction.

Keywords: Steel strands, Reinforced concrete, Seismic behaviour, Constitutive model, High-strength steel, Anchorage design, longitudinal reinforcement.

INTRODUCTION

Design standards across the world restrict the maximum strength of reinforcing steel that could be used in concrete elements. In this regard, ACI-318 (ACI 318, 2019) restricts the specified yield strength to be limited to a maximum of 550 MPa, 690 MPa, and 550 MPa for longitudinal reinforcement, concrete confinement, and shear reinforcement, respectively for columns in special moment frames. This capping of steel strength primarily arises from the lack of comprehensive experimental tests and systematic studies to develop necessary design guidelines to enable the use of steels with higher yield strengths (Aoyama, 2001; NIST, 2014). This led to significant research in the past three decades in exploring the possibilities of using high-strength deformed bars. However, high-strength deformed bars are not readily available today, especially in developing countries. In contrast, steel strands widely used for prestressing applications are. The use of steel strands with significantly high yield stress (Grade 1860 MPa) also offers an economic advantage due to reduced shipment costs, labour charges, and low cost per unit strength. For instance, in Taiwan, the low relaxation Grade 1860 MPa seven-wire steel strands confirming to ASTM 416 (ASTM A416, 2010) used in the current study approximately resulted in a 40% reduction in cost per unit strength (Ou et al., 2020).

However, no prior study, which uses unstressed steel strands as the sole longitudinal reinforcement in concrete columns and beam-column joints has been reported in the literature. Thus, the objective of the current study is to critically evaluate the feasibility of using unstressed Grade 1860 MPa seven-wire steel strands as longitudinal reinforcement in place of conventional deformed bars in reinforced concrete columns and beam-column joints designed to resist seismic loading. To achieve the

above objective, an extensive experimental program was carried out, in which multiple flexurally dominant columns, shear-critical columns, and beam-column joints were cyclically loaded. Backed up by the results of the experiment, design constitutive models for steel strands were proposed for strength prediction. The proposed strand constitutive model addresses the strand response for both compression and tension regimes, provided the steel strands are embedded in concrete. The classically available strand constitutive models in the literature were defined only for tension loading (Caltrans, 2013). Finally, the use of steel strands with considerably higher yield stress also necessitated the development of special design details to effectively anchor the strands at the column end and in the beam-column joint region.

It is to be noted that the emphasis of this study was on columns and beam-column joints which were subjected to combined axial load and bending moment; and was designed to resist seismic loads. Under combined bending and axial loads, and to ensure the toughness necessary in structures to resist seismic loads, it is preferable to size columns so that the expected axial load demand falls below the balanced point. In this domain, the moment capacity of the column is controlled by the reinforcement in tension, which suggests that the use of high-strength reinforcement may be beneficial. Columns subjected to high axial load (axial loads above 0.3 $f_c'A_g$) were not considered and are a topic for future research.

A BRIEF SUMMARY OF THE EXPERIMENTAL PROGRAM

An extensive experimental program comprising flexurally dominant columns, shear-critical columns, and beam-column joint specimens was conducted. The specimens were subjected to displacement-controlled cyclic loading and were tested at the National Center for Research on Earthquake Engineering (NCREE) in Taiwan.

Column Flexure Specimens

To evaluate the flexural response of columns with unstressed steel strands (Grade 1860 MPa) as longitudinal reinforcement, a total of eight large-scale column specimens were cyclically loaded under constant axial load. The columns were tested in a double curvature fashion where both ends of the column were fixed. Out of the total ten specimens, three specimens used conventional rectilinear ties while the rest specimens used multi-spiral transverse reinforcement detailing. The transverse reinforcement in all specimens used conventional deformed bars (Grade 420 MPa) allowing the specific evaluation of the change in structural behaviour caused by the replacement of conventional deformed bars with unstressed steel strands. Further, the volumetric ratio of the transverse reinforcement in all the specimens considered in this study slightly exceeded the minimum confining steel requirement of ACI 318. All the test specimens had a column height of 2.4 m and a square cross-section of 600×600 mm and were designed to have a flexural failure mode. Two grades of concrete (35 and 70 MPa) and two axial load levels (0.1 and 0.3 $f_c'A_g$) were considered in the evaluation of flexural behaviour. Further details of the test specimens and experimental setup can be found elsewhere (Ou et al., 2020, 2022c).

Column Shear Specimens

To evaluate the shear behaviour of the columns with unstressed steel strands (Grade 1860 MPa) as longitudinal reinforcement, six large-scale shear-critical columns were designed and cyclically loaded under constant axial load. All the columns had a square cross-section of 600×600 mm and a column height of 1.8 m. The columns were tested in a double curvature fashion with all specimens having a span-to-effective depth ratio (a/d) of 1.875. Further, all the columns had a design compressive strength of 49 MPa and transverse reinforcement used grade 420 MPa deformed bars. As shear behaviour was under consideration, two types of transverse reinforcement layouts in the form of rectilinear ties and multi-spiral transverse reinforcement were considered. Finally, two axial load levels (0.1 and 0.3 $f_c'A_g$) were considered in the evaluation of shear behaviour Further details of the test specimens and experimental setup can be found elsewhere (Ou et al., 2022b).

Beam-Column Joint Specimens

Five beam-column joint specimens: three exterior and two interior specimens were subjected to cyclic loading to investigate the effectiveness of using unstressed steel strands (Grade 1860 MPa) as full/partial replacement for the conventional Grade 420 MPa deformed bars as beam longitudinal reinforcement. All the specimens were designed to fail through plastic hinge formation in the beams. Thus. This study also allows the evaluation of the beam flexural behaviour. The columns in all the test specimens were the same, with an effective column height of 3.2 m and a square cross-section of 800 × 800 mm. The beams in the test specimens had the same cross-section dimension of 400 × 700 mm. Also, the same transverse reinforcement detailing was adopted in all specimens. The transverse reinforcement detailing adopted satisfied the confinement requirement of ACI 318 (ACI 318, 2019). Further, all the specimens had a design compressive strength of 42 MPa. The major difference between test specimens was in the use of longitudinal reinforcement, where steel strands fully/partially replaced conventional deformed bars. A special hooked anchorage was developed to anchor the steel strands in the joint region. Further details of the test specimens and experimental can be found elsewhere (Ou et al., 2022a).

SPECIAL DESIGN DETAILS DEVELOPED

An important aspect that needed special attention was finding an effective method to anchor the unstressed steel strands. The seven-wire steel strand requires a considerably larger development length owing to the high tensile strength of the strand, and its relatively inferior bond characteristics compared to conventional deformed bars. Hence, two special anchorage details were developed as a part of the study to anchor steel strands at column/beam ends and at the joint region.

Special Two-way Anchorage System at Member Ends

If the strands were to develop their capacity (1860 MPa), the development length that would be required is equal to 4049 mm according to ACI-318 (ACI 318, 2019). Hence, the strands were anchored with the aid of steel end plates. A special two-way anchorage system, which locked the strand in both directions was specially developed. This special two-way anchorage system is important because the conventional anchors available in the market can lock the strand in tension only. As the strands are expected to undergo tension-compression cycles under cyclic loading, effectively locking the strands in both directions is necessary at the column/beam ends. The anchorage system consisted of steel strands locked in both directions by wedges, and the barrel which holds the wedges was in turn welded to the steel end plates. For the purpose of specimen design considered in the study, the entire anchorage system was conservatively designed such that the strands could develop the tensile strength of 1860 MPa. Figure 1 depicts the anchorage system and its layout. Further details of the anchorage system can be found elsewhere (Ou et al., 2022c).

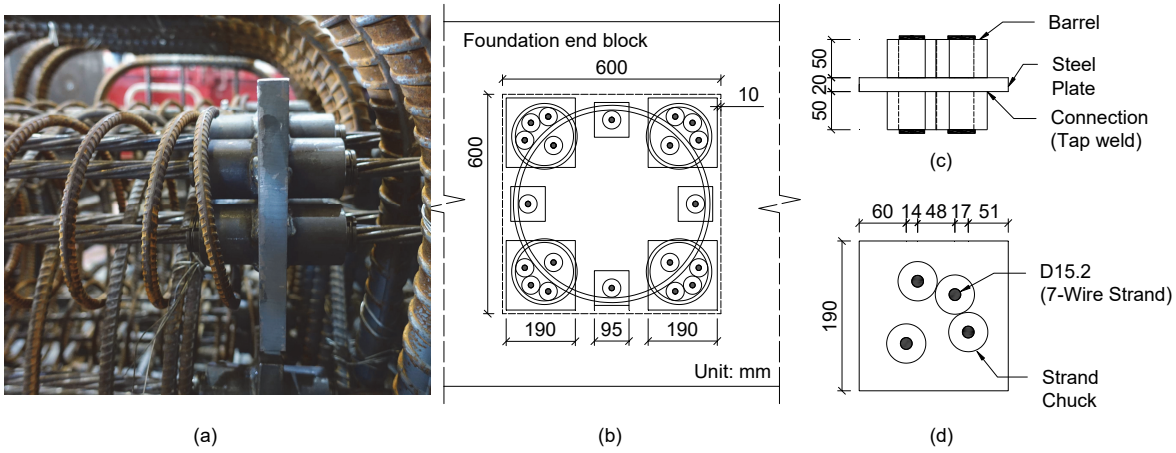

Figure 1. (a) Anchorage system kept in position inside the reinforcement cage; (b) anchorage system layout of columns with multi-spiral layout; (c) elevation of a typical corner anchorage; and (d) plan of a typical corner anchorage.

Special Hooked Anchorage System at Beam-Column Joints

Typical columns' available straight development length (in the joint region) will be insufficient to anchor steel strands with very high tensile strengths (Grade 1860 MPa steel strand). For instance, the required column depth to anchor a steel deformed bar of yield stress 1674 MPa that passes through an interior column equals 80 d_b (d_b =bar diameter) as per ACI 352 (ACI 352, 2010). Thus, in the case of a deformed steel bar with a bar diameter, same as the D15.2 (Grade 1860 MPa) steel strand used in the study; the minimum required column depth turns out to be 1211 mm. Thus, allowing longitudinal reinforcements of high yield capacities to pass through the beam-column joint will result in substantially large column sizes to satisfy the bond requirements alone. Hence, a special hooked anchorage system was developed to anchor the steel strands. The required joint straight development length (for hooked anchorage) was estimated using the current ACI 318-19 provisions for Type 2 joints, which is given by Equation 1:

$$l_{dh} = \frac{f_y d_b}{5.4\sqrt{f_c'}}(MPa) = \frac{1674 \times 15.2}{5.4\sqrt{42}} = 727\ mm \quad (1)$$

Though Equation 1 was initially developed for joints with deformed bars, the same equation has been used to estimate the joint development requirement for steel strands. Figure 2 shows a three-dimensional view of the joint, which illustrates the hooked anchorage provided for the strands at the joint. The joint confinement reinforcement is not depicted in Figure 2 to clearly illustrate the hooked anchorage detail. In the special hooked anchorage system developed, the beam longitudinal steel strands were bent 180° backwards and taken back to the same beam. Additional anchor bars were appropriately placed in the joint in addition to the longitudinal column reinforcement, as shown in Figure 2, to assist the anchorage of the steel strand at the 180° hook. The experimental study revealed that the proposed anchorage detail was effective. The fracture of steel strands at the beam plastic hinge location confirmed that the special hooked anchorage detail developed was efficient in anchoring the steel strands. Further details of the anchorage system can be found elsewhere (Ou et al., 2022a).

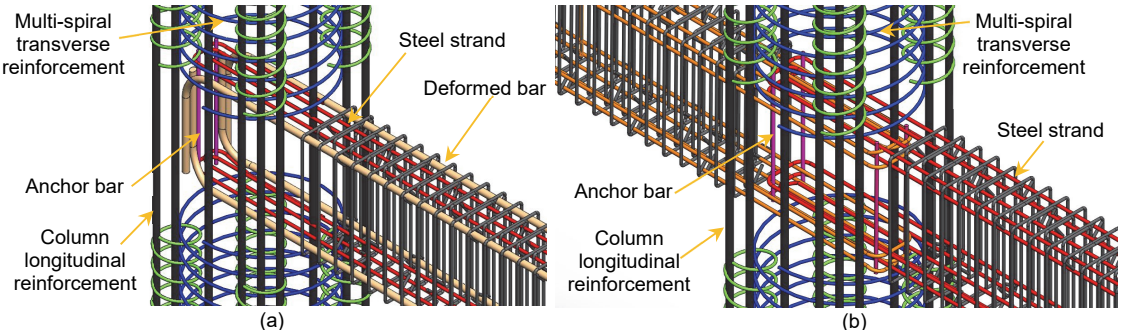

Figure 3. Joint reinforcement detail of (a) Exterior joint specimen with partial replacement of deformed bars by strands; and (b) Interior joint specimens with full replacement of deformed bars by strands.

KEY FINDINGS FROM THE EXPERIMENTAL PROGRAM

Conventional wisdom suggests that steel strands are effective only in tension and are too flexible to sustain any sort of compressive loading. However, steel strands can sustain compressive stresses to a limited extent when the strands are embedded in concrete. The experimental program conducted as part of this study provided valuable data to quantify the behaviour of unstressed steel strands embedded in concrete. Also, the experimental program highlighted the satisfactory seismic performance of columns and beam-column joint specimens. Procedures to estimate the strength of the specimens for design purposes were also developed.

Strand Constitutive Model

The experimental results showed that strands under compression tend to bulge and unwind, and subsequently lose their capacity to sustain compressive stresses. This happened once the surrounding confinement weakened. The experimental results also showed that strands straightened up to sustain tensile stresses under load reversals (see Figure 3). Therefore, in the proposed constitutive model, strands are conservatively assumed to effectively sustain compressive stresses same as tensile stresses till a compressive strain of 0.002, and thereafter the compressive stress in strands drops to zero. The strain of 0.002 corresponds approximately to the strain at the peak compressive stress of cover concrete. As strands straightened up to sustained tensile stresses under load reversal even after experiencing bulging and unwinding under compression, the strands are considered effective in tension even after experiencing compressive strains exceeding 0.002. The strain data recording obtained from the strands also agrees with the above observations. Thus, two constitutive models; one which considers strain hardening (Model A) and the other which assumes an elasto-perfectly plastic response in tension (Model B) were proposed for strands. Equations 2, 3, and 4 are used to construct Model A. And equations 2, 3, and 5 are used to construct Model B.

$$\varepsilon_s < -0.002 : f_s = 0 \tag{2}$$

$$-0.002 < \varepsilon_s < \varepsilon_{ys} : f_s = E_s \varepsilon_s \tag{3}$$

$$\varepsilon_{ys} < \varepsilon_s < 0.03 : f_s = A - \frac{B}{\varepsilon_s - C} \tag{4}$$

$$\varepsilon_{ys} < \varepsilon_s < 0.03 : f_s = E\varepsilon_{ys} \tag{5}$$

where the values of yield strain (ε_{ys} = 0.0086), strand elastic modulus (E_s = 191349 MPa), and the constants (A = 2021, B = 1.72 and C = 0.004) are obtained to closely match the experimental stress-strain response of the steel strands. Figure 4 illustrates Model A, Model B, and the Caltrans strand model and how those compare with the experimental tensile test data. Details on the development of the bilinear and strain hardening strand constitutive models can be found elsewhere (Ou et al. 2022c).

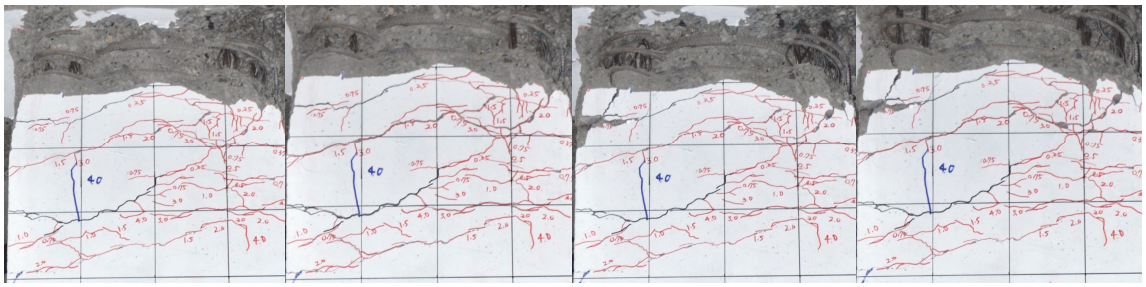

Strand unwrapped + 5% (1st cycle) | Strand straightened - 5% (1st cycle) | Strand unwrapped + 6% (1st cycle) | Strand straightened - 6% (1st cycle)

Figure 3. View of a typical column specimen during cyclic loading at the drift levels specified in the figure.

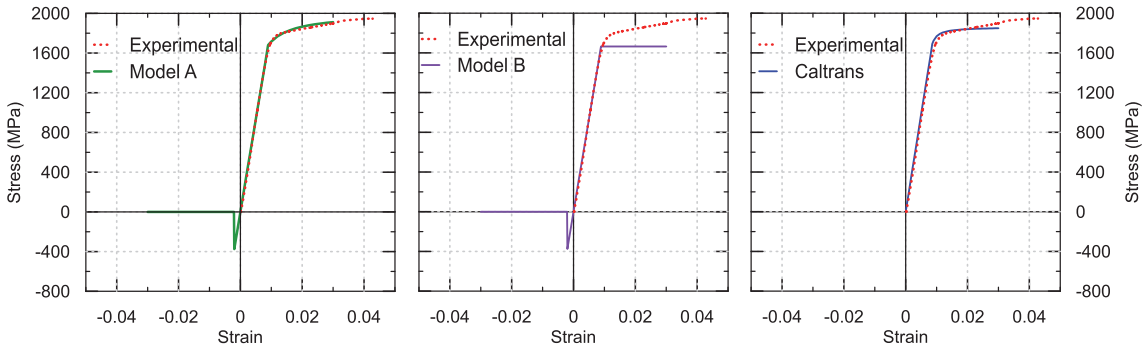

Figure 4. Stress-strain relationship of seven-wire steel strands.

Column Flexural Behaviour

The failure mode of column specimens with strands as longitudinal reinforcement was due to a combination of strand fracture and core concrete crushing. Columns with unstressed steel strands as longitudinal reinforcement exhibited drift capacities ranging between 4.96-5.70%, which is well over the conventional expectation of 3.50% drift requirement for columns in special moment frames. Specimens with strands exhibited fewer and wider cracks, in comparison with the control specimen which used deformed bars as longitudinal reinforcement. Further, the specimens exhibited lower energy dissipation but enhanced re-centering capability owing to the fact that the strands have significantly higher tensile yield capacity compared to deformed bars (see Figure 5). The hysteretic response was close to a flag-shaped one for a drift ratio till 4.0%, indicative of its self-centering capability. A reduction in effective elastic stiffness was also observed as the post-cracking stiffness of specimens with strands dropped due to the low longitudinal reinforcement ratio provided.

The proposed strand constitutive models, Model A and Model B were used for flexural strength prediction. Model A when used in the detailed moment-curvature analysis was able to produce reasonably accurate estimates for flexural strength. Both constitutive models when used in the simplified analysis which considers equivalent stress block (similar to ACI flexural strength prediction procedure) for concrete was able to consistently produce conservative estimates of flexural strength, which is suitable for design purposes.

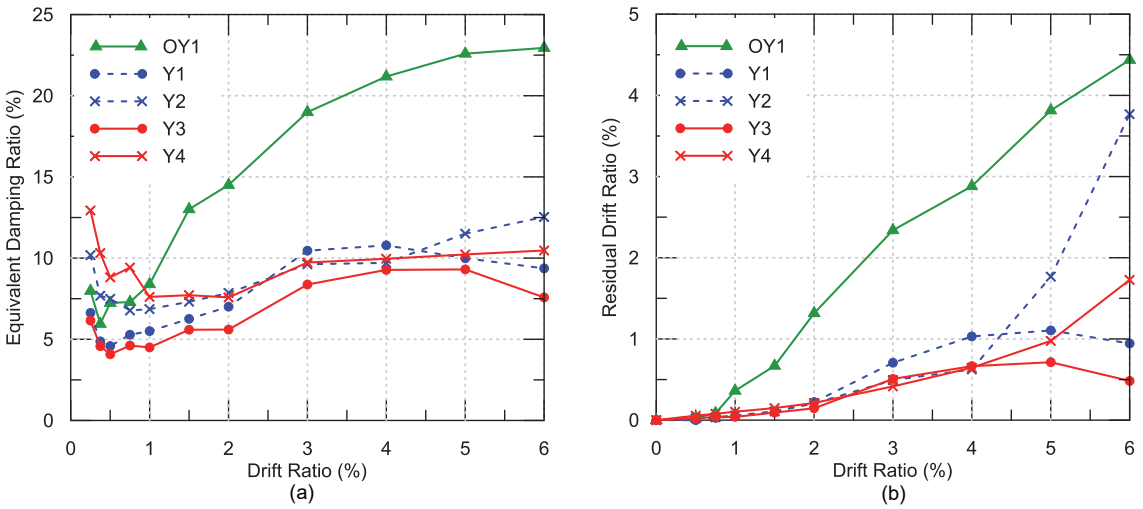

Figure 4. (a) Equivalent damping ratios; and (b) residual drift, of columns with multi-spiral transverse reinforcement layout (Ou et al., 2022c).

Column Shear Behaviour

The experimental tests indicated that the specimens with strands as longitudinal reinforcement failed in shear as intended in the design. Specimens with strands exhibited long diagonal shear cracking and transverse reinforcement yielding at or before the attainment of peak load sustained during cyclic loading. The yielding of transverse reinforcement for all the specimens (see Figure 5) suggests that the use of strands as longitudinal reinforcement did not hamper the transverse reinforcement in developing stresses expected in design to resist shear loads. The behaviour of specimens with unstressed steel strands as longitudinal reinforcement varied considerably depending upon the type of transverse reinforcement layout adopted. The multi-spiral transverse reinforcement layout was able to better confine the core concrete and restrain the longitudinal reinforcement compared to rectilinear ties. Finally, both the ACI-318 simplified and detailed shear strength prediction methods were able to conservatively estimate the shear strength of the test specimens. In comparison with the ACI-318 simplified method, shear strength prediction by the ACI-318 detailed method was able to produce safer estimates with less variation. In addition to the ACI method to estimate steel contribution to shear strength, modified discrete computational shear strength (mDCSS) model was also used for columns with multi-spiral

transverse reinforcement (Ou et al., 2021). The mDCSS method provided more accurate result with less variation than the ACI method.

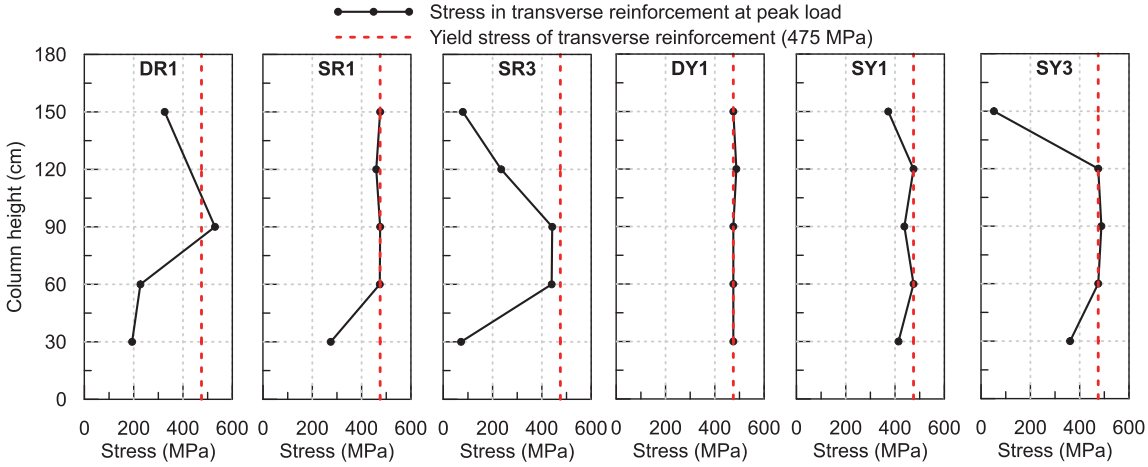

Figure 5. Stress distribution in transverse reinforcement of column specimens at their corresponding peak load (Ou et al. 2022b).

The Behaviour of Beam-Column Joints

All the beam-column joint test specimens failed by beam plastic hinge formation near the column face as intended in design, with drift capacities between 5.12 % and 7.57%, which is well over the ACI 374.1 (ACI 374.1, 2005) requirement of 3.50% drift in special moment frames. In specimens where strands partially (50%) replaced the deformed bars as beam longitudinal reinforcement, drift capacities ranged between 6.74-7.57%, comparable to the 6.92% drift capacity of the control specimen which had deformed bars as beam longitudinal reinforcement. However, the full (100%) and partial (50%) replacement of deformed bars by strands led to a 58% and 28% decrease in average relative energy dissipation. Despite this, the full/partial replacement of deformed bars by strands as beam longitudinal reinforcement resulted in enhanced reentering capabilities. Fracture of longitudinal steel strands observed in the beam plastic hinge region at the end of the test indicated the effectiveness of the special hooked anchorage detail in allowing steel strands to develop their capacity. Further, the flexural strength of the beams of test specimens was evaluated through a detailed moment-curvature analysis, which predicted the beam flexural strength with high accuracy and less variation (mean = 1.01, standard deviation = 0.02). After that, beam flexural strengths were evaluated following the ACI 318 (ACI 318, 2019) procedure modified to include the proposed bilinear strand model, which produced conservative estimates of beam flexural strength (mean = 1.15) suitable for design. Also, the procedure to estimate the beam's probable flexural strength is presented. Finally, required modifications to the conventional seismic design procedure were proposed to incorporate the use of strands as beam longitudinal reinforcement. Specific details can be found elsewhere (Ou et al. 2022a).

CONCLUSIONS AND SCOPE FOR FUTURE WORK

The study comprehensively evaluated the seismic response of columns and beam-column joints with unstressed steel strands as longitudinal reinforcement. This being the first ever extensive study reported in the literature, further research is required before using strands as the sole longitudinal reinforcement in concrete elements. The behaviour of columns under high axial load levels, long-term durability considerations, and serviceability criteria are the three main areas where further research is required. Despite the above-mentioned shortcomings, the present study provided valuable information regarding the behaviour of concrete columns and joints with strands as longitudinal reinforcement. Also, the special anchorage details developed as a part of this research performed as intended during the experimental tests. Further, the study demonstrated the satisfactory seismic response of concrete elements with strands as longitudinal reinforcement. The specimens exhibited adequate drift capacity

with enhanced re-centering capabilities which are promising. Furthermore, the study based on experimental observations developed constitutive models for steel strands embedded in concrete, which considers the response of steel strands in both tension and compression. Finally, the constitutive models, when used for flexural strength prediction of columns and beams produced reasonably accurate results with less variation which is suitable for design purposes.

ACKNOWLEDGMENTS

The authors would like to thank the support from the Ministry of Science and Technology of Taiwan under Contract Nos. 106-2221-E-002 -233 -MY3, from the Ruentex Engineering & Construction Co., Ltd of Taiwan, and from the National Center for Research on Earthquake Engineering (NCREE) of Taiwan.

REFERENCES

ACI 318. (2019). *Building Code (ACI 318-19) and Commentary on Building Code Requirements for Structural Concrete (ACI 318R-19)*. *American Concrete Institute*. Farmington Hills, MI.

ACI 352. (2010). *Recommendations for Design of Beam-Column Connections in Monolithic Reinforced Concrete Structures*. Farmington Hills, MI.

ACI 374.1. (2005). *Acceptance Criteria for Moment Frames Based on Structural Testing and Commentary: an ACI Standard*. *American Concrete Institute.*

Aoyama, H. (2001). *Design of modern high-rise reinforced concrete structures*. London, UK: Imperial College Press.

ASTM A416. (2010). *Standard Specification for Steel Strand, Uncoated Seven-Wire for Prestressed Concrete*. West Conshohocken, PA.

Caltrans. (2013). *Seismic Design Criteria Version 1.7*. *Caltrans*. Sacramento, CA.

NIST. (2014). *Use of High-Strength Reinforcement in Earthquake-Resistant Concrete Structures*. Gaithersburg, MD.

Ou, Y. C., J. Joju, and M. Y. Hsieh. (2022a). "Seismic Behavior of Reinforced Concrete Beam-Column Joints with Unstressed Steel Strands Fully or Partially Used for Beam Longitudinal Reinforcement." *Journal of Building Engineering (Forthcoming)*.

Ou, Y. C., J. Joju, and W. C. Hsu. (2022b). "Cyclic behavior of shear-critical concrete columns with unstressed steel strands as longitudinal reinforcement." *Engineering Structures*, 264: 114465.

Ou, Y.-C., J. Joju, and Y.-C. Liu. (2022c). "Cyclic Behavior of Reinforced Concrete Columns with Unstressed Steel Strands as Longitudinal Reinforcement." *Journal of Structural Engineering*, 148 (9): 04022125.

Ou, Y. C., J. Y. Li, and H. Roh. (2021). "Shear strength of reinforced concrete columns with five-spiral reinforcement." *Engineering Structures*, 233: 111929.

Ou, Y. C., S. Y. L. Yin, Y. Q. Liu, and J. C. Wang. (2020). "Cyclic Behavior of a Reinforced Concrete Column with Unstressed Seven-Wire Steel Strands as Longitudinal Reinforcement." *Special Publication*, 341: 97–104.

SEISMIC PERFORMANCE OF RESILIENT FRAME-CORE TUBE STRUCTURE

Shurong Li[1,2] and Huanjun Jiang[3]
1. Key Laboratory of Building Structural Retrofitting and Underground Space Engineering, Ministry of Education, Shandong Jianzhu University, Jinan, China
2. School of Civil Engineering, Shandong Jianzhu University, Jinan, China
3. State Key Laboratory of Disaster Reduction, Tongji University, Shanghai, China
Email: lishurong20@sdjzu.edu.cn

ABSTRACT

This study evaluates the seismic performance of a new type of resilient frame-core tube structure with replaceable components. Two frame-core tube structures with 32 stories, including one conventional structure and one new structure with replaceable components, were designed. Nonlinear numerical models were developed using software Perform-3D and nonlinear dynamic analysis was carried out. The responses of two structures under different levels of earthquake were analyzed and compared. The results indicate that the seismic performance of resilient structure improves significantly.

Keywords: resilient structure, replaceable components, numerical simulation, seismic performance

INTRODUCTION

Previous earthquakes(Wallace 2012; Kawashima et al. 2009) indicated that the coupling beams and the bottom corners of wall piers suffered severe damage. The damage not only is difficult to repair, also the related cost and time of repair are high.

Many researchers have put forward various types of energy-dissipation devices (replaceable part) installed at the mid-span of coupling beams, such as steel damper(Ji et al. 2016; Fortney, Shahrooz, and Rassati 2006; Lu, Chen, and Jiang 2018), friction damper(Qu et al. 2020), viscoelastic damper (Montgomery and Christopoulos 2015)and combined damper(Kim et al. 2012). During earthquakes, the energy-dissipation devices dissipate energy and protect the main structure. After earthquakes, the devices can be replaced. Christopoulos and Montgomery (2013) analyzed the wind and earthquake response of two high rise buildings incorporating viscoelastic damper installed at the middle of coupling beams. Ji conducted the seismic performance evaluation of a tall building with replaceable coupling beams. Based on the FEMA P-58 method, the repair time and cost of the building were estimated. Compared with conventional building, the repair cost and time reduced significantly. Lu(Lu et al. 2013) developed a replaceable corner component(RCC) installed at the bottom corner of wall piers to reduce the damage of the wall corner.

Considering that the coupling beam and the bottom corners of wall piers are vulnerable to severe damage during strong earthquakes, a resilient coupled shear wall with replaceable coupling beams and RCCs was developed. And two finite element models, including one conventional frame-core tube structure and one frame-core tube structure with resilient shear wall, were established using software Perform-3D. And the seismic responses of two structures were compared.

DESCRIPTION OF RESILIENT SHEAR WALL

Figure 1 illustrates the resilient coupled shear wall with replaceable components. A composite damper, which consists of metallic damper and viscoelastic damper, is installed at the mid span of coupling

beams. Replaceable corner components (RCCs) installed at the bottom corner of wall piers, and it consists of buckling-restrained mild steel core and the concrete filled steel tube. During earthquakes, composite damper and RCC yield successively and dissipate energy, protecting the other parts of the coupled shear wall. The details of composite damper and RCC can refer to reference (Huanjun Jiang et al. 2022). Cyclic loading tests on the resilient coupled shear wall were carried out and the test results show that this wall has superior seismic performance (Huanjun Jiang et al. 2022).

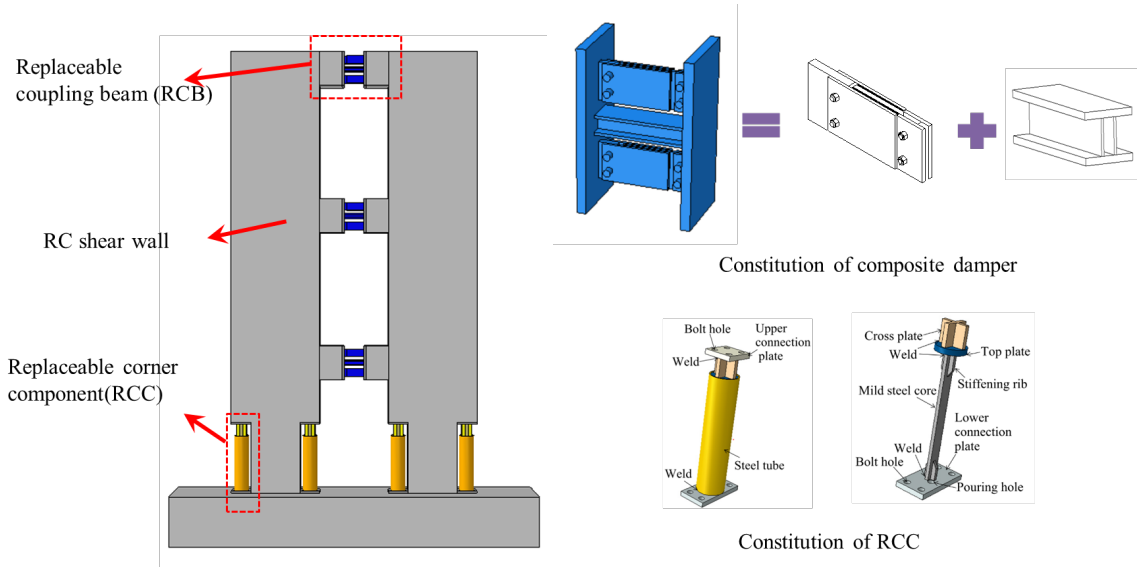

Figure 1. Resilient coupled shear wall

CASE STUDY

Project profile

A typical frame-core tube structure with 32 stories was designed. The height of the floor was 4m, except for the first floor with a height of 5m. The conventional structure is referred as CS. The coupling beams and the bottom corner of wall piers with high force were replaced by the replaceable components. The RCCs were located at the first floor and the replaceable coupling beams were located at 2-20 stories. The layout of replaceable components is illustrated in Figure 2.

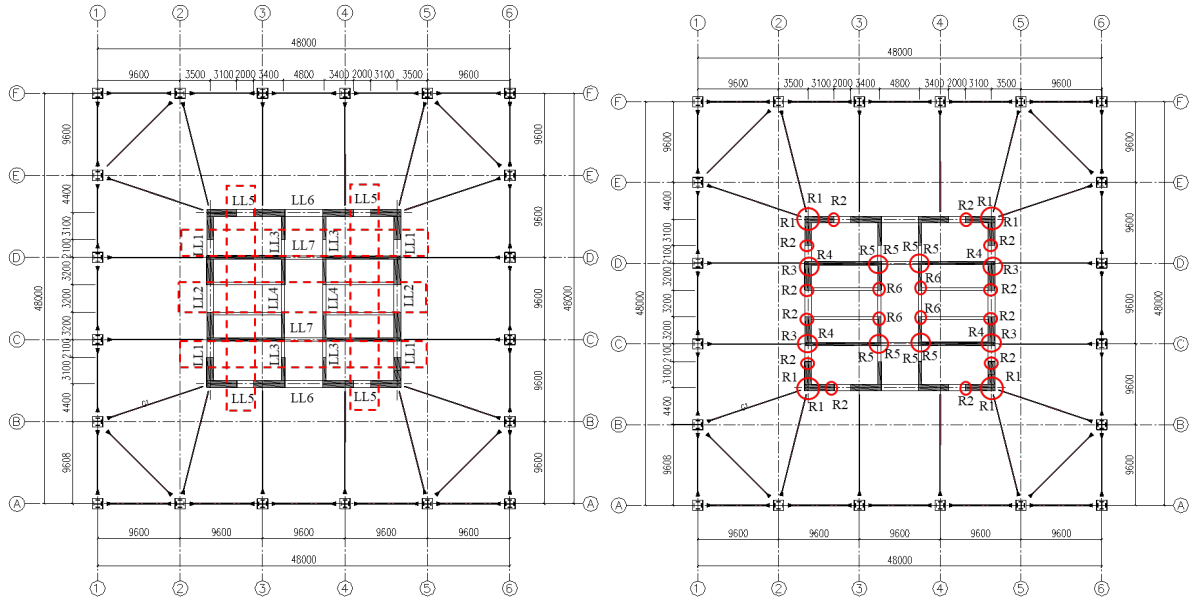

(a) Replaceable coupling beams (b) RCCs

Figure 2. Layout of replaceable components

The finite element models of the conventional frame-core tube structure (CS) and the new frame-core tube structure with replaceable components (NS) were established by software Perform-3d. P-delta effect was considered. The damping ratio was 0.04 for minor earthquakes and 0.05 for basic earthquakes and rare earthquakes. According to Chinese seismic design code, 7 earthquakes waves, including 5 natural waves and 2 artificial waves were used.

Analytical results

Dynamic characteristics

It can be found from Table 1 that the period of the new structure with replaceable components was larger than that of conventional structure, but the difference was small.

Table 1. Characteristics of the first six natural vibration modes

Mode number	Vibration form	Period/s		Difference
		CS	NS	/%
1	Translation in Y direction	2.528	2.617	3.52
2	Translation in X direction	2.476	2.492	0.65
3	Torsion	2.253	2.398	6.44
4	Torsion	0.7766	0.8057	3.75
5	Translation in Y direction	0.748	0.7803	4.32
6	Translation in X direction	0.6937	0.7018	1.17

Inter-story drift ratio

The average maximum inter-story drift ratio in Y direction under three levels of earthquakes is shown in Figure 3. Under minor earthquakes, the average maximum inter-story drift ratio for CS and NS was almost the same. Under moderate earthquakes and rare earthquakes, the maximum inter-story drift ratio of NS was reduced significantly.

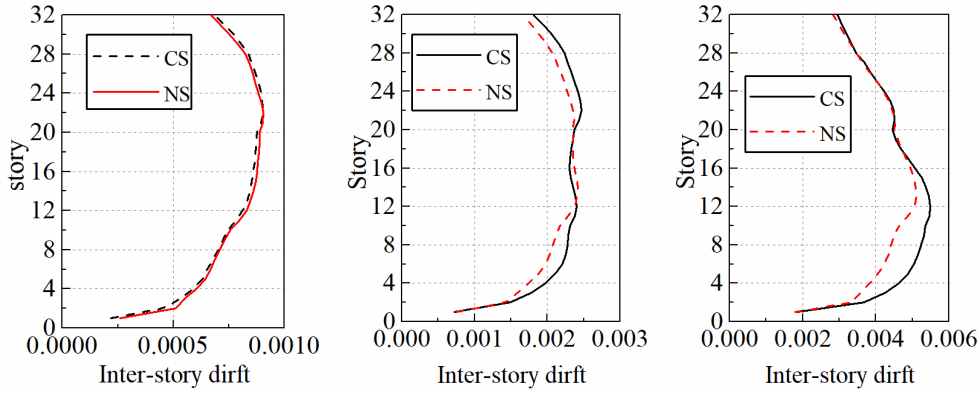

(a) Minor earthquakes (b) Moderate earthquakes (c) Rare earthquakes

Figure 3. Average maximum inter-story drift ratio in Y direction

Damage state

Figure 4 shows the damage state of coupling beams under rare earthquakes. In the new structure, all coupling beams are at the IO level and the maximum ratio of actual deformation to the limit value of IO level is 0.4, indicating that the damage of the replaceable coupling beams in NS is very slightly under rare earthquake. Figure 5 illustrates the damage state of shear walls under rare earthquakes. Different colors refer to the ratio of the steel bar strain to the yield strain. It can be found that the steel

bars remain elastic in the NS while part of steel bars in the bottom corner of wall pies of conventional structure yield. Above all, the damage concentrated on the replaceable components and the main structure was well protected.

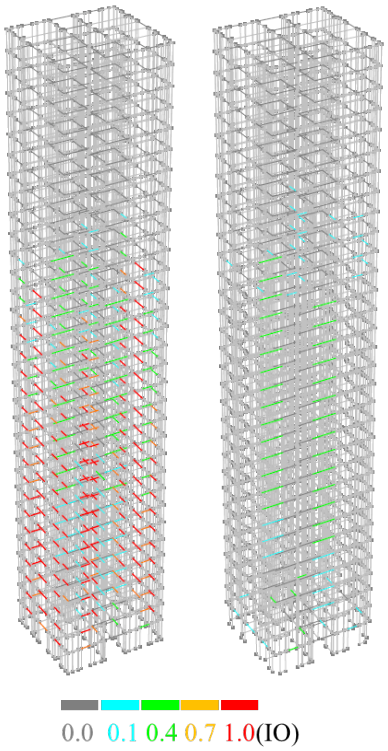

（a）CS（NGA55） （b）NS（NGA55）

Figure 4. Damage state of coupling beams under rare earthquakes

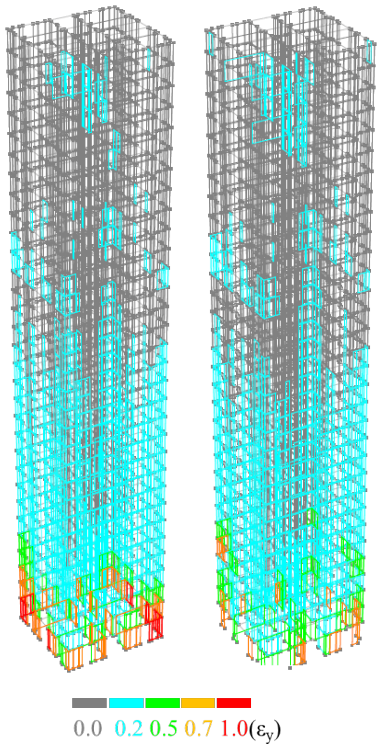

Figure 5. Damage state of shear wall under rare earthquakes

CONCLUSIONS

This study assesses the seismic performance of frame-core tube structure with resilient shear wall. The finite element analysis results indicate that the lateral stiffness of the resilient structure is slightly smaller than the conventional structure. Under strong earthquakes, the inter-story drift ratio of NS is reduced significantly and the damage occurs in the replaceable components.

ACKNOWLEDGMENTS

The authors would like to thank the support from Shandong Provincial Natural Science Foundation under Grant No. ZR2021QE268 and the National Natural Science Foundation of China under Grant No. 52038006.

REFERENCES

Christopoulos, C., and M. Montgomery (2013). "Viscoelastic Coupling dampers (VCDs) for Enhanced Wind and Seismic Performance of High-Rise Buildings," *Earthquake Engineering & Structural Dynamics* **42**(15), 2217-33.

Fortney, P. J., B. M. Shahrooz, and G. A. Rassati (2006). "The Next Generation of Coupling Beams," *Composite Construction in Steel and Concrete V*, 619-30.

Huanjun Jiang, Shurong Li, John E. Bolander, and Sashi K. Kunnath (2022). "Seismic Performance of a New Type of Coupled Shear Wall with Replaceable Components: Experimental Validation," *Journal of Earthquake Engineering*, 1-23.

Ji, X. D., Y. D. Wang, Q. F. Ma, and T. Okazaki. 2016. "Cyclic Behavior of Very Short Steel Shear Links." *Journal of Structural Engineering,* **142**(2), 04015114.

Kawashima, K., Y. Takahashi, H. B. Ge, Z. S. Wu, and J. D. Zhang (2009). "Reconnaissance Report on Damage of Bridges in 2008 Wenchuan, China, Earthquake," *Journal of Earthquake Engineering,* **13**(7), 965-96.

Kim, HJ, KS Choi, SH Oh, and CH Kang (2012). Comparative Study on Seismic Performance of Conventional RC Coupling Beams and Hybrid Energy Dissipative Coupling Beams Used for RC Shear Walls. Proceedings of the 15th World Conference on Earthquake Engineering, Lisbon, Portugal.

Lu, X. L., Y. J. Mao, Y. Chen, J. J. Liu, and Y. Zhou (2013). "New Structural System for Earthquake Resilient Design," *Journal of Earthquake and Tsunami*, **7**(3), 1350013.

Lu, Xilin, Yun Chen, and Huanjun Jiang (20180. "Earthquake Resilience of Reinforced Concrete Structural Walls with Replaceable "Fuses"," *Journal of Earthquake Engineering*, **22**(5), 801-25.

Montgomery, Michael, and Constantin Christopoulos (2015). "Experimental Validation of Viscoelastic Coupling Dampers for Enhanced Dynamic Performance of High-Rise Buildings," *Journal of Structural Engineering*, **141**(5),04014145.

Qu, Zhe, Xiaodong Ji, Xiao Shi, Yandong Wang, and Hanquan Liu (2020). "Cyclic Loading Test of Steel Coupling Beams with Mid-Span Friction Dampers and RC Slabs," *Engineering Structures,* **203**(1), 109876.

Wallace, John W (2012). "Behavior, Design, and Modeling of Structural Walls and Coupling Beams — Lessons from Recent Laboratory Tests and Earthquakes," *International Journal of Concrete Structures and Materials,* **6**(1), 3-18.

DEVELOPMENT OF PRECAST UHPC PANELS FOR SEISMIC STRENGTHENING OF RC FRAMES

Cheng-Hao Huang [1], Jing-Ya Wei [2] and Chung-Chan Hung[3]

1. Graduate Student, Department of Civil Engineering, National Cheng Kung University, 1 University Rd, Tainan City 701, Taiwan
2. Graduate Student, Department of Civil Engineering, National Cheng Kung University, 1 University Rd, Tainan City 701, Taiwan
3. Professor, Department of Civil Engineering, National Cheng Kung University, 1 University Rd, Tainan City 701, Taiwan

Email:, ken472513@gmail.com, g489518525@gmail.com, cchung@mail.ncku.edu.tw

ABSTRACT

This research takes the advanced concrete material Ultra-High Performance Concrete (UHPC) as the idea, and uses its high compressive strength, tensile strength, and crack control ability to establish a strengthening method for adding precast panels to improve the earthquake resistance of buildings. The research method is to design a reinforced concrete frame and a UHPC precast panel in frame, and use the strengthening or not and changing the location of retrofit as variables to study the effectiveness and characteristics of the strengthening.

The research results show that the strength of the retrofit frame is 2.8 times that of the original frame, and the stiffness is 4.1 times that of the original frame. Using UHPC as the precast panel material can inhibit the development of cracks and concrete crushing through its internal fiber bridging effect, thereby improving its shear strength and exhibiting ductile behavior. Moreover, due to its high strength properties, it can reduce the size of components to minimize the impact on occupants. And using the precast method also can reduce the disturbance to the occupants during the construction period, furthermore, precast method does not affect its earthquake-resisting capacity.

Keywords: seismic retrofit; UHPC; precast; panels; stub column

INTRODUCTION

When general concrete increases the depth of the component, it often leads to the formation of short columns or even walls, therefore engineers can only choose either ductility or strength. The mechanical properties and material properties of UHPC can provide high shear resistance, and maintain high shear strength when the depth of the component increases. In addition, it can maintain strength control by the bending moment strength, exhibiting ductile behavior.

In this study, designed seismic components whose aspect ratio was set as 2, and the construction method chose precast to conform to modern use, also make good use of the high bond ability of UHPC to establish a high-efficiency seismic retrofit method.

This paper presents the details of the UHPC precast panels retrofit scheme, the connections between the panel and the frame, and the experimental and analytical studies on the seismic behaviors of two half-scale, one-story, single-bay RC frames and one specimen only the precast panel.

MATERIALS AND METHODS

In this study, an earthquake-resistant panel and two strengthening frame specimens were designed, all specimens designed as a double-curvature behavior. The precast panels added diagonal reinforcement to increase energy dissipation capacity. The details of the specimen shown in Figure 1. The detailed design content includes strength design, joint design, and boundary beam capacity, first to ensure that the force between the retrofit member and the frame is effectively transmitted, and second, to check the retrofit does not cause a burden that which frame can’t afford.

Regarding the strength design, first calculating the bending moment strength with the contribute by diagonal bar's longitudinal component. Second, using softened strut-and-tie model to design the shear strength of the B-region (indicating a Bernoulli region) and D-region (indicating a disturbed region) shear strength to insure the maximum strength control by the flexural strength, for details, please refer to Hwang's research. Additionally, the frame design refers to the specimen designed by Hung et al, and the results of the non-retrofit frame is used as the control group of this study for comparison.

The experiment test in the Bi-Axial Testing System (BATS) of the National Earthquake Research Center in Tainan, using cyclic loading to test the capability of the retrofit method. By observing the experiment and analyzing the test results to evaluate the benefit and feasibility of the retrofit.

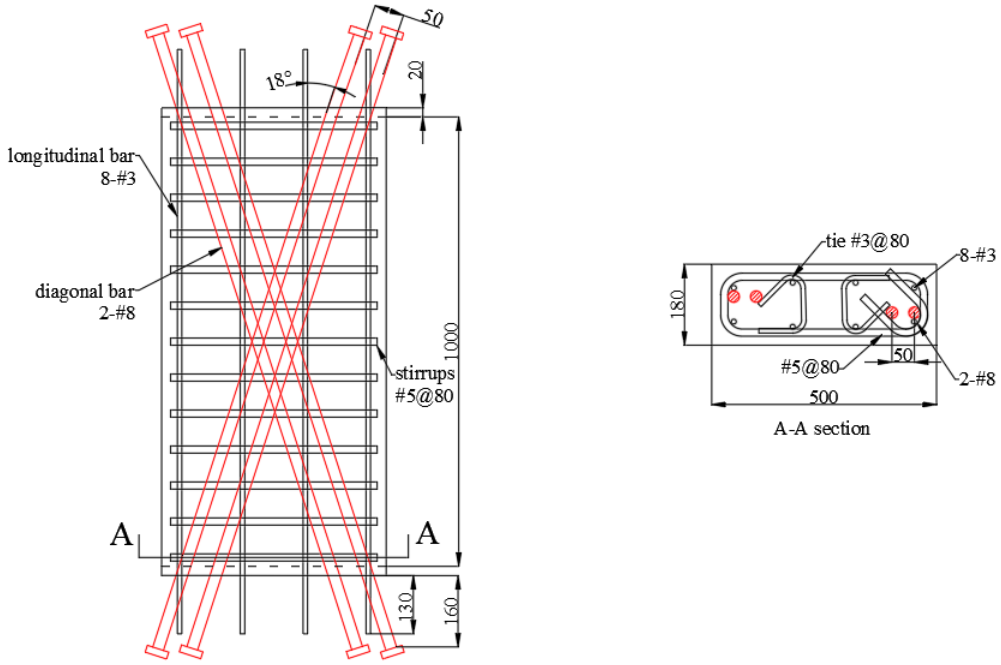

(a) Elevation (b) Cross section

Figure 1 reinforcement drawing of precast UHPC panels

RESULTS AND DISCUSSION

According to the experiment results, the precast UHPC panel greatly improves the overall lateral strength and stiffness. The lateral strength of the frame was increased by 2.8 times and increased initial stiffness by about 4.1 times compared to the non-retrofitted frame. In addition, the strength maintains above 2 times of the non-retrofitted frame until the end of the test. Subsequently, to compare the influences of change in the retrofit position, only the ductile behavior of F-SP has slightly promoted by jointed the connecting part to the frame column. Figure 2 shows the hysteresis loop of all specimens, the abbreviation F-N, F-MP, F-SP, and U/P represent the non-retrofit frame, retrofit panel in the middle of the frame, retrofit panel in the side of the frame, and UHPC panel respectively. And the horizontal dotted line means the nominal strength for the member has a diagonal bar from ACI 318, and another dotted line means flexural strength which considers the contribution from the longitudinal component of the diagonal bar. One can see that the strength predicted from ACI 318 was too conservative because it only considers the shear strength contributed by the diagonal bar. However using the bending strength while considering the contributed by the diagonal bar's longitudinal component, can precisely predict the strength of UHPC panels. In addition, the softening strut-and-tie model can conservatively predict shear strength, the specimens all have ductile behavior with the ultimate strength being controlled by the bending strength.

In summary, seismic strengthening by precast UHPC panels can significantly improve the seismic capacity of the frame, and the strength can estimate accurately by the flexural strength with diagonal bar contribution. Furthermore the retrofit didn't cause the brittle failure on the frame by checking the boundary beam capacity method.

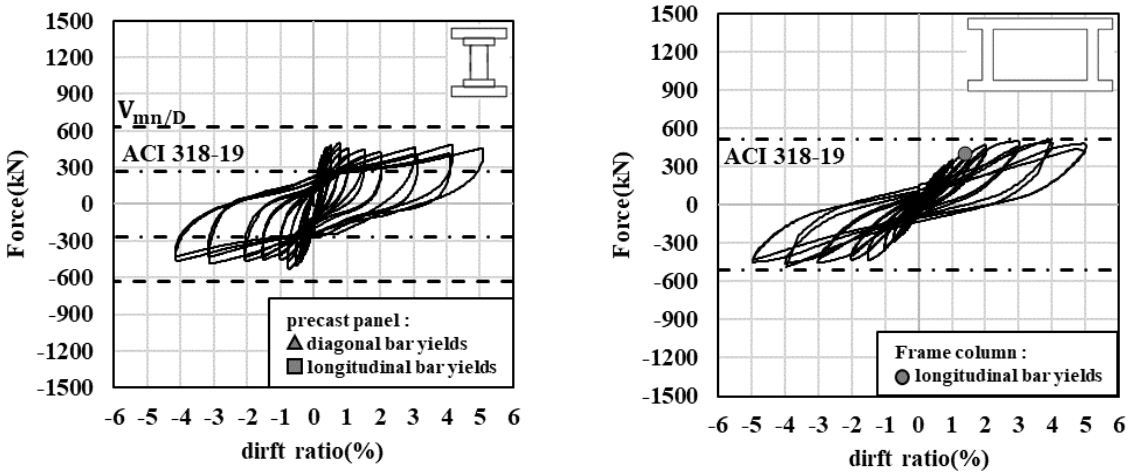

(a) U/P (b) F-N (Hung et al. 2021)

(c) F-MP (d) F-SP

Figure 2 Load-deflection curves

CONCLUSIONS

In this study, precast UHPC panels were used to strengthening the frame, and three specimens were made to test the feasibility, effectiveness and impact to the frame. The test method is carried out with cyclic loading to study the behavior of the specimen including its ultimate strength, ductile behavior, energy dissipation, and failure mode. After observed and analyzing the test results, the following conclusions can be drawn:

1. The use of UHPC in the seismic panels can give full play to its material properties to increase the shear resistance of the component, and develop the component geometry that is normally considered to be controlled by shear strength into a ductile flexural behavior.
2. Retrofitting the frame using 1precast UHPC panels can significantly increase the frame's strength to 2.8 times after seismic strengthening, and its initial stiffness can also be substantially improved to 4.1 times after retrofit.
3. The flexural strength which considers the contribution of the diagonal rebar can accurately predict the strength generated by the UHPC panels, which is beneficial for engineers to carry out practical design. And the shear strength of the specimen can be conservatively estimated by the

softening strut-and-tie model, the test strength is greater than the estimated shear strength. As the result of the test, specimens are not controlled by shear failure.

4. In this study, the boundary beam capacity method was used to check the retrofitted frame. The final test results showed that the beams which UHPC panels connect did not have obvious damage, which indicated that the method could accurately evaluate the maximum degree of seismic strengthening it could bear.

ACKNOWLEDGMENTS

This study was sponsored in part by the Ministry of Science and Technology, Taiwan, under Grant No. 110-2636-E-006-020. The opinions, findings, and conclusions expressed in this paper are those of the authors and do not necessarily reflect those of the sponsor.

REFERENCES

Hung, C.-C., Chen, Y.-T., & Yen, C.-H. (2020). Workability, fiber distribution, and mechanical properties of UHPC with hooked end steel macro-fibers. Construction and Building Materials, 260, 119944.

Hung, C.-C., & Chueh, C.-Y. (2016). Cyclic behavior of UHPFRC flexural members reinforced with high-strength steel rebar. Engineering Structures, 122, 108-120.

Hung, C.-C., Lee, H.-S., & Chan, S. N. (2019). Tension-stiffening effect in steel-reinforced UHPC composites: Constitutive model and effects of steel fibers, loading patterns, and rebar sizes. Composites Part B: Engineering, 158, 269-278.

Hung, C.-C., Li, H., & Chen, H.-C. (2017). High-strength steel reinforced squat UHPFRC shear walls: Cyclic behavior and design implications. Engineering Structures, 141, 59-74.

Yang, C., Chen, S.-C., Yen, C.-H., & Hung, C.-C. (2022). Behaviour and detailing of coupling beams with high-strength materials. Journal of Building Engineering, 47, 103843.

Naaman, A. E., & Reinhardt, H.-W. (2006). Proposed classification of HPFRC composites based on their tensile response. Materials and structures, 39(5), 547-555.

ACI Committee, A. C. I. (2019). Building code requirements for structural concrete (ACI 318-19) : an ACI standard ; Commentary on building code requirements for structural concrete (ACI 318R-19).

Paulay, T. (1975). Design aspects of shear walls for seismic areas. Canadian Journal of Civil Engineering, 2(3), 321-344.

Paulay, T., Priestley, M., & Synge, A. (1982). Ductility in earthquake resisting squat shearwalls. Journal Proceedings,

Wallace, J. W. (2007). Modelling issues for tall reinforced concrete core wall buildings. The structural design of tall and special buildings, 16(5), 615-632.

Wallace, J. W. (2012). Behavior, design, and modeling of structural walls and coupling beams—Lessons from recent laboratory tests and earthquakes. International Journal of Concrete Structures and Materials, 6(1), 3-18.

Hwang, S.-J., & Lee, H.-J. (2002). Strength prediction for discontinuity regions by softened strut-and-tie model. Journal of structural engineering, 128(12), 1519-1526.

Lim, E., Hwang, S.-J., Cheng, C.-H., & Lin, P.-Y. (2016). Cyclic Tests of Reinforced Concrete Coupling Beam with Intermediate Span-Depth Ratio. ACI Structural Journal, 113(3).

Lim, E., Hwang, S.-J., Wang, T.-W., & Chang, Y.-H. (2016). An investigation on the seismic behavior of deep reinforced concrete coupling beams. ACI Structural Journal, 113(2), 217.

Tsai, K. C., Hsu, C. H., Li, C. H., & Chin, P. Y. (2018). Experimental and analytical investigations of steel panel dampers for seismic applications in steel moment frames. Earthquake Engineering & Structural Dynamics, 47(6), 1416-1439.

Structural Engineering Institute, (2017). ASCE standard, ASCE/SEI, 41-17 : seismic evaluation and retrofit of existing buildings.

EXPERIMENTAL INVESTIGATION OF DEVELOPED VERTICAL CONNECTIONS BETWEEN PC WALLS FOR ENHANCED SHEAR STRENGTH

Kyo Young Moon[1], Ingeun Jeon [2] and Sung Jig Kim [3]

1. Ph.D. Candidate, Department of Architectural Engineering, Keimyung University, Daegu, South Korea
2. Graduate Student, Department of Architectural Engineering, Keimyung University, Daegu, South Korea
3. Associate Professor, Department of Architectural Engineering, Keimyung University, Daegu, South Korea

Email: mky9404@gmail.com, inkn97@gmail.com, sjkim4@kmu.ac.kr

ABSTRACT

The paper introduces the large-scale testing program for the newly developed vertical connections between Precast Concrete (PC) wall panels to improve their in-plane shear and drift capacity. One of the developed vertical connections has the dovetail-shaped metal lath with headed rebars. Others are similar to the traditional connection but have more reinforcements and shear keys. A total of four specimens including the conventional and developed vertical connections were designed and constructed. The first specimen is PC walls with the widely used conventional connection using the wire loop system. The constructed specimens were experimentally investigated through static cyclic loading tests with a constant axial load. The observed damage, hysteretic behavior, and strength are investigated and compared with the cases of specimens with conventional connections. Experimental results indicate that the seismic performance of PC walls with developed vertical connections is comparable to the widely accepted connection.

Keywords: Precast concrete wall, Vertical connection, Cyclic loading test, Seismic performance

INTRODUCTION

Precast Concrete (PC) systems could ensure high and uniform quality of structure members and shorten the construction period (Dang *et al*., 2021; Brunesi *et al*., 2018). The PC structural members are typically prefabricated at manufacturing plants and transported to the construction site. Due to limitations of transportation and erection equipment, the size of the fabricated PC members is restricted and thus connections between members are essential. Such connections can significantly affect the structural performance and cause severe damage to PC structures under earthquake loads. The observed earthquake damage and failures of PC structures were mainly due to brittle behavior of poor connection details between the precast elements, poor detailing of the elements and poor design concepts (FIB, 2003). Specifically, connections between PC wall panels need to be designed to provide sufficient stiffness, strength, or ductile capacity so that the performance of the PC systems should be either equivalent to or superior to that of monolithic Reinforced Concrete (RC) structures.

Typical PC walls with lapped reinforcing bars in concreted or grouted connections are expected to have enough stiffness and strength to allow composite action like a monolithic cast-in-place RC wall. However, such traditional wet connections could easily suffer damage due to the insufficient in-plane shear capacity and limited ductility, resulting in the deterioration of structural performance. Thus, several connections to ensure structural integrity have been proposed and studied (Zhi *et al*., 2019; Kang *et al*., 2010). Figure 1(a) presents one of the widely used wet connections, the so-called wire loop connection (Jorgensen and Hoang, 2015). The wire rope with a high tensile strength is stressed in tension to transfer shear force across the connection. In addition, the wire loop connection makes the vertical installation of the PC walls easier. However, once the large deformation of the system occurs, the tensile force of the wire rope is significantly developed. Thus, high concentrated stresses in the joint mortar confined by the overlapping wire loops could be developed, resulting in brittle failure of the connection (Soudki *et al*., 1996; Jorgensen and Hoang, 2015). Therefore, in this study vertical connections between

PC wall panels are newly proposed to prevent such brittle failure and provide sufficient shear strength and ductility. A total of four specimens were constructed and investigated through static cyclic loading tests. The in-plane shear and drift capacity of developed connections are evaluated by comparing those of the wire loop connection.

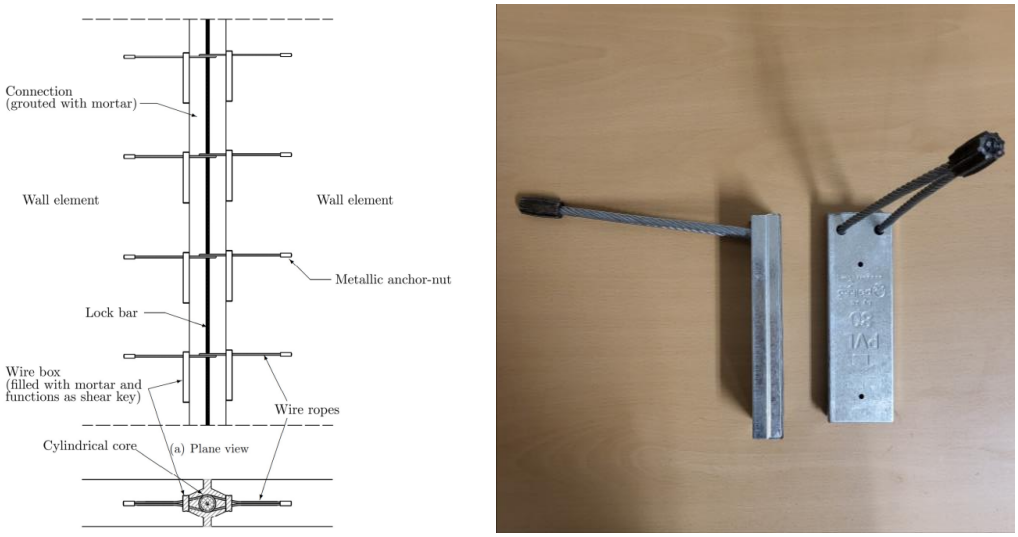

(a) Elevation and plan views (b) Details of wire loop

Figure 1. Wire loop connection

DEVELOPED VERTICAL CONNECTION SYSTEM OF PC WALL

Three vertical connections between PC wall panels to improve the shear strength are proposed as shown in Figure 2. The first one is a dovetail-shaped metal lath with headed rebars as illustrated in Figure 2 (a). The dovetail-shaped metal lath with rough surfaces works as a permanent form for cast-in-situ mortars to improve the construction quality. The reinforcing bars with terminator are placed in the inner space of the dovetail-shaped joint and are expected to enhance the stiffness, ductility, and shear strength of the connection. A slit between PC walls is designed to be 20 mm by Korea Design Standard (KDS 41 17 00). The second and third connections are similar to the traditional connection but have a higher transverse rebar ratio and provide enough space as well as shape to improve construction. The only difference between the two connections is shear keys on the surface as shown in Figure 2 (b).

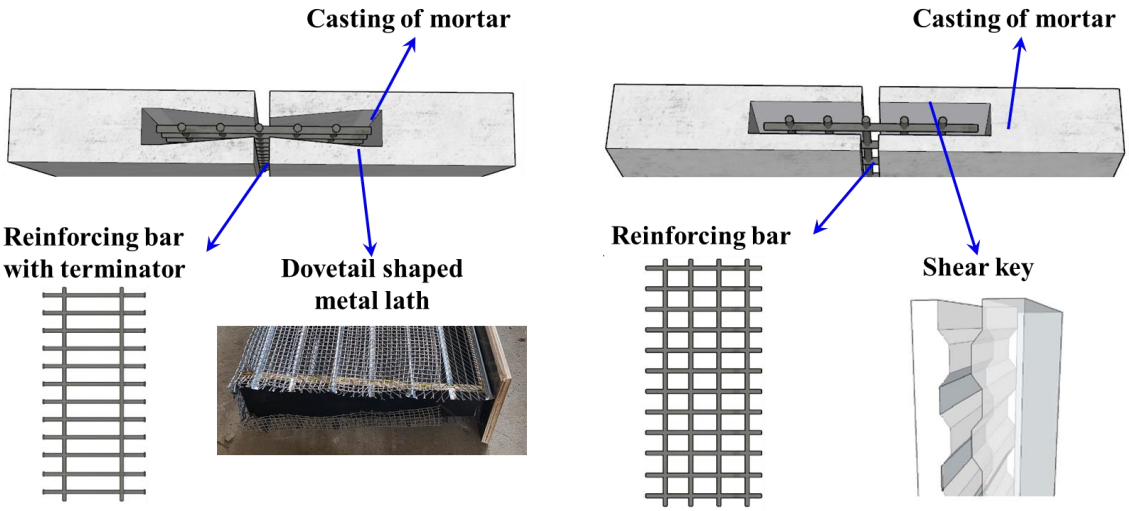

(a) Dovetail-shaped joint (b) Joint with rebars and shear keys

Figure 2. Developed vertical connections

EXPERIMENTAL PROGRAM

The experimental program aims to investigate the effect of the developed vertical connections on the behavior of PC walls. Table 1 summarizes the details of all specimens. All specimens have identical configuration except panel width. This is because the slits between PC walls are different depending on the type of vertical connections. The clear height and thickness of PC walls are 2700 mm and 200 mm, respectively. The compressive strengths of concrete shown in Table 1 were obtained when each structural testing was conducted.

Table 1. Details of specimen

Specimen Name	Description of vertical connection	Geometric configuration		Material strength and section details			
		slit (mm)	panel width (mm)	$f_c{}'$ (MPa)	f_m (MPa)	ρ_v (%)	ρ_h (%)
PWL	With wire loop	100	860	32.13	52.16	0.33	0.34
PWD	With metal lath and reinforcing bars	20	900	33.33	57.81	0.32	0.34
PWR	With reinforcing bars	20	900	27.44	60.34	0.32	0.34
PWRS	With reinforcing bar and shear keys	20	900	30.04	63.43	0.32	0.34

Where, f_c' is concrete strength of PC wall. f_m is mortar strength of the vertical connection. ρ_v and ρ_h are vertical and horizontal reinforcement ratio, respectively.

The PC wall with a wire loop connection (PWL) is selected as a reference structure for an existing vertical joint. For the specimen PWL, PVL80 in Peikko Group is selected as a wire loop system and is required to have the slit of 100 mm (Peikko, 2020). As described previously, specimens with the developed dovetail-shaped joint (PWD) and traditional joints with improved rebar ratio (PWR) and shear keys (PWRS) were also designed and constructed. Elevation and section details of the specimens are shown in Figure 3. In addition, the horizontal connections between walls and footing were designed based on ACI 318-19 and constructed with widely used corrugated tubes along with dowel rebars.

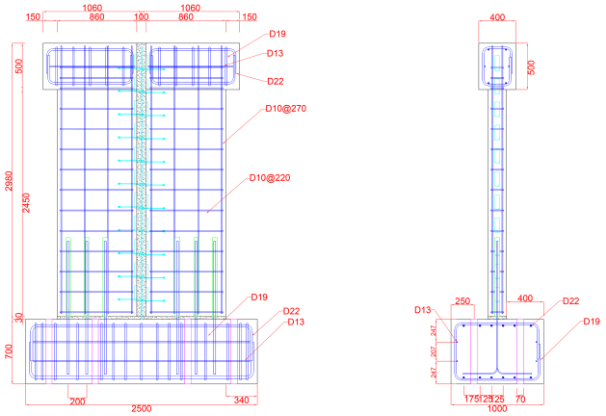

(a) PWL

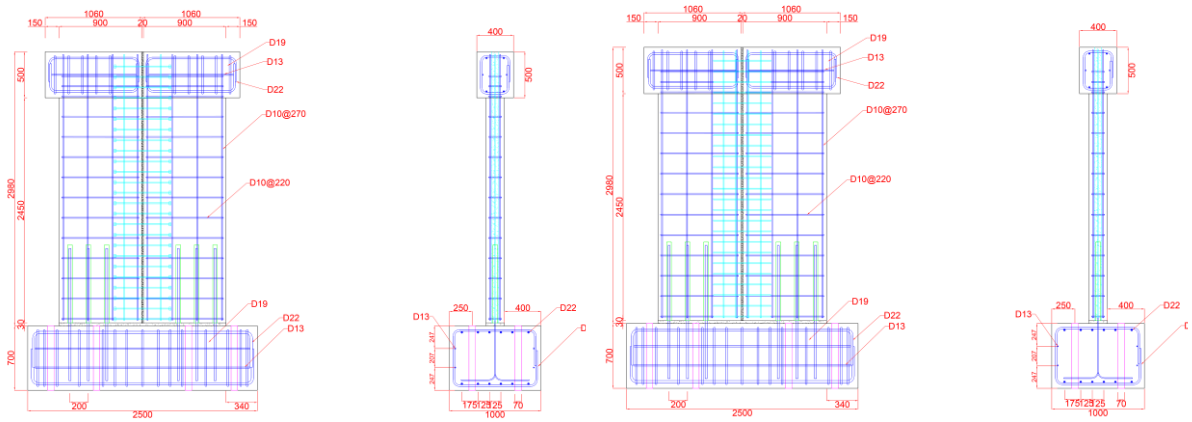

(b) PWD (c) PWR & PWRS

Figure 3. Elevation and section of specimens

Figure 4 illustrates the overview of test setup including a test specimen and loading devices. The horizontal actuator was used to apply lateral forces and the vertically installed two hydraulic jacks were responsible for the compression axial load. 17 LVDTs were installed to measure the displacement and shear deformation of each specimen. Figure 5 shows the applied lateral displacement history for the static cyclic tests with a constant axial load. The imposed lateral displacement history includes multiple cycles at each displacement level to reflect the effect of strength degradation characteristics. The applied axial load was 1092kN which is approximately 10%of the column axial capacity ($0.1A_g f_c$).

Figure 4. Experimental setup

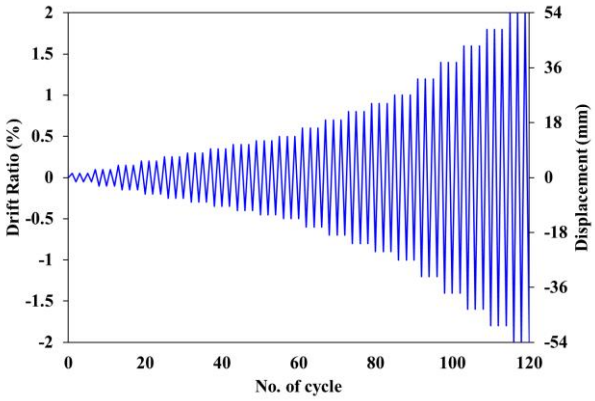

Figure 5. Loading history

EXPERIMENTAL RESULTS

Figure 6 presents crack patterns of all specimens at the drift ratio of 1.0%. The initial horizontal cracks of specimens PWL, PWR and PWRS occurred at the horizontal connection between the PC wall and horizontal mortar pad at the drift ratio of 0.05%, while those cracks of the specimen PWD occurred at the drift ratio of 0.1%. Crack development of all specimens had similar pattern as shown in Figure 6. For specimens PWL, PWD and PWR, the flexural cracks at the bottom of specimens occurred around the drift ratio of 0.1%, while the flexural cracks of the specimen PWRS occurred around the drift ratio of 0.15%. In addition, the diagonal cracks of the specimen PWR were developed at the bottom and middle of specimens around the drift ratio of 0.15%, and the rest of specimens occurred around at the drift ratio of 0.2%. The specimen PWL suffered the most severe damage with large cracks. Note that more cracks of specimen PWR were observed, but their size was smaller than that of specimen PWL. In the case of the specimen PWD, few cracks were observed at the vertical connection. However, a number of cracks were observed at a distance of around 340 mm from the vertical connection, where the wall has the smallest thickness due to the dovetail-shaped permanent form. Compared with crack patterns of the specimen PWR, much smaller cracks were observed in the specimen PWRS, presumably due to the effect of shear keys on the connection surface.

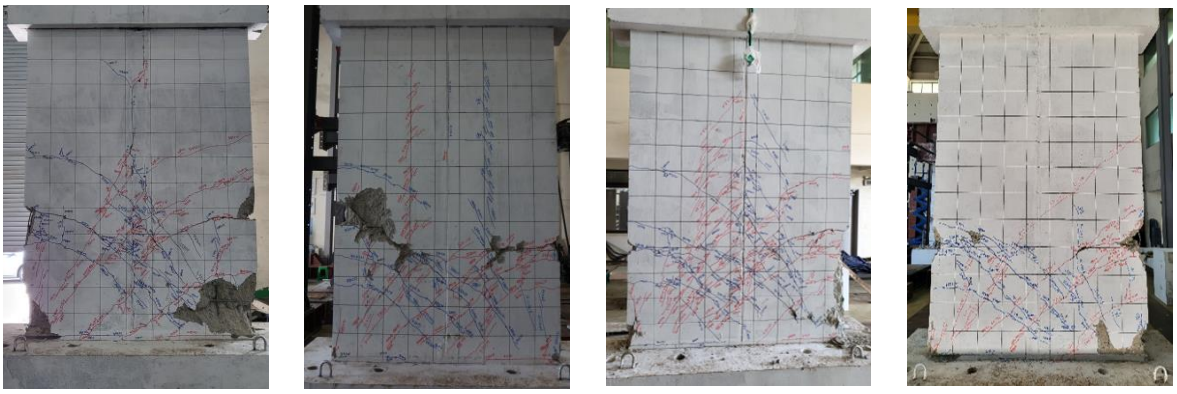

(a) PWL (b) PWD (c) PWR (d) PWRS

Figure 6. Cracks patterns of specimens

Figure 7 presents the relationship between the drift ratio and lateral force for all specimens. The ultimate drift ratio is determined at the point of 15% drop in strength from the peak of the maximum applied load. The measured maximum forces of specimens PWL, PWD, PWR, and PWRS are 559.42kN, 590.35kN, 545.88kN and 578.87kN, respectively. Compared with the specimen PWL, the maximum lateral force of the specimen PWR decreased up to 2.42%, while those of specimens PWD and PWRS increased by 5.53% and 3.48%, respectively. Compared with the specimen PWL, the ultimate drift ratio of the specimen PWD increased by 20%.

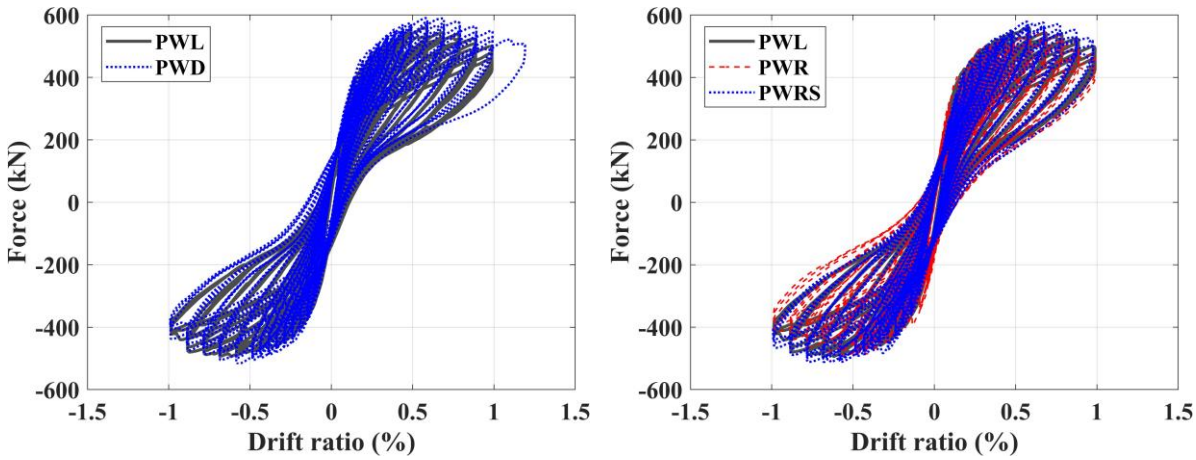

(a) PWL and PWD (b) PWL, PWR and PWRS

Figure 7. Force-drift ratio relationship

CONCLUSION

The paper presents the experimental investigation on the seismic performance of PC walls with newly developed vertical connections. To improve the shear strength of the vertical connection, innovative dovetail-shaped metal lath with headed rebars is developed. In addition, the improved traditional connection with shear keys is proposed. Experimental results in terms of observed damage, hysteretic behavior, and strength are investigated and compared with the cases of specimens with a widely used and existing vertical joint. Compared with the specimen with conventional specimen, the maximum lateral force of the specimen with the developed connection increased by up to 5.53%. The drift capacity also increased by up to 20%. Therefore, taking into account the observations from the experimental program described above, it is concluded that the proposed connections can improve the seismic performance of PC walls.

ACKNOWLEDGMENTS

This research was supported by a grant (22TBIP-C161540-02) from Technology Business Innovation Program funded by Ministry of Land, Infrastructure and Transport of Korean government.

REFERENCES

ACI Committee 318. (2019). "Building Code Requirements for Structural Concrete (ACI318-19)," American concrete institute, Farmington Hills, MI

Architectural Institute of Korea. (2019). "In Seismic Building Design Code (KDS 41 17 00)," Ministry of Land: Seoul, Korea

Brunesi, E., Peloso, S., Pinho, R., & Nascimbene, R. (2018). "Cyclic testing of a full-scale two-storey reinforced precast concrete wall-slab-wall structure," *Bull. Earthq. Eng*, 16(11), 5309-5339.

Dang, L., Liang, S., Zhu, X., Zhang, M., & Song, Y. (2021). "Seismic performance of precast concrete wall with vertical energy-dissipating connection," *Struct. Des. Tall Spec. Build*, 30(2), e1820.

Fib Commission 7.3. (2003). "State-of-art report on seismic design of precast concrete building structures," New Zealand

Jorgensen, H. B., & Hoang, L. C. (2015). "Load Carrying Capacity of Keyed Connections Reinforced with High Strength Wire Rope Loops Proceedings of fib symposium: Concrete-Innovation and Design"

Kang, S. M., Oh, J. K., Kim, O. J., Lee, D. B., & Park, H. G. (2010). "Development of a precast concrete structural wall adopting improved connections in the plastic hinge region," *EESK*, 14(2), 15-26.

Peikko. (2020). "Technical manual. PVL connecting loop-Wall connecting loop box with single wire"

Pekau OA, Hum D (1991). "Seismic response of friction jointed precast panel shear walls," *PCI J*, 36(2), 56–71

Soudki, K. A., West, J. S., Rizkalla, S. H., & Blackett, B. (1996). "Horizontal connections for precast concrete shear wall panels under cyclic shear loading," *PCI J*, 41(3), 64-80.

Zhi, Q.; Zhou, B.B.; Zhu, Z.F. (2019). "Evaluation of load–deformation behavior of reinforced concrete shear walls with continuous or lap-spliced bars in plastic hinge zone," *Adv. Struct. Eng*, 22, 722–736.

EXPERIMENTAL STUDY ON SEISMIC RETROFIT OF CONCRETE FRAMES USING STEEL SUPPLEMENTAL BEAMS

Chao-Hsun Huang[1], Min-Lang Lin[2], and Zhen-Jun Zheng[3]
1. Associate Professor, National Taipei University of Technology, Taipei, Taiwan
2. Associate Research Fellow, National Center for Research on Earthquake Engineering, Taipei, Taiwan
3. Graduate Student, National Taipei University of Technology, Taipei, Taiwan
Email: steve@mail.ntut.edu.tw, qsc870521456@gmail.com

ABSTRACT

Structural analysis in previous studies have shown the effectiveness of steel supplemental beams in the seismic retrofit of existing structures. To check the actual performance of this technique, a quasi-static experiment was conducted on a pair of full-scale frames in this study. It is observed that the lateral strength of the frame is significantly increased after the retrofit, which shows that the proposed technique can be used to enhance the seismic resistance of existing concrete structures.

Keywords: Seismic retrofit, steel supplemental beam, push-over analysis

INTRODUCTION

Recognizing the vulnerability of old buildings during earthquakes, the Taiwanese government has been encouraging building owners to examine the seismic safety of their homes and perform rehabilitation if necessary. So far, the program is going well for public buildings. For privately owned structures, however, the progress is extremely slow due to technical, financial, and sometimes political reasons. To increase the chance of survival of such buildings in future earthquake, the Department of Interior announced a "multi-phase rehabilitation plan" and offers a financial incentive for building owners to improve the seismic performance of their structures to a certain level. Among these buildings, the most common structural problem is "vertical stiffness irregularity", also known as "soft-story", which is a product of local building regulations in Taiwan. To improve the seismic resistance of buildings with a soft story, a rehabilitation technique is proposed by installing inter-story beams between adjacent columns. In this study, a concrete frame is retrofitted with a so-called "steel supplemental beam" and tested under lateral load to verify the effectiveness of such technique. A comparison between specimens with and without the retrofit will be presented in this paper.

TEST SPECIMENS

Two full-scale specimens were tested in this experiment. The prototype, denoted as Proto, is constructed based on the member size of a 7-story building evaluated in a preliminary study (Liu, 2021), as shown in Fig. 1(a). The beam and column sections of the frame are given in Fig. 2. The yield strengths of the longitudinal and transverse reinforcement are specified at 412 MPa and 275 MPa, respectively, and the compressive strength of the concrete is 20.6 MPa.

The retrofitted specimen, denoted as Retro-1, has a frame completely identical to Proto except that a RH450x200 steel beam was connected to the frame (columns) through a pair of jacket-type connections, as shown in Fig. 1(b). The strength of such connection has been examined by Lin before this test (Lin, 2021). The yield and ultimate strengths of the steel beam are 250 MPa and 400 MPa, respectively, and the dimensions of the beam section is given in Table 1.

Table 1. Dimensions of the steel beam

Designation	d	b_f	t_w	t_f
RH450x200	450 mm	200 mm	9 mm	14 mm

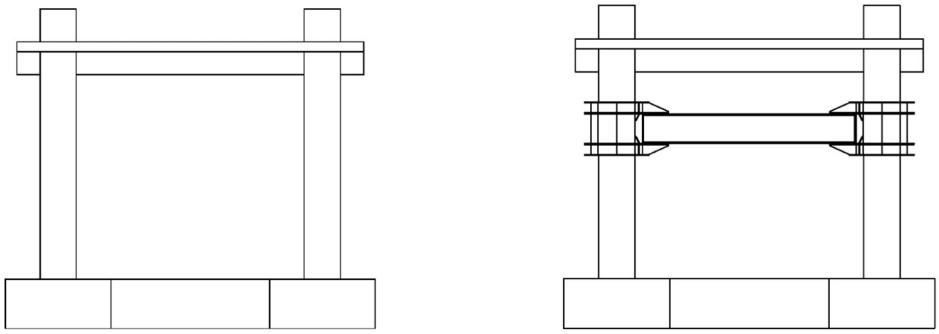

(a) Proto (b) Retro-1

Figure 1. Test specimens

(a) Beam section (40 cm x 50 cm) (b) Column section (55 cm x 55 cm)

Figure 2. Beam and column sections of the concrete frame

EXPERIMENTAL PROGRAM

A quasi-static test was conducted at the Structural Lab. Of the National Center for Researches on Earthquake Engineering (NCREE) in Taipei. The experimental setup of the specimen is shown in Fig. 3. The frame was fixed to the strong floor by 8 pre-stressed anchors (4 on each side). A pair of hydraulic jacks were attached to the top of the specimen (the extended sections of the T-beam) through loading blocks (one at each end) and 4 pre-stressed ties. To prevent out-of-plane twisting during the experiment, bracing frames were provided on both sides of the specimen (not shown in the figure).

The lateral load was applied in a reversed cyclic pattern according to ACI 374 (ACI, 2005). The lateral displacement of the frame was measured at the top of the frame by a linear variable differential transformer (LVDT). The drift ratio in each loading cycle is calculated as

$$DR\ (Drift\ Ratio) = \frac{\Delta}{H} \times 100\% \quad (1)$$

in which

Δ = lateral displacement of the steel beam at the top of the frame

H = the story height of the concrete frame = 3,600 mm.

To observe the strain progress in both the steel beam and rebars, stain gages were also attached to these elements.

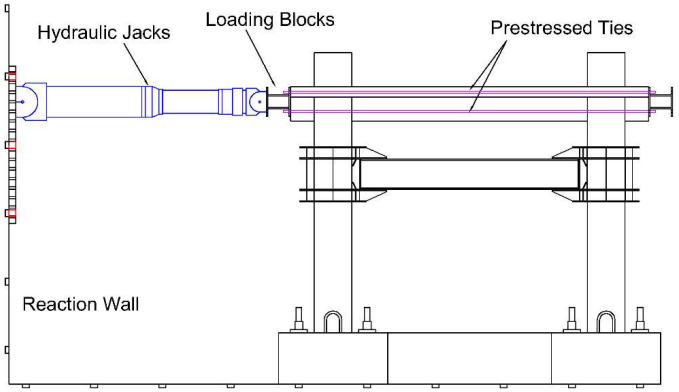

Figure 3. Experimental setup

EXPERIMENTAL RESULTS

Fig. 4 shows the hysteresis loops of specimen Proto under the prescribed loading cycles. A maximum load of 923 kN takes place at *DR* = 3%, at which a clear shear crack could be observed in the T-beam. As the drift ratio reaches 4%, shear failure occurred at both ends of the T-beam and the lateral strength of the frame drops more than 20%. By examining stain gage recordings, it was found that the longitudinal reinforcement in the concrete beam yielded at *DR* = 1.25% and the transverse reinforcement yielded at *DR* = 1%, which agrees with the experimental observations.

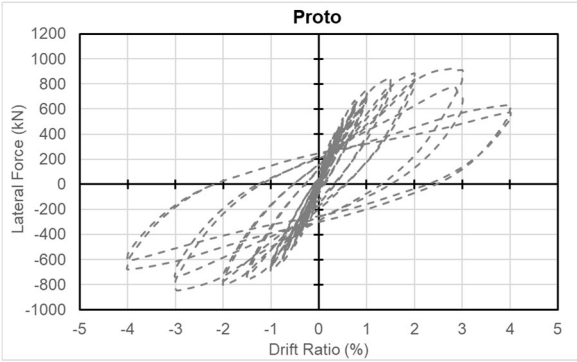

Figure 4. Hysteresis loops of frame Proto

Fig. 5 shows the hysteresis loops of specimen Retro-1. The lateral strength of 1558 kN was recorded at *DR* = 3%, posting a strength boost of 69% from the prototype. As the drift ratio reaches 4%, flexural-shear failure occurred at the bottom of both columns, and the frame strength also drops more than 20%. By examining stain gage recordings, it was found that the longitudinal reinforcement in the concrete column yielded at *DR* = 1% and the transverse reinforcement yielded at *DR* = 1.5%, which also agrees with the observations.

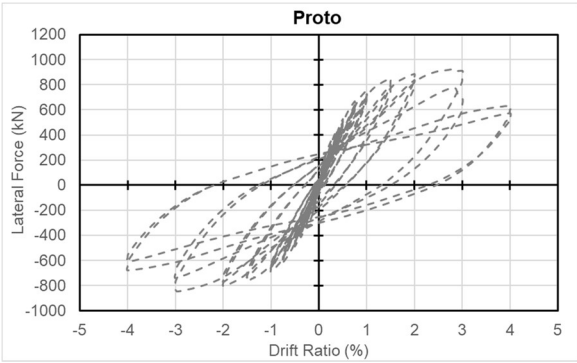

Figure 5. Hysteresis loops of frame Retro-1

DISCUSSIONS

From the experimental observation, it is found that the strength of frame Proto is governed by the shear failure of the T-beam during the test. In frame Retro-1, such failure did not happen throughout the test, however, flexural-shear damage was discovered at the bottom of both columns. These unexpected failure modes might have resulted from the computer program used for the push-over analysis, TEASPA 3.1 (NCREE/SINOTEC, 2019), which does not follow the code instruction to neglect the shear strength provided by concrete when the axial compressive load in the member is less than $0.05A_g f'_c$ (ACI, 2019), causing an overestimation of shear strength for both columns and the T-beam. In addition, the extra strength in frame Retro-1, which is contributed by the overstrength and stain-hardening of both steel beam and steel reinforcement, also raised the shear demand of the columns. To avoid such problems in actual construction, it is recommended that the engineer double check the shear strength of frame members with code provisions and strengthen the members if necessary.

CONCLUSIONS

A quasi-static experiment was performed on full-scale concrete frames in this study to check the effectiveness of steel supplemental beams in seismic retrofit of concrete structures. Ii is found that the lateral strength of the frame was raised from 923 kN for the prototype to 1558 kN for the retrofitted frame, or an increase 69% in lateral strength. With the saving of construction time and space, this technique can be as competitive as other rehabilitation options. However, it is recommended that the engineer should check the increase shear demand in the columns and conduct shear strength if necessary.

ACKNOWLEDGMENTS

The authors would like to thank the Ministry of Science and Technology (Taiwan) for financially sponsoring this project (Project No. MOST 110-2224-E-027-001). The authors also want to thank the National Center for Research on Earthquake Engineering for providing the test laboratory and technical assistance and Ya Tung Ready Mixed Concrete Co. for providing the concrete used in the construction of specimens.

REFERENCES

ACI Committee 318. (2019) “Acceptance Criteria for Moment Frames Based on Structure Testing and Commentary Building Code Requirements for Structural Concrete and Commentary,” American Concrete Institute, Farmington Hills, MI, USA.

ACI Committee 374. (2005) “Acceptance Criteria for Moment Frames Based on Structure Testing and Commentary,” American Concrete Institute, Farmington Hills, MI, USA.

Lin, E. (2021) “Seismic Retrofit of Reinforced Concrete Building using Steel Supplemental Beams and Jacket Connection,” *Master’s Thesis*, National Taipei University of Technology. (in Chinese)

Liu, C. Y. (2021) “Seismic Rehabilitation of RC Buildings with Soft Story using Steel Supplemental Beams,” *Master’s Thesis*, National Taipei University of Technology. (in Chinese)

NCREE/SINOTEC. (2019) “Taiwan Earthquake Assessment for Structures by Pushover Analysis (TESPA) v3.1,” National Center for Research on Earthquake Engineering and Sinotech Engineering Consultants, Inc., Taipei, Taiwan.

(3c) Advances in earthquake engineering research

CONSIDERATIONS FOR SEISMIC RATCHETING

Gregory A. MacRae[1], Chin-Long Lee[1] and Trevor Yeow[2]
1. Civil Engineering, University of Canterbury, New Zealand
2. Earthquake Research Institute, The University of Tokyo, Bunkyo-ku, Tokyo, Japan 113-0032
Email: gregory.macrae@canterbury.ac.nz, chin-long.lee@canterbury.ac.nz, tyeow.work@gmail.com

ABSTRACT

This paper describes recent research conducted to understand the effects of structural characteristics on seismic ratchetting of structures. From analyses conducted of cantilever structures with fibre hinges representing steel and reinforced concrete structures, it was shown that as the difference in strength in the forward and reverse directions increased, the tendency for increased seismic displacements in one direction increased. Ratcheting of the model representing steel structures was significantly greater than that of the model representing reinforced concrete structures. From the results obtained, simple recommendations are provided for use in structural earthquake standards.

Keywords: earthquake engineering, ratcheting

INTRODUCTION

For an inelastically responding structure subjected to earthquake shaking, seismic ratcheting describes the progressive deformation of the structure in one direction. Seismic analysis methods used for design which do not explicitly consider the possibility of seismic ratchetting may underestimate the likely displacement demands so amplifications of structural displacements are required.

For structures with symmetric strength, stiffness and loading, ratcheting may occur due to (i) the characteristics of ground motions, (ii) hysteretic effects (such as degrading strength and stiffness), and (iii) *P*-delta effects. They may also occur in structures with different stiffnesses / strengths in different directions, or in structures subject to eccentric gravity loading.

This paper relates only to structures with different lateral force resistance in opposite directions. This difference in lateral force resistance may result from the difference in structural strength, or it may be due to gravity loading eccentricity.

Figure 1 shows that for a 5 storey steel moment frame subject to an earthquake record that displacements tend to occur about the origin when there is no ratchetting tendency (i.e. a concentric axial force) with the blue line. However, when the net axial force considering cantilever sections of the frame, is to the left of the centre, this causes the frame to tend to ratchet toward the left, and there are larger peak and permanent displacements in that direction (red line). Here, the “representative displacement” is the multi-degree-of-freedom displacement response condensed to an equivalent SDOF displacement.

While some previous studies have been undertaken previously on ratchetting, there is the concern that either they are too simple to represent the increases in displacement in structures with different levels of ratchetting tendency, or too complex for use in realistic design. As a result there is a need to obtain simple, and reasonable approaches for displacement increase due to structural ratchetting that may not be in other standards.

This paper seeks to address this need by seeking answers to the following questions:

1) What studies have been conducted in seismic ratcheting?
2) What structural parameters affect the tendency for seismic ratcheting?
3) How are different structural forms sensitive to ratcheting?
4) Can simple ratcheting provisions be proposed for seismic standards?

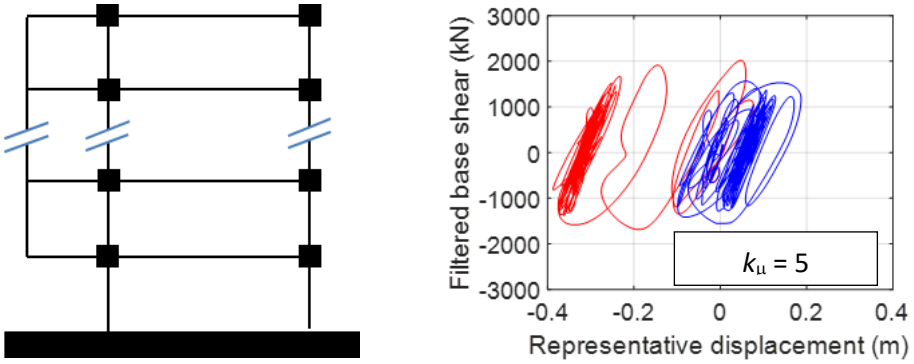

(a) Frame (b) Hysteresis response

Figure 1. Hysteretic response for 5 storey steel moment frame subject to shaking equal to 5 times that expected to cause yield at the fundamental period (i.e. $k_\mu = 5$) (i) with no structural ratchetting tendency (blue), and (ii) with a structural ratchetting tendency (red) (Yeow and Kusunoki, 2022).

PREVIOUS WORK

The Japan Road Association (JRA, 1990) standard for bridge columns was among the first to consider ratchetting. It recognises that when gravity force does not act vertically through the centre of a column, then there is a moment at the column base equal to the vertical force multiplied by the eccentricity, M_E. JRA requires that bridge columns with such a base moment be provided with extra flexural strength (reinforcing) in one direction to resist that moment.

MacRae and Kawashima (1993) developed concepts describing the tendency for a structure to yield primarily in one direction using the *hysteresis centre curve* (HCC) concept and defining hysteresis loop *dynamic stability*. They showed that in order to minimise ratcheting of a bridge column with elastically-perfectly plastic (EPP) behaviour, the additional flexural strength in the direction of eccentric moment should be $2M_E$. The JRA standard only considered 1.0 M_E.

Masuno et al. (2011) obtained a relationship between displacement increase and initial out-of-plumb for 9 storey steel buildings designed to have (i) constant strength/stiffness up the height, and (ii) constant interstorey over the height due to the code lateral force distribution. An empirical relationship was obtained to describe the increase in displacement. It was shown that the residual/permanent displacement increased much faster with out-of-straightness than did the peak displacement.

Yeow et al. (2013) conducted time history analyses of eccentrically loaded bridge columns. Analyses were conducted of cantilever structures with the records both in the positive and negative directions. These showed that for elastic-perfectly plastic (EPP) hysteresis loops, the additional column base flexural strength required in one direction, M_{add}, is exactly twice the eccentric moment, M_e. That is, $M_{add} = 2M_e$. This is consistent with MacRae et al. (1993). However, for structures with EPP hysteresis loops and P-delta, $M_{add} \approx 2\ M_e/(1-\theta)$, where θ (= P/(KL)) is the stability coefficient, where P is the gravity axial force, and K is the initial lateral stiffness, and L is the height to the centre of mass. For Takeda hysteresis loops, the flexural strength required was slightly greater than for EPP loops and it was recommended that the $M_{add} \approx 2.3\ M_e$.

Dupuis et al. (2014) conducted analyses of symmetric structures subject to eccentric moment. They recommended the displacement amplifications in Table 1, where β is the ratio between the applied eccentric moment, and the member yield capacity in the eccentric moment direction. It is noted that this relationship is not dependent on ductility, although when the structure is fully elastic it would be expected that there would be no ratcheting effect. These were incorporated into the Canadian seismic provisions (NBCC, 2015).

Table 1. Canadian Ratcheting Provisions (Dupuis et al. 2014)

Systems with self-centering characteristics	Other systems	Code requirement
$0.0 \leq \beta \leq 0.1$	$0.0 \leq \beta \leq 0.03$	No requirements
$0.1 < \beta \leq 0.2$	$0.03 < \beta \leq 0.06$	Multiply displacements by 1.2
$0.2 < \beta$	$0.06 < \beta$	Nonlinear response history analysis

The 2016 amendments to Part 5 of the New Zealand Structural Design Actions standards, NZS1170.5 (2016), were also based around RC structures. A ratchetting index, r_i, given in Equation 1 was introduced, where S_f is the lateral force resistance in the forward direction (being the direction of higher lateral resistance including gravity load effects), and S_r is the lateral force resistance in the reverse direction including gravity load effects. When there was also a change in lateral strength, the ratchetting index was modified. The main issues with this approach were that it was complex, it had an error in the definitions, and that it was conceptually difficult to understand what was happening, and it was non-conservative in terms of accuracy.

$$r_i = S_f / S_r \tag{1}$$

Saif (2017) and Saif et al. (2017) conducted time history analyses of eccentrically loaded bridge columns under a suite of earthquake records to obtain the increase in displacement due to eccentricity. The earthquake records were applied in both directions to mitigate the record directionality effect. Columns, used a fibre element at the column base. For steel columns, the fibres had the same strength in tension and compression and this resulted in something close to an elastic-perfectly plastic hysteretic loop. For reinforced concrete structures, the concrete was assumed to carry compression only and this resulted in a pinched hysteretic loop and also a variation in stiffness in the loading and reloading directions. Relationships were developed to determine the increase in displacement due to gravity load eccentricity as a function of α which is the ratio of the eccentric gravity moment, M_E, to the yield moment assuming no gravity moment, M_y. This parameter resulted from earlier work by MacRae (1994).

$$\alpha = M_E/M_y \tag{2}$$

For buildings which had been pushed out-of-straight by earthquake shaking, Rad (2018, 2020) experimentally and numerically studied the effect of increasing the strength only in the deformed direction by installing tension-only braces. These braces, which added stiffness and strength, meant that aftershocks tended to restraighten the structure, and mitigate the possibility of collapse due to further displacements in the same direction. The average amount of restraightening achieved (considering shaking in reverse directions to eliminate the record ratcheting effects), could be understood using the energy concepts.

A proposed 2019 Amendment to NZS1170.5 was developed, and the key aspects of this are discussed in the following section.

Yeow and Kusunoki (2022) conducted studies on multistorey structures to evaluate proposed code clauses for ratcheting displacements considering eccentric loading. A number of provisions including from Canada (based on Dupuis, 2013), the 2016 provision for the New Zealand earthquake loading standard (NZS1170.5 Amendment 1 2016), and the proposed 2019 provisions for Amendment 2, were evaluated. The proposed 2019 provisions were based on the thesis of Saif (2017), and the same as those given in this change proposal. Yeow and Kusunoki found that the 2016 provision average displacement increases due to seismic ratcheting were generally non-conservative as shown in Table 2. The "2019 draft provisions" provided better estimates of the average increase for the records considered. The National Building Code of Canada (NBCC, 2015) provisions were generally conservative for both steel and RC buildings, although they only permit a small range of eccentricity. The post-elastic stiffness, number of inelastic response cycles, record duration, and shaking intensity, all influenced displacement

increases. It is noted that Yeow and Kusunoki (2022) used the maximum increase in displacement from the two directions of each ground motion considered, rather than the average value of the 2 values. As a result, the average increase for all motions and all directions are slightly smaller than the values they reported. Even with this, personal discussion with Yeow indicates that the 2016 provisions for steel structures are significantly non-conservative especially for steel structures, and this is consistent with Saif (2017). The ratchetting effect was also found to be relatively independent of ductility demand (or lateral force reduction factor) for the range of structures considered, and this was consistent with Dupuis et al. (NBCC, 2013) and Saif (2017).

Table 2. Code-based Displacement Modifier Exceedance Percentage (Yeow and Kusunoki, 2022)

Number of floors	NZS1170.5 (2016)		NZS1170.5 (2019)		NBCC (2015)	
	Steel	Concrete	Steel	Concrete	Steel	Concrete
1	90%	71%	55%	68%	38%	0%
3	87%	61%	25%	58%	28%	1.3%
5	86%	65%	28%	63%	18%	0%
10	90%	68%	68%	65%	22%	0.9%

BACKGROUND ANALYSES FOR RATCHETING RECOMMENDATIONS

The recommendations are modified from the work of Saif (2017). They were originally proposed for the 2019 Amendment to NZS1170.5. Saif conducted analyses for structures with both pinched (using fibre elements to model reinforced concrete) and elastoplastic (using fibre elements to model steel without buckling) hysteretic loops subject to a suite of earthquake records. In both cases a fibre hinge was used. The magnification of displacement due to ratchetting was given by a displacement magnification factor, r_{dmf}, as shown in Equation 3, where Δ_{ur} and Δ_u are the peak displacements considering and ignoring ratcheting respectively.

$$\Delta_{ur} = r_{dmf} . \Delta_u \quad (3)$$

Relationships for displacement magnification factor, r_{dmf} (= Average PD(α)/PD(α=0)) were obtained from many analyses by Saif (2017) as shown in Figure 2 as a function of α. Here, R is the lateral force reduction factor (also known as k_μ), the S_p factor is taken as unity, T is the fundamental period, and the axial force ratio is P/P_o.

It was decided to use the NZS1170.5 Amendment 1 (2016) ratcheting index in Equation 1, so the results of Saif (based on a given in Equation 2) were first transformed into functions of r_i following Equation 4.

$$\alpha = 0.4 (r_i - 1) \quad (4)$$

For reinforced concrete columns Equation 5 was obtained. This is similar to NZS1170.5 Amendment 1 (2016) where $r_{dmf} = 0.75r_i + 0.25$. For steel columns without buckling, Equation 6 resulted.

$$r_{dmf,RC} = 1 + 2\alpha = 0.8\, r_i + 0.2 \quad (5)$$

$$r_{dmf} = 1 + 10\alpha = 4r_i - 3 \quad (6)$$

Saif (2017) showed that for structures with unbalanced strength, the displacement increase, r_{dmf}, for different ratchetting indices is given below. P-delta effects were included in these analyses and the design ductility was 4. This is approximately the largest ductility expected in a design level earthquake as the serviceability factor $R_s = 0.25$. For lower design ductilities (and lateral force reduction factors, k_μ), smaller displacement increases result, but the relationship between displacement increase and lateral force reduction factor is not linear. Therefore, as per NZS1170.5 Amendment 1, one relationship is

suggested for all design ductilities except those below the nominally ductile (μ = 1.25) level where ratchetting is not considered.

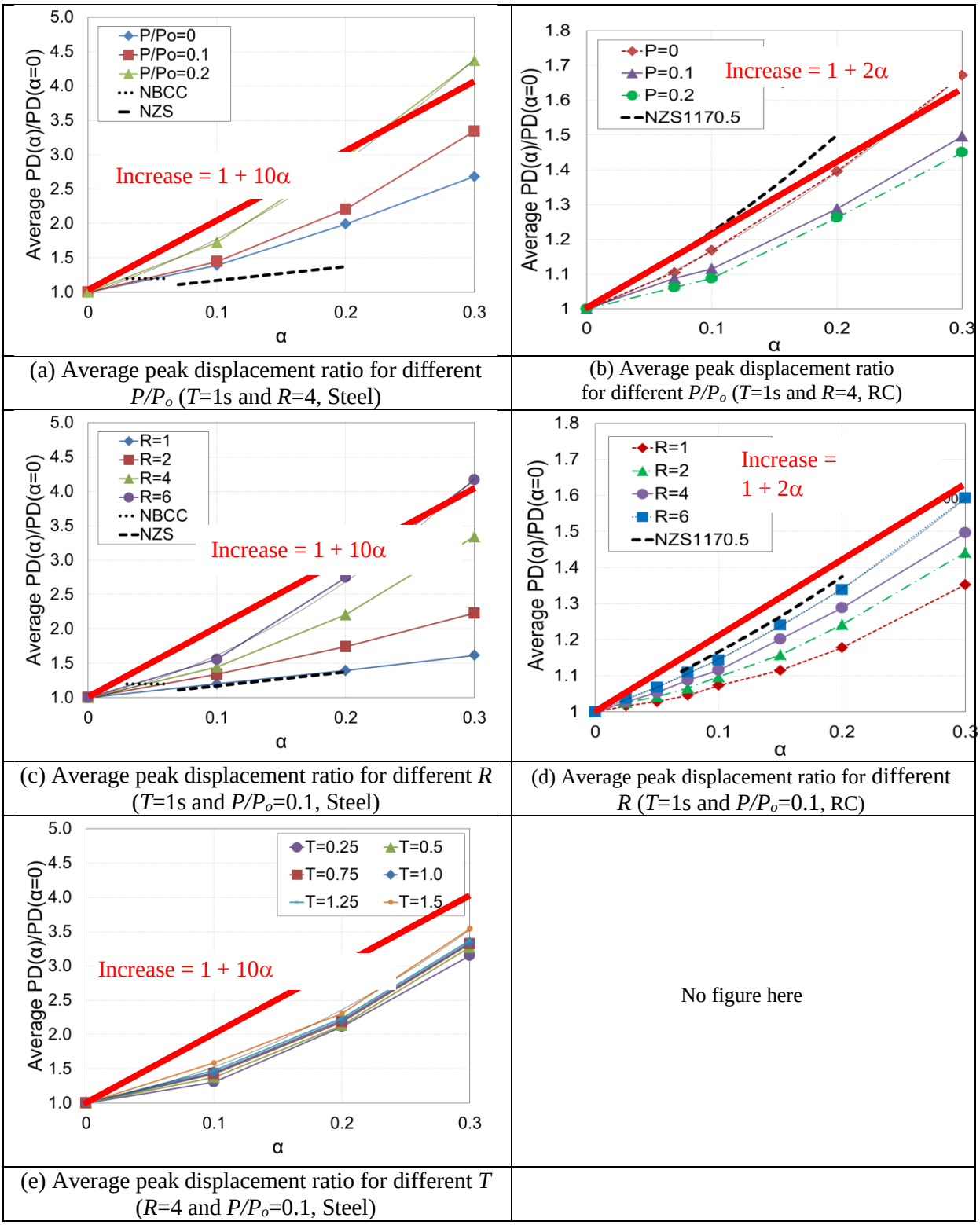

(a) Average peak displacement ratio for different P/P_o (T=1s and R=4, Steel)

(b) Average peak displacement ratio for different P/P_o (T=1s and R=4, RC)

(c) Average peak displacement ratio for different R (T=1s and P/P_o=0.1, Steel)

(d) Average peak displacement ratio for different R (T=1s and P/P_o=0.1, RC)

(e) Average peak displacement ratio for different T (R=4 and P/P_o=0.1, Steel)

No figure here

Figure 2. Steel and Concrete (RC) results with P-delta (Saif, 2017)

It is apparent that the steel hysteretic loop results in significantly greater ratcheting than the reinforced concrete hysteretic loop. If the increase in displacement due to ratchetting needs to only be considered when the displacement increase is more than 12% (i.e. $r_{dmf} > 1.12$), say, then ratchetting does not need

to be considered when $r_i < r_{im}$, where r_{im}, is 1.15 for pinched loops (representing reinforced concrete structures), and r_{im} is 1.03 for elasto-plastic structures.

PROPOSED PROVISIONS FOR NZ SEISMIC STANDARDS

Ductile and limited ductile structures, which have been designed either using the equivalent static or modal response spectrum methods of analysis, shall be assessed for their potential increase in lateral displacements due to ratcheting by calculating the ratcheting index, "r_i" as given in Equation 1, where S_f is the lateral force resistance in the forward direction, being the direction of higher lateral resistance including gravity load effects and S_r is the lateral force resistance in the reverse direction including gravity load effects.

Ratcheting considerations for the ultimate limit state (i.e. 500 year shaking) are required unless one of the following applies:

(a) The assigned structural ductility factor is less than or equal to 1.25;

(b) The structural ductility demand at the ultimate limit state is less than or equal to 1.25

(c) The value of the ratcheting index, r_i, is less than or equal to r_{im}, where:

r_{im} = 1.15 for structures with pinched hysteretic behaviour; and

= 1.03 for structures with elastoplastic hysteretic behaviour.

When r_i exceeds 1.5, the nonlinear numerical integration time history method of analysis shall be used.

When amplification of deflections due to ratcheting are required, then displacements in the reverse direction shall be multiplied by the ratcheting displacement magnification factor, r_{dmf}, where:

r_{dmf} = $0.8r_i + 0.2$ for structures with pinched hysteretic behaviour

= $4r_i - 3.0$ for structures with elastoplastic hysteretic behaviour

CONCLUSIONS

This paper describes recent research conducted to understand the effects of structural characteristics on the seismic ratchetting of structures. Inelastic time history analyses were conducted on cantilever structures with fibre hinges representing steel and reinforced concrete structures. It was shown that:

1) A number of studies have been previously conducted to evaluate the ratchetting effect, but none directly consider the continuous relationship between seismic ratchetting and increase in response in a simple way appropriate for design standards.
2) As the difference in strength in the forward and reverse directions increased, the tendency for increased seismic displacements in one direction increased.
3) Ratcheting of the model representing steel structures was significantly greater than that of the model representing reinforced concrete structures.
4) From the results obtained, simple recommendations are provided for use in structural earthquake standards.

ACKNOWLEDGMENTS

The first author wishes to acknowledge the NZ Ministry of Business Innovation and Enterprise (MBIE) who has encouraged the writing of these provisions in a format suitable for use in NZ design and assessment of structures. Also, to Rob Jury who was involved with the formatting of this work in a form used in a 2019 proposal for inclusion in the NZ seismic design standard, and to Khaled Saif who conducted some of the analyses on which the recommendations are based.

REFERENCES

Dupuis, M. R., Best, T. D. D., Elwood, K. J., & Anderson, D. L. (2014). Seismic performance of shear wall buildings with gravity-induced lateral demands. Canadian Journal of Civil Engineering, 41(4), 323-332.

Japan Road Association, “Design Specifications for Road Bridges, Part V, Seismic Design, February 1990.

MacRae G. A. and Kawashima K., "The Seismic Response of Bilinear Oscillators Using Japanese Earthquake Records", Journal of Research of the Public Works Research Institute, Vol. 30, Ministry of Construction, Japan, 1993.

MacRae G. A., "P-Δ Effects on Single-Degree-of-Freedom Structures in Earthquakes", Earthquake Spectra, Vol. 10, No. 3, August 1994, pp. 539-568.

Masuno T., MacRae G.A., Sadashiva V.K. and Wada A., “Effect Of Building Out-Of-Straightness On Seismic Response”, Sixth International Conference of Seismology and Earthquake Engineering (SEE6), Tehran, Iran, 16-18 May, 2011.

National Building Code of Canada (NBCC). Issued by the Canadian Commission on Building and Fire Codes. National Research Council of Canada, Ottawa, Ontario, 2015.

Rad, A. Seismic Ratchetting of Steel Low-Damage Buildings, PhD Thesis, University of Canterbury, Christchurch, New Zealand. December 2017. https://www.dropbox.com/s/uwyaqvjeuad3m8c/2018_03_AliAbdoahiRad_PhDThesis.pdf?dl=0

Rad A. and MacRae G. A. (2020). "Seismic Ratcheting of Steel Structures with Unbalanced Stiffness/Strengths - Shaking Table Study", 17th World Conference on Earthquake Engineering, Sendai, Japan, September, 2020. Paper 2g-0063 (C000730).

Saif K., “Seismic Ratchetting of RC Columns with Eccentric Gravity Loadings and Non-Symmetric Lateral Stiffness/Strength”, ME Thesis, University of Canterbury, supervised by Lee CL. and MacRae G. A., 2017. https://www.dropbox.com/s/j0qrwva6wtorpqj/2017_ME_KhaledSaif_Ratchetting.pdf.pdf?dl=0

Saif K.Z., C.-L. Lee, G.A. MacRae & T.Z. Yeow. (2017) Effect of Eccentric Moments on Seismic Ratcheting of Single-Degree-Of-Freedom Structures. New Zealand Society for Earthquake Engineering conference. New Zealand, Wellington.

Saif K., Lee C.L., Yeow T. and MacRae G.A., "Seismic Ratchetting of Single-Degree-of-Freedom Steel Bridge Columns", Steel Structures in Seismic Areas (STESSA) Conference, Christchurch, 14-16 February 2018, Key Engineering Materials, Vol. 763, pp. 295-300, 2018.

Saif K. Z., Yeow T. Z., Lee C.-L., and MacRae G. A. “Interpretation and Evaluation of NZS1170.5 2016 Provisions for Seismic Ratcheting”, Bulletin of NZSEE, Accepted May 2022.

Standards New Zealand. (2016). NZS1170.5:2004 Structural Design Actions Part 5 Earthquake actions New Zealand. Incorporating Amendment 1, 2016.

Yeow T., MacRae G. A., Kawashima, K and Sadashiva V. K. Dynamic Stability and Design of C-Bent Columns, Journal of Earthquake Engineering, 17(5), 2013, pp. 750-768.

Yeow T. and Kusunoki K., 2022. Seismic Ratcheting of Eccentric Gravity Loaded Moment-Resisting Frame Buildings, Journal paper submitted for publication.

TIME-DEPENDENT BEHAVIOUR OF CONCRETE-FILLED STEEL TUBE

Doan-Binh Nguyen[1], Wen-Cheng Liao[1]
1. Department of Civil Engineering, College of Engineering, National Taiwan University, Taipei, Taiwan, R.O.C.
Email: d07521014@ntu.edu.tw, wcliao@ntu.edu.tw

ABSTRACT

Concrete-filled steel tube (CFT) represents the advantageous combination of concrete and steel tube for structural applications in comparison with ordinary steel and reinforced concrete. According to the investigation of the time-dependent deformation of this composite material using high strength self-compacting concrete, the results showed that both of the shrinkage and creep of CFT was lower significantly than that of concrete without steel tube confined in a long period up to about 400 days. Moreover, the vertical strains of steel tube and concrete core were almost identical show the advantage of interaction between two components of CFT. However, the stress transfer is notable and cannot be neglected in CFT design. The vertical stress of steel increased 35.5 percent, whereas the vertical stress of concrete decreased 15.8 percent at 389 days after loading age.

Keywords: time-dependent behaviour, strain, stress, creep, shrinkage, concrete-filled steel tube

INTRODUCTION

Concrete-filled steel tubes are a combination outer steel tube and inner concrete core so that these composite columns had the advantages of both types of materials (Bergmann, Matsui, & C. Meinsma, 1995). These composites haves been used popularly in practical fields because of its high ductility, high strength, good fireproof properties, excellent seismic resistance, low creep and shrinkage benefits in comparison with reinforced concrete or steel structures (Morino, Uchikoshi, & Yamaguchi, 2001) (Han, Li, & Bjorhovde, 2014).

Most experiments performed the time-dependent behavior of the concrete-filled steel tube (CFT) with various affecting parameters, including structure shapes, types of concrete and steel tubes, and applied stress. Y. Wang *et al* (Wang Y. , Geng, Ranzi, & Zhang, 2011) and Ma *et al.* (Ma & Wang, 2012), determined the creep behaviour of concrete-filled steel tubes using normal strength concrete and high strength concrete, respectively, they found the creep strain of CFT specimens to be significantly lower than that for unconfined concrete. Similar dimensions of specimens were tested by Ma (Ma & Wang, 2012), D. J. Zhang *et al.* (Zhang, Ma, & Wang, 2015), the researchers measured the creep and stress-strain relation of the CFT. R. Zhang *et al.* (Zhang R. , et al., 2019) studied the creep behaviour of CFT with various content of expansive agent and indicated that the creep coefficient of the concrete structure increases as well as reducing number of expansive additive. Lehman *et al.* (Lehman, Kuder, Gunnarrson, Roeder, & Berman, 2015) compared the strain of CFT using self-consolidating concrete and supplementary cementitious materials concrete. Moreover, Lai *et al.* (Lai & Chen, 2016) investigated the shrinkage strain of CFT specimens base on changing the size of steel tube, compressive strength and amount of fly ash.

Additionally, some researchers tested on the strain and stress of steel tube and concrete core of the CFT member. Ichinose *et al.* (Ichinose, Watanabe, & Nakai, 2001) and Y. Wang *et al.* (Wang & Zhao, 2018) determined the strain of concrete core and steel tube due to creep and shrinkage with different location of the gauges. Ichinose carried out condition in which the humidity and temperatures were constant but Wang tested on ambient environment. The results showed the different data of strains between steel tube and concrete core. Kwon *et al.* (Kwon, Kim, & Kim, 2005) indicated that the strains within CFT components have the same magnitude over time, while vertical stress in the steel tube increases with time and the vertical stress of the concrete decreases over time. Wang *et al.* (Wang

Y. Y., Geng, Chen, & Zhao, 2019) showed the effects of different load ratios impact on the stress of concrete core and steel tube with higher sustained loading.
Although some researchers have performed analyses of the properties of long-term behaviours, the time-dependent deformation of CFT under long-term loading has not been fully studied. Notably, a few studies investigated the stress transfer between the steel tube and concrete due to creep. In this study, the time-dependent behaviour of CFT using high strength self-compacting concrete (SCC) was carried out in long term up to 400 days. Moreover, the estimation of the stress transfer between the concrete core and steel tube under a sustained load were also analysed.

1. Experimental program

1.1 Materials and mix proportion

Cementitious materials (cm), aggregates, superplasticizer (SP), expansive additive (EA), and water are used materials in mix proportion of SCC. The cementitious materials were combined cement and supplementary cementitious material including granulated blast-furnace slag (GGBS) and silica fume (SF). Original portland cement was satisfied type II of ASTM C150 with fineness 347 m^2/kg, while ground-granulated blast-furnace slag and silica fume had a specific surface area of 435 m^2/kg and 15000 m^2/kg, respectively. Aggregates had fine aggregate with a fineness modulus of 3.1 and sandstone as coarse aggregate (CA) with a nominal maximum size of 12 mm. To enhance the workability, high-range water-reducing agent (type F) was used as the superplasticizer admixture. Expansive additive was incorporated into all specimens to reduce the shrinkage. The dosage of SP and EA was approximate 2% and 3% by weight of cementitious material, respectively. The mix proportion of the concrete is presented in Table 1. The concrete had ratio of sand to aggregates (s/a) of 0.48 and water-cementitious material ratio (w/cm) of 0.24.

Table 1. Mix proportion of SCC.

Mix proportion, kg/m^3								Slump flow, mm	Setting time, min.	
Cement	GGBS	SF	Sand	CA	Water	SP	EA		Initial	Final
384	256	50	730	789	165	14.3	20	570	539	729

1.2 Specimens design

Total six CFT were 108 mm in outer diameter, thickness of 3 mm, 300 mm in height. The CFT specimens have the ratio of diameter to thickness (D/t) of 36, and the steel ratio (proportion of steel area to concrete area) of 12.1%. The steel tube had the yield strength of 250 MPa, grade satisfied ASTM A36. The composite members were not only carried out on the creep and shrinkage tests but also used to determine the strain and stress behaviour of steel tube and concrete core. The plain concrete were conducted on cylindrical specimens of 100 x 300 mm for creep and shrinkage, and 100 mm by 200 mm dimensions for the experiment of compressive strength and modulus of elasticity. Three specimens were prepared for each type and age of testing. The specimens were designated for creep, shrinkage of CFT and SCC as presented in Table 2.

Table 2. Specimens design for creep and shrinkage tests.

Specimens	Test age, days	Curing condition	Quantity
CFT	14	Steel tube	6
SCC-M	14	Moisture	6
SCC-D	14	Drying	6

1.3 Experiment methods

In the fresh stage, properties of SCC were determined the slump flow as ASTM C1611, and setting time with the penetration resistance according to ASTM C403. After the specimens were cast in the required moulds for each test, the top surface of all specimens was covered immediately with a plastic sheet to prevent water evaporation. The specimens were demoulded after 24 h and cured in a standard

condition (temperature of 23 ± 2^0C, relative humidity of 95% above) until the ages of testing. The compressive strength and the modulus of elasticity were tested according to ASTM C39 and ASTM C469, respectively.

All time-dependent deformation of cylindrical specimens was measured with the embedded vibrating wire strain gauges (VWSG) that were installed in the longitudinal axis and center of the mould. The strain gauges model 9200A with temperature compensation function which measured exactly the vertical strain as well as temperature of concrete specimens were made from stainless steel and had length of 155 mm, diameter of 19 mm. Beside the VWSG, the CFT specimens had two other resistive strain gauges installed outside of specimens for recording the strain of steel tube, as illustrated in Figure 1(a). These collected strains were stored in the datalogger which was connected to the computer as presented in Figure 1(b).

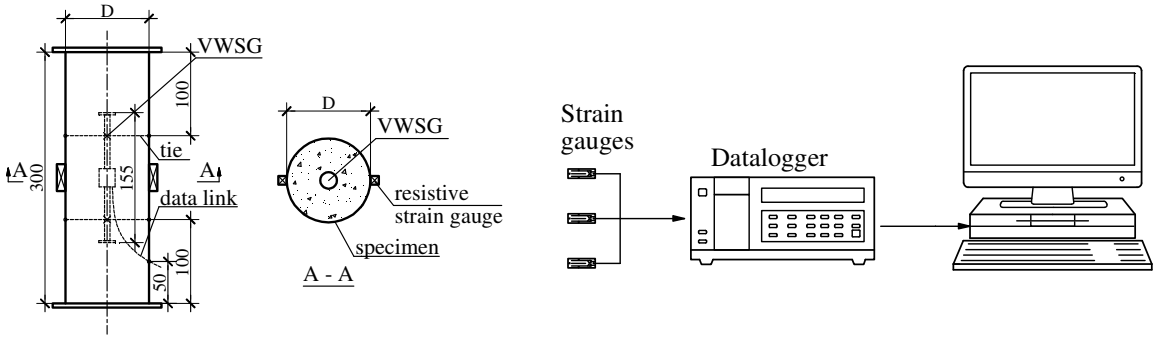

(a) (b)

Figure 1. Diagram of strain measurement
(a) positions of strain gauges, (b) connection of strain gauge and computer.

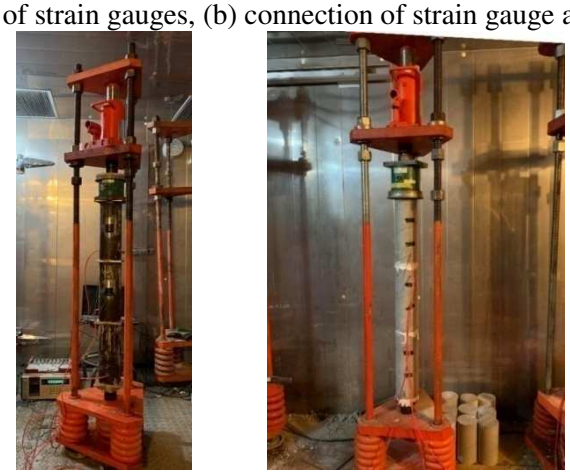

(a) (b)

Figure 2. Setup for creep test with loading frame
(a) CFT specimens, (b) SCC specimens.

The creep of both the CFT and SCC specimens was conducted according to ASTM C512. At age of loading, the creep specimens were grinded for smooth, and the CFT specimens was welded additionally the another steel plate with sizes of 13 cm × 13 cm to seal the concrete core. Then, the specimens were connected and put in the loading frame under applied sustainable stress which was calculated exactly base on their compressive strengths as shown in Figure 2. Whereas, CFT and SCC-D specimens were removed to the drying environment (temperature of 23 ± 2^0C, relative humidity of 50 ± 2%), the last ones still was put in the moisture room (temperature of 23 ± 2^0C and relative humidity of 95% above). The shrinkage strain was measured under the condition accompany the creep tests. The shrinkage and creep strains were determined in long time over a year.

2. Results and discussion

2.1 Workability and mechanical properties

As presented in Table 1, the SCC concrete had a slump flow value of 570 mm, the initial setting time of 539 minutes and final setting time of the concrete of 729 minutes, respectively. The mechanical properties of SCC included the compressive strength and modulus of elasticity which was investigated in different ages of concrete at 7, 14, 28, 56, and 91 days as shown in Figure 3. According to the results, the compressive strength developed significantly at first week up to 81 percent of the 28-day strength. The evolution of elastic modulus related directly to the strength and both of the properties tended to stabilize after 28 days.

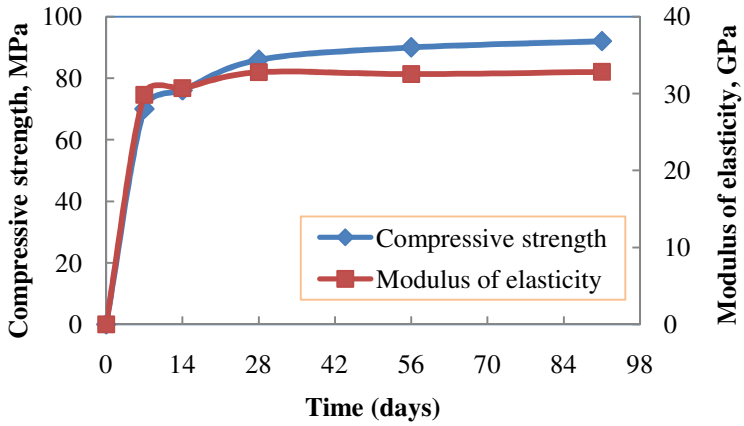

Figure 3. Compressive strength and elastic modulus of SCC.

2.2 Stress conversion

The CFT is combined concrete and steel tube so that the stress impacts on these specimens not same plain concrete. It is well known that creep and shrinkage of concrete core affect directly to time-dependent deformation of CFT. According to the theory of elasticity, the stress of CFT is converted to find exactly applied loading value on the specimens. The theory load of CFT can be expressed as

$$N_{cft} = N_{cft,s} + N_{cft,c} \quad (1)$$

Where N_{cft}, $N_{cft,c}$, $N_{cft,s}$ are axial load of CFT specimen, concrete and steel component, respectively (kN).

It is assumed that plane section remains plane under axial compression, which is essence of strain compatibility so that the steel strain is same as concrete strain at all locations and can be calculated by following equation

$$\varepsilon_{cft,s} = \varepsilon_{cft,c} = \frac{N_{cft,c}}{A_{cft,c} \cdot E_c} \quad (2)$$

The load applies on steel tube can be calculated on that of concrete core as

$$N_{cft,s} = \sigma_{cft,s} \cdot A_{cft,s} = \left(E_s \cdot \varepsilon_{cft,s}\right) A_{cft,s} \quad (3)$$

In which $A_{cft,c}$, $A_{cft,s}$ are cross section of concrete core and steel tube, respectively (mm^2); E_c, E_s are elastic modulus of concrete core and steel tube, respectively (MPa); $\varepsilon_{cft,c}$, $\varepsilon_{cft,s}$ are elastic strain of concrete core and steel tube, respectively.

The loading force of concrete core of CFT can be calculated same with SCC specimens

$$N_{cft,c} = N_c = n_c \cdot f'_c(t_0) \cdot A_c \quad (4)$$

Where N_c is axial load (kN); n_c is stress ratio; $f'_c(t_0)$ is compressive strength at loading age t_0 (MPa); A_c is cross section of concrete component (mm^2).

When CFT is under axial loading, various cylinder stresses appear in the composite member including vertical stress of steel tube ($\sigma_{cft,s}$ or $\sigma_{s,v}$) and vertical stress of concrete core ($\sigma_{cft,c}$), circumferential stress in steel tube ($\sigma_{s,c}$), radial stress (σ_r) as shown in Figure 4.

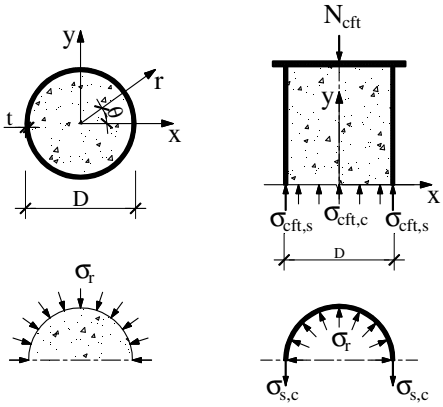

Figure 4. Different stresses in concrete filled steel tube.

The stress occurs on loading of the composite specimen found to be directly proportional to the strain. The stress-strain relationship of CFT subjected to axial compression follows Hook's law within the elastic range.

$$\begin{bmatrix}\sigma_{s,v}\\ \sigma_{s,c}\end{bmatrix}=\frac{E_s}{1-\upsilon_s^2}\begin{bmatrix}1 & \upsilon_s\\ \upsilon_s & 1\end{bmatrix}\begin{bmatrix}\varepsilon_{s,v}\\ \varepsilon_{s,c}\end{bmatrix} \tag{5}$$

The vertical stress of steel tube $\sigma_{cft,s}$ and concrete core $\sigma_{cft,c}$ can be calculated by

$$\sigma_{cft,s}=\sigma_{s,v}=\frac{E_s}{1-\upsilon_s^2}\left(\varepsilon_{s,v}+\upsilon_s\varepsilon_{s,c}\right) \tag{6}$$

$$\sigma_{cft,c}=\frac{N_{cft,c}}{A_{e,cft,c}}=\frac{N_{cft}-N_{cft,s}}{A_{e,cft,c}} \tag{7}$$

In which $\sigma_{s,v}$, $\sigma_{s,c}$ are vertical and circumferential stress in steel tube (MPa), respectively; $\varepsilon_{s,v}$, $\varepsilon_{s,c}$ are vertical and circumferential strain of steel tube (με); υ_s is Poisson's ratio of steel ($\upsilon_s = -\varepsilon_{s,c}/\varepsilon_{s,v}$); $A_{e,cft,c}$ is conversion area of concrete core of CFT (mm^2).

Additionally, when the specimens CFT and plain concrete are embedded the VWSG inside the specimen, the conversion area can be obtained by following general equation

$$A_{e,c}(t_0)=n(t_0)\cdot A_{vw}+A_c \tag{8}$$

$$n(t_0)=\frac{E_{vw}}{E_{mts}(t_0)} \tag{9}$$

Where A_{vw} is cross section of the VWSG (mm^2); $n(t_0)$ is conversion factor; E_{vw} is modulus of elasticity of the VWSG (MPa); $E_{mts}(t_0)$ is elastic modulus of test specimens at loading age t_0.

The conversion stress $\sigma_c(t_0)$ and stress ratio $n_c(t_0)$ are determined by following equations

$$\sigma_c(t_0)=\frac{N_c(t_0)}{A_{e,c}(t_0)} \tag{10}$$

$$n_c(t_0)=\frac{\sigma_c(t_0)}{f_c(t_0)} \tag{11}$$

According to the loading force equations with the stress ratio (n_c) of 0.3, the load value of SCC specimens is 180 kN and 202 kN at 14 days and 28 days, respectively, and the axial load of CFT specimens (N_{cft}) is 325kN at 14 days. The elastic strain of the concrete core and steel tube can be determined by the strain gauges. The elastic modulus of steel tube and stainless steel of VWSG are 200 GPa and 195 GPa, respectively. Poisson's ratio of steel υ_s is 0.3. The creep parameters of the specimens after conversion are given in Table 3.

Table 3. Conversion of stress ratio with consideration of VWSG.

Specimens	Designated stress ratio, n_c	Axial load $N_{cft,c}$ (N_c), kN	Elastic modulus $E_{mts}(t_0)$, MPa	Factor $n(t_0)$	Area $A_{e,c}(t_0)$, mm^2	Stress $\sigma_c(t_0)$, MPa	Real stress $n_c(t_0)$
CFT	0.3	219	44510	4.4	9132	24.0	0.32
SCC		180	30680	6.4	9386	19.2	0.25

2.3 Strain behaviour

Figure 5 shows the shrinkage strains of specimens accompany the creep condition and total strains which was measured base on the creep tests at loading age of 14 days. As the results, shrinkage increased significantly under drying condition, the specimens SCC-D had the highest rate of shrinkage at the initial month after loading age and it could be attained 55 percent value of the final shrinkage strain at 389 days. The shrinkage of these specimens depended mainly on the rate of water loss which is being expelled during the shrinkage process. On the other hand, the swelling phenomenon seemed to occur on the specimens store in the moisture environment and the specimens SCC-M were expanded slightly 74 (10^{-6}mm/mm) in the final time of test. The key reason for the reversible shrinkage of specimens is an incorporation of additional water from humid environment into the porous as well as an increase of water content of adsorbed layers in the concrete structure. While the shrinkage of the plain concrete was affected by the ambient conditions, the shrinkage of specimens CFT was occurred only due to self-desiccation with the negligible final value of only 53 (10^{-6}mm/mm). This value of CFT was nearly 86% smaller than that of the plain concrete in drying test. The issue is considered that the confining effect of steel tube not only restraints significantly the shrinkage of concrete but also prevents the swelling because of expansive agent. The shrinkage of concrete core reduces significantly because the concrete is cured in an enclosed moist environment by steel tube, which has important role prevents the water inside of the concrete evaporate to the environment. In other previous study, Lehman *et al.* showed that shrinkage of self-consolidating concrete filled steel tube specimen was only 200 (10^{-6}mm/mm) at 126 days, which is equal to 44 percent of SCC specimen at the same time.

The total strain occurred from the immediate onset of loading and developed larger in the first week but stabilized then. The data showed that the total strain of CFT was about 16% and 81% less than that of unconfined concrete specimens SCC-M and SCC-D at 389 days after loading age, respectively. Therefore, the steel tube was not only prevented the shrinkage efficiently but also improves significantly the deformation capacity of concrete core due to the restrains concrete dilation and passive confinement of steel tube. Although applied stress is sustainable, the ratio of stress to strength is lower because the strength of concrete improved by confinement effect of steel tube more than plain concrete. On the other hand, the stress of concrete component is relaxed due to possible stress transfer between concrete and steel tube so that the total of CFT is reduced.

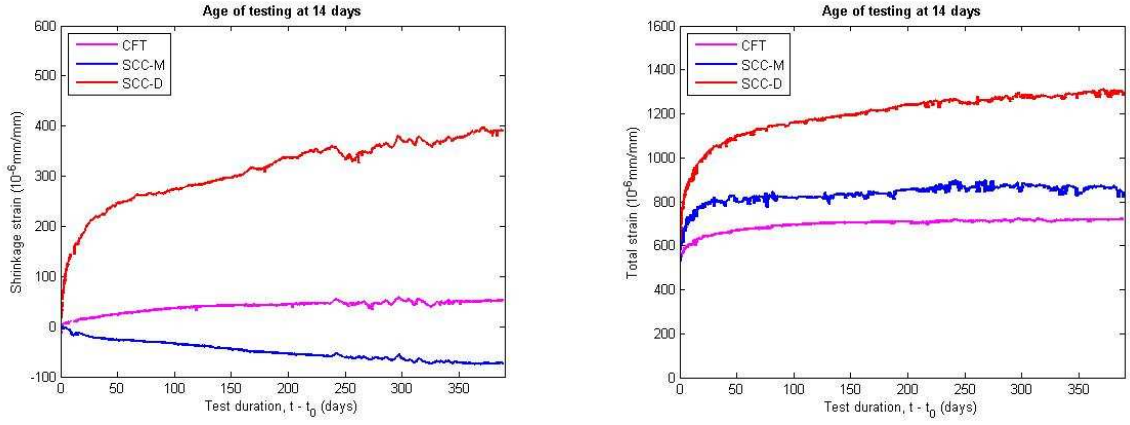

(a) (b)

Figure 5. Strains of CFT and SCC at test age of 14 days.
(a) Shrinkage strain, (b) Total strain

According to the results of the total strain and shrinkage strain, the strain creep and the other parameters such as creep coefficient, specific creep, and compliance function could be determined exactly through the Eqs. 12, 13, 14, and 15, respectively (Bažant, 1988) (Neville, Dilger, & Brooks, 1983). When the temperature is stable same as the testing condition, the creep strains can be obtained by subtracting shrinkage strains from measured total strains as following

$$\varepsilon_{cc}(t,t_0) = \varepsilon(t,t_0) - \varepsilon_e(t_0) - \varepsilon_{cs}(t,t_c) \quad (12)$$

Creep coefficient is expressed as

$$\phi(t,t_0)=\frac{\varepsilon_{cc}(t,t_0)}{\varepsilon_e(t_0)} \tag{13}$$

Specific creep (creep compliance) is determined as

$$C_{sp}(t,t_0)=\frac{\varepsilon_{cc}(t,t_0)}{\sigma(t_0)} \tag{14}$$

Compliance function (creep function) is calculated by

$$J(t,t_0)=\frac{\varepsilon_e(t_0)+\varepsilon_{cc}(t,t_0)}{\sigma_c(t_0)} \tag{15}$$

In which $\varepsilon(t,t_0)$ is total strain (10^{-6}); $\varepsilon_{cs}(t,t_c)$ is the shrinkage strain (10^{-6}); $\varepsilon_e(t_0)$ is elastic strain (10^{-6}); $\varepsilon_{bc}(t,t_0)$ is basic creep strain (10^{-6}); $\varepsilon_{dc}(t,t_0)$ is drying creep strain (10^{-6}); $\sigma_c(t_0)$ is applied stress (MPa).
According to the values of creep parameters summarized in Table 4, the plain concrete which was cured in different environment conditions had rather similar the results including creep strain, creep coefficient, specific creep and creep compliance. However, these parameters of CFT were decreased significantly in comparison with the plain concrete. For instance, creep strain, creep coefficient, specific creep, and creep compliance of CFT specimens were about 53%, 48%, 63%, and 42% lower than those of the SCC specimens under drying environment, respectively. These results indicated again the improvement of the composite structure base on steel tube and concrete core.

Table 4. Basic and total creep results of specimens.

Specimen	Applied stress, σ_c (MPa)	Elastic strain, ε_e (10^{-6})	Creep parameters at 389 days after loading.					
			Total strain, ε (10^{-6})	Shrinkage strain, ε_{cs} (10^{-6})	Creep strain, ε_{cc} (10^{-6})	Creep coefficient, ϕ	Specific creep, C_{sp} (10^{-6}/MPa)	Creep compliance, J (10^{-6}/MPa)
CFT	24.0	502	721	53	166	0.33	6.9	27.8
SCC-M	19.2	540	837	-74	371	0.69	19.3	47.4
SCC-D	19.2	556	1304	390	358	0.64	18.6	47.6

2.4 Strain and stress of CFT

The strains of CFT components were measured by separate strain gauges. As can be observed in Figure 6(a), the values raises quickly at initial 21 days and become stably after about 50 days. The vertical strains of steel tube and concrete began at the time of applied loading and increased gradually to 389 days after applied stress. The two components of the composite member had the similar magnitude of vertical strain between steel tube and concrete core. In the initial period after loading, the steel tube had vertical strain value higher than the concrete core because the Poisson's ratio of concrete is lower than that of the steel. The difference of vertical strains of CFT components also indicates longitudinal slipping between the steel tube and concrete can occur in this stage. The vertical strain of concrete was higher with time due to creep as well as the larger lateral strain. However, the deformation of the concrete core is restrained by confinement effect of steel tube so that the vertical strain of the concrete increases equally with steel. The result confirms the plane section remain plane as well as compatibility between steel and concrete components. The test data compared suitably with those of Kwon (Kwon, Kim, & Kim, 2005), who determined that vertical strains within the steel tube and concrete core have the same magnitude.
When the CFT specimens were sustained load 325kN with conversion stress ratio of 0.32, the stress of components can be evaluated according to data of strain gauges. Figure 6(b) illustrates that the vertical stress transfer on steel tube increases 35.5 percent at 389 days after loading age, whereas that on concrete core drops 15.8 percent of vertical stress at the same time. The stress of composite member is influenced by strain variation, and the stresses of CFT components are unstable due to no restraint effects on the concrete core at initial several weeks. It also can be observed clearly that the stress magnitude of fluctuation of steel tube is much large in this time. The stress transfer only occurs from a radial pressure develops at steel-concrete interfacial bond because the lateral expansion of the concrete core increases larger than steel tube. The various magnitude of stress of steel tube also gets smaller with time. On the other hand, the reason of stress redistribution is concrete possess the creep properties but steel does not perform creep deformation. Furthermore, the interconnection between steel tube and

concrete core of CFT, which has sufficient strength and stiffness to combine steel tube and concrete core work as a unity member, also is an important role influence on the behaviour of the composite structure. The stress result of the composite components varied over time had also been shown by researches of Kwon (Kwon, Kim, & Kim, 2005) and Wang (Wang Y. Y., Geng, Chen, & Zhao, 2019). Kwon (Kwon, Kim, & Kim, 2005) explained that the value of the vertical stress variation in the concrete core is smaller than that in the steel tube because the cross-sectional area of the concrete is much larger than the area of steel. Wang (Wang Y. Y., Geng, Chen, & Zhao, 2019) indicated that the vertical stresses in the steel tubes were about 310 to 320 MPa under sustained loading between 40% and 80% of the strength, whereas vertical stress in the concrete core basically maintains a constant value of 29 to 30 MPa for specimens with 1 meter in length at 300 days.

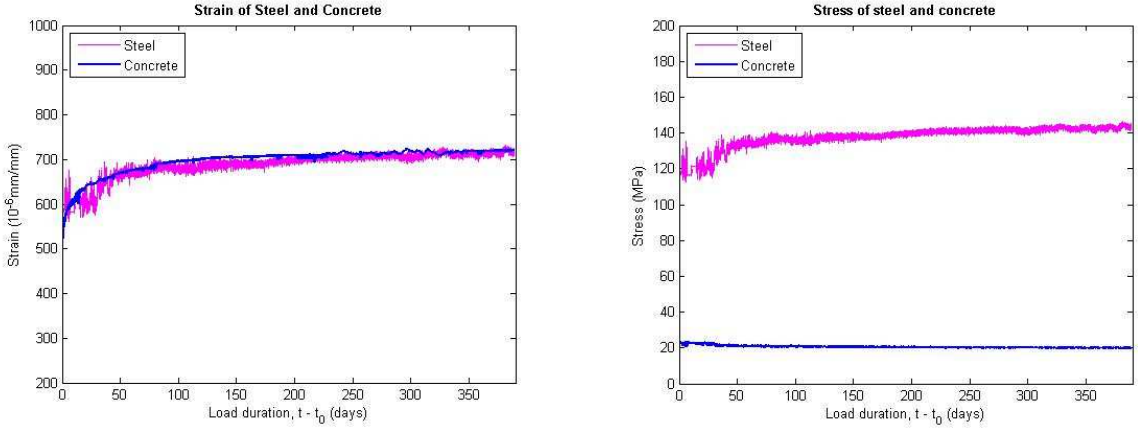

(a) (b)

Figure 6. Strains and stresses of steel tube and concrete core
(a) vertical strains, (b) vertical stresses.

The vertical strains, vertical stresses, and stress transfer of CFT components were changed by various days, as can be seen in Table 5.

Table 5. Vertical strains, stresses and stress transfer of CFT member.

Load duration $t-t_0$, days	Steel tube			Concrete core		
	Strain, με	Stress, MPa	Stress transfer, %	Strain, με	Stress, MPa	Stress transfer, %
0	536	107	0.0	502	24.0	0.0
21	630	126	+17.8	642	21.9	-8.8
389	723	145	+35.5	721	20.2	-15.8

CONCLUSIONS

Base on the experimental results of CFT and plain concrete in a long term, the main conclusions of the study can be drawn as follows:

- The advantage of interaction between steel tube and concrete core reduced significantly the time-dependent deformation of CFT. The shrinkage strain of CFT was negligible, while creep strain of this composite material was 53 percent lower than that of concrete without steel tube in drying condition, respectively.
- The vertical strain of CFT components had the similar magnitude of vertical strains between steel tube and concrete core so they can be considered as fully composite member.
- The vertical stress of steel increased 35.5 percent but vertical stress of concrete decreased 15.8 percent at 389 days after applied loading. This stress transfer magnitude cannot be neglected put considerations in CFT design.

ACKNOWLEDGMENTS

The research reported in this paper was supported by Ministry of Science and Technology (MOST) of Taiwan (No. 109-2224-E-002 -007-).

REFERENCES

Bažant, Z. P. (1988). *Mathematical modeling of creep and shrinkage of concrete.* John Wiley & Sons.

Bergmann, R., Matsui, C., & C. Meinsma, D. D. (1995). *Design Guide for concrete filled hollow section columns under static and seismic loading.* Germany: Verlag TÜV Rheinland.

Han, L.-H., Li, W., & Bjorhovde, R. (2014). Developments and advanced applications of concrete-filled steel tubular (CFST) structures: Members. *Journal of Constructional Steel Research , 100*, 211-228.

Ichinose, L., Watanabe, E., & Nakai, H. (2001). An experimental study on creep of concrete filled steel pipes. *Journal of Constructional Steel Research , 57*, 453-466.

Kwon, S. H., Kim, Y. Y., & Kim, J. K. (2005). Long-term behaviour under axial service loads of circular columns made from concrete filled steel tubes. *Magazine of Concrete Research , 57* (2), 87-99.

Lai, X., & Chen, B. (2016). Shrinkage predicted model of concrete filled steel tube and shrinkage stress of concrete filled steel tubular arch. *8th International Conference on Arch Bridges*, (pp. 909-920).

Lehman, D. E., Kuder, K. G., Gunnarrson, A. K., Roeder, C. W., & Berman, J. W. (2015). Circular Concrete-Filled Tubes for Improved Sustainability and Seismic Resilience. *Journal of Structural Engineering , 141* (3), (1-12) B4014008.

Ma, Y. S., & Wang, Y. F. (2012). Creep of high strength concrete filled steel tube columns. *Thin-Walled Structures , 53*, 91-98.

Morino, S., Uchikoshi, M., & Yamaguchi, I. (2001). Concrete-filled steel tube column system-its advantages. *Steel Structures , 1*, 33-44.

Neville, A. M., Dilger, W. H., & Brooks, J. J. (1983). *Creep of plain and structural concrete.* Construction Press.

Wang, Y. Y., Geng, Y., Chen, J., & Zhao, M. Z. (2019). Testing and analysis on nonlinear creep behaviour of concrete-filled steel tubes with circular cross-section. *Engineering Structures , 185*, 26-46.

Wang, Y., & Zhao, R. (2018). Experimental Study on Time-dependent Behavior of Concrete Filled Steel Tubes in Ambient Environment. *KSCE Journal of Civil Engineering , 23* (1), 200-209.

Wang, Y., Geng, Y., Ranzi, G., & Zhang, S. (2011). Time-dependent behaviour of expansive concrete-filled steel tubular columns. *Journal of Constructional Steel Research , 67*, 471-483.

Zhang, D. J., Ma, Y. S., & Wang, Y. (2015). Compressive behavior of concrete filled steel tubular columns subjected to long-term loading. *Thin-Walled Structures , 89*, 205-211.

Zhang, R., Ma, L., Wang, Q., Li, J., Wang, Y., Chen, H., et al. (2019). Experimental Studies on the Effect of Properties and Micro-Structure on the Creep of Concrete-Filled Steel Tubes. *Materials , 12*.

ANALYTICAL METHOD FOR PUNCHING OF REINFORCED CONCRETE FLAT SLABS WITHOUT STIRRUPS

Srinivas Mogili,[1] Hsiang-Yun Lin[2] and Shyh-Jiann Hwang[3]
1. Post-doctoral Researcher, Department of Civil Engineering, National Taiwan University, Taipei, Taiwan
2. Graduate Student, Department of Civil Engineering, National Taiwan University, Taipei, Taiwan
3. Professor, Department of Civil Engineering, National Taiwan University, Taipei, Taiwan
Email: smogili@connect.ust.hk, r09521203@ntu.edu.tw, sjhwang@ntu.edu.tw

ABSTRACT

Flat slabs are characterized by an absence of beams framing into columns. The limited depths of flat slabs result in the development of severe stresses near the column-slab joints, which typically results in brittle punching of the column into the slab, especially when transverse reinforcement is not provided. It is thus important to accurately assess the punching capacity of such members in design and preclude such brittle failures. In this paper, an analytical model based on the softened strut-and-tie model is presented to estimate the punching capacity of flat slab members without transverse reinforcement. The proposed model is efficient in capturing key parameters such as concrete strength, column size, slab thickness, and longitudinal reinforcement. The accuracy of the analytical model when verified using the test data from 44 flat slab test specimens in the literature is reasonable with an average test-to-calculated capacity ratio of 1.22 and a coefficient of variation of 0.15. Comparisons are also made with the estimates based on ACI 318 and Eurocode 2 recommendations to assess the current design scenario. This work lays a foundation for the punching of flat slabs under lateral loading.

Keywords: reinforced concrete, flat slabs, punching, concrete strut, softened strut-and-tie model

INTRODUCTION

Reinforced concrete flat slabs are quite commonly observed in buildings due to the advantage of clear height of the floor, the convenience and the overall cost of construction. However, such members are at risk of catastrophic failure due to their limited strength, particularly near the column-slab joints, resulting in the punching of columns through slabs. The absence of beams and limited depth of flat slabs severely limit the shear capacity of these members near the joints. Although shear capacity can be generally enhanced in reinforced concrete members through the addition of transverse reinforcement, the limited thickness of flat slabs makes it quite difficult to place stirrups in these members. Thus, it is quite common to encounter flat slabs with little or no transverse reinforcement in practice, because of which it is of interest for researchers to study, assess and improve the punching capacity of flat slabs without transverse reinforcement.

Several investigations (Elstner and Hognestad, 1956; Regan, 1986; Rankin and Long, 1987; Marzouk and Hussein, 1991) have been conducted to analyze the behavior and strength of reinforced concrete flat slabs without shear reinforcement under vertical monotonic loading – with a major focus on the parametric variation of key parameters such as concrete strength, longitudinal reinforcement, thickness (and effective depth), span, column dimensions, etc. The addition of tension reinforcement can greatly improve the punching capacity of flat slabs with low tension reinforcement ratios through the enhancement of the flexural capacity of the slab. At higher tension reinforcement ratios, improvement in flexural capacity could sometimes trigger a more brittle shear punching in flat slabs (Rankin and Long, 1987). The improvement in shear capacity was also observed with more reinforcement concentrated under the column region as compared to the reinforcement spread uniformly across the slab (Regan, 1986; Rankin and Long, 1987). Conversely, a reduction in the capacity of flat slabs was observed when tension reinforcement does not pass through the slab-column connections – adversely impacting the

shear punching capacity (Pérez Caldentey *et al.*, 2013). Thus, both the area and format of tension reinforcement influence the punching capacity of flat slabs.

Similarly, the increase in slab thickness is also beneficial to the punching capacity of flat slabs (Regan 1986; Rankin and Long 1987). While the improvement in flexural capacity with effective depth is clear through the sectional analysis, the improvement in shear capacity is due to a greater concrete contribution toward the load resistance. The trend of improvement in shear capacity with thickness does not hold at higher thicknesses where the shear strength reduces with an increase in thickness due to the size effect (Guandalini *et al.*, 2009; Lips *et al.*, 2012). Thus, a reduction in the load-carrying capacity needs to be considered with an increase in thickness over a certain limit. American design code (ACI 318, 2019) prescribes 250 mm as a limit above which size effect should be considered. A larger column area also showed improvement in the punching strength due to the beneficial reduction in the bearing stresses which are inversely proportional to the column area (Elstner and Hognestad, 1956; Regan, 1986). Another key parameter for improving the capacity of flat slabs is the concrete compressive strength. An increase in concrete strength enhances the capacity with an improvement of strut strength. However, using high-strength concrete reportedly resulted in rather brittle failures as compared with normal-strength concrete (Marzouk and Hussein, 1991; Ramdane, 1996).

To summarize, test results from the literature indicate that the load-carrying capacity of flat slabs under vertical loading without shear reinforcement is influenced by key parameters such as longitudinal reinforcement area & layout, thickness (or effective depth), column dimensions, and concrete strength. Therefore, a reliable analytical model for the strength estimation should reflect the influence of these parameters, such that engineers can vary these parameters to achieve desired design requirements. While the flexural estimations are rather straightforward using the sectional analysis through the yield line theory, there is however no consensus on the estimation of the shear strength among major design codes due to the omission of key parameters in the empirical expressions recommended for the calculation of shear strength.

For instance, the ACI code (ACI Committee 318, 2019) prescribes that flat slabs are designed as per the two-way shear requirements through the empirical equation shown in Eq 1. Although this expression includes the effective depth d and the column geometry (indirectly through critical perimeter), it cannot capture the influence of longitudinal reinforcement on the shear strength. The lack of reinforcement factor in Eq. 1 was reported to result in unsafe designs in flat slabs with low reinforcement ratios (Muttoni, 2008). For members with high reinforcement ratios, ACI underestimates the capacity leading to inefficient and perhaps costly design. The size effect factor is equal to 1.0 for flat slabs where the effective depth does not exceed 250 mm. However, for larger slabs, the reduction factor λ_s should be determined. b_o represents the perimeter of the critical section located at a distance of $0.5d$ and f_c' is the concrete compressive strength.

$$V_c = 0.33 \times \lambda_s \times \sqrt{f_c'} \times b_o d \quad \text{where} \quad \lambda_s = \sqrt{2 \Big/ \left(1 + \frac{d\ (\text{mm})}{250}\right)} \leq 1 \tag{1}$$

The European design standard Eurocode 2 (CEN 1992-1-1, 2004) considers the effect of longitudinal reinforcement for shear strength through a 1/3 power function, as shown in Eq. 2, where b_o represents the perimeter of the critical section at a distance of $2d$ away from column. The effect of size is considered through the factor k for slabs effective in slabs with depth over 200 mm. It is noteworthy that the definition of the critical section is different from that of the ACI code.

$$V_c = 0.18 \times k \times \left[100 \rho f_c'\right]^{1/3} \times b_o d \quad \text{where} \quad k = 1 + \sqrt{200/d\ (\text{mm})} \leq 2 \tag{2}$$

Thus, the design codes are somewhat inconsistent in the treatment of flat slabs concerning the inclusion of key parameters for shear strength estimation. The resulting estimations cannot accurately capture the

variation in the capacity of flat slabs associated with the parametric variations. This is especially important for flat slab members where designers are often challenged with improving the capacity with a controlled variation of one or more key parameters. For example, improving the shear punching capacity through the inclusion of additional tension reinforcement and likewise. Hence, it is important to develop an accurate and reliable analytical method for the shear punching capacity of flat slabs which can incorporate the effects of key parameters outlined hitherto. This paper presents an analytical model based on the softened strut-and-tie model (Hwang and Lee, 2002) to estimate the shear capacity of flat slabs while capturing the influence of key parameters that generally influence flat slab behavior. The flexural capacity is calculated according to the commonly accepted yield line theory with the critical sections at the edges of the column. The verification of the proposed model was carried out using the experimental data consisting of 44 flat slab specimens under monotonic/gravity loading from the literature (Rankin and Long, 1987; Marzouk and Hussein, 1991). The proposed model is introduced in the following section.

PROPOSED ANALYTICAL METHOD

The development of the analytical method for the shear punching capacity of flat slabs is based on the authors' previous analytical work (Mogili and Hwang, 2021) on the estimation of the punching capacity of pile caps. The monotonic load applied to the column is resisted through the formation of concrete struts in different directions. The formation of concrete struts in a typical flat slab with loading from a square column is shown in Fig. 1. Four struts are developed, one in each direction from the edge of the column to resist the column load. The strengths of the diagonal struts determine the overall punching shear capacity of the flat slab member.

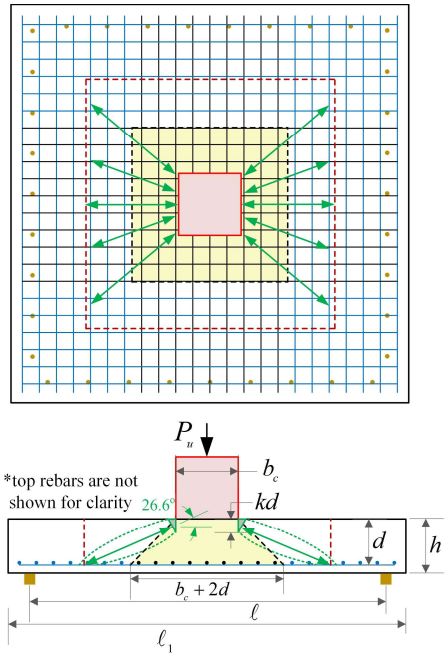

Figure 1. Formation of concrete struts within the flat slab under monotonic loading

The diagonal struts typically extend from the column towards the supports, i.e., the inclination typically depends on the span-to-depth ratio. While this is reasonable in members like pile caps and deep beams, it is not suitable for flat slabs where inclination based on span-to-depth ratio will result in struts with very small angles which are not practical. (Grob and Thürlimann, 1976) suggested a lower limit of 26.6° for the concrete struts for stability. This is commonly accepted among designers and engineers alike with the ACI code (ACI Committee 318, 2019) adopting similar lower limits (rounded off to 25°) for a design using strut-and-tie methods. In this study, the diagonal concrete struts are assumed to be inclined

at an angle of 26.6°, forming a D-B-D region in the flat slabs as opposed to D-regions in deep beams and pile caps.

The proposed method considers that the region surrounding the area directly underneath the column exhibits severe stresses that eventually result in the punching of the slab. The severe stresses in this region are a result of bearing stresses from the column load and flexural compressive stresses generated within the slab. The strut formation occurs at an early stage of loading where the tension reinforcement over the entire width of the slab is not effective. For the purpose of calculation of the flexural compression zone, the reinforcement that falls within the 45° pyramid is considered. This follows the general consideration of 1:1 spread in two-way members to define yield lines (in plan) and bearing zone (in elevation). This assumption can explain the particular benefit to shear capacity with an addition of concentrated tension reinforcement under the column region as discussed previously. For a flat slab shown in Fig. 1 with a total area of tension reinforcement in one direction A_s uniformly distributed over the entire width, the area of the effective reinforcement A_{se} for strut in one direction is given by Eq. 3.

$$A_{se} = A_s \times \left(b_c + 2d\right) / \ell_1 \tag{3}$$

The width of this activated zone near the column is defined as the effective loading width b_e. The concrete from this width is assumed to be effective in supporting the diagonal concrete struts and therefore b_e is adopted as the width of the concrete strut. The depth of the elastic compression zone with width b_e generated through the tension reinforcement A_{se} is taken as the strut depth. It must be highlighted that the compression reinforcement is assumed to not affect b_e, a consideration which is consistent with the previously reported conclusion that compression reinforcement does not affect the shearing strength of flat slabs (Elstner and Hognestad, 1956). b_e is determined by considering a consistent interaction of the flexural and shear actions developed within the slab. This follows an iterative procedure as shown in Fig. 2. kd from the final iteration is assumed to be equal to the depth of the strut. Thus, the area of the diagonal strut is calculated as follows:

$$A_{str} = b_e \times kd \tag{4}$$

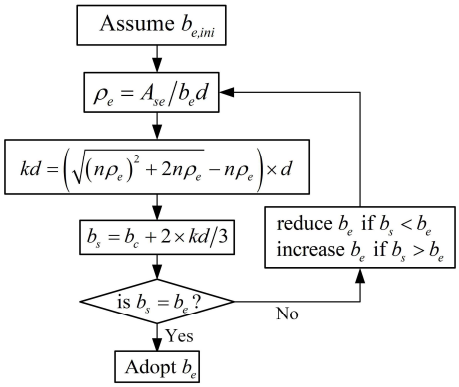

Figure 2. Iteration for the calculation of effective loading width

The compression capacity of the strut is calculated as given by Eq. 5 (Hwang and Lee, 2002).

$$C_d = \xi f_c' \times A_{str} \tag{5}$$

where ξ represents the softening behavior of the concrete which accounts for the reduction in the concrete strength due to the development of transverse tensile strains in the strut. The approximation for softening coefficient ξ is given by Eq. 6 based on the related work by (Hwang *et al.*, 2017).

$$\xi = 3.35 \Big/ \sqrt{f_c' \text{ (MPa)}} \leq 0.52 \tag{6}$$

The vertical load required to develop the capacity of the diagonal strut is determined by assuming the angle of inclination of the strut as 26.6° as discussed previously. Thus, for a two-way symmetric slab with a square column, the vertical load corresponding to the shear capacity is calculated as follows:

$$P_{shear} = 4 \times C_d \sin 26.6° \tag{7}$$

The flexural capacity is determined through Bernoulli sectional analyses at critical sections considered at each edge of the column over the entire width of the slab. The total area of both the compression and tension reinforcement at the critical section is considered for the flexural analysis. The nominal flexural capacity M_n corresponds to the strain in extreme concrete compression reaching 0.003. The corresponding vertical load for generating M_n is derived by dividing it by the clear span. Thus, the vertical load corresponding to the flexural capacity is calculated as:

$$P_{flex} = 4 \times M_n \Big/ \left(\frac{\ell}{2} - \frac{b_c}{2} \right) \tag{8}$$

The overall punching capacity of a flat slab member P_{SST} is determined as the minimum of the shear and flexural punching capacities calculated by Eqs. 7 and 8, respectively.

$$P_{SST} = \min\left(P_{shear}, P_{flex} \right) \tag{9}$$

VERIFICATION

The accuracy of the proposed analytical model is assessed using test results from 44 flat slab specimens without shear reinforcement reported in the literature (Rankin and Long, 1987; Marzouk and Hussein, 1991). Only specimens with symmetric geometry and reinforcement layouts were chosen for verification. The specimens collated include a wide range of parametric variations such as concrete strength, column dimension, slab thickness, span, and reinforcement ratio. (Marzouk and Hussein, 1991) is a full-scale flat slab experimental study comprising 17 specimens with a controlled variation of parameters such as reinforcement ratio (both tension and compression), slab thickness, and column dimension on the punching capacity in specimens with normal and high-strength concrete. (Rankin and Long, 1987) is a half-scale flat slab study comprising 27 singly reinforced specimens with a variation in slab thickness and tension reinforcement ratio. The failure modes reported included a mix of both flexural and shear failures. The accuracy of the proposed model can be adjudged by verifying how well the measured capacities are replicated in estimates with different parametric variations. In addition, the estimates for 44 specimens are also calculated according to the ACI 318 (ACI) and Eurocode 2 (EC2) design recommendations which are introduced earlier in this manuscript. The material, geometric details, as well as prediction accuracies in terms of the test-to-calculated capacity ratios for all 44 specimens are listed in Table 1.

A comparison of the overall strength ratios shows that the proposed analytical model is accurate in estimating the punching capacity of the specimens in the collated database with a mean of 1.22 and a low coefficient of variation (COV) of 0.15. The flexural punching failure is predicted in only six specimens, and shear failure in the rest. The estimates from EC2 are also quite reasonable with a mean of 1.24 and COV of 0.12. EC2 predicted flexural failure in only three specimens and shear failure in the rest. In comparison, the punching estimates by ACI are underestimated with an overall mean capacity ratio of 1.45 and a COV of 0.23, with five specimens failing in flexure and the rest in shear. Accurate predictions using the proposed analytical procedure highlight that the proposed model can capture the effect of key parameters such as reinforcement, thickness, span, and column dimension on the capacity

reasonably well. The reasonable estimates from EC2 can also be attributed to the consideration of the longitudinal reinforcement ratio that is included in shear capacity estimation using Eq. (2). ACI on the other hand, does not consider any effect of reinforcement on the shear capacity which resulted in underestimation, especially for specimens with high reinforcement ratios.

Table 1. Properties and predictions of flat slabs without shear reinforcement

S. No.	f_c' (MPa)	f_y (MPa)	ρ_t %	ρ_c %	d (mm)	b_c (mm)	ℓ (mm)	P_{test} (kN)	P_{SST} (kN)	$\frac{P_{test}}{P_{SST}}$	$\frac{P_{test}}{P_{ACI}}$	$\frac{P_{test}}{P_{EC}}$
1	42	490	1.17%	0.24%	95	150	1500	320	270.9	1.18	1.61	1.21
2	67	490	0.39%	0.24%	95	150	1500	178	185.9	0.96(F)	0.96(F)	0.96(F)
3	70	490	0.68%	0.24%	95	150	1500	249	250.2	1.00	0.97	0.95
4	74	490	0.97%	0.24%	95	150	1500	356	296.7	1.20	1.35	1.18
5	69	490	1.17%	0.24%	95	150	1500	356	313.6	1.14	1.39	1.14
6	66	490	2.19%	0.58%	90	150	1500	418	370.7	1.13	1.80	1.20
7	30	490	0.54%	0.19%	120	150	1500	396	206.4	1.92	1.69	1.44
8	68	490	0.54%	0.19%	120	150	1500	365	305.5	1.19	1.03	1.01
9	70	490	0.54%	0.19%	120	150	1500	489	307.9	1.59	1.37	1.34
10	69	490	1.04%	0.43%	120	150	1500	436	408.3	1.07	1.23	0.96
11	74	490	1.56%	0.43%	120	150	1500	543	492.8	1.10	1.48	1.02
12	80	490	2.08%	0.43%	120	150	1500	645	565.4	1.14	1.69	1.08
13	70	490	0.79%	0.33%	70	150	1500	196	180.0	1.09(F)	1.15	1.19
14	75	490	1.25%	0.33%	70	150	1500	258	223.6	1.15	1.47	1.31
15	68	490	1.58%	0.33%	70	150	1500	267	238.6	1.12	1.59	1.29
16	72	490	1.17%	0.24%	95	220	1500	498	418.3	1.19	1.49	1.39
17	71	490	1.17%	0.24%	95	300	1500	560	503.9	1.11(F)	1.34	1.38
18	31	530	0.42%	-	40.5	100	640	36.42	33.4	1.09(F)	1.09(F)	1.09(F)
19	31	530	0.56%	-	40.5	100	640	49.08	39.5	1.24	1.18	1.25
20	31	530	0.69%	-	40.5	100	640	56.55	43.1	1.31	1.36	1.34
21	35	530	0.82%	-	40.5	100	640	56.18	51.0	1.10	1.27	1.20
22	35	530	0.88%	-	40.5	100	640	57.27	52.6	1.09	1.29	1.20
23	35	530	1.03%	-	40.5	100	640	65.58	56.0	1.17	1.48	1.30
24	30	530	1.16%	-	40.5	100	640	70.94	51.8	1.37	1.73	1.43
25	30	530	1.29%	-	40.5	100	640	71.09	53.8	1.32	1.74	1.38
26	30	530	1.45%	-	40.5	100	640	78.6	56.4	1.39	1.92	1.47
27	30	530	0.52%	-	40.5	100	640	43.59	37.4	1.17	1.08(F)	1.14
28	30	530	0.80%	-	40.5	100	640	55	44.8	1.23	1.34	1.25
29	30	530	1.11%	-	40.5	100	640	67.06	51.1	1.31	1.63	1.37
30	34	530	0.60%	-	40.5	100	640	49.39	43.9	1.12	1.13	1.18
31	34	530	0.69%	-	40.5	100	640	52.45	46.7	1.12	1.20	1.20
32	34	530	1.99%	-	40.5	100	640	84.84	70.9	1.20	1.94	1.36
33	29	530	0.44%	-	46.5	100	640	45.19	40.3	1.12	0.99(F)	1.01
34	29	530	0.69%	-	46.5	100	640	66.24	48.6	1.36	1.37	1.28
35	29	530	1.29%	-	46.5	100	640	89.72	62.5	1.44	1.86	1.40
36	31	530	1.99%	-	46.5	100	640	97.43	77.7	1.25	1.95	1.29
37	38	530	0.42%	-	35	100	640	28.85	25.1	1.15(F)	1.15(F)	1.15(F)
38	38	530	0.69%	-	35	100	640	37.63	40.1	0.94(F)	0.98	1.05

39	38	530	1.29%	-	35	100	640	56.67	54.7	1.04	1.48	1.28
40	31	530	1.99%	-	35	100	640	72.52	54.8	1.32	2.09	1.52
41	28	530	0.42%	-	53.5	100	640	62.74	45.9	1.37	1.10	1.14
42	32	530	0.69%	-	53.5	100	640	87.86	63.8	1.38	1.42	1.29
43	32	530	1.29%	-	53.5	100	640	124.14	82.0	1.51	2.01	1.48
44	28	530	1.99%	-	53.5	100	640	125.94	85.3	1.48	2.20	1.36
Note: Flexural mode of failure is indicated by the superscript F on the corresponding strength ratio, the failure mode is shear otherwise.									**AVG** **COV**	**1.22** **0.15**	**1.45** **0.23**	**1.24** **0.12**

The comparison of capacity estimates using the three procedures is also presented in Fig. 2 showing the variation of respective capacity ratios with concrete compressive strength and tension reinforcement ratio separately. The visual comparison shows that both the proposed SST approach and EC2 approach resulted in reasonable estimates for specimens with normal strength concrete. In the case of specimens with high-strength concrete, the SST approach provided more accurate estimations as compared with EC2. In both these cases, ACI considerably underestimated the capacities. Furthermore, the ACI estimates vary from unsafe in specimens with low tension reinforcement ratios to severe underestimation in specimens with high tension reinforcement ratios. This trend can be accounted to the influence of longitudinal reinforcement on the punching shear capacity – which is ignored by ACI. EC2, which includes a factor for reinforcement ratio for estimating the shear capacity (refer to Eq. (2)) performs better with more consistent ratios over the entire range of tension reinforcement ratios indicating that such a factor is reasonable for the estimation of shear capacity in flat slabs. The consistent estimates of the SST method also highlight that the effect of longitudinal reinforcement on shear capacity is well captured through the calculation of kd. With regards to the failure mode, it appears that tension reinforcement is the most important factor for EC2 and ACI methods – with flexural failure associated with tension reinforcement ratios lower than 0.42% and 0.52%, respectively. The SST approach on the other hand predicted flexural failure even at higher tension reinforcement ratios up to 0.7% – and in one case at 1.2% where b_c/d is very high (3.2). Although other factors impact the modes of failure, based on the accurate estimates through the SST approach, it can be inferred that the tension reinforcement ratio lower than 0.75% generally tends to result in flexural failure of flat slabs.

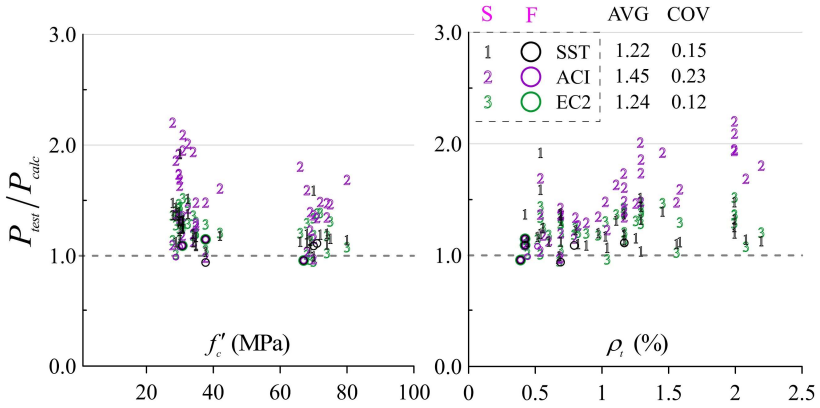

Figure 2. Comparison of strength estimations

CONCLUSIONS

An analytical model based on the softened strut-and-tie model to estimate the punching capacity of reinforced concrete flat slabs without shear reinforcement is presented. The proposed approach assumes the formation of concrete struts inclined at an angle of 26.6° in determining the shear capacity. Flexural capacity is estimated through yield line theory with the nominal bending capacity of the flexure critical section at the edge of the column. The verification of the proposed model was carried out using the data from 44 symmetric flat slab members without transverse reinforcement. The collated database is

comprised of a variety of parameters such as concrete strength, column geometry, tension and compression slab reinforcement, span, and thickness. The strength prediction using the proposed model is compared with the estimates using the ACI 318 and Eurocode 2 recommendations for punching strength of flat plates. Comparisons showed that the proposed model reasonably captured the influence of key parameters which resulted in the average test-to-estimated strength ratio of 1.22 and a low coefficient of variation of 0.15. The proposed approach is simple and accurate and can be adopted for design purposes. The proposed approach can be further customized for the punching of flat slabs under lateral loading.

ACKNOWLEDGMENTS

Funding support from the Ministry of Science and Technology, Taiwan under the grant numbers 109-2221-E-002-007-MY3 and 110-2811-E-002-549-MY2 is gratefully acknowledged.

REFERENCES

ACI Committee 318. (2019). *Building Code Requirements for Structural Concrete (ACI 318-19): Commentary on Building Code Requirements for Structural Concrete (ACI 318R-19)*. American Concrete Institute, Farmington Hills, Detroit MI.

Elstner, R. C., and Hognestad, E. (1956). "Shearing Strength of Reinforced Concrete Slabs," *ACI Journal Proceedings*, **53**(7), 29–58.

European Committee for Standardisation (CEN) 1992-1-1. (2004). *Eurocode 2: Design of concrete structures - Part 1-1 : General rules and rules for buildings*. European Committee for Standardization, Brussels.

Grob, J., and Thürlimann, B. (1976). "Ultimate Strength and Design of Reinforced Concrete Beams under Bending and Shear," *Ultimate Strength and Design of Reinforced Concrete Beams under Bending and Shear / Résistance et dimensionnement des poutres en béton armé soumises à la flexion et à l'effort tranchant / Bruchwiderstand und Bemessung von Stahlbetonbalken unter Biegung un*, Birkhäuser Basel, Basel, 107–120.

Guandalini, S., Burdet, O. L., and Muttoni, A. (2009). "Punching Tests of Slabs with Low Reinforcement Ratios," *ACI Structural Journal*, **106**(1), 87–95.

Hwang, S.-J., and Lee, H.-J. (2002). "Strength Prediction for Discontinuity Regions by Softened Strut-and-Tie Model," *ASCE Journal of Structural Engineering*, **128**(12), 1519–1526.

Hwang, S. J., Tsai, R. J., Lam, W. K., and Moehle, J. P. (2017). "Simplification of Softened Strut-and-tie Model for Strength Prediction of Discontinuity Regions," *ACI Structural Journal*, **114**(5), 1239–1248.

Lips, S., Ruiz, M. F., and Muttoni, A. (2012). "Experimental Investigation on Punching Strength and Deformation Capacity of Shear-Reinforced Slabs," *ACI Structural Journal*, **109**(6), 889–900.

Marzouk, H., and Hussein, A. (1991). "Experimental Investigation on the Behavior of High-Strength Concrete Slabs," *ACI Structural Journal*, **88**(6), 701–713.

Mogili, S., and Hwang, S.-J. (2021). "Softened Strut-and-Tie Model for Shear and Flexural Strengths of Reinforced Concrete Pile Caps," *ASCE Journal of Structural Engineering*, **147**(11), 04021169.

Muttoni, A. (2008). "Punching Shear Strength of Reinforced Concrete Slabs without Transverse Reinforcement," *ACI Structural Journal*, **105**(4), 440–450.

Pérez Caldentey, A., Padilla Lavaselli, P., Corres Peiretti, H., and Ariñez Fernández, F. (2013). "Influence of stirrup detailing on punching shear strength of flat slabs," *Engineering Structures*, **49**, 855–865.

Ramdane, K.-E. (1996). "Punching Shear of High Performance Concrete Slabs," *4th International Symposium on Utilization of High Strength High Performance Concrete*, Paris, France, 1015–1026.

Rankin, G. I. B., and Long, A. E. (1987). "Predicting the Punching Strength of Conventional Slab-Column Specimens," Proceedings of the Institution of Civil Engineers, **82**(2), 327–346.

Regan, P. E. (1986). "Symmetric punching of reinforced concrete slabs," *Magazine of Concrete Research*, **38**(136), 115–128.

LOADING TESTS FOR REINFORCED CONCRETE FRAMES RETROFITTED BY ATTACHING STEEL MEMBERS

Yi-Hsuan Tu[1] and Wei-Chun Lian[2]
1. Professor, Dept. of Architecture, National Cheng Kung University, Tainan, Taiwan
2. Master of Science, Dept. of Architecture, National Cheng Kung University, Tainan, Taiwan
Email: yhtu@mail.ncku.edu.tw, lianweichun95@gmail.com

ABSTRACT

Street houses in Taiwan are typically vulnerable to earthquakes because of their soft first story and nonductile columns. The applicability of regular retrofitting techniques to street houses is limited by the typical layouts of the houses. This study established a simple retrofitting method that involves attaching steel members to the inside of the RC frame. The method was validated through lateral load tests on three full-size frame specimens: one unretrofitted frame and two retrofitted frames with different joint designs. Shear failure occurred at the column tops of the unretrofitted frame when its strength, which is governed by flexure, reached its maximum value. The retrofitted frames also underwent shear failure, which occurred at the column bottom in specific directions because the retrofit steel members were not connected to the foundation. Although the failure modes were similar, the initial stiffness, ultimate strength, and energy dissipation of both retrofitted frames were higher than those of the unretrofitted frame. The specimen with moment-connected retrofitting was stronger and had lower deformation capacity than the specimen with compression-only retrofitting because the latter specimen was actively retrofitted in only one of the two columns in each loading direction.

Keywords: lateral load test, reinforced concrete, seismic retrofit, soft first story

INTRODUCTION

Street houses are the most common building type in southern central Taiwan. These houses are typically single-span units composed of a confined masonry (CM) or reinforced concrete (RC) frame with several intact partition walls between adjacent units. The partitions in the street's direction are often removed or contain eccentric doors for access, as illustrated in Fig. 1. Therefore, existing street houses have been severely damaged or have collapsed after earthquakes because of their soft first story and nonductile columns.

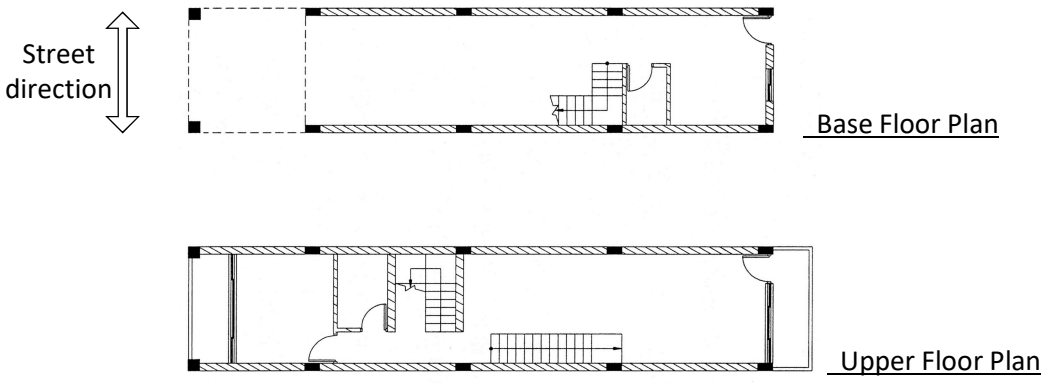

Figure 1. Floor plans of typical street-houses.

Regular seismic retrofitting methods—such as adding RC shear walls and side-walls (Hayashi *et al.*, 1980; JBDPA, 2005) and jacketing columns with RC (Júlio *et al.*, 2003), steel, or fiber—have been effective in low-rise RC school buildings in Taiwan (Hsiao *et al.*, 2013). The addition of steel braces

has also been a popular retrofitting method for buildings with soft and weak stories (JBDPA, 2005, Teresa Guevara-Perez, 2012). However, these methods are difficult to apply to street houses because of the partition walls between adjacent house units (column jacketing) or the negative influence of the retrofitting on the interior features (walls and braces). Furthermore, excavating the foundation of added members and concrete casting for RC retrofitting are expensive and time-consuming. These factors make street house owners relatively resistant to seismic retrofitting.

This study established a simple seismic retrofitting method that responds to the needs of street house owners. The efficiency of the proposed method was verified using full-size frame specimens that were tested under constant vertical force and cyclic lateral load.

PROPOSED SIMPLE RETROFITTING METHOD

To reduce the cost and construction time and to minimize disturbance to the interior space, the method using herein involves 1) dry construction, 2) no excavation of the foundation, and 3) installation of all retrofitted members from the interior of the frame. Fig. 2(a) illustrates the prototype of the retrofitted frame. The retrofit steel members are attached to the interior of the RC frame by using chemical anchors, as illustrated in Fig. 2(b). The bottom ends of the retrofit steel columns are not connected to the foundation; thus, no excavation of foundation is required. The steel beam–column joints carry only compression, as illustrated in Fig. 2(c). The compression-only joints are designed to minimize the tension demand of the retrofit steel beam anchors and prevent a decrease in ductility of the RC column by strengthening the tensile side of the section. However, only one of the two columns is actively retrofitted (the leeward column is retrofitted with steel on the compressive side). Therefore, this paper also proposes an alternative design in which moment-connected joints are used, as illustrated in Fig. 3(d).

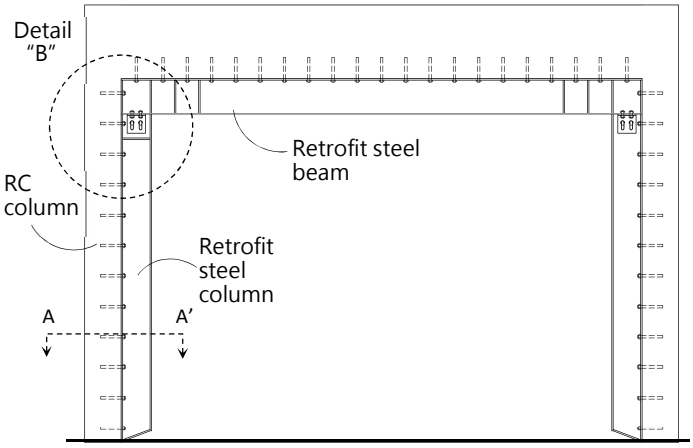

(a) Prototype of the retrofitted frame

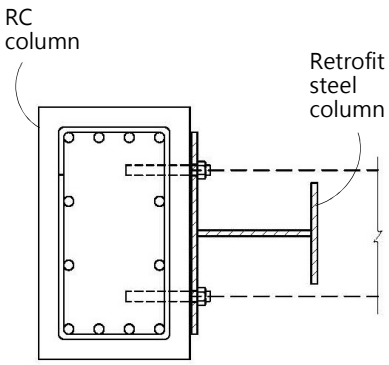

(b) Section A-A'

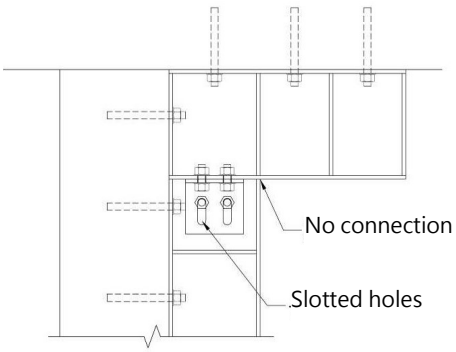

(c) Detail "B" – compression-only connection

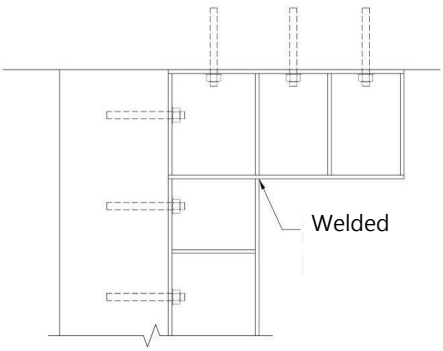

(d) Detail "B" – moment connection

Figure 2. Design and joint details of the proposed simple retrofitting method.

SPECIMENS AND TEST APPARATUS

Fig. 3 illustrates the dimensions of three specimens tested in this study. Specimen F0 is the frame with no retrofitting; Specimens FR-C and FR-M are the retrofitted frames with compression-only connections and moment connections, respectively. The RC frames used in the three specimens were identical. Table 1 shows the details of the designed member section of the frames. The RC column sections were designed to simulate the nonductile columns in existing street houses. The cantilevers of the longitudinal beam were enlarged for the connections with the loading devices.

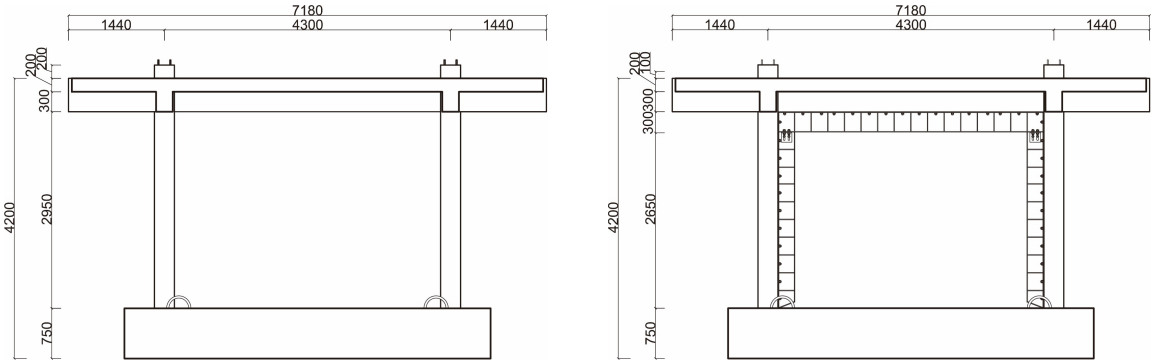

(a) Specimen F0

(b) Specimen FR-C

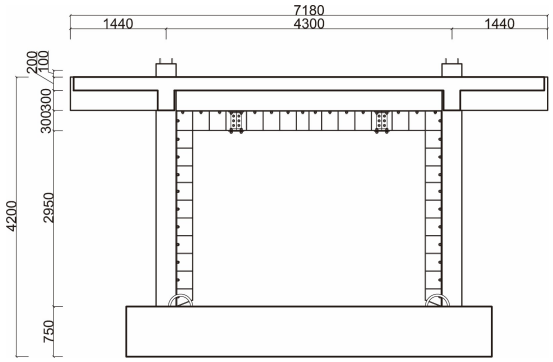

(c) Specimen CR-M

Figure 3. Dimensions of the test specimens. (unit: mm)

Table 1. Details of member sections of the tested RC frames (unit: mm)

Member	Column	Beam			
		Longitudinal (inner ends)	Longitudinal (middle)	Longitudinal (cantilevers)	Lateral
Section				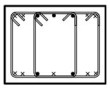	
Size	300x500	350x500	350x500	650x500	250x500
Longitudinal reinforcement	4 – #7 8 – #6	7 – #7 2 – #6	7 – #7 2 – #6	5 – #7 9 – #6	4 – #7 2 – #6
Steel ratio	2.56%	1.25%	1.25%	1.56%	0.96%
Hoops	#3@250	#3@150	#3@250	#3@100	#3@100

Fig. 4 illustrates the sections of the retrofit steel members. The flanges attached to the RC frames were designed to be wide to facilitate anchor installment. The ends of the retrofit steel beam of the Specimen FR-M were welded to the retrofit steel column in a factory and bolted to the middle section so that on-site welding did not have to be performed.

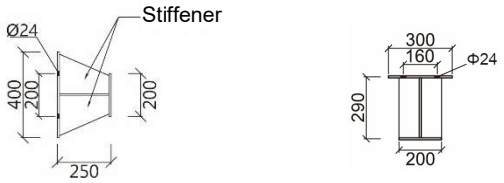

(a) Column (b) Beam

Figure 4. Sections of the retrofit steel members. (unit: mm)

Fig. 5 illustrates the lateral loading test apparatus. A constant axial force of 1020.87 kN representing the dead load at the base floor of a three-story street house was applied using two jacks fixed to the top of each of the two columns in the specimen. Rollers between the jacks and the reaction beam enabled the jacks to move with the specimen. The lateral load was cyclic and displacement-controlled. The lateral drift started from 0.125% and increased to 0.25%, 0.375%, 0.5%, 0.75%, 1.0%, 1.5%, 2.0%, and 3.0% with three cycles in each loading stage. Testing was terminated when the strength in any direction decreased to lower than 85% of the maximum strength if axial failure of the column had not yet occurred. Two vertical actuators were installed on the side of the specimen to obtain a force couple for maintaining the top beam's horizontal direction during lateral loading and thus enabling a double-curvature loading scheme.

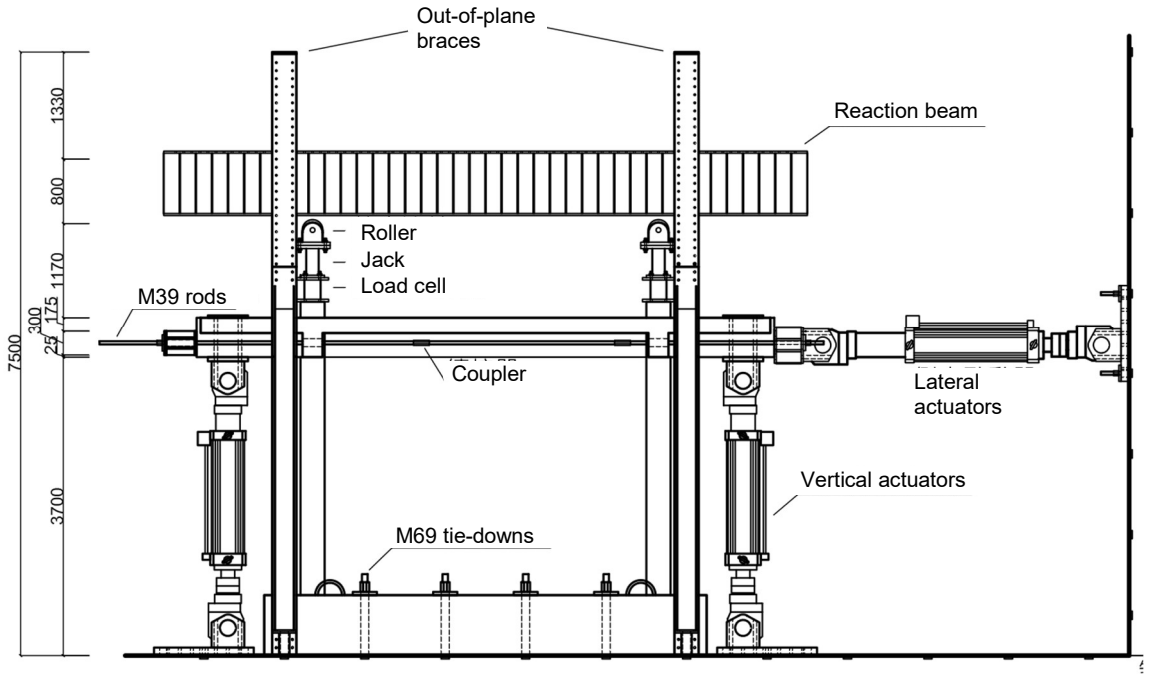

Figure 5. East elevation of the test apparatus

Linear variable differential transformer gauges and an optical measuring system were used to record the deformation of the specimens and to monitor the out-of-plane displacement. Strain gauges were installed on the longitudinal and transverse reinforcements in the RC column and on the retrofit steel to measure the variation in stress. The concrete strength obtained through the cylinder tests was 31.27 MPa. The yield strength of the #3, #6, and #7 bars used in the RC columns was 368.7, 465.4, and 438.5 MPa, respectively. The yield strength of the retrofit steel was 321.4 MPa.

TEST RESULTS

Fig. 6 illustrates the crack patterns of the east elevation of the specimens when their maximum strength was reached. Fig. 7 displays images captured from the west side of the specimens at the end of each test. All three tests were terminated at the 3.0% stage. However, the full three cycles of the stage were

performed only for Specimen FR-C. Specimens F0 and FR-M failed during the second and first cycles, respectively. The mechanism of damage in the specimens is summarized in this section.

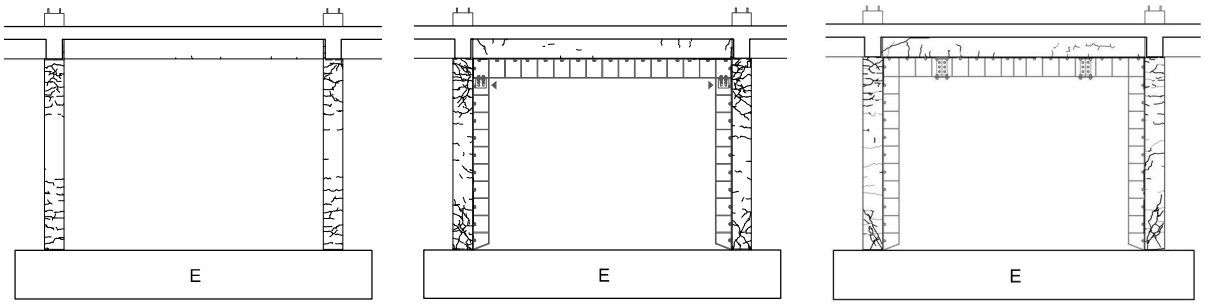

(a) F0 (−2.0%) (b) FR-C (−2.0%) (c) FR-M (+1.5%)

Figure 6. Crack patterns when the maximum strength was reached

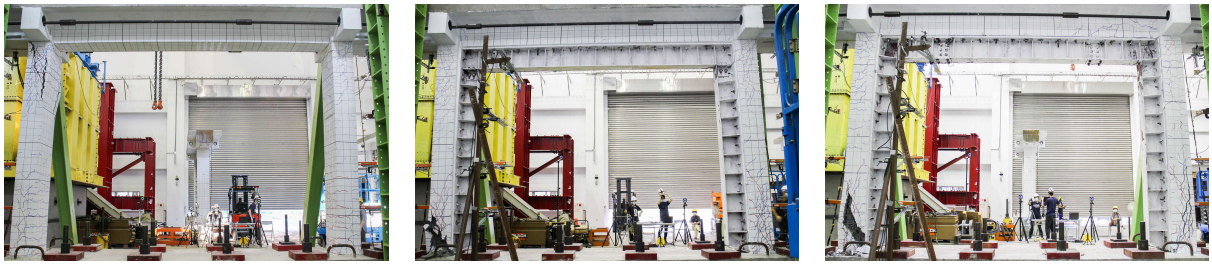

(a) F0 (b) FR-C (c) FR-M

Figure 7. Images of the specimens at the end of the tests (west elevation)

Specimen F0

Flexural cracks appeared on the ends of both columns during the 0.125% to 0.5% stages. Inclined shear cracks appeared on one of the column tops during the 0.75% stage and started to propagate during the 1.0% stage. The flexural cracks widened considerably during the 1.5% stage. The concrete surface spalled at the compression corners of the top and bottom ends of both columns during the 1.5% and 2.0% stages. The specimen exhibited maximum strength in the push (+252.84 kN) and pull (−285.15 kN) directions in the 2.0% stage. Shear failure occurred at the top of the north column during the second cycle of 3.0% drift, and the resistance of the specimen decreased to 70% of its maximum strength. The lateral actuator automatically stopped working because of the sudden decrease in resistance, and the test was terminated. Although the columns exhibited flexural shear failure, the beam was negligibly damaged during the test. This so-called strong beam–weak column behavior is typical of nonductile RC frames.

Specimen FR-C

Flexural cracks appeared on the RC column ends at the sides opposite to the retrofit steel in the 0.125% to 0.375% stages. The flexural cracks were longer than those in Specimen F0. Inclined shear cracks started to appear in the bottom ends of both columns during the 0.25% stage in specific directions. The inclined cracks only appeared on the bottom of the north column when the load was a push load, and then symmetrical inclined cracks appeared on the bottom of the south column when the load was a pull load. During the 0.5% to 1.0% stages, the flexural cracked area extended from the ends to the middle sections of the columns, shear cracks appeared on the column tops, and the shear cracks at the bottom of the columns extended upward. Inclined and short vertical cracks appeared at the ends of the beam during the 1.0% and 1.5% stages, respectively. The concrete surface spalled at the compression corners of the top and bottom ends of both columns during the 2.0% stage. Buckling also occurred at the top ends of free-side flanges of the retrofit steel columns during the 2.0% stage. The specimen exhibited maximum strength in the push (+460.93) and pull (−466.99 kN) directions in this stage (2.0%). The shear crack at the north column bottom widened during the first cycle of the 3.0% stage. The resistance

of the specimen gradually decreased during the following cycles and decreased to 72% of the maximum strength. The concrete at the bottom of the north column was crushed, and the 90° hook of the hoop had become loose at the end of the 3.0% stage. The test was terminated because of safety concerns.

Specimen FR-M

The development of flexural and shear cracks in this specimen was similar to that in Specimen FR-C. However, the interface between the RC frame and retrofit steel cracked during the 0.375% stage. Vertical cracks corresponding to the anchor positions appeared on the beam during the 0.75% stage because of tension in the retrofit steel column. Shear cracks also appeared at the middle of the columns during the 0.75% stage. The shear cracks at the bottom of the columns extended upward during the 1.0% and 1.5% stages. Shear cracks on the column tops became dense and an inclined crack appeared at the south end of the beam during the 1.5% stage. The specimen exhibited maximum strength in the pull direction (−604.58 kN) in the 1.5% stage. Inclined cracks opposite to the existing shear cracks at the column bottoms appeared during the 2.0% stage. Buckling also occurred at the top ends of the free-side flanges of the retrofit steel columns during the 2.0% stage, and the specimen exhibited maximum strength in the push direction (+600.83 kN). Shear failure occurred at the bottom of the north column during the first cycle of the 3.0% stage, and the testing system terminated because of sudden failure. The loading was restarted and the specimen was pushed to 3.0% drift because the resistance of the specimen was not lower than 85% of the maximum strength, and a 3.0% drift did not occur. The resistance decreased to 53%, and the test was terminated due to safety concerns.

Load–Displacement Relationships and Failure Modes

Fig. 8 displays the load–displacement relationships of the three specimens. All three specimens exhibited a symmetric load–displacement relationship. The push (+) strength and pull (−) strength were almost equal. A slight pinching effect was observed in the hysteresis loop of Specimen FR-C but not in that of Specimen FR-M. However, the columns in Specimen FR-C exhibited a flexure–shear failure mode with concrete spalling; this represented the ultimate flexural behavior that occurred before shear failure. The columns in Specimen FR-M exhibited shear failure without concrete spalling at the compression corners. The larger hysteresis loop of Specimen FR-M might be attributed to the energy dissipation of the retrofit steel members.

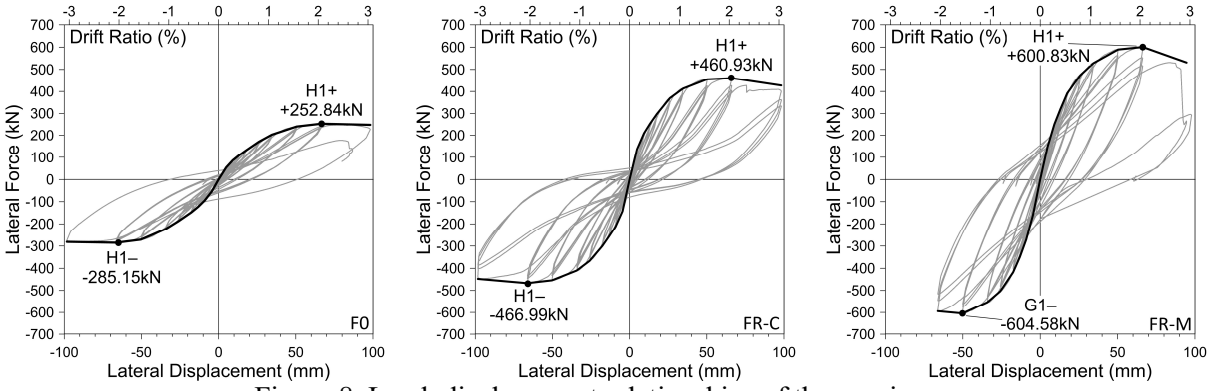

Figure 8. Load–displacement relationships of the specimens

COMPARISON AND DISCUSSIONS

Table 2 summarizes the performance of the three specimens. The actual loaded drifts were slightly different from the expected drifts because of errors due to the actuators. Figs. 9 and 10 compare the load–displacement characteristics and energy dissipation. The two retrofitted specimens exhibited higher strength and initial stiffness than did the specimen without retrofitting. Specimen FR-M exhibited the highest strength and energy absorption because steel was actively retrofitted on both columns in both loading directions. However, this specimen exhibited earlier strength degradation and lower deformation capacity. Although the steel in Specimen FR-C was actively retrofitted in only one of the columns in

each loading direction, the increases in stiffness and strength were still notable, and the specimen did not have decreased deformation capacity.

Table 2. Load and drift performance of the three specimens

Specimen	Initial cracking		Push strength		Pull strength		Ultimate drift	
	Drift (%)	Load (kN)	Drift (%)	Load (kN)	Drift (%)	Load (kN)	Drift (%)	Load (kN)
F0	+0.15	+53.78	+2.08	+252.84	–2.07	–285.15	+3.07	+176.99
FR-C	+0.15	+136.90	+2.06	+460.93	–2.07	–466.99	–3.07	–385.62
FR-M	+0.15	+148.12	+2.07	+600.83	–1.57	–604.58	+2.96	+531.29

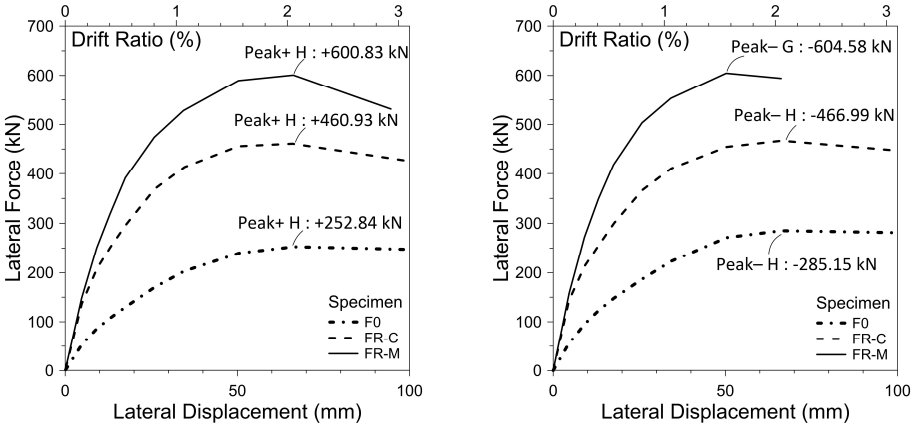

Figure 9. Comparison of the load–displacement envelopes

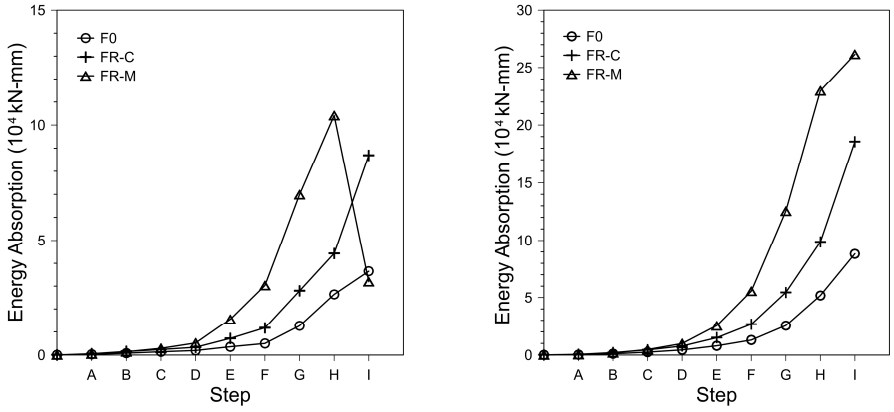

(a) Energy dissipated in each stage (b) Cumulative energy dissipation

Figure 10. Comparison of energy dissipation

The higher stiffness of the retrofitted specimens was attributed to the retrofit steel members that stiffened the RC columns. The stiffened columns in the retrofitted specimens were subjected to higher shear stress than was Specimen F0 at the same lateral displacement. Therefore, the shear cracks in the retrofitted specimens appeared at an earlier stage. The final failure modes of the three specimens were governed by shearing, but the failure position and the strength were different. Shear failure occurred at the top of a column in Specimen F0. Both retrofitted specimens exhibited shear failure at the bottom of columns in a specific direction, as indicated by the unretrofitted shear failure line (gray) in Fig. 11. Although the shear failure lines for Specimens FR-C and FR-M did not directly pass though the retrofitted steel, the exhibited strengths were considerably higher than that of Specimen F0, meaning that the retrofitting increased the shear capacity of the columns. Failure occurring at the column bottom rather than the top is preferable for maintaining the integrity of the superstructure.

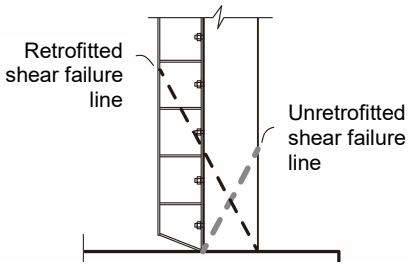

Figure 11. Potential shear failure

CONCLUSIONS

Cyclic lateral loading tests using full-size frame specimens were performed to verify the efficiency of the simple retrofitting method established in this study; the method was found to be suitable for the typical street houses in Taiwan. The design of the method was aimed at reducing the cost and time required for construction by using prefabricated steel members and avoiding the excavation of house foundations. The following conclusions were drawn.

1) The two retrofitted specimens had higher initial stiffness and strength than the unretrofitted specimen. The specimen with moment-connected retrofit members exhibited the highest strength and energy absorption. However, it also had low deformation capacity and its strength decreased earlier.
2) The moment-connected joint design caused tension in the anchors of the beam retrofit steel. Cracks corresponding to the anchor position appeared on the beam in Specimen FR-M. However, the beams in all three specimens were mostly undamaged and did not affect the frame failure mode.
3) The unretrofitted specimen and the retrofitted specimen with compression-only connected retrofit members both exhibited flexure–shear failure. The retrofitted specimen with moment-connected retrofit members exhibited shear failure that caused early strength degradation and low deformation capacity. Although the final failure modes of the RC columns were similar, the retrofitted specimens were stronger, indicating that the retrofitted steel members increased the shear capacity of the columns.
4) The proposed retrofitting method can increase frame stiffness and may prevent the development of a soft first story. The retrofitting also alters the failure position from the column top to the column bottom; this is desirable because the change in failure position helps maintain the integrity of the superstructure.

ACKNOWLEDGMENTS

The authors are grateful to the Ministry of Science and Technology (MOST) for financially supporting this research (MOST 107-2625-M-006-009) and to the laboratory staff of National Center for Research on Earthquake Engineering, Taiwan, for their assistance.

REFERENCES

Hayashi, T, H. Niwa, and M. Fukuhara (1980). "The strengthening methods of the existing reinforced concrete buildings," *Proceedings of the 7th World Conference on Earthquake Engineering*, **4**, 89-97.

Hsiao, F. P., L.L. Chung, Y.K. Yeh, W.Y. Chien, W.C. Shen, T.C. Chiou, T.K. Chow, Y.F. Chao, P.W. Weng, Y.S. Yang, Y.L. Chu, Y.S. Tu, J.F. Chai, and S.J. Hwang (2013). "Technology Handbook for Seismic Evaluation and Retrofit of School Buildings – Third Edition," NCREE Technical report, NCREE-13-023.

JBDPA (2005). *English Version of the Standard and Guidelines for Seismic Evaluation of Existing Reinforced Concrete Buildings, 2001, and the Technical Manual for Seismic Evaluation and Seismic Retrofit of Existing Reinforced Concrete Buildings, 2001*, The Japan Building Disaster Prevention Association.

Júlio, E.S., F. Branco, and V.D. Silva (2003). "Structural rehabilitation of columns with reinforced concrete jacketing", *Progress in Structural Engineering and Materials*, **5**, 29-37.

Teresa Guevara-Perez, L. (2012). "Soft story and weak story in earthquake resistant design: A multidisciplinary approach", *Proceedings of 15th World Conference on Earthquake Engineering*, paper no. 0183.

EVALUATION OF THE BASE SHEAR CONTRIBUTION OF MOMENT-RESISTING FRAMES IN HIGH-RISE REINFORCED CONCRETE NON-REGULAR DUAL SYSTEMS

Jerson S. Rabadon[1] and Pher Errol B. Quinay, D. Eng.[2]
1. Structural Design Engineer, RB Sanchez Consulting Engineers, Philippines.
2. Associate Professor, Institute of Civil Engineering, University of the Philippines Diliman, Philippines.
Email: jersonrabadon@gmail.com, pbquinay2@up.edu.ph

ABSTRACT

Dual systems are one of the most used lateral load-resisting structural systems for mid-to-high rise structures. The lateral load resistance of a dual system combining reinforced concrete (RC) shear walls and beam-column moment resisting frames (MRF) is studied. Past studies show that shear walls reduce the effects (e.g., stress concentration and torsion) of plan non-regularities in buildings. Currently, NSCP (2015) specifies the design requirements for dual systems to the following: MRFs should be capable of independently resisting at least 25% of the seismic forces. Results show that the structural models followed the NSCP provision for dual systems as the moment-resisting frames (columns) took over at least 25% of the base shear in both X and Y directions, except for models with a large percentage of re-entrant corner non-regularity. The shear walls in these models are found to carry greater lateral load, provide the strength and stiffness, and control the horizontal displacements and inter-story drifts. Also, the study shows that as the percentage of re-entrant corner non-regularity increases along a horizontal direction, the base shear contribution of columns along the perpendicular horizontal direction decreases.

Keywords: base shear distribution, dual systems, RC buildings, re-entrant corner, linear static analysis

INTRODUCTION

In high-rise buildings at regions of low to moderate seismic risk, a dual system can be effectively utilized because both the frames and shear walls mutually contribute to resisting the lateral loads. Dual systems are a common choice for multi-story RC buildings (Paulay and Priestley, 1992) since they control horizontal displacements both in the lower and in the upper part of the building. At the upper part, dual systems are more efficient in resisting seismic forces than building frame systems or moment-resisting frame systems (Shin *et al.*, 2010). Additionally, the National Structural Code of the Philippines 2015 defines a dual system as a combination of moment-resisting frames and shear walls or braced frames in which the moment-resisting frames shall be designed to independently resist at least 25% of the design base shear.

Sigmund *et al.* (2008) showed that the wall contribution in dual systems diminishes as the plastic deformation increases. Shear walls take 83 to 93% of the total base shear in the elastic range. However, as the structures entered the nonlinear range, frames are taking over larger part of the base shear as walls took over only 48 to 83% of the total base shear. Although walls dominated the dynamic response, there was still a higher-than-expected nonlinear behavior of the wall and frame elements because of the contribution of the higher modes. Thus, to ensure structural stability, the contribution of the frame elements should be considered.

With advances in technology, structures are now more complex in shape and contain multiple non-regularities. Non-regular structures have significant physical discontinuities in configuration or in their lateral-force-resisting systems. In the case of this study, only the issue of re-entrant corners will be examined. A re-entrant corner non-regularity is a type of horizontal structural non-regularity where

both plan projections of the structure beyond a re-entrant corner are greater than 15% of the plan dimension of the structure in the given direction. The percentage of re-entrant corner non-regularity can be computed using A/L in Fig. 1.

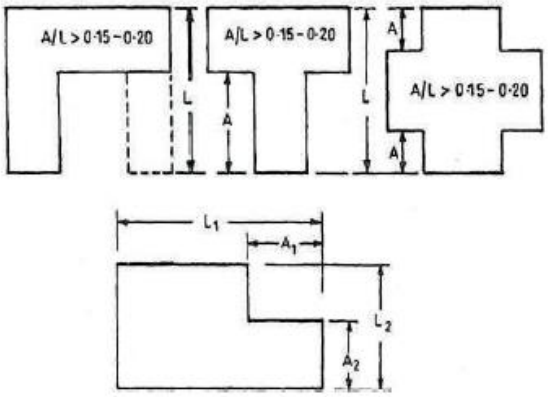

Figure 1. Types of re-entrant corners. Figure taken from IS 1893: Part 1 (2002)

Shreyasvi and Shivakumaraswamy (2015) studied the effect of re-entrant corners on buildings in different seismic zones. They found that re-entrant buildings undergo larger displacement as compared with regular buildings. Since re-entrant buildings have lesser time periods, they are more susceptible to ground motions and the probability of undergoing damage due to high frequency ground motions is high.

The main objective of this study is to evaluate the base shear contribution of moment-resisting frames and shear walls for high-rise, reinforced concrete, non-regular dual structural systems. This can be achieved by creating computational models, performing linear static analysis, and providing a summary of the results with emphasis on relationship between base shear distribution and building parameters (e.g., building height and percentage of re-entrant corner non-regularity).

Recent studies confirm dual systems as being effective in reducing drift and resisting large earthquakes. However, the consequences of the 25% rule have not been directly addressed. This paper presents an evaluation of the NSCP (2015) (Section 208.4.6.4) provision for dual systems. This specific task is accomplished by a series of structural modelling and stability checks that is succeeded by a careful analysis of the resulting data.

METHODOLOGY

Modelling of structures

Model creation and analysis are done using ETABS Ultimate 16.2.1. In this study, the 15-story regular RC dual system building from Nikzad and Yoshitomi (2019) is selected as the benchmark (BM) model. Section sizes produced by their optimizer are considered for beams, columns, and shear walls for every three floors where the column has a square shape, and beam and shear wall have rectangular shapes. These are listed in Table 1. The BM model is modified to contain re-entrant corners with varying percentage of non-regularity and will be labeled as Model RE1 and Model RE2. The compressive strength of concrete is 27 MPa and yield strength of reinforcement is 414 MPa for all member sizes. The plan areas of BM, RE1, and RE2 has been made approximately equal in order to facilitate the comparison.

Table 1. Section sizes of structural elements of BM, RE1, and RE2
Table taken from Nikzad and Yoshitomi (2019)

Element Type	Story Number	Section Sizes, width x depth (cm)	
		Central	Edge
Column	1-3	100x100	87x87
	4-6	100x100	85x85
	7-9	100x100	79x79
	10-12	95x95	76x76
	13-15	59x59	47x47
Beam	1-3	36x61	41x62
	4-6	38x57	43x65
	7-9	41x65	43x65
	10-12	41x62	43x65
	13-15	37x63	40x65
Shear Wall	1-12	40 (thickness)	
	13-15	36 (thickness)	

Models BM, RE1, and RE2 have 15 stories with typical height of 3 m. The models have eight 3 m-wide shear walls that are located at the perimeter of the building and slabs with thickness of 200 mm. Figs. 2 and 3 show the plan and 3D view of the models.

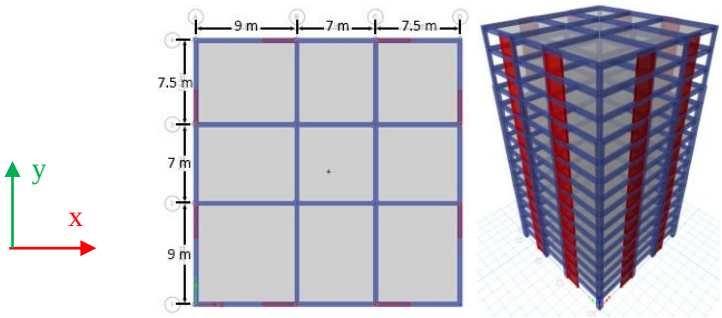

Figure 2. Plan and 3D view of model BM.

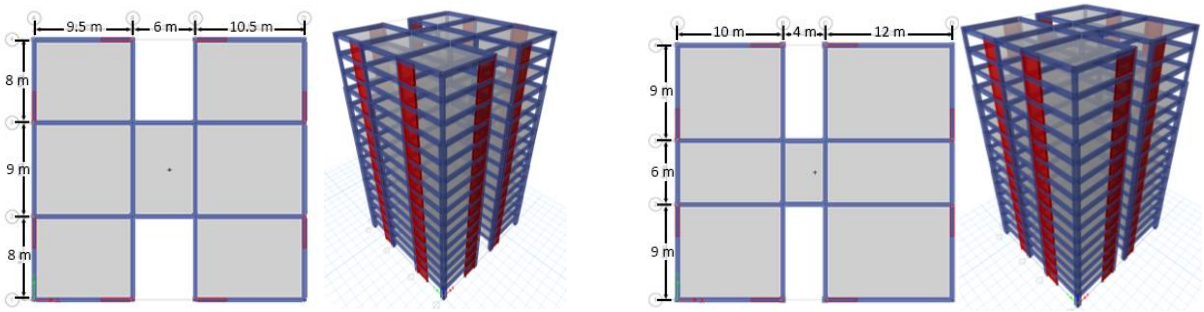

(a) Model RE1 (b) Model RE2

Figure 3. Plan and 3D view of re-entrant corner models.

Lastly, an existing building design is modeled to extend the understanding into taller and more realistic buildings. Section sizes for the beams, columns, slabs, and shear walls are taken from the existing structural plans of the building. RE46 is a 46-story building model that is 67 m long and 27.6 m wide. A large percentage of re-entrant corner non-regularity is found along the X-direction with a value of 80%. Table 2 shows the section sizes of structural elements of RE46, while Fig. 4 illustrates the plan and 3D view of Model R46.

Table 2. Section sizes of the structural elements of model RE46

Element Type	Story Number	Section Sizes, width x depth (cm)	
		Central	Edge
Column	1-46	75x100	75x100
Beam	1-10	50x60	40x75
	11-20	50x60	40x60
	21-30	50x60	40x60
	31-46	50x60	40x60
Shear Wall	1-46	40 (thickness)	

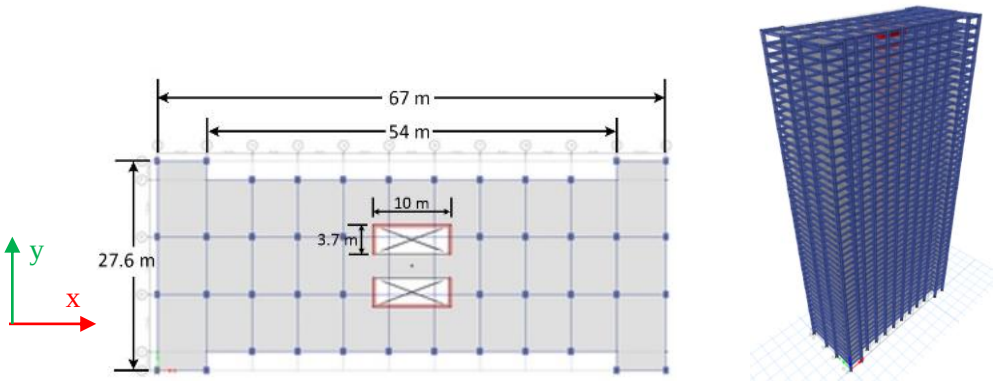

Figure 4. Plan and 3D view of model RE46.

Loadings and load combinations

The frames are assigned with a uniform dead load of 2 kN/m and slabs are assigned with 2 kN/m^2 of uniform dead and live loads. Only gravity and lateral loads are considered while wind loads are neglected. The load combinations used are:

$$U = 1.4D \quad (1)$$

$$U = 1.2D + 1.6L \quad (2)$$

$$U = 1.2D + 1L \pm 1E \quad (3)$$

$$U = 0.9D \pm 1E \quad (4)$$

where U corresponds to the required strength of members' resisting factored loads in a load combination, D stands for dead loads, L stands for live loads, and E stands for earthquake loads. According to Nikzad and Yoshitomi (2019), lateral loads are calculated based on ASCE 7-10, where the site class of the structure is D, response modification factor (R) of 6, short period spectral response (S_1) of 0.51 and 1-sec spectral response (S_s) of 1.28. Table 3 summarizes all the seismic load parameters used.

Table 3. Seismic parameters for models BM, RE1, and RE2

Parameter	Value
Occupancy category	III
Site class	D
Importance factor (I)	1
Seismic response coefficient (Cs)	0.17
Response modification factor (R)	6
Site coefficient (F_a)	1
Site coefficient (F_v)	1.5

For RE46, the frames are assigned with a uniform dead load of 2 kN/m and slabs are assigned with 2 kN/m^2 of uniform dead and live loads, and 1 kN/m^2 of uniform superimposed dead load. Only gravity

and lateral loads are considered while wind loads are neglected. A summary of the site geology and seismic factors used is shown in Table 4. The lateral loads are computed using UBC (1997).

Table 4. Site geology and seismic factors for RE46

Parameter	Value	Source
Site location	Ermita, Manila	User - Defined
Soil profile type	S_C	NSCP 2015 Table 208 - 2
Seismic zone	4	NSCP 2015 Figure 208 - 1
Nearest active fault trace	West Valley Fault	PHIVOLCS FaultFinder
Distance from nearest active fault	9.1 km	PHIVOLCS FaultFinder
Seismic source type	A	NSCP 2015 Table 208 - 4
Occupancy category	III	NSCP 2015 Table 208 - 1
R	8.5	NSCP 2015 Table 208 - 11A
Seismic coefficient, C_a	0.4	NSCP 2015 Table 208 - 7
Seismic coefficient, C_v	0.672	NSCP 2015 Table 208 - 8

RESULTS AND DISCUSSION

The structural models have no torsional irregularity, stiffness irregularity, and mass irregularity, and P-Delta effects need not be considered. The maximum inter-story drifts occurred at Story 8 and Story 9 for Models BM, RE1, and RE2.

Inter-story drift

Based on Fig. 5, the inter-story drifts of models with re-entrant corners (RE1 and RE2) are larger than that of Model BM. Model RE2 which has 37.5% re-entrant corner non-regularity along Y produced greater drifts along X than Model RE1 which has 32% re-entrant corner non-regularity along Y. On the other hand, Model RE1 which has 23% re-entrant corner non-regularity along X produced greater drifts along Y than Model RE2 which has 15% re-entrant corner non-regularity along X. The calculated story drifts are within the allowable of 0.020 times the story height as per ASCE 7-10 and NSCP 2015.

This is worth noting that as the percentage of re-entrant corner non-regularity increases along a horizontal direction, the inter-story drifts along the perpendicular horizontal direction becomes larger (i.e., higher percentage of re-entrant corner non-regularity along Y produces larger inter-story drifts along X).

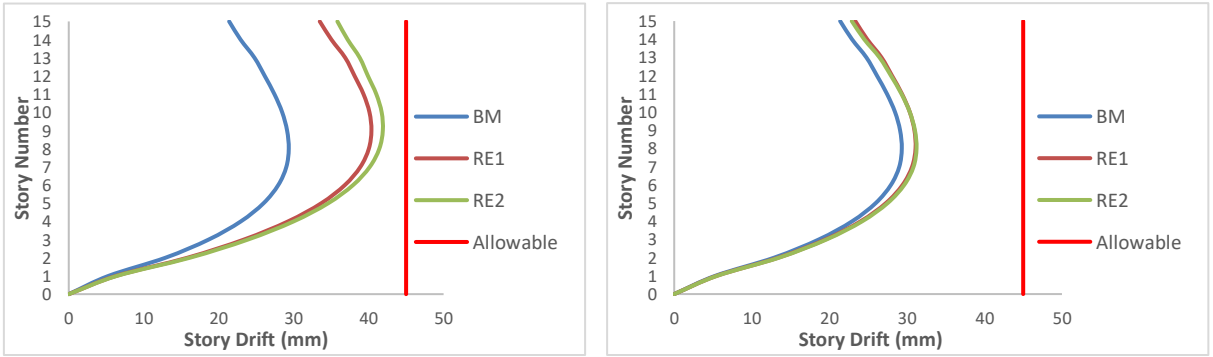

(a) along X-direction (b) along Y-direction

Figure 5. Inter-story drifts of Models BM, RE1, and RE2.

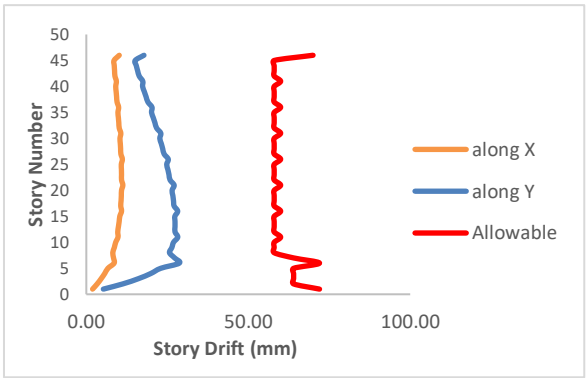

Figure 6. Inter-story drifts of Model RE46.

In Fig. 6, the inter-story drifts of Model RE46 along Y are greater than the inter-story drifts along X due to the presence of re-entrant corners along X and may also be affected by higher stiffness in X that is influenced by the plan configuration.

Base shear contribution of columns and walls

Based on Fig. 7, the base shear contribution of the columns from the models with re-entrant corners (RE1 and RE2) are much lesser than that of Model BM. Also, it can be seen that a higher percentage of re-entrant corner non-regularity along Y decreases the base shear contribution of columns along X and vice-versa. Note that the percentages of re-entrant corner non-regularity of Model RE1 in the X-direction and Y-direction are 23% and 32%, respectively, while Model RE2 has 15% and 37.5%, respectively.

The four models followed the NSCP provision for dual systems as the moment-resisting frames (columns) took over at least 25% of the base shear in both X and Y directions, except for Model RE2 and Model RE46 which is just below 25% in X-direction. The presence of a large percentage of re-entrant corner non-regularity in X-direction of Models RE2 and RE46 may have caused the shear walls to carry greater lateral load and control the horizontal displacements and inter-story drifts.

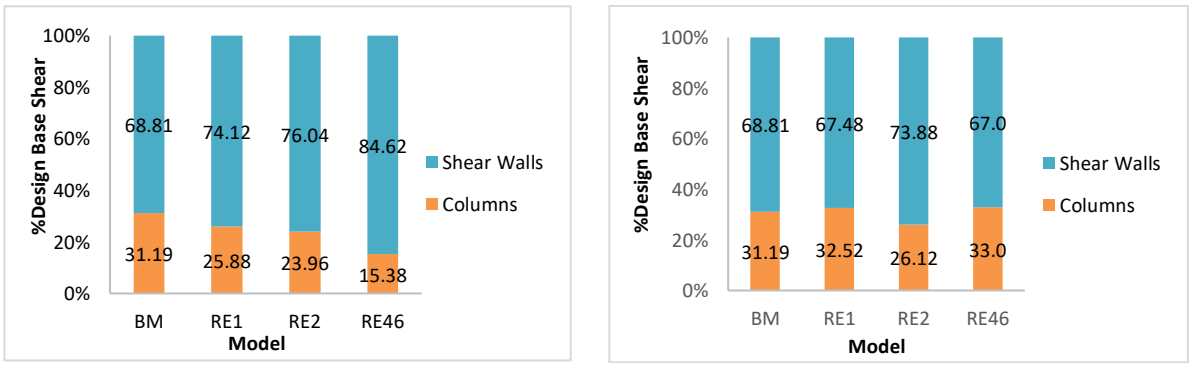

(a) along X-direction (b) along Y-direction

Figure 7. Base shear contribution of columns and walls.

Response of central columns containing the re-entrant corners

The four interior columns are further analyzed because they take over the largest part of the base shear among all the columns. Fig. 8 shows the location of the columns and their number assignments.

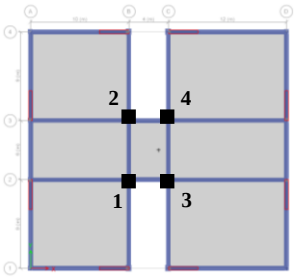

Figure 8. Interior columns and their number assignments.

Based on Fig. 9, the columns in Model RE2 had the greatest base shear contribution in both X and Y directions as compared to Models BM and RE1. In Model BM, the four columns collectively resisted 8.95% of the base shear in the X and Y directions. The base shear contribution of these columns in Model RE1 and Model RE2 ranges from 8-10%. This is considerably large in comparison to the total contribution of all the other 12 columns.

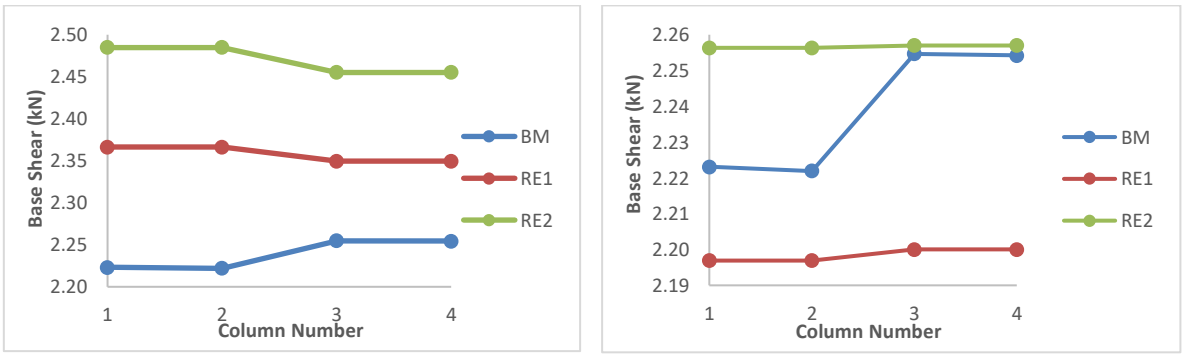

(a) along X-direction (b) along Y-direction

Figure 9. Total base shear at interior columns.

CONCLUSIONS AND RECOMMENDATIONS

The conducted analyses show that as the percentage of re-entrant corner non-regularity increases along a horizontal direction, the base shear contribution of columns along the perpendicular horizontal direction decreases. Moreover, the models with re-entrant corners undergo larger displacements and drifts as compared with the regular model. The inter-story drifts and displacements were greater when the percentage of re-entrant corner non-regularity in the horizontal perpendicular direction is also large. The columns containing the re-entrant corners (or the central columns) resist greater base shear as compared to the other columns. Thus, they should be designed with much more strength than the other columns. Overall, the four models followed the NSCP provision for dual systems as the moment-resisting frames (columns) took over at least 25% of the base shear in both X and Y directions, except for Model RE2 and Model RE46 which is just below 25% in X-direction. The presence of a large percentage of re-entrant corner non-regularity in X-direction of Models RE2 and RE46 may have caused the shear walls to carry greater lateral load and control the horizontal displacements and inter-story drifts. It is recommended to perform nonlinear analysis to study the change in the parameters as the structures undergo nonlinear behavior. Further studies should be conducted on buildings with various geometries (e.g., varying locations of re-entrant corner, taller buildings with other horizontal and vertical non-regularities) to validate the findings of this study and propose final design recommendations.

REFERENCES

American Society of Civil Engineers (2010). "Minimum design loads for buildings and other structures," *ASCE/SEI 7-10,* Reston, VA.

Association of Structural Engineers of the Philippines (2015). "National Structural Code of the Philippines (NSCP)," Seventh edition, Quezon City, Philippines.

Code, U. B. (1997). "International building code," *International Code Council*, USA.

IS 1893 Part I: (2002). "Criteria for Earthquake Resistant Design of Structures," *Bureau of Indian Standards*, New Delhi.

Nikzad, H. and Yoshitomi, S. (2019). "Design Application Procedures of 15 Storied 3D Reinforced Concrete Shear Wall-Frame Structure," *International Journal of Structural and Construction Engineering*, 13(2), 67-78.

Paulay, T. and Priestley, M. N. (1992). "Seismic design of reinforced concrete and masonry buildings," *Vol. 768*, New York: Wiley.

Shin, M., Kang, T. H. K., and Grossman, J. S. (2010). "Practical modelling of high-rise dual systems with reinforced concrete slab-column frames," *The Structural Design of Tall and Special Buildings*, 19(7), 728-749.

Shreyasvi, C. and Shivakumaraswamy, B. (2015). "A Case Study on Seismic Response of Buildings with Re Entrant Corners," *IJRET: International Journal of Research in Engineering and Technology eISSN*, 2319-1163.

Sigmund V., Guljas I., and Hadzima-Nyarko M. (2008). "Base shear redistribution between the R/C dual system structural components," *14th WCEE*, Beijing.

A CASE STUDY ON THE CONVERGENCE IMPROVEMENT OF NONLINEAR STATIC PUSHOVER ANALYSIS

Chien-Chun Liu[1], Chi-Hang Li[1], Jian-Hwang Weng[2] and Qiang Xue[3]
1. Research Fellow, CHRC Center, Sinotech Engineering Consultants, Inc., Taipei, Taiwan, R.O.C.
2. Structural Engineering Section Chief, CHRC Center, Sinotech Engineering Consultants, Inc., Taipei, Taiwan, R.O.C.
3. Deputy Director, CHRC Center, Sinotech Engineering Consultants, Inc., Taipei, Taiwan, R.O.C.
Email: chien@sinotech.org.tw

ABSTRACT

When performing nonlinear static pushover analysis (NSPA) using commercial software to assess seismic performance of buildings, we may encounter a convergence problem resulting in an incomplete capacity curve. In this paper, a case study is carried out to demonstrate how to solve this problem by a slight modification of the backbone curves of the plastic hinges.

Keywords: nonlinear, pushover, seismic performance, convergence, capacity curve, backbone curve

INTRODUCTION

NSPA has been widely used for seismic performance assessment of buildings for years. Based on feedback from engineering practice, even though all simulation settings are correct, it's still common to encounter a convergence problem which causes the analysis stopped earlier before the maximum base reaction is reached. In such a case, the last point of the capacity curve is usually regarded as the state corresponding to the maximum base reaction of the building. Seismic capacity of a building in such a case is underestimated. Seismic performance of the building is not completely captured. The analytical results are hard to use for further engineering decision making.

In this paper, we carried out a case study to explain how such convergence problem occurs, what are the possible causes and how to solve them.

SEISMIC PERFORMANCE ASSESSMENT OF A CASE BUILDING

Overview of the Case Building

The case building adopted is a 3storey reinforced concrete (RC) dormitory, built in 1968. The building has no basement. The total floor area is about 2,200 m^2. The structural system is regular in plane and elevation. The typical size of main column is 30 cm x 30 cm. The typical beam size is 30 cm x 65 cm, and the partition walls are 0.5B brick walls.

Original Results of NSPA

As shown in Fig. 1(a), numerical model of the case building is built using SAP2000 v20. Based on Taiwan Earthquake Assessment for Structure by Pushover Analysis (TEASPA) website (NCREE and SECI, 2020) and the official TEASPA technical manuals (Chiou et al., 2020; NCREE and SECI, 2021), plastic hinge properties of this structural members has been assigned using TEASPA v4 method. After confirming that all processes and settings are in accordance with the official TEASPA guidelines, NSPA is carried out. The original capacity curve obtained from the NSPA is shown in Fig. 1(b). The capacity curve was terminated before the base reaction dropped. The maximum base reaction and its corresponding displacement are denoted as $V_{max,1}$ and $D_{max,1}$.

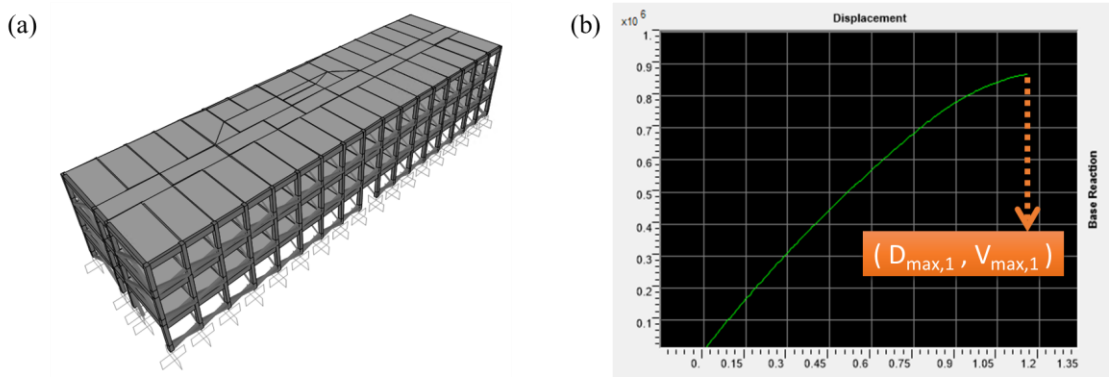

Figure 1. (a)The case building model. (b)The original resulting capacity curve from NSPA.

If such an incomplete capacity curve from NSPA is used as the result, the following concerns will be raised:

1. The base reaction at the last point of the capacity curve may not be the real maximum base reaction of the building.
2. Using incomplete capacity curve as the basis for subsequent assessment may underestimate the seismic performance of the building.

In summary, use of the incomplete capacity curve without the decrease of the base reaction will not be able to accurately evaluate the seismic performance of the structure, which may lead to doubts in the review or additional verification. Therefore, this case building will be used to demonstrate how to identify the convergence problem and how to improve the analytical results by solving such a problem of nonlinear analysis.

SOLVING THE CONVERGENCE PROBLEM

Evidence of the Convergence Problem

It is important to confirm that all settings of necessary process of seismic performance assessment are correct. After carrying out the NSPA, we need to observe if the computational efficiency is severely reduced. This can be done by checking the *Analyzing* interface which is shown in Fig. 2 displayed by the commercial software during the analysis process. The computational convergence problem is identified according to the following phenomena:

1. The *Null Steps* increase much more than the *Saved Steps* as the *Total Steps* increase.
2. The *Max Sum of Steps* does not change and *Curr Step Size* is keeping less than 1.00E-10.

When both the above two phenomena occur, it can be inferred that commercial software is in a situation where NSPA is difficult to converge.

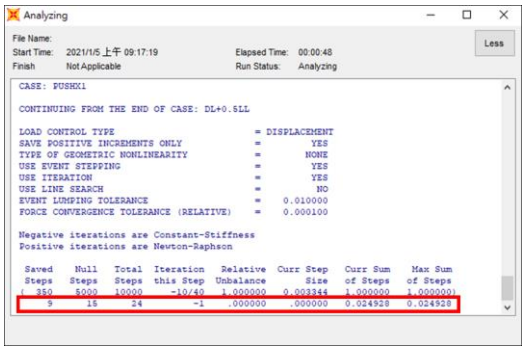

Figure 2. *Analyzing* interface displayed by SAP2000 v20.

For the case building, based on the above description, we found that the NSPA process encountered a computational convergence problem, resulting in an incomplete capacity curve with no drop in base reaction.

Method to Solve the Convergence Problem

The computational convergence of NSPA is related to the nonlinear iterative parameters set in the commercial software and the degree of nonlinearity. Since the stability of the implicit method of nonlinear analysis is influenced by the step size and tolerance, although the commercial software has a default set of parameters, it may not be suitable for all cases. Furthermore, due to the degree of nonlinearity, when the variation of the building stiffness occurs, the computation of NSPA will be accompanied by nonlinear iterations. If the stiffness varies significantly from one step to the next, a large number of iterations are needed. Therefore it is computationally time consuming. For TEASPA, this situation is usually occurred when the axial force nonlinear hinge properties of the brick wall or the shear force nonlinear hinge properties of the RC column and the RC wall change from a state with positive stiffness to that with negative stiffness in the backbone curve. The higher the number of such nonlinear hinges, the more significant the convergence problem.

There're two proposed methods to solve the above-mentioned convergence problem:

1. Adjustment of the nonlinear iterative parameters of the commercial software.
2. Slightly modification of the backbone curve of the nonlinear hinges.

Since the backbone curve of TEASPA nonlinear hinge has been validated experimentally, it's recommended to use method 1 first. Method 2 is suggested to use only if method 1 is still not effective.

Rules for adjusting the nonlinear iterative parameters of the commercial software in method 1 vary from case by case upon experience. A larger number of total steps is usually needed so that the step size is small enough to produce a convergent solution without a lot of iterations.

In this case study, after adopting method 1, we still couldn't obtain a complete capacity curve. The resulting capacity curve from NSPA was almost the same as that shown in Fig. 1(b). Therefore, we adopted method 2 to improve the computational convergence.

Method 2 is to reduce the computational complexity of nonlinear analysis by changing the variability of the stiffness of the nonlinear hinge backbone curve. It is only suitable to use when the analysis is difficult to converge and the stiffness state of a structural component has a tendency to change significantly.

For the case building, the convergence problem leads to the termination of NSPA. Distribution of the nonlinear hinges as the analysis terminates is shown in Fig. 3(a). The overall structural damage is slight. There are many axial plastic hinges of brick walls in a state of exceeding the yielding strength. Significant changing in stiffness can be found as shown in Fig. 3(b). It's suitable for using method 2 to improve computational convergence.

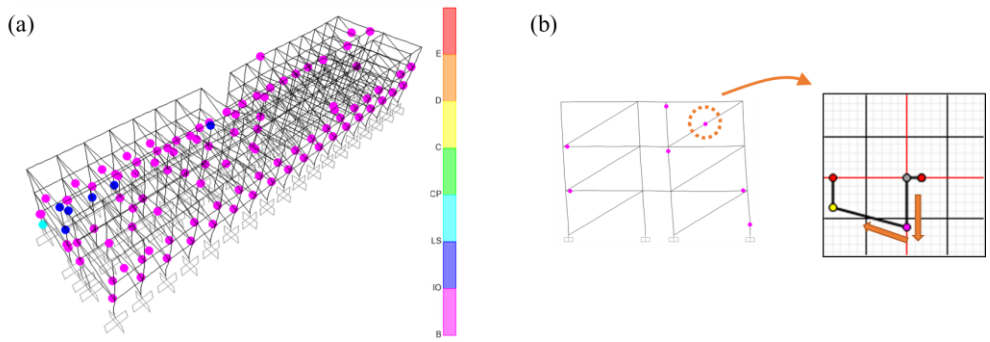

Figure 3. (a)Distribution of plastic hinges. (b)Significant change in stiffness at yielding point.

It's not necessary to change the shape of the backbone curve significantly. What we need is to trim the curve at a strength level a bit smaller than the yielding point. As shown in Fig. 4, finding a point just below the yielding point and creating a small platform can slow down the degree of the sudden change in stiffness. Other hinge properties remain the same.

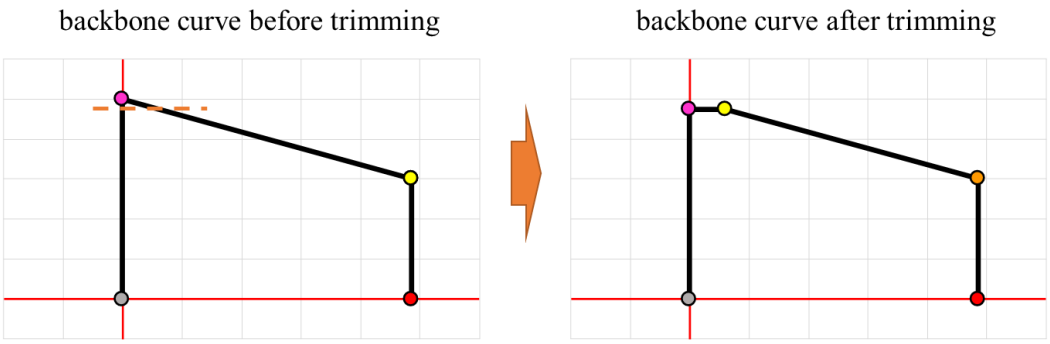

Figure 4. Trim the backbone curve slightly at the yielding point.

The ratio of the platform strength to the original yielding strength has different effects on the computational convergence case by case. It's recommended that this ratio shouldn't be too small to avoid distortion of the properties of the nonlinear hinges, which may affect the accuracy of the overall analysis results.

For the case building, a ratio of 0.95 is used to modify the plastic hinge properties of the brick wall component, as shown in Fig. 5. It's worth noticing that this modification affects the color rendering of the nonlinear hinges, special attention should be paid to avoid misjudging the component damage degree.

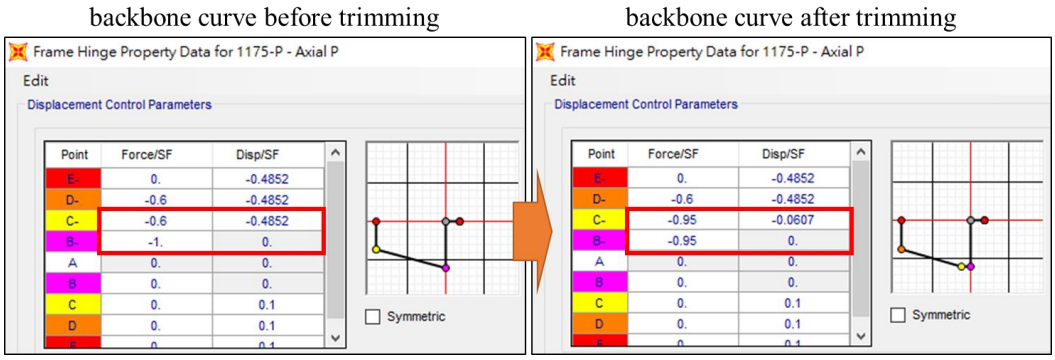

Figure 5. Modification of the backbone curve in the case building.

Results of NSPA after Convergence Improvement

After adopting the two afore-mentioned methods, the computational convergence of NSPA of the case building has been improved. Not only the time spent on NSPA was significantly reduced, but also the capacity curve corresponding to different performance level of the structure was obtained successfully. The final capacity curve and the overall structural nonlinear hinge development at the maximum base reaction are shown in Fig. 6(a) and 6(b). The maximum base reaction and its corresponding displacement are denoted as $V_{max,2}$ and $D_{max,2}$, respectively. Comparing these value with $V_{max,1}$ and $D_{max,1}$ in Fig. 1(b), we can see that the maximum base reaction and its corresponding displacement have increased significantly. Besides, the nonlinear hinge development at the maximum base reaction point indicating severe damage as shown in Fig. 6(b) is more reasonable comparing with that in Fig. 3(a). With the improved computational convergence, the results from NSPA will provide a more accurate insight into the seismic performance of the building.

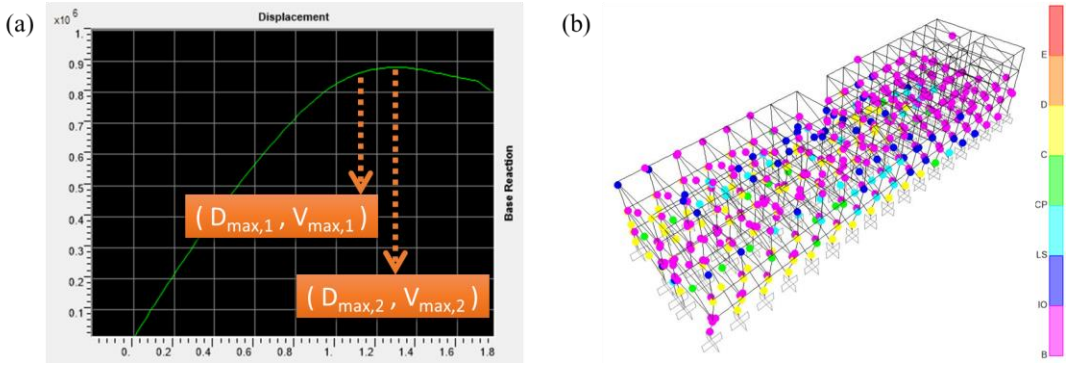

Figure 6. (a)The complete capacity curve. (b)Plastic hinge distribution at the maximum base reaction.

CONCLUSIONS

In engineering practice, it happens to encounter a convergence problem resulting in an incomplete capacity curve from NSPA even after a correct building model has been produced. The convergence improvement methods described in this paper consist of adjustment of the nonlinear iterative parameters of commercial software and trimming the plastic hinge backbone curve slightly at the yielding point. They are based on engineering practice experience and should allow engineers to obtain a completed capacity curve when conducting NSPA. However, in the adjustment process, attention must be paid to the rationality of the analysis results in order to solve the problem of poor computational convergence and obtain a complete capacity curve without losing accuracy.

ACKNOWLEDGMENTS

Thanks to the participation of Dr. Chyuan Chang and research fellow Tien-Hung Chiu from ASTRC, Sinotech Engineering Consultants, Inc., Taipei, Taiwan, R.O.C. in the discussion of similar topics.

REFERENCES

National Center for Research on Earthquake Engineering and Sinotech Engineering Consultants Inc. (2020), *Taiwan Earthquake Assessment for Structures by Pushover Analysis*. https://teaspa.ncree.org.tw.

Chiou, T.C., et al. (2020), *Taiwan Structural Seismic Assessment and Rehabilitation Technical Manual (TEASPA V4.0)*, National Center for Research on Earthquake Engineering, Report No.: NCREE-20-005.

National Center for Research on Earthquake Engineering and Sinotech Engineering Consultants Inc. (2021), *Taiwan Earthquake Assessment for Structures by Pushover Analysis, TEASPA v4.1 online web service user manual*.

ASSESSING THE SEISMIC PERFORMANCE OF BUILDING STRUCTURES USING AN IMPROVED PUSHOVER ANALYTICAL METHOD

Po-Chien Hsiao[1] and Aman Mola Worku[2]
1. Associate Professor, National Taiwan University of Science and Technology, Taipei, Taiwan, R.O.C.
2. Graduate Student, National Taiwan University of Science and Technology, Taipei, Taiwan, R.O.C.
Email: pchsiao@mail.ntust.edu.tw

ABSTRACT

With the aim of performance-based design of building structures, nonlinear response history analysis (NRHA) procedures are required to reliably obtain the realistic responses which, however, involve much complex procedures and reduce the feasibility of the practical uses. Nonlinear static procedure (NSP) analysis conventionally solely based on the first-mode of the structure are typically adopted in the design practice for approximately assessing seismic performances. Modal pushover analysis (MPA) and other modified NSP procedures were developed to include the higher-mode-effects in the NSP analysis, while they are still not feasible for the general practical uses. The study proposed a relatively simple procedure, named the modified first-mode-based pushover analysis (MFPA), for accurately assessing the seismic performance of buildings through a single-step pushover process with a novel load pattern until a target displacement. Against mathematical approaches, a wide range of model building cases, including five-, ten-, fifteen-, and twenty-story buildings of special moment resisting frames (SMRFs) with two types of story heights were designed and examined in the study to verify the validity of the MFPA procedures. The results verified that the proposed MFPA procedures enabled to consistently more accurately assess the peaks and distributions of the inter-story responses of buildings obtained by others.

Keywords: Nonlinear static procedures, Seismic performance, Nonlinear response history analysis, Modal pushover analysis

INTRODUCTION

Performance-based design (PBD) has been the major trend of tomorrow's seismic building codes (Ghobarah 2001), as the current building codes are typically based on the force-based design (FBD). To achieve the PBD, the seismic performances of structures under various seismic-hazard-level events should be assessed in the design process, especially that under the maximum considered earthquakes (MCE) which is far beyond the first yield in the structures that the FBD is upon. The nonlinear response history analysis (NRHA) are typically required to assess seismic performances of building structures. However, the NRHA procedures usually require the consideration of a number of seismic events and high computational effort, which requires advanced analytical skill and structural engineering software. It significantly reduces the feasibility of the practical applications.

To significantly simplify the evaluation procedures of seismic performance of steel frames, Montuori et al. (2020) have developed a simplified performance-based method to assess the pushover curves whose trend can be approximated to a trilinear capacity curve of the existing special moment-resisting frame (SMRF) buildings. The approach is simple and accurate to reflect the overall performances, yet might have limitation to present the deformation distributions within the structures, e.g. inter-story drift and plastic hinge distributions.

With the aim to achieve the performance-based and more economical design of the buildings, acquiring the ultimate seismic demands at each level of the building are required, yet it usually relies on performing the NRHA procedures which is practically too complicated, while performing the nonlinear static procedures (NSP) to a certain target roof displacement might significantly lose the accuracy of response distributions through the height (Park et al. 2007, Rofooei et al. 2012, Jan et al.

2004). Dorri et al. (2019) developed a specific load pattern for the NSP analysis of eccentrically braced frames, the development of a non-complex procedure is therefore needed for one to access the ultimate seismic performance or demands of the SMRF buildings. To increase the feasibility of the practical use, simplification of the NSPs need to be compromised, and the conventional NSPs required to be modified to improve the representation. In the study, an intermediate and alternative pushover analysis procedure has been proposed, named the modified first mode-based pushover analysis (MFPA), in aim to both covering the high mode effects beyond the fundamental mode, and maintaining the simplification of the procedures. In the MFPA procedure, a single-step pushover analysis is involved with a novel lateral force pattern modified from the first mode load vector. To validate the proposed MFPA procedures, multiple five-, ten-, fifteen-, and twenty-story SMRF buildings covering a wide range of structures and fundamental periods were analytically evaluated. The results of the MFPA were compared to that of the NRHA under MCE level events, the conventional NSPs, and the MPA procedures followed by an error analysis among those. It should be stated that the proposed NSP method was not developed through mathematical approaches, and therefore might have limitations for being applied for other structural systems of steel buildings which are not considered and validated in the study. The applicable scope of the MFPA might be limited to only the steel SMRF buildings under 20-story height.

MODIFIED FIRST-MODE-BASED PUSHOVER ANALYSIS (MFPA) PROCEDURES

In conventional NSP analysis, a distribution of lateral loads based on the first mode shape of the frames representing inertia forces in earthquakes is typically applied and monotonically increased until the roof floor reaching the target displacement and formation of plastic hinges in the systems. However, the conventional NSPs usually give very different distribution of inter-story drifts leading to the deformations of lower floors in the mid- to high-rise buildings are usually significantly overestimated as the top floors are comparable compared to the counterpart NRHA. The amount of the overestimation would vary with floor heights and the fundamental periods of the structures. To overcome the demerit yet maintaining the simplicity of the NSPs, the study proposes to apply an enhanced lateral load pattern in the NSPs with a novel lateral force distribution, modified from the load vector of the first mode shape to simulate the effects of higher modes, and so-called MFPA. Instead of combing the first mode distribution with higher modes used in the existing procedures, the modification factors were adopted to modify the first-mode load pattern upon the empirical observation, as illustrated in Fig. 1. The modified first-mode load pattern can be acquired and presented by Eq. (1).

$$S_j^* = \beta_j m_j \phi_{1j} S_a(T_1, \xi_1) \tag{1}$$

Where the j denotes the floor number; denotes the first mode shape; Sa denotes the spectral pseudo acceleration upon the fundamental period (T_1) and damping ratio (ξ_1); presents the major modification of the load pattern in the study, as defined in Eq. (2).

$$\beta_j = \left| \left(1 - 2h_j / h_r\right)^{\frac{T_1}{2}} \right| \tag{2}$$

Where is the floor height of the *j*th floor from the ground; h_r is the height of the roof level. through. The modification factors (β_j) were developed to vary with not only the floor heights but also the fundamental period of the considered building. It should be noted that to mimic the high-mode effects of the building, the developed modification aims to relatively enlarge the load proportions at upper stories and relatively mitigate that at mid-height stories according to the empirical observations that the typical NSP procedures usually underestimate the inter-story drifts at upper and mid-height stories as match the inter-story drifts at the bottom stories with respect to the dynamic responses. Moreover, the developed modification was designed to vary with the structural period (T_1) considering the high mode effects are usually more severe in taller buildings, with greater structural period (T_1), observed in

the literature. The resulting formula and the coefficients of Eq. (2) were empirically acquired upon several times iterations of analysis on the adopted model buildings in the development of the study for minimizing the differences from the responses of the counterpart NRHA as remaining the simplicity of equation.

In the aim of simulating and establishing the seismic responses of the NRHA, a target displacement of the roof level corresponding to the hazard level under consideration should be set up for the NSPs. In the MFPA procedures, the target displacement, , has been determined following the empirical formula used in the nonlinear static procedure analysis of FEMA-356 (2000) as shown in Eq. (3) along with the resulting capacity curve obtained from the pushover analysis, as illustrated in Fig. 2.

$$\delta_t = C_0 C_1 C_2 S_a \frac{T_e^2}{4\pi^2} g \tag{3}$$

Where C_0, C_1 and C_2 are modification factors, which have been specified and guided in FEMA 440 (2005); S_a denotes the response spectrum acceleration at the effective fundamental period (T_e) and damping ratio of the building under consideration; T_e denotes effective fundamental period of the building in the direction under consideration determined by modifying the fundamental period; g denotes the gravity acceleration.

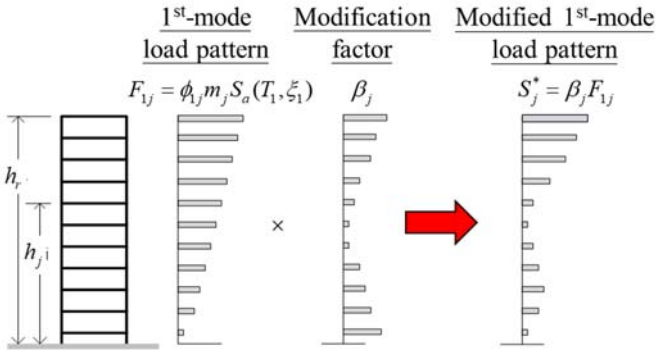

Figure 1. Schemes of the proposed load patterns of MFPA

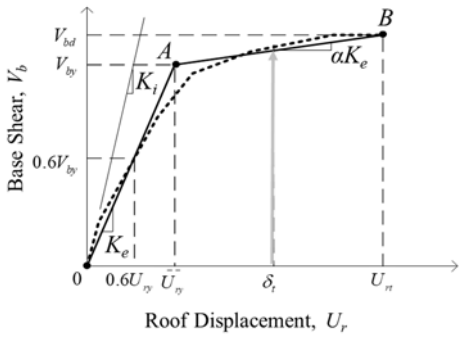

Figure 2. Illustration and idealization of base shears versus roof displacement pushover curves [33]

ANALYTICAL PROGRAM

To verify the validity and feasibility of the MFPA procedures, instead of using mathematic approaches, a series of prototype building structures has been designed and analytically evaluated through various static pushover and dynamic response history analysis. The considered prototype buildings include five-, ten-, fifteen-, and twenty-story SMRF structures to uniformly cover low- to high-rise buildings which would potentially adopt SMRF systems. In addition, to further include the effects of story heights of the buildings and wider the structural period ranges of the buildings in the study, two story-heights were considered for each building height. The results of the MFPA procedures were then compared to that of the multiple NSPs recommended in the literature, the MPA, and the NRHA. It should be noticed that application scope of the MFPA procedures might thereby be limited to only the range of buildings covered in the study. Upon the comparisons, the merits and demerits of each procedure are later discussed and evaluated upon the results of the program. The series of SMRFs in the study contained eight model buildings with various building heights, covering four numbers of stories, 5-, 10-, 15-, and 20-story, as shown in Fig. 3. All considered model buildings had 5-by-5 bays, while the span lengths varied with the total number of floors of the building from 6.1m to 9.1m long.

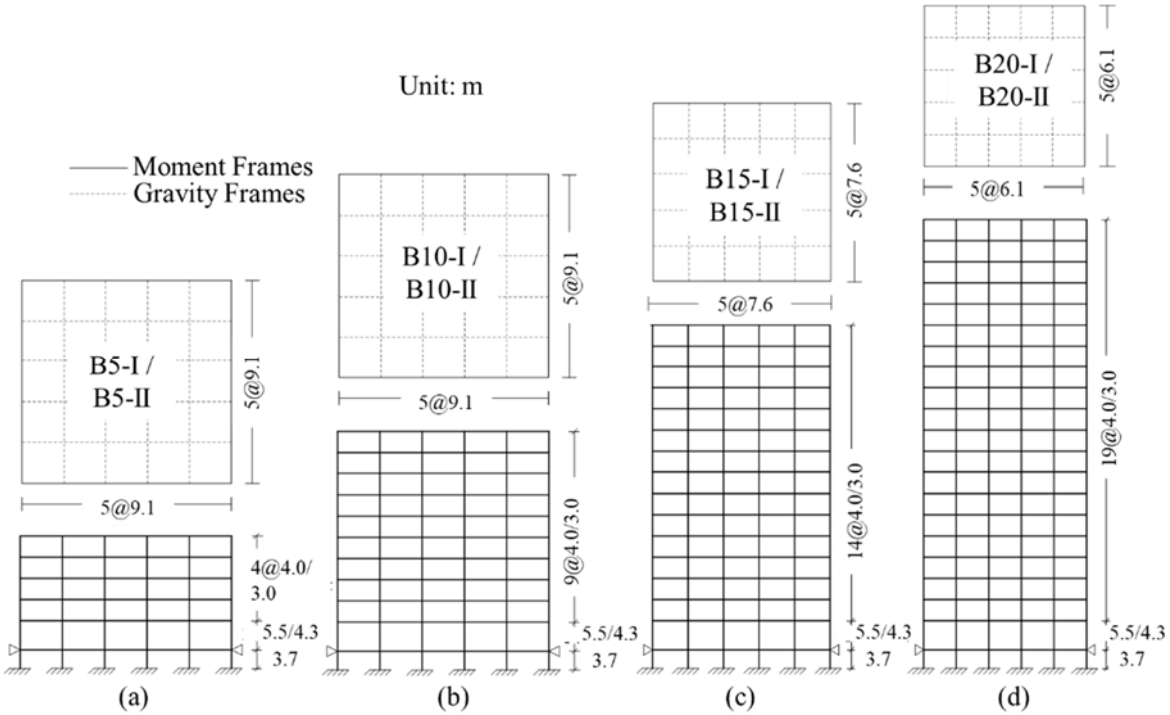

Figure 3. Floor plans and elevations of (a) 5-, (b) 10-, (c) 15-, and (d) 20-story prototype buildings

Numerical Modelling

Two-dimensional nonlinear discrete models of one planer SMRF at the building perimeter were established in the open system for earthquakes engineering simulation (OpenSees) framework (2009) to represent the buildings in the study. Figure 4 shows an illustration of the adopted numerical model of the SMRF planers in the study. All beams and columns in the frames were modeled using "nonlinearBeamColumn" element combined with "fiber section" model allowing the simulation of the distributed plasticity on the section. The "Steel02" material model with the nominal yield stresses (F_y) of 350MPa, the poisson's ratio (υ) of 0.3, the elastic modulus (E) of 200GPa and post-yield stiffness slope (b) of 0.03 was consistently applied for all members in the analysis. The rigid end zone effects of the beam-to-column joints were included by rigid offsets to simulate the rigidity of the joints in the frames. To include the P-Δ effect, a leaning column consisting of several rigid trusses and the pinned column base as shown was adopted for each building model. The Rayleigh damping was considered by a 5% damping ratio for the first three modes of the structural models. The models developed for each model building were used to compute their mode shapes, structural periods, various pushover and dynamic responses history analysis.

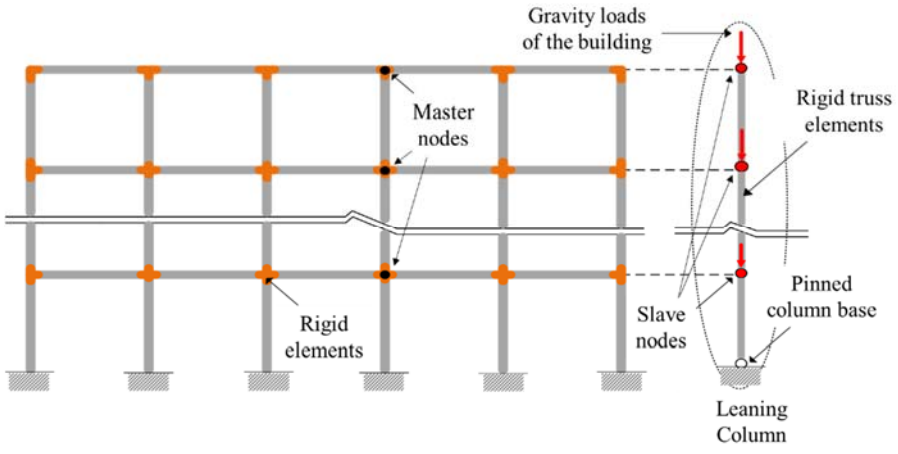

Figure 4. Illustration of the adopted OpenSees numerical model of SMRFs

Seismic Excitation

To provide the seismic excitation at MCE hazard level for the NRHA, the set of far-field ground motions per FEMA P-695 (2009) are used including 44 ground motions. According to the recommendation of NEHRP [39], the scaling was individually conducted for each record rather than scaling them as pairs. The provisions specify that the ground motions should be scaled such that the average value of 5% damped response spectral accelerations should not fall below the target spectrum within the period range of 0.2T to 1.5T, where T is the computed fundamental period of the considered structure, as shown in Fig. 5 taking B5-I and B15-II model buildings as examples. The period 0.2T was selected as the lower bound to ensure that important higher modes of vibration are sufficiently excited. The NRHA was aimed for acquiring the extreme responses under events of the 2% probability of exceedance in 50 years (2/50), representing the maximum considered earthquakes (MCEs).

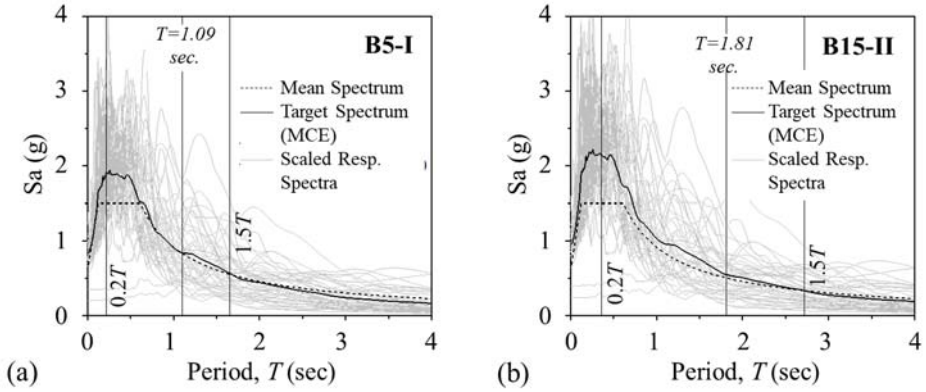

Figure 5. Scaled responses and mean spectra compared to the target spectrum for (a) B5-I and (b) B15-II buildings

Analytical Dynamic Responses

The responses of the NRHA, such as maximum absolute lateral floor displacements normalized by the building height and inter-story drifts of the frames, for 5- and 20-story buildings are shown in Figs. 6 and 7 as examples, respectively. It should be noted that the maximum responses through the height of the frames for a given event as shown in the figures might occur at different times during the event. The medium responses with single standard deviation (S_{dv}) among the set of ground motions are given in the figures, while the medium responses are adopted as representing seismic performance of each building at the MCE level. The results show that the median inter-story drifts of all considered buildings generally distributed uniformly throughout the heights and were around inter-story drifts of 1-2% radians, as the roof drifts were around 1.0% to 1.5% radians. It should be noted that maximum medium inter-story drifts of some considered buildings seem over the drift limitation per ASCE 7-16 standard (ASCE 7-16, 2016), it might be due to the slight over-scaled seismic excitation adopted in the study as shown in Fig. 5. However, all considered buildings were designed to meet the period and displacement limits per ASCE 7-16 standard in the typical design procedure, which implies the member sizes of the buildings have generally been designed efficiently and appropriately. The distributions of the inter-story drifts of the Type-I buildings along the building heights were similar with the counterpart Type-II ones. It implied the buildings having the same number of stories and stiffness distribution over the height would have similar dynamic characteristics and seismic performance, even though their structural periods and floor weights were different. Moreover, beam plastic-hinge distributions of each building based on the NRHA are also recorded and will be later discussed and compared with the responses of other NSP analysis.

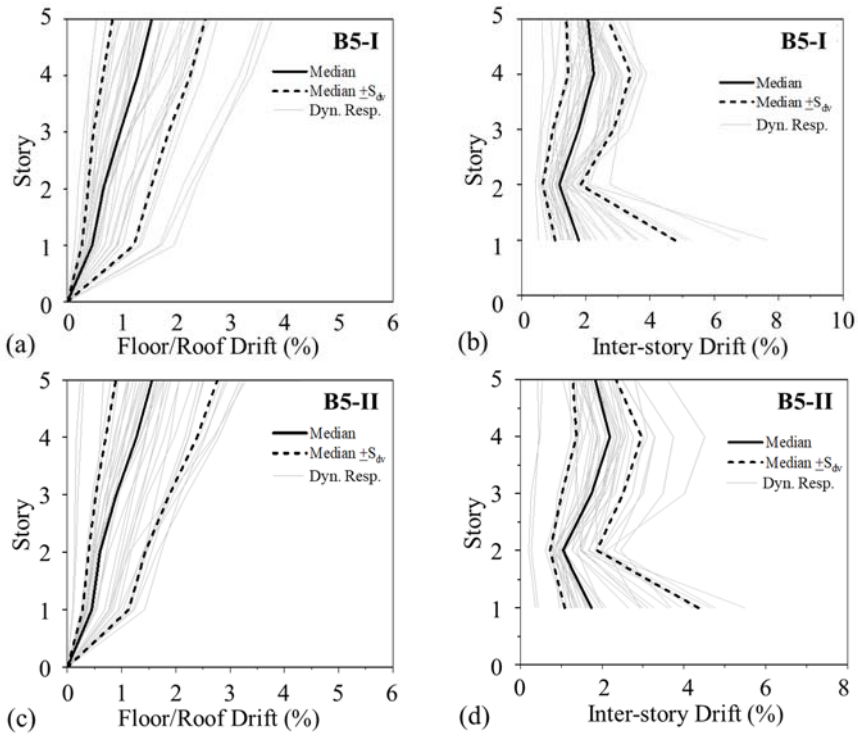

Figure 6. Dynamic responses of the NRHA for 5-story buildings on (a), (c) roof drifts and (b), (d) inter-story drifts

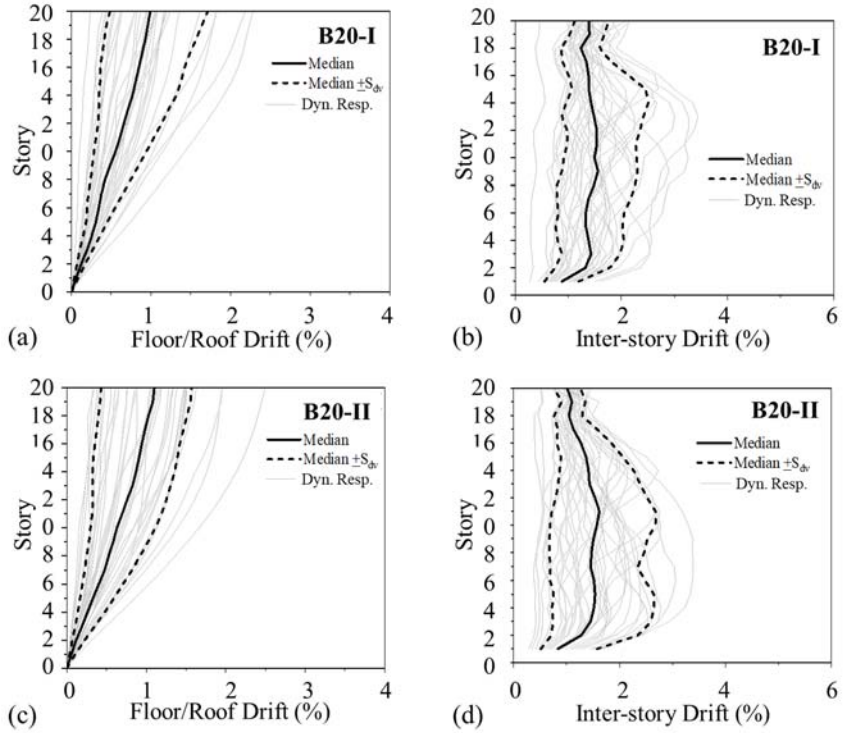

Figure 7. Dynamic responses of the NRHA for 20-story buildings on (a), (c) roof drifts and (b), (d) inter-story drifts

Performance and Comparisons of Various Procedures

The proposed MFPA procedures have been performed for all considered buildings in the study, and the results were compared with that of the NRHA, the MPA and other conventional NSPs using the

suggested lateral force distributions of the ELF and SRSS. In the comparisons, the medium values of the maximum dynamic responses by the NRHA were used to represent the exact responses of the considered buildings under MCE-level events, and adopted to recognize the accuracies of other procedures. In terms of the MPA, the effects of first three modes were considered, while it was confirmed that the first three modes had covered over 90% mass participation for each considered buildings. The extracted modal responses were then combined using SRSS approach to acquire the overall responses of the systems prior to comparing with that of the NRHA. The NSPs with lateral load patterns of ELF and SRSS approaches, denoted as ELF and SRSS hereinafter, were performed until the roof lateral displacements reached the target deformations corresponding to the applied load patterns. It should be noted that different NSPs may lead to different target roof displacements due to the difference of the applied load patterns. The responses at the final stage of the pushover analysis of the various NSPs were compared with that of the NRHA.

For quantifying the accuracy, the errors of responses of each NSP were presented in percentages by Eq. (4).

$$Er\,(\%) = \frac{\left(r_{\max,j}\right)_{NSP} - \left(r_{\max,j}\right)_{NRHA}}{\left(r_{\max,j}\right)_{NRHA}} \times 100 \tag{4}$$

where denotes the maximum dynamic responses of the NRHA at the *j*th story, and denotes the maximum responses of each NSPs, either the MFPA, ELF or SRSS, at the *j*th story. Figure 8 shows the errors of the inter-story drifts of the MPA, ELF, SRSS, and MFPA procedures for 5- to 20-story buildings with respect to that of the NRHA.

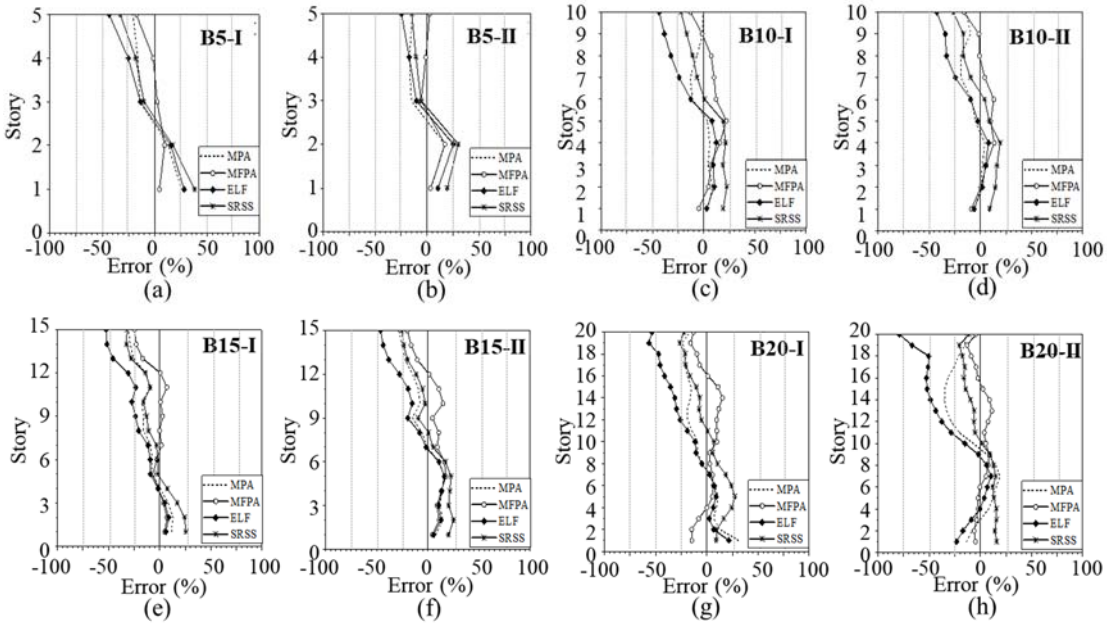

Figure 8. Errors of inter-story drifts of (a) B5-I, (b) B5-II, (c) B10-I, (d) B10-II, (e) B15-I, (f) B15-II, (g) B20-I, and (h) B20-II buildings

It is verified that the ELF procedures would underestimate the inter-story drifts of the stories above the mid-height by 25% to 75%, which would be enlarged with the building heights. The SRSS procedures would also underestimate the inter-story drifts of the stories above the mid-height yet reduced to 15% to 25%, while the overestimation of the inter-story drifts at the bottom stories were enlarged to around 25%. The MPA procedures provided very similar inter-story results with the SRSS for the stories above mid-height, but much smaller errors by15% in average at the bottom stories. The proposed MFPA procedures could eliminate the above mentioned underestimation of story drifts above the mid-height, and also further reduce the overestimation of story drifts at the bottom stories compared to that of the MPA procedures. It led to that the MFPA procedures provided the most accurate estimations of the dynamic responses upon the NRHA. It could be summarized that, in general, the proposed MFPA

procedures could consistently provide the best estimations of the inter-story drifts with the maximum errors through the building height within 25%, while the MPA as well as ELF and SRSS led to more significant deviation with the maximum errors through the building height varying around 25% to 75%.

CONCLUSIONS

A modified NSP analysis upon the modified first-mode shape of the building, named MFPA, has been proposed in the study to effectively achieve the seismic performance assessment of building structures of SMRF systems under MCE events. Several remarks have been concluded based on the results and evaluations of the study as listed follows:

- The SRSS and proposed MFPA procedures would predict similar and more conservative target roof displacements compared to the ELF and MPA procedures with respect to the medium maximum dynamic responses by the NRHA.
- The proposed MFPA procedures upon a novel load pattern based on empirical observation and against mathematics to simulate high-mode effects were verified to improve the accuracies of the estimations of both peak values and distribution shapes of inter-story drifts over the building heights compared to the MPA and other conventional NSP procedures as remaining the simplicity of the NSP approaches.
- The ELF procedures, typically used in the current practice, were verified to generally significantly underestimate the inter-story drifts from mid-height to upper stories of the buildings, especially for the high-rise buildings, while the peak inter-story drift over the height of the building could be reasonably captured.

REFERENCES

Ghobarah A. (2001), "Performance-based design in earthquake engineering: state ofdevelopment," Engineering Structures, 23, pp. 878–884.

FEMA 356 (2000), "Prestandard and commentary for the seismic rehabilitation of buildings," Federal Emergency Management Agency, Report FEMA 356, Washington D.C.

Park, H.G., Eom, T. and Lee, H. (2007), “Factored Modal Combination for Evaluation of Earthquake Load Profiles,” Journal of Structural Engineering, 133(7), pp. 956-968.

Rofooei, F.R., Mirjalili, M.R. and Attari, N.K.A. (2012), “Modal spectra combination method for pushover analysis of special steel moment resisting frames,” International Journal of Civil Engineering, 10(4), pp. 245-252.

Jan, T.S., Liu, M.W. and Kao, Y.C. (2004), “An upper-bound pushover analysis procedure for estimating the seismic demands of high-rise buildings,” Engineering Structures, 26(1), pp. 117-128.

Montuori, R., Nastri, E., Piluso, V., Todisco, P. (2020), " A simplified performance based approach for the evaluation of seismic performances of steel frames," Engineering Structures, 224, No.111222.

Dorri, F., Ghasemi, S.H. and Nowak, A.S. (2019), " Developing a Lateral Load Pattern for Pushover Analysis of EBF System," Reliability Engineering and Resilience, 1(1), pp.42-54.

FEMA 440 (2005), "Improvement of nonlinear static seismic analysis procedures," Federal Emergency Management Agency, Report FEMA 440, Washington D.C.

ASCE 7-16 (2016), “Minimum Design Loads and Associated Criteria for Buildings and Other Structures”, American Society of Civil Engineers (ASCE), Reston, Virginia.

Mazzoni, S., McKenna, F., Scott, M.H. and Fenves, G. (2009), "OpenSees user command language manual," Pacific Earthquake Engineering Research (PEER) Center, University of California, Berkeley.

FEMA P-695 (2009), "Quantification of Building Seismic Performance Factors," Federal Emergency Management Agency, Report FEMA P-695, Washington D.C.

EXPERIMENTAL STUDY ON SEISMIC PERFORMANCE OF INNOVATIVE REINFORCED-CONCRETE COUPLING BEAMS

Min-Chin Lin[1], Min-Lang Lin[2] and Chao-Hsun Huang[3]
1 Project Assistant Technologist, National Center for Research on Earthquake Engineering
2 Research Fellow, National Center for Research on Earthquake Engineering
3 Associate Professor, National Taipei University of Technology

Email: minchin@narlabs.org.tw

ABSTRACT

Short-span reinforced-concrete (RC) coupling beams are prone to shear failure and slip failure of the main steel bars. Therefore, this study proposes two schemes to improve the seismic performance of traditional coupling beams with straight-through main reinforcement. In the first scheme, a sheet steel plate is placed inside the traditional coupling beam to increase the shear strength. In the second scheme, the traditional coupling beam is cladded with additional reinforcement and concrete, but leaving a gap at the ends of the coupling beam such that the end portions have the same dimensions as the original dimensions. The cladded RC can only improve the shear strength of the original beam section and the bond strength of the main steel bar but not the moment strength of the original beam section. The test results show that the two schemes exhibit good ductility performance, and neither shear failure nor main steel bar splitting failure occurs. Plastic hinges occur for both specimens at the ends of the beams; this suggests the ideal flexural failure mode, thus meeting the expected behavior.

Keywords: coupling beam, shear plate, shear capacity, shear demand, bond strength, bond demand, double-layer stirrup

INTRODUCTION

A coupling beam is an important member of the ductile reinforced-concrete (RC) shear wall system. In the current Taiwan Civil 401 [1] and ACI 318 [2] design codes, coupling beams with a span-to-depth ratio of less than 2 and shear requirements must be configured with diagonal reinforcement. However, it is very difficult to apply diagonal reinforcement in an actual construction site.

According to previous research results, the traditional coupling beam with straight-through reinforcement has a bending moment capacity similar to that of the diagonally reinforced beam but lower ductility performance. Embedding steel plates in a traditional straight reinforced coupling beam can increase the shear strength of the beam and delay its degradation. This may in turn improve the ductility of the beam. Therefore, traditional straight reinforced coupling beams composited with steel plates may exhibit good seismic performance and can address the problem of difficult construction of diagonal steel bars.

In this study, cyclic loading tests were conducted on high-strength RC coupling beams embedded with steel plates for shear walls to evaluate the behavioral response of the coupling beams. Furthermore, the proposed steel plate and beam composite and steel plate end anchor design theory were verified.

[1] Research Fellow, National Center for Research on Earthquake Engineering
[2] Associate Professor, National Taipei University of Technology
[3] Master, National Taipei University of Technology

It was observed that the embedded steel plate increases the beam's shear capacity. However, it also increases the bending moment capacity, which in turn increases the beam shear requirements. To reduce the increase in the bending moment capacity of the beam caused by the embedded steel plate, the embedded steel plate needs to be partially cut off in the plastic hinge zone of the beam.

SPECIMEN DESIGN

An experiment to simulate the behavior of a coupling beam under the action of seismic force was conducted in the reaction wall and strong floor test area at the National Center for Research on Earthquake Engineering. The simulation causes double curvature deformation of the testing frame. To accommodate the limitations of the test structure, a beam section of 30 cm × 50 cm with a length of 100 cm was selected. According to Ci-Hong Chen3's literature, the test specimen number of CB20SW1 was adopted as the standard specimen, and two coupling beam specimens with a span–depth ratio of 2 were designed and constructed.

This experiment specimen CB2-1 and CB2-2 are embedded in comb-shaped cutting steel plates, with Ci-Hong Chen3 CB20SW3 as the model, having a beam section of 30 cm × 50 cm, beam lengths 100 cm and 150 cm, and span–depth ratios of 2 and 3, respectively. The two test specimen reinforcing steel configuration are as follows: twelve straight-through reinforcing steel #6-SD420, transverse tie reinforcements #4-SD420, and stirrups #3-SD420, with a 10 cm spacing; In the boundary column, there are six main rebars #7-SD420, and stirrups #3-SD420, with a 6 cm spacing. Concrete strength is 42 MPa. This test mainly aimed to reduce the number of main reinforcements and the spacing of the stirrups as well as increase the reinforcement as the main variables.

The experiment specimen CB2-2 has an middle section of 45 cm × 65 cm and the standard section of 30 cm × 50 cm is retained at 5 cm in front of and behind the beam section in both ends.

The reinforcement configuration for CB2-2 is the same as that for the CB20SW1 specimen: six straight-through rebars #8-SD420, transverse reinforcements #4-SD420, and stirrups #3-SD420, with a 10 cm spacing. Then, a second layer of stirrups and tie ribs is inserted in the middle section to observe. At the end of the experiment, we can observed toughness of the test specimen and possible to avoid splitting failure or shear failure.

Table 1. Specimen design parameters.

Specimen	Section	Steel plate ratio	Steel plate thickness	Steel plate anchor length
CB2-1	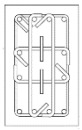	1.33%	t = 1.0 cm (cut 50%)	45 cm
Specimen	Section	original	Expanded section	
CB20SW1		30 cm × 50 cm	-	
CB2-2	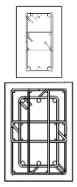	30 cm × 50 cm	45 cm × 65 cm	

Table 2. Specimen size chart (mm).

CB20SW1	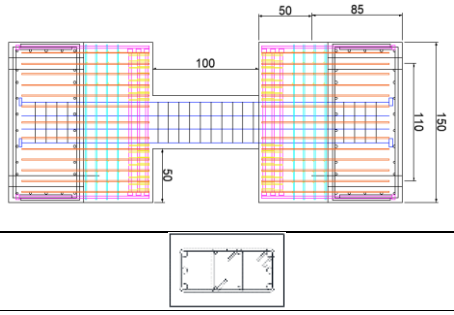
CB2-1	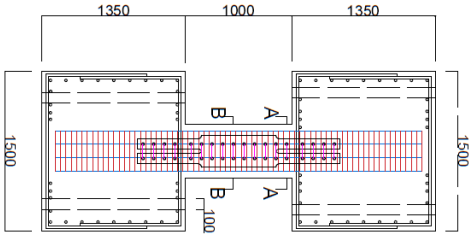 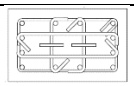 Section A-A 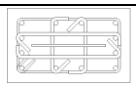 Section B-B
CB2-2	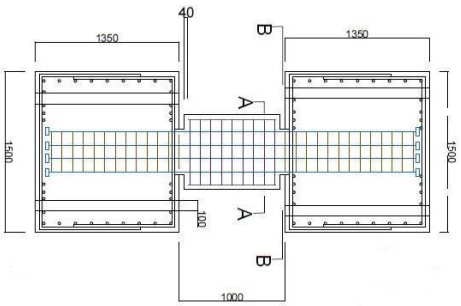 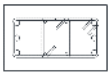 Section B-B 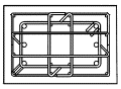 Section A-A

TEST SETUP AND CYCLIC LOADING TESTS

This test simulates the double curvature deformation of the specimen when it is subjected to a seismic force. An L-shaped steel frame and two vertical MTS actuators were used to ensure that the upper foundation did not rotate during the test. Two horizontal MTS actuators were used to apply a progressively increasing displacement to the test specimen. The test setup for the test is shown in Figure 1.

Figure 1. Test setup

To simulate the repetitive characteristics of earthquakes, this test referred to the loading protocol of ACI 374.1-05. A total of two loops were performed for each displacement load. The lateral displacement increments were 0.25%, 0.375%, 0.5%, 0.75%, 1%, 1.5%, 2%, 3%, 4%, 5%, 6%, 8%, and 10%, respectively, as shown in Figure 2.

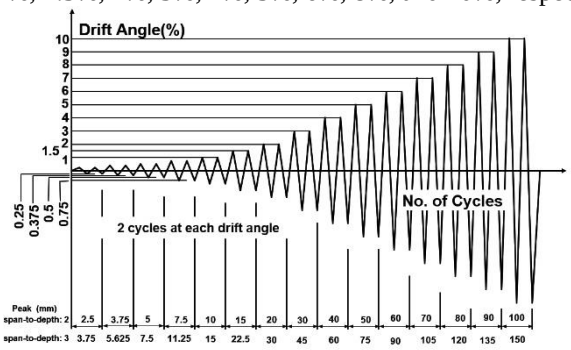

Figure 2. Test protocol.

TEST RESULTS

Figure 3 shows the load and displacement hysteresis cycles of each specimen. The extremum of the first cycle of each interlayer displacement is plotted as an envelope, and the ultimate interlayer displacement of each specimen is calculated, as shown in Figure 4. Table 3 lists the initial strength value of each specimen, and Figure 5 shows the failure of each specimen.

The ultimate interlayer displacement of the standard specimen CB20SW1 is only 2.22% (negative), which implies that the displacement toughness of the coupling beam with traditional reinforcement is poor and the energy dissipation ability is the worst.

For cutting steel plate specimens, the part with span–depth ratio 2 is compared with the Ci-Hong Chen3 standard specimen CB20SW1 and cutting steel plate CB20SW3. Specimen SW3 has a maximum strength point of approximately 2% interlayer displacement and a maximum lateral force of 760.8 kN; CB2-1 has a maximum strength of 3%, which is similar to that of CB20SW3 (approximately 4%) and approximately 40% higher than the maximum lateral force of the standard specimen. From the perspective of the ultimate interlayer displacement, the steel plate specimen CB2-1 was configured to be approximately 2.46 times higher than the standard specimen and approximately 1.73 times higher than CB20SW3 and the cumulative dissipation energy when 7% interlayer displacement is reached is 1.5 times that of the CB20SW3. After the standard specimen is configured with the steel plate, the cladded part must be considered so that with the increase in the lateral force, the strength of the specimen does not decay rapidly in the later stage, thereby fully taking advantage of the ability of the steel plate.

For the cladded concrete specimen, CB20SW1 was used as the prototype to cover the concrete in the middle section of the beam to increase the shear strength while the shear demand remains unchanged. The maximum lateral force of CB2-2 is approximately 1.5 times that of CB20SW1 at 861 kN; its displacement capacity is 5.81%, which is approximately 2.1 times that of the standard specimen; the cumulative dissipation energy of CB2-2 when 5% interlayer displacement is reached is approximately 2.25 times that of CB20SW1, and the maximum lateral force increase results in an increase in accumulated dissipative energy. The above analysis results indicate that the configuration of double-layer stirrup-cladded concrete in the middle section of the beam can effectively improve its interlayer displacement and increase the maximum lateral force as well as the accumulated energy.

The intensity decay of each specimen shows that, among all specimens, CB20SW1 has the maximum strength before the interlayer displacement of 3%, and there is no obvious attenuation; Furthermore, rapid decay in the standard specimen strength is observed after the interlayer displacement of 4%. Below, the configuration of the cutting steel plate specimen and the cladded concrete specimen is maintained at the maximum lateral force strength of more than 80%, with the decay in the later stage being relatively less. It can be seen that the initial strength of the CB2-1 steel plate with 50% of the cutting area of the comb-shaped steel plate is the initial stiffness of the CB2-2-coated concrete specimen, which is 81.1 kN/mm; it is approximately 3% lower than that of the standard specimen 0.6%. This indicates that irrespective of whether CB2-1 is placed in steel plates or cladded on concrete, the initial stiffness is relatively unaffected.

Table 3. Initial stiffness of specimens.

Specimen	Initial stiffness (kN/mm)			
	+	-	Average	Increase
CB20SW1	82.4	81.1	81.7	-
CB2-1	85.8	83.6	84.7	+3.0%
CB2-2	82.9	79.3	81.1	−0.6%

The deformation of CB20SW1 mainly occurs in the beam body, which is shear force deformation, while the boundary structure remains intact. The deformation of CB20SW3 occurs in the beam body, where it is curved deformation in the early stage and grip wrapping deformation in the later stage. Deformation of the CB2-1 and CB2-2 specimens occurs at the junction of the beam and foundation, while the core concrete remains intact. Plastic hinges are generated at the end of the beam, which is a flexural failure.

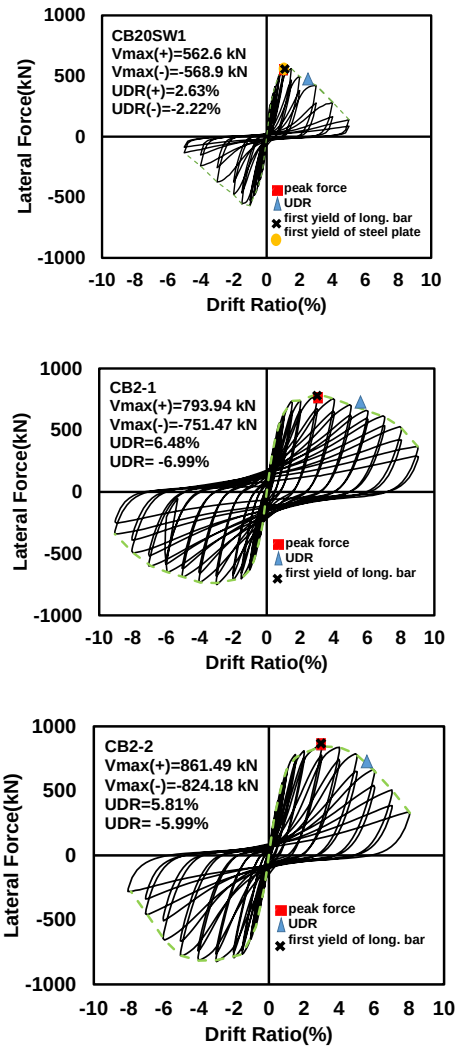

Figure 3. Hysteretic loops of specimens.

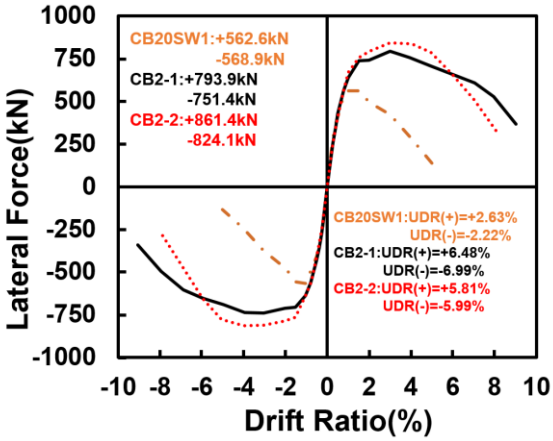

Figure 4. Envelope curves of specimens.

CB20SW1 CB2-1 CB2-2

Figure 5. Failure mode of specimens

CONCLUSIONS

In this study, two reinforced-concrete (RC) coupling beam specimens with a span–depth ratio of 2 were designed and tested. The test results revealed that plastic hinges were generated on the specimens mainly at the end of the beam, which is an ideal flexural failure. Good ductility performance was observed for the specimens used in the two design schemes. The comprehensive experimental results confirmed that the proposed RC coupling beam schemes have good seismic performance and can be used for engineering applications in practice.

REFERENCES

1. Chinese Society of Civil and Hydraulic Engineering, "Concrete Design Codes and Explanations (Civil Engineering 401-100)", 2011.
2. ACI Committee 318, Building Code Requirements for Structural Concrete (ACI 318-19) and Commentary (ACI 318R-14), American Concrete Institute, Farmington Hills, 2019.
3. Min-Lang Lin, Shan-Chun Yang(2014) “Study on Seismic Behavior for High Strength Reinforced Concrete Coupling Beams of Shear Walls” NCREE, Taipei.
4. Min-Lang Lin, Chao-Hsun Huang, Sung-Yi Yang and Ci-Hong Chen(2019), “Study on Seismic Behavior for Steel-Plate-Embedded Reinforced-Concrete Coupling Beams of Shear Walls” NCREE, Taipei.
5. ACI Committee 374, Acceptance Criteria for Moment Frames Based on Structural Testing and Commentary, American Concrete Institute, Farmington Hills, 2013.

EXPERIMENTAL INVESTIGATION ON SEISMIC PERFORMANCE OF REINFORCED CONCRETE SANDWICH WALL PANELS

Sushil Kumar[1], Binqi Chen[2], Yuye Xu[3], Jian-guo Dai[4,*]

1. Sushil Kumar, Department of Civil and Environmental Engineering, The Hong Kong Polytechnic University, Hong Kong, China
2. Binqi Chen, College of Civil Engineering, Huaqiao University, Xiamen, China
3. Prof. Yuye Xu, College of Civil Engineering, Huaqiao University, Xiamen, China
4. Prof. Jian-guo Dai, Department of Civil and Environmental Engineering, The Hong Kong Polytechnic University, Hong Kong, China
*Email: cejgdai@polyu.edu.hk

ABSTRACT

This paper presents the findings of an experimental investigation study conducted to understand the seismic performance of reinforced concrete sandwich wall panels (SWPs). A SWP consists of an insulation layer sandwiched between two reinforced concrete wythes, which are laterally linked with connectors. A total of six BFRP grid/steel-reinforced geopolymer concrete SWPs were prepared and tested under in-plane cyclic shear loading. A solid wall panel was also prepared and tested to distinguish the seismic performance of solid and sandwich wall panels. The test parameters included axial load ratio, shear span to length ratio and type of wall shear reinforcement. The failure modes, hysteretic curve, energy dissipation characteristics, ductility and deformability characteristics of SWPs are presented and discussed. The BFRP grid reinforced slender SWPs failed due to strength deterioration from wide diagonal cracks and a long vertical crack. The drift at ultimate load for BFRP grid reinforced SWPs ranged from 1.34% to 1.81%. The seismic performance of the BFRP grid reinforced solid wall panel and steel-reinforced SWPs was found to be relatively better than that of the counterpart BFRP grid reinforced SWPs. Therefore, existing seismic design guidelines for solid wall panels may not be suitable for SWPs and requires modifications.

Keywords: Sandwich wall panel, BFRP reinforcement, geopolymer concrete, seismic performance

INTRODUCTION

The precast concrete sandwich wall panels (SWPs) have been used for decades in building envelopes to provide thermal insulation. A SWP consists of an insulation layer sandwiched between two reinforced concrete wythes, which were laterally linked with connectors. Since the 1960s, considerable research has been conducted on the seismic performance of solid shear wall panels, and these have been used as a primary seismic load resisting system. However, only a limited number of studies are available on the seismic performance of SWPs. A few studies have recently been conducted on the seismic responses of steel-reinforced ordinary Portland cement (OPC) concrete SWPs designed with different types of sectional configurations, connectors, and a range of axial load ratios [1-5]. The seismic response of SWPs is not well understood yet.

For the last few decades, researchers have focused more on sustainable alternatives to existing construction materials. The authors of this research group have proposed a sustainable alternative to traditional reinforced concrete (RC) SWPs, i.e., Basalt FRP (BFRP) grid-reinforced geopolymer concrete SWPs enabled with Glass FRP (GFRP) tubular connectors. The proposed novel type of SWP has already been tested to assess its flexural [6] and axial performances [7, 8]. This study investigated the in-plane cyclic shear behavior of the proposed novel type of SWP.

EXPERIMENTAL PLAN

Test Specimens

The experimental program consisted of six SWPs and one solid wall panel designed with different test parameters. The details of tested specimens (i.e., SWPs and a solid wall panel) are given in Table 1. Fig. 1 shows the typical geometry of a SWP. An XPS insulation layer was sandwiched between two BFRP grid/steel-reinforced geopolymer concrete wythes. The two wythes and an insulation layer were connected laterally with several Glass FRP (GFRP) tubular connectors. All the SWPs were provided with longitudinal steel bars confined with steel stirrups concentrated at both edges of each wythe, called edge boundary elements. The web region (See Fig. 1) of the BFRP grid reinforced SWPs (i.e., CS1, CS3, CS4, CS5 and CS6) and steel-reinforced SWPs (i.e., CS2 and CS7) were reinforced with the two layers of BFRP grid and a single layer of steel bar, placed at the mid-thickness of each wythe, respectively. The cross-sections of typical BFRP grid-reinforced SWPs are shown in Fig. 2.

Table 1. Details of testes specimens

Panel ID	ALR	Wall web reinforcement	SLR
CS1-SQ-0.1-BG	0.1	BFRP G	1.25
CS2-SQ-0.1-St	0.1	Steel bar	
CS3-SQ-0.3-BG	0.3	BFRP G	
CS4-SL-0.2-BG*	0.2	BFRP G	2.38
CS5-SL-0.1-BG	0.1	BFRP G	
CS6-SL-0.2-BG	0.2	BFRP G	
CS7-SL-0.1-St	0.1	Steel bar	

Note: ALR – Axial load ratio; SLR – Shear span to length ratio; *CS4 is a solid wall panel (i.e. no insulation), all other wall panels are sandwich wall panels; BFRP G – Basalt FRP grid

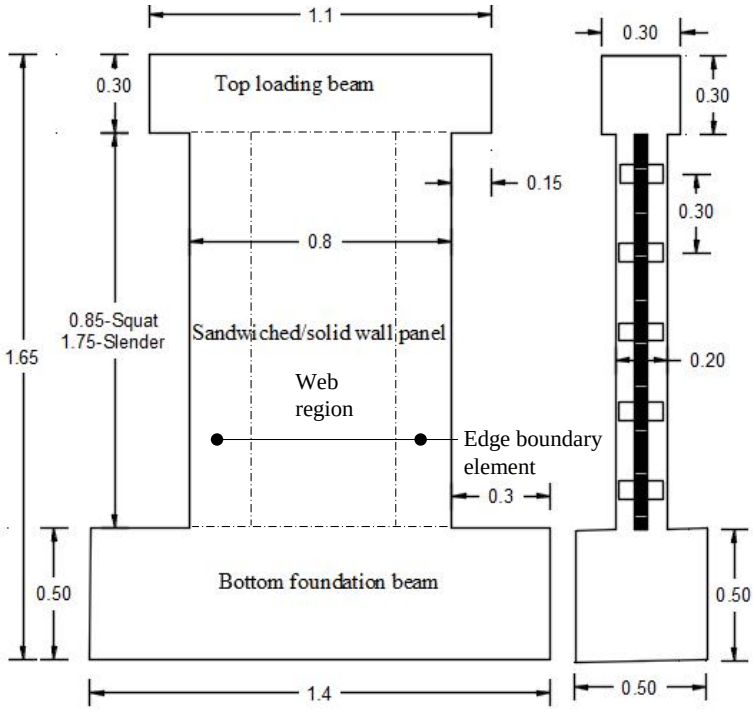

Figure 1. Typical layout of a specimen (all dimensions are in m)

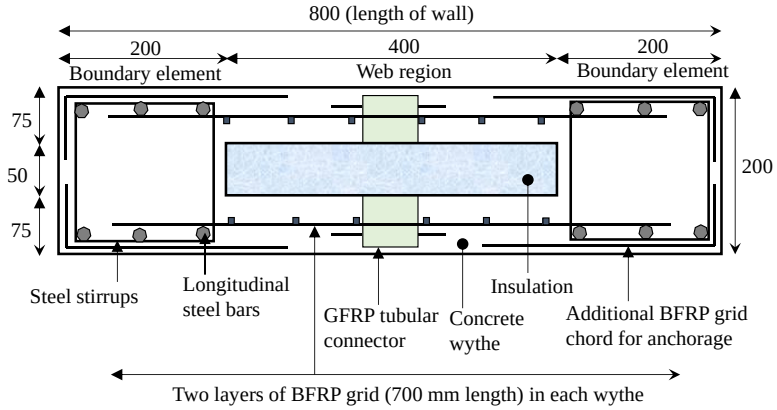

Figure 2. Coss-section of specimens CS1, CS3, CS5 and CS6

Materials

All the specimens were prepared using geopolymer concrete which was produced using slag, Class-F fly ash, sodium-hydroxide flakes, sodium silicate solution, aggregates (i.e., coarse and fine), and tap water. The two-part mixing method was used to prepare the geopolymer concrete. The compressive test-day cube strength of all specimens was 68.1 MPa, except for CS4, for which it was 55.5 MPa. XPS insulation layer of 50 mm thickness was used. The BFRP grid had elastic modulus, ultimate tensile capacity and ultimate tensile strain of 54750 MPa, 977 MPa and 1.74%, respectively. The yield and ultimate tensile strength of steel bars were 442 MPa and 682 MPa, respectively.

Fabrication of Specimens

Each specimen consisted of an RC sandwiched/solid wall panel, a top RC beam and a bottom RC foundation beam. The top and bottom beams were cast monolithically with the wythes of the wall panel. The specimens were fabricated in a horizontal position. The construction sequence was – a) casting of the bottom layer with geopolymer concrete, b) placing of insulation on top of the bottom layer and casting of the top layer with geopolymer concrete, and c) casting of top and bottom beams with high strength OPC concrete.

Instrumentation, Test-Setup and Test Procedure

The specimens were mounted with LVDTs to measure lateral deflections, diagonal shear deformations, rocking displacements and horizontal slip between specimen and bottom beam. Further, strain gauges (SGs) were glued to reinforcement and connectors to record the local strain.

Fig. 3 shows a sketch of the test setup. The quasi-static loading method is adopted in the test. A pre-determined axial force was applied gradually to the top of the SWP and kept constant for the whole test duration. Lateral displacement loading was applied at the centroid of the top beam following the protocol in Table 2. Visual inspections were done at the end of each drift cycle.

Table 2. Displacement loading scheme – squat wall panels

Displacement angle θ, rad	1/800	1/500	1/250	1/200	1/150	1/100	1/70	1/50	1/35	1/25	1/20
No of cycles	One					Three					

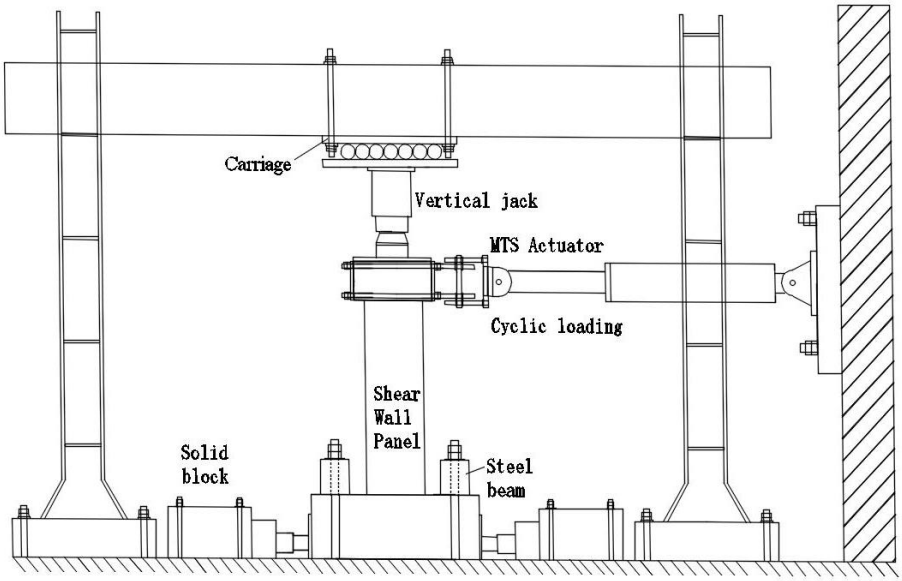

Figure 3. Test setup sketch

TEST RESULTS

Table 3 presents the failure modes, normalized average shear stress, drifts at peak and ultimate load and ductility of all the specimens. The squat specimens had shear failure. The slender solid wall panel CS4 and steel-reinforced SWP CS7 had flexural compression failure. The slender BFRP grid reinforced SWPs (i.e., CS5 and CS6) had wide diagonal cracks and developed a long vertical crack connecting the interconnecting points of the forward and diagonal cracks. Fig. 4 shows the photos of specimens at failure.

CS1-SQ-0.1-BG CS4-SL-0.2-BG (solid wall) CS6-SL-0.2-BG

Figure 4. Photos of specimen at failure

The average normalized shear stress (*Ks*) varied from 0.39 to 0.86 (Table 3). For squat specimens, it was higher than that of slender specimens. In the case of squat specimens, the shear plays a prominent role; therefore, web reinforcement becomes governing. The value of *Ks* of the steel-reinforced squat specimen (i.e., CS2) was higher than that of the counterpart BFRP grid reinforced squat specimen (i.e.,

CS1) because of the higher elastic modulus of steel bars. The value of K_s of the slender sandwich wall panel (i.e., CS6) was found to be around 15% lower than that of the corresponding slender solid wall panel (i.e.. CS4), which was due to the presence of cavity (i.e., insulation has no structural contribution) or discontinuity of material in CS6.

Table 3. Failure modes, average shear stress, drift and ductility of the specimens

Specimen ID	Failure mode	K_s = P_{peak}/A_{cv} /Sqrt(fck')	Drift (%)		Ductility, μ
			Δ_{peak}	Δ_{ult}	
CS1-SQ-0.1-BG	Diagonal shear compression	0.53	1.55	1.55	1.96
CS2-SQ-0.1-St	Diagonal shear compression	0.71	1.43	2.01	2.30
CS3-SQ-0.3-BG	Compression strut failure	0.86	1.34	1.34	1.71
CS4-SL-0.2-BG*	Post-flexure shear compression failure	0.52	1.96	2.70	2.77
CS5-SL-0.1-BG	Flexural compression at peak, and wide diagonal cracks with a vertical crack at ultimate	0.39	1.42	1.81	2.29
CS6-SL-0.2-BG	The wide diagonal cracks, and a vertical crack developed due to strength deterioration and non-uniformity of cracks in two wythes	0.45	1.40	1.40	2.09
CS7-SL-0.1-St	flexural compression failure with the formation of a plastic hinge	0.41	1.47	2.90	3.56

The hysteretic curves of squat and slender BFRP grid reinforced SWPs, a slender BFRP grid reinforced solid wall panel, and a slender steel-reinforced SWP are shown in Fig. 5. The ultimate drift of the slender sandwich wall panel (i.e., CS6) was found to be significantly lower than that of the counterpart slender solid wall panel (i.e.. CS4). Also, the ultimate drift of slender steel-reinforced SWP (i.e., CS7) was higher than that of BFRP grid-reinforced SWP (i.e., CS5). The ductilities of steel-reinforced SWPs (i.e., CS2 and CS7) and BFRP grid reinforced solid wall panels (i.e., CS4) were much higher than that of counterpart BFRP grid reinforced SWPs.

The total energy dissipations of steel-reinforced SWPs were higher than that of counterpart BFRP grid-reinforced SWPs due to the rounded hysteretic loops and late failure of steel-reinforced SWPs. Also, the total energy dissipation of a slender BFRP grid-reinforced solid wall panel was higher than that of counterpart BFRP grid-reinforced SWPs due to the late failure of steel-reinforced SWPs

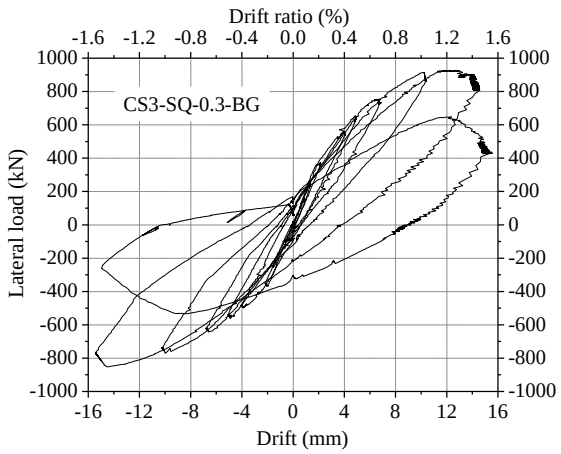

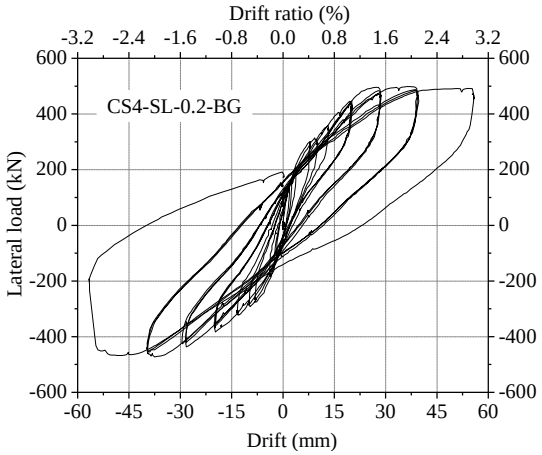

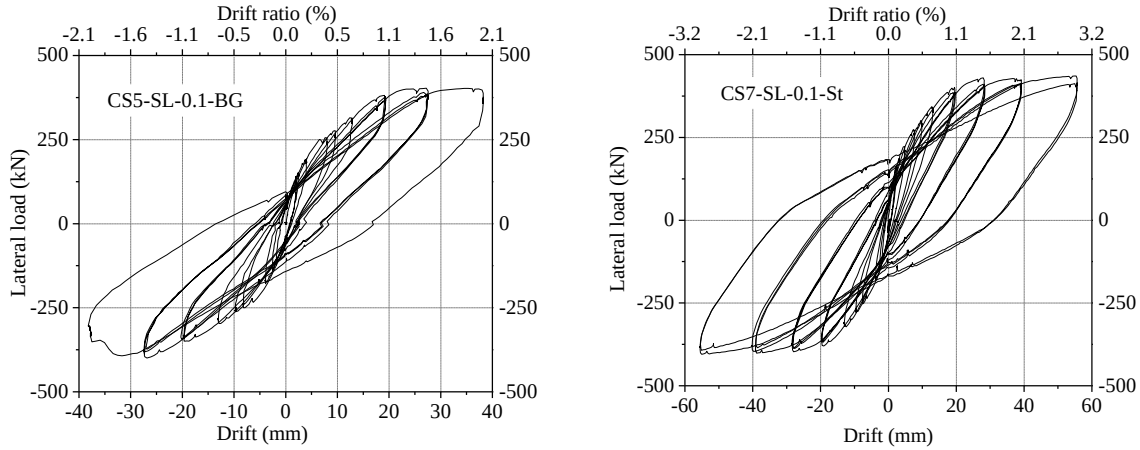

Figure 5. Hysteretic response of specimens

Fig. 6 shows the comparison of stiffness degradation curves of different specimens. The BFRP grid reinforced specimen CS3 with higher ALR had the highest stiffness until its failure due to higher applied axial load. The BFRP grid reinforced specimen CS1 and steel-reinforced specimen CS2 had almost the same stiffness at the initial drift level before cracking. Owing to the higher stiffness of steel bars than that of BFRP bars, the secant stiffness of specimen CS2 was higher than that of CS1 after cracking. The stiffnesses of slender specimens were nearly the same at all drift levels, irrespective of test parameters.

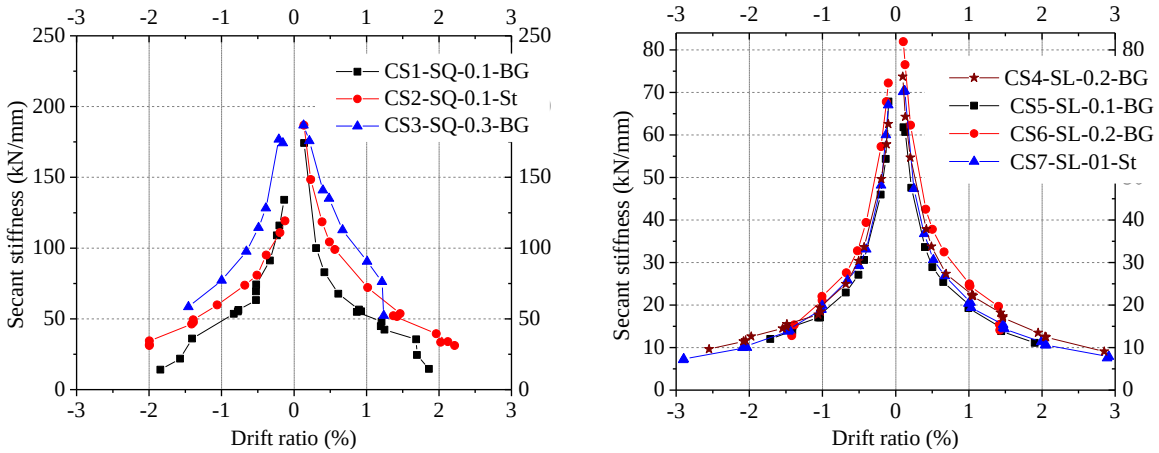

Figure 6. The comparison of stiffness degradation curves of different specimens

CONCLUSIONS

The following conclusions were drawn from this study.

1. The squat SWPs had shear failure. The slender solid wall panel had post-flexure shear compression failure. The BFRP gird reinforced slender SWPs had strength deterioration at ultimate load with the formation of a vertical crack connecting the intersection points of diagonal shear cracks. The steel bar reinforced slender SWPs had flexural compression failure followed by the formation of a plastic hinge.
2. The connector located at the mid-height of SWP was subjected to direct tension and bending. The resulting maximum recorded tensile strain of each BFRP grid reinforced SWPs varied from 1304 με to 6892 με.
3. The seismic performance of the slender solid wall panel was better than that of the counterpart slender sandwich wall panel. The average shear stress, ultimate drift, ductility, and total energy dissipation of the slender solid wall panel were significantly more than that of the corresponding slender SWP. This implies that the design guidelines given in the Code of Practice and

methodologies proposed by various researchers for solid shear walls may not be suitable for the seismic design of SWPs.

4. The SWPs with wall web reinforced with steel reinforcement displayed better seismic performance than that of BFRP grid reinforced SWPs. The average shear stress, ultimate drift, ductility, and energy dissipation of squat and slender steel reinforcement SWPs was higher than that of counterpart BFRP grid reinforced SWPs.
5. All tested squat and slender SWPs had ultimate drift greater than 1%. The drift at ultimate load for BFRP grid reinforced SWPs ranged from 1.34% to 1.81%.

ACKNOWLEDGMENTS

The authors are also grateful to the College of Civil Engineering, Huaqiao University, Xiamen, China, for providing access to the lab facility to carry out experimental works.

REFERENCES

[1] Aldemir, A., B. Binici and E. Canbay (2017). "Cyclic Testing of Reinforced Concrete Double Walls," *ACI Structural Journal*, **114**, 395-406.
[2] Huang, J.Q. and J.G. Dai (2020). "Flexural performance of precast geopolymer concrete sandwich panel enabled by FRP connector," *Composite Structures*, **248**, 112563.
[3] Jiang, Q., J. Shen, X. Chong, M. Chen, H. Wang, Y. Feng and et al. (2021). "Experimental and numerical studies on the seismic performance of superimposed reinforced concrete shear walls with insulation," *Engineering Structures*, **240**, 112372.
[4] Kumar, S., B. Chen, Y. Xu and J.G. Dai (2021). "Structural behavior of FRP grid reinforced geopolymer concrete sandwich wall panels subjected to concentric axial loading," *Composite Structures*, **270**, 114117.
[5] Kumar, S., B. Chen, Y. Xu and J.G. Dai (2022). "Axial-flexural behavior of FRP grid-reinforced geopolymer concrete sandwich wall panels enabled with FRP connectors," *Journal of Building Engineering*, **47**, 103907.
[6] Li, Y., W. Xue, Y. Yun and H. Ding (2022). "Reversed cyclic loading tests on precast concrete sandwich shear walls under different axial compression ratios," *Journal of Building Engineering*, **54**, 104619.
[7] Lu, Z., Y. Wang, J. Li and L. Wang (2019). "Experimental study on seismic performance of L-shaped insulated concrete sandwich shear wall with a horizontal seam," *The Structural Design of Tall and Special Buildings*, **28**, 1551.
[8] Qiao, W., J. Yuan, D. Wang, X. Yin and L. Meng (2021). "Pseudo-static experimental study on insulated sandwich concrete wall with embedded columns," *Journal of Building Engineering*, **34**, 101926.

RECORDED GROUND MOTION SELECTING, SCALING, AND ORIENTING FOR NONLINEAR RESPONSE HISTORY ANALYSIS: OVERVIEW OF ASCE 7 STANDARDS

Hsun-Jen Liu[1], Yin-Nan Huang[2], and Wen-Yu Jean[3]

1. Assistant Researcher, Earth Sciences and Geotechnical Engineering Division, National Center for Research on Earthquake Engineering, Taipei, Taiwan, R.O.C.
2. Associate Professor, Department of Civil Engineering, National Taiwan University, Taipei, Taiwan, R.O.C.
3. Researcher, Earth Sciences and Geotechnical Engineering Division, National Center for Research on Earthquake Engineering, Taipei, Taiwan, R.O.C.

Email: hjliu@narlabs.org.tw, ynhuang@ntu.edu.tw, wychien@narlabs.org.tw

ABSTRACT

In recent decades, response history analysis has been widely used in academic researches and generally accepted in engineering practices. After review of seismic design codes regarding selection and modification of ground motions for response history analysis, however, the ambiguity and inconsistency often exist in provisions. This study aims at the seven editions of the ASCE 7 Standard from 1996 to 2022 as well as at the three structure types of building structures, seismically isolated structures, and structures with damping system, to conduct an overall discussion on selecting, scaling, and orienting procedures focused on nonlinear response history analysis. The intent of this paper is to investigate and compare the criteria of recorded input excitations in the ASCE 7 provisions, and to summarize key requirements from the different editions of the ASCE 7 Standard. In Taiwan, lately a website for input motion selection and scaling has been developed, while the more practical code provisions for ground motion selection and modification still need to be improved.

Keywords: ASCE 7 Standard, nonlinear response history analysis, recorded ground motion selection, amplitude scaling, component orientation, seismic design

INTRODUCTION

The principal advantages of response history analysis, as known as time history analysis, is providing information on the force state, deformation situation, and nonlinear behavior of the structure over time during and after the application of a real earthquake load. For design purpose, the fundamental goal of response history analysis is to predict the unbiased seismic demand with relatively limited variation in results. Because these estimations of structural responses are highly depended on the characteristics of input ground motions, the there are two basic principles for the input excitations. The first principle is that a suite of input excitations is necessary for observing the difference in structural response resulting from differences in ground motion characteristics. The second principle is that the input excitations should reflect the site-specific characteristics generated by the seismic hazards and site effects. Owing to the limitation on software performance and suitable seismic data recordings, however, until 2010 the benefits of response history analysis were infrequently achieved in practice.

In recent decades, using actual recorded earthquake ground motions to perform response history analysis has been widespread apply in academic researches and generally accepted in engineering practices. Meanwhile, many of national seismic design codes actively improved and detailed the procedures regarding selection and modification of recorded ground motions for response history analysis, such as the National Building Code of Canada (NBC), the New Zealand Standard (NZS), and the U.S. building codes provided by the American Society of Civil Engineers (ASCE). The ASCE 7 Standard entitled *Minimum Design Loads for Buildings and Other Structures*, is not only the authoritative source for general structural design in the U.S., but also among the most commonly used building codes in various parts of the world. The ASCE 7 provisions regarding input ground motions for response history analysis were firstly specified in the ANSI/ASCE 7-95 edition, and till the current ASCE/SEI 7-22 edition a total of six revisions was made.

In view of active revision (period of about 4.5 years) on the international structural design code of the ASCE 7 Standard, it is necessary to review the technical bases of the changes. This study aims at the seven editions of the ASCE 7 Standard from 1996 to 2022 as well as at the three structure types including building structures, seismically isolated structures, and structures with damping system, to conduct an overall discussion on selecting, scaling, and orienting procedures focused on nonlinear response history analysis. The intent of this paper is to investigate and compare the input motion procedures in the ASCE 7 provisions, and to summarize key requirements from the different editions of the ASCE 7 Standard. Lastly, this paper briefs the current practices of the input motion procedures in Taiwan and provides directions for future revision of the Taiwan Building Code (CPAMI, 2022).

REVIEW OF PROVISIONS DEVELOPMENT

In the U.S., the requirements for input ground motion selection and modification were explicitly specified in the building codes, which was caused by the significant amount of research, development, and application activity in seismic isolation from late 1970s. The design code development for seismically isolated structures occurred throughout the late 1980s and began at the reginal provisions. In 1990, the Structural Engineers Association of California (SEAOC) Seismology Committee published an appendix to the fifth edition of the SEAOC Blue Book entitled, "*General Requirements for the Design and Construction of Seismic-Isolated Structures*." In addition, the ASCE was based on the national provisions for new building design developed by the Federal Emergency Management Agency (FEMA) in 1994, as known as FEMA-222A, to firstly specify the criteria for seismically isolated structures including ground motion in the ANSI/ASCE 7-95. Afterwards, the provisions for ground motion selection and modification for building structures and structures with damping system were initial specified in the SEI/ASCE 7-02 and the ASCE/SEI 7-05, respectively.

Overall, the typical requirements of response history analysis in the ASCE 7 Standards, for ground motion selection are (1) the comparability of seismic hazard (controlling magnitude and distance), site condition, and spectral shape, (2) the minimum number of motions, (3) the time history components (single, pair, or triplet), and (4) the recorded spectrum type (geometric mean or maximum direction); for ground motion modification are (1) the period range of interest, (2) the lower limit of ratio of scaled recorded spectrum to target spectrum (record-to-target ratio, RTR) for any period within the period range of interest, and (3) the orientation of horizontal ground motion components for near-fault sites. Moreover, the target spectrum can be categorized as (1) the approach of design spectrum determination (uniform hazard or uniform risk), (2) the design ground motion level (design earthquake, DE or maximum considered earthquake, MCE), and (3) the design spectrum type.

GROUND MOTION REQUIREMTS IN ASCE 7 STANDARDS

Table 1 summarizes the key requirements regarding recorded ground motion selecting, scaling, and orienting for nonlinear response history analysis from the seven editions of the ASCE 7 Standard from ANSI/ASCE 7-95 to ASCE/SEI 7-22. The requirements in Table 1 are individually listed for the three structure types: (1) building structures, (2) seismically isolated structures, and (3) structures with damping system. The review and perspective of the requirements in Table 1 are discussed below.

Minimum Number of Selected Motions

Before the ASCE/SEI 7-16, response history analysis was performed with at least 3 pairs of horizontal ground motions, except that for building structures are additionally allowed to use at least 3 singles of horizontal ground motions. In the ASCE/SEI 7-16, the minimum number of selected motions was increase to 7 for structures with isolation or damping system and 11 for building structures. In the ASCE/SEI 7-22, the minimum number of selected motions requires 11 for all structure types. When fewer than 7 selected motions are analyzed, the maximum response is used for design. When 7 or more selected motions are analyzed, then the average response is used for design.

Table 1. Summary of ground motion requirements regarding selecting and scaling, and orienting for nonlinear response analysis from ASCE 7 Standards

Edition of ASCE 7	ANSI/ASCE 7-95 (1996)	ASCE 7-98 (2000)	SEI/ASCE 7-02 (2003)	ASCE/SEI 7-05 (2005)	ASCE/SEI 7-10 (2013)	ASCE/SEI 7-16 (2017)	ASCE/SEI 7-22 (2022)
Building Structures							
Provision Sections			9.5.7.2; 9.5.8.2	16.1.3; 16.2.3	16.1.3; 16.2.3; C16.1.3	16.2; C16.2	16.2; C16.2
Minimum Number of Selected Motions			3 singles or 3 pairs	3 singles or 3 pairs	3 singles or 3 pairs	11 pairs or 11 triplets	11 pairs or 11 triplets
Recorded Spectrum (RecSA) Type			· For single: RS · For pair: SRSS	· For single: RS · For pair: SRSS	· For single: RS · For pair: SRSS	· For H: RotD100 · For V: RS	· For H: RotD100 · For V: RS
Target Spectrum (TarSA) Type			Geomean (DE or MCE)	Geomean (DE or MCE)	RotD100 (DE or MCE_R)	· For H: RotD100 (MCE_R) · For V: RS (MCE_R)	· For H: RotD100 (MCE_R) · For V: RS (MCE_R)
Lower Limit of Period Range (s)			0.2T	0.2T	0.2T	· For H: min{$T_{m90\%}$, $0.2T_{1L}$} · For V: max{0.1 s, T_{vL}}	· For H: min{$T_{m90\%}$, $0.2T_{1L}$} · For V: max{0.1 s, T_{vL}}
Upper Limit of Period Range (s)			1.5T	1.5T	1.5T	· For H: $2.0T_{1H}$ · For V: $2.0T_v$ (unclearly defined)	· For H: $2.0T_{1H}$ · For V: $2.0T_v$ (unclearly defined)
Requirements of Amplitude Scaling			· For single: $RecSA_{avg} \geq DE$ · For pair: $RecSA_{avg} \geq 1.3 \times MCE$	· For single: $RecSA_{avg} \geq DE$ · For pair: $1.1 \times RecSA_{avg} \geq 1.3 \times MCE$	· For single: $RecSA_{avg} \geq DE$ · For pair: $RecSA_{avg} \geq MCE_R$	· For H: $RecSA_{avg} \geq 0.9 \times TarSA$ · For V: $RecSA_{avg} \geq TarSA$	· For pair: $RecSA_{avg} \geq 0.9 \times TarSA$ · For V: $RecSA_{avg} \geq TarSA$
Seismically Isolated Structures							
Provision Sections	9.2.6.4.4.2	9.13.4.4.2	9.13.4.4.2	17.3.2	17.3.2 (follow 16.1.3.2); C17.3.2	17.3; C17.3; C17.6.3.4	17.3 (follow 16.2); C17.3
Minimum Number of Selected Motions	3 pairs	3 pairs	3 pairs	3 pairs	3 pairs	7 pairs or 7 triplets	11 pairs or 11 triplets
Recorded Spectrum (RecSA) Type	SRSS	SRSS	SRSS	SRSS	SRSS	· For H: SRSS · For V: RS	· For H: RotD100 · For V: RS
Target Spectrum (TarSA) Type	Geomean (DE or MCE)	Geomean (DE or MCE)	Geomean (DE or MCE)	Geomean (DE or MCE)	RotD100 (DE or MCE_R)	· For H: RotD100 (MCE_R) · For V: RS (MCE_R)	· For H: RotD100 (MCE_R) · For V: RS (MCE_R)
Lower Limit of Period Range (s)	T_I - 1.0	$0.5T_D$	$0.5T_D$	$0.5T_D$	$0.5T_D$	· For H: $0.75T_{ML}$ · For V: $0.2T_v$	· For H: min{$T_{m90\%}$, T_{fb}} · For V: max{0.1 s, T_{vL}}
Upper Limit of Period Range (s)	T_I + 1.0	$1.25T_M$	$1.25T_M$	$1.25T_M$	$1.25T_M$	· For H: $1.25T_{MH}$ · For V: $1.5T_v$	· For H: $1.25T_{MH}$ · For V: $2.0T_v$ (unclearly defined)
Requirements of Amplitude Scaling	$1.1 \times RecSA_{avg} \geq 1.3 \times TarSA$	$1.1 \times RecSA_{avg} \geq 1.3 \times TarSA$	$1.1 \times RecSA_{avg} \geq 1.3 \times TarSA$	$1.1 \times RecSA_{avg} \geq 1.3 \times TarSA$	$RecSA_{avg} \geq TarSA$	· For H: $RecSA_{avg} \geq TarSA$ · For V: SF_{pair} or least-squares fit	· For H: $RecSA_{avg} \geq 0.9 \times TarSA$ · For V: $RecSA_{avg} \geq TarSA$
Structures with Damping System							
Provision Sections				18.2.3.2 (follow 17.3.2)	18.2.3.2 (follow 17.3.2)	18.2.2; C18.3	18.2.2 (follow 16.2); C18.2.2.2
Minimum Number of Selected Motions				3 pairs	3 pairs	7 pairs	11 pairs
Recorded Spectrum (RecSA) Type				SRSS	SRSS	SRSS	RotD100
Target Spectrum (TarSA) Type				Geomean (DE or MCE)	RotD100 (DE or MCE_R)	RotD100 (DE or MCE_R)	RotD100 (DE or MCE_R)
Lower Limit of Period Range (s)				$0.5T_{1D}$	$0.5T_{1D}$	$0.2T_{1D}$	min{$T_{m90\%}$, $0.2T_{1DL}$}
Upper Limit of Period Range (s)				$1.25T_{1M}$	$1.25T_{1M}$	$1.25T_{1M}$	$2.0T_{1MH}$
Requirements of Amplitude Scaling				$1.1 \times RecSA_{avg} \geq 1.3 \times TarSA$	$RecSA_{avg} \geq TarSA$	$RecSA_{avg} \geq TarSA$	$RecSA_{avg} \geq 0.9 \times TarSA$

The minimum number of recorded ground motions is subjectively selected 3 at before and 11 in the current. The considerations for this judgment are summarized as follows (ASCE/SEI 7-16, 2017):

1. The round motion database are well improved in quantity and quality, such as PEER NGA-West2 database (Ancheta *et al.*, 2013) and PEER NGA-East database (Goulet *et al.*, 2014).
2. The mean structural response can be estimated with more reliability.
3. The possibilities of difference in structure response for varied ground motion characteristics can be more adequately observed. That is, the unacceptable response possibility can be found to check whether the structure will meet the goal of 10% conditional collapse probability (Risk Category I or II) or not.

For the second consideration, having the higher spectral shape similarity between recorded and design ground motions is also an important factor to predict the stable mean response. For the last consideration, the uncertainty in the estimated collapse probability depends on the total number of ground motions, and the number of required ground motions and the maximum number of unacceptable responses may be established clearly in the future ASCE 7 provisions.

Time History Components

Before the ASCE/SEI 7-16, for structures with isolation or damping system, 3-D structural analysis was performed and simultaneously applied pairs of horizontal history motions; for building structures, 2-D and 3-D structural analysis are permitted with singles and pairs of horizontal history motions, respectively. Since vertical design spectra were specified in the ASCE/SEI 7-16, pairs of horizontal components or triplets of horizontal and vertical components were considered for building structures and seismically isolated structures.

According to the statement of the ASCE 7 Standard, 2-D structural analysis is simply for initial studies as well as specific issue examinations; however, 3-D structural analysis is the proper approach for confirmation of structural performance in the final stage. Besides, for most structures, it is adequate to only consider response to horizontal ground motions; however, for buildings near to faults and structures with suspended ceiling systems, long spans, prestressed construction, or vertical discontinuities, it is necessary to consider the response to vertical ground motions.

Recorded Spectrum Type

In the past ASCE 7 Standards, each pair of horizontal ground motions was constructed as a square root of the sum of the squares (SRSS) spectrum. For all structure types in the ASCE/SEI 7-22, each pair of horizontal ground motions is constructed as a maximum direction spectrum which is identical with the definition of the horizontal design spectra.

Maximum direction spectrum is identical to RotD100 (Rot: rotary; D: period-dependent; 100: 100th-percentile) that represents the maximum spectral amplitude of a pair of horizontal ground motions over all non-redundant rotation angles (Boore, 2010). RotD100 is independent of the in situ orientations of the sensor recordings. SRSS spectrum represents the combined spectral maxima of two horizontal components. SRSS spectrum is frequently used in previous building codes and is commonly accepted among structural engineers involved in seismic design and analysis, although amplitude of SRSS spectrum is higher than amplitude of RotD100 and geometric mean (geomean) spectra.

Target Spectrum Type

For the approach of development of horizontally probabilistic ground motion spectra for design, uniform hazard concept was adopted before the ASCE/SEI 7-10 while uniform risk concept was used since the ASCE/SEI 7-10. Moreover, the two levels of design ground motion spectra are constructed in the ASCE 7 Standard: the maximum considered earthquake (MCE) and the design earthquake (DE). The return periods for hazard-based MCE and DE are 2,475 years and 475 years, respectively, except

that the MCE return period is about 950 years in the ANSI/ASCE 7-95. The performance goal of risk-targeted maximum considered earthquake (MCE_R) is defined by 1% absolute collapse probability within a 50-year period.

The hazard-based MCE spectra were established as geomean type, which was related to the earlier ground motion attenuation relationships for the geometric mean of horizontal ground motions. The risk-based MCE_R spectra were established as RotD100 type, which was related to the rising value of structural reliability analysis as well as the code consideration of using the largest maximum response over all orientations. Moreover, in the ASCE 7 Standards, the DE is two-thirds of the MCE or MCE_R, except that in ANSI/ASCE 7-95 the particular equations for MCE and DE were specified.

The vertical design ground motion spectra were explicitly specified since the ASCE/SEI 7-16. Compared to the traditionally method using the simple two-thirds value of vertical-to-horizontal (V/H) spectral ratio, the equations for vertical design spectra were based on the V/H ratios observations from seismic data recordings. The characteristics of observed V/H ratios include high period-dependent, significant short-period spectral content, and high attenuation rate of vertical ground motion with decreasing distance from the earthquake (Bozorgnia and Campbell, 2004; FEMA P-750, 2009). The limit imposed on the MCE_R vertical design spectra was that the spectral ratios of the vertical MCE_R to the horizontal MCE_R are not less than 0.5.

Lower Limit of Record-to-Target Spectral Ratio

For the identical spectrum type in the recorded and target ground motions, the lower limit of ratio of scaled recorded spectrum to target spectrum (record-to-target ratio, RTR) for any period within the period range of interest, is typically required as 0.9. This judgment threshold could be traced to the NUREG-75/087 of the initial nuclear regulation published in 1975.

When lower limit RTR for horizontal directional ground motions is examined, the representative of the scaled recorded spectra is the average of the SRSS or RotD100 type from all the selected motions ($\overline{RecSA}$), and the target spectrum ($TarSA$) can be the MCE or DE level with geomean or RotD100 type. It should be noted that the different spectrum type definitions on the recorded and target spectra cause the different relatively lower limit RTR requirements. Taking building structures as an example, there are four statements for the relatively lower limit RTR requirements in the different editions of ASCE 7 Standard. The mathematical expressions and its coefficients descriptions are as follows:

1. $\boldsymbol{\overline{RecSA}_{SRSS} \geq 1.3 \times TarSA_{geom} \Rightarrow \overline{RecSA}_{SRSS}/TarSA_{geom} \geq 1.3/1.0}$ **(SEI/ASCE 7-02)**
   If the two horizontal ground motion components are perfectly correlated, which means both directions with the identical spectral amplitudes, the proportional coefficient of SRSS spectrum to geomean spectrum is 1.4 ($=\sqrt{(1)^2+(1)^2}/\sqrt{1\times1}$). In comparison, this RTR requirement value (1.3/1.0=1.3) in SEI/ASCE 7-02 is relatively consistent with the essential value (1.4×0.9≈1.3).
2. $\boldsymbol{1.1\times\overline{RecSA}_{SRSS} \geq 1.3 \times TarSA_{geom} \Rightarrow \overline{RecSA}_{SRSS}/TarSA_{geom} \geq 1.3/1.1}$ **(ASCE/SEI 7-05)**
   Since actual ground motions are not perfectly correlated, it is reasonable that the proportional coefficient of SRSS spectrum to geomean spectrum can be less than 1.4. In addition, the SRSS spectrum has to equal or exceed 1.3 times the target spectrum (geomean type), this judged criteria was explicitly required in FEMA 222A (provisions) and FEMA 223A (commentary) in 1995. As a result, this RTR requirement value (1.3/1.1≈1.18) in ASCE/SEI 7-05 relatively corresponds to the essential value (1.3×0.9≈1.17).
3. $\boldsymbol{\overline{RecSA}_{SRSS} \geq TarSA_{RotD100} \Rightarrow \overline{RecSA}_{SRSS}/TarSA_{RotD100} \geq 1.0/1.0}$ **(ASCE/SEI 7-10)**
   Based on the studies of the 50 ground motions with earthquake magnitude 6.5 to 7.9 for both far- and near-field records and for period range from 0.1 to 3.0 seconds indicate that the SRSS spectrum tending to be approximately 1.16 times the RotD100 spectrum (FEMA P-750, 2009). In comparison, this RTR requirement value (1.0/1.0=1.0) in ASCE/SEI 7-10 is relatively consistent with the essential value (1.16×0.9≈1.0).

4. $\overline{RecSA}_{RotD100} \geq 0.9 \times TarSA_{RotD100} \Rightarrow \overline{RecSA}_{RotD100}/TarSA_{RotD100} \geq 0.9/1.0$ **(ASCE/SEI 7-16)**
The recorded and target ground motion are with identical spectrum type of RotD100, hence, the RTR requirement value (0.9/1.0=0.9) in ASCE/SEI 7-16 and ASCE/SEI 7-22 is absolutely correspond to the essential value (1.0×0.9=0.9).

For the vertical ground motion scaling, in the ASCE/SEI 7-16, using the same scale factor as the horizontal ground motion, or using different scale factor by using a least-squares fit method, was available for seismically isolated structures. In the ASCE/SEI 7-22, the lower limit RTR is required as 1.0 for the structures sensitive to vertical response. Because the vertical spectral shape is usually significantly different than the horizontal spectrum, especially at higher frequencies (shorter periods), using the separate scale factor to vertical and horizontal and a conservatively lower limit RTR may be proper. No specific lower limit RTR requirements in the ASCE 7 Standard for structures with damping system which is insensitive to vertical response.

Period Range for Amplitude Scaling

The period range for checking spectral shape and amplitude of scaled ground motions, which is required to cover the dynamic response characteristics of the structures included the following: (1) the fundamental period of the structure; (2) the period elongation effects associated with inelastic response; and (3) the shorter period effects associated with higher modes response. The observations regarding period range for scaling in the seven editions of the ASCE 7 Standard are summarized below.

1. ***Expanding the lower and upper limits of the period range.*** The typical period range for horizontal ground motion scaling are $0.2T$ to $1.5T$ and $0.5\ T_D$ to $1.25\ T_M$, respectively; where T is the primary period of the structure and T_D and T_M are the effective periods of the structures with damping system at the design and maximum displacements, respectively. Experience has shown that the higher modes effects generate a significant response for tall buildings, long-period structures, and isolated superstructures. Accordingly, in the ASCE/SEI 7-22, for all structure types the lower limit should extra capture the periods achieved for 90% mass participation in both directions of the building ($T_{m90\%}$). In addition, larger inelastic response can be expected at the MCE_R ground motion level, hence the upper limit period is increased to $2.0T$ and $2.0T_M$ for building structures and structures with damping system, respectively; however, the upper limit period is remained $1.25T_M$ for seismically isolated structures due to the less nonlinearity is expected.
2. ***Considering the uncertainty in fundamental period.*** Since the ASCE/SEI 7-16, the structural primary period should be selected as the smallest and largest first-mode periods (T_{1L} and T_{1H}), to determine the lower and upper limit periods, respectively. Especially for seismically isolated structures, the smallest and largest effective periods (T_{ML} and T_{MH}) have to be determined using the maximum and minimum isolation system properties, respectively, which is used to account for variation of the nominal design parameters such as effective stiffness.
3. ***Including the period range for vertical component.*** When vertical response is considered, the lower limit period is selected as the larger of 0.1 seconds or the smallest period including significant mass participation (T_{vL}); the upper limit period is $2.0T_v$ obscurely; where T_v is the primary structural vertical period.

Ground Motions Orientation and Application

The structural analysis results are highly depended on the orientation of the two horizontal ground motion components. Unfortunately, the record orientation is unpredictable due to the complexity of the seismic source, seismic wave transmission, and site effects. In most engineering practices, the pairs of horizontal recorded ground motions are treated as a random event and then directly applied to the building's orthogonal orientation without rotating. However, when sites located close to the faults which have potential for inducing large-magnitude earthquakes, the ground motions perpendicular to the fault can be stronger than that parallel to the fault caused by large velocity pulse, especially site-to-

fault distance within 5 km (Huang *et al*., 2009). Therefor, for near-fault sites, the recorded ground motion components should be rotated to the fault-normal (FN) and fault-parallel (FP) directions and applied to corresponding orientations of the structure.

Table 2 summarizes the ground motion requirements regarding orientation and application. In the ASCE/SEI 7-10, the initial criteria required the orientation of all records of near-fault sites, and the lower limit of average of all FN spectra ($FnSA_{avg}$). Then the ASCE/SEI 7-16 added the specific definitions of near-fault sites, and the constraint on spectral shape similarity for sites that are not near-fault (far-fault sites), which the average of the recorded component spectra in each direction ($UniSA_{avg}$) is with in ±10% of the average of the all recorded component spectra ($BiSA_{avg}$). The ASCE/SEI 7-22 changes that orientation is only needed for the records of a nearby fault source.

As shown in Table 2, currently the requirements of ground motions orientation and application are united to all structures types. For checking whether the site is classified as near-fault site, it may be inconvenient to collect the fault parameters regarding geometries, activities, and potential magnitudes in practices.

Table 2. Summary of ground motion requirements regarding orientation and application

Edition of ASCE 7	ASCE/SEI 7-10 (2013)	ASCE/SEI 7-16 (2017)	ASCE/SEI 7-22 (2022)
Building Structures	· **Definition of near-fault sites:** $R_x \le 5$ km · **For near-fault sites:** (1) rotating to FN and FP directions for all motions; (2) $FnSA_{avg} \ge MCE_R$ within the period range from 0.2T to 1.5T	· **Definition of near-fault sites:** (1) $R_x \le 15$ km & $M_w \ge 7.0$, or $R_x \le 10$ km & $M_w \ge 6.0$; (2) net slip rate ≥ 1 mm/yr; and (3) $R_x = 0$ defined as the portion of the surface projection of the fault depth ≤ 10 km · **For near-fault sites:** (1) rotating to FN and FP directions for ALL motions and applying all motions to building in such orientations · **For far-fault sites:** (1) applying all motions to building's orthogonal orientations; (2) $0.9\times BiSA_{avg} \le UniSA_{avg} \le 1.1\times BiSA_{avg}$, within the period range from $\min\{T_{m90\%}, 0.2T_{1L}\}$ to $2.0T_{1H}$	· **Definition of near-fault sites:** (1) $R_x \le 15$ km & $M_w \ge 7.0$, or $R_x \le 10$ km & $6.0 \le M_w < 7.0$; (2) net slip rate ≥ 1 mm/yr; and (3) $R_x = 0$ defined as the portion of the surface projection of the fault depth ≤ 10 km · **For near-fault sites:** (1) rotating to FN and FP directions ONLY for the near-fault motions and applying these motions to building in such orientations; (2) according to the far-fault sites requirements for the OTHER motions · **For far-fault sites:** (1) applying all motions to building's orthogonal; (2) $0.9\times BiSA_{avg} \le UniSA_{avg} \le 1.1\times BiSA_{avg}$, within the period range from $\min\{T_{m90\%}, 0.2T_{1L}\}$ to $2.0T_{1H}$
Seismically Isolated Structures	· Same as building structures, except that the period range replacing as $0.5T_D$ to $1.25T_M$	· **Definition of near-fault sites:** $R_x \le 5$ km · **For near-fault sites:** (1) rotating to FN and FP directions for all motions; (2) $FnSA_{avg} \ge MCE_R$ and $FpSA_{avg} \ge 0.5\times MCE_R$, within the period range from $0.2T_M$ to $1.25T_M$	· Same as building structures, except that the period range replacing as $\min\{T_{m90\%}, T_{fb}\}$ to $1.25T_{ML}$
Structures with Damping System	· Same as building structures, except that the period range replacing as $0.5T_{1D}$ to $1.25T_{1M}$	· Same as seismically isolated structures, except that the period range replacing as $0.2T_{1D}$ to $1.25T_{1M}$ · **For far-fault sites:** (1) applying all motions to building's orthogonal orientations; (2) $0.9\times BiSA_{avg} \le UniSA_{avg} \le 1.1\times BiSA_{avg}$, within the period range from $0.2T_{1D}$ to $1.25T_{1M}$	· Same as building structures, except that the period range replacing as $\min\{T_{m90\%}, 0.2T_{1DL}\}$ to $2.0T_{1MH}$

CONCLUSIONS AND CURRENT PRACTICES IN TAIWAN

In this study, the recorded ground motion selecting, scaling, and orienting procedures for nonlinear response analysis are overall discussed and compared, which is focused on the seven editions of the ASCE 7 Standard and the three structure types including building structures and structures with isolation or damping system. Table 1 and 2 summarize the key requirements of these procedures.

ASCE 7 Standard gradually has consistent requirements, still the provisions in vertical ground motions and period range limits could be more detailed and clear for practices. For the current ASCE/SEI 7-22, the design basis spectra are constructed as the risk-based MCE_R with horizontal and vertical components; the input ground motions are required for the maximum direction spectra and a suit of 11 pairs or triplets; the amplitude scaling procedures include the lower limit RTR and period range for horizontal and vertical components; the records orientation and application are required for near-fault and far-fault sites. These development work of input ground motions can be assisted by PEER Ground Motion Database, ASCE 7 Hazard Tool, and other commercial programs.

In Taiwan, the 2022 edition of Taiwan Building Code (TBC) basically specifies the same requirements of ground motion selecting and scaling for the above-mentioned three structure types, which includes: (1) no fewer than 3 horizontal recorded ground motions (spectrum type and history component are not clearly defined); (2) the period range from 0.2*T* to 1.5*T* (*T* is for the direction under consideration); (3) the lower limit RTR is 0.9 for each ground motion (unreasonable requirement); and (4) the average of scaled recorded spectra shall not fall below the target spectrum (contradiction with previous criterion). Lately, a website of Input Motion Selection for Taiwan (INMOST) with user-friendly features has been launched by the National Center for Research on Earthquake Engineering (NCREE) to provide proper recorded ground motions with similar spectral shapes to target spectra as well as useful parameters regarding seismic sources, strong-motion stations, and ground motions (Liu *et al.*, 2022). For next TBC edition, we suggest that the revised ground motion criteria for response history analysis should aim at clear definitions, practical scaling procedures, and near-fault motions orientation.

REFERENCES

Ancheta, T.D., R.B. Darragh, J.P. Stewart, E. Seyhan, W.J. Silva, B.S.J. Chiou, K.E. Wooddell, R.W. Graves, A.R. Kottke, D.M. Boore, T. Kishida, and J.L. Donahue (2013). *PEER NGA-West2 Database*, Pacific Earthquake Engineering Research Center, Berkeley, CA.

ANSI/ASCE 7-95 (1996). *Minimum Design Loads for Buildings and Other Structures*, American Society of Civil Engineers, Reston, Virginia.

ASCE 7-98 (2000). *Minimum Design Loads for Buildings and Other Structures*, American Society of Civil Engineers, Reston, Virginia.

ASCE/SEI 7-05 (2005). *Minimum Design Loads for Buildings and Other Structures*, American Society of Civil Engineers, Reston, Virginia.

ASCE/SEI 7-10 (2013). *Minimum Design Loads for Buildings and Other Structures*, American Society of Civil Engineers, Reston, Virginia.

ASCE/SEI 7-16 (2017). *Minimum Design Loads and Associated Criteria for Buildings and Other Structures*, American Society of Civil Engineers, Reston, Virginia.

ASCE/SEI 7-22 (2022). *Minimum Design Loads and Associated Criteria for Buildings and Other Structures*, American Society of Civil Engineers, Reston, Virginia.

Boore, D.M. (2010). "Orientation-Independent, Nongeometric-Mean Measures of Seismic Intensity from Two Horizontal Components of Motion," *Bull. Seism. Soc. Am.*, **100**(4), 1830-1835.

Bozorgnia, Y. and K.W. Campbell (2004). "The Vertical-to-Horizontal Response Spectral Ratio and Tentative Procedures for Developing Simplified V/H and Vertical Design Spectra," *J. Earthq. Eng.*, **5**(8), 175-207.

CPAMI (2022). *Seismic Design Specifications and Commentary of Buildings*, Construction and Planning Agency, Ministry of the Interior, Taiwan. (In Chinese)

FEMA 222A (1995). *NEHRP Recommended Seismic Provisions for Seismic Regulations for New Buildings: Prat 1 - Provisions*, 1994 Edition, Federal Emergency Management Agency, Washington, D.C.

FEMA 223A (1995). *NEHRP Recommended Seismic Provisions for Seismic Regulations for New Buildings: Prat 2 - Commentary*, 1994 Edition, Federal Emergency Management Agency, Washington, D.C.

FEMA P-750 (2009). *NEHRP Recommended Seismic Provisions for New Buildings and Other Structures*, 2009 Edition, Federal Emergency Management Agency, Washington, D.C.

Goulet, C.A., T. Kishida, T.D. Ancheta, C.H. Cramer, R.B. Darragh, W.J. Silva, Y.M.A. Hashash, J. Harmon, J.P. Stewart, K.E. Wooddell, and R.R. Youngs (2014). *PEER NGA-East Database*, Pacific Earthquake Engineering Research Center, Berkeley, CA.

Huang, Y.N., A.S. Whittaker, and N. Luco (2009). "Orientation of Maximum Spectral Demand in the Near-Fault Region," *Earthq. Spectra*, **25**(3), 707-717.

Liu, H.J., X.M. Lu, and W.Y. Jean (2022). *Platform of Input Motion Selection for Taiwan (INMOST)*, 2021 NCREE Research Programs and Accomplishments, 173-176.

NUREG-75/087 (1975). *Standard Review Plan for the Review of Safety Analysis Reports for Nuclear Power Plants*, LWR Edition, U. S. Nuclear Regulatory Commission, Washington, D.C.

SEAOC Seismology Committee (1990). *Recommended Lateral Force Requirements and Commentary*, Fifth Edition, Structural Engineers Association of California, Sacramento, CA.

SEI/ASCE 7-02 (2003). *Minimum Design Loads for Buildings and Other Structures*, American Society of Civil Engineers, Reston, Virginia.

VERTICAL DISPLACEMENT AND STRAIN MEASUREMENTS OF RC WALLS USING FIBER-OPTIC SENSORS AND CONVENTIONAL INSTRUMENTATION

Ryan D. Hoult[1], Alex Bertholet[2], and João Pacheco de Almeida[3]

1. Postdoctoral Researcher, Institute of Mechanics, Materials and Civil Engineering, UCLouvain, Louvain-la-Neuve, Belgium.
2. Technical Project Manager, LEMSC, Institute of Mechanics, Materials and Civil Engineering, UCLouvain, Louvain-la-Neuve, Belgium.
3. Professor, Institute of Mechanics, Materials and Civil Engineering, UCLouvain, Louvain-la-Neuve, Belgium.

Email: ryan.hoult@uclouvain, alex.bertholet@uclouvain.be, joao.almeida@uclouvain.be

ABSTRACT

High resolution, distributed reinforcement strain measurements can provide invaluable information for developing and evaluating numerical and analytical models of reinforced concrete structures. An ongoing testing campaign in the iMMC institute at UCLouvain, Belgium, is employing fibre optic sensors along several longitudinal rebars in three reinforced concrete U-shaped wall specimens. To the knowledge of the authors, this is the first example where distributed fibre optic sensors are used to measure the longitudinal strain profiles in reinforcement embedded in structural walls and to such a high resolution. This paper presents some of the preliminary results from two of the tested wall units, which include the vertical strain and displacement distributions. The strains and displacements are compared to other more common instrumentation used in the tests, including the linear variable differential transformers (LVDTs). The strain penetration length into the foundation is estimated using the strain and displacements derived from the two types of instrumentation used. This state-of-the-art measurement technique has the potential to help solving many long-standing questions on RC member response and quantifying phenomena that are currently only known qualitatively.

Keywords: optical fibre, reinforced concrete, core walls, U-shaped, yield penetration

INTRODUCTION

The ability to measure the entire reinforcement strain profile within reinforced concrete (RC) structures has the potential to help solving many long-standing questions on the mechanisms involved in their response and quantify different phenomena that are currently only known qualitatively. Until recently, many “spot sensors”, such as strain gauges, were required to be used along the length of the rebar to derive the strain profile, a time consuming and costly exercise. For example, an investigation on tension stiffening effects installed 84 strain gauges within a single longitudinal reinforcing bar (Scott & Gill, 1987). Strain gauges also impose other limitations, including an alteration of the characteristic behaviour of the reinforcing steel, as well as affecting the bond performance to the surrounding concrete (Mata-Falcón *et al.*, 2020). Alternatively, meshes of light-emitting diodes (LEDs) for camera tracking have also been glued at regular spacing to steel rebars in concrete holes left during the casting phase (Tarquini *et al.*, 2019). Recent technological improvements to Distributed Fibre Optic Sensors (DFOS) have the potential to measure the full strain profile of steel reinforcement embedded in concrete structures. When the fibres, acting as the sensor, are subjected to an extension or contraction, the frequency of the backscattered light is altered due to the change in distance between the imperfections caused in the cylindrical geometry of the fibres (Malek *et al.*, 2019). A measurement system, known as an interrogator, is then able to analyse the characteristics of the backscattered light and provide strain data. A more complete and detailed explanation of this process can be found in the literature (Bado & Casas, 2021; Zhang *et al.*, 2022). Some of the unique features of DFOS include, but are not limited to, its high

accuracy (e.g., ±25 με), repeatability, stability, resistance to electromagnetic interference, protection from corrosion, light mass, small size (e.g., diameter of 125 μm), and low cost (Malek *et al.*, 2019).
Despite recent advances in the last decade, the application of DFOS in RC structures is still in its infancy (Zhang *et al.*, 2022). However, there has been some recent research using DFOS embedded in RC structures (Malek *et al.*, 2019; Zdanowicz *et al.*, 2022; Zhang *et al.*, 2022). To the authors knowledge, only one experimental investigation used DFOS in RC walls. In the study by Woods *et al.* (2017), DFOS was bonded to the surface of the outermost layer of carbon fiber reinforced polymer to measure the strain distribution over the entire face of the strengthened RC wall. No experimental investigation using DFOS bonded to the longitudinal reinforcing steel in RC walls has been found.
In this paper, a summary is provided of an ongoing experimental campaign the Université catholique de Louvain (UCLouvain), Belgium, in the technological platform LEMSC (Laboratoire Essais Mécaniques, Structures et Génie Civil) of the Institute of Mechanics, Materials and Civil Engineering (iMMC). The experimental program involved testing three large-scale RC U-shaped walls subjected to different combinations of flexure and torsion. State-of-the-art technology, based on the DFOS system, was used to capture the strain profiles along the entire length of several longitudinal reinforcing bars in each wall unit. The authors will herein present some of the experimental observations obtained thus far, with a direct comparison between the strains and displacements from the DFOS system and those obtained by more conventional instrumentation, namely linear variable differential transformers (LVDTs). The authors are currently preparing to submit a paper manuscript that will provide a more extensive set of experimental results and findings, including additionally comparisons with micrometres and digital image correlation techniques. For the sake of brevity, in this conference paper, only one channel of the DFOS system, which reads the strain data from longitudinal bars located in the boundary end of the wall West flange (see next section), will be used to compare against the measurements from an array of LVDTs. An introductory general summary of the experimental program and some of the instrumentation used is given in the next section.

SUMMARY OF EXPERIMENTS AND INSTRUMENTATION

Two of the three wall units in the test programme are presented in this paper: wall units UW1 and UW2 are half-scale specimens of a 6-story prototype core wall. The test specimens correspond to approximately 1.5 stories, where an overturning moment was applied to the collar (i.e., head) of test specimen UW1 to increase the shear span to one characteristic of a 6-storey building. The U-shaped wall test specimens have a thickness (t_w) of 100 mm, web length (L_w) of 1300 mm, and flange length (L_f) of 1050 mm. The geometry with reinforcement detailing is illustrated in Figure 1a, and the elevation view of the test specimen is given in Figure 1b.

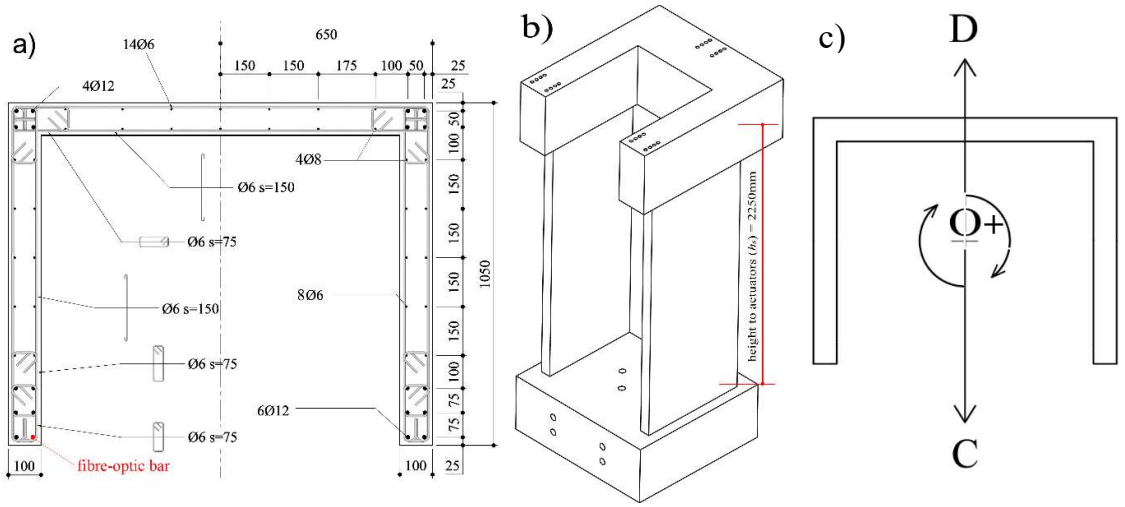

Figure 1. (a) Cross-section and reinforcement detailing of the wall specimens and (b) elevation view (c) loading positions of the wall

Ductile Class C reinforcing steel was used for the longitudinal and transverse reinforcement in the wall in accordance with Eurocode 8 (CEN, 2004). The corresponding mechanical properties of the rebars used in the wall units are given in Table 1.

Table 1. Mechanical properties of the Class C (CEN, 2004) bars used in the U-shaped wall units

d_{bl}	f_y	f_u	ε_{sy}	ε_{su}	E_s
[mm]	[MPa]	[MPa]	[mm/m]	[mm/m]	[GPa]
6	550	676	2.7	9.5	207
8	538	664	2.7	12.0	196
12	580	690	2.9	10.1	199

Specimen UW1 was loaded parallel to the flanges in the north-south direction (according to the cardinal points in Figure 1a). Two wall positions, C and D (Figure 1c), correspond to bending about the minor axis (i.e., parallel to the flanges) with web in tension and web in compression, respectively. Unit UW2 was subjected to pure torsion by applying a rotation from the two horizontal actuators located at 2.25m above the foundation of the wall. The authors have defined the rotational positions as O+ and O-, as depicted in Figure 1c (i.e., a positive twist is defined as a clockwise rotation). A constant axial load ratio (*ALR*) of 5% was subjected to both units prior to the flexural or torsional loading.

For the sake of brevity, the focus of the discussion on the instrumentation will be limited to the information needed for the results provided in this brief paper. For complete information on all the instrumentation used, see Hoult *et al.* (2022). The DFOS was implemented using the ODiSI 6000 Series sensing platform (Luna Innovation Inc). Four fibre-optics were attached to a total of eight longitudinal reinforcing bars in each wall unit to investigate the strain profile in the core of the wall. For this paper, the focus is on the strain and displacement measurements from channel 4 of the DFOS system (see Figure 2a), and on the innermost longitudinal rebar (d_{bl}=12mm) in the West flange boundary end, as indicated in Figure 1a. A polyimide coated, single-mode sensing fibre housed in polytetrafluoroethylene tubing was used. A small groove (i.e., slit of 1 mm width and depth) was cut along the longitudinal ribs of the rebar, which has been widely practiced in previous research for attaching the DFOS to steel reinforcement and to help prevent a premature failure of the fibre (Bado *et al.*, 2020; Michou *et al.*, 2015; Quiertant *et al.*, 2012; Zdanowicz *et al.*, 2022; Zhang *et al.*, 2021). A general-purpose adhesive (cyanoacrylate) was used to bond the fibre into the grove of the bar, which has also been successfully used in the literature for this purpose (Barrias *et al.*, 2018; Berrocal *et al.*, 2021; Brault & Hoult, 2019; Zdanowicz *et al.*, 2022). An epoxy was also used to provide a coating of further protection between the glued-fibre and the concrete. To compare with the DFOS measurements, an array of LVDTs attached to the West flange boundary end (Figure 2b) will be used (i.e., LVDTs 50A, 50B, 10A, 10C, 5A in Figure 2b). The location of the DFOS and the array of LVDTs provides a specific opportunity to make comparisons between the strain and displacement measurements of each system.

In comparison to the DFOS measurements at the base, the LVDT at the base (i.e., 50A in Figure 2b) is likely to provide a larger strain reading over its gauge length unless a strain penetration length (L_{sp}) into the foundation is considered to this gauging length. Thus, an estimate of the L_{sp} into the foundation is required. It is herein calculated with Equation 1, which uses both the displacement reading Δ_{LVDT} from the 50A base LVDT and the average of the strains measured by the DFOS system ($\varepsilon_{DFOS.avg}$) over the gauge length of such LVDT (l_{LVDT} = 450mm). If the information from both the LVDTs and the DFOS was not available, a more general empirical expression for L_{sp} would need to be employed, e.g. Priestley *et al.* (2007). The calculation of L_{sp} using Equation 1 will necessarily provide different values for different imposed displacements or twists. Furthermore, the base LVDT reading will be omitted from the comparisons to the DFOS for the obvious reasons stated above.

$$L_{sp} = \frac{\Delta_{LVDT}}{\varepsilon_{DFOS.avg}} - l_{LVDT} \quad (1)$$

The calculated L_{sp}, using Equation 1, for each level of drift or rotation considered here also provides an opportunity to compare the values with the expressions previously proposed by other researchers.

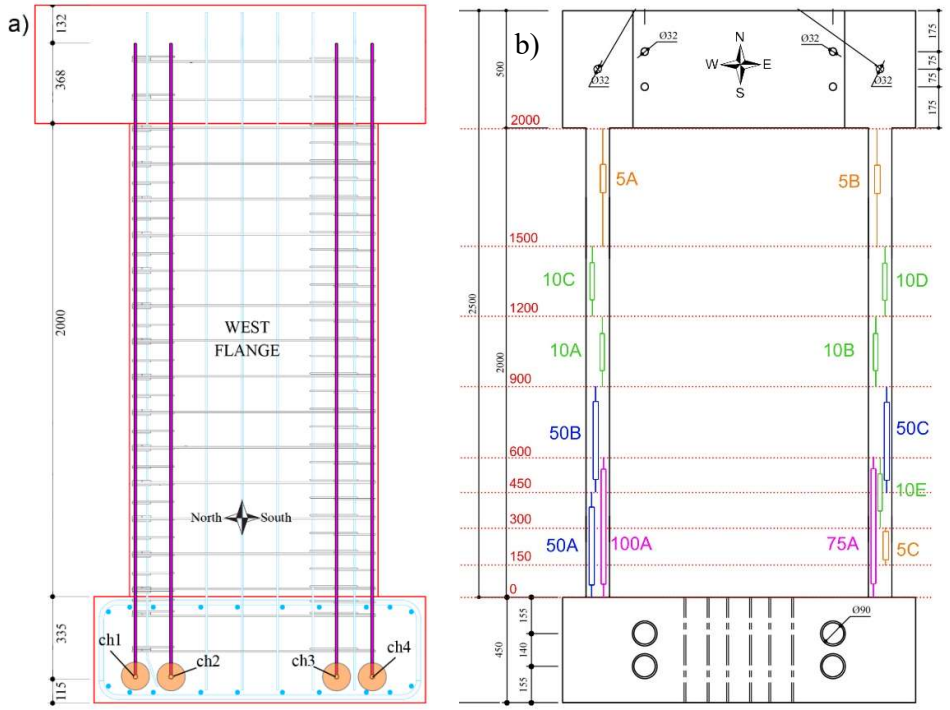

Figure 2. (a) Elevation view of the West flange with fibre-optics installed on the longitudinal reinforcing bars (purple, full opacity bars) (b) chain of LVDTs installed on the flange boundary ends

STRAIN AND DISPLACEMENT FROM FIBER-OPTIC AND LVDTS

The strain profiles determined from the LVDTs and measured from the DFOS system for wall units UW1 and UW2 are presented in Figure 3. To emphasise, these are the strain values in the West flange boundary end of the two wall units and for a limited value of drift levels. It was found that the DFOS measurements became unreliable once the bars behave inelastically (i.e., for strains greater than approximately 2.7 mm/m), corroborating other research (Brault & Hoult, 2019; Zdanowicz *et al.*, 2022; Zhang *et al.*, 2022).

For wall unit UW1 (Figure 3a), which was subjected to pure flexure, a reasonably good match between the DFOS strain measurements and the strains calculated using the LVDT displacement s is achieved. For larger levels of drift (δ), the highest located LVDT (5A in Figure 2b) gives larger strain estimates compared to the DFOS measurements in this region. It is possible that the steel rebar strains into the collar of the wall (i.e., the strain penetration into the collar), which are not presented in Figure 3a, are contributing to the displacement recorded by this LVDT. Local strain peaks can be observed up the wall height, as measured by the DFOS system, which correspond to the spacing of the stirrups (≈75mm) – substantiating previous observations of DFOS installed in beams (Zhang *et al.*, 2022).

In contrast to the comparisons for UW1, the calculated strains from the LVDTs for wall unit UW2 (Figure 3b), which was subjected to pure torsion, is more poorly correlated with the measured strains by the DFOS system. This observation applies particularly higher up the wall than at the base – although, to emphasise, the base strains from the LVDTs have been manipulated to give a good match to the DFOS measurements using a calculated L_{sp} (i.e., see previous section and Equation 1). An obvious reason for this poor correlation higher up the wall could simply be the difference in locations of the LVDTs in comparison to the DFOS embedded in the wall, if one recalls the existence of a cover of approximately 25 mm in both transversal directions. This could emphasise the importance of surface instrumentation placement during testing of experimental specimens, which could in turn be dependent on the type of applied loading. Furthermore, the strain gradient is more inclined for UW2 (Figure 3b) than UW1 (Figure 3a) because of the overturning moment applied to UW1 to increase its shear span; this could not

be applied to UW2 with pure torsion. Also observe that, although the torsional load was applied to UW2 at a height of 2.7 m above the strong floor (i.e., 2.25 m above the foundation), it appears that a bi-moment exists at the head of the wall resulting in negative strains at a height above the foundation of approximately 1.5 m (Figure 3b). This was unexpected; under idealized conditions, the tensile strain gradient was expected to converge to zero at the height of the load application. Instead, this height has been significantly reduced (≈30%), which in turn has increased the expected torque demand.

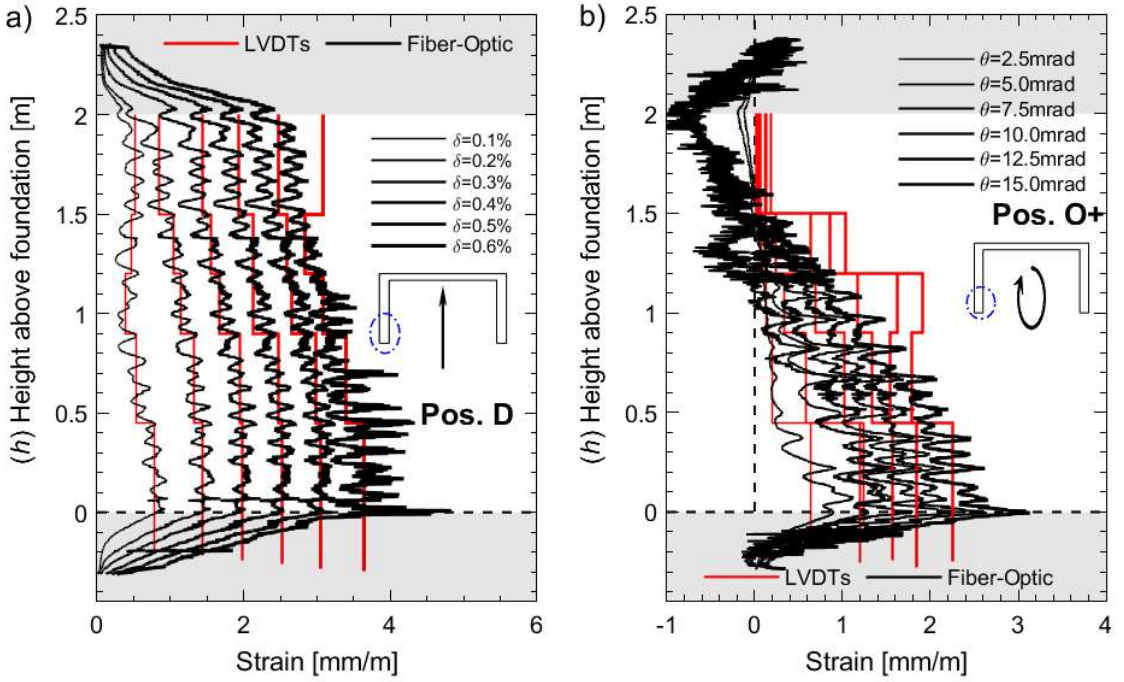

Figure 3. Strain profiles as measured by the DFOS system (solid black) and as calculated by the LVDTs (solid red) (a) wall unit UW1 and (b) wall unit UW2. The shaded-grey regions represent the foundation and collar (head) of the wall units.

Using the strain measurements from the DFOS, the vertical displacement of the rebar can be calculated and compared to the measurements of the LVDTs, which are presented in Figure 4. For these calculations, the L_{sp} was not considered for the base LVDT gauge length. For both wall units UW1 and UW2, the vertical displacement measured by the LVDTs are greater than the calculated displacement of the longitudinal rebar using the DFOS strain measurements. This is particularly visible for wall unit UW2 (Figure 4b), where the maximum displacement measured by the LVDTs at the top of the wall ranged between 30% to 80% greater than the calculated DFOS displacement values. In fact, the shape of the vertical displacement profiles in Figure 4b are different between each of the instrumentation used. A bend can be observed at the top of the wall for the displacement calculated with the DFOS, which is a result of the negative strain values measured in this region, as mentioned above. This is not present in the displacement from the LVDTs, which measured the concrete surface displacement rather than the direct bar displacement.

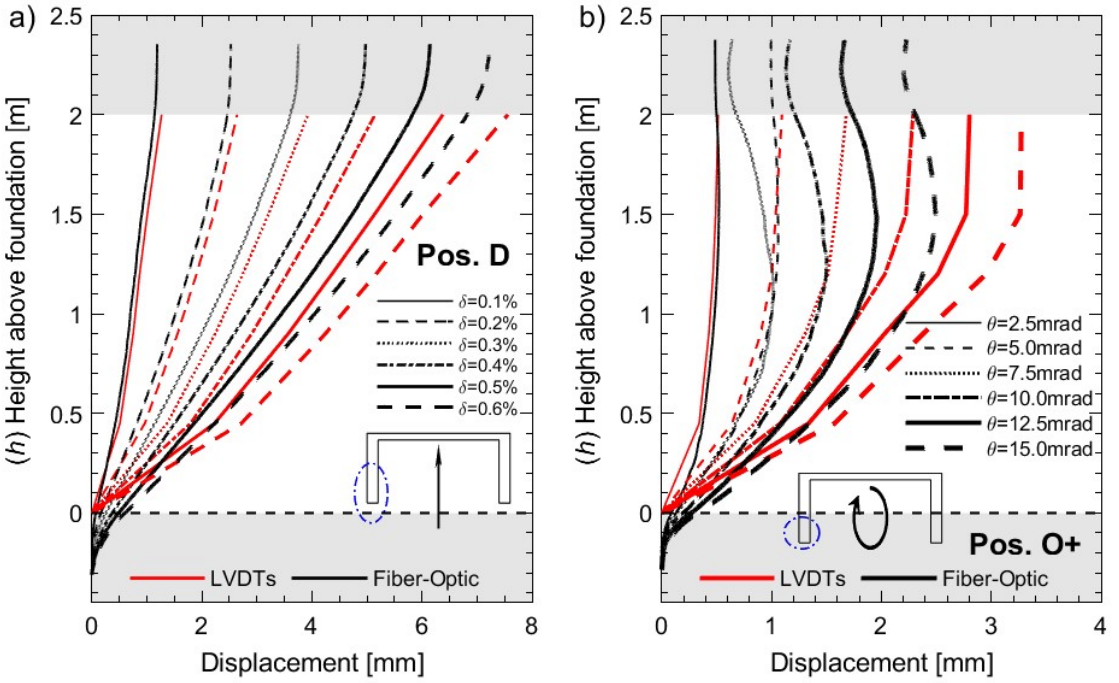

Figure 4. Vertical displacement profiles as calculated from the DFOS strains (black lines) and as measured by the LVDTs (red lines) (a) wall unit UW1 and (b) wall unit UW2. The shaded-grey regions represent the foundation and collar (head) of the wall units.

The strain penetration (L_{sp}) values calculated using Equation 1 are presented in Table 2. These values were used to modify the strain calculations for the base LVDT to include the displacement measured into the foundation. In general, the L_{sp} values appear to increase as a function of the drift imposed, or as the strain in the foundation increases, which is particularly true for the values obtained for unit UW1. The average L_{sp} of all values listed in Table 1 is 222 mm.

Table 2. Strain penetration lengths (L_{sp})

Unit	Position	Drift (%)	Rotation (mrad)	d_{bl} (mm)	L_{sp} (mm)
UW1	D	0.1	-	12	200.55
UW1	D	0.2	-	12	216.63
UW1	D	0.3	-	12	241.08
UW1	D	0.4	-	12	260.13
UW1	D	0.5	-	12	282.08
UW1	D	0.6	-	12	297.44
UW2	O+	-	2.5	12	88.44
UW2	O+	-	5.0	12	69.21
UW2	O+	-	7.5	12	252.80
UW2	O+	-	10.0	12	239.33
UW2	O+	-	12.5	12	276.95
UW2	O+	-	15.0	12	246.73
				AVG:	222.62

Deriving the L_{sp} from a combination of the LVDT and DFOS measurements gives a unique opportunity to compare the experimental values to some of the expressions in the literature. Priestley *et al*. (2007) presented Equation 2 for estimating the strain penetration length (L_{sp}).

$$L_{sp} = 0.022 f_y d_{bl} \quad (2)$$

where f_y is the yield strength of the reinforcing steel and d_{bl} is the diameter of the longitudinal reinforcing steel. These values can be obtained from Table 1.

Sezen and Moehle (2004) proposed Equation 3 for the elastic L_{sp} of limited-ductile RC columns assuming a uniform bond stress.

$$L_{sp} = \frac{f_y d_{bl}}{4\sqrt{f'_c}} \quad (3)$$

where f'_c is the concrete strength (≈38 MPa for units UW1 and UW2).

Table 3 presents the two L_{sp} values calculated using Equation 2 and 3. The value determined from Priestley *et al*. (2007) provides a somewhat conservative value in comparison to those determined experimentally in Table 2. On the other hand, the value from Sezen and Moehle (2004) is estimated to be larger than those values determined experimentally. However, it is worth emphasising that Equation 3 was derived for limited-ductile columns and not ductile RC walls. Despite subsequent yielding into the foundation contributing to the overall displacement capacity of these structures, there has been little research on the strain and yield penetration length of RC walls. One reason for this, until now, was the technological limitation in deriving strain profiles of rebars embedded in concrete elements. The DFOS system can currently overcome such difficulties and provide insights into this phenomenon, as well as others. Therefore, it would be worth if future studies focus on the strain and yield penetration lengths of rebar embedded in concrete structures using this technology.

Table 3. Calculated elastic strain penetration lengths ($L_{sp.elastic}$)

Authors	Equation	$L_{sp.elastic}$ (mm)
Priestley and Paulay (2002)	2	153.12
Sezen and Moehle (2004)	3	282.27

CONCLUSIONS

A recent experimental program used Distributed Fibre Optic Sensors (DFOS) embedded in reinforced concrete walls subjected to different loading protocols, to measure the strain profiles of the reinforcing steel. This paper showed and discussed the differences between surface and rebar strain measurements in a flange of such RC walls. This is important, considering that the large majority of previous experimental tests on RC walls have relied on surface measurements for salient engineering parameters, such as base strains and strain profiles. Thus, DFOS has the potential of providing further insights on many long-standing questions on the response of RC structures. A small example was provided in this paper, where the strain penetration length was calculated based on both DFOS and LVDT measurements. To the authors knowledge, the L_{sp} of steel reinforcement into the foundation of RC walls has never been quantified to such a high-resolution due to the difficulty in measuring the strain profile below the walls' surface. The authors plan to submit soon a journal paper, which will present more results from the DFOS system implemented in these RC wall tests, including additionally comparisons to digital image correlation measurements.

ACKNOWLEDGMENTS

This work was supported by the Fonds de la Recherche Scientifique – FNRS under Grant nº F.4501.21.

REFERENCES

Bado, M. F., & Casas, J. R. (2021). "A Review of Recent Distributed Optical Fiber Sensors Applications for Civil Engineering Structural Health Monitoring," *Sensors,* **21**(5).

Bado, M. F., Casas, J. R., Dey, A., & Berrocal, C. G. (2020). "Distributed Optical Fiber Sensing Bonding Techniques Performance for Embedment inside Reinforced Concrete Structures," *Sensors,* **20**(20), 5788.

Barrias, A., Casas, J. R., & Villalba, S. (2018). "Embedded Distributed Optical Fiber Sensors in Reinforced Concrete Structures—A Case Study," *Sensors,* **18**(4), 980.

Berrocal, C. G., Fernandez, I., & Rempling, R. (2021). "Crack monitoring in reinforced concrete beams by distributed optical fiber sensors," *Structure and Infrastructure Engineering,* **17**(1), 124-139.

Brault, A., & Hoult, N., A. (2019). "Distributed Reinforcement Strains: Measurement and Application," *ACI Structural Journal,* **116**(4)

Hoult, R., Doneux, C., & Almeida, J. P. d. (2022). "Data Paper: Tests on Reinforced Concrete U-shaped Walls Subjected to Torsion and Flexure," *Submitted to Earthquake Spectra*.

Malek, A., Scott, A., Pampanin, S., & Hoult, N. A. (2019). "Postyield Bond Deterioration and Damage Assessment of RC Beams Using Distributed Fiber-Optic Strain Sensing System," *Journal of Structural Engineering,* **145**(4), 04019007.

Mata-Falcón, J., Haefliger, S., Lee, M., Galkovski, T., & Gehri, N. (2020). "Combined application of distributed fibre optical and digital image correlation measurements to structural concrete experiments," *Engineering Structures,* **225**.

Michou, A., Hilaire, A., Benboudjema, F., Nahas, G., Wyniecki, P., & Berthaud, Y. (2015). "Reinforcement–concrete bond behavior: Experimentation in drying conditions and meso-scale modeling," *Engineering Structures,* **101**, 570-582.

Priestley, M., & Paulay, T. (2002). "What is the stiffness of reinforced concrete walls?," *SESOC Journal,* **15**(1), 30-34.

Priestley, M. J. N., Calvi, G. M., & Kowalsky, M. J. (2007). "Displacement-based seismic design of structures," Pavia : IUSS Press : Fondazione Eucentre, 2007.

Quiertant, M., Baby, F., Khadour, A., Marchand, P., Rivillon, P., Billo, J., . . . Cordier, J. (2012, May 22-24). "Deformation monitoring of reinforcement bars with a distributed fiber optic sensor for the SHM of reinforced concrete structures," *Paper presented at the 9th International Conference on NDE in Relation to Structural Integrity for Nuclear and Pressurized Components*, Seattle, Washington, USA.

Scott, R., & Gill, P. A. (1987). "Short-term distributions of strain and bond stress along tension reinforcement," *The Structural Engineer,* **65**(2), 39-43.

Sezen, H., & Moehle, J. P. (2004). "Strength and deformation capacity of reinforced concrete columns with limited ductility," *Paper presented at the Proceedings of the 13th World Conference on Earthquake Engineering*.

Tarquini, D., Almeida. J.P., Beyer, K. (2019). "Uniaxial cyclic tests on reinforced concrete members with lap splices," *Earthquake Spectra*, **35**(2), 1023-1043.

Woods, J. E., Lau, D. T., Bao, X., & Li, W. (2017). "Measuring strain fields in FRP strengthened RC shear walls using a distributed fiber optic sensor," *Engineering Structures,* **152**.

Zdanowicz, K., Gebauer, D., Koschemann, M., Speck, K., Steinbock, O., Beckmann, B., & Marx, S. (2022). "Distributed fiber optic sensors for measuring strains of concrete, steel, and textile reinforcement: Possible fields of application," *Structural Concrete*.

Zhang, S., Liu, H., Coulibaly, A. A. S., & DeJong, M. (2021). "Fiber optic sensing of concrete cracking and rebar deformation using several types of cable," *Structural Control and Health Monitoring,* **28**(2), e2664.

Zhang, S., Liu, H., Darwish, E., Mosalam, K. M., & DeJong, M. J. (2022). "Distributed Fiber-Optic Strain Sensing of an Innovative Reinforced Concrete Beam-Column Connection," *Sensors,* **22**(10).

(3e) Practice case studies in innovative structural design

PERFORMANCE UPGRADING OF CONCRETE ENCASED STEEL COMPOSITE BEAMS

1. Yuan-Tao Weng[1] ,Min-Lang Lin[1] and Chyuan-Fong Li[2]
2. Associate Researcher, National Applied Research Laboratories, National Center for Research on Earthquake Engineering, Taipei, Taiwan, R.O.C.
3. Civil Engineer, Jiuyu Development Co., Ltd., Taichung, Taiwan, R.O.C.
Email: ytweng@narlabs.org.tw, mllin@narlabs.org.tw

ABSTRACT

Steel beam encased with concrete cover is rather common used in new constructed steel structures in Taiwan. This research conducted experiments to enhance the performance of this kind of composite beam. And how to evaluate the moment capacity of this composite beam influenced by the external concrete cover is introduced. Four improvement schemes are proposed, such as (1) steel beam flanges with expanded wings after cutting, (2) no concrete filling on both sides of steel beam webs, (3) increasing the cutting depth of steel beam flanges and (4) lengthening the trimming section of steel beam flanges. Therefore, five specimens are designed, fabricated and tested under cyclic loading tests. In this study, the flexural strength estimation and ductility improvement methods of such beams are tested and analyzed, and the contribution of the concrete cladding part of such components to the flexural strength and the simple calculation method is proposed. According to the failure mechanism, it is proposed that (1) the steel girder wing is cut with expanded wings, (2) the two sides of the steel girder web are not filled with concrete, (3) the cutting depth of the steel girder wing plate is increased, and (4) the cutting section of the steel girder wing plate is lengthened. Test results revealed that (1) the flexural strength provided by the concrete part should be properly considered when designing this type of beam member, and (2) when designing the cutting section of the steel beam flanges, at least the bending moment strength of this composite beam member must be lower than that of the other. The bending moment needs to be more than 10%, so that the section can be smoothly and obviously plastically deformed.

Keywords: steel beam with concrete cover, ductility, reduced beam section, cyclic test

INTRODUCTION

Traditional steel structures usually require fire cladding treatments such as sandblasting due to the need for fire protection. However, such fire retardant treatments are often expensive and harmful to health. In recent years, concrete is often used as the fire cladding material for steel beam members in the industry. Such steel-reinforced concrete beams (hereinafter referred to as SC beams) components can not only reduce the cost of fire cladding, but also are suitable for connecting with reinforced concrete exterior walls. Moreover, SC beams are more suitable for building structures with long beam spans because they are easier to control their serviceability. However, how to properly consider the contribution of clad concrete to member stiffness and bending moment strength for such beam members are still unclear. In addition, the reduced steel beam flange plates of the SC beams are constrained with concrete, so that the SC beams are not easy to meet strength and ductility requirements smoothly. This study presents a strengthening scheme include the use of extending steel beam flanges at the beam-to-column interface to make beam yielding prior to fractures of a welding connection, and three weakening schemes include the use of a reduced steel beam flanges near the beam-to-column interface to improve the ductility of an entire connection.

Cyclic testing was performed on five exterior moment connections. A strengthening scheme was proposed to strengthen one connection by extending steel beam flanges at the beam-to-column interface. The extending steel beam flanges are intended to help transfer some beam moments to the column because the existing beam flange welded joints could sustain modest inelastic deformation

before fracturing (AISC, 2010a; Chen at el., 1996; Chen and Tu, 2004). Three weakening schemes were proposed as: (1) no concrete filling on both sides of steel beam webs in the reduced steel beam section, (2) increasing the trimming depth of steel beam flanges and (3) lengthening the reduced beams section. This research investigated experimentally the cyclic responses of these proposed schemes to validate the performance upgrading schemes. Design procedure for each performance upgrading scheme is presented based on the test results.

DESIGN OF SC BEAMS

Flexural Strength

As Figure 1 shown, since the longitudinal reinforcements of the SC beam do no to pass through the beam-to-column connection, the strength of the longitudinal reinforcements could be neglected in calculating for the flexural capacity of the SC beams. In addition, the compressive strength of the concrete part should be included in the strength calculation properly. Therefore, the simplified full-plastic method is proposed in this study, in which the areas of the flanges and web of the steel beam are concentrated on the centerline of the flange and web respectively, as shown in Figure 1a. It is assumed that plane sections remain plane, the stress distribution of the equivalent rectangular stress block of the compressed concrete part and the steel material are all in the full-plastic state. The stress distribution of the section is shown in Figure 1b or Figure 1c. For the simplified full-plastic method, assume that the cross section of the SC beam is doubly symmetric. Assume that c is small than d_s', while the steel beam is full cross-sectional plastic, c can be calculated by force equilibrium principle. Then the flexural strength of the SC beam can be calculated if c is small than d_s'; If c is larger than d_s', the one flange of steel beam is in compression and the another flange is in tension. It can be simplified as the tension and pressure of the upper and lower flanges cancel each other, so when solving the value of c, only needs to consider the contribution of the web of the steel beam, then the flexural strength of the SC beam can be calculated; If c is equal to d_s', the web and the lower flange of the steel beam are in compression, which need to be considered when calculating the flexural strength of the SC beam. The detailed procedure of the simplified full-plastic method is as follows:

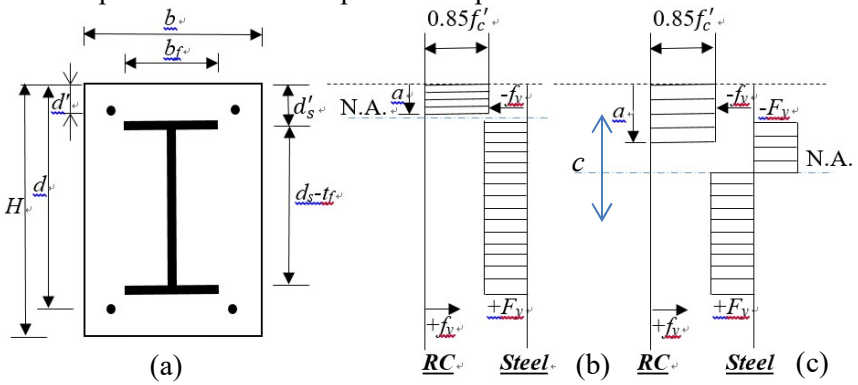

Figure 1 The simplified cross-section of SC beam and its stress distribution

(1) The neutral axis is above the upper flange of the steel beam:

As Figure 1b shown, the Eq. (1) can be obtained from the force equilibrium principle in longitudinal direction of the SC beam:

$$(A_{sb} - A'_{sb})f_y + A_{ss}F_y = 0.85f'_c ab \tag{1}$$

where A_{sb} is the cross-sectional area of the tensile steel bar; A'_{sb} is the cross-sectional area of the compression steel bar; A_{ss} is the total cross-sectional area of the steel frame; f_y is the yielding strength of the steel bar; f'_c is the compressive strength of the concrete; F_y is the yielding strength of the steel beam; b is the beam Section width; a is the depth of concrete pressure block. Then a and c can be obtained from Eq. (1) as follow:

$$a = \frac{(A_{sb}-A'_{sb})f_y+A_{ss}F_y}{0.85\ f'_c b} \tag{2a}$$

$$c = \frac{(A_{sb}-A'_{sb})f_y+A_{ss}F_y}{0.85\beta_1 f'_c b} \quad (2b)$$

where β_1 is the ratio of a to c. According to the ACI specification (2002), when $f'_c \le 280\ kg/cm^2$, β_1=0.85, and if f'_c exceeds $280\ kg/cm^2$, each increase of $70\ kg/cm^2$, the β_1 value is reduced by 0.05 and the β_1 must not be less than 0.65. If the value of c obtained by Eq. (2b) is less than or equal to d'_s, the flexural strength M of the SC beam can be calculated according to the Eq. (3):

$$M = A_{sb}f_y(d-c) + A_{ss}F_y\left(\frac{H}{2}-c\right) + 0.85\beta_1 f'_c c^2 b\left(1-\frac{\beta_1}{2}\right) + A'_{sb}f_y(c-d') \quad (3)$$

where d is the distance from the outer edge of the pressure side of the SC beam to the center of the tension steel bar (Fig. 1a); d' is the distance from the outer edge of the pressure side to the center of the compression steel bar. If the value of c obtained by Eq. (2b) is greater than d'_s, it is necessary to enter the following step (2) as follow.

(2) The neutral axis is located below the upper flange of the steel beam:

As Figure 1c shown, the Eq. (4) can be obtained from the force equilibrium principle in longitudinal direction of the SC beam:

$$(A_{sb}-A'_{sb})f_y + (A_{sst}-A_{ssc})F_y = 0.85f'_c cb \quad (4)$$

where A_{sst} and A_{ssc} are the tensile area and the compression area of the steel beam respectively, so the tension and pressure of the upper and lower flanges cancel each other, so the value of c can be solved by Eq. (5):

$$c = \frac{(A_{sb}-A'_{sb})f_y+Ht_wF_y}{2t_wF_y+0.85\beta_1 f'_c b} \quad (5)$$

where t_w is the thickness of the steel web. If the value of c obtained by Eq. (5) is larger than d'_s, the flexural strength M of the SC beam can be calculated according to the Eq. (6):

$$M = F_y\left[z - t_w\left(\frac{H}{2}-c\right)^2\right] + (A_{sb}+A'_{sb})f_y\left(\frac{d-d'}{2}\right) + 0.85\beta_1 f'_c cb\left(\frac{H-\beta_1 c}{2}\right) \quad (6)$$

where z is the plastic modulus of the steel beam. If the value of c obtained by Eq. (5) is less than d'_s, it means that the neutral axis coincides with the upper flange (c=d'_s), then proceed to step (3) for calculation.

(3) The neutral axis is located on the upper flange:

When c is equal to d'_s, that is a=$\beta_1 d'_s$, the flexural strength M of the SC beam can be calculated according to the Eq. (7):

$$M = A_{sb}f_y(d-c) + A'_{sb}f_y(c-d') + F_y(d_s-t_f)\left(A_f+\frac{A_w}{2}\right) + 0.85\beta_1 f'_c c^2 b\left(1-\frac{\beta_1}{2}\right) \quad (7)$$

where $A_w = (d_s-2t_f)t_w$ is the sectional area of the steel beam web; $A_f = b_f \times t_f$ is the sectional area of the steel beam flange, and b_f is the width of the steel beam flange.

Shear Strength

The available shear strength of SC beams is based on the web of the steel beam bearing all the shear force, and considering the shear force caused by the plastic bending moment of the beam end, then the design shear strength is calculated according to the ANSI/AISC 360-16 specification (AISC, 2010b).

Design Detailing

(1) Longitudinal reinforcement of SC beams

The upper and lower sides of the SC beam must have at least two longitudinal steel bars running through the entire length of the beam, and the tensile or compression reinforcement ratio of the SC beam must not exceed 0.025.

(2) transverse stirrups of SC beams

Diameter of tie bar shall be at least No. 3, and the minimum spacing should not be less than 75 mm. When the size of the stirrups of the beam is No. 3, the spacing should not be greater than half of the beam depth, and must be less than 250 mm. When using larger diameter stirrups, the spacing can be appropriately increased, but still not more than half of the beam depth, and must be less than 450 mm; and the minimum stirrup ratio $(r_w)_{min}$ should not be less than 0.1%, where $r_w = A_v/(bS)$, A_v is the cross-sectional area of the stirrup within the range of the spacing S.

In addition, closed stirrups must be arranged within twice the beam depth at the interface of the beam-column joint and twice the beam depth on the left and right sides where plastic hinges may occur. The first closed stirrup shall be arranged within 50 mm of the interface with the beam-column joint. The spacing between closed stirrups shall not exceed: (a) the effective depth of a quarter beam

section; (b) eight times the minimum diameter of the longitudinal reinforcement; (c) 24 times the diameter of the closed stirrups; (d) 300 mm. Where the closed stirrups do not need to be arranged, the full length of the web reinforcement should be arranged, and the spacing should not be greater than one-half the effective depth of the beam section [6].

(3) Regarding the arrangement of the net spacing between the longitudinal reinforcement and the steel beam, when the longitudinal reinforcement is parallel to the surface of the steel beam, the clear spacing shall be kept at least 25 mm, and shall not be less than 1.25 times the maximum grain size of the coarse reinforcement; when the main reinforcement is perpendicular to the surface of the steel beam, the spacing is not limited by this. The stirrups shall not be closely attached to the surface of the steel beam, and the net spacing shall be kept more than 25 mm.

(4) The minimum thickness of the concreter cover of the steel beam should take into account the needs of the configuration and construction of the reinforcement. When the steel plate is parallel to the main reinforcement, the thickness of the concrete cover of the steel beam should generally be more than 100 mm. When the size of the longitudinal bar is above No. 7, the concrete cover of the steel beam must be above 125 mm.

Design of reduced steel beam section

The intent of the reduced beam section (RBS) is to move the plastic hinge region away from the weld between the beam flanges and column. The reduced section creates a weaker location where yielding and plastic hinge formation are expected to occur. The plastic deformation of RBS moment connection comes mainly from yielding of the steel plate and avoids stress concentration on the weld. By forcing yielding to occur in the steel plate, the sensitivity of welding is relaxed and energy dissipation becomes much more reliable. The decrease of stiffness due to the tapered flange is only 3% and is considered acceptable. The proposed connection under a dynamic load also shows satisfactory energy dissipation compared to conventional design that fails from brittleness. The design of the proposed moment connection is suggested as follows. The connection details are shown in Fig. 2. Chen et al. (1996) suggested that trim the flanges so that the provided plastic moment capacity is 5-10% less than that of the demand values. Start to trim the flange at the location beyond the weld access hole (10-15 cm from the column face) and use a smooth transition area about 5~10 cm long before and after the object area. The length of the object area should be about $0.5d_s$ ~$0.8d_s$, where d_s is the steel beam depth, and d_t should be about 15 cm.

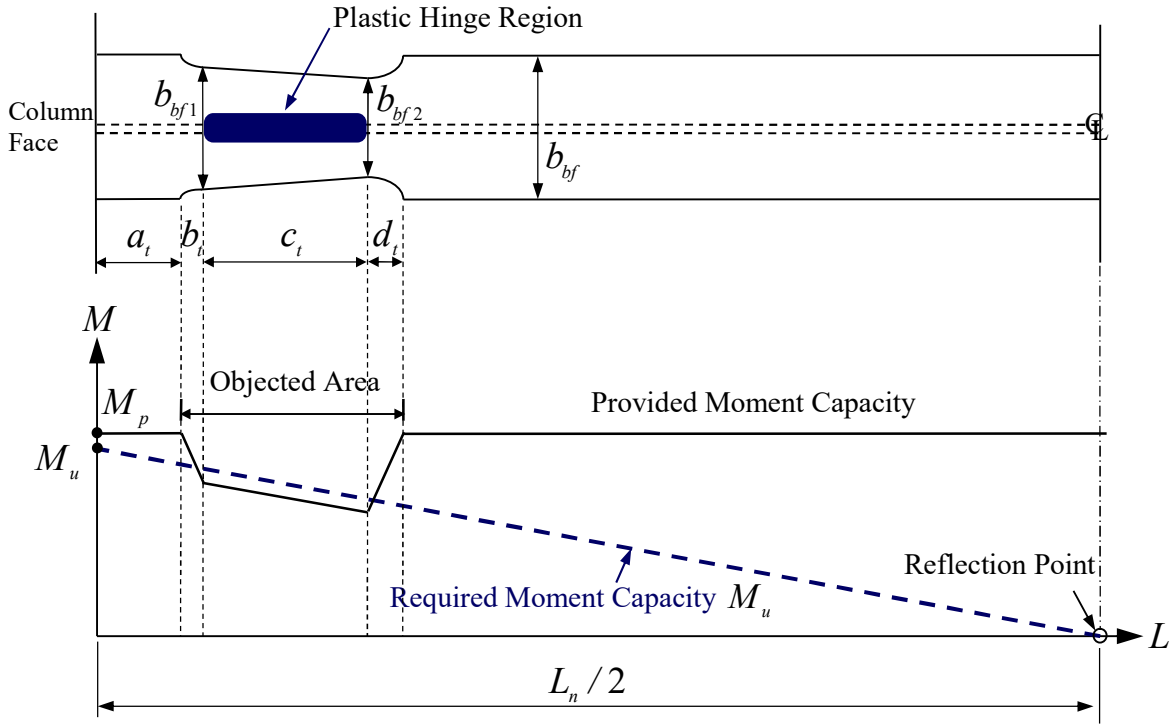

(a)

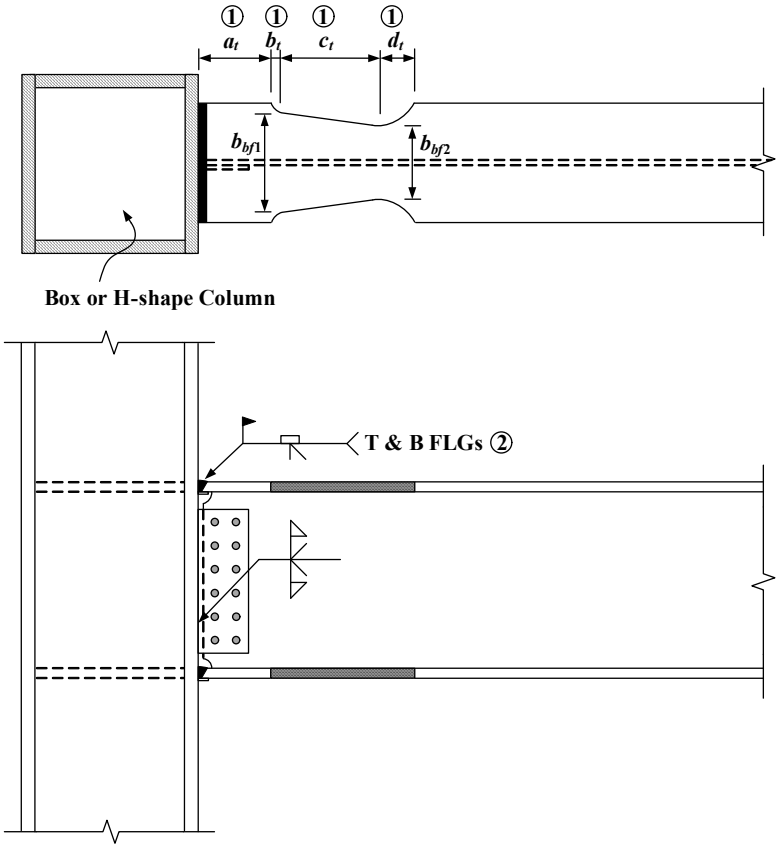

(b)

Figure 2 The detailing and geometry of the RBS connections.

Table 1. Member size of the SC beam specimens

Spec.	SC01	SC02	SC03	SC04	SC05
Steel Beam Section	BH 750x400x12x32				
$L_n/2$	3350 mm				
Beam Size	950x600				
Steel Column Size	BOX 700x700x28				
`	3600				
CFT Column Size	900x900				

EXPERIMENTAL DESCRIPTION

Connection specimens

Five specimens are designed, fabricated and tested under cyclic loading tests, each of which represented an exterior moment connection with one SC beam and one box column. Member sizes and material properties are listed in Tables 1 and 2. SN490B steel was utilized for the box columns and steel beams; All steel beams were BH 750x400x12x32, and all box columns were BOX 700x700x28. Each specimen is equipped with shear nails on the lower flange side of the steel beam with a spacing of 200 mm.

Specimen SC01 designed according to the common engineering practice and was tested as a benchmark, which the steel beam flanges are tapered according to the moment gradient so as to produce an enlarged area of plastic hinge. The moment gradient is calculated only considering the steel beam part of the SC beam. In addition, because the steel beam is surrounded by concrete, the plastic hinging did not occur in the region of the steel beam weakened in the reduced beam section

scheme that indirectly causes the maximum tensile force of the beam section to be concentrated on the steel beam near the beam-column joint. The beam flanges near the column face were damaged by tension. The cyclic loading test results of the specimen SC01 show that the plastic rotation can reach 3.99%, the unexpected tensile failure occurred on the steel beam flanges.

表 2 試體實際鋼材及混凝土強度

Specimen	Yielding strength of the steel (MPa)			the compressive strength of the concrete f'c (MPa)
	Beam Flange	Beam Web	Column	
SC01 SC04 SC05	429	409	392	23.4
SC02 SC03	366	366	370	30.9

In order to develop a method for preventing the unexpected failure occurred easily near the column face, and ensure plastic deformation can produce in the reduced steel beam flanges zone, specimen SC02 was designed using widening steel beam flanges at the beam end to increase the flexural strength of the beam may not be less than the flexural strength of the SC beam considering the compressive contribution of the concrete, and the width b_f of the steel beam after the expansion should still be smaller than the width b of the SC beam. Before the steel beam flanges are not expanded (as the specimen SC01), the flexural strength not considering the contribution of the concrete compressive strength is 4550 kN-m, so the width of the steel beam flanges at the beam-column joint is widened by 50 mm on the left and right sides, respectively. The thickness of the steel beam flange t_f remains unchanged, the flexural strength of the pure steel beam at beam end is increased from the original 3890 kN-m to 4690 kN-m (greater than 4550 kN-m).

As to Specimen SC03, in order to ensure the plastic hinging could be occurred in the RBS zone, styrofoam blocks were put in the reduced steel beam flanges zone and on both sides of the web, so as to reduce the lateral restraint of the steel beam.

As to Specimen SC04, in order to ensure the plastic hinging could be occurred in the RBS zone, the trimming amount of the steel beam flanges is appropriately increased to enhance its deformation capacity. Considering the concrete may contribute another 10%~12% to the sectional bending moment strength of the SC beam, it suggested that trim the flanges so that the provided plastic moment capacity is 15-25% less than that of the demand value. If the steel beam flange width was trimmed halving, the sectional bending moment strength of the SC beam would be reduced 15%~25% that of the prototype, and the steel beam is bound by concrete cladding, so that the lateral torsional stiffness of the beam will not be too low, which can avoid local buckling of the steel beam. For the specimen SC04, the minimum steel beam flange width was reduced from 400 mm to 200 mm, thereby reducing the bending moment gradient of the trimming section by 26%.

Because the moment capacity of the SC beam would be decreased with elongating the length of the plastic hinge region, the Specimen SC05 was designed to lengthen the length of the plastic hinge region to enable plastic hinge to occur in the expected plastic zone. The length of the plastic hinge region increases from $0.5d_b$ of the first four groups of specimens to $0.75d_b$, and the minimum steel beam flange width is reduced from 400 mm to 210 mm.

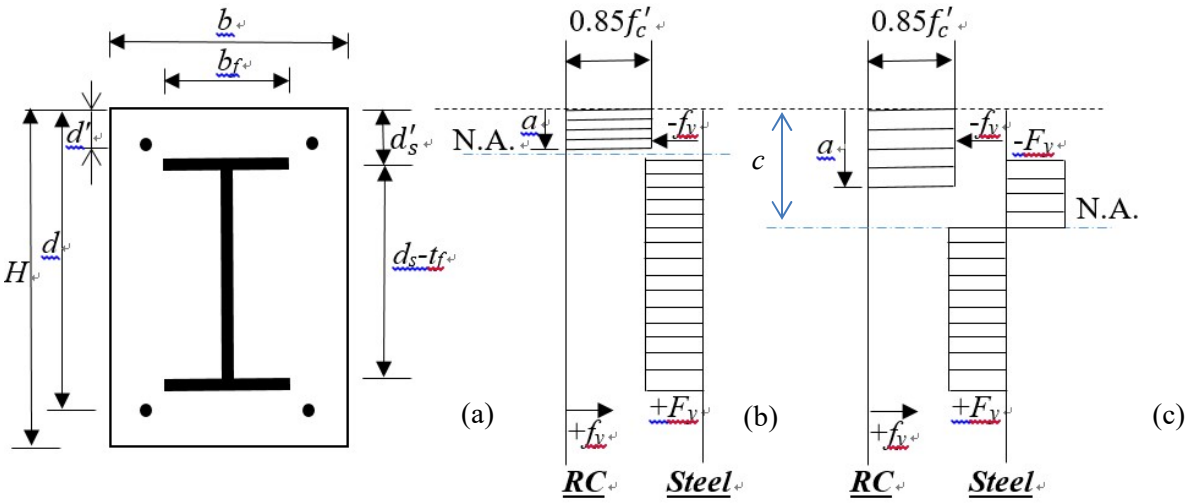

Figure 1 The simplified cross-section of SC beam and its stress distribution

SUMMARY AND CONCLUSIONS

This study firstly proposes how to properly consider the moment strength estimation method contributed by concrete when designing SC beams, and proposes four methods for improving the performance of the SC beam, through a series of the cyclic loading tests and analysis lead to the following conclusions and suggestions:

1. The simplified full-plastic method proposed in this study can appropriately consider the contribution of concrete to the bending moment strength of SC beams, so that the analysis results of the bending moment requirements and capacity of SC beams are more reasonable, and the performance of SC beams can be accurately grasped.
2. Specimen SC02 is a steel beam flanges trimming with a wing expansion mechanism. The purpose is to expand the wing before the cutting section to provide the bending moment strength near the beam-column interface, so that the steel beam wing cutting section can be used first. Plastic deformation occurs, but the bending moment capacity in this section is only about 3% to 7% lower than the bending moment requirement, so slight plastic deformation occurs in the cutting section. Compared with the control sample SC01, the wing expansion mechanism can effectively avoid the tearing of the steel beam and the wing near the beam-column junction, and can also slightly increase the plastic deformation capacity of the SC beam (the plastic turning angle is increased from 3.99% to 4.05%).
3. Specimen SC03 is a steel beam wing cutting section with no concrete filled on both sides of the web, in order to weaken the bending moment strength of the cutting section and reduce the deformation range of the concrete beam steel beam, but due to the steel in this section Although the beam web has not been restrained by concrete, the steel beam wing area where plastic deformation mainly occurs is still partially restrained by concrete, and the bending moment capacity of this section is only about 5% to 7% lower than the bending moment requirement. %, so the plastic deformation capacity of the SC beam is only slightly increased (the plastic turning angle is increased from 3.99% to 4.02%), and the tearing of the steel beam wing near the junction of the beam column can also be avoided.
4. Specimen SC04 is designed to deepen the cutting section. The minimum width of the steel girder flange after cutting is changed from 400 mm to 200 mm, the bending moment strength of the section is reduced by at most about 26% compared with the demand, and the cutting is expected to be reduced. The section can produce plastic deformation smoothly. The test results show that its plastic turning angle reaches 4.96%, which is 24% higher than that of the specimen SC01, that is, its toughness capacity is obviously improved, and it is proved that this specimen has a larger cutting amount of the wing plate. However, there is concrete cladding as the lateral restraint of the steel beam, so there is no lateral torsional buckling of the steel beam.

5. For specimen SC8, the length of the cutting section is elongated from 0.5db to 0.75db, and the minimum width of the steel beam flange after cutting is changed from 400 mm to 210 mm. The purpose is to increase the length of the cutting section to increase. The cutting depth of the steel beam wing also expands the plastic deformation range. The test results show that its plastic turning angle reaches 5.82%, which is about 46% higher than that of the specimen SC01, and its steel beam, beam wing and beam web can obviously produce plastic deformation.
6. The two methods of improving the performance of SC beams, which are suggested by this study, can effectively avoid the tearing and damage of the steel beam at the junction of the beam-column. Improving its plastic deformation capacity has limited effect.
7. There are two suggestions for improving the performance of SC beams by increasing the trimming depth of the steel beam flanges and lengthening the length of the RBS region, which can not only significantly improve its plastic deformation capacity, but also avoid the tearing of the steel beam at the beam-column junction. In particular, lengthening the trimming section of the steel beam flanges has the most excellent effect in improving the performance of the SC beam.
8. When designing the trimming section of the steel beam flanges of the SC beam, the bending moment strength must be at least 10% lower than the bending moment requirement, so that the section can be smoothly and obviously plastically deformed.

REFERENCES

AISC, "*Seismic Provisions for Structural Steel Buildings, ANSI/AISC 341-10, American Institute of Steel Construction, Chicago, IL.*", USA, 2010a.

AISC, "*Specifications for Structural Steel Buildings, ANSI/AISC 360-10, American Institute of Steel Construction, Chicago, IL.*", USA, 2010b.

ACI, "*Buildings Code Requirements for Structural Concrete (ACI 318-05) and Commentary (ACI 318R-05), American Concrete Institute*," USA, 2002.

American Institute of Steel Construction (AISC). *Seismic Provisions for Structural Steel Buildings*, AISC, Chicago, IL, 2005.

Chen, S.J., Yeh, C.H. and Chu, J.M., "Ductile Steel Beam-to-Column Connections for Seismic Resistance," *Journal of Structural Engineering* (ASCE), 1996, 122(11), pp. 1292-1299.

Chen, S.J. and Tu, C.T., "Experimental Study of Jombo Size Reduced Beam Section Connections Using High-Strength Steel," *Journal of Structural Engineering* (ASCE), 2004, 130(4), pp. 582-587.

DESIGN EQUATION FOR SHEAR STRENGTH OF UHPC BEAMS

Manuel Bermudez[1] and Chung-Chan Hung[2]
1. PhD. Student, Department of Civil Engineering, National Cheng Kung University, Tainan City, Taiwan
2. Professor, Department of Civil Engineering, National Cheng Kung University, Tainan City, Taiwan
Email: n68077063@gs.ncku.edu.tw

ABSTRACT

It is reasonable that when new technologies arise, they are received with appropriate skepticism, especially if these technologies can make extraordinary claims such as a hundred years of low or no maintenance. However, the research on ultra-high-performance concrete (UHPC) during the last three decades proves that this revolutionary material is able to reframe the future of the concrete industry. This study acknowledges that there are multiple challenges in the design of UHPC structural components. In the case of the basic structural engineering principles such as shear and flexure, these challenges are associated with including the post cracking strength of the UHPC material and having an additional resisting mechanism that can also have collateral effects on well-known load transfer mechanisms. Specifically for shear, in reinforced concrete design, the shear strength has been traditionally related to the tensile of the concrete matrix and recently, many studies have taken the tensile strength of UHPC as a predictor for beam shear. Due to the lack of a widely accepted tension test, this study provides a practical approach for structural engineers and practitioners to accurately quantify the shear strength of UHPC beams to allow its use in shear critical members.

Keywords: Shear strength design, ultra-high performance concrete, shear span to effective depth ratio, effective depth, fiber reinforcement, direct tensile strength, indirect tensile test

INTRODUCTION

It is a recurrent question from practitioners and engineers of the construction industry to ask if the response of structural members made of ultra-high-performance concrete (UHPC) follows the traditional principles that have been characterized in reinforced concrete (RC). The answer to this question is both yes and no. UHPC is a result of the evolution of advanced cementitious composites and has a discontinuous pore structure that enhances its durability when compared to RC (Hung et al. (2017), Hung et al. (2018), Hung et al. (2019), Hung et al. (2020), and Hung et al. (2021)). What makes UHPC special is its outstanding post-cracking strength that can sustain tensile strengths greater than 5 MPa. This means that in terms of flexure, although the basic structural engineering principles of the Euler-Bernoulli beam theory are still valid for UHPC, in this material there is a contribution to the flexural capacity provided by the fibers in the tension zone. This opposes the assumption done for the flexural design of RC members in which the tensile strength is neglected due to the low tensile strength of the RC matrix. In the case of shear, several experimental studies in the last three decades have confirmed that the mechanisms that have been identified by the report of the ACI-ASCE Committee (1973), namely, the contribution of the concrete in the compression zone, the dowel action, and the residual tensile strength across the tensile cracks, are still valid for UHPC members. The study of Bermudez and Hung (2022) collected relevant shear tests that revealed the importance of the shear resisting mechanisms identified for RC and in that study, Bermudez and Hung (2022) provided additional evidence of the individual contribution of the fiber reinforcement to the shear strength as well as its collateral effects on the other shear resisting mechanisms.

The real challenges that UHPC has to be fully implemented in structural design are 1. A reduction of the cost of UHPC raw materials and 2. Structural guidance for designing efficient UHPC members. The rise of nonproprietary UHPC mixes has significantly reduced the cost when compared to the cost of prebagged materials because it allows concrete producers to make use of constituent materials that are locally available (El-Tawil et al. (2018), Lawler et al. (2019), Tadros et al. (2020), El Tawil (2020)). Generally, satisfactory results of mechanical properties can be obtained from well-designed nonproprietary UHPC mixes. Therefore, one can be optimistic that the current progress in developing

UHPC mixes will lead to an optimization of both cost and structural performance. The development of design guidelines, on the other hand, still needs further study and refinement. UHPC is an expensive solution for structural designers if the structural properties are not properly assessed. In the case of flexural strength, UHPC can increase the bending capacity of a beam with continuous longitudinal steel reinforcement by 10 to 20%. If the traditional Euler-Bernoulli beam theory is used to design the flexural strength of a UHPC member, this additional percentage will be ignored. It must be mentioned that in the tension zone, the UHPC material can reach a strain of 3/1000 which is higher than the yield strength of steel reinforcement. Although the underestimation of the flexural capacity of UHPC members can be tolerated, in the case of shear, if the shear strength prediction of ACI 318 (2019) is used, the underestimation can be 3 to 5 times the capacity of UHPC, making this material not competitive when compared to other solutions. The high shear resistance of UHPC represents a promising solution for shear critical members because it can reduce or eliminate the stirrups which simplify the design and both in-place and precast concrete production. This is particularly important in seismic regions where congested reinforcement results from following the requirements specified by the relevant construction codes. Therefore, the objective of this study is to provide a practical approach for predicting the shear strength of UHPC so it can be implemented by structural engineers to simplify design and concrete production.

THE SHEAR STRENGTH OF UHPC

Why not rely on the tensile strength of UHPC?

Since the report of the ACI-ASCE Committee (1962), the shear strength of an RC member has been related to the tensile strength of the RC matrix. However, the relationship between the shear strength and the tensile strength has always been indirectly estimated by an indirect relationship of the tensile strength of RC with the square root of the material's compressive strength. This indirect relationship was developed because of the lack of a proper tensile test for RC materials.

In the case of UHPC, one of its most important characteristics is that this material can sustain post-cracking tensile strengths greater than 5 MPa while displaying a strain hardening response specially when its strain is above 5/1000 (Naaman and Shah 2022). However, UHPC's research community has not been able to generate a satisfactory tensile test that can be generalized so that structural engineers can get this important engineering property. The issue with the tensile strength of a fiber-reinforced UHPC is that the tensile response is not an intrinsic property (Maya Duque and Graybeal 2017). UHPC has two important points in the stress-strain curve that are affected by the anisotropy of the material: the first cracking strength and the post-cracking strength. These two points in the stress-strain curve will vary depending on the element dimensions, the casting method, the flow direction during casting, fiber alignment, the fiber dimensions, the fiber type, and other factors.

Until now, two methods are used to obtain the tensile properties of UHPC. One method is through a direct tensile test. Usually, this test method is performed by pulling a dog bone shaped specimen using a displacement-controlled procedure with a loading rate of 0.01 mm/min. Besides the inherent variability generated in the specimen due to fiber orientation, in the last three decades, in less than 30% of the almost 200 beams that claimed a shear failure, their authors reported the direct tensile strength of the UHPC material. This under-reporting combined with the lack of a standard that generalizes the specimen's dimension as well as the test setup requirements makes it complicated for design engineers to accept and incorporate the tensile strength as a predictor of the shear strength of UHPC. A recent publication by El-Helou and Graybeal (2022) has developed their shear model associating a derivation of the modified compression field theory (MCFT) with the direct tensile strength of a prism specimen. The tension test using a prism that has been accepted by AASHTO under the standard T-397 (AASHTO 2022) promises to generate a more consistent methodology that can characterize properly the tensile strength of UHPC and will eliminate the bias by generating more objective considerations of the data obtained from the test. Until the research community implements this standard and reports the tensile strength of their UHPC material, then the shear strength should not be associated with the direct tensile strength of UHPC.

The other method that some researchers and construction codes such as the French standards (AFGC (2013) and NF P18-710 (2016)), the Swiss standards (SIA 2052 (2016)), and the Canadian standards (CSA 2019) use to predict the shear strength is by obtaining a residual tensile strength from an inverse analysis of a flexural test. There are mainly two standards that are used for this test, namely ASTM C1609 and EN 14651. These two standards were developed for fiber reinforced concrete (FRC) that have compressive strengths as high as 60 MPa. However, even for FRC, both standards generate high variability of the residual tensile strength of FRC and Bencardino et al. (2013) have documented well different flaws associated with these standards. It is, therefore, an unnecessary risk to depend on this test method and fortunately, future editions of constructions codes and guidelines of UHPC will not recommend this test method as a predictor of the shear strength of UHPC members.

Development of the shear strength design equation for UHPC

In the last three decades, researchers from all over the world have done numerous experiments to understand the shear behavior of such revolutionary material. Currently, there have been reported almost 200 shear tests of non-prestressed beams made of advanced cementitious materials. The objectives of these experimental campaigns have been focused on the use of fibers as shear reinforcement, the use of different types of fibers, the shear slenderness (a/d) ratio, and the presence/absence of coarse aggregate. Numerous efforts from the research community have been devoted to obtaining a sufficient understanding of the shear behavior of UHPC to develop rational design equations. However, due to the complex behavior associated with the shear failure in concrete, until now, no general agreement has been reached on the shear design of UHPC members.

Although almost 200 tests of non-prestressed beams have reported a shear failure, a more thorough examination of the data shows that some of these beams had indeed flexure-shear failure or even flexure failure. In this investigation, a database with strict filtering criteria has been developed considering the evolution of UHPC. The coefficients of the proposed shear design equation (1) were optimized using the evaluation database that contained 110 beams that fulfilled the filtering criteria.

$$V_u = \sqrt{\frac{2}{1+\frac{d}{254}}}\left[2.25e\left(f'_c\rho_w\frac{d}{a}\right)^{0.57} + (1.80v_b)^{1.28}\right]\left(\frac{b}{b_w}\right)^{0.35} \quad \text{(MPa)} \qquad (1)$$

where:

e = dimensionless factor that accounts the arching action: 1 for a/d >3.4, 3.4(d/a) for a/d ≤ 3.4.

d = effective depth (mm)

f'_c = compressive strength of a cylinder (MPa)

b = for isolated beams, the width of the flange of the beam; for intermediate T-beams, $2h_f + b_w$ (mm)

b_w = width of the web of the beam (mm)

h_f = top flange thickness (mm)

v_b = fiber term to account for the direct contribution of the fibers to shear resistance: 0.41τF

τ = average fiber-matrix interfacial bond stress: 4.15 MPa for steel fiber (Swamy et al. (1974)), and 0.04 MPa for PVA fiber (Hong et al. (2020)).

F = fiber factor calculated as follows for monofiber or hybrid fibers

$$F_{Total} = \left(\frac{L_1}{D_1}\right)V_{f1}d_{f1} + \left(\frac{L_2}{D_2}\right)V_{f2}d_{f2} + \left(\frac{L_3}{D_3}\right)V_{f3}d_{f3} \qquad (2)$$

where the variables with subscript 1, 2, and 3 corresponds to the characteristics of each fiber type used, L/D is the aspect ratio, where L is the length of the fiber in mm and D is the diameter of the fiber in mm, V_f is the volume fraction of fibers, d_f is the bond characteristics of the fiber where for straight steel fibers or round fibers is 0.5, for hooked end fibers or crimped fibers is 0.75, for indented fibers is 1, and for PVA fibers is 0.25.

The proposed equation (1) can predict the shear strength of both deep and slender beams with either monofiber or hybrid fibers reinforcement. The criteria used for optimizing the equation were to make it simple for practitioners to use it, as it requires basic experimental data to predict the shear strength of

UHPC beams without stirrups. The design equation (1) is a modification of the shear model presented by Kwak et al. (2002) and it has two additional factors that are necessary to have rational predictions of large UHPC members. Since UHPC beams are intended to reduce the size of the structural members, a factor derived by Placas and Regan (1971) to account for the shape of the beam was included. The size effect factor recommended by ACI 318 (2019) was incorporated in the equation for beams with effective depths larger than 254 mm. Equation 2 is the modification of the fiber factor proposed by Narayanan et al. (1987). This adaptation of the fiber factor allows the structural engineer to quantify the shear strength of UHPC when using steel monofibers, hybrid fibers as well as when using synthetic fibers.

The advantage of using this semi-empirical equation to predict the shear strength of UHPC is that the structural designer knows all the required parameters and it is only required that the laboratory provides the compressive strength of UHPC. Depending only on the most used property of concrete reduces the possibility of erroneous comparisons like the ones that surge with the direct tensile tests in which researchers use different specimens for their tensile tests. This design equation facilitates a broad number of practitioners and designers a practical tool that can capture the full potential of shear capacity provided by the UHPC material and gives them a reasonable justification for the high initial cost of the cementitious material. It is important to note that laboratories do not need to change their testing equipment for obtaining the compressive strength according to ASTM C39 and they only need to modify the loading rate as specified by ASTM C1856. This design equation acknowledges the fiber orientation effect by considering that only 41% of the fibers are going to be aligned perpendicular to the diagonal crack (Romualdi et al. (1964)). This consideration of limiting the fiber efficiency is fundamental in one-way shear because there is no structural redundancy, which is the issue that arises when depending solely on the tensile strength, and therefore the optimum percentage prescribed in the equation is conservative enough to ensure an appropriate structural response under shear loading.

RESULTS AND DISCUSSION

Statistical analysis was done to examine the accuracy of Equation 1. As shown in Figure 1, the shear design equation was able to generate rational and accurate predictions for the shear strength of the 110 UHPC beams that were evaluated. The ratio between the experimental shear strength and the prediction was 1.00 with a coefficient of variation of 22%, an average absolute error of 19%, with a root-mean-square deviation of only 2.34. Figure 1 shows the predictive power of this equation that had a coefficient of determination (R^2) of 0.84 with mean values that were clumped inside the 95% confidence interval that ranged between 0.96 to 1.04. The confidence interval (CI) bands shown in Figure 1 indicates how precise the data is been defined by the trend line and, on average, the predictions using Equation 1 will tend to fall in the conservative range. The prediction interval (PI) bands shown in Figure 1 are just to illustrate the interval in which 95% of the future predictions will probably fall since it is based on the observed variation in the dataset.

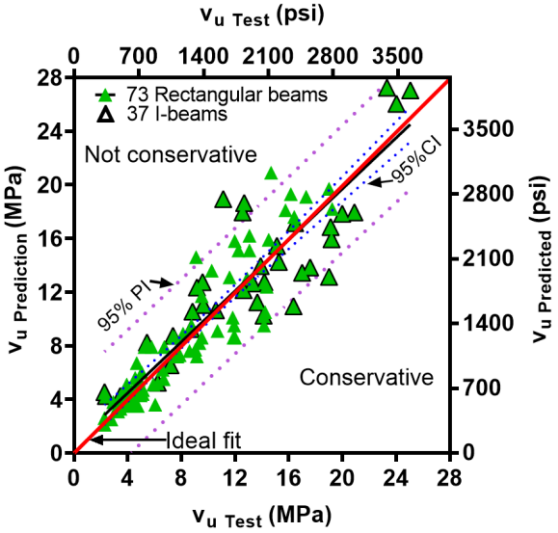

Figure 1. Evaluation of the shear design equation

The high predictive capacity of this equation is emphasized in large UHPC beams, as shown in Figure 2. The size effect factor proposed by ACI 318 (2019) seems to generate reasonable predictions of I-shaped UHPC beams with effective depths larger than 254 mm. This figure shows that the equation underestimated the shear strength of the 10 beams that had effective depths larger than 559 mm by only 6%. Until the size effect is properly quantified in UHPC beams, it is recommended to use the factor proposed by ACI 318 (2019).

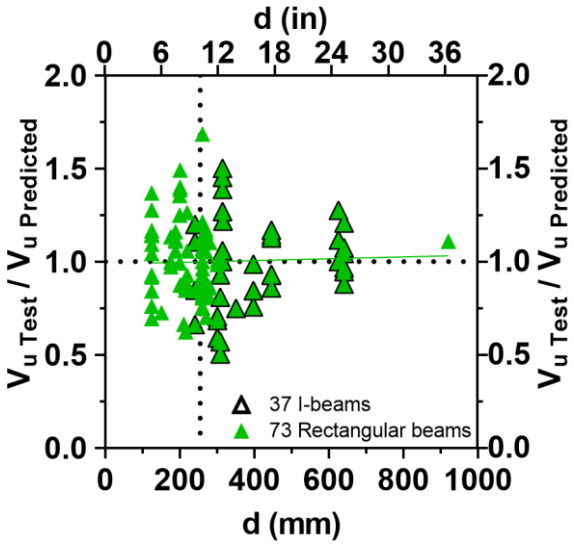

Figure 2. Shear strength ratio vs effective depth

CONCLUSIONS

This paper shows the development of a design equation for the shear strength of UHPC applications. Throughout the paper, it is discussed the need of having readily available engineering properties that can be used as predictors for structural design calculations. The goal of this study was to provide structural engineers and practitioners with a practical tool that will generate accurate predictions of the shear strength and therefore prove that the fiber-reinforced UHPC material justifies its initial cost due to its outstanding shear strength capacity that on the field can be translated as reductions in the construction time, reduction of the labor force, increase of the expected service life, no maintenance or if any, maintenance of tightly spaced small width cracks. The shear strength design equation was obtained from the accumulated knowledge developed from shear tests during the last three decades. The semi-empirical equation that relied on basic experimental data accurately predicted the shear strength of 110 non-prestressed fiber-reinforced UHPC beams that had a shear failure. The statistical analysis revealed the predictive power of the equation which had good performance in both rectangular and I-shaped beams, in a range of shear span to effective depth ratio between 1 and 4.5, reinforced with either monofibers or hybrid fibers. Although most of the laboratory shear tests were conducted on beams with relatively small depths, the equation only had an underestimation of 6% of the shear strength of the ten beams that had effective depths larger than 559 mm (22 in). The shear design equation of this study intends to advance the use of UHPC in large structural members and to provide a reasonable estimation of the shear capacity when considering the use of this material in seismic regions.

ACKNOWLEDGMENTS

This study was sponsored in part by the Ministry of Science and Technology, Taiwan, under Grant No. 109-2636-E-006-015. The opinions, findings, and conclusions expressed in this paper are those of the authors, and do not necessarily reflect those of the sponsor.

REFERENCES

AASHTO. 2022. Standard method of test for uniaxial tensile response of ultra-high performance concrete. AASHTO T 397. Washington, DC: *AASHTO.*

ACI Committee 318. Building Code Requirements for Structural Concrete (ACI 318-19): An ACI Standard: Commentary on Building Code Requirements for Structural Concrete (ACI 874 318R-19); *American Concrete Institute*, Farmington Hills, Michigan, USA, 2019, ISBN 978-1641950565.

ASCE-ACI Committee 326. (1962). "Shear and diagonal tension." *ACI J.*, 59(1), 1-30, 277-344, 352-396.

ASCE-ACI Committee 426. (1973). "The shear strength of reinforced concrete members." *J. Struct. Div.*, ASCE, 99(6), 1091-1187

Association Francaise de Genie Civil (AFGC). (2013) Scientific and Technical Document on Recommendations for Ultra High Performance Fibre-Reinforced Concrete; Revised Edition; *Association Francaise de Genie Civil (AFGC)*: Paris, France.

Bencardino, F., Rizzuti, L., Spadea, G., & Swamy, R. N. (2013). Implications of test methodology on post-cracking and fracture behaviour of steel fibre reinforced concrete. Composites Part B: Engineering, 46, 31-38.

Bermudez, M., Wen, K. W., & Hung, C. C. (2022). A Comparative Study on the Shear Behavior of UHPC Beams with Macro Hooked-End Steel Fibers and PVA Fibers. *Materials*, 15(4), 1485.

CSA A23.1:19/CSA A23.2:19, "Concrete Materials and Methods of Concrete Construction/Test Methods and Standard Practices for Concrete," *Canadian Standards Association*, Toronto, ON, Canada, 2019.

El-Helou, R. G., & Graybeal, B. A. (2022). Shear Behavior of Ultrahigh-Performance Concrete Pretensioned Bridge Girders. *Journal of Structural Engineering*, 148(4), 04022017.

El Tawil, S., Tai, Y. S., Meng, B., Hansen, W., & Liu, Z. (2018). Commercial Production of Non Proprietary Ultra High Performance Concrete (No. RC 1670). Michigan. Dept. of Transportation. Research Administration.

El Tawil, S., Tai, Y. S., Belcher II, J. A., & Rogers, D. (2020). Open Recipe Ultra High Performance Concrete. *Concrete International*, 42(6), 33 38.

Hong, L., Chen, Y. D., Li, T. D., Gao, P., & Sun, L. Z. (2020). Microstructure and bonding behavior of fiber-mortar interface in fiber-reinforced concrete. *Construction and Building Materials*, 232, 117235.

Hung, C.-C.; Li, H.; Chen, H.-C. High-strength steel reinforced squat UHPFRC shear walls: Cyclic behavior and design implications. *Eng. Struct*. 2017, 141, 59–74.

Hung, C.-C.; Hu, F.-Y.; Yen, C.-H. Behavior of slender UHPC columns under eccentric loading. *Eng. Struct*. 2018, 174, 701–711.

Hung, C.-C.; Lee, H.-S.; Chan, S.N. Tension-stiffening effect in steel-reinforced UHPC composites: Constitutive model and effects of steel fibers, loading patterns, and rebar sizes. *Compos. Part B: Eng.* 2019, 158, 269–278.

Hung, C.-C.; Chen, Y.-T.; Yen, C.-H. Workability, fiber distribution, and mechanical properties of UHPC with hooked end steel macro-fibers. *Constr. Build. Mater*. 2020, 260, 119944.

Hung, C.-C.; El-Tawil, S.; Chao, S.-H. A review of developments and challenges for UHPC in structural engineering: Behavior, analysis, and design. *J. Struct. Eng*. 2021, 147, 03121001.

Kwak, Y. K., Eberhard, M. O., Kim, W. S., & Kim, J. (2002). Shear strength of steel fiber-reinforced concrete beams without stirrups. *ACI Structural Journal*, 99(4), 530-538.

Lawler, J. S., Tadros, M. K., Lampton, M., & Wagner, E. N. (2019, June). Development of Non-Proprietary UHPC for Florida Precast Applications. In International Interactive Symposium on Ultra-High Performance Concrete (Vol. 2, No. 1). Iowa State University Digital Press.

Maya Duque, L. F., & Graybeal, B. A. Correlation between the material tensile properties and the flexural response of UHPFRC panels. Proceedings of UHPFRC 2017 Designing and Building with UHPFRC: New large-scale implementations, recent technical advances, experience and standards. *RILEM Publications SARL*, 2017, 385 – 394.

Naaman, A. E., & Shah, S. P. (2022). Strain Capacity of Strain-Hardening Ultra-High-Performance Concrete with Steel Fibers. *ACI Materials Journal*, 119(2), 171-180.

Narayanan, R., & Darwish, I. Y. S. (1987). Use of steel fibers as shear reinforcement. *Structural Journal*, 84(3), 216-227.

NF P18-710, "National Addition to the Eurocode 2—Design of Concrete Structures: Specific Rules for Ultra High Performance Fiber- Reinforced Concrete (UHPFRC)," *Association Française de Normalisation (AFNOR - French Standard Institute)*, Paris, France, 2016.

Romualdi, J. P., & Mandel, J. A. (1964, June). Tensile strength of concrete affected by uniformly distributed and closely spaced short lengths of wire reinforcement. In Journal Proceedings (Vol. 61, No. 6, pp. 657-672).

Placas, A., & Regan, P. E. (1971, October). Shear Failure of Reinforced Concrete Beams. In Journal Proceedings (Vol. 68, No. 10, pp. 763-773).

SIA 2052, "Recommendation: Ultra-High Performance Fiber-Reinforced Cement-based Composites (UHPFRC) Construction Material, Dimensioning, and Application," *Swiss Federal Institute of Technology*, Lausanne, Switzerland, 2016.

Swamy, R. N., Mangat, P. S., & Rao, C. K. (1974). The mechanics of fiber reinforcement of cement matrices. *Special Publication*, 44, 1-28.

Tadros, M. K., Gee, D., Asaad, M., & Lawler, J. (2020). Ultra-high-performance concrete: A game changer in the precast concrete industry. *PCI J*, 65, 3-06.

STUDY ON LIGHTWEIGHT TRUSS-TYPE COMPOSITE TEMPORARY BRIDGES FOR EMERGENCY DISASTER RELIEF

Fang-Yao Yeh[1], Bo-Han Lee[2], Sheng-Yuan Shiao[3], Chi-Lon Jang[3], Kuo-Chun Chang[4], Yao-Yu Yang[5] and Chia-Ming Chang[6]

1. Division Director, National Center for Research on Earthquake Engineering, Taipei, Taiwan, R.O.C.
2. Associate Researcher, National Center for Research on Earthquake Engineering, Taipei, Taiwan, R.O.C.
3. Associate Technologist, National Center for Research on Earthquake Engineering, Taipei, Taiwan, R.O.C.
4. Distinguished Professor, Department of Civil Engineering, National Taiwan University, Taipei, Taiwan, R.O.C.
5. Ph. D. Candidates, Department of Civil Engineering, National Taiwan University, Taipei, Taiwan, R.O.C.
6. Associate Professor, Department of Civil Engineering, National Taiwan University, Taipei, Taiwan, R.O.C.

Email: fyyeh@narlabs.org.tw

ABSTRACT

Typhoons and earthquakes, which occur frequently in Taiwan, often lead to traffic disruption and many other disaster conditions because of bridge failures such as washout or collapse. Therefore, constructing an effective temporary rescue bridge is crucial for alleviating the impacts of disasters. In this study, a truss-type composite temporary rescue bridge is proposed to improve the stiffness of longer span (50 m) bridges. A 50-m span asymmetric self-anchored truss-type cable-stayed bridge is carefully designed and experimentally validated. The rapid assembly technology proposed for construction is validated via simulations. Furthermore, in order to improve worker safety during the installation of a temporary rescue bridge, two construction processes, namely the cantilever erection method and the incremental launching method, are compared in this study. Moreover, it is found that the assembly process actually improved worker safety during bridge construction and shortened the assembly duration.

Keywords: temporary rescue bridge, asymmetric cable-stayed bridge, truss-type composite structure, glass fiber-reinforced plastic, safety of workers, rapid assembly

INTRODUCTION

Typhoons and earthquakes, which occur frequently in Taiwan, often cause to traffic disruption and many other disaster conditions because of bridge failures such as washout or collapse. Thus, building a temporary rescue bridge in a very short time provides an effective disaster relief option when the structure of a bridge loses its workability. Yeh *et al.*, 2015 applied glass fiber-reinforced plastic (GFRP) material to a segmental temporary rescue bridge design, making it lightweight and reusable. The live load capacity of the GFRP bridge was 5 tons and the span length was 20 m. Nevertheless, the safety of on-site construction workers should also be considered since workers sometimes need to install a temporary rescue bridge under severe weather conditions. In addition, workers' exposure risks may increase because of the unsuitable bridge span length. These difficulties should be observed when designing a temporary rescue bridge.

To address these problems, a truss-type segmental structure is used here to improve the stiffness of a longer span (50 m) bridge, and the process of constructing the GFRP temporary rescue bridge is analyzed. Obviously, the assembly process is critical, as it significantly affects construction progress and worker safety during bridge construction. In terms of worker safety, two different processes, namely the cantilever erection and incremental launching methods, are compared in this study.

DESIGN AND EXPERIMENT OF A COMPOSITE TEMPORARY BRIDGE

Design of a Truss-type Composite Bridge

For the design, a case of communities isolated by Typhoon Morakot in 2009 was considered. A river bridge with a 50 m span length was washed away by the floods, paralyzing traffic of surrounding areas. In order to transport disaster relief materials into the isolated area, a temporary rescue bridge was required to endure small trucks weighing 3.5 tons.

A temporary rescue bridge system adapting a self-balancing approach with a cantilever erection method and incremental launching method is herein developed and an asymmetric self-anchored truss-type segmental composite cable-stayed bridge is proposed. And truss-type GFRP segmental bridge systems were studied to assess the structural requirements necessary to meet the following design requirements recommended by USDA, 2011: 50-m span, 3-m width, 5-ton live load capability, and a deflection-to-span ratio of L/400. Figs. 1(a) and 1(b) present the finite element method (FEM) model and design results of the asymmetric self-anchored truss-type segmental composite cable-stayed bridge. The main girders of the bridge system with truss-type structural segments were composed of 203 mm × 60 mm × 9.5 mm C-shaped and 101 mm × 101 mm × 6 mm box-shaped GFRP composite members. The GFRP had the Young's modulus of 20.03 GPa, a density of 1.72 g/cm^3, and an allowable stress of 207 MPa. Figs. 1(c) and 1(d) demonstrate the deformed shape and deflections under various loading positions. As a result, the maximum displacement was 10.67 cm, which meets the design requirements for a deflection-to-span ratio of L/400.

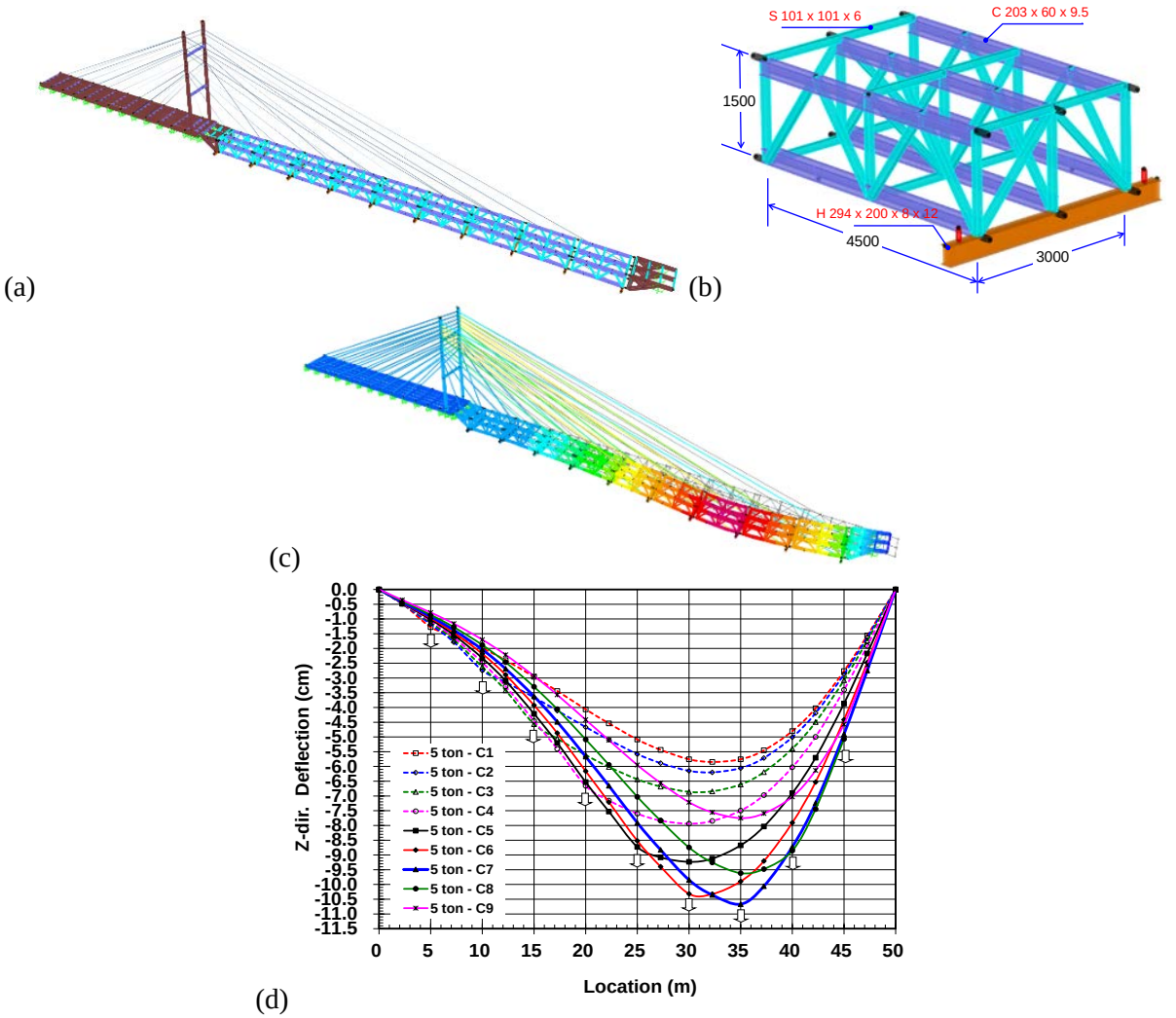

Figure 1. Design results for a 50-m span temporary rescue bridge: (a) FEM model, (b) truss-type composite segment (unit: mm), (c) the deformed shape and (d) deflections (for various loading positions).

Experiment for a Truss-type Composite Segment

Preparation of specimen for truss-type segments of composite temporary rescue bridges as shown in Fig. 2. The typical experimental setup for a flexural test is shown in Fig. 3. The test program included a flexural test to measure the deflection and stiffness of the truss-type composite segment to calibrate the FEM model.

The specimen was tested using flexural loadings applied at the mid-span of the specimen. The tests were performed by controlling the load with a design target loading of 50 kN. Comparisons of laboratory measurements and analytical results obtained using the FEM model are presented in Fig. 4, showing the deflection of the G2 girder at an applied load of P = 20–50 kN at the mid-span. The solid and dashed lines denote the analytical results and experimental measurements, respectively. These figures show the FEM model can predict the GFRP bridge deflection with satisfactory accuracy. Therefore, the FEM model was validated by comparing the analytical and experimental results.

(a)

(b)

(c)

Figure 2. Preparation of specimens, (a) assemble of truss-type main girder, (b) completion of truss-type main girders, (c) completion of the truss-type composite segment.

Figure 3. Experimental setup for the flexural test with the applied loading at the mid-span of the specimen.

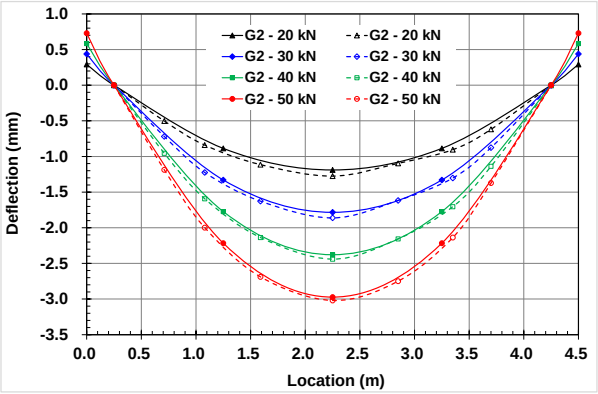

Figure 4. Comparison of results for the deflection of the specimen at an applied load of P = 20–50 kN.

Fig. 5 presents the strain measurement positions at the top of the upper chord, bottom of the upper chord, vertical strut, diagonal brace, top of the lower chord, and bottom of the lower chord. Fig. 6 describes that the maximum longitudinal strains were 3.23×10^{-4}, which occurred in the main girder G2, on the bottom of the upper chord. Nevertheless, the minimum longitudinal strains were -3.51×10^{-4}, which occurred in the main girder G2 on the top of the upper chord.

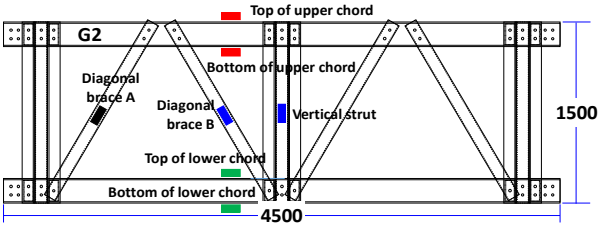

Figure 5. Location of strain gauges for main girder G2 of the specimen.

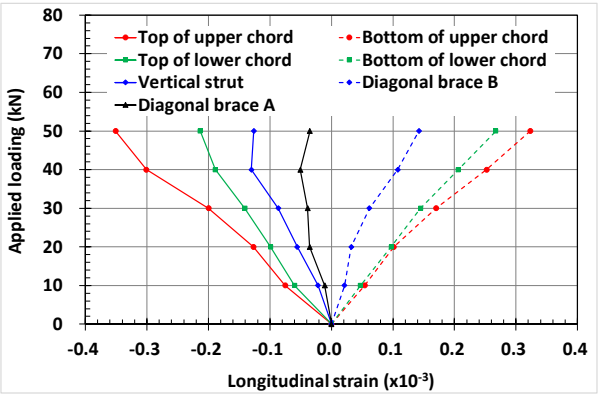

Figure 6. Test results for the longitudinal strains of main girder G2 at the applied load of P = 0–50 kN.

RAPID ASSEMBLY TECHNOLOGY FOR CONSTRUCTION

Design of Truss-type Segment Joints

The pin connection is the key component of the joint design when considering the force transmission and ease of assembly. Fig. 7 shows the design results for the segmented male joint, the female joint, and the combined joint. This joint only transmits axial and shear forces.

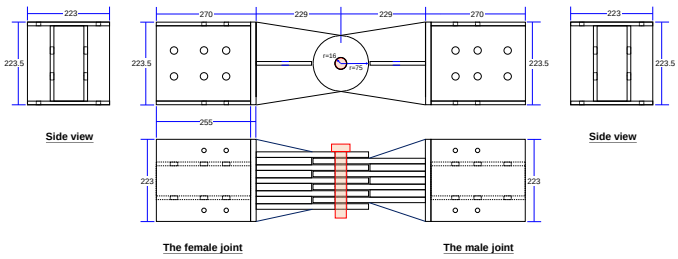

Figure 7. Design drawing of the truss-type segment joints (unit: mm).

Development of Rapid Assembly Technology

The joint between the segments of the cantilever erection method is guided by the central joint of the upper chord, after which the bottom chord joint would be assembled in a rotating manner. In the proposed construction method (Fig. 8), the section can be hoisted by a miniature crawler crane. The upper chord joint section is first combined with a bolt, then the section is assembled in a rotating manner.

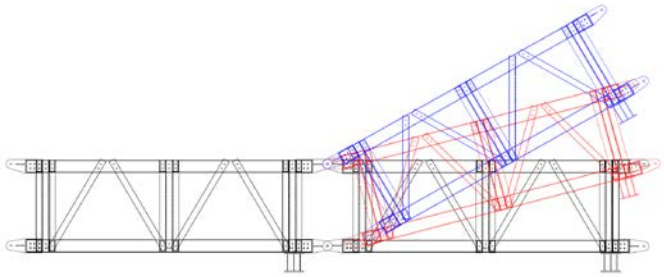

Figure 8. Segment joint assembly by the rotation method.

CONSTRUCTION OPERATIONAL EFFICIENCY AND SAFETY ANALYSIS

Description of Efficiency Analysis

The operational efficiency for the disaster relief task using temporary rescue bridges were evaluated between the cantilever erection method (Figs. 9 and 10) and the incremental launching method (Figs. 11 and 12). Hence, the indicators of operational efficiency were created in order to analyse the efficiency between these two methods. The efficiency indicators include (1) worker safety, (2) construction time, (3) equipment and labour requirements for the construction, and (4) counterweight demand.

In fact, worker safety is the first indicator under consideration. For the cantilever erection method, a mini-crawler crane is used instead of workers for the river-crossing process, thus improving worker safety. For the incremental launching method, the assembly is performed on the riverbank, after which the bridge is pushed forward to the isolated end to avoid construction over the river, which ensures worker safety.

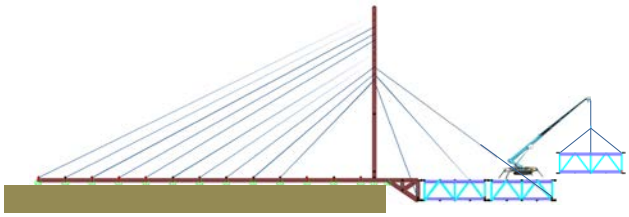

Figure 9. Cantilever erection method for rescue bridges.

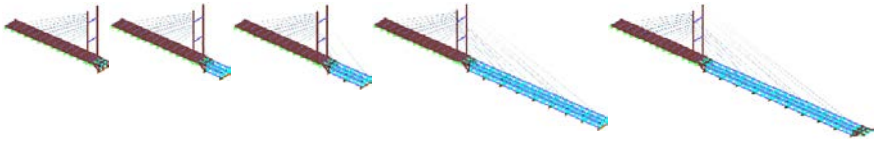

(a) (b) (c) (d) (e)

Figure 10. Cantilever erection method for rescue bridge construction, (a) assemble segments of the weight-balance module, (b) assemble the first GFRP truss segment of crossing structural module and lifting to cross the river, (c)(d) repeat stage (b) for a second to ninth GFRP truss segments, (e) completed the construction sequence to cross the river.

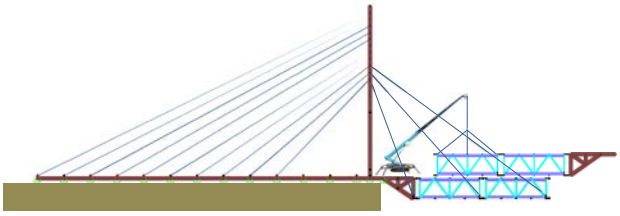

Figure 11. Incremental launching method for rescue bridges.

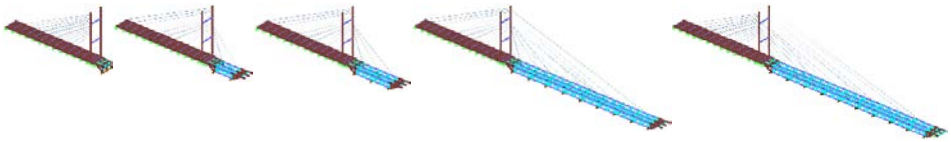

(a) (b) (c) (d) (e)

Figure 12. Incremental launching method for rescue bridge construction, (a) assemble segments of the weight-balance module, (b) assemble the first GFRP truss segment and install launching noise, (c) assemble the second GFRP truss segment and push it forward, (d) repeat stage (c) for third to ninth segments (e) completed the construction sequence to cross the river.

Construction Time Analysis

Subsequently, the construction time analysis for a 50-m span temporary rescue bridge was also examined. Thus, the total construction time among the original construction method (without assembly technology), the cantilever erection method (with rapid assembly technology), and the incremental launching method were compared in the study.

Fig. 13 presents the construction time results for the three different construction processes for a 50-m span temporary rescue bridge. The gray line represents the original construction method, whose total construction time was approximately 540 minutes. Nevertheless, this does not meet the requirement of being within eight hours. The red line represents the cantilever erection method. Owing to the rapid assembly technology, the total construction time was shortened to 430 minutes, thus attaining the < 8-hr requirement. And the blue line represents the incremental launching method. Accordingly, as the

construction process over the river was avoided, the total construction time was drastically shortened to 370 minutes, thus meeting the < 8-hr requirement.

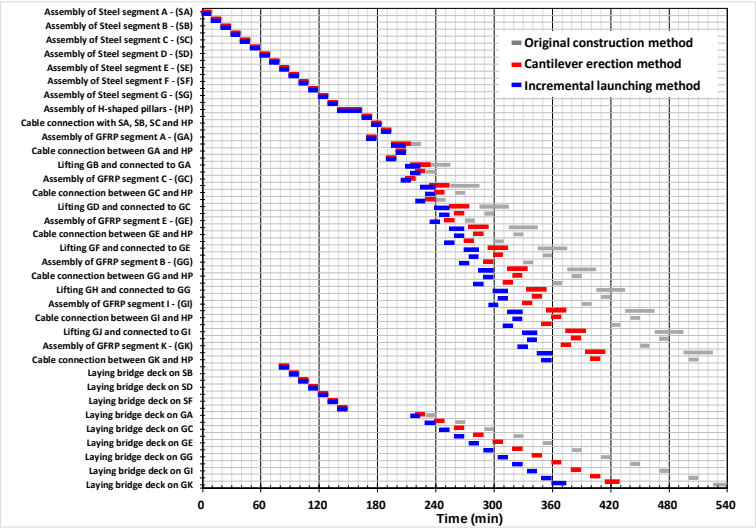

Figure 13. Results of construction time analysis of the three construction processes for a 50-m-span temporary rescue bridge.

Demand for Additional Counterweight

The truss-type composite temporary rescue bridge was constructed using a self-balancing approach with either the cantilever erection method or the incremental launching method. Before completion of the composite bridge, an additional counterweight is needed for balancing the weight of the mini-crawler crane and the self-weight of composite segments during construction.

Fig. 14 shows the results for additional counterweight demand of both construction processes for a 50-m span temporary rescue bridge. The red line represents the cantilever erection method, where the required additional counterweight was 1.8–25.8 tons during the river-crossing process. And the blue line represents the incremental launching method, where the required additional counterweight was 3.8–8.9 tons during the river-crossing process.

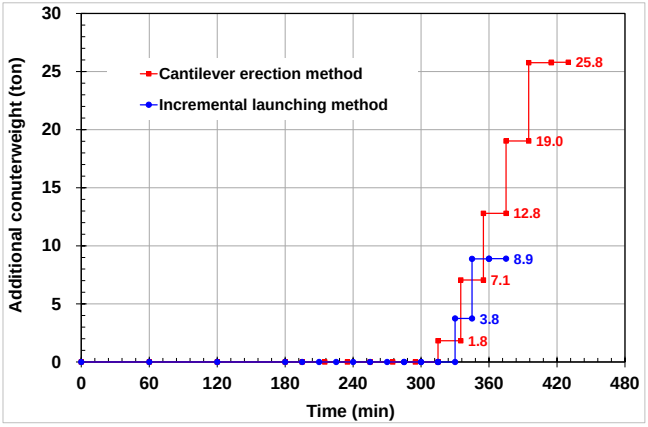

Figure 14. Results of additional counterweight demand for the two construction processes for a 50-m span temporary rescue bridge.

Analysis of Wind Effects during Construction

During the erection of the temporary bridge for disaster relief, the lateral wind was the most important factor affecting construction safety. Wind force calculations were performed according to current highway bridge design specifications. Fig. 15 shows the lateral displacement of the front end of the

bridge under different wind speeds at a length of 42.5 m (before bridge completion) for a 50-m span truss composite disaster relief bridge. As the skew angle of the wind increased, the maximum lateral displacement was decreased accordingly. Conversely, as the wind speed increased, the maximum lateral displacement was increased rapidly.

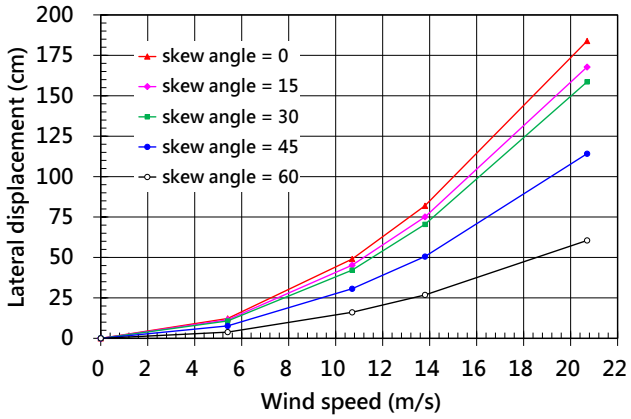

Figure 15. Lateral displacements under different wind speeds for a 50-m span temporary rescue bridge.

CONCLUSIONS

To sum up, this study identifies that (1) a truss-type segmental composite bridge can improve the stiffness of a 50-m span rescue bridge to meet the required deflection-to-span ratio, (2) rapid assembly technology for bridge construction can contribute significantly to improving worker safety and shortening assembly time of rescue bridges, (3) the incremental launching method has greater operational efficiency than the cantilever erection method, (4) the incremental launching method can avoid construction over the river, thus ensuring better worker safety, and (5) the maximum allowable wind speed for construction environment should be regulated for ensuring construction and worker safety.

ACKNOWLEDGMENTS

This work was supported by the Ministry of Science and Technology of Taiwan R.O.C., under the grant number MOST 107-2119-M-492-004. Also, the National Center for Research on Earthquake Engineering (NCREE) is gratefully acknowledged for technical assistance and facilities support.

REFERENCES

Yeh, F.Y., K.C. Chang, Y.C. Sung, H.H. Hung and C.C. Chou (2015). "A Novel Composite Bridge for Emergency Disaster Relief: Concept and Verification," *Composite Structures*, **127**, 199-210.

USDA Forest Service (2011). *A guide to fiber-reinforced polymer trail bridges*, 2nd edition, United States Department of Agriculture.

Numerical Studies on Flexural Performance of Geopolymer Concrete Beams with Varied Depth under Cyclic Loading

Mohammad Rizwan Bhina[1a], Waseem Khan[1b], Kuang-Yen Liu[2]*, Saleem Akhtar[3] and Ellena Kalmansur[4]

[1a]Department of Civil Engineering, National Cheng Kung University, Taiwan
[1b]Department of Civil Engineering, UIT, RGPV, India
[2*]Department of Civil Engineering, National Cheng Kung University, Taiwan
[3]Department of Civil Engineering, UIT, RGPV, India
[4]Department of Civil Engineering, National Cheng Kung University, Taiwan

E-mail: n68097039@gs.ncku.edu.tw, wkrgpv@gmail.com, kyliu@gs.ncku.edu.tw, sargpv@gmail.com, ellenpk.11@gmail.com.

ABSTRACT

This study investigated the flexural performance of Geopolymer concrete beam under varied cyclic loading with varied depth and performed numerical studied by ABAQUS a finite element analysis tool. The variation in the depth of beam considered from 250 mm to 750 mm and analyzed under variation of magnitude on cyclic loading. A Concrete damaged plasticity (CDP) model has used to modeled the GPM beam with the use of ABAQUS (FE) software. Deformation behavior, yield strength with ultimate and failure strength with displacement have examined under cyclic loading. A comparative studied of cyclic loads for load-deformation curve also performed in this study. Finite Element (FE) analysis results were also compared with conventional concrete of similar compressive strength. The result revealed that the performance of Geopolymer concrete under tension was slightly better than conventional concrete with similar compressive strength. Performance of Geopolymer beam was good to high-performance concrete beam under cyclic loading due to elongated shape of Ground Granulated Blast-furnace Slag particle. The Geopolymer beam was lighter in weight due to fly ash and Ground Granulated Blast-furnace. However, cost analysis indicated that geopolymer beam was slightly expansive than High performance concrete beam.

Keywords: Geopolymer concrete, Flexural strength, Cyclic Load, Geopolymer Damage Plasticity Model, Finite Element Model.

1. INTRODUCTION

Concrete is a most important construction material and used in the second to water across the world. America's Infrastructure report card stated that concrete structure play an important role for the country's economic stability by infrastructure developments (ASCE, 2009)). It was observed that Government spends billions of dollar on the infrastructure development work of concrete structure each year (Purvis, 2003). However, concrete industries emitted 5-7 % of CO_2 into environment and responsible for global warming (Benhelal et al., 2013). The demand of concrete increased by 4% per year due to huge infrastructure development projects (Syverson, 2011). Therefore, concrete industries demanded a material to reduce carbon emission from cement production. US Geological Survey stated that the replacement of cement concrete was the most challenging task, as it required a green concrete material which have similar mechanical and durability properties (Garside, 2021). Geopolymer concrete known for its early high strength, freeze-thaw resistance, low shrinkage, and the usage of industrial waste as its main constituents for the development of Geopolymer concrete (Davidovits, 2002). Geopolymer

[1a] Ph.D Candidate, Department of Civil Engineering, National Cheng Kung University.
[1b] Ph.D Candidate, Department of Civil Engineering, UIT, RGPV, India.
[2*]Associate Professor, Department of Civil Engineering, National Cheng Kung University.
[3] Professor, Department of Civil Engineering, UIT, RGPV, India.
[4] MSc. Student, Department of Civil Engineering, National Cheng Kung University.

materials reduced carbon footprint by 80%, and energy demand by up to 40 % from cement industries. (Duxson et al., 2007; Juenger et al., 2011). Fly ash can substitute cement up to 50 to 70% (Atiş, 2002). Fly ash, Ground granulated blast-furnace slag and alkali solution (NaOH/KOH) are the main binder of Geopolymer concrete (Mehta et al., 2020; Mehta & Monteiro, 2017). The main constituents of fly ash are SiO_2 and $Al2O_3$ (Ghosh & Ghosh, 2012). The polymerization reaction take place on Si-Al minerals in an alkaline environment, which produces a three-dimensional polymeric chain and ring structure made up of Si-O-Al-O links (Davidovits, 1999).

GGBS and fly ash are the main constituents for the development of Geopolymer material (Islam et al., 2014). Adding of GGBS may enhanced the mechanical properties of GPC (Bernal et al., 2010). Elongated and sharp edges of GGBS particle enhanced the tensile strength of GPC and may be affected the setting time and workability properties of Geopolymer material(Vikas & Rao, 2021). Furthermore, ambient curing may affect the mechanical properties of Geopolymer material (Vijai et al., 2010; Vora & Dave, 2013). Hot air curing for more than one day enhance the compressive strength of Geopolymer material(Singh et al., 2015; Xuequan et al., 1987). Hot curing may accelerate the rate of polymerization reaction (Lee et al., 2002). Hence, this research considered fly ash to GGBS ratio 1:1 and room temperature curing to develop Geopolymer concrete.

Relaxation behavior of joint investigated with help of X-ray diffraction procedure under cyclic loading and calculated residual stress (Yonezawa et al., 2020). A nonlinear finite element models used to evaluate the effect of CFRP rod and GFRP rod on structure behavior.(Ftai khan et al., 2019). Tsutsumi et al. (2019) analyzed load-carrying capacity of a bridge pier under cyclic loading. Numerical analysis of inelastic response of reinforced-concrete beam-column joints has performed and indicated fundamental characteristics of joints under cyclic loading (Lowes & Altoontash, 2003). However, structural behavior of Geopolymer concrete is still under consideration. Few researchers have investigated flexural performance of Geopolymer beam under cyclic loading with varied depth (Noushini et al., 2018). Limited information is available on the complex behavior of Geopolymer concrete materials beam under static and dynamic loading (Pham et al., 2021). Failure of the previous investigations to examine the characteristics of Geopolymer beam under cyclic loading motivated the present research work.

Flexural performance of Geopolymer concrete beam with fly ash to GGBS ratio 1:1 and 10 molarity alkali solution were numerically investigated under varied cyclic loading and depth with the used of ABAQUS finite element (FE) program. This study investigated the flexural performance of Geopolymer concrete beam under varied cyclic loading with varied depth and performed numerical studied by ABAQUS a finite element analysis tool. The variation in the depth of beam considered from 250 mm to 750 mm and analyzed under variation of magnitude on cyclic loading. A Concrete damaged plasticity (CDP) model has used to modeled the GPM beam with the use of ABAQUS (FE) software. Deformation behavior, yield strength with ultimate and failure strength with displacement have examined under cyclic loading. A comparative studied of cyclic loads for load-deformation curve also performed in this study.

II. NUMERICAL MODELING

Numerical analysis of geopolymer and high strength concrete beam were executed by using finite element-based software package ABAQUS version 11.2. Geopolymer and high strength concrete beam were modelled in ABAQUS by using C3D8 brick element. The C3D8 brick element considered eight nodes, and each node have three degrees of freedom, to analyse the compressive as well as tensile characteristics of Geopolymer and high strength concrete. The compressive strength properties, modulus of elasticity calculated by experiments and used during the modelling of beam.

Geometry of Beam:

Geopolymer concrete and high strength concrete rectangular beam with cross-sectional area of 200 mm × 250 mm, and effective length of 500 mm have been modelled and numerically evaluated in ABAQUS software. Table 4 indicates the beam dimensions. Table 5 shows the material properties of Geopolymer concrete and High-performance concrete gotten by performing lab experiments at Structure laboratory, Department of Civil Engineering, National Cheng Kung University, Taiwan.

Table 1: Beam specification

Beam	Width (mm)	Depth (mm)	Effective length (mm)
B-1	100	150	500
B-2	200	350	500
B-3	200	500	500
B-4	200	600	500
B-5	200	750	500

Table 2 Experimental results for Geopolymer and high-performance concrete

Material	Compressive strength f'_{ck} (MPa) at 28 days	Split tensile strength f_{tk} (MPa) at 28 days
Geopolymer concrete	60.5	5.04 MPa
High Strength Concrete	61.25	4.60 MPa

Damage plasticity model:

Figure 1 shows the damaged plasticity model of Geopolymer concrete (CDP) developed based on Lubinar Model. Nonlinear behavior of Geopolymer concrete can be simulated by CDP model. The force-deformation characteristics of Geopolymer concrete, compression and tension load behavior can be predicted from damage plasticity model.

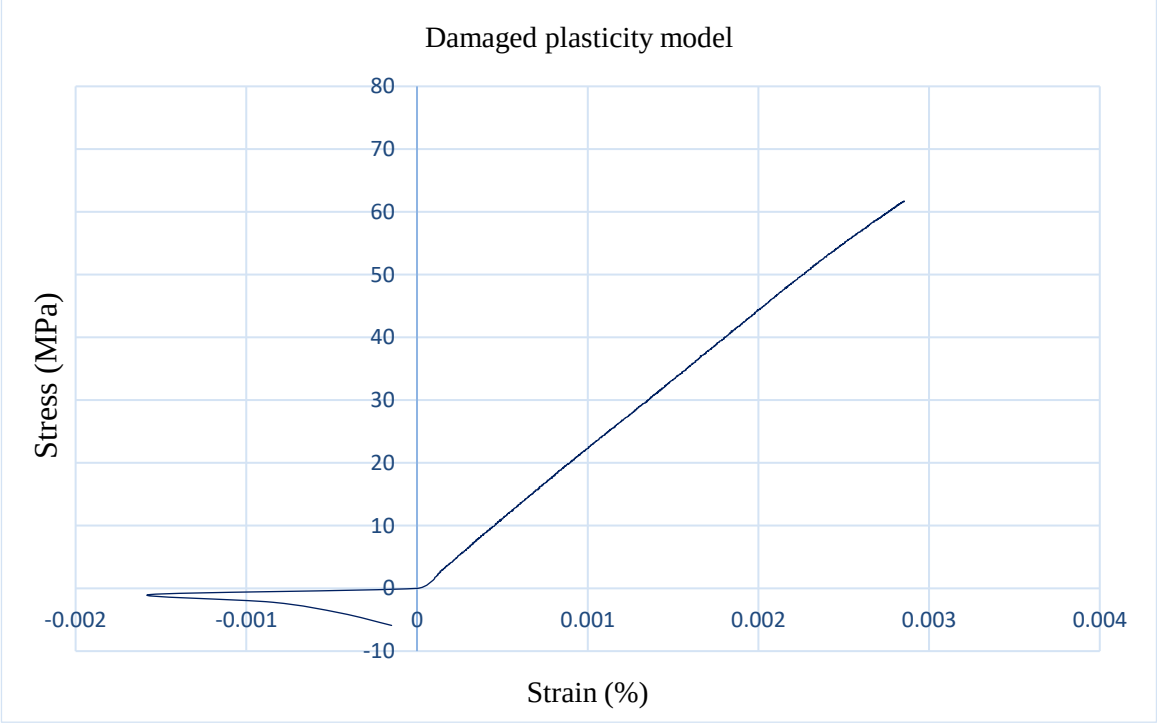

Figure 1 Damaged plasticity model for Geopolymer concrete based on Lubinar Model

Support conditions, loading, and post simulated axial deformation of reinforced concrete beam:

Figure 2 shows beam model in flexural using ABAQUS. The FE model of the beam included nodes and element.

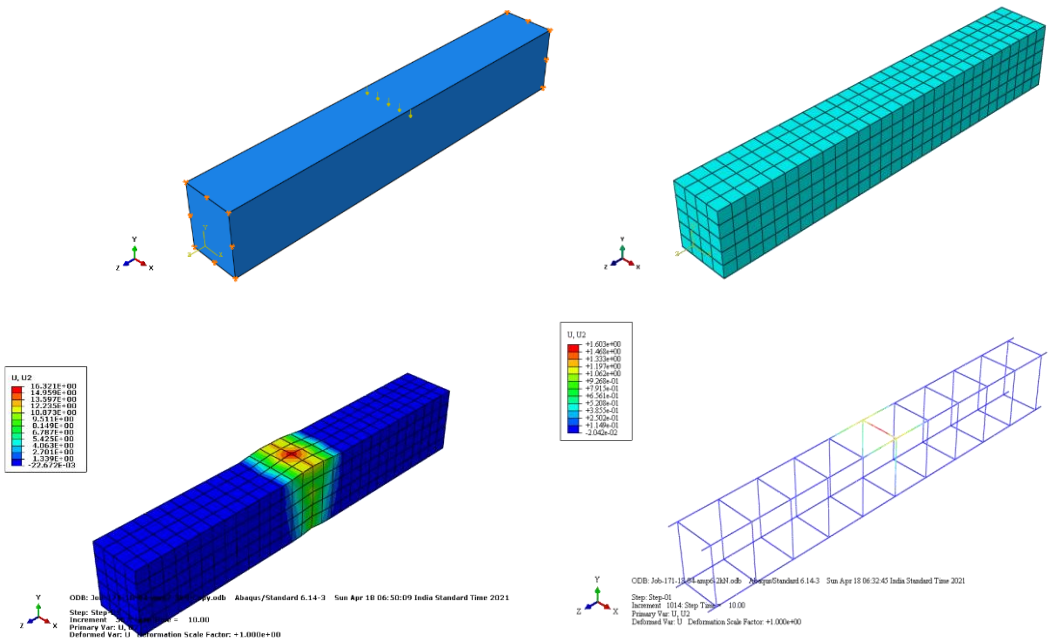

Figure 2 Finite Element model of reinforced concrete beam

Boundary conditions: The beams have analyzed as a simply supported beam by providing one end hinged (U_x, U_y, U_z are constrained) and other end roller support (U_y, U_z, constrained). The beam was examined under four-point loading condition. Mesh size was adopted as 10 mm.

I. RESULTS AND DISCUSSION

Table 2 shows the compressive strength test results and split tensile strength of Geopolymer concrete and high strength concrete at 28 days.

On the based on results shown in Table 2 that split tensile strength of Geopolymer concrete more than to high performance concrete, this may be because of GGBS particle have elongated shape which may enhanced the tensile strength of Geopolymer concrete.

Furthermore, comparative study of Geopolymer concrete and Conventional concrete have been carried out in this research. Geopolymer concrete and conventional reinforced concrete beam with similar cross-section and dimension and percentage of reinforcement have been examine by using the ABAQUS software.

Simulation result of Finite Element analysis of rectangular RC beam and Geopolymer concrete are indicated in Table 3, Table 4, and Figure 3. Simulation results of cyclic load displacement of reinforced beam of Geopolymer concrete beams and High-performance concrete beams from ABAQUS shown in Table 3 and Table 4.

Table 3 plastic deformation for Geopolymer and high-performance concrete beam

Beam Designation	First Plastic Displacement (mm) for High performance concrete	First Plastic Displacement (mm) for Geopolymer concrete
B-1	0.26	0.20
B-2	0.15	0.13
B-3	0.05	0.03
B-4	0.03	0.01

B-5	0.02	0.005

Table 4 Plastic Load for Geopolymer and High-performance concrete Beam

Beam Designation	**First Plastic Load (N) for High performance concrete**	**First Plastic Load (N) for Geopolymer concrete**
B-1	19988	23000
B-2	24932	27139
B-3	29768	29768
B-4	32000	38000
B-5	41000	51000

Table 5 Cost analysis of Geopolymer and concrete Beam

Materials	Cost in NTD (excluding overheads)	Ultimate load (kN)	Cost/ultimate load
Geopolymer concrete	16840	55.3	304.52
High strength concrete	15704	54.2	283.97

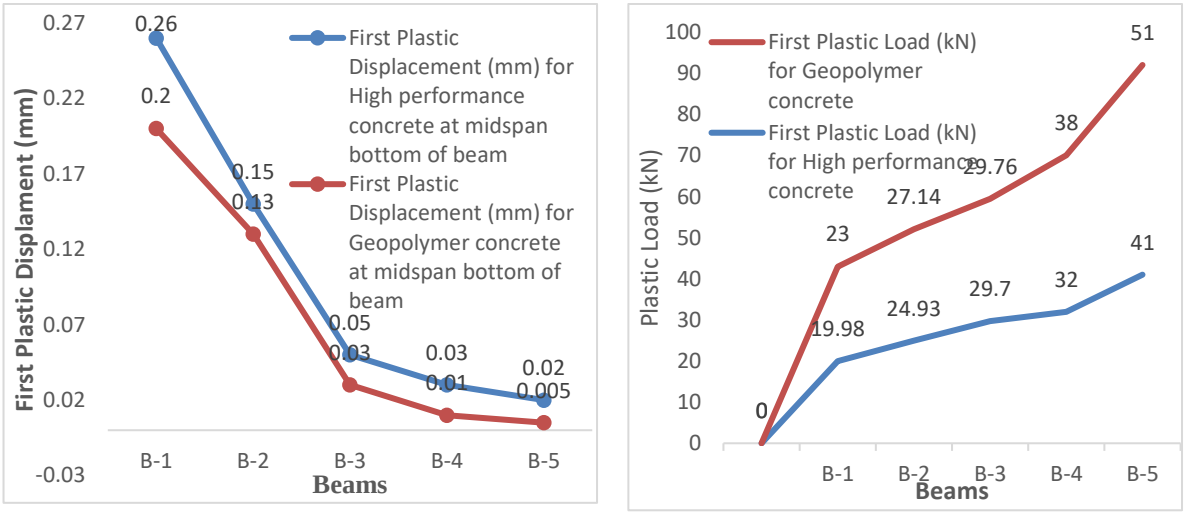

Figure 3 Plastic deformation and cyclic load curve for Geopolymer and high-performance concrete beams.

CONCLUSION

- A three-dimensional finite element analysis of 500mm×100mm×100mm of Geopolymer beam and high-performance concrete beam for cyclic load has been done.
- Total 10 number beam has been analyzed for cyclic load.
- Performance of Geopolymer beam is good to high-performance concrete beam due to GGBS particle have elongated shape.
- In cost analysis Geopolymer is slightly expansive then to high performance concrete.
- For further research work fracture energy analysis will explore for more accuracy of analysis of Geopolymer beam.

REFERENCES

Alanazi, H., Yang, M., Zhang, D., & Gao, Z. J. (2016). Bond strength of PCC pavement repairs using metakaolin-based geopolymer mortar. *Cement and concrete composites*, *65*, 75-82.
ASCE. (2009). 2009 report card for America's infrastructure.
Assi, L. N., Deaver, E. E., ElBatanouny, M. K., & Ziehl, P. (2016). Investigation of early compressive strength of fly ash-based geopolymer concrete. *Construction and building materials*, *112*, 807-815.
Atiş, C. D. (2002). High volume fly ash abrasion resistant concrete. *Journal of materials in civil engineering*, *14*(3), 274-277.
Benhelal, E., Zahedi, G., Shamsaei, E., & Bahadori, A. (2013). Global strategies and potentials to curb CO2 emissions in cement industry. *Journal of Cleaner Production*, *51*, 142-161.
Bernal, S., De Gutierrez, R., Delvasto, S., & Rodriguez, E. (2010). Performance of an alkali-activated slag concrete reinforced with steel fibers. *Construction and building materials*, *24*(2), 208-214.
Chindaprasirt, P., De Silva, P., Sagoe-Crentsil, K., & Hanjitsuwan, S. (2012). Effect of SiO2 and Al2O3 on the setting and hardening of high calcium fly ash-based geopolymer systems. *Journal of Materials Science*, *47*(12), 4876-4883.
Concrete, A. I. C. C. o., & Aggregates, C. (2013). *Standard Test Method for Bond Strength of Epoxy-resin Systems Used with Concrete by Slant Shear1*. ASTM International.
Davidovits, J. (1999). Chemistry of geopolymeric systems, terminology. Geopolymer,
Davidovits, J. (2002). years of successes and failures in geopolymer applications. Market trends and potential breakthroughs. Geopolymer 2002 conference,
Ghosh, K., & Ghosh, P. (2012). Effect of Na2O/Al2O3, SiO2/Al2O3 and w/b ratio on setting time and workability of fly ash based geopolymer. *International Journal of Engineering Research and Applications*, *2*(4), 2142-2147.
Lee, S. y., Lai, Y. l., & Hsu, T. s. (2002). Influence of polymerization conditions on monomer elution and microhardness of autopolymerized polymethyl methacrylate resin. *European Journal of Oral Sciences*, *110*(2), 179-183.
Lowes, L. N., & Altoontash, A. (2003). Modeling reinforced-concrete beam-column joints subjected to cyclic loading. *Journal of Structural Engineering*, *129*(12), 1686-1697.
Mehta, A., Siddique, R., Ozbakkaloglu, T., Shaikh, F. U. A., & Belarbi, R. (2020). Fly ash and ground granulated blast furnace slag-based alkali-activated concrete: Mechanical, transport and microstructural properties. *Construction and building materials*, *257*, 119548.
Mehta, P. K., & Monteiro, P. J. (2017). *Concrete microstructure, properties and materials*.
Nath, P., & Sarker, P. K. (2014). Effect of GGBFS on setting, workability and early strength properties of fly ash geopolymer concrete cured in ambient condition. *Construction and building materials*, *66*, 163-171.
Noushini, A., Hastings, M., Castel, A., & Aslani, F. (2018). Mechanical and flexural performance of synthetic fibre reinforced geopolymer concrete. *Construction and building materials*, *186*, 454-475.
Pham, D. Q., Nguyen, T. N., Le, S. T., Pham, T. T., & Ngo, T. D. (2021). The structural behaviours of steel reinforced geopolymer concrete beams: An experimental and numerical investigation. Structures,
Purvis, R. (2003). Bridge deck joint performance: A synthesis of highway practice (NCHRP Synthesis 319). *Washington, DC: Transportation Research Board*.
Singh, B., Ishwarya, G., Gupta, M., & Bhattacharyya, S. (2015). Geopolymer concrete: A review of some recent developments. *Construction and building materials*, *85*, 78-90.
Tsutsumi, S., Fincato, R., & Momii, H. (2019). Effect of tangential plasticity on structural response under non-proportional cyclic loading. *Acta Mechanica*, *230*(7), 2425-2446.
Vora, P. R., & Dave, U. V. (2013). Parametric studies on compressive strength of geopolymer concrete. *Procedia Engineering*, *51*, 210-219.
Yonezawa, T., Shimanuki, H., & Mori, T. (2020). Influence of cyclic loading on the relaxation behavior of compressive residual stress induced by UIT. *Welding in the World*, *64*(1), 171-178.
Zhu, X., Tang, D., Yang, K., Zhang, Z., Li, Q., Pan, Q., & Yang, C. (2018). Effect of Ca (OH) 2 on shrinkage characteristics and microstructures of alkali-activated slag concrete. *Construction and building materials*, *175*, 467-482.

(3f) Case studies on use of emerging technologies

APPLICATION OF ROBOTIC WELDING TECHNOLOGY TO CONTINUITY PLATE WELD WITHIN STEEL BUILT-UP BOX COLUMNS IN TAIWAN

Chung-Che Chou[1], Gee-Jin Yu[2], Kung-Juin Wang[3], Wei-Tze Chang[4], Chiun-Lin Wu[5], Charlene Chin-Jie Zhao[6], Keng-Li Lin[7], Zhi-Long Jian[8], Chung-Hsun Tsai[9], Yan-Song Lin[10], Ming-Ti Chou[11]

1. Director General, National Center for Research on Earthquake Engineering, Taipei, Taiwan, R.O.C.
2. Associate Technologist, National Center for Research on Earthquake Engineering, Taipei, Taiwan, R.O.C.
3. Principal Engineer, National Center for Research on Earthquake Engineering, Taipei, Taiwan, R.O.C.
4. Assistant Researcher, National Center for Research on Earthquake Engineering, Taipei, Taiwan, R.O.C.
5. Deputy Director General, National Center for Research on Earthquake Engineering, Taipei, Taiwan, R.O.C.
6. Undergraduate Student, Mechanical Science & Engineering, University of Illinois Urbana-Champaign, Illinois, U.S.A.
7. Chairman, Evergreen Steel Corporation, Taipei, Taiwan, R.O.C.
8. Deputy General Manager, Evergreen Steel Corporation, Taipei, Taiwan, R.O.C.
9. Manager, Evergreen Steel Corporation, Taipei, Taiwan, R.O.C.
10. General Manager, Farmost Industrial Company Limited, Taichung, Taiwan, R.O.C.
11. Engineer, Farmost Industrial Company Limited, Taichung, Taiwan, R.O.C.

Email: gjyu@narlabs.org.tw

ABSTRACT

This paper describes an effort to preliminarily verify the feasibility of adopting the technology of robotic welding in the manufacturing process of steel built-up box columns in Taiwan. Small-scale specimens emulating the key components in steel beam-to-column moment connections for the special moment frame (SMF) were manufactured. The specimens were made by including a gas metal arc welding (GMAW) performed by a robotic manipulator and a flux-cored arc welding (FCAW) performed manually by a skilled welding worker. The specimens passed by ultrasonic testing were tested by three mechanical ways including tensile tests, bending tests, and cyclic loading tests. Test results indicated that the robotic GMAW weld met the requirements specified in related codes and exhibited satisfactory mechanical properties and ductility.

Keywords: Robotic Welding, Built-Up Box Column, Internal Continuity Plate, GMAW, Special Moment Frame

INTRODUCTION

The demand of steel construction has increased rapidly in recent years in Taiwan. However, the steel fabrication industry is facing the challenge of an increasingly tough situation of welder shortage, significantly affecting the industry development. As a result, the research and industry communities are planning to use advanced robotic welding technology to substitute the traditional manual operation for this predicament. Technologies of robotic welding have been applied in many fields, such as shipbuilding (Lee 2014), pressure chamber processing (Jin et al. 2017), automobile manufacturing (Liu et al. 2010), aircraft component bonding (Zhang 2010) and train carriage manufacturing (Kochan 2000). There are also some successful practices in the building construction industry, including in-factory and on-site welding. In Taiwan, to reduce the manufacturing cost, in the processes of cutting the plates or the assembling units the manufacturing discrepancy or the geometric error is typically not rigorously controlled. This results in difficulty of directly applying the existing robotic welding technology that highly depend on the high geometric accuracy of the components to be welded. Therefore, developing an advanced robotic welding technology is one of the most important goals for the steel industry in Taiwan.

Taiwan is located in the circum-Pacific seismic belt; hence, earthquakes occur frequently and sometimes cause severe damages. Built-up box columns are widely used in steel structures in Taiwan due to the construction practice and excellent flexural capacity for earthquake resistance (Chou and Wu 2019, Chou and Chen 2020, Lin and Chou 2022, Chou et al. 2022a, 2022b). To provide the desired capacity of moment resistance at the beam-to-column connections, continuity plates inside the box column are welded at the elevations of the beam flanges. The welding quality of the continuity plates crucially affects the moment capacities of the beam-to-column connections and the corresponding seismic performance of steel frames.

The production process of built-up box columns in Taiwan is shown in Figure 1. Almost the whole process has been assisted by automated manufacturing equipment such as cutting and performing the web to flange welding using submerged arc welding (SAW). But the welding between the continuity plates and the column plates requires quite amount of skilled labor to carry out. Although it is a typical groove welding with high repeatability, due to a high variety of the customized column design, imperfection of the plate cut, and assembly with non-computerized machining, significant variance exists in the task of welding of continuity plates in the steel box column. This might be challenging for automatic manufacturing which highly depends on the controllable working environment. Therefore, it is urgent to develop an appropriate robotic welding technology to meet the requirements of automatic welding for the continuity plates in the steel box column.

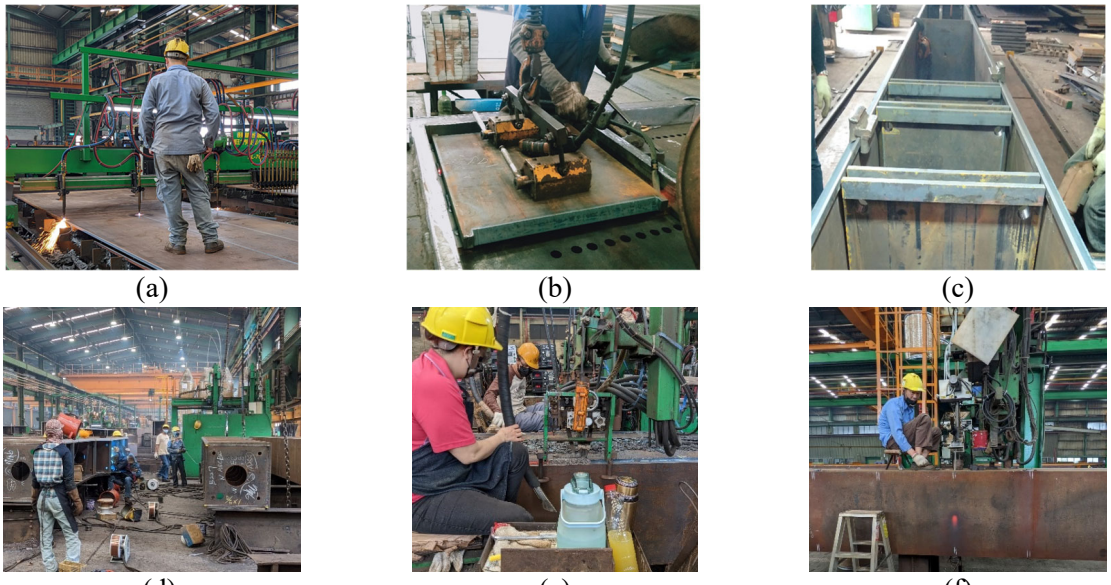

Figure 1 The production process of a built-up box column in Taiwan: (a) CNC flame cuts the steel plate, (b) assemble continuity plates, (c) assemble three column plates and the continuity plates, (d) weld the two sides of the continuity plates by GMAW, (e) weld the fourth column plates by SAW, and (f) weld the other two sides of the continuity plates by ESW

SPECIMENS USING ROBOTIC WELDING AND FCAW

Figure 2 shows a fabrication procedure of small-scale specimens in this study. The procedure was designed to emulate that by which the continuity plate, the column plate, and the beam flange are connected in an actual building construction. Figure 2 (a) shows the state in which the continuity plate (marked by yellow) is to be welded on the column flange (marked by orange). The continuity plate and the column plate were firstly temporarily assembled as shown in Figure 2 (b). Then, a different sets of trial parameters for the automatic welding were used to connect the continuity plate and the column plate by a robotic manipulator performing multi-layer and multi-pass welding, as shown in Figure 2(c). If the welding quality was passed by the ultrasonic testing (UT), another steel plate representing the beam flange was manually welded by the Flux-Cored Arc Welding (FCAW) to the opposite side of the column plate [see Figure 2(d)]. The specimens were made of SN490 steel plates with a thickness of 25

mm and a weld path length of 450 mm as shown in Figure 3. Finally, steel coupons are made by cutting and grinding specimens for subsequent material testing (see Figure 4).

Material testing includes tensile tests, cyclic loading tests, and bending tests. Figure 5 shows the configuration of tensile test and cyclic loading test. According to the American Structural Welding Code (AWS 2013), the Welding Procedure Qualification Tests (WPQT) should include both tensile and bending tests. The tensile tests were planned as per the ASTM E8 code (ASTM 2016) to investigate the mechanical properties of the welding. The tests were conducted for steel coupons sampled from the specimens (i.e., the coupon containing the base and welding materials) and the coupons made of the base material (SN490 steel). In addition, since continuity plates in the columns participate in transferring force from the beam flanges during seismic motion, bending and cyclic loading tests were planned to investigate the ductility and the hysteretic response of the welding. The dimension of the coupons for cyclic loading test followed the specification in ASTM E606 code (ASTM 2004). The cyclic loading was conducted in strain control with a strain command increasing from 1% to 4.5% as shown in Figure 5(c).

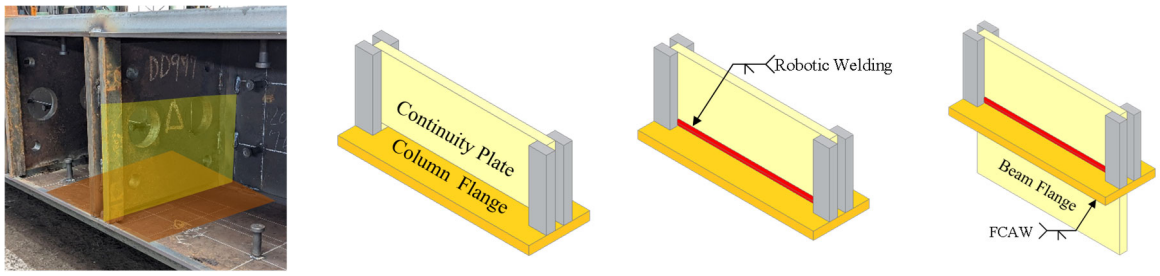

(a) (b) (c) (d)

Figure 2 Process of manufacturing the specimen: (a) A real box column in the manufacturing process, (b) Temporary assembling, (c) Robotic welding of the continuity plate, and (d) Manual welding of the beam flange

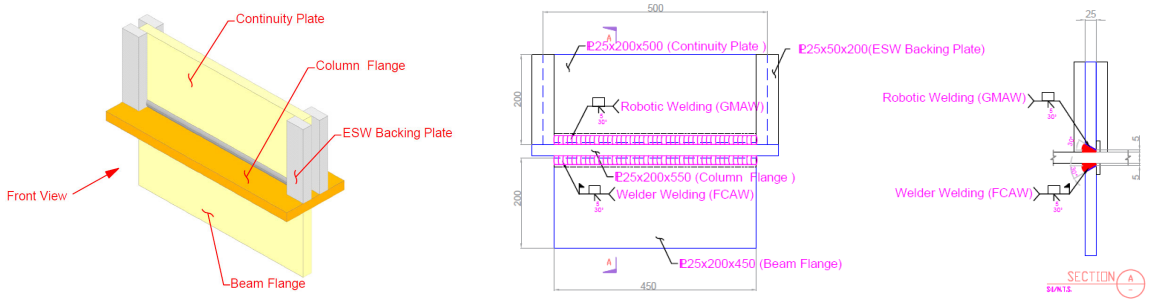

(a) (b)

Figure 3 Specimen details: (a) Schematic, and (b) Shop drawing (Unit: mm)

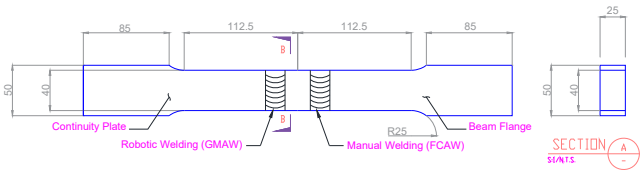

(a) The tensile test coupon

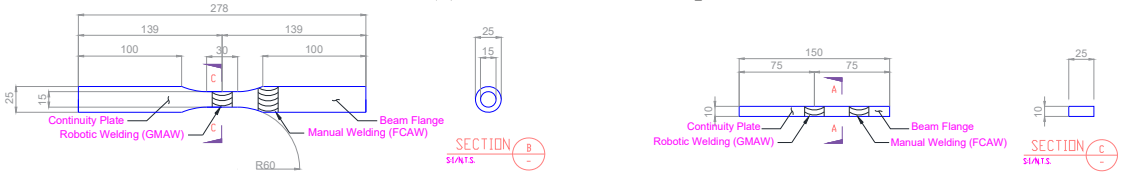

(b) The cyclic loading test coupon (c) The bending test coupon

Figure 4 The dimensions of material test coupons (Unit: mm)

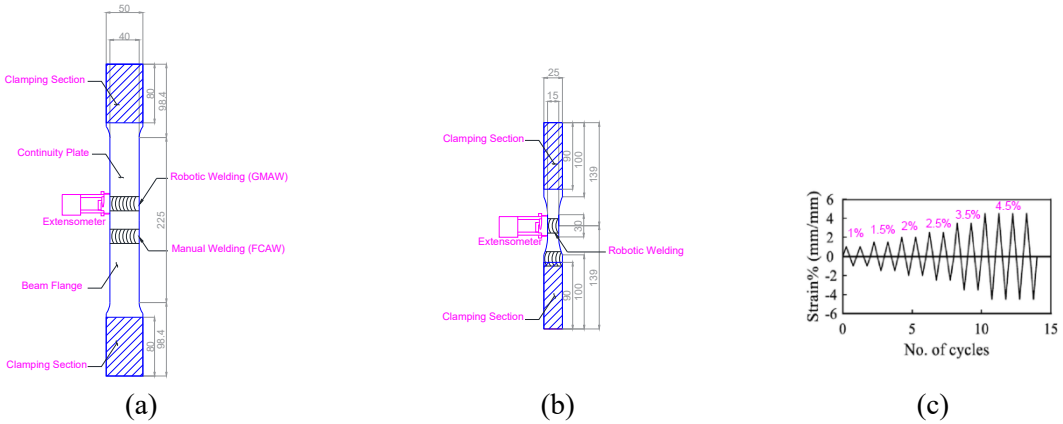

(a) (b) (c)

Figure 5 Configurations of tests: (a) tensile test, (b) cyclic loading, and (c) cyclic loading protocol.

GMAW WELDING PARAMETERS

The gas metal arc welding (GMAW) is the welding process in which with the heat supplied by electrical current two metals are melt and fused under the shield of flowing gasses. The tip of the electrode – in this case, the filler metal – must contact the metal workpiece to establish an electrical arc to begin the welding process. The filler metal is consumed by melting into the workpiece and is dispensed at a constant rate. Some of the most important welding parameters for GMAW are: voltage, current, travel speed, wire feed speed (WFS), working and travel angles, manipulation, electrode extension, and arc length. In addition, gas flow rate and gas composition are also important factors. Each parameter can affect the weld quality. The voltage and current have a directly proportional relationship with the heat input and melting rate of the filler metal. Travel speed and WFS are distinct parameters; travel speed is the rate at which the welder moves along the workpiece, and the WFS is the rate at which the filler metal is shot through the nozzle. Increasing the WFS may require an increase in travel speed and vice versa. The working and travel angles are the angles between the electrode and workpiece and the angles along the direction of travel, respectively. The manipulation is done with either stringer or weave beads. Stringer is a linear welding trajectory along the weld profile, while weaving is a patterned movement, which aids in achieving the desired geometry and heat input. Single-pass and multi-pass dictate the number of welding passes. Electrode extension is the length from the welding gun's contact tip to the tip of the filler metal. Arc length is the distance of the electrical arc generated, which is usually not accounted for since it is mostly imperceptible to the human eye.

Gas flow rate is essential in GMAW because it directly affects the effects of shielding the metal from externalities during solidification. It also helps in stabilizing the electrical arc. Oxidation and premature cracking due to improper gas shield coverage can jeopardize welds. Transfer methods include the short circuit, globular, and spray methods, and the classifications are dictated by the current, voltage, and gas composition administered. Since globular is affordable with a 100% CO_2 gas shield which is a more cost-effective option as compared to the more expensive argon, this study adopted the globular method.

ROBOTIC WELDING AND TEST RESULTS

Small-scale steel specimens emulate the assembly of the continuity plate and the column flange in actual built-up box columns. In this study, the robotic welding adopted the manipulator "Yaskawa AR1440" and the welding machine "MOTOWELD-X350". The ER48S-G with a diameter of 1.2 mm was adopted as the welding wire, and 100% CO_2 was chosen as the shielding gas. The welding environment is shown in Figure 6(a). Before welding, a groove profile of a specimen was scanned by the laser profiler shown in Figure 7(a). Figure 7(b) shows a typical output of the laser profiler. Figure 6 Figure 7 (c) shows the detailed measured results and the corresponding discrepancies. It is evident that despite complying with the tolerance specified in AWS D1.1, non-negligible assembly errors existed, especially for the root gap and the groove angle. This is resulted from the attempt to reduce the manufacturing cost, which is prevalent in practice in the construction industry in Taiwan. The plates are typically flame cut without

utilizing a more advanced but more expensive computer numerical control (CNC) and machining. In addition, after the plates are cut, they are usually assembled without using advanced equipment for accurately position of the workpieces.

(a) (b) (c)

Figure 6 (a) The welding environment, (b) robotic GMAW welding, and (c) manual FCAW welding

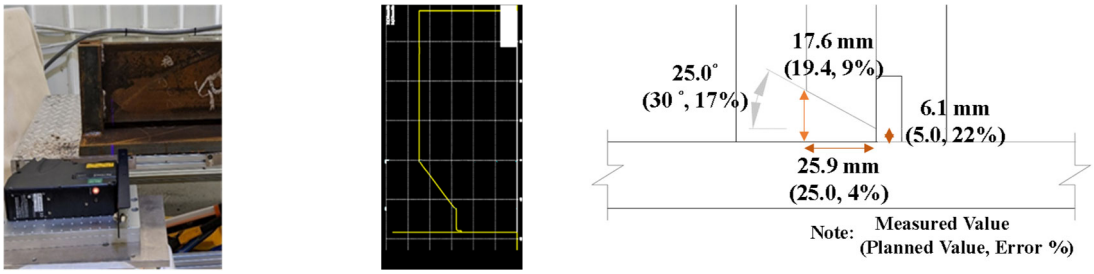

(a) (b) (c)

Figure 7 Laser profiler measurement of the groove profile of the specimen: (a) laser profiler, (b) laser profiler output, and (c) measured results and discrepancies

Welding Parameters

The quality of the GMAW weld highly depends on the selection of the input parameter values, regardless of the manner of welding (manually or robotically). In this study, values of the welding parameters suggested by professional welding workers were initially adopted to increase the likelihood of good-quality welds. These values were adjusted according to the actual welding results. The polarity setting of Direct Current Electrode Positive (DCEP) was used, and globular mode was adopted as the method to transfer the filler metal across the arc to the base metal. After a number of trials, some important input parameter values and findings are listed below.

1. The size of the bead is controlled by speed, current and voltage. Therefore, appropriate combination of the speed, current, and voltage is important especially for the last layer since the remaining space limits the size of the weld. In general, the size of weld bead generated with 280 volts and 30 amps is about 15 mm wide and 5 mm high on a flat surface.
2. When it is close to the end of a pass that the arc should be extinguished, it is suggested that the "back up crater filling technique" (Guo et al. 2009) should be used to reduce the chance of a crater crack as it would fill the weld crater, slow the cooling rate, and fill the undercut. It is suggested that the arc should be extinguished in a two-stage gradual manner: (1) reducing both the voltage and current by 10%, then holding still for about 0.5 seconds, and (2) further reducing the voltage and current by 10%, then holding still for about 3 seconds.
3. Before arc ignition, it is suggested to start the flow of the shielding gas for at least 0.2 second to cover the space of the weld bead to be formed.
4. The angle of the welding torch affects the stacking of beads. After the test, it is recommended to adjust the angle approaching to 90 degrees to obtain better results.
5. After each welding procedure is completed, the slag should be removed.

With the welding parameter values mentioned above, it required a four-layer weld for the small-scale specimen. The welding pass sequence is shown in Figure 8. Details of each layer are as follows:

1. The first layer: it adopted a combination of 280 volts, 30 amps, and a traveling speed in 3.3 mm/s for the root pass to ensure that the root gap can indeed be filled. Since the root gap is 5 mm, the previous welding parameters are sufficient to fill the root gap.
2. The second layer: Three welding passes (the 2nd - 4th passes) were planned for the second layer weld. The second and third passes are welded on the bottom of the second layer to provide a base with sufficient width for the fourth pass. At the same time, in order to reserve enough space on top of the two passes for the melted filler metal to fill in the fourth pass, the voltage and the current of the second pass and the third pass were slightly reduced. In order to avoid the bead being too large and therefore to slip off, the fourth welding pass was performed at a faster speed.
3. The third layer and fourth layer: Three welding passes (the 5th - 7th passes and the 8th - 10th passes) were planned for the third layer and fourth layer, respectively. They are stacked sequentially from bottom to top. Lower voltage, current and higher welding speed were used for the three passes in the third layer.

Figure 6(b) shows the robotic welding process for a specimen. The quality of the resulting weld was then examined by UT and was capable of meeting the acceptance criteria. Then the beam flange was manually welded to the opposite side of the column plate with the FCAW process by a skilled welder [see Figure 6(c)]. After the manufacturing processes completed, the specimen was cut and ground to make coupons for the subsequent mechanical tests. Figure 9 shows the specimen's cross section which contains two welds, made by the manipulator and the welder. The surface of the weld made by the welder is much smoother than that made by the manipulator, indicating that humans tend to be more adaptable to variations in the welding process.

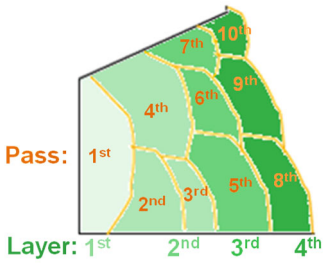

Figure 8 Welding pass sequence in multi-layer and multi-pass welding with robotic welding

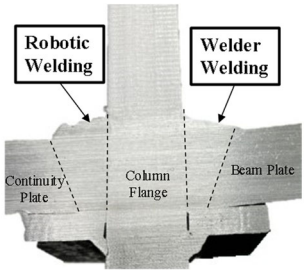

Figure 9 Photographical view of the specimen's cross section

Welding Test

In order to investigate the mechanical properties of the weld made by the robotic manipulator, a tensile test, cyclic loading test, and side bending test were performed on the coupons according to the ASTM E8, ASTM E606, ASTM E190, respectively.

Figure 10(a) shows the configuration photo of the tensile test. From top to bottom, the coupon was actually composed of 5 components: the continuity plate, the GMAW weld by the robotic manipulator, the column flange along its thickness direction, the weld with the FCAW process by the welder, and the beam flange. During the test, necking concentrated at the continuity plate before failure occurred. Figure 10(b) and (c) show the front and the side views of the coupon after the test. It is evident that the weld was not damaged in the tensile test, thus meeting the requirement in AWS D1.1. The force-displacement

curve of the welding specimen is similar to the base metal as shown in Figure 11(a). The stress-strain curve in Figure 11 (b) showed that the strain of the weld zone could exceed 7%, indicating the satisfactory ductility exhibited by weld. Figure 10(c) shows the stress-strain curve obtained from the cyclic loading test; the hysteretic loop of the weld by robotic welding is very stable up to an axial strain of 4.5%. No visual damage or cracks on the surface of the coupon were found after the low cycle fatigue test. The lateral bending test was conducted as specified in ASTM E190 (ASTM 2021), using a 100 ton universal testing machine, which pressed down coupon until the inner curvature radius of the coupon reached 20 mm [see Figure 11(d)]. Since neither cracks nor other visible defects were found on the outside of the curved part of the weld, it can be concluded that the weld made by the robotic manipulator met the requirements of the specification.

(a) (b) (c)

Figure 10 Coupon tensile test: (a) tensile test, (b) Coupon front view after test, and (c) Coupon side view after test

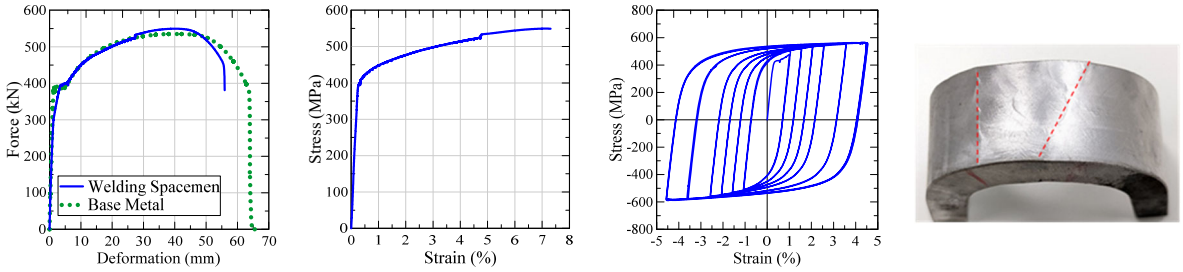

(a) (b) (c) (d)

Figure 11 Mechanical test results: (a) force-displacement relationship (tensile test), (b) stress-strain relationship of the weld zone (tensile test), (c) stress-strain relationship of the weld zone (cyclic test), and (d) coupon after the bending test

CONCLUSIONS

This study evaluated the feasibility of using a robotic technology to welds between the internal continuity plate and the column plate in steel built-up box columns. The experimental results revealed that the weld made by a robotic manipulator exhibited satisfactory mechanical properties. A set of suggested values of welding parameters was provided in this study for multi-layer and multi-pass slot welding.

To speed up the development of the robotic welding technology, the National Center for Research on Earthquake Engineering (NCREE) has launched a three-year research project with the steel industry in Taiwan (Figure 12) to integrate the Artificial Intelligence (AI) and advanced sensing technology to build an adapted smart robotic welding system. It is expected that the efficiency and quality of welding in the steel building construction industry can be significantly improved in the future.

Figure 12 A meeting (2022.5.19) for facilitating industry-academia cooperation on the development of robotic welding (NCREE, the four major steel manufacturing companies, and Farmost Industrial Company)

ACKNOWLEDGMENTS

The specimen fabrication was sponsored by Evergreen Steel Corporation Company, Taiwan. The robotic welding was conducted by Farmost Industrial Company, Taiwan. We would like to thank both companies for their support in this research work.

REFERENCES

ASTM. (2004). *Standard Practice for Strain-Controlled Fatigue Testing*, American Society for Testing and Materials International, ASTM E606-04.

ASTM. (2016). *Standard Test Methods for Tension Testing of Metallic Materials*, American Society for Testing and Materials International, ASTM E8/E8M.

ASTM. (2021). *Standard Test Method for Guided Bend Test for Ductility of Welds*, American Society for Testing and Materials International, ASTM E190-21.

AWS. (2020). *Structural Welding Code - Steel*, American Welding Society, AWS D1.1.

Chou, C. C., Xiong H. C., Kumar A., Lai Y. C., Uang, C. M. (2022a). "Test and Finite Element Analysis of Two-Story Steel Subassemblage Frames with Highly and Moderately Ductile Box Columns", *8th Asia Conference on Earthquake Engineering*, Taipei, Taiwan.

Chou, C. C., Lai, Y. C., Xiong, H. C., Lin, T. H., Uang, C. M., Mosqueda G., Ozkula, G., El-Tawil, S., McCormick, J.P. (2022b). "Effect of Boundary Condition on the Cyclic Response of I-Shaped Steel Columns: Two-Story Subassemblage versus Isolated Column Tests," *Earthquake Engineering and Structural Dynamics,* DOI: 10.1002/eqe.3730.

Lin, T. H., Chou, C. C. (2022). "High-Strength Steel Deep H-Shaped and Box Columns under Proposed Near-Fault and Post-Earthquake Loadings." *Thin-Walled Structures*, 172, 108892.

Chou, C. C., Chen, G. W. (2020). "Lateral Cyclic Testing and Backbone Curve Development of High-Strength Steel Built-Up Box Columns Under Axial Compression. *Engineering Structures* 223, 111147.

Chou, C. C., Wu S. C. (2019). "Cyclic Lateral Load Test and Finite Element Analysis of High-strength Concrete-filled Steel Box Columns under High Axial Compression. *Engineering Structures,* 189(15), 89-99.

Asif, K., Zhang, L., Derrible, S., Indacochea, J.E., Ozevin, D., Ziebart, B. (2022). "Machine Learning Model to Predict Welding Quality Using Air-coupled Acoustic Emission and Weld Inputs," *Journal of Intelligent Manufacturing*, 33: 881–895.

Jin, Z., Li, H., Zhang, C., Wang, Q., Gao, H., (2017). "Online Welding Path Detection in Auto-matic Tube-to-tubesheet Welding using Passive Vision," *International Journal of Advanced Manufacturing Technology*, 90: 3075-3084.

Liu, Z., Bu, W., and Tan, J. (2010). "Motion Navigation for Arc Welding Robots based on Feature Mapping in A Simulation Environment," *Robotics and Computer-Integrated Manufacturing*, 26: 137-144.

Kochan, A. (2000). "Automating the Construction of Railway Carriages," *Industrial Robot*, 27: 108–110.

Zhang, Z., Gao, H., Han, Q., Huang, R., Rong, J., and Wang, Y. (2015). "Hand-eye Calibration in Robot Welding of Aero Tube," *Journal of Shanghai Jiao Tong University*, 49(3): 392-394.

STUDY ON DEVELOPMENT LENGTH IN TENSION AND BOND SPLITTING PERFORMANCE OF CONCRETE FOR REBAR

Kai-Ning Chi[1] and Ker-Chun Lin[2] and Sheng-Jhih Jhuang[1]
1. Assistant Researcher, Building Engineering Division, National Center for Research on Earthquake Engineering, Taipei, Taiwan, R.O.C.
2. Researcher Fellow, Building Engineering Division, National Center for Research on Earthquake Engineering, Taipei, Taiwan, R.O.C.
Email: knchi@narlabs.org.tw, kclinncree@narlabs.org.tw, sjjhuang@narlabs.org.tw

ABSTRACT

For ACI 318-19 Code, a modification factor of steel grade of Ψ_g that is equal to 1.15 or 1.3 for 550 or 690 MPa grade of steel bar exceeding 420 MPa was added to increase straight development length in tension for deformed bar. It is known that the design equation of development length stipulated in the existing ACI 318 Code was obtained based on a mechanism of concrete splitting primarily dominated by contact characteristics between concrete and steel bar. This paper was intended to investigate the rationality of the Ψ_g included in the design equation of development length. A total of 20 beam-end specimens was carried out to study bond behaviors of concrete splitting with a deformed bar in this research. Based on analysis overcomes of the test bond stress in this research, it was confirmed that under upper limitations of 70 MPa for the concrete strength and 2.5 for the split index, the average bond stresses of the three various grade bars for ACI 318-14 Code ranged from 1.72 to 2.4. The modification factor of steel grade of Ψ_g seemed to not be needed in the provisions of straight development length of ACI 318-19 Code.

Keywords: ACI 318-19, development length, splitting, bond stress, split index.

INTRODUCTION

In the current domestic design specifications for concrete structures, the formula for the development length of deformed bars in tension mainly follows the relevant provisions of the ACI 318-05 specification. The ACI 318-19 specification also uses the same formula, which provides that in addition to raising the upper limit of the applicable longitudinal bar strength from 420 MPa to 690 MPa, also adds the coefficient Ψ_g of reinforcement strength grade. The development length L_d of rebar in tension, ld, is shown in Eq. (1).

$$L_d = 0.9\frac{f_y}{\lambda\sqrt{f_c'}}\frac{\psi_t\psi_e\psi_s\psi_g}{\left(\frac{c_b+K_{tr}}{d_b}\right)}d_b,\ K_{tr}=\frac{40A_{tr}}{sn},\ 1.0\le\left(\frac{c_b+K_{tr}}{d_b}\right)\le 2.5 \quad (1)$$

where f_y is the specified yield stress of a reinforcing bar (MPa); f_c' is the specified compressive strength of concrete (MPa); d_b is the nominal diameter of a reinforcing bar (mm); c_b is the smaller of the distance from the center of a reinforcing bar to the nearest concrete edge or half center-to-center spacing of the bars (mm); K_{tr} is the transverse reinforcement index; A_{tr} is total sectional area of all transverse reinforcement within spacing s that crosses the potential plane of splitting through the reinforcement being developed or developed along the plane of splitting (mm2); s is center-to-center spacing of the transverse reinforcement (mm); and n is number of reinforcing bars being developed along the splitting plane; Ψ_g is the reinforcement strength grade coefficient.

According to the relevant provisions of the ACI 318-19 code, the coefficient Ψ_g for yield strengths of 420 MPa (60 ksi), 550 MPa (80 ksi), and 690 MPa (100 ksi) are 1.0, 1.15, and 1.3, respectively. The revision of this coefficient is based on the research of Orangun *et al*. (1977) and Canbay and Frosch

(2005). From their conclusions, it is known that "the splice strength of reinforcement is linearly related to the parameter of splice length $\sqrt{l_s}/d_b$," and this was based on the rebar lapped test without confinement. As for the development length of confined longitudinal reinforcement in beam members, the conclusions still need to be further verified. In addition, the development increment of the splice strength of rebar decreases with the increase in the lap length; however, the increase in the splice length is not only related to the strength of the rebar. Although increasing the strength of the rebar requires a longer splice length, it is also possible to shorten the lap length requirement by increasing the strength of the concrete.

EXPERIMENTAL PLAN

Test specimen

In this study, 20 sets of bonding test specimens were used to investigate the bonding behavior of threaded bars in HSRC members. The width, height and length of each bonding test specimen was 180 mm, 450 mm, and 1000 mm, respectively (Figure 1). As shown in Fig. 1, a beam type of bonding specimen is used herein to determine the bond characteristics of the reinforcements for most RC members. The purpose is to simulate the actual behaviors of bonded longitudinal bars if beam members under the combined effects of flexure and shear. Therefore, the testing reinforcements are unsymmetrically placed in the specimens. To simulate as accurately as possible and to conveniently adjust bonded length, two polyvinyl chloride (PVC) pipes are installed at both bond ends of the bonded reinforcement in each specimen to isolate the reinforcement from the concrete. All specimens in this paper are designed based on Eq. (1). Table 1 presents the study parameters. Primary parameters of this study include the specified yield strength f_y of the deformed bar, specified compressive strength f_c' of concrete, splitting index $(c_b+K_{tr})/d_b$ and relative rib area R_r (ratio of rib height to rib spacing for reinforcement). Figure 2 shows the different surface geometric shapes (parallelogram and diamond) of the reinforcing bars that were used in this study. Each specimen used a single #10 tensile bar with three strength grades (420, 550, 690 MPa) and five concrete strengths (28, 49, 70, 85, 100 MPa). Two $(c_b+K_{tr})/d_b$ splitting indices of values 3.87 and 4.92 were used for all specimens.

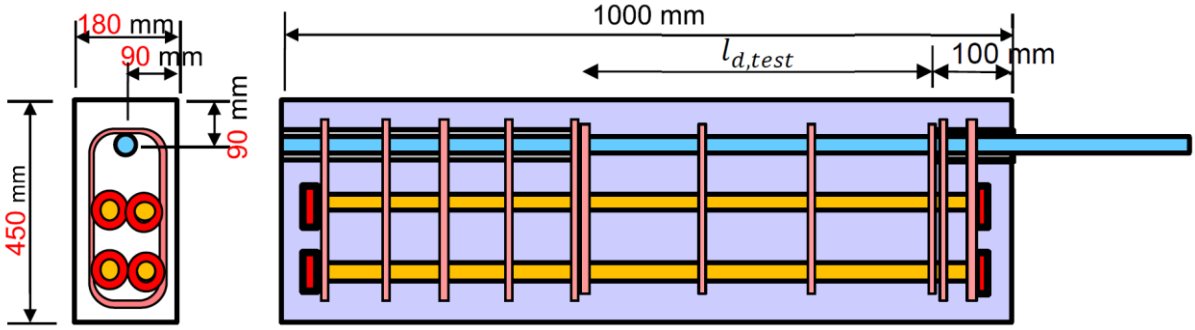

Figure 1. Schematic diagram of the specimens and the mechanical mechanism of the bond tests.

(a) Deformed bars (Parallelogram type) (b) Deformed bars (Diamond type)

Figure 2. Details of the deformed bars.

Test setup

Figure 3 schematically depicts the test setup and presents the photograph. This test setup is intended to simulate the actual mechanism of bonded straight reinforcement in structural members combining

moment and shear forces. The L-shape reaction frame is designed as subjected reactions mechanism to the specimens and its source of reaction force is from its right and left sides in the Figure 3. On the right side of the reaction frame, a hollow cylinder oil jack, a hollow cylinder load cell and a double-web H-section member are placed in order as force source, a force measuring device and reaction force to this test setup. The loaded end of the testing reinforcement is designed to extend through the oil jack, load cell and the double-web H-section member and it is then fastened by a nut. A monotonically increasing tensile load is manually applied using the oil jack to each specimen. Each increment in the load is 5% of the yield strength of the tested reinforcement. Bonding force of the reinforcement comes from the maximum reading from load cell during the test. The maximum readings of the test are monitored at all times through the outputs shown on the computer's screen.

Table 1. Design parameters of specimens.

Specimens	f_c' (MPa)	f_y (MPa)	d_b (mm)	R_r	$C_{b,s}$ (mm)	$C_{b,t}$ (mm)	S_s (mm)	$\frac{(C_b + K_{tr})}{d_b}$	$l_{d,14}$ (mm)	$l_{d,test}$ (mm)	$\frac{l_{d,test}}{l_{d,14}}$
BC28Y42S15De	28	420	32	0.097	90	90	150	3.87	914	450	0.492
BC28Y55S15De	28	550	32	0.094	90	90	150	3.87	1197	600	0.501
BC28Y42S15Di	28	420	32	0.154	90	90	150	3.87	914	450	0.492
BC28Y55S15Di	28	550	32	0.133	90	90	150	3.87	1197	600	0.501
BC49Y42S15De	49	420	32	0.090	90	90	150	3.87	691	450	0.651
BC49Y55S15De	49	550	32	0.097	90	90	150	3.87	905	600	0.663
BC49Y42S15Di	49	420	32	0.145	90	90	150	3.87	691	450	0.651
BC49Y55S15Di	49	550	32	0.138	90	90	150	3.87	905	600	0.663
BC70Y42S15De	70	420	32	0.087	90	90	150	3.87	578	450	0.779
BC70Y55S15De	70	550	32	0.094	90	90	150	3.87	757	450	0.594
BC70Y42S15Di	70	420	32	0.134	90	90	150	3.87	578	450	0.779
BC70Y55S15Di	70	550	32	0.130	90	90	150	3.87	757	450	0.594
BC85Y55S75De	85	550	32	0.099	90	90	75	4.93	757	450	0.594
BC85Y69S75De	85	690	32	0.102	90	90	75	4.93	950	450	0.474
BC85Y55S75Di	85	550	32	0.121	90	90	75	4.93	757	450	0.594
BC85Y69S75De-BC	85	690	32	0.101	90	90	75	4.93	950	450	0.474
BC10Y55S75De	100	550	32	0.093	90	90	75	4.93	757	450	0.594
BC10Y69S75De	100	690	32	0.095	90	90	75	4.93	950	450	0.474
BC10Y55S75Di	100	550	32	0.136	90	90	75	4.93	757	450	0.594
BC10Y69S75De-BC	100	690	32	0.099	90	90	75	4.93	950	450	0.474

Note: The diameter of the stirrup is 13 mm; f_y denotes the specified yield strength of the deformed bar; f_c' denotes the specified compressive strength of concrete; d_b denotes the nominal diameter of a reinforcing bar (mm); R_r denotes the relative rib area of the bar surface (ratio of rib height to rib spacing for reinforcement); $c_{b,s}$ and $c_{b,t}$ represent the distance from center of a bar to side and top concrete surface; S_s denotes the spacing of confined stirrups between the region of development bonded length; c_b is the smaller of $c_{b,s}$ and $c_{b,t}$; K_{tr} is the transverse reinforcement index; $l_{d,14}$ represents

the reinforcement development length calculated using Eq. (1) without Ψ_g; $l_{d,test}$ represents the testing embedded length of bar.

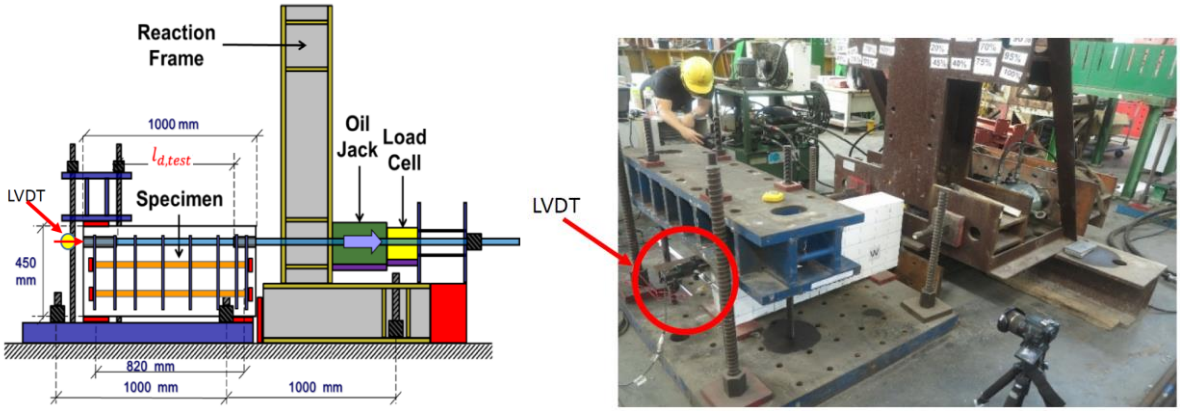

Figure 3. Test setup of Bonding Test.

RESULTS AND DISCUSSION

Strength and Failure Mode

The test results such as the test strength and failure modes of each specimen are listed in Table 2, where P_{test} is the maximum tensile strength of the specimen. The ratio of P_{test} to P_y in Table 2 shows that except for specimens BC28Y55S15De and BC28Y55S15Di which are slightly less than 1.0, the rest of the specimens are all greater than 1.0, and the maximum can reach 1.49. The results show that when the ratio of the average rib height to the average rib spacing of the deformed bar was not less than 0.087 and the splitting index was not less than 3.87, the straight development length of the rebar calculated using ACI 318-14 or ACI 318-19 without considering the coefficient Ψ_g of reinforcement strength grade (i.e., $\Psi_g = 1.0$) is still quite conservative. In addition, four failure modes were identified, namely concrete splitting, bar fracture, splice fracture, and rod fracture, as portrayed respectively in Figure 4. Except for the bar fracture of specimens BC85Y55S75De, BC10Y55S75De and BC10Y69S75De, the rod and coupler fracture of the BC10Y55S75Di and the BC10Y69S75De-BC, which were unexpected failures, the remaining 15 specimens all occurred concrete splitting failure as expected. Examining the 5 specimens with unexpected failure, it was found that their concrete strengths were all higher than 70 MPa and $(c_b+K_{tr})/d_b$ was 4.93. Discussion of the results shows that this situation is related to the contribution of high concrete strength (above 70 MPa) and high splitting index$(c_b+K_{tr})/d_b$, resulting in a significant increase in the bond strength capacity, which in turn affects the rod and coupler of BC10Y55S75Di and BC10Y69S75De-BC. In addition, the developed bars of the other three specimens were bar fracture.

Figure 4. Failure modes.

Bond Stress

The ratios of test bond stress are expressed as $R_{u14,lim}$ and $R_{u19,lim}$ with the upper limit of the concrete strength of 70 MPa and the splitting index value of 2.5 stipulated in specification ACI 318-14 and -19 for development length, as shown in Figure 3. The figure on the left shows that the average values of

$R_{u14,unl}$ corresponding to the three steel strength grades are 1.72, 1.89, and 2.4, which are approximately equal. This is a conservative result. The figure on the right shows that the average value of the test bond stress ratio $R_{u19,unl}$ are 1.73, 2.17, and 3.17 for the three grades (420, 550, and 690 MPa), respectively.

In addition, the ratios of test bond stress are expressed as $R_{u14,unl}$ and $R_{u19,unl}$ without the upper limit of the concrete strength of 70 MPa and the splitting index value of 2.5 stipulated in specification ACI 318-14 and -19 for development length, as shown in Figure 4. The figure on the left shows that the average values of $R_{u14,unl}$ corresponding to the three steel strength grades are 1.10, 1.05, and 1.12, which are approximately equal. This is a conservative result. The figure on the right shows that the average value of the test bond stress ratio $R_{u19,unl}$ are 1.10, 1.21, and 1.46 for the three grades (420, 550, and 690 MPa), respectively. Based on the ratio $R_{u19,unl}$ of the 420 strength grade, the average bond stresses of grades 550 and 690 are 1.1 and 1.33, respectively. This ratio roughly corresponds to the coefficient Ψ_g in Eq. (1), showing that this formula is already sufficiently conservative, and therefore, there is no need to add the coefficient Ψ_g.

Table 2. Test results of bond tests.

Specimens	f'_{ca} (MPa)	f_y (MPa)	d_b (mm)	P_y (kN)	P_{test} (kN)	$\frac{P_{test}}{P_y}$	Failure Mode
BC28Y42S15De	43.9	420	32	338	342	1.012	Concrete splitting
BC28Y55S15De	43.9	550	32	442	421	0.952	Concrete splitting
BC28Y42S15Di	43.9	420	32	338	339	1.003	Concrete splitting
BC28Y55S15Di	43.9	550	32	442	427	0.966	Concrete splitting
BC49Y42S15De	63.5	420	32	338	394	1.166	Concrete splitting
BC49Y55S15De	63.5	550	32	442	509	1.152	Concrete splitting
BC49Y42S15Di	63.5	420	32	338	427	1.263	Concrete splitting
BC49Y55S15Di	63.5	550	32	442	552	1.249	Concrete splitting
BC70Y42S15De	73.5	420	32	338	505	1.494	Concrete splitting
BC70Y55S15De	73.5	550	32	442	476	1.077	Concrete splitting
BC70Y42S15Di	73.5	420	32	338	448	1.325	Concrete splitting
BC70Y55S15Di	73.5	550	32	442	457	1.034	Concrete splitting
BC85Y55S75De	79.1	550	32	442	569	1.287	Bar fracture ✖
BC85Y69S75De	79.1	690	32	555	631	1.137	Concrete splitting
BC85Y55S75Di	79.1	550	32	442	582	1.317	Concrete splitting
BC85Y69S75De-BC	79.1	690	32	555	625	1.126	Concrete splitting
BC10Y55S75De	91.1	550	32	442	583	1.319	Bar fracture ✖
BC10Y69S75De	91.1	690	32	555	641	1.155	Bar fracture ✖
BC10Y55S75Di	91.1	550	32	442	600	1.357	Splice fracture ○
BC10Y69S75De-BC	91.1	690	32	555	640	1.153	Rod fracture □

The following specific conclusions can be obtained from the results and discussion of the development of the experimental bond stress. If the upper limit conditions of the concrete strength of 70 MPa and

the splitting index of 2.5 are lifted, the straight development length of the specification ACI 318-14 can still obtain accurate results. And there is still a conservative margin of more than 10% on average. Therefore, it is suggested that when calculating the development length of high-strength deformed bars at the critical section for members with transverse reinforcement to provide confinement, the ACI 318-14 straight development length model (Eq.(1) without Ψ_g) can be used. However, the upper limit of concrete strength and splitting index can be adjusted to 100 MPa and 5.0 respectively.

From the results of the bond test of deformed bars with a relative area R_r value not less than 0.0087 in this study, the development length provided by Eq. (1) is about 1.7 times (considering Ψ_g factor) more than the actual development length requirement under the condition of developing the same tensile strength.

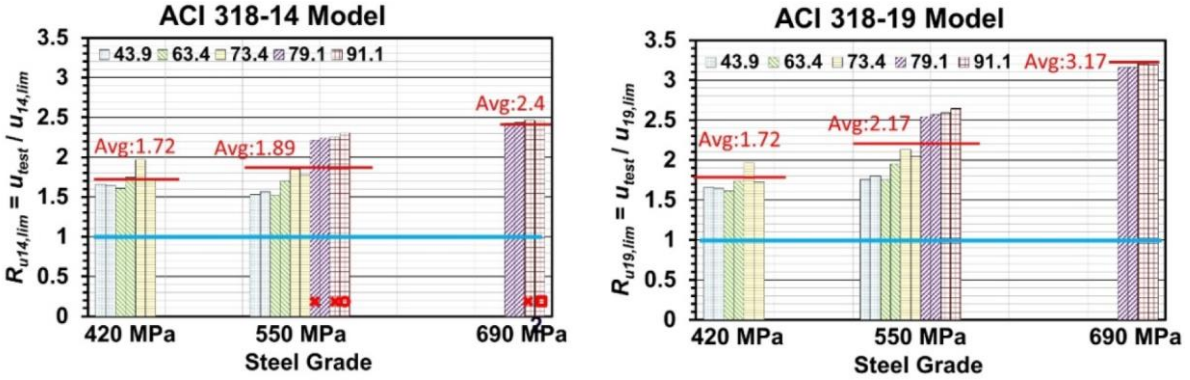

Figure 3. Bond stress ratio with considering the upper limit of the splitting index and concrete strength.

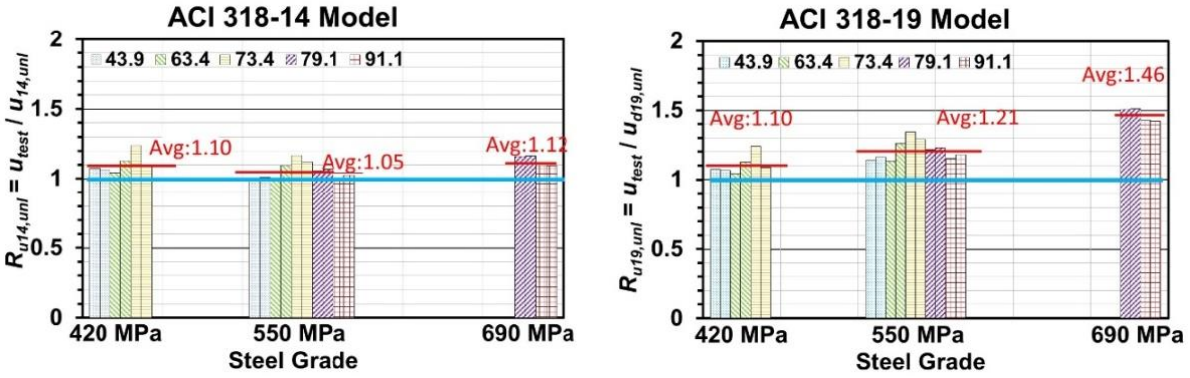

Figure 4. Bond stress ratio without considering the upper limit of the splitting index and concrete strength.

CONCLUSIONS

The surface relative rib area R_r value of steel bars not less than 0.087 are used to discuss the bond performance in this study. The following conclusions and suggestions can be summarized from the test and analysis results.

(1) There are four failure modes in this study, including concrete splitting, bar fracture, splice fracture and rod fracture. The failure modes are listed in Table 2.

(2) From the test failure mode, it is found that the specimen with a splitting index of 4.93 still exhibits splitting crack. By combining with past bond tests, it has been shown that the bond stress, normalized to the square root of the concrete strength $\sqrt{f_c'}$, increases approximately linearly with the splitting index.

(3) When the upper limits of concrete strength 70 MPa and splitting index 2.5 are used to calculate the development length, respectively, the average bond stresses of developed bars with different strength grades of 420, 550 and 690 MPa are 1.72, 1.89 and 2.40 for ACI 318-14, and the

formula can provide sufficient safety factor, which is better than 1.72, 2.17 and 3.17 for ACI 318-19.

(4) When the upper limits of concrete strength and splitting index are lifted to 70 MPa and 2.5, and the upper limits of the value are adjusted to 100 MPa and 5.0, respectively, the development length model of ACI 318-14 can be obtained results with a conservative margin of about 10%. The mean values of the bond stress of the bars corresponding to strength grades 420, 550 and 690 MPa are 1.10, 1.05 and 1.12, respectively.

ACKNOWLEDGMENTS

A donation of high-strength reinforcements from Tung Ho Steel Co. and Feng Hsin Steel Co. is gratefully appreciated. The authors would like to thank the Ministry of Science and Technology (MOST) of Taiwan on financial support under the No. 108-2625-M-492-006.

REFERENCES

ACI Committee 318 (2014, 2019). *Building Code Requirements for Structural Concrete (ACI 318-14 and ACI 318-19): Commentary on Building Code Requirements for Structural Concrete (ACI 318R-14 and ACI 318R-19)*. American Concrete Institute, Farmington Hills, Detroit MI.

ACI Committee 408 (2003). *Bond and Development of Straight Reinforcing Bars in Tension*, American Concrete Institute, Farmington Hills, Detroit MI.

Orangun, C. O.; Jirsa, J. O.; and Breen, J. E. (1977), "A Reevaluation of Test Data on Development Length and Splices," *ACI Journal Proceedings*, **74** (3), 114-122. Doi: 10.14359/10993.

Kai-Ning Chi, Chien-Kuo Chiu, Ker-Chun Lin (2018), "Study on straight development length of tensile threaded bars in high strength reinforced concrete members," *Construction and Building Materials*, **Vol. 183**, 661-674. (https://doi.org/10.1016/j.conbuildmat.2018.06.180)

Yuan-Yan Lin (2021), "Behavior of Straight Split-Bond for High-Strength Deformed Bars in Concrete," National University of Science and Technology, Master Thesis.

Bo-Da Li (2019), "Study on Straight Bond Behavior of Deformed Bars in Reinforced Concrete," National University of Science and Technology, Master Thesis.

Yuan-Yan Lin (2021), "Behavior of Straight Split-Bond for High-Strength Deformed Bars in Concrete," National Central University, Master Thesis.

(3g) Seismic isolation, energy dissipation and vibration control of structures

EXPERIMENTAL STUDY OF SHAKING TABLE TEST WITH DISPLACEMENT-DEPENDENT TUNED MASS DAMPERS

Bo-Han Lee[1], Chun-Chung Chen[2], Sheng-Yuan Shiao[3], Chi-Rung Jiang[3], Fang-Yao Yeh[4]

1. Associate Researcher, Bridge Engineering Division, National Center for Research on Earthquake Engineering, Taipei, Taiwan, R.O.C.
2. Research Fellow, Bridge Engineering Division, National Center for Research on Earthquake Engineering, Taipei, Taiwan, R.O.C.
3. Associate Technologist, Bridge Engineering Division, National Center for Research on Earthquake Engineering, Taipei, Taiwan, R.O.C.
4. Division Director, Bridge Engineering Division, National Center for Research on Earthquake Engineering, Taipei, Taiwan, R.O.C.

Email: bhlee@narlabs.org.tw, jingochen@narlabs.org.tw, shengyuan@narlabs.org.tw, chilonjang@narlabs.org.tw, fyyeh@narlabs.org.tw

ABSTRACT

Tuned mass dampers reduce vibrations of high-rise buildings due to wind disturbance. Specifically, the displacement-dependent tuned mass damper (DTMD) is an effective vibration energy absorber connected to a primary structure to reduce the vibration response of the structure under harmonic and external force disturbances. Its natural frequency is adjusted to be close to the fundamental vibration frequency of the primary structure; this leads to an antiphase resonance that dissipates the external force-induced disturbance energy. Several studies have proposed different optimization design objective functions and developed active and semi-active tuned mass damping systems to improve control efficiency significantly. Therefore, in this study, a reasonable mass and an objective function were considered using a simplified degree-of-freedom structural model (DTMD and primary structure) to derive an optimized design method and evaluate the feasibility of structural reinforcement through numerical analysis of the tuned mass damper and shaking table tests. The fundamental retrofit design process used in this study can facilitate the development of a specialized tuning mass damper that can be used in practical engineering applications, such as improving the seismic resistance of ancient and low-rise buildings.

Keywords: Tuned mass damper, Seismic performance, Shaking table test

INTRODUCTION

In recent years, many studies have focused on structural components or materials that undergo long-term aging and deterioration, affecting structural safety; low floors account for the majority of such components. Therefore, the use of reinforcement design methods to improve earthquake resistance is a common countermeasure for this problem. The earthquake resistance of a degraded structure can be enhanced by improving its strength, increasing the damping ratio, and extending the primary vibration period. In the past, many studies applied the tuned mass damper (TMD) concept in the seismic design of civil structures. Housner GW et al. proposed developing structural control devices and algorithms for passive control of nonlinear systems, concentrating on energy-saving methods and hardware to handle strong inputs. The primary structural system was subjected to harmonic excitation of fixed acceleration and displacement amplitudes without damping. The theoretical formulae of the optimal TMD damping ratio and the primary structure's frequency ratio under the minimum steady-state response was derived. Warburton derived the optimal TMD design formula for the damping of a single degree of freedom (SDOF) system in a primary structural system subjected to harmonic external and white noise random excitation. However, structural systems experience damping effects, and the influence of structural damping needs to be considered for optimal TMD design. Therefore, Warburton used the value method to investigate the behavior of a primary structural system with damping. TMD design parameters were optimized, and a chart was created for practical design reference. Tsai and Lin used the curve-fitting

method to confirm the optimized TMD design parameter formula. Villaverde and Toshihiko et al. proposed another optimal damping ratio design formula and conducted a series of numerical simulations to verify its applicability. However, this formula is not applicable when the tuning mass is greater than the primary structure mass. Moreover, the results obtained using the optimized damping ratio formula do not correspond to the damping ratios of the first two modes of vibration. Matta discussed the effectiveness of a TMD with regard to the input pulse of the base excitations. Sadek et al. used the state space method to derive theoretical formulas for optimal TMD frequency and damping ratios, under the following condition: for the main structure containing the TMD, the first two modes have the most extensive and almost equal damping ratios. Numerical analysis proved that an increase in mass ratio results in a smaller design frequency ratio and a larger design damping ratio. The objective function of TMD design is to optimize the dynamic characteristics. Generally, when designing TMD parameters, it is considered that when the primary structural system is subjected to harmonic excitations, the formula or regression chart obtained in the linear elastic phase is still applicable. TMD system design based on the harmonization of external excitations can reduce the response of the primary structure.

In Rana and Soong's research, an SDOF structure was equipped with a TMD. The TMD design parameters were based on a formula derived from the harmonic excitations. Time history analysis results under the action of an earthquake suggested that the TMD had a seismic reduction effect. Additionally, after the primary structural system began yielding, the TMD's natural frequency decreased with a reduction in stiffness. Consequently, the effectiveness of the TMD system decreased owing to the detuning effect. Soong TT et al. discuss different types of energy dissipation devices and also discuss numerous examples and case studies, including devices in currently installed structures and possible future developments in this field. Pinkaew et al. simulated a 20-story structure equivalent to an SDOF system. Under seismic excitations, the frame equipped with a TMD experienced less structural damage after yielding than the frame without a TMD. Kaneko K describes the passive control method of TMD for reducing seismic response in reinforced concrete buildings. The displacement-dependent optimal tuning ratios of linear TMDs for nonlinear response were formulated to reduce seismic response in a wide range of solid ground motion levels. This study explores the application of a displacement-dependent TMD (DTMD) to enhance structural seismic performance. To evaluate the feasibility of such an enhancement, shaking table tests were conducted to compare the responses of a two-story bare frame with and without displacement-type tuned mass dampers. The duration of the test earthquake was decided considering different peak ground acceleration (PGA) and seismic characteristics.

Shaking table test

This section describes the test specimens, DTMD mechanism design, input seismic excitations, and measurement details of the shaking table tests. The numerical analysis is also discussed, including comparisons of the displacement responses, inter-story drifts, and acceleration responses of the test specimens. The reduction in the dynamic responses of the specimens with DTMDs under different input seismic excitations is explored. Conclusions and suggestions regarding the feasibility of DTMDs for enhancement of structural seismic performance are presented. The long-stroke high-velocity seismic simulation shaking table used for the tests has a plane size of 8 m × 8 m, a mass of 92000 kg, a maximum load of 250000 kg, and four pressure actuators in each axis. The shaking table can simulate seismic response for six degrees of freedom along three axes. The maximum displacements of the shaking table are ±100 cm, ±100 cm, and ±40 cm in the longitudinal direction (X), lateral direction (Y), and vertical direction (Z), respectively. The maximum accelerations of the empty table surface in the X, Y, and Z directions are ±2.5 g, ±2.5 g, and ±3.0 g, respectively. As per the shaking table specifications, the existing two-story steel frame of the National Center of Research on Earthquake Engineering (NCREE) in Taiwan was selected as the test specimen. The specimen with a DTMD (DTMD specimen) was compared with the specimen without a DTMD (bare specimen) in this study. Each floor of the test frame is 3500 mm long, 3500 mm wide, and 3000 mm high. The cross-section of the column member of the test specimen is H-shaped steel with dimensions 340 mm × 250 mm × 9 mm × 14 mm; the beam cross-section is C-shaped steel with dimensions 300 mm × 90 mm × 12 mm; the girder cross-section is H-shaped steel with dimensions 340 mm × 250 mm × 9 mm × 14 mm. The steel used satisfied the following specifications: SN490B (equivalent to A572), SN400B (equivalent to A36). The weights of the bare and DTMD test specimens included the load of each floor and the weight of the specimen itself. The load on the floors was 15000 kg, and the test specimen load was 11400 kg. Modal analysis revealed that the

long-direction (X) fundamental modal period was 0.2 s; the elevation of the specimens is depicted in Fig. 1.

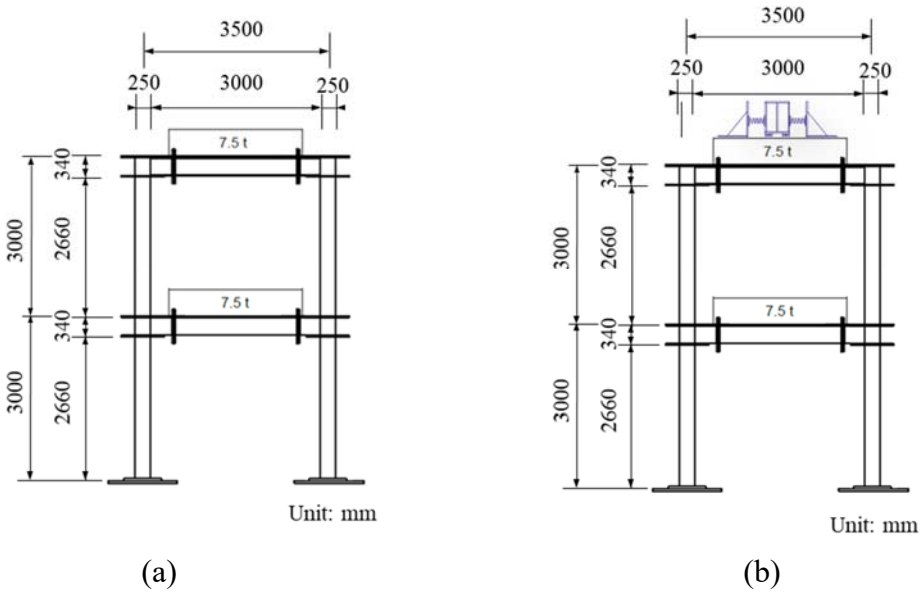

Figure 1. Elevations of test specimens: (a) Bare specimen, (b) DTMD specimen

The equations of motion that govern the response of a structure when it is subjected to ground excitation can be expressed as follows:

$$\mathrm{M}\ddot{u}(t)+\mathrm{C}\dot{u}(t)+\mathrm{K}u(t)=-\mathrm{MR}\ddot{u}_g(t)$$

$$\begin{bmatrix} m_p & 0 \\ 0 & m_t \end{bmatrix}\ddot{u}(t)+\begin{bmatrix} c_p+c_t & -c_t \\ -c_t & c_t \end{bmatrix}\dot{u}(t)+\begin{bmatrix} k_p+k_t & -k_t \\ -k_t & k_t \end{bmatrix}u(t)=-\begin{bmatrix} m_p & 0 \\ 0 & m_t \end{bmatrix}\begin{Bmatrix} 1 \\ 1 \end{Bmatrix}\ddot{u}_g(t) \tag{1}$$

where M, C, and K are the mass, damping, and stiffness matrices of the structure, respectively; $\ddot{\boldsymbol{u}}(t)$, $\dot{\boldsymbol{u}}(t)$, and $\boldsymbol{u}(t)$ are the acceleration, velocity, and displacement vectors, respectively, of the structure relative to the ground; **R** is the influence coefficient vector, which represents the displacement vector; $\ddot{\boldsymbol{u}}_g(t)$ is the acceleration of the input ground motion; m_p is effective mass of a primary structure; k_p is elastic stiffness of a primary structure; c_p is the damping coefficient of a primary structure. For a linear DTMD, an optimal tuning ratio f^{opt} and an optimal damping ratio ξ_t^{opt} are expressed in the following form.

$$f^{opt}=\frac{\sqrt{1-\bar{\mu}/2}}{1+\bar{\mu}},\ \bar{\mu}=\psi^2\frac{m_t}{m_p}\ \text{for linear DTMDs} \tag{2}$$

$$\xi_t^{opt}=\frac{1}{2}\sqrt{\frac{\bar{\mu}(1-\bar{\mu}/4)}{(1+\bar{\mu})(1-\bar{\mu}/2)}} \tag{3}$$

$$\frac{\boldsymbol{\phi}^T\mathbf{M}\mathbf{r}}{\boldsymbol{\phi}^T\mathbf{M}\boldsymbol{\phi}}\boldsymbol{\phi}=(\psi)^T,\ \mathbf{r}=(1,1,\cdots,1)^T \tag{4}$$

Where ψ is the participation vector on the top floor, the modal vector $\boldsymbol{\phi}$ is considering a structure with DTMD, and **M** is the corresponding mass matrix. The remaining design parameter is the coefficient friction α_a, which needs to be tuned to obtain the optimal hysteretic damping in the DTMD. For convenience, a standardized coefficient $\bar{\alpha}$ is defined in the following form.

$$\bar{\alpha}=\frac{\alpha_a}{\alpha_b} \tag{5}$$

For linear elastic structures, a base shear coefficient of the controlled structure replaced the parameter α_b is defined in the following form. Where Q_b and g are the peak base shear and gravity acceleration; S_a is the spectral acceleration for specified ground motion.

$$\alpha_b=\frac{\max_t Q_b(t)}{(m_p+m_t)g}\approx\frac{S_a(\omega_p,\xi_p)}{g} \tag{6}$$

For nonlinear structures, the parameter α_b is defined in the following form.

$$\alpha_b=\frac{Q_y}{(m_p+m_t)g} \tag{7}$$

Where Q_y is the maximum shear strength of the simplified lumped-mass structure model, the optimal coefficient $\bar{\alpha}$ is approximately the value of 0.25 using numerical optimizations based on time history analysis.

$$\bar{\alpha}^{opt}\approx 0.25 \tag{8}$$

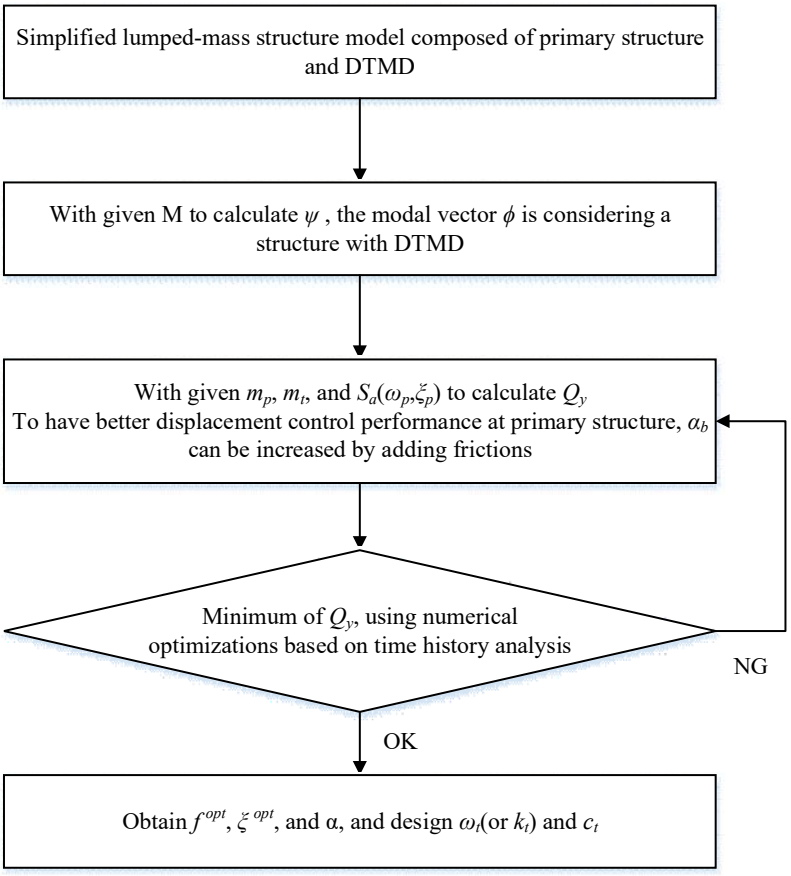

Figure 2. Design procedure of DTMD proposed in this study

With the experimental and numerical verification aforementioned, a preliminary design procedure of the DTMD approach is provided based on the simplified lumped-mass structure model, as presented in Fig. 2. Under the objective function of minimizing the structural base shear, a numerical model was developed by SAP2000 software for time-history analysis using TMD properties and checking whether the structural response reduction and TMD deformation were acceptable. If response reduction is insufficient, the TMD mass should be increased; it does not satisfy the constraint, the damping coefficient should be increased. Then, perform time history analysis again. In the range of alpha 0.2 to 0.25, the anti-phase difference motion between the TMD and the controlled structure is more noticeable when the external force is applied. Therefore, the seismic response of the controlled structure can be decreased based on the anti-phase motion. In a non-linear system, a value is sensitive to the frequency ratio between the TMD and the controlled structure. Therefore, the $\bar{\alpha}^{opt}$ is calculated by the time-history analysis results of the seismic response.

We considered the influence of input excitations with different characteristics on the DTMD. The experiment involved near-fault, far-fault, and long-term ground motions, including earthquake excitations measured at stations TCU047 and TCU068 for the 1999 Chi-Chi earthquake in Taiwan, at station I-ELC270 for the 1940 Northridge Earthquake in California, at station KJM000 for the 1995 Hanshin Earthquake in Japan, and at station MYG013 for the 2011 Tohoku Earthquake in Japan. Researchers often use the uniform frequency connotations of the far-fault El Centro earthquake and near-fault Kobe earthquake with the velocity pulse period. There are two different station records of the Chi-Chi earthquake. TCU047 was a far-fault earthquake, and TCU068 was a near-fault earthquake with a high peak ground velocity (PGV) and an extensive velocity pulse. The maximum PGV of TCU068 reached 383 cm/s, surpassing the previous highest PGV value measured during the 1994 Northridge earthquake. On record, the 2011 off-the-Pacific-coast-of-Tohoku earthquake was Japan's first earthquake with a moment magnitude scale of more than 9.0, with a long-term duration of more than 2 min. The displacement and acceleration response of the structure in the 0~5 period under the single-degree-of-freedom system is observed in the normalized 1g response spectrum and the dynamic response of the test structure to avoid damage in the test process. To compare the seismic response of the DTMD under different seismic conditions, a numerical analysis was conducted. This analysis included three different magnifications for each seismic excitation before the test. The maximum drift ratio of each floor was less than 0.01, and the stroke of the friction device was less than the design stroke. The earthquake magnification was determined based on the analysis results and the details of the seismic excitations, which are shown in Table 1. Eq. (1), (2), and (3) represent small, medium, and large scaling test excitations, respectively.

Table 1 Details of seismic excitations

PGA of time histories of seismic excitations for bare and DTMD specimens								
Earthquake	Latitude	Longitude	Depth (km)	Magnitude (Mw)	Acceleration (g)	Eq. (1)	Eq. (2)	Eq. (3)
El Centro	32.73 °N	115.50 °W	16.0	6.9	Scaling	100%	80%	60%
					PGA	0.349	0.279	0.209
Kobe	34.59 °N	135.07 °E	17.6	6.9	Scaling	30%	20%	10%
					PGA	0.250	0.167	0.083
TCU047	23.85 °N	120.82 °E	8.0	7.6-7.7	Scaling	60%	40%	20%
					PGA	0.241	0.160	0.080
TCU068	23.85 °N	120.82 °E	8.0	7.6-7.7	Scaling	120%	100%	80%
					PGA	0.434	0.362	0.290
THU	38.30 °N	142.37 °E	29.0	9.1	Scaling	40%	20%	10%
					PGA	0.132	0.066	0.033

Comparison of seismic responses of bare and DTMD specimens for shaking table tests

For an intuitive and comprehensive comparison, the ratio of the maximum accelerations of the DTMD and bare specimens (AR_{max}) and the ratio of the minimum accelerations of the DTMD and bare specimens (AR_{min}) at 2F under the five seismic excitations were calculated using Eqs. (9) and (10), respectively; the values are depicted in Fig. 3. The abscissas in the figure indicate the different PGA ratios for the input seismic excitations. If the ordinate value is greater than 100%, the 2F response is amplified.

$$AR_{max} = \text{MAX}Acc_{DTMD,i} / \text{MAX}Acc_{Bare,i} \quad (9)$$

$$AR_{min} = \text{MIN}Acc_{DTMD,i} / \text{MIN}Acc_{Bare,i} \quad (10)$$

where the subscript i indicates the maximum X-directional acceleration responses at the i^{th} floor of the specimens. On average, the 2F acceleration response of the DTMD specimen under the El Centro, Kobe, and THU seismic excitations was reduced by approximately 7%, with different magnification ratios of excitations from the test results. The interaction between the DTMD and the structure out of phase motion of the larger PGA reduces the structural response under earthquake excitations. Thus, it is verified that the DTMD provides effective vibrate reduction under the TCU047, TCU068, and THU earthquakes.

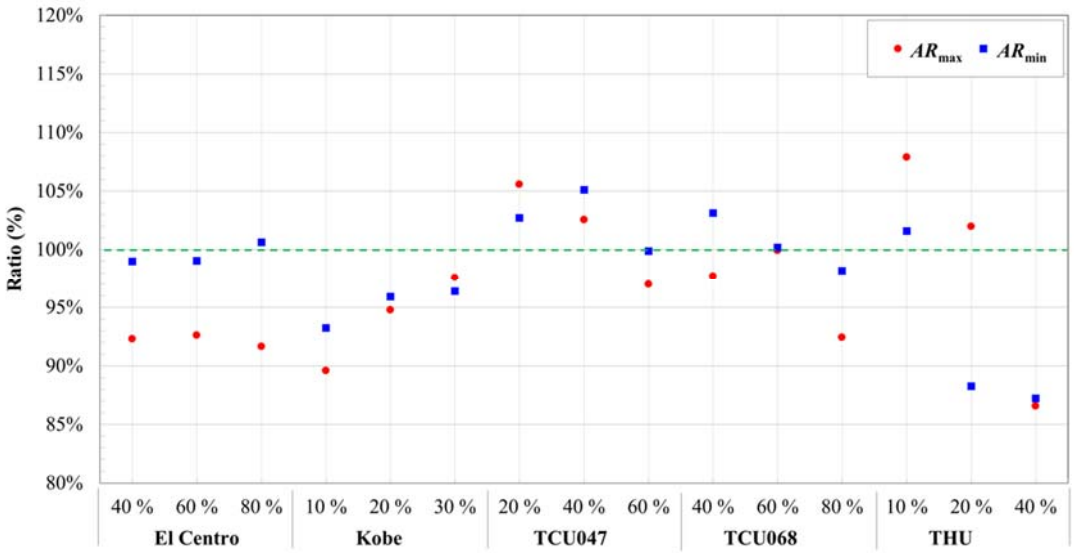

Figure 3. AR_{max} and AR_{min} for the DTMD and bare specimens

For an intuitive and comprehensive comparison, the maximum relative displacement RD_{max} and minimum relative displacement RD_{min} of the DTMD with respect to the bare specimen at 2F under the five seismic excitations were calculated using Eqs. (11) and (12), respectively; the values are depicted in Fig. 4. The DTMD and test specimen remained stable throughout the shaking table tests; no torsion or rotation was generated. Therefore, the design of the proposed mechanism is considered feasible for enhancing structural seismic performance using a DTMD.

$$RD_{max} = \text{MAX}(Disp_{DTMD,i} - Disp_{Bare,i}) \quad (11)$$

$$RD_{min} = \text{MIN}(Disp_{DTMD,i} - Disp_{Bare,i}) \quad (12)$$

where the subscript i indicates the maximum X-directional displacement responses at the i^{th} floor of the test specimens.

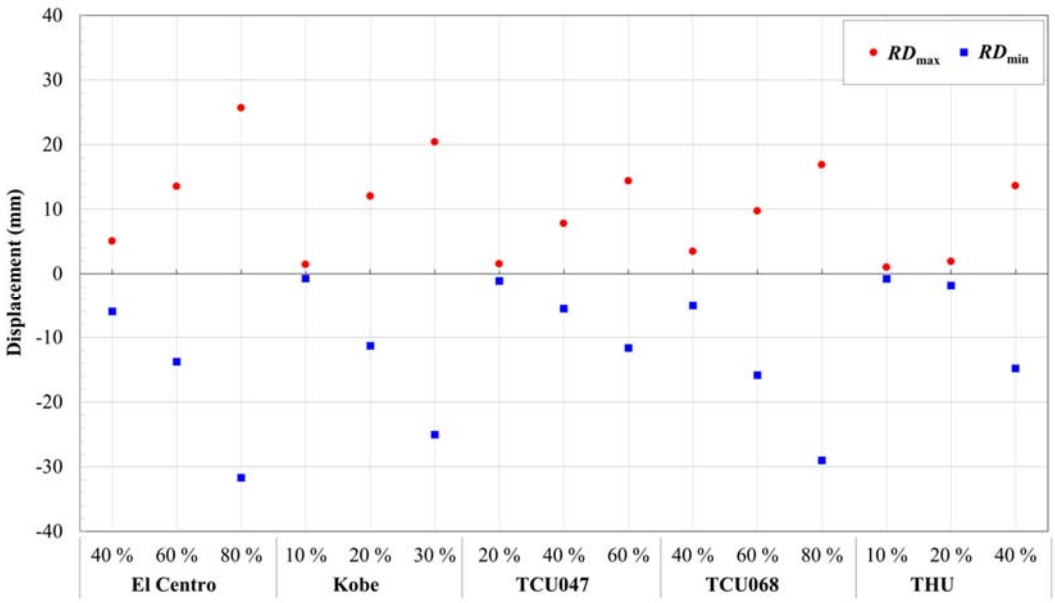

Figure 4. RD_{max} and RD_{min} of DTMD with respect to bare specimen

CONCLUSIONS

In this study, we considered different PGAs and seismic excitations for a two-story scaling test specimen to verify the reduction in structural responses achieved using a DTMD. In previous studies, TMDs have been used for wind-resistant design of high-rise buildings. In this study, the used of DTMDs was proposed to improve the seismic performance of ancient and low-rise buildings with insufficient seismic resistance. This design method provides a buffer solution for ancient and low-rise buildings that have not yet undergone urban renewal, ensuring safety under strong earthquakes. In this study, a two-story steel structure was used to simulate a low-rise RC building for the shaking table test, and the maximum responses of positive and negative directions between the bare and DTMD specimens during the earthquake excitations experience were observed. The test results show that DTMD can effectively reduce the structure's response. Furthermore, the strokes of DTMD in the positive and negative directions during the seismic excitations are less than the design value of 50 mm, indicating the structure's stability and response reduction are representative.

In summary, the DTMD, which produces an antiphase resonance to dissipate the external force disturbance energy, enhances structural seismic performance. The test results reveal that the test specimen equipped with a DTMD did not exhibit a significantly reduced inter-story drift ratio. The reduction in the acceleration response of the DTMD specimen can be increased beyond 10% with a properly designed DTMD mechanism and parameters. Moreover, the use of compression springs to provide stiffness and friction supports to provide energy dissipation is feasible. Thus, the modularly designed mass, compression springs, and friction supports together form a viable mechanism to enhance structural seismic performance.

ACKNOWLEDGMENTS

The study was financially aided by the Ministry of Science and Technology (MOST) of Taiwan [108-1903-02-17-04]. The authors would like to thank Kuochen & Associates Engineering Technology Co., Ltd.; Tokyo Institute of Technology; Kozo Keikaku Engineering Inc.; and Shimizu Corporation for the experimental planning, numerical analysis, and suggestions for ensuring a smooth test process. We would also like to thank the reviewers for their constructive comments that helped us in improving the quality of the paper.

REFERENCES

Housner GW, Bergman LA, Caughey TK, Chassiakos AG, Claus RO, Masri SF, Skelton RE, Soong TT, Spencer Jr. BF, Yao JTP. Structural control: past, present and future. J Eng Mech - ASCE 1997;123(9):897–971. doi:10.1061/(asce)0733-9399(1997)123:9(897)

Den Hartog JP. Mechanical vibrations. 4th ed. New York: McGraw-Hill; 1956.

Warburton GB. Optimal absorber parameters for various combinations of response and excitation parameters. Earthq Eng Struct Dyn 1982;10(3):381-401. https://doi.org/10.1002/eqe.4290100304.

Warburton GB, Ayorinde EO. Optimum absorber parameters for simple systems. Earthq Eng Struct Dyn 1980;8(3):197-217. https://doi.org/10.1002/eqe.4290080302.

Warburton GB. Optimum absorber parameters for minimizing vibration response. Earthq Eng Struct Dyn 1981;9(3):251-62. https://doi.org/10.1002/eqe.4290090306.

Tsai HC, Lin GC. Optimum tuned-mass dampers for minimizing steady-state response of support-excited and damped systems. Earthq Eng Struct Dyn 1993;22(11):957-73. https://doi.org/10.1002/eqe.4290221104.

Villaverde R. Reduction seismic response with heavily-damped vibration absorbers. Earthq Eng Struct Dyn 1985;13(1):33-42. https://doi.org/10.1002/eqe.4290130105.

Villaverde R. Seismic control of structures with damped resonant appendages. Proceedings of the First World Conference on Structural Control 1994, Los Angeles, California, United States.

Villaverde R, Koyama LA. Damped resonant appendages to increase inherent damping in buildings. Earthq Eng Struct Dyn 1993;22(6):491-507. https://doi.org/10.1002/eqe.4290220603.

Asami T, Wakasono T, Kameoka K, Hasegawa M, Sekiguchi H. Optimum design of dynamic absorbers for a system subjected to random excitation. JSME Int J III-Vib C 1991;34(2):218-26. https://doi.org/10.1299/jsmec1988.34.218.

Matta E. Effectiveness of tuned mass dampers against ground motion pulses. J Struct Eng 2013;139(2):188-98. https://doi.org/10.1061/(ASCE)ST.1943-541X.0000629.

Sadek F, Mohraz B, Taylor AW, Chung RM. A method of estimating the parameters of tuned mass dampers for seismic applications. Earthq Eng Struct Dyn 1997;26(6):617-35. https://doi.org/10.1002/(SICI)1096-9845(199706)26:6<617::AID-EQE664>3.0.CO;2-Z.

Rana R, Soong TT. Parametric study and simplified design of tuned mass dampers. Eng Struct 1998;20(3):193-204. https://doi.org/10.1016/S0141-0296(97)00078-3.

Soong TT, Dargush GF. Passive Energy Dissipation Systems in Structural Engineering, John Wiley & Sons: Chichester, 1997.

Pinkaew T, Lukkunaprasit P, Chatupote P. Seismic effectiveness of tuned mass dampers for damage reduction of structures. Eng Struct 2003;25(1):39-46. https://doi.org/10.1016/S0141-0296(02)00115-3.

Kaneko K. Performance-based design of tuned mass damper mounted on rooftop of buildings considering type of seismic ground motions. J Struct Constr Eng Trans AIJ 2016;81(730):2057-67. https://doi.org/10.3130/aijs.81.2057.

Kaneko K. Optimal design method of tuned mass damper effective in reducing overall bending vibration in steel buildings with inter story dampers. J Struct Constr Eng Trans AIJ 2017;82(737):1003-12. https://doi.org/10.3130/aijs.82.1003.

Kaneko K, Takahashi K, Zhang KW, Chen TW, Lee BH and Chen CC. Nonlinear response analysis-based control performance diagrams for TMDs mounted on reinforced concrete buildings. Japan Association for Earthquake Engineering (JAEE) 2021;21(4):34-48. https://doi.org/10.5610/jaee.21.4_34

Bo-Han Lee, Chun-Chung Chen, Tsung-Wu Chen, Sheng-Yuan Siao, Chi-Rung Jiang, Fang-Yao Yeh, “Enhancement of Structural Seismic Performance of Low-Rise Buildings using Displacement-Dependent Tuned Mass Damper”, Structures, 2022.(SCI)(IF: 4.01, Ranking 43/138 in Engineering, Civil)

SEISMIC DESIGN OF DAMPED-OUTRIGGER WITH BUCKLING-RESTRAINED BRACE FOR BUILDINGS WITH VARIOUS HEIGHTS

Pao-Chun Lin[1] and Shou-June Tsai[2]
1. Assistant Professor, Department of Civil Engineering, National Cheng Kung University, Tainan, Taiwan.
2. Graduate Student, Department of Civil Engineering, National Cheng Kung University, Tainan, Taiwan.
Email: pclin@gs.ncku.edu.tw, n66081383@gs.ncku.edu.tw

ABSTRACT

The keen purpose of this study is to investigate the seismic performance of buildings equipped with damped-outrigger system using the buckling-restrained brace (BRB) system (BRB-outrigger) and to propose the optimal design recommendation for buildings with a different height. The numerical models with building heights of 72, 144, 216 and 288m, each contains two layers of BRB-outrigger and a 40m by 40m structural plan are analyzed using response spectral analysis and nonlinear response history analysis procedures. To get closer to the actual reality, the member-by-member benchmark models are designed based on the seismic code requirement. In the response spectral analysis procedure, the equivalent damping ratio is computed in order to include the BRB's inelastic response. For the main purpose of parametric study, a simplified model which will be using a Timoshenko beamcolumn element in order to capture shear-type to flexural-type lateral deformation for a lower to higher raising buildings are proposed. The dimensionless parameters that actually describe the relationships between the core structure stiffness, outrigger flexural stiffness, the axial stiffness of BRB and perimeter column in the parameter study are considered. Based on the analyzed result, the ranges of optimal design parameters vary in the different optimization targets and building heights.

Keywords: tall buildings, outrigger system, buckling-restrained brace, nonlinear response history analysis, response spectral analysis

INTRODUCTION

Most of the tall buildings are composed of a stiff core structure and surrounded by perimeter columns, which mainly support the gravity loads from the slabs. This core-tube type building is suitable for utilizing outrigger system to reduce the seismic response. As shown in Fig. 1, the outrigger truss connects the core structure to the perimeter columns. Under lateral seismic loads, the core structure deformation rotates the outrigger truss. The perimeter columns are therefore subjected to tension or compression and then apply a resisting moment on the core structure. The outrigger system has been developed and utilized in real constructions for several decades (Ali and Moon, 2007). A numerous researches have focused on an optimal design for conventional outrigger systems, including the outrigger numbers and locations (Smith and Salim, 1981). In addition to the viscous dampers, the buckling-restrained brace (BRB) (Watanabe *et al*., 1988) was included into the damped-outrigger system as an energy dissipation mechanism (Lin *et al*., 2018). If compared with the viscous damper, the BRB provides a larger stiffness and strength. During service level earthquakes, the BRBs remain elastic and the BRB-outrigger works as conventional outrigger. During design base and maximum considered earthquakes, the BRBs develop inelastic deformation and dissipate seismic energy. Most of the researches have adopted the simplified model (SM) as shown in Fig. 1a for simplicity and analysis efficiency. As the outrigger is commonly considered to be effective only for tall buildings, most of the studies utilized a cantilever Euler-Bernoulli beam to model the core structure. However, such type of SM is suitable to model tall buildings with flexural-type lateral deformation but may not be suitable to model mid-rise to low-rise buildings with shear-type lateral deformation. In the other hand, the parametric studies on the optimal design in the past researches did not take the practical design into consideration, such as the available structural sections. This can lead to a proposed optimal solution but in fact cannot be achieved by practical design. In this study, the benchmark models with 20, 40, 60 and 80 stories steel structures equipped with two layers of BRB-outrigger are developed. The detail element

sizes are designed based on the code seismic requirement, thus, a more real lateral deformation characteristic of the building can be captured. The SM in this study utilizes a Timoshenko beam to model the building core structure in order to capture the lateral deformation types for low-rise, mid-rise and high-rise buildings. The response spectral analysis (RSA) using the concepts of equivalent damping ratio and equivalent displacement proposed in this study is conducted in order to investigate the optimal design of BRB-outrigger system. The RSA results are confirmed by performing nonlinear response history analysis (NLRHA). The optimal design of BRB-outrigger system for low-rise to high-rise buildings including the outrigger elevations and the relationships between BRB axial stiffness, core structure flexural stiffness and perimeter column axial stiffness are finally concluded.

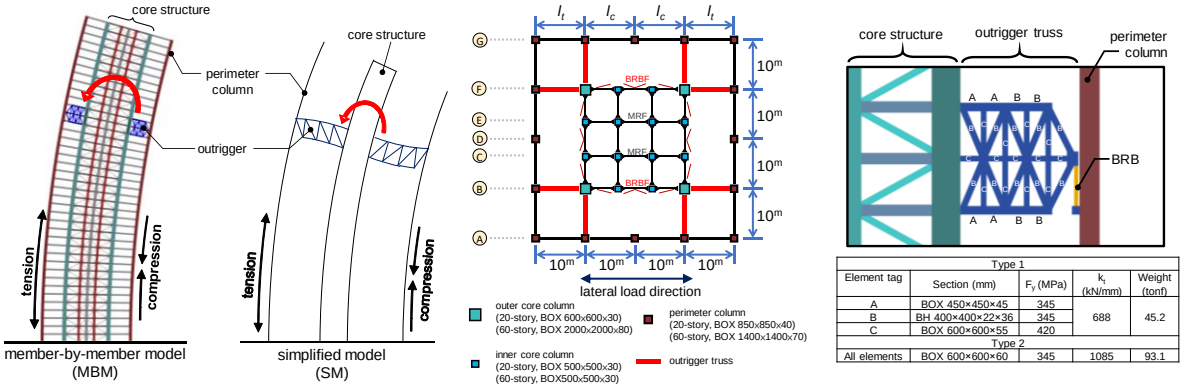

Type 1				
Element tag	Section (mm)	F_y (MPa)	k_t (kN/mm)	Weight (tonf)
A	BOX 450×450×45	345	688	45.2
B	BH 400×400×22×36	345		
C	BOX 600×600×55	420		
Type 2				
All elements	BOX 600×600×60	345	1085	93.1

(a) (b) (c)

Figure 1. Illustration of (a) elevation (b) structural plan, and (c) BRB-outrigger detail for core-tube type building with outrigger.

NUMERICAL MODELS

Member-by-member models

Fig.1b shows the structural plan of the numerical model analyzed using OpenSees. The story heights are 3.6m for all the models. In order to simplify the analysis, it is assumed that the structural plans are the same in all such models. In addition, the beam, column and brace element sizes do not change with the stories. The live (LL) and dead loads including element self-weight (DL) are assumed to be 0.3 tonf/m^2 and 0.8 tonf/m^2, respectively. The dead load is also considered as the mass of the model. The lateral force resistance of the core structure is composed of two buckling-restrained braced frames (BRBF) and two moment-resisting frames (MRF). In this study, the 20-story and 60-story MBM models are built. The detailed element sizes have been designed according to the code requirement are shown in Fig. 1b. All the steel materials are to be SM570 with a yield strength 420 MPa. All the elements of the MBM models are modeled using fiber sections and bilinear material model with a post-yield stiffness ratio of 0.02 in OpenSees. The fundamental periods of the 20-story ($T_{1,20}$) and 60-story ($T_{1,60}$) MBM models are 2.63 and 6.13 second, respectively. The elastic design base shear coefficient is 0.083 for all the models. A total of 10 BRBs with the axial yielding forces (P_y) ranging from 1750kN to 17500kN are designed, so that the ratio (R_{dc}) of BRB axial stiffness (k_d) to the perimeter column axial stiffness (k_c) ranges from 1 to 10. The axial yielding deformations of all the BRBs are 5.1 mm. The steel core of the BRB is made by using A572 Gr. 50 steel material with a yield strength of 345MPa. The length of each BRB equals to the story height (3600mm). For the benchmark model in this study, the outrigger truss depth is set to across two-story height as shown in Fig. 1c. Two types of outrigger truss are designed and the member sizes are listed in Fig. 1c.

Simplified models

In order to model the MBM model in a more efficient way, the SM shown in Fig. 2 is established using OpenSees. The core structure SM is modeled using Timoshenko beamcolumn element. The mass of each story is concentrated at the core structure. The perimeter columns and outrigger trusses are modeled using elastic beamcolumn elements they are designed to remain elastic during the earthquakes. The BRBs are modeled using truss elements with bilinear material model using a post-yield stiffness ratio of 0.05. The core structure flexural (EI_{core}) and shear ($GA_{v,core}$) stiffness of the SM are being determined

by using the trial and error procedure, by actually comparing the periods and mode shapes differences between the MBM model and the SM for the first six modes, where E (200 GPa) and G (77 GPa) are the Young's modulus and shear modulus, respectively. The dimensionless parameter κ^2 which indicates the relationship between the shear and flexural-type deformations is defined as follows (Miranda, 1999):

$$\kappa^2 = \frac{GA_{v,core}H}{EI_{core}/H} \tag{1}$$

The value of κ^2 is mostly larger for taller building due to a more obvious flexural-type lateral deformation. Table 1 shows the values of $A_{v,core}$ and I_{core} for the numerical models which are determined by assuming that the value of κ^2 is linearly proportional to the building height. The first mode shapes of the four SM, 20-story (MBM20) and 60-story (MBM60) MBM models are shown in Fig. 3.

Table 1 Parameters of the numerical models

model	H (m)	I_{core} (mm^4)	$A_{v,core}$ (mm^2)	κ^2	Perimeter column (box)		1st mode period (sec)	
					width (mm)	thickness (mm)	SM	MBM
20-story	72	3.04×10^{13}	4.69×10^{4}	3.08	850	40	2.63	2.63
40-story	144	8.38×10^{13}	1.45×10^{5}	13.82	1200	55	4.52	N.A
60-story	216	2.02×10^{14}	2.77×10^{5}	24.56	1400	70	6.13	6.13
80-story	288	3.92×10^{14}	4.34×10^{5}	35.31	1650	80	7.60	N.A

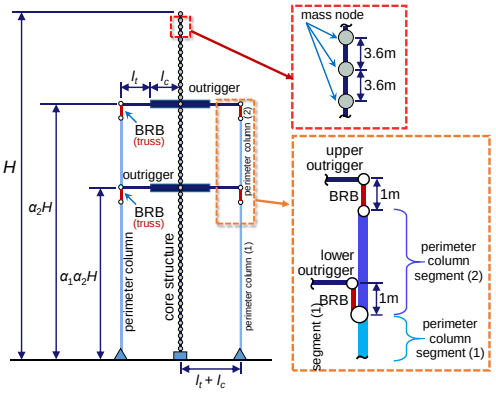

Figure 2. The simplified model.

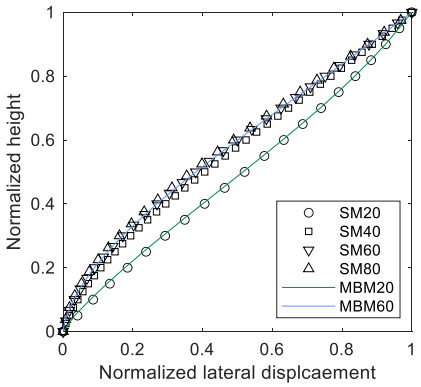

Figure 3. Comparison of the first mode shapes between SM and MBM.

ANALYSIS METHODS

Response spectral analysis

The response spectral analysis (RSA) is adopted to evaluate the seismic performance of the SMs. The single-degree-of-freedom (SDOF) model responses of the first six modes are considered individually and then combined by using the square root of sum of squares (SRSS) rule. In this study, the SDOF model's force and deformation relationship of the i^{th} mode is primarily obtained by applying i^{th} mode modal pushover analysis (MPA) (Chopra and Goel, 2002) on the SM. The MPA result of the roof displacement (Δ) and base shear (P) relationship is shown in Fig. 5a. When the first and second BRB yields, the corresponding roof displacements are $\Delta_{top,y1}$ and $\Delta_{top,y2}$, respectively, and the corresponding base shear are P_{y1} and P_{y2}, respectively. μ is the ductility ratio and $\mu\Delta_{top,y1}$ is the maximum roof displacement. Fig. 5b shows the force and deformation relationship of the SDOF model, which is converted from the MPA results by linearly scaling the roof displacement so that the elastic stiffness k_{fi} satisfies the following equation:

$$k_{fi} = \left(2\pi/T_i\right)^2 m_{eq,i} \tag{2}$$

where T_i and $m_{eq,i}$ are the period and effective mass of the i^{th} mode, which are obtained from the eigenvalue analysis in OpenSees. The force and displacement relationship of the SDOF model is assumed to have the same post-yield stiffness ratio with the MPA result. As shown in Fig. 5c, when the maximum displacement of $\mu\Delta_{eq,y1}$ is reached, E_d is the energy dissipation of the SDOF model that performs one hysteretic loop, E_s is the strain energy and $k_{eq,i}$ is the equivalent stiffness. The equivalent

damping ratio ($h_{eq,i}$) of the i^{th} mode due to the inelastic response of the BRBs can be calculated as follows (Kasai *et al.*, 1998):

$$h_{eq,i} = h_0 + \frac{1}{\mu}\int_1^{\mu} h' d\mu' = h_0 + \frac{1}{\mu}\int_1^{\mu} \frac{E_d(\mu')}{4\pi E_s(\mu')} d\mu' \tag{3}$$

where h_0 = (0.02) is the inherent damping ratio and μ' is the damping ratio within the range between 1 and μ. $E_d(\mu')$ and $E_s(\mu')$ are the energy dissipation in one hysteretic loop and strain energy under the ductility of μ'. The reduction factor (D_h) in spectral velocity (S_{pv}) due to the increased damping ratio $h_{eq,i}$ can be computed as follows, which is commonly used in seismic building design in Japan:

$$D_{h,i} = \left(1+10h_0\right) \Big/ \left(1+10h_{eq,i}\right) \tag{4}$$

The spectral displacement of the SDOF model under the equivalent period ($T_{eq,i}$) and damping ratio, S_d (T_{eq}, h_{eq}), can be calculated as follows:

$$S_d\left(T_{eq,i}, h_{eq,i}\right) = D_{h,i}\sqrt{\frac{k_{fi}}{k_{eq,i}}}\frac{S_{pv}\left(T_{eq,i}, h_{eq}\right)}{S_{pv}\left(T_i, h_0\right)} S_d\left(T_i, h_0\right), \quad \text{where } T_{eq,i} = 2\pi\sqrt{\frac{m_{eq,i}}{k_{eq,i}}} \tag{5}$$

The i^{th} mode's maximum deformation of the SM is obtained by multiplying S_d ($T_{eq,i}$, $h_{eq,i}$) with the i^{th} mode shape and modal participation factor. The maximum deformation of the SM is obtained by using SRSS combination considering the first six modes (i = 1 to 6).

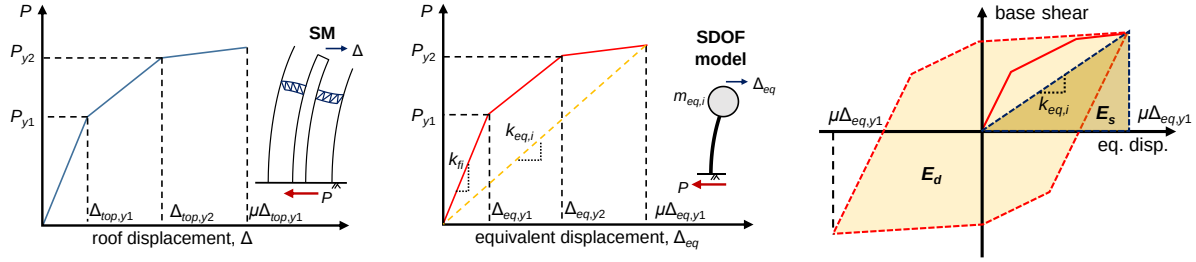

(a) (b) (c)

Figure 4. The force and deformation relationships: (a) MPA result, (b) SDOF model, and (c) SDOF model with one hysteretic loop

Nonlinear response history analysis

The nonlinear response history analysis (NLRHA) is adopted to evaluate the seismic performance of the BRB-outrigger systems. In addition, the NLRHA results are being compare with the RSA results. The 20 ground motions LA01 to LA20 provided in the SAC steel project are used as the input ground motions in the NLRHA. The average of those 20 NLRHA results are used to compare with the RSA results. The input ground motions are scaled to the design spectrum within the range of $0.2T_1$ to $1.5T_1$ (ASCE, 2016), where T_1 is the fundamental period of the SM without considering the outriggers.

Analysis procedure

In this study, five dimensionless parameters are defined and their various ranges are shown in Table 2. The α_1 and α_2 define the lower and upper outrigger elevations, as indicated in Fig. 2. R_{dc} defines the ratio of the axial stiffness of BRB in upper outrigger (k_{d2}) to the perimeter column axial stiffness considering the building height of H (k_c). The value of R_{dc} ranges from 1 to 10. R_{tc} defines ratio of outrigger flexural stiffness to the perimeter column axial stiffness, which are based on the member sizes of the outrigger design. R_{dd} defines the axial stiffness ratio of the BRB in the upper outrigger (k_{d2}) to one in the lower outrigger (k_{d1}). The parametric study is separated into two stages, first one (stage I) assumes that the axial stiffness of the upper and the lower outrigger BRBs are same (R_{dd} = 1). The second stage analysis (stage II) investigates the effect of R_{dd} on the response.

Table 2 The range of dimensionless parameters

Parameters	α_2	α_1	R_{dc}	R_{tc}	R_{dd}
range	0.1~0.9	0.3~0.7	1~10	2.03, 3.19	0.5~2.0

ANALYSIS RESULTS

Stage I analysis

Fig. 7 shows the relationships between the maximum roof drift and outrigger elevations, when R_{dc}=5 and R_{tc}=3.19 for all the models obtained from RSA and NLRHA. The maximum roof drift response is mainly affected by the upper outrigger elevation (α_2). In addition, changing α_2 results in greater influence on maximum roof drift in taller buildings. In summary, the optimal α_2 in order to best reduce roof drift is around 0.7 to 0.9 and is higher for taller building. The lower outrigger elevation (α_1) only affects in a slight range to the response of maximum roof drift and the optimal α_1 is around 0.6. Under the optimal α_2 and α_1, the maximum roof drift can be reduced around 15% when compared with the building without equipping BRB-outriggers. The larger maximum roof drift responses are found in the RSA results, when compared with the NRLHA results for taller building models. This is because the acceleration spectra of the input ground motions cannot be perfectly fit with the design spectra. However, the trends obtained from RSA and NLRHA are similar to each other and the results of optimal outrigger elevation should not be affected. Fig. 6 shows the relationship between the maximum base shear and outrigger elevations. Similar to the maximum roof drift responses, the maximum base shear is mainly affected by α_2. However, as shown in the SM20 response, when α_1 is lower, the maximum base shear can be even more reduced in a better effect. It appears that, the outrigger with a lower elevation can effectively reduce the base shear for low-rise buildings with shear-type lateral deformation. It is suggested that the base shear can be best reduced when α_2 and α_1 equals to 0.7 and 0.5, respectively.

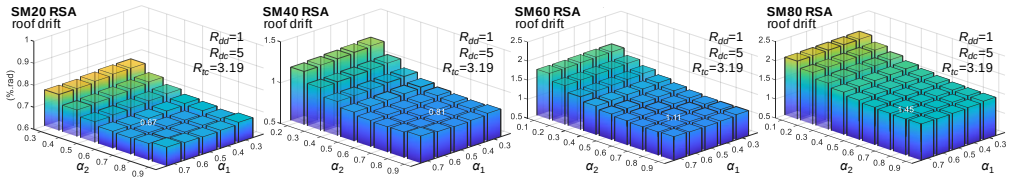

(a)

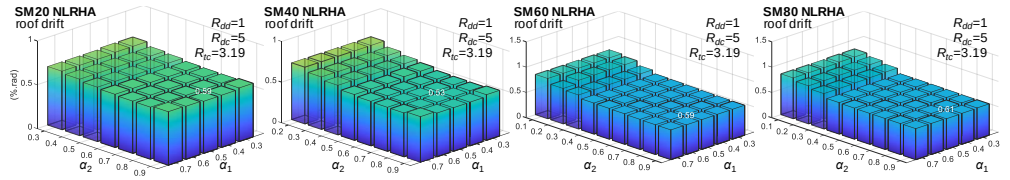

(b)

Figure 5. Relationships between roof drift, α_2, and α_1 obtained from (a) RSA and (b) NLRHA

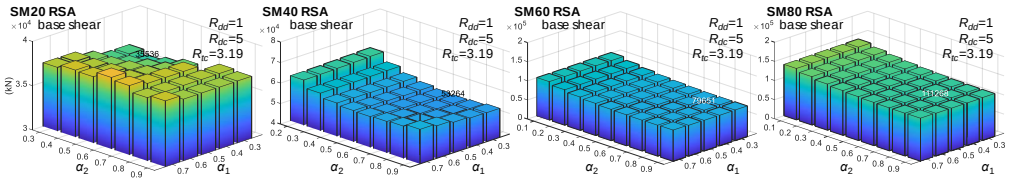

(a)

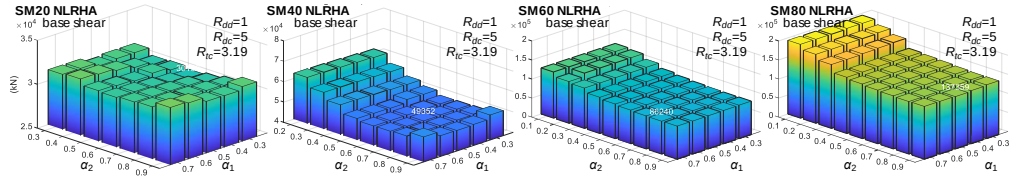

(b)

Figure 6. Relationships between base shear, α_2, and α_1 obtained from (a) RSA and (b) NLRHA

Fig. 7 shows the average cumulative plastic deformation (CPD) which is gained from the BRBs in the upper and lower outriggers. Fig. 8 shows the ratio of energy dissipated by each of the BRB, to the total input energy. Based on the analysis results, the BRBs in the upper outrigger generally shows a higher energy dissipation performance when compared with the BRBs in the lower outrigger because of larger core structure rotation demand in the upper outrigger triggers larger BRB axial deformation. Because the BRB axial yielding deformations with a different value of R_{dc} are the same (5.1 mm), the system

with a larger value of R_{dc} results in a smaller CPD response. For high rise building (SM60 and SM80), the high CPD values (greater than 500) in the BRBs in upper outrigger with small R_{dc} values can fracture even before the end of an earthquake. Therefore, selecting a suitable value of R_{dc} (greater than 3) for taller buildings is more essential. Based on the analysis results, around 30% and 10% of the input seismic energy can be dissipated by the BRBs in the upper and lower outrigger, respectively. For low-rise buildings (SM20), it is suggested to select R_{dc} to be smaller than 3, in order to develop sufficient BRB energy dissipation. For mid- rise (SM40) to high-rise buildings (SM60 and SM80), it is suggested to set the R_{dc} value to be greater than 3 to 5 in order to prevent BRB early fracture.

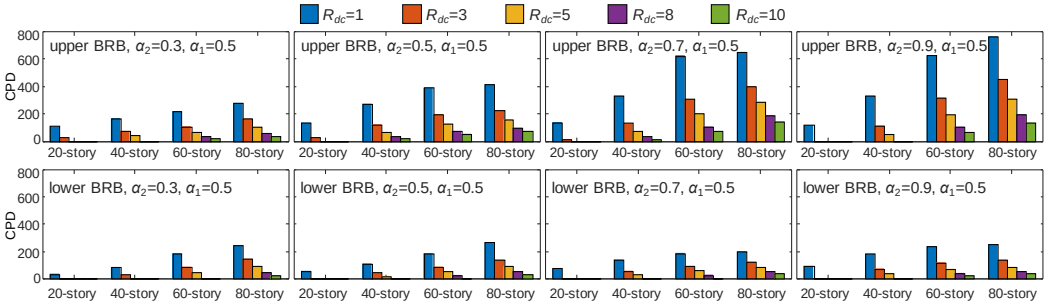

Figure 7. The CPD of upper and lower BRBs obtained from NLRHA

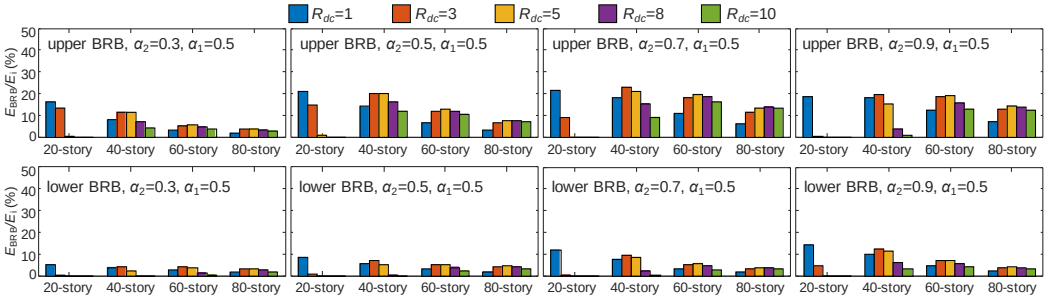

Figure 8. The energy dissipation of upper and lower BRBs obtained from NLRHA

Stage II analysis

The stage II aims to investigate the effect of the axial stiffness ratio (R_{dd}) of the BRB in upper outrigger to the BRB in lower outrigger on the seismic performance. The ratio of upper BRB axial stiffness to the perimeter column axial stiffness is defined as $R_{dc,2}$. The ratio of lower BRB axial stiffness to the perimeter column axial stiffness is defined as $R_{dc,1}$. Fig. 9 shows the relationship between roof drift, $R_{dc,2}$, and $R_{dc,1}$ for the building models with four different heights when α_2=0.7 and α_1=0.5 using contour plots. The roof drift can be better reduced with larger R_{dd}, which suggests that the reduction in roof drift is more efficient when the axial stiffness of BRBs in upper outrigger is greater than the lower ones.

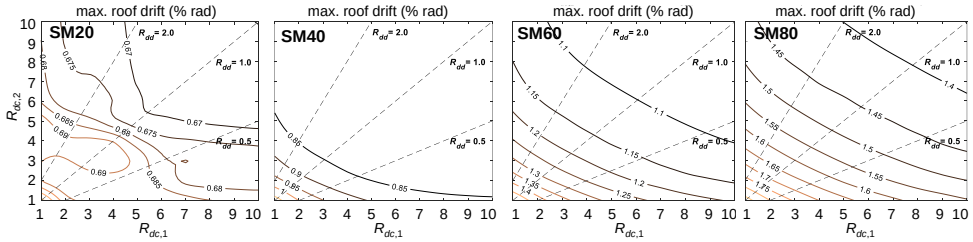

Figure 9. Relationships between roof drift, R_{dc2}, and R_{dc1} for the SM20 obtained from RSA

Fig. 10 shows the relationship between core structure base shear under different values of $R_{dc,2}$ and $R_{dc,1}$ when α_2=0.7 and α_1=0.5. For the SM20, the larger values of $R_{dc,2}$ and $R_{dc,1}$ generally result in larger core structure base shear due to the increased spectral acceleration demand. However, for the SM40, SM60 and SM80, the core structure base shear can be the best reduced aspect, when R_{dd} is around 0.5 to 1.0.

This suggests that, the core structure base shear can be better reduced when the BRBs in lower outrigger are stiffer than the upper outrigger ones. Similar to the roof drift reduction responses, the core structure base shear reduction is not proportional to the increase of $R_{dc,2}$ and $R_{dc,1}$. It is suggested to select R_{dd} equals to 0.5 with smaller $R_{dc,2}$ and $R_{dc,1}$ values ($R_{dc,2}$=1, $R_{dc,1}$=2) for low-rise buildings and larger values ($R_{dc,2}$=3, $R_{dc,1}$=6) for mid-rise and high-rise buildings, respectively.

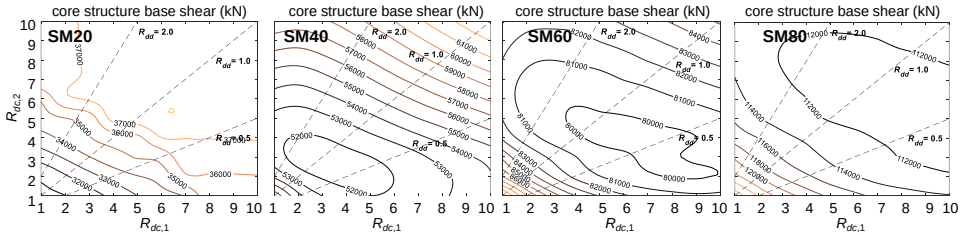

Figure 10. Relationships between core base shear, R_{dc2}, and R_{dc1} for SM20 obtained from RSA

Fig. 11 and Fig. 12 show the CPDs gained by the BRBs in the upper and lower outriggers and the ratio of energy dissipated by BRBs in upper and lower outriggers to the total input energy, when α_2=0.7, α_1=0.5 and R_{tc}=3.19. The larger values of $R_{dc,2}$ and $R_{dc,1}$ results in smaller CPD values and the CPD values are larger in taller buildings, because of larger BRB deformation demands. In addition, the CPD gained by each BRB is only related to its own axial stiffness and has nothing to do with the stiffness of the BRB in another outrigger. The BRBs in the upper outrigger will gain more CPD than the BRBs in lower outrigger and dissipate more seismic energy, than the BRBs in the lower outrigger. Though the larger values of $R_{dc,2}$ and $R_{dc,1}$ results in smaller CPD values, the BRB energy dissipation efficiency is highest when $R_{dc,2}$ and $R_{dc,1}$ are around 6 for mid-rise and high-rise building models (SM40, SM60 and SM80). For those building models, the BRBs in the upper and lower outriggers dissipate around 15% to 20% and 5% to 10% of the total input energy, respectively. For the low-rise building models (SM20), the values of Rdc,2 and Rdc,1 are suggested to be less than 3 in order to develop sufficient BRB energy dissipation efficiency.

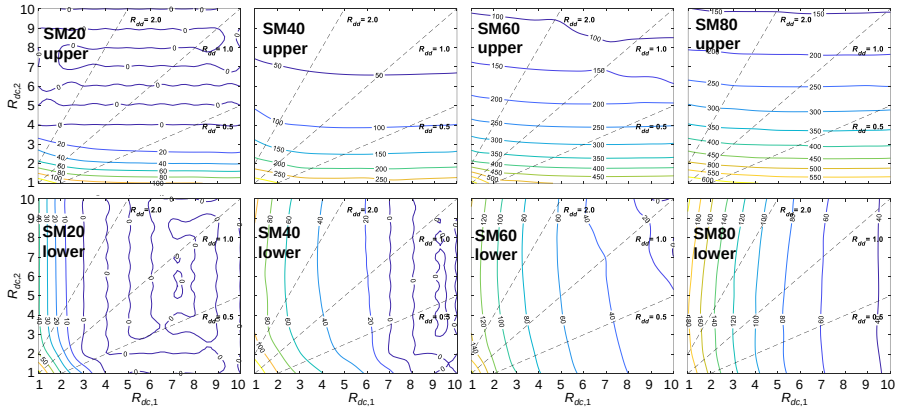

Figure 11. The CPDs gained by the BRBs in upper and lower outriggers obtained from NLRHA

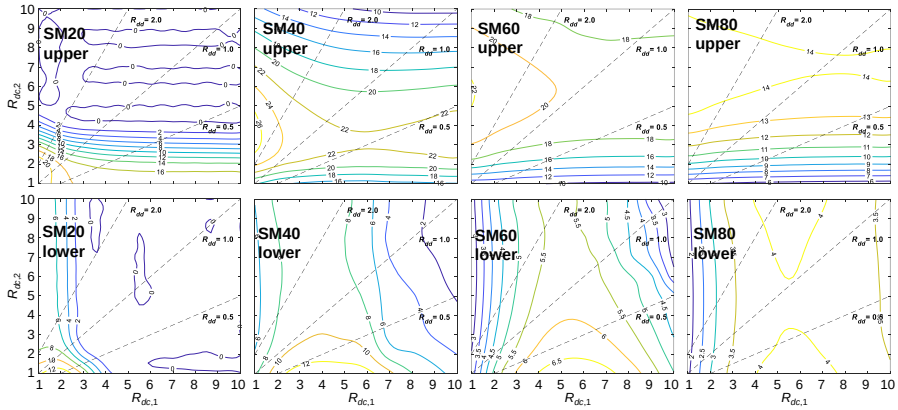

Figure 12. The ratio (%) of energy dissipated by BRBs in the upper and lower outriggers to the total input energy obtained from NLRHA

CONCLUSION

1. The BRB-outrigger system can efficiently reduce the seismic responses for low-rise, mid-rise and high-rise buildings. In general, the larger outrigger flexural stiffness (k_t) better reduces the seismic responses.
2. The proposed SM using Timoshenko beamcolumn element to model the core structure can represent the MBM model based on the modal analysis results. The SM core structure modeled by using Timoshenko beam element well simulate the flexural-type and shear-type lateral deformations of the core structure of MBM model by adjusting the ratio of shear to flexural stiffness (κ^2).
3. The optimal upper BRB-outrigger elevation (α_2) varies from different design targets. In order to reduce the roof drift response, the optimal α_2 is around 0.6 to 0.9 and is higher for taller buildings. Based on the models used in this study, the roof drift can be reduced by 30% to 40% if compared with the buildings without BRB-outriggers. In order to reduce the core structure base shear, the optimal α_2 is around 0.4 to 0.8 for low-rise and mid-rise buildings and is around 0.6 to 0.9 for high-rise buildings. Based on the models used in this study, the core structure base shear can be reduced by around 15% to 25% if compared with the buildings without BRB-outrigger.
4. For low-rise buildings, the values of $R_{dc,2}$ and $R_{dc,1}$ are suggested to be lower than 3, in order to increase the energy dissipation efficiency for the BRBs. For mid-rise and high-rise buildings, the $R_{dc,2}$ and $R_{dc,1}$ are suggested to be greater than 3 in order to prevent gaining a too large CPD value for the BRB.
5. Based on the models used in this study and the NLRHA results, under the optimal design parameters, the BRBs in the BRB-outrigger system dissipate around 30%, 30%, 25% and 20% of the total input seismic energy.

REFERENCES

Ali, M. M., and Moon, K. S. (2007). "Structural developments in tall buildings: current trends and future prospects," *Architectural science review*, **50**(3), 205-223.

American Society of Civil Engineers. (2000, February). "Minimum design loads for buildings and other structures. American Society of Civil Engineers".

Chopra, A. K., and Goel, R. K. (2002). "A modal pushover analysis procedure for estimating seismic demands for buildings," *Earthquake engineering & structural dynamics*, **31**(3), 561-582.

Kasai, K., Fu, Y., and Watanabe, A. (1998). "Passive control systems for seismic damage mitigation," *Journal of Structural Engineering*, **124**(5), 501-512.

Lin, P. C., Takeuchi, T., and Matsui, R. (2018). "Seismic performance evaluation of single damped-outrigger system incorporating buckling-restrained braces," *Earthquake Engineering & Structural Dynamics*, **47**(12), 2343-2365.

Miranda, E. (1999). "Approximate seismic lateral deformation demands in multistory buildings," *Journal of structural engineering*, **125**(4), 417-425.

Smith, B. S., and Salim, I. (1981). "Parameter study of outrigger-braced tall building structures," *Journal of the Structural Division*, **107**(10), 2001-2014.

Watanabe, A., Hitomi, Y., Saeki, E., Wada, A., and Fujimoto, M. (1988, August). "Properties of brace encased in buckling-restraining concrete and steel tube," *Proceedings of ninth world conference on earthquake engineering* (Vol. 4, pp. 719-724).

APPLICATION OF HARDWARE-IN-THE-LOOP SIMULATION WITH DIGITAL TWIN TO REAL-TIME HYBRID TEST

Shih-Yu Chu[1], Chan-Jung Kang[2], Hao-Siang Syu[3], Liang-Yu Lin[4], Meng-Ze Deng[5], Jhih-Yuan Huang[6], Ting-Ru Liang[7], Yong-Kai Zou[8]

1. Associate Professor, Department of Civil Engineering, National Cheng Kung University, Taiwan, e-mail: sychu@mail.ncku.edu.tw
2. Ph.D. Candidate, Department of Civil Engineering, National Cheng Kung University, Taiwan; e-mail: kang830927@gmail.com
3. Structural engineer, Toward Engineering Consultants Co., Ltd.
4. Structural engineer, John-Tai Structural Engineer & Associates
5. Assistant engineer, TASA Construction Corporation.
6. Equipment engineering, Taiwan Semiconductor Manufacturing Company,Ltd.
7. Supervisor, Department of Civil Engineering and Architecture Section, Likees Tech-Service Co., Ltd.
8. Engineer, Wang-Lian Construction Co., Ltd.

ABSTRACT

The Real-time hybrid test (RTHT) can effectively reduce the cost and time compared to the traditional test. However, the technical barrier of RTHT for experimenters is much higher, because not only the knowledge of civil engineering but also mechanical control is required. Therefore, this study proposes a hardware-in-the-loop simulation (HILS) technology as a tool to assist in the development of the RTHT. The HILS is commonly used in aerospace, machinery, and electrical engineering fields that can ensure the embedded software test is completed in the early stage of development. When the system is integrated with the real hardware, the embedded software that has been tested can be directly integrated with the hardware. In this paper, an Active Mass Damper (AMD) is installed on a vibration isolation floor system with variable curvature friction pendulum isolators to verify whether AMD can reduce the acceleration and isolation displacement at the same time. The shake table test (STT) and the RTHT are carried out and compared with each other to verify whether the STT can be perfectly replaced with the RTHT. Furthermore, the real-time simulator in HILS is developed to simulate the environment of the actual configuration of the RTHT, and the addition of the digital-twin technology is developed to identify abnormal operations, malfunctions, and possible sources of error in the integrated testing facilities.

Keywords: Hardware-in-the-loop simulation, Digital twin, Real-time hybrid test, Active mass damper, Base-isolated system

INTRODUCTION

Active control

The application of active control in the field of civil engineering structures has been developed for over 30 years [1] [2], and different active control systems have also been installed on high-rise buildings and bridge structures. It is well known that time delay easily leads to the instability of controlled structures. Agrawal et al. (1993) [3] have solved the analytical formula for the maximum allowable delay time of an undamped single-degree-of-freedom system using state feedback and direct velocity feedback control. Inaudi et al. (1994) [4] also examined the time delay effect of active isolation structures using velocity feedback and obtained an expression for the maximum allowable delay time related to active damping. Agrawal et al. (1997) [5] proposed a set of approximate methods to determine the maximum allowable delay time of multi-degree-of-freedom systems. Lin et al. (1996) [6] defined the meaning of the critical delay time and found that for state and velocity feedback control, the increase or decrease of the critical delay time of a single-degree-of-freedom pre-stressing tendons system is related to the initial damping and initial frequency of the structure. Chu et al. (2002) [7] investigated the hybrid mass damper (HMD)

system, when the direct output feedback method is adopted and the optimal delay time is selected, this control force with time-delay can instead increase the modal damping ratio of the control system. The maximum allowable delay time defined at the onset of instability of controlled system can be the optimal delay time that reaches the optimal control performance if the delay time is considered in the delayed feedback gains. The inclusion of sampling period and delay time in the optimization process for discrete-time control illustrates the beneficial effect under the same delay time.[8]

Real-time hybrid test

The real-time hybrid test (RTHT) is developed from the pseudo-dynamic test. The concept of the pseudo-dynamic test was first proposed by Hakuno et al. (1969) [9]. Takanashi et al. (1975) [10] first applied the concept of pseudo-dynamic test to structural experiment. Dermitzakis et al. (1985) [11] proposed the application of substructure experiments. Nakashima et al. (1992) [12] proposed the concept of the real-time pseudo-dynamic test, which adopted the central difference method for numerical operation. Chung et al. (1999) [13] formally combined the shaking table test (STT) and the pseudo-dynamic test. In their research, the STT of the low-rise isolation structure was firstly conducted, and then the pseudo-dynamic test was carried out to compare it. In the same year, Horiuchi et al. (1999) [14] used a shake table as an actuator to verify the feasibility of the real-time pseudo-dynamics test in multi-DOF structures. Reinhorn et al. (2003) [15] proposed the RTHT of structure with middle layer isolation, using the shaking table and the actuator to simulate the response of the upper and lower structures at the same time, to understand the relationship between the interaction effect.

Hardware-in-the-loop simulation

"Hardware-in-the-loop Simulation (HILS)" is commonly used in aerospace, machinery, and electrical fields, such as new-type mechanical testing [16], controller design [17][18], and self-driving automobiles and airplanes [19]. HILS can ensure the completion of embedded software tests in the early stage of development. When the system is integrated with real hardware, the embedded software has been tested and can be directly connected to the hardware for testing. At present, more and more scholars have proposed the development process of HILS. Tutunji [20] applied online system identification technology to the HILS. The application of the above concepts in civil and architectural tests is the prototype of the RTHT. This study will use the HILS technology to establish the fail-safe test process of the RTHT.

INTRODUCTION OF SPECIMEN AND DEVICE

In this research, the configuration is to simulate the installation of AMD on the isolation system to explore the influence of the active control mechanism on the stroke of the isolation system. The isolation system is the Polynomial Sliding Isolator with Variable Curvature (PSIVC) [21]. It is mainly composed of an upper curved plate, lower curved plate, ball and socket support, friction element, and friction material, as shown in Figure 1(a). The AMD is as shown in Figure 1(b), which is controlled by the LabVIEW software. The control method is to transmit the displacement command to the servo motor controller through the PCI-7340 motion control card. After the controller receives the command, it will drive the servo motor, and the motor will drive the screw to rotate, which drives the AMD to move. In addition, the potentiometer on the AMD will measure the actual displacement at the same time and transmit the measured value to the computer through the PCI-7340 motion control card.

(a) (b)

Figure 1. Photograph of the specimens (a) PSIVC; (b) AMD

NUMERICAL SIMULATION

At the beginning, the control efficiency of AMD can be verified by numerical simulation. This research adopts discrete-time linear quadratic regulator (LQR) as the control algorithm of AMD and is extended with the consideration of delay time. The optimal feedback gain is then obtained by assuming the delay time of AMD is 0.01sec. Different earthquakes (El Centro & Imperial Valley) with different PGAs are used in numerical simulation, the aim is to investigate whether the AMD can reduce the relative displacement of PSIVC, but only with small increment on absolute acceleration. The results are shown in Table 1. It can be observed that the relative displacements of PSIVC with AMD are smaller than Uncontrolled. Meanwhile, the absolute accelerations of PSIVC with AMD are amplified compared to those of Uncontrolled in small PGAs, but the opposite trend occurs in the cases of larger intensities. This is in line with the expected control effectiveness.

Table 1. Peak response of PSIVC in numerical simulation

	Peak relative displacement (mm)		Peak absolute acceleration (gal)	
	With AMD	Uncontrolled	With AMD	Uncontrolled
El Centro_150 gal	1.24	1.33	108.08	104.56
El Centro_200 gal	3.57	4.77	122.66	118.15
El Centro_250 gal	9.32	11.40	133.91	129.02
El Centro_400 gal	27.37	30.36	151.73	142.97
El Centro_600 gal	71.05	80.85	159.12	162.30
El Centro_800 gal	116.67	124.50	291.95	327.72
IV_125 gal	0.52	0.95	103.05	99.13
IV_200 gal	8.13	9.85	130.63	124.94
IV_300 gal	36.40	43.63	150.75	141.15
IV_400 gal	86.89	96.88	163.72	188.45

SHAKING TABLE TEST

Configuration of STT

The shaking table used in this research is called the MAST (shown in Figure 2) which is equipped in the Tainan Lab. of NCREE. MAST is a six-degree-of-freedom vibration simulation platform which is usually used to test smaller structural components, can also be applied in some non-structural fields such as server or car assembling. The setup of shaking table test is shown in Figure 3. The PSIVC with the

AMD is directly mounted on the MAST, and different kinds of sensors are installed on the platform, PSIVC, and AMD, respectively, to measure the response of the whole physical system.

Results of STT

Due to the performance of the MAST (the limitation on stroke is $\pm 20cm$), PGA of different earthquake cases are first screened according to the results of numerical simulation. Only PGA which is smaller than 250 gal. for the El Centro, and smaller than 150 gal. for the Imperial Valley can be conducted. In this paper, the case of El Centro 200 gal. is taken as an example. The results are shown in Figure 4 and Figure 5. It can be observed that the case (with AMD) reduces the relative displacement compared to that of Uncontrolled, and the results of STT and numerical simulations are very similar. These results indicate the control effectiveness of AMD installed on the PSIVC system, and the derived numerical model can precisely predict the behavior of the whole physical system.

Figure 2. Multi-Axial Seismic Test System, MAST (NCREE)

(a) (b)

Figure 3. Photographs of shaking table test

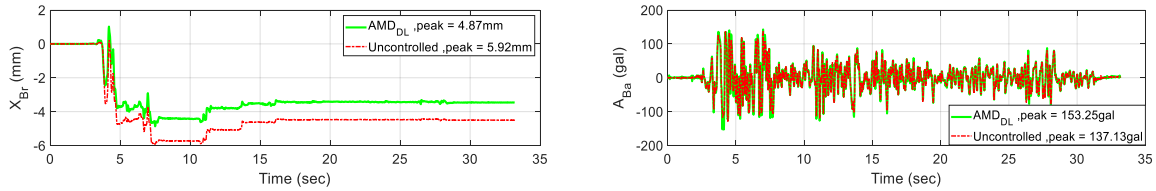

(a) (b)

Figure 4. Comparison of response of PSIVC between with AMD and uncontrolled state (a) Relative displacement; (b) Absolute acceleration

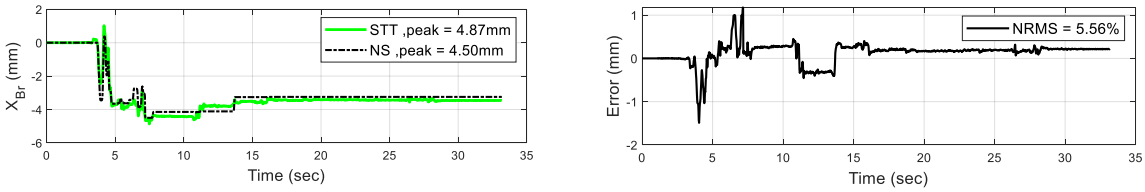

(a) (b)

Figure 5. Comparison of relative displacement of PSIVC (STT vs. Numerical simulation) (a) Time history; (b) Error

HARDWARE-IN-THE-LOOP SIMULATION

The framework of the HILS proposed in this research is shown in Figure 6. The objective is to help the experimenters remotely and safely predict the stability and safety of their RTHT setups. The essential part of this proposed HILS is the real-time simulator, which must have an I/O interface for signal transmission between the numerical models of the actuator, device, sensor, etc. The shared common memory technique (SCRAMNet) is utilized for signal transmission in the proposed framework of HILS. The ARX model with the recursive least square method is used to identify the characteristic of MAST, and the identified transfer function is shown in Figure 7. In this proposed framework, the real-time simulator receives the simulated response of the PSIVC and outputs the response of the numerical model of AMD to the Target PC1 (shown in Figure 6), which simultaneously calculates the next-step response of the PSIVC by the receiving AMD response and defined input (e.g., Earthquake). In this paper, because the AMD can be actively actuated, it is possible to replace the virtual AMD with the real physical AMD with a real sensor installed on it. This change may make the results of HILS closer to the real experimental configuration of the RTHT. After the HILS is completed, the left-hand part in Figure 7 can then be taken apart and embedded in the control system in the RTHT. The virtual reality (VR) technique is also adopted in this proposed framework to create the digital twins of the device, specimen, and actuator. The digital twins can respond to the same stimuli as their physical counterparts and help identify abnormal operations, malfunctions and identify the sources of error. The digital twins in this research are shown in Figure 8. It is helpful for the experimenters to avoid any dangerous situation and make reasonable plans for their RTHT.

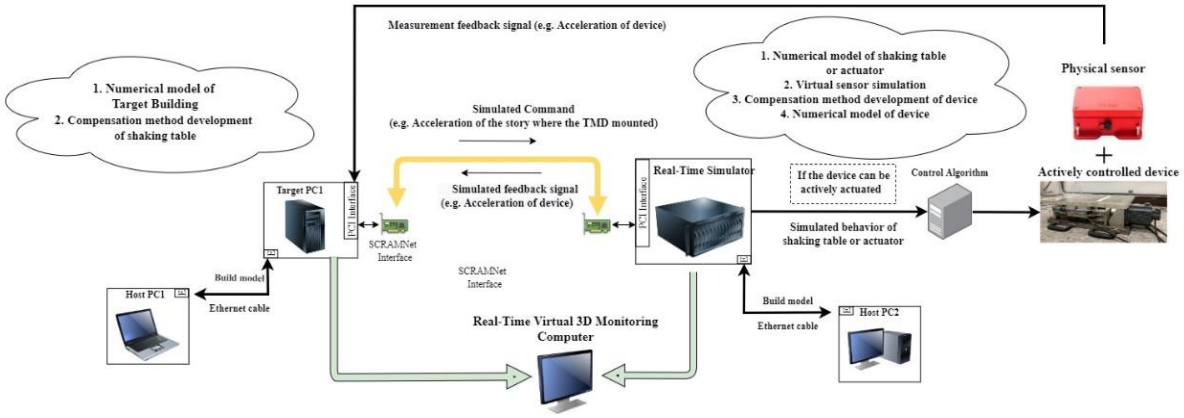

Figure 6. Diagram of the HILS

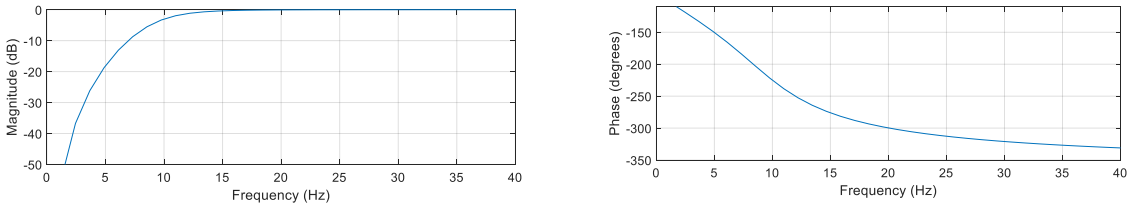

(a) (b)

Figure 7. Transfer function of MAST (a) Amplitude; (b) Phase

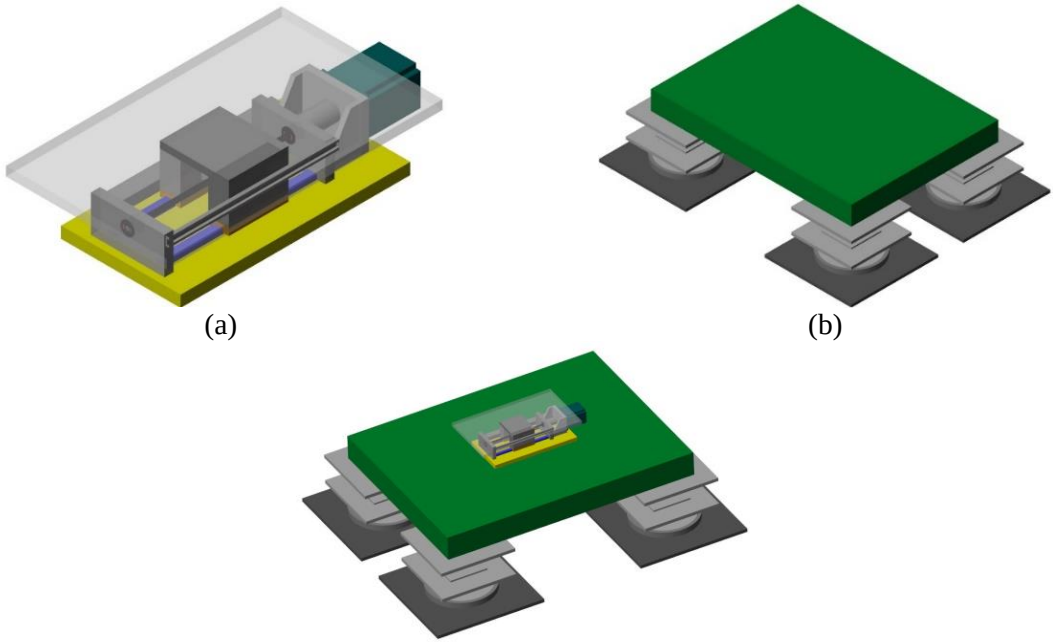

(a) (b)

(c)

Figure 8. Digital twins of AMD and PSIVC (a) AMD; (b) PSIVC; (c) STT

REAL-TIME HYBRID TEST

The concept of the RTHT in this research is to replace the primary structure with its numerical model. An AMD is directly installed on the MAST in the RTHT compared to the STT, and the behavior of the PSIVC is displayed by the MAST. The results are shown in Figure 9. It can be observed that the relative displacement of PSIVC in the RTHT is roughly similar as that in the STT during strong-motion stage, but quite different during the residual-motion stage. This means there are still many sources of error between the RTHT and the STT that needed to be clarified. However, it can be noticed that the difference between the RTHT and the HILS is obviously smaller than that of RTHT and STT. The results of other cases are shown in Table 2. The accuracy of numerical model is verified in section of shaking table test, the reason of difference between numerical model of the PSIVC and the real one can be excluded. Another reason may cause this difference is speculated as the performance of the MAST. It is known from Figure 7 that the characteristic of MAST is like a high-pass filter, this may cause a large influence on the RTHT especially the PSIVC is kind of like a low natural frequency system. Because the HILS has first included the identified MAST features in the real-time simulator, making the HILS closer to its RTHT results, which indirectly means that the HILS can indeed effectively predict the RTHT results in advance.

Table 2. Comparison of response of PSIVC (RTHT vs. HILS & RTHT vs. STT)

	RMS of relative displacement (mm)		RMS of absolute acceleration (gal)	
	HILS	STT	HILS	STT
El Centro_150 gal	0.1063	0.8816	4.2064	8.7168
El Centro_200 gal	0.3109	2.835	7.264	13.395
El Centro_250 gal	1.2122	5.5423	6.2195	12.8590
IV_125 gal	0.0220	0.0583	2.6922	6.0237

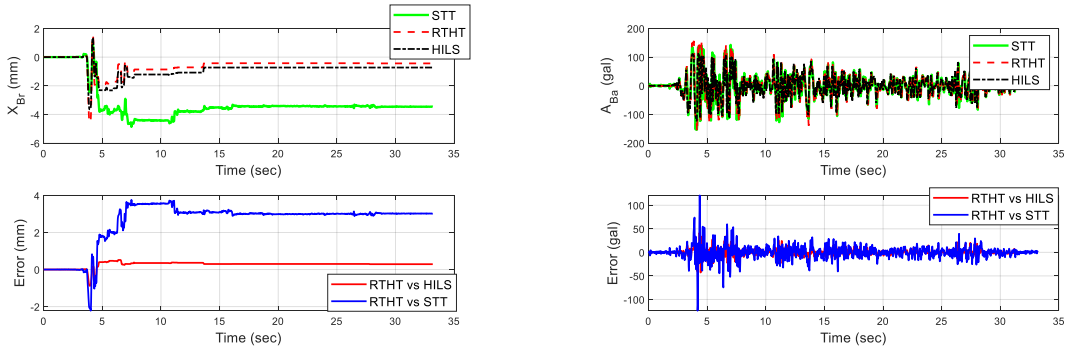

(a) (b)

Figure 9. Comparison of response of PSIVC between RTHT, STT and HILS (a) Relative displacement; (b) Absolute acceleration

CONCLUSIONS

There are still many sources of error between the RTHT and the STT that need to be addressed. These errors may cause the failure of the test, or even cause possible damage to the equipment. Therefore, this paper develops a framework of HILS suitable for current RTHT as a fail-safe test, experimenters can safely test and develop embedded software and hardware in the laboratory prior to the RTHT. Even helpful for them to predict the results and any possible problems in advance. In addition, by introducing the application of VR technology, the experimenter can easily observe any dangerous or strange situation and make reasonable judgements during the RTHT in advance. According to the above-mentioned results, the HILS can indeed effectively predict the behavior of the RTHT. Therefore, it is recommended that the method proposed in this paper can be used for security confirmation before each RTHT.

ACKNOWLEDGMENTS

This research was supported in part by Ministry of Science and Technology of the Republic of China under grant MOST 110-2625-M-002-017 and the in-house project of the National Center for Research on Earthquake Engineering of Taiwan (0611A2500). These supports are greatly appreciated.

REFERENCES

1 Soong, T. T. (1990). *Active Structural Control: Theory and Practice*, John Wiley, New York.

2 Chu, S. Y., Soong, T. T. & Reinhorn, A. M. (2005). *Active, Hybrid and Semi-Active Structural Control – A Design and Implementation Handbook*, John Wiley & Sons Ltd, West Sussex, UK.

3 Agrawal, A. K., Fujino, Y., & Bhartia, B. K. (1993). "Instability due to time delay and its compensation in active control of structures," *Earthquake Engineering & Structural Dynamics*,

22(3), 211-224.

4 Inaudi, J. A., & Kelly, J. M. (1994). "A robust delay-compensation technique based on memory," *Earthquake Engineering & Structural Dynamics*, 23(9), 987-1001.

5 Agrawal, A. K., & Yang, J. (1997). "Effect of fixed time delay on stability and performance of actively controlled civil engineering structures," *Earthquake Engineering & Structural Dynamics*, 26(11), 1169-1185.

6 Lin, C. C., Sheu, J. F., Chu, S. Y., & Chung, L. L. (1996). "Time-delay effect and its solution for optimal output feedback control of structures," *Earthquake Engineering & Structural Dynamics*, 25(6), 547-559.

7 Chu, S. Y., Soong, T. T., Lin, C. C., & Chen, Y. Z. (2002). "Time-delay effect and compensation on direct output feedback controlled mass damper systems," *Earthquake Engineering & Structural Dynamics*, 31(1), 121-137.

8 Chu, S. Y., Lin, C. C., Chung, L. L., Chang, C. C. and Lu, K. H. (2008), "Optimal Performance of Discrete-time Direct Output Feedback Structural Control with Delayed Control Forces", *Structural Control and Health Monitoring*, 15(1), 20-42.

9 Hakuno, M., Shidawara, M., & Hara, T. (1969). "Dynamic destructive test of a cantilever beam, controlled by an analog-computer," *Japan society of civil engineers, 1969*(171), 1-9.

10 Takanashi, K., Udagawa, K., Seki, M., Okada, T., & Tanaka, H. (1975). "Nonlinear earthquake response analysis of structures by a computer-actuator on-line system," *Transactions of the Architectural Institute of Japan, 8*, 1-17.

11 Dermitzakis, S. N., & Mahin, S. A. (1985). "Development of substructuring techniques for on-line computer controlled seismic performance testing". University of California, Berkeley.

12 Nakashima, M., Kato, H., & Takaoka, E. (1992). "Development of real-time pseudo dynamic testing," *Earthquake Engineering & Structural Dynamics, 21*(1), 79-92.

13 Chung, W. J., Yun, C. B., Kim, N. S., & Seo, J. W. (1999). "Shaking table and pseudodynamic tests for the evaluation of the seismic performance of base-isolated structures." *Engineering Structures, 21*(4), 365-379.

14 Horiuchi, T., Inoue, M., Konno, T., & Yamagishi, W. (1999). "Development of a Real-Time Hybrid Experimental System Using a Shaking Table：(Proposal of Experiment Concept and Feasibility Study with Rigid Secondary System)," *International Journal Series C Mechanical Systems, Machine Elements Manufacturing, 42*(2), 255-264.

15 Reinhorn, A. M., Bruneau, M., Chu, S. Y., Shao, X and Pitman, M. C. (2003), "Large scale real time dynamic hybrid testing technique - shake tables substructure testing. *Structures Congress and Exposition: Engineering Smarter*. Seattle, WA, United states, 67-72.

16 G. Stoepler, T. Menzel and S. Douglas. (2005). "Hardware-in-the-loop simulation of machine tools and manufacturing systems," *IEE Computing and Control Engineering*, Vol. 16, pp. 10-15.

17 R. Isermann and N. Müller. (2003). "Design of computer controlled combustion engines," *Mechatronics*, Volume 13, Issue 10, Pages 1067-1089.

18 C. Lin, C. Tseng and T. Tseng. (2006). "A hardware-in-the-loop dynamics simulator for motorcycle rapid controller prototyping," *Control Engineering Practice,* Volume 14, Issue 12, Pages 1467-1476.

19 L. f. Xu, J. q. Li, J. f. Hua, X. j. Li and M. g. Ouyang. (2009). "Hardware in the loop simulation of vehicle controller unit for fuel cell/battery hybrid bus," *2009 IEEE Vehicle Power and Propulsion Conference*, pp. 1777-1782, doi: 10.1109/VPPC.2009.5289701.

20 Tutunji, Tarek & Saleem, Ashraf. (2008). "A method for on-line identification and control based on hardware-in-the-loop concept," *2008 5th International Multi-Conference on Systems*, Signals and Devices, SSD'08. 1-6. 10.1109/SSD.2008.4632896.

21 L.Y. Lu, T.Y. Lee, S.W. Yeh. (2011). "Theory And Experimental Study For Sliding Isolators With Variable Curvature," *Earthquake Engineering & Structural Dynamics*, 40, 1609-1627.

CONTROL PARAMETERS DESIGN OF TUNED MASS DAMPERS WITH ACTIVE VARIABLE INERTER

Chang-Ching Chang[1], Jer-Fu Wang[2] and Chi-Chang Lin[3]
1. Associate Researcher, National Center for Research on Earthquake Engineering, Taipei, Taiwan.
2. Department of Civil and Disaster Prevention Engineering, National United University, Miaoli, Taiwan
3. Department of Civil Engineering, National Chung Hsing University, Taichung, Taiwan.
Email: ccchang@narlabs.org.tw

ABSTRACT

A conventional tuned mass damper (TMD) is a popular and generally accepted vibration control device in the field of passive structural control. However, it was found that the control efficacy of a conventional TMD may significantly degrade when the TMD's frequency does not tune to its desired value. In addition, the vibration energy of the controlled structure transferred into the TMD is dissipated by a viscous or friction damper and becomes waste heat. In this study, a flywheel with variable mass moment of inertia could be introduced into the transmission system of the TMD to adjust TMD's frequency to mitigate the frequency-detuning effect and to enhance the control efficacy of TMD system. In addition, a tuned mass damper with active variable inerter (TMDAVI) is developed to improve the flexibility of variable inertia adjustment. The theoretical derivation is performed to generate the relationship between the DC motor and the transmission system of the TMDAVI by active control theory. An optimal design method of the TMDAVI will be developed for torsionally-coupled shear building.

Keywords: Tuned mass damper, Inerter, Electromagnetic damper, Vibration Control, Active control.

INTRODUCTION

Tuned mass damper (TMD) has been a widely-used vibration control system for civil engineering structures since 1970s, where the first TMD idea can be traced back to 1911(Frahm 1911; DenHartog 1985). A conventional TMD consists of a mass connected to the controlled structure with stiffness and damping components of constant coefficients. Electromagnetic dampers are one type of damping devices that have been used as damping components of TMDs.

Recently, the idea of using an electromagnetic damper as the TMD damping device for vibration control and simultaneously for energy-harvesting has been proposed. Liu et al. (2016) proposed energy-harvesting series electromagnetic-tuned mass dampers (EMTMDs). They derived the analytical solution for performance indices of vibration control and energy-harvesting and conducted experiments to verify the vibration control effectiveness of EMTMDs is better than conventional TMDs, with additional advantage of energy-harvesting. Tang and Zuo (2012) and Shen et al. (2012) used a rotational motor as an electromagnetic damper for a TMD and performed tests to verify the vibration control and energy-harvesting abilities of the TMD. Gonzalez-Buelga et al. (2014) proposed a TMD/H (Tuned mass damper/harvester) with a linear motor and successfully achieved semi-active control using the harvesting energy from the TMD itself.

Using variable mass rather than a fixed mass is another idea to increase the adaptiveness of a TMD, where an inerter is a device that can achieve this purpose. Smith (2002) proposed an inerter mechanism that can generate a force proportional to the relative acceleration of two ends of the device. The linear relation between the force and the relative acceleration is called Inertance. An inerter usually consists of flywheels and gears/chain drives (Papageorgiou and Smith 2005; Chuan et al. 2011) and the inertance of an inerter can be several times the mass of the inerter. Later on, researchers (Giaralis et al. 2016; Gonzalez-Buelga et al. 2015; Luo et al. 2017) began to combine an electromagnetic damper and an inerter in a TMD with different inerter types with analytical simulations.

In this study, a flywheel with variable mass moment of inertia could be introduced into the transmission system of the TMD to adjust TMD's frequency to mitigate the frequency-detuning effect and to enhance

the control efficacy of TMD system. In addition, a tuned mass damper with active variable inerter (TMDAVI) is developed to improve the flexibility of variable inertia adjustment. The theoretical derivation is performed to generate the relationship between the DC motor and the transmission system of the TMDAVI by active control theory. An optimal design method of the TMDAVI will be developed for torsionally-coupled shear building.

MODELLING OF ELECTROMAGNETIC TMD INERTER

The paper proposes a tuned mass damper with active variable inerter (TMDAVI), of which the viscous damper or friction damper is replaced by the electromagnetic motor connected with adjustable resistance and an inerter-like flywheel mechanism, as shown in Figure 1, so that a more flexible viscous damping can be achieved and part of the energy originally dissipated by the dampers could be harvested. A flywheel with variable mass moment of inertia will be introduced into the transmission system of the TMD to adjust the TMD's frequency to mitigate the frequency detuning effect and to enhance the control efficacy of TMD system.

The electromagnetic damper is a device that provides an opposing force to the imparted movement. It is mainly composed of a transducer (generator) which converts energy between mechanic form and electric form. The composing transducers can be classified into two main groups based on the type of motion provided by the mover: rotational motion transducers and linear motion transducers.

In this paper, DC motors are used as rotary electromagnetic transducers. Hereinafter the rotary permanent magnet DC motor will be referred to as a generator. The electromagnetic transducer and the circuit can be modeled as an ideal transducer shunted with an RLC circuit (Liu et al. 2016, Tan et al. 2013). The generator can be modeled as series connection of an inductor L_{gen}, a resistor R_{gen} and a dependent voltage source e_{gen}. If the generator is attached to a rotating mechanical system, according to Faraday's law of electromagnetic induction, the magnitude of induced electromotive force (EMF) e_{gen} will depend on the relative angular velocity $\dot{\theta}_{gen}$ of the mechanical system. Based on Lorentz force law, induced electric current $\dot{q}$ in the generator coil will further produce a torque τ_{gen} back into the mechanical system following the relationship

$$e_{gen}(t) = k_e \dot{\theta}_{gen}(t) \tag{1}$$

$$\tau_{gen}(t) = k_t \dot{q}(t) \tag{2}$$

where k_e and k_t are the motor back EMF constant and motor torque constant, respectively. The constants k_e and k_t are determined by the transducer properties. The relation $k_e = k_t$ is held for an ideal transducer without energy loss. In the resonator circuit, the closed-loop voltage drop is zero according to Kirchhoff's voltage law. Thus, we have

$$e_{gen}(t) - L_{gen}\ddot{q}(t) - (R_{gen} + R_{load})\dot{q}(t) = 0 \tag{3}$$

where L_{gen} represents the internal inductance of the generator; R_{gen} is the internal resistance of the generator; R_{load} is the external load resistance. Due to the typically low frequency feature of the primary building (civil buildings) and the relative small value of L_{gen} of the generator, that is $L_{gen}\ddot{q} \ll (R_{gen} + R_{load})\dot{q}$, the torque of the generator can be rewritten as

$$\tau_{gen}(t) = \left(\frac{k_e k_t}{R_{gen} + R_{load}} \right) \dot{\theta}_{gen}(t) \tag{4}$$

In addition, considering the transmission efficiency ratios of the gearbox to the gear (β_{gh}) and the gear to rack (β_{pin}) in the motor transmission system, and the torque equations between the motor and the flywheel, between the motor and the gearbox, and between the gear and the rack, it can be seen that the force and reaction force applied by the motor transmission system to the TMD and the primary structure are composed of the relative speed-dependent damping force and the relative acceleration-related inertial force, which can be expressed

$$F(t) = \left(\frac{I_{pin}}{r_{pin}^{\ 2}} + \frac{I_{gh} n_{gh}^{\ 2}}{\beta_{pin} r_{pin}^{\ 2}} + \frac{\left(I_{gen} + I_{fw}\right) n_{gh}^{\ 2}}{\beta_{gh}\beta_{pin} r_{pin}^{\ 2}} \right) \ddot{v}_s(t) + \left(\frac{k_e k_t n_{gh}^{\ 2}}{\beta_{gh}\beta_{pin} r_{pin}^{\ 2} \left(R_{gen} + R_{load}\right)} \right) \dot{v}_s(t) \tag{5}$$

where I_{fw} , I_{gen} , I_{pin} indicate the moment of inertia of flywheel, motor, gearbox, and pinion, respectively; r_{pin} is the radius of gearbox; n_{gh} is the pinion ratio of gearbox; θ_{fw} is angle velocity of flywheel; τ_{gen} and θ_{gen} are toque and angle velocity, respectively, of motor; τ_{gh} and θ_{gh} are toque and angle velocity, respectively, of gearbox; τ_{pin} , θ_{pin} are toque and angle velocity, respectively, of pinion. From eq. (5), the inertance and electromagnetic damping coefficient can be express as

$$b_s = \frac{I_{pin}}{r_{pin}^{\ 2}} + \frac{I_{gh} n_{gh}^{\ 2}}{\beta_{pin} r_{pin}^{\ 2}} + \frac{\left(I_{gen} + I_{fw}\right) n_{gh}^{\ 2}}{\beta_{gh}\beta_{pin} r_{pin}^{\ 2}} \tag{6}$$

$$c_e = \frac{k_e k_t n_{gh}^{\ 2}}{\beta_{gh}\beta_{pin} r_{pin}^{\ 2}\left(R_{gen} + R_{load}\right)} \tag{7}$$

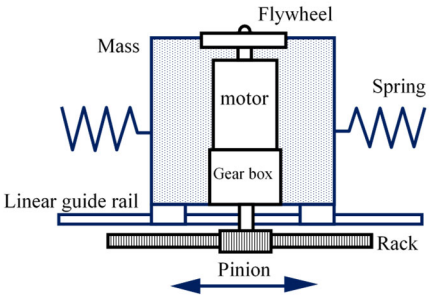

Figure 1. Schematic of a mechanical model of TMDAVI system

DYNAMIC EQUATION OF BUILDING-TMDAVI SYSTEM

For a torsionally coupled N -story building with TMDAVI and subjected to bi-lateral ground acceleration, $\ddot{x}_g$ and $\ddot{y}_g$, is shown in Figure 2. The dynamic equation of motion for combined building-TMDAVI system subjected to bi-lateral ground acceleration $\ddot{\mathbf{u}}_g$ can be written as

$$\mathbf{M}\ddot{\mathbf{x}}(t) + \mathbf{C}\dot{\mathbf{x}}(t) + \mathbf{K}\mathbf{x}(t) = \mathbf{B}_0 u_d(t) + \mathbf{E}_0 \ddot{x}_g(t) \tag{8}$$

where $\mathbf{M}$, $\mathbf{C}$ and $\mathbf{K}$ are the $N \times N$ (where $N = n+1$) system mass, damping and stiffness matrices, respectively, and can be expressed in detail as

$$\mathbf{M} = \begin{bmatrix} m_p & -b_{AVI} \\ m_s & m_s + b_{AVI} \end{bmatrix}; \mathbf{C} = \begin{bmatrix} c_p & -c_s \\ 0 & c_s \end{bmatrix}; \mathbf{K} = \begin{bmatrix} k_p & -k_s \\ 0 & k_s \end{bmatrix}; \mathbf{x}(t) = \begin{Bmatrix} x_p(t) \\ v_s(t) \end{Bmatrix}; \mathbf{E}_0 = \begin{Bmatrix} -m_p \\ -m_s \end{Bmatrix} \tag{9}$$

where m_{p_i} , and m_s represent the masses of the ith DOF and TMDAVI, respectively; c_{p_i} , and c_s represent the damping coefficients of the ith DOF and TMDAVI, respectively; k_{p_i} , and k_s represent the stiffness coefficients of the ith DOF and TMDAVI, respectively. The natural frequency and damping ratio of the TMDAVI can be expressed as

$$\omega_s = \sqrt{\frac{k_s}{m_s + b_s}}\ ;\ \xi_s = \frac{c_s}{2(m_s + b_s)\omega_s} \tag{10}$$

From Eq. (10), it can be seen that the planar TMDAVI position are optimally determined based the mode shapes of the controlled mode for a torsionally coupled building. A TMDAVI is optimally designed to control the modes that make the greatest contribution to the modal responses of the primary structure. In addition, the mass ratio μ and the inerter mass μ_b ratio of the TMDAVI to the primary system can be expressed as

$$\mu = \frac{m_s}{m_p},\ \mu_b = \frac{b_{em}}{m_s} \tag{11}$$

Represented in state-space form, equation (9) can be rewritten as

$$\dot{\mathbf{X}}(t) = \mathbf{A}\mathbf{X}(t) + \mathbf{E}\ddot{x}_g(t) + \mathbf{B}\mathbf{u}(t) \tag{12}$$

where

$$\mathbf{X}=\begin{Bmatrix}\dot{\mathbf{x}}\\ \ddot{\mathbf{x}}\end{Bmatrix},\ \mathbf{A}=\begin{bmatrix}\mathbf{0} & \mathbf{I}\\ -\mathbf{M}^{-1}\mathbf{K} & -\mathbf{M}^{-1}\mathbf{C}\end{bmatrix},\ \mathbf{B}=\begin{Bmatrix}\mathbf{0}\\ -\mathbf{M}^{-1}\mathbf{B}_1\end{Bmatrix},\ \mathbf{E}=\begin{Bmatrix}\mathbf{0}\\ -\mathbf{M}^{-1}\mathbf{E}_1\end{Bmatrix} \tag{13}$$

are $2N\times 1$ state vector, $2N\times 2N$ system matrix, $2N\times 1$ controller location matrix and $2N\times 1$ external excitation location matrix, respectively.

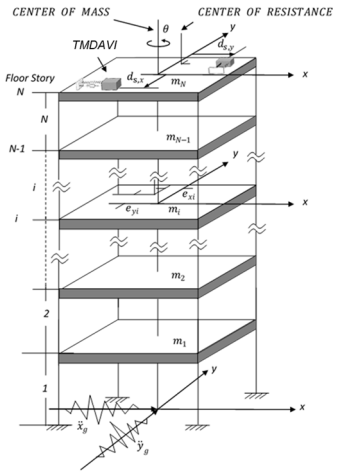

Figure 2. N -story general torsionally coupled building-TMDAVI system

$\mathbf{H}_\infty$ DIRECT OUTPUT FEEDBACK CONTROL THEORY

Define a $p\times 1$ control output vector $\mathbf{Z}(t)$ and an $s\times 1$ output measurement vector $\mathbf{y}(t)$ as

$$\mathbf{Z}(t)=\mathbf{C}_1\mathbf{X}(t)+\mathbf{D}\mathbf{u}(t) \tag{14}$$

$$\mathbf{y}(t)=\mathbf{C}_2\mathbf{X}(t) \tag{15}$$

where $\mathbf{C}_1$, $\mathbf{D}$ and $\mathbf{C}_2$ are $p\times 2N$, $p\times q$ and $s\times 2N$ matrices. The direct output feedback control force is calculated by

$$\mathbf{u}(t)=\mathbf{G}\mathbf{y}(t)=\mathbf{G}\mathbf{C}_2\mathbf{X}(t) \tag{16}$$

where $\mathbf{G}$ is a $q\times 2s$ time-invariant feedback gain matrix. According to H_∞ control algorithm, the H_∞ norm of transfer function matrix $\mathbf{T}_{\mathbf{Zw}}(j\omega)$ of control output $\mathbf{Z}(j\omega)$ with respect to external excitation $\mathbf{w}(j\omega)$ takes the form

$$\left\|\mathbf{T}_{\mathbf{Zw}}(j\omega)\right\|_\infty=\sup\frac{\left\|\mathbf{Z}(j\omega)\right\|_2}{\left\|\mathbf{w}(j\omega)\right\|_2} \tag{17}$$

where $j=\sqrt{-1}$, and sup is defined as the supremum over all $\mathbf{w}(t)$. According to the optimal H_∞ control algorithm (Yaesh and Shaked 1997), the H_∞ norm of transfer function matrix $\mathbf{T}_{\mathbf{Zw}}(j\omega)$ satisfies the following constraint

$$\left\|\mathbf{T}_{\mathbf{Zw}}(j\omega)\right\|_\infty=\sup\frac{\left\|\mathbf{Z}(j\omega)\right\|_2}{\left\|\mathbf{w}(j\omega)\right\|_2}<\gamma \tag{18}$$

where γ is a positive attenuation constant which denotes a measure of control performance. Adopting a smaller value of γ means that more stringent performance of control system is required. It has been proved (Lin and Chang 2006) that an optimal H_∞ control system is asymptotically stable if there exists a matrix $\boldsymbol{P}\geq 0$ that satisfies the following Riccati equation

$$(\mathbf{A}+\mathbf{B}\mathbf{G}\mathbf{C}_2)^{\mathrm{T}}\mathbf{P}+\mathbf{P}(\mathbf{A}+\mathbf{B}\mathbf{G}\mathbf{C}_2)+\frac{1}{\gamma^2}\mathbf{P}\mathbf{E}\mathbf{E}^{\mathrm{T}}\mathbf{P}+(\mathbf{C}_1+\mathbf{D}\mathbf{G}\mathbf{C}_2)^{\mathrm{T}}(\mathbf{C}_1+\mathbf{D}\mathbf{G}\mathbf{C}_2)=\mathbf{0} \tag{19}$$

One way to design the optimal H_∞ output feedback gain is to solve Eq. (10) with minimizing the Entropy of $\mathbf{T}_{\mathbf{Zw}}(j\omega)$ which takes the form (Lin and Chang 2013)

$$E_n(\mathbf{T}_{\mathbf{Zw}},\gamma) = tr\{\mathbf{E}\mathbf{E}^{\mathrm{T}}\mathbf{P}\mathbf{E}\} \tag{20}$$

where tr{-} denotes the trace of a square matrix. Then, the optimization problem to obtain gain matrix $\mathbf{G}$ is converted to minimize the Entropy in Eq. (20) subject to the constraint of Eq. (10). The Lagrangian L can be introduced as

$$L(\mathbf{G},\mathbf{P},\boldsymbol{\lambda}) \equiv tr\left\{\mathbf{E}^{\mathrm{T}}\mathbf{P}\mathbf{E} + \boldsymbol{\lambda}[(\mathbf{A}+\mathbf{B}\mathbf{G}\mathbf{C}_2)^T\mathbf{P} + \mathbf{P}(\mathbf{A}+\mathbf{B}\mathbf{G}\mathbf{C}_2) + \frac{1}{\gamma^2}\mathbf{P}\mathbf{E}\mathbf{E}^T\mathbf{P} + (\mathbf{C}_1+\mathbf{D}\mathbf{G}\mathbf{C}_2)^T(\mathbf{C}_1+\mathbf{D}\mathbf{G}\mathbf{C}_2)]\right\} \tag{21}$$

where λ is a 8×8 Lagrangian multiplier matrix. For simplicity and without loss of generality, the necessary and sufficient conditions for minimization of $L(\mathbf{G},\mathbf{P},\boldsymbol{\lambda})$ are derived and expressed by

$$\frac{\partial L}{\partial \boldsymbol{\lambda}} = (\mathbf{A}+\mathbf{B}\mathbf{G}\mathbf{C}_2)^{\mathrm{T}}\mathbf{P} + \mathbf{P}(\mathbf{A}+\mathbf{B}\mathbf{G}\mathbf{C}_2) + \frac{1}{\gamma^2}\mathbf{P}\mathbf{E}\mathbf{E}^{\mathrm{T}}\mathbf{P} + (\mathbf{C}_1+\mathbf{D}\mathbf{G}\mathbf{C}_2)^{\mathrm{T}}(\mathbf{C}_1+\mathbf{D}\mathbf{G}\mathbf{C}_2) = 0 \tag{22a}$$

$$\frac{\partial L}{\partial \mathbf{P}} = (\mathbf{A}+\mathbf{B}\mathbf{G}\mathbf{C}_2 + \frac{1}{\gamma^2}\mathbf{E}\mathbf{E}^{\mathrm{T}}\mathbf{P})\boldsymbol{\lambda} + \boldsymbol{\lambda}(\mathbf{A}+\mathbf{B}\mathbf{G}\mathbf{C}_2 + \frac{1}{\gamma^2}\mathbf{E}\mathbf{E}^{\mathrm{T}}\mathbf{P})^{\mathrm{T}} + \mathbf{E}\mathbf{E}^{\mathrm{T}} = 0 \tag{22b}$$

$$\frac{\partial L}{\partial \mathbf{G}} = \mathbf{B}^{\mathrm{T}}\mathbf{P}\boldsymbol{\lambda}\mathbf{C}_2^{\mathrm{T}} + (\mathbf{C}_2{}^{\mathrm{T}}\mathbf{G}^{\mathrm{T}}\mathbf{D}^{\mathrm{T}}\mathbf{D})^{\mathrm{T}}\mathbf{G}\mathbf{C}_2\boldsymbol{\lambda}\mathbf{C}_2^{\mathrm{T}} = 0 \tag{22c}$$

The gain can be obtained by solving equations (22a)-(22c) for the direct output feedback. The required inerter could be obtained from the gain.

CONCLUSIONS

In this paper, TMDAVI is developed.by replacing the viscous dampers with electromagnetic rotary transducers so that a more flexible viscous damping can be achieved and part of the energy originally dissipated by the dampers could be harvested. A flywheel with variable mass moment of inertia will be introduced into the transmission system of the TMD to adjust TMD's frequency to mitigate the frequency detuning effect and to enhance the control efficacy of TMD system. The theoretical derivation is performed to generate the relationship between the DC motor and the transmission system of the TMDAVI by active control theory. The active mechanism to improve the flexibility of variable inertia adjustment.

ACKNOWLEDGMENTS

This work is supported by the National Science and Technology Council of the Republic of China (Taiwan) under grant No. MOST 110-2625-M-492-009. This support is greatly appreciated

REFERENCES

H. Fhram, "Device for damping vibration of bodies," U.S. Patent No. 989-958, 1911.

J. P. Den Hartog, Mechanical vibrations, 4th edition, McGraw-Hill, New York, 1956.

Y. Liu, C. C. Lin, J. Parker, and L. Zuo, "Exact H2 optimal tuning and experimental verification of energy-harvesting series electromagnetic tuned-mass dampers," Journal of Vibration and Acoustics, vol.138, Article ID 061003, 2016.

X. Tang and L. Zuo, "Simultaneous energy harvesting and vibration control of structures with tuned mass dampers," Journal of Intelligent Material Systems and Structures, vol. 23, pp. 2117–2127, 2012.

W. A. Shen, S. Zhu, and Y. L. Xu, "An experimental study on self-powered vibration control and monitoring system using electromagnetic TMD and wireless sensors," Sensors and Actuators A: Physical, vol.180, pp.166–176, 2012.

A. Gonzalez-Buelga, L. R. Clare, A. Cammarano, S. A. Neild, S. G Burrow, and D. J. Inman, "An optimised tuned mass damper/harvester device," Structural Control and Health Monitoring, vol21, pp.1154–1169, 2014.

M. C. Smith, "Synthesis of mechanical networks: the inerter," Institute of Electrical and Electronics Engineers. Transactions on Automatic Control, vol.47, no.10, pp.1648–1662, 2002.

C. C. Lin, C. C. Chang, H. L. Chen, "Optimal H_∞ Output Feedback Control System with Time Delay", Journal of Engineering Mechanics (ASCE) vol 132 pp1096-1105, 2006

C. C. Lin and C. C. Chang, "Optimum Design Strategy for H_∞ Control of Time-Delayed Velocity Feedback Control", Journal of Engineering Mechanics (ASCE) vol 139 pp 1460-1469, 2013

C. Papageorgiou and M. C. Smith, "Laboratory experimental testing of inerters," IEEE Conference on Decision and Control, 44, 2005.

L. Chuan, M. Liang, Y. Wang, and Y Dong, "Vibration suppression using two terminal flywheel. Part I: Modeling and Characterization," Journal of Vibration and Control, vol.18, pp.1096-1105, 2011.

A. Gonzalez-Buelga, L. R. Clare, S. A. Neild, J. Z. Jiang, and D. J. Inman, "An electromagnetic inerter-based vibration suppression device," Smart Materials and Structures, vol 24, 55015-55024, 2015.

J. Salvi and A. Giaralis, "Concept study of a novel energy harvesting-enabled tuned massdamper-inerter (EH-TMDI) device for vibration control of harmonically excited structures," Journal of Physics: Conference Series, 744, Article ID 012082, 2016.

Y. Luo, H. Sun, X. Wang, L. Zuo, and N. Chen, "Wind induced vibration control and energy harvesting of electromagnetic resonant shunt tuned mass-damper-inerter for building structures," Shock and Vibration, vol. 2017, article ID 4180134, 13 pages, 2017.

Z. Li, L. Zuo, G. Luhrs, L. Lin, and Y. Qin, "Electromagnetic energy-harvesting shockabsorbers: design, modeling, and road tests," IEEE Transactions on Vehicular Technology, vol.62, pp.1065–1074, 2013.

LOADING TESTS ON BUCKLING-RESTRAINED BRACES WITH MULTIPLE ROUND STEEL CORE BARS

Sijin Zhang[1], Hiroshi Tagawa[2], Xingchen Chen[3]
1. Graduate Student, Graduate School of Adv Sci and Eng, Hiroshima University, Japan.
2. Professor, Graduate School of Adv Sci and Eng, Hiroshima University, Japan.
3. Assistant Professor, Graduate School of Adv Sci and Eng, Hiroshima University, Japan.
Email: d211700@hiroshima-u.ac.jp, htagawa@hiroshima-u.ac.jp, xchen@hiroshima-u.ac.jp

ABSTRACT

This study conducted loading tests on a novel buckling-restrained brace (BRB) using multiple round steel core bars to increase the feasible strength of BRBs utilizing steel bars with roll-threaded screw ends. The buckling restraining members of the proposed BRB consisted of multiple primary tubes and a secondary tube. The primary tube directly restrained the buckling of each core bar, and the secondary tube restrained the buckling of the primary tube through spacers. This paper first describes the configuration of the proposed BRB. Subsequently, cyclic loading tests of three specimens with different spacer spacing are presented to demonstrate the mechanical behavior of the proposed BRB. The test results indicated that fulfilling the requirement of spacer spacing is essential for achieving stable behavior of the primary tubes and steel core bars.

Keywords: Buckling-restrained braces, multiple round steel core bars, cyclic loading tests

INTRODUCTION

Commonly used BRBs often adopt steel plates or steel tubes as core members, which are designed to yield under cyclic axial loads and remain buckling-restrained under compression. Besides steel plates, round steel bars are becoming popular core members for energy dissipation devices. Buckling-restrained round steel bar dampers have been used in beam-to-column connections (Tagawa et al. 2020), spine frames (Mateus et al. 2021), and knee braces (Munkhunur et al. 2022). Previous studies (Fujii and Tagawa 2010, 2011; Mateus et al. 2019) investigated BRBs using round steel bar cores with roll-threaded screw ends. One benefit of using such core bar is their low cost for manufacturing rather long core members. The roll-threaded screw ends ensure sufficient plastic deformation capacity of the bar shank. Thus, milling down the bar shank is unnecessary. In addition, the clearance between the bar shank and inner surface of the buckling restraining tube can be minimized because of the proximity of the shank diameter and the screw diameter. Thus, grouting around the bar shank is unnecessary.

As mentioned previously, BRBs using single-round steel core bars have been well developed and investigated. However, the feasible bar diameter has an upper limit in the roll-threading process, which limits the maximum strength of the BRB. This study investigated a novel BRB comprising multiple core bars to increase the feasible maximum strength of BRBs using round steel bars.

PROPOSED BRB

Fig. 1 presents the configuration of the proposed BRB which uses multiple round steel core bars with roll-threaded screws at the bar ends. There are two types of buckling-restraining members: primary and secondary tubes. The primary tube directly restrains the core bar buckling while the secondary tube restrains the buckling of the primary tube through the spacers. The spacer spacing is assumed to be the buckling length of the primary tube, thus, an increase in the number of spacers reduces the buckling length of the primary tube. The secondary tube penetrates the central coupler and is fixed using allen bolts. The secondary tube also restrains the overall buckling of the BRB.

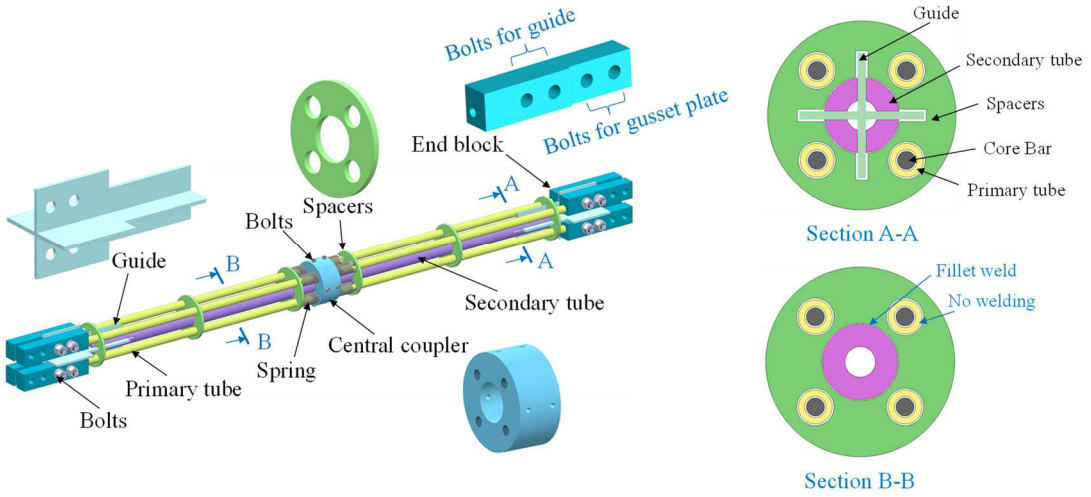

Figure 1. Configuration of proposed BRB.

During the construction of buildings, BRBs are often connected to frames using gusset plates. This study adopted steel block members, referred to as end blocks, to connect the multiple core bars with the gusset plates. Because the long-uncovered and exposed portions of the core bar are likely to exhibit local buckling under compressive loads, four contraction allowance zones were provided to reduce the length of each exposed portion. Two zones were located at both sides of the central coupler while two were located near the end blocks.

LOADING TESTS

Description of test specimens

Three test specimens were fabricated and tested to investigate the structural performance of the proposed BRB. The dimensions and configurations of specimens are presented in Fig. 2. For all specimens, the primary and secondary tubes have circular hollow steel sections of 27.2 × 5.0 (diameter × thickness) and 60.5 × 18.0, respectively. The core bars of the ABR400 specification have M16-roll threaded screws at both ends, and the diameter of their non-threaded part is 14.5 mm. The clearance between the core bar shank and primary tube is 2.7 mm. The plastic-deformation portion of each core bar is 958 mm long; thus, the total length of the plastic-deformation portion of the specimen is 1916 mm. All specimens have a total length of 2592 mm.

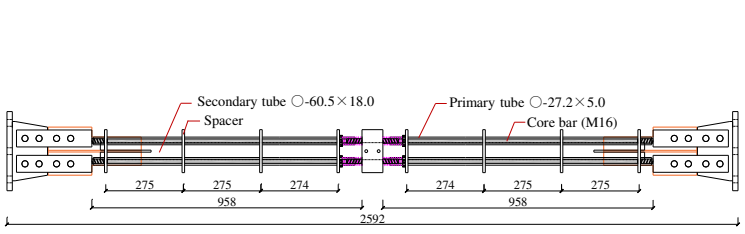

(a) Specimen A-1

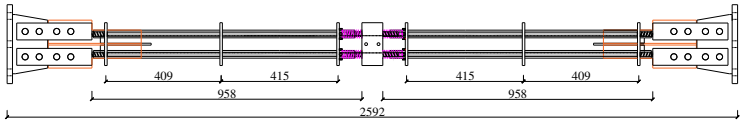

(b) Specimen A-2

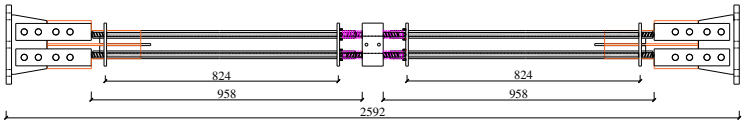

(c) Specimen A-3

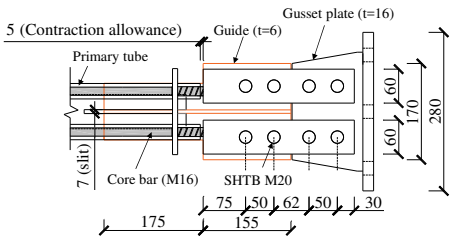

(d) Connection details

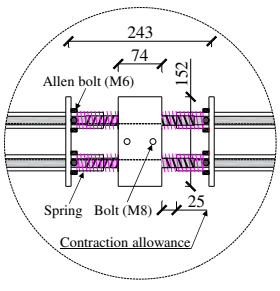

(e) Details near the central coupler

Figure 2. Configuration of specimens. (units: mm)

Table 1. Material properties of the main components of the specimens

Component	Material and Geometry	Yield stress (N/mm^2)	Ultimate strength (N/mm^2)	Elongation (%)
Core bar	ABR400 (ϕ14.5-M16)	295	452	29
Primary tube	STKM13A ($D \times t$: 27.2×5.0)	488	514	33
Secondary tube	STKM13A ($D \times t$: 60.5×18.0)	274	451	66

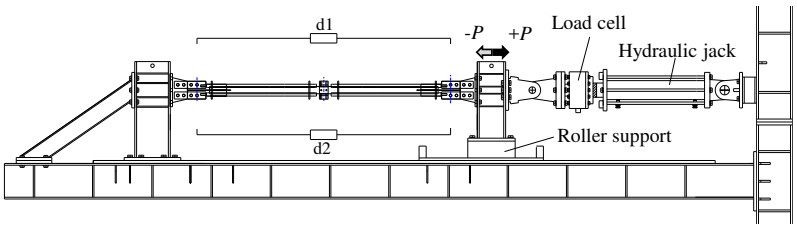

Figure 3. Test setup and measuring system.

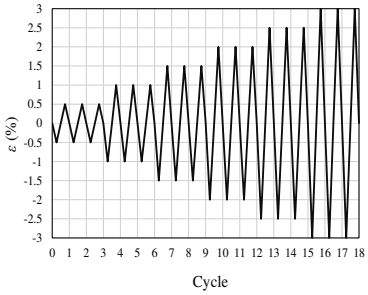

Figure 4. Loading protocol.

Each specimen had a different maximum spacer spacing, namely, 275, 415, and 824 mm for A-1, A-2, and A-3, respectively. According to Architectural Institute of Japan (2009) for the design principle of BRB, the limit of the maximum spacer spacing was determined as 687 mm. Therefore, the primary tubes of specimens A-1 and A-2 were predicted to exhibit no buckling, whereas those of specimen A-3 were predicted to buckle during the loading test.

Fig. 2(d) shows the details of this connection. Super high-strength bolts (SHTB) M20 were used to connect the specimen to the gusset plate. A length of 5 mm was set for each contraction allowance zone at the end of the block. Fig. 2(e) shows the details of the central portion of the BRB. The allen bolts M6 are screwed to the primary tubes and restrict the movement of the primary tube. A length of 25 mm was assigned for each contraction allowance zone at a side of the central coupler. The total contraction allowance of 60 mm was determined to allow a maximum average strain of 3 %, which corresponds to an axial deformation of 57.5 mm (= 1916 mm × 3 %).

The material properties of the main components of the test specimens are listed in Table 1. The values for the core bars were obtained based on the coupon tests, while those for the other components were provided by the steel inspection certificate.

Testing setup and loading protocol

The test specimens were placed horizontally and fixed onto the loading frame, as shown in Fig. 3. A hydraulic jack was used to conduct cyclic load experiments by means of displacement control. The axial deformation U of the test specimens was measured between the first bolts at the brace ends using displacement sensors d1 and d2. The average strain ε of the BRB was calculated as $\varepsilon = U/1916$.

The loading protocol is shown in Fig. 4, which compares the number of cycles against the average strain ε of the BRB. Based on the Building Center of Japan (BCJ) specification (2016) for the BRB, a gradually increasing symmetric protocol comprising three cycles at each amplitude, was adopted. The amplitude of the average strain ε was gradually increased from 0.5 % up to 3.0 %.

Test results

Fig. 5 presents the lateral load P and average strain ε relationships. Specimen A-1 exhibited stable hysteretic loops. Nevertheless, the lateral strength of the compression side (negative side) gradually

increases more than that of the tension side as the loading cycle increases because of the friction between the core bar and primary tube during compression. Subsequently, overall buckling occurs in the second cycle at ε =3.0 %, the lateral strength increases sharply and reaches approximately 480 kN. Visual inspection after the experiment revealed that the core bars deformed over their entire length, which was attributed to the presence of four contraction allowance zones. Consequently, specimen A-1 demonstrated a satisfactory energy dissipation capacity.

Specimen A-2 also exhibits stable hysteretic loops. The maximum restoring force reached about 463 kN in the third cycle at ε =3.0 %. In the subsequent tensile loading process, the local accumulation of plastic strain in one core bar induces its sudden brittle failure, and the other three core bars rupture almost simultaneously. Nevertheless, specimen A-2 also exhibits satisfactory energy dissipation capacity, similar to that observed for specimen A-1.

As described previously, the maximum spacer spacing for specimen A-3 was larger than the limit value. Therefore, the buckling of primary tubes was observed on the left side of the BRB for the first cycle at ε =1.5 %. For the subsequent loading cycles, the behavior deteriorates, as shown in Fig. 5. Finally, buckling of the primary tubes on the right side was also observed.

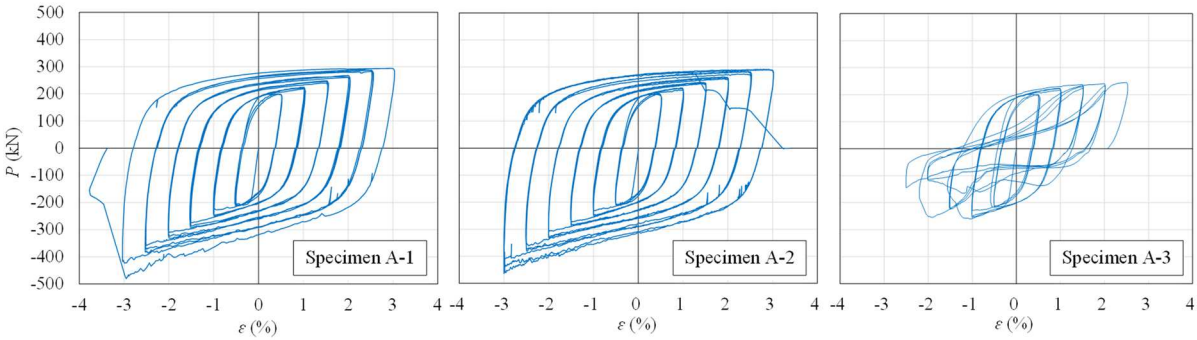

Figure 5. Lateral load P and average strain ε relationships.

CONCLUSIONS

In this study, the structural performance of a new type of buckling-restrained brace using multiple round steel core bars was assessed by performing cyclic loading tests on three specimens with different spacer spacing. In the test results, specimens A-1 and A-2, which satisfied the requirement of the maximum spacing of spacers, exhibited stable and similar hysteretic behaviors. For these specimens, the failure occurred in the loading cycle for an average strain ε of 3 %, which indicated their good energy dissipation capacity to meet effective seismic design criteria. In contrast, specimen A-3 exhibited an earlier deteriorating behavior induced by the buckling of the primary tubes, which did not satisfy the requirement of the maximum spacing of the spacers.

ACKNOWLEDGMENT

This study was partially supported by JSPS KAKENHI (Grant Number JP19K04711).

REFERENCES

Architectural Institute of Japan (2009): *Recommendations for Stability Design of Steel Structures*, Sec. 3.5 Buckling restrained braces (in Japanese).

Building Center of Japan (2016). *Specifications for BRB certification* (in Japanese).

Fujii S., H. Tagawa (2010). "Experimental study on buckling-restrained braces using round steel bar cores and double steel tubes," *J Struct Constr Eng Trans AIJ*;75(650):879-885 (in Japanese).

Fujii S., H. Tagawa (2011). "Behavior characteristics of buckling-restrained braces using round steel bar cores and double steel tubes," *J Struct Constr Eng Trans AIJ*;76(659):167-174 (in Japanese).

Mateus J.A.S., H. Tagawa, X. Chen (2019). "Buckling-restrained brace using round steel bar cores restrained by inner round steel tubes and outer square steel tube," *Engineering Structures*, 197, 109379.

Mateus J.A.S., H. Tagawa, X. Chen (2021). "Buckling-restrained steel bar damper for spine frame system," *Engineering Structures,* 229, 111593.

Munkhunur T., H. Tagawa, X. Chen (2022). "Steel rigid beam-to-column connections strengthened by buckling-restrained knee braces using round steel core bar dampers," *Engineering Structures,* 250, 113431.

Tagawa H., Y. Nagoya, X. Chen (2020). "Bolted beam-to-column connection with buckling-restrained round steel bar dampers," *Journal of Constructional Steel Research,* 169, 106036.

DESIGN OF OPTIMAL PASSIVE TUNED MASS DAMPER USING DIRECT OUTPUT FEEDBACK CONTROL ALGORITHM

Yong-An Lai[1], Chi-Hung Chang[2] and Hsuan-Ying Lin[2]
1. Assistant Professor, Department of Civil Engineering, National Central University, Taoyuan, Taiwan, R.O.C.
2. Graduated Student, Department of Civil Engineering, National Central University, Taoyuan, Taiwan, R.O.C.
Email: laiyongan@ncu.edu.tw

ABSTRACT

In this paper, the optimal passive tuned mass damper (TMD) design problem is been recast into an optimal control problem, so that a general passive TMD optimization design methodology is proposed. The proposed method, which combines the direct output feedback algorithm (also known as the static output feedback algorithm) and parameter updating iterative procedure, can be applied to single-degree-of-freedom (SDOF) or multi-degree-of-freedom (MDOF) structure, damped structure or undamped structure, subjected to base excitation or wind force. To achieve different structural vibration reduction objective when subjected to certain external loadings, the proposed method only requires to select different output matrices to cast the corresponding weighting matrix and quadratic initial condition matrix for computation. The optimization procedure is not changed. Using a SDOF structure as the main structure, the design parameter results verify that the obtained optimal design parameters of passive TMD are equal to the analytic solution or close to the approximate solution. Finally, a MDOF structure is used as the main structure for demonstration a TMD design. The numerical simulation results confirm that the proposed design method is accurate and feasible to minimize the mean square response of structure.

Keywords: tuned mass damper; passive control; optimal design; direct output feedback; base excitation; wind loads

INTRODUCTION

The tuned mass damper is a passive structural vibration control device, as a substructure system assembled by mass, damping and stiffness. The substructure system employing on the main structure can change its dynamic characteristics. When the natural frequency of the substructure is close to the vibration frequency of the main structure, the vibration energy of the main structure is transferred to the substructure system according to the resonance effect. This reduces the vibration energy of the main structure, thereby decreasing the dynamic response and enhancing the safety and comfort of the main structure. Den Hartog, 1956 incorporated the TMD into the undamped SDOF structure subjected to harmonic external disturbance, and used the "fix-point" in the frequency response function to deduce a set of optimal design formulae. Tsai and Lin, 1993 proposed an optimal design formula for the undamped SDOF structure in the harmonic base excitation in the concept of fix-point theory, and further obtained the design formula for damped structure by regression. Warburton, 1982 proposed the optimization formula to minimize the mean square response of structural displacement or velocity for undamped structures subjected to wind load or earthquake load. Korenev and Reznikov, 1993 compiled and proposed the optimization formula of analytic solutions or approximate solutions for various cases of objective and disturbance. Bakre and Jangid, 2007 obtained the optimal design formula by regression for mean square response minimization of structural displacement and velocity of the damped structure under random wind force or earthquake force. In 2012, Tigli, 2012 deduced the approximate solution design formula for mean square response minimization of displacement and acceleration for damped structure under random wind force. Tigli,2012 further derived the design formula of analytic solution for mean square response minimization of structural velocity for damped structure. The aforementioned design formulae are applied for SDOF structures. In practical application, the MDOF structure needs to be simplified to a SDOF system so that the TMD design formula is applicable.

In this paper, a general passive TMD optimization design method is proposed. The passive TMD design parameters are reconfigured in equation of motion, so that the optimal design problem of the TMD could be transformed into the gain matrix optimization problem as in the active control field. The direct output feedback algorithm is then applied to obtain the conditionally optimal gain matrix. In order to determine the optimal TMD design parameters without regarding the regulator of direct output feedback and reach the minimization of the mean square of structural responses, the parameter updating iterative procedure is further presented. Therefore, a passive TMD optimization design method is proposed, which combines the direct output feedback algorithm and parameter updating iterative procedure.

Equation of Motion

The equation of motion of a *N*-DOF structure installed with a TMD, as shown in Figure 1, is expressed as:

$$\mathbf{m}\ddot{\mathbf{x}}(t)+\mathbf{c}\dot{\mathbf{x}}(t)+\mathbf{k}\mathbf{x}(t)=\mathbf{e}\mathbf{w}(t) \tag{1}$$

where, $\mathbf{x}(t)=\begin{bmatrix} x_d(t) \\ \mathbf{x}_s(t) \end{bmatrix}$ is the displacement vector; $\mathbf{m}=\begin{bmatrix} m_d & \mathbf{0}_{1\times N} \\ \mathbf{0}_{N\times 1} & \mathbf{M}_s \end{bmatrix}$ is the mass matrix of system; $\mathbf{c}=c_d\mathbf{d}^T\mathbf{d}+\begin{bmatrix} 0 & \mathbf{0}_{1\times N} \\ \mathbf{0}_{N\times 1} & \mathbf{c}_s \end{bmatrix}$ is the damping matrix of system and $\mathbf{d}_{1\times(N+1)}=\begin{bmatrix} 1 & \mathbf{0}_{1\times(N-j)} & -1 & \mathbf{0}_{1\times(j-1)} \end{bmatrix}$ is the vector indicates TMD location configuration; $\mathbf{k}=k_d\mathbf{d}^T\mathbf{d}+\begin{bmatrix} 0 & \mathbf{0}_{1\times N} \\ \mathbf{0}_{N\times 1} & \mathbf{k}_s \end{bmatrix}$ is the stiffness matrix of system; $\mathbf{e}$ is the external force configuration matrix, which varies according to the external force form of the system ($\mathbf{e}=-\mathbf{m1}$ for base excitation or $\mathbf{e}=\begin{bmatrix} \mathbf{0}_{1\times N} \\ \mathbf{I}_{N\times N} \end{bmatrix}$ for wind loads); $\mathbf{w}(t)$ is the external force of the system, which can be seismic force or wind force.

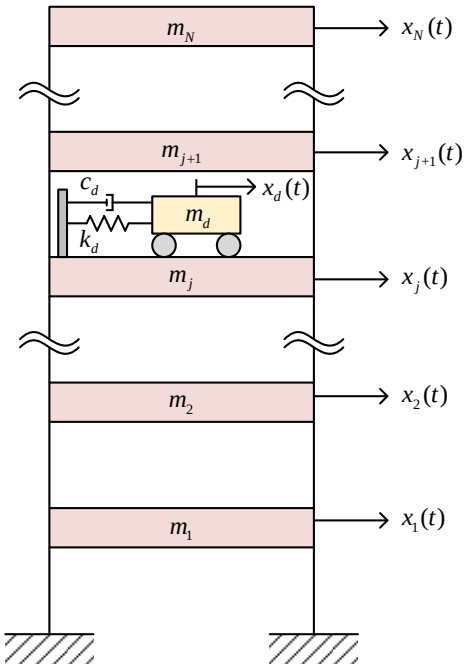

Figure 1. Schematic diagram of a MDOF structure equipped with a TMD

To determine the optimal design of the TMD stiffness and damping coefficient, as well as to maintain the solution stability in the design process which uses the direct output feedback algorithm, the stiffness and damping coefficient of TMD are set as:

$$k_d = k_{d0} + k_{d1} \tag{2}$$

$$c_d = c_{d0} + c_{d1} \tag{3}$$

where k_{d0} and c_{d0} are the initial stiffness and damping coefficient, respectively. In order to keep the solution stable, k_{d0} and c_{d0} must be greater than 0 to ensure the overall system asymptotically stable. The sum of the restoring force and damping force of TMD is the partial interaction force of TMD and structure, expressed as:

$$u(t) = k_{d1}(x_d - x_j) + c_{d1}(\dot{x}_d - \dot{x}_j) \tag{4}$$

This restoring force $u(t)$ can be regarded as a control force requiring optimal design. The feedback signals of Eq. (6) are the TMD stroke and the velocity of TMD relative to the structure, so that k_{d1} and c_{d1} are the gains of this control force. The equation of motion of the system can be transformed into a form with active control forces:

$$\mathbf{m}\ddot{\mathbf{x}}(t) + \bar{\mathbf{c}}\dot{\mathbf{x}}(t) + \bar{\mathbf{k}}\mathbf{x}(t) = \mathbf{b}u(t) + \mathbf{e}\mathbf{w}(t) \tag{5}$$

where $\bar{\mathbf{c}}$ and $\bar{\mathbf{k}}$ are the damping matrix and stiffness matrix without including k_{d1} and c_{d1}; $\mathbf{b} = -\mathbf{d}^T$ is the location vector of the control force. The equation of motion of Eq. (5) can be converted to the state-space expression:

$$\dot{\mathbf{z}}(t) = \mathbf{A}\mathbf{z}(t) + \mathbf{B}u(t) + \mathbf{E}\mathbf{w}(t) \tag{6}$$

where **z**(t) is the state vector. **A** is the system matrix; **B** is the state-space control force location vector; **E** is the state space external force location matrix. And Eq. (4) can also be expressed as:

$$u(t) = \begin{bmatrix} k_{d1} & c_{d1} \end{bmatrix} \begin{bmatrix} \mathbf{v}_{rd} \\ \mathbf{v}_{rv} \end{bmatrix} \begin{bmatrix} \mathbf{x} \\ \dot{\mathbf{x}} \end{bmatrix} = \mathbf{G}\mathbf{V}\mathbf{z}(t) \tag{7}$$

where $\mathbf{G} = \begin{bmatrix} k_{d1} & c_{d1} \end{bmatrix}$ is the undetermined stiffness and damping coefficient; **V** is the matrix of the corresponding output vector combination. And the design can be completed by solving the optimal gain matrix.

Gain Matrix Design for Minimizing Response

It can be seen from Eq. (7) that there is a partial state relationship between the system and the control force, not full-state feedback. Therefore, the traditional LQR optimization method cannot be used to obtain the gain matrix. However, the direct output feedback method can be used to design the gain matrix. The relationship between the system, gain matrix and signal feedback is shown in Figure 2.
The state-space expression, besides the system state equation of Eq. (6), is often accompanied by an output equation. Its relation to the state **z**(*t*), input *u*(*t*), and output ***y***(*t*) of the system is expressed as:

$$\mathbf{y}(t) = \mathbf{C}\mathbf{z}(t) + \mathbf{D}u(t) + \mathbf{F}\mathbf{w}(t) \tag{8}$$

where $\mathbf{y}(t)$ is the output, which can be a single output or multiple outputs. **C** is the output matrix; **D** is the control force feedforward matrix; **F** is the external force feedforward matrix; **C**, **D**, and **F** matrices can be selected according to the desired output.

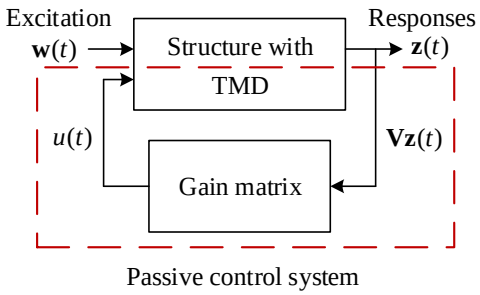

Figure 2. Schematic diagram of gain coefficient and feedback signal of control force

Optimal Design of Direct Output Feedback

The direct output feedback is a method to design an optimal active control gains. It uses output feedback instead of state feedback. The control effect of direct output feedback is usually not identical to the traditional LQR optimization because the initial conditions have to be considered. The control force applied to the system aims to enhance the dynamic characteristics of the system and reduce its response when encountering external forces, so if the system is stationary and the external force is impulse load at a time $t=0$, this external impulse can be transformed into the initial conditions of the system while satisfying the following state equation:

$$\dot{\mathbf{z}}(t)=[\mathbf{A}+\mathbf{BGV}]\mathbf{z}(t),\ \mathbf{z}(0)=\mathbf{E}\bar{\mathbf{1}} \tag{9}$$

where $\bar{\mathbf{1}}$ is the column vector of ones where the dimension is the number of external forces. The output function can also be expressed as:

$$\mathbf{y}(t)=\mathbf{C}\mathbf{z}(t)+\mathbf{D}u(t) \tag{10}$$

To obtain the optimal gain matrix **G**, the quadratic effectiveness objective function J of output $\mathbf{y}(t)$ minimization is set up:

$$\begin{aligned} J &= \int_0^\infty [\mathbf{y}^T(t)\mathbf{y}(t)+u^T(t)Ru(t)]dt \\ &= \int_0^\infty [\mathbf{z}^T(t)\mathbf{Q}\mathbf{z}(t)+2\mathbf{z}^T(t)\mathbf{N}u(t)+u^T(t)\bar{R}u(t)]dt \end{aligned} \tag{11}$$

where $\mathbf{Q}=\mathbf{C}^T\mathbf{C}$ is the positive semidefinite weighting matrix of the system state; $\mathbf{N}=\mathbf{C}^T\mathbf{D}$ is the weighting matrix of state and control force coupling term; $\bar{R}=\mathbf{D}^T\mathbf{D}+R$ is the control force regulator and R is a positive definite weight coefficient. The quadratic efficiency objective function J is required to satisfy the constraints of dynamics, so that the Lagrangian multipliers is used. After partial differentiation of the independent variables in the constrained objective function, it becomes:

$$(\mathbf{A}+\mathbf{BGV})^T\mathbf{H}+\mathbf{H}(\mathbf{A}+\mathbf{BGV})+(\mathbf{Q}+2\mathbf{NGV}+\mathbf{V}^T\mathbf{G}^T\bar{R}\mathbf{GV})=\mathbf{0} \tag{12}$$

$$\mathbf{Z}_0+\mathbf{L}(\mathbf{A}+\mathbf{BGV})^T+(\mathbf{A}+\mathbf{BGV})\mathbf{L}=\mathbf{0} \tag{13}$$

$$\mathbf{G}=-\bar{R}^{-1}\left(\mathbf{B}^T\mathbf{HLV}^T+\mathbf{N}^T\mathbf{LV}^T\right)\left(\mathbf{VLV}^T\right)^{-1} \tag{14}$$

where **H** is a constant coefficient positive definite matrix; **L** is a Lagrange multiplier matrix; $\mathbf{Z}_0$ is a quadratic initial state matrix, which is related to the external force configuration matrix in the state space according to the different types of external forces. The algebraic equations of Eq. (12) to Eq. (14) are solved simultaneously to obtain the gain matrix **G**, i.e. the direct output feedback design method of active control (Chung *et al*., 1993).

Optimal TMD Parameter Design Process

The gain matrix **G** obtained by solving Eq. (12) to Eq. (14) is a conditionally weight balanced optimal solution of output $\mathbf{y}(t)$ and control force $u(t)$, that is not the most general optimal solution of the sum of square regarding only the output $\mathbf{y}(t)$

$$J = \int_0^\infty [\mathbf{y}^T(t)\mathbf{y}(t)]dt \tag{15}$$

Therefore, a parameter updating iterative procedure is further proposed to obtain the general optimal value of Eq. (15). Moreover, through the parameter updating iterative procedure, the optimal TMD design parameters can be obtained without regarding the assign value of weight *R*.
The gain matrix **G** calculated by direct output feedback can improve the dynamic response of the system, so that k_{d1} and c_{d1} can be used to update the initial stiffness k_{d0} and initial damping coefficient c_{d0} of the TMD. After the TMD design parameters in the system matrix are updated by the obtained gain matrix, the gain matrix **G** is recalculated by direct output feedback. Through this iterative gain matrix **G** recalculated operation, the gain matrix **G** must converge and approach to 0. The TMD design parameters (k_{d0} and c_{d0}) in the system matrix are updated to the optimal design parameters. Therefore, the iterative operation is completed.

The iterative procedure combined with direct output feedback as follows:

1. The structural parameters $\mathbf{m}_s$, $\mathbf{c}_s$, $\mathbf{k}_s$ and TMD mass m_d are known. The initial stiffness k_{d0} and initial damping coefficient c_{d0} of TMD are set up. The system matrices $\mathbf{m}$, $\bar{\mathbf{c}}$ and $\bar{\mathbf{k}}$, control force location vector $\mathbf{b}$, and external force configuration matrix $\mathbf{e}$ are established.
2. The state-space system matrix **A**, control force location vector **B**, and external force location matrix **E** are established. The matrix **V** is established according to the TMD location. The optimal output target matrices **C** and **D** are selected and the initial condition $\mathbf{Z}_0$ is calculated.
3. The weighting matrices **Q** and **N** are calculated accordingly and the initial gain matrix $\mathbf{G} = [k_{d1} \quad c_{d1}] = [0 \quad 0]$ is set up.
4. A regulator weight *R* is selected.
5. Eq. (12) to (14) of direct output feedback is solved simultaneously to obtain an optimal gain matrix $\mathbf{G} = [k_{d1} \quad c_{d1}]$. If simultaneous solving fails, return to Step 4 to modify regulator *R*.
6. If the absolute values of elements of the gain matrix **G** are converged and smaller than the preset micro value ε, approaching 0, proceed to Step 7. If the absolute values of elements of the gain matrix **G** are still larger than micro value ε, $k_{d0} = k_{d0} + k_{d1}$ and $c_{d0} = c_{d0} + c_{d1}$ are updated. After $\bar{\mathbf{c}}$ and $\bar{\mathbf{k}}$ are updated, return to Step 2.
7. If the conditionally optimal gain matrix $\mathbf{G} = [k_{d1} \quad c_{d1}]$ solved by direct output feedback has converged and approached 0, the optimal design parameters of TMD are $k_d^{opt} = k_{d0}$ and $c_d^{opt} = c_{d0}$. The optimal design is completed.

Numerical Simulation and Verification of SDOF Structure with a TMD

This section takes a SDOF structure with a TMD as an example to compare and verify the analytical solution or approximate solution formula in the reference. The mass and natural frequency of the SDOF structure is given, and the structural damping ratios varies form 0~0.1. The mass ratio of the TMD varies form 0.01~0.2. After the optimal design parameters k_d^{opt} and c_d^{opt} of TMD are obtained by the proposed method, the optimal frequency ratio R_f and the optimal damping ratio ζ_d of the TMD are further calculated. The case of considering the minimization of structural displacement, structural velocity and structural acceleration under seismic force is analyzed and compared with the analytical method, as shown in Table 1 to Table 3.

Table 1. Comparison of optimal TMD design parameters of structural displacement minimization under earthquake force

	Structural Damping Ratio ζ_s											
	0				0.02				0.05			
	Proposed Method		Warburton		Proposed Method		Bakre and Jangid		Proposed Method		Bakre and Jangid	
R_m	R_f	ζ_d	R_f	ζ_d	R_f	ζ_d	R_f	ζ_d	R_f	ζ_d	R_f	ζ_d
0.01	0.98762	0.04981	0.98762	0.04981	0.98190	0.04982	0.98124	0.04981	0.97040	0.04982	0.96994	0.04981
0.02	0.97548	0.07019	0.97548	0.07019	0.96781	0.07019	0.96724	0.07019	0.95344	0.07020	0.95264	0.07019
0.05	0.94040	0.10981	0.94040	0.10981	0.92916	0.10982	0.92915	0.10981	0.90956	0.10985	0.90947	0.10981
0.10	0.88607	0.15273	0.88607	0.15273	0.87136	0.15278	0.87146	0.15273	0.84676	0.15288	0.84696	0.15273
0.20	0.79057	0.20972	0.79057	0.20972	0.77211	0.20994	0.76864	0.20972	0.74215	0.21032	0.73521	0.20975

Table 2. Optimal TMD design parameters of structural velocity minimization under earthquake force

	Structural Damping Ratio ζ_s											
	0		0.01		0.02		0.05		0.075		0.1	
R_m	R_f	ζ_d	R_f	ζ_d	R_f	ζ_d	R_f	ζ_d	R_f	ζ_d	R_f	ζ_d
0.01	0.99010	0.04975	0.98852	0.04973	0.98676	0.04969	0.98035	0.04957	0.97380	0.04944	0.96627	0.04929
0.02	0.98039	0.07001	0.97824	0.06996	0.97590	0.06990	0.96782	0.06969	0.95994	0.06948	0.95114	0.06923
0.05	0.95238	0.10911	0.94918	0.10899	0.94581	0.10885	0.93474	0.10840	0.92451	0.10797	0.91351	0.10751
0.10	0.90909	0.15076	0.90491	0.15052	0.90057	0.15028	0.88678	0.14948	0.87447	0.14876	0.86155	0.14800
0.20	0.83333	0.20412	0.82817	0.20370	0.82291	0.20326	0.80653	0.20189	0.79233	0.20069	0.77775	0.19947

Table 3. Optimal TMD design parameters of structural absolute acceleration minimization under earthquake force

	Structural Damping Ratio ζ_s											
	0		0.01		0.02		0.05		0.075		0.1	
R_m	R_f	ζ_d	R_f	ζ_d	R_f	ζ_d	R_f	ζ_d	R_f	ζ_d	R_f	ζ_d
0.01	0.99257	0.04981	0.99208	0.04981	0.99160	0.04981	0.99022	0.04982	0.98924	0.04985	0.98854	0.04990
0.02	0.98528	0.07019	0.98460	0.07019	0.98394	0.07019	0.98203	0.07021	0.98065	0.07025	0.97960	0.07034
0.05	0.96421	0.10977	0.96320	0.10977	0.96220	0.10978	0.95938	0.10983	0.95733	0.10993	0.95568	0.11013
0.10	0.93154	0.15254	0.93023	0.15254	0.92895	0.15255	0.92534	0.15266	0.92273	0.15287	0.92061	0.15325
0.20	0.87401	0.20871	0.87244	0.20872	0.87091	0.20874	0.86666	0.20897	0.86361	0.20940	0.86114	0.21012

The results show that for the undamped structure, the optimal parameters obtained by the proposed method are equal to the analytic solution proposed by Warburton,1982. For the damped the structure, the obtained optimal parameters are close to the approximate solution proposed by Bakre and Jangid,2007. The feasibility of the H_2-norm optimization according to the proposed method is validated.

Numerical Verification of Optimal Design a TMD for the MDOF Structure

The results of a five-story MDOF structure (Lin *et al*., 2001) with a TMD installed on its fourth floor is shown in this section. The MDOF structure cannot always be simplified to a SDOF structure directly, or the simplified SDOF is likely to have larger differences than the original MDOF structure for some reason. In addition to being applied to a SDOF structure case, the optimal TMD design method proposed in this paper is also applicable to a MDOF structure directly. The mass matrix, damping matrix, and stiffness matrix of the five-story structure are shown in Table 4. The design objective is to reduce the response of the top floor slab of the structure under earthquake force.

Table 4. System parameters of a 5-story structure

Mass matrix $\mathbf{m}_s$ (kg)	$\begin{bmatrix} 19.57 & 0 & 0 & 0 & 0 \\ 0 & 19.57 & 0 & 0 & 0 \\ 0 & 0 & 19.57 & 0 & 0 \\ 0 & 0 & 0 & 19.57 & 0 \\ 0 & 0 & 0 & 0 & 19.57 \end{bmatrix}$
Damping matrix $\mathbf{c}_s$ (N-s/m)	$\begin{bmatrix} 15.93 & -14.28 & 0.11 & 0.46 & 0.06 \\ & 34.26 & -16.46 & -1.04 & 0.30 \\ & & 36.22 & -15.61 & -0.79 \\ & sym. & & 37.46 & -13.67 \\ & & & & 47.19 \end{bmatrix}$
Stiffness matrix $\mathbf{k}_s$ (N/m)	$\begin{bmatrix} 14621 & -22962 & 7463 & 1169 & -211 \\ & 52688 & -36587 & 5481 & 1612 \\ & & 58344 & -35825 & 4549 \\ & sym. & & 58596 & -36564 \\ & & & & 77108 \end{bmatrix}$
Modal frequencies $\mathbf{f}_s$ (Hz)	$[0.915 \quad 3.371 \quad 7.107 \quad 10.657 \quad 12.728]$
Modal damping ratios $\boldsymbol{\zeta}_s$	$[0.02 \quad 0.02 \quad 0.02 \quad 0.02 \quad 0.02]$

The mass of the TMD is set as 2.8 kg. According to the design process of this paper, the displacement response of the top floor of the structure is minimized under the earthquake force. The obtained optimal stiffness of TMD k_d^{opt} is 78.0786 N/m and the optimal damping coefficient c_d^{opt} is 3.7613 N-s/m. The frequency response function is shown in Figure 3.

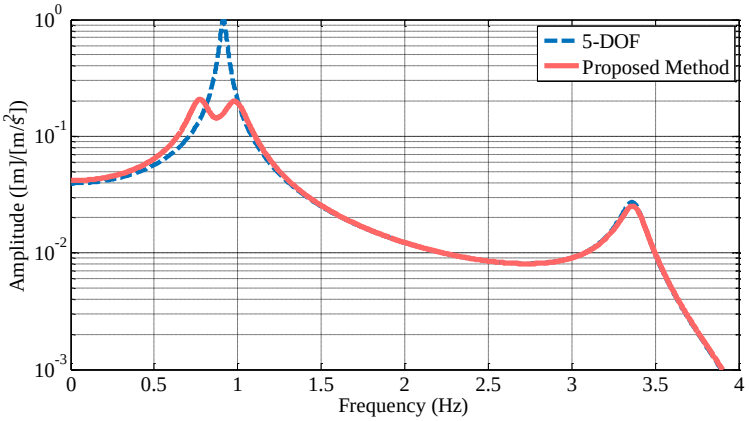

Figure 3. Top floor displacement frequency response function of the MDOF structure under earthquake force

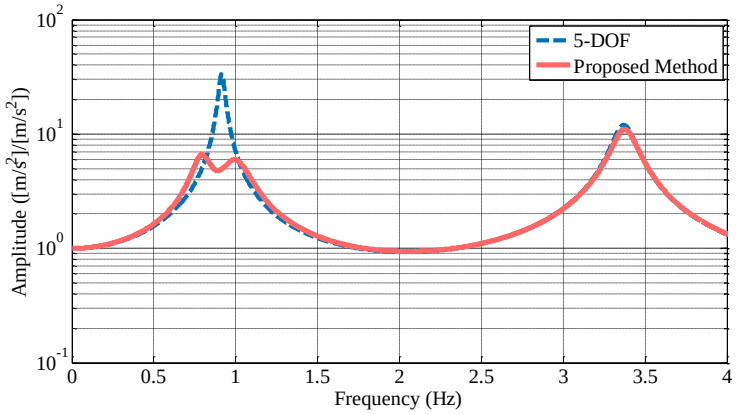

Figure 4. Top floor absolute acceleration frequency response function of the MDOF structure under earthquake force

If the optimization goal is to minimize the acceleration response of the top floor, the optimal stiffness of the TMD can be obtained as $k_d^{opt} = 84.2040$ N/m ; the optimal damping coefficient is $c_d^{opt} = 4.1494$ N-s/m and the frequency response function is shown in Figure 4. The top floor absolute acceleration of the first mode can be reduced effectively. This verifies that the method proposed in this paper can also be applied for case of the MDOF structure, and the TMD can be installed on various location of the structure.

CONCLUSIONS

By appropriate parameter reconfigured in the design of passive TMD parameters, the optimization parameter design issue can be transformed into the gain matrix optimization problem in the direct output feedback (or called static output feedback) of active control. Given this, this paper further developed a parameter updating iterative procedure to associate with the direct output feedback, so as to propose a general optimization method for the passive TMD design. The proposed method can be applied to SDOF or MDOF structure, damped structure or undamped structure, subjected to base excitation or wind force. The design results confirm that the proposed method is equal to the analytic solutions of some specific cases, so that the accuracy and feasibility of the proposed method is verified.

REFERENCES

Bakre S.V. and Jangid R.S., (2007) "Optimum parameters of tuned mass damper for damped main system", *Structural Control and Health Monitoring*, **14**, 448-470.

Chung L.L., Lin C.C. and Chu S.Y., "Optimal direct output feedback of structural control", *Journal of Engineering Mechanics*, **119**, 2157-2173 (1993).

Den Hartog, J.P., (1956) *Mechanical Vibrations*, 4th Edition, McGraw-Hill, New York.

Korenev B.G. and Reznikov L.M., (1993) *Dynamic Vibration Absorbers, Theory and Technical Applications*, Wiley, New York.

Lin C.C., Wang J.F. and Ueng J.M., (2001) "Vibration control identification of seismically excited m.d.o.f structure-PTMD systems", *Journal of Sound and Vibration*, **240**(1), 87-115.

Tigli O.F., (2012) "Optimum vibration absorber (tuned mass damper) design for linear damped systems subjected to random loads", *Journal of Sound and Vibration*, **331**,3035-3049.

Tsai H.C. and Lin G.C., (1993) "Optimum tuned-mass dampers for minimizing steady-state response of support-excited and damped systems", *Earthquake Engineering and Structural Dynamics*, **22**(11), 957-973.

Warburton G.B., (1982) "Optimum absorber parameters for various combinations of response and excitation parameters", *Earthquake Engineering and Structural Dynamics*, **10**,381-401.

IMPROVING SEISMIC PERFORMANCE OF SKEWED HIGHWAY BRIDGES WITH MULTIDIRECTIONAL ENERGY DISSIPATORS

Fernando Barriuso[1], Jorge Gonzalez[1] and Ramiro Bazaez[1*]
1. Departamento de Obras Civiles, Universidad Técnica Federico Santa María, Valparaíso, Chile.

*Corresponding author. Email address: ramiro.bazaez@usm.cl, fernando.barriuso.14@sansano.usm.cl, jorge.gonzalezgal.13@sansano.usm.cl

ABSTRACT

In this paper, the seismic performance of skewed highway bridges with multidirectional energy dissipators based on U-Shaped components is assessed. With that aim, an experimental campaign was carried out to characterize the hysteretic behavior of U-Shaped dampers. Then, finite element models of U-Shaped components and multidirectional energy dissipators were performed in ANSYS to calibrate model parameters based on the experimental results. Finite element models were also performed in OpenSees to include the behavior of the multidirectional energy dissipator in macro-models of skewed highway bridges. Finally, multi-stripe analyzes were performed to obtain analytical fragility curves and assess the effectiveness of including multidirectional energy dissipators in skewed highway bridges.

Keywords: Skewed highway bridges, fragility curves, energy dissipation devices, hysteretic behavior.

INTRODUCTION

During the Mw 8.8 2010 Maule, Chile earthquake, several simply supported skewed highway bridges were severely damaged and some even collapsed, (Kawashima, *et al*., 2011). In order to increase the seismic performance of this type of bridge we propose to include multidirectional energy dissipators between the superstructure and substructure as shown in Fig. 1(a). The multidirectional energy dissipator is based on U-shaped dampers arranged in a radial configuration as shown in Fig. 1(b). In this context, a multidirectional energy dissipator consists of a device that can dissipate energy independent of the direction of the displacement demand that is applied. A U-Shaped damper consist of a bended steel plate that can dissipate energy through the yielding of the material. The first time this was conceived was with the work of Kelly (1972) and they have been used and studied in several investigations (Deng, *et al*., 2013; Baird, *et al*., 2014; Ene, *et al*., 2016).

To assess the effectiveness of multidirectional dissipator in skewed highway bridges, fragility curves are generated using tridimensional finite element (FE) models and multi-stripe analysis (MSA) (Jalayer & Cornell, 2009). The finite element models for the U-Shaped dampers were developed in ANSYS and OpenSees (McKenna, *et al.*, 2010) and were calibrated with experimental results.

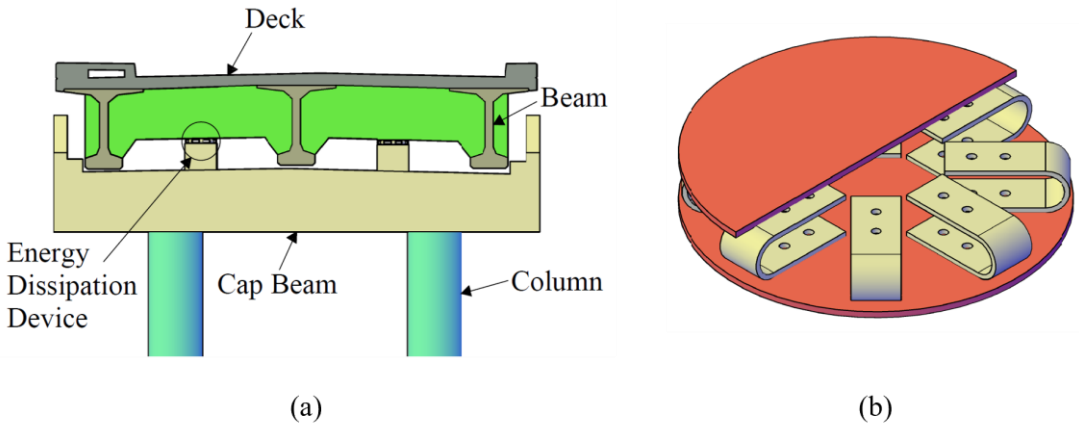

Figure 1. (a) Location of the device in the bridge. (b) Multidirectional U-Shaped energy dissipator.

CALIBRATION OF NUMERICAL MODELS BASED ON EXPERIMENTAL DATA

Experimental program

The experimental test was carried out using an MTS-810 testing machine. A pair of steel U-Shaped elements were installed in a steel frame (as can be seen in Fig. 2(a)) and then were subjected to a vertical displacement protocol.

Finite element models in ANSYS

Force-displacement curves were obtained from the experimental program and were used to calibrate a finite element (FE) model in the program ANSYS 2020 R2 as shown in Fig.2(b). The U-Shaped damper was modeled with isotropic elasticity in the linear part, and for the post yielding behavior the models of Chaboche kinematic hardening and the Voce hardening law were used. Several parameters of the material used in the model were calibrated to minimize the difference in total energy dissipated. The difference between the experimental and numerical energy dissipated was 12.6%, and for the maximum force was a 4.9%. Fig.2(c) shows both curves and the similarity between them.

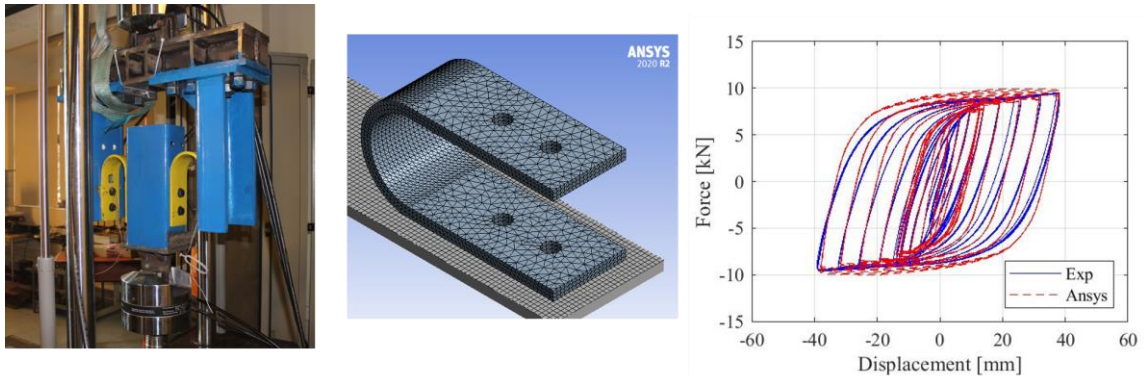

(a) (b) (c)

Figure 2. (a) Experimental test of U-Shaped elements. (b) FE model in ANSYS. (c) Comparison between numerical model and experimental results.

Once the model parameters were calibrated in ANSYS, a FE model of a multidirectional dissipator was generated. This device is made of U-Shaped elements disposed in a circular arrangement (see Fig. 3) to have the same unidirectional behavior independent of the direction of the demanded displacement. This model was subjected to 3 cycles of 8.3, 16.7 and 25 [mm] in only one direction and in a circular pattern to obtain the force-displacement behavior of the multidirectional energy dissipator.

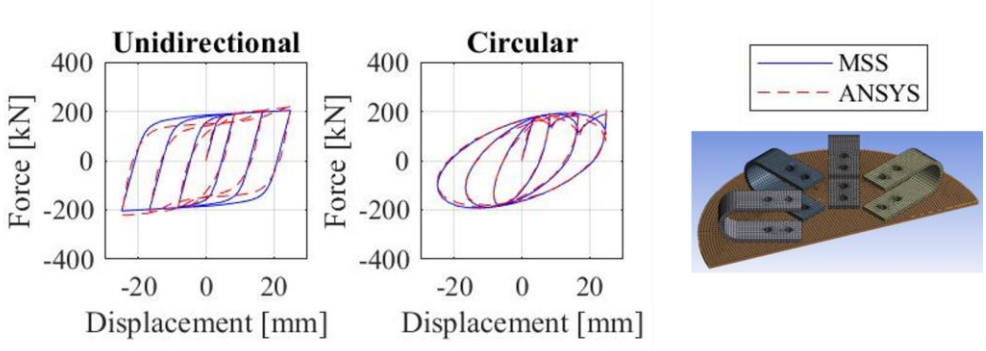

Figure 3. Force-displacement curves of multidirectional hysteretic damper and model made in Ansys.

Finite Element Model in OpenSees

FE models were developed in OpenSees by using the multiple shear spring (MSS) element. This element corresponds to a radial array of springs which resembles the proposed multidirectional energy dissipator. The material selected to characterize the springs was Steel4. The Steel4 parameters were calibrated to minimize the mean squared error for the unidirectional and circular displacement shown in Fig. 3. This was done by using a pattern search minimization algorithm in Matlab (R2021a).

CASE STUDY

The selected case studies for this research were obtained using Latin hypercube sampling. We selected 30 bridges that resemble typical Chilean skewed bridges. Using the Least Squares Method, the best probability density function (pdf) was adjusted for 9 geometric parameters: n° of spans, n° of columns, n° of beams, column width, column height, skew angle, span length, deck thickness and width. In Table 1 is shown the probabilistic adjustment assigned to each geometric parameters, and in Table 2 is presented the geometric characteristics of the bridges considered in this study.

Table 1. Parameters used in probabilistic adjustment.

Geometrical Parameters	pdf	Par. 1	Par. 2
N° of Spans	Geometric	0.22	-
N° of Columns	Poisson	3.77	-
N° of Beams	Poisson	3.93	-
Skewed [°]	Normal	25.50	12.92
Column height [cm]	Weibull	603.50	4.36
Column width [cm]	Log-Normal	4.81	0.16
Span length [cm]	Gamma	7.14	390.90
Deck thickness [cm]	Normal	20.95	2.00
Deck width [cm]	Gamma	11.84	99.44

Table 2. Geometry and characteristics of bridges selected.

Samples	N° Spans / Columns / Girders	Skew Angle [°]	Column height [cm]	Column diameter [cm]	Span length [cm]	Deck thickness [cm]	Deck width [cm]
B1	3 / 3 / 3	15.4	450	130	1760	25	530
B2	3 / 4 / 5	25.6	480	130	3630	25	1060
B3	3 / 5 / 5	9.5	780	140	1940	18	1010
B4	4 / 5 / 5	27.3	670	130	1890	22	1040
B5	5 / 2 / 4	3.5	630	120	1380	21	770

Modeling details for the case studies

Tridimensional non-linear finite element models were performed in OpenSees to represent the case studies. A sketch of the model is shown in Fig. 4. In this model, the superstructure is modeled as a grid where each longitudinal element represents a girder with its composite area, meanwhile the transversal element represents the interaction between the girders through the deck. The bridge superstructure was

modeled using *ElasticBeamColumn* elements since it is supposed to remain elastic during the expected loads (Kaviani, *et al.*, 2012). Columns were modeled using *ForceBeamColumn* elements with fiber sections and using *Concrete02* and *Steel02* materials. Cap beams were modeled using *ElasticBeamColumn* elements. Foundations were represented through elastic translational and rotational springs (Gazetas, 1991). Abutments were modeled using *ElasticBeamColumn* elements to represent the abutment wall. Impact between the superstructure and abutments was modeled using an *Impact* material representing a Hertz model modified by Muthukumar (2003). The passive soil resistance at the abutment was modeled with an *HyperbolicGap* material following the recommendations from Caltrans (2019) and Shamsabadi et al. (2007). Interface elements between superstructure and substructure as shear keys, seismic bars and elastomeric bearings were modeled as follows. Internal concrete shear keys were modeled through *ElasticPPGap* materials, according to Megally, et al. (2002). External concrete shear keys were modeled using an *ElasticPPGap* material in parallel to a hysteretic material, according to Goel & Chopra (2008), while the seismic bars were modeled using a *Hysteretic* material, following the recommendations of Aldea, et al. (2021). Finally, non-anchored elastomeric bearings were modeled through *FlatSliderBearing* elements (Aldea, *et al.*, 2021), following Steelman et al. (2013) recommendations. More detailed modeling features are specified in Aldea, et al. (2021).

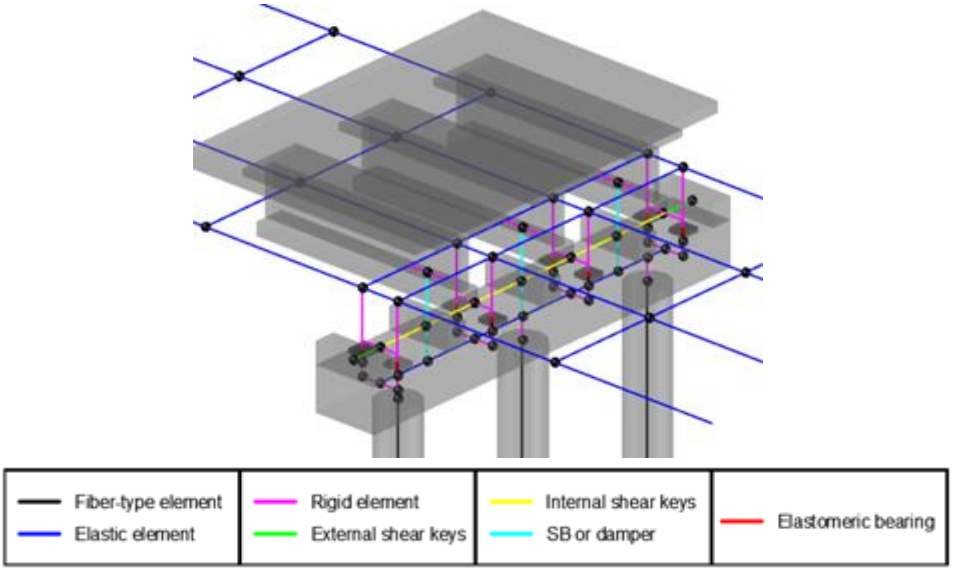

Figure 4. Three-dimensional models of the case studies in OpenSees.

Selection of ground motion records

Ground motion records were selected considering northwest Santiago (Chile's capital) as the location of interest and a soil type 2 according to Idini et al. (2017), which has an averaged shear-wave velocity in the first 30 meters (Vs30) of 600 [m/s]. For the MSA, four stripes are considered with ground motion levels of 100, 475, 975 and 2475-year return period. The intensity measure (IM) adopted is the 5% damped spectral acceleration ordinate at 0.7 [s] (fundamental period of the bridge) or S_a (0.7s). 30 records were selected for each stripe by matching them to their conditional spectrum using Baker et al. methodology (2008). The acceleration records were obtained from the SIBER-RISK database (Castro, *et al.*, 2021). The amplitude scaling factor was limited to 4 in order to prevent excessive bias in the ground motion selection. The 5% damped spectra for the selected records are shown in Fig. 5.

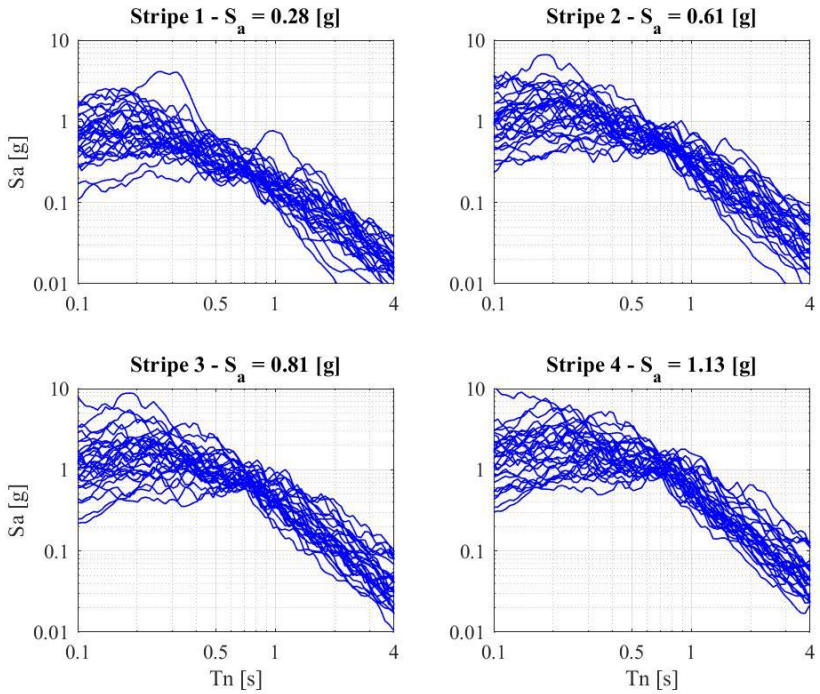

Figure 5. 5% damped acceleration spectra for the selected records.

Multidirectional energy dissipator design and modeling

Multidirectional dampers are included in the superstructure-substructure interface of the sampled skewed highway bridges. The preliminary design of the dampers was done following the procedure proposed by Xiang et al. (2019) . This procedure allows obtaining the initial stiffness and the yield strength of the devices. It is worth noting that the elastomeric bearings act in parallel with the multidirectional energy dissipators, and these in series with the multi-column reinforced concrete (RC) bent. For design purposes only, bilinear behavior was considered for the multidirectional dissipators and for elastomeric bearings, and linear behavior was considered for the RC bent.

The design procedure is applied using spectral acceleration obtained at a hazard level of 975-year return period. The spectral accelerations are obtained from a probabilistic seismic hazard analysis (PSHA) (Baker, 2008). Finally, we propose that the design of the multidirectional energy dissipator needs to be verified to ensure that the probability of damage is lower than 30 %.

The damper design methodology is applied to each case study. The design results for each bridge are shown in Table 3, where, F_{yd} is the total yield strength of the dampers of the bent, while d_y is the yield displacement of the dampers. A diagram of the force-displacement behavior of the multidirectional damper is shown in Fig. 6.

ANALYSIS AND RESULTS

Seismic fragility assessment

MSAs were performed to obtain analytical fragility curves for the case studies. Using Eq. 1 the discreet probability of exceeding a Damage State (DS) conditioned to an intensity measure value (P[DS|IM]) is obtained. Then, a log-normal cumulative function is fitted to the discreet exceedance probability points using the least squares method. Damage states (DSs) are specified in Table 4 and dispersion values recommended by Nielson (2005) are considered.

$$P[DS|IM] = \int P[DS|EDP(IM)]f(EDP|IM)dEDP \quad (1)$$

Table 3. Yield parameters of the damper for each bridge.

Samples	F_{yd} [kN]	d_y [mm]
B1	417	4.6
B2	2200	5.7
B3	666	4.7
B4	789	4.8
B5	247	4.6

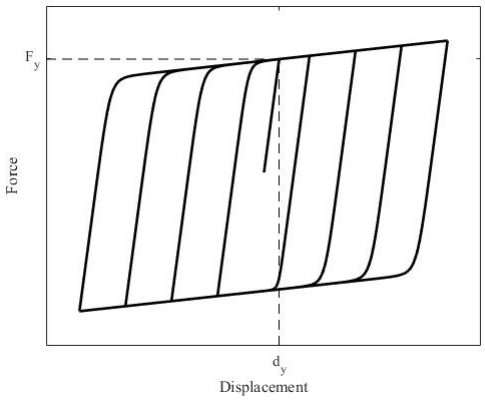

Figure 6. Hysteretic behavior of the damper in OpenSees.

Table 4. Damage State parameters.

EDP	Slight Damage		Moderate Damage		Extensive Damage	
	Median	Dispersion	Median	Dispersion	Median	Dispersion
Superstructure to substructure maximum displacement [cm]	-	-	-	-	20	0.46
Elastomeric bearing maximum shear strain [%]	100	0.25	250	0.46	-	-

From the fragility curves shown in Fig. 7, it is obtained that the probability for each DS in average decreases 63%, 43% and 62% for slight damage, moderate damage, and extensive damage, respectively, when the multidirectional dissipator is included. The results also show that the bridges with larger skew angles (i.e., samples B1, B2 and B4) have a greater decrease in the probability of exceeding the damage states when the multidirectional dissipator is included.

Fig. 8 presents the exceedance probability for the moderate damage state for a specific earthquake matching the 975-year return period stripe. It shows that the seismic performance for the bridges with multidirectional dissipators are successfully verified with less than 30% probability of exceedance, except for the sample B2. It is worth noting that the skewed bridges without the multidirectional dissipator did not achieve that performance objective.

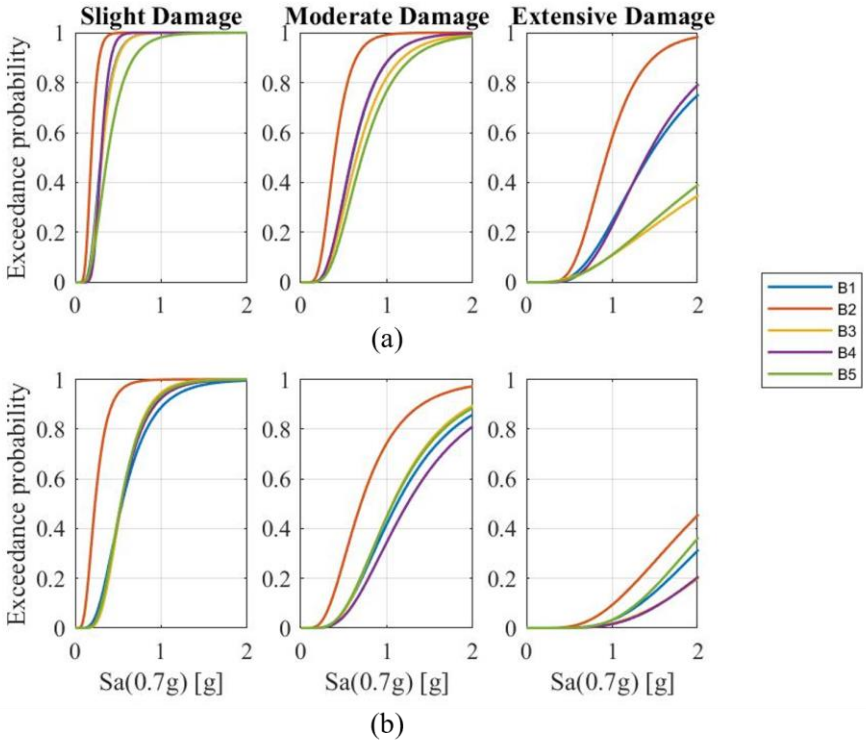

Figure 7. Fragility curves for (a) Bridges w/o damper (b) Bridges with damper.

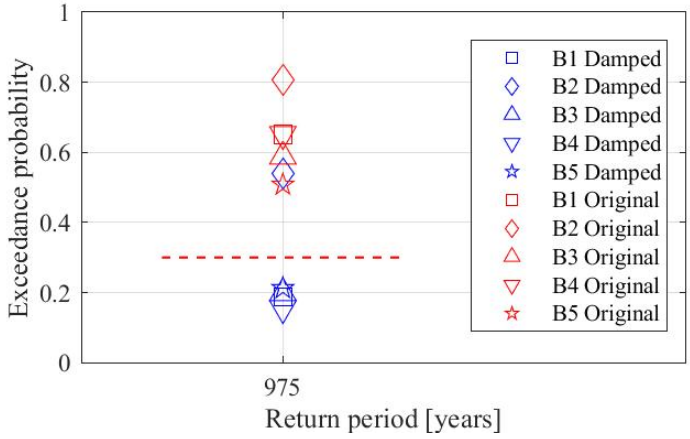

Figure 8. Exceedance probability for moderate damage.

CONCLUSIONS

- Finite element models in ANSYS and OpenSees can adequately represent the behavior of U-Shaped hysteretic dampers. Finite element models calibrated with experimental data offer an alternative to study the behavior of multidirectional devices based on the response of single U-Shaped dampers, which avoid making several experimental tests to have knowledge of a multidirectional device. The MSS element in OpenSees can capture the behavior of a multidirectional hysteretic damper to be used in macro-models of other large structures.
- The inclusion of multidirectional energy dissipators in the interface between substructure and superstructure can significantly improve the overall seismic performance of skewed highway bridges, especially in those with larger skew angles. This is represented in lower probabilities of exceeding a particular damage state when the dissipator was included.

The fragility curves presented in this paper are only valid for the case study analyzed and should neither be used for seismic assessment of other bridge types nor for regional seismic risk assessment. Finally, full-scale experimental test of the multi-directional dissipator is still required to have more reliable data.

ACKNOWLEDGMENTS

This study was funded by the National Agency for Research and Development (ANID) under the Scholarship Program/ Magister Becas Chile 2021 - 22210688 and FONDECYT grant #11180882.
The strong motion database was provided by the SIBER-RISK project: Simulation Based Earthquake Risk and Resilience of Interdependent Systems and Networks.

REFERENCES

Aldea, S., Bazaez, R., Astroza, R. & Hernandez, F., 2021. Seismic fragility assessment of Chilean skewed highway bridges. *Engineering Structures,* Volumen 249, p. 113300.

Baird, A., Smith, T., Palermo, A. & Pampanin, S., 2014. *Experimental and numerical Study of U-Shape Flexural Plate (UFP) disspators.* Christchurch, New Zealand, s.n.

Baker, J. W., 2008. An introduction to probabilistic seismic hazard analysis (PSHA). *White paper, version,* Volumen 1, p. 72.

California Department of Transportation, 2019. *Seismic design criteria.* s.l.:CALTRANS.

Castro, S. y otros, 2021. A Consistently Processed Strong Motion Database for Chilean Earthquake. Submitted.

Deng, K., Pan, P. & Chaoyi, W., 2013. Development of crawler steel damper for bridges. *Journal of Constructional Steel Research,* Volumen 85, pp. 140-150.

Ene, D. y otros, 2016. Experimental study on the bidirectional inelastic deformation capacity of U-shaped steel dampers for seismic isolated buildings. *Earthquake Engineering & Structural Dynamics,* 45(2), pp. 173-192.

Gazetas, G., 1991. Foundation Vibrations. En: *Foundation engineering handbook.* Boston, MA: Springer, pp. 553-593.

Goel, R. K. & Chopra, A. K., 2008. Role of shear keys in seismic behavior of bridges crossing fault-rupture zones. *Journal of Bridge Engineering,* 13(4), p. 398.

Idini, B., Rojas, F., Ruiz, S. & Pastén, C., 2017. Ground motion prediction equations for the Chilean subduction zone. *Bulletin of Earthquake Engineering,* 15(5), pp. 1853-1880.

Jalayer, F. & Cornell, C. A., 2009. Alternative non-linear demand estimation methods for probability-based seismic assessments. *Earthquake Engineering & Structural Dynamics,* 38(8), pp. 951-972.

Kaviani, P., Zareian, F. & Taciroglu, E., 2012. Seismic behavior of reinforced concrete bridges with skew-angles seat-type abutments. *Engineering Structures,* Volumen 45, pp. 137-150.

Kawashima, K., Unjoh, S., Hoshikuma, J.-I. & Kosa, I., 2011. Damage of Bridges due to the 2010 Maule, Chile, Earthquake. *Journal of Earthquake Engineering,* 15(7), pp. 1036-1068.

Kelly, J. M., Skinner, R. I. & Heine, A. J., 1972. Mechanisms of energy absorption in special devices for use in earthquake resistant structures. *Bulletin of the New Zealand Society for Earthquake Engineering,* 5(3), pp. 63-88.

Kohnke, P. C., 1982. Ansys. *Finite Element Systems,* pp. 19-25.

McKenna, F. y otros, 2010. *OpenSees,* Berkeley: University of California.

Megally, S. H., 2002. *Seismic Response of Sacrificial Shear Keys in Bridge Abutments.* San Diego, s.n.

Muthukumar, S., 2003. *A contact element approach with hysteresis damping for the analysis and design of pounding in bridges.* Georgia Institute of Technology: s.n.

Nielson, B. G., 2005. *Analytical fragility curves for highway bridges in moderate seismic zones.* Georgia Institute of Technology: s.n.

Pagani, M. y otros, 2014. Openquake engine: An open hazard (and risk) software for the global earthquake model.. *Seismological Researh Letters,* 85(3), pp. 692-702.

Shamsabadi, A., Rollins, K. M. & Kapuskar, M., 2007. Nonlinear soil-abutment-bridge structure interaction for seismic performance-based design. *Journal of geotechnical and geoenvironmental engineering,* 133(6), pp. 707-720.

Steelman, J. S., Fahnestock, L. A. & Filipov, E. T., 2013. Shear and friction response of nonseismic laminated elastomeric bridge bearings subject to seismic demands. *Journal of Bridge Engineering,* 18(7), pp. 612-623.

Xiang, N., Alam, M. S. & Li, J., 2019. Yielding steel dampers as restraining devices to control seismic sliding of laminated rubber bearings for highway bridges: analytical and experimental study. *Journal of Bridge Engineering,* 24(11), p. 04019103.

NUMERICAL AND EXPERIMENTAL VERIFICATION OF ECCENTRIC ROLLING ISOLATION SYSTEM WITH CONVEX GUIDE

Zhen-Wei Hong[1], Yu-Jen Lai[2], Dn, Chiao[3], Cho-Yen Yang [4], and Yong-An Lai[5]

1. Graduate Student, National Central University, Taoyuan, Taiwan, R.O.C
2. Graduate Student, National Taiwan University, Taipei, Taiwan, R.O.C.
3. Graduate Student, National Taiwan University, Taipei, Taiwan, R.O.C.
4. Associate Researcher, National Center for Research on Earthquake Engineering, Taipei, Taiwan, R.O.C.
5. Assistant Professor, Department of Civil Engineering, National Central University, Taoyuan, Taiwan, R.O.C.

Email: qqaazz10708@gmail.com, cpes40913@gmail.com, jordan860426@gmail.com, choyen@narlabs.org.tw, laiyongan@ncu.edu.tw

ABSTRACT

In this study, Eccentric Rolling Isolation System with Convex Guide (CERIS) possessing a nonlinear restoring force is proposed. The CERIS is composed of circular isolators and convex guides. The isolated object mounted on the isolation platform is pin connected to the circular isolators eccentrically. Based on the mechanism idea of the CERIS above, the equation of motion is derived considering the inertia of the circular isolator. The seismic performance and the inertial effect of the circular isolator of the CERIS subjected to ground excitation are numerically investigated. Finally, the shaking table test is conducted to verify the feasibility of the mechanism and also validate the mathematical model. Consequently, the proposed CERIS with appropriate design indeed shows its effectiveness to reduce the acceleration response subjected to ground motions and the prototype of the mechanism successfully works.

Keywords: seismic isolation, rolling, nonlinear, convex, shaking table test

INTRODUCTION

The main concept of the current seismic design code in Taiwan is divided into three performance levels, “no damage,” “repairable,” and “no collapse” under weak, moderate, and strong earthquakes, respectively. Isolation technologies are good solutions and have already been implemented widely to ensure the seismic performance of buildings meets the requirement of the design code. However, the near-fault earthquake with low-frequency content may be an issue that affects the isolation performance of important equipment or valuable items even structure with conventional seismic isolation systems. The reason is that, for a near-fault earthquake with a velocity pulse in which the dominant period usually lies two to three seconds, this range of period is close to the fundamental period of isolation systems. This issue may potentially result in large amplification of seismic response even pounding or damage to the conventional isolation systems. To avoid or mitigate the resonant issue of conventional isolation systems, recently, many researchers changed their focus from linear isolation systems to nonlinear isolation systems. The eccentric rolling isolation system (ERIS) proposed by Chung *et al*. is one of them. In that research, the effectiveness of the ERIS subjected to near-fault earthquakes is numerically verified. To improve the seismic performance, the effectiveness of the ERIS equipped with an additional viscous damper was also investigated. (Chung *et al*., 2011). However, in the previous two research on the ERIS, the ERIS is hard to practically implement due to the large size of the mechanism and lack of numerical verification. Therefore, Lai, 2020 modified the concept of the ERIS by introducing a convex guide mounted below the circular isolator of the ERIS, by doing so, the isolation period remains long without using the circular roller with a large radius. Besides, the experimental verification of the ERIS by uniaxial shaking table test is conducted by Chiao,2021. In that research, the effectiveness and the feasibility of the prototype of the ERIS are successfully verified by a series of tests considering various ground motions.

Chung *et al.*, 2011 added viscous damping based on ERIS. In addition, the mathematical model has been modified by additionally considering the effect of the inertia of circular rollers, this modification is also verified by comparing the experimental and resimulation results.

In this study, the advantages of the ERIS due to modifications proposed by previous research are further combined and considered in this paper including the effect of roller inertia and convex guide, and the uniaxial prototype of the ERIS mechanism is also upgraded to work under bilateral ground excitation. The sensitivity study is conducted to investigate the effect of several design parameters, and then, the experimental study is also carried out on validating the mathematical model and verifying the feasibility of the new mechanism.

Equation of Motion

The 3D schematic diagram of upgraded bilateral CERIS is shown in Figs. 1. Orthogonally stacking could be the simplest way to modify the original mechanism effectively working under bilateral ground excitation. For the upper layer, the isolation platform with four rigid links is eccentrically pin-connected to the circular isolators. To derive the equation of motion, the coordinate with origin defined in the center of the circular isolator is shown in Figs. 2. r and R are the radius of the circular isolator and the radius of curvature of the convex guide, respectively. α represents the eccentricity. Point A and B are, respectively, the initial and displaced contact point between the circular isolator and the convex guide. m_s and m_r are mass of the superstructure and isolator, respectively. The mass ratio is defined as $\frac{m_r}{m_s}$. θ represents the rolling angle of the circular isolator, and ψ is the angle of the convex guide with respect to the rolling angle θ. x_g represents ground displacement. In this study, the dynamic behavior of the bilateral mechanism is assumed to be decoupled under bilateral excitation. Thus, for each layer, the rolling angle, θ, is the degree of freedom of this system.

When the system is in a displaced position (Figs. 1), the relationship between the two angles is expressed as follows:

$$r\theta = R\psi \tag{1}$$

By introducing the ratio of radius β defined as $\frac{r}{R}$, Eq. (1) can be turned into Eq. (2) shown as follows,

$$\beta\theta = \psi \tag{2}$$

The absolute displacement of the mass of the circular isolator and superstructure can be described as,

$$\begin{aligned} X_r &= r(1+\frac{1}{\beta})\sin(\beta\theta) + x_g \\ Y_r &= -r(1+\frac{1}{\beta})[1-\cos(\beta\theta)] \end{aligned} \tag{3}$$

$$X_s = r(1+\frac{1}{\beta})\sin(\beta\theta) - \alpha r\sin((1+\beta)\theta) + x_g$$
$$Y_s = -r(1+\frac{1}{\beta})[1-\cos(\beta\theta)] - \alpha r\cos((1+\beta)\theta) + \alpha r \quad (4)$$

Taking the second-order time derivative, the absolute acceleration for the circular isolator and superstructure are shown as follows,

$$\ddot{X}_r = r(1+\beta)\cos(\beta\theta)\ddot{\theta} - r(\beta+\beta^2)\sin(\beta\theta)\dot{\theta}^2 + \ddot{x}_g$$
$$\ddot{Y}_r = -r(1+\beta)\sin(\beta\theta)\ddot{\theta} - r(\beta+\beta^2)\sin(\beta\theta)\dot{\theta}^2 \quad (5)$$

$$\ddot{X}_s = r(\beta+1)[\cos(\beta\theta) - \alpha\cos((1+\beta)\theta)]\ddot{\theta}$$
$$+r[\alpha(1+\beta)^2\sin((1+\beta)\theta) - (\beta^2+\beta)\sin(\beta\theta)]\dot{\theta}^2 + \ddot{x}_g$$
$$\ddot{Y}_s = -r(\beta+1)[\alpha\sin((1+\beta)\theta) - \sin(\beta\theta)]\ddot{\theta} \quad (6)$$
$$+r[\alpha(1+\beta)^2\cos((1+\beta)\theta) - (\beta^2+\beta)\cos(\beta\theta)]\dot{\theta}^2$$

In this study, the equation of motion is derived by introducing Lagrange's equation,

$$\frac{d}{dt}\left(\frac{\partial L}{\dot{\theta}}\right) - \frac{\partial L}{\theta} = Q^{\mathrm{N}} \quad (7)$$

where L is Lagrangian defined as difference between the kinetic and potential energy of the system; Q^{N} is nonconservative force. Since this degree of freedom is a rotation angle θ, the non-conservative force Q^{N} should be a moment. The horizontal friction f_r between the circular isolator and convex guide is assumed to be large enough to ensure only rolling behavior occurs. For such a mechanism, the friction for the whole system may be complicated and caused from several positions, such as pin and rolling friction between circular isolator and convex guide. The friction of pin connection is f_{b}. The moment of f_{b} causes to the center of the circular isolator is $f_{\mathrm{b}}\alpha R\cos\theta$. The friction torque generated by the deformation of the contact point between the gear and the rack is $N\delta$,where N is the normal force, δ is the horizontal displacement between the normal force and the center of the circular isolator. Thus, effective friction moment M_{fr} is considered to represent a total frictional damping for one layer (one direction). Therefore, the effective friction moment and the nonconservative force could be defined as follows:

$$M_{\mathrm{fr}} = N\delta + f_{\mathrm{b}}\alpha R\cos\theta$$
$$= (m_s + m_{\mathrm{r}})g\delta + f_{\mathrm{b}}\alpha R\cos\theta \quad (8)$$

$$Q_i^N = -M_{fr} \quad (9)$$

From Eqs. (3) and (4), the Lagrangina can be calculated, then substituting the result with Eqs. (9) into Eq. (7), the equation of motion can be obtained and shown as follows:

$$
\begin{aligned}
&[m_s r^2(1+\beta)^2(1-2\alpha\cos\theta+\alpha^2)+m_r r^2(1+\beta)^2+I_r]\ddot{\theta} \\
&+[m_s\alpha r^2(1+\beta)^2\sin\theta]\dot{\theta}^2+[m_s\alpha(1+\beta)\sin((1+\beta)\theta)-(1+\beta)\sin\beta\theta(m_s+m_r)]rg \\
&=-M_{fr}+(m_s\alpha\cos((1+\beta)\theta)-(1+\beta)\cos(\beta\theta)(m_s+m_r))r\ddot{x}_g
\end{aligned} \tag{10}
$$

where $I_r=\frac{1}{2}m_r r^2$ is the moment of inertia of the circular isolator. If the rolling angle is quite small, the system can be linearized by replacing the $\sin\theta$ and $\cos\theta$ term by θ and one, respectively (i.e. $\sin\theta\approx\theta$, $\cos\theta\approx 1$). If the high-order term, $m_s\alpha(1+\beta)^2\theta\cdot\dot{\theta}^2$, in Eq. (10) is neglected, the fundamental frequency can be determined as linear system by considered the equivalent mass $m_s(1+\beta)^2(1-\alpha)^2+m_r(1+\beta)^2+\frac{1}{2}m_r$ and the equivalent stiffness $[m_s\alpha(1+\beta)^2-(\beta+\beta^2)(m_s+m_r)]\cdot\frac{g}{r}$. Consequently, the fundamental frequency from linearized equation of motion can be expressed as follows:

$$
f_0=\frac{1}{2\pi}\sqrt{\frac{[m_s\alpha(1+\beta)^2-(\beta+\beta^2)(m_s+m_r)]}{m_s(1+\beta)^2(1-\alpha)^2+m_r(1+\beta)^2+\frac{1}{2}m_r}}\cdot\sqrt{\frac{g}{r}} \tag{11}
$$

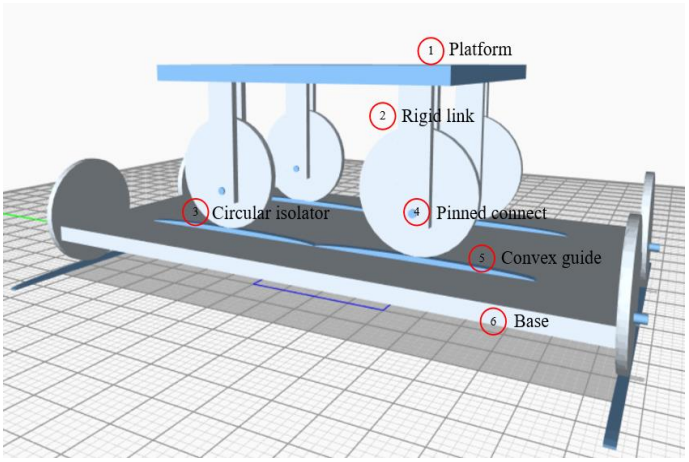

Figure 1. schematic diagram of the two-direction CERIS

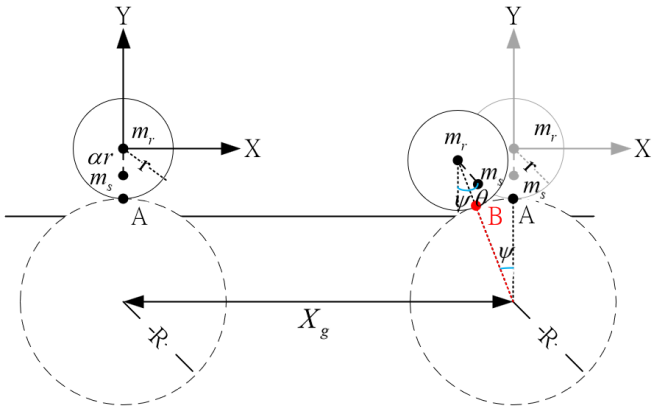

Figure 2. Mathematical model of CERIS.

In original ERIS case, the displacement limitation is $180°$. However, after we add the convex guide, the displacement limitation become smaller than $180°$. For example, the displacement limitation of system parameter lists in Table 1 is $130.49°$.

Foe Free Vibration

In this section, the sensitivity of ratio of radius β is investigated and demonstrated by free vibration with initial angle θ_0 equal to $90°$. The system parameters are tabulated in Table 1. The horizontal displacement time histories and absolute acceleration time histories for the three cases with β =0.005 and 0.03 and 0.05 are compared and shown in Figs. 3(a) and (b). For the three cases of β =0.005 and 0.03 and 0.05, the initial displacement is 0.1011m and 0.0959m and0.0988m, respectively. After one cycle of oscillation, the displacement become 0.038m and 0.051m and 0.045m, respectively. Therefore, the greater ratio of radius, the decay of CERIS become faster. Besides, the linearized frequency is 0.7563 and 0.7015 Hz and 0.6554Hz, respectively. The frequency decreases with increase of radius of ratio β. In other words, the greater ratio of radius, the longer isolation period. Thus, to meet the familiar isolation period within 2 to 5 seconds in practical application, a greater ratio of radius could be considered, which may further reduce the requirement of radius of circular isolator.

Table 1. Design parameters of CERIS

m_r(kg)	m_s(kg)	r_m	β	α	μ	r (cm)
8	10	0.8	0.05	0.3	0.02	7.5

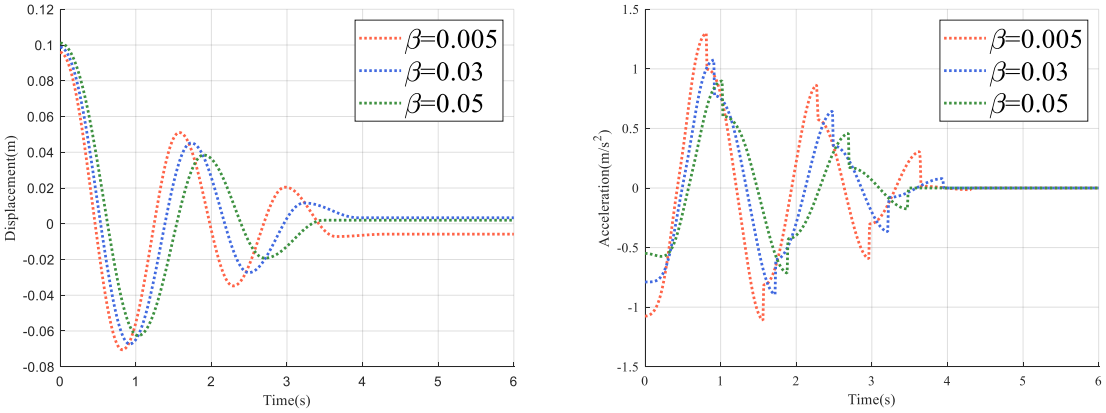

(a) displacement (b) abs. acceleration

Figure 3. Time histories of CERIS under free vibration.

Forced Vibration: Sinusoidal Excitation

In this section, the dynamic response of CERIS and a linear isolation system subject to sinusoidal excitation with different frequencies is numerically studied. A performance index, r_a is defined as the maximum absolute horizontal acceleration divided by the peak ground acceleration.

$$r_a = \frac{\max\left|\ddot{x}_{s,abs}(t)\right|_{\text{w/isolation}}}{\max\left|\ddot{x}_{g,abs}(t)\right|} \tag{12}$$

The Acceleration ratio r_a indexes the effectiveness of the isolation system. If r_a is much smaller than one, the performance of the isolation system is effective in terms of reducing the acceleration response. According to the design parameters of the CERIS tabulated in Table 1, an equivalent single-degree-of-freedom linear isolation system is also considered to be compared with the proposed CERIS The parameters of the linear isolator are specified as follows: the mass of the linear system is the same as

CERIS; the fundamental frequency (f_0) is equal to the linearized frequency of CERIS; the damping ratio equal to 10.74% is determined from the decaying envelope of CERIS under free vibration.

The amplitude equal to 0.3 m/sec^2 is assigned, and the duration equal to 100 seconds, Δt equal to 0.01 second, the frequency ratio from 0.05 to 3 in the interval of 0.05(i.e. frequency ratio is defined as the frequency of excitation divided by the linearized frequency) are considered in numerical simulation. The response of the CERIS tends to be steady-state after roughly 40 cycles. Therefore, the peak value shown in the frequency response is determined from the response after 40 cycles (Figs. 4). Different from the linear system, the resonance of the CERIS does not occur at the frequency ratio equal to one but occurs at the frequency ratio smaller than one. In contrast to the CERIS, the resonance of the linear isolation system occurs when the frequency ratio is equal to one. From the comparison between the two systems, it is obvious that the amplification of the CERIS is lower than the linear system when the frequency ratio is close to one. Besides, the greater eccentricity, where r_a is less than 1 in the curve, move to the left. The CERIS has wider range of isolation effect with the greater eccentricity. Eventually, when the external force is high frequency, r_a is less than 1. The CERIS has good isolation effect under high frequency of external force.

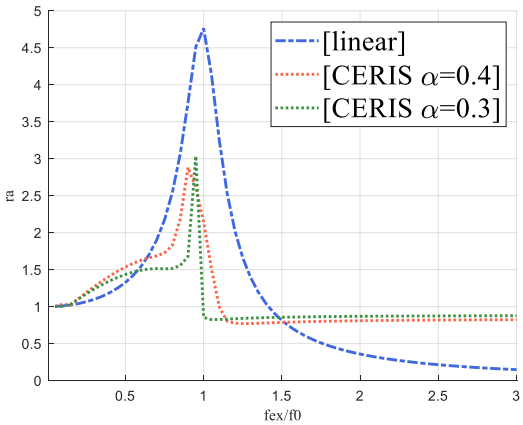

Figure 4. The frequency response under sine wave

Forced Vibration: Seismic Excitation

To investigate the effect of the inertia of the circular isolator on both the dynamic behavior and the seismic performance of the CERIS, the seismic input is considered in this section. The same system parameters listed in Table 1 are adopted here. The seismic responses of the CERIS under Chi Chi earthquake (TCU102 EW) with PGA scaled to 1.2 m/s^2 are shown in Table2 and the hysteresis loop of CERIS are shown in Figs. 5(a)、(b)、(c). For the three cases of the CERIS with the mass of the circular isolator equal to 0 and 4 and 8 kg, the acceleration ratios are 1.5346 and 1.2035 and 0.8659, respectively. Only one case is effective to mitigate the acceleration response. Thus, the effect of the inertia of the circular isolator should not be neglected. Besides, the greater mass of the circular isolator, the smaller linearized frequency. On the other word, the stiffness of CERIS become smaller leading to the greater maximum displacement response and the smaller maximum absolute acceleration response. So, if the inertia of isolator is not enough, the isolation effect will not show out. Last but not least, with smaller displacement response, the hysteresis loop doesn't show the nonlinear characteristic. This is another reason for the poor isolation effect.

Table2. CERIS response under Chi Chi earthquake

	m_r =0	m_r =4	m_r =8
Maximum displacement (m)	0.0274	0.0522	0.0885
Maximum abs.acceleration (m/s^2)	1.8415	1.4442	1.0391
r_a	1.5346	1.2035	0.8659
linearized frequency (Hz)	1.3063	0.8494	0.6554

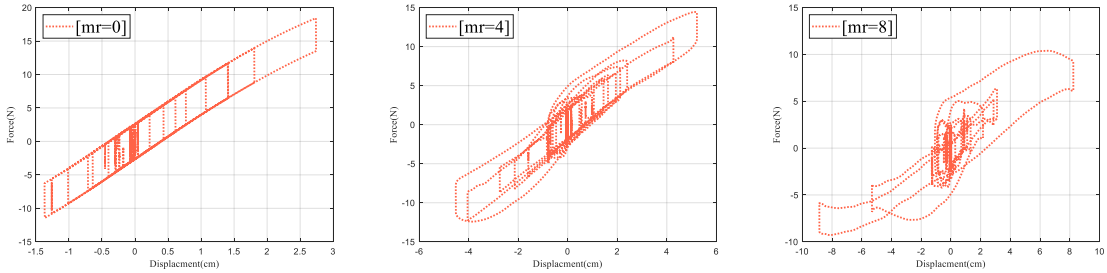

(a) m_r =0 (b) m_r =4 (c) m_r =8

Figure 5. the hysteresis loop of CERIS under Chi Chi earthquake

Shaking Table Test

The experimental verification is conducted by a uniaxial shaking table in the National Center for Research on Earthquake Engineering. The instrument layout is shown in Figs. 6, a total of four accelerometers are installed to measure the acceleration responses, one for the shaking table, two for the horizontal acceleration of the platform, and the rest one for the vertical acceleration of the platform. Besides the acceleration, the isolation displacement is also important, thus a laser displacement transducer is installed on the shaking table to record the horizontal displacement of the CERIS relative to the ground (shaking table). In this case, the convex guide is not included, which means the radius ratio equal to zero is taken into consideration. A near-fault Chi-Chi earthquake with PGD equal to 75 mm (Chi-Chi TCU102EW) is used as input excitation of the shaking table. The experimental and resimulation results are compared and illustrated in Figs. 7. The acceleration ratios r_a of the experimental and the simulation results are 0.845 and 0.853, respectively. Both the acceleration responses from the experimental and resimulation results indicate that the CERIS is effective to mitigate the ground acceleration transmitting to the superstructure. The error of r_a between the two cases is 0.92% which is quite small and implies that the dynamic behavior could be accurately simulated by the mathematical model.

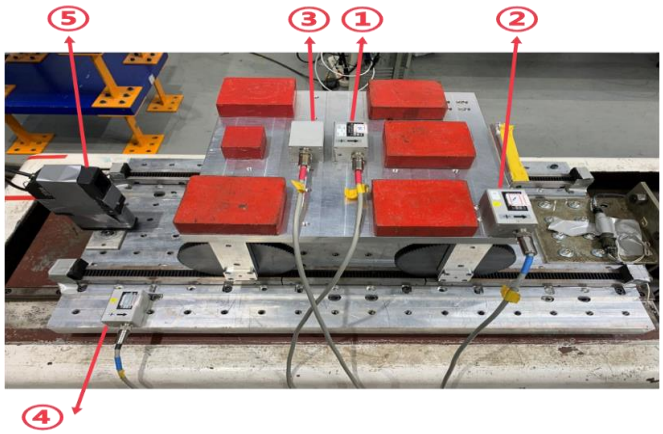

Figure 6. Isolator and sensor configuration

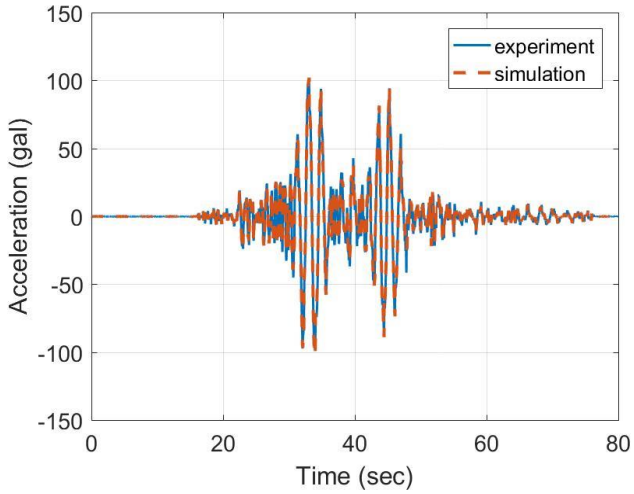

Figure 7. Time histories of abs. acceleration under Chi-Chi earthquake TCU102 (PGD: 75MM)

CONCLUSIONS

In this study, the inertia of the circular isolator and convex guide are both considered to implement and improve the seismic performance of the eccentric rolling isolation system. The effect of several design parameters is numerically investigated by sensitivity study, and the feasibility of the modified mechanism is experimentally verified. By introducing the convex guide and consideration of the inertia of the circular isolator, a greater radius of the circular isolator is no longer necessary to achieve a long isolation period, which means the size of the mechanism could be significantly reduced. Moreover, in frequency response, the CERIS has good isolation effect under high frequency of excitation. Finally, when the system is excited by near-fault ground motion, the amplification of the CERIS considering the inertia of isolator is lower than a without considering the inertia of isolator one. Thus, the feasibility of the CERIS in practical application is also remarkably imporved.

ACKNOWLEDGMENTS

This study was supported by the Ministry of Science and Technology of the Republic of China (MOST 108-2625-M-492-005).

REFERENCES

Chung LL, Yang CY, Chen HM, Lu LY, (2009) "Dynamic behavior of nonlinear rolling isolation system," *Structural Control and Health Monitoring*, **16**(1), 32-54.

Yang CY, Hsieh CH, Chung LL, Chen HM, Wu LY, (2012) "Effectiveness of an eccentric rolling isolation system with friction damping," *Journal of Vibration and Control*, **18**(14), 2149-2163.

Chiao D. (2021), Numerical and Experimental Verification of Eccentric Rolling Isolation System, *Master. Thesis*, National Taiwan University. (in Chinese)

Lai Y J. (2020), Study on Eccentric Rolling Isolation System with Convex Guide, *Master. Thesis*, National Taiwan University. (in Chinese)

Chung LL, Hsieh CH, Yang CY, Wu LY, Chen HM, (2011) "Study on nonlinear rolling isolation system with linear viscous damper" *Journal of the Chinese Institute of Civil and Hydraulic Engineering*, **23**(2), 175–186, 2011 (in Chinese)

ACTIVE SEISMIC CONTROL SIMULATION OF NONLINEAR STRUCTURES USING OPENSEES-SIMULINK CONNECTION

Pei-Ching Chen[1] and Danny Gho[2]
1. Associate Professor, National Taiwan University of Science and Technology, Taipei, Taiwan, R.O.C.
2. Graduate Student, National Taiwan University of Science and Technology, Taipei, Taiwan, R.O.C.
Email: peichingchen@mail.ntust.edu.tw, m10905839@mail.ntust.edu.tw

ABSTRACT

Structural control has been generally utilized to ensure a building's performance during seismic events. One of the active control methods named active base isolation, has been investigated multiple times in previous researches. However, these analyses often employ simplified and elastic shear building model because it is difficult to simulate complex structural models in MATLAB/Simulink, the mainstream program for simulation of active control algorithms. This paper presents the usage of TCP/IP-based connection between Simulink and OpenSees, a popular open-source software for structural analysis. Validation of the connection and OpenSees accuracy for active structural control simulation is presented. A single-degree-of-freedom structure model is controlled using active base isolation in the OpenSees-Simulink and the result is compared to the pure Simulink model. It demonstrates that the usage of OpenSees-Simulink non-linear structural analysis offers additional insight which linear-elastic model may not be able to represent for structural control performance investigation.

Keywords: Active control, Simulink, OpenSees, TCP/IP

INTRODUCTION

Active structural control is one of the methods employed to suppress dynamic response of buildings subjected to earthquake excitation (Chen & Chien, 2020). In active structural control, a control algorithm computes the control force required to suppress the dynamic response of structures (Chu *et al*., 2005). The control force is then imposed on the structure by control devices, such as active mass damper (Chen *et al*., 2021) and active base isolation (Chang & Spencer, 2010). However, the usage of active structural control comes with drawbacks. One of the major drawbacks is that if the control algorithm used for active control is not proper, the active structural control performance could become inferior. Even worse, the dynamic response could be amplified and damage of the structure may occur. Therefore, a rigorous numerical simulation of the active structural control must be conducted to ensure that the algorithm deployed is stable and robust enough.

Large amounts of numerical simulation of active structural control were conducted using linear shear building model with state-space formulation in MATLAB/Simulink (Chen *et al*., 2021; Liao & Thedy, 2021). The prevalent usage of MATLAB/Simulink for active structural control simulation is due to its relative friendliness for users, extensive library, and its adoption by multitude of control textbooks as the control engineering software (Chu *et al*., 2005). Despite MATLAB/Simulink advanced capabilities, it may be difficult to model a complex structure with non-linear material and complex geometry using MATLAB/Simulink. Although it is possible to program a non-linear finite element submodule for MATLAB/Simulink, currently developed submodules have limited material model and capabilities compared with stand-alone finite element software such as OpenSees. (Castaneda *et al*., 2015; Ohtori *et al*., 2004).

OpenSees is a powerful and extensible finite element software with libraries of linear and nonlinear material models which is able to model highly complex structures (McKenna *et al*., 2010). However, it is not simple to use the OpenSees interpreter to conduct control system simulation due to the limitation of TcL and Python built-in capabilities in control system. However, previous researches have shown

that it is possible to use the powerful OpenSees capabilities with other software by using a 'adapter' or 'coupling'. Previous usages of such technique are for connecting OpenSees with other finite element softwares or for hybrid simulation (H. Schellenberg *et al.*, 2019; Xu *et al.*, 2021).

In this study, OpenSees was connected to MATLAB/Simulink using TCP/IP connection, a simple protocol which would not require installation of additional software. The usage of MATLAB/Simulink allows the practice of standard software for control engineering with the powerful finite element capabilities of OpenSees for active structural control simulation; therefore, numerical simulation of active control algorithm with complex structures can be performed. A further analysis of nonlinear behavior of actively-controlled structure is also then discussed in this paper.

METHODOLOGY

Architecture Overview

Since OpenSees are using TcL and/or Python as an intermediary language between the user and the C/C++ finite element engine, a TCP/IP-based communication can be developed using the built-in language feature of both TcL (socket command) and Python (socket library). This allows both OpenSees and Simulink to send and receive data from each other. The communication method between two softwares is illustrated in Fig. 1 and described as follows in order:

1. OpenSees sends the simulation time and the feedback signal (or other data) set by the user. Unless initial displacement or other forces are set (such as gravity analysis), the feedback signal should be zero.
2. Simulink receives the data sent from OpenSees and sends the feedback signal to the control algorithm. The resulting control force is then sent back to OpenSees.
3. OpenSees receives the control force and the Simulink simulation time. If the simulation time does not match with OpenSees time, the analysis breaks. If the time matches, the control force parameter is updated, and the structural model analysis continues to the next time step.

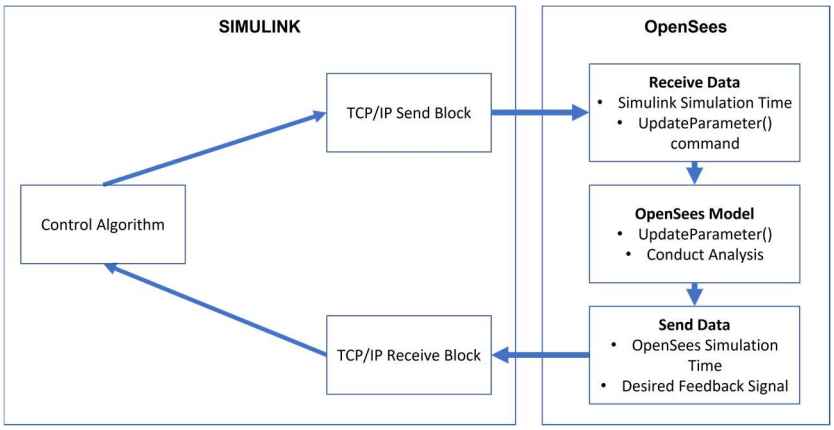

Figure 1. Architecture overview of TCP/IP connection between OpenSees and Simulink.

Modelling of Active Base Isolation

The numerical model of active base isolation in this study was created by simulating the excitation received by the building (hereafter referred as applied acceleration). The applied acceleration received by the building was defined as the sum of ground excitation and the control acceleration. The applied acceleration was configured in the OpenSees model using the UniformExcitation command, which applied the acceleration to all the dynamic degrees of freedom (DOFs) of the structure. An overview of the implementation is depicted in Fig. 2.

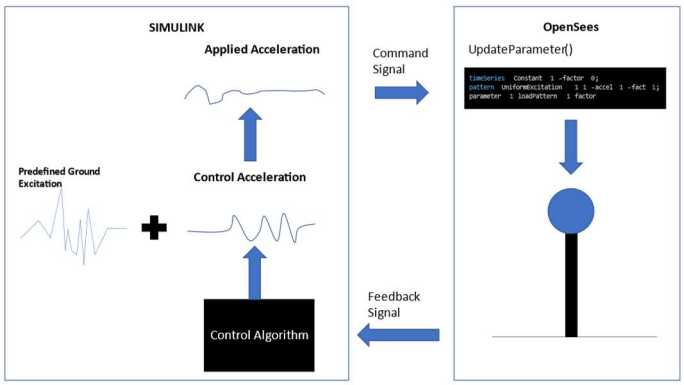

Figure 2. Implementation of active base isolation.

SIMULATION RESULTS

Verification of Connection Correctness

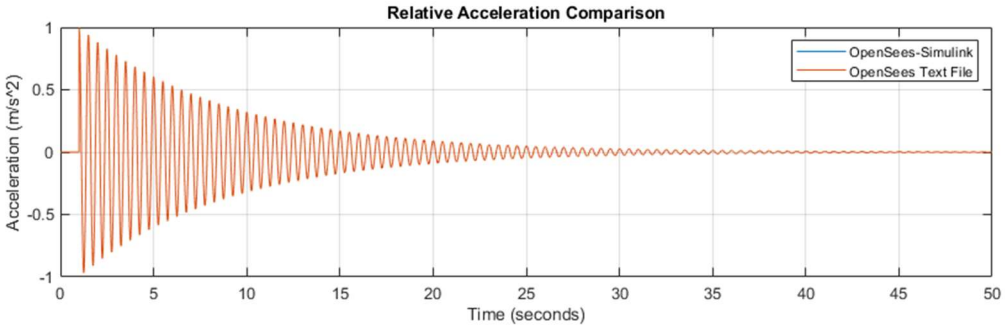

Figure 3. Comparison between OpenSees-Simulink and OpenSees Text File Input for Step Function Excitation.

To verify the correctness of the implementation, the connection was used to communicate ground acceleration command from Simulink to OpenSees and send acceleration of a single-degree-of-freedom (SDOF) structure. The SDOF structure had a mass of 5000 N-s^2/m and a stiffness of 789,570 N/m. The damping ratio of the SDOF structure was set as 1%. Two excitations were used for testing. The first one is a step excitation and the second one is the 1940 El Centro earthquake ground motion record. Performance of the structure was then compared with an equivalent state-space model as well as an OpenSees model where the ground motion was from OpenSees text file. The setting of the OpenSees transient analysis is shown in Table 1.

Table 1. Parameter of OpenSees transient analysis

Parameter	Value
Convergence Test	NormDispIncr with Tolerance of 10^{-6}
Algorithm	Newton
Integrator	Newmark Method with Alpha of 0.5 and Beta of 0.25
dt	0.005 second

Acceleration timeseries of the free end of the SDOF structure can be seen in Figs. 3 and 4. For OpenSees-Simulink and OpenSees text input, after adjusting for timestep difference, the result was virtually identical. However, for the OpenSees-Simulink and Simulink state-space model, differences existed. The difference is shown at Fig 5, as an example. The root-mean-square error (RMSE) of the OpenSees-Simulink connection with step excitation and the El Centro ground motion was 0.0101 m/s^2 and 0.0288 m/s^2, respectively. The RMSE difference between the OpenSees-Simulink and Simulink state-space

model was due to the different integrator techniques used by OpenSees and Simulink. If the timestep was progressively decreased, the RMSE value became smaller. For a time step of 0.00005 sec (20,000 hz), the RMSE became 6.3008 x 10^{-5} m/s^2 and 2.1930 x 10^{-4} m/s^2 for step excitation and the El Centro excitation, respectively. Note that the running time also increased in a near proportional manner with the decrease of time step. Furthermore, the running time was taken from the connection operating on the Ubuntu 22.04 LTS. Running the connection on Windows-based computer may result in significant running time for unknown reasons at this time. Considering all of that, a time step of 0.0005 sec was taken as a balance between accuracy and running time. Table 2 summarizes the simulation results for evaluate the accuracy and running cost.

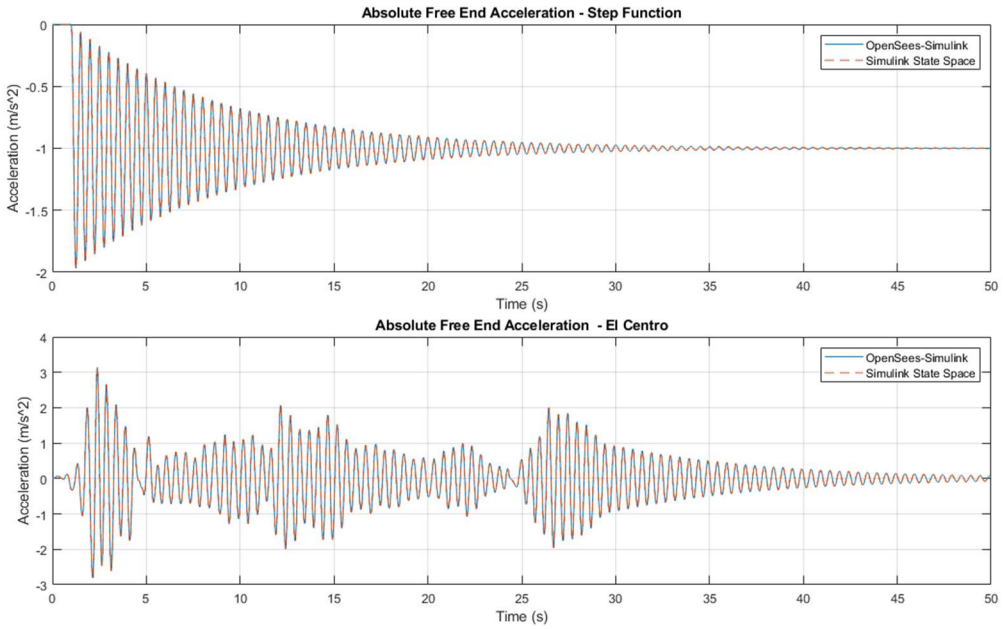

Figure 4. Comparison between OpenSees-Simulink and Simulink state-space model.

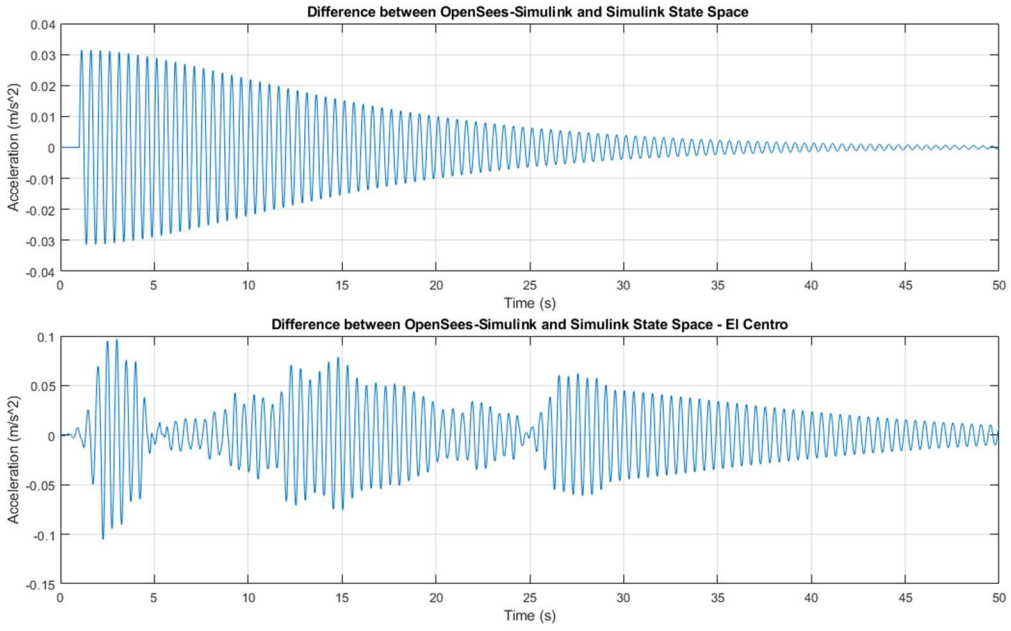

Figure 5. Difference between OpenSees-Simulink and Simulink state-space model.

Table 2. Running time of the connection with different timestep.

Excitation	Timestep (second)	RMSE (m/s^2)	Running Time (second)
1940 El Centro Ground Motion	0.005	0.0288	24
	0.0005	0.022	231
	0.00005	2.1930×10^{-4}	2121

Active Control Performance

After the simulation accuracy was proved, the connection was then used to perform active base isolation control using the same SDOF structure. In this study, the control algorithm used for active base isolation was proportional-integral-derivative (PID) control. The PID controller was manually tuned, and the gains of the PID were set to be 40 for proportional gain, 10 for integral gain, and 10 for derivative gain. The control performance of the structure can be seen in Fig. 6. The results provided from the OpenSees-Simulink and Simulink state-space model are nearly identical, with a RMSE of only 1.3909×10^{-4} m/s^2.

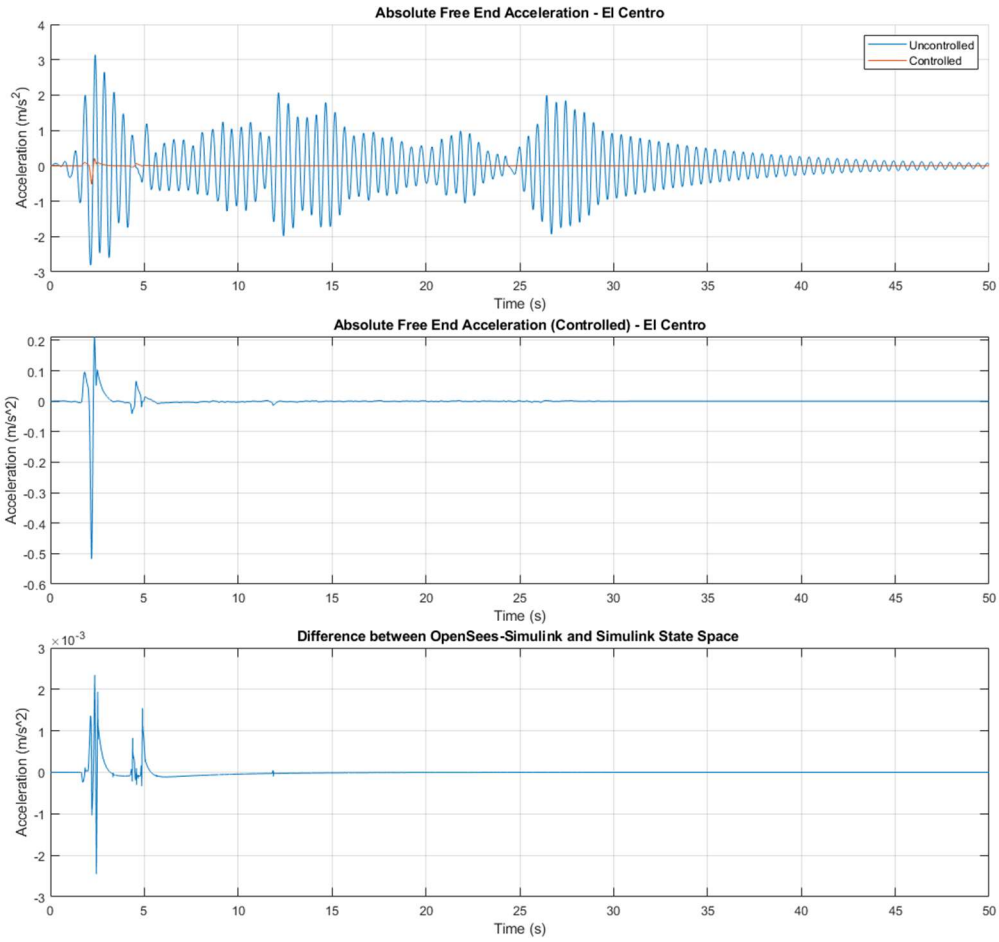

Figure 6. Absolute acceleration time histories of active base isolation of free end and difference between OpenSees-Simulink and Simulink state-space model.

Active Control of Nonlinear SDOF

Taking the advantages of wide and diverse nonlinear material library of OpenSees, active base isolation of a nonlinear structure was conducted. A 12-feet structure, using American standard W-section, was taken from the Example 4.1 of Dynamics of Structure textbook (Chopra, 2012) and modeled using OpenSees with Uniaxial Elastic material, Steel01 (Bilinear material model for steel) and Steel02 (Giuffré-Menegotto-Pinto with Isotropic hardening material model for steel). The W-section, for all material model, use Grade 50/A572 steel with E_s of 30,000 ksi and strain hardening of 1% for the

nonlinear Steel01 and Steel02 material. The structure has a natural period of 0.5 second and damping ratio of 2%

The PID controller was also tuned with the same procedure used to tune the previous example structure, and the proportional gain, integral gain, and derivative gain were tuned as 3.0, 5.0 and 1.0, respectively. After the tuning, 18 structural analyses were conducted. The parameters varied for structural analyses were the peak ground acceleration (PGA), with control or without control, maximum control saturation, and material type. The excitation used for the simulation was the 1940 El Centro earthquake ground motion. The seismic performance of the controller can be seen in Table 3. For the controlled system without saturation limit, the performance was identical as expected. However, for the controlled system with a control force saturation of 0.05 g, the system had significant difference in performance, especially on larger PGA. The difference in performance, as can be seen in Fig. 7, was caused by different hysteretic behaviors. The Steel02 material has a more significant strain behavior. The difference is exemplified in Figs. 8 and 9. With 1 g excitation, structures with nonlinear material type have a significant plastic strain at the end of the analysis. The plastic strain causes a permanent deformation after the earthquake.

Table 3. Excitation performance of the nonlinear SDOF structure.

PGA	Control Type	Material Type	Max. Disp. (Inch)	Max. Abs. Acc. (g/gravity)	RMS Disp. (Inch)	RMS Abs. Acc (g/gravity)
0.5 g	Uncontrolled	Elastic	3.5739	1.4631	0.9052	0.3705
		Steel01	3.2922	1.2745	0.9112	0.3671
		Steel02	3.3322	1.2332	0.8434	0.3264
	Controlled	Elastic	0.0999	0.041	0.0212	0.0087
		Steel01	0.0999	0.041	0.0212	0.0087
		Steel02	0.0999	0.041	0.0212	0.0087
	Saturation	Elastic	3.4434	1.4097	0.8110	0.3320
		Steel01	2.5093	1.0273	0.4213	0.1725
		Steel02	2.4672	0.9906	0.4191	0.1695
1 g	Uncontrolled	Elastic	7.1478	2.9261	1.8104	0.7411
		Steel01	5.8491	1.3828	1.6708	0.5678
		Steel02	8.8327	1.355	1.8376	0.3521
	Controlled	Elastic	0.1999	0.0820	0.0424	0.0173
		Steel01	0.1999	0.082	0.0424	0.0173
		Steel02	0.1999	0.082	0.0424	0.0173
	Saturation	Elastic	7.0098	2.8697	1.7093	0.6997
		Steel01	5.7589	1.3797	1.1197	0.3683
		Steel02	7.2285	1.327	1.4542	0.2868

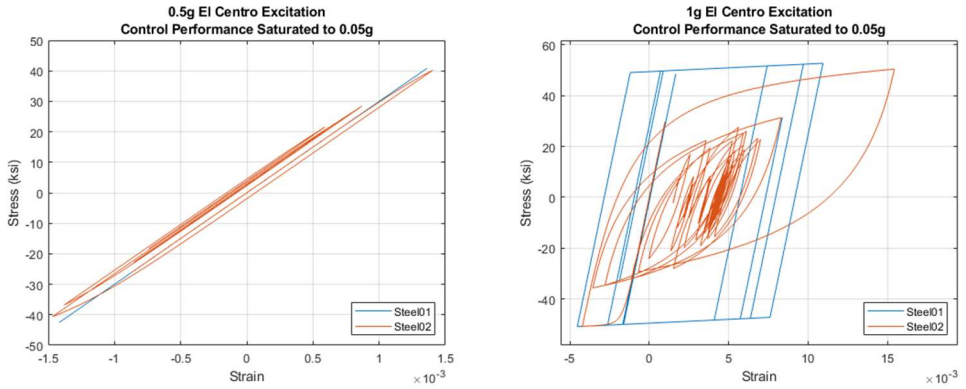

Figure 7. Hysteresis curve of the building under controlled subjected to the El Centro excitation with force saturation (Steel01 and Steel02)

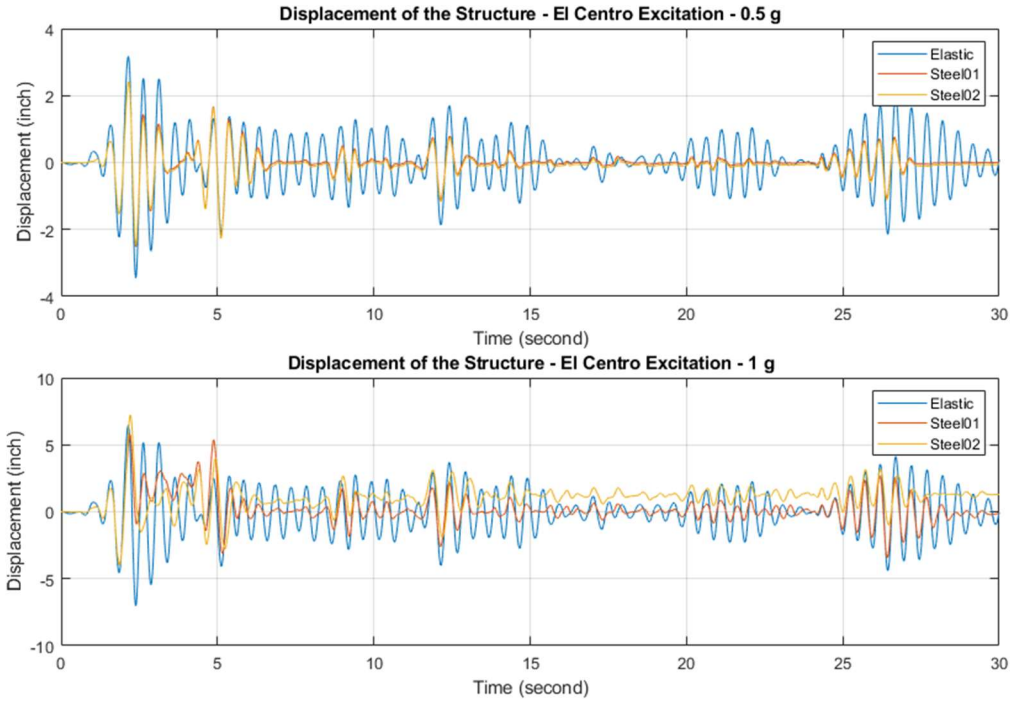

Figure 8. Displacement time histories of the nonlinear SDOF structures.

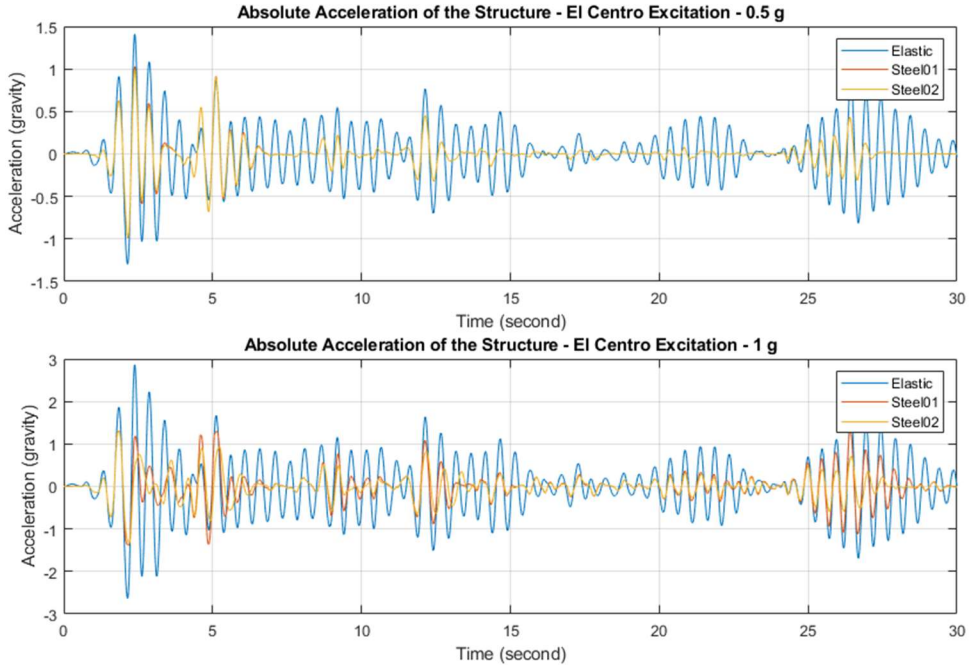

Figure 9. Absolute acceleration time histories of the nonlinear SDOF structures.

CONCLUSIONS

Using a TCP/IP connection between OpenSees and Simulink, a comparison between active base isolation control of a SDOF structure with elastic, bilinear strain hardening, and Giuffré-Menegotto-Pinto steel model was shown in this study. It is found that the usage of an elastic structure with force saturation may not represent a realistic performance for a sufficiently large excitation with the control force under the saturation limit. Specifically, after yielding occurs, it does not consider the plastic deformation and thus does not consider the drifting. This may present a problem for a structure that has a dominant importance on deformation control. However, for structures that acceleration control become

critical, the usage of elastic models may result in conservative analyses. Furthermore, the usage of bilinear strain hardening model may underestimate the maximum strain of the element/section. Earthquake excitation often changes from positive acceleration to negative acceleration (cyclic-reversal) and conceivably have compression and tension yield. Nonlinear material that accounts for Bauschinger effect (such as Steel02) may reflect a more accurate displacement behavior due to the increased plastic strain. As in the previous discussion, this behavior is exacerbated for excitation with higher PGA which may cause higher non-linearity. Summarily, the usage of a non-linear structure for structural control analysis is suggested, especially when deformation control is the utmost concern. Due to the wide availability of material models and advanced numerical features, the OpenSees program is suggested as the non-linear finite element engine for the simulation.

ACKNOWLEDGMENTS

The authors are thankful for the support of National Center for Research on Earthquake Engineering (NCREE) for the computational support provided by Small-Scale Structural Laboratory.

REFERENCES

Castaneda, N., Gao, X., & Dyke, S. J. (2015). "Computational Tool for Real-Time Hybrid Simulation of Seismically Excited Steel Frame Structures", *Journal of Computing in Civil Engineering*, *29*(3)

Chang, C.-M., & Spencer, B. F. (2010). "Active base isolation of buildings subjected to seismic excitations", *Earthquake Engineering & Structural Dynamics*, *39*(13), 1493–1512.

Chen, P.-C., & Chien, K.-Y. (2020). "Machine-Learning Based Optimal Seismic Control of Structure with Active Mass Damper", *Applied Sciences*, *10*(15), 5342.

Chen, P.-C., Sugiarto, B. J., & Chien, K.-Y. (2021). "Performance-based optimization of LQR for active mass damper using symbiotic organisms search", *Smart Structures and Systems*, *27*(4), 705–717.

Chopra, A. K. (2012). *Dynamics of structures: Theory and applications to earthquake engineering* (4th ed). Prentice Hall.

Chu, S. Y., Soong, T. T., & Reinhorn, A. M. (2005). *Active, hybrid, and semi-active structural control: A design and implementation handbook*. Wiley.

H. Schellenberg, reas, Huang, Y., & A. Mahin, S. (2019). "Structural Finite Element Software Coupling Using Adapter Elements", *Computer Modeling in Engineering & Sciences*, *120*(3), 719–737.

Liao, K.-W., & Thedy, J. (2021). "Probabilistic optimal control parameters with incomplete information on design variables using a heuristic algorithm", *Applied Soft Computing*, *110*, 107586.

McKenna, F., Scott, M. H., & Fenves, G. L. (2010). "Nonlinear Finite-Element Analysis Software Architecture Using Object Composition", *Journal of Computing in Civil Engineering*, *24*(1), 95–107.

Ohtori, Y., Christenson, R. E., Spencer, B. F., & Dyke, S. J. (2004). "Benchmark Control Problems for Seismically Excited Nonlinear Buildings", *Journal of Engineering Mechanics*, *130*(4), 366–385.

Xu, Z.-D., Dong, Y.-R., Chen, S., Guo, Y.-Q., Li, Q.-Q., & Xu, Y.-S. (2021). "Development of hybrid test system for three-dimensional viscoelastic damping frame structures based on Matlab-OpenSees combined programming", *Soil Dynamics and Earthquake Engineering*, *144*, 106681.

STUDY ON CRACK INITIATION MECHANISM OF OZONE-DETERIORATED RUBBER DAMPER

Kazutoshi Nagata[1], Shintaro Sawada[2], Kouta Kawa[3],
Suguru Kodaka[4], Zhengyan Wang[5] and Kunitomo Sugiura[6]

1. Associate Professor, Department of Civil and Environmental Engineering, Nagoya Institute of Technology, Nagoya, Japan
2. Maeda Corporation, Tokyo, Japan
3. Chubu Regional Development Bureau, Ministry of Land, Infrastructure, Transport and Tourism, Shizuoka, Japan
4. Undergraduate student, Department of Civil and Environmental Engineering, Nagoya Institute of Technology, Nagoya, Japan
5. Master student, School of Civil Engineering, Tongji University, Shanghai, China
6. Professor, Kyoto University, Kyoto, Japan

Email: nagata@nitech.ac.jp, s.sawada.873@stn.nitech.ac.jp, k.kawa.911@stn.nitech.ac.jp, s.kodaka.914@stn.nitech.ac.jp, 821863759@qq.com, sugiura.kunitomo.4n@kyoto-u.ac.jp

ABSTRACT

Rubber dampers are used to reduce the response of structures during earthquakes. In recent years, crack damage has occurred in rubber dampers, possibly due to ozone degradation. In order to elucidate the mechanism of this crack initiation, this study conducted an accelerated ozone degradation test of rubber and numerical analysis of rubber dampers. The results of the accelerated test showed that crack initiation occurs when the pre-strain is greater than 70%. Furthermore, numerical analysis showed that this magnitude of strain occurs in the coated rubber near the lower steel plate of the rubber damper.

Keywords: rubber damper, crack damage, accelerated ozone degradation test, numerical analysis

INTRODUCTION

In Japan, the effectiveness of rubber-based devices, or rubber bearings and rubber dampers, was confirmed during the 1995 Hyogo-ken Nanbu earthquake (Editorial Committee for the Report on the Hanshin-Awaji Earthquake Disaster, 1997). Since then, these devices have been actively used to improve the seismic performance of bridges (Subcommittee on Support Functions of Steel Bridges, Committee on Steel Structures, 2008). However, in recent years, crack damage has been found in these rubber devices, as shown in Fig. 1, and there is concern that the seismic performance of these devices may deteriorate (D. Daimon *et al.*, 2015). These rubber devices are subjected to shear deformation due to the elongation and contraction that occurs in the structure as a result of temperature changes throughout the year. It has also been shown that rubber is degraded by ozone, heat, and ultraviolet rays. Although ozone and thermal degradation studies on rubber and rubber devices have been conducted (M. Hirohata *et al.*, 2015; T. Zheng *et al.*, 2021), the mechanism of ozone-induced crack initiation in rubber

Figure 1. Crack damage near lower steel plate of rubber damper

dampers has not been clarified. Therefore, in this study, ozone accelerated degradation tests and numerical analysis of rubber dampers used in bridges were conducted to clarify the crack initiation mechanism of ozone-induced cracks in rubber dampers.

ACCELERATED OZONE DEGRADATION TEST USING DUMBBELL SPECIMENS

In this study, specimens were prepared using a rubber compound used in rubber dampers, which were actively used after the Hyogo-ken Nanbu Earthquake and are now facing the problem of crack damage due to ozone. Based on JIS K 6251, No. 3 dumbbell specimens were prepared as shown in Fig. 2 (Japanese Industrial Standards, 2017). Then, in this study, to eliminate variations in tensile strain, three dumbbell specimens were simultaneously tested using the stretching apparatus shown in Fig. 3.

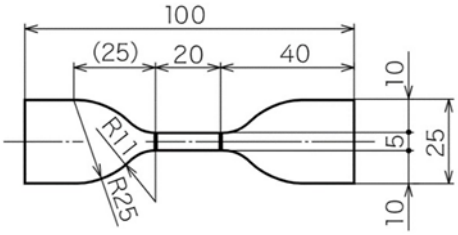

Figure 2. No. 3 Dumbbell specimen (mm)

Figure 3. Stretching apparatus

In this study, ozone accelerated degradation tests were conducted using the testing machine shown in Fig. 4. The ozone concentration and temperature in this ozone degradation test were 50 pphm and 40°C, respectively. One cycle was conducted for 2 hours in this test. Fourteen cases were tested with tensile strain increased by 10% from 20% to 150% in increments of 10%.

Figure 4. Ozone accelerated deterioration testing machine

Cracks were evaluated based on JIS K 6259 using a combination of the number of cracks, crack size and depth shown in Table 1 (Japanese Industrial Standards, 2004). As an example, if the number of cracks is small and the size and depth of the cracks are visible to the naked eye, the evaluation is given as A-2.

Table 1. List of crack ratings

Number of cracks	Crack size, depth
A: Few cracks B: Many cracks C: No cracks	1: Items that are not visible to the naked eye but can be seen with a 10x magnifying glass. 2: Visible to the naked eye 3: Crack depth is less than 1 mm 4: Crack depth between 1 mm and 3 mm Likely to cause a crack or amputation greater than 5.3 mm

As shown in Fig. 5, no cracks were observed in cases with tensile strains lower than 60%. However, slight crack initiation was observed in the 70% and 80% tensile strain cases, and similar cracks were observed in the higher strain cases. In particular, as shown in Fig. 6, crack propagation was observed for cases with tensile strains of 90% and higher. As shown in Fig. 7, the crack depth and the number of cracks tended to increase at higher tensile strains, such as 150% tensile strain. In the case of crack initiation, it was also observed that smaller cracks merged with each other over time, resulting in the initiation of larger cracks.

The following is a summary of the ozone accelerated degradation tests. Crack initiation was observed in cases where the tensile strain was greater than 70%. In particular, it was confirmed that in the case of cracks with tensile strains of more than 90%, further propagation was observed after the cracks appeared.

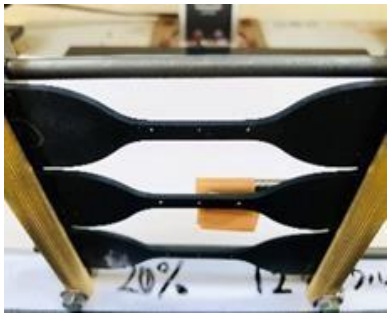

Figure 5. Strain 20%
(Rank: No cracks)

Figure 6. Strain 90%
(Rank: B-2)

Figure 7. Strain 150%
(Rank: C-4)

NUMERICAL ANALYSIS OF RUBBER DAMPER

Ozone accelerated degradation tests showed that tensile strain affects crack initiation. Therefore, the tensile strain in the rubber coating of the rubber damper was numerically analyzed. In this analysis, the rubber damper installed on the urban expressway shown in Fig. 8 was used as the analysis target. This rubber damper has a laminated structure consisting of six layers of 12 mm thick rubber and five layers of 3 mm thick internal steel plates. The general-purpose finite element analysis program ABAQUS was used in this analysis. A half model of the rubber damper shown in Fig. 9 was generated in this analysis. In this analytical model, solid elements (C3D8RH) were used for both the rubber layers and the inner steel plates. Young's modulus and Poisson's ratio of the steel used in this analysis were 2.1E05MPa and 0.3, respectively. The Ogden model of the strain energy function shown in Equation (1) was used for the rubber material as superelastic.

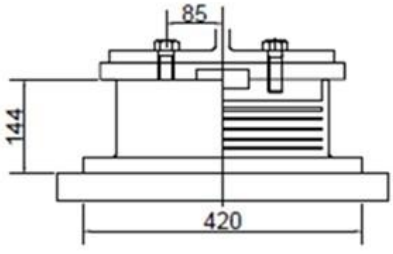

Figure 8. Rubber damper (unit: mm)

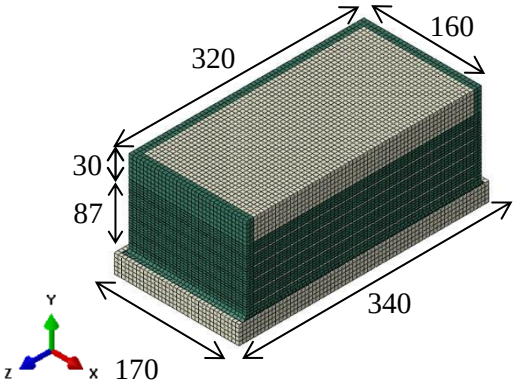

Figure 9. Analysis model (1/2 model, Unit: mm)

$$W = \sum_{n=1}^{N} \frac{\mu_n}{\alpha_n} \left({\lambda_1}^{\alpha_n} + {\lambda_2}^{\alpha_n} + {\lambda_3}^{\alpha_n} - 3 \right) \quad (1)$$

$\lambda_i (i = 1,2,3)$: Elongation ratio in each direction

The parameters of the Ogden model used in this analysis are listed in Table 2. These parameters were obtained from material tests on rubber. The lower steel plate of the rubber damper was kept completely fixed, and shear deformation was applied to the rubber damper by applying forced displacement to the top surface of the upper steel plate. According to the Road Bridge Bearing Handbook (Japan Road Association, 2019), the allowable shear deformation is 70% for normal conditions and 150% for wind conditions. Therefore, in the numerical analysis, the shear deformation was varied from 70% to 150% in the Z-axis direction as shown in Fig. 10. For each shear deformation, elongation strain was evaluated at the center of the width direction of the rubber damper as shown in Fig. 10.

Table 2. Ogden Model Parameters

α_n (−)		μ_n(N/mm^2)	
α_1	0.677	μ_1	-252
α_2	0.940	μ_2	123
α_3	0.435	μ_3	129

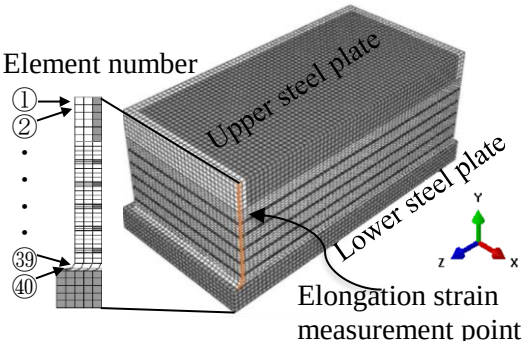

Figure 10. Elongation strain measurement point

The shear deformation of the rubber damper by numerical analysis is shown in Fig. 11. From this figure, it can be seen that elongation strain is generated in the rubber coating of the rubber damper. Therefore, the elongational strain in the rubber damper's coated rubber elements was investigated in detail.

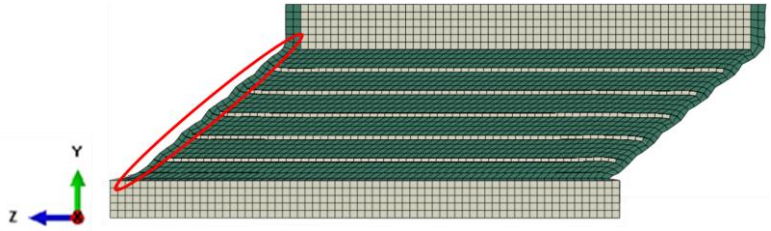

Figure 11. Shear deformation of rubber damper

The elongation strain of the coated rubber surface during shear deformation in the negative z-axis direction is shown in Table 3. Cells showing strains greater than 70% where cracks occurred during the ozone accelerated degradation test and greater than 90% where larger cracks occurred were colored. From 100% shear deformation, elongational strain greater than 70% occurred in the rubber near the lower steel plate and near the inner steel plate. As shear deformation increased, the number of elements with elongational strain greater than 70% increased, and some elements had elongational strain greater than 90%. The elongation strain of the coated rubber on the rubber damper surface during shear deformation in the positive z-axis direction is shown in Table 4. Table 3 and Table 4 show that the elongation strain on the coated rubber on the surface of the rubber damper under shear deformation in the positive and negative directions of the z-axis is different.

In the ozone accelerated degradation test, crack initiation was observed at 70% elongational strain, and crack propagation was observed at elongational strains above 90%. Numerical results indicate that shear deformation of the rubber damper causes elongation strain of more than 70% in the rubber coating on the surface of the rubber damper. The results of ozone accelerated degradation tests and numerical analysis indicate that ozone degradation may cause cracks in the rubber damper surface coating.

Table 3. Elongation strain during shear deformation in the negative Z-axis direction

	Shear deformation			
Element number	100%	130%	140%	150%
㉑ (Rubber)	27.97	47.02	54.39	62.24
㉒ (Rubber)	38.56	59.55	67.38	75.47
㉓ (Upper rubber near the inner steel plate)	40.97	60.46	66.80	72.80
㉔ (Lower rubber near the inner steel plate)	35.18	48.42	52.39	56.04
㉕ (Rubber)	18.26	25.10	27.41	30.35
㉖ (Rubber)	32.84	54.81	62.23	69.43
㉗ (Rubber)	32.26	51.40	58.61	66.14
㉘ (Rubber)	43.81	64.92	72.53	80.25
㉙ (Upper rubber near the inner steel plate)	45.65	64.91	70.84	76.24
㉚ (Lower rubber near the inner steel plate)	37.66	50.50	54.27	57.69
㉛ (Rubber)	25.99	38.17	43.35	49.23
㉜ (Rubber)	39.44	59.29	65.88	72.53
㉝ (Rubber)	42.04	61.66	68.72	75.98
㉞ (Rubber)	55.12	76.84	84.04	91.39
㉟ (Upper rubber near the inner steel plate)	52.53	71.11	76.55	81.55
㊱ (Lower rubber near the inner steel plate)	43.67	59.99	65.63	70.22
㊲ (Rubber)	47.36	65.33	71.57	78.01
㊳ (Rubber)	55.27	75.57	82.50	89.55
㊴ (Fillet)	74.13	97.16	104.79	112.41
㊵ (Fillet)	41.24	52.17	55.64	59.01

Table 4. Elongation strain during shear deformation in the positive Z-axis direction

	Shear deformation			
Element number	100%	130%	140%	150%
⑦ (Rubber)	39.71	53.98	59.51	65.59
⑧ (Rubber)	28.04	45.63	52.85	60.80
⑨ (Rubber)	31.72	50.74	57.54	64.70
⑩ (Rubber)	15.80	20.64	23.32	26.90
⑪ (Upper rubber near the inner steel plate)	35.48	47.08	50.52	53.81
⑫ (Lower rubber near the inner steel plate)	40.37	57.69	63.41	69.37
⑬ (Rubber)	37.68	56.49	63.76	71.50
⑭ (Rubber)	27.92	45.89	52.86	60.41
⑮ (Rubber)	28.72	49.60	57.26	65.12
⑯ (Rubber)	15.79	22.41	25.17	28.58
⑰ (Upper rubber near the inner steel plate)	33.99	46.43	49.97	53.12
⑱ (Lower rubber near the inner steel plate)	39.14	57.69	63.62	69.23
⑲ (Rubber)	36.45	56.54	64.13	72.10
⑳ (Rubber)	26.61	45.06	52.12	59.61

CONCLUSIONS

In order to elucidate the mechanism of this crack initiation, this study conducted an accelerated ozone degradation test of rubber and numerical analysis of rubber dampers. In the ozone accelerated degradation test, crack initiation was observed at tensile strains above 70%, and crack propagation was observed at tensile strains above 90%. Numerical results indicate that shear deformation of the rubber damper causes elongation strain of more than 70% in the rubber coating on the surface of the rubber damper. It was found that shear deformation causes elongation strain in the rubber coating of rubber dampers. It should be noted that rubber dampers subjected to shear deformation may crack due to ozone degradation.

REFERENCES

Editorial Committee for the Report on the Hanshin-Awaji Earthquake Disaster (1997). Report on the Hanshin-Awaji Earthquake Disaster, Japan Society of Civil Engineers.

D. Daimon, H. Nakayama, A. Mizutani, S. Hayashida, M. Suzuki and Y. Goto (2015). “Confirmation test of seismic performance of rubber damper (HDR-S) damaged by aging and discussion a,” *Proceedings of the 16th Symposium on Performance-based Seismic Design Method for Bridges*, Japan Society of Civil Engineers, 487-492.

Japan Road Association (2019). Road Bridge Bearing Handbook.

JIS K 6251 (2017). "Vulcanized and thermoplastic rubbers - Determination of tensile properties," *Japanese Industrial Standards*.

JIS K 6259 (2004). "Vulcanized and thermoplastic rubbers - How to determine ozone resistance," *Japanese Industrial Standards*.

M. Hirohata, Y. Itoh and S. Wang (2015). “Crack initiation of base-isolated natural rubber bearing subjected to environmental deterioration factors and strain,” *Journal of structural engineering*, Japan Society of Civil Engineers, 302-312.

Subcommittee on Support Functions of Steel Bridges, Committee on Steel Structures (2008). Improvement and maintenance technology for bearing support system of highway bridges, Japan Society of Civil Engineers.

T. Zheng, X. Zheng, S. Zhan, J. Zhou. And S. Liao (2021). “Study on the ozone aging mechanism of Natural Rubber,” *Polymer Degradation and Stability*, **186**, 109514.

SEISMIC FRAGILITY EVALUATION FOR CROSSOVER PIPING SYSTEM OF SEISMICALLY ISOLATED APR1400 NPPS

Da-Woon Yun[1], Bub-Gyu Jeon[1], Sung-Wan Kim[1], Jae-Bong Kim[1] and Sang-Ho Lee[2]
1. Researcher, Pusan National University, Seismic Research and Test Center, Yangsan, Korea.
2. Director, Pusan National University, Seismic Research and Test Center, Yangsan, Korea.
Email: ardw818@pusan.ac.kr, bkjeon79@pusan.ac.kr, swkim09@pusan.ac.kr, kjb@pusan.ac.kr, sangho@pusan.ac.kr

ABSTRACT

An isolation system installed in a nuclear power plant (NPP) could increase seismic safety during seismic events. On the other hand, a more significant relative displacement may occur due to the isolation system. The seismic risk could be increased in the case of a crossover piping system that connects isolated and non-isolated structures. Therefore, it is necessary to consider the piping systems when evaluating the safety of isolated-NPPs. This study performed seismic fragility analysis with isolated APR1400 nuclear power plants with the main steam piping. The main steam piping is the crossover pipe connecting the isolated auxiliary building and the turbine building. The failure mode for seismic fragility analysis was defined as cracks caused by leakage. The experimental and numerical analysis results quantified the leak-through crack point as a damage index. The seismic fragility curves were suggested based on peak ground acceleration and the relative displacement between the isolated and non-isolated buildings.

Keywords: base isolation, crossover piping, fragility analysis, seismic performance

INTRODUCTION

In this study, seismic fragility analysis was performed with seismically isolated APR1400 nuclear power plants and main steam line. The main steam line is the crossover piping system connecting the base-isolated auxiliary building and the turbine building. The failure mode for seismic fragility analysis was defined as leak-through crack. Leak-through crack point was quantified as a damage index through experimental and numerical analysis results and used as a failure criterion for seismic fragility analysis. Seismic fragility curves were suggested based on PGA and Relative displacement between isolated-non isolated building.

INPUT MOTION

The crossover piping system which is connecting isolated structures and non-isolated structure could be damaged by relative displacement. Therefore, this paper conducted seismic response analysis of isolated structure and relative displacement was calculated. A seismic responses of isolated structure is dominant by isolatory behavior, therefore an upper structure was simplified to a point-mass with 2 degree of freedom in two directions (x, y). A seismic response analyses were performed using the Opensees program (Eem *et al*., 2021).

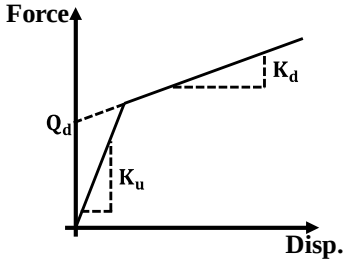

Parameters	Values
K_{eff}	2939.72 MN/m
K_u	19620.51 MN/m
K_d	1962.05 MN/m
Q_d	329.43 Mn

Figure 1. Mechanical properties of the isolation system.

The target NPP is APR1400 which is a Korean standard NPP. It was assumed that the isolation system was applied to nuclear island which is the foundation of the containment and auxiliary buildings. It was assumed that the isolation system has bilinear characteristics as shown in Fig. 1. The isolation system had an effective period of 2.5 sec and a damping ratio of 20% for a PGA of 0.5 g as design levels.

Input earthquakes were modified to satisfy the response spectrum of Reg. Guide 1.60 using the RSPmatch program, with the seismic records provided by the Pacific Earthquake Engineering Research Center (PEER). The input earthquake was composed of a total of 30 sets from EQ1 to EQ30 in horizontal bi-directions (x, y), and artificial earthquakes were generated in units of 0.5 g from 1.0 g to 3.0 g with PGA level. Fig. 3 shows a response spectrum for each direction of the generated input earthquake.

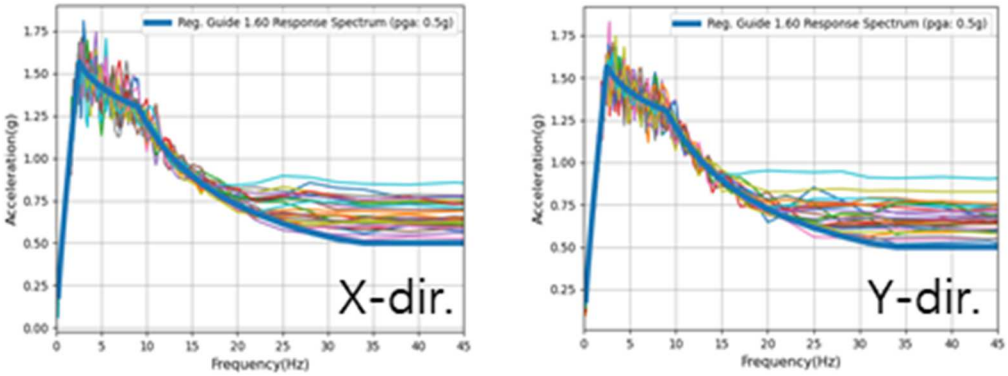

Figure 2. Response spectrums.

SEISMIC RESPONSE ANALYSIS

In this paper, the crossover piping system is a main steam line with multiply supported and arranged by an auxiliary building on the isolated APR1400 NPP nuclear island and a turbine building which is a non-isolated structure. A finite element model of the piping system is modeled using ABAQUS 6.14 (Dassault systems, 2020). Fig. 3 shows the crossover piping system which is the main steam line of APR1400 NPP. The material of pipe is assumed to be carbon steel SA106 and Grade B of ASME B36.10M, which are commonly used in NPPs.

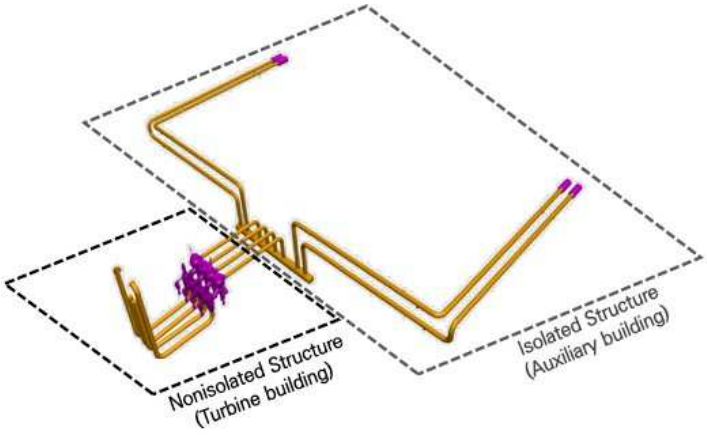

Figure 3. Main steam line of isolated APR1400 NPP.

The finite element model of connection pipes was modeled using the shell element, so that the effect of elliptical deformation of pipes could be considered. Nonlinear seismic response analysis was performed by the direct integration method while applying pressure inside the crossover piping system and maintaining the stress caused by internal pressure. In consideration of the reliability and convergence of the analysis, the input earthquake was used as input displacement, and the stress and strain in the circumferential direction were obtained from elbow's crown in Fig. 4.

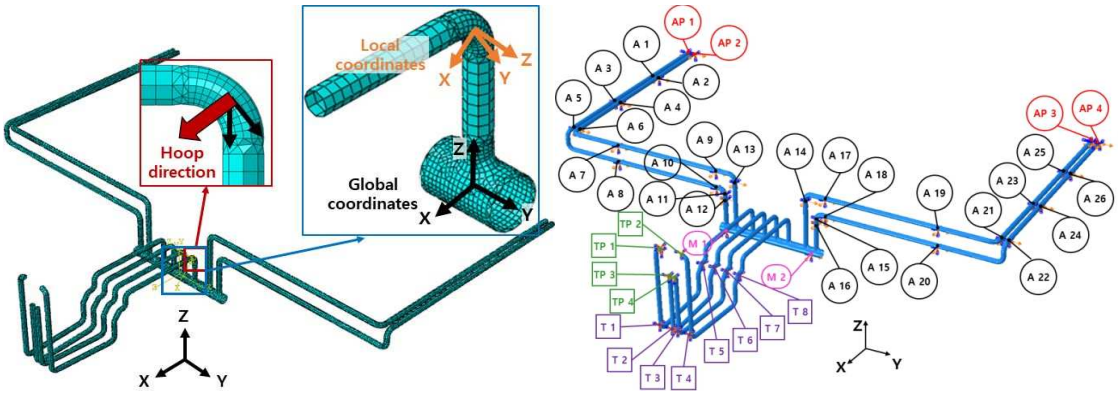

Figure 4. Finite element model of MS line.

FAILURE CRITERIA

The actual failure to the pipe observed by the test is leakage-through cracks. Therefore, in this paper, leakage-through cracks, which can cause serious damage such as loss of function of pipes and radiation leakage, were defined as failure. In general, failure to pipe elements under repeated large dynamic loading such as a seismic load is LCF(low cycle fatigue failure) (Takahashi *et al*., 2009). In a previous study, the failure tests by in-plane cyclic loading were conducted on the elbow of carbon steel pipe. As a result, failure of pipe by LCF could be quantified by using the damage index. Therefore, in this paper, damage index was used for failure criteria of seismic fragility analysis was damage index for leakage (Kim *et al*., 2019), It is a 35.25.

PERFORMANCE EVALUATION

Fig. 5 shows the damage index distribution. When MRD is used as a seismic intensity, the maximum response is dispersed according to the size of MRD of each input ground motion as shown in Fig 5. The larger the size of PGA, the wider the distribution of MRD and damage index. In particular, even if the size of the PGA is small, the size of the MRD and the value of the damage index may be larger. For the design of isolation system of NPP, it is necessary to calculate the probability of damage of crossover piping system. Here, MRD is the maximum relative displacements between isolation-non isolation building. Fig. 6 shows the fragility curve prepared using MRD as seismic intensity. The MRD with a 5% probability of damage is 1156 mm, and the median of the seismic fragility curve is 1800 mm.

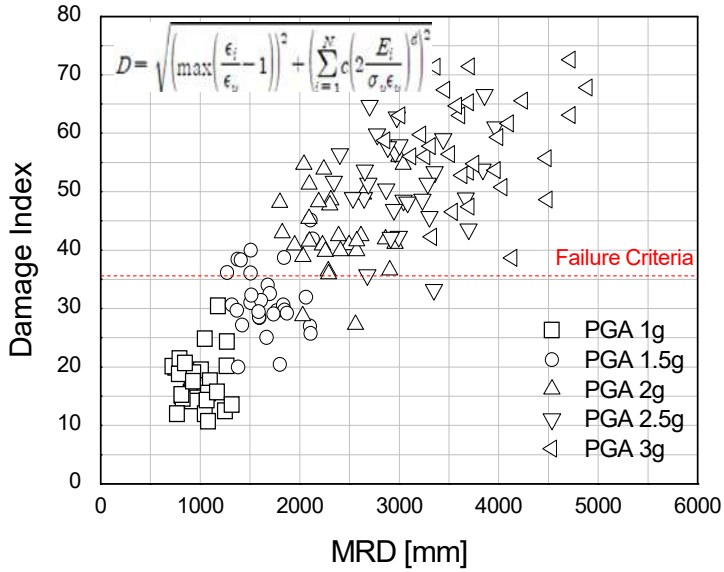

Figure 5. Damage index.

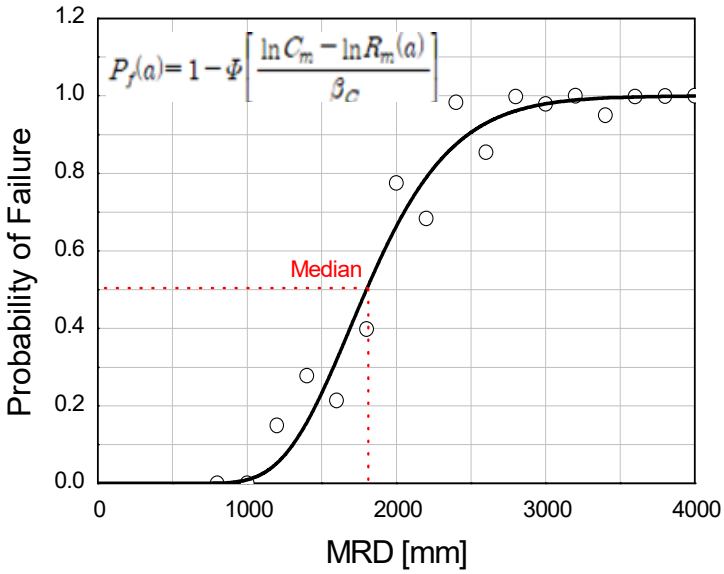

Figure 6. Fragility curve.

CONCLUSIONS

The probability of failure to the seismically isolated pipe could be one of the considerations when designing the seismic isolator of a nuclear power plant. The results of this study can be useful for the design of isolators.

This paper performed the seismic fragility analysis targeted with the main steam line, a crossover piping system of a Korea standard nuclear power plant applied with isolation system. For the accurate seismic fragility analysis, the damage index for leakage-through cracks, which is an Actual failure, was used as the fragility criterion. As a result of nonlinear seismic response analysis, according to the size of MRD of each input ground motion, the damage indices are dispersed. The larger the size of the PGA, the wider the distribution of MRD and damage index. Even if the size of the PGA is small, the size of the MRD and the value of the damage index can be larger. It is necessary to calculate the probability of damage of crossover piping system for the design of isolation system of NPP.

ACKNOWLEDGMENTS

This work was supported by the Korea Institute of Energy Technology Evaluation and Planning (KETEP) and the Ministry of Trade, Industry & Energy (MOTIE) of the Republic of Korea (No.20217910100150).

REFERENCES

Dassault systems (2020). ABAQUS Ver. 6.14.

Eem, S.H., I.K. Choi, S.L. Cha and S.Y. Kwag (2021). “Seismic Response Correlation Coefficient for the Structures, Systems and Components of the Korean Nuclear Power Plant for Seismic Probabilistic Safety Assessment,” *Annals of Nuclear Energy*, **150**, 107759.

Kim, S.W., B.G. Jeon, D.G. Hahm and M.K. Kim (2019). “Seismic Fragility Evaluation of the Base-Isolated Nuclear Power Plant Piping System Using the Failure Criterion Based on Stress-Strain,” *Nuclear Engineering and Technology*, **51**(2), 561-572.

Takahashi, K., S. Watanabe, K. Ando, A. Hidaka, M. Hisatsune and K. Miyazaki (2009). “Low Cycle Fatigue Behaviors of Elbow Pipe with Local Wall Thinning,” *Nuclear Engineering and Design*, **239**(12), 2719-2727.

PHASE CONTROL ACTIVE TUNED MASS DAMPER FOR STRUCTURAL VIBRATION MITIGATION

Yong-An Lai[1], Wei-Chen Luo[2] and Han-Tzuo Lin[2]
1. Assistant Professor, Department of Civil Engineering, National Central University, Taoyuan, Taiwan, R.O.C.
2. Graduated Student, Department of Civil Engineering, National Central University, Taoyuan, Taiwan, R.O.C.
Email: laiyongan@ncu.edu.tw, weichen.luo@g.ncu.edu.tw, 110322096@cc.ncu.edu.tw

ABSTRACT

The phase control active tuned mass damper (PC-ATMD) is developed by achieving PC-ATMD 90-degree phase lag of structure, so that the maximum power flow of PC-ATMD can be realized. By utilizing the ATMD velocity relative to structure and structural displacement or absolute acceleration feedback, two PC-ATMD are thus developed individually as denoted as PCD-ATMD or PCA-ATMD, respectively. The control algorithm of PC-ATMD is smooth, proportional and full-state system measurement or estimation is not required. The optimal control gains of PCD-ATMD or PCA-ATMD can be determined by direct output feedback optimization method. A structure implemented with PC-ATMDs subjected to earthquakes are investigated and verified by numerical simulations and shaking table experiments. The results indicate that after implemented with the PCD-ATMD or PCA-ATMD, the peak displacement and absolute acceleration of the primary structure are both well suppressed. Moreover, the PCD-ATMD has comparable effectiveness with LQR control, while the PCA-ATMD is only a few less performance but more feasible to apply in tall building structure.

Keywords: active tuned mass damper; phase control; structural control; direct output feedback; seismic excitation; shaking table experiment

INTRODUCTION

The active tuned mass damper (ATMD) is an active structural vibration control device, as a substructure system assembled by mass, damping, stiffness and actuator. Since Chang and Soong (1980) proposed the idea of active control technology incorporated with TMD and numerically investigated the feasibility of the ATMD, the superior performance of ATMD is attracted interest and attention for many scholars including Yang (1987), Loh and Chao (1996), Nagashima (2001), Mitchell *et al*.,(2012). Although the ATMD exhibits excellent performance to suppress the structural vibration than the passive TMD, the issues arising in ATMD, such as the need of high instant power consumptions and equipment maintaining, prevent their widespread use in past decades. However, due to the progress of the control technology, the above mentioned issues is no longer an unsolvable subject especially for ATMD applied in full-scaled building structure (Saaed *et al*.,(2013) and Lai *et al*.,(2022)).

In this paper, the phase control active tuned mass damper (PC-ATMD) is developed. The essential of the proposed active phase control algorithm is to minimize the trajectory error when ATMD is out of 90-degree phase lag of the structure. According to different utilized signals feedback by the main structure, the PC-ATMD can be separated as phase control displacement-feedback active tuned mass damper (PCD-ATMD) and phase control acceleration-feedback active tuned mass damper (PCA-ATMD). For the PCD-ATMD, control force is calculated by using the structural displacement and ATMD relative velocity feedback. On the other side, the PCA-ATMD control force is calculated by using the structural absolute acceleration and ATMD relative velocity feedback. The optimal control gains of PCD-ATMD and PCA-ATMD can be determined by direct output feedback method. A shear building structure implemented with PC-ATMDs subjected to earthquake are investigated to verify the effectiveness of structural vibration mitigation. The feasibility of the PC-ATMDs are examined by numerical simulations and shaking table experiments. The performance of PC-ATMDs is also assessed through comparing with a traditional linear quadratic designed ATMD (LQR-ATMD).

MODELING OF SDOF STRUCTURE WITH ATMD

For a SDOF structure implemented with a ATMD, as shown in Fig. 1, the equation of motion of the system is:

$$\mathbf{M}\ddot{\mathbf{x}}(t)+\mathbf{C}\dot{\mathbf{x}}(t)+\mathbf{K}\mathbf{x}(t)=\mathbf{b}u(t)-\mathbf{M}\mathbf{1}\ddot{x}_g(t) \tag{1}$$

where $\mathbf{x}(t)=\begin{bmatrix}x_d(t)\\x_s(t)\end{bmatrix}$, $x_d(t)$ is the ATMD displacement and $x_s(t)$ is the structure displacement; $\mathbf{M}=\begin{bmatrix}m_d+m_i & -m_i\\-m_i & m_i+m_s\end{bmatrix}$ is the mass matrix, m_d and m_i are the mass and inerter of the ATMD, respectively, as well as m_s is the mass of the SDOF structure; $\mathbf{C}=\begin{bmatrix}c_d & -c_d\\-c_d & c_d+c_s\end{bmatrix}$ is the damping matrix, c_d is the damping coefficient of ATMD and c_s is the damping coefficient of structure; $\mathbf{K}=\begin{bmatrix}k_d & -k_d\\-k_d & k_d+k_s\end{bmatrix}$ is the stiffness matrix, k_d and k_s are the stiffness of ATMD and structure, respectively. $\mathbf{b}=\begin{bmatrix}-1\\1\end{bmatrix}$ is active control force location vector. $u(t)$ is the active control force. $\mathbf{1}=\begin{bmatrix}1\\1\end{bmatrix}$ is base excitation location vector and $\ddot{x}_g(t)$ is the base acceleration.

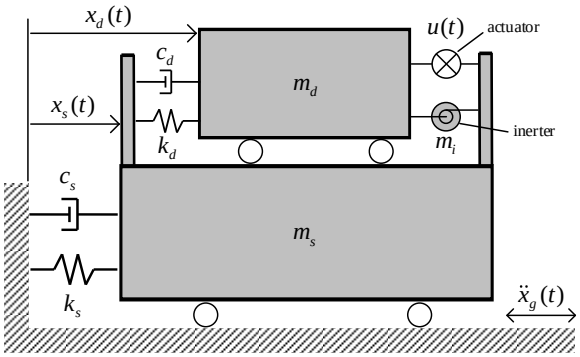

Figure 1. The model of SDOF structure implemented with a AMD

Eq. 1 can be transferred to a first-order state-space equation:

$$\dot{\mathbf{z}}(t)=\mathbf{A}\mathbf{z}(t)+\mathbf{B}u(t)+\mathbf{E}\ddot{x}_g(t) \tag{2}$$

where $\mathbf{z}(t)=\begin{bmatrix}\mathbf{x}(t)\\\dot{\mathbf{x}}(t)\end{bmatrix}$ is the state vector of the system; $\mathbf{A}=\begin{bmatrix}\mathbf{0} & \mathbf{I}\\-\mathbf{M}^{-1}\mathbf{K} & -\mathbf{M}^{-1}\mathbf{C}\end{bmatrix}$ is the system matrix; $\mathbf{B}=\begin{bmatrix}\mathbf{0}\\\mathbf{M}^{-1}\mathbf{b}\end{bmatrix}$ is the state-space control force location vector. $\mathbf{E}=\begin{bmatrix}\mathbf{0}\\-\mathbf{1}\end{bmatrix}$ is the state-space external excitation location vector.

ACTIVE PHASE CONTROL ALGORITHM

Since Soong and Dargush (1997) proposed the power flow theory – a passive TMD can exert the best performance to mitigate structural vibration when the passive TMD is at 90° phase lag relative to the primary structure. The phase issue of the TMD is been carrying out. However, the passive TMD can only achieve the 90-degree phase lag precisely when the external excitation is resonance with the natural frequency of the main structure. Therefore, the efficiency of passive TMD is limited in some excitation

cases. In order to exert the maximum performance of TMD system, the active phase control algorithm is proposed to regulate ATMD phase relative to the structure by applying active control force.

Phase control algorithm for PCD-ATMD

For a vibrating object, the object velocity is 90-degree phase lead to the displacement. Therefore, if a TMD is just 90-degree phase lag of the structure, the TMD relative velocity (relative to the structure) is just the same phase (zero phase difference) with structure displacement (relative to base) as shown in Fig. 2.

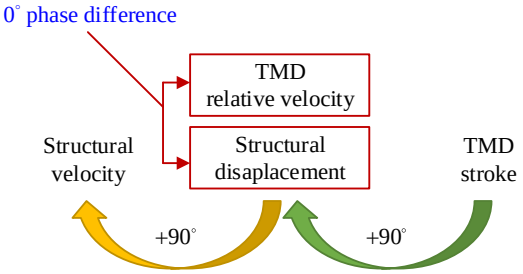

Figure 2. Phase relationship of TMD relative velocity and structural displacement when TMD is just 90-degree phase lag of the structure.

Consequently, as shown in Fig. 2, if a TMD is just 90-degree phase lag of the structure, the TMD relative velocity and structural displacement should be observed as only different in amplitude:

$$\dot{x}_d(t) - \dot{x}_s(t) = g_d x_s(t) \tag{3}$$

where g_d is the amplitude ratio of TMD relative velocity to structural displacement. If the TMD is not just 90-degree phase lag of structure, the difference of TMD relative velocity and structure displacement will have a trajectory error $e_d(t)$:

$$e_d(t) = [\dot{x}_d(t) - \dot{x}_s(t)] - g_d x_s(t) \tag{4}$$

he trajectory error in Eq. 4 can be used for representing the phase error because of larger phase error resulting in larger trajectory error. So the active phase control force of PCD-ATMD is now designed as:

$$u(t) = G_d e_d(t) = G_d[\dot{x}_d(t) - \dot{x}_s(t)] - G_d g_d x_s(t) \tag{5}$$

where G_d is the gain parameter of the active control force. The design purpose of Eq. 5 is that if the trajectory error becomes larger, then the control force is also larger to reduce the trajectory error by negative feedback. Note that, in the phase control algorithm, the measurement is only the PCD-ATMD relative velocity and structure displacement (where the TMD installed floor). The full-state feedback of the system is not required. In order to optimal design the control gains, by Eq. 5, the control force can be further rearranged as:

$$u(t) = G_d e_d(t) = \mathbf{G}_d \mathbf{D}_d \mathbf{z}(t) \tag{6}$$

where $\mathbf{G}_d = \begin{bmatrix} G_1 & G_2 \end{bmatrix} = \begin{bmatrix} G_d & -G_d g_d \end{bmatrix}$ is the gain matrix for structural displacement feedback phase control force; $\mathbf{D}_d = \begin{bmatrix} 0 & 0 & 1 & -1 \\ 0 & 1 & 0 & 0 \end{bmatrix}$ is the corresponding local output matrix. In Eq. 6, because the desired phase control force $u(t)$ is actually designed as proportional to the system state, the optimal gain matrix $\mathbf{G}_d = \begin{bmatrix} G_1 & G_2 \end{bmatrix}$ can be conducted by the linear quadratic regulator with direct output

feedback optimization (Lai *et al*.,(2022)). Thus, after the gain matrix $\mathbf{G}_d$ is optimized by direct output feedback method, the optimal design of the gain parameter G_d and amplitude ratio g_d of PCD-ATMD can then be obtained.

Phase control algorithm for PCA-ATMD

For tall buildings, the structural displacement (relative to ground) is not easy to measure. Moreover, the structural absolute acceleration is almost just opposite phase (180-degree phase difference) of the structural displacement as shown in Fig. 3.

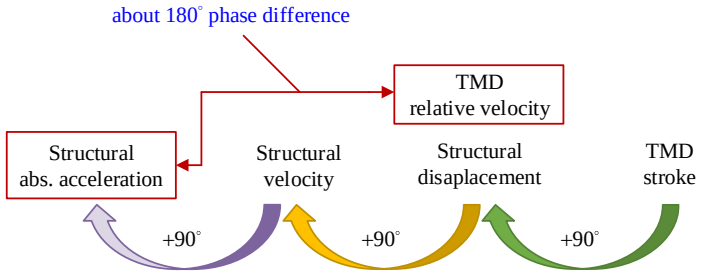

Figure 3. Phase relationship of TMD relative velocity and structural absolute acceleration when in situation of maximum power flow.

As shown in Fig. 3, the structural absolute acceleration with negative sign can be used to replace the displacement signals. Thus, if a TMD is just 90-degree phase lag of the structure, the difference of TMD relative velocity and structural absolute acceleration should satisfy the follows:

$$\dot{x}_{\mathrm{d}}(t)-\dot{x}_{\mathrm{s}}(t)=-g_a\ddot{x}_s^t(t) \tag{7}$$

where g_a is the amplitude ratio of TMD relative velocity to structural absolute acceleration. If the TMD is not in the right phase relative to the structure, the difference of TMD relative velocity and structural absolute acceleration will also have a trajectory error $e_a(t)$:

$$e_a(t)=[\dot{x}_d(t)-\dot{x}_s(t)]+g_a\ddot{x}_s^t(t) \tag{8}$$

So the active phase control force of PCA-ATMD is now designed as:

$$u(t)=G_a e_a(t)=G_a[\dot{x}_d(t)-\dot{x}_s(t)]+G_a g_a\ddot{x}_s^t(t) \tag{9}$$

where G_a is the gain parameter of the active phase control force by using structural absolute acceleration feedback. Substitute Eq. 2 into Eq.9, the phase control force can be further rearranged as:

$$u(t)=G_a e_a(t)=\mathbf{G}_a\mathbf{D}_a\mathbf{z}(t) \tag{10}$$

where $\mathbf{G}_a=\left[\frac{G_a}{1-G_a g_a\mathbf{d}_{sa}\mathbf{B}}\quad\frac{G_a}{1-G_a g_a\mathbf{d}_{sa}\mathbf{B}}\right]$ is the gain matrix for structural absolute acceleration feedback phase control force which can also be optimal designed by direct output feedback optimization; $\mathbf{D}_a=\begin{bmatrix}\mathbf{d}_{rv}\\ \mathbf{d}_{sa}\mathbf{A}\end{bmatrix}$ is the corresponding location output matrix; $\mathbf{d}_{rv}=\begin{bmatrix}0 & 0 & 1 & -1\end{bmatrix}$ is the TMD relative-velocity output vector and $\mathbf{d}_{sa}=\begin{bmatrix}0 & 0 & 0 & 1\end{bmatrix}$ is the output vector for structural absolute acceleration.

Note that the term $\mathbf{d}_{sa}\mathbf{B}$ is a scaler, and $\mathbf{d}_{sa}\mathbf{B} = \frac{m_d}{\det(\mathbf{M})}$. The close loop control flow chat of PCD-ATMD and PCA-ATMD is shown in Fig. 4.

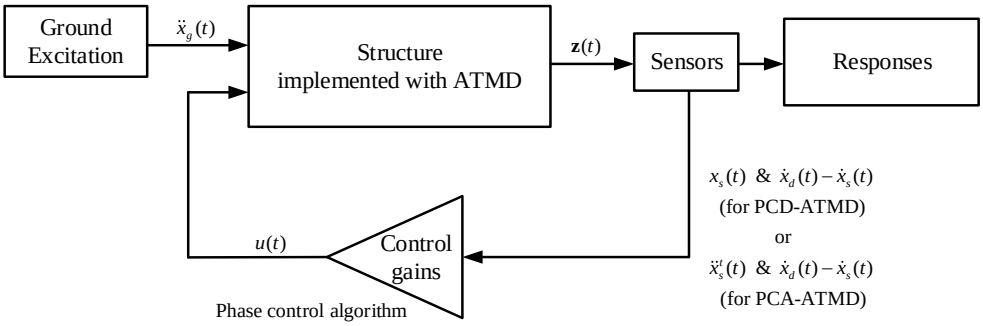

Figure 4. Control flow chat of PCD-ATMD and PCA-ATMD.

NUMERICAL SIMULATION AND EXPERIMENTAL RESULTS

A one-story shear building specimen as shown in Fig. 5 is using as a SDOF benchmark structure. The structure is made by aluminum 6061 with structural mass is 45.0 kg. The natural frequency and damping ratio of the structure is 0.925 Hz and 0.003, respectively. A motor-driven ball screw linear guider is used as the ATMD in this demonstration. The motor-driven linear guider consists of a moving mass, a ball-screw guider, and a AC-driven motor to provide a control forces is shown in Fig. 6. The SDOF structure and ATMD parameters are list in Table 1.

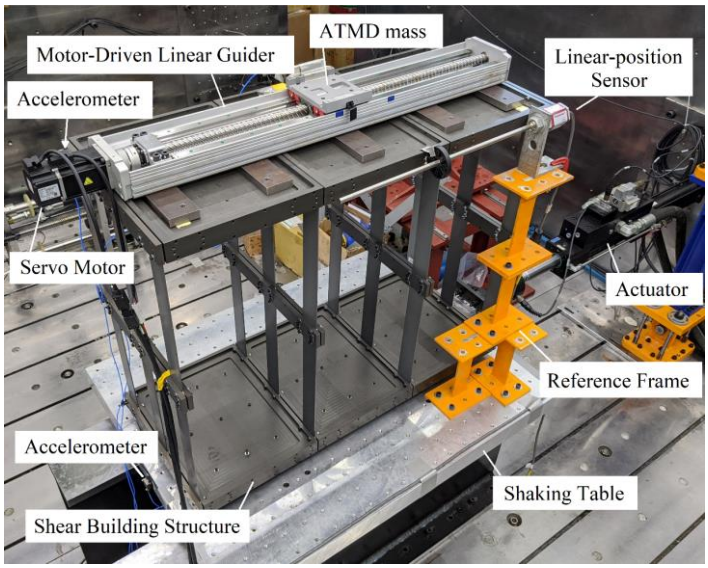

Figure 5. Configuration of the experimental specimen

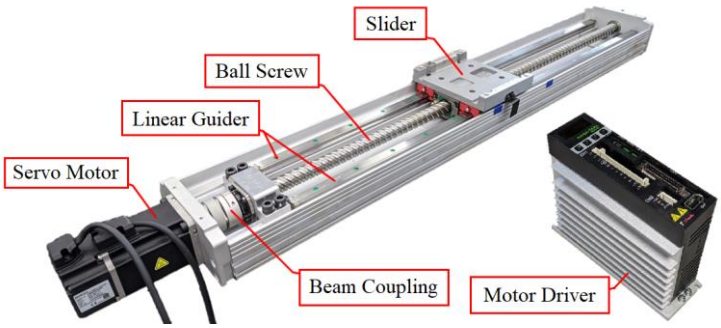

Figure 6. Mechanism of the motor-driven ball screw linear guider

Table 1. SDOF shear building structure and ATMD parameters

Mass (kg)	45.0
Stiffness (N/m)	1521.4
Frequency (Hz)	0.9254
Damping ratio	0.003
Damping coefficient (N-sec/m)	1.57
ATMD mass ratio (%)	3.11
ATMD mass (kg)	1.40
ATMD inerter (kg)	3.73
ATMD imitate stiffness (N/m)	173.5
ATMD damping coefficient (N-s/m)	11.94

the optimal control gains of PCD-ATMD are $G_d^{opt} = 8.0224$ and $g_d^{opt} = 99.6576$. The optimal control gains of PCA-ATMD are $G_a^{opt} = 5.5805$ and $g_a^{opt} = 3.7105$. For comparison, the optimal gain matrix of the LQR-ATMD is designed $G_{lqr} = [0.0000 \quad -799.2390 \quad 8.0077 \quad -8.3263]$

Frequency Response Function

The performance of controlled active tuned mass damper is herein investigated by frequency response functions for the cases of: (1) the SDOF structure without using ATMD (Uncontrolled), (2) the structure with traditional LQR-ATMD, (3) the structure with PCD-ATMD, or the structure with PCA-ATMD are individually simulated when subjected to ground acceleration. The H_2 norm is also calculated for comparison.

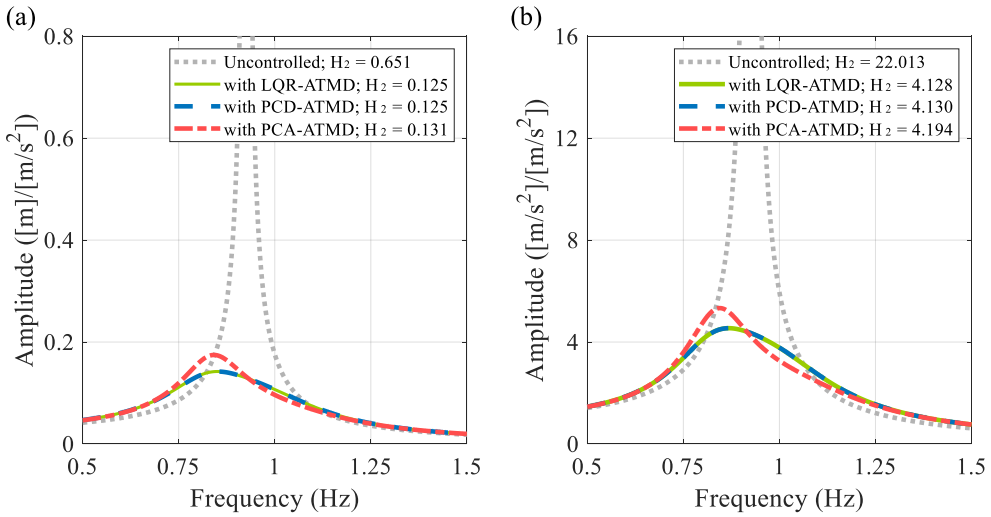

Figure 7. Frequency responses function of structure of (a) displacement and (b) absolute acceleration

The frequency response functions of the structural displacement and absolute acceleration are shown in Fig. 7(a) and Fig. 7(b), respectively. The response curves show that all of the ATMDs are well behaved to suppress the peaks of structural displacement and absolute acceleration responses, the H_2 norm of the structural responses can be reduced significantly. Moreover, using the same controller design weighting, the performance of the PCD-ATMD is almost identical with the traditional LQR-ATMD. It is also worth remarking that in Fig. 7, the PCA-ATMD performed slightly less than the LQR-ATMD to suppress structural responses using the same regulator. Therefore, the regulator of the PCA-ATMD can be appropriately adjusted to enlarge the control force to meet the desired performance.

Shaking Table Experimental Verification

The experimental results are shown in this section. The uniaxial shake table is actuated by the hydraulic actuator with force and stroke capacity of 15 kN and ±127 mm, respectively (Fig. 5). To apply the controller of the ATMD, a Micro-Box 2000 x86 based controller, developed by TeraSoft Inc., is adopted for xPC target to rapid control prototype application. The low noise and high-resolution MEMS accelerometers (3711E112G) manufactured by PCB Group Inc., with measurement range ±2g are installed on the top of the shear building structure. The Temposonics G-Series linear-position sensor (GHS0400MRB12V2), manufactured by MTS System Corporation, with a stroke capacity of 400 mm is installed on the reference frame to measure the shear building structure displacement relative to the shaking table. The incremental encoder, manufactured by HIWIN®, with a high resolution of 131072 counts/rev is installed in the AC servo motor for obtaining ATMD stroke and relative velocity.
The cases of (1) the SDOF structure without using ATMD (Uncontrolled), (2) the structure with LQR-ATMD, and (3) the structure with PCD-ATMD or PCA-ATMD are subjected to a 1940 El Centro earthquake, scaled to PGA 150 gal. The experiment results show that with the PCD-ATMD, the peak structural displacement is 4.4 cm (Fig. 8(a)), and the peak structural absolute acceleration is 216.7 gal (Fig. 8(b)). The peak displacement of applying PCD-ATMD is reduced about 53.2% and the peak absolute acceleration is reduced about 34.3% of the case of without ATMD (Uncontrolled). For the case of with PCA-ATMD, the peak structural displacement is 5.0 cm (Fig. 9(a)), and the peak structural absolute acceleration is 232.4 gal (Fig. 9(b)). The peak displacement of applying PCA-ATMD is reduced about 47.0%, and the peak absolute acceleration reduction is reduced about 29.5% of the case of without ATMD. The performance of PCD-ATMD and PCA-ATMD are similar with traditional LQR-ATMD. The detail of SDOF shear building structure and PCA-ATMD peak responses are listed in Table 2.

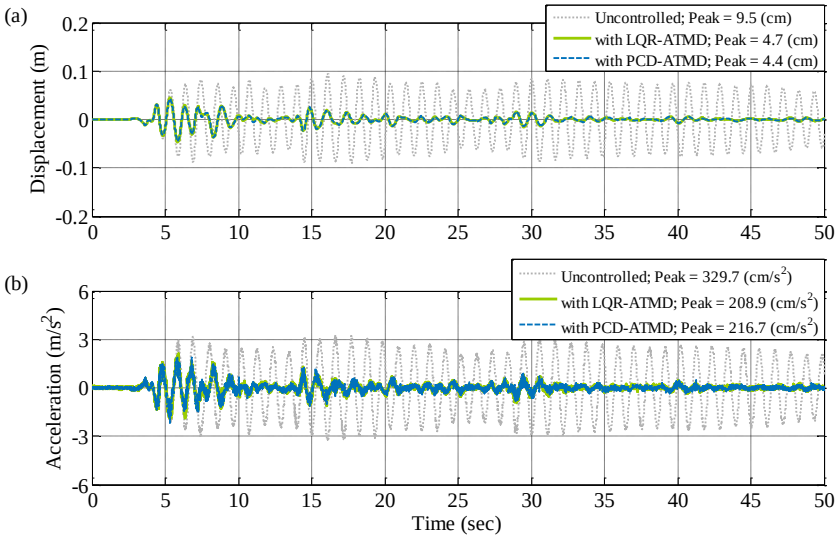

Figure 8. Structural responses with PCD-ATMD: (a) displacement and (b) absolute acceleration

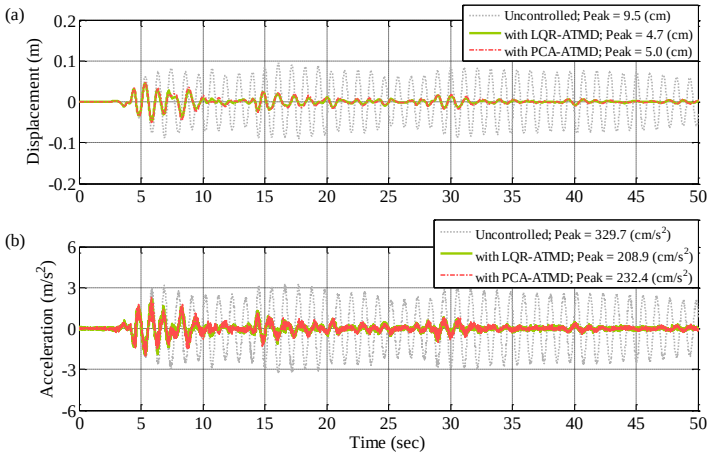

Figure 9. Structural responses with PCA-ATMD: (a) displacement and (b) absolute acceleration

Table 2. Experimental peak responses of structure and ATMD

	Uncontrolled	LQR-ATMD	PCD-ATMD	PCA-ATMD
Structural peak displacement (cm)	9.5	4.7	4.4	5.0
Displacement reduction ratio	--	50.6%	53.2%	47.0%
Structural peal acceleration (gal)	329.7	208.9	216.7	232.4
Acceleration reduction ratio	--	36.6%	34.3%	29.5%
ATMD stroke (cm)	--	30.4	31.2	27.9
ATMD apply force (N)	--	108.1	109.9	106.5

CONCLUSIONS

In this paper, the performance of the PCD-ATMD and the PCA-ATMD are presented. The PCD-ATMD uses the structural displacement and ATMD relative velocity signals to calculate active phase control force. In addition, the PCA-ATMD uses the structural absolute acceleration and ATMD relative velocity signals to obtain active control force. Both algorithms achieve the merit of smooth proportion and because they only use local measurements, full-state system measurement or estimation is not required. The optimal control gains of the PCD-ATMD or PCA-ATMD can be designed by the direct output feedback optimization method. The performance of the proposed PCD-ATMD and PCA-ATMD are investigated by numerical simulation and shaking table experiments. The results show that the PCD-ATMD and PCA-ATMD both exhibit good performance in suppressing structural responses. In comparison to the PCD-ATMD, the PCA-ATMD is much more feasible than the PCD-ATMD in tall building structures because absolute acceleration of structure is much easier to measure.

ACKNOWLEDGMENTS

This research was supported in part by the Ministry of Science and Technology of the Republic of China (MOST 109-2222-E-008-001-MY2). This support is greatly appreciated.

REFERENCES

Chang, J.C.H and Soong, T.T. (1980), "Structural control using active tuned mass dampers," *Journal of Engineering Mechanics*, **106**, 1091-1098.

Yang, J.N. (1987), "New optimal control algorithms for structural control," *Journal of Engineering Mechanics*, **113**, 1369-1386.

Loh, C.H. and Chao, C.H. (1996), "Effectiveness of active tuned mass damper and seismic isolation on vibration control of multi-storey building, " *Journal of Sound and Vibration*, **193**, 773-792.

Nagashima, I. (2001), "Optimal displacement feedback control law for active tuned mass damper," *Earthquake Engineering and Structural Dynamics*, **30**, 1221-1242.

Mitchell, R., Kim, Y., El-Korchi, T. and Cha, Y.J. (2012) "Wavelet-neuro-fuzzy control of hybrid building-active tuned mass damper system under seismic excitations," *Journal of Vibration and Control*, **19**, 1881-1894.

Saaed, T.E., Nikolakopoulos, G., Jonasson, J.E. and Hedlund, H. (2013), "A state-of-the-art review of structural control systems," *Journal of Vibration and Control*, **21**, 919-937.

Lai, Y.A., Luo, W.C., Huang, S.K., Yang, C.Y and Chang C.M. (2022), "Seismic control of structure with phase control active tuned mass damper," *Structural Control and Health Monitoring*, **29**(7), e2946.

Soong, T.T. and Dargush, G.F. (1997) *Passive Energy Dissipation Systems in Structural Engineering*, Wiley, New York.

(3h) Seismic performance design, evaluation and retrofit for non-structural components

EXPERIMENTAL STUDY OF GLASS-TYPE STATIC SMOKE BARRIERS BY USING LARGE-SCALE SHAKING TABLE

T. C. Lin [1] and G. C. Yao [2]

1. Assistant Researcher, Center for Architecture Performance Certification, NCKU Research and Development Foundation, Tainan City, Taiwan.
2. Professor, Dept. of Architecture, National Cheng Kung University, Tainan City, Taiwan.

Email: tclin.nckurdf@gmail.com

ABSTRACT

The glass-typed static smoke barriers usually used in public and commercial buildings in Taiwan and Japan are often damaged in major earthquakes. In the scenario of fires following earthquakes, the smoke control performance of the SHCS will be reduced and the fallen sharp glass will have the people and firefighters injured. In this study, 7 specimens subjected to a large-scale shaking table tests in the out-of-plane direction. According to the findings of the tests, a modified empirical equation to predict the natural frequency and improvement measures of the glass-typed static smoke barriers is proposed and found effective. This equation could be used to improve the seismic performance of glass-typed static smoke barriers.

Keywords: glass-type smoke barrier, shaking table test, natural frequency, seismic performance improvement

INTRODUCTION

Smoke barriers contain the movement of fire effluent inside construction works in the event of a fire and play a key role in a Smoke and Heat Control System (SHCS) (ISO, 2008). Under the aesthetics consideration, architects usually use the glass-type static smoke barriers (SSB) in commercial and public buildings in Taiwan. The SSB usually are damaged in major earthquakes in Taiwan and Japan (Yao *et al.*, 2019). In the fires following earthquakes, the performance of the SHCS may be reduced and allow smoke to spread quickly, and the glass fragments fall on the ground to obstruct the escape and rescue. This will lead to severe casualties and property damage. The seismic design guideline to assure the efficacy of the smoke leakage and fire protection performance of SSBs should be established as soon as possible. Yao (Yao *et al.*, 2019) proposed an empirical equation for 0.5m deep smoke barrier to predict the natural frequency of straight-line type as follows,

$$f = \frac{24}{L} \tag{1}$$

where f and L are the natural frequency (Hz) and the total length of the glass-type smoke barrier (m), respectively. Furthermore, the applications of SSB in commercial and public buildings usually have a long span, different configurations, such as L-shaped, T-shaped, cross-shaped, etc., and boundary conditions. It's necessary to investigate the effect of the construction variables of the SSB related to seismic performance in advance.

EXPERIMENTAL SETUP AND PROTOCOL

To investigate the variables of the configuration layout, boundary condition, and length between support of SSB, 7 specimens are subjected to out-of-plane shaking table tests in conjunction with the exposed ceiling system (11m wide x 11m long) which were installed in accordance with ASTM E 580(ASTM, 2008) in the test frame, as Figs 1 and 2, at the Tainan Laboratory of National Center for Research on Earthquake Engineering (NCREE), Taiwan.

The construction details of the glass-type smoke barriers are demonstrated in Fig 3 and the experimental factors of the specimen are as shown in Table 1. Specimen B is the controlled one of which boundary condition is both-end restrained by silicone sealant. Specimen C and D are the experimental group of which boundary condition are one-sided unrestrained and both-sided unrestrained respectively using the silicone sealant and fireproof airtight strip. Specimen A and F are the experimental group of which boundary condition are both-sided restrained and T-conjunction at the one-fourth and the middle length of specimen using the silicone sealant.

At the beginning of the test, a white noise test was conducted to evaluate the natural frequency of the specimen. In order to excite the maximum response of the controlled specimen, the natural frequency of the controlled specimen estimated by Yao's equation is $f = 24 / 11 \fallingdotseq 2.2$ Hz. The excitation wave with the natural frequency 2.7 Hz was chosen which obtained by the sensor installed in the building at 921 earthquake in Taiwan, and the test sequence of peak acceleration which are 100 gal, 200 gal, 400 gal, 600 gal and 800 gal was carried out at the out-of-plane direction to determine the seismic performance of the specimen.

Totally 42 accelerometers, as shown in Fig 4, were located on the specific position of the test frame, ceiling system, the upper horizontal aluminum channel, and the lower edge of the glass to record the history of acceleration of the specimens.

EXPERIMENTAL RESULTS AND ANALYSIS

In Table 2, a summary of damage observations at different excitation levels is given. In the shaking table test, there are three damage phenomena such as silicone detached, glass breakage, and ceiling tiles damaged. The glass breakage occurred at the excitation levels of 400 gal, 600 gal and 800 gal for specimen A, B and G respectively. The wire glass of specimen C and D maintained sound even when the excitation level 800 gal reached.

Table 3 shows the natural frequency of each specimen obtained by Frequency Response Function (FRF) method in accordance with the time-history acceleration record from the sensor of the lower edge of the wired glass to the upper channel of the specimen. The natural frequency of specimen B, C, and D which is the straight-lined type of specimens, are 2.2 Hz, 2.0 Hz, and 2.0 Hz respectively. The natural frequencies of the T-shaped configuration of specimen A are 6.6 Hz at the A-1 section and 3.0 Hz at A-2 section, at which the acceleration sensors are located in the middle of the three-fourth length and one-fourth length of the specimen respectively. The natural frequency of the T-shaped configuration of specimen G is 3.8 Hz.

Obviously, the natural frequency of the A-1 section (3.0 Hz) of specimen A is closer to the frequency of the excitation wave (2.7Hz) than specimen B (2.2Hz). The resonance effect made the damage phenomena of specimen A occurr prior to all specimens. The fireproof airtight strip will improve the seismic performance of SSB than silicone sealant.

Fig 1. Test Frame

Fig 2. Specimen installed under the exposed ceiling

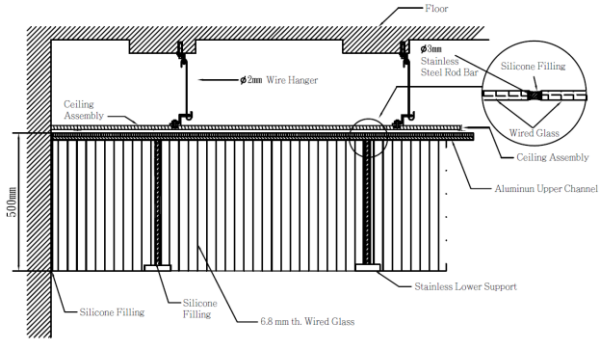

Fig 3. Elevation of the glass-typed smoke barrier[2]

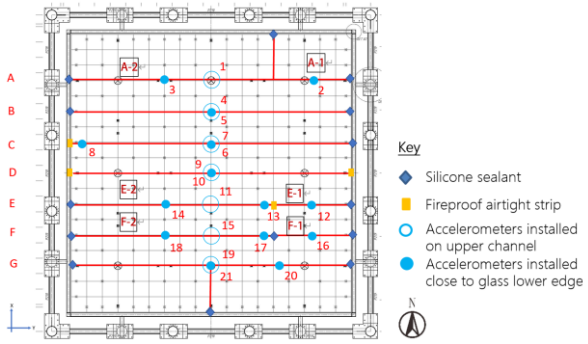

Fig 4. Specimens and accelerometers layout on the test frame

Table 1 Experimental factors and variables

	Configuration		Gap treatment		Effective Length			
No	Straight-lined	T-shaped	Silicone Sealant	Fireproof Airtight Strip	L_0	$L_0/4$	$L_0/2$	$3L_0/4$
A		●	●			●		●
B	●		●(@both end)		●			
C	●		●(@east end)	●(@west end)	●			
D	●			●(@both end)	●			
E	●		●(@both end			●		●
F	●		●(@both end)	●(@L0/4 gap))		●		●
G		●	●				●	

Table 2 Test observations in shaking table test

Test #	Accel. (gal)	Observation
1	100	No apparent failure
2	200	Silicone detached at west end of specimen A.
3	400	Glass breakage at the west end of specimen A. Silicone detached at the west end of specimen A, $L_0/4$ of specimen F and T-shaped conjunction of specimen G.
4	600	Glass breakage at middle-span of specimen A and at the west end of specimen B. Silicone detached at the west end of specimen E, specimen F and east end of specimen G. Ceiling tiles damage at specimen E and F.
5	600	Glass breakage at the west end of specimen E.
6	800	Glass breakage at the west end of specimen G.

Table 3 Natural frequency obtained by FRF

Specimen No.	A		B	C	D	E		F		G
	A-1 section	A-2 section				E-1 section	E-2 section	F-1 section	F-2 section	
Natural Frequency (Hz)	6.6	3.0	2.2	2.0	2.0	5.4	2.2	2.2	2.2	3.8

According to the test result of the natural frequency of specimen B, it approved the empirical equation proposed by Yao (Yao *et al.*, 2019) could predict the natural frequency of the straight-lined glass-type SSB of which the boundary condition is both-end restrained. The additional assembly perpendicular to a straight-lined one which the T-shaped configuration consisted of will change the natural frequency of the straight-lined SSB. Although the straight-lined configuration specimen C of which boundary condition is one-end unrestrained, the natural frequency is similar to the specimen D of which boundary condition is both-end unrestrained. It seems that as the length of the SSB is longer the natural frequency will be lower and approach to a specific boundary value. We also found that the natural frequency is independent of the total length of the SSB when the boundary condition of the SSB both-end is unrestrained. Additionally, the natural frequency is measured as 1.8 Hz by the same construction and 1.6m long specimen on the small-scale shaking table at the laboratory (Lin & Yao, 2020). Hence, the modified Yao's equation is proposed as follow (Lin, 2021),

$$f = \frac{24}{L}, \quad f \geq 1.8\text{Hz} \tag{3}$$

where f and L are the natural frequency (Hz) and the total length of the glass-type smoke barrier(m), respectively.

CONCLUSIONS

The specimens of glass-type static smoke barriers with different variables related to configuration and boundary condition were conducted on a large-scale shaking table test. According to the results of the test and analysis, there are some findings as follows,

1. A mathematical model of the glass-type static smoke barrier with both-end unrestrained was proposed. It proved when the boundary condition of SSB is with both-end unrestrained or longer enough, the natural frequency will be independent of the length of the SSB and approach to a specific value.
2. A modified empirical equation of the natural frequency of the straight-line type SSB with the both-end restrained is proposed and predicts the natural frequency of the straight-line type SSB accurately.
3. Additional assembly perpendicular to a straight-lined SSB will change the natural frequency, and the fireproof airtight strip will improve the seismic performance of SSB.

According to the investigations of major earthquakes, SSBs are usually severely damaged in public and commercial buildings. These findings could provide a safe environment for SSB by tuning its natural frequency away from the building's resonance frequency such as changing length, configurations and boundary conditions.

ACKNOWLEDGMENTS

This study was supported by the Ministry of Science and Technology, Taiwan (MOST 105-2221-E-006-031-MY3). The authors are grateful to this support.

REFERENCES

International Organization for Standardization. (2008) Smoke and heat control systems - Smoke and heat control systems (ISO 21917-1:2008).

Yao, G.C. T.C. Lin and P.A. Chen. (2019): A Study on Seismic Performance of Glass-Type Static Smoke Barriers. *Journal of Architecture* 2019; (107): 43-55.

American Society of Testing and Materials. (2008). Standard Practice for Installation of Ceiling Suspension Systems for Acoustical Tile and lay-in Panels in Areas Subject to Earthquake Ground Motions (ASTM E580/E580M-08).

Lin, T.C. and G.C. Yao. (2020): A Study on Natural Frequency and Seismic Performance Improvement of Glass-Type Static Smoke Barriers. *Journal of Architecture* 2020; (112): 83-97.

Lin, T. C. (2021). A Study on Seismic and Fire Protection Performance of Glass-Type Static Smoke Barriers (Unpublished Doctoral dissertation). National Cheng Kung University, Tainan, Taiwan.

NUMERICAL STUDY ON SEISMIC EFFECT AND RETROFIT STRATEGY OF LIQUID SLOSHING MODE IN TANKS

Wei-Hung Hsu[1], Juin-Fu Chai[2] and Fan-Ru Lin[3]

1. Assistant Researcher, National Center for Research on Earthquake Engineering, Taipei, Taiwan, R.O.C.
2. Deputy Director General and Division Director, National Center for Research on Earthquake Engineering, Taipei, Taiwan, R.O.C.
3. Associate Researcher, National Center for Research on Earthquake Engineering, Taipei, Taiwan, R.O.C.

Email: mikehsu@narlabs.org.tw, chai@narlabs.org.tw, frlin@narlabs.org.tw

ABSTRACT

Sloshing refers to any motion of liquid inside containers. The liquid must have free surface to induce this kind of hydrodynamic behavior when the containers are disturbed. The container shape also affects the motion of the free liquid surface. However, storage tanks are common containers to store various liquids, such as water, petroleum, liquefied natural gas, industrial chemicals and so on, in industry. They can be vertical or horizontal tanks with circular and rectangular shapes. In view of past failure events of storage tanks, sloshing of liquid was considered as an important factor to damage of the tanks. And sloshing of liquid inside storage tanks is often caused by earthquake; thus, the seismic capacity of the tanks becomes an important performance objective in tank design. From the failure events of storage tanks in industry, it can be observed some damage on tank roofs or at the top parts of tank walls caused by sloshing. For nuclear power plants, the liquid inside the spent fuel pool may be splashed out of the pool by sloshing. Therefore, the sloshing height of the liquid may affect tank failure mode. The reduction in sloshing height is expected to be able to mitigate damage. In this study, the numerical approach is adopted to discuss the effect of the additional installed baffle on sloshing height of liquid in tanks. From the changes of the sloshing frequencies and the sloshing heights, and seismic characteristics, the effects of the baffle on mitigating sloshing height can be figured out.

Keywords: liquid storage tank, sloshing mode, seismic retrofitting, sloshing height

INTRODUCTION

Liquid containers are very common equipment and facilities in the daily life. Most of the containers are partially filled with liquid; thus, liquid inside the containers may experience sloshing when the containers are disturbed. Liquid sloshing often occurs in moving containers, such as fuel tanks of aircraft and rocket, ballast or fuel tanks of large ships, fuel or cargo tanks of automotive vehicles, and railroad tank cars (Abramson, 1966). It also occurs in the storage tank subjected to lateral excitation, e.g., earthquake. Sloshing of liquid inside the storage tank induced by earthquake often causes catastrophic damage to tanks such as seal fire in the floating roof tanks. Damage on tank roofs or at the top parts of tank walls, which was caused by liquid sloshing due to the low frequency content of the earthquake, are common failure events of storage tanks. To mitigate damage to tanks in the earthquake events, the seismic isolation system and energy dissipation system are main seismic retrofit approaches which were discussed in many literatures. The friction pendulum system (FPS) is commonly used for base isolation of liquid storage tanks since the period of the isolation system is independent of the storage level (Panchal and Jangid, 2008; Abalı and Uçkan, 2010; Soni *et al.*, 2011). The baffles were extensively used in moving liquid containers especially in space vehicles to reduce the sloshing effects such as hydrodynamic pressure and sloshing amplitude. The effects of the baffles on liquid oscillations can be divided into changes in frequency and damping ratio of sloshing mode (Maleki and Ziyaeifar, 2007; Maleki and Ziyaeifar, 2008). For changes in frequency, this is due to changes in the effective depth and the effective movement dimension of liquid. For changes in damping ratio, this is due to energy dissipation when liquid flows through the baffles.

In this study, the numerical models of a small-scale rigid rectangular tank are built. Near-fault ground motions with pulse-like property are picked out from PEER NGA West database to be input motion of the models. The vertical rigid baffle is installed in the middle of the tank. The effect of the baffle on sloshing amplitude of liquid in tank for different ground motions are discussed by comparing analysis results.

SLOSHING FREQUENCY AND HEIGHT

According to the linear sloshing model proposed by Housner (Housner, 1957), the hydrodynamic pressure can be divided into two parts: impulsive pressure and convective pressure. The impulsive pressures are generated by the impulsive movement of the wall of the storage tank. The convective pressures are generated by the oscillation of the liquid. Housner simplified the complex sloshing behavior into an equivalent hydrodynamic model to consider pressures caused by the impulsive mode and the asymmetric convective mode. In the model, the impulsive mass M_0 is connected rigidly to the wall of the tank, and the convective mass M_n (n = 1, 3, 5,…) is spring mounted on the wall, as shown in Figure 1. In the figure, only two asymmetric modes are shown. Housner used the approximate method to derive the formula for calculating the frequency of the asymmetric convective mode in the rectangular tank, as below:

$$\omega_n^2 = \sqrt{\frac{5}{2}}\frac{g}{(l/n)}\tanh\left(\sqrt{\frac{5}{2}}\frac{h}{(l/n)}\right) \tag{1}$$

where ω_n is the nth (n = 1, 3, 5,…) convective frequency, g is the gravitational acceleration, l is the half length of the tank parallel to the shaking direction, and h is the liquid level. The formula was adopted in guidance of the Electric Power Research Institute (EPRI, 2013) to evaluate sloshing in the spent fuel pool. In the guidance, the maximum sloshing height (h_{s1}) for the fundamental sloshing mode can be estimated from:

$$h_{s1} = l(\frac{Sa}{g}) \tag{2}$$

where Sa is 0.5% damped horizontal spectral acceleration at the top of the pool wall at the fundamental frequency in the direction of motion, the low damping ratio was suggested by the guidance (EPRI, 2013). In order to account for higher sloshing modes and nonlinear sloshing effects, the theoretical sloshing height predicted by Eq. (2) may be increased by 20%. Thus, the total estimated sloshing height becomes:

$$h_s = 1.2l(\frac{Sa}{g}) \tag{3}$$

The maximum sloshing height estimated by Eqs. (2) and (3) are only for unidirectional shaking, the total sloshing height (h_{st}) for two horizontal direction (x- and y-direction) shaking can be estimated from:

$$h_{st} = [h_{sx}^2 + h_{sy}^2]^{0.5} \tag{4}$$

where h_{sx} and h_{sy} are sloshing heights due to x and y shaking, respectively.

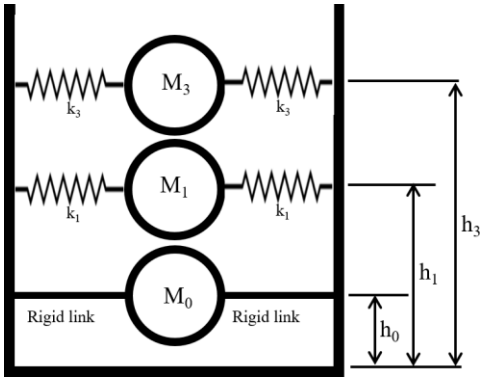

Figure 1. Illustration of hydrodynamic model provided by Housner.

NUMERICAL MODEL

In the study, the software Abaqus was adopted to simulate sloshing behavior of water in storage tank. In the numerical model, the tank, the baffle and the water are simulated by Lagragian elements. Contact element is used to transfer forces among them to consider Fluid-Structure Interaction (FSI) effect. The tank and the baffle are assumed to be rigid and the interior dimensions of the tank are 1 m in length, 0.5 m in width, and 1.5 m in height. The baffle, which is installed in the middle of the tank, does not penetrate the entire depth of the water. Figure 2 shows numerical model of small-scale rigid rectangular tanks with the water level of 0.5m. The units used in the model are shown in Table 1. In sloshing problem, the water can be considered an incompressible and inviscid fluid. Per Abaqus documentation (Dassault Systemes, 2014a), an effective method for modeling the water is to use a simple Newtonian viscous shear model and a linear U_s-U_p equation of state for the bulk response. The bulk modulus functions as a penalty parameter for the incompressible constraint. Since sloshing problems are unconfined, the bulk modulus chosen can be two or three orders of magnitude less than the actual bulk modulus and the water will still behave as an incompressible medium. The shear viscosity also acts as a penalty parameter to suppress shear modes that could tangle the mesh. The shear viscosity chosen should be small because water is inviscid. Table 2 gives material properties of the water used in the numerical model. The parameters c_0 and s in Table 2 are the linear relationship between the shock velocity, U_s, and the particle velocity, U_p, as follows (Dassault Systemes, 2014b):

$$U_s = c_0 + sU_p \tag{5}$$

Near-fault ground motions with pulse-like property are picked out from PEER NGA West database to be input motion of the numerical model. The database provides period of velocity pulse (T_p) of the Fault-normal (FN) and the Fault-parallel components of each ground motion through wavelet analysis and the period of peak spectral velocity (T_{Sv}) of the FN component of each ground motion as well. Table 3 lists information of the near-fault ground motions used in the study.

Table 1. Units used in the numerical model.

Quantity	Length	Force	Mass	Time	Stress	Energy	Density
SI (mm)	mm	N	tonne	s	MPa	mJ	tonne/mm^3

Table 2. Material properties of the water used in the numerical model.

Parameter	Density (tonne/mm^3)	Viscosity (MPa-sec)	c_0 (mm/s)	s	Γ_0
Value	9.832 x 10^{-10}	1.036 x 10^{-10}	45850	0	0

Table 3. Information of the near-fault ground motions.

RSN	Event	Station	FN T_p (s)	FP T_p (s)	FN T_{Sv} (s)
451	Morgan Hill	Coyote Lake Dam (SW Abut)	0.95	1.08 (X-dir.)	0.69
459	Morgan Hill	Gilroy Array #6	1.23 (X-dir.)	1.21	1.13
568	San Salvador	Geotech Investig Center	0.85	1.81 (X-dir.)	0.65
1051	Northridge-01	Pacoima Dam (upper left)	0.90	0.46 (X-dir.)	0.73
1120	Kobe, Japan	Takatori	1.63 (X-dir.)	2.96	1.28
828	Cape Mendocino	Petrolia	2.81	0.96 (X-dir.)	0.73

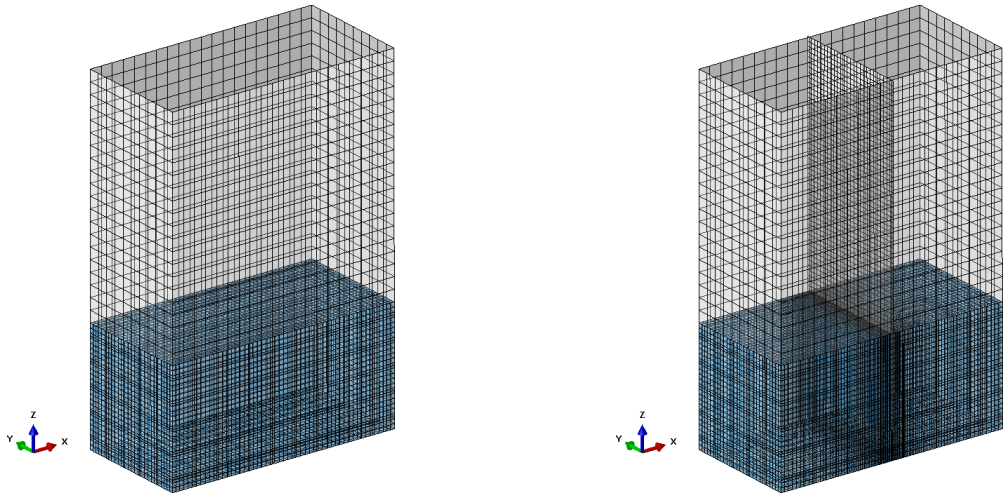

(a) Rigid rectangular tank *(b) Rigid rectangular tank with a baffle in the middle*

Figure 2. Numerical model of small-scale rigid rectangular tanks.

RESULTS AND DISCUSSIONS

This study aims to discuss the effect of the baffle on sloshing height of liquid in tanks. The numerical analysis is performed to compare the sloshing height of the water in tank with and without the baffle qualitatively. The frequencies of the fundamental convective mode are also discussed later.

Fundamental Sloshing Frequencies

The fundamental convective mode is an important characteristic to liquid sloshing behavior. According to Housner's study, it is an asymmetric mode. Eq. (1) gives the relationship between the sloshing frequencies and depth of stored water-to-the half length of the tank parallel to the shaking direction ratio (h/l) for two horizontal directions as solid lines in Figure 3. The scattered points in the figure are sloshing frequencies obtained from the numerical analysis. The result shows that the sloshing frequency will become higher and converge to a constant value as h/l increasing for both theoretical and numerical values. From the figure, it can be observed that the numerical sloshing frequency is slightly smaller than the theoretical one for two horizontal directions. This shows the numerical approach used in the study is suitable for liquid frequency analysis.

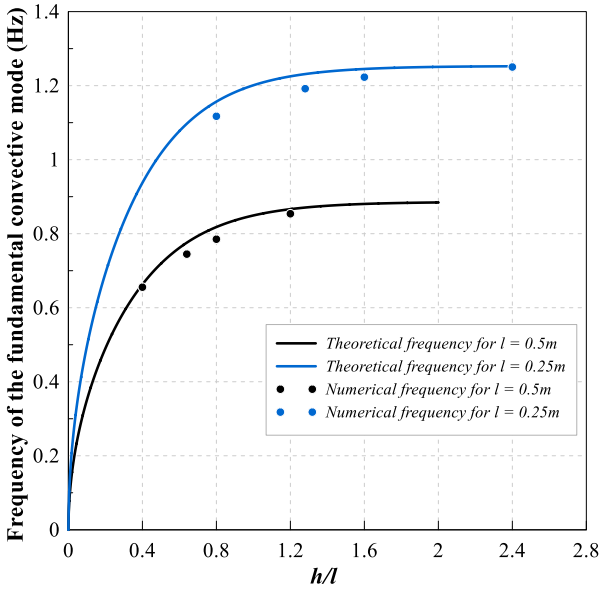

Figure 3. Relationship between the fundamental convective frequency and the ratio of h/l of the rectangular tank under the X- and the Y- direction excitations.

Sloshing Height

The sloshing height is another important characteristic to liquid sloshing behavior. According to Eqs. (2) and (3), it can be known that the sloshing height is related to tank dimensions and horizontal spectral acceleration at the fundamental frequency in the direction of motion. Therefore, the greater the tank is, the higher the sloshing height is. It also has high correlation with intensity of input motion. To reduce the sloshing height, the approach of the reduction in space of liquid motion, the vertical rigid baffle installed in the middle of the tank, is adopted. In the analysis, only the results of the point 1 on water surface as shown in Figure 4 under X-direction excitation are discussed.
Figure 5 shows comparison between numerical and theoretical results for the case with and without baffle. Each ratio in the figure defines the ratio of numerical result to theoretical result, e.g., the frequency ratio is the ratio of the fundamental sloshing frequency obtained from numerical analysis to that calculated by Eq. (1), Sa ratio is the ratio of the horizontal spectral acceleration at the numerical frequency to that at the theoretical frequency, and hmax ratio is the ratio of the maximum sloshing height obtained from numerical analysis to that estimated by Eq. (2) or Eq. (3). From the comparison, it can be concluded that the fundamental sloshing frequency obtained from the numerical approach used in the study is slightly smaller than theoretical value under the near-fault ground motions used here for both cases. This slight difference leads to slight difference of the horizontal spectral acceleration and then leads to difference of the maximum sloshing height. For the case without baffle, the maximum sloshing height obtained from numerical analysis is close to that estimated by Eq. (2) except for the RSN828 ground motion; for the case with baffle, the maximum sloshing height obtained from numerical analysis for the RSN459 and RSN828 are obviously smaller than that estimated by Eq. (2). From the results show in Figure 5, it can be known that Eq. (3) gives conservative estimated sloshing height under the near-fault ground motions used in the study. Figure 6 shows X-direction 0.5% damping ratio acceleration response spectra of the near-fault ground motions. The red dotted line in the figure indicates the fundamental sloshing frequency for water in the tank; the blue dotted line in the figure is the fundamental sloshing frequency for water in the tank with a baffle in the middle. It roughly shows the horizontal spectral acceleration will increase due to increasing sloshing frequency caused by the existing baffle. This is not beneficial to reduce the sloshing height according to knowledge from the estimated sloshing height formula. But the existing baffle decreases the space of liquid motion, this in turn is beneficial to reduce the sloshing height. Figure 7 discusses the existing baffle effect on the horizontal spectral acceleration and maximum sloshing height. The solid lines in the figure show variation of the horizontal spectral acceleration; the dotted lines show variation of the maximum sloshing height. Except for the RSN828 ground motion, the maximum sloshing height reduces even if the horizontal spectral acceleration increases due to the existing baffle. Therefore, although the existing baffle reduces the space of liquid motion to half of the original space, it cannot guarantee that the sloshing height can be lowered. The sloshing height has high correlation with intensity of input motion. Figure 8 shows the relationship between the horizontal spectral acceleration and maximum sloshing height for the case with and without baffle. The dotted lines in the figure are linear fitting lines. It can be known that there is a linear relationship among them and it is consistent with the estimated sloshing height formula.

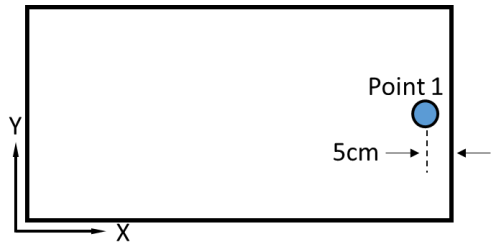

Figure 4. Illustration of the point 1 on water surface.

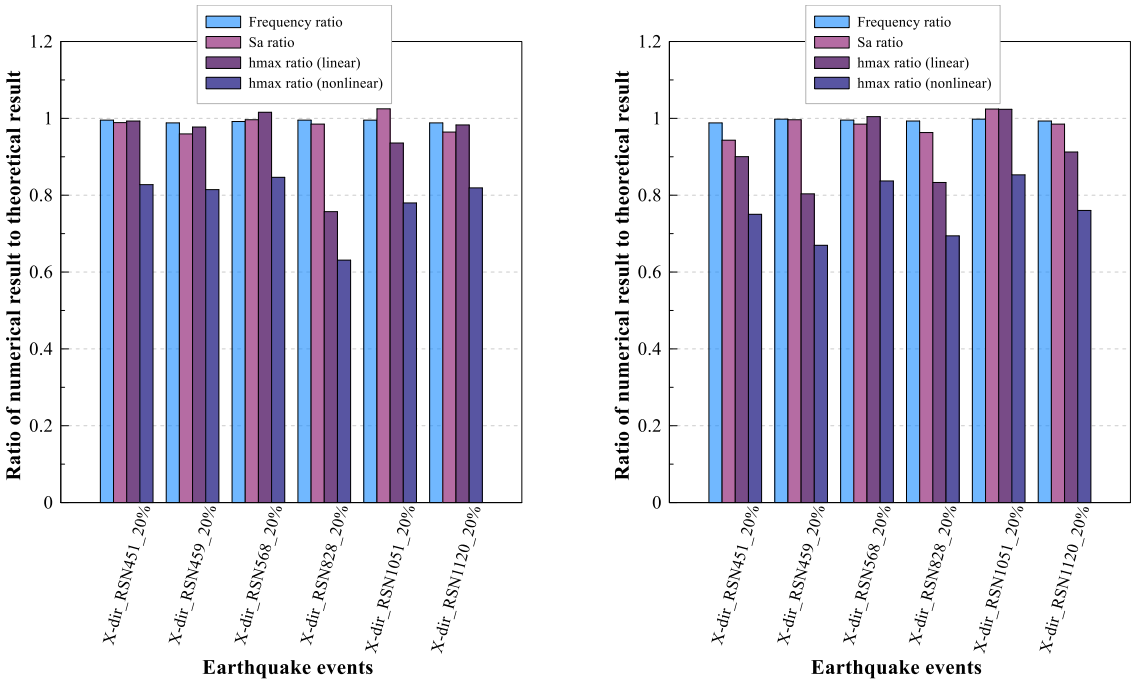

(a) Without baffle *(b) With baffle*

Figure 5. Comparison between numerical and theoretical results.

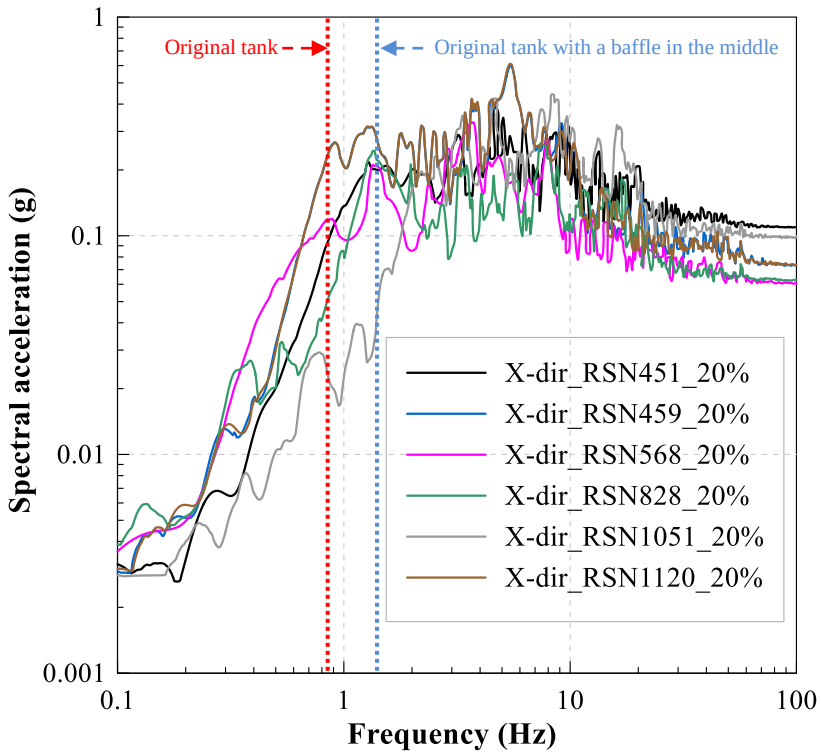

Figure 6. X-direction 0.5% damping ratio acceleration response spectra of the near-fault ground motions.

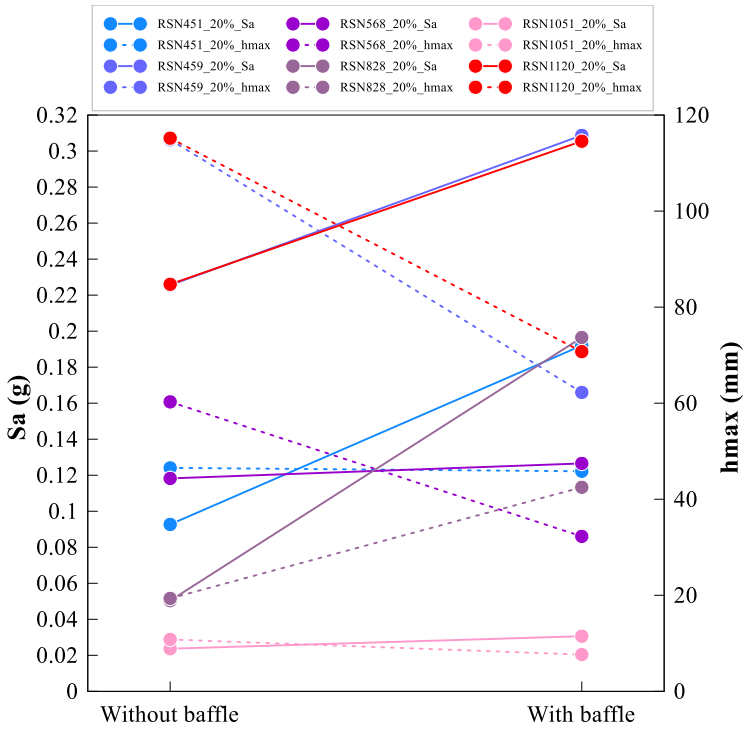

Figure 7. The existing baffle effect on the horizontal spectral acceleration and maximum sloshing height.

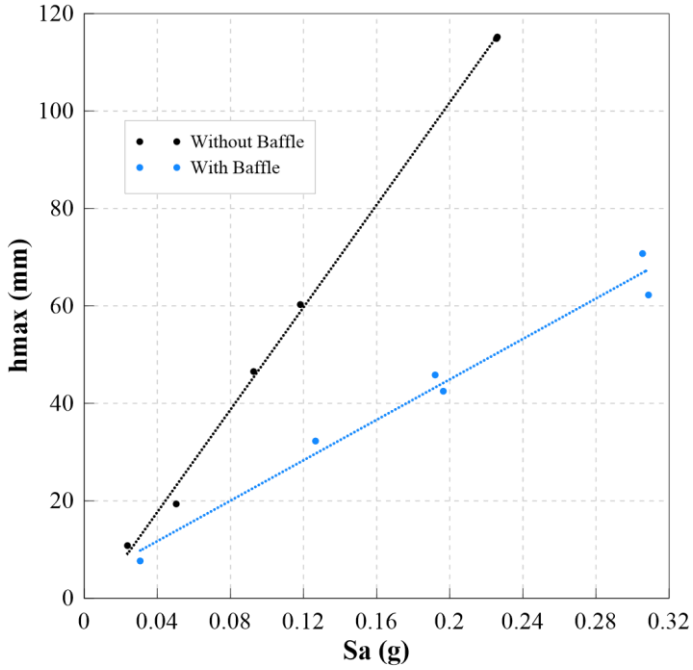

Figure 8. The relationship between the horizontal spectral acceleration and maximum sloshing height.

CONCLUSIONS

This study aims to discuss the effect of the additional installed baffle on sloshing height of liquid in tanks by using numerical approach. Only the analysis under X-direction excitation are performed and discussed. The existing baffle in the middle of the tank changes the sloshing frequency and reduces the space of liquid motion. From the results of most of the near-fault ground motions used in the study, the baffle reduced the maximum sloshing height because of the shortened length of the tank parallel to the shaking direction. The results of one of the near-fault ground motions showed increased maximum sloshing height due to the baffle because of larger spectral acceleration. Therefore, the baffle used in the tank cannot guarantee that the sloshing height can be lowered. The sloshing height has high

correlation with intensity of input motion and length of the tank parallel to the shaking direction. The results also showed that there is a linear relationship between the horizontal spectral acceleration and maximum sloshing height and it is consistent with the estimated sloshing height formula. The design of the baffle configuration is needed to study further to find a better seismic retrofit strategy.

REFERENCES

Abalı, E. and Uçkan, E. (2010). "Parametric analysis of liquid storage tanks base isolated by curved surface sliding bearings," *Soil Dynamics and Earthquake Engineering*, **30**, 21-31.

Abramson, H. N. (Ed) (1966). "The dynamic behavior of liquids in moving containers, with applications to space vehicle technology," *NASA SP-106*.

Dassault Systemes. (2014a). "The Abaqus Example Problems Guide", *the Abaqus documentation collection*.

Dassault Systemes. (2014b). "The Abaqus Analysis Guide", *the Abaqus documentation collection*.

EPRI (The Electric Power Research Institute). (2013). "Seismic evaluation guidance – Screening, prioritization and implementation details (SPID) for the resolution of Fukushima Near-Term Force Recommendation 2.1: Seismic," *EPRI-1025287*.

Housner, G.W. (1957). "Dynamic pressures on accelerated fluid containers," *Bull. Seismol. Soc. Am.*, **47(1)**, 15-35.

Maleki, A. and Ziyaeifar, M. (2007). "Damping enhancement of seismic isolated cylindrical liquid storage tanks using baffles," *Engineering Structures*, **29**, 3227-3240.

Maleki, A. and Ziyaeifar, M. (2008). "Sloshing damping in cylindrical liquid storage tanks with baffles," *Journal of Sound and Vibration*, 311, 372-385.

Panchal, V.R. and Jangid, R.S. (2008). "Variable friction pendulum system for seismic isolation of liquid storage tanks," *Nuclear Engineering and Design*, **238**, 1304-1315.

Soni, D.P., Mistry, B.B. and Panchal, V.R. (2011). "Double variable frequency pendulum isolator for seismic isolation of liquid storage tanks," *Nuclear Engineering and Design*, **241**, 700-713.

TO OBTAIN EFFECTIVE ELASTIC MODULUS OF STRAIGHT BUSWAY BY SIMPLE TESTING

Yu-Chiau Huang[1], Chuan-Cheng Lee[2], Chao-Yu Tu[3], Wei-Chung Chen[4], Juin-Fu Chai[5], Fan-Ru Lin[6], Bai-Yi Huang[7]

1. Assistant Researcher, National Center for Research on Earthquake Engineering, Tainan, Taiwan, R.O.C.
2. Graduate student, Department of Architecture, National Cheng Kung University, Tainan, Taiwan, R.O.C.
3. Assistant Researcher, National Center for Research on Earthquake Engineering, Tainan, Taiwan, R.O.C.
4. Assistant Researcher, National Center for Research on Earthquake Engineering, Tainan, Taiwan, R.O.C.
5. Deputy Director General, National Center for Research on Earthquake Engineering, Taipei, Taiwan, R.O.C.
6. Associate Researcher, National Center for Research on Earthquake Engineering, Taipei, Taiwan, R.O.C.
7. Assistant Researcher, National Center for Research on Earthquake Engineering, Tainan, Taiwan, R.O.C.

Email: yuchiau@narlabs.org.tw, g122359189@gmail.com, 2106018@narlabs.org.tw, chenwc@narlabs.org.tw, chai@narlabs.org.tw, frlin@narlabs.org.tw, byhuang@narlabs.org.tw

ABSTRACT

Busway System has been applied widely in many buildings of major utilities, commercial and IT centers and etc., which is critical in maintaining buildings' functionality. However, most domestic and international test standards and study documents are focus mainly on electricity power, anti-rust and fireproof, only a few with simple test on mechanics properties such as loading and impact, but lack of any study about seismic test. Therefore, variety of mechanics parameters cannot be obtained by the existing test method and standard to make seismic design and analysis on busway system. Based on that, this study is targeted on straight busway in this stage to design 3 major corresponding mechanics testing: (1) tensile strength of metal material of busway component, (2) compression strength of straight busway, (3) impulse excitation of vibration testing of straight busway. The major purpose is to generate relevant mechanics properties of straight busway for further studies in the future.

Keywords: busway, component testing

INTRODUCTION

Busway system (or called as Busbar Trunking System, BTS) was originated from Detroit mobile industry (IEEESA, 2013) in late 1920. Benefited by the modularized design, busway system is not only easy to assemble and maintain, but also more safe than traditional power supply system constituted by cable. From then on, it becomes more and more popular and is used widely in variety of structures and facilities such as critical utilities, technology plants, commercial buildings, IT centers and etc. Busway system has been proven itself to be decisive in maintaining functionality of structures and facilities in the modern world.

Busway system is designed as suspension type and is classified to several different categories, in which feeder busway is the most important one. Feeder busway is usually used in large scale factories or commercial buildings, its length may goes to tens of meters in vertical or hundreds of meters in horizontal which restrains it from monolithic design in production. As the result, 3 major types of feeder busway are born: straight busway, elbow busway and tee/cross type busway, which separate parts are connected to each other by bridge joint to meet the field layout requirement. Furthermore, to prevent damage by its own weight, busway is usually reinforced by suspension system in horizontal and by spring hanger in vertical which is fixed by every other spacing or on specific site designed. Bridge joint (by red circle), suspension system (by red arrow) and spring hanger (by red frame) are shown as figure 1.

Figure 1. Physical joint and fixing of busway

Domestic and international standards of busway are made to ensure its functionality and safety. By the defined test method and criteria, busway quality can be checked whether meets the required standard. Variety of busway properties can also be obtained through the test, which is useful for further analysis and design. Existing busway standards are, for example, in domestic, CNS 14286 (BSMI, 2016), CNS 61439-6 (BSMI, 2021) published by BSMI (Bureau of Standards, Metrology and Inspection, M.O.E.A., Taipei), and in international, IEC 61439-6 (IEC, 2012) published by IEC (International Electrotechnical Commission, Switzerland) and IEEE 3001.5 (IEEESA, 2013), IEEE 344 (IEEESA, 2013), IEEE 693 (IEEESA, 2018) published by IEEESA (Institute of Electrical and Electronics Engineers Standards Association, U.S.), and so forth.

However, after study domestic and international standards mentioned above, most standards of busway are focus mainly on electricity power, anti-rust and fireproof. Comparatively, only 2 major tests about force load are found: (1) impact hammer test (2) simple static loading test against straight busway and its joints. Apart from these 2 mechanics tests, most standards are without any test about other components of busway, nor seismic test. IEEE 344 (IEEESA, 2013) and IEEE 693 (IEEESA, 2018) are the only 2 standards found covering seismic test, which are targeted only on non-structural components such as equipment and suspended distribution systems in nuclear power plant or electrical substation to set up uniform seismic test standard. Therefore, in practice, even with the same busway specimen, every testing design may generate various results to each other which always harass both the user and designer.

This study refers to existing test standard, and takes straight busway of the feeder busway category as testing target at this stage to set up straight busway testing method and obtain its mechanics properties. Testing is designed with 3 major parts: (1) tensile strength testing of metal material, to obtain material elastic modulus of specific single metallic material , then effective elastic modulus of straight busway can be derived accordingly. This study follows CNS 2112 (BSMI, 1996) and CNS 2111 (BSMI, 1996) published by BSMI which provide standards to conduct tensile strength testing on metal material. (2) compression strength testing of straight busway, to obtain effective compression elastic modulus, (3) impulse excitation of vibration testing of straight busway, to obtain flexural rigidity. Considering the length of straight busway is too long to be assembled on the testing machine of regular materials, this study follows the standard of ASTM E1876-01 (ASTM, 2002) published by ASTM (American Society for Testing and Materials International, United States) that applies to straight specimen with uniform cross section, cross section in homogeneous or sandwich structure, which is similar to the cross section structure of straight busway. Also, flexural rigidity can be obtained without material testing machine. Based on above, this study takes ASTM E1876-01 (ASTM, 2002) to conduct impulse excitation of vibration testing to obtain flexural rigidity.

INTRODUCTION OF STRAIGHT BUSWAY SPECIMEN

Straight busway discussed in this study is with a cross section similar to I-beam, as shown in figure 2. Its inner composition is made out of several pieces of metal conductor wrapped by insulation material,

and clamped by 2 pieces of C-shape metal web in both lateral sides. And, without any adhesive, it's fixed to the upper and bottom metal flanges by screw.

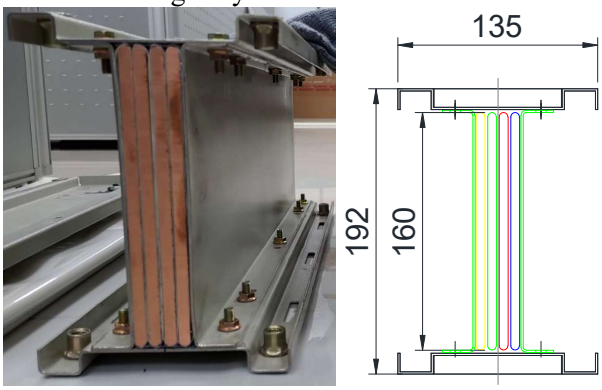

Figure 2. Physical cross section of straight busway (unit: mm)

TENSILE STRENGTH TESTING OF METAL MATERIAL

Straight busway trends to have flexural deformation in earthquake, so the effective elastic modulus such as axial tension and axial compression must be obtained in studying the behavior of straight busway in earthquake. Be made by composite material, it's difficult to fix the both ends of straight busway by welding or fixture to conduct testing of integral tensile strength. Besides, considering the strength of fastening screw and insulation material are much less than the inner conductor and enclosure, it's reasonable to treat axial elastic modulus of straight busway as the weighted average of axial elastic moduli of conductor and enclosure, in which the weighted value is calculated by the cross-sectional area ratio. The obtained elastic moduli of conductor and enclosure are helpful to make theoretical calculation to verify the reasonableness of further testing results. To get elastic moduli of conductor and enclosure, straight busway is disassembled, and CNS 2112 (BSMI, 1996) is followed to make standard test pieces of tensile strength as shown in figure 3.

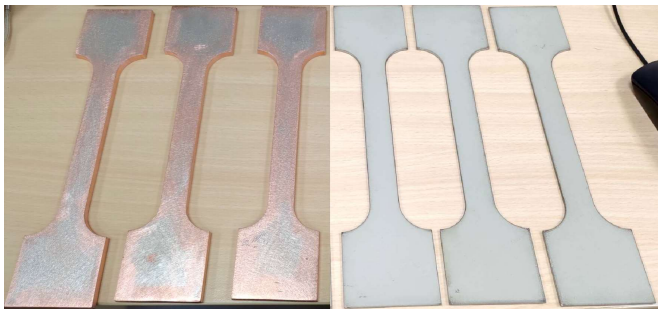

Figure 3. Test pieces of tensile strength testing (conductor/left, enclosure/right)

According Standard CNS 2111 (BSMI, 1996) to conduct testing of tensile strength, the layout is shown as figure 4. Cutting the standard test pieces, then stick strain gauge to the center of test pieces in both of the front and back sides to measure strain duration, and by calculating cross-sectional area and load history in the center of test pieces to get stress history. Then, stress-strain curve is generated to acquire elastic moduli of both components under tension, and finally the effective elastic modulus of straight busway tensile strength can be obtained.

Figure 5 and 6 show the stress-strain curve obtained from tensile strength testing of conductor and enclosure. As shown, there is mutual consistency among stress-strain curves of different specimen of conductors. As for enclosure, although some differences are observed, but the slope difference in elastic stage is very limited. By straight segment of the curve, elastic moduli of conductor and enclosure are to be derived, and based on that to get the elastic moduli of conductor and enclosure as 8.82 tf/mm^2 and 19.39 tf/mm^2 respectively.

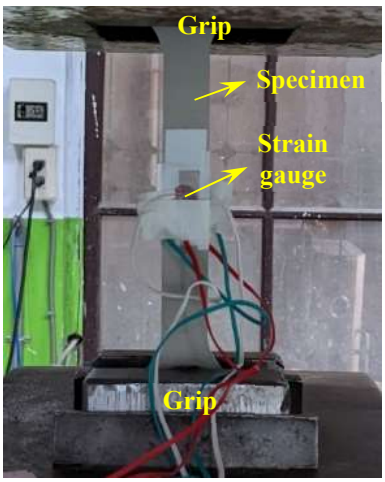

Figure 4. Layout of tensile strength testing

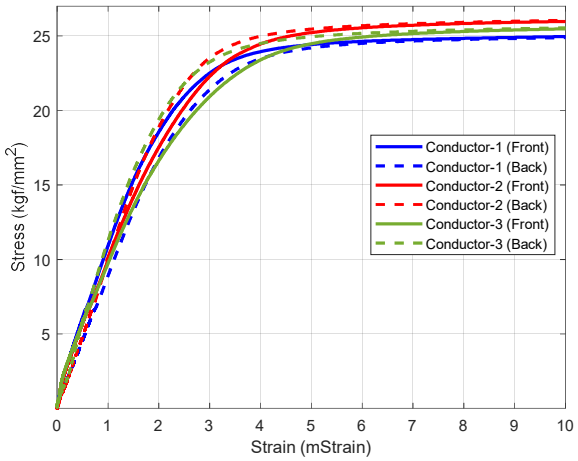

Figure 5. Stress-strain curve of conductor derived from tensile strength testing

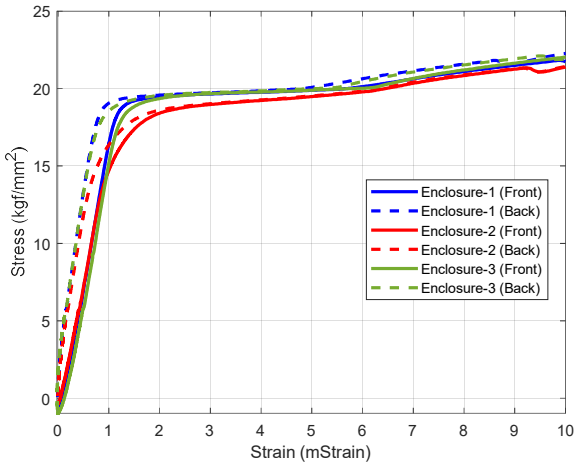

Figure 6. Stress-strain curve of enclosure derived from tensile strength testing

COMPRESSION STRENGTH TESTING OF STRAIGHT BUSWAY

In the initial study of straight busway installation, 2 major points are found about straight busway under compression: (1) Made out of metal material, too long specimen of straight busway trends to generate buckling. So, the length of specimen must be restricted. (2) Tabulate conductor is fixed by the clamping force of the screw which is hard to keep constant strength under axial compression during

the testing. Therefore, inconsistent deformation between conductor and enclosure is expected to happen.

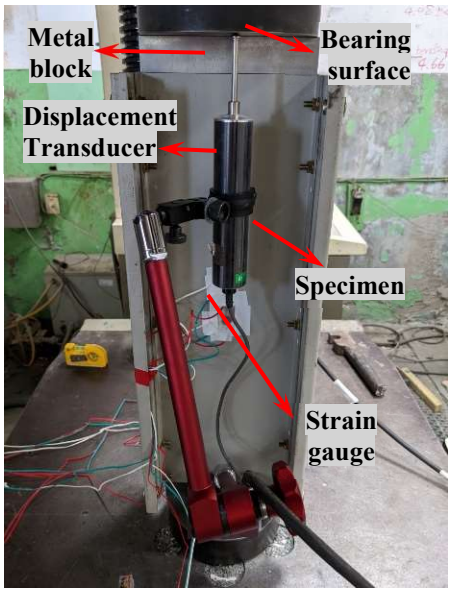

Figure 7. Layout of compression strength testing

With consideration of above 2 points, layout of compression strength testing of straight busway is suggested to be as shown in figure 7. Two pieces of metal block are placed in both ends of 50 cm length straight busway testing specimen, metal block's area matches exactly the cross-sectional area of straight busway conductor to prevent from compressing enclosure during the testing. Use displacement transducer and strain gauge simultaneously to measure entire and partial deformation of straight busway. In addition to stick to the enclosure, strain gauge can also be placed in a rectangular hole in the central area of specimen to observe the different deformation between conductor and enclosure. Finally, conduct the testing by layout described above to obtain effective elastic modulus of straight busway under compression.

Force-displacement curve generated from compression strength testing of straight busway is shown as figure 8. Effective elastic modulus of straight busway under compression can be derived by straight segment and cross-sectional area & length of inner conductor as 44.90 tf/mm^2.

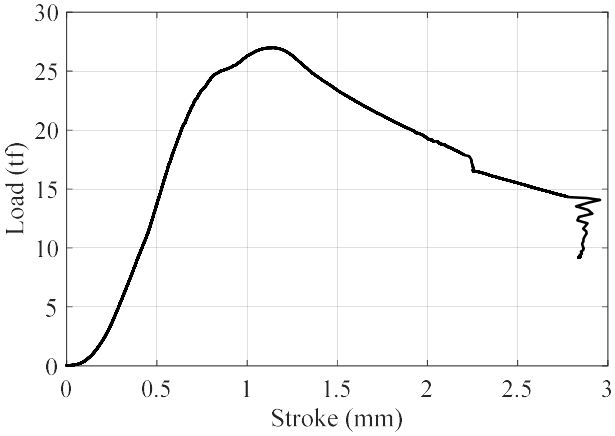

Figure 8. Force-displacement curve generated from compression strength testing

IMPULSE EXCITATION OF VIBRATION TESTING OF STRAIGHT BUSWAY

Been made out of composite material and with high ductility & big volume, it's difficult to obtain the flexural rigidity of straight busway by traditional 3-point/4-point loading test. So, this study takes Standard ASTME1876-01 (ASTM, 2002) and makes a little modification to obtain flexural rigidity of

straight busway. Testing layout is as shown in figure 9, with 2 supports placed at 0.224 ratio of total length of straight busway to both ends. According to the test standard, straight busway is to be placed in the form of simple supported beam on the top of proper fixture, and accelerometers are to be set in the midpoint and support points of straight busway.

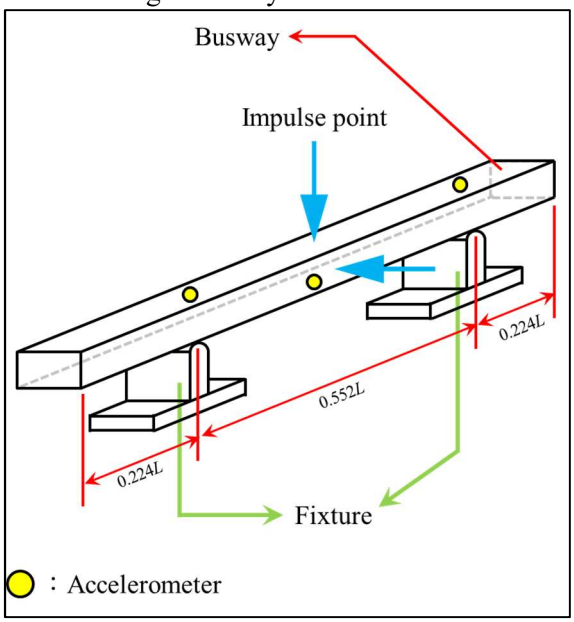

Figure 9. Specified test layout of ASTM E1876-01 (ASTM, 2002)

When the layout is completed, strike the upper surface and lateral central area of straight busway specimen by impact hammer. The fundamental vibration frequency in different direction of the specimen can be obtained by subsequent data analysis. Then, the flexural rigidity of specimen is derived by following formula:

$$EI = 0.0789mf^2L^3 \tag{1}$$

Above formula is derived by vibration formula of Euler beam and figure 9 where EI represents flexural rigidity, m is mass of specimen, f is fundamental vibration frequency obtained from impulse excitation testing, L is length of specimen.

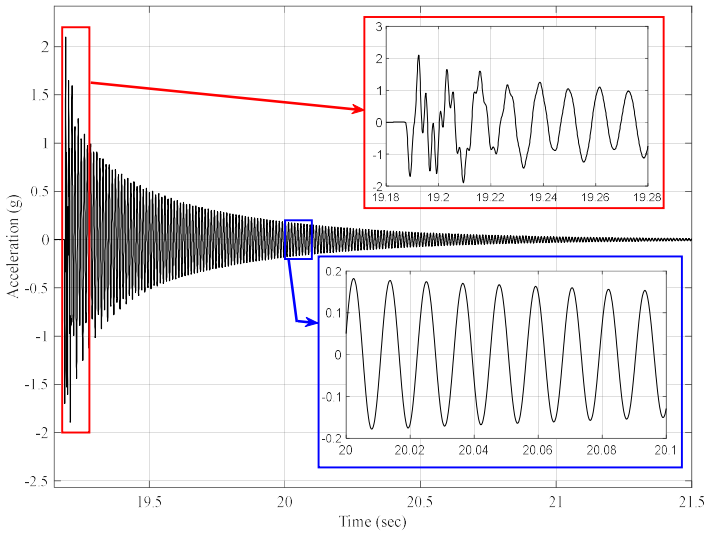

Figure 10. Acceleration history recorded from impulse excitation testing

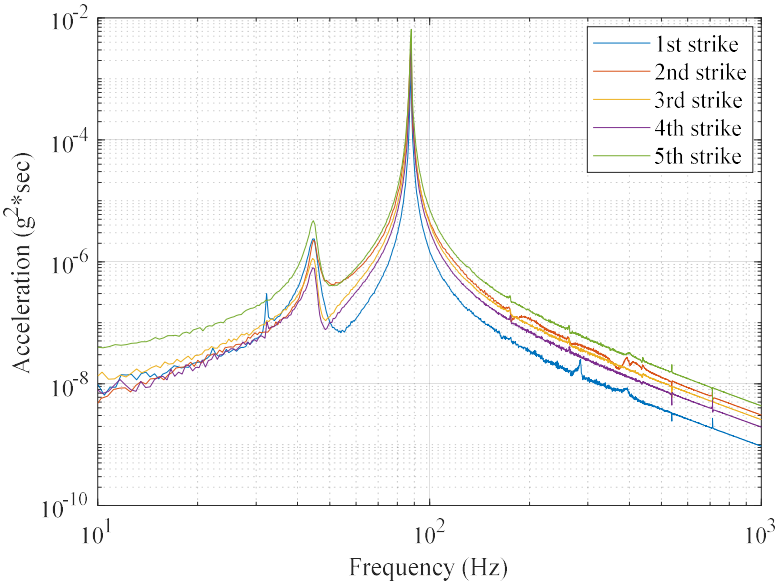

Figure 11. Power spectra derived from impulse excitation testing

The impulse excitation testing is conducted by making 5 strikes along with the weak-axis (strong-axis bending) of busway in length about 3 meters and with weight about 130 kilograms. The vertical acceleration history of a strike midpoint is shown as figure 10. In practice, it's infeasible to seek for perfect striking during the testing. Also, fundamental vibrational frequency is the only parameter needed to derive flexural rigidity. From the enlargement of figure 10, it's found the frequency content of fore history is wider, while frequency content of free decay of post history is approaching to single frequency. Therefore, this study takes history of free decay to make Fourier transform to identify fundamental vibration frequency.

As displayed in figure 10, Power spectra derived from free decay history of 5 strikes is shown as figure 11 where the frequency is identified to be 87.97 Hz. Calculating the fundamental vibration frequency of busway by the cross-sectional area of tensile strength testing and figure 2 stated above, the result comes to be 85.36 Hz which is with error rate of 3.05% to the said 87.97 Hz. To calculate further, flexural rigidity and elastic modulus can be derived as 1.69×10^{8} (tf·mm^2) and 11.96 (tf/mm^2) respectively, both error rates of flexural rigidity and elastic modulus is 6.20% which falls within the acceptable range.

CONCLUSIONS

Based on sufficient results obtained, this study verifies the applicability of testing described above. Further testing will be designed in the future to obtain mechanics parameters of other components of straight busway such as spring shock absorber, bridge type joint and etc.

ACKNOWLEDGMENTS

With deep gratitude to President Jasper Liu of Zhongfu Enterprise Co., Ltd., for his kind sponsoring busway specimen in this study.

REFERENCES

ASTM E1876-01 (2002). *Standard Test Method for Dynamic Young's Modulus, Shear Modulus, and Poisson's Ratio by Impulse Excitation of Vibration*, American Society for Testing and Materials International, United States.

CNS 2111 (1996). *Method of Tensile Test for Metallic Materials*, Bureau of Standards, Metrology and Inspection, M.O.E.A., Taipei.

CNS 2112 (1996). *Method of Tensile Test for Metallic Materials*, Bureau of Standards, Metrology and Inspection, M.O.E.A., Taipei.

CNS 14286 (2016). *Low voltage busways*, Bureau of Standards, Metrology and Inspection, M.O.E.A., Taipei.

CNS 61439-6 (2021). *Low-voltage switchgear and controlgear assemblies, Part 6: Busbar trunking systems (busway)*, Bureau of Standards, Metrology and Inspection, M.O.E.A., Taipei.

IEC 61439-6 (2012). *Low-voltage switchgear and controlgear assemblies - Part 6: Busbar trunking systems (busways)*, International Electrotechnical Commission, Switzerland.

IEEE Std. 344 (2013). *IEEE Standard for Seismic Qualification of Equipment for Nuclear Power Generating Stations*, Institute of Electrical and Electronics Engineers Standards Association, U.S.

IEEE Std. 693 (2018). *IEEE Recommended Practice for Seismic Design of Substations*, Institute of Electrical and Electronics Engineers Standards Association, United States.

IEEE Std 3001.5™ (2013). *IEEE Recommended Practice for the Application of Power Distribution Apparatus in Industrial and Commercial Power Systems*, Institute of Electrical and Electronics Engineers Standards Association, United States.

EVALUATION OF NONSTRUCTURAL SEISMIC DEMAND BASED ON SHAKE-TABLE TESTING OF STEEL RACKS INSTALLED ON FULL-SCALE 2-STORY MOMENT FRAME

Su-Chan Jun[1] Cheol-Ho Lee[2] Chang-Jun Bae[3] and Bong-Ho Cho[4]

1. Graduate student, Seoul National University, Department of Architecture and Architectural Engineering, Seoul, Korea
2. Professor, Seoul National University, Department of Architecture and Architectural Engineering, Seoul, Korea
3. Graduate student, Seoul National University, Department of Architecture and Architectural Engineering, Seoul, Korea
4. Professor, Ajou University, Department of Architectural Engineering, Suwon, Korea

Email: corrora90@snu.ac.kr, ceholee@snu.ac.kr, changjun0125@snu.ac.kr, bhcho@ajou.ac.kr

ABSTRACT

This study conducted shake-table tests of a full-scale 2-story steel moment frame to investigate the seismic demand on nonstructural elements. The main objective of this study was to evaluate the effects of structural and nonstructural nonlinearities on the peak floor acceleration (PFA) and the peak component acceleration (PCA). The PCA was measured through steel racks which are one of the most widely used types of floor-mounted nonstructural elements. The steel rack specimens were installed on access floors to utilize a more realistic installation configuration. Based on test results, the relationship between the PFA reduction and structural ductility prescribed by ASCE 7-22 were evaluated, along with the relationship between the PCA reduction and component ductility. It was observed that the PFA reduction was generally overestimated by ASCE 7-22 until the frame developed a low-to-moderate ductility level. Also, the importance of structural ductility on the elastic C_{AR} (=PCA/PFA) was highlighted, where the high resonant PCA around the fundament structural mode was effectively decreased as the test frame experienced a moderated level of ductility; PCA was lowered by 36 % and 25 % on the 2nd and roof floor, respectively. Due to the pinching hysteretic behavior of the access floor-mounted steel rack specimens, the PCA reduction was generally less than the relevant provisions of ASCE 7-22 through all the component ductility levels. Effects of inferior energy-dissipating capacity of steel rack specimens were discussed.

Keywords: Nonstructural elements, shake-table test, seismic demand, nonlinear behavior

INTRODUCTION

Nonstructural elements have suffered significant seismic damage during past major earthquakes not just because of their poor force-resisting structural configuration but also because they are usually subjected to a highly amplified ground acceleration which is caused by the structural and nonstructural dynamic behaviors. Therefore, ideally, ensuring the satisfactory seismic performance of nonstructural elements involves explicit consideration of the entire influence chain composed of input ground motion, supporting structure as well as nonstructural elements.

The seismic demand on nonstructural elements can be understood as a two-stage cascade amplification. The first amplification is caused by the amplification of the input ground motion by the supporting structure (or in-structure amplification). The second amplification is related to the resonance between the supporting structure and nonstructural elements (or component amplification). Significant efforts have been made during past decades to provide more rational and engineering-based methods to determine the nonstructural seismic demands and to fulfill the increasing expectations on seismic performance of nonstructural elements. In the recently published ASCE 7-22 (ASCE/SEI, 2022), a much more advanced procedure was proposed, which reflected the effects of structural and component

nonlinearity on the seismic demand. However, despite the improvements made, there still remains room for further advancement because the proposed procedure was developed largely based on numerical analysis using idealized mathematical models, especially when nonlinear behavior was involved.

In this study, a series of shake-table tests were performed on a full-scale 2-story steel moment frame, which was conducted as part of a Korean government-funded joint research project. A total of 5 universities with more than 10 industry sponsors collaborated to systematically investigate the seismic performance on nonstructural elements. Various architectural nonstructural elements were installed on the test frame. This study focused on analyzing the seismic demand on nonstructural elements and evaluating the effects of component nonlinearity based on steel rack specimens installed on the roof floor of the testing frame.

SEISMIC DESIGN FORCE FOR NONSTRUCTURAL ELEMENTS

This section summarized the equivalent static method recommend by ASCE 7-22. The seismic design force F_p is determined according to the formula given below.

$$F_p = 0.4S_{DS}\left(\frac{H_f}{R_\mu}\right)\left(\frac{C_{AR}}{R_{po}}\right)W_p I_p \tag{1}$$

where F_p = seismic design force; S_{DS} = spectral acceleration at short period; H_f = factor for force amplification as a function of height in the structure; R_μ = structure ductility reduction factor; C_{AR} = component resonance ductility factor that converts the peak floor or ground acceleration into the peak component acceleration; R_{po} = component strength factor; W_p = component operating weight; I_p = component importance factor.

In Eq. (1), the ground acceleration at the base, $0.4S_{DS}$, is intended to be the same as the design ground acceleration for the supporting structure, determined considering the seismic hazard and the soil condition of the building site. The in-structure amplification is reflected by H_f as below.

$$H_f = 1 + a_1\left(\frac{z}{h}\right) + a_2\left(\frac{z}{h}\right)^{10} \tag{2}$$

where $a_1 = 1/T_a \leq 2.5$; $a_2 = [1-(0.4/T_a)^2]$; z = height in structure of the highest point of attachment of component with respect to the base; h = average roof elevation of structure above the base; T_a = lowest approximate fundamental period of supporting building in either orthogonal direction.

Eq. (2) is a newly introduced distribution in ASCE 7-22, expressed as a function of the approximate fundamental period of a supporting structure (T_a). For longer-period buildings, the amplification profile becomes more vertical; almost no amplification occurs along the height except at the roof level. If the approximate structural period is unknown, the linear distribution can be utilized, which amplifies the peak floor acceleration (PFA) up to 2.5 at the roof level.

One of the major features introduced in ASCE 7-22 is the reduction of the component and floor acceleration considering the structure and component ductility level. The reduction in PFA resulting from structural ductility was given with the factor R_μ which can be calculated as below.

$$R_\mu = \left[\frac{1.1R}{I_e\Omega_0}\right]^{1/2} \geq 1.3 \tag{3}$$

where R = structure response modification factor; I_e = structure importance factor; Ω_0 = structure overstrength factor.

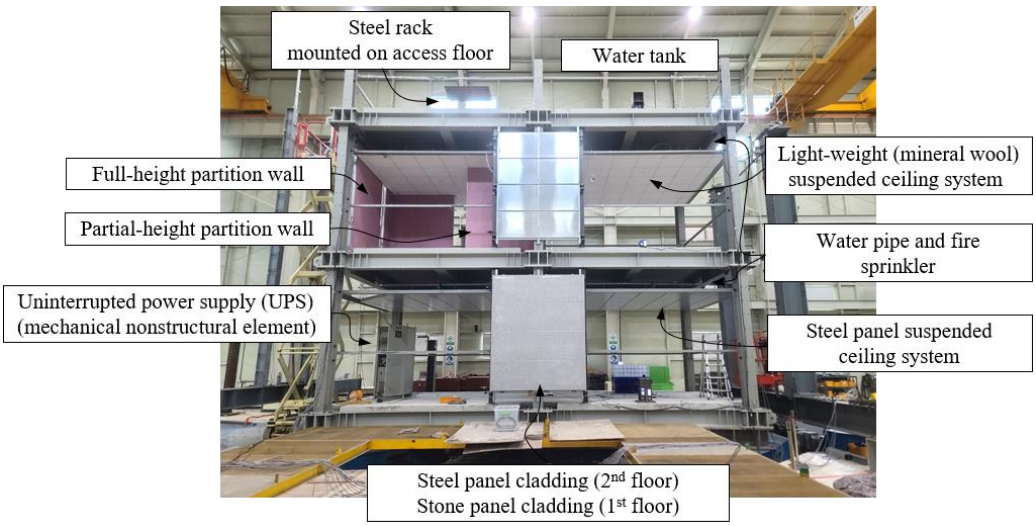

Figure 1. Full-scale 2-story steel moment frame installed with various nonstructural elements

Eq. (3) shows that the amount of PFA reduction depends on both the structure response modification factor (R) and the structure overstrength factor (Ω_0). Using the definition of R factor given by SEAOC (1999) and taking the structure importance factor (I_e) as 1.0, Eq. (3) can be reduced as follows.

$$R_\mu = [\frac{1.1R}{I_e\Omega_0}]^{1/2} = [R_D]^{1/2} \simeq [u_m / u_y]^{1/2} \quad (4)$$

where R_D = global ductility factor at design earthquake level; u_m = maximum roof displacement of supporting structure; u_y = yield roof displacement of supporting structure.

Eq. (6) implies that the PFA reduction is proportional to the square roof of the structure global ductility level which can be approximated as the ratio of the maximum roof displacement normalized by the yield roof displacement of the structure (NIST, 2018).

C_{AR} represents the component acceleration amplification that occurs when the component is tuned to one of the major modes of supporting structure. In ASCE 7-22, C_{AR} was provided with respect to the component ductility level, and a lower C_{AR} is assigned to the component of higher ductility (see Table 1).

EXPERIMENTAL PROGRAM

Test set-up and measurement

A two-by-two bay steel moment frame was fabricated, which had a plan dimension of 4.5 m × 9.0 m and a total height of 6.75 m as shown in Fig. 1. A total of 10 types of nonstructural elements were

Table 1. Component ductility categories (ASCE 7-22, 2022)

Ductility category	Assumed component ductility	PCA/PFA (= C_{AR})
Elastic	1.00	4.00
Low	1.25	2.80
Moderate	1.50	2.20
High	2.00	1.40

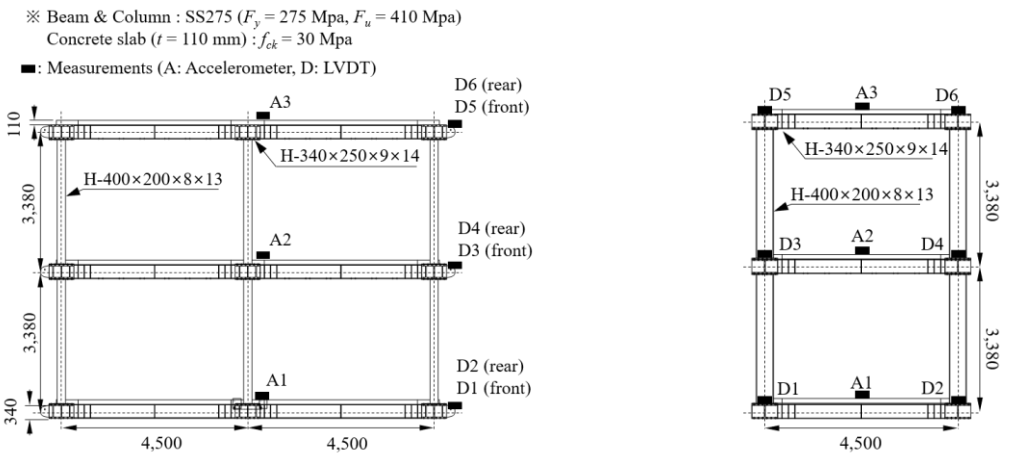

(a) Front veiw (b) Side view

Figure 2. Dimensions and measurement plan of 2-story steel moment frame

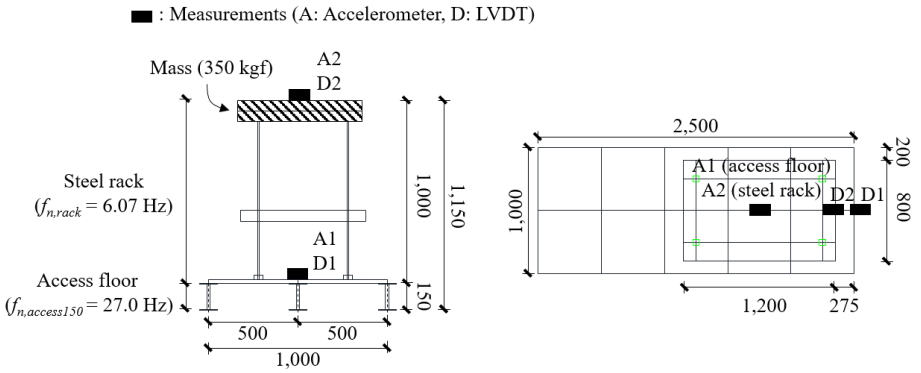

(a) Steel rack specimens mounted on 300 mm-high access floors (FH300-series)

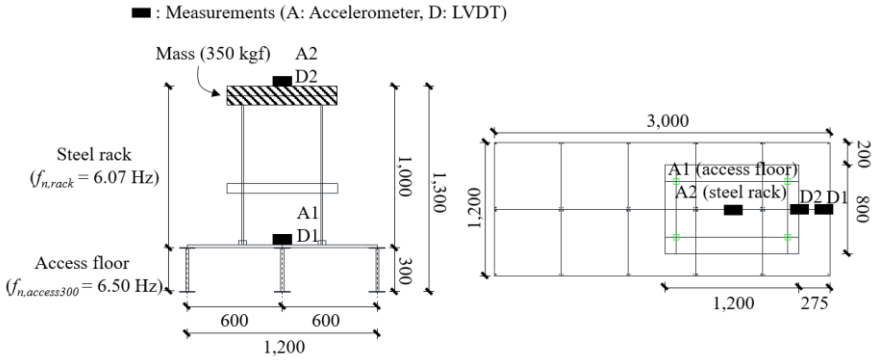

(b) Steel rack specimens mounted on 150 mm-high access floors (FH150-series)

Figure 3. Dimensions and measurement plan of access floor-mounted steel rack specimens

installed in the 2-story test frame by the collaborative research team. The nonstructural elements included stone and steel panel exterior claddings, metal panel and lightweight suspended ceiling systems, full- and partial-height partition walls, steel racks mounted on access floor, water tanks, pipes, fire sprinklers, and UPS (mechanical nonstructural elements). Tests were performed in two stages where the non-seismic test specimens were tested first, and then the performance of seismic-designed test specimens was evaluated.

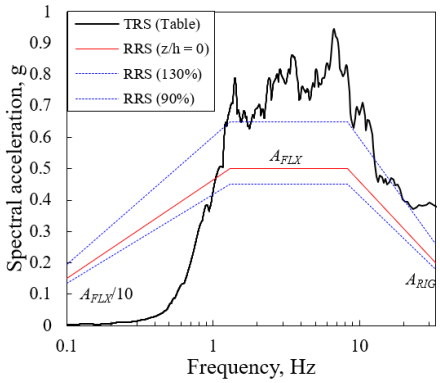

Figure 4. Artificial input motion generated to envelop ICC-AC156 required response spectrum

The steel frame was mounted on an array of two isolated shake tables and incremental uniaxial tests were conducted by shaking the two tables synchronously. The measurement plan using the accelerometers and LVDTs is shown in Fig. 2.

The 1st- and 2nd-mode natural frequencies of the test frame measured from white-noise excitation were 1.50 Hz (0.67 sec.) and 4.59 Hz (0.22 sec.), respectively. The measured damping of the 1st mode was 1.5% of the critical damping.

On the roof floor of the test frame, steel rack specimens were installed to measure the peak component acceleration (PCA). A total of four access floor-mounted steel rack specimens were tested, which are rigidly mounted on four different types of access floors. The natural frequency of the steel rack was measured as 6.07 Hz, and the critical damping ratio was approximately 1.0 %. The access floors had variations in their height and the base-fixing method. FH300-series specimens utilized 300 mm-high flexible access floors, whereas the more rigid 150 mm-high access floors were employed for FH150-series specimens. The natural frequencies of the 300 mm- and 150 mm-high access floors were measured as 6.5 Hz and 27.0 Hz, respectively. Specimens denoted with -F were rigidly fixed to the concrete floor slab through concrete nails, whereas the specimens with -S had no positive base fixtures such that some sliding movement could occur. The detailed dimension and measurement plan are shown in Fig. 3.

Input Motion for Shake-Table Test

Incremental shake table tests were performed using artificial input motions generated following ICC-AC 156 (2010). The required response spectrum for generating input motion was constructed using S_{DS} = 0.50 g, which corresponds to the highest seismic demand according to Korean Design Standards (KDS 41 17 00, 2019). As shown in Fig. 4, the artificial input motions well enveloped the RRS specified by ICC-AC 156.

TEST RESULTS

Effect of Structural Ductility on Floor Response Spectrum

Fig. 5(a) shows the in-structural amplification measured during the incremental shake table tests. It can be observed that the overall amplification along the height reduced as the frame underwent nonlinear behavior. The tested steel frame was yielded when subjected to 60 % RRS (PGA = 0.21 g) input motion. To evaluate the effects of structural nonlinearity on PFA reduction, the nonlinear response parameters used to define PFA reduction in ASCE 7-22 (see Eq. 4) were utilized. The u_{max} and u_y were obtained based on the cyclic roof displacement and the base shear relationship of the tested frame (Fig. 5(b)). Only the data measured at 30 % and 60 % RRS tests were presented due to the space limitation.

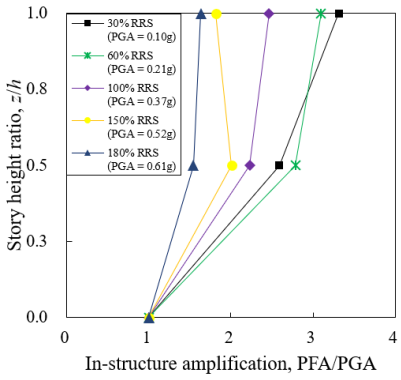

(a) Decreasing in-structure amplification

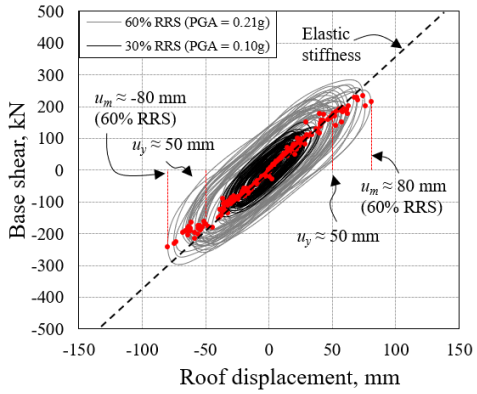

(b) Determination of yield and maximum roof displacements

Figure 5. Effects of structural nonlinearity and measurement of structural ductility level

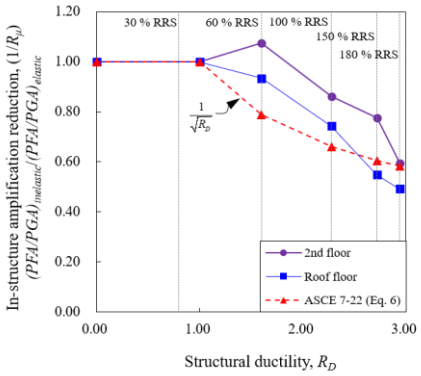

(a) PFA reduction depending on structural ductility

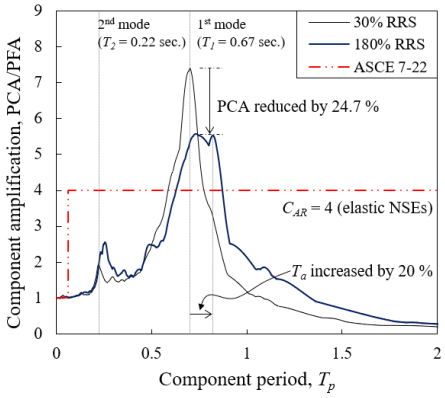

(b) Elastic PCA reduction caused by structural nonlinearity (roof floor)

Figure 6. Effects of structural ductility on PFA and elastic PCA

The relationship between the measured PFA reduction and the structural ductility (R_D) was summarized in Fig. 6(a). Overall, the PFA was much more reduced on the roof floor than on the 2nd floor. The PFA at the structural ductility level of 3 was 40 % - 50 % of the elastic PFA. The difference in PFA reduction between 2nd and roof floors may have resulted from the non-uniform yielding of the test frame. The PFA reduction was generally overestimated by ASCE 7-22 until the test frame achieved a low-to-moderate level of structural ductility (R_D = 2.94).

To evaluate the effect of structural ductility on the PCA of elastic components, the component amplification spectrum was constructed in Fig. 6(b). As the frame yielded, the shift in the fundamental structural period was noticed, and a high reduction in the component amplification was observed on both floors. Under a low-to-moderate level of structural ductility (R_D = 2.94 at 180 % RRS), the elastic resonant PCA around the fundamental period was reduced by 36 % and 25 % on the 2nd and roof floor, respectively. The effects of structural nonlinearity on PCA are currently not addressed by ASCE 7-22. Further study needs to be conducted to avoid the overdesign of elastic components mounted on elastic supporting structures.

Effect of Component Ductility on Peak Component Acceleration

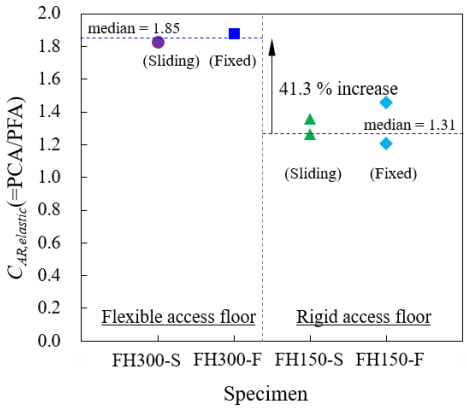

Figure 7. Effects of flexibility of component mountings on the PCA

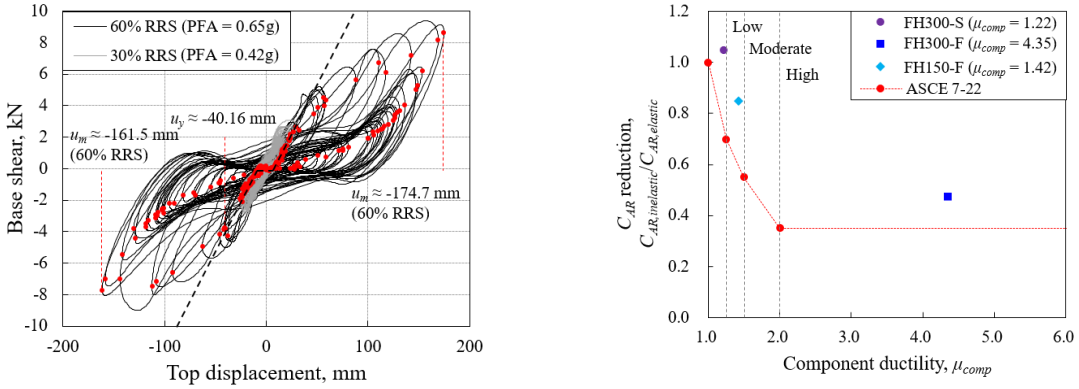

(a) Pinched hysteretic behavior of FH300-F specimen

(b) Comparison of measured and ASCE 7-22 CAR reduction depending on component ductility level

Figure 8. Pinched hysteretic behavior of access floor-mounted steel rack specimen and its effects on PCA reduction

Fig. 7 presents the elastic C_{AR} evaluated before the steel rack specimens yielded. The PCA measured at the top of the steel rack was normalized by the PFA to obtain the elastic C_{AR}. It is shown that the base sliding FH300- and FH150-S specimens seemed to have a minor effect on the component response, which might have been caused by a very small sliding movement of the specimens (approximately 4 mm). Steel rack specimens mounted on flexible 300 mm-high access floor (FH300-series specimens) were subjected to higher C_{AR} than FH150-series specimens due to the large period shifting of FH300-series specimen systems. The natural period of FH300-series specimens became closer to the 2nd mode of the test frame ($T_{1,FH300}/T_{2,frame}$ = 0.76), resulting in more than 40 % higher PCA compared to that of FH150-series specimens. These results clearly indicated that possible interaction between nonstructural elements and non-rigid mounting needs to be properly considered in their seismic design.

Fig. 8 summarizes the test results analyzing the effects of component nonlinearity on the PCA reduction. First, it was observed that all the steel rack specimens showed a highly pinched behavior caused by the loosely connected beam-to-column tab joints in the access floor (see Fig. 8(a)). The noticeable pinching behavior of test specimens might be related to the underestimation of C_{AR} made by ASCE 7-22, as shown in Fig. 8(b), which was proposed based on the bilinear hysteretic model. It is well known that systems with pinched hysteretic behavior generally exhibit inferior energy-dissipating capacities. Considering that many of the floor-mounted nonstructural elements (such as steel racks and partition walls) frequently involve pinched hysteretic behavior of tabbed or hooked joints, further investigation

including the pinching model is warranted to establish a more realistic relationship between the component ductility and C_{AR}.

SUMMARY AND CONCLUSIONS

In this study, the seismic demand on nonstructural elements was evaluated through shake-table testing of a full-scale 2-story steel moment frame. Various types of nonstructural elements were installed in the 2-story frame by the collaborative research team. This study discussed the effects of structural and nonstructural nonlinearities on the peak floor and peak component acceleration. The results of this study can be summarized as follows:

1. The PFA reduction suggested by ASCE 7-22 to account for structural nonlinearity was larger than the experimental results until the 2-story test frame developed a moderate level of ductility (Rd = 2.94). Because of the non-uniform yielding of the test frame, the PFA reduction was more pronounced on the roof floor than on the 2nd floor, which implies that the PFA reduction overestimation made by ASCE 7-22 could be much more severe for lower floors. Additional studies on supporting structures with a moderate-to-high level of ductility seem desirable.

2. The resonant PCA was also significantly affected by structural nonlinearity. For elastic nonstructural elements resonating to the fundamental mode of the test frame, the PCA was reduced by 30 % as the test frame reached a moderate level of structural ductility (R_D = 2.94). The effects of structural nonlinearity on the response of elastic component needs to be systematically addressed.

3. The results of steel rack specimens evidently showed that the flexibility of the mountings (in this study, access floor) needs to be properly considered in the design. About 40 % higher PCA was observed for FH300-series steel rack specimens mounted on flexible access floors.

4. The PCA reduction depending on the component ductility level was generally less than the prediction made by ASCE 7-22. Such differences are speculated to be caused by the inferior energy-dissipating capacity of steel rack specimens which showed a pinched hysteretic behavior. Considering that the pinching behaviors are commonly reported for the floor-mounted components, a more refined analysis using the pinching model needs to be conducted to establish a more realistic PCA and component ductility relationship.

ACKNOWLEDGMENTS

This research was supported by a grant (21AUDP-C146352-04) from Architectural & Urban Development Research Program funded by Ministry of Land, Infrastructure and Transport of Korean government.

REFERENCES

ASCE/SEI, 7-22 (2022). *Minimum design loads and associated criteria for buildings and other structures*. American Society of Civil Engineering, VA, USA.

SEAOC (1999). *Recommended lateral force requirements and commentary, 7th edition*. Seismology Committee Structural Association of California, San Francisco, CA.

NIST (2018). "Recommendations for improved seismic performance of nonstructural components (NIST GCR 18-917-43)", National Institute of Standards and Technology.

ICC (2010). *Acceptance criteria for seismic certification by shake-table testing of nonstructural components, ICC-ES-AC156*. International Code Council, Whittier, CA.

AIK (2019). *Seismic building design code, KDS 41 17 00*. Architectural Institute of Korea, Seoul, Korea (in Korean)

EXPERIMENTAL STUDY OF SUSPENDED BUSWAY SYSTEMS

Wei-Chung Chen[1], Zeng-Wei Zeng[2], Fan-Ru Lin Fan-Ru Lin[3], and Juin-Fu Chai [4]
1. Assistant Researcher, National Center for Research on Earthquake Engineering, Tainan, Taiwan, R.O.C.
2. Graduate Student, National Cheng Kung University, Tainan, Taiwan, R.O.C.
3. Associate Researcher, National Center for Research on Earthquake Engineering, Taipei, Taiwan, R.O.C.
4. Deputy Director General, National Center for Research on Earthquake Engineering, Taipei, Taiwan, R.O.C.
Email: 2006023@narlabs.org.tw

ABSTRACT

Damage to nonstructural components during past seismic events has been shown to be not only a critical threat to life in extreme cases but has also led to a substantial reduction in the functionality of buildings and other facilities. Suspended busway systems are among the important yet lesser understood nonstructural components of a building for which the current standards provide only limited seismic design guidance due to their heterogeneous and complex construction. In order to understand the dynamic behavior of suspended busway systems, a series of full-scale shaking table tests were conducted at National Center for Research on Earthquake Engineering Tainan Laboratory. This paper presents details of this experimental study, including the test setup and configurations, the test motions, and the failure patterns of the busway systems observed during the tests.

Keywords: suspended busway systems, cast resin busway, metal busway, shaking table tests, nonstructural components

INTRODUCTION

The busway (Figure 1) is a suspended electrical distribution system that uses copper or aluminum busbars with suitable enclosures and a significant amount of protection to prevent the inside conductors from damage caused by foreign bodies. It has a compact design and the compressed flat conductors can pass through the enclosure. Due to this compact design, busway systems require less space than traditional cable systems do and this is a major advantage when thousands of amperes of electricity need to be transmitted. These systems can also be used in any kind of structure and with any configuration. They are easily modifiable and hence an extra room or any mechanical equipment can be easily added, and they also help to facilitate the efficient and safe distribution of lines with junction boxes located where they are required. The data junction boxes can be easily increased in number and changed whenever and wherever in the future. In addition to the convenience and safety factors, there are several other advantages that the busway systems have over the traditional cable systems and that is the reason they are becoming commonly used in important buildings and facilities (Figure 2).

Figure 1. The busway system

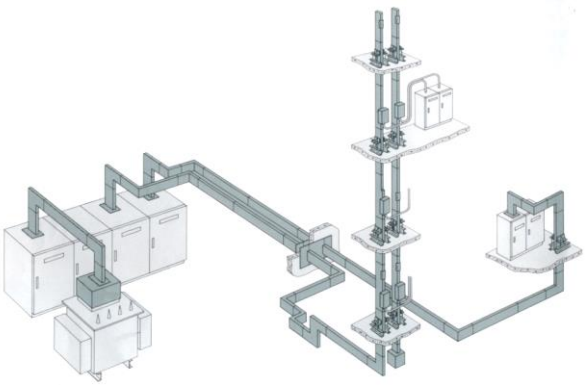

Figure 2. Typical busway layout in buildings

Dating back to the 1999 Chi-Chi earthquake, seismic events had caused documented damage to suspended busway systems stated in several subsequent post-earthquake studies. Common damage primarily consisted of fractured elements, damaged trapeze systems, joint connection failure, and anchorage failure. In more serious cases, misaligned joint connections resulted in the electrical short-circuit of the busway system, as shown in Figure 3. Loss of power was shown to be not only a critical threat to life but also led to a substantial reduction in the functionality of important facilities.

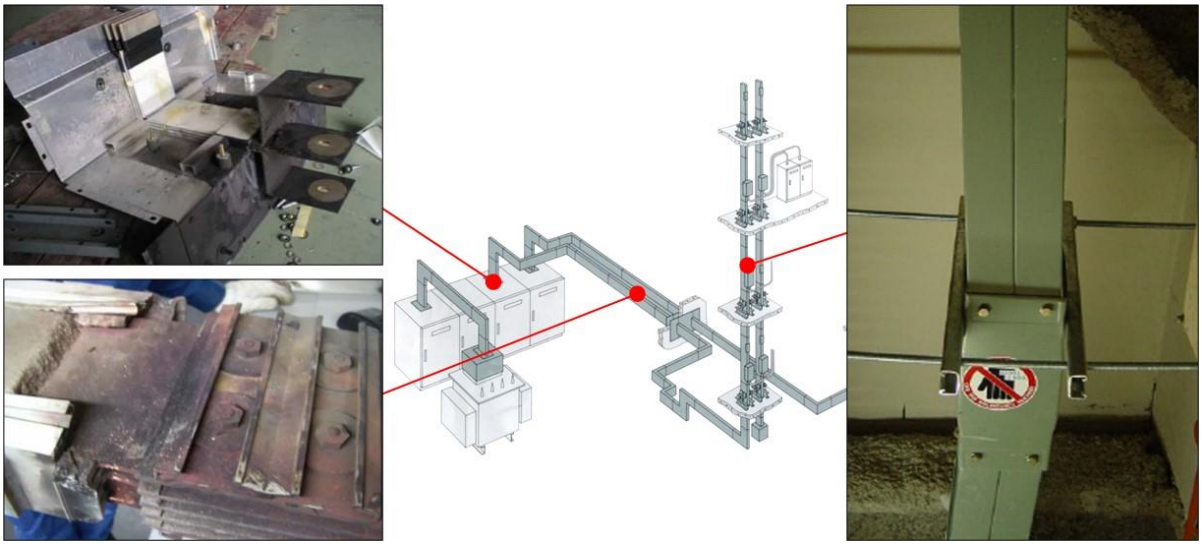

Figure 3. Electrical short-circuit caused by misaligned joint connections

Suspended busway systems are composed of combinations of many discrete components, which makes it difficult to determine the strength capacity of the entire system. In order to understand the seismic performance and the dynamic behavior of busway systems subjected to earthquake induced excitation, a series of full-scale shaking table tests were performed using a long-stroke and high-speed earthquake simulator at the National Center for Research on Earthquake Engineering (NCREE) Tainan Laboratory. This paper presents the test setup, specimen configurations, input test motions, and failure mechanisms of the busway systems observed during the experiments.

TEST SETUP

A three-story test frame 5 m × 5 m in area and 12.7 m high was mounted on the shaking table at National Center for Research on Earthquake Engineering (NCREE) Tainan Laboratory for a series of full-scale dynamic tests. The steel structure is shown in Figure 4. For the purpose of achieving a larger inter-story drift, an increased mass was added to the floor decks. The weight of the three-story test frame without the busway system was approximately 46t. The dynamic properties of the bare test frame were obtained using transfer functions, Hanning window with 8192 window points from data, calculated from acceleration histories (white noise tests) between the shaking table and the roof center. The fundamental frequencies of the test frame in the two horizontal directions were both 1.1 Hz, while the frequency in the vertical direction was 11.7 Hz.

In order to measure the response of the test system, various instruments as shown in Table 1 including accelerometers, displacement transducers, and motion capture systems were installed to the shaking table, the test frame, and the busway systems.

Figure 4. The three-story test frame

Table 1 List of instrumentation

Instrumentation	Quantity
Tri-axial accelerometer (Dytran)	34
Single-axis accelerometer (Setra)	9
Temposonis (MTS)	21
DP-E Displacement Transducer (Tokyo Measuring Instruments Lab.)	8
Motion capture system (Optitrack)	40

TEST BUSWAY CONFIGURATIONS

Two types of suspended busway systems were constructed inside the three-story test frame to investigate the influence of various input motions and layout parameters. The first system was the metal sandwich busway system, in which the inner conductor and insulator are protected by a metal shell structure (Figure 5). The other system was the cast resin busway system (Figure 6) that uses a mixture of epoxy resin and insulating filler as a shell to protect the inner conductor.

Figure 5. The metal busway system

Figure 6. The cast resin busway system

Figure 7. The test busway configurations

Figure 7 shows the test configurations of the suspended busway systems on different floors, which consist of series of line elements joined by different types of connections. A distribution box was installed at the center of the first floor, and two complete metal busway systems with different configurations were developed from the distribution box through the second floor to the third floor. The primary test parameters of these two systems were the plenum heights which were 1.5m and 3.0m respectively. A portion of a typical cast resin busway system was installed on the second floor. This test specimen was designed to explore the seismic performance of the cast resin busway system and to investigate the effects of different plenum heights at the same time.

All of the test busway systems were made in compliance with the current construction method in Taiwan. The trapeze systems (see Figure 8(a)) hanging the main runners were placed at an interval of 150cm, and two types of braced frames were adopted for busway systems with different plenum heights, as shown in Figure 8(b, c).

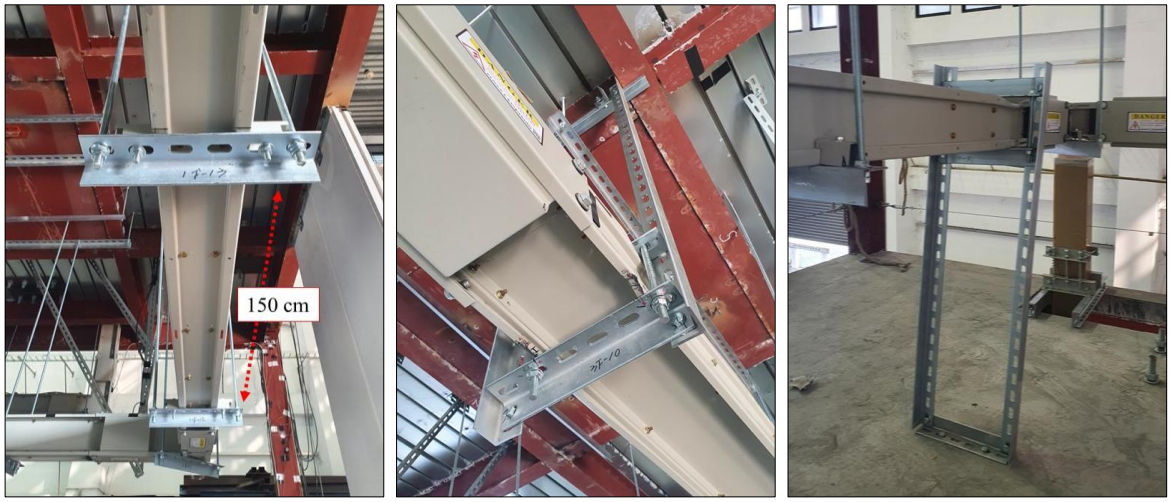

(a) (b) (c)

Figure 8. (a) The trapeze systems; (b) The suspended braced frame; (c) The grounded braced frame

TEST MOTIONS

Various input motions were used for different purposes. White noise tests, sine-beat tests, and sine sweep tests were performed to identify the dynamic characteristics of the test busway systems, whereas ground motion tests were implemented to simulate realistic earthquake events. Table 2 summarizes the information of the selected earthquake events, and these events were scaled down to target levels to prevent the test frame from suffering severe structural damage. A conceptual computer model (Figure 9) was created using SAP2000 to assess the strength capacity of the test frame, which took into account the interaction between the test frame and the busway systems.

Table 2 Description of the test motions

Events	Station	Scaling
Kobe EQ	JMA	20%
	Takatori	20%
	Shin-Osaka	60%
Northridge EQ	Rinali Receiving	20%
	Beverly Hill	30%
Chi-Chi EQ	CHY101	40%
	CHY025	90%

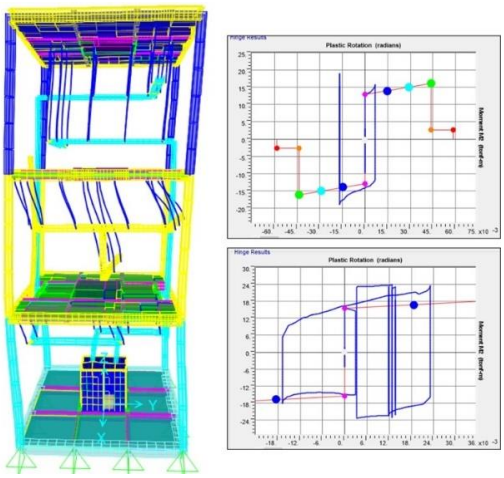

Figure 9. The SAP2000 numerical model

The test busway systems were subjected to incremental base motions, starting from 10% of the target level of each earthquake event until substantial and unrepairable damaged was observed in the test specimens. After each step of every seismic event, the busway systems were visually inspected to record the changes and to document damage. It was noted that any damage to the test specimens can only be simply repaired, resulting in accumulated damage to the busway system in the following test steps.

TEST RESULTS

The test results of the primary failure patterns of the busway systems are presented in this section. Three main failure patterns were identified: (i) failure of the trapeze systems, (ii) failure of the braced frames, and (iii) failure of the line elements.

Failure of the trapeze systems

Slip between the line elements of the busway and the trapeze systems was the early observation inspected during the experiment, which happened at low intensity of the input excitation which the PFA (peak floor acceleration) was 250gal. The moment when the slip occurred can further be found from the monitor videos, as presented in Figure 10, showing the response acceleration of the busway element was approximately 600 gal.

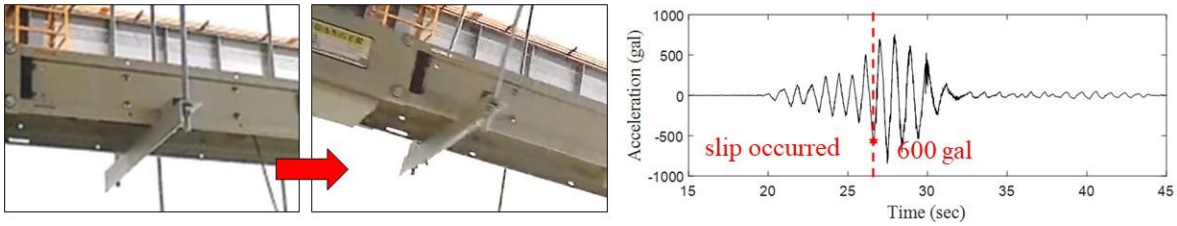

Figure 10. Slip between the busway elements and the trapeze systems

This failure of one trapeze system resulted in progressively missing vertical supporting and uneven loading distribution of the busway systems, which led to other more severe failure. Figures 11(a) and (b) show the failure of the trapeze rods and trapeze attachments with a corresponding PFA of 450 gal and 500 gal, respectively. The most serious damage to the trapeze systems was observed when the PFA exceeded 650 gal, as shown in Figure 11(c).

(a) (b) (c)

Figure 11. (a) Failure of the rods; (b) Failure of the attachments; (c) Complete failure of the trapeze

(a) (b)

Figure 12. (a) Deformation of the ground braced frame; (b) Failure of the anchor bolt

Failure of the braced frames

Visible deformation of the grounded braced frames (Figure 12(a)) was recorded with a PFA of 300 gal and this caused slip between the line elements of the busway and the braced frames. Eventually the grounded braced frames were pulled out when the PFA exceeded 650 gal, as shown in Figure 12(b). The failure patterns of the suspended braced frames were similar to those of the grounded braced frames. Visible deformation and complete failure (Figure 13) were observed with a PFA of 400 gal and 700 gal, respectively.

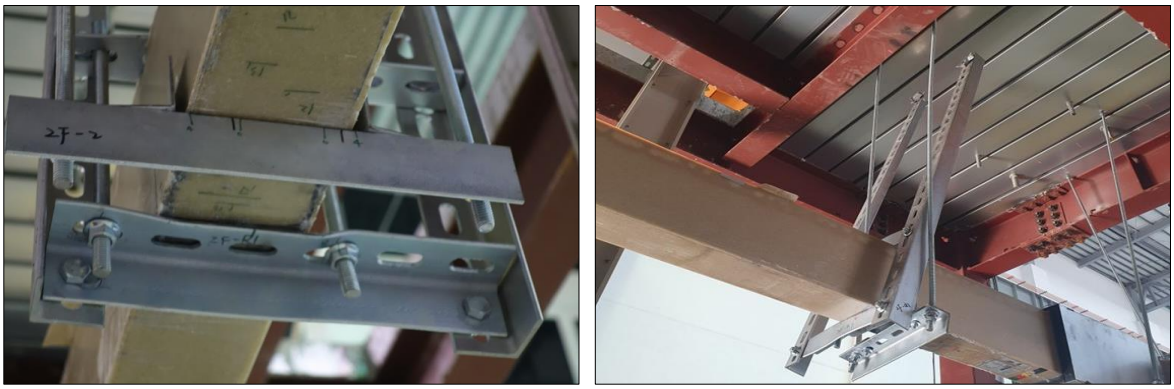

(a) (b)

Figure 13. (a) Deformation of the suspended braced frame; (b) Complete failure of the braced frame

Failure of the line elements

Damage to the line elements (Figure 14(a)) occurred primarily in the cast resin busway system when the PFA exceeded 200 gal. The worst case resulted in exposure of the conductor and was recorded with a PFA of 650 gal, as shown in Figure 14(b). In terms of the metal busway system, it was only observed that the metal shell damaged during the tests, as shown in Figure 14(c).

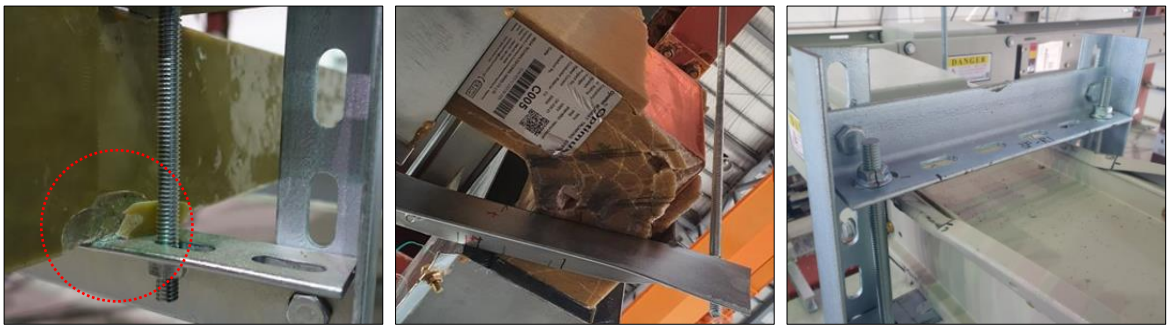

(a) (b) (c)

Figure 14. (a) Fracture of the line element; (b) Complete failure; (c) Metal busway system

CONCLUSIONS

Although the busway systems are commonly used in recent years, the current standards provide only limited seismic design guidance due to their complex construction. Based on the test result, several failure patterns were identified with respect to the busway systems made in compliance with Taiwan construction method. Among all the failure patterns, fractures in the cast resin busway system requires special attention. For this system, a mixture of epoxy resin and insulating filler is used as a shell to protect the inner conductors. However, this material lacks of ductility and gets cracked while suffering concentrating loads. In the most dangerous situation, even a small crack appears inside the element of the cast resin busway system, free electrons will flow from one conductor to another and consequently

lead to electrical short-circuit or fire disaster. Therefore, it is necessary to improve the seismic safety of the busway systems in buildings.

ACKNOWLEDGMENTS

This study was supported by OPTIMUS technology co., Ltd. The authors are grateful to this support.

REFERENCES

American Society of Civil Engineers (ASCE), 2016. “Minimum design loads for buildings and other structures”, ASCE/SEI 7- 16, ASCE, Reston, VA.

Federal Emergency Management Agency (FEMA 273), 1997. “NEHRP Guidelines for the Seismic Rehabilitation of Buildings.” FEMA 273, Applied Technology Council, Redwood City, CA, USA.

Federal Emergency Management Agency (FEMA 302), 1997. “NEHRP Recommended Provisions for Seismic Regulations for New Buildings and Other Structures: Part 1, Provisions.” FEMA 302, Building Seismic Safety Council, Washington, DC, USA.

Federal Emergency Management Agency (FEMA P695), 2009. “Quantification of Building Seismic Performance Factors.” FEMA P695, Building Seismic Safety Council, Washington, DC, USA.

EXPERIMENTAL STUDIES OF STRENGTHENING STRATEGIES FOR SMALL-BORE PIPING OF FIRE PROTECTION SPRINKLER PIPING SYSTEMS

Fan-Ru Lin[1], Chun-Yu Chen[2], Zen-Yu Lin[3], Wen-I Liao[4], and Juin-Fu Chai[5]

1. Associate Researcher, National Center for Research on Earthquake Engineering, Taipei, Taiwan, R.O.C.
2. Graduated Student, National Taipei University of Technology, Taipei Tech, Taipei, Taiwan, R.O.C.
3. Assistant Researcher, National Center for Research on Earthquake Engineering, Taipei, Taiwan, R.O.C.
4. Professor and Department Head, National Taipei University of Technology, Taipei Tech, Taipei, Taiwan, R.O.C.
5. Division Director and Deputy Director General, National Center for Research on Earthquake Engineering, Taipei, Taiwan, R.O.C.

Email: frlin@ncree.narl.org.tw, zylin@ncree.narl.org.tw, wiliao@ntut.edu.tw, chai@ncree.narl.org.tw

ABSTRACT

In recent years, due to the vigorous development of performance design concepts, the seismic resistance of building structures has been improved, and the main disasters and economic losses caused by earthquakes have shifted from structural to non-structural systems. This study takes a hospital as an example to explore the seismic performance of pipelines subjected to different types of earthquakes, damage to ceilings, water leakage, partial collapse, and other failure modes. The results of shaking table tests and numerical model analysis are used to verify the simplified evaluation methods.

Keywords: fire protection sprinkler system, shaking table tests, seismic strengthening devices, numerical analysis, simplified evaluation

INTRODUCTION

During small- and medium-scale earthquakes, a fire-protection sprinkler system might be damaged and cause leakage of small-bore piping, and sprinkler heads might impact ceiling boards resulting in falling dusts and debris. In large-scale earthquakes, anchorage or supports of sprinkler piping systems might lose seismic capacity. Damage related to sprinkler piping may cause interruption of the normal medical functions of hospitals and fail to prevent secondary disasters such as fires after earthquakes. Therefore, improvement of seismic performance designs of fire-protection sprinkler systems is necessary.

In this study, a full-scale fire-protection sprinkler piping system with an area of approximately 10 m x10 m was suspended on the shaking table in the Tainan Laboratory of the National Center for Research on Earthquake Engineering. Shaking table tests were carried out to compare the effects of different seismic strengthening configurations. Floor responses of two kinds of buildings under far-field or near-fault earthquakes were adopted as input motions. Numerical models simulating the seismic response of the hospital pipeline system were established to verify the simplified evaluation method. The research contents are briefly described as follows:

1. Taking the fire-protection sprinkler piping system of a hospital damaged during the 2010 Jiaxian earthquake as an example, a full-scale fire-protection sprinkler piping system was recreated and hung by a rigid test frame in the laboratory. As shown in Fig. 1, the tested sprinkler piping specimen covered two sickrooms and an outside corridor. The part of the sprinkler piping damaged during the Jiaxian earthquake was tested. The real main pipe of the sprinkler system along the corridor exceeds the range of the shaking table. Therefore, the boundary condition of the tested partial main pipe was designed according to initial simulation results of moment distribution under earthquakes. In addition to the original configuration, three types of seismic strategies were adopted: braces of the main pipe, diagonal cables for branches or sprinkler heads, and flexible hoses for small-bore piping at wall penetrations.

2. The seismic behavior of the sprinkler piping system covering the entire floor plan was evaluated by numerical analysis with SAP2000 software. Comparing numerical analysis and shaking-table test results of part of the piping system, the accuracy or conservativism of analysis parameters of nonlinear dynamic analysis were verified and then applied to the complete numerical model of the sprinkler piping system covering the entire floor plan. Component parameters of seismic devices including bracing attachments, wire cables, and flexible hoses were set according to the results of specific cyclic-loading tests.
3. In order to enable engineers to design sprinkler piping conservatively without complex numerical analysis, the seismic behavior of the sprinkler piping observed in shaking table tests was used to adjust parameters of the simplified evaluation method (Tsai, 2018) and thus improve its effectiveness and accuracy, as shown in Fig. 2.

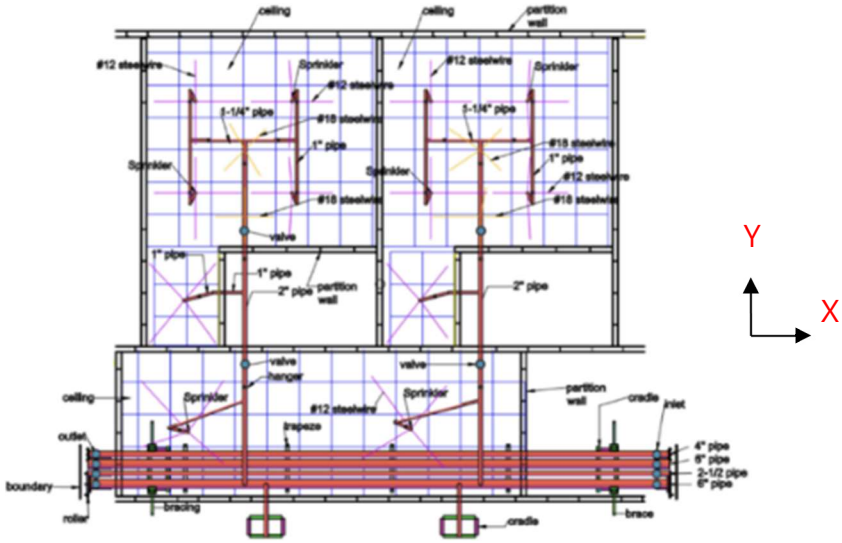

Figure 1. Test specimen of sprinkler piping (Su, 2020)

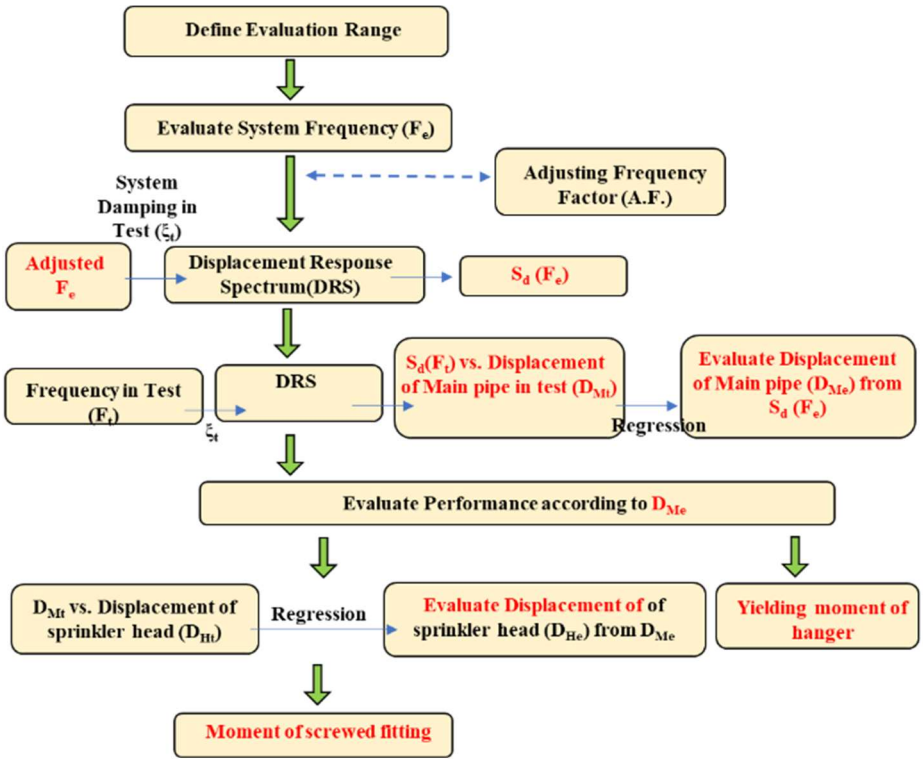

Figure 2. Simplified evaluation flowchart

EFFECTIVENESS OF SEISMIC IMPROVEMENT STRATEGIES FOR SPRINKLER PIPING

Seismic Strategies

Based on the National Fire Protection Association NFPA13 standard, this research proposes four seismic improvement strategies for the example case. Table 1 lists the strengthening devices of each strategy. Strengthening devices used are main pipe bracing, flexible hose, and diagonal steel-wire cables.

Seismic Performance of Sprinkler Piping with Strengthening Devices

1. Axial force of main pipe bracing

As shown in Fig. 1, based on the damaged example case, the main source of inertia force is from the main pipe along the corridor in the X direction. Therefore, the seismic response of the piping system in the Y direction is controlled by the fundamental mode of lateral movement of the main pipe, which can be evaluated by the corresponding spectral acceleration of input motion in the Y direction. Figure 3 depicts the comparison of axial forces of the diagonal braces of the main pipe due to the floor spectral acceleration for three configurations: SBH, AXX, and AXF cases. The spectral acceleration values corresponding to the piping system frequency in the Y direction were obtained from the response spectrum of the test frame. The axial forces of the braces on both sides were derived from the measured maximum strain values under each shaking table test. Comparing the SBH and AXF cases indicated in Fig. 3, due to the smaller frequency of the AXF system, both the spectral acceleration value and axial force of braces were amplified under the same input motion (3DNDL40). On the other hand, the flexible hoses decreased the effects of the partition walls on the response of piping, so that both the displacement response of the pipeline system and the axial force of the diagonal brace were amplified. From test results, it can be seen that more consideration should be given to the seismic capacity of diagonal braces while installing flexible hoses arranged near wall penetrations.

Table 1. Test configurations

	Seismic brace of main pipe (A、S)	Restraint of branch lines (B)		Restraint of sprinkler heads (H)		Flexible pipe (F)
		Left room	Right room	Left room	Right room	
Case 1 (SBH)	V	V	V	V	V	
Case 2 (AHLABR)	V		V	V		
Case 3 (AXX)	V					
Case 4 (AXF)	V					V
Original (XXX)						

V: installed devices

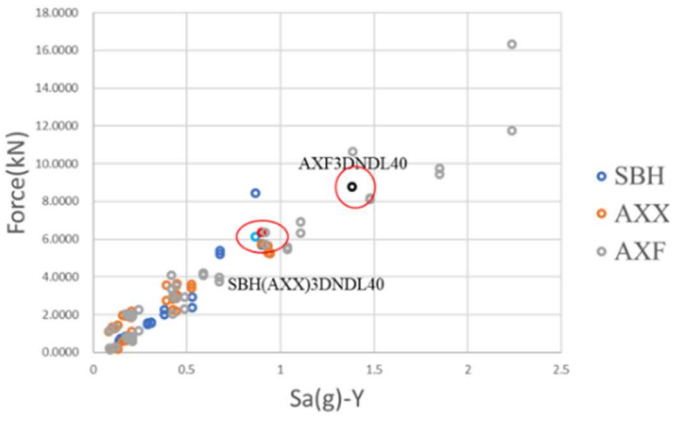

Figure 3. Comparison of axial forces of braces

2. Leakage situation

The example case shows that the damaged threaded joint of the one-inch drop could easily cause leakage in the hospital. Therefore, the seismic capacity of the threaded joint of the one-inch branch pipe is also one of the important factors in the design of the fire sprinkler system. Table 2 depicts a comparison of the bending moment and water pressure of the one-inch pipe when each test configuration was damaged or reached the maximum input motion. Table 2 also shows that there was no leakage in terms of the SBH and AXF tests. The test results verify the effectiveness of the steel-wire cables to branches and drops. In addition, the use of small-bore flexible hoses near wall penetrations increases the displacement response of the piping system during earthquakes, but it can reduce the damage at the threaded joints of the one-inch branch pipes.

Table 2. Bending moment of one-inch pipe and leakage situation

Configuration		Input motion	Water pressure (kgf/cm2)	1" pipe moment (kgf-cm)
AXF	Left room	3DNDL60 no leakage	no leakage	338
				-410.3
AXX		3DNDL40	no leakage	3110
				-3179
SBH		3DFDH60 no leakage	no leakage	547.6
				-110.5
XXX		1YNDL10	6.87	5540
			6.996	-5061
Configuration	Right room	Input motion	Water pressure (kgf/cm2)	1" pipe moment (kgf-cm)
AXF		3DNDL60 no leakage	no leakage	606.4
				-436.7
AXX		3DNDL40	6.758	3851
			6.77	-2898
SBH		3DFDH60 no leakage	no leakage	565.4
				-277.4
XXX		1YNDL10	no leakage	5504
				-2264

3. Effects on adjacent ceiling systems

For commercial buildings, sprinkler heads of the fire protection system are generally arranged at the center of ceiling boards. Therefore, excessive relative movement between sprinkler piping and suspended ceiling systems could easily result in impacts between ceiling boards and sprinkler heads. From previous studies and component tests of ceiling boards (Tsai, 2018), when the displacement of a sprinkler head is equal to or greater than 16.6 mm, it is judged that the mineral-fiber ceiling board was torn and damaged. Figure 4 compares the sprinkler head displacement of each configuration due to the spectral floor acceleration to evaluate the ceiling failure situation. The displacement of the sprinkler head in the original configuration (XXX) greatly exceeds 16.6 mm. It can be seen that under the same spectral acceleration, the displacement of the sprinkler head in the SBH configuration is small. Therefore,

the seismic steel-wire cables and braces of the main pipe are verified to decrease effects on the adjacent ceiling system. On the other hand, from the comparison between the AXX case and the AXF case, although the installation of the flexible hoses reduces the bending moment of the one-inch branch pipe, it also causes an increase of sprinkler head displacement due to the lower displacement limitation offered from the partition wall. Therefore, the displacement response of sprinkler heads in the AXF case was larger than that in the AXX case.

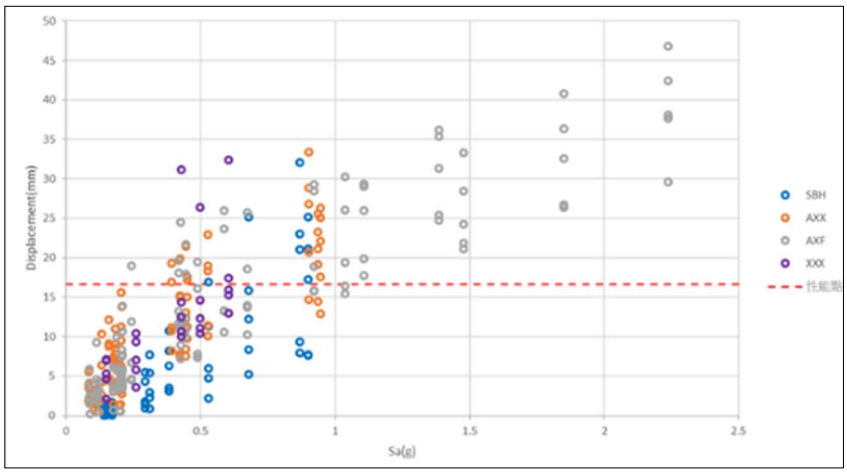

Figure 4. Comparison of sprinkler head displacement

NUMERICAL MODEL ANALYSIS

In this study, SAP2000 software was used to establish numerical models of each test configuration (Fig. 5). The parameter settings of the numerical models were verified with shaking table tests, and these were extended to the numerical model of the complete hospital pipeline system (Fig. 6).

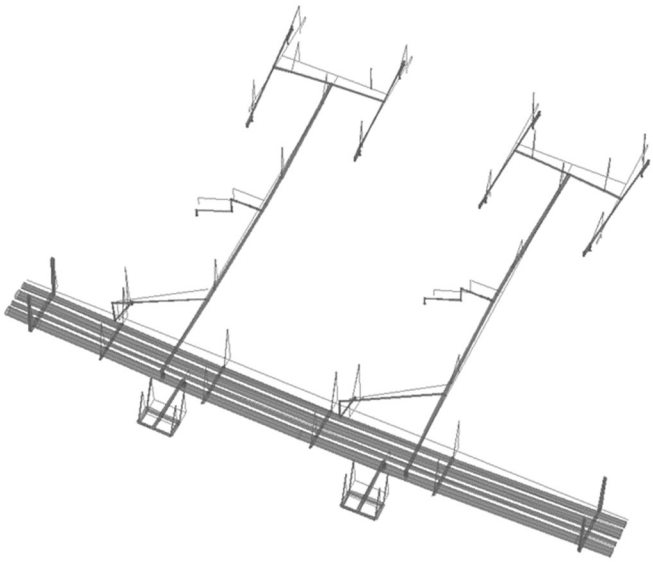

Figure 5. Numerical model of partial pipeline system

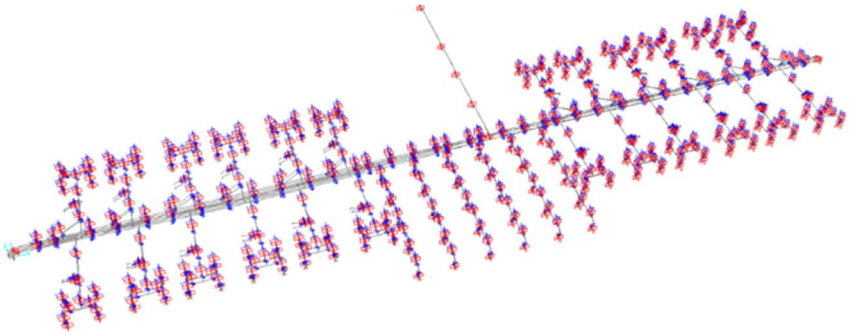

Figure 6. Numerical model of whole pipeline system

Fig. 7 depicts displacement responses of the main pipe of the tested AXX case (blue line), the corresponding numerical model (red line), and the numerical model covering the whole floor plan (black line). It can be seen that due to the nonlinear response of sprinkler piping under large-scale floor motion, the numerical peak value (red line) and the tested value (blue line) are different. Numerical responses of the main pipe of partial (red line) and complete (black line) models are quite similar due to the boundary condition of the partial main pipe; this boundary condition was carefully designed based on the location of the inflection point of the main pipe shown in the initial numerical modal analysis of the complete piping system. Figure 8 depicts the comparisons of maximum main pipe displacement of tests and numerical results for four tested cases. Most of the numerical results are smaller than test results; this unconservative tendency requires attention. According to test and analysis results, a safety factor for numerical analysis is proposed to bring the numerical analysis results closer to the real response of the main pipe.

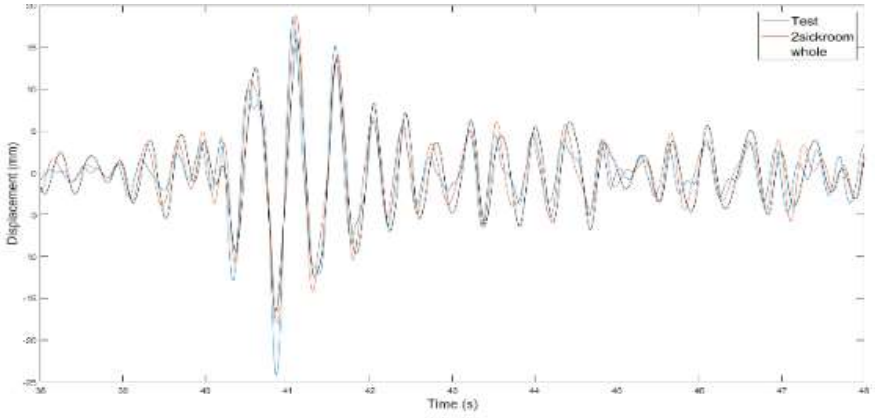

Figure 7. Displacement response of the main pipe in the AXX case

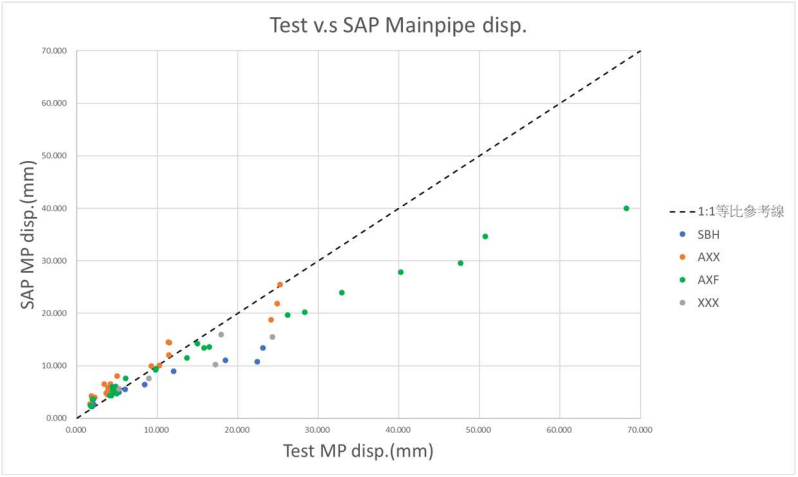

Figure 8. Maximum displacement of the main pipe

SIMPLIFIED EVALUATION AND VERIFICATION

The third part of this study uses the floor spectral displacement to evaluate the displacement response of the main pipe along the corridor, and then estimates the dynamic response of related branch lines covering sickroom systems from the displacement response of the main pipe. As shown in Fig. 9, the relationship between spectral displacement and the displacement response of the main pipe is adopted to evaluate the displacement response of the main pipe.

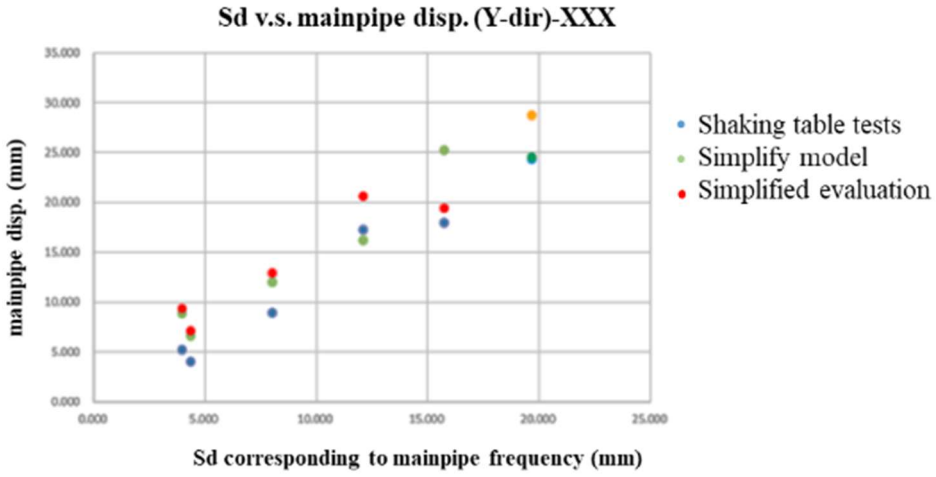

Figure 9. Relationship between responses of main pipe and spectral displacement

CONCLUSIONS

The effectiveness of three types of seismic restraint device were tested: braces with well-designed attachments for the main pipe, steel cables for branch lines, and flexible hoses for penetrations. Braces on main pipes with well-designed attachments were found to be most critical in controlling the majority of inertial forces acting on the piping system. Steel cables restrain displacements of sprinkler heads but effectiveness is decreased due to the necessity of maintaining slack to keep the piping level with the ceiling system. Flexible hoses were effective in decreasing local impact forces near wall penetrations. While bracing can reduce damage from impacts onto adjacent ceiling systems and architectural components, the optimum strategy to avoid leakage is to strengthen the main pipe with braces and to use flexible hoses near wall penetration to decrease demands on screwed fittings, or to use braces and steel cables to limit the movements of the main pipe and branch lines, respectively.

References

National Fire Protection Association (2019). Standard for the Installation of Sprinkler Systems, NFPA 13, U.S.

Yung-An Tsai (2018). Seismic Performance Assessment of Strengthened Fire Protection Sprinkler Piping Systems in Hospitals.

Pei-Ru Wu (2020). Seismic Performance of Flexible Hose of Fire Protection Sprinkler Piping Systems.

Shao-Chun Tseng (2020). A Study on Seismic Behavior of Fire Protection Sprinkler Piping Systems in Hospital.

Cheng-Yen Su (2020). A Study on Seismic Displacement-Limiting Devices of Fire Protection Sprinkler Piping System.

FUNDAMENTAL STUDY ON SEISMIC PERFORMANCE OF STONE BRIDGES FOCUSING ON SIZE OF FILLING MATERIAL

Aiko Furukawa[1], Yusuke Higashi[1] and Junji Kiyono[1]
1. Department of Urban Management, Graduate School of Engineering, Kyoto University, Kyoto, Japan
Email: furukawa.aiko.3w@kyoto-u.ac.jp, higashi.yusuke.83e@st.kyoto-u.ac.jp, kiyono.junji.5x@kyoto-u.ac.jp

ABSTRACT

Several stone bridges were damaged during the 2016 Kumamoto earthquake. The most severe damage was the collapse of the stone walls. It is reported that the condition of filling materials has a strong influence on the stone wall collapse of the Futamata Fukura Bridge. With this evidence, this study focuses on the size effect of filling stones on the seismic strength of stone bridges. We carried out shaking table tests using two simplified stone bridge models with different crushed stone sizes. It was observed that the model filled with larger crushed stones could resist higher acceleration than the model filled with smaller crushed stones. The numerical simulations using the refined DEM were conducted, and the same tendency that larger crushed stones improve seismic resistance was obtained.

Keywords: stone bridge, seismic resistance, filling material, shaking table test, DEM

INTRODUCTION

Stone bridges were introduced from overseas in the Edo period (1603-1868), and many stone bridges have been built throughout Japan, especially in the Kyushu region. At the end of the Taisho era (1912-1926), when the largest number of stone bridges were constructed, there were as many as 70,000 stone bridges in Japan, and even today, many stone bridges remain. Earthquakes have damaged these stone bridges, but their seismic resistance and damage mechanisms are still unknown. During the Kumamoto earthquake, there was little damage to the ring stones, and most of the damage was caused by the collapse of wall stones. The wall stones and filling material collapsed in the orthogonal direction to the bridge axis, suggesting that the bridge collapsed due to orthogonal vibration. Some damage to stone walls may have been caused by the filling material inside the stone bridge. As for the actual condition of the filling material in the stone bridge, a detailed survey of the stone bridge damaged during the Kumamoto earthquake was conducted. In many cases, gravel and soil were mixed, but there was also a case where the bridge was filled only with crushed stones as large as the wall stones. Although the size of the filling material in the actual stone bridge varies, there is no research on the relationship between the size of the filling material and the earthquake resistance.

As a previous study on the seismic resistance of stone bridges, Fujita et al. (2013) made an arch model using stones similar to those used in actual stone bridges and clarified the cracking mechanism of the ring stones. Asai et al. (2009) evaluated the static and dynamic behavior of stone arch bridges in two dimensions using FEM, and Setoyama et al. (2017) conducted a three-dimensional static and dynamic strength analysis using FEM. Kiyono et al. (2015) conducted seismic assessment of a stone arched bridge using the three-dimensional DEM. However, these analyses focused on the vibration characteristics of the whole arch structures and did not model the individual filling materials in detail.

Fukumoto et al. (2014) conducted centrifuge model tests on the seismic deformation behavior of stone walls with different stone shapes. They found that the differences in deformation behavior could be reproduced using the three-dimensional DEM. In a similar study, Murakami et al. (2014) conducted seismic response analysis of a stone wall using the extended DEM (EDEM) and showed the effectiveness of anchor reinforcement. Nakajima et al. (2015) conducted seismic reinforcement of masonry retaining walls using a combination of collapse prevention net and ground reinforcement. They evaluated the reinforcement effect by nonlinear beam-spring analysis considering the interlocking resistance of stones. However, the structure of the stone walls is different from that of the stone bridge.

In the present study, firstly, the size effect of the filling material used in the stone bridge on the seismic resistance was examined by the shaking table test and the numerical analysis by the refined DEM.

SHAKING TABLE TEST

Outline of Experiment

In the shaking table test, a cross-sectional model of a stone bridge was vibrated in the direction orthogonal to the bridge axis, as shown in Photo 1. Two types of filling materials were prepared. The large crushed stone has the same size as the wall stone, and the small crushed stone is about half the size. The sinusoidal acceleration was input, and the amplitude was gradually increased. The earthquake resistance was evaluated by the acceleration at which the collapse occurred.

Experimental Apparatus

The detailed dimensions of the experimental apparatus are shown in Figure 1. The experimental apparatus was made using wood (backside), L-shaped metal fittings, and acrylic plates (front side). A string was tied between the top of the wood plate and the acrylic plate to prevent the acrylic plate from tilting. The wall of the cross-sectional model is constructed using concrete blocks with 7 cm width, 8 cm depth, and 6 cm height and assembled in seven sections. The concrete blocks on the front and back sides of the even-numbered sections are 4 cm deep (Photo 1(b)). The bottom block was fixed to the wood with L-shaped corners from both sides. For the inner filling material, crushed stones with 40-100mm and 20-30mm are used as large and small crushed stones, respectively. The direction of vibration is the left-right direction of Photo 1(a), orthogonal to the bridge axis. A high-speed camera, an accelerometer, and a digital camera were used for the measurements.

Material Properties

For the numerical simulation, the material properties of the test specimen were measured. First, the density of concrete blocks and crushed stones were measured, and they were 2.2 t/m^3 and 3.2 t/m^3.
Next, the friction coefficient was measured using a spring scale. The results are shown in Table 2. Since the friction coefficient between crushed stones was difficult to measure using a spring scale, the angle of repose was measured instead of using the small crushed stone (20~30mm). The angle of repose is measured by the discharge method. A container of 13.5 cm (width) × 13.5 cm (depth) × 15 cm (height) was filled densely with crushed stone, and the container was pulled upward, and the angle of repose was measured as shown in Photo 2. The mean angle of repose was 19.45 degrees with a standard deviation of 3 degrees.

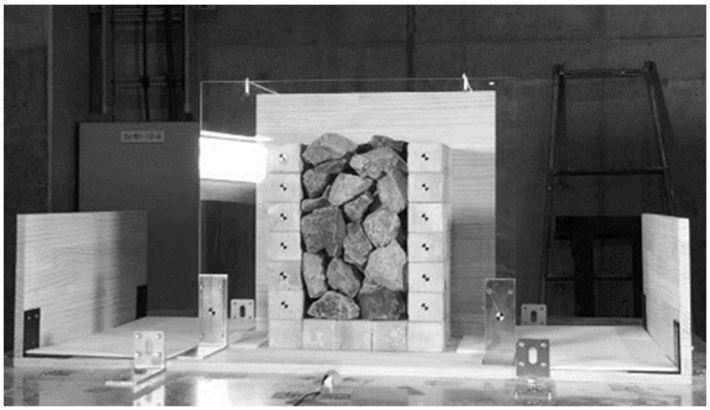

(a) Front view (left-right direction is the excitation direction)

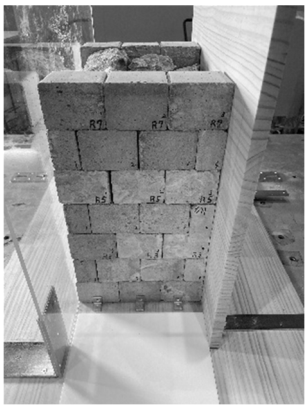

(b) Side view

Photo 1. Test specimen on the shaking table

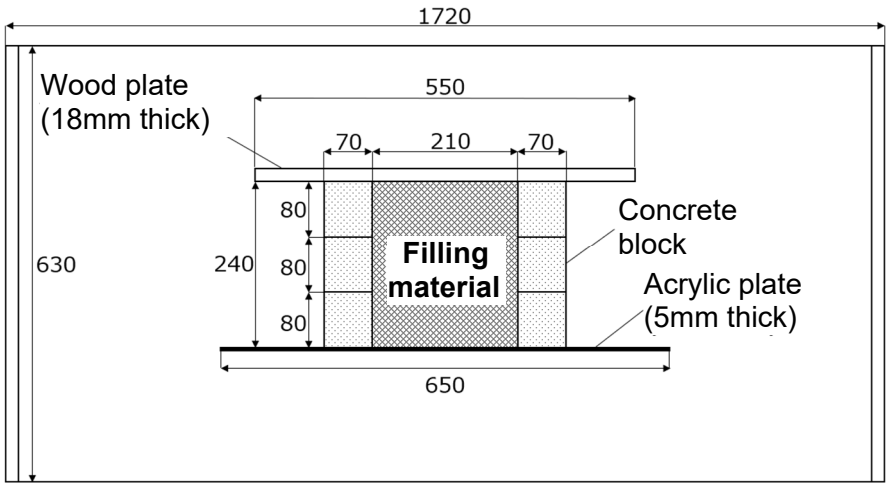

(a) View from the top

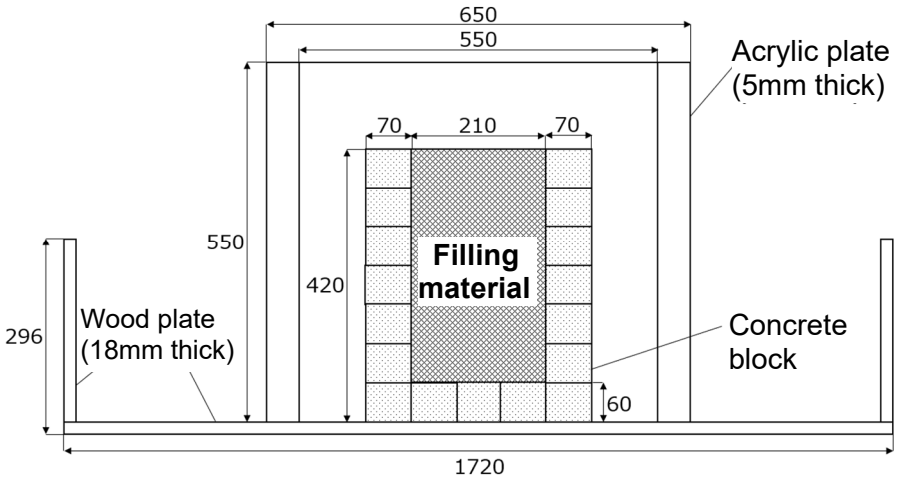

(b) Front view

Figure 1. Dimensions of test apparatus and test specimen (mm)

Table 2. Measured friction characteristics

Materials	Friction coefficient
Concrete-Concrete	0.666
Concrete-Wood	0.516
Concrete-Acrylic plate	0.279
Concrete-Crushed stone	0.772
Crushed stone-Acrylic plate	0.152
Crushed stone-Wood	0.707

Photo 2. Experiment to measure the angle of repose

Experimental Results

Resonance Curve

A resonance curve was obtained for models with large and small crushed stones. The shaking table was vibrated with a small displacement of about 2 or 3 mm, and then the frequency was gradually increased. The ratio of the acceleration Fourier spectra measured on top of the wall stone and the shaking table was computed as shown in Figure 2. The resonance curve confirmed that there was almost no effect of resonance up to around 30 Hz in this test specimen.

Sinusoidal excitation

The sinusoidal excitation with a constant frequency was conducted. The test specimen was excited with four types of sinusoidal waves (2, 4, 6, and 8 Hz), and the amplitude was gradually increased. The input acceleration when the collapse occurred was examined.
The acceleration at which the wall collapsed is shown in Figure 3. The overall tendency of the experimental results is that the model with large crushed stone can resist larger acceleration and thus has higher seismic resistance.
Next, Photo 3 shows the collapse behavior for the cases with 2Hz and 8Hz shaking. It was confirmed that the small crushed stone collapsed and formed a slope, while the large crushed stone was less likely to collapse. Furthermore, comparing the middle photo in Photos 6(c) and 6(d) for 8Hz, there is no gap between the right wall and the small crushed stones (Photo 3(c)), while there is a gap between the wall and the large crushed stones (Photo 3(d)). The large crushed stones did not fill the gap indicates that the large crushed stone wall is more resistant to collapse.
Based on these results, the mechanism of wall collapse is that the concrete blocks are displaced outward by vibration, and the filling material is dragged into the space created between the blocks. Then the filling material causes the collapse of the wall. Since the filling material made with the large crushed stones is more difficult to collapse than with the small ones, the wall with large crushed stones resisted large acceleration.

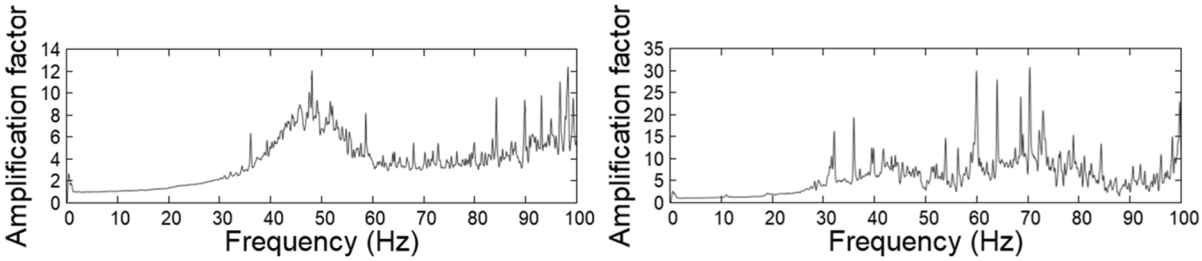

(a)Small crushed stones (b)Large crushed stones

Figure 2. Resonance Curve

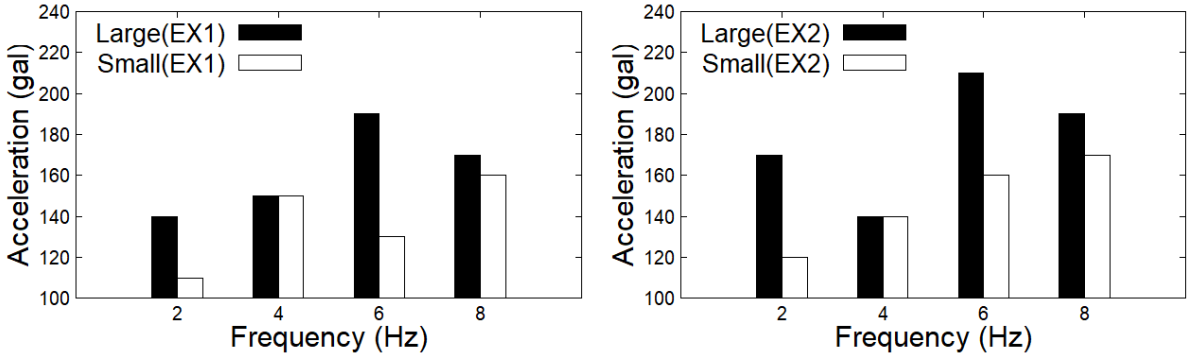

(a)1st experiment (b)2nd experiment

Figure 3. Input acceleration at which the collapse occurred during the experiment

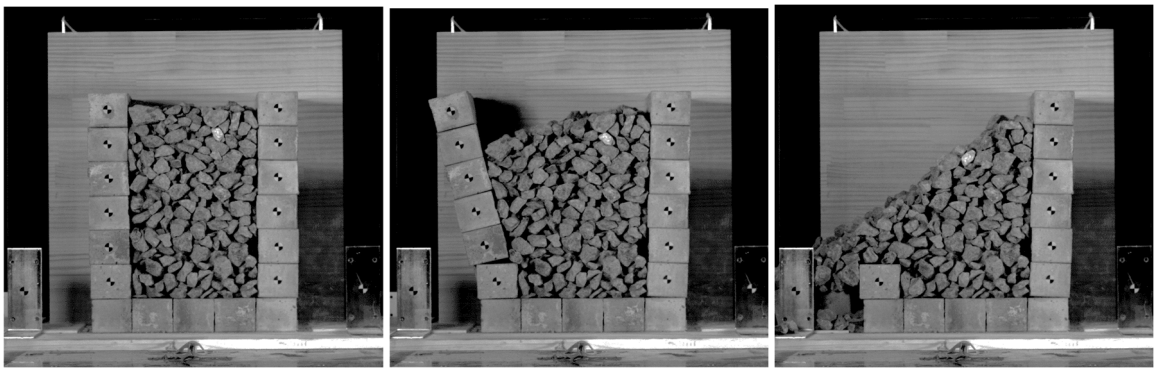

(a) Small crushed stones (2Hz, collapsed at 110gal)

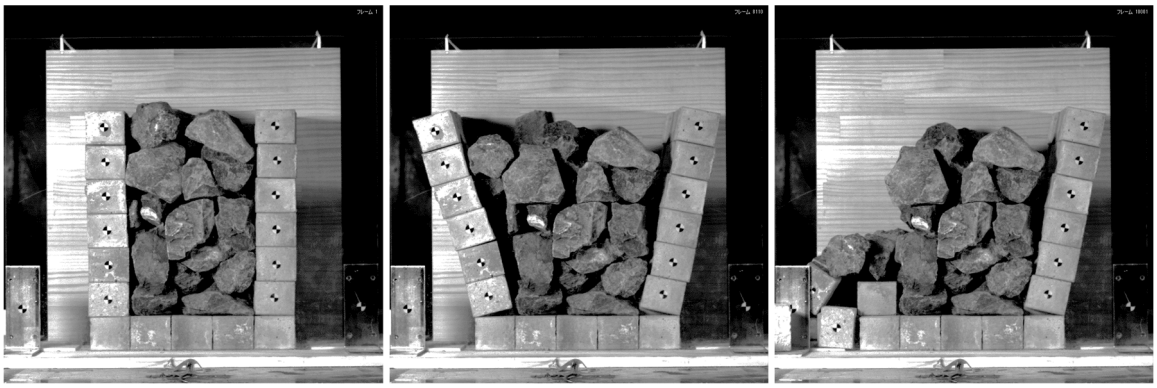

(b) Large crushed stones (2Hz, collapsed at 114gal)

(c) Small crushed stones (8Hz, collapsed at 160gal)

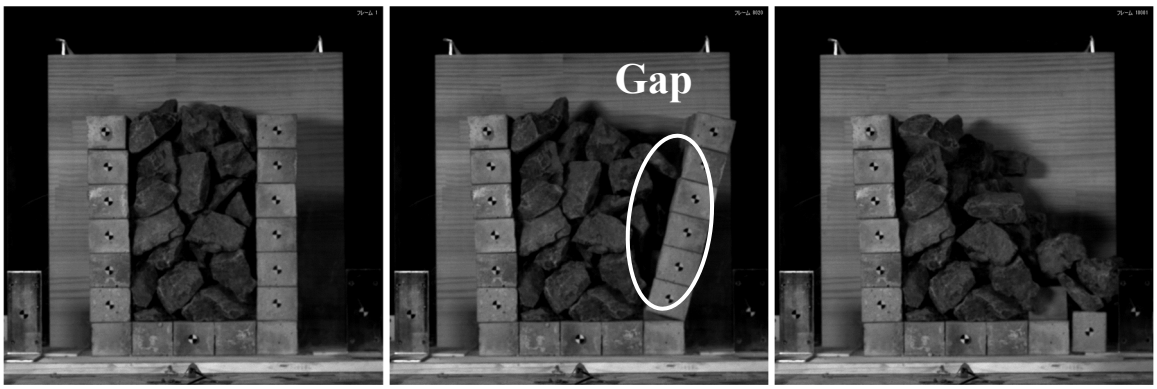

(d) Large crushed stones (8Hz, collapsed at 170gal)

Photo 3. Collapse behavior (Left: pre-collapse, Middle: during the collapse, Right: post-collapse)

NUMERICAL SIMULATION

Analytical Condition

The shaking table test using sinusoidal excitation is simulated using the refined DEM (Furukawa et al., 2011). DEM is selected because of its extensive experience in the numerical analysis of vibration, collapse and overturning of stones (Furukawa et al, 2005; Kiyono et al., 2015; Furukawa et al., 2019). The decahedral element shown in Figure 4 was newly introduced to model the filling material. Since the sizes of the large and small crushed stones used in the experiments were 40-100mm and 20-30mm, respectively, the longest edge of the crushed stones was set to 60mm and 25mm, respectively.

The numerical analysis model is shown in Figure 5. In the experiment, acrylic and wooden walls were installed at the front and back to prevent the filling material from falling. These walls are modeled with transparent elements. The filling ratio of the large model was 53.2%, and that of the small model was 58.6%, which was similar to the experimental results.

The analysis parameters are shown in Tables 2(a) and 3. The friction coefficient between the crushed stones was determined to be 0.2. Then the angle of repose by the numerical analysis matches the average angle of repose by the experiment shown in Table 2(b). Material properties not measured in the experiment were set by referring to previous studies (Furukawa et al., 2019; Hoshino and Negishi, 1970; Sawada, 1936; Kawaguchi, 2004).

The acceleration data measured on the shaking table during the second sinusoidal excitation was input. The time interval is 2.5×10^{-6} sec.

Results

Figure 6 shows the input acceleration at which the collapse occurred in the numerical analysis. Table 4 compares the input accelerations at which the collapse occurred among the numerical analysis and two shaking table results for each case. The numerical results for all eight cases show the same trend as the experiment; the seismic performance is improved by using large crushed stones.

As an example, Figure 7 shows the collapse behavior under 8Hz excitation. In the case of the large crushed stone, there was a gap between the wall and the crushed stones, while in the case of the small crushed stone, there was no gap between the wall and the crushed stone, indicating a similar tendency to the experiment.

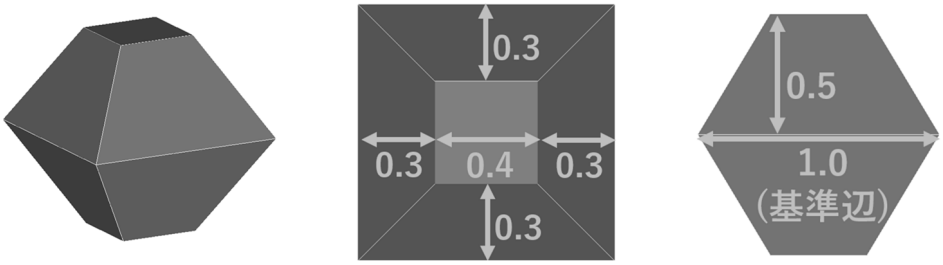

Figure 4. Modeling crushed stone using a decahedron element

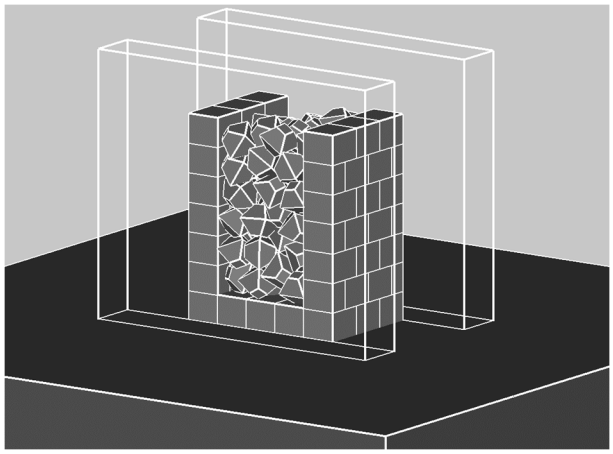

Figure 5. Numerical analysis model

Table 3. Analysis parameters

Material	Density [t/m^3]	Young's Modulus [N/m^2]	Poisson's ratio
Concrete block	2.20	3.3×10^{10}	0.20
Crushed stone	3.20	5.3×10^{9}	0.18
Wood	0.50	1.7×10^{8}	0.40
Acrylic plate	1.19	3.0×10^{9}	0.35

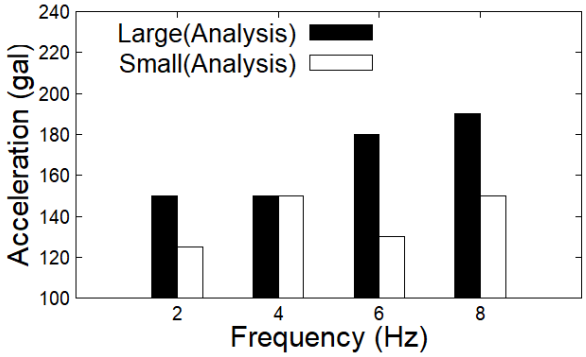

Figure 6. Input acceleration at which the collapse occurred by the numerical analysis

Table 4. Comparison of input acceleration at which the collapse occurred

Input frequency(Hz)	Crushed stone	Input acceleration at which the collapse occurred (gal)		
		Numerical analysis	Shaking table test (1st)	Shaking table test (2nd)
2	Small	125	110	120
2	Large	150	140	170
4	Small	150	150	140
4	Large	150	150	140
6	Small	130	130	160
6	Large	180	190	210
8	Small	150	160	170
8	Large	190	170	190

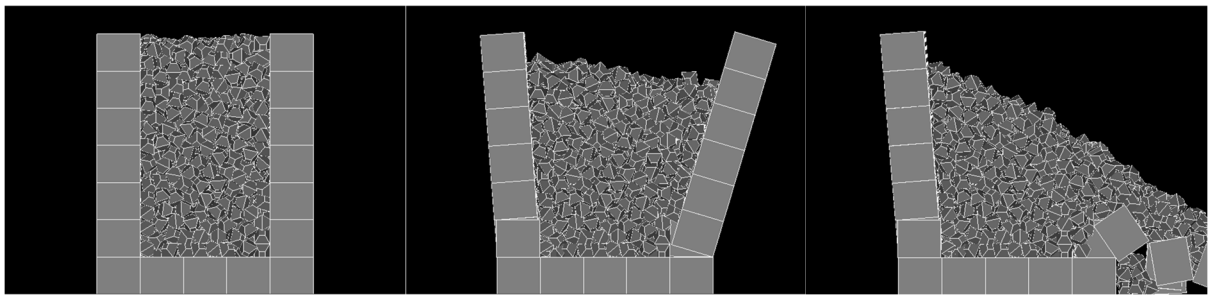

(a) Small crushed stone (8Hz, collapsed at 150 gal)

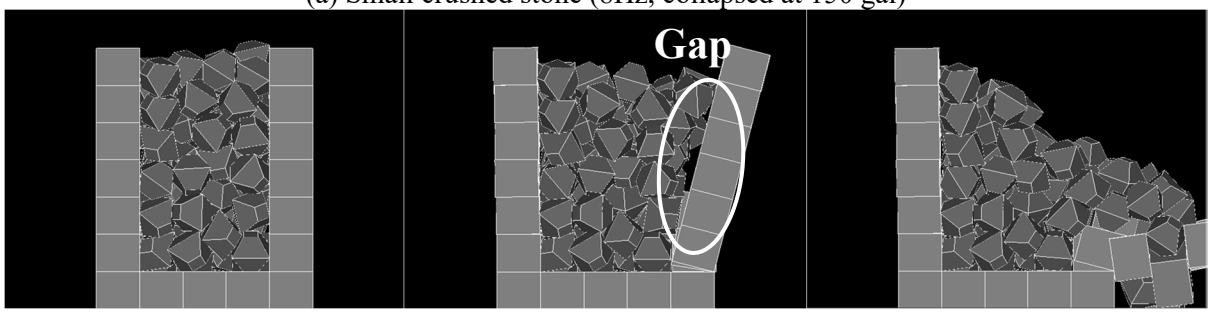

(b)Large crushed stone (8Hz, collapsed at 190 gal)

Figure 7. Collapse behavior by the numerical analysis
(Left: pre-collapse, Middle: during the collapse, Right: post-collapse)

CONCLUSIONS

In order to investigate the size effect of the filling material on the seismic performance of stone bridges, shaking table experiments and numerical analyses were conducted.
In the shaking table test, the model with large crushed stones could resist larger input acceleration than the model with small crushed stones, indicating the possibility that the seismic performance can be improved by using larger crushed stones. It was observed that the wall gradually tilted as the filling material pushed the wall outward. When the wall tilts, the gap is generated between the wall and the filling material. It was observed that the small crushed stones moved outward and filled the cap while the gap remained for the large crushed stones.
In the analysis, the crushed stones were modeled by decahedral elements, and the refined DEM simulated the shaking table test. The numerical analysis observed a similar tendency to the shaking table test

ACKNOWLEDGMENTS

We would also like to thank Prof. Tomomi Yagi, Prof. Tomoki Shiotani, and Prof. Katsufumi Hashimoto of Kyoto University for providing experimental equipment.

REFERENCES

Asai, M., Yamashita, K., Yamazaki, R., Araki, K.(2009). "Evaluation of static and dynamic strength of stone arch bridge using discrete finite element model", *Journal of Structural Engineering, JSCE*, **55A**, 172-180. (in Japanese)

Fujita, C., Yamao, T., Koga, K., Ogura, M. (2013). "Static Behavior by Stone Arch Model and Mechanism of Cracking of Arch Ring Stone", *Journal of Structural Engineering*, **59A**, 26-36. (in Japanese)

Fukumoto, Y., Yoshida, J., Sakaguchi, H., Murakami, A. (2014). "The Effects of Block Shape on the Seismic Behavior of Dry-Stone Masonry Retaining Walls, A Numerical Investigation by Discrete Element Modeling", *Journal of Soil and Foundation*, **54**(6), 1117-1126. (in Japanese)

Furukawa, A., Kiyono, J., Shigeru, M. (2005). "Collapse Mechanism of Gravestones during 1995 Kobe Earthquake using Physics-based Simulation", *Journal of Social Safety Science*, **7**, 221-230. (in Japanese)

Furukawa, A., Kiyono, J., Toki, K. (2011). "Proposal of a Numerical Simulation Method for Elastic, Failure and Collapse Behaviors of Structures and its Application to Seismic Response Analysis of Masonry Walls", *Journal of Disaster Research*, **6**(1), 51-69.

Furukawa, A., Yoshikawa, H., Kiyono, J. (2019). "Investigation of the Tsujun Bridge Damage Mechanism during the 2016 Kumamoto Earthquake", *Journal of Natural Disaster Science*, **38**(S06), 1-23.

Hoshino, M. and Negishi, M. (1970). "An Experiment on Mechanical Properties of Rocks", *Applied Geology*, **11**(3), 91-96. (in Japanese)

Kawaguchi, N. (2004). "Fundamental Reinforced Concrete Engineering", Toyo Shoten, Tokyo. (in Japanese)

Kiyono, J., Furukawa, A., Toki, K. (2015). "Seismic Assessment of Stone Arched Bridges", *Proceedings of the 15th World Conference on Earthquake Engineering*, Paper No.1036.

Murakami, T., Numata, M., Meguro, K. (2014). "Seismic Response Analysis of Stone Wall Structures using Two-Dimensional Extended Discrete Element Method", *Journal of JSCE Ser. A1*(*Structural Engineering & Earthquake Engineering*), **70**(4), I_506 - I_512. (in Japanese)

Nakajima, S., Watanabe, K., Kanda, M., Fujiwara, T., Takasaki, H., Ikemoto, H. (2015). "Development of Reinforcement Method for Existing Masonry Wall Using Collapse Prevention Net and Ground Reinforcement Material", *Proceedings of JSCE*, **71**(4), 317-334. (in Japanese)

Sawada, M. (1936). "Elasticity and Strength of Wood as Orthotropic Anisotropic Material", *Zairyo*, **12**(121), 749-753. (in Japanese)

Setoyama, O., Asai, M., Harasaki, K., Kawasaki, T. and Fukuda, H. (2017). "Static and Dynamic Strength Analysis of Masonry Arch Bridge by Three-Dimensional Discrete Finite Element Model", *Journal of Structural Engineering, JSCE*, **63A**, 36-48. (in Japanese)

(4a) Social impacts and resilience

SUPPORT FOR LONG-TERM EVACUEES BASED ON THE CASE OF THE GREAT EAST JAPAN EARTHQUAKE -FOCUSING ON KYOTO, OSAKA, AND OKAYAMA PREFECTURES

Maki Koyama[1], Kohei Tsuchida[2], Daisuke Matsushita[3], and Kiyotaka Ogata[4]
1. Associate Professor, River Basin Research Center, Gifu University, Gifu, Japan.
2. Former student, Graduate School of Natural Science and Technology, Gifu University, Gifu, Japan.
3. Professor, School of Human Life and Ecology, Osaka Metropolitan University, Osaka, Japan.
4. Former part-time lecturer, Okayama University of Science, Okayama, Japan.
Email: maki_k@gifu-u.ac.jp

ABSTRACT

In the wake of the Great East Japan Earthquake, many people were evacuated to other prefectures over long periods of time. Because such disasters are expected to occur in Japan in the future, it is important to propose appropriate support measures for such long-term evacuees. Therefore, this study conducted a questionnaire survey of evacuees in Kyoto, Osaka, and Okayama prefectures, as well as interviews with support groups. Consequently, housing and employment were found to be major issues. In addition, the activities of support groups revealed that it is necessary to provide support tailored to the needs of each disaster victim.

Keywords: 2011 Great East Japan Earthquake, livelihood reconstruction, disaster relief organizations, long-term evacuation, interview

INTRODUCTION

During the Great East Japan Earthquake of 2011, in addition to residents who suffered direct damage to their homes, many others were forced to evacuate for long periods of time or to move far away from their homes because of the establishment of evacuation zones following the accident at the Fukushima Daiichi Nuclear Power Plant. In addition, many people in areas outside the evacuation zone evacuated voluntarily, fearing the radiation effects. Most disaster-related deaths are caused by deteriorating living conditions. During the Great East Japan Earthquake, 3,789 disaster-related deaths occurred (Reconstruction Agency, 2022), and improving the living environment of evacuees was a major challenge. This study examines the difficulties faced by evacuees and assistance provided to them to examine the measures needed for long-term evacuees. We then identify the challenges and propose ways to improve the livelihood support for evacuees.

QUESTIONNAIRE SURVEY FOR LONG-TERM EVACUEES

The following items were extracted from the survey data: personal attributes (sex and age); household attributes (household type, presence of children, and type of home ownership); social indicators (employment status before and after evacuation); economic indicators (household income before and after evacuation); health indicators (items measuring physical and mental health status); and current problems and concerns. The items related to current problems and anxieties were used to identify the problems that evacuees face during their evacuation and the attributes of evacuees who are at high risk of poverty and may need assistance.

Outline of the Survey

The survey conducted in Kyoto Prefecture included evacuees and individuals living there. The evacuees in Kyoto Prefecture included all evacuees registered in the prefecture. The survey forms were distributed to survey participants through the Kyoto prefectural government and collected by

mail. Residents of Kyoto Prefecture were also surveyed as a comparison group. The number of survey targets was set to equal the number of evacuees. All the household members were included in the survey. The survey of evacuees in Osaka and Okayama Prefectures covered all evacuee household heads registered as evacuees in Osaka and Okayama Prefectures, respectively. These questionnaires were distributed through the prefectural government of each prefecture and collected by mail. Both the surveys were conducted in 2016.

The purpose of the evacuee surveys was twofold. First, it aimed to identify the attributes of evacuees who were at a high risk of deprivation and were likely to need further assistance. Second, it aimed to understand the problems faced by the evacuees during evacuation. We used the mathematical quantification theory class II for the first point to clarify the extent to which each attribute (sex, age, employment status, presence or absence of children, household type, housing tenure, and household income) affects the value of K6 (Kessler *et al*., 2003), an indicator of depressive tendencies. The K6 is a widely used indicator of psychological stress. The second point was extracted from the responses to the survey items regarding current problems and concerns.

Number of dispatched and collected questionnaires and collection rate

The number of questionnaires sent and collected, and the collection rates are shown in Table 1. Because the questionnaires in Kyoto Prefecture were divided into individual and household questionnaires, the number of questionnaires collected for each is shown.

Table 1. Number of questionnaires sent and collected, and the collection rate

	Number of Target Households	Number of Households Collected	Collection Rate	Number of Individuals Collected
Kyoto Residents	250	76	30.4%	140
Evacuees to Kyoto Prefecture	223	47	21.1%	62
Evacuees to Osaka Prefecture	188	33	17.6%	33
Evacuees to Okayama Prefecture	216	69	31.9%	69
Total	877	225	25.7%	304

Results

Mathematical quantification theory class II

Mathematical quantification theory class II is a method for predicting the objective variable using the explanatory variables when both explanatory and objective variables are categorical data. In this study, the classification of the degree of depressive tendency by the K6 was used as the objective variable, and sex, age, employment status, presence of children, household type, home ownership status, and household income were used as explanatory variables.

To ensure the number of responses per category necessary for analysis, the explanatory variables were age (20s and 30s, 40s and 50s, and 60s and older), employment status (full-time employment, part-time employment, unemployed), children (children present, no children present), and household composition (single-person household, mother-child household, "other household"). Households were categorized as either "public housing" or "other." The objective variable (K6) had the following four categories: "negative," "mild," "moderate," and "severe." To ensure that the number of respondents

was sufficient to withstand analysis, the four categories were divided into two: "negative" and "positive." Note that positive includes three categories and negative includes one.

The category scores for each explanatory variable obtained from the analysis are presented in Figure 1, and the ranges for each explanatory variable are presented in Table 2. The category score indicates the extent to which each explanatory variable affects the target variable. The greater the range of the category scores listed in Table 2, the more likely the item is to affect the target variable. In this analysis, the further to the left the category score, the more likely the item is to contribute negatively to the objective variable; the further to the right, the more likely the item is to contribute positively to the objective variable. Table 2 shows that the range for employment status was 2.06, indicating that it had a significant impact on depressive tendencies.

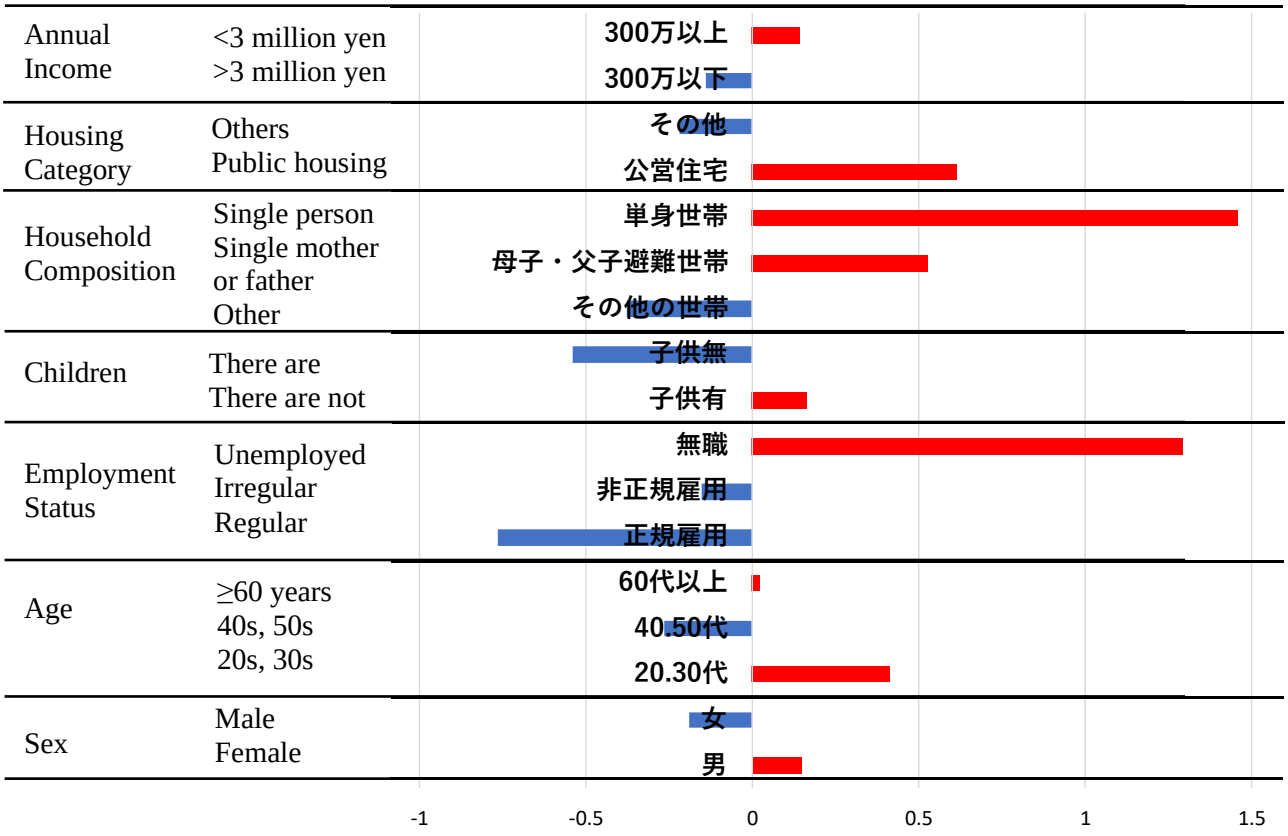

Figure 1. Category score

Table 2. Range of each explanatory variable

Attributes	Range
Annual Household Income	0.28
Housing Category	0.83
Household Composition	1.84
Children	0.7
Employment Status	2.06
Age	0.68
Sex	0.34

Problems in long-term evacuation

The top three concerns for evacuees of the Kyoto Prefecture were "work," "housing," and "living expenses or income;" for those to the Osaka Prefecture were "housing," "living expenses or income," and "information about previous housing;" and for those to the Okayama Prefecture were "education," "mental and physical health," and "housing." Problems with "housing" were found among long-term evacuees in all three prefectures.

In the free responses, ten out of 29 evacuees to Kyoto and Osaka Prefectures indicated that they had problems with "future housing, expiration of public housing, and moving from a familiar place to a new place." Unlike evacuees to Kyoto and Osaka Prefectures, few evacuees to Okayama Prefecture live in public housing. However, six of their 32 free responses were related to housing. The most common statement regarding housing was the burden of double-living in the original house and the new house at the evacuation site." Many of the evacuees to Okayama Prefecture were from the Kanto area, and a substantial number had evacuated not because of damage to their buildings but because they feared the effects of radiation. Some respondents described how the evacuation of a few household members resulted in the double burden of rent and living expenses in their original and evacuated homes.

INTERVIEW SURVEY OF SUPPORTERS

This study aimed to clarify the actual situation of impoverishment and support for evacuees, and to examine how support should be provided. Focusing on the problems of long-term evacuees identified in the previous chapter and the attributes (employment and housing) that put them at a high risk of impoverishment, interviews were conducted with private support groups that provide assistance to long-term evacuees. Organize the support provided by each organization, the consultation received from evacuees, and the issues faced by each organization (those considered important for the continuation of support for evacuees in the future).

Survey Overview

In the field of disaster relief, the importance of tripartite cooperation among the government, disaster relief volunteer centers, and private support groups has been pointed out, and much assistance has been provided based on this cooperation during the Great East Japan Earthquake. In addition to the government, private support groups play a major role in assisting disaster victims. Private support groups provide support tailored to the needs of each individual (e.g., consultation services, accompaniment to various contact points) and are considered to have a better grasp of the actual situation of evacuees.

In this study, private support groups based in Kyoto, Osaka, and Okayama Prefectures were surveyed. Although there are several support groups in each prefecture that provide assistance to long-term evacuees, this survey focuses on organizations commissioned by Fukushima Prefecture to provide support to evacuees after the Great East Japan Earthquake. The names of the organizations and dates of the survey are as follows:

- Kyoto Prefecture
  Survey Date: Tuesday, December 22, 2020, 10:00–11:00 a.m.
  Survey subject: Mx. Otsuka, non-profit corporation, Nagomi
- Osaka Prefecture
  Survey date: Wednesday, December 29, 2020, from 9:00–10:30 a.m.
  Survey subject: Mx. Furube, Marutto Nishinihon
- Okayama Prefecture
  Survey Date: Saturday, January 9, 2021, from 5:30–7:00 p.m.
  Survey subject: Mx. Hattori, General Incorporated Association Hot Okayama

The interview items were: (a) related to housing (i.e., support provided, consultation with evacuees provided to your organization, needs of evacuees that could not be met, and difficulties in providing

support); (b) related to employment (i.e., support provided, consultation with evacuees provided to the organization); and (c) other items (funding for activities and what is needed to continue supporting evacuees ten years after the disaster).

Results

This section summarizes the results of (1) the support provided by each organization, (2) consultations with evacuees, and (3) issues faced by each organization (those deemed important for the continued support of evacuees in the future). The results for (1) and (2) are summarized for housing and employment, respectively.

Assistance provided by each agency

- Housing-related

  All three organizations provided housing-related support in the form of consultation and housing information. However, there were some differences in the support provided by "Nagomi," "Marutto Nishinihon," and "Hot Okayama." In Kyoto and Osaka Prefectures, support from local governments focused on the provision of emergency temporary housing. The provision of emergency temporary housing was initially limited to a maximum of two years under the provisions of the Disaster Relief Law, but it was repeatedly extended in response to requests from the affected prefectures. Extensions were reviewed and decided every year (April–May); thus, long-term evacuees would be unaware if they could continue to live in their current housing, until the decision was made. Hence, the volatile housing situation made it difficult for them to plan long-term. Therefore, long-term evacuees were in a constant state of uncertainty regarding their housing. Nagomi and Marutto Nishinihon summarized the deadline for providing emergency temporary housing each time it was extended and published it as an information magazine (Disaster Response Letter, Marutto Nishinihon NEWS). In addition, as the provision of emergency temporary housing was sequentially terminated at each shelter in March 2016, some evacuee households had to move out of the houses they had been living in. Both organizations provided assistance in developing relocation plans tailored to each household's situation.

  Hot Okayama's support consisted mainly of providing information on vacant houses so that the Okayama Prefecture government could match evacuees with private vacant houses. However, in some cases, vacant houses that had been uninhabited for long periods of time had problems such as ticks, roof leaks, and missing floors, and needed repairs. The agency provided consultation on how to improve the living infrastructure.

- Employment

  All three organizations provided employment support through counseling services. Marutto Nishinihon connected evacuees who wanted to find employment with organizations that provided career counseling and accompanied them to find employment, whereas Hot Okayama introduced job information to evacuees. Unlike these two organizations, Nagomi provided "restaurant management." In September 2013, they opened "Kitchen Nagomi" to create a place where evacuees could work together and employed 16 evacuees, including office staff.

Consultation from evacuees

- Housing

  Of the housing-related problems faced by the evacuees, the three organizations had one thing in common: the problem of guarantors. Kurashiki City in Okayama Prefecture has a system in which the city’s taxpayers serve as guarantors. However, for evacuees who had evacuated from far away and had no relatives or friends in Kurashiki, it was very difficult to set up a guarantor. Therefore, Hot Okayama accompanied the evacuees to the guarantee company and residential support network to assist them in setting up a guarantor. However, many evacuees have no ties with support groups, and it is very difficult to find someone to act as a guarantor at the evacuation site. Therefore, it is necessary to review the guarantor system itself, for example, by relaxing the requirements for guarantors.

- Employment
  A common issue raised by the three groups regarding employment was cultural differences such as dialects and conversational styles. While some evacuees were able to adapt to these cultural differences, not all were able to do so. Those who could not adapt, have difficulty building relationships in the workplace. Consequently, many reportedly have been forced to change their jobs.

Issues faced by each organization

In common with the three organizations, they identified the following two issues necessary to realize sustainable support for evacuees: (1) stabilizing funding for activities, and (2) addressing issues beyond the scope of evacuee support. Each organization's activities were funded by grants, but in most cases, the grants are for a single year, with no guarantee that they will be funded again the following year. Stabilization of funding is one of the conditions for achieving sustainable support for evacuees, as it will be difficult to maintain evacuee support activities if subsidies are not obtained continually.

All three organizations were confirmed to be involved in daily life support activities, such as welfare and nursing care, as well as matters directly related to disasters. Because evacuees from distant areas often have no one to turn to at their evacuation sites and do not know of any organizations that provide support, a situation has arisen in which support groups for disaster victims provide consultation for all types of problems faced by evacuees. The most frequently consulted issues were those related to welfare. Therefore, it is desirable for the national government and public administration, the main actors in the support system, to provide one-stop services that seamlessly link support during normal times and times of disaster. Disaster case management will prove effective in providing tailored support for each evacuee.

CONCLUSIONS

The major housing-related problems of long-term evacuees were uncertainty about how long they could continue to live there and the problem of guarantors. In particular, with regard to the guarantor issue, it is necessary to review the guarantor system for evacuees, for example, by relaxing the requirements for guarantors. Regarding employment, we have seen cases where evacuees have had difficulty building relationships in the workplace due to differences in dialect and culture, and consequently, they have been forced to change jobs because they could not adjust to the workplace atmosphere. Therefore, while job placement support is important, mental care to help evacuees recover to a state in which they can work is also important. Another candidate for employment support would be to create a place like "Nagomi" where evacuees can work together. Two things are necessary for sustainable support: securing stable funding for activities, and addressing issues beyond the scope of evacuee support.

ACKNOWLEDGMENTS

We would like to thank Editage (www.editage.com) for English language editing.

REFERENCES

Cabinet Office, Government of Japan (2018), “Guidebook for Collaboration of Administrations with NPOs, Vol unteers, etc. in Disaster Prevention,” http://www.bousai.go.jp/kaigirep/kentokai/bousai_volunteer_kankyoseibi/pdf/h3004guidebook.pdf (in Japanese)

Kessler RC, Barker PR, Colpe LJ, Epstein JF, Gfro-erer JC, Hiripi E, et al. (2003), “Screening for serious mental illness in the general population,” Arch Gen Psychiatry, **60**, 184-189.

Reconstruction Agency (2022), “Number of earthquake-related deaths in the Great East Japan Earthquake,” https://www.reconstruction.go.jp/topics/main-cat2/sub-cat2-6/20220630_kanrenshi.pdf. (in Japanese)

STUDY ON PRE-DISASTER RECOVERY PLANNING FOR THE EARTHQUAKE RESILIENT COMMUNITY: TAKE MIN-AN VILLAGE OF TAMSUI DISTRICT AS AN EXAMPLE

Sawyer Mars[1] and Pei-Chun Shao[2]
1. AKA Shyh-Yuan Maa, Associate Professor, Department of Urban Planning and Disaster Management, Ming-Chuan University, Taipei, Taiwan, R.O.C.
2. Professor, Department of Land Management and Development, Chang Jung Christian University, Tainan, Taiwan, R.O.C.
Email: swymars@mail.mcu.edu.tw, peicshao@mail.cjcu.edu.tw

ABSTRACT

At present, the pre-disaster recovery workshop has been implemented in Taiwan not long ago, and the public is relatively unfamiliar with the entire promotion process and content. In recent years, there has been no major disaster, and the public's awareness of disaster prevention has gradually weakened. Although the residents of Min-An Village have been trained by two workshops, has a certain awareness and ideas about the pre-disaster recovery planning, but at present it is still needed more practice to build the consensus, and can directly discuss the regional recovery plan and future rebuild scenarios, so that can better meet the needs of the community and achieve a build back better future.

Keywords: disaster resilient community, pre-disaster recovery planning

INTRODUCTION

In recent year, large-scale disasters occurred frequently, the governance of natural disasters much more focused on non-engineering than engineering countermeasures. Mitigation and adaptation to strengthen resilience becomes the important concept in disaster management. In Taiwan, the policy of resilient communities was decided in 2018. The goals of the policy are to establish the mechanism of communication between the central and local governments, to plan strategies for promoting resilient communities, to educate volunteers related to handling disaster management and so on. The Tamsui community was taken as a case study to discuss the pre-earthquake recovery plan. The purposes are to verify the issues of promoting resilient communities and pre-disaster recovery planning to be the basis for strengthening resilience.

LITERATURE REVIEW

Resilient Communities and Disaster Management

The concept of resilient was proposed by Holling who an ecologist is. He defined that the resilience means flexible ability against external disturbance (Holling, 1973). The concept of resilient also applied in the field of disaster management, such as Hyogo Framework for Action 2005-2015 pointed out building resilience of nations and communities to disasters, and Sendai Framework for Disaster Risk Reduction 2015-2030 was created as an attempt to broaden and enhance responses to disasters and allow for resilience measurements. Thus, the resilient community could be defined as the ability to resist, to absorb and to accommodate and to recover while communities face the impact of disasters.

Difference between Disaster Prevention Community and Disaster Resilient Community

In Taiwan, the disaster prevention communities focused on debris flow areas evacuation after the No. 8 typhoon hit in 2001 which caused serious landslides in mountain villages impacted by the 1999 Chi-Chi earthquake as well. After the Typhoon Morakot in 2009, it pointed out the problem of easily isolated villages in the mountains which were short of ability for self-disaster-management and storage

for food and equipment during large scale landslides occur. To deal with such problems, the Water Resources Agency started the policy of flood indigenous prevention community to strengthen residents' emergency ability from 2012 until now. Simultaneously, the National Fire Agency began to implement countermeasures related to strengthening local governments' capability of emergency management since 2009 to 2017 (Disaster Management Capacity Building Project for Local Government Phase I & II, DMCB). Both countermeasures of the Water Resources Agency (WRA) and the National Fire Agency (NFA) focused on disaster preparedness and response. However, the NFA and its collaborative consulting team (Ridge EM Consulting Co.) started to implement countermeasures including the disaster resilient community with pre-disaster recovery planning, disaster mitigation, local business participation, disaster relief volunteer training which based on the applying the concept of resilience in DMCB Project Phase III from 2018 to 2022. The WRA also executed the "water-resilient cities" policy to improve the ability to protect against floods during climate change. The central government began to change the disaster management policy to loop resilient concept in since 2017, which are not only for emergency response and waiting for post-disaster recovery, but also emphasizing on the importance of pre-disaster recovery planning.

Post- and Pre-disaster Recovery Planning

The definition of post-disaster recovery from UNISDR means the decision or action was made to improve the situation suffered from destruction and to reduce the risk of disaster after disaster, which focuses on reconstruction, recovery, restoration, and rehabilitation (UNISDR, 2005). Thus, a post-recovery plan usually means restoring to a living level. Such a level may not be equal to the same level or higher level before disaster occurred. To compare to a post-disaster recovery plan, a pre-disaster recovery planning means to implement mitigation or grasping pre-disaster issues or needs for the recovery plan. Namely, the purpose of a pre-disaster recovery planning is to strengthen the efficiency of implementing a post-recovery plan; to make a recovery plan in advance would promote achieving the goal of recovery plan and to improve results of post-disaster recovery plan. Whether in the U.S. or Japan, to make the recovery plan in advance to a catastrophe becomes the trade of mitigation and disaster management to avoid the crisis of implanting post-disaster recovery.

Hint from Implement of Pre-disaster Recovery Planning in Japan

In Japan, the experts proposed the process of making pre-disaster recovery planning which are:

- Communicating with community and local governmental officers.
- Considering disaster scenarios to discuss the organization for recovery plan.
- Practicing the local government officers to join the discussion of recovery scenarios.
- Recovery plan including not only hardware facilities, but software like community culture and the way of living.

What the key points from literature review would be the principles or rules to case study in the Ming-An community in Tamsui in Taiwan.

IMPLEMENTING AND DISCUSSION OF RESILIENT COMMUNITY

This paper takes Ming-An Community of Tamsui District in New Taipei City as an example to discuss pre-disaster recovery training for facing with earthquake threats. We set the scenario of damage in an certain magnitude earthquake as the basis for study. Through choosing the case, setting the issues of recovery for the community, simulating recovery scenarios and so on, the process and mechanism were made for strengthening the ability of pre-disaster recovery planning for the large scale earthquake.

Background of the Community

Ming-An Community located in Tamsui District along the Tamsui River, where is a historic area with several cultural and historical heritages and important sightseeing resources. To be aware of its vulnerable environment may be destroyed by tsunami after a great earthquake, the local government began the resilient community project with the New Taipei City Fire Department and Department of

Urban Planning and Disaster Management of Ming-Chuan University. The location of Ming-An Community is shown as figure 1.

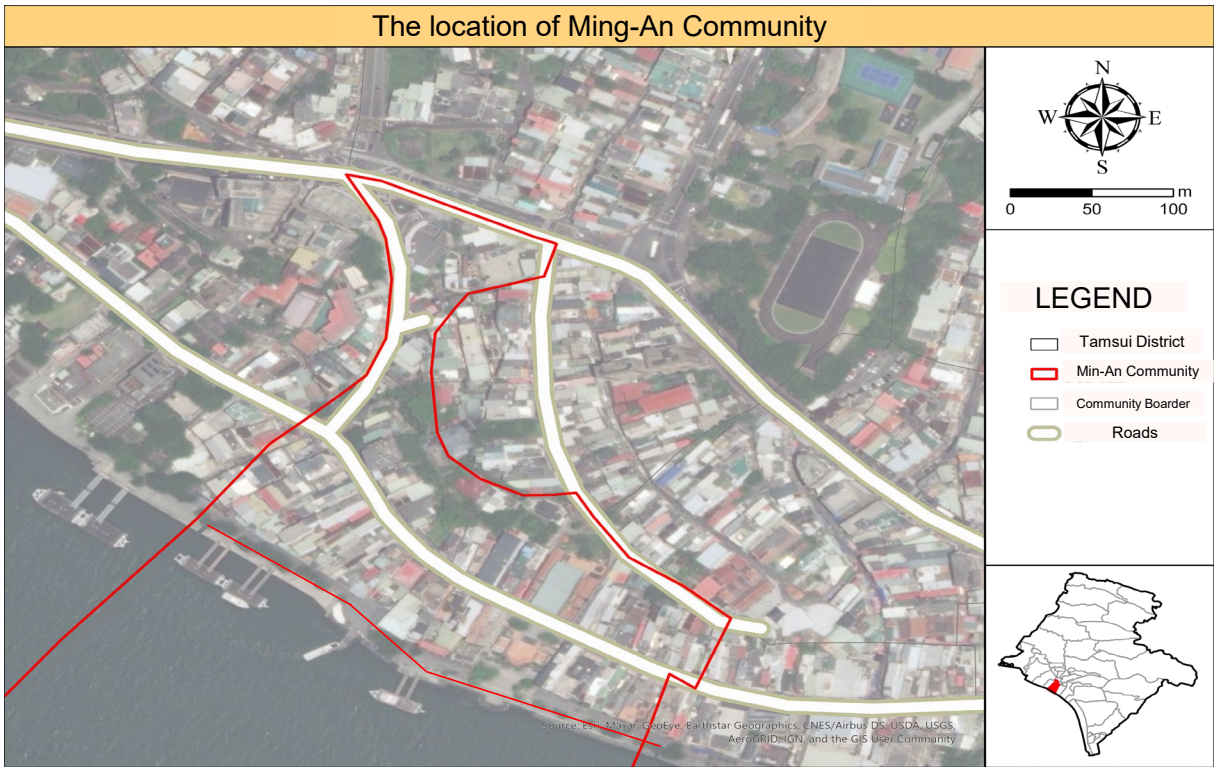

Figure 1 The location of Ming-An Village

Methodology for Pre-disaster Recovery Planning

Except the process of pre-disaster recovery planning, other steps for implementing disaster resilient community are similar to disaster prevention community, therefore, the research focuses on the recovery plan training part. Taking the experience from Japan, the first step of pre-disaster recovery planning is to visit local governmental officers and community's leaders to realize the possible difficulties of recovery issues in the local community. After communicating with local stakeholders, the steps for pre-disaster recovery planning will be set as follows.

Selecting the Presentive Case for Discussing Pre-disaster Recovery

To communicate with residents would be important to discuss the thinking of housing recovery and living rehibition. Therefore, to interview with the community's leader to realize the types of householders, to select the householders may probably be damaged seriously after the earthquake to join the workshop for discussing the baseline of recovery analysis. For example, a commercial householder was selected to analyze business and housing reconstruction.

Setting the Recovery Organization

To face the scenario of post-earthquake recovery, residents would talk about needs of recovery in the workshop. To deal with the issues and needs of recovery from the workshop, the organization for recovery would be re-organized from the organizations already existing in the community to address new tasks related to recovery working.

The Recovery Scenario-based Local Spatial Analysis

Due to the long-term process for recovery needed, based on the time series for reconstruction with different stakeholders' situations in different blocks were shown in a matrix discussion. The tasks of different stages in the matrix addressed as the key works of organizations for recovery in the short term, interim, medium term and long-term period. this would guide the land using and make a concrete recovery-scenario in the community. See figure 2.

The process of community for implementing pre-disaster recovery is shown in Table 1.

Table 1 The process of community for implementing pre-disaster recovery

Steps	Summary
1. Establishment of recovery organization	Community residents, external groups and professionals discuss the organizational structure, cooperation intention and future vision of recovery.
2. Understand the potential impact to the community	Using vulnerability analysis data or disaster potential map data, assuming the extent of the disaster in the community, determine the time and mechanism required for each stage of recovery.
3. Build consensus on recovery	Confirm work items and responsible units, dissemination the outcome and build consensus
4. Identify available resources	Confirm the required resources and provide organization and resource inventory
5. Check the recovery matters and sign the memorandum of cooperation	Check whether there are any missing items in the restoration and reconstruction work, and ensure that the units and personnel who can provide assistance, including work priorities, expected goals, etc.
6. Regularly PDCA and update the recovery mechanism	Test feasibility and improve, and regularly discuss the corrective recovery and reconstruction mechanism.

ANALYSIS AND DISCUSSION

According to the workshop, the concrete discussions were as follows.

Analysis of Damaged Based on the Hypothesis of Earthquake

The elderly people and children are approximately 35% by all residents. When the earthquake was set as Magnitude 8.3, the Ming-An community would be struck by the intensity of scale 6-weak. Thus, the vulnerable people would be injured as an important issue. Besides, several historic blocks and traditional businesses located in the center of the community, and the earthquake could make the brick-made old buildings collapse mainly in the sightseeing areas. The long-term refugee services and business rebuild become necessary in the future.

The Working Groups Supporting for Recovery

The working groups after the earthquake includes patrol, evacuating, rescue, administration and nursing. To face the tasks of recovery, divisions of nursing and administration would transfer to support long-term living in the shelters. The divisions of patrol and evacuating would support rebuilding the historic blocks. Namely, to grasp the needs of recovery, the divisions of emergency response would transfer their tasks to supporting the long-term recovery affairs. See figure 3.

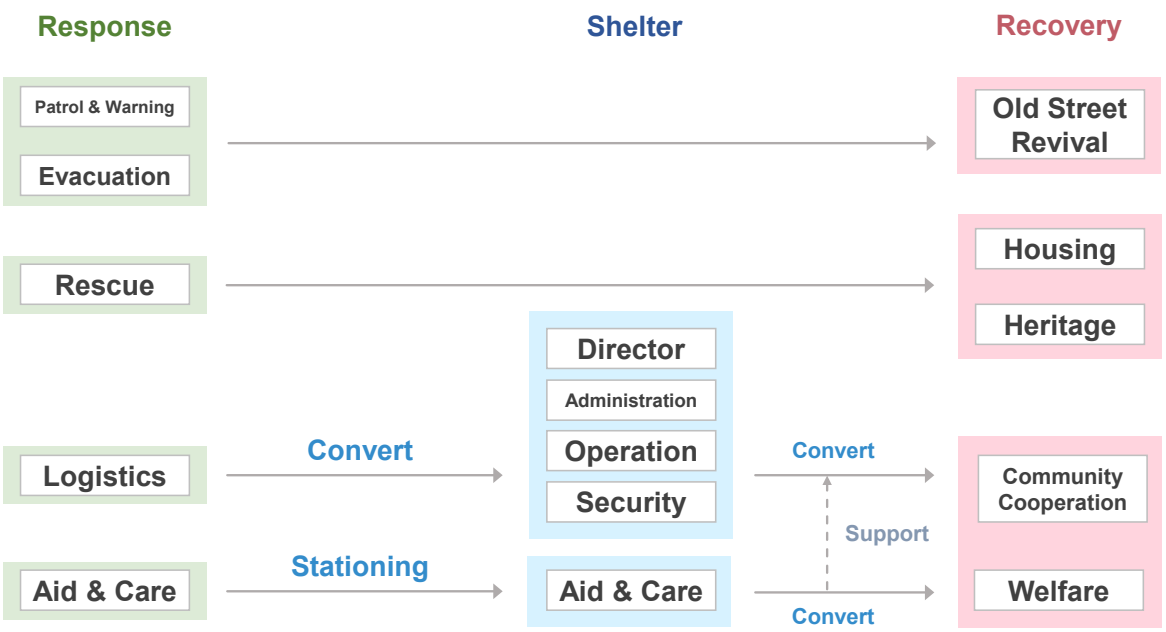

Figure 3 Tasks transfer to support the long-term recovery.

Interim Schedule for Recovery

Due to old and weak buildings concentrated on Ming-An community, the key points for recovery are relief and the need to keep business operating. Besides, to revive the economy of historic blocks and sightseeing in local areas are also another issue for community recovery. Thus, to meet the needs of recovery after the earthquake, a temporary business area, temporary housing area and revival historic and sightseeing area were taken into consideration in the recovery planning.

The Recovery Planning to Fit the Local Environmental Characteristics

To Consider the key points of recovery mentioned above, the three areas located in the community are as follows.

1. Heritage area: the function is to integrate with the historic treasures and education
2. Sightseeing and leisure area: the function is to construct leisure with business.
3. Lifestyles of health: the function is to improve seismic for old buildings to strengthen living quality and to solve the issues of public safety.

CONCLUSIONS

Through the literature review, the research pointed out the importance of resilient community policy and international definition. Besides, from the viewpoint of mitigation to realize the resilient community related to not only emergency response, but to implement pre-disaster recovery planning positively.

This paper also showed the results from the case study on Ming-An Community including:

1. To transfer the functions of emergency response organizations to recovery ones for supporting community recovery planning.
2. To meet the needs from discussion of the pre-disaster recovery planning, several key areas are addressed including “temporary living”, “temporary business”, and “revitalizing historic and sightseeing blocks”.
3. To the recovery vision of the community, three areas are including “Heritage area”, “Sightseeing and leisure area” and “Lifestyles of health area”.

However, still several research issues related to how to integrate the inner and external resources to build the resilience of community by participation of residents and how to make residents understand

the vision of recovery to achieve the consensus for pre-disaster recovery with sustainability become necessary in the deeper discussion in the next stage.

ACKNOWLEDGMENTS

The study was funded by the research projects of MOST 109-2625-M-130-005 and MOST110-2625-M-309 -003. The authors would like to express their gratitude to the National Science and Technology Council (Former Ministry of Science and Technology).

REFERENCES

Holling, C. S. (1973). Resilience and Stability of Ecological Systems, Annual Review of Ecology and Systematics, 4, 1-23.

International Strategy for Disaster Reduction (2005), Hyogo Framework for Action 2005-2015: building the resilience of nations and communities to disasters, World Conference on Disaster Reduction 18-22 January 2005, Kobe, Hyogo, Japan.

Riyanti Djalante, Cameron Holley and Frank Thomaslla (2011), “Adaptive Governance and Managing Resilience to Natural Hazards”, Int. J. Disaster Risk Sci. 2011, 2 (4): 1–14

Pei-Chun Shao and Shyh-Yuan Maa (2021), Discussing on Model of Pre-earthquake Community-based Recovery Planning in Japan, Annual Meeting of Urban Planning 2021, Kaohsiung, Taiwan (Traditional Chinese Version)

National Fire Agency (2017), The DMCB Project Phase III (Disaster Management Capacity Building for Local Governments Project), Taipei, Taiwan (Traditional Chinese Version)

(4b) Seismic hazards and vulnerabilities

SEISMIC DEAGGREGATION ANALYSIS FOR SELECTED MAJOR CITIES IN NORTHERN SOUTH EAST ASIA

Teraphan Ornthammarath[1] and Pennung Warnitchai[2]
1. Associate Professor, Department of Civil and Environmental Engineering, Faculty of Engineering, Mahidol University THAILAND.
2. Professor., Asian Institute of Technology, Pathumthani, THAILAND.
Email: teraphan.orn@mahidol.edu, pennung@ait.ac.th

ABSTRACT

In this study, seismic deaggregation analysis is applied for selected major cities in Northern South East Asia to assess the combined effect of all magnitudes and distances on the probability of exceeding a given ground motion level. Deaggregation of peak ground acceleration and spectral acceleration at 1 s at 2475 year return periods are derived. From comparing the hazard maps from different major cities, it could be concluded that some cities have similar hazard estimates for considered return periods but by deaggregating the hazard, the controlling earthquake scenarios are different, partly due to the location of considered cities and seismicity level of background seismicity and considered active faults. The deaggregation results presented here can be helpful to both private and public stakeholders for many applications. For example, they can be used by structural engineers to select appropriate ground-motion records for testing the adequacy of the design of new structures or the response of existing ones.

Keywords: Seismic hazard, Deaggregation, Northern South East Asia, Indochina

INTRODUCTION

An attempt to assess seismic hazard and quantify epistemic uncertainties in Northern South East Asia has been made by several past PSHA studies. One of the benefits of probabilistic seismic hazard assessment is that it sums the hazard to a site from all relevant earthquake sources. However, this summation may hamper the application of PSHA since it does not represent any specific earthquake scenarios. To get intuitive understanding of the controlling hazard will not only help in engineering seismic design but it could also improve communication link between engineers and relevant stake holders (e.g. building owners, policy makers, etc.). For example, structural engineers generally require appropriated time histories analysis for engineering seismic design as an input to perform nonlinear time history dynamic analysis. While, a seismic loss assessment of any city area, a set of realistic earthquake scenarios have to be defined. With respect to seismic hazard, these scenarios should cover all possible earthquakes events so that the results of seismic loss estimation can be utilized in developing an effective and versatile earthquake disaster contingency plan. For this purpose, deaggregation analysis has generally been used to examine the spatial and magnitude dependence of PSHA hazard results.

In order to define magnitudes, M, distances, r, and epsilons, ε, the number of standard deviations from the median ground motion as predicted by an ground motion model (GMM) that contribute to the specific return period and at a structural period considered in engineering seismic design and other purposes. The deaggregation process has been performed following the approach described by Bazzurro and Cornell, (2004) and Harmsen et al., (1999). This paper, in connection with Ornthammarath et al. (2020), supplements those results through deaggregation analysis which could help to explain the typical size and distance of earthquakes making the largest contributions to the seismic hazard for the 2% probability of exceedance in 50 years on stiff site (760 m/s average shear wave velocity in the upper 30 m) condition. Deaggregation is applied for cities in Northern South East Asia to assess the combined effect of all magnitudes and distances on the probability of exceeding a

given ground motion level, for both smoothing seismicity and fault models. These findings could lead to better understanding of the hazard analysis results and providing indication for further research in reducing existing uncertainty. Important contributions to seismic hazard deaggregation methods and applications are found in Stepp et al. (1993), Chapman (1995), McGuire (1995), Cramer and Petersen (1996), and Bazzurro and Cornell (1999).

METHODOLOGY

PSHA integrates over all potential earthquake occurrences and ground motions to estimate the mean frequency of exceedance, ν, of any given spectral acceleration at the site. occurring at different locations in different seismic sources at difference probabilities of occurrence. By this reason, it is difficult to get an intuitive understanding of what earthquake scenarios are controlling the hazard of the project site. To provide insight into what earthquake scenarios are the most important for the hazard, the hazard is broken down into its contributions from different earthquake scenarios. This process is called "Seismic Hazard Deaggregation Analysis (SHDA)" (Harmsen and Frankel, 2001). The results of this SHDA will later on guide us on how to select ground motions that represents the hazard controlling earthquake scenarios.

In general, it is important to provide an overview of the procedure developed by Ornthammarath et al. (2020) for the evaluation of seismic hazard for Northern South East Asia. The seismic hazard maps for Northern South East Asia has been developed by using combination of smoothed gridded seismicity, crustal-fault, and subduction source models. For smooth seismicity, where earthquakes are usually assumed to be point sources, the rate at which the ground motion from the ith source exceeds the test level z at the site, is given by

$$\nu_i\left(Sa > z\right) = N_i\left(M_{\min}\right)\int_{r=0}^{\infty}\int_{m=M_{\min}}^{M_{\max}}\int_{\varepsilon=\varepsilon_{\min}}^{\varepsilon_{\max}} f_{m_i}(m)\, f_{r_i}(r)\, f_{\varepsilon}(\varepsilon)\, P\left(Sa > z \middle| M, r, \varepsilon\right) dr\, dm\, d\varepsilon \qquad (1)$$

where Ni(Mmin) is the rate of earthquakes with magnitude greater than Mmin from the i^{th} source, Mmin = 4.5 for background seismicity in BG I and M_{min} = 5.0 for background seismicity in BG II, r is the distance metric, m is magnitude, ε is the number of standard deviations of the ground motion from the median ground motion, Mmax is the maximum magnitude (for the i^{th} source), Mmax = 6.5 for background seismicity in BG I and Mmax = 7.5 for background seismicity in BG II, fm(m), and fr(r) are probability density functions for the magnitude, and distance which describe the relative likelihood of different earthquake scenarios, fε(ε) is the probability density function for a ground motion variability and P(SA > z|m,r, ε) is either 0 or 1. It is an indicator for the SA of z ground motion (generated by source i) of magnitude M, distance r, and ε standard deviations away from the median with respect to level z. This indicator function is equal to 1 if predicted SA(M,r, ε) as computed from the GMM is greater than z and 0 otherwise.

Two-dimensional deaggregation in terms of magnitude and distance is the most common form of deaggregation representation; however, three-dimensional deaggregation in terms of magnitude, distance, and epsilon would provide insight into the difference between probabilistic ground-motion estimates and ground motions from deterministic scenarios. The deaggregation can be selected reference to PGA, SA, etc. It allows the definition of the earthquake controlling the local seismic hazard (dominant scenario earthquake). The dominant scenario earthquake might be defined by mean or modal values of M and r. Mean values are simple to understand, communicate, and compute but do not always represent a realistic scenario (i.e., the most likely M and r that might induce the specified IM at the site). However, although mean values of M and r do not correspond to any realistic scenario, they appear more appropriate when the hazard is calculated from areal sources rather than faults. The mode corresponds to the M-r group that gives the largest contribution to the hazard (the largest deaggregation value) and, consequently, corresponds to a realistic source, at least within the resolution of the magnitude and distance binning. The main disadvantage of using modal values is that they are

sensitive to the bin size. In this study, seismic hazard deaggregation maps for mean and modal values of M, r, and ε for PGA at 2% of probability in 50 years have been derived.

SEISMIC HAZARD DEAGGREGATION ANALYSIS (SHDA) FOR SELECTED CITIES

In this study, a SHDA for Mandalay, Yangon, Vientiane, and Bangkok are carried out. Of major cities in the Northern South East Asia, Mandalay has the highest seismic hazard for all considered structural periods and probabilities of exceedance. For short and long ground motions (PGA and SA at 1.0s), the predicted high ground motions are about 100% g for 2% probability of exceedance in 50 years, Table 1, due to observed seismicity and the Sagaing fault located in the western part of Mandalay. On the other hand, Yangon has lower hazard levels with 30% g for PGA for 2% probability of exceedance in 50 years. On the other hand, Vientiane has lower hazard levels with 9% g for PGA for 2% probability of exceedance in 50 years. A lower seismic hazard level is found for Bangkok than for Mandalay, Yangon, and Vientiane because Bangkok is far from high seismicity areas and its location which is away from any known active faults, Figure 1.

Table 1. Probabilistic ground motions with 5 % damping for selected cities at 2% probability of exceedance in 50 years based on Ornthammarath et al. (2020) (standard site condition: V_{S30} = 760 m/s)

City	PGA (g)	SA (T = 1s)
Mandalay	1.00	1.00
Yangon	0.35	0.3
Vientiane	0.09	0.06
Bangkok	0.05	0.07

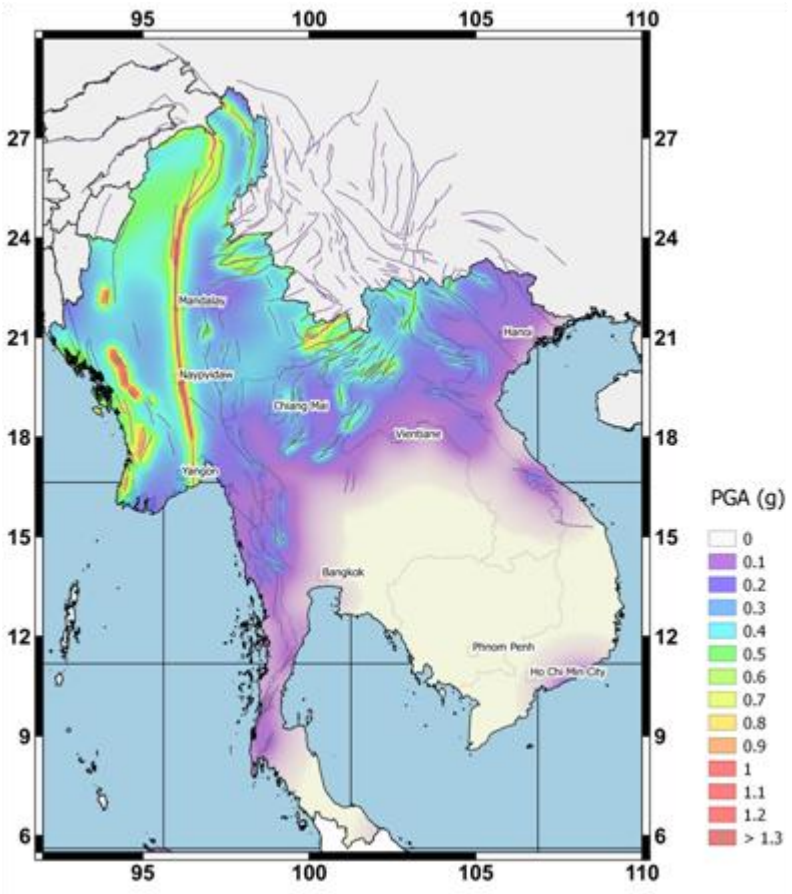

Figure 1. Probabilistic seismic hazard map for mean PGA at 2 % exceedance in 50 years.

Some of the SHDA results for Mandalay, Yangon, Vientiane, and Bangkok are presented by 3D bar graphs in Figures 2 to 5, where the height of each bar shows the contribution to hazard by the earthquake scenario that the bar represents, while the location of the bar shows the magnitude (M_W) and source-to-site distance (R) of the earthquake scenario. The hazard is represented by the PGA and SA at structural periods of 1.0 sec for return periods of 2475 years.

The SHDA results show that the seismic hazard at Mandalay at return period of 2,475 is dominated by earthquakes of magnitude around 7.75 from the Sagaing fault central segment, which is less than 12 km distance to the city center for both PGA and SA (T=1.0s), Figure 2. On the other hand, Yangon is mostly contributed by two types of earthquake scenarios. The first type (type 1) is the scenarios where an earthquake with magnitude 6.5 to 7.5 is occurring at a distance of 40 to 50 km from Yangon. They are shallow crustal earthquakes along the Sagaing fault and nearby areas. The second type (type 2) is the scenarios where an earthquake with magnitude 8.0 to 8.5 is occurring at a distance of 40 to 50 km from the Arakan Megathrust Subduction Zone. These scenarios are large subduction interface earthquakes occurring in subduction source zones (SD-A), Figure 3.

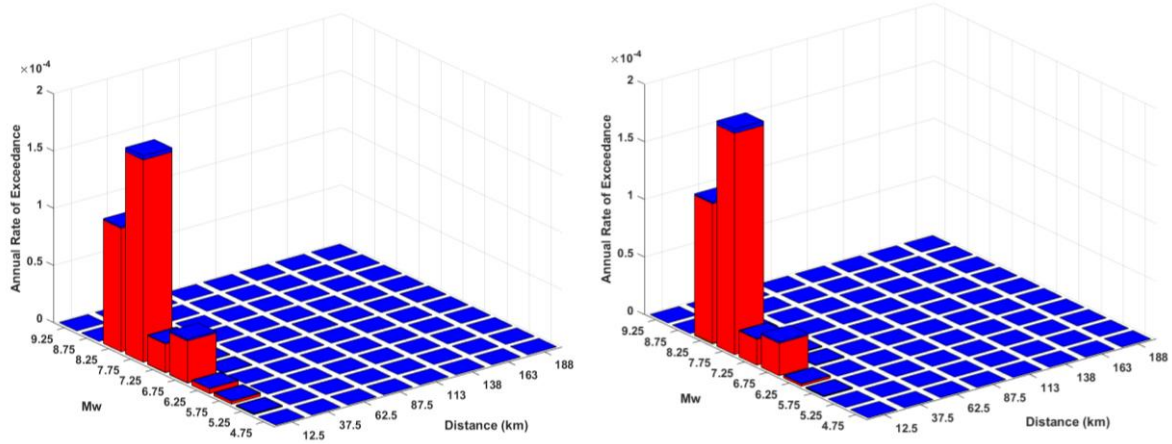

Figure 2. The 3-D deaggregation for PGA and SA (T-1.0s) at Mandalay at 2,475-year return period corresponding to 2 % of excceedance in 50 years.

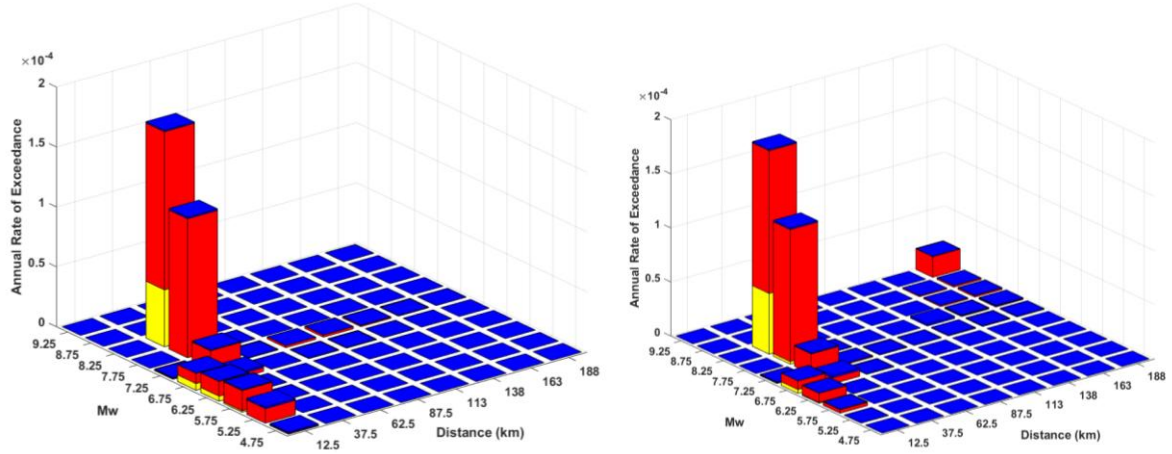

Figure 3. The 3-D deaggregation for PGA and SA (T-1.0s) at Yangon at 2,475-year return period corresponding to 2 % of excceedance in 50 years.

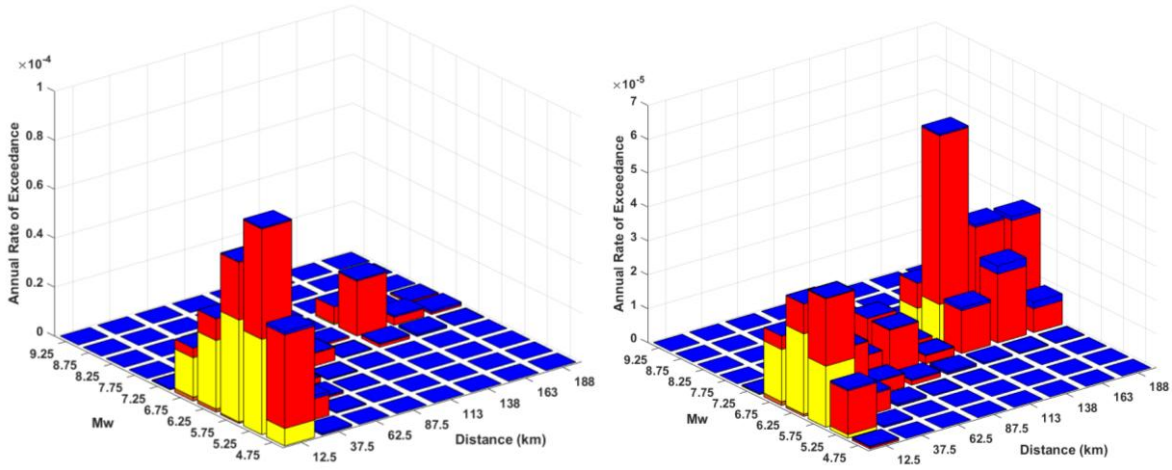

Figure 4. The 3-D deaggregation for PGA and SA (T=1.0s) for Vientiane at 2,475-year return period corresponding to 2 % of excceedance in 50 years.

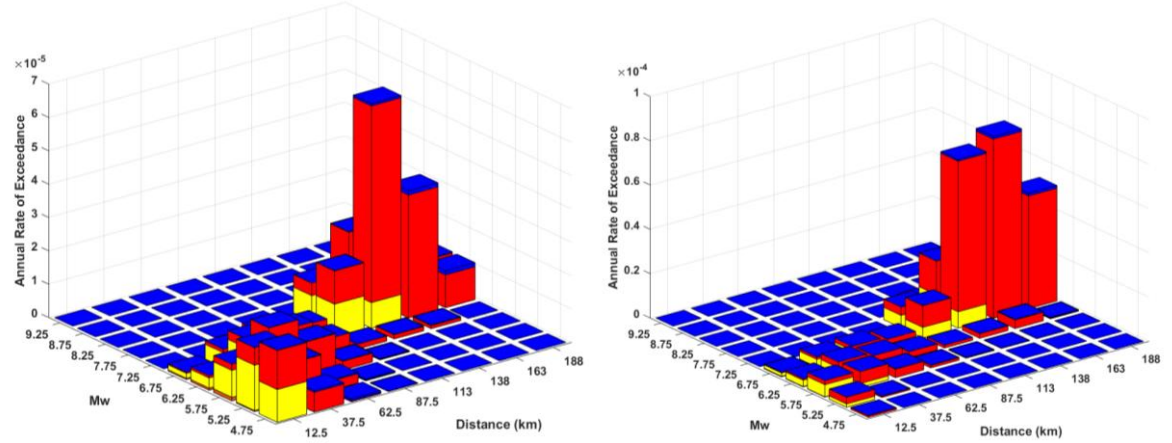

Figure 5. The 3-D deaggregation for PGA and SA (T=1.0s) for Bangkok at 2,475-year return period corresponding to 2 % of excceedance in 50 years.

For Vientiane, the deaggregation for PGA at 2475-year return periods (Figure 4) was computed, and local seismicity is the controlling earthquake with moderate magnitude of 5.25 at distance less than 12 km. In contrasting to the PGA, the deaggregation result from the SA (T = 1.0s) is highly contributed from the magnitude of 7.75 at distance less than 140 km with some contribution from background seismicity. Lastly, the SHDA results for Bangkok show that, for return period of 2475 years, the controlling scenarios for PGA and SA at (1.0 sec) is the active fault with magnitude of 7.25 at distance between 100 and 150 km, Figure 5. They are shallow crustal earthquakes in Kanchanaburi province and nearby areas.

CONCLUSIONS

From comparing the hazard and deaggregation results from recent seismic hazard assessment model, it could be concluded that different major cities in Northern South East Asia subjected to different degree of seismic hazard. The seismic hazards for different cities seem to be similar but by deaggregating the hazard, the controlling earthquake scenarios are different, partly due to observed seismicity and location of major active faults with different degrees of magnitude-frequency relationships. So the deaggregation results, therefore, reveals different earthquake scenarios that controlling the hazard, which could be useful for urban planning and seismic risk reduction in the future. It is then sensible to consider these deaggregation results for further studies (e.g. selection of ground motion records for engineering design, etc.).

REFERENCES

Bazzurro, P., and C. Allin Cornell (1999). Disaggregation of seismic hazard. Bull. Seism. Soc. Am . 89,501 –520.

Bazzurro, P., Cornell, C.A. (2004) "Disaggregation of Seismic-Hazard," Bull Seismol Soc Am, Vol. 89, No. 2, pp. 501-520.

Cramer, C. H., and M. D. Petersen (1996). Predominant seismic source distance and magnitude maps for Los Angeles, Orange, and Ventura Counties, California, Bull. Seism. Soc. Am . 86,1645 –1649.

Chapman, M. C. (1995). A probabilistic approach for ground motion selection for engineering design, Bull. Seism. Soc. Am . 85,937 –942.

Harmsen, S., Frankel, A. (2001) Geographic Deaggregation of Seismic Hazard in the United States, Bull. Seism. Soc. Am . 91 (1): 13–26. https://doi.org/10.1785/0120000007

Harmsen, S., D. Perkins, and A. Frankel (1999). Deaggregation of probabilistic ground motions in the central and eastern United States, Bull. Seism. Soc. Am . 89,1 –13.

McGuire, R. K. (1995). Probabilistic seismic hazard analysis and design earthquakes: closing the loop. Bull. Seism. Soc. Am . 85,1275 –1284.

Ornthammarath,T., Warnitchai, P., Chan, C.H., Wang, Y., Shi, X., Nguyen, P.H., Nguyen, L.M., Kosuwan, S., Thant, M. Probabilistic seismic hazard assessments for Northern Southeast Asia (Indochina): Smooth seismicity approach Earthquake Spectra, 36 (2020), pp. 69-90, 10.1177/8755293020942528

Stepp, J. C., W. J. Silva, R. K. McGuire, and R. W. Sewell (1993). Determination of earthquakes design loads for a high level nuclear waste repository facility, in Proc. of the Natural Phenomena Hazards Mitigation Conference, Atlanta, Georgia, 19–22 October 1993, Vol. II, 651–657.

(4c) Earthquake loss estimation

RECENT PROGRESS OF TAIWAN EARTHQUAKE LOSS ESTIMATION SYSTEM

Chin-Hsun Yeh[1]
1. Division Director, Seismic Disaster Simulation Division, National Center for Research on Earthquake Engineering, Taipei, Taiwan, ROC.
Email: chyeh@narlabs.org.tw

ABSTRACT

After the Chi-Chi, Taiwan earthquake in 1999, a project to develop Taiwan Earthquake Loss Estimation System (TELES) was initiated at the National Center for Research on Earthquake Engineering (NCREE). Since then, NCREE has collected and calibrated various nationwide seismic source, geologic, and inventory databases. NCREE has also studied seismic hazard analysis, damage assessment, and loss estimation models and calibrated the associated parameter values to meet local engineering practices and socio-economic environments. The disaster simulation results due to several probable maximum earthquakes may provide helpful information in disaster reduction, emergency response, and risk management of the study region. The application software integrates a geographic information system (GIS) to store geologic and inventory data spatial variation. The GIS kernel related to the application software's database management engine and map display interface has been under reconstruction using open-source libraries recently.

Keywords: Chi-Chi Taiwan Earthquake, scenario earthquake, seismic disaster simulation, geographic information system

APPLICATIONS OF SCENARIO-BASED SEISMIC DISASTER SIMULATION

The Taiwan Earthquake Loss Estimation System (TELES) includes various analysis models (Yeh et al., 2006). The analysis framework of TELES is shown in Figure 1(a). It can estimate the potential earth science hazards, direct or indirect physical damages, and socio-economic losses under any scenario earthquake. All analysis models require a localized database and site-dependent parameters to obtain valuable and reliable estimates. Therefore, ground-motion prediction models, soil liquefaction assessment methods, building damage and casualty assessment, etc., have been studied to meet observations in the Chi-Chi Taiwan earthquake.

The evaluation targets cover structural types such as buildings, bridges, facilities, and buried pipelines. According to functionality, it may be divided into general building stocks, essential facilities, transportation, and utility systems. Since 2011, TELES has been decomposed into several subsystems shown in Figure 1(b) to satisfy individual user demands. Each subsystem may run independently and target different subjects, including Tgbs for general building stocks, Tschool for school buildings, Thighway for highway systems, Trailway for railway systems, and Twater for potable water systems. For example, rescue and firefighting services can obtain information from Tgbs about the estimated number of building collapses, casualties, post-quake fires, and the various demands for rescue and evacuation. Water departments can utilize Twater to assess the water shortage, repair cost, and interruption time due to damages to water treatment plants, storage tanks, and buried pipeline systems.

Seismic disaster simulation has many applications in disaster prevention and risk management. However, it should be noted that we need to update its databases and improve its estimation models from time to time to ensure the validity of simulation results. We also need to promote its applications and share the estimation results through the Internet. The following sections briefly introduce recent advances in data manipulation and assessment models.

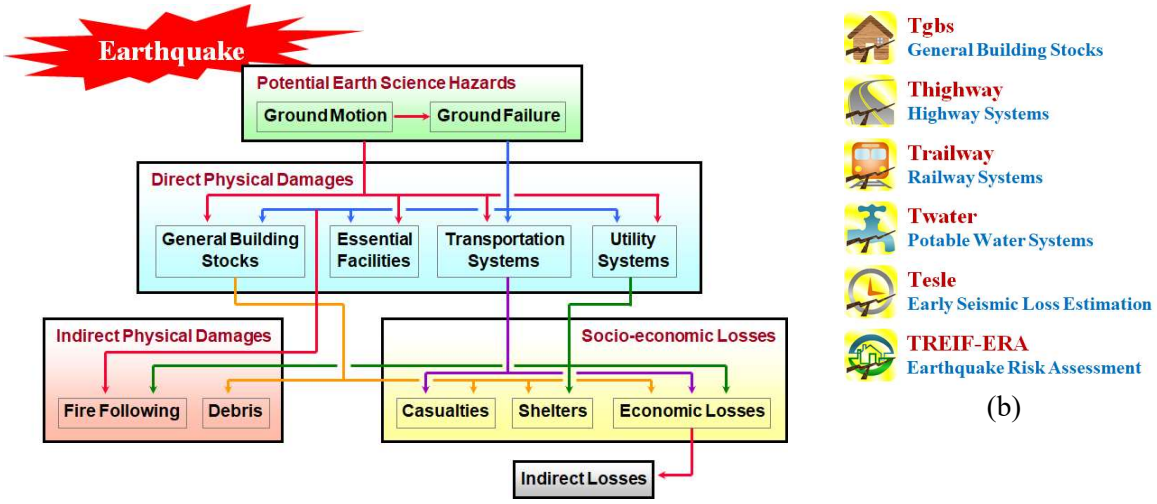

Figure 1 (a) Analysis framework of Taiwan Earthquake Loss Estimation System (TELES); (b).Subsystems of TELES

DISTRIBUTION AND STATISTICS OF EXPOSURES

Original building tax data and insurance policy records do not have precise location information to assign each risk exposure to individual villages. We have developed an address location technology that may find the geographic coordinates of the building through its address. Using the address location technology, we may simultaneously retrieve the seismic attributes and the coordinates of individual houses in the building tax data. In other words, we may establish a building inventory database with reliable features, including structural type, construction year, height, occupancy class, and coordinates, to increase the validity and precision of estimation results. These features help assess probable damages, losses, and casualties under any scenario earthquake. The address location technology may also increase the accuracy of the insured policy distribution in the earthquake risk assessment model.

Obtaining the individual coordinates of houses and insurance policies enables analysis of general building stocks and risk assessment in villages or street-block units. There are 7 833 villages and 77 773 street blocks in Taiwan. Thus, a street-block-based approach vastly increases the resolution of exposure distribution and estimation results in metropolitan areas, as shown in Figure 2. The high resolution in the inventory database and estimation results makes it possible to study urban spatial planning and post-quake road blockage risk due to nearby building collapse.

GROUND MOTION PREDICTION MODEL

Estimating local seismic hazards, including ground excitation, soil liquefaction, landslide, etc., is the first step in structural damage assessment over a wide area due to any scenario earthquake. Furthermore, estimating ground-motion intensity is the basis for other seismic hazards, such as soil liquefaction or landslide potential. The ground-motion prediction model may roughly be divided into two steps: path attenuation and site amplification.

The ground-motion prediction equation (GMPE) Chao19 uses the moment magnitude scale, distinguishes the seismic source types and fault rupture mechanisms, and is based on the regression results of strong-motion records in Taiwan over the past two decades. Despite the advantages above, due to insufficient strong-motion records of large magnitude earthquakes near the fault rupture in Taiwan, Chao19 may underestimate the ground-motion intensity within 10 km of fault ruptures compared with existing GMPE in TELES and other GMPEs (Chiou et al., 2019). Therefore, we

examined how to specify the depth of the rupture top (Z_{tor}) (Yeh et al., 2022). It is found that the discrepancy of ground-motion intensities may be reduced if the seismogenic rupture top has been considered in the specification Z_{tor} .

A new generation GMPE, such as Chao19, has considered linear and nonlinear site effects in the prediction model. Geological data such as V_{s30} (averaged shear-wave velocity to a depth of 30 m) and $Z_{1.0}$ (depth at which shear-wave velocity is 1000 m/s) are generally used in the GMPEs to reflect site-effect. However, other factors such as terrain and landform may affect the ground-motion intensity. In addition, the V_{s30} and $Z_{1.0}$ are unavailable in most places. The site-effect models in GMPEs are generally unsuitable for large areas seismic hazard analysis or loss assessment. Therefore, based on the existing ground-motion modification model in TELES, we have combined the new GMPE and the strong-ground-motion databases in Taiwan to develop and assess a site-effect model suitable for wide-area seismic damage assessment (Yeh et al., 2021).

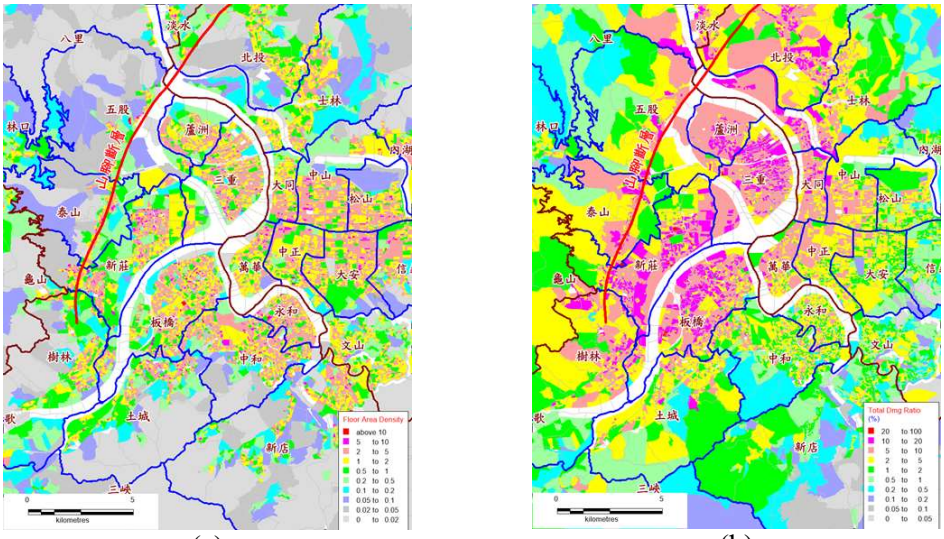

(a) (b)

Figure 2 Distribution of building (a) floor-area densities and (b) damage ratios in street-block units in the metropolitan Taipei area under a scenario earthquake of magnitude 6.6 due to rupture of the Sanchiao fault.

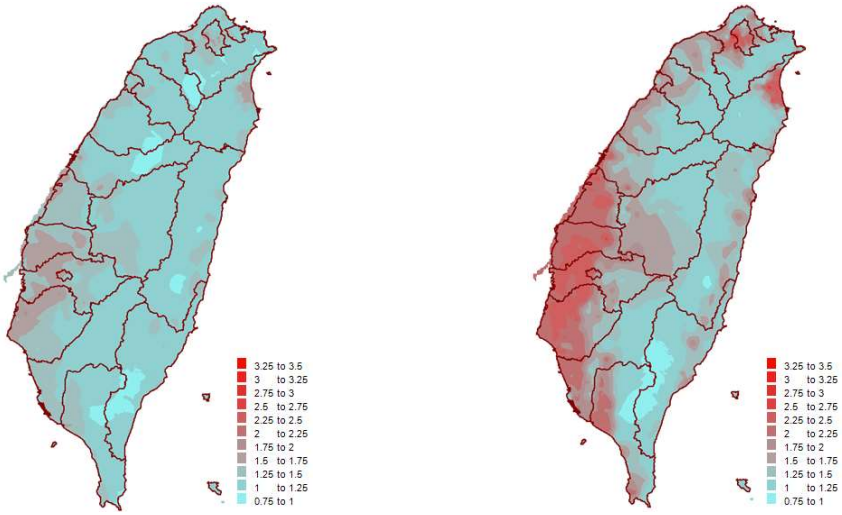

(a) reference site $S_{a03} = 0.2g$ (b) reference site $S_{a10} = 0.1g$

Figure 3 Ground-motion amplification of (a) short-period and (b) 1-second-period structure spectral accelerations at the specified reference intensity

CLASSIFICATION SCHEME OF MODEL BUILDING TYPES AND DAMAGE FUNCTIONS

We have proposed an updated model building classification scheme, classifying all buildings into 18 categories depending on their structural types and heights. Since information about concrete shear walls or ductile moment frames does not exist, the lateral structural resisting system is not used to distinguish model building types. The structural types include reinforced concrete, steel, steel-reinforced concrete, reinforced masonry, unreinforced masonry, and wood structures. Since the sizes of newly constructed buildings increase over time, besides the original categories of low-rise (1F-3F) and mid-rise (4F-7F) buildings, buildings that have over eight floors are further classified into high-rise (8F-18F) and super-high-rise (19F and over) buildings.

A capacity curve reflects the seismic strength of a model building type. The influence factors include the minimum design base shear, the seismic zonation scheme, the short-period and 1-second-period spectral accelerations, the local site condition, and the importance factor specified by the seismic design codes. In addition, a set of fragility curves is used to reflect the deformability within different damage states of a model building type. Since the ratio of buildings that comply with design and construction specifications increases with time, the building fragility also seems highly dependent on the construction periods. The medians of fragility curves are calibrated by disaster reconnaissance and analytic models, which are compatible with capacity curves.

STRUCTURAL AND NON-STRUCTURAL DAMAGE ASSESSMENT

Building damages can be roughly divided into those of the structural system and the non-structural components. Structural damages relate to the life safety of human beings, while non-structural damages relate to the economic losses and the facility's functionalities. For example, the amount of post-quake casualties, the required rescue-task forces, the short-term shelter needs, etc., are closely related to structural damages. However, if we want to evaluate the economic losses, the functionality failures, the business interruption time, etc., a non-structural damage assessment of individual components and equipment is essential.

We are applying the disaster simulation technology in the seismic insurance business and post-quake emergency medical-care needs. Thus, it is necessary to assess the damage and possible function losses of non-structural parts, equipment, content, etc., and evaluate the business interruption time after a scenario earthquake. The non-structural damage assessment model can also be applied to assess post-earthquake healthcare performance.

MIGRATION TO OPEN GIS

Information about the seismic attributes and the spatial distribution of risk exposure is essential in a seismic disaster simulation and can be easily manipulated in a geographic information system (GIS). The original software of TELES was written in C++ programming language and Microsoft Foundation Class (MFC) Library and integrated with commercial GIS desktop software MapInfo to store the risk exposures' seismic attributes and spatial information. However, MapInfo has stopped supporting an integrated map technology through the MFC framework. Therefore, searching for an alternative approach to managing GIS databases and displaying input/output maps is required.

After careful evaluations of database management capabilities, including computation efficiency, thematic map capability, acquisition cost, etc., the open-source GIS libraries Spatialite and MapWinGIS were selected for future development. Since these GIS libraries can integrate with the MFC library, all existing analysis modules are still valid with only minor modifications. However, the open GIS libraries do not provide a user-friendly graphical user interface to control map windows' appearance and exchange data between different libraries. In other words, we need to develop a graphical user interface and integrate the two independent GIS libraries. Despite these difficulties, we plan to complete the migration of Tgbs by the end of 2022.

CLOUD INFORMATION SERVICES

We are developing an online seismic damage assessment service called TELES Onlin. The seismic source parameters, including the fault name, earthquake magnitude, rupture length, and width of the scenario earthquake, are to be specified by users. Through asynchronous computation technology, when the TELES server completes the seismic damage assessment, the server will inform the user to log in to the website to inquire about or download the damage and loss assessment results online.

Taking advantage of the 3D map services launched by the Ministry of the Interior in November 2020, our goal is to put the existing products and research results on the 3-D Web GIS to enhance the comprehensibility of the estimation results.

REFERENCES

Chao, S.-H., B. Chiou, C.-C. Hsu, P.-S. Lin, 2019, "Development of Horizontal and Vertical Ground Motion Models for Crustal Earthquakes and Subduction Earthquakes in Taiwan," NCREE-19-003.

Chiou, B. and P.-S. Lin, 2019, "Adjusted Foreign GMPEs for Taiwan," part of GMC Technical Report, Development of the Hazard Input Document for Taiwan using SSHAC Level 3 Methodology, Taiwan Power Company.

Yeh, C. H., Loh, C. H., and Tsai, K. C., 2006, "Overview of Taiwan Earthquake Loss Estimation System," Natural Hazards, 37, pp. 23-37.

Yeh, C.-H., L.-H. Huang and Y.-N. Huang, 2021, "Site-effect Model for Wide-area Seismic Damage Assessment," 2020 NCREE Research Programs and Accomplishments.

Yeh, C.-H. and L.-H. Huang, 2022, "Applicability of the Ground Motion Prediction Equations for Wide-area Seismic Damage Assessment," 2021 NCREE Research Programs and Accomplishments.

SURVEY ON THE STRUCTURAL CHARACTERISTICS ASSOCIATED WITH SEISMIC CAPACITY OF MASONRY TEMPLES IN TAIWAN

Keng-Chang Kuo[1] and Wei-Hsiang Hung[2]
1. Assistant Professor, National Kaohsiung University of Science and Technology, Kaohsiung, Taiwan
2. Master, National Kaohsiung University of Science and Technology, Kaohsiung, Taiwan
Email: kkuo@nkust.edu.tw

ABSTRACT

Masonry temples are the most familiar historic buildings to people in Taiwan. For temples located in such earthquake-prone area, it is critical to ensure their seismic capacity. The goal of this study is to survey the structural characteristics which allow masonry temples to survive past earthquakes. Temples in the strong shaking areas of the Chi-Chi and Chiayi earthquakes of 1999 were selected and an in-situ survey was conducted to measure the statistics of structural characteristics, including weight of unit roof area and shear strength. Meanwhile, ambient vibration measurements were conducted to investigate natural frequencies of temples. A good correlation was found between measured natural frequency and shear coefficient, serving as an indicator of shear strength. Lastly, the threshold of applied inertia force for moderate and minor damages were identified.

Keywords: 1999 Chi-Chi Earthquake, masonry temples, structural characteristics, natural frequencies

INTRODUCTION

Masonry temples are the most familiar historic buildings to people in Taiwan because of Taoism and Buddhism (Fig. 1). Since 1999, when the Chi-Chi earthquake caused unprecedented damage to architectural heritage (Hsu *et al.*, 2000), the seismic performance of historical buildings has drawn research attention such as push-over tests on brick walls with lime-cement mortar (Chen *et al.*, 2012). During the Chi-Chi earthquake, many masonry temples were severely damaged, while in the same areas there were still temples undergoing minor or no damage (Chang *el al.*, 2001). The goal of this study is to identify the relationship of damage to brick walls and the structural characteristics which allow masonry temples to survive past earthquakes. The structural characteristics associated with seismic capacity such as weight of unit roof, plan eccentricity and shear strength are measured. Temples in the strong shaking areas of the Chi-Chi and Chiayi earthquakes of 1999 were selected and an in-situ survey was conducted to measure the statistics of structural characteristics. In addition, ambient vibration measurements were conducted to identify the natural frequencies of masonry temples. Correlation of theoretical shear strength and natural frequency was identified.

OUTLINE OF THE SURVEY AND AMBIENT VIBRATION MEASUREMENTS OF MASORY TEMPLES

Fig. 2 shows the spatial distribution of surveyed temples and the shaking intensity levels regulated by the Central Weather Bureau (CWB), Taiwan for the two earthquakes. They were mainly distributed over the central and south part of the island. Temples located within 5 km of CWB earthquake stations with seismic intensity exceeding level 5 (PGA greater than 80gal) were selected so that reliable input ground motions were available. For many sites, there were typically two to three masonry buildings aligned in sequence to provide different space functions. Each building was counted as an individual sample. In total, 31 samples from 19 sites were investigated, among which damage along in-plane and out-of-plane directions of brick walls were observed for nine and two cases.

While conducting ambient vibration measurements, sensors were installed on walls or timber frames depending on in-situ conditions (Fig. 3). It is indicated by Chang (2001) that installation of vibration

sensors to either brick walls or timber frames immediately adjacent to walls will obtain approximate natural frequencies. For three-gate hall styles, brick walls only exist on two sides. Thus, for such symmetric distributions of brick walls, only one vibration sensor was installed on either side. By contrast, layouts with main and back halls have one back wall in addition to side walls. As the distribution of brick walls is a U shape, each side wall required one sensor to capture planar torsional vibration modes.

Figure 1. Photograph of the surveyed temples in central and south Taiwan.

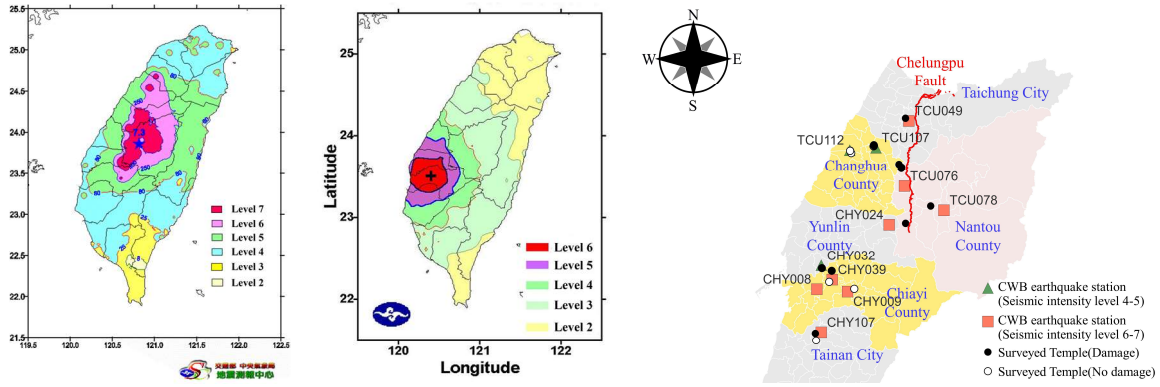

(a) (b) (c)

Figure 2. (a, b) Epicenter and shaking intensity of the Chi-Chi and Chiayi earthquakes of 1999 (edited from Central Weather Bureau, Taiwan). (c) Spatial distribution of surveyed temples and earthquake stations.

Figure 3. Photograph of vibration sensors installed on wall (left) and adjacent timber frame (right).

STRUCTURAL CHARACTERISCTICS ASSOCIATED WITH SEISMIC CAPACITY

Temples commonly contain heavy roofs due to the requirement of religious customs. The induced large inertia force for a heavy roof is a major factor causing damage to temples in earthquakes. Based on the survey results (Fig. 4), the weight of unit roof areas mainly ranged within 200~275 kgf/m^2 and showed no relation with the temples' plan areas. Meanwhile, the plan areas of the surveyed temples mainly ranged within 40~140m^2. There are two types of tiles commonly used for the roof: Tongban, convex tile; and Yanho, red tile (Fig. 5). Roofing weight is transferred to timber frames and brick walls by purlins. On the whole, roofs constructed with Yanho tiles showed larger weight of unit roof area than those with Tongban tiles. This is because Yanho tiles are overlapped at a certain distance so that above each tile three to four are laid up. As a result, more Yanho tiles are used than Tongban tiles within a

given length. Calculation of roof weights included ridges and purlins so that the obtained values were much higher than the design values suggested by domestic codes. For reference, the regulated weight of unit area for roofs with Japanese-style black and cement tiles should be greater than 60 and 45kgf/m^2, respectively.

Brick walls in perimeters provide the main resistance to seismic force for temples. Except for a three-gate hall (the temple's entrance portico), walls are located in a U shape for the main and back halls such that the plan eccentricity of brick walls is of concern. As shown in Fig. 6, generally larger eccentricity was observed for the samples with larger area. For the temples with approximate plan areas, plan dimensions are considered to affect eccentricity. Hence, the relationship between ratio of plan width to length and eccentricity is furthermore verified. There can be seen a clear linear relationship between eccentricity of brick walls and length-to-width ratio of plans, corresponding to narrower geometries.

Shear strength is calculated using a method proposed by domestic researchers (Chen *et al.*, 2012). For the ultimate strength P of masonry wall under in-plane lateral loading, based on the damage mode of diagonal shear cracks, a wall is modeled as a network of oblique compressive trusses at an angle α to the vertical direction, Y-axis as illustrated in Fig. 7. By coordinate transformation, shear stress of the wall, τ_{xy}, can be calculated from principal compressive stress of truss, f_m'. From experimental results, it is known that cracks occur between brick and mortar because the strength of lime-cement mortar used in historic buildings is much lower than that of bricks. Thus the lateral strength of the wall depends on the shear strength of the brick-mortar interface, and can be determined by Mohr-Coulomb theory: $\tau_m=\tau_0+\mu N$. By stress transformation, $\tau_m=f_m'\cdot\sin\alpha\cdot\cos\alpha$. τ_0 is the shear strength of the interface without vertical loads. The friction coefficient μ is taken as 0.4 based on reference. The normal force, N, includes upper dead load σ_y, such as the roof, applied to the wall and σ is transformed from f_m' by the stress transformation $\sigma = f_m'\cdot\cos2\alpha$. As a result, f_m' can be determined as $(\tau_0+0.4\cdot\sigma_{y0})/(\sin\alpha\cdot\cos\alpha-0.4\cdot\cos2\alpha)$, and the ultimate lateral strength of the wall is calculated by $P=\tau_{xy}\cdot B\cdot T$, where B and T are the breadth and thickness of the wall. For the interface of mortar and brick, the shear strength was set 2.0 kgf/cm^2. Fig. 8(a) displays the relationship between shear strength of brick wall and plan area. On the whole, temples with larger plan areas showed higher shear strength. However, as the scale of temples increases, the variation in shear strength increases. For example, the sample with plan area of 125m^2 has the lowest shear strength of 100tf while the highest one approximately attains 180tf. Shear strength was mainly determined by the section area of brick walls. Since the breadth of a wall is approximate, Fig. 8(b) compares shear strength with length of plan instead. As seen in the figure, temples with larger length showed higher shear strength.

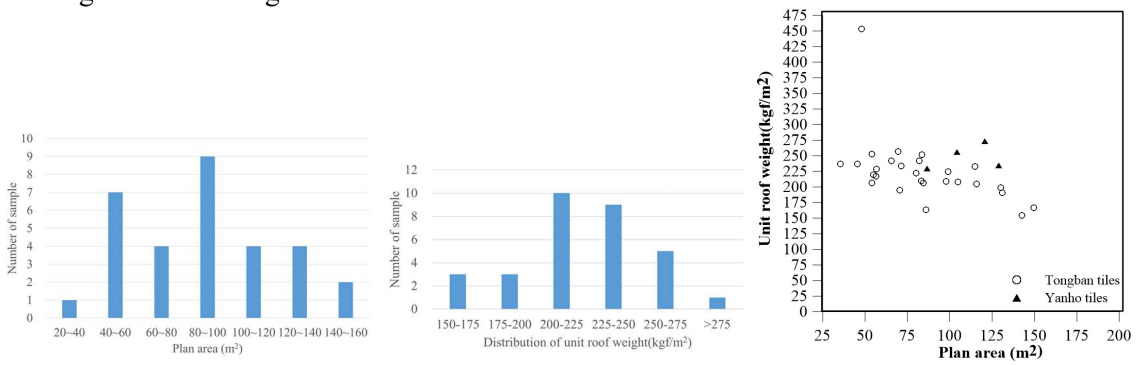

(a) Distribution of plan area. (b) Distribution of unit roof weight. (c) Unit roof weight and plan area.
Figure 4. Statistics of plan area and unit roof weight of surveyed temples

Figure 5. Conventional roofing tiles of masonry temples. Left: Tongban, convex tile; Right: Yanho, red tile.

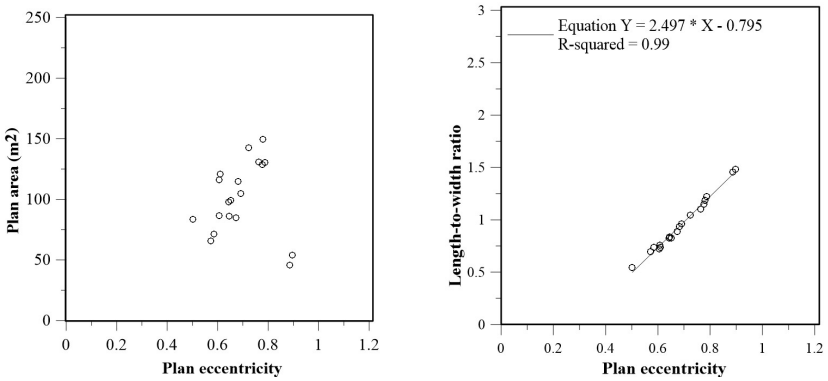

(a) Plan eccentricity and plan area. (b) Plan eccentricity and length-to-width ratio.

Figure 6. Statistics of plan eccentricity of surveyed temples.

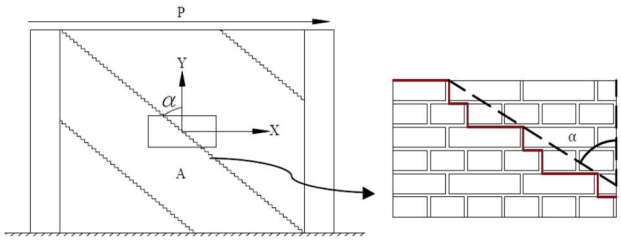

(a) A wall is modeled as a network of oblique compressive trusses.

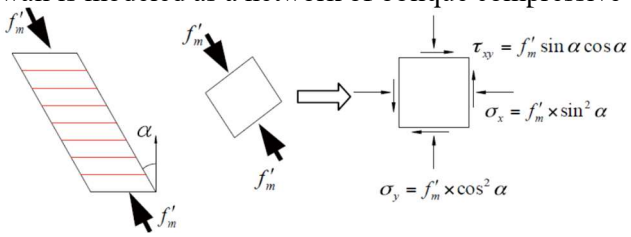

(b) Stress transformation of principal compressive stress fm' to shear stress τ_{xy} between brick and mortar.

Figure 7. Theoretical model for calculation of shear strength of brick wall.

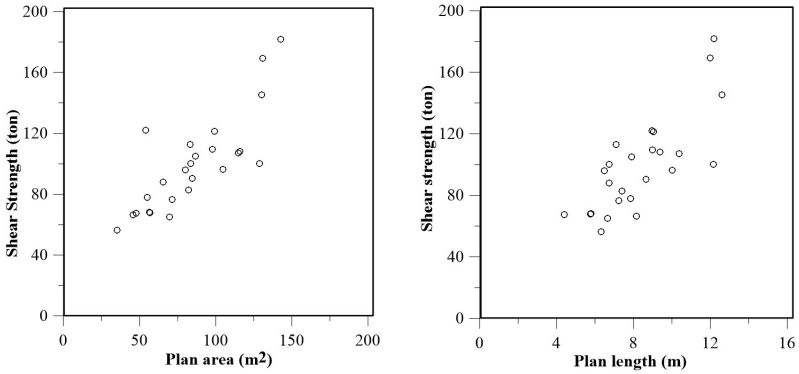

(a) Shear strength vs plan area. (b)Shear strength vs plan length.

Figure 8. Statistics of shear strength of surveyed temples.

NATURAL FREQUENCIRS OF MASONRY TEMPELS AND THE RELATIONSHIP WITH SHEAR CAPACITY

Based on ambient vibration measurements, natural frequencies of masonry temples were identified. The natural frequencies ranged within 10~15Hz and 4~8Hz for in-plane and out-of-plane directions of side walls, respectively, corresponding to the length and width directions of temple plans. In Taiwan seismic code, fundamental periods of buildings are regulated. Masonry structure is classified in the category of other structure systems and fundamental period T is calculated by $T=0.05H^{3/4}$, in which H represents the building height in meters. Fig. 9(a) shows a good relationship between measured period and $H^{3/4}$. The regression equation is $T=0.027H^{3/4}$ with R-square value of 0.93. The coefficient in the regression equation was only half that proposed by seismic code. It implies that masonry temples hold much larger lateral stiffness than that regulated by code. By modeling the building as a single-degree-of-freedom lumped mass model (Chang, 2001), the natural frequency can be derived and is proportional to wall ratio, *R*, and building height, *H*. Fig. 9(b) displays a good correlation between the theoretical and measured frequencies.

Fig. 10 correlates base shear coefficient and measured natural frequency. Base shear coefficient, C, was calculated dividing shear strength by weight of the temple. As evident in the figure, C shows a good correspondence to natural frequency as the value of R-square exceeds 0.80. Thus we can easily measure the natural frequency of a temple and use it as a proper indicator for its shear strength. In the figure, more than half damage cases were on the left part. It implies that temples with lower natural frequencies may have a higher likelihood of damage.

Since ambient vibration measurements were conducted, applied inertia force to the temples is obtained from the acceleration response spectrum of the nearest earthquake station according to the identified predominant period of the temple. From Fig. 11, it is found that minor and moderate damages occur when inertia force exceeds 4.0% and 19.0% of shear strength, respectively. The threshold of applied inertia force for moderate damage was about 5 times that for minor damage.

CONCLUSIONS

In this study, the statistics of structural characteristics associated with seismic capacity of masonry temples were considered. Temples in the strong shaking areas of the Chi-Chi and Chiayi earthquakes of 1999 were selected and an in-situ survey was conducted to measure the statistics of structural characteristics. The weight of unit roof areas mainly ranged within 200~275 kgf/m^2 and showed no relation with the temples' plan areas. Temples with larger plan areas showed higher shear strength. Meanwhile, ambient vibration measurements were conducted to investigate natural frequencies of temples. A good correlation was found between measured natural frequency and shear coefficient, serving as an indicator of shear strength. From the comparisons of shear strength and applied inertia force, it is found that the threshold of applied inertia force for moderate damage was about 5 times that for minor damage.

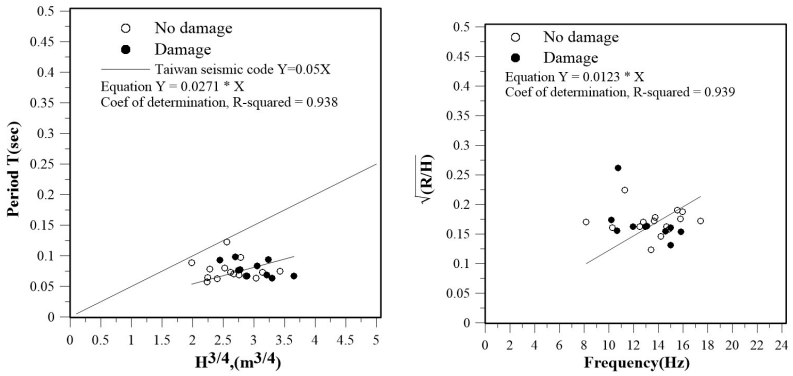

(a) Correlation of in-plane predominant period and height. (b) Correlation of measured and theoretical natural frequencies. (R: wall ratio; H: building height)

Figure 9. Correlation of in-plane predominant period and height.

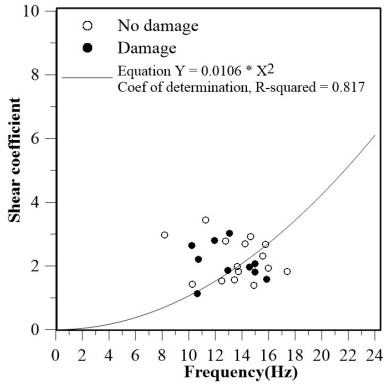

Figure 10. Relationship between natural frequency and shear coefficient.

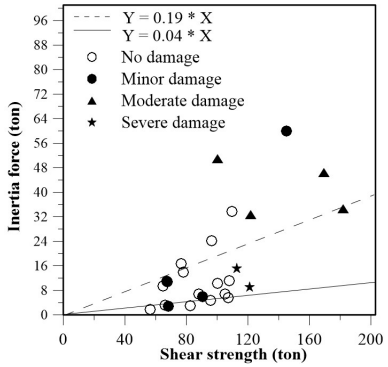

Figure 11. Threshold of applied inertia force for moderate and minor damages.

ACKNOWLEDGMENTS

Special thanks for generous support from the Ministry of Science and Technology, Taiwan, under research program No. MOST 106-2221-E-327-009, and the collaboration of the staff of temples during the survey.

REFERENCES

Chen, T.N., Chang, J.S., Huang, H.H. (2012). "Performance of URM wall with opening under in-plane horizontal loading," *The 15th World Conference on Earthquake Engineering*, Lisboa, Portugal.

Chang, W.S. (2001). *Ambient Vibration Measurement of Listed Masonry Wall Mixed with Timber Frame Historic Buildings.* Department of Architecture, National Cheng Kung University, Tainan, Taiwan.

Chang, J.S., Hsu, M.F. and Chen, C.C. (2001). "*Research on Earthquake Damages and Maintenances of Historic Buildings (2) Masonry Structures*, " National Cheng Kung University Research and Development Foundation.

Fu, C.C. (2009) Reading Tainan: a historic city of cultural heritage. Taiwan Architecture and Cultural Property Press, Tainan, Taiwan.

Hsu, M.F., Li, L.F., Wang, C.F., Fang, H.S., and Lin, T.S. (2000). *A Report on Primary Investigation of The Damages to Cultural Properties and Historic Buildings After 1999 Chih-chih Earthquake*, National Center for Research and Preservation of Cultural Properties. Taiwan.

Nambu, Y., Takiyama, N., and Hayashi, Y. (2013). " Changes in Out-of-plane Vibration Characteristics of Unreinforced and Reinforced Walls of Historic Masonry Buildings," *AIJ Journal of Technology and Design*, Japan, **19**(41), 165-168.

MESHED-BASED SEISMIC IMPACT ANALYSIS AND APPLICATION ON DISASTER MITIGATION PLANNING

Bing-Ru Wu[1], Siao-Syun Ke[2], Chih-Hao Hsu[1] and Sheu-Yien Liu[3]

1. Associate Researcher, National Science and Technology Center for Disaster Reduction, New Taipei City, Taiwan, R.O.C.
2. Researcher, National Science and Technology Center for Disaster Reduction, New Taipei City, Taiwan, R.O.C.
3. Assistant Researcher, National Science and Technology Center for Disaster Reduction, New Taipei City, Taiwan, R.O.C.

Email: brwu@ncdr.nat.gov.tw, opbook@ncdr.nat.gov.tw, willie2567@ncdr.nat.gov.tw, lsy@ncdr.nat.gov.tw

ABSTRACT

The disaster vulnerability has increased in recent years because of population concentration and complex infrastructures constructed in Taiwan. The seismic resistant capacity subjected to large-scale earthquakes in metropolitan cities should be evaluated for disaster management. We developed a mesh-based scenario simulation tool which is capable of analyzing the ground motion, casualty, damage of buildings and infrastructures. We present analytical results in terms of major theme maps for disaster mitigation planning, including emergency rescue and medical care, evacuation and shelter, and government operation. Our research accomplishment has been applied on the National Earthquake Drills for governments. The quantitative impact analysis by scenario simulation in details could be helpful to elaborate a thorough mitigation planning for enhancing the disaster resilience of society.

Keywords: earthquake, scenario simulation, disaster reduction planning

INTRODUCTION

As located on the subduction zone between the Philippine Sea Plate and the Eurasia Plate, more than a dozen of disastrous earthquakes have occurred in Taiwan. The most severe events in the western Taiwan are the Meishan earthquake in 1906 (M_L=7.3, 1,258 death), the Hsinchu-Taichung earthquake in 1935 (M_L=7.1, 3,276 death), and the Chi-Chi earthquake in 1999 (M_L=7.3, 2,415 death). Figure 1 displays locations of 14 disastrous earthquakes and the population distribution in 500 m x 500 m mesh. Approximately 70% of the population (23 million in total) clusters in 6 metropolitan cities in the western plain areas. In recent decades, the disaster vulnerability in urban areas has risen because of population concentration and complex infrastructures constructed in cities. Two major earthquakes, 2016 Meinong earthquake (M_L=6.6, 117 death) and 2018 Hualien earthquake (M_L=6.2, 17 death) called Taiwanese attention to potential seismic threat. If a large-scale earthquake like the Chi-Chi event occurred in urban areas again, the induced casualties and losses would be more extensive than those in 1999.

After the Chi-Chi earthquake, the disaster management framework was established in 3 levels of government organizations, i.e., central ministries, cities/counties, and townships, following the Disaster Prevention and Response Act issued in 2000. Accordingly, central ministries formulate the Operation Plans of Disaster Prevention and Response for each type of disaster defined in the Act, such as earthquake, typhoon, flood, drought, fire, debris flow, etc. City/county governments drew up the Local Plan of Disaster Prevention and Response covering each specified disaster. Scenario simulations were carried out to analyze possible damages subjected to specific earthquake sources in some cities/counties. However, the simulation results have not been properly applied on configuration of corresponding countermeasures. Therefore, we developed a mesh-based scenario simulation tool to reveal weak exposures and their distribution which are informative for effective mitigation planning using limited resources. Furthermore, we collaborated with academic institutions to perform a serious of large-scale

earthquake scenario simulations and promoted their application on the operation of the National Earthquake Drill in Taiwan.

No.	Earthquake	Date	Magnitude (M_L)	Depth (km)	Casulties	
					Ceased	Injured
1	Douliou	1904/11/06	6.1	7.0	145	158
2	Meishan	1906/03/17	7.1	6.0	1,258	2,385
3	Nantou Series	1916/08/28	6.8	45.0	71	285
		1916/11/15	6.2	3.0		
		1917/01/05	6.2	0.0		
		1917/01/07	5.5	0.0		
4	Hsinchu-TaiChung	1935/04/21	7.1	5.0	3,276	12,053
5	Chungpu	1941/12/17	7.1	12.0	358	766
6	Hsinhua	1946/12/05	6.1	5.0	74	182
7	Longitudinal Valley Series	1951/10/22	7.3	4.0	>85	>1,000
		1951/10/22	7.1	1.0		
		1951/10/22	7.1	18.0		
		1951/11/25	6.1	16.0		
		1951/11/25	7.3	36.0		
8	Hengchun	1959/08/15	7.1	20.0	17	85
9	Paiho	1964/01/18	6.3	18.0	106	653
10	Hualien	1986/11/15	6.5	15.0	13	45
11	Chi-Chi	1999/09/21	7.3	8.0	2,415	11,305
12	Tauyuan	2010/03/04	6.4	5.0	0	96
13	Meinong	2016/02/06	6.6	14.6	117	551
14	Hualien	2018/02/26	6.2	6.3	17	291

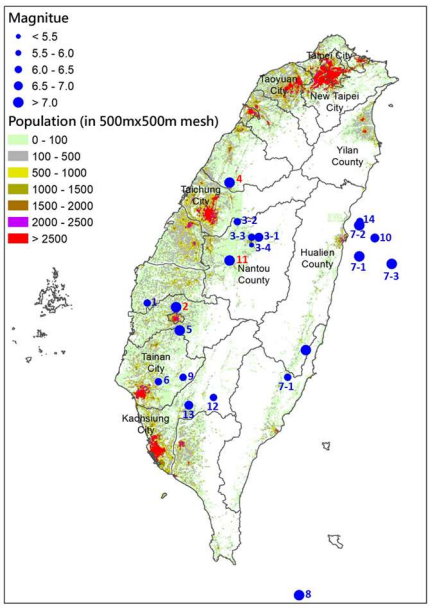

Figure 1. Disastrous earthquakes and population distribution in Taiwan

EARTHQUAKE SCENARIO SIMULATION TOOL

We build the Taiwan Earthquake Impact Research and Information Application Platform (TERIA) with the state-of-the-art analysis techniques in conjunction with the inventory database on the basis of mutual cooperation among the academic institutions and governmental agencies (Figure 2). Considerable efforts were devoted to construct the inventory database, including building, population, infrastructure, and lifeline system. The TERIA can analyze the ground motion response, potential of liquefaction and landslide, casualty, damages of buildings, roads, bridges, electricity, and portable water facilities. We used fragility curves to estimate possible damages of buildings and facilities (Wu, et al., 2014; Liu, et al., 2014). The analytical results in a 500 m × 500 m mesh at different layers can be integrated to interpret the disaster scenario in details.

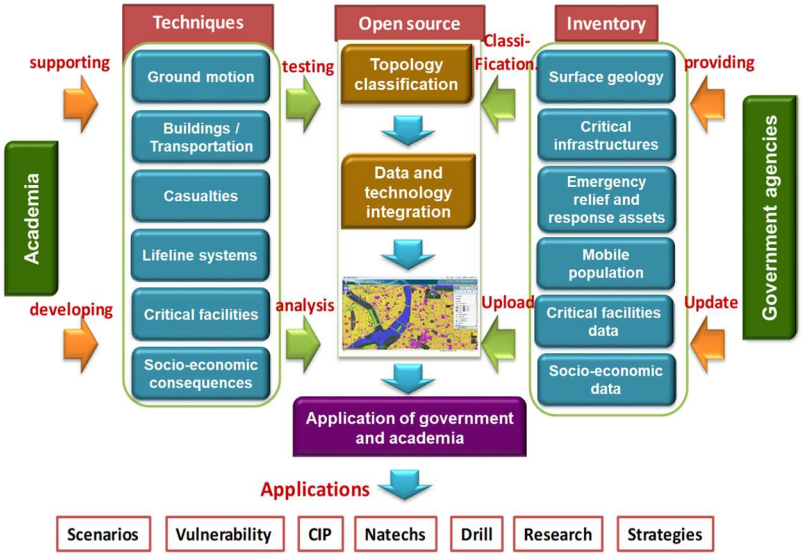

Figure 2. TERIA platform framework

Major functions of TERIA comprises: (1) Query basic information: Users can query basic information of building, population distribution, road, bridge, electricity, and portable water facility online from inventory database. (2) Impact analysis module: Point sources, line sources (active faults identified by the Central Geological Survey), and user-defined ground motion distribution are available options for input sources. (3) Display results: An interactive interface displays mesh-based analytical results with figures and statistic charts for each item. Users can download the digital files for their own purposes (Figure 3). (5) Theme maps for the Local Plans: We provided analytical results for 33 active faults with default parameters in a package of five theme maps, including building, casualty, shelter demand, transportation, and resource demand which are useful for Local Plan of Disaster Prevention and Response.

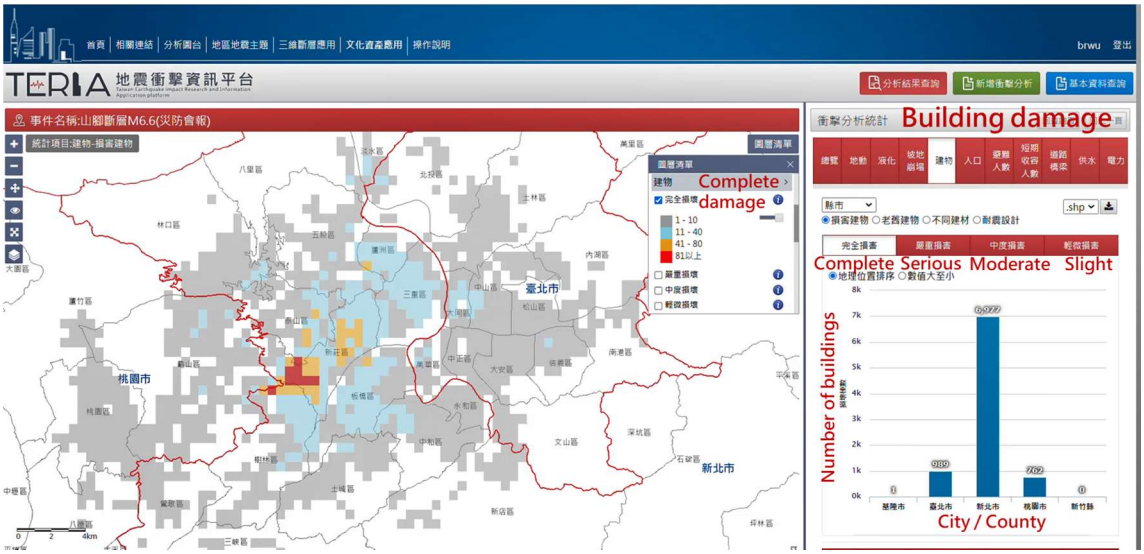

Figure 3. Demonstration of scenario simulation results in TERIA

LARGE-SCALE EARTHQUAKE SCENARIO SIMULATIONS IN TAIWAN

Based on the minutes of the 36th meeting of the Central Disaster Prevention and Response Council in 2017, a task force "Scenario Simulation for Large-scale earthquakes" was initiated by the central government consisting of the groups of the Earthquake Source, Loss Estimation, and Corresponding Countermeasure (Figure 4). The Earthquake Source Group provides the ground simulation results as the input motions to the Loss Estimation Group for the damage assessment of buildings and infrastructures, which both are organized by the National Science and Technology Council. According to the damage assessment results, central ministries and city governments formulate corresponding countermeasures. Such scenario-based disaster mitigation planning enables limited resources to be effectively applied to improve the seismic resistant capacity of infrastructures and reduce disaster losses.

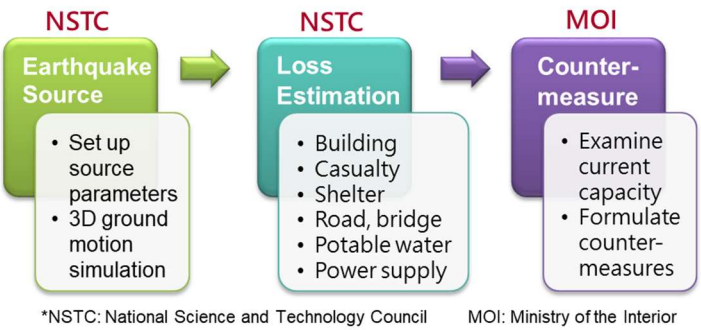

Figure 4. Task force for the large-scale earthquake scenario simulation

In consideration of both the occurrence potential of large-scale earthquakes and the importance of political and economic conditions, the Sanchiao Fault (M_w 6.6), Chung-Chou seismogenic structure (M_w 6.9), and Hualien offshore earthquake (M_w 8.0) were chosen as input sources (Figure 5).

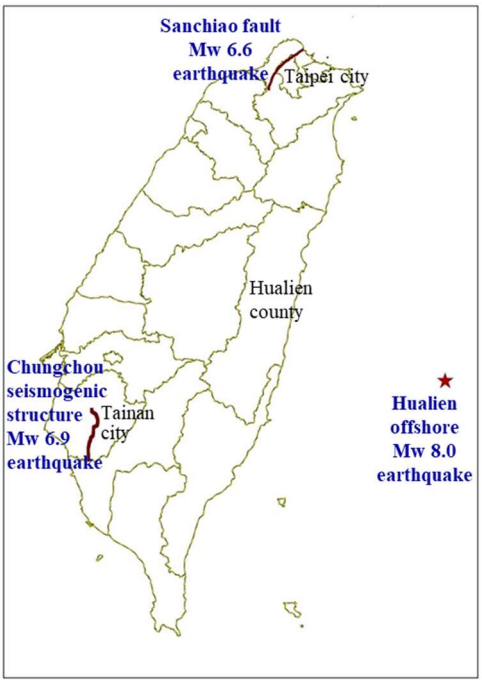

Figure 5. Three earthquake sources for scenario simulations

As the Sanchiao Fault located in the capital area where the population of surrounding 4 cities is approximately 9 million people, an M_w 6.6 earthquake was assumed for scenario simulation in the northern Taiwan. According to the occurrence probability in 50 years proposed by the Taiwan Earthquake Research Center (2022), the Chungchou seismogenic structure has the highest potential (39%) for an M_w 6.9 earthquake in the southern Taiwan. More than 70% of earthquakes occurred in the eastern offshore area where is the subduction zone between the Philippine Sea Plate and the Eurasia Plate. An M_w 8.0 earthquake in the Hualien offshore area was assumed as the source for scenario simulation since an M_w 8.0 earthquake occurred in 1920 in this area. Three dimensional ground motion simulation and damage assessments were performed for these three scenarios. These simulation results have been submitted to the Ministry of the Interior and applied on the configuration of the 2018, 2020, and 2022 National Earthquake Drills, respectively. The research accomplishment for the Hualien offshore M_w 8.0 earthquake is illustrated in the following.

Three Dimensional Ground Motion Simulation

The Earthquake Source Group performed the three dimensional ground motion simulation for an M_w 8.0 earthquake in the Hualien offshore area which is located in the subduction zone (Figure 6). The regional underground seismic wave velocity profile, topography and site effects are considered in the simulation. The computed peak ground acceleration (PGA), peak ground velocity (PGV), peak ground displacement, spectrum acceleration at 0.3 second (Sa-0.3), and spectrum acceleration at 1.0 second (Sa-1.0) in a 500 m × 500 m mesh are the input motions of the following damage assessment. According to the intensity scale defined by the Central Weather Bureau, the intensity map for the M_w 8.0 Hualien offshore earthquake is shown in Figure 7 using the estimated PGA and PGV values.

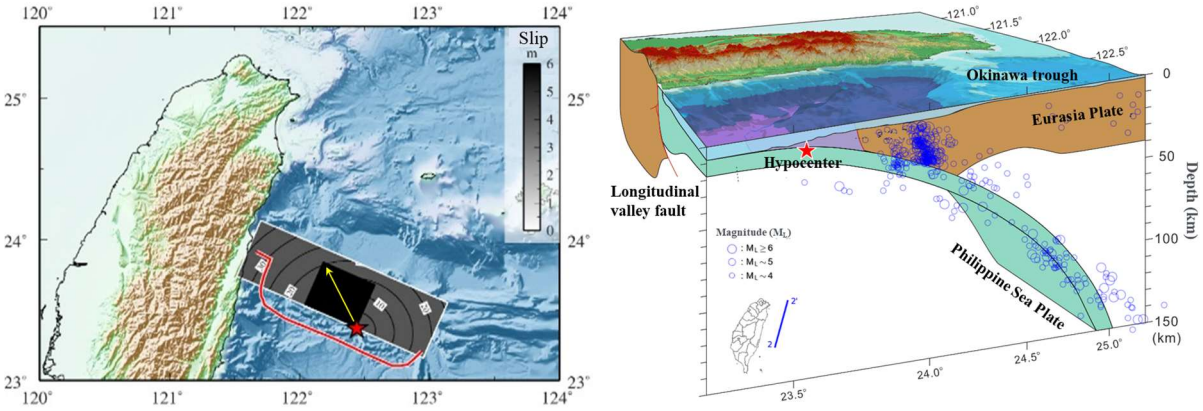

(a)Source model (b)Hypocenter location and plate structure

Figure 6. Earthquake source and plate structure for the Hualien offshore M_w 8.0 earthquake

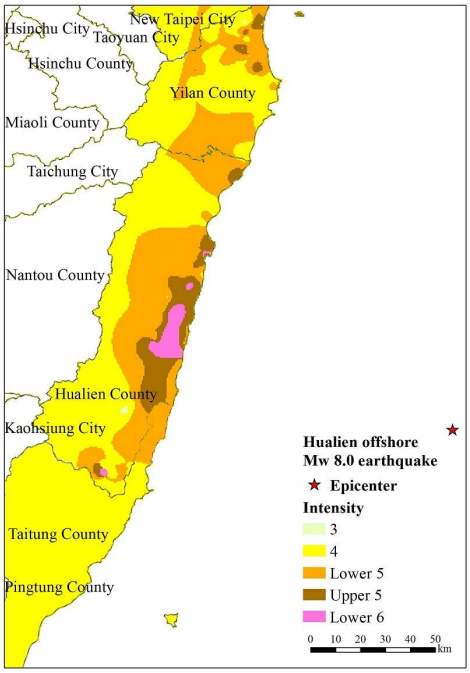

Figure 7. Intensity map for the Hualien offshore M_w 8.0 earthquake

Damage Assessment Results

This study adopted TERIA to analyze the ground failure, building damages, casualty, shelter demand, and damages of transportation and lifeline systems induced by the Hualien offshore M_w 8.0 earthquake. To interpret the disaster scenario, the impact theme maps were generated with integration of various analytical items for disaster mitigation planning, including emergency rescue and medical care, evacuation and shelter, and government operation (Figure 8).

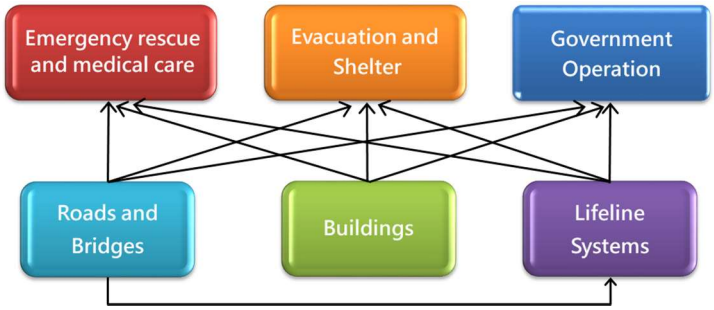

Figure 8. Impact theme maps for disaster mitigation planning

The impact theme map for emergency rescue and medical care is chosen as an example. The estimated number of people being medium injury plus serious injury is defined as the hospitalization need. The hospitalization need in Hualien city is 299 people. As suggested by the 7th Disaster Prevention and Protection Expert Consultation Committee, the Executive Yuan, the available number of beds is suggested as 10% of the total number of beds in a hospital. Thus, the available number of beds in Hualien city is 203 which is less than the hospitalization need. More than 90 patient would be transported to the hospitals in the south of Hualien county. However, some roads and bridges may be suffered from medium to high risk of closure from the evaluation (Figure 9). The transportation of patients would be influenced by closure of roads and bridges. Alternative transportation routes should be configured in advance.

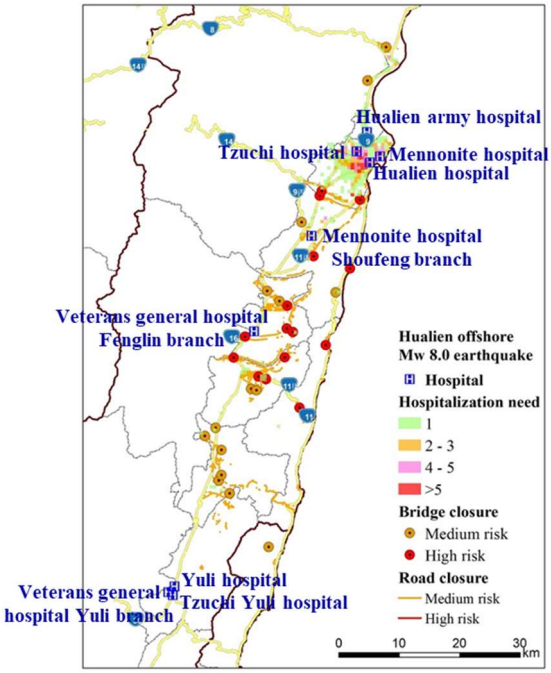

Figure 9. Emergency rescue influenced by interruption of transportation

The operation of hospitals relies on the supply of electric power and potable water. However, the electric power system and water supply system may be malfunction from the evaluation. As shown in Figure 10(a), two substations in Hualien city are subjected to medium damages which would influence the power supply to the hospitals. Besides, two treatment plants and water pipes in Hualien city are subjected to medium damages which would affect the water supply to hospitals as demonstrated in Figure 10(b). Corresponding countermeasures to the interruption of electric power and potable water should be formulated to ensure the functionality of hospitals.

APPLICATION OF SCENARIO SIMULATION ON DISASTER REDUCTION PLANNING

We submitted the damage assessment results for the Hualien offshore M_w 8.0 earthquake to the Ministry of the Interior and applied on the configuration of the 2022 National Earthquake Drills. Three applications in the operation of the earthquake drill are illustrated in the following.

Mobilization and Transportation for Emergency Rescue

According to the damage assessment results, the major impact area is Hualien county and Yilan county. The search and rescue (SAR) teams from other cities/counties would assemble to the Hualien county stadium and Yilan sport park. However, the transportation of SAR teams would be interrupted by the closure of roads and bridges between Yilan county and Hualien county. In addition to vehicles, railway, aircrafts, and naval ships are selected to transport the rescue teams and equipment from other cities/counties. As shown in Figure 11(a), the SAR teams from Taoyuan city, Hsinchu city and Hsinchu

county (in yellow color) were transported by vehicles to Yilan Sport Park. The SAR teams from Miaoli county, Taipei city, New Taipei city and Keelung city (in pink color) drove to the Su'ao railway station then took trains to the Hualien railway station. Their heavy equipment and vehicles were transported by naval ships to the Hualien harbor. The SAR teams from 9 cities/counties (in blue color) were conveyed by C-130H aircrafts from the Taichung, Chiayi and Pingtung airports. Detail transportation routes from the Hualien airport, Hualien railway station, and Hualien harbor to the Hualien county stadium were shown in Figure 11(b). These routes were available for transportation without risks of closure.

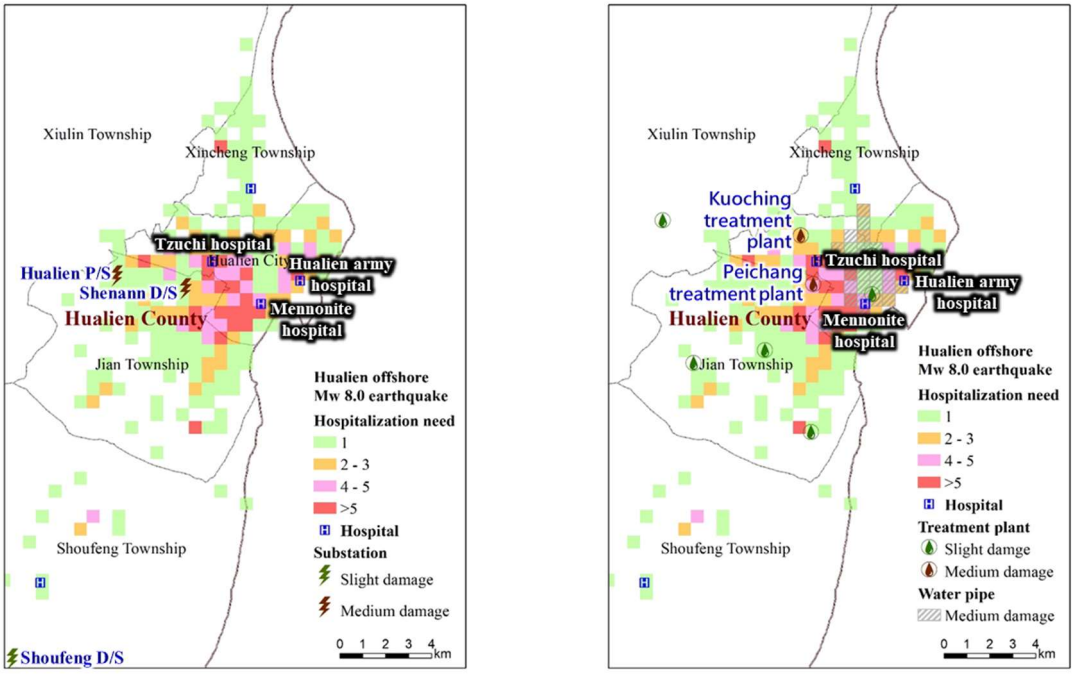

(a)The influence of electric power (b)The influence of potable water

Figure 10. Medical care influenced by the interruption of electric power and potable water supply

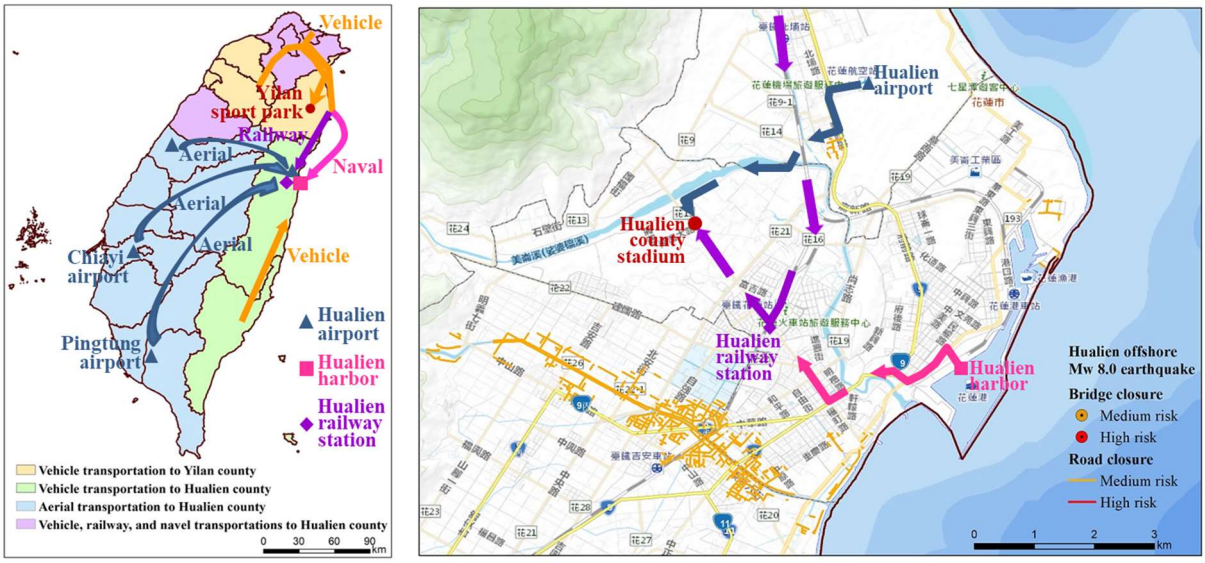

(a)Transportation to Yilan and Hualien counties (b)Transportation routes to the Hualien county stadium

Figure 11. The transportation for rescue teams to Yilan county and Hualien county

Allocation of searching district

According to the estimation of casualty, the searching districts were designated as Figure 12. The SAR teams from western cities/counties in Taiwan and foreign SAR teams are allocated to these districts. One USAR coordination Cell (UCC) and two Sector Coordination Cells (SCCs) were established to coordinate the searching actions. The UCC is in charge of coordinating D, E, D, and G districts which are the most affected areas. The Assessment Search Rescue (ASR) actions in 4 levels were deployed following the commands given by UCC, SCC1 (coordinating A, B, C districts) and SCC2 (coordinating H, I, J districts). The operation status for SCC1 and SCC2 should be reported to UCC.

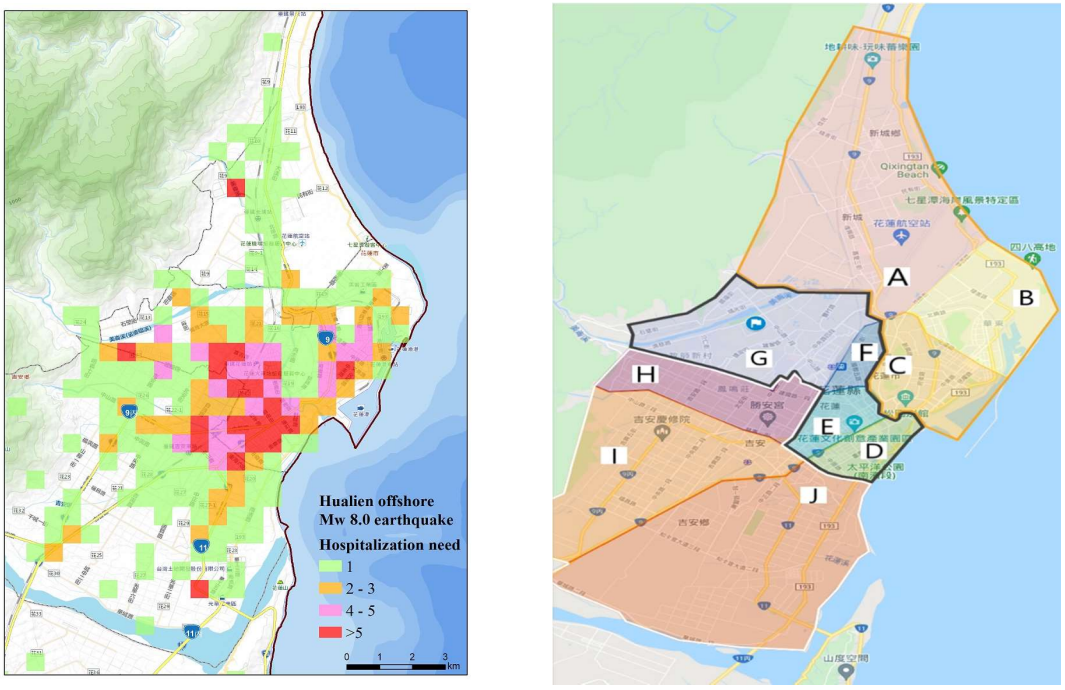

(a)Estimated hospitalization need (b)Allocation of searching district

Figure 12. Estimated hospitalization need and allocation of searching district

CONCLUSIONS

The mesh-based earthquake assessment tool, TERIA, can be applied to evaluate the seismic impact to exposures and reveal the spatial distribution of damages. With integration of several layers of analytical results, impact theme maps are proposed to present the disaster scenario for hazard mitigation planning. Our research accomplishments have been applied to the operation of the National Earthquake Drills for central governments. Currently we are collaborating with the National Fire Agency on a pilot project to promote the scenario-based disaster reduction planning for local governments. These applications would be helpful to allocate limited resources effectively and enhance the seismic capability against disasters.

REFERENCES

Taiwan Earthquake Research Center (2022). "The occurrence probability map for potential earthquakes in 50 years induced by seismogenic structures in Taiwan," (in Chinese).

Ministry of the Interior (2022). 2022 National Earthquake Rescue and Mobilization Drill Plan (in Chinese).

Liu, S. Y., C. R. Wu, C. Y. Lee, M. C. Deng, Y. N. Lee, C. S., Lee, S. S. Ke, and S. W. Chien (2014). "Scenario Simulation for Taipei Metropolitan Area II: Road, Bridge, Portable Water, Electricity, and Important Infrastructure," National Science and Technology Center for Disaster Reduction, Taiwan (in Chinese).

Wu, T. H., M. W. Huang, B. R., Wu, C. Y., Chen, C. L., Su, C. S., Lee, and S. S. Ke (2014). "Analysis of Disaster Potential, Buildings, and Casualty for the Large-Scale Earthquake Scenario in Taipei Metropolitan Area," National Science and Technology Center for Disaster Reduction, Taiwan (in Chinese).

(4d) Disaster risk assessment for earthquakes

IMPLEMENTATION OF TWATER FOR SEISMIC RISK ASSESSMENT OF WATER SUPPLY SYSTEMS – A CASE STUDY

Gee-Yu Liu[1], Chin-Hsun Yeh[2] and Gee-Jin Yu[3]
1. Research Fellow, National Center for Research on Earthquake Engineering, Taipei, Taiwan, R.O.C.
2. Research Fellow, National Center for Research on Earthquake Engineering, Taipei, Taiwan, R.O.C.
3. Assistant Researcher, National Center for Research on Earthquake Engineering, Taipei, Taiwan, R.O.C.
Email: karl@narlabs.org.tw, chyeh@narlabs.org.tw, gjyu@narlabs.org.tw

ABSTRACT

This investigation implemented Twater to the seismic risk assessment of water supply system in Hsinchu, Taiwan. Twater is a scenario-based analysis tool employed specialized for predicting the damage and loss of a water supply system, and its serviceability following earthquake. The assessment has successfully provided the estimates of damage in aqueducts, pipelines, critical facilities, and the number of households without water of four earthquake scenarios. According to the assessment results, some of the key seismic concerns of the water supply system in Hsinchu have been identified.

Keywords: water supply system, seismic risk assessment, scenario simulation

INTRODUCTION

Taiwan is located on the circum-Pacific seismic belt, one of the most earthquake-prone regions in the world. Many of its densely populated cities and industrial clusters are exposed to high seismic hazards. Evidence indicates that the widespread disruption of water supply on this island, which has occurred in the past in the presence of major earthquakes, will occur again in future earthquake events. It will cause inconvenience to the daily life of people in disastrous areas. Medical caring, sanitation, fire-fighting may be seriously affected, too. The time needed for resuming water supply is usually much longer than power and telecommunication due to the difficulties in detecting and repairing buried pipe damage. Therefore, it is highly desirable to facilitate water utilities with a seismic risk assessment tool that will be of help in seismic risk management.

As early as the 1980s, pioneer research work has been performed on this topic. Water network flow analyses were explored to assess system reliability and serviceability via the Monte Carlo method (Shinozuke et al. 1981; Hwang et al. 1998). A methodology involving sophisticated hydraulic models for pipe break and leak simulation has been employed in the software GIRAFFE (Graphical Iterative Response Analysis for Flow Following Earth quakes) by the research team led by Prof. T. D. O'Rourke (Shi 2006). The Los Angeles Department of Water and Power has formally adopted GIRAFFE as a decision-supporting tool for its water system.

A GIS-based Windows application Taiwan Earthquake Loss Estimation System (TELES) has been developed (Yeh et al. 2006) by the National Center for Research on Earthquake Engineering (NCREE), Taiwan. Recently, TELES has been re-developed for the scenario-based seismic risk assessment of water supply systems. This new software is called Twater, a subsystem of TELES. It can simulate the damage, loss, and post-earthquake performance of a water supply system. Twater inherits the seismic hazard modulus of TELES, which means that it can simulate the strong motions and ground failures (due to fault rupture and soil liquefaction) given an earthquake event defined by appropriate earthquake source parameters. Models of seismic fragility and reduction of functionality for various types of water supply facilities and aqueducts/pipes have been developed and integrated into Twater (Yeh et al. 2017). Twater has first been employed to analyze the water supply systems in the Greater Kaohsiung Area, Taiwan (Liu et al. 2019).

This investigation focused on the seismic risk assessment of the water supply system in Hsinchu, where the Hsinchu Science Park, a cluster of dominant producers of semiconductors in the world, is located. Unfortunately, there are three known active faults right beneath Hsinchu. As a result, the seismicity there is very high. It is expected that a disruption of water supply to the Hsinchu Science Park, whether or not due to a major earthquake there, will inevitably generate large impacts to elsewhere in the world through the disconnection of high-tech supply chains.

METHODOLOGIES OF TWATER SOFTWARE

A water supply system can be simplified as Figure 1. As the input data, Twater utilizes the inventory and hierarchy of relevant system components including, from upstream to downstream, raw water aqueducts, water treatment plants, clear water trunks, and water transmission and distribution pipeline networks, of a water supply system. When an earthquake occurs, each component may sustain a reduction in functionality due to its damage, as shown by the gray area in Figure 1, whilst all service areas will experience water outages of varying severity.

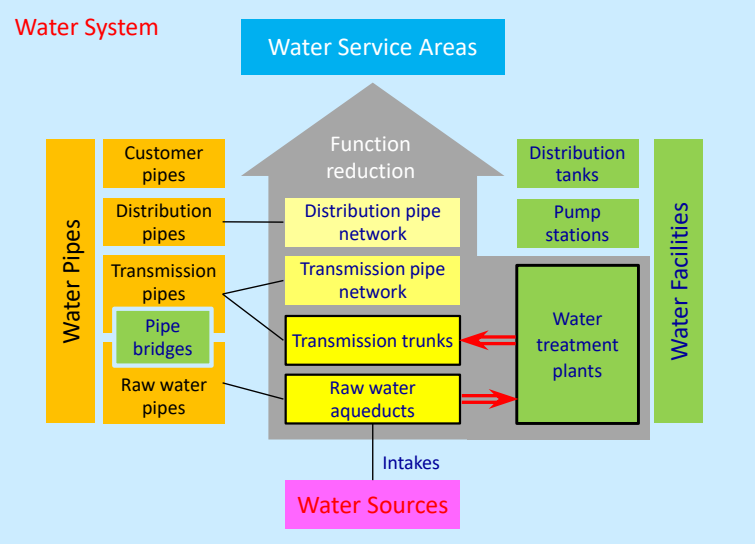

Figure 1. Conceptual diagram of a water supply system with reduction in component functionality following earthquake.

Twater uses the following procedure to complete the seismic risk assessment of a water supply system:

- Divide a large water system into several smaller water service areas (WSAs), according to the actual water supply condition; WSAs are the basic units of assessment;
- Specify the water treatment plants and clear water transmission trunks associated with each WSA;
- Specify the raw water aqueducts associated with each water treatment plant;
- Divide the remaining pipelines into each WSA; classify and separate the pipelines into the transmission and distribution pipe networks according to pipe diameter;
- Perform the assessment and decide: (1) the damage to all raw water aqueducts, water treatment plants, and transmission trunks, (2) the reduced functionality of these components, (3) the average repair rates for the transmission and distribution pipe networks of each WSA;
- Compute the water supply shortage rate and household outage rate of each WSA by considering the serviceability reduction of components as per previous step.

SEISMIC RISK ASSESSMENT OF THE WATER SYSTEM IN HSINCHU

The System

The Hsinchu Water Supply System (HWSS), as depicted in Figure 2, provides water to customers in the Hsinchu City and Hsinchu County except some of the peripheral mountainous areas. It also supplies water to the Hsinchu Science Park (HSP), the first and largest science park of its kind in Taiwan. HSP is one of the most important clusters of semiconductor manufacturing in the world. In 2017, HSP alone contributed 6% of Taiwan's gross domestic product.

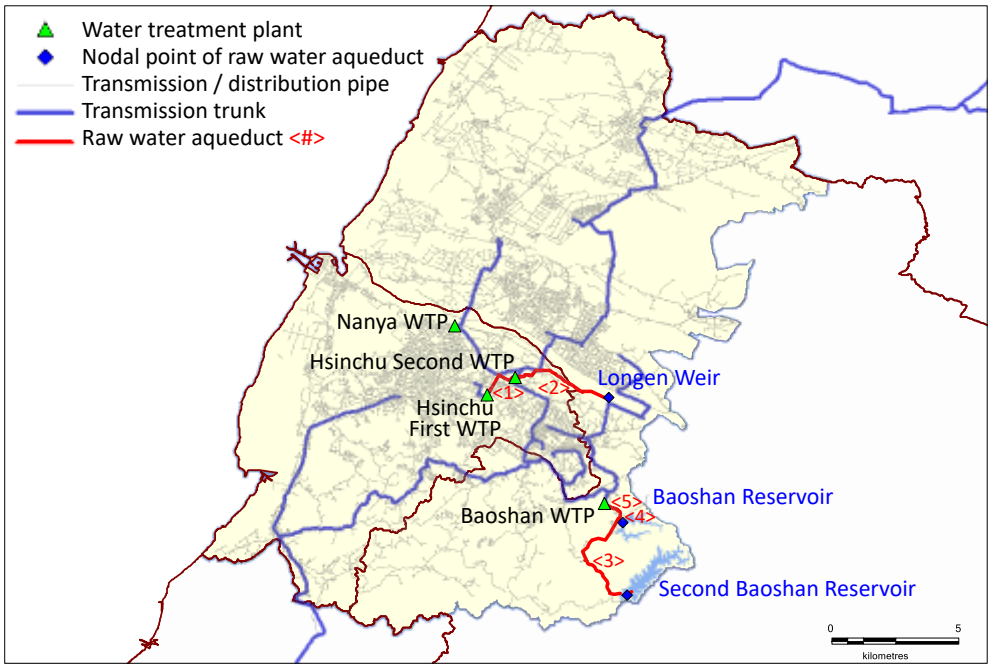

Figure 2. The Hsinchu Water Supply System (HWSS) and its raw water aqueducts, four water treatment plants, and clear water transmission trunks.

HWSS has a capacity of 739,000 CMD (cubic meters per day) of clear water production. It supplies 530,000 CMD of water to a total population of 780 thousand. It consists of four water treatment plants (WTPs): Baoshan (60.9% of total capacity), Hsinchu First (12.0%), Hsinchu Second (21.7%), and Nanya (5.4%). The largest Baoshan WTP receives raw water from both the Baoshan Reservoir and the Second Baoshan Reservoir. It takes the advantage of higher elevation and supplies clear water by gravity to the south of HWSS and all the way to downtown Hsinchu. The Hsinchu First and Second WTPs both locate at heart of Hsinchu and intake raw water from the Taoqianxi River via the Longen Weir. The smallest Nanya WTP also intakes raw water from the same River. The five major raw water aqueducts of HWSS are depicted in Figure 2, too, as <1> to <5>. Because the quantity of raw water from the Taoqianxi River is not sufficient sometimes, HWSS needs external support. To be precise, it requests 60,000 CMD of clear water from the northern neighbor utility (via the Pingzhen and Shihmen WTPs) and another 50,000 CMD from the southern neighbor utility (via the Dongxing WTP), respectively.

In this investigation, HWSS is spatially divided into seven water service areas (WSAs), as depicted in Figure 3, according to the actual system operation for water transmission. They are [Hukou Xinfeng], [Zhubei], [HSP], [Hsinchu Downtown], [Hsinchu East], [Hsinchu Xiangshan], and [Baoshan], among which [HSP] stands for the (water service) area of the Hsinchu Science Park. It is overlaid mostly on [Hsinchu East], has 394 customers, and consumes water most. Quantitative water supply data within HWSS were established and employed for scenario simulation by Twater software.

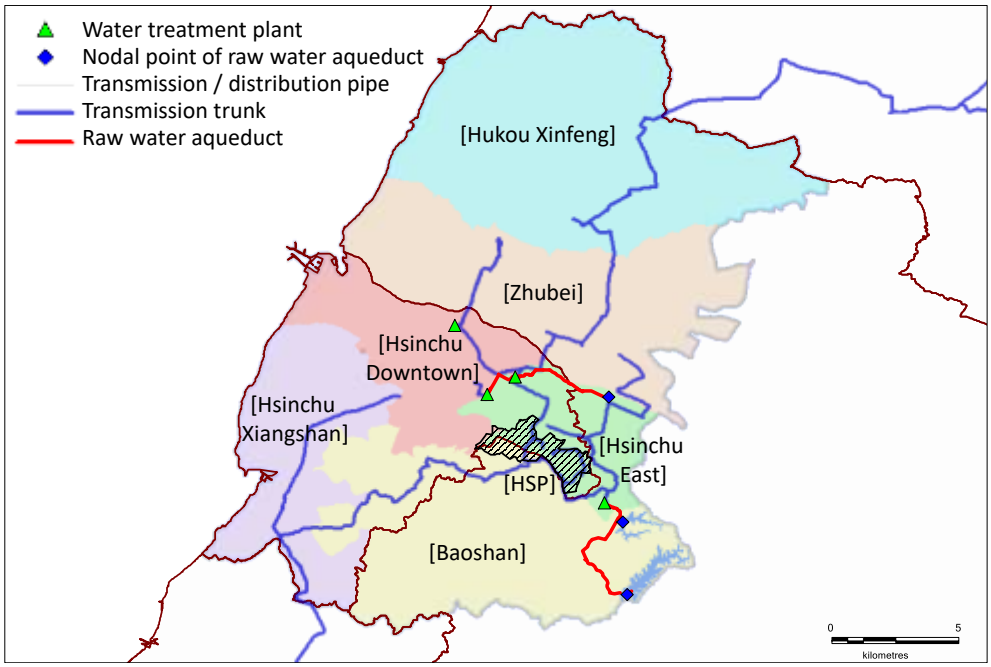

Figure 3. The division of water service areas of HWSS.

Earthquake Scenarios

According to the active fault map published by the Central Geological Survey (CGS), Ministry of Economic Affairs, there are three active faults in Hsinchu: Hsincheng (Category I), Hsinchu, and Hukou (both Category II). By CGS definition, faults of Category I activate within past 10,000 years and are considered more active, while faults of Category II activate within past 100,000 years and less active. It is worth notice that both the Hsinchu First and Second WTPs locate in the vicinity of the Hsinchu fault, with the former on the footwall and the later hanging wall. The raw water aqueduct from the Longen Wein to these two WTPs actually has two fault crossings. Furthermore, in the south of HWSS, the two transmission trunks leaving the Baoshan WTP are also crossed by the Hsincheng fault. Historically, an M7.1 earthquake called Shinchiku-Taichū earthquake occurred in the south of this area in 1935. It was the deadliest earthquake in Taiwan's recorded history, claiming 3,276 lives and causing extensive damage. Consequently, the seismic threat arising from these faults should not be overlooked.

Four scenario earthquakes have been selected for the assessment. The first three, termed #1, #2, and #3, refer to the events of entire rupture of the Hsincheng, Hsinchu, and Hukou faults, of which the earthquake magnitudes can be decided by using the empirical formula of Wells and Coppersmith (1994). In addition, the fourth scenario, termed as #4, is included in the analysis to take into account the high seismicity of the neighborhood. Its source is specified as a shallow point source with a focal depth of 5 km right beneath the most populated part of the study region. The seismic source parameters of the four earthquake scenarios are summarized in Table 1. Figure 4 depicts fault rupture planes of the scenarios #1~#3 and the epicenter of #4.

Table 1. The seismic source parameters of the four earthquake scenarios.

Scenario ID	Source (fault name)	Source type	Earthquake magnitude	Rupture Width (km)	Rupture Length (km)	Dip Angle (deg)
#1	Hsincheng	Reverse	6.8	15.6	28	40
#2	Hsinchu	Reverse	6.8	13.1	26	50
#3	Hukou	Reverse	6.6	10.4	20	60
#4	Local shallow	Point	6.5	-	-	-

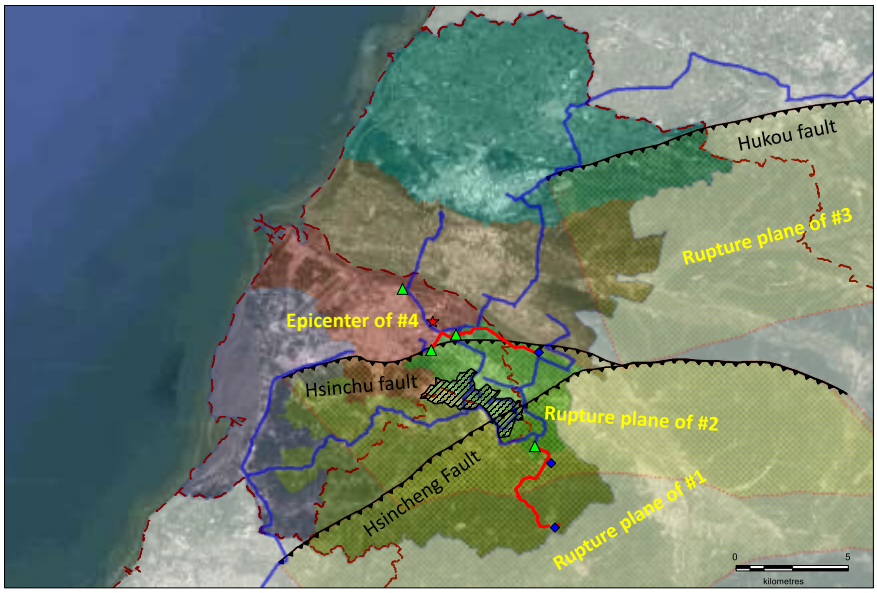

Figure 4. The fault rupture planes of the scenarios #1~#3 and the epicenter of #4.

Assessment Results

Table 2 summaries the estimates of casualties, injuries, damages and water outage of the four scenarios. Tables 3 to 7 summarizes the performance of major raw water aqueducts, water treatment plants (including three external WTPs), and the pipe damages, water supply condition, and serviceability of the water service areas.

There are three important rates in Table 6, namely (A) the water availability rate (to a WSA), (B) the network transmission rate (within a WSA), and (C) the network distribution rate (within a WSA). A value of 1.0 and 0.0 for these rates refers to no and complete loss of water supply or functionality, respectively. The water supply shortage rate (X) in Table 7 can decided from these rates. One of the merits of Twater is that the causes of water outage of each water service area can be easily identified through a comparison among the key performance of various system components.

Overall, the worst impact to HWSS is expected from #2, with an average water outage rate of 0.61 or, equivalently, 148,285 households (customers) left without water. It is followed by #1, with an average water outage rate of 0.51 (or 87,066 households left without water), and then followed by #4 (0.42, 93,511) and #3 (0.38, 81,961). The details of each scenario can be summarized as below.

- #1: [Hsinchu East] and [HSP] sustain the highest water supply shortage rates of 0.68 and 0.65, respectively. Mostly, this is due to the likely damage of the two transmission trunks from the Baoshan WTP by fault rupture. The pipe damage in their internal transmission and distribution network is severe, which also leads to the result of high water shortage rate.
- #2: [Hsinchu Downtown] and [Hsinchu East] sustain the highest water supply shortage rates of 0.83 and 0.76, respectively. The rest WSAs sustain water supply shortage, too, with the rates varying between 0.53 and 0.74. The only exception is [Hukou Xinfeng], with a rate of 0.21. The major cause is that the water output rates of both the Hsinchu First and Second WTPs are reduced to 0.69 and 0.33, respectively. Similar to #1, the pipe damage in the internal transmission and distribution network of most WSAs is severe, leading to the result of high water shortage rate.
- #3: [Hukou Xinfeng] and [Zhubei] sustain the highest water supply shortage rates of 0.64 and 0.59, respectively. There are two major causes. One is that the transmission trunk forwarding clear water from the northern neighbor utility is likely damaged by fault rupturing. As a result, the water availability rate of [Hukou Xinfeng] is reduced to 0.74. The other is that pipe

damages will reduce the internal network transmission and distribution rate of both [Hukou Xinfeng] and [Zhubei], who are closest to the seismic source.

- #4: The water supply shortage rates of [Hsinchu Downtown], [Zhubei], and [Hsinchu East], right above the epicenter (point seismic source), are very high due to the reduction of internal network transmission and distribution rate caused by pipe damages.

Table 2. The estimates of casualties, damages and water outage of HWSS.

Scenario ID		#1	#2	#3	#4
No. of casualties and serious injuries		345	836	267	367
No. of WTPs exceeding slight damage state		1	4	0	1
No. of damages in raw water pipes (aqueducts)		4.8	4.3	0.3	1.1
No. of damages in clear water pipes	Distribution pipes (ϕ100-450mm)	648.0	1183.1	608.4	687.4
	Transmission pipes (ϕ≥500mm)	5.6	8.3	4.3	4.8
	Total (including customer pipes)	1773.9	3290.2	2348.1	2105.2
Average water outage rate		0.47	0.61	0.38	0.42
Households w/o water		87,066	148,250	81,961	93,511

Table 3. The estimated number of damage and conveyance rate of major water aqueducts.

Raw water aqueduct	Flow capacity (CMD)	No. of damages				Raw water conveyance rate			
		#1	#2	#3	#4	#1	#2	#3	#4
<1>	89,000	0.0	0.3	0.0	0.1	0.97	0.72	0.98	0.95
<2>	249,000	0.2	0.8	0.1	0.2	0.84	0.48	0.87	0.83
<3>	518,400	3.2	1.8	0.0	0.5	0.00	0.38	0.98	0.70
<4>	1,382,400	1.0	0.7	0.1	0.2	0.52	0.62	0.89	0.84
<5>	450,000	0.0	0.0	0.0	0.0	0.98	0.99	1.00	1.00

Table 4. The estimated damage state and output rate of each water treatment plant.

WTP	Capacity (CMD)	Damage state				WTP output rate			
		#1	#2	#3	#4	#1	#2	#3	#4
Baoshan	450,000	Moderate	Slight	None*	None*	0.71	0.82	0.98	0.96
Hsinchu Second	160,000	None*	Slight	None*	Slight	0.78	0.33	0.81	0.78
Hsinchu First	89,000	None*	Slight	None*	None*	0.90	0.69	0.95	0.84
Nanya	40,000	None*	Slight	None*	None*	0.94	0.82	0.92	0.84
Dongxing (Ext.)	240,000	Slight	None*	None	None	0.69	0.94	1.00	1.00
Pingzhen (Ext.)	185,000	None	None*	Moderate	None	1.00	0.85	0.55	1.00
Shihmen (Ext.)	120,000	None	None	Slight	None	1.00	1.00	0.00	1.00
Ext.: external WTP supporting HWSS; None*: status between none and slight damage.									

Table 5. The estimates of damage of water pipes of each water service area.

WSA	No. of damages in internal transmission pipe network				No. of damages in internal distribution pipe network			
	#1	#2	#3	#4	#1	#2	#3	#4
[Hukou Xinfeng]	0.3	0.4	1.1	0.4	42.1	70.3	203.8	66.5
[Zhubei]	1.0	1.9	1.7	1.5	118.6	219.4	188.9	162.1
[HSP]	1.2	0.7	0.2	0.3	56.2	73.5	16.3	32.2
[Hsinchu Downtown]	0.8	2.0	0.7	1.4	139.0	357.5	109.2	235.9
[Hsinchu East]	1.6	1.9	0.5	0.8	110.3	168.7	47.9	79.7
[Hsinchu Xiangshan]	0.5	1.1	0.1	0.3	67.5	154.2	22.5	59.7
[Baoshan]	0.2	0.3	0.0	0.1	114.3	139.5	19.9	51.4
Total	5.6	8.3	4.3	4.8	648.0	1183.1	608.4	687.4

Table 6. The estimates of water supply condition of each water service area.

WSA	(A) Water availability rate (to WSA)				(B) Network transmission rate (within WSA)				(C) Network distribution rate (within WSA)			
	#1	#2	#3	#4	#1	#2	#3	#4	#1	#2	#3	#4
[Hukou Xinfeng]	1.00	1.00	0.74	1.00	0.96	0.93	0.82	0.93	0.91	0.85	0.63	0.86
[Zhubei]	1.00	0.82	1.00	1.00	0.72	0.56	0.60	0.63	0.78	0.64	0.68	0.72
[HSP]	0.93	1.00	1.00	1.00	0.79	0.88	0.97	0.95	0.47	0.40	0.78	0.62
[Hsinchu Downtown]	0.84	0.51	1.00	0.95	0.87	0.71	0.88	0.79	0.72	0.47	0.77	0.58
[Hsinchu East]	1.00	1.00	1.00	1.00	0.58	0.55	0.84	0.76	0.55	0.43	0.76	0.64
[Hsinchu Xiangshan]	0.88	0.77	1.00	1.00	0.83	0.67	0.96	0.89	0.71	0.50	0.89	0.74
[Baoshan]	1.00	1.00	1.00	1.00	0.92	0.91	0.99	0.97	0.57	0.52	0.90	0.77

Table 7. The estimates of performance and serviceability of each water service area.

WSA	Demand (CMD)	(X) Water supply shortage rate				Households without water			
		#1	#2	#3	#4	#1	#2	#3	#4
[Hukou Xinfeng]	106,779	0.13	0.21	0.62	0.20	3,683	6,190	20,843	5,838
[Zhubei]	74,113	0.44	0.71	0.59	0.55	18,159	32,386	26,023	23,695
[HSP]	160,482	0.65	0.65	0.24	0.41	225	224	72	130
[Hsinchu Downtown]	107,600	0.48	0.83	0.32	0.57	35,985	71,877	23,186	44,332
[Hsinchu East]	35,105	0.68	0.76	0.37	0.52	16,702	19,239	8,030	11,934
[Hsinchu Xiangshan]	29,212	0.48	0.74	0.14	0.34	7,696	13,110	2,067	5,256
[Baoshan]	20,060	0.47	0.53	0.11	0.26	4,616	5,224	918	2,326
Total (average)	533,351	0.47	0.61	0.38	0.42	87,066	148,250	81,139	93,511

Observations and Recommendations

As mentioned above, the worst scenario is #2, which results in an average water outage rate of 0.61. In this scenario, the water availability rate of the most populated WSA, namely [Hsinchu Downtown], is reduced to merely 0.51. This is a result of low water output rates of the Hsinchu First and Second WTPs, 0.69 and 0.33, respectively. There are two reasons behind. The first is the low raw water conveyance rates of the associated aqueducts <1> and <2>, 0.72 and 0.48, respectively, as summarized in Table 3. As depicted in Figure 5, the aqueducts <1> and <2> have a fault crossing each and probably perform poor in #2. The other is that both WTPs are found to sustain slight damage in Table 4, and their functionality would to reduced, accordingly. Moreover, the damage of (internal) transmission / distribution pipe networks of some of the WSAs is severe. For [Hsinchu Downtown], the resulted network transmission and distribution rates are reduced to 0.71 and 0.47, respectively. The factors of 0.51, 0.71, and 0.47 yield the final water supply shortage rate of [Hsinchu Downtown] as 0.83 (i.e. $1-0.51\times0.71\times0.47$). Following #2, it is recommended that the raw water aqueducts <1> and <2> should be retrofitted at the fault crossings. The Hsinchu First and Second WTPs should be enhanced seismically as they are too close to the Hsinchu fault and have a high probability of being damaged.

For the Hsinchu Science Park, or [HSP], the water supply shortage rate is the same value of 0.65 in both #1 and #2. According to Table 6, the major cause is its low network distribution rate. The minor cause is its low network transmission rate. The effect from water availability rate seems little to no. As [HSP] is crossed by the Hsincheng fault, and located on the hanging wall of the Hsinchu fault, severe pipe damage is inevitable in either #1 or #2. To be precise, the estimates of damage in distribution pipes are 52.6 and 73.5, which result in the network distribution rates of 0.47 and 0.40 for #1 and #2, respectively. In order to most reduce the likely huge loss to the manufacturers in the Hsinchu Science Park due to water outage, the authorities should take action to (1) retire the existing distribution pipes

to seismically resistant pipes, and (2) to secure the availability of large number of water tank trucks in case of emergency.

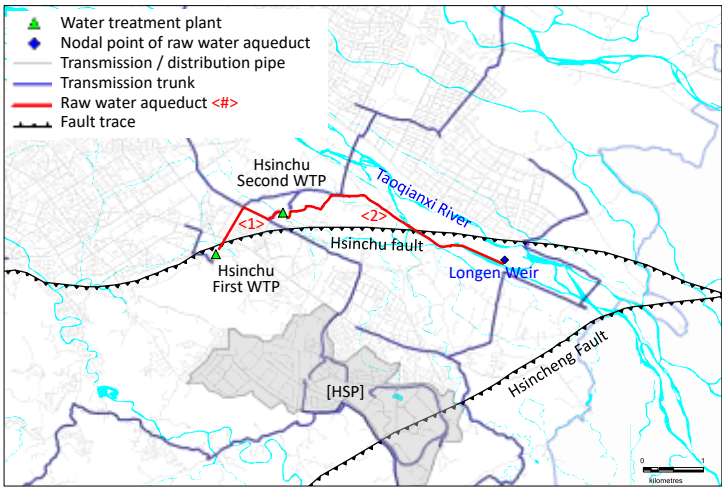

Figure 5. The Hsinchu First and Second WTPs and their environment.

Finally, #4 of a shallow M6.5 earthquake also causes substantial pipe damage and water outage. There are around 700 damages in water pipes, which result in an average water outage rate of 0.42, leaving more than 93,000 households without water. Considering the fact of high seismicity of the entire region of Taiwan, such event is not rare. It is recommended that the local water utility should be well prepared for the occurrence of such event and its consequence.

CONCLUDING REMARKS

Software Twater for the seismic risk assessment of water supply systems has been implemented to the system in Hsinchu, Taiwan, for the sake of seismic hazard mitigation. According to the assessment results, it is identified that: (1) the clear water transmission trunks from the Baoshan Water Treatment Plant, the largest in the system, needs retrofit against fault offset; (2) the smaller but crucial Hsinchu First and Second Water Treatment Plants and their shared raw water aqueduct need retrofit for surviving any earthquake right beneath them; (3) the Hsinchu Science Park, now a hub of semiconductor manufacturing in the world, sustains high risk of water outage due to the vulnerability of its own water distribution network.

REFERENCES

Hwang, H. H. M., H. Lin and M. Shinozuka (1998). "Seismic Performance Assessment of Water Distribution Systems," *J. Infrastructure Systems*, **4**(3), 118-125.

Liu, G.-Y., C. H. Yeh, L.-H. Huang, G.-J. Yu and T.-J. Chiu (2019). "Seismic Risk Assessment of Water Supply Systems in the Greater Kaohsiung Area," *Proc. 11-th WRF/JWWA/CTWWA Water System Seismic Conference*, 99-106, Los Angeles, CA.

Shi, P., T. D. O'Rourke and Y. Wang (2006). "Simulation of Earthquake Water Supply Performance." *Proc. 8th U.S. Nat. Confer. Earthquake Eng.*, Paper No. 1295, San Francisco, CA.

Shinozuka, M., R. Y. Tan and T. Toike (1981). "Serviceability of Water Transmission Systems under Seismic Risk." *Lifeline Earthquake Engineering, the Current State of Knowledge*, ASCE, New York, NY.

Wells, D. L. and K. J. Coppersmith (1994). "New Empirical Relationships Among Magnitude, Rupture Length, Rupture Width, and Surface Displacement," *Bull. Seism. Soc. Am.*, **84**, 974-1002.

Yeh, C. H., C. H. Loh and K. C. Tsai (2006). "Overview of Taiwan Earthquake Loss Estimation System," *Natural Hazards*, **37**, 23-37.

Yeh, C. H., G.-Y. Liu and H.-Y. Hung (2017). "Seismic Scenario Simulation of Water Supply Systems," *Proc. 10-th JWWA/WRF/CTWWA Water System Seismic Conference*, 209-216, Tainan, Taiwan.

A STUDY FOR RC STRUCTURE SAFETY REDUCTION ASSESSMENT IN SEISMIC RESPONSE AFTER REGIONAL FIRE DAMAGE

Ren-Jwo Tsay[1]
1. Associate Professor, Department of Internal Design and Civil Engineerig, Vanung University, Taoyang, Taiwan, R.O.C.
Email: trj@vnu.edu.tw

ABSTRACT

Building safety doubts caused by fire damage often cause users' subsequent use troubles, especially how to provide earthquake-resistant safety assessment of buildings after regional fire damage is a very important issue in practice for the currently common reinforced concrete structures. In this study firstly analyzes the material strength changes after fire damage, and then uses SAP software to evaluate the seismic safety impact of RC structures that may be caused by changes in temperature of the overall structure with dynamic load, and provides suggestions for rapid assessment of RC structures after fire damage. From the analysis results, it can be seen that the RC structure is easily deformed and the bending moment force of the rod is reduced when the temperature exceeds 500 °C. On the other hand, the structural safety affected by dynamic loading will increase for high temperature causes RC material strength soften. .

Keywords: RC, regional fire damage, dynamic loading, SAP

INTRODUCTION

For the RC structure, due to the temperature sensitivity of the constituent materials, it often causes safety concerns when a fire occurs. So engineers must to find a safety assessment method to confirm building safe after fire damage. There are many research studied in RC building safety after fire. Kodur et al. [1] used full scale beam sample fire test compare with different numerical failure criterion to confirm the feasibility of the analysis model. Whitney [3] developed a simple RC frame moment strength capacity method. Terro [4] discuss different codes for building deflection to confirm the effect for building safety. Yang [5] developed concrete soften strength formulation by laboratory test. Chang [6] discussed RC structure fire damage behavior by experiment and thesis discussion. Bratina et al. [7] analysis time-dependent thermal and mechanical loads for RC beam then use FE method compare with the test results.
In former studies may be confined in RC structure element response with fire temperature but can't understand the effect for whole building. In this paper we applied SAP program to setup numerical method for local region fire which induce the change of RC material strength to assessment the real building response after fire damage.

FIRE-DAMAGED MATERIAL PROPERTIES AND STRUCTURAL TEMPERATURE OF REINFORCED CONCRETE IN SEISMIC SAFETY ASSESSMENT

Building fire temperature assessment

Among the methods for evaluating the maximum temperature of concrete fire damage, the results of the loss-on-ignition method are the most reliable. The evaluation methods and steps are suggested as Eq.(1)

$$T = 1000 - 10 \times IL \quad (1)$$

Where T : fire temperature(℃)
IL : normalized loss on ignition (%)

High temperature reduce concrete strength assessment

Yuang 1996[5] promotion concrete residual strength as Eq.(2) and Eq.(3) shown.

$$\sigma_c = \begin{cases} f_{fr}\left[1-(\dfrac{\varepsilon_{\max}-\varepsilon_c}{\varepsilon_{\max}})^2\right], \varepsilon_c \le \varepsilon_{\max} \\ f_{fr}[1-\dfrac{(\varepsilon_{\max}-\varepsilon_c)}{\eta\times\varepsilon_{\max}}], \varepsilon_c > \varepsilon_{\max} \end{cases} \quad (2)$$

Where

$\varepsilon_{\max}$: concrete stress of residual compress strength in fire effect

$$\varepsilon_{\max} = 0.0022 + (0.25T + 0.15T^2)\times 10^{-7}$$

$$\eta = \begin{cases} 2.5, T \le 400^o C \\ 3, T > 400^o C \end{cases}$$

f_{fr} : concrete residual compress strength in fire effect

$$f_{fr} = \begin{cases} f_c^{'}(1.02-0.001T) \le f_c^{'}, 25^o C \le T \le 400^o C \\ f_c^{'}(1.38-0.0019T), 400^o C < T \le 600^o C \\ f_c^{'}(0.66-0.007T) \ge 0.05 f_c^{'}, T > 600^o C \end{cases} \quad (3)$$

Fire effect steel strength

From Chang [6] experiment results in Fig. 1 the steel yield stress could be shown as Table. 1.

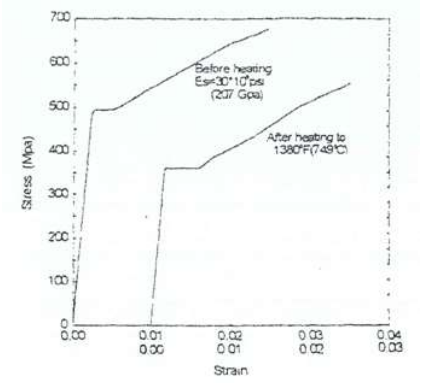

Fig. 1 Stress-Strain Relationship Curve for Steel in High Temperate by Tension [6]

Table 1. Steel yield stress by fire effect [6]

$f_{yr} = f_y$	when T≦500°C
$f_{yr} = (-0.108T+154.27)*0.01*f_y)$	when 500°C≦T≦750°C
$f_{yr} = (0.196T-73.863)*0.01*f_y)$	When 750°C≦T≦800°C
$f_{yr} = 0.83f_y$	When T≧800°C

RC elements moment **strength Analysis**

Witney 1937[3] promotion a simple RC bending strength by steel ratio as Eq(4) to Eq(6) shown.

$$\rho_b = 0.456\frac{f_c'}{f_y} \tag{4}$$

$$\rho < \rho_b \ , \ M = \rho bd^2 f_y(1-0.59\frac{\rho f_y}{f_c'}) \tag{5}$$

$$\rho > \rho_b \ , \ M = \frac{bd^2}{3} f_c' \tag{6}$$

In this paper, we comparison between the allowable strength of the reinforced concrete section at different stages fire temperature and the actual member strength will be used to define the failure condition of the RC members.

SAP program Numerical Fire Damage and Seismic Load Analysis

In the structure analysis SAP program users can import temperature and seismic dynamic load to analysis the structure behavior. The Fig. 2 we show the structure temperature load in local roof area by 300℃. So we can found the deformation and the roof slab moment distribution after temperature load as Fig. 3.

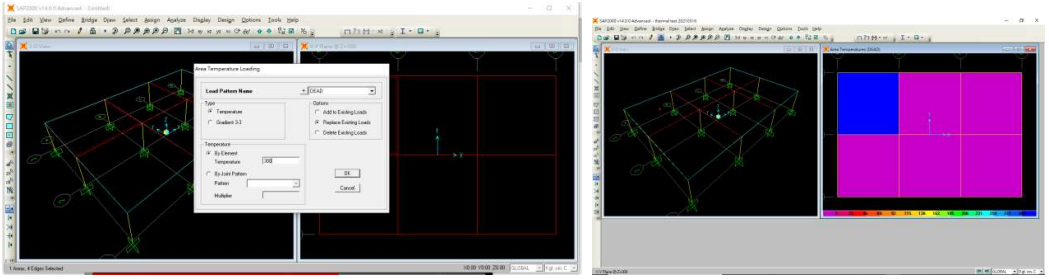

Figure 2 diagram of structural system temperature loading input and area

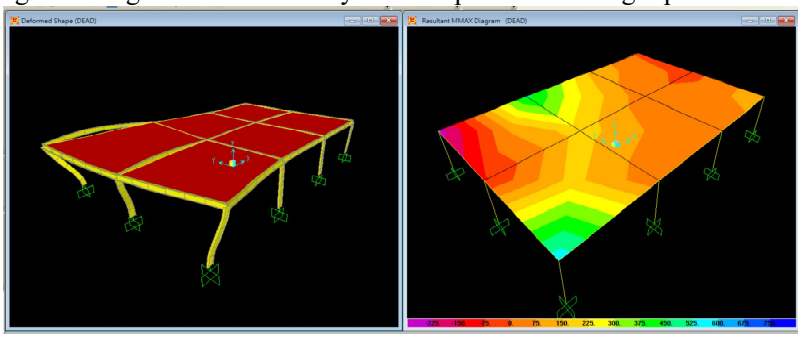

Figure 3 Moment distribution and deformation by temperature load

Seismic Load Applied in RC building

The dynamic load of building will induce more member strength after fire damage. In order to get the response we applied numerical program SAP applied the time history load to fire damage building to understand the response in earthquake. In this paper we apply 1999 GiGi earthquake time history record as Fig. 4 as building dynamic loading import.

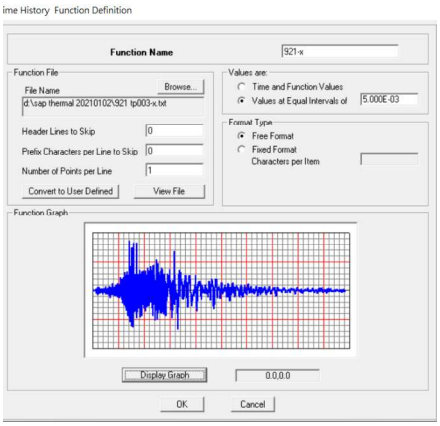

Fig. 4 Dynamic loading acceleration time history input sample

NUMERICAL ANALYSIS APPLICATION

Structure system setup

In this paper analysis the structural safety of a 5F RC apartment after the 4F is damaged by fire. The architectural and structural systems are shown in Figure 5.

Figure 5. Analysis case architectural and structure map

Material properties setting

We set the initial RC material strength as

Concrete compression strength $f_c' = 210\ ^{\mathrm{kg}}/_{\mathrm{cm}^2}$ andSteel yield strength $f_y = 2800\ ^{\mathrm{kg}}/_{\mathrm{cm}^2}$

Beam and column section are $24cm \times 50cm$, 12cm brick wall, 15cm RC slab. The SAP numerical material sections were seated as Fig. 6.

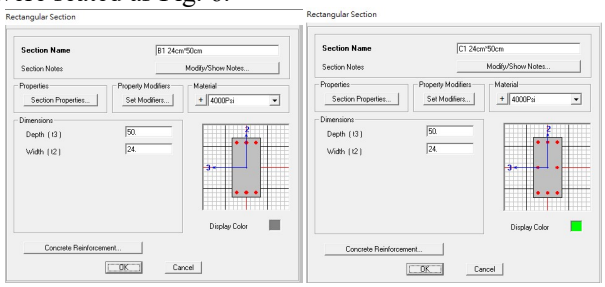

Figure 6. SAP RC beam column properties setting

Temperature effect structure element strength analysis

In order to get element strength capacity when applied Eq(3) and Table 1 formulation so we can get concrete compression strength and steel yield stress at different temperate as Table 2 shown.

Table 2. Table of permissible material strength under different fire damage temperatures

Temperature(℃)	fc(kg/cm^2)	fct(kg/cm^2)	0.05fc	fy(kg/cm^2)	fyr(kg/cm^2)
200	210	172.2		2800	2800
300	210	151.2		2800	2800
400	210	130.2		2800	2800
500	210	90.3		2800	2800
600	210	-743.4	10.5	2800	2505.16
700	210	-890.4	10.5	2800	2202.76
750	210	-963.9	10.5	2800	2047.836
800	210	-1037.4	10.5	2800	2322.236
900	210	-1184.4	10.5	2800	2324
1000	210	-1331.4	10.5	2800	2324

Then we applied the material strength and RC section sizes and reinforce steel to get element max strength at different temperature as Figure 7 and Figure 8 shown.

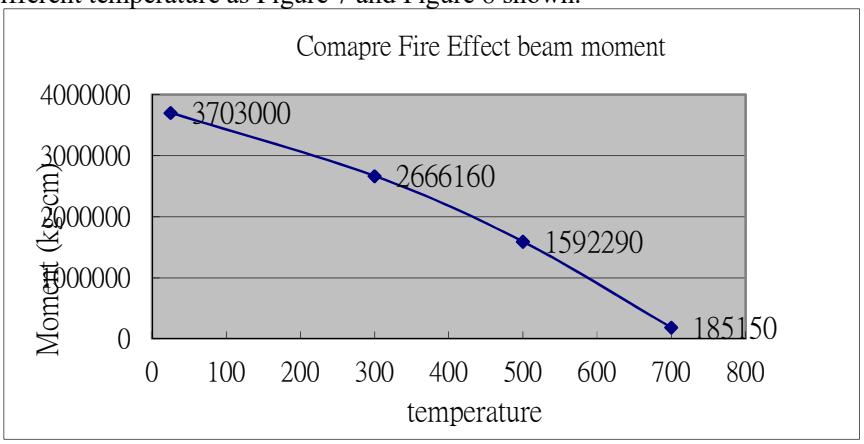

Figure 7. Compare the RC beam capacity moment at different temperate

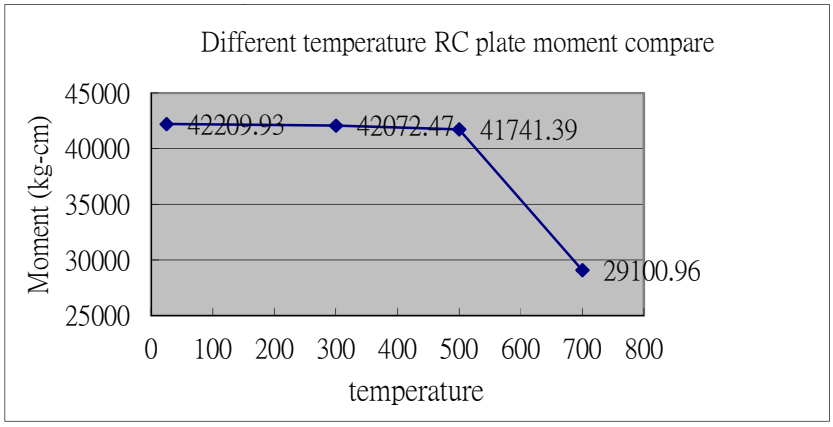

Figure 8. Compare the RC plate capacity moment at different temperate

Building Fire Hazard numerical simulation

We simulate the local temperature 700℃ fire point at 5F RC floor for RC building as Fig. 10 shown.

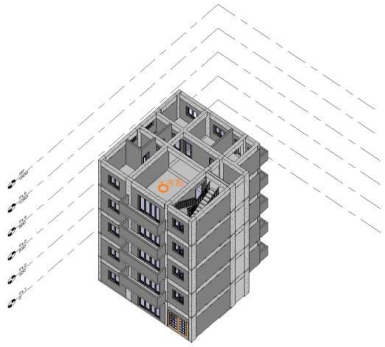

Figure 9. 3D diagram of the fire point

SAP numerical model and temperature load setting

We applied the structure system define to setup SAP numerical model as Fig. 10 shown.

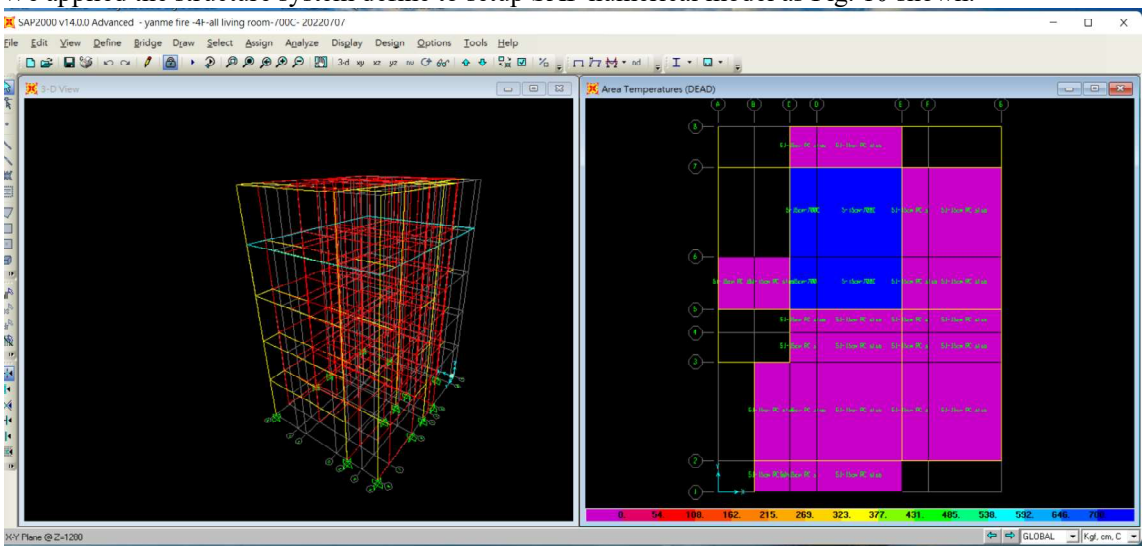

Figure 10. SAP 3D model and plane map with temperate region load setting

Comparison the soften material effect by temperature

In order to understand the RC building behavior by temperature effect we applied different temperature in region area floor. In Fig. 11 is the result when 700℃ loading at 4F floor so we can found the different between material soften effect.

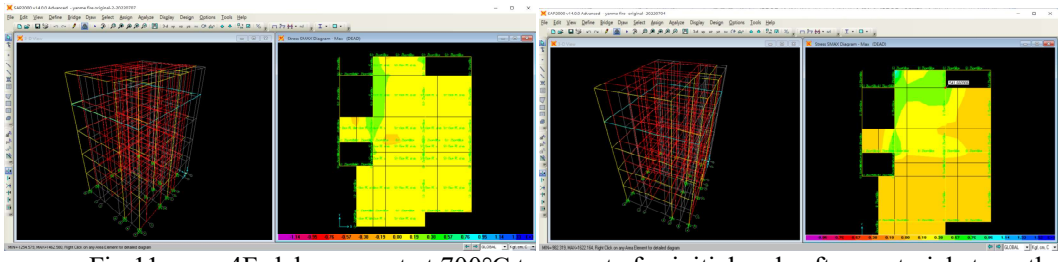

Fig.11 max 4F slab moment at 700℃ temperate for initial and soften material strength

Dynamic response after fire effect

In order to understand the RC building dynamic response after fire damage we applied time history load to SAP program to compare the different. In Fig. 12 is the comparison initial condition and building effect by 700°Croof max dynamic deformation. From table 3 we can get the different RC building response for fire damage.

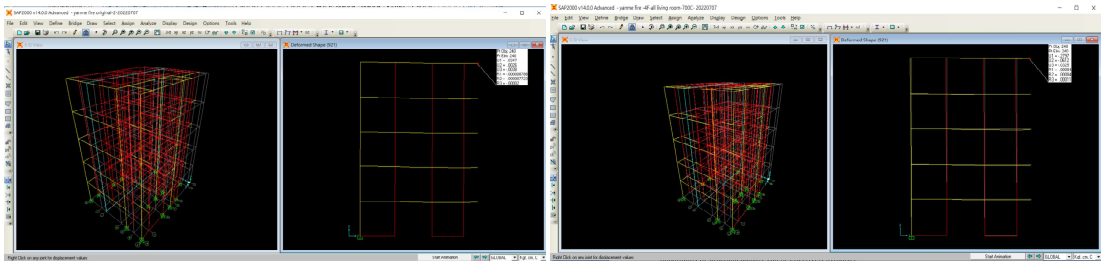

Figure 12. Dynamic load roof floor deformation for initial and fire damage condition

Table 3. Comparison the dynamic response on 5F RC building roof for initial and 700°C

	Ux(cm)	Uy(cm)	Uz(cm)	Total deformation(cm)
Initial condition	0.0347	0.0026	0.0038	0.035004
Fire damage (700°C) 4F on region area	0.2797	0.0612	0.03825	0.288861
Multiple ratio with initial condition				8.252191

CONCLUSIONS

From the above analysis, it can get follow conclusions.

(1). The impact of regional fire damage will be mainly in the area where fire damage occurs, and there will be concentrated temperature stress distribution at the top of the internal partition wall.

(2). The RC structural member will generate the bending moment at the rod end after being damaged by fire, so this effect can be used as a repair criterion for RC reinforcement after being damaged by fire.

(3). From the case analysis, it can be seen that the fire damage exceeding 500℃ will be the critical value of RC structural damage. Therefore, if a cooling mechanism can be provided in the early stage of fire damage, the opportunity of structural damage can be effectively avoided.

(4). In regional fire damage will larger the temperature moment of building frame so maybe induce 8 times in 700°C. So we must careful confirm building safety after building fire.

REFERENCES

Kodur , V.K.R., Dwaikat, M.(2008) "A numerical model for predicting fire resistance of reinforce concrete Beams," *Cement and Concrete Composites,* 30(5), 431-443.

SFPE(2002), "Handbook of Fire Protection Engineering", Third Edition

Whitney, C. S. (1937), "Design of Reinforced Concrete Members Under Flexure or Combined Flexure and Direct Compression", *International Concrete Abstracts Portal*, **33**(3), 483-498

Terro, M. J. (1998), "Numerical modeling of the behavior of concrete structures in fire," *ACI Structural Journal,* **95**(2), 183-193

Yang , M. S., (1996) "Torsional Behavior of Reinforced Concrete Rods after Fire Damage, " *Ph.D. Thesis*, Department of Construction, National Taiwan University of Science and Technology.

Chang, S. T. (1999), "Building fire damage and post-disaster safety assessment method," *Science and Technology Press*.

Bratina, S., Planinc, I., Saje, M., and Turk, G. (2003)," Non-linear fire-resistance analysis of reinforced concrete beams," *Structural Engineering and mechanics*., 16(6), 695–712.

ASSESSING HOSPITAL NON-STRUCTURAL FAILURE AFTER AN EARTHQUAKE WITH STRUCTURAL DAMAGE AS A NEW FACTOR

Chi-Hao Lin[1] and You-Xuan Lin[2]
1. Associate Researcher, National Center for Research on Earthquake Engineering, Taipei, Taiwan, R.O.C.
2. Research Assistant, National Center for Research on Earthquake Engineering, Taipei, Taiwan, R.O.C.
Email: chihao@narlabs.org.tw, yxlin@narlabs.org.tw

ABSTRACT

Emergency medical care capacities of hospitals after seismic disasters are largely determined by the remaining functionality of hospital non-structural systems. Studies in the past have worked on developing approaches for non-structural failure estimations. However, the indirect damage to non-structures caused by structural damage is less concerned. In this study, a new estimation approach is proposed to represent the added effects of structural damage on non-structural damage. The structure is viewed as a component linked to every individual non-structural component in the fault tree analysis, representing that the integrity of each non-structural component is dependent on the structural integrity. Accordingly, the failure probability of the non-structural system is a function of failure probabilities of both structures and non-structural components. Moreover, the concept of damage states is incorporated to non-structural failure estimations, where the damage state dependent fragility functions are exploited. A case study based on a Richter magnitude 6.6 scenario earthquake induced by Sanchiao Fault is conducted to assess the failure probabilities of beds and operation rooms of an intermediate level emergency responsibility hospital. The results of bed and operation room failure probabilities show that, without considering the possibility of structural damage undermining non-structures, the potential non-structural failure is underestimated.

Keywords: non-structural damage estimation, structural damage, damage states, fragility function, fault tree analysis

INTRODUCTION

Emergency healthcare functionality of medical institutes after earthquakes has long been a concern for decision-makers, practitioners, and researchers in the field of disaster management and reduction. There are historical records of massive earthquakes damaging hospitals and causing delays and shortage of emergency medical aids, e.g., the 1971 San Fernando earthquake and the 1994 Northridge earthquake in California, the Great Hanshin Earthquake Disaster of 1995, and the 1999 Chi-Chi earthquake in Taiwan. In order to predict and prepare for the possible functionality reduction under the impact of earthquakes, efforts have been made to develop estimation approaches for the hospital structural and non-structural failure and recovery considering the complex interdependent relationship between components, subsystems, and even exterior lifelines and road networks (Hassan *et al.*, 2018; Hassan *et al.*, 2019; Yu *et al.*, 2019; Shang *et al.*, 2020). Extensive and complete damage in building structures implies misfunction of a hospital, and, therefore, a complete loss of emergency medical supply is inevitable. However, effects of structural damage at moderate or lower levels, where some wall and beam surfaces may exhibit cracks and spalling depending on the building type being discussed (FEMA, 2020), on the medical supply have yet been thoroughly considered and incorporated into the system of failure assessment.

As a generally agreed-upon practice in literature, the dependence of non-structural components on structures is commonly attended by using the structural response, specifically floor accelerations and inter-story drifts, as the seismic demand in the non-structural fragility function. The damage estimated by this approach is determined solely by qualities of the components, including their intrinsic seismic capacity and installation details. Together with fault tree analyses, a hospital or the system of a

medical institute is treated as a top event whose functionality is supported by lower events linked with each other either by “and” gates or “or” gates. The failure of the top event, a hospital, is attributed to failures of structural functional units and non-structural functional units, which are linked and together yielding bottom-up effects (Hassan *et al.*, 2019).

Given that individual items of the non-structural functional units are placed inside the structures, in addition to the top system, individual items in the system are subject to indirect damage caused by structures. Effects of falling debris, large cracks, and rotated walls or beams that characterize structural damage on non-structural damage should be considered from the perspective of probability especially when issues of medical capacity reduction and repair are to be addressed.

To fill up the gaps in non-structural damage and loss estimations, a method is proposed in this study. Failure probabilities of each component and exceedance probabilities of moderate structural damage are jointly considered to obtain a failure probability that manifests the effects of indirect damage to non-structural components due to structural damage. On the other hand, different from previous studies where only a single value of failure probability is computed to represent the chance of damage and non-damage, in this study, we introduce the concept of damage states to non-structures. The degrees of damage severity are differentiated so that the estimation of lengths of repair time for damage states of different components can be precisely defined for practical purposes. In this paper, methods of state-dependent non-structural failure probabilities coupled with structural failure probabilities will be elaborated. Non-structural components are primarily sensitive to accelerations or drifts. An exclusive focus of this paper will be on acceleration-sensitive components.

STATE-DEPENDENT FRAGILITY FUNCTIONS FOR NONSTRUCTURAL COMPONENTS

Fragilities describe the potential damage at given seismic demands. The relationship is assumed to be a lognormal function defined by two parameters, median and standard deviation. Hazus technical manual (FEMA, 2020) assumed homogeneous fragilities of non-structural components in a building of the same design code and of a particular structural type (e.g., mid-rise concrete moment frame, or C1M). Lin *et al.* (2017; 2019) adapted performance modification factors (PMFs) developed by Multidisciplinary Center for Earthquake Engineering Research (MCEER) and established a set of fragility functions for individual components of emergency power systems. Fragility parameters are tuned to match levels of installation qualities that have an impact on seismic performance of components, e.g., anchorage. Still other studies derived fragility functions from simulations. For instance, Zolfaghari *et al.* (2012) focused on free standing hospital components (e.g., beds) and acquired fragility functions by simulating overturning and sliding due to seismic ground motions.

Since detailed and specialized fragility data for every important hospital equipment (e.g., those addressing PMFs and features of equipment) are yet thoroughly studied and established, an alternative is to apply a generic function for components wherever a specialized function is inaccessible. For large-scale studies involving several hospitals, like an aim to build a non-structural fragility database for all emergency responsibility hospitals in Taiwan (a total of 205 verified hospitals), PMF-based fragility is unrealizable without an investment of a huge amount of time and labor for its necessity of on-site surveys. Instead, the model proposed in Hazus that requires only features of buildings where components are placed is relatively viable. In this study, we exploited fragilities from Hazus (FEMA, 2020) as a generic function to address non-structural components except beds. Figure 1 shows an example of generic fragility curves for components placed in a C1H building with the peak floor acceleration (PFA) in gal as the variable. The curve indicates the probability of damage exceeding a particular state. Resistance level of components is assigned by referring to the building’s year of construction that reflects seismic capacities as regulated in the corresponding seismic codes; that is, high code points to buildings abiding by the relatively recent codes and should be of higher standards.

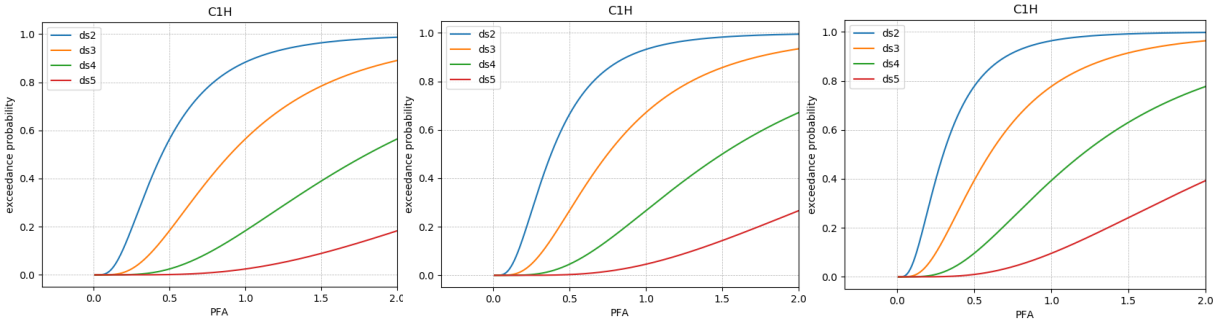

(a) High code (b) Mid code (c) Low code

Figure 1. Generic fragility functions for non-structural components placed in buildings of the C1H structure indicating exceedance probabilities of four damage states in response to PFA.

Regarding a component whose fragility data is available, a specialized function can be adopted to better capture its seismic response. In this study, we adapted and extended the specialized fragility function for beds by Zolfaghari *et al.* (2012) to remain a consistent assessment structure. Specifically, assuming that the proposed fragility in Zolfaghari *et al.* is for beds at the high seismic resistance level which corresponds to high code in the Hazus system, and that the two damage states defined in that paper based on minimum displacement (100 mm and 200 mm) are analogous to the slight and moderate damage states, we scaled up and down the parameters proportionally to reach the parameters for resistance levels of mid and low codes, as well as extensive and complete damage (Fig. 2).

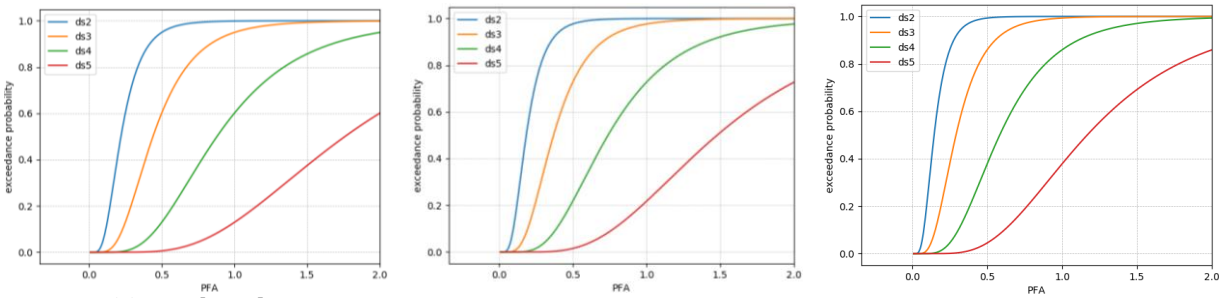

(a) High code (b) Mid code (c) Low code

Figure 2. Specialized fragility functions for beds indicating exceedance probabilities of four damage states in response to PFA, adapted from Zolfaghari et al. (2012).

PEAK FLOOR ACCELERATION

For non-structural functional components and equipment that are placed on or attached to floors of a building, once an earthquake happens, the trigger for non-structural damage is the response of the floor to the ground motion. Therefore, to establish damage assessment models for non-structures in the hospital buildings, calculating floor response at a specific seismic scenario is indispensable. According to FEMA P-58 (FEMA, 2012), PFA of each floor can be obtained by regression, taking in peak ground acceleration (PGA) of the site and structural characteristics. The PFA of the first floor (or the ground floor) equals to PGA. On the i^{th}floor, the PFA can be achieved by the following equation:

$$PFA_i = F_i(S, T, H, h_i) \times PGA \tag{1}$$

where $F_i(S, T, H, h_i)$ is the acceleration correction factor obtained from:

$$\ln(F_i) = a_0 + a_1 T_1 + a_2 S + a_3 \frac{h_i}{H} + a_4 \left(\frac{h_i}{H}\right)^2 + a_5 \left(\frac{h_i}{H}\right)^3 \tag{2}$$

with coefficients a_0 to a_5 determined by the frame types and the floor height, as listed in Table 1. H is the total height of the building; $h_i$is the height of the floor i; S is the strength ratio which is

related to spectral response accelerations at the first mode period $S_a(T_1)$, yield strengths V_{y1}, and the weight of the building W, as described in Eq. 3.

$$S = \frac{S_a(T_1)W}{V_{y1}} \tag{3}$$

Table 1. Coefficients of the acceleration correction factor for 2-story to 9-story buildings

Frame Type	a_0	a_1	a_2	a_3	a_4	a_5
Braced	0.66	-0.27	-0.089	0.075	0	0
Moment	0.66	-0.25	-0.080	-0.039	0	0
Wall	0.66	-0.15	-0.084	-0.26	0.57	0

Since design drawings of hospital buildings are not available in this study, the yield strength is unknown. As a compromise, the equation of base shear in seismic codes were utilized; that is, V_{y1} is assumed to be:

$$V_{y1} = \frac{S_{aD}I}{1.4\alpha_y F_u}W \tag{4}$$

The equation to compute the strength ratio is then modified accordingly with the new V_{y1} applied:

$$S = \frac{1.4S_a(T_1)\alpha_y F_u}{S_{aD}I} \tag{5}$$

As for the first mode period, the total building height can be used for estimation. The empirical equations for different structure types are as follows:

$$\text{Steal structure: } T_1 = 0.085H^{3/4} \tag{6}$$

$$\text{Reinforced concrete structure: } T_1 = 0.070H^{3/4} \tag{7}$$

$$\text{Other types: } T_1 = 0.050H^{3/4} \tag{8}$$

Based on the simple model adopted from FEMA P-58, standard response spectra, and data of hospital buildings, the acceleration correction F_i can be reached, and, accordingly, the PFA is obtained.

HYPOTHETICAL LAYOUT OF NON-STRCUTURAL SYSTEMS AND COMPONENTS

To deal with a lack of real surveyed data of the hospital layout and equipment placement which are required to compute PFA, as an interim solution, we made some analogies and reasonable guesses about the setting of non-structural functional systems, the buildings where components are placed, and the floor. A database of hospital buildings had been established by collating the House Tax data of Taiwan recording characteristics of buildings, e.g., the year of construction, the total number of floors, structure types, and so on, whereas the information required to derive PFA is not directly available. To be specific, one medical institute may own more than one building, but, in the database, the building usage and the floor information of each and every building are not documented. While all important information can be sorted out by visiting or consulting hospitals, the expense is remarkable to go over a total of 205 emergency responsibility hospitals.

The focus of this study is on four functional units, emergency power systems, operation rooms, laboratories, and beds. For emergency power systems, we resorted to previous studies and took the documented hospital data in the studies as the prototypes. Some previous efforts had been made to execute site surveys to gather overall information of hospitals as well as the setting of emergency

power systems (Yao, 2000; Lin *et al.*, 2017). Inspired by these studies, we took the surveyed hospitals as the prototypical hospitals and assumed that the setting and layout of emergency power systems of other hospitals should be comparable to the prototypes if they belong to the same level of emergency capacity on the three-level emergency responsibility scale (advanced, intermediate, and general levels). For the advanced level, National Taiwan University Hospital was taken as the prototype; Zhongxing branch of Taipei City Hospital was selected as the prototype for the intermediate level; as for the general level, Puli branch of Taichung Veterans General Hospital was referred to. By comparing hospitals to the prototypical hospitals of the corresponding level, a database of emergency power system for all 205 hospitals was established.

As for other functional units, reasonable guesses were made based on observations and common sense. For instance, in light of the observation that wards are less likely to be set up on lower floors, beds are assumed to be placed at the three fourths of the total floors. When a hospital has multiple buildings, in addition to matching the prototypes, we also assumed that hospitals would prefer buildings of higher resistance level, i.e., the newly constructed buildings. Note that issues pertaining to arrangement of hospital space and equipment setting are out of the scope of this study. Details of the placement and justifications of our assumptions will not be further discussed in this paper.

FAILURE PROBABILITY ESTIMATION FOR NONSTRUCTURAL COMPONENTS

Fault Tree Analysis and Damage Estimation of Non-structural Functional Units

Fault tree analysis was applied to depict the relationship between non-structural components forming a system, and their separate or joint contributions to the failure probability of the whole system. To illustrate the logical relationship between components and exemplify the computation of the failure probability of a system through fault trees, the damage estimation of laboratory rooms and operation rooms will be demonstrated in the following.

As displayed by Figure 3, components are linked with each other by certain gates. Components linked by the "or" gate should be simultaneously operational for an upper event to work; that is one component fails will lead to a shutdown of the upper event. For example, for an operation room to work, all the constituent parts are required to remain functional, including medical equipment and the space for medical behaviors to happen (Fig. 3a). Components linked by the "and" gate are mandatorily selective for an upper event to work. At least one component remaining functional is sufficient for the upper event to work. As shown by Fig. 3b, laboratory rooms are not damaged if one functional unit, Xray or blood and urine tests, can remain functional.

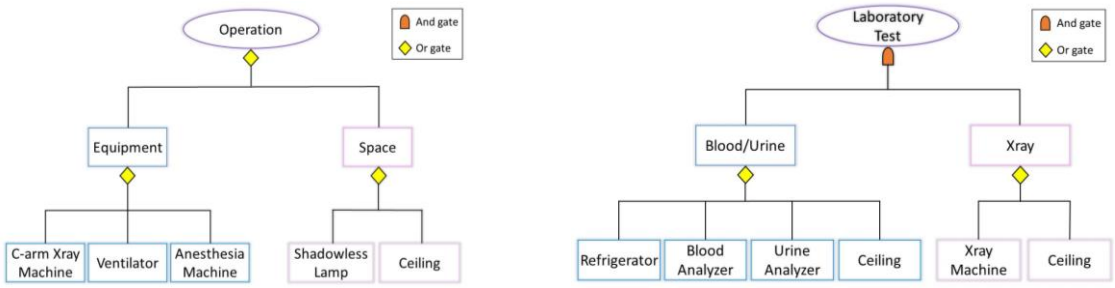

(a) Operation room (b) Laboratory room

Figure 3. Fault tree analysis.

With the fault tree revealing the relationship, the failure probability of upper events can be computed. For an upper event composed of lower events connected by "or" gates, the failure probability is:

$$P[u] = 1 - \prod_{i=1}^{n}(1 - P[l_i]) \tag{9}$$

where $P[u]$ is the failure probability of the upper event consisting of n lower events whose components have a probability $P[l_i]$ to fail for each lower event i. This equation states that an upper event fails if the functionality of its every component is not guaranteed. As for the lower components linked by "and" gates, they generate an upper event whose failure probability being calculated as follows:

$$P[u] = \prod_{i=1}^{n} P[l_i] \tag{10}$$

saying that the upper event fails only when components fail altogether.

Notice that computation with the equations above (Eqs. 9 and 10) depends only on the probability of failure or non-failure of the components. However, damage state dependent fragility analysis generates not only probabilities of failure but also of failure at different damage states. To incorporate the concept of damage states to non-structural damage estimation, the component failure probability $P[l_i]$ in Eqs. 9 and 10 should be substituted with the exceedance probability of slight damage (as in Eqs. 11 and 12). By the new equation, the derived system failure probability $P'[u]$ implies only a probability of failure. The degrees of damage severity of the upper event are governed by component failure probabilities at each state. In short, the number of $P'[u]$ tells is the system is, more or less, damaged.

$$P'[u] = 1 - \prod_{i=1}^{n}(1 - P_{ds2}[l_i]) \tag{11}$$

$$P'[u] = \prod_{i=1}^{n} P_{ds2}[l_i] \tag{12}$$

Estimation of Non-structural Damage Coupled with Structural Damage

Considering the effects of structural damage on non-structural damage is to add on structures to the fault tree of non-structural functional units. Structures are linked to each component by the "or" gate to reflect the indirect damage caused by structural damage. While, structural failure is also estimated by damage state dependent fragility, different from non-structures whose damage has a direct impact on the whole functional system regardless of the state, for structural damage to induce indirect damage, structures are expected to have undergone intermediate damage and above, which is characterized by large cracks, rotation, and spalling by the definition in Hazus. Therefore, in the computation of system failure, as described in Eq. 13, it is the exceedance probability of moderate structural damage $P_{ds3}[s]$ being deducted from 1 to determine the probability of structures of no significant damage. Slight damage and below was considered of no effects for non-structures, and, thus, is analogous to no damage in this respect.

$$P'_{ds2}[l_i] = 1 - (1 - P_{ds3}[s])(1 - P_{ds2}[l_i]) \tag{13}$$

The obtained new probability $P'_{ds2}[l_i]$ is then further taken to compute the system failure probability by Eq., 9 and 10. Note that, the failure probability of non-structural components coupled with structures through Eq.13 will be different from $P_{ds2}[l_i]$. To garner the probability of other damage states, the difference between two exceedance probabilities, $P'_{ds2}[l_i]$ and $P_{ds2}[l_i]$, is distributed to exceedance probabilities of other states, $P'_{ds3}[l_i]$, $P'_{ds4}[l_i]$, and $P'_{ds5}[l_i]$, which will be:

$$z = P[l_i]'_{ds2} - P[l_i]_{ds2} \tag{14}$$

$$P[l_i]'_{ds(j)} = P[l_i]_{ds(j)} + \frac{z(6-j)}{4}, 3 \le j \le 5 \tag{15}$$

RESULTS OF A CASE STUDY

To exemplify the proposed estimation methods, we conducted a case study to show the effects of structural damage on the non-structural damage. The case is based on a Richter magnitude 6.6 seismic scenario caused by a displacement of the Sanchiao Fault. An intermediate emergency responsibility hospital located at Datong District is the research target. At this seismic scenario, the site PGA of the hospital is 0.41g. The exceedance probability of structural moderate damage is 0.179. The estimation results of the bed and operation room failures are presented in Table 2. Here, beds are estimated as stand-alone equipment instead of as a system composed of multiple components, like operation rooms. The results show that in general, without considering the indirect damage caused by moderate structural damage and above, the failure probabilities of non-structural functional units are underestimated.

Table 2. Estimation results

	$P[u]$	$P'[u]$
Bed	0.971	0.977
Operation Room	0.992	0.998

DISCUSSION

The major contributions of this study are: (1) damage state dependent failure estimation, and (2) a new approach for non-structural damage that observes indirect image caused by structural damage. One of the benefits of distinguishing damage states is that the downtime and repair cost can be more delicately modeled by assigning different parameters for different components suffered different damage states. Researchers have been interested in medical resilience under the impact of the fluctuation of medical supply as a result of seismic damage and repair, and the patient surge. One strain of studies is to incorporate functionality failures to patient flow analysis and examine the consequences of the increased demand with the decreased supply (Favier *et al.*, 2019; Romani, 2021). Less considered is that downtime or functionality loss is correlated to the degrees of damage severity. A separation of damage states should grant more flexibility to approach the real-world situations and help gain a complete picture of patient flow after earthquakes.

On the other hand, joining structural damage to the non-structural damage emphasizes the subordinate status of non-structural components to structures. While the structures of a hospitals may be exempt from damage that is severe enough to evacuate patients and reject requests for medical help, the functional components inside are still susceptible to indirect damage. The joint estimation can also be integrated to Monte Carlo method-based patient flow analyses (e.g., Lin *et al.*, 2020) where the effects of structural damage on the hospital capacity, either a complete shutdown or an increased probability of non-structural failure, are determined by sampling.

CONCLUSION

In this paper, a damage state dependent estimation approach joining non-structural damage and structural damage has been introduced. It views structural damage over moderate states as another threat to non-structural damage. Results of a case study have shown that the non-structural system failure probabilities are underestimated without considering indirect damage. Moreover, this approach is damage state dependent. The information of component damage states provides flexibilities for applications in other studies, e.g., patient flow analysis concerning the length of downtime of medical supplies. Due to limitations of a lack of detailed hospital data regarding equipment installation, and setting and layout of functional units, the parameters for PFA functions and system fault trees are established by an interim solution. In the future, the relevant data can be elaborately collected and documented by means of questionnaires or site surveys to improve the reliability of estimation results.

REFERENCES

Favier, P., A. Poulos, J.A. Vásquez, P. Aguirre and J.C. DeLa Llera (2019). "Seismic risk assessment of an emergency department of a Chilean hospital using a patient-oriented performance model," *Earthquake Spectra*, **35**(2), 489–512.

FEMA (2012). Seismic performance assessment of buildings, Volume 1 – Methodology.

FEMA (2020). Hazus earthquake model technical manual.

Hassan, E. M. and H. Mahmoud (2018). "A framework for estimating immediate interdependent functionality reduction of a steel hospital following a seismic event," *Engineering Structures*, 168, 669–683.

Hassan, E. M. and H. Mahmoud (2019). "Full functionality and recovery assessment framework for a hospital subjected to a scenario earthquake event," *Engineering Structures*, **188**, 165–177.

Lin, C.H., C.T. Yang, Y.X. Lin and K.C. Chen (2019). Assessing Seismic Failure Probability of Hospital Emergency Power Supply Systems and Software Development. Presented at 5th International Conference on Smart Monitoring, Assessment and Rehabilitation of Civil Structures, August 2019 in Potsdam, Germany (SMAR 2019).

Lin, C.H., X.Q. Liu, C.T. Yang, Y.K. Pan and Y.C. Liao (2017). "Approaches for evaluating failure probability of emergency power supply systems in hospitals," *International Journal of Safety and Security Engineering*, **7**(4), 568 – 576.

Lin, Y.X., C.H. Lin and C.H. Lin. (2020). "A challenge for healthcare system resilience after an earthquake: The crowdedness of a first-aid hospital by non-urgent patients," *Plos One*, **16**(4), e0249522.

Romani, G.M P. (2021). Evaluating post-earthquake functionality and surge capacity of hospital emergency departments using discrete event simulation. *Master's Thesis*, The University of British Columbia, Vancouver.

Shang, Q., T. Wang and J. Li (2020). "A quantitative framework to evaluate the seismic resilience of hospital systems," *Journal of Earthquake Engineering*, **26**(7), 3364-3388.

Yao, G.C. (2000). Damage to functional facilities, *Investigation and Analysis of Building Disaster in Chi-Chi Earthquake*, NCKU Architecture, Tainan.

Yu, P., W. Wen, D. Ji, C. Zhai and L. Xie. (2019). "A framework to assess the seismic resilience of urban hospitals," *Advances in Civil Engineering*, **2019**, 1-11.

Zolfaghari, M.R. and S. Jahanbakhsh (2012). Development of seismic fragility curves for hospital equipment. Presented at 15th World Conference on Earthquake Engineering 2012, September 24-28 in Lisbon Portugal (15 WCEE).

SIMULATIONS FOR SEISMIC BEHAVIOR OF RUNNING VEHICLES ON CURVED PART OF EXPRESSWAY

Masaki Tsuda [1], Junji Kiyono [2], Ryoichi Kawai [3], Takumi Moro [3]
1. Graduate School of Engineering, Kyoto University
2. Professor, Graduate School of Engineering, Kyoto University
3. Technology Promotion Office, Engineering Department, Hanshin Expressway Co. Ltd.
Email: tsuda.masaki.57a@st.kyoto-u.ac.jp, kiyono.junji.5x@kyoto-u.ac.jp, kawai-ryoichi@hanshin-exp.co.jp, moro-takumi@hanshin-exp.co.jp

ABSTRACT

When a large earthquake occurs, estimation of damage to expressway and running vehicles is essential because it plays an important role for emergency restoration and supplies to the affected area. Simulations of running vehicles during an earthquake is necessary for damage estimation. In this study, we develop an extended driving model for curvilinear routes based on the simulations that has been conducted for straight routes in the past in order to realize a more general driving simulation during earthquakes. In the developed model, the acceleration/deceleration during curve entry and exit, and the steering wheel operation during curve following are implemented. The reproducibility of the model was confirmed by comparison with the results of DS experiments. Finally driving safety during the actual earthquake occurred in 2018 is discussed by the plural vehicle-running simulation model on curved sections of the expressway.

Keywords: earthquake, driving model, car-following model, expressway

1. INTRODUCTION

With the possibility of large-scale damage from a Nankai Trough earthquake or direct earthquake under the metropolitan area, it is very important to analyze vehicle behavior during earthquakes and to calculate the scale of damages from the viewpoint of the functions of expressways such as emergency transportation routes in the event of earthquakes. In previous studies (Murakami, 2017; Fukunaga, 2020), vehicle behavior analysis has been conducted for straight sections of expressways during earthquakes. However, the actual expressway consists of a complex alignment with a combination of arcs and transition curves. Therefore, it is necessary to conduct the analysis considering curved roads in order to estimate the damage on the expressway more accurately in the event of an actual huge earthquake. In this study, we made a curve-following model based on the Driving Simulator experiment (hereinafter called "DS experiment") and extended the vehicle running model under the earthquake excitation on a straight road by Murakami *et al.* (2017) to curve-following driving simulation on an expressway with a complex road alignment.

2. ANALYSIS METHOD OF VEHICLE BEHAVIOR

2.1 Vehicle Model

The vehicle model is a six-degree-of-freedom model that considers translation and rotation in the forward-backward, left-right, and up-down directions. The model shown in Fig.1. In Fig.1, the lower springs represent the tire stiffness and the upper springs represent the suspension springs. The upper mass (above the springs) represents the mass of the vehicle body, and the lower mass (below the springs) represents the mass of the wheel. All parameters for each wheel are assumed to be equal.

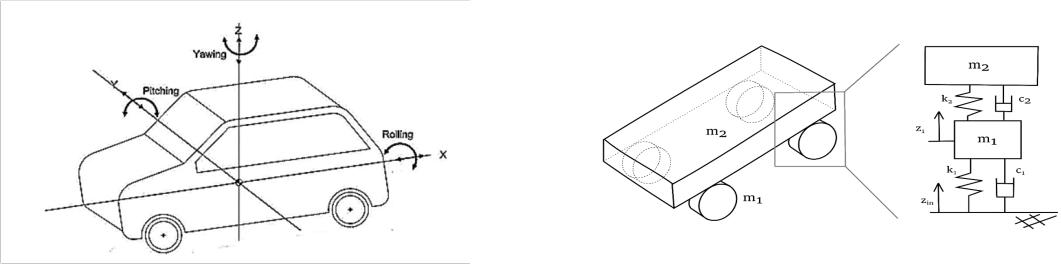

Figure 1. Vehicle Model

2.2 Vehicle Running Model under an Earthquake

In this study, we extended the previous vehicle following model (Murakami, 2017; Fukunaga, 2020) so that it can be applied to driving on curves. The basic equations of the model are shown below.

$$m_i \cdot \ddot{x}_i(t) = (1-\alpha)(F_{i1} + F_{i2} + F_{i4}) + \alpha F_{i3} \quad [1]$$

Where i denotes the vehicle number. F_{i1} represents the autonomous force, and F_{i2} represents the interaction force with the vehicle ahead, which are determined based on the existing models (Murakami, 2017). F_{i3} represents the deceleration force under an earthquake, and F_{i4} represents the acceleration /deceleration force during running on a curve. α is a weight coefficient, which indicates the degree to which each driver is inclined to brake operation in an emergency.

Regarding α and F_{i3}, Fukunaga developed a brake operation model focusing on the difference of running speeds by analyzing the video images during the earthquake (Fukunaga, 2021). Based on the maximum deceleration during braking (hereinafter called "brake strength") determined from the model and the results of past DS experiments (Transportation laboratory; 2016), the brake operation is approximated by a normal distribution shape, and the mean and standard deviation values are determined form DS experimental results. F_{i3} acts when the input seismic motion exceeds 50[gal] for the first time. This is because it was confirmed in the DS experiment that about 95% of all drivers started braking within a few seconds when the input seismic motion exceeds 50[gal].

F_{i4} is the force to control acceleration/deceleration during curve driving, which was added in this study based on the previous study (Takahashi *et al.*, 2012), and is calculated by the following equation.

$$F_{i4} = -m_i C \dot{\kappa}_{pv} \dot{x}_i^2(t) \quad [2]$$

This system generates a force corresponding to the time variation of the curvature κ_{pv} of the point that the driver is gazing at during driving. In addition, due to the velocity component in the equation, even when running on the same curve, a greater deceleration is generated as the vehicle enters the curve at a higher speed. C is a constant that represents the acceleration/deceleration rate when running on a curve, and is assumed to be independently recognized by the driver. In this study, we reproduced the driving conditions described in previous study (Takahashi *et al.*, 2012) and set the value of C to have the same speed profile as that of expert drivers.

2.3 Driver Model

The forward gaze model shown in Fig.2 is adopted as a steering model. The path tracking is realized by feedforward (FF) control based on the target course curvature and feedback (FB) control based on the position and yaw angle deviation from the target course. L is the forward looking distance, T_p is the forward looking time, V is the longitudinal speed, and y_{cr} and y_{sr} are the deviation from the target course at the vehicle center of gravity and the forward looking point, respectively. In this study, T_p is set to 1.0 second.

Fig.3 shows a block diagram of driver model based on previous study (Noguchi and Kageyama, 2016). δ represents the steering angle, y and ψ are the vehicle center of gravity and yaw angle respectively, and ϵ_y and ϵ_ψ are the deviation of y and ψ from the forward gaze point, respectively. In the FF control, since the paper (Noguchi and Kageyama, 2016) shows a high correlation between road curvature and steering angle, the curvature of the gaze point is used as an input, and the front wheel steering angle δ_{ff} is output by adding a dead time factor and a first-order lag factor. The FB part takes as inputs the deviation of the vehicle center of gravity from the center position of the lane calculated based on the forward gaze model and the deviation of the yaw angle, and outputs the steering angle by applying proportional, integral, and differential factors to each of them.

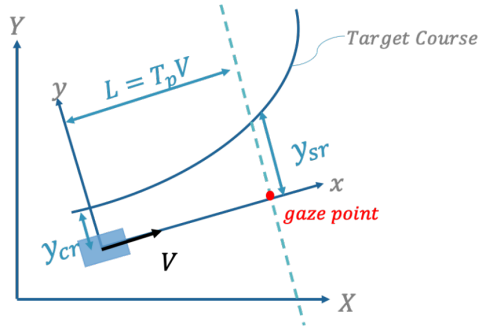

Figure 2. Forward looking model

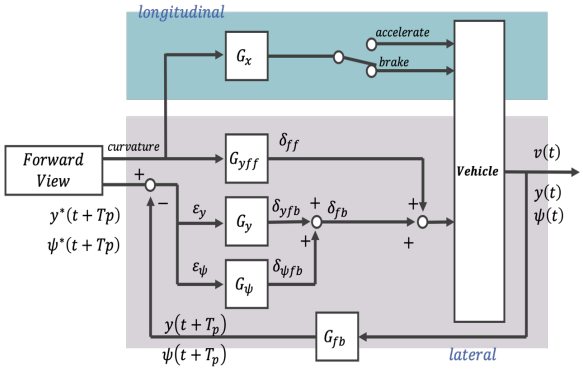

Figure 3. Block Diagram of Driver Model

3. COMPARISON OF DS EXPERIMENTAL RESULTS WITH SIMULATION

In this chapter, we examine the validity of the model by conducting single vehicle driving simulations using the developed model and comparing them with the results of the DS experiment. First, we reproduce the target route that the driver assumed in the DS experiment. Two vehicles (car1 and car2) that showed clear road-shoulder evacuation behavior in the DS experiment are extracted, and a road-shoulder evacuation route that the driver would expect is created based on the speed, yaw angle, and time history of the transversal displacement of the lane. In order to ensure the difference of the curvature, a point-symmetric path with a curve that has diminishing sine wave curvature is assumed. Figs.4 and 5 show the trajectories of the two vehicles and the created road-shoulder evacuation routes.

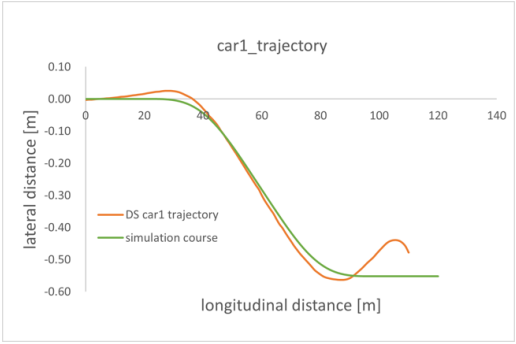

Figure 4. Assumed shoulder evacuation route (car1)

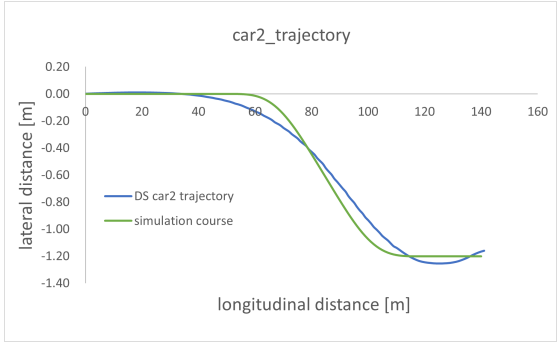

Figure 5. Assumed shoulder evacuation route (car2)

Then, we calculate the brake strength required for the simulation. The acceleration time histories are calculated from the velocity time histories obtained from the DS experiment (Fig.6), and the brake strength of each vehicle is obtained by approximating it with a normal distribution shape. The approximated acceleration time histories are shown in Fig.7.

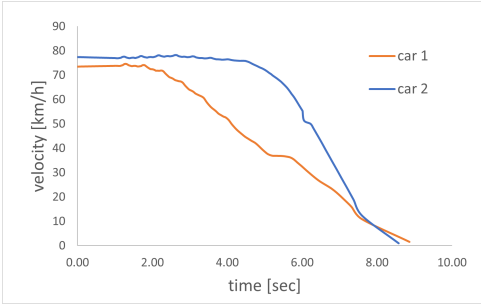

Figure 6. velocity time history

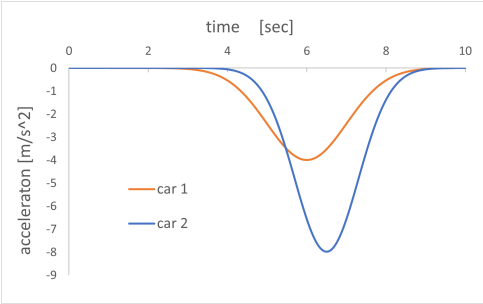

Figure 7. acceleration time history

The calculated brake strength is assigned to each car, and the same JMA seismic intensity of 5+ as in the DS experiment is input to each car to simulate the following of the created road-shoulder evacuation route. Figs.8 and 9 show the time histories of perpendicular displacement and velocity for car1 and car2, respectively. The solid lines in the figures are the results of the DS experiment, and the dashed lines are the results of the seismic input simulation. The simulation and the DS experimental are in good agreement for the vehicle behavior during the earthquake.

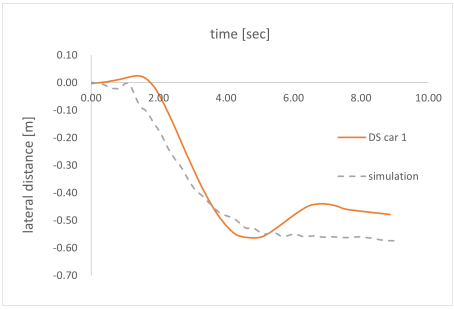

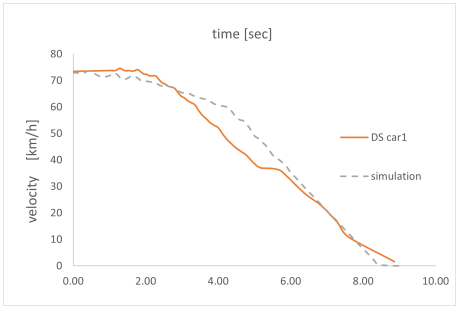

Figure 8. Left: Lateral displacement time history Right: Velocity time history (car1)

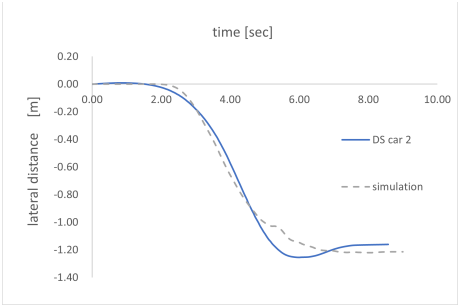

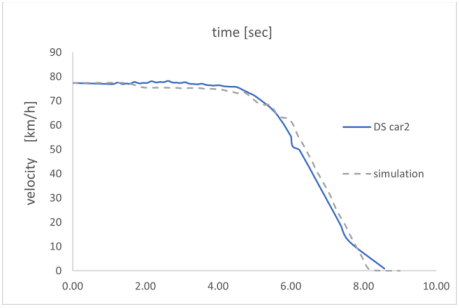

Figure 9. Left: Lateral displacement time history Right: Velocity time history (car2)

4. SIMULATIONS OF DRIVING ON REAL EXPRESSWAY

4.1 Input Seismic Wave

The input seismic motions are the data observed at the expressway pier top in the 2018 Northern Osaka Prefecture earthquake at the Moriguchi Observatory.

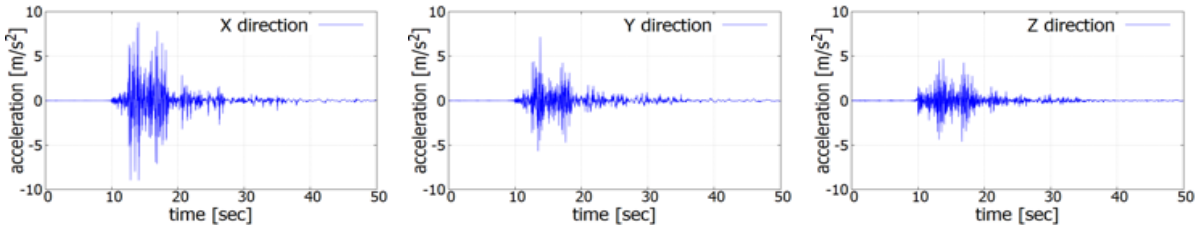

Figure 10. Input seismic waveform (Moriguchi Observatory, Seismic intensity 5+)

4.2 Parameters of Traffic Flow

On a real expressway, the distance between vehicles and vehicle speed are not constant. Therefore, we determined the mean values and standard deviations as shown in the Table 1 based on the speed limits at the earthquake observation points, and the values at the start of running were generated by normal random numbers.

Table 1. Parameters of Traffic Flow

average speed of a lane	60 km/h
Lane speed standard deviation	10 km/h
lane average vehicle headway time	1.5 sec
Lane headway time standard deviation	0.5 sec

4.3 Driving Test Course

In order to study driving safety during earthquakes on curved sections of expressways, we modeled the running route of the area where earthquake records are observed. The driving course model is made based on the road alignment data of the Osaka Moriguchi line (Kp7.5-Kp10.5) provided by Hanshin Expressway Co. Ltd.. Fig.11 shows the original course location map, and Figs.12 and 13 show the created driving course and curvature.

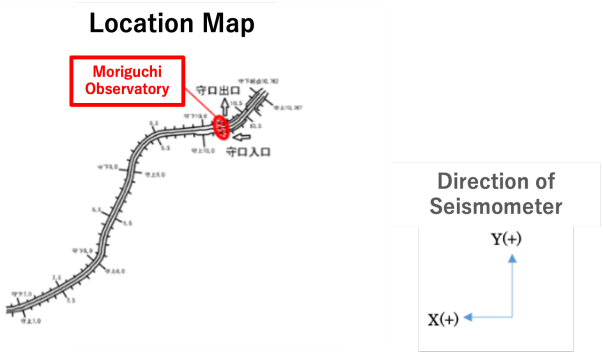

Figure 11. Location map of driving course

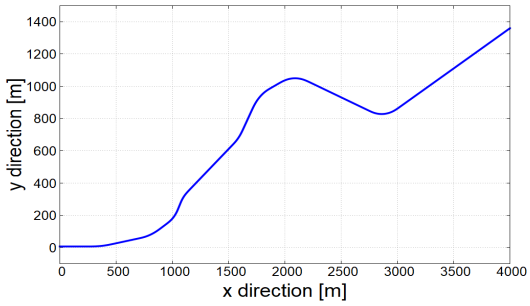

Figure 12. Test Course

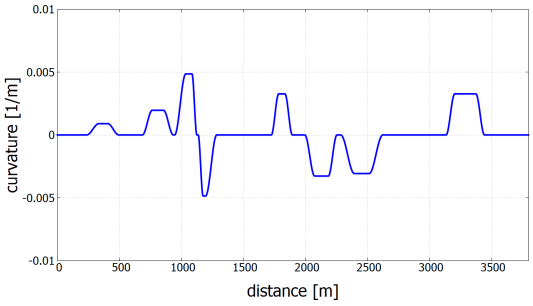

Figure 13. Course Curvature

4.4 Analysis Conditions

As shown in Fig.14, five vehicles are assumed to drive in the same lane, and 100 samples with initial vehicle speed and distance are created for the simulation. The input points of seismic motion are set to be four curved sections of the running course, and the peak of the seismic waveform is set to occur when the leading vehicle of the group passes the midpoint of the arc section of each curve. The seismic input points and the road alignment at each point are shown in Fig.15 and Table 2, respectively.

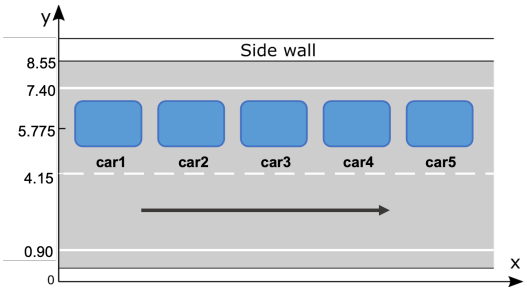

Figure 14. Road Coordinate System

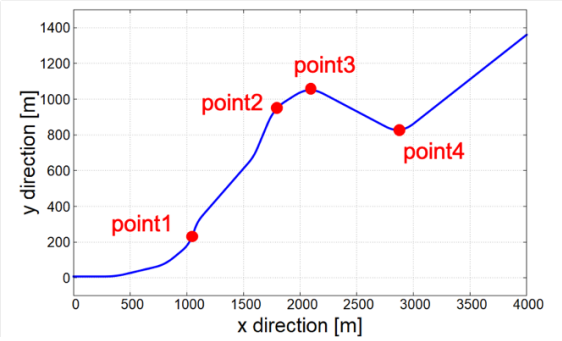

Figure 15. Seismic input point

Table 2. Road Alignment

Number	Transition curve length [m]	Maximum curvature [1/m]
point 1	84.9	4.86×10^{-3}
point 2	73.6	3.27×10^{-3}
point 3	110.8	3.07×10^{-3}
point 4	73.6	3.27×10^{-3}

4.5 Analysis Results

Figs.16 ~ 19 shows an example of one of the 100 analysis patterns under the earthquake excitation. The start time of earthquake motion is indicated by yellow lines in the figure. Table 3 shows the initial conditions of vehicles at the time of data output. For each figures, from left to right, the velocity time history, the time history of the deviation between center of the lane and the vehicle center of gravity, and the distance between vehicles time history are shown.

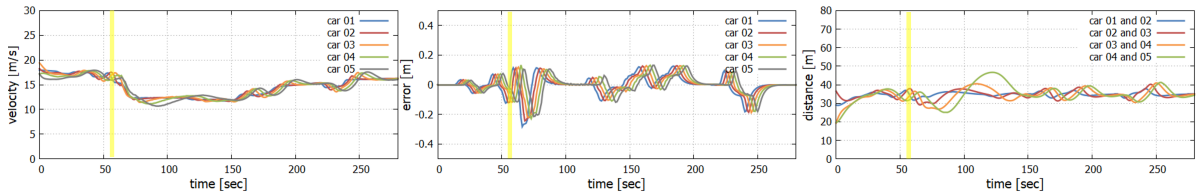

Figure 16. Vehicles behavior time history (point 1)

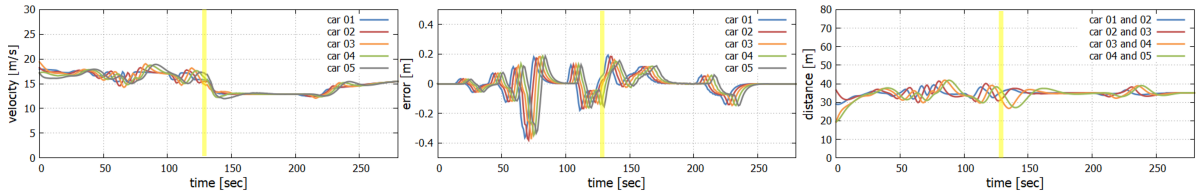

Figure 17. Vehicles behavior time history (point 2)

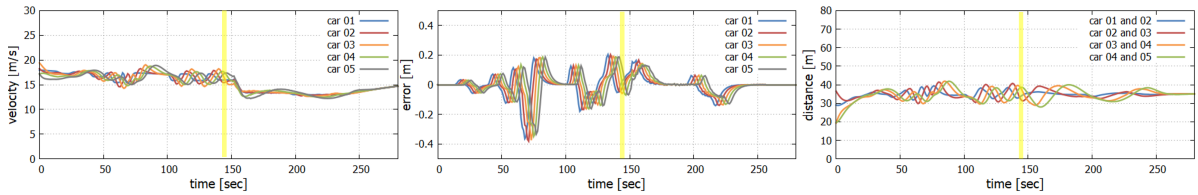

Figure 18. Vehicles behavior time history (point 3)

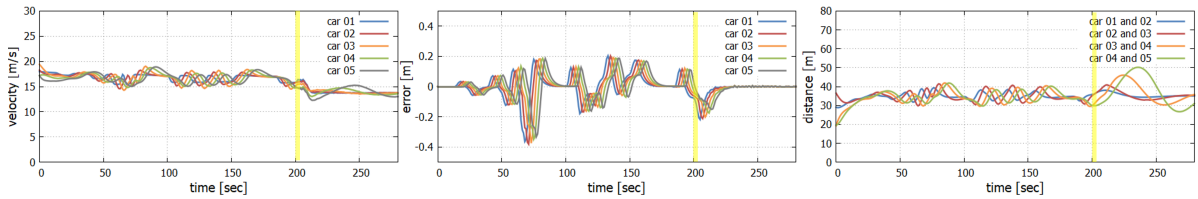

Figure 19. Vehicles behavior time history (point 4)

Table 3. Vehicle Initial Conditions

	Distance from the front vehicle [m]	Initial Speed [m/s]
car1	-	17.1
car2	21.2	17.4
car3	33.2	18.8
car4	27.8	18.1
car5	29.4	18.3

From Figs.16 ~ 19, a maximum lateral deviation is about 0.4[m] at the time of earthquake motion. Moreover, neither lane departure nor collision occurred in all 100 patterns due to the sufficient tracking performance. While accidents have occurred due to excessive braking in previous studies, the results show that, by changing the brake strength, the vehicle is able to maintain a sufficient distance between vehicles while decelerating under the influence of seismic motion. The results of the above analysis trace the fact that no accidents were actually observed on the Moriguchi Line during the 2018 Northern Osaka Prefecture earthquake.

5. CONCLUSION AND DISCUSSION

In this study, the vehicle running model during an earthquake in a straight section is extended to a curved section. The conclusions obtained are as follows.

(1) The braking behavior based on the results of DS experiments, which had been used in previous studies, was converted into a braking behavior based on the results of video analysis. In this model, the vehicle does not decelerate excessively even when an earthquake occurs, and no collision or lane departure occurs on the expressway when the earthquake intensity is about 5 or higher. In fact, no collision accident has been occurred at the points in the 2018 Northern Osaka Prefecture earthquake.

(2) A driving model of vehicles on a curved section of an expressway during an earthquake was developed. In the model, the acceleration/deceleration during curve entry and exit, and the steering wheel operation during the curve running are implemented. The reproducibility of the model was confirmed by comparison with the results of DS experiments. It is expected that by increasing the number of vehicles, a larger scale simulation during an earthquake should be done to evaluate the danger of driving vehicles on expressway.

REFERENCES

Hanshin Expressway Co.Ltd. (2020). "*Regulated speeds on Hanshin Expressway (enlarged image)*", Hanshin Expressway Drivers Site. https://www.hanshin-exp.co.jp/drivers/driver/rule/speed/speed_big.html

Junya Takahashi, Masakoto Yamakado, Shinji Saito (2012). *A Study of Acceleration/Deceleration Model Based on the Time Variation of Road Curvature Ahead*, Transactions of the Society of Automotive Engineers of Japan, Inc. Vol.43, No.1, pp.7~14 (in Japanese)

Kenji Fukunaga, Junji Kiyono, Ryotaro Mabuchi, Seiji Shinohara and Takafumi Ito (2020). *Collisions of Vehicles Running on Highway during an Earthquake*, Proc. of the Journal of Japan association for Earthquake Engineering, Vol.20, No.7, p.7.35-p.7.45

Kenji Fukunaga (2021). *Validation of vehicle running model by video analysis during the 2018 Northern Osaka Prefecture Eathquake*, Master course thesis, Kyoto University (in Japanese)

Murakami, R. (2017). *A study on the safety running of vehicles during an earthquake*, Master course thesis, Kyoto University (in Japanese)

Makoto Yamakado, Masato Abe, Yoshio Kano, Yuu Sato, Yuusuke Tanaka, Junya Takahashi, Kenta Maeda (2019). *Formulation of Trajectory of Vehicle that Accelerates and Decelerates in Coordination with Lateral Motion*, Transactions of the Society of Automotive Engineers of Japan, Inc. Vol.50, No.2, pp.383~389 (in Japanese)

Takahiro Noguchi, Ichiro Kageyama (2016). *Study on Algorithm for Autonomous Vehicle*, Proc. of the 49th Annual Conference of College of Industrial Technology, Nihon University, pp.591~592 (in Japanese)

Transportation laboratory (2016). *Analysis of vehicle behavior during an earthquake by using driving simulator*, Technical Report of Transportation laboratory, Kyoto University

SOFTWARE DEVELOPMENT OF RESCUE ROUTE PLANNING AND SEISMIC RISK ASSESSMENT

Cheng-Tao Yang [1], Wen-Yuan Wu [2], Yi-Chang Chu [3], Ya-Chu Tsao [4]

1. Associate Researcher, National Center for Research on Earthquake Engineering, Taipei, Taiwan, R.O.C.
2. Student, Dept. of Civil Eng., National Taiwan University, Taipei, Taiwan, R.O.C.
3. Graduate Student, Dept. of Civil Eng., National Taiwan University, Taipei, Taiwan, R.O.C.
4. Research Assistant, National Center for Research on Earthquake Engineering, Taipei, Taiwan, R.O.C.

Email: ctyang@narlabs.org.tw[1]

ABSTRACT

Rescue routes play an important role in pre-earthquake preparedness and post-earthquake rescue response. This study aims to develop a standard database and software in the Taiwan region to assist local government in response to earthquake disasters. The establishment of the database mainly considers the rescue of injured and trapped victims a crucial factor and collects basic data, including road conditions, population distribution, building locations, and rescue nodes (i.e., institutions that offer rescue services, for example, hospitals and fire stations) in metropolitan areas. The software provides two major modules, rescue route planning and seismic risk assessment. It is able to provide route planning between rescue nodes and severely-stricken areas. In addition, according to these planned routes, it estimates seismic risk in adjacent areas and blocks under earthquake scenarios; then identifies the rescue route with the least blocking probability after the earthquake.

Keywords: Rescue routes, Software engineering, Seismic risk

INTRODUCTION

Metropolitan areas are the places where population, buildings, and infrastructure (e.g., road networks, fire stations, and hospitals) are densely distributed. Earthquake disaster management in these areas requires considerations of interdependence between lifelines and critical infrastructure to effectively estimate various possible scenarios caused by large-scale earthquakes and avoid chain effect that expands disasters due to damages to some facilities or systems. As a result, the development of this software considers the interrelationship of the rescue of injured and trapped victims, collapsed buildings, and blocked rescue routes.

Over the years, NCREE has continuously offered disaster potential data, earthquake loss estimation, and training programs to disaster prevention departments. Through the experience of interactions with these institutions in recent years, we generalized the need for a more detailed loss risk estimation in three aspects: the identification of critical rescue areas, the recognition of the risk of blocked rescue routes, and the resilience assessment of rescue locations. First, according to the previous earthquake loss estimation tool, the basic evaluation unit is village and grid. However, it doesn't apply to metropolitan areas. Therefore, it is unable to identify areas with high seismic risk and greater demand for earthquake resistance. Second, since the previous tool doesn't integrate the data, including hot zone of casualties, on-street building collapse, and blockage on critical bridges, we are not able to evaluate and improve the rescue routes. Third, it is necessary to assess the residual rescue capacity after earthquakes so that we can determine the impairment loss in hospitals and fire stations.

This study aims to provide solutions to the aforementioned two aspects (i.e., the identification of critical rescue areas and the recognition of the risk of blocked rescue routes). Under the need for rescue preparedness and disaster prevention planning in densely populated metropolitan areas, we established software with two main functions: automatic route planning and blocking probability estimation of the rescue route under scenario earthquake. In this investigation, the Taipei Metro Area served as an instance

to develop the software and database prototype. We cooperated with the fire department of Taipei City government, collected disaster potential data in recent years, utilized the TELES (Yeh 2003) developed by NCREE, and established the database and software. The following sections will introduce requirements analysis, software framework design, and software development status.

REQUIREMENTS ANALYSIS AND DATABASE ENTITY–RELATIONSHIP MODEL

The requirements analysis of this software is based on the feedback of practitioners in disaster prevention departments of local governments in the Taipei Metro Area. According to the requirements, we established a relational database. In this database, locations and seismic properties of all the buildings, road network, population distribution, rescue nodes, and block distribution in the Taipei Metro Area are integrated, as shown in Figure. 1. With the help of local governments, we acquired the updated raw data, including house tax data in 2020, TGOS data in 2019, and the newest lists of rescue nodes and distressed areas.

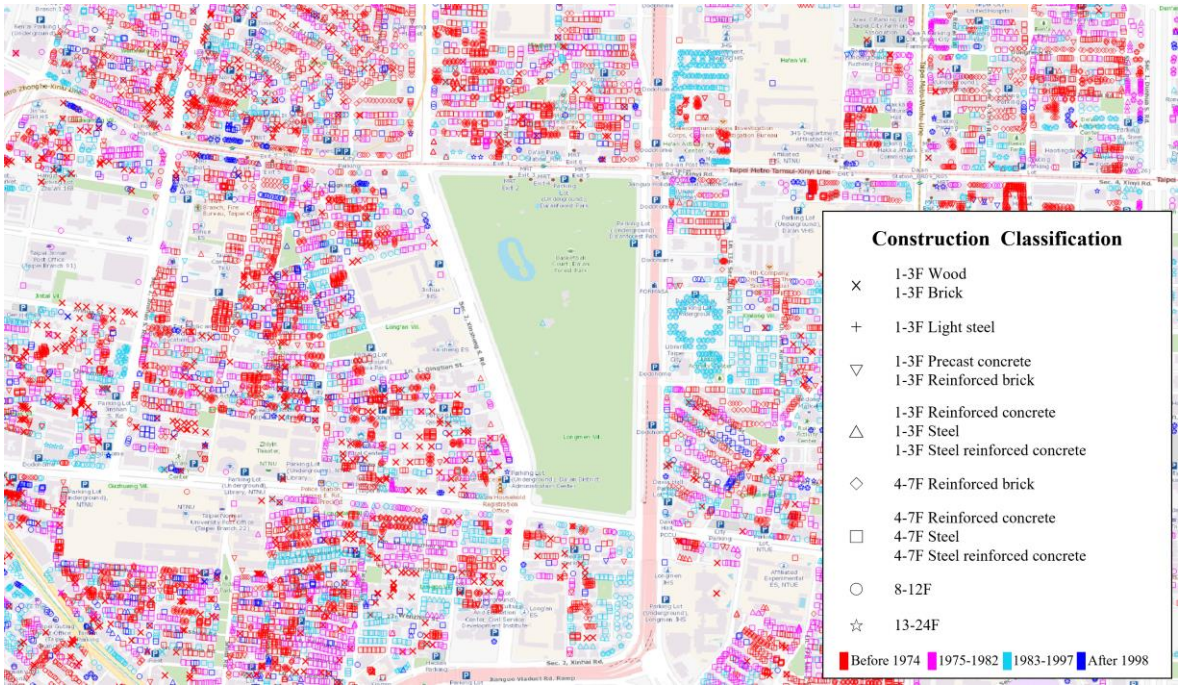

Figure 1. The distribution of building construction classification in the Taipei Metro Area

Since the vast territory in New Taipei City results in complex terrains, the administrative districts are not completely located in urban areas. Some are even in mountainous areas. Consequently, **rescue nodes** and road data in those remote places are unable to update immediately. Furthermore, New Taipei City was just a county before becoming a special municipality. Because of historical factors, the road level here is more complicated and disordered compared to that of Taipei City. For example, the road width in front of some fire stations in New Taipei City is only 4 meters. Hence, we held the workshop of rescue route planning in New Taipei City. During this workshop, requirement analysis and the ER Model were discussed, checked, and revised. In addition, we designed a questionnaire and distributed it to each district department in New Taipei City, each municipal bureau, and various experts through official documents and online forms. At the beginning of the questionnaire, the link and QR Code of the rescue route plan are offered, and the responses are collected through not only true or false but also short answer questions. At last, a total of 44 responses are received, including 34 district officers, 4 municipal bureau personnel, and 6 experts. These responses are beneficial to requirements analysis and ER Model correction as well.

SOFTWARE FRAMEWORK DESIGN

The design of this software is based on QGIS software then develops as an extended Plugin. In the framework for GIS modeling, we integrated the interface, including ER Model, transportation planning model, and rescue route planning. The development of this software mainly consists of two information technologies: relational database and QGIS Plugins. Below will introduce these two technologies in sequence.

1. Relational database

The database adopts SpatiaLite and GeoPackage data format to implement relational data model of disaster prevention information. According to the model, disaster potential data, road network, building distribution, population agglomeration, rescue nodes, and infrastructure data (e.g., bridges) were collected. SpatiaLite is a simple spatial database (henceforth, GeoDB) derived from a number of open-source software. It has three fundamental GIS operation functions. First, it is a SQL Database. Different from other client-server ones, it directly reads a single data and simplifies the installation process of the software. Second, it is able to adopt as an In-Memory Database, which is beneficial to the development of parallel and distributed algorithms. Third, it consists of Virtual Shapefile tables. With the function of virtualization, it is able to deal with relational spatial queries between several Shapefiles without occupying too many executive resources. In sum, compared to commercial software, open-source software is more flexible to adapt to the special needs of developers.

2. QGIS Plugins

QGIS is a free and open-source desktop GIS application that supports viewing, editing, and analyzing geospatial data. Since QGIS supports the integration of SpatiaLite and GeoPackage, its development environment is highly compatible with Geographic Information & Novel Notion Yolk (Yang 2016) developed by us in recent years. In addition, it supports almost all the GIS data, including Shapefiles, CSV files, and MapInfo TAB formats. With this wide range, it is beneficial to process a large amount of GIS data and basic data. With this integration function, we can transform all the data into SpatiaLite formats. Most important of all, compared to other open-source software, the description files of QGIS are widely utilized; therefore, it is easier to obtain related support services.

SOFTWARE DEVELOPMENT STATUS

This software is named ROSA. Since it is designed as QGIS Plugins, we need to execute QGIS software before loading ROSA. As shown in Figure 2, when executing ROSA, a toolbar is displayed. The definitions of each icon are demonstrated in the general table of ROSA in Table 1. To utilize these functions, users can click Plugins and ROSA from the top or just click the icons in the toolbar. Recently, ROSA is still in the prototype stage. The completed functions include layer setting, rescue node management, candidate route management, project management, administrative district management, relief road planning, rescue nodes and routes, rescue route planning and seismic risk assessment, as shown in Figure 3. Although this software is still a prototype program, its analysis result has been provided to Taipei City for reviewing its rescue routes and provided to the New Taipei City Government as a topic for disaster prevention drills. Its feasibility and practicability have been preliminarily verified. In the future, we hope that it can be extended to other cities through more practical applications.

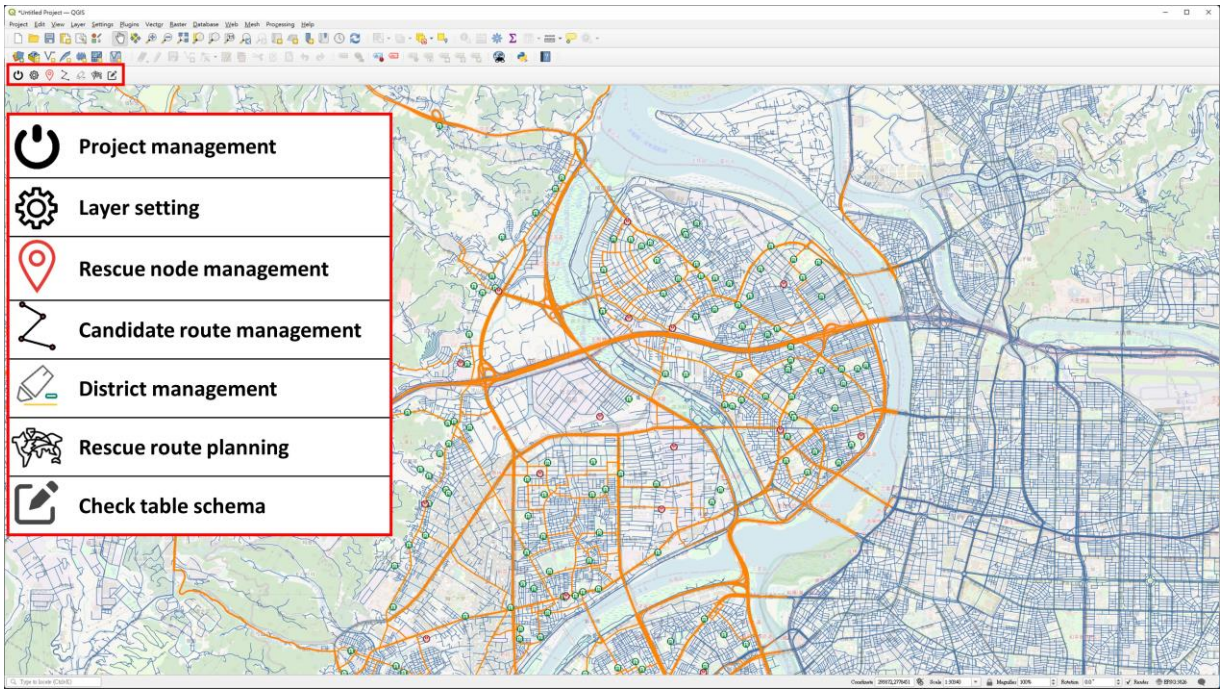

Figure 2. Interface of ROSA

Table 1 Functions and Icons of ROSA

Icon	Function	Description
	Project management	switch all the executing functions in ROSA.
	Layer setting	Set the required layer files and save them together.
	Rescue node management	View, select, and edit POIs (e.g., shelters and fire stations).
	Candidate route management	Set information about road network levels.
	Administrative district management	Set a mask for the area outside the administrative district that you want to highlight.
	Rescue route planning	Rescue route planning between between rescue nodes and severely-stricken areas
	Check table schema	Check the format of input data.

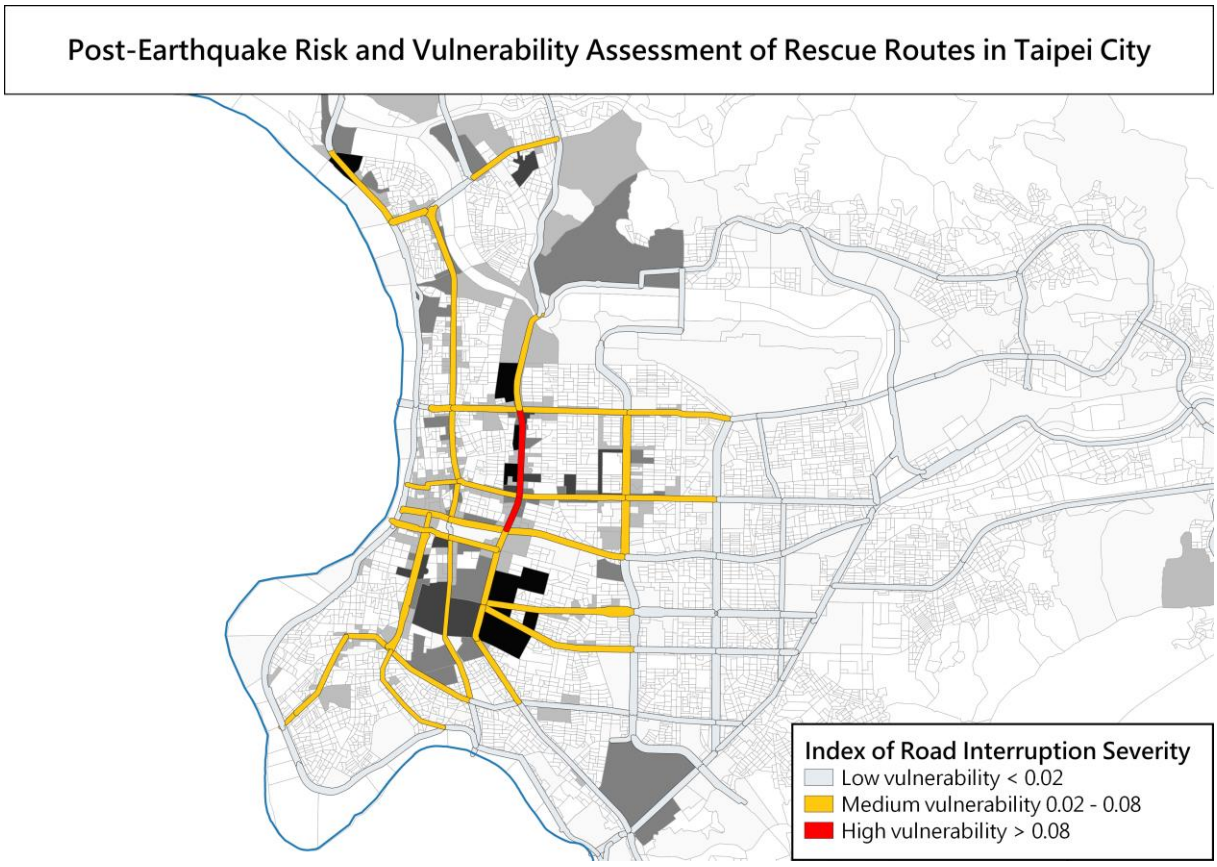

Figure 3. Risk and vulnerability assessment of rescue routes

CONCLUSION

This study introduces our recently developed software, ROSA. It assists local government in rescue route planning and seismic risk assessment. During its establishment, we cooperated with the local governments in the Taipei Metro Area to ensure that its functions meet the needs. Now, the disaster potential data and the analysis results have been offered to the Taipei City government to help estimate the blocking risk of the existing rescue route. Based on these data and results, the local government can further examine the earthquake resistance on not only the high seismic risk buildings adjacent to the rescue route but also the high seismic risk bridges connecting the Taipei Metro Area. In the future, ROSA will help extend the rescue network in the adjacent cities of the Taipei Metro Area, assess the seismic risk of the main road, and assist the local government in establishing relief roads when earthquake hits.

REFERENCES

Yeh, Chin-Hsun, Chin-Hsiung Loh, and Keh-Chyuan Tsai. (2006) "Overview of Taiwan earthquake loss estimation system". *Natural hazards* **37**.1-2: 23-37.

Yang, Cheng-Tao, Yeh, Chin-Hsun, Lin, Chi-Hao. (2016)「Developer's Manual of Geographic Information & Novel Notion Yolk 1st」(in Chinese)Technical Reports (NCREE-16-018)。

CASCADING EFFECTS OF SEISMIC IMPACT ON INTERCONNECTED URBAN INFRASTRUCTURE

Chih-Hao Hsu[1] Min-Cheng Teng[1] and Siao-Syun Ke[3]

1. Associate Researcher Fellow, Earthquake and Man-made Disaster Division, Nation Science and Technology Center for Disaster Reduction, New Taipei City, 23143, Taiwan, R.O.C.
2. Associate Researcher Fellow, Earthquake and Man-made Disaster Division, Nation Science and Technology Center for Disaster Reduction, New Taipei City, 23143, Taiwan, R.O.C.
3. Division Director, Earthquake and Man-made Disaster Division, Nation Science and Technology Center for Disaster Reduction, New Taipei City, 23143, Taiwan,, R.O.C

Email: willie2567@ncdr.nat.gov.tw, jack@ncdr.nat.gov.tw, opbook@ncdr.nat.gov.tw

ABSTRACT

Infrastructure is defined as an aggregation of numerous facilities that constitute the backbone of urban operations. Moderate-to-large earthquakes adversely affect infrastructure, severely impairing most urban functions. Both the water supply system and electronic power system have interdependencies; thus, damage to one system can potentially cause a chain reaction, triggering failures in related and connected systems that then lead to a cascade of disasters. Taiwan is located in the Circum-Pacific seismic zone, and earthquakes frequently occur. Therefore, understanding the effects of moderate-to-large earthquakes on water supply and electronic power systems, as well as how those effects contribute to disaster scenarios in urban areas, is a critical issue for the Taiwanese government. This study aims to consider the characteristics of earthquake disaster management, such as seismic ground shaking and cascading effects, to perform develop a method for assessing potential damage and therefore plan earthquake disaster response. The results of this study may assist the authorities in making effective decisions regarding water supply and electronic power facility disaster and resource management.

Keywords: urban infrastructure, cascading effects, seismic impact chain

INTRODUCTION

Lifelines are essential infrastructure, such as water and electricity supply systems, that are required for normal urban operation. In a seismic event, ground shaking may damage these critical facilities, causing serious disruption to the urban service functionality. Because these events impact social, economic, industrial, and commercial activities, society as a whole might be extensively affected at both large and small scales over varying degrees of time and space. In Taiwan, urban communities are rapidly developing and that growth, in combination with the flourishing technology industry, has led to a gradual increase in the dependence on lifelines. The facilities management ensures that equipment and operation maintenance are performed daily, and maintains an emergency response plan to keep lifelines stably operating. In recent years, significant earthquakes in Taiwan have demonstrated that lifelines in areas which experience a magnitude six earthquakes or higher are often damaged, and thereby indirectly impact various other critical infrastructure (Table 1).

Table 1. Significant earthquake disasters event in Taiwan (2010~2018)

Year	Area	Earthquake Magnitude (M_L)	Focal Depth (K_m)	Direct Impact	Indirect Impact
2010	Jiasian	6.4	22.64	• Power electronic • Water system	• Power outage → Communication base stations

				• Roadway, bridge (*Ke et al.*, 2010; *NCREE*, 2010)	
2013	Nantou	6.5	14.5	• Power electronic • Water system • Roadway, bridge (*CEOC*, 2013; *NCDR*, 2013)	• Power Outage → Railway • Roadway blackout → Scenic area
2016	Meinong	6.6	14.6	• Power electronic • Water system • National gas • Roadway, bridge (*NCDR*, 2016)	• Water system shortage → Medical and care center • Power outage → Technology industry, Communication base station, Traffic signs
2018	Hualein	6.2	10	• Power electronic • Water system • Roadway, bridge (*CEOC*, 2018)	• Power outage → Communication base stations

CASCADING EFFECTS MODEL

Life During a seismic event, ground shaking may cause damage to critical urban facilities that supply electrical power, water, transportation, and other important services. These lifelines are increasingly reliant on each other for varying required functionalities, and are therefore interdependent. These operational interactions significantly increase the likelihood that even minor disruptions in a single facility will lead to a cascade impact. The characteristics are as follows:

- The system dependencies lead to impacts that propagate to other systems
- The combined impacts of the propagated event are of greater consequence than the root impacts
- Multiple stakeholders and/or responders are involved

Hassel et al. (2014) Proposed a conceptual model of indirect disaster impact (Figure 1). The figure shows that during the initiating event, the original system(s) is/are directly impacted (first-order). Once the systems internal equipment/components are damaged, the external chain system is impacted (second-order), or derives other systems (third-order)

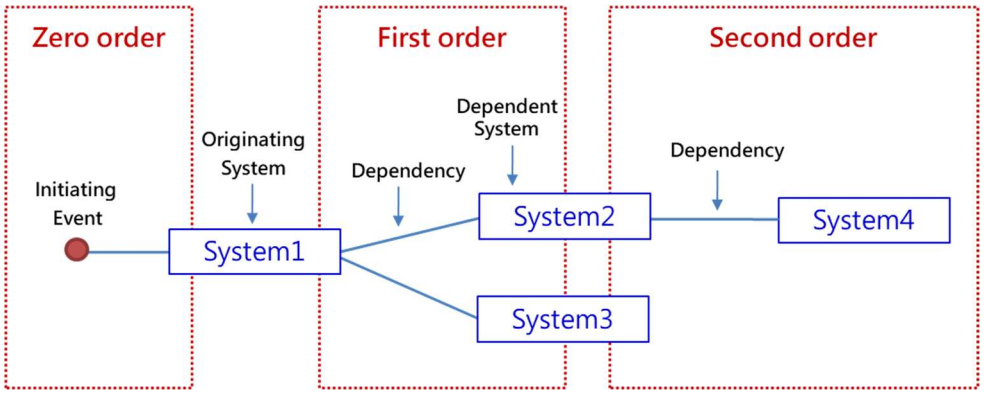

Figure 1. Sample of dependencies between systems (*Hassel et al.,* 2014)

There are many important assets in the lifelines infrastructure that are used to produce and transfer resources. Under normal operating conditions, the facilities depend on external sources to operate. (*Rinaldi et al,.* 2001) proposed that the system relationships can be classified into the following categories: 1) "dependency" where the facility depends on external resources for daily operations, e.g., the substation step-down depends on the power generated at and transferred from the plant power; and 2) "interdependency" where the facilities interdependent on each other's resources to maintain operations, i.e., the power plant needs cool water, but pumping water requires external power. Figure 2 depicts the infrastructure interdependencies of the emergency service system.

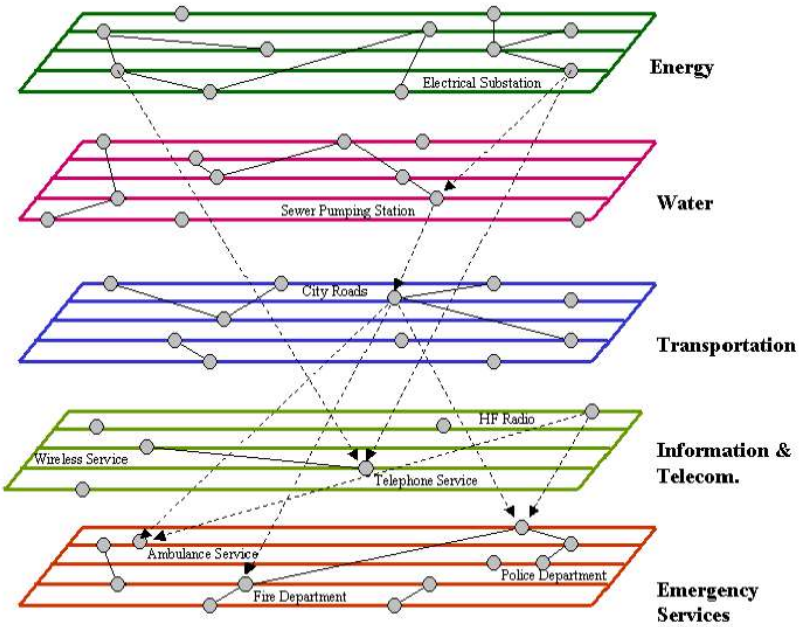

Figure 2. Infrastructure interdependencies (*Dudenhoeffer et al.,* 2006)

FRAMEWORK AND EVALUATION METHOD

A seismic impact chain developed for urban areas (Figure. 3) should consider major factors such as emergency response issues (emergency rescue, rescue supplies delivery, and special space rescue), evacuation shelter issues (homecoming transportation, large crowd evacuation, and resettlement of vulnerable ethnic groups), and continuity management issues (government functional services, critical infrastructure recovery, and business continuity management).As past experience shows that the lifeline infrastructure is susceptible to both direct and indirect damages, we consider both types of effects in this study. the procedure for assessing seismic impacts with the consideration of cascading effects. The procedural steps are as follows:

1. Basic data on lifeline infrastructure facilities, including treatment plants, pumping stations, and pipelines within water systems, were obtained from the Taipei Water Department and Taiwan Water Corporation. The original files were in various formats (e.g., the shapefile shape format).
2. By using the ground–motion attenuation equation and the site effect coefficient, ground motion parameters, such as peak ground acceleration, peak ground velocity, and peak ground displacement, were estimated from the seismic parameters (e.g., epicenter location, focal depth, and earthquake magnitude).
3. The seismic assessment of lifeline systems enables the quantification of the direct damage related to the seismic hazard intensity. The vulnerability functions used, which were probabilistic relationships based on the fragility curves, depended on the input earthquake hazard scenario.
4. According to the results regarding the direct impacts caused by ground shaking, a cascading effects model was developed. Subsequently, the matrix method was used to examine the factor of infrastructure impact. Finally, the topic chart was constructed.

Figure 3. Main factors of a seismic impact chain for emergency response

The procedural of seismic impact evaluation of lifeline infrastructure, the first step is to set the seismic parameters, including the earthquake epicenter, focus depth, and earthquake magnitude. Second, we assess the direct damages caused to the facilities by seismic ground motions and consider the cascading-effects model, which is shown in Figure. 4. The figure shows that when the electricity, water supply, and transportation services (roadways and bridges) are affected by an earthquake and not restored promptly, they indirectly affect other critical infrastructure operations.

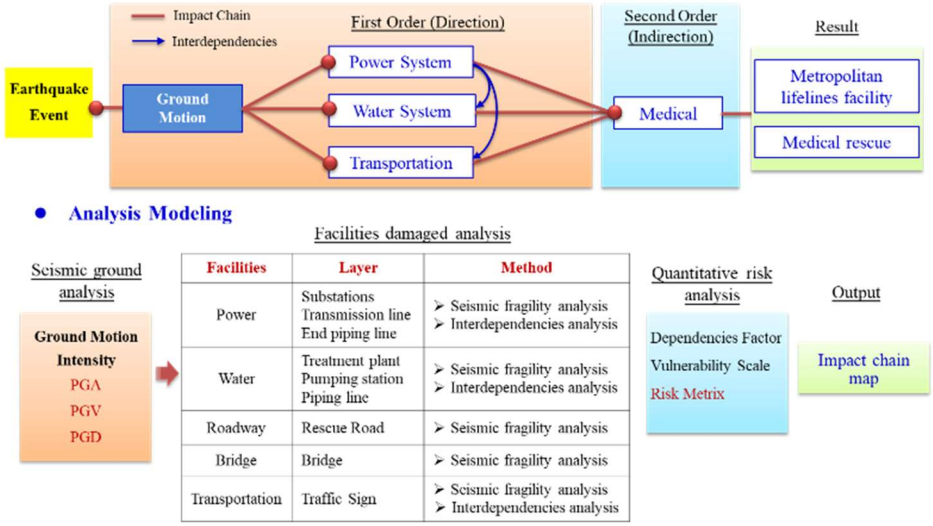

Figure 4. Framework of the model of cascading effects caused by the simulated earthquake

CONCLUSIONS

1. The lifelines are an aggregation of facilities that constitute the backbone of urban operations. For this reason, damage to individual systems can trigger chain effects and cause failures to related and connected systems, which lead to cascading disasters. The operation state and interdependency among lifeline facilities during an earthquake is, therefore, a major concern for disaster reduction of urban areas.
2. In this study, we considered the direct seismic damage and the cascading effects to develop a method for assessing potential damage and therefore plan earthquake disaster response. Therefore, the result of this study will assist the authorities in making intelligent decisions regarding lifeline infrastructure and resource management.

REFERENCES

Ke S.S, Huang M.W, Su W.R, Yeh C.C, Liu, S.Y, Ke, M.C, Wu B.R, Wu T.H, and C.Y Chen (2010). *Summary report of 20100304 Jiasian Earthquake No. 57, National Science and Technology Center for Disaster Reduction E-paper*, Taipei, Taiwan (in Chinese)

NCREE (2010). Reconnaissance report on Jiaxian earthquake in Kaohsiung on March 4, 2010. *Report No. NCREE-10-010*, National Center for Research on Earthquake Engineering, Taipei, Taiwan (in Chinese)

NCDR (2013). *Preliminary information summary of 0602 Nantou Earthquake*, National Science and Technology Center for Disaster Reduction, Taipei, Taiwan (in Chinese)

CEOC (2013). *Convened the Work Report: for 0602 earthquake in Nantou*, Central Emergency Operation Center, Taipei, Taiwan (in Chinese)

NCDR (2016). *0206 earthquake disaster investigates and losses summary in Meinong*, National Science and Technology Center for Disaster Reduction, Taipei, Taiwan (in Chinese).

CEOC (2018). *Convened the Work Report for 0206 Earthquake in Hualien*, Central Emergency Operations Center, Taipei, Taiwan (in Chinese)

Hassel, H., Johansson, J., and A. Cedergren (2014). "Method to study cascading effects," *D2.1.CascEff Project (FP7 EU project 607665).*

Rinaldi, Steven M., James P. Peerenboom, and K.K. Terrence (2001). "Identifying, Understanding, and Analyzing Critical Infrastructure Interdependencies," *IEEE Control Systems Magazine*, **1**, 11-25.

Dudenhoeffer, D. D., Permann, M. R., and M. Manic (2006). "CIMS: a framework for infrastructure interdependency modeling and analysis". Proceedings of the 2006 Winter Simulation Conference, Monterey, California, USA, pp. 478- 485.

(5a) Structural health monitoring and early warning system

RAPID POST-EARTHQUAKE RESPONSE ASSESSMENT OF HIGH-RISE BUILDINGS USING ACCELERATION RESPONSE TIME HISTORIES

S. M. Ziauddin[1] and Pennung Warnitchai[2]

1. Senior Manager (AIT Solutions) and Doctoral Student, Department of Civil & Infrastructure Engineering, Asian Institute of Technology, Bangkok, Thailand.
2. Department Head, Civil and Infrastructure Engineering, Asian Institute of Technology, Bangkok, Thailand.

Email: ziau@ait.ac.th, pennung@ait.ac.th

ABSTRACT

This study investigated two different interpolation techniques, modal approach and filter approach, to estimate motion based responses of non-instrumented floors of a symmetric building structure. Efficacy of interpolation methods are verified by comparing their outputs with simulated Non-Linear Response History Analysis (NLRHA) responses. Obtained results suggests that the filter approach underestimates acceleration responses as it completely filters quasistatic and inertial responses. Moreover, resonant response estimation by the method is unreliable as it assumes that predominant response for all the modes can be obtained from roof floor acceleration. Test results encouraged this study to continue investigation of force based responses using modal approach. All previous studies commonly practiced motion based seismic damage evaluation even though force related seismic demands in comparison to design consideration is a well-recognized seismic damage evaluation approach for engineering community. Estimated force based responses by modal approach confirmed that it is not necessary to instrument a structure with accelerometers at every floor. Adequate number of accelerometers recordings can be utilized to accurately estimate both motion based and force related responses along the height of the structure using suitable interpolation technique.

Keywords: Strong motion instrumentation programs, rapid post-earthquake response assessment, non-linear response history analysis, modal approach for interpolation, filter approach for interpolation, motion based response, force based response.

INTRODUCTION

Strong motion instrumentation programs initiated numerous research studies which paved the way for improved building codes, performance based seismic design and advancement in mathematical model for nine decades. Despite all the evolution in structural design, an earthquake of moderate magnitude still creates agitation amongst the inhabitants. It triggered the need for a new research area namely rapid post-earthquake response assessment to prevent confusion by making early decisions on the severity of damage to a building after an earthquake event. Strong motion instrumentation programs throughout the world responded by installing earthquake recording instruments such as accelerometers in increasing numbers of high-rise buildings expecting engineers to utilize acceleration records for evaluating structural performance during earthquake events through estimation of motion based structural response (e.g., accelerations, displacements, inter-story drifts). However, it is not feasible to install acceleration sensors at each floor of a building structure due to financial constraints. Hence, a number of interpolation theories have developed over the years to estimate acceleration responses of non-instrumented floors (Goel, 2008; Kaya *et. al.*, 2015; Naeim *et al.*, 2004; Sinthumongkhonchai, 2020; Tsuchihashi and Yasuda, 2009). This study examined two approaches, Mode Based Interpolation (MBI) proposed by Goel, 2008 and Mode Shape Based Estimation (MSBE) proposed by Kaya *et. al.*, 2015.

Improvement in computing technology allows engineers to estimate seismic damages of structures using finite element analysis. However, numerical analyses are time consuming, and outputs are dependent on the model assumptions. Hence, motion based response evaluation is commonly practiced by the industry (ANSS, 2005; Çelebi *et al.*, 2004; Goel and Chadwell, 2007; Tsuchihashi and Yasuda,

2009) even though force related responses are well understood by engineers for seismic damage assessment. Therefore, a simple data-driven force based analysis scheme is presented in this study.

THEORETICAL BACKGROUND

Theoretical background of MBI and MSBE are explained in this section followed by theoretical background for estimation of force related responses.

Mode Based Interpolation (MBI)

MBI procedure is proposed by Goel, 2008 based on theory originally developed by Chopra, 2007 that, floor displacements and accelerations can be calculated by the superposition of modal displacements and accelerations. This theory can be presented in mathematical form as shown in Eq. 1.

$$\ddot{\mathbf{u}}(\mathrm{t}) = \boldsymbol{\Phi}\, \ddot{\boldsymbol{q}}(t) \tag{1}$$

Where $\ddot{\mathbf{u}}(\mathrm{t})$ represents time history of relative floor acceleration response. $\boldsymbol{\Phi} = [\boldsymbol{\phi}_{\mathrm{ij}}]$ is normalized mode shape matrix where subscripts i and j represents ith floor and jth mode respectively. Time history of modal acceleration is presented as $\ddot{\boldsymbol{q}}(t) = [\ddot{q}_{\mathrm{j}}(t)]$.

Imagine an eight storied building, and the structure is equipped with accelerometers at five floor levels including ground floor. Therefore, relative acceleration responses of four floor levels such as 8th floor, 6th floor, 4th floor, and 2nd floor can be estimated after an earthquake event. Normalized mode shapes can be obtained from modal analysis of Finite Element Model (FEM). Thus, modal accelerations $\ddot{q}_1(t)\,, \ddot{q}_2(t)\,, \ddot{q}_3(t), \ddot{q}_4(t)$ can be estimated by solution of Eq. 1.

$$\begin{bmatrix} \ddot{\boldsymbol{u}}_8(t) \\ \ddot{\boldsymbol{u}}_7(t) \\ \ddot{\boldsymbol{u}}_6(t) \\ \ddot{\boldsymbol{u}}_5(t) \\ \ddot{\boldsymbol{u}}_4(t) \\ \ddot{\boldsymbol{u}}_3(t) \\ \ddot{\boldsymbol{u}}_2(t) \\ \ddot{\boldsymbol{u}}_1(t) \end{bmatrix} = \begin{bmatrix} \boldsymbol{\phi}_{81} & \boldsymbol{\phi}_{82} & \boldsymbol{\phi}_{83} & \boldsymbol{\phi}_{84} \\ \boldsymbol{\phi}_{71} & \boldsymbol{\phi}_{72} & \boldsymbol{\phi}_{73} & \boldsymbol{\phi}_{74} \\ \boldsymbol{\phi}_{61} & \boldsymbol{\phi}_{62} & \boldsymbol{\phi}_{63} & \boldsymbol{\phi}_{64} \\ \boldsymbol{\phi}_{51} & \boldsymbol{\phi}_{52} & \boldsymbol{\phi}_{53} & \boldsymbol{\phi}_{54} \\ \boldsymbol{\phi}_{41} & \boldsymbol{\phi}_{42} & \boldsymbol{\phi}_{43} & \boldsymbol{\phi}_{44} \\ \boldsymbol{\phi}_{31} & \boldsymbol{\phi}_{32} & \boldsymbol{\phi}_{33} & \boldsymbol{\phi}_{34} \\ \boldsymbol{\phi}_{21} & \boldsymbol{\phi}_{22} & \boldsymbol{\phi}_{23} & \boldsymbol{\phi}_{24} \\ \boldsymbol{\phi}_{11} & \boldsymbol{\phi}_{12} & \boldsymbol{\phi}_{13} & \boldsymbol{\phi}_{14} \end{bmatrix} \begin{bmatrix} \ddot{q}_1(t) \\ \ddot{q}_2(t) \\ \ddot{q}_3(t) \\ \ddot{q}_4(t) \end{bmatrix} \tag{2}$$

Thereafter, Eq. 1 can be presented as Eq. 2 where all the parameters at right hand side of the equation are known. Normalized mode shapes along the height of the structure are obtained from modal analysis of FEM, modal accelerations are calculated using Eq. 1. Therefore, relative acceleration responses at the non-instrumented floors such as 7th floor, 5th floor, 3rd floor, and 1st floor can be estimate using Eq. 2. Estimated acceleration responses are double integrated to obtain displacement responses and inter-story drift responses are calculated from story displacement responses.

Mode Shape Based Estimation (MSBE)

Theoretical background of MBI approach suggests that accuracy of the method is dependent on number of instrumented floors. Thus, hunt for better method brings this study to filter approach proposed by Kaya *et. al.*, 2015 and named as MSBE. This method requires acceleration data of only three floor locations: ground acceleration, roof acceleration and acceleration of second floor. From Fast Fourier Transformation (FFT) of the absolute acceleration of roof and second floor, Transfer Ratio (TR) is obtained by using Eq. 3.

$$\mathrm{TR} = \frac{\mathrm{FFT}\,\{\ddot{\boldsymbol{A}}_{\mathrm{Roof}}(\mathrm{t})\}}{\mathrm{FFT}\,\{\ddot{\boldsymbol{A}}_{\mathrm{2nd\ Floor}}(\mathrm{t})\}} \tag{3}$$

TR is used to identify natural frequency clearly where each spike in TR plot represents one natural frequency. Fig. 1 showing distinguishable natural frequency of first 10 modes obtained through TR. Upon obtaining TR, band of frequency are defined around modal frequency where lower cutoff frequency is the frequency when TR started to increase, and upper cutoff frequency is the frequency when TR is minimum for each mode. Thereafter, Narrow bi-directional band-pass Butterworth filters around band of each identified frequencies are applied to relative acceleration response of roof floor to obtain modal accelerations. Even though the methodology of computing modal acceleration responses is different, but MBI and MSBE shares the same second step of calculating floor acceleration responses. Thus, Eq. 1 can be used to estimate acceleration time histories at non-instrumented floors.

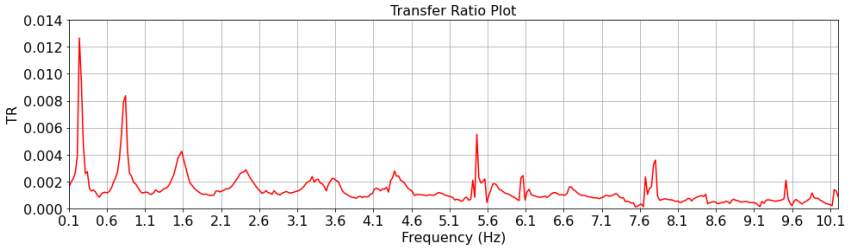

Figure 1: TR of roof acceleration with respect to second floor acceleration for Y direction.

Estimation of force related responses

Force related responses are obtained in this study by solution of equation of motion as shown in Eq. 4.

$$\mathbf{M\ddot{u}}(t) + \mathbf{C\dot{u}}(t) + \mathbf{F}(t) = -\mathbf{M}\boldsymbol{l}\,\ddot{u}_g(t) \quad (4)$$

$$\mathbf{M\ddot{u}}(t) = \mathbf{M}\,\boldsymbol{\Phi}\,\ddot{\boldsymbol{q}}(t) \quad (5)$$

$$\mathbf{C\dot{u}}(t) = 2\,\boldsymbol{\zeta}\,\mathbf{M}\,\boldsymbol{\omega}\,\boldsymbol{\Phi}\,\dot{\boldsymbol{q}}(t) \quad (6)$$

Where $\mathbf{M\ddot{u}}(t)$ represents inertial force, $\mathbf{C\dot{u}}(t)$ stands for damping force and $\mathbf{M}\boldsymbol{l}\,\ddot{u}_g(t)$ is external force coming from ground acceleration. $\boldsymbol{l}$ is the influence vector of which every element is equal to unity. Floor acceleration responses $\mathbf{\ddot{u}}(t)$ can be estimated by using modal approach or filter approach. Modal velocity responses $\dot{\boldsymbol{q}}(t)$ are calculated through integration of modal acceleration responses $\ddot{\boldsymbol{q}}(t)$. Mass matrix of the structure $\mathbf{M}$ is obtained from Finite Element Model (FEM). Ground acceleration $\ddot{u}_g(t)$ can be retrieved from installed accelerometer at ground floor level. Damping force $\mathbf{C\dot{u}}(t)$ is computed using Eq. 6 where $\boldsymbol{\zeta}$ is matrix of modal damping ratio assumed to be 2.5% for all the modes and $\boldsymbol{\omega}$ is circular natural frequency matrix extracted from modal analysis of FEM. Thus, resisting force $\mathbf{F}(t)$ can be calculated. Thereafter, story shear force $\boldsymbol{V}_k(t)$ and story overturning moment $\boldsymbol{M}_k(t)$ demands of k^{th} floor are estimated using Eqs. 7 and 8 respectively where $\boldsymbol{F}_i(t)$ is resisting force time history of i^{th} floor and N is total number of floors.

$$\boldsymbol{V}_k(t) = \sum_{i=k}^{N} \boldsymbol{F}_i(t) \quad (7)$$

$$\boldsymbol{M}_k(t) = \sum_{i=k}^{N} (h_i - h_k)\boldsymbol{F}_i(t) \quad (8)$$

CASE STUDY BUILDING

Case study building chosen for this study is a forty storied 120 meters tall residential building structure. The building has a width of 49 meters in X direction and 26.3 meters in Y direction. Gravity loads are resisted by 175mm thick two-way slabs supported by concrete girders and columns. Lateral forces are mainly resisted by the reinforced concrete shear walls and moment-resisting concrete frames. Detailed structural drawings of the case study building were used to prepare nonlinear FEM utilizing commercial software Perform 3D. Two sets of ground accelerations are applied to FEM in both X and Y directions to conduct NLRHA. Applied ground accelerations were recorded during Loma Prieta

earthquake in 1989 from station at Saratoga-aloha Avenue, USA. Peak Ground Acceleration (PGA) for first set of ground motions is 0.5g in both directions. As PGA of 0.5g is very much near to Maximum Considered Earthquake (MCE) for many regions (Ishiyama, 2008) and a structure is expected to exhibit inelastic response subjected to these earthquakes, therefore, a second set of ground accelerations with PGA of 0.05g is applied to FEM where amplitude is scaled down by tenfold.

RESULTS AND DISCUSSIONS

NLRHA responses are used as a benchmark in this study because of the global acceptance of this meticulous analysis procedure (Goel, 2008). Thus, accuracy of modal and filter approaches are verified by comparing the outcomes with simulated NLRHA responses.

Estimation of acceleration responses using modal approach

Implementation of modal approach started with the assumption that the case study building is equipped with accelerometers at 11 floors, positioned at center of geometry of the structure, uniformly placed from ground floor to roof deck. Ground acceleration and acceleration of 10 other floors are recorded during an earthquake event. Therefore, acceleration of 10 modes in both X and Y direction can be computed using Eq. 1. Computed modal accelerations are utilized in second step as an input of extended Eq. 1 to calculate relative floor accelerations along the height of the structure as depicted in Fig. 2. Results suggests that relative floor acceleration responses can be accurately estimated by using 10 modes or 11 instrumented floors acceleration data with error of around 8% calculated by Eq. 9 where ε_i is error function, $\mathbf{r}$ (t) stands for recorded and $\mathbf{c}$ (t) stands for estimated responses. Moreover, time history of relative acceleration responses of 35th floor and 21st floor as presented in Fig. 2 proves that, not only envelope responses, MBI with 11 instrumented floors acceleration data can accurately estimate acceleration response time history of non-instrumented floors.

$$\varepsilon_i = \sqrt{\left(\frac{\sum_{t=1}^{A}\{\mathbf{r}(t) - \mathbf{c}(t)\}^2}{\sum_{t=1}^{A}\{\mathbf{r}(t)\}^2}\right)} \tag{9}$$

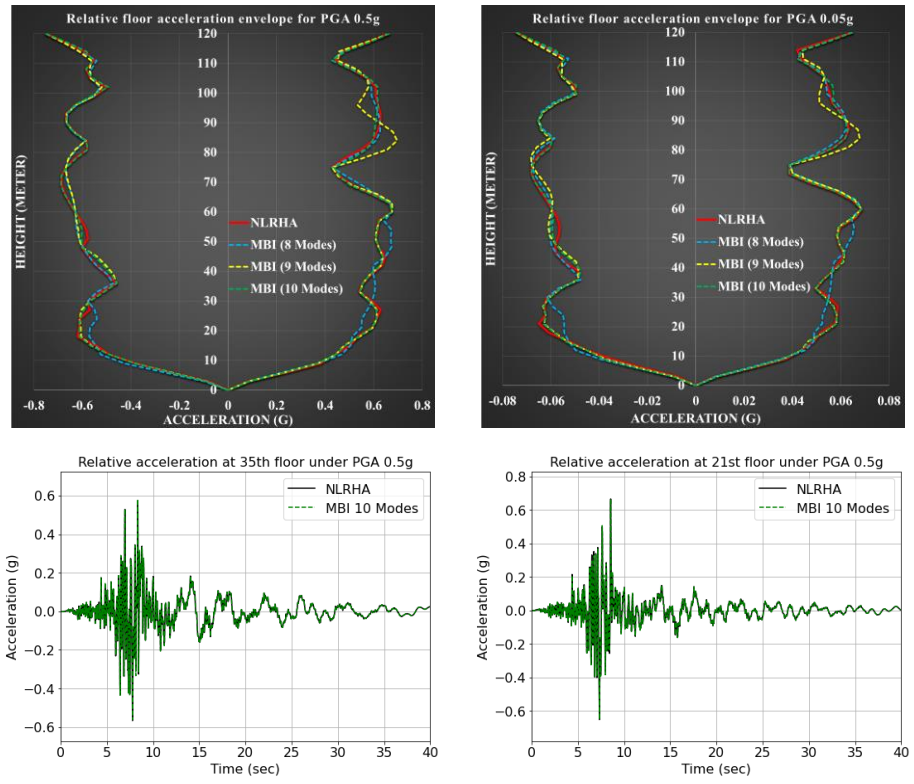

Figure 2: Estimated acceleration responses by MBI method compared to NLRHA.

It is understood that not all building owners can afford to have accelerometers installed in 11 floors. Therefore, optimum number of instrumented floors is identified in this study as demonstrated in Fig. 2. It is notable from the results that accuracy of acceleration estimation is increasing with the increase of considered modes. Lastly, a second set of ground motions with PGA of 0.05g is applied in FEM for NLRHA to observe contrast of responses compared to PGA 0.5g outcomes. Envelope results show that contribution of higher modes is still critical in estimation of acceleration responses.

Estimation of acceleration responses using filter approach

In filter approach, narrow bi-directional band-pass Butterworth filters are applied to relative acceleration response of roof floor to obtain modal accelerations. Fig. 3 showing obtained modal acceleration of first mode compared with the outcome of modal approach. It is visible from result that high frequency contents of the time history are completely filtered by MSBE. Peak and time history of relative acceleration responses by MSBE method are shown in Fig. 4. Significant deviation of responses compared to NLRHA outcomes increases curiosity to identify shortcomings of this approach. Investigation started with Power Spectral Density (PSD) of 21st floor's relative acceleration responses. It can be observed from Fig. 4 that MSBE or the filter approach completely filters high frequency portions of acceleration response and underestimated the response from 4 to 5 Hz frequency. Same underestimation is observed around 1 Hz frequency as well. Fig. 5 is showing spectrum of 6th mode acceleration. It is apparent that modal acceleration between 4 to 5 Hz is underestimated by filter approach because the method assumes that predominant response for all the modes can be obtained from roof floor acceleration. It turns out, roof floor acceleration does not contain predominant response of all the modes. It can be noticed from Fig. 5 that at some frequencies, such as around 1 Hz and 5 Hz frequencies, relative acceleration of 21st floor is higher than roof floors acceleration. Moreover, PSD of 5th and 7th mode acceleration in Fig. 5 showing that filter approach only retains resonant responses. It completely filters quasistatic and inertial responses. For 5th mode, inertial response after resonance and for 7th mode quasistatic response before resonance is completely filtered. Drawbacks of filter approach as demonstrated in this study was not identified in previous study (Kaya *et. al.*, 2015) because instead of directly comparing estimated outputs from MSBE approach with recorded acceleration, authors decided to filter acceleration records to discard noise.

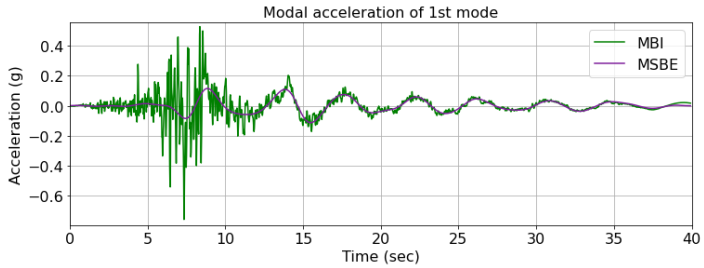

Figure 3: Estimated modal acceleration of first mode by MSBE method compared to MBI.

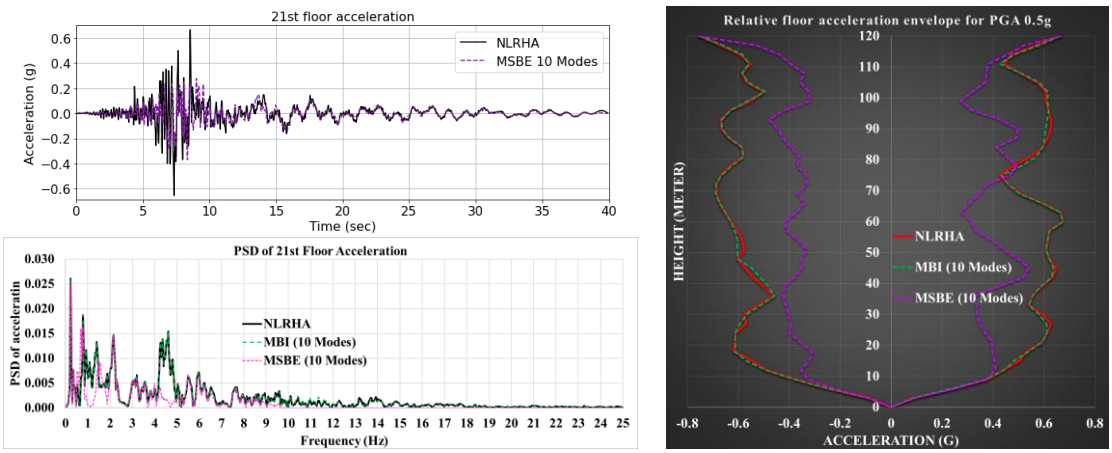

Figure 4: Estimated relative floor acceleration responses by MSBE and MBI compared to NLRHA.

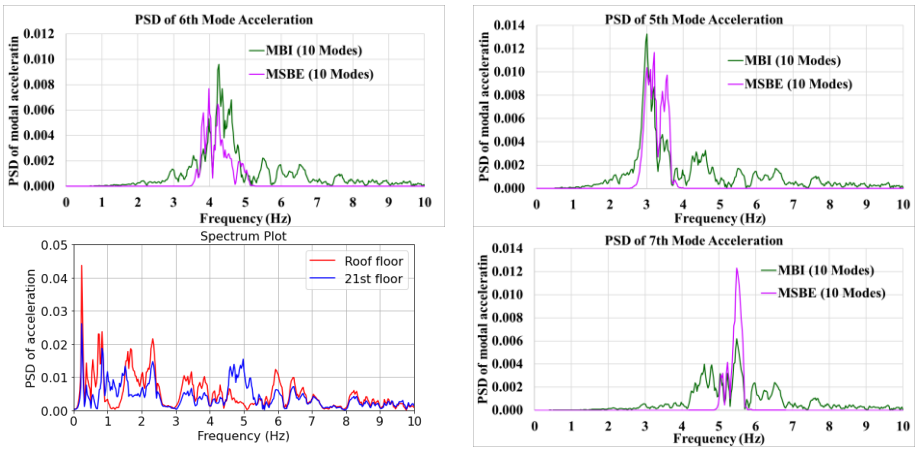

Figure 5: PSD of acceleration responses obtained using MSBE and MBI approaches.

Estimation of displacement responses

Due to its shortcomings, filter approach is discontinued from this section. Acceleration responses estimated by modal approach are double integrated to obtain displacement response. A Python script is written which performs recurrent cubic polynomial curve fitting and subtracts cumulative error created by double integration process. Results in Fig. 6 depicts that, irrespective of ground motions amplitude, 3 modes or installation of 4 accelerometers is enough to accurately estimate displacement response at non-instrumented floors.

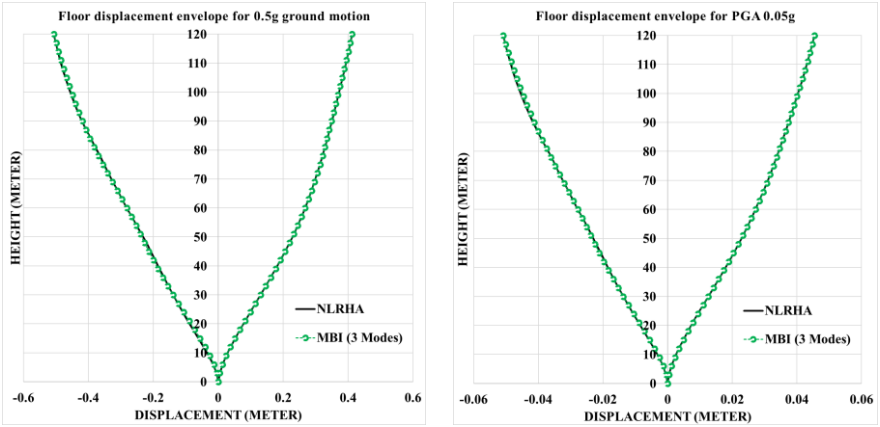

Figure 6: Estimated displacement responses by MBI method compared to NLRHA.

Estimation of inter-story drift responses

Inter-story drift responses are calculated from story displacement responses using Eq. 10. It is noticed that irrespective of ground motions amplitude, 6 modes or installation of 7 accelerometers is enough to accurately estimate inter-story drift responses along the height of the structure as shown in Fig. 7.

$$\boldsymbol{d}_i(t) = \frac{\boldsymbol{u}_i(t) - \boldsymbol{u}_{i-1}(t)}{h_i - h_{i-1}} \tag{10}$$

Estimation of force related responses

Estimation of force related responses started with calculation of resisting force $\mathbf{F}(t)$ using Eq. 4. Estimated resisting force time history of 21st floor is compared to NLRHA outcomes, good agreement between the results is displayed in Fig. 8. In estimation of resisting force, acceleration responses were calculated by MBI using contribution of 8 modes. Velocity responses are estimated by integrating acceleration responses. Envelope of story shear force and overturning moment can be estimated from

resisting force using Eqs. 7 and 8 respectively. Installation of accelerometers at 9 floor levels found to be adequate for estimation of story shear and overturning moment responses as depicted in Fig. 9.

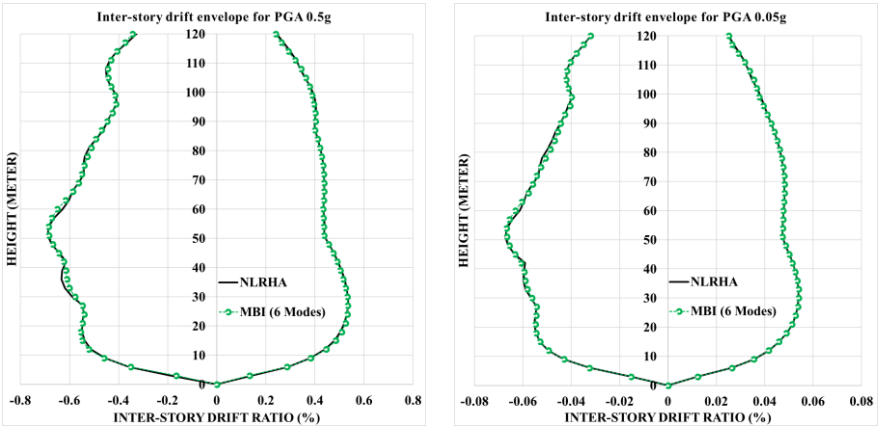

Figure 7: Estimated inter-story drift responses by MBI method compared to NLRHA.

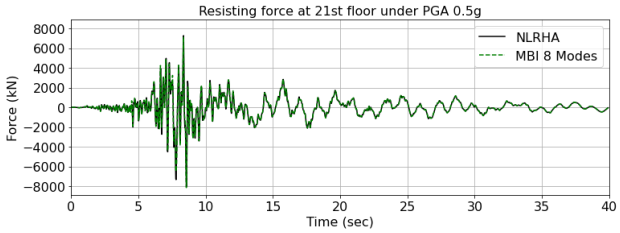

Figure 8: Estimated resisting force time histories by MBI method compared to NLRHA.

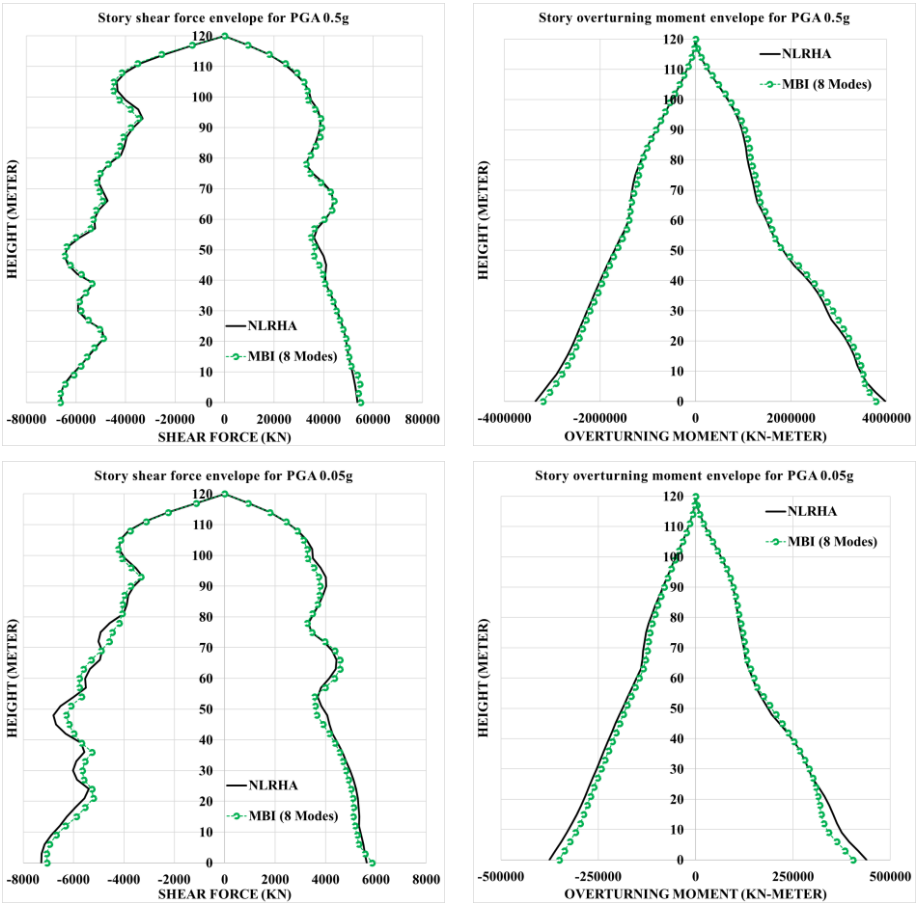

Figure 9: Estimated force related global responses by MBI method compared to NLRHA.

CONCLUSIONS

Motion and force based responses are estimated in this study using acceleration response time histories generated by NLRHA of a detailed numerical model of case study building to highlight limitations of two different interpolation techniques. It is observed from results that filter approach underestimates acceleration response because it completely filters quasistatic and inertial responses. Resonant response estimation by the method is also unreliable as it assumes that predominant response for all the modes can be obtained from roof floor acceleration. However, it is observed that instrumenting a structure with accelerometers at every floor is not necessary, adequate number of accelerometers recordings can be utilized to accurately estimate both motion and force related responses along the height of the structure using suitable interpolation technique such as modal approach. Contribution of higher modes is found to be critical in estimation of acceleration and force related responses irrespective of ground motions amplitude. In contrast, contribution from fewer mode is adequate to accurately estimate displacement and inter-story drift responses. Hence, inter-story drift based damage detection is mostly practiced in industry, even though force based global responses can be estimated by instrumenting two additional floors. It is worth mentioning that required floor acceleration data was generated by NLRHA to avoid on-site measurement errors so that the study can focus only on the accuracy of interpolation methods. Moreover, this study was limited to global responses. Acquiring local responses and analysis of asymmetric structures are future scopes of this study.

REFERENCES

ANSS (2005). *Guideline for ANSS Seismic Monitoring of Engineered Civil Systems – Version 01*, U.S. Geological Survey open-file report 2005-1039.

Çelebi, M., Sanli A., Sinclair M., Gallant S., Radulescu D. (2004). "Real-time seismic monitoring needs of a building owner and the solution - a cooperative effort," *In: Proceedings of 13th World Conference on Earthquake Engineering, Vancouver, Canada*, 333-346.

Chopra, A. K. (2007). *Dynamics of structures: theory and applications to earthquake engineering*, Prentice-Hall, Inc., NJ.

Goel, R. K. (2008). "Mode-based procedure to interpolate strong motion records of instrumented buildings," *ISET Journal of Earthquake Technology*, **45**(3-4) 97–113.

Goel, R. K., Chadwell C. (2007). *Evaluation of current nonlinear static procedures for concrete buildings using recorded strong-motion data*, California Geological Survey, Sacramento.

Ishiyama, Y. (2008). *Seismic codes and structural dynamics (in Japanese)*, Sanwa-shoseki, Osaka.

Kaya, Y., S. Karakalpak, E. Safak (2015). "System identification and model calibration of multistory buildings through estimation of vibration time histories at non-instrumented floors," *Bull Earthquake Eng* **13**, 3301–3323.

Naeim, F., H. Lee, H. Bhatia, S. Hagie, K. Skliros (2004). "CSMIP Instrumented Building Response Analysis and 3-D Visualization System (CSMIP-3DV)," *In: Proceedings of SMIP04 Seminar on Utilization of Strong-Motion Data, Sacramento, USA*, 83-102.

Sinthumongkhonchai, C. (2020). Evaluation of seismic damage of tall buildings from acceleration response time histories by a modal decomposition approach, *Master Thesis*, Asian Institute of Technology, Bangkok.

Tsuchihashi, T., M. Yasuda (2009). "Rapid diagnosis systems using accelerometers in seismic damage of tall buildings," *International journal of high-rise buildings*, **6(**3), 207-216.

DATA ANOMALY DETECTION AND CLASSIFICATION WITH STATISTICS AND MACHINE LEARNING TECHNIQUES

Shieh-Kung Huang[1*], Tian-Xun Lin[2] and Jau-Yu Chou[3]
1. Assistant Professor, Department of Civil Engineering, National Chung-Hsing University, Taiwan, R.O.C.
2. Graduate Student, Department of Civil Engineering, National Chung-Hsing University, Taiwan, R.O.C.
3. Ph. D., Department of Civil Engineering, National Taiwan University, Taiwan, Taiwan, R.O.C.
Email: skhuang@nchu.edu.tw

ABSTRACT

Structural health monitoring (SHM) and structural integrity management (SIM) are emerging recently. To continuously track the condition and constantly detect early deterioration of the infrastructure, huge amounts of data are produced and abnormal measurement is inevitable. The corrupted data can produce a lot of problems and, generally, they are examined and classified by humans. In this study, the detection and classification are replaced by the techniques of machine learning (ML) and improved by using statistical information. The neural networks based on 1-dimensional and 2-dimensional data are studied via a field dataset collected from a long-span cable-stayed bridge. The results show that both models can detect and classify the data anomalies and the usage depends on the assigned application and the trade-off between computation and performance.

Keywords: data anomaly, sensor faults, machine learning, deep learning, structural health monitoring

INTRODUCTION

Smart cities have been attracting attention as an innovative paradigm to realize sustainable construction and maintenance in a high-tech aspect. As one of the most important technologies, structural health monitoring (SHM) and structural integrity management (SIM) serve as a key to continuously track the condition and constantly detect early deterioration of the infrastructure, especially for large-scale structures, such as buildings, bridges, dams, and tunnels (Karbhari and Ansari, 2009).

Huge amounts of data are produced during long-term monitoring; in the meantime, harsh environments, damaged components, or calibration errors decrease the performance of sensors and corrupt the measurement from civil structures (Yi *et al.*, 2017). The abnormal measurement can significantly misjudge the structural conditions via SHM or SIM applications. Obviously, the corrupted data can make distortion while signal processing, inaccuracy while system identification, and falseness while damage detection.

Sensor data anomalies (e.g., sensor faults) are generally examined and classified in accordance with the features of the time history measurement data. So far, detecting and classifying the anomaly data is always done by humans. The task is laborious and tedious and not to mention that all humans make mistakes. Therefore, developing efficient techniques to autonomously detect and classify different types of anomalies are essential to reliable SHM or SIM applications.

For data anomaly detection and classification, conventional physics-based strategies can be categorized as model-based methods and model-free methods. Recently, data-driven methods leveraging machine learning (ML) have been exploited to handle the task directly. In general, data-driven methods can achieve high precision compared to physics-based methods, but nevertheless, typical challenges of data-driven methods include the requirement of extensive datasets for training and difficulties to achieve high accuracy for all anomalies (Chou *et al.*, 2022). In this study, taking the advantage of statistics, the accuracy of data anomaly detection and classification can be improved. To do so, a field dataset collected from a long-span cable-stayed bridge is used to explore the possibility of detecting and classifying data anomalies via the techniques of ML. Furthermore, the neural networks based on 1-dimensional and 2-dimensional data are sequentially studied, the classification results are compared, and the performance is summarized.

MONITORING DATASET AND DATA ANOMALIES

The quality of measurement and monitoring data is essential to SHM and SIM. However, abnormal measurement sometimes happens, and detecting the anomaly data is laborious and tedious. In this study, a field dataset is used and six data anomalies are defined to explore the possibility of data anomaly detection and classification using the techniques of ML.

Field Dataset of Long-span Cable-stayed Bridge

The field dataset used in this study is acceleration responses collected from a long-span cable-stayed bridge in China. The bridge has a main span of 1,088 meters, two side spans of 300 meters each, and two towers of 306 meters in height. The acceleration responses are measured from accelerometers and the locations of the accelerometers are illustrated in **Fig. 1** (Tang *et al.*, 2019) The total number of channels is 38, including 16 biaxial accelerometers on the deck and the top of the towers, and 2 triaxial accelerometers at the bottom of the towers. The dataset is a full month measurement (744 hours) in January 2012 with a sampling rate of 20 Hz.

The data in each hour and channel are manually marked by 7 different labels, including *normal data* and 6 types of data anomalies. The data anomalies include *missing*, *minor*, *outlier*, *square*, *trend*, and *drift* and **Fig. 2** shows the 7 different labels in terms of time history responses. These labeled data are provided by the 1st international project competition for structural health monitoring (Bao *et al.*, 2021). Admittedly, the distribution of the labels is imbalanced because most of the monitoring data is expected to be *normal data*. **Fig. 3** exhibits the number and the distribution of 7 different labels and *normal data* accounts for almost half (48%) of the dataset; on the other hand, *outlier* possess less than 2% of the dataset (only 527 hour-channel). The imbalanced distribution gives ML a challenge during classification and the difficulty is studied hereinafter (Chawla, 2009).

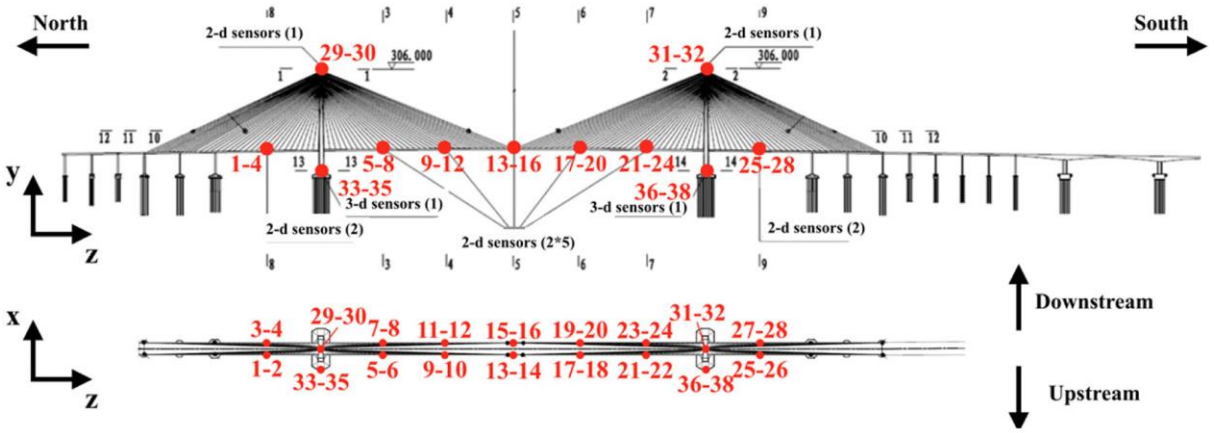

Figure 1. Illustration of the long-span cable-stayed bridge and the configurations of the accelerometers (Tang *et al.*, 2019).

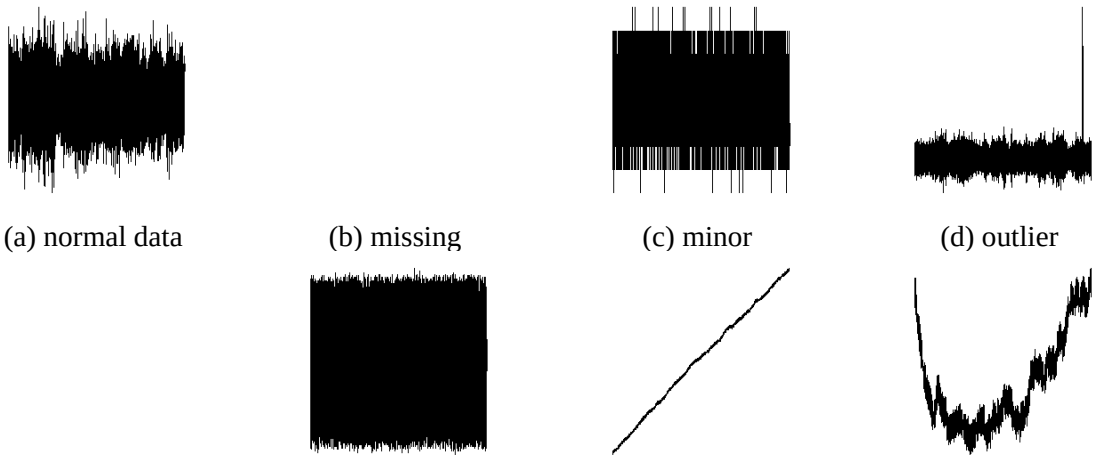

(a) normal data (b) missing (c) minor (d) outlier

(e) square (f) trend (g) drift

Figure 2. Types of labels and the typical responses in terms of time history.

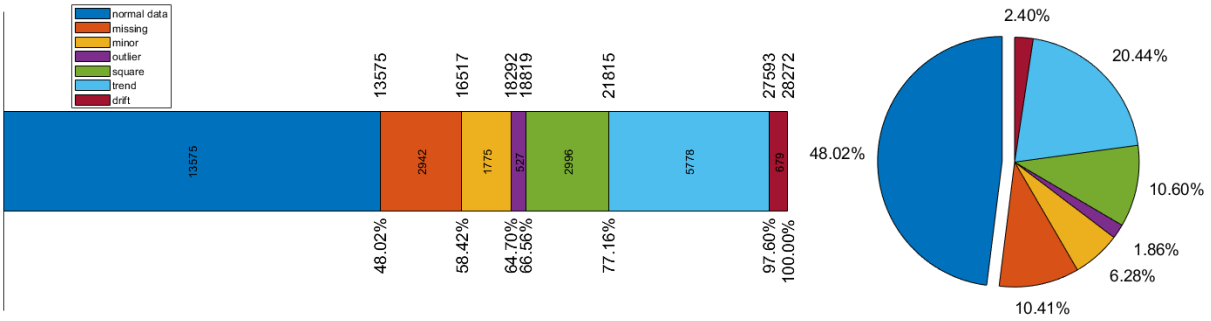

Figure 3. Number and the distribution of different labels.

MACHINE LEARNING FOR DETECTION AND CLASSIFICATION

To classify the six anomalies and, furthermore, detect the anomaly data beforehand, the techniques of ML are exploited in this study. Neural networks based on 1-dimensional and 2-dimensional data are sequentially studied for the task of data anomaly detection and classification. Instead of using time-domain data only, the proposed models use statistics to improve the performance, especially when differentiating some anomalies.

Neural Networks based on 1-dimensional Data - Pattern Recognition Network

The first model is a typical pattern recognition network, which is a multi-layer feedforward (MLF) network that can be trained to differentiate inputs by target labels. In this study, several statistics parameters, including the probability distributions (histograms), arithmetic means, ranges, standard deviations, quartiles, and standard scores (z-scores), are exploited as inputs. Considering the similarity between probability distributions and standard scores, only the difference between the maximum and minimum standard scores is used, as

$$z_{\text{diff}} = z_{\max} - z_{\min} = \frac{x_{\max} - x_{\min}}{\sigma} \tag{1}$$

where z is the standard scores, x is the measured data, and σ is the standard deviation. Through the range rule of thumb, z_{diff} can represent the type of distribution, for example, the range is about four times the standard deviation for normal distribution (Ramirez and Cox, 2012). To be efficient, the network is comprised sequentially by an input layer, two to four hidden layers, and an output layer. All these layers are fully connected layers. The hyperbolic tangent is selected as the activation function except for the output layer; the layer activated by the softmax activation function. The cross-entropy is chosen to measure the training performance because it's a multi-class classification problem in this study.

First, the weights and bias values in each neuron are initialized using the Nguyen-Widrow algorithm (Pavelka and Procházka, 2004). The network then updates the weight and bias values in accordance with the backpropagation learning; the learning and optimizing step is accomplished by the one-step secant backpropagation. Training is terminated when the minimum gradient or maximum epochs is reached. Besides, to avoid overfitting, partial data is pre-isolated and serves as a validation subset (Tetko *et al.*, 1995). The training process is forced to stop when the losses of the training and validation subset are decreased and increased respectively for several steps. That is, if the accuracy over the training subset increases but the accuracy over the validation subset remains the same or decreases, the training process is early terminated to hold the generalization. It's called validation checks the network starts to overtrain and overfit the training subset. This check yields an inevitable trade-off similarly to the problem of curve fitting, where a higher number of degrees of freedom in the approximating function results in greater flexibility and better fitting performance for the input data. However, considering that the data may be affected by noise, a generalized model is preferred even with little inaccuracy.

Neural Networks based on 2-dimensional Data - GoogLeNet

The second model is a more sophisticated network, which is a convolution neural network (CNN) that can see the 2-dimensional image to distinguish between different labels. CNN is also a kind of MLF network and LeNet is proposed in this study to process the image (LeCun *et al.*, 1989). To improve the performance, a deeper CNN architecture has been demonstrated to be effective (Krizhevesky *et al.*, 2012). Moreover, GoogLeNet has been proven to be capable of extracting more detailed patterns because of the dense and complicated layers, called Inception, within the network (Szegedy *et al.*, 2015). As the result, it was employed to classify 1000 types of objects, such as keyboard, mouse, pencil, and many animals, and was rewarded with 1st place in the ImageNet Large Scale Visual Recognition Challenge (ILSVRC) in 2014. Despite other competent networks, such as AlexNet (Krizhevesky *et al.*, 2012), ZFNet (Zeiler and Fergus, 2014), VGGNet (Simonyan and Zisserman, 2014), and ResNet (He *et al.*, 2016), GoogLeNet is utilized in this study to classify the anomalies using 2-dimensional images.
The time history responses and the probability distribution are plotted, overlaid, and resized to 224×224 pixels to reduce computational loading. The layers in GoogLeNet include convolution layers, max pooling layers, average pooling layers, inception layers, a fully connected layer, and a softmax layer. Furthermore, the inception layers contain convolution layers, ReLU (rectified linear unit) layers, and depth concatenation layer. There are totally 22 layers (144 layers if flattened) and more details can be found in the literature (Szegedy *et al.*, 2015). To be noticed, the model is a pre-trained model so it's a kind of transfer learning in this study. To this end, the fully connected layer, the softmax layer, and the last classification layer are replaced from 1000 to 7 types of objects, representing 7 different labels.
The same with the first model, the validation subset is pre-isolated from the training subset and the training process performs validation checks to avoid overfitting. The network learns and is optimized by stochastic gradient descent with momentum (SDGM). Considering the hardware environment and the training efficiency, the initial learning rate is 0.001, the maximum epochs set to 6, and the minimum batch size is set to 10. For other training parameters, the model directly uses the default.

DATA ANOMALY DETECTION AND CLASSIFICATION

After the models are built, the field dataset is assigned as the inputs and the various labels are assigned as the outputs to perform supervised training. Hence, the training process and their performance can be studied and the advantage of statistics can be examined. In this section, the results regarding two neural networks are discussed and summarized.

Performance of Pattern Recognition Network

In pattern recognition network, *missing* can be identified beforehand as two kinds of measurement are labeled as *missing* in the field dataset. The first one is the data with NAN (not a number); these data cannot generate any statistics parameters so can be easily identified while preparing the input data. The other kind is constant measurements. These data have monotonous statistics parameters and, most importantly, the range is always zero. Thus, the measurement can also be classified as *missing* while

preparing the input data. A pre-screening step is facilitated to detect this data anomaly before implementing the neural network and the number of labels is reduced from 7 to 6.

To study the necessary statistics parameters, several models are built and trained. First, four models with different histograms (e.g. with 3, 11, 21, and 31 sections equally distributed between ±2 standard deviations) are trained to compare the accuracy. The histogram with 3 sections displays the worst results and the other 3 histograms show no significant difference. Since the histogram is only used to provide the information on probability distributions and the number of other statistics parameters is only 6, 11 sections are selected for the pattern recognition network to keep it simple compared to GoogLeNet. Then, the other statistics parameters (e.g. arithmetic means, ranges, standard deviations, quartiles, and standard scores) are sequentially examined. The standard score is found to advance the accuracy, especially for *outlier* and *drift*. Both of the anomalies have wider ranges and, consequently, larger standard scores compared to *normal data*.

The number of hidden layers and neurons is also studied in pattern recognition network and several models with different configurations are trained to compare the accuracy. Unlike the results from statistics parameters, the differences between those models are quite small. For example, the network with only two hidden layers can produce a fair good performance, and the performance of four hidden layers is better. The overall accuracy of two and four hidden layers is 98.8% and 98.9%, respectively. Consequently, the number of hidden layers is four for the final model and the performance is shown in **Fig. 4**.

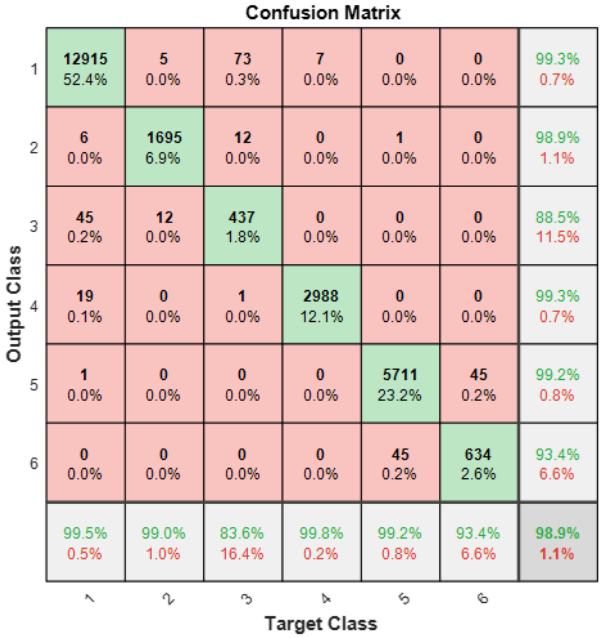

Figure 4. Confusion matrix for pattern recognition network (number 1 to 6 is for *normal data*, *minor*, *outlier*, *square*, *trend*, and *drift*, respectively).

Performance of GoogLeNet

Since the model of GoogLeNet is a pre-trained model, there are not many modifications in this study. Instead, the effect of using statistics is discussed via GoogLeNet.

In the first model, the time history responses are plotted and resized for training. Then, the time history responses and the probability distribution are plotted, overlaid, and resized for the second model. **Fig. 5** exhibits the comparison between the two models. To be noted that only the results of the validation subset are shown in this figure for simplicity. Obviously, the first model is kind of incompetent to differentiate drift, resulting in 82.4% recall and 91.8% precision. In other ways, the second model has 94.1% recall and 90.1% precision although the accuracy of both models is equal. In addition, some unclear labels or mislabels are found during training and manually removed to further improve the performance of models, as shown in **Fig. 6(a)**. By doing so, recall is escalated from 93.8% to 97.3% for

minor and the accuracy is increased to 99%. Hence, incorporating probability distribution clearly improves the model and produces a better result.

The ML under an imbalanced dataset is prone to bias toward prevalent classes and, as the result, samples belonging to the small classes will be misclassified more often than others. The effect of imbalanced data is studied using GoogLeNet. Typically, there are two approaches for handling an imbalanced dataset, namely under-sampling and over-sampling. Considering the huge ratio between the largest and smallest classes in this field dataset, under-sampling, which reduces the prevalent classes to balance the sample number, is used. The model randomly selects 500 samples from each label and divides them into the training and validation subsets with a 7:3 ratio, respectively. The results are displayed in **Fig. 6(b)** and, again, only the results of the validation subset are shown in this figure for simplicity. Admittedly, recall is leveled in all labels except normal data; in the meantime, precision is slightly better. The comparison of the confusion matrix demonstrates that the imbalanced dataset affects the trained model and some approaches can improve the performance, especially for those classes with small numbers.

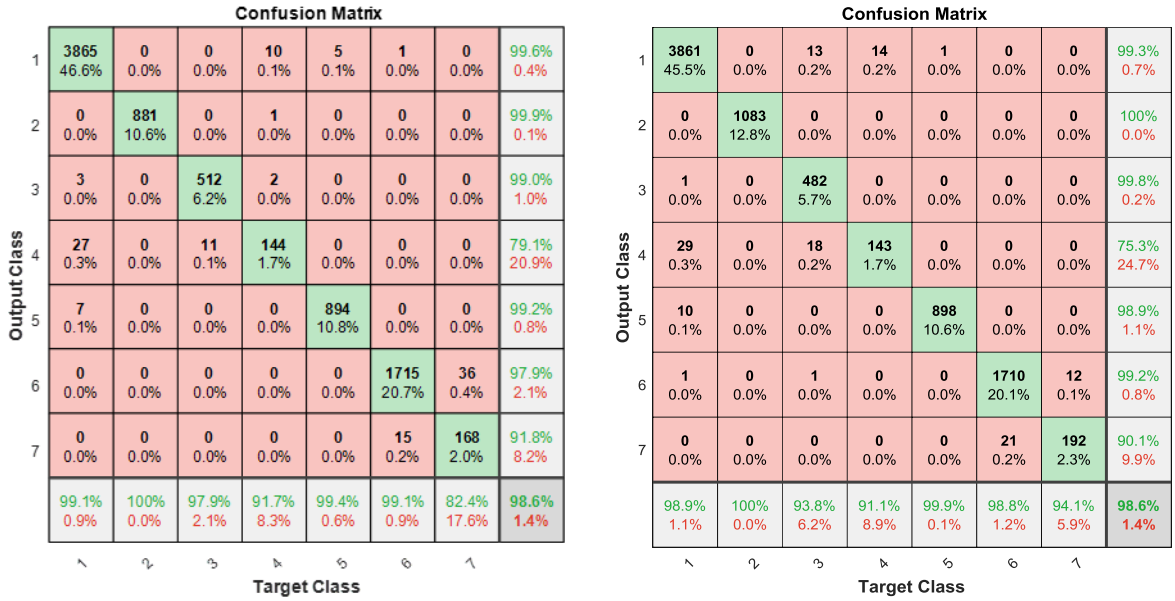

(a) time history data only (b) time history data and probability distribution

Figure 5. Comparison of confusion matrix for GoogLeNet (number 1 to 7 is for *normal data*, *missing*, *minor*, *outlier*, *square*, *trend*, and *drift*, respectively).

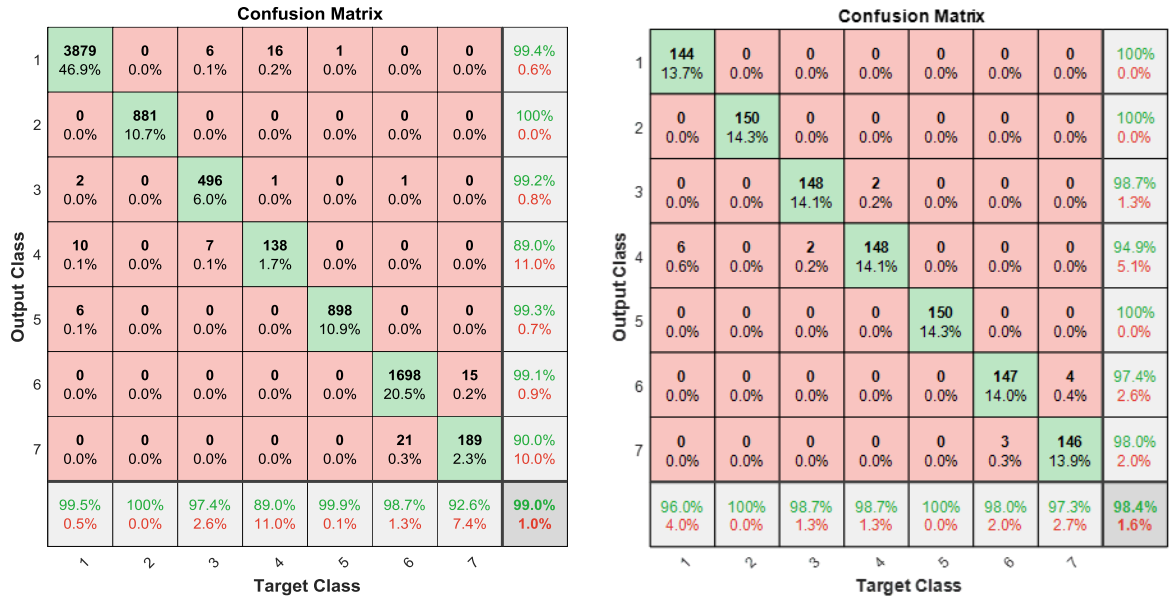

(a) imbalanced dataset (b) balanced dataset

Figure 6. Comparison of confusion matrix for GoogLeNet (number 1 to 7 is for *normal data*, *missing*, *minor*, *outlier*, *square*, *trend*, and *drift*, respectively).

Discussion of Two Models

Finally, the performance and the possible application of pattern recognition network (as shown in **Fig. 4**) and GoogLeNet (as shown in **Fig. 6(b)**) are discussed. Overall, the performance of GoogLeNet overwhelms the one used pattern recognition network; however, the difference isn't dramatic. For example, the maximum difference in recall between two models is 15.2% for *outlier* and the other differences are less than 4%. Similarly, the maximum difference in precision is 6.4% for *outlier* and others are less than 4.5%. Furthermore, it's noted that the complexity of the two models is significant. The training of pattern recognition network takes 10 to 20 minutes but it spends around 120 minutes for GoogLeNet under the same hardware specification, using a computer with i7-11700 CPU, RTX3080 GPU with 10 gigabits of VRAM, and 64 gigabits of RAM. Although a model based on GoogLeNet has excellent performance and is suitable for a large and efficient system, a model based on pattern recognition network is preferable for an application using a small or portable device.

CONCLUSIONS

This study demonstrates the detection and classification of data anomalies using ML techniques. By taking the advantage of statistics, the accuracy can be improved and both the neural networks based on 1-dimensional and 2-dimensional data are performed well for the task. Based on the results, conclusions can be summarized as follows:

- Both pattern recognition network and GoogLeNet can detect and classify the data anomalies although the performance is slightly different.
- The performance can be improved by using statistical information and the balanced dataset can further boost the results.
- Models based on both ML techniques produce acceptable accuracy; the usage of ML techniques depends on the application and the trade-off between computation and performance.

ACKNOWLEDGMENTS

The results published here are in whole or in part based on data obtained from the 1st international project competition for structural health monitoring (http://sstl.cee.illinois.edu/ipc-shm2020/).

REFERENCES

Bao, Y., Li, J., Nagayama, T., Xu, Y., Spencer Jr, B. F., & Li, H. (2021). "The 1st international project competition for structural health monitoring (IPC-SHM, 2020): a summary and benchmark problem," *Structural Health Monitoring*, 20(4), 2229-2239.

Chawla, N. V. (2009). "Data mining for imbalanced datasets: An overview," *Data mining and knowledge discovery handbook*, 875-886.

Chou, J. Y., Fu, Y., Huang, S. K., & Chang, C. M. (2022). "SHM data anomaly classification using machine learning strategies: A comparative study," *Smart Structures and Systems*, 29(1), 77-91.

He, K., Zhang, X., Ren, S., & Sun, J. (2016). "Deep residual learning for image recognition," *In Proceedings of the IEEE conference on computer vision and pattern recognition*, 770-778.

Karbhari, V. M., & Ansari, F. (2009). *Structural health monitoring of civil infrastructure systems*, Elsevier.

Krizhevsky, A., Sutskever, I., & Hinton, G. E. (2012). "Imagenet classification with deep convolutional neural networks," *Advances in neural information processing systems*, 25.

LeCun, Y., Boser, B., Denker, J. S., Henderson, D., Howard, R. E., Hubbard, W., & Jackel, L. D. (1989). "Backpropagation applied to handwritten zip code recognition," *Neural computation*, 1(4), 541-551.

Pavelka, A., & Procházka, A. (2004, November). "Algorithms for initialization of neural network weights," *In Proceedings of the 12th annual conference, MATLAB*, 453-459.

Ramirez, A., & Cox, C. (2012). "Improving on the range rule of thumb," *Rose-Hulman Undergraduate Mathematics Journal*, 13(2), 1.

Simonyan, K., & Zisserman, A. (2014). "Very deep convolutional networks for large-scale image recognition," arXiv preprint arXiv:1409.1556.

Szegedy, C., Liu, W., Jia, Y., Sermanet, P., Reed, S., Anguelov, D., ... & Rabinovich, A. (2015). "Going deeper with convolutions," *In Proceedings of the IEEE conference on computer vision and pattern recognition*, 1-9.

Tang, Z., Chen, Z., Bao, Y., & Li, H. (2019). "Convolutional neural network-based data anomaly detection method using multiple information for structural health monitoring," *Structural Control and Health Monitoring*, 26(1), e2296.

Tetko, I. V., Livingstone, D. J., & Luik, A. I. (1995). "Neural network studies. 1. Comparison of overfitting and overtraining," *Journal of chemical information and computer sciences*, 35(5), 826-833.

Yi, T. H., Huang, H. B., & Li, H. N. (2017). "Development of sensor validation methodologies for structural health monitoring: A comprehensive review," *Measurement*, 109, 200-214.

Zeiler, M. D., & Fergus, R. (2014, September). "Visualizing and understanding convolutional networks," *In European conference on computer vision*, 818-833. Springer, Cham.

DYNAMIC CHARACTERISTICS OF A STEEL-FRAMED HIGH-RISE BUILDING BASED ON STRONG MOTION DATA ANALYSIS

Toshihide Kashima[1]
1. Research Engineer, Building Research Institute, Tsukuba, Japan
Email: kashima@kenken.go.jp

ABSTRACT

A 15-story steel-framed building in Sendai city was equipped with strong motion instruments in 1989 as one of research activities of the Building Research Institute (BRI) of Japan. Over the last 33 years, more than 300 strong motion data have been accumulated. Dynamic characteristics of the building were minutely investigated using the strong motion data. Fundamental natural frequencies in both horizontal directions were close to each other and showed values from 0.5 Hz to 0.57 Hz. Despite the violent shaking, the changes in the dynamic characteristics of the building during the 2011 Tohoku Earthquake were slight. The apparent amplitude-dependence in the natural frequencies and damping ratios of the building could be recognized. The natural frequencies and damping ratios decrease as the response amplitudes increase. The regression analysis of the natural frequency and the maximum displacement angle revealed changes in the natural frequency before and after the Tohoku Earthquake.

Keywords: Strong motion observation, system identification, structure health monitoring, 2011 Tohoku Earthquake

INTRODUCTION

The Building Research Institute (BRI) of Japan is a national institute engaged in research and development in the fields of architecture, building engineering and urban planning. As one of its research activities, BRI operates a strong motion network that covers buildings in major cities across Japan. A great number of strong motion data has been accumulated in the long history of the BRI strong motion network. This paper discusses the dynamic behavior of a building, which has the longest history of observation in the network.

TARGET BUILDING AND INSTRUMENTATION

The building is in the central part of the city of Sendai, in the north-eastern region of Japan. The building completed in 1973 is a 15-storey steel-framed structure having two basement floors and a two-story penthouse. The building is supported by the mat foundation at 10 meters below the ground level. The building is referred to as the SND building hereinafter. External view of the SND building is shown in Figure 1.

BRI started seismic monitoring with old mechanical strong motion instruments when construction was completed. The old instruments were replaced by digital one having feedback sensors in 1989. The sensor configuration is illustrated in Figure 2. Acceleration sensors are placed on the second basement floor (B2F), on the fifteenth floor (15F), and at 40 meters below the ground level (G40). The G40 sensor was installed in 1972 and was continuously used by connecting it to the strong motion instrument replaced in 1989. This sensor worked normally until 2006 but is no longer working. The sensors are installed along the building axis, and the direction closer to the east is treated as X and the direction closer to the south as Y in this paper as shown in Figure 2.

Figure 1. Exterior view of the SND building.

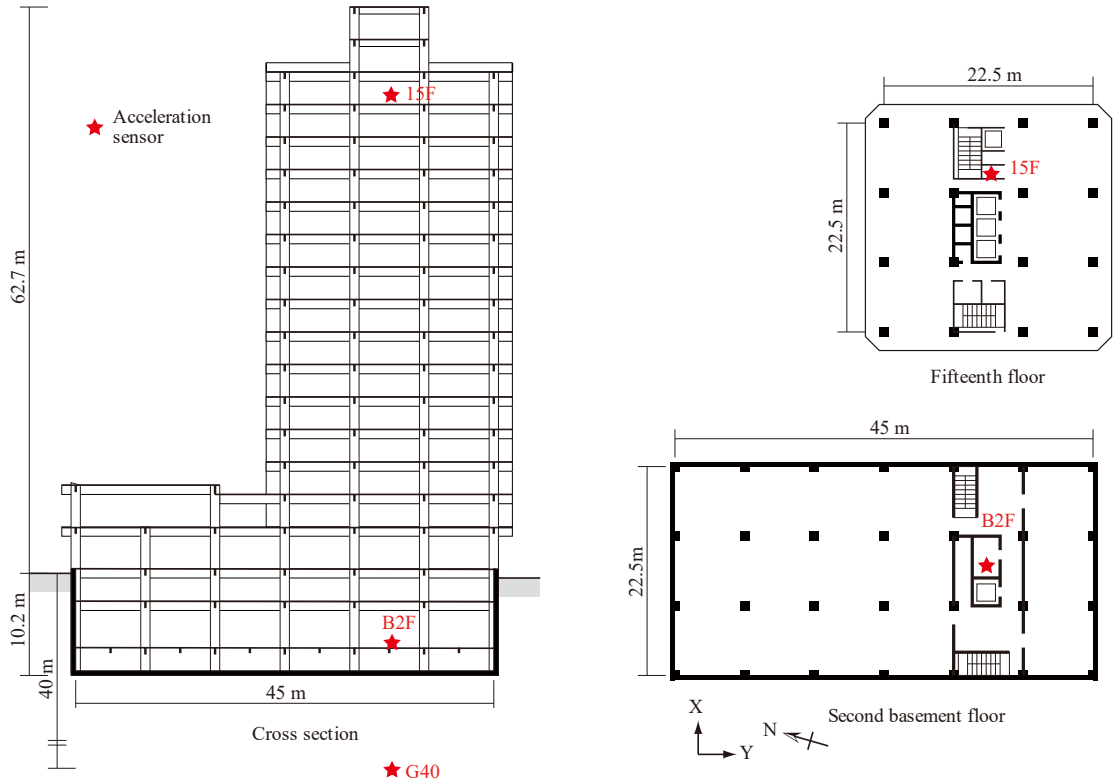

Figure 2. Sensor configuration at the SND building.

STRONG MOTION DATA

This paper discusses strong motion data since 1989. Over 300 strong motion data have been obtained over the last 33 years. Epicenters of the recorded strong motion data are plotted in Figure 3. The location of the instrumented building is indicated by a black diamond. The magnitude of the

earthquake ranges from 3.4 to 9.0, and the epicenter distance ranges from 5 km to 1157 km. The maximum accelerations at the second basement floor (B2F) are distributed between 0.02 and 2.59 m/s^2. The strongest ground motion was caused by the 2011 off the Pacific coast of Tohoku Earthquake of March 11, 2011. The earthquake is referred to simply as the Tohoku Earthquake hereinafter.

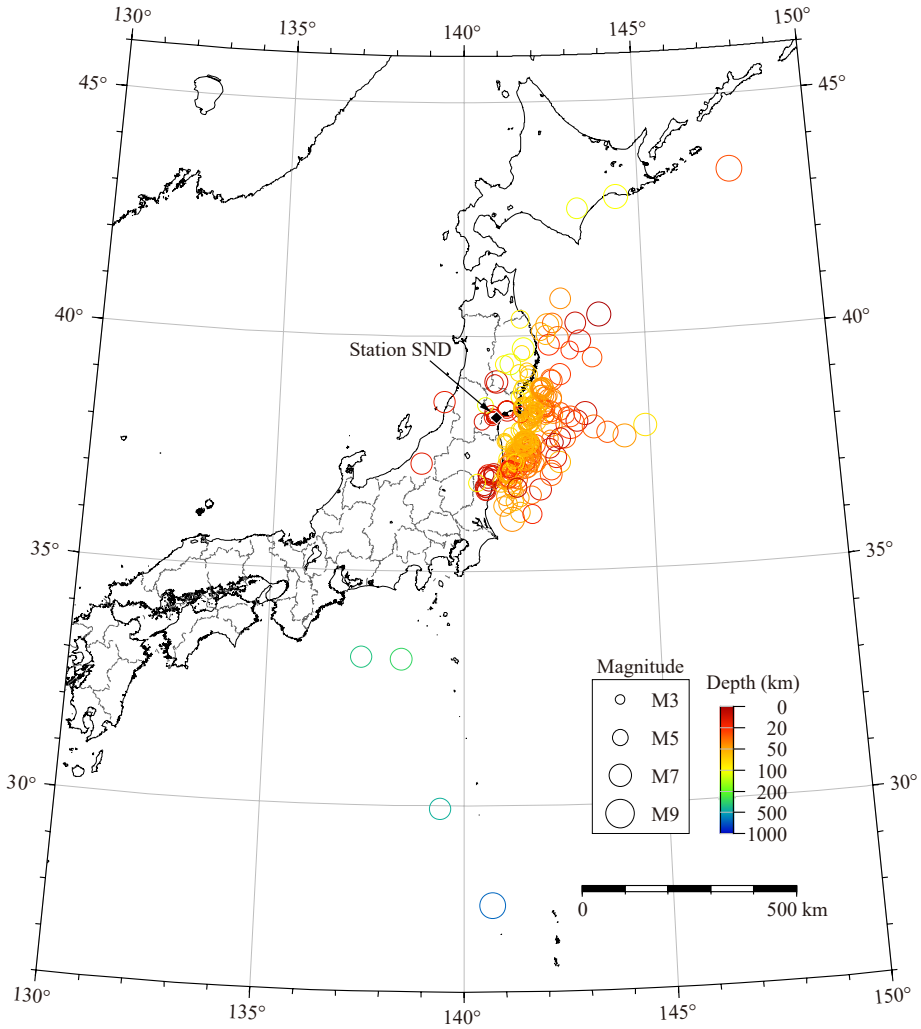

Figure 3. Epicenters of earthquakes recorded at the SND building.

TRANSITION OF DYNAMIC CHARACTRISTICS

From each strong motion data, the fundamental natural frequencies and damping ratios in two horizontal directions of the SND building were identified using a parameter optimization technique introduced by Kashima et al. (2006). With a single-degree-of-freedom system, the natural frequency and damping ratio that had the most fitted response displacement were determined using the grid search. Strong motion data on the second basement and fifteenth floors were adopted as the input and output motions, respectively.

Figure 4 shows the transition of the natural frequencies and damping ratios of the SND building over the past 33 years. Red circles and blue triangles correspond to values in X- and Y-directions, respectively. The orange dashed line represents the time of the Tohoku earthquake. First, it can be pointed out that seismic activity has become active since the Tohoku Earthquake, and strong motion records have increased sharply. Second, the natural frequencies are generally distributed between 0.5 Hz and 0.57 Hz in both directions. The damping ratios are approximately 1% to 3%, and the values in the X-direction are slightly larger than those in the Y-direction. The natural frequencies and damping ratios fluctuate greatly, and it is hard to read any tendency from this figure.

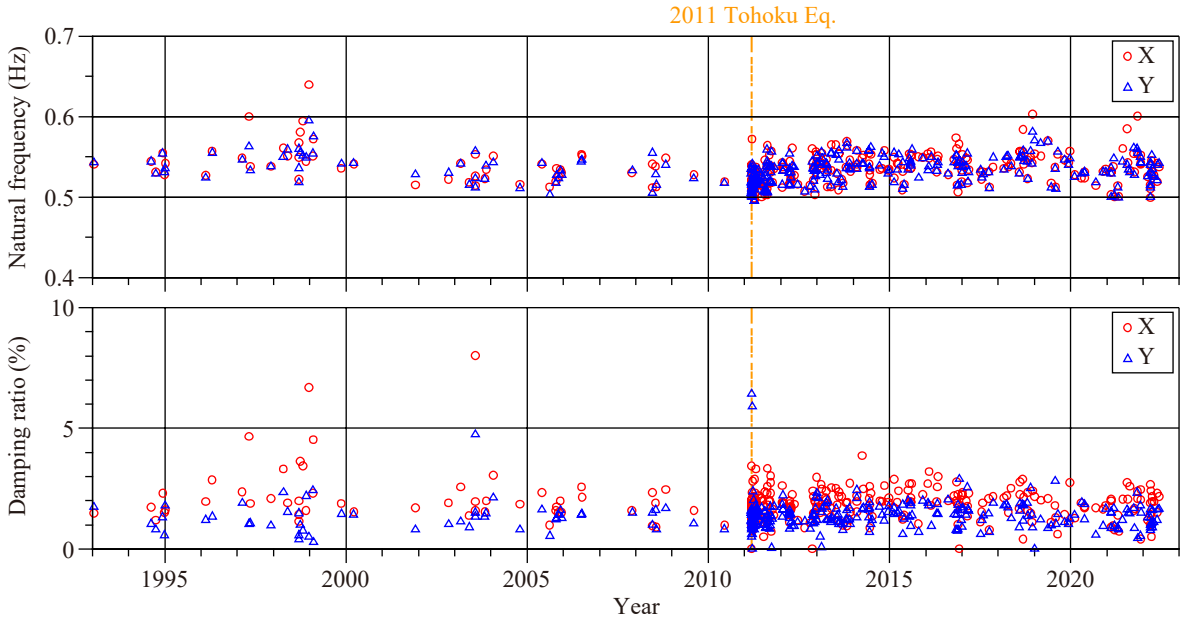

Figure 4. Change in identified natural frequencies (upper) and damping ratios (lower) with time.

DYNAMIC BEHAVIOR DURING THE TOHOKU EARTHQUAKE

The Tohoku Earthquake caused severe shaking of the SND building as reported by Kashima et al. (2012). The magnitude of the Tohoku Earthquake was 9.0 and the focal depth was 24 km. The SND building was 175 km west of the epicenter.

The peak accelerations and velocities recorded in the SND building are listed in Table 1. This is the strongest earthquake motion at the SND building in the past.

Table 1. Peak accelerations and velocities recorded in the SND building during the Tohoku Earthquake

Location	Peak acceleration (m/s^2)			Peak velocity (m/s)		
	X	Y	Z	X	Y	Z
B2F	1.63	2.59	1.47	0.331	0.348	0.136
15F	3.61	3.46	5.43	0.979	0.889	0.201

Acceleration time histories recorded in the SND building during the Tohoku Earthquake are shown in Figure 5. Figures 5 (a) and (b) correspond to X- and Y-directions, respectively. Bold dark and thin light lines indicate accelerations on the second basement floor (B2F) and fifteenth floor (15F), respectively. The duration of the earthquake motion is extremely long, close to 200 seconds. It is notable that several wave groups with large amplitudes come repeatedly.

Building displacements, which are relative displacements of 15F to B2F, in X- and Y-directions are plotted in Figures 5 (c) and (d), respectively. Peak building displacements reached nearly 0.3 m in both directions.

Natural frequencies and damping ratios identified every 5 seconds during the Tohoku Earthquake are indicated in Figures 5 (e) and (f), respectively. Red circles and blue triangles correspond to values in X- and Y-directions, respectively. Despite the extremely large shaking, the fluctuation of the natural frequencies is extremely small. Looking at Figure 5 (e) carefully, the natural frequencies near 200 seconds are slightly lower than those around 50 seconds. The damping ratios are also stable at about 2% or less.

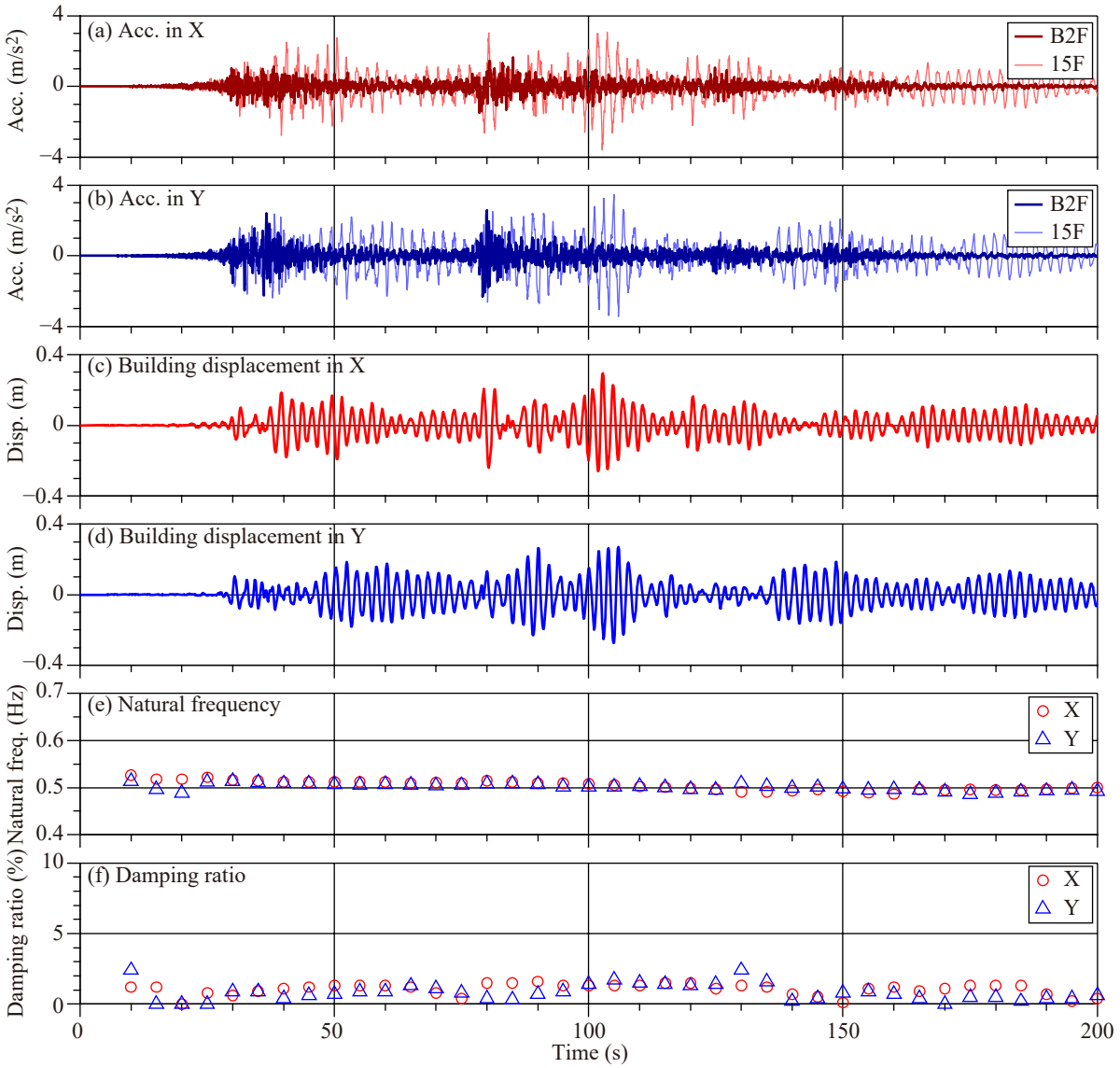

Figure 5. Time histories of acceleration and building displacement, and transitions of natural frequencies and damping ratios during the Tohoku Earthquake.

AMPLITUDE-DEPENDENCY OF DYNAMIC CHARACTRISTICS

Dependence of dynamic characteristics on response amplitude is examined using the maximum displacement angle $\theta_{\max}$ defined by Eq. (1).

$$\theta_{\max} = |x_{15F}(t) - x_{B2F}(t)|_{\max}/H \quad (1)$$

where, $x_{15F}(t)$ and $x_{B2F}(t)$ are the time histories of the displacements on the fifteenth and second basement floors, respectively, and H is the height of the fifteenth-floor level from the first-floor level. The relation of the natural frequency and damping ratio to the maximum displacement angle $\theta_{\max}$ is plotted in Figure 6. Red circles and blue triangles indicate the values in the X- and Y-directions, respectively. Hollow and solid symbols represent the values before and after the Tohoku Earthquake, respectively.

There is apparent amplitude dependence in the natural frequencies. In both directions, the natural frequencies decrease as the response amplitudes increase. Similarly, the damping ratios decrease as the response amplitudes increase.

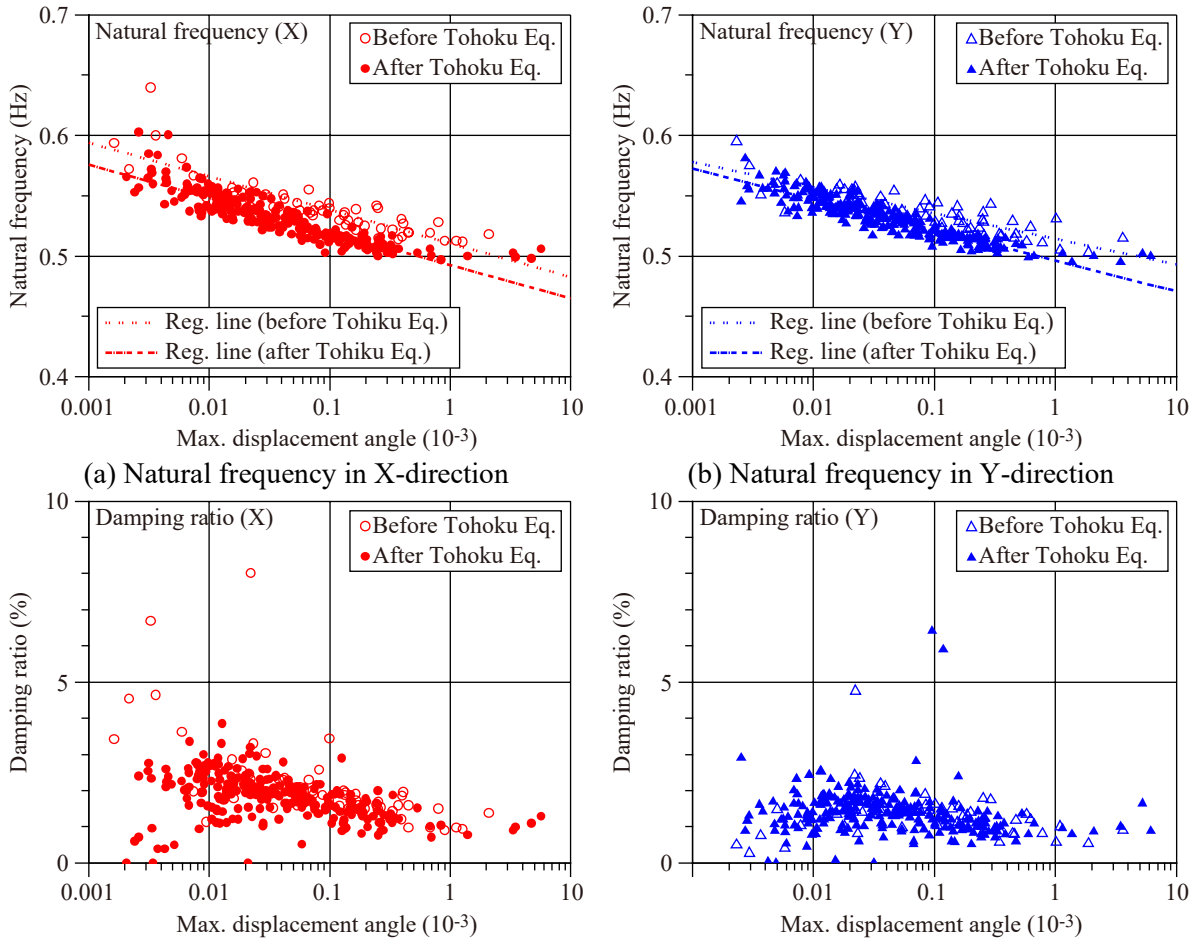

(a) Natural frequency in X-direction (b) Natural frequency in Y-direction

(c) Damping ratio in X-direction (d) Damping ratio in Y-direction

Figure 6. Relation of identified natural frequencies and damping ratios to maximum displacement angle

To clarify the relation of the natural frequency to the response amplitude, a single regression analysis was performed using a regression model shown in Eq. (2). The analysis was performed separately for the observation period before and after the Tohoku Earthquake in each direction.

$$f = a + b \log_{10} \theta_{\max} \tag{2}$$

Regression coefficients as the results of the regression analysis are shown in Table 2. Since the adjusted coefficients of determination (R^2) show high values, the regression equations can be considered significant. It is shown that the natural frequencies decrease by 0.021 Hz to 0.028 Hz when the response amplitudes increase by 10 times.

Table 2. Regression coefficients

Period	Direction	a	b	R^2
Before Tohoku Earthquake	X	0.4270	-0.02781	0.7470
	Y	0.4505	-0.02127	0.7559
After Tohoku Earthquake	X	0.4094	-0.02774	0.7977
	Y	0.4500	-0.02540	0.8375

R^2: Adjusted coefficient of determination

The regression lines are plotted in Figures 6 (a) and (b). Dotted line and dashed-and-dotted line indicate the regression lines before and after the Tohoku Earthquake, respectively. The regression analysis makes the difference in the tendency before and after the Tohoku earthquake becomes clear. Around the maximum displacement angle of 10^{-4}, the natural frequencies after the Tohoku Earthquake are 0.014 Hz to 0.018 Hz lower than those before.

CONCLUSIONS

The dynamic characteristics of a 15-story steel-framed building were examined minutely using the strong motion data obtained over the last 33 years. The findings can be summarized as follows.

- Fundamental natural frequencies in both horizontal directions are close to each other and showed values from 0.5 Hz to 0.57 Hz. Damping ratios were distributed between 1% and 3%.
- Despite the violent shaking, the changes in the dynamic characteristics of the building during the Tohoku Earthquake were slight. Therefore, it is probable that the impact of the Tohoku Earthquake on the building structure was small.
- The natural frequencies and damping ratios of the building showed the apparent amplitude-dependence. The natural frequencies and damping ratios decrease as the response amplitudes increase.
- The regression analysis of the natural frequency and the maximum displacement angle revealed changes in the natural frequency before and after the Tohoku Earthquake.

ACKNOWLEDGMENTS

Maps and some figures in the paper are drawn using GMT6 developed by Wessel et al. (2019). I thank for this useful and irreplaceable tool.

REFERENCES

Kashima, T., Koyama, S., Okawa, I. and Iiba, M. (2012). "Strong Motion Records in Buildings from the 2011 Great East Japan Earthquake," *Proceeding of the 15th World Conference on Earthquake Engineering (15WCEE)*, #1762.

Kashima, T. and Kitagawa, Y. (2006). "Dynamic Characteristics of Buildings Estimated from Strong Motion Records," 8th National Conference on Earthquake Engineering, San Francisco, U.S.A.

Wessel, P., Luis, J. F., Uieda, L., Scharroo, R., Wobbe, F., Smith, W. H. F., and Tian, D. (2019). "The Generic Mapping Tools version 6", *Geochemistry, Geophysics, Geosystems*, 20, 5556–5564. https://doi.org/10.1029/2019GC008515

VIBRATION-BASED STRUCTURAL HEALTH MONITORING OF THE NCREE BUILDING UNDER A SERIES OF ENVIRONMENTAL AND EARTHQUAKE LOADINGS

Yu-Tzu Huang[1], Wen-Hui Chen[2], Chung-Che Chou[3] and Chin-Hsiung Loh[4]

[1]Graduate Student, Dept. of Civil Eng., National Taiwan University, Taipei, Taiwan, R.O.C.
[2]Senior Engineer, P-Waver Inc., Taipei, Taiwan
[3]Director, National Center for Research on Earthquake Engineering, Taipei, Taiwan, R.O.C.
Professor, Dept. of Civil Eng., National Taiwan University, Taipei, Taiwan, R.O.C.
[4]Adjunct Professor, Dept. of Civil Eng., National Taiwan University, Taipei, Taiwan, R.O.C.
Adjunct Professor, Dept. of SME, University of California at San Diego, Lo Jolla, CA. USA.
email: a706304@gmail.com, wendy@pwave.com, cechou@ntu.edu.tw, lohc0220@ntu.edu.tw

ABSTRACT

This paper was aimed to develop a systematic way of structural health monitoring for buildings by using data collected from a long-term seismic monitoring system. Continuous monitoring data for the 13-story NCREE building in Taipei is used as an example, studying the building response under daily-operating condition and the building seismic response data for a safety assessment. From the analysis of long-term monitoring data, the stochastic subspace identification and time-frequency analysis of floor response are used to extract the building dynamic characteristics. A cross safety assessment on the extracted features of the building is used to examine the changes of the extracted features. Furthermore, the earthquake response data is also investigated through the principal component analysis (PCA) and Q-index to investigate and locate abnormal response locations of the building. The results highlight the applicability of the signal processing-based approach (without a physical analysis of the wave propagation process) for the structural damage assessment.

Keywords: system identification, principal component analysis, structural health monitoring, building safety assessment

INTRODUCTION

A civil infrastructure during its service life may be subjected to different environmental loadings, such as earthquake excitation. It is important to know the current state of the structure after the external loading. In this regard, appropriate data analysis and feature extraction techniques are required to interpret the measured data and to identify the state of the structure and, if possible, to detect the damage that might have been caused by severe external loadings. Through a series of strong motion data, acquired from structure during seismic events, can play a vital role in gaining insight into the system behavior if a systematic procedure is adopted in analyzing the acquired data. Two different data sets can be collected from a building monitoring system: structural response under daily-operating condition and seismic response data. Several analytical algorithms had been developed to extract the dynamic features from the vibration signal of structure. For multi-channel signal processing tools, the Frequency Domain Decomposition (FDD) [Brinker et.al., 2001; Pioldi et.al., 2016] and the Covariance-drive Stochastic Subspace Identification (SSI-COV) [Overschel et.al., 1996; Mrabet et.al., 2014] can be applied to the ambient vibration data. Besides, the time-frequency analysis (continuous wavelet analysis) on each individual measurement can provide direct visualization on the vibration characteristics of the building [Noh et.al., 2011; Todoravska, M.I., 2001]. Moreover, in structural health monitoring (SHM), PCA has been extensively applied to measured vibration signals for dimensionality studies, for extracting structural damage features to discriminate features from damaged and undamaged structures. In this paper, continuous monitoring data of the NCREE building (National Center for Research on Earthquake

Engineering), including the earthquake response data and ambient vibration data, are analyzed for the performance assessment.

INSTRUMENTATION OF EARTHQUAKE MONITORING SYSTEM IN NCREE BUILDING

The National Center for Research on Earthquake Engineering (NCREE) was built in 1997. It was a 6-story reinforced concrete (RC) structure. In the year of 2020, a 7-story steel structure was added to the top of the original 6-story RC building to become a 13-story NCREE building. Considering this newly compound building structure with two different construction materials, a 24-hours seismic monitoring system has been implemented to this building since 2021 to collect the vibration of building under the operating condition as well as the earthquake excitation. High resolution accelerometers (AS-301 series with Uni-axis model) for seismic measurement were installed in this building. Figure 1 shows the instrumentation layout. Each floor, from 1st to 5th and 8th to 12th floors, was installed with three uni-axial accelerometers and B1 floor, 6th to 7th floor and 13th floor were installed with tri-axial accelerometers. The type of data logger for this monitoring system is National Instruments NI PXIe-1082. Table 1 listed a series of seismic event data recorded from the building SHM system during the period of Feb. 2021 to March 2022.

The SHM system of this building was designed by selecting a pre-seismic event, post-seismic event, and seismic event data to conduct a safety assessment of the building. Once the earthquake monitoring system was triggered by the earthquake P-wave arrival, the recorded data would be automatically downloaded from the data logger for analysis. As shown in Figure 2, once the seismic event was detected, a 30 sec of pre-memory data together with a pre-assigned 90 sec of seismic-event data was automatically downloaded. This seismic event data with a duration of 120 sec is defined as the seismic-event data. To avoid the missing of the seismic event data in a longer excitation another 120 sec post-event data, following the seismic event data, was also automatically downloaded for analysis. Besides, to catch the dynamic behavior of the building under operating condition, a duration of 120 sec pre-event data right before the seismic event data was also downloaded to serve as the reference information of the building before earthquake excitation. Therefore, a total of 360 sec of data was used for the online analysis. This download data with 360 seconds in three different consecutive sets of back-to-back data (each with 120 second of duration) was used for SHM of the building.

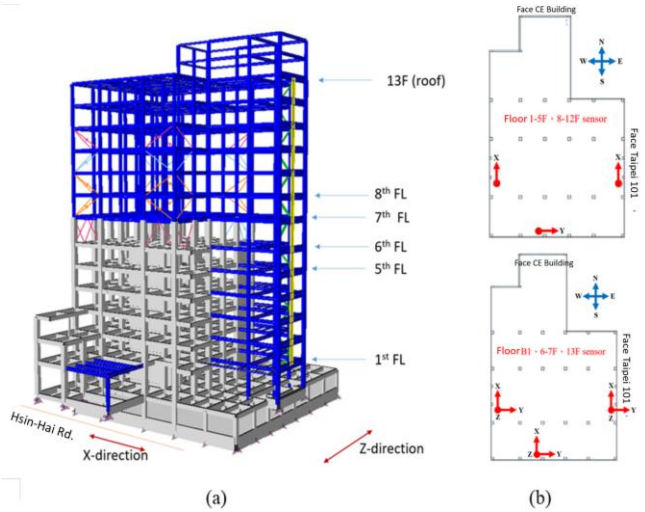

No.	Event No.	Time	Magnitude	Depth (km)	Epicenter Dis. (km)
1	110014	2021-02-09 00:58:02	5.6	24.7	86.3
2	110025	2021-04-18 22:11:39	5.8	16.3	127.3
3	110026	2021-04-18 22:14:37	6.2	14.4	128.4
4	110047	2021-06-23 13:40:24	4.8	23.6	105.1
5	110049	2021-06-29 13:30:56	4.9	71.1	83.6
6	110055	2021-07-08 06:11:55	5.5	8.2	125.0
7	110077	2021-08-05 05:50:45	6.0	7.0	81.8
8	110079	2021-08-06 16:11:04	5.6	13.3	69.8
9	110103	2021-10-24 13:11:34	6.5	66.8	59.4
10	110104	2021-10-24 13:12:42	5.5	64.1	54.8
11	111001	2022-01-03 17:46:37	6.0	19.4	128.1
12	111007	2022-01-25 22:35:53	5.1	64.7	59.1
13	111011	2022-02-07 18:58:25	5.5	33.2	81.5
14	111012	2022-02-12 00:43:13	5.6	26.4	131.6
15	111019	2022-03-23 01:41:38	6.7	25.7	179.2
16	111020	2022-03-23 01:43:25	6.2	22.6	177.3

Figure 1. Sketch of the NCREE building & location of strong motion instrumentation (Also list the recorded seismic event data of the building)

ANALYSIS OF BUILDING VIBRATION DATA UNDER OPERATING CONDITION

In this section, the response of the structure to the unmeasured operational loading is recorded, and the dynamic features and modal parameters of the building are extracted from the output-only data (pre-event data). Two different algorithms are used to analyze the ambient data: (1) correlation study on floor

responses using response spectrogram**,** (2) identification of the building dynamic characteristics (natural frequencies and mode shapes) and the variabilities.

Correlation Study on Floor Responses Using Response Spectrogram

Take the advantages of continuous wavelet transform, the spectrogram from each recoded floor response under operating condition can be calculated through time-frequency analysis (continuous wavelet transform). For this analysis, the Modified Complex Morlet Wavelet (MCMW) with variable central frequency was used [Wen et. al., 2022]. The dominant frequency of the floor vibration can be observed through the visualization of the peaks in the marginal spectrum, defined as

$$H^i(f) = \sum_t \left| W_\psi{}^i[x](t,f) \right| \tag{1}$$

where $\left| W_\psi{}^i[x](t,f) \right|$ is the wavelet coefficient from a specific sensor "i". By checking the identified dominant frequency of each calculated floor marginal spectrum, the variation of dominant frequency can be detected immediately. Figure 2 shows the marginal spectrum of each floor response data (for pre-event data of No.110103 & N0.110079). The fundamental dominant frequency of each floor response is between 1.46 Hz and 1.48 Hz. To quantify the difference of the estimated marginal spectrum between two consecutive floors, the correlation coefficient, defined as follows, is used to check the correlation of the marginal spectrum:

$$\rho = \frac{\sum_f [M_i(f) \times M_{i+1}(f)]}{\sqrt{\sum_f [M_i(f)]^2 \times \sum_f [M_{i+1}(f)]^2}} \tag{2}$$

where $M_i(f)$ is the marginal spectrum of the i[th] floor acceleration data. Figure 2 plots the correlation coefficient between the two consecutive floors of the building from pre-event data of No.110103 and No. 110079, respectively. High correlation of the marginal spectrum between the two consecutive floors indicates no dramatically change on the floor response of the building under operating condition.

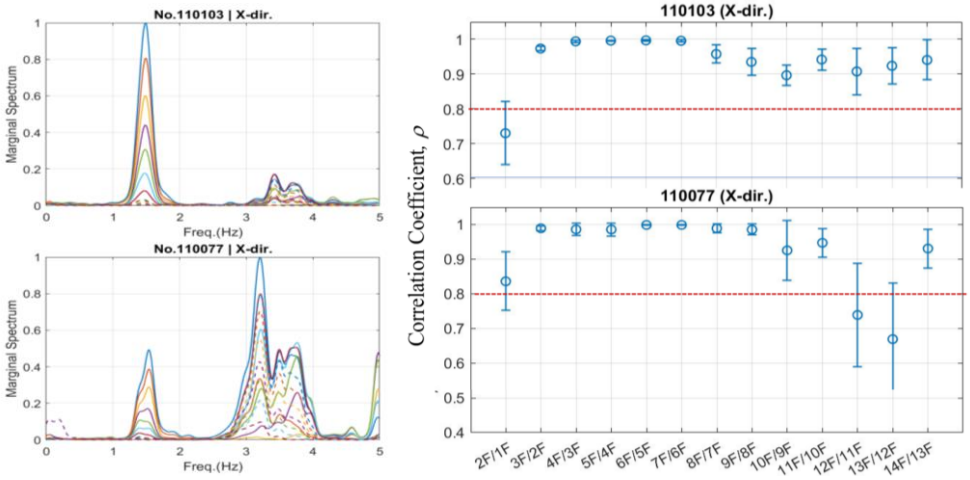

Figure 2. (a) Marginal spectrum of floor pre-event data, (b) Correlation coefficient of inter-story floor marginal spectrum

Application of Covariance-driven Stochastic Subspace Identification (SSI-COV)

Instead of using spectrogram to check the variability of floor response, the SSI-COV stems from the need to solve the problem through identifying a stochastic state-space model (system matrix **A** and observation matrix **C)** from output-only measurement. Based on the data Hankel matrix, the Toeplitz matrix can be obtained by a multiplication between future and transpose of past measurements. Based on the stochastic property, the Toeplitz matrix can be factorized into the extended observability matrix $\mathbf{O}_i \in \Re^{li \times 2n}$ and the reversed extended stochastic controllability matrix $\mathbf{\Gamma}_i \in \Re^{2n \times li}$. Perform singular value decomposition on Toeplitz matrix one can also directly obtain the factorization, and the system matrices

(**A**) can be obtained from the extended observability matrix $\mathbf{O}_i \in \Re^{li \times 2n}$. The modal parameters of the building can be identified from the extracted system matrix **A**. Note that the identified mode shapes from structural modal identification (SSI-COV algorithm) are in a complex form, and one needs to transform this damped normal mode as the real normal mode [Imregun and Ewins, 1993]. The SSI-COV approach was applied to analyze all the pre-event data (ambient data); the identified modal frequencies were plotted with respective to each recorded pre-event data (from event No.110025 to event No.111019), as shown in Figure 3. The identified three fundamental modes of the building (from the pre-event data of No.110103) is also shown. Note that the three fundamental modal frequencies decrease about 4.5% from April 2021 to March 2022 during the period of service time. Besides, the extracted mode shapes from all the pre-event data (ambient data) are also examined. The modal assurance criterion (MAC) is used to pair mode shapes obtained from the pre-event data. Since the MAC can detect the differences between mode shapes from two different sets, Figure 4 shows the calculated MAC value from two consecutive pre-event data. Basically, the overall MAC value is larger than 0.9 (good correlation on mode shape in general).

To explain the reduction of modal frequencies during the last year service time of the building, the mode shape curvature was used to assess the difference on the identified mode shapes from two pre-event data. The mode shape curvature was calculated based on the identified mode shapes from Event No.110025 (April 2021) and Event No.111019 (March 2022). The difference on the curvature from these two pre-events data is very clear. As shown in Figure 5, the mode shape curvature along the X-direction at the top floor and above the 8th floor is larger in the pre-event of No.111019 (either positive or negative) then in the pre-event of No.110025. Similar phenomenon is also observed for the mode shape curvature in the torsion mode. The calculated larger mode shape curvature at the 2nd floor and floors above 8th floor from No.111019 can be explained as the decrease of modal frequencies during the past one-year service life of the building. More detail study on the seismic response data is required about this reduction of modal frequencies.

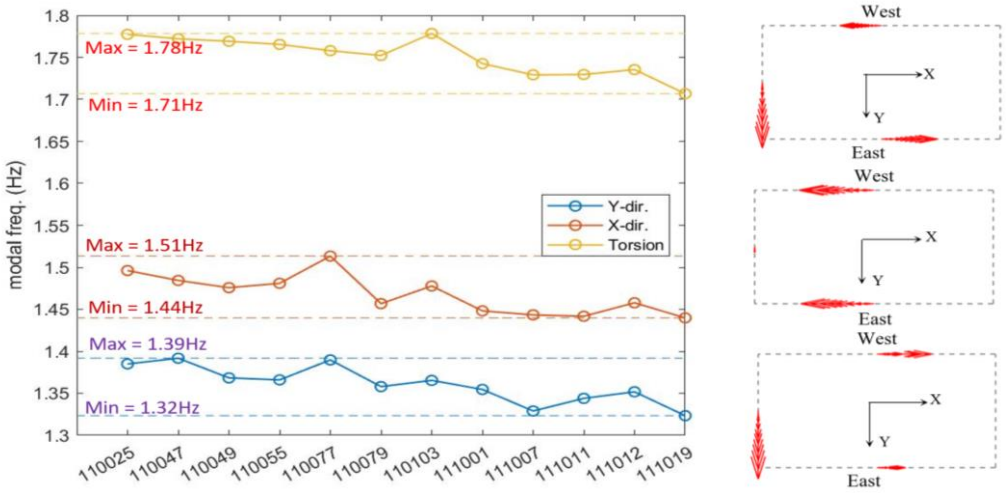

Figure 3. Identified three fundamental modal frequencies (Y-direction, X-direction & Torsion) and its corresponding mode shape (from Pre-event No.110103)

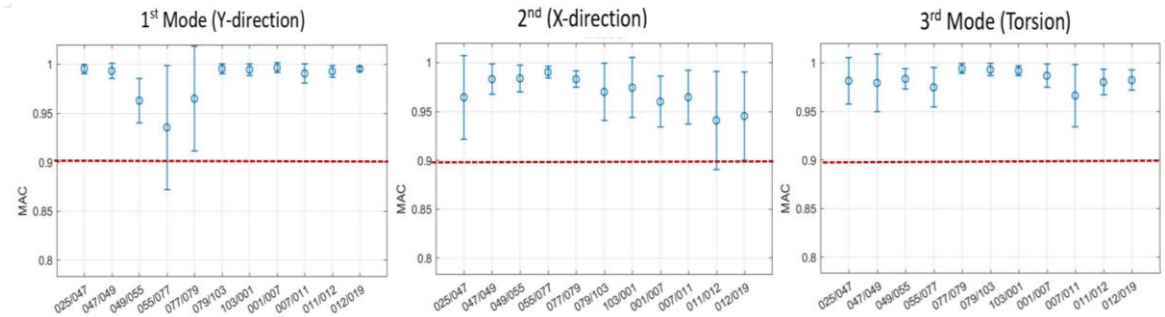

Figure 4: Calculated modal assurance criteria (MAC) from two consecutive pre-event data.

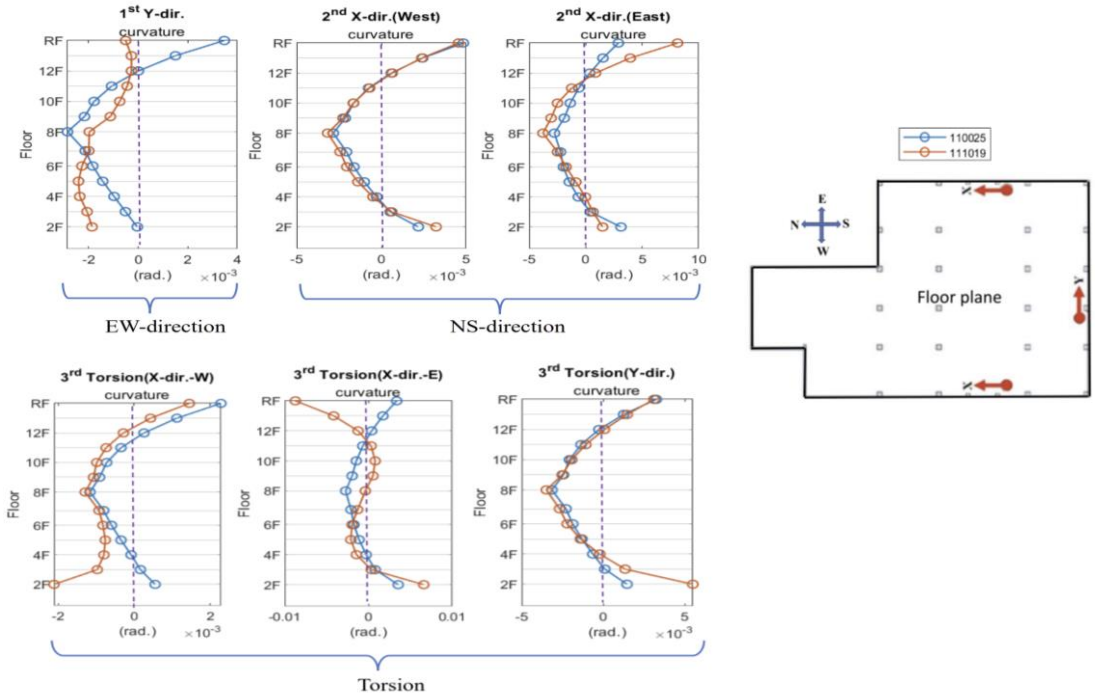

Figure 5. Comparison on the mode shape curvature (Y-direction, X-direction, and Torsion) between two pre-event data of No.110025 and No.111019.

DAMAGE ASSESSMENT OF NCREE BUILDING USING SEISMIC RESPONSE DATA

To analyze the building seismic response data, the input ground motion acceleration response spectrum is generated first, as shown in Figure 6. It is observed that most of the peak ground acceleration (PGA) recorded at the basement of the building is less than 10 gal, and only two events, No.110103 and No.111001, with PGA larger than 30 gal. In this section, the floor frequency response function (FRF) from each seismic monitoring data of the building (from April 2021 to March 2022) is used for safety assessment of the building. The FRF is estimated by using the ARX model (Recursive Auto-Regressive model with eXternal input). Two different approaches on the damage assessment are used: one is to examine the changes of FRF between each floor during an earthquake and the other is to perform the damage assessment of floor response through a series of earthquake excitation using reference test cases.

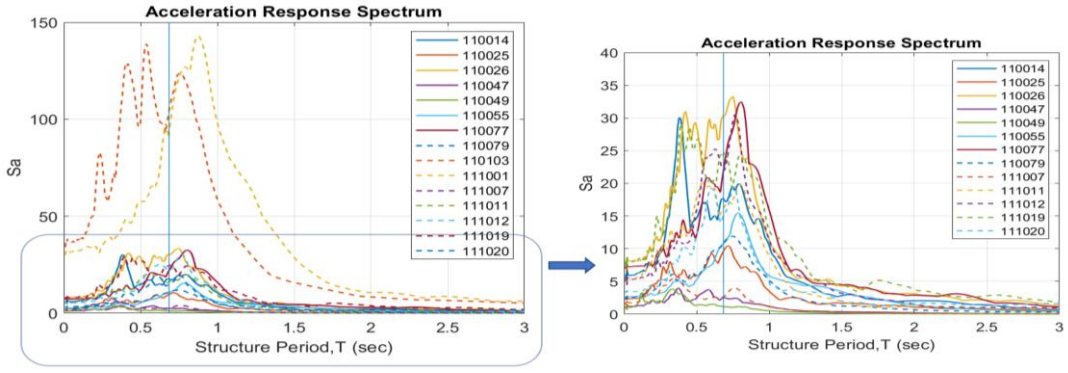

Figure 6. Acceleration response spectrum of the recorded basement motion of NCREE.

Assessment of Floor FRF Between Two Earthquake Excitations Using 2D-PCA Map

The ARX model can be used to identify the building frequency response function (FRF) of each floor during earthquake excitation. Two-dimension PCA mapping technique is developed for assessing the variability of floor FRF between two different earthquake excitations. To examine the variability of the

building floor FRF between two seismic events, a 2-dimension PCA mapping technique is used. Assume 'm' is the floor number, "A-i" is the FRF data from i-th sensor of "A" event and "B-i" is the FRF from i-th sensor of "B" event, and 'N' is the number of data point to be considered in frequency domain (or frequency band). Then, the data [X] matrix is formed by using the floor FRF from two seismic events, as shown in the following equation:

$$[X] = \begin{bmatrix} senser\ A-1 \\ senser\ A-2 \\ \vdots \\ sensor\ A-m \\ sensor\ B-1 \\ Sensor\ B-2 \\ \vdots \\ Sensor\ B-m \end{bmatrix}_{2m\times N} \tag{3}$$

The Covariance matrix $[C]_{2m\times 2m}$, defined in Eq. 4, is calculated:

$$[C]_{2m\times 2m} = cov(X) = \frac{XX^T}{M-1} \tag{4}$$

Then solve the eigenvalue problem of $[C]_{2m\times 2m}$, from which the eigenvalue is $[\Lambda] = diag(\lambda_1, \cdots, \lambda_{2m})$ and the corresponding eigenvectors is $[\boldsymbol{P}]$. It is believed that the largest two eigenvalues will contain most of the component energy of the data. Based on the distribution of eigenvalues, one can select the two major principal components (PCs), to construct the 2-D PCA map, $[X]_{2D-PCA}$. From two set of pre-event data, plot the $[X]_{2D-PCA}$ on a complex plain, as defined $\boldsymbol{P_{A/B}}$

$$\boldsymbol{P_{A/B}} = \begin{Bmatrix} \vec{p}_1 \\ \vec{p}_2 \\ \vdots \\ \vdots \\ \vec{p}_{2m} \end{Bmatrix} = \begin{Bmatrix} \vec{p}_1 = x_{1.1} - ix_{1.2} \\ \vec{p}_2 = x_{2.1} - ix_{2.2} \\ \cdots\cdots \\ \cdots\cdots \\ \cdots\cdots \\ \vec{p}_{2m} = x_{2m.1} - ix_{2m.2} \end{Bmatrix} \tag{5}$$

Since $\boldsymbol{P_{A/B}}$ contains two information in one vector form: one is the reference case $\boldsymbol{P_{ref}}$ and the other is the test cased $\boldsymbol{P_{test}}$, therefore, one can identify the difference between the test case and the reference case at each measurement node. Note that using different frequency bandwidth from FRF may have different representation of 2-D PCA map.

Figure 7 plots the 2D-PCA map of two seismic events (No.110079 vs. No.110103 and No.110103 vs. No.111001, respectively) using two different frequency bands from the identified FRF.

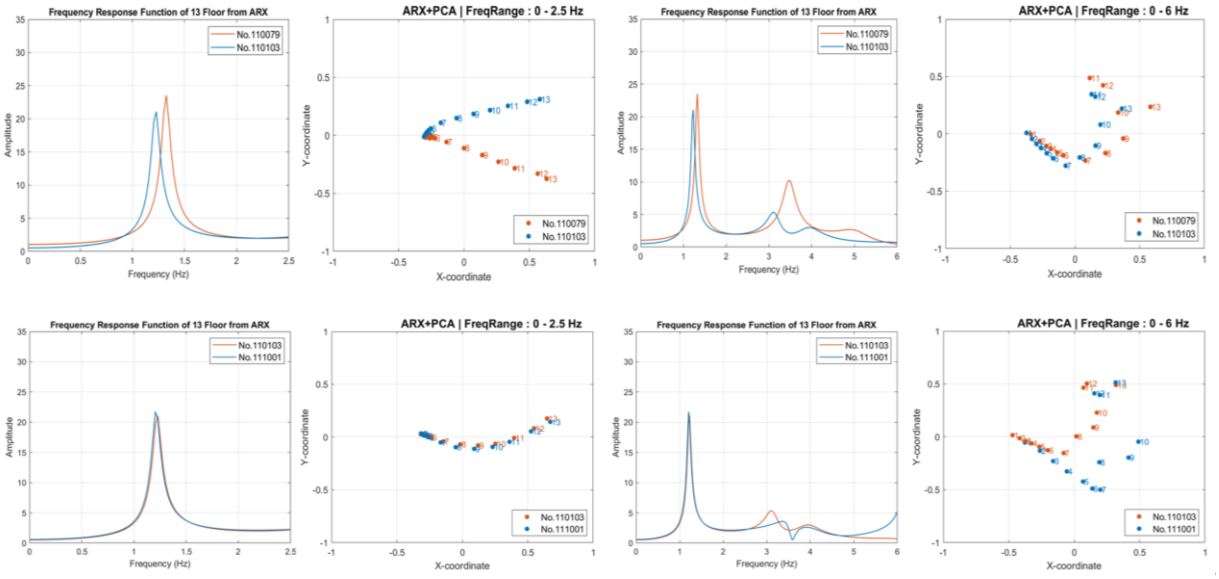

Figure 7: Comparison of 2-diension PCA map between two seismic events (No.110079 vs. No.110103 and No.110103 vs. No.111001) using two frequency band from the identified FRF.

The FRF at the 13th floor is also plotted. Consider the frequency band between 0.0 Hz ad 2.5 Hz in the analysis, no big difference from 2D-PCA map between No.110103 vs. No.111001 (the FRF at 13th floor from these two test cases is almost the same). But for No.110079 and No.110103, the fundamental frequency (bandwidth 0.0 Hz ~ 2.5 Hz) was shifted so that the 2D-PCA map showed different phases and differences of distance at each floor. If the bandwidth of FRF included high frequency (i.e., from 0.0 Hz to 6.0 Hz) in the analysis, the distance of $\boldsymbol{P_{A/B}}$ in 2D-PCA map became larger due to the variation of FRF in the 2nd mode. The distance between two test cases, particularly in between No.110079 and No.110103, is much larger in the upper floors because of the big difference of FRF between these two test cases. It is concluded that through the 2D-PCA map, the difference from two seismic events from floor FRF and the corresponding mode can be identified easily.

Measured Difference Between Test Case and Reference Case Through PCA

As shown in Figure 8, the reference model created from the seismic response data (or experiments) performed over the healthy structure. Since these seven seismic response data are collected under earthquake excitation with PGA less than 10 gal, FRF collected from the initial seven seismic response data performs the health structure. PCA is applied to the matrix that contains dynamical responses (FRF in this study) at a specific floor location from all reference test cases. From which the major principal components $\tilde{P}$ are formed. With the new test (new seismic response data) a test FRF is calculated. The Q-index is a measure of the difference, or the residual between a test sample and its projection into the reference model. The Q-index of the i-th sample (from new experiment) vector x_i is defined as follows:

$$Q_i = e_i e_i^T = x_i (I - \tilde{P}\,\tilde{P}^T) x_i^T = x_i x_i^T - x_i \tilde{P}\,\tilde{P}^T x_i^T \quad (6)$$

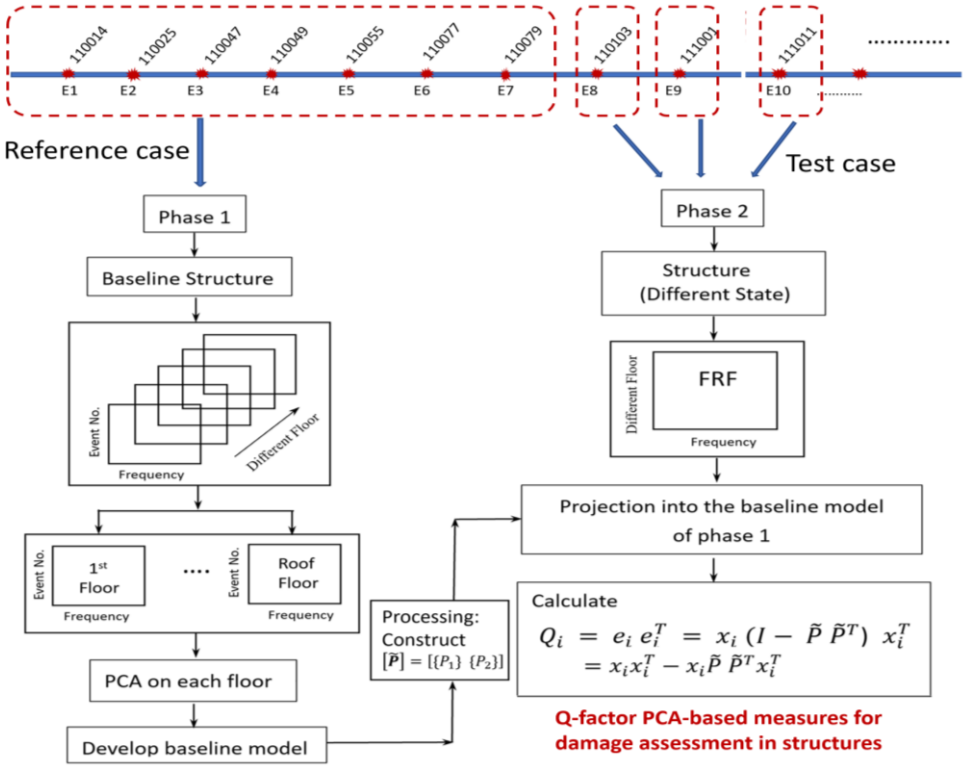

Figure 8: General scheme based on PCA for detecting and distinguishing damages structures.

Figure 9 shows values of the Q-index from serval test cases. It is observed that the Q-index values from test cases No.110103, No.111001 and 111019 are higher in upper floors (above 9th floor) than other test cases. The Q-index from event No,110103 test case shows a highest value among all test cases in every floor of the building. Q-index indicates how well each test case conforms to the PCA model. It is a measure of the difference or the residual between a test case and its projection into the principal components retained in the model. A large Q-index means the difference on FRF at that particular floor.

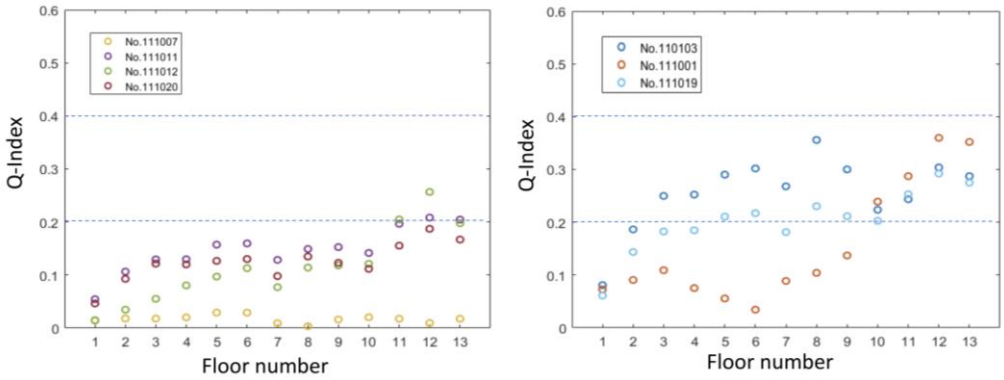

Figure 9. Projection of several test cases in to the PCA model (from reference model): Q-index.

ONCLUSIONS

This paper presents the use of signal analysis techniques to detect and distinguish the abnormal structural responses during a series of earthquake excitations. Through the correlation analysis of floor response spectrogram (via continuous wavelet analysis and the stochastic subspace identification on the building response under operating condition), the long-term variation of dominant frequencies and mode shape curvatures of the building can be identified. Moreover, the use of the principal component analysis (PCA) and the Q-index may detect and locate the change of the building seismic response. The results verify the applicability of a signal processing-based approach (without a physical analysis of the wave propagation process) to distinguish abnormal vibrations of an existing building (i.e. a new 13-story compound NCREE building) during earthquake excitations.

ACKNOWLEDGMENTS

The authors are grateful to the Structural Monitoring and Control Division of NCREE and P-Waver Inc. to provide the building vibration data for this study.

REFERENCES

Brincker, R., L.M. Zhang, and P. Andersen (2001) “Modal identification from output-only system using frequency domain decomposition,” Smart Materials and Structures, Vol.10, No.3, pp. 441-445.

Chen, W.H., Hseuh, W. Loh, K., Loh, C.H. (2022) “Damage evaluation of seismic response of structure through time-frequency analysis technique,” Structural Monitoring and Maintenance, *9(2) 107-127.*

Imregun, M., and Ewins, D.J., (1993)," Realization of complex mode shapes", Proceeding. of 11th International Modal Analysis Conference, pp. 1303·1309.

Mrabet, E., M. Abdelghani, and N.B. Kahla (2014) “A New Criterion for the Stabilization Diagram Used with Stochastic Subspace Identification Methods: An Application to an Aircraft Skeleton,” Shock and Vibration, vol.2014, pp.1-8.

Noh, H. Y., K. K., Nair, D. G., Lignos, and A. S., Kiremidjian (2011) “Use of Wavelet-Based Damage-Sensitive Features for Structural Damage Diagnosis Using Strong Motion Data,” Journal of Structural Engineering, Vol.137, No.10, pp.1215-1228.

Overschee, P. Van, and B. De Moor (1996) “Implementation and Applications,” *Subspace Identification for Linear Systems*, pp.161-196.

Pioldi, F., R. Ferrari, and E. Rizzi (2016) “Output-only modal dynamic identification of frames by a refined FDD algorithm at seismic input and high damping,” Mechanical Systems and Signal Processing Vol.68-69, pp.265-291.

Todorovska, M. I. (2001) “Estimation of Instantaneous Frequency of Signals Using the Continuous Wavelet Transform,” University of Southern California, report CE pp.01-07.

AN EXPERIMENTAL STUDY ON SEISMIC RESPONSE ESTIMATION USING MEASURED ACCELERATION DATA

Abhishek Regmi[1] and Pennung Warnitchai[2]
1. Research Associate, Structural Engineering, Department of Civil and Infrastructure Engineering, Asian Institute of Technology, Thailand.
2. Professor, Structural Engineering, Department of Civil and Infrastructure Engineering, Asian Institute of Technology, Thailand.
Email: abhishek.regmi53@gmail.com, pennung.ait@gmail.com

ABSTRACT

This paper presents an experimental study to test a seismic response estimation method by using limited acceleration data. Unlike many other techniques, this method estimates both the displacement as well as force-based seismic responses. This will eventually help in a rapid and accurate identification of structural damage. In this study, a multi-degree freedom steel cantilever system was built for the experiment. The specimen was placed on a shaking table with which real ground motions were simulated for the test. Acceleration sensors were attached at a few levels of the given specimen. The recorded acceleration time-history signals were then passed through a proposed orthogonal filter to extract the modal accelerations. These modal accelerations were converted to modal coordinates by double integration. After combining the modal coordinates with the dynamic properties of the specimen identified from the ambient vibration test, the responses in each mode were obtained. Then, the overall seismic responses were estimated by summing up the modal responses. Finally, the given method was validated by comparing the estimated shear and bending strain responses with the strain values directly obtained from the strain gauges attached to the specimen.

Keywords: seismic responses, orthogonal filter, modal concept, shaking table test

INTRODUCTION

Earthquake related hazards can cause severe damage to the built infrastructures. Also, there may be damage in the important structures such as highway bridges, hospital buildings, etc. This may cause significant physical and economical loss if not identified and restrengthened within a certain time. From the Great East Japan earthquake in 2011, it was realized that the people faced a lot of difficulty to return to their home. and also there was no any system to rapidly diagnose the structural damage that resulted to a chaotic situation (Tsuchihashi & Yasuda, 2017). Thus, an early detection of damage has a significant role both in preventing the panic condition and also minimizing the physical and economical loss after an earthquake.

The field of structural health monitoring has developed several ways to detect the damage in the structure. Vibration based damage detection approach is one of them (Doebling et al., 1996). Damage in any structural system can be directly linked to the change of its dynamic properties (Rytter, 1993). Here, in the vibration-based approach, the acceleration response of the structure is monitored either under ambient condition or with some forced excitation. These responses are then used to extract the dynamic characteristics of the given structure such as Eigen frequencies, mode shapes, and damping. Analyzing those dynamic properties, the structural performance can be evaluated (Frigui et al., 2018; Slawu, 1997). The change in dynamic properties of the structure is normally small even when the damage is severe, and this small change may be masked by the variation of these properties from some environmental factors such as temperature, wind, etc. (Saisi et al., 2015). Due to this, the study of change in dynamic properties is not enough for the detection of structural damage.

Damage to structural and non-structural components is associated with some response parameters. The structural response in terms of acceleration can be related to the falling of ceilings, toppling of non-structural components. Similarly, the inter-story drift can be used to evaluate the damage in infill walls and also the shear force and bending moment can be related to the damage of structural components such as beams and columns. So, the damage evaluation should be more accurate, if we could either measure these response parameters directly or estimate them from other responses. Since the acceleration responses are relatively easier to measure compare to other response parameters, here the measured acceleration responses will be used to estimate other damage-related responses. In this study, the main idea is to measure the acceleration responses from the structure and extract the modal responses in terms of modal coordinates using a modal decomposition approach. Then by applying the modal concept, taking the modal coordinates, other responses will be evaluated. For this it would be ideal to have acceleration sensors installed in every floor. But in reality, acceleration sensors are installed only on some floors in most of the cases. Thus, the methodology needs to be based in these limited acceleration data.

This technique of computing response parameters using limited acceleration data has already been carried out by Mori Buildings, a real estate company in Japan. A modal synthesis approach has been used by Kasai Laboratory to get the modal accelerations from the measured acceleration data (Tsuchihashi & Yasuda, 2017). Using this approach, the floor acceleration in non-instrumented floors and inter-story drift were computed. Then the maximum responses computed were compared with acceptance limits to determine the level of damage. However, the force-related responses were not computed using this approach and also, the least square technique for modal decomposition was used which do not take into account the orthogonality of the modes. With regard to this, (Sinthumongkhonchai, n.d.), identified the orthogonal filter approach to extract the modal acceleration responses using the limited number of acceleration responses measured. Here, both the displacement and force related responses were computed. Though this method was numerically tested in different structures, the experimental verification was yet to be done.

Thus, in this research, with the intent of experimentally studying the seismic response estimation method along with using the orthogonal filter approach, 2-meter-tall laboratory model was built in the structural engineering lab at Asian Institute of Technology. The model consisted of eight vertical levels with the same quantity of mass attached to it in order to depict it as a multi-degree freedom structural system. This model was subjected to several real ground motions simulated using a shaking table. Accelerometers were attached at three different levels along with some strain gauges at the base and at the mid height. The orthogonal filter approach was used to extract the modal accelerations and those modal accelerations were then converted to modal coordinates using the double integration. These modal displacements were then used to compute all the modal responses. Then all the displacement and force based seismic responses were estimated in each degree of freedom combining the modal responses. Finally, the seismic response estimation approach was verified by comparing its strain results with the one directly obtained from the strain gauges attached to the specimen.

SEISMIC RESPONSE ESTIMATION METHOD

This research study focuses on deriving the overall seismic responses of the structure just by using the acceleration response data of the given structure. The acceleration responses are measured only from the limited number of nodes of the given structure. For this the sensors should be placed in such a way that the optimum results can be obtained. During any seismic events these sensors will record the acceleration responses from some locations of the given structure. Here, in this section, the technique of estimating the overall seismic responses of the structure using the limited acceleration data will be discussed.

Consider the multi-degree freedom system as shown in Figure 1 of which the overall responses are to be evaluated using the measured acceleration data. This structure is also supposed to be vibrating along the uniaxial direction thus having a total of 8 degrees of freedom. Using the concept of modal

orthogonality (Chopra & Goel, 2004), the measured acceleration responses can be decomposed using the orthogonal filter approach.

The orthogonal Filter Approach is based on the concept of orthogonality of the modes i.e., the mode shape vectors, ($\boldsymbol{\phi_n}$), are orthogonal to each other with respect to the mass($\mathbf{M}$) and stiffness matrix($\mathbf{K}$) as shown in Eqs. 1a, 1b, 2a, and 2b.

$$\boldsymbol{\phi_n^T}\mathbf{M}\boldsymbol{\phi_r} = 0, \qquad for\ n \neq r \tag{1a}$$

$$\boldsymbol{\phi_r^T}\mathbf{M}\boldsymbol{\phi_r} = M_r \tag{1b}$$

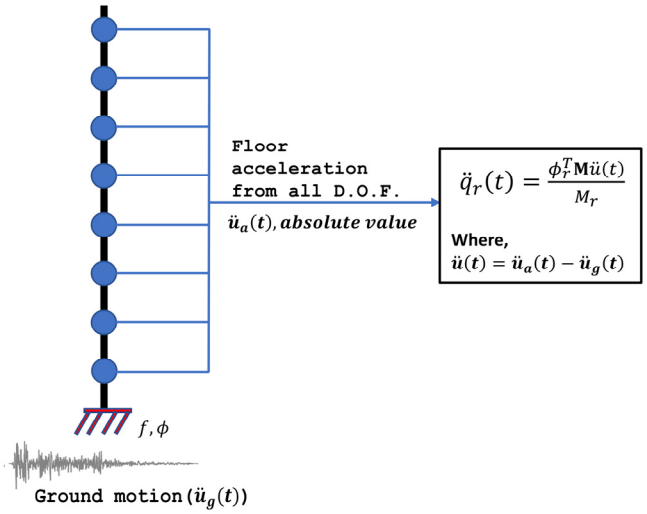

Figure 1. Extraction of modal acceleration from a multi degree freedom system with acceleration measured from all Degrees of Freedom (DOF)

$$\boldsymbol{\phi_n^T}\mathbf{K}\boldsymbol{\phi_r} = 0, \qquad for\ n \neq r \tag{2a}$$

$$\boldsymbol{\phi_r^T}\mathbf{K}\boldsymbol{\phi_r} = K_r \tag{2b}$$

M_r and K_r, represents the modal mass and modal stiffness at r^{th} mode respectively.

Now, using the modal concept, relative acceleration vector, $\ddot{\boldsymbol{u}}(\boldsymbol{t})$, at any location can be expressed as the sum of many modal responses. This relative acceleration vector is obtained by deducting the acceleration at the base from the acceleration at the given floor level.

$$\ddot{\boldsymbol{u}}(\boldsymbol{t}) = \sum_{n=1}^{m} \boldsymbol{\phi_n}\ddot{q}_n = \boldsymbol{\phi_1}\ddot{q}_1 + \boldsymbol{\phi_2}\ddot{q}_2 + \boldsymbol{\phi_3}\ddot{q}_3 + \cdots + \boldsymbol{\phi_r}\ddot{q}_r + \ldots + \boldsymbol{\phi_m}\ddot{q}_m \tag{3}$$

On multiplying Eq. 3 by $\boldsymbol{\phi_r^T}\mathbf{M}$ and applying the modal orthogonality concept from Eqs.1a, and 1b we get,

$$\boldsymbol{\phi_r^T}\mathbf{M}\ddot{\boldsymbol{u}}(\boldsymbol{t}) = \boldsymbol{\phi_r^T}\mathbf{M}\boldsymbol{\phi_r}\ddot{q}_r(t) = M_r\ddot{q}_r(t) \tag{4}$$

Hence,

$$\ddot{q}_r(t) = \frac{\boldsymbol{\phi_r^T}\mathbf{M}\ddot{\boldsymbol{u}}(\boldsymbol{t})}{M_r} \tag{5}$$

Thus, in this way the modal acceleration, $\ddot{q}_r(t)$, can be determined for any given r^{th} mode. As per the above derivation, the acceleration response from each and every floor should be known. Since in reality, the acceleration sensors are placed only on some floor levels, this approach needs some modification.

Now, let's take the accelerations from just three floor levels as shown in Figure 2**.** with the reduced relative acceleration vector, $\ddot{u}_R(t)$, and reduced mode shape vector, ϕ_{nR}, which is obtained by taking the mode shape vectors only at the instrumented floor level. Since we are dealing with the acceleration vectors only at few floor levels, the reduced mode shape vectors need to be used unlike the mode shape vectors used earlier. To extract the modal acceleration in a similar way as shown in Eq. 5, we need to find a new matrix in place of **M,** where all these reduced mode shape vectors are orthogonal to each other. This new matrix is named as matrix **A.** Thus, using matrix **A**, Eqs. 6a, and 6b can be written.

$$\phi_{nR}^T \mathbf{A} \phi_{rR} = 0 \quad , \; for\; n \neq r \tag{6a}$$

$$\phi_{rR}^T \mathbf{A} \phi_{rR} = A_r \tag{6b}$$

The matrix, **A**, is the symmetrical matrix with the row and column equal to the number of D.O.F on which the acceleration sensors are placed. For the given MDOF system with three accelerometers attached, matrix **A** is the 3X3 symmetrical matrix.

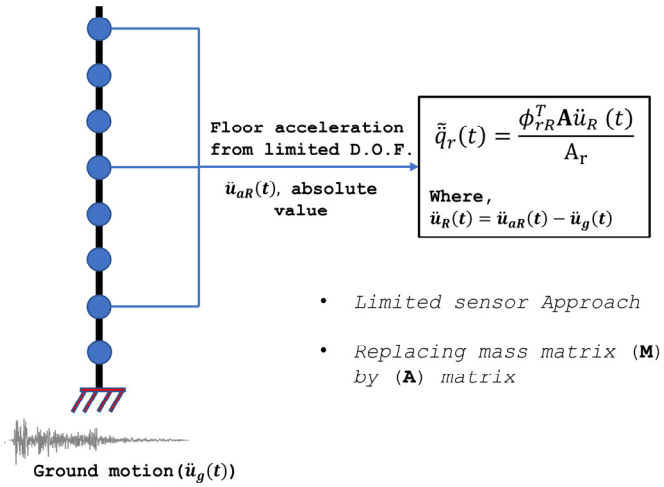

Figure 2. Extracting modal accelerations from a multi degree freedom system with acceleration measured from limited number of nodes

It is possible to find the matrix **A** that satisfies Eqs. 6a, and 6b, which can then be used to extract the modal acceleration from limited acceleration data as shown in Eq. 7.

$$\tilde{\ddot{q}}_r(t) = \frac{\boldsymbol{\phi_{rR}^T \mathbf{A} \ddot{u}_R(t)}}{A_r} \tag{7}$$

Here, $\tilde{\ddot{q}}_r(t)$ is the modal acceleration of the r^{th} mode obtained from the orthogonal filter approach using limited acceleration data.

Now the modal accelerations obtained are doubly integrated to compute the modal coordinates. Then the displacement-based responses such as displacement, inter-story drift, etc. can be computed by combining these modal coordinates with the mode shape vectors obtained from the modal identification as shown in Figure 3. The force-based responses like shear force and bending moment, can be estimated by using the modal coordinates along with the modal frequencies, mode shape

vectors and generalized force factor as illustrated in Figure 4. This approach is for the linear system where all the force-related responses in each mode are linearly proportional to the modal coordinate and their relationship can be derived as illustrated in Figure 4. However, if the structural response exceeds elastic limit, the concept of Uncoupled Modal Response History Analysis (UMRHA) needs to be applied, and the deformation-related responses are still approximately proportional to the modal coordinate but the force-related responses are not. They are proportional to modal force parameter (Mehmood et al., 2018). The concept is believed to be applicable in the nonlinear range, but it is beyond the scope of this study.

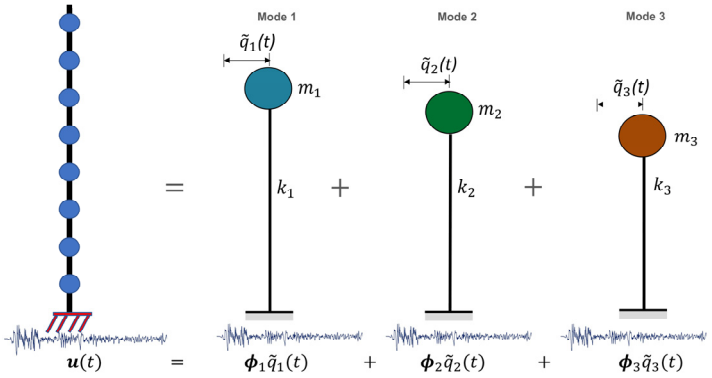

Figure 3. Illustration of modal concept to obtain the response by combining the modal responses

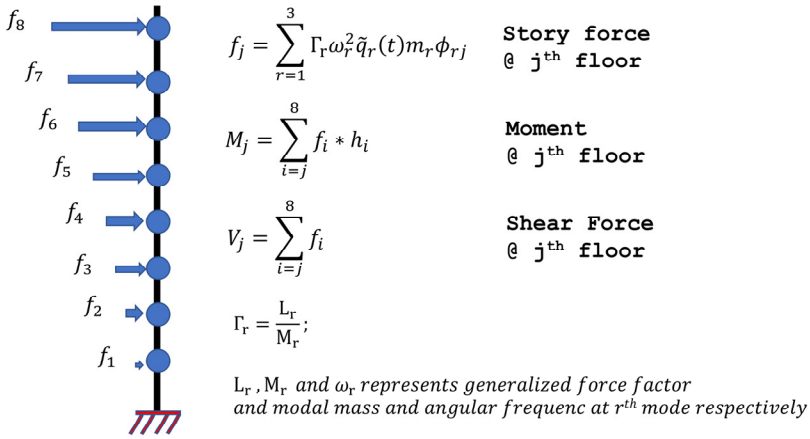

Figure 4. Computation of force-based seismic responses

EXPERIMENTAL VALIDATION AND RESULTS

Experimental study was done by taking a 2-meter-tall steel cantilever beam with equal masses attached at eight equal levels. Rectangular hollow steel tube segment measuring 50 mm by 25 mm and having a 2 mm thickness was used as a cantilever beam. The tensile yield strength of the steel was 235Mpa. Steel plates with combined mass of 10.85kg was used at each node. The specimen was installed on the shaking table with its base plate using nut-bolt connection. The shaking table driven by the servo-controlled hydraulic actuator, with the maximum displacement of 75mm, was used to simulate the real ground motions.

Modal Identification

After fixing the model on the table, ambient vibration test was conducted to determine its modal properties. The piezo-resistive strain gauge-based type acceleration transducers with the frequency response from DC to 60Hz, were used as the acceleration sensors. Sensors were placed in each level

with one placed on the top as a reference station. While conducting the Ambient vibration Test, external ambient forces from the table fan and floor tapping were used. Modal frequencies and mode shapes of the structure were determined by transforming the time signal obtained to the frequency response using Fast Fourier transformation. Thus, obtained mode shapes were then used for developing the orthogonal filter.

Application of ground motions and results obtained

The experimental set up was done as shown in Figure 5**.** Considering the limitations of shaking table, the design of model and the selection of ground motion was done. Several ground motions were simulated for the test. Here, only two of them having different response spectrum are presented, as listed in Table 1. In order to record the acceleration, accelerometers, as shown at the left-hand side of the Figure 5, were placed at 2nd, 5th, and 8th level. One accelerometer was placed on the shaking table to measure the applied input ground motion. Two diagonal strain gauges and two vertical strain gauges, as shown in the right-hand side of the Figure 5, were attached for measuring the shear strain and bending strain respectively.

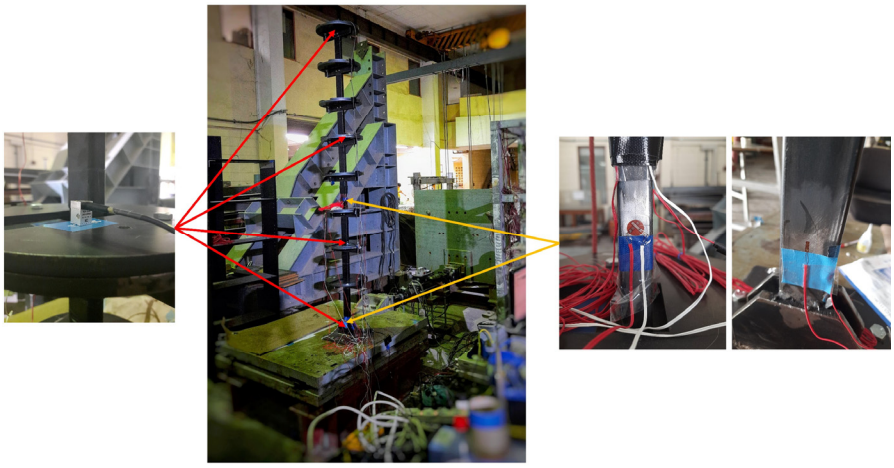

Figure 5. Experimental setup showing the steel cantilever specimen installed on the shaking table with accelerometers and strain gauges attached to it

Table 1 Selected earthquake motions for simulation

No.	Earthquake	Year	Station	PGA(g)	Scale Factor	Applied PGA(g)
1.	Kobe (Japan)	1995	Kakogawa (CUE90)	0.3447	0.1	0.03447
2.	Friuli (Italy)	1976	Tolmezzo (000)	0.3513	1.8	0.63234

The acceleration data recorded was processed as per the method discussed in section 2. The modal accelerations were extracted using the orthogonal filter approach and then converted to the modal coordinates. By using the modal coordinates and the dynamic properties obtained from the ambient vibration test, modal responses were computed. Finally, the modal responses were combined to obtain the displacement and force-based seismic responses. Basically, after computing the bending moment and shear force at those two locations, the corresponding strains were computed. In order to validate the responses computed from this technique, the results of shear and bending strains were compared with those directly obtained from the strain gauges. This comparison is illustrated in Figure 6 and Figure 7. For both figures, the upper plot is for the strain at base and the lower one for that at mid-level. Here, the case for Kobe earthquake depicts the very low magnitude seismic event whereas the Friuli earthquake has a very high peak ground acceleration of approximately 0.6g. The time history results of estimated strain values of both bending and shear are found to be perfectly matching to the reference

measurement obtained directly from the strain gauges. Also, the measured acceleration time histories and the estimated strain time histories were found to be different. This demonstrates that the proposed modal based method is able to estimate the force-based responses which are different from the measured ones.

The measured bending strain results show higher percent contribution from the 2nd mode at the mid height point than that at the base. Unlike this, the higher contribution of shear strain from the 2nd mode was seen at the base than that at the mid height. However, all these are accurately estimated by the proposed approach.

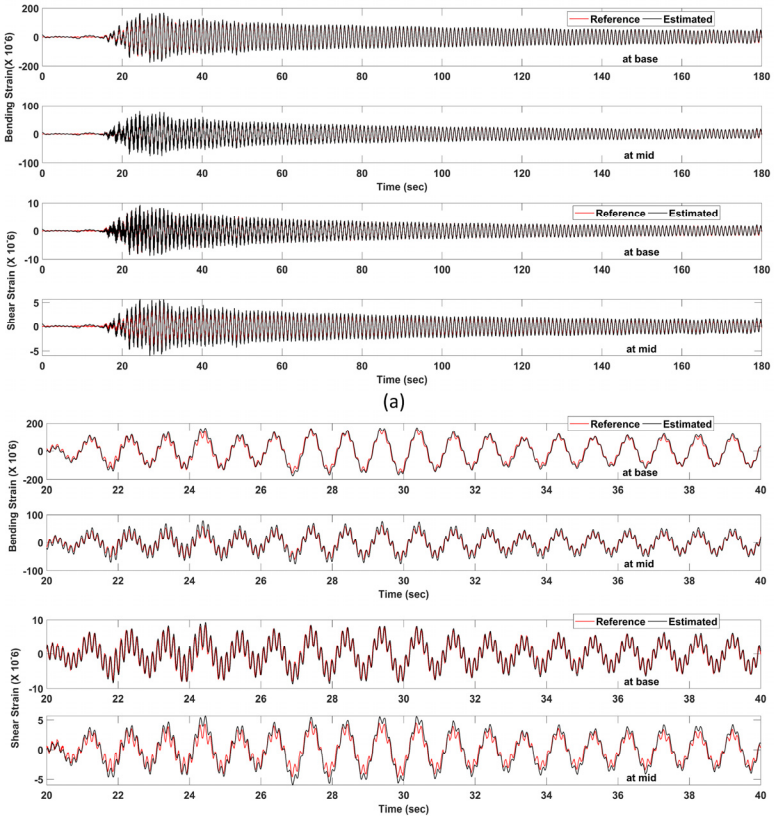

Figure 6 Comparison of bending and shear strain for Kobe earthquake; a) entire time; b) from 20s to 40s

CONCLUSIONS

Thus, in this study a new methodology to estimate the overall seismic responses by only measuring the limited floor accelerations is proposed and experimentally tested. It is based on the concept of modal decomposition where the measured acceleration responses are decomposed into modal coordinates. Then by applying the concept of proportionality of force and displacement-based responses with the modal coordinates, all the seismic responses are computed. For this, a shaking table test of a multi-degree-of-freedom steel vertical column is conducted where the accelerometers were placed only at few floor levels along with the strain gauges attached at two levels for measuring the bending and shear strain. The bending and shear strain computed after obtaining the force-related responses are then compared with those obtained directly from the strain gauges. The results show that the estimated and measured strain responses are exactly matching with each other which verifies the key concept of modal decomposition used in this research. The methodology used is able to give accurate estimate of all the force and displacement-based seismic responses. Furthermore, future work to check the effectiveness of this method in the inelastic range is being planned.

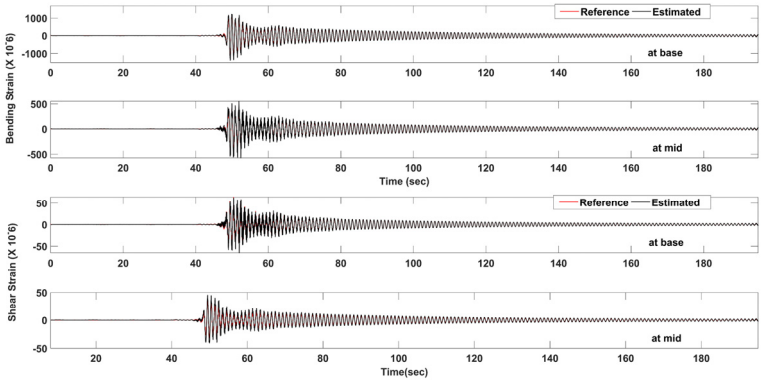

(a)

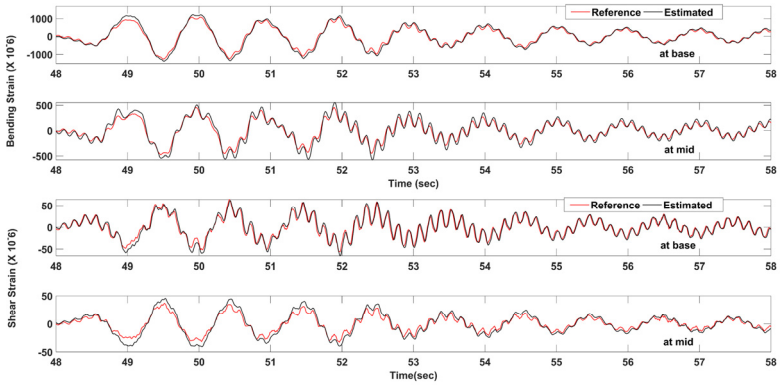

(b)

Figure 7. Comparison of bending and shear strain for Friuli earthquake; a) entire time; b) from 48s to 58s

REFERENCES

Chopra, A. K., & Goel, R. K. (2004). A modal pushover analysis procedure to estimate seismic demands for unsymmetric-plan buildings. *Earthquake Engineering and Structural Dynamics*, *33*(8), 903–927. https://doi.org/10.1002/eqe.380

Doebling, S. W., Farrar, C. R., Prime, M. B., & Shevitz, D. W. (1996). *Damage identification and health monitoring of structural and mechanical systems from changes in their vibration characteristics: A literature review*. https://doi.org/10.2172/249299

Frigui, F., Faye, J.-P., Martin, C., Dalverny, O., Pérès, F., & Judenherc, S. (2018). Global methodology for damage detection and localization in civil engineering structures. *Engineering Structures*, *171*, 686–695.

Mehmood, T., Warnitchai, P., & Suwansaya, P. (2018). Seismic Evaluation of Tall Buildings Using a Simplified but Accurate Analysis Procedure. *Journal of Earthquake Engineering*, *22*(3), 356–381. https://doi.org/10.1080/13632469.2016.1224742

Rytter. (1993). *Aalborg Universitet Vibrational Based Inspection of Civil Engineering Structures Rytter , Anders*.

Saisi, A., Gentile, C., & Guidobaldi, M. (2015). Post-earthquake continuous dynamic monitoring of the Gabbia Tower in Mantua, Italy. *Construction and Building Materials*, *81*, 101–112.

Sinthumongkhonchai, C. (n.d.). *Evaluation of Seismic Damage of Tall Buildings from Acceleration Response Time Histories by a Modal Decomposition Approach*. *December 2020*.

Slawu, O. S. (1997). Detection of structural damage through changes in frequency: a review. *Engineering Structures*, *19*(9), 718–723.

Tsuchihashi, T., & Yasuda, M. (2017). Rapid Diagnosis Systems Using Accelerometers in Seismic Damage of Tall Buildings. *International Journal of High-Rise Buildings*, *6*(3), 207–216. https://doi.org/10.21022/ijhrb.2017.6.3.207

EXTRACTING BUILDING RESPONSE FROM THE LOW-COST QSIS SEISMIC NETWORK (QSN) FOR STRUCTURE INTEGRITY MONITORING

Wen-Tzong Liang[1] Utpal Kumar[2] and Kuo-Fong Ma[1]
1. Institute of Earth Sciences, Academia Sinica, Taipei, Taiwan, R.O.C.
2. Berkeley Seismological Laboratory, University of California, Berkeley, CA, USA
Email: wtl@earth.sinica.edu.tw, utpalkumar@berkeley.edu, fong@earth.sinica.edu.tw

ABSTRACT

To monitor the structural integrity, we have extracted the building response, shaking intensity, and associated resonance parameters from the seismic records by the newly developed QSIS (Quake Structure Integrity Sensor) Seismic Network (QSN). The development of QSN aims to support the community with an affordable and reliable building health monitoring system, which is composed of three primary components of low-cost and high-sensitivity sensor devices, data acquisition system and web data services. After shaker testing with standard seismometer, the collected acceleration records has been proven to be reliable with a root-mean-square noise level of 0.15 gal. Both the dominant resonance frequencies and the building response extracted from QSN by using the seismic interferometry can reveal the seismic wavefield in the building, which can be used to characterize the shaking behavior of the building. With the design of QSN, the building monitoring for seismic risk assessment and the rapid array mobilization for aftershocks become easier for researchers.

Keywords: low-cost seismic network, QSIS, building health monitoring

INTRODUCTION

Buildings might be damaged due to the natural hazards, such as earthquakes and winds, and man-made accidents, such as fires and gas explosion, during their long-term use. To understand the integrity of the building, the continuous structural health monitoring (SHM) has become an important issue for sustainable development of urban cities and seismic hazard mitigation. A low-cost but reliable monitoring system is essential to widely promote the SHM for mitigating any potential hazards to the building (Clayton et al., 2011;2015). We have developed a new SHM system which comprises low-cost MEMS sensor device, data acquisition system and web data services. Both triggered mode (event-based data transmission) and the continuous data streaming are included in the system. In this paper, we will introduce the latest achievement of the QSIS seismic network.

QSIS SEISMIC NETWORK

The QSN is composed of three primary components, they are the QSIS sensor device, the QSIS data acquisition system, and the web data services.

- QSIS sensor device
  To design an affordable and reliable accelerometer, we adopt a high-sensitivity and low-cost MEMS sensor together with a micro-computer to not only record and stream ground motion data, but also process the data in real-time. Alerts can be issued onsite based on customized criteria.
- QSIS Data Acquisition System
  The data collected on each device will be transmitted to the cloud server in either triggered mode or continuous mode. An associator module is running on the server to associate the record to any events occurred within a reasonable time window. In addition to the earthquakes,

we have also successfully recorded thunder signals in two buildings during a thunderstorm. Figure 1 shows the concept of the QSIS data acquisition system.

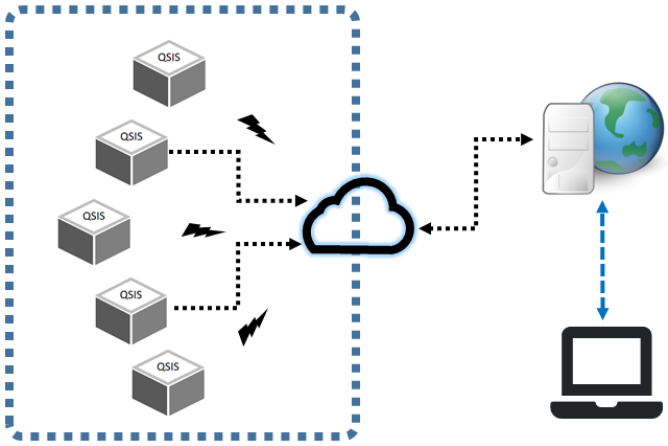

Figure 1. The concept of the QSIS Data Acquisition System. The data collected by those QSIS devices in a building will be transmitted to the cloud server in either triggered mode or continuous mode. Users can browse these data or information at the QSN website.

- Web Data Services
  To manage both the data and the status of health (SOH) of sensor devices, we have developed codes to demonstrate event data and SOH of each device. The dominant frequencies and associated spectral amplitudes, shaking intensity, H/V spectral ratios and the building responses will be computed regularly once the event data arrived at the server. In this case, the long-term building health monitoring can be achieved by examining the outcomes from these analyses. Figure 2 demonstrates the basic web services from event selection, building/site selection and seismic waveforms viewing functions. The color of marks on the map represents focal depth and PGAs respectively.

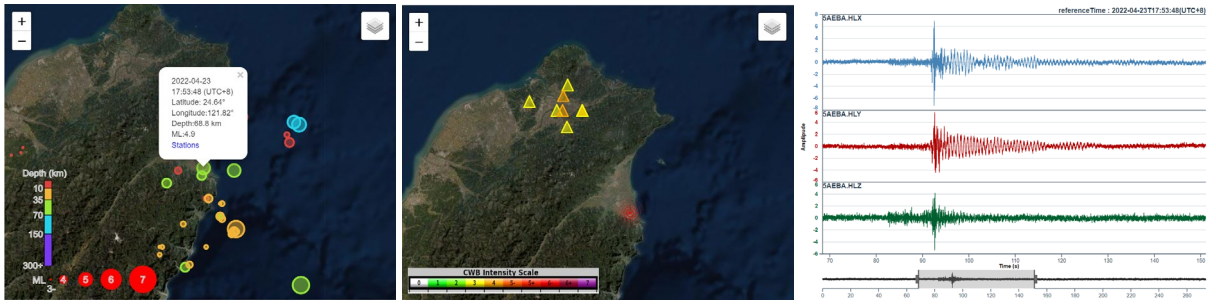

Figure 2. Some functions of QSN web data services. Participants can select any earthquake event to see the records associated to individual building/site from these web services.

QSIS WAVEFORM DATA

Most of the QSIS devices are aligned to the wall to constrain the shaking behavior related to the building geometry. Conventionally, the Y-axis is oriented along the longer axis of the building. Figure 3 shows the waveforms recorded at a 9-story building and generated by a ~50-kilometer-away M4.9 earthquake with a depth of 69 km beneath the Ilan, Taiwan on 2022-04-23. A significant long-lasting resonance at longer period above the third floor can be easily identified. On the other hand, a higher frequency shaking around the S arrival is amplified at the fifth and sixth floors. This pattern can be verified in the frequency domain as shown in the Figure 4. We believe these two dominant natural frequencies (f_1, f_2) are comparable to the fundamental and the first higher translational modes of the building. The f_2/f_1 ratios (4.51/1.39=3.24) in the Y directions are slightly smaller than the ratios

(5.073/1.434=3.54) in the X directions, which means that the shear stiffness relates in different way to the bending stiffness for both directions (*Kohler et al., 2013*). These frequencies and ratios can be used to indicate if the building behavior deviates from the normal condition. It is worthwhile to notice that there are two fundamental natural frequencies, 1.39 and 1.50 Hz, in the X-direction. This accounts for the beating envelope in the higher floor resonance in the X-direction (Fig. 5, right). Furthermore, the f_2 splits into 4 frequencies (4.42, 4.59, 5.05, and 5.26 Hz). Noticeably, the shaking pattern in the X-direction is more complicated than that in the Y-direction.

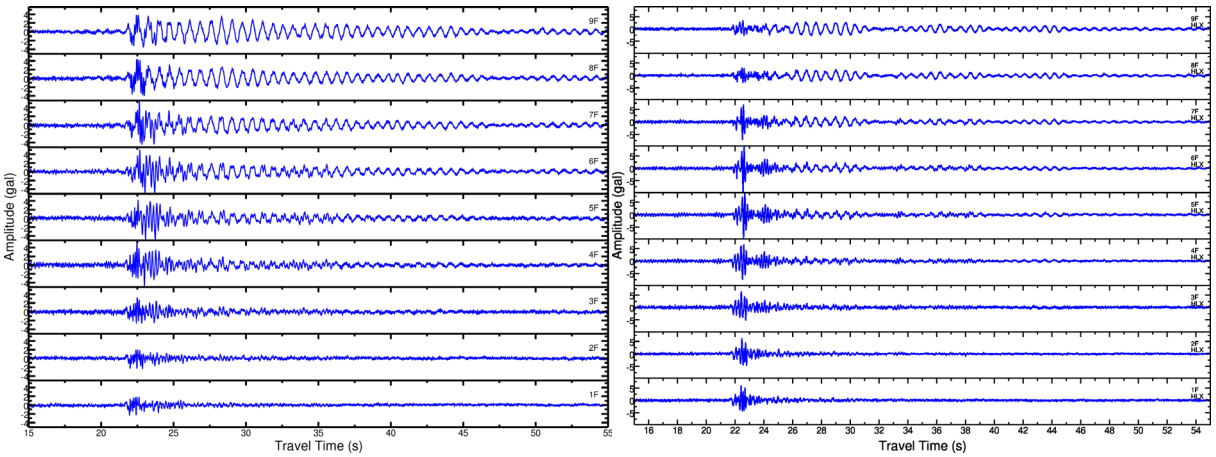

Figure 3. QSN seismic waveforms recorded at a 9+ story building in Taipei that is ~50 km away from the M4.9 2022-04-23 earthquake, which is located 69 km beneath the Ilan, Taiwan area. (left) Y-direction, (right) X-direction.

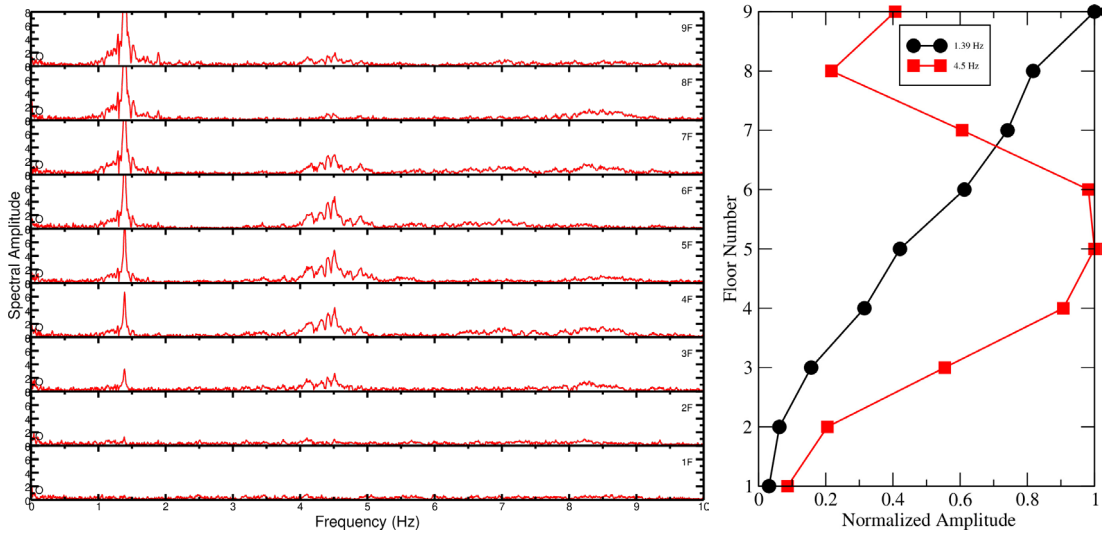

Figure 4. (left) Stacked amplitude spectra for each floor of the 9+-story building in the Y direction in Taipei. The frequencies of 1.39 and 4.51 Hz correspond to the fundamental and first higher mode of building resonance. (right) Normalized amplitudes for each floor for the first two dominant natural frequencies.

BUILDING RESPONSE FROM SEISMIC INTERFEROMETRY

We apply the seismic interferometry method proposed by *Snieder and Şafak* (2006) to those waveform data recorded by the QSIS sensor devices installed in the building. Figure 5 shows the waveforms deconvolved with the signal recorded on the first floor. The first onset of the deconvolved waveforms is a wave that propagates upward in the building. The reflection of this wave by the top of the building

is visible as the second peak in the waveforms that propagate downward (*Snieder and Şafak*, 2006). To further investigate the shear wave velocity propagating in the building, we selected the deconvolved waveform for the 5th floor, which shows two clear peaks in the early part of the waveform. The estimated shear velocity in the building is 231.4 m/s, which is generally in agreement with the relation derived from a pure shear beam model, $c=4Hf_1=4\times45.6\times1.39=253.5$ m/s (*Snieder and Şafak*, 2006). The shear velocity propagating in the building is widely accepted in the SHM studies (e.g., *Clotaire and Guéguen*, 2018). Unfortunately, we do not have a QSIS device installed on the roof because of the shortage of power supply. Therefore, the method to deconvolve the waves with the signal recorded on the 9th floor is not applied in this work.

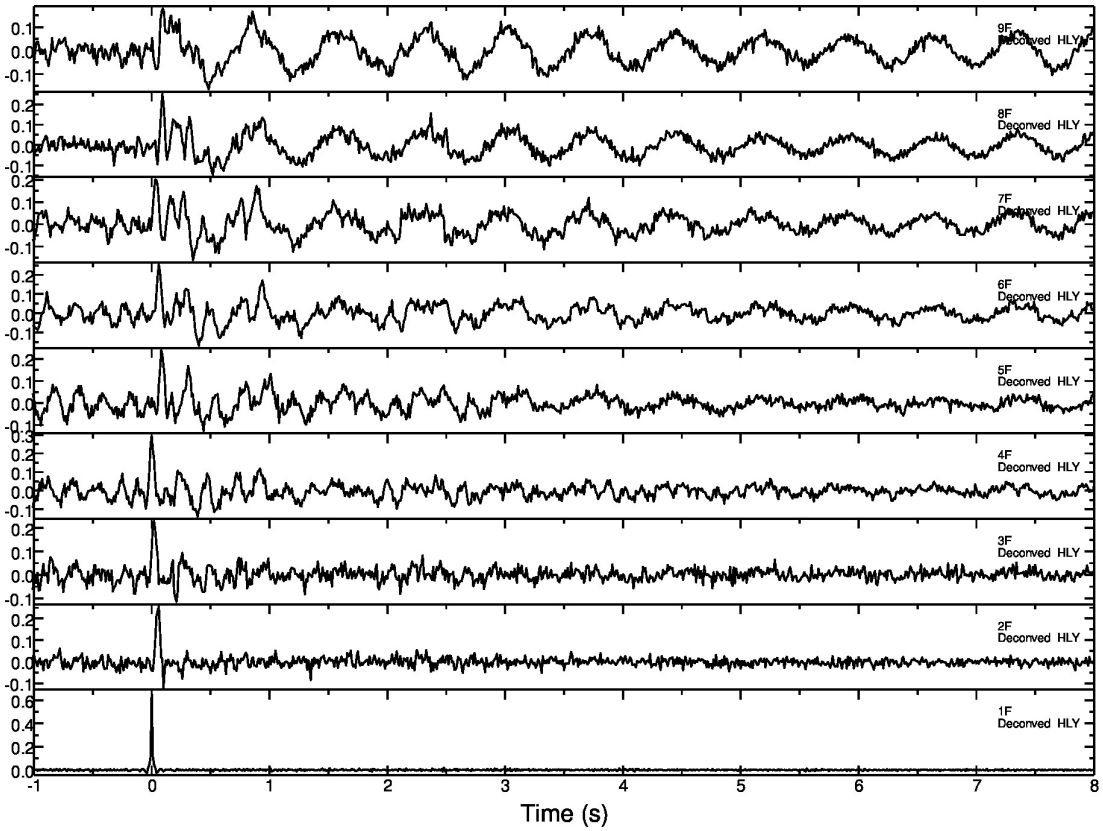

Figure 5. Waveforms deconvolved with the signal recorded at the first floor. The natural frequencies of the fundamental mode at higher floors are significant.

CONCLUSIONS

The development of the QSIS seismic network (QSN) is aimed at supporting the long-term structural health monitoring. The signals recorded by QSN from moderate to large earthquakes have been proven suitable for research-based studies. A further step toward more practical application is on-going.

ACKNOWLEDGMENTS

We thank Mr. Hao-Te Chiu and Mr. Chung-Hung Lo for their technical support on both hardware implementation and web service coding. This work is supported by the Ministry of Science and Technology, Taiwan under the Belmont Forum project of resilient societies through smart-city technology: Assessing earthquake risk in ultra-high resolution with Grant MOST-111-2124-M-008-001.

REFERENCES

Clayton, R. W., T. Heaton, M. Chandy, A. Krause, M. Kohler, J. Bunn, R. Guy, M. Olson, M. Faulkner, M. H. Cheng, L. Strand, R. Chandy, D. Obenshain, A. Liu, and M. Aivazis (2011) "Community Seismic Network," *Annals of Geophysics*, 54, 6.

Clayton, R. W., T. Heaton, M. Kohler, M. Chandy, R. Guy, and J. Bunn (2015) "Community Seismic Network: a dense array to sense earthquake strong motions," *Seis. Res. Lett.*, 86, 1354-1363.

Clotaire M. and P. Guéguen (2018). "Interpretation of the velocity measured in buildings by seismic interferometry based on Timoshenko beam theory under weak and moderate motion," *Soil Dynamics and Earthquake Engineering*, 104, 131-143.

Kohler, M. D., T. H. Heaton, and M. H. Cheng (2013) "The Community Seismic Network and Quake-Catcher Network: enabling structural health monitoring through instrumentation by community participants," *Proceedings of the SPIE Smart Structures/Non-destructive Evaluation Conference, San Diego, CA, March* 10-14, 2013.

Snieder R and E. Safak (2006) "Extracting the building response using seismic interferometry: theory and application to the Millikan Library in Pasadena, California," *Bull Seismol Soc Am,* 96, 586–598.

NUMERICAL MODELING OF THE STEEL ARCH BRIDGE TO IDENTIFY THE CABLE FORCE WHICH VALIDATED BY THE FIELD MEASUREMENT

Alfinna Mahya Ummati[1,3*] and Chung-Yue, Wang[2]
[1] Ph.D. Candidate, Department of Civil Engineering, National Central University, Taoyuan, Taiwan, R.O.C.
[2] Professor, Department of Civil Engineering, National Central University, Taoyuan, Taiwan, R.O.C.
[3] Assistant Professor, Department of Civil Engineering, Institut Teknologi Sumatera, Lampung, Indonesia
Email: *alfinnamahya@g.ncu.edu.tw, cywang@cc.ncu.edu.tw

ABSTRACT

Structural health monitoring was performed for a steel arch bridge in Taiwan, to monitor the cable force by the sensor in the field and compare it with the numerical analysis. Since the bridge with cable achieved the architectural preferably, low-cost efficiency, and high strength capability, it cannot be avoided that the cables become a critical element of the bridge. Therefore, a double measurement by field inspection and validated by the numerical analysis is performed in order to achieve the reasonable behavior of the bridge that in further as the reference of decision making to prevent the worst damage that most likely happens in the cable bridge.

Keywords: numerical analysis, cable force, steel arch bridge, monitoring, moving load

INTRODUCTION

Structural Health Monitoring System (SHMS) become the first priority as the part of real time maintenance system of a bridge especially for those which located with high catastrophe possibility (Meng et al., 2019), such as the bridge which located near the fault rupture zone and the bridge which located in the high salinity environment which lead to corrosion. Nanfang'ao bridge in Taiwan that collapsed in 2019 due to the cable corrosion become an alert for engineers around the world to enhance the SHMS which can detect the real time bridge behavior and prevent the damage and causalities with a certain action (Fan, 2021). Cable bridge is widely used especially for the long span bridge regarding its architectural view yet their tension contribution is able to improved the bridge capacity, thus either the stayed or suspension cable provide the preferable looks and strength (Huang & Chen, 2019). However, the cable become the critical and sensitive element regarding the vibration and environmental condition. Lin et al. proposed a cable damage detection within virtual distortion method (Lin et al., 2017). Meanwhile, Sun et al. performed a monitoring investigation of a suspension bridge to evaluate the premature damage (Sun et al., 2017). Shi et al. compare the mitigation of cable vibration which using passive negative stiffness dampers and active control to identify the method with the best cable vibration achievement (Shi et al., 2017). Study in determining such a reasonable state of spatial cable of the suspension bridge which combined with the finite element modelling to determine the reasonable state of the cable suspension to avoid the theoretical derivation proposed by Xiao et al. as the part of the numerical analysis (Xiao et al., 2017), Genetic algorithm and particle swarm optimization proposed as the method in estimating the cable tension bridge (Ehsan et al., 2017). Overall, beside the efficiency and preferable architectural design of a bridge with the cable support, the intensive maintenance and field monitoring as the part of SHMS are necessary to conduct and the validation of the numerical analysis is also an important role to predict every possibility that might be happen in the future. This research proposed a procedure of modelling to create the bridge model in computational program which represent the real condition of a steel arch bridge, this research concern on the cable force monitoring to prevent the bridge from the cable failure possibilities.

A mid-road steel arch Bridge was open for traffic in January 2014. In order to prevent the disaster and ensure the safety of the arch bridge which located on Hualien County, Taiwan. The Bridge Monitoring conduct with the aim is to prevent the sudden security incident caused by the damage occurs by the steel

cable that belongs to Fracture Control Member (FCM). The real bridge view as in Fig. 1, total length of the span is 186.4 meters and width 23.5 meters. The maximum height of the center point of arc to the deck is 21.256 meters. Equipped with 4 meters clear space for bicycle lane, 2.5 and 1.5 meters for the pedestrian way on both side, overall structure built by steel and concrete which composite with the longitudinal girder (LG).

Fig. 1 Bridge view

BRIDGE MODEL

The steel arc bridge is the steel bridge with the cable hanger to enhance the bridge performance with the material properties as in Table 1. Basically, most of the girders made from square hollow beam with the stiffener inside, Main girder indices by (GA/GB), Steel arc (CA/CB), Steel connection between arc and main girder (GL), Transverse girder which varies in several locations (F1-X, F2-X, F3-X) and Bracing arc (F4), all of these sections typically are square hollows with the stiffener inside. Meanwhile, the bracing along the main span (ST), and girder stiffeners are made by I and C-beam. The bridge deck has the thickness of 27 cm (22 cm concrete + 5 cm asphalt) which composited with the longitudinal girder (LG). Overall, the section properties of all members listed on Table 2.

Table 1 Materials Properties

No	Parameters	Concrete Deck	Steel Girder	Cable Hanger
1	Standard	ASTM(RC) Grade C3500	ASTM(S) A36 Grade 36	
2	Young's Modulus (MPa)	2.4×10^4	2×10^5	2×10^5
3	Poisson Ratio	0.2	0.3	0.3
4	Thermal Coefficient (1/F)	5×10^{-6}	6.5×10^{-6}	1.15×10^{-5}
5	Weight Density (kg/m^3)	2403	7861	7861

Table 2 Section Properties of the Steel Girders

No	Girder	Type	Height (mm)	Width (mm)	Web Thickness (mm)	Flange Thickness (mm)
1	Main Girder (GA/GB)	Hollow Square	2400	1600	80	80
2	Arc (CA/CB)		2000	1600	80	80
3	Longitudinal Girder (GL)		1490	1440	32	32
4	Transverse Girder (F1-X)		1404~1938	1400	50	50
5	Transverse Girder (F2-X)		1574~2106	900	50	50
6	Transverse Girder (F3-X)		1424~1958	1400	50	50
7	Bracing Arc		650	1200	22	22
8	Main Bracing	I-Shape	250	370	12	16
9	Secondary Bracing	C-Shape	300	90	10	15.5

Numerical analysis has been done within Midas Civil 2021 V.1.1. Midas geometry modelling following the geometry map in design drawing, Midas modelling shown in Fig. 2. For the cable hanger, there are 11 hanger point in each side, 22 hanger points totally in both sides, whereas there are 2 cables in every point. Totally, there are 44 cables in this bridge. Cable diameter measured 70 mm, with the Young's modulus is 19500 kgf/mm^2.

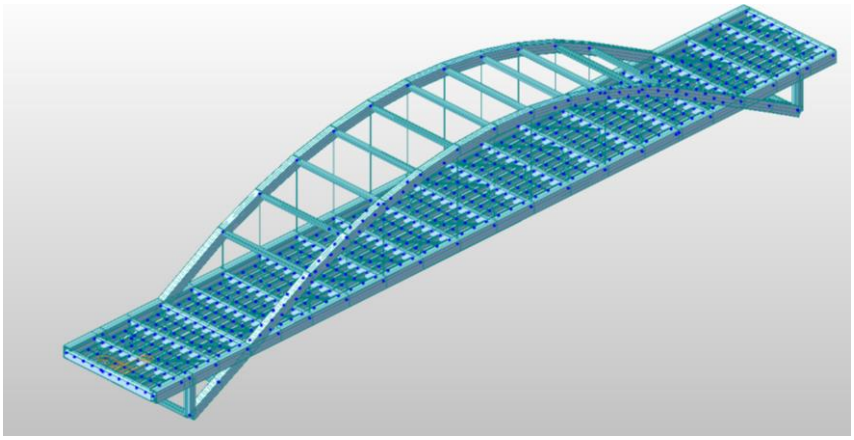

Fig. 2 Geometry Modelling of the Arc Bridge

NUMERICAL MODELING AND ANALYSIS

Loadings

The bridge designed to sustain the deadload as a static loading such as: Self-weight, Pedestrian Path, Road Blocks, and Fence. The self-weight is the weight of the structure influenced by the gravity. Pedestrian path located on the left and right side of the bridge. Both sides pedestrian assumed as the distributed load in the Main Girder GA/GB, thickness = 0.29 m, width = 2.5 m, pedestrian path constructed by the concrete and modelled as the distributed loading of 1742.18 kg/m along the main girder GA and GB. Road blocks as the boundary blocks made from concrete that use to separate the bicycle path with the vehicle lanes, with the height = 0.4 m and width = 1 m, these road blocks modelled as the distributed loading as amount 961.2 kg/m in total and placed on the longitudinal girder GL-3 and GL-4. Fence is the element which put for the safety reason for the vehicle and pedestrian who passing through the bridge, the fence modelled as the distributed loading which sustained by the main girder GA/GB as amount 285.77 kg/m.

Beside the static load, the bridge also loaded by the moving load of four axle loads of the vehicle test as in Fig. 3. The bridge consists of pedestrian way and bicycle lane in upstream side, and 2 lanes with different traffic direction. This moving load analysis consider the cross-beam method, where the vehicle load will distribute in every cross beam as the bridge loading. Moving load case will be: 2 vehicles with 4 wheels pass through lane 1 and lane 2.

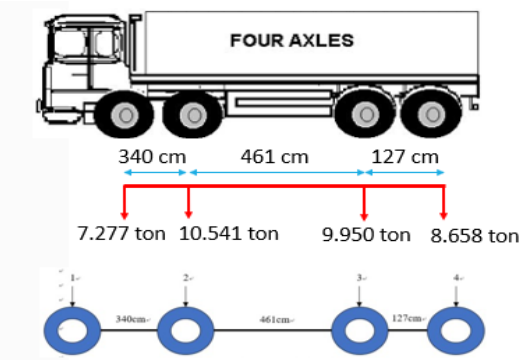

Fig. 3 Vehicle type

Static Analysis

Total reaction in vertical direction of the bridge is 10362.378 tonf and it reflects the total weight of the superstructure. In global axes, Z assumed as the vertical direction, x is horizontal direction along the bridge span, and y is horizontal direction along the bridge width. The maximum displacement on z, x, y directions are 10.352 cm, 0.442 cm, and 0.04 cm.

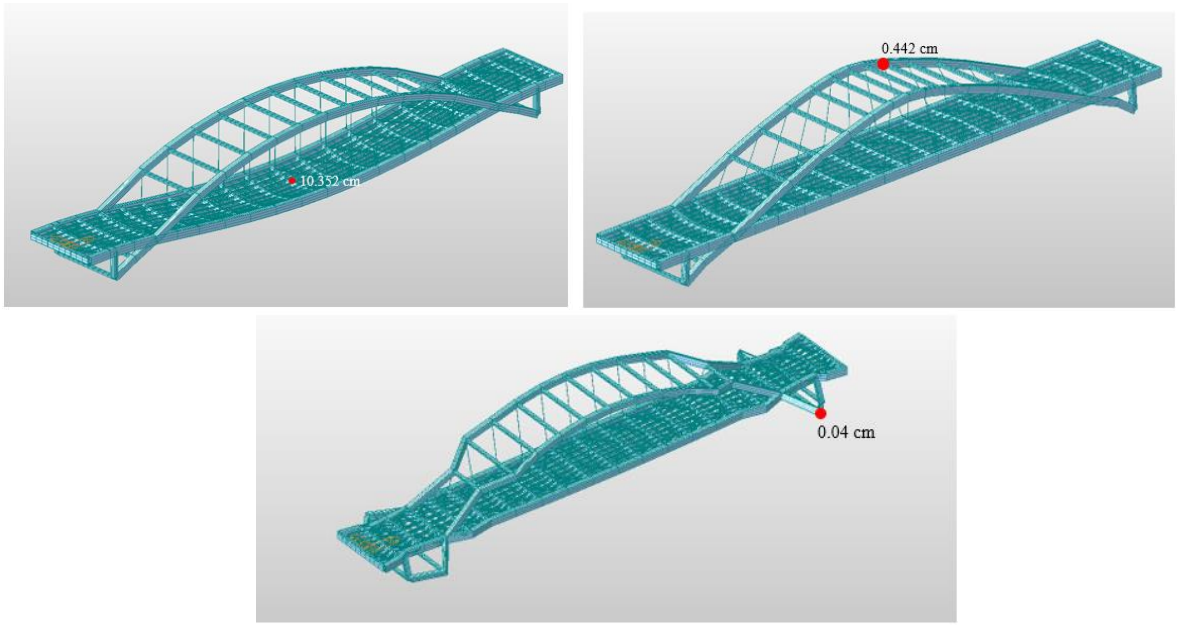

Fig. 4 Maximum displacement on: (Top Left) Z direction, (Top Right) X direction, (Bottom) Y Direction

Modal Analysis

Modal analysis uses the overall mass and stiffness of a structure to find the various periods and frequencies, also the bridge natural modes. For the modal analysis, table below mention the first fifth cyclic frequencies (Hz.), and periods (sec). Fig. 5 shows the structural shape of the bridge in mode 1 until mode 3.

Table 3 Frequencies and Periods

Mode No	Frequency Hz	Period (sec)
1	3.368	0.297
2	3.467	0.288
3	5.407	0.185
4	5.773	0.173
5	6.767	0.148

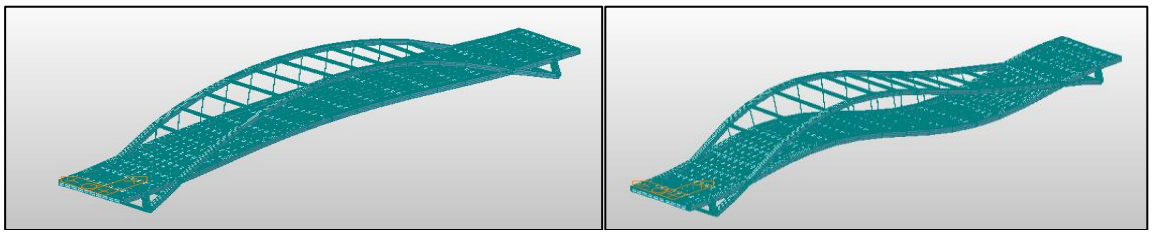

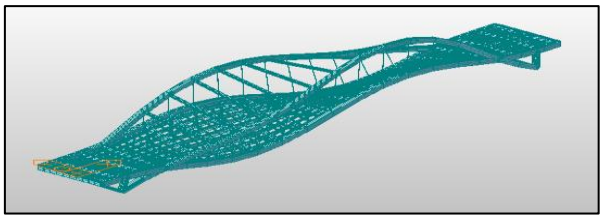

Fig. 5 (Top Left) Mode 1, (Top Right) Mode 2, (Bottom) Mode 3

Moving Load Analysis

As mentioned before the case of moving load will be: 2 vehicles with 4 wheels pass through lane 1 and lane 2. The moving load analysis has the purpose to analyze the moment and displacement influence in three location on the outermost girder: ¼, ½, and ¾ of the total length of bridge span.
The influence bridge displacement looks when the 4 wheels vehicle testing passing through each location described as in Fig. 6 and the results of the influence displacement and moment are listed on Table 4 and Table 5.

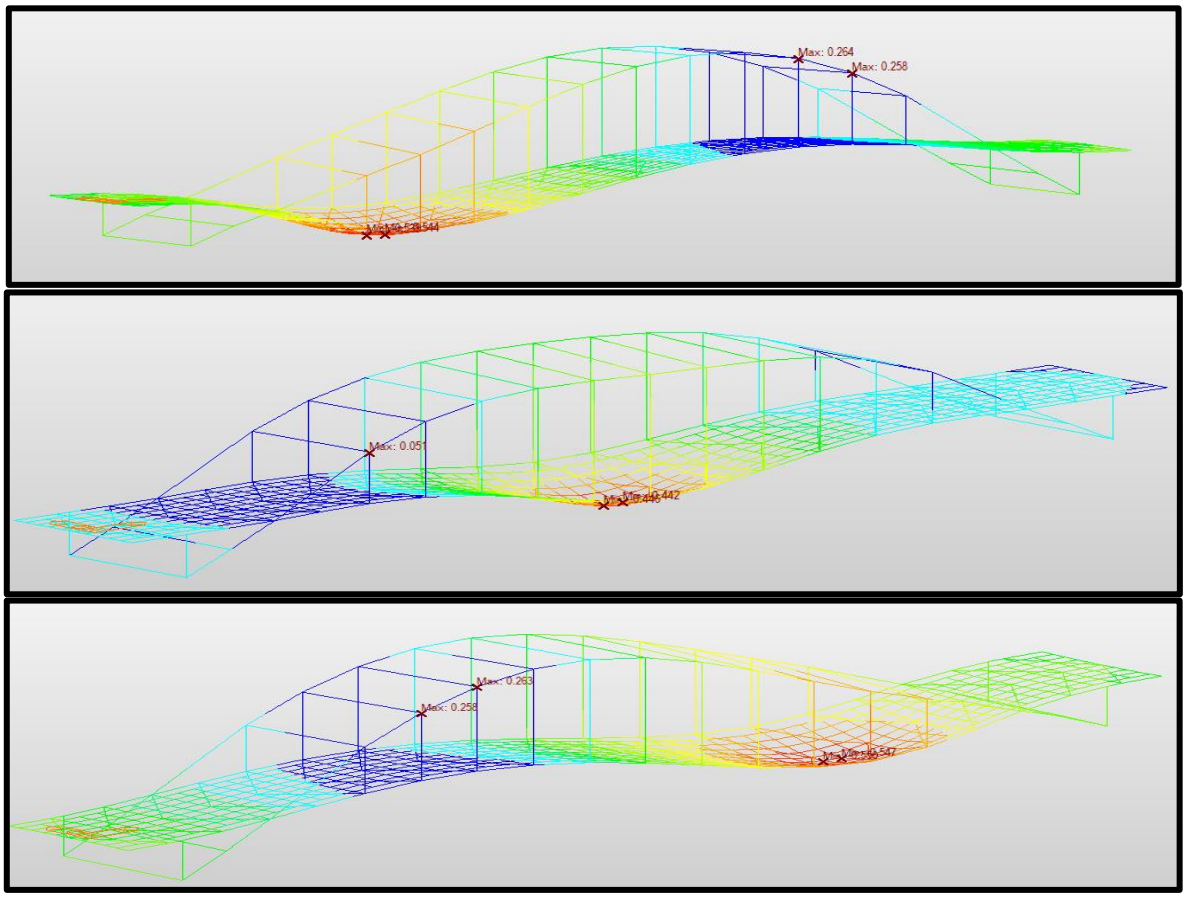

Fig. 6 Influence displacement when the vehicle 4 wheels passing through: (Top) Quarter span, (Middle) Half Span, (Bottom) Three-Quarter Span

Table 4 Influence displacement

Influence Displacement (cm)		Location of the Truck		
		¼ L	½ L	¾ L
Outer beam location	¼ L (23)	-0.443	0.033	0.204
	½ L (28)	0.124	-0.305	-0.140
	¾ L (32)	0.246	-0.037	-0.439

Table 5 Influence Moment

Influence Moment (tonf-cm)		Location of the Truck		
		¼ L	½ L	¾ L
Outer beam location	¼ L (23)	15012.9	-6059.73	-5326.15
	½ L (28)	-4915.9	12295.8	-3036.68
	¾ L (32)	-3546.3	-5211.03	15155.1

CABLE FORCE MONITORING AND ANALYSIS COMPARISON

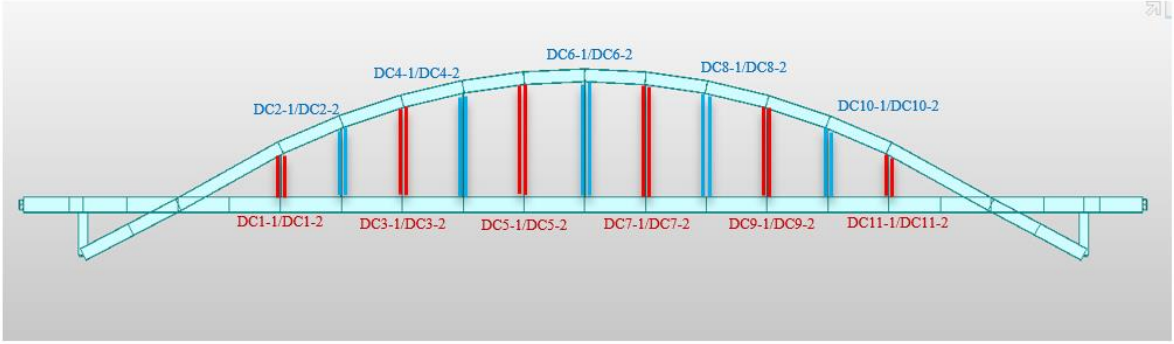

Fig. 7 Cable force in downstream side

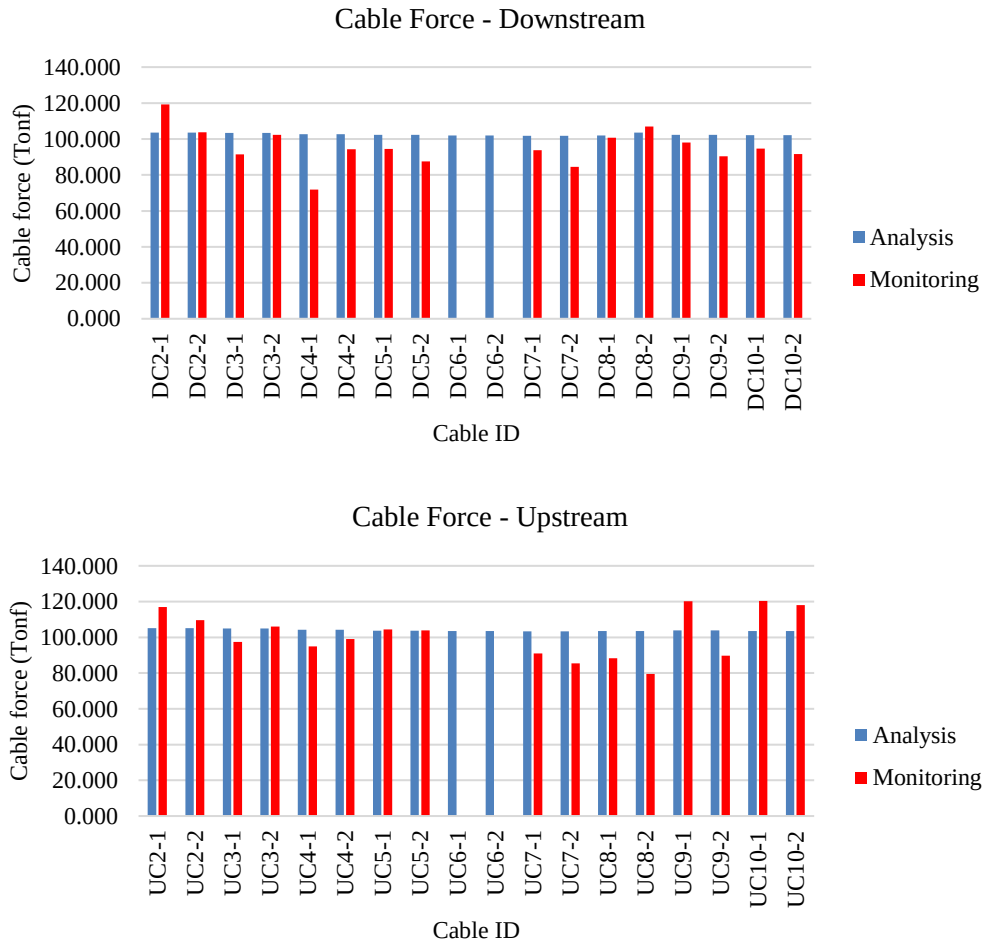

Fig. 8 Cable force comparison of the numerical analysis and field monitoring: (Top) Downstream side, (Bottom) Upstream side

The left and right side of the bridge defined as downstream (D) and upstream (U) side, there are 11 hanger points in each side, and 2 cables in each hanger point, totally 44 cables hang in the bridge. There are 2 lines which represent there is 2 cables in one hanger point, for example in hanger point 1, there are 2 red lines, they are cable DC1-1 and cable DC1-2, 1 and 2 is the sequence of the cable. Field monitoring have been done to get the cable force in order to identify the recent condition of the bridge within some sensors which fix on the bridge, in the same configuration as the upstream side.
The comparison of the cable force measurement between the numerical analysis and field monitoring shown on the bar chart on Fig. 8.

CONCLUSION

In order to prevent the disaster and ensure the safety of the steel arch bridge which located on Highway in east coast of Taiwan. Bridge Monitoring have the aim to prevent the sudden security incident caused by the damage occurs by the steel cable that belongs to Fracture Control Member (FCM) was conduct and the conclusion of the research are as follows:

1. Under the static loading analysis, the vertical reaction directly shows the superstructure weight, under the static load the total vertical reaction is about 10362.378 tonf, the bridge vertical displacement is about 10.352 cm, the displacement in horizontal along (x) and (y) directions are about 0.442 cm and 0.04 cm. Under the modal analysis, the first period and cyclic frequency of the bridge is 0.297 sec and 3.368 Hz, respectively.
2. Influence moment which observe in position of 1/4L, 1/2L, and 3/4L are 15012.9 tonf-cm, 12295.8 tonf-cm, and 15155.1 tonf-cm. Meanwhile the influence displacement which observe in the same position of 1/4L, 1/2L, and 3/4L are 0.443 cm, 0.305 cm, and 0.439 cm, respectively.
3. Numerical analysis was done in order to identify the current cable force based on the numerical simulation in Midas Civil software and validate the field measurement result. According to Numerical Analysis, the maximum cable force in downstream side is about 103.561 tonf, upstream side is about 105.114 tonf. Field monitoring was done in order to identify the current cable force, according to field monitoring, the maximum cable force in downstream side is about 119.200 tones, upstream side is about 120.300 tones. Numerical analysis and field monitoring provide 13% cable force difference for the extreme value, which is this difference is under tolerate and permissible. The numerical modelling can reflect the real structure as in further prediction matter.

REFERENCES

Ehsan, S., Agha, H., Zarbaf, M., Norouzi, ; Mehdi, Randall, ;, Allemang, J., Victor, ;, Hunt, J., & Helmicki, A. (2017). "*Stay Cable Tension Estimation of Cable-Stayed Bridges Using Genetic Algorithm and Particle Swarm Optimization*". *Journal of Bridge Engineering*, 22(10), 05017008 1-9

Fan, C. L. (2021). *"Detection of multidamage to reinforced concrete using support vector machine-based clustering from digital images". Structural Control and Health Monitoring*, *28*(12), 1-22

Huang, D., & Chen, W. (2019). *"Cable Structures in Bridge Engineering". Journal of Bridge Engineering*, *24*(8), 02019001 1-3

Lin, S.-W., Yi, T.-H., Li, H.-N., & Ren, L. (2017). *"Damage Detection in the Cable Structures of a Bridge Using the Virtual Distortion Method". Journal of Bridge Engineering*, *22*(8), 04017039 1-14

Meng, X., Nguyen, D. T., Owen, J. S., Xie, Y., Psimoulis, P., & Ye, G. (2019). *"Application of GeoSHM system in monitoring extreme wind events at the forth Road Bridge". Remote Sensing*, *11*(23), 2-19

Shi, X., Zhu, S., & Nagarajaiah, S. (2017). *"Performance Comparison between Passive Negative-Stiffness Dampers and Active Control in Cable Vibration Mitigation". Journal of Bridge Engineering*, *22*(9), 04017054 1-15

Sun, Z., Ning, S., & Shen, Y. (2017). *"Failure Investigation and Replacement Implementation of Short Suspenders in a Suspension Bridge". Journal of Bridge Engineering*, *22*(8), 05017007 1-9

Xiao, R., Chen, M., & Sun, B. (2017). "*Determination of the Reasonable State of Suspension Bridges with Spatial Cables". Journal of Bridge Engineering*, *22*(9), 04017060 2-12

(5c) Geochemical and seismological investigations

ANALYSIS OF CONTINUOUS RADON MONITORING DATA OF SAN-JIE STATION IN NORTHERN TAIWAN FOR SEISMIC STUDIES

Arvind Kumar[1], Vivek Walia[2], Shih-Jung Lin[3], Ching-Chou Fu[4]
1. Associate Researcher, National Center for Research on Earthquake Engineering, Taipei, Taiwan, R.O.C.
2. Research Fellow, National Center for Research on Earthquake Engineering, Taipei, Taiwan, R.O.C.
3. Research Assistant, National Center for Research on Earthquake Engineering, Taipei, Taiwan, R.O.C.
4. Assistant Research Fellow, Institute of Earth Science, Academia Sinica, Taipei, Taiwan, R.O.C.
Email: kumar@ncree.narlabs.org.tw, walia@ncree.narlabs.org.tw, sjin@ncree.narl.org.tw,ccfu@earth,scinica.edu.tw

ABSTRACT

In the present study, soil-gas radon data generated from San-Jie monitoring station in northern Taiwan have been analyzed. The hourly radon time series has been decomposed into three component series (seasonal, trend, and random) for recognizing the authentic anomalous values. The irregular patterns in hourly and residual radon data have been associated with earthquake events and rainfall. Our Preliminary results have shown that this method is helpful to recognize the radon anomalous values that are suppressed by rainfall or other meteorological parameters. Additionally, to find a radon correlation with temperature, pressure, humidity, and rainfall Pearson correlation has been used.

Keywords: Radon time series, Pearson correlation, Decomposition, Earthquake Precursor, northern Taiwan

INTRODUCTION

Predicting earthquakes is still a concerning issue in Earth Sciences. Globally we don't have any model or procedure to forecast the coming seismic event. However possible geochemical precursors have been recorded hours to months before some major earthquakes at many countries (Yang *et al.*, 2006; Cicerone *et al*., 2009; Matsumoto and Koizumi, 2011; Martinelli, 2015; Fu *et al*., 2017a). Among the all geochemical precursors, radon (^{222}Rn) is recognized as one of the most promising geochemical precursors (Walia *et al*., 2009a, 2009b; Nicoli *et al*., 2019; Fu *et al.*, 2017b, 2017c). Radon monitoring both in soil and in groundwater have shown that spatial and temporal variations can give clue about geodynamical events.

While, soil gas radon emanation from beneath the earth towards the surface is also affected by environmental parameters such as rainfall, temperature relative humidity and pressure (Kumar et al., 2015; Arora *et al*., 2017). As the radon emanation is not only affected by seismic events but also by meteorological parameters. Therefore, it is often not possible to identify radon anomalies or radon irregular patterns caused by seismic events, and those merely caused by climate changes. Some anomalies are hidden whereas some anomalies are erroneously considered as earthquake precursors. These necessities the usage of statistical and computational tools to minimize the effects of meteorological parameters on radon emission (Torkar *et al*., 2010; Kumar *et al*., 2015; Arora *et al*., 2017).

In Taiwan, we have four radon monitoring stations along different faults (Fig.1) in the Hsinchu (HC) (i.e., along Hsincheng fault), Tainan (HH) (along Hsinhua Fault), Ilan (at Jaosi (JS)), and in Yangmingshan area (along Shanchiao fault (SJ)) regions of Taiwan to study temporal geochemical variations of soil-gas composition. In the present study, soil-gas radon time-series data from San-Jie monitoring station in northern Taiwan (Fig.1) have been examined statistically. To find a radon correlation with temperature, pressure, humidity, and rainfall Pearson correlation has been used. Further, radon time series data has been decomposed into three component series (seasonal, trend, and random).

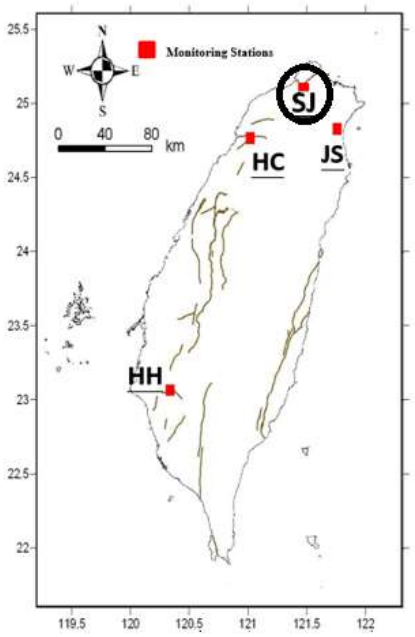

Fig.1. Map showing the location of

METHODS AND INSTRUMENTATIONS

Pearson correlation coefficient:

Pearson's correlation coefficient or Pearson's r is defined in statistics as the measurement of the strength of the relationship between two variables and their association with each other. In simple words, Pearson's correlation coefficient calculates the effect of change in one variable when the other variable changes. The correlation coefficient formula finds out the relation between the variables. It returns the values between -1 and 1. Use the below Pearson coefficient correlation calculator to measure the strength of two variables.

Pearson correlation coefficient formula:

$$r = \frac{N\Sigma xy - \Sigma x \Sigma y}{\sqrt{[N\Sigma x^2 - (\Sigma x)^2][N\Sigma y^2 - (\Sigma y)^2]}} \qquad (1)$$

Where:

N = the number of pairs of scores

Σxy = the sum of the products of paired scores

Σx = the sum of x scores

Σy = the sum of y scores

Σx^2 = the sum of squared x scores

Σy^2 = the sum of squared y scores

Time Series Decomposition:

Time series data can exhibit a variety of patterns, and it is often helpful to split a time series into several components, each representing an underlying pattern category. The three types of time series patterns: trend, seasonality and cycles. When we decompose a time series into components, we usually combine the trend and cycle into a single trend-cycle component (sometimes called the trend for simplicity). Thus we think of a time series as comprising three components: a trend-cycle component, a seasonal component, and a remainder component (containing anything else in the time series). If we assume an additive decomposition, then we can write

$$Y_t = S_t + T_t + R_t \qquad (2)$$

Where Y_t is the data, S_t is the seasonal component, T_t is the trend-cycle component, and R_t is the remainder component, all at period t. Alternatively, a multiplicative decomposition would be written as

$$Y_t = S_t * T_t * R_t \qquad (3)$$

The additive decomposition is the most appropriate if the magnitude of the seasonal fluctuations, or the variation around the trend cycle, does not vary with the level of the time series. Whereas, when the variation in the seasonal pattern, or the variation around the trend-cycle, appears to be proportional to the level of the time series, then a multiplicative decomposition is more appropriate. Multiplicative decompositions are common with economic time series. An alternative to using a multiplicative decomposition is to first transform the data until the variation in the series appears to be stable over time, then use an additive decomposition. When a log transformation has been used, this is equivalent to using a multiplicative decomposition because

$Y_t = S_t * T_t * R_t$ is equivalent to: $LogY_t = LogS_t + LogT_t + LogR_t$. (4)

Radon Monitoring:

To carry out the investigation, temporal soil-gas radon composition variations were measured 15 minutes intervals at the above-mentioned continuous earthquake monitoring stations using RAD7 (Durridge USA). The meteorological and seismic data were taken from Center weather bureau, Taiwan. Rainfall data was available with hourly sampling, so for the sake of uniformity and comparison 15-minutes radon, temperature, Humidity and pressure data have been reduced to Hourly averages.

RESULTS AND DISCUSSIONS

To make the continuity and regularity of the data, the data has been carefully selected for intervals with minimum breaks. The selected soil-gas radon concentrations data along with temperature, pressure, humidity, and rainfall from June 01, 2019 to May 31, 2020 are shown in figure 2.

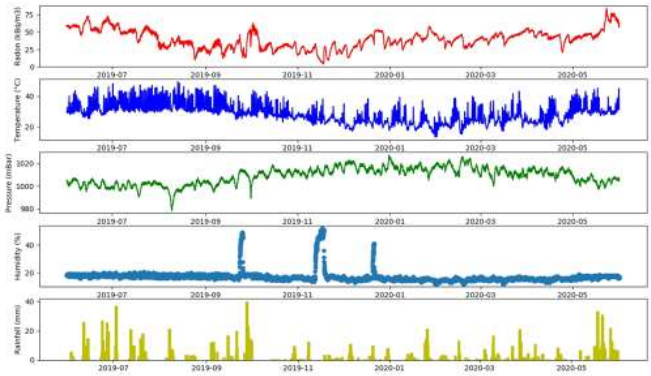

Fig. 2. Recorded soil radon concentrations along with temperature, pressure, humidity, and rainfall at the JS monitoring station from June 01, 2019 to May 31, 2020.

Table 1 and Figures 3 a, b, c, & d shows the radon correlation with temperature, pressure, humidity, and rainfall observed in the present study using Pearson's method. The computed overall Pearson (r) of radon with temperature, pressure, humidity, and rainfall are 0.11, -0.3, -0.16, and 0.06 respectively.

Table 1: Computed radon correlation with temperature, pressure, humidity, and rainfall using Pearson's method.

Correlation using Pearson's method (r)			
Radon & Temperature	**Radon & Pressure**	**Radon & Humidity**	**Radon & Rainfall**
0.11	-0.3	-0.16	0.06

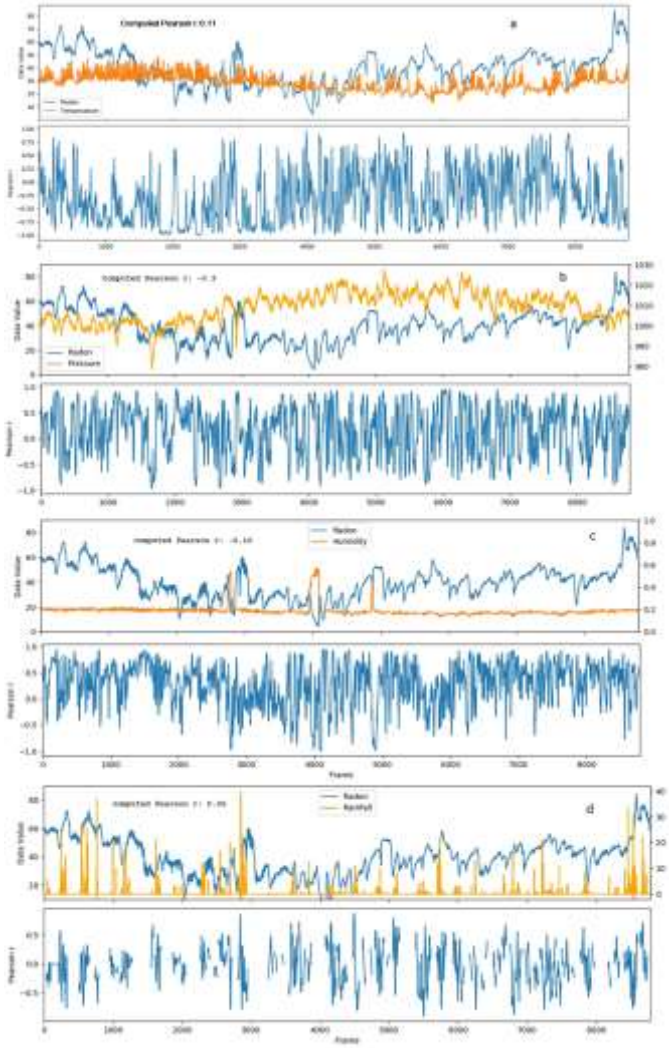

Fig. 3. The computed overall Pearson (r) and moment-to-moment, local synchrony using Pearson correlation, repeated along with a rolling window of 30 days of radon with temperature (a), pressure (b), humidity (c), and rainfall (d)

The overall Pearson (r) is a measure of global synchrony that reduces the relationship between two signals to a single value. Nonetheless, there is a way to look at moment-to-moment, local synchrony, using Pearson correlation. One way to compute this is by measuring the Pearson correlation in a small portion of the signal, and repeat the process along with a rolling window until the entire signal is covered. In our study, we have measured Pearson correlation in the radon signal, and have repeated the process along a rolling window of 30 days until the entire signal is covered. It has been observed from this studies (Fig. 3 a, b, c, & d) that radon is not only control by a single metrological parameter but multi metrological parameters. In comparison with the effect of other meteorological parameters, it is seen that there is a significant correlation in relation of the exhalation rate with the precipitation. Thereafter, we have used Panda's library for the radon time series decomposition, which offers a lot of flexibility when manipulating data, and allowing to perform statistical computing in Python. Radon time series decomposition has been done by a polynomial fitting method. Here we have defined an order of polynomial three to fit in our data and find out the coefficient. Firstly, we found the overall trend in the radon time series and then we have reduced the overall trend component from the original radon time series. After that, we found seasonal component and then we have reduced this seasonal component from the original radon time series. Finally overall trend and seasonal component have been reduced from the original radon time series to reach at the residual component. Figure 4 shows the decomposition of radon time series (observed radon, de-trend, de-seasonal, and residual) using a polynomial fitting method. There are irregular patterns in residual radon data.

To correlate the residual radon data with the earthquake that occurred in the study area during the

observation time, only earthquakes with a local intensity of one or more, depth ≤40 km, epicentral distance (R) < 100 km and D/R ratio ≥ 1 (where D= $10^{0.43M}$ theoretical strain radii of impending earthquakes proposed by Dobrovolsky, 1979) have been selected. Also in the case of a group of earthquake that are close together reported during our study time, we have selected the largest earthquake prior to the anomaly (Kumar *et al*., 2009). Also in our study, radon concentration the statistical threshold value of gas anomalies or irregular patterns is fixed at the Avg. + 2σ. Figure 5 shows the hourly radon, residuals radon calculated from the polynomial fitting method along with seismic events and rainfall that occurred during the study time.

During this study time, eight earthquakes have been observed, those fit our criteria. The red rectangle shows the earthquake events recorded but no irregular patterns in daily radon as well as residual radon data or vice versa. The yellow rectangle shows the earthquake events recorded after and before the irregular patterns in hourly radon or residual radon data. For the events 3, 4, and 5 hourly radon data have not shown any anomalous value but residual radon data has shown the anomalous value before these events. The possible reason for not showing any anomalous value in hourly radon data is rainfall during this time period, which hide the anomalies.

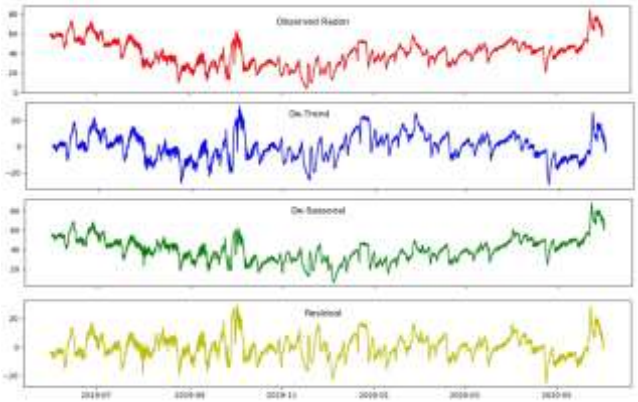

Fig. 4. Decomposition of the radon time series (from top first panel is observed radon, second panel is De-trend, third panel is De-seasonal, and fourth panel is residual) using polynomial fitting method

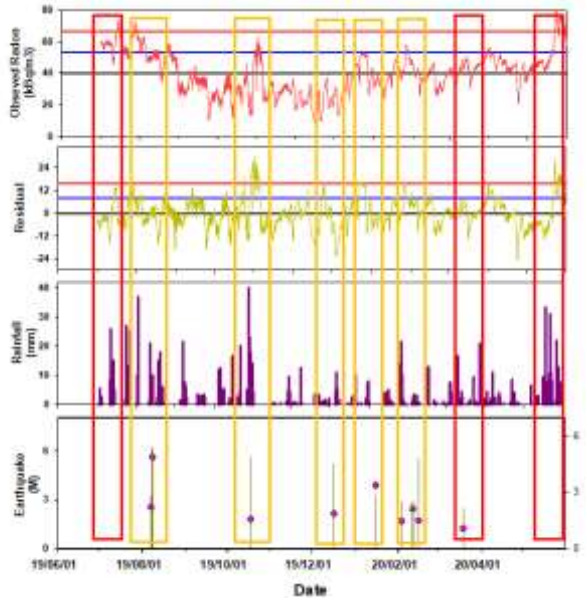

Fig. 5. Correlation of radon anomalies (from top, first panel is hourly radon, second panel is residual from polynomial fitting method) with rainfall (third panel) and seismic events (forth panel) occurred during the study time.

CONCLUSIONS

The soil-gas radon data generated from San-Jie monitoring station in northern Taiwan have been analyzed. The hourly radon time series has been decomposed into three component series (seasonal, trend, and random) for recognizing the authentic anomalous values. The irregular patterns in hourly and residual radon data have been associated with earthquake events and rainfall. This study results show that this technique is helpful to recognize the radon anomalous values that are suppressed by rainfall or other meteorological parameters.

ACKNOWLEDGMENTS

The authors are thankful to the Ministry of Science and Technology of Taiwan for funding this research under the projects 108-2116-M-492 -003 and 111-2811-M-492-001

REFERENCES

Arora BR, A. Kumar, V. Walia, T.F. Yang, C.C. Fu, T.K. .Liu, K.L. Wen, C.H. Chen (2017). Cleaning Soil-gas Radon at Hsinchu, Taiwan for Contamination from Meteorological and Hydrological Parameters: A Step Forward to Identify Earthquake Precursors. *J Asian Earth Sci* **149**, 49-63.

Cicerone RD, J.E. Ebel, J. Britton (2009). A systematic compilation of earthquake precursors. *Tectonophysics* **476**, 371–396.

Dobrovolsky I.P., S.I. Zubkov, V.I. Miachkin (1979). Estimation of the size of earthquake preparation zones. *Pure Appl Geophys* 1**17**, 1025–1044.

Fu CC, T.F. Yang, C.H. Chen, L.C. Lee, Y.M. Wu, T.K. Liu, V. Walia, A. Kumar, T.H. .Lai (2017b) Spatial and temporal anomalies of soil-gas in northern Taiwan and its tectonic and seismic implications. *J Asian Earth Sci* 1**49**, 64-77.

Fu CC, T.F. Yang, M.C. Tsai, L.C. Lee, T.K. Liu, V. Walia, C.H. Chen, W.Y. Chang, A. Kumar, T.H. Lai (2017a) Exploring the relationship between soil degassing and seismic activity by continuous radon monitoring in the Longitudinal Valley of eastern Taiwan. *Chem Geol* **469**, 163-175.

Fu CC, V. Walia, T.F. Yang, L.C. Lee, T.K. Liu, C.H. Chen, A. Kumar, T.H.Lai, K.L.Wen (2017c). Preseismic anomalies in soil-gas radon associated with 2016 M6.6 Meinong earthquake, Southern Taiwan. *Terr Atmos Ocean Sci* **28(5),** 787-798.

Kumar A, s. Singh, S. Mahajan, B.S. Bajwa, R. Kalia, S. Dhar (2009) Earthquake precursory studies in Kangra valley of north-west Himalayas, India, with special emphasis on radon emission. *Appl Radiat & Isot* **67**, 1904–1911.

Kumar A, V. Walia, B.R. Arora, T.F. Yang, S.J. Lin, C.C Fu, C.H. Chen, K.L. Wen (2015) Identifications and removal of diurnal and semi-diurnal variations in radon time-series data of Hsinhua monitoring station in SW Taiwan using singular spectrum analysis. *Nat Hazards* **79(1),** 317-330.

Martinelli G (2015) Hydrogeological and geochemical precursors of earthquakes: an assessment for possible applications. *Boll di Geofis Teor ed Appl* **56(2**), 83-94.

Matsumoto N, N. Koizumi (2011) Recent hydrological and geochemical research for earthquake prediction in Japan. *Nat Hazards* **69**, 1247-1260.

Nicoli L, G. Massimiani, S. Segantin, M. Zucchetti (2019) Detection of radon emissions during 2016/2017 earthquakes in abruzzo (Italy). Fresenius Environ Bull **28(2)**, 672-680.

Smetanová I, K. Holý, M. Müllerová, P. Anna (2010) The effect of meteorological parameters on radon concentration in borehole air and water. *J Radioanal Nucl Ch* **283**, 101-109.

Torkar D, B. Zmazek, J. Vaupotic, I. Kobal (2010) Application of artificial neural networks in simulating radon levels in soil gas. *Chem Geol* **270(1–4),** 1–8.

Walia V, T.F. Yang, S.J. Lin, W.L. Hong, C.C. Fu, K.L. Wen, C.H. Chen (2009b) Continuous temporal soil-gas composition variations for earthquake precursory studies along Hsincheng and Hsinhua faults in Taiwan. *Radiat Meas* **44,**934-939.

Walia V, T.F. Yang, S.J. Lin, W.L.Hong, C.C. Fu, K.L. Wen, C.H. Chen (2009a) Geochemical variation of soil-gas composition for fault and earthquake precursory studies along Hsincheng fault in NW Taiwan. *Appl Radiat Isot* **67**, 1855-1863.

Yang TF, C.C Fu, V. Walia, C.H. Chen, L.L. Chyi, T.K. Liu, S.R. Song, M. Lee, C.W Lin, C.C. Lin (2006) Seismogeochemical variations in SW Taiwan: multi-parameter automatic gas monitoring results, *Pure Appl Geophys* **163**, 693– 709.

DISCUSSION OF THE ACTIVITY OF THE TATUN VOLCANO GROUP FROM RECENT MONITORING RESULTS

Hsiao-Fen Lee [1], Ya-Chuan Lai[2], Min-Hung Shih[3], Cheng-Horng Lin[4], Ching-Hua Lo[5], Guo-Teng Hong[6]

1. Associate Researcher, National Center for Research on Earthquake Engineering, Taipei, Taiwan, R.O.C.
2. Associate Researcher, National Center for Research on Earthquake Engineering, Taipei, Taiwan, R.O.C.
3. Assistant Researcher, National Center for Research on Earthquake Engineering, Taipei, Taiwan, R.O.C.
4. Distinguished Research Fellow and Deputy Director, Institute of Earth Sciences, Academia Sinica, Taipei, Taiwan, R.O.C.
5. NTU Chair Professor, Department of Geosciences, National Taiwan University, Taipei, Taiwan, R.O.C.
6. Assistant Technical Specialist, Central Geological Survey, MOEA, New Taipei City, Taiwan, R.O.C.

Email: hflee@narlabs.org.tw, yclai@narlabs.org.tw, shinmh@narlabs.org.tw, lin@earth.sinica.edu.tw, chlo@ntu.edu.tw, gthong@moeacgs.gov.tw

ABSTRACT

Taiwan Volcanic Observatory-Tatun (TVO) was established in 2011 to monitor the volcanic activity using various methods, including seismic activity, fluid geochemistry, and ground deformation. According to recent monitoring data, the volcano was relatively quiet from 2017 to 2018. However, magma or deep hydrothermal fluids might have upwelled at the end of 2018 due to increased hydrogen chloride and helium levels in the fumarolic gas. In the second half of 2020, the cation concentration of hot spring in the Dayoukeng geothermal area also increased sharply, which also indicated a large amount of upwelling deep hydrothermal fluid. The seismic activity increased in 2019 to approximately 1.5 times the background value. In 2020, it increased to as much as twice the background value. In addition to the significant increase in the number of microseisms, earthquakes with ML greater than 3.0 have also increased. These anomalies indicate that the TVG has become more active. The current monitoring work will continue to focus on whether there are more magmatic signals and on possible disasters caused by hydrothermal activities.

Keywords: Tatun Volcano Group, volcano monitoring, micro-earthquake, geochemistry

INTRODUCTION

Hot springs and other geothermal activities of the Tatun Volcano Group (TVG) are still quite evident. The results of investigations over recent decades, including high helium isotopic ratios (~5–7 RA) and increased seismicity, emission of volcanic gases, geothermal activity, and occurrence of hot springs, indicate that volcanic activity may not have stopped. Moreover, such observations imply that a magma reservoir exists beneath the TVG (Song et al., 2000; Yang et al., 1999). The last eruption at the TVG was 5–6 thousand years ago, as determined from ash dating (Belousov et al., 2010). It has been concluded that the TVG is an active volcano. Furthermore, the magma reservoir has been identified by seismic signal analysis and located in the Wanli area (Lin, 2016; Huang et al., 2021). A conduit with clustered seismicity was found beneath the Dayoukeng geothermal area, which is one of the strongest fumaroles in the TVG, and is connected to a fracture zone. Such clustered seismicity may be triggered by volcanic gases and fluids ascending from a deep magma reservoir and would be the likely pathway for ascending magma for a TVG eruption in the future (Pu et al., 2020).

The magmatic system of the TVG is stable overall, and no immediate eruption can be expected. However, the possibility of future eruption must still be considered, and, given the substantial hydrothermal activity of the TVG, eruption may be phreatic. Hence, detailed monitoring must be continued in order to detect significant volcanic activity. Recent monitoring data, especially important geochemical indicators, show that the activity in the TVG has changed. This study reports these unusual observations of the TVG, and the corresponding changes in various data.

MONITORING METHODS

The Taiwan Volcanic Observatory-Tatun (TVO) continues to employ a variety of monitoring methods, including seismic monitoring, geochemical analysis, study of surface deformation, and geothermal measurements. The results of seismic and geochemical monitoring are presented here.

The geochemical method used in the present study is direct sampling. Fumarolic gas was sampled by using the Giggenbach bottle to analyses almost all gas species. This method is commonly used by volcanologists (Giggenbach, 1975). Helium isotopic value was collected and stored in another vacuum glass bottles and analyzed in the laboratory in National Taiwan University. For water samples, temperature, conductivity, and other parameters were measured in situ at each site and filtered water samples were brought back to the laboratory for analysis. The analyses included determination of concentrations of main anion and cation components.

For Seismic monitoring, a dense seismic network was established for monitoring and investigating the seismicity of the TVG. To date, forty seismic broadband stations have been installed in the TVG, with the majority distributed southeast of the Shanjiao fault. With good network coverage of the Mount Cising, Dayoukeng, and Bayan areas, micro-earthquakes can be readily detected. When magma rises or a hydrothermal fluid migrates, many micro-earthquakes may be triggered along the path due to changes of stress in the rocks. This means that seismicity can be used to obtain important information.

The distribution of geochemical sampling sites and seismic stations are shown in Figure 1.

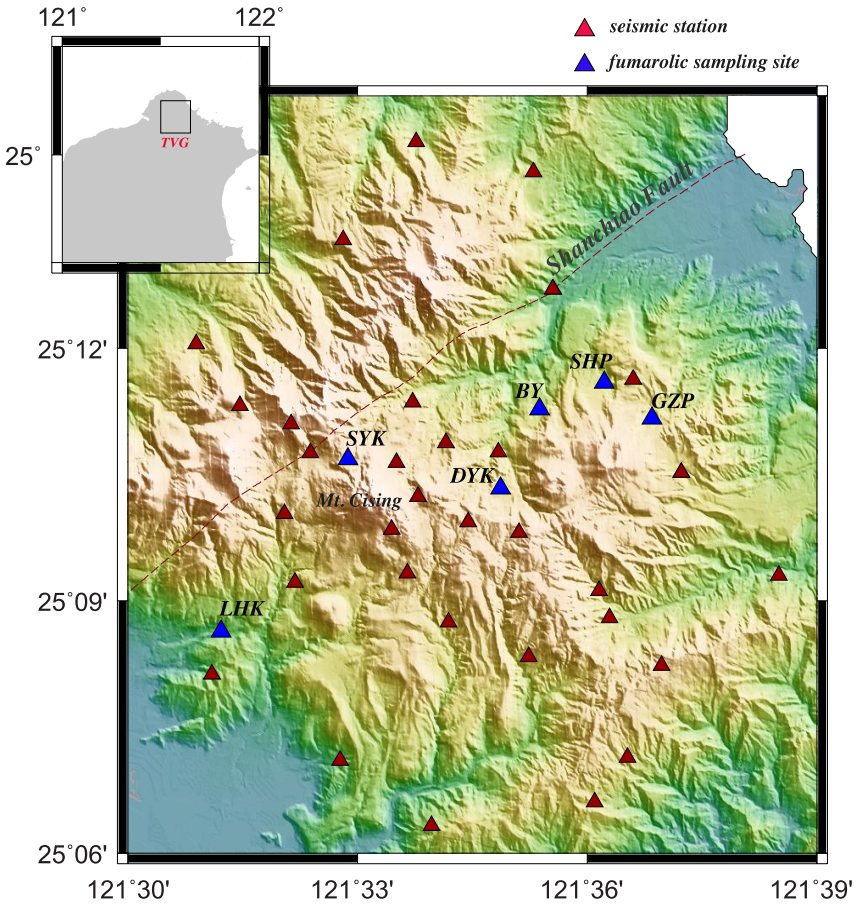

Figure 1. Distribution map of seismic stations and fumarolic sampling sites. DYK: Dayoukeng; SYK: Shiaoyoukeng; BY: Bayen; LHK: Liaohuangkuo; SHP: Sihuangping; GZP: Gengziping. Hot spring samples were collected in DYK ares.

RESULTS AND DISCUSSION

Between the end of 2018 and 2021, the geochemical signatures have changed dramatically. This study focuses on changes in fumarolic gas and water composition, and compares them with seismic monitoring results.

In gas composition, the ratio of hydrogen chloride to carbon dioxide (HCl/CO_2) is one of the parameters often used to distinguish between magmatic and hydrothermal activity. Figure 2a shows the variation of the HCl/CO_2 ratio at each sampling site from 2016 to 2021. The red dotted line is the international empirical threshold separating hydrothermal from magmatic activity. From 2016 to 2018, which was a relatively stable period, the HCl/CO_2 ratio did not change significantly, except in the Dayoukeng (DYK) area. At the end of 2018, however, there was a sudden and significant increase in HCl in the whole area, and this trend continued until 2021. This means that, during this period, although the volcanic system was still dominated by a hydrothermal environment, more magmatic material was added into the system.

The ratio of helium to argon (He/Ar) is also a parameter that determines the relative importance of a magmatic source. The atmosphere is the main source of argon, while the sources of helium are ^4He in the crust and ^3He in the mantle. Figure 2b shows the variation of the He/Ar ratio in the fumarolic gas with time over 2016 to 2021. Two earthquakes, with ML larger than 3, occurred in the TVG area in January and February of 2019. A significant increase in the concentration of helium was observed after the earthquakes, especially in the Bayan area. It is noted that, the helium isotopic ratio ($^3He/^4He$) did not change significantly, indicating that both ^3He and ^4He concentrations increased. One of the possible reasons for this phenomenon is that the pathway for the gas became smoother, so helium could escape more easily than before 2019. It also means that the magma might have a chance of rising up through the smoother path. Dramatic changes in helium are concentrated in 2019 and 2021.

Figure 2. Variations of the HCl/CO_2 and He/Ar ratio in the fumarolic gas with time.

The DYK area has the highest helium isotopic ratio (~6.7RA) in the TVG. Such a high helium isotopic value indicates that (1) the DYK area may be closer to the magma reservoir or (2) the pathway of the fluid is smoother than at other sites. From other studies (Lin et al, 2016; Huang et al, 2021), it is known that the location of the magma reservoir is still some distance from the DYK area, so it can be inferred that the pathway of fluid under this area is much smoother than at other sites.

There are two stages of variation displayed in the monitoring results of hot springs in the DYK area (Figure 3). First, the chloride concentration began to increase since 2019, which is consistent with the abnormal trend of fumarolic gas. The second phase of variation began in the second half of 2020, when a greater number of cations were detected and the anions also changed drastically. In summary, both the fumarolic gas and hot spring compositions indicate the relative importance of magmatic or hydrothermal activity, although their anomalies do not correspond exactly in time.

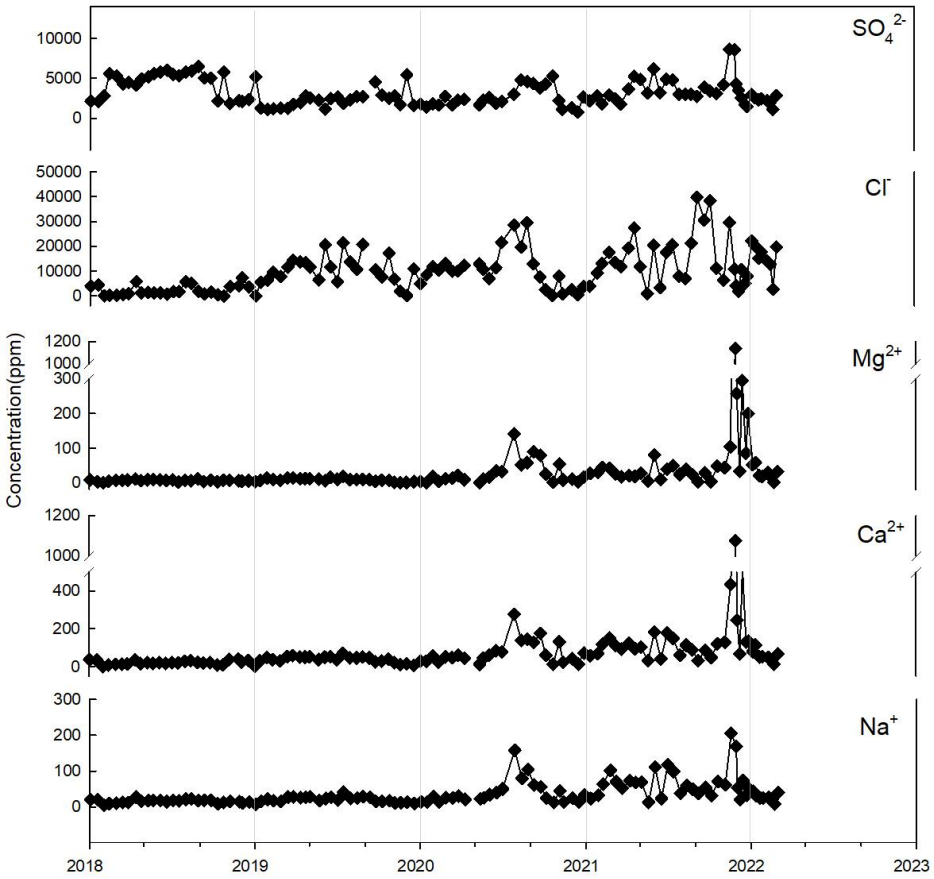

Figure 3. Variation of the major ion concentration of hot springs in Dayoukeng with time.

A large number of seismic events was observed in 2019, and this increased significantly in 2020 (Figure 4). In 2020, the number of microseisms was as high as 4,550 which is twice the background micro-seismic activity level in the TVG area, approximately 2,000 to 2,500 each year. Moreover, the epicentral depth was deeper than previously. The number of earthquakes decreased slightly in 2021. It is worth noting that the seismic activity in 2020 was mainly concentrated in the first half of the year, and the cation anomaly happened just after the most intense period of seismic activity.

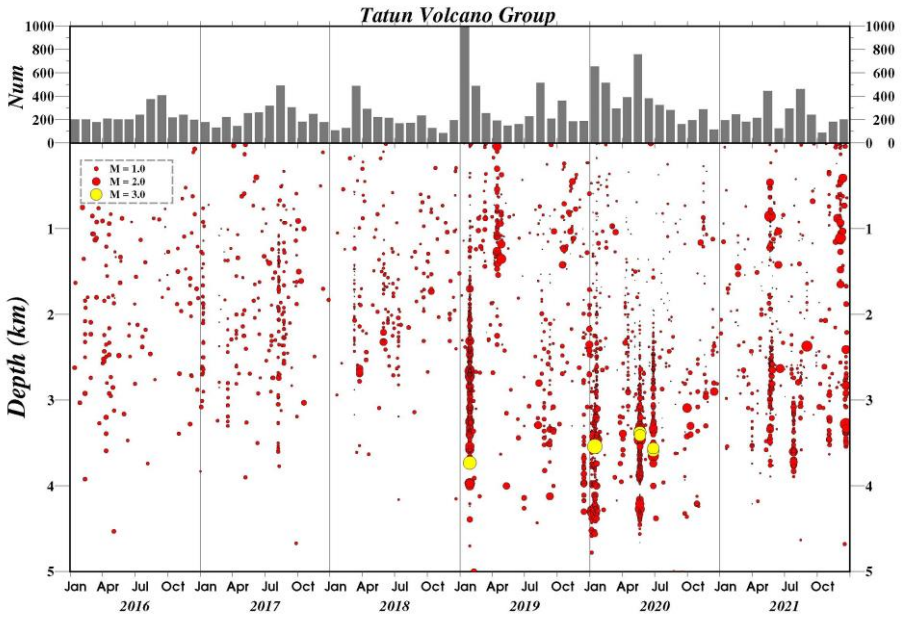

Figure 4. Distribution of the number, scale, and depth of microseisms in the TVG area.

Pu et al. (2021) established a volcanic activity model by comparing the focal mechanism of the DYK earthquake with observations of volcanic gas releasing. When deep material, such as magma, begins to rise, it squeezes the formation, causing pressure in the deep surrounding rock to increase. At this time, the seismic activity indicates thrust faulting (compression). Due to the blocking of caprock, only part of the fumarolic gas escapes. Shallow earthquakes then occur primarily as extensional normal faults when material moves upward and begins to be released near the surface. After the release is complete, seismic activity decreases. Therefore, the peaks of fumarolic gases do not exactly coincide with the peaks of seismic activity. Based on this model, the peak of the fumarolic gas anomaly should follow the seismic event. However, the observed fumarolic gas anomalies did not fit the model with the sequence of seismic events. This means that the model of volcanic activity in the TVG could be more complex. It is unclear whether the anomaly in 2021 is a follow-up event to that in 2019 or another new event.

CONCLUSIONS

By comparing recent anomalies of fumarolic gas, hot springs and seismic activity, it can be divided into several stages. 1) At the end of 2018, high concentrations of hydrogen chloride in fumarolic gas were detected. Upwelling of a magmatic or deep hydrothermal fluid should have commenced during this stage. The fumarolic gas exhibited the characteristics of deep material, but the amount had not yet reached its peak value. This probably due to the caprock was not severely fractured at this stage. 2) Helium concentration increased with several larger and deeper earthquakes in early 2019. The anion concentration of the hot spring also increased significantly, which should be affected by more escaping acidic gas composition. 3) The seismic activity peaked in 2020. Significant changes in cations were observed after the seismic activity. This might be due to the rupture of the cap rock causing large amounts of deep fluid to be added to the original system. In any case, these unusual phenomena suggest that the TVG is currently in a stage with more activity than previously.

ACKNOWLEDGMENTS

The authors would like to thank the National Science and Technology Council and Central Geological Survey, MOEA for their long-term support and cooperation.

REFERENCES

Belousov, A., M. Belousova, C. H. Chen, G. F. Zellmer (2010). Deposits, character and timing of recent eruptions and gravitational collapses in Tatun Volcanic Group, Northern Taiwan: Hazard-related issues. *J. Volcanol. Geotherm. Res.*, 191, 205-221.

Giggenbach, W.F. (1975) A simple method for the collection and analysis of volcanic gas samples. *Bull. Volcanol.* 36, 132-145.

Huang, HH., ES. Wu, C.H. Lin, J. Y.-T Ko, M.H. Shih, I. Koulakov (2021). Unveiling Tatun volcanic plumbing structure induced by post-collisional extension of Taiwan mountain belt. *Scientific Reports*, 11, 5286.

Lin, C.H. (2016). Evidence for a magma reservoir beneath the Taipei metropolis of Taiwan from both S-wave shadows and P-wave delay, Scientific Reports, Vol. 6, 39500.

Pu, H. C., C. H. Lin, Y. C. Lai, M. H. Shih, L. C. Chang, H. F. Lee, P.T. Lee, G.T. Hong, Y.H. Li, W.Y. Chang, C. H. Lo (2020). Active Volcanism Revealed from a Seismicity Conduit in the Long-resting Tatun Volcano Group of Northern Taiwan, *Scientific Reports*, 10.

Pu, H. C., C. H. Lin, H. F. Lee, Y. C. Lai, L. C. Chang, M. H. Shih (2021). Ascending Volcanic Fluids Portended by Spatiotemporal Variations of the Earthquake Mechanisms in the Tatun Volcano Group in Northern Taiwan, *Geophysical Research Letters* 48(9).

Song, S.R., T.F. Yang, Y.H. Yeh, S.J. Tsao, H.J. Lo (2000). The Tatun volcano group is active or extinct? *J. Geol. Soc. China*, 43, 521–534.

Yang, T. F., Y. Sano, S. R. Song (1999). 3He/4He ratios of fumaroles and bubbling gases of hot springs in Tatun Volcano Group, North Taiwan. *Il Nuovo Cimento Soc. Ital. Fisica C*, 22, 281-286.

(6a) Advanced techniques for simulations in earthquake engineering

STRUCTURAL PERFORMANCE ANALYSIS OF A SEISMIC DAMAGED BRIDGE WITH LOADING TEST

Po-Hsin Lee[1], Feng-Kai Chang [2], and Yu-Chi Sung[3]

1. Ph.D. Student, Department of Civil Engineering, National Taipei University of Technology, Taipei, Taiwan, R.O.C.
2. Master, Department of Civil Engineering, National Taipei University of Technology, Taipei, Taiwan, R.O.C.
3. Professor, Department of Civil Engineering, National Taipei University of Technology, Taipei, Taiwan, R.O.C.

Email: [1] t108428001@ntut.org.tw, [3] sungyc@ntut.edu.tw

ABSTRACT

This study adopted a 3D finite element model optimized by a genetic algorithm to evaluate Provincial Highway 86 Bridge No. 24, severely damaged by the Meinong earthquake in 2016. The finite element model was established according to the design drawings and on-site investigation. However, the 3D finite element model with numerous elements increases the model complexity and computation cost. Therefore, the study adopted a response method of experimental design function, which replaced the static and dynamic analysis and reduced the computation cost. The response surface functions are checked against R-squared to ensure sufficient accuracy to represent the finite element analysis results. Subsequently, the parameters are optimized with the genetic algorithm and fed back to the finite element model. The comparison results show that the optimized finite element model can accurately reflect the static and dynamic behavior of the bridge.

Keywords: 2016 Meinong Earthquake, moving load, gene algorithm

INTRODUCTION

The Meinong earthquake occurred on February 6, 2016. According to the data released by the United States Geological Survey (USGS), as shown in Figure 1, the sensed vibration was between very strong and severe. Provincial Highway 86 is one of Taiwan's east-west viaduct highways. The Meinong earthquake caused severe damage to the girders of Bridge No. 24, resulting in large lateral deformation, as shown in Figure 2. Huang et al. (2017) conducted the bridge investigation and repair design. The report mentioned that the maximum lateral displacement of the bridge was about 49 cm and proposed superstructure repair and seismic capacity reinforcement projects.

Subsequently, the on-site loading tests were conducted by National Center for Research on Earthquake Engineering (NCREE) to ensure the safety of the bridges. The report by Zeng et al. (2019) shows that the deformation and frequency at each span of the girders are stable. Therefore, the bridge is judged to still be in service, but long-term monitoring is required. Finally, the warning and action values of the deformation are defined according to the results of numerical analysis, loading tests, and temperature influence range from March 2017 to February 2019.

This study takes Bridge No. 24 of Provincial Highway 86 as an example. A 3D finite element model was established according to the design drawings using the commercial software Midas Civil and adjusted based on experimental data. In order to reduce the computational cost, the study adopts the design parameters based on the response surface methodology (RSM). Subsequently, the parameters are optimized by the genetic algorithm and fed back to the finite element model. The comparison of finite element analysis and measurement results will be discussed in the study. The results show that the optimized finite element model can match the static and dynamic characteristics of the actual bridge.

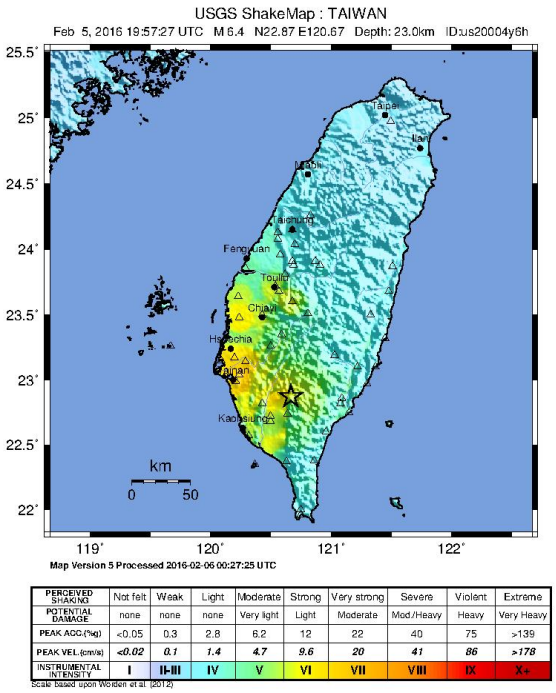

Figure 1. Seismogram released by USGS of the Meinong Earthquake

(a) Excessive lateral displacement of girder

(b) Concrete pier damage

Figure 2. Damage photos of Provincial Highway 86 Bridge No. 24

EXPERIMENTAL INVESTIGATION

This study focuses on the eastbound viaduct of Provincial Highway 86 Bridge No. 24, which can be divided into two vibration units, A1~RP7 (A1) and RP7~A2 (A2). Each unit comprises 7 spans of continuous prestressed box girders, as shown in Figure 3. The bridge's support system adopts pot bearing, including free movement, sliding guided, and rigid. Figure 4 illustrates the bearing configuration of the bridge.

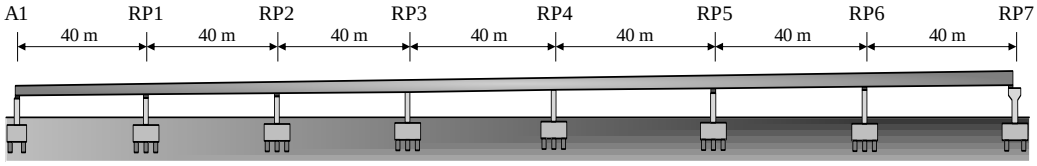

(a) A1~RP7 (A1 unit: 7@40 m)

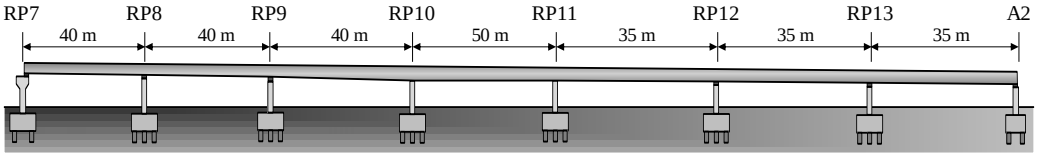

(b) RP7~A2 (A2 unti: 3@40+50+3@35 m)

Figure 3. Basic information of the eastbound viaduct of Provincial Highway 86 Bridge No. 24

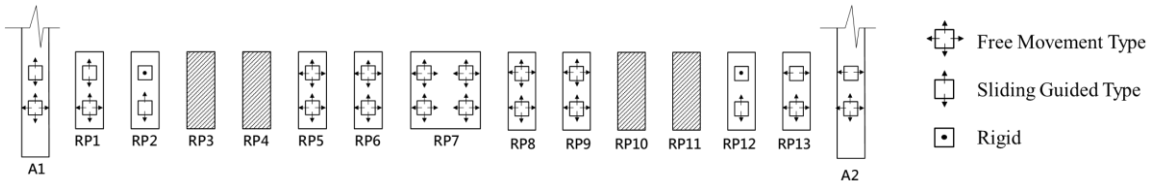

Figure 4. Bearing configuration of the bridge

Measurement Sensor Layout

Figure 5 illustrates the deployment of the measuring instruments used in the loading tests. The measuring instruments are installed between 5~7 spans of the A1 unit and 8~10 spans of the A2 unit, with 12 displacement transducers and 6 laser rangers. The displacement transducer adopts SDP-50C and SDP100C (Figure 6) produced by Tokyo Sokki Kenkyujo, and the laser ranger adopts Disto X310 (Figure 7) produced by Leica, having an accuracy of 1mm.

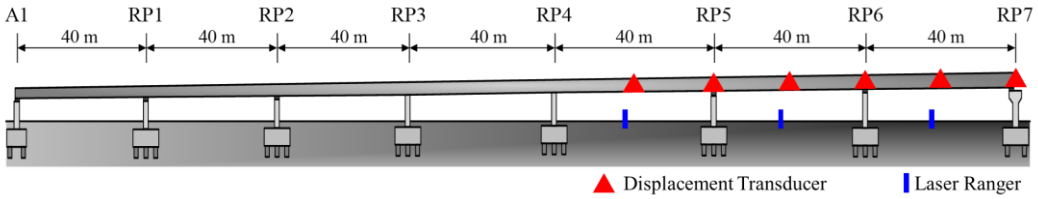

(a) A1 unit (6 displacement transducers + 3 laser rangers)

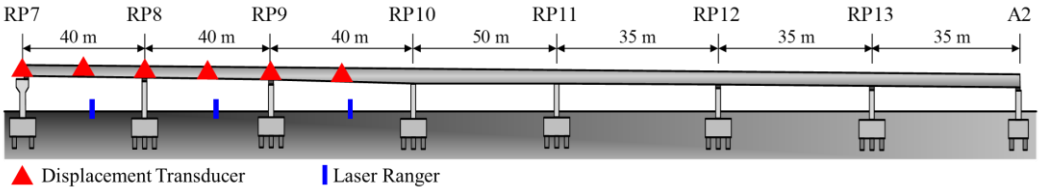

(b) A2 unit (6 displacement transducers + 3 laser rangers)

Figure 5. Deployment of the measuring instruments

Figure 6. Displacement transducer (SDP-C)

Figure 7. Laser ranger (Disto X310)

General Information of Field Test

The static loading tests are divided into A1 and A2 units, each with four cases, and Table 1 describes the configuration of each case. The maximum design live load calculated according to the bridge design specification is about 144 tons. Therefore, the static loading test adopts a maximum of 6 trucks, each weighing 24 tons, evenly distributed on the bridge deck. The maximum displacement measured in each test is about 5~8mm.

Table 1 Controlled loading tests

Unit	Case	Span	Number of Vehicles	Results (mm)
A1~RP7	Case1_A1	RP6-RP7	4	7.00
	Case2_A1	RP5-RP6	4	6.40
	Case3_A1	RP4-RP5	4	5.48
	Case4_A1	RP4-RP5	6	7.90
RP7~A2	Case1_A2	RP7-RP8	4	7.92
	Case2_A2	RP8-RP9	4	6.72
	Case3_A2	RP9-RP10	4	4.96
	Case4_A2	RP9-RP10	6	6.56

In the dynamic loading tests, a single truck passed through 5~7 spans at 20, 40, and 60 km/hr, respectively. Figure 8 shows the dynamic measurement results at the midspan of the 6th span.

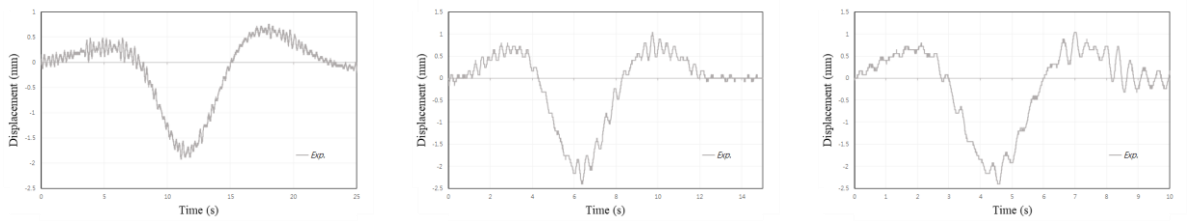

(a) Case1 (20 km/hr) (b) Case2 (40 km/hr) (c) Case3 (60 km/hr)

Figure 8. Dynamic measurement results at the midspan of the 6th span

FINITE ELEMENT MODEL OPTIMIZATION

To simulate the behavior of the case bridge, a 3D finite element model was established using Midas Civil. Figure 9 shows the numerical model with two different analytical elements. Concrete box girders are modeled by solid elements with a total of 320,085 meshes, and prestressed tendons are simulated by truss elements with 4,771 meshes. The compressive strength of the concrete is 350 kgf/cm^2; the ultimate tensile strength of the tendon is 19,000 kgf/cm^2, and the yield stress is 17,080 kgf/cm^2.

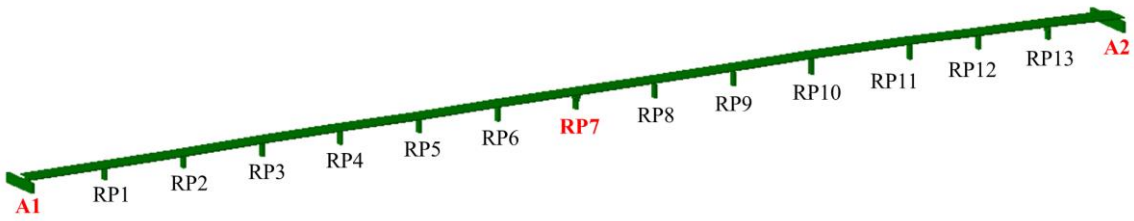

Figure 9. 3D finite element model of the eastbound viaduct in Midas Civil

To reduce the errors between the experimental data and finite element analysis, the study uses the genetic algorithm to optimize the design parameters of the finite element model. However, the complexity and computational cost of the 3D finite element models are too high, resulting in poor optimization efficiency. RMS can effectively solve the problem of excessive analysis costs and increase optimization efficiency. The optimization process of the genetic algorithm based on RSM is as follows:

1. Define the experimental points and the number of cases according to the finite element model.
2. Define control factors and normalize variation ranges.
3. Perform finite element analysis and output displacement of the experimental points.
4. Fit the response surface function according to the finite element analysis results, and check the accuracy of the response surface function by R-squared.
5. Genetic algorithm parameter initialization.
6. Fitness calculation: evaluate the fitness value of each chromosome.
7. Selection: keep good gene sequence according to fitness value.
8. Crossover: randomly select gene positions in chromosomes for crossover operation.
9. Mutation: randomly select gene positions in chromosomes for mutation operation.
10. Convergence check; otherwise, repeat steps 6 to 9.

Response Surface Function

In this study, the elastic modulus E was used as the optimization variable for the finite element model. The variables are set to x_1~x_6 with the symmetrical span and normalized to three levels, as shown in Figure 10 and Table 2. The upper and lower limit of the elastic modulus is 2.81×10^5 and 1.77×10^5 kgf/cm^2, respectively. The middle displacements of each span in the static loading tests (cases 1 to 4) are selected as the optimization objectives. According to the Box-Behnken design method, at least 54 sets of data are required as input parameters, which are obtained by finite element analysis.

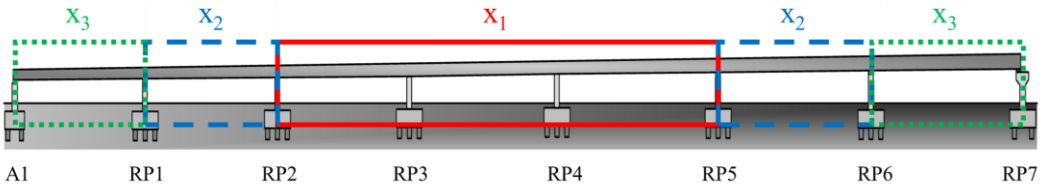

(a) A1 unit (x_1~x_3)

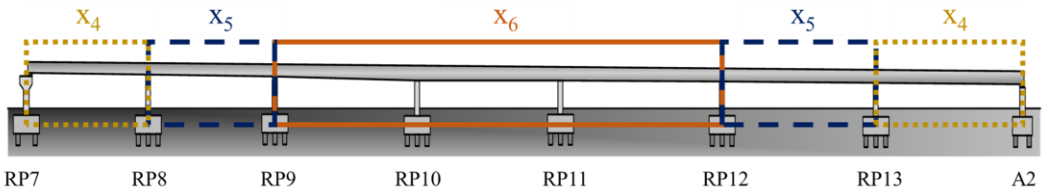

(b) A2 unit (x_4~x_6)

Figure 10. Deployment schematic of the bridge design parameters

Table 2 Range of normalization parameters

Design Parameters	x_1~x_6		
Normalization	1.0	0	-1.0
Elastic modulus (kgf/cm^2)	2.81 E+05	2.29 E+05	1.77 E+05

In the RSM, second-order polynomials are used to fit the eight optimization objectives, given as (1)~(8), to replace the finite element analysis. Table 3 shows the fitting results of the coefficients for the polynomials. Furthermore, the functions are checked against R-squared to ensure sufficient accuracy. The R-squared results are close to 1.00, indicating that the response surface functions are accurate enough to represent the finite element analysis.

Case1_A1: $$f_1(x_i) = A + Bx_1 + Cx_2 + Dx_3 + Ex_2^2 + Fx_3^2 + Gx_2x_3 \quad (1)$$

Case2_A1: $$f_2(x_i) = A + Bx_1 + Cx_2 + Dx_3 + Ex_1^2 + Fx_2^2 + Gx_3^2 + Hx_1x_2 + Ix_1x_3 + Jx_2x_3 \quad (2)$$

Case3_A1: $$f_3(x_i) = A + Bx_1 + Cx_2 + Dx_3 + Ex_1^2 + Fx_2^2 + Gx_1x_2 \quad (3)$$

Case4_A1: $$f_4(x_i) = A + Bx_1 + Cx_2 + Dx_3 + Ex_1^2 + Fx_2^2 + Gx_1x_2 \quad (4)$$

Case1_A2: $$f_5(x_i) = A + Bx_4 + Cx_5 + Dx_6 + Ex_4^2 + Fx_5^2 + Gx_4x_5 \quad (5)$$

Case2_A2: $$f_6(x_i) = A + Bx_4 + Cx_5 + Dx_6 + Ex_4^2 + Fx_5^2 + Gx_6^2 + Hx_4x_5 + Ix_4x_6 + Jx_5x_6 \quad (6)$$

Case3_A2: $$f_7(x_i) = A + Bx_4 + Cx_5 + Dx_6 + Ex_5^2 + Fx_6^2 + Gx_4x_6 + Hx_5x_6 \quad (7)$$

Case4_A2: $$f_8(x_i) = A + Bx_4 + Cx_5 + Dx_6 + Ex_5^2 + Fx_6^2 + Gx_4x_6 + Hx_5x_6 \quad (8)$$

Table 3 Results of the fitting coefficients for each function

	A	B	C	D	E
Case1_A1	-0.7791	0.0022	0.0318	0.1230	-0.0039
Case2_A1	-0.6368	0.0234	0.0833	0.0254	-0.0028
Case3_A1	-0.5158	0.0796	0.0186	0.0013	-0.0140
Case4_A1	-0.6417	0.0979	0.0237	0.0016	-0.0171
Case1_A2	-0.8152	0.1359	0.0339	0.0024	-0.0248
Case2_A2	-0.6441	0.0276	0.0847	0.0229	-0.0028
Case3_A2	-0.5349	0.0015	0.0201	0.0815	-0.0021
Case4_A2	-0.6675	0.0019	0.0255	0.1007	-0.0027
	F	G	H	I	J
Case1_A1	-0.0218	-0.0053	-	-	-
Case2_A1	-0.0136	-0.0025	-0.0029	-0.0013	-0.0046
Case3_A1	-0.0018	-0.0038	-	-	-
Case4_A1	-0.0023	-0.0049	-	-	-
Case1_A2	-0.0040	-0.0064	-	-	-
Case2_A2	-0.0138	-0.0026	-0.0048	-0.0014	-0.0030
Case3_A2	-0.0144	-0.0003	-0.0039	-	-
Case4_A2	-0.0176	-0.0004	-0.0050	-	-

Genetic Algorithm Optimization

According to the genetic algorithm, the optimal solution of the finite element model based on the RSM is carried out. The genetic algorithm adopts binary coding, including 500 generations, 80 chromosomes, and 12 genes, with a mating rate of 0.65, a mutation rate of 0.1, and a retention strategy of 0.05. The fitness function can be expressed as:

$$\begin{cases} \min \ fitness = \sqrt{\sum_{i=1}^{8}\left[(f_i(x_j) - F_i)^2 \times P_{s_i} \right]} \\ s.t. \qquad -1 \le x_j \le 1 \qquad j = 1 \sim 6 \end{cases} \tag{9}$$

where f_i is the calculation result of the response surface function, F_i is the on-site test result, x_j is the optimized design parameters, and P_{si} is the penalty function. Each objective error is used as a penalty function, and there is no penalty if the error is less than 5%; otherwise, the penalty function is given as:

$$P_{s_i} = \begin{Bmatrix} 1 & , & \left| \frac{f_i(x_j) - F_i}{F_i} \times 100 \right| \le 5\% \\ \left| \frac{f_i(x_j) - F_i}{F_i} \times 100 \right| & , & \left| \frac{f_i(x_j) - F_i}{F_i} \times 100 \right| > 5\% \end{Bmatrix} \tag{10}$$

The optimization analysis converges on the 410th generation, as shown in Figure 11, and Table 4 shows the optimization results of 6 design parameters, which meet the specified upper and lower limits.

Table 4 Optimization results of 6 design parameters

	x_1	x_2	x_3	x_4	x_5	x_6
Normalization	-0.978	0.0728	0.7456	0.33037	-0.4946	0.3745
Design Parameters	1.79E+05	2.33E+05	2.68E+05	2.45E+05	2.04E+05	2.48E+05

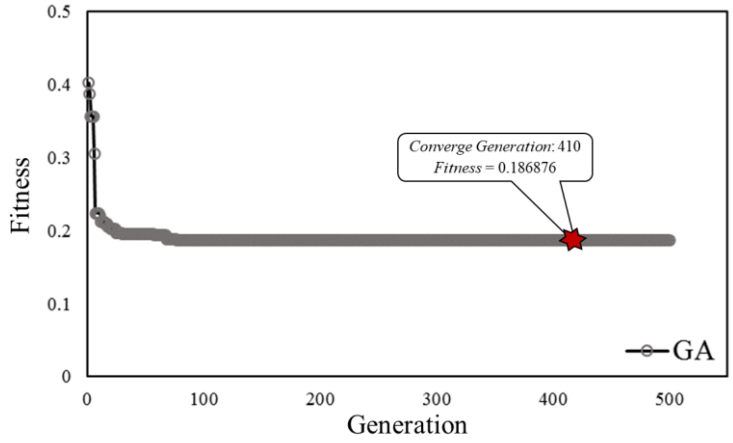

Figure 11. Genetic algorithm offline performance

SIMULATION RESULTS AND COMPARISONS

Table 5 compares the results of the static loading tests and the finite element analysis. The maximum error occurs in Case3_A1 about 0.56 mm, and it is judged that the finite element model is sufficient to simulate the static behavior of the bridge.

The dynamic time history analysis is performed using a single truck passed through 5~7 spans at 20, 40, and 60 km/hr, respectively. The moving load is simulated by defining the delay of the time history functions at each node. Figure 12 shows the comparison results of the dynamic loading tests at the midspan of the 6th span (A1 unit). The results show that the finite element model can reflect the dynamic behavior of the bridge.

Table 5 Comparison results of the static loading tests

Case	Span	Number of Vehicles	Measurement Results (mm)	Analysis Results (mm)	Error (%)
Case1_A1	RP6-RP7	4	7.00	7.01	0.13
Case2_A1	RP5-RP6	4	6.40	6.38	0.30
Case3_A1	RP4-RP5	4	5.48	6.04	10.2
Case4_A1	RP4-RP5	6	7.90	7.80	5.09
Case1_A2	RP7-RP8	4	7.92	7.93	0.14
Case2_A2	RP8-RP9	4	6.72	6.71	0.16
Case3_A2	RP9-RP10	4	4.96	5.16	4.10
Case4_A2	RP9-RP10	6	6.56	6.45	1.68

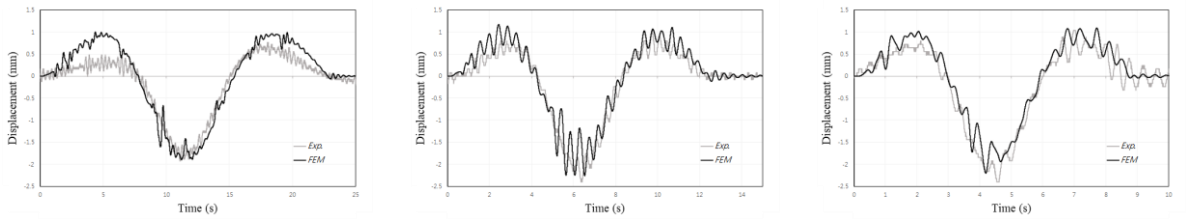

(a) Case1 (20 km/hr) (b) Case2 (40 km/hr) (c) Case3 (60 km/hr)

Figure 12. Comparison results of the dynamic loading tests

CONCLUSIONS

In this study, a 3D finite element model was established based on the design drawings, and RSM was adopted to replace the finite element analysis to reduce the computational cost. Subsequently, the genetic algorithm is used to optimize the input parameters based on the data of the static loading tests. The comparison results of optimized finite element analysis and experimental data show that the numerical model can well reflect the static and dynamic behavior of the bridge. The conclusions and contributions of this study are as follows:

1. The RSM is established through the concept of statistics and experimental design, which can effectively solve the high computation cost caused by the 3D finite element model with numerous elements.

2. In this study, the optimization method of the genetic algorithm is used to optimize under two unconstrained conditions. The results show that the genetic algorithm performs well in global and local search ability.

3. The numerical model optimized by the method combined with RSM and the genetic algorithm can well simulate the static and dynamic behavior of the bridge. However, the efficiency may be reduced if the optimization problem is too complex. Other algorithms with better search ability can be used in these cases, such as the multi-objective hybrid genetic algorithm and ant colony algorithm.

REFERENCES

Huang, P.H., C.H. Chiang and Y.H. Chen (2017). "Introduction of Lateral Displacement and Restoration of Provincial Highway 86 Bridge No. 24 After The Meinong Earthquake," *Journal of Chinese Institute of Civil and Hydraulic Engineering*, **44**(3), 20-26.

Yeh, F.Y., B.H. Lee, Z.K. Lee, C.C. Hsu, C.C. Chen, L.S Lee, C.L. Jang, Y.C. Sung, K.C. Chang and K.Y Liu (2019). "Damage Investigation and Response Strategy of Bridge due to The Meinong Earthquake," *Journal of Chinese Institute of Civil and Hydraulic Engineering*, **31**(5), 431-441.

Zeng, W.L., C.R. Zhang, K.Z. Chen, C.H. Ku, Y.C. Sung, F.Y. Yeh, Z.K. Lee, C.C. Hsu, B.H. Lee, C.C. Chen (2019). "Long-Term Monitoring and Loading Test Analysis of Provincial Highway 86 Bridge No. 24," *Taiwan Highway Engineering*, **45**(12), 2-17.

Chang, F.K., and Y.C. Sung (2017). Loading Test Analysis of Earthquake Damaged Bridge and Study on Long-Term Health Diagnostic Method for Retrofitted Bridge, *Academic Thesis*, National Taipei University of Technology, Taipei.

Chiu, Y.T. (2016). Optimal Identification of Bridge Structure and Its Application on Safety Evaluation Based on Long-term Monitoring Data, *Ph.D. Thesis*, National Taipei University of Technology, Taipei.

Sung, Y.C., C.Y. Wang, E.H. Teo (2016) "Application of particle swarm optimization to construction planning for cable-stayed bridges by the cantilever erection method," *Struct. Infrastruct. Eng.*, **12**(2), 208-222.

Holland, J.H. (1975). "Adaptation in Natural and Artificial Systems: An Introductory Analysis with Applications to Biology, Control, and Artificial Intelligence," *U Michigan Press.*

Negaendra, S., D. Jestin, Z. Gurdal, R.T. Haftka and L.T. Watson (1996). "Improved Genetic Algorithm for The Design of Stiffened Composite Panels," *Comput. Struct.*, **58**(3), 543-555.

Wang, H., and H. Ohmori (2013). "Elasto-Plastic Analysis Based Truss Optimization Using Genetic Algorithm," *Eng. Struct.*, **50**, 1-12.

Box, B.E.P., and K.B. Wilson (1951). "On the Experimental Attainment of Optimum Conditions," *Journal of the Royal Statistical Society. Series B (Methodological)*, **13**(1), 1-45.

Box, B.E.P., and K.B. Wilson (1960). "Some New Three Level Designs for the Study of Quantitative Variables," *Technometrics*, **2**(4), 455-475.

INFRASTRUCTURE CONSTRUCTION OF A WEB APPLICATION SYSTEM FOR STRUCTURAL ANALYSIS

Kuang-Wu Chou[1], Chia-Chuan Hsu[2], and Chang-Wei Huang[3]

1. Associate Researcher, Bridge Engineering Division, National Center for Research on Earthquake Engineering, Taipei, Taiwan, R.O.C.
2. Assistant Researcher, Bridge Engineering Division, National Center for Research on Earthquake Engineering, Taipei, Taiwan, R.O.C.
3. Professor, Department of Civil Engineering, Chung Yuan Christian University, Taoyuan, Taiwan, R.O.C.

Email: kwchou@narlabs.org.tw, chiachuan@narlabs.org.tw, cwhuang@cycu.edu.tw

ABSTRACT

This study aims to develop a system that can perform structural analysis on the web. To support such analysis, we build this system's infrastructure that comprises an efficient back-end system and a responsive front-end system. The JavaScript framework Angular is used to provide the front-end system with a responsive web user interface. The computer graphics engine WebGL is utilized to render 3D structural models in the canvas of this web user interface. A simple example demonstrates that the document-oriented database technology MongoDB can straightforwardly describe and efficiently store a structural model. The back-end technology Node.js works smoothly with the MongoDB database, providing the front-end system with a web application programming interface. Through this programming interface, the back-end system can feed the front-end with data of a structural model.

Keywords: numerical analysis, structural model, cloud computing

INTRODUCTION

Developers prefer to create native desktop applications instead of applications of other types such as console and web applications. This is because desktop applications provide users with rich and diverse native graphical user interfaces (GUI) while the others seem unable. Nevertheless, recently, popular and powerful desktop applications like Atom, Visual Studio Code, Microsoft Teams, and Facebook Messenger were developed with the web technologies supported by a famous framework Electron. They offer native GUIs for Windows, macOS, and Linux. And Their being developed with the same source code suffices to make them cross-platform.

Web technologies keep developing and get improved so fast that we cannot ignore them. While most of numerical analysis software are developed with desktop application technologies other than web technologies, this study intends to examine if developing numerical analysis software could benefit from applying web technologies.

As a procedure of numerical analysis, finite element analysis or structural analysis is essential to simulate mechanical behaviors of bridge or building structures and to examine their health. This study therefore aims to develop a system that can perform structural analysis on the web. This system will be implemented as a web application, which never needs users to install and update it frequently while desktop applications need both. Besides, Electron can easily transform this web application into a desktop application without modifying the code of this web application.

Before implementing structural analysis into this web system, we build this system's infrastructure comprising a back-end system and a front-end system. This infrastructure should support this web system to effectively manipulate and display structural models, to offer users responsive interface, and

to perform time-consuming computations. This infrastructure is described in the following. A minimal example is also given to demonstrate how this web system's prototype works.

INFRASTRUCTURE

The client-server architecture is applied to develop this web system. This means that this system comprises a back-end system and a front-end system. These two subsystems are illustrated as follows.

Back-end System

The back-end system takes charge of providing clients with the resources it manages. One important resource is the front-end system, which is described later. Another important resource the back-end manages and provides is data of structural models. To effectively manage structural model data, the back-end utilizes a MongoDB database to store the data. This database stores data in documents. Documents are more flexible than fixed rows and columns, which traditional, relational SQL databases utilize to manage data (MongoDB, 2022). In addition, the way of describing documents in MongoDB fits how a structural model is defined by finite element software. This is demonstrated in the next section (Prototype Demonstration).

Directly manipulating the database of structural models, the back-end is supposed to perform numerical analysis on these models and thus should work with corresponding analysis modules by calling them. These modules will be implemented in C++, ensuring that those analyses can be efficiently executed. Nevertheless, we consider that these C++ modules may be called by not only the back-end, but also the front-end. That is, our system might let users choose which end to perform analysis.

The back-end is implemented as a web API (Application Programming Interface) for any front-end program or system to call. To fulfil the tasks mentioned above, the web API is supposed to provide manipulation and analysis on structural models.

The web API is implemented by utilizing a cross-platform back-end web technology: Node.js. It is a JavaScript runtime that is built and runs on Chrome's V8 JavaScript engine (OpenJS Foundation, 2022; Wikipedia, 2022). Node.js enables the usage of the programming language JavaScript, which is essential for front-end development, to develop and to run back-end systems.

The API of Node.js suffices to do many things like creating web APIs and using databases (especially MongoDB databases). To simplify our codes and ensure the stability and reliability of our web systems, we use a framework for building Node.js web applications: Express. Express is minimal and flexible, treated as the de facto standard server framework for Node.js.

Node.js offers transparent ways for a JavaScript module to call C++ modules. More importantly, the C++ modules can run asynchronously in a Node.js application without blocking this application's main thread. This means that a Node.js application can run time-consuming tasks and respond to user requests at the same time. That is why this study chooses Node.js to examine if structural analyses that likely consume much CPU time may run along with web applications.

Front-end System

The front-end system provides this web system's GUI. This GUI helps clients send requests on structural model data to the back-end system. To build a responsive web GUI that feels like a native desktop GUI, this study adopts the SPA (Single Page Application) approach. This approach prevails over the "traditional" MPA (Multiple Page Application) approach. At the client side, SPA retrieves the single web page only once from the server. After that, according to user requests, SPA will send data to the server or get data from the server to update the content of this page. Under such pattern of communication between clients and the server, the server takes charge of only receiving and providing

data that users concern about. That is why we design the back-end system as a web API, which provides user with manipulation on structural model data.

There are JavaScript frameworks or libraries for building SPAs. Three main streams are Facebook's React, Google's Angular, and Vue. Currently, this study adopts Angular because it is a full-featured framework and because its programming language is Typescript that we prefer to utilize. Typescript is a strict syntactical superset of JavaScript. Typescript is statically typed so that some errors may be caught in compile time. For dynamically typed JavaScript, compile time never exists to detect errors. Besides, Angular Material is used to design the front-end system's web GUI while Angular Material supplies high quality UI design components for developing Angular applications.

In addition to offering the web GUI, the front-end system is supposed to show 3D structural models in browsers. To ensure that this system can efficiently display objects in 3D, this study uses a low-level JavaScript API that can command a GPU (Graphics Processing Unit) to draw with minimal overheads. Currently, only two APIs may be utilized: WebGL and WebGPU. Because WebGPU is still a W3C working draft, we adopt WebGL and would try WebGPU which is claimed faster than WebGL.

PROTOTYPE DEMONSTRATION

Considering that structural analysis procedures will be implemented and tested on this web system, simple examples detailing for verifying the analysis results are required. Here we borrow Example 5.9 from McGuire *et al*. (2000). This example shows a portal frame that comprises three structural members (See Fig. 1). Each member has its section properties. Fig. 2 shows that the structural model of this frame is defined and stored as a JSON (JavaScript Object Notation) document object in this system's MongoDB database. A JSON object is described with its properties surrounded by two curly braces {}. Each property is represented by a key-value pair. The JSON object that describes this frame has the key "_id", "name", "nodes", "elements", "materials", and "sections". The "name" key has a string value. Each of the key "nodes", "elements", "materials", and "sections" has an array value.

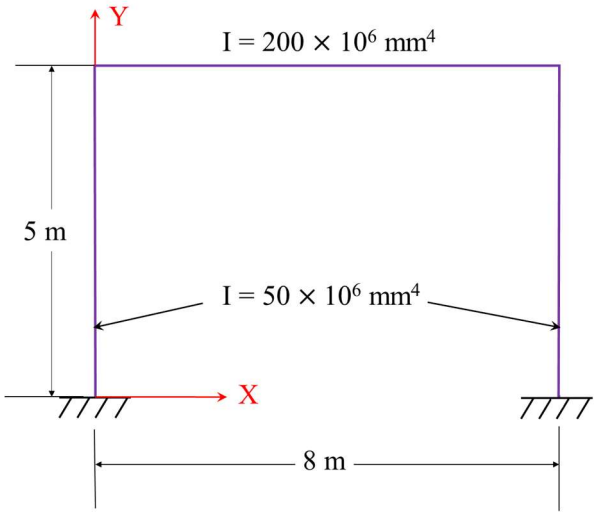

Figure 1. A portal frame.

The array value of the key "nodes" has four members each representing a node while this frame has four nodes. As a node, each member is described by an array having three floating-point values that are the node's coordinates.

Since this frame has three elements, the array value of the key "elements" has three members representing these elements, respectively. To sufficiently describe an element, each member is defined as a JSON object owning the property (or key) "nodes" and "section". This property "nodes" describes

an element's nodes with an array of node indices. The "section" property has a string value that is the name of a section. A section is also described with a JSON object, as a member of the property "sections" of the root JSON object describing a structural model. Expanded in Fig. 2, the second member of the property "elements" has the property "nodes" containing the index 1 and 2 and the property "section" whose value is "beam". This value is the name of a section object defined in the property "sections" of the root JSON object (while Fig. 2 shows the first, expanded section object has a different name "column").

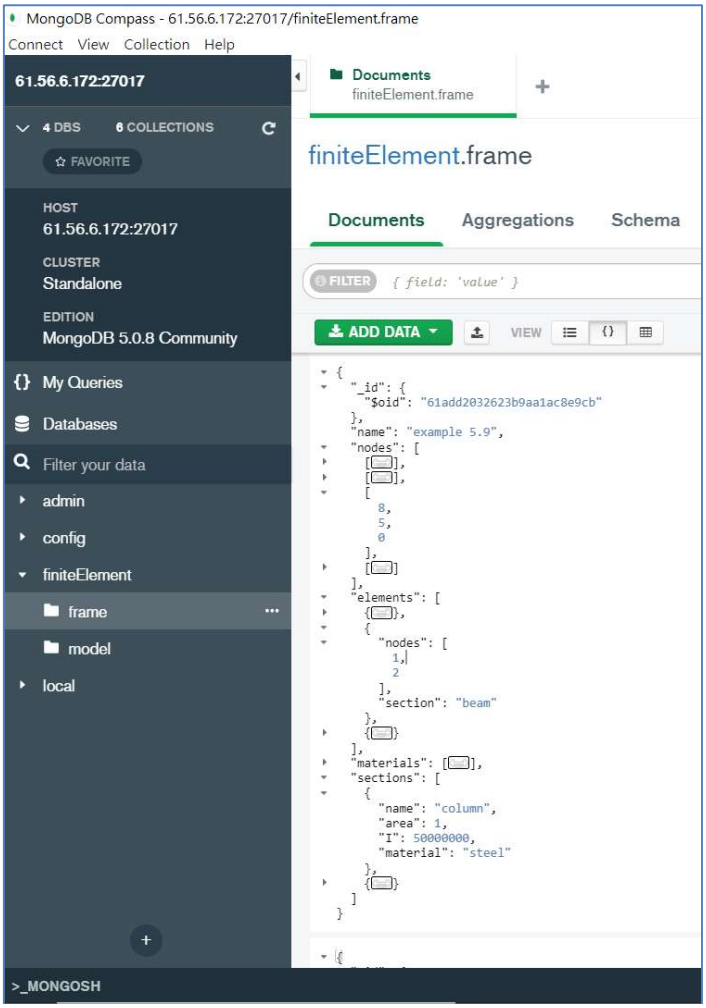

Figure 2. A JSON object represents a MongoDB document that describes the structural model of a portal frame.

Fig. 3 shows that a browser gets the structural model of this frame in JSON format by calling the web API of this system prototype. The JSON object looks almost the same as in Fig. 2. The URL (Uniform Resource Locator) of the web API is http://61.56.6.172:8080/frames/61add2032623b9aa1ac8e9cb. The identifier at the end of this URL matches the value of the property "_id" of the JSON object describing this frame in the MongoDB database. The web API uses this identifier to find a structure model from this database.

A minimal web application of the system prototype is demonstrated in Figs. 4 and 5. The two figures show the node data and the frame element data of this portal frame, respectively. Furthermore, the two figures show different perspective views of this frame while users can move, rotate, and zoom in or out any structural model displayed on the 3D canvas by manipulating their computer mice. In fact, this minimal calls the web API along with the aforementioned URL. Then, this minimal gets the model data of this frame from the server and shows the model data by calling Angular Material UI (User Interface) components. Because this model data sufficiently describes this frame's geometry, this

minimal can use this data to display a 3D view of this frame by calling the 3D graphics engine WebGL.

CONCLUSIONS

This study created a system prototype that provides a web API and a web application. This practice shows that the document-oriented database technology MongoDB can effectively describe, store, and disseminate structural models with JSON document objects.

Utilizing Node.js, we quickly prototyped a web server (the back-end system) in JavaScript. This server may manage the MongoDB database, providing other systems with a web API to access the structural models stored in the database.

The front-end JavaScript framework Angular and its UI design component, Angular Material, suffice to create a responsive UI for the system prototype. By consuming the web API, this UI can show the data that defines a frame model. This practice also shows that Angular can smoothly work with the 3D graphics JavaScript API, WebGL.

REFERENCES

McGuire, W., Gallagher, R.H., and Ziemian, R.D. (2000). *Matrix Structural Analysis*, *2nd Edition*, Faculty Books, **7**, 119-120, https://digitalcommons.bucknell.edu/books/7.

MongoDB, Inc (2022). *What is a Document Database?*, https://www.mongodb.com/document-databases.

OpenJS Foundation (2022). *Node.js*, https://nodejs.org.

Wikipedia (2022). *Node.js*, https://en.wikipedia.org/wiki/Node.js.

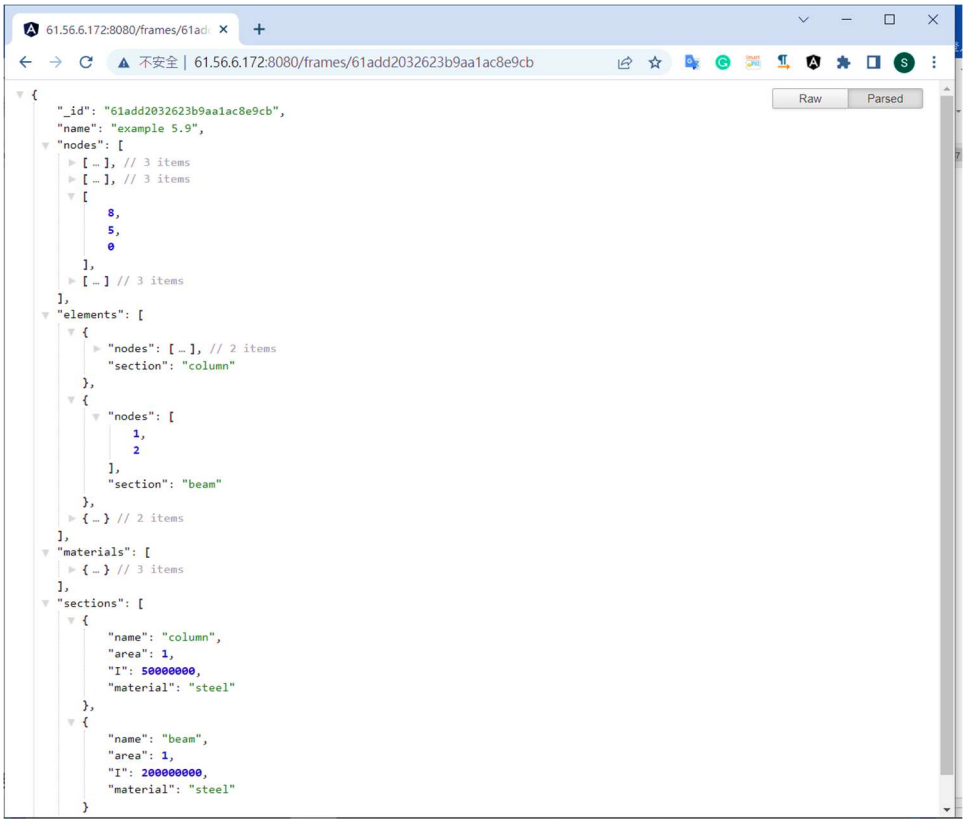

Figure 3. The web API of the system prototype returns a structural model as a JSON object to a Chrome browser.

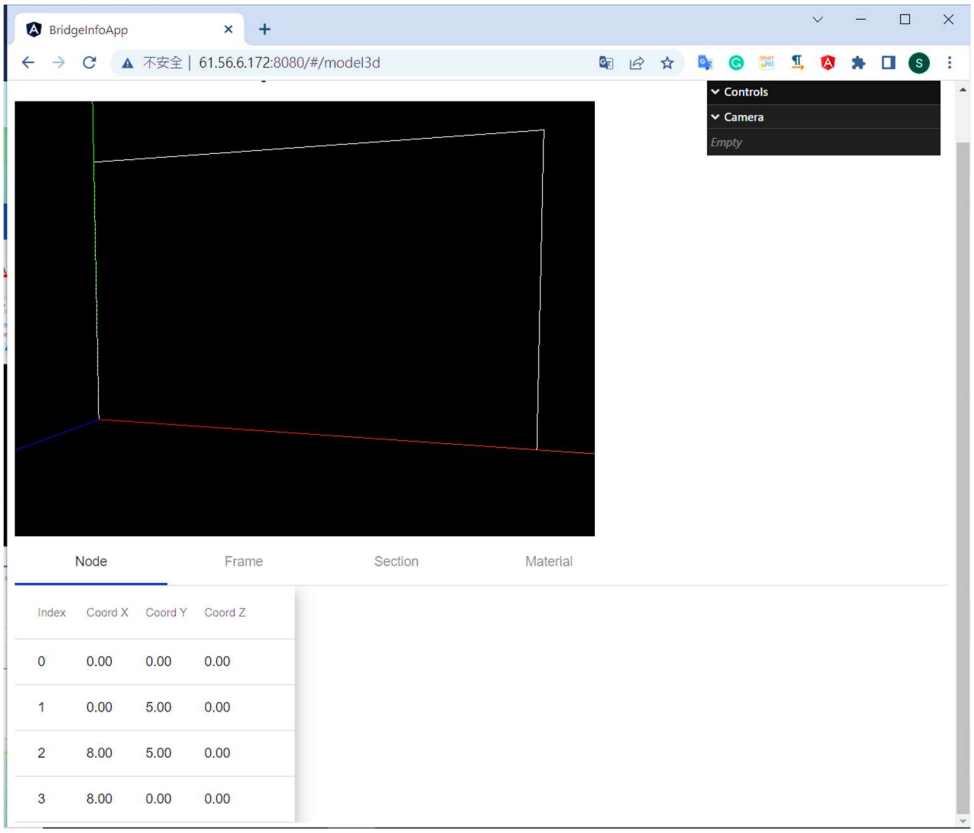

Figure 4. Node data of a portal frame.

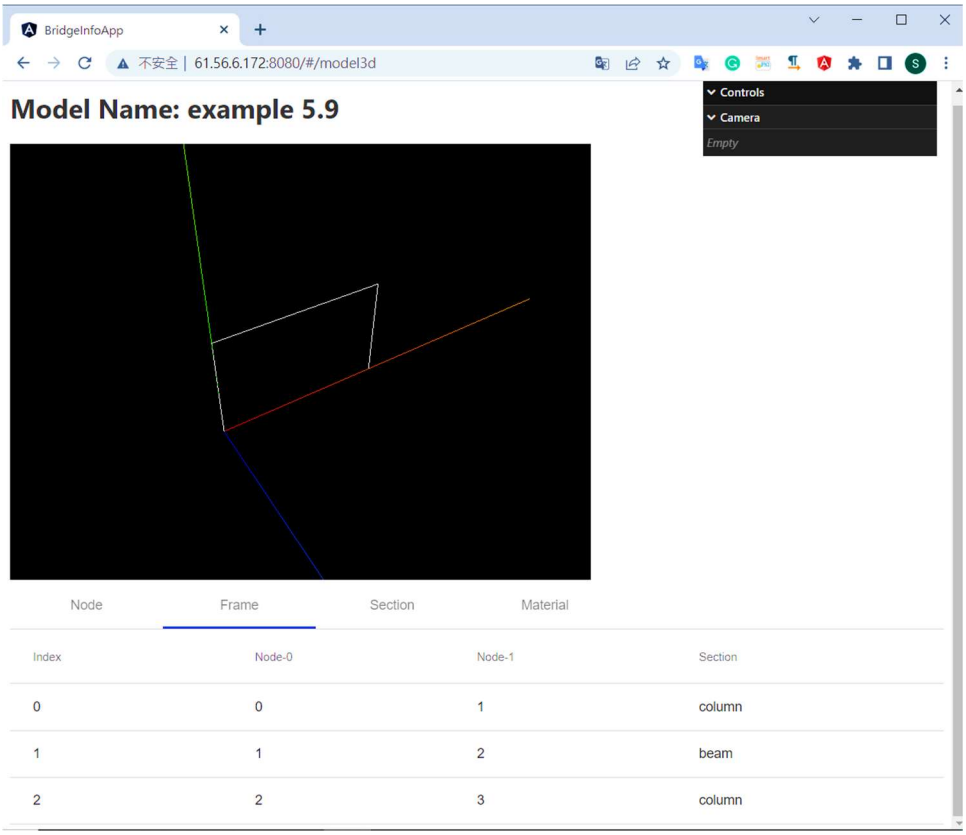

Figure 5. Frame element data of a portal frame.

SEISMIC FRAGILITY ASSESSMENT OF A NON-CONFORMING RC FRAME CONSIDERING SHEAR DEFORMATION OF VERTICAL MEMBERS

Won Jun Hwang[1] and Sung Jig Kim[2]
1. Ph. D. Student, Department of Architectural Engineering, Keimyung University, Daegu, Korea.
2. Associate Professor, Department of Architectural Engineering, Keimyung University, Daegu, Korea.
Email: hwangwj94@kmu.kr, sjkim4@kmu.ac.kr

ABSTRACT

The paper presents the seismic vulnerability of a non-conforming RC frame by utilizing the analytical model considering nonlinear shear deformations of RC columns. The predictive equations for shear spring parameters of the Pinching4 model in OpenSees are modified using the experimental data and the existing shear spring models. The constructed numerical model using the shear spring is evaluated by comparing with the experimental data in terms of the initial stiffness, maximum strength, strength degradation, and pinching behavior. In addition, seismic fragility curves of the non-conforming RC frame are derived by utilizing the numerical models with and without the shear spring, and the effect of shear deformation on the damage probability is evaluated. The analytical results indicate that the seismic vulnerability of the selected structure significantly increases when the shear deformation of RC columns is considered.

Keywords: seismic fragility, shear spring, RC column, non-seismic details

INTRODUCTION

Reinforced Concrete (RC) columns with inadequate details are vulnerable to shear damage when subjected to earthquake loads. Due to this shear distress, the axial capacity of the columns is degraded, showing brittle fracture behavior, and amplifying damage to a RC structure. To prevent this situation, it is necessary to identify vulnerable members through a rigorous numerical analysis. However, it is difficult to accurately simulate the shear behavior of RC columns with the fiber section element-based analysis programs. As shown in Figure 1, many studies have focused on simulating the shear behavior by adding a shear spring element to the numerical analysis program of the macroscopic modeling technique (Elwood, 2004; Haselton, 2006; Leborgne, 2012; Lee, 2018). In this study, the predictive equations for the shear spring parameters are developed by utilizing experimental data and existing shear spring models. In addition, the seismic fragility of the RC frame with non-seismic details is evaluated by applying the proposed shear spring, and the difference in damage probability is compared with the model without the shear spring.

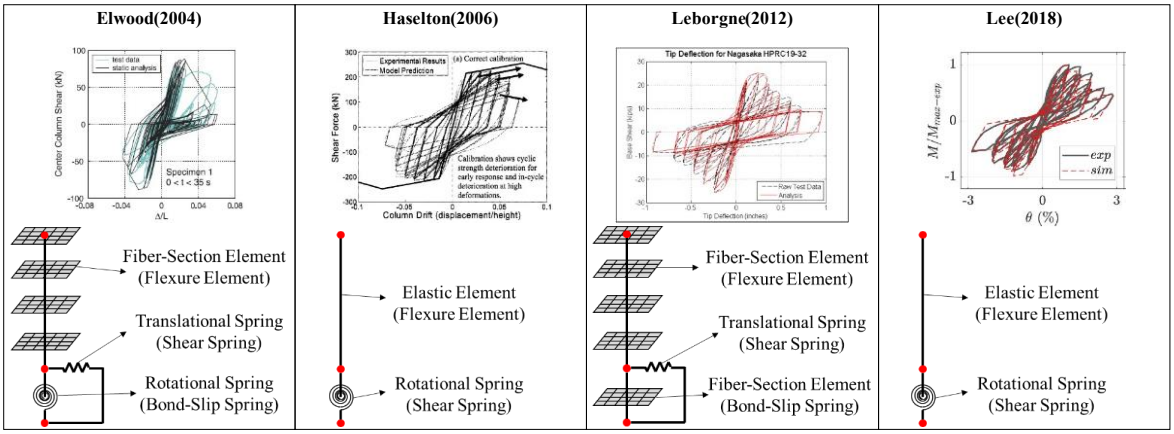

Figure 1. Various shear spring models.

SHEAR SPRING PARAMETERS

The parameters of the shear spring are determined based on the experimental data and physical properties of the RC columns obtained from the PEER structural performance database (Berry et al., 2004). Experimental data used in this study satisfies the followings:

1. Rectangular cross section.
2. Compressive strength of concrete less than 40 MPa.
3. Shear failure or shear-flexural failure.
4. Incremental cyclic loading.

The numerical analysis program used to simulate the shear spring in this study is OpenSees (McKenna, 2011), and the shear spring is implemented using the Pinching4 model (Lowes et al., 2004) in OpenSees. Using the collected force-displacement data, the backbone curve parameters having four points: cracking, yielding, maximum force, and ultimate state are calibrated as shown in Figure 2. Parameters related to reloading and unloading stiffness, strength degradation, and pinching effect are also calibrated. The variables of the predictive equations of shear spring for the Pinching4 model are determined through regression analyses using the calibrated parameters and the physical properties. The basic formulations of predictive equations are based on the relationship proposed by Lee (Lee, 2018). A numerical model is constructed using the derived regression coefficients and predictive equations for shear spring parameters. The constructed numerical model is evaluated by comparing with the experimental data. Figure 3 compares the force-displacement relationships of the selected RC columns obtained from numerical simulation and experimental data. Figure 3 demonstrates that the numerical model can similarly simulate the initial stiffness, maximum strength, strength degradation, and pinching behavior.

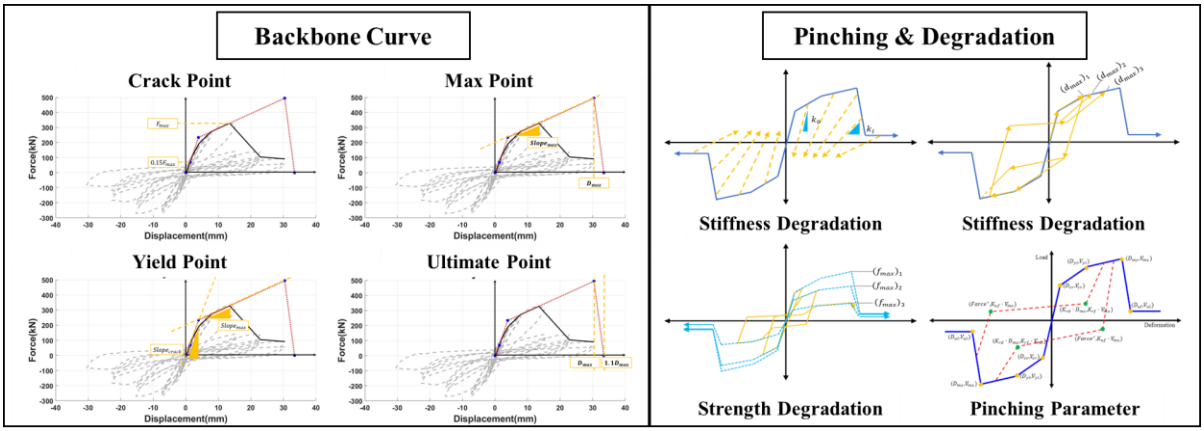

Figure 2. Shear spring parameter at Pinching4 model in OpenSees

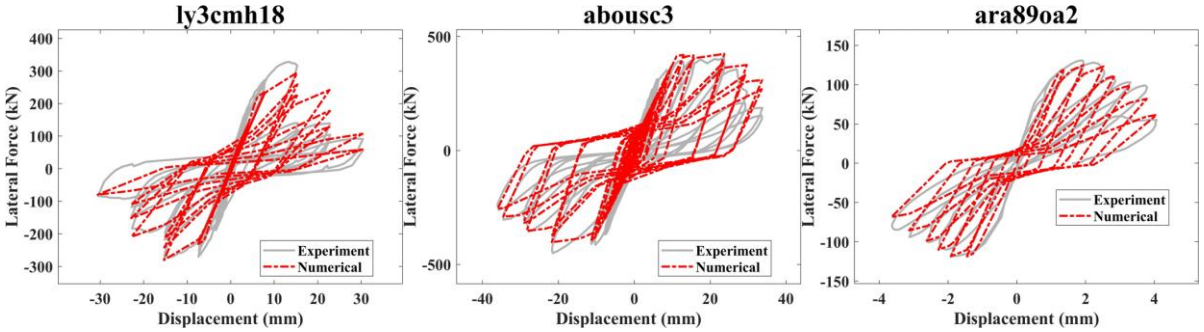

Figure 3. Experiment result (grey solid) versus analytical model with shear spring (red dashed)

SEISMIC FRAGILITY ASSESSMENT

A non-conforming RC frame is selected to evaluate the effect of shear deformation of RC columns on the seismic fragility of a RC structure. Figure 4 shows the plan view and elevation of the selected RC structure with a story height of 3.3m. The selected structure complies with the 1980s Standard Drawings for School Buildings provided by the Ministry of Education, South Korea. The cross-sections with rebar details of RC columns are shown in Table 2. The longitudinal rebar ratios of C1, C2, and C3 shown in Table 2 are 1.54%, 2.74%, and 1.13%, respectively, while the volumetric ratios of transverse rebar are 0.30%, 0.34%, and 0.34%, respectively, which indicates the low confinement. According to the 1980s specifications for School Buildings in South Korea, the compressive strength of concrete and yield strength of rebar are defined as 21 MPa and 340 MPa, respectively.

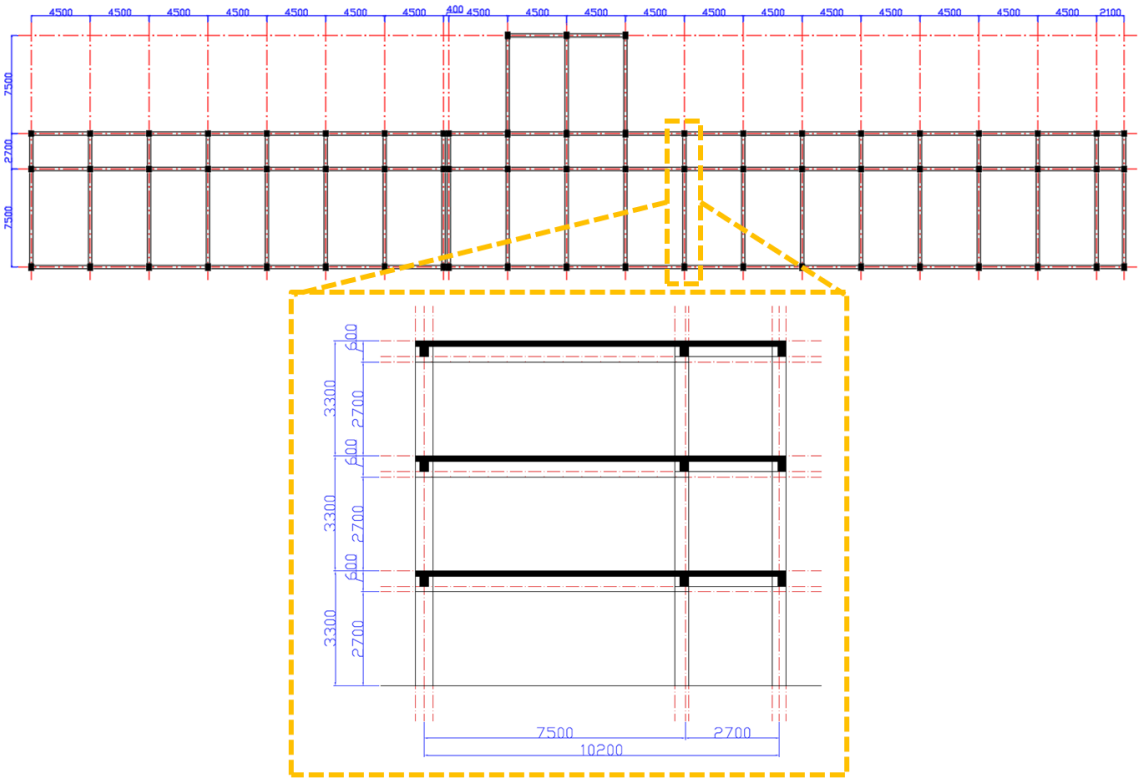

Figure 4. Plan view and elevation of the selected RC structure (mm)

Table 1. Section details of RC columns (mm)

Section name	C1		C2		C3	
Section Detail	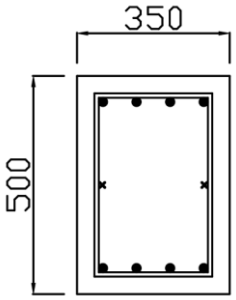		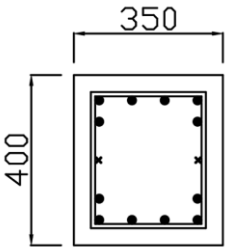		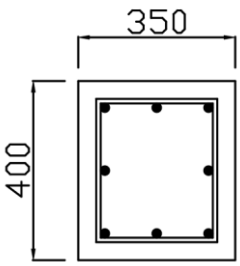	
Longitudinal Rebar	o	8-D19	o	12-D19	o	8-D16
	x	2-D16	x	2-D16	-	
Transverse Rebar	D10@300		D10@300		D10@300	

Numerical models of the selected RC structure were implemented and analyzed using the OpenSees software package, which is a finite element analysis platform. As shown in Figure 5, two analytical models are constructed with and without the shear spring. The RC frame members are modeled by the Displacement-Based Beam-Column Element with the material constitutive laws of Concrete02 and Steel02 for concrete and steel, respectively. To take into account the shear deformation of RC columns, the shear springs at both ends of each column are implemented by utilizing the Pinching4 model.

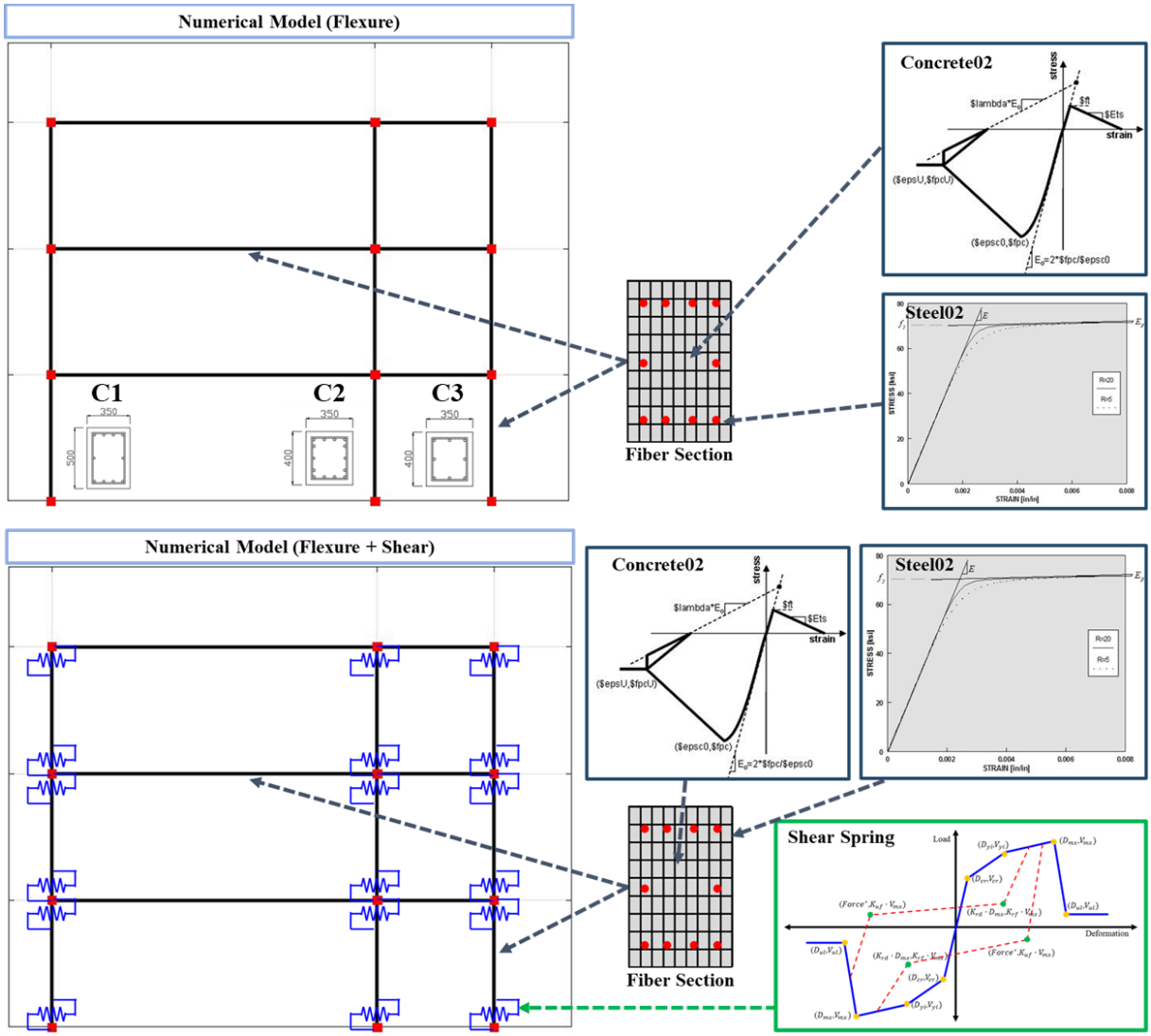

Figure 5. Numerical model with or without shear deformation consideration

The three limit states associated with the structural performance levels for the selected structure are defined: serviceability, damage control, and collapse prevention (Kwon and Elnashai, 2006). The serviceability level is defined when longitudinal reinforcement reaches yielding and the damage control level is defined when concrete strain reaches the maximum confined stress. The collapse prevention level is defined when concrete strain reaches the ultimate confined strain that is suggested by the Eurocode 8. Earthquake ground motions from 100 stations were collected from the PEER strong motion database (Bozorgnia et al., 2014) to conduct nonlinear dynamic analyses of the selected structures. Figure 6 shows the response acceleration spectra of selected records along with the fundamental period (0.26s) of the selected structure.

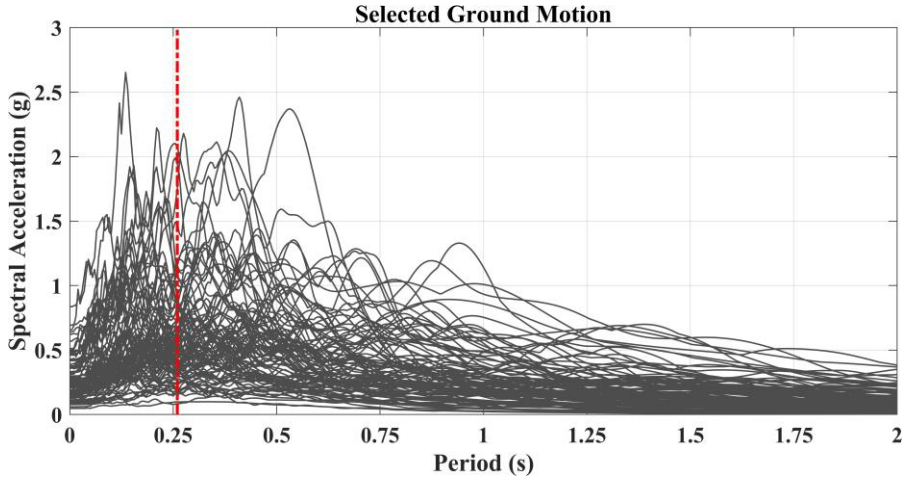

Figure 6. Response spectra of selected ground motions.

Figure 7 shows the seismic fragility curves of the selected frame derived from analytical models with and without the shear spring. Compared to the analytical model without the shear spring, the seismic vulnerability significantly increases when the shear deformation of RC columns is considered in the analytical model. For example, the exceedance probability at the Sa of 1.0g of the serviceability level in the analytical model without the shear spring is 0.84, while that of the analytical model with the shear spring is 0.96. In the case of the damage control level, the exceedance probability at the Sa of 1.0g is changed from 0.30 to 0.66, resulting in the increase of 120%, when the shear deformation of RC columns is considered. The exceedance probability at the Sa of 1.0g of the collapse prevention dramatically increases from 0.03 to 0.21 when the shear spring is implemented in the analytical model. Therefore, Figure 7 clearly shows that the seismic fragility of the non-conforming RC frame is significantly affected when the shear deformation of vertical members is considered.

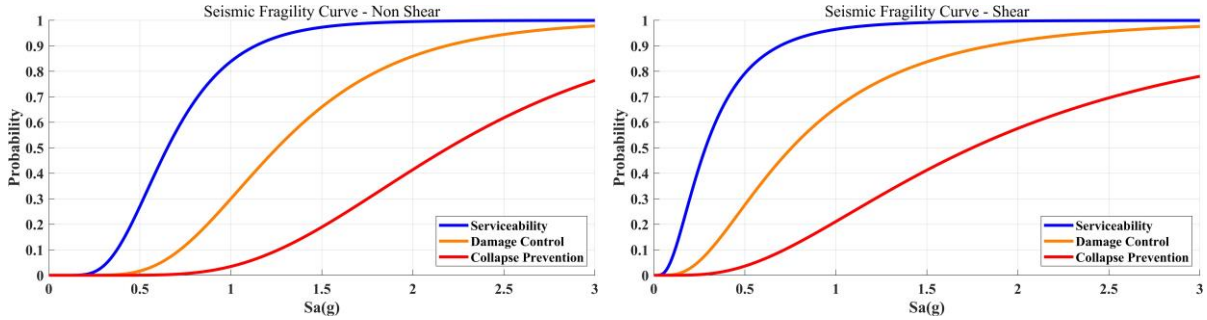

(a) model without the shear spring (b) model with the shear spring

Figure 7. Seismic fragility curves of the selected frame.

CONCLUSIONS

In this study, to derive the seismic fragility curve of the non-conforming RC frame by considering nonlinear shear deformation of RC columns, predictive equations for parameters of a force-deformation-based shear spring are developed using the experimental data and the existing shear spring models. The numerical model using the proposed predictive equations shows the force-displacement relationship matched well with the experimental data in terms of the initial stiffness, maximum strength, strength degradation, and pinching behavior.

The constructed shear spring model is utilized in the analytical model of the non-conforming RC frame to derive the seismic fragility curve. It is observed that the exceedance probabilities of performance levels of the selected structure significantly increase when the shear deformation of RC columns is considered. Therefore, taking into account the observations from the study described above, it is recommended that the realistic shear deformation of RC columns be considered in the analysis for the reliable seismic vulnerability assessment of the non-conforming RC frame.

ACKNOWLEDGMENTS

This research was supported by Korea Basic Science Institute (National Research Facilities and Equipment Center) grant funded by the Ministry of Education. (2021R1A6C103A412)

REFERENCES

Berry, M., Parrish, M., and Eberhard, M. (2004). *PEER structural performance database user's manual* (version 1.0). University of California, Berkeley.

Bozorgnia, Y., Abrahamson, N. A., Atik, L. A., Ancheta, T. D., Atkinson, G. M., Baker, J. W., ... and Youngs, R. (2014). "NGA-West2 research project," *Earthq Spectra*, **30**(3), 973-987.

Elwood, K. J. (2004). Modelling failures in existing reinforced concrete columns. *Can. J. Civ. Eng.*, **31**(5), 846-859.

Haselton, C. B. (2006). Assessing seismic collapse safety of modern reinforced concrete moment frame buildings *Ph.D. Thesis*, Stanford University

Kwon, O. S., and Elnashai, A. (2006). "The effect of material and ground motion uncertainty on the seismic vulnerability curves of RC structure," *Eng. Struct.*, **28**(2), 289-3S03.

LeBorgne, M. R. (2012). Modeling the post shear failure behavior of reinforced concrete columns, *Ph.D. Thesis*, University of Texas at Austin, Austin

Lee, C. S. (2018) Analytical model for non-ductile moment frames with masonry infill walls and retrofit method using friction dampers., *Ph.D. Thesis*, Hanyang University.

Lowes, L. N., Mitra, N., and Altoontash, A. (2004). A beam-column joint model for simulating the earthquake response of reinforced concrete frames. *PEER Report 2003/10*. University of California, Berkeley.

McKenna, F. (2011). "OpenSees: a framework for earthquake engineering simulation," *Comput. Sci. Eng.*, **13**(4), 58-66.

European Committee for Standardization. (2004). "Eurocode 8. Design provisions for earthquake resistance of structures - Part 1: General rules, seismic actions and rules for buildings", Brussels.

MATERIAL-POINT-METHOD IMPLEMENTATION OF TRACTION-BASED DOMAIN REDUCTION SCHEME FOR SOIL-STRUCTURE INTERACTION PROBLEMS

Wen-Chia Yang
Assistant Professor, National Chung Hsing University, Taichung, Taiwan, R.O.C.
Email: yangwc@nchu.edu.tw

ABSTRACT

Soil-structure interaction analyses allow engineers and researchers to better understand the seismic performance of structures, and are generally required in the structural design of important, unusual, and sensitive buildings, e.g., nuclear power plants and dams. Among many modeling techniques, finite element modeling of soil and structures simultaneously in the time domain is a popular choice, especially when a high degree of plasticity is expected. However, in practice, only part of the soil in the real field is (and can be) included in analyses. Therefore, numerical modeling techniques are necessary to define appropriate boundary conditions at the underground surface. The traction-based domain reduction scheme is one of them. The material point method has a computational kernel similar to the finite element method and is powerful in problems involving large deformation. This study implements the traction-based domain reduction scheme in the material point method and tests it with a one-dimensional dynamic problem. Surface particles are adopted for applying traction boundary conditions. The result shows that the domain reduction scheme works fine in the material point method. Further study will be necessary to understand the cause of the minor numerical reflection.

Keywords: material point method, domain reduction scheme, absorbing boundary, soil-structure interaction, semi-infinite domain

INTRODUCTION

The material point method (Sulsky *et al.*, 1994; Sulsky *et al.*, 1995) has a Lagrangian finite element computational kernel and is free from element distortion problems. Therefore, this method is especially suitable for history-dependent materials undergoing large deformation and large displacement, e.g., landslides. The traction-based domain reduction scheme (Chang *et al.*, 2022) is derived based on continuum mechanics and hence is compatible with any Lagrangian numerical methods solving the momentum equation. This study proposes an approach to implement the traction-based scheme in the material point method to expand the method to applications addressing seismic-induced failures. In this article, the traction-based scheme is first introduced, followed by a brief introduction to the material point method. The implementation approach and performance tests are then presented.

TRACTION-BASED DOMAIN REDUCTION SCHEME

Consider a structure sitting on soil excited by an earthquake. The dynamic motion of the soil can be described with the partial differential equation

$$\rho \boldsymbol{a} = \operatorname{div} \boldsymbol{\sigma} + \rho \boldsymbol{b} \tag{1}$$

and satisfies the boundary conditions

$$\boldsymbol{v} = \boldsymbol{v}^* \quad \text{on } \Gamma^v \tag{2}$$
$$\boldsymbol{\tau} = \boldsymbol{\tau}^* \quad \text{on } \Gamma^\tau \tag{3}$$

where ρ is the mass density of soil, $\boldsymbol{a} = D\boldsymbol{v}/Dt$ is acceleration, $\boldsymbol{v}$ is velocity, t is time, $\boldsymbol{\sigma}$ is Cauchy stress, $\boldsymbol{b}$ is body force, $\boldsymbol{\tau} = \boldsymbol{\sigma} \cdot \boldsymbol{n}$ is surface traction, $\boldsymbol{n}$ is outward normal to the boundary Γ of the domain Ω in consideration, $\boldsymbol{v}^*$ is a prescribed velocity field on boundary Γ^v, and $\boldsymbol{\tau}^*$ is a prescribed traction field on boundary Γ^τ. $\Gamma^v \cup \Gamma^\tau = \Gamma$ and $\Gamma^v \cap \Gamma^\tau = \emptyset$. Since the velocity and traction at the underground surface of the soil mass Ω are both unknown, modeling techniques are necessary to define appropriate boundary conditions at the surface. The traction-based domain reduction scheme is one of these modeling techniques.

The traction-based domain reduction scheme (Chang *et al.*, 2022) separates the surface traction and velocity at underground boundaries Γ^U of the soil mass into the contribution of static equilibrium ($\boldsymbol{\tau}^{st}$), free-field excitation ($\boldsymbol{v}^f$ and $\boldsymbol{\tau}^f$) and dynamic influence of the structure ($\boldsymbol{v}^b$ and $\boldsymbol{\tau}^b$), i.e.

$$\boldsymbol{v} = \boldsymbol{v}^f + \boldsymbol{v}^b \quad \text{and} \quad \boldsymbol{\tau} = \boldsymbol{\tau}^{st} + \boldsymbol{\tau}^f + \boldsymbol{\tau}^b \quad \text{on } \Gamma^U. \tag{4}$$

$\boldsymbol{\tau}^{st}$ is evaluated with static analyses and is the initial condition before excitation. $\boldsymbol{v}^f$ and $\boldsymbol{\tau}^f$ are responses to site response analyses that represent the best "guess" of the dynamic responses at the domain boundaries. $\boldsymbol{v}^b$ and $\boldsymbol{\tau}^b$ are the differences between the real and the assumed responses and can be interpreted as the influence of the existence of the structures. Assuming the influence only propagates out of the domain, and $\boldsymbol{\tau}^b$ can be expressed as a function of $\boldsymbol{v}^b$ at the boundary Γ^U,

$$\boldsymbol{\tau}^b = -\eta_p \boldsymbol{v}^b \cdot (\boldsymbol{n} \otimes \boldsymbol{n}) - \eta_s \boldsymbol{v}^b \cdot (\boldsymbol{I} - \boldsymbol{n} \otimes \boldsymbol{n}) \quad \text{on } \Gamma^U \tag{5}$$

with coefficients, η_p and η_s, derived from elastic wave propagation theory. (These coefficients are called damping or viscous coefficients in the classic absorbing boundary condition proposed by Lysmer and Kuhlemeyer (1969).) Then, a prescribed surface traction $\boldsymbol{\tau}^*$ at the underground boundary Γ^U can be defined with

$$\begin{aligned} \boldsymbol{\tau}^* = \boldsymbol{\tau}^{st} + \boldsymbol{\tau}^f + \boldsymbol{v}^f \cdot \left[\eta_p(\boldsymbol{n} \otimes \boldsymbol{n}) + \eta_s(\boldsymbol{I} - \boldsymbol{n} \otimes \boldsymbol{n})\right] \\ -\boldsymbol{v} \cdot \left[\eta_p(\boldsymbol{n} \otimes \boldsymbol{n}) + \eta_s(\boldsymbol{I} - \boldsymbol{n} \otimes \boldsymbol{n})\right] \quad \text{on } \Gamma^U \in \Gamma^\tau. \end{aligned} \tag{6}$$

MATERIAL POINT METHOD

The material point method (Sulsky *et al.*, 1994; Sulsky *et al.*, 1995) is an extension of FLIP (Brackbill and Ruppel, 1986; Brackbill *et al.*, 1988), a particle-in-cell method for fluid simulation, to solid mechanics. This method discretizes a continuum with a finite number of particles and adopts Lagrangian grids to evaluate the motion and the deformation of the continuum at each time step. Since continuum states are recorded with these particles, the grids are generally called computational grids to address that the grids are only used for computation and can be reselected at each time step.

The grid interpolates the acceleration and velocity field with

$$\boldsymbol{a}^h(\boldsymbol{x}, t) = \sum_i N_i(\boldsymbol{x})\boldsymbol{a}_i(t) \quad \text{and} \quad \boldsymbol{v}^h(\boldsymbol{x}, t) = \sum_i N_i(\boldsymbol{x})\boldsymbol{v}_i(t). \tag{7}$$

in which the superscript h means an approximated function, the subscript i indicates node number, N_i is a nodal shape function, $\boldsymbol{a}_i$ is nodal acceleration, and $\boldsymbol{v}_i$ is nodal velocity. At a computational step, say the nth time step, nodal acceleration is evaluated on the grid using a weak formulation of the momentum equation (Eq. 1),

$$m_i \boldsymbol{a}_i = \boldsymbol{f}_i^{int} + \boldsymbol{f}_i^{ext} \tag{8}$$

where nodal mass m_i, nodal internal force $\boldsymbol{f}_i^{int}$, and nodal external force $\boldsymbol{f}_i^{ext}$ are computed based on the configuration of the continuum body at t_n,

$$m_i = \int_{\Omega^{(n)}} \rho^{(n)} N_i dV \tag{9}$$
$$\boldsymbol{f}_i^{int} = -\int_{\Omega^{(n)}} \mathrm{grad}\, N_i \cdot \boldsymbol{\sigma}^{(n)}\, dV \tag{10}$$
$$\boldsymbol{f}_i^{ext} = \int_{\Omega^{(n)}} N_i \rho^{(n)} \boldsymbol{b}^{(n)}\, dV + \int_{\Gamma^{\tau(n)}} N_i \boldsymbol{\tau}^{*(n)}\, dA \tag{11}$$

Because the continuum only encapsulates its states at particles, these particles are selected as integration points for the volume integrals. Hence, Eqs. 9 to 11 yield

$$m_i \approx \sum_p m_p N_{ip} \tag{12}$$
$$\boldsymbol{f}_i^{int} \approx -\sum_p m_p N_{ip} \tilde{\boldsymbol{\sigma}}_p^{(n)} \cdot (\mathrm{grad}\, N_i)_p \tag{13}$$
$$\boldsymbol{f}_i^{ext} \approx \sum_p m_p N_{ip} \boldsymbol{b}_p^{(n)} + \int_{\Gamma^{\tau(n)}} N_i \boldsymbol{\tau}^{*(n)}\, dA \tag{14}$$

Besides, nodal velocity is also evaluated to update displacement and deformation of the continuum,

$$m_i \boldsymbol{v}_i = \int_{\Omega^{(n)}} \rho^{(n)} \boldsymbol{v}^{(n)} N_i dV \tag{15}$$
$$\approx \sum_p m_p N_{ip} \boldsymbol{v}_p^{(n)} \tag{16}$$

In the end of *n*th time step, velocity increment, location change and rate of deformation at each particle can be computed from the grid values,

$$\Delta \boldsymbol{v}_p^{(n)} = \Delta t \sum_i \boldsymbol{a}_i N_{ip} \tag{17}$$
$$\Delta \boldsymbol{x}_p^{(n)} = \Delta t \sum_i (\boldsymbol{v}_i + \Delta t \boldsymbol{a}_i) N_{ip} \tag{18}$$
$$\dot{\boldsymbol{F}}_p^{(n)} = \sum_i (\boldsymbol{v}_i + \Delta t \boldsymbol{a}_i) \otimes (\mathrm{grad}\, N_i)_p \tag{19}$$

MPM IMPLEMENTATION OF THE DOMAIN REDUCTION SCHEME

The traction-based domain reduction scheme (Chang *et al.*, 2022) adopts a traction boundary condition for the underground soil boundaries Γ^U and hence is compatible with any Lagrangian numerical methods solving the momentum equation shown in Eq. 1.

To implement the scheme in the material point method, the second term of the right-hand side of Eq. 14 has to be evaluated. In this study, surface particles are proposed for the surface integral. The surface particles are similar to the particles used for volume integral but contain no mass because these surface particles support areas but not volumes. With these particles on Γ^U, Eq. 14 becomes

$$\boldsymbol{f}_i^{ext} \approx \sum_p m_p N_{ip} \boldsymbol{b}_p^{(n)} + \sum_q N_{iq} A_q^{(n)} \boldsymbol{\tau}_q^{*(n)} \tag{20}$$

with

$$\boldsymbol{\tau}_q^* = \boldsymbol{\tau}_q^{st} + \boldsymbol{\tau}_q^f + (\boldsymbol{v}_q^f - \boldsymbol{v}_q) \cdot \left[(\eta_p)_q (\boldsymbol{n}_q \otimes \boldsymbol{n}_q) + (\eta_s)_q (\boldsymbol{I} - \boldsymbol{n}_q \otimes \boldsymbol{n}_q) \right] \quad \forall \boldsymbol{x}_q \in \Gamma^U. \tag{21}$$

At the end of a computational time step, surface particles also need velocity increment, location change, and rate of deformation (Eqs. 17 to 19) to update velocity, location, and the particle-supported surface.

NUMERICAL EXAMPLE: ONE-DIMENSIONAL IMPACT PROBLEM

Consider a one-dimensional bar impacting against a rigid wall as displayed in Fig. 1. This bar is fixed to the wall on the left-hand side and free at the other, and has elastic modulus $E = 2$, a constant cross-sectional area $A = 1$, an initial mass density $\rho_o = 0.5$, and an initial length L_o. Initial velocity

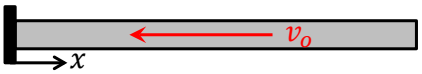

Figure 1. Illustration of the model example: a one-dimensional bar impacting against a rigid wall.

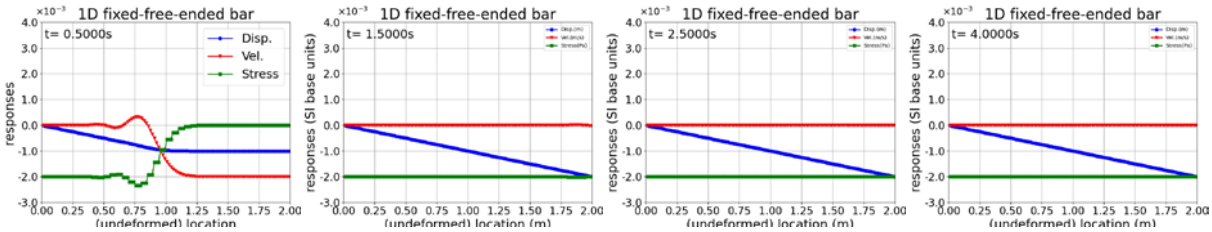

Figure 2. Simulation results of full-domain model at time 0.5, 1.5, 2.5 and 4.0. ($L_o = 8, L_{model} = 8$)

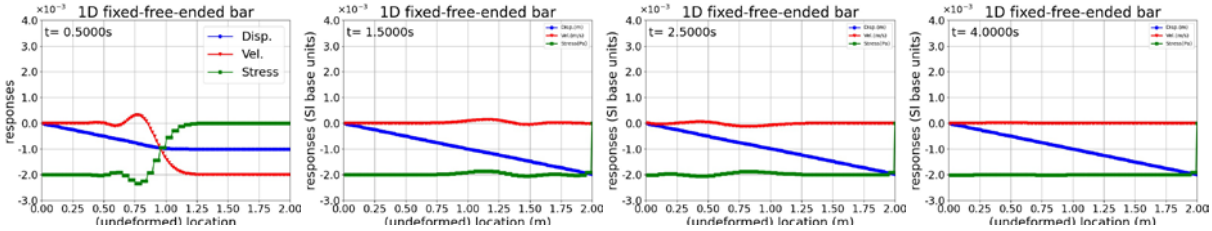

Figure 3. Simulation results of sub-domain model at time 0.5, 1.5, 2.5 and 4.0. ($L_o = 8, L_{model} = 2$)

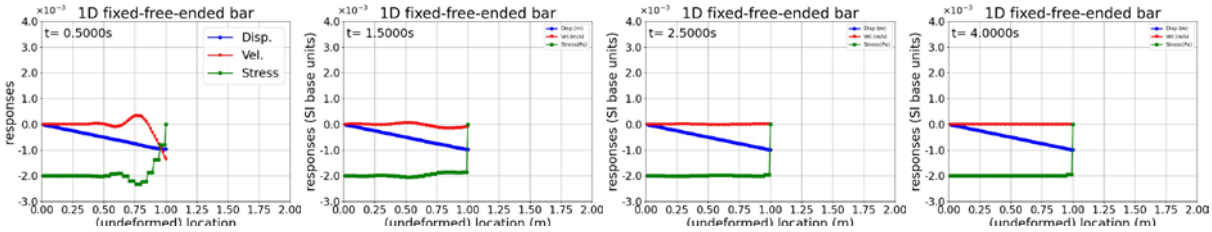

Figure 4. Simulation results of sub-domain model at time 0.5, 1.5, 2.5 and 4.0. ($L_o = 8, L_{model} = 1$)

$v(x, 0) = -0.002$ is assigned to the bar and immediately induces a shock wave propagating to the right at a speed of $c = \sqrt{E/\rho} \approx 2$. Element size The viscous coefficient $\eta_p = \sqrt{E\rho_o} = 1$.

In the first test, $L_o = 8$, the cell size is 0.05 and the number of particles per cell is 3. The time increment is 0.0125 which is half of the critical time step estimated with the Courant-Friedrichs-Lewy (CFL) condition. The simulated time is 4. Fig. 2 shows the simulation results of a full-domain model and displays only in the range of $0 \leq x \leq 2$. Since the wave speed is 2, there is no wave bouncing back from the free end before the simulation is stopped. Figs. 3 and 4 show the results of sub-domain models with lengths of 2 and 1, respectively. Wave reflection at the traction boundaries has been observed. The reflected waves have amplitudes much smaller than those of the major shocks.

The second test (plotted in Figs. 6 and 7) uses the same setup as the first one except $L_o = 3$. With this length, the shock front of the wave, reflected from the free end of the bar, arrives $x = 1$ at $t = 2.5$. The front bounces back and reaches $x = 2$ at $t = 4.0$ after hitting the rigid wall at $t = 3.0$. In this case, a minor reflecting wave can be observed in the sub-domain model again. Besides, by comparing the third plots of Figs. 6 and 7, the sub-domain model maintains a sharper wave front than the full-domain model. That is because waves travel a shorter distance in a sub-domain model than in a full-domain model, and hence diffuse less.

The numerical reflection observed in both tests (Figs. 2 to 6) might come from the shape function inconsistency of the velocity and stress fields, or the incomplete stress updating that pushing forward of the stress tensor is ignored in these simulations. More studies will be necessary to improve the accuracy of the traction-based domain reduction scheme in the material point method.

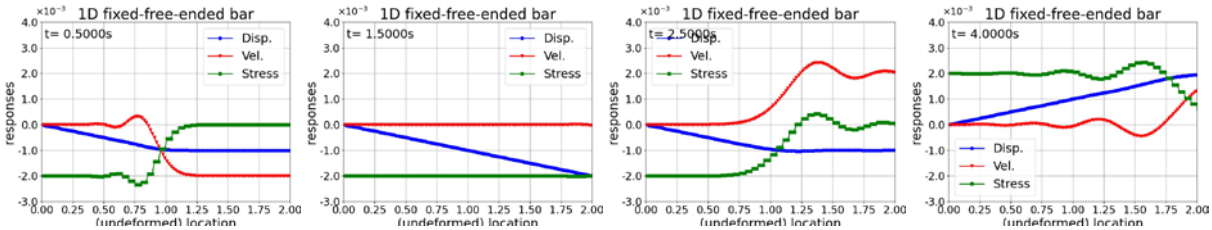

Figure 5. Simulation results of full-domain model at time 0.5, 1.5, 2.5 and 4.0. ($L_o = 3, L_{model} = 3$)

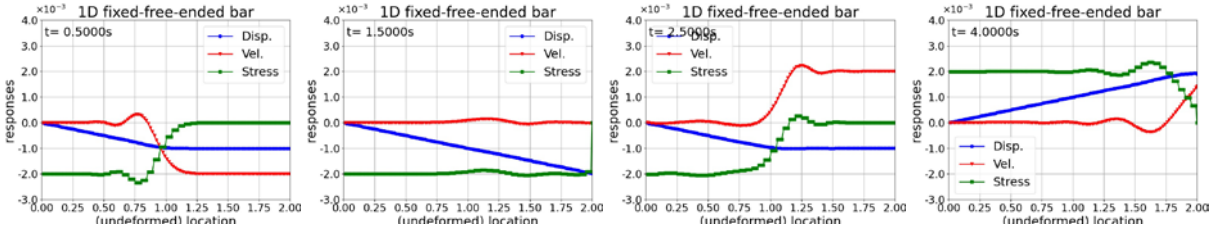

Figure 6. Simulation results of sub-domain model at time 0.5, 1.5, 2.5 and 4.0. ($L_o = 3, L_{model} = 2$)

CONCLUSIONS

This study presents an approach to implement the traction-based domain reduction scheme in the material point method. Surface particles are introduced for applying traction boundary conditions. One-dimensional impact problems are used to evaluate the performance of the traction-based scheme. Results show the scheme works fine with the material point method. However, more works addressing the causes of the minor numerical reflection are necessary to improve the accuracy of the boundary modeling scheme in the method.

REFERENCES

Brackbill, J. U., and Ruppel, H. M. (1986). "FLIP: a method for adoptively zoned, particle-in-cell calculations in two dimensions," *J. Comput. Phys.*, **65**, 314-343.

Brackbill, J. U., Kothe, D. B., and Ruppel, H. M. (1988). "FLIP: a low-dissipation, particle-in-cell method for fluid flow," *Comput. Phys. Commun.*, **48**, 25-38.

Chang, C.-Y., Yang, W,-C., and Kuo, C.-H. (2022). "Traction-based domain reduction scheme for soil-structure interaction analyses," (in preparation).

Lysmer, J., and Kuhlemeyer, R. L. (1969). "Finite dynamic model for infinite media," *Journal of the Engineering Mechanics Division*, **95**(4), 859-878.

Sulsky, D., Chen, Z., and Schreyer, H. L. (1994). "A particle method for history-dependent materials," *Comput. Meth. Appl. Mech. Engrg.*, **118**, 179-196.

Sulsky, D., Zhou, S.-J., and Schreyer, H. L. (1995). "Application of a particle-in-cell method to solid mechanics," *Computer Physics Communications*, **87**, 236-252.

(6b) Advanced hybrid simulations with online model updating

HYBRID SIMULATION OF A SEVEN-STORY STEEL FRAME CONSIDERING COLUMN SHORTENING DUE TO LOCAL BUCKLING

Kung-Juin Wang[1], Chung-Che Chou[2], Cheng-Wei Huang[3], Hou-Kuan Shen[3], Man-Hong Tam[3], Claudio Sepulveda[4], Gilberto Mosqueda[5], and Chia-Ming Uang[5]

1. Principal Engineer, National Center for Research on Earthquake Engineering, Taipei, Taiwan, R. O. C.
2. Director General, National Center for Research on Earthquake Engineering, Taipei, Taiwan, R.O.C.
3. Graduate Student, Dept. of Civil Engineering, National Taiwan University, Taipei, Taiwan, R.O.C.
4. Graduate Student, Dept. of Structural Engineering, University of California San Diego, La Jolla, USA.
5. Professor, Dept. of Structural Engineering, University of California San Diego, La Jolla, USA.

Email: kjwang@narlabs.org.tw, cechou@ntu.edu.tw, andy1002011@gmail.com, r08521262@ntu.edu.tw, manhong9707@gmail.com, csepulve@eng.ucsd.edu, gmosqueda@eng.ucsd.edu, cmu@ucsd.edu

ABSTRACT

This paper presents an implementation of a series of hybrid simulation (HS), with the considered structure a two-dimensional seven-story two-bay steel frame subjected to near-fault ground motions. The specimen is a full-scale cruciform beam-column connection subassembly and is controlled by the actuation system that provides four degree-of-freedom (DOF) mixed displacement and force control. The structural analysis program "Platform of Inelastic Structural Analysis for 3D Systems" (PISA3D) is used as the analysis kernel for the HS. Preliminary PISA3D and Abaqus FEA (ABAQUS) simulations were conducted to confirm the adequacy of the control method and test assumptions. By applying a set of additional time-varying fictitious force in the HS, this work addressed one of the principal challenges: to incorporate the column shortening due to local buckling into PISA3D analysis in the HS. In addition, the shortening of the two other first-story columns was also considered by incorporating preliminary ABAQUS simulation results in the HS. Test results confirmed that the proposed modeling and control methods could successfully integrate the information available only in the laboratory or ABAQUS simulation into the PISA3D analysis in HS, and provide more realistic structural responses otherwise cannot be obtained by traditional numerical simulation or testing methods.

Keywords: hybrid simulation, local buckling, force control, displacement compatibility

INTRODUCTION

In quake-prone and typhoon-prone areas in Asia, box columns are widely used in buildings because they can be easily built by welding four plates together and can provide the same stiffness and strength for both horizontal directions. In high-rise buildings, local buckling can occur at the base of the first-story columns when the axial force and the frame drift is large. The columns might be significantly shortened due to the occurrence of local buckling [Nakashima and Liu 2005; Fadden and McCormick 2011; Wang *et al*. 2014; Onogia *et al*. 2019; Chou and Wu 2019; Chou and Chen 2020], and different amount of shortenings can occur for different first-story columns in earthquake events because of different magnitudes of the axial force induced by the overturning effects of the swaying frame. Such phenomena have not been experimentally studied in the past and therefore this work aims to investigate this effects via hybrid simulation (HS). A specimen of full-scale steel cruciform beam-column subassembly was fabricated and tested in National Center for Research on Earthquake Engineering (NCREE). The specimen includes the first-story interior column and is a part of a two-dimensional seven-story two-bay steel frame. The structural analysis program "Platform of Inelastic Analysis for 3D Systems" (PISA3D) [Lin *et al*. 2009] was adopted as the analysis kernel in the HS.

PISA3D MODEL AND EXPERIMENTAL SETUP

Fig. 1 (a) shows the elevation of the prototype frame, which is a dual system consisting of a special moment frame (SMF) and a buckling-restrained braced frame (BRBF) at the left and the right bay, respectively. This building is located on a hard site which is 3.5 km away from the Xinhua fault in southern Taiwan. The columns are fabricated by SM570 steel, while the beams and the buckling-restrained braces (BRBs) are made of SN490 steel. The left column (C1) is a wide-flange column while the interior and the right columns (C2 and C3) are built-up box shaped.

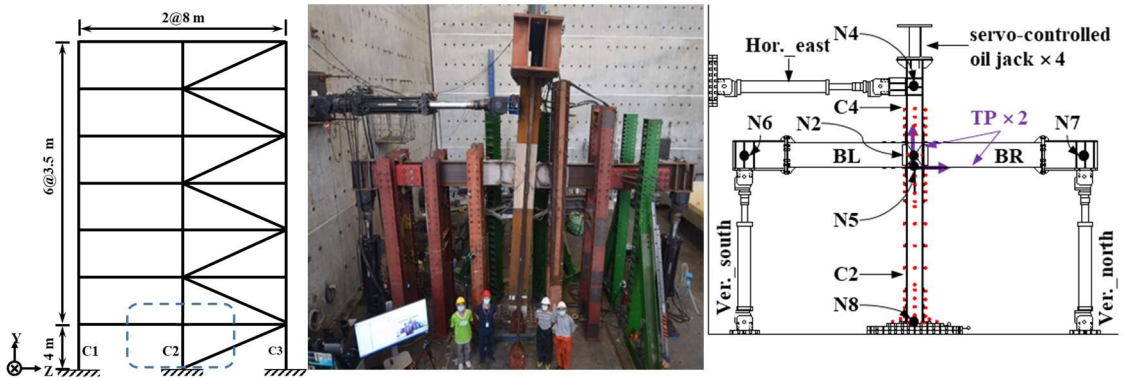

(a) Prototype frame (b) Specimen (c) Test setup

Figure 1. The prototype frame, the PISA3D model, the specimen, and the test setup

A two-dimensional PISA3D model was created for the prototype frame. All the beams and columns are modeled by using the PISA3D *BeamColumn* elements, which concentrate the inelastic behaviors in the plastic hinges at their two end nodes. Each beam was modeled by several *BeamColumn* elements such that the reduced beam sections (RBSs) can be properly modeled. All the braces are modeled by the *Truss* elements and all the beam-column connections (panel zones, PZs) are modeled by the *Joint* elements. The PISA3D *Hardening* material which considers both kinematic and isotropic hardening rules was used for all the beams, columns, and BRBs. The material parameters were obtained by calibration to experimental data of previously conducted cyclic tests [Lin and Chou 2022; Chou *et al.* 2012]. The PZ was designed to remain elastic and therefore the *Elastic* materials were used to model them. The designed dead load (DL) and live load (LL) for each floor are 9.8 and 1.96 kPa, respectively. Nodal mass was calculated based on the tributary area of the DL and LL, and was assigned for both the horizontal and vertical DOFs. The gravitational second-order effect was not considered. Rayleigh damping was specified based on the assumption of 3% damping ratios for the first and the second mode. The TCU052 (1999 Taiwan Chi-Chi earthquake) EW component was selected as the input ground motion. It was scaled to two levels, maximum considered earthquake (MCE) and 1.5 times the MCE (1.5MCE), to be used in two HS tests, respectively.

Fig. 1 (b) shows the specimen which is the part enclosed by the dash-line box in Fig. 1 (a). It includes the first-story column, two half-span of the second-story beams, and the lower-half of the second-story column. Fig. 1 (c) shows the test setup. Four servo-controllable actuators were used to impose the displacement and four servo-controllable oil jacks were installed on top of the second-story column such that time-varying force can be imposed on the specimen to simulate the axial force subjecting the specimen. Two digital displacement transducers (TPs) were mounted on top of the first-story column such that the achieved horizontal and vertical displacements of node N5 can be calculated on a real-time basis (1024 Hz). Miscellaneous sensors including strain gauges, PI gauges, 3D optical displacement trackers, and other traditional displacement sensors were used to monitor the responses of the specimen during the tests.

HYBRID SIMULATION METHOD

Physical Substructure and Control Targets

The complete specimen can be chosen as the physical substructure (PS) for the HS. However, this would cause the PS to interface with the numerical substructure (NS) with three interfacing points (nodes N4, N6, and N7). As a results, in practice it would be impossible for the laboratory to provide the required support of imposing the nine-DOF commands and measuring the corresponding nine-DOF specimen force. Therefore, only the first-story column was chosen as the PS and the rest part in the specimen was considered the fixture for the PS. In this manner, there is only one interfacing point (node N5) and the communication between the PS and the NS consists of only three-DOF displacement ($u_{z,5}$, $u_{y,5}$, and $\theta_{x,5}$) and the corresponding force values. In addition, this selection of PS equipped the PS with the actual boundary condition (BC) which enhances the simulation fidelity.

As mentioned above, the achieved horizontal displacement at node N5 ($u_{z,5}$) can be calculated jointly by the measurement of two TPs, and can be controlled mainly by the two horizontal actuators. Although the achieved vertical displacement ($u_{y,5}$) can also be obtained in the same manner, this vertical DOF was chosen to be controlled by force control mode. This is because bad control results can be expected if this DOF is displacement-controlled due to the high-stiffness associated with this DOF. To this end, in each integration time step, after the axial resisting force of the PZ was recovered, it was conveyed out as the axial force command for the PS, and the four servo-controlled oil jacks were used to impose the time-varying force command on the PS. Regarding the rotational DOF, it was also difficult to accurately control $\theta_{x,5}$ due to the long distance between the point of actuation and the point to be controlled. Fortunately, since the other part of the specimen served as an actual BC for the PS, the $\theta_{x,5}$ might automatically achieve the desired displacement level if the control of $u_{z,5}$, $u_{y,6}$, and $u_{y,7}$ is reasonably correct. The effect of not directly controlling $\theta_{x,5}$ is numerically investigated by performing a PISA3D displacement-control analysis on a model that represented the specimen. The simulation results verified that $\theta_{x,5}$ can be achieved accurately enough without being explicitly controlled [Wang *et al.* 2022].

Enforcing Displacement Compatibility in PISA3D

As a result of the force-control for the vertical DOF, the corresponding displacement response $u_{y,5}$, which can consist of significant column shortening due to local buckling when the axial load and the frame drift is large, can be measured during the tests. This displacement ($u_{y,5}$) would not be the same as that predicted by PISA3D because PIAS3D does not support modeling the buckling behavior of structural members subjected to axial load. Column shortening can cause redistribution of the resisting force of other members in the system. However, in the past such phenomenon were usually neglected. This study implemented an innovative method [Sepulveda *et al*. 2022] to address this issue of displacement incompatibility. The idea is to apply a set of equivalent fictitious force on the structural system such that the additional displacement caused by column buckling can be included in prediction of the displacement in the time-history response analysis (THRA). In each integration time step, in addition to those conventionally executed tasks, the following three tasks are added to consider the column shortening in the analysis: (1) The magnitudes of the shortening due to buckling of the three first-story columns were measured or estimated, before assembled into a displacement vector $\{u_y^{bcl}\}$. (2) A fictitious force vector $\{F_{eq}\}$ was calculated by multiplying a condensed elastic stiffness matrix associated with the three vertical DOFs with assembled $\{u_y^{bcl}\}$. (3) The vector $\{F_{eq}\}$ is added as an additional term of the external force into the system equations in the next integration time step in the THRA.

Without considering the geometric deformation, the total column axial deformation consists of that due to the gravity and seismic load, and that due to local buckling. The total axial deformation can be measured for column C2 from the test, and estimated by previously conducted offline ABAQUS analyses for columns C1 and C3. In each integration time step, once these vertical displacement values were obtained, they can be assembled to construct a vector $\{u_y^{tol}\}$ and then the deformation caused by local buckling $\{u_y^{bcl}\}$ can be calculated by Eq. 1, where the $\{u_y^{ref}\}$ is the axial deformation due to gravity and seismic load. Note that the $\{u_y^{ref}\}$ can be obtained by a conventional THRA that does not consider the measured or estimated column shortenings.

$$\{u_y^{bcl}\} = \{u_y^{tot}\} - \{u_y^{ref}\} \quad (1)$$

Software Framework

To incorporate $\{u_y^{bcl}\}$ in the HS by the aforementioned method, it requires to run two instances of PISA3D simultaneously in the HS. Fig. 2 shows the numerical model and the details of the two models used in HS. The "Reference model" is constructed by replacing the numerical *BeamColumn* element C2 with an experimental element E2, which was responsible to return the measured resisting force to the THRA. The "Hybrid simulation model" was constructed by adding three experimental elements E1, E2, and E3, which were responsible to return the measured resisting force and the fictitious pull-down force to the THRA. The experimental element was developed based on a communication protocol "Remote Experimental Control and Data Exchange (Recdex)" [Wang and Tsai, 2015]. The testing was implemented by using the software package "Software Framework for Quasi-static Structural Testing" [Wang and Tsai, 2011].

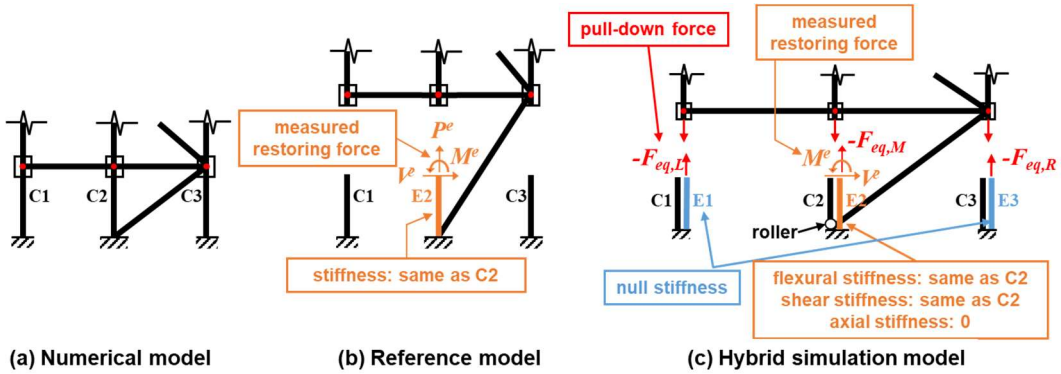

Figure 2. The prototype frame, the PISA3D model, the specimen, and the test set

TEST RESULTS

Two HS tests were conducted with MCE and 1.5MCE magnitude levels, respectively. Fig. 3 (a) – (d) show the observation at the column base and the beam ends. Local buckling did not occur at the column base in the MCE test while minor buckling was observed in the RBS of the beams. In the 1.5MCE test, significant local buckling was observed at the column base and the permanent shortening of the column was about −10 mm at the end of the test.

(a) Column base (MCE)

(b) Beam ends (MCE)

(c) Column base (1.5MCE)

(d) Beam ends (1.5MCE)

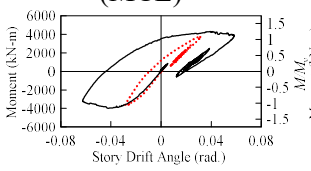

(e) Column base

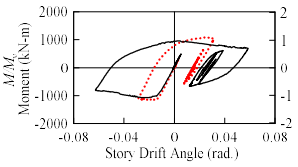

(f) South beam end

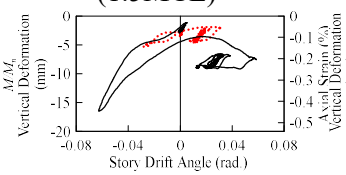

(g) Column vertical deformation

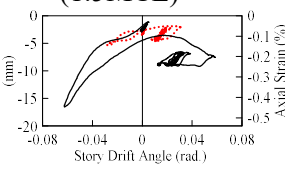

(h) Column axial force

··· 1.0 MCE — 1.5 MCE

Fig. 3 Test observation and specimen responses

Fig. 4 shows the time histories of the calculated fictitious equivalent force. Fig. 5 shows the vertical displacements of the top nodes of the three first-story columns. "PisaRef" and "PisaHS" refer to the PISA3D analyses performed on the "Reference model" and "Hybrid simulation model", respectively. It is clear that the vertical displacements obtained from PisaHS agreed well with the measured displacement (for C2) and that estimated by the offline ABAQUS analyses (for C1 and C3). It is also evident that they were significantly larger than the corresponding values obtained from PisaRef which did not consider the experimentally measured or ABAQUS predicted column shortenings due to local buckling. This verified the effectiveness of the proposed method to address the issues of displacement compatibility when the associated DOF is force-controlled.

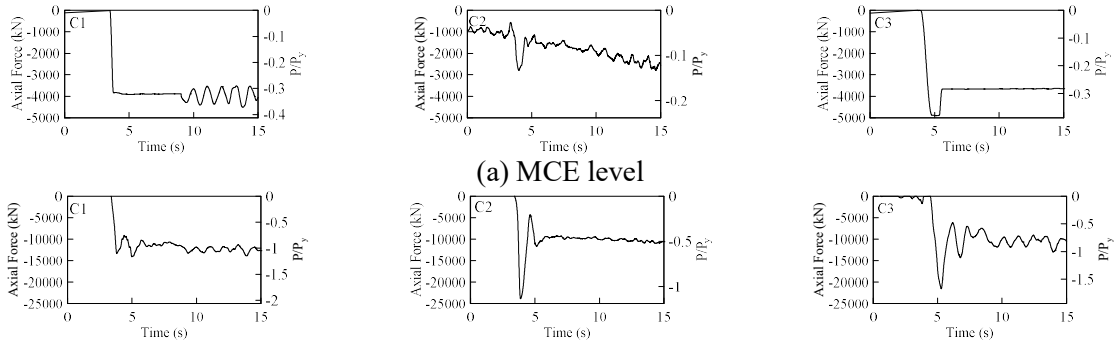

(a) MCE level

(b) 1.5MCE level

Fig. 4 Fictitious equivalent force time history

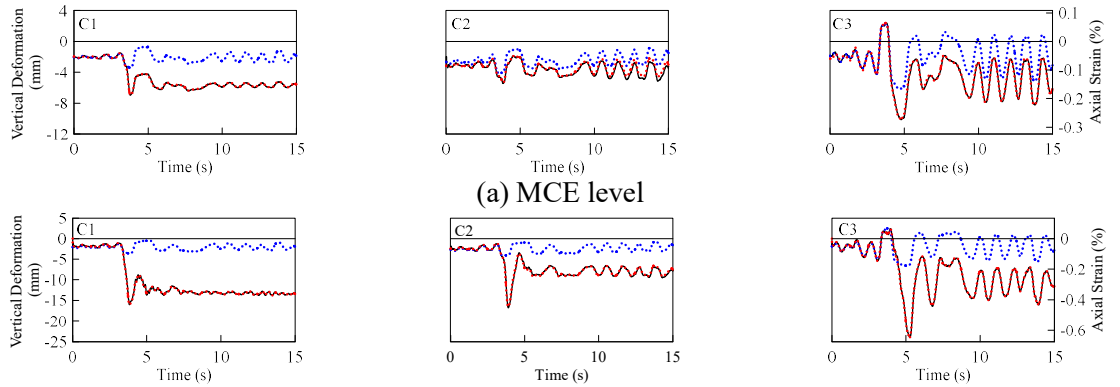

(a) MCE level

(b) 1.5MCE level

PisaRef — PisaHS ····· Measured or ABAQUS

Fig. 5 Vertical displacement of column top in different analyses

CONCLUSIONS

This study investigated the seismic responses of a seven-story steel frame subjected to near-fault ground motion via HS. The specimen was a full-scale beam-column subassembly but only the first-story column was treated as the PS. To reduce the chance of error propagation in the HS, different control targets were selected for different DOFs. The horizontal and the vertical DOFs were controlled by displacement and force control modes, respectively. The rotational DOF was not controlled because the effects are acceptable as verified by previously conducted numerical analysis results. The vertical deformation of the three first-story columns were measured (for the interior column) during the tests and estimated by offline ABAQUS analyses before the HS (for the two exterior columns). They were used to calculate an additional set of fictitious equivalent force to be added into the system motion equations in each

integration time step such that the THRA in PISA3D can consider the column shortenings due to local buckling. The test results verified the validness of the proposed method, and is able to provide more realistic structural responses otherwise cannot be obtained by traditional numerical simulation or testing methods.

ACKNOWLEDGMENTS

This work is funded by the Ministry of Science and Technology under the project number MOST 109-2625-M-002-005, Taiwan. Additional support from the National Institute of Standards and Technology under Award 70NANB171TZ91, USA to UC San Diego for the international cooperation is also appreciated. Sincerest gratitude also goes to NCREE staff for the exceptional laboratory support.

REFERENCES

Nakashima, M., & Liu, D. (2005). "Instability and complete failure of steel columns subjected to cyclic loading," *Journal of Engineering Mechanics*, 131(6), ASCE, 559-567.

Fadden, M., McCormick, J. (2011). "Cyclic quasi-static testing of hollow structural section beam members," *J. Structural Engineering*, ASCE, 138(5), 561-570.

Wang, Y. B., Li, G. Q., Cui, W., & Chen, S. W. (2014). "Seismic behavior of high strength steel welded beam-column members," *J. Constructional Steel Research*, 102, 245-255.

Onogia, T. Sato, A., and Yoshioka, Y. (2019). "Experimental study on square steel tubular columns under compressive axial force with cyclic biaxial bending moment," XII Conference on Steel and Composite Construction, Coimbra, Portugal.

Chou, C. C., Wu, S. C. (2019). "Cyclic lateral load test and finite element analysis of high-strength concrete-filled steel box columns under high axial compression," *Engineering Structures*, 189, 89-99.

Chou, C. C, and Chen, G. W. (2020). "Lateral cyclic loading testing and backbone curve development of high-strength steel built-up box columns under axial compression," *Engineering Structures* 223 (2020) 111147.

Lin, B.Z., Chuang, M.C. and Tsai, K.C. (2009). "Object-oriented Development and Application of a Nonlinear Structural Analysis Framework," *Advances in Engineering Software*, 40, pp. 66-82.

Lin T.H. and Chou, C. C. (2022). "High-strength steel deep H-shaped and box columns under proposed near-fault and post-earthquake loadings," *Thin-Walled Structures*, https://doi.org/10.1016/j.tws.2022.108892.

Chou, C. C., Liu, J. H., Pham D. H. (2012). "Steel buckling-restrained braced frames with single and dual corner gusset connections: seismic tests and analyses," *Earthquake Engineering and Structural Dynamics*, 7(41): 1137-1156.

Wang, K. J., Chou, C. C., Huang, C. W., Shen, H. K., Sepulveda, C., Mosqueda, G., and Uang, C. M. (2022). "Hybrid simulation of a steel BRBF with a first-story beam-to-column subassemblage using a mixed control mode for considering column shortening," *Earthquake Engineering and Structural Dynamics*, (in preparation).

Sepulveda, C., Mosqueda, G., Uang, C. M., Chou, C. C., Wang, K. J. (2022). "Hybrid simulation using mixed displacement and equivalent-force control to capture column shortening in frame structures," Proceedings of the 12th National Conference in Earthquake Engineering, Earthquake Engineering Research Institute, Salt Lake City, UT.

Wang, K.J. and Tsai, K.C. (2011). "A software framework for quasi-static structural testing," NCREE technical report, NCREE-11-007, Taipei, Taiwan, 2011.

Wang, K.J. and Tsai, K.C. (2015). "A uniform method to integrate test equipment for large-scale quasi-static structural testing," Proceedings of the 6th International Conference on Advances in Structural Engineering, University of Illinois, Urbana-Champaign, United States, 2015.

HYBRID SIMULATION OF MOMENT FRAMES WITH DEEP COLUMNS EXPERIENCING AXIAL SHORTENING

Claudio Sepulveda[1], Gilberto Mosqueda[2], Chia-Ming Uang[2], Gulen Ozkula[3], Kung-Juin Wang[4], Chung-Che Chou[5], Po-Chia Huang[6], Cheng-Wei Huang[6], Mao Cheng[7] and Tracy Becker[8]

1. Research Assistant, University of California San Diego, California, USA
2. Professor, University of California San Diego, California, USA
3. Assistant Professor, Dept. of Civil Engineering, Tekirdağ Namik Kemal University, Tekirdağ, Turkey
4. Principal Engineer, National Center for Research on Earthquake Engineering, Taipei, Taiwan, R.O.C
5. Director General, National Center for Research on Earthquake Engineering, Taipei, Taiwan, R.O.C
6. Research Assistant, National Center for Research on Earthquake Engineering, Taipei, Taiwan, R.O.C
7. Research Assistant, University of California Berkeley, California, USA
8. Professor, University of California Berkeley, California, USA

Email: csepulve@eng.ucsd.edu

ABSTRACT

Wide flange steel column elements have been commonly used for steel moment frames in seismic regions. To economically comply with drift limit requirements, the moment of inertia of the section is increased by choosing slender and deep sections. However, deep columns are susceptible to local buckling and subsequent axial shortening when subjected to a combination of high axial forces and cyclic lateral loads. The interaction between the shortening columns and the surrounding structural framing system can result in a redistribution of axial loads, which has not been examined in detail. Here, this interaction is studied through a hybrid simulation of a full-scale steel moment frame subassembly using advanced hybrid simulation algorithms with new capabilities developed for this test. A new mixed displacement and force control framework is implemented to capture the coupled nature of the column axial behavior during shortening. The lateral behavior of the frame is highly dependent on the moment frame with reduced beam sections considered in this study. The experimental cruciform subassemblage includes beam-to-column connections and this measured plastic hinge response is utilized through online model updating to update parameters in the nonlinear numerical beam models. Preliminary tests are presented for these ongoing experiments.

Keywords: Hybrid simulation, steel moment frames, axial shortening, online model updating

INTRODUCTION

Building design codes currently impose maximum drift requirements for buildings (ASCE 2022). The use of deeper and thinner sections for columns has been common practice to meet drift requirements with an economical solution. However, deep columns are susceptible to localized buckling that can result in axial shortening. A series of experiments have been carried out on individual column members to characterize this phenomenon under quasi-static load patterns of axial loads and lateral drifts (Ozkula et al., 2021; Elkady and Lignos, 2017). Such quasi-static testing of isolated columns and subassemblies have shown the importance of the axial load, inelastic deformation, and boundary conditions on the axial shortening severity (Chansuk et al., 2021; Chou et al., 2022). Nevertheless, the impact of column shortening on the system-level behavior of the frame has only been addressed through pure numerical simulation (Wu et al., 2018), without experimental system-level testing verification. This project aims to experimentally assess the system behavior of moment frame structures with deep columns by conducting hybrid simulations including full-scaled cruciform subassemblies. To include axial shortening in the hybrid simulation, a new mixed displacement and force control method is proposed and implemented to achieve equilibrium of forces and displacement compatibility. Moreover, to overcome the limitations in the experimental setup, an overlapping substructuring method is used to simplify the boundary conditions of the physical substructure. In

addition, an online model updating scheme is included to that utilized data measured during the test to update parameters of hysteretic models for the reduced beam section.

HYBRID EXPERIMENTAL AND NUMERICAL MODEL

Hybrid simulation or pseudodynamic testing (Mahin et al., 1985) is a technique where the complete structural model is divided into different substructures. At least one of the substructures is experimental, while the rest of the system is simulated using a numerical model. All substructures interact with each other sharing displacements and forces through the degrees of freedom at the boundary conditions of each subsystem (Shing and Mahin, 1984). Similar to a shake table test, it can be used to experimentally evaluate a structural system under a given ground motion record. Although a shake-table test can be considered a more realistic way to replicate the real behavior of a structure subjected to seismic loads, hybrid simulation is a cost-effective alternative because only the key components or subsystems are tested in the laboratory. With inertial and other rate dependent force simulated numerically, the test can be performed at a slower velocity, reducing laboratory equipment requirements, and allowing for large scale testing as demonstrated here.

For this project, the prototype structure considered is a steel moment frame with 18ft height at the first story plus five floors at 14ft each over four bays each spanning 26ft. Column sections are W24x131 and beams are W27x94 for the first three stories, while for the upper stories columns are W24x117 and beams are W27x84. Reduced beam sections (RBS) are designed for beam-column connection. Figure 1 shows the prototype structure and a scheme of the numerical model used for the numerical substructure.

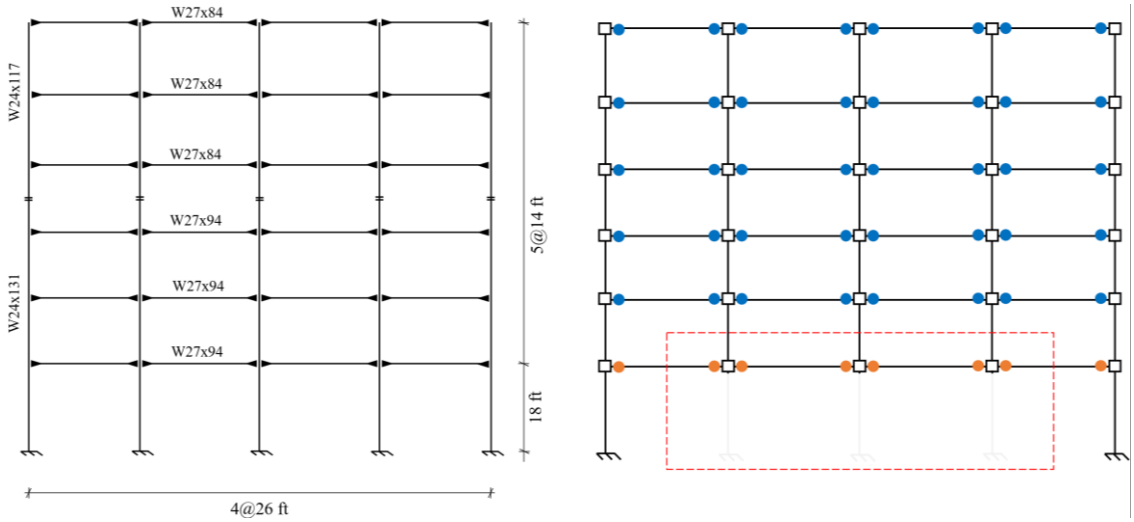

Figure 1. Prototype structure and numerical model

The numerical nonlinear substructure is modeled in OpenSees (McKenna et al., 2009) for the hybrid simulation. Columns are modeled using distributed plasticity elements with a displacement-based formulation. The panel zone deformation is simulated using the parallelogram approach (Gupta and Krawinkler, 1999) with a rotational spring in one of the corners. Beams are modeled considering an elastic beam-column element for the middle section with each end having rigid offsets plus a lumped plasticity spring. Above the second story (blue hinges in Figure 1) the beam hinges are simulated using Ibarra-Medina-Krawinkler (IMK) model (Ibarra et al., 2005). However, for beam hinges at the first story, a modified version of Bouc-Wen model (Cheng and Becker, 2021) are used with the ability of having updatable parameters to be used in the online model updating scheme explained later. Figure 2 shows a schematic of the typical numerical elements used.

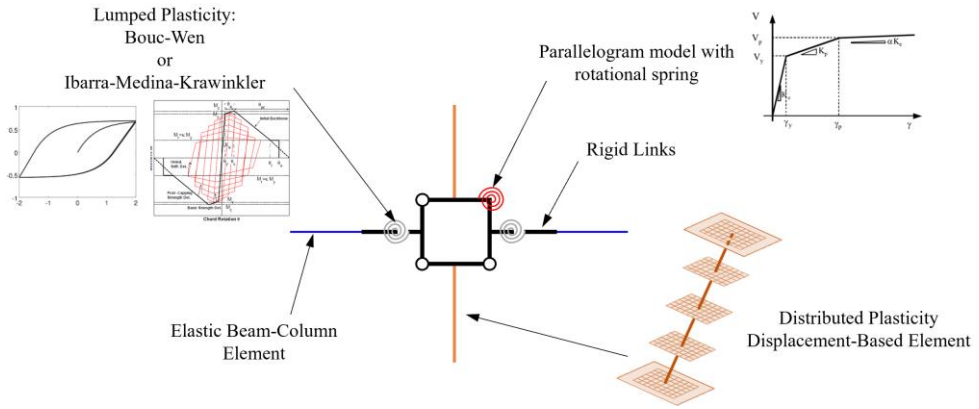

Figure 2. Details of the numerical model

SUBSTRUCTURING METHOD AND EXPERIMENTAL SETUP

The physical substructure is a cruciform beam-column subassembly depicted in Figure 3. The column is one and one-half story heigh with a pair of parallel pinned-connected actuators located on top of the specimen to control the horizontal displacement of the system. The control point of the actuators in the horizontal and vertical direction is located at the top end of the first story column to ensure displacement compatibility at the first floor level with the numerical substructure. Since axial shortening is expected at the base of the column and the specimen is an interior column, one vertical pinned-connected actuator controls each beam end following the vertical displacement measured at the vertical control point. Axial forces are applied by the four hydraulic jacks located on top of the specimen in force control mode. Preliminary numerical studies indicate that the three interior columns are expected to have similar behavior, thus, the one experimental specimen is selected to represents the three interior columns. To overcome the large number of DOFs at the boundaries of the experimental substructure (rotation and displacements at the member ends) an overlapping substructure approach is implemented for this test (Hashemi and Mosqueda, 2014). In this approach, a zone of the system is overlapped in both domains in order to minimize the effects of limiting the controlled DOFs such as neglecting rotation at the boundaries. For this test, the commanded signals from the numerical substructure are the horizontal displacement at the floor level, and the axial load obtained from the second story column. The feedback signals are the moment M and shear force V calculated at the top end of the first story column in the physical substructure, plus the vertical displacement measured at the same point. This last signal is converted into an equivalent vertical force F_{eq}, to impose a vertical displacement in the numerical model that is compatible with the measured displacement as explained later.

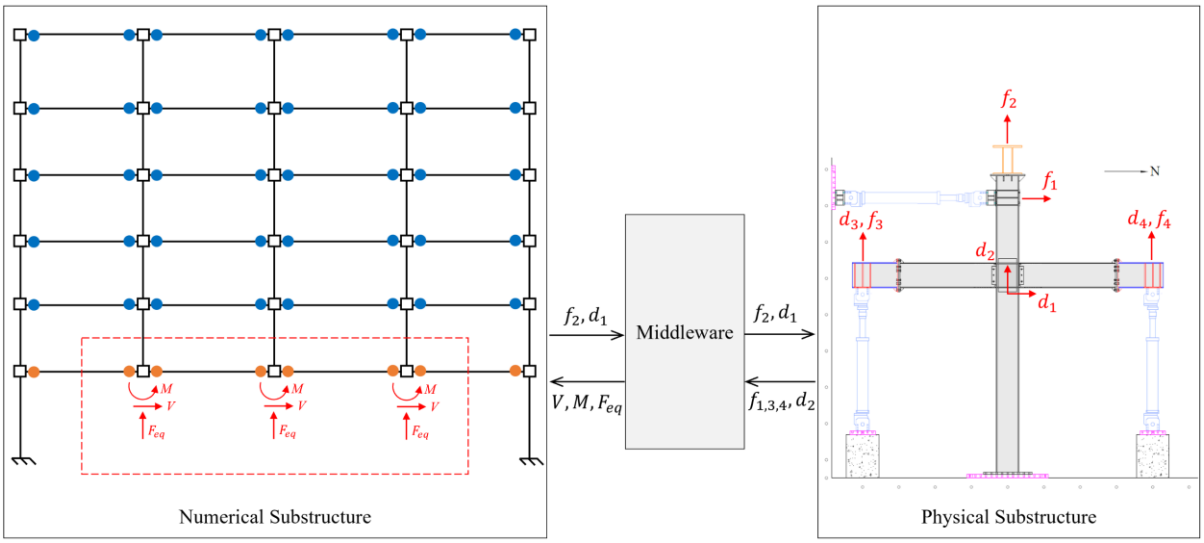

Figure 3. Experimental setup and hybrid loop.

COMUNICATION PROTOCOL

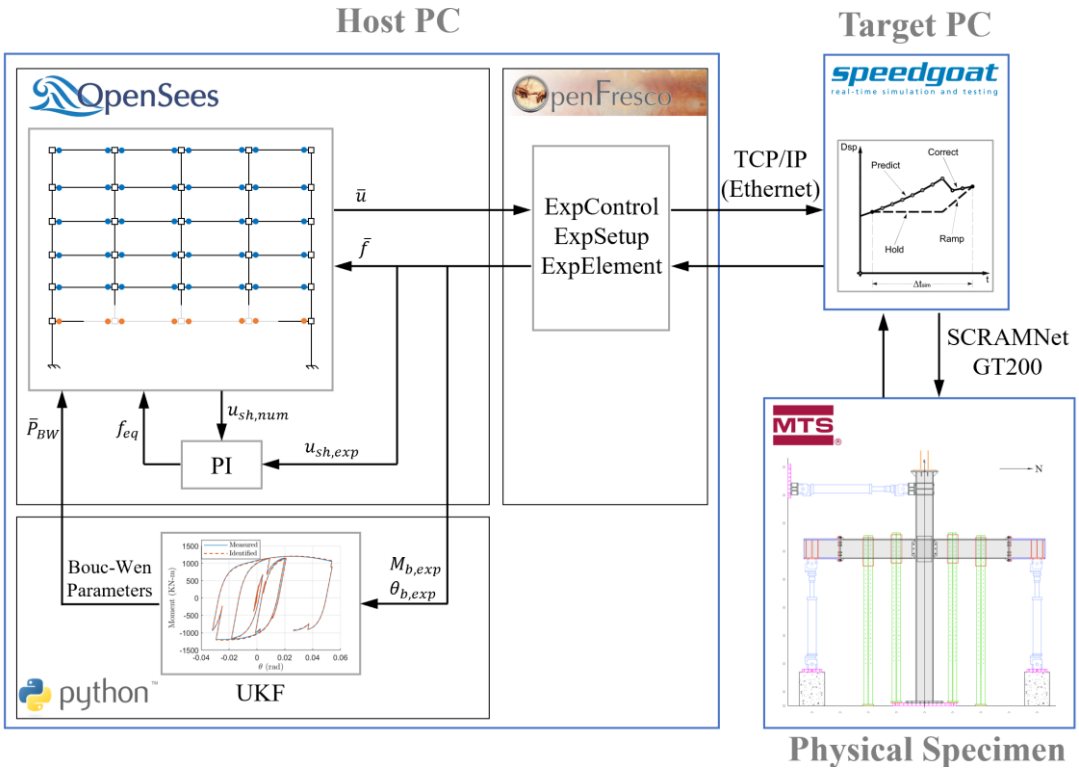

Figure 4. Flowchart of the hybrid simulation with closed-loop-based mixed displacement/force control algorithm and online model updating.

Figure 4 shows a flowchart of the hybrid simulation scheme. The structural analysis software OpenSees (McKenna et al., 2009) is used for the numerical substructure with OpenFresco (Schellenberg et al., 2009) as middleware to connect the numerical domain with the physical domain. OpenFresco exchanges information with a real-time target machine (Speedgoat xPC Target), which converts discrete signal coming from the numerical domain into a more continuous signal series using a predictor-corrector algorithm (Stojadinovic et al., 2016). Then this signal with scaled velocity is sent to the MTS controller to command the actuators. The host PC, running OpenSees, Python and OpenFresco, is connected to the real-time machine through TCP/IP connection (Ethernet), which, in turn, is connected to the MTS actuator controller through a shared memory network (SCRAMNetGT).

In the host PC, where the nonlinear finite elements model is running, two subprocesses are running in parallel. Within the OpenSees model, the vertical displacement measured in the test is transformed into the equivalent force F_{eq} shown in Figure 3 on every integration time-step. In the same computer, an online model updating algorithm is running in Python to update the parameters of the beam hinge in the numerical model. The details of these features are explained below.

ONLINE MODEL UPDATING

In a hybrid simulation, the numerical substructure is typically based on the region that can be simulated more accurately while the experimental substructure consists of components that are more difficult to model. In some cases, the complex behavior can be distributed throughout the whole structure. If components similar to the experiment exist in the numerical model, but experience slightly different deformation pattern, the measured behavior of the specimen can be used to update the model parameters of numerical substructure during the hybrid simulation (Hashemi et al., 2014). A few applications of this technique have been developed and applied recently, including a hybrid simulation carried out at Lehigh University using one nonlinear viscous damper as physical substructure and using the measured data to update the parameters of the rest of the dampers within the numerical substructure (Al-Subaihawi et al., 2022). Cheng and Becker (Cheng and Becker, 2021)

developed a modified unscented Kalman filter (UKF) which combines the robustness of the constrained UKF, the ability of learning new features from adaptive UKF, and including an additional weighting on learning based on the magnitude of the input. This weighted adaptive constrained unscented Kalman filter (WACUKF) algorithm was implemented in Python, and able to update parameters in OpenSees through a network socket connection. These past studies have verified the ability to identify and update parameters using a modified Bouc-Wen model. The current version of the hysteretic model used here captures hardening or softening behavior beyond the linear range without influencing its accuracy for smaller deformations.

For the application proposed here, the WACUKF algorithm was used to identify the moment-rotation behavior of the reduced beam section (RBS) assuming that the hysteresis can be represented by the Bouc-Wen model. To obtain the required data from the experiment, the moment is calculated as the actuator force at the beam end multiplied by the distance to the center of the RBS. The relative rotation of the hinge zone is calculated as the difference between two displacement transducers: one of them located at the bottom flange and the other one located on the top flange of the beam. The measured moment-rotation hysteresis is received in the host PC and sent through OpenFresco to OpenSees, and from this stage, both signals are sent to a Python-Based code running the online model updating algorithm. The identified parameters of the Bouc-Wen model are the initial stiffness, yielding moment, and post-yielding stiffness ratio. The rest of the parameters used by Bouc-Wen model are defined offline before the test. These parameters are then sent back to the numerical substructure to update the models of the first story beam plastic hinges. Figure 5 illustrates the process.

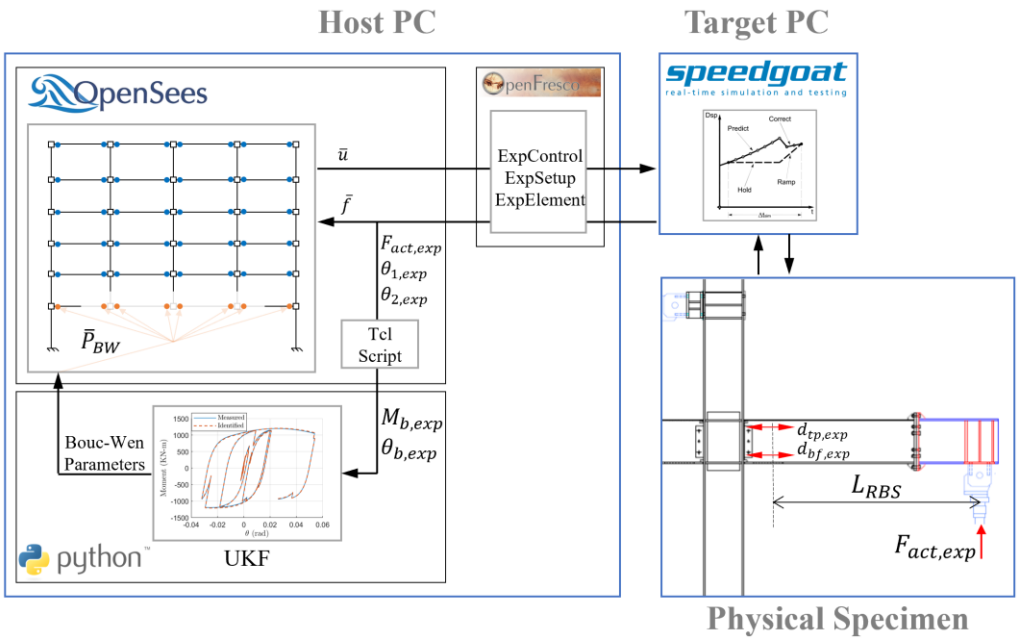

Figure 5. Flowchart of the model updating algorithm

CLOSED-LOOP MIXED DISPLACEMENT/FORCE CONTROL

Performing a hybrid simulation using conventional displacement-control mode can be challenging for highly rigid DOFs because small displacement increments result in large variations in the applied force. Also, since the expected displacement increments are small, they can be even smaller than the resolution of the actuator (Pan et al., 2005). In this case, hybrid simulation with actuators in force-control can overcome this issue imposing a commanded force and sending back displacement feedback (Wu et al., 2007) to the numerical substructure. However, a specialized integration algorithm is needed because traditional finite element platforms are displacement based, sending displacements and receiving forces from each element. Past applications of hybrid simulations have utilized force control for stiff DOFs but neglected displacement compatibility (Del Carpio et al.,2015). In this test, a new closed-loop-based mixed displacement/force control approach is used to overcome issues with rigid DOFs while capturing column shortening (Sepulveda et al. 2022). The method is formulated for

application in a traditional finite element platform like OpenSees, sending displacements for each element and receiving forces. For stiff DOFs, the command is converted to an equivalent force to be applied by the actuators in force control and the feedback is the measured displacements converted into equivalent forces. A recent test of a mixed displacement and force control including feedback forces assumed linear vertical stiffness for the columns and led to small errors in vertical displacement compatibility (Wang et al., 2022). To correct for nonlinearities in the numerical model, the equivalent force is calculated here using a closed-loop proportional-integral (PI) controller. For the closed-loop controller, the target is the feedback displacement being measured in the test u_{exp}, while the current displacement in the numerical substructure u_{num} is the observed variable. The PI controller uses the error (u_{exp} - u_{num}) to calculate the change in equivalent force F_{eq} in the numerical substructure. For every time integration step, the equivalent force is calculated based on the error and imposed in the numerical substructure as an external force.

For this hybrid simulation, the axial force command for the hydraulic jacks applying the axial load on top of the specimen is the internal axial force of one of the second story columns at the overlapped zone boundary of the numerical substructure. The vertical displacement is then measured at the top end of the first story column in the physical substructure. The feedback displacement is sent back to the numerical model and converted into the equivalent force to apply displacement compatibility between both substructures. With this method, the axial force can be imposed in the specimen and the measured displacement can be fed back into the numerical model, allowing to simulate the system behavior of the structure when column axial shortening occurs in the specimen.

RESULTS FROM HYBRID SIMULATION

A hybrid simulation was carried out using a specimen previously tested under a quasistatic protocol. The ground motion recorded during the M_w 6.9 Loma Prieta Earthquake was scaled by a factor of 1.86 to target MCE level. The axial load on the column is equivalent to 10% of the yield load. The objective of these tests was to verify the hybrid simulation algorithms including the features described previously. Additional tests are planned on undamaged specimens.

Figure 6(a) shows the column shear versus drift ratio of the specimen. The sudden drop in the resisting force is evident due to a fracture of one of the beam flanges near -3% drift ratio. Figure 6(b) shows the hysteresis for the measured response of a beam plastic hinge, the numerical hinge model at the 1st story with parameters updated from the measured response, and a numerical hinge model from the 2nd story. After the fracture of the south beam there was a problem in the rotation measurement that produced a sudden rotation increment at the north beam, which was used for model updating. Because of this, the parameters started to adapt to the measured behavior and then the test was stopped.

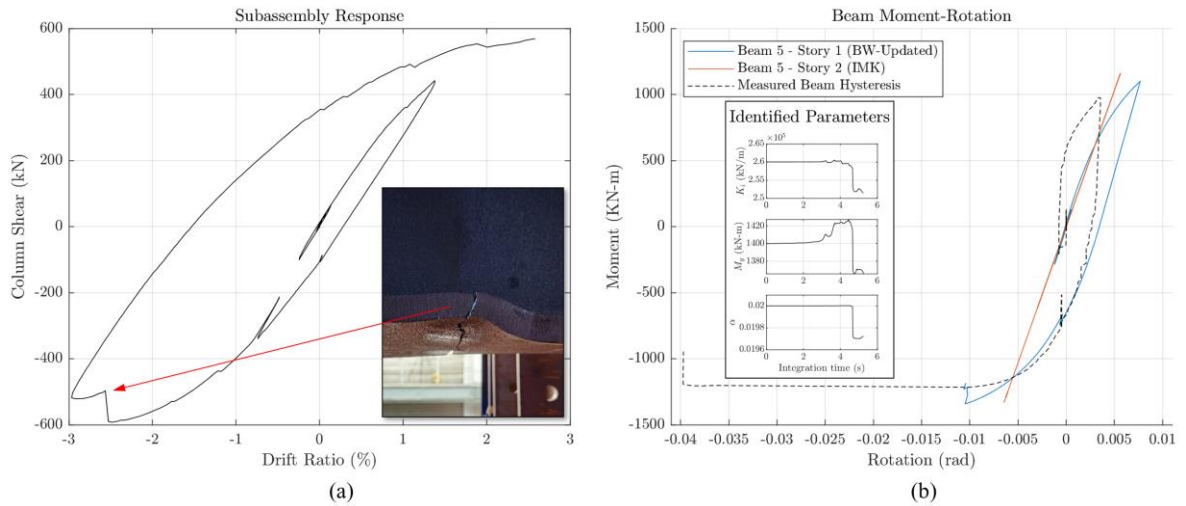

Figure 6. Force response of experimental column in horizontal direction and beam hysteresis

The performance of the closed-loop mixed-control model is verified by the equilibrium and compatibility between the experimental and numerical model in the vertical direction. Figure 7(a)

shows the commanded axial load generated from the numerical substructure, and the axial load measured during the test. The initial axial load applied is 935 kN with the zoom plot showing noise on the order of 0.1 kN that is within the expected precision for using hydraulic jacks. More importantly, the axial load begins to drop as shortening increases demonstrating that the hybrid model captures this interaction. Figure 7(b) shows the measured vertical displacement due to the applied axial load including shortening and the displacement in the numerical substructure imposed through the equivalent force F_{eq} using the closed-loop approach. It can be observed that there is a small delay in the displacement imposed in the numerical substructure. This was expected because the PI controller used to estimate F_{eq} was tuned for stability instead of a faster response that could be excited by the high frequency noise in the displacement measurement. Overall, this approach can capture the coupling between the numerical and experimental substructures in the vertical direction.

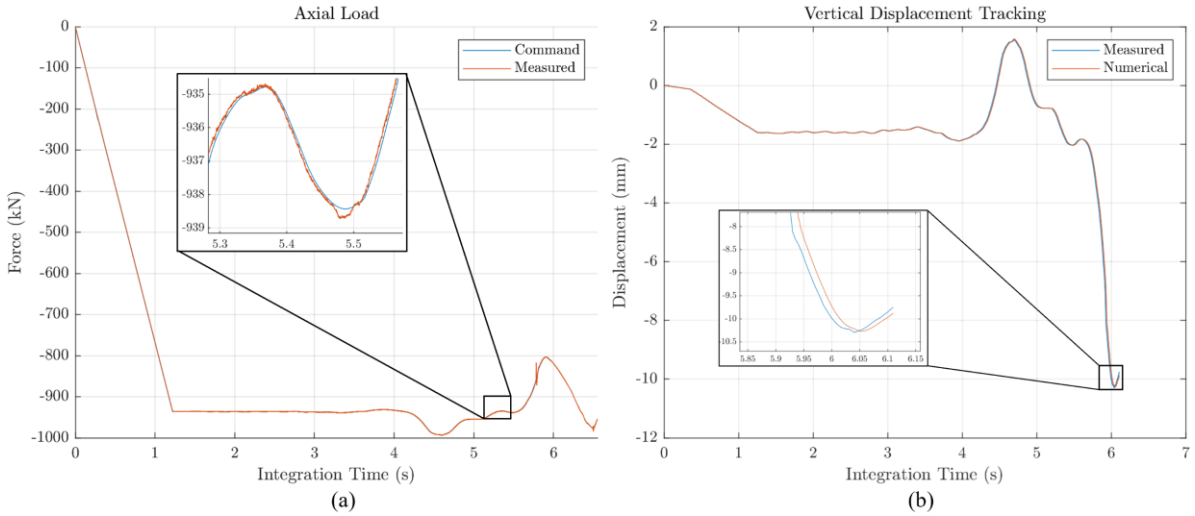

Figure 7. Examination of the vertical response in the numerical and experimental substructures

CONCLUSIONS

A hybrid simulation framework was developed and applied to study the complex behavior of deep slender columns under seismic loads and their interaction with the frame system. The substructuring method simplify the experimental setup to work within the limitations of the experimental facility. To improve the numerical models for beam plastic hinges, an online model updating algorithm is used to update the model parameters according to the measured data. The algorithm was tested using a virtual hybrid simulation and will be fully tested to future hybrid test. A closed-loop-based algorithm is proposed to implement a mixed displacement/force control mode to apply displacements in the numerical model compatible with the measured axial shortening in the experiment. Tests results showed that the axial behavior of the system can be simulated successfully using the proposed method. The complete framework will be implemented to simulate the nonlinear response of the system subjected to several high intensity ground motions in planned tests.

ACKNOWLEDGMENTS

This project was funded by NIST under Award 70NANB171TZ91 to University of Michigan and UC San Diego. Hybrid testing at National Center for Research on Earthquake Engineering (NCREE) is supported by the Ministry of Science and Technology (MOST 110-2625-M-002-015), Taiwan. The support of Andreas Schellenberg and M. Javad Hashemi in the implementation of the hybrid testing is gratefully acknowledged.

REFERENCES

Al-Subaihawi, Safwan, J. M. Ricles, and S. Quiel (2022). “Online Explicit Model Updating of Nonlinear Viscous Dampers for Real Time Hybrid Simulation,” *Soil Dynam Earthq Eng*, 154, 107108.

ASCE. 2022. Minimum Design Loads and Associated Criteria for Buildings and Other Structures (7-22). *ed. American Society of Civil Engineers.*

Del Carpio, M., G. Mosqueda, and M.J. Hashemi. (2015). "Large-Scale Hybrid Simulation of a Steel Moment Frame Building Structure through Collapse." *J Struct Eng*, 142(1), 04015086

Chansuk, P., G. Ozkula, C.-M. Uang, and J.L. Harris. (2021). "Seismic Behavior and Design of Deep, Slender Wide-Flange Structural Steel Beam-Columns," *Technical Note (NIST TN).*

Cheng, Mao, and Tracy C. Becker. (2021). "Performance of Unscented Kalman Filter for Model Updating with Experimental Data." *Earthq Eng Struct Dynam*, 50(7), 1948–66

Chou, Chung-Che, Y.-C. Lai, H.-C. Xiong, T.-H. Lin, C.-M. Uang, G. Mosqueda, G. Ozkula, S. El-Tawil, J. McCormick (2022). "Effect of Boundary Condition on the Cyclic Response of I-shaped Steel Columns: Two-story Subassemblage versus Isolated Column Tests." *Earthq Eng Struct Dynam*, 1–22.

Elkady, A., and D. Lignos (2017). "Full-Scale Testing of Deep Wide-Flange Steel Columns under Multiaxis Cyclic Loading: Loading Sequence, Boundary Effects, and Lateral Stability Bracing Force Demands." *J Struct Eng*, 144(2).

Gupta, A., and H. Krawinkler (1999). "Seismic Demands For Performance Evaluation Of Steel Moment Resisting Frame Structures." *John A. Blume Earthquake Engineering Center*, Report No. 132

Hashemi, M.J., A. Masroor, and G. Mosqueda (2014). "Implementation of Online Model Updating in Hybrid Simulation." *Earthq Eng Struct Dyn*, 43(3), 395–412.

Hashemi, J., and G. Mosqueda (2014). "Innovative Substructuring Technique for Hybrid Simulation of Multistory Buildings through Collapse." *Earthq Eng Struct Dyn*, 43(14), 2059–74

Ibarra, L.F., R.A. Medina, and H. Krawinkler (2005). "Hysteretic Models That Incorporate Strength and Stiffness Deterioration." *Earthq Eng Struct Dyn*, 34(12), 1489–1511.

Mahin, S. & P.S. Shing. (1985). "Pseudodynamic Method for Seismic Testing." *J Struct Eng*, 111(7), 1482–1503.

McKenna, F., M.H. Scott, and G.L. Fenves. (2009). "Nonlinear Finite-Element Analysis Software Architecture Using Object Composition." *J of Comput in Civil Eng*, 24(1), 95–107.

Ozkula, G., C.-M. Uang, and J. Harris (2021). "Development of Enhanced Seismic Compactness Requirements for Webs in Wide-Flange Steel Columns," *J Struct Eng*, 147(7), 04021100.

Pan, P., M. Nakashima, and H. Tomofuji (2005). "Online Test Using Displacement-Force Mixed Control." *Earthq Eng Struct Dyn*, 34(8), 869–88.

Schellenberg, A., S. Mahin, and G. L Fenves (2009). "Advanced Implementation of Hybrid Simulation," *Pacific Earthquake Engineering Research Center*, Berkeley, Report 2009/104

Sepulveda, C., G. Mosqueda, C.M. Uang, C.C. Chou, K.J. Wang (2022). "Hybrid Simulation Using Mixed Displacement and Equivalent-Force Control to Capture Column Shortening in Frame Structures." *12th National Conference on Earthquake Engineering, Salt Lake City, USA.*

Shing, P. S. B, and S. A. Mahin (1984). "Pseudodynamic Test Method for Seismic Performance Evaluation: Theory and Implementation," *Pacific Earthquake Engineering Research Center*, Berkeley, EERC-84/01

Stojadinovic, B., G. Mosqueda, and S. Mahin (2016). "Event-Driven Control System for Geographically Distributed Hybrid Simulation," *J Struct Eng*, 132(1), 0733-9445

Wang, K.-J., C. C. Chou, C. W. Huang, H. K. Shen, M. H. Tam, C. Sepulveda, G. Mosqueda, and C. M. Uang (2022). "Hybrid Simulation of a Seven-Story BRBF Using a Mixed Displacement and Force Control Method on the First-Story Beam-to-Column Subassemblage." *12th National Conference on Earthquake Engineering, Salt Lake City, USA.*

Wu, B., Q. Wang, P.S. Shing, and J. Ou (2007). "Equivalent Force Control Method for Generalized Real-Time Substructure Testing with Implicit Integration," *Earthq Eng Struct Dyn*, 36(9), 1127-1149

Wu, T.-Y., S. El-Tawil, and J. McCormick (2018). "Seismic Collapse Response of Steel Moment Frames with Deep Columns," *J Struct Eng*, 144(9)

(8a) Reconnaissance, lessons learned from recent earthquakes, and post-earthquake assessment and response

RECONNAISSANCE OF THE DAMAGES CAUSED BY THE FEBRUARY 6, 2018, EARTHQUAKE IN HUALIEN, TAIWAN

Jui-Liang Lin [1], Chun-Hsiang Kuo [1], Yu-Wen Chang [1], Shu-Hsien Chao [1], Yi-An Li [1], Wen-Cheng Shen [1], Chung-Han Yu [1], Cho-Yen Yang [1], Fan-Ru Lin [1], Hsiao-Hui Hung [1], Chun-Chung Chen [1], Chin-Kuo Su [1], Shang-Yi Hsu [1], Chih-Chieh Lu [1], Lap-Loi Chung [1], and Shyh-Jiann Hwang [1]

1. National Center for Research on Earthquake Engineering, Taipei, Taiwan, R.O.C.
Email: jllin@narlabs.org.tw

ABSTRACT

An earthquake with an epicenter offshore of Hualien City in eastern Taiwan occurred at midnight on February 6, 2018. The Richter magnitude (ML) of the earthquake was 6.26 and the seismic intensity ranged up to level VII, the strongest seismic intensity level regulated in Taiwan. Almost all the major damage resulting from this seismic event was occurred near both sides of the Milun Fault, where records from nearby strong motion stations displayed the characteristics of near-fault ground motions. In order to examine the seismic damage states before they could be altered by rescue and restoration efforts, Taiwan's National Center for Research on Earthquake Engineering (NCREE) sent its first reconnaissance team to Hualien City in the early morning of February 7, 2018. The seismic reconnaissance team collected information on the geology and damage states of buildings, non-structural components, bridges, and ports. The main seismic damage was the collapse of four buildings with soft bottom stories, one of which resulted in fourteen of the seventeen total fatalities. Comparing the acceleration response spectra with the design response spectra sheds light on the effects of near-fault ground motions on the collapsed buildings.

Keywords: Seismic reconnaissance, 0206 Hualien earthquake, Milun fault, near-fault ground motion, building collapse

GROUND MOTION CHARACTERISTICS

According to Taiwan's Central Weather Bureau (CWB), this earthquake event occurred on February 6, 2018, at 23:50 local time (GMT+8). The Richter magnitude (M_L) was 6.26. The epicenter was at 24.1 °N, 121.73 °E, approximately 20 km off Taiwan's east coast and close to Hualien City. The depth of the hypocenter was 6.31 km. The observed peak ground acceleration (PGA) was 594 cm/s^2 at the strong motion station HWA057, which is 12.7 km away from the epicenter. The observed peak ground velocity (PGV) was 146 cm/s at the strong motion station HWA014, which is 19.1 km away from the epicenter. The PGAs of five strong motion stations reached Taiwan's strongest intensity level VII (*i.e.*, PGA > 400 gal). Additionally, there were ten strong motion stations with PGVs greater than 75 cm/s. Figs. 1a to c show the maps of PGA, spectral acceleration at 0.3 s (denoted by S_a (T = 0.3 s)) divided by 2.5, and spectral acceleration at 1.0 s (denoted by S_a (T = 1.0 s)), respectively. Taiwan's Central Geological Survey (CGS 2018) reported that all the serious seismic damages in Hualien City were approximately located within the geologically sensitive zone of the Milun Fault, *i.e.*, the 300-m-wide strip along the Milun Fault. In addition, some ruptures and dislocations on the ground surface along the Milun Fault were observed. Thus, it was confirmed that the Milun Fault was dislocated in this seismic event. Among the eighteen strong motion stations with seismic intensity equal to or greater than level VI (*i.e.*, PGA $\geqq$ 250 gal), there are seven stations (*i.e.*, HWA009, HWA011, HWA012, HWA013, HWA014, HWA028, and HWA050) with vertical PGAs greater than both the horizontal PGAs. In addition, all the PGVs of these seven stations are beyond 60 cm/s.

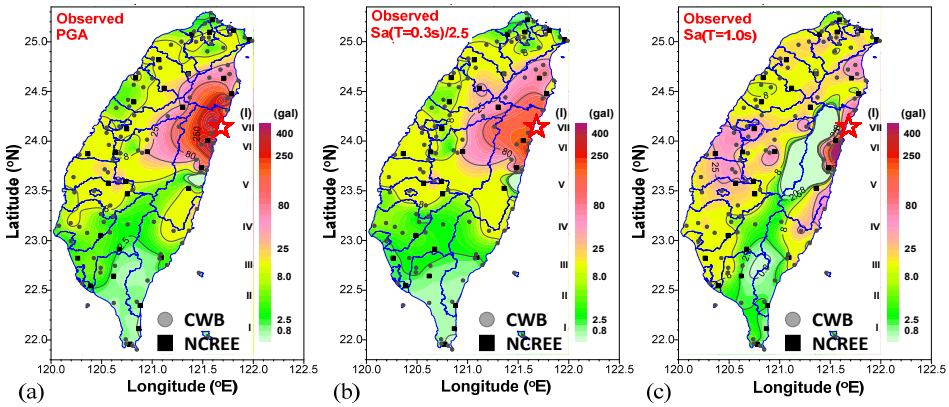

Figure 1. Maps of (a) PGA, (b) S_a (T = 0.3 s)/2.5, and (c) S_a (T = 1.0 s) across Taiwan.

Based on the pulse indicator proposed by Shahi and Baker (2014), the velocity histories recorded at the strong motion stations near the Milun Fault were analyzed to determine whether the ground motion records possess the characteristics of near-fault velocity pulses. The green arrows shown in Fig. 2 represent the magnitudes and directions of the velocity pulses observed at 17 strong motion stations in the Hualien area. In addition, the three contours of the PGVs equal to 40 cm/s, 80 cm/s, and 120 cm/s are also illustrated. Figure 2 indicates that all the records of the strong motion stations near the Milun Fault exhibit velocity pulses, most of which are toward the E-W direction, *i.e.*, perpendicular to the Milun Fault. Figure 3 shows the velocity histories of strong motion stations HWA014 and HWA019, whose PGVs, the greatest two of all strong motion stations, are greater than 120 cm/s.

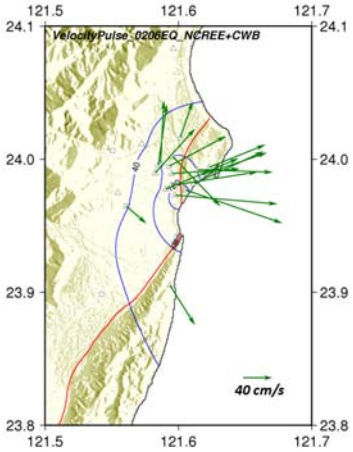

Figure 2. Magnitudes and directions of the velocity pulses observed at the strong motion stations in the Hualien area.

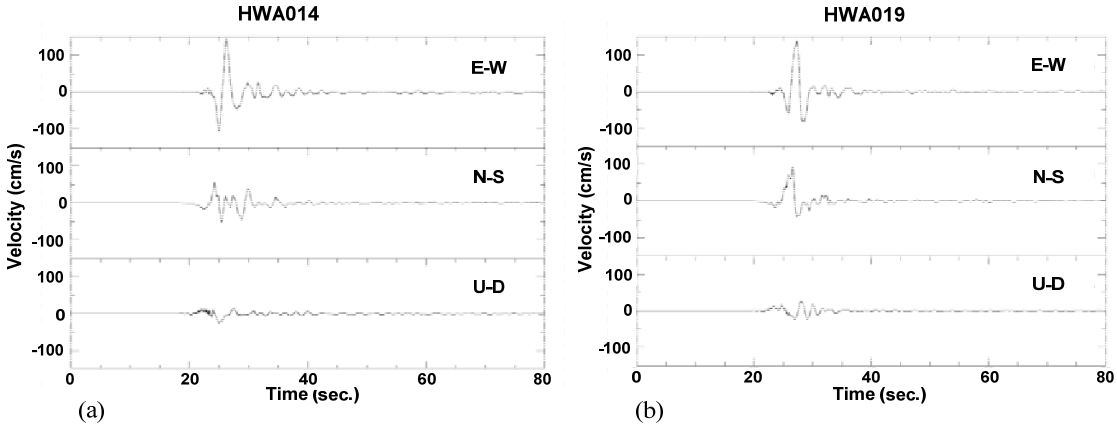

Figure 3. Velocity histories of strong motion stations (a) HWA014 and (b) HWA019. From top to bottom, the plots show velocities in the E-W, N-S, and U-D directions.

Figure 4a shows the distribution of the strong motion stations with PGA greater than 300 cm/s^2. Their acceleration response spectra are compared with the 475- and 2500-year-return-period design response spectra in Fig. 4b. Figure 4b indicates that the spectral accelerations at 2.5 s and 1.0 s of the response spectra of strong motion stations HWA019 and HWA060, respectively, have a significant peak. The aforementioned spectral acceleration peaks, which are relatively larger than the corresponding values of the design response spectra with a 2500-year return period, imply that the medium-to-high-rise building structures around the two strong motion stations are likely to be seriously damaged. In contrast, the acceleration response spectra of the other four strong motion stations (*i.e.*, ILA050, A210, HWA057, and HWA058) have peaks at short periods. Some of these peaks are larger than the corresponding values of the design response spectra with 475- or 2500-year return periods. It is thus reasonable to expect that some slight to medium damages might occur in low-rise buildings located around these four stations.

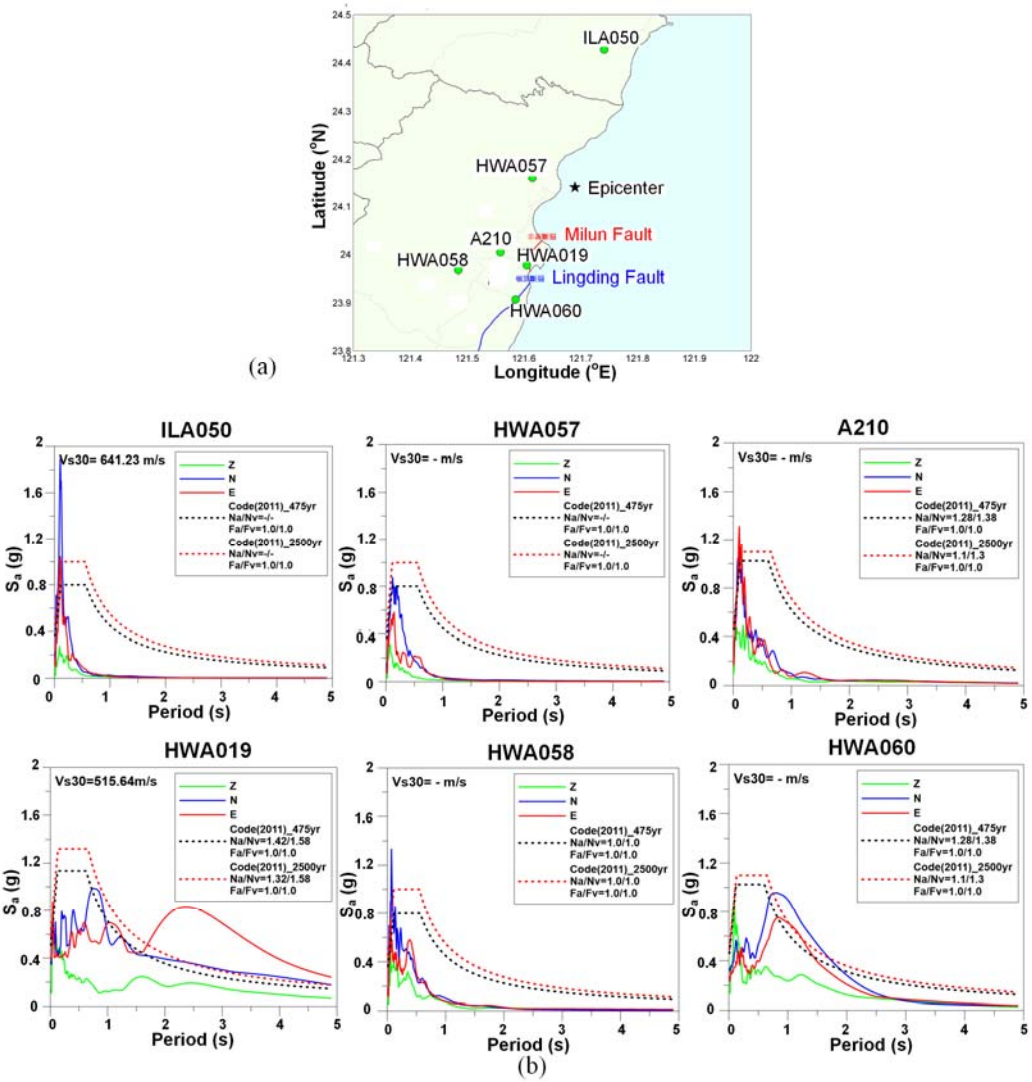

Figure 4. (a) Distributions of the strong motion stations with PGA greater than 300 cm/s^2 and (b) their acceleration response spectra compared with the 475- and 2500-year-return-period design response spectra.

BUILDINGS

The Hualien earthquake resulted in four buildings collapsing and one being seriously damaged. The four collapsed buildings were a 12-story mixed-use apartment block, a 6-story apartment building, a 9-story apartment building, and an 11-story hotel. The seriously damaged building was a 12-story department store. The collapsed buildings, all of which were constructed before 1999 Chi-Chi earthquake, had soft bottom stories and were located along the Milun Fault (Fig. 5). Because Taiwan's near-fault provisions were enacted in 2005, the design procedures at the times of construction of the four collapsed buildings did not include the near-fault provisions. Besides the four collapsed buildings, Fig. 5 also shows the location of a damaged bridge crossing the Milun Fault.

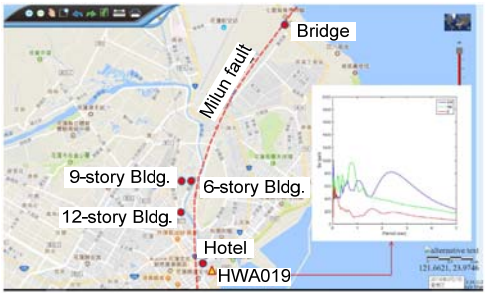

Figure 5. Locations of the four collapsed buildings and one damaged bridge relative to the Milun Fault.

The collapse of this 12-story reinforced concrete (RC) building resulted in the severest number of fatalities, *i.e.*, fourteen out of the total of seventeen in this earthquake. Figures 6a and b respectively show the front and rear sides of the collapsed building, which was built in 1994. The yellow steel struts shown in Fig. 6a are temporary measures to prevent the building from further collapse, which might threaten the lives of the rescuers. The floor plan of the building (Fig. 6c) indicates that the front of the building is to the south-west. In addition, the building is relatively plan-asymmetric. Due to the significantly high peaks of the E-W acceleration response spectra between 1.5 s and 2.5 s (Fig. 4), the building whose dominant vibration period was highly likely within the stated period range collapsed toward the front (*i.e.*, the south-west direction). It is worth noting that the first and second stories of the building were commercially used as a hotel with large open spaces in its lobby/reception hall. Figures 6d to f show the damaged columns that had overly large spacing of stirrups, which was approximately equal to 25 cm to 30 cm. In addition, the splices of all the column reinforcements appeared at the same height (Fig. 6f), which was contrary to the current code requirements (CICHE 2011). Figure 6f shows that the column moved upward and failed where splicing of reinforcements was deficient.

(a) (b) (c)

(d) (e) (f)

Figure 6. (a) Front view, (b) back view, (c) drawing of floor plan, (d) corner column, and (e) and (f) bottom columns of the collapsed 12-story mixed-use apartment block.

Figures 7a and b show the front and back of the tilted 9-story apartment building, which was built in 1994. Figure 7c is a close-up photograph of the bottom story shown in Fig. 7a. The bottom story of this building was used as a parking lot. Figure 7c indicates that there were two spans (*i.e.*, three columns) along the direction shown in the photograph. The front, middle, and back columns circled in yellow were all bent at their tops. In addition, all three columns were inclined toward the inside of the building, and the inclinations sequentially increased from the front column to the back column (Fig. 7c). As a result, the extent of the damages at the tops of the three columns sequentially increased from the front to the back columns. In detail, the top of the front column remained joined to the upper column. In contrast, the top of the middle column was almost entirely separated from the above column. Additionally, the surface of the break at the top of the middle column appeared smooth and there appears to be almost no reinforcements going through that surface. The back column, which was the most severely damaged among the three columns, was almost laid down as a rigid block. The back column shown in Fig. 7c can also be seen from the rear side of the apartment building shown in Figs. 7b and d. Figure 7d is a close-up photograph of the bottom story shown in Fig. 7b. Figure 7d indicates that the back column remained essentially intact except that the column's top was broken. The reinforcements and stirrups at the top portion of the back column were insufficient (Fig. 7c). Additionally, the concrete in the core of the back column appeared inferior, lacking proper cementation. Moreover, the appearances of the 2nd-story columns atop the three 1st-story columns were all torn off at different lengths and this sequentially increased from the front column to the back column (Fig. 7c). From Fig. 7d, the ends of the reinforcements of the beam connected to the back column were bent downward. The bending direction for the ends of the bottom reinforcements of the beams is upward rather than downward. Figure 7e shows the broken exterior walls and the detachment of the exterior tiles of the 9-story apartment building. From the broken section of the exterior walls, there seem to have been very few reinforcements in the exterior walls.

In light of the above-mentioned substantially unequal inclinations and damage extents of the three bottom columns shown in Fig. 7c, the frame consisting of these three columns very likely underwent rotation-induced out-of-plan displacements. In other words, the apartment building was probably plan-asymmetric, which had stiff and flexible sides at the front and back columns of Fig. 7c, respectively. In addition, according to the situations of the reinforcements and concretes exposed at the tops of the bottom columns, the construction appears to have been poor and perhaps was not built following the design drawings. Furthermore, it is worth noting that the color of the exterior tiles on the top three stories was obviously darker than those on the below six stories (Figs. 7a and b). According to statements from the residents of the building, the top three stories were added later, *i.e.*, the original building was a six-story building. Whether or not the added top three stories were legal may require investigation by authorities. If the added top three stories were illegal, then the original six-story building would very likely not have had sufficient capacity to sustain the additional weight and lateral inertial force induced by the added three stories during an earthquake.

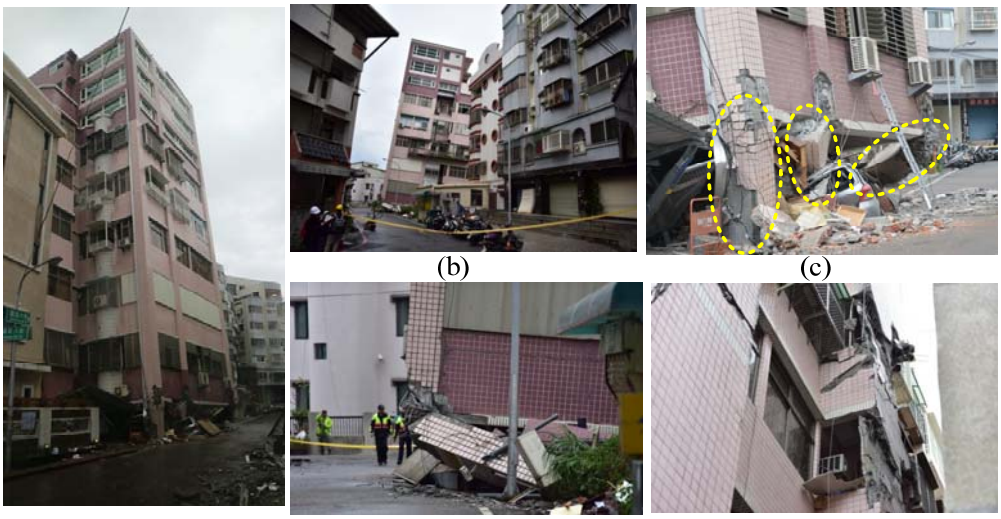

(a) (b) (c) (d) (e)

Figure 7. (a) Front and (b) back views of the collapsed 9-story apartment building. (c) and (d) Close-up photographs of the bottom story shown in (a) and (b), respectively. (e) Exterior walls of the collapsed building.

BRIDGES

Soon after the Hualien earthquake, passage over four bridges, namely the Qixingtan Bridge, Hualien Bridge, Hualien City No. 3 Bridge, and Shangzhi Bridge, were temporarily blocked for safety inspections. The Qixingtan Bridge and Hualien Bridge cross the northern parts of the Milun Fault and the Lingding Fault, respectively (Fig. 8a). Figures 8b and c illustrate the directions of the Qixingtan and Hualien Bridges relative to the Milun and Lingding Faults. The two bridges are shown as blue strips in Figs. 8b and c, in which the abutments are denoted as A1 and A2. The strong ground motion stations HWA028 and HWA060 are close to Qixingtan Bridge and Hualien Bridge, respectively (Fig. 8a). Both the PGAs recorded at HWA028 and HWA060 were over 400 cm/s^2, which is Taiwan's strongest seismic intensity level VII. The reconnaissance results for Qixingtan Bridge are as follows (Hung *et al*. 2018).

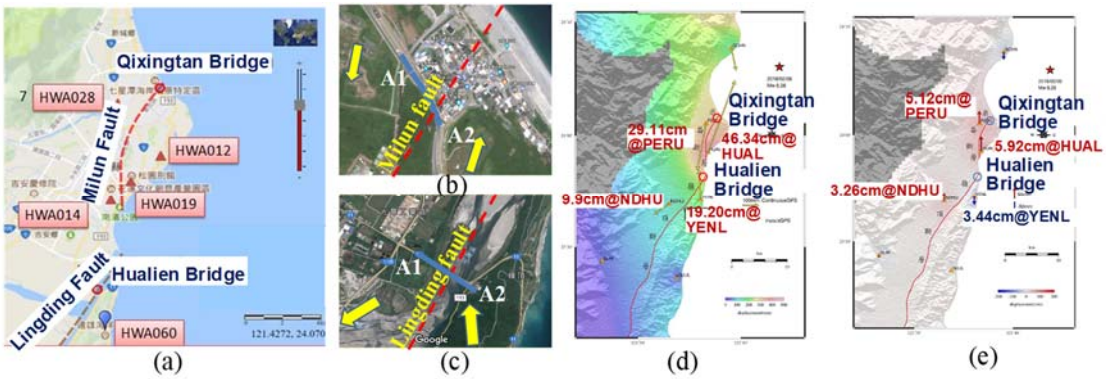

Figure 8. (a) Locations of the Qixingtan Bridge and Hualien Bridge. (b) The direction of Qixingtan Bridge relative to the Milun Fault. (c) The direction of the Hualien Bridge relative to Lingding Fault. The (d) horizontal and (e) vertical displacements of land surfaces on the two sides of the Milun Fault and Lingding Fault (CGS 2018).

Figures 8d and e respectively show the horizontal and vertical displacements of land surfaces measured through the global positioning system (GPS) by Taiwan's Central Geological Survey (CGS 2018). The lengths and directions of the arrows shown in Figs. 8d and e represent the magnitudes and directions of the displacements. The GPS monitoring stations HUAL and PERU are on the hanging wall (or east side) and footwall (or west side) of the Milun Fault, respectively. The horizontal displacements at the HUAL and PERU stations were 46.34 cm toward the north-east direction and 29.11 cm toward the south-west direction, respectively (Fig. 8d). That is to say, the relative horizontal displacement between the hanging wall and the footwall of the Milun Fault, dislocated in the Hualien earthquake, was over 70 cm. Additionally, the vertical displacements at the HUAL and PERU stations were 5.92 cm and 5.12 cm, respectively, both of which were upward (Fig. 8e). Moreover, the GPS monitoring stations YENL and NDHU are on the hanging wall (or east side) and footwall (or west side) of Lingding Fault, respectively. The horizontal displacements at the YENL and NDHU stations were 19.2 cm toward the north-west direction and 9.9 cm toward the south-west direction, respectively (Fig. 8d). The vertical displacements at the YENL and NDHU stations were downward 3.44 cm and upward 3.26 cm, respectively (Fig. 8e). The directions of the yellow arrows shown in Figs. 8b and c are the same as those of the arrows shown in Fig. 8d. Figures 8b and c clearly indicate that the overall land displacements of Qixingtan Bridge and Hualien Bridge were counterclockwise. Differential land displacements indeed existed in each of the bridges. In addition, the major land displacements of Qixingtan Bridge and Hualien Bridge were on the hanging wall (or east side), *i.e.*, on the abutment A2 side.

Figure 9a depicts a plan and elevation layouts of Qixingtan Bridge, which was opened for traffic in 2013. Abutment A1 to pier P1 is a 60-m-span simply supported vibration unit where the bearing at abutment A1 is longitudinally moveable and the bearing at pier P1 is a hinge. Pier P1 to abutment A2 is another vibration unit that is a two-span, 90 m + 90 m, continuous girder rigidly connected to pier P2 (Fig. 9a). In this two-span vibration unit, both the bearings at pier P1 and abutment A2 are moveable in the longitudinal direction and fixed in the transverse direction, and vertically adjustable. Abutment A2 is skewed relative to the direction of traffic flow. The superstructure of the bridge consists of pre-stressed concrete two-cell box girders. The substructure of the bridge is single-column RC piers with elliptical cross-sections and pile foundations. In addition, there is a culvert integrated with abutment A2 (Fig. 9a). Figures 9b and c show respectively a satellite image and a photograph of the Qixingtan Bridge. The serial numbers of the piers and abutments are marked in the photographs (Figs. 9b and c).

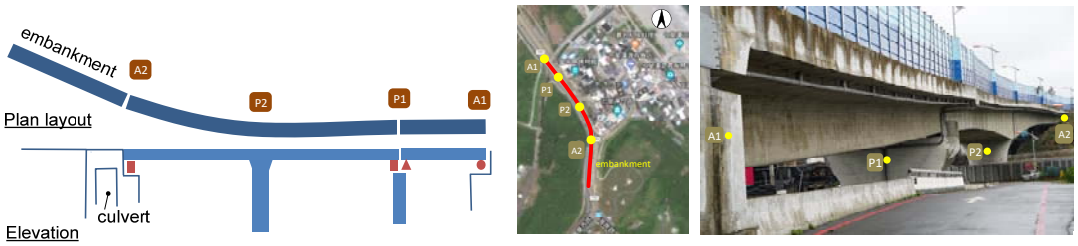

(a) (b) (c)

Figure 9. Qixingtan Bridge: (a) diagrams of the plan and elevation layouts, (b) satellite image, and (c) photograph.

Figures 10a and b show the upheaval of the road embankment approaching abutment A2. In light of the displacements of the land surface shown in Figs. 8b and d, there was a thrust from the embankment toward abutment A2, by which the aforementioned upheaval was manifested. Additionally, that is why the noise barriers at the top of the upper-left corner of the culvert were pushed against each other (Fig. 10c). Figure 10d shows the cracked seismic stopper at abutment A2. This slightly damaged seismic stopper implies an inclined rather than perpendicular collision between the girder and the seismic stopper because abutment A2 is skewed relative to the direction of traffic flow. Pier P2 was intact (Fig. 10e), whereas pier P1 had obvious damage (Figs. 10f and g) caused by the collision between the girder and the seismic stopper. This collision also resulted in the surrounding concrete flaking off pier P1. Nevertheless, through detailed visual inspection, there were no visible flexural or shear cracks at the bottom of pier P1. The damage to the seismic stoppers (Figs. 10d, f, and g) reflects that the seismic stoppers functioned properly. Figure 10h shows the essentially intact expansion joint at abutment A1. Nevertheless, it is noted that the red traffic markings on the opposite sides of the expansion joint were not in line with each other (Fig. 10h). This indicates that different transverse displacements occurred on the two sides of abutment A1. Considering the large dislocation of the Milun Fault and the structural integrities of piers P1 and P2 (Figs. 10e and f), Qixingtan Bridge performed well in this seismic event.

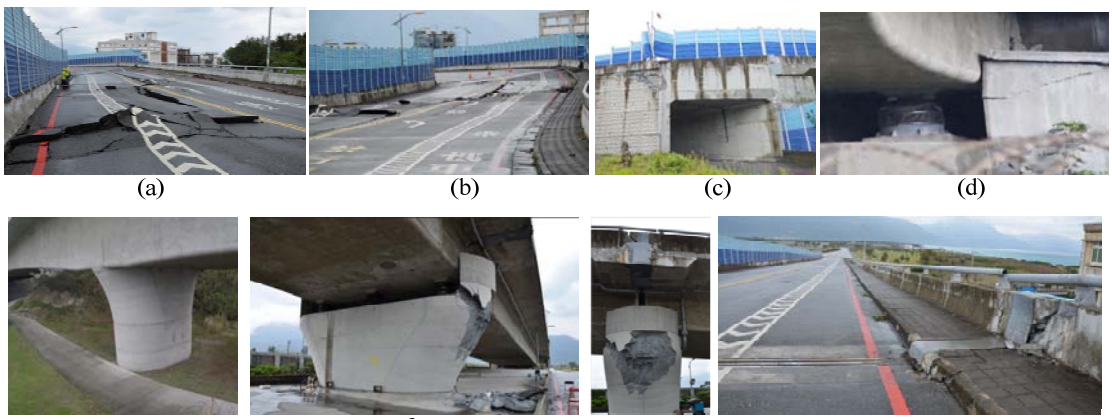

(a) (b) (c) (d)

(e) (f) (g) (h)

Figure 10. (a) and (b) Upheavals of the road embankment approaching abutment A2. (c) The damaged noise barriers above the culvert. (d) The cracked seismic stopper at abutment A2. (e) The intact pier P2. (f) and (g) The damaged pier P1. (h) The expansion joint of abutment A1.

CONCLUSIONS

The main characteristics of this seismic event were near-fault ground motions and damages to structures located close to the active faults. The locations of the structures that suffered severe damage in the seismic event are distributed along the sides of the Milun Fault. From the acceleration response spectra obtained from the strong motion stations around the severely damaged structures, the spectral accelerations at medium to long vibration periods are significantly higher than the design response spectra. The large spectral accelerations resulting from the effect of near-fault ground motions were perhaps one of the main factors causing the structural damage. Therefore, the seismic design of medium to high-rise buildings close to active faults should be comprehensively reviewed. A limit on construction of such buildings may be a possible alternative. Besides the poor construction and the large seismic demands imposed by the near-fault ground motions, the soft and/or weak bottom stories resulting from these open spaces could be one of the key factors causing the building collapses. The significant differential displacements of land surfaces on the two sides of the active faults where Qixingtan Bridge and Hualien Bridge crossed over the faults were identified. When bridges inevitably cross active faults, the seismic mechanisms and capacities of the bridges for accommodating possible large differential displacements on the two sides of the active faults should be determined.

REFERENCES

CGS (2018). “Geological survey report on 20180206 Hualien earthquake,” Central Geological Survey, Ministry of Economic Affairs, Taiwan, R.O.C. (in Chinese).

Shahi, S.K. and Baker, J.W. (2014). “An efficient algorithm to identify strong-velocity pulse in multicomponent ground motions,” *Bull. Seism. Soc. Am* **104**(5), 2456-2466.

CICHE (2011). “Application of design codes of concrete engineering,” *Civil 404-100*, Chinese Institute of Civil and Hydraulic Engineering, Taipei, Taiwan (in Chinese).

Hung, H.H., Chen, C.C., Su, C.K., Lee, B.H., Jang, C.L. and Sung, Y.C. (2018). “Reconnaissance observation and analysis on bridge damage caused by the 0206 Hualien earthquake,” The 4th National Conference on Earthquake Engineering, Taichung, Taiwan, 6-8 November, 2018. Paper No. 24014 (in Chinese).

EVALUATING RECOVERY EXPENSES OF INFRASTRUCTURE DAMAGED BY EARTHQUAKES

Saki Yotsui[1], Tomohiro Tanaka[2], Kazuyuki Izuno[3]
1. Assistant Professor, College of Science and Engineering, Ritsumeikan University, Shiga, Japan.
2. Student, College of Science and Engineering, Ritsumeikan University, Shiga, Japan.
3. Professor, College of Science and Engineering, Ritsumeikan University, Shiga, Japan.
Email: s-yotsui@fc.ritsumei.ac.jp

ABSTRACT

This study aims to develop a simple equation that can estimate the expenses of a project to recover public civil engineering works damaged by earthquakes (referred to as recovery expenses). The explanatory variables are the number of fatalities, the population exposed to earthquakes, and the number of buildings affected by earthquakes. The results of this study can be summarized as follows. (1) In contrast to the direct cost of damage to ports and public facilities worth around 2,500 billion JPY in the 1995 Hyogo-ken Nanbu Earthquake, disaster recovery expenses from 2007 to 2020 have since steadily declined as a result of the promotion of damage mitigation measures, such as earthquake resistance and seismic isolation using the latest construction technology. (2) We found that disasters with high fatalities and damage level tend to cause significant damage to infrastructure facilities. (3) The coefficient of determination of the adjusted multiple regression is an estimating equation with high predictive accuracy. (4) We proposed the equation that estimates disaster recovery expenses by local governments for disaster resilience as a part of the disaster reduction measures.

Keywords: natural disaster, earthquake, recovery expenses, infrastructure, fatalities

INTRODUCTION

Various disasters have occurred within a year, and there are concerns about the concurrence of multiple disasters and the consequent widespread damage. Infrastructure, such as roads and bridges, which forms the basis of industry and social life and enable people to lead safe, secure, and prosperous lives, is damaged by natural hazards. According to the Swiss Re (Swiss Re Institute, 2022), the number of natural catastrophe events has been increasing globally.

The early restoration of infrastructure is important as natural hazards are becoming more widespread and severe. However, the following problems have been cited in Japan (MLIT, 2016; Aota *et al.*, 2010). (1) Lack of human resources capable of responding to large-scale disasters in each municipality; (2) increased burden of administrative procedures; and (3) delays in support measures caused by delays in understanding the damage. If disaster recovery expenses can be estimated in advance, restoration can begin almost immediately. Therefore, it is important to rapidly formulate a restoration policy against the damage expected from the Nankai Trough Mega Earthquake that is likely to occur in the future. The purpose of this study is to analyze the changes in disaster recovery expenses of public civil engineering facilities after a disaster has occurred. Furthermore, the relationship between the damage scale and recovery expenses can be used to examine the financial preparedness for restoration in future disaster scenarios.

FINANCIAL SUPPORT FROM THE JAPANESE GOVERNMENT FOR THE RESTORATION OF INFRASTRUCTURES DAMAGED BY NATURAL DISASTERS

Various methods exist for disaster recovery, such as the restoration of infrastructure, railways, airports, and residential properties. This study focused on the restoration of infrastructure managed by local governments. The Ministry of Land, Infrastructure, Transport, and Tourism (MLIT) in Japan has a

system called the project of restoring infrastructure damaged by natural disasters (MLIT, 2010). It includes facilities related to rivers, coasts, ports, roads, bridges, harbors, parks, sewers and landslide prevention. The costs of restoring infrastructure can be immense and variable. Because it is difficult for local governments to pay these costs, the National Government Defrayment Act for Reconstruction of Disaster Stricken Public Facilities was enacted in 1951 for enabling the local governments to receive financial aid from the national government. When a natural disaster reaches certain criteria and damages infrastructure beyond a certain level, most of the disaster recovery expenses are covered by the national treasury to avoid affecting the finances of the local government.

When a disaster occurs, local governments apply for disaster recovery for the affected area. A disaster assessment is conducted based on the application to determine the amount of financial support it should be allotted. The steps of the disaster recovery project are as follows. Damage assessment and emergency work, surveying and designing, placing an order for construction, and commencing work. Moreover, disaster recovery work can begin immediately after the disaster without waiting for the government's disaster assessment. The following two types of financial support are available:

- restoration to the original state
- restoration to an improved state to prevent the repetition of disasters

Disaster statistics are publicly available on the internet (MLIT, 2022). Fig. 1 shows the disaster recovery expenses for infrastructure caused by earthquakes from 2007 to 2020. We extracted the disaster recovery expenses for infrastructure from both prefectures and municipalities. For disaster recovery expenses from 2007 to 2020, a price index from 1 to 1.17 was required to reach the 2020 values. Therefore, it should be noted that actual cost of disaster recovery was higher than that shown in Fig. 1. The years 2011 and 2016 were prominent because of the Great East Japan Earthquake and Tsunami, and the Kumamoto Earthquake, respectively. The accumulated disaster recovery expenses for the earthquakes were approximately 3.18 trillion JPY.

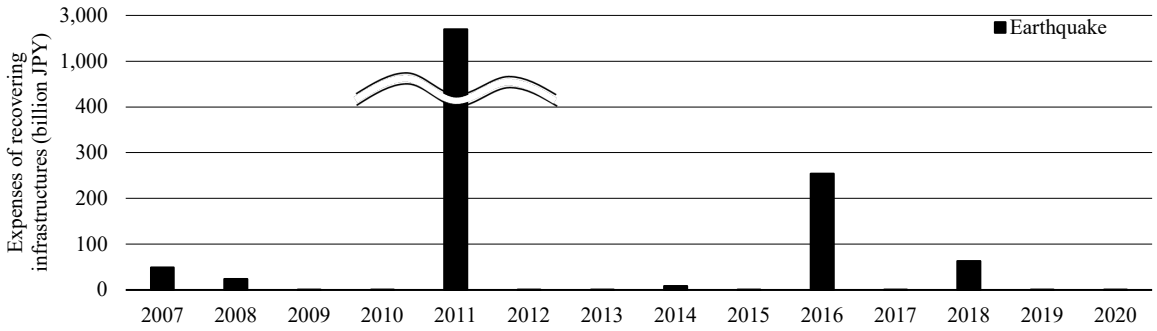

Figure 1. Disaster recovery expenses of infrastructure caused by earthquakes from 2007 to 2020

METHODOLOGY

Datasets

We analyzed earthquakes with a focus on the number of dead and missing persons and damaged buildings as a numerical representation of the extent of the damage caused. Table 1 lists the earthquake data used for statistical analysis. An overview of the data used is as follows.

1. Disaster statistics under the jurisdiction of the MLIT (MLIT, 2022): The Public Civil Engineering Facility Disaster Recovery Project, combined with expenditure for prefectures and municipalities, was used. We used a total of eight listed earthquakes from 2007 to 2018. This study covered severe disasters that exceeded the designation criteria on a national scale. In addition, the 2018 Osaka Northern Earthquake data were included, although this was not a severe disaster. The 2011 Great East Japan Earthquake and Tsunami data were much larger than the others in terms of both damage and recovery expenses (approximately 8,000 and 11 times larger than that of the 2018 Osaka Northern Earthquake and 2016 Kumamoto Earthquake, respectively). Thus, the 2011

Great East Japan Earthquake and Tsunami data were excluded from the statistical analysis because the correlation depended on itself.

2. The population data from the National Census (Statistics Bureau of Japan, 2005, 2010, 2015): 2005, 2010, and 2015 were used.
3. Number of dead and missing persons (fatalities): Data from the Cabinet Office's White Paper on Disaster Management in 2020 were used for the earthquake, only direct deaths were included.
4. Number of damaged buildings: The number of totally collapsed, half-collapsed, and partially collapsed dwellings from the Cabinet Office's White Paper on Disaster Management in 2020 were used.

Table 1. List of earthquake data used for statistical analysis

Year	Earthquake name	Dead and missing persons	Exposed population (1,000 people)	Damaged buildings	Expenses (100 million JPY)
2007	Niigataken Chuetsu-oki	11	957	44,342	292
2007	Noto Hanto	1	180	29,384	200
2008	Iwate-Miyagi Nairiku	17	1,137	2,697	232
2014	Northern Nagano	0	406	1,640	85
2016	Kumamoto	50	1,180	206,886	2,517
2016	Tottori	0	768	14,562	21
2018	Osaka Northern	4	3,854	27,600	4
2018	Hokkaido Eastern Iburi	42	832	14,729	626

Method of analysis

We conducted a statistical analysis based on these four datasets. As a prerequisite, the population exposed to earthquakes was calculated based on the census conducted before the earthquake, which indicates the population in areas where the seismic intensity was 5 or higher. The number of fatalities, exposed population, and the number of damaged buildings, which are indicators of the scale of the disaster, were used as explanatory variables.

First, a statistical analysis of the relationships among (1) the number of fatalities and the number of damaged buildings, (2) the number of damaged buildings and exposed population, and (3) the exposed population and number of fatalities were conducted for the earthquake. Second, the disaster recovery expenses from 2007 to 2018 were used to examine the relationships among the disaster recovery expenses and the number of fatalities, the exposed population, and the number of damaged buildings. Finally, an estimation equation for the disaster recovery expenses was constructed using multiple regression analysis.

RESULTS AND DISCUSSION

Relationship between the damage caused by earthquakes and disaster recovery expenses

Trends in disaster recovery expenses

Compared to the direct cost of damage to ports and public facilities worth 2,488 billion JPY in the 1995 Hyogo-ken Nanbu Earthquake, disaster recovery expenses have since steadily declined as a result of the promotion of damage mitigation measures, such as earthquake resistance and seismic isolation using the latest construction technology (Hyogo Earthquake Memorial 21st Century Research Institute, 2006). As shown in Table 1, the number of people exposed to a seismic intensity of 5 or higher was approximately 3.85 million in the 2018 Osaka Northern Earthquake and approximately 1 million in the other seven earthquakes, which indicates that the earthquakes in relatively rural areas have caused more damage in recent years.

Statistical analysis of earthquakes

Fig. 2 shows the correlations between the number of fatalities and the number of damaged buildings, the number of damaged buildings and the exposed population, and the exposed population and the number of fatalities in earthquakes. No significant correlations were found between the explanatory variables. The correlation between the number of fatalities and the number of damaged buildings by the earthquake is not simply based on the number of damaged buildings in response to the shaking caused by the earthquake. Rather, it also includes the effects of landslides and other factors, which may have contributed to the lack of a significant correlation. Fig. 3 shows the correlation between disaster recovery expenses and (1) the number of dead and missing persons, (2) the exposed population, and (3) the number of totally, half, and partially damaged buildings. The correlation coefficient values were 0.78 and 0.93, respectively, which indicates a strong correlation.

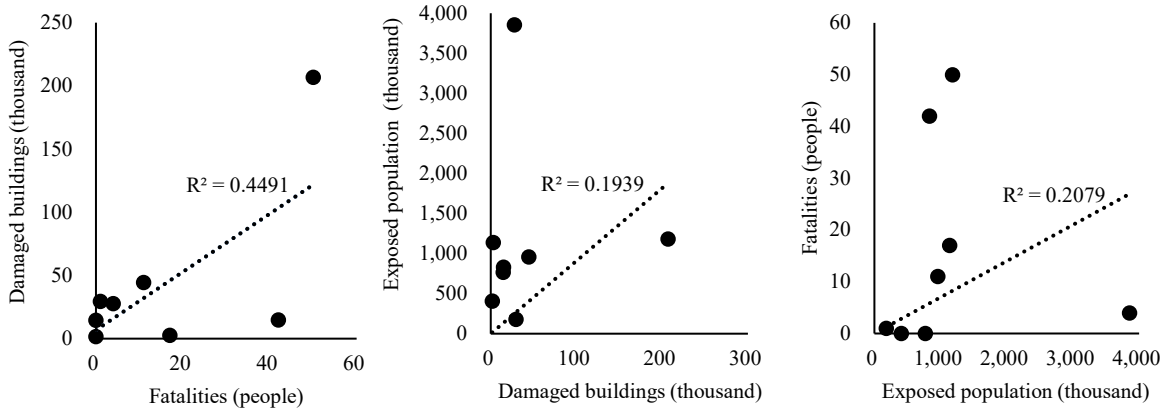

Figure 2. Relationship between damages

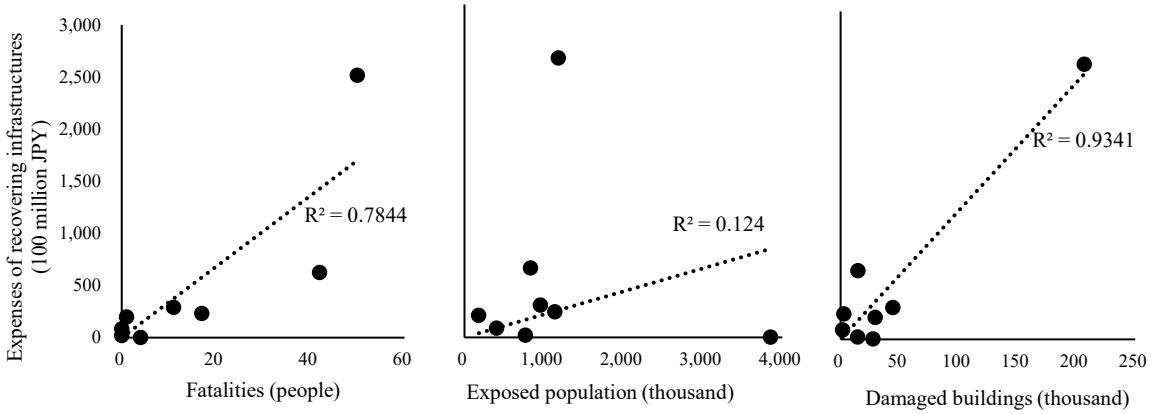

Figure 3. Relationship between disaster recovery expenses caused by earthquakes and damages

Construction of the disaster recovery expenses estimation equation

The explanatory variables used in the equation are the number of fatalities, damaged buildings, and exposed population. Based on the results shown in Fig. 3, the 2016 Kumamoto Earthquake was excluded from the construction of the equation. Consequently, Eq. 1 was derived, and Table 2 lists the statistical analysis results.

$$y = 74.31 + 13.06x_1 - 0.06x_2 + 0.003x_3 \qquad (1)$$

where y is the disaster recovery expenses (100 million JPY), x_1 is the number of dead and missing persons, and x_2 is the exposed population (thousand people), x_3 is the number of totally, half, and partially damaged dwellings.

Table 2. Results of statistical analysis

Numeric category	Constant term	x_1	x_2	x_3
P value	0.105	0.001	0.027	0.069

Seven samples were used, and the coefficient of determination of the adjusted multiple regression, which is an estimating equation with high predictive accuracy, was set to 0.96. Focusing on the p-values for each of the explanatory variables listed in Table 2, the results of the explanatory variables of fatalities and exposed population are statistically significant at a significance level of less than 5 %. Assuming the same number of fatalities, we found that the disaster recovery expenses are low if the damage level (ratio of damaged buildings to the exposed population) is low.

It should be noted that this estimation equation for earthquakes is based on the results of disasters under 50 dead and missing persons, excluding the 2011 Great East Japan Earthquake and Tsunami and the 2016 Kumamoto Earthquake. Fig. 4 shows that the average error is the difference between the actual disaster recovery and estimated expenses calculated to check the accuracy of the equation. The average error calculated using Eq. 2 was approximately 2 billion JPY.

$$E_a = \frac{1}{N}\sum_1^N |Y - y| \qquad (2)$$

where E_a is the average error (100 million JPY), N is the number of disasters analyzed, Y is the actual disaster recovery expenses (100 million JPY), and y is the estimated disaster recovery expenses (100 million JPY).

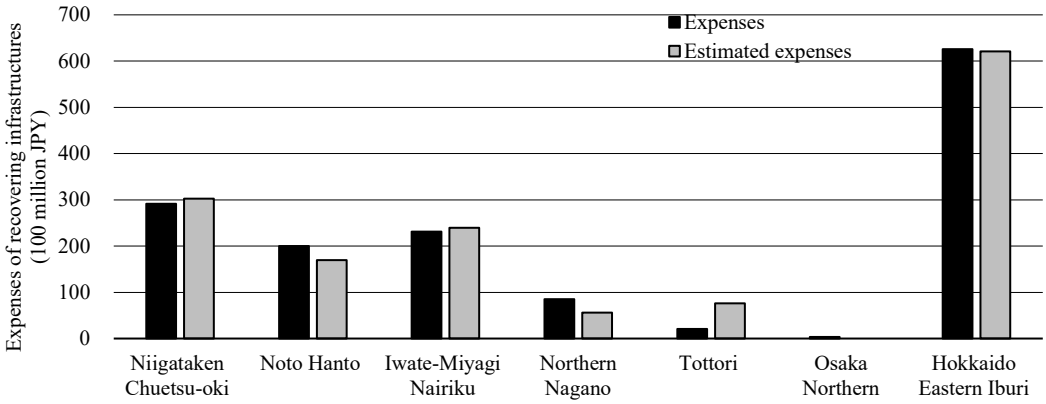

Figure 4. Estimated results for disaster recovery expenses for earthquake disasters

Validation of the estimation equation

Eq. 1 confirmed that the relationship between damage information and disaster recovery expenses is significantly affected by the number of fatalities and damage level. The disaster recovery expenses of the 2004 Niigata-Chuetsu Earthquake, calculated using Eq. 1 and the data in Table 3, were approximately 63.7 billion JPY. However, as of January 7, 2009, it was approximately 112 billion JPY, which results in an underestimation of approximately half of the actual value (Cabinet Office, 2009). The data used for the calculation of the estimation equation refers to earthquake disasters between 2007 and 2018, influenced by the revision of the Seismic Design Edition of the Guidelines for Highway Bridges in 2002 and 2012. The 2004 Niigata-Chuetsu Earthquake was considered a disaster in which damage to infrastructure with insufficient seismic design occurred. A comparison of the disaster recovery expenses of the 2004 Niigata-Chuetsu Earthquake with the disaster recovery expenses in the estimation formula indicated that the disaster recovery expenses in the estimation formula are approximately half of those of the 2004 Niigata-Chuetsu Earthquake. This is because of the small number of samples used in the construction of the earthquake estimation formula, the special characteristics of the 2004 Niigata-Chuetsu earthquake, and the influence of the earthquake-resistant design.

Table 3. 2004 Niigata-Chuetsu Earthquake data

Dead and missing persons	Exposed population (1000 people)	Damaged buildings
16	552	122,667

CONCLUSIONS

In this study, the number of fatalities (dead and missing persons), damaged buildings (totally, half, and partially damaged dwellings), and exposed populations were surveyed. This information was collected by municipalities as part of their post-disaster housing damage assessment work, and its relationship with the disaster recovery expenses of public infrastructure was identified. This study also examined the relationship between the number of fatalities and the number of damaged buildings. The relationships between the number of fatalities, damaged buildings, and exposed population were used as explanatory variables to construct an estimation equation for disaster recovery expenses in the case of earthquakes. Therefore, disasters with high fatalities and damage level tend to cause significant damage to infrastructure facilities. However, the estimation equation for earthquakes was not valid owing to the small sample size. Thus, further studies are required for application in cases other than those analyzed.

The estimation equation was characterized such that it can be used to estimate disaster recovery expenses easily after a disaster occurred. Recently, the concept of disaster resilience, which refers to the recovery of an organization or community and emphasizes the reduction of damage caused by disasters, early commencement of recovery activities, and efficiency of recovery activities, has attracted attention (Komuro, 2018). The equation for estimating disaster recovery expenses is used by local governments for disaster resilience as a part of the disaster reduction measures, considering the hazard and expected damage in the area. In the future, it can be used for disaster resilience assessments at the prefectural level. We will focus on disaster recovery expenses at the prefectural level considering the number of days required for recovery to improve the estimation formula.

ACKNOWLEDGMENTS

We gratefully acknowledge the work of past laboratory members, especially Ms. Hanaka Kato. We would like to thank Editage (www.editage.com) for the English language editing.

REFERENCES

Aota R., Ebara A., Tsukui S., Yamanaka S., and Yamamoto S. (2010). “A Method of the Disaster Recovery and Revitalization Project: Perspectives on the Creation of New Type Subsidies,” *Studies in Disaster Recovery and Revitalization*, 2,117-132.

Cabinet Office (2009). “2004 Niigata-Chuetsu Earthquake,” Available: http://www.bousai.go.jp/kaigirep/houkokusho/hukkousesaku/saigaitaiou/output_html_1/case200404.html. [in Japanese, Accessed: July 2022]

Cabinet Office (2020). “White Paper on Disaster Management,” Available: http://www.bousai.go.jp/kaigirep/hakusho/r02/honbun/3b_6s_09_00.html. [in Japanese, Accessed: July 2022]

Hyogo Earthquake Memorial 21st Century Research Institute (2006). “Research report on financial management of local governments in the 1995 Hyogo-ken Nanbu Earthquake,” Available: https://www.hemri21.jp/contents/images/2019/06/01678c56e4406ec100c83a3f2ddb49e5.pdf. [in Japanese, Accessed: July 2022]

Komuro T. (2018). “Frameworks and Problems of Disaster Resilience Studies,” *Treatises and studies by the Faculty of Kinjo Gakuin University*,14(2),1-12.

Ministry of Land, Infrastructure, Transport and Tourism (2016). “Current status and issues of municipalities in the event of a large-scale disaster,” Available: https://www.mlit.go.jp/river/shinngikai_blog/shityosonshien/dai01kai/pdf/2_genjotokadai.pdf. [in Japanese, Accessed: July 2022]

Ministry of Land, Infrastructure, Transport and Tourism (2010). “The project of restoring infrastructure damaged by natural disasters,” Available: https://www.mlit.go.jp/river/hourei_tsutatsu/bousai/saigai/hukkyuu/ppt.pdf. [in Japanese, Accessed: July 2022]

Ministry of Land, Infrastructure, Transport and Tourism (2022). “Disaster statistics,” Available: https://www.mlit.go.jp/statistics/details/river_list.html. [in Japanese, Accessed: July 2022]

Statistics Bureau of Japan (2005). “Population data from the National Census,” Available: http://www.stat.go.jp/data/kokusei/2005/index.html. [in Japanese, Accessed: July 2022]

Statistics Bureau of Japan (2010). “Population data from the National Census,” Available: http://www.stat.go.jp/data/kokusei/2010/index.html. [in Japanese, Accessed: July 2022]

Statistics Bureau of Japan (2015). “Population data from the National Census,” Available: http://www.stat.go.jp/data/kokusei/2015/kekka.html. [in Japanese, Accessed: July 2022]

Swiss Re Institute (2022). “Natural catastrophes in 2021,” Available: https://www.swissre.com/institute/research/sigma-research/sigma-2022-01.html. [Accessed: July 2022]

RECOVERY MONITORING OF MINAMI-ASO AREA AFTER THE 2016 KUMAMOTO EARTHQUAKE BASED ON REMOTE SENSING DATA

Fumio Yamazaki[1] and Wen Liu[2]
1. Research Fellow, National Research Institute for Earth Science and Disaster Resilience (NIED), Tsukuba, Japan
2. Assistant Professor, Chiba University, Chiba, Japan
Email: fumio.yamazaki@bosai.go.jp, wen.liu@chiba-u.jp

ABSTRACT

The recovery process of Minami-Aso Village from the April 2016 Kumamoto earthquake was monitored using multi-temporal PALSAR-2 data and the results were compared with optical images from Google Earth and our field survey data. Significantly changed areas, such as slope protection works and reconstruction of Aso-Ohashi Bridge and road ways, were recognized from the SAR data because the SAR backscattering intensity increased or decreased significantly for these areas. Thus, remote sensing images are considered useful for monitoring wide areas in a long term after a natural disaster strikes.

Keywords: Synthetic Aperture Radar, Google Earth, UAV, reconstruction, bridges

INTRODUCTION

Information gathering after a natural disaster strike is often hindered by the disruption of road networks and telecommunication systems. Remote sensing technologies have been used to assess the extent and degree of various damages (Dong and Shan, 2013) without accessing the stricken areas. There are mainly two categories of remote sensing: passive (optical and thermal sensors) and active (mainly radar sensors) remote sensing. Optical satellite systems work in the daytime and cannot observe objects under cloud-cover conditions. However, a radar system as Synthetic Aperture Radar (SAR) overcomes this problem and has been used in all-day and all-weather conditions (Dell'Acqua and Gamba, 2012). Both optical and SAR sensors onboard satellites have been used in emergency response to extract heavily affected areas after major earthquakes, such as the 2011 Tohoku earthquake (Liu *et al*., 2013) and the 2015 Gorkha, Nepal, earthquake (Watanabe *et al*., 2016).

Satellite remote sensing can also be used to monitor the recovery and reconstruction processes after major disasters (Ghaffarian *et al*., 2018). Using very high-resolution optical images, Meslem *et al*. (2012) observed the damage situation and recovery of Boumerdes City after the 2003 Algeria earthquake. Hoshi *et al*. (2014) conducted urban recovery monitoring of Pisco City after the 2007 Central Peru earthquake. Hashemi-Parast *et al*. (2017) evaluated the urban reconstruction process of Bam City, Iran, after the 2003 Bam earthquake. These studies used high-resolution optical satellite images because they are easy to understand and different satellite sensors can be used for long-term monitoring.

Satellite SAR sensors are more difficult to use for long-term monitoring because different SAR sensors cannot be used for change detection due to different radar wavelength and spatial resolution. Even using the same SAR sensor, observation conditions are not always the same due to different flight paths and radar incidence angles, and in such cases, the multi-temporal change detection becomes difficult. Another drawback of SAR sensors is their short lifespans. For example, PALSAR sensor onboard ALOS satellite (JAXA, 2022) had been in operation from January 2006 to April 2011. Although PALASAR provided a lot of images before and just after the 2011 Tohoku earthquake, its data could not be used for recovery monitoring. The successor of PALSAR is PALSAR-2 onboard ALOS-2 satellite, which was launched in May 2014 and has been in operation up to now (July 2022). Since PALSAR-2 has higher spatial resolution than PALSAR, the direct comparison of their images is not possible.

For the April 2016 Kumamoto earthquake, the authors conducted damage detection of Mashiki Town, the most heavily affected area in the earthquake using PALSAR-2 data (Liu and Yamazaki, 2017) and Lidar data (Moya *et al*., 2020). The recovery process of Mashiki Town was also monitored using multi-temporal PALSAR-2 data (Yamazaki and Liu, 2022). In this study, the recovery process of Minami-Aso Village, which was hit by strong motion and numerous landslides, is attempted using PALSAR-2 data and the results are compared with optical images and our field investigation data.

THE 2016 KUMAMOTO EARTHQUAKE AND ITS DAMAGES IN MINAMI-ASO VILLAGE

A Mw-6.2 earthquake hit Kumamoto Prefecture in the western Japan on April 14, 2016 at 21:26 (JST). Considerable structural damages and human casualties had been reported due to this event, including 9 deaths. The epicenter was in the Hinagu fault with a shallow depth. On April 16, 2016 at 01:25 (JST), about 28 hours after the first event, another earthquake of Mw 7.0 occurred in the Futagawa fault, closely located with the Hinagu fault. Thus, the first event was called as the "foreshock" and the second one as the "main-shock". A total of fifty (50) direct-cause deaths were accounted by the earthquake sequence, mostly due to the collapse of wooden houses and landslides (Yamazaki and Liu, 2016).

Figure 1 shows the location of the causative faults and Japanese national GNSS Earth Observation Network System (GEONET) stations, operated by the Geospatial Information Authority of Japan (GSI), in the source area. The displacement of 75 cm to the east-northeast (ENE) was observed at the Kumamoto station while that of 97 cm to the southwest (SE) was recorded at the Choyo station in the main-shock. These observations validated the right-lateral strike-slip mechanism of the Futagawa fault. A detailed distribution of coseismic displacements in Mashiki Town was estimated by Moya *et al.* (2017) using the airborne Lidar data acquired before and after the April 16 main-shock.

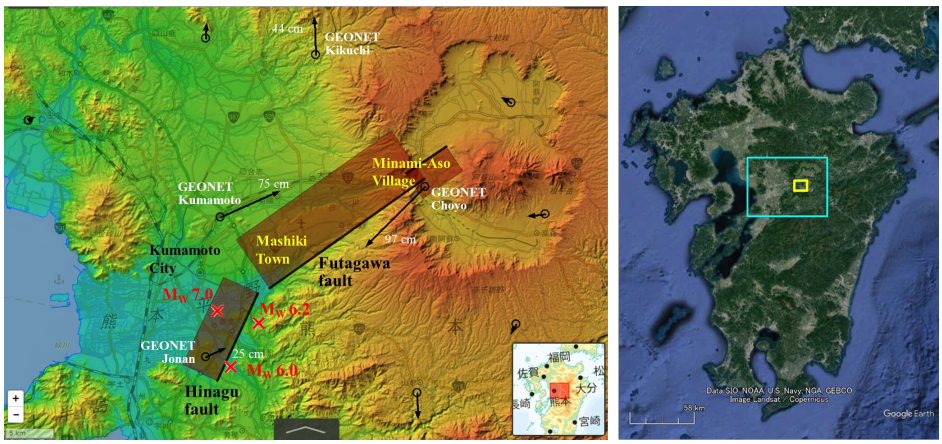

Figure 1. Location of causative faults and GNSS stations in the 2016 Kumamoto earthquake on a GSI map (left) and the extent of the left map (blue square) and Minami-Aso Village (yellow square) in Kyushu Island (right).

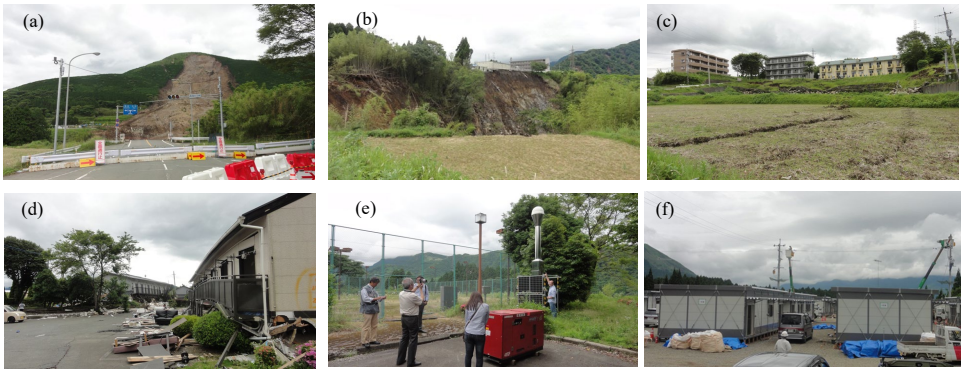

Figure 2. Damage situation of the Minami-Aso Village on June 7, 2016; (a) the largest landslide in Tateno district, (b) a landslide, (c) surface faulting and (d) collapsed apartment buildings in Kawayo district, (e) GEONET station and (f) temporary housing units under construction in Choyo district.

Figure 2 shows the on-site photos of the Minami-Aso Village taken in our field survey on June 6, 2016. The large landside, which caused the collapse of the Aso-Ohashi bridge, and ground failures including surface faulting and collapsed apartment buildings were seen in Kawayo district of the village. Temporary housing units were under-construction near the Choyo GEONET station when we visited.

MULTI-TEMPORAL PALSAR-2 DATA FOR RECOVERY MONITORING

The study area focuses on the heavily affected districts (Tateno and Kawayo) of Minami-Aso Village. Eight pre- and post-event PALSAR-2 data were used in this study as shown in **Figure 3**. These images were taken in the StripMap mode by the HH polarization from the descending path No. 23. The acquisition conditions are also shown in the figure. In order to avoid seasonal changes of vegetation in change detection, the scenes taken in the same month (November) were selected to monitor the recovery process. The image taken two days after the main-shock (2016/4/18) was also included to observe the impact from the event. The SAR data were provided as Level 1.1 data in the slant range, represented by complex I and Q channels to preserve the amplitude and phase information.

The eight datasets were registered in a sub-pixel level before the change extraction. A globally available digital elevation model (SRTM: Shuttle Radar Topography Mission) was used to compensate the image distortion caused by the terrain heights. The datasets were projected to a World Geodetic System (WGS) 84 reference ellipsoid with a resampled square pixel size of 2.5 m. The amplitude information was converted to the backscattering coefficient (sigma naught) in the dB unit, using the calibration factor by JAXA (2022).

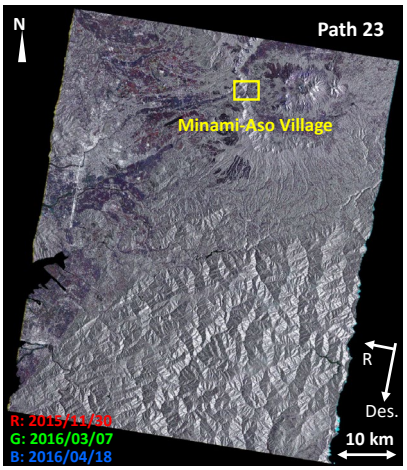

Observation Condition

Off-nadir angle	32.4
Polarization	HH
Ascending node	Descending
Node ID	301
Observation Mode	SM1
Observation Direction	Right
Beam No.	U2-7

Observation Time (UTC)

2015-11-30T03:17:50Z
2016-04-18T03:17:54Z
2016-11-14T03:17:45Z
2017-11-13T03:17:43Z
2018-11-12T03:17:44Z
2019-11-11T03:17:45Z
2020-11-09T03:17:46Z
2021-09-13T03:17:46Z

Figure 3. Color composite of the geo-coded pre- and post-event PALSAR-2 backscattering coefficient images taken from the path 23. The observation year/data/time of 8 PALSAR-2 data and their acquisition condition are also shown in the figure.

Figure 4 shows the study area of a part of Minami-Aso Village, which is located in the western outer rim of the Aso volcanic crater. The area is mostly mountainous, where the Kurokawa river runs from the north to the south and the Shirakawa river from the south to the north. The two rivers merge at the area C in the figure and the mainstream of the Shirakawa river goes to the west to the sea.

Figure 4 (a) shows the color composite of the pre-event (2015/11/30) and post-event (2016/04/18) PALSAR-2 intensity images for the study area. The area is mostly covered by forests, grasslands and agriculture fields. Manmade objects such as buildings and roads are not so clearly recognized in this scale. The difference of the sigma naught values is shown in **(b)**, showing the increase (red) and decrease (blue) of the value. The intensity correlation **(c)** and coherence **(d)** of the two SAR data were also shown in the figure. The both values are large for built-up areas and small for agricultural lands and trees, but it looks difficult to observe the damage situation only from these values. Optical images acquired on 2016/4/15 (e) and 2017/9/2 (f) from Google Earth are also shown in the figure. From the post-event image, numerous landslides and ground failures can be observed in this area.

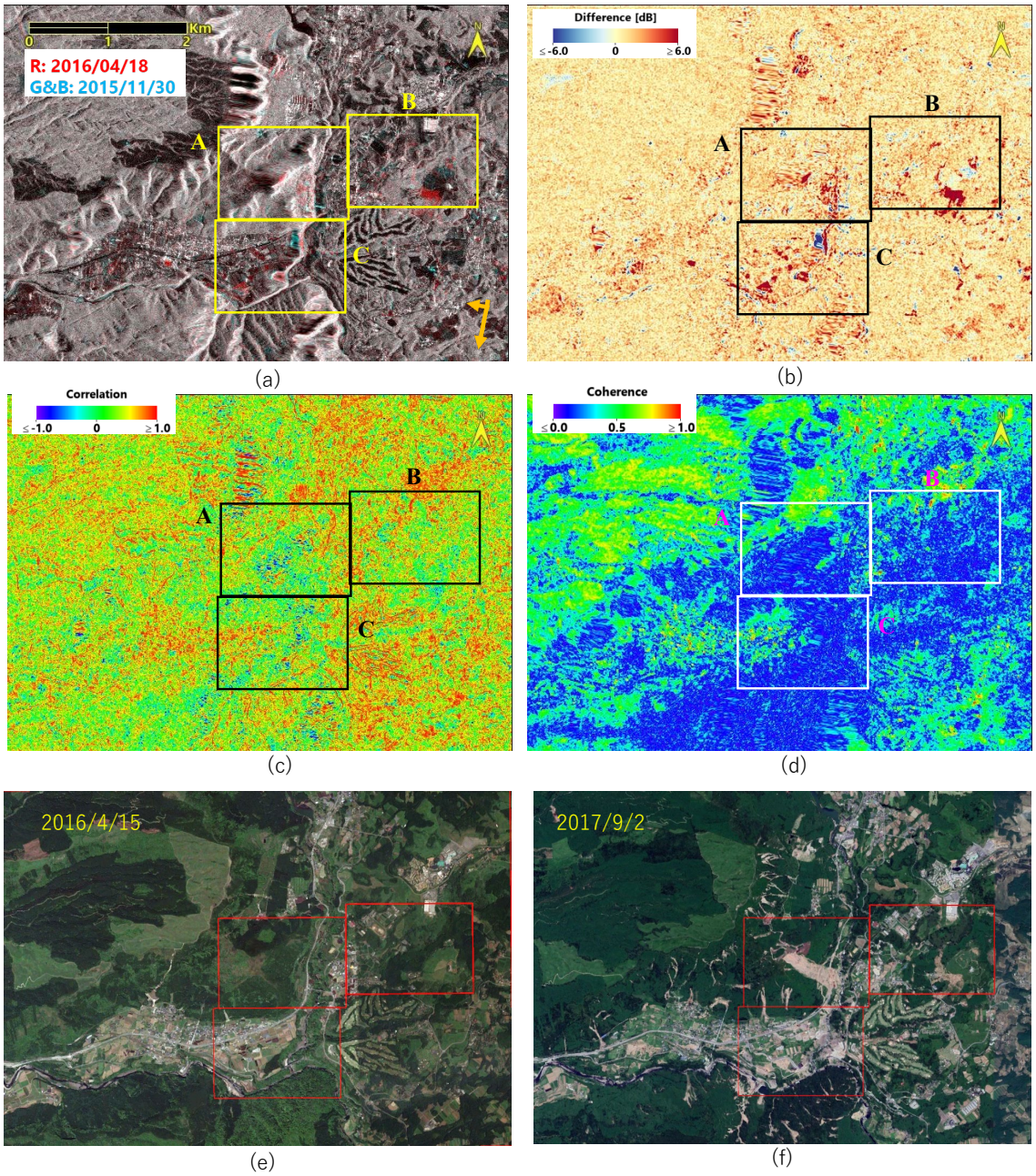

Figure 4. The color composite (a), difference (b), correlation (c), and coherence (d) of the two-temporal PALSAR-2 images (2015/11/30 vs 2016/04/18) for the Minami-Aso area. The optical images from Google Earth on 2016/4/15 (e) and 2017/09/02 (f). The locations of three significantly changed areas are shown by squares (A, B, C).

The recovery process of the Minami-Aso Village was further examined for the three sample areas. **Figure 5** shows the color composite of the two-temporal PALSAR-2 images for three time-spans and the optical images from Google Earth on 2017/9/2, 2018/8/19 and 2020/11/21 for the three sample areas in the Minami-Aso Village.

Area **A** (Tateno landslide) is in the center of the study area, which includes the largest landslide in the 2016 Kumamoto earthquake. By this landslide, Aso-Ohashi bridge (steel arch structure, length: 206m, width: 8 m) fell to the Kurokawa valley (Tanabe *et al.*, 2018). The collapsed bridge is clearly seen in the color composite in cyan colour. After the earthquake, the slope stability works were carried out and the National Highway No. 57 was restored as seen in the optical images. Due to topographic effects, it is difficult to extract recovery process from the SAR color composite images.

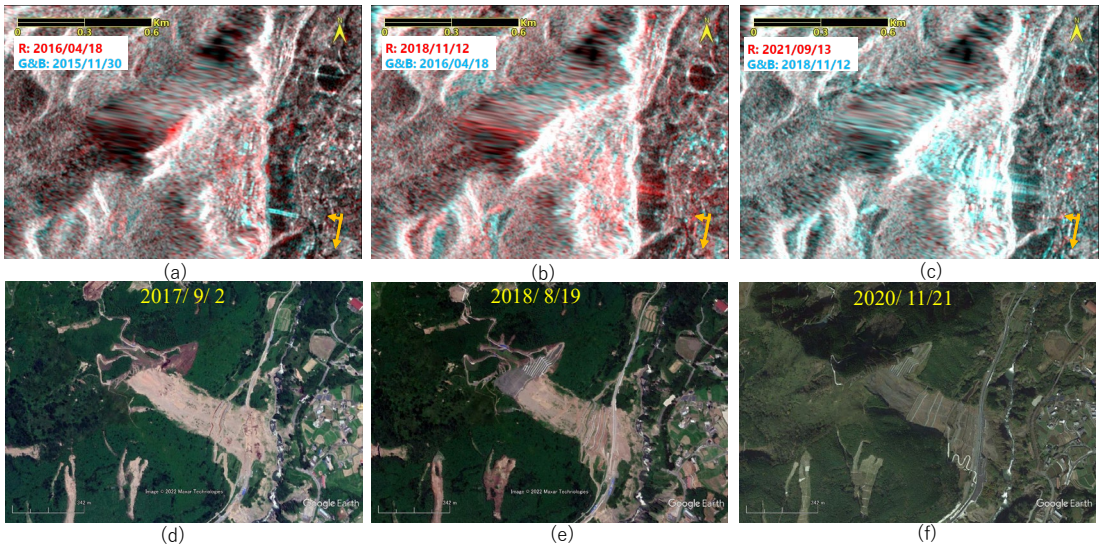

(a) Close-up of Area **A** (Tateno landslide)

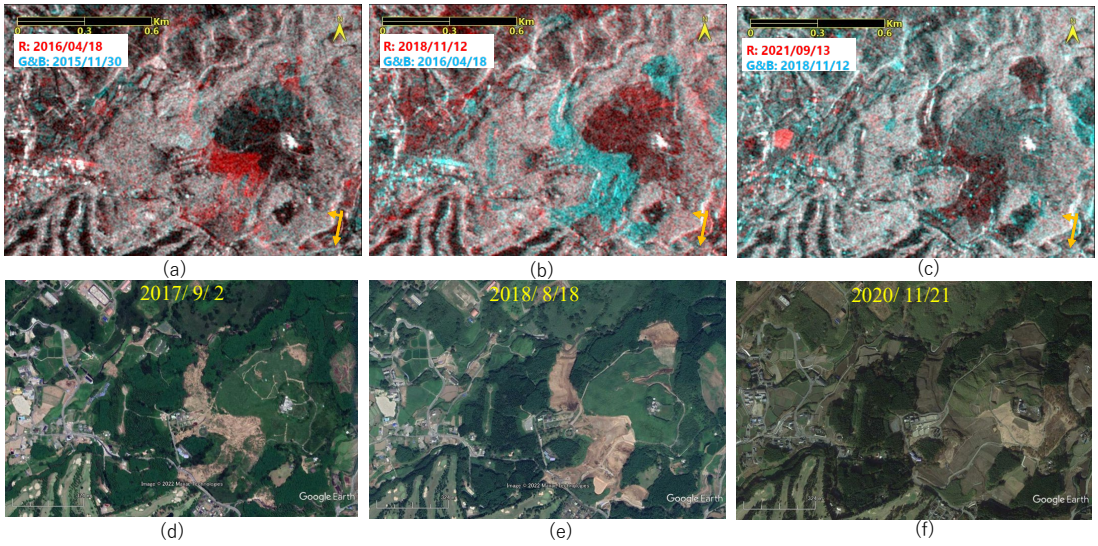

(b) Close-up of Area **B** (Kawayo district)

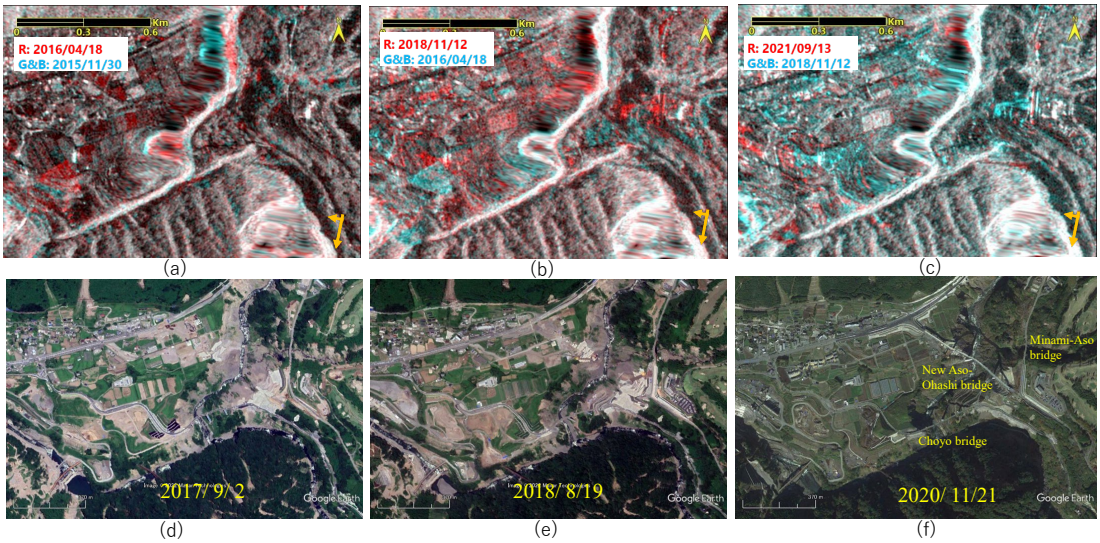

(c) Close-up of Area **C** (Tateno district)

Figure 5. The color composite (a-c) of the two-temporal PALSAR-2 images and the optical images from Google Earth on (d) 2017/9/2, (e) 2018/8/19, and (f) 2020/11/21 for the three sample areas.

Area **B** (Kawayo district) is located on the left bank of the Kurowaka river and has hilly topography. The surface faulting passed through the district (**Fig. 2c**) in the main shock. Due the strong shaking several apartment buildings were totally collapsed (**Fig. 2d**). The school of Agriculture of Tokai University was located here before the earthquake. But the earthquake damage to the university campus was severe, the campus was closed and moved to Kumamoto City after the earthquake. Several large landslides were also triggered by the earthquake and they were clearly seen in the optical images. The landslide areas can be recognized as red color in **(a)** due to increased backscatter and cyan color in **(b)** after the recovery works.

Area **C** (Tateno district) is located on the right bank of the Kurokawa and Shirakawa rivers. Landslides and ground failures were also extensive in the area, as clearly seen in the optical images. In this area, Minam-Aso bridge (steel arch structure, length: 110 m) and Choyo bridge (concrete continuous girder, length: 276m) sustained moderate damage to their abutments and foundations (Tanabe *et al*., 2018). More importantly, the reconstruction of the collapsed Aso-Ohashi bridge started in this area and the New Aso-Ohashi bridge opened for traffic on March 7, 2021. In the color composites of the SAR images, the bridge construction was partially recognized.

FIELD SURVEYS OF MIMANI-ASO VILLAGE AND UAV FILIGHTS

For gathering the damage and reconstruction information of the Minami-Aso Village from the 2016 Kumamoto earthquake, the authors have conducted field surveys of the affected area a total of five times (2016/06/6-7, 07/3-4, 08/8-9, 2021/07/21, 2021/12/23-24). We flew a UAV (DJI Phantom 4) over some affected areas in the survey during 2016/08/8-9 (Yamazaki *et al*., 2017; Cheng *et al*., 2022).

(a) Slope stability works for Tateno landslide

(b) Kawayo district and collapsed Aso-Ohashi bridge

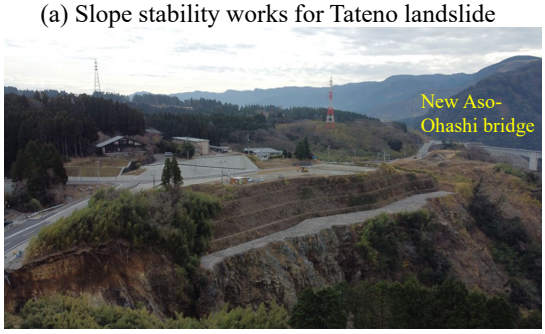

(c) Slope stability works in Kawayo district

(d) Repaired Minami-Aso bridge

(e) New Aso-Ohashi bridge

(f) Choyo bridge under repair works

Figure 6. UAV photos in our field survey (2021/12/23-24) for the areas A and C.

In the field survey during 2021/12/23-24, we also flew a very small UAV (DJI Mini 2, 199 g) form off-road open space. **Figure 6** shows aerial images recorded by a 4K camera, taken from the UAV at the altitude about 30-50 m. Figure **(a)** shows the restoration works of the largest landslide and the reconstructed National Highway No. 57 in Tateno district. **(b)** shows an overview of Kawayo district, where the collapsed Aso-Ohashi bridge still exists. The slope stability works for a landslide in Kawayo (**Fig. 2d**) is seen in **(c)**. The repaired Minami-Aso bridge is shown in **(d)**, the newly constructed Aso-Ohashi bridge in **(e)**, and the Choyo bridge was still under repair works in **(f)**. Aerial survey from UAV is quite useful to monitor the recovery process for wide areas.

CONCLUSIONS

In this study, the damage and recovery process of Minami-Aso Village from the 2016 Kumamoto earthquake was monitored using multi-temporal PALSAR-2 data and the results were compared with optical images from Google Earth and our field survey data. Significant changes such as large landslides and their restoration works were recognized from the SAR data because of the increase or decrease in the SAR backscattering intensity. Although it was not so easy to extract small changes from the change parameters from the SAR intensity data, the constant acquisition of SAR data for a long time is useful to monitor and overview the resilience of affected areas after natural disasters.

ACKNOWLEDGMENTS

The ALOS-2 PALSAR-2 data used in this study are owned by the Japan Aerospace Exploration Agency (JAXA) and were provided through the research program of the satellite image analysis support team (R03) of JAXA. This research was partially supported by JSPS KAKENHI Grant Number 21H01598, Japan.

REFERENCES

Cheng, M.L., Matsuoka, M., Liu, W., Yamazaki, F. (2022). "Near-real-time gradually expanding 3D land surface reconstruction in disaster areas by sequential drone imagery," *Automation in Construction*, 135, 104105, https://doi.org/10.1016/j.autcon.2021.104105.

Dell'Acqua, F., Gamba, P. (2012). "Remote sensing and earthquake damage assessment: Experiences, limits, and perspectives." *Proceedings of the IEEE*, 100 (10): 2876-2890.

Dong, L., Shan, J. (2013). "A comprehensive review of earthquake-induced building damage detection with remote sensing techniques," *ISPRS Journal of Photogrammetry and Remote Sensing*, 84: 85–99, http://dx.doi.org/10.1016/j.isprsjprs.2013.06.011

Ghaffarian, S., Kerle, N., Filatova, T. (2018). "Remote sensing-based proxies for urban disaster risk management and resilience: a review," *Remote Sensing*, 10, 1760; doi:10.3390/rs10111760

Hashemi-Parast, S.O., Yamazaki, F., Liu, W. (2017). "Monitoring and evaluation of the urban reconstruction process in Bam, Iran, after the 2003 Mw6.6 earthquake," *Natural Hazards*, 85(1): 197-213, doi: 10.1007/s11069-016-2573-9

Hoshi, T., Murao, O., Yoshino, K., Yamazaki, F., Estrada, M. (2014). "Post-disaster urban recovery monitoring in Pisco after the 2007 Peru earthquake using satellite image," *Journal of Disaster Research*, 9(6): 1059-1068, doi: 10.20965/jdr.2014.p1059

Liu, W., Yamazaki, F., Gokon, H., Koshimura, S. (2013). "Extraction of tsunami-flooded areas and damaged buildings in the 2011 Tohoku-Oki Earthquake from TerraSAR-X intensity images," *Earthquake Spectra*, 29(S1): S183-S200.

Liu, W., Yamazaki, F. (2017). "Extraction of collapsed buildings due to the 2016 Kumamoto earthquake based on multi-temporal PALSAR-2 data," *Journal of Disaster Research*, 12(2): 241-250, doi: 10.20965/jdr.2017.p0241

Meslem, A., Yamazaki, F., Maruyama, Y., Benouar, D., Kibboua, A., Mehani, Y. (2012). "The effects of building characteristics and site conditions on the damage distribution in Boumerdes after the 2003 Algeria earthquake," *Earthquake Spectra*, 28(1): 185–216, doi: 10.1193/1.3675581

Moya, L., Yamazaki, F., Liu, W., Chiba, T. (2017). "Calculation of coseismic displacement from lidar data in the 2016 Kumamoto, Japan, earthquake," *Natural Hazards and Earth System Sciences*, 17: 143-156, https://doi.org/10.5194/nhess-17-143-2017

Moya, L., Mas, E., Yamazaki, F., Liu, W., Koshimura, S. (2020). "Statistical analysis of earthquake debris extent from wood-frame buildings and its use in road networks in Japan," *Earthquake Spectra*, 36(1): 209-231, https://doi.org/10.1177/8755293019892423

Japan Aerospace Exploration Agency (JAXA) (2022). ALOS Research and Application Project. https://www.eorc.jaxa.jp/ALOS/en/index_e.htm

Tanabe, R., Yamazaki, F., Liu, W. (2018). "Damage analysis of landslides and bridges in Minami-Aso village due to 2016 Kumamoto earthquake using full-polarimetric airborne SAR images," *Proc. 39th Asian Conference on Remote Sensing*, Kuala Lumpur, Malaysia, 1545-1553.

Yamazaki, F., Liu, W. (2016). "Remote sensing technologies for post-earthquake damage assessment: A case study on the 2016 Kumamoto earthquake," *Proc. of 6th Asia Conference on Earthquake Engineering*.

Yamazaki, F., Kubo, K., Tanabe, R., Liu, W. (2017). "Damage assessment and 3D modeling by UAV flights after the 2016 Kumamoto," Japan earthquake, *Proc. of 2017 IGARSS*, 3182-3185.

Yamazaki, F., Liu, W. (2022). "Monitoring of the recovery and reconstruction process after the 2016 Kumamoto earthquake based on multi-temporal remote sensing data," *Proc. of the 3rd European Conference on Earthquake Engineering & Seismology*, Bucharest, Romania.

Watanabe, M., Thapa, R.B., Ohsumi, T., Fujiwara, H., Yonezawa, C., Tomii, N., Suzuki, S. (2016). "Detection of damaged urban areas using interferometric SAR coherence change with PALSAR-2," *Earth Planets and Space*, 68 (131), https://doi.org/10.1186/s40623-016-0513-2

STUDY ON PRE-EVENT COMMUNITY-BASED RECOVERY PLANNING FOR THE EARTHQUAKE MITIGATION IN JAPAN

Pei-Chun Shao[1] and Shyh-Yuan Maa[2]
1. Professor, Department of Land Management and Development, Chang Jung Christian University, Tainan, Taiwan, R.O.C.
2. Associate Professor, Department of Urban Planning and Disaster Management, Ming-Chuan University, Taipei, Taiwan, R.O.C.
Email: peicshao@mail.cjcu.edu.tw , swyrmars@mail.mcu.edu.tw

ABSTRACT

Past earthquake disaster experience in Japan has caused disasters and impacts on cities. More specific examples include the Great Hanshin Earthquake in Japan and the Great East Japan Earthquake. A large number of collapses were caused by insufficient earthquake resistance in areas with dense old houses, and a large number of wooden buildings were burnt down due to local urban fires. Due to the destruction of a large number of buildings and houses, the victims have lived in the shelter for too long, and there is not enough space in urban areas to build modular houses to accommodate the victims. The victims are mostly low-income elderly people living in the shelter for a long time, resulting in loneliness and other problems; at the same time, the community foundation Industries, shopping streets, markets, etc. collapsed and burned down, and large areas of the city must be rezoned and reconstructed. This also prevents residents from returning to the original community for life reconstruction, which affects the efficiency of urban area reconstruction. Based on this, Japan has actively promoted pre-disaster community recovery planning since the Hanshin Earthquake. Through table-top exercise and disaster recovery imagery, people have been able to think about the reconstruction of communities and households before the earthquake. Through the analysis of Japanese experience, the focus of the promotion model is to focus on the community environment, simulate the disaster situation, improve the professionalism of public sector staff, and integrate live making issues. At the same time, it also provides reference for the seismic reinforcement of old residential buildings in the region or community and how to improve efficiency.

Keywords: community-based recovery planning, earthquake-mitigation planning, resilience

INTRODUCTION

From the experience of earthquake, such as the Hanshin-awaji great earthquake in 1995, the Chi-Chi earthquake in 1999 and the great east Japan earthquake in 2011, the same characteristics in the damaged areas were most old buildings lacking of seismic collapsed, destroyed life infrastructure for long-term recovery, urban areas lacking of spatial for temporary housings, most areas needed land regeneration, isolated death issues related to the elderly people and so on. The complex recovery issues occurred after great earthquake, and this would affect the recovery speed in the post-earthquake reconstruction go smoothly or not. To face such kinds of problems, how to recovery efficiently in the damaged areas or cities becomes a big issue after great earthquakes.

Based on the claim in the world conference on disaster risk reduction, to keep reduce disaster risk, to invest the mitigation behavior before disaster, and to strengthen the resilience of nations and communities not only for emergency response but also for building back better from the disaster would be necessary in the disaster management planning (United Nations, 2015). Especially for the post-earthquake recovery, to take consideration on recovery plan in advanced before the earthquake become more and more important in Japan recently. In order to grasp the mechanism of pre-event recovery

planning in the communities, this study tried to analyze the cases recently in Japan. The experience from Japan would be taken as reference for Taiwan.

LITERATURE REVIEW

Definition of Post-disaster and Pre-event Recovery

UNISDR defined the post-disaster recovery as the decision making or action after the disasters to reduce risks occurred followed the disasters (International Strategy for Disaster Reduction, 2005). Quarantelli pointed out that most recovery actions related to reconstruction, restoration and rehabilitation. The post-disaster recovery could build the damaged areas back to the same living level or higher one before disaster. To compare to post-disaster recovery, pre-event recovery means planning recovery based on the possible post-disaster issues or needs from a mitigation viewpoint before occurrence of disaster. The purpose of pre-event recovery planning is to strengthen the efficiency of post-disaster recovery to meet the goals of recovery to improve the results of reconstruction. Pre-event recovery plan also could establish the vision for development of areas (National Firefighting Agency, 2017). Thus, in FEMA of U.S. and Japan, promoting the pre-event recovery planning to reduce the crisis of post-disaster recovery plan recently become a trade recently.

Stages and Contents of Post-disaster Recovery

Through the literatures related to post-disaster recovery, the stages and time of post-disaster recovery would be different due to the scale of the disasters. It is usually defined the first 24 hours as emergency response period, and to seek for evacuating life as period of temporary settle down (Pei-Chun Shao, 2003a). According to the scale of the disasters, following temporary settle down, returning to the original living quality and building the damaged areas better as period of reconstruction would happen. The issues and key points for each stage after disaster are shown in Table 1 as follows.

Table 1. Key points and issues in stages of post-disaster recovery

Stage of recovery	Key points of works	Characteristics
Emergency response	Urgent relief, recovery of public facilities, decision making and so on	Live saved, Basic life required
Settle down	Temporary housing	Needs for living
Recovery	Living environment equipped	Needs for living, working of social system
Reconstruction	Living rehabilitation, mitigation	Strengthening whole environmental quality

Source: Pei-Chun Shao, 2003a

Stakeholders for Post-disaster Recovery

From personal recovery to communities' reconstruction, several kinds of problems would be faced such as housing, living environment, industry, culture and so on. Thus, many post-disaster works need to be cooperated or to be empowerment by specialists, NGOs, local governmental officers and residents. The basic concept of community-based empowerment for post-disaster recovery is the bottom-up mechanism not only to consider community's construction but also to build the software related to welfare, education, health and so on (Pei-Chun Shao, 2003b). The factors related to community-based empowerment for post-disaster recovery include leadership of recovery organizations, communicating

and participating with residents, variety of recovery issues and extension, institutional permission and funding supporting.

ANALYSIS OF PRE-EVENT COMMUNITY PLANNING IN JAPAN

Through the experience of Great Hanshin-awaji Earthquake in 1995, most victims were elderly people and economy-weak householders. Thus, the isolated death of the elderly people without protecting living to prevent living recovery became a big issue after the earthquake. Besides, the economic weakness of householders had to leave the damaged area becoming an obstacle to community and local areas' reconstruction, and slim chance of achieving the vision of urban recovery. The reconstruction after Hanshin-awaji Great Earthquake took almost 20 years to reach the living level equaling to level before earthquake. In the case of Great East Japan Earthquake in 2011, most people evacuated to other prefectures, such as residents would not like to return to the communities for reconstruction due to the nuclear disaster in Fukushima prefecture. Therefore, the goals of community recovery and the vision of urban reconstruction have close relationship with living supporting after the earthquake. Based on the experience of post-earthquake recovery recently, the local governmental officers, urban planning specialists and scholars began to promote the pre-event recovery planning to consider the recovery tasks before the earthquake to reduce the difficulties in the recovery to make post-earthquake reconstruction implement smoothly in the future. This section would analyze the experience of pre-event recovery plan for communities in the periods of the Great Hanshin-awaji Earthquake and the Great East Japan Earthquake.

Period of Great Hanshin-awaji Earthquake

Many problems and crisis occurred related to evacuating life, community recovery and urban reconstruction. Thus, how to equip the long-term evacuating living, to make the decision related to the housing and urban reconstruction become important issues after a mega earthquake (Ministry of Land, Infrastructure, Transport and Tourism, 2018). The metropolitan of Tokyo and prefecture of Shizuoka proposed the manual of urban reconstruction to practice the public sectors' officers grasping the recovery main affairs related to different stages after the earthquake. Simultaneously, through the survival camp of earthquake, the residents participated in the recovery to discuss the possible issues in post-earthquake reconstruction in the temporary blocks. Besides, the urban-disaster scholars also tried to dig out the issues related to pre-event recovery planning from the workshops and imaging games (Ministry of Land, Infrastructure, Transport and Tourism, 2017). In this period, issue-driven simulation of recovery and imaging-game-based cooperation with the public- private sectors were proposed.

Issue-driven simulation of recovery

Yoshigawa pointed out the conflicts occurred among the vision of urban reconstruction, living rehabilitation and community recovery. Thus, how to make the consensus of urban-reconstruction vision and living rehabilitation, it is necessary to adopt the viewpoint for pre-event-recovery simulation (Yoshigawa Tadahiro, 2007). The procedures of pre-event-recovery simulation are as follows:

1. Step 1 "to grasp the local recovery issues": based on the damaged situation after the earthquake, to build the recovery-issue map to consider the necessity of local regeneration.
2. Step 2 "to image living rehabilitation": to propose the problems of living rehabilitation after a earthquake by role playing to generalize the living issues. Through the discussion to establish the pre-event solving methodology and routes.
3. Sept 3 "to consider the changes and spatial arrangement in urban areas according to the time span": to consider the spatial arrangement and influence by imaging the different recovery-stage after a earthquake. The model could be used in various blocks to seek for the vision of urban space.
4. Step 4 "to make the recover plan for the communities": through the participating of residents, specialists and the public sectors to make decision on the basic structure and contents of recovery plan for the communities to complete the spatial arrangements related to land using and urban planning.

Imaging-game-based cooperation with the public- private sectors

Ichiko and Nakabayashi suggested that the pre-event recovery workshop could applied for the residents participating to discuss the works in the post-earthquake local reconstruction. Simultaneously, to take reference to the "Manual of post-earthquake reconstruction for Tokyo Metropolitan", the local governmental officers also attended the workshop for simulation practice (Ichiko Taro and Nakabayashi, 2006). Under the hypothesis of earthquake was earthquake intensity 7 within 300 ha urban areas, the local government had to set up the reconstruction headquarter in a week after the earthquake to invest the damaged areas and to draw the housing-damaged maps. The main tasks for practicing were to divide the damaged areas into four types according to the damaged level, building restriction and time span which were key areas for reconstruction, promoting recovery areas, recovery leading areas and general areas. Through the practice, the officers learned to make the recovery goals for damaged areas, to decide the rules for arranging the facilities in the urban space and to establish the methodology or skill for implementing recovery.

Period of Great East Japan Earthquake

Through the questionnaire conducted in 2014 to the local governments suffered in the Great East Japan Earthquake, the recovery issues mainly focused on "the damaged areas needed to be corrected according to the changes of residents' living rehabilitation", "the scale and function for the points of recovery needed to be long-tern examined" and "the officers in the damaged areas unfamiliar to the affairs of recovery". Thus, the main tasks in pre-event recovery planning are related to establish the institution for reconstruction and to cultivate human resource. After the Great East Japan Earthquake, the pre-event recovery planning for communities adopted the model with thinking of scenario-based needs of recovery under time span.

Scenario-based Time-space Supporting Model

After the Great East Japan Earthquake, the scholars from university of Tokyo developed the pre-event recovery imagination training to combine living rehabilitation with urban reconstruction. The concept based on both speeding the personal living rehabilitation and rebuilding better urban environment at the same time. The procedures are: "to set the scenario of damage in the earthquake", "to decide the damaged areas and householders", "to discuss the needs both for personal living rehabilitation and urban reconstruction", and "from the viewpoint of living rehabilitation to verify the issues related to living rehabilitation with urban reconstruction" (Tokyo Metropolitan, 2015). Through model, the compatibility between supporting strategies for living rehabilitation and styles of urban reconstruction could be examined to adjust to meet the goals and vision for local reconstruction. (Kato Takaaki and Nakamura Hitoshi, 2011)

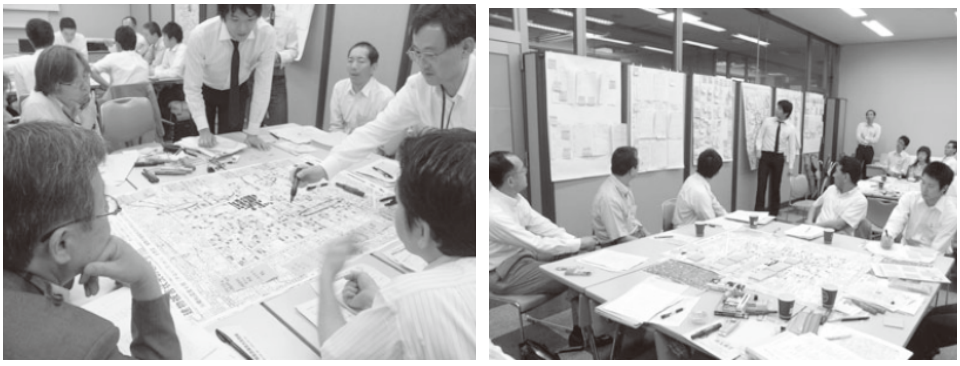

Source: Kato Takaaki and Nakamura Hitoshi, 2011

Figure 1 The workshop for pre-event recovery planning for the local governmental officers.

Land-using-based Recovery Imagination Training

After the Great East Japan Earthquake, to the post-earthquake problems of land using, the scholars planned to seek for recovery strategies to examined. The purposes are to let the local governmental officers realize how to equip for recovery, and to make the residents participate in the recovery planning

and know the needs for rehabilitation in advanced. The Figure showed the results of training for pre-event recovery planning in different types of urban communities by the Tokyo Metropolitan (Tokyo Metropolitan, 2016)). Through the figure, the officers and the residents could discuss the issues under time span in different recovery stages. Such kind of training could also accumulate the resilience for the communities and local areas.

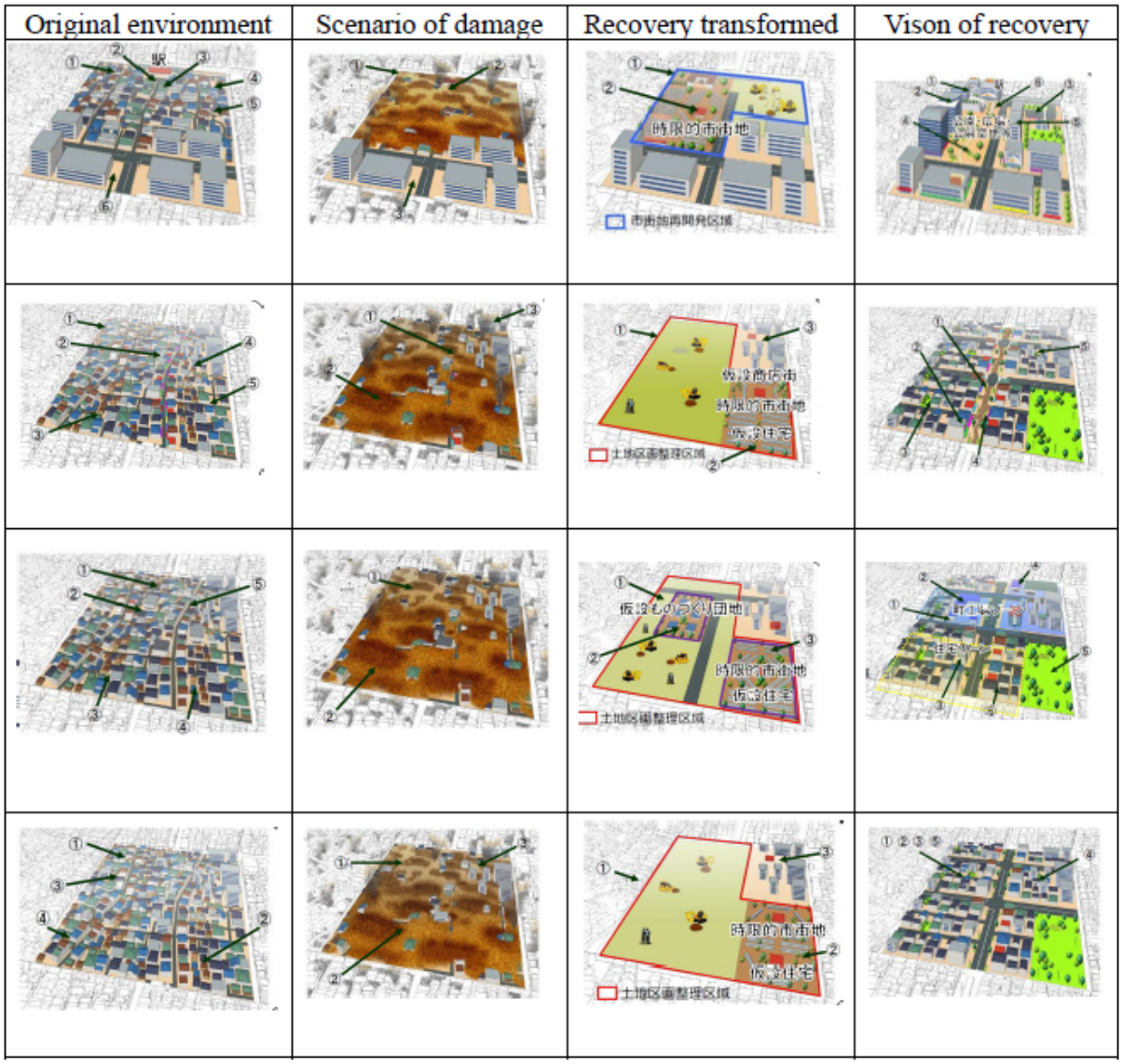

Source: Tokyo Metropolitan, 2016

Figure 2. Training for Pre-event recovery planning.

CONCLUSIONS

Through the experience of pre-event recovery plan practice in Japan, the Ministry of Land, Infrastructure, Traffic and Tourism established the manual to promote the mechanism of pre-event recovery planning to accumulate the resilience from the viewpoint of mitigation. From the models developed by different scholars, the key points of implementation are as follows:

1. Community-based operation: through the communicating with specialists, officers and the residents in the community, the equipped pre-event recovery plan could be the basis for improving environment of the community to reduce the destroyed risks from the disasters.
2. Scenario-based consideration: under the scenario of damage, the organizations of the community and urban reconstruction could be discussed to propose the concrete works related to reconstruction.
3. Concrete training and participating for the public officers: the pre-event recovery training could let

the officers realize the affairs of post-earthquake recovery. Besides, it is helpful for the officers to grasp the issues of recovery and implement the reconstruction plan efficiently.

4. Not only local hardware construction but considering needs for living rehabilitation: to combinate the urban reconstruction with living rehabilitation of residents, it would reduce the conflicts of living and housing to support several types of recovery for the householders.

In Taiwan, the community-based disaster management exercise run many years, and the resilient community also proposed to implement recently. In the resilient community, the pre-event recovery planning is also adopted. The experience of pre-event recovery planning in Japan could be taken as reference in the future. Especially for the old block or areas in the urban cities, the seismic-performance issues for the old buildings could be improved through the discussing via pre-event recovery planning. To meet the different needs for recovery of the residents, the acceptable seismic reinforcement with living rehabilitation could be equipped to strengthen the local safety.

ACKNOWLEDGMENTS

This study was found by the research project: MOST109-2625-M-309-003. The authors would express their gratitude to the Ministry of Science and Technology (Reorganized as National Science and Technology Council).

REFERENCES

United Nations (2015), Sendai Frame work for Disaster Risk Reduction 2015-2030.

International Strategy for Disaster Reduction (2005), Hyogo Framework for Action 2005-2015: building the resilience of nations and communities to disasters, World Conference on Disaster Reduction 18-22 January 2005, Kobe , Hyogo, Japan.

National Firefighting Agency (2017), The third reinforcement disaster management plan, Taipei, Taiwan (Chinese Version)

Pei-Chun Shao (2003a), Mechanism of post-earthquake community reconstruction, Journal of urban planning Vol.30(4), pp.371-389, Taiwan. (Chinese version)

Pei-Chun Shao (2003b), The comparative research on the Housing Reconstruction in Chi-Chi Earthquake of Taiwan and Great Hanshin-awaji Earthquake of Japan, MOIS 921012, Taipei, Taiwan. (Chinese version)

Ministry of Land, Infrastructure, Transport and Tourism (2018): The guideline for pre-event urban reconstruction plan, Tokyo, Japan (Japanese version)

Ministry of Land, Infrastructure, Transport and Tourism (2017), Manual of imagination training for urban reconstruction, Tokyo, Japan. (Japanese version)

Tokyo Metropolitan (2015), Manual of pre-event urban reconstruction, Tokyo, Japan. (Japanese version)

Tokyo Metropolitan (2016), The countermeasure of pre-event reconstruction, Tokyo, Japan. (Japanese version)

Yoshigawa Tadahiro (2007), Pre-event recovery and issues from the lessons of the disasters, Guidance of Urban Reconstruction, pp.66-75, Tokyo, Japan. (Japanese version)

Ichiko Taro and Nakabayashi Itsuki (2006), Disaster imagination in urban reconstruction for pre-event reconstruction planning, Journal of Japan Institution of Urban Planning, No.11-3, pp. 607-612, Japan. (Japanese version)

Kato Takaaki and Nakamura Hitoshi (2011), The scenario and issues of urban recovery from the development of imagination training for pre-event urban recovery, Research and Production Vol.63(4), pp. 109-118, Japan. (Japanese version)

(8b) Intersection of earthquake engineering with social justice

THE EVOLUTION OF TAIWAN EARTHQUAKE INSURANCE CLAIMS MECHANISM FOR BUILDING DAMAGE CAUSED BY SOIL LIQUEFACTION

Hsuan-Chih Yang[1], Che-Yu Chang [2], Chih-Chieh Lu [3], Jin-Hung Hwang [4], Yu-Ying Lin [5]

1. Associate Researcher, Earth Sciences and Geotechnical Engineering Division, National Center for Research on Earthquake Engineering, Taipei, Taiwan, R.O.C.
2. Assistant Researcher, Earth Sciences and Geotechnical Engineering Division, National Center for Research on Earthquake Engineering, Taipei, Taiwan, R.O.C.
3. Research Fellow, Earth Sciences and Geotechnical Engineering Division, National Center for Research on Earthquake Engineering, Taipei, Taiwan, R.O.C.
4. Professor, Department of Civil Engineering, National Central University, Taoyuan, Taiwan, R.O.C
5. Research Assistant, Earth Sciences and Geotechnical Engineering Division, National Center for Research on Earthquake Engineering, Taipei, Taiwan, R.O.C.

Email: hcyang@narlabs.org.tw, cheyu@narlabs.org.tw, chchlu@narlabs.org.tw, hwangjin@ncu.edu.tw, yylin@narlabs.org.tw

ABSTRACT

Taiwan is located in the seismic belt around the Pacific Ocean, at the junction of the Eurasian plate and the Philippine plate. Therefore, Taiwan is rich in geographical features such as mountains, forests, basins, plains, and bays. It also has geological features such as alluvial and backfill that are prone to soil liquefaction. When a catastrophic earthquake occurs, it is accompanied by great social impact and economic losses. The 921 Chi-Chi earthquake in 1999 was the largest destructive earthquake ever recorded in Taiwan. It also began to develop residential earthquake insurance in Taiwan and established a benchmark for total loss appraisal of buildings. The insurance claim evaluation criteria design before upgrade is mainly aimed at the damage caused by the earthquake to the destruction of the beams, columns and wall or the excessive displacement between floors. There is no clear indicator for the damage of residential buildings due to soil liquefaction. This study develops earthquake insurance claim criteria for building damage caused by soil liquefaction in Taiwan. Considering other international practices, current building codes in Taiwan, and existing building conditions, guidelines and indices, settlement and tilt were added to the current criteria. This study divides the claims evaluation and judgment into three parts: total loss claims, professional appraisal, and non-claims for minor damages. Based on conservativeness and reference to Japanese insurance regulations, the suggested criteria in this study has been accepted by Taiwan Residential Earthquake Insurance Fund (TREIF) with a slight adjustment.

Keywords: earthquake insurance, soil liquefaction, damage assessment

INTRODUCTION

Taiwan is located in the seismic belt around the Pacific Ocean, at the junction of the Eurasian plate and the Philippine plate. Therefore, Taiwan is rich in geographical features such as mountains, forests, basins, plains, and bays. It also has geological features such as alluvial and backfill that are prone to soil liquefaction. When a catastrophic earthquake occurs, it is accompanied by great social impact and economic losses. The 921 Chi-Chi earthquake in 1999 was the largest destructive earthquake ever recorded in Taiwan. According to statistics from the Fire Department of the Ministry of the Interior, the economic and property damage caused by Chi-Chi earthquake which caused a total of 2,454 deaths, 50 missing and 11,305 injuries is ranked 13th among the earthquake disasters in the world. After the earthquake, it also began to develop residential earthquake insurance in Taiwan and established a benchmark for total loss appraisal of buildings.

In the Meinong Earthquake on February 6, 2016, Tainan, the damage patterns of buildings that can be observed in Figure 1 are obviously different. One is the structural system damage of the building due to insufficient seismic design capacity, or weak floors caused by secondary construction (Figure 1a). The damage assessment of such buildings usually focuses on the damage ratio of main structural systems such as beams, columns, and load-bearing walls. The calculation is also the current appraisal standard of the earthquake insurance. The other is that the structure of the building is intact, but it is damaged due to terrestrial disasters such as soil liquefaction (Figure 1b). This phenomenon will cause the building to sink or tilt but the internal beams and columns will not be damaged.

The insurance claim evaluation criteria design is mainly aimed at the damage caused by the earthquake to the destruction of the beams, columns and wall or the excessive displacement between floors. There is no clear indicator for the damage of residential buildings due to soil liquefaction. Therefore, it is an important issue to establish the definition and identification criteria of total loss of buildings exclusively for soil liquefaction disasters.

(a)Structural damage (b)Building settlement by soil liquefaction

Figure 1. The damage model of buildings in 20160206 Meinong earthquake

THE EVOLUTION OF INSURANCE CLAIM EVALUATION CRITERIA

The main insurance coverage for earthquake disasters in Taiwan is that buildings collapse or become uninhabitable due to earthquakes or earthquake-induced fires, explosions, ground subsidence, cracks, breaches, etc. When the house is judged as a total loss due to the earthquake, each household can receive up to NTD $1.5 million in compensation and $0.2 million in temporary accommodation costs. There are two criteria for the assessment of total loss of buildings. One is the damage of residential buildings is "unable to live and must be demolished and rebuilt", and the another is the damage of residential buildings is "uninhabitable without repairs and the repair cost is more than 50% of the replacement cost when the danger occurs". The definition of "uninhabitable and must be demolished and rebuilt" is that the building collapses as a whole or partially collapses, and the overall inclination rate of the building or the inclination rate of some floors of the building is more than 1/30.

The ratio of the repair cost to the reconstruction cost is usually called the story repair cost ratio (SRCR) or the local repair cost ratio (LRCR). The reconstruction cost is estimated based on the current price index, while the repair cost is calculated using the following steps.

Step 1: The story damage factor (SDFj) for each story is computed as:

$$SDF_j = \frac{w_C \frac{\sum_{i=1}^{n_C} DF_{C,i}}{n_C} + w_B \frac{\sum_{i=1}^{n_B} DF_{B,i}}{n_B} + w_W \frac{\sum_{i=1}^{n_W} DF_{W,i}}{n_W}}{w_C + w_B + w_W} \quad (1)$$

where

$$w_C \frac{\sum_{i=1}^{n_C} DF_{C,i}}{n_C} = \frac{0.1 \times C_I + 0.2 \times C_{II} + 0.3 \times C_{III} + 0.65 \times C_{IV} + C_V}{C} \quad (2)$$

$$w_B \frac{\sum_{i=1}^{n_B} DF_{B,i}}{n_B} = \frac{0.1 \times B_I + 0.2 \times B_{II} + 0.3 \times B_{III} + 0.65 \times B_{IV} + B_V}{B} \quad (3)$$

$$w_W \frac{\sum_{i=1}^{n_W} DF_{W,i}}{n_W} = \frac{0.1\times W_I + 0.2\times W_{II} + 0.3\times W_{III} + 0.65\times W_{IV} + W_V}{W} \quad (4)$$

in which

(1) C, B, and W indicate the total structural components of column, beam, and wall, respectively

(2) wC = wB = wW = 1

(3) i = the ith component; j = the jth floor

(4) n = the total count or length of the corresponding component on the jth floor

(5) DF = damage factor (0.1, 0.2, 0.3, 0.65, and 1 for damage levels I, II, III, IV, and V, respectively)

(6) CI to CV, BI to BV, and WI to WV are the counts for damage levels I, II, III, IV, and V, respectively

Step 2: The maximum value of SDFj is taken as the story damage factor, SDF. If SDF is greater than 0.4, the damage is severe and "SRCR > 85%" is recorded; otherwise, Step 3 is implemented.

Step 3: SRCR is computed from SDF as follows:

$$SRCR(\%) = -5.2171 \times \mathrm{SDF}^2 + 4.2401 \times SDF - 0.051\,, \quad (5)$$

THE INSURANCE CLAIM EVALUATION CRITERIA BEFORE RENEWAL

The earthquake geotechnical engineering practices from the New Zealand Geotechnical Society (NZGS) categorize the degree of damage with damage levels. These levels are based on fissure width, settlement depth, and structural damage, and range from L0, no apparent land damage, to L5, very severe land damage as shown in figure 2. Van Ballegooy et al. (2014) used these damage levels to evaluate the soil liquefaction-induced building damage during the 2010 Canterbury earthquake. Shen et al. (2018) also used these levels to quantify the soil liquefaction-induced building damage during the 2011 Christchurch earthquake. Bray and Stewart (2000) established the ground failure (GF) index using settlement, tilt, and lateral movement to evaluate building damage from the Kocaeli earthquake on 17 August 1999 in Turkey. There are four GF levels, denoted GF0, GF1, GF2, and GF3, which indicate no observable GF, minor GF, moderate GF, and significant GF, respectively. Taking settlement as an example, 10 cm and 25 cm are the dividing points. Settlement of less than 10 cm defines the minor damage level, while settlement between 10 cm and 25 cm is moderate GF, and significant GF occurs when the settlement is larger than 25 cm. Bjerrum (1963) conducted a series of studies on structural tilt and settlement limits. The potential damage to structural components may occur when the building distortion is larger than 1/150 radians.

Yasuda and Hashimoto (2002) and Yasuda (2004) investigated a considerable number of buildings affected by soil liquefaction during the 2000 Tottori earthquake. There were 116 out of 169 buildings under investigation that were tilted by more than 0.29° (5/1000 radians). These studies indicated a tilt of 0.6° (10/1000 radians) reported by the residents as the bearable limit and concluded that repair is necessary for buildings with a tilt above 0.6°. Kohiyama and Keino (2012) investigated damaged buildings in Mihama Ward, Chiba City during the Tohoku earthquake. The maximum bearable tilt reported by the residents was 0.7° (13/1000 radians). When the tilt was larger than 1° (1/60 radians), more than 60% of the residents felt uncomfortable and 50% experienced dizziness.

In the Japanese earthquake insurance policy, the criteria for determining the level of soil liquefaction-induced building damage includes building tilt angle and settlement. There are four levels of damage: significant damage, moderate damage, minor damage, and very little damage. The significant damage level is defined by a tilt angle larger than 1° or settlement of more than 30 cm.

This study develops tilt criteria for Taiwan earthquake insurance claims for building damage caused by soil liquefaction that are based on the total loss of a building being a tilt of 1/30 radians (as in the current Taiwan earthquake insurance policy), international practices of evaluation criteria for earthquake insurance claims, and the effect of building tilt on human health. Building settlement is not

considered in the current evaluation criteria for Taiwan earthquake insurance. However, it plays an important role in international practices, such as the building damage investigation processes in Japan, the United States, and New Zealand. This study suggests taking into account the building settlement as one of the indices for the evaluation criteria for earthquake insurance claims in Taiwan. Given that building settlement due to soil liquefaction is usually differential settlement, the definition of settlement in this study is the maximum settlement of the structure.

Land Damage Zone Description	Description	Performance Level From NZGS (2010)
Very Severe Land Damage	Extensive lateral spreading (>1 m) and liquefaction evidence, large open cracks (>100mm) with surface rupture extending through the ground surface, with very severe horizontal and vertical displacement (>200 mm). Heavy structural damage to buildings includes obvious lateral and vertical displacements and stretching, twisting and cracking of the structures. Damage to roads/services/houses and structures likely to require significant remedial actions or demolition. Generally, affected buildings are beyond economic repair and in most cases likely to be uninhabitable.	L5
Major Land Damage	Extensive liquefaction evidence, large cracks from ground oscillations extending across the ground surface, with horizontal and vertical displacement across crack (>50 mm). Damage to structures includes major differential settlement (>100 mm settlement over 10 m horizontal distance) with obvious lateral and vertical displacements along with twisting/cracking of the structures. Damage to roads/services/houses and structures likely to require major remedial actions or demolition. Generally, affected buildings are beyond economic repair and in most cases are likely to be either uninhabitable, or only habitable in the short-term.	L4
Moderate Land Damage	Visible signs of liquefaction (ejected sand), small cracks from ground oscillations (<50 mm) in paved surfaces but limited depth into the underlying ground, no vertical displacement of cracks. Damage to structures includes moderate differential settlement (<100 mm settlement over 10 m horizontal distance) and twisting/cracking of structures. Remedial work likely to be required in streets and within houses mainly being to walls and ceilings as cracking will be evident. Many foundations will likely require repairs, and remediation may be significantly complicated by differential settlement of the structure. Buildings likely to be habitable in the medium-term, but with reduced serviceability (jamming doors & windows, uneven floors and non-level surfaces) but are variable with respect to the cost to repair them. Within this moderate damage area, localised areas of more major land damage may exist which were not captured by mapping.	L2 to L3
Minor Land Damage	Shaking-induced land damage resulting from cyclic ground deformation and surface-waves. Land damage likely limited to minor cracking (tension) and buckling (compression). No signs of liquefaction obviously visible at the surface, nor of lateral/vertical displacements. Minor remedial work may be required within the street, pavements and landscaping. Land damage may have caused minor damage to houses, which may require minor repair/ relevelling work.	L0 to L3
No Apparent Land Damage (Building damage still possible)	No apparent land damage or signs of liquefaction obviously visible at the surface. Any damage to structures likely to due to earthquake shaking rather than land damage.	L0

Figure 2. Land damage level classification (Jacka and Murahidy, 2011).

Complete information on building tilt and settlement as discussed above for the suggested earthquake insurance claim criteria is summarized in Table 1 and Figure 3(a). Based on conservativeness and reference to Japanese insurance regulations, the suggested criteria in this study has been accepted by Taiwan Residential Earthquake Insurance Fund (TREIF) with a slight adjustment. The constructive total loss is determined when the maximum building settlement due to soil liquefaction is larger than 30 cm, as shown in Figure 3(b).

Table 1. The suggested earthquake insurance claim evaluation criteria by this study.

<table>
<tr><td colspan="2" rowspan="2">Suggested criteria</td><td colspan="4">Building tilt (radians)</td></tr>
<tr><td>≥1/30</td><td>≥1/60 & <1/30</td><td>≥1/150 & <1/30</td><td><1/150</td></tr>
<tr><td rowspan="4">Building settlement (cm)</td><td>More than 50 cm</td><td rowspan="4">Total loss</td><td colspan="3">Total loss</td></tr>
<tr><td>25–50 cm</td><td rowspan="2">Constructive total loss</td><td colspan="2">Constructive total loss</td></tr>
<tr><td>10–25 cm</td><td rowspan="2">Further assessment</td><td>Further assessment</td></tr>
<tr><td>Less than 10 cm</td><td>Further assessment</td><td>No indemnification</td></tr>
</table>

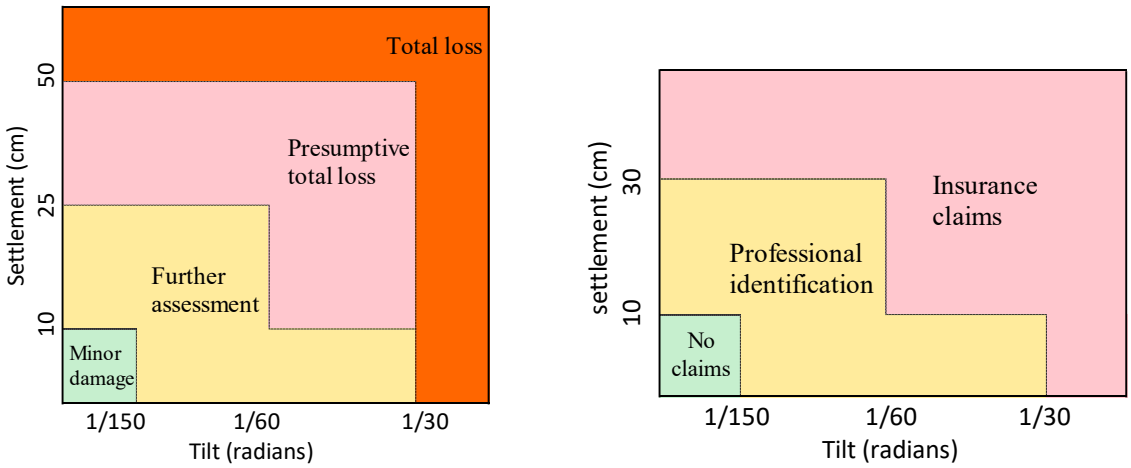

(a) Suggested by this study (b) Final decision by TREIF

Figure 3. The suggested earthquake insurance claim evaluation criteria for building damage caused by soil liquefaction.

SUGGESTIONS FOR ON-SITE MEASURING INSTRUMENTS

Considering the preliminary earthquake insurance claims appraisal is performed by insurance practitioners. Therefore, we recommend measuring instruments based on the principles of portability and ease of operation and exclude technically difficult and complex measuring techniques. This study suggests that the tools to be carried include a plumb line, a spirit level /inclinometer (or a mobile phone), a laser rangefinder, a tape measure, a shovel, an engineering calculator (or a mobile phone), a camera (or a mobile phone), etc. The plumb line and the inclinometer (or mobile phone) are the tools for measuring the title; the laser rangefinder, tape measure, shovel, engineering calculator (or mobile phone) are the measurement and evaluation tools for the settlement; the camera (or mobile phone) is the tool for documenting the current situation.

Table 2 shows the advantages and disadvantages of measuring instruments for the title angle of buildings. Considering the construction conditions and measurement accuracy of the exterior wall of the building. This study preferentially recommends using the plumb line to measure the title angle to reduce the influence of the construction quality of the building and the uneven wall surface, and to obtain a credible building inclination rate by a large-scale point measurement method.

Table 2. Efficiency comparison of measuring instruments for title angle of building

Item	Plumb line	Spirit level	Inclinometer / Mobile phone
Precision	-	★	★
Portability	★	▲	★
Accuracy	★	●	▲
Operability	▲	●	★
Suggested order	①	②	③
Photo			

★ : Excellent ●: Good ▲: Poor

CONCLUSIONS

The purpose of this study was to develop earthquake insurance claim criteria for building damage caused by soil liquefaction in Taiwan are summarized as follows:

(a) Including the maximum settlement of the building as one of the parameters for evaluating the damage of the structure caused by soil liquefaction, the damage of the structure due to soil liquefaction can be described more specifically.

(b) The proposed measure instruments will make it easier for non-professionals to make measurements and judgments, which will reduce claims disputes.

(c) Based on conservativeness and reference to Japanese insurance regulations, the suggested criteria in this study has been accepted by TREIF with a slight adjustment. The constructive total loss is determined when the maximum building settlement due to soil liquefaction is larger than 30 cm.

ACKNOWLEDGMENTS

This research was funded by the Taiwan Residential Earthquake Insurance Fund (TREIF) to establish the insurance claim criteria of building damage caused by liquefaction. Their support is greatly appreciated.

REFERENCES

Bjerrum, L., 1963. Allowable settlement of structures, 3, 135-137, in Proceedings, European Conference on Soil Mechanics and Foundation Engineering, 1963, Wiesbaden, Germany.

Bray, J. D. and Stewart, J. P., coordinators, 2000. Chapter 8: Damage patterns and foundation performance in Adapazari, Kocaeli, Turkey Earthquake of August 17, 1999 Reconnaissance Report, T.L. Youd, J.P. Bardet, and J.D. Bray, eds., Earthquake Spectra, Supplement A to Vol. 16, 163-189, 2000.

Jacka, M. E. and Murahidy, K. M., 2011. Observation and characterization of land damage due to liquefaction and lateral spreading, in Proceedings, 9th Pacific Conference on Earthquake Engineering, 14-16 April, 2011, Auckland, New Zealand

Kohiyama, M. and Keino, C., 2012. Health disturbance of residents in houses tilted due to liquefaction during the great east Japan earthquake, in Proceedings, 15th World Conference on Earthquake Engineering, 24-28 September, 2012, Lisbon, Portugal.

Shen, M., Chen, Q., Zhang, J., and Juang, C. H., 2018. Case histories of liquefaction-induced building damage-focusing on the 22 February 2011 Christchurch earthquake, International Foundations Congress & Equipment Expo, 5-10 March, 2018, Orlando, Florida.

Van Ballegooy, S., Malan, P., Lacrosse, V., Jacka, M. E., Cubrinovski, M., Bray, J. D., O'Rourke, T. D., Crawford, S. A., and Cowan, H., 2014. Assessment of liquefaction-induced land damage for residential Christchurch, Earthquake Spectra, 30(1), 31-55.

Yasuda, S. and Hashimoto, T., 2002. Liquefaction-induced settlements of houses during the western Tottori prefecture earthquake (title translated by the authors), 1029-1030, in Proceedings, 57th Annual Conference of the Japan Society of Civil Engineers, Sep. 25-27, Sapporo, Hokkaido, Japan. (in Japanese)

Yasuda, S., 2004. Damage of housing estate due to the western Tottori prefecture earthquake (title translated by the authors), Sougou-Ronbun-Shi (New Frontiers in Architecture for Damage Mitigation and Recovery from Disasters), Architectural Institute of Japan, 2, 45-46. (in Japanese)

(SS1) Artificial intelligence and big data for earthquake engineering

APPLICATION OF ARTIFICIAL-INTELLIGENCE ON QUICK SEISMIC ESTIMATION OF THE BUILDING STRUCTURES IN TAIWAN

Jin-Biau Wei[1] Yu-Chi Sung[2] Chung-Min Chiu[3] Chia-Hsuan Li[4],
Sheng-Wei Kuo[5], Zhi-Yuan Chen[6], Siao-Syun Ke[7], Chih-Hao Hsu[8]

1. Ph.D. Student, Department of Civil Engineering, National Taipei Univ. of Technology, Taiwan, R.O.C.
2. Professor, Department of Civil Engineering, National Taipei Univ. of Technology, Taiwan, R.O.C.
3. Master Student, Department of Civil Engineering, National Taipei Univ. of Technology, Taiwan, R.O.C.
4. Master, Department of Civil Engineering, National Taipei Univ. of Technology, Taiwan, R.O.C.
5. Master Student, Department of Civil Engineering, National Taipei Univ. of Technology, Taiwan, R.O.C.
6. Master Student, Department of Civil Engineering, National Taipei Univ. of Technology, Taiwan, R.O.C.
7. Supervisor, Earthquake and Man-Made Disaster Division, Nation Science and Technology Center for Disaster Reduction, Taiwan, R.O.C.
8. Assistant Research Fellow, Earthquake and Man-Made Disaster Division, Nation Science and Technology Center for Disaster Reduction, Taiwan, R.O.C.

Email: t106429007@ntut.edu.tw, sungyc@ntut.edu.tw, t110428016@ntut.edu.tw, t108428017@ntut.edu.tw, t109428122@ntut.edu.tw, t110428006@ntut.edu.tw, opbook@ncdr.nat.gov.tw, willie2567@ncdr.nat.gov.tw

ABSTRACT

In the third quarter of 2021, the real estate information platform provided by Ministry of the Interior (MOI) Taiwan reported there are about 8.93 million buildings in Taiwan. Among which, there are 4.49 million buildings serviced over 30 years and, generally speaking, they may not have qualified seismic capacity due to either material aging or outdated design standard. Supported by MOI, the preliminary seismic evaluation (PSE) of over 5,286 existing buildings with high potential seismic risk was performed in the past few years. Accordingly, the buildings with poor seismic capacity can be captured and renewing of them is encouraged. Limited by the budget, the seismic evaluation of the other 8.92 million existing buildings has not been totally performed yet. To deal with this problem, a quick and effective seismic estimation based on PSE experience is needed. Through the quite limited information provided by the building tax data or usage license, the present paper intends to complete the quick seismic estimation of the existing buildings by using artificial intelligence (AI) based on the database established from PSE. The results obtained could help government establish the potential risk map related with seismic capacity of all the existing buildings and list priority of renewing process in a short time.

Keywords: preliminary seismic evaluation (PSE), Back-Propagation Neural Network (BPNN), urban renewal, disaster prevention

INTRODUCTION

The real estate information platform provided by Ministry of the Interior (MOI) Taiwan reported, in the third quarter of 2021, there are about 8.93 million buildings in Taiwan. Among which, there are 4.49 million buildings serviced over 30 years and, generally speaking, they may not have qualified seismic capacity due to either material aging or outdated design standard. How to deal the numerous existing buildings unqualified in earthquake resistance and activate necessary retrofit or renewing works as soon as possible becomes a hot issue in disaster prevention.

The preliminary seismic evaluation (PSE) is suitable to rapid screening numerous buildings by surveying some elementary data related to seismic capacity. Even the complicated numerical analyses are unnecessary for consideration of short-time work, the survey of structural members, on ground floor at least, capable of resisting earthquake force in the building are still unable to be exempted. The engineers should go to the building site to investigate the current situation of the building and check the consistency with original design data. Identification of the structural system as well as the availability of the structural members should be confirmed and serving as the input data. The evaluation platform

known as preliminary seismic evaluation of reinforced concrete building (PSERCB, Sung et al. 2016) was authorized by MOI since 2016 and opened to all the licensed civil/structural engineers and architectures for purpose of preliminary seismic evaluation of buildings.

In view of numerous existing buildings without PSE yet, a quick estimation of their approximate seismic capacity for target searching of successive PSE process is important and should be performed by a simple way without practical survey works but still having reliable results. A reasonable approach is proposed by use of artificial intelligence (AI) technique to deal with. The individual visit to numerous buildings for survey is impossible, therefore, the limited information such as the total floor area, total number of floors, total building height, building location and year of use, etc. recorded in the building tax data or usage license, according to Taiwan Building Act, are available for use of the quick estimation. Although these data just belong to a subset of all the input data from the practical survey recorded in PSERCB platform, they can be screened through sensitive analysis. Those that are found to have the significant influence on seismic capacity will be chosen as the necessary parameters as input of quick estimation.

Limited by the budget, the seismic evaluation of the other 8.92 million existing buildings has not been totally performed yet. To deal with this problem, a quick and effective seismic evaluation based on PSE experience is needed. Through the quite limited information provided by the building tax data or usage license, the present paper intends to complete the quick seismic estimation of the building structures (QSEBS) by using artificial intelligence (AI) based on the database preserved in PSERCB system.

DATA ARRANGEMENT OF PRELIMINARY SEISMIC EVALUATION OF BUILDINGS

Contents of PSERCB

Sung and Tsai (2014) developed a cloud-operation system of PSERCB that was authorized by MOI in 2016 as official standard for PSE to the buildings by professional civil/structural engineers and architectures. Both the qualitative and quantitative evaluation contents are included. PSERCB has the major advantages: (1) qualitative evaluation allows professional engineering judgement provided by the experienced engineers; (2) quantitative evaluation prevents subjective man-made obstinateness; (3) cloud-operation system accelerates the evaluation activity and eases the data preservation. The officials, government employee, professional association, professional engineers and students, etc. can use PSERCB system up to different purposes. All the seismic capacity evaluated and the survey data for each one building that has been performed with PSE are preserve in the system and relative statistical analyses can be shown in the platform. Associated with Geographic Information System (GIS), all the results are able to be displayed on the map, helping a wider observation on strategy of urban disaster prevention.

As of February 9, 2021, there are 5,286 buildings evaluated by PSERCB. The data accumulated would be provided as basis for quick estimation of seismic capacity of all the buildings in Taiwan.

Pre-arrangement of Data in PSERCB for Application to QSEBS

In the PSERCB platform, there are totally thirty-two parameters such as total floor area, number of floor, usage partition, year of design code, soil type of foundation, number/dimension of column and wall on ground floor, dead load, live load, material strength estimated, etc., recorded and related to seismic capacity of the existing building. Most of them are determined by the professional judgement of the engineers via the in-situ survey or the necessary tests. For application of QESBS to the numerous existing buildings without PSE, it's impossible to consider all the parameters in PSERCB platform because it needs considerable finance and time to carry out. On the other hand, there are eight parameters sensitive to seismic capacity recorded by tax data/usage license of every building, such as building location, total floor area, the maximum number of floor, material classification of building structure, etc., those are well preserved in the construction institute of government. The mutual parameters included in both PSERCB platform and tax data/usage license of buildings are (1) total floor area (floor_area), (2) number of floor (floor_number), (3) building type of housing (build_type), (4) soil type of foundation (st_f), and (5) year of seismic design code (year_code), and therefore available for purpose of quick seismic estimation of the existing buildings particularly without in-situ survey. They are served

as the input data of artificial neural network (ANN) for QESBS to determine three target outputs including the equivalent total area of column and wall (ETRC) and the equivalent width/depth per column and wall (E_W/CW, E_D/CW) on ground floor, of the buildings. As a result, the seismic capacity can be obtained.

The parameters (1) and (2), i.e. floor_area and floor_number, belong to the continuous variable, and the others are able to be classified as label variables. The process of data cleaning of them is illustrated as follows.

Data Cleaning of Continuous Variables

All the six input parameters in the 5,286 cases of buildings with PSE preserved in PSERCB platform were picked up and complied by JSON file. However, not all the cases provide representative information, based on statistical theory, the data cleaning work to screen out the non-representative cases are necessary.

Physically speaking, the vertical/horizontal force bearing system of a building structure to resist the gravity and earthquake loads is mainly provided by columns/walls. The quantity of total floor area, (floor_area), indicates the gravity load. On the other hand, the total sectional area of columns and walls, (column&wall_section_area), reflects the resistance to the load. Therefore, the total floor area divided by the total column and wall area reflects the ratio of load/resistance related to gravity load and should has a reasonable distribution range for the building structure. Therefore, this ratio serves as a metadata and also a screen index of data cleaning. In addition, (column&wall_section_area) related seismic capacity is, of course, considered as the second index of data cleaning.

The data cleaning of these two continuous variables were determined by the box plot. In which, the invalid data by identifying the outliers of the index and sort in order of size. For all the data, the first- and third- quartile of the index are determined as Q1 and Q3, respectively. The difference between them, represented by Q3-Q1, is defined as interquartile range (IQR). The data with index outliers within the ranges either less than $(Q1-1.5\times IQR)$ or greater than $(Q3+1.5\times IQR)$ should be removed from the set of original data.

The following efforts were conducted and the conclusions were obtained in the process:

1. Removing of duplicate cases: The building owner might offer one case to different professional engineers and the duplicate data for a building may be stored in the system. To prevent the incorrect training samples in the succeeding ANN model, they should be removed in advance. As a result, the original 5,286 cases were screened effectively to 3,133 cases left.
2. The box plot in Figure 1 represents the distribution of index (floor_area/unit_area_column&wall). In which, the values of Q1, Q3 and IQR are 44.29, 81.46 and 37.17, respectively. When the value is less than zero or greater than 136.49, the data is considered as the outlier and removed. After this process, the number of effective cases is reduced to 3,072.

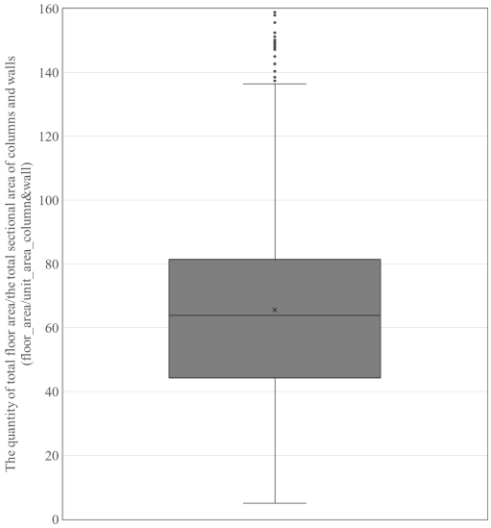

Figure 1. Box plot diagram of distribution of index (floor_area/unit_area_column&wall)

3. Figure 2 shows the scatter diagram representing relationship between (floor_number) and (column&wall_section_area) and the corresponding box plots are shown in Figure 3. As can be seen in Figure 2, the relationship between (column&wall_section_area) and (floor_number) reveals a linear distribution for (floor_number) >5; and a constant for (floor_number). The identification of the outliers of index (column&wall_section_area) can be grouped for these two different situations. The corresponding values of Q1, Q3 and IQR are listed, respectively, in Table 1.

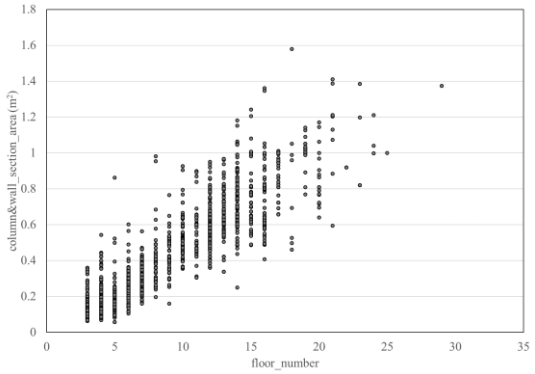

Figure 2. Scatter diagram of (column&wall_section_area) and (floor_number)

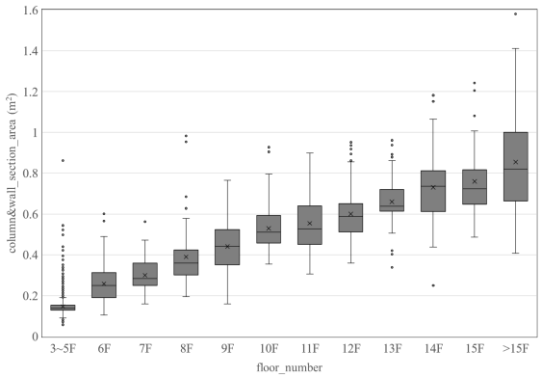

Figure 3. Box plot of (column&wall_section_area) and (floor_number)

Table 1. Outliers range of index (column&wall_section_area)

	The first quartile, Q1	The third-quartile, Q3	The interquartile range, IQR	Q1 - 1.5×IQR	Q3 + 1.5×IQR
3~5F	0.129	0.154	0.025	0.091	0.191
6 F	0.192	0.312	0.121	0.010	0.493
7 F	0.250	0.360	0.110	0.085	0.525
8 F	0.303	0.424	0.121	0.122	0.605
9 F	0.353	0.522	0.169	0.101	0.775
10 F	0.458	0.590	0.133	0.258	0.790
11 F	0.452	0.640	0.188	0.170	0.922
12 F	0.513	0.649	0.136	0.309	0.852
13 F	0.615	0.710	0.095	0.472	0.853
14 F	0.614	0.810	0.196	0.321	1.104
15 F	0.649	0.815	0.166	0.401	1.063
>15 F	0.664	1.000	0.336	0.161	1.503

Through the process of data cleaning, there are 2,805 cases available and served as the input of the succeeding ANN efforts.

Significant Difference between Label Variables and Continuous Variables

The nonparametric statistics is suitable to data population with the uncertain distribution, small sample, non-normal distribution, etc. and is good to deal with the label variables. The Kruskal-Wallis H test is a rank-based nonparametric test and used to determine if there are statistically significant differences between two or more groups of an independent continuous variable. Because the post-sequencing data are often not normal distribution and have some significant outliers, use of ranks is more reasonable than that of actual values to avoid the test affected by the presence of outliers. The present study adopted the Kruskal-Wallis H test to justify the statistical significance between the continuous variable in the set of target output (ETRC, E_W/CW and E_D/CW) and the variables in the set of label variables (build_type, st_f, year_code), one by one. All the nonparametric statistics data are shown in Table 2.

Table 2. The evaluated Chi-square value for the continuous variables together with label variables

	Chi-square	degrees of freedom	χ^2(k-1,0.05)	significant difference
χ^2 (year_code v.s. ETRC)	594.94	3	7.81	V
χ^2 related to (year_code v.s. E_W/CW)	950.386	3	7.81	V
χ^2 related to (year_code v.s. E_D/CW)	730.425	3	7.81	V
χ^2 related to (st_f v.s. ETRC)	328.841	5	11.07	V
χ^2 related to (st_f v.s. E_W/CW)	440.139	5	11.07	V
χ^2 related to (st_f v.s. E_D/CW)	464.678	5	11.07	V
χ^2 related to (build_type v.s. ETRC)	420.266	3	7.81	V
χ^2 related to (build_type v.s. E_W/CW)	818.905	3	7.81	V
χ^2 related to (build_type v.s. E_D/CW)	587.563	3	7.81	V

BPNN MODEL FOR QUICK SEISMIC EVALUATION OF BUILDINGS

Model Illustrations

Back-Propagation Neural Network (BPNN) is used as the first step in the process of quick seismic evaluation of the buildings. The input variables include: (1) total floor area (floor_area), (2) number of floor (floor_number), (3) building type of housing (build_type), (4) soil type of foundation (st_f) and (5) year of seismic design code (year_code). The arrangement of all the variables in BPNN model is illustrated as follows:

1. The (floor_area) and (floor_number) are both continuous variables and the quantities of them, serving as input, can be arranged by single individual neuron, respectively.
2. Generally speaking, there are six different building types of housing (build_type) for practical engineering application in Taiwan, namely apartment, congregate housing, hybrid area of commerce and residence, shopping mall and office building, etc., belonging to label variables and are arranged by six individual neurons, respectively.
3. According to Seismic Design Code of Buildings in Taiwan (2011), four soil types of foundation are classified, respectively, belonging to label variables, therefore (st_f) are arranged by four individual neurons, respectively.
4. Four different ranges for year of seismic design code and dealt by discrete variables with integrals 1 to 4, (year_code) is arranged by one single neuron.

As a result, the input layer of BPNN contains thirteen neurons.

In order to reflect the nonlinear mapping relation and find the better precision of the mapping model, through the well-tried tests, five hidden layers with different neurons as shown in Table 3 and Figure 4 are adopted. Two BPNN models are considered for output finding of ETRC and the set of (E_W/CW, E_D/CW), respectively. Between the two models, the only difference in the model structure is the number of neuron in the output layer for different purposes of output finding. The models are constructed by the function of RandomSearch in python KerasTuner. The activation functions of ReLU, tanh, Sigmoid, respectively, are compared and it showed that the former one has a better performance.

Table 3. Sketch of two BPNN models

Parameters / Model structure	Model-1 ETRC	Model-2 E_W/CW, E_D/CW
No. of hidden layer	5	
No. of neurons in hidden layer	8、14、14、8、6	
Input layer	13 neurons for floor_area (1); floor_number (1); build_type (6); st_f (4) and year_code (1)	
Output layer	ETRC	E_W/CW, E_D/CW
Activation function	Relu	
No. of iteration	4000	750

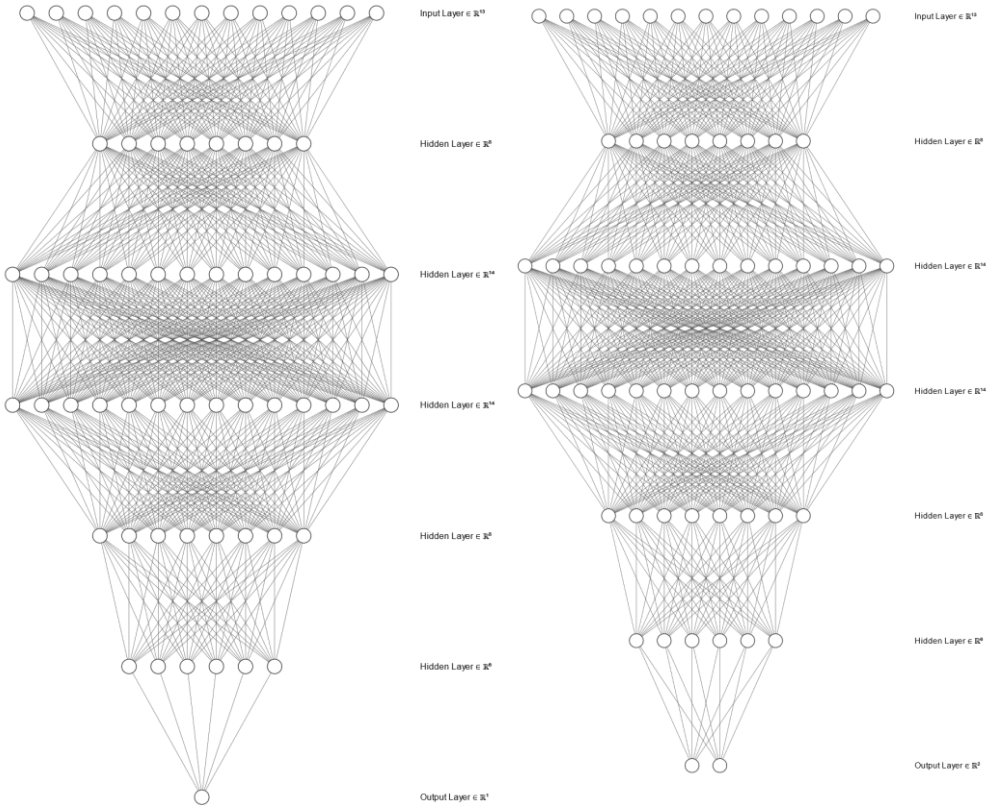

(a) Model 1 (b) Model 2

Figure 4. Schematic of BPNN models established

Model Validation

After data cleaning, there are 2,805 cases collected in PSERCB platform and partitioned into training data (1795, 64%), validation data (449, 16%) and test data (561, 20%), respectively, for BPNN models. Figure 5 reveals the convergence situation of loss function in model 1, the coefficient of determination (R^2) obtained is 0.841 and the Root-Mean-Square Error (RMSE) is 37332.168 cm^2. Figure 6 shows the R^2 in model 2 are 0.8739. On the other hand, the R^2 and RMSE for EW/C are found to be 0.882 and 7.29 cm, respectively, and those for ED/C are 0.851 and 8.07 cm, respectively. These two figures indicate they have the good convergences. It shows that the reliability of the BPNN model constructed is able to be verified.

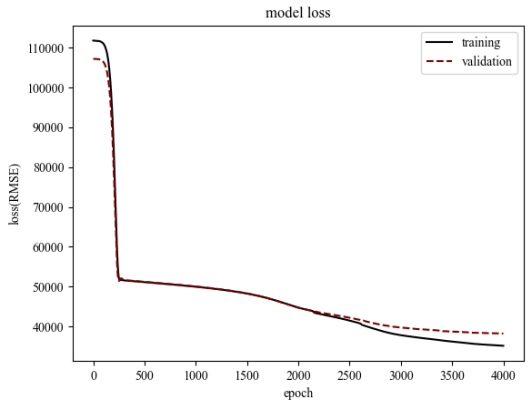

Figure 5 Loss function of Model 1

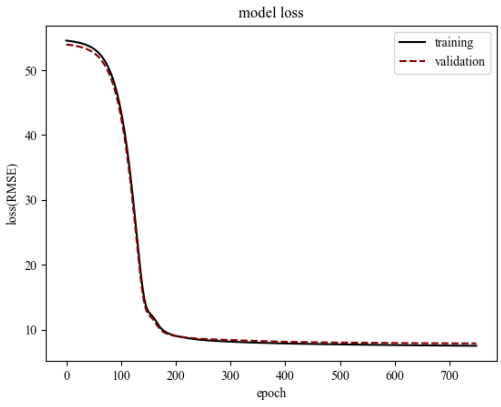

Figure 6 Loss function of Model 2

RESULTS OF QSEBS

Comparisons between Data of PSERCB and Results Estimated from QSEBS

Figure 7 shows the relationship of occurrence probability versus index $\frac{A_{C2}}{IA_{2500}}$ between data preserved in PSERCB and the result estimated from QSEBS. Those relationships reveal the mutual tendency of normal distribution and they have a high degree of consistency in cumulative probability distribution. The difference between the data in PSERCB and the result estimated from QSEBS is found to be insignificant. As can be seen in Figure 7, the dangerous building with index $\frac{A_{C2}}{IA_{2500}} \le 0.35$ takes about percentage of 25.9% in the total samples in PSERCB and seems somewhat higher than 24.3% from QSEBS, however, it is acceptable for purpose of practical application.

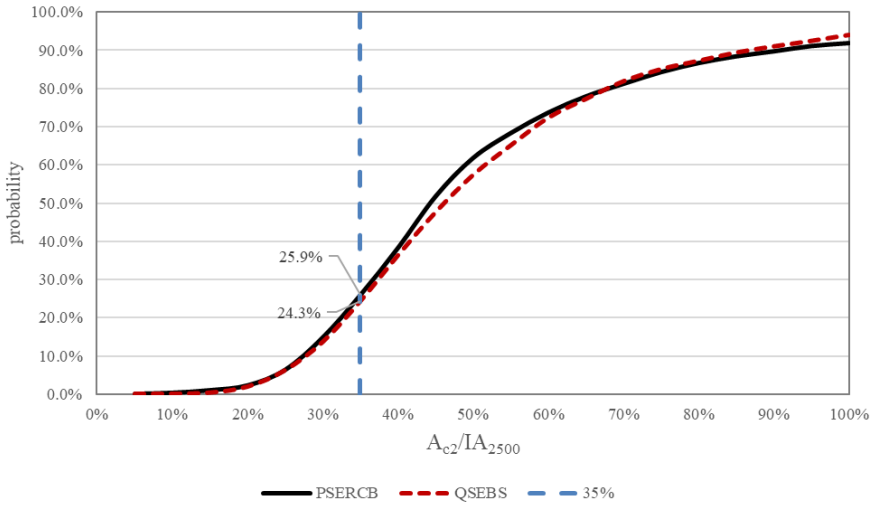

Figure 7. Cumulative probability distribution of $\frac{A_{C2}}{IA_{2500}}$ between data in PSERCB and result estimated from QSEBS

CONCLUSIONS

The present paper used the quite limited information inventoried in the building tax data or usage license of the existing buildings, well preserved in construction institute of government, associated with the data recorded in the PSERCB platform for the building cases that have been proceed with preliminary seismic evaluation (PSE) to develop a method for quick seismic estimation of building structures (QSEBS). For the purpose of practical application, the dominated parameters mutually kept in both the building tax data or usage license and PSERCB platform were planning as the input data. The mapping relationship between them and the indicators related to seismic capacity, as the output data, were determined by BPNN model. The outlier data of continuous variables were screened out through the statistical theory and expressed by box plot, on the other hand, the statistical significance between the label variables and the output was identified by the Kruskal-Wallis H test method. After a series of data cleaning, the data of original 5,286 cases were screened to 2,805 cases for having the effective analysis data. Different structures of BPNN model were proceed by well-tried tests and established for comparisons of analysis results to determine the suitable one for the mapping relationship between I/O. Eventually, the QSEBS are able to be fulfilled.

The conclusions obtained are drawn as follows:

1. The cumulative probability distribution of (A_{C2}/IA_{2500}) estimated from QSEBS were found to be very close the data preserved in PSERCB, which means that the precision of QSEBS is acceptable for practical application.
2. According to the real estate information platform provided by Ministry of the Interior (MOI) Taiwan, third quarter of 2021, there are 4.49 million buildings already serviced over 30 years and, generally speaking, they may not have qualified seismic capacity due to either material aging or outdated design standard. The present study estimates their seismic capacity approximate to the results of PSE, based on the inventoried data in the building tax data or usage license. By the QSEBS, the quick estimation for all the buildings doesn't need the in-situ survey, considerable finance and work time, etc. Because the seismic capacity of the individual building can be estimated and the list sorting of the succeeding efforts on seismic retrofit or reconstruction can be made, QSEBS could help the government facilitate the urban renewal works.

ACKNOWLEDGMENTS

This study supported by National Science and Technology Center for Disaster Reduction, NCDR, Taiwan through the grant numbers NCDR NCDR-S-111012 is gratefully acknowledged.

REFERENCES

Freeman, S.A. (1998). "Development and use of capacity spectrum method," *In The 6th US National Conference on Earthquake Engineering/EERI*, Seattle, Washington.

Freeman, S.A. (1975). "Evaluations of existing buildings for seismic risk-A case study of Puget Sound Naval Shipyard," *In Proc. 1st US Nat. Conf. on Earthquake Engrg*., Bremerton, Washington.

Molas, G.L. and F. Yamazaki (1995). "Neural networks for quick earthquake damage estimation." *Earthquake engineering & structural dynamics*, **24** (4), 505-516.

Morfidis, K. and K. Kostinakis (2018). "Approaches to the rapid seismic damage prediction of r/c buildings using artificial neural networks," *Engineering Structures*, **165**, 120-141.

Huang, C.S., S.L. Hung, C.M. Wen, and T.T. Tu (2003). "A neural network approach for structural identification and diagnosis of a building from seismic response data." *Earthquake engineering & structural dynamics*, **32** (2), 187-206.

De Lautour, O.R., and P. Omenzetter (2009). "Prediction of seismic-induced structural damage using artificial neural networks," *Engineering Structures*, **31** (2), 600-606.

Arslan, M.H. (2010). "An evaluation of effective design parameters on earthquake performance of RC buildings using neural networks." *Engineering Structures*, **32** (7), 1888-1898.

Arslan, M.H., M. Ceylan, and T. Koyuncu (2015). "Determining earthquake performances of existing reinforced concrete buildings by using ANN." *International Journal of Civil and Environmental Engineering*, **9** (8), 1097-1101.

Caglar, N. and Z.S. Garip (2013). "Neural network based model for seismic assessment of existing RC buildings." *Computers and Concrete*, **12** (2), 229-241.

Rofooei, F.R., A. Kaveh, and F.M. Farahani (2011). "Estimating the vulnerability of the concrete moment resisting frame structures using artificial neural networks." *International Journal of Optimization in Civil Engineering*, **1** (3), 433-448.

Ghosh Mondal, T., M.R. Jahanshahi, R.T. Wu, and Z. Y. Wu (2020). "Deep learning-based multi-class damage detection for autonomous post-disaster reconnaissance." *Structural Control and Health Monitoring*, **27**(4), e2507.

(SS2) Seismic design, analysis and qualification for off-shore wind turbines

SOIL-STRUCTURE INTERACTION ON JACKET-SUPPORT OFFSHORE WIND TURBINES UNDER SEISMIC LOADING

Pei-Hsuan Yu[1], I-Yan Chen[2], Xiao-Qin Liu[3], Yu-Chi Sung[4], Chin-Kuo Su[5] and Tzu-Chi Chien[6]

1. Assistant Research, Research Center of Offshore Wind Power Engineering, National Taipei University of Technology, 10608 Taipei, Taiwan, R.O.C.
2. Ph.D. student, Department of Civil Engineering, National Taipei University of Technology, 10608 Taipei, Taiwan, R.O.C.
3. Postdoc, Research Center of Offshore Wind Power Engineering, National Taipei University of Technology, 10608 Taipei, Taiwan, R.O.C.
4. Distinguished Professor, Department of Civil Engineering, National Taipei University of Technology, 10608 Taipei, Taiwan, R.O.C.
5. Project Manager, Research Center of Offshore Wind Power Engineering, National Taipei University of Technology, 10608 Taipei, Taiwan, R.O.C.
6. Assistant Research, Research Center of Offshore Wind Power Engineering, National Taipei University of Technology, 10608 Taipei, Taiwan, R.O.C.

Email: sungyc@ntut.edu.tw

ABSTRACT

This study focused on the jacket-support structure and proposed a tentative approach for time-domain seismic analysis of jacket-supported offshore wind turbine system. Unlike the conventional response spectrum method, which is based on the linear assumption of the overall structural system, the proposed approach considers the soil-structure interaction effect by integrating a series of nonlinear soil springs. Moreover, this study takes into account of ground multi-excitation inputs through the site response analysis. Through numerical implementation of the soil-structure interaction and site response analysis, a finite element simulation analysis of a jacket-supported offshore wind turbine system subjected to a seismic time-history was conducted. The von Mises stress of the jacket members and the pile head rotation were obtained and then verified to comply with the required design limits, thereby confirming the feasibility of the proposed approach.

Keywords: Jacket-Support Structure, Site Response analysis, Soil-Structure Interaction, Time-history Seismic Analysis, Nonlinear Soil Spring, Ground Acceleration.

INTRODUCTION

To respond to the global green movement, the countries across the world are all seeking for efficient energy alternatives for fossil fuel resources. Offshore wind is deemed a key player in the transition to net-zero cutting greenhouse gas emissions. Offshore wind turbine (OWT) systems, consisting of the slender tower with a heavy rotor-nacelle mass at the tower top, are rather sensitive to earthquake-induced hazards in seismic zones, therefore requiring appropriate seismic analysis and design.

Conventionally, engineers use the response spectrum method (RSM) for seismic design, which assumes the structure as a linear system. However, offshore wind turbine systems do not fit such assumptions due to their highly nonlinear characteristics. Moreover, according to DNV-RP-0585, the RSM is only applicable for low seismic risk areas due to limited accuracy caused by simplified linear assumptions. As for moderate to high seismicity, the DNV-RP-0585 suggests that the time-history seismic analysis method should be applied for more conservative consideration.

The site response analysis (SRA) is often used to predict the surface ground motion for the development of the design response spectra, and to evaluate dynamic stresses and strains for evaluation of liquefaction

hazards, and to determine the earthquake-induced forces that can lead to instability of earth and earth-retaining structures (Kramer, 1996).

The soil-structural interaction (SSI) refers to an exchange of mutual stresses between the structure and underlying soil, and the SSI mechanism is often governed by the properties of both soil and superstructure. Various combinations of soil and structure may generate amplify or diminish movement and subsequent damage, which is significant in earthquake-prone areas.

To account for the aforementioned affecting aspects, this study proposed a framework for the time-domain seismic analysis of jacket-support offshore wind turbines. In this framework, the soil-structure interaction is integrated using a series of nonlinear soil springs, and the site response analysis is implemented to acquire seismic multi-excitation inputs. Furthermore, the Newton–Raphson method is used to solve for the defined nonlinear time-domain analysis. An implementation study of the proposed framework was conducted on an OWT model to verify the proposed framework.

METHODOLOGY

The proposed numerical analysis for OWTs under time-domain seismic loads is described in Figure 1. First, use geotechnical software to conduct site-specific responses. Second, use the beam on the nonlinear Winkler foundation (BNWF) model to account for soil-structure interaction, this is also known as p-y, t-z, and q-z curve analysis.

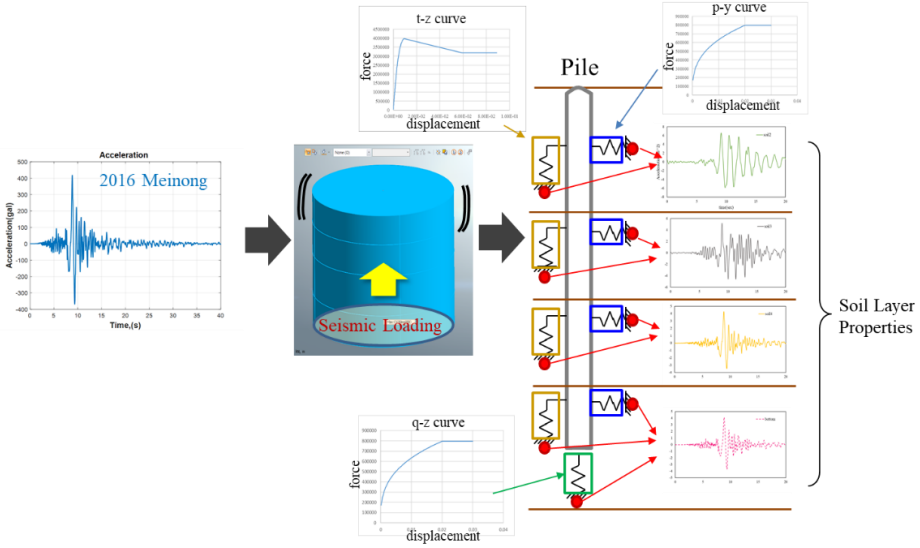

Figure 1 Schematic of OWTs subject seismic loads analysis flow.

Site-specific response analysis (SSRA)

Through the SSRA, the earthquake excitation signals in terms of ground acceleration were obtained at different soil depths (DNV-RP-0585, 2021). This study used the commercial software MIDAS GTS to conduct the SSRA. Based on the assumption of infinitely extending horizontal soil layers, the seismic motion is caused by the horizontal shear wave propagating vertically upward from the seabed, as known as one-dimensional wave propagation. The seismic acceleration time history at each depth level of the site can be obtained through the MIDAS modeling.

SSI

The American Petroleum Institute (API, 2002) code recommends using the p-y, t-z, and q-z curve nonlinear springs to simulate the SSI. The p-y spring is defined in Eq. 1, where A is a factor that depends

on the type of loading, p_u is ultimate resistance depends on the depth x and inertial friction angle, and k is the initial modulus of subgrade reaction.

$$p=Ap_u \tanh\left(\frac{kx}{Ap_u}y\right) \quad (1)$$

The numerical model involves nonlinear and time-variant processes, to solve such processes, the full Newton-Raphson option embedded in ANSYS is thus used.

CASE STUDY

Finite element model

This case analyzed the NREL 5-MW baseline OWT with the jacket-supported structure under IEC 61400-3 Class IA (Jonkman et al., 2009). This average water depth was set to be 50 m. The basic parameters of this wind turbine and the jacket substructure are enlisted in Table 1. Multiple loading conditions including seismic, wind, wave, and current loads were considered as the model inputs.

This paper employed the commercial software ANSYS for constructing the jacket OWT finite element (FE) modeling, namely using Pipe 288 elements to simulate the columns, bracings, piles, Beam 188 elements for the tower, and CONTA 175 element for the rigid links connecting the tower and jacket (Figure 2).

Table 1 Basic Parameters of NREL 5-MW Baseline Wind Turbine

Parameter	Value
Rated power	5 MW
Number of blades	3
Rotor diameter	126 m
Cut in, Rated, Cut out wind speed	3 m/s, 11.4 m/s, 25 m/s
Cut in, Rated Rotor speed	6.9 rpm, 12.1 rpm
Rotor mass	110,000 kg
Nacelle mass	240,000 kg
Hub mass	56,780 kg
Blade mass	53,220 kg
Tower mass	347,460 kg
Tower height	87.6 m
Hub height	90.55m
Base diameter, thickness	6 m, 0.027 m
Top diameter, thickness	3.87 m, 0.019m

Table 2 Basic parameters of Jacket substructure

Parameter	Value
Length of jacket legs	70 m
Diameter of jacket legs	1.2 m
Wall thickness of jacket legs	0.05 m
Diameter of diagonal bracing	0.8 m
Diameter of mudline bracing	0.8 m
Wall thickness of bracing	0.02 m
Steel density	8,500 kg/m^3
Steel yield strength	355 MPa
Steel Yong's modulus	2.00×10^8 kN/m^2
Steel shear modulus	8.08×10^7 kN/m^2
Steel Poison's ratio	0.3

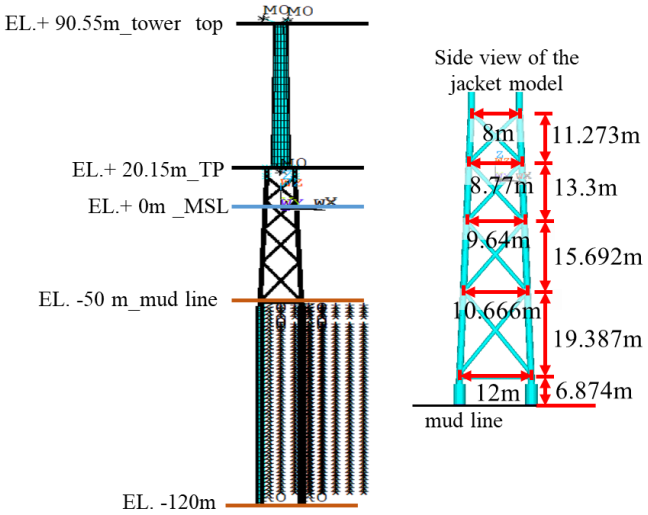

Figure 2 5MW jacket-type OWT numerical modeling

Wind and wave loading

This study focused on the structural responses under seismic loads. On top of the seismic loads, the input wind, wave, and current loads were determined based on IEC 61400-3. The aerodynamic load is calculated with the blade element momentum (BEM) theory with the assumed wind speed of 11.4 m/s. The marine environment loads for the jacket substructure are related to the water depth, wave and current status. This study used the JONSWAP spectrum theory to model ocean waves considering the 1-year return period wave height of 7.65 m and the current speed of 1.436 m/sec. The wave and current loads acting on the jacket structure were subsequently evaluated using Morison's equation.

Ground motion inputs

This study employed the MIDAS GTS program to conduct the SSRA in order to evaluate the ground acceleration time-history at each predefined soil layers. According to the Mohr-Coulomb failure criterion, the soil was modeled as an elastic-plastic body with free-field boundaries. The seismic input took the form of the east-west ground acceleration time-history of the 2016 Meinong earthquake from the CHY 063 station. Through the SSRA, the equivalent depth-varying acceleration time-histories with the duration of 40 sec were obtained at the designated soil layers. These equivalent acceleration time-histories were then used for the following OWT dynamic analysis.

SSI model

The results of a geotechnical survey of an existing offshore wind farm (OWF) in the Taiwan strait were employed as the basis for constructing the soil spring submodel. The surveyed (Taiwan Power Company, 2013) soil body has a profile of distinct layers: silt sand (SP), silt (ML), clay of low plasticity (CL), and inclusions clay. Therefore, the nonlinear depth-varying p-y, t-z, and q-z soil springs were accordingly defined, with the spring parameters presented in Table 3.

Table 3 Soil properties

Depth Range (m)	Density (kg/m^3)	Young's Modulus (MPa)	Shear Modulus (MPa)	Poisson's Ratio	Cohesion (kN/m^2)	Friction Angle (°)
0-22.1	1788.494	155.162	59.683	0.3	50624.43	29.625
22.1-45.7	1770.891	212.684	81.795	0.3	77755.51	0
45.7-76.1	1825.243	416.048	160.016	0.3	64906.58	24.741
76.1-100	1856.874	681.8	372	0.3	0	30

Results and discussion

By conducting the Newton-Raphson analysis, the maximum von Mises stress was determined with the value of 199.23 MPa occurring at the 9.26 sec, as shown in Figure 3, which was lower than the steel yield stress of 355 MPa.

According to the DNV-ST-0126, the limiting total and permanent tilt rotation of 0.5˚ is suggested, this allows for permanent deformations in the soil to develop and implicate a nominal additional tilt rotation of the axis of 0.25˚. The maximum pile head rotation was 0.184˚ occurring in 10.76 sec, as shown in Figure 4, which is lower than the DNV suggested limitations. Such fulfillment of the OWT design requirements indicates the feasibility of the proposed time-history seismic analysis of jacket-supported OWT system.

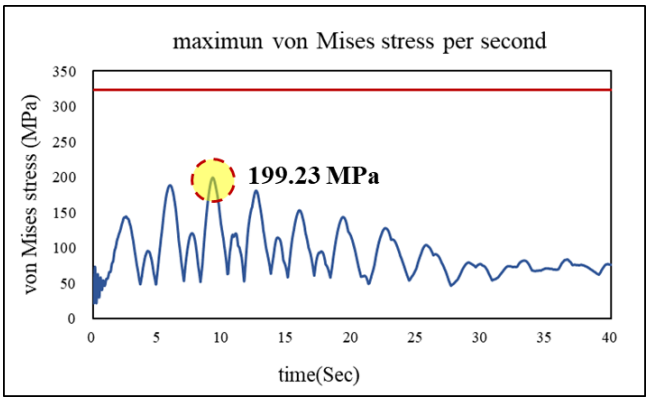

Figure 3 maximum von Mises stress

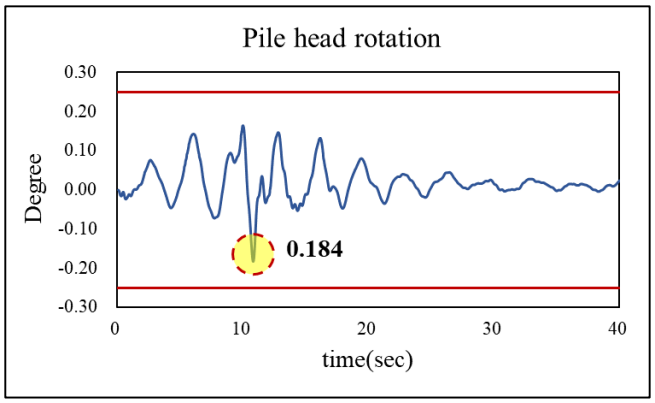

Figure 4 pile head rotation

CONCLUSION

This study explored a tentative procedure for time-history seismic analysis of jacket-support OWT system. To account for the soil-related nonlinear and wave propagation effects, the SSI and SRA are integrated into the procedure by using the BNWF spring models and ground multi-excitation inputs. The ground multi-excitation inputs take the form of depth-variant ground acceleration time-histories derived using the geotechnical software, MIDAS GTS. A case study was conducted to implement the proposed procedure on the NREL 5MW jacket OWT system, and the geotechnical conditions of a real OWF site were used for constructing the soil spring models and SRA settings. The results reveals that the maximum von Mises stress and the maximum pile top rotation were within about 38% and 28% of the design bounds, respectively, thereby indicating the feasibility of the proposed procedure.

REFERENCE

API (2002). Recommended practice for planning, designing and constructing fixed offshore platforms - working stress design. API Recommended Practice 2A-WSD (RP 2A-WSD), 21st Edition, Dallas: API.

DNV. (2021). Seismic design of wind power plants. Report No: DNV-RP-0585, *Det Norske Veritas*, Høvik, Norway.

DNV (2021). Support structures for wind turbines. Report No: DNV-ST-0126, *Det Norske Veritas*, Høvik, Norway.

IEC (2019).Wind energy generation systems – Part3-1: Design requirements for fixed offshore wind turbines.

Jonkman, J., S. Butterfield, W. Musial, and G. Scott (2009). "Definition of a 5-MW reference wind turbine for offshore system development," *Office of Scientific Technical Information Technical Report*, NREL, US.

Kramer SL (1996) "Geotechnical earthquake engineering," I*n: Prentice-Hall international series in civil engineering and engineering mechanics*. Prentice-Hall, New Jersey

Taiwan Power Company (2013). Feasibility Study of Offshore Wind Farm in Taiwan—Stage I; *TPC: Taipei, Taiwan,* in Chinese.

NUMERICAL VIBRATIONAL ANALYSES OF SCOUR EFFECTS ON A JACKET-SUPPORTED OFFSHORE WIND TURBINE

Xiao-Qin Liu[1], I-Yan Chen[2], Po-Hung Liu[3], Yu-Chi Sung[4], and Jin-Hung Hwang[5]

1. Postdoc, Research Center of Offshore Wind Power Engineering, National Taipei University of Technology, Taipei, Taiwan
2. Ph.D. student, Department of Civil Engineering, National Taipei University of Technology, Taipei, Taiwan
3. Master student, Department of Civil Engineering, National Taipei University of Technology, Taipei, Taiwan
4. Distinguished Professor, Department of Civil Engineering, National Taipei University of Technology, Taipei, Taiwan
5. Professor, Department of Civil Engineering, National Central University, Taoyuan, Taiwan

Email: lisaliu@ntut.edu.tw, qwer336987@gmail.com, t108428094@ntut.org.tw, sungyc@ntut.edu.tw, hwangjin@ncu.edu.tw

ABSTRACT

This study focused on the jacket support structure and explored scour effects on the vibrational behaviors of a virtual 5-MW offshore wind turbine (OWT) system. A numerical model of the virtual OWT system was constructed using commercial software ANSYS. Meanwhile, adopting the p-y curve method, soil-structure interaction was modeled as discrete lateral and axial springs along the pile side. The OWT system model was deliberately validated before a subsequent scour investigation. The vibration responses of the simulated OWT system subjected to dynamic wind and cyclic wave loads were obtained and analyzed for designated scour cases. The results indicated that the natural frequency of the OWT model decreases, along with the structural stiffness, as the scour depth increases. Critically, the frequency analyses revealed that intense scour is likely to subject the OWT system to a 1P or 3P resonance regime, thereby threatening structural safety. Therefore, the study suggests that scour-induced resonance must be considered in the design and that monitoring of scour or structural resonance is fairly necessary.

Keywords: jacket support structure, offshore wind turbine (OWT), resonance response, scour, soil-structure interaction (SSI)

INTRODUCTION

Ocean scour around the offshore wind turbine (OWT) foundation is considered critical in reducing the foundation lateral resistance, and thus even causing fatal damages to OWT systems (Sumer and Fredsøe, 2001). Contrary to numerous studies on bridge scour (Sumer et al., 1992; Sung et al., 2013; Kobayashi and Oda, 1994), offshore scour studies are relatively limited and majorly focused on scour at monopiles. Rather few studies regard scour of OWT systems with jacket-type support structures.

OWT systems withstand various frequency excitations, including excitations of the rotor (1P) and the blade-pass (3P for a three-bladed turbine) frequencies. When the OWT system's natural frequency coincides with its 1P or 3P frequency, resonance-type failure can occur. Scour changes the dynamic performance of OWT systems and possible risks the OWT systems to resonance damage (Malhotra, 2011).

The study employed the commercial software ANSYS for numerically modeling a jacket-supported OWT system. Meanwhile the soil-structure interaction (SSI) was integrated by using a series soil springs featuring p-y curves. The scour investigation was then conducted based on the developed model. Through evaluating variations of the structural frequency with respect to the scour depth, the study presented an insight into how scour affects dynamic performance and resonance response of a jacket-supported OWT system.

ANALYSIS MODEL

SSI-Embedded Structural Model

Rather than a real wind turbine, a NREL 5-MW virtual wind turbine supported by a jacket support structure was used as the prototype for constructing the OWT model. The geometrical sizes are demonstrated in Fig. 1(a). Detailed information about modeling properties of the NREL turbine could be referred to Jonkman et al.'s work (2009) and Popko et al.'s work (2012). The eccentric masses of the rotor and nacelle were assumed lumped at the hub elevation.

As shown in Fig. 1(b), the jacket support structure is composed of a 4-leg jacket structure, a transition piece, and a tower. The members of the towel and jacket structure all take forms of steel tubes.

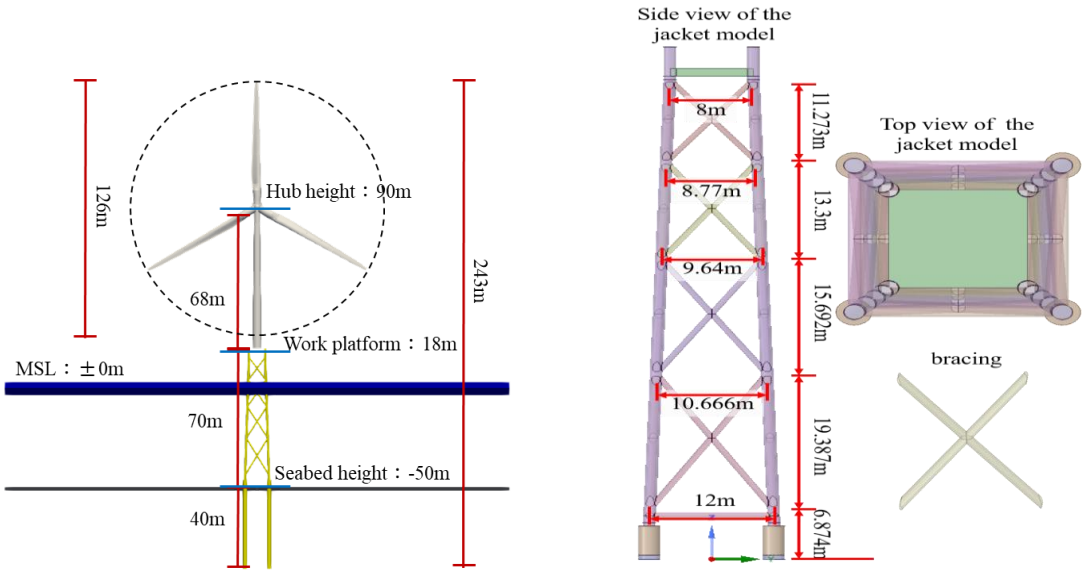

(a) (b)

Figure 1. Schematic figures of a) the NREL 5-MW OWT system and b) the jacket substructure model

According to the American Petroleum Institute (API 2002), the Winkler model was applied to account for the SSI of the pile foundation. The Winkler model regards a discrete number of nonlinear springs acting on an elastic pile beam. For implementation, the p-y, t-z, and Q-z curves, with the curve parameter in Table 1, were used to define the nonlinear spring stiffness separately in the three translational directions, as shown in Fig. 2.

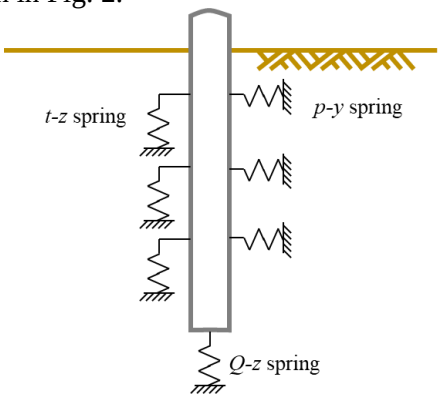

Figure 2. Schematic figure of the SSI springs

Table 1. Properties of the jacket support structure

SSI Springs	Parameter	Value	SSI Springs	Parameter	Value

p-y spring	ϕ' (deg)	37.5	t-z spring	r_f	0.9
	D (m)	2.082		t_{max} (kPa)	235.2
	γ' (kN/m^3)	11	Q-z spring	ϕ' (deg)	37.5
	K (MPa/m)	30		Nq*	81.5
t-z spring	G_0 (kN/m^2)	5.0×10^4		σ_v' (kPa)	440

In the table, ϕ' denotes the soil internal friction angle, D is the pile diameter, γ' is the soil effective unit weight, K is the initial modulus of subgrade reaction, G_0 denotes the soil initial shear modulus, r_f is a curve fitting parameter, t_{max} is the maximum skin resistance, and σ_v' is the vertical soil pressure.

Scour Consideration

Referring to DNVGL-ST-0126 (2016), lack of lateral resistance down to the depth of scour was considered by removing the corresponding SSI springs (i.e., the p-y and t-z springs) from the model, and then the effective stiffness of the remaining SSI springs was adjusted according to the new mudline level or embedment depth.

RESULTS AND DISCUSSIONS

Scour and Natural Frequency Responses

The constructed ANSYS model was verified through a comparative study with Damiani et al.'s FAST model (2013), before used for studying scour effects on dynamic responses of the jack-supported OWT system. Four scour depths were considered: s = 0D, 1D, 1.5D, and 2D; and D (= 2 m) is the diameter of the pile.

Scour was implemented by removing the corresponding SSI springs as well as simultaneously adjusting the effective stiffness of the remaining SSI springs. For the four scour cases, the resultant natural frequencies in the X and Y directions are presented in Table 2. As shown, the natural frequency of all cases drops as the scour depth increases, and the maximum reduction reaches as large as 15.40% for the 3st mode in Y direction.

Table 2. Scour effects on the modal frequency

Mode ID.	s/D				Frequency Difference (%)
	0	1	1.5	2	
1st in X dir.	0.3019	0.2993	0.2978	0.2963	1.89%
2st in X dir.	0.8683	0.8143	0.7869	0.7596	14.31%
3st in X dir.	2.0100	1.8574	1.7956	1.7420	15.38%
1st in Ydir.	0.3022	0.2996	0.2981	0.2966	1.89%
2st in Y dir.	0.8703	0.8160	0.7885	0.7611	14.35%
3st in Y dir.	2.0181	1.8646	1.8026	1.7488	15.40%

Foundation Dynamics

For the NREL 5-MW OWT in the study, the OWT's cut-in and rated rotor speed = 6.9 and 12.1 rpm, which are associated with the 1P and 3P frequencies = 0.115–0.2 Hz and 0.345–0.6 Hz, respectively. These ranges also define the corresponding resonance regimes. A Campbell diagram is plotted in Fig. 3 to identify such resonance regimes. As shown, the rotor speed zone of 6.9–12.1 rpm and the 1P and 3P frequency bands together outline the lower and upper resonance regimes, respectively.

To assess occurrence of scour-induced resonance, either the lower or upper resonance, the natural frequency of the jacket-supported OWT system was evaluated for particular scour cases (including

silting above the original seabed height): s = -3D (silting), -2D (silting), 0D, 1D, 2D, 6D, 9D, 12D, and 15D. The results in terms of the first natural frequencies in either the X or Y direction are presented in Fig. 3 and Table 3.

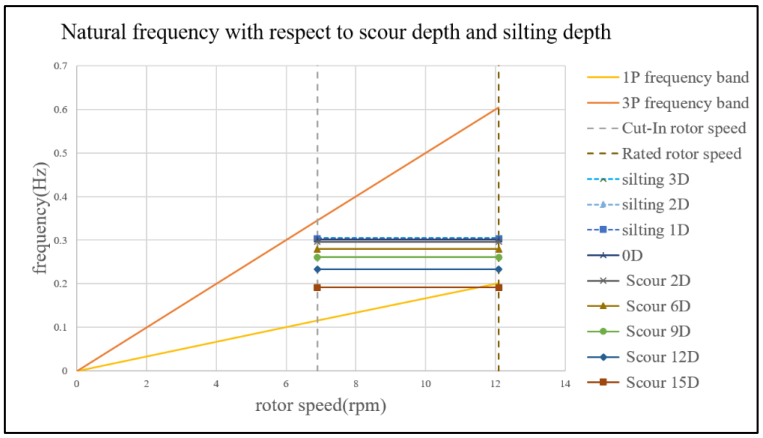

Figure 3. Campbell diagram of natural frequency with respect to scour depth

Table 3. First natural frequency of the OWT model for different scour cases

Dir.	s/D									
	-3	-2	-1	0	1	2	6	9	12	15
X	0.3052	0.3044	0.3035	0.3019	0.2993	0.2963	0.2797	0.2611	0.2331	0.1918
Y	0.3055	0.3047	0.3035	0.3022	0.2996	0.2966	0.2800	0.2613	0.2332	0.1918

As shown in Fig. 3, when scour depth reaches as large as 15D (= 30 m), the natural frequency (= 0.1918 Hz in both X and Y directions) fairly approaches the 1P frequency upper margin (= 0.2 Hz). This indicates that further scour is highly likely to induce resonance effect on the OWT system. On the other hand, when silting occurs, the first natural frequency increases but to a minor extent, remaining in the resonance-free zone.

CONCLUSIONS

This study conducted a numerical investigation on the effect of ocean scour on the vibrational behaviors of a jacket-support OWT system. The SSI-embedded OWT model was constructed and verified with the reference study by Damiani et al. (2013). Scour was then taken into accounted by removing the corresponding SSI springs from the numerical model. The results of the numerical scour investigation indicated the following conclusion:

1. The natural frequency of the OWT system drops as the scour depth increases.
2. During the typical seabed scour and silting processes, resonance failure was likely occur to the OWT system. Therefore, it is recommended that scour-induced resonance must be considered in the design stage, and monitoring of scour or structural resonance responses is fairly necessary during the OWT operation and maintenance phases.

ACKNOWLEDGMENTS

The research was supported by the project grants “Research on Site Survey and Design of Offshore Wind Turbines (Project No. 1D171090507-59)”, the Bureau of Standards, Metrology and Inspection of Taiwan.

REFERENCES

Damiani, R., H. Song, A. Robertson, and J.M. Jonkman (2013). "Assessing the importance of nonlinearities in the development of a substructure model for the wind turbine CAE tool FAST," in: Proceedings of the 32nd Int. Conf. on Ocean, Offshore, and Arctic Eng. Jun 2013, Nantes, France.

Jonkman, J., S. Butterfield, W. Musial, and G. Scott (2009). "Definition of a 5-MW reference wind turbine for offshore system development," Office of Scientific Technical Information Technical Report, NREL, US.

Kobayashi, T. and K. Oda (1994). "Experimental study on developing process of local scour around a vertical cylinder," in: Proceedings of the 24th Int. Conf. on Coastal Eng Oct 1994, Kobe, Japan.

Malhotra, S. (2011). "Selection, design and construction of offshore wind turbine foundations," *Wind Turbines*. 231–264.

Popko, W. et al. (2012). "Offshore code comparison collaboration continuation (OC4), phase I – results of coupled simulations of an offshore wind turbine with jacket support structure," in: Proceedings of the 22nd Int. Soc of Offshore and Polar Eng Conf Jun 2012, Rhodes, Greece.

Sumer, M., N. Christiansen, and J. Fredsøe (1992). "Time scale of scour around vertical pile," in: Proceedings of the 2nd Int. Offshore and Polar Eng Conf Jun 1992, California, USA.

Sumer, M. and J. Fredsøe (2001). "Scour around pile in combined waves and current," *J of Hydraul Eng*, 127(5), 403–411.

Sung, Y.C., and C.Y. Wang (2013). "A study on damage assessment of the scoured bridges," *J of the Chin Inst of Eng*, 36(8), 994–1007.

A LITERAL REVIEW ON THE SEISMIC OR VIBRATION TEST REQUIREMENTS FOR WIND ENERGY EQUIPMENT

Bai-Yi Huang[1], Juin-Fu Chai[2], Fan-Ru Lin[3], Wei-Hung Hsu[1], Tzu-Chieh Chien[4], Zhen-Yu Lin[1] and Chin-Xin Wang[5]

1. Assistant Researcher, National Center for Research on Earthquake Engineering, Taiwan, R.O.C.
2. Research Fellow and Deputy Director General, National Center for Research on Earthquake Engineering, Taiwan, R.O.C.
3. Associate Researcher, National Center for Research on Earthquake Engineering, Taiwan, R.O.C.
4. Associate Technologist, National Center for Research on Earthquake Engineering, Taiwan, R.O.C.
5. Research Assistant, National Center for Research on Earthquake Engineering, Taiwan, R.O.C.

Email: byhuang@narlabs.org.tw, chai@narlabs.org.tw, frlin@narlabs.org.tw, mikehsu@narlabs.org.tw, tcchien@narlabs.org.tw, zylin@narlabs.org.tw, cxwang@narlabs.org.tw

ABSTRACT

Taiwan has been developing on-shore wind turbine for decades, and aims to increase offshore wind power installed capacity due to the abundant wind resources in the west coast. The first offshore wind farm in Taiwan had started commercial operation at the end of 2019, which represents an important milestone of the energy policy transition in Taiwan. However, natural hazards such as typhoons or earthquakes threaten all the time. BSMI Taiwan cooperated with NCREE and announced the amended edition of the national standard, CNS 15176-1-2018, on design requirements of wind turbines. The standard includes the seismic design requirements to improve the safety of wind turbine supporting structures. However, it's also important to verify the seismic safety of the instruments inside the wind turbine or substation. This article briefed the seismic or vibration testing requirements of present design standards or operational documents of wind turbines issued by internationally recognized organizations, such as IEC, DNV GL or IEEE.

Keywords: offshore wind turbine, seismic qualification, vibration test

INTRODUCTION

At each phase of wind power plant life cycle, such as development phase, construction phase or operation phase, relevant inspections or verifications need to be carried out in accordance with the specific standards provided by the accreditation body. In addition, prototype certification and component certification require the submissions of qualified documents corresponding to the test or acceptance standards for design evaluation or manufacturing evaluation. The standards adopted depend on the accreditation or certification bodies. Commonly, standardization bodies can be classified into international (ISO, IEC, IEEE, etc.), regional (EU, CEN or CENELEC, etc.) or national (BSMI in Taiwan, BSI in British, API in U.S., BSH in German, NEK and PSA in Norway, etc.). On the other hand, classification societies such as ABS in the United States, ClassNK in Japan, BV and DNV GL, etc., have been dedicated to the field of maritime engineering for a long time, and transferred into a certification bodies. Therefore, these classification societies established technical standards for ships and offshore structures. (Norsk Industri AS, 2020).

This article reviews the requirements for the seismic or vibration testing of wind turbines described in the documents issued by the internationally recognized organizations, such as IEC, DNV GL or IEEE. These requirements can be used as the reference materials to improve the safety of wind turbine in Taiwan to mitigate the seismic hazard. In addition, some of the standards described sampling or testing methods for site investigation or liquefaction resistance, which are also helpful for improving the seismic safety of wind turbine. However, this article focused the requirements on shaking table testing for seismic qualification or vibration test.

IEC

The International Electrotechnical Commission (IEC) is an authoritative international standards organization formed more than a century ago. IEC prepares and publishes a large number of international standards for all electrical, electronic and related technologies, and cooperates with several major standards development organizations, such as ISO, International Telecommunication Union (ITU), and IEEE etc. In order to facilitate international trade in equipment and services for use in renewable energy sectors, IEC established the IECRE system, which aims to offer a harmonized application around the globe for certification to standards relating to equipment used in solar PV energy, wind energy and marine energy. The standards applied to wind energy are the IEC 61400 series, which are also the bellwether in the field of wind energy. The design requirement standards issued by Bureau of Standards, Metrology and Inspection, CNS 15176-1 (BSMI, 2018), and similar standards issued by other national standardization organizations are based on IEC 61400-1 and harmonized according to local environmental conditions and needs.

Table 1. Design evaluation requirements in OD-501-7

Component	**Standard**	**Scope of evaluation**
Generator	60034 series	● heat-run test results (converter operated, if applicable), ● other type/prototype test results, ● vibration test results as applicable, ● routine test plan, ● bearing rating life calculation (ISO 281), ● cooling system, ● cable connection and interfaces, ● installation and environment, ● protection and earthing ● Direct drive generators shall be documented according to an agreed design basis as IEC ● 60034 does not account for the special issues related to direct drives systems.
Converter	62477-1 or 61800-4 (if Ur > 1kVa.c.)	● EMC according to IEC 61800-3 or equivalent, ● IEC type and routine tests such as protective bonding impedance test, impulse ● withstand voltage test, touch current measurement, thermal performance test, etc., ● insulation design (including environmental categories according to IEC 60721, ● overvoltage categories, clearance and creepage distance, etc.).
Transformer	60076 series	● type and routine tests, ● vibration test, ● environmental testing, ● cooling system, ● installation and earthing ● protection and monitoring equipment
Switchgear	62271 series	The switchgear arrangement for the main power line between generator and grid and its ratings shall be compared with assumptions made in the design basis. For high-voltage switchgear internal faults testing, pressure relief measures and their possible influence on the installation environment shall be checked in addition.

The main IEC relevant standards that cover wind energy generation systems are the IEC 61400-series, which aim to ensure the wind turbines are appropriately engineered against damage from hazards within the planned lifetime. Among this series, IEC 61400-1 standard specifies the basic design

requirements for the subsystems of wind turbines, such as control and protection mechanisms, internal electrical systems, mechanical systems and support structures. It describes the assessment of earthquake conditions, and the seismic load should be carried out according to local codes (IEC, 2019). By contrast, the requirements related to seismic or vibration testing were described in the withdrawn IEC 61400-22, which was replaced with the deliverables for the wind sector (WE-OMC) contained in the IECRE. The IECRE provided the operational document OD-501, which specifies procedures for the type certification scheme, with respect to specific standards and other technical requirements, and it's applicable for both onshore and offshore wind turbine and not limited to wind turbine of any particular size a type. The type certification scheme also covers prototype certification including procedures related to evaluation of the safety of operating a prototype in order to enable testing of a new wind turbine type (IECRE, 2018). In order to reduce the complexity of the certification procedure for the applicant, the document describes procedures for conformity assessment relating to design, testing and manufacturing. Based on OD-501, IECRE provided a series of sub-document that defines the conformity assessment and certification of specified components of wind turbine by renewable energy certification bodies (RECB), which including blade (OD-501-1), gearbox (OD-501-2), tower (OD-501-3), loads (OD-501-4), control and protection system (OD-501-5) and main electrical components (OD-501-7). Among these sub-documents, the requirements relate to seismic or vibration tests are described in OD-501-7, and the applicable standards, scopes of evaluation for specific electrical components are shown in Table 1 (IECRE, 2019).

Table 2. Relevant IEC standards with seismic or vibration testing requirement

Standard	Title	Test method
IEC/IEEE 60076-16 2018	IEC/IEEE International Standard - Power transformers - Part 16: Transformers for wind turbine applications (seismic qualification required in IEC 60076-11)	IEC 60068-3-3
IEC 62271-207 2012	High-voltage switchgear and controlgear –Part 207: Seismic qualification for gas-insulated switchgear assemblies for rated voltages above 52 kV	IEC 60068-3-3
IEC 62271-210 2013	High-voltage switchgear and controlgear –Part 210: Seismic qualification for metal enclosed and solid-insulation enclosed switchgear and controlgear assemblies for rated voltages above 1 kV and up to and including 52 kV	IEC 60068-3-3 IEC 60068-2-57
IEC 62271-300 2006	High-voltage switchgear and controlgear – Part 300: Seismic qualification of alternating current circuit-breakers	IEC 60068-2-57
IEC 60255-21-1 1988	Electrical relays - Part 21: Vibration, shock, bump and seismic tests on measuring relays and protection equipment - Section One: Vibration tests (sinusoidal)	IEC 60068-2-6
IEC 60255-21-3 1993	Electrical relays - Part 21: Vibration, shock, bump and seismic tests on measuring relays and protection equipment - Section 3: Seismic tests	IEC 60068-2-6 IEC 60068-2-57 IEC 60068-3-3

Among the applicable standards listed in Table 1, there are no environmental test requirements in the IEC 60034 series. The vibration test results should be the vibration measurement results induced by the operation of rotating electrical machines; IEC 60076-16 is the applicable standard for dry-type or liquid-immersed transformers used in wind turbines. The climatic and environmental test requirements shall follow the service conditions specified in IEC 60076-11 (dry-type transformers), and IEC 60076-11 referred to IEC 60068-3-3 for seismic test; IEC 62271 series are standards for high-voltage switchgear and controlgear, and the sub-documents IEC 62271-207, -210 and -300 provided the requirements of seismic qualification for high-voltage gas-insulated switchgear assemblies, metal enclosed and solid-insulation enclosed switchgear and controlgear assemblies, and alternating current circuit-breakers, respectively. These standards referred to the IEC 60068 series for the seismic or vibration testing procedures; there is no environmental testing requirement described in IEC 62477-1 and 61800-4 (which was replaced by IEC 61800-2) for converter.

DNV

Det Norske Veritas (DNV) and Germanischer Lloyd (GL) are both long-established classification societies, and they merged in 2013. They had accumulated maritime engineering experience for more than a century, and delivered classification, certification and advisory services for relevant industries. Recently, DNV had built a complete set of standards and recommended practices for wind power plants including turbines, bottom-fixed and floating support structures, cables, and offshore substations. Therefore DNV and IEC are the leading organizations that have published the most extensive documents related to offshore wind turbine. Nowadays not only offshore but also onshore wind power assets are included in the scope of the certification service provided by DNV, shown in figures 1 and 2.

The service document system is organized according to a three-level document hierarchy. Service specification (SE) provides principles and procedures related to certification and verification services, and present the scope and extent DNV GL's services. Standard (ST) issued as neutral technical standards to enable their use by national authorities, as international codes and as company or project specifications without reference to DNV GL's services. Recommended practices (RP) provide DNV GL's interpretation of safe engineering practice for general use by the industry (DNV GL, 2018).

DNVGL-ST-0145 (2020) provides design requirements for offshore substations, including structural design, electrical design and so on. Major electrical equipment shall comply with the corresponding requirements, such as IEC 62271-203 (high voltage switchgear), IEC 62271-200 (medium voltage switchgear), IEC 62271 series (switchgear in general), IEC 60076 series (transformer in general), IEC 60076-15 (gas insulated transformers), IEC 60099-4 (surge arresters) etc. Most of the standards referred to IEC 60068 series as the seismic or vibration testing method as well.

DNVGL-ST-0076 (2015) provides design principles and technical requirements for electrical installations in onshore or offshore wind turbines. It states in Chapter 11 that the Electrical equipment for measurement and control use and its accessories for wind turbine applications shall comply with part of IEC 60068 series, and the parameters of the tests required for a specific product shall be determined on a case by case basis depending on the product and its use. Furthermore, the standards referred for fire hazard (IEC 60695, laser products (IEC 60825-1) require vibration test in accordance with IEC 60068-2-6.

Although DNVGL-RP-0585 (2021) is a recommended practice for seismic design of wind farms, and focuses on site investigation and soil dynamic analysis. However, seismic qualification for components is not required in the document. As an internal summary, the design or certification requirements for wind turbines issued by DNV basically refer to other international standards or specifications due to DNV and GL were formerly classification societies. In terms of electronic or electrical equipment, IEC 60068 series is referred for vibration test or seismic qualification.

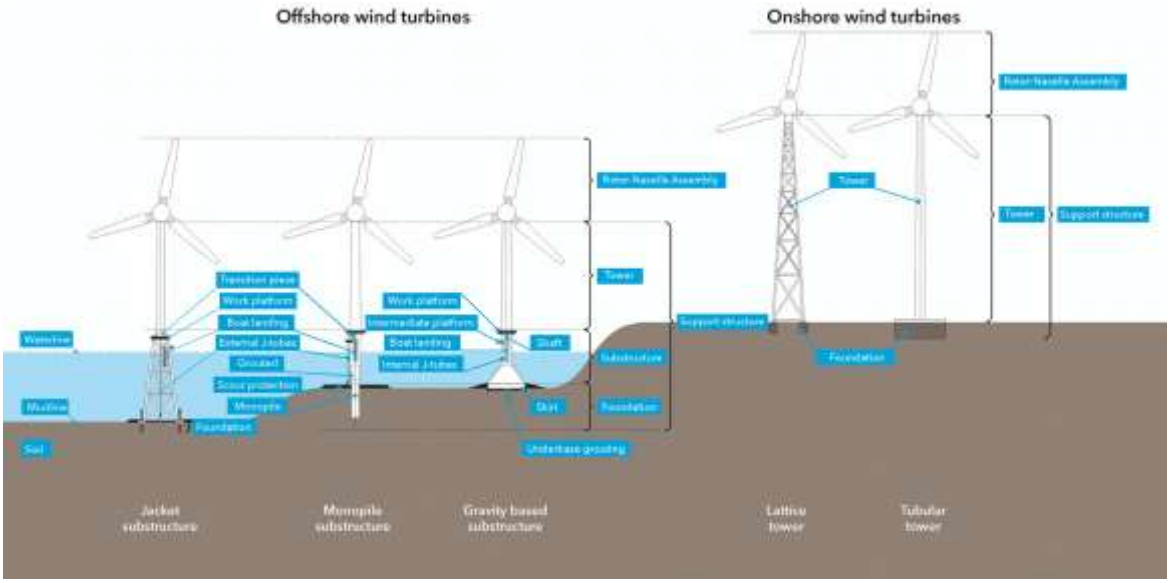

Figure 1. Definition of offshore and onshore wind turbine components (DNV, 2015)

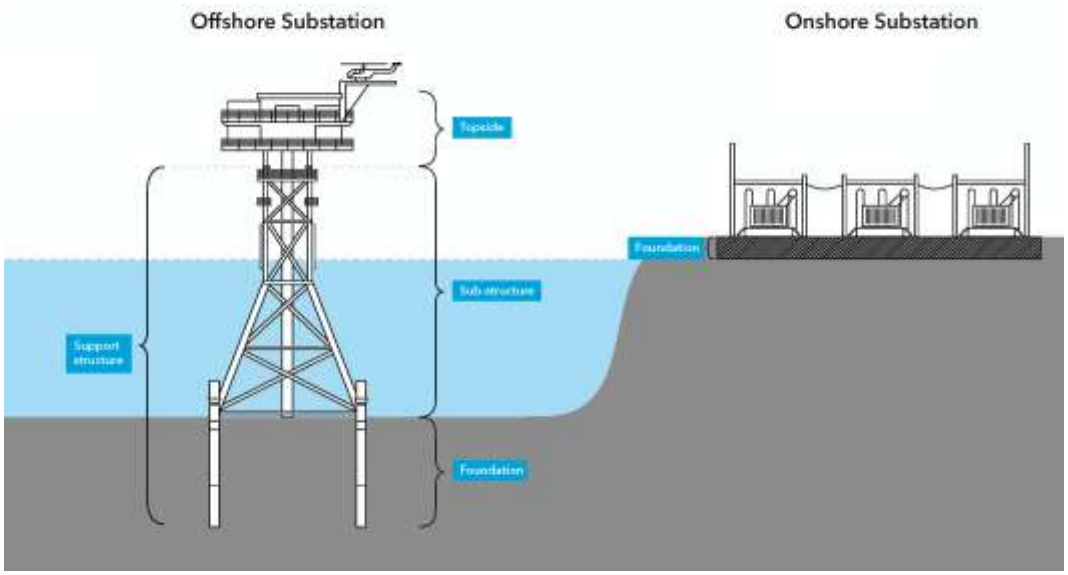

Figure 2. Definition of offshore and onshore substation components (DNV, 2015)

OTHER ORGANIZATIONS

The standards related to wind turbine issued by the International Organization for Standardization (ISO) independently include the blade coating inspection (ISO 19392 series), mechanical vibration (ISO 10816-21:2015), and Condition monitoring and diagnostics of wind turbines (ISO 16079), etc., and the joint standard IEC 61400-4:2012 for gearboxes with IEC, which are listed in table 3. Although there is no relevant standards particularly for seismic design or testing of offshore or onshore wind turbines. However, some seismic design requirements for offshore wind turbine supporting structure given by other specifications, such as DNV-OS-J101, referred to ISO 19901-2 as the basis for offshore structural design methods, but there is no description on vibration or seismic testing as well.

Table 3. ISO standards related to wind turbine.

Standard	Title
ISO 19392-1~3:2018	Paints and varnishes — Coating systems for wind-turbine rotor blades
ISO 10816-21:2015	Mechanical vibration — Evaluation of machine vibration by measurements on non-rotating parts — Part 21: Horizontal axis wind turbines with gearbox
ISO 16079-1:2017	Condition monitoring and diagnostics of wind turbines — Part 1: General guidelines
ISO 16079-2:2020	Condition monitoring and diagnostics of wind turbines — Part 2: Monitoring the drivetrain
ISO 29400:2020	Ships and marine technology — Offshore wind energy — Port and marine operations
ISO 29404:2015	Ships and marine technology — Offshore wind energy — Supply chain information flow
IEC 61400-4:2012 (Published by IEC)	Wind turbines — Part 4: Design requirements for wind turbine gearboxes

The standards related to wind turbine issued independently by Institute of Electrical and Electronics Engineers (IEEE) include personnel safety (IEEE 2760-2020), acoustic noise measurement techniques (IEEE 2400-2016) or technical supervision code for rotor systems (IEEE 1834-2019), and the joint standard IEC/IEEE 60076-16-2018 for transformers with IEC. In the aspect of electrical power systems applied to offshore facilities, IEEE provided IEEE 1662 (IEEE, 2016) for the power electronics (PE), which referred to IEC 60068-2-6 as the basis of vibration test method. Furthermore, for the PE installed in seismic active areas and emergency standby power systems, it's suggested in IEEE 1662 to withstand physical shocks and multi-axis accelerations as specified in the International Building Code (IBC) or other applicable local building codes. IBC states in Section 1705.14.2 that the

nonstructural components shall qualified by analysis, testing or experience data specified in Section 13.2.1 of ASCE 7 (ICC, 2021), and ASCE 7 required in Section 13.2.6 that the seismic qualification shall be in accordance with the nationally recognized testing standard procedure, such as ICC-ES AC156 (ASCE, 2022). IEEE 693 is the authoritative standard for the seismic design of the structure and seismic qualification on equipment of the substation (IEEE, 2018). In addition, formula of the required response spectra given in IEEE 693 were adopted by relevant standards issued by IEC, such as IEC 62271-207, -210.

Table 4 IEEE standard related to wind turbine and power electronics

Standard	Title	Test method
IEEE 2400 2016	IEEE Standard for Wind Turbine Aero Acoustic Noise Measurement Techniques	-
IEEE 1834 2019	IEEE Standard for Technology Supervision Code for Wind Turbine Rotor Systems	-
IEEE 2760 2020	IEEE Guide for Wind Power Plant Grounding System Design for Personnel Safety	-
IEC/IEEE 60076-16 2018-09	IEC/IEEE International Standard - Power transformers - Part 16: Transformers for wind turbine applications	IEC 60068-3-3 (in IEC 60076-11)
IEEE 1580	IEEE Recommended Practice for Marine Cable for Use on Shipboard and Fixed or Floating Facilities	IEC 60068-2-6
IEEE 1662	IEEE Recommended Practice for the Design and Application of Power Electronics in Electrical Power Systems	IEC 60068-2-6 and local building code
IEEE 693	IEEE Recommended Practice for Seismic Design of Substations	IEEE 693

CONCLUSIONS

This article reviewed the design requirements or project certification specifications for wind turbines. In the aspect of improving the structural integrity and reliability, the effect of earthquake is usually taken into consideration the load combination with other environmental conditions, such as wind, waves and currents, during structure design phase. However, earthquake is considered as regional hazard, therefore the relevant requirement should be given by the local seismic code. Most of the reviewed specifications lay stress on site inspection to identify the earthquake or liquefaction hazard, and there are not too many detailed instructions on the seismic qualification of equipment.

In order to find out the practical measures, this article reviewed the relevant standards specified or referred in the guidance documents or standards further. It turns out that the standards of the specified equipment or component give the testing requirements or acceptance criteria, and refer to other standards for detailed testing or qualifying procedure. Commonly, the environmental test methods referred by the standards are IEC 60068 series, especially the IEC 60068-2-6 for sinusoidal vibration test and IEC 60068-3-3 for seismic test. These standards provided the method and guidance to conduct the seismic or vibration test. However, there is no specific testing parameter given. It's necessary to determine the suitable parameters based on the local seismic and structural characteristics through analysis or simulation. On the other hand, IEEE 693 played an important role in qualifying the seismic performance on electrical power equipment. Not only the substation and its components can be designed and qualified in accordance with IEEE 693, but also the required response spectra given in relevant standards issued by IEC, such as IEC 62271-207, -210, are originated from IEEE 693.

ACKNOWLEDGMENTS

This study was supported by Bureau of Standards, Metrology and Inspection and Metal Industries Research & Development Centre, Taiwan. The authors are grateful to this support.

REFERENCES

Norsk Industri AS. (2020). *Overview of offshore wind standards and certification requirements in selected countries* (Report No.: 2020-1194, Rev. 01). DNV GL.

BSMI. (2018). *Wind turbines − Part 1: Design requirements* (CNS 15176-1).

IEC. (2019). *Wind energy generation systems - Part 1: Design requirements* (IEC 61400-1).

IECRE. (2018). *Type and Component Certification Scheme* (OD-501).

IECRE. (2019). *Conformity assessment and certification of Main Electrical Components by RECB* (OD-501-7).

DNV GL. (2015). *Design of electrical installations for wind turbines* (DNVGL-ST-0076).

DNV GL. (2018). *Certification of floating wind turbines* (DNVGL-SE-0422).

DNV GL. (2020). *Offshore substations* (DNVGL-ST-0145).

DNV GL. (2021). *Seismic design of wind power plants* (DNVGL-RP-0585).

DNV GL. (2014). *Design of Offshore Wind Turbine Structures* (DNV-OS-J101).

DNV GL. (2015). *Project certification of wind power plants* (DNVGL-SE-0190)

IEEE. (2016). *IEEE Recommended Practice for the Design and Application of Power Electronics in Electrical Power Systems* (IEEE 1662-2016).

International Code Council. (2021) *International Building Code* (IBC).

American Society of Civil Engineers. (2022). *Minimum Design Loads and Associated Criteria for Buildings and Other Structures* (ASCE/SEI 7-22).

IEEE. (2018). *IEEE Recommended Practice for Seismic Design of Substations* (IEEE 693-2018).

(SS3) Structural collapse behavior under near-fault earthquake effect

PARAMETER OPTIMIZATION FOR PIVOT HYSTERESIS MODEL OF REINFORCED CONCRETE SHEAR WALLS WITH DIFFERENT FAILURE MODES

Yu-Che Ling[1], Srinivas Mogili[2] and Shyh-Jiann Hwang[2]
1. PhD Student, Dept. of Civil Engineering, National Taiwan University, Taiwan, R.O.C.
2. Post-doctoral researcher, Dept. of Civil Engineering, National Taiwan University, Taiwan, R.O.C.
3. Professor, Dept. of Civil Engineering, National Taiwan University, Taiwan, R.O.C.
Email: d08521005@ntu.edu.tw, smogili@ntu.edu.tw, sjhwang@ntu.edu.tw

ABSTRACT

Reinforced concrete walls as the major vertical reinforced concrete members resisting lateral loading in the reinforced concrete structures located in seismic regions. Hence, the hysteresis behavior prediction of reinforced concrete walls is important for earthquake-resistant design. Currently, the Pivot hysteresis model is used to predict the hysteretic behavior with parameters α and β representing the unloading stiffness and pinching, respectively, determined using the geometric and reinforcement details in column members. In this paper, an effort is made to improve the existing application of the Pivot hysteresis model to reinforced concrete walls. The key variables to control α and β are axial load ratio, wall height-to-length ratio, web reinforcement indices, boundary element reinforcement indices, and length-to-effective thickness ratio. Equations for α and β were calibrated through optimization of energy dissipation from 61 wall specimens subjected to cyclic loading and exhibiting different failure modes. The calibration was based on the optimization of energy dissipation for specimens from the collated database - a numerically complex task achieved through a superior optimization technique known as Simulated Annealing. The proposed formulations can improve the accuracy of the Pivot hysteresis model for walls by capturing pinching and stiffness degradation more reasonably under different failure modes.

Keywords: reinforced concrete walls, hysteresis, energy dissipation, optimization, pivot hysteresis model

INTRODUCTION

Reliable hysteretic modeling is essential for the evaluation of existing reinforced concrete buildings. Also, tall buildings and other structures of high importance require reasonably accurate seismic nonlinear time-domain analysis for design, which includes the nonlinear response characteristics, namely load-displacement behavior and hysteretic modeling of structural members. Reinforced concrete (RC) walls are a commonly-used lateral loading resisting system in RC buildings located in seismic regions. The accurate prediction of the nonlinear response characteristics of RC walls is particularly important in such dynamic analyses.

Currently, several general hysteretic models have been proposed by researchers (Takeda *et al.*, 1970; Baber and Wen, 1981; Baber and Noori, 1985; Kunnath *et al.*, 1990; Dowell *et al.*, 1998) and these are broadly classified into two categories. The first category, "smooth" hysteresis models, refers to the prediction of smooth loops that can effectively trace continuous changes in cyclic responses. An example of a smooth hysteresis model is the Bouc-Wen-Baber-Noori (BWBN) model (Baber and Wen, 1981; Baber and Noori, 1985), which was later modified in the context of RC walls (Sengupta and Li, 2014). The second category is referred to as "polygon" hysteresis models. Polygonal hysteresis models generalize the responses into piecewise linear curves, which are separately defined by simple hysteresis rules at different deformation levels, such as cracking, yielding, and post-yielding levels. A few examples of the polygonal hysteresis models are the Takeda model (Takeda *et al.*, 1970), the Three-parameter model (Kunnath *et al.*, 1990), the Pivot hysteresis model (Dowell *et al.*, 1998), etc. The

Takeda model includes realistic conditions for the reloading curves and considers stiffness degradation due to increasing damage upon further loading, but it discounts the pinching phenomenon making it unsuitable for shear critical members. The Three-parameter model is derived based on three parameters that capture stiffness degradation, pinching behavior, and strength degradation. The Pivot hysteresis model, as in Fig. 1, models the hysteresis behavior based on two pivot points (α and β) that represent the unloading stiffness and the pinching phenomenon.

Although both the smooth-type and polygon-type models are suitable for research applications, the complex hysteresis rules and high computational demands of the smooth hysteretic models are major hurdles for design applications. On the other hand, the polygon-type hysteretic models are relatively less complex and more user-friendly, making them desirable for popular commercial design software since they can feature the cyclic responses of structural elements with acceptable accuracy and less computational time. For instance, the modified pivot hysteresis model (Sharma *et al.*, 2013) provides equations to determine the pivot parameters of a column based on the physical parameters of the members. The ease and objective determination of the pivot parameters make the Pivot hysteresis model the preferred choice for design applications. This has led to the adoption of this model in popular commercial software such as ETABS and SAP2000. A subsequent study (Ling *et al.*, 2022) further improved the Pivot hysteresis model to include more comprehensive physical parameters in deriving the pivot parameters separately for flexure and shear failure hinges; however, the applicability of this model is limited to column members.

In this paper, an effort is made to fill this gap in deriving the equations for pivot parameters pertaining to RC walls exhibiting flexural and shear failure modes. The current work can improve the overall nonlinear modeling of RC walls with accurate hysteresis predictions that can be easily adopted in popular design programs. The application of the failure mode dependent pivot parameters in walls is aided through the representation of walls using the equivalent column model (Chung *et al.*, 2009). The hinge definition of the equivalent column representation for walls is highlighted in Fig. 2. Analyzing RC walls using the hinge definitions of the equivalent column has been shown to produce reasonably good seismic evaluations of buildings with RC walls in Taiwan. The failure mode dependent hysteresis parameter recommendation proposed in this study can be embedded in the equivalent column model to analyze the nonlinear behavior of RC walls.

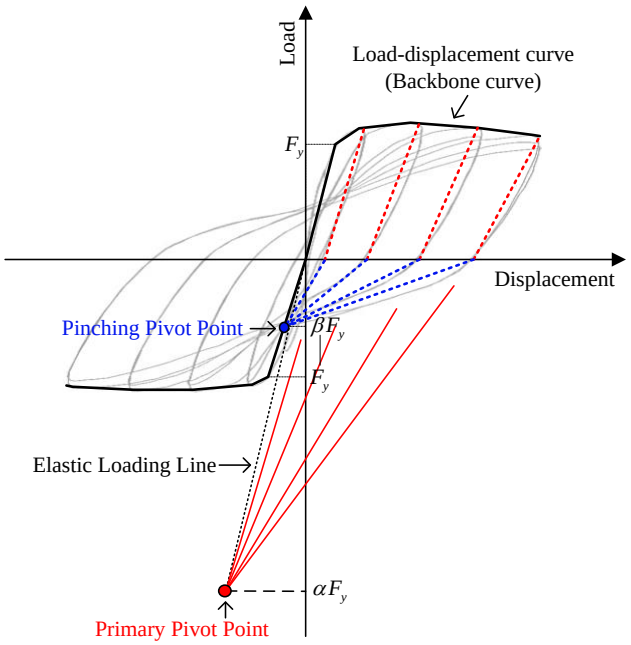

Figure 1. Pivot points for hysteresis loops as per the Pivot hysteresis model

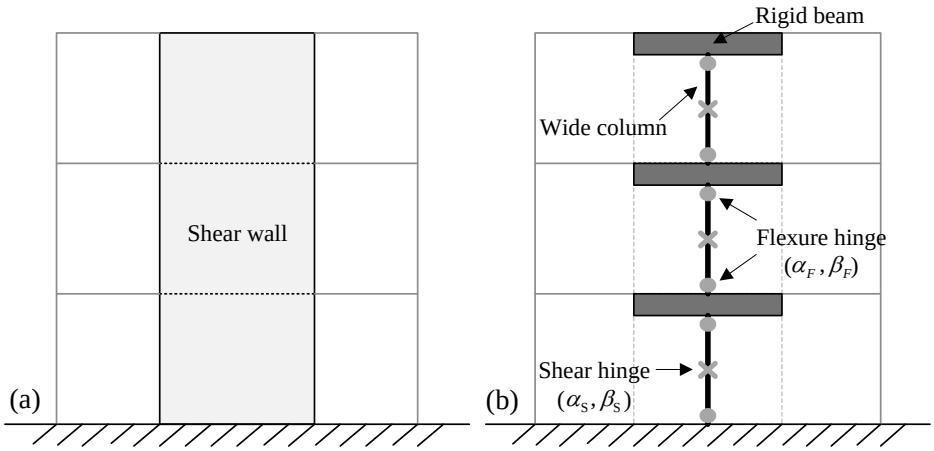

Figure 2. Nonlinear models of RC walls: (a) typical wall frame buildings; (b) equivalent column models

EXPERIMENTAL DATABASE

This study establishes an experimental database with hysteresis data for 61 single-story, one-bay reinforced concrete wall specimens for pivot parameter optimization. Most of the specimens are extracted from SERIES Database (SERIES, 2013) and remaining part of test data is newly collected by the authors. The database included both rectangular and barbell shaped walls. Among the test specimens collected, 40 walls were identified as flexure-dominant and 21 walls as shear-dominant walls.

The distributions of physical parameters that are relevant to the performance of RC walls are shown in Figure 3. The parameters of interest are as follows: (1) axial load ratio $P/A_g f_c'$; (2) wall height-to-length ratio H/ℓ_w; (3) web reinforcement index $\rho_w f_{y,w}/f_c'$; (4) boundary element longitudinal reinforcement index $\rho_c f_{y,c}/f_c'$; (5) boundary element transverse reinforcement index $\rho_{ct} f_{y,ct}/f_c'$; and (6) length-to-effective thickness ratio ℓ_w/t_e. The effective thickness t_e adopted from AIJ Standard (AIJ, 2018) to represent the contribution of wall thickness from additional concrete portions in boundary elements in barbell shaped walls can be calculated as:

$$t_e = A_g/\ell_w \tag{1}$$

where A_g is the wall gross section; t_w is the wall thickness.

Due to the high correlation (0.83) between web horizontal and vertical reinforcement indices, this study merges these two indices as web reinforcement index $\rho_w f_{y,w}/f_c'$. The concept of $\rho_w f_{y,w}/f_c'$ was adopted from the recommendations of Hwang and Lee (Hwang and Lee, 2002) based on the force transfer mechanism within the RC discontinuity regions. The contributions of the vertical and horizontal web reinforcements depend on the wall height-to-length ratio H/ℓ_w. When $H/\ell_w \geq 1$, the web horizontal reinforcement plays a more important role in transferring the lateral force as compared with that of the web vertical reinforcement. In this case, the rebar ratio and yield strength of web reinforcement were assumed to be equal to that of the horizontal web reinforcement, i.e., $\rho_w = \rho_{wh}$ and $f_{y,w} = f_{y,wh}$. Conversely, when $H/\ell_w < 1$, the web vertical reinforcement is more significant, ρ_w was defined as the vertical web reinforcement ratio ($\rho_w = \rho_{wv}$), and $f_{y,w}$ is the yield strength of the vertical web reinforcement ($f_{y,w} = f_{y,wv}$).

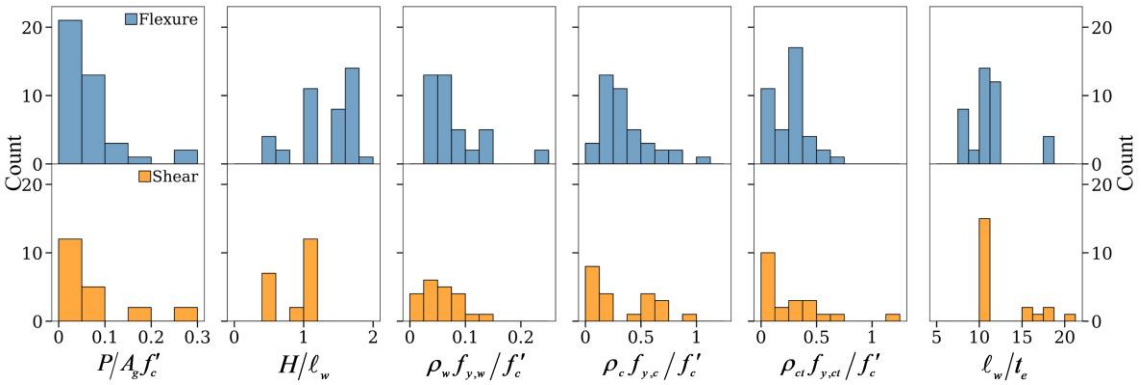

Figure 3. Distribution of physical parameters

PARAMETER OPTIMIZATION

The optimization procedure is to carry out the optimization of α and β as a function of multiple input physical features. The generalized form of parametric equations for α and β are given by Eqs. 2 and 4, respectively. Furthermore, to prevent over-emphasis on a single feature, the coefficients were limited within practical ranges shown in Eqs. 3 and 5.

$$\alpha = a_0 \times p_1^{a_1} \times p_2^{a_2} \ldots \times p_k^{a_k} + a_{k+1} \le 10 \tag{2}$$

$$0 < a_0 \le 1;\ 0.1 \le |a_1, a_2, \ldots, a_k| \le 3;\ 0 \le a_{k+1} \le 3 \tag{3}$$

$$\beta = b_0 \times p_1^{b_1} \times p_2^{b_2} \ldots \times p_k^{b_k} + b_{k+1} \le 1 \tag{4}$$

$$0 < b_0 \le 1;\ 0.1 \le |b_1, b_2, \ldots, b_k| \le 3;\ 0 \le b_{k+1} \le 1 \tag{5}$$

where p_1 to p_k are selected geometric or reinforcement input features, and a_0 to a_{k+1} and b_0 to b_{k+1} are the coefficients that control the influence of each chosen feature on α and β, respectively.

The optimization problem is two-fold: choosing the features and computing the coefficients for the selected features. The selection of features was carried out in a forward-selection manner by adopting a greedy strategy (Guyon and Elisseeff, 2003), i.e., choosing the feature that provided the best reduction in error, followed by the addition of the next best feature, and so on. In the first run, a single feature that provided the greatest reduction in the error was selected. In the next run, another feature was selected in such a way that the new feature, in combination with the previously selected feature, would be the best choice for error reduction. Therefore, for each pivot parameter, six runs were performed in total, with the addition of one feature per run.

At each run, the determination of the best feature choice involved the calibration of coefficients for the selected features in that run by running an optimization algorithm based on energy dissipation. In order to use energy dissipation in numerical optimization, the authors defined two kinds of indicators that collectively quantified the variation of energy dissipation. These two indicators could capture the differences between model hysteretic prediction and experimental response: one at the single loop level and the other at the specimen level. The first kind of energy dissipation indicator, named the "loop energy index," was defined at the loop level to measure the calibration difference within a single loop. The loop energy index is a dimensionless ratio of model-to-test energy dissipation estimated separately at each loop in designated drift regions. Loop energy indices for parameter α (unloading behavior) and β (pinching phenomenon) are given by Eqs. 6 and 7, respectively.

$$I_\alpha^{j+} = \left(A_\alpha^{j+}\right)_{model} \Big/ \left(A_\alpha^{j+}\right)_{test};\ \ I_\alpha^{j-} = \left(A_\alpha^{j-}\right)_{model} \Big/ \left(A_\alpha^{j-}\right)_{test} \tag{6}$$

$$I_\beta^{j+} = \left(A_\beta^{j+}\right)_{model} \Big/ \left(A_\beta^{j+}\right)_{test};\ \ I_\beta^{j-} = \left(A_\beta^{j-}\right)_{model} \Big/ \left(A_\beta^{j-}\right)_{test} \tag{7}$$

where $j\pm$ represents the target loop in positive and negative directions; I_α and I_β are the loop energy indicators for α and β, respectively; A_α and A_β are the local energy dissipation areas corresponding to α and β, respectively, as shown in Figs. 4 and 5.

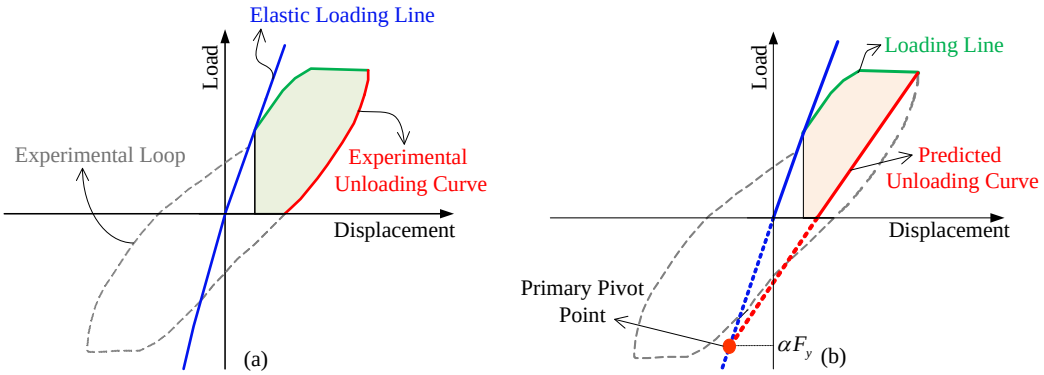

Figure 4. Energy dissipation area A_α^{j+} for loop energy indices I_α^{j+}: (a) experiment $\left(A_\alpha^{j+}\right)_{test}$ and (b) analysis $\left(A_\alpha^{j+}\right)_{model}$

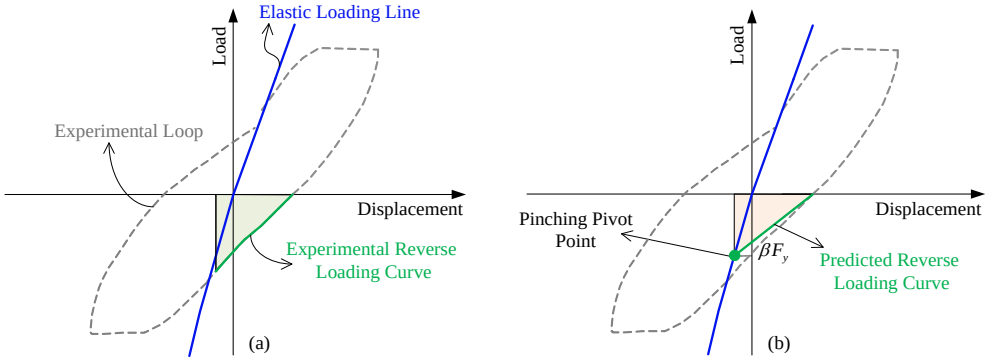

Figure 5. Energy dissipation area A_β^{j-} for loop energy indices I_β^{j-}: (a) experiment $\left(A_\beta^{j-}\right)_{test}$ and (b) analysis $\left(A_\beta^{j-}\right)_{model}$

The second kind of indicator, called the "average energy index," was used to perform the overall calibration accuracy at a specimen level by weighted averaging the individual loop indices. The average energy indices for α and β are given in Eqs. 8 and 9, respectively.

$$I_\alpha^{avg} = \sum_{j=1}^{m}\left(A^{j+}\times I_\alpha^{j+} + A^{j-}\times I_\alpha^{j-}\right) \Big/ \sum_{j=1}^{m}\left(A^{j+} + A^{j-}\right) \tag{8}$$

$$I_\beta^{avg} = \sum_{j=1}^{m}\left(A^{j+}\times I_\beta^{j+} + A^{j-}\times I_\beta^{j-}\right) \Big/ \sum_{j=1}^{m}\left(A^{j+} + A^{j-}\right) \tag{9}$$

where weighting factor $A^{j\pm}$ is the energy dissipation of each target loop in either direction and m is the number of target loops. Having the energy dissipations as weighted factors ensured that loops with high energy dissipation were more important for the optimization.

Following these indicators, the cumulative difference in energy dissipation between the model and test response in each failure mode case, corresponding to α and β, can be calculated by the summed squared error for each specimen given by Eqs. 10 and 11, where n represents the total number of specimens. The procedure for deriving E_α is outlined in Fig. 6.

$$E_\alpha = \sum_{i=1}^{n}\left(I_{\alpha,i}^{avg} - 1\right)^2 \tag{10}$$

$$E_\beta = \sum_{i=1}^{n}\left(I_{\beta,i}^{avg} - 1\right)^2 \tag{11}$$

For each run with selected features, the optimization was carried out to minimize E_α and E_β to derive coefficients for equations pertaining to α and β. The procedure for deriving optimized coefficients, as a high dimensional minimization problem, is very complex and requires an efficient optimization approach to solve it. To address this issue, the authors adopted a specialized algorithm known as Simulated Annealing (Kirkpatrick *et al.*, 1983). In each run, the optimization was carried out to derive the coefficients of the features involved in the respective run. Due to space limit, A more comprehensive discussion of Simulated Annealing optimization can be found in reference.

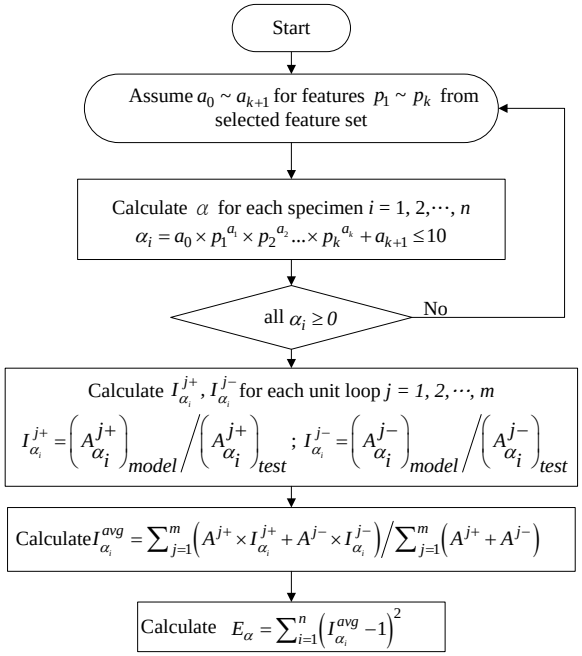

Figure 6. Flowchart for calculating the total error for α

Table 1 represents the order of feature selection and the reduction in error with addition for each run of the four pivot parameters. For the proposed model to have practical utility, the model selection had to be carried out parsimoniously, i.e., the model that could provide reasonably acceptable results with the smallest subset of features was chosen. This was established by comparing the error in energy dissipation with the addition of the new feature in each step. If the selected model could not be improved further by more than 5% with the addition of a new feature, the features at the prior step were selected to represent the most parsimonious model.

Table 1. Feature selection based on the "greedy" strategy

Order	α_F	E_α (%)	β_F	E_β (%)	α_S	E_α (%)	β_S	E_β (%)
I	$P/A_g f_c'$	0.488 (----%)	$P/A_g f_c'$	1.810 (----%)	$P/A_g f_c'$	0.175 (----%)	$P/A_g f_c'$	2.293 (----%)
II	H/ℓ_w	0.365 (-25%)	H/ℓ_w	1.337 (-26%)	$\rho_c f_{y,c}/f_c'$	0.128 (-27%)	H/ℓ_w	0.752 (-67%)
III	$\rho_c f_{y,c}/f_c'$	0.344 (-5.9%)	$\rho_{ct} f_{y,ct}/f_c'$	1.143 (-15%)	$\rho_w f_{yw}/f_c'$	0.120 (-6.5%)	ℓ_w/t_e	0.630 (-16%)
IV	ℓ_w/t_e	0.332 (-3.3%)	$\rho_w f_{yw}/f_c'$	1.000 (-13%)	$\rho_{ct} f_{y,ct}/f_c'$	0.117 (-2.7%)	$\rho_c f_{y,c}/f_c'$	0.590 (-6.4%)
V	$\rho_{ct} f_{y,ct}/f_c'$	0.327 (-1.6%)	ℓ_w/t_e	1.035 (+3.5%)	ℓ_w/t_e	0.116 (-0.5%)	$\rho_{ct} f_{y,ct}/f_c'$	0.588 (-0.2%)
VI	$\rho_w f_{yw}/f_c'$	0.322 (-1.4%)	$\rho_c f_{y,c}/f_c'$	1.053 (+1.8%)	H/ℓ_w	0.116 (+0.0%)	$\rho_w f_{yw}/f_c'$	0.619 (+5.2%)

PROPOSED PARAMETRIC FORMULATIONS

The specimens with different failure mode were used for optimization based on energy dissipation. Two sets of equations for α and β were derived – one for flexural and the other for shear dominant walls.

For flexure hinges, the parametric formulations for α_F and β_F are as follows:

$$\alpha_F = 0.55 \times \left(\frac{P}{A_g f_c'}\right)^{-1.2} \times \left(\frac{\rho_c f_{y,c}}{f_c'}\right)^{0.50} \times \left(\frac{H}{\ell_w}\right)^{-1.3} \leq 10 \quad (12)$$

$$\beta_F = 1.1 \times \left(\frac{P}{A_g f_c'}\right)^{0.17} \times \left(\frac{\rho_w f_{y,w}}{f_c'}\right)^{0.21} \times \left(\frac{\rho_{ct} f_{y,ct}}{f_c'}\right)^{0.10} \times \left(\frac{H}{\ell_w}\right)^{0.27} + 0.03 \leq 1 \quad (13)$$

For shear hinges, the parametric formulations for α_S and β_S are as follows:

$$\alpha_S = 0.18 \times \left(\frac{P}{A_g f_c'}\right)^{-2.3} \times \left(\frac{\rho_c f_{y,c}}{f_c'}\right)^{0.90} \times \left(\frac{\rho_w f_{y,w}}{f_c'}\right)^{0.20} + 0.55 \leq 10 \quad (14)$$

$$\beta_S = 0.11 \times \left(\frac{P}{A_g f_c'}\right)^{0.31} \times \left(\frac{\rho_c f_{y,c}}{f_c'}\right)^{-0.12} \times \left(\frac{\ell_w}{t_e}\right)^{1.1} \times \left(\frac{H}{\ell_w}\right)^{2.4} + 0.09 \leq 1 \quad (15)$$

The hysteretic predictions from the proposed equations are compared with experimental responses in Fig. 7 to show the relevance of the Pivot hysteresis model in prediction and improvement in such predictions with the proposed parametric formulations. Furthermore, the model-to-test cumulative energy dissipation ratio (R_d) up to the ultimate point (20% drop in peak strength) as shown in Fig. 8 was used to represent the accuracy in predicting the overall dissipation energy. The results show that predictions using the proposed equations have resulted in good hysteretic predictions. Using different equations of α and β separately for flexure and shear failure modes through proposed formulations has improved the hysteretic predictions and captured the behavioral differences with failure modes reasonably well.

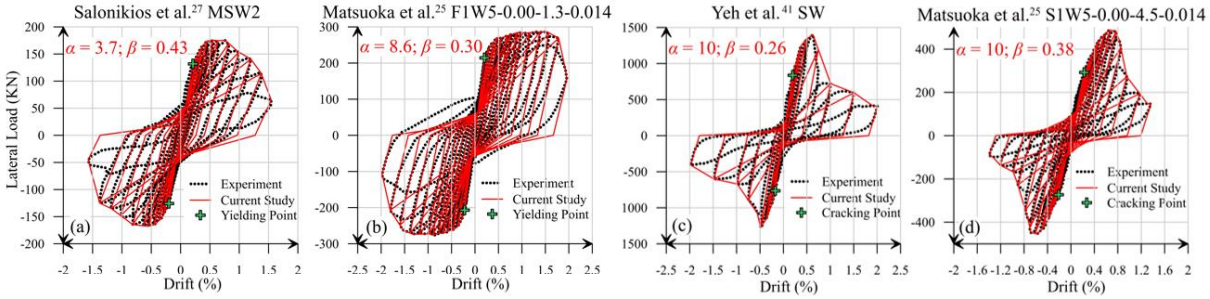

Figure 7. Comparison between the experimental and analytical hysteresis plots for (a) flexure dominant rectangular wall; (b) flexure dominant barbell wall; (c) shear dominant rectangular wall; (d) shear dominant barbell wall

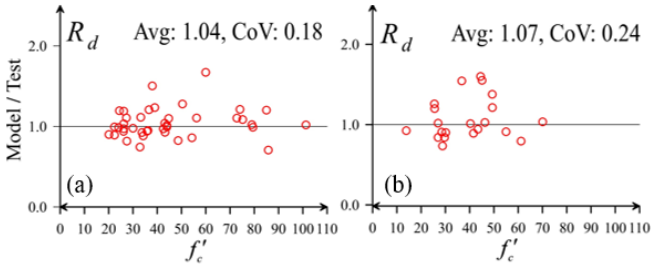

Figure 8. The cumulative energy dissipation ratio driven from the proposed equations in (a) flexural group and (b) shear group

CONCLUSIONS

This paper proposes a series of failure mode dependent parametric equations for the Pivot hysteretic model to predict the hysteretic behavior of reinforced concrete walls. The proposed parameters were derived using optimization techniques such as Simulated Annealing to calibrate the proposed model with the experiment results from 61 specimens in total. The results showed that failure mode predominantly affects the hysteresis behavior of walls and that these behavioral variations are captured reasonably well through the proposed parametric formulations. This study will help engineers to carry out more reliable and accurate nonlinear time-domain analysis of tall buildings and complex structures.

ACKNOWLEDGMENTS

The authors gratefully acknowledge the Ministry of Science and Technology, Taiwan, for offering their support under grant numbers 110-2625-M-002-025. Also, the authors are thankful to National Taiwan University, Taiwan for providing the Elite Doctoral Scholarship to the first author.

REFERENCES

Architectural Institute of Japan (AIJ). (2018). *AIJ Standard for structural calculation of reinforced concrete structures (revised)*. Architectural Institute of Japan, Tokyo, Japan. (in Japanese)

Baber, T.T. and Noori, M.N. (1985). "Random vibration of degrading pinching systems," *J. Eng. Mech.*, **111**(8), 1010–1026.

Baber, T.T. and Wen, Y.K. (1981). "Random vibrations of hysteretic degrading systems," *J. Eng. Mech.*, **107**(6), 1069–1087.

Chung, L.L., Yeh ,Y.K., Chien, W.Y., Hsiao, F.P., Shen, W.S., Chiou, T.C., Chow, T.K., Chao, Y.F., Yang, Y.S., Tu, Y.S., Chai, J.F., Hwang, S.J. and Sun, C.H. (2009). "Technology Handbook for Seismic Evalulation and Retrofit of School Buildings Second Edition," *Technical Report No. NCREE-2009-023*, Taipei, Taiwan. (in Chinese)

Dowell, R.K., Seible, F. and Wilson, E.L. (1998). "Pivot Hysteresis Model for Reinforced Concrete Members," *ACI Struct J.*, **95**(5), 607-617.

Guyon, I. and Elisseeff, A. (2003). "An introduction to variable and feature selection," *J. Mach Learn Res*, **3**, 1157-1182.

Hwang, S.J. and Lee, H.J. (2002). "Strength Prediction for Discontinuity Regions by Softened Strut-and-Tie Model," *J .Struct. Eng. (ASCE)*, **128**(12), 1519-1526.

Kirkpatrick, S., Gelatt, C.D. and Vecchi, M.P. (1983). "Optimization by Simulated Annealing," *Science*, **220**(4598), 671-680.

Kunnath, S.K., Reinhorn, A.M. and Park, Y.J. (1990). "Analytical Modeling of Inelastic Seismic Response of RC Structures," *J. Struct. Eng. (ASCE)*, **116**(4). 996–1017.

Ling, Y.C., Mogili, S. and Hwang, S.J. (2022). "Parameter optimization for Pivot hysteresis model for reinforced concrete columns with different failure modes," *Earthquake Engng. Struct. Dyn.* doi:10.1002/eqe.3658

Seismic Engineering Research Infrastructures For European Synergies (SERIES) (2013). SERIES RC Walls Database. http://www.dap.series.upatras.gr.

Sengupta, P and Li, B. (2014). "Hysteresis Behavior of Reinforced Concrete Walls," *J. Struct. Eng. (ASCE)*, **140**(7), 04014030.

Sharma, A., Eligehausen, R. and Reddy, G.R. (2013). "Pivot Hysteresis Model Parameters for Reinforced Concrete Columns, Joints, and Structures," *ACI Struct J.*, **110**(2),217-228.

Takeda, T., Sozen, M.A. and Nielsen, N.N. (1970). "Reinforced Concrete Response to Simulated Earthquakes," *J. Struct. Div.* **96**(12), 2557-2573.

EXPERIMENTAL STUDY OF A 7- STORY REINFORCED CONCRETE BUILDING USING REAL-TIME HYBRID TESTING METHOD

Shih-Wei Yeh[1] Lyan-Ywan Lu[2*] Fu-Pei Hsiao[3] and Fan-Po Chang[4]

1. Associate Technician, National Center for Research on Earthquake Engineering, Taipei, Taiwan, R.O.C.
2. Corresponding Author, Professor, Department of Civil Engineering, National Cheng Kung University, Tainan, Taiwan, R.O.C.
3. Director of Tainan Experimental Technology Division, National Center for Research on Earthquake Engineering, Taipei, Taiwan, R.O.C.
4. Graduate Student, Department of Civil Engineering, National Cheng Kung University, Tainan, Taiwan, R.O.C.

Email: swyeh@narlabs.org.tw, lylu@ncku.edu.tw, fphsiao@narlabs.org.tw, showman875@gmail.com

ABSTRACT

Shaking table test (STT) which is one of well-known efficient experimental methods to evaluate the seismic performance of structures. However, STT may be hard to be conducted for a full-scale reinforced concrete (RC) building due to the limitation of specimen cost and test equipment capacity. To solve this problem, a novel experimental method called Real-time hybrid testing (RTHT) can be utilized. The concept of RTHT is to divide a structural system into a primary structure whose dynamic responses is simulated by a numerical substructure, and a physical substructure which is experimentally tested with an actuator. The purpose of this study is to develop a RTHT with a virtual spring. To validate the proposed test method, a RTHT with a virtual spring for a 7-story RC building is conducted. The test results show the RTHT with a virtual spring can overcome the problem of system instability and reduce the control error caused by hardware equipment. When compared with the theoretical results, the peak error of each floor response in the RTHT results is merely about 1%. The comparison of the RTHT and the STT results shows that floor acceleration responses in the RTHT are very close to those of the STT.

Keywords: real-time hybrid testing, virtual spring, unstable system, control error, reinforced concrete building, high-to-mid rise building

INTRODUCTION

To study the dynamic responses of structures under seismic excitations, many experimental methods have been developed. Shaking table test (STT) is one of the well-known efficient experimental methods to evaluate the seismic performance of structures (Li and Kong, 2019). The idea of shaking table is to use a plate on which a test specimen is installed and to simulate earthquake ground motion with the plate. Therefore, the seismic performance of the specimen can be record and studied. However, the STT may be hard to be conducted for a full-scale reinforced concrete (RC) building due to the limitation of specimen cost and test equipment capacity. Although, the specimen cost can be reduced by applying a reduced-scale RC building (Tashkov and Krstevska, 2013), the dynamic responses of the reduced-scale RC building may not be the same as those of the full-scale RC building (Hu and Duan, 2010).

To solve this problem, a novel experimental method called Real-time hybrid testing (RTHT) can be utilized. The concept of RTHT is to divide a structural system into a primary structure whose dynamic responses is simulated by a numerical substructure and a physical substructure which is experimentally tested with an actuator. The actuator simulates the displacement of the numerical substructure and applies the displacement on the physical substructure, while the measured reaction force of the physical substructure is transmitted to a computer that determines the next step structural displacement by using the feedback reaction force, the numerical model, and an integration algorithm. Therefore, the seismic responses of the structural system can be simulated by using RTHT.

However, the time step in a RTHT is usually very small and the loading rate of RTHT is very high. This means the response of the numerical substructure has to be computed and the actuator should move to the target displacement within a very small time step in the RTHT. Therefore, the control system may become unstable due to the control delay time (Horiuchi *et al.*, 1999) or the accuracy of the test results should be validated due to control error caused by of hardware equipment. These problems may affect the reliability of the RTHT result and become a challenge to the RTHT (Bursi *et al.*, 2010).

The purpose of this study is to develop a RTHT with a virtual spring which can improve the reliability of RTHT results. In this paper, the equations of a RTHT with a virtual spring is derived. To validate the proposed test method, a RTHT with a virtual spring for a 7-story RC building, whose STT has been executed in the Tainan laboratory of the National Center for Research on Earthquake Engineering (NCREE), is also conducted, and the RC building seismic responses of the RTHT can compared with those of the STT.

(a) Overall view of the specimen (Hsiao, 2019)

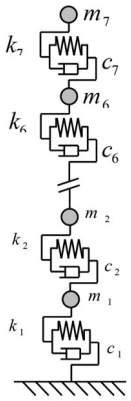

(b) simplified numerical model

Figure 1. 7-story RC benchmark structure.

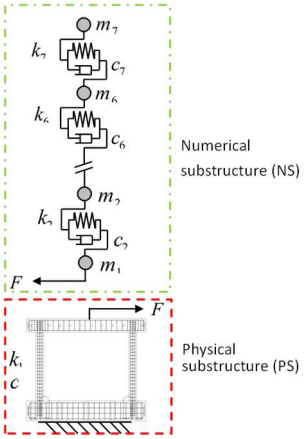

Figure 2. Substructuring of RTHT for the 7-story RC building.

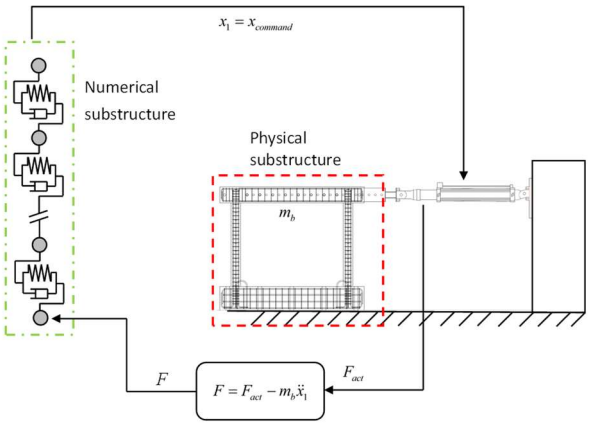

Figure3. Control flow diagram of RTHT.

RTHT OF THE 7-STORY RC BUILDING

To study the seismic response and failure modes of medium- and high-rise RC buildings under near-fault earthquakes, the National Center for Research on Earthquake Engineering (NCREE) conducted a STT of a 1/2-scaled 7-story RC building at the Tainan laboratory in November 2018, as shown in Fig. 1 (a) (Hsiao, 2019). The RC building also is the benchmark structure in this paper. To carry out the RTHT for the RC building, it is necessary to model the RC building by using a simplified numerical model, so that the next step of the numerical substructure responses can be calculated in real-time during

the experiment. As shown in Fig. 1 (b), the shear building model is chosen to be the simplified numerical model of the RC building.

Table 1. Basic parameter of a simplified numerical model of 7-story RC building

Parameter name	Value	Parameter name	Value
Lumped mass of each floor	m_1 =18516.35 kg	Frequency of each mode	f_1 =1.57 Hz
	m_2 =18705.56 kg		f_2 =7.69 Hz
	$m_3 \sim m_6$ =20597.75 kg		f_3 =9.51 Hz
	m_7 =17002.6 kg		f_4 =15.88 Hz
Stiffness of each floor	k_1 =4.31×10^7 N/m		f_5 =21.95 Hz
	k_2 =2.14×10^7 N/m		f_6 =26.47 Hz
	$k_7 \sim k_3$ =1.84×10^8 N/m		f_7 =29.19 Hz
Rayleigh damping coefficient	α_R =1.6056	Damping ratios of first two-mode	ζ_1 =0.0890
	β_R =0.0016		ζ_2 =0.0549

Fig. 2 shows the schematic diagram of the RTHT in this paper. The frame selection in the dashed box represents the primary structure, which is simulated by the simplified numerical substructure (NS) mentioned above. The detailed parameters are shown in Table 1. Fig. 3 is the control flow chart of RTHT for the 7-story RC building. The physical substructure (PS) shown on the right side of Fig. 2 is an RC frame with a 50-ton high-performance actuator connected to clamped beams and a force-transmitting steel beam. The actuator is set up on the reaction wall. The numerical substructure outputs the displacement response (x_1) of the first floor as the control command of the actuator, then feeds back the force of the actuator (F_{act}). After deducting the inertial force ($m_b\ddot{x}_1$) caused by the acceleration of the beams, the corrected force (F) is fed back to the numerical substructure for the next calculation of the control command. In this way, the dynamic responses of the 7-story RC frame under the action of earthquake force can be simulated repeatedly. Fig. 4 shows the PS appearance and experimental assembly photos of RTHT.

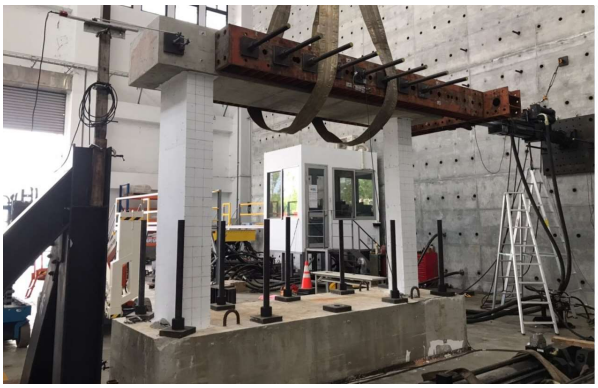

Figure 4. Test setup of the RTHT of the 7-story RC building.

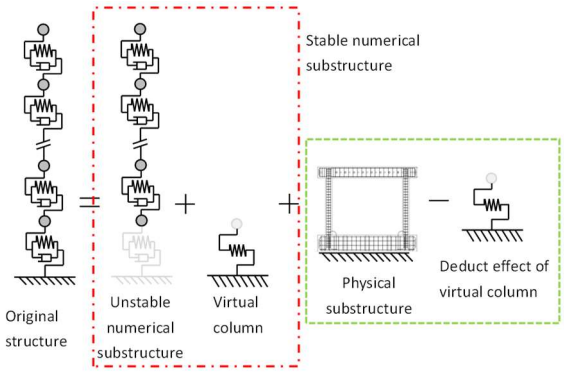

Figure 5. Schematic diagram of the introduction of virtual springs in RTHT

PRINCIPLE OF RTHT WITH A VIRTUAL SPRING

If the numerical substructure (NS) in RTHT is an unstable structure, the RTHT results will diverge. So, this paper introduces virtual springs into the NS of RTHT for stabilization. Fig. 5 is a conceptual diagram of the virtual spring compensation method. After the virtual spring be introduced to the unstable NS, the original unstable NS will become stable. However, since the stiffness of the virtual spring is artificially added, it must be deducted the effect caused by the virtual spring. So that it will not affect the results of the RTHT. Fig. 6 is the first-floor free body diagram of the theoretical 7-story building, F in the figure is the force feedback by the PS and $\hat{k}_1$ is the stiffness of the PS, and its equation of motion is

$$m_1\ddot{x}_1 + (\hat{k}_1 + k_2)x_1 - k_2x_2 = -m_1\ddot{x}_g \quad (1)$$

Fig. 7 is the first-floor free body diagram after introducing the virtual spring. In the figure, k' is the stiffness of the virtual spring. If the control error of the actuator is considered, its equation of motion can be expressed as

$$m_1\ddot{x}_1 + (\hat{k}_1 + k_2)x_1 - k_2x_2 = -m_1\ddot{x}_g - (\hat{k}_1 - k')\Delta x_1 \quad (2)$$

From Eqs. 1 and 2, it can be known that if the stiffness of the virtual spring is equal to the stiffness of the PS, the control error can be eliminated.

Table 2 Peak displacement comparison of RTHT and theoretical results (stiffness ratio =1)

Excitations	PGA (g)	Top floor displacement (mm)			First-floor displacement (mm)		
		Theory	RTHT	Error ratio [1]	Theory	RTHT	Error ratio
El Centro	0.05	11.63	10.99	-5.54%	3.80	3.60	-5.15%
Kobe	0.1	17.71	16.73	-5.54%	6.05	5.48	-9.39%
Chi-Chi (TCU075)	0.05	8.58	8.13	-5.32%	2.98	2.98	-0.04%
Meinong (CHY015)	0.118	18.00	17.66	-1.93%	6.10	6.01	-1.45%
Meinong (CHY063)	0.233	55.00	53.36	-2.98%	19.31	19.51	1.01%
Average [2]				4.26%			3.41%

[1] Error ratio =(Maximum of RTHT-maximum of theory)/ maximum of theory。
[2]The mean of the absolute value of the error ratio。

Table 3 Peak acceleration comparison of RTHT and theoretical results (stiffness ratio =1)

Excitations	PGA (g)	Top floor acceleration (g)			First-floor acceleration (g)		
		Theory	RTHT	Error ratio	Theory	RTHT	Error ratio
El Centro	0.05	0.12	0.11	-7.62%	0.09	0.09	0.02%
Kobe	0.1	0.18	0.18	-2.20%	0.11	0.11	3.81%
Chi-Chi (TCU075)	0.05	0.09	0.09	-0.92%	0.07	0.08	7.96%
Meinong (CHY015)	0.118	0.19	0.19	-0.11%	0.12	0.13	4.88%
Meinong (CHY063)	0.233	0.54	0.52	-2.32%	0.31	0.36	18.67%
Average [2]				2.63%			7.07%

[1] Error ratio =(Maximum of RTHT-maximum of theory)/ maximum of theory。
[2]The mean of the absolute value of the error ratio。

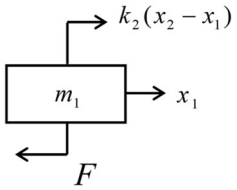

Figure 6. Theoretical first-floor free body diagram

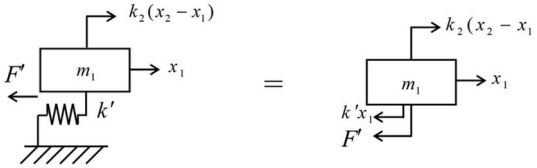

Figure 7. Free-body diagram of the first floor by introducing virtual spring

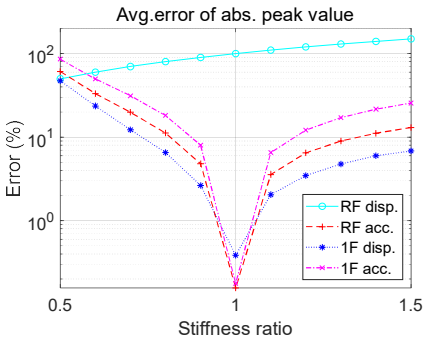

(a) Average peak error of the top floor and the first floor

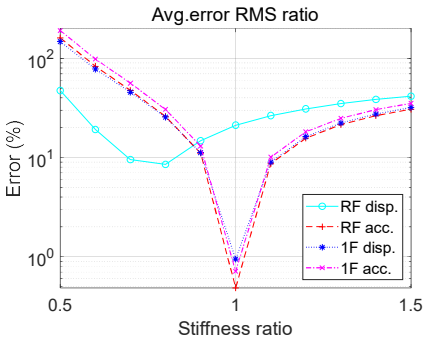

(b) The average error RMS ratio of the top floor and the first floor

Figure 8. The comparison of average error for different virtual spring stiffness

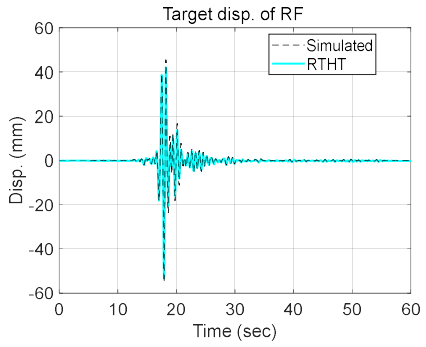

(a) Relative displacement of the top floor

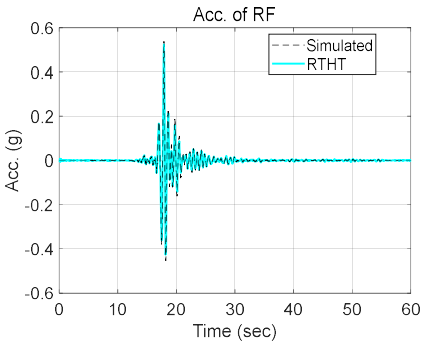

(b) Absolute acceleration of the top floor

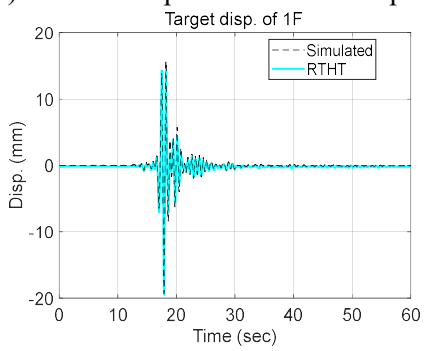

(c) Relative displacement of the first floor

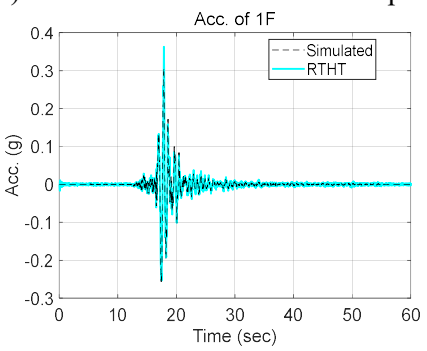

(d) Absolute acceleration of the first floor

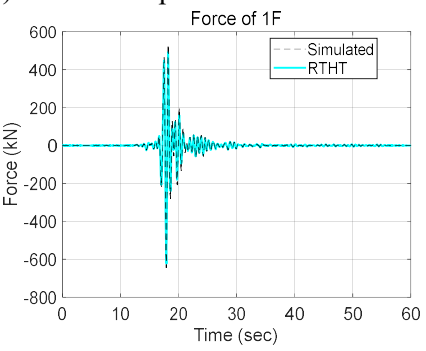

(e) Base shear

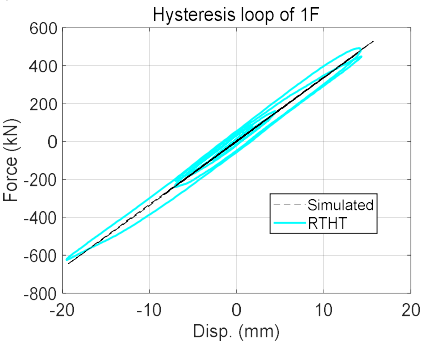

(f) Hysteresis loop of the first floor

Figure 9. Time plot comparison between uncompensated RTHT and theoretical values (CHY063，PGA=0.233g，virtual spring stiffness ratio =1)

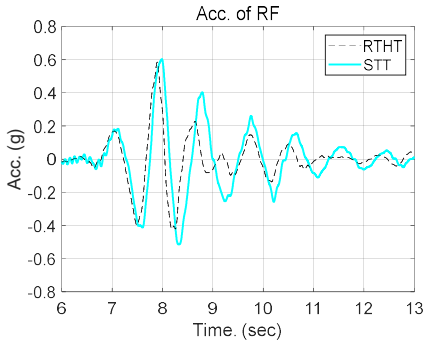

(a) Acceleration of RF

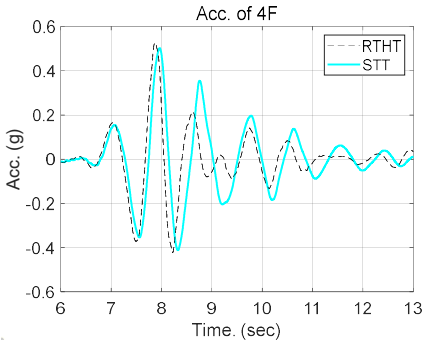

(b) Acceleration of 6F

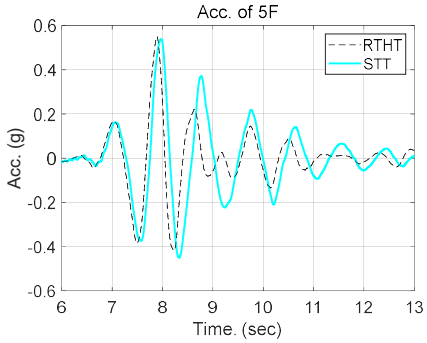

(c) Acceleration of 5F

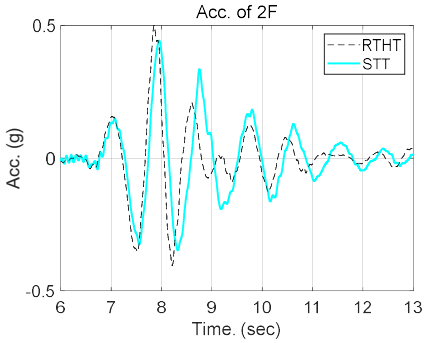

(d) Acceleration of 4F

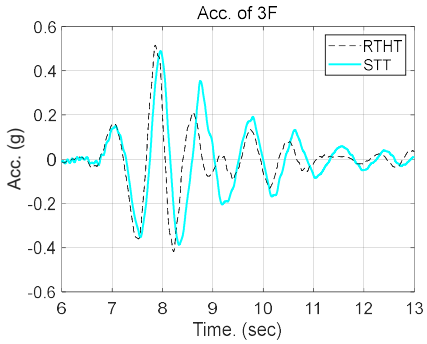

(f) Acceleration of 3F

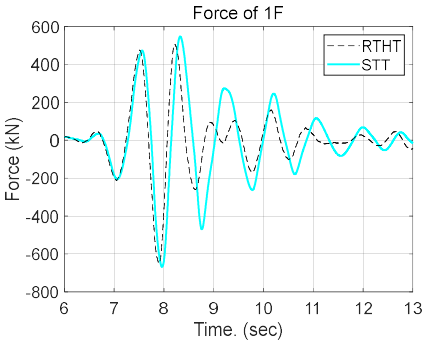

(f) Acceleration of 2F

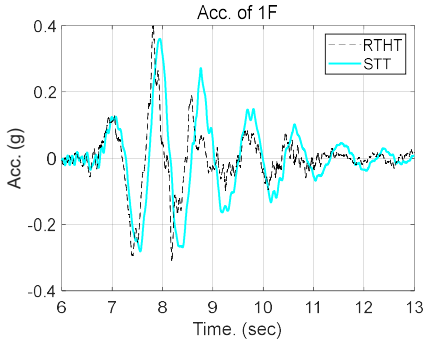

(g) Acceleration of 1F

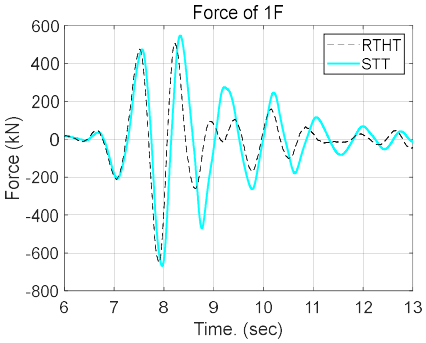

(h) Base shear

Figure 10. Comparison of acceleration between RTHT and STT of 7-story RC building with compensation (CHY063，PGA=0.233g，virtual spring stiffness ratio =1)

RESULTS AND DISCUSSIONS

Comparison of RTHT results and theory

Although the unstable NS can be stabilized by the virtual spring, its optimal parameter still needs to be determined. Therefore, this paper uses virtual real-time hybrid testing (V-RTHT) to verify the optimal stiffness ratio of the virtual spring. Fig. 8 is a comparison of errors for different virtual spring stiffness

ratios averaged by each earthquake. In Fig. 8, it can be found that except for the top floor displacement, the rest of the responses have the smallest peak error when the virtual spring stiffness ratio is equal to 1. Therefore, the virtual spring stiffness ratio 1 is the best parameter, which can minimize the error of most responses. Tables 2 and 3 compare the peak response errors between the RTHT and theoretical results when the stiffness ratio of the virtual spring is 1. The average peak error ratio of the responses between the top floor and the first floor is about 7%, which means that the virtual spring can make the NS stable, it can also reduce the experimental error. Fig. 9 is a comparison of the response time histories between the RTHT and the theoretical results under the CHY063 earthquake. By observing each subplot in Fig. 9, it can be found that no matter what kind of response is, the RTHT results are quite close to the theoretical results and thus are quite accurate.

CONCLUSIONS

Due to the complex mechanical properties of the RC building, it is difficult to precisely control the hydraulic servo actuator, which may easily lead to experimental instability. If the NS in RTHT is a system with unstable supports, it may cause the calculated commands of the RTHT to diverge and lead to the experiment failure. Therefore, in this paper, a virtual spring is introduced into the NS of the RTHT to enhance the computational stability and accuracy of the NS, which can avoid the divergence of the RTHT. The experimental results show that the virtual spring is very effective for improving the stability of the NS with unstable supports in the RTHT, and enables the impossible experiments become stable, and can compensate for the control errors at the same time. Also, the RTHT results are similar to the STT results.

ACKNOWLEDGMENTS

This research was supported in part by the Ministry of Science and Technology of R.O.C. (Taiwan) through grant MOST 110-2625-M-492-008.

REFERENCES

Bursi, O.S., D.P. Stoten, N. Tondini and L. Vulcan (2010). “Stability and accuracy analysis of a discrete model reference adaptive controller without and with time delay,” *Int. J. Numer. Methods Eng.*, **82**, 1158-1179.

Horiuchi, T., M. Inoue, T. Konno and Y. Namita (1999). “Real-time hybrid experimental system with actuator delay compensation and its application to a piping system with energy absorber,” *Earthq Eng Struct Dyn*, **28**(10), 1121-1141.

Hsiao, Y.H. (2019). “Seismic isolation design and its probabilistic performance assessment considering near-fault pulse effect,” *Master thesis*, National Cheng Kung University (in Chinese).

Hu, X. and K. Duan (2010). “Mechanism behind the Size Effect Phenomenon,” *J. Mech. Eng.*, **136**(1), 60-68.

Li, S., C. Wu, and F. Kong (2019). “Shaking Table Model Test and Seismic Performance Analysis of a High-Rise RC Shear Wall Structure,” *Shock. Vib.*, **2019**, 1-17.

Tashkov, L. and L. Krstevska (2013). “Shaking Table Test of 1/30 Scale Model of Palasport in Bologna with Timber Shell Roof Structure,” *Adv. Mat. Res.*, **778**, 503-510.

8th Asia Conference on Earthquake Engineering
Taipei, Taiwan ■ November 9-11, 2022

In-plane Experimental Study on an Attached RC Frame Using High Strength Anchor Bolts

Kai-Wen Teng[1]、Tsung-Chih Chiou[2]、Lap-Loi Chung[2]、Jing-Fang Liang[1]、Tzu-Lun Lee[1]
1. Department of Civil Engineering, National Taiwan University
2. National Center for Research on Earthquake Engineering
Taipei, Taiwan, R.O.C.
Email: 0306045@narlabs.org.tw

ABSTRACT

Attaching external reinforced concrete (RC) frames to existing buildings not only enhances the seismic capacity of existing structures but also reduces the interruption in the use of buildings during retrofitting. The mechanisms of force transmission between the interface of attached and existing frames are significant in design technology. Therefore, improvement in the confidence of connections is essential during construction. This study proposes using high strength anchor bolts for connection instead of adhesive rebar, as this can improve the quality control of connection. Three frame tests, a prototype RC fame, an attached RC frame using an adhesive rebar connection, and an attached RC frame using an anchor bolt connection, are reported. Comparison of the connections using adhesive rebar and anchor bolts is discussed. Testing results indicate that the lateral strength of the retrofitted frames is significantly increased and the deformation capacity is also improved when the frame is attached using anchor bolts rather than adhesive rebar connections.

Keywords: seismic retrofit, reinforced concrete frame, adhesive rebar, anchor bolt, existing building

INTRODUCTION

Seismic retrofit of existing public school buildings has been implemented in the past decade in Taiwan. Most of the public school buildings were retrofitted by reinforced concrete (RC) jacketing columns, wing walls, RC walls etc. These traditional retrofitting schemes can be conducted on school buildings because the schools have summer and winter vacations. However, many existing buildings, such as hospitals, factories, and residential buildings, cannot lose functionality for two to three months for retrofitting. Attaching external RC frames to existing buildings can not only enhance the seismic capacity of existing structures but also reduce the interruption to the use of buildings during the retrofitting.

Attaching external RC frames to the outside of existing buildings has been widely applied to schools in Japan. Takeda et al. (2013) adopted a new RC slab for connection between the attached and existing frames by adhesive rebar. However, the construction quality control may be an issue in Taiwan. This study proposes attaching new RC frames to the existing frames without a connecting slab. The interface between the attached new beams and existing beams is connected by high strength anchor bolts. The construction procedure is simplified to drilling holes in the existing RC beams, placing the high strength anchor bolts in the holes, reserving a suitable embedded length of bolts in the steel cages of the new attached beam, and finally casting the concrete of the newly attached beam. No cleaning holes and injection of adhesive paste are required. This can significantly improve the construction quality of connections.

This study conducted cyclic loading tests on three RC frames, a prototype RC frame, an attached RC frame using an adhesive rebar connection, and an attached RC frame using anchor bolt connections, in the structural laboratory of National Center for Research on Earthquake Engineering (NCREE) in Taiwan. Different connections for the interface between the attached beam and existing beam are clarified and discussed in conjunction with the experiments. In the following sections, the retrofitting design and test program, results of cyclic loading tests, analysis and comparison of testing results, and conclusions are reported.

RETROFITTING DESIGN AND TEST PROGRAM

The tests were conducted in the Multi-Axial Testing System (MATS) in NCREE. The specimens simulated the existing school building frames at a scale of 0.45 due to the limitation of MATS. The attached external frame was designed with higher lateral stiffness and strength than the existing frame. Therefore, the new frame will develop its ultimate strength under a small deformation while the existing frame would still remain in the elastic range, as shown in Figure 1.

To test the effectiveness of retrofitting using an external frame, a prototype existing frame and an attached external frame were designed for investigating the behavior. The dimensions of the test frames are shown in Figure 2, and detailed sections of the frames are shown in Figure 3. To test the connection between the beam interfaces, the external frame attached with high strength anchor bolts and with adhesive rebar were tested. The connection details of the beam interfaces are illustrated in Figure 4.

CYCLIC LOADING TESTS

The existing prototype frame is abbreviated as PT, the external frame attached with high strength anchor bolts as AB, and the external frame attached with adhesive rebar as PB. The material properties are reported in Table 1 and Table 2.

The tested behavior of specimen PT is summarized as follows. The frame remained elastic while the inter-story drift ratio was less than $\pm 0.5\%$ o. The ultimate lateral strength occurred when the inter story drift ratio reached $\pm 1.5\%$, of inter story drift ratio and the ultimate lateral strength was 4.84 tf and 5.39 tf, respectively. The cracking pattern at the ultimate lateral strength is shown in Figure 5. Above 2.0% of inter story drift ratio, the lateral strength slowly decreased. The test was terminated at the first cycle of 5.0% inter story drift ratio due to loss of axial loading capacity of the columns; at this point the lateral strength decreased to 2.05 tf. The hysteresis loop of lateral strength versus displacement of specimen PT is shown in Figure 6.

The behavior of specimen AB is as follows. Frame AB remained elastic while the inter story drift ratio was below $\pm 0.5\%$ of. The ultimate lateral strength was reached when the inter story drift ratio reached $\pm 3.0\%$, and it was 13.84 tf and 11.41 tf, respectively. The cracking pattern at the ultimate lateral strength is shown in Figure 7. Above 4.0% of inter story drift ratio, the lateral strength slowly decreased. The test was terminated at the second cycle of 10% inter story drift ratio due the loss of axial loading capacity of the columns, and the residual lateral strength was only 2.02 tf. The hysteresis loop of lateral strength versus displacement of specimen AB is shown in Figure 8.

The behavior of the specimen PB is as follows. PB remained elastic below $\pm 0.375\%$ of inter story drift ratio. The ultimate lateral strength was reached when the inter story drift ratio reached $\pm 1.5\%$ of inter story drift ratio and was 14.23 tf and 12.93 tf, respectively. Significant flexural cracks occurred in the columns of the existing frame, and. the cracking pattern at the ultimate lateral strength is shown in Figure 9. After 2.0% inter story drift ratio, the lateral strength decreased significantly. The test was terminated at the first cycle of 8.0% inter story drift ratio due to loss in the axial loading capacity of the columns, and the residual lateral strength was only 6.72 tf. The hysteresis loop of lateral strength versus displacement of the specimen PB is shown in Figure 10.

ANALYSIS AND COMPARISON OF TEST RESULTS

Comparison of the ultimate lateral strength of the three specimens is shown in Table 3. The test results indicate that the ultimate lateral strength of the retrofitted frames was significantly increased, with strength values more than double that of the prototype frame.

Comparing the anchoring effect using the different connections indicates that the lateral force was well transmitted between the interface of the existing and new beams by both the anchor bolts and the adhesive rebar. However, the beam connection with high strength anchor bolts (specimen AB) could retain its post strength toughness more effectively than the connection with adhesive rebar (specimen PB), as shown in Figure 11.

CONCLUSIONS

The study conducted cyclic loading tests of three RC frames, a prototype existing RC frame, an attached RC frame using an adhesive rebar connection, and an attached RC frame using an anchor bolt connection. Based on the test results, the following conclusions can be drawn.

1. Retrofitting frames with attached external frames significantly increases the ultimate lateral strength, with strength values more than double that of the prototype frame.

2. Retrofitted frames with attached external frames have increased deformation capacity, with values more than double or triple that of the prototype frame.

3. Both the proposed connection using high strength anchor bolts and that using adhesive rebar transmit the lateral force between the interface of the existing and new beams well.

4. The proposed beam connection using high strength anchor bolts performs better with regard to post strength toughness than that using adhesive rebar.

ACKNOWLEDGMENTS

We would like to thank the Ministry of Science and Technology for providing research programs and funding subsidies (project number: 109-2625-M-492 -006 -), which enabled the smooth progress of this research.

REFERENCES

Chiou, T.-C., Chung, L.-L., Tu, Y.-C., Lai, Y.-C., Tseng, C.-C. Weng, P.-W., Chuang, M.-C., Yeh, Y.-K., Li, C.-H., Lin, M.-L, Wang, J.-X., Shen, W.-C., Hsiao, F.-P., Xue, Q., Hwang, S.-J. (2020), “Technical Hand Book for Taiwan Earthquake Assessment and Strengthening of Structures by Pushover Analysis (TEASPA4.0)”, National Center for Research on Earthquake Engineering, report number：NCREE-20-005, Taipei, 2020.

Japan Building Disaster Prevention Association, “ollection of seismic reinforcement construction method” 2008.

Kiyoji Takeda, Kyoya Tanaka, Toshiaki Someya, Asao Sakuda, and Yoshiteru Ohno, “Seismic retrofit of reinforced concrete buildings in Japan using external precast, prestressed concrete frame”, PCI Journal, pp.41-61, 2013.

Liang, J.-F. (2021) “Retrofitting Method by Connecting External Reinforced Concrete Frame with High-Strength Anchor Bolts”master thesis, dept. of civil engineering, NTU.

Lin, S.-S., Lai, Y.C., Lai, T., Chung, L.-L., Huang, G.-L., Tseng, C.-C. (2009), “seismic Retrofit by External Reinforced Concrete Frames – Using School Building of HOU-JIA Junior High School as Example” Journal of Institute of Structural Engineering, Vol. 31. No4. pp.19-37, 2009.

Lai, Y.-C., Lin, S.-H., Chung, L.-L., Tseng, C.-C., Huang, G.-L. and Lai, T. (2018). “Experimental study on retrofit with external reinforced concrete frame and its application on seismic retrofit of hospital”, Journal of Chinese Institute of Civil and Hydraulic Engineering, Vol. 30. No. 1. pp. 61-72, 2018.

Tsung-Chih Chiou, Jing-Fang Liang, Tzu-Lun Lee, Lap-Loi Chung, Yu-Chih Lai, Kai-Wen Deng, “In-Plane Test of Attached RC Frame Using High-Strength Anchor Bolts Connection”, National Center for Research on Earthquake Engineering, report number：NCREE-22-005, Taipei, 2022.

伊藤宰、辻聖晃、吉富信太、竹脇出，「アウトフレーム連結制振耐震補強のための連結ダンパーの合理的決定法，日本建築学会構造系論文集，第 74 巻，第 636 號，273-218，2009。

辻聖晃、中川大輔、吉富信太、竹脇出，「アウトフレーム型連結制振構法におけるアウトフレーム及び連結ダンパーの応答低減比マップを用いた設計法」，日本建築学会構造系論文集，第 75 巻，第 648 號，337-346，2010。

Table 1. Compressive strength of concrete

f_c' (kgf/cm^2)	PT	AB	PB
Existing frames	356	419	421
Attached frames	-	452	427

Table 2. Tensile strength of rebar

f_y (kgf/cm^2)	Existing frames	Attached frames
#2	3647	3647
#3	3632	4490
#4	3466	-

Table 3. Comparison of ultimate lateral strength of the three specimens.

$V_{max.}$ $(tonf)$	ultimate lateral strength	$\frac{V_{max.}}{V_{max.}^{PT}}$
PT	5.39	1.0
AB	13.84	2.57
PB	13.12	2.43

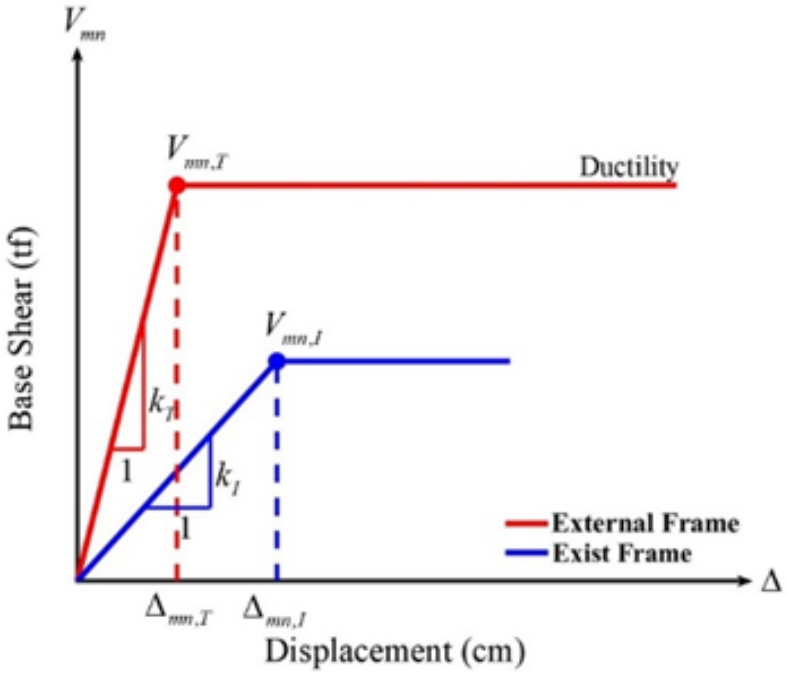

Figure 1. Design concept of retrofit by external frame

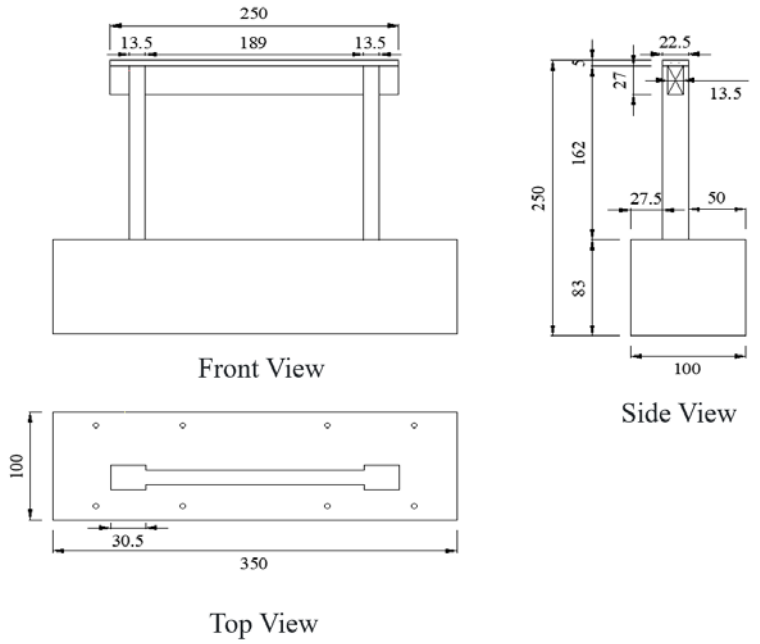

(a) Prototype frame

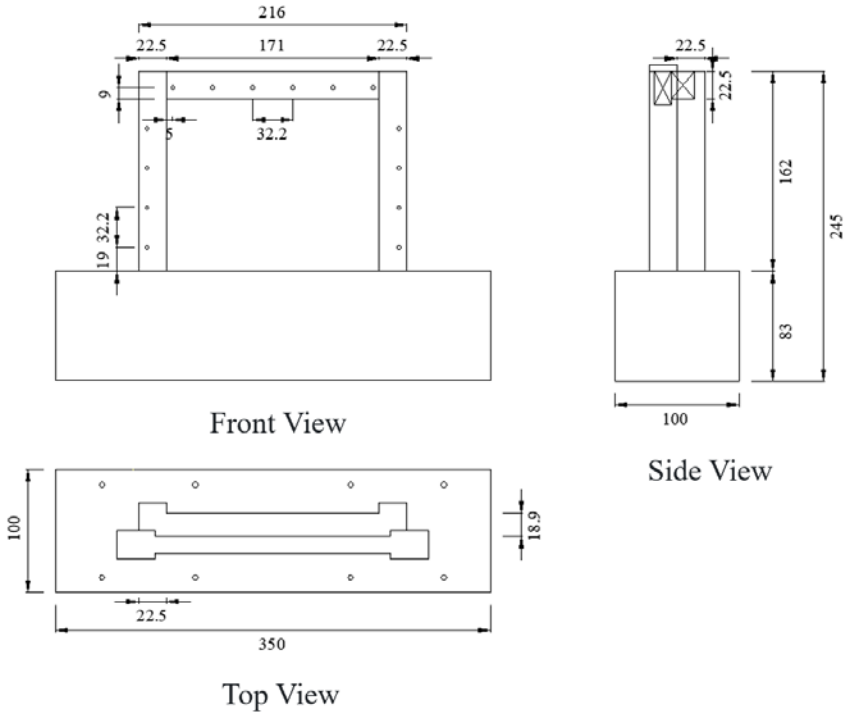

(b) Retrofitted frames

Figure 2. Dimensions of prototype and retrofitted RC frames

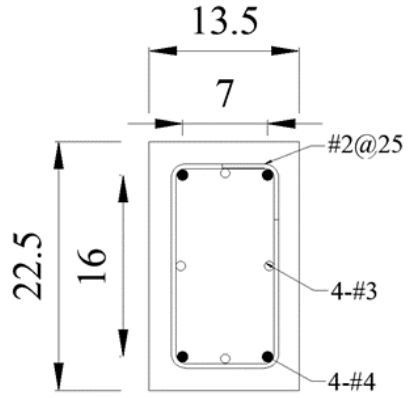

(a) Column section of prototype frame

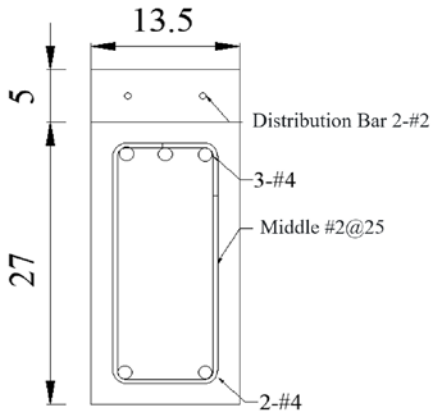

(b) Beam section of prototype frame

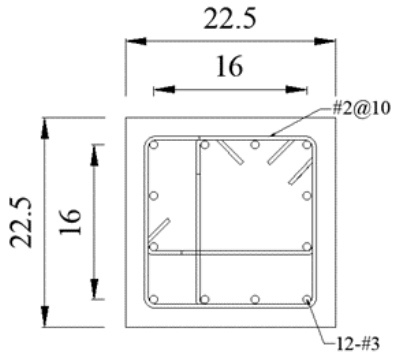

(c) Column section of retrofitted frames

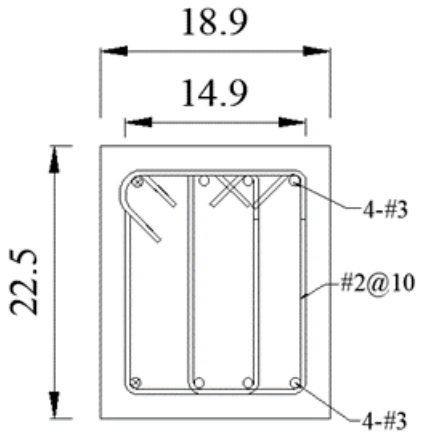

(d) Beam section of retrofitted frames

Figure 3. Detailed sections of prototype and retrofitted RC frames

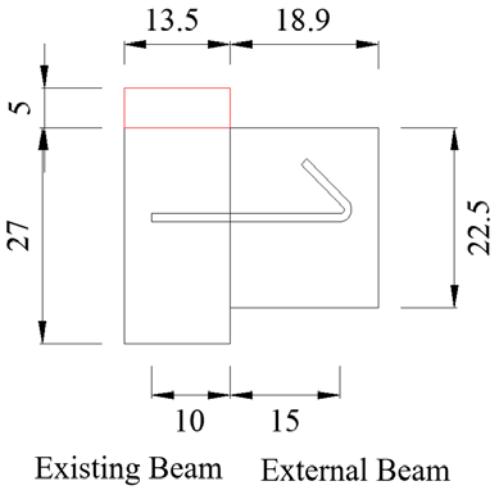

(a) Adhesive rebar

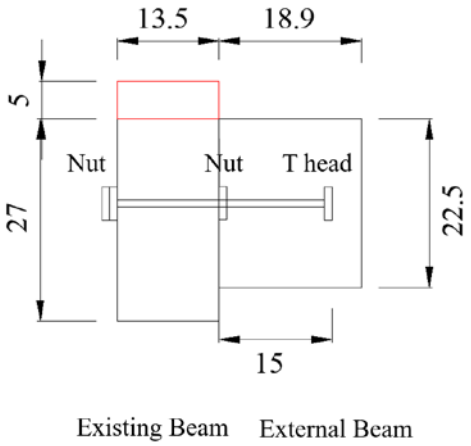

(b) Anchor bolts

Figure 4. Different connections of prototype and retrofitted RC frames

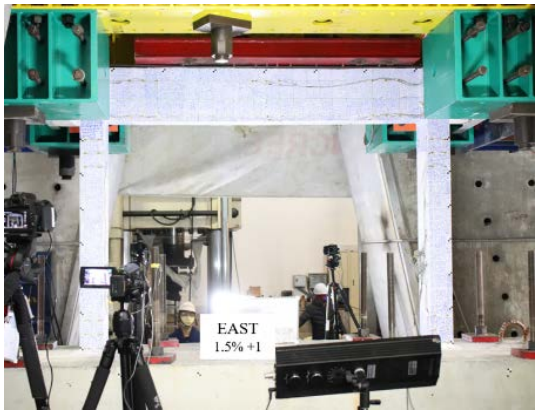

Figure 5. Cracking pattern of specimen PT at the ultimate lateral strength.

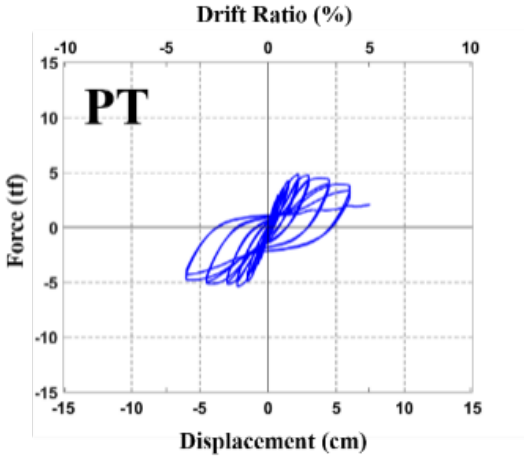

Figure 6. Hysteresis loop of lateral strength versus displacement of specimen PT.

Figure 7. Cracking pattern of specimen AB at the ultimate lateral strength.

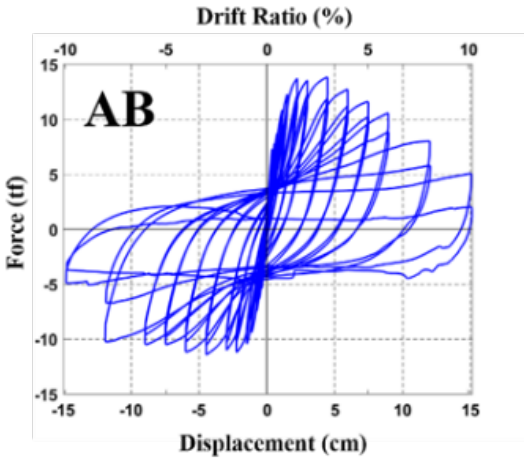

Figure 8. Hysteresis loop of lateral strength versus displacement of specimen AB.

Figure 9. Cracking pattern of specimen PB at the ultimate lateral strength.

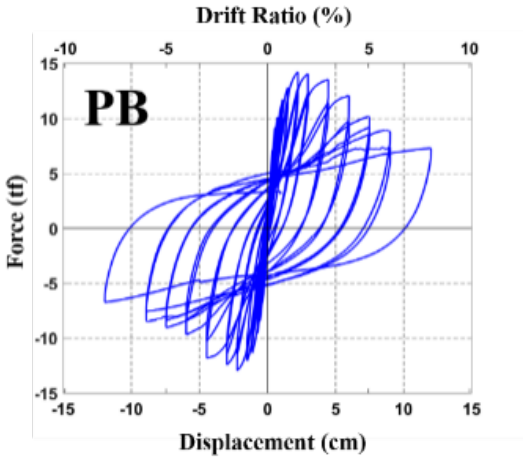

Figure 10. Hysteresis loop of lateral strength versus displacement of specimen PB.

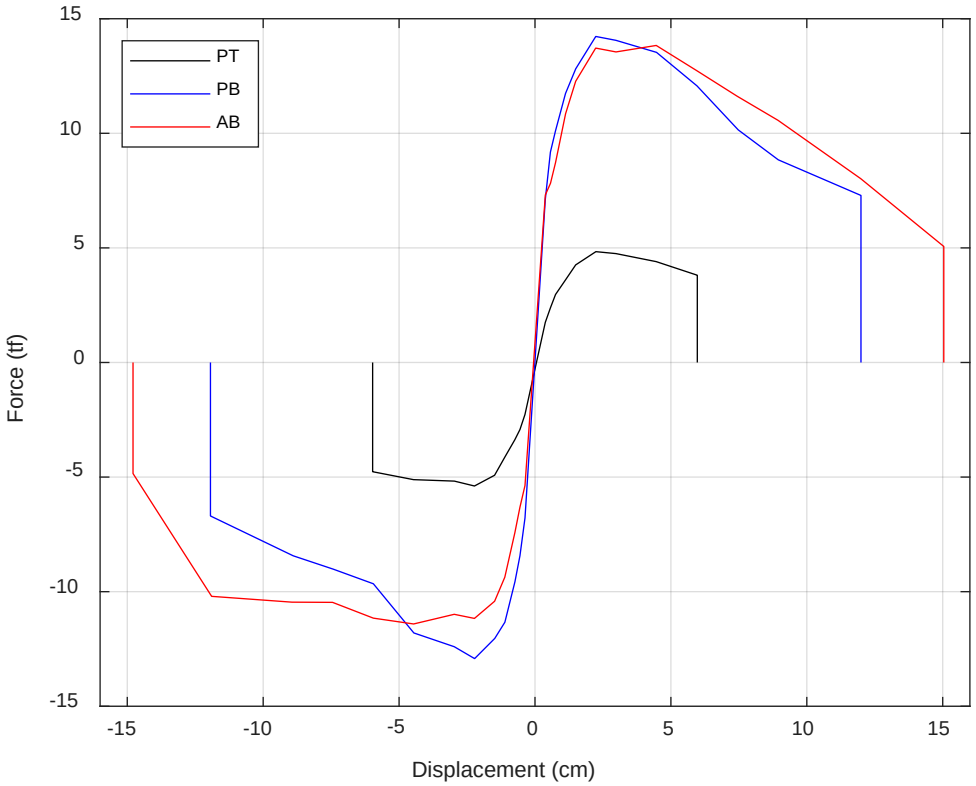

Figure 11. Envelopes of the hysteresis loops of the three specimens.

ON THE PREDICTION OF FLEXURAL PERFORMANCE OF RC BEAMS STRENGTHENED WITH EXTERNAL STEEL WIRE ROPES: A NUMERICAL STUDY

Yanuar Haryanto[1], Hsuan-Teh Hu[2], Ay Lie Han[3], Fu-Pei Hsiao[4] and Chia-Chen Lin[5]

1. Associate Professor, Department of Civil Engineering, Jenderal Soedirman University, Purwokerto, Indonesia; Ph.D, Department of Civil Engineering, National Cheng Kung University, Tainan, Taiwan
2. Professor, Department of Civil Engineering, National Cheng Kung University, Tainan, Taiwan; Professor, Department of Civil and Disaster Prevention Engineering, National United University, Miaoli, Taiwan
3. Professor, Department of Civil Engineering, Diponegoro University, Semarang, Indonesia
4. Research Fellow, National Center for Research on Earthquake Engineering, Taipei, Taiwan; Joint Appointment Professor, Department of Civil Engineering, National Cheng Kung University, Tainan, Taiwan
5. Associate Technologist, National Center for Research on Earthquake Engineering, Taipei, Taiwan

Email: yanuar.haryanto@unsoed.ac.id, hthu@mail.ncku.edu.tw, hanalylie@live.undip.ac.id, fphsiao@ncree.narl.org.tw, chiachen@ncree.narl.org.tw

ABSTRACT

Strengthening method of using external steel wire ropes has been considered to be an effective way to increase the strengthening efficiency. This paper focuses on predicting the flexural performance of reinforced concrete (RC) beams which strengthened by external steel wire ropes. Finite element (FE) analysis is presented to validate against laboratory tests of three beams. All beams have the same rectangular cross-section geometry and are loaded under four point bending, but different in the steel wire ropes. The smeared-crack model for concrete, bilinear model for steel, and an elastic-linear model for steel wire rope, are evaluated with respect to their ability to describe the behavior of the beams. The results show good agreement with the experimental data regarding load-displacement response, ultimate flexural load, and the stiffness. In conclusion, engineers and researchers could use the developed FE model as a valuable numerical tool to predict the effect of several parameters on the flexural performance of externally strengthened RC beams with steel wire ropes.

Keywords: finite element analysis, RC beam, steel wire rope, strengthening

INTRODUCTION

The strengthening and rehabilitation of existing structures is now a challenging problem facing civil engineers all over the world. Many RC structures constructed in the past are no longer considered safe due to increase in live loads, change in design codes and specifications or due to the effect of carbonation, corrosion or chloride attacks (Abhikary *et al.*, 2000). Steel wire rope, commonly used in civil and mechanical applications (Fontanari *et al.*, 2015), is a promising material for strengthening RC structures due to its high strength, light weight and high flexibility properties. Behavior of RC structures strengthened with steel wire rope has been extensively investigated in recent years and some of the main findings and conclusions were adopted by JGJ / T325-2014 guide (General Administration of Quality Supervision, Inspection and Quarantine of the People's Republic of China, 2014). Haryanto *et al.* (2014) conducted an experimental test on T-section RC beams strengthened in the negative moment region with bonded steel wire ropes. Furthermore, an FE simulation by applying an initial pre-stress force on this strengthening technique resulted in an initial 20% pre-stress force, which provided a 52.15% higher flexural strength improvement. Finally, the load-displacement relationship resulting from FE simulation was found to be identical to that resulting from the experimental test (Haryanto *et al.*, 2017).

Another approach is to add steel rebars on the compression block for the T-section RC beams strengthened with steel wire ropes in the negative moment region, resulting in an increase in flexural

strength with a ratio of 2.09 (Haryanto *et al.*, 2019). Haryanto *et al.* (2018) also conducted a study on streel wire rope performance as the external strengthening of RC beams with different end-anchor. The aim of the present study is to develop FE models that can predict the performance of RC beams strengthened with externally steel wire ropes. This paper is based upon previous work conducted by the authors (Haryanto *et al.*, 2021). In this study, three FE models were developed using the finite element software, ATENA (Cervenka *et al.*, 2017). The models consider material constitutive laws of the smeared-crack model for concrete, bilinear model for steel, and an elastic-linear model for steel wire rope. The model is validated by comparing the predicted load-deflection response results with the measured experimental data at all stages of loading.

METHODS

Experimental Setup

The experimental program [8] consisted of two strengthened RC beams with two and four 6 mm diameter steel wire ropes (B26 and B46) in addition to an unstrengthened specimen to serve as a control beam (B0). The beams had a total length of 1000 mm and of rectangular cross-section having a width and depth of 100 mm and 150 mm, respectively. The steel reinforcement consisted of two 6 mm diameter bars in both of the tension the compression zone. In addition, 6 mm diameter steel stirrups were used as shear reinforcement spaced 50 mm apart. The tested beams geometric details are presented in Figure 1 (Haryanto *et al.*, 2021).

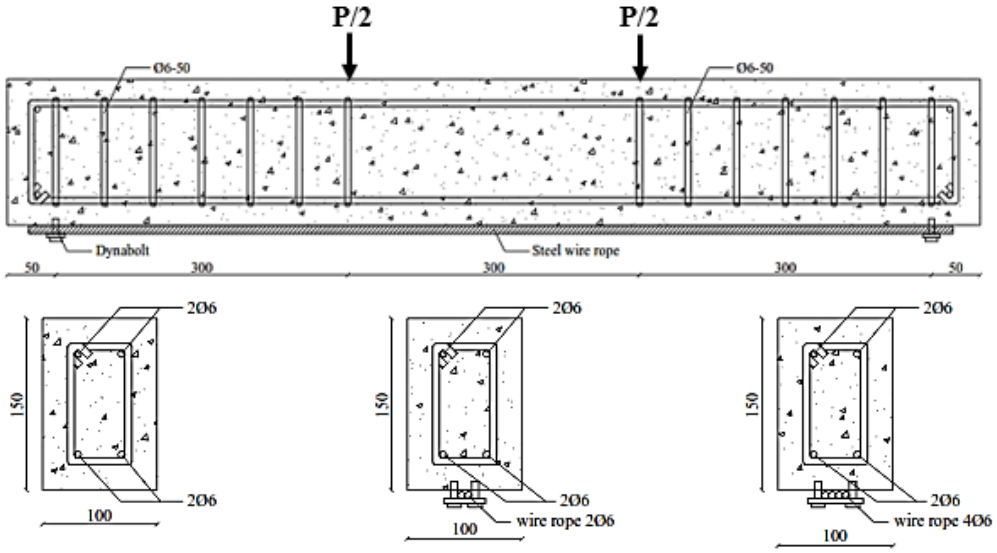

Figure 1. Geometric details of beam specimens (Haryanto *et al.*, 2021).

Geometry of the Developed FE Models

Figure 2 displays the unstrengthened beam FE model. The strengthened beams were also modelled but not presented for the sake of saving space. For the reason of reducing the cost of calculation, only half of the beam was modelled and the whole beam results could be obtained according to the symmetry of the beam.

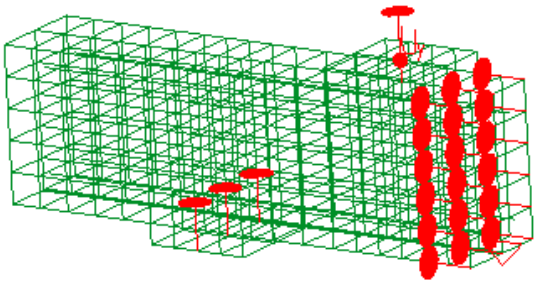

Figure 2. Loading and boundary conditions

For the loading and boundary conditions, the nodes at the centerline of the bottom surface of the support plate were pinned with restraints in the vertical direction. The area at the right end of the model was restrained with symmetric boundary conditions. Vertical displacement was applied to the nodes at the centerline of the bottom surface of the beam

Element Description

The materials and type of elements used in the modeling are summarized in Figure 3 and Table 1. An 8-noded solid element that assumes a hardening regime before reaching compressive strength, CC3DnonLinCementitious2, was used to model the concrete. Longitudinal reinforcements and wire ropes were modeled using CCReinforcement elements that have the ability to disable reinforcement's compressive response. Loading and supporting plates were modeled using the 8-noded solid element CC3DelastIsotropic, as it simulates linear isotropic materials for 3D. The concrete with stirrups was modeled using the 8-noded CCCombinedMaterial element that can be used to create a composite material consisting of various components, e.g. concrete with smeared reinforcement in different directions.

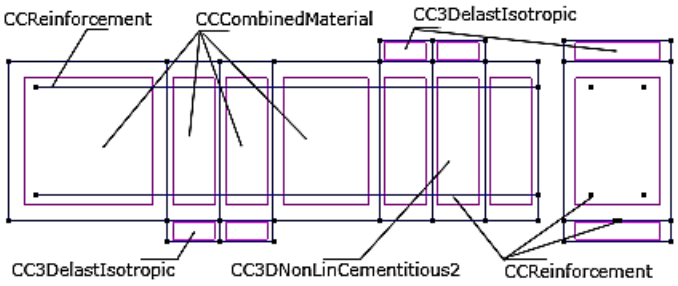

Figure 3. Model of finite element analysis for half of a section

Table 1. Materials and types of elements

Materials	Element type	Properties	Data
Concrete	*CC3DnonLinCementitous2*	Compression strength	30.45
		Young's modulus, E_c	25220.262
Steel reinforcement Ø6	*CCReinforcement*	Young's modulus, E_s	195900
		Ultimate stress, f_u	540.63
		Yield stress, f_y	369.40
		Area of reinforcement, A	0.00002827
Steel wire rope Ø6	*CCReinforcement*	Young's modulus, E_s	32568
		Ultimate stress, f_u	599.48
		Yield stress, f_y	-
		Area of reinforcement, A	0.0000283
Concrete stirrup	*CCCombinedMaterial*	Ratio of direction x reinforcement (1)	0
		Ratio of direction y reinforcement (2)	0,011309734
		Ratio of direction z reinforcement (3)	0,007539822
Loading and support plates	*CC3DElastIsotropic*	Young's modulus, E_s	200000
		Poisson's ratio, v	0.3

Material Modeling

The steel reinforcement constitutive model is based on bilinear laws, while the tensile behavior of the steel wire rope is characterized by a linearly elastic stress-strength relationship until failure as shown in Figure 4. Furthermore, the constitutive basic models of concrete in ATENA use the concept of smeared cracking and the fracture mechanics approach as shown in Figure 5.

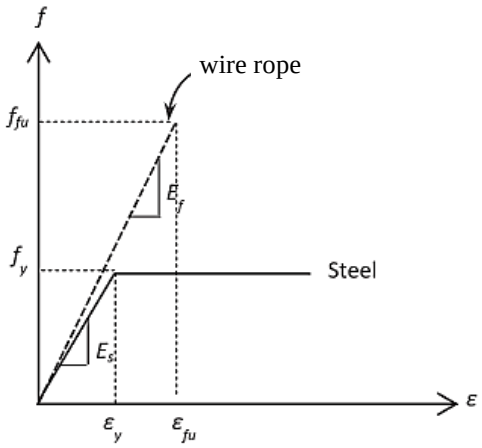

Figure 4. Stress-strain law for steel reinforcement and steel wire rope

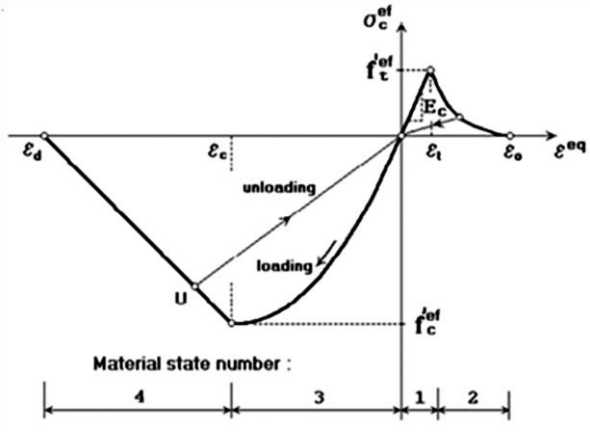

Figure 5. Uniaxial stress–strain law for concrete

RESULTS AND DISCUSSION

Load-deflection Curves

It can be observed from Figure 6 that the beam strengthened with external steel wire ropes seems to have a reasonable enhancement on the flexural strength. The unstrengthened beam (B0) experienced 18.59 kN ultimate load and 12.49 mm corresponding deflection. An ultimate load-carrying capacity of 30.81 kN was achieved by the beam strengthened with two 6 mm diameter of steel wire ropes (B26) with a corresponding mid-span deflection of 20.24 mm. Beam B26 yielded 66% extra strength gain over the control specimen. The ultimate load acquired for the beam strengthened with four 6 mm diameter of steel wire ropes (B46) was equal to 57.33 kN which is equivalent to 208% gain in the load-carrying capacity compared to the unstrengthened control beam. The deflection achieved corresponding to the ultimate load was 29.19 mm for this beam.

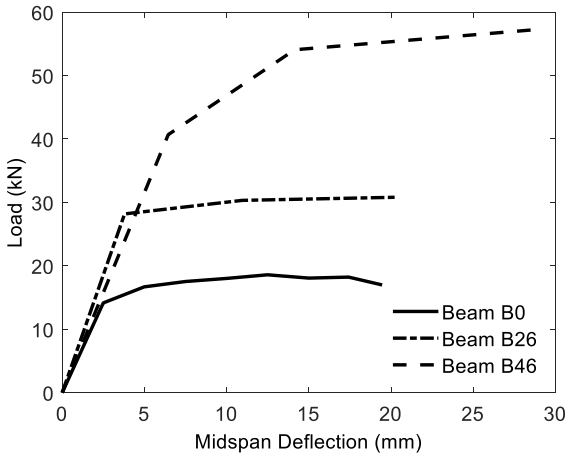

Figure 6. Load-midspan deflection curves of the developed FE models

FE Model Validation

The developed FE models are validated and verified using the results of load and midspan deflection from experimental testing [8]. Figure 7 shows the predicted load versus mid-span deflection response curves for three of the tested specimens at all loading stages till failure. Table 2 summarizes the ultimate carrying load capacity and the corresponding midspan deflections for the tested beams obtained from the experiments and developed FE models. It can be clearly indicated from Figure 7 and Table 2 that there is an excellent correlation between the numerical and experimental results at all loading stages.

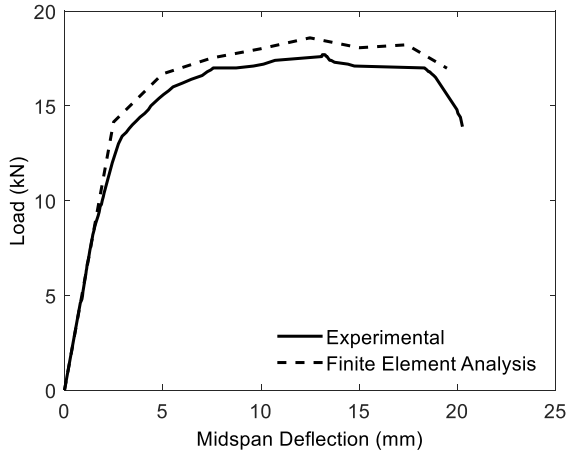

(a) Beam B0

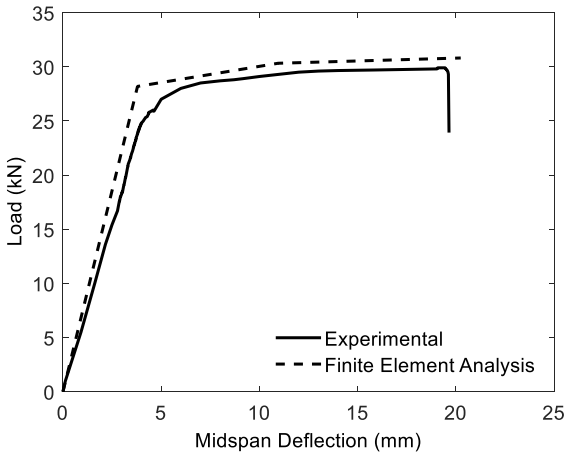

(b) Beam B26

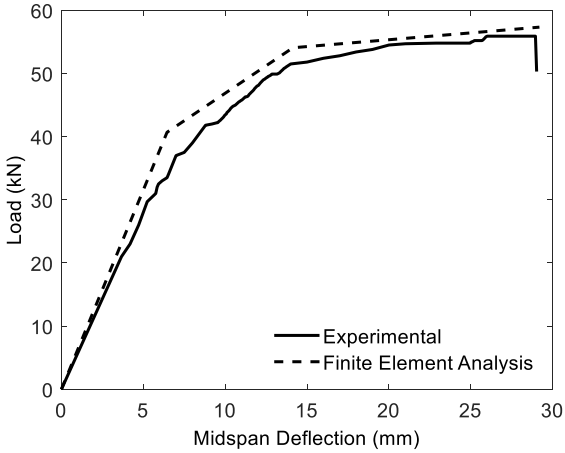

(c) Beam B46

Figure 7. Load-deflection curve comparisons between FEA and experimental

At ultimate, the model was able to predict the ultimate load-carrying capacity and associated deflection with a difference ranging from 2.49 to 4.78% and 0.82 to 6.18% respectively. The FE results had a higher stiffness, especially when the beams were at nonlinear stage. This could be explained that the perfect bond assumption between steel and concrete, which ignored the bond-slip relationship, would enhance the flexural stiffness of the beams and cause overestimated strain concentration in steel at the locations of cracks. However, these results verify the accuracy of developed FE models in predicting RC beams strengthened with external steel wire rope response and performance.

Table 2. FE versus experimental results

Specimen	$P_{u\,(FE)}$ (kN)	$\delta_{u\,(FE)}$ (mm)	$P_{u\,(Exp)}$ (kN)	$\delta_{u\,(Exp)}$ (mm)	% Difference	
					P_u	δ_u
B0	18.59	12.49	13.26	20.25	4.78	-6.18
B26	30.81	20.24	29.90	19.49	2.95	3.71
B46	57.33	29.19	55.90	28.95	2.49	0.82

CONCLUSIONS

This paper presented the development of three 3D nonlinear finite element (FE) models for the evaluation and prediction of the response of three tested specimens conducted by the authors in a

previous investigation. The three FE models were developed and the results were validated by comparing the predicted FE load-deflection response with the measured experimental data. It can be concluded from this study that:

- The load–midspan deflection responses of the developed FE models are in good agreement with the measured experimental data at all stages of loading till failure of the specimens.
- The beams strengthened with two and four 6 mm diameter of external steel wire ropes achieved an increase in ultimate strength by 66% and 208% over the control beam, respectively.
- The proposed modeling technique predicts structural behaviors of RC beams with external steel wire ropes accurately.
- The FE model can be improved with proper consideration of the bond-slip relationship.
- The developed and validated FE models presented in this study could serve as a numerical platform to investigate the behavior and predict the performance of RC beams externally strengthened in flexure with external wire ropes.

For further investigation on the flexural performance of RC beams strengthened with external steel wire ropes, a parametric study with different prestressing level is warranted in a future investigation to develop acceptable guidelines for such strengthening material with its desirable ductile.

ACKNOWLEDGMENTS

This work was financially supported by the Jenderal Soedirman University, Indonesia, under the contract number 3747/UN23.14/PN/2018.

REFERENCES

Abhikary, M., B.B. Mutsuyoshi and H. Sano (2000). "Shear Strengthening of Reinforced Concrete Beams Using Steel Plates Bonded on Beam Web: Experiments and Analysis," *Constr. Build. Mater.*, **14**(5), 237-244.

Cervenka, V., J. Cervenka, Z. Janda, D. Pryl (2017). *ATENA Program Documentation Part 8; User's Manual for ATENA-GiD Interface*, Cervenka Consulting, Prague.

Fontanari, V., M. Benedetti, D.B. Monelli, F. Degasperi (2015). "Fire Behavior of Steel Wire Ropes: Experimental Investigation and Numerical Analysis," *Eng. Struct.*, **84**, 340-349.

General Administration of Quality Supervision, Inspection and Quarantine of the People's Republic of China (2014). *JGJ/T 325-2014 Technical Specification for Strengthening Concrete Structures with Prestressed High Strength Steel Wire Ropes*, Ministry of Housing and Urban-Rural Development of China, Beijing, [in Chinese].

Haryanto, Y., A.L. Han, H.-T. Hu, F.-P. Hsiao, B.A. Hidayat, A. Widyaningrum (2021). "Enhancement of Flexural Performance of RC Beams with Steel Wire Rope by External Strengthening Technique," *J. Chin. Inst. Eng.*, **44**(3), 193-203.

Haryanto, Y., B.S. Gan, A. Maryoto (2017). "Wire Rope Flexural Bonded Strengthening System on RC-beams: A Finite Element Simulation," *Int. J. Technol.*, **8**(1), 134-144.

Haryanto, Y., B.S. Gan, A. Widyaningrum, N.G. Wariyatno, A. Fadli (2018). "On the Performance of Steel Wwire Rope as the External Strengthening of RC Beams with Different End-anchor Type," *J. Teknol. (Sci. Eng.)*, **80**(5), 145-154.

Haryanto, Y., H.-T. Hu, A.L. Han, A.T. Atmajayanti, D.L.C. Galuh, B.A. Hidayat (2019). "Finite Element Analysis of T-section RC Beams Strengthened by Wire Rope in the Negative Moment Region with An Addition of Steel Rebar at the Compression Block," *J. Teknol. (Sci. Eng.)*, **81**(4): 143-154.

Haryanto, Y., I. Satyarno, D. Sulistyo (2012). "Strength and Ductility of Reinforced Concrete T-beams Strengthened in The Negative Moment Region with Wire Rope and Mortar Composite," *Civ. Eng. For.*, **21**(1), 1163-1169.

HYBRID TESTING APPLICATION OF OPENFRESCO IN MULTIPLE PHYSICAL SUBSTRUCTURES OF THE SEVEN-STORIES RC STRUCTURE

Fu-Pei Hsiao[1], Lyan-Ywan Lu[2*], Shih-Wei Yeh[3] , Bo-Tse Hsu[5], Hsuan-Wen Huang[4], Cheng Hung[5]

1. Division Director, National Center for Research on Earthquake Engineering, Professor (Joint Appointment), Department of Civil Engineering, National Cheng Kung University
2. Professor, Department of Civil Engineering, National Cheng Kung University, Adjunct Researcher, National Center for Research on Earthquake Engineering (*corresponding author)
3. Associate Technologist, National Center for Research on Earthquake Engineering
4. Master, Department of Civil Engineering, National Cheng Kung University
5. Graduate Assistant, Department of Civil Engineering, National Cheng Kung University

Email: fphsiao@narlabs.org.tw,lylu@ncku.edu.tw

ABSTRACT

The structural behavior of RC structures is relatively complicated, it is difficult to accurately simulate its seismic dynamic response using a finite element software. This study aims to establish an hybrid testing (HT) platform suitable for testing RC structures for NCREE. HT is a research approach that combines numerical simulation and structural testing. The proposed platform is a combination of OpenSees, OpenFresco and MTS CSIC.A shaking table test of a 1/2-scaled seven-story RC structure was conducted in the Tainan Laboratory of NCREE. This study intends to reproduce the results of the shaking table test through the established HT platform. In this study, the OpenFresco hybrid model was built based on the OpenSees model and used to conduct the HT for the RC structure under median to extreme seismic loadings. The HT results of the seven-story RC structure show that it is quite consistent with the simulated results of the numerical model built by the OpenSees. It is also demonstrated that the dynamic responses of the shaking table test can be partially reproduced by the HT method. Therefore, the feasibility of the hybrid testing platform developed in this study for the application of large-scale RC structures is verified.

Keywords: hybrid testing, reinforced-concrete frame, OpenSees, OpenFresco, MTS CSIC.

INTRODUCTION

In order to investigate the response and characteristics of the structural systems under seismic forces, the research methods often adopted can be roughly divided into two categories: numerical simulation and shaking table tests (STTs). Because the former method only relies on numerical tools, the simulated results may be considerably different from the actual structural behavior due to model errors. While the latter is able to more accurately reflect the behavior of the overall structural system, it is often too costly to build full- or reduced-scale structure for the STT. Especially, for experiment of full-scale RC structures, the experiment of the STT will become very expensive. In view of this, this study aims to develop a hybrid testing (HT) approach to mitigate the above-mentioned problems encountered in the seismic research of RC structures, so the structural behavior and structural response of RC structures under seismic forces can be obtained in a more economical and efficient way.

Hybrid testing is an advanced experimental technology that combines the technologies of numerical simulation and structural testing. The method usually divides the target structure to be investigated into a numerical substructure (NS) and a physical substructure (PS). Since the structural behavior of the NS in the HT is usually more easily predicted by a numerical model, it is simulated by a structural analysis software. While the seismic response of the PS is tested physically by an experimental setup,

because the PS usually involves more complex structural behavior that is hard to be predicted numerically. In order to conduct the HT for various large-scale RC structures, this study presents a HT platform consists of the finite-element software OpenSees (2015), middle software OpenFresco (2014) and MTS CSIC controller software. Both OpenSees and OpenFresco are open-source software developed by the Pan Pacific Earthquake Engineering Research Center (PEER) at the University of California, Berkeley, while the MTS CSIC software is developed by MTS company. The test result of the developed HT platform on a RC frame is expected to reproduce the results of a shaking table test conducted to investigate the seismic performance of a large-scale RC structures.

TARGET STRUCTURE – SEVEN-STORY RC BUILDING

The hybrid testing sample is a seven-story reinforced concrete frame composed of the physical and numerical substructure. This composite model refers to the seven-story building conducted in the Tainan Laboratory, National Center for Research on Earthquake Engineering, in July and November 2018. The RC building shaking table specimen is a 1/2 scale model. The total height of the building is 12.73 meters. The clear height of the first story is 300 cm, and the clear height of each other story is 150 cm. There are two types of column sizes. The size of the column on the left is 30x30 centimeters, and the dimension of the column on the right is 30x75 centimeters; in addition, the section of the foundation column is 115x75 centimeters, the thickness of the slab is 10 centimeters, and the dimensions of the beam section are 25x45 centimeters. There are shear walls above the building, with a thickness of 15 cm, to simulate the weak story effect of middle- to high-rise buildings.
OpenFresco is conducted to establish the model as the numerical simulation. The six columns at the first story are the physical substructure (Fig.1), the experiment is carried out with the U-shaped frame in the middle span (Fig.2), and the others are the numerical substructure. This paper will discuss the experimental results when the ground motion is CHY063 400gal.

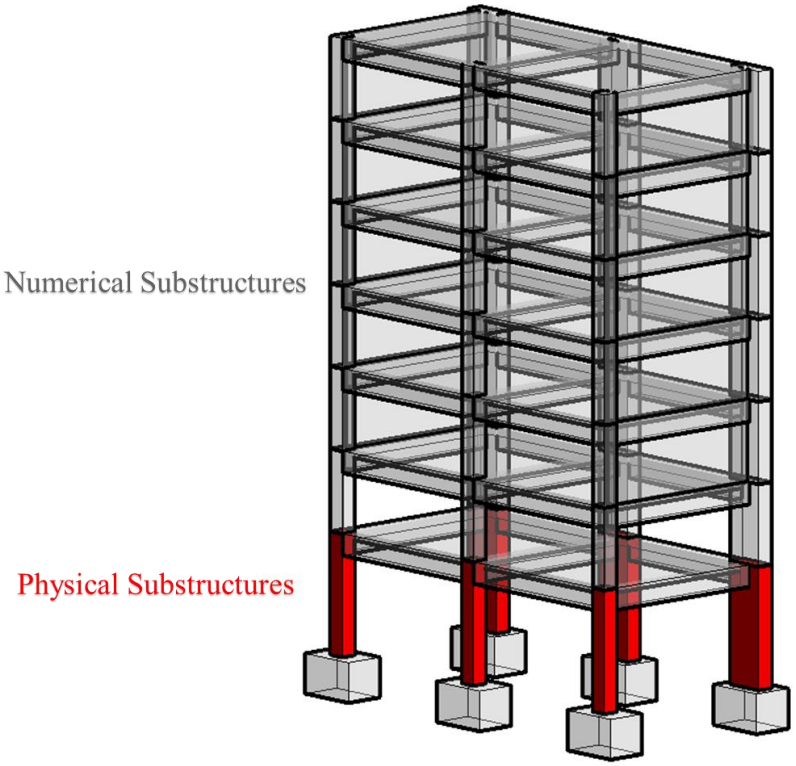

Figure 1 Hybrid simulation model of the seven-story RC building

Figure 2 Setup of hybrid simulation test

HYBRID TESTING WITH OPENFRESCO FRAMEWORK

Figure 3 is a schematic diagram of the process of this hybrid testing experiment. The software and hardware devices used are OpenSees and OpenFresco to build a hybrid testing model. Then the displacement command is output by the hybrid testing model through the MTS CSIC system to the MTS 793 control software to drive the actuator. Apply displacement on the specimen, and finally, the hybrid testing model analyzes the following displacement command through the feedback reaction force. For data recording, the MGCPlus data acquisition system is used to record the actuators' actual commands and feedback signals.
As a bridge between the numerical and the actual space, OpenFresco includes Experimental Element, Experimental Site, Experimental Setup, and Experimental Control and communicates with the MTS CSIC system.
The Experimental Elements of this study use Generic elements, which can define any number of nodes and degrees of freedom so that the six columns at the first story of the seven-story RC building can be established with a single Experimental Element to achieve the goal of multi-channel hybrid testing.
It can be seen from Figure 3 that this hybrid testing only controls the one-directional degree of freedom of the specimen, and the hybrid testing model simulates the other degrees of freedom. Therefore, in order to match this experimental configuration, this paper assumes that the RC structure model of the seven-story building is a double-curvature column model. In addition, in order to ensure that the structural responses of the other two-span U-shaped frames at the first story in the numerical model are the same as the results of the actual experiment. This paper assumes that the structural responses of the three-span U-shaped frames at the first story are the same, expanding the virtual channel and adjusting the feedback.
As shown in Fig. 4, the numerical model of this study will output the displacement commands to the top of the column with the six columns at the first story, which will first be sent to the MTS CSIC system, and then sent to the six channels established by the MTS FT-100 controller. The six channels are "five virtual channels that do not send commands to the actuator" and a "single actual channel that outputs to the actuator and pushes the specimen." The feedback force of the virtual channel is set to be the same as the actual channel, and the displacement commands of the six columns at the first story are also the same value based on the assumption of a rigid diaphragm. So, the displacement command of any column can be arbitrarily used as the output of the actual channel. Next, because the reaction force feedback by the actuator

is the reaction force of the whole structure, the coefficient of the feedback force needs to be adjusted by the program command of OpenFresco, which is determined by the stiffness of the columns.

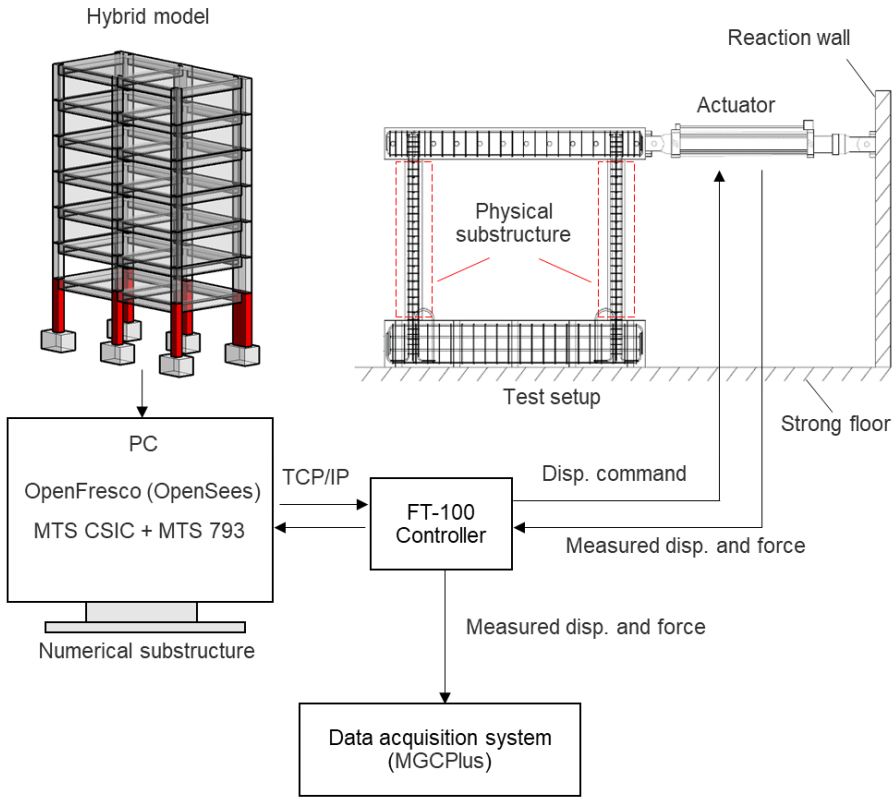

Figure 3 Schematic diagram of hybrid testing (six columns as physical substructures)

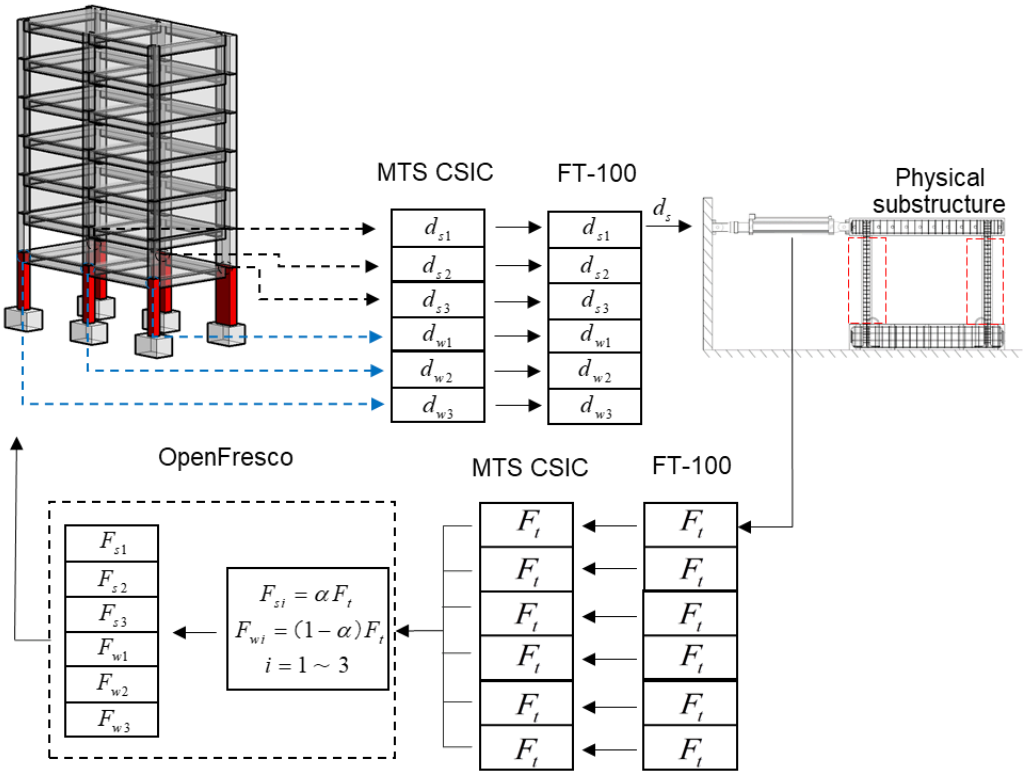

Figure 4 Schematic diagram of the command and feedback channels by the seven-story RC structure

RESULTS AND DISCUSSIONS

1. Comparison of hybrid testing and numerical simulation results

In order to verify the results of this hybrid testing, this paper uses virtual hybrid testing for comparison. The parameters of this comparison include:

- The displacement at the roof.
- The acceleration at the roof.
- The story drifts from the second story.
- The story drifts from the first story.
- The base shear.
- Hysteresis loop from the first story.

As shown in Fig. 5, the ground motion CHY063 400gal was carried out in this experiment. The comparison results show that they have a certain degree of agreement, and each peak values and frequencies are consistent.

2. Comparison of hybrid testing and shaking table results

The research purpose of this paper is to replace the shaking table experiment through hybrid testing technology. In order to verify whether this paper can achieve this purpose of hybrid testing, the shaking table experiment of the seven-story RC structure is reproduced. The results are compared with the shaking table experiments, as shown in Fig. 6. The ground motion CHY063 400gal is considered in the hybrid testing.

The parameters of this comparison include:

- The displacement at the roof.
- The acceleration at the roof.
- The story drifts from the second story.
- The story drifts from the first story.
- The base shear.
- Hysteresis loop from the first story.

The comparison results show that the acceleration at the roof, The story drifts from the second story, the base shear, and the hysteresis loop from the first story have a certain degree of agreement. The experiment result has a certain residual displacement, but the hybrid testing does not, and the peak value is relatively different. The reason is that the specimen in the hybrid testing is newer and more robust than the specimen in the shaking table test. The specimen was slightly damaged before the experiment, which was judged to be caused by the difference of the specimens.

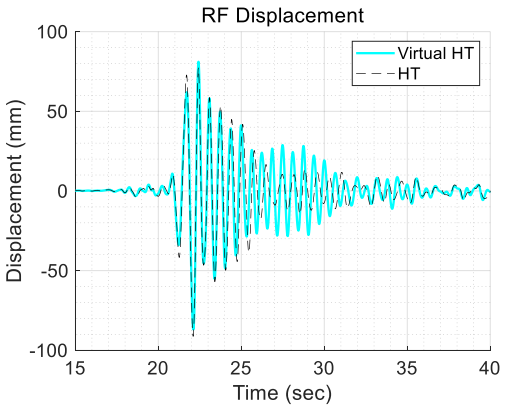

(a) Displacement at the roof

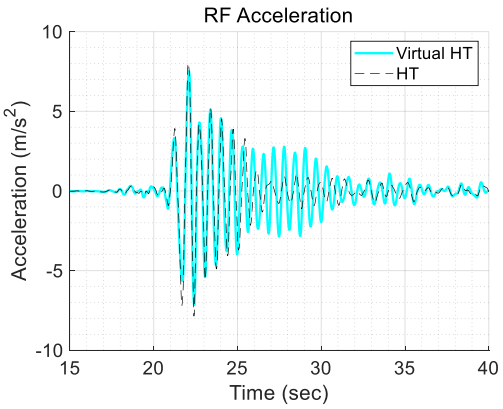

(b) Acceleration at the roof

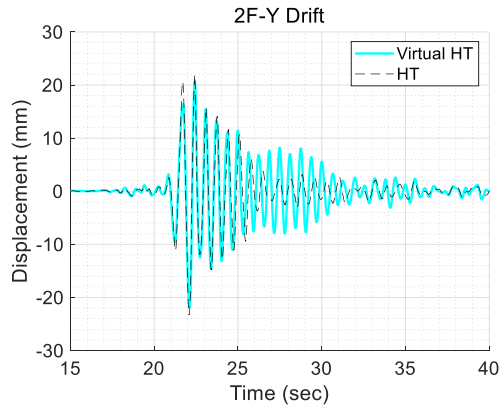

(c) Story drift from the second story

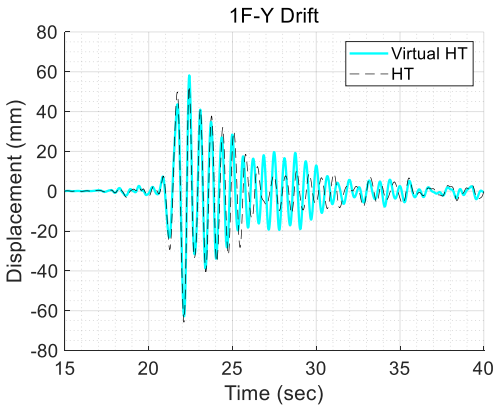

(d) Story drift from the first story

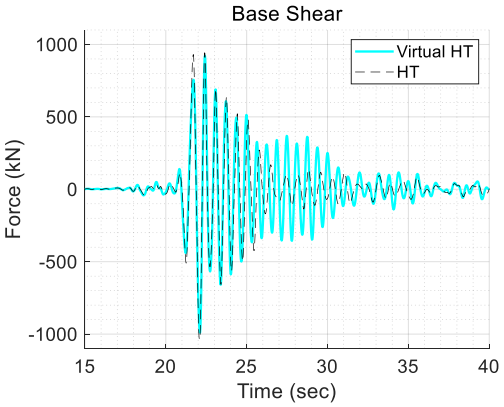

(e) Base shear

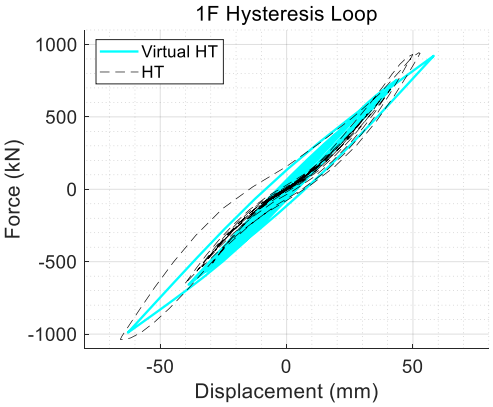

(f) Hysteresis loop from the first story

Figure 5 Comparison of hybrid test and numerical simulation results (six columns as physics substructure, CHY063, 400gal)

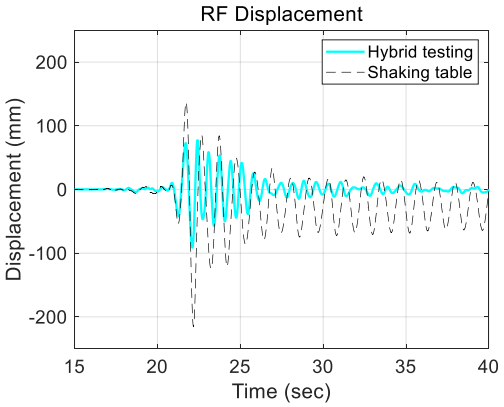

(a) Displacement at the roof

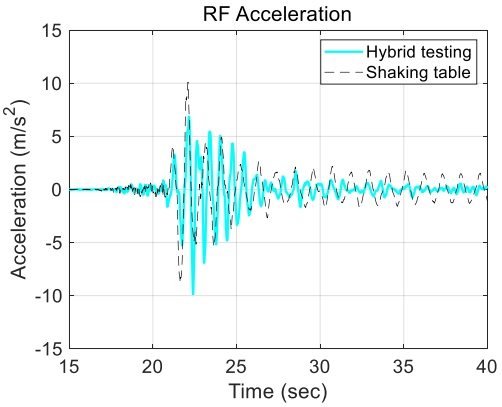

(b) Acceleration at the roof

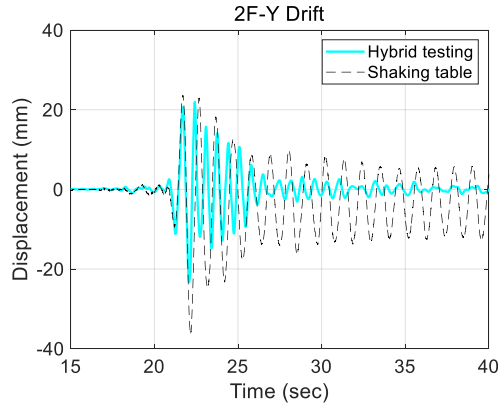

(c) Story drift from the second story

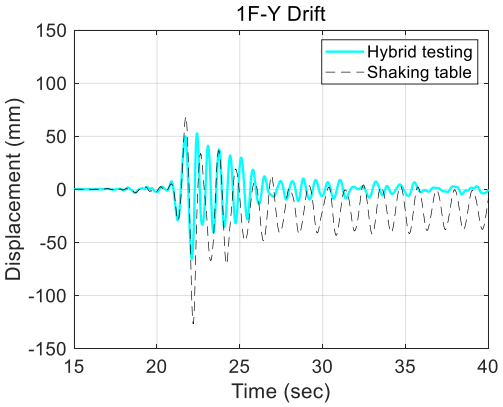

(d) Story drift from first story

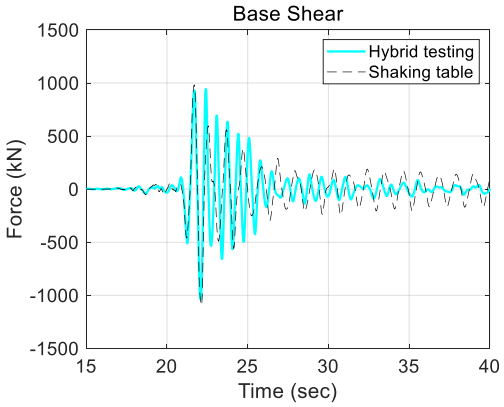

(e) Base shear

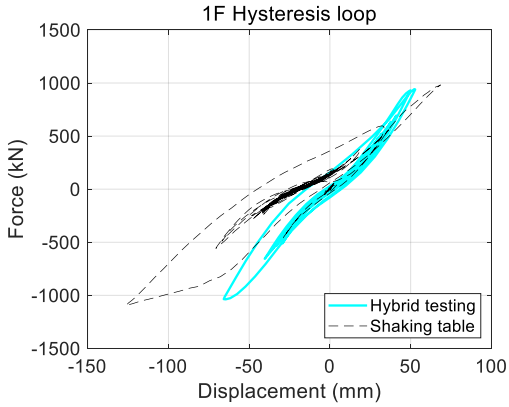

(f) Hysteresis loop from the first story

Figure 6 Comparison of hybrid test and shaking table test (six column as physics substructure, CHY063, 400gal)

CONCLUSIONS

This study uses OpenSees and OpenFresco with MTS CSIC to conduct slow hybrid testing. It cooperates with the facility to confirm its feasibility in the Tainan Laboratory, National Center for Research on Earthquake Engineering. The study results show insignificant differences between the hybrid testing and the numerical simulation. It can confirm the correctness of the hybrid testing and successfully use the Generic Element to perform a three-dimensional hybrid testing in which multiple columns are physical substructures. According to the characteristics of the Generic Element, an arbitrary number of nodes and degrees of freedom determine the feasibility and correctness of multi-channel control and can conduct slow hybrid testing through real and virtual channels in this research.

ACKNOWLEDGMENTS

This study was supported by research grants from National Science and Technology Council (MOST 110-2625-M-492-015). Authors also thanks to Tainan Laboratory, National Center for Research on Earthquake Engineering, and Assistant Technologist Ms. An Hsu for providing technical support.

REFERENCES

1. Andreas H. Schellenberg, Hong K. Kim, Yoshikazu Takahashi, Gregory L. Fenves, and Stephen A. Mahin (2009), “OpenFresco Command Language Manual”.
2. Andreas H. Schellenberg, Stephen A. Mahin, Gregory L. Fenves (2009), “Advanced Implementation of Hybrid Simulation” *PEER*, 09-104.
3. Maikol Del Carpio Ramos, M. Javad Hashemi, Gilberto Mosqueda (2013), “Large-Scale Hybrid Simulation of a Steel Moment Frame Building from the Onset of Damage Through Collapse” *5th International Conference on Advances in Experimental Structural Engineering*, Taipei, Taiwan.
4. M. Javad Hashemi, Yassamin Al-Ogaidi, Riadh Al-Mahaidi, Robin Kalfat, Hing-Ho Tsang, John L. Wilson (2016), “Application of Hybrid Simulation for Collapse Assessment of Post-Earthquake CFRP-Repaired RC Columns” *Journal of Structural Engineering*, ASCE. 143(1).
5. Hsuan-Wen Huang (2021). Application and Verification of OpenFresco in Hybrid Testing of Reinforced Concrete Frame, *Master's thesis*, National Cheng Kung University. (in Chinese)
6. Hsuan-Wen Huang, Bo-Tse Hsu, Lyan-Ywan Lu, Fu-Pei Hsiao, Shih-Wei Yeh (2021). Analysis and Application of the Open Earthquake Engineering Simulation System (OpenSees) in Nonlinear Structures with Plastic Hinges, *NCREE-2021-013*, National Center for Research on Earthquake Engineering. (in Chinese)

(SS4) Advanced earthquake engineering techniques for seismic resistance and disaster mitigation

THE DEVELOPMENT OF AN APPLICATION PROGRAM FOR SEISMIC FRAGILITY ANALYSES OF STRUCTURES

Ming-Chieh Chuang[1], Jui-Liang Lin[2], You-Jin Zhong[3] and Chao-Hsien Li[4]

1. Associate Researcher, National Center for Research on Earthquake Engineering, Taipei, Taiwan, R.O.C.
2. Division Director, Building Engineering Division, National Center for Research on Earthquake Engineering, Taipei, Taiwan, R.O.C.
3. Research and Development Engineer, Phison Electronics Corp., Miaoli, Taiwan, R.O.C.
4. Senior Research Engineer, CoreBrace, LLC, UT, U.S.A.

Email: mcchuang@narlabs.org.tw, jllin@narlabs.org.tw, r06521207@ntu.edu.tw, chaohsien.li@corebrace.com

ABSTRACT

This paper presents a special-purpose application program for the seismic fragility analysis named Fragility Analyses of STructures (FAST). To investigate the seismic fragility of structures, FAST adopts the incremental dynamic analysis (IDA) that is conducted to obtain seismic demand and capacity by using a series of nonlinear response history analyses at different ground-motion intensity levels. To enhance the effectiveness of multi-record IDAs that require enormous nonlinear response history analyses, not only the hunt-and-fill-tracing algorithm but also the multi-thread mechanism were implemented in the FAST. Through the validation with the illustrative case of a nine-story steel building, it shows that the FAST is an effective tool for users to engage in the research and practice related to seismic fragility analysis of structures.

Keywords: seismic performance, fragility curve, incremental dynamic analysis, IDA curve, seismic fragility analysis

INTRODUCTION

For the goals of performance-based earthquake engineering, seismic fragility analysis (SFA) is the crucial technique. In general, three main methods for the seismic fragility analysis include cloud analysis, incremental dynamic analysis (IDA) and multiple strip analysis (MSA). Both IDA and MSA methods require enormous nonlinear response history analyses (NRHA) at different ground-motion intensity levels. In order to offer a time-saving and cost-effective tool for both IDA and SFA, the authors developed the application program named Fragility Analyses of STructures (FAST) by using C# programming language.

THE PROTOTYPE OF THE APPLICATION PROGRAM

To effectively conduct the IDA and SFA, the Taiwan National Center for Research on Earthquake Engineering (NCREE) researchers (Lin *et al.*, 2021) have developed a solution using MATLAB. Moreover, the finite element analysis program "Platform of Inelastic Structural Analysis for 3D Systems" (PISA3D) (Lin *et al.*, 2009) was used as the analysis engine for NRHA to generate IDA curves. The MATLAB-based solution is the prototype of the FAST presented in this study. As shown in Figs. 1 and 2, The MATLAB-based software has been used in performing both IDA and SFA in the previous study (Lin *et al.*, 2021).

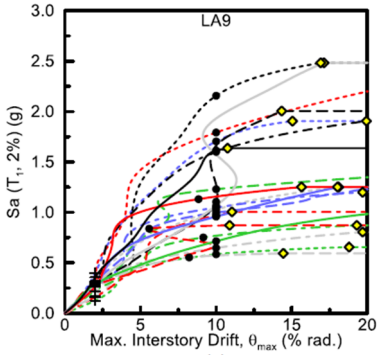

Figure 1. IDA curves (Lin *et al*., 2021).

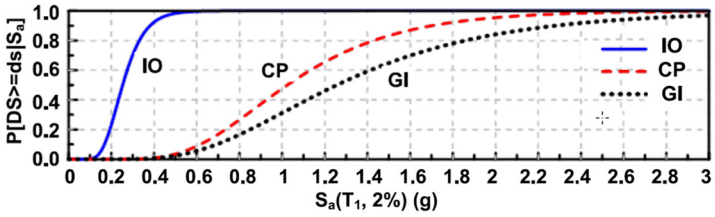

Figure 2. Seismic fragility curves (Lin *et al*., 2021).

Fig. 3 shows the technical framework of the MATLAB-based prototype comprising (1) the pre- and post-processor and (2) the analysis engine (i.e., PISA3D). The pre- and post-processor implemented using MATLAB not only provides the interface to read information from the text-based input file but also generates the corresponding PISA3D input files for NRHA. Furthermore, it can process the results of IDAs using PISA3D to generate the IDA curves. Based on the IDA curves, the seismic fragility curves can be constructed accordingly.

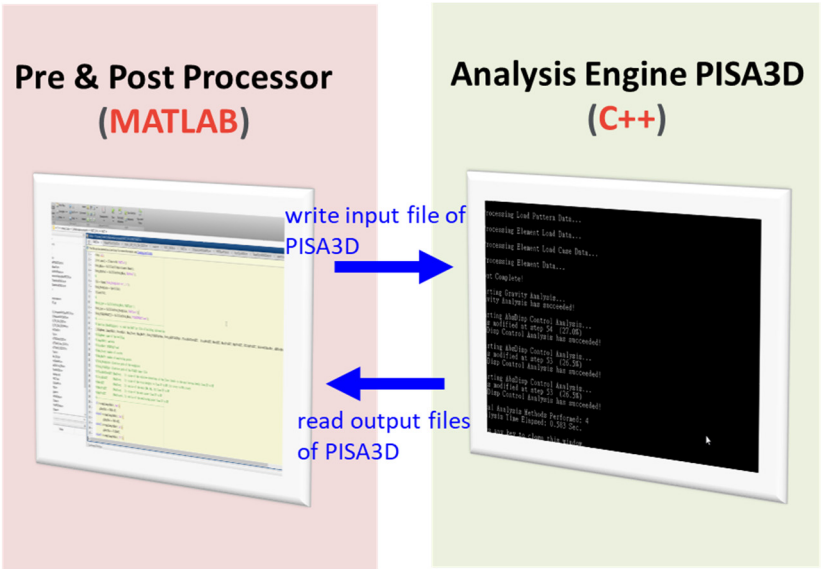

Figure 3. Technical framework of the MATLAB-based prototype.

THE NEWLY-DEVELOPED APPLICATION PROGRAM: FAST

Based on the MATLAB-based prototype, the authors have developed the application program named FAST. The objectives of the development of the FAST include (1) developing a user-friendly IDA and SFA tool, (2) building the novel mechanisms to enhance efficiency of IDA and SFA, and (3) broadening PISA3D applications.

The Features of FAST

A flexible framework for extended applications

To take advantage of the object-oriented programming for a flexible framework, the C# programming language and the .NET Framework were utilized in the development of the FAST. Through the migration from MATLAB to C# programming language, the redesigned system framework of the FAST has been done in this study (Fig. 4). The object-oriented framework allows that the researcher can conveniently enhance the modules of computing logics (e.g., run dynamic analysis).

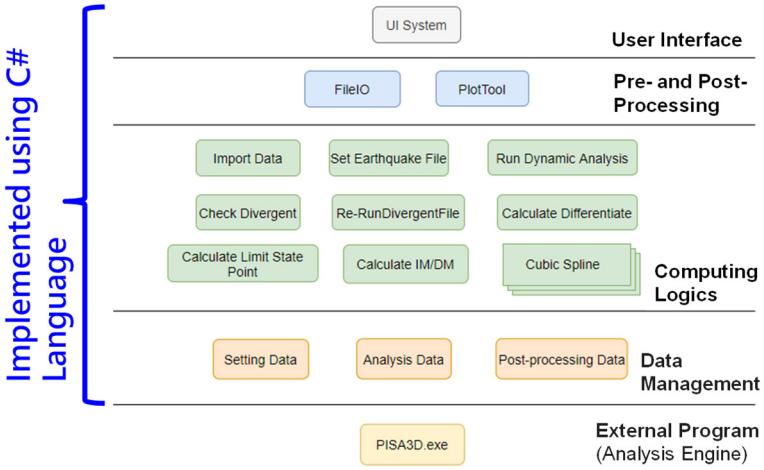

Figure 4. Newly designed architecture of the FAST

The concise and friendly user interface

Through the .NET Framework, the concise and friendly user interface can be implemented as shown in Fig. 5. For a user, only four steps are required to conduct SFA including (1) input model, (2) select ground motions, (3) run analysis, and (4) check results. In contrast to the text-based input file used in the MATLAB-based prototype, FAST possesses an easy-to-use interface for researchers and engineers to conveniently conduct the IDA and SFA.

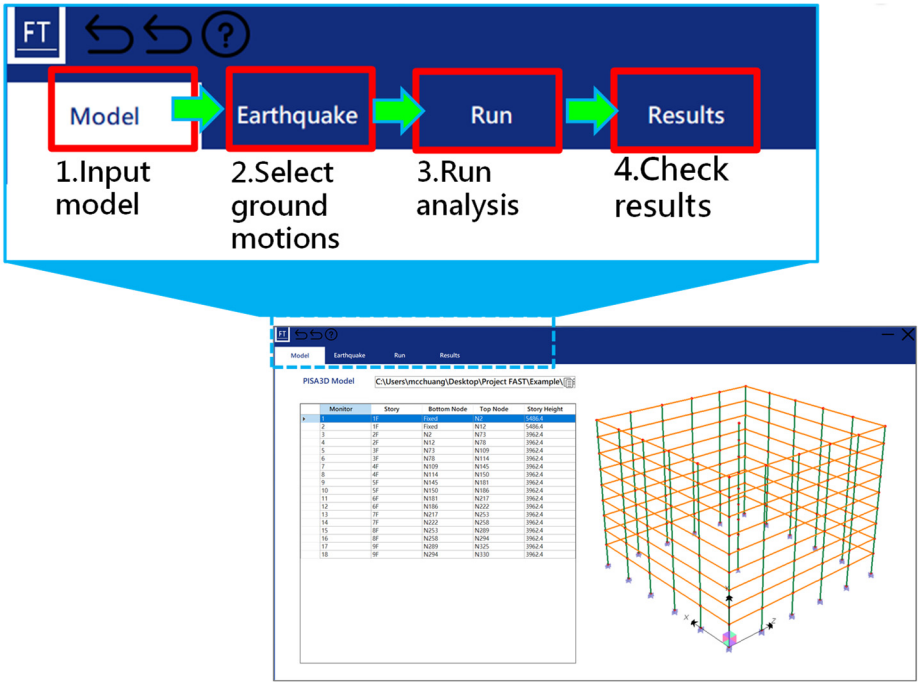

Figure 5. Overview of FAST interface

The relatively effective multi-record IDA

The multi-thread mechanism was implemented in FAST for parallel track of conducting IDAs (Fig. 6). Through the multi-thread mechanism, the multi-record IDAs can be conducted in parallel. The time consumption spent on generating the IDA curves can be reduced accordingly to enhance the SFA efficiency.

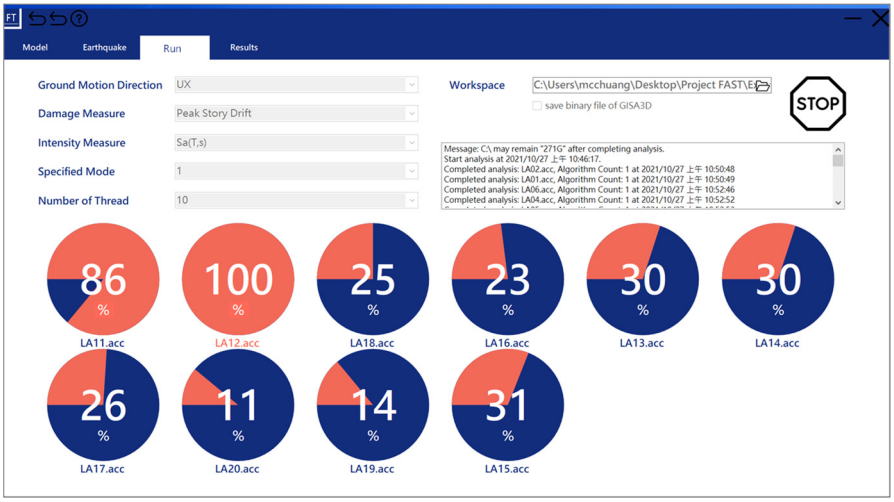

Figure 6. Parallel track of conducting IDAs

Illustrative Case for Verification

To comprehensively investigate the seismic performance of steel framed buildings with varied plan-asymmetric properties, Lin *et al*. (2021) constructed a PISA3D model of the nine-story symmetrical steel building that was investigated by the SAC steel research project (SAC Joint Venture, 2000) for buildings located in Los Angeles. For brevity, this building is designated as LA9 hereafter. Furthermore, twenty earthquake records used in the SAC project for the hazard level of a 475-year return period in Los Angeles are selected for the multi-record IDAs. The seismic fragility curves of building LA9 are constructed according to the aforementioned IDAs with the MATLAB-based prototype. The detailed description of building LA9 and its IDA results, which is available in literature (Lin *et al*., 2021) is not repeated in this paper.

In this study, building LA9 is utilized as an illustrative case to verify the effectiveness of the FAST. The author utilized the FAST to conduct the aforementioned IDAs with the same PISA3D model and earthquake ground motion records. According to the results of IDAs and specified damage states (DS), the fragility curves are constructed and shown in Fig. 7. Fig. 7 gives the fragility curves of building LA9 corresponding to three damage states including immediate occupancy (IO), collapse prevention (CP), and global instability (GI) obtained from the FAST and the MATLAB-base prototype. Obviously, the results show that the fragility curves corresponding to three damage states computed by FAST coincide very well with those computed by the MATLAB-base prototype.

With the hunt-and-fill-tracing algorithm developed by Vamvatisikos and Cornell (2002), it could reduce the number of NRHAs necessary to generate an IDA for a single ground motion. For example of building LA9, one IDA curve can be generated through 12 NRHAs corresponding to 12 ground motion intensity levels. For an ensemble of 20 ground motions, a total of 240 NRHAs are required. The 20-record IDA using the MATLAB-based prototype requires about 15 hour of computing on the computer with an Intel Core i7-10700K processor (8 cores, up to 5.10 GHz) and 32 GB of RAM. However, it is worth noting that that the time consumption of the IDA with FAST with 10 threads can be dramatically reduced from 15 hours to 2.5 hours. This confirms the effectiveness of the FAST.

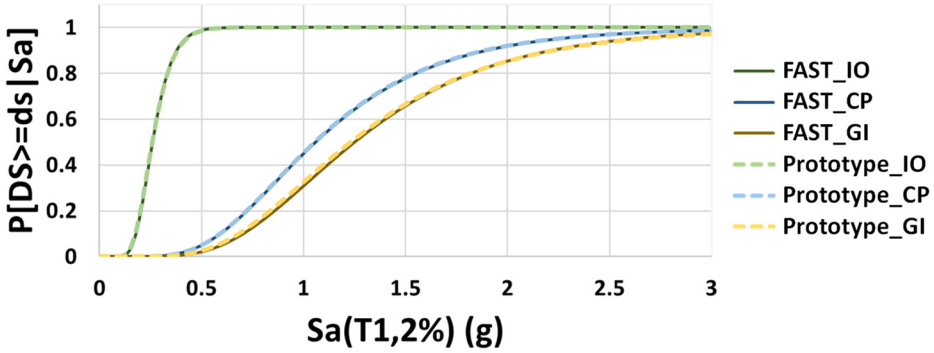

Figure 7. Results of SFA (FAST vs. MATLAB-based prototype)

CONCLUSIONS

The FAST, developed in NCREE, is a special-purposed software for the seismic fragility analysis of structures. The FAST can not only automatically generate the PISA3D input file for conducting NRHA but also effectively conduct NRHA through the multi-thread mechanism. The effectiveness of the FAST has been demonstrated using the building LA9. In LA9 model example, the time consumption of FAST with 10 threads can be dramatically reduced from 15 hours to 2.5 hours. In other words, the efficiency of IDAs is increased to 6 times. The effectiveness of the multi-thread mechanism has been verified accordingly. As a result, the FAST is an effective tool for users engage in the research and practice related to seismic fragility analysis of structures.

REFERENCES

SAC Joint Venture (2000). "State of the Art Report on Systems Performance of Steel Moment Frames Subject to Earthquake Ground Shaking," *FEMA-355C*, FEMA.

Lin, B.Z., M.C. Chuang and K.C. Tsai (2009). "Object-oriented Development and Application of a Nonlinear Structural Analysis Framework," *Advances in Engineering Software*, 2009, **40**(1), 66-82.

Lin, J.L., T.K. Chow, C.H. Li and Y.K. Yeh (2021). "A Comparative Study of Seismic Performance of Steel Framed Buildings with Varied Plan-Asymmetric Properties," *Journal of Earthquake and Tsunami*, **15**(04), 2150016.

Vamvatisikos, D, CA Cornell (2002). "Incremental dynamic analysis," *Earthquake Engineering and Structural Dynamics*, **31**, 491-14.

THE RESPONSE OF STEEL-REINFORCED CONCRETE (SRC) COLUMNS JACKETED BY FRP-WRAPPED SPIRAL CORRUGATED TUBE (FWSCT) UNDER AXIAL COMPRESSION

Chung-Sheng Lee, Obed Adi Kusuma, Ren-Kang Su

Department of Civil and Disaster Prevention Engineering, National United University,
Miaoli, Taiwan, R.O.C.
Email: lee.cs@nuu.edu.tw

ABSTRACT

This paper presents the research work on steel-reinforced concrete (SRC) columns jacketed by FRP-wrapped steel corrugated tube (FWSCT) under axial compression. A total of 48 FWSCT-jacketed SRC columns were fabricated with various types of shaped steel reinforcement: hollow-shaped steel, cross-shaped steel, and W-shaped steel. Meanwhile, they were jacketed by steel tubes or the FWSCTs with different layers of CFRP or GFRP. On the other hand, the numerical simulation on each specimen was performed and compared with its experimental results in axial and lateral directions.

Keywords: steel-reinforced concrete (SRC), confined concrete, fiber-reinforced polymer (FRP), steel corrugated tube, axial compression test

INTRODUCTION

Steel reinforced concrete (SRC) structures have been widely used in recent years because of their advantages. The shaped steel embedded in the concrete enhances the stiffness and the strength, and the surrounding concrete protects the shaped steel reinforcement from buckling, fire damage, and chemical corrosion. In addition, the axial compressive capacity and flexural strength of the SRC columns can be increased by the lateral confinement to generate the confining effectiveness for concrete [1]. Although SRC columns have many advantages, the required steel rebars in hoop and axial directions brought the complexity and challenges in construction.

To meet the requirements of the axial strength and seismic resistance, SRC columns need to have additional steel rebars to confine their cross sections. Several studies have shown that with inadequate confinement, the compression members will buckle and lose its strength [2,3]. Steel-confined concrete has better axial compressive strength and deformation capacity. However, due to the elastic-plastic behavior, the steel confinement will not be able to provide concrete with a higher confining pressure after it yields. In contrast, fiber-reinforced polymer (FRP) is a linear elastic material. It can provide an increased confining pressure to the concrete until it ruptures [4-8]. Typical mechanical responses of the steel-confined and the FRP-confined concrete cylinders with different level of confinement are depicted in Figure 1.

Combining the advantages of the FRP material and the corrugated steel tube, a high-performance tubular structure, FRP-wrapped steel corrugated tube (FWSCT), has been developed [9,10]. FWSCT has the advantages of lightweight, high strength, and tailored design. Considering the advantages of the SRC column and FWSCT, this study is to develop an innovative seismic-resistant structural member through the application of FWSCT-jacketed SRC columns. The objective of applying FWSCT on the SRC column are to reduce the use of the steel stirrups and the difficulty in SRC column construction. Additionally, the development of FWSCT-jacked SRC columns is to increase the axial strength and seismic resistance capacities.

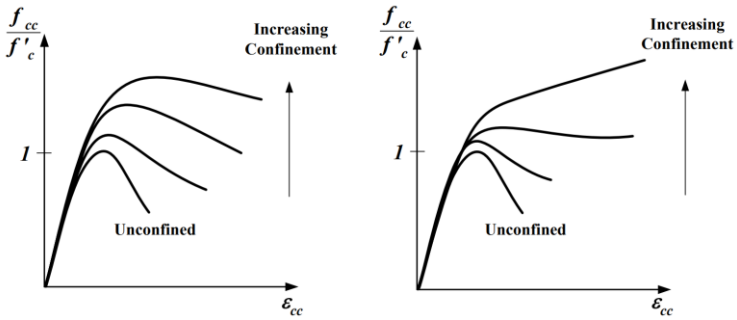

(a) Steel-confined concrete (b) FRP-confined concrete

Figure 1 Typical mechanical response of steel-confined concrete and FRP-confined concrete with different levels of confinement (Lee and Hegemier, 2006)

AXIAL COMPRESSION EXPERIMENTAL TESTS

Test Matrix and Specimen Details

The test matrix for this program is shown in Table 1. A total of 48 specimens with the diameter of 150 mm and the height of 300 mm were fabricated. These specimens were categorized into 24 types: one type of pure concrete column, three types of steel-reinforced concrete (SRC) column, 16 types of FWSCT-jacketed SRC column, and four types of SRC filled steel tube column. Three shaped-steel types included hollow, cross, and W shapes. The steel corrugated tubes were wrapped by given layers of FRP composites made by glass or carbon fabrics. As shown in Table 1, each specimen has its specific code. The first letter represents the confinement placed on the outer surface of the specimen, where G stands for glass fiber, C stands for carbon fiber, and S stands for steel. The second letter represents the shaped-steel section embedded in the concrete, where S stands for solid specimen, HK stands for the hollow-shaped steel, X stands for cross-shaped steel, and W stands for W-shaped steel section. The third digit represents the number of the FRP layers, where 2 represents two layers of FRP, 4 represents four layers of FRP. Each type has two specimens that will be tested represented by the code "-1" and "-2" as a distinction.

Table 1 Specimen Test Matrix

	Unconfined	GFRP2	GFRP4	CFRP1	CFRP2	Steel Tube
Solid Concrete	S-1	GS2-1	GS4-1	CS1-1	CS2-1	SS-1
	S-2	GS2-2	GS4-2	CS1-2	CS2-2	SS-2
Hollow-shaped Steel	HK-1	GHK2-1	GHK4-1	CHK1-1	CHK2-1	SHK-1
	HK-2	GHK2-2	GHK4-2	CHK1-2	CHK2-2	SHK-2
Cross-shaped Steel	X-1	GX2-1	GX4-1	CX1-1	CX2-1	SX-1
	X-2	GX2-2	GX4-2	CX1-2	CX2-2	SX-2
W-shaped Steel	W-1	GW2-1	GW4-1	CW1-1	CW2-1	SW-1
	W-2	GW2-2	GW4-2	CW1-2	CW2-2	SW-2

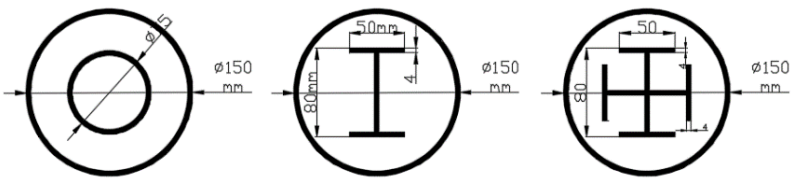

Figure 2 Specimen Cross-section Details

As shown in Figure 2, the steel sections used in the SRC columns are hollow-shaped steel, cross-shaped steel, and W-shaped steel, which are made of 4-mm thick steel plates. The steel tube confinement has the inner diameter of 150 mm, with the thickness of 4 mm. The yield strength of the steel section and the steel tube confinement is 320 MPa, with the ultimate strength of 370 MPa. The 300 mm-long spiral corrugated steel tube has an inner diameter of 150 mm, with the thickness of 0.35 mm. The spiral thread of the corrugated tube has a depth of 5 mm and a width of 12 mm, with the spacing between each spiral thread of 24 mm. The yield strength of the steel corrugated tube is 150 MPa, with the ultimate strength of 280 MPa. The filler on the surface of the corrugated steel tube is made of AEROSIL silica and ETERSET 2960PT-S vinyl ester resin applied prior to wrapping the FRP materials. In this study, the FRP materials wrapped on the surface of the spiral corrugated steel tube is made of the L900-E uniaxial 0-degree woven glass fiber cloth and L250-C uniaxial 0-degree woven carbon fiber cloth. The overlapping length of each FRP layer is 150 mm. The compressive strength of the concrete used in this experiment is 20 MPa.

Instrumentations and Testing Procedure

Figure 3(a) shows the instrumentations installed on the specimens. Each specimen was equipped with two sets of strain gauges to measure the axial and lateral strain. Four uniaxial strain gauges were placed at the center of the specimen. Two strain gauges were arranged in the hoop direction and the other two strain gauges were arranged in the longitudinal direction perpendicular to the fiber direction. They are denoted by the letter SL and ST in Figure 3(a), respectively. In addition, two linear variable displacement transducers (LVDT) were installed to measure the axial displacement.

As shown in Figure 3(b), all the tests were conducted by the 500-ton universal testing machine at the National Center for Research on Earthquake Engineering (NCREE). All the specimens in this study were subjected to unidirectional loading test with displacement control. The applied loading rate was 0.039 mm/sec, maintained until the strength of the specimens dropped to 1/3 of the maximum strength or when the displacement reached 20 mm.

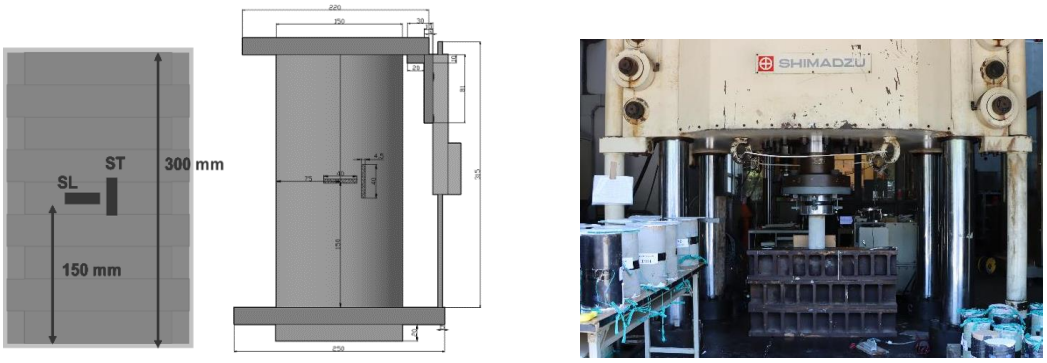

(a) Instrumentations (b) Test Setup

Figure 3 Instrumentations and Test Setup

Experimental Results

Figure 4 shows the photographs of the specimen W-1, representing the behavior of the unconfined SRC columns under axial compression. The failure mode of specimen W-1 is discussed by the observed crack pattern. For the unconfined specimen, the vertical cracking was initiated along the height of the specimen. The cracks become more obvious as the increase of the axial load before reaching its peak value. After reaching the peak load, the force-strain curve in Figure 4(c) shows descending trend. The strain remains constant while the resistance is decreasing. At this point, the concrete cracks become more pronounced.

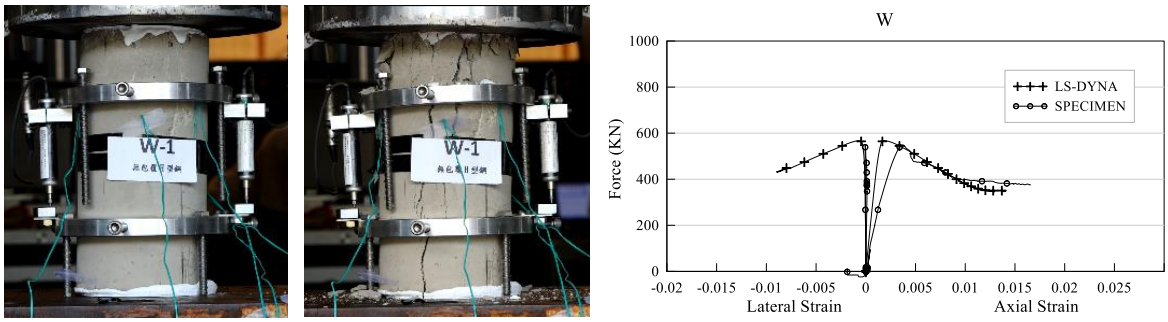

(a) Before the Test (b) After the Test (c) Specimen Response during the Test

Figure 4 Photograph of specimen W-1 during the test

Figure 5 shows the photographs of the specimen GW4-1, representing the behavior of the FWSCT-jacketed SRC columns. As can be seen in Figure 5(c), the specimens, either wrapped by the glass fiber or the carbon fiber, exhibit a strain hardening behavior during the test. Due to the massive deformation, the strain gauges were all peeled off from the FRP surface before the failure of the specimen, with the result that the maximum strain of the specimens were not well measured. It was observed that the FWSCT-jacketed SRC columns lose their axial strength after the tensile failure of the FRP.

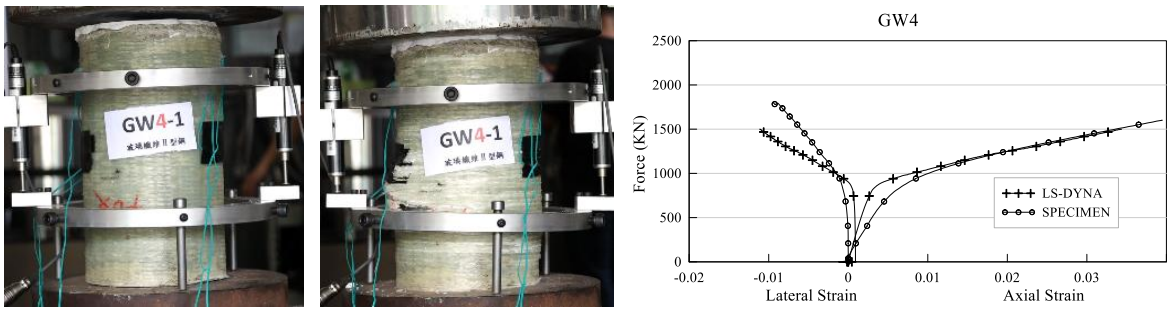

(a) Before the Test (b) After the Test (c) Specimen Response during the Test

Figure 5 Photograph of specimen GW4-1 during the test

The behavior of the steel-confined concrete columns represented by specimen SX-1 can be seen in Figure 6. It can be observed in Figure 6(c) that after reaching the peak strength, the axial strength remains flat with the increase of the axial and lateral strain. In the later stage during the compression, the outer steel tube was partially buckled at the upper and lowers ends of the specimens.

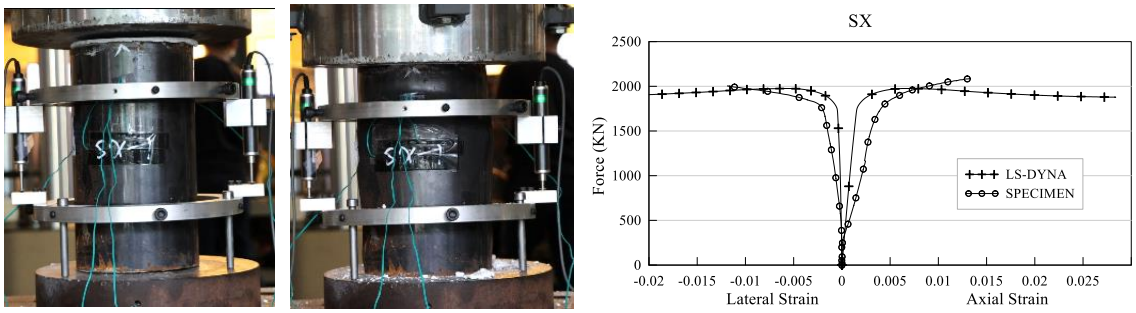

(a) Before the Test (b) After the Test (c) Specimen Response during the Test

Figure 6 Photograph of specimen SX-1 during the test

Test Results and Simulation Comparisons

Figure 7 to Figure 9 show the force-strain response curves comparing the numerical results with the experimental results. Observing the mechanical behavior between specimen X and GX2, it can be seen that the FRP-wrapped spiral corrugated tube can increase the axial strength as well as the strain capacity

of the SRC specimens. Nevertheless, the force-strain curve between specimen GX2 and SX showed different mechanical behavior. The force-strain curve of Specimen GX2 exhibits a bilinear with a strain hardening response. By contrast, the axial strength of specimen SX exhibits a rapid increase before reaching its peak strength. The force response of the specimen SX tends to be flat after entering the plastic zone. The comparison between numerical and experimental results of all specimen types is given in Appendix.

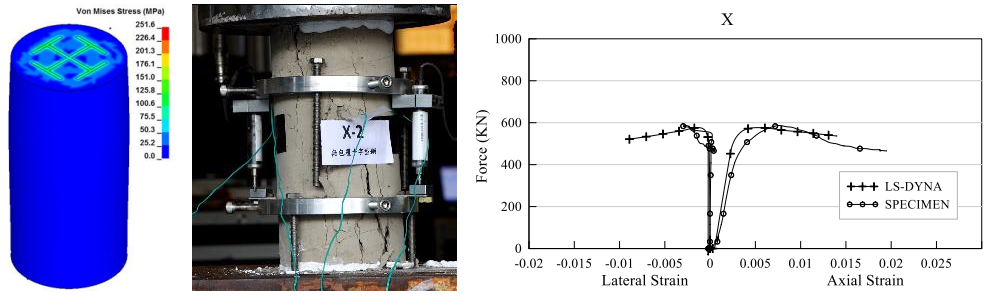

Figure 7 Numerical and Experimental Results Comparison of Specimen X

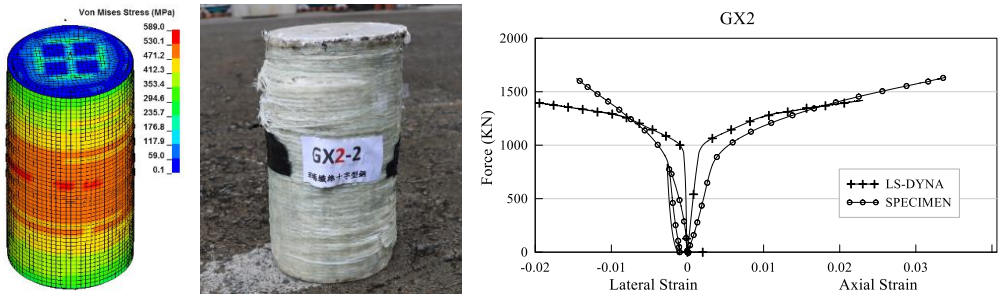

Figure 8 Numerical and Experimental Results Comparison of Specimen GX2

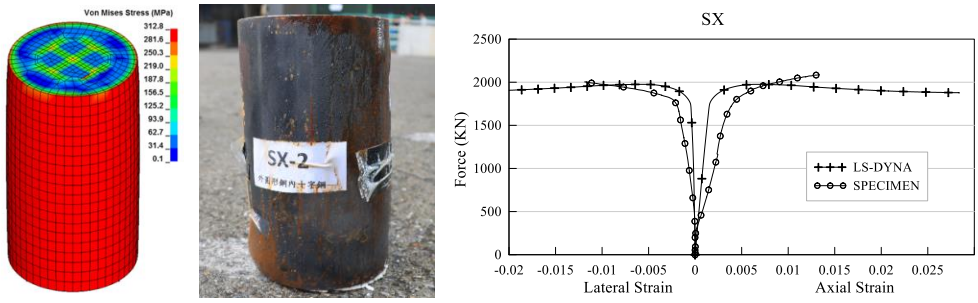

Figure 9 Numerical and Experimental Results Comparison of Specimen SX

SUMMARY AND CONCLUSION

The main purpose of this study is to verify the mechanical behavior of the SRC column jacketed by FRP-wrapped spiral corrugated tube (FWSCT) and develop the design method. The main research work includes: (1) Conducting axial compression experimental tests; (2) Developing numerical simulation methods; and (3) Examining the mechanical behavior of FWSCT-jacketed SRC columns under axial compression. This study has verified the behavior of the SRC columns jacketed by FRP-wrapped spiral corrugated tube (FWSCT) under axial compression. Confining the SRC column with FWSCT can provide an effective confinement effect on the concrete, which can improve the axial strength of the specimens. In addition, the use of FWSCT to confine the SRC column can improve the axial strain capacity of the specimens, which is similar to the effect of the steel tube confinement. By utilizing this feature, it can provide a higher deformation capacity in the plastic region. This study will further analyze the mechanical behavior of the FWSCT-jacketed SRC columns, including the influence of the steel section on the confined concrete and the contribution of each material system to the axial strength of the specimen.

ACKNOWLEDGMENTS

This research project was funded by the Ministry of Science and Technology, Taiwan, under Program No. MOST 109-2625-M-239-001. The experimental work was conducted at the Materials Testing Center at National United University (NUU) and the National Center for Research on Earthquake Engineering (NCREE) in Taiwan. Assistance from the technical staff is acknowledged.

REFERENCES

1. Construction and Planning Agency, Ministry of the Interior, Taiwan (2011), Design Specifications and Commentary of Steel Reinforced Concrete Structures.
2. Di, Jiang (2005), Behavior of SRC Columns in Axial load, Master Thesis, Department of Construction Engineering, National Taiwan University of Science and Technology.
3. Lin Wang (2010), Numerical Simulation on Mechanical Behavior and Confinement Effect of SRC Columns, Master Thesis, Department of Civil Engineering, National Chiao Tung University.
4. Begum M, Driver RG, Elwi AE. Behaviour of partially encased composite columns with high strength concrete. Eng Struct 2013;56:1718–27.
5. De Sousa BMJ, Jr Caldas, R.B.. Numerical analysis of composite steel-concrete column of arbitrary cross section. J Struct Eng 2005;131(11):1721–30.
6. Ding F, Ding X, Liu X, Wang H. Mechanical behavior of elliptical concrete-filled steel tubular stub columns under axial loading. Steel Compos Struct 2017;25(3):375–88.
7. Lam J, Ho J, Kwan A. Flexural ductility of high-strength concrete columns with minimal confinement. Mater Struct 2009;42(7):909–21.
8. Mursi M, Uy B. Strength of slender concrete filled high strength steel box columns. J Constr Steel Res 2004;60(12):1825–48.
9. Chou, C. C., Lee, C. S., Tan, H. H., Wu, K.Y., (2017a) “FRP composite wrapped Grooved-wall lining tubular structure, and method of manufacturing.” U.S. Patent US9566748 B2.
10. Lee, C. S., Chou, C. C., Tan, H. H., Chin, V.L., Axial Behavior and Test of Concrete-Filled Spiral Corrugated Steel Tubes Wrapped with Glass Fiber Reinforced Polymer, Structural Engineering, Vol. 35, No.1, pp.52- 77, March 2020.

SEISMIC BEHAVIOR OF BRIDGE COLUMNS BY NON-PRESTRESSED STEEL STRANDS

Jhen-Wei Wu[1] and Yu-Chen Ou[2]

1. PhD Student, Department of Civil Engineering, National Taiwan University, Taipei, Taiwan, R.O.C. E-mail: d06521007@ntu.edu.tw
2. Professor, Department of Civil Engineering, National Taiwan University, Taipei, Taiwan, R.O.C.

ABSTRACT

A new self-centering concrete bridge column has been developed by the authors. The proposed bridge column uses unstressed seven-wire steel strands as elastic elements to reduce the residual displacement of the column after a strong earthquake. This research uses the Matlab software to develop a pushover model of unstressed steel strands column (PM-USSC). According to the comparison between the model establishment and the test result, it is observed that the steel strand slips at the anchorage system, and the anchorage system is considered through the modified formula relationship. The effect of anchorage system slip can be accurately captured before the envelope response of the unstressed steel strands column reaches the ultimate state.

Keywords: self-centering, strand, residual displacement

INTRODUCTION

Taiwan experiences frequent seismic activity and has a high population density. According to data released, there are approximately one-third of the population of Taiwan lives within 10 km of an active fault and is threatened by near-fault earthquakes. Earthquake observations have revealed that the ground motion displacement and velocity near a fault rupture zone are considerably different from those observed far from this zone. In a near-fault region, a large displacement of the ground in one direction and high-speed pulses over a short time are typically observed. Structures cannot efficiently dissipate an earthquake's energy by swinging, and conventional reinforced concrete (RC) bridge columns might exhibit large residual displacement after an earthquake, which substantially reduces the safety and serviceability of the bridge.

This research proposed a self-centering RC bridge column. ASTM 416 Grade 270 (1860-MPa) seven-wire steel strands were used as the elastic element to provide stiffness and self-centering capability to the column after yielding of the conventional longitudinal steel reinforcement during an earthquake. Although the yield strength of the steel strand was extremely high, the steel strand could still yield when the column was subjected to a large displacement. To prevent the yielding of the steel strand before a 5% drift ratio of the column was achieved, the tape was used to wrap a certain length of the steel strand extending upward from the plastic hinge area of the column. The steel strand was not prestressed, which reduced the construction cost of the column compared to the post-tensioned self-centering bridge column. Moreover, concrete creep due to prestressing can be avoided.

UNSTRESSED STEEL STRANDS COLUMN

In the bridge column developed by this research, in addition to the traditional deformed bar, the longitudinal reinforcement is added with high-strength steel strands for unstressing. After the earthquake force coming, it can provide the stiffness of traditional longitudinal steel bars after yielding, reduce the residual displacement of the bridge column after the earthquake, and improve the self-recentering ability. A 7-wire steel strand with a nominal ultimate strength of 1860 MPa and a diameter of 15.2 mm was used in this study.

In the use of bridge columns, steel strands will be subjected to repeated tension and compression when the bridge column is subjected to cyclic lateral force, so the anchoring at both ends must be anchored by tension and compressive anchoring. For this purpose, a tension-compression anchor is specially developed, which consists of two tension anchors. The anchor is designed with an steel plate to assist the concrete bearing.

In addition, the equipment and labor required for prestressing are not required. Compared with post-tensioning bridge columns, the construction cost can be greatly reduced, and since there is no prestressing, the concrete creep caused by prestressing can be avoided. Although the yielding stress of the steel strand is extremely high, it may still yield when the column is subjected to large displacement. In order to prevent the steel strand from yielding before the displacement ratio of 5%, the steel strand is wrapped with tape and extends upward for a length from the plastic hinge area of bridge column. In order to avoid the grip between the steel strand and the concrete, thereby reducing the stress of the steel strand. Figure 1(a) is the design drawing of the unstressed steel strand column. Two sets of wedges were used for the two back-to-back anchors to anchor the strands in both tension and compression as illustrated in Figure 1(b). The steel plates were used to provide bearing areas to anchor the strands in concrete. Figure 1(c) illustrates the construction of specimen. The yellow duct tape used to unbond the strands can be seen in the figure.

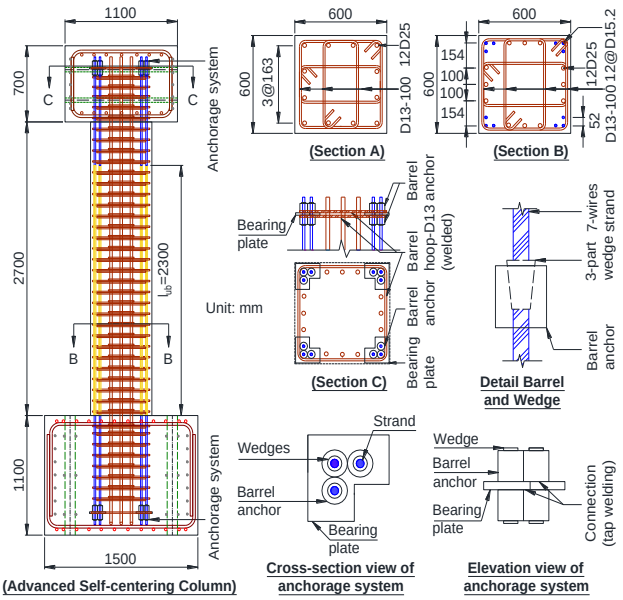

(a) Cross-sectional and elevation view of specimen

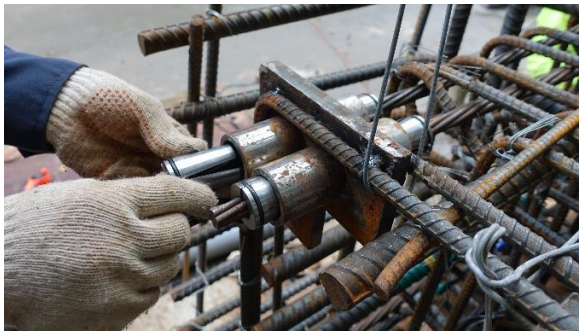

(b) Adding wedges to strand anchors

(c) Construction of unstressed steel strand column

Figure 1 Design and construction of specimens

TEST RESULTS

The specimens were tested in a cantilever fashion with the base of the specimen fixed to the strong floor. The test setup is shown in Figure 2. A horizontal actuator was used to apply lateral cyclic loading to the column to nominal drift ratios of 0.25, 0.375, 0.5, 0.75, 1.0, 1.5, 2.0, 3.0, 4.0, 5.0, 6.0, 7.0, and 8.0%. For each drift level, the drift ratio that was actually achieved was smaller and was measured by an optical system. Each drift ratio was repeated twice. The drift ratio is defined as the lateral displacement divided by the distance from the center of the lateral loading to the base of the column, 3050 mm.

According to the test and analysis results, the bridge column with the unstressed steel strand has a higher yielding force, ultimate force and post-yield stiffness ratio than the traditional bridge column. The addition of steel strands not only improves the overall strength and hysteresis energy dissipation capacity of the bridge column, but also provides the ability to self-recentering after earthquakes by increasing the post-yielding stiffness.

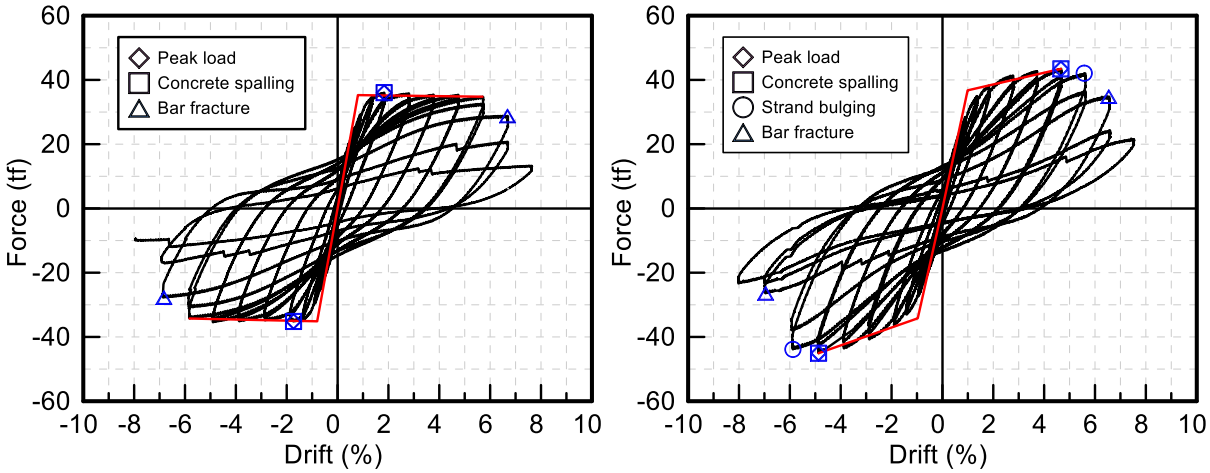

(a) Traditional bridge column (b) Unstressed steel strand bridge column

Figure 2 Lateral force-drift behavior

Table 1. Characteristics of lateral force-displacement responses

Type	D_y (%)	P_y (tf)	D_u (%)	P_u (tf)	k_i (tf/m)	k_2 (tf/m)	α (%)
Traditional bridge column	0.80	35.2	5.76	34.5	1440	-4	-0.3
Unstressed steel strand bridge column	0.98	35.5	4.77	44.3	1186	76	6.4

PUSHOVER MODEL

The pushover model of unstressed steel strands column (PM-USSC) developed on the Matlab platform can accurately predict the seismic behavior of the unstressed steel strands column specimen under the lateral force test. The stress and strain distribution of each material, and the curvature, displacement, bending moment and reaction force of the bridge column specimen. During the establishment of PM-USSC, the strain distribution of longitudinal deformed bars follows the conventional method. The strain in the part of column is determined according to the curvature of the section, and the part of foundation is determined according to the slip behavior of the deformed bar; while the strain elevation distribution of the steel strand assumes that the unbonded part has the same strain, and the part of column without unbonded length is the same as the deformed bar, the strain is determined according to the curvature of the section, but it should be noted that when the bonding force between the steel strand and the concrete is insufficient, the behavior will change from the bending behavior to the slip behavior, The part of foundation is also the same as the deformed bar, as shown in Figure 3. Through the comparison between the model establishment and the strain gage data, it is found that the steel strand will slip at the anchorage system. The influence of the anchorage system slip is considered through the modified formula relationship, and the envelope response of the unstressed steel strand bridge column can be accurately captured when it reaches the ultimate state. The phenomenon of the steel strand slip at the anchorage system will reduce the post-yield stiffness ratio of the unstressed steel strand bridge column.

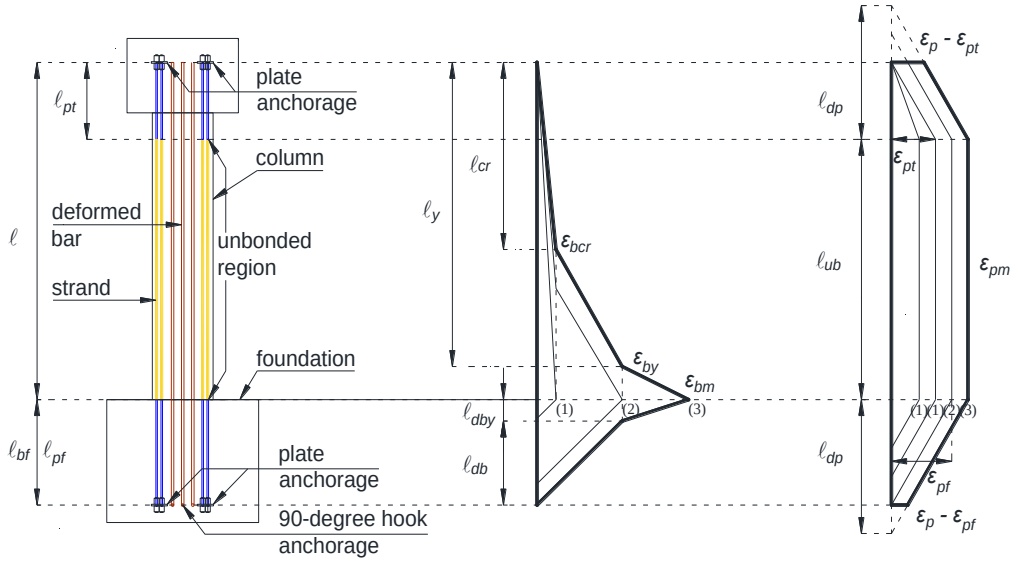

Elevation view of specimen (a) Strain of deformed bar (b) Strain of strand

Figure 3 Distribution of strain along a deformed bar and a strain

CONCLUSIONS

In this study, the unstressed steel strand is used as the elastic element of the bridge column, so that it remains elastic after the traditional longitudinal deformed bar yielding, as to improve the post-yield stiffness of the bridge column and reduce the residual displacement after a near-fault earthquake. A pushover model of unstressed steel strand column (PM-USSC) was developed by the Matlab platform, which can accurately predict the seismic behavior of the unstressed steel strand bridge column specimen under the lateral force test. Strain distribution, curvature, displacement, bending moment and reaction force reacted with the bridge column specimen. In addition, through the development of PM-USSC, it can be used to understand the influence on the post-yield stiffness ratio and seismic performance of the new self-recentering bridge column.

ACKNOWLEDGMENTS

The authors would like to thank the support from the Ministry of Science and Technology of Taiwan under Contract Nos. 110-2625-M-002-013-.

REFERENCES

Ou YC, Wu JW, Pratiwi AY. (2022). “Cyclic behavior columns with partially unbonded seven-wire steel strands to increase post-yield stiffness”. Eng Struct; 258: 114112.

Ou, Y.C., Wu, J.W., and Pratiwi A.Y. (2022). "Effect of the Concrete Cover Thickness Ratio on the Post-yield Stiffness of Bridge Columns with Partially Unbonded Unstressed Steel Strands." Advances in Bridge Engineering. (Under Review)

EFFECT OF CURING CONDITIONS ON THE STRENGTH OF BIO-TREATED SAND SPECIMENS

Yu-Syuan Jhuo[1], Hui-Ee Wong[2], Amali Gitanjali Rayappan Kennedy[3] and Louis Ge[4]
1. Postdoctoral Researcher, Civil Engineering, National Taiwan University, Taipei, Taiwan, R.O.C.
2. Graduate Student, Civil Engineering, National Taiwan University, Taipei, Taiwan, R.O.C.
3. Ph.D. candidate, Civil Engineering, National Taiwan University, Taipei, Taiwan, R.O.C.
4. Professor, Civil Engineering, National Taiwan University, Taipei, Taiwan, R.O.C.
Email: ymca0777@gmail.com, r09521128@ntu.edu.tw, d07521017@ntu.edu.tw, louisge@ntu.edu.tw

ABSTRACT

Microbiological induced calcium carbonate precipitation (MICP) is a sustainable and environmental protectable technique in geotechnical engineering. There are many factors that affect the formation of calcium carbonate cementation. In this study, the effect of urea and calcium ion concentration and curing time on the shear strength of treated sand specimens was discussed. Calcium chloride was selected as calcium source, the concentrations were 0.25, 0.5, 1.0 M, similar to the urea concentrations. Percolation method was used to inject the single-phase treatment solution into the specimens from the top. The curing days were 7 and 14 days. Saturated consolidated drained test was conducted to examine mechanical behavior of the treated specimens. The results show that the peak strengths were proportional to the concentration of urea and calcium chloride, but the residual strengths have no significant difference. The strength of treated specimens increases with curing time with one cycle treatment. As the strength of the treated specimen increases, the volume change also tends to increase.

Keywords: Microbiologically induced calcium carbonate precipitation, soil improvement, shear strength, sustainable engineering

INTRODUCTION

Microbiologically induced carbonate cementation as the functions of pore filling and particle capturing have begun with the process of sediment rock formation. In recent years, with the rising awareness of environmental protection, the application of this function to issues related to geotechnical engineering has been regarded as a sustainable method (DeJong et al., 2010; Khodadadi et.al., 2017). Microbiologically induced carbonate precipitation can be divided into aerobic and anaerobic processes. The use of aerobic urea hydrolysis to generate calcium carbonate cements has been widely discussed in soil improvement. The effectiveness of microbial soil improvement is affected by a number of factors, including physical, chemical, and environmental factors. For example, bacterial species, bacterial growth, temperature, pH, the composition and concentration of treatment solution, injection method, and soil properties. Depending on the materials and purpose, it can be adjusted. For the purpose of increasing uniformity of treated specimens, this study used the surface percolation method to inject single-phase treatment solutions into sand specimens, and discussed the effect of different concentrations of urea and calcium and curing time on the strength of treated specimens.

MATERIAL AND METHOD

Materials

This study used Vietnam silica sand as a MICP-improved target. The distribution of the sand is shown in Fig. 1, which is poor graded sand according to USCS soil classification. The maximum and minimum dry unit weight are 1.690 and 1.392 g/cm^3, respectively. The specific gravity is 2.66. *Bacillus pasteurii* (Bioresource Collection and Research Center 11596) was used in this study which is commonly applied to MICP-related research. It has urease to decompose urea into ammonia and carbon dioxide, the

reaction is as Eq. 1. An alkaline substance such as ammonia raises the pH value of proximal environments and promotes the formation of calcium carbonate by combining calcium ions with carbonate ions (Eq. 2). Medium for solid and culture solution which containing distilled water 1 L, yeast extract 3 g, peptone 5 g, and 5% urea, to which 1.5% agar was added to make a solid medium for the stock culture. The initial pH of the medium is 6.81. Bacteria was frozen with 15% glycerol stocks in -80°C for long-term storage.

$$CO(NH_2)_2 + 3H_2O \rightarrow 2NH_4^+ + 2OH^- + CO_3^{2-} \quad (1)$$

$$Ca^{2+} + HCO_3^{2-} + OH^- \rightarrow CaCO_3 \downarrow + H_2O \quad (2)$$

Preparation of bacterial solution

The bacterial solution was prepared in a way that we mixed 1 ml of thawed frozen bacteria with 55 ml culture solution, and put it on orbital shaker with 100 rpm in a 25°C incubator for 24 hours. The OD_{600} value after 24 hours was between 1.450 to 1.500, and the range of pH value was 9.50 to 9.55 and is referred to as bacterial solution 1. This study attempted to use single-phase MICP treatment solution to inject into specimens by surface percolation method for increasing the uniformity of treated specimens. Single-phase treatment solution contains bacteria solution, urea, and calcium chloride. It is necessary to keep the pH value of the bacteria solution under 9.0 to prevent calcium carbonate precipitating quickly and causing cementation to accumulate on the top of the treated specimen. To reduce the pH value around 8.70-8.90, 5% of bacteria solution 1 was added to the urea-free culture solution, this solution was referred to as bacterial solution 2 and the OD600 was 0.100-0.200. Added urea and calcium chloride to bacterial solution 2 and inject into specimens within 30 minutes.

Preparation of treated specimen

This study adopted cylindrical paper molds, with a closed base and an open top, for producing lots of treated specimens. The diameter of specimen is 7.2 cm and the height is 15 cm. The sand was remolded in the mold with 50% relative density. The closed end of the mold was drilled few holes and with tapes on before sand was poured in. The treatment solution was injected slowly into specimen from the top of the mold to avoid disturbing the specimen. The sand was soaked in the solution. At the fourth day of curing, the tapes were removed to make sure the specimen was dry enough and easy to conduct the triaxial test. The amount of MICP treatment solution was determined by calculating the saturated water content of the specimen, which was 300 ml of each specimen. All of the specimens were treated once. The factors that discussed in this study are the concentration of urea and calcium chloride (0.25, 0.5, 1.0 M) and curing time (7 and 14 days).

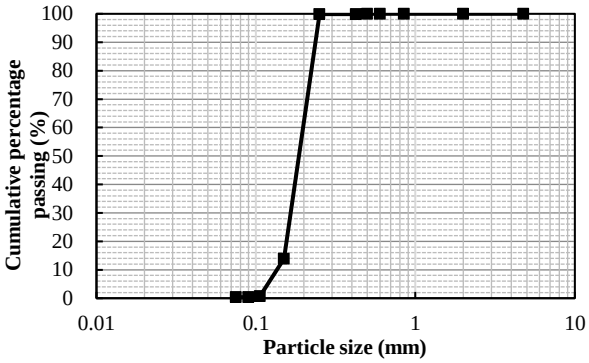

Figure 1 Particle distribution of Vietnam silica sand

RESULTS

Uniformity of treated specimens

The treated specimens were divided into three parts (top, middle and bottom) where 30 g of each part was taken and acid digested with 4 M hydrochloric acid to observe the homogeneity of the specimens. Fig. 2 shows the results of acid digestion of the triaxial specimens treated with calcium chloride. The

concentration of urea and calcium was 0.5 M. Each part of specimen exhibits similar amount of calcite content. Thus, the method of specimen preparation mentioned in this study does result in a uniform distribution of calcium carbonate for both small and large specimens.

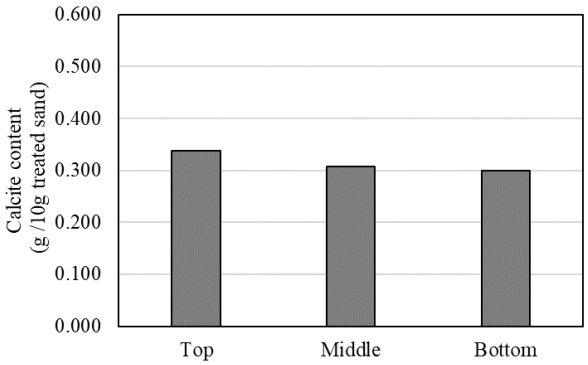

Figure 2. Acid digestion results of triaxial specimens treated with calcium chloride.

Effect of urea and calcium chloride concentration on treated specimens

This study used the same concentrations of urea and calcium chloride, 0.25, 0.5, and 1.0 M. In Fig. 3, the results of a 14-day curing time are shown. The peak deviator stress of the MICP-treated specimen is proportional to the concentration of urea and calcium chloride. From small to large, the peak stress of the three concentrations are 369.46, 378.00, and 399.66 kPa, respectively, and 353.48 kPa for pure sand. The residual stress of all the treated specimens is similar to that of the untreated specimen after the peak. The peak stress happened corresponding to the axial stress of the treated specimens is larger than that of untreated specimen. In the treated specimens, the peak stress occurred corresponding to the axial strain is greater than in the untreated specimens. All treated specimens expanded during shearing and were larger than pure sand specimens at post peak.

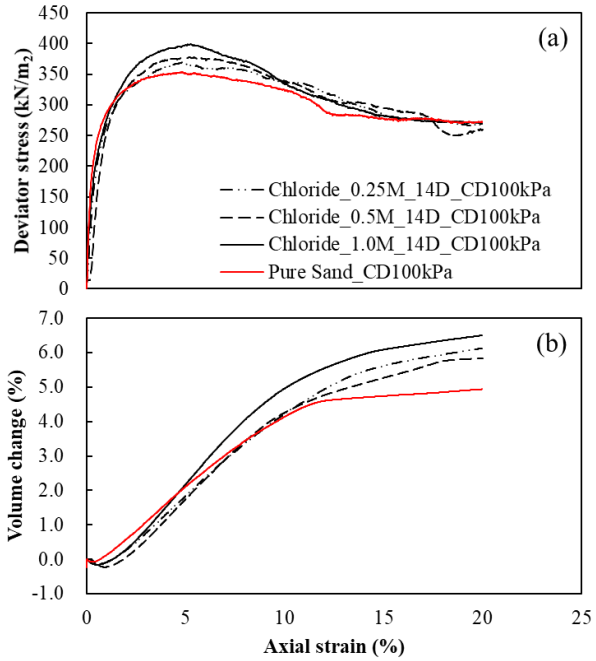

Figure 3 Triaxial CD test results for three different concentrations at confining pressure of 100 kPa: (a) deviator stress; (b) volume change.

Effect of curing time on the treated specimens

After being injected with single-phase treatment solutions for 7 and 14 days, the strength of the treated MICP sample with 1.0 M of urea and calcium chloride concentration was 379.31 kPa and 399.66 kPa, respectively (Fig. 4). It indicates that the peak strength of treated specimens increases with curing time with one cycle curing. In either case, the residual strength after the peak is very similar, which is the same as that of pure sand. The volume changes also increased with the curing time.

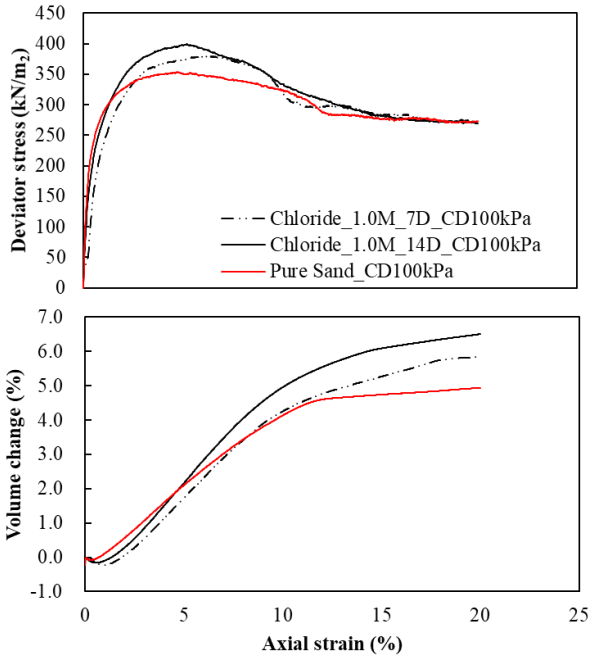

Figure 4 Triaxial CD test results for 7 and 14 curing days at confining pressure of 100 kPa: (a) deviator stress; (b) volume change.

Strength of treated specimens under different confining pressures

Fig. 5 shows the results for calcium chloride and urea concentrations of 0.5 M and 14 days curing. The peak stresses at confining pressure 50, 100, 200 kPa are 209.30, 371.75, 697.90 kN/m^2, respectively. As a result of different confining pressures, the cohesion of the pure sand specimen is 0 kPa, and the friction angle is 39.45°. Upon improvement, the cohesion is increased to 11.20 kPa and the friction angle is slightly reduced to 38.22°. It shows that calcium carbonate is cemented between the pores of the sand and provides the bonding force between particles.

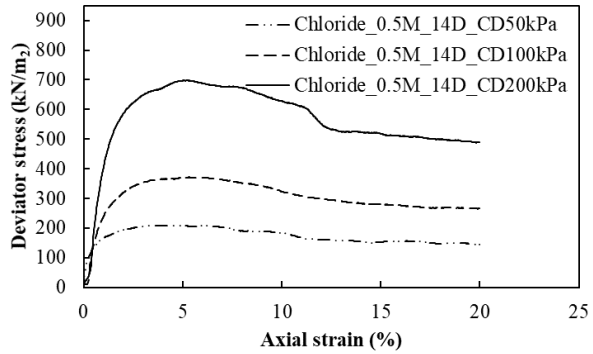

Figure 5 Triaxial CD test results for different confining pressure with 0.5 M urea and calcium chloride at 14 days curing days

CONCLUSIONS

In this study, a single-phase MICP treatment solution was used to inject into the sand specimens through the surface percolation method, and only one cycle of curing was applied. The volume of the improvement solution was the same as the calculated saturated water content of the sand specimens. The peak stresses of the MICP-treated specimens were higher than that of untreated specimens, which was proportional to the concentration of urea and calcium chloride and the curing time. The axial strains corresponding to the occurred the peak strength of treated specimens were larger than that before the improvement, and the residual strength has no significant difference. The cohesion of the treated specimens was increased by 11.20 kPa compared with that of untreated specimens. This indicates that the calcium carbonate cement caused by microbes can increase the bonding force between sand particles and enhance the strength of the soil itself.

ACKNOWLEDGMENTS

The authors would like to acknowledge the financial support from National Taiwan University "Higher Education Sprout Project & NTU Core Consortiums" (project number 110L891306) is acknowledged. Their support has made this study and potential future investigations possible.

REFERENCES

Castanier, S., Merayer-Levrel, G. L. and Perthuisot, J. P. (1999). "Ca-carbonates precipitation and limestone genesis – the microbiologeologist point of view," *Sediment Geology*, **126**(1-4), 9-23.

Ehrlich, H. L. (1999). "Microbes as geologic agents: Their role in mineral formation," Ecological Engineering, **36**(2), 197-210.

DeJong, J. T., Mortensen, B. M., Martinez, B. C., and Nelson, D. C. (2010). "Bio-mediated soil improvement, "*Ecological Engineering*, **36**, 197-210.

Khodadadi, T. H., Kavazanjian, E., Paassen, L., and DeJong, J. (2017). "Bio-grout materials: A review," *Grouting 2017*, GSP 288.

Mahawish, A., Bouazza, A., and Gates, W. P. (2018). "Strengthening crushed coarse aggregates using bio-grouting," *Geomechanics and Geoengineering*, **14**(1).

Tang, C. S., Yin L. Y., Jiang N. J., Zhu C., Zeng H., Li H., and Shi B. (2020). "Factors affecting the performance of microbial-induced carbonate precipitation (MICP) treated soil: a review," *Environmental Earth Sciences.* 79: 94.

Zamani, A., Montoya, B., and Gabr M. A. (2019). "Investigating the challenges of in situ delivery of MICP in fine grain sands and silty sand," *Canadian Geotechnical Journal*, **56**(12).

THE TEST PROGRAM OF STEEL-REINFORCED CONCRETE (SRC) COLUMNS JACKETED BY FRP-WRAPPED STEEL CORRUGATED TUBE (FWSCT) UNDER FOUR-POINT BENDING

Chung-Sheng Lee[1] and Obed Adi Kusuma[2]
1. Department of Civil and Disaster Prevention Engineering, National United University, Miaoli, Taiwan, R.O.C.
2. Department of Civil and Disaster Prevention Engineering, National United University, Miaoli, Taiwan, R.O.C.
Email: lee.cs@nuu.edu.tw, M1015012@O365.nuu.edu.tw

ABSTRACT

The flexural behavior of Steel-Reinforced Concrete (SRC) columns jacketed by FRP-Wrapped Steel Corrugated Tube (FWSCT) under four-point bending is investigated. Five SRC columns with different types of confinement, including the steel tube and FRP-Wrapped Steel Corrugated Tube (FWSCT) with different layers of CFRP and GFRP will be tested and studied. A numerical model will be developed and validated with the experimental work. A cross-section analysis was performed to examine the moment-curvature relationship of the specimens. The analysis shows that the specimen SW confined with 5.50-mm thick steel tube has the highest moment capacity compared to the specimens confined with FWSCT. Comparing the specimens confined with FWSCT, specimen C2G3W has higher moment capacity, indicating that two layers of CFRP arranged in longitudinal direction (0 degree) can increase the energy dissipation higher than three layers of GFRP arranged in longitudinal direction (0 degree).

Keywords: confined concrete, steel-reinforced concrete (SRC), FRP, steel corrugated tube, four-point bending test

INTRODUCTION

Concrete filled steel tubular (CFST) columns have been shown to provide superior static and dynamic resistant properties such as high ductility, high strength, and great energy absorption capacity (Sangeetha et al., 2018). However, with the enlargement of the cross-section sizes needed for larger structures, the self-weight of the members increases and the construction becomes impractical (Wang et al., 2021; Chou et al., 2018). In order to overcome this issue, the emerging solution is to replace the outer steel tube with the Fiber Reinforced Polymer (FRP). Fiber Reinforced Composites are considered as alternative of steel reinforcement due to the light weight, high strength, high stiffness-to-weight ratio, good corrosion resistance and easy installation (Chou et al., 2018).

Different types of advanced FRP composite-jacketed column systems have been developed and investigated, ranging from hand layup of carbon or glass fabrics to premanufactured layered carbon or glass shell systems (Seible and Karbhari, 1996). Seible et al. (1996) developed a Carbon Shell System (CSS) concept that has internal ribs on the surface inside the tube for bond and force transfer to the concrete core. However, the implementation of FRP ribs in the tube increases the construction difficulty.

In recent years, a comprehensive research program was undertaken in developing a hybrid confinement tube, FRP-Wrapped Steel Corrugated Tube (FWSCT), which made of a steel corrugated tube wrapped with FRP composites (Tan, 2014; Wu, 2015). The inner surface of the spiral corrugated tube features ribs to improve the bonding and force transfer between the FRP composites and the concrete core. Furthermore, the premanufactured FWSCT can also be utilized as the stay-in-place column formwork. Previous research conducted by Tan (2014) has indicated that the FWSCT can improve the strength and the ductility of the members. Although various studies have been conducted, further investigation is necessary to examine the flexural behavior of the FWSCT- jacketed SRC columns. In this study, 5 types

of Steel Reinforced Concrete (SRC) column jacketed by FRP-Wrapped Steel Corrugated Tube (FWSCT) will be tested to investigate the flexural behavior of the members under four-point bending test.

TEST PROGRAM

Test Matrix and Specimen Details

The test matrix for this program is shown in Table 1. Test number 1 is an 1800-mm long Steel-Reinforced Concrete Filled Steel Tubular (SRCFST) column, while test number 2 to 5 are four 1800-mm long Steel Reinforced Concrete (SRC) columns jacketed by FRP-Wrapped Steel Corrugated Tube (FWSCT). A total of 5 specimens will be subjected to four-point bending. As shown in Table 1, each specimen is identified by the specimen code, which illustrates the confinement and the reinforcement type. For the test number 1, the first letter represents the confinement, where S stands for steel tube; and the second letter represents the steel reinforcement embedded in the concrete, where W stands for w-shaped steel. For the test number 2 to 5, the first letter and digit represent the FRP composite applied longitudinally (0 degree) and the number of layers, respectively. In test number 2, the code "00" means that there is no FRP composite wrapped in longitudinal direction. In test number 3 and 5, G stands for glass fiber and digit 3 stands for three layers of GFRP in longitudinal direction. In test number 4, C stands for carbon fiber and digit 2 stands for two layers of CFRP in longitudinal direction. The second letter and digit in test number 2 to 5 represent the FRP composite applied transversely (90 degrees) and the number of layers, respectively. In test number 2 to 5, G stands for glass fiber and digit 3 stands for 3 layers of GFRP in hoop direction. The last letter code in test number 2 to 5 represents the type of shaped steel embedded in the concrete, where W stands for W-shaped steel and H stands for hollow-shaped steel. The steel corrugated tube will be wrapped sequentially in hoop direction first before being wrapped in longitudinal direction.

Table 1 Specimen Test Matrix

Test Number	Specimen Code	Specimen Dimensions (mm)		Laminate Code	Steel Section
	(L/H/S)	Length	Inside Diameter		
1	SW	1800	260	-	W-shaped Steel
2	00G3W	1800	260	$[90_3^G]$	W-shaped Steel
3	G3G3W	1800	260	$[0_3^G/90_3^G]$	W-shaped Steel
4	C2G3W	1800	260	$[0_2^C/90_3^G]$	W-shaped Steel
5	G3G3H	1800	260	$[0_3^G/90_3^G]$	Hollow Steel

Figure 1 shows the cross-section details of the specimens. The SRC will be reinforced by two types of steel section embedded in the concrete, including the W-shaped steel and hollow-shaped steel. The W-shaped steel has the cross-sectional dimensions of 150x150x7x10x8 mm, and the hollow-shaped steel has an outer diameter of 130 mm, with the thickness of 5.50 mm. The steel tube confinement has an inner diameter of 260 mm, with the thickness of 5.50 mm. The steel corrugated tube has an inner diameter of 260 mm, with the thickness of 0.35 mm. The spiral thread of the corrugated tube has a depth of 5 mm and a width of 12 mm, with the spacing between each spiral thread of 24 mm. The filler on the surface of the corrugated steel tube is made of AEROSIL silica and ETERSET 2960PT-S vinyl ester resin applied prior to wrapping the FRP materials. The spiral corrugated tube will be wrapped by different layers of GFRP and CFRP in accordance with the laminate code given in Table 1. The overlapping length of each FRP layer is 150 mm.

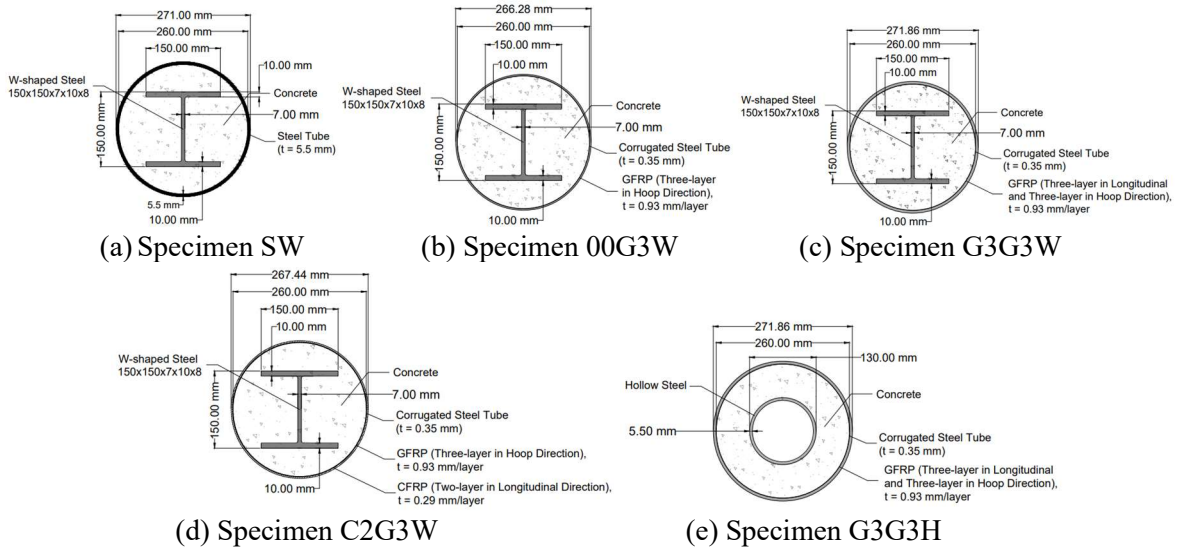

(a) Specimen SW (b) Specimen 00G3W (c) Specimen G3G3W

(d) Specimen C2G3W (e) Specimen G3G3H

Figure 1 Specimen Cross-section Details

Table 2 illustrates the material properties of the FRP. The maximum longitudinal (0 degree) tensile strength of the CFRP and GFRP is 1665.3 MPa and 690 MPa, respectively. In this study, the FRP materials wrapped on the surface of the spiral corrugated steel tube is made of the L900-E uniaxial 0-degree woven glass fiber cloth and L250-C uniaxial 0-degree woven carbon fiber cloth. The compressive strength of the concrete used in this experiment is 20 MPa. The steel tube confinement and the steel section reinforcement have a yield strength of 315 MPa. The spiral corrugated steel tube has a yield strength of 150 MPa, with the ultimate strength of 280 MPa.

Table 2 Material Properties of FRP

Properties	Carbon (L250-C)	Glass (L900-E)	Unit
Longitudinal Stiffness (0°)	92520	24800	MPa
Transversal Stiffness (90°)	9250	2900	MPa
Ultimate Tensile Strength (0°)	1665.3	690	MPa
Ultimate Tensile Strain	0.018	0.028	
Thickness per ply	0.29	0.93	mm/layer

Test Setup and Instrumentation

Figure 2(a) shows the four-point bending test setup for the FWSCT-jacketed SRC columns. The specimen will be settled on two 340-mm wide steel saddles at its two ends. Under the steel saddle, a steel support will be placed to form a pin-pin support condition that allow the rotation at pile ends during testing. The force will then be transferred to the I-beam and then to the strong floor. Two loading points were designed at location 450-mm away from the pin support at the pile ends, as illustrated in Figure 2(a). At each loading point, a loading block made of steel will be arranged and the distance between the two loading points is 600 mm.

Figure 2(b) illustrates the instrumentation on the FWSCT-jacketed SRC columns. On each specimen, 22 strain gauges will be used to measure the longitudinal and hoop strains on the specimen surface at the locations indicated. Meanwhile, five linear variable displacement transducers (LVDT) will be placed at the specimen bottom face to measure the deflections. A LVDT will be placed at the top end of the specimen cross-section as illustrated Figure 2(b) to measure the slippage between the outer confinement and the concrete core.

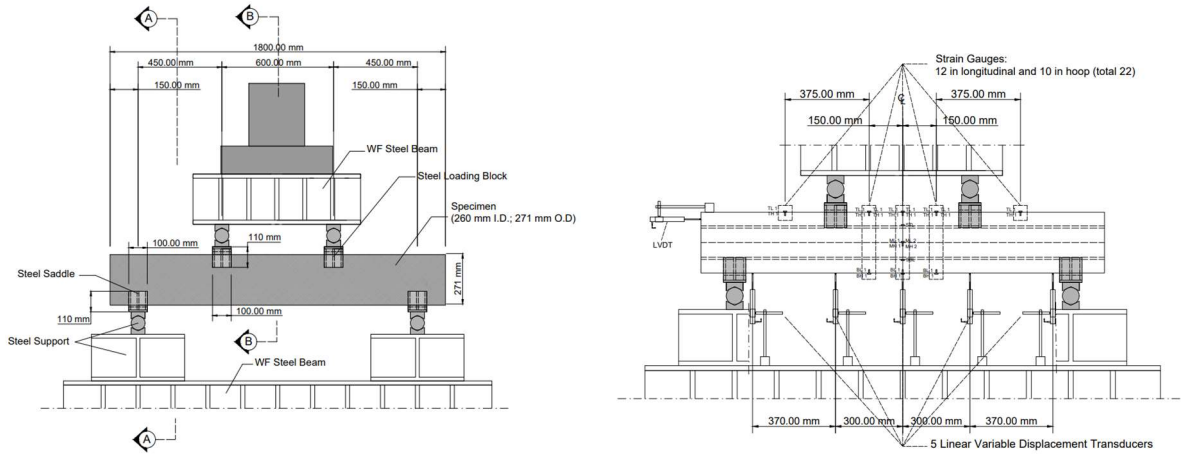

(a) Test Setup (b) Instrumentation

Figure 2 Test Setup and Instrumentation

Cross Section Analysis

A cross section analysis using Engineering Software Solution (EngiSSol) was conducted to analyze the moment-curvature relationship of the specimen. Figure 3 shows the specimen cross-section modeled in the analysis program. The material properties of the steel members were defined as a bilinear material and the FRP composite was defined as a linear material. In this analysis, the concrete was defined as a confined concrete. The resulted moment-curvature curve of each specimen will then be compared.

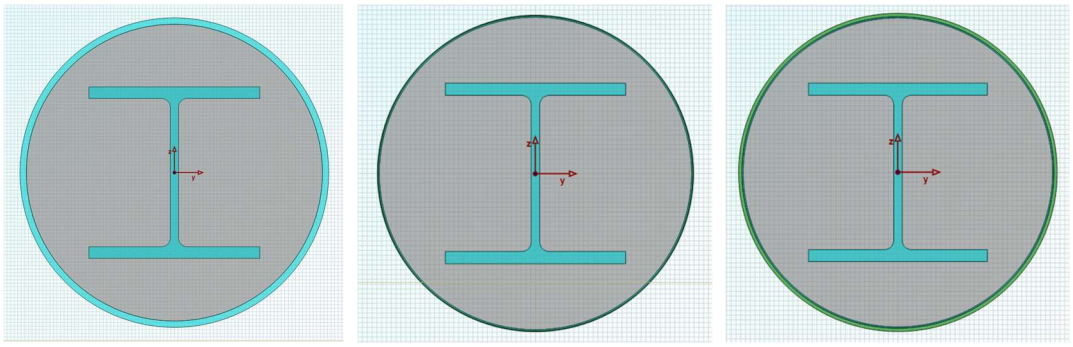

(a) Specimen SW (b) Specimen C2G3W (c) Specimen G3G3W

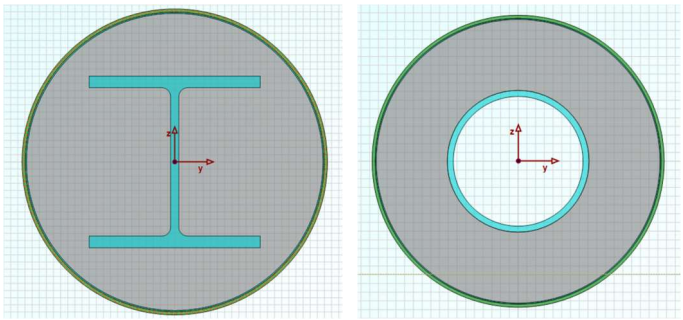

(d) Specimen 00G3W (e) Specimen G3G3H

Figure 3 The cross-section model of the specimens

Figure 4 shows the graph comparing the resulted moment-curvature curve of each specimen. The moment-curvature curves shown in Figure 4 exhibit a ductile behavior for all specimens. It can be seen that the moment capacity of the 5.50-mm thick steel tube is higher than that of FRP composites. Comparing the moment-curvature curve of the specimens confined with FWSCT, specimen C2G3W

shows higher moment capacity compared to the other FWSCT-jacketed specimens. This indicates that the two layers of CFRP arranged in longitudinal direction in specimen C2G3W can increase the amount of energy that can be absorbed before failure, representing a good indicator of ductility. Meanwhile, specimen G3G3H shows the lowest moment capacity.

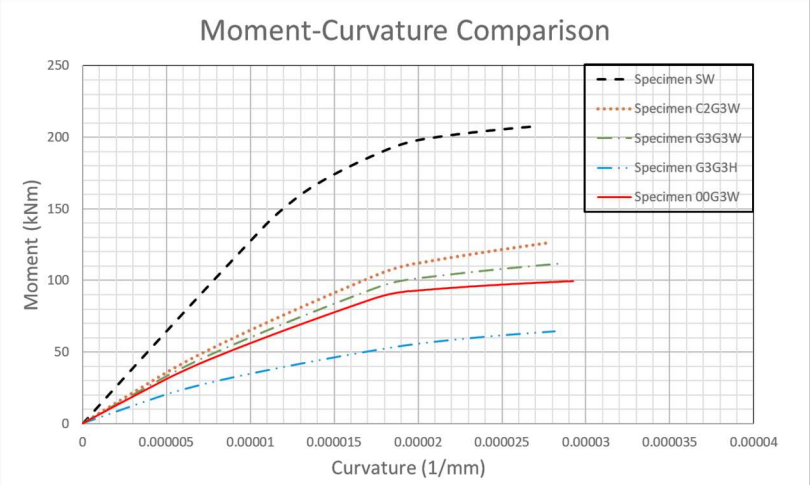

Figure 4 Moment-curvature Comparison

CONCLUSION AND SUGGESTION

The main purpose of this study is to investigate the flexural behavior of the SRC column jacketed by FRP-wrapped spiral corrugated tube (FWSCT). The main research work includes: (1) Conducting four-point bending tests; (2) Developing numerical analysis methods; (3) Examining the flexural behavior of FWSCT-jacketed SRC columns under four-point bending test. In this study, the cross-section analysis was conducted to predict the moment-curvature relationship of the specimens. Observing the moment-curvature curve, all the specimens show ductile responses. The specimen confined with the 5.50-mm thick steel tube has the highest moment capacity compared to the specimen confined with the FRP composites. Confining the SRC column with two layers CFRP arranged in longitudinal direction (0 degree) provides higher moment capacity compared to the SRC column confined with GFRP, indicating that the CFRP increase the energy dissipation of the SRC column. However, the theoretical results need to be validated by the experimental results.

ACKNOWLEDGMENTS

This research was funded by MOST 110-2625-M-239-001, Taiwan. The experimental work was conducted at the National Center for Research on Earthquake Engineering (NCREE) in Taiwan. Assistance from the technical staff is acknowledged.

REFERENCES

Chung-Che Chou, Chung-Sheng Lee, Kai-Yi Wu, V-Liam Chin, Development and validation of a FRP-wrapped spiral corrugated tube for seismic performance of circular concrete columns, Construction and Building Materials, Volume 170, 2018, Pages 498-511, ISSN 0950-0618, https://doi.org/10.1016/j.conbuildmat.2018.03.047.

C.S. Lee, G.A. Hegemier, Model of FRP-confined concrete cylinders in axial compression, J. Compos. Constr. 13 (5) (2009) 442–454.

D. Innamorato, F. Seible, G.A. Hegemier, M.J.N. Priestley, Carbon Shell Jacket Retrofit Test of a Circular Shear Column with 2.5% reinforcement Report No. ACTT-95/19, University of San Diego, California, 1995.

Fangying Wang, Ben Young, Leroy Gardner, Testing and numerical modelling of circular CFDST cross-sections with stainless steel outer tubes in bending, Engineering Structures, Volume 247, 2021, 113170, ISSN 0141-0296, https://doi.org/10.1016/j.engstruct.2021.113170.

F. Seible, R. Burgueño, M.G. Abdallah, R. Nuismer, Development of advanced composite carbon shell systems for concrete columns in seismic zones, Proc., 11th World Conf. Earthquake Engineering, Elsevier Science, Oxford, UK: Pergamon, 1996.

F. Seible, M.N. Priestley, G.A. Hegemier, D. Innamorato, Seismic retrofit of RC columns with continuous carbon fiber jackets, J. Compos. Constr. 1 (2) (1997) 52–62.

Ju Chen, Yahui Zhu, Fangying Wang, Bing Feng, Experimental and analytical study of hollow section concrete-filled GFRP tubes in bending, Thin-Walled Structures, Volume 177, 2022, 109297, ISSN 0263-8231, https://doi.org/10.1016/j.tws.2022.109297.

K.Y. Wu, Seismic Tests of Circular Reinforced Concrete Columns Confined with a Spiral Corrugated Tube and Glass Fiber Reinforced Polymer (GFRP) Materials, Department of Civil Engineering, National Taiwan University, Taiwan, 2015 (in Chinese).

Muhammad N.S. Hadi, Qasim S. Khan, M. Neaz Sheikh, Axial and flexural behavior of unreinforced and FRP bar reinforced circular concrete filled FRP tube columns, Construction and Building Materials, Volume 122, 2016, Pages 43-53, ISSN 0950-0618, https://doi.org/10.1016/j.conbuildmat.2016.06.044.

M.J.N. Priestley, F. Seible, Seismic assessment and retrofit of bridges. Structural systems research project, Rep. No. SSRP-91/ 03, M. J. N. Priestley, F. Seible, University of California, San Diego, Calif (1991).

P., S., R.M., A. M., G., D., M., D., S., J. and Madumathi, S. (2018) “Behaviour of Concrete Filled Steel Tubes”, Journal of Informatics and Mathematical Sciences, 10(1-2), pp. 297–304. doi: 10.26713/jims.v10i1-2.1056.

Yu-Hang Wang, Wei Wang, Ju Chen, Seismic behavior of steel tube confined RC columns under compression-bending-torsion combined load, Journal of Constructional Steel Research, Volume 143, 2018, Pages 83-96, ISSN 0143-974X, https://doi.org/10.1016/j.jcsr.2017.12.025.

STRAIN-BASED SEISMIC EVALUATION OF A MULTI-SPAN REINFORCED CONCRETE BRIDGE

Erwin Lim[1], Dyah Kusumastuti[1*], Rildova[1], Mario Asneindra[1], Silvester Sandy Mulyadi[1]
1. Department of Civil Engineering, Faculty of Civil and Environmental Engineering, Institut Teknologi Bandung, West Java, Indonesia
*Email: dkusumastuti@gmail.com

ABSTRACT

The need to seismically evaluate the structural performance of an existing infrastructure is getting more important in Indonesia nowadays as the discovery of new faults and updating of the national seismic hazard map. This paper analyzes an existing eleven-span reinforced concrete bridge which was designed using a seismic hazard map developed some 30 years ago. Strength evaluation based on the latest seismic hazard map shows that the existing bridge still satisfies the strength and serviceability requirement despite the increase in seismic demand. In addition, a nonlinear time history analysis is conducted based on eleven pairs of site-specific ground motion developed based on the latest discovery of nearby faults. Using the average inelastic longitudinal reinforcement and concrete strain at bridge pier and comparing them to the strain-based performance criteria given in NCHRP 949, this study concludes that the bridge is still "fully operational" and "life safety" when subjected to the lower level (100 year return period) and the upper level (1000 year return period) ground motions, respectively.

Keywords: strain-based based model, multi-span reinforced concrete bridge, hazard map, NCHRP 949, NLTHA

INTRODUCTION

An existing eleven-span reinforced concrete bridge located in a high seismicity area was designed using a hazard map developed some 30 years ago (SNI 2833:1992). Due to the advancement in science and technology, and as more ground motion records are available, in 2017, an update on Indonesian seismic hazard map was published. Therefore, it is of interest to reevaluate the bridge's structural performance using the latest seismic hazard using nonlinear time history analysis. The Federal Highway Administration categorizes the performance level of an existing bridge based on the anticipated service life, bridge importance, and service life category. The performance is evaluated under two levels of ground motion, i.e., the lower level (corresponding to earthquake with return period of 100 years) and the upper level (corresponding to earthquake with return period of 1000 years) as shown in Table 1. Unfortunately, this document does not provide a clear approach on how to quantify the expected performance. This problem remained until 2020, when NCHRP 949 was published. This guideline fills the gap of FHWA's previous publication and provides quantitative criteria for the two levels of evaluated earthquakes, using strain limit as the key parameter. The guideline states that bridges are categorized into standard and essential bridges, with four level of performance based on their anticipated service life (see Table 1). The strain limit for longitudinal pier reinforcement and extreme concrete compression fiber under three different level of performances with minimum requirements is given in Table 2. Table 2 tabulates the maximum strain of concrete and longitudinal reinforcement bar under three different performance levels predetermined in Table 1. The strain criteria for the reinforcement bar is governed by buckling mode, while that of concrete is limited by the crushing strain of concrete core.

In order to apply this strain-based criteria, the cross sections of all piers are discretized into concrete and steel fibers. For each concrete fiber and longitudinal steel reinforcement fiber, the stress strain curve is then explicitly defined using commonly accepted material model. Hence, it can also capture implicitly the flexural stress-strain behavior of the section along the length through the integration process by

assuming plane sections remain plane. Since the length to depth ratio of all piers are larger than 4 and the piers satisfy capacity design check for shear, the shear degradation behavior is not modeled herein.

Table 1. Performance level

EARTHQUAKE GROUND MOTION	BRIDGE IMPORTANCE and SERVICE LIFE CATEGORY					
	Standard			Essential		
	ASL 1	ASL 2	ASL 3	ASL 1	ASL 2	ASL 3
Lower Level Ground Motion 50 percent probability of exceedance in 75 years; return period is about 100 years.	PL0[4]	PL3	PL3	PL0[4]	PL3	PL3
Upper Level Ground Motion 7 percent probability of exceedance in 75 years; return period is about 1,000 years.	PL0[4]	PL1	PL1	PL0[4]	PL1	PL2

Notes:

1. Anticipated Service Life categories are:
   - ASL 1: 0 – 15 years
   - ASL 2: 16 – 50 years
   - ASL 3: > 50 years
2. Performance Levels are:
   - **PL0: No minimum** level of performance is recommended.
   - **PL1: Life safety.** Significant damage is sustained and service is significantly disrupted, but life safety is preserved. The bridge may need to be replaced after a large earthquake.
   - **PL2: Operational.** Damage sustained is minimal and service for emergency vehicles should be available after inspection and clearance of debris. Bridge should be reparable with or without restrictions on traffic flow.
   - **PL3: Fully Operational**. No damage is sustained and full service is available for all vehicles immediately after the earthquake. No repairs are required.
3. Spectral ordinates and peak ground accelerations may be found as described in Chapter 2.
4. Bridges assigned a Performance Level of PL0 have 15 years, or less, anticipated service life (ASL) and are candidates for replacement or rehabilitation. If the bridge is replaced or rehabilitated, the ASL category will change and so will the required Performance Level.

Table 2. Strain limit under targeted performance level

Design Parameter	Performance Level		
	PL1: Life Safety	PL2: Operational	PL3: Fully Operational
Reinforcement tensile strain limit *(RC Column)*	$\varepsilon_{s\ buckling}^{bar} = 0.032 + 790\rho_s \frac{f_{yhe}}{E_s} - 0.14\frac{P}{f'_{ce}A_g}$	$\varepsilon_s = 0.8\,\varepsilon_{s\ buckling}^{bar}$	≤ 0.010
Concrete compressive strain limit *(RC Column)*	$\varepsilon_c = 1.4\left(0.004 + 1.4\frac{\rho_v f_{yh}\varepsilon_{su}}{f'_{cc}}\right)$	$\varepsilon_c = \left(0.004 + 1.4\frac{\rho_v f_{yh}\varepsilon_{su}}{f'_{cc}}\right)$	≤ 0.004

EXISTING BRIDGE INFORMATION

The bridge under evaluation consists of 11 spans. The first (A1-P1) and last spans (A2-P10) connected to abutments are simply supported, while P1-P6 and P6-P10 spans are continuous as shown in Fig. 1. The typical span length is approximately 42 m, while the pier height varies from 13.5 m at P1 to 27 m at P6. The substructure was assumed to be adequate to resist all loads, and analysis was limited to the upper structures.

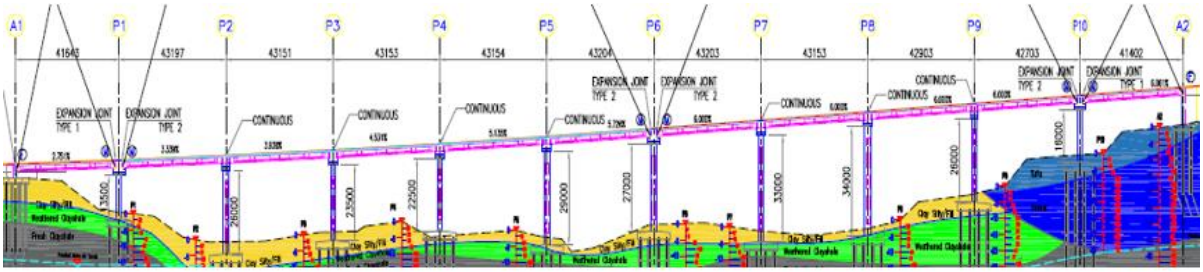

Figure 1. Longitudinal bridge profile [in mm]

The typical transverse section of bridge is shown in Fig. 2a. In the longitudinal direction, the piers behave under single curvature, while in the transverse direction they behave in double curvature. Typical pier dimension is 2 m x 3.5 m, with concrete strength equivalent to 30 MPa. The piers' main longitudinal reinforcements are of D25 rebar with steel ratio ranges from 0.7 % to 1.2 % as shown in Fig. 2b. Meanwhile, typical hoops and cross ties use D13 rebar.

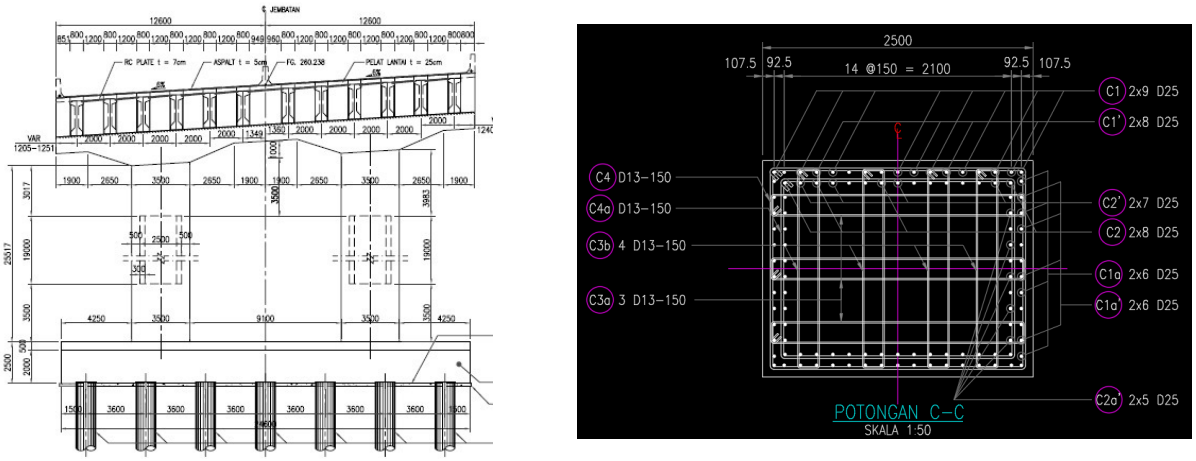

(a) Transverse bridge profile (b)Typical pier dimension and reinforcement

Figure 2. Transversal and Pier Detailing

ELASTIC ANALYSIS

The 3D model was developed using the properties specified in construction drawing and shown in Fig. 3. From eigen value analysis, the first dominant mode shape is in transverse direction with the predominant period of 0.82 second. A simple check on the strength adequacy based on the response spectrum (Fig. 4) analysis was carried out. The strength evaluation on piers showed that flexural capacity of piers was sufficient, as shown in the P-M diagram in Fig. 5. Moreover, it was verified that the piers fulfilled the shear capacity design requirement. In this calculation, the shear strength is compared to the plastic shear demand due to the formation of plastic hinges in piers.

The inspection on shear strength is very important because using the nonlinear time history analysis, only flexural behavior can be modeled and captured. Therefore, by ensuring the shear capacity is adequate, it can be inferred that the flexural behavior of piers can be fully developed and strength degradation due to shear behavior can be delayed. In addition, this check is also important because the pier is analyzed using distributed inelasticity model which cannot capture the degradation behavior well.

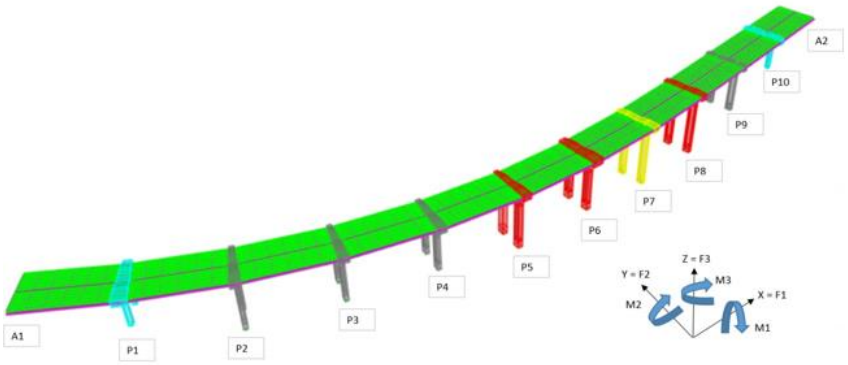

Figure 3. Three-dimensional modeling

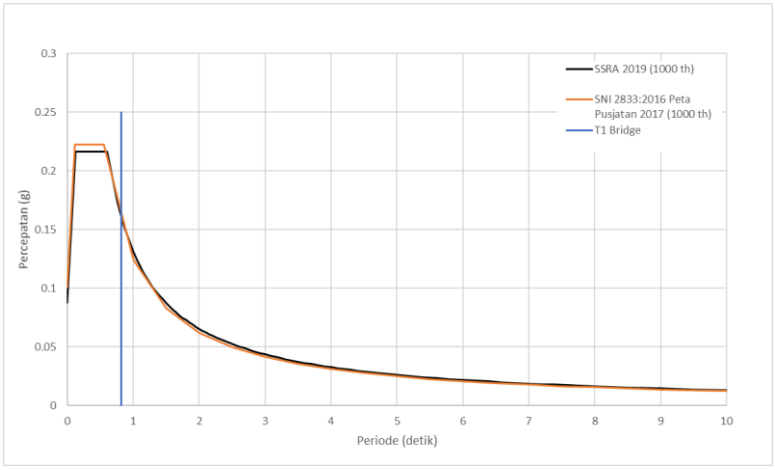

Figure 4. Inelastic response spectrum

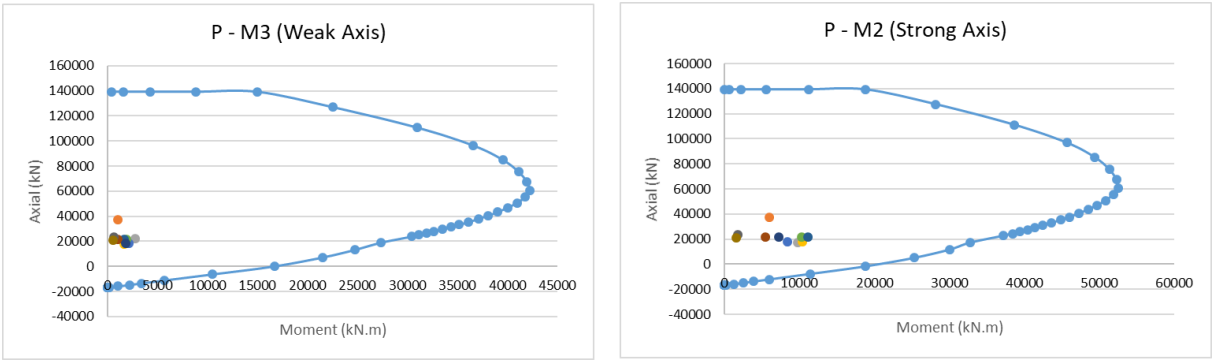

Figure 5. Typical PM Diagram for piers

NONLINEAR TIME HISTORY ANALYSIS

As mentioned in NCHRP 949, the criteria of performance level under two levels of earthquake is evaluated using the strain values, both in piers' extreme concrete fiber and in longitudinal reinforcement bars. Therefore, the fiber model was generated using commercial software and is presented in Fig. 6. First, the pier section was modeled and the concrete material was discretized into 9x9 elements. The longitudinal reinforcements were modeled individually, as indicated in Fig. 6.

The material constitutive equations for confined concrete and longitudinal steel reinforcement under monotonic loading followed those shown in Fig. 7. The monotonic relationships were then transformed into hysteretic relationships. For concrete material, Takeda model was adopted, while kinematic model was used for the reinforcement bar.

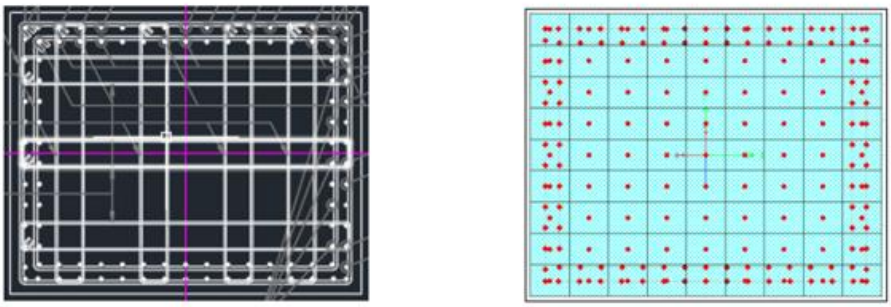

a. Pier section b. Section discretization

Figure 6. Discretization of pier cross section

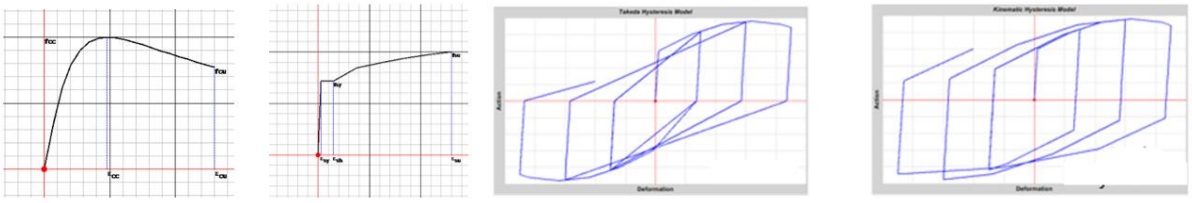

a. Monotonic confined concrete | b. Monotonic reinforcement steel | c. Hysteretic confined concrete | d. Hysteretic reinforcement steel

Figure 7. Constitutive relationship for material

To conduct nonlinear time history analysis, eleven pairs of ground motions were developed considering all major earthquake mechanisms within 500 km radius from the site, as shown in Table 3. Figure 8 plots the acceleration histories for these ground motions. It is noteworthy to mention that time history for two levels of earthquake were developed, i.e., for 100 years return period (lower level) and 1000 years return period (upper level).

Table 3. Summary of ground motions

No	Ground Motion	Time (second)	Direction	100 years rp		1000 years rp	
				Min Acc. (g)	Max Acc. (g)	Min Acc. (g)	Max Acc. (g)
1	Shallow Crustal A-GRN	19.995	A-GRN180	-0.2122	0.1585	-0.4213	0.3375
			A-GRN270	-0.1190	0.1562	-0.2203	0.3045
2	Shallow Background FDS	39.98	FDS262	-0.1936	0.1452	-0.3670	0.2644
			FDS172	-0.1715	0.1269	-0.3383	0.2953
3	Benioff Padang30sept	100	Padang30sept2009EW	-0.0283	0.0492	-0.0620	0.0939
			Padang30sept2009NS	-0.2156	0.2823	-0.5471	0.4786
4	Shallow Crustal A-HMC	17.995	A-HMC180	-0.1145	0.1078	-0.2406	0.2176
			A-HMC270	-0.1458	0.2349	-0.2703	0.4578
5	Shallow Background H-VC4	29.985	H-VC4000	-0.2052	0.1569	-0.4055	0.3031
			H-VC4090	-0.1384	0.1592	-0.2733	0.3162
6	Megathrust-HWA026	89.995	HWA026-W	-0.1459	0.2182	-0.2884	0.4230
			HWA026-N	-0.1096	0.1473	-0.2820	0.2951
7	Megathrust-MYG 013	299.99	MYG013110311146EW	-0.1059	0.1232	-0.2050	0.2386
			MYG013110311146NS	-0.1642	0.2446	-0.3484	0.4614
8	Shallow Crustal PKC	39.975	PKC360	-0.2051	0.1837	-0.4118	0.3631
			PKC090	-0.1594	0.1194	-0.3153	0.2408
9	Megathrust-HKD12	123.99	HKD1260309260450 EW	-0.1085	0.1915	-0.2335	0.3673
			HKD1260309260450 NS	-0.0913	0.1923	-0.2017	0.3737
10	Megathrust-KAU078	89.995	KAU078-W	-0.2277	0.1771	-0.3601	0.4430
			KAU078-N	-0.0866	0.1283	-0.2567	0.2195
11	Benioff KSH	32.975	KSH-T1	-0.1841	0.1481	-0.3599	0.2924
			KSH-L1	-0.1874	0.1372	-0.3648	0.2603

After conducting nonlinear time history analyses using eleven pairs of ground motions, the stress and strain histories of extreme concrete fibers and longitudinal reinforcement bars were plotted and examined. An example of the plot is given in Fig. 9. For evaluation on the acceptance criteria, the average of the maximum value obtained for each pair of ground motions is calculated at extreme fibers. These values are then compared with the NCHRP 949's criteria shown in Table 2.

The so-called engineering design parameters values shown in Table 2 links the analysis results to decide the performance level. For the life safety level, the reinforcement strain limit of longitudinal bar is based on its tensile limit to prevent bar fracture. Meanwhile, the concrete compressive strain limit is based on Mander's model (1988) with a factor of 1.4 to account for the inherited conservatism. For operational level, the tensile steel strain limit is based on statistical data, in which less than 10% of rebars are expected to buckle, while the concrete compression limit is based on the work of Mander et al. (1988).

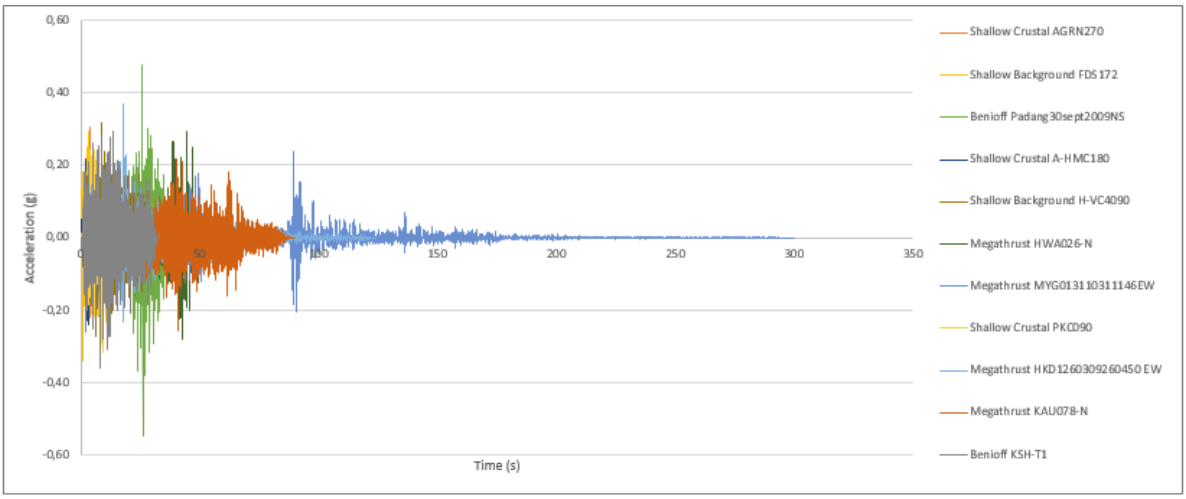

Figure 8. Acceleration history of 11 ground motions

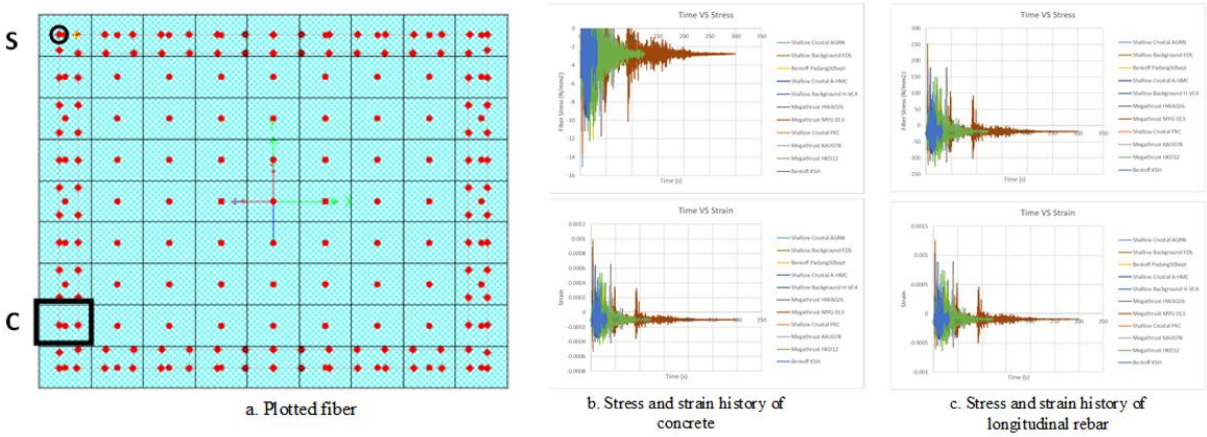

a. Plotted fiber

b. Stress and strain history of concrete

c. Stress and strain history of longitudinal rebar

Figure 9. Stress and strain history for extreme fiber subjected to eleven pairs of ground motion

The comparisons show that for the lower level earthquake ground motion (return period of 100 years), the attained performance level is fully operational, which complies with the FHWA requirement in Table 1. For the upper level earthquake ground motion (return period of 1000 years), the achieved performance level is life safety, which also satisfies the FHWA requirement. Therefore, the existing bridge shows adequate capacity under the current seismic load.

CONCLUSIONS

This study adopts the latest strain-based criteria set by NCHRP 949 Guideline to quantitatively evaluate the performance level of an existing multi-span reinforced concrete bridge. The bridge was designed using a previous code and is evaluated using the latest seismic hazard. Nonlinear time history analysis using eleven pairs of ground motions generated specifically for the site was conducted. The stress and strain histories of extreme concrete fibers and longitudinal reinforcement bars were evaluated and then compared with the NCHRP 949's criteria. The study reveals that the performance level of this bridge still satisfies the requirement of FHWA, which is "fully operational" under the lower level ground motion earthquake (return period 100 years) and "life safety" under the upper level ground motion earthquake (return period 1000 years).

ACKNOWLEDGMENTS

The authors wish to thank Prof. I Wayan Sengara, Mr. Det Komardevi, and team for developing eleven pairs of ground motions at the site under evaluation.

REFERENCES

American Association of State Highway and Transportation Officials. (2020). *Guidelines for Performance-Based Seismic Bridge Design*, Washington DC, 75 pp.

Badan Standardisasi Nasional. (1992). *Code of Highway Bridge Design - Tata Cara Perencanaan Ketahanan Gempa untuk Jembatan Jalan Raya (SNI 2833)*, 76 pp. (in Indonesia)

Badan Standardisasi Nasional. (2016). *Code for Bridge Seismic Design - Perencanaan Jembatan terhadap Gempa (SNI 2833)*, 60 pp. (in Indonesia)

Badan Standardisasi Nasional. (2019). *Code for Seismic Resistant Design for Buildings and Non-Buildings - Tata Cara Perencanaan Ketahanan Gempa untuk Struktur Bangunan Gedung dan Non-Gedung (SNI 1726)*, Jakarta, 236 pp. (in Indonesia)

Federal Highway Administration. (2006). *Seismic Retrofitting Manual for Highway Structures*, Virginia, 610 pp.

Mander, J. B., Priestley, M. J. N., Park, R. (1988). *Theoretical Stress-Strain Model for Confined Concrete*, ASCE Journal of Structural Engineering, Vol. 114, No. 8, pp. 1804-1826.

National Academies of Sciences, Engineering, and Medicine. (2013). *NCHRP Synthesis 440 - Performance Based Seismic Bridge Design*, Washington DC, 127 pp.

National Academies of Sciences, Engineering, and Medicine. (2020). *NCHRP Research Report 949 - Proposed AASHTO Guidelines for Performance-Based Seismic Bridge Design*, Washington DC

Pusat Studi Gempa Nasional. (2017), *Indonesia Seismic Hazard Map - Peta Sumber dan Bahaya Gempa Indonesia Tahun 2017*, Bandung, 376 pp. (in Indonesia)

Sengara, W.S. and Komardevi, D., personal communication, Bandung, 2021.

SEISMIC PERFORMANCE OF A SELF-CENTERING PRECAST REINFORCED CONCRETE ROCKING WALL WITH EXTERNAL SMA RODS

Ahmed M. Elnady [1,2,3] and Huanjun Jiang [1,2]
1. State Key Laboratory of Disaster Reduction in Civil Engineering, Tongji University, Shanghai 200092, China;
2. Department of Disaster Mitigation for Structures, Tongji University, Shanghai, China;
3. Zagazig University, Arab Republic of Egypt
Email: amelnady@zu.edu.eg , jhj73@tongji.edu.cn

ABSTRACT

This research aims to propose an alternative way to provide a recentering force to a pre-cast unbonded post-tensioned reinforced concrete rocking wall (RW) using shape memory alloy (SMA) bars. The physical and mechanical properties, such as fatigue, corrosion resistance, and large damping capacity, qualify the SMA to be at the forefront of materials used in structural engineering applications. In this study, the SMA bars replace the post-tensioned tendons to minimize the permanent deformation resulting from the system's exposure to the lateral loading coming from the seismic events. The SMA bars are attached externally to the wall and fixed with the base to facilitate the installation process and reduce the repairing time if a failure occurs under unexpected events. The proposed system shows that the SMA rods can play the same role as the PT tendons to minimize the residual displacement while also providing an acceptable level of energy dissipation to the system.

Keywords: rocking wall (RW), shape memory alloy (SMA), energy dissipation, post-tensioned, self-centering, resilient system.

1 INTRODUCTION

Design of buildings to sustain fewer damages from earthquakes is a crucial component of resilience-based design, which concerns the quick ability of the organization or community to recover and gain its post-earthquake functionality after extreme future events. According to the resiliency concept, earthquakes cause direct economic loss from damage to structural and nonstructural components and indirect economic loss from the downtime due to the temporary suspension of productivity and living, which may be higher than the direct losses (Cimellaro et al. 2006). Economic losses can be significantly reduced if the structure can rapidly retain or restore its function after an earthquake (Lu and Jiang 2014).

The use of rocking walls (RW) as earthquake-resilient systems in structures was a transition in the world of construction and considered a viable option for buildings in regions of high seismicity (Parsafar and Moghadam 2017). A restoring force, such as unbonded post-tensioned (PT), must be applied to retain the wall in the undeformed shape after any expected events along with the RW (Elgawady et al. 2010). The nonlinear behavior of these structures is governed by the opening of gaps at the joints between the structural members (Kurama et al. 1999b). The unbounded PT-RW exhibits narrow hysteresis loops under cyclic loading (Kurama et al. 1999a). This is due to the absence of energy dissipation components that control the shape of the hysteretic response (Chancellor et al. 2014). The primary source to dissipate the energy is the impact between the wall and the base. Due to the deficiency of these systems alone to provide the required seismic performance, supplementary yielding elements should be utilized to enhance their performance and dissipate more energy (Eatherton et al. 2014).

The unbonded PT structures may encounter several issues due to yielding or fracture of the PT strand systems (Masrom and Hamid 2020) or deterioration of PT steel tendons, such as corrosion and fatigue due to live loads. Corrosion is promoted by the ingress of chlorides and other deleterious agents through vulnerable areas such as anchorages, joints, cracks, and porous concrete cover (Fuzier et al. 2005). Rehabilitation of these damages requires a great deal of effort and time to replace the corroded or damaged tendons. This process requires breaking part of the base and the wall to complete the process of repairing and rehabilitation.

An alternative way to apply the restoring force to the structure is by using the SMA. The SMA is a unique material that can undergo large deformation but fully recover upon load removal. The SMA was used in critical regions to eliminate the permanent deformation in concrete structures, such as RC columns (Saiidi and Wang 2006), shear walls (Cortés-Puentes et al. 2018), column-beam connection (Oudah and El-Hacha 2017), and RC beams (Mas et al. 2017). All the previous works used the SMA bars as embedded elements. The downside of this method is that it is difficult to repair or replace the SMA bars in the event of any potential damage. Another technique is to utilize the SMA externally, for instance, using the SMA as bolts or rods connections (Wang et al. 2019), or SMA rod with a buckling-restrained device (BRD) (Wang and Zhu 2018). The most characteristic of this technique is the ease of installing and performing the monitoring operations and repairing or replacing SMA components as they work as a structural fuse.

The current study presents an earthquake resilient RW with a self-centering mechanism instead of the ordinary post-tensioned tendons. The restoring force system comprises an SMA bar restrained by BRD attached externally to the wall and fixed with the base. The hysteretic behavior of the BRD with the SMA bar is investigated first under cyclic loading, then a numerical model for an ordinary unbonded pre-cast RC-RW is established and verified by representative test results. Lastly, the hybrid RW with SMA-based BRD attached externally to the wall is numerically analyzed and compared with the ordinary RW.

2 HYSTERETIC BEHAVIOR OF THE SMA ROD

A commercial superelastic NiTi-based alloy is utilized as the SMA material used in this research for its excellent superelasticity and high fatigue and corrosion resistance compared to the other SMA alloys. The SMA specimen was machined to a dog-bone shape. The bar reduced diameter is 8 mm and 12 mm for the virgin diameter, and the length of the reduced part is 250 mm. The potential lateral deformation of the bar was prevented by encasing the rod using a steel buckling restrained device (BRD) with a 1.0 mm clearance to minimize the friction with the BRD inner surface and allow a smooth movement for the rod. The dimensions of the specimen, including the SMA rod and the steel BRD, are provided in Figure 1.

2.1 Test results

In the current research, SMA rods are mainly subjected to tensile force while the wall rocks. The hysteretic behavior of the SMA rods was obtained by applying a cyclic tension loading with increasing strain amplitudes (0.5%, 1.0%, 2.0%, 3.0%, 4.0%, 5.0%, 6.0%, 7.0%), with two cycles for each amplitude and a constant loading and unloading strain rate of 0.0005 s^{-1} using an MTS machine, as illustrated in Figure 2. Before the loading, SMA was trained for approximately ten cycles at strain levels of approximately 5% until the hysteretic loops stabilized. A representative stress-strain relationship of the tested NiTi coupon is presented in Figure 4, showing satisfactory flag-shaped loops without strength degradation. The start and finish stresses for the forward phase transformation are 335 MPa and 510 MPa, with a corresponding strain of 1% and 6%, respectively. The start and finish stresses and strains for the reverse transformation phase are 230 MPa, 5%, and 80 MPa, 0.6%, respectively, and the residual strain was almost 0.2% after 14 cycles when unloading from the peak strain of 6%.

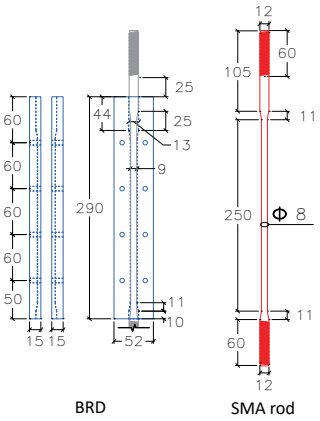

Figure 1 Specimen dimensions

Figure 2 Test setup for the SMA rod.

2.2 FEA for the SMA rod with BRD

As shown in Figure 3 (a) and (b), the ABAQUS program's FE model consists of two main components, the BRD and SMA rod. For simplicity, BRD is modeled using one solid part with a hole along its height. The SMA rod and the BRD are modeled using an eight-node solid element with reduced integration and hourglass control (C3D8R). The elasto-plastic material with linear strain isotropic hardening is used with the BRD steel part, wherein the yield and ultimate strengths were 400 MPa and 500 MPa, respectively. A built-in superelastic material model in ABAQUS is employed to represent the cyclic behavior of the SMA rod with with a Young modulus of the austenite and martensite of 31 and 24 GPa, respectively. Starting and finishing stress induced marensie phase transformation are 335 and 510 MPa, respctivily. However, the starting and finishing stresses for the austenite phase transformation are 230 and 80 MPa. The compressive stress of martensite starts at 350 MPa.

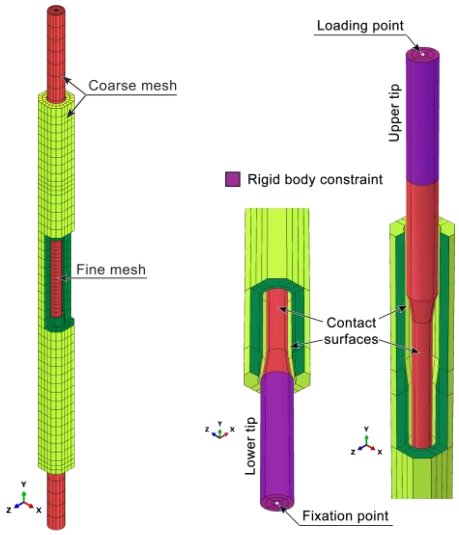

(a) (b)

Figure 3 FE model of SMA rod and the BRD: (a) meshed assembly, (b) loading point, fixation point, and contact surfaces.

As can be seen in Figure 3 (b), the cyclic loading is applied on the top surface of the upper tip through a rigid body reference point constrained with the upper tip surface as a rigid body region. Similarly, the lower tip is fixed through a reference point at the bottom, constrained with the lower tip surface as a rigid body region. The fixation point is constrained for all degrees of freedom. Likewise, the loading point got the same

constraints except that the direction of loading is free. The surface-to-surface contact type with 'hard' contact and no penetration for normal behavior and a small friction coefficient of 0.1 for the tangential behavior is adopted to describe the contact behavior between the SMA rod and the BRD, as described in Figure 3 (b).

2.3 Numerical simulation results

As shown in Figure 4, the stress-strain hysteresis loops under incremental loading amplitudes are used to compare the test results with the FE analysis outputs. Stable and satisfactory flag-shaped hysteresis loops without any strength degradation for both experimental and FEA are observed. The FE modeling using the ABAQUS program gave an excellent simulation to the cyclic loading test result of the SMA rod. This was evident through accurate tracing of austenite and martensite stiffness for each loading cycle and the forward and reverse transformation paths from austenite to martensite and vice versa. Unlike the tested specimen, the FEA shows no residual strain for the SMA rod due to the ideal behavior of the built-in superelasticity model in ABAQUS. Nevertheless, the current modeling accuracy is sufficient to explore the global behavior of the SMA rod with BRD and is reliable enough to build up the proposed model of the unbonded post-tensioned RC rocking wall with externally attached SMA rods restrained with steel BRDs.

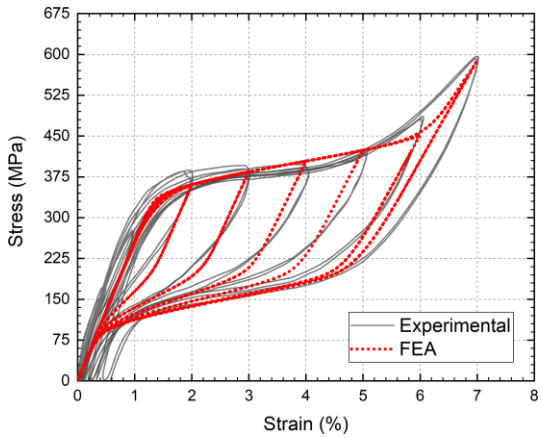

Figure 4 Stress-strain hysteretic curves for restrained SMA rod.

3 BEHAVIOR OF UNBONDED POST-TENSIONED ROCKING WALL

The experimental results of the unbonded post-tensioned rocking wall (PRW) conducted by (Twigden et al. 2017) were adopted as a reference model. Based on these results, the efficiency of the proposed hybrid RW is numerically verified under the influence of cyclic loads. The wall dimensions were selected to represent a target range of a low-to-mid-rise multi-story building in a region with medium to high seismic hazards. The wall dimensions and the reinforcement details are illustrated in Figure 5. The horizontal reinforcement was arranged at 100 mm centers along the wall height and 40 mm centres at the wall base spaced over 200 mm up the wall. The wall was tested under pseudo-static cyclic loading following (ACI ITG-5.1 2007) standard up to a maximum drift of 2%, while the numerical model was loaded up to a lateral drift of 2.9% to study the wall behavior beyond the PT tendon yielding. And an external axial load of 2500 N was applied on the top beam to verify the axial force ratio of 2.49%.

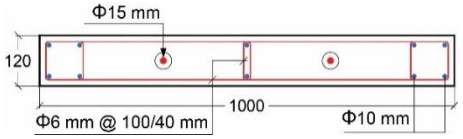

Figure 5 Wall geometry and details.

3.1 Finite element modeling

Due to symmetry, half of the model is only considered. The concrete damage plasticity (CDP) built-in model is used to define the concrete. The reinforcements and the post-tensioned tendons are modeled using elasto-plastic material with linear strain isotropic hardening. The boundary element of the PRW wall was modeled with a confined concrete model based on (Mander et al. 1988) and (ACI ITG-5.2 2009).

All the concrete, including the unconfined and the confined parts, are meshed and discretized using an 8-node linear brick with reduced integration and hourglass control element (C3D8R). The PT tendon and reinforcement rebars are simulated and discretized with a 2-node linear 3-D truss element (T3D2). The top tip of the PT tendon is embedded in the top beam to simulate the upper anchorage system, the same as the web reinforcement in the wall part, while the lower tip of the PT tendon is fixed at the foundation beam base level. The surface-to-surface contact type with 'hard' contact and no penetration for normal behavior and a friction coefficient of 0.4 for the tangential behavior was adopted to describe the contact behavior between the wall base and the foundation beam.

3.2 Numerical analysis results

The FEA results using ABAQUS program give a reasonable simulation for the experimental data, as represented in Figure 6 and Figure 7. There is an almost perfect match between the experimental and the numerical analysis results in the negative loaded cycles for the lateral load-lateral displacement relationship. And there is a slight variation in the plastic response of the positive displacement, which may be due to the imperfection of the experimental results in the reverse loading direction. The definition of the anchorage of the PT tendons as an embedded part at the top tip zone and fixed at the foundation beam may be the reason for the slight variance in the lateral displacement with force in PT tendons relationship.

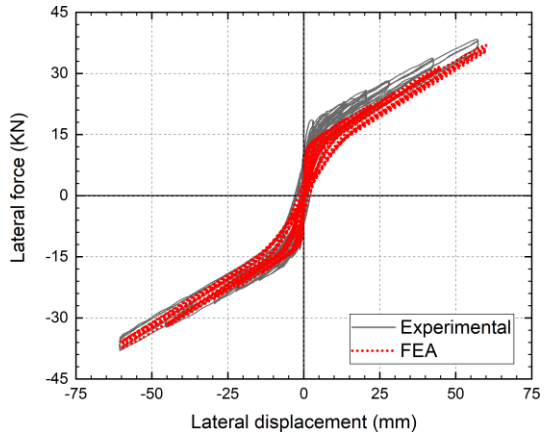

Figure 6 Lateral top displacement versus lateral top force relationship.

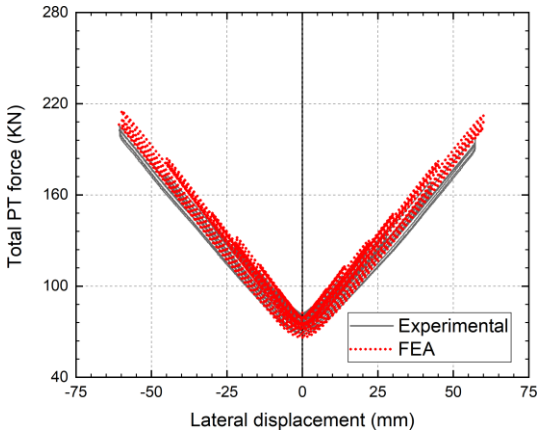

Figure 7 Lateral top displacement versus total force in post-tensioned tendons relationship.

4 BEHAVIOR OF HYBRID ROCKING WALL WITH SMA RODS

The proposed hybrid rocking wall, which RWS denotes, is composed of a pre-cast RC wall connected to the foundation beam by a group of SMA rods attached externally to the wall and fixed with the foundation beam, as shown in Figure 8. A BRD restrains the SMA rods with a 1.0 mm clearance to prevent any predicted lateral displacement for the SMA rods. The length of the SMA rods is determined based on the maximum permissible strain of the SMA rod at the maximum uplift value at the outermost SMA rod. The SAM rods are located at the same position as the PT tendon in the PRW model. The amount of the SMA rods is obtained to provide the same axial strength as the PT tendons at the yielding point at a drift angle

associated with lateral displacement of 60 mm. The SMA rods are 10 mm in diameter and 250 mm long. Figure 8 shows cross-sectional dimensions, reinforcement details, and the SMA rods' location and length of the RWS wall model.

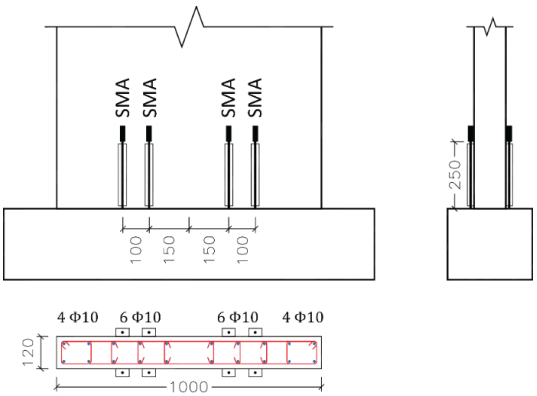

Figure 8 Hybrid rocking wall with SMA-based self-centering system (RWS).

The purpose of studying the hybrid wall behavior is to investigate the efficiency of the SMA rods with the rocking wall compared to the PT tendons as in the PRW model. The wall model is designed to behave linearly during all the loading stages up to the allowable drift angle with the same geometric dimension of the PRW reference wall. The wall was loaded with the same axial load as the PRW wall with an axial force of 2500 N to provide an AFR of 0.34%. The wall boundary element dimensions and reinforcement ratio are designed according to (ACI ITG-5.2 2009) and (ACI Committee 318 2014). Additional longitudinal reinforcement is added at the SMA rods' zone to resist the generated tensile force in the wall transferred by the stretched SMA rods during wall rocking.

4.1 Numerical analysis

The RWS walls were modeled in the same way as the reference model, using the same element types, material properties for all the concrete parts and steel reinforcement, interaction characteristics, and loading protocol. Due to the symmetry of the wall, only half of the model was considered using symmetric boundary conditions.

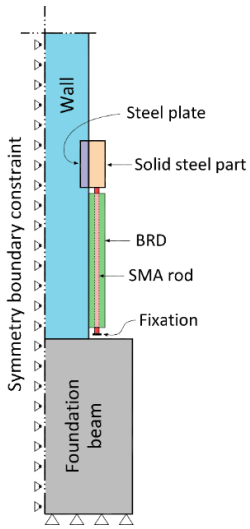

Figure 9 Detailed side view for the connection of the EDD with the wall.

The contact surfaces between every two adjacent parts are modeled as a tie constraint except for the contact between the SMA rod and the BRD and between the wall base and the foundation beam. As can be seen in Figure 9, the SMA rods are fixed to the wall by connecting a solid steel part to the upper tip of the SMA rod and a steel plate to the wall and connecting them using tie constraint. The lower tip surface of the SMA rods is fixed just over the upper surface of the foundation beam.

4.2 Results and discussions

In this section, the analysis results of the hybrid wall are explored using the lateral load-lateral displacement hysteretic response, self-centering behavior, and the energy dissipated by the system. The wall experienced linear behavior during all cyclic loading beyond the specified drift angle ($\theta = 2\%$) showing no crushing for any particles.

The self-centering capability was assessed by measuring the uplift value of the wall base center at the end of the third cycle of each sequence of cycles. As shown in Figure 10, the uplift for both models was almost identical, proving the ability of each model to return to the undeformed shape after the cyclic load is complete. The maximum permanent uplift at the limiting drift angle is 0.37mm and less than the permissible value specified by the (ACI ITG-5.1 2007), which is 0.8mm.

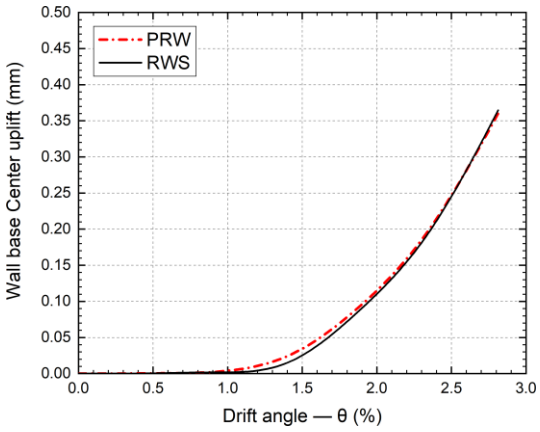

Figure 10 Uplift of wall base center.

Both systems were designed to have the same lateral stiffness at a drift of 2% associated with a lateral displacement of 60 mm so that the lateral load-carrying capacity at the same displacement was equal under the cyclic loading, as shown in Figure 11. The RWS exhibited fatter hysteresis loops, indicating relatively greater energy absorption than the PRW model due to the flag-shaped behavior of the SMA material during stress-induced martensite transformation. The behavior of the PRW model is characterized by bilinear behavior with narrow loops up to the drift of 2% absorbing a small amount of energy. For the RWS model, the force-displacement loops dissipate much more energy due to the flag-shaped behavior of the SMA. The PT tendon changed to the post-yielding stage after a drift of 2%, resulting in softening the hysteresis loops due to stiffness degradation of the system. In the case of the RWS, the SMA rod started to behave plastically after the same displacement, negatively affecting the energy-dissipation and self-centering capability.
The PRW system didn't contain any members that experienced plastic behavior at low drift levels; consequently, the system's energy dissipation was not sufficient. Figure 12 represents the relative energy dissipated ratio (REDR) of the two models, calculated at the last loop of each loading amplitude. It expresses the efficiency of each system in dissipating energy compared to its stiffness. The REDR concept is similar to the equivalent viscous damping concept for designing and evaluating seismically isolated structures used in (FEMA-302 and FEMA-303 1997). According to (ACI Committee 374.1 2005) standards, the PRW did not meet the minimum requirement, which shall not be less than 0.125 for the third complete cycle at the

limiting drift. It can be noticed that the PRW's REDR increased slightly after a drift of 2% where the PT tendon reached the plastic state.

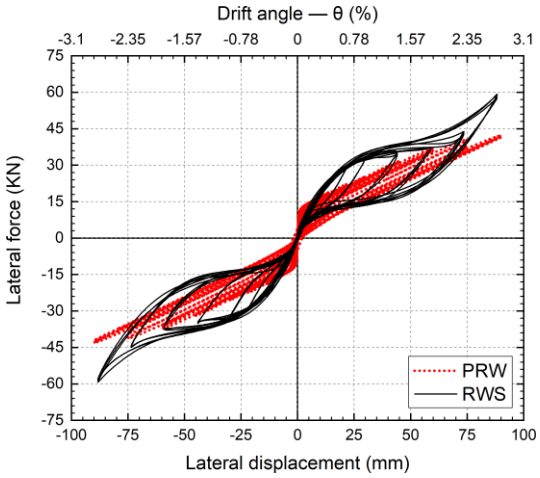

Figure 11 Lateral load-lateral displacement relationship up to drift of 2.8%.

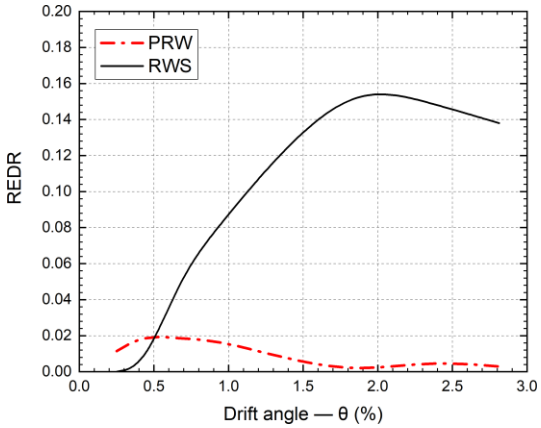

Figure 12 REDR for the PRW and RWS models.

Similarly, for the RWS model, the total energy increased, accompanied by an increase in the REDR. Afterward, the rate of increase noticeably decreased after the design drift ($\theta = 2\%$) because the SMA rod started to exhibit plasticly after reaching the maximum strain of the superelastic rang behavior. Then the rate of increase in the area of hysteresis loops of the SMA material began to decrease compared to the peak lateral load, causing the REDR to decrease. Therefore, it is essential to keep the strain of the SMA material to remain in the superelasticity range, and it can be controlled by the proper design of the SMA rod length and its location relative to the wall's rotation point. By comparing the total absorbed energy for the PRW and RWS models, it was found that due to the flag-shaped hysteresis behavior of the SMA material, the RWS model could dissipate ten times more energy than the PRW model.

5 CONCLUSIONS

This paper presented a novel self-centering rocking wall system with SMA rods (RWS). First, the SMA rod with BRD was experimentally and numerically studied under cyclic loading. Then, the FE model for the pre-cast unbonded post-tensioned RC rocking wall (PRW) was validated. Finally, the seismic performance of the RWS was then compared with the PRW. The proposed hybrid system proves that the SMA rods can provide the self-centering capability the same way the PT tendons do to the rocking wall system to minimize the residual displacement while also providing an acceptable level of energy dissipation to the system at the specified AFR. The energy absorbed by the hybrid system depends mainly on the flag-shaped behavior of the SMA rods.

6 REFERENCES

ACI Committee 318 (2014), *Building Code Requirements for Structural Concrete (ACI 318-14): Commentary on Building Code Requirements for Structural Concrete (ACI 318R-14): an ACI Report, American Concrete Institute.*, ACI.

ACI Committee 374.1 (2005), *Acceptance Criteria for Moment Frames Based on Structural Testing and Commentary: an ACI Standard, American Concrete Institute.*, ACI.

ACI ITG-5.1 (2007), *Acceptance Criteria for Special Unbonded Post-Tensioned Precast Structural Walls Based on Validation Testing and Commentary: an ACI Standard, American Concrete Institute.*, ACI.

ACI ITG-5.2 (2009), *Requirements for Design of a Special Unbonded Post-Tensioned Precast Shear Wall Satisfying ACI ITG-5.1 (ACI ITG-5.2-09) and Commentary: an ACI Standard, American Concrete Institute.*, ACI.

Chancellor, N., Eatherton, M., Roke, D., and Akbaş, T. (2014), "Self-Centering Seismic Lateral Force Resisting Systems: High Performance Structures for the City of Tomorrow," *Buildings*, 4, 520–548. https://doi.org/10.3390/buildings4030520.

Cimellaro, G. P., Reinhorn, A. M., and M. Bruneau (2006), "Quantification of Seismic Resilience," in *the 8th U.S. National Conference on Earthquake Engineering*, San Francisco, California, USA, p. 10.

Cortés-Puentes, L., Zaidi, M., Palermo, D., and Dragomirescu, E. (2018), "Cyclic loading testing of repaired SMA and steel reinforced concrete shear walls," *Engineering Structures*, Elsevier, 168, 128–141. https://doi.org/10.1016/j.engstruct.2018.04.044.

Eatherton, M. R., Ma, X., Krawinkler, H., Deierlein, G. G., and Hajjar, J. F. (2014), "Quasi-Static Cyclic Behavior of Controlled Rocking Steel Frames," *Journal of Structural Engineering*, 140, 04014083. https://doi.org/10.1061/(asce)st.1943-541x.0001005.

Elgawady, M., Booker, A. J., and Dawood, H. M. (2010), "Seismic Behavior of Posttensioned Concrete-Filled Fiber Tubes," *Journal of Composites for Construction*, 14(5), 616–628.

FEMA-302, and FEMA-303 (1997), *NEHRP Recommended Provisions for Seismic Regulations for New Buildings and Other Structures, Part 1: Provisions (FEMA 302), and Part 2: Commentary (FEMA 303)*, *Federal Emergency Management Agency*, Washington, D.C.

Fuzier, J., Ganz, H., and Matt, P. (2005), *Durability of post-tensioning tendons, fédération internationale du béton (fib) Bulletin No. 33*.

Kurama, Y., Pessiki, S., Sause, R., and Lu, L.-W. (1999a), "Seismic behavior and design of unbonded post-tensioned precast concrete walls," *PCI Journal*, 44, 72–89.

Kurama, Y., Sause, R., Pessiki, S., and Lu, L. W. (1999b), "Lateral load behavior and seismic design of unbonded post-tensioned precast concrete walls," *ACI Structural Journal*, 96, 622–632. https://doi.org/10.14359/700.

Lu, X., and Jiang, H. (2014), "Recent progress of seismic research on tall buildings in China Mainland," *Earthquake Engineering and Engineering Vibration*, 13, 47–61. https://doi.org/10.1007/s11803-014-0239-8.

Mander, J. B., Priestley, M. J., and Park, R. (1988), "Theoretical stress-strain model for confined concrete," *Journal of Structural Engineering*, 114, 1804–1826. https://doi.org/10.1061/(ASCE)0733-9445(1988)114:8(1804).

Mas, B., Biggs, D., Vieito, I., Cladera, A., Shaw, J., and Martínez-Abella, F. (2017), "Superelastic shape memory alloy cables for reinforced concrete applications," *Construction and Building Materials*, Elsevier Ltd, 148, 307–320. https://doi.org/10.1016/j.conbuildmat.2017.05.041.

Masrom, M. A., and Hamid, N. H. A. (2020), "Review on the rocking wall systems as a self-centering mechanism and its interaction with floor diaphragm in precast concrete structures," *Latin American Journal of Solids and Structures*, 17, 1–29. https://doi.org/10.1590/1679-78256115.

Oudah, F., and El-Hacha, R. (2017), "Joint performance in concrete beam-column connections reinforced using SMA smart material," *Engineering Structures*, Elsevier Ltd, 151, 745–760. https://doi.org/10.1016/j.engstruct.2017.08.054.

Parsafar, S., and Moghadam, A. S. (2017), "Development of a rocking R/C shear wall system implementing repairable structural fuses," *International Journal of Advanced Structural Engineering*, Springer Berlin Heidelberg, 9, 247–258. https://doi.org/10.1007/s40091-017-0161-1.

Saiidi, M. S., and Wang, H. (2006), "Exploratory study of seismic response of concrete columns with shape memory alloys reinforcement," *ACI Structural Journal*, 103, 435–442.

Twigden, K. M., Sritharan, S., and Henry, R. S. (2017), "Cyclic testing of unbonded post-tensioned concrete wall systems with and without supplemental damping," *Engineering Structures*, Elsevier Ltd, 140, 406–420. https://doi.org/10.1016/j.engstruct.2017.02.008.

Wang, B., and Zhu, S. (2018), "Cyclic tension–compression behavior of superelastic shape memory alloy bars with buckling-restrained devices," *Construction and Building Materials*, Elsevier Ltd, 186, 103–113. https://doi.org/10.1016/j.conbuildmat.2018.07.047.

Wang, B., Zhu, S., Qiu, C. X., and Jin, H. (2019), "High-performance self-centering steel columns with shape memory alloy bolts: Design procedure and experimental evaluation," *Engineering Structures*, Elsevier, 182, 446–458. https://doi.org/10.1016/j.engstruct.2018.12.077.

SEISMIC PROTECTION OF ESSENTIAL COMPONENTS AND EQUIPMENT USING ISOLATION WITH GEOMETRICALLY NONLINEAR VISCOUS DAMPER

Chieh-Yu Liu[1] and Chia-Ming Chang[2]
1. Ph.D. Student, National Taiwan University, Taipei, Taiwan.
2. Associate Professor, National Taiwan University, Taipei, Taiwan.
Email: d10521011@ntu.edu.tw, changcm@ntu.edu.tw

ABSTRACT

Seismic isolation with supplemental damping devices is one of effective strategies to mitigate structural responses. To date, this control strategy has been implemented in many building structures. However, the performance of damping devices would be limited, e.g., satisfied and reduced effectiveness in the design level and other levels of earthquakes, respectively. In this study, an adaptive isolation system with a geometrically nonlinear damping device, which is initially placed with an oblique angle to the isolation motion direction (i.e., horizontally uniaxial direction), is proposed. First, the dynamic characteristics of the proposed isolation system with geometrically nonlinear damping are investigated. A stochastic design method is developed to fulfill multi-objective performance for this system such as better reducing the absolute isolation acceleration in small earthquakes as well as lowering the isolation displacements in large earthquakes. Moreover, the proposed system is also experimentally verified for the displacement-force and velocity-force relationships. As seen in the results, the proposed system can adaptively achieve different control objectives for various levels of earthquakes.

Keywords: Seismic Isolation; Geometric Nonlinearity; Viscous Damper; Dynamic Characteristics; Multiple Performance Objectives

INTRODUCTION

Earthquakes pose risks to essential components and equipment (ECEs) that can lead to significant economic loss. A wide range of ECEs is vulnerable to earthquake loadings, e.g., apparatuses in the manufacturing process of semiconductors, storage facilities for fragile high-tech products, and essential information technology equipment. Sometimes these ECEs are concurrently sensitive to floor accelerations and displacements. Therefore, seismic protection of ECEs becomes a crucial issue.

Seismic isolation is a common and effective strategy that has been widely used to concur seismic hazards for elongating the structural vibration period. Robinson (1982) proposed the lead rubber bearing for base-isolated buildings, which is the most commonly used foundations isolation method today. Harvey and Gavin (2014) proposed a double rolling isolation system with two stacking layers that can avoid potential damage to essential equipment. Hamidi and El Naggar (2007) developed a sliding con-cave foundation system that can change the isolation period to 8-10 seconds. These strategies can efficiently mitigate the isolation accelerations, but excessive isolation displacements were produced if suffering impulse or severe excitation. Thus, supplemental damping devices are recommended to install along the isolation layer to reduce excessive displacements at the isolation layer. This control strategy can reduce isolation displacements by adding damping, but the superstructure's absolute acceleration and story drift will be amplified in the meantime (Kelly, 1999; De Domenico and Ricciardi, 2018; Providakis, 2008; Providakis, 2009). Designing seismic isolation is a trade-off problem between isolation displacement and acceleration and must be solved by adaptive damping.

This research proposes an isolation system with a geometrically viscous damper. The dynamic characteristics of the proposed isolation system are first investigated. Then, a design method based on stochastic linearization is established to determine the parameters in the proposed isolation system. In this design method, the proposed system should produce better reductions of absolute accelerations than a linearized isolation system against small-to-moderate earthquakes. Meanwhile, this system should outperform isolation displacements in the linearized system against severe earthquakes. Consequently, the isolation system with a geometrically nonlinear viscous damper can be designed with multiple

performance objectives. In addition, the geometrically nonlinear damping is experimentally verified through performance testing. As a result, the damping with geometric nonlinearities generates the adaptive effectiveness and displacement-dependent feature against different levels of earthquakes.

NUMERICAL MODEL OF ISOLATION SYSTEM WITH GEOMETRICALLY NONLINEAR DAMPING

Consider an isolation system with a geometrically nonlinear viscous damper as illustrated in Fig. 1.

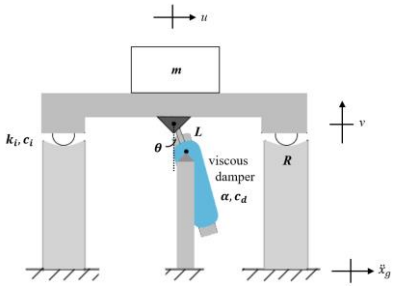

Figure 1. Schematic diagram of the proposed isolation system

Thus, the equation of motion for the proposed system can be written by

$$m\ddot{u} + c_i\dot{u} + k_i u + f_d = -m\ddot{x}_g \tag{1}$$

where $\ddot{x}_g$ represents the ground motion; u, $\dot{u}$, and $\ddot{u}$ are represent the relative displacement, velocity, and acceleration to the ground. The isolation platform with mass m and the inherent damping coefficient c_i. The friction-type isolation bearings with a single curvature provide the equivalent stiffness k_i. The viscous damper has a damping coefficient c_d and velocity exponent α, and pin-to-pin length of the damper is L. The initial oblique angle between the gravitational direction and viscous damper at the equilibrium is θ. Moreover, f_d is the geometrically nonlinear damping force provided by a viscous damper and written by

$$f_d = c_d \cdot sgn(\dot{u}) \cdot \left| \frac{(Lsin\theta+u)\dot{u}}{\sqrt{(Lsin\theta+u)^2+(Lcos\theta)^2}} \right|^{\alpha} \frac{|(Lsin\theta+u)|}{\sqrt{(Lsin\theta+u)^2+(Lcos\theta)^2}} \tag{2}$$

In this study, the velocity exponent is considered to be 1 to eliminate the material nonlinearity in a damper with nonlinear viscosity.

DESIGN METHOD USING STOCHASTIC LINEARIZATION

A design method is developed to determine the viscous damping coefficient in the proposed isolation system with a given pin-to-pin length and initial oblique angle. In this design method, the proposed nonlinear system is stochastically linearized, assuming Gaussian noise as the ground excitation (Caughey, 1963; Lutes and Sarkani, 2004). Thus, Eq. 1 can be linearized and rewritten by

$$m\ddot{u} + c_i\dot{u} + k_i u + b_1 u + b_2\dot{u} = -m\ddot{x}_g \tag{3}$$

where

$$b_1 = 0$$

$$b_2 = \frac{c_d}{\sigma_u \sigma_{\dot{u}}{}^3 \pi} \Gamma\left(\frac{\alpha+2}{2}\right)(2\sigma_{\dot{u}}{}^2)^{\frac{\alpha+2}{2}} \int_0^\infty \left(\frac{Lsin\theta - u}{\sqrt{(Lsin\theta-u)^2+(Lcos\theta)^2}}\right)^{\alpha+1} e^{-\frac{u^2}{2\sigma_{\dot{u}}{}^2}} du \quad (4)$$

In Eq. 4, b_2 is a function of displacement and velocity variances. Therefore, if b_2 in Eq. 3 is linearly determined by seismic design, then the damping coefficient of the geometrically nonlinear viscous damper can be computed by Eq. 4.

Stochastic Design

To fulfill the multiple performance objectives of the proposed system, the performance indices in small-level and large-level earthquakes are defined such as

$$J_u^e = \frac{\sigma_u^e}{\sigma_u^D}; J_{\ddot{x}_a}^e = \frac{\sigma_{\ddot{x}a}^e}{\sigma_{\ddot{x}_a}^D} \quad (5)$$

where the superscript e indicates the earthquake intensity, e.g., e = S, D, and L representing the small-, design-, and large-level earthquakes. $\sigma_{\blacksquare}^{\blacksquare}$ and $\sigma_{\ddot{x}_a}^{\blacksquare}$ denote the standard deviations (or root-mean-square responses, RMS responses) of the isolation displacement and absolute acceleration. For the multiple performance objectives, the proposed system should satisfy

$$J_{\ddot{x}_a}^S < \frac{\sigma_{\ddot{x}_g}^S}{\sigma_{\ddot{x}_g}^D}$$

$$J_u^L < \frac{\sigma_{\ddot{x}_g}^L}{\sigma_{\ddot{x}_g}^D} \quad (6)$$

In this study, a design example is provided. An isolation system has platform mass $m = 1$ kg, inherent damping coefficient $c_i = 0.05$ N · sec/m (i.e., 2% damping ratio), and stiffness $k_i = 1.58$ N/m (i.e., 0.2-Hz resulting natural frequency). Assumed the initial oblique angle is 30°, b_2 in Eq. 3 is determined by minimizing the RMS absolute acceleration in design-level earthquakes and equals 0.766 N-sec/m. Thus, the relationship between the damping coefficient of the viscous damper and the pin-to-pin length can be obtained by Eq. 4 and shown in Fig. 2.

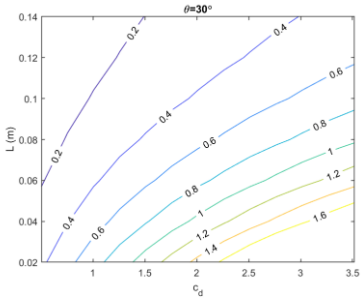

Figure 2. Relationship between the damping coefficient and pin-to-pin length for the design-level earthquakes

In the performance evaluation, 43 earthquake records in the 2016 Meinong earthquake in Kaohsiung are employed as design-level earthquakes and converted into spectrum-compatible ones. As seen in Fig. 3, all RMS responses in small or large-level earthquakes are normalized to the RMS responses in design-

level earthquakes. In this example, the intensities of small- and large-level earthquakes are 1/3 ($\frac{\sigma^S_{\ddot{x}_g}}{\sigma^D_{\ddot{x}_g}}$) and 3 ($\frac{\sigma^L_{\ddot{x}_g}}{\sigma^D_{\ddot{x}_g}}$) times that of the design-level earthquakes. If the proposed system is appropriately designed for the multiple performance objectives, both Eqs. 5-6 should be satisfied. As seen in Fig. 3(a), the proposed system can effectively reduce the RMS isolation accelerations in the small-level earthquakes. Meanwhile, the RMS isolation displacement is significantly lowered in the large-level earthquakes, as shown in Fig. 3(b). Note that the red stars and blue circles represent the performance for the design-level earthquakes. Through this design procedure, the proposed isolation system with a geometrically nonlinear viscous damper can realize multiple performance objectives in different levels of earthquakes.

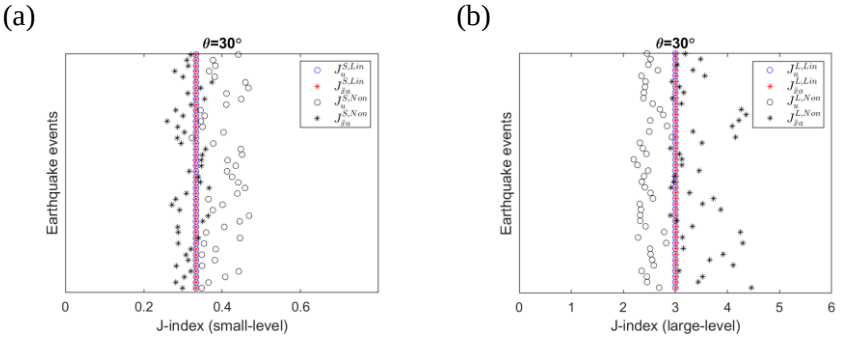

Figure 3. Performance evaluation results (a) performance indices in the small-level earthquakes (b) performance indices in the large-level earthquakes, where superscripts Lin and Non indicate the optimally linear system and the proposed nonlinear system, respectively.

EXPERIMENTAL VERIFICATION

To verify the mathematical model of the geometrically nonlinear damping, a small-scale experiment is carried out and illustrated in Fig. 4. A platform is connected to a hydraulic actuator on its top and supported by linear guides. One piston rod end of the viscous damper is pin-connected to the bottom of the platform and moves together with the platform. Two plates clamping to the top of the damper cylinder are pinned to the fixed brackets. The pin-to-pin length L can be adjusted to 0.25 m and 0.21 m. The servo-hydraulic actuator has a stroke of ±127 mm and a maximum force of 15 kN. The viscous damper is manufactured by Taylor Devices and has a damping coefficient $C_d = 3{,}450$ N-sec/m and a velocity exponent of 1. In the experiment, displacement u is measured by the actuator's internal linear variable displacement transducer (LVDT); absolute acceleration is measured by a force balance accelerometer; the actuator force is measured by the load cell on the back of the actuator. The geometrically nonlinear damping behavior can finally be verified through this configuration.

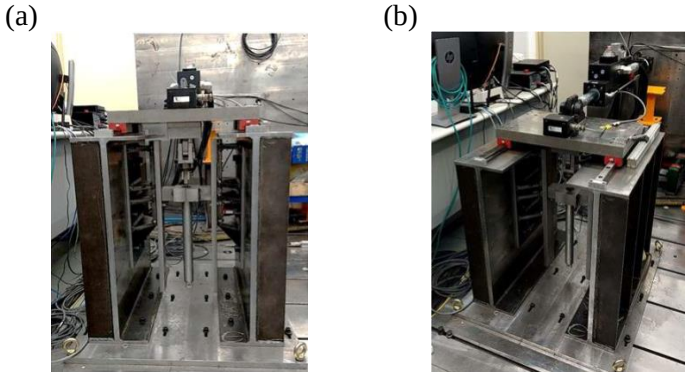

Figure 4. Experimental setup: (a) front view; (b) overview.

Fig. 5 demonstrates the results of the performance test. This performance test considers a sinusoidal displacement input to the guided platform, where the input displacement varies from 0.07~0.10 m with a constant excitation frequency of 1.5 Hz. In this experimental setup, the initial oblique angle remains zero. In this figure, $f_{\mathrm{ec,m}}$ is the calculated force by Eq. 2, while $f_{\mathrm{ec,mx}}$ is the measured force by the platform inertial force (i.e., the platform mass times the absolute acceleration). Due to the special configuration, the weight of the eccentric viscous damper would introduce a variable moment and result in a force proportional to the displacement in the horizontal direction. Thus, the measured and calculated forces include this rotational effect, and the hysteretic loops in Fig. 5 behave both damping and stiffness-like characteristics. As seen in this figure, this geometrically nonlinear damping is realizable. The hysteretic loops present a butterfly shape whereby this configuration generates a tiny damping force around the equilibrium. When the maximum horizontal displacement is achieved, the damping force remains zero because of zeroed velocities. The maximum damping force occurs when the displacement is roughly 2/3 of the maximum. Therefore, the viscous damper with the proposed geometrical configuration can yield adaptive damping forces.

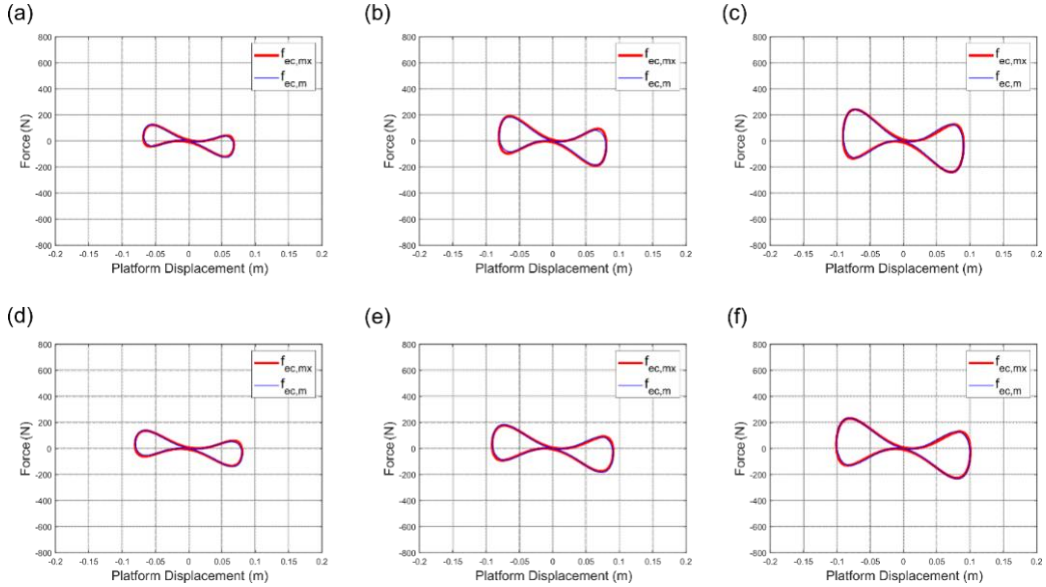

Figure 5. Experimental results (a) $U = 0.07$ m and $L = 0.21$ m, (b) $U = 0.08$ m and $L = 0.21$ m, (c) $U = 0.09$ m and $L = 0.21$ m, (d) $U = 0.08$ m and $L = 0.25$ m, (e) $U = 0.09$ m and $L = 0.25$ m, and (f) $U = 0.10$ m and $L = 0.25$ m.

CONCLUSIONS

This study proposed an isolation system with geometrically nonlinear damping. The geometrically nonlinear damping was realized by a viscous damper obliquely placed between the gravitational and damper axial directions at the equilibrium. The resulting damping force was a function of isolation displacement and velocity. A design procedure was developed using a stochastic approach to determine the parameters in the geometrically nonlinear damping. Given an initial oblique angle, a series of damping coefficients and pin-to-pin lengths can be optimally designed in accordance with the design-level earthquakes. Using the criteria in Eqs. 5-6, the proper damping coefficient and pin-to-pin were selected from the optimally designed ones and allowed for achieving multiple performance objectives. The multiple performance objectives yielded reduced isolation absolute accelerations and displacements in the below and beyond design-level earthquakes compared to the optimally conventional isolation system. As seen in the performance evaluation results, the designed equipment isolation system consequently satisfied the multiple performance objectives when 43 spectrum-compatible earthquake records were input into the system.

ACKNOWLEDGMENTS

This work was supported in part by the Ministry of Science and Technology in Taiwan under grant numbers of MOST 107-2628-M-002-007-MY3 and MOST 109-2224-E-002-005.

REFERENCES

Robinson, W. H. (1982). Lead-rubber hysteretic bearings suitable for protecting structures during earthquakes. *Earthquake engineering & structural dynamics*, *10*(4), 593-604.

Harvey Jr, P. S., and Gavin, H. P. (2014). Double rolling isolation systems: a mathematical model and experimental validation. *International Journal of Non-Linear Mechanics*, *61*, 80-92.

Hamidi, M., and El Naggar, M. H. (2007). On the performance of SCF in seismic isolation of the interior equipment of buildings. *Earthquake engineering & structural dynamics*, *36*(11), 1581-1604.

Kelly, J. M. (1999). The role of damping in seismic isolation. *Earthquake Engineering & Structural Dynamics*, ***28***(1), 3-20.

De Domenico, D., and Ricciardi, G. (2018). An enhanced base isolation system equipped with optimal tuned mass damper inerter (TMDI). *Earthquake Engineering & Structural Dynamics*, ***47***(5), 1169-1192.

Providakis, C. P. (2008). Effect of LRB isolators and supplemental viscous dampers on seismic isolated buildings under near-fault excitations. *Engineering Structures*, ***30***(5), 1187-1198.

Providakis, C. P. (2009). Effect of supplemental damping on LRB and FPS seismic isolators under near-fault ground motions. *Soil Dynamics and Earthquake Engineering*, ***29***(1), 80-90.

Jensen, H. A., & Sepulveda, A. E. (2000). Optimal design of uncertain systems under stochastic excitation. *AIAA journal*, ***38***(11), 2133-2141.

Caughey, T. K. (1963). Equivalent linearization techniques. *The Journal of the Acoustical Society of America*, ***35***(11), 1706-1711.

Lutes, L. D., and Sarkani, S. (2004). *Random vibrations: analysis of structural and mechanical systems*: Butterworth-Heinemann.

AN EVALUATION OF THE EQUIVALENT LINEAR METHOD FOR LEAD-RUBBER-BEARING SYSTEMS SUBJECTED TO PULSE-LIKE GROUND MOTIONS

Yin-Nan Huang[1] and Julian Adiputra[2]
1. Associate Professor, Department of Civil Engineering, National Taiwan University, Taipei, Taiwan, R.O.C.
2. Graduate Student, Department of Civil Engineering, National Taiwan University, Taipei, Taiwan, R.O.C.
Email: ynhuang@ntu.edu.tw, julianadiputro@gmail.com

ABSTRACT

Pulse-like ground motions (PLGM) can produce severe damage and large demands for base-isolation systems. Additional dampers can reduce the large displacement demand, but additional force will be transmitted to the superstructure. However, only a few studies investigated the efficacy of the commonly used equivalent-linear design procedure of isolation systems compared to the nonlinear response-history analysis subjected to PLGMs. This study thoroughly evaluates (1) the efficacy of the equivalent linear method specified in ASCE 7-16 and AASHTO 2010 and the equivalent linear method without damping reduction factor for the design of LRB systems with additional viscous dampers subjected to PLGMs and (2) the influences of damping exponential (α_d) on structural responses. The results show that both methods still deliver unconservative results on displacement. The accuracy of both methods is highly dependent on the effective period and the characteristic strength of LRBs.

Keywords: Lead rubber bearing, viscous damper, pulse-like ground motion, equivalent linear method

INTRODUCTION

Pulse-like ground motions are defined as ground motions, typically observed at sites located near the fault, with one or more pulses in the ground velocity history. Earlier, Bertero et al. (1978) and Anderson and Bertero (1987) indicated that the pulse feature located in ground motions and the relationship between the pulse period and the structural period are the reasons for enormous demands on multistory buildings. They also point out that the structural response caused by pulse-like ground motions will be more than non-pulse-like ground motions given the same PGA. The performance of isolation systems subjected to pulse-like ground motions is different from the performance of isolation systems subjected to non-pulse-like ground motions where: (1) there will be an excessive displacement on the isolation systems; (2) transmitting higher forces into the superstructure; (3) resonance-like behavior if the pulse period is close to the period of the isolation system.

One method that can address these problems is by using additional dampers. Several studies investigated the effect of supplemental viscous damping devices on seismically isolated structures. A similar conclusion was obtained that supplemental viscous dampers will help to control the large deformation demand of the isolators in exchange for a moderate increase in superstructure forces and acceleration (e.g., L. P. Carden et al., 2005; C. P. Providakis, 2008).

Moreover, only a few studies investigated the efficacy and accuracy of the current design procedure of isolation systems compared to the nonlinear response history analysis. The widely used equivalent linear (EL) method has been challenged on its possible lack of accuracy and efficacy in predicting the peak nonlinear responses of an isolation system subjected to pulse-like ground motions. Dicleli and Buddaram (2007) used several synthetic near-fault ground motions with a forward rupture directivity effect (the term used in the original paper) to evaluate the accuracy of the equivalent linear method provided by AASHTO (1990). They concluded that the equivalent linear method would produce an unconservative prediction on the responses of seismically isolated bridges when the ratio between the post-elastic period of the system and the ground velocity pulse period is much greater or much smaller

than one. Moreover, Alhan and Özgür (2015) checked the accuracy of the equivalent linear method provided by the ASCE/SEI 7-05 standard (2006) using four pulse-like ground motions and concluded that the EL method underestimates the nonlinear responses (displacements and forces) of the isolation systems with flexible superstructures.

LRB SYSTEMS, GROUND MOTION DATABASE, AND METHODS

In this study, 21 SDOF models of LRB systems with additional viscous dampers were used. Two characteristics are set as constant values: (1) yield displacement (D_y = 0.01m), (2) post-yield period (T_{post} = 3.5 sec), and (3) weight (W = 547.7 tons). Moreover, three variables are set as parametric studies: (1) characteristic strength (Q_d = 0.03W, 0.06W, and 0.09 W), (2) damping ratio of the viscous damper (ξ_d = 0%, 10%, and 20%), and (3) damper exponential (α_d = 0.5, 1.0, and 1.5).

In this study, 220 pulse-like ground motions (109 in Taiwan and 111 outside Taiwan) are obtained from the PEER NGA West2 project and the SSHAC Level-3 project of NCREE Taiwan. These ground motions are scaled into four ground motions intensity levels (2/3 DBE, DBE, 1.5 DBE, and 2 DBE) in the target seismic area of Taipei Basin second zone.

In this study, three analysis methods are used: (1) nonlinear response-history analysis (NRHA), (2) equivalent linear (EL), and (3) equivalent linear (EL) without B factor. The NRHA method is performed using SAP2000 and OPENSEES and is stated as method 1. The EL method is performed using MATLAB and based on ASCE 7-16 and AASHTO 2010. Moreover, this method is stated as method 2. The EL method without B factor utilizes the response history analysis with the Newmark-β method to obtain the displacement spectrum. This method is performed using MATLAB and is stated as method 3.

ANALYSIS RESULTS

The results obtained from the NRHA method are displacement and acceleration. The example of NRHA results is given in Figure 1. Figure 1 shows the results for the model with Q_d = 0.03W, ξ_d = 10%, and three types of α_d subjected to pulse-like ground motions with intensity levels of 1.5 DBE and 2 DBE. The trend shown in Figure 1 is the same for all the models performed in this study. From these figures, it can be observed that for a large ground motion intensity level, α_d greater than 1 provides smaller displacement with a small or insignificant increase in terms of acceleration.

Moreover, because this study also aims to check the efficacy and accuracy of methods 2 and 3, the displacement results obtained from the NRHA method are used as the benchmark for the displacement results obtained from methods 2 and 3. The ratio between the displacement of method 2 (or3) and the displacement of method 1 then could be obtained where a ratio below 1 means unconservative and a ratio above 1 means conservative. Figure 2 shows us the example of the T_{eff} vs ratio for both methods. All models and cases have a similar trend to the one shown in Figure 2. It can be observed that on average, the results delivered by both methods 2 and 3 are still below 1.

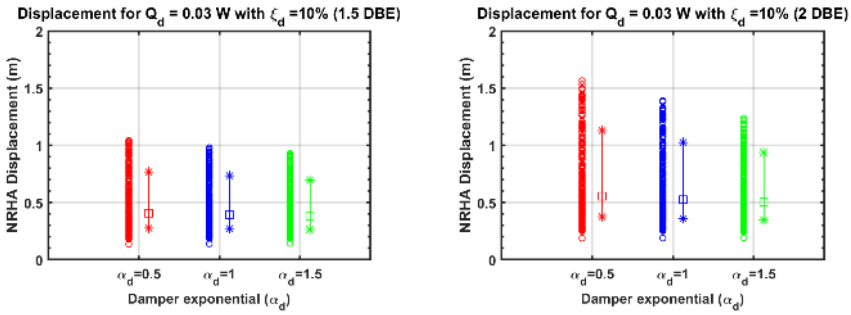

(a) Disp (1.5 DBE)

(b) Disp (2 DBE)

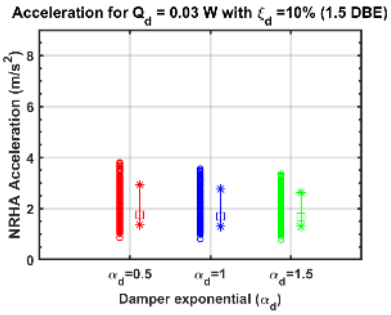

(c) Acc (1.5 DBE)

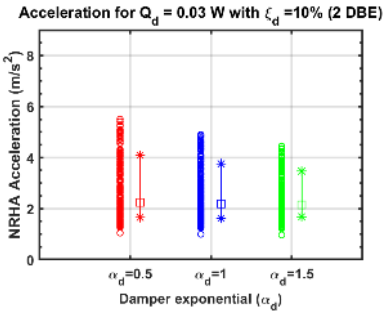

(d) Acc (2 DBE)

Figure 1 NRHA displacement and acceleration

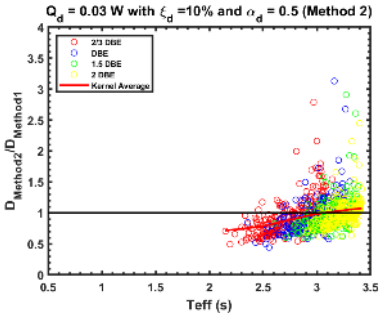

(a) Method 2

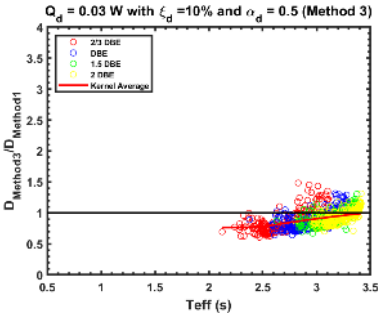

(b) Method 3

Figure 2. T_{eff} vs ratio

Figure 3 (a) and (b) shows the example of the average trend of cases with the same ξ_d and α_d, but different Q_d, meanwhile Figure 3 (c) and (d) show the example of the average trend of cases with the same Q_d but different ξ_d and α_d. From figures (a) and (b), it can be observed that T_{eff} and Q_d have some influences on the efficacy of methods 2 and 3. Meanwhile, it can be observed from figures (c) and (d) that the influences of ξ_d and α_d on the efficacy of methods 2 and 3 are very minor as the trends are pretty close and similar for each ξ_d and α_d.

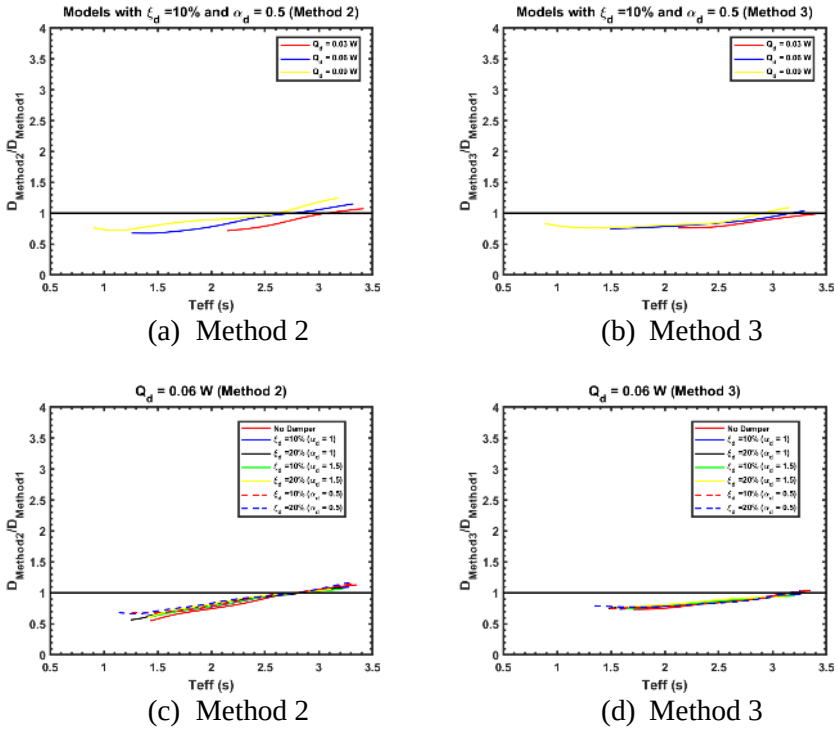

(a) Method 2 (b) Method 3

(c) Method 2 (d) Method 3

Figure 3. Average trend of the T_{eff} vs ratio

CONCLUSIONS

On average, the results of both methods 2 and 3 produce unconservative results on displacement and are highly dependent on the effective period (T_{eff}) of the structures and the characteristic strength (Q_d) of the LRB.

From the results of the nonlinear response-history analysis, it is observed that in the large ground motion intensity level, α_d greater than 1 provides smaller displacement with a small or insignificant increase in terms of acceleration.

ACKNOWLEDGEMENTS

The research presented in this paper was supported by National Taiwan University (Grant Number 110L891304). The support is deeply appreciated.

REFERENCES

Alhan, C., & Ozgur, M. (2015). Seismic responses of base-isolated buildings: efficacy of equivalent linear modeling under near-fault earthquakes. *Smart Structures and Systems*, *15*(6), 1439-1461.

American Association of State, H., Transportation Officials, S. o. B., & Structures. (2010). *Guide specifications for seismic isolation design*. American Association of State Highway and Transportation Officials.

Anderson, J. C., & Bertero, V. V. (1987). Uncertainties in Establishing Design Earthquakes. *Journal of Structural Engineering*, *113*(8), 1709-1724.

ASCE. (2016). "Minimum design loads for buildings and other structures." ASCE 7-16, ASCE, Reston, VA

Bertero, V. V., Mahin, S. A., & Herrera, R. A. (1978). Aseismic design implications of near-fault san fernando earthquake records. *Earthquake Engineering & Structural Dynamics*, *6*(1), 31-42.

Carden, L., Davidson, B., Larkin, T., & Buckle, I. (2005). Retrofit of seismically isolated structures for near-field ground motion using additional viscous damping. *Bulletin of the New Zealand Society for Earthquake Engineering*, *38*, 106-118.

Dicleli, M., & Buddaram, S. (2007). Equivalent linear analysis of seismic-isolated bridges subjected to near-fault ground motions with forward rupture directivity effect. *Engineering Structures - ENG STRUCT*, *29*, 21-32.

Providakis, C. (2008). Effect of LRB isolators and supplemental viscous dampers on seismic isolated buildings under near-fault excitations. *Engineering Structures*, *30*, 1187-1198.

EFFECTS OF NEAR-FIELD AND FAR-FIELD EARTHQUAKES ON SEISMIC RESPONSE OF EXTENDED PILES UNDER EXTREME SCOURING CONDITIONS

Mohammad Asif Raja[1] and Jiunn-Shyang Chiou[2*]
1. Ph.D. Candidate, Department of Civil Engineering, National Taiwan University, Taipei, Taiwan, R.O.C.
2. Associate Professor, Department of Civil Engineering, National Taiwan University, Taipei, Taiwan, R.O.C.
Email: asif.best1989@gmail.com, jschiou@ntu.edu.tw

ABSTRACT

Scouring causes damage to and failure of several structures such as bridges, wind turbines and electric towers every year around the world. In this study, a long pile with variable diameters is subjected to extreme scour. Modal analyses are used to observe the effect of the length-to-diameter ratio on the period of soil-pile systems. The results show that small diameter piles have higher periods than large diameter piles. Furthermore, the rate of change of period is higher for smaller scour depths and become constant for large diameter piles (D > 2.5 m). Modal analyses on soil in free-field conditions are also performed to observe the kinematic effect and found that the period of the free-field ground is close to large diameter piles. Time history analyses are performed to observe the dynamic response of piles subjected to near-filed and far-field earthquakes. Results are discussed in the form of envelopes of acceleration, velocity, displacement, shear, and moment. For generalization, results are normalized with maximum input values of ground motions. Results show that different behavior of piles is evident under near-field and far-field ground motions.

Keywords: Extreme scouring, Near-field earthquake, Far-field earthquake, Kinematic effect, Inertial effect.

INTRODUCTION

Scouring is one of the devastating natural phenomena which occurs regularly in soil with flowing water and it becomes severe problems for geotechnical engineers when water flows with very high speed such as during flood, tsunami, and heavy rainfall. When the rate of scour is very high in a short period of time under high speed water effluent, it can be considered as extreme scour and due to sudden removal of soil support from the foundations such as piles, monopole, and caisson can lead to local damage to or failure of the entire structures supported by these foundations. Controlling and mitigation of scouring is complex and costly and may be less effective in most of the cases due to extreme water effluent with a swift speed and hence, it is necessary to design the foundation is such a way that it should not be damaged under extreme scouring. Removal of soil support around the foundation is defined as scouring (Maddison, 2012; Prendergast et al., 2013; Raja and Chiou et al., 2022) which leads to reduction and soil stiffness around the foundation and ultimately failure of the structure (Bolduc et al., 2020; Raja and Chiou et al., 2022). Several studies have been performed on the behavior of piles subjected to scouring. The scouring in clay under cyclic loading forms gaps in between pile and soil results in reduction of soil stiffness with loading cycles (Reese et al., 1989). Avent and Alawady (2005) studied the effect of scouring in group piles under lateral loading and concluded that buckling increases with scour in the pile. Hughes et al. (2007) studied effect of extreme scour and modulus of soil subgrade reaction on bridge piles to investigate the lateral and buckling behavior of the pile. Kishore et al., (2009) conducted 1g small-scale centrifuge test on piles in marine clay under monotonic and cyclic loadings and concluded that due to scouring, bending moment and deflection of pile increase with scour. Li et al. (2013) cooducted numerical analyses on the behavior of laterally loaded single pile in clay subjected to scouring and found that the depth of scour hole has a larger impact than width in local scour. Prendergast et al., (2013) investigated the effect of scour on the frequency of a driven pile using laboratory and field tests and concluded that scouring causes a reduction in the natural frequency. Raja and Chiou (2022) studied the combined effect of scour and water on piles under seismic loading and concluded that the

acceleration initially attenuated and later on amplified at the pile top. There are limited studies on the behavior of scoured piles under seismic loading. Effects of near-field and far-field earthquakes on scoured piles with various diameter and scour depth have not studied yet. This study focuses on the effect of scour on the period of the soil (free-field) and soil-pile systems (with different L/D ratios). Furthermore, this study focuses on the effects of near-field and far-field earthquakes on the dynamic responses of the pile.

PROBLEM STATEMENT

For this analysis, a 35 m-long extended single pile with variable diameters (0.5-5 m) is installed on saturated dense sand subjected to extreme scouring conditions under heavy water flow. A pile head (4.5 m × 4.5 m × 2.5 m) on the top of the pile is simulated as an equivalent length (behave as rigid bar) of 1.25m, mass of 121.27 Mg and mass moment of inertia of 267.804 Mg-m^2. The unit weight of the reinforced concrete is 23.5 kN/m^3 with Poisson's ratio of 0.2 is used for the pile. The modulus of elasticity of concrete of the pile is 2.5×10^7 kN/m^2. Initially, the pile is 25 m embedded in saturated sand with a relative density of 70%, saturated unit weight of 20.5 kN/m^3 and angle of friction of 39° is adopted. The effect of water is ignored for the sake of simplicity in the calculation of complex soil-structure interaction problem. The saturated sand is later on subjected to four scouring depths (s = 2 m, s = 4 m, s = 6 m, and s = 8 m) under extreme water flow conditions. A combined shear beam and soil-structure interaction model (Fig.1b) is used to simulate the soil-pile system which is based on beam-on-nonlinear-Winkler-foundation (detail description is available, Raja and Chiou 2022; Chiou et al., 2020). For the free-field response, the shear beam model is used alone. The schematic diagram of the soil-pile system and their equivalent model is shown in Fig. 1(a).

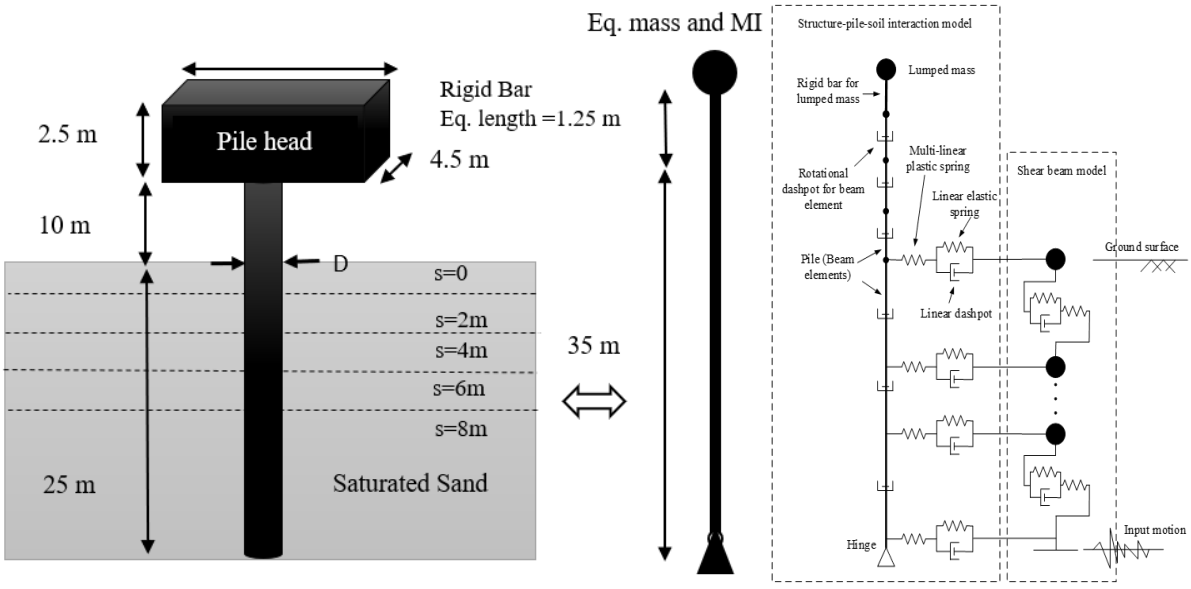

Figure 1. (a) Schematic diagram of soil-pile system with different scouring depths (s), (b) Combined shear beam and soil-structure interaction model (Chiou et al., 2020).

EFFECT OF SCOURING ON TIME PERIODS

Modal analyses are conducted to observe the free-field responses of different scouring depths using shear beam model. Fig. 2 shows the variation of period for three modes of vibration with increasing scour depths. Periods for all three modes linearly decrease with increasing scour depths and the fundamental periods are much higher than the periods of 2nd and 3rd modes. The rate of change of periods with increasing scour depths are least in modes 2nd and 3rd as compared with the first mode of vibration. Figures 3, 4, and 5 show the variation period with increasing diameters (decreasing length L/ diameter

D ratio) for 1st , 2nd, and 3rd modes of vibration of the soil-pile systems, respectively. From Fig. 3, it is observed that the small diameter piles (D = 0.5, 1, 1.5, 2 and 2.5 m) have higher periods which decreases sharply as compared to the higher diameter piles (D > 2.5m) which remains almost constant with increasing scour depths. Simultaneously, it is further observed that higher scour depths have higher period for small diameters piles and remains low and constant for large diameter piles. Therefore, it can be concluded that smaller diameter piles will have lower kinematic effect due to the ground movement as compared with larger diameter piles and with increasing scour depths the kinematic effect increases (inertial interaction will reduce) as the period approaches with free-field ground periods when subjected to seismic loading. Fig. 4 and Fig. 5 show that the initially high period in small diameter piles and later on low periods for higher scouring depths in large diameter piles. The 2nd and 3rd modes of vibration have periods closer to the free-field ground condition and hence, will produce a large kinematic effect under dynamic loading.

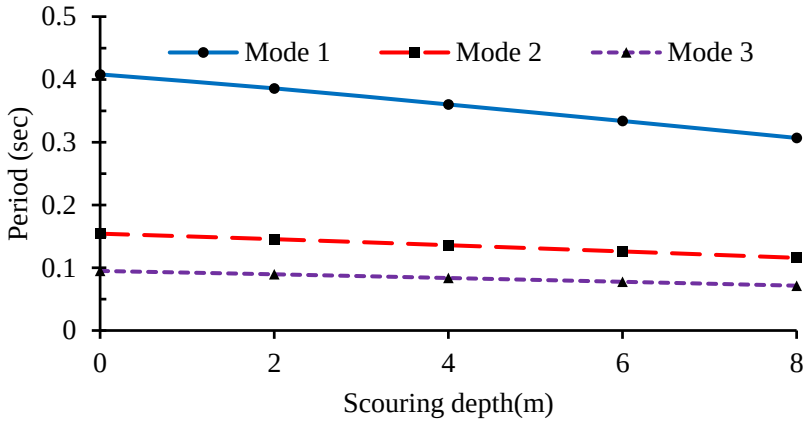

Figure 2. Variation of period in free-field condition with increasing scouring depths

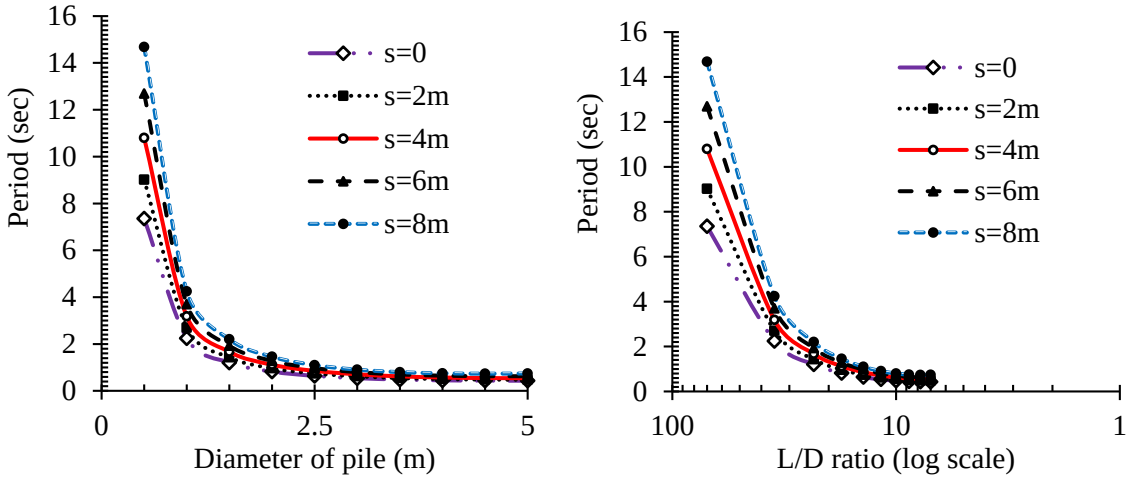

Figure 3. Variation of fundamental period of soil-pile system with increasing scouring depths

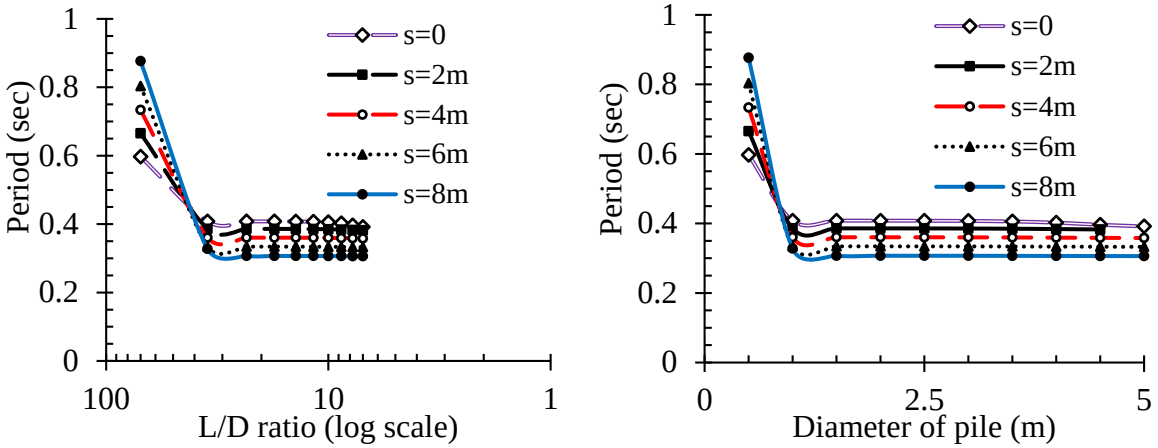

Figure 4. Variation of period of 2nd mode of soil-pile system with increasing scouring depths

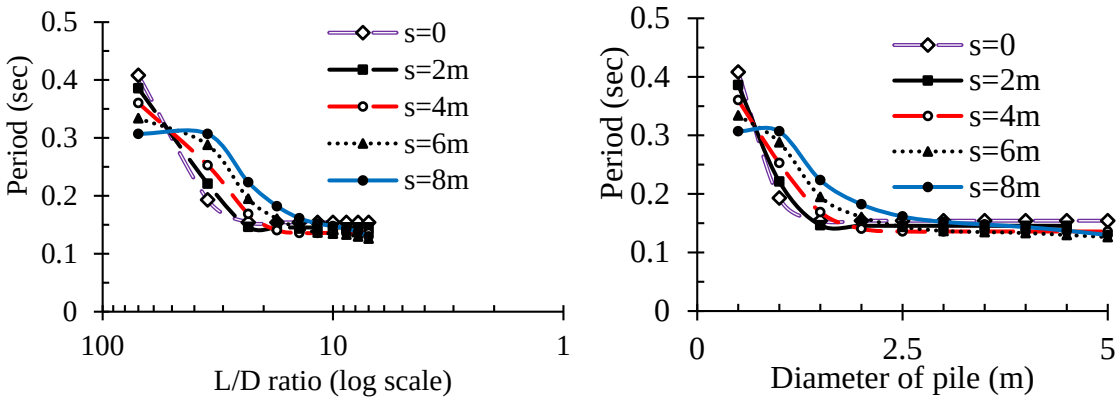

Figure 5. Variation of period of 3rd mode of soil-pile system with increasing scouring depths

INPUT MOTION CHARACTERESTICS

The Kobe earthquake is a great earthquake due to its high magnitude (M_w=6.9) and high peak ground acceleration (PGA), peak ground velocity (PGV), and high peak spectral acceleration (PSG) in near-field conditions. It occurred on 16th January 1995 at a latitude of 34.5948 and a longitude of 135.0121 with a focal depth of 17.9 km and having a strike-slip (strike: 230, dip: 85, rake: 180) mechanism (PEER, 2022). The parallel component of ground motion records of two different stations of Kobe earthquake is chosen in such a way that one of the ground motions should behave as a near-field motion (KJMA site, JMA station, Japan) and another one should behave as a far-field motion (Tadoka site, CEOR station, Japan). The near-field motion has high PGA, PGV, PSG and low PGD as compared with far-field motion (Fig. 6). However, the near-field motion was recorded of 48 seconds, while the far-field motion was recorded for 140 seconds. The characteristics of these two ground motions are listed in Table 1 (PEER, 2022).

Table 1. Characteristics of Kobe (1995) earthquake of KJMA site (near-field) and Tadoka (far-field)

Name (Site)	Distance to fault (km)	Hypocentral Distance (km)	PGA(g)	PGV(m/s)	PGD(m)	PSA(g)	Predominant Periods (sec)
Kobe (KJMA)	1	25.6	-0.805	-0.771	-0.176	2.681	0.345
Kobe (CEOR)	31.7	42.6	-0.288	0.239	-0.245	1.317	0.197

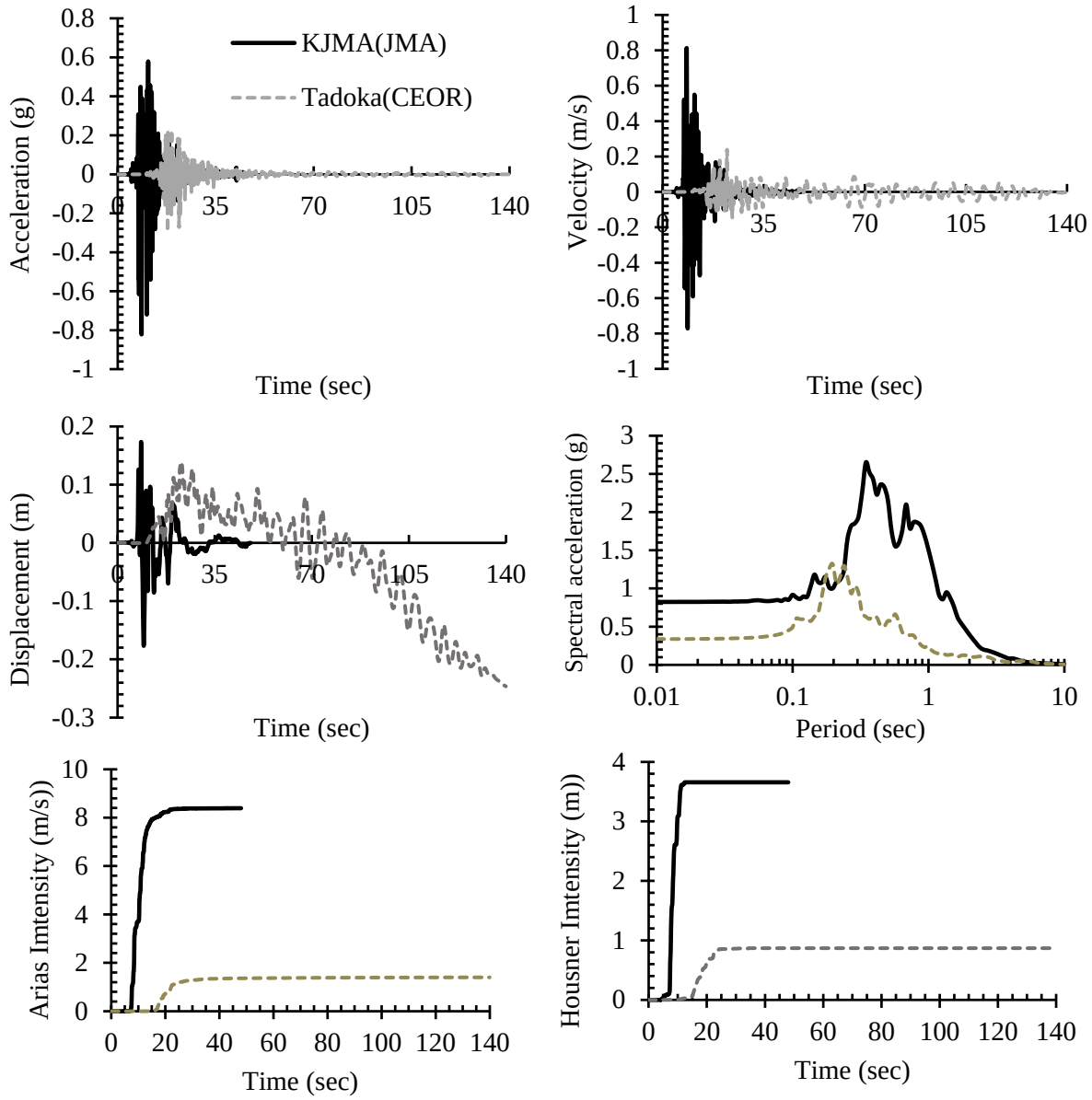

Figure 6: Comparison of acceleration, velocity and displacement time histories, response spectra, and energy intensities of Kobe (1995) earthquake of KJMA and Tadoka sites (PEER, 2022)

EFFECTS OF NEAR-FIELD AND FAR-FIELD EARTHQUAKES

A nonlinear direct integration time history analysis is performed using SAP 2000. Modal analysis shows that very high L/D ratio is too flexible and after a certain low L/D ratio (around 17), the periods of the pile-soil systems do not change much for all three modes of vibration. Therefore, a 2-m diameter pile is used in the time history analysis keeping length of the pile as constant. Results are presented in the form of envelopes of acceleration, velocity, displacement, shear force, and bending moment with respect to scour depth (s) to the pile length. Acceleration, velocity and displacement are normalized with input PGA, PGV, and PGD, respectively, to generalize the behavior of pile in near-field and far-field ground motions. Fig. 7 shows that the acceleration initially decreases for small s/L ratios and later increases for the near-field earthquake, while for the far-field earthquake, it initially decreases and later on remains constant for a higher s/L ratio. Normalized acceleration shows that for a smaller s/L ratio, the far-field earthquake shows higher responses, but for a higher s/L ratio, the near-field earthquake shows higher responses. Fig 7. also shows that for the near-field earthquake, the velocity and displacement initially

decrease and later on increase sharply under a higher s/L ratio, while for the far-field earthquake, the velocity initially decreases and later remains constant. Displacement remains constant for the far-field earthquake and normalized displacement shows high sensitivity of displacement for the near-field earthquake and it further increases with increasing s/L ratio which implies high inertial effects. Therefore, it is important to note that far-field earthquakes should be considered even though a structure is located far away from active faults.

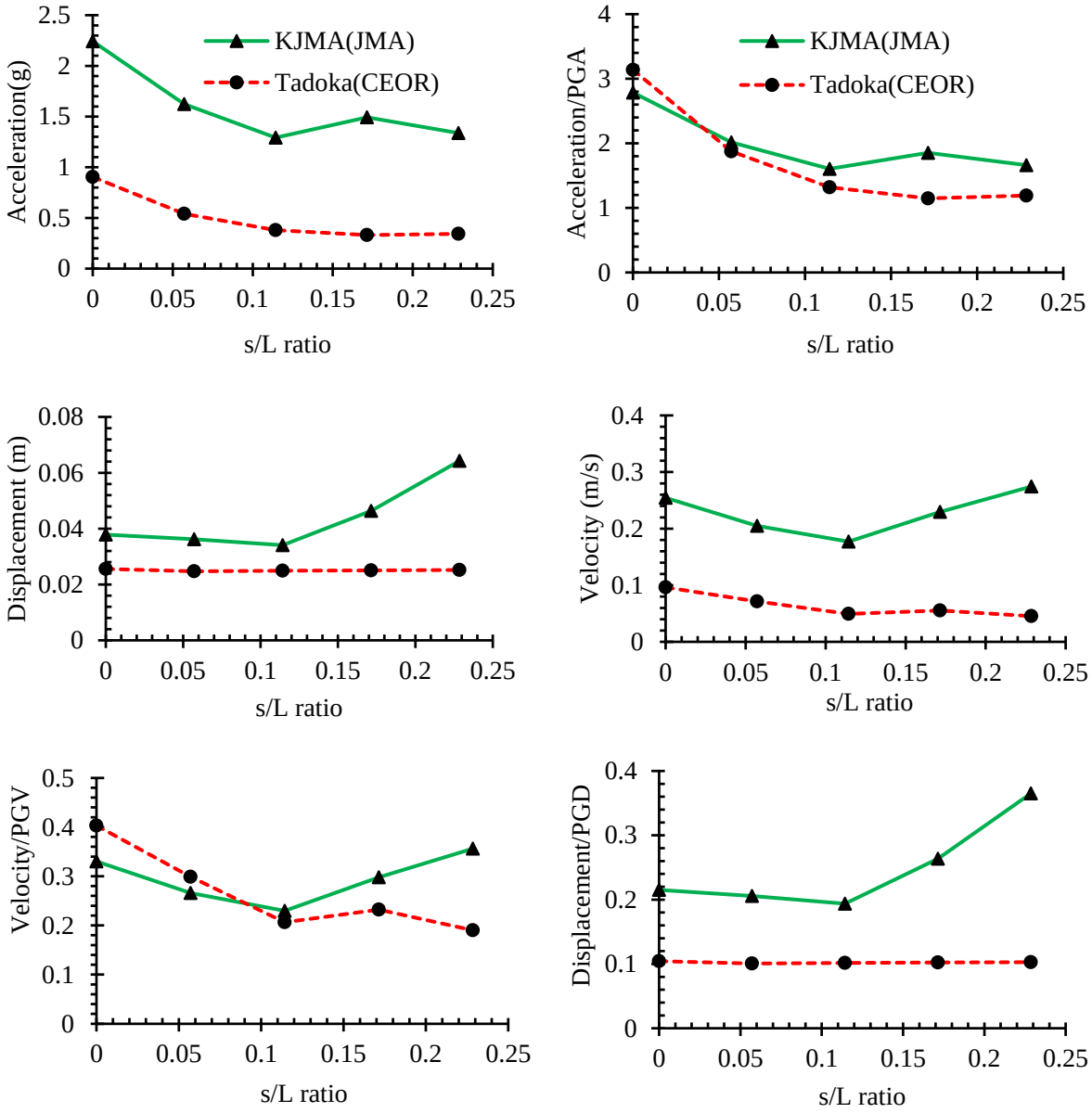

Figure 7. Variation of envelopes of acceleration, velocity, and displacement with increasing scour depth(s)/length of pile (L) ratio

Fig. 8 shows the variation of maximum shear force and normalized shear force with increasing s/L ratio. The shear force initially decreases then decreases for the near-field earthquake, while for the far-field earthquake it continuously decreases. The similar pattern is also observed for the maximum bending moment as shown in Fig. 8. It can be further observed that the maximum shear force is least for the s/L ratio greater than 0.1 in near-field and far-field earthquakes, while the maximum bending moment is least in between 0.9 to 0.12 in case of the near-field earthquake. Therefore, to observe the minimum shear force and bending moment, the pile length should be selected based on maximum potential scour depth so that the s/L ratio is between 0.1 and 0.15.

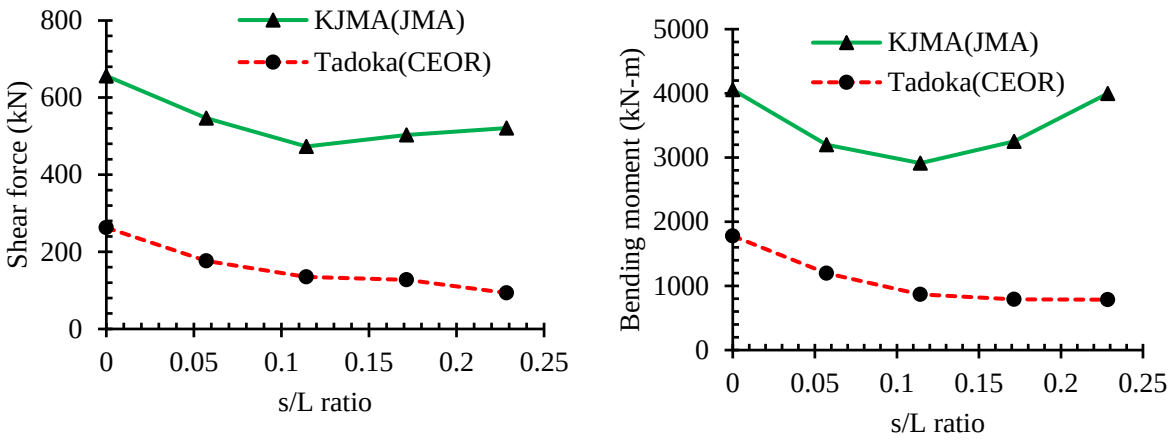

Figure 8. Variation of envelopes of shear force and bending moment with increasing scour depth(s)/length of pile (L) ratio

CONCLUSIONS

Based on the aforementioned studies, the following conclusions can be drawn:

1. The fundamental period of soil-pile system increases with increasing scouring depths, while it decreases with increasing L/D ratio and remains constant for a high L/D ratio.
2. Piles with small L/D ratios have very high period with increasing scour depths, i.e., very high inertial effects when subjected to seismic loading. Therefore, it should be avoided when soil is subjected to extreme scour.
3. The fundamental period of soil-pile systems is close to free-field soil for a higher L/D ratio, i.e., a high kinematic effect will be observed under seismic loading.
4. Higher mode of vibrations of soil-pile systems and free-field soil have very close periods and it may result in resonance.
5. The s/L is a critical component to observe the minimum acceleration, velocity, and displacement while designing for near-field earthquake. The s/L equal to 0.1 to 0.12 provides the minimum response.
6. For lower s/L value, near-filed and far-field earthquakes behave similar. Therefore, with s/L lower than 0.1, far-field earthquakes should be considered even though a structure is located far away from active faults.
7. The minimum shear force and bending moment can be observed when s/L lies in between 0.1 to 0.15. Therefore, length of pile should be selected based on the maximum potential scour depth.

ACKNOWLEDGMENTS

The authors would like to thank the Ministry of Science and Technology of Taiwan (Grant no. 111-2221-E-002-066) and the National Taiwan University (Grant no. NTU-CC-111L890705) for financial support. The authors also would like to thank the Center of Earthquake Engineering Research, National Taiwan University to fund this study.

REFERENCES

Avent, R. R., and Alawady, M. (2005). "Bridge scour and substructure deterioration:Case study." *J. Bridge Eng.*, **10**(3), 247-254.

Bolduc, L. C., Gardoni, P., & Briaud, J. L. (2008). "Probability of exceedance estimates for scour depth around bridge piers". *J. Geotech. Geoenviron. Eng.*, **134**(2), 175–184

Chiou, J. S., Hung, W. Y., Lee, Y. T., & Young, Z. H. (2020). "Combined dynamic structure-pile-soil interaction analysis considering inertial and kinematic effects". *Computers and Geotechnics*, **125**, 103671.

Hughes, D., Ramey, G. E., & Hughes, M. L. (2007). "Effects of Extreme Scour and Soil Subgrade Modulus on Bridge Pile Bent Buckling". *Practice Periodical on Structural Design and Construction*, **12**(2), 96–108.

Kishore, Y.N., Rao, S.N., Mani, J.S., 2009. "The behavior of laterally loaded piles subjected to scour in marine environment". *KSCE J. Civ. Eng*., **13**, 403–408.

Li, F., Han, J., & Lin, C. (2013). "Effect of scour on the behavior of laterally loaded single piles in marine clay". *Marine Geores. Geotech.*, **31**(3), 271-289.

Maddison, B. (2012). "Scour failure of bridges," *Proc. Inst. of Civil Engineers – Foren. Eng.*, **165**(1), 39–52.

Pacific Earthquake Engineering Research Center (2022). "PEER Ground Motion Database Web Application".

Prendergast, L. J., Hester, D., Gavin, K., & O'sullivan, J. J. (2013). "An investigation of the changes in the natural frequency of a pile affected by scour". *J. Soun. Vib.*, **332**(25), 6685-6702.

Raja, M. A., & Chiou, J. S. (2022). "Seismic analysis of extended piles in sand considering effect of scouring and effect of water as added mass". *In E3S Web of Conf., EDP Sciences*., **347**, 3017-3028

Reese, L. C., Wang, S. T., & Long, J. H. (1989). "Scour from cyclic lateral loading of piles". *In Offshore Technology Conference. Houston, Texas OnePetro*.

Test and Finite Element Analysis of Two-Story Steel Subassemblage Frames with Highly and Moderately Ductile Box Columns

Chung-Che Chou[1], Hou-Chun Xiong[2], Agam Kumar[2], Yun-Chuan Lai[2], Chia-Ming Uang[3]
1. Director General, National Center for Research on Earthquake Engineering, Taiwan
Professor, Department of Civil Engineering, National Taiwan University, Taiwan
2. Master Student, Department of Civil Engineering, National Taiwan University, Taiwan
3. Professor, Department of Structural Engineering, University of California, San Diego, USA
Email[1]: cechou@ntu.edu.tw

ABSTRACT

A two-story steel subassemblage frame with a built-up square box column and I-shaped steel beams was studied to evaluate the cyclic behavior of first-story columns. A constant axial compression load, representing 40% of the column axial yield load, was applied to columns before cyclic lateral test. A finite element analysis was then conducted on the two-story subassemblage frame specimens for a correlation study and on isolated column counterparts with a fixed-fixed boundary condition to investigate the boundary effect. The study showed that the moderately ductile box column performs as well as the highly ductile box column. The columns with a fixed-fixed boundary condition have higher flexural stiffness, strength, axial shortening, and severe local buckling at column ends than those with an actual boundary condition. The inflection point of the first-story column in the two-story subassemblage frame moves upward with increasing drifts so that most of the moment from beam plastic hinging is distributed to the bottom end of the second-story column rather than the top end of the first-story column. This leads to yielding, un-symmetric response, or sway to one direction of the columns, indicating that the strong column/weak beam requirement in AISC 341-16 (2016) cannot eliminate yielding at the bottom end of the second-story box column at large drifts.

Keywords: Built-up Box Column, Two-Story Subassemblage Frame, Cyclic Test, Finite Element Analysis

INTRODUCTION

In Asian countries, hollow structural section (HSS) or built-up box columns are common for the construction of Special Moment Frame (SMF), but wide-flange columns are widely used in North America. To simplify the test setup for column research, most of the laboratory testing was conducted on isolated columns with either a cantilever or fixed-fixed boundary condition. Recognizing that the top end of first-story columns would rotate while experiencing lateral drift, some isolated columns have been conducted. For example, Elkady and Lignos [1] and Chansuk et al. [2] tested isolated columns with a fixed column base and a predefined rotation at the top end, where the imposed rotation was synchronized with cyclic lateral drifts.

The top end of first-story columns in a moment frame is connected to beams and the column above through a panel zone. When flexural yielding occurs at the column base, the inflection point would move upward, decreasing the moment at the top end. Although the column in the second story is expected to remain elastic, flexural yielding as well as potential panel zone yielding would alter the rotational restraint at the top end of the first-story columns and the moment distribution in the first- and second-story columns. Since the effects mentioned above cannot be reproduced from isolated column tests, two subassemblies representing two-and-a-half story in a frame using steel built-up square box columns and steel beams at two floors were tested in this research (see Figure 1). Then, finite element (FM) analyses including a correlation

study were conducted to further investigate the effects of boundary conditions on the first-story column response. A parallel study with wide-flange columns is reported in Reference [3].

TEST PROGRAM

The overall dimensions of the half-scale subassemblage frames are shown in Figure 1. SM570MB steel with a nominal yield strength of 420 MPa was specified for the square built-up box columns, and SN490B steel with a nominal yield strength of 325 MPa was specified for the built-up, I-shaped beams. According to AISC 341-16 [4], the limiting width-to-thickness ratios, *b/t*, for the flanges of highly ductile (λ_{hd}) and moderately ductile (λ_{md}) built-up box sections are 12.9 and 23.5, respectively. The cross section of Specimen HBC-12-S was 190 mm×190 mm×13 mm with a *b/t* ratio of 12.6, thus meeting the highly ductile requirement. The column of Specimen HBC-16-S (230 mm×230 mm×13 mm) was classified as moderately ductile because the *b/t* ratio was 15.7. These two columns satisfy the most compactness requirement (=21.7) for welded built-up box columns in Taiwan [5]. The previous study [6] indicated that the highly-ductile compactness requirement in AISC 341-16 [4] may be too stringent for similar seismic response of the wide-flange and built-up box columns. Built-up I-shaped beams (256 mm×101 mm×6 mm×12 mm) with a Reduced Beam Section (RBS) moment connection were used for both specimens. The strong column-weak beam (SCWB) ratios are 1.2 and 1.8 for Specimens HBC-12-S and HBC-16-S under the $0.4P_y$ axial load, respectively, where P_y represents the actual yield strength of the column.

With the presence of an axial load P_c, the reduced plastic moment, M_y, in this study is computed as:

$$M_y = \alpha_y M_p \left(1 - \frac{P_c}{P_y}\right) \quad (1)$$

where M_p is the plastic moment based on the measured yield stress, and α_y (=1.31) is a coefficient determined from a plastic analysis at the section level. Values of M_y are 214 and 322 kN-m for Specimens HBC-12-S and HBC-16-S, respectively. The testing was conducted in a displacement-controlled mode by imposing δ_H through the horizontal actuator such that the measured first-story drift angle was close to that specified in AISC 341-16 [4] for testing SMF connections (see Figure 1). The inflection point of each beam on the third floor was simulated by connecting a vertical actuator at the free end of each beam; the measured vertical actuator forces were used to compute the beam shears and moments [3]. Two pin-ended vertical rigid links were used to maintain floor spacing. Forces measured by the load cell installed at the top end of each link were then used to determine the beam shears and moments in the second floor.

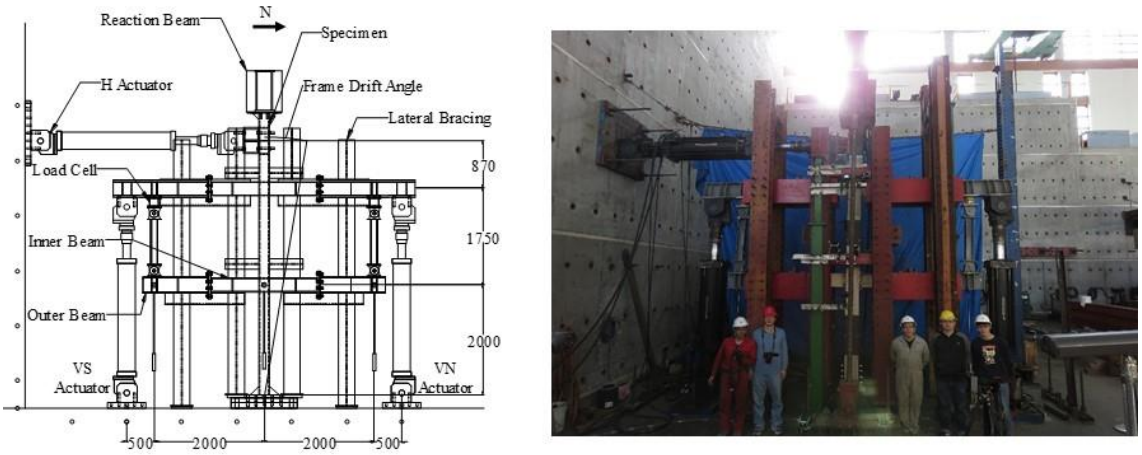

(a) Test Setup (b) HBC-16-S

Figure 1. Two-story subassemblage frame specimen

TEST RESULT

Specimen HBC-12-S

Figure 2(a) shows the response of the horizontal actuator force versus frame drift angle. The specimen started to show yielding in the beam flanges and the column base when the frame drift angle reached 0.0105 and 0.02 rad, respectively. Local buckling was observed in the beam webs and the column base at a frame drift angle of 0.035 rad, where the buckling amplitudes were about 1 to 2 mm. At a frame drift angle of 0.045 rad, significant local buckling was observed in the beam webs and minor local buckling was visible in the column webs [Figure 2(b)]. The specimen showed significant strength degradation during the first cycle at 0.055 rad drift [Figure 2(a) and (c)]. This was caused by the top flange fracture of the south beam at the third-floor level and lateral-torsional buckling of the north beam at the second-floor level. But fracture and lateral-torsional buckling of the beams did not affect the column to carry the axial load throughout the test.

Figure 3(a) and (b) show the response plots of the columns in the first and second stories. The moment at the bottom end was larger than that at the top end in each story, indicating that the inflection point was above the mid-height of the column. Figure 3(a) shows that local buckling at the column base did not decrease the column's flexural strength. Note that the moment at the bottom end of the second-story column significantly exceeded the reduced plastic moment, M_y, at a story drift angle of 0.02 rad [Figure 3(b)], which was not expected when the strong column-weak beam design (i.e., 1.2 for this specimen) was adopted in AISC 341-16 [4].

(a) Hysteretic Response (b) Column Buckling (0.045 rad) (c) Deformation (0.055 rad)

Figure 2 Response and observed performance of specimen HBC-12-S

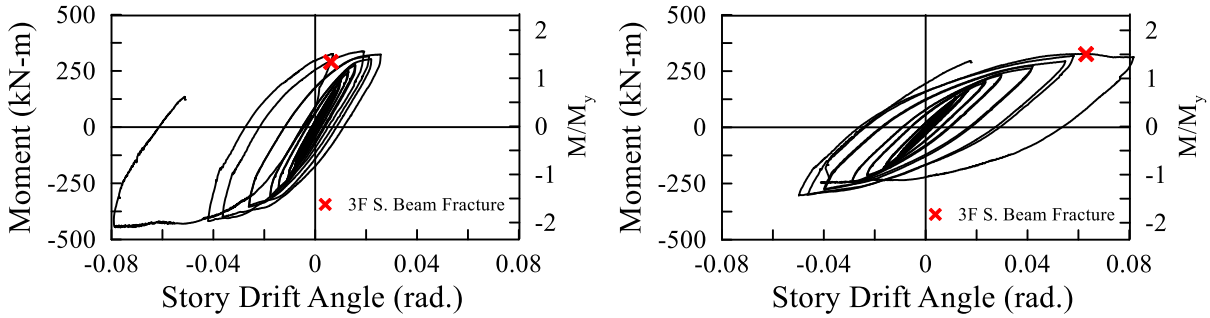

(a) Column Base ($M_{1F,CB}$) (b) Second-Story Column Bottom ($M_{2F,CB}$)

Figure 3 Hysteretic response at the column base and bottom end of the second-story column (HBC-12-S)

Specimen HBC-16-S

Specimen HBC-16-S behaved similarly as Specimen HBC-12-S up to a frame drift angle of 0.0105 rad. The column base showed yielding at 0.0145 rad drift, earlier than that observed in Specimen HBC-12-S. Minor local buckling was observed in the beam webs and the column base at a frame drift angle of 0.025 rad. The specimen developed its peak strength during the first cycle at a frame drift angle of 0.045 rad. It then showed a significant strength degradation during the first cycle to -0.045 rad drift due to the fracture of the south beam bottom flange at the third floor level. During the second cycle of the same frame drift angle, another fracture was observed at the bottom flange of the north beam at the third floor level. The magnitude of column flange buckling at the base was about 2 to 3 mm, similar to that observed in Specimen HBC-12-S.

Figure 4(a) shows that the column at the base did not exhibit strength degradation associated with minor local buckling. It was observed that the moment at the bottom end of the second-story column also exceeded the reduced plastic moment, M_y, at a story drift angle of 0.03 rad [Figure 4(b)]. The story drift angle when yielding at the bottom end of the second-story column occurred was delayed from 0.02 to 0.03 rad in Specimen HBC-16-S when compared to Specimen HBC-12-S. Note from Figures 3 and 4 that the second-story column reached larger drift angle than the first-story column.

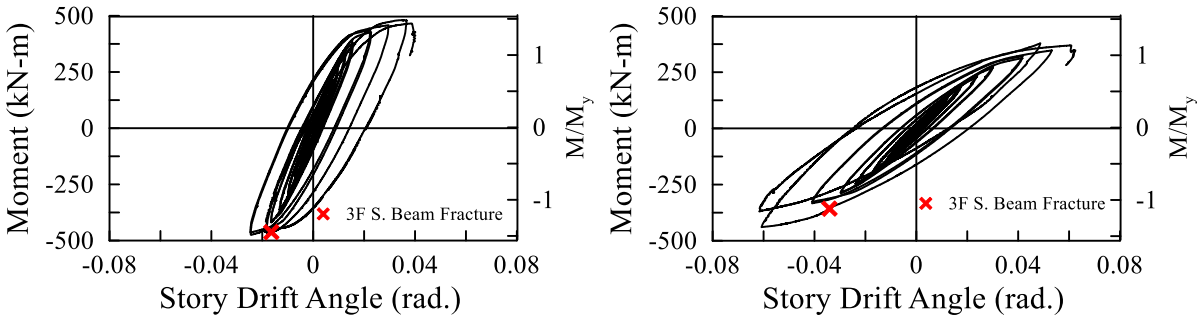

(a) Column Base ($M_{1F,CB}$) (b) Second-Story Column Bottom ($M_{2F,CB}$)

Figure 4 Hysteretic response at the column base and bottom end of the second-story column (HBC-16-S)

FINITE ELEMENT ANALYSIS

Finite element (FE) analyses was conducted by using ABAQUS [7] to further study the cyclic behavior of the two-story subassemblges, the boundary effect on the first-story column response, and the moment distribution in the first-story and second-story columns.

Subassemblage Frame Model

All members in the subassemblage frame specimens were modelled by using four-node S4R shell elements (Figure 5). A seed size of 60 mm and 50 mm was used for HBC-16-S and HBC-12-S columns, respectively; it was done so that both columns had four elements along their webs. Fine mesh was used for the beams near the column. Coupons, made of SN490B and SM570MB steels, were fabricated based on ASTM standard and tested to obtain material properties for modeling. Figure 5 shows the comparison of the hysteresis responses of Specimen HBC-12-S from both the test and analysis. Moment versus story drift angle response is plotted at the end of the first-story column. The finite element model reasonably predicts the test response, but cannot simulate the column response at 0.055 rad drift when the beam fractures, marked as a yellow solid circle.

Isolated Column versus Two-Story Subassemblage Column

To examine the effect of boundary conditions on the cyclic response of first-story columns, two isolated columns with a fixed boundary condition at both ends were modeled by using the computer program ABAQUS. Figure 6 shows that plastic hinges developed at both ends of the isolated column models; local buckling occurrs not only at the column base but also at the column top end. Figure 7 shows the hysteretic response at the column base of the first-story column. Both the elastic flexural stiffness and the maximum strength of isolated columns are higher than those of the columns with an actual boundary condition in the two-story subassemblage frame. No strength degradation is found from both the two-story subassemblage and isolated column models with a *b/t* ratio of 12 (i.e., a highly ductile box column). However, the first-story column in the subassemblage model shows un-symmetric hysteresis (i.e., particularly in the negative drift), which is not observed in the isolated column under a symmetric cyclic loading. For a column with a *b/t* ratio of 16 (i.e., a moderately ductile box column), the moment in the isolated column model decreases after 0.03 rad drift, which is not seen in the two-story subassemblage model counterpart.

CONCLUSIONS

Two-story steel subassemblage frames with a built-up box column and I-shaped beams at two floors were tested to evaluate the effect of boundary condition on the cyclic behavior of the first-story columns and the associated damage progress in the columns. The column sections satisfied the compactness limits of highly ductile and moderately ductile members, respectively, in AISC 341-16 [4]. Large local buckling in the beam webs initiated beam lateral-torsional buckling or fracture at 0.045 or 0.055 rad drifts, respectively, leading to a strength degradation of both subassemblages. Minor local buckling was observed at the base of both columns, but no strength degradation was observed in both column responses (Figures 3 and 4), indicating that Specimen HBC-16-S with a *b/t* ratio 15.7 (classified as moderately ductile per [4]) can perform as well as the highly ductile column in HBC-12-S. No yielding was observed at the top end of the first-story column, but yielding at the bottom end of the second-story column was observed at 0.025 and 0.035 rad drift for HBC-12-S and HBC-16-S, respectively. This indicated that the SCWB ratio that exceeds the required limit (i.e., =1 in AISC 341-16 [4]) cannot eliminate the plastic hinge formation at the bottom end of the second-story column under a high axial load (= $0.4P_y$) at large drifts. The behavior led to the un-symmetric reponse (or sway) of the first-story column and larger drift in the second-story column than in the first-story column. The un-symmetric response was not observed in the isolated column models or column specimens [8] under a symmetric cyclic loading.

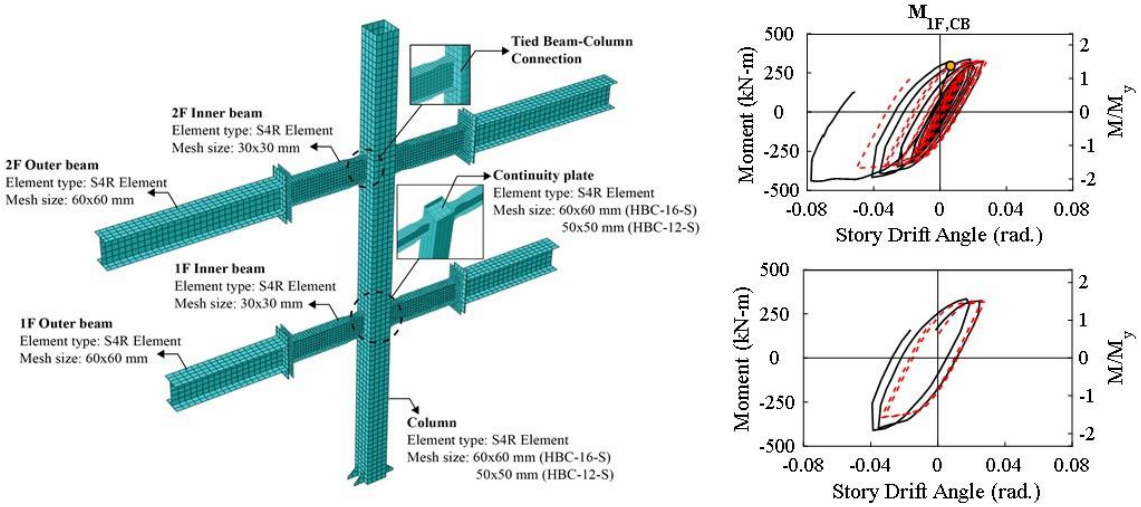

Figure 5 Finite element model and comparison of hysteretic response (HBC-12-S)

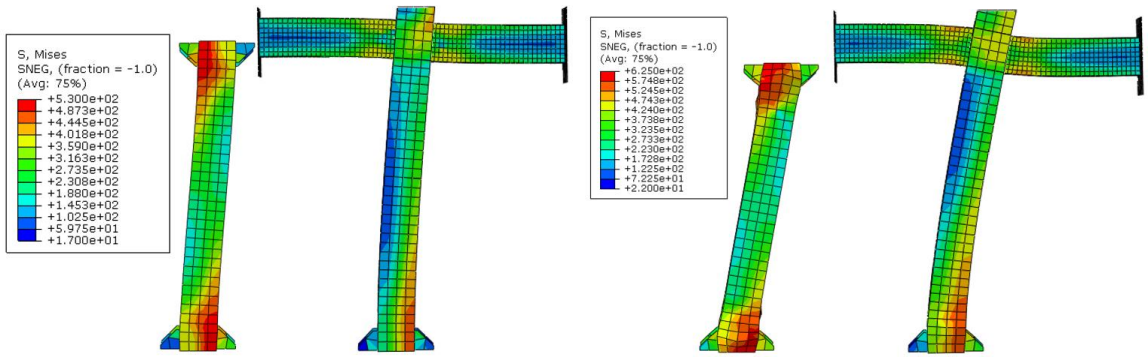

(a) 0.025 rad. (b) 0.055 rad.

Figure 6 Column deformed shapes in different boundary conditions (*b*/*t*=16)

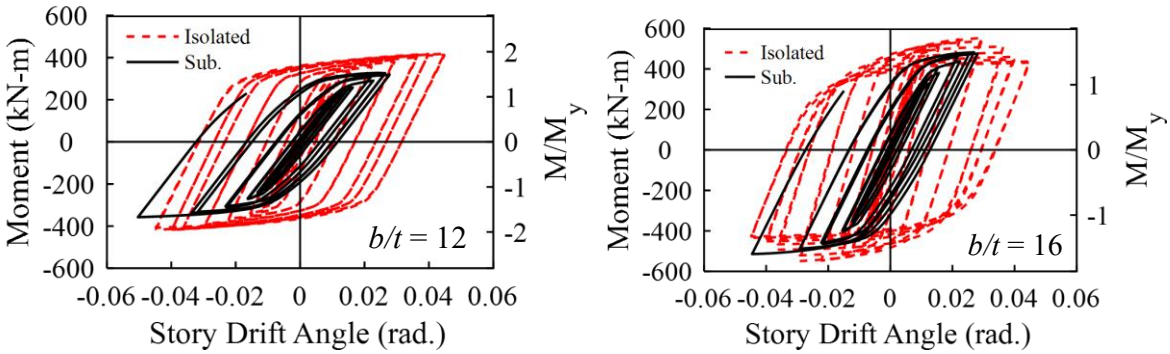

Figure 7 Columns response in subassemblage frame and fixed-fixed boundary conditions

ACKNOWLEDGEMENTS

The research project was supported by the Ministry of Science and Technology (108-2625-M-002-003), Taiwan. The technician support from NCREE is appreciated. The assistance by Tung Ho Steel Enterprise Corporation, Taiwan on the specimen fabrication is gratefully acknowledged.

REFERENCES

[1] Elkady, A., Lignos, D. G. (2018). Full-Scale Testing of Deep Wide-Flange Steel Columns under Multiaxis Cyclic Loading: Loading Sequence, Boundary Effects, and Lateral Stability Bracing Force Demands. *Journal of Structural Engineering*, 2018, 144(2): 04017189

[2] Chansuk, P., Ozkula, G., Uang, C. M., and Harris, J. L. (2021). *Seismic Behavior and Design of Deep, Slender Wide-Flange Structural Steel Beam-Columns*. Technical Note 2169, National Institute of Standards and Technology, Gaithersburg, MD.

[3] Chou, C. C., Lai, Y. C., Xiong, H. C., Lin, T. H., Uang, C. M., Mosqueda G., El-Tawil, S., McCormick, J. P. (2022). Seismic Response of I-Shaped Steel Columns in Two-Story Subassemblage Frames, *12th National Conference in Earthquake Engineering*, Salt Lake City, USA.

[4] AISC Committee. (2016). *Seismic Provisions for Structural Steel Buildings*, *ANSI/AISC 341–16*. American Institute of Steel Construction Inc., Chicago, IL.

[5] Taiwan Code. (2010). *Design and Technique Specifications of Steel Structures for Buildings*. Taiwan: Construction and Planning Agency, Ministry of the Interior.

[6] Lin, T. H., Chou, C. C. (2022). High-Strength Steel Deep H-Shaped and Box Columns under Proposed Near-Fault and Post-Earthquake Loadings. *Thin-Walled Structures*, 172, 108892.

[7] ABAQUS/CAE User's Guide 6.13. 2016.

[8] Chou, C. C., Chen, G. W. (2020). Lateral Cyclic Testing and Backbone Curve Development of High-Strength Steel Built-Up Box Columns Under Axial Compression. *Engineering Structures*, 223, 111147.

Analysis and Test Plan for a Three-Story Steel BRBF with a Sliding Slab to Reduce Seismic Lateral Force in Shake Table Tests

Chung-Che Chou[1], Alvaro Córdova[2], Huang-Zuo Lin[3], Jian-Ming Chen[3], Yen-Hsun Chou[4], Shu-Hsien Chao[5], Shih-Ho Chao[6], Georgios Tsampras[7], Chia-Ming Uang[8], Hsin-Yang Chung[9], Hsuan-Teh Hu[10], Chin-Hsiung Loh[11]

1. Director General, National Center for Research on Earthquake Engineering, Taipei, Taiwan Professor, National Taiwan University, Taipei, Taiwan
2. Ph.D. student, National Taiwan University, Taipei, Taiwan
3. Master student, National Taiwan University, Taipei, Taiwan
4. Master student, National Cheng Kung University, Tainan, Taiwan
5. Research Fellow, National Center for Research on Earthquake Engineering, Taipei, Taiwan
6. Professor, University of Texas, Arlington, USA
7. Assistant Professor, University of California, San Diego, USA
8. Professor, University of California, San Diego, USA
9. Associate Professor, National Cheng Kung University, Tainan, Taiwan
10. Professor, National Cheng Kung University, Tainan, Taiwan
11. Adjunct Professor, National Taiwan University, Taipei, Taiwan

Email: cechou@ntu.edu.tw

ABSTRACT

A new system for reducing the seismic force of traditional steel buildings is investigated through a collaboration work between the US and Taiwan. It involves a set of horizontal energy dissipating devices, working with the traditional Lateral Force Resisting System to speed up the on-site construction and enhance the seismic performance of steel buildings. This is achieved by allowing the slab to slide with respect to the steel frame, activating a horizontal energy dissipation device (i.e., horizontal buckling-restrained brace, HBRB) connected to the slab and beam to provide resistance. A design procedure based on ASCE/SEI 7-16 (2016) was validated through nonlinear time history analyses, conducted on a three-story steel Buckling-Restrained Braced Frame (BRBF) with different sets of horizontal devices. The analysis showed that by using this design procedure, the deformation of the horizontal device could limit to an axial strain of 4.5% during a strongest near-fault earthquake motion, and the peak frame roof drift could be about 1%. A full-scale, three-story steel frame with a sliding slab linked to a HBRB at each floor will be tested by using a shake table at NCREE to validate the proposed design procedure.

Keywords: Horizontal buckling-restrained brace, sliding slab, Near-fault motion, Shake table test, Time history analysis.

INTRODUCTION

A new system is investigated in this work by introducing a horizontal energy dissipation device between the slab and beams in the Lateral Force Resisting System (LFRS); no shear studs are used between the steel beam and slab as in the conventional steel frame system. The slab slides with respect to the beam, allowing energy dissipation devices to provide horizontal resistance (called “New System” in this work) in addition

to the conventional moment-resisting system that accounts on the ductility of vertical frame members. The new system aims to decrease forces and drifts developed in the LFRS, and total accelerations developed in the floors. Among a variety of ductile devices, a sandwich buckling-restrained brace (SBRB) that was verified to provide stable hysteretic response and deformation capacity (Chou and Chen 2010, Chou et al. 2012, 2016) will be used between the slab and beams in this new steel frame. Currently, there are no guidelines to size these horizontal energy dissipating members for steel buildings with slabs that are allowed to slide relative to a steel frame. Tsampras et al. (2022) proposed a step-by-step method for the design of connections that limit the forces transferred from conventional gravity load resisting systems to LFRS with flexural yielding base mechanism (e.g. structural walls) or rocking base mechanism (e.g., steel self-centering concentrically braced frames or rocking post-tensioned structural walls in Tsampras 2016, Tsampras et al., 2016, Zhang et al., 2018, Tsampras et al. 2022). This conference paper proposes a procedure to calculate initial design forces for the Horizontal BRBs (HBRB) that connect the sliding slab with the LFRS in a three-story steel buckling-restrained braced frame (BRBF) based on ASCE/SEI 7-16 section 12.10.1 (2016). The building was modeled as a 2D frame using nonlinear time history analyses (NLTH) in the PISA3D computer program. A full-scale, three-story steel frame with a sliding slab connected to HBRBs at each floor will be tested by using a shake table at Tainan Lab, NCREE to validate the proposed design procedure in November 2022.

THREE-STORY STEEL PROTOTYPE FRAME

Fig. 1 shows a prototype, which is a steel dual system composed of a Special Moment Frame (SMF, left bay) and a BRBF (right bay). All columns are steel built-up box columns that satisfy the moderately ductile member requirement in AISC 341-16 (2016); similar columns, tested by Chou and Chen (2020) and Chou et al. (2022), showed good cyclic performance at 4% drift. All three HBRBs are sandwiched buckling-restrained braces, designed based on a design procedure in Chou and Chen (2010). The HBRBs were modeled using a truss element and the steel core properties were based on kinematic hardening material parameters in Chou et al. (2012). All masses were lumped at one end of the HBRBs for inelastic time history analysis of the frame, and the damping ratio was 2%. In Fig. 1, a symbol Δ_{Hx} is the HBRB displacement at floor x; Δ_{Fx} is the frame displacement at floor x, and Δ_{Dx} is the diaphragm displacement at floor x.

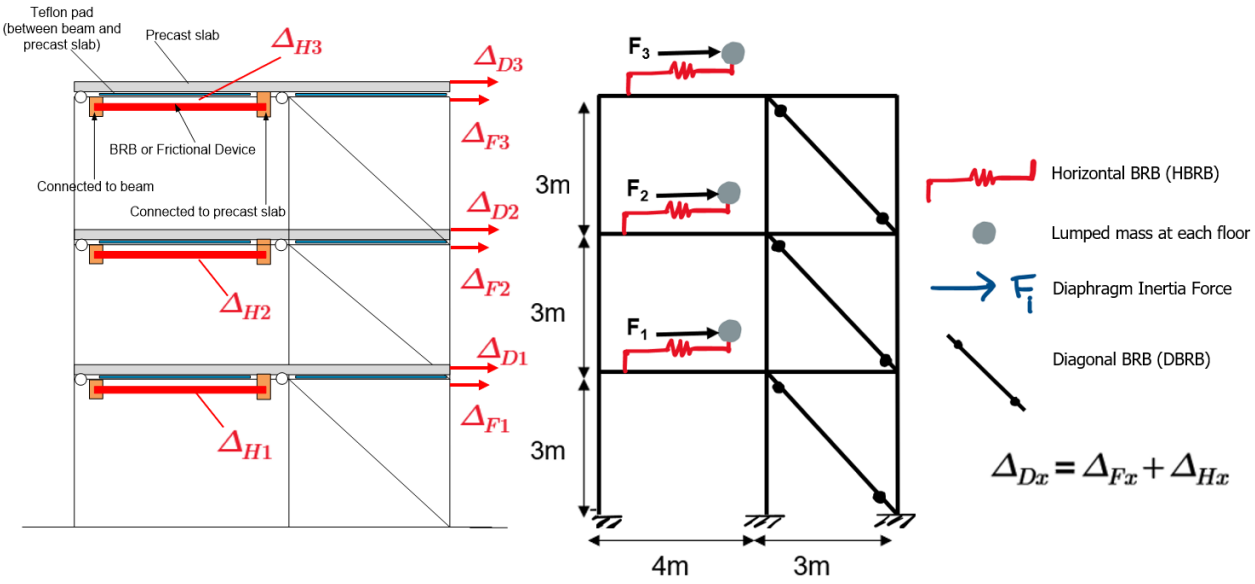

(a) Original building system (b) Structural model

Figure 1. Three-story prototype with BRBF, SMF and sliding slabs.

Proposed Design Procedure

The section 12.10.1 of ASCE/SEI 7-16 (2016) has a procedure to compute diaphragm design forces for buildings. This force level represents the absolute maximum floor acceleration during a given earthquake, thus representing an acceleration envelope. For this procedure, it is first required to obtain the base shear from the Equivalent Lateral Force (ELF) procedure, and then, given the floor masse w_x, and height h_x, to compute floor force F_x [Eq. (1)]. A parameter, k, accounts for higher mode contribution in upper floors (Lopez and Cruz 1996). Eq. (2) is used to determine the diaphragm design forces, where the numerator is F_x in Eq. (1). In addition, there is a lower bound, $0.2S_{DS}I_e w_{px}$, and an upper bound, $0.4S_{DS}I_e w_{px}$, which represent 0.5 and 1.0 times the Peak Ground Acceleration (PGA), respectively (where S_{DS} is the design spectral acceleration for short periods and I_e is the importance factor). The code recommends that floor acceleration should exceed at least 0.5PGA. These limits are independent of the system ductility R and Ω_o because the diaphragm detailing usually doesn't depend on the selected structural system. Eq. (2) provides a larger set of forces than Eq. (1), more significant in lower floors resulting in a steeper slope of the floor force distribution. For example, for same floor masses, w_x, and heights, h_x, in all three floors, Eq. (1) results in force ratios of 1, 2, and 3, and Eq. (2) results in force ratios of 1, 1.25, and 1.5. Although this design method still considers the vertical ductility of the traditional system (i.e., the horizontal ductility of the new system is not considered), it was shown to provide an acceptable initial design for the horizontal devices.

While F_{px} forces at each floor are obtained from Eq. (2), the HBRB core area at each floor can be computed based on LRFD procedure. For this model, the calculated parameters are as follows: $w_x = w_{px} =$ 327 kN, $h_x = 3$ m (for all floors), $k = 1.0$, $C_s = 0.242$ g for Tainan and the base shear is $V = 237.4$ kN. Forces from ELF procedure are: $F_1 = 39.6$ kN, $F_2 = 79.1$ kN and $F_3 = 118.7$ kN. Diaphragm forces for the DBE level are: $F_{p1} = 79.1$ kN, $F_{p2} = 98.9$ kN, $F_{p3} = 110.88$ kN. Diaphragm forces for the maximum-considered earthquake (MCE) level are: $F_{p1} = 118.65$ kN, $F_{p2} = 148.35$ kN, $F_{p3} = 166.32$ kN. The HBRB core can be determined based on $\phi P_n > P_u$, where $P_n = A_{sc}F_y$, A_{sc} and F_y are the HBRB steel core area and the yield strength, respectively, and $\phi = 1.0$. Since the diaphragm force, F_{px}, is transferred directly to the HBRB, replacing P_u in the later equation by F_{px} at the MCE level. The resulting core areas are 163 mm^2, 204 mm^2 and 228 mm^2 for 2nd, 3rd and roof floor, respectively, as listed in Table 2. Two HBRBs per floor are considered to avoid force eccentricities.

$$F_x = \frac{w_x \cdot h_x^{\,k}}{\sum_{i=1}^{n}\left(w_i \cdot h_i^{\,k}\right)} \cdot V \quad (1)$$

$$F_{px} = \frac{\sum_{i=x}^{n} F_i}{\sum_{i=x}^{n} w_i} w_{px} \quad (2)$$

ANALYSIS AND RESULTS

Fig. 2 shows eleven near-fault motions and eleven far-field motions, scaled to match the Design Based Earthquake (DBE) for the three-story prototype frame based on Lin and Chou (2022). The two green motions NF6 and FF4 are the most representative to the system, as shown in Fig. 2(a) and (b). The NF6 motion was used as an example for the illustration of the prototype under the near-fault earthquake motion.

-NF1 Chi-Chi-CHY101-E
-NF2 Chi-Chi-TCU029-E
-NF3 Chi-Chi-TCU029-W
-NF4 Chi-Chi-TCU031-E
-NF5 Chi-Chi TCU053-E
-NF6 Chi-Chi-TCU068-EW
-NF7 El Centro-#6-230
-NF8 Landers LCN-260
-NF9 Northridge-01 Sta-360
-NF10 Kobe-KJMA-000
-NF11 Christchurch-PRP-W

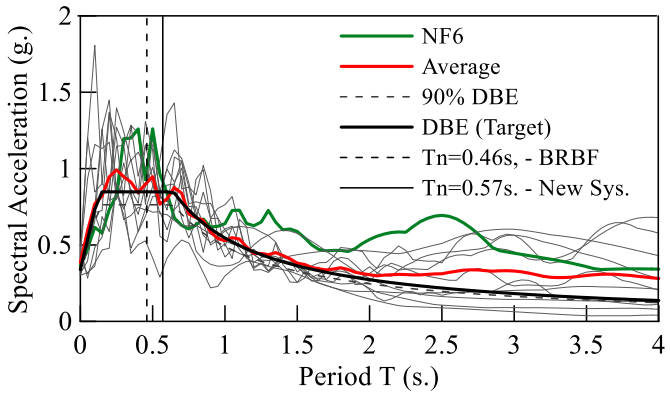

(a) Eleven near-fault motions

-FF1 Chi-Chi - TCU095NS
-FF2 Chi-Chi - CHY015NS
-FF3 Chi-Chi - CHY015EW
-FF4 Jiasian - CHY099NS
-FF5 Wutai - CHY099NS
-FF6 Meinong - CHY133NS
-FF7 Whittire Narrows - ALT360
-FF8 Northridge - CNP196
-FF9 Landers - IND090
-FF10 Kobe - ABN090
-FF11 Christchurch - RHSCS04W

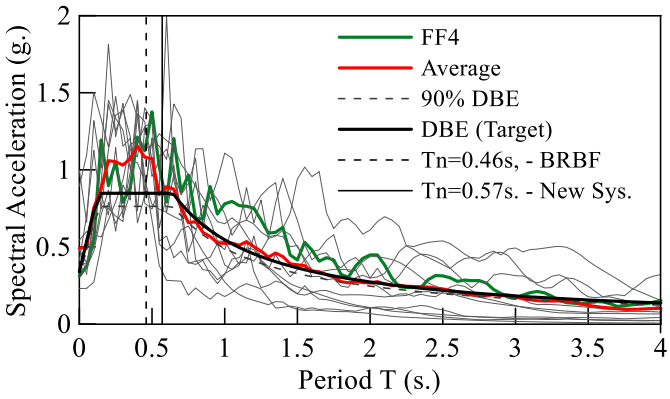

(b) Eleven far-field motions

Figure 2. Earthquake motions for time history analysis of the frame.

The two controlling parameters for all analyses are that (1) the HBRBs shouldn't exceed an axial strain of 4.5% and (2) HBRB strain along the building height should be uniformly distributed. An effort was made to optimize the design based on these two constraints. This was achieved by trying different sets of HBRBs, called "Cases" as listed in Table 1. Peak strains of HBRB at each floor in five cases are plotted in Fig. 3. The best case (i.e., labeled by Case 3* in this work), based on these two controlling parameters, was very close to results based on Eq. (2) at the MCE level as design forces (5% difference). Fig. 3 shows a summary of the results where the horizontal axis represents cases with different sets of HBRBs (five cases are shown). HBRBs in case 1 were designed based on the lowest forces, thus having the smallest BRB cores; HBRBs in case 5 were designed based on the largest forces, thus having the largest BRB cores. The HBRBs exceeded the deformation capacity in cases 1 and 2, and the HBRBs in cases 4 and 5 did not fully develop the maximum deformation capacity. Case 3* shown below is the result of using Eq. (2) for design; the HBRB showed not only a peak strain of 4.3% at the roof (very close to the deformation target of HBRB), but also a more uniform strain distribution along the building height compared to other cases (see Tables 1 and 2). Table 2 shows the maximum strains of HBRBs and diagonal BRBs (DBRB) at each floor; Fig. 3 also shows the maximum force of DBRBs (as shown by $P/P_y > 1$), which increases with the case number since the force demand is larger as the HBRB core area increases (higher P_y of HBRB).

Table 1: Core yield forces (P_y), areas (A_{sc}) and peak strains for five HBRB cases using NF6 motion.

	CASE 1			CASE 2			CASE 3*			CASE 4			CASE 5		
Floor	HBRB Py (kN)	HBRB Asc (mm^2)	HBRB Max. Strain (%)	HBRB Py (kN)	HBRB Asc (mm^2)	HBRB Max. Strain (%)	HBRB Py (kN)	HBRB Asc (mm^2)	HBRB Max. Strain (%)	HBRB Py (kN)	HBRB Asc (mm^2)	HBRB Max. Strain (%)	HBRB Py (kN)	HBRB Asc (mm^2)	HBRB Max. Strain (%)
Roof	60	165	7.5%	40	110	11.5%	83	228	**4.3%**	91	250	2.8%	102	280	1.3%
3rd	40	110	10.5%	33	90	13.2%	74	204	1.3%	82	225	0.6%	91	250	0.2%
2nd	22	60	20.6%	27	75	16.2%	59	163	2.3%	66	180	0.7%	73	200	0.4%

(Note: Case 3* corresponds to results using ASCE/SEI 7-16 method at MCE level.)

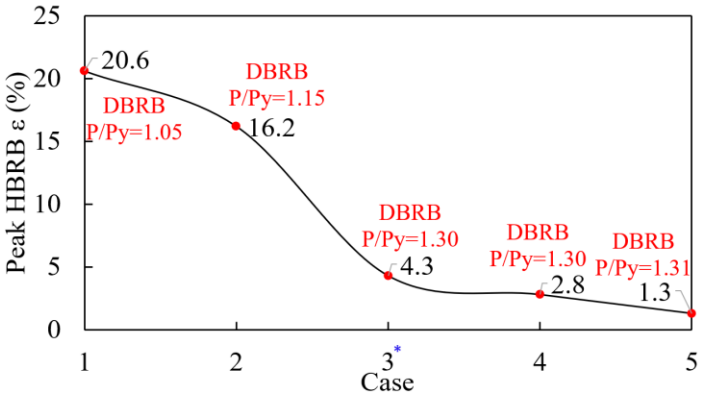

Figure 3. Peak HBRB strains vs. different cases of HBRB for NF6 motion.

Table 2. HBRB and DBRB properties and main results for all three floors (case 3* for NF6 motion).

Floor	HBRB Py (kN)	HBRB Asc (mm^2)	HBRB Max. Strain (%)	HBRB Max. P/Py	DBRB Max. Strain (%)	DBRB Max. P/Py
Roof	83	228	4.3%	1.34	0.44%	1.20
3rd	74	204	1.3%	1.23	0.75%	1.27
2nd	59	163	2.3%	1.31	0.94%	1.29

Fig. 4(a) shows the roof displacement response of both the traditional frame and new system (case 3*) under the strongest motion (NF6, Chi-Chi-TCU068). The maximum roof drift for the traditional and new system is 1.95% and 1.14%, respectively, and the corresponding maximum residual drift is 0.71% and 0.15%. Fig. 4(b) shows a similar plot for the frame under FF4 motion, where the peak roof drift for the traditional and new system is 1.10% and 0.85%, respectively, and the corresponding maximum residual drift is 0.19% and 0.05%. Fig. 5(a) and (b) shows the force-displacement response for HBRBs at all floors, showing larger energy dissipation at the roof. Fig. 6(a) and (b) shows the interstory displacement response of the slab at each floor, which can move with respect to the beam. For NF6 motion, the peak drifts are 3.5%, 1.2%, 3.7% and the residual drifts are 1.9%, 0.6% and 2.7% for the 2nd, 3rd and roof floors respectively. For FF4 motion, the peak drifts are 1.13%, 0.91%, 1.80% and the residual drifts are 0.09%, 0.11% and 0.39% for the 2nd, 3rd and roof floor respectively. Average peak interstory frame and slab drifts are plotted in Fig. 7 for the new system (case 3*) under 11 far-field and 11 near-fault motions. Traditional frame drifts are also plotted for comparison. In this figure, frame drifts are reduced by using the new system, thus reducing the frame ductility demand. However, the slab drift in the new system increases compared to the traditional frame system, indicating a possible tradeoff behavior (i.e., frame drift decreases while slab drift increases by allowing their relative movement). This observation is also shown in Fig. 6, where slab drifts, both peak and residual, are significant, particularly for NF6 motion.

Fig. 8 shows the force-displacement response of the first-story DBRB in both the traditional and new system under NF6 and FF4 motions. The new system shows a considerable reduction in the brace ductility demand, particularly for NF6 motion where the peak DBRB strain is reduced from 1.97 to 0.94% compared to the traditional frame system.

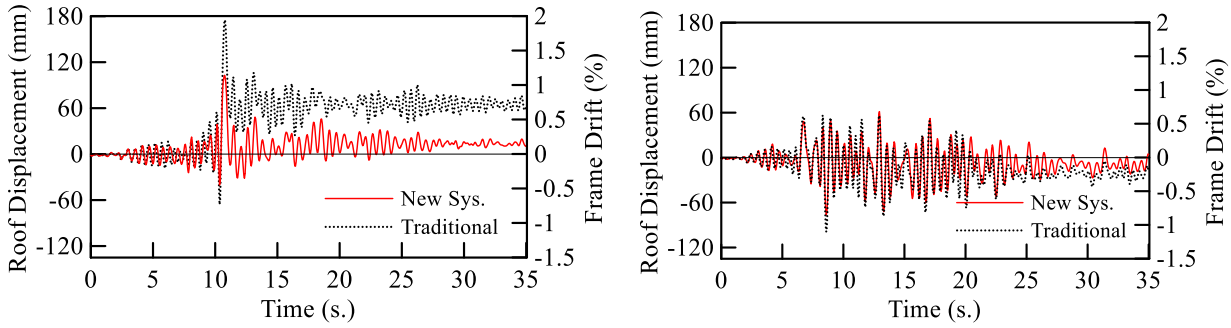

(a) NF6 motion. (b) FF4 motion.

Figure 4. Steel frame displacement response at roof level for the traditional and new system (case 3*)

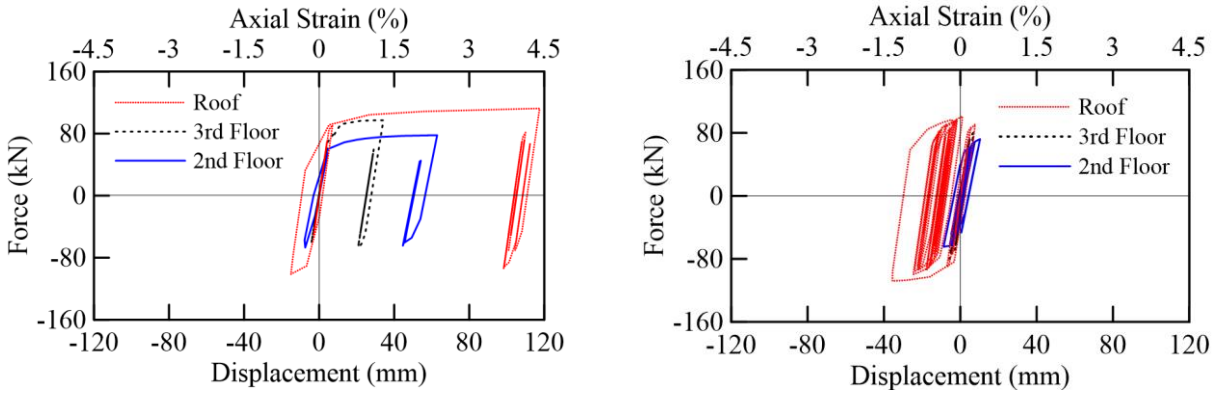

(a) NF6 motion. (b) FF4 motion

Figure 5. HBRB force vs. displacement response at all floors for NF6 and FF4 motions (case 3*)

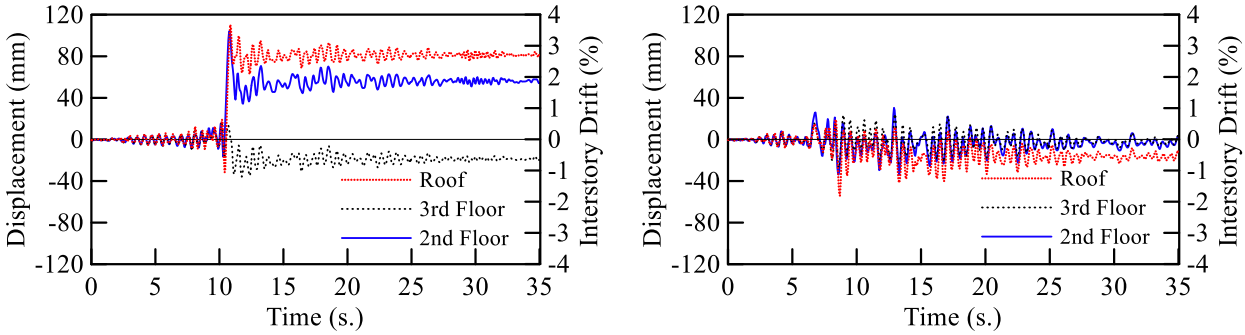

(a) NF6 motion. (b) FF4 motion.

Figure 6. Interstory slab displacement response at all floors for NF6 and FF4 motions (case 3*)

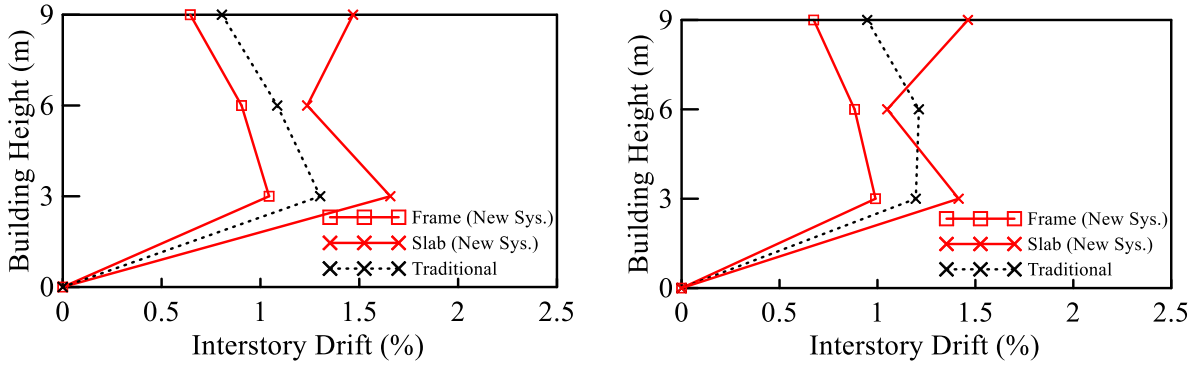

(a) Near-fault motions. (b) Far-field motions.

Figure 7. Average maximum drifts along building height for the traditional and new system (case 3*).

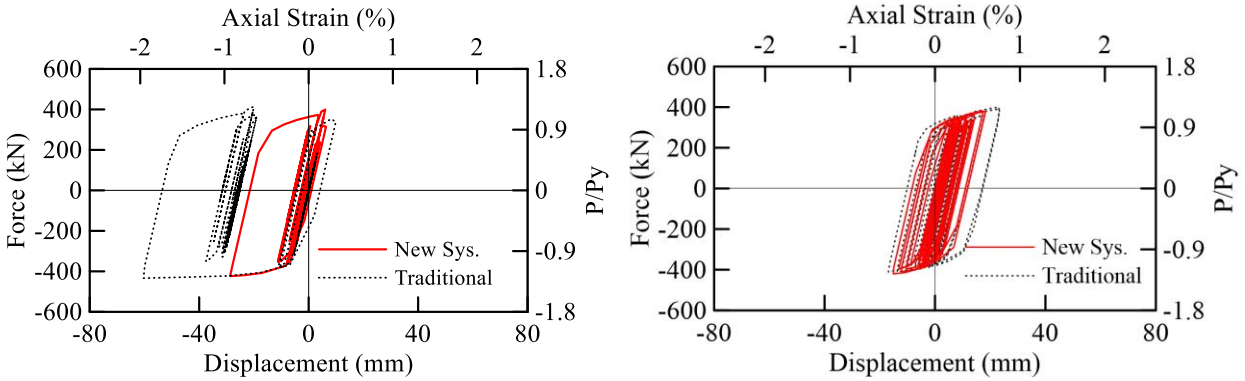

(a) NF6 motion. (b) FF4 motion.

Figure 8. First floor DBRB response for both the traditional and new system (case 3*)

SHAKE TABLE TESTS FOR A THREE-STORY FRAME

A full-scale, three-story prototype frame with a sliding concrete slab was designed and planned for shake table tests in Tainan laboratory. Fig. 9(a) shows the three-dimensional view of the specimen, Fig. 9(b) is the elevation view of B line and Fig. 9(c) is the elevation view of Lines 1 and 3. The B Line frame represents the Lateral Force Resisting System (LFRS), which is composed of a Special Moment Frame (SMF) on the left-hand side bay and a BRBF on the right-hand side bay. The Gravity Load Resisting System (GLRS) is located in the perimeter of the 3D frame and designed with pin connections for members. After adding concrete blocks, there are around 330 kN at 2FL and 3FL, and 350 kN at the roof. The total weight of the specimen is around 1000 kN. The P/P_y from columns SC1 to SC3 are 5.72%, 11.92% and 3.34% respectively.

Table 3 shows the section of each member. The width-to-thickness ratios (b/t) of box columns are 20.5 and 21.1, respectively, which are between the highly ductile member (b/t = 15.4) and moderately ductile (b/t = 28) member requirement in AISC 341-16 (2016). These similar box columns showed good response up to 4% drift in static cyclic loading based on previous isolated column or subassemblage tests (Chou and Chen 2020, Chou et al. 2022).

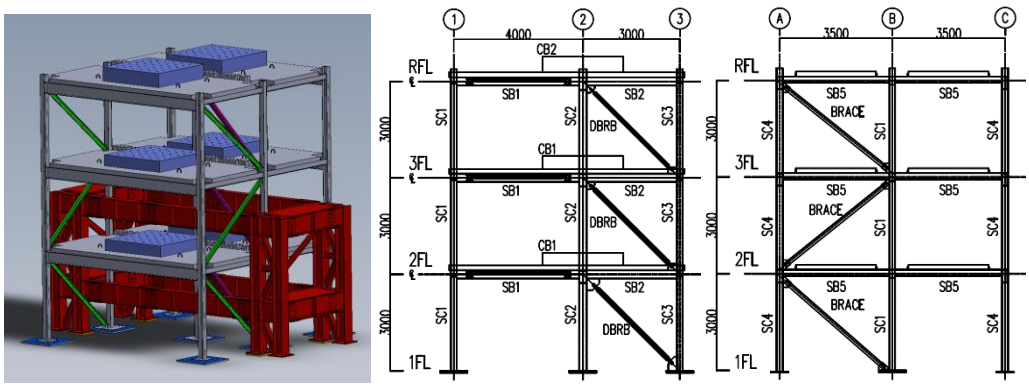

(a) 3D view (b) Line B (c) Lines 1 and 3

Figure 9. Full scale three-story steel frame specimen for shake table test (unit: mm)

Two test phases are planned to be conducted on the three-story dual frame system. In phase one, the frame with a precast sliding slab at each floor will be tested by using one of the motion in Fig. 2. Teflon pads will be placed between the slab and steel beams to reduce the interface friction force. These slabs connected to the steel beams in the LFRS through HBRBs are allowed to slide with respect to the frame in horizontal earthquake loading. Since the steel frame is expected to deform less than 1% drift (Fig. 7), the same frame will be tested in the second phase to investigate the seismic behavior of moderately ductile columns in the traditional dual system. To investigate the seismic behavior of the box columns in the dual system, the HBRB at each floor will be replaced by a structural T member designed to simulate a rigid connection between the slab and beams.

To minimize the out of plane movement of the sliding slabs during the test, vertical steel pads are positioned on the top of the beam flange on the periphery of the slab (see Fig. 10). A wide flange member as shown in Fig. 11(a) is fixed to the slab to provide lateral support to the steel beam at each floor in SMF and BRBF bays. Moreover, a slab at each floor is composed of two slabs bolted together as a unit [Fig. 11(b)].

Table 3. Member Section in Three-Story Frame

Type	Label	Section (mm)
Column	SC1, SC3	BOX 185x185x8
	SC2	BOX 225x225x10
	SC4	H 200x200x8x12
Beam	SB1, SB2	H 257x102x6x9
	SB3, SB4	H 400x200x8x13
	SB5	H 200x100x5.5x8
Type	Story	Section (mm)
BRACE	1F, 2F, 3F	DL 130x130x12
Structural T	1F, 2F, 3F	CT 145x200x8x13
Type	Place	Core area (mm^2)
DBRB	1F, 2F	900
	3F	400
HBRB	1F	162
	2F	204
	3F	228

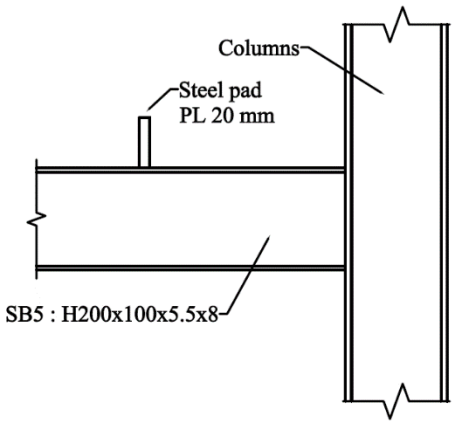

Figure 10. Steel pads to avoid rotation and lateral displacement of slab

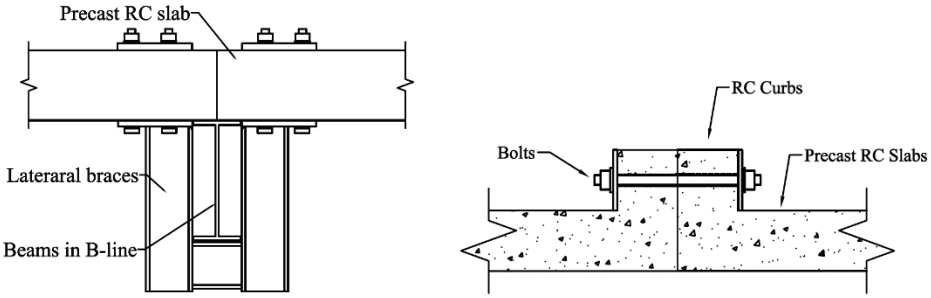

(a) Lateral bracing setup (b) Bolted connection between precast slabs

Figure 11. Beam lateral braces and slab connection

CONCLUSIONS

This paper presents preliminary time analysis results for a three-story steel dual frame with a sliding slab at each floor, designed to reduce the seismic lateral force demand to the earthquake-resisting frame during earthquake motion. The HBRBs that are used to connect the sliding slab and the Lateral Force Resisting System (LFRS) were detemined based on the diaphragm design method in ASCE/SEI 7-16, 12.10.1 (2016), considering the maximum considered earthquake (MCE) force level. The design procedure limited the axial strain of HBRBs below 4.5% under 22 motions, scaled to the MCE level. The new system showed a considerable reduction in terms of the maximum frame drifts; however, its slab interstory drift was larger than that in the traditional dual frame. A shake table test will be conducted on the full-scale, three-story frame in Novemebr 2022 to validate the design procedure and the seimic response with either a sliding slab or rigidly-connected slab in earthquake motions.

ACKNOWLEDGEMENTS

This work is funded by the National Science and Technology Council under the project number MOST 111-2625-M-002-006, Taiwan and the 2022 Innovative Project of National Applied Research Laboratories.

REFERENCES

ASCE/SEI 7-16. Minimum design loads and associated criteria for buildings and other structures. American Society of Civil Engineers. 2016

Chopra, A. K., Newmark, N. M. (1980). Analysis, Chapter 2 in Design of Earthquake Resistant Structures. *ed. E. Rosenblueth, Pentech Press Ltd., London*.

Chou, C. C., Lai, Y. C., Xiong, H. C., Lin, T. H., Uang, C. M., Mosqueda G., Ozkula, G., El-Tawil, S., McCormick, J.P. (2022). "Effect of Boundary Condition on the Cyclic Response of I-Shaped Steel Columns: Two-Story Subassemblage versus Isolated Column Tests," *Earthquake Engineering and Structural Dynamics*, DOI: 10.1002/eqe.3730.

Chou, C. C., Xiong H. C., Kumar A., Lai Y. C., Uang, C. M. (2022). "Test and Finite Element Analysis of Two-Story Steel Subassemblage Frames with Highly and Moderately Ductile Box Columns", *8th Asia Conference on Earthquake Engineering*, Taipei, Taiwan.

Chou, C. C., Chen, G. W. (2020). "Lateral Cyclic Testing and Backbone Curve Development of High-Strength Steel Built-Up Box Columns Under Axial Compression. *Engineering Structures* 223, 111147

Chou, C. C., Chung, P. T., Cheng, Y. T. (2016). "Experimental Evaluation of Large-Scale Dual-Core Self-Centering Braces and Sandwiched Buckling-Restrained Braces." *Engineering Structures*, 116, 12-25.

Chou, C. C., Liu, J. H., Pham D. H. (2012). "Steel Buckling-Restrained Braced Frames with Single and Dual Corner Gusset Connections: Seismic Tests and Analyses." *Earthquake Engineering and Structural Dynamics,* 7(41): 1137-1156.

Chou, C. C., Chen, S. Y. (2010). "Subassemblage Tests and Finite Element Analyses of Sandwiched Buckling-restrained Braces." *Engineering Structures*, 32, 2108-2121.

Ghosh, S. K. (2016). Alternative diaphragm seismic design force level of ASCE 7-16. *Structure magazine*, 18-22.

Lin, T. H., Chou, C. C. (2022). "High-Strength Steel Deep H-Shaped and Box Columns under Proposed Near-Fault and Post-Earthquake Loadings." *Thin-Walled Structures*, 172, 108892

Lopez, O. A., Cruz, M. (1996). Number of modes for the seismic design of buildings. *Earthquake engineering & structural dynamics*, *25*(8), 837-855.

Tsampras, Georgios. "Force-Limiting Floor Diaphragm Connection for Earthquake-Resistant Buildings." PhD, Lehigh University, 2016. https://preserve.lehigh.edu/etd/2851.

Tsampras, G., Sause, R., Zhang, D., Fleischman, R. B., Restrepo, J. I., Mar, D., & Maffei, J. (2016). Development of deformable connection for earthquake-resistant buildings to reduce floor accelerations and force responses. *Earthquake Engineering & Structural Dynamics*, *45*(9), 1473-1494.

Tsampras, G., Sause, R. (2022). Force-Based Design Method for Force-Limiting Deformable Connections in Earthquake-Resistant Buildings. *Journal of Structural Engineering*, *148*(10), 04022150.

Tsampras G., Sause R., Fleischman R. B., Restrepo J. I., Nema A., Zhang Z., Practical force-limiting deformable connections in buildings with rocking base mechanism and limited higher-mode responses. *Proceedings of the 12th National Conference in Earthquake Engineering*, Earthquake Engineering Research Institute, Salt Lake City, UT. 2022.

Zhang, Z., Fleischman, R. B., Restrepo, J. I., Guerrini, G., Nema, A., Zhang, D., Ulina, S., Tsampras, G., Sause, R., (2018). Shake-table test performance of an inertial force-limiting floor anchorage system. *Earthquake Engineering & Structural Dynamics*, *47*(10), 1987-2011.

(SS5) Structural assessment and health monitoring for bridge and civil structures

EXPERIMENTAL STUDY ON THE EVALUATION METHOD FOR BRIDGE STRUCTURES BY USING LOAD TESTS

Chun-Chung Chen[1], Bo-Han Lee[2], Chi-Rung Jiang[3] and Sheng-Yuan Siao[4]

1. Research Fellow, National Center for Research on Earthquake Engineering, Taipei, Taiwan, R.O.C.
2. Associate Researcher, National Center for Research on Earthquake Engineering, Taipei, Taiwan, R.O.C.
3. Associate Technologist, National Center for Research on Earthquake Engineering, Taipei, Taiwan, R.O.C.
4. Associate Technologist, National Center for Research on Earthquake Engineering, Taipei, Taiwan, R.O.C.

Email: jingochen@narlabs.org.tw, bhlee@narlabs.org.tw, 0906164@narlabs.org.tw, shengyuan@narlabs.org.tw

ABSTRACT

For bridges that are old or have unique structural systems, the field load test can effectively and accurately assess and verify the safety of the bridge structure. This paper describes the experimental studies of the evaluation methods for bridges using loading tests. The study conducted a series of flatcar loading tests to evaluate the structural safety of bridges. Improving bridge evaluation technologies can effectively assist bridge authorities in implementing bridge maintenance and management operations and extend the service life of bridges to perform service functions. With the development trend of artificial intelligence analysis technology and the demand for practical applications, transforming a large amount of bridge inspection and monitoring database data into information that can assist in evaluation processes is needed. Thus, this study applied data science methods to deal with the experimental data. Intelligent information promotes effective bridge disaster prevention decision-making and management and maintenance actions to ensure safety during the life cycle of bridge services, improve bridge disaster prevention technology and implement application business.

Keywords: bridge, structural evaluation, load test

INTRODUCTION

The bridge vehicle load test is a direct method to evaluate and verify the actual structural bearing capacity of the field bridges. Generally, there are static load tests and dynamic load tests. The static load test can understand the stress behavior of the bridge structure to judge the characteristics of the bridge structure and check the safety of the bridge structure, verify the bridge structure design theory and calculation method, and then feed the results back to similar structural bridges. During the design and construction, the dynamic load test can determine the dynamic characteristics of the bridge structure, such as the natural vibration frequency, vibration state, or damping characteristics of the bridge structure. Besides, it can also understand the dynamic impact effect of the bridge when the heavy vehicle passes. The vehicle load test must use a loading vehicle with a known weight as the test load. Thus it has to record the actual vehicle load before entering the bridge deck for the test and move slowly to the expected position according to experimental plans. The static vehicle load test mainly measures the relative vertical deflection of each measuring point of the bridge deck or the change of the bridge profile under experimental loadings. Moreover, the test data should also include the inclination or displacement of the related static parameters of the bridge structure. Since the load-bearing capacity and deformation behavior of the system are related to the time characteristics of the loaded weight, the loading program must be carefully selected to correctly understand the load-bearing capacity and deformation behavior of the structure. There must be enough interval time between each loading case. To obtain the essential dynamic characteristics of the bridge by measuring the vibration acceleration at different positions of the bridge, including the fundamental vibration frequency, representative vibration state, or damping. The dynamic vehicle load test should install vibration signal measuring instruments and equipment on the bridge to record the bridge vibration signal during the dynamic vehicle load driving.

Since the load test is a valuable way to assess the safety of bridge structures, the method that can effectively quantify and evaluate structural safety still needs to be studied. This research explores the method of assessing the safety of bridge structures by an experimental load test platform. The study designs and perform a series of load test cases with scaled bridge specimen applies controllable static and dynamic loads in the laboratory and measures the response of the bridge specimen.

APPLICATION OF DATA SCIENCE METHODS

In recent years, artificial intelligence and big data analysis technology have received attention from many research fields, and practical application requirements have gradually developed. Data science is a multidisciplinary field of application technology, including statistical scientific methods and data analysis and processing. This study integrates the bridge load test data into the monitoring and inspection data processing with life-cycle-based bridge management and maintenance thoughts.

This research carries out flatcar load tests. The known load-bearing load can be used as the input value to measure the output response of the bridge specimen structure. The applicability of the data science analysis method is applied to deal with a series of experimental data. A series of experimental data science models can be used for long-term monitoring data references. Figure 1 shows the application of scientific data analysis methods to select parameter categories. Data processing tools can be divided into three categories: structural analysis, data regression, and structural status classification. The input parameters of structural analysis include structural system characteristics, geometric dimensions, material parameters, and boundary support conditions. The corresponding output continuity long-term monitoring data can cover field and laboratory test data. The traditional analysis method can build a structural analysis model for verification. The structural analysis model can be appropriately evaluated for structural response.

Regression analysis is one of the data processing methods commonly used in the collection of long-term monitoring data. It is suitable for exploring the long-term trend of monitoring data to determine the relative management and maintenance value. Field bridge monitoring items usually include physical quantities such as temperature, strain, displacement, inclination, and velocity or acceleration, directly feedback into the structural safety assessment method. Regarding the structural state classification method, the structural safety level classification of the structural assessment results must rely on a large amount of measurement or monitoring data. In addition to the structural safety level, the classified output can also be used to estimate the limit state of the structure, predict possible disaster modes in advance, and prepare for disasters when they occur.

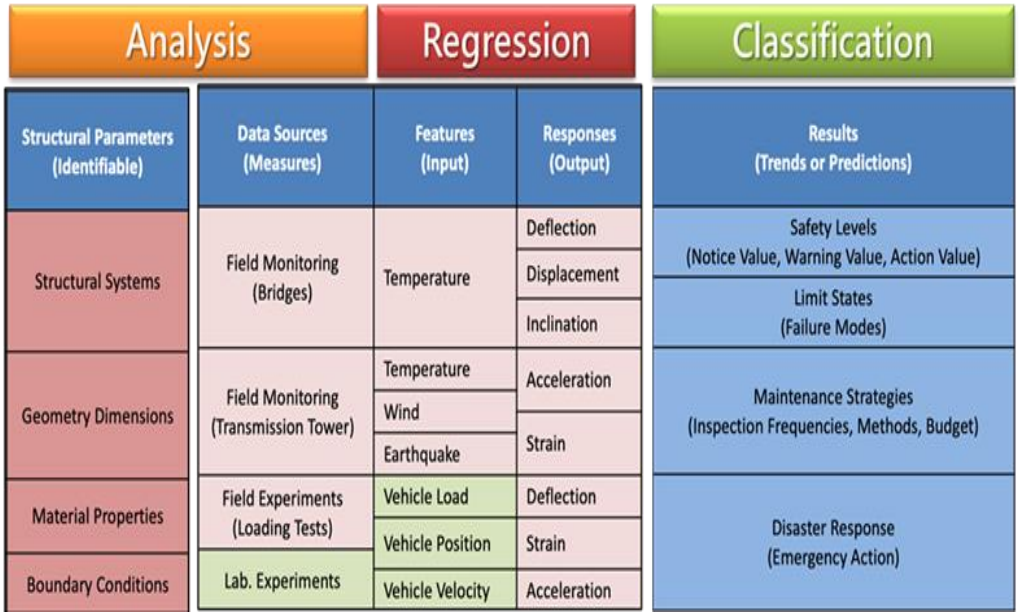

Figure. 1. Selected parameters of data science analysis method in this study

LABORATORY EXPERIMENTS OF LOADING TESTS

The planned experimental research analysis process and studied content are shown in Figure 2. Based on the case of the field bridge long-term monitoring system and the load test of the experimental specimen, a considerable amount of measurement data can be obtained. This study conducted the verification of scientific analysis methods with data. The on-site monitoring data mainly uses the environmental temperature change as the input parameter and matches the filed vehicle load test results. The laboratory load test can accurately know the applied load value and the loading position and conditions and measure the precise response of the structural specimen. In addition to the traditional finite element analysis method using the structural model for analytical solution analysis, the load test can also be analyzed by the structural influence line theory to obtain the analytical solution under the corresponding load condition.

The structural analysis model and test measurement data can be compared with the structural analysis model and test measurement data for further discussion. The data science method can perform regression calculations and classification analysis. It is necessary to sort out and screen the data first and formulate applicable data scientific analysis process to analyze monitoring data or measurement data and define representative measurement parameters corresponding to safety and then develop a quantitative index process for assessing bridge safety and disaster prevention.

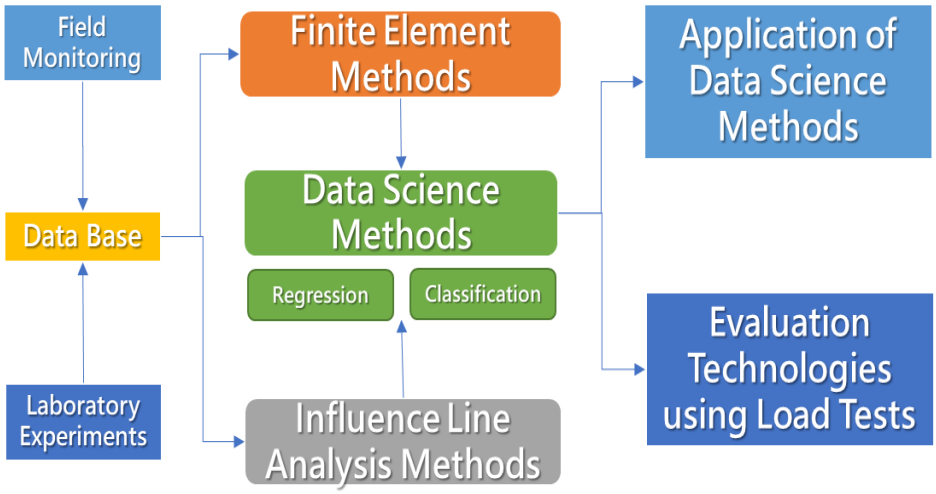

Figure 2. Test research analysis process and studied content

This study designs and plans a set of research and development platforms for load test technology. The hardware components of the platform include test landslide lanes for loaded flatcars and bridge specimens, as shown in Figure 3. The test platform can carry out static load and dynamic load tests. The static load test is equipped with various flatcar loads at the different location on the bridge specimen and conduct static data measurement. In the dynamic load test, a pulley system is installed above the landslide section. The pulley system and the counterweight device behind the ramp section connect a flatcar with a given load to a steel cable. The steel cable lifts the flatcar to a specific elevation and is fixed temporarily.

Furthermore, the decoupling release allows the test flatcar to detach from the steel cable during the test. The flatcar will freely slide down by gravity and enter the test section lane of the bridge specimen. Because gravitational potential energy may be converted to other forms of energy, such as kinetic energy, the free sliding entry speed of the flatcar at a specific height can be calculated. The bridge specimen currently used in this study is a single-span simply-supported steel bridge with a span of 3 meters, a bridge deck width of 1 meter, and two-way lanes. The structural system includes three steel girders (section H150x45x2.3) and a steel bridge deck (thickness 5 mm). Figure 4 shows the configuration plan of the load test measuring instrument. The measuring instruments include the optical fiber and electronic strain gauges installed on the steel member to measure the strain response of the girders when the load is applied. Furthermore, an optical displacement measuring instrument is

used to record the output response of the dynamic relative displacement of the bridge specimen as flatcars traveling through the test section. Besides, because of the possible vibration problems caused by vehicles passing over the bridge, this test technology research platform is planned to combine the development requirements of structural vibration reduction technology in the future, such as coordinated mass dampers mounted on the bridge specimen, and conduct vibration reduction experiments.

Figure 3. Load test landslide lane and test bridge specimen

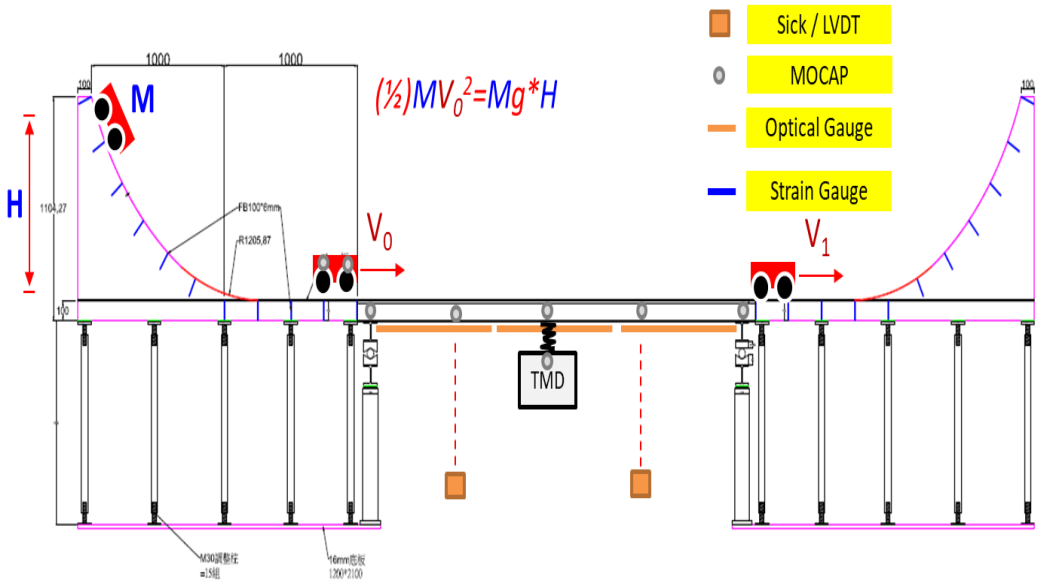

Figure 4. Load test measurement instrument configuration planning

The research work adopts the commercial structural analysis software MIDAS Civil to build the bridge specimen's structural analysis model shown in Figure 5. The main components of the analysis model include three girders and the bridge deck. The measurement data of the test load applied during the test can feedback analysis model, and the simulation can further evaluate the ultimate state and the related dynamic characteristics of the bridge specimen. During the test, the input and output parameters of the measurement record must be defined. This research applied the data science method to analyze the experimental data. Thus the test loading cases must be planned more systematically. In the dynamic load test, it is necessary to release the elevation from the landslide, calculate and set the

average speed of the test vehicle on the bridge deck, and measure the displacement and stress of the main girder and deck plate of the test bridge, as well as structural vibration signals.
Through a series of flatcar load tests, the maximum displacement or strain data can be obtained, and the test load and average speed of the corresponding flatcar can be input as key analysis parameters. In this study, the data science analysis method explores the correlation and establishes a data science analytical model. The established data scientific analysis model can evaluate the safety level or state of the bridge structure. Figure 6 shows the test measurement record input and output parameter table.

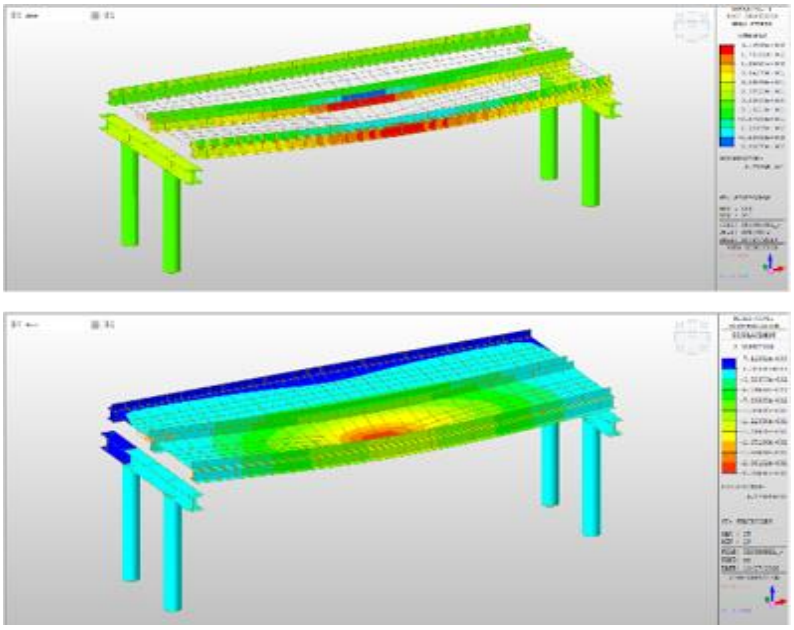

Figure 5. Structural analysis model of bridge specimen

Figure 7 shows the preliminary static load tests in this study. The maximum vertical load of each flatcar with eight layers of mass slices is 125 kg in total weight. There are four sets of flatcar that can be used with different layers of mass slices so that various vertical loads can be carried out according to the test configuration of different flatcar positions. For the dynamic load test, each test flatcar is equipped with a sliding rail support frame and low-friction bearings so that the moving flatcar can run smoothly on the deck lane without deviating from the lane, and at the same time, to ensure that the test flatcar can pass the full-bridge more smoothly. The steel plate elevation of the expansion joint between the landslide section and the bridge deck must be smooth.

	Ramp Load Testing Bridge (Measurement / Input)					Target (Response)	
Time / Items	Loading (Li)	Velocity (Ti)	Deflection (Di)	Stress (Si)	Acceleration (Ai)	Max Deflection (Dmax)	Loading (Li)
$Record_1$	L_1	V_1	D_1	S_1	A_1	Dmax	L_1
$Record_2$	L_2	V_2	D_2	S_2	A_2		L_2
.	.	.	.	.	.		.
.	.	.	.	.	.		.
$Record_n$	L_n	V_n	D_n	S_n	A_n		L_n
Weightings	Try to find the "key feature" / Representative sensors or locations					Safety / Warning / Action	

Figure 6. Test measurement record input and output parameters

Figure 7. The static load test configuration with flatcars

CONCLUSIONS

This study proposed an innovative experimental platform for the developing technologies of evaluation bridge structures by load tests. The research conducts a series of flatcar load tests and applies data science methods to deal with the test data for the safety assessment of bridge structures. The feasibility of the dynamic load test is presented in the laboratory. To select and discuss the applicability of data science method models, it has to collect a large amount of data through experiments or field projects. For old bridges or bridges with unique structural systems, the field load test is a practical way that can provide a detailed assessment of structural safety. With the development trend of artificial intelligence analysis technology, a large amount of data from field monitoring or inspection, or experiments can be obtained and be transformed into information that can assist in evaluation through scientific data analysis methods. Now we are moving towards intelligent bridge disaster prevention decision-making and management actions, ensuring bridge services safety during the life cycle, achieving complete life cycle management and maintenance, improving bridge disaster prevention technology, and implementing application business.

(SS6) Advancements in earthquake early warning systems

SEISMIC SITE EFFECTS IMPLICATION ON EEW PARAMETER ESTIMATION

Mugesh. A[1], Aniket Desai[2], Ravi S Jakka[2], Kamal[1]

1. Research Scholar, Centre of Excellence in Disaster Mitigation and Management, IIT-Roorkee, India.
2. Research Scholar, Department of Earthquake Engineering, IIT-Roorkee, India.
2. Associate Professor, Department of Earthquake Engineering, IIT-Roorkee, India.
1. Professor, Centre of Excellence in Disaster Mitigation and Management, IIT-Roorkee, India.

Email: amugesh@dm.iitr.ac.in, dsanjay@eq.iitr.ac.in, ravi.jakka@eq.iitr.ac.in, kamalfes@iitr.ac.in

ABSTRACT

In the Earthquake Early Warning (EEW) system, the current practices of early warning prediction are based on the initial three seconds of the P wave onset. The most commonly used EEW parameter is peak displacement amplitude (P_d). Still, the warning prediction algorithm is formulated with the source and path characteristics of the motion, and the site characteristics influence-based studies are very limited. In this study, the work focused on the local site parameter Vs_{30} (Time-average shear wave velocity) influence on the P_d characteristics for site class C (Soft rock type) and site class D (stiff soil type). The linear scaling relationship was analyzed between the magnitude and the logarithmic peak displacement amplitude. The strong motion records of the vertical component with 14 magnitudes (range 5-7.3) of the KIK-Net database in Japan are considered for this study. The three seconds of the motion time window after the onset of the P wave is used. The linear fit line comparison of the P_d parameter with the function of magnitude is made for the site classes C and D. The outcome shows that P_d was found higher in stiff soil sites compared to the soft rock type. The results from the stiff soil sites signified that the influence of the local site effect is more prominent in the EEW amplitude parameter estimation.

Keywords: Peak displacement Amplitude (P_d), Vs_{30} (Time-Average Shear wave velocity), Stiff soil, soft rock, Local Site Effect.

INTRODUCTION

Seismological hazard management can be enhanced by seismological early warning systems by reducing losses due to damaging earthquakes (Nakamura, 1988; Allen and Kanamori 2003). Sites that are close to earthquake sources can implement an onsite earthquake early warning system with effective results (Kanamori, 2005). Within the first three seconds of a P wave motion, the peak displacement amplitude (P_d) is calculated and is shown to be well correlated with magnitude, hypocentral distance, and peak ground velocity (Wu and Kanamori, 2005b). Based on the regression analysis using the P wave vertical component motion, linear relationships were assumed for the logarithmic peak displacement amplitude (log P_d), magnitude M. It was suggested that the correlation coefficient (R) is more inevitable in the statistical analysis (Wu and Zhao, 2005). Any site that has a logarithmic term of Pd > 0.5 cm is likely to experience significant damage from the earthquake (Wu et al., 2007). P_d showed a significant correlation with seismic event sizes between 5.0 and 8.0 in the KIK-Net database for Japan (Huang et al., 2015). According to Li et al. (2017), the peak displacement amplitude (P_d) of EEW systems provides the most reliable correlation with magnitude prediction since it has a cutoff frequency of 0.075-3 Hz. Every station in the KIK-Net network is equipped with three component accelerometers, one in the borehole and one on the surface (AOI et al., 2000). A site's soil conditions have a significant impact on the nature and characteristics of shaking. During intense ground shaking, sites with V_{S30} below 400 m/s demonstrated strong nonlinearity, so these types of sites were preferred (Zalachoris & Rathje, 2015). This study focuses on the local site condition effect influences on the earthquake early warning parameter, peak displacement amplitude (P_d).

The vertical motion (UD- component) of the surface 3 seconds time window is used to find the P_d parameter. Based on the site classification, the records are categorized. The sites considered for the analysis mostly fall under the site classes C (Vs30 ranges 360 to 760 m/s) and D (Vs30 ranges 180 to 360 m/s) as per the (NEHRP, 2009) site classification guidelines. The linear relationship comparison of the logarithmic P_d parameter for the stiff soil sites and soft rock sites is made. The results ensure that the stiff soil site P_d parameters have been significantly influenced by local soil site condition variation. (A. Mugesh et al., 2021) considered site parameter Vs30 influences EEW parameters.

SEISMIC DATASET

The Japanese strong motion dataset (KIK-Net database) containing records of 14 events (magnitude range 5.0-7.3) from 2008-2018 is used in this study. The following criteria were used to select earthquakes and records: (a) The earthquake magnitude is greater than 5; (2) Hypocenter Distances < 100 km; (3) Peak ground acceleration of the surface records in Vertical component > 50 cm/s^2; (4) 3-seconds motion time window in UD component is considered for the calculation of EEW parameter P_d. The event and site details are listed in Tables 1 and 2.

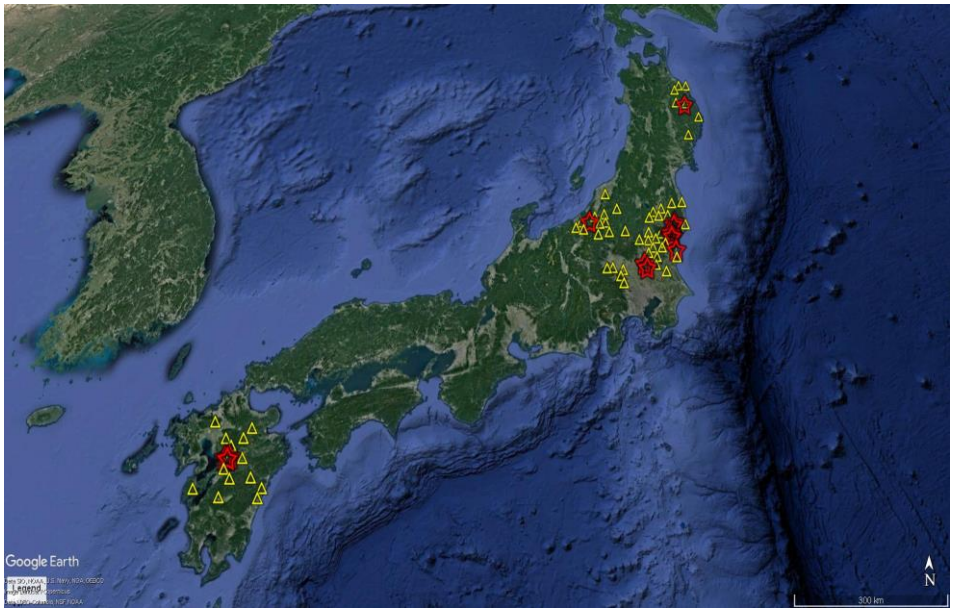

Figure 1. Map of 14 Event Epicenters (red stars) and 60 sites (yellow triangle) in the Japanese Strong motion network (KIK-Net).

Table 1. Event epicentre details

S. No	Magnitude	Latitude	Longitude	Focal Depth (km)
1	5	36.17	139.81	53
2	5.3	36.44	140.62	56
3	5.4	36.72	140.61	7
4	5.5	36.8	140.53	9
5	5.6	36.09	139.86	47
6	5.8	32.77	130.85	8
7	5.9	37	140.7	17
8	6.1	36.78	140.57	5
9	6.3	36.72	140.57	11
10	6.5	32.74	130.81	11
11	6.7	37.34	139.31	8
12	6.8	39.7	141.6	108
13	7	36.95	140.67	6
14	7.3	32.75	130.76	12

Table 2. KIK-Net station details

S. No	Station	Latitude	Longitude
1	FKSH08	37.2822	140.2144
2	FKSH09	37.353	140.4264
3	FKSH10	37.1616	140.093
4	FKSH12	37.2169	140.5703
5	FKSH21	37.3421	139.3147
6	GNMH12	36.144	138.9129
7	IBRH12	36.8369	140.3181
8	IBRH15	36.5566	140.3013
9	IBRH16	36.6405	140.3976
10	IBRH18	36.3631	140.6198
11	IBRH19	36.2137	140.0893
12	IWTH02	39.825	141.3826
13	IWTH03	39.802	141.652
14	IWTH07	40.2705	141.5709
15	IWTH12	40.1533	141.4245
16	IWTH21	39.4734	141.9336
17	IWTH27	39.0307	141.532
18	KMMH01	33.1089	130.6949
19	KMMH02	33.122	131.0629
20	KMMH03	32.9984	130.8301
21	KMMH06	32.8114	131.101
22	KMMH09	32.4901	130.9046
23	KMMH10	32.3151	130.1811
24	KMMH12	32.2054	130.7371
25	MYZH04	32.5181	131.3349
26	MYZH08	32.2132	131.5309
27	MYZH15	32.3654	131.5893
28	NGNH29	36.9102	138.4408
29	NIGH11	37.1728	138.744
30	NIGH12	37.2239	138.9821
31	NIGH13	37.0544	138.3966
32	NIGH14	37.0303	138.8521
33	NIGH15	37.0533	138.9951
34	NIGH19	36.8114	138.7849
35	OITH11	33.2844	131.2118
36	SAGH04	33.3654	130.4046
37	SITH05	36.1509	139.0504
38	SITH06	36.1131	139.2894
39	SITH10	35.9964	139.2191
40	SITH11	35.8637	139.2726
41	TCGH06	36.4458	139.9509

42	TCGH07	36.8817	139.4534
43	TCGH10	36.8578	140.0225
44	TCGH13	36.7342	140.1781
45	FKSH11	37.2006	140.3386
46	FKSH14	37.0264	140.9702
47	FKSH19	37.4703	140.7227
48	FKSH20	37.4911	140.9871
49	GNMH13	36.862	139.0627
50	IBRH10	36.1112	139.9889
51	IBRH11	36.3701	140.1401
52	IBRH13	36.7955	140.575
53	IBRH17	36.0864	140.314
54	IWTH08	40.2686	141.7831
55	KMMH14	32.6345	130.7521
56	KMMH16	32.7967	130.8199
57	NIGH06	37.6527	139.0676
58	NIGH18	36.9425	138.2594
59	TCGH11	36.7084	139.7694
60	TCGH12	36.6959	139.9842
61	TCGH16	36.548	140.0751

The collected records are in the form of uncorrected digital data. The signal processing was performed to get the corrected signal. The Bandpass Butterworth filter with the cutoff frequency range of 0.075-30 Hz in second-order was applied in the accelerograms to remove the drift in the records. The signal processing technique is used in MATLAB (2020b) and the corrected surface motion of the three seconds time window is involved in the calculation of EEW parameter P_d.

RESULTS AND DISCUSSIONS

Peak displacement amplitude versus Magnitude in stiff soil site (site class-D) and soft rock (site class-C)

The results of this study found in the form of the linear relationship between the magnitude (M) and the peak displacement amplitudes (P_d) for the site classes C and D are shown in Figures 2a and 2b. The P_d values are averaged in each bin of the magnitudes, and linear scaling analysis has been carried out between the magnitudes and average P_d values. In both site classes, such as stiff soil site and soft rock site, the mean values of the P_d increased with increasing magnitudes. Least-square fit line relationship adopted based on the fit line equation $\log(P_d) = a(M) - b \pm \sigma$, where P_d is the peak displacement amplitude in 3 seconds, M represents the magnitude; a and b are constants, and σ is the standard deviation error in linear scaling analysis. The standard deviation error from the fit line is slightly smaller for the regression model from the site class D contrast to site class C. The stability of the correlation is represented in terms of R for both regression models. In figure 2b the correlation coefficient value (R) is relatively smaller, it happens because, the records used in the site class D models are limited.

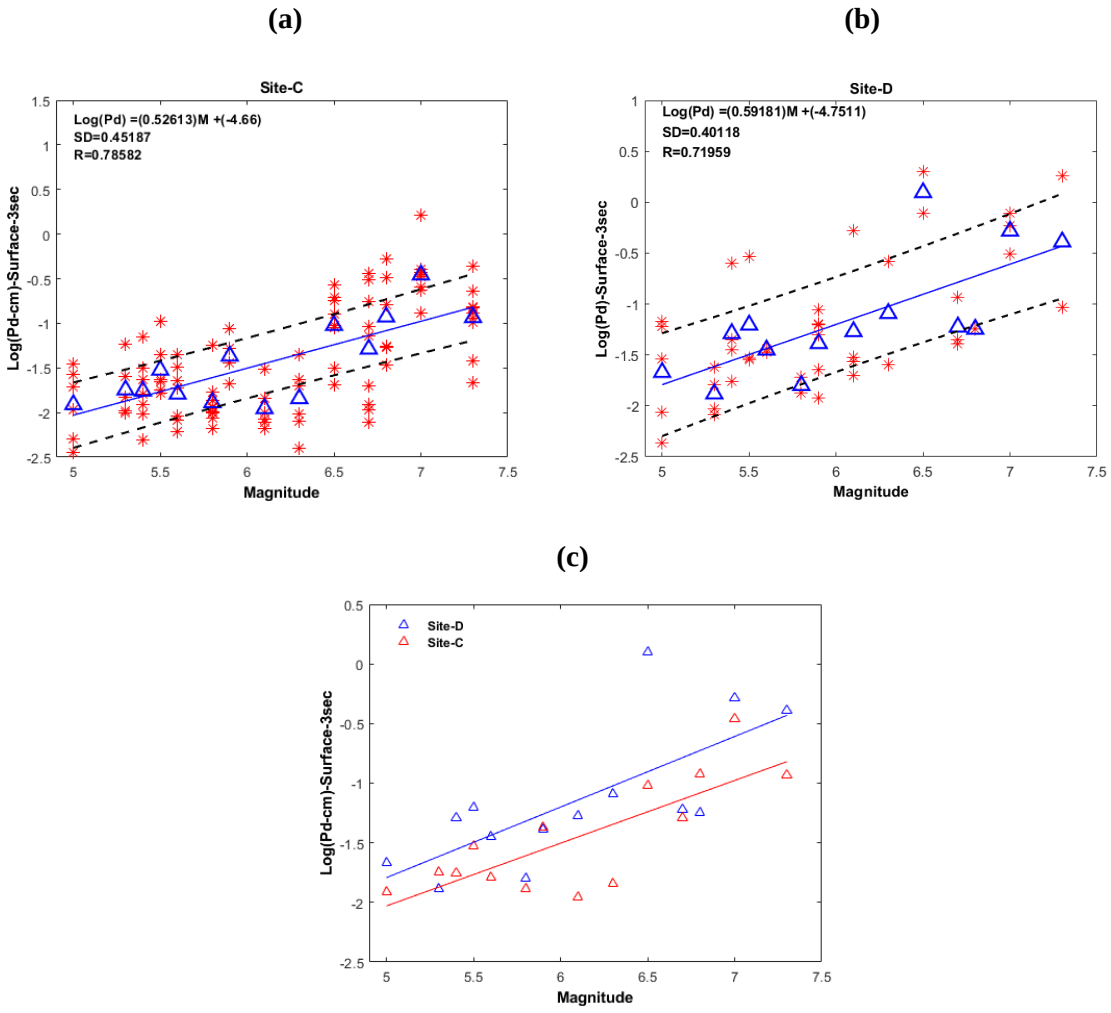

Figure 2. Linear scaling relationship between the magnitude (M) and logarithmic peak displacement amplitude (P_d) for the site classes C and D (a, b). Linear fit line comparison of the Log (P_d) for stiff soil sites and soft rock sites (c).

In figure 2(c), the linear regression fit line comparison was made for the log (P_d) parameters in terms of site classes C and D. The slope of the line shows higher in site class D (stiff soil sites) than site class C (soft rock sites). It implies that the P_d parameter from the stiff soil sites shows higher amplitude compared to soft rock sites. The sites which have a lower range of time-averaged shear wave velocities (low stiffness on the surface) amplified the displacement amplitude in contrast to sites which has a high-velocity range (higher stiffness). Specifically, in magnitude 5.3, the P_d parameter from site D shows a low value compared to site C, because it might be the damping effect of the motion being high in stiff soil sites as compared to soft rock sites.

For Site Class- C (dense soil & soft rock site)

$$\log (P_d) = 0.526\ (M) - 4.660 \pm 0.452 \quad (1)$$

For Site Class- D (stiff soil site)

$$\log (P_d) = 0.592\ (M) - 4.751 \pm 0.401 \quad (2)$$

CONCLUSIONS

This study initiated a local site class-based approach for the EEW parameter peak displacement amplitude estimation in the form of linear scaling relationships. The P_d parameter shows the increment with the magnitude increases for the stiff soil site (site class-C) and soft rock sites (site class-D). In soil sites, the log Pd prediction from the stiff soil shows slightly less standard deviation error compared to the soft rock sites. In Figure 2c, due to its local site condition variation, the site effects on the amplitude-based parameter (P_d) is revealed. It was found that the sites which have a low range of time-averaged shear wave velocity amplified the displacement amplitude in the initial three seconds of the P wave motion more as compared to sites which have high time-averaged shear wave velocity. Based on the findings, it was concluded that the vertical component of the motion is influenced by the soil site parameter Vs_{30} (Time averaged shear wave velocity). Though, the strong motion record and the site details used in this study are limited. Further justifying the results, a strong motion dataset and the site details are required more to estimate the site effect's impact on the EEW system.

REFERENCES

Allen, R .M., and Kanamori, H. (2003). The potential for earthquake early warning in Southern California *Science 300 786–9*

AOI, S., KUNUGI, T., & FUJIWARA, H. (2004). STRONG-MOTION SEISMOGRAPH NETWORK OPERATED BY NIED: K-NET AND KiK-net. *Journal of JAEE Journal of Japan Association for Earthquake Engineering*, 4(3), 65–74. https://doi.org/10.5610/jaee.4.3_65

Building Seismic Safety Council [BSSC]. NEHRP recommended provisions for seismic regulations for new buildings and other structures. *(FEMA P-750 report). 2009 edition. Washington, D.C.: Federal Emergency Management Agency; 2009.*

Huang P L, Lin T L and Wu Y M (2015) Application of τ_c*Pd in earthquake early warning *Geophys .Res. Lett.* 42 1403–10

Li H, Zhang .J. and Tang, Y., (2017)Testing earthquake early warning parameters, τ_{pmax}, τ_c and Pd, for rapid magnitude estimation in the Sichuan, *China, region Bull. Seismol. Soc. Am.* 107 1439–50

MATLAB (2020b), *The MathWorks Inc*. https://in.mathworks.com/help/signal/index.html

Mugesh, A., Desai, A., Jakka, R.S., Kamal (2022). Local Site Effects Influence on Earthquake Early-Warning Parameters, Earthquake Geotechnics. Lecture Notes in Civil Engineering, vol 187. Springer, Singapore. https://doi.org/10.1007/978-981-16-5669-9_10

Nakamura, Y., (1988). On the urgent earthquake detection and alarm system (UrEDAS*) Proc. 9th World Conf. Earthquake Eng.* vol 7, pp 673–8.

Wu, Y. M., & Kanamori, H. (2005). Experiment on an onsite early warning method for the Taiwan early warning system. *Bulletin of the Seismological Society of America*, 95(1), 347–353. https://doi.org/10.1785/0120040097

Wu, Y. M., and H. Kanamori (2005b), Rapid assessment of damaging potential of earthquakes in Taiwan from the beginning of P Waves, *Bull. Seismol. Soc. Am*., 95, 1181–1185.

Wu, Y. M., Kanamori, H., Allen, R. M., & Hauksson, E. (2007). Determination of earthquake early warning parameters, τc and Pd, for southern California. *Geophysical Journal International*, 170(2), 711–717. https://doi.org/10.1111/j.1365-246X.2007.03430.x

Wu, Y. M., Yen, H. Y., Zhao, L., Huang, B. S., & Liang, W. T. (2006). Magnitude determination using initial P waves: A single-station approach. *Geophysical Research Letters*, 33(5), 5–8. https://doi.org/10.1029/2005GL025395

Zalachoris, G., & Rathje, E. M. (2015). Evaluation of one-dimensional site response techniques using borehole arrays. *Journal of Geotechnical and Geoenvironmental Engineering*, 141(12), 1–15. https://doi.org/10.1061/(ASCE)GT.1943-5606.0001366

UTTARAKHAND EARTHQUAKE EARLY WARNING SYSTEM: PERFORMANCE AND VALIDATION

Pankaj Kumar[1], Kamal[2] and M.L. Sharma[3]

1. Project Fellow, Earthquake Early Warning System Laboratory, Centre of Excellence in Disaster Mitigation & Management, Indian Institute of Technology Roorkee, India
2. Professor, Department of Earth Sciences, Indian Institute of Technology Roorkee, India
3. Professor, Department of Earthquake Engineering, Indian Institute of Technology Roorkee, India

Email: pkumar@dm.iitr.ac.in, kamal@es.iitr.ac.in, m.sharma@eq.iitr.ac.in

ABSTRACT

The earthquake early warning system (EEWS) laboratory, centre of excellence in disaster mitigation & management, Indian institute of technology Roorkee, has developed an earthquake early warning system for the Uttarakhand region. Seismic sensors have been installed in the central seismic gap region, an area where strong and higher magnitude earthquakes are long due. In total, 167 sensors have been installed in this seismically active region, and a control server has been established in the EEWS laboratory. The data is streamed in the laboratory through the dedicated private network. Server continuously performs processing of the fetched data. Warning of the earthquakes that occur in the instrumented region is issued through two modes. In the first mode, the warning is issued to the public by sirens installed in the government-owned buildings of Dehradun, Haldwani and district emergency operation center (DEOC) of all thirteen districts of Uttarakhand. In the second mode, warnings of earthquakes are issued by the warning server and received by the mobile app installed on users' mobile phones. Since 2014, the starting year of this project, no strong earthquake has occurred in the instrumented region. For a few light earthquakes that occurred in the instrumented region, notification alerts were issued to the public. These few events have boosted our confidence and we hope for the best performance during strong earthquakes.

Keywords: Earthquake Early Warning, Lead Time, Alerts, Uttarakhand

INTRODUCTION

The Himalayas is one of the most seismically active regions of the world. The geodynamic system in the Himalayas has produced many devastating earthquakes; the most recent one was on April 25th, 2015, M_w: 7.6 Nepal earthquake. This earthquake caused substantial economic loss to the Himalayan country (Gauchan et al., 2017). Less frequent but highly devastating earthquakes call for immediate mitigation measures—hence, disaster risk reduction strategies need to be implemented in the Himalayan region on a priority basis. After studying the high seismic risk and sporadic distribution of the vulnerable zones in the central seismic gap (Bajaj and Sharma, 2019; Chaudhary and Sharma, 2017; Choudhary and Sharma, 2018; Srivastava et al., 2015), an earthquake early warning system (UEEW) has been developed for the Uttarakhand region (Bhardwaj et al., 2016; Chamoli et al., 2019; Kumar et al., 2022; Mittal et al., 2018). The unpredictable nature of earthquakes makes them more dangerous than other hazards. Therefore, a fully automatic regional earthquake early warning system can perform the task of alerting people with sufficient lead time required to take precautionary measures and shut down the key facilities but not necessarily determine exact earthquake parameters. Under the setup of the UEEW system, seismic sensors are installed on the ground floor of government-owned offices of Base Transceiver Station (BTS) of Bharat Sanchar Nigam Limited (BSNL) and Point of Presence (PoP) of State Wide Area Network (SWAN) available in Uttarakhand. The instrumented array comprises 167 accelerometers with an inter-station spacing of about 10 to 20 Km. The installed sensors transmit ground motion data to the server installed in the EEWS Laboratory over a dedicated private network on 24×7 basis in real-time.

The seismic data is streamed continuously at the central server set-up in the EEW system laboratory, IIT Roorkee. A computer program, PICK_EEW, continuously monitors the p-onset. For this, an

improved standard short-term average (STA) and long-term average (LTA) algorithm is used (Allen, 1982, 1978; Chen et al., 2015). The threshold value for P-pick is the ratio of STA/LTA (i.e., 6.0). At least four stations must trigger simultaneously to certify that the earthquake event is true.

The hypocenter of the earthquake is estimated in two steps. In the first step, the Geiger method is applied to find the epicenter (Geiger, 1912). This method needs a P-wave velocity profile of the instrumented region. A half-space velocity model of the Uttarakhand region as suggested by one of the studies carried out in this region has been selected (Kanaujia et al., 2015). In the second step, the grid search method with a depth ranging from 0 to 50 Km is applied to find out the actual depth of the earthquakes. In the grid search method, theoretical travel times to each triggered station are calculated and compared with the observed depth at each step. The step at which minimum residual is found is considered as the depth of the earthquake. Initially, at least four triggered stations are used, and the search point which gives minimum residual is picked as the focus. As soon as the hypocenter is estimated, the TCPD module estimates the magnitude based on a regression model. The mathematical form of the applied model is:

$$M_{pd} = \mathrm{A}\times \log(P_d) + \mathrm{B}\times \log(R) + \mathrm{C} \quad (1)$$

where, M_{pd} is P_d based on magnitude, R is hypocentral distance and $R = \sqrt{d^2 + h^2}$, d is epicentral distance, and h is depth of the focus. The coefficients of Eq. (1) change with the variation of the data set of different regions and are region-specific. The coefficients A, B, and C are estimated for the model (Eq.1) as 0.35, 0.06 and 0.15, respectively using earthquake records from 2005 to 2020 in the Uttarakhand region (Kumar, 2020).

The module TCPD generates a report and stores it in a user-defined location for archive purposes. As soon as a report is generated, a warning is issued to the public on the mobile and by blowing the installed sirens in the state. Notification on the mobile app is sent for light earthquakes as they do not create discernible damage while warnings are issued for moderate and higher magnitude earthquakes on both the mobile app and by blowing sirens.

PERFORMANCE

A light earthquake of magnitude 4.6 was triggered in the Pithoragarh region of Uttarakhand on May 11, 2022, 10:03:09 IST. Figure 1 shows the locations of the sensors where records of this earthquake were recorded by the installed sensors.

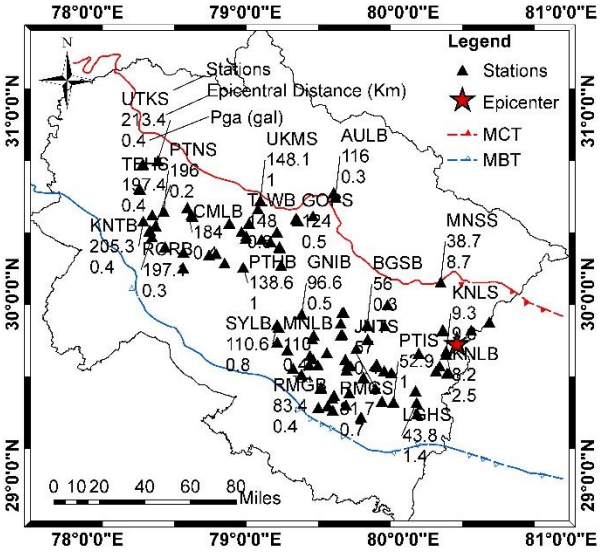

Figure 1. Location of the sensors with epicentral distance, estimated peak ground acceleration at site and epicenter of the earthquake.

The lead time for the user is important. It is the remaining time for the S-waves to reach at the target site. Lead time varies depending on the location of the user from the epicenter of the earthquake (Bhardwaj et al., 2018; Mittal et al., 2019). A user at a far distance would get more lead time than the

users at the nearest locations. The existing system is developed based on the regional EEW concept. Therefore, it takes a few seconds to process and then issue warnings. These few seconds are elapsed time to get at least 3 seconds of data from at least four sensors and time needed for transmission, processing, magnitude and hypocenter estimation, and then sending the decision to the warning server. The lead time can be calculated as per Eq (2) (Satriano et al., 2011), where reporting time (Tr) is the time needed (Td) to trigger and record the sufficient length of the waveforms and the time (Tpr) required to process the waveforms for the hypocenter and magnitude determination. The earthquake early warning time (Tw) is given by:

$$Tw = Ts - Tr \tag{2}$$

and

$$Tr = Td + Tpr \tag{3}$$

where, Ts is the destructive S-wave travel time. For the advanced warning, we must have Tw > 0. Clearly, this requires Ts > (Td + Tpr). The locations for which Tw < 0 are considered as the blind zone.

Figure 2 shows a diagram that describes the discrete times using the results of the Pithoragarh earthquake. The Baluakot (BLKB) site was 12 Km away from the epicenter (Lat: 29.91, Long: 80.38), and Bhilangana (BHLS) site was at a distance of 180 Km. The Td was 7.36 seconds measured from the origin time to the triggering and recording of the data. The processing (Tpr) took 6.25 seconds to compute the hypocenter and magnitude. Therefore, an early-warning time (Tw) of 33.48 seconds was for the BHLS site before the arrival of the destructive wave.

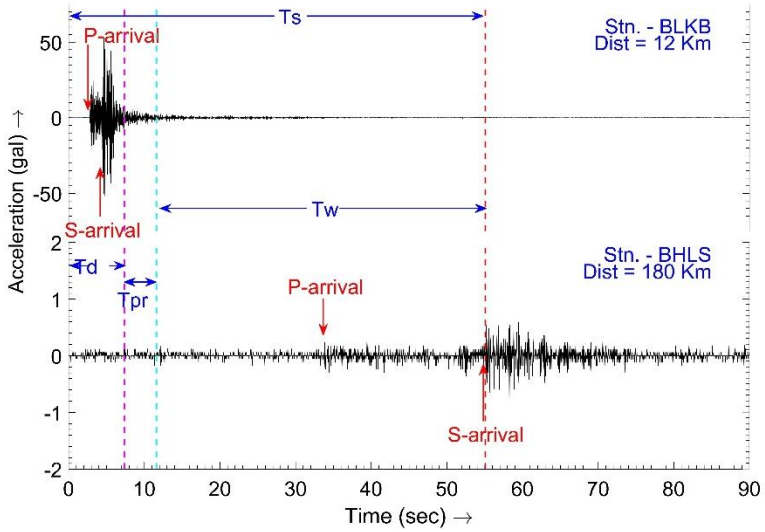

Figure 2. The diagram shows data-recording time (Td), data-processing time (Tpr), event-reporting time (Tr), target-area early-warning time (Tw), shear-wave travel time (Ts) at Bhilangna station (BHLS). The target area, BHLS station (180 Km away from the epicenter) gets an early warning (Tw) with a lead time of ~33.48 seconds.

An alert message was issued about this earthquake to the public which was received by the user through the installed mobile application "Uttarakhand Bhookamp Alert". This mobile app was developed by the EEW System laboratory, IIT Roorkee, in collaboration with the Government of Uttarakhand. It is freely available on the play store and app store.

VALIDATION

The central server generated five reports during this earthquake. The first two reports were considered as confirmation of the earthquake, and three alerts were issued (Figure 3) to the public based on the remaining three reports. The third report was generated by analyzing data from six stations and an alert was issued at 10:03:18.23 UTC. The fourth report was generated when records were found on three

more stations, thus a total of nine stations were used to create the report and an alert was issued at 10:03:22.99 UTC. The fifth report was generated when one more station was triggered and thus a total of ten station based report was created by the server and an alert was issued at 10:03:26.53 UTC.

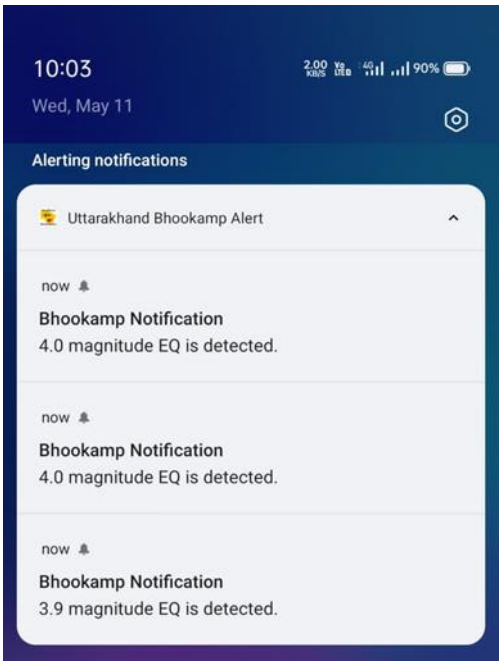

Figure 3. Screenshot of mobile application during receiving of alerts of the Pithoragarh earthquake.

The Pithoragarh earthquake was a light earthquake. If it would be a strong earthquake then what could be the lead time for the major cities of Uttarakhand? Considering the Pithoragarh earthquake as a strong earthquake, the probable lead time for major cities is estimated (Table 1).

Table 1. The lead time for the major cities in view of the Pithoragarh earthquake.

S.No.	City	Epicentral Distance (km)	Lead Time (sec)	S.No.	City	Epicentral Distance (km)	Lead Time (sec)
1	Bageshwar	59	5	**17**	Ukhimath	141	28
2	Champawat	69	8	**18**	Agustmuni	141	28
3	Almora	79	10	**19**	Kashipur	158	33
4	Dwarhat	93	14	**20**	Srinagar	159	33
5	Ramgarh	96	16	**21**	Lansdown	163	35
6	Ranikhet	97	16	**22**	Devprayag	173	37
7	Tanakpur	97	16	**23**	Pratapnagar	192	43
8	Auli	104	18	**24**	Tehri	195	44
9	Naintal	107	18	**25**	Chamba	197	44
10	Joshimath	107	18	**26**	NarendraNagar	203	46
11	Haldwani	113	20	**27**	Rishikesh	204	46
12	Adibadri	114	21	**28**	Uttarkashi	207	47
13	Chamoli	115	21	**29**	Haridwar	214	49
14	Gopeshawar	116	21	**30**	Dehradun	230	54
15	Karnprayag	119	22	**31**	Roorkee	240	56
16	US Nagar	140	28	**32**	Chakrata	257	61

DISCUSSION AND CONCLUSION

The Uttarakhand earthquake early warning system has demonstrated its performance during light earthquake events. Since the launch of the mobile application on August 4th, 2021, seven light earthquakes have occurred in the Uttarakhand region. Alerts were issued to the public for earthquakes listed in Table 2. In this table, there was one minor earthquake mentioned at serial number two for which server generated reports and alerts were issued to the public.

Table 2. Earthquakes triggered in Uttarakhand region.

S.No.	Date	Time UTC	Mag	Depth	Region
1	23/05/2021	19:01:45	4.3	22	Chamoli, Uttarakhand
2	28/06/2021	06:48:05	3.7	10	Pithoragarh, Uttarakhand
3	11/09/2021	00:28:33.18	4.7	5	Chamoli
4	29/12/2021	19:08:21	4.1	10	Pithoragarh
5	24/01/2022	19:39:00	4.3	10	Pithoragarh
6	11/02/2022	23:33:34	4.1	28	Tehri Garhwal
7	09/04/2022	11:22:36	4.1	10	Uttarkashi
8	11/05/2022	04:33:09	4.6	5	Pithoragarh

As the alerts were issued for all light earthquakes to the public, this built up our confidence that this system would be a success in issuing warnings for moderate and higher magnitude earthquakes in the future. This early warning system will save lives, jobs, infrastructure and support for long-term sustainability. It strengthens government officials and administrators in their planning, saving money in the long run and protecting the economy. The Government of Uttarakhand conducts mock drills in coordination with EEWS Laboratory, IIT Roorkee. These mock drills help to create awareness among people regarding earthquakes and motivate them to follow the guidelines given in the dos and don'ts list. The line departments take mock drills seriously to examine their preparation and rehearse their standard operating procedures. The mock drill would help them during post-earthquake operations.

ACKNOWLEDGEMENT

The authors are thankful to the Uttarakhand State Disaster Management Authority, Dehradun, Government of Uttarakhand for providing funds to run this project, and the National Center for Seismology (NCS) Ministry of Earth Sciences, Government of India for funding the pilot project. The discussions held with the National Disaster Management Authority of India, Uttarakhand administration and NCS officials are gratefully acknowledged. The help provided by the Centre of Excellence in Disaster Mitigation & Management and the Department of Earthquake Engineering, IIT Roorkee, is thankfully acknowledged.

REFERENCES

Allen, R., 1982. Automatic phase pickers: Their present use and future prospects. Bull. Seismol. Soc. Am. 72, S225-242.

Allen, R. V., 1978. Automatic earthquake recognition and timing from single traces. Bull. Seismol. Soc. Am. 68, 1521–1532.

Bajaj, S., Sharma, M.L., 2019. Modeling Earthquake Recurrence in the Himalayan Seismic Belt Using Time-Dependent Stochastic Models : Implications for Future Seismic Hazards. Pure Appl. Geophys. 176, 5261–5278.

Bhardwaj, R., Sharma, M.L., Chen, Z., 2018. Lead time for cities of Northern India by using multiparameter EEW algorithm. Int. J. Geophys. 2018.

Bhardwaj, R., Sharma, M.L., Kumar, A., 2016. Multi-parameter algorithm for Earthquake Early Warning.

Geomatics, Nat. Hazards Risk 7, 1242–1264.
Chamoli, B.P., Kumar, A., Chen, D.Y., Gairola, A., Jakka, R.S., Pandey, B., Kumar, P., Rathore, G., 2019. A Prototype Earthquake Early Warning System for Northern India. J. Earthq. Eng. 25, 2455–2473.
Chaudhary, C., Sharma, M.L., 2017. Probabilistic Models For Earthquakes With Large Return Periods In Himalaya Region. Pure Appl. Geophys. 174, 4313–4327.
Chen, D.Y., Hsiao, N.C., Wu, Y.M., 2015. The earthworm based earthquake alarm reporting system in Taiwan. Bull. Seismol. Soc. Am. 105, 568–579.
Choudhary, C., Sharma, M.L., 2018. Global strain rates in western to central Himalayas and their implications in seismic hazard assessment. Nat. Hazards 94, 1211–1224.
Gauchan, D., Joshi, B.K., Ghimire, K., 2017. Impact of 2015 Earthquake on Economy , Agriculture and Impact of 2015 Earthquake on Economy , Agriculture and Agrobiodiversity in Nepal. In: Proceedings of Sharingshop on Germplasm Rescue. pp. 19–25.
Geiger, L., 1912. Probability method for the determination of earthquake epicenters from the arrival times only. Bull. Saint Louis Univ. 8, 60–71.
Kanaujia, J., Kumar, A., Gupta, S.C., 2015. 1D velocity structure and characteristics of contemporary local seismicity around the Tehri region, Garhwal Himalaya. Bull. Seismol. Soc. Am. 105, 1852–1869.
Kumar, P., 2020. Earthquake Early Warning System : Site Classification, Intensity Map and Attributes. Thesis, Centre of Excellence in Disaster Mitigation & Management, Indian Institute of Technology Roorkee, India.
Kumar, P., Pandey, B., Kamal, Kumar, A., 2022. Site classification of seismic recording stations of Garhwal region of earthquake early warning system for Uttarakhand, India. Vietnam J. Earth Sci. 44, 369–394.
Mittal, H., Wu, Y.M., Lal, M., Benjamin, S., Yang, M., Gupta, S., 2018. Testing the performance of earthquake early warning system in northern India. Acta Geophys.
Mittal, H., Wu, Y.M., Sharma, M.L., Yang, B.M., Gupta, S., 2019. Testing the performance of earthquake early warning system in northern India. Acta Geophys. 67, 59–75.
Satriano, C., Wu, Y.M., Zollo, A., Kanamori, H., 2011. Earthquake early warning: Concepts, methods and physical grounds. Soil Dyn. Earthq. Eng. 31, 106–118.
Srivastava, H.N., Verma, M., Bansal, B.K., Sutar, A.K., 2015. Discriminatory characteristics of seismic gaps in Himalaya. Geomatics, Nat. Hazards Risk 6, 224–242.